ELSEVIER

HANDBOOK OF **CRYSTAL GROWTH**

SECOND EDITION

II

BULK CRYSTAL GROWTH:

BASIC TECHNIQUES, AND GROWTH MECHANISMS AND DYNAMICS

EDITED BY PETER RUDOLPH

Handbook of Crystal Growth

Bulk Crystal Growth: Basic Techniques

VOLUME II, Part A

Second Edition

Editor-in-Chief

Tatau Nishinga

The University of Tokyo
Hongo, Bunkyo-ku, Tokyo, Japan

Volume Editor

Peter Rudolph

Crystal Technology Consulting (CTC)
Schönefeld, Germany

Amsterdam • Boston • Heidelberg • London
New York • Oxford • Paris • San Diego
San Francisco • Singapore • Sydney • Tokyo

Handbook of Crystal Growth

Bulk Crystal Growth: Growth Mechanisms and Dynamics

VOLUME II, Part B

Second Edition

Editor-in-Chief

Tatau Nishinga

The University of Tokyo
Hongo, Bunkyo-ku, Tokyo, Japan

Volume Editor

Peter Rudolph

Crystal Technology Consulting (CTC)
Schönefeld, Germany

Amsterdam • Boston • Heidelberg • London
New York • Oxford • Paris • San Diego
San Francisco • Singapore • Sydney • Tokyo

Elsevier
Radarweg 29, PO Box 211, 1000 AE Amsterdam, The Netherlands
The Boulevard, Langford Lane, Kidlington, Oxford OX5 1GB, UK
225 Wyman Street, Waltham, MA 02451, USA

First edition 1993

Second edition 2015

Copyright © 2015, 1993 Elsevier B.V. All rights reserved.

The crystals on the front cover are high-quality synthetic diamond crystals grown by Sumitomo Electric Industries, LTD by a temperature gradient method under high pressure and high temperature. The yellowish crystals are ordinarily synthetic diamonds containing nitrogen impurity of several tens of ppm (type Ib). The colorless ones are high-purity synthetic diamonds free of impurities (type IIa). The size of the largest high-purity crystal (lower left) is about 12 mm in diagonal length. The photo was provided by Dr. Hitoshi Sumiya.

No part of this publication may be reproduced or transmitted in any form or by any means, electronic or mechanical, including photocopying, recording, or any information storage and retrieval system, without permission in writing from the publisher. Details on how to seek permission, further information about the Publisher's permissions policies and our arrangements with organizations such as the Copyright Clearance Center and the Copyright Licensing Agency, can be found at our website: www.elsevier.com/permissions.

This book and the individual contributions contained in it are protected under copyright by the Publisher (other than as may be noted herein).

Notices
Knowledge and best practice in this field are constantly changing. As new research and experience broaden our understanding, changes in research methods, professional practices, or medical treatment may become necessary.

Practitioners and researchers must always rely on their own experience and knowledge in evaluating and using any information, methods, compounds, or experiments described herein. In using such information or methods they should be mindful of their own safety and the safety of others, including parties for whom they have a professional responsibility.

To the fullest extent of the law, neither the Publisher nor the authors, contributors, or editors, assume any liability for any injury and/or damage to persons or property as a matter of products liability, negligence or otherwise, or from any use or operation of any methods, products, instructions, or ideas contained in the material herein.

British Library Cataloguing-in-Publication Data
A catalogue record for this book is available from the British Library

Library of Congress Cataloging-in-Publication Data
A catalog record for this book is available from the Library of Congress

SET Volume ISBN: 978-0-444-63303-3
Volume 2, Part A–978-0-444-63332-3
Volume 2, Part B–978-0-444-63331-6

For information on all Elsevier publications visit our website at http://www.store.elsevier.com/

Printed and bound in the UK.

Contents

General Preface ix

Preface to Volume II xi

List of Contributors xiii

Part A. Basic Techniques

1. Crystal Growth in Geology: Patterns on the Rocks 1
Juan Manuel García-Ruiz, Fermín Otálora

2. Czochralski Growth of Silicon Crystals 45
Jochen Friedrich, Wilfried von Ammon, Georg Müller

3. Liquid Encapsulation and Related Technologies for the Czochralski Growth of Semiconductor Compounds 105
J. Brian Mullin

4. Czochralski Growth of Oxides and Fluorides 131
Nobuhiko Sarukura, Teruhiko Nawata, Hiroyuki Ishibashi, Mitsuru Ishii, Tsuguo Fukuda

5. Czochralski and Flux Growth of Crystals for Lasers and Nonlinear Optics 169
Jiyang Wang, Guochun Zhang, Haohai Yu, Yan Wang, Chuantian Chen

6. Growth Measures to Achieve Bulk Single Crystals of Transparent Semiconducting and Conducting Oxides 209
Zbigniew Galazka

7. Floating Zone Growth of Silicon 241
Andris Muiznieks, Janis Virbulis, Anke Lüdge, Helge Riemann, Nico Werner

8. Floating Zone Growth of Oxides and Metallic Alloys 281
Hanna A. Dąbkowska, Antoni B. Dąbkowski, Regina Hermann, Janis Priede, Gunter Gerbeth

9. Vertical Bridgman Growth of Binary Compound Semiconductors 331
Manfred Jurisch, Stefan Eichler, Martin Bruder

10. Multicrystalline Silicon Crystal Growth for Photovoltaic Applications 373
Chung-wen Lan, Chuck Hsu, Kazuo Nakajima

11. The Unidirectional Crystallization of Metals and Alloys (Turbine Blades) 413
Krzysztof Kubiak, Dariusz Szeliga, Jan Sieniawski, Arkadiusz Onyszko

12. Crystal Growth by Traveling Heater Method 459
Robert Triboulet

13. Growth of Bulk Nitrides from a Na Flux 505
Yusuke Mori, Mamoru Imade, Mihoko Maruyama, Masashi Yoshimura, Hisanori Yamane, Fumino Kawamura, Takahiro Kawamura

14. Hydrothermal Growth of Crystals—Design and Processing 535
Kullaiah Byrappa, Namratha Keerthiraj, Shayan M. Byrappa

15. High-Pressure, High-Temperature Solution Growth and Ammonothermal Synthesis of Gallium Nitride Crystals 577
Dirk Ehrentraut and Michal Bockowski

16. Vapor Transport Growth of Wide Bandgap Materials 621
Matthias Bickermann, Tania Paskova

17. Crystal Growth of Diamond 671
Yuri N. Palyanov, Igor N. Kupriyanov, Alexander F. Khokhryakov, Victor G. Ralchenko

18. Wafer Processing 715
Hans-Joachim Möller

Part B. Growth Mechanisms and Dynamics

19. Capillarity and Shape Stability in Crystal Growth from the Melt 757
Thierry Duffar

20. Heat Transfer Analysis and Design for Bulk Crystal Growth: Perspectives on the Bridgman Method 793
Jeffrey J. Derby, Andrew Yeckel

21. Fluid Dynamics: Modeling and Analysis 845
Koichi Kakimoto, Bing Gao

22. The Role of Marangoni Convection in Crystal Growth 871
Takao Tsukada

23. Flow Control by Magnetic Fields during Crystal Growth from Melt 909
Daniel Vizman

24. Oscillatory-Driven Fluid Flow Control during Crystal Growth from the Melt 951
Peter Capper, Evgeny Zharikov

25. Segregation and Component Distribution 995
Aleks G. Ostrogorsky, Martin E. Glicksman

26. Thermal Stress and Dislocations in Bulk Crystal Growth 1049
Noriyuki Miyazaki

27. Defect Generation and Interaction during Crystal Growth 1093
Helmut Klapper, Peter Rudolph

28. Automation of Crystal Growth from Melt 1143
Jan Winkler, Michael Neubert

29. Fundamentals of Crystal Growth from Solutions 1185
Igor Pritula, Keshra Sangwal

30. Crystallization Mechanisms of High Critical Temperature Superconductors 1229
Yuh Shiohara, Teruo Izumi

31. Crystallization in Gels 1277
Abel Moreno, Ma Eugenia Mendoza

32. Fundamentals of Industrial Crystallization 1317
Joop H. ter Horst, Christiane Schmidt, Joachim Ulrich

Index 1351

General Preface

The history of crystal growth is long as those of the universe and the earth. Meteorites contain pyrites and olivine crystals which indicate these crystals were grown when the planets were born. Crystals naturally produced are used as gems from the early time of the human history. In Exodus, it is written that breast-piece was decorated by ruby, emerald, sapphire, amethyst, and other gems.

There are a lot of crystals around us. As examples, we can find snowflakes falling down from the sky, ice crystals in a lake in winter, salt and sugar crystals in the pots of our kitchen. But, it was after the invention of point contact and junction transistors, respectively in 1947 and 1948, that the industry paid a great interest on the crystal growth. Without the growth of high purity and highly perfect single-crystal semiconductor, at that time of Ge, the invention of the transistors will never happen.

It is well known that the modern information society will be not realized without electronic and optical devices. One finds large-scale integrated circuits of Si in every computer from laptop to super computers. For high speed and mass transmission of information, compound semiconductor devices are indispensable.

These devices are fabricated almost all by using single crystals of semiconductors and oxides. When we look into the history of the devices, we always see that an invention of crystal growth technique makes it possible to bring out new device. As we saw, the invention of transistor was possible only after the growth of high-quality Ge single crystal. The growth of large-diameter dislocation-free Si crystal has enabled the production of large-scale integrated circuit. Due to the invention of liquid-phase epitaxy, it became possible to realize light-emitting diode (LED) and laser diode (LD) in real use. Drastic technological improvement in highly lattice mismatch heteroepitaxy made it possible to realize blue ∼ ultraviolet LED and LD and it can be said that the success in the growth of high-quality nitride semiconductor gave the blue light all over the world. Hence, we should understand that new technology of crystal growth has always created new electronic and optical devices.

It is extremely good news for the community of crystal growth that 2014 Nobel Prize in Physics was awarded to Professors Isamu Akasaki, Hiroshi Amano and Shuji Nakamura for the invention of efficient blue light-emitting diodes which has enabled bright and energy-saving white light sources. This invention is based on the growth of nitride semiconductors employing a low-temperature buffer layer on sapphire substrate in heteroepitaxy. We are happy that Professor Hiroshi Amano, one of the winners, is contributing to this Handbook as an author of Chapter 16 in Vol. IIIA.

The first edition of the Handbook of Crystal Growth was edited by D.T.J. Hurle. This Handbook was composed of three volumes and published in 1993–1994. The present second edition of the Handbook also consists of three volumes. Each volume was edited by separate editors. Volume I is edited by T. Nishinaga and the volume covers the basic aspects of crystal growth. In Volume IA, fundamentals and kinetics of crystal growth are described and in IB, advanced problems of transport and stability are discussed. Volume II is edited by P. Rudolph and this volume covers bulk crystal growth. Volume IIA presents basic technologies of bulk growth and IIB does growth mechanism and dynamics. Volume III was edited by T. F. Kuech and the volume covers thin film growth and epitaxy. Volume IIIA discusses basic techniques and IIIB does growth mechanisms and dynamics.

Present Handbook project was created in March, 2011 and six advisors were appointed. They are T. F. Kuech, G. B. Stringfellow, J. B. Mullin, J. J. Derby, R. Fornari, and K. H. Ploog. I am very much grateful for their important and valuable suggestions.

Finally, all editors would like to express their sincere thanks to Shannon Stanton, Elsevier, for her strong and well cared support to this work.

Tatau Nishinaga
Editor in Chief

Preface to Volume II

In Volume II, application of the science from Volume I to the development of technology in the field of bulk crystallization on both industrial and research scales is reviewed. While Volume IIA demonstrates important growth practices, Volume IIB presents the process fundamentals, including capillarity, segregation phenomena, and transport of heat and mass. Of course, even for crystal growth not always is such a division into methodical and elementary parts sustainable due to its requirement of ever-coincidental combination between engineering and science. Therefore, most chapters in both issues A and B connect simultaneously the experiences with backgrounds or vice versa.

Chapter 1 is an introduction to the formation of minerals because from an historical point of view humans learned from nature about the basic crystal formation parameters. Then, today's state-of-the-art of crystallization practice is discussed. Along with the demonstration of a high material versatility, special emphasis is placed on mono- and polycrystalline silicon for microelectronics and photovoltaics, respectively. The Czochralski and float zone growth of dislocation-free silicon are discussed in great detail in Chapters 2 and 7, as well as the directional solidification of multi- and quasimonocrystalline silicon ingots in Chapter 10. The importance of Czochralski, flux growth, and floating zone techniques for production of dielectric and conducting oxide crystals for lasers and nonlinear optics as well as for metallic alloys are reported in Chapters 4–6 and 8. A compromised review on liquid encapsulation Czochralski technique is also added in Chapter 3.

As it is well known, the Bridgman method became an exciting renaissance during the last decades due to the high accuracy of the crystal diameter and relative low defect density. Today, the rapid developments of computer processing, ingredient and engineering improvements have led to the vertical gradient freeze process for many important materials, such as GaAs, CdTe for HF electronics and IR imaging, as shown in Chapter 9. The unidirectional solidification of super alloys in the shape of crystalline turbine blades is especially of increasing importance for the aircraft as well as other industries, as argued in Chapter 11.

The treatment of solution growth techniques starts with the traveling heater method in Chapter 12 being particularly favorable for obtainment of homogeneous mixed crystals. Chapters 13–16 discuss flux, ammono- and hydrothermal, as well as vapor growth techniques focusing on bulk growth of very topical GaN, AlN, and SiC crystals as substrates for optoelectronics and high-power devices. Then, in Chapter 17 the spectacular production measures of diamond crystals are reviewed. Lastly, Chapter 18 shows modern

cutting methods to separate the as-grown crystals into wafers for further applications, e.g., as substrates for epitaxy (Volume III).

Volume IIB continues with Chapter 19 on fundamentals of capillarity and shape stability analysis including dewetted Bridgman growth arrangement. Then the transport processes are discussed. Before the atoms or molecules pass over from a position in the fluid medium (gas, melt, or solution) to their place in the crystalline face, they must be transported over macroscopic distances by diffusion, buoyancy-driven convection, surface-tension-driven convection, and forced convection (rotation, acceleration, vibration, magnetic mixing) as outlined in Chapters 21–24. Further, the heat of fusion and the part carried by the species on their way to the crystal must be dissipated in the solid phase by well-organized thermal conductions and radiation to maintain a stable propagating interface, as shown in Chapter 20. The segregation and component distribution encountered in Czochralski, directional solidification, and zone-melting processes are treated on a modernized level in Chapter 25.

Today, the increase of high-quality crystal yield, its size enlargement and reproducibility are imperative conditions to match the strong economy. Thus, the application of both global simulation for optimum growth design and advanced automation process are shown to be crucial. Whereas the implicit use of tools of computer modeling runs through many chapters, a special overview about the strategies for the automatic control of crystal growth from melt is given in Chapter 28. It is shown that model-based tools are an essential resource for the control performance optimization. Prior to that, in Chapters 26 and 27 the origins of defect generation in growing crystals are described. Beside the thermomechanical stress, the point defect-assisted dislocation dynamics, but also grain patterning, foreign phase particle formation, and twinning are discussed in detail and controlling measures are proposed.

Finally, selected fundamentals and methodical consequences at bulk growth from solutions are shown in Chapter 29. In Chapter 30, special attention is given on the growth of high-T_C superconductors accentuating the common problem of twinning. Then, the mechanisms of protein crystal growth from gels are discussed in Chapter 31. Volume IIB closes with Chapter 32 on mass crystallization being of highest importance for food and pharmaceutical industries.

In summary, this volume demonstrates the enormous progress of bulk crystal growth technology and deepening of process understanding especially during the last 20 years. Of course, this volume cannot claim to be complete, but it constitutes a very good complement to the 1994 handbook.

This editor would like to extend his deep thanks to all authors of Volume II for their constructive cooperation and excellent contributions. In spite of their heavy workloads, all authors completed their chapters with great enthusiasm and on time.

Peter Rudolph
July 2014

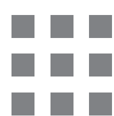

List of Contributors

Matthias Bickermann Leibniz Institute for Crystal Growth, Berlin, Germany; Institute for Chemistry, Technical University Berlin, Berlin, Germany

Michal Bockowski Institute of High Pressure Physics Polish Academy of Sciences and TopGaN Ltd., Warsaw, Poland

Martin Bruder AIM Infrarot Module GmbH, Heilbronn, Germany

Kullaiah Byrappa Center for Materials Science and Technology, University of Mysore, Mysore, Karnataka, India

Shayan M. Byrappa Department of Materials Science and Engineering, Stony Brook University, State University of New York at Stony Brook, Stony Brook, NY, USA

Peter Capper Selex ES, Southampton, UK

Chuantian Chen Beijing Center for Crystal Research and Development, Key Laboratory of Functional Crystals and Laser Technology, Technical Institute of Physics and Chemistry, CAS, Beijing, China

Hanna A. Dąbkowska Brockhouse Institute for Materials Research, McMaster University, Hamilton, ON, Canada

Antoni B. Dąbkowski Brockhouse Institute for Materials Research, McMaster University, Hamilton, ON, Canada

Jeffrey J. Derby Department of Chemical Engineering and Materials Science, University of Minnesota, Minneapolis, MN, USA

Thierry Duffar SIMaP-EPM, Saint Martin d'Hères, France

Dirk Ehrentraut Soraa, Inc., Goleta, CA, USA

Stefan Eichler Freiberger Compound Materials, Freiberg, Germany

Jochen Friedrich Fraunhofer Institute IISB, Erlangen, Germany

Tsuguo Fukuda Fukuda Crystal Lab Co., Ltd, Sendai, Miyagi, Japan

Zbigniew Galazka Leibniz Institute for Crystal Growth, Berlin, Germany

Bing Gao Research Institute for Applied Mechanics, Kyushu University, Kasuga, Fukuoka, Japan

Juan Manuel García-Ruiz Instituto Andaluz de Ciencias de la Tierra, Laboratorio de Estudios Cristalográficos CSIC-Universidad de Granada, Granada, Spain

Gunter Gerbeth Helmholtz-Zentrum Dresden-Rossendorf, Dresden, Germany

Martin E. Glicksman Mechanical & Aerospace Engineering Department, Florida Institute of Technology, Melbourne, FL, USA

Regina Hermann Leibniz Institute for Solid State and Materials Research Dresden, Dresden, Germany

Chuck Hsu Sino-American Silicon Productions Inc., Hsin-chu, Taiwan

Mamoru Imade Osaka University, Suita, Osaka, Japan

Hiroyuki Ishibashi Hitachi Chemical Co., Ltd., Ibaraki, Japan

Mitsuru Ishii Shonan Institute of Technology, Higashiyamato, Tokyo, Japan

Teruo Izumi Superconductivity Research Laboratory, International Superconductivity Technology Center, Kawasaki, Kanagawa, JAPAN

Manfred Jurisch Freiberger Compound Materials, Freiberg, Germany

Koichi Kakimoto Research Institute for Applied Mechanics, Kyushu University, Kasuga, Fukuoka, Japan

Fumino Kawamura National Institute for Materials Science, Tsukuba, Ibaraki, Japan

Takahiro Kawamura Mie University, Tsu, Mie, Japan

Alexander F. Khokhryakov V.S. Sobolev Institute of Geology and Mineralogy, Siberian Branch of the Russian Academy of Sciences, Novosibirsk, Russia; Novosibirsk State University, Novosibirsk, Russia

Helmut Klapper Institute of Crystallography, RWTH Aachen University, Aachen, Germany

Krzysztof Kubiak The Faculty of Mechanical Engineering and Aeronautics, Department of Materials Science, Rzeszow University of Technology, Rzeszow, Polish, Poland

Igor N. Kupriyanov V.S. Sobolev Institute of Geology and Mineralogy, Siberian Branch of the Russian Academy of Sciences, Novosibirsk, Russia; Novosibirsk State University, Novosibirsk, Russia

Chung-wen Lan Department of Chemical Engineering, National Taiwan University, Taipei, Taiwan

Anke Lüdge Leibniz Institute for Crystal Growth, Berlin, Germany

Mihoko Maruyama Osaka University, Suita, Osaka, Japan

Ma Eugenia Mendoza Instituto de Física, Benemérita Universidad Autónoma de Puebla, Puebla, Mexico

Noriyuki Miyazaki Kyoto University, Kyoto, Japan; Kyushu University, Fukutsu-shi, Fukuoka, Japan

Hans-Joachim Möller Fraunhofer Technology Center for Semiconductor Materials, Freiberg, Germany; Technical University Bergakademie Freiberg, Institute for Experimental Physics, Freiberg, Germany

Abel Moreno Instituto de Química, Universidad Nacional Autónoma de México, Mexico

Yusuke Mori Osaka University, Suita, Osaka, Japan

Andris Muiznieks Department of Physics, University of Latvia, Riga, Latvia; (Deceased 5 April 2013)

Georg Müller Crystal Consulting, Langensendelbach, Germany

J. Brian Mullin Electronic Materials Consultancy, Poole, UK

Kazuo Nakajima Graduate School of Energy Science, Kyoto University, Yoshida, Sakyo-ku, Kyoto, Japan

Namratha Keerthiraj Center for Materials Science and Technology, University of Mysore, Mysore, Karnataka, India

Teruhiko Nawata Tokuyama Corporation, Yamaguchi, Japan

Michael Neubert Leibniz Institute for Crystal Growth, Berlin, Germany

Arkadiusz Onyszko The Faculty of Mechanical Engineering and Aeronautics, Department of Materials Science, Rzeszow University of Technology, Rzeszow, Polish, Poland

Aleks G. Ostrogorsky Mechanical & Aerospace Engineering Department, Illinois Institute of Technology, Chicago, IL, USA; Research on segregation was partially supported by NASA

Fermín Otálora Instituto Andaluz de Ciencias de la Tierra, Laboratorio de Estudios Cristalográficos CSIC-Universidad de Granada, Granada, Spain

Yuri N. Palyanov V.S. Sobolev Institute of Geology and Mineralogy, Siberian Branch of the Russian Academy of Sciences, Novosibirsk, Russia; Novosibirsk State University, Novosibirsk, Russia

Tania Paskova Department of Electrical and Computer Engineering, North Carolina State University, Raleigh, NC, USA

Janis Priede Applied Mathematics Research Center, Coventry University, UK

Igor Pritula Institute of Single Crystals, National Academy of Sciences of Ukraine, Kharkov, Ukraine

Victor G. Ralchenko Prokhorov General Physics Institute, Russian Academy of Sciences, Moscow, Russia

Helge Riemann Leibniz Institute for Crystal Growth, Berlin, Germany

Peter Rudolph Crystal Technology Consulting, Schönefeld, Germany

Keshra Sangwal Department of Applied Physics, Lublin University of Technology, Lublin, Poland

Nobuhiko Sarukura Institute of Laser Engineering, Osaka University, Suita, Osaka, Japan

Christiane Schmidt Martin-Luther-Universitaet Halle-Wittenberg, Zentrum für Ingenieurwissenschaften, Halle, Germany

Yuh Shiohara Superconductivity Research Laboratory, International Superconductivity Technology Center, Kawasaki, Kanagawa, JAPAN

Jan Sieniawski The Faculty of Mechanical Engineering and Aeronautics, Department of Materials Science, Rzeszow University of Technology, Rzeszow, Polish, Poland

Dariusz Szeliga The Faculty of Mechanical Engineering and Aeronautics, Department of Materials Science, Rzeszow University of Technology, Rzeszow, Polish, Poland

Joop H. ter Horst Intensified Reaction & Separation Systems, Process & Energy Department, Delft University of Technology, Delft, The Netherlands; EPSRC centre for Innovative Manufacturing in Continuous Manufacturing and Crystallisation, Strathclyde Institute of Pharmacy and Biomedical Sciences, University of Strathclyde, Glasgow, U.K.

Robert Triboulet CNRS/GEMAC, Versailles Cedex, France

Takao Tsukada Department of Chemical Engineering, Tohoku University, Sendai, Japan

Joachim Ulrich Martin-Luther-Universität Halle-Wittenberg, Zentrum für Ingenieurwissenschaften, Halle, Germany

Janis Virbulis Department of Physics, University of Latvia, Riga, Latvia

Daniel Vizman Faculty of Physics, Department of Physics, West University of Timisoara, Timisoara, Romania

Wilfried von Ammon von Ammon Consulting, Roth, Germany

Jiyang Wang State Key Laboratory of Crystal Materials, Shandong University, Jinan, China

Yan Wang Fujian Research Institute of Matter Structures, CAS, Fuzhou, China

Nico Werner Leibniz Institute for Crystal Growth, Berlin, Germany

Jan Winkler Institut für Regelungs- und Steuerungstheorie, Technische Universität Dresden, Dresden, Germany

Hisanori Yamane Tohoku University, Aoba-ku, Sendai, Miyagi, Japan

Haohai Yu State Key Laboratory of Crystal Materials, Shandong University, Jinan, China

Andrew Yeckel Department of Chemical Engineering and Materials Science, University of Minnesota, Minneapolis, MN, USA

Masashi Yoshimura Osaka University, Suita, Osaka, Japan

Guochun Zhang Beijing Center for Crystal Research and Development, Key Laboratory of Functional Crystals and Laser Technology, Technical Institute of Physics and Chemistry, CAS, Beijing, China

Evgeny Zharikov D. Mendeleyev University of Chemical Technology of Russia, Moscow, Russia

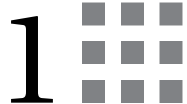

Crystal Growth in Geology: Patterns on the Rocks

Juan Manuel García-Ruiz, Fermín Otálora

INSTITUTO ANDALUZ DE CIENCIAS DE LA TIERRA, LABORATORIO DE ESTUDIOS CRISTALOGRÁFICOS CSIC-UNIVERSIDAD DE GRANADA, GRANADA, SPAIN

CHAPTER OUTLINE

1.1 Introduction **1**
1.2 Geological Scenarios for Crystal Growth **4**
1.2.1 Magmatic Environments 5
1.2.2 Metamorphic Environments 8
1.2.3 Hydrothermal Environments 9
1.2.4 Sedimentary Environments 10
1.2.5 Biomineralization and Biologically Induced Crystallization 11
1.3 Deciphering Geological Information from Crystal Morphology **12**
1.4 Decoding Polycrystalline Textures from Nucleation and Growth **16**
1.5 The Case of Giant Crystals **21**
1.6 Decoding Disequilibrium Mineral Patterns **24**
1.6.1 Compositional Zoning 25
1.6.2 Liesegang Structures 28
1.6.3 Fractal Dendrites 30
1.7 Early Earth Mineral Growth, Primitive Life Detection, and Origin of Life **32**
1.8 From Deep Earth to Outer Space **36**
Acknowledgments **39**
References **39**

1.1 Introduction

Rock-forming minerals are mostly crystalline. In most cases, rock minerals are micrometric in size and are irregularly embedded within other minerals, so they are not really attractive to the naked eye. However, in a few cases, minerals display their geometrical beauty as isolated single crystals of several centimeters or even larger in size. The geometry of crystals (as those shown in Figure 1.1), which is so different than any other

Handbook of Crystal Growth. http://dx.doi.org/10.1016/B978-0-444-63303-3.00001-8
Copyright © 2015 Elsevier B.V. All rights reserved.

FIGURE 1.1 Minerals have played a main role in the history of crystals and crystal growth. The morphology of crystals found in nature was the most astonishing feature to explain, the main challenge. The law of constancy of angles rediscovered up to four times until his definitive discovery by Rome de L'Isle- and the concept of the "molécule intégrant" of René Haüy set the basis for the development of morphological crystallography in XIX century. Minerals were also the targets that triggered the development of the first crystallization technology to grow synthetic crystals. Natural samples of minerals: (a) Galena, (b) Calcite, (c) Pyrite, (d) Quartz.

natural object, triggered the curiosity of rational thinkers such as Theophrastus, who classified minerals by their physical properties [1]; Pliny the Elder, who wrote what was for centuries the most extensive and rational approach to minerals [2]; Kepler, who envisaged the internal order of ice crystals [3]; Biringuccio, who studied metals; Stenon, who discovered the morphological properties of quartz crystals [4]; and Romé de L'Isle, who demonstrated unambiguously the law of constancy of angles [5].

The science of crystals began historically with the study of minerals, and the same goes for the study of crystals' formation and growth. In his prodromus, Nicolas Steno provided a rational analysis of crystal growth and concluded that crystals do not grow by germination or vegetative growth, as thought at his time, but by accretion of growth units. Until the late nineteenth century, most crystallographic studies were devoted to the morphology and symmetry properties of single and twinned mineral specimens [6]; the main crystal growth challenge was the synthesis of natural crystals in the laboratory, from common minerals to precious stones [7]. The progress of these studies during the twentieth century powered the emergence of a huge industry related to crystal growth, not only for gems but also for single crystals for new technologies [8a,b].

Most of the chapters in this book deal with the study of the formation of crystals in the laboratory or industry. In those cases, it is possible to obtain reproducible and comprehensible data about the composition of the mother phase under highly precise and stable conditions of pressure, temperature, and compositional purity, thus providing

feedback about the growth conditions and products of the crystallization process. In this chapter, we face a completely different problem. Here, the crystals to be studied already formed during the long history of this planet, a history that dates back 4500 million years. Except for the contemporary surface or near-surface geological scenarios, the composition of the mother phase or the crystallization conditions of those crystals is not known and the temperature, pressure, and composition are not controlled. These parameters change with time, sometimes even suddenly. A large number of reactions proceed simultaneously in a complex, multicomponent fluid, including chemicals that modify crystallization behavior in many nonlinear ways. In addition, these processes are usually difficult (or even impossible) to observe, particularly those occurring at very high temperatures and pressures, and the typical timeframe for geological processes spans a range from a few seconds to a few million years.

In mineral growth studies, there is nothing but crystals. In fact, the main contribution expected from crystal growth to this field is to decode the information contained in these crystalline rock-forming minerals to reveal the physicochemical scenario from which they grew—that is, to help uncover the geological history of this planet. This is not an easy task because the relevant information derived from classical crystal growth studies is rather scarce. We have adequate knowledge on crystallization to control the nucleation flow and crystal growth rates at the laboratory and industrial scales. However, we still have difficulties understanding in detail the variables that control crystal growth morphology and crystal defects, which are the crystal properties most used to understand mineral growth thanks to the pioneering work of Sunagawa [9]. Therefore, we need to continue the analysis and interpretation of single crystal features—morphology, impurities, inclusions, surface topography, and isotopic signature—to better understand their geological context. However, it is very important to note that minerals almost never appear as single crystals in rocks. They only rarely appear as the beautiful well-faceted single or twin crystals displayed in museums and sold in mineral shops. In most cases, minerals appear on forming rocks as polycrystalline materials [10]. Unfortunately, the information on polycrystalline crystallization was only interesting for metallurgists, so it is scarce and restricted to alloys. Crystal growth studies will only be useful for earth and planetary sciences if there is an extensive exploration of pattern formation, such as how minerals self-assemble into peculiar structures and how they do so when crystallizing massively from seas and lakes, from magma and vapor, and how they experience phase transitions during their spatiotemporal trip triggered by the slow but continuous dynamics of the planet.

All of these circumstances and drawbacks make it very difficult to understand crystal nucleation and growth in geological media; however, at the same time, they make crystals richer in behavior and products and open up the possibility of performing studies at the frontier of science and technology. It is essential to push a new research program in crystal growth beyond classic studies because novel theoretical and experimental tools are necessary to understand what mineral crystals can tell us about the past of this planet, as well as its current inner and outer dynamic; they will also allow us

to properly analyze the results of our incipient exploration of solar planets and extraterrestrial images. This chapter reviews the current status and the future trends of this fascinating research program.

1.2 Geological Scenarios for Crystal Growth

Minerals form in a variety of different geological environments, such as solutions, melts, or vapor, as well as by solid–solid transition. Therefore, it is convenient to analyze the different geological scenarios in order to understand how they work in terms of crystallization. Figure 1.2 shows the main processes in the Earth's crust. The solid arrows indicate processes of crystallization, whereas the dashed arrows indicate dissolution or melting; the dotted arrows correspond to the transport of material. The two gray rectangles contain the fluids from which crystallization proceeds in the majority of geological crystallization processes: magmas and solutions of different origin and properties. For simplicity, the atmosphere is not included, although it plays a very important role, along with life, in processes such as the precipitation of carbonates. Igneous rocks are formed by the crystallization of magmas, either in the interior of the crust (plutonic rocks) or at the surface (volcanic rocks). Crystallization produces fractionation and liquids with increasing concentration of metals and other ions that do not enter into the crystal lattice of the crystallized minerals. Finally, a high-temperature solution remains, which gives rise to hydrothermal deposits and contributes to the composition of surface waters through volcanoes and smokers. All types of rocks at the Earth's surface undergo weathering owing to the interaction with meteoric waters, the atmosphere, and living organisms. This produces fragments of rocks (clasts) and dissolved species in the surface waters that, after precipitation, can combine with the

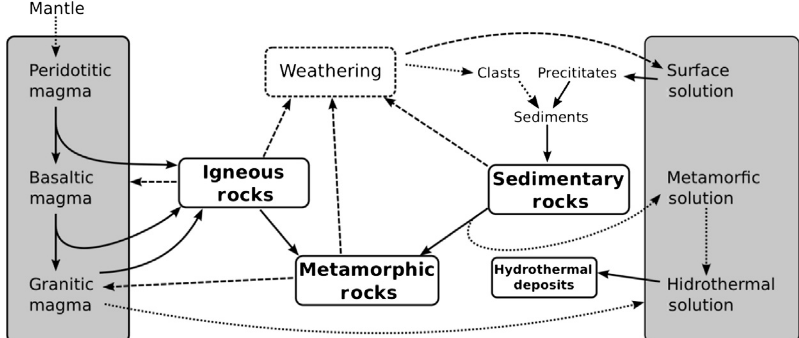

FIGURE 1.2 Sketch of the relation between the main crystallization/dissolution processes in the Earth's crust that produce minerals from solutions or melts. Solid line arrows indicate processes of crystallization, dashed line arrows indicate dissolution or melting and dotted line arrows correspond to transport of material. The two gray rectangles contain the sources from which crystallization proceeds in virtually all geological crystallization processes: magmas and solutions having different origin and properties. For simplicity, the effects of atmosphere or life are not included, although they play an important role in processes like the precipitation of carbonates.

clasts into sediments. Compaction, crystallization, and recrystallization of minerals during diagenesis transform these sediments into sedimentary rocks. The minerals of any rock can become unstable with temperature and pressure changes. This can lead to dissolution, recrystallization, and nucleation of new phases during metamorphism. Sedimentary rocks, forming at the surface and later buried by new sediments, typically suffer modification by changes of pressure, temperature, and redox potential.

1.2.1 Magmatic Environments

Crystallization from the melt, as in the case of Czhochralsky growth of semiconductors, is characterized by high temperature, very condensed systems, small or no interaction with solvents, and continuous growth of rough interfaces. However, this only applies to the solidification of single phases from a melt of their components. Magmatic crystallization normally implies that the growing crystals are in contact with a complex multicomponent melt that acts as a solvent. Crystals in most magmatic solidification scenarios grow by layer growth, not by continuous growth; therefore, faceted crystals are far more common than rounded or dendritic forms. For these reasons, magmatic mineral growth can be considered as high-temperature, high-viscosity solution growth with silicates and volatile components acting as solvents, rather than melt growth [11]. Due to the high viscosity, mass transport is slow and growth kinetics are controlled by the transport of latent crystallization heat rather than by mass transport, although mass transport may become very important for several processes.

Magmas can be either generated from materials in the mantle, such as peridotitic magmas, or from the melting of igneous or metamorphic rocks, typically in subduction zones. Crystallization of magmas upon cooling deep into the crust is slow, starting with crystals having the highest fusion temperature among all the possible minerals that can be nucleated from the composition of the magma. This first crystallization produces a melt that is enriched in the component not present in the first crystals produced, which eventually gives rise to new minerals with a lower fusion temperature. As a consequence, the composition of the melt evolves with time. This evolution, along with the movement of the magma within the crust, differentiates the various types of igneous rocks and magmas that contain the remaining components. The large number of degrees of freedom characterizing a crystallizing magma can be summarized in the form of a phase diagram containing the most relevant chemical species and divided into a series of stability fields for different minerals. The crystallization of one of them—the most stable one for the composition of the magma—moves the position of the magma within this diagram, eventually entering the stability field of a different mineral that starts crystallizing. This trajectory around the phase diagram is called the solidification path, which leads to magma differentiation in the sense of the classic Bowen's reaction series. The minerals present in the resulting rock and the textural relations between them encode the solidification path, which can be investigated looking at the phase relations in the phase diagram. The main variables to be considered when dealing with mineral growth

in magmatic environments are the latent heat value for each of the crystallizing minerals, the nucleation, growth thermodynamics and kinetics, the rate of convective flow, the temperature of the melt, and the constraints (e.g., the thermal contrast between magma and country rock) if the temperature is not constant.

Along with metamorphic media (see below), crystal growth in magmatic environments is difficult to study experimentally because of the high temperatures and pressures involved, and it is almost inaccessible in in-situ studies, although some experiments have been successfully performed [12,13]. Most of the experimental investigations in igneous petrology have studied magmas at equilibrium, with the aim of obtaining thermodynamic data on mineral/melt and mineral/mineral partition coefficients to study the genesis of igneous rocks by analytical methods on geological samples. Unsteady systems have also been studied to investigate the crystallization of magmas upon cooling in closed (magmatic chambers) [14] and open (magmatic ocean) [15] conditions. Experiments in which magma was cooled to reproduce crystallization conditions [16] have been used to investigate crystal growth in magmatic environments, particularly the dependency of crystal growth rates on temperature and convective mass transport, the texture, crystal shape and composition as a function of cooling rate, and the development of compositional zonation.

Upon the nucleation of crystals in the magma and after a highly transient stage, crystallization tends toward equilibrium between heat production (latent heat release) and heat loss. Because the main controlling factor is the fast release of latent heat during the nucleation and the first stages of fast growth, nucleation usually is the rate-limiting process, occurring as sharp pulses, producing thermal oscillations, and followed by longer periods of crystal growth. The main parameters controlling crystal size distribution, especially close to the margins of cooling igneous bodies, are the initial thermal conditions and the nucleation and growth kinetics of the main minerals [16]. Crystal size, number, and shapes resulting from crystal growth kinetics have important consequences on the fractionation of magmas and their rheological properties. Fractional crystallization occurs when crystals can freely sediment within the magma and accumulate at the bottom of the magmatic chamber, leaving the fluid depleted in the chemicals entering their composition, which leads to a chemical evolution of magmas. This process is responsible for the differentiation of the light minerals making up the Earth's crust. On the other hand, nonfractional crystallization implies differentiation within the melt percolating the already-crystallized solid matrix; the crystal size distribution determines the degree of differentiation in this regime due to the competition between percolation and solidification rates. The crossover between fractional and nonfractional crystallization, and the chemical and mineralogical evolution of the magma in both cases, are controlled by the crystal size and shape [15], which are the macroscopic output of the nucleation and growth kinetics operating in the magmatic body.

The rheological properties of the lava that produces volcanic rocks are also controlled by crystal nucleation and growth kinetics. The content and shape of the crystals determine the formation of basic lava crusts and their rheological properties [17]. In volcanic

rocks, and in general in magmatic rocks for which temperature and pressure can change quickly during the growth of crystals, the crystallization conditions are usually encoded in the crystal compositional zoning, morphology, and texture, either in the different parts of large crystals (phenocrystal cores crystallized deeper than their rims), or in different crystals of the same composition (microphenocrystals and microlites formed at subaerial conditions) [14].

Many natural rocks contain clear evidence of disequilibrium, such as compositional zoning, because they have formed from magmas crystallizing along nonequilibrium, time-dependent pathways [12,18]. The main contribution of crystal growth to igneous petrology is probably the interpretation of the features related to mineral growth during the time-dependent evolution of these igneous systems. Changes in temperature, pressure, and composition of the magma do modify crystal growth kinetics, so the history of the rock is recorded in the disequilibrium geochemical features and the petrographic texture of the rock. An example of this approach to decoding the genetic information contained in igneous rocks is the application of growth rate studies into zoning profiles in plagioclase crystals. This problem has been modeled and tested against experimental data [19]. Recent models, including nonlinear multicomponent diffusion equations, show that growth rate and crystal composition may vary stepwise, even under linear cooling of the magma [20].

The nonequilibrium features of crystal growth are relevant for the fine-tuning of the thermodynamic indicators used in petrology. Crystal geothermometers and geobarometers are extensively used in igneous and metamorphic petrology. They are based on the temperature-dependent partition coefficient of a component or a chemical species between coexisting phases, with at least one of them being a crystal, such as clinopyroxene-melt, orthopyroxene-melt, or orthopyroxene-clinopyroxene. The process of impurity trapping depends on the thermodynamics of lattice-strain accumulation within the crystal lattice, as well as on the growth kinetics and the crystal growth mechanism, which makes them sensitive to changes in both the overall growth rate [21] and the relative growth rate of different crystal faces (i.e., to the morphology and sectorial structure) [22]. These features can hinder the use of geothermometers or make them less accurate, but they also open the possibility for advanced experimental methods, such as using single-crystal thermometers in which the partition coefficient between different growth sectors is used as a geothermometer or geobarometer, thus avoiding any assumption about the thermodynamic equilibrium between two phases in contact.

Extreme examples of crystal growth are found in pegmatites, which are very coarse-grained intrusive igneous rocks made of interlocking crystals, from millimeter size up to large crystals of tens of meters in length. The genesis of pegmatites is still controversial, and there is not a model explaining all the features of these rocks. The most accepted model is the formation of granitic pegmatites from residual melts derived from the crystallization of granitic plutons. Shallow-level pegmatites cool much more rapidly than previously believed [23]. This is consistent with the disequilibrium crystal growth

features observed in these rocks, including skeletal, radial, and graphic morphologies; strong compositional zoning patterns; sharp changes in grain size; and anisotropic, oriented fabrics such as comb structures. These features seem contradictory to the existence of large crystals, which in classical petrology textbooks are identified as having slow-cooling rates. The exceptional textural properties of these rocks are most probably due to the uncommon composition of the residual magmas from which they grow. After magmatic differentiation, these magmas are enriched in rare, incompatible components, and they have high concentrations of fluxes and volatiles. In these conditions, one can expect anomalously high mass transport rates and solubility and anomalously low crystallization temperatures, nucleation rates, and melt polymerization [24]. The joint effect of these anomalies leads to wide metastability ranges and rapid depletion of the high-mobility growth units, which can explain the development of large crystals due to inhibited nucleation rates and enhanced growth rates.

1.2.2 Metamorphic Environments

Metamorphic rocks undergo changes in texture, mineralogy, and chemical composition through partial or complete recrystallization of their minerals, either solid-state or solution-mediated [25–27]. These rocks remain essentially solid during metamorphism, but they can flow in a plastic-like manner due to differential pressure. The main factors driving metamorphism are temperature, pressure, the presence of fluids, and the composition of the original rock. Temperature drives the chemical changes that result in the recrystallization of existing minerals, destabilization of previous ones (particularly hydrated minerals), or the nucleation and growth of new phases. Many crystals will grow larger than they were in the parent rock. Pressure, like temperature, increases with depth and contributes to changes in a rock's mineralogy and texture. Confining pressure (in all directions) causes the spaces between mineral grains to close, producing a more compact rock. Directed pressure, on the other hand, guides the shape and orientation of the new metamorphic minerals, producing plate-like crystals extended in the directions perpendicular to the pressure gradient. Fluids (mostly water but also other volatile components, such as carbon dioxide) play an important role in metamorphism, dissolving and transporting ions along the boundaries between crystals or catalyzing some reactions during metamorphism. Clay minerals can contain up to 60% water in their crystal structure, which is mobilized when these minerals are transformed during metamorphism. Apart from this loss or accumulation of volatiles, most metamorphic rocks have the same overall composition as the parent rock from which they were formed.

Metamorphism creates new textures on the rock, and it is the realm of recrystallization and transformation of some of the original minerals into new ones that grow at high temperatures and pressures. Metamorphic rocks can exhibit great variation in crystal size; in general, the size of crystals increase as the grade of metamorphism increases. During the recrystallization process, certain metamorphic minerals, including

garnet, staurolite, and andalusite, tend to develop a few large crystals [28,29]. In contrast, minerals such as muscovite, biotite, and quartz typically form a large number of small crystals. The mineral grain shape and orientation is also altered: changes in orientation lead to foliation, whereas the most relevant effect of crystal size increases in some minerals is the development of granoblastic textures. Foliation can develop by solid-state plastic flow because of the intracrystalline movement of lattice defects within each grain or due to the dissolution of crystals from areas of high stress, transport along the intercrystalline surface, and deposition in low-stress areas [30,31]. Granoblastic rocks, such as quartzite, have a massive or coarse granular appearance that is produced by recrystallization during metamorphism [32,33] and exhibit no directional deformation. They are composed mainly of crystals that grow in equidimensional shapes in restricted spaces. Aside from quartzite, the most common granoblastic rock is marble, resulting from the metamorphism of limestone or dolostone leading to a complete recrystallization of the original rock into a polygonal interlocking mosaic of calcite, aragonite, and/or dolomite crystals [34]. Metamorphic rocks are classified by their metamorphic grade, which is defined as the maximum temperature and pressure to which the rock was subjected. However, metamorphism is a dynamic process, and a metamorphosed rock may have a very complex history. This history influences the successive stages of crystal growth or dissolution; therefore, it is encoded in the crystallography, chemistry, and texture of the minerals that grow during metamorphism (i.e., in the properties of the crystals making up the rock). For example, by studying the compositional zoning of the growth rims or the inclusions into crystals of garnet, it is possible to reconstruct complex metamorphism sequences [35].

1.2.3 Hydrothermal Environments

After the solidification of magmas, high-temperature hypersaline solutions enriched in elements incompatible with magmatic minerals remain close to the magmatic chamber and flow through the pores or fractures, provoking leaching of rocks and the precipitation of some of the most important ore deposits. The growth of hydrothermal minerals occurs in relatively open spaces and with a continuous supply of ions from solution, which produces large-faceted crystals that stand out among the most beautiful crystal specimens in mineralogical collections; some of them show very interesting growth structures, such as the quartz specimens from the Alpine veins [36]. Hydrothermal systems comprise solutions of magmatic origin but also meteoric waters, which can account for up to 95% of the waters transported during cooling of an intrusion in the shallow crust [37]. Hot springs and volcanic fumaroles are the active, observable equivalents to these systems.

Compositional zonation is very common in hydrothermal crystal growth due to the open character of the system with continuous restoring of solution. This zonation records information on the hydrothermal processes. An interesting example is the zonation patterns of the andradite-rich garnets in a contact aureole in Drammen

granite, which record at least five intermittent growth periods related to changes in the oxygen fugacity [38].

1.2.4 Sedimentary Environments

Crystallization from low-temperature aqueous solutions in sedimentary or diagenetic environments has traditionally been a prolific field of collaboration between geology and crystal growth, mainly because of the ease for laboratory experimentation and the widespread distribution of sedimentary rocks. The main topics of this collaboration have been carbonates, evaporates, and clay minerals. The studies have focused mostly on the morphology of crystals in relation to growth conditions [39] and the use of morphology as a geological indicator [40].

Three main scenarios are common in solution growth studies in geologic media: (1) the crystallization of minerals from free superficial brines, (2) the precipitation of minerals in the pore space in sediments, and (3) the crystallization and transformation of minerals during diagenesis. The temperature as well as the pressure increase from scenario (1) to scenario (3), while the volume of solution and the effect of living organisms decrease. These differences obviously influence the thermodynamics and the kinetics of mineral growth, but also the degree of equilibration with the hosting sediments and the morphology of the resulting crystals. The driving force for crystallization is produced in surface waters by evaporation or by the mixing of solutions of different compositions. These processes are usually fast, so nucleation and growth rates tend to be high in comparison with diagenetic environments, where the supersaturation develops because of the destabilization of minerals and slow mixing of phreatic waters. The effect of living organisms is also mostly restricted to superficial solutions, although investigations suggest a deep biosphere that is more active than thought [41].

The range of temperatures and pressures involved makes the laboratory study of these crystal growth processes possible; therefore, sedimentary environments are the most-often addressed environment for experimental studies in mineral crystal growth. Abundant literature is available on the thermodynamics, kinetics, and mechanisms of crystal nucleation, growth, and dissolution, as well as the effect of mass transport and the morphology of the grown crystals.

Nucleation and crystal growth play a fundamental role in the deposition of chemical and biochemical sediments, as well as the compaction and cementation of sedimentary rocks. Chemical and biochemical processes in the sedimentary environment lead to the precipitation of minerals such as calcite, gypsum, halite, or apatite and to the formation and deposition of calcareous or siliceous plant or animal parts, such as shells. The rocks resulting from these precipitation processes are limestones, cherts, evaporates, or phosphorites. During the burial diagenesis of any type of sediment, authigenic minerals (e.g., quartz, feldspars, clay minerals, calcite, gypsum, hematite) precipitate, compacting the rock and partially changing its chemical composition.

Carbonate rocks account for 20–25% of the sedimentary record. They are mainly made of calcium carbonate (mostly calcite and aragonite) or calcium magnesium carbonate (dolomite) in many different forms, from chemically precipitated fine lime mud to small grains (peloids) generally formed by biological activity to skeletal grains or carbonate-coated grains such as ooids. The texture of these constituents depends on the genetic processes involved in their precipitation. For instance, when ooids [42] are made of randomly oriented aragonite crystals, a marine origin is indicated. On the other hand, the presence of radially distributed aragonite crystals can indicate marine, lacustrine, or hypersaline environments. Tangentially distributed aragonite crystals in an ooid are only possible in high-temperature environments. If the crystals are made of calcite, ooids are of nonmarine origin; a tangential distribution of the crystals indicates that they formed in a caliche, while radial or random crystal orientations can form in lakes and radial distributions are only possible in caves of fluvial deposits. “Sparry calcite” is the term used for large crystals formed during diagenetic cementation. They usually have rich textures: granular fillings of voids, fibrous overgrowths of grains, and even large monocrystalline overgrowths on echinoderm fragments. Carbonate crystallization leading to carbonate rocks in sedimentary environments occurs at close to ambient temperatures (typically 0–40 °C) from sea (salinity 3.0–4.5%) or continental waters.

Crystallization in porous media can be successfully mimicked by crystal growth in gels [43,44]. Actually, gels such as silica gels, agarose, or the use of other substrate (e.g., clays, bentonites, sands, muds) that reduce convective mass transport can be used as laboratory-analogous crystallization [45,46]. The technique has great potential, but the complex spatiotemporal pattern of supersaturation, ratio of concentration of reactants, and speciation of reactants, among other factors (see Section 1.6.2) makes analysis of the experiment very demanding and difficult to extrapolate to the natural-analogous.

1.2.5 Biomineralization and Biologically Induced Crystallization

The impact of life on the nucleation and growth of minerals is qualitative and quantitatively important. First, there is a direct impact on mineral formation because living organisms have managed a way to produce minerals themselves, the so-called biominerals. Everything—the nucleation, crystal phase, crystal morphology, texture, and growth mechanisms of biominerals—was dramatically affected by biological molecules and macromolecules, as it is today. Secondly, beyond biomineralization, there is an indirect but important influence of life on the chemical history of the ocean and atmosphere. An evident example is the impact that photosynthetic bacteria had on the oxygenation of the hydrosphere and then on the atmosphere of the planet, starting 2.5 billion years ago [47]. However, this chapter will not deal with the growth of biominerals; instead, we refer the reader to Chapters 19 and 20 in Volume IB and Chapter 31 of Volume IIB in this book. We will only discuss the problem of life detection and the morphogenesis of microstructures and macrostructures that have an ambiguous origin, either biologically or geochemically induced.

1.3 Deciphering Geological Information from Crystal Morphology

The feature of the minerals most often used in geological studies aimed at decoding genetic information during crystal growth is crystal morphology. The external morphology of a crystal is the result of its growth history; fortunately, this history (the evolution of the crystal morphology during crystal growth) is accessible through the zonal and sectorial structure of the crystal. Changes in the composition, temperature, or concentration of impurities in the fluid phase in contact with the crystal produce distortions in the crystal lattice, which result in greater incorporation of impurities or inclusions (either liquid or solid), changes in the composition of the crystalline phase, or accumulation of stress or nucleation of crystal defects. All of these defective lattice volumes, called the *zonal structure*, appear within the crystals at the positions where the crystal surface was at the time of the change in the fluid phase; they allow the reconstruction of the morphological history of the crystal during growth.

Faceted crystals are made of pyramidal volumes left behind on a single face during the growth of the crystal. Each such pyramid is called a *sector*. The distribution and properties of sectors is called the *sectorial structure* of the crystal. Stress accumulates into the surfaces joining two nonequivalent sectors due to the anisotropic growth and impurity accumulation kinetics, producing slight misfits at the edges of the crystal (a common place for the accumulation of defects). The presence of these defects may render may render the sectorial structure visible. Both the zonal and the sectorial structure of crystals, when observable, make it possible to study the growth history of crystals.

As in any type of crystal, mineral morphology is a function of the supersaturation at which the crystal grew (Figure 1.3). This is due to the different growth mechanisms as a function of supersaturation or supercooling. At very low supersaturation, crystals grow by screw dislocations and develop slightly convex faces containing dislocation hillocks on an essentially flat surface. Above a given supersaturation, the dominant growth mechanism is two-dimensional nucleation on the crystal faces, which are flat with some roughness where two-dimensional (2D) islands are growing. This growth mechanism becomes unstable at higher supersaturation values due to the higher supply of growth units at the edges and vertices of the crystal, which start growing faster, producing the concave crystal faces typical of hopper crystals, but are mostly flat. Further increases of supersaturation make continuous growth the dominant process and the surface becomes rounded, giving rise to the unstable growth of dendrites, spherulites, and bow-tie morphologies. Even higher supersaturation values produce fractal aggregates and coagulation textures.

Crystals grown at variable supersaturations can show their morphological history in their sectorial and, more likely, zonal structures. The inset in Figure 1.3 shows the zonal structure of a crystals that, after growing for some time at high supersaturation as dendrite, underwent a change of growth conditions to a lower supersaturation; it

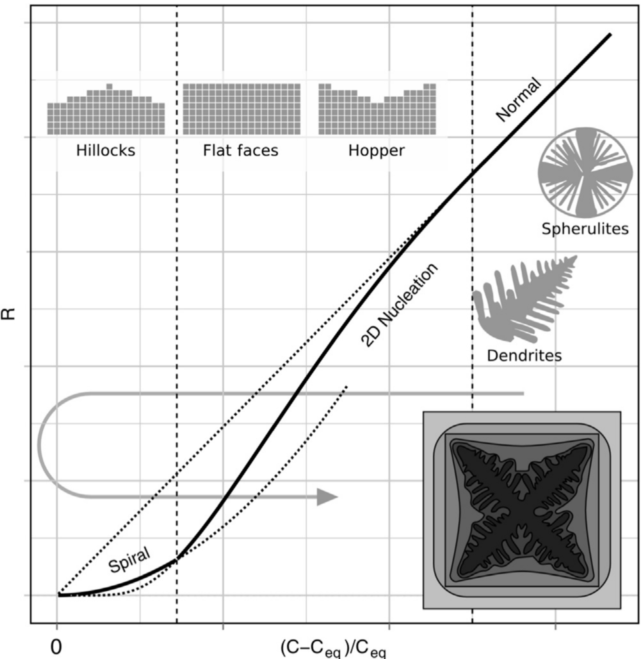

FIGURE 1.3 Growth rate and surface growth mechanism as a function of supersaturation. Vertical dashed lines indicate the crossover between the spiral growth, 2D nucleation and Normal growth regimes. The typical morphology of the crystal surface is sketched for spiral and 2D nucleation mechanisms. The overall morphology of the dendritic crystals and the spherulitic aggregates is also shown at the supersaturation values where they develop. The inset at bottom right shows consecutive morphologies of a crystal grown at decreasing (and later increasing) supersaturation illustrated by the gray "c"-shaped curve. The crystal displays a morphological sequence from dendritic crystal to hopper crystal and then a faceted morphology followed by a dissolution period (rounded edges) when supersaturation falls below 0, and finally a new growth period at low supersaturation. The consecutive morphologies can show in the zonal structure of the crystal.

gradually changed morphology to a hopper crystal and then a polyhedral shape with flat faces. After growing in this regime for some time, further decreases of supersaturation made the fluid undersaturated with respect to the crystal, provoking dissolution of the crystals with rounded edges. After this period, the supersaturation raised again to moderate values, and the crystals restarted their growth until their final size.

Figure 1.3 shows a cubic crystal. However, in general, supersaturation at the crystal surface is controlled by the specific surface energy, depending on the structure of the crystal surface and, consequently, is anisotropic. The relative growth rate of different faces in the crystal changes with supersaturation; this change leads to changes in the crystal habit and to a supersaturation-dependent growth morphology. An extreme example of this fact is ice: the faces parallel to the hexagonal axis grow very fast by continuous growth under atmospheric conditions, while the faces perpendicular to this axis grow slowly layer by layer, producing the well-known flat, dendritic snowflakes. In general, the observed morphologies of minerals are growth morphologies, which deviate from the equilibrium

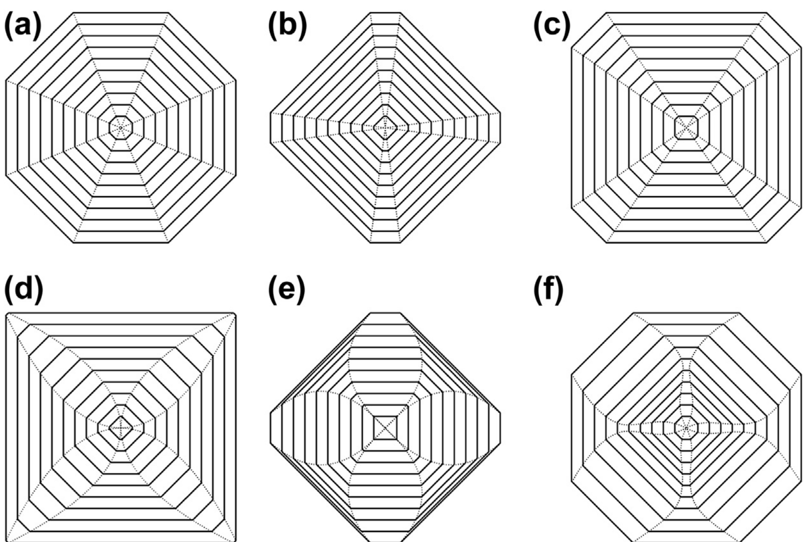

FIGURE 1.4 Morphological evolution of crystals growing at constant (top row) and variable (bottom row) supersaturation. (a) Development for $R_{100} = R_{101}$ (R_{hkl} being the growth rate of the (hkl) face). (b) $0.8R_{100} = R_{101}$. (c) $R_{100} = 0.8R_{101}$. (d) R_{100} = constant, $R_{101} = 0.77R_{100}–1.40R_{100}$ (linear). (e) R_{100} = constant, $R_{101} = 1.40R_{100}–0.80R_{100}$ (linear). (f) R_{100} = constant, $R_{101} = 1.00R_{100}–0.75R_{100}–1.00R_{100}$.

or structural morphology, resulting from the bonding energies of each face; they can be computed using methods such as the Hartman and Perdok PBC (Periodic Bond Chain) theory [48].

Differential changes of the growth rate as a function of supersaturation among different faces of the same crystal can be studied through the zonal and sectorial structure of the crystal to get information on the compositional, thermal, or flow history of the environment. Figure 1.4 shows sketches of the growth morphology of a simple cubic crystal with two families of faces: {100} faces (those vertical or horizontal) and {101} faces (the diagonal ones). Zonal structure is shown as solid lines and sectorial structure as dashed lines. The growth rate of the {100} faces is constant for all cases. The three sketches on top show cases in which the {101} growth rate is also constant. Figure 1.4(a) shows the morphological evolution when the {100} and {101} growth rates are equal, leading to an octagonal shape of increasing size. In Figure 1.4(b), the growth rate of the {101} faces is constant and 20% smaller than that of {100}. The slowest faces {101} are more developed, but the morphology (the relative development of each face) is preserved over time. The opposite situation, with the growth rate of {101} being 20% larger than the growth rate of {100}, is illustrated in Figure 1.4(c). Again, the slowest faces—those corresponding to the form {100} in this case—are more developed, but the relative size of faces is preserved along the growth history.

The sketches on the bottom row show the cases in which supersaturation changes with time. In all of them, the {100} growth rate is assumed to be constant (i.e.,

independent of supersaturation). In Figure 1.4(d), the growth rate of {101} linearly increases from 77% that of {100} (leading to diamond shaped crystals in the first stages) to 140% that of {100} (leading to square-shaped crystals in the last stages). The opposite situation is shown in Figure 1.4(e), where the growth rate of the {101} faces linearly decreases from 140% that of {100} at the beginning to 80% by the end of the growth history. Finally, Figure 1.4(f) shows the morphological output of a more complex situation where the growth rate of the {101} faces first decreases smoothly from 100% of the growth rate of {100} to 75% of this value by the fifth outline; it then increases smoothly back to 100% the growth rate of the {100} face by the last stage.

As the number of crystals increases at higher nucleation rates, the interrelation between different crystals—that is, their relative orientation, size distribution, geometrical interrelations, and grain boundaries—start to play an important role, restricting the growth of crystals and their morphology. This collective morphological control by the ensemble of crystals in the system can be the most determinant aspect of mineral growth in cases such as the development of granoblastic textures (Figure 1.5(a)), made by an interlocked, space-filling set of crystals of similar size. This texture is characteristic of marbles and quartzites and develops by regrowth of a large density of crystals. When the growth is only restricted in two spatial dimensions but is unrestricted in the third one, competitive growth develops crystal aggregates; characteristic parallel, columnar textures of partially oriented crystals also develop as an emergent property (Figure 1.5(b)). This kind of texture is typical of hydrothermal veins, geodes, and druses. Crystals oriented with faster growth rates in the direction allowing unrestricted growth will overtake their less favorably oriented neighbors, thus stopping their growth. Competitive growth selects the crystals that will continue growing and the ones that will be buried behind the advancing front. This collective growth as a front made of closely oriented crystals

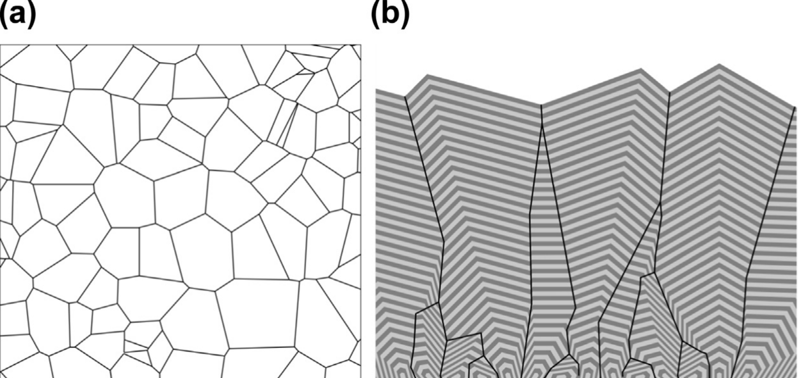

FIGURE 1.5 Textures produced by competition for space. Granoblastic textures (a) are generated by three-dimensional competition by growing crystals. Sub-parallel growth textures (b) are generated by one or two-dimensional competition for space.

synchronizes the zonal structure of the crystals contributing to the front and can lead to banding parallel to the substrate.

In natural environments, other actors can play a major role in determining the crystal growth morphology, notably the action of living organisms and the presence of impurities increasing or reducing the relative growth rate in different directions. Life effects are discussed elsewhere in this volume (see Section 1.2.5). The effect of impurities is thoroughly explained in Ref. [49].

1.4 Decoding Polycrystalline Textures from Nucleation and Growth

The texture of a rock is defined by the crystal size distribution—that is, the distribution for each mineral of crystals having a given size. This distribution is determined by both nucleation and growth kinetics. In natural crystallization, heterogeneous nucleation is expected to be the dominant process by far because homogeneous nucleation requires larger activation energy. This is mainly due to the large number of impurities, as well as the widespread presence of particles of different natures and multiphase, rough surfaces. Secondary nucleation can be important in superficial waters moving by turbulent flow, such as in a river or at a coastline.

A simple model for the dynamics of nucleation and growth is the Johnson-Mehl-Avrami-Kolmogorov model, which describes phase transformations by nucleation and growth [50–52]. This theory was initially formulated by Kolmogorov to explain the solidification of metals, but it is general enough to be applied to many different nucleation/growth processes because it is a geometrical formalism without any energetic term and only involves generic nucleation and growth rates $I(t)$ and $G(t)$. Assuming that crystals grow spherically and that the growth rate is independent of crystal size, it is possible to write the volume, at time t, of a crystal nucleated at time τ as follows:

$$V = \frac{4\pi}{3}\left(\int_{\tau}^{t} G dt\right)^3$$

The number of such crystals is $V_{sys} I(\tau) d\tau$, where V_{sys} is the volume available for nucleation. Therefore, at time t, the total volume of crystals nucleated between τ and $\tau + d\tau$ is

$$dV = \frac{4\pi}{3} V_{sys} I(\tau) d\tau \left(\int_{\tau}^{t} G(t') dt'\right)^3$$

Finally, by integrating over all times, it is possible to compute the total volume of crystals in the system:

$$V_{ext} = \frac{4\pi}{3} V_{tot} \int_{0}^{t} I(\tau) \left(\int_{\tau}^{t} G(t') dt'\right)^3 d\tau$$

The process is illustrated in Figure 1.6. We can see crystals nucleating at random positions with a given frequency $I(t)$ (constant in Figure 1.6, top) and then growing at a given rate $G(t)$ (also constant in the illustration). The process is straightforward and well described by the previous equations until $t = 7$. At this time, crystals start impinging during growth on other crystals and with the boundaries of the system. The equations then start to fail because these interactions are not included in the model. This is indicated in the last equation by writing V_{tot} (the total volume of the system) instead of V_{sys} (the volume available for nucleation, which is hard to compute after crystals start to interact) and V_{ext} (the fictitious crystal volume if interactions are ignored) instead of V (the actual crystal volume that indicated in the last equation) by writing V_{tot} (the total volume of the system) instead of VV (the actual crystal volume that, again, is too difficult to compute). In the Avrami formulation, this approximation is handled correcting the equations using the mean field approximate relationship:

$$dV = \left(1 - \frac{V}{V_{tot}}\right) dV_{ext}$$

Integrating both sides of this relation and solving for V, we get

$$\frac{V}{V_{tot}} = 1 - \exp\left(-\frac{V_{ext}}{V_{tot}}\right)$$

Inserted into the expression for V_{ext}, that produces

$$\varphi \equiv \frac{V}{V_{tot}} = 1 - \exp\left(-\frac{4\pi}{3}\int_0^t I(\tau)\left(\int_\tau^t G(t')dt'\right)^3 d\tau\right)$$

That is the general form of the Avrami equation. For constant nucleation and growth rates, the equation reduces to

$$\varphi = 1 - \exp\left(-\frac{4}{3} I G^3 t^3\right)$$

The equation is commonly used for interpreting experimental results as $\varphi = 1 - \exp(-kt^n)$, which has the well-known sigmoidal form shown in Figure 1.6 (down). The low transformation rates at the beginning and at the end are due to, respectively, the limited number of nuclei existent at the beginning and the limited volume of liquid feeding growth at the end. Using this equation, experimental data can be analyzed by plotting $log(log1/1 - \varphi)$ as a function of $log(t)$, which produces a linear plot with slope n and intercept $log(k)$. An example of these curves from experimental data is shown in Figure 1.7, where selected data on the transformation of aragonite into calcite are shown using this type of plot (data from Ref. [53]). The curvature in the plot is due to the nonlinear behavior of $I(t)$ and $G(t)$, which is assumed to be constant in the equations.

The next step in developing a model relating the nucleation and growth rates measurable in the laboratory with the actual texture of mineral grains in a rock is to

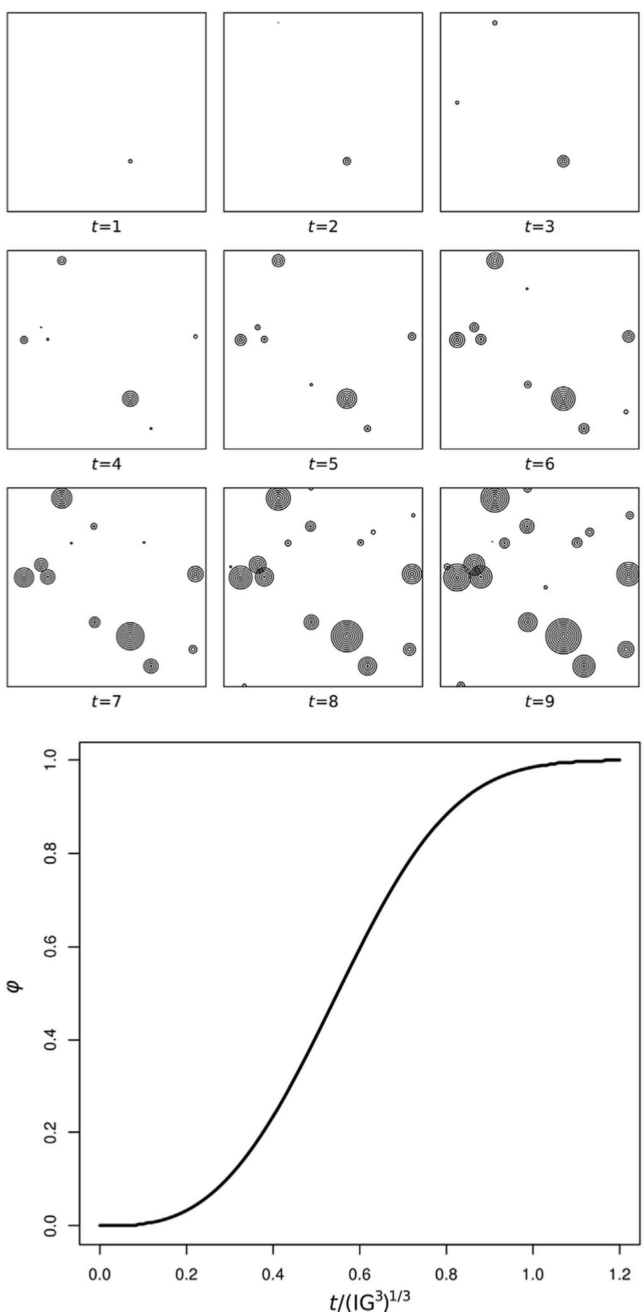

FIGURE 1.6 Time evolution of the crystal size distribution of crystals nucleating and growing at a constant rate (top). Notice the overlapping of crystal "volumes" for $t > 7$. Evolution of the crystallized volume fraction φ (bottom).

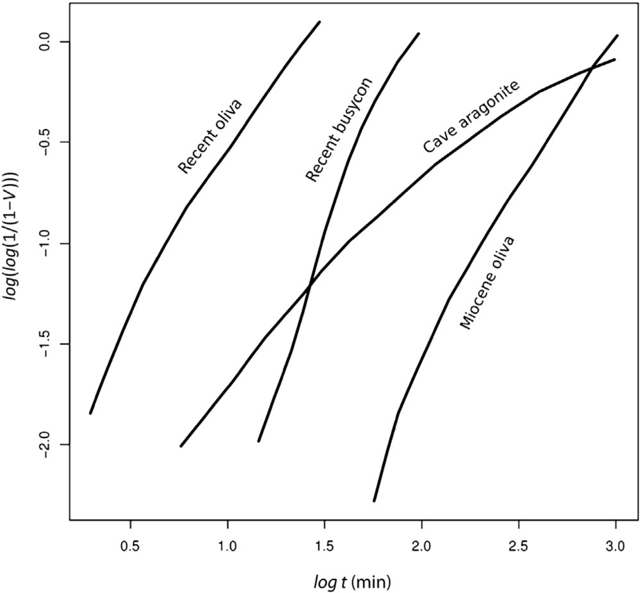

FIGURE 1.7 Plot of selected data on the aragonite/calcite transformation *(From Ref. [53].)* in $log(log(1/(1-V)))$ versus $log\ t$ coordinates used to estimate the kinetic constants n and k from experimental data using the approximate Avrami equation.

develop a model for the number of crystals of a given length per unit length per unit volume. This quantity n is called the *population density*:

$$n \equiv \frac{dN}{dL}$$

where N is the number of crystals per unit volume with size less than L. To obtain an expression for n, we will use the Avrami formalism to define efficient rates of nucleation and growth ($I_{eff}(t)$ and $G_{eff}(t)$), related to the laboratory measured values without inter-crystals interferences $I(t)$ and $G(t)$.

$$I_{eff} = I(t)(1 - \varphi(t))$$

The exponent 1/3 in the growth rate equation is due to $G_{eff}(t)$ being defined as a linear growth rate because we are interested in the linear size L of the crystals.

Given these values, we can compute the size at time t of a crystal nucleated at time τ:

$$L = \int_{\tau}^{t} G_{eff}(t')dt'$$

This equation introduces a functional dependency of τ on L, so we can write the time at which a crystal having size τ nucleated $\tau(L)$. In these terms, the number of crystals nucleated between τ and $\tau + d\tau$ is, using the Avrami corrected nucleation rate,

$$dN = I_{eff}(\tau)d\tau = I(\tau(L))(1 - \varphi(\tau(L)))d\tau$$

and, from the definition of n,

$$n \equiv \frac{dN}{dL} = -I(\tau(L))(1 - \varphi(\tau(L)))\frac{d\tau}{dL}$$

The minus sign in this equation comes from the inverse relationship between $d\tau$ and dL: higher $d\tau$ means shorter L. Using the previous equation for L, this equation can be rewritten as follows:

$$n = I(\tau(L))(1 - \varphi(\tau(L)))\frac{1}{G_{eff}(\tau(L))}$$

This equation, along with the Avrami equation for φ, defines a fully general model for the relationship between the experimental nucleation and growth kinetics and the population density (i.e., the texture of the rock resulting from the crystallization of the mineral grains). The inversion of this equation, along with values of the dependency of the experimental rates on some variable, such as temperature, allows the decoding of the evolution of this variable during the growth of mineral grains. By modeling the time-dependent nucleation and growth rates in a functional form, we can use the previous equation to compute population density curves. Assume, for example, that you can model the nucleation and growth rates by Gaussians:

$$I(t) = I_0 \exp\left(-A_I\left(t - t_0^I\right)^2\right)$$

$$G(t) = G_0 \exp\left(-A_G\left(t - t_0^G\right)^2\right)$$

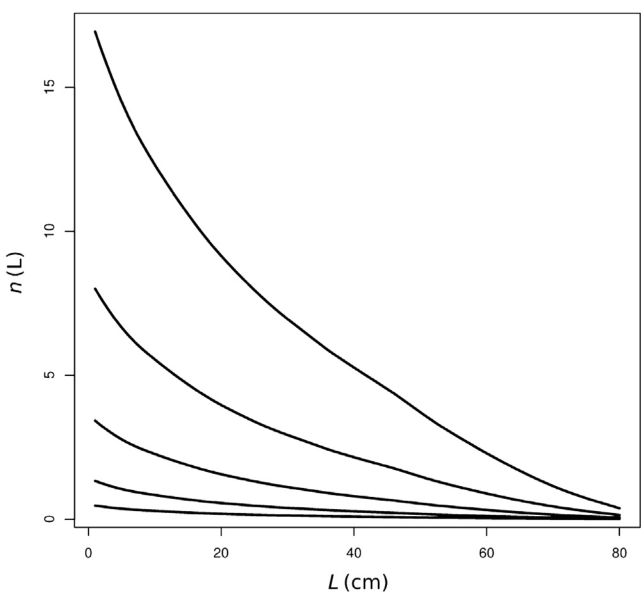

FIGURE 1.8 Computed distribution of the number of crystals of a given length per unit length per unit volume (population density) as a function of crystal size. The five curves correspond to increasing from bottom to top.

with three adjustable parameters each. Using these functions, Figure 1.8 shows the evolution of a typical population density for five different values of time (60, 70, 80, 90, and 100 years).

1.5 The Case of Giant Crystals

Beyond their beauty, the spectacular giant crystals of gypsum found in the Naica mine (Chihuahua, Mexico) offer a typical example of how knowledge of crystal growth can be used to decode geological information present in mineral crystals grown in geological settings [54,55]. Crystal growth in the laboratory often assumes equilibrium, or at least steady-state, but the time scales for laboratory studies are too short for close-to-equilibrium studies. However, crystal growth in natural media proceeds over millions of years, providing a singular and extremely valuable opportunity to study close-to-equilibrium growth processes. This is the case of the giant crystals from Naica.

Among the many caves and cavities filled with gypsum crystals within the limestones of the mountain of Naica, the best known are the Cave of Swords [56,57] and the Cave of Crystals [54]. The walls of the former cave are completely covered with crystals of several centimeters in length displaying two different morphologies (one elongated along the c-axis and the other more equidimensional). By contrast, in the Cave of Crystals, there are fewer crystals, but they are larger and more transparent; they also display the same morphologies as in the Cave of Swords. In addition to these notable differences, the number of crystals differs between the caves. In the upper cave, the crystals are smaller but more abundant than in the Cave of Crystals, where there are fewer crystals but of much bigger size. The existence of large crystals can be explained by nucleation. The nucleation rate is an exponential function of supersaturation, so the probability of having a nucleation event is very unlikely for small supersaturation values; however, beyond a critical value, the rate increases so fast that small changes in supersaturation can lead to orders-of-magnitude changes in the number of crystals produced. Therefore, nucleation kinetics is an extremely sensitive probe for chemical conditions during crystal nucleation and growth. The low number of crystals in the Cave of Crystals allows the crystals to grow to a very large size, which is due to the fact that they nucleated at very low supersaturation. In addition, supersaturation must be kept low enough, without large fluctuations, during the entire crystal growth history to avoid triggering further massive nucleation.

García-Ruiz et al. [54] have shown that the only geologically plausible mechanism capable of producing this large and steady supply of Ca^{2+} and SO_4^- ions is a self-feeding mechanism based on a solution-mediated anhydrite-gypsum phase transition occurring in a slow and smooth cooling scenario. Calcium sulfate may precipitate as different hydrates, with each of them being stable in a different temperature range. Among them, the dihydrate is the less soluble phase at low temperatures (below 54.5°) and the anhydrous calcium sulfate is the stable phase above this temperature. The existence of a crossover between the solubility of anhydrite and gypsum provides the “ion pump”

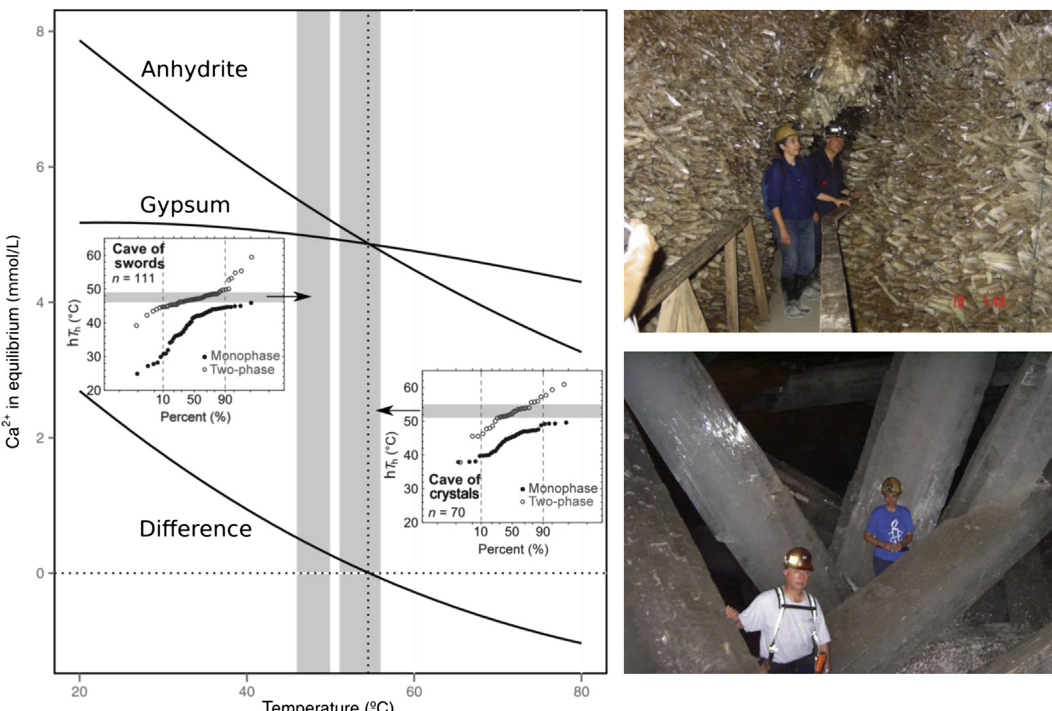

FIGURE 1.9 Plot of the solubility of gypsum and anhydrite (left). Gypsum is the stable phase to the left of the dotted vertical line and will grow from dissolving anhydrite. The amount of transferred Ca and sulfate is the difference in solubility also plotted. The two vertical gray bars indicate the range of crystal growth temperatures for the Cave of Swords (right top) and the Cave of Crystals (right bottom) in the Naica mine. These ranges were obtained from the statistical analysis of fluid inclusion homogenization temperatures (insets) measured in samples from these caves. The crystals in the Cave of Crystals grew very close to equilibrium from a very low driving force.

required for a steady and continuous supply of growth units. Figure 1.9 shows the solubility of gypsum and anhydrite plotted against temperature along with the difference in solubility, which is the maximum amount of Ca^{2+} and SO_4^- ions transferred from anhydrite to gypsum as a function of temperature. This amount is small enough to ensure a slow and steady supply (-10^{-3} to 10^{-3} mol/L in the 40–80 °C range). This extremely slow cooling rate leads to the close-to-equilibrium anhydrite dissolution and gypsum growth at progressively lower levels within the phreatic layer.

For this mechanism to operate, there must be enough anhydrite in the area, and the temperature at which the crystals grow must be close to the transition temperature. Both conditions are met in the Naica mines. The temperature of both current groundwaters and the solution in equilibrium with the crystals during their growth (obtained from fluid inclusions trapped in the crystals [58]) show that current groundwaters have a mean temperature of $T = 53.2$ °C, whereas fluid inclusions indicate that $T = 52.5$ °C during crystal growth. These temperatures correspond to a very low undersaturation value for anhydrite ($\Delta\mu = -0.04$), which makes the self-feeding mechanism possible. Additional

pieces of evidence supporting this self-feeding mechanism for the nucleation and growth of the giant gypsum crystal [54] are the low salinity values of the mother waters, the isotopic composition of these crystals, and the presence of celestite coating the walls of the Cave of Crystals, as a result of the excess Sr that the structure of anhydrite can hold with respect to that of gypsum.

The giant gypsum crystals also offer a unique opportunity to study the mechanisms and kinetics of crystal growth at very low supersaturation values, as well as the agreement between the morphology of crystals growing in this regime and the equilibrium morphology. Obviously, the giant crystals of the Naica mines must have grown very slowly at very low supersaturation, but what was their growth rate? The supersaturation values of the current Naica waters are below the experimental error of modern analytical techniques for measuring concentrations. Therefore, measurement of growth kinetics in the laboratory using Naica's waters must be performed with well-designed growth cells in a short period of time, because significant shifts in supersaturation could be produced if the solution evaporates. Experimental studies of gypsum crystal growth kinetics show that the growth of gypsum crystals at low supersaturation proceeds mainly by two-dimensional nucleation on {010} faces and the advance of steps, usually as macrosteps [59]. Even at lower supersaturation values, crystal growth kinetics have been measured for the {010} face of gypsum in contact with waters collected from the Naica mine using an advanced high-resolution white-beam phase-shift interferometry microscope [60]. The growth rates found in this work for temperatures in the range of 50–55 °C are extremely slow, ranging from 1.6×10^{-6} to 2.1×10^{-5} nm/s. This very small growth rate can be enhanced by screw dislocations and similar crystal defects, colloidal particles incorporated into the crystal surface, or surface instabilities such as macrosteps or fluid inclusions, which are quite frequent on the surface of gypsum crystals.

As previously mentioned, gypsum crystals in the Naica mines show two completely different morphologies, both of which have been described by Foshag in the Cave of Swords [56]: blocky crystals, which in some cases cluster to form parallel or radial aggregates, and much more elongated crystals that grow from some groups of blocky crystals. Neither of these morphologies agree with the classical equilibrium morphology of gypsum [61,62]. The more developed faces in the giant crystals are the {1k0} family instead of {010}, as would be predicted by theory. Several faces in this family (at least $2 \leq k \leq 6$) appear with an overall orientation of {140} instead of the predicted {120}. In addition, {−111} is more developed than {011}. These contradictions gave rise to new investigations on the equilibrium morphology of gypsum, leading to refinements of the surface energy calculations that considered surface relaxation and semi-empirical potentials, which were carefully selected for each interaction that predicts equilibrium morphologies showing better agreement with the giant Naica crystals [63]. The origin of the striated {1k0} forms was also explained using similar methods [64].

The second type of morphology, the colossal beams, is more challenging and is not predicted by any of the existent theories. An explanation for this morphology has

been proposed [55]. It has been observed that the Naica beams are {100} contact twins showing reentrant dihedral angles between {−111} faces. These reentrant angles are known to (1) operate as an additional source of steps under low supersaturation in crystals containing few or no screw dislocations (although this is less effective with an increasing number of these defects) [65]; (2) produce elongated morphology due to the enhanced growth rate in the crystallographic direction of the reentrant angle; and (3) produce crystals that are much larger than the coexisting single crystals and show crystal faces that are uncommon in single crystals. All of these features are exhibited by the twin beams in the Cave of Crystals, which makes them so different from the blocky crystals precisely because of these characteristics. Consequently, the elongated giant crystals in Naica are crystals that developed, by chance, {100} contact twins with the reentrant angle between their {−111} faces pointing approximately upwards.

1.6 Decoding Disequilibrium Mineral Patterns

In geological terms, self-organized processes leading to pattern formation operate at all scales, from the atomic scale, as in the case of the kinetic behavior of cation ordering in crystal lattices such as Na feldspars with partially ordered Al, Si positions [66], to the tectonic processes controlling the distribution of tectonic plates at the scale of the whole planet [67]. There are two requirements for self-organization: the system is sufficiently far from equilibrium and at least two active processes in the system are coupled [68]. Because several types of reaction-transport loops can operate in geochemical systems and because these systems are most often out of equilibrium, geochemical self-organization should be expected to be commonplace [69,70].

Crystallization is an inherently nonequilibrium process in which surface aggregation processes and mass transport often operate simultaneously and with comparable rates. Consequently, pattern formation during crystallization is a common phenomenon. In natural systems, this is facilitated by the ubiquitous presence of noise in all the variables involved. In the laboratory, it is usual practice to work with smooth containers having constant and isotropic chemical and physical properties to hold ultrapure solutions of well-defined composition at constant temperature and pressure. In a natural system where minerals are nucleating and growing, this is not the case. Self-organization can be thought of as the ability of a system to select one pattern from all possible noise-generated patterns and amplify it by feedback loops into a well-ordered observable structure [71].

Mineral pattern formation can be the result of the following: (1) intrinsic instabilities during the growth of the crystal, as in the case of Mullins–Sekerka instability leading to dendritic crystals or the compositional zonation of crystals; (2) self-organized processes involving coupled mass transport and precipitation, as in the case of Liesegang structures; or (3) the mineralization of patterns produced by biological or convective mass transport processes, as in the case of stromatolitic structures or fractal dendritic

structures. Examples of these processes are provided in this section. More information on mineral pattern formation in geological media can be found in references [72–75].

1.6.1 Compositional Zoning

The chemical composition of minerals may change within the crystal volume in a distinctive (patterned) way. This is very common in solid solutions and in the minor element compositions of many minerals. The kinetics of the incorporation of impurities and minor components to the surface of a growing crystal are anisotropic, as for the regular molecules or ions making up the crystal. As a result, the composition of a crystal may vary from sector to sector. This phenomenon called sectorial zonation, is well known in minerals such as quartz, calcite, staurolite, topaz, and zircon [76–79]; it is a result of the differences in the structures of the surface, bond distribution, and specific energy of the different faces of the crystal. In addition, the presence of structurally nonequivalent growth steps, typically at adjacent flanks of polygonized spiral growth hillocks, can result in differential incorporation of minor components into symmetry-equivalent growth sectors or even in the same sector [80]. This feature, called intrasectorial zoning, has been described for calcite [81,82]; it illustrates both the fundamental need for crystal growth knowledge for the decoding of geological information encoded in mineral features and the stringent requirements for these studies, which can go up to the atomic details of the surface of growing crystals.

Compositional zoning along volumes parallel to the growing crystal surface is commonly associated with, and more common than, sectorial zoning. This compositional zoning occurs in most major classes of minerals in a wide range of geological environments. When this zoning is quasi-cyclic, such as the well-known compositional alternation in plagioclase crystals, it is called oscillatory zoning. This rhythmic pattern of chemical composition or physical properties can be alternatively explained as the result of (1) self-organized coupling between the interface kinetics and the diffusion of chemical species in the melt or (2) changes in the chemical composition of the magma from which crystals grow. Moreover, both types of effects can happen simultaneously; in both cases, the information on the conditions during crystal growth is encoded within the pattern [83,84]. Oscillatory zoning has been explained by changes in the crystal growth regime due to changes in the concentration in the boundary layer [85,86], changes in the crystal growth kinetics as a function of the undercooling [19], the nonlinearities of the partitioning coefficient of anorthite concentration [87], and the cross-terms in the component diffusion coefficients [20,88]. All these models explain to some degree the oscillatory zoning of plagioclase and have their particular drawbacks. More studies, particularly with the support of experimental data, are required to understand this process and to be able to use oscillatory zoning as a tool for decoding the genetic information contained in plagioclase crystals. Notable advances are being achieved in this direction for the case of decompression-driven crystallization of volcanic rocks. Both the morphology and the composition of plagioclase in

decompression experiments have been demonstrated to be a function of the decompression rate [89,90].

Other minerals—at least 75 rock-forming and accessory minerals comprising most major mineral classes—show oscillatory zoning [91]. The widespread presence of oscillatory zoning in natural minerals contrasts with the very limited observation of this phenomenon in the laboratory. This fact leads to the common interpretation of oscillatory zoning being due to systematic variations in the crystal growth environment (extrinsic mechanism) instead of being a result of self-organized nonlinear behavior in systems driven far from thermodynamic equilibrium (intrinsic mechanisms). Several models for self-organized oscillatory zoning in natural systems have been proposed for plagioclase [92]. The model most accepted by geologists is the interpretation of this zoning in terms of extrinsic mechanisms based on relative reductions and increases of the total pressure during convective movement of the magma, leading to higher and lower Ca concentrations within the plagioclase crystal, respectively.

The best-known case of a clearly intrinsic mechanism producing oscillatory zoning is the barite ($BaSO_4$)–celestite ($SrSO_4$) solid solution system [93–96]. These studies correspond to the observation of spontaneous oscillatory growth of Ba and Sr sulfate-rich terms of the solid solution under controlled experimental conditions; therefore, the observation cannot extend to extrinsic mechanisms, as it qualifies as a self-organized oscillatory mineral pattern [94]. This behavior is explained by the coupling of diffusive mass transport of growth units to the surface of the crystal and the autocatalytic continuous growth, with a rate dependent on the mineral surface composition [97]. The incorporation of cations at kink sites is energetically favored at sites having the same sulfate species as neighbors. Therefore, when the surface is composed of mostly $BaSO_4$, more Ba is incorporated into the crystal and the solution in contact with the crystal gets enriched in Sr. This increasing concentration of Sr leads to a progressively larger incorporation of this cation to the surface, which, after some time, will start favoring the incorporation of Sr Replenishment of the two cations by diffusive mass transport keeps this oscillatory growth going. This interplay between mass transport and surface kinetics is summarized by these authors [97] in a balance equation for mass transport at the liquid/crystal interface:

$$\frac{\partial m_i}{\partial t} = D_i \frac{\partial^2 m_i}{\partial x^2} + V \frac{\partial m_i}{\partial x}$$

where m_i and D_i are the concentration and diffusion coefficients of the ith species in solution. The crystal growth kinetics are

$$V = V_b + V_c$$
$$V_b = \beta_b \left(m_{Ba} m_{SO_4} - m^0_{Ba} m^0_{SO_4} \right) (X + p_b)^2$$
$$V_c = \beta_c \left(m_{Sr} m_{SO_4} - m^0_{Sr} m^0_{SO_4} \right) (1 - X + p_c)^2$$

where the b and c subscripts stand for barite and celestite, respectively; V is the growth rate, β is a kinetic coefficient; m^0 is the equilibrium concentration; and p is the

probability for the attachment of a Ba-unit (Sr-unit) on a pure Sr (Ba) surface. X is the solid-phase barite mole fraction having dynamics modeled by

$$\alpha L \frac{dX}{dt} = [X + (1 - X)\alpha]^2 [V_b - X(V_b + V_c/\alpha)]$$

where α is the ratio between the barite and celestite molar volumes and L is the effective thickness that characterizes the roughness of the interface between the crystal and the aqueous solution.

This model accounts for different crystal growth regimes in the barite ($BaSO_4$)–celestite ($SrSO_4$) solid solution system, including the oscillatory compositional zoning observed experimentally [93,94,95,96]. It is therefore demonstrated to be an intrinsic, self-organized behavior of the system. Separate regions of stable (SF), unstable (UF), and multistable (MS) composition during crystal growth appear in the phase space, as shown in Figure 1.10(a) and (b), corresponding to two different concentration values. Within the stable zone, compositional fluctuations do not exist or are quickly damped to a constant value of the Ba/Sr ratio (Figure 1.10(c), point *c* in the phase space plot). Conditions within the unstable zone (Figure 1.10(d) and Figure 1.10(e)) show sustained, self-organized compositional zoning of different

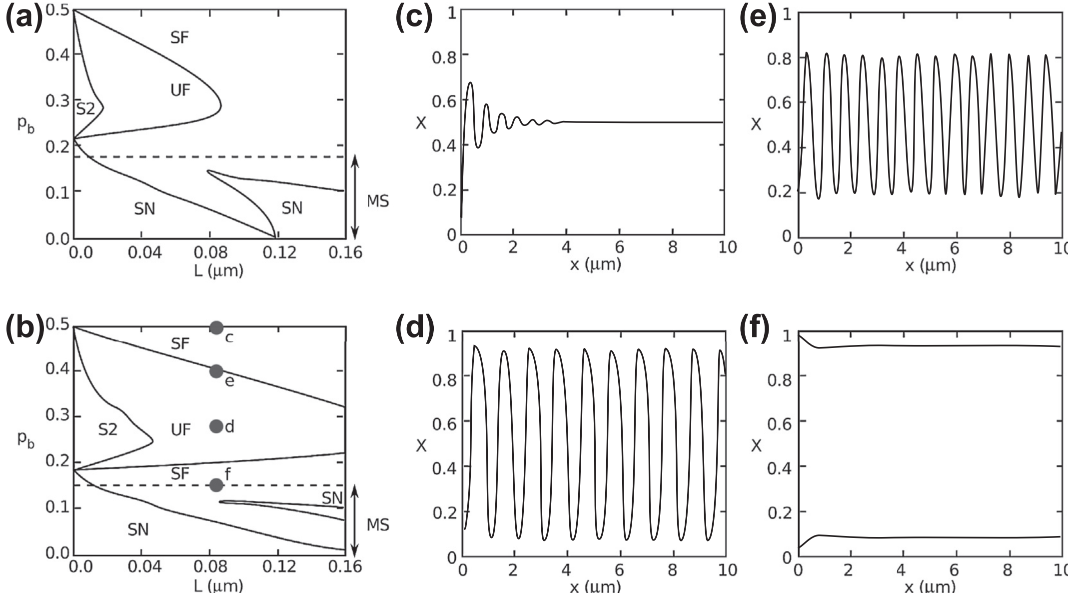

FIGURE 1.10 Stability phase diagram (left) in the (p_b,*L*) space. SF = stable focus, UF = unstable focus, S2 = saddle, SN = stable node, and MS = multistability. The upper phase diagram corresponds to bulk concentrations of 10 mM (a) and 15 mM (b). The four plots c–f show the molar fraction of barite in the resulting crystal as a function of the distance from the crystal nucleus. They illustrate the behavior at conditions labeled c–f in the phase diagram at the bottom b *(Adapted from Ref. [97].)*.

frequencies and amplitudes. Finally, two different Ba/Sr ratios may coexist in the multistable zone (Figure 1.10(f)).

The fact that these types of self-organized oscillatory zoning processes are widespread in nature but difficult to observe in the laboratory is commonly explained by noise-induced effects [98], which are very common in nature but almost absent under controlled laboratory conditions.

Beyond the single crystal scale, rhythmic patterns are also very common in geological environments. Again, the periodic changes in composition or other properties may arise from environmental variations or from self-organization.

1.6.2 Liesegang Structures

On a larger scale, compositional banding due to precipitated minerals is also common in the form of concentric or parallel stripes reminiscent of Liesegang bandings in many geological systems, such as agates, cherts, rhyolites, sandstones, and limestones [99,100]. Liesegang bandings form sequentially and can be explained in the context of Ostwald's supersaturation theory when one or more of the reacting species diffuses into a space occupied by other species. Figure 1.11 shows a sketch of the coupled mass transport of a reactant A into a space initially filled with a homogeneous concentration of reactant B. The supply of A molecules from the left side induces the supersaturation with respect to the precipitating phase until nucleation happens at a region where the concentration of A (C_A) reaches a critical value C_A^*. This region, where the concentration of reactants is close to the equilibrium value C_A^0 because crystals are growing, typically has the shape of a band parallel to the diffusion front because all the points having a given value of supersaturation are located in this band. The precipitated band is marked as a gray bar in the plots. This nucleation event and the further growth of the precipitating phase depletes the concentration of both A and B (plot at t_2), preventing the nucleation of further mineral near the precipitated band (see the trajectories in phase diagrams for the points x_2 and x_3 near time t_2). Continuous diffusion of A eventually increases the supersaturation value at points distantly ahead of the previously deposited bands, where the concentration stays close to equilibrium as long as precipitation continues. At these points, supersaturation can grow past the critical value required for nucleation, and a new band is formed (t_3). The process repeats itself until the full region is homogenized by the diffusive supply of reactants and their consumption by nucleation and growth processes.

The bands produced by this phenomenon are regularly spaced in space and time. The spacing law, first described by Jablczinsky in 1923 [101], states that the positions where bands form follow a geometrical series. That is, the ratio between the positions of any pair of consecutive bands in the pattern is constant:

$$P = \frac{x_{n+1}}{x_n}$$

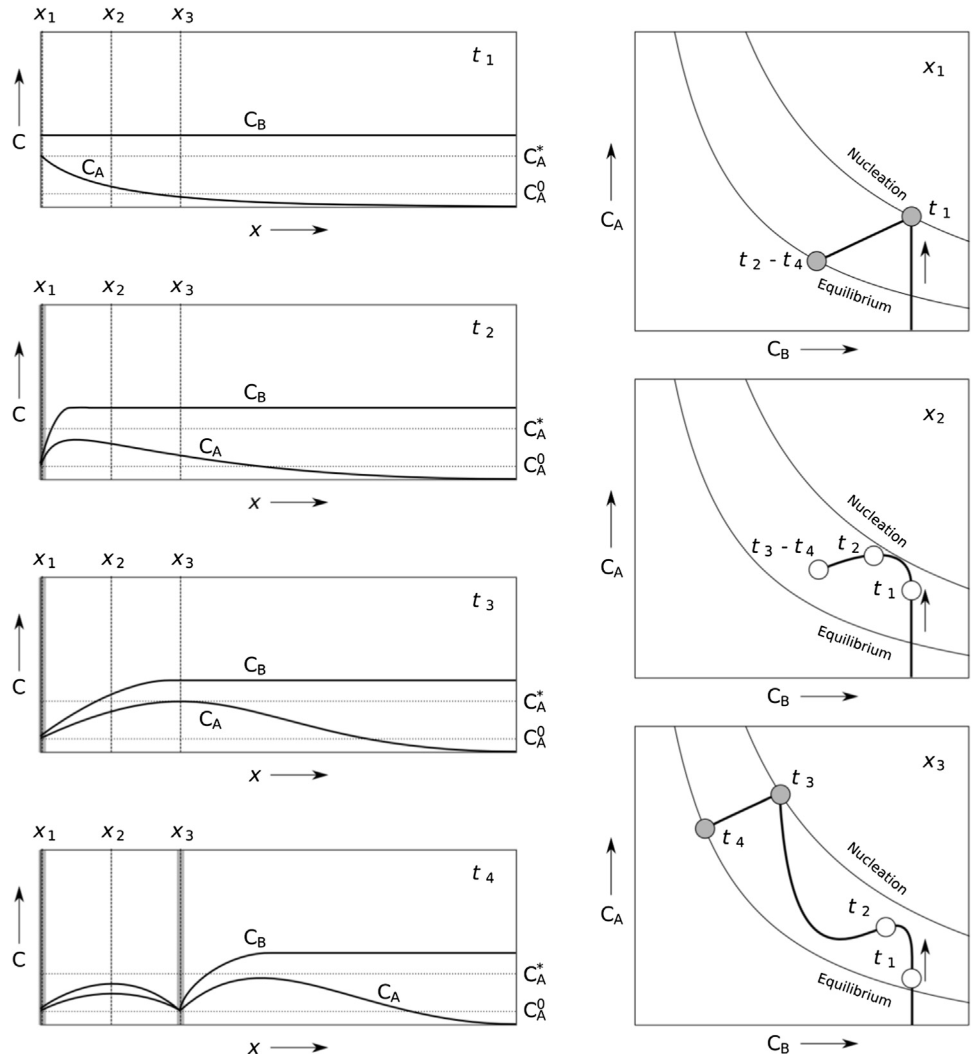

FIGURE 1.11 Sketch of the coupled diffusion and crystal growth processes producing Liesegang rings. To the left a series of four consecutive time snapshots is shown as plots of the A and B concentration profiles (C_A, C_B), the critical (nucleation) and equilibrium concentration values (C_A^*, C_A^0). Three points are marked x_1–x_3. The time evolution of A and B concentrations is shown in the three plots to the right. In these phase diagram sketches, the equilibrium (solubility) and nucleation curves are shown. The instants illustrated in the left plots are marked by dots in the phase diagrams.

The time periodicity of the pattern is controlled by the dynamics of diffusive mass transport. The time at which the *n*th band forms is proportional to the square of the distance at which the band forms:

$$K = \frac{x_n^2}{t_n}$$

1.6.3 Fractal Dendrites

Self-organized kinetic instabilities at the surface of growing crystals, generally interpreted under the Mullins-Sekerka stability model, occur at high supersaturation (or undercooling) on surfaces growing by continuous growth. In these conditions, the competition between capillary forces and diffusion kinetics (as opposed to interface kinetics) favors configurations in which the growing surface has as large a surface area as possible, which allows, for example, a faster dissipation of latent heat [102]. The best-known example of this kind of instability is the development of snowflakes, with their distinctive dendritic development in the hexagonal direction and their unique shape reflecting the relative changes in temperature and humidity as the crystal moves within the cloud during its growth. In mineralogy, the most common occurrence of this phenomenon is among metal ores, where dendritic growth is typically associated with framboidal and colloform textures.

Single-crystal dendrites are thoroughly discussed in Chapter 16 of Volume IB of this handbook [103]. Here, we will concentrate on a type of mineral precipitation commonly called "dendrites," although they form by entirely different processes. "Pyrolusite dendrites" is a somewhat misleading name for the beautiful tree-like fractal patterns formed by manganese and iron oxyhydroxide minerals. Because of their very common occurrence, knowledge of the genetic conditions of manganese and iron dendrites would be of great practical interest in understanding geological environments. These fractal dendrites are sometimes embedded in quartz crystals and agates, but the most common and geologically significant are associated with cracks and sedimentary laminations or, in general, with quasi two-dimensional spaces. They appear on or inside many different types of rocks, such as limestone and sandstone, which suggests that the mineralogy of the host rock is not a limiting factor for their formation.

There are two different mechanisms that may explain the formation of these structures. Chopard et al. proposed that pyrolusite dendrites can be explained by a diffusion-limited aggregation (DLA) [104–106], a mechanism that may work for tridimensional iron and manganese dendrites found in quartz and agates. Alternatively, García-Ruiz et al. showed that manganese and iron dendrites are the mineral record of Saffman-Taylor instability [107]. Both mechanisms can plausibly operate in geological environments, and only a thorough study of the mineralogical and textural properties of the minerals and the geological environment can shed light on the actual origin of the patterns. The controversy illustrates very well the pathway of decoding genetic information in mineral patterns and also is an example that morphology, by itself, does not contain genetic information [108]. The values of the fractal dimensions measured for these mineral dendrites are compatible with both proposed mechanisms.

The fractal dendrites analyzed by García-Ruiz et al. appear in the sedimentary laminations of sandstones from the flysch of Tarifa (Spain). Their fractal dimension, as measured by box-counting methods, was l.69, matching that for Laplacian growth patterns. They appear to be associated with other deposits of the same composition and

aspect that have higher fractal dimensions. As conjectured by Van Damme [109] for manganese dendrites, this is consistent with a genetic mechanism based either on DLA, which implies the irreversible aggregation of diffusing units to a stationary growing pattern, or on viscous fingering [110], which is produced when a fluid is injected into a more viscous and non-Newtonian one. In any case, it must be assumed that the formation of the dendrites occurs under highly irreversible conditions that are far from equilibrium, in which the nucleation kinetics are faster than the pattern formation process.

Infrared spectroscopic studies of these deposits [111] showed that they are formed by nonsingular, variable mineral associations, including various species of the Romanecheita and Hollandite groups, along with minor and optional iron oxides that, when present, can also form dendritic tree-like patterns. All of these minerals have low crystallinity, as shown by powder X-ray diffraction and high-resolution electron microscopy. The very low crystallinity of the precipitates is a clear indication of very fast growth kinetics and therefore high supersaturation, which is consistent with the fractal geometry of the patterns. Under scanning electron microscopy, the material forming the dendrite shows a colloidal aspect and appears to be coating the mineral grains forming the matrix rock.

The colloidal texture of manganese oxides, the manganese concentration profile around the dendrites, and the coexistence of well-differentiated Mn and Fe dendrites are difficult to explain by a diffusion reaction mechanism, at least in the cases where these patterns appear to be associated to sedimentary laminations (Figure 1.12). In these cases, a genetic model based on the mineral record of fluid flow structures is more plausible. Viscous fingering is a pattern created when one fluid pushes another of higher viscosity in a confined quasi-2D space. In porous media for very low velocities, the flow provokes a percolation pattern with a fractal dimension of 1.82, which decreases for higher velocities as the flow patterns become reminiscent of DLA patterns with a dimension of 1.70 [112]. These patterns fit very well with the geometrical properties of manganese dendrites and related structures with higher fractal dimensions. Consequently, the most probable genetic mechanism for the formation of manganese dendrites is based on the mineralization of flow structures formed during the invasion of sedimentary discontinuities by Mn- and Fe-bearing fluids rising through cracks. For this process to operate, the host rock body to be injected must be at least partially cemented and the injected fluid must displace another of higher viscosity. Both facts are possible during diagenesis, when a colloidal suspension fills the interbedding laminations and cavities of partially cemented sediments. Under these conditions, the parameters controlling the great variety of dendritic and nondendritic patterns observed in field studies are the width and thickness of the uncemented muddy lamina, the roughness of the cemented surfaces, the pressure of the injection, and the viscosity of the pushed fluid. Sediments containing Mn^{4+} and Fe^{3+} compounds are reduced upon burial below the anoxic-oxic interphase and thus become enriched in Mn^{2+} and Fe^{2+}. Solutions containing these cations can migrate upwards through the cracks of the sedimentary body

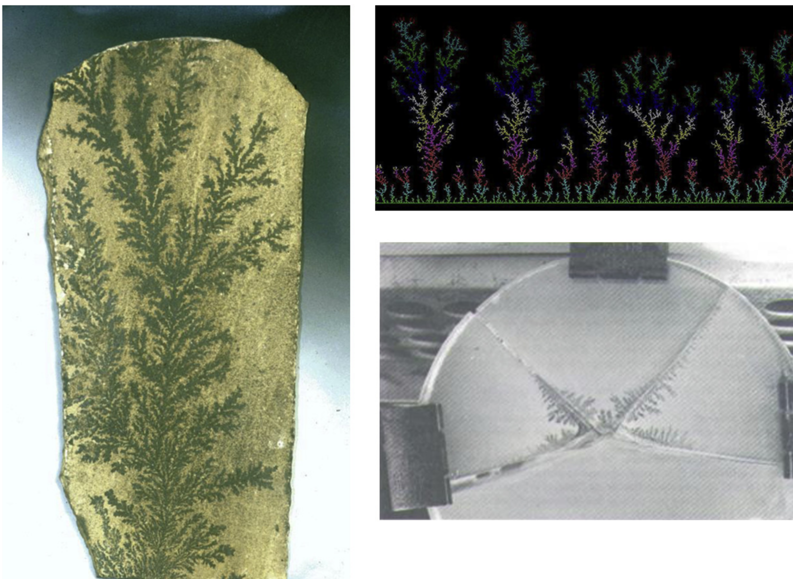

FIGURE 1.12 On the left, a mineral dendrite of iron and manganese oxi-hydroxides. The vertical length of the rock is 45 cm. This type of dendrites with fractal dimension close to 1.68 can be generated either by a diffusion limited aggregation mechanism (top right) or by a viscous fingering mechanism (bottom right). This is an example that the morphology of an object—by itself—does not contain information about its genesis.

and invade the upper alkaline and oxygenated zones, pushing the colloidal suspension that fills the sedimentary laminations and consequently forming the dendritic patterns. Finally, preservation of the pattern can be due to the cementation of the host rocks, plugging of the system by the formation of colloidal iron oxides, and the exhaustion of the source of reducing chemicals.

1.7 Early Earth Mineral Growth, Primitive Life Detection, and Origin of Life

Once living organisms appeared on our planet, most crystal growth phenomena occurring in surface and subsurface environments were affected by life. If life appeared near or within hydrothermal vents, not only the hydrosphere and atmosphere but also the fluid transport and geochemistry of hydrothermal systems were deeply affected by the influence of living organisms. This influence started more than 3 billion years ago, and today it is ubiquitous and evident.

Thus, it is not strange that when the geological record is analyzed with the *actualistic* view characteristic of geological studies, biomimetic structures are interpreted by comparison with contemporary structures created by processes working today—that is, processes on which life plays an important role. Mineral textures and structures that look

like biofilms [113], microfossils [114], or extant stromatolitic structures [115] were straightforwardly interpreted as life remnants, as real fossils, because it was thought that such complex structures could not be produced by mineral processes alone. This is no longer true since the discovery of silica biomorphs [116,117], which are self-organized mineral structures with hierarchic textures and shapes of continuous curvature, such as those thought to be exclusive of life. They can be produced not only without the aid of life but even without organic compounds. In fact, there are several physicochemical routes to producing inorganic materials displaying shapes reminiscent of life, but silica-carbonate biomorphs have an exceptional relevance for life detection. This is because of the formidable mimicking of the structures proposed to be the earliest remnants of life, but mostly because they self-assemble from a simple chemical cocktail that is geochemically plausible and similar to the chemistry of the rocks in which these putative microfossils are embedded.

The elements required to form silica biomorphs in the laboratory—silicon, water, and alkaline earth metals, particularly calcium and barium—were all abundant in Archean times. In addition, all the Archean putative microfossils reported to date were found in cherty rocks (i.e., rocks that either formed from silica sols or were silicified by silica-rich fluids). More astonishingly, in several cases the rocks containing the oldest putative remnants of life were barium-rich cherts [114,118]. With such a geochemical framework, silica biomorphs are a clear inorganic alternative explanation to some of the microstructures considered to be the oldest remnants of life on the planet. Further experiments also showed that the carbonaceous composition of the kerogen decorating Archean putative microfossils and claimed to be a proof of biogenesis [119] could also be obtained when silica biomorphs are grown with the same chemical recipe used to create inorganic hydrocarbons from siderite decomposition [120,121]. The Raman spectra of both Archean putative microfossils and their laboratory inorganic counterpart are characteristic of graphite-like and diamond-like carbon (see Figure 1.4 in Ref. [122]).

Figure 1.13 shows a selection of images illustrating the morphological variety of silica biomorphs. Each of these structures are made by millions of nanocrystals of barium, strontium, or calcium carbonate, which remain co-oriented to each other no matter the curvature of the shape. They are obtained either in single-pot solution experiments or by the counterdiffusion technique in gels, where these millions of nanocrystals self-assemble to create the bioforms. How do these bizarre structures crystallize? Everything starts with an initial single crystal of the orthorhombic carbonate (witherite, strontianite, or aragonite), followed by the breaking of the symmetry of the crystal structure. This occurs by fibrillation, by the splitting of the two ends of the single crystal corresponding to their basal faces. The continuous splitting creates fractal cauliflower-like structures that are characteristic of pH values in the range of 9–10. At higher pH values, the fibrillation takes place by nucleation events rather than by splitting, thus creating 2D lamellae that grow radially until the lamellae curl on their own in some singular point of the growth front. Then, the radial growth stops and the curls propagate along the rims of the structure. All the precise morphological diversity of the biomorphs

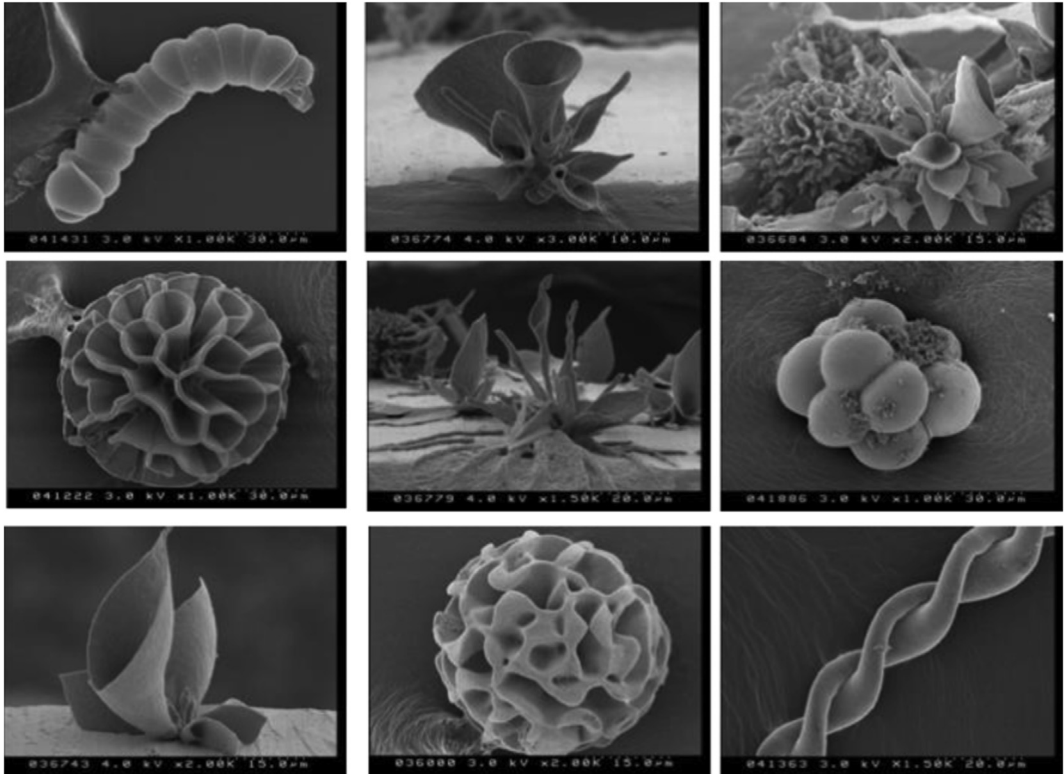

FIGURE 1.13 Complex self-assembled inorganic materials from chemical coupling: a selection of images illustrating the morphological variety of silica/carbonate biomorphs.

(e.g., globular, twisted ribbons, spirals, worms) can be explained by three parameters of a pair of counterpropagating curls, namely their relative chirality, their propagation velocity with respect to the radial growth velocity of the lamellae, and their relative radius of curling.

All of the above phenomenology are driven by the role that polymeric silica plays as a modifier and inhibitor of carbonate precipitation. What is singular in this case is the chemical coupling between the growing carbonate crystals and the silica impurities. They have reverse solubility with respect to pH. Thus, as shown in Figure 1.14, there is a feedback that provokes the oscillatory behavior of the supersaturation of both phases, as the very growth of the carbonate induces the precipitation of the impurity and, reversely, the precipitation of the impurity provokes the precipitation of the carbonate [123].

Beyond the impact on life detection, the morphology of silica biomorphs, as in the case of fractal dendrites, does not by itself contain genetic information; therefore, it cannot be used as an unambiguous tool to decipher the formation mechanism. Another example of this misuse of morphology is the case of nanobacteria, which are living organisms less than a micron in size that have been claimed to play important roles in

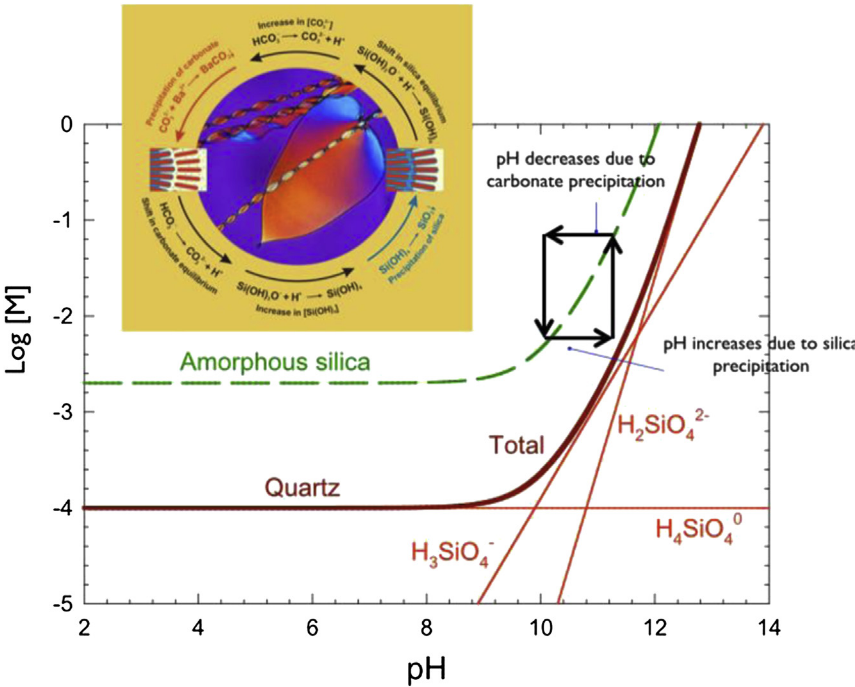

FIGURE 1.14 Mineral complexity requires a feedback mechanism to trigger autocatalysis. In the case of self-assembled silica biomorphs the mechanism is the reverse solubility of silica and carbonate versus pH.

several diseases. It has been demonstrated that abiotic nanostructures formed of amorphous calcium carbonate meet existing criteria for identification as living nanobacteria [124,125]. Today, most paleontologists realize that morphology cannot be claimed as a proof of biogenicity for Archean microstructures [78,79,89,90,126]. However, none of the putative Archean microfossils have been demonstrated to be unequivocally silica biomorphs, either. A deeper investigation to search and decipher putative, dubio, and nonfossil microstructures in Archean rocks should be carried out in the future.

In parallel, the search for self-organized biomimetic structures in current alkaline silica-rich environments must be performed. The precipitation of tubular structures of calcium-silicate-hydrated phases have been found during the alkaline weathering of granites (Figure 1.15). These tubules have been demonstrated to be reverse silica gardens formed by the leaching of silica from plagioclase and quartz in the presence of an alkaline, calcium-rich solution flow [127]. This finding is important because alkaline silica-rich environments are natural locations investigating the complexity of and pathways to prebiotic chemistry. Serpentinization reactions known to yield alkaline solutions and be the main source of abiotic organic carbon will therefore be investigated in the future [128].

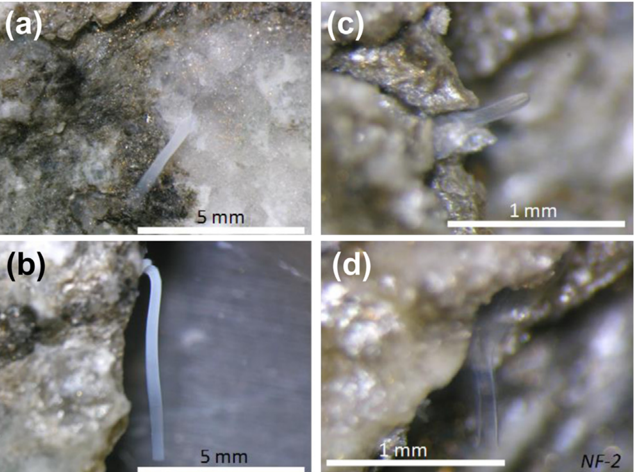

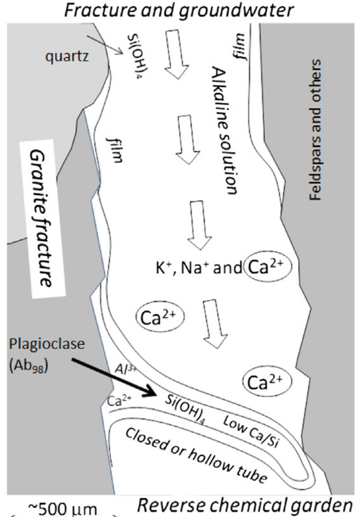

FIGURE 1.15 Top: tubular structures of calcium silicate hydrate forming by the weathering of granitic rocks by highly alkaline water flow. Below: scheme of the proposed origin as reverse silica garden. *From Ref. [127].*

1.8 From Deep Earth to Outer Space

A new challenge for crystal growers is to unravel the structure of minerals in the deep Earth. Until recently, information about the layered structure of the interior of our planet was mainly provided by the analysis of the propagation of seismic waves. The development of new technologies for high-pressure, high-temperature crystal growth opened a new field of study of geological interest. The goal is to know how mineral phases change under the pressure and temperatures found in the interior of the planet. The discontinuities that are delimited by the change of the speed of the seismic waves (e.g., at

660 km, dividing the upper and lower mantle) can now be understood from the physical properties of the phases that are stable below and above the pressure-temperature conditions of these discontinuities. The new diamond anvils are simple but fascinating machines, allowing one to reach pressure values characteristic of the lower mantle (tens to hundreds of GP) at laser-induced high temperatures while recording in situ the phase transformations by X-ray diffraction [129].

The field is ready for discoveries of surprises, such as the exotic $NaCl_3$ phase found when NaCl is squeezed at 20 GP [130]. Experimental studies on the phase transitions observed when the main minerals forming the upper mantle (namely pyroxene, olivine, and garnets) undergo high pressure have already started to shed light on the structure of the Earth. Thus, the silicate with perovskite structure $(Mg,Fe)SiO_3$ undergoes a transformation to postperovskite at pressure-temperature conditions of 2900 km deep where the mantle–core discontinuity is located [131,132]. More detailed experiments will be performed in the near future. There is much to discover, and certainly laboratory studies will try to reach the pressure values required to mimic the actual core below the deep lower mantle.

The formation of the solar system can be described as a history of phase transitions from gas, melt, and vapors to solid phases, which in most cases ends with a crystalline mineral. Thus, in some way, understanding our solar system is a matter of crystallization. Therefore, decoding growth information contained in the earliest crystals ever formed can, in turn, be useful for revealing the actual history of the solar system they have helped to create. The exposed rocks of our own planet contribute poorly to that research program because there is no geological record older than 4.0 billion years, with the exception of some zircon crystals recycled from the oldest extinct rocks [133,134]. Our solar systems started 4.6 billion years ago with a solar nebulae from which chondrules, meteorites, and interstellar dust particles started to form. These objects are the main pieces of information, and their study in terms of crystal growth is one of the research avenues for the future. In addition, the exciting robotic missions to the moon and Mars are sending important analytical information, allowing for the first time the study of extraterrestrial mineral growth processes that are vital for the future of planetary missions [135,136]. Some examples of what we call *astrocrystallization* are described here.

The nucleation and growth of silicate melts in space has been studied in the laboratory, both on Earth and also under microgravity conditions. For instance, small silicate spherules called chondrules are a major component of primitive meteorites; therefore, they have been extensively studied in the past. Computer simulation and experimental work performed under microgravity conditions provided new insights on the subject. Crystallization experiments using a floating melt droplet by gas-jet levitation found that heterogeneous nucleation by collisions of tiny cosmic dust particles likely explain the formation of crystalline chondrules. Homogeneous nucleation is very difficult, and the melted spheres are able to crystallize only at significantly high supercooling temperatures ($\sim$1000 K) [137]. These studies have also successfully mimicked the textures of chondrules. For instance, to form the rim characteristic of some chondrules, a

temperature difference of ~ 100 K is required between the center and the surface of the droplet. Such a large difference in temperature can be achieved in the case of rapid cooling at a rate of $\sim 10^3$ K/s [138].

The formation of nanometer-sized cosmic dust has been also reproduced in the laboratory based on nanoscale properties, such as a decrease of melting point by 50% [139] and an increase in the diffusion coefficient of more than nine orders of magnitude [140], as well as the fusion of nanoparticles [141]. Indeed, various analogs of cosmic dust have been reproduced in laboratories and successfully proposed in growth processes, such as silicate nanoparticles having non-mass-dependent oxygen isotope fractionation formed in a plasma field [142], composite particles of TiC-core and carbon-mantle formed by decomposition of CO gas [143], fullerene and its existence around evolved stars [144], and carbonaceous hollow particles [145].

Another application of crystal growth in astrocrystallization is the study of the formation process of framboidal magnetite. These are particles made of three-dimensionally aligned nanocrystals of magnetite found in fractures of the parent asteroid and formed in microgravity as the result of shaking due to collision with other solar bodies [146]. The uniformity of the size distribution and the similar morphology of the magnetite nanoparticles in each of the colloidal crystals suggest that they were formed through homogeneous nucleation from a highly supersaturated isolated solution in a single nucleation event. The colloidal nanomagnetites arrange by repulsive force to form a colloidal crystal in the solution. To overcome this force, the density of magnetite particles in a solution must be sufficiently high in an isolated solution. The diameter of each droplet is roughly 25% larger than that of the final product (several micrometers in diameter). The increase in the volume fraction of magnetite can be achieved through the evaporation of water. If the distance between particles and the Debye screening length of each particle is equivalent, they can arrange and make a colloidal crystal. Further evaporation reduces the interparticle spaces until the colloidal crystals are stabilized by desiccation. The very last droplets of aqueous solution in an ancient asteroid are very important because the mutual interaction of minerals and organics in water-concentrated chemical species play critical roles in the final minerals in meteorites and in the early evolution of organics.

One of the most pristine materials in our solar system that we can collect on earth are interplanetary dust particles (IDPs). Their mineralogy has been investigated and compared with the spectra of dust around other stars [147,148], showing that they have similar mineral phases. It is still unclear when and from where all these minerals originate, if all of them formed in the solar nebula, or if some components have a presolar origin. One of the more intriguing components of IDPs is glass with embedded metals and sulfides, which may have a presolar origin. It seems that silicates and other minerals in IDPs formed directly out of the gas phase, so that gas-to-solid condensation is the fundamental mechanism of grain growth in nebula environments [149]. Beyond the information provided by observational astronomy, it seems clear that future experimental crystal growth studies will be key for revealing the formation mechanism of the

components of IDPs and the particles themselves, as well as for a better understanding of the formation of the solar system.

Acknowledgments

We acknowledge support from ‘‘Factoría de Cristalización’’ (Consolider Ingenio 2010, Spanish MINECO), the Junta de Andalucía (project RNM5384), and the Spanish MICINN (projects CGL2010-16882 and AYA2009-10655). We thank our colleagues M. Prieto and C. Ayora for useful discussions and suggestions.

References

[1] Caley ER, Richards JFC. Theophrastus on stones. Colombia: Ohio State University; 1956.

[2] [Heales JF, Trans.] Pliny the elder, natural history. Harmondsworth: Penguin; 1991.

[3] Kepler J. Strena Seu de Nive Sexangula. Frankfurt: Godfrey Tampach; 1611 [Hardie C, Trans.]. The Six-Cornered Snowflake, Oxford, Clarendon Press, 1966.

[4] Steno N, De Solido Intra Solidum Naturaliter Contento Dissertationis Prodromus, Florence, 1669, [Winter JG, Trans.] The prodromus of Nicolous Steno’s Dissertation concerning a solid body enclosed by process of nature within a solid, New York, Hafner, 1968.

[5] Burke JH. Origin of the science of crystals. Berkeley: University of California Press; 1966.

[6] Amorós JL. La gran aventura del cristal. Editorial Universidad Complutense. Madrid 1978.

[7] Scheel HJ. Historical aspects of crystal growth technology. J Cryst Growth 2000;211:1.

[8] [a] Galazka Z. Hand book of crystal growth: bulk crystal growth. In: Rudolph P, editor. Growth measures to achieve bulk single crystals of transparent semiconducting and conducting oxides vol. 2; 2014.
[b] Wang J, Zhang G, Haohai Y, Wang Y, Chen C. Hand book of crystal growth: bulk crystal growth. In: Rudolph P, editor. Czochralski and flux growth of crystals for lasers and nonlinear optics vol. 2; 2014.

[9] Sunagawa I. In: Hurle DTJ, editor. Handbook of Crystal Growth, vol. 2. Amsterdam: Elsevier; 1994. [Chapter 1], pp. 2–49.

[10] Grigoriev DP. Ontogeny of minerals. Jerusalem (Israel): Israel Program for Scientific Translation; 1965.

[11] Sunagawa I. Dev Sedimentol 1994;51:19.

[12] Nakamura H, Tsukamoto K, Sunagawa I. J Cryst Growth 1990;99:1227.

[13] Tsukamoto K, Abe T, Sunagawa I. J Cryst Growth 1983;63:215.

[14] Brandeis G, Jaupart C. Contrib Mineral Petrol 1987;96:24.

[15] Solomatov SV, Stevenson DJ. J Geophys Res 1993;98(E3):5407.

[16] W Dunbar N, Jacobs GK, Naney MT. Contrib Mineral Petrol 1995;120(3–4):412.

[17] Hoover SR, Cashman KV, Manga M. J Volcanol Geotherm Res 2001;107:1.

[18] Muncill GE, Lasaga AC. Am Mineral 1987;72:299.

[19] Lasaga AC. Am J Sci 1982;282:1264.

[20] Gorokhova NV, Melnik OE. Fluid Dyn 2010;45:679.

[21] Lofgren GE, Huss GR, Wasserburg GJ. Am Mineral 2006;91:1596.

[22] Hinsberg VJ, Schumacher JC. Contrib Mineral Petrol 2006;153:289.

[23] Chakoumakos B, Lumpkin G. Can Mineral 1990;28:287.

[24] Simmons WBS, Webber KL. Eur J Mineral 2008;20:421.

[25] Barker AJ. Introduction to metamorphic textures and microstructures. Kluwer Academic Publishers; 1990. ISBN 10: 0216926858/0-216-92685-8.

[26] Bard JP. Microtextures of igneous and metamorphic rocks. Series: petrology and structural geology, IX. Springer-Verlag; 1986. 264 p.

[27] Kretz Ralph. Metamorphic crystallization. Wiley; 1994. 530 p. ISBN: 978-0-471-94214-6.

[28] Kretz R. Lithos 1974;7:123.

[29] Thanh NX, Sajeev K, Itaya T, Windley BF. Lithos 2011;127:552.

[30] Imon R, Okudaira T, Kanagawa K. J Struct Geol 2004;26:793.

[31] Wassmann S, Stöckhert B, Stöckhert. J Struct Geol 2013;46:200.

[32] Augenstein C, Burg J-P. J Struct Geol 2011;33:244.

[33] Otani M, Wallis S. Geology 2006;34:561.

[34] Barnhoorn A, Bystricky M, Burlini L, Kunze K. J Struct Geol 2004;26:885.

[35] Zhou L-G, Xia Q-X, Zheng Y-F, Chen R-X. Lithos 2011;127:101.

[36] Jourdan A-L, Vennemann TW, Mullis J, Ramseyer K, Spiers CJ. Eur J Mineral 2009;21:219.

[37] Hedenquist JW, Lowenstern JB. Nature 1994;370:519.

[38] Jamtveit B, Wogelius RA, Fraser DG. Geology 1993;21:113.

[39] Sunagawa I. Crystals: growth, morphology and perfection. Cambridge University Press; 2005. 295 pp.

[40] Rodriguez-Clemente R. Estud Geol 1982;38:55.

[41] Edwards KJ, Becker K, Colwell F. Annu Rev Earth Planet Sci 2012;40:551.

[42] Richter DK. In: Peryt TM, editor. Coated grains. Berlin: Springer; 1983. p. 71.

[43] García-Ruiz JM. In: Rodríguez R, Sunagawa I, editors. Crystal growth processes in sedimentary enviroments. Estudios Geológicos, vol. 38; 1982. p. 209.

[44] García-Ruiz JM. Key Eng Mater 1991;58:87.

[45] Cody RD, Shanks HR. J Cryst Growth 1974;23:275.

[46] van Rosmalen GM, Marchée WGJ, Bennema P. J Cryst Growth 1976;35:169.

[47] Holland HD. Philos Trans R Soc Biol Sci 2006;361:903.

[48] Hartman P. In: Hartman P, editor. Crystal Growth: an Introduction. Amsterdam: North-Holland Publishing Cy; 1973 [Chapter 14]. pp. 367–402.

[49] Sangwal K. Impurities and crystal growth. Pergamon; 1996. 169 p.

[50] Avrami M. J Chem Phys 1939;7:1103.

[51] Avrami M. J Chem Phys 1940;8:212.

[52] Avrami M. J Chem Phys 1941;9:177.

[53] Kunzler RH, Goodell HG. Am J Sci 1970;269:360.

[54] García-Ruiz JM, Villasuso R, Ayora C, Canals A, Otálora F. Geology 2007;35:327.

[55] Otálora F, García-Ruiz JM. Chem Soc Rev 2014;43:2013.

[56] Foshag W. Am Mineral 1927;12:252.

[57] Degoutin N. Soc Cient Antonio Alzate Rev 1912;32:35.

[58] Krüger Y, García-Ruiz JM, Canals A, Marti D, Frenz M, Van Driessche AES. Geology 2013;41:119–22.

[59] Van Driessche AES, García-Ruiz JM, Delgado-López JM, Sazaki G. Cryst Growth Des 2010;10:3909.

[60] Van Driessche AES, García-Ruiz JM, Tsukamoto K, PatiñoLopez LD, Satoh H. PNAS 2011;108:15721.

[61] Simon B, Bienfait M. Acta Cryst 1965;19:750.

[62] Weijnen MPC, van Rosmalen GM, Bennema P, Rijpkema JJM. J Cryst Growth 1987;82:509.

[63] Massaro FR, Rubbo M, Aquilano D. Cryst Growth Des 2010;10:2870.

[64] Massaro FR, Rubbo M, Aquilano D. Cryst Growth Des 2011;11:1607.

[65] Kitamura M, Hosoya S, Sunagawa I. J Cryst Growth 1979;47:93.

[66] Salje E. J Phys Condens Matter 1993:4775.

[67] Anderson DL. Geology 2002;30:411.

[68] Nicolis G, Prigogine I. Self-organization in nonequilibrium systems: from dissipative structures to order through fluctuations. New York: Wiley; 1977. 491 p.

[69] Hergarten S. Self-organized criticality in earth systems. Berlin Heildelberg: Springer-Verlag; 2002. 250 p.

[70] Ortoleva P, Merino E, Moore C, Chadam J. Am J Sci 1987;287:979.

[71] Ortoleva P, Chadam J, Merino E, Sen A. Am J Sci 1987;287:1008.

[72] Jamtveit B, Meakin P, editors. Growth, dissolution, and pattern formation in geosystems. Dordrecht and Boston: Kluwer Academic Publishers; 1999. p. 409.

[73] Meakin P, Jamtveit B. Proc R Soc A 2010;466:659.

[74] Turcotte DL. In: Fractals and Chaos in geology and geophysics. 2nd ed. Cambridge: Cambridge University Press; 1997. p. 416.

[75] Bak P. How nature works, the science of self-organized criticality. New York: Copernicus Press; 1996. 212 p.

[76] Hollister LS. Am Mineral 1970;55:742.

[77] Dowty E. Am Mineral 1976;61:460.

[78] Reeder RJ, Paquette J. Sediment Geol 1989;65:239.

[79] Vavra G. Contrib Mineral Petrol 1990;106:90.

[80] Reeder RJ, Rakovan J. In: Jamtveitand B, Meakin P, editors. Growth, dissolution and pattern-formation in geosystems. Dordrecht: Kluwer; 1999. p. 143.

[81] Paquette J, Reeder RJ. Geology 1990;18:1244.

[82] Paquette J, Reeder RJ. Geochim Cosmochim Acta 1995;59:735.

[83] Cashman KV. Contrib Mineral Petrol 1992;109:431.

[84] Gorokhova NV, Melnik OE, Plechov PY, Shcherbakov VD. J Volcanol Geotherm Res 2013;263:172.

[85] Allègre CJ, Provost A, Jaupart C. Nature 1981;294:223.

[86] Tsune A, Toramaru A. Am Mineral 2007;92:1071.

[87] L'Heureux I, Fowler AD. Geophys Res Lett 1996;23:17.

[88] Oishi Y. J Chem Phys 1965;43:1611.

[89] Brugger CR, E Hammer J. J Petrol 2010;51:1941.

[90] Mollard E, Martel C, Bourdier J-L. J Petrol 2012;53:1743.

[91] Shore M, Fowler AD. Can Mineral 1996;341:111.

[92] L'Heureux I, Fowler AD. Can Mineral 1996;34:1137.

[93] Putnis A, Fernandez-Diaz L, Prieto M. Nature 1992;358:743.

[94] Prieto M, Putnis A, Fernandez-Diaz L. Geol Mag 1993;130:289.

[95] Prieto M, Fernandez-González A, Putnis A, Fernandez-Diaz L. Geochim Cosmochim Acta 1997;61:3383.

[96] Pina CM, Enders M, Putnis A. Chem Geol 2000;168:195.

[97] L'Heureux I, Katsev S. Chem Geol 2006;225:230.

[98] Horsthemke W, Lefever R. In: Noise-induced transitions: theory and applications in physics, chemistry, and biology, vol. 15. Berlin Heidelberg: Springer Series in Synergetics; 1984. p. 318.

[99] Stern KH. Chem Rev 1954;54:79.

[100] Jamtveit B, Hammer Ø. Geochem Perspect 2012;1:341.

[101] Jablczinsky K. Bull Soc Chim Fr 1923;4:592.

[102] Langer JS. Rev Mod Phys 1980;52:1.

[103] Glicksman M. Handbook of Crystal Growth, vol. IB. Amsterdam: Elsevier; 2014. [chapter 03].

[104] Witten TA, Sander LM. Phys Rev B 1983;27:5686.

[105] Chopard B, Herrmann HJ, Vicsek T. Nature 1991;353:409.

[106] Witten TA, Sender LM. Phys Rev Lett 1981;47:1400.

[107] Garcia-Ruiz JM, Otálora F, Sanchez-Navas A, Higes-Rolando FJ. In: Kruhl JH, editor. Fractals and dynamic systems in geoscience. Berlin: Springer-Verlag; 1994. p. 307.

[108] García-Ruiz JM. In: García-Ruiz JM, Louis E, Meakin P, Sander L, editors. Growth patterns in physical sciences and biology. Pergamon Press; 1993. p. 183.

[109] Van Damme H. Flow and interfacial instabilities in newtonian and colloidal fluids. In: Avnir D, editor. The fractal approach to heterogeneous chemistry. Chichester: John Wiley & Sons; 1989. p. 199.

[110] Vicsek T. In: Fractal growth phenomena. Singapore: World Scientific; 1989. p. 495.

[111] Potter RM, Rossman GR. Am Mineral 1979;64:1199.

[112] Lenormand R, Daccord G. Flow patterns in porous media. In: Stanley HE, Ostrowsky N, editors. Random fluctuations and pattern growth. Dordrecht: Kluwer Academic Publishers; 1988. p. 69.

[113] Noffke N, Christian D, Wacey D, Hazen RM. Astrobiology 2013;13:1.

[114] Schopf JW. Science 1993;260:640.

[115] Allwood AC, Walter MR, Kamber BS, Marshall CP, Burch IW. Nature 2006;441:714.

[116] García-Ruiz JM. Biosphere 1994;24:451.

[117] García-Ruiz JM. Geology 1998;26:843.

[118] Buick R, Dunlop JSR, Groves DI. Alcheringa 1981;5:161.

[119] Schopf JW, Kudryavtsev AB, Agresti DG, Wdowiak TU, Czaja AD. Nature 2002;416:73.

[120] McCollom TM. Geochim Cosmochim Acta 2003;67:311–7.

[121] Zuilen MA, van Lepland A. Arrhenius G. Nature 2002;418:627.

[122] García-Ruiz JM, Hyde ST, Carnerup AM, Christy AG, Van Kranendonk MJ, Welham NJ. Science 2003;302:1194–7.

[123] Garcia-Ruiz JM, Melero E, Hyde ST. Science 2009.

[124] Martel J, Young JD. Proc Natl Acad Sci USA 2008;105:5549.

[125] Wu C-Y, Young L, Young D, Martel J, Young JD. Bions: a family of biomimetic mineralo-organic complexes derived from biological fluids. PLoSONE 2013;8(9):e75501. http://dx.doi.org/10.1371/journal.pone.0075501.

[126] Martel J, Young D, Peng H-H, Wu C-Y, Young JD. Annu Rev Earth Planet Sci 2012;40:167.

[127] Satoh H, Tsukamoto K, García-Ruiz JM. Formation of chemical gardens on granitic rock: a new type of alteration for alkaline systems. Eur J Mineral 2014;26(3):415–26. http://dx.doi.org/10.1127/0935-1221/2014/0026-2378.

[128] NcCollom TM, Seewald JS. Elements 2013;9:129.

[129] Duffy TS. Rep Prog Phys 2005;68:1811.

[130] Zhang W, Oganov AR, Goncharov AF, Zhu Q, Boulfelfel SE, Lyakhov AO, et al. Unexpected stable stoichiometries of sodium chlorides. Science 2013;342(6165):1502–5. http://dx.doi.org/10.1126/science.1244989.

[131] Organov AR, Ono S. Nature 2004;430:445.

[132] Hirose K, Brodholt J, Lay T, Yuen D, editors. An introduction to post-perovskite: the last mantle phase transition. American Geophysical Union; 2007. http://dx.doi.org/10.1029/174GM02.

[133] Wilde SA, Valley JW, Peck WH, Graham CM. Nature 2001;409:175.

[134] Bell EA, Harrison TM, McCulloch MT, Young ED. Geochem Cosmochim Acta 2011;75:4816.

[135] Bish DL, Blake DF, Vaniman DT, Chipera SJ, Morris RV, Ming DW, et al. Science 2013;341:1238932.

[136] Vaniman DT, Bish DL, Ming DW, Bristow TF, Morris RV, Blake DF, et al. Science 2013;343:1243480.

[137] Nagashima K, Tsukamoto K, Satoh H, Kobatake H, Dold P. J Cryst Growth 2006;293:193–7.

[138] Miura H, Yokoyama E, Nagashima K, Tsukamoto K, Srivastava A. J Appl Phys 2010;108:114912.

[139] Lee J, Tanaka T, Mori H. Nanotechnology 2009;20:475706.

[140] Mori H, Komatsu M, Takeda K, Fujita H. Philos Mag Lett 1991;63:173.

[141] Kimura Y. In: Mann I, Meyer-Vernet N, Czechowski A, editors. Nanodust in the solar system: discoveries and interpretations. Springer-Verlag; 2012. pp. 31–46.

[142] Kimura Y, Nuth III JA, Chakraborty S, Thiemens MH. Meteorit Planet Sci 2007;42:1429.

[143] Kimura Y, Nuth III JA, Ferguson FT. Meteorit Planet Sci 2006;41(5):673.

[144] Kimura Y, Nuth III JA, Ferguson Frank T. Astrophys J Lett 2005;632:L159.

[145] Saito M, Kimura Y. Astrophys J Lett 2009;703:L147.

[146] Kimura Y, Sato T, Nakamura N, Nozawa J, Nakamura T, Tsukamoto K, et al. Nat Commun 2013;4:2649.

[147] Malfait K, Waelkens C, Waters LBFM, Vandenbussche B, Huygen E. Graauw MS van. Astron. Astrophys 1998;332:L25.

[148] Molster FJ, Waters LB, Tielens A, Koike C, Chibara H. Astron Astrophys 2002;382:241.

[149] Apal D, Lauretta DS, editors. Protoplanetary dust. Cambridge University Press; 2010. p. 396.

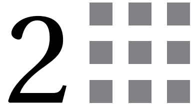

Czochralski Growth of Silicon Crystals

Jochen Friedrich[2], Wilfried von Ammon[1], Georg Müller[3]

[1]VON AMMON CONSULTING, ROTH, GERMANY;
[2]FRAUNHOFER INSTITUTE IISB, ERLANGEN, GERMANY;
[3]CRYSTAL CONSULTING, LANGENSENDELBACH, GERMANY

CHAPTER OUTLINE

2.1 Introduction **46**
2.2 Description of the Czochralski Process **47**
2.2.1 Principle 47
2.2.2 Setup of a Silicon Czochralski Pulling Apparatus 48
2.2.3 Procedure of the Czochralski Growth Process 51
2.3 Global Heat Transfer and Convective Flow **58**
2.3.1 Growth Kinetics and Interface Shape 59
2.3.2 Heat Transfer and Growth Rate 59
2.3.3 Convective Flow in the Silicon Melt 61
2.3.4 Modeling of Heat and Species Transfer 66
2.3.5 Magnetic Fields 67
2.4 Transport and Incorporation of Dopants and Impurities **69**
2.4.1 General Considerations 69
2.4.2 Segregation Coefficient *k* 69
2.4.3 Distribution of Species in the Crystal 72
2.4.3.1 Numerical Modeling of Species Transport 72
2.4.3.2 Longitudinal (Axial) Concentration Profiles 72
2.4.3.3 Continuous Czochralski 73
2.4.3.4 Lateral (Radial) Nonuniformity 74
2.4.4 Constitutional Supercooling in Heavy-Doping Cz Growth 75
2.4.5 Microsegregation: Striations 76
2.4.6 Intentional Doping during the Cz Process 77
2.4.6.1 Donors and Acceptors 77
2.4.6.2 Other Intentional Doping Elements (Ge, N, H) 78
2.4.6.3 Co-Doping of Solar-Grade Silicon 78

Handbook of Crystal Growth. http://dx.doi.org/10.1016/B978-0-444-63303-3.00002-X
Copyright © 2015 Elsevier B.V. All rights reserved.

2.4.7 Unintentional Impurity Incorporation during the Cz Process 79
2.4.7.1 Oxygen 79
2.4.7.2 Carbon 81
2.5 Oxygen in Silicon 82
2.5.1 Technical Relevance of Oxygen Effects in Silicon Crystals 82
2.5.2 Atomistic Configurations of Oxygen in Silicon Crystals 82
2.5.3 Solubility of Oxygen in Silicon Crystals 83
2.5.4 Diffusivity of Oxygen in Silicon Crystals 83
2.5.5 Formation of Oxygen-Related Thermal Donors in Silicon Crystals 84
2.5.6 Reaction and Aggregation of Oxygen in Silicon Crystals 84
2.5.7 Formation of Oxidation-Induced Stacking Faults 86
2.6 Intrinsic Point Defects and Their Aggregates 88
2.6.1 The Importance of Intrinsic Point Defects and Their Aggregates 88
2.6.2 Incorporation of Intrinsic Point Defects into the Growing Crystal 90
2.6.3 Influence of Crystal Growth Parameters on the Intrinsic Point Defect Behavior 91
2.6.4 Calculation of the Aggregation of Intrinsic Point Defects 92
2.6.5 Impact of Impurities on the Intrinsic Point Defect Aggregation 93
2.7 Economic Aspects of Cz Growth 94
2.7.1 General Remarks 94
2.7.2 Factors that Impact the Yield of Dislocation-Free Cz Grown Crystals 95
2.7.3 Factors that Impact Cycle Time and Other Costs 96
2.7.4 Special Issues of Cz Growth of Silicon Crystals for Solar Cells 97
References 98

2.1 Introduction

In 1916, Prof. Jan Czochralski demonstrated that crystals can be grown from the melt by a pulling mechanism [1]. Three decades later, the first silicon (Si) single crystals were grown using the Czochralski (Cz) technique [2]. This pioneering work initiated tremendous developments in the field of microelectronics, information technology, power electronics, and photovoltaics. Today, Si crystals with diameters up to 300 mm and weights of more than 300 kg are industrially produced by the Cz technique. The technical feasibility to pull Si crystals with 450-mm diameters has also been demonstrated [3]. In the field of photovoltaics, monocrystalline Si crystals with diameters of approximately 210 mm and weights up to 200 kg are industrially produced by the Cz technique [4]. It is estimated that approximately 250,000 tons of Si crystals per year are currently manufactured worldwide for the semiconductor and photovoltaic industry [5].

The process of pulling Si crystals by the Cz technique from the first crystal until now was evolutionary, but it was also characterized by technological and scientific

breakthroughs: the purification of Si by the Siemens process [6], the elimination of dislocations by the Dash procedure [7], the theory of Hurle [8] about the control of the crystal diameter, the capability of oxygen for gettering impurities [9], the growth velocity (V)/temperature gradient (G) criterion introduced by Voronkov for the incorporation of intrinsic point defects [10], the application of magnetic fields to control the melt flow [11], and the development of growth processes that yielded so-called defect-free or "perfect" silicon [12] were some of these milestones.

2.2 Description of the Czochralski Process

2.2.1 Principle

The principle of the Cz process is illustrated in Figure 2.1 which shows the setup of an industrial-like Si Cz puller. In this process, the polycrystalline silicon feed material is loaded into a cylindrical, bowl-shaped silica crucible and melted at approximately

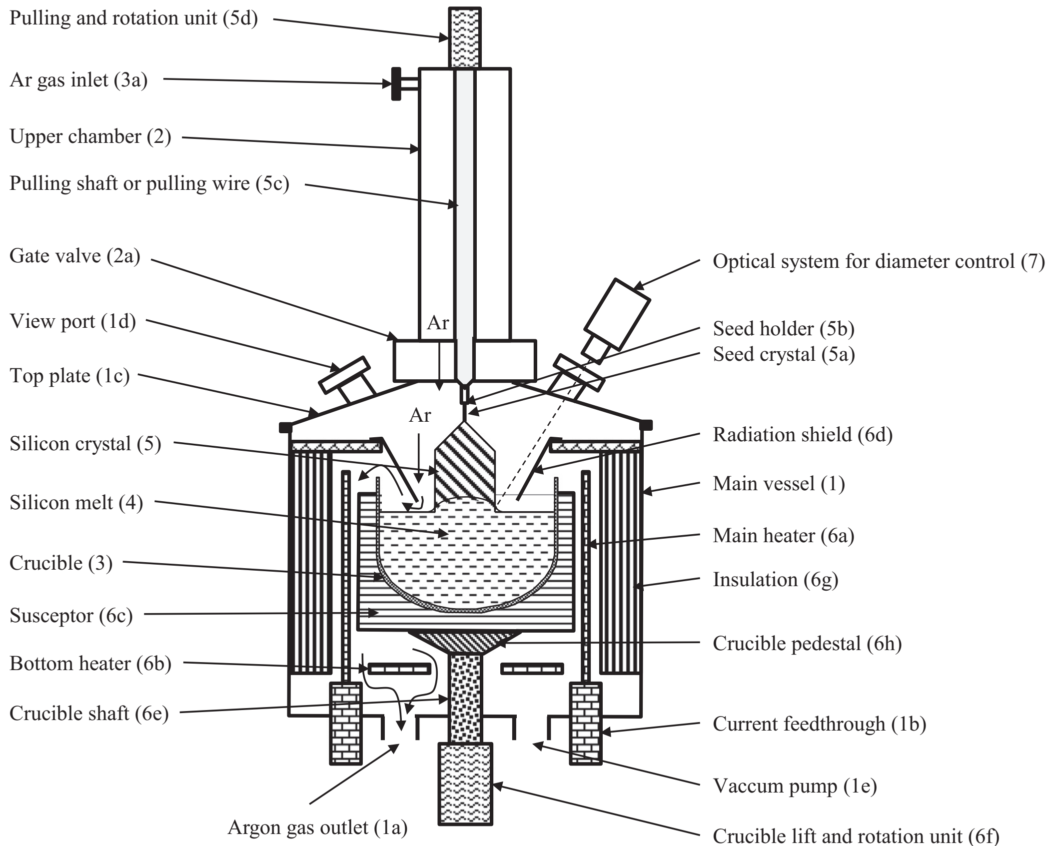

FIGURE 2.1 Schematic setup of an industrial-like silicon Czochralski puller.

1413 °C in an inert gas (argon) atmosphere. Crystal growth is initiated by dipping a silicon seed crystal (which is mounted on a moveable pull rod) into the free surface of the silicon melt. The seed is then slowly withdrawn from the melt, which causes the crystallization of silicon atoms at the melt–crystal interface of the seed by forming a new crystal portion. The diameter of the growing crystal is first increased until a nominal diameter is achieved. This diameter is kept constant to provide a cylindrical shape of the crystal body throughout the total growth process. Finally, when most of the melt is consumed, the crystal diameter is decreased again to form the shape of a cone and the crystal is removed from the residual melt. After cooling down, the as-grown crystal is removed from the growth facility.

2.2.2 Setup of a Silicon Czochralski Pulling Apparatus

This section explains the various components of the Czochralski apparatus shown in Figure 2.1.

Main Vessel: The main parts of a Cz setup are placed in a vacuum-proof cylindrical main vessel (1) with water-cooled steel walls. The bottom plate contains a flange for evacuation (1a) and several feed-throughs like electrodes (1b) for the power supply of the heaters (6a and 6b). The top plate (1c) is equipped with a viewport (1d) for visual observation of the seeding process and the growing crystal. Optical viewports are also used for optical diameter control (7). The top plate can be removed for mounting purposes and for insertion and removal of the crucible (3) in the main vessel.

Upper Chamber: Directly connected with the main vessel (1) is the upper chamber (2), in which the as-grown crystal (5) is moved vertically by the pulling shaft or pulling wire (5c). Optionally, the upper chamber and the main vessel can be separated from each other by a valve (2a). This optional device has an advantage: the cooled crystal can be removed from the growth chamber without letting air into the main vessel while the hot zone is still at high temperature. The crucible (3) can now be filled again with polysilicon and used for a further growth run. This procedure is called "multipulling" [13]. It is considered to be a promising technique for cost reduction in the growth of Si crystals for photovoltaic applications.

Crucible: The crucible is one of the most important components of a Cz puller. Apart from the poly-Si, the crucible material has to be considered as a major source of impurity contamination to the Si crystal because it is in contact with the Si melt throughout the whole growth process.

Several crucible materials have been tested in the past [14]. However, the only material that meets the requirements of purity, mechanical stability, and chemical inertness is fused silica. The silica crucibles are fabricated from pure silicon dioxide powder, called "quartz sand," mostly by a flame fusion technology.

Other possible crucible materials, such as silicon nitride or silicon carbide, would also meet the requirements of mechanical stability and purity. However, they cannot be used for the following reason. Both materials are attacked by the Si melt, which leads to a

contamination of the melt by nitrogen or carbon, respectively. Both nitrogen and carbon have relatively low vapor pressures in the Si melt, which causes a relatively quick increase of their concentration during Cz growth. If the solubility limit in the melt (in the range of $5 \cdot 10^{18}$ atoms/cm^3 [15]) is exceeded during growth, small particles of Si_3N_4 or SiC can form in the melt [15]. Such particles, however, would prevent the growth of dislocation-free Si crystals by the Cz technique.

Fortunately, the situation with silica is more favorable, as the oxygen concentration in the melt can be kept below the solubility limit where SiO_2 precipitates would be formed. This will be explained in the following paragraphs.

Silica crucibles are not totally chemically inert to the Si melt. A surface reaction takes place, which is given in Eqn (2.1) in a simplified form:

$$\mathrm{Si\ (melt)} + \mathrm{SiO_2(crucible)} \rightarrow 2\mathrm{SiO} \tag{2.1}$$

SiO (silicon monoxide) is dissolved in the Si melt, leading to oxygen contamination of the melt. In contrast to other crucible materials, such as the above-mentioned Si_3N_4 or SiC, the vapor pressure of SiO in the Si melt is much higher than that of N and C [16]. Therefore, it is possible to avoid exceeding the saturation value of approximately 3×10^{18} O atoms/cm^3 in the melt by appropriate measures (see further below).

The dissolution rate of the silica crucible depends on several parameters, such as the temperature and flow rate in the melt, argon pressure, and flow rate in the gas above the melt surface, as well as on the morphology and composition of the silica crucible. It is typically in the range of 10–50 μm/h [17]. However, the reaction rate (Eqn (2.1)) is not uniformly at the crucible wall; rather, it depends on the crucible temperature and on the structural morphology of the silica surface (e.g., cristobalite or vitreous silica) [14]. In particular, pit corrosion also can be a problem with respect to the mechanical stability of the crucible. In fact, the vitreous silica content causes a certain loss of mechanical stability by creeping at elevated temperatures, so-called sagging of the crucible wall. Therefore, the silica crucible must be surrounded by a graphite shell to stabilize the walls (called the susceptor (6c) in Figure 2.1). This crucible support causes a new problem by the chemical reaction between graphite and silica, which produces gaseous carbon monoxide (see Section 2.4.7.2).

Silicon Melt: The Si melt is kept in a temperature range slightly above the melting point ($T_m = 1413\ °C$) by the aid of the heaters (6a, 6b) and the power control system. A melt temperature that is too high increases the crucible corrosion and decreases its mechanical stability. Usually, the melt temperature is not directly used for the control of the crystal diameter. The heat transfer into the melt occurs mainly from the cylindrical side heater(s) (6a) via the crucible wall; bottom heating (6b) can be additionally used. The coldest region of the melt is at the growth interface in the central region of the free melt surface. This temperature distribution causes a strong buoyancy-driven flow, which interacts with the forced convective flow driven by the crystal and crucible counter-rotation and the capillary-driven flow originating from temperature differences at the melt surface.

The purity of the melt determines the purity of the growing crystal. Impurities and dopants in the melt are incorporated into the crystal by the segregation mechanism. The contamination of the Si melt by the dissolution of the silica crucible was already mentioned. The dissolved oxygen is transported through the Si melt by convective flows and reaches the free melt surface as well as the crystal–melt interface. This convective transport is of high importance for the control of the oxygen content of the crystal. The high vapor pressure of the SiO leads to strong evaporation of SiO from the free surface of the Si melt, which is beneficial for keeping the oxygen concentration in the melt below the solubility limit. In fact, Zulehner and Huber [14] give an estimated value that nearly 99% of the oxygen that dissolves at the crucible wall can be removed from the melt by evaporation via the melt surface. Therefore, the SiO evaporation is used as an important parameter to control the oxygen content of the Si crystal. For that purpose, the flow of the Ar gas, which is fed in at the top (3a) of the upper chamber (2), is guided downwards to the surface of the melt. Here, the Ar gas flows very close along the melt surface by the aid of the heat radiation shield (6d) and thereby removes part of the SiO, which evaporates from the melt surface.

Because the segregation coefficient of oxygen in Si is close to unity, oxygen is incorporated into the crystal with nearly the same concentration as in the melt. Typical concentrations are in the range of $3 \cdot 10^{17} - 9 \cdot 10^{17}$ atoms/cm^3. The oxygen content of the crystal plays an important role with respect to lattice hardening and the formation of gettering centers for impurities.

Silicon Crystal and Pulling Unit: The Si crystal (5) is held by the seed (5a), which is mounted in a seed holder (5b), typically made from molybdenum. The seed holder is connected to either a solid pulling shaft (5c) or a pulling wire. Both options are in use. One main advantage of the shaft system is its higher mechanical stability against an orbiting movement of the seed or the crystal, respectively. This allows for higher rotation rates, which are beneficial for uniform oxygen incorporation. The wire rope has the advantage that it can be wound up at the top of the upper chamber (2) which reduces the height of the puller. The pulling unit (5d) is mounted outside, on top of the upper chamber (2). In addition to the vertical movement (pulling), it also provides the rotation of the crystal. The pulling rates depend strongly on the crystal diameter and on the hot-zone geometry. Typical rates are 1 mm/min for pulling and approximately 20 rpm for crystal rotation.

Hot Zone: The “hot zone” is the key part in controlling the growth process, the melt and gas flow, and the concentration of the intrinsic point defects and their aggregates. The hot zone consists of the main heater (6a) and optionally a bottom heater (6b). All heaters are fabricated from pure solid graphite, which is powered by an electric current (mainly DC). The resistance of the heaters is adjusted by a meander-like structure, which is also beneficial for minimizing the Lorentz forces caused by the current that would introduce mechanical forces on the heater. The heat from the heaters is transferred by radiation to the graphite susceptor (6c). The susceptor has two main tasks: uniform heat transfer and mechanical support of the crucible. The susceptor is positioned on a

pedestal (6h) and a shaft (6e) at the bottom of the main vessel. This shaft is connected to a unit (6f) that provides vertical movement as well as rotation of the crucible. The vertical movement is used to adjust the level of the melt surface with respect to the main heater, which is necessary for the optical diameter control system. The rotational movement in the range of 0.5–20 rpm (mostly counterrotation to the crystal) is used to create certain convective melt flows. The heat losses from the heaters to the cooled walls of the main vessel are reduced by several heat shields or insulation parts (6g) typically made from graphite felt or foils.

A further important element of the hot zone is the radiation shield (6d). It is mounted on a circular ring-shaped cover plate in the upper region of the hot zone and made from, for example, molybdenum or graphite [14]. More sophisticated heat shields are being investigated, consisting of a combination of different materials, including an active water-cooling system [18]. The heat shield is very important because it has to provide several functions. It shields the growing crystal from the radiation of heat from the hot crucible walls. This shielding improves the radiative heat transfer from the crystal surface, which allows for an increase of the pulling rate. Furthermore, the axial temperature gradient can be increased, which is important with respect to the incorporation of intrinsic point defects. Secondly, the shield reduces the radiative heat loss from the hot melt surface to the cooled top plate (1c) of the main vessel (1). Thirdly, the shield guides the Ar flow closely along the melt surface to efficiently remove the evaporating SiO. The design of the heat shield on the heat and mass transport has been studied in several investigations (see e.g., Ref. [18]).

Argon gas flow (3a to 1a): Both chambers (2 and 1) of the Cz puller are purged with Ar gas from the beginning to the end of the growth process. The gas inlet (3a) is on the top of the puller; the outlet (1a) is in the bottom plate. The main purpose of the Ar flow is to prevent the contamination of the Si melt by residual gases such as CO and H_2O and to remove the evaporating SiO from the melt surface. For that purpose, the Ar flow is guided along the melt surface with a high flow rate, which occurs mainly by the aid of the heat shield (6d). Furthermore, the Ar flow transports the SiO away from the hot zone in such a way that possible reaction products stemming from a reaction of SiO with surrounding graphite parts could not fall down to the melt surface and cause growth defects.

Magnet: Cz pullers, which are used for Si crystals with diameters of 300 mm or larger, are mostly equipped with an external magnet to control the oxygen transport via the convective flow (see Section 2.4).

2.2.3 Procedure of the Czochralski Growth Process

The typical sequence of steps in the Cz growth process is shown in Figure 2.2 and is explained here in more detail.

Charging of the crucible with polysilicon: The silica crucible is charged with very pure poly-Si chunks outside of the growth chamber under clean room conditions. The

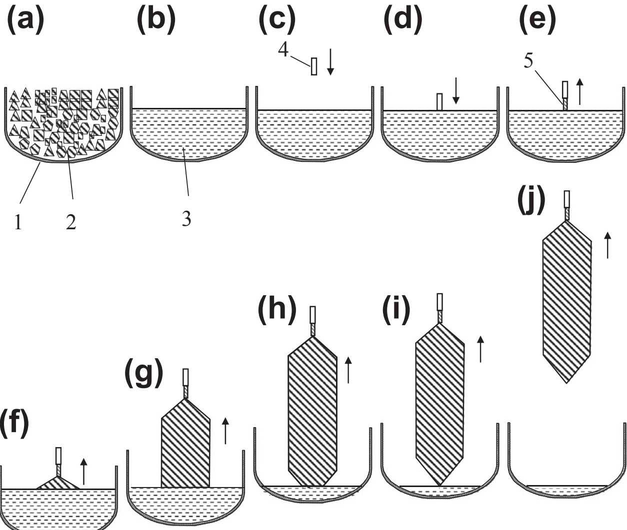

FIGURE 2.2 Schematic illustration of the different steps (a–j) of the Cz process for growing a silicon crystal (5). (a) The polycrystalline feedstock (2) is melted (b) in a silica crucible (1). (c, d) Seeding procedure: The Si seed crystal (4) is dipped into the melt (3), followed by the Dash procedure (e) of growing a neck (5) (e), shouldering (f), cylindrical growth (g), growth of end cone (f), lift off (i), and cooling down and removing of the crystal (j).

chunks are usually cleaned by a wet-chemical treatment. The typical impurity concentrations of different types of feedstock materials (electronic grade, solar grade, and upgraded metallurgical silicon) are compiled in Table 2.1. Doping atoms are either added as elements to the charge or as highly pre-doped Si chunks. The charging of the Si chunks has to be carried out carefully by hand. The spatial distribution of the differently sized chunks within the crucible has to be considered in such a way as to avoid heavy movements of the chunks during melting. Such movements could cause a splashing of the melt, which would damage parts of the hot zone. The open spaces between the chunks can be filled with granular Si material in order to get as much

Table 2.1 Typical Impurity Concentrations in Different Types of Silicon Feedstock Materials: Electronic-Grade Silicon (EG) for Microelectronics, and Solar-Grade Silicon (SoG) and Upgraded Metallurgical Silicon (UMG), Both for Photovoltaic Applications

Impurity	EG	SoG	UMG
Total metallic impurities (ppm(w))	<0.001	<0.05	1
B (ppm(a))	<0.0001	<0.0005	<5
P (ppm(a))	<0.0005	<0.005	<5
O (ppm(w))	<1	<5	<100
C (ppm(w))	<0.1	<5	<50

Adapted from Ref. [19].

charge as possible into the crucible. The filled crucible is loaded into the main vessel of the Cz puller and positioned on top of the crucible pedestal. The main vessel is then closed and evacuated.

Melting of the polysilicon: The heater power has to be adjusted to achieve melting of the poly-Si in a controlled way. The heating time should be kept short for economic reasons, but the temperature of the silica crucible wall should not exceed values that would destabilize its mechanical stiffness and intensify its corrosion. The melting process is carried out under Ar atmosphere in a pressure range of approximately 20–500 mbar. A flow of the Ar gas is used to remove desorbing species from the heated poly-Si and the melt. The temperature distribution in the melt is adjusted in such a way that the coldest region is at the center of the free melt surface, with a temperature slightly above the melting point, in order to enable the seeding process.

Stabilization of the melt temperature: After the silicon melt is heated up to its defined temperature condition, the heater power is kept constant in order to achieve stable thermal conditions. This process phase can take several hours depending on the melt volume. The melt temperature will not really achieve steady conditions as the convective flows in the melt are unsteady, even turbulent.

Seeding: After a stabilization of the melt temperature is achieved, the Si seed is carefully lowered by the pull facility (under rotation) to a position closely above the melt surface for preheating. This procedure is mandatory to minimize a "thermal shock" when the lower end of the seed is subsequently dipped into the melt. The thermal boundary conditions of the melt near the surface area where the seed comes in contact must be adjusted carefully by temperature control and rotational movements of the seed and crucible. The conditions are optimal if a small portion of the seed is melted and a stable melt meniscus between the melt surface and lower seed surface is formed. This remelted, freshly formed seed surface is the starting melt–crystal interface where the growth of the new crystal is initiated by adding Si atoms from the melt to the seed interface. Now, the pulling process is started. The rotational movements of the pulling shaft or wire are maintained during the whole process in a range of 10–20 rpm, whereas the crucible has a counterrotation in the range of 0.5–20 rpm; lower values are used for larger crucibles.

Necking: One of the big advantages of the Cz technique is the possibility of growing large crystals "dislocation free."[1] If there are no disturbances of the growth process, the generation of dislocations is suppressed because the energy for the formation of dislocations in Si is much higher than in other semiconductor materials. The seed crystals for the Cz process are prepared from dislocation-free bulk crystals. However, even after having used a careful seeding procedure, it is inevitable that dislocations are created by the thermal stress during the dipping process. Because these dislocations have

[1]The term *dislocation-free* is used to mean "free of dislocations with dislocation lines extending through a larger crystal range." In fact, the so-called dislocation-free Si crystals can contain small dislocation loops in the microscale with closed dislocation lines around clusters of intrinsic point defects and oxygen. Details about these defects and their generation are given in Sections 2.5 and 2.6.

dislocation lines that terminate at the growth interface, they will continue to grow and increase their density by multiplication. This problem can be overcome by a procedure consisting of several measures, which are summarized as "necking." In the late 1950s, methods to eliminate these dislocations were discovered, such as using a tapered thin seed [20], the growth of a long thin neck (diameter 2–4 mm, length about 30 mm) [7], and an increased growth rate (pulling rate up to 6 mm/min) [21] (see Figure 2.3). The proper combination of these measures will cause the dislocation lines to terminate at the surface of the growing thin neck, where they cannot continue. If the measures are carried out properly, all dislocations are eliminated after a grown length of the neck of

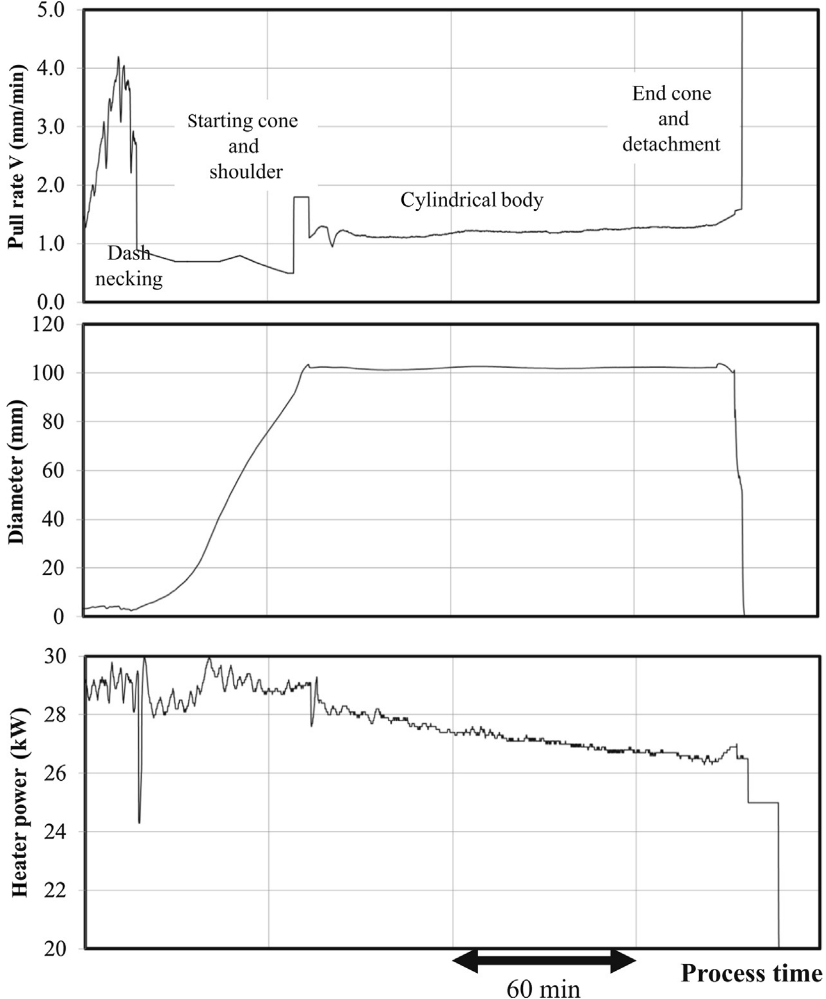

FIGURE 2.3 Pull rate (V, top), crystal diameter (middle, as detected by the control system), and heating power (bottom) versus process time for Cz pulling of a silicon crystal with a diameter of 100 mm in the cylindrical part (body) [22]. *Courtesy of A. Molchanov.*

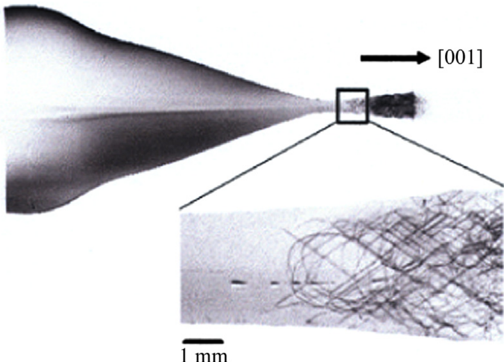

FIGURE 2.4 Longitudinal section of the seed and cone region of a Cz-grown Si crystal. Dislocation lines are visualized by X-ray topography. Enlargement (right): dislocations are eliminated within the neck. *Reprinted from Ref. [23] with permission from IOP Publishing.*

approximately 30 mm, as shown in Figure 2.4. A summary of scientific explanations of the dislocation elimination during necking can be found in [14].

Even if the neck has a diameter only in the range of a few millimeters, it can hold large and heavy Cz crystals with a weight up to 300 kg [24]. Without dislocations, no creeping effect occurs, which would narrow down the neck diameter and break it. Instead, the loading capacity of the neck is only determined by the theoretical tensile strength of the Si crystal lattice and the diameter of the neck. For that reason, the neck diameter may not fluctuate during the necking process. Any restrictions of the neck diameter that could be caused by temperature fluctuations of the melt would be a weak point. A crack of the neck at a later growth stage could be very dangerous because of possible breakage of the crucible and leakage of the melt. In fact, leakage of the melt is one of the most hazardous incidents in the Cz process because liquid Si can destroy the cooling system and react with the cooling water to form an explosive gas mixture. Fluctuations of the neck diameter caused by temperature fluctuations can be avoided by using magnetic fields, which damp the flow and reduce the temperature oscillations in the melt.

For Si crystals with a weight above 300 kg (e.g., crystals with diameters of 300 and 450 mm), alternative solutions and improvements of the necking procedure have been developed. A possible solution to overcome the risk of neck breaking is to use a mechanical device that grips the crystal at a position far below the neck and at a growth stage when the weight limit is not yet exceeded. Another solution is to grow a double cone shape and use a mechanical device that grips the crystal behind it (see Figure 2.5). An alternative method uses a highly doped, dislocation-free seed crystal that can withstand the dipping process without formation of dislocations due to the lattice hardening effect of the high doping [25]. The most commonly used method in industrial Si crystal growth is the double cone technique.

Crystal shoulder: After the necking procedure is finished, the diameter of the crystal has to be increased up to the target value of the cylindrical body. In doing so, the crystal gets a conical shape, which is called the "crystal shoulder." For economic reasons, the

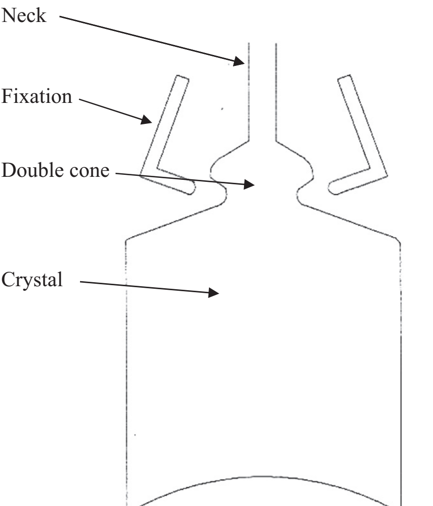

FIGURE 2.5 Illustration of the double cone with mechanical fixation used to grow Si crystals after Dash necking with a weight of more than 300 kg.

shape of this cone should be as flat as possible. This rapid increase of the crystal diameter requires major changes in various process parameters, especially a reduction of the pulling speed, as shown in Figure 2.3.

Growth of crystal body and control of diameter: The economically important part of the crystal is the cylindrically shaped crystal body, with typical nominal diameters of 100 mm up to 450 mm. The pull rate during growth of the crystal body depends on the crystal diameter and on the hot-zone geometry. It is typically around 1 mm/min or less for crystals with a diameter of 300 mm and larger and up to 2 mm/min for smaller diameters. The length of the grown crystal can be in the range up to 2 m.

Physically, the diameter of the growing crystal is determined by the angle of the melt meniscus at the triple point of the crystal–melt interface and thus by its height and width. A CCD camera (7 in Figure 2.1) detects the melt meniscus, which is visible as a bright ring that stems from the light reflection of the hot crucible wall. The position of the bright meniscus is used as a signal for the automatic diameter control. An instantaneous lifting of the pulling shaft (rope) increases the meniscus height, which will instantaneously decrease the crystal diameter, while a lowering reduces the height and thus increases the diameter. For the optical diameter control system, the position of the melt surface must be kept constant, which is achieved by moving the crucible pedestal. The heater power can be used as control parameter for slow changes in the long term only. For details on the control system, the reader is referred to the literature (e.g., Ref. [8]) and to Chapter 19 in Volume IIB of this handbook.

Decreasing the crystal diameter (end cone): At the end of the growth of the cylindrical crystal body, the diameter of the crystal must be reduced gradually and always kept in

contact with the residual melt. If one would simply detach the crystal from the melt, the crystal would experience a "thermal shock" and dislocations would be formed. These dislocations can propagate back into the dislocation-free cylindrical crystal part, which is still at a high temperature. The distance that the dislocations propagate back corresponds roughly to the crystal diameter [14]. Thus, it is necessary to reduce the diameter at the end of the growth by growing a so-called end cone. For stable growth of this end cone, a sufficient volume of residual melt is indispensable.

Detaching the crystal end from the residual melt and cooling the crystal: If the diameter of the end cone is small enough, the crystal can be detached from the melt without dislocation formation in the crystal body. Now, a rather high velocity is used to withdraw the crystal from the melt region, but not too fast, in order to avoid a thermal shock causing plastic deformation in the lower part of the crystal. The importance of appropriate control of the cooling conditions (temporal behavior of withdrawing speed and heater power) in this phase of the growth process was investigated in Ref. [26]. In the considered case, a reduction in the cooling time by approximately 30–50% is possible during cooling down of an Si crystal with a 200-mm diameter in comparison to the reference case under optimized conditions.

Opening of the growth vessel and removal of the crystal: The crystal is finally pulled into the upper chamber, where it cools down. It can be removed from the puller by opening the main vessel (1) if it is cooled down to room temperature. If the upper chamber (2) can be separated from the main chamber by the gate valve (2a), the crystal can be removed in an earlier phase of the cooling process, even if it has still a temperature around 100 °C.

Habitus of the as-grown crystal: Figure 2.6 shows a photograph of an <100> oriented Si crystal with a 300 mm diameter grown by the Cz method. The neck and crystal shoulder can clearly be seen. On the crystal shoulder, there are four (111) facets along the four <110> directions. Along the crystal body, the facets are also visible but smaller; they are reduced to lines, which are called ridges or habitus lines. The different sizes of these

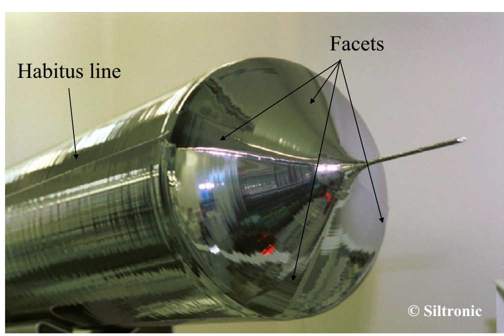

FIGURE 2.6 <100>-oriented Cz-grown Si crystal with a 300 mm diameter. On the shoulder, four (111) facets are visible along the four <110> directions. On the cylindrical surface, the facets shrink to the so-called habitus lines. *Courtesy of Siltronic.*

facets are caused by the different temperature gradients and pulling speeds during growth of the shoulder and body.

The observation of the presence of facets and ridges on the crystal surface can be used during growth as a distinct sign that the crystal grows as a single crystal and dislocation free. The formation of the facets and ridges can be explained by considering the growth kinetics of the different crystal faces. For an atomically rough interface (which are most of the Si faces), the growth rate V is proportional to the supercooling with a proportionality kinetic coefficient a of approximately 0.1 cm/s K [27]. As the growth rates V in Cz growth of Si are on the order millimeters per minute, a rough interface like the (100) face grows with a supercooling ΔT of less than a millidegree. Thus, the solid–liquid interface can be assumed to be identical to the melting point isotherm. However, for atomically smooth interfaces, such as the (111) faces (called facets), the growth mechanism is different. Growth on atomistic smooth faces needs the formation of a two-dimensional nucleus, which grows laterally until the layer is completed. The formation of this nucleus needs a supercooling of a few degrees [27]. In the case of Cz growth of <100>-oriented Si crystals, four (111) faces occur in the four <110>-directions. Only at the periphery of the crystal the conditions are fulfilled so that a supercooling of the melt in the vicinity of the (111) planes can occur. Here the Gibbs–Thomson effect plays a certain role by reducing the melting temperature at regions of the interface with a strong curvature [28]. In <111> oriented crystals, there are six (111) facets along the [211] directions. From the six facets three can typically clearly be seen on the crystal surface. In addition, a central facet can easily form in the case of <111>-oriented crystals if the interface is bent downwards to the melt (see also Section 2.3).

The facet effect does not occur if dislocations are present in the (111) plane. In this case, a two-dimensional nucleus and the corresponding supercooling are not necessary because the growth kinetics at dislocations are more like that at a rough interface. This also explains the fact that the occurrence of facets and ridges can be used as a criterion for dislocation-free growth.

2.3 Global Heat Transfer and Convective Flow

The Cz growth process is like other melt growth processes governed by heat transfer phenomena. Of special importance are the convective flows in the Si melt, which have a strong influence on the shape of the solid–liquid interface, on the growth process itself via the shape and stability of the melt meniscus, on the concentration and distribution of intrinsic point defects (by their impact on the temperature gradient in the growing crystal at the solid–liquid interface), and on extrinsic point defects in the crystal.

In this section, the basics of heat transfer mechanisms in relation to the Cz process are introduced. For an extensive treatment of the mechanisms of heat transfer in crystal growth, the reader is referred to textbooks [29] as well as to Chapter 20 in Volume IIB of this handbook.

2.3.1 Growth Kinetics and Interface Shape

Si crystals grow with a so-called rough interface, except the (111) faces, which grow with an atomically smooth interface—a “faceted” interface. Therefore, the shape and position of the solid–liquid interface can be considered to be identical to the melting point isotherm T_m (1413 ± 2 °C [16]) if the facet formation is negligible.

However, for an atomically smooth interface like on (111) faces, the kinetic growth mechanism is totally different from that of the rough interfaces. As a consequence, on (111) facets, the shape and position of the interface is actually not identical to the melting point isotherm. Also, the incorporation of dopants and impurities differs from growth with a rough interface. In the case of convex interface shapes (i.e., bent downwards toward the melt), facets can form in the vicinity of the crystal surface close to the triple point. In case of the <111>-oriented growth direction, a central facet can additionally form. However, convex shapes are commonly not used in industrial Si Cz growth for economic reasons because of the less efficient transfer of the heat of crystallization away from the growth interface.

The most common interface shape in Si Cz growth for typical pulling speeds used in industrial production is concave (i.e., bent upwards toward the crystal). In this configuration, no central facet should actually occur, even for the <111>-orientation. However, it should be mentioned that the appearance of a central (111) facet was reported in the literature if the interface was not convex. In such a case, faceting may form by a partial remelting of the curved solid–liquid interface [30]. However, the authors could not fully explain this effect, which seems to contradict the growth mechanism with supercooling on a facet.

2.3.2 Heat Transfer and Growth Rate

The previous section on growth kinetics has shown that the growth rate of a Si crystal in the Cz process is controlled by the supercooling ΔT at the growth interface—that is, it is controlled by the transfer of heat via the crystal–melt interface into the crystal. The heat balance at the solid–liquid interface during crystal growth can be formulated in one dimension (z) as follows:

$$\lambda_s \left({\partial T}/{\partial z} \right)_s = \lambda_l \left({\partial T}/{\partial z} \right)_l + \rho V L \tag{2.2}$$

where λ_s and λ_l are the thermal conductivity of crystal (s) and melt (l), V is the growth rate, ρ is the density, and L is the latent heat and the temperature gradients along the growth direction z in the crystal (s) and melt (l) at the interface position. This equation also explains why the temperature gradient in the crystal must be much larger than in the melt (consider $\lambda_l \sim 3 \cdot \lambda_s$). The heat flux through the crystal (left side of Eqn (2.2)) must dissipate the heat flux arriving from the melt (first term of the right side of Eqn (2.2)) and the heat of crystallization, which is proportional to the growth or pulling rate V (second term of the right side of Eqn (2.2)). The heat is transported away from the

interface through the crystal by heat conduction to the crystal surface, where the heat is transferred by radiation to cooler parts in the Cz pulling chamber.

From this consideration, it follows that the growth rate V itself is not limited by growth kinetics, but rather by the rate of heat transfer. This can be illustrated by a simple mathematical model that allows one to estimate the maximum growth rate V_{max} in dependence from the crystal radius R [31]. Although the model strongly overestimates V_{max}, it hints that, with increasing crystal diameter, the maximum growth rate decreases because the cooling of the crystal becomes less efficient. According to this simplified model, two measures can be used to achieve high growth rates. First, the radiative heat flux at the crystal surface must be increased. As described in Section 2.2, the crystal has to be efficiently shielded from the hot crucible wall and the hot heater surface to achieve efficient cooling of the crystal by radiation from its surface. The flow of the cool argon gas also supports the cooling of the crystal, because the flow is guided from the inlet on the top of the puller to the crystal (see Figure 2.1). However, the cooling effect of the gas at the crystal surface is of minor importance compared to radiation because the gas pressure and flow rates are relatively low [32]. The second approach is to keep the heat flux from the melt to the interface as small as possible. The heat flux in the melt is mainly determined by the convective flows inside the melt.

However, in industrial Cz pulling, there are other important constraints that limit the growth rate in the Cz growth of Si crystals besides the heat transfer. For example, as discussed in Section 2.6, the growth rate may also be limited by the requirement to achieve certain types and concentrations of intrinsic point defects. In Section 2.7, it will be shown that the dislocation-free growth of Si crystals with large diameters may also be limited by the growth rate related to thermal stress in the growing crystal, which may cause plastic deformation in the material. In addition, a too-high growth rate may flatten the radial temperature gradient at the melt surface in the vicinity of the triple point, which will distort the cylindrical shape of the growing crystal.

Figure 2.7 gives a schematic representation of the mechanisms of heat transfer in a Cz growth configuration. The radiative heat transfer occurs in all cavities of the whole growth facility between the surfaces of the various materials, which are at elevated temperatures ($T > 800\,°C$). This holds true especially for the heat transfer from the heaters to the crucible support, cooling of the crystal, and heat loss from the melt surface. The latter two effects are the main reasons for installing a heat shield. In the crystal and melt. Internal radiative heat transport is negligible [16].

It is also important to note that the radiative heat transfer often changes during a Cz growth run and/or from one growth run to the other. First, the geometry changes due to the growing crystal, the decrease of the melt level, and vertical movements of the crucible. Furthermore, a part of the radiating materials, such as graphite, typically changes its emissivity due to aging effects, mainly by adsorption of SiO, which evaporates from the melt and deposits locally in form of different chemical products on certain graphite parts, resulting in nearly whitish to greenish films [33,34].

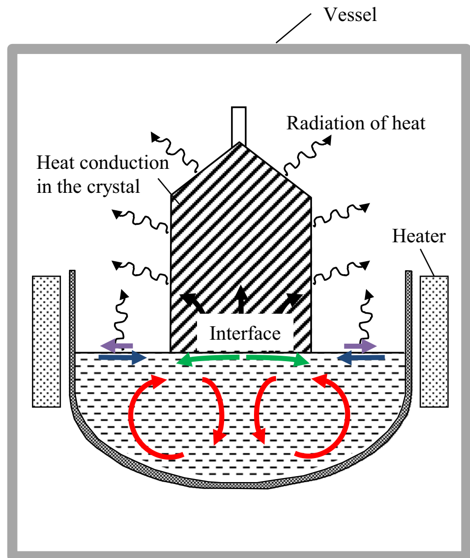

FIGURE 2.7 Sketch of a Si Cz setup with the basic physical mechanisms of heat transfer: conduction, radiation, and convection and their mathematical descriptions. The melt flow is driven by buoyancy, capillary effects, rotation of the crystal (interface) and crucible, and shear stress at the surface due to the argon flow. The corresponding equations are given in Section 2.3.4. Important for the solution of the equations are the internal heat sources and sinks and the boundary conditions. Heat is generated in the heaters and at the crystal–melt interface (heat of crystallization). Heat is dissipated into the cooled walls of the growth vessel.

2.3.3 Convective Flow in the Silicon Melt

In Cz configurations, convection is the dominant mechanism of heat transfer within the Si melt, although it is a small Prandtl-number (Pr) fluid (see Eqn (2.3)) in which the ratio of viscosity to heat diffusivity is small. The reason is that the forces driving the flow are very strong.

$$\mathrm{Pr} = \nu / \kappa \tag{2.3}$$

where κ is the thermal diffusivity and ν is the kinematic viscosity. The material properties of Si are compiled in Table 2.2. For the Si melt, $\mathrm{Pr} = 0.01$.

In a Cz melt, there are typically three different mechanisms that drive convective flows: buoyancy-driven convection, capillary convection, and forced convection (compare to Figure 2.7). Buoyancy and capillary convection are both driven by temperature and concentration gradients; therefore, they are sometimes called natural convection. Forced convection is always driven by external forces, such as rotational movements of the crystal and crucible, by the shear stress at the free melt surface generated by the argon flow, or by Lorentz forces induced in the melt (e.g., by applying a magnetic field).

Convective flows and their contribution to the heat and species transport can be calculated by solving the corresponding system of transport and conservation equations.

Table 2.2 Properties of Silicon at the Melting Point T_m that Are Important for Heat Transport

Interface	Melting Point T_m	1686 K
	Latent heat, L	$1.8 \cdot 10^6$ J/kg
	Growth angle	11°
Liquid	Density, ρ	2570 kg/m^3
	Thermal conductivity, λ_l	60–66 W/(m K)
	Heat capacity, C	915 J/(kg K)
	Electrical conductivity, σ	$1.2 \cdot 10^6$ S/m
	Emissivity, ε_l	0.3
	Kinematic viscosity, ν	$3 \cdot 10^{-7}$ m^2/s
	Thermal expansion coefficient, β	$1.4 \cdot 10^{-4}$/K
	Surface tension, γ	$875 \cdot 10^{-3}$ N/m
	Marangoni parameter, $d\gamma/dt$	$2.2 \cdot 10^{-4}$ N/(m K)
Solid	Density, ρ	2300 kg/m^3
	Thermal conductivity, λ_s	$96017/T^{1.149}$ W/(m K)
	Heat capacity, C	1000 J/(kg K)
	Electrical conductivity, σ	$1.2 \cdot 10^{-4}$ S/m
	Emissivity, ε_s	0.7

A detailed compilation of the physical-chemical properties of liquid and solid silicon can be found in Ref. [16].

A short comprehensive treatment is given in Section 2.3.1. For a more detailed description of this subject, the reader is referred to Chapter 21 in Volume IIB of this handbook.

Buoyancy convection occurs in Si Cz due to the temperature differences within the Si melt as the melt density decreases with temperature (β in Table 2.2). Hotter (lighter) melt portions rise from the hot crucible walls and bottom to the coldest melt region below the growing crystal, where the heavier (colder) melt portions are descending, as shown by the red arrows in Figure 2.7. The melt density can also be changed by its composition. However, this effect is negligible for Si, with the exception of germanium-rich SiGe melts [35].

The vigor of buoyancy convection is typically described by the Grashof number (Gr):

$$Gr = \frac{g \cdot \beta \cdot \Delta T \cdot l^3}{\nu^2} \tag{2.4}$$

where g is the gravitational constant, β is the volumetric thermal expansion coefficient, l is the characteristic length, and ΔT is the characteristic temperature difference.

The definition of the Gr number relates to fluid layers, which have theoretically an infinite extension in the dimension perpendicular to the temperature gradient. Nevertheless, it can be used for the Cz melt geometry. In a Si Cz melt, both lateral and vertical temperature differences are present. Therefore, the Gr number can be defined either by choosing a characteristic radial temperature difference ΔT_r for ΔT and the radius of the crucible r_c as characteristic length l or by choosing a characteristic vertical temperature difference ΔT_h and the height of the melt h. As the aspect ratio (h/r_c) of the

Table 2.3 Typical Charge Sizes and Crucible Diameters Used for Industrial Production of Si Crystals with Different Diameters [38]

Crystal Diameter (mm)	Charge Size (kg)	Crucible Diameter $2 \times r_c$ (mm)	*Gr*	*Ma*
100	28–32	356	2.E + 09	2.E + 08
125	28–50	356–457	4.E + 09	2.E + 08
150	42–70	357–457	4.E + 09	2.E + 08
200	65–120	457–610	1.E + 10	3.E + 08
300	200–400	711–914	3.E + 10	5.E + 08

The fourth and fifth columns contain the corresponding *Gr* and *Ma* numbers, assuming a typical temperature difference ΔT of 40 K and using the maximum of the crucible radius r_c as the characteristic length l [39].

Si melt changes during growth, one has to consider that $Gr = f(h/r_c)$. The most important conclusion that can be drawn for a Cz setup from a consideration of the Gr number is its dependence on the third power of the characteristic length l. In other words, the larger the crucible, the stronger the buoyant convection becomes. Therefore, the control of melt flow for growing Si crystals with diameters of 300 mm or more is much more difficult than for smaller crystal and crucible diameters. Therefore, the influence of buoyancy convection decreases considerably for shallow melt levels. This phenomenon is used in the continuous Czochralski (CCz) technique, for which a flat crucible can be used (see Sections 2.4.6 and 2.7).

It was shown in the literature that flows in fluids with a low Pr number, such as Si, are time-dependent and even turbulent [36,37] at higher values of the Gr number (about $Gr > 10^6$). For the typical parameters used in the field of Si Cz growth, the resulting Gr numbers are far above such values (see Table 2.3).

Capillary convection: At the free surface of the Si melt adjacent to the Ar atmosphere, convective flows are generated by a capillary phenomenon called Marangoni effect. It originates from the temperature (and concentration[2] [40]) dependence of the surface tension γ. Because γ is larger for lower temperature and vice versa, the so-called *thermocapillary* flow is directed at the melt surface from the hotter crucible wall to the colder crystal, as sketched by the blue arrow in Figure 2.7.

The strength of capillary-driven convection can be expressed in terms of the dimensionless Marangoni number Ma. For thermocapillary convection:

$$Ma = \frac{-(d\gamma/dT) \cdot \Delta T \cdot l}{\nu \cdot \kappa} \tag{2.5}$$

with surface tension γ, characteristic temperature difference ΔT, and characteristic length l (e.g., distance from crucible wall to crystal periphery at the free surface).

Typical values of the thermal Ma number in Si Cz are given in Table 2.3. The influence of the thermocapillary flow is mainly restricted to the melt region close to the free

[2]It is especially discussed that the oxygen concentration in the Si melt can affect the capillary flow. Therefore, near the silica crucible wall where the gradient of the oxygen concentration is high, a certain influence on capillary flow might be expected.

surface (blue arrow in Figure 2.7). However, its influence on the regions at the melt–crystal meniscus and melt–crucible meniscus can be very important. An appropriate consideration is only possible by using numerical simulation. For a more detailed treatment of thermocapillary flows, the reader is referred to Chapter 19 in Volume IIB of this handbook.

The following external forces also generate convective flows, called "forced convection."

Crystal rotation: In a Cz melt, forced convection is induced by the rotation of the crystal with a certain rotation rate ω_X. The Si melt sticks to the crystal interface, which transfers its rotational movement to the melt region below the interface by the viscous forces in the melt. The centrifugal forces of this rotational motion cause an outward flow (compare the green arrows in Figure 2.7). This radial flow induces, by continuity, an axial flow back to the interface. This effect results in a very important flow phenomenon, the formation of a stable boundary layer in front of the solid–liquid interface. This boundary layer enables a uniform incorporation of dopants (see Section 2.4) while counteracting the deleterious influences of nonuniform and unsteady buoyancy and capillary-driven flows. Therefore, the formation of this boundary layer by crystal rotation is one of the strengths of the Cz method.

Crucible rotation: Similarly to the crystal rotation, the crucible rotation generates a contact force at the melt–crucible interface, leading to forced convection in the form of a primary azimuthal flow. The rotational movement of the crucible is typically in the opposite direction as the crystal (i.e., counterrotation). In analogy to the crystal rotation, a boundary layer is formed along the interface between the melt and crucible wall. This boundary layer has some importance with respect to the transport of oxygen, which comes from the surface of the dissolving silica crucible.

The crucible rotation has a stabilizing influence on the melt flow. As shown in Figure 2.8 temperature fluctuations caused by unsteady melt flow can be damped by

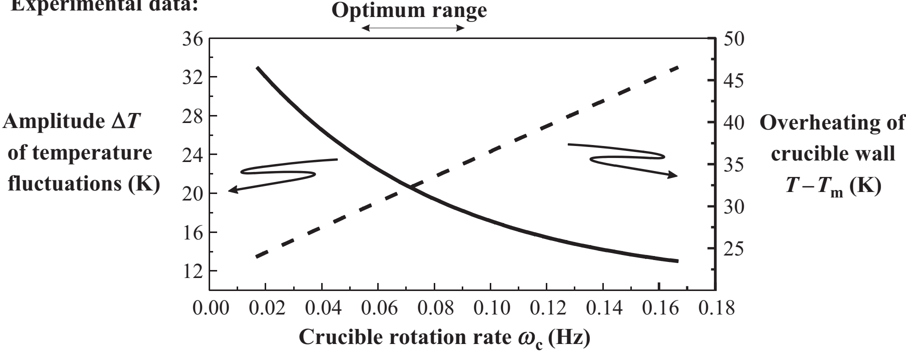

FIGURE 2.8 Amplitude ΔT of temperature fluctuations obtained from in-situ measurements in a 20 kg Cz Si melt versus rotation rate of the crucible ω_c. The dashed line shows the trend of the dependence of the overheating $T-T_m$ measured at the crucible wall versus the crucible rotation rate. T_m = melting point. *Adapted from Ref. [41].*

increasing the crucible rotation rate, which reduces its deleterious influence on the growing crystal. However, rotational movements that are too strong can cause overheating of the crucible wall because the forced azimuthal flow suppresses the convective heat transfer in the radial direction [42] (compare also Figure 2.9). Overheating of the crucible reduces its mechanical and chemical stability; therefore, it has to be controlled carefully. In addition, the crucible rotation has a strong impact on the oxygen concentration, which is incorporated in the growing crystal.

The counterrotation of the crucible and crystal has a certain influence on the overall convective flow in the melt volume, mainly by interacting with the buoyancy-driven flow. This interaction of different convection phenomena causes typically rather complex flow structures in the melt, which have a mostly unsteady character. For example, several authors [45,46] observed flow structures in Si Cz melts with azimuthally moving patterns of varying multiplicity depending on the crucible rotation rate, including the meteorological phenomenon of baroclinic waves.

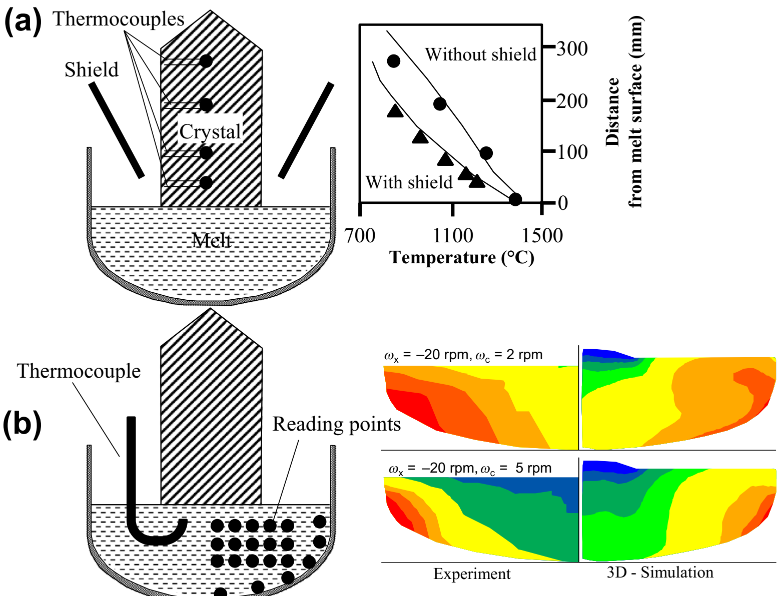

FIGURE 2.9 (a) *Left:* Measurement of temperatures inside a specially prepared Si crystal (diameter 100 mm) with thermocouples in four axial positions. The crystal is positioned in contact with the melt in an industrial Si Cz puller with and without heat shield. *Right:* Measured (symbols) and simulated (solid lines) temperatures in the crystal with (triangles) and without (dots) heat shield. *(Adapted from Ref. [43].)* (b) *Left:* In-situ temperature measurement in the melt of an industrial Si Cz puller (crucible diameter = 360 mm and crystal diameter = 100 mm) by specially designed thermocouples covered by a silica tube and stabilized by glassy carbon. The black dots mark the reading points of the stepwise measurement (mapping) in the bulk melt and at the crucible wall during the Cz growth process. *Right:* Comparison of the experimental (left) and three-dimensional numerical simulation results (right) for two different crucible rotation rates (ω_c). ω_x = crystal rotation rate. *(Adapted from Ref. [42,44].)*

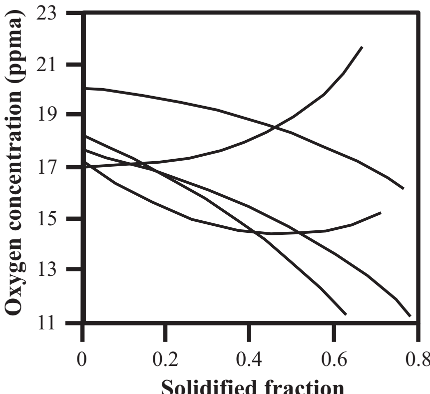

FIGURE 2.10 Oxygen concentration in Si crystals versus solidified fraction. Axial oxygen profiles of silicon crystals grown by the Cz process are shown for several combinations of crystals and crucible rotation rates. *Adapted from Ref. [47].*

The rotational movement of the crucible not only affects the heat transport, but it also has an influence on the oxygen transport. That means the crucible rotation rate can be used as a parameter to control the transfer of oxygen from the crucible wall into the bulk melt and from here into the crystal. This effect is demonstrated in Figure 2.10, which shows that the axial oxygen concentration in the crystal can strongly be influenced by the combination of crucible and crystal rotation rates [47].

Forced convection by argon flow: The argon gas is guided by the aid of the radiation shield, almost parallel over a big portion of the free melt surface (compare Figure 2.1). This flow introduces a shear stress at the free melt surface, which counteracts the Marangoni flow (see Figure 2.7). Therefore, the gas flow can have a certain influence on the heat and oxygen transport in the melt.

2.3.4 Modeling of Heat and Species Transfer

Experimental studies prove that the flow in the Si melt is in a turbulent flow state for large crucibles (>300 kg melt) [42]. Various approaches for turbulence modeling have been tested in the past. Meanwhile, the modeling of heat and species transfer during the Cz growth of large Si crystals has advanced to a point where it can be successfully applied to optimize the puller setup and the crystal growth process; examples of the state of the art can be found elsewhere [34,48–55]. However, until a model has reached the state of a reliable tool, it needs several steps of development. One important step is the experimental validation of the model. In this context, the role of Cz model experiments should be mentioned, which provide temperature distributions in the crystal or at various positions in the melt and hot zone, for example. Figure 2.9 gives examples of such in-situ temperature measurements in Si Cz pullers. More details can be found elsewhere [42–45].

2.3.5 Magnetic Fields

In the growth of large Si crystals from crucibles with diameters of 80–90 cm, it is very difficult to control the melt flow and the oxygen transport in the melt by using only the parameters crystal and crucible rotation. Therefore, steady magnetic fields, mainly cusp or horizontal configurations, are well established to damp undesired temperature fluctuations [56], as well as to grow crystals with low oxygen concentrations ($<5\cdot10^{17}$ atoms/cm^3) and improved axial and radial homogeneity [56,57]; they also are very helpful for the production of so-called defect-free silicon. For a detailed treatment of magnetic fields, the reader is referred to Ref. [58] and Chapter 23 in Volume IIB of this handbook.

An external *steady magnetic field* can act on the melt motion because the Si melt behaves like a metallic melt with a high electrical conductivity σ (see Table 2.2). Thus, a Lorentz force is generated in the melt due to the convective flow velocity. Usually, relatively high values of the magnetic induction B, on the order of some hundreds of milli-Tesla, are necessary for efficient control of the melt flow. The required magnetic systems are either large electromagnets or expensive superconducting magnets [3].

Figure 2.11 illustrates how the flow velocity in the Si melt in a small-scale Cz puller is reduced under the influence of a magnetic field [59]. In this case, both the experimental and numerical results show that the fluid flow velocity and its oscillation amplitudes (vertical bars in Figure 2.11) are efficiently damped by applying a cusp magnetic field. Theoretically, for buoyancy convection, it can be shown that the damping influence of a magnetic field on the flow velocity follows a reciprocal dependency of the square of the magnetic induction B [60]. It should be also noted that for precise calculations of the effects of steady magnetic fields on the heat and mass transport in Si Cz, the electrical conductivity of the crystal must also be considered, although at high temperatures it is one order of magnitude smaller than that of the melt [61,62].

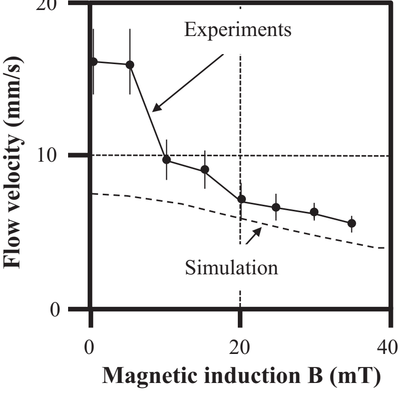

FIGURE 2.11 Flow velocity in molten silicon measured by tracer particles and X-ray radiography (symbols) in a small-scale Cz puller and by numerical simulation (dashed line) as a function of the magnetic induction B. *Adapted from Ref. [59].*

However, steady magnetic fields are not only beneficial by damping convective flows. They can also have detrimental influence on the shape of the solid–liquid interface [56,58] and flow conditions. This has consequences for the lateral uniformity of the distribution of point defects. For example, in the case of *axial magnetic fields*, flow instabilities can occur in the melt, the radial dopant distribution becomes nonuniform, and the crucible wall temperature rises strongly [56]. Therefore, the application of this type of magnetic field was stopped early.

An externally vertical steady magnetic field was also used in combination with an externally applied DC electric current through the melt and crystal in the so-called electro-magnetic-field-Czochralski method (EMCZ) for growing Si crystals without crucible rotation [63,64] (see also Chapter 23 in Volume IIB of this handbook). The interaction of the vertical magnetic field with the radial current results in an azimuthally oriented Lorentz force, causing a primary flow in the azimuthal direction. The EMCZ process allows the control of the oxygen transport [63] as well as of the shape of the solid–liquid interface [63,64]. However, no real industrial application was found. One reason might be the graphite electrodes, which are inserted into the melt and may thus cause a contamination of the melt with carbon, leading to particle formation.

The use of *time-dependent magnetic fields* in the growth of Si Cz crystals was also studied. Much lower field strengths compared to steady fields, on the order of only some milli-Tesla, are needed if time-dependent fields are applied. They do not damp the flow, but they are well suited for establishing different flow regimes in the melt, depending on the configuration of the magnetic field. The time-dependent magnetic field configurations most frequently analyzed are the so-called rotating magnetic field (RMF), the alternating magnetic field (AMF), and the traveling magnetic field (TMF) (see Ref. [58] or Chapter 23 in Volume IIB of this handbook for more details).

For a RMF, it was demonstrated [65] that it is possible to grow Si crystals by Cz without crystal and crucible rotation. However, because no clear advantage of using a RMF was found, this approach was not pursued further. The same statement holds also for the AMF. The AMF improves the mixing in the melt and changes the flow pattern in such way that SiO is transported directly from the crucible to the solid–liquid interface, with less evaporation at the free melt surface. Therefore, a high oxygen concentration is observed in crystals grown in an AMF [56]. In contrast to RMF and AMF, the TMF was demonstrated to be advantageous for the Si Cz process. The application of a TMF in Cz crystal growth causes a change of the flow pattern, which makes it possible to grow Si crystals with 300 mm diameters in a TMF at field strengths of only approximately 2–6 mT, with low and axially very uniform oxygen distributions [56]. However, the use of an external TMF requires the replacement of a part of the steel vessel by a non-electrically-conducting material in order to efficiently couple the electromagnetic field into the melt. Otherwise, too-high currents through the coils would be necessary [66]. Therefore, the use of an external TMF has not become accepted in industrial Si Cz growth.

One elegant way to overcome the problem of the shielding effect of the vessel is to use an internal heater magnet module, as proposed in [66]. The heaters are supplied with a

superposition of a DC current for heating and an AC current for generation of the TMF. Under optimized conditions, it was shown that silicon crystals grown in a TMF exhibit radially and axially very homogeneous distributions of oxygen. Because the TMF allows the achievement of Cz growth with a low and stable radial temperature gradient in the order of 1–2 K/cm at the periphery of the crystal, the growth of four long (110)-facets is stable, resulting in <100>-oriented Si crystals with almost quadratic cross-sections [67].

2.4 Transport and Incorporation of Dopants and Impurities

2.4.1 General Considerations

The usual starting materials for the Si Cz process is the so-called electronic-grade polysilicon, or for certain solar cell applications, the less pure solar-grade polysilicon. The purity of these starting materials is defined by the specifications given by the producer (see Table 2.1). The impurities in the feedstock have their origin in the basic raw material (natural SiO_2) and remain after the various steps of purification by the Siemens process for the production of poly-Si (see e.g., Ref. [19]). A special group of impurities that are intentionally added to the poly-Si before crystal growth are the dopants. Further impurities can be added unintentionally during breaking of the poly-Si rods. For that purpose, a wet-chemical cleaning step is used before the poly-Si chunks are put into the silica crucible. An important unavoidable contamination of the Si by oxygen occurs during the Cz process as soon as the poly-Si becomes molten in the silica crucible, because oxygen is transferred into the melt by corrosion of the silica crucible.

All impurity atoms—whether they are added intentionally or not—follow the same diffusive-convective mechanisms of transportation in the melt toward the growth interface. At the melt–crystal interface, they are incorporated into the crystal according to thermodynamics and growth kinetics. Within the as-grown crystal solid-state diffusion, reaction with other defects, supersaturation, and eventually formation of precipitates occur.

The key for influencing the incorporation of species into the crystal lies in the "species transport" in the melt. Therefore, the transport of impurity atoms in the melt is of great importance. Its physical mechanisms, diffusion and convection, are the same as discussed in Section 2.3 for the transport of heat in the melt. A very special phenomenon of species incorporation into the crystal is *segregation*. Figure 2.12 schematically shows the relevant mechanisms of the transport of species during the Cz process and their incorporation into the growing crystal.

2.4.2 Segregation Coefficient *k*

In most cases, Si grows with the continuous kinetic mode of a rough interface. This allows one to assume that the incorporation of foreign atoms (dopants and impurities)

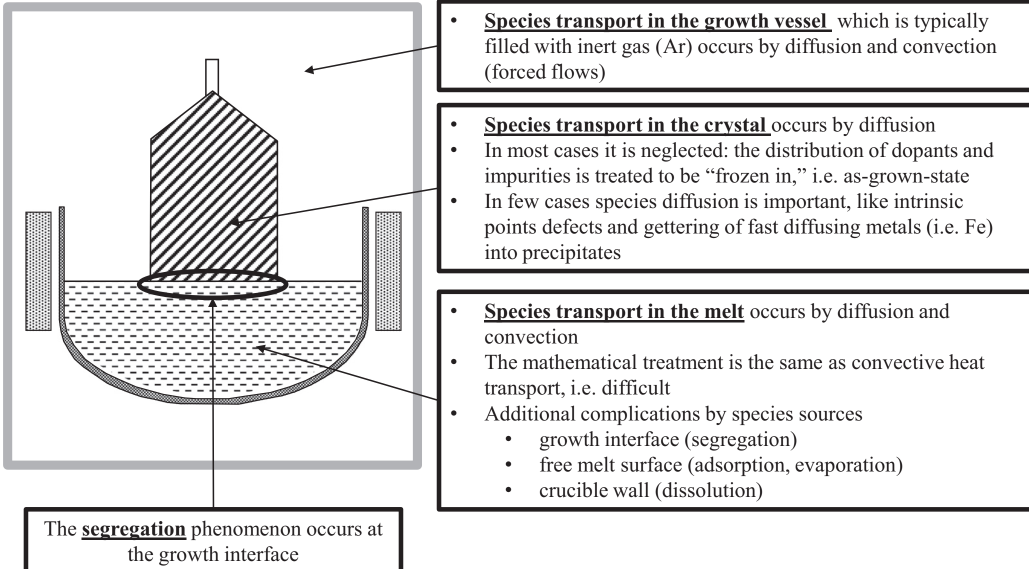

FIGURE 2.12 Schematic representation of the relevant mechanisms of species transport (dopants and impurities) during the Cz process and their incorporation into the crystal during growth.

occurs at the growth interface according to the law of equilibrium thermodynamics. The ratio of the solute concentration C_S in the crystal to its concentration C_L in the melt is defined as the (equilibrium) segregation coefficient: $k = C_S/C_L$ (see Chapter 25 in Volume IIB of this handbook).

In Table 2.4, the segregation coefficients k for various elements in Si are compiled. The data were taken from Ref. [16]. Most metallic impurities in Si have a segregation coefficient of $k << 1$—that is, the feedstock is purified upon melting and solidification during the growth process. Doping elements such as B, P, and As have segregation coefficients closer to 1. Boron is a very favorable dopant because a k value of 0.8 allows one to obtain very uniform electronic properties throughout the crystal. The special case of oxygen with a segregation coefficient k close to 1 will be described in detail in Section 2.4.7.1.

In practical crystal growth, it is useful to relate the dependence of the species concentration C_S of the crystal on certain growth parameters, such as pulling rate, crystal rotation, and crucible rotation rate, to the given concentration C_L of the species in the melt. Such a general relationship is possible if one considers the influence of the relevant Cz parameters by the effective segregation coefficient k_{eff}. The oldest and most popular model of an effective segregation coefficient k_{eff} was introduced by Burton, Prim, and Slichter [68]. According to them, k_{eff} is defined as follows:

$$k_{eff} = \frac{k}{k + (1 - k) \cdot \exp(-V \cdot \delta / D)} \tag{2.6}$$

Table 2.4 Segregation Coefficient k, Maximum Solubility C_S^m, Diffusion Coefficient D in the Melt, and Evaporation Rate g_{ev} for Various Impurities in Silicon

Solute	k	C_S^m (atoms/cm^3)	D (10^4 cm^2/s)	g_{ev} (cm/sec)
H		1.7e19		
Li	0.01	6.5e19		
Cu	4.0e-4	1.5e18		8.0e-5
Ag	1.0e-6	2.0e17		
Au	2.5e-5	1.2e17		
Zn	1.0e-5	1.2e17		
Cd	1.0e-6	0.1–0.3e16		
B	0.8	6.0e20	1.8	8.0e-6
Al	2.0e-3	2.0e19	5.3	1.6e-4
Ga	8.0e-3	4.0e19	3.6	2.0e-3
In	4.0e-4	0.4–2.0e18	5.2	8.0e-3
Tl	1.7e-4	8.8e17	5.9	
Ti	3.6e-4	–		
C	0.07	3.0e17	1.5	
Ge	0.33			
Sn	0.016	5.0e19		
Ta	1.0e-7			
N	7.0e-4	4.5e15		
P	0.35	1.3e21	3.9	1.4e-4
As	0.3	1.8e21	2.5	8.0e-3
Sb	0.023	7.0e19	1.1	0.13
Bi	7.0e-4	8.0e17	0.76	
Cr	1.1e-5	1.0e14		
O	~1	3e18	0.7–2 [70]	1.4e-3 [71]
S	1.0e-5	3.0e16		
Se		7.0e16		
Mn	1.0e-5	3.0e16		4.0e-4
Fe	8.0e-6	3.0e16	0.1	4.0e-5
Co	8.0e-6	2.0e16		
Ni	8.0e-6	8.0e17		

Adapted from Ref. [16].

where δ is a free fit parameter that is often approximated by a boundary layer thickness, D is the diffusion coefficient of the solute in the melt, and V is the pulling rate. In the case of Si Cz, the boundary layer thickness δ at the melt-crystal interface can be calculated by using the model of a rotating disk with infinite diameter in contact with a liquid [69]. In the literature, more complex models exist in order to calculate the boundary layer thickness δ and thus the effective segregation coefficient k_{eff} more accurately (see Chapter 25 in Volume IIB).

It follows from Eqn (2.6) that, in the practical range of growing Si crystals by the Cz technique (i.e., for pull rates $V < 2$ mm/min), the effective segregation coefficient k_{eff} for all species is not so much different from the equilibrium segregation coefficient k.

It should be mentioned that the growth of an Si crystal with a (111) facet results in segregation with an effective segregation coefficient that is higher than the equilibrium segregation coefficient. The reason can be explained by the discontinuous stepwise growth mechanism on a facet. Foreign atoms that are adsorbed on the growth facet are incorporated in a higher concentration compared to thermodynamic equilibrium due to the very rapid lateral growth velocity. Obviously, the desorbed atoms are overgrown by the layer [27]. This phenomenon can be formally expressed by a facet segregation coefficient k_{fac}. For example, k_{fac} (P) = 1.4k (P) for phosphorous and k_{fac} (As) = 1.2k (As) for arsenic [72].

2.4.3 Distribution of Species in the Crystal

The distribution of species, especially of dopants in the growing crystal in the axial and radial directions as well as on the microscale, is of great importance. Therefore, prediction of the influence of Cz growth parameters on the distribution of the various species is of great interest.

2.4.3.1 Numerical Modeling of Species Transport

Figure 2.12 gives an overview of the processes of species transport in Cz growth of Si. Species transport in the crystal is described by Fick's laws of diffusion, while the species transport in both fluid media, the gas atmosphere, and the melt is governed by the equation of convective diffusive species transport. The convective flow in the "bulk" fluid, either Ar in the gas space or Si melt within the crucible, is computed by the same formalism that was shown in the previous section about melt flow. In the species case, one has to consider a boundary condition for species incorporation at the crystal–melt interface by the segregation coefficient. For oxygen transport, further special boundary conditions exist: the inner crucible surface acts as a source, whereas the free melt surface and crystal interface act as a sink (for details, see Section 2.4.7.1).

It should be mentioned here that the thickness of the species boundary layer is smaller than the thermal boundary layer. Therefore, a finer numerical mesh—especially near the crystal–melt interface, the free melt surface, and the melt–crucible interface—is needed. The number of mesh points per unit area determines the accuracy of the numerical solution. As a rule, one should have at least five grid elements within the width δ of the boundary layer [73]. Therefore, in practice, for an accurate resolution of the boundary layer, a spatial resolution of the mesh points of less than 10 μm might be required [54].

2.4.3.2 Longitudinal (Axial) Concentration Profiles

In the Cz pulling process, the starting material is completely molten at the beginning. During crystal growth, the melt volume decreases continuously, which increases the solute concentration in the melt due to the enrichment by segregated species. If the system is conservative—that is, no component is lost or added during growth—and assuming total mixing by convection, the solute concentration C_S in the crystal can be

described by Scheil's equation (Eqn (2.7), [74]) depending on the solidified fraction g, the segregation coefficient k, and the starting concentration C_0:

$$C_S = k \cdot C_0 \cdot (1 - g)^{k-1} \tag{2.7}$$

Instead of k, one can also use k_{eff}. By using Eqn (2.7), it can be easily shown that the variation of the species concentration from the seed to the tail end is smaller the closer k is to unity. This is the reason why B with $k = 0.8$ is the preferred dopant.

The description of the longitudinal concentration distribution by Scheil's equation can be applied to nonvolatile and moderately volatile species, such as B, P, Ga, and Al. In the case of volatile species such as As, In, and Sb, which have a vapor pressure that is considerably higher than the vapor pressure of Si, their evaporation may compensate or even overcompensate the enrichment of the melt due to the segregation effect. In fact, the species concentration in the melt can be controlled by the pressure of the argon gas inside the puller and the gas flow conditions over the free melt surface [14]. This effect of evaporation can be taken into account in Scheil's equation by an additional parameter k_{ev} [75], resulting in

$$C_S = k \cdot C_0 \cdot (1 - g)^{k + k_{ev} - 1} \tag{2.8}$$

Several models for k_{ev} can be found in the literature [75–77], from which measures can be determined to grow the crystal with a uniform species concentration in the case of volatile dopants.

2.4.3.3 Continuous Czochralski

For nonvolatile elements, other measures are needed to overcome the problem of an increase of the species concentration in the decreasing melt volume with increasing solidified fraction (i.e., during pulling of the silicon crystal). One possible option is in-situ replenishment of the melt by nondoped silicon material. For that purpose, special feeder recharging systems were developed, which allow refilling of the melt by adding undoped or properly doped silicon, either in form of chunks or by a polycrystalline rod that is melted by immersing it into the melt. The technological development of this approach is known as the CCz technique. Figure 2.13 shows a sketch of a CCz setup with a feeder system for recharging of the melt with granules using a tube typically made from silica. Often, an inner crucible is used to reduce the risk that solid silicon particles are transported to the interface. The CCz hot zone usually consists of a shallow crucible containing less melt volume in comparison to a conventional "batch" Cz setup (see Figure 2.1). This has several advantages: the melt is less turbulent, the hot zone can be made smaller, and the thermal budget and energy demand is reduced. The main advantage of the CCz method is that the longitudinal species distribution of the CCz grown crystal is very uniform because the melt volume can be kept constant while feeding it with undoped silicon during pulling of the crystal [78].

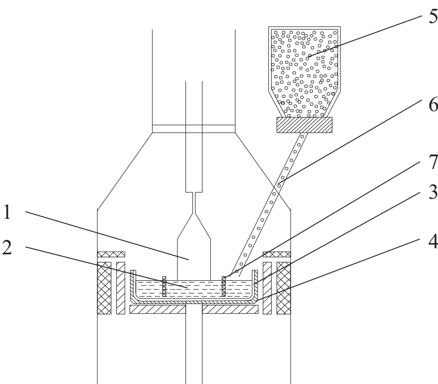

FIGURE 2.13 Sketch of a Cz setup with the crystal (1) and melt (2). Continuous recharging (CCz) of poly-Si chunks (5) by a feeding tube (6) into the silica crucible (3) surrounded by the support crucible (4) is shown. The silica crucible (3) has a second inner wall, with openings (7) to prevent the transport of floating solid Si particles to the growth interface.

However, the risk of structure loss caused by Si particles floating on the melt surface and arriving at the melt meniscus is high. It was also observed that the use of granular feeding material caused the formation of holes within the growing crystal, with diameters up to several micrometers [79]. A further disadvantage of the CCz technology is the fact that a crystal usually cannot be dumped back into the melt and the growth process cannot be restarted if a structure loss occurs. These problems caused a shutdown of the CCz technology, even after a longer period of development. Most companies that are growing microelectronic-grade Si crystals gave up this technology due to the above-mentioned yield problems. Recently, interest in the CCz method has increased for growing n-type Si crystals for solar cells. For solar cells, the requirements for the Si wafer are not as strict as for their use in microelectronics; therefore, the above-mentioned problems might not be as harmful.

2.4.3.4 Lateral (Radial) Nonuniformity

Lateral (radial) nonuniformity in the Si crystal during Cz growth can be caused by the following mechanisms: curvature of the growth interface (1), nonuniform species transport within the melt to the growth interface and away from it (2), and growth with a faceted interface (i.e., in the <111>-direction) (3).

(1) The growth interface in Si Cz is typically bent with a concave shape. Thus, the center of the growing crystal is solidified at a later time, t_2, than the rim of the crystal which was grown at a time $t_1 < t_2$. As the solute concentration in the melt increases with increasing time for nonvolatile species with $k < 1$, the solute concentration C_s is higher at the center (grown at t_2) than at the rim (grown at t_1) on a wafer which is cut perpendicular to the crystal axis. This effect is smaller for Si crystals with larger diameters because of the relatively lower bending of the solid–liquid interface.

(2) The solute transport in the melt is controlled by diffusion and convective flow. In the vicinity of the growth interface, a solute boundary layer is formed with a thickness δ_c. Due to radial nonuniformity of convective flows, δ_c(r) can vary radially. Considering the dependence of k_{eff} on the thickness of the boundary layer (see Section 2.4.1) and Eqn (4.6) (Scheil's law) for the segregation with a radially varying δ_c(r), one has to expect "transport-induced" radial nonuniformity with the incorporation of dopants and other impurities.

(3) A further cause of nonuniform incorporation of the solute is the presence of (111) facets. When pulling a <111>-oriented silicon crystal, a (111) facet may form in the center. In this case, the faceted core region of the crystal exhibits a higher doping concentration than the nonfaceted periphery, which grows with an atomically rough interface. Therefore, the radial doping nonuniformity of faceted crystals (i.e., the resistivity nonuniformity) can be drastic and much higher than for nonfaceted crystals (e.g., <100>-oriented).

2.4.4 Constitutional Supercooling in Heavy-Doping Cz Growth

Typically, the Si melt in a Cz run contains at least one doping element in the concentration range of 10^{17}–10^{20} atoms/cm^3, meaning that the melt is a binary or, generally speaking, multicomponent system. In such cases, the enrichment of the solute in front of the interface results in a locally dependent liquidus temperature; in combination with the diffusion boundary layer, this can lead to the phenomenon of constitutional supercooling—a morphological instability of the melt–crystal interface (cellular structure, in Si with microfacets). In Cz growth with heavy doping (i.e., concentration $>10^{19}$ atoms/cm^3), the phenomenon of constitutional supercooling is the main reason for an increased probability of the formation of dislocations. Such high doping concentrations are needed for certain applications of Si crystals in power electronics [80]. In Ref. [81], a detailed review of the impacts of constitutional supercooling on the Cz growth of heavily doped Si crystals is given.

Tiller [82] and Hurle [83] derived a stability criterion for growth with a stable interface. According to these authors, constitutional supercooling and interface instability can be avoided for $k < 1$ if

$$\frac{G_L}{V} > \frac{(1-k)\cdot(-m)\cdot C_L}{k\cdot D}\cdot k_{eff} \tag{2.9}$$

where G_L is the axial temperature gradient in the melt at the interface, V is the growth rate, m is the slope of liquidus line, k is the segregation coefficient, D is the diffusion coefficient, and k_{eff} is the effective segregation coefficient.

From this criterion, one can conclude that the following measures should be considered to avoid constitutional supercooling in the Cz growth of heavily doped Si crystals: (1) Optimization of the hot zone of the puller, such as by introducing additional heat shields in order to establish a higher temperature gradient G_L. (2) Decrease of the pulling speed V, which has the effect of an increase of G_L as less heat of crystallization is

produced; additionally, it decreases the pileup of doping atoms in the melt in front of the growth interface. (3) Increased convective melt transport to decrease the pileup of doping atoms in the melt in front of the growth interface (i.e., to match $k_{eff} \rightarrow k_o < 1$).

However, it is not desirable to decrease the pulling rate V for economic reasons. Furthermore, an increase of the temperature gradient G_L in the melt results in an increase of the temperature gradient in the crystal G_S, mostly leading to an increase of the thermal stress and, thus, formation of crystal defects, such as dislocations. Therefore, an increase of the convective species transport in front of the melt–crystal interface might be the best measure to prevent instability of the interface.

It is also discussed in literature that the occurrence of structure loss during Cz growth of heavily doped silicon crystals can be affected by oxygen or intrinsic point defects, e.g., [80,84]. High doping concentrations of B, P, and As can have considerable influence on the formation of voids, oxygen precipitates, and the position of the oxidation-induced stacking fault (OSF) ring [84]. However, no clear picture exists so far. Currently, it remains difficult to prove whether constitutional supercooling is responsible for a structure loss or whether other phenomena are limiting the dislocation-free growth of heavily doped Si crystals.

2.4.5 Microsegregation: Striations

It is a well-known phenomenon that melt-grown crystals often exhibit a microscopically nonuniform incorporation of dopants (impurities), which display the shape of the solid–liquid interface at certain time steps of growth. Longitudinal sections of such crystals reveal the patterns of these nonuniformities as striations (see Figure 2.14).

In general, the occurrence of striations in melt growth is mainly caused by fluctuations of the growth rate V, which influences the incorporation of the solute according to the segregation effect. Formally, the striation effect can be deduced from the dependence of the effective segregation coefficient $k_{eff}(V)$ from the growth rate V (compare to Eqn (2.6)). At this point, it must be noted that the actual growth rate on the microscopic level can significantly deviate from the pulling speed. Fluctuations of the growth rate are the result of unsteady (fluctuating) heat transfer. Generally, unsteady heat transfer in melt growth is caused by the unsteady characteristics of convective flows, which are

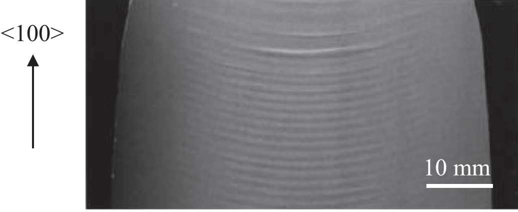

FIGURE 2.14 X-ray topography of a longitudinal section of a silicon Cz crystal grown under the influence of a cusp magnetic field. The nonuniform incorporation of dopants causes the occurrence of growth striations displaying the shape of the solid–liquid interface. *Reprinted from Ref. [85] with permission from Elsevier.*

therefore a typical reason for the occurrence of striations (e.g., Ref. [29]). However, in the case of the Cz process, the origin of striation formation is mostly the rotation of the crystal [86]. Because the temperature field of the hot zone in a Cz puller is never ideally axi-symmetric, the rotation of the crystal causes the interface to move periodically from a region of higher temperature to a region of lower temperature. The effect of this fluctuating temperature adds to the constant pulling rate and results in a time-dependent growth rate. Therefore, the distance of the striations on a longitudinal cut (e.g., Figure 2.14) can be correlated to the crystal rotation period [87]. On a wafer cut from the crystal perpendicular to the pulling direction, the striations exhibit a ring-like structure (see Figure 2.15) and are therefore also called rotational striations. Other sources of striations can be mechanical vibrations and fluctuations of the power control. For a detailed discussion of the fundamentals of convection and inhomogeneities in crystal growth from the melt, the reader is referred to a review article by one of the authors [29].

2.4.6 Intentional Doping during the Cz Process

2.4.6.1 Donors and Acceptors

Any technical application of Cz-grown Si crystals needs a certain electrical resistivity value with either n-type or p-type conductivity. This property is achieved in principle by adding either donor (P, As) or acceptor elements (B, Al, Ga) to the feedstock. However,

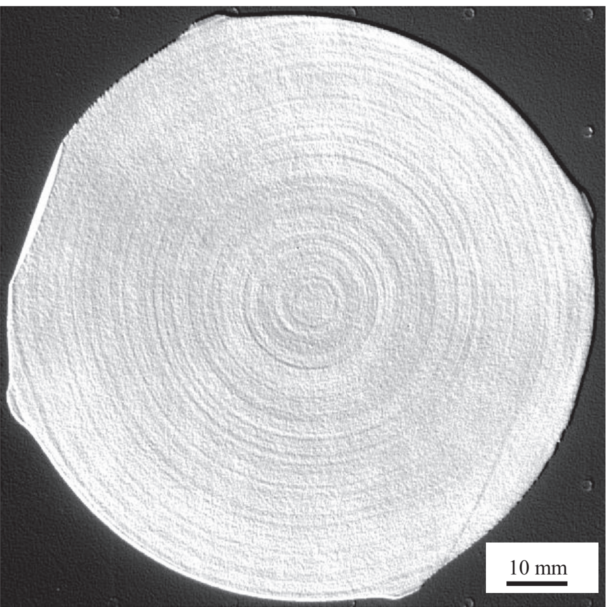

FIGURE 2.15 Visualization of rotational striations in a highly arsenic-doped silicon wafer (diameter approximately 100 mm) using a photoluminescence technique. *Courtesy of Fraunhofer IISB.*

depending on the chemical properties and segregation coefficient, the doping process can be rather sophisticated. For growing p-type or n-type silicon crystals with shallow doping levels ($<10^{19}$ atoms/cm^3) by the Cz technique, the dopant atoms are added in elementary form (e.g., B or Ga) to the silicon feedstock while loading the crucible.

For volatile dopants such as As, P, Sb, or In, doping is much more complex. In some cases, As and P pre-doped silicon chunks can be used. However, the loss of such volatile dopants during the homogenization and seeding phases must be considered. For example, in the case of a repeated seeding process, additional doping is necessary to compensate for the losses by evaporation. Particular care is needed in the case of heavily doped material. Special sophisticated techniques were developed, in which the dopants are added only after the silicon becomes completely molten in order to prevent an evaporation of the volatile elements during heating (e.g., Ref. [88]).

2.4.6.2 Other Intentional Doping Elements (Ge, N, H)

Germanium as doping element in Cz Si has attracted attention for microelectronic and photovoltaic applications because it is isoelectronic and does not induce electrically active levels in Si. If the Ge concentration is less than 10^{19} atoms/cm^3, no significant influence on the stability of the growth of Cz Si is observed. Ge is sometimes also added to the Si melt as a co-dopant of B in order to compensate for the small atomic radius of B, which causes stress in the Si lattice as a substitutional defect. Ge has a certain influence on the formation of oxygen precipitates, intrinsic defects, and thermal donors. For a review of the use of Ge as dopant in Cz Si crystal growth, the reader is referred to Ref. [89].

Nitrogen is also used to influence the nucleation and agglomeration of the intrinsic point defects. It is introduced in the Si melt via the gas atmosphere by using a mixture of argon and nitrogen or nitrogen-containing compounds (e.g., Ref. [90]). The partial pressure of nitrogen in the gas mixture has to be well controlled to prevent the formation of Si_3N_4 particles in the melt by keeping the nitrogen concentration in the melt below the solubility limit.

Hydrogen can also be added via the gas atmosphere in order to modify the grown-in microdefects [91].

2.4.6.3 Co-Doping of Solar-Grade Silicon

In the case of Si for photovoltaic applications, it was investigated whether a less-pure feedstock can be used for the growth of Si crystals (e.g., Ref. [92]). Often, the less-pure feedstock contains a higher amount of the acceptor B and the donor P. This donor–acceptor compensation effect reduces both the mobility and the minority carrier lifetime within the Cz Si crystals. However, even worse, it could result in a change of the type of conductance from p-type to n-type after a certain crystal length due to the different segregation coefficients of B and P. Therefore, several attempts were made to co-dope Si with other p-type dopants, such as Ga, to avoid the conversion from p-type to n-type material [92]. Another problem of the usage of B as a dopant for p-type Si for solar cells results from the formation of the B–O complex, which causes the so-called

light-induced degradation of solar cells [93]. The acceptor Ga does not have the property of forming a deleterious oxygen complex. However, Ga doping has a severe disadvantage because of its small segregation coefficient ($k = 0.008$). In this case, co-doping with n-type dopants (especially with P) was investigated to properly compensate for the segregation of Ga [92].

2.4.7 Unintentional Impurity Incorporation during the Cz Process

In addition to the intentionally added dopants and impurity elements of the Si starting material that one has to consider in the Cz process for Si, the two major impurities—oxygen and carbon—are inherently related to the Cz processing itself. The main source of oxygen is the silica crucible, while the main source of carbon is the graphite parts of the hot zone. Details of the route of contamination are discussed in the following sections. The behavior of these impurities in the Si crystal, especially its reaction with intrinsic defects, is discussed in Sections 2.5 and 2.6.

2.4.7.1 Oxygen

The Si melt reacts with the silica crucible and dissolves its surface gradually. It is not quite clear whether the oxygen in the melt has to be considered as dissolved SiO or just as dissolved O. In any case, it is known that oxygen evaporates from the Si melt as (SiO) vapor with a relatively high vapor pressure of 12 mbar at the melting point of Si [16]. Furthermore, it is known that oxygen has a segregation coefficient k that is close to 1. A precise determination of k (oxygen) is difficult because it would need a conservative closed system without supply and removal of oxygen.

Both effects—the high evaporation rate of SiO via the free melt surface and the absence of segregation-induced pileup of oxygen in front of the growth interface—are favorable. They avoid the occurrence of supersaturation and hence the formation of SiO_2 particles in front of the growth interface, which would cause the generation of dislocations followed by structure loss. Therefore, as a first target of Cz processing, one has to avoid an increase of the oxygen concentration in the Si melt beyond the saturation value of $2–3 \cdot 10^{18}$ atoms/cm^3 [16]. This means that the relatively high flux of oxygen coming from the crucible dissolution rate has to be compensated for by the transport rate within the melt to the free surface and the removal from the free surface by the flow of Ar. The dissolution rate of the silica crucible wall was determined by several authors to be in the range of 1 mg SiO_2/h cm^2 [17].

In the development of Cz silicon for the fabrication of integrated circuits, it soon became clear that an oxygen concentration in the Si crystal in the range of about $3–9 \cdot 10^{17}$ atoms/cm^3 is very useful. Therefore, it is extremely important to adjust the concentration of oxygen in the growing crystal to a nominal value given by the user of the wafers. It has to be controlled by carefully considering all the phenomena and parameters that are influencing the oxygen incorporation into the crystal. In Ref. [50], a commonly accepted numerical model for simulating the oxygen transport during Cz growth of Si can be found.

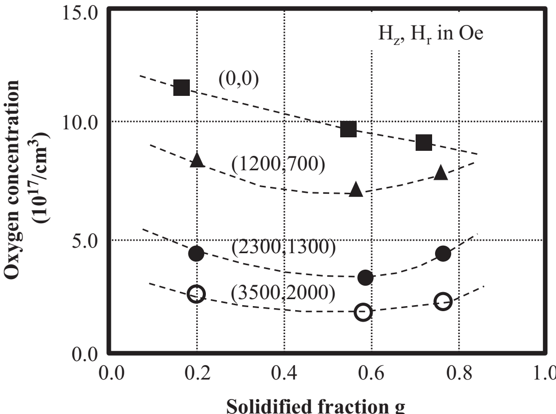

FIGURE 2.16 Oxygen concentration in Cz Si crystals with 75-mm diameters versus solidified fraction g (i.e., axial position in the crystal) grown under a cusp magnetic field with different field strengths (H_z-axial component, H_r-radial component.) *Adapted from Ref. [95].*

The following phenomena and parameters are important for the incorporation of oxygen into the growing Si crystal:

- The *input of oxygen* by dissolution of the crucible wall is directly proportional to the reaction rate, which depends exponentially on the absolute temperature of the crucible wall [94].
- The *transport of oxygen* within the Si melt occurs via the diffusive-convective mechanisms. Hence, the rotation rates of the crucible and crystal are important parameters to control the oxygen transport and thus the oxygen distribution in the crystal (see Figure 2.10). Static magnetic fields are very useful to decrease the transport of oxygen from the crucible wall to the bulk melt. Typically, low oxygen content ($<4 \cdot 10^{17}$ atoms/cm^3) of the crystal is only achievable by the use of static magnetic fields (see Figure 2.16). Therefore, in order to achieve a uniform axial distribution of the oxygen concentration at a certain level, an adjustment of various process parameters is needed.
- *Incorporation of oxygen into the growing crystal and segregation at the interface*: Most investigations of the incorporation of oxygen into the growing Si crystal come to the conclusion that the segregation coefficient of oxygen is very close to 1 [14,16].
- *Evaporation of SiO from the free melt surface*: The oxygen that is transported to the free surface of the Si melt is removed by evaporation as molecular SiO. The vapor pressure of SiO is > 12 mbar for temperatures above the melting point of Si [14]. The flux of oxygen across the melt surface depends strongly on the conditions in the region above the Si melt surface. Here, the flow of the Ar gas plays a very important role. The Ar gas flow is guided within the Cz puller from the top region down to the crystal and then tightly along the free melt surface by the aid of the heat shield. The flux rate of evaporation can be strongly increased by a proper

design of the lower portion of the heat shield. Furthermore, it is important that the Ar flow containing SiO is guided to lower regions of the Cz puller in order to avoid a deposition of SiO at parts of the hot zone from where SiO particles could fall into the melt.
- *Oxygen is incorporated into the crystal*, typically in an interstitial position. Its properties and behavior during cooling of the crystal are extensively discussed in Section 2.5.

2.4.7.2 Carbon

Many parts of the hot zone of a Cz puller are made from graphite. Therefore, carbon is a potential candidate for contamination of the melt and hence the crystal. The main route of contamination is via the gas phase by carbon monoxide (CO). CO reaches the free melt surface, is absorbed there, and is transported through the melt. The solubility of C in the Si melt is $5 \cdot 10^{18}$ atoms/cm^3 [15]. C is incorporated into the Si crystal with a segregation coefficient of $k = 0.07$, which means that a strong pileup of C in front of the growth interface takes place. Therefore, it is important to keep the C concentration in the melt below the limit of homogeneous nucleation of SiC. Otherwise, SiC particles coming to the growth interface could cause structure loss. Another reason to keep the C concentration low is the fact that C in Si can increase the leakage current of devices and modify the properties of microdefects.

The presence of CO in the gas atmosphere is a result of chemical reactions between SiO evaporating from the melt and graphite parts (at lower temperatures), as well as of a reaction between the silica crucible with the surrounding support crucible made from graphite (at higher temperatures) [33] and of residual oxygen that reacts with graphite. These reactions also lead to the formation of solid Si or SiC on the graphite parts in the hot zone. Fortunately, the formation of SiC needs very high temperatures. Therefore, it preferentially takes place in the hottest parts of the heaters and not at the heat shield. This is important because flaking SiC particles that fall into the melt and reach the growth interface must be avoided.

Another problem is the different thermal expansion between graphite and SiC and Si layers, which results in surface damage of the graphite parts. Graphite parts with highly corroded surfaces can eject particles into the gas atmosphere, which may fall into the melt and again cause structure loss. The hot-zone parts that have predominant corrosion are the heat shield, the graphite susceptor that holds the silica crucible, and the heaters.

A measure for keeping the carbon concentration in the Si melt low is to prevent the CO from getting to the free melt surface. Furthermore, SiC and Si particles should be prevented from falling to the melt surface. Both effects can be achieved by a corresponding guidance of the Ar flow first along the crystal and melt surface, then along the hottest parts of the hot zone, and by using the properly designed heat shield.

2.5 Oxygen in Silicon

2.5.1 Technical Relevance of Oxygen Effects in Silicon Crystals

Typically, Cz-grown Si crystals contain oxygen with concentrations between $3 \cdot 10^{17}$ atoms/cm^3 and $9 \cdot 10^{17}$ atoms/cm^3. Before 1970, this comparably high oxygen content in Cz-grown Si crystals was considered to be a disadvantage because the formation of oxygen-related precipitates could have a negative impact on device performance. To avoid oxygen contamination, the crucible free floating zone (FZ) technique was developed, and silicon crystals were preferably produced by this technique until the 1970s. Then, the importance and advantage of oxygen in silicon was recognized to obtain high yields during device processing. Oxygen turned out to impede the mobility and multiplication of dislocations, which makes the silicon wafer more resistant to slippage during device processing [96]. In addition, oxygen-related precipitates were found to be capable of gettering fast-diffusing metallic impurities such as Fe, Ni, and Cu [97], which can severely degrade device functionality. Furthermore, the development of the "denuded zone" technique—that is, the outdiffusion of oxygen in the near-surface region to the wafer surface and the diffusion of metallic contaminants into gettering centers in the bulk of the wafer during the high-temperature process steps—remedied the oxygen-related defect problem. The discovery of these favorable effects launched immense research activities for further improvement of the wafer quality. It was particularly important to overcome the negative effects of oxygen doping, namely wafer warpage and the formation of thermal donors during device processing. The former is caused by excessive oxygen precipitation [97]; thus, its remedy required a thorough understanding of the aggregation of oxygen atoms. The latter is related to the formation of oxygen complexes, of which its nature is still debated. A negative effect of oxygen is also the stabilization of vacancy aggregates.

Today, the semiconductor industry has optimized the favorable effects of oxygen. However, this is not true for high-power devices where the electric current is directed through the wafer bulk. For these devices, oxygen precipitates in the bulk are usually detrimental. Consequently, they are still produced on FZ wafers.

With regard to solar cells, oxygen usually is an undesirable impurity because it degrades the minority carrier lifetime in the wafer bulk by forming oxygen precipitates [98,99] and B-O complexes [100].

2.5.2 Atomistic Configurations of Oxygen in Silicon Crystals

Oxygen atoms are incorporated in the silicon lattice on an interstitial position (denoted by O_i), where the oxygen atom sits in an almost bond-centered position between two adjacent Si atoms [101]. Several of the local vibration modes are infrared (IR) active. The predominant IR line at 1104/cm (at room temperature) was calibrated with respect to other analytical methods, such as gas fusion and several radioactive techniques, and is used as the standard method for the quantitative determination of the oxygen content in

as-grown silicon crystals (as-grown silicon usually contains only a negligible amount of precipitated oxygen).

Oxygen can also form dimers. The dimer has a significant concentration at low temperatures (<700 °C) which results in a drastic change in the oxygen diffusivity. More recently, oxygen trimers have also been investigated [101], but their concentration is only detectable in irradiated silicon. In irradiated silicon, oxygen on a *substitutional* position or a vacancy–oxygen complex can also be produced [102]. The defect is known as A-center, which can be detected by IR measurements because it has local vibration modes (LVM) at 835/cm and 885/cm [103]. It can be removed by annealing at approximately 300 °C.

2.5.3 Solubility of Oxygen in Silicon Crystals

The data on the solubility of oxygen as found in the literature over time are substantially scattered, because the detection limit of Secondary Ion Mass Spectrometry (SIMS), which is the mostly applied direct tool for the measurement, is only approximately $1 \cdot 10^{17}$ atoms/cm^3. Therefore, the ^{18}O isotope is often used [104]. Reasonable data have also been obtained from indirect methods, such as the monitoring of oxygen precipitation [105]. More recent data yielded the following equation [106]:

$$C_s(O_i) = 9.1 \times 10^{22} \times \exp(-1.57\ \mathrm{eV/kT}) \tag{2.10}$$

which is relatively close to previous data [107]. The maximum solubility is slightly above 10^{18} atoms/cm^3. Below 800 °C, the data of many measurements are obscured by small oxygen precipitates.

It should be noted that the oxygen solubility is increased if the sample is heat treated in an oxidizing ambient. At low temperatures, this increase can reach up to almost an order of magnitude [106].

2.5.4 Diffusivity of Oxygen in Silicon Crystals

The following value for the diffusion coefficient of the interstitial oxygen atom is generally accepted [108]:

$$D_O = 0.13 \times \exp(-2.53\ \mathrm{eV/kT}) \tag{2.11}$$

This value was mainly determined from SIMS measurements of diffused profiles (at high temperatures) and of the relaxation of stress-induced dichroism (at low temperatures) over a total temperature range of 250–1400 °C. The diffusion of oxygen does not involve interactions with vacancies or Si interstitials.

Below 700 °C, however, interstitial oxygen atoms are more and more transformed into dimers, which diffuse much faster than the single atom. From measurements of dislocation unlocking, an activation energy of approximately 1.5 eV has been found for the dimer diffusion coefficient [109].

It was reported that oxygen diffusivity notably slows down for heavy B and As doping (>10^{18} atoms/cm^3), whereas heavy Sb doping has no effect [110]. However, in the

temperature range of 350–550 °C, the opposite effect was found for heavy B doping [111]. The diffusivity was almost a factor of 50 higher than for low B doped samples.

2.5.5 Formation of Oxygen-Related Thermal Donors in Silicon Crystals

Oxygen can form so-called thermal donors. In the temperature range of 300–500 °C (most pronounced near 450 °C), the well-known *double donors* are generated [112]. Depending on the annealing time and the oxygen content, the concentration of these donors can reach more than $10^{16}/cm^3$, which corresponds to a resistivity of 0.5 Ωcm [14]. Thus, the resistivity of the silicon crystal can be considerably altered by the donor formation and can even result in a change of the conductivity type. With respect to as-grown crystals, the donor formation is much stronger at the seed end as compared to the tail end because the seed end is higher in oxygen and the exposure time to 450 °C is longer. The thermal donors can be easily destroyed by annealing above 500 °C and subsequent rapid cooling to temperatures below 300 °C.

Usually, the donors are assumed to have a common core, onto which supersaturated oxygen atoms are aggregated. The double donors represent a whole family of donors with slightly different ground-state energies [113–115]. With regard to their impact on minority carrier lifetime, it was found that the recombination activity of the donors is rather small [116] in contrast to larger oxygen precipitates.

So-called *new donors* can be additionally generated in the temperature range of 550–800 °C, but their concentrations are usually much lower as compared to the “old” (450 °C) donors. Although the old donors have distinct energy levels, the new donors exhibit a continuous distribution of trap states [117]. Unlike the old donors, the formation of new donors is significantly enhanced in the presence of carbon [118]. Their structural nature has not been revealed yet.

2.5.6 Reaction and Aggregation of Oxygen in Silicon Crystals

When the growing crystal cools down, the solubility of oxygen in the silicon lattice decreases rapidly; hence, an increasing supersaturation of oxygen builds up, which will eventually result in the formation of oxygen precipitates. The behavior of these oxygen precipitates upon further heat treatment strongly depends on the grown-in size distribution and on the heat treatment itself. If the average size of the grown-in precipitates is too small, the precipitates are dissolved during heat treatment and their technically important gettering capability is lost. If the average size is too large, the precipitates can grow during the heat treatment and reach a size where they exert enough stress on the silicon lattice so that dislocations are generated. Therefore, the density and size distribution of oxygen precipitates must be well controlled and adjusted during crystal growth.

Experimentally, the aggregation of oxygen can easily be monitored by measuring the decrease of the concentration of interstitial oxygen upon thermal treatment. A standard heat treatment for the formation of oxygen precipitates is a nucleation step at 780 °C or 800 °C (3–4 h), followed by a 1000 °C (16 h) growth step. The increase of the precipitated

oxygen depends on the initial oxygen concentration and the thermal history, which is different for the seed and tail end of the crystal. The morphology of the oxygen precipitates depends on the annealing temperature. Roughly, three temperature regimes can be distinguished. Below 800 °C, ribbon or rod-like shapes are found [119]; in the temperature range of 800–1050 °C, a plate-like morphology often accompanied by prismatic dislocation loops occurs [119]. Above 1050 °C, a regular or truncated octahedron is observed [119]. However, the three regimes considerably overlap.

The chemical composition of the precipitates appear to be SiO_2, which replaces about 2.25 unit volumes of 1 Si atom in the silicon lattice. This enlargement of volume generates substantial strain energy in and around a precipitate. The minimization of the strain energy is, therefore, the driving force for the different morphologies in the various temperature regimes. At high temperatures, the lattice can easily reduce the strain by the generation of dislocations. Thus, the minimization of the interface energy dominates; the (111) plane, which has the lowest interface energy, is preferred as the interface of the Si host matrix. At lower temperatures, the strain energy increasingly dominates over the interface energy. Consequently, the precipitate has to minimize the strain by a favorable shape, such as the ribbon geometry. The exact composition and morphology are still being debated, except for the low-temperature regime, where coesite has been identified [119]. Coesite only exists under high pressure (>25 kbar), which demonstrates that Si is very brittle in this temperature range and cannot generate dislocations or move Si atoms into interstitial positions in order to reduce stress.

Similar to intrinsic point defect aggregation, the aggregation of oxygen occurs if the oxygen supersaturation is high enough for nucleation. However, due to the large volume change that occurs when a precipitate is formed, the nucleation of oxygen precipitates depends on additional parameters, such as the supersaturation of vacancies and Si interstitials. In case of a vacancy supersaturation, the embryo precipitate can absorb vacancies; thus, nucleation can occur without the generation of stress on the surrounding Si matrix. This favors nucleation, whereas a supersaturation of Si interstitials inhibits nucleation because the precipitate cannot easily emit Si interstitials to reduce the buildup of strain. In the literature, expressions for the critical precipitate radius, at which the precipitate is stable, are given [120].

Until recently, the models for oxygen precipitation were based on the homogeneous nucleation of incoherent Si_xO_y clusters. These models yield reasonable results only if the strain of the growing nuclei is relieved by the absorption of vacancies or by the emission of Si interstitials. A more advanced kinetic model describes the nucleation at 800 °C, a temperature at which most of the vacancies are bound in VO_2 complexes and which are thus the actual vacancy source [121]. More recent models of incoherent nucleation consider the segregation of emitted Si interstitials to the precipitate nuclei [122] or the direct participation of the VO_2 complexes in the nucleation process [123].

The oxygen precipitate density, which is typically in the range between $1 \times 10^7/cm^3$ up to $1 \times 10^{10}/cm^3$ after the heat treatment of the Si wafer, has a major impact on the minority carrier lifetime [98,99]. It was found that the lifetime decreases by about one

order of magnitude when the precipitate density increases by two orders of magnitude. Thus, the inverse lifetime of minority carriers is roughly proportional to the square root of the precipitate density. The precipitation of oxygen can be considerably enhanced in the presence of certain impurities. Besides vacancies, nitrogen appears to have the most pronounced impact [124]. The increase is already detectable at rather low nitrogen concentrations on the order of 10^{14} atoms/cm^3 and is particularly visible at low oxygen concentrations (<4–5·10^{17} atoms/cm^3), where precipitation is negligible without nitrogen doping. At higher oxygen concentrations, the effect is obscured by the strong homogeneous nucleation of oxygen clusters [125].

Carbon is also well known to enhance oxygen precipitation [126], but only at higher concentrations (>10^{16} atoms/cm^3). Because carbon predominantly resides on substitutional sites, it is very unlikely that, as in the case of nitrogen doping, a higher residual vacancy concentration is responsible for the stronger oxygen precipitation. On the other hand, the small size of a carbon atom exerts a local tensile strain on the surrounding lattice and attracts Si interstitials to form carbon–Si (interstitial) complexes. Thus, Si interstitials ejected into the lattice by growing oxygen precipitates are effectively removed and, in turn, further precipitate growth is not retarded by a buildup of Si interstitial supersaturation. The origin of the enhanced oxygen precipitation may also be related to heterogeneous nucleation at small carbon aggregates [127]. A significant enhancement of oxygen precipitation is also observed for crystals that are highly doped with boron [128], for germanium doping [129], and metal contamination [130].

2.5.7 Formation of Oxidation-Induced Stacking Faults

A well-known defect structure in Cz-grown Si crystals is the OSF ring, which marks the boundary between the vacancy and the Si interstitial-dominated region (V/I boundary). This famous ring is generated by oxygen precipitates with a platelet shape, which grow to a particularly large size at the edge of the void region and, there, exceed a critical size that is necessary to form stacking faults in a subsequent wafer oxidation [131]. The critical size of these grown-in platelets is approximately 70 nm. The large oxygen precipitates then act then as the nuclei for the aggregation of Si interstitials generated by the oxidation at the wafer surface. The aggregated Si interstitials form the actual extrinsic OSF with the oxygen precipitate in its center [14]. OSFs usually cannot be detected on (111) surfaces. It should also be noted that the formation and detection of OSFs is strongly dependent on the temperature and time of the oxidation process. The standard tests work with wet oxidation and temperatures between 1000 and 1200 °C for 2–3 h.

An illustration of the defect formation is given by the schematic representation in Figure 2.17. The reason for the enhanced growth of oxygen precipitates at the edge of the vacancy-rich region is a local maximum of the residual vacancy concentration, which develops there after void formation has stopped (compare Figure 2.17, middle). The absorption of free vacancies allows the oxygen precipitate to nucleate and grow without building up notable strain energy.

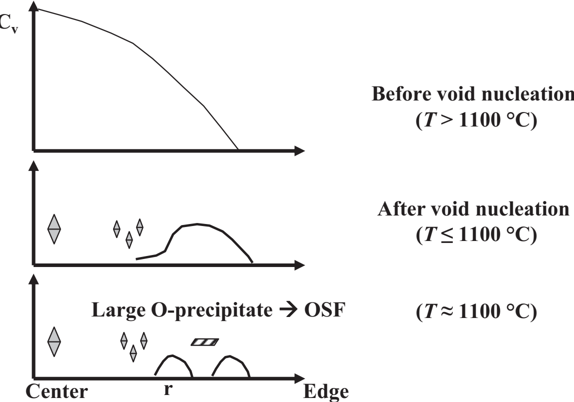

FIGURE 2.17 Schematic representation of the concentration of vacancies C_v versus radial position r in Si crystals at three different temperature regimes during cooling. The sequence illustrates the evolution of the radial vacancy profile and the accompanying formation of voids (diamond symbols) and large O_i-precipitates (shaded rhomboid) at decreasing temperatures. *Adapted from Ref. [132].*

The qualitative explanation of this local maximum is fairly simple [38]: The original radial vacancy profile decreases from the crystal center toward the crystal rim (Figure 2.17, top). Therefore, the critical supersaturation for void formation is first reached at the crystal center at relatively high temperatures, and the free vacancies are quickly consumed in this area (Figure 2.17, middle). As the cooling of the crystal proceeds, voids are also nucleated in the regions of lower initial vacancy concentrations; thus, vacancies are now also consumed further away from the center. Because the removal of vacancies works better at higher temperatures, the concentration of free vacancies finally turns into a minimum in the center, and the maximum of the residual vacancies gradually moves toward the V/I boundary upon further cooling. Nevertheless, the concentration at the maximum of residual vacancies continues to decrease. Thus, the void nucleation temperature decreases, too.

As free vacancies favor the nucleation of oxygen precipitates upon further cooling, a temperature is reached where the probability for the nucleation of precipitates is higher than that for the formation of voids (Figure 2.17, bottom). Thus, oxygen aggregates are formed at this local maximum close to the V/I boundary on the vacancy-rich side in competition with the formation of voids. The relatively high nucleation temperature at this radial position results in a larger size but lower density of the corresponding precipitates as compared to those nucleated at lower temperatures away from the V/I boundary. Consequently, they preferably reach the critical size for OSF formation in a subsequent wafer-oxidation process. At sufficiently fast cooling rates of the growing crystal, the oxygen precipitates are formed with a higher density but a smaller size and cannot grow until they reach the critical size. Thus, OSF formation is prevented in agreement with experimental findings. The same density/size effect is obtained if the oxygen content is lower; thus, the OSF formation is suppressed. The size of oxygen precipitates can also be reduced by carbon or hydrogen doping, which also reduces the

OSF formation. On the other hand, strongly enhanced generation of OSFs is observed in the presence of some metallic impurities, such as copper and, in the case of nitrogen, even at rather low levels (10^{13}–10^{14} atoms/cm^3) [132].

2.6 Intrinsic Point Defects and Their Aggregates

2.6.1 The Importance of Intrinsic Point Defects and Their Aggregates

For thermodynamic reasons, even a highly ordered material like a silicon single crystal must have some disorder. It has to contain a certain amount of vacancies (V) and Si atoms on interstitial positions I (called interstitials) in order to minimize its Gibbs free energy. In silicon, the equilibrium concentrations of these intrinsic point defects are rather low ($\leq 10^{15}/cm^3$) at growth temperatures. In the 1970s, it was found that aggregates of Si interstitials, creating local networks of dislocation loops as secondary defects, cause severe problems for device performance. When the interstitials begin to aggregate during the cooling of the growing crystal, they first form a stacking fault [133]. If the stacking fault reaches a critical size, the strain exerted on the crystal lattice is relaxed by the generation of dislocation loops of several micrometers in size around the stacking fault. This defect is the so-called A-swirl or L-pit [134,135] (see Figure 2.18). Self-interstitial clusters with a size below the critical limit [137] are called B-swirls [138,139]. A- and B-swirl defects often coexist in the same crystal region. L-pits/A-swirls are extremely stable and cannot be destroyed by high-temperature processes, whereas B-swirls can be dissolved by wafer annealing at temperatures above 1000 °C.

Another defect type, which started to puzzle the manufacturers of memory devices in the 1980s, is the aggregation of Si vacancies, which results in the formation of voids in the crystal [140] (see Figure 2.19). Although the voids are much smaller than the A-swirl/L-pit defects, they generate an early breakdown of the gate oxide of MOS transistors [142].

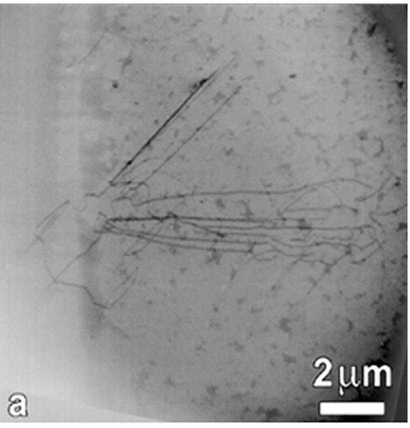

FIGURE 2.18 Transmission electron microscopy (TEM) picture of an L-pit in a Cz-grown Si crystal. *Reprinted from Ref. [136] with permission from Trans Tech Publications.*

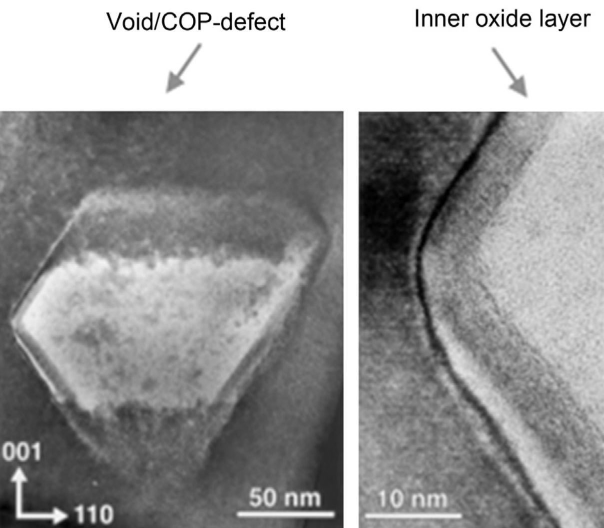

FIGURE 2.19 TEM picture of a void/COP in a Cz-grown Si crystal (left). The inner surface of the void is covered by an oxide layer (right). *Reprinted from Ref. [141] with permission from Trans Tech Publications.*

The void defect can be delineated by different detection methods. Originally, the defect was discovered on cut and acidic-etched (polish-etched) wafers by an additional, agitated Secco etch [143]. It was denoted as a flow-pattern-like defect [144] or D-defect [145]. Later, the void defect was also observed as a light point defect on the surface of polished wafers. Because the defects could not be cleaned off, they were called crystal originated particles (COP) [146]. Voids can also be detected by laser light scattering tomography (LST), which is the only method to measure them in the wafer bulk. In this case, they were called LST defects. Using atomic force microscopy, the void defect at a polished surface can be measured as a dimple with a certain depth that relates rather well to the size of the void. Furthermore, the voids were analyzed in detail by transmission electron microscopy (TEM) investigations.

Voids are bound by (111) planes and usually exhibit an octahedral morphology, as shown in Figure 2.19. However, voids can change their shape to a platelet- or even rod-like habitus if the crystal is doped with nitrogen [147]. They can also appear as twins or triplets. In contrast to A-swirl/L-pits, a strain field around the void is generally not observed. Due to the relatively high content of oxygen in Cz-grown crystals, the sidewalls of the void are lined with an oxide layer of approxmately 2–5 nm [148]. This oxide layer stabilizes the void defect and prevents its dissolution in thermal processes up to temperatures of 1200 °C.

The size of the voids is considerably smaller (70–150 nm) compared to A-swirl/L-pit defects. In modern devices with design rules well below 100 nm, the voids can significantly affect the device performance. A-swirl or L-pits are always detrimental to devices because they always destroy a relatively large area.

The performance of solar cells is not so much affected by A-swirl/L-pits and voids because these defects have only a weak influence on the minority carrier lifetime, which is the most important material parameter of solar cells. A stronger effect is observed from the grown-in oxygen precipitates in Cz Si, which notably decreases the minority carrier's lifetime [99].

2.6.2 Incorporation of Intrinsic Point Defects into the Growing Crystal

By comparing atomistic simulations with the different available experimental data, a parameter set was established over the years that seems to be rather accurate and allows one to predict defect aggregation well in agreement with the experimental observations [149]. It is now widely accepted that the uncertainty of the current data set of thermophysical properties is in the order of 50% or less.

The driving forces for the incorporation of intrinsic point defects at the interface of a growing crystal were first analyzed by Voronkov [10]. To understand the defect behavior in silicon crystals within the Voronkov model, it is important to note that the vacancy equilibrium concentration is slightly higher (approximately 30%) than the respective Si interstitial concentration at the melting point, while the vacancy diffusivity is significantly smaller than the Si interstitial diffusivity [150]. Based on this knowledge, Voronkov considered two competing fluxes—one of the vacancies and the other of the interstitials. Each flux, in turn, consists of two terms, originating from Fickian diffusion and from "convection." The Fickian diffusion is proportional to the temperature gradient (G) of the growing crystal at the growth interface, whereas the convection term is proportional to the growth rate (V) of the crystal. The origin of the Fickian diffusion is the recombination between vacancies and interstitials. Both equilibrium concentrations strongly decrease with decreasing temperature. Thus, the Fickian diffusion is directed from the interface into the crystal, where the equilibrium concentrations C_V^{eq} and C_I^{eq} are lower. The convection term, on the other hand, is related to the advancing growth interface. Mathematically, the moving growth interface is set to be the origin of the coordinate system, which establishes a "convective" species flow into the crystal, in the same direction as the Fickian diffusive flows.

At the growth interface, the vacancy concentration is always higher than the self-interstitial concentration. Consequently, the vacancy flux will dominate over the self-interstitial flux if the growth rate V is sufficiently fast. In the other extreme case, if the growth rate V is very low, then the Fickian diffusion dominates; that is, the concentration of the interstitials exceeds that of the vacancies, owing to the much higher interstitial diffusivity D_I. If the vacancy and interstitial fluxes are equal, neither of the two species can survive the recombination process. Hence, the concentrations of both species decrease when the as-grown crystal cools down. As shown by Voronkov, this situation occurs if the parameter V/G is equal to a critical value, which was later determined to be $\xi_{tr} = 1.38 \cdot 10^{-3}\ \mathrm{cm^2/min/K}$ [150]. For $V/G > \xi_{tr}$, vacancies dominate, whereas $V/G < \xi_{tr}$ favors self-interstitials. It should be noted that G has to be calculated directly at the interface [151]. If G is calculated as an average value over a certain range from the interface, incorrect results are obtained.

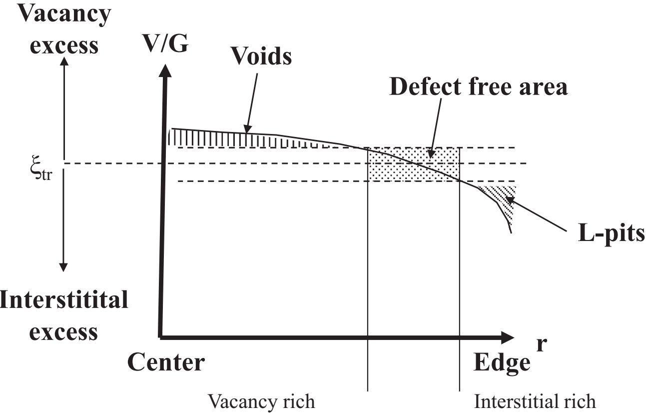

FIGURE 2.20 Schematic representation of V/G versus radial position r. The radial variation of the dominating defect type is given. The occurrence of the vacancy aggregates (voids) and interstitial aggregates (L-pits) is explained in Section 2.6.4. *Adapted from Ref. [132].*

Surprisingly, it turns out that the V/G values of standard Si Cz growth processes are rather close to the critical value ξ_{tr}. As a consequence, Si crystals often contain two regions with different dominating intrinsic point defects—V-rich and I-rich, which are separated in radial direction as schematically shown in Figure 2.20. This behavior is explained by the radial variation of the axial temperature gradient G(r). Usually, G increases from the center toward the crystal rim due to the heat loss through the crystal surface by radiation. Thus, V/G(r) decreases accordingly, and a crossover from vacancy to self-interstitial type defects occurs. The small ring-shaped transition region between the two defect areas where the vacancy and the self-interstitial fluxes are equal and, hence, $V/G(r) = \xi_{tr}$, usually contains oxidation-induced stacking faults (OSF) (for details, see Section 2.5.7). A variation of the growth rate *V* significantly shifts the radial position of the transition region according to $V/G(r) = \xi_{tr}$. It is therefore possible to grow crystals that are either fully vacancy or interstitial rich, respectively, by adjusting the pulling rate V. This situation is peculiar for silicon and is not found in other materials such as germanium, where the crystals are always found to be vacancy rich.

It should be noted that the Voronkov model has been challenged [152]. However, the proposed alternative approach has not found wide acceptance. A further theoretical discussion focuses on the influence of thermal stress on the transition value ξ_{tr} [153,154]. However, a final conclusion has not been reached.

2.6.3 Influence of Crystal Growth Parameters on the Intrinsic Point Defect Behavior

It was noticed early that the void region together with the OSF-ring expands with an increasing pull rate while the width of the outer A-swirl/L-pit region shrinks, and vice versa [135]. If the pull rate V is sufficiently high, the void region finally extends to the cylindrical crystal surface and the entire crystal volume contains only voids. On the other

hand, if the pull rate V is sufficiently low, the void region shrinks to zero and only A-swirl/L-pits are observed. This experimental observation is now well understood within the model of Voronkov. It was also found that the critical pull rate, at which the void region shrinks to zero and A-swirl/L-pits remain as the only defect type, is proportional to the axial temperature gradient G of the growing crystal at the growth interface [155], which is exactly in accordance with the Voronkov model [10]. It should be emphasized that it is of great technological importance that a complete change of the defect type can be achieved within the regime of technically feasible pull rates V. It is also economically very favorable that crystals containing only the less harmful voids can be grown at high pull rates and, thus, at lower cost.

The *aggregation of intrinsic point defects* was intensively experimentally investigated by transient growth experiments. The results of such experiments demonstrate that the nucleation and growth of voids occurs between 1070 and 1100 °C. At lower temperatures, the growth stops due to the strong decrease of vacancy diffusivity and the oxidation of the inner void surface. L-pits seem to nucleate in a similar temperature range as voids [156].

It was experimentally found that the void density increases with an increasing cooling rate by following a 2/3 power law [132]. The void size decreases with increasing cooling rate and vice versa [157]. A characteristic change in the defect density and size distribution is also observed across the crystal diameter [158]. While in the crystal center large voids of low density prevail, the distribution gradually shifts to small sizes and high density toward the boundary of the crystal or the void region, respectively. Because the cooling rates of the crystal center and rim are nearly the same, this remarkable variation of the density and size distribution cannot be related to the cooling rate. The effect must be a consequence of the radial variation of the point defect concentrations due to the radial dependence of V/G(r).

2.6.4 Calculation of the Aggregation of Intrinsic Point Defects

The aggregation of a species is driven by the gain of Gibbs free energy due to the agglomeration of the species. For vacancies, the Gibbs free energy change then reads as:

$$F_n = n \cdot k \cdot T \cdot \log \frac{C_V}{C_V^{eq}} + \lambda \cdot n^{2/3} \tag{2.12}$$

for an aggregate of size n (number of vacancies in the aggregate). The first term is the volume energy, whereas the second term represents the surface energy, with λ as the specific surface energy of the aggregate. The critical size beyond which the aggregate is stable is found by setting the derivative of F_n to zero (maximum of F_n).

The nucleation of aggregates can be visualized as follows. At a high temperature, a distribution of aggregates with size n exists. However, almost none of the aggregates are stable because the critical size $n_{\max}$ is very large as supersaturation is negligible. Therefore, no nucleation occurs. When the temperature is lowered and supersaturation becomes appreciable, the critical size significantly decreases; now, a measurable part of the larger aggregates is above the critical size (see Figure 2.21). These stable aggregates act as nuclei and can further grow in size.

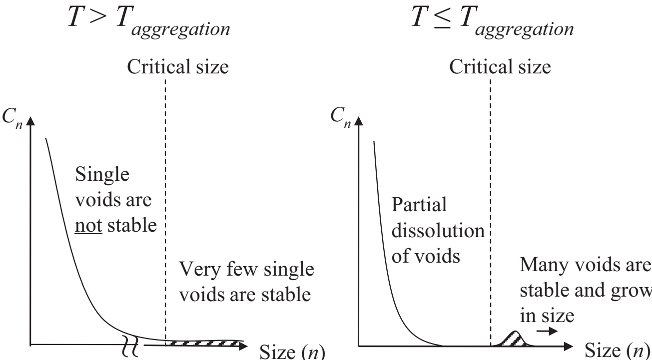

FIGURE 2.21 Number of aggregates C_n with size n versus the size n for a temperature T above (left) and below (right) the aggregation (nucleation) temperature $T_{aggregation}$.

Most aggregation models have focused on the nucleation and growth of voids because they are technologically most relevant. A model for the aggregation of vacancies was first derived by Voronkov and Falster [159]. This theoretical model predicts a $q^{3/2}$ dependence of the void density on the cooling rate q, which is in excellent agreement with the experimental data. Furthermore, the model also predicts that the void density is proportional to $C_V^{-0.5}$. As for a fully vacancy-rich crystal, the vacancy concentration decreases from the center toward the crystal rim due to the decrease of V/G(r) (as shown in Figure 2.20); the void density should increase toward the crystal rim while the void size decreases, which is again well in accordance with the experimental findings [132].

In principle, a similar approach should also be applicable to the aggregation of Si interstitials, but the details of interstitial nucleation are different.

2.6.5 Impact of Impurities on the Intrinsic Point Defect Aggregation

Impurities can dramatically alter the point defect aggregation. The impurity with the most pronounced effect is nitrogen, particularly in oxygen-lean materials such as FZ-grown crystals (oxygen concentration $< 10^{17}$ atoms/cm^3) [160]. In this case, voids as well as A-swirl/L-pits are suppressed simultaneously at rather low N concentrations ($<10^{14}$ atoms/cm^3). The suppression effect was attributed to a reaction between nitrogen and intrinsic point defects [161]. For the oxygen-rich Cz crystals, the desirable defect suppression by nitrogen is not observed. However, a notable effect on the defect size distribution is still detectable. With increasing nitrogen concentration, the void size is reduced, but its density is increased [162]. It was also found that nitrogen systematically changes the void morphology [147]. Furthermore, nitrogen doping strongly enhances oxygen precipitation [124], which, however, can also have an undesirable effect on the OSF formation [125]. Both the reduction of void size as well as the stronger oxygen precipitation can be technologically useful [163], but the enhanced formation of OSFs must be avoided.

There were many attempts to explain the effect of nitrogen on point defect aggregation [164–166], but a final model is still under discussion, particularly for Cz material. It should also be mentioned that, in FZ-grown crystals, the OSF ring is replaced by a ring-like area where no defects are observable [167] because of the comparatively very low oxygen content of FZ-grown crystals.

At high concentrations (10^{18}–10^{19} atoms/cm^3), doping elements such as boron, arsenic, and phosphorus exhibit similar effects on the intrinsic point defect aggregation as nitrogen [84,168,169]. In the case of boron, it was found that the void region as well as the diameter of the OSF ring starts to shrink when the boron content exceeds a level of $5 \cdot 10^{18}$ atoms/cm^3. At approximately 10^{19} atoms/cm^3, the voids and the OSF ring disappear in the center of the crystal. Despite the disappearance of the void region and the OSF ring, no L-pits are observed. Originally, it was suspected that the high dopant content results in a change of the equilibrium concentrations and diffusivities of intrinsic point defects, which would modify the transition value ξ_{tr} of the parameter V/G as a function of the boron content [170]. Although this model can explain the shrinkage of the void region with increasing boron content, it would entail a simultaneous appearance of L-pits in the outer crystal region, which is in conflict with the experimental results. Another attempt [171] considers reversible reactions between boron and intrinsic point defects, particularly Si self-interstitials. The situation is more complex for highly arsenic- or phosphorus-doped silicon. With increasing doping level, the void density first rises gradually and then sharply, before it abruptly collapses to very low values at a certain dopant concentration (1–$3 \cdot 10^{19}$ atoms/cm^3). One study tried to explain this behavior by the formation of vacancy-dopant and Si interstitial–dopant complexes [170].

The impact of carbon doping ($>10^{17}$ atoms/cm^3) on intrinsic point defect aggregation differs from the behavior of the above-mentioned impurities. It was found that the void region in the crystal center disappears upon carbon doping [172], while the region of L-pits/A-Swirl is widened. Furthermore, it was reported that carbon doping reduces the void size in Cz-grown crystals [173].

A slight effect on void size is also reported for germanium doping of Cz crystals [174]. With increasing doping levels (10^{15}–10^{18} atoms/cm^3), the void density is shifted to higher values, while the average void size continuously decreases. Unlike carbon, germanium doping is not known to enhance the formation of L-pits/A-swirls.

Hydrogen doping in the Cz growth of Si crystals induces the formation of very large voids with sizes of several micrometers [79]. The mechanism for the formation of these defects is poorly understood.

2.7 Economic Aspects of Cz Growth

2.7.1 General Remarks

In the progress toward better economic capability of the Cz process, the biggest challenge is the improvement of the good-for-order yield [175]. This includes not only the

minimization of losses due to structure loss, but it also considers useless crystal portions that do not meet the material requirements of the customer. Yield has the most notable impact on the cost of ownership for Cz crystal growth processes, mostly due to the cost of the feedstock material. All measures, even if they are costly at first sight, usually pay off if they result in a higher yield.

2.7.2 Factors that Impact the Yield of Dislocation-Free Cz Grown Crystals

Quality of silica crucibles. Improvements in the crucible quality are of great importance for the economy of the Cz process. Due to pitting corrosion, the cristobalite layer formed on the inner side of the crucible becomes a source of particles, which are released into the melt and may stop dislocation-free growth. The formation of cristobalite islands is strongly dependent on the original cleanliness of the inner crucible surface. Another corrosion effect that eventually results in the release of particles into the melt is the existence of tiny bubbles below and near the inner crucible surface [176]. During the growth process, the bubbles grow in size and can also form bubble clusters. Due to the progressing dissolution of the inner crucible surface, more and more bubbles are opened and silica particles can be released into the melt. Today, most high-quality crucibles are equipped with an additional lining of the inner crucible surface by a synthetic silica layer [177]. This layer is very clean and dense and contains nearly no bubbles. However, it substantially increases the manufacturing cost of such crucibles; consequently, the yield improvement must be notable in order to justify the higher crucible costs. In particular, large-diameter growth processes (e.g, 300 mm) that have a rather high thermal budget achieve higher yields with these crucibles.

Quality of polysilicon. The reasons for the impact of polysilicon on the generation of dislocations during growth are significantly less known as compared to crucible effects. The general belief is that polysilicon may contain particles, such as silicon nitride or silicon carbide, that dissolve very slowly in the silicon melt; hence, they can exist long enough to drift to the growth interface. It also seems that the rough, popcorn-like surface of the polysilicon chunks has a negative effect. This is probably due to their increased surface and related difficulties in cleaning them. If granular polymaterial is used, the formation of microholes (several micrometers) in the growing crystal is observed. This holds true especially for the CCz-process [79]. The actual cause for this effect may be the introduction of notable amounts of hydrogen into the melt, which results in the formation of the well-known hydrogen-induced defects (see e.g., Ref. [79]).

Particles in the gas ambient. A common source of particles in the gas ambient is corroded graphite parts on which a SiC layer has formed. From this layer, SiC particles tend to flake off the graphite. Another source is condensed layers of SiO on hot-zone parts, which can be detached from the surface. In general, the particle issue can be well handled by an appropriate design and management of the gas flow, and a careful maintenance of the hot zone and vessel.

Temperature fluctuations. Abrupt temperature changes significantly increase the risk of structure loss. The origin is often instabilities in the melt flow pattern, such as the formation of hot plumes drifting from the crucible bottom to the growth interface [178].

Process parameters. The set point curve and control of the heater power has to match with the desired pull rate scheme as a function of crystal length. A particular critical process phase in this regard is the shoulder growth and rollover to the body growth phase. During this period, large changes in the deflection of the growth interface as well as in the pull rate and power can occur (see Figure 2.3), which must be well balanced.

Out-of-specification losses. Materials for the semiconductor industry usually have to meet rather tight specifications. The most important parameters are resistivity, oxygen concentration and grown-in oxygen precipitates, size/density distribution of intrinsic point defect aggregates, and oxidation-induced stacking faults. The real challenge is to find a suitable compromise for the growth parameters as, with the exception of resistivity, all other material parameters depend on the same process parameters, but their dependencies are quite different and often contrary to each other. Owing to the problematic shoulder and rollover phase, the first few centimeters of body growth usually has to be scrapped because at least one material parameter (e.g., oxygen concentration) is out of specification. For solar applications, the situation is more relaxed because nearly all specifications are comparatively wide.

Other losses. Unavoidable losses are the seed and tail end cones as well as the residual melt, which is needed to grow the end cone. These losses obviously depend on the diameter/length ratio of the grown crystal. Typical values are in the range of 20–40%, with 450 mm crystals representing the higher value. Additional losses occur by grinding the as-grown crystals to a precise diameter and cylindrical shape.

2.7.3 Factors that Impact Cycle Time and Other Costs

Pull rate. With the introduction of heat shields in the 1970s, the pull rate V could be greatly increased. A further substantial increase was obtained by water-cooled heat shields in the 1990s. The challenge of this technology was the safety issue. Today, they are used in mass production and severe malfunctions have not been reported. For Cz growth with water-cooled heat shields, the upper limit of the growth rate is determined by the increasing thermal stress in the growing crystal, which must not exceed a critical value [179]. For certain growth processes, the pull rate may also be limited by a destabilization of the growth process, which manifests itself by a loss of the cylindrical shape of the growing crystal [56].

Thermal budget. The thermal budget of the growth process is predominantly determined by the crystal diameter. Besides the pull rate, the thermal budget of the hot zone has the biggest impact on the cycle time because it determines the duration of the warm-up, melt-down, stabilization, and cool-down phases of the process. For large diameter processes (e.g., 300 mm), these process phases can add up to more than 1 day and, in the case of 450 mm, they reach up to several days. The thermal budget can be reduced by

using thinner CFC material instead of graphite for the hot zone parts. However, CFC is much more expensive than graphite.

Other process times. Further actions that add to the cycle time are the insertion of the charged crucible into the hot zone, the evacuation of the vessel after process start, the removal of the grown crystal and the silica crucible with the residual melt, as well as the cleaning of the hot zone and vessel at the end of process. The latter is necessary in order to remove SiO deposits, which stick to the surface of various hot-zone parts and the walls of the upper vessel section. The major fraction of evaporated SiO is collected in certain areas or containers, where it must be removed for disposal after every run.

Besides the cost for the feedstock material, the next largest contribution to the cost of ownership is usually the silica crucibles. In particular, 300 mm and 450 mm growth processes require rather expensive crucibles with long lifetimes owing to their long cycle times. The graphite parts for a complete hot zone are a substantial investment, which can reach a price of more than €100,000 for large diameter processes. However, only those parts that are exposed to excessive SiO vapor during the process time have to be replaced after a certain number of runs and, thus, add to the operating costs. The major part of the hot zone has a lifetime of many years and can be considered as part of the initial investment.

The initial investment, which is mainly the puller, is usually the third largest contribution to the cost of ownership, followed by the cost for personnel. The reason for this can be attributed to the high level of process automation.

Energy and argon consumption often have a minor impact in comparison to the above-mentioned cost factors. However, the prices for energy and argon can vary considerably depending on the location of a factory, which may change the ranking of the expenses.

Finally, it should be mentioned that the costs per kilogram of grown ingot strongly increase for larger diameters, such as 300 mm and, in particular, 450 mm [180]. The main reason is the significantly higher cycle time. In addition, the occurrence of structure loss has dramatic consequences for larger diameters. As nearly a length of one diameter of already dislocation-free grown material has to be scrapped upon structure loss, which means almost half a meter in the case of 450 mm, the yield is lowered. Furthermore, the ratio of diameter to crystal length, which also impacts the yield, becomes more and more unfavorable. It is therefore expected that 450 mm, which is currently being introduced into mass production as the next standard crystal diameter, will be the largest diameter for the time being.

2.7.4 Special Issues of Cz Growth of Silicon Crystals for Solar Cells

The share of expenses of a Si wafer in electronic devices is probably only a few percent [181]; in a solar cell, however, it is about one third [181]. Therefore, the main targets in optimization of the Cz process for the growth of photovoltaic (PV) Si are (1) a reduction

of costs by improvement of crystal yield and increase of material throughput and (2) tailoring the material quality for the PV application.

The cost reduction must be achieved without a decrease in the solar cell efficiency. On the other hand, it might not be necessary to grow Si crystals for PV applications with the same high material quality as needed for microelectronic devices. This is true for wider radial variations of oxygen and dopants. On the other hand, the minority carrier lifetime is a rather critical parameter for solar applications, which must not drop below a specific value depending on the solar cell concept. Therefore, one must carefully analyze which defects in which concentration can be tolerated in a "solar-grade" Cz-grown Si crystal.

To optimize the Si Cz process for PV applications, all single process steps, except the growth of the cylindrical crystal, should be reduced in time. In principle, this latter step could also be shortened by an increase of the growth rate beyond the present rates of 1–2 mm/min. However, an increased growth rate means an increase in heat transfer and increased thermal stress in the crystal, which was previously discussed. A considerable shortening or even saving of the time period for certain Cz process steps is possible by using the multiple Cz growth technology (also called multipulling, multiple charge technique, and multiple batch technique), which was described in Section 2.2, and the CCz method, which was introduced in Section 2.4.3.3. As explained in Section 2.7.2, the poly-Si charge and the crucible represent a considerable amount of the expenses of a Cz growth run together with the consumption of energy, argon gas, and graphite parts for the hot zone. Therefore, the use of cheaper feedstock material is one further option to reduce costs [182] Also, proper design of the hot zone can lead to cost reduction by reducing heat losses and thus energy [4].

The continuous optimization of the Cz technology for PV applications has contributed to the fact that almost every second solar cell made today is based on a Si Cz wafer [4]. It could be expected that the future use of Si Cz for solar cell applications will increase even further compared to competing technologies, if a further cost reduction is possible.

In conclusion, the growth of silicon crystals by the Czochralski method has developed into a highly sophisticated industrial production technology that has achieved high reproducibility and good yield results. However, the ongoing demands for further improvements in productivity and yield at a high material quality for device applications, including solar cells, require further progress in the optimization of the Czochralski process. This progress will only be possible by continued growth of the knowledge base on the relevant physicochemical phenomena.

References

[1] Czochralski J. J Phys Chem 1918;91:219.

[2] Teal GK, Buehler E. Phys Rev 1952;87:190.

[3] Shiraishi Y, Takano K, Matsubara J, Iida T, Takase N, Machida N, et al. J Cryst Growth 2001;229:17.

[4] Müller G, Friedrich J. AIP Conf Proc 2010;1270:255.

[5] http://www.pv-magazine.com/news/details/beitrag/polysilicon-industry-to-resume-growth-in-2013_100009775/#axzz2Xo5cPQrU.

[6] Siemens & Halske: BRD Patents 1.102.117 and 1.140.549 filed 1954, issued 1956.

[7] Dash WC. J Appl Phys 1958;29:736.

[8] Hurle DTJ. J Cryst Growth 1977;42:473.

[9] Tan TY, Gardner EE, Tice WK. Appl Phys Lett 1977;30:175.

[10] Voronkov VV. J Growth 1982;59:625.

[11] Series RW, Hurle DTJ. J Cryst Growth 1991;113:305.

[12] Eidenzon AM, Puzanov NI. Inorg Mater 1997;33(3):219.

[13] Shimura F. Semiconductor silicon crystal technology. San Diego (USA): Academic Press; 1988.

[14] Zulehner W, Huber D. Crystals, vol. 8. Berlin: Springer; 1982. 1.

[15] Reimann C, Trempa M, Jung T, Friedrich J, Müller G. J Cryst Growth 2010;312:878.

[16] Hull R, editor. Properties of crystalline silicon. London (United Kingdom): INSPEC, The Institution of Electrical Engineers; 1999.

[17] Mühe A, Müller G. Microelectron Eng 2001;56(1–2):147.

[18] Krause M, Friedrich J, Müller G. Mater Sci Semicond Process 2003;5:361.

[19] Ceccaroli B, Lohne O. Solar grade silicon feedstock. In: Luque A, Hegedus S, editors. Handbook of photovoltaic science and engineering. 2nd ed. Chichester (United Kingdom): John Wiley & Sons; 2011. p. 169.

[20] Keller W, Muehlbauer A. Floating-zone silicon. In: Wilcox WR, editor. Preparation and properties of solid state materials, vol. 5. New York (USA): Marcel Dekker; 1981.

[21] Ziegler G. Z Naturforsch 1961;16a:219.

[22] Molchanov A, private communication.

[23] Kawado S, Taishi T, Iida S, Suzuki Y, Chikaura Y, Kajiwara K. J Phys D Appl Phys 2005;38:A17.

[24] Kim KM, Smetana P. J Cryst Growth 1990;100:527.

[25] Huang X, Taishi T, Yonenaga I, Hoshikawa K. Jpn J Appl Phys 2000;39(11B):1115.

[26] Friedrich J. Further developments of software tools and their usage for description of the Czochralski growth of silicon crystals for photovoltaic applications. Final report of BMBF project 03SF0379C; 2012. http://dx.doi.org/10.2314/GBV:747129797.

[27] Jackson K. Actual concepts of interface kinetics. In: Müller G, Metois JJ, Rudolph P, editors. Crystal growth – from fundamentals to technology. Amsterdam (The Netherlands): Elsevier; 2004. p. 27.

[28] Voronkov VV. J Cryst Growth 1981;52:311.

[29] Müller G. Crystal growth from the melt. Crystals, vol. 12. Berlin (Germany): Springer; 1988.

[30] Ciszek TF. J Cryst Growth 1971;10:63.

[31] Liaw HM. Crystal growth of silicon. In: O'Mara WC, Herring RB, Hunt LP, editors. Handbook of semiconductor technology. Park Ridge (USA): Noyes Publications; 1990. p. 94.

[32] Kalaev VV, Evstratov IY, Makarov YN. J Cryst Growth 2003;249:87.

[33] Schmid F, Khattak CP, Digges TG, Kaufman L. J Electrochem Soc 1979;126(6):935.

[34] Lan CW, Hsieh CK, Hsu WC. Czochralski silicon crystal growth for photovoltaic applications. In: Nakajima K, Usami N, editors. Crystal growth of silicon for solar cells. Berlin (Germany): Springer; 2009. p. 25.

[35] Campbell TA, Schweizer M, Dold P, Cröll A, Benz KW. J Cryst Growth 2001;226:231.

[36] Krishnamurti R. J Fluid Mech 1973;60(2):285.

[37] Gräbner O, Mühe A, Müller G, Tomzig E, Virbulis J, von Ammon W. Mater Sci Eng B 2000;73:130.

[38] von Ammon W. Silicon crystal growth. In: Müller G, Metois JJ, Rudolph P, editors. Crystal growth – from fundamentals to technology. Amsterdam (The Netherlands): Elsevier; 2004. p. 27.

[39] Muiznieks A, Krauze A, Nacke B. J Cryst Growth 2007;303:211.

[40] Hibiya T. J Mater Sci 2005;40:2417.

[41] Müller G, Gräbner O, Vizman D. Simulation of crystal pulling and comparison to experimental analysis Cz-process. In: Oral presentation, Electrochemical Society meeting, ninth international symposium on silicon materials science and technology, Philadelphia, USA; May 12–17, 2002.

[42] Gräbner O, Müller G, Virbulis J, Tomzig E, von Ammon W. Microelectron Eng 2001;56:83.

[43] Dornberger E, Tomzig E, Seidl A, Schmitt S, Leister H-J, Schmitt Ch, et al. J Cryst Growth 1997; 180:461.

[44] Vizman D, Friedrich J, Müller G. J Cryst Growth 2001;230:73.

[45] Seidl A, McCord G, Müller G, Leister H-J. J Cryst Growth 1994;137:326.

[46] Kishida Y, Tanaka M, Hisao E. J Cryst Growth 1993;130:75.

[47] Lin W, Benson KE. Annu Rev Mater Sci 1987;17:273.

[48] Su W, Zuo R, Mazaev K, Kalaev V. J Cryst Growth 2010;312:495.

[49] Gao B, Kakimoto K. J Cryst Growth 2010;312:2972.

[50] Smirnov AD, Kalaev VV. J Cryst Growth 2008;310:2970.

[51] Kalaev VV. J Cryst Growth 2007;303:203.

[52] Raufeisen A, Breuer M, Botsch T, Delgado A. Int J Heat Mass Transfer 2008;51:6219.

[53] Kirpo M. J Cryst Growth 2013;371:60.

[54] Jung T, Seebeck J, Friedrich J. J Cryst Growth 2013;368:72.

[55] Collet Y, Magotte O, Van den Bogaert N, Rolinsky R, Loix F, Jacot M, et al. J Cryst Growth 2012;360:18.

[56] von Ammon W, Gelfgat Y, Gorbunov L, Muehlbauer A, Muiznieks A, Makarov Y, et al. In: Proceedings of 6th PAMIR international conference on fundamental and applied MHD; 2005. p. 41.

[57] Tomzig E, Virbulis J, Ammon W, Gelfgat Y, Gorbunov L. Mater Sci Semicond Process 2002; 5(4–5):347.

[58] Friedrich J. Control of melt convection in VGF and CZ crystal growth configurations by using magnetic fields: theory and examples. In: Dost S, Okano Y, editors. Crystal growth under applied Fields. Kerala (India): Transworld Research Network 37/661(2); 2007. p. 32.

[59] Kakimoto K, Yi K-W. Phys B Condens Matter 1996;216:406.

[60] Friedrich J. [Ph.D. thesis]. Germany: University Erlangen – Nuremberg; 1996.

[61] Langlois WE, Hjellming LN, Walker JS. J Cryst Growth 1987;83:51.

[62] Vizman D, Friedrich J, Mueller G. In: Proceedings of the 5th international Pamir conference, fundamental and applied MHD; 2002. p. 19.

[63] Watanabe M, Eguchi M, Wang W, Hibiya T, Kuragaki S. J Cryst Growth 2002;237–239:1657.

[64] Watanabe M, Vizman D, Friedrich J, Mueller G. J Cryst Growth 2006;292(2):252.

[65] Brueckner FU, Schwerdtfeger K. J Cryst Growth 1994;139(3–4):35.

[66] Rudolph P. J Cryst Growth 2008;310:1298.

[67] Rudolph P, Czupalla M, Lux B, Kirscht F, Frank-Rotsch Ch, Miller W, et al. J Cryst Growth 2011;318:249.

[68] Burton JA, Prim RC, Slichter WP. J Chem Phys 1953;21:1987.

[69] Cochran WG. Math Proc Cambridge Philos Soc 1934;30(3):365.

[70] Kakimoto K, Ozoe H. J Electrochem Soc 1998;145(5):1692.

[71] Liu L, Nakano S, Kakimoto K. J Cryst Growth 2007;299:48.

[72] Wilke KT, Bohm J. Kristallzüchtung. Frankfurt: Harry Deutsch Verlag; 1988.

[73] von Karman T. Nachrichten von der Gesellschaft der Wissenschaften zu Göttingen. Fachgruppe 1 (Mathematik) 1930;5:58.

[74] Scheil E. Z Met 1942;34:70.

[75] Bkadshaw SE, Mlavsky AI. J Electron Control 1956;2(2):134.

[76] Hobgood HM, Braggins TT, Sopira MM, Swartz JC, Thomas RN. IEEE Trans Electron Devices 1980;27(1):14.

[77] Liu Z, Carlberg T. J Electrochem Soc 1993;140(7):2052.

[78] Fiegl G. Solid State Technol August 1983:121.

[79] Iino E, Takano K, Kimura M, Yamagishi H. Mater Sci Eng B 1996;36:146.

[80] Scala R, Porrini M, Borionetti G. Cryst Res Technol 2011;46(8):749.

[81] Friedrich J, Stockmeier L, Müller G. Acta Phys Pol A 2013;124(2):219.

[82] Tiller WA, Jackson KA, Rutter JW, Chalmers B. Acta Metall 1953;1(4):428.

[83] Hurle DTJ. Solid Sate Electron 1961;3:37.

[84] Voronkov VV, Falster R, Porrini M, Duchini J. Phys Status Solidi A 2012;209(10):1898.

[85] Watanabe M, Eguchi M, Hibiya T. J Cryst Growth 1998;193:402.

[86] Carruthers JR, Benson KE. Appl Phys Lett 1963;3:100.

[87] Barthel J, Jurisch M. Krist Tech 1973;8:199.

[88] Chiou HD. J Electrochem Soc 2000;147(1):345.

[89] Chen J, Yang D. Germanium doped czochralski silicon. In: Chu PK, editor. Advances in solid state circuits technologies. Croatia: INTECH; 2009. p. 446.

[90] Yu X, Chen J, Ma X, Yang D. Mater Sci Eng R 2013;74:1.

[91] Becker P, Bettin H, Kuetgens U, Hallmann-Seiffert B, Riemann H. J Phys D Appl Phys 2005;38:4109.

[92] Forster M, Fourmond E, Einhaus R, Lauvray H, Kraiem J, Lemiti M. Phys Status Solidi C 2011;8(3):678.

[93] Häßler C, Höfs H-U, Koch W, Stollwerck G, Müller A, Karg D, et al. Mater Sci Eng B 2000;71:39.

[94] Müller G, Mühe A, Backofen R, Tomzig E, von Ammon W. Microelectron Eng 1999;45:135.

[95] Hoshikawa K, Huang X. Mater Sci Eng B 2000;72:73.

[96] Hu SM, Patrick WJ. J Appl Phys 1975;46:1869.

[97] Rozgonyi GA, Deysher RP, Pearce CW. J Electrochem Soc 1976;123:747.

[98] Kissinger G, Vanhellemont J, Simeon E, Claeys C, Richter H. Mater Sci Eng B 1996;36:225.

[99] Kirscht FG, Furukawa Y, Seifert W, Seifert K, Schmalz K, Buczkowski A, et al. Mater Sci Eng B 1996;36:230.

[100] Schmidt J, Aberle AG, Hezel R. In: Proceedings of the 26th IEEE photovoltaic specialists conference Anaheim, USA; 1997. p. 11.

[101] Murin LI, Tolkacheva EA, Markevich VP, Peaker AR, Svensson BG, Lindström JL. Phys Status Solidi C 2011;8(3):709.

[102] Watkins GD, Corbett JW. Phys Rev 1961;121:1001.

[103] Watkins GD, Corbett JW. Phys Rev 1961;121:1015.

[104] Mikkelsen JC. Appl Phys Lett 1982;41:871.

[105] Wijaranakula W. Appl Phys Lett 1991;59(10):1185.

[106] Barcz A, Panas A, Jakiela R. Semicond Sci Technol 2004;19:1311.

[107] Mikkelsen JC. Mater Res Soc Symp Proc 1986;59:19.

[108] Newman RC. Mater Sci Eng B 1996;36:1.

[109] Senkader S, Wilshaw PR, Falster RJ. J Appl Phys 2001;89(9):4803.

[110] Ono T, Rozgonyi G, Asayama E, Horie H, Tsuya H, Sueoka K. Appl Phys Lett 1999;74(24):3648.

[111] Murphy JD, Wilshaw PR, Pygall BC, Senkader S, Falster RJ. J Appl Phys 2006;100:103531.

[112] Fuller CS, Ditzenberger JA, Hannay NB, Buehler E. Phys Rev 1954;96:833.

[113] Öder R, Wagner P. Mater Res Soc Symp Proc 1983;14:171.

[114] Suezawa M, Sumino K. Phys Status Solidi A 1984;82:235.

[115] Götz W, Pensl G, Zulehner W. Phys Rev B 1992;46:4312.

[116] Binetti S, Acciarri M, Brianza A, Savigni C, Pizzini S. Mater Sci Tecnol 1995;11:655.

[117] Pensl G, Schulz M, Hölzlein K, Bergholz W, Hutchison JL. Appl Phys A 1989;48:49.

[118] Knamori A, Kanamori M. J Appl Phys 1979;50:8095.

[119] Bender H. Phys Status Solidi A 1984;86:245.

[120] Vanhellemont J, Claeys C. J Appl Phys 1987;62(9):3960.

[121] Voronkov VV, Falster R. J Appl Phys 2002;91(9):5802.

[122] Vanhellemont J, De Gryse O, Clauws P. Appl Phys Lett 2005;86:221903.

[123] Kissinger G, Dabrowski J, Sattler A, Seuring C, Müller T, Richter H, et al. J Electrochem Soc 2007;154:H454.

[124] Shimura F, Hockett RS. Appl Phys Lett 1986;48:224.

[125] von Ammon W, Hoelzl R, Wetzel T, Zemke D, Raming G, Blietz M. Microelectron Eng 2003;66:234.

[126] Kishino S, Kanamori M, Yoshihizo N, Tajima M, Iizuka T. J Appl Phys 1978;50:8240.

[127] Shimura F. J Appl Phys 1986;59:3251.

[128] Gupta S, Messoloras S, Schneider JR, Stewart RJ, Zulehner W. J Appl Cryst 1991;24:576.

[129] Chen J, Yang D, Li H, Ma X, Que D. J Appl Phys 2006;99:073509.

[130] Jablonski J, Shen B, Mchedlidze TR, Imai M, Sumino K. Mater Sci Forum 1995;196–201:1859.

[131] Sueoka K, Akatsuka M, Nishihara K, Yamamoto T, Kobayashi S. Mater Sci Forum 1995;196–201:1737.

[132] von Ammon W. Defects in monocrystalline silicon. In: Kasap S, Capper P, editors. Springer handbook of electronic and photonic materials. Berlin (Germany): Springer Science and Business Media; 2006. p. 101.

[133] Nakai K, Hasebe M, Ohta K, Ohashi W. J Cryst Growth 2000;210:20.

[134] Petroff PM, de Kock AJR. J Cryst Growth 1975;30:117.

[135] Sadamitsu S, Umeno S, Koike Y, Hourai M, Sumita S, Shigematsu T. Jpn J Appl Phys 1993;32:3675.

[136] Schmolke R, Angelberger W, von Ammon W, Bender H. Solid State Phenom 2002;82–84:231.

[137] Föll H, Gösele U, Kolbesen BO. J Cryst Growth 1977;40:90.

[138] de Kock AJR. Philips Res Rep 1973;(Suppl. 1).

[139] Föll H, Kolbesen BO. Appl Phys 1975;8:319.

[140] Itsumi M, Akiya H, Ueki T, Tomita M, Yamawaki M. J Appl Phys 1995;78(10):5984.

[141] Vanhellemont J, Dornberger E, Esfandyari J, Kissinger G, Trauwaert M-A, Bender H, et al. Trans. Tech. Publications, Switzerland Mater Sci Forum 1997;258–263(1):341.

[142] Bergholz W, Mohr W, Drewes W. Mater Sci Eng 1989;B4:359.

[143] d' Aragona F Secco. J Electrochem Soc 1972;119(7):948.

[144] Yamagishi H, Fusegawa I, Fujimaki N, Katayama M. Semicond Sci Technol 1992;7:A135.

[145] Roksnoer PJ, Van de Boom MMB. J Cryst Growth 1981;53:563.

[146] Ryuta J, Morita E, Tanaka T, Shimanuki Y. Jpn Appl Phys 1990;29:L1947.

[147] Takahashi J, Nakai K, Kawakami K, Inoue Y, Yokota H, Tachikawa A, et al. Jpn J Appl Phys 2003; 42:363.

[148] Nishikawa H, Tanaka T, Yanase Y, Hourai M, Sano M, Tsuya H. Jpn J Appl Phys 1997;36:6595.

[149] Sinno T. In: Huff HR, Fabry L, Kishino S, editors. Proc. 9th int. symp. on silicon materials science and technology. Semiconductor silicon 2002. Pennington (USA): The Electrochemical Society; 2002. p. 212.

[150] Sinno T, Dornberger E, von Ammon W, Brown RA, Dupret F. Mater Sci Eng 2000;28:149.

[151] Voronkov VV, Falster R. J Appl Phys 1999;86(11):5975.

[152] Abe T, Takahashi T. J Cryst Growth 2012;334:16.

[153] Vanhellemont J. J Cryst Growth 2012;352:21.

[154] Sueoka K, Kamiyama E, Kariyazaki H. J Appl Phys 2012;111:093529.

[155] von Ammon W, Dornberger E, Oelkrug H, Weidner H. J Cryst Growth 1995;151:273.

[156] Furukawa J, Tanaka H, Nakada Y, Ono N, Shiraki H. J Cryst Growth 2000;210:26.

[157] Dornberger E, Esfandyari J, Gräf D, Vanhellemont J, Lambert U, Dupret F, et al. In: Kolbesen B, Stallhofer P, Claeys C, Tardiff F, editors. Crystalline defects and contamination control: their impact and control in device manufacturing II. Pennington (USA): The Electrochemical Society; 1997. p. 40.

[158] Dornberger E, Esfandyari J, Vanhellemont J, Gräf D, Lambert U, Dupret F, et al. In: Huff H, Gösele U, Tsuya H, editors. Semiconductor silicon. Pennington (USA): The Electrochemical Society; 1998. p. 490.

[159] Voronkov VV, Falster R. J Cryst Growth 1998;194:76.

[160] Abe T, Kimura M. In: Huff HR, et al., editors. Semiconductor silicon 1990. Pennington (USA): The Electrochem. Soc.; 1990. p. 105.

[161] von Ammon W. Extended Abstracts. In: Huff HR, Gösele U, Tsuya H, editors. Semiconductor silicon 1998, PV 98-1. Pennington (USA): The Electrochemical Society; 1998. Abstract No. 512.

[162] von Ammon W, Hölzl R, Virbulis J, Dornberger E, Schmolke R, Gräf D. J Cryst Growth 2001;226:19.

[163] Gräf D, Lambert U, Schmolke R, Wahlich R, Siebert W, Daub E, et al. Electrochem Soc Proc 2000; 2000-17:319.

[164] Voronkov VV, Falster R. J Electrochem Soc 2002;149(3):G167.

[165] Ono T, Umeno S, Tanaka T, Asayama E, Hourai M. In: Proceedings of the forum on the science and technology of silicon materials 2001; 2001. p. 95.

[166] Nakamura K, Saishoji T, Togawa S, Tomioka J. In: Proceedings of the forum on the science and technology of silicon materials 2001; 2001. p. 109.

[167] Yamagishi H, Fusegawa I, Takano K, Iino E, Fujimaki N, Ohta T, et al. In: Huff HR, Bergholz W, Sumino K, editors. Semiconductor silicon 1994, PV 94-10. Pennington (USA): The Electrochemical Society; 1994. p. 124.

[168] Suhren M, Gräf D, Lambert U, Wagner P. Electrochem Soc Proc 1996;96(13):132.

[169] Borionetti G, Gambaro D, Porrini M, Voronkov VV. Electrochem Soc Proc 2002;2002(2):505.

[170] Voronkov VV, Falster R. J Appl Phys 2000;87(9):4126.

[171] Sinno T, Susanto H, Brown R, von Ammon W, Dornberger E. Appl Phys Lett 1999;75:1544.

[172] Abe T, Masui T, Harada H, hikawa JC. In: Bullis WM, Broyda S, editors. VLSI science and technology. Pennington (USA): The Electrochem. Soc.; 1985. p. 543.

[173] Takeda R, Minami T, Saito H, Hirano Y, Fujimori H, Kashima K, et al. Electrochem Soc 2000;PV 2000-17:331.

[174] Yang D. Phys Status Solidi A 2005;202(5):931.

[175] von Ammon W. J Jpn Assoc Cryst Growth 2000;27(2):8.

[176] Minami T, Maeda S, Higasa M, Kashima K. J Cryst Growth 2011;318:196.

[177] Kemmochi K, Mosier RO, Spencer PG, EP1319736 A1.

[178] Raufeisen A, Breuer M, Botsch T, Delgado A. Comput Fluids 2009;38:1549.

[179] von Ammon W, Dornberger E, Hansson PO. J Cryst Growth 1999;198/199:390.

[180] von Ammon W. In: Umeno M, editor. Proceedings of the 2nd international symposium on advanced science and technology of silicon materials; 1996. p. 233.

[181] Merker R. Silizium – das High-Tech Erfolgsmaterial der Mikroelektronik erobert neue Einsatzgebiete. at 6th Leibniz Conf. of Advanced Science; 2008. www.leibniz-institut.de.

[182] Pizzini S. Sol Energy Mater Sol Cells 2010;94(9):1528.

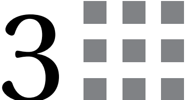

3 Liquid Encapsulation and Related Technologies for the Czochralski Growth of Semiconductor Compounds

J. Brian Mullin

ELECTRONIC MATERIALS CONSULTANCY, POOLE, UK

CHAPTER OUTLINE

3.1 Introduction ... 106
3.1.1 Historical Background ... 106
3.1.2 Significant Semiconductor Properties ... 107
3.2 Pressure-Balancing Czochralski Growth ... 108
3.2.1 Vapor Pressure–Controlled Cz Growth ... 109
3.2.2 Liquid-Encapsulated Czochralski ... 113
3.2.2.1 InAs and GaAs ... 113
3.2.2.2 InP and GaP ... 114
3.2.2.3 CdTe, ZnTe, and ZnSe ... 118
3.2.3 Magnetic Liquid–Encapsulated Kyropoulos ... 119
3.3 Growth Constraints to Crystal Quality in LEC and Related Technologies ... 119
3.3.1 Evaporative Group V Loss from the Crystal Emerging from the B_2O_3 ... 119
3.3.2 Point Defects ... 120
3.3.3 Facets and Twinning ... 121
3.3.4 Growth from Nonstoichiometric and Alloy Melts ... 124
3.3.5 Role of B_2O_3 ... 126
3.4 Summary ... 127
References ... 128

Handbook of Crystal Growth. http://dx.doi.org/10.1016/B978-0-444-63303-3.00003-1
Copyright © 2015 Elsevier B.V. All rights reserved.

3.1 Introduction

It is now more than half a century since the pioneering work on the semiconducting properties of germanium, with its potential device applications stimulated a curiosity to investigate the related properties of silicon and those of the III-Vs, II-Vs, and other potential semiconductors. The explosion of knowledge of these and related materials has fueled the evolution of our current technological age, an age that can be compared in its importance to the Industrial Revolution. The literature on the semiconducting compounds is vast, and this review will be limited to the evolution of some key developments of our knowledge on the growth of those significant compounds, which have been grown by liquid-encapsulated Czochralski (LEC), pressure balancing (PB), or vapor pressure–controlled (VCz) Czochralski-related techniques. The primary focus of the chapter will be on those compounds that dissociate at melting point, especially the compounds of major commercial importance (GaAs and InP), but also InSb, GaSb, GaP, and CdTe are considered.

It is significant that, although the development of semiconductor grade Ge took approximately a decade, the comparable research and development effort to produce single crystal compounds suitable for high-performance devices of the readily dissociable III-V compounds has followed a much slower evolution and is still in progress. But, as a result, the detailed scientific studies required to solve the problematic growth problems limiting the development of these materials have created a vast wealth of crystal growth knowledge.

3.1.1 Historical Background

One's vision of the context of the evolution of any technology is a personal one. The author is no exception and would apologize for any lack of appreciation of a more accurate appraisal.

The early development of the application of Czochralski (Cz)–related growth technologies to the growth of semiconducting compounds has been reviewed by Hurle and Cockayne in volume 2 of the first edition of this handbook [1]. A less accessible review on III-V compounds by the author in 2004 [2] provides the background for this review. Other reviews [3–7] provide additional background information to early work on compound semiconductors.

However, to provide a framework for this review, it is appropriate to highlight and revisit some of the key characteristics of the Czochralski-related pulling technique to the growth of these compounds.

The essence of the original method is the use of a small, single, crystal seed that acts as a nucleus on which to propagate a larger single crystal from a melt. Czochralski [8] used the method to pull metal crystals from a molten metal source. But, it was the work on germanium and the search for knowledge and understanding of semiconductors that brought about literally a revolutionary development. Teal and Little [9] applied controlled rotation to the seed during the pulling process [see review Teal [10]]. Rotation

helped to bring about a more controllable environment in the melt and a more uniform deposition of layers of crystal from the melt. But, to fully understand its significance, one needs to understand the scientific environment that produced this technology. Our knowledge of the science of semiconductors has required the relentless pursuit of two key requirements: first, there is an imperative need for high purity material; and second, there is a need to grow the material having an exceptionally high state of crystalline perfection to achieve effective semiconductor behavior.

Both of these factors are key considerations driving the development of the Czochralski-related pulling technique and will be reviewed in the analysis of the various developments. Device applications involving commercial exploitation are now a major driving force in the development of the technology of crystal growth. Roughly, the market is divided into two similarly sized fields of application, essentially the electronic field driven by high-frequency application and optoelectronics, which is driven by optical applications. They require differently specified material, which has affected the evolution and relative importance of different growth technologies.

Here, one must recognize that our knowledge from the commercial world is restricted and detailed knowledge of evolving technology is limited not only by commerciality but by the escalating cost of the increasingly large and costly crystal growth systems. Also, it is important to appreciate that crystal growth is a multivariant process, so that, for example, growth of a particular semiconductor by one technology may require a different technology, even for growth of material having the same specification if larger crystals are required to be more cost-effective.

First, then, the growth techniques themselves will be considered and, second, the growth phenomena that can impair crystalline perfection and potential device performance are examined.

3.1.2 Significant Semiconductor Properties

The key properties of the semiconductors that have to be taken into account in the development of a crystal growth technology are their melting points and the vapor pressures at their melting points. In addition, other critical properties for the semiconductors considered in the following review are listed in Table 3.1.

The benign properties of InSb enabled it to be developed as a semiconducting compound readily in the era before the introduction of LEC technology. Thus, semiconductor behavior was demonstrated in InSb in a matter of months. This was a consequence of its negligible vapor pressure, 4×10^{-8} bar [2], at its low melting point (525 °C). However, it has taken several years to achieve an equivalent state of development for GaP. This is a consequence of its relatively high vapor pressure of 32 bar at its correspondingly high melting point of 1465 °C. Micklethwaite [11] has reviewed the Cz growth of InSb from a commercial aspect, highlighting the critical growth aspects in meeting device specifications, especially for infrared detector applications; they are still a major driving force in its use. Here, the material requirements are dominated by the commercial need for large

Table 3.1 Semiconductor Properties: Potential Constraints to Crystal Growth

Semiconductor	Melting Point (°C)	Dissociation Pressure at m.pt. (bar)	CRSS (Mpa) Near m.pt.	Thermal Conductivity κ (W/cm k) Near m.pt.
Si	1420		6–9	0.21
InSb	525	4×10^{-8}		0.04
GaSb	712	1×10^{-6}		0.09
InAs	943	0.33		0.08
GaAs	1238	2.2	0.3–0.5	0.07
InP	1062	27.5	0.6	0.09
GaP	1465	32		0.8
CdTe	1092	0.07	0.2	0.009

uniform crystals. Micklethwaite et al. [12], in 1996, reported the growth of 3-inch-diameter wafers using a conventional non-LEC pulling technology. More recently, Martinez [13], of Galaxy Semiconductors, now part of the IQE group, has reported the production of 125-mm (5-inch)-diameter InSb and 100-mm (4-inch)-diameter GaSb.

3.2 Pressure-Balancing Czochralski Growth

Before the introduction of the LEC technology to the growth of InAs and GaAs, a PB technology was developed at the Royal Radar Establishment (RRE) subsequently renamed Royal Signals and Radar Establishment (RSRE) the author's laboratory [14]. The technology is illustrated in Figure 3.1. Here, the crystal was grown in a hot pulling chamber, which prevented continuous loss of As vapor. The walls of the pulling chamber were sufficiently hot to prevent condensation of As, a hot wall concept. The versatility of the system is discussed herein, where the ability to form the III-Vs in situ and by implication the ability to control the group V pressure independently from a separate source are discussed. A novel feature of the system is the use of a liquid seal of B_2O_3, which allowed one to equilibrate the pressure in the system; one could pressure balance the evaporative As pressure. The problem anticipated in the system was the prevention of As escaping from the pulling chamber between the pull rod bearing and the pull rod. This was achieved by means of a thread on the BN (boron nitride) bearing, which acted as an Archimedes' screw and prevented the B_2O_3 from running down the pull rod as it rotated.

A detailed account of the design and application of the technique to the growth of crystals of InAs and GaAs is given in the publication [14]. The technique worked effectively well and demonstrated the system's potential.

Some 10 years later, in 1983, Azuma [15] patented a related technology for the growth of InP. The design incorporated a separate source of phosphorus. The phosphorus could be deposited on the heated walls of the upper part of the chamber. The temperature of the P_4 source could be adjusted to maintain a balancing vapor pressure of P_4 that prevented evaporative loss from the crystal as it emerged through the surface of the B_2O_3. In addition, the pull rod was pulled through a cup-shaped reservoir of B_2O_3 that acted as a liquid seal.

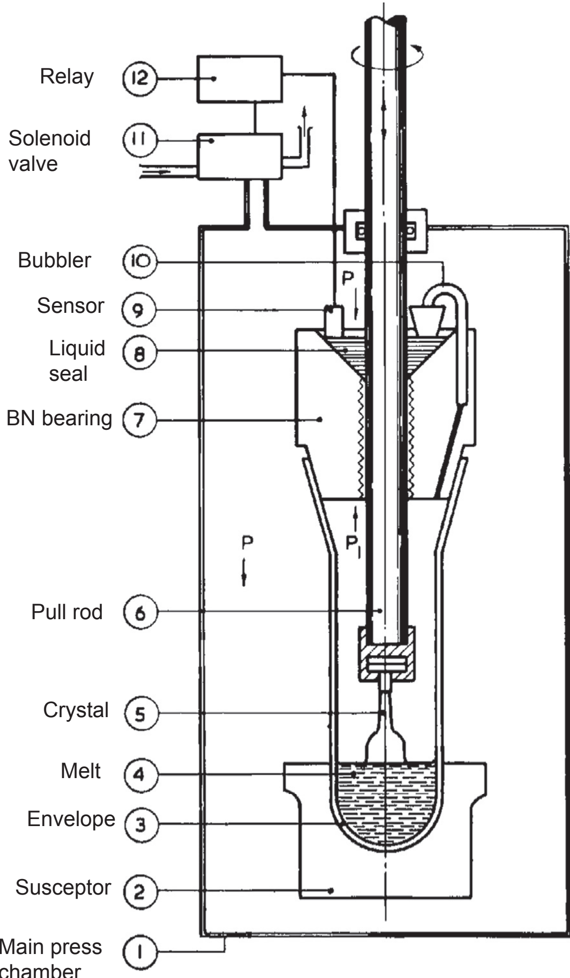

FIGURE 3.1 A schematic diagram showing the principle of pressure balancing. The walls of the inner quartz envelope are maintained at temperature to prevent group V condensation. The inert gas pressure P in the outer chamber is maintained at a pressure to balance the dissociation pressure of the group V component, which is sensed by the surface position of the B_2O_3 liquid seal. *Original after Mullin et al. [14] schematic [2] with permission of Elsevier.*

3.2.1 Vapor Pressure–Controlled Cz Growth

Tada and Tatsumi [16], in a review, reported a similar concept but omitted the B_2O_3 upper seal (see patent in 1984). This type of technology was initially reviewed by Neubert and Rudolph [3]. They assessed the advantages and disadvantages of the technique and compared the technique to the then known status of LEC. A significant problem in the growth of LEC GaAs is the thermoelastic stress, which can readily cause slip and dislocation formation in the newly formed crystal. Crucially, the critical resolved shear stress (CRSS) for GaAs at the growth temperature is sufficiently low for slip and dislocation

production to occur: it is ~0.5 MPa for GaAs compared with 6–9 Mpa for Si, a stronger group IV semiconductor. This CRSS problem is exacerbated in the conventional Cz LEC growth of GaAs because of the relatively high temperature gradients and the curvature they impart to the growth surface. Even a small departure from planarity of the growth surface can produce a stress greater than the CRSS. The ease of dislocation multiplication is enhanced with an increase in crystal diameter because the acting shear stress is proportional to the crystal diameter. Interface shape is, therefore, a controlling factor. In addition, the point defects can condense on cooling and initiate the formation of dislocation loops and the formation of precipitates and microvoids. The higher the concentration of point defects, the lower the CRSS. Jordan et al. [17]. have performed a useful thermoelastic analysis of the effect of stress in LEC GaAs and InP and have shown that dislocation multiplication is a result of glide caused by excessive stress. They concluded that reducing the temperature gradient in the crystal during growth could be beneficial, as could moderate appropriate doping. Neubert and Rudolph [3] also highlighted the need to reduce the temperature gradients and noted the difficulty in achieving near-interface planarity as the crystal diameter is increased. In their VCz design, they introduced an internal heater arrangement to the system in an effort to reduce the temperature gradients. A carefully designed As source was used to maintain an As pressure sufficient to prevent loss of As from the crystal growing under the lower temperature gradient conditions as it emerged from the B_2O_3. Thus, it was possible to dispense with or retain the B_2O_3 in their VCz growth system. They developed their technique to commercialize its use for the growth of single crystals of GaAs. A diagram showing the concept of their apparatus is shown in Figure 3.2. However, the lower

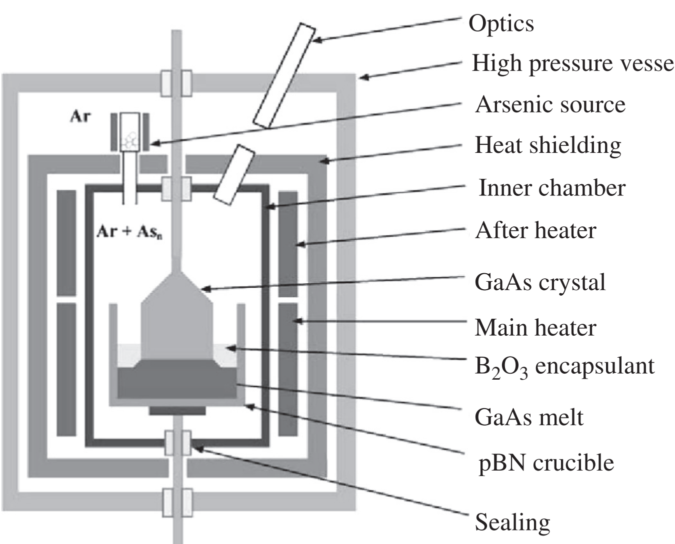

FIGURE 3.2 Schematic diagram of the vapor pressure controlled (VCz) system. The As source is designed to provide a controlled pressure of arsenic vapor sufficient to prevent As loss from the grown crystal. *After Neubert and Rudolph [3] with permission of Elsevier.*

temperature gradients that are a feature of this VCz technology have the potential to create a stability control problem; the control of crystal growth can be more difficult than with conventional LEC Cz technology. The need for careful thermal design has required the development of ever more sophisticated thermal modeling, such as that reported by Yakovlev [18], or the three-dimensional modelling, as shown by Vizman et al. [19], who advocated the use of magnetic fields.

Despite its potential stability problem, the lower temperature gradients using VCz technology provide a significant advantage over conventional LEC Cz technology. An important gain is the production of crystals having significantly lower dislocation densities than had been achieved by LEC growth. In their initial work, they reported high-quality crystals 10 mm in diameter with etch pit densities $<10^4$ cm^3. This is to be compared with typical LEC crystals having an inhomogeneous radial distribution in the range from 0.5 to 1×10^5 cm^2.

Kiessling et al. [20] used this VCz apparatus but dispensed with the use of B_2O_3 to grow from Ga-rich melts. This was achieved by controlling the As vapor pressure during growth. This needed a temperature-controlled source of As with access to the inner pulling chamber, whose walls were separately heated. The low-temperature gradients were advantageous in minimizing the dislocation density of the GaAs crystals. The principle advantages with regard to the quality of the grown crystals were a much reduced boron concentration and the ability to reduce and control the carbon content of the GaAs. Kiessling et al. [21] have reported a further more detailed review of this work, highlighting the reduction in the effect of As precipitates with increase in the melt Ga content, although a Ga-rich melt can enhance the probability of Ga inclusions. The ability to grow GaAs crystals that were twin free and without Ga inclusions has subsequently been reported in a later study by Rudolph and Kiessling [22]. It is a clear example of the value of the VCz technique without B_2O_3, where the melt composition can be independently controlled. The technique highlights the importance of definitive studies on the chemistry of point defect formation.

In a more recent development of the VCz system, Neubert et al. [23] reintroduced the use of B_2O_3 in a novel way to reduce temperature gradients. Their design (Figure 3.3) incorporates a silica tube sealed against a flat upper platform. The silica tube or bell dips into a layer of B_2O_3 covering the melt of GaAs contained in a heated crucible. A bearing is joined to the top of the platform, allowing a pull rod to pass through so that a crystal could be pulled from the melt. The bearing is attached to a separate pulling system, which could adjust the position of the dipping position of the silica tube or bell in the B_2O_3 at an appropriate level during growth. The crucible is surrounded with heaters. The whole assembly rests inside the main outer chamber, which had bearings for both pull rods. The silica tube isolates the growing crystal from the insulation and the cold crucible walls, providing a more uniform temperature environment. The design reduced the temperature gradients and the dimensions of any potential Bénard cells (Section 3.1) and, hence, minimize convection and potential turbulence.

The significance and potential role of this development can be seen in the elegant 160-mm-diameter VCz GaAs crystal Figure 3.4 grown using this technology and reported by Neubert et al. [23].

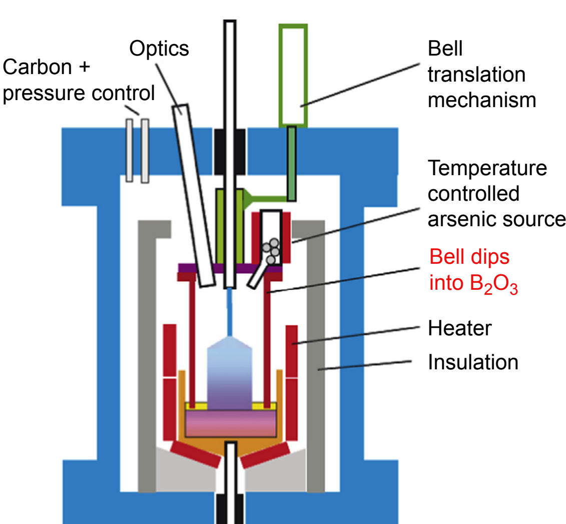

FIGURE 3.3 Schematic diagram of a modified vapour pressure–controlled (VCz) system which provides a silica tube or "bell" aimed to isolate the growing crystal from turbulent convection and provide a lower temperature gradient environment. *After Neubert et al. [23] with permission of Elsevier.*

FIGURE 3.4 The 160-mm diameter GaAs grown by the modified vapour pressure–controlled (VCz) inside the diving bell using As vapor pressure control. *After Neubert et al. [23] with permission of Elsevier.*

3.2.2 Liquid-Encapsulated Czochralski

3.2.2.1 InAs and GaAs

The exploitation of the liquid encapsulation technique, [24] subsequently called the LEC process, has made a decisive impact on the growth technologies for all the III-Vs. The principle involved in liquid encapsulation was initially used by Metz, Miller, and Mazelsky [25] for growing the volatile compounds PbTe and PbSe to prevent their volatilization during Cz growth of these compounds. The essential feature of the B_2O_3 in the LEC process is the role it plays in encapsulating the melt, but it can also coat the crystal as it emerges from the melt surface with a film of B_2O_3 if there are appropriate temperature conditions. The B_2O_3 also coats the silica crucible.

A typical low-pressure apparatus is illustrated in Figure 3.5. It was used for the growth of both InAs and GaAs.

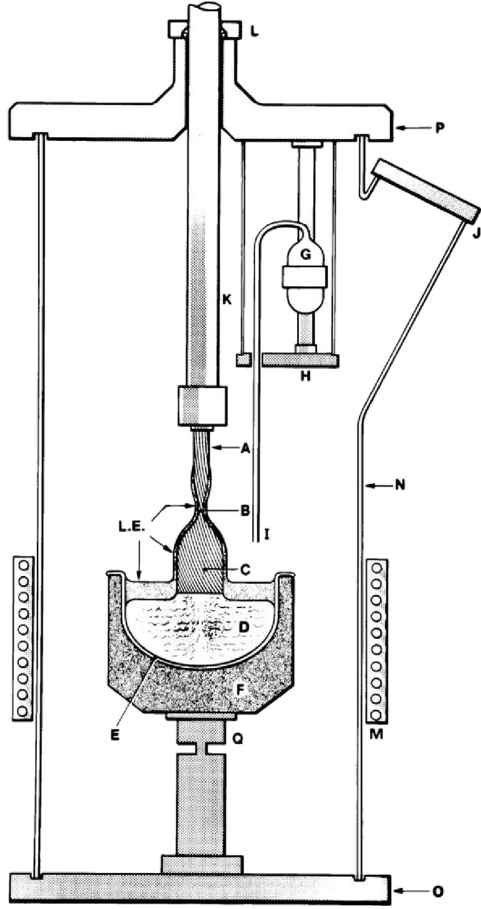

FIGURE 3.5 Cz liquid-encapsulated Czochralski (LEC) low pressure growth apparatus for InAs and GaAs. The silica outer vessel or growth chamber N which is some 150 mm in diameter is held between end plates O and P. The viewing port J is demountable. The induction heating coils couple into the graphite surround F mounted on Q. The seed A is fixed in the chuck on the pull rod K that rotates and moves through the bearing and seal L. The crystal C grows from the seed through a necking process at B, and on withdrawal pulls out a layer of B_2O_3 over its surface. *After Mullin et al. [2,24] with permission of Elsevier.*

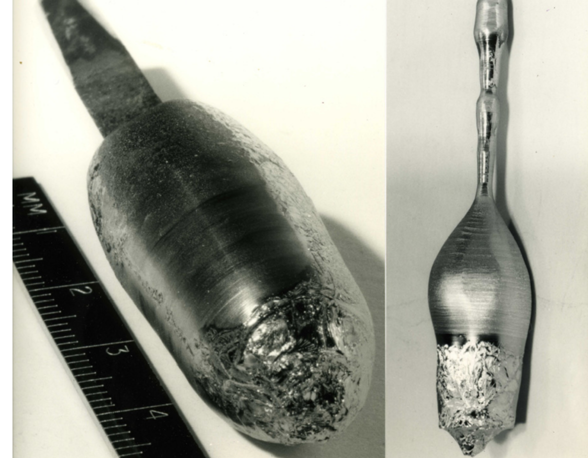

FIGURE 3.6 Two of the original crystals grown by the liquid-encapsulated Czochralski (LEC) technique (1965). Left InAs; right GaAs; note no scale but maximum diameter ~30/40 mm. *Courtesy of the author (original).*

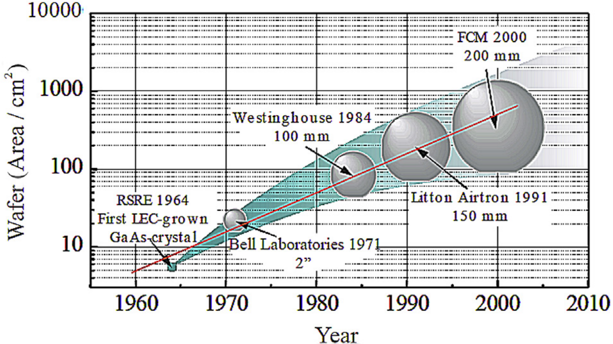

FIGURE 3.7 Diameter of SI GaAs single crystals grown by the liquid-encapsulated Czochralski (LEC) method. *Taken from Jurisch M, Eichler St. Extended abstract of Czochralski-symposium 03. Torun/Kcynia, Poland; April 26–27, 2003.*

Because the low-pressure system uses a silica growth chamber some 150 mm in diameter, the inert gas pressure required to suppress evaporation of the group V component must be limited to a few atmospheres on grounds of safety.

Examples of the original InAs and GaAs crystals grown by the LEC process are shown in Figure 3.6 and the typical properties reported in Ref. [24]. Now, some 35 years later, the LEC growth of GaA monocrystals with diameters between 75 and 150 mm is well established in mass production. Because lower specific costs per die are the main driving force in device manufacturing, the transition from laboratory scale to mass production has followed the inevitable logic for an increase in crystal (wafer) diameter and length exactly tailored to device-relevant properties. By 2009, the technology for industrial transfer of even 200-mm diameter crystals had been developed as reported by Jurisch et al. [27] (Figure 3.7).

3.2.2.2 InP and GaP

The growth and properties of the single crystals of both InP and GaP that were initially grown by the LEC technique are discussed by Mullin et al. [28] At the same time, Bass

et al. [29] reported the growth of GaP. The growth of group IV doped InP has also been reported Mullin et al. [30]. Examples of the first single crystals of InP and GaP are shown in Figure 3.8

Most of the phosphide publications concern InP and the need to prepare large-diameter, dislocation-free doped InP because its principle application is its role as a substrate material for laser fabrication. An example of a 3-inch LEC InP crystal is shown in Figure 3.9.

An interesting feature of the development involved in the technology required to grow such crystals, as reported by the authors, is the use of a magnetic field in a VCz puller, which stabilized the temperature fluctuations and enabled twin-free growth (Figure 3.9)

The principle problem with the growth of InP and GaP is the need to design a system to cope with dissociation pressures of ~27.5 and 32 atm, which are generated at their respective melting points of 1062 and 1465 °C. A really safe pressure vessel in a laboratory working environment is essential. A fully developed apparatus for growing InP or GaP is shown in Figure 3.10. The growth apparatus is fitted with a weighing machine, which could be programmed to control the crystal diameter during growth. In addition, there is a TV-viewing system. The theory of the weighing technique has been published as a

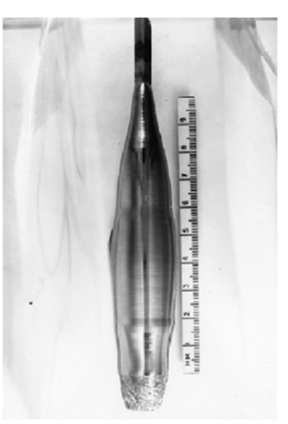

FIGURE 3.8 Examples of the first single crystals of InP and GaP grown using the liquid-encapsulated Czochralski (LEC) technique in a high pressure puller. *Reproduced from Ref. [6] with permission of Elsevier.*

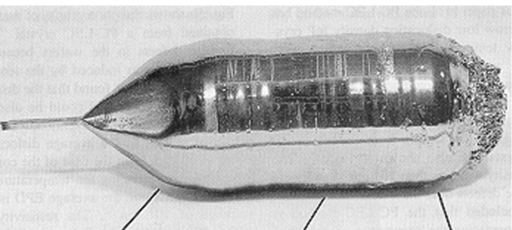

FIGURE 3.9 A 3-inch liquid-encapsulated Czochralski (LEC) InP. *Reproduced from Kawase et al. In: Proceedings of international conference on InP and related Materials (Nara 2001). p.13.*

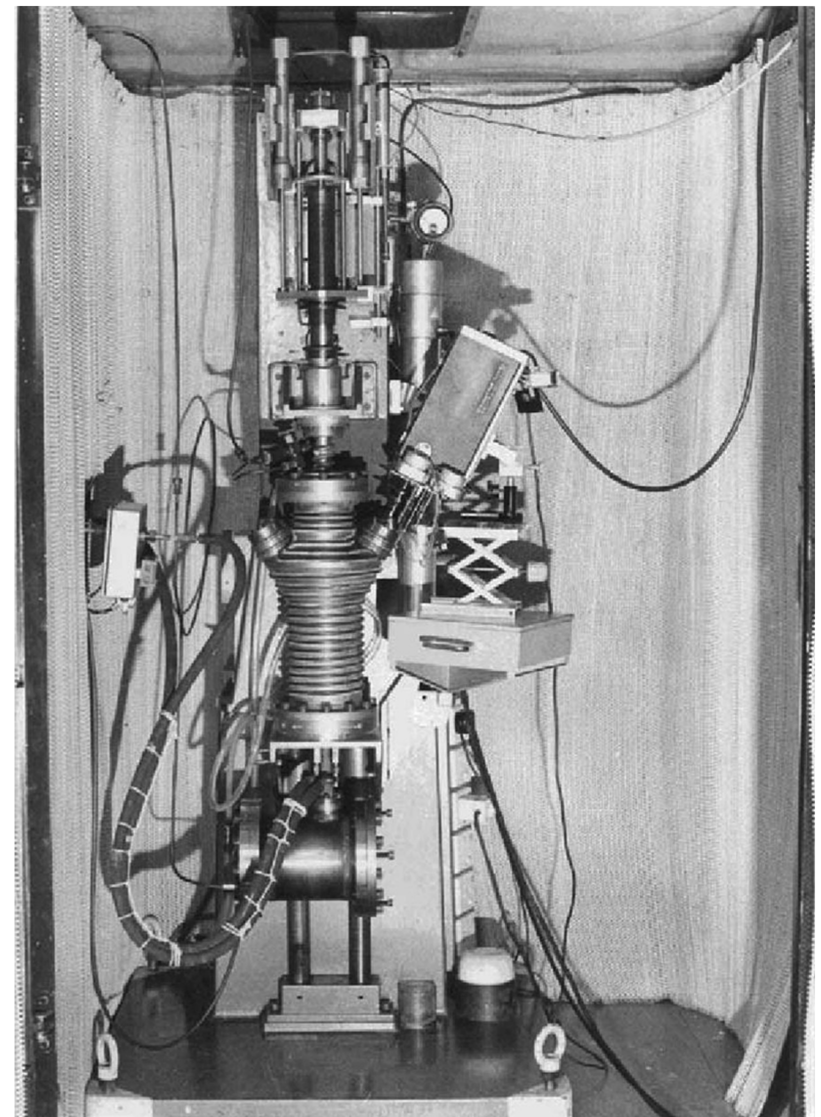

FIGURE 3.10 High-pressure liquid-encapsulated Czochralski (LEC) crystal puller developed at RSRE, showing water-cooled steel pressure vessel and two optical ports for viewing, one fitted with a video camera. Below the steel pressure vessel is a large chamber containing the weighing cell designed to provide data for controlling the crystal diameter. *After Ref. [2] with permission of Elsevier.*

low-order mathematical model by Satunkin [31], but more recently, he has published a seminal review [32]. The use of a custom-built pressure vessel is essential. The initial design and development with automatic diameter control is reviewed in reference [2].

The development of the pressure vessel design (Figure 3.11) involved many unexpected problems. The initial aim was to manufacture the pressure vessel as a

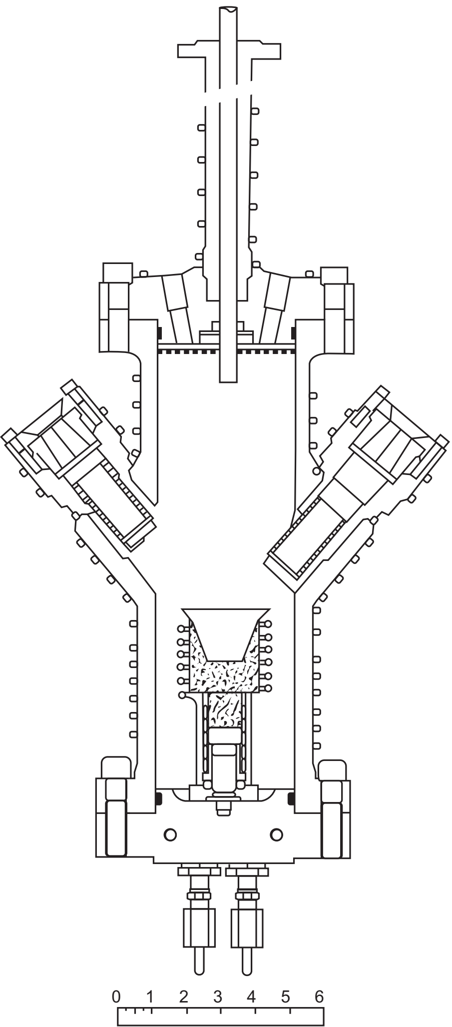

FIGURE 3.11 High-pressure liquid-encapsulated Czochralski (LEC) crystal puller developed at RSRE, showing water-cooled steel pressure vessel and two optical ports for viewing, one fitted with a video camera. Below the steel pressure vessel is a large chamber containing the weighing cell designed to provide data for controlling the crystal diameter. *After Ref. [2] with permission of Elsevier.*

casting, but the then current technology could not cope with the required size and quality of the pressure vessel. The working system was machined from a specially prepared high-quality steel ingot. The design was intended to grow crystals up to 200 bar. Flat silica windows were considered to be unsafe. A cone-shaped window of silica was used. The cone was fitted into the inverse cone-shaped steel holder using a thin In seal, which would be capable of strain relief at room temperature. The design ensured that the gas pressure would subject the silica to compression; it would not be safe under tension.

There was an imperative need also to demonstrate that appropriately designed pressure vessels could be safe to operate in the laboratory for the growth of these III-Vs. The solution to this problem was relatively straightforward. A growth chamber was taken to an experimental explosives establishment, completely filled with cordite (effectively gun powder), and when suitably located in a safe bunker the charge was ignited. The pressure in the chamber increased to some 10,000 atm in a few milliseconds. The chamber bulged, but held the pressure. The silica windows were undamaged. The experiment clearly demonstrated that the vessels offered a considerable margin of safety. There were many other technical problems which I will not go into. The 200-bar design was intended to grow II-VIs, but the development did not materialize because of the relative incompatibility of II-VIs with B_2O_3.

3.2.2.3 CdTe, ZnTe, and ZnSe

The LEC procedure, although initially aimed at the III-Vs, has also attracted limited application to some of the tellurides and selenides. The early studies identified some of the difficult growth control problems. A study on its application to CdTe has been reported by the author [33]. Crystals were pulled from the melt, but the quality of the crystals was poor. The crystals were twinned and had many large grains and dislocations. Hobgood et al. [34] have reported the growth of 1-kg crystals some 50 mm in diameter, but they, too, experienced twinning and polycrystallinity. They were able to seed <III> CdTe crystals of CdTe doped with Mn up to 0.20 mol fraction and this reduced the extent of the polycrystallinity, but there were still grains and twins. They noted that the crystals had a significant concentration of boron.

There are serious growth control problems. One of the design difficulties for the growth is to deal with the poor thermal conductivity of CdTe (Table 3.1). Some of the fundamental problems in the growth of CdTe have been reviewed by Rudolph [26]. The analysis was obtained during a study of the Bridgman growth of CdTe.

The LEC process has also been used by Hruban et al. [35] to prepare charges of ZnSe and to pull Cz crystals. A floating Si_3N_4 matrix or plate, which floated on the B_2O_3, substantially separated it from the melt. Immediately under the growing face of the growing crystal, the angular matrix protruded into the melt in an effort to limit the effects of the convecting melt. They also used the Kyropoulos procedure. This latter Kyropoulos procedure, which involved an LEC process, was used by Ashi et al. [36] to grow 80-mm-diameter single crystals of ZnTe.

In a review article on the melt growth of large-diameter elemental and compound semiconductors, Thomas et al. [37] proposed the use of magnetic fields greater than 2000 G to limit the thermal fluctuations. They also contrast the growth of these semiconductors together with their property-controlling properties that affect the quality of the crystals. The review provided the then (1993) current knowledge for a useful comparison of the growth of CdTe. It is evident that the knowledge being gained from the advanced LEC growth of the III-Vs is benefitting the growth of these materials.

3.2.3 Magnetic Liquid–Encapsulated Kyropoulos

A novel alternative way of using an encapsulant has been reported by Bliss et al. [38]. The technique, called magnetic liquid–encapsulated Kyropoulos (MLEK), involves the growth of the crystal under the encapsulant. This ensures growth occurs under a low-temperature gradient. The applied magnetic field dampens convection and potential turbulence. They were able to grow twin-free InP crystals with a convex growth surface that minimized the formation of edge facets and twins.

3.3 Growth Constraints to Crystal Quality in LEC and Related Technologies

3.3.1 Evaporative Group V Loss from the Crystal Emerging from the B_2O_3

The development of the high-pressure technology, however, poses more problems than simply designing a pressure vessel capable of withstanding the inert gas pressure.

Melts of the III-Vs rapidly lose their group V component, unless there is a pressure higher than the melt at least equal to the equilibrium vapor pressure of the group V component over the melt. This applies to all the arsenides and phosphides. As the crystal emerges above the surface of the B_2O_3, it can lose its inert protective layer. The inert gas pressure then cannot prevent group V evaporation from the exposed surface of the crystal. In the case of GaAs, a problem can arise with the Ga, which is liberated. It forms droplets that migrate under the applied temperature gradient into the crystal by temperature gradient zone melting. Ultimately, because the crystal grows faster than the droplet motion, the latter freezes in the solid. The resulting differential contraction between the frozen liquid droplet and the surrounding GaAs causes dislocation clusters.

The problem with InP is exacerbated by the relatively high inert gas pressure (in excess of 28 atm). Pressures in excess of 50 atm were often used in the mistaken belief that the higher the pressure, the greater the reduction in evaporative loss. Unfortunately, the higher pressures can result in turbulent gaseous convection. This major problem arises as a consequence of the additional potentially high-temperature gradients resulting from the need to keep the walls of the pressure vessel at a low temperature for safety reasons. This can generate large temperature gradients across the gas phase. The high gas velocities are the result of Rayleigh convection, which is driven by the high pressure, the large temperature differences, and the relatively large dimensions of the Bénard cells.

The convection can be assessed by consideration of the dimensions of the Bénard cells in the pressure vessel; its magnitude correlates with the value of the Rayleigh number Ra given as follows:

$$R_a = (T_h - T_c) g\, d^3\, P^2 / [T_m\, k\, \nu] \quad (3.1)$$

where $T_h - T_c$ is the vertical temperature difference across the volume of the convecting gas (the temperature difference between surfaces driving the Bénard cell), and T_m is an average gas temperature, g is the gravity, d is the depth of volume of the convecting gas, k is the thermal diffusivity, ν is the kinematic viscosity, and P is the gas pressure. The critical significance of Ra is that its magnitude depends on the square of the gas pressure, the cube of d, and the temperature difference between surfaces driving the convective Bénard cell. It is important, therefore, in the pulling systems, to avoid large free volumes with large temperature differences between hot and cold surfaces. The judicious use of baffles can reduce the dimensions of the Bénard cells and their associated temperature gradients. Although turbulence may be reduced or avoided, convection can still be present and its control is important. The problem of turbulence and excessive convection can be a significant problem as the size and diameter of crystals and their melts increase.

3.3.2 Point Defects

Our knowledge of the source of defect-related problems in the growth of the III-Vs has been stimulated by the drive to meet ever more demanding device specifications. It is a major topic beyond the scope of this chapter. Nevertheless, it is worth highlighting some of those significant aspects that are relevant to LEC-related growth. Each III-V and even minor variations in the growth technology of the same specified III-V can result in significantly different defect-related properties. Each specification could provide a review on its own; hence, only a more generalized assessment can be given here.

Even in the case of Si, which has received a longer and more sustained period of scientific study than any of the III-Vs, our knowledge is by no means complete. As temperatures increase higher than absolute 0, the number and complexity of point defects in materials increase. In the case of the III-V compounds, the process is additionally more complicated than for Ge or Si by the two different lattice sites, which can produce antisite locations for atoms, in addition to the interstitial and vacancy opportunities for each atom. That the component atoms can also produce charged species adds to the difficulties in understanding and controlling the properties of III-Vs grown from the melt. In addition, for the III-Vs, the equilibrium concentration of point defects at their melting points is generally significantly higher than is the case for Ge and Si.

Most of the defect- and dislocation-related studies in the III-Vs concern GaAs and InP, a consequence of their important device applications. For the crystal grower, Kröger's [39] fundamental study on defects in semiconductor compounds generally remains a seminal study. In this regard, a useful overview of defect formation, segregation, faceting, and twinning as a historical perspective to the melt growth of most semiconductors, not just III-Vs, was published in 2004 by Hurle and Rudolph [40].

They highlighted the difficulties in identifying and controlling defects. They consider that the identification of the various types and a knowledge of their concentrations

under different growth conditions to be one of the most important challenges facing the development of the III-Vs. Hurle pioneered a thermodynamic approach in 1995 [41] in an attempt to quantify the behavior of the point defects controlling the properties of GaAs. The model was able to relate to the concentration of As-vacancies or As-interstitials in the resulting crystal as a function of melt composition.

More recently, he has published a seminal article [42] in which he has extended his thermodynamic model to analyze all the binary zinc blended III-V compounds (Ga–In)-(P, As, Sb) using all the known important defects for which there is reasonable evidence in these materials. By using these data, he has been able to construct solidus curves for GaAs, InP, InSb, GaSb, and InAs. The model identified the dominant point defects in the arsenides and the phosphides to be vacancies and interstitials on the group V sites, whereas in the case of the antimonides, the dominant defects are vacancies on both lattice sites. Perhaps even more important, the concentrations of the charged native defects significantly exceed the intrinsic electron hole concentration at the melting point for GaAs, GaP, and GaSb. This means that the Fermi level in these materials at high growth temperatures is controlled by the native point defects, principally the group V vacancies, not by electron hole pair generation. The model provides a splendid framework for understanding what can happen not only during growth, but also as the crystal is cooled down, and also if it is subsequently annealed.

3.3.3 Facets and Twinning

Facet development during the melt growth of the III-Vs can be a significant limitation to the growth of all single crystal III-V compounds. Early work on the growth of InSb illustrated some of the main characteristics of facet behavior and provides a useful framework for comparing the behavior of other III-Vs. The early studies on InSb showed that the formation of facets was associated with two prominent phenomena, facet-related solute incorporation and twinning.

The first of these phenomena, the Facet Effect [43], was discovered in the course of initial studies during the crystal growth of pure InSb crystals. During their growth, an enhanced carrier concentration correlated directly with growth in a region where (111) facetted growth had occurred. The enhanced carriers were presumed to be due to a residual impurity Te. A detailed study [44] on the Facet Effect was performed using radioactive tellurium, ^{127}Te, which served as a marker for the history of facet formation and twinning behavior. The presence and relative concentration of ^{127}Te in cross-sectional slices of Cz grown ^{127}Te InSb was recorded using autoradiographs. The study revealed a significant difference in the behavior of (111) planes terminating in In atoms and those terminating in Sb atoms so called (111)In and (111)Sb, respectively. Twinning was more prevalent during the growth of (111)In planes. Figure 3.12 is a composite diagram showing clearly the difference in behavior of the (111)Sb and the (111)In facets.

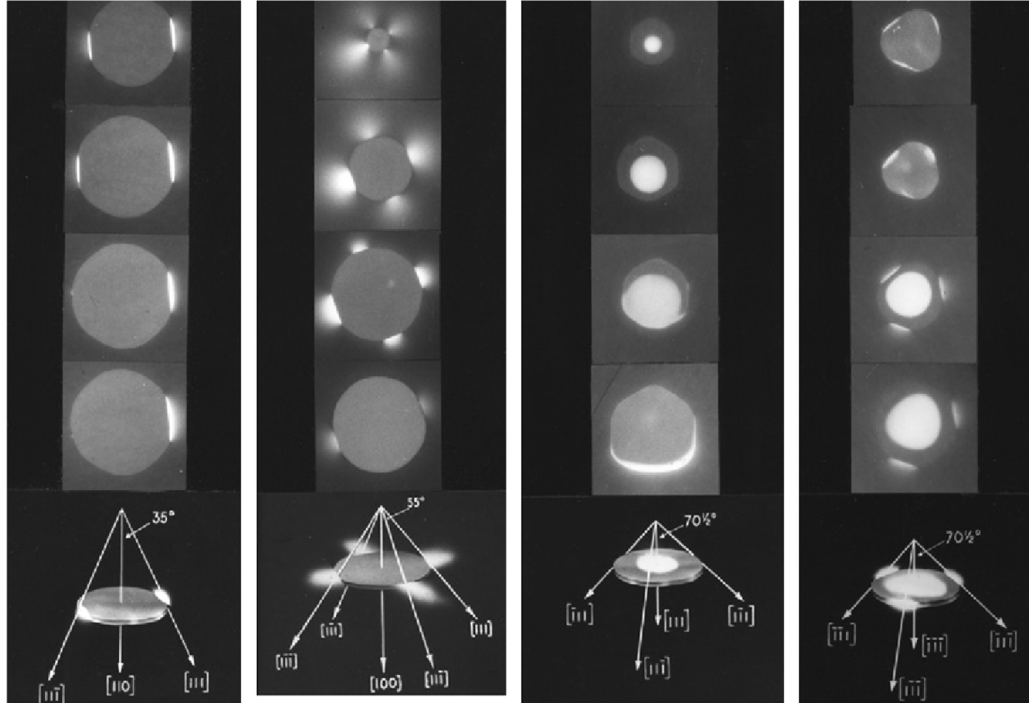

FIGURE 3.12 Effect of {111} facet evolution during the growth of InSb crystals grown in different growth directions as revealed by auto radiographic monitoring of the radioactive ^{127}Te doping: left to right <110>, <100>, <111> Sb and <111> In crystals. The bright regions reveal the presence of facets. In the <110> crystal, the (111)Sb edge facets develop preferentially and are larger than the (111)In facets. This is also obvious in the <100> crystal where the (111) Sb facets persist with growth in the fourth slice. Only the central or principle Sb facet can be seen in the <111> Sb grown crystal. For the <111> In grown crystal (111)Sb edge facets develop in addition to the central (111)In facet. In this crystal, the first two slices show regions of the principle (111)In facet. In the third section, three (111)Sb edge facets can be seen, but in the fourth section twinning has occurred and eliminated one of the (111)Sb facets. It is very rare to be able to grow twin free <111> In crystals. It was achieved by using an initially concave growth surface. *After Ref. [6] with permission of Elsevier.*

Twinning was so prevalent for growth in the (111)In direction that it was almost impossible to grow single crystals in that direction. Growth in the (111)Sb direction was less problematic with regard to twinning but not with regard to the uniformity of the radial ^{127}Te incorporation. It is evident that the central or principle (111)Sb facet, which is normal to the growth direction, produces a significantly enhanced ^{127}Te concentration. The principle (111)In facet during growth in the (111)In direction also causes marked radial nonuniformity. The development of edge facets can also cause radial nonuniformity, but not to the same extent. The magnitude of the Facet Effect has been assessed as the ratio of the concentration in the impurity or solute incorporated in a facetted region to that in an adjacent region in the nonfacetted region of growth. The magnitude of the facet ratio for Te was $\sim$6. Facet ratios for several solutes ranged from apparently 1 [45] for Ge to $\sim$6 for Te. The residual impurities in high purity InSb also showed a marked Facet Effect.

The presence of edge facets could be correlated with the incidence of twinning, where the (111)Sb facet, not the principle facet, was the most twin prone. The avoidance of edge facets enables the growth of twin-free, relatively radially uniform crystals. Facet development appears to be a necessary, but not sufficient, cause for twinning.

An elementary explanation of the Facet Effect can be appreciated by considering the nature of growth on the facetted surface compared with that at the edges adjacent to the facet. The facet forms as a consequence of the difficulty of nucleation on the smooth (111) surface. A region of supercooling thus develops adjacent to the facet when the growth surface is convex or flat but not concave. Nucleation, when it does occur under intense supercooling, produces a driving force, which causes rapid lateral growth of atomic layers on the facet. An impurity, such as Te, which is chemically adsorbed on the surface, can be trapped under nonequilibrium conditions by the rapid advance of such growth layers. The adjacent edges of the crystal, however, provide easy nucleation sites, where growth can occur under a condition of thermodynamic equilibrium.

Thus, to minimize the nonuniformity caused by either the principle (111) facet or the edge facets, it has been necessary to grow doped InSb crystals on a non <111> axis, while maintaining as far as possible a near planar growth surface. Considerable success was achieved by using the <311> Sb axis using a specially designed system involving electromagnetic stirring [46,47]. This or similarly related growth orientations have been used in the manufacture of large antimonide crystals. The problem appears to be no longer a significant limitation with the availability of large diameter seeds that can provide and maintain a flat or only slightly convex growth surface.

Twinning in relation to facet formation is a problematic, often controversial, growth phenomenon. It can occur generally not just in pulling crystals but also during crystal growth in any growth technology. In the case of the III-Vs, it involves a rotation of the lattice structure by 60° in approximately a <111> direction, where the twin plane forms on an orthogonal (111) plane. Chen et al. [48] examined GaAs, GaP, and InAs crystals, and all the twins found were rotation twins in approximately a <111> direction, but not all facets produced twins. Twinning can be a serious limitation to the yield of device quality material. Another manifestation of this twinning phenomenon is the formation of lamellar twins, where rotation of the lattice by 60° occurs repeatedly after a short period of growth after each twinning event. The phenomenon has occurred during the growth of InP, while increasing the diameter from a narrow seed [49]. Many factors have been cited to enhance the probability of twinning and include facet size, seed orientation, interface shape, temperature gradient, and temperature fluctuations at the three-phase boundary (TPB), surface scum, and the quality of the B_2O_3. Both facet phenomena and twinning can occur in any of the III-Vs, but twinning is most pronounced in the In-containing III-Vs. The avoidance of facet development is clearly a significant requirement in the growth of high-quality uniformly doped crystals.

As mentioned, it is important to maintain a planar interface during growth, a point stressed by Bonner [49] in a study of the growth of twin-free InP. In addition, he claimed

a need to limit the angle the sides of the crystal made with the principle growth direction as the crystal was increased in diameter. He recommended limiting the angle to be $\leq 19.68^\circ$ during growth. This is the angle a twin would make with a <111> growth direction. He identified laminar twin formation with growth widening through an angle greater than previously described. Once the crystal had grown sufficiently long so that the laminar formation no longer intersected the interface, larger-growth angles could be used to achieve single crystals with increased diameters. Again, however, there is a need to use a planar or weakly convex growth surface. Other factors were claimed to affect twinning, such as the quality of the B_2O_3, especially its water content.

Although these various factors clearly were significant in influencing the twinning behavior, there was no formal mechanism that could relate measureable control parameters to a scientifically assessable model. After an initial proposal and stimulated by earlier studies of Voronkov [50], Hurle [51] modeled a potential mechanism for the formation of twins during Czochralski-related growth and encapsulated vertical Bridgman growth. In the thermodynamic model, it was argued that twinning occurred at the TPB at a sufficiently large supercooling because the free energy of formation of a twinned nucleus is less than that for nucleation on any other orientation. This will occur only if a critical angle of conical growth presenting a portion of the surface normal a <111> is sampled during growth; an experimental situation may be more likely under poor growth conditions, where the melt is oscillating. It requires the edge facet to intersect the TPB. In his landmark analysis, he was able to quantify the situation and apply it InSb, InP, GaAs, Ge, and Si. The model is a proposal and would require more precise data to fully test the theory. The data have been reviewed subsequently after a detailed crystallographic study involving the use of Synchrotron white beam X-ray topography, together with chemical etching by Dudley et al. [52]. They examined the presence of twin formation using cross sections of [001] S-doped LEC InP, grown by an MLEK Czochralski technique [Bliss 38]. In a detailed statistical study, Neubert, Kwasniewski, and Fornari [53] have argued that twin formation in LEC InP is closely connected to the crystal growth rate and its fluctuations and that the angles predicted by Hurle's theory for twinning to occur are not statistically found. Hurle and Dudley [54] have responded and argued that it is difficult to experimentally assess the actual angle at which twinning occurs because of, for example, melt fluctuations; thus, at this stage, the evidence does not invalidate the theory. Some more twinning and faceting features are given in Chapter 27 in Vol. IIB.

3.3.4 Growth from Nonstoichiometric and Alloy Melts

The growth of III-Vs from nonstoichiometric melts can result in constitutional supercooling, a well-researched phenomenon in crystal growth, which is discussed in Chapter 9 in volume IIb of this handbook. Some of the earliest work in the case of the III-Vs was reported for InSb [55], where, as shown in Figure 3.13, one can see that growth from a slightly nonstoichiometric melt can cause severe nonuniformity.

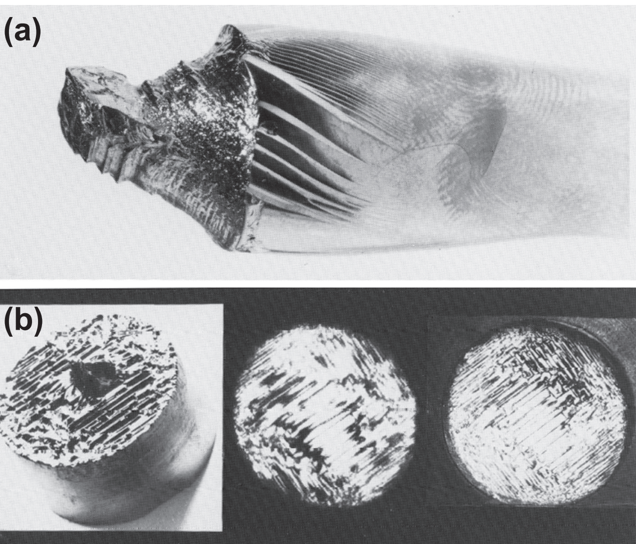

FIGURE 3.13 Effects of nonstoichiometric growth on InSb crystals. (a) A photo showing the effect of the cellular growth on the edges and bottom of the crystal. (b) Crystal end and results from adjacent slices of a <100> grown InSb crystal from an In-rich melt. The left photo shows the (111) facetted cellular structure of the ^{127}Te-radioactively doped crystal. The middle photo shows an autoradiograph image of a cross sectional slice showing the enhanced ^{127}Te incorporation on the {111} facetted cells. The right hand photo shows an etched slice which was cut adjacent to the middle slice. *After (a) Ref. [4]; (b) Hurle et al. [55] with permission of Elsevier.*

It can occur in the case of any of the III-Vs when growth is attempted from non-stoichiometric melts; the greater the deviation from the stoichiometric composition of the melt and/or the faster the growth rate, the more likely it is to occur. It appears not to be a problem in the case of the growth of SI-GaAs from the usual slightly As-rich solutions, provided high growth rates are not used. However, Kiessling et al. [21] found, for growth from Ga-rich melts, using VCz without B_2O_3, a method used to minimize the formation As precipitates, that the ratio of the grow rate to the temperature gradient may need to be carefully controlled if one is to avoid Ga inclusions.

Dutta [56] has reviewed the growth of bulk ternary alloy III-Vs for substrate applications from alloy melts. Even in the case of the growth of the lower vapor pressure III-V alloys by non-LEC techniques, lack of singularity and nonuniformity appear to be a significant limitation to quality. However, an encouraging development was the use of quaternary melts at low growth temperatures. In a more recent article, Gennett, Lewis, and Dutta [57] have used low-temperature quaternary solutions for bulk alloy growth. In the case of $Ga_{1-x}In_xP$, they grew from InSb rich $Ga_{1_x}In_xP_ySb_{1_y}$ melts and so avoided the technical difficulty of growth at high group V vapor pressures. Bulk alloys were grown but were not single and showed evidence of multiphase microstructure. Tsaur and Kou [58] have also achieved some success with the growth of $Ga_{1-x}In_xSb$ using a floating crucible technique. Here, the aim was to maintain the composition of the growth melt by replenishing it with a second alloy melt of appropriate composition via a narrow capillary. The capillary size and design length were chosen to avoid back diffusion. They were able to grow relatively uniform single crystals of 2 mol% InSb. But hydrodynamic instability appears to be a problem. Constitutional supercooling is still an unfortunate

limitation to the bulk growth of single crystal alloys of the III-Vs. Overcoming the problem represents a major challenge for the crystal grower.

3.3.5 Role of B_2O_3

The role of B_2O_3 on the growth and properties of III-Vs has attracted significant research with the development of devices with enhanced device specifications. A useful perspective view of the role of manufacturing III-Vs up to 2001 has been published by Grant [59]. He drew on the experience of his company's (Wafer Technology Ltd) experience in the development of III-Vs for device applications. He drew attention to the importance of controlling the water content of the B_2O_3 because it plays an important role chemically in the composition and purity of the III-Vs grown by LEC. Subsequently, Yamada et al. [60] reported a study in which they considered the potential reactions of the B_2O_3 with the gaseous atmosphere and the crucible containers. They equilibrated GaAs and InP melts with a B_2O_3 flux in a silica crucible with and without a BN crucible. The boron content deceased with increasing nitrogen pressure in both melts equilibrated with B_2O_3 and BN. In the case of the equilibration with the silica crucible, the boron content was much larger than the equivalent with the BN crucible. It was proposed that the Si introduced into the melt from the silica crucible was responsible for increasing the boron content of the melt. A detailed account of existing knowledge of the chemistry involved in the LEC and VCz related growth technologies due to the B_2O_3 is complex and beyond the scope of this chapter, but the role of the significant sources of information will be considered.

One of the more demanding materials grown by LEC requiring property-specific properties is GaAs. The Freiberger Compound Materials Group [61] has published a truly illuminating review of the problematic aspects of not only the role of the B_2O_3 on the quality of SI-GaAs but also the role of the complex environment issues that beset the manufacture of specific device quality crystals and by implicating other related III-Vs. In the case of SI GaAs, the resistivity is controlled by the deep donor As antisite EL2 and the concentration of the shallow acceptor C if the latter dominates any effect from residual impurities. The source of the impurities can be the B_2O_3, the crucible materials, such as pyrolytic BN [62], silica, and the gaseous environment. The chemical reactions of the water in the B_2O_3 with the GaAs melt can produce relatively high B contents in grown GaAs crystals.

Both B and Si on As sites act as acceptors, whereas Si on a Ga lattice site acts as a donor. The latter can include the CO due to its formation by reaction of the graphite components with the boron oxides present in the B_2O_3 due to its water content. High-resistivity GaAs requires the concentration of the EL2 to be greater than the concentration of the shallow acceptors, principally C: also, the total of all shallow acceptors needs to be in excess of the shallow donors. Device specifications for SI-GaAs can require specific closely controlled resistivity properties involving precise control of the C concentration. The water content of the B_2O_3 is required to be appropriately

controlled. But, control of the CO and O_2 levels in the growth environment is essential. Oates and Wenzl [63] reviewed the thermodynamic aspects of the growth environment with a view to establishing more effective models for growing property-specific GaAs. They highlighted an extremely important consideration. Because the growth process is a dynamic one, it is inappropriate to attempt a full equilibrium analysis using standard chemical reactions. Their thermodynamic analysis involved the use of a Gibbs minimization procedure to provide graphical representations of the behavior of C, B, Si, and O at the growth temperature. They also advocated the use of initially equilibrating, in effect dominating, the starting conditions using known concentrations of CO or H_2/CO_2, thereby reducing the thermodynamic degrees of freedom to 0 and simply consider the thermodynamic behavior of the C, B, Si, and O components as functions of the intensive properties of the system. In a related, but more detailed, thermochemical analysis, Korb [64] developed the chemistry and, by implication, the chemical role of B_2O_3 on the properties of LEC grown GaAs and showed additional insights into the complexity of defect-related phenomena in GaAs. The starting material for LEC growth was, as noted, equilibrated initially during its period of formation so that it was possible to consider the status of boron, oxygen, nitrogen, hydrogen, and carbon during crystal growth. Their concentrations were effectively controlled by the chemical potentials of the carbon and oxygen, which were determined by the initial water content of the B_2O_3, the nitrogen fugacity, and the carbon as the controlled input of carbon (as CO). By using a working knowledge of the C and O concentrations/activities in the B_2O_3 and the melt, one can establish a working model for controlling the C incorporation in the crystal during growth. In modelling the growth of GaAs to provide a uniform crystal, Eichler et al. [65] took into account the transport of C, which has a segregation coefficient of C $\sim$2 through the B_2O_3. They also needed to make use of a modified Scheil equation by considering the diffusivity of C through the B_2O_3 in terms of its height and surface area. The use of the empirical model was reported to be effective and became a reliable manufacturing technology. The effectiveness of the LEC technology in this respect, together with its comparison with VGF technology, has been reviewed by Jurisch et al. [27]. It is now abundantly clear that to prepare closely specified properties of Cz III-Vs, it is essential to take into account not only the environmental contents of the growth system and the growth conditions but to understand and control the complex behavior of the crystal defects involved during growth and subsequent treatment.

3.4 Summary

The growth of the III-Vs, but particularly GaAs and InP, by LEC-related growth technologies continues to provide an important route to the preparation of a range of material specifications for an ever-increasing device market. The demand for higher-quality material has stimulated a vast increase in the number and range of fundamental scientific studies aimed at understanding the role of the property controlling

factors involved in the growth of crystals and their subsequent preparation. The role of point defects and their quantitative behavior is an essential requirement for our understanding, as is the total chemical environment involved in crystal growth. It is evident that the chemical and physical role of B_2O_3 encapsulant plays a significant role in determining the properties of the grown crystals. One result continues to be the development of vapor-controlled Cz technologies both with and without the use of B_2O_3.

The importance of modelling for the total physical and chemical environment in aiding the design and improvement of these crystal growth technologies will continue to be a critical requirement for future development.

Whether by LEC or an alternative technology, the ability to grow high-quality single crystal alloys would open up a major source of valuable materials for device development.

References

[1] Hurle DTJ, Cockayne B. Handbook of crystal growth, vol. 2A. Amsterdam: North Holland; 1994. p. 99–211.

[2] Mullin JB. J Cryst Growth 2004;264:578–92.

[3] Neubert M, Rudolph P. Progress in crystal growth and characterisation; 2001. p. 119–185.

[4] Mullin JB. In: Cahn RW, Haasen P, Kramer EJ, editors. Materials science and technology. Jackson KA, editor. Processing of semiconductors, vol. 16. Weinheim: VCH; 1996. p. 1 [Chapter 1].

[5] Mullin JB. In: Malik RJ, editor. III-V semiconducting materials and devices. Amsterdam: Elsevier Science Publishers BV; 1989. p. 63.

[6] Mullin JB. J Cryst Growth 2008;310:1315–23.

[7] Rudolph P, Jurisch M. J Cryst Growth 1999;198/199:325–35.

[8] Czochralski J. Z Physik Chem 1917;92:219.

[9] Teal GK, Little JB. Phys Rev 1950;78:647.

[10] Teal GK. In: Bridges HE, Scaff JH, Shive JN, editors. Introduction to transistor technology. New York: Van Nostrand; 1958 [Chapter 4].

[11] Micklethwaite WFH. Bulk crystal growth of electronic, optical and optoelectronic materials. In: Peter Capper, editor. Van Nostrand, New York: John Wiley and Sons, Ltd; 1958 [Chapter 4]. 2005.

[12] Micklethwaite WF, Fines RG, Freschi DJ. III-Vs Rev June 1996;9(3):51–5.

[13] Martinez R, Amirhaghi S, Smith B, Mowbray A, Furlong Mark J, Flint JP, et al. Quantum sensing and nanophotonic devices X. Proc SPIE 2013;8631:8 [SPIE Homepage] article id. 86311N.

[14] Mullin JB, MacEwan WR, Holliday CH, Webb AEV. J Cryst Growth 1972;13/14:629–34.

[15] Azuma K. Japanese Patent 60–11299. Furukawa Industries; 1983.

[16] Tada K, Tatsumi M. Japanese Patent 60–264390.

[17] Jordan AS, Von Neida AR, Caruso R. J Cryst Growth 1984;70:555–73.

[18] Yakovlev EV, Kalaev VV, Evstratov I Yu, Frank-Rotsch Ch, Neubert M, Rudolph P, et al. J Cryst Growth 2003;252:26–36.

[19] Vizman D, Eichler S, Friedrich J, Muller G. J Cryst Growth 2004;266:396–403.

[20] Kiessling FM, Neubert M, Rudolph P, Ulrici W. Mater Sci Semicond Process 2003;6:303–6.

[21] Kiessling F-M, Rudolph P, Neubert M, Juda U, Naumann M, Ulrici W. J Cryst Growth 2004;269: 218–28.

[22] Rudolph P, Kiessling FM. J Cryst Growth 2006;292:532–7.

[23] Neubert M, Rudolph P, Frank-Rotsch Ch, Czupalla M, Trompa K, Pietsch M, et al. J Cryst Growth 2008;310:2120–5.

[24] Mullin JB, Straughan BW, Brickell WS. J Phys Chem Solids April 1965;26(4):782–4.

[25] Metz EPA, Miller RC, Mazelsky R. J Appl Phys 1962;33(6):2016.

[26] Rudolph P. Prog Cryst Growth Charact Mater 1994;29:275–381.

[27] Jurisch M, Börner F, Bünger Th, Eichler St, Flade T, Kretzer U, et al. J Cryst Growth 2005;275:283–91.

[28] Mullin JB, Heritage RJ, Holliday CH, Straughan BW. J Cryst Growth 1968;3,4:281.

[29] Bass SJ, Oliver PE, Birbeck FE. J Cryst Growth 1968;2:169–70.

[30] Mullin JB, Royle A, Straughan BW, Tufton PJ, Williams EW. J Cryst Growth 1972;13/14:640–6.

[31] Satunkin G. J Cryst Growth 1995;154:172–88.

[32] Satunkin G. J Cryst Growth Prog Cryst Growth Charact Mater 2010;56:1–121.

[33] Mullin JB, Straughan BW. Proceedings of the international symposium on CdTe Strasbourg 1976. Rev.de Phys Appliquée 1977;12(2):105.

[34] Hobgood HM, Swanson BW, Thomas RN. J Cryst Growth 1987;85:510–20.

[35] Hruban A, Dalecki W, Nowysz K, Strzelecka S, Gladski A. J Cryst Growth 1999;198/199:282–6.

[36] Asahi T, Yabe T, Sato K. J Electron Mater 2004;33(6):651–3.

[37] Thomas RN, Hobgood HM, Ravishankar PS, Braggins T. Prog Cryst Growth Charact Mater 1993;26: 219.

[38] Bliss David F, Hilton Robert M. J Cryst Growth 1993;128:451–6.

[39] Kröger FA. The chemistry of imperfect crystals. Amsterdam: North Holland; 1973.

[40] Hurle DTJ, Rudolph P. J Cryst Growth 2004;264:550–64.

[41] Hurle DTJ. J Appl Phys 1995;85:6957.

[42] Hurle DTJ. J Appl Phys 2010;107:121301.

[43] Hulme KF, Mullin JB. Philos Mag 1959;4:1286.

[44] Mullin JB. Compound semiconductors. In: Willardson RK, Goering HL, editors. Preparation of III-V compounds, vol. 1. New York: Reinhold; 1962. p. 365.

[45] Mullin JB, Hulme KF. J Phys Chem Solids December 1960;17(1–2):1–6.

[46] Mullin JB, Benz KW. Historical introduction to “The role of magnetic fields in crystal growth”. Prog Cryst Growth Charact Mater 1999;38:1.

[47] Hulme KF, Mullin JB. Solid-state eletronics, vol. 6. Pergamon Press; 1962. p. 211–247.

[48] Chen TP, Chen FR, Chuang YC, Guo YD, Peng JG, Huang TS, et al. J Cryst Growth March 1992; 118(1–2):109–16.

[49] Bonner WA. J Cryst Growth 1981;54:21–31.

[50] Voronkov VV. Sov Phys Cryst 1975;19:573.

[51] Hurle DTJ. J Cryst Growth 1995;147(3–4):239–50.

[52] Dudley M, Raghothamachar B, Guo Y, Huang XR, Chung H, Hurle DTJ, et al. J Cryst Growth 1998; 192:1–10.

[53] Neubert M, Kwasniewski A, Fornari R. J Cryst Growth 2008;310:5270–7.

[54] Hurle DTJ, Dudley M. J Cryst Growth 2010;312:1659–60.
[55] Hurle DTJ, Jones O, Mullin JB. Solid State Electron 1961;3:317–20.
[56] Dutta PS. J Cryst Growth 2005;275:106–12.
[57] Gennett A, Lewis D, Dutta PS. J Cryst Growth 2010;312:1080–4.
[58] Tsaur SC, Kou S. J Cryst Growth 2007;307:268–77.
[59] Grant IR. Encyclopedia of materials: science and technology. 2nd ed. 2001. p. 1441–1452.
[60] Yamada T, Kudo T, Tajima K, Otsuka A, Narushima T, Ouchi C, et al. J Cryst Growth 2004;211:174–8.
[61] Jurisch M, Börner F, Bünger Th, Eichler St, Flade T, Kretzer U, et al. J Cryst Growth 2005;275:283–91.
[62] Fischer L, Lambertb U, Nagelb G, Riifer H, Tomzig E. J Cryst Growth 1995;153:90–6.
[63] Oates WA, Wenzl H. J Cryst Growth 1998;191:303–12.
[64] Korb J, Flade T, Jurisch M, Köhler A, Reinhold Th, Weinert B. J Cryst Growth 1999;198/199:343–8.
[65] Eichler S, Seidl A, Börner F, Kretzer U, Weinert B. J Cryst Growth January 2003;247(1–2):69–76.

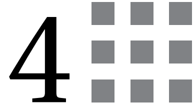

4 Czochralski Growth of Oxides and Fluorides

Nobuhiko Sarukura[1], Teruhiko Nawata[2], Hiroyuki Ishibashi[3], Mitsuru Ishii[4], Tsuguo Fukuda[5]

[1]*INSTITUTE OF LASER ENGINEERING, OSAKA UNIVERSITY, SUITA, OSAKA, JAPAN;* [2]*TOKUYAMA CORPORATION, YAMAGUCHI, JAPAN;* [3]*HITACHI CHEMICAL CO., LTD., IBARAKI, JAPAN;* [4]*SHONAN INSTITUTE OF TECHNOLOGY, HIGASHIYAMATO, TOKYO, JAPAN;* [5]*FUKUDA CRYSTAL LAB CO., LTD, SENDAI, MIYAGI, JAPAN*

CHAPTER OUTLINE

4.1 Introduction 132
4.2 Sapphire Single Crystals 132
4.2.1 Growth Apparatus 134
4.2.2 Growth Technique 135
4.2.2.1 High Frequency Heater 135
4.2.2.2 Resistance Heater 136
4.3 Calcium Fluoride Crystals 137
4.3.1 Growth Technique 138
4.3.2 Starting Materials 139
4.3.3 Growth Apparatus 140
4.3.4 Technical Challenges 140
4.3.5 Double-Crucible System 142
4.3.6 Annealing Process 146
4.4 Large Fluoride Crystals 146
4.4.1 Growth Technique 147
4.4.2 As-Grown Crystals 148
4.4.3 Transmission Properties 148
4.4.4 Solid-state Lasers 150
4.4.5 Chirped-pulse Amplification 152
4.5 Scintillator Crystals 152
4.5.1 Bismuth Germinate 154
4.5.2 Cadmium Tungstate 157
4.5.3 Lead Tungstate 158
4.5.4 Gadolinium Silicate 160

Handbook of Crystal Growth. http://dx.doi.org/10.1016/B978-0-444-63303-3.00004-3
Copyright © 2015 Elsevier B.V. All rights reserved.

4.5.5 Lutetium and Other Silicates ... 163
4.5.6 Scintillator Applications ... 163
4.5.6.1 X-ray Computer Tomography ... 163
4.5.6.2 Positron Emission Tomography ... 164
4.5.6.3 High Energy Physics ... 164
4.5.6.4 Other Applications ... 165
4.6 Summary and Outlook ... 165
References ... 165

4.1 Introduction

Oxide and fluoride crystals are useful in many practical applications, ranging from smartphone components, semiconductor substrates, optical materials, and light sources to scintillators and radiation detectors. Many growth methods are available to produce these oxide and fluoride crystals. Techniques include Czochralski, Stepanov, EFG, Bagdasarov, VHGF, Bridgman–Stockbarger, and Verneuil methods to name a few. Among all of these techniques, Czochralski (CZ) promises high production efficiency for highly oriented and sufficiently large crystals. The crystals grown by the CZ technique have promising characteristics that make them useful in their respective applications. Given the advantages of the CZ method, large and high quality oxide and fluoride crystals such as sapphire (Al_2O_3), calcium fluoride (CaF_2), colquirite ($LiCaAlF_6$), scheelite ($LuLiF_4$), bismuth germinate, and silicates among others are produced. The actual growth implementation has some modifications depending on the material and on the technical challenges and desired output. For example, high frequency heaters and resistance heaters are used for sapphire single crystals. On the other hand, the double-crucible system and annealing are done for the growth of CaF_2 crystals. Details on these growth procedures as well as the material applications are discussed in this chapter.

4.2 Sapphire Single Crystals

Sapphire (Al_2O_3) exists naturally as corundum. As a well-known gem, sapphire is either colored blue or red. The red sapphire has some impurities and is commonly known as ruby. An artificial sapphire with 2040 °C melting point can be grown by the Verneuil method using oxyhydrogen flame [1]. Sapphire is doped with titanium (Ti) as impurity, and ruby is doped with chromium (Cr). By using high purity starting materials, a colorless and transparent single crystal called “white sapphire,” now also referred to as sapphire, can be grown. This sapphire has a high Mohs hardness of 9, next to diamond among naturally existing materials. White sapphire has been used for applications such as mechanical bearings, watch windows, and phonograph needles.

Table 4.1 Properties of a Single Sapphire Crystal

Crystal System	Hexagonal
Space group	R3c
Crystal habit	Massive and granular
Lattice parameters	a = 4.675
	c = 13.001
Melting point	2053 °C
Reference density	3.97 g/cm^3
Thermal expansion	9.0×10^{-6} along c-axis
Thermal conductivity at 20 °C	42 W/m K
Mohs hardness	9
Index of refraction	No = 1.768
	Ne = 1.760
Cleavage	None

After the developments of ruby (Cr-doped Al_2O_3) lasers and Ti:sapphire tunable lasers, the CZ method has been implemented for the growth of high purity sapphire. Sapphire has been used in various applications because of its thermal and chemical stability around 2000 °C. Focusing on the insulation properties of sapphire, the semiconductor silicon on sapphire (SOS) devices have already been put to practical use in smartphone electronic components. The raw materials of sapphire occur widely throughout nature. Sapphire is also used for optical components because of mechanical strength and of high transmittance in a broad spectral range from the ultraviolet (UV) to infrared (IR) regions. These properties are suitable for smartphone panels. The chemical and physical properties of sapphire are shown in Table 4.1.

Many growth methods for sapphire were reported for various applications. Stepanov and EFG methods were used to make single crystal fibers, tubes, and rod-shaped sapphire [2,3]. Thick, broad-shaped sapphire was prepared by Bagdasarov and VHGF techniques [4]. Kyropoulos and heat exchange methods were utilized to grow huge sapphire crystals [4,5]. Molybdenum (Mo) or tungsten (W) crucible was being used in all cases.

In recent years, sapphire served as substrate for gallium nitride (GaN) light-emitting diodes (LED). GaN LEDs are widely used for illumination though the price optimization and new markets for their used are still being explored. Figure 4.1 shows the applications, market trends, and predictions of the wafer sizes of sapphire. Mostly the c-plane wafers are used for GaN LED substrates. Two-inch diameter wafers were mainly produced in 2008 by EFG, Kyropoulos, and CZ methods with the a-axis as the pulling direction; two- to four-inch-diameter wafers were used as the standard in 2013. Looking toward 2020, six- to eight-inch wafers are now being developed in response to the expanding markets. In addition, new growth techniques such as VHGF, VB, heat exchange, and arc-energy methods are being developed [6,7]. The c-plane wafers are

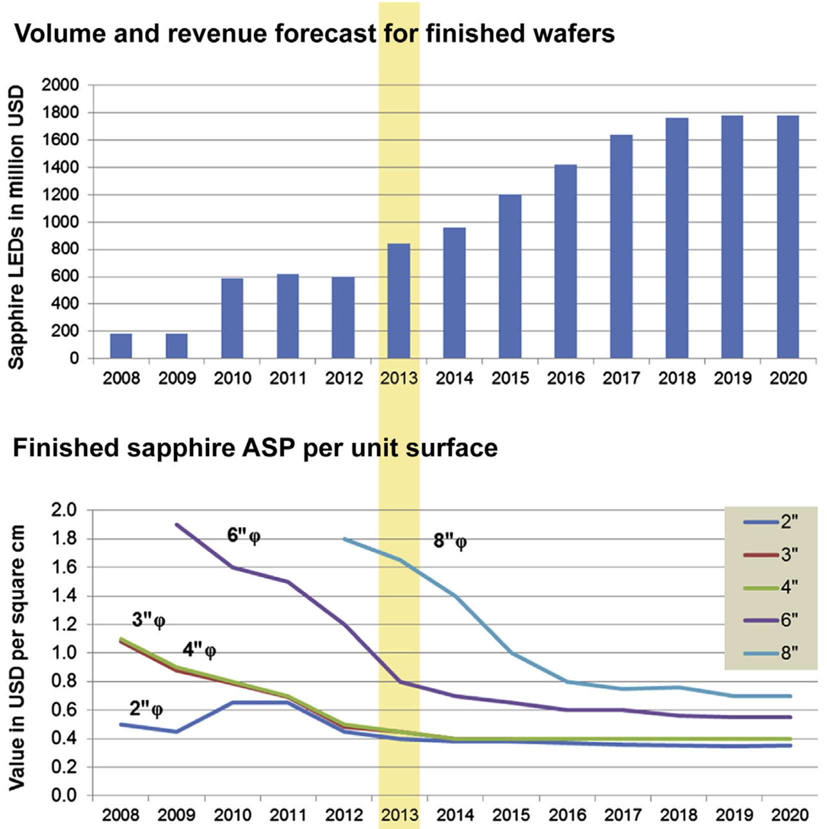

FIGURE 4.1 Market trends and applications of sapphire substrates. *After Ref. [83] with permission of the publisher.*

basically made by cutting the a-axis grown crystals with CZ or arc-energy methods for LED substrate applications. The a-plane, m-plane, and r-plane substrates are also being increasingly studied. The r-plane wafers are scaled up from six to eight inches in size for semiconductor SOS device application. In the decade ahead, anticipated developments of the CZ method include high quantity output of large size grown crystals and on-axis growth for high frequency devices, power devices, and SAW device substrates.

4.2.1 Growth Apparatus

The demand for sapphire crystals of six to eight inches in diameter has gradually increased. There have been few reports of the mass production by CZ method of crystals with over 2000 °C melting point, and as yet there are no reports of the growth of crystals of over four inches in diameter.

Sapphire crystals were grown by CZ method utilizing either a high frequency (inductive) heater or a resistance heater. Figure 4.2 shows the schematic diagrams of the

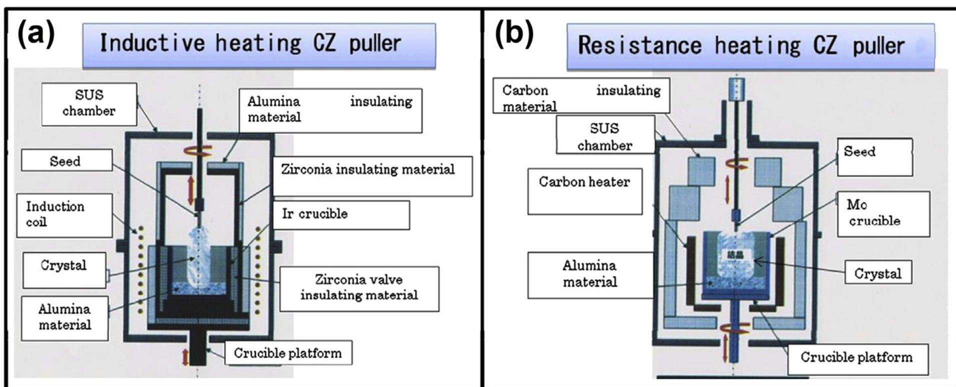

FIGURE 4.2 Schematic diagrams of Czochralski growth apparatuses implementing (a) inductive heating and (b) resistive heating.

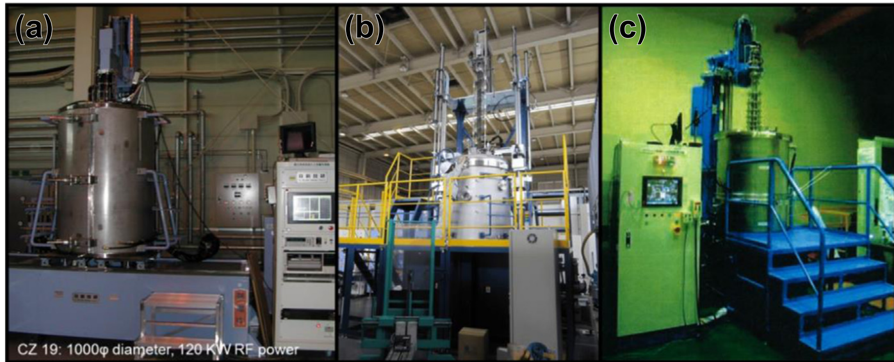

FIGURE 4.3 Czochralski growth setups with high frequency (inductive) heating pullers for (a) 6″ φ to 8″ φ crystals *(courtesy of Nissin Gikenn)* and (b) for 8″ φ to 10″ φ crystals *(courtesy of Daiichi Kiden)* and with resistance heating puller for (c) 6″ φ to 8″ φ crystals *(courtesy of Nittetsu Sumikin Fine Tech)*.

two types of CZ growth apparatuses. In a high frequency heater, sapphire is melted in an iridium (Ir) or iridium–rhenium (Ir–Re) crucible. On the other hand, in a resistive heater, the crystal is melted in a Mo, W, or Mo-W alloy with carbon (C) in argon (Ar) atmosphere. Figure 4.3 contains the photographs of actual CZ growth setups.

4.2.2 Growth Technique

4.2.2.1 High Frequency Heater

Figure 4.2 illustrates the crystal growth with a high frequency heater in terms of the furnace structure. For GaN LED substrate application, a c-plane grown crystal is used. As compared to the a-axis direction, pulling along the c-axis causes subgrain and displacements because of the high thermal gradient. For the currently available two- to four-inch-diameter wafers, the a-axis is standard in EFG, Kyropoulus, and VHGF

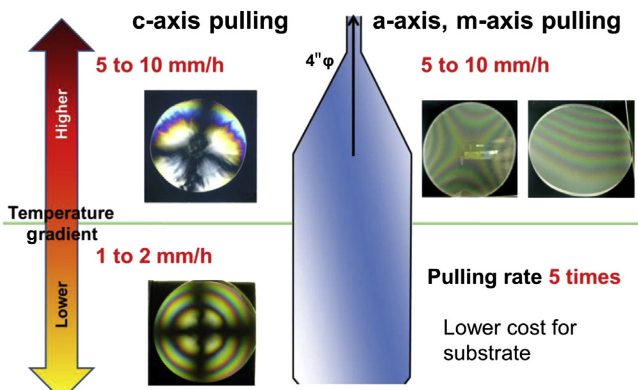

FIGURE 4.4 Comparison of the Czochralski growth of sapphire crystals with c-, a-, and m-axis pulling.

methods. The c-plane wafers are hewed out from the a-axis grown crystals. In most cases, crystals by CZ method are grown parallel to the a-axis. The low concentration gradient is required for a high quality crystal in any growth direction. The growth rate of four-inch-diameter crystals pulled along the c-axis is about 1–2 mm per hour (mm/h). The growth rate along the a-axis is five to ten times faster than the growth rate along the c-axis. Figure 4.4 compares the growth of sapphire crystals along different pulling directions.

A low thermal gradient decreases the defects such as cracks, thermal strain, sub-grains, and displacement in CZ-grown sapphire crystals. Figure 4.5 presents some crystals grown in larger crucibles. Using a larger crucible lowers the thermal gradient. The grown crystal has curves and small bubbles because of supercooling effects. Bubbles, discoloration, holes, and light scattering also exist in sapphire. These problems can be solved by controlling the natural and forced convections in the crucible by optimizing the growth temperature and rotation speed.

Figure 4.5 shows the photographs of sapphire crystals grown by high frequency heating using Ir crucible. Large diameter crystals, from four to ten inches, are grown along the a-axis, c-axis, and even r-axis. The CZ growth technique can utilize different growth directions.

4.2.2.2 Resistance Heater

The CZ growth with a resistance heater is basically similar to that with a high frequency heater as shown in Figure 4.2. The main difference between the two methods is the high vacuum condition and Ar atmosphere requirement for the resistance heater because of the use of carbon components and Mo or W crucible. In addition, the natural convection and thermal gradient are low in CZ growth with resistance heating because the crucible itself is not a heater. A major drawback of this technique is that the growing crystal gets through the melting area. Figure 4.6 shows the sapphire crystals grown by resistance heating.

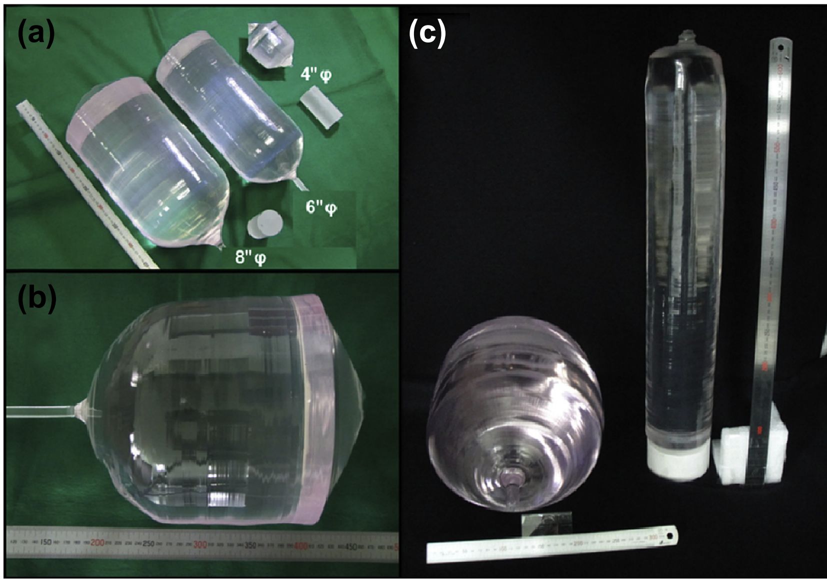

FIGURE 4.5 Sapphire crystals grown by Czochralski method with high frequency (inductive) heating using large crucibles with different pulling directions: (a) 4″ φ, 6″ φ, and 8″ φ crystals along the c-axis; (b) 8″ φ crystals along the r-axis; and, (c) 10″ φ crystal along the a-axis and 4″ φ crystal with 500 cm length along the c-axis. *Courtesy of Fukuda Crystal Lab Co., Ltd.*

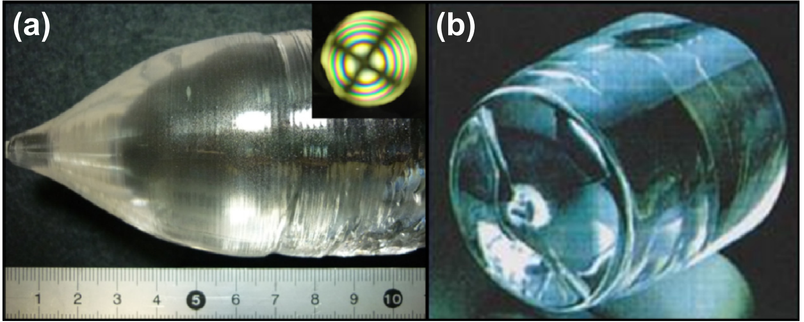

FIGURE 4.6 Distinctive sapphire crystals grown by Czochralski method with resistance heating pullers: (a) grown into crucible and (b) square-shaped shoulders. *Courtesy of Fukuda Crystal Lab Co., Ltd.*

4.3 Calcium Fluoride Crystals

Calcium fluoride (CaF_2) crystal is a natural fluoride having transparency over a wide wavelength range. Being chemically and physically stable, it has been used in optical equipment windows, lenses, and prisms. Highly crystalline and pure CaF_2 single crystals are particularly required for apparatuses using an excimer laser light source, for example, a lithographic exposure apparatus using F_2 and ArF excimer laser. High quality crystals have been produced using various growth techniques such as CZ, vertical gradient

freezing (VGF), and Bridgman-Stockbarger (BS) methods [8]. Among these techniques, the BS method was the first to successfully produce high quality CaF_2 for industrial applications.

There has been active development of F_2 lithography since 2001 when we started developing a CaF_2 single crystal. Low cost and large CaF_2 crystals were required as optical materials for a F_2 excimer laser because CaF_2 is transparent up to 157 nm. The mass production technology had not yet been established, and the supply shortage was a concern [9]. Because the crystal system of CaF_2 is cubic, the intrinsic birefringence is almost negligible when CaF_2 is used as a conventional optical component. In a F_2 excimer laser stepper, the intrinsic birefringence is not negligible because the laser operates at a very short wavelength (157 nm) [10]. To compensate for the intrinsic birefringence of optics in a F_2 excimer laser stepper, the combination technique of CaF_2 lens with <100> plane orientation was then proposed [11].

In conventional techniques such as VGF and BS methods, the crystal growth is greatly influenced by the dominant growth direction. Establishing a growth method for a large lens block with <100> surface orientation is a problem. Since CZ method is capable of producing orientation-controlled crystal in large quantities, the authors have developed a manufacturing technology for a large single crystal of CaF_2 by modifying this method.

4.3.1 Growth Technique

CaF_2 shows a melting point of around 1420 °C, and it has high reactivity in a molten state. For these reasons, only a high purity carbon can be used for the constructional elements of a hot zone in a furnace. Since the solarization and transmittance are significantly deteriorated by oxygen and water in the growth atmosphere, it is necessary to pay careful attention to the moisture desorbed from the furnace wall and from the leakage into the furnace. As previously mentioned, CaF_2 single crystals are conventionally produced using the VGF and BS methods. In these methods, the molten raw material is filled in the crucible with a scavenger such as lead fluoride (PbF_2) and slowly crystallizes afterward. The permeability of the crucible is adjusted by changing the size and number of vent holes on the crucible's upper lid. Changing the crucible's permeability enables maintaining a vacuum state inside the furnace during crystal growth. This is also very effective in preventing impurities from being incorporated into the crystal. The VGF and BS methods can produce crystals as large as the crucible and, in principle, can be considered as growth techniques for large size single crystals. However, since the crystal grows in contact with the crucible, problems with crystallinity arise. Polycrystalline samples are grown because of the formation of crystal nuclei in the crucible wall and of the increased residual strain due to the difference in the expansion rate of the crystal and the crucible material. By these methods, large crystals with a desired orientation are difficult to produce.

CZ method is a typical production technology for large silicon single crystals for the semiconductor industry. The control of crystal orientation is relatively easy because the

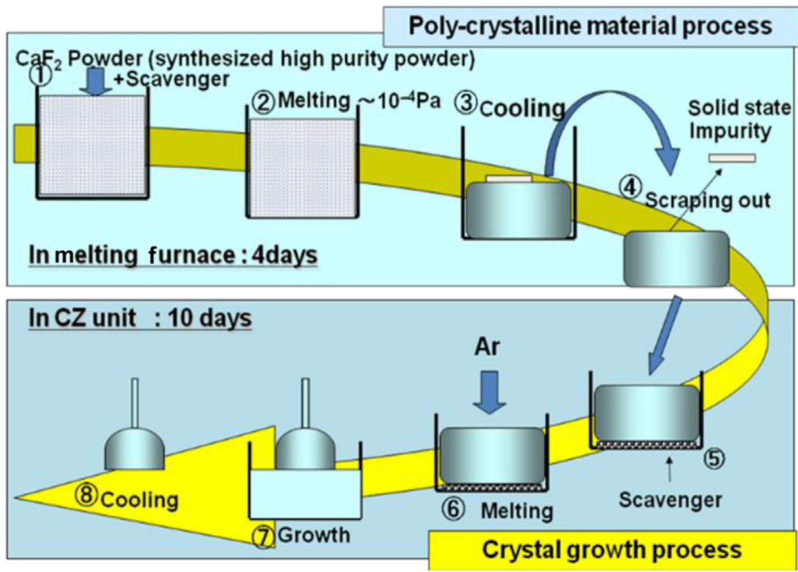

FIGURE 4.7 Process flow for the purification of raw materials for CaF_2 lens block crystal growth.

state of the seeding process can be easily observed by eyesight and by weight measurement. On the other hand, since the convection and temperature fluctuation of the molten material become violent as the crucible size increases, the incorporation of voids and the stabilization of growth at the interface are challenging problems. In addition, the CZ furnace configuration is more complicated than other conventional methods because the precise mechanisms of crystal pulling and rotation, of crucible raising and rotation, etc. are necessary.

In the 1960s [12], a CaF_2 single crystal with one-inch diameter was reported to be grown by CZ method. In the following years, CaF_2 grown by CZ method was rarely reported until Fukuda et al. in the 1990s [13]. From their results, the authors started to study the industrialization of large, high quality CaF_2 single crystals by CZ method. Figure 4.7 shows the entire manufacturing flow of a large CaF_2 single crystal ingot using CZ method. It takes about 4 days to produce a purified block raw material and 10 days to grow a single crystal. These two processes are carried out by different furnaces from viewpoints of throughput of the entire process.

4.3.2 Starting Materials

Crystals are used as optics for vacuum ultraviolet (VUV) applications, for example, a lens material in semiconductor lithography. Since rare earth elements contain natural fluorides causing an emission or absorption center, it is necessary to use high purity CaF_2 produced by chemical synthesis. In producing high purity CaF_2 raw material, the method to react the high purity hydrogen fluoride (HF) and high purity calcium

carbonate ($CaCO_3$) is generally used. A synthetic CaF_2 is a white powder with several micrometer particle sizes. The powder material has large specific area and easily absorbs moisture, so it cannot be used as raw material for crystal growth. The powder material also has low bulk density, so it cannot be set in large quantity in a crucible, leading to the decrease of production efficiency. It is thus necessary to place purified block materials in a crucible in order to efficiently grow a high quality crystal. Raw powder materials are purified by mixing CaF_2 with a few percent of fluorine agent such as a scavenger. As described in the following chemical equations, the scavenger works to remove impurities such as moisture and oxygen [14]:

$$CaO + PbF_2 \rightarrow CaF_2 + PbO \tag{4.1}$$

$$H_2O + PbF_2 \rightarrow PbO + 2HF\uparrow \tag{4.2}$$

$$2PbO + C \rightarrow Pb\uparrow + CO_2 \tag{4.3}$$

The raw powder material is perfectly dried by keeping the furnace at high vacuum pressure while increasing the temperature to 200–300 °C. This procedure is necessary because CaF_2 reacts with fractional moisture, thus forming stable oxides at 300 °C or higher. The unwanted reaction leads to deterioration of the crystal quality such as clouding. Carbon-related foreign materials also adhere to the surface of block-like materials after solidification. The foreign materials have to be removed by a diamond grinder before setting into the crucible puller.

4.3.3 Growth Apparatus

Figure 4.8 shows a CZ apparatus used for the growth of large CaF_2 single crystals. The CZ apparatus is composed of a water-cooled chamber, a hot zone, resistive heaters, and a pulling mechanism, among others. The basic configuration is similar to that of the semiconductor silicon's puller. A vacuum exhaust system is installed, and gas tightness is ensured to maintain a high vacuum less than 10^{-4} Pa in the growth furnace. These are necessary to make the hot zone and raw material dry prior to the melting process so that CaF_2 would not react to moisture at high temperatures. High performance vacuum pumps, such as a cryosorption pump, are recommended to efficiently remove the moisture in the furnace. The hot zone structure is designed considering the low distortion of the crystal and the resulting optimal temperature gradient during growth by computer simulation.

4.3.4 Technical Challenges

The growth of a large CaF_2 crystal, like a 300-mm-diameter boule (Figure 4.8(C)), is faced with various technical challenges as illustrated in Figure 4.9.

For lithography lens material applications, the optical absorption in the VUV region induced by laser irradiation must be inhibited, and incorporation of oxygen impurities must be prevented as much as possible [15]. The change in the VUV light transmittance

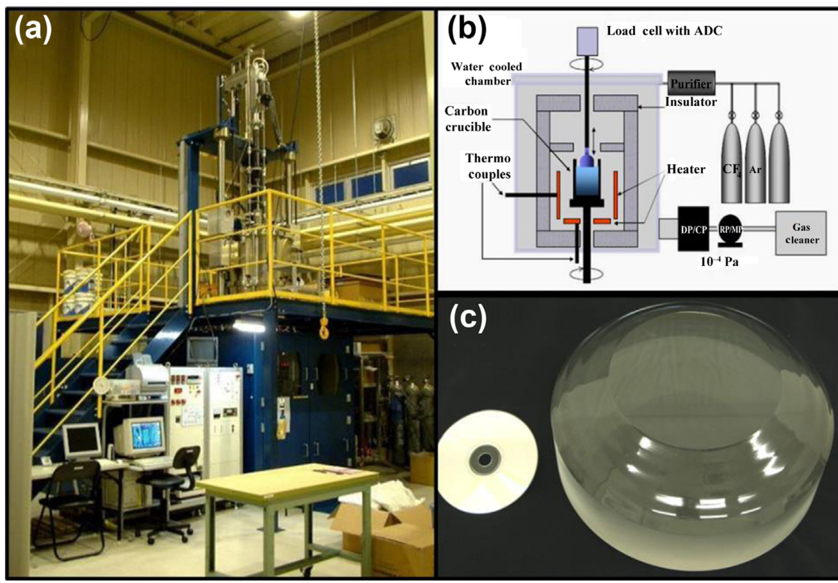

FIGURE 4.8 The (a) actual photograph and (b) schematic diagram of a Czochralski apparatus for (c) large (e.g., 300-mm diameter) CaF_2 single crystals.

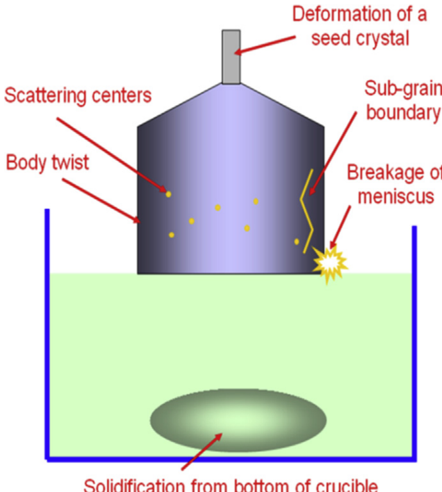

FIGURE 4.9 Technical issues from the growth of large CaF_2 crystals by Czochralski method.

with the introduction of oxygen or moisture to the CZ furnace is investigated. As compared to oxygen, moisture has more impact on the deterioration of the transmittance in the VUV region. The moisture contamination happens when the raw material is contaminated, when carbon members are desorbed, and when there is leakage from outside the furnace. A furnace with excellent airtightness, baking, and furnace

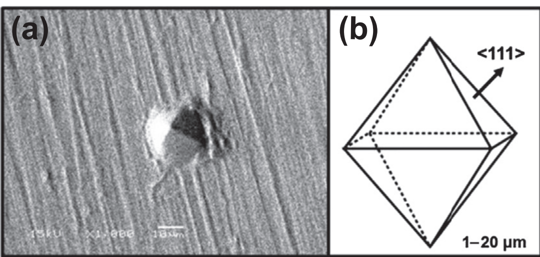

FIGURE 4.10 The (a) SEM image and (b) schematic diagram of a scattering center (SC) in a Czochralski-grown CaF_2 single crystal.

member management and with thorough water removal using a hydrofluoric agent before melting the raw material is required in order to produce a high quality CaF_2 single crystal.

In addition, stress birefringence and refractive index homogeneity are important for lithography lens material applications. The stress birefringence of the crystal can be reduced by high temperature annealing. On the other hand, refractive index homogeneity is closely related to low angle grain boundaries, so it is hardly improved by post-growth processes such as annealing.

The most troubling problem of the CZ growth of large CaF_2 crystals is the formation of light scattering centers (SCs) in the crystal. Most SCs are small octahedral negative crystals that scatter irradiated light depending on the incidence angle. A scanning electron micrograph and schematic diagram of a sample SC are shown in Figure 4.10.

4.3.5 Double-Crucible System

Complex flows are generated in the melt within the forced convection brought upon by the rotation of the grown crystal and the natural convection from the melt's temperature gradient. These complex flows generate negative crystals inside the crystal. To reduce the fluctuations of the temperature and melt flow, an original double crucible method was developed. By utilizing this procedure, SCs and bubbles are significantly reduced. The Grashof number is an index of intensity of the buoyancy in the convection. It is proportional to the cube of the depth of the melt and can be expressed as:

$$\mathrm{Gr} = g \cdot \beta \cdot \Delta T \cdot d^3 / V^2 \tag{4.4}$$

where g is the acceleration due to gravity, β is the volume expansion coefficient, ΔT is the temperature difference between the crystal and crucible, d is the depth of the melt, and v is viscosity.

In growing a large crystal, a large crucible is often used to contain a lot of raw materials. Figure 4.11 shows the differences of the CZ growth of a large CaF_2 crystal using different types of crucibles. A crystal grown using a normal crucible filled with a lot of molten material exhibits many SCs, while the crystal grown from shallow molten material exhibits fewer SCs. The double crucible method can constantly keep the shallow

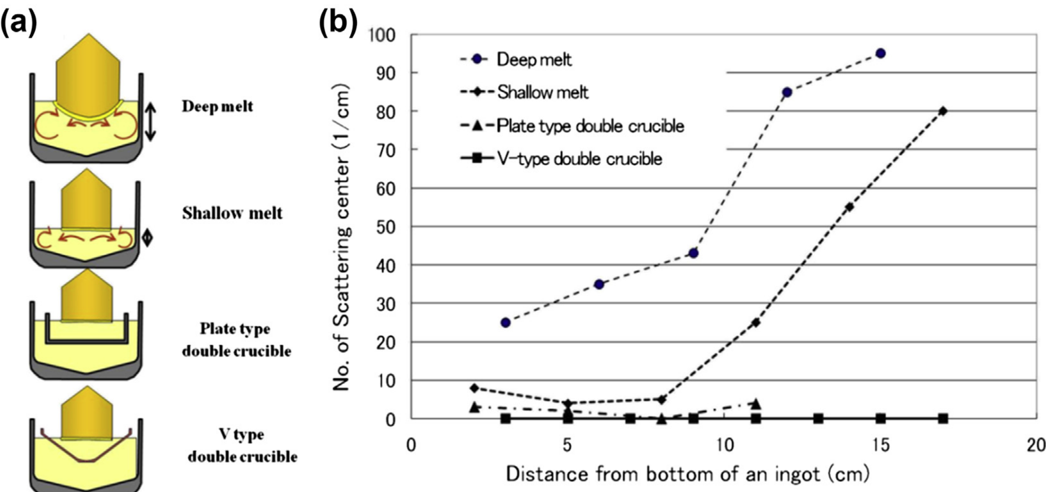

FIGURE 4.11 Effects of an inner crucible's shape on the diminishing scattering centers (SCs) of a Czochralski-grown CaF_2 single crystal.

depth of the melt. As a result, when the double crucible method is applied, the amount of the SCs is substantially reduced. The SCs are further decreased when the double crucible method implementing an inner crucible with V-type cross-section is used. It is also possible to reduce the downward flow in the melt just below the double crucible, and the supercooling and solidification at the bottom of the crucible can be inhibited. With these possibilities, the stable crystal growth for an extended period of time and the production of large-diameter, long body crystals can both be realized. The double crucible system is advantageous in removing carbon matter suspended on the melt before the start of the crystal growth. The double crucible system is also employed for the growth of large halide scintillation crystals in both radial and axial directions [16].

Figure 4.12 shows the analytical results of the melt flow in the crucible calculated by using commercially available software. Figure 4.12(A) shows the case of a single crucible with inner diameter of 360 mm and filled with melt of 250 mm depth. Figure 4.12(B) shows the case of a double crucible system with V-shaped inner crucible and with the inner crucible filled with melt of 100 mm depth. The melt flow rate obviously becomes slower for the double crucible system. The average flow rate is about one-tenth of the conventional crucible system. The fluctuation of melt temperature is also much lower, thus the double crucible method can provide a very stable environment for crystal growth.

Figure 4.13 shows the optimization of the shape of the inner crucible and of the arrangement of the holes. By optimizing the shape and the arrangement, the temperature fluctuation of the melt can be further suppressed. In the case depicted in Figure 4.13(B), small holes are distributed all over the crucible, and the hole size and placement are optimized by computer simulation to minimize the melt flow rate.

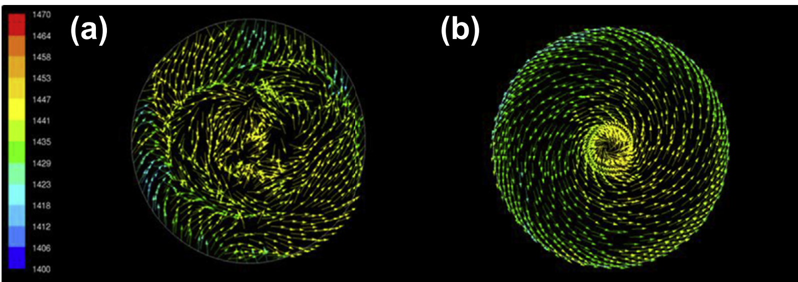

FIGURE 4.12 Melt surface flow in (a) conventional single crucible and in (b) inner crucible of the developed double crucible system. The arrows indicate the flow direction and melt velocity.

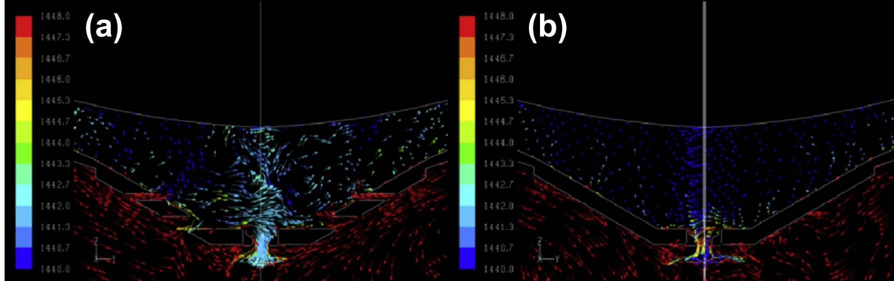

FIGURE 4.13 Optimization of the hole arrangement of an inner crucible with (a) several large holes around the bottom of the crucible and (b) many small holes distributed all over the crucible. The arrows indicate the flow direction and melt velocity.

A schematic diagram of the growth process in a double crucible system for large CaF_2 single crystals is shown in Figure 4.14. A similar illustration can also be found in Ref. [16] with specific details on the technological hardware facilities. The crucible system is composed of a movable outer crucible and a fixed inner crucible. The small holes at the bottom of the inner crucible allow the exchange of molten material between the two crucibles.

First, the outer crucible is filled with purified block material and a small amount of fluorinating agent serving as a scavenger (Figure 4.14(A)). Since residues cause absorption peaks in the VUV region, the raw materials should be perfectly removed before reaching the melting temperature of CaF_2. Lead fluoride (PbF_2) has long been used as a scavenger for the growth of CaF_2 crystals. Zinc fluoride (ZnF_2) has a lower vapor pressure at high temperatures compared to PbF_2, so ZnF_2 can serve as a better scavenger at higher temperatures. Trace amounts of ZnF_2 do not affect the optical properties of the grown crystal. ZnF_2 is then considered as a more suitable scavenger for the CZ method. For the CZ method, unlike other techniques such as the BS method, the crucible has no lid that prevents the evaporation of raw material. The crystal growth is thus performed in an atmosphere of inert gas near the vapor pressure. After placing the raw material, the temperature is raised slowly while keeping the vacuum atmosphere in the furnace to

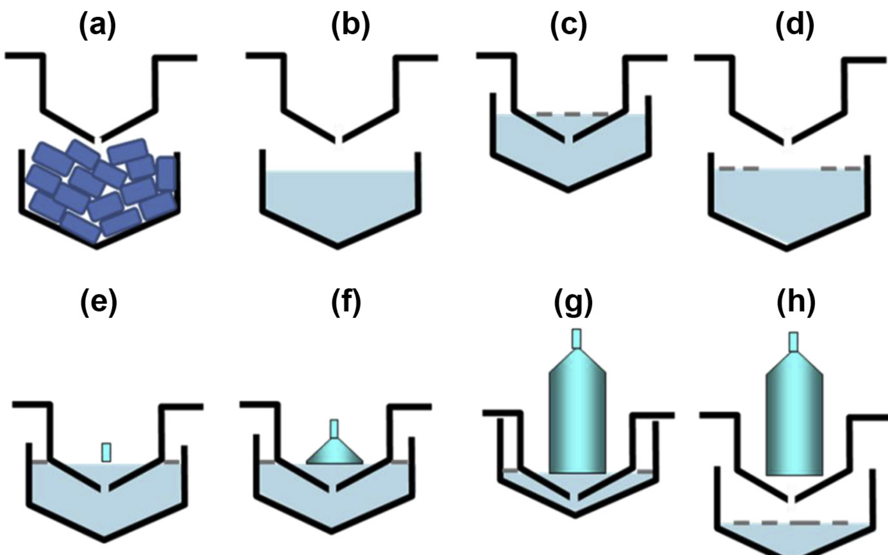

FIGURE 4.14 Czochralski growth process using double crucible system for large CaF_2 single crystals: (a) setting and baking raw materials; (b) melting; (c and d) cleaning melt surface; (e–g) growing a crystal; and (h) cooling down.

efficiently remove moisture adsorbed on the raw material itself, the carbon members, and the furnace wall. High purity argon gas is introduced into the furnace at a temperature just below the CaF_2 melting point. The raw material is perfectly melted after heating to over the melting temperature (Figure 4.14(B)). Once the temperature of the molten material is stabilized, the outer crucible is lifted near the inner crucible. The molten material enters through holes and fills the inner crucible. In most situations, film-like carbon forms on the surface of the molten material. Although the cause is still unclear, the carbon floats are attributed to fine powders from the surface of the graphite crucible or to products of some chemical reactions. It is necessary to completely remove the carbon floats because they will cause polycrystallization that will interfere with the seeding process. Charging and discharging molten material are repeated several times to remove carbon floats. Charging and discharging are done by raising the outer crucible near the inner crucible (Figure 4.14(C)) and by lowering the outer crucible (Figure 4.14(D)), respectively. Since the carbon floats tend to move to the periphery due to the surface tension of the molten material, the carbon floats can be removed from the inner crucible by repeating the charging and discharging procedures. A seed crystal is dipped on the surface of the molten material (Figure 4.14(E)) and is then rotated and pulled upward (Figure 4.14(F)). The seed crystal is connected to a load cell via a pulling shaft, and the crystal's weight is measured every minute during the growth process. The weight data from the load cell are transferred to a computer system to control the crystal diameter. The diameter of the growing crystal is calculated from the change in weight,

and the computed value is fed back to the heater control system, thus attaining an automated diameter control (Figures 4.14(G) and (H)). Moreover, the rate of lifting the outer crucible is calculated from the consumption rate of the molten material and is determined to keep a constant amount of molten material in the inner crucible. The possibility of maintaining a stable temperature and convection during a growth process leads to the possibility of producing large and high quality single crystals with fewer voids and scattering centers. At the end of the procedure, the crystal is removed from the melt and cooled slowly (Figure 4.14(H)). This prevents heat shock and strong strain on the newly formed crystal. Requisite cooling time depends on the size of a crystal. As-grown crystals with a diameter of 200 mm or more need at least 24 h to avoid cracks when cooling and cutting.

4.3.6 Annealing Process

During growth or cooling, a large temperature distribution is created, and large thermal strain can remain in the as-grown crystal. If the residual strain is very large, such as when an ingot cracks when cutting, it is necessary to perform annealing. The residual strain causes stress birefringence even if the residual strain is relatively small and does not require the ingot to be annealed. The crystal cannot then be used for VUV light lithography applications. Slip planes are commonly generated in as-grown crystals, and these planes can be removed by annealing. Because CaF_2 has a transition point at around 950 °C [17], the residual strain and the slip plane can be reduced by annealing at 1000 °C or more.

A crystal with small stress birefringence (<0.5 nm/cm) can be used as a lens material for VUV lithography. The as-grown crystal should be heated to a temperature (>1300 °C) close to the melting point. Removing the residual strain in a large crystal with a diameter exceeding 200 mm by annealing is more intricate. The cooling program should be optimized, and the hot zone in an annealing furnace should be designed to avoid a temperature distribution in the crystal during cooling. A technique to calculate the relationship between the birefringence generated by the thermal annealing history of CaF_2 was developed and used to optimize the annealing conditions [17]. The birefringence distribution of CaF_2 discs with a diameter of 300 mm is shown in Figure 4.15. The upper and lower parts indicate the states before and after annealing, respectively. Before annealing, various strong patterns of stress birefringence can be identified. After annealing, stress birefringence has become very weak, and the requirements for a lithographic lens material are satisfied. It takes about a month or more to complete this annealing process.

4.4 Large Fluoride Crystals

Ultraviolet (UV) light sources are useful in many practical applications in medicine, material processing, optical communications, and remote sensing [18]. Although excimer and tunable color-centered lasers have been used as UV sources, their utilization

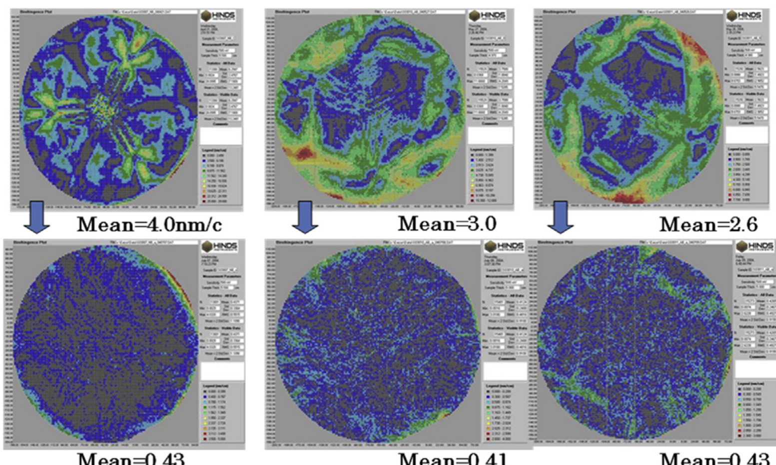

FIGURE 4.15 Stress birefringence distribution maps of a 300-mm diameter CaF_2 crystal. Upper and lower pictures indicate states before and after annealing, respectively.

has been limited due to low temperature operation and to material deterioration. Fluoride-based $LiCaF_6$ and $LiLuF_4$ crystals have been investigated as efficient and convenient solid-state UV laser media [19–22]. It is difficult however to obtain a high energy output from cerium ion (Ce^{3+})-doped crystals due to a limited crystal size. The growth of these crystals has been known to be challenging. A fluorination process using gases like HF [23] is usually performed to purify both the precursor materials and the resulting crystals.

The growth of fluoride crystals as potential UV light sources is hereby presented. The CZ method is used to grow large-size crystals to about 120 mm in diameter. The crystals' optical properties and laser applications are also discussed. The CZ-grown large crystals have high potential as optical materials not only in the UV range but also in the vacuum ultraviolet (VUV) region.

4.4.1 Growth Technique

Fluorides such as $LiCaAlF_6$ (LiCAF), $LiSrAlF_6$ (LiSAF), $LuLiF_4$ (LuLiF), $KMgF_3$ (KMF), and $BaLiF_3$ (BLF) were prepared by the CZ growth method [24–28]. Stoichiometric and/or excess amounts of high purity and commercially available fluoride compounds served as the precursors. The powders were mixed and placed in a glassy carbon or platinum (Pt) crucible. The growth chamber was equipped with an automatic diameter system and with resistive heater and thermal insulators made from high purity graphite. Vacuum thermal treatment was performed on the chamber prior to the actual growth. The chamber was evacuated to about 10^{-2} to 10^{-5} Torr using rotary and diffusion pumps. This procedure ensured elimination of water and oxygen from the chamber and precursor materials. Subsequent heating from room temperature to 550–850 °C for 12 h was

then performed. Argon (Ar) or carbon tetrafluoride (CF_4) gas was slowly introduced to the system. The mixture was then melted to the glass melting temperature. The growth direction was controlled by an oriented seed crystal. The procedure was implemented with 0.5–1.5 mm per hour pulling rate and 10 rpm rotation rate. The fluoride crystals were grown without the use of hydrofluoride (HF) gases and without the hydrofluorination of raw materials. Table 4.2 summarizes the preparation parameters used for the CZ growth of fluoride crystals.

4.4.2 As-Grown Crystals

Figure 4.16 shows the CZ-grown fluoride crystals. For the preparation of Ce-doped LiCAF and LiSAF, high purity CeF_3 and NaF were used with a concentration of 1 mol% [30]. Na^{3+} was co-doped with Ce^{3+} to maintain charge neutrality. For Ce-doped LuLiF, the starting composition was enriched with 1 mol% LiF and mixed with 1 mol% Ce^{3+} [26]. The KMF precursor was also enriched with 4 mol% KF to compensate for the vaporization of KF from the melt [27]. Since BLF melts incongruently, the starting material was composed of 43% BaF_2 and 57% LiF [28]. Previous samples exhibited white foreign substances on their surfaces. The growth parameters have been optimized to avoid this formation along with inclusions and cracks. Several modifications were also implemented to enable reproducibility. As a result, cracks, bubbles, or inclusions have not been observed. Large crystal boules have also been realized. Table 4.3 shows the summary of the dimensions of CZ grown fluoride crystals.

4.4.3 Transmission Properties

Fluoride crystals are ideal optical materials in the UV and VUV regions. They are also nonhydroscopic and have better mechanical processing properties. The transmission characteristics of 1-mm-thick LiCAF and LiSAF crystals were investigated using the Ultraviolet Synchrotron Orbital Radiation (UVSOR) facility of the Institute for Molecular Science (IMS) [31]. The Seya-Namioka monochromator with 1-m focal length and the photo multiplier with 290 nm band-pass filters were used. The monochromator, crystal, and photo multiplier were aligned inside a chamber evacuated to 10^{-9} Torr by an ion pump. The monochromator set the excitation wavelength, while the photo multiplier detected the transmitted signal from the sample. The beam flux incident to the sample was approximately 1010 photons per second around 200-nm wavelength with 0.1-mm slit width. The transmission edge was defined by the 1% transmission point on the transmission spectra. A 1% transmission is dark enough to use a material not only for a laser crystal but also for a practical window in the UV and VUV regions. Figure 4.17 shows the transmission spectra of the LiCAF and LiSAF. The transmission edges of LiCAF and LiSAF are located at 112 and 116 nm, respectively [31]. A new excitation channel around 112 nm is discovered for Ce:LiCAF crystal originating not from the cerium ions but from absorption around the band gap of the host crystal. On the other hand, transmission properties of KMF and BLF were analyzed by a VUV 5530

Table 4.2 Preparation Parameters for Fluorides by the Czochralski Growth Technique

		Vacuum Thermal Treatment							
Fluoride Crystal	**Precursor Powders**	**Temperature (°C)**	**Time (h)**	**Pressure (Torr)**	**Background Gas**	**Melting Temperature (°C)**	**Pulling Rate (mm/h)**	**Rotation Rate (rpm)**	**Seed Crystal**
$LiCaAlF_6$	LiF CaF_2 AlF_3	700	12	10^{-2} [24] 10^{-5} [25]	Ar [24] CF_4 [25]	825 [24] 820 [25]	1	10	Cr^{3+}:LiCAF
$LiSrAlF_6$ [25]	LiF SrF_2 AlF_3	700	12	10^{-5}	CF_4	820	1	10	Cr^{3+}:LiSAF
$LuLiF_4$ [26]	LiF LuF_2	700	12	10^{-4}	CF_4	N/A	1	15	LuLiF
$KMgF_3$ [27]	KF MgF_2	850	12	10^{-5}	CF_4	1100	0.5–1.5	15	CaF_2 $KMgF_3$
$BaLiF_3$ [28]	BaF_2 LiF	550	12	10^{-3}	CF_4	N/A	1	10	$BaLiF_3$

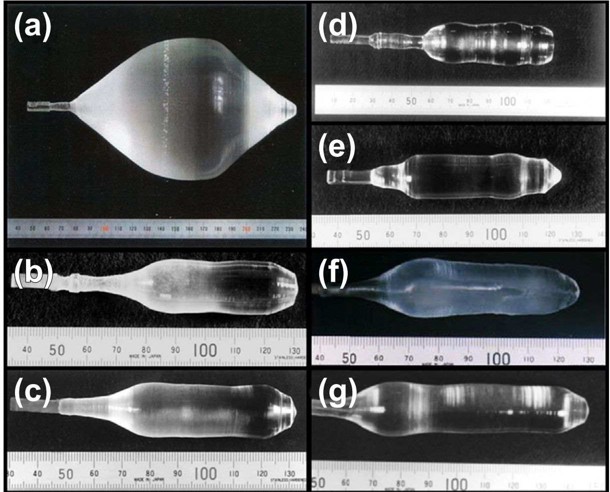

FIGURE 4.16 As-grown fluorides by Czochralski method: (a) 12-cm diameter LiCAF boule with growth direction along the axis (after Ref. [29] with permission of the publisher); as-grown 18-mm diameter Ce-doped (b) LiCAF and (c) LiSAF single crystals pulled along the a-axis (after Ref. [25] with permission of the publisher); (d) undoped and (e) Ce-doped LuLiF (after Ref. [26] with permission of the publisher); (f) 20-mm diameter $KMgF_3$ single pulled along the <111> direction (after Ref. [27] with permission of the publisher); and, (g) $BaLiF_3$ single crystal pulled along the <100> orientation. *After Ref. [28] with permission of the publisher.*

Table 4.3 Dimensions and Transmission Edges of Fluorides Prepared by the Czochralski Growth Technique

Fluoride	Diameter (mm)	Length (mm)	Transmission Edge (nm)
$LiCaAlF_6$	120 [29]	100 [29]	112 [25]
$LiSrAlF_6$ [25]	18	60	116
$LuLiF_4$ [26]	18	50	N/A
$KMgF_3$ [27]	20	90	115
$BaLiF_3$ [28]	20	80	123

spectrophotometer at room temperature under vacuum. KMF wafers with <111> orientation were cut and polished from grown crystals. A BLF wafer with <100> orientation and 2-mm thickness was cut and polished from a BFL boule. The transmission edges for KMF and BLF are determined to be at 115 nm and 123 nm, respectively [27,28]. Table 4.3 also lists the transmission edges of each fluoride crystals. The samples grown by the CZ technique have superior transmission properties and high potential as optical materials in the UV and VUV regions.

4.4.4 Solid-state Lasers

Ce^{3+}-doped fluorides have been identified as efficient and convenient UV solid-state laser media [32]. Since large fluoride crystals have been made available by the CZ

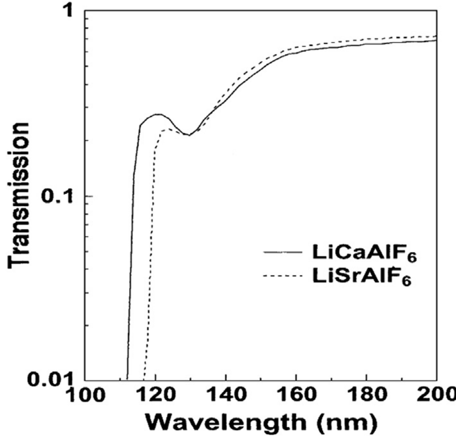

FIGURE 4.17 Transmission characteristics of LiCAF and LiSAF at room temperature. *After Ref. [31] with permission of the publisher.*

growth method, it is then possible to obtain high energy output from a Ce:LiCAF and Ce:LuLiF laser. High power pulses were generated from a Ce:LiCAF laser quasicoaxially pumped by two Nd:YAG lasers [33]. The fourth harmonics of two simultaneously Q-switched Nd:YAG lasers were used as the pumping sources. Three beams were focused on the Ce:LiCAF crystal using a 40-cm focal length lens. The beams were incident to the crystal's surface with approximately 6-mm spot size. The Ce:LiCAF crystal with 15-mm aperture and 10-mm length doped by 1.2 mol% Ce^{3+} was placed between a flat high reflector and a flat output coupler. The reflector and the coupler with 30% reflection were separated by 4 cm and were used to establish a laser resonator. With 85% of the total 230-mJ pumping energy being absorbed, the Ce:LiCAF laser produced 60-mJ pulses with 10-Hz repetition rate and 289-nm wavelength. This output power is twice as high as what we have previously demonstrated [34]. No significant power decrease was observed due to thermal effects for the 10-Hz operation compared to that of 1-Hz operation. LiCAF's negative change of refractive index with temperature [35] contributing to the thermal lens tends to cancel the positive effects of thermal expansion. Thermal lensing tends to be very low in LiCAF crystals. Moreover, a 27-mJ pulse was generated from a Ce:LuLiF oscillator pumped transversely by a KrF excimer laser [36]. The 10-mm Ce:LuLiF crystal was obtained by cutting an as-grown boule in the middle along its axis and by cutting the side window and end surfaces. The side window and end surfaces were not coated with dielectric materials. The laser resonator was established by using a flat high reflector and a flat output coupler. The laser cavity has a length of 6 cm. A randomly polarized KrF excimer laser operating at 248-nm wavelength and 1-Hz frequency served as the pump laser. The laser pulses were softly focused on the side window of the Ce:LuLiF crystal using a 50-cm focal length spherical lens under a normal incidence side pumping condition. The crystal absorbed almost all of the pumping pulse energy with 230 mJ maximum. The maximum output pulse reached 27 mJ with the

230-mJ pumping pulse energy and corresponding 0.6 J/cm^2 pumping fluence. The highest output energy was obtained with the coupler with 45% transmission. The free-running Ce:LuLiF laser operated with 309-nm wavelength.

4.4.5 Chirped-pulse Amplification

We have also successfully demonstrated chirped-pulse amplification in the UV region using a broadband Ce:LiCAF laser medium [37]. Figure 4.18 illustrates the schematic diagram of the experimental setup. The femtosecond seed pulses with 290-nm wavelength and 1-kHz repetition rate from the third harmonics of a Ti:sapphire laser. The seed pulse has a duration of 210 fs and a spectrum bandwidth of 1.0 nm. Seed pulses without any dispersion compensation were guided to an eight-pass quartz-prism pulse stretcher with reflective optics. This expanded the pulse duration to 2.6 ps and avoided spatial chirping and aberration. Stretched seed pulses of 2.6-ps pulse duration, 290-nm wavelength, and 33-μJ energy were guided to a modified bow-tie-style four-pass Ce:LiCAF amplifier after being selected by a mechanical shutter [38]. The 100 mJ, 266 nm, 10 Hz, 10 ns pump pulses from a synchronously operated Q-switched Nd:YAG laser were softly focused with a 70-cm focal length lens. The diameter of the seed beam was approximately 1.5 mm for the first and second passes and was expanded to 3 mm for the third and fourth passes to avoid deep gain quenching and possible damage to the amplifier optics. The maximum output energy was 6 mJ with a net gain of 180 for the 33-μJ input pulse. The corresponding fluence was approximately 90 mJ/cm^2, which was near the saturation fluence of the Ce:LiCAF crystal. The amplified spontaneous emission was below the 20 μJ detection limit when no seed pulse was input into the amplifier. The energy-extraction efficiency for the absorbed pump power reached 7.3%. The total gain factor was 370 for the transmission pulse when the output energy was 4.5 mJ. After dispersion compensation, the output pulses are compressed to 115 fs.

4.5 Scintillator Crystals

Since its discovery by Hofstadter in 1948, NaI:Tl scintillators have been widely used as detectors for radiation [39,40]. With the development and market penetration of medical equipment such as X-ray computed tomography (X-ray CT) in 1973 [41] and positron emission tomography (PET) in 1975 [42], dense scintillator oxide crystals have been developed as alternatives to NaI:Tl. These include bismuth germinate ($Bi_4Ge_3O_{12}$ or BGO), cadmium tungstate ($CdWO_4$ or CWO), lead tungstate ($PbWO_4$ or PWO), cerium-doped gadolinium silicate (Gd_2SiO_5:Ce or GSO), and cerium-doped lutetium silicate (Lu_2SiO_5:Ce or LSO). These scintillators have good radiation sensitivity because of their density and their constituent elements with high atomic numbers. They are used in nuclear and high energy physics research as well as detectors for the above-mentioned medical equipment to downsize the radiation detector, resulting in better image quality.

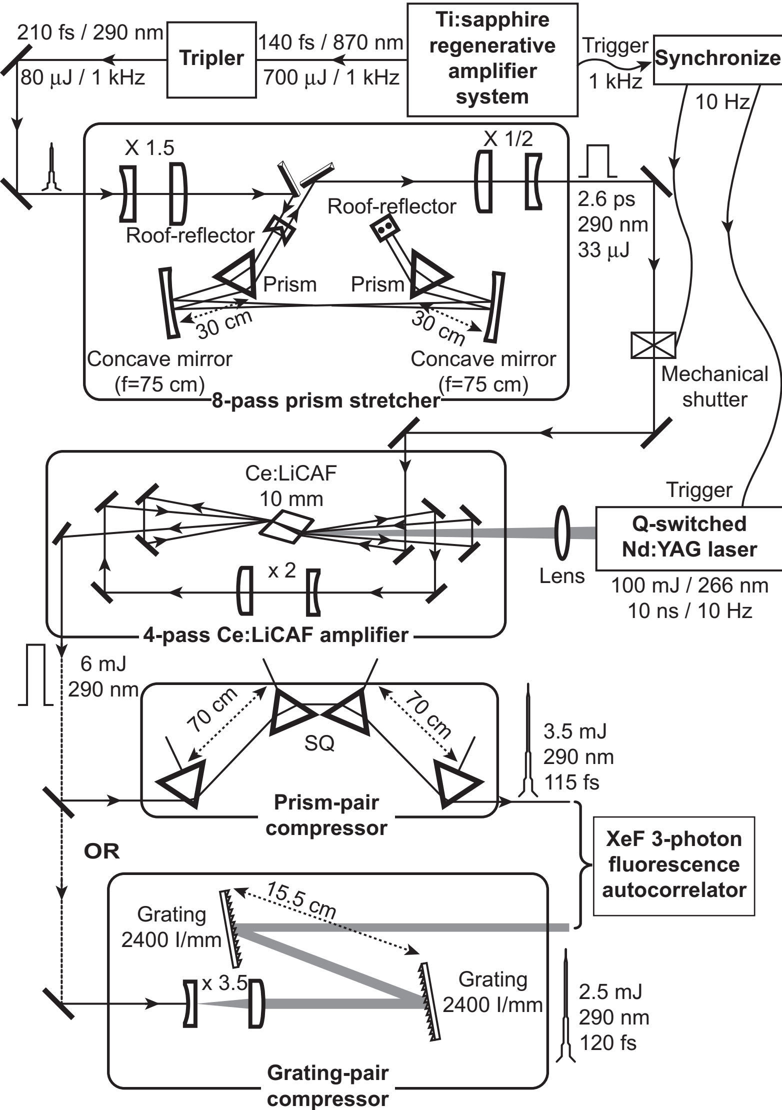

FIGURE 4.18 Experimental setup of the Ce:LiCAF CPA laser system with SQ as synthetic quartz. *After Ref. [37] with permission of the publisher.*

A scintillator crystal must produce luminescence from an incident radiation and serve as a guide to transfer the scintillation light efficiently to a detector such as a photomultiplier tube (PMT) or photodiode. To be able to do so, many scintillators are made from high purity single crystals with great performance because of few defects and fewer grain boundaries to avoid light scattering.

Table 4.4 Comparison in Properties of Typical Scintillators

Scintillators		NaI:Tl	BGO	CWO	PWO	GSO	LSO	LGSO	LYSO
Density (g/cm^3)		3.67	7.13	7.90	8.28	6.71	7.4	7.2	6.0
Decay time (ns)	Fast	230	300	5000	~3	30–60	41	40–44	40–44
	Slow				<40	600			
Light output (relative)	Fast	100	7–10	30	0.26	18	40–75	~80	~80
	Slow				0.04	2			
Emission λ_{em} (nm)	Fast	415	480	480	440	430	420	420	420
	Slow					430			
Refractive index at λ_{em}		1.85	2.15	2.25	2.2	1.85	1.82	1.82	1.82
Rad. hardness (gray)		10^3	10^{2-3}	10^4	$>10^5$	$>10^6$	$>10^5$	–	$>10^4$
Effective atomic number		51	74	64	73	59	66	64	64
Radiation length (cm)		2.59	1.12	1.10	0.89	1.38	1.14	1.16	1.16
Hygroscopicity		Yes	No	No	No	No	No	No	No
Radioactivity		No	No	No	No	No	Yes	Yes	Yes
Melting point (°C)		651	1050	1272	1123	1950	2150	2100	2100
Growth method		BR	CZ,BR	CZ,BR	CZ,BR	CZ	CZ	CZ	CZ

This section reviews crystal growth technology and the scintillation characteristics of germinates such as BGO, tungstates such as CWO and PWO, and rare earth silicates such as GSO and LSO. These crystals have distinguishing features and are applied to radiation detectors especially for medical equipment and high energy physics. The scintillators are grown by the Czochralski method with a large diameter for practical use. Triggered by the rapid expansion of the PET market and by the plans of large accelerator experiments in 1990s, new single crystal scintillators are being developed aggressively [43–45]. Table 4.4 shows the properties of typical scintillators grown by Czochralski method compare to a standard scintillator, NaI:Tl. These scintillators are currently used as radiation detectors because of their density and large absorption coefficients. For reviews of crystal growth for other new inorganic scintillators, see Refs [45–47].

4.5.1 Bismuth Germinate

Bismuth germinate or BGO ($Bi_4Ge_3O_{12}$) has the best sensitivity for gamma (γ) rays with 511 keV for PET because it is composed of elements with high atomic numbers. The BGO scintillator was discovered by Weber in 1973 [48]. Scintillation in BGO crystal originates from the s-p transition in the Bi atom. Nestor and Huang revealed that BGO was the most promising scintillator for high energy γ-ray detectors because of its high absorption coefficient, Z, and density [49]. BGO was initially used for X-ray detectors in X-ray CTs. Since PET became available, BGO has been used for PET γ-ray detectors [50].

A BGO single crystal was first grown by Nitsche to study its electro-optic effects [51]. After that, the BGO was grown by CZ method as host laser material [49,52]. Bridgman–Stockbarger and heat exchange methods were also implemented to grow BGO

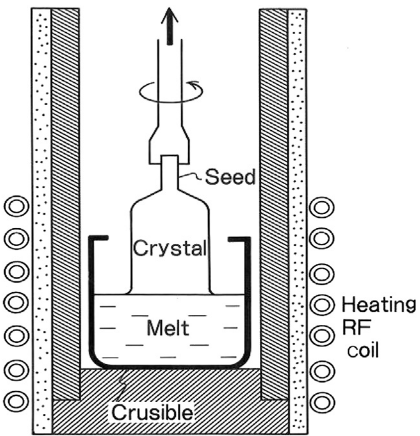

FIGURE 4.19 Typical Czochralski growth principle for BGO.

scintillators [51,53]. The stoichiometric composition of BGO with 1044 °C melting point is a congruent composition that produces luminescence at room temperature. The crystal structure of BGO is cubic with $\overline{4}3m$ space group. BGO has thermal expansion of 5×10^{-6}/°C and Mohs hardness of 5. BGO is chemically stable in any solvent including water but is soluble in acid. Figure 4.19 shows the typical CZ growth principle where a platinum (Pt) crucible is conduction heated by radio frequency and heat insulated by alumina-based refractories for BGO.

For the growth of BGO with good scintillation performance, raw materials of Bi_2O_3 and GeO_2 with 99.999 (5N) to 99.9999% (6N) purity must be used. Decomposition by vaporization of raw materials from the melt during the growth due to overheating or insufficient oxygen in the atmosphere must be prevented. Figure 4.20 shows the measured distribution of scintillation performance of light output as a function of longitudinal position in an ingot and as a function of the number of times of repeating

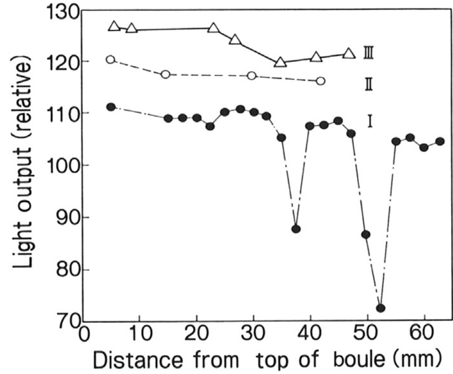

FIGURE 4.20 Effects of multipurification on light output of BGO. *After Ref. [54] with permission of the publisher.*

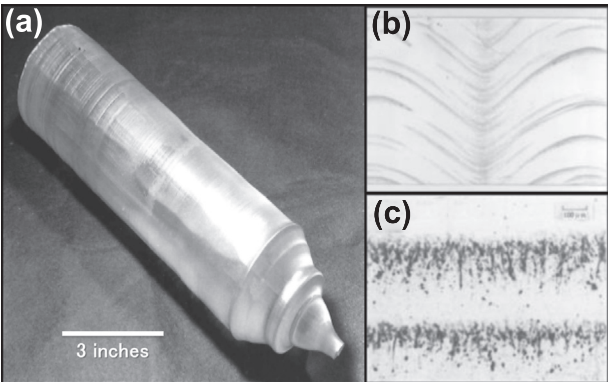

FIGURE 4.21 (a) Three-inch diameter BGO crystal grown by CZ method and the (b) macroscopic and (c) microscopic appearance of typical voids in the crystal. *After Ref. [43] with permission of the publisher.*

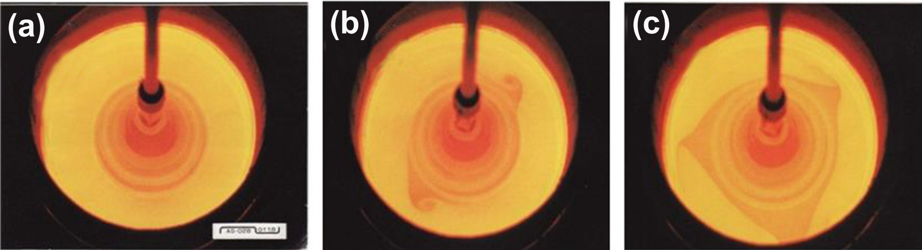

FIGURE 4.22 Flow patterns during the CZ growth of BGO: (a) before melt; (b) start of melt; and, (c) after melt.

crystallization. The growth parameter I, II, III denotes the number of repeated crystallization [54]. Two sharp drop-offs in the light output of growth parameter I are caused by voids.

Figure 4.21(A) shows a single crystal of BGO with a diameter of 7.5 cm and a length of 25 cm grown by CZ method. Voids usually form easily during crystal growth. Figure 4.21(B) and (C) are the typical macroscopic and microscopic appearances of voids in BGO, respectively [43]. Voids appear from a shrinkage hole caused by dendrite growth particular to a BGO melt having large supercooling and high viscosity. These voids are located in the center and bottom of the crystal because of large supercooling during crystal growth in these areas.

During the shoulder growth of BGO, typical flow patterns of CZ growth (Figure 4.22) can be observed. Natural convection (Figure 4.22(A)) can be seen in the flow pattern at the initial stages of the growth. After a certain period and reaching a certain diameter, forced convection can be identified as seen in Figure 4.22(B) and (C). The flow pattern with forced convection seems to start to melt back at the solid–liquid interface of the BGO crystal in the melt, which commonly occurs in some CZ-grown crystals.

A low-thermal-gradient CZ technique (LTG CZ) has been adapted for BGO growth by Gusev et al. [55]. In this method, thermal conditions of the growth are selected to provide

a complete faceting of the crystallization front. LTG CZ allows the growth of BGO crystals up to 130 mm in diameter and up to 400 mm in length [56].

4.5.2 Cadmium Tungstate

Cadmium tungstate or CWO ($CdWO_4$) is one of the good candidates for X-ray detectors because of its density and large light output. It is not used for γ-ray detectors of PET due to a long decay time. Kroger did the first systematic study on the luminescence characteristics of various tungstate powders in 1948 [57]. Magnesium (Mg), calcium (Ca), and zinc (Zn) tungstates also show good scintillation characteristics at room temperature. Single crystals of $CaWO_4$ and CWO were grown in 1950 by Gillette [58] employing the Verneuil method and were evaluated as γ-ray detectors. CWO was first used as X-ray fluorescent intensifying screens and then as detectors for X-ray CT [59]. The detector application has led to serious work on the development of CWO single crystals [57,58]. Studies were also made on $ZnWO_4$ for the same purpose [60,61].

Robertson et al. reported the crystal growth of CWO by CZ method [62]. CWO has a melting point of 1272 °C. Besides the minimization of impurities, control of the composition of CdO/WO_3 is important in growing high quality single crystals. CdO and WO_3 powders with impurities less than 10 ppm are used as raw materials. The precursors are mixed and pretreated at 1000 °C for 12 h. CWO crystal has monoclinic structure of the wolframite type, which can be considered as a distortion of the scheelite structure spatial symmetry group P_2, P_2/c [63].

CWO single crystals are grown from the melt contained inside a Pt crucible. If the melt has an excess of WO_3, the grown crystals are colored green. On the contrary, if the melt has 5 mol% excess of CdO, the grown crystals are colored light yellow, especially at the top of the boule. When the melt composition has a remarkable excess of CdO over the stoichiometric condition, precipitates similar to brown CdO can be observed in the grown crystals. A CWO crystal grown from a stoichiometric composition has yellow-green precipitates at the bottom of the boule [43].

Figure 4.23 shows a CZ-grown CWO single crystal having a diameter of 75 mm and a length of 300 mm. Since CWO tends to have a faceted growth, the ingots may have an

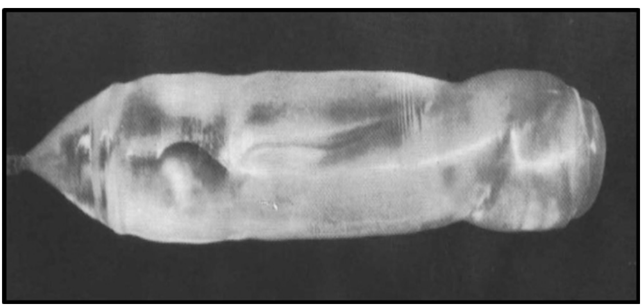

FIGURE 4.23 CWO crystal grown by CZ method.

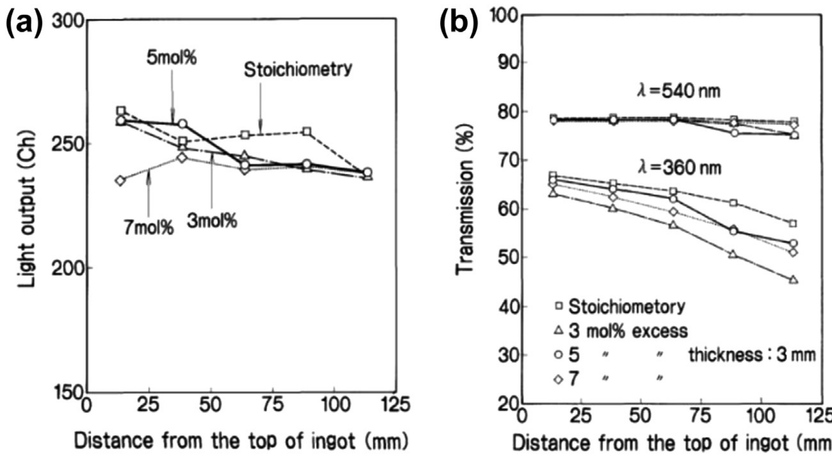

FIGURE 4.24 Distribution of (a) light output and (b) optical transmission in CWO grown from various melt compositions. *After Ref. [43] with permission of the publisher.*

elliptical cross-section or may become polycrystalline. Furthermore, CWO crystals tend to crack easily. The cracks are mainly caused by large anisotropy in the thermal expansion coefficient. Cracks may also be due to the existence of cleavage in (100) plane, and to avoid such cleavage, the recommended growth axis of the crystal boule must be parallel with (100).

Optimizing the starting melt composition is important to eliminate the composition variation due to CdO vaporization and the occurrence of macroscopic defects such as precipitates. Figure 4.24 shows the dependence of the light output and the optical transmission on the longitudinal position of boules grown from the starting melt with stoichiometric compositions and with 3 mol%, 5 mol%, and 7 mol% excess of CdO. In most cases, both light output and transmission are high at the top of boule and slightly decrease toward the bottom. The almost flat distribution of light output versus position is consistent with that of the optical transmission at 540 nm, the peak of the emission wavelength for X-ray excitation. The heat insulation improvement of the growth station including the crucibles and the avoidance of overheating in melting are also important to eliminate vaporization [43].

4.5.3 Lead Tungstate

Lead tungstate or PWO ($PbWO_4$) has high density, nonhygroscopicity, low radiation length, high efficiency in detecting ionizing radiation, fast response, and sufficient radiation hardness. These properties have attracted much interest in PWO as an electromagnetic calorimeter scintillator. PWO was proposed as a promising scintillator for high energy physics by Derenzo after observing scintillation from many kinds of powdered oxides, fluorides, and chlorides containing lead (Pb), hafnium (Hf), ytterbium (Yb), cadmium (Cd), and tungsten (W) metals [64]. In 1992, at Crystal 2000, the first

international conference on inorganic scintillators in Chamonix, France, the PWO crystal raised attention for the first time for its potential use in high energy physics calorimetry [44]. After improvements in its crystal growth technology and scintillation performance, PWO was employed as electromagnetic calorimeters for the Large Hadron Collider (LHC) built by the European Organization for Nuclear Research (CERN) [62], which recently contributed to the investigation of the Higgs boson.

PWO occurs in nature as tetragonal scheelite type as well as monoclinic respite. Synthetic PWO crystal, however, grown from a melt is scheelite only. It belongs to the $I4_1/a$ space group and has a melting point of 1123 °C. PWO crystals can be grown by the CZ and Bridgman methods using standard equipment. By the CZ method, PWO is grown from the stoichiometric mixture of raw materials in a Pt crucible. Crystal ingots are annealed in atmosphere inside nongradient ovens to minimize radial and axial stress of ingots before mechanical treatment.

The first results on the optical transmission and radiation damages for CZ-grown PWO crystals were obtained by Kobayashi et al. and Nagornaya et al. in 1992 [65,66]. Significant improvement in the transmittance of PWO by trivalent ion doping, with lanthanum (La^{3+}) for example, was obtained [67]. The transmittance of PWO doped with more than 85 ppm La improved in the near absorption range. The trivalent ion doping also affects the scintillation decay of PWO as shown in Figure 4.25 [65]. Here, the radiation damage μ_{ir} is expressed as

$$\mu_{ir} = (1/d)\text{In}(T_0/T) \tag{4.5}$$

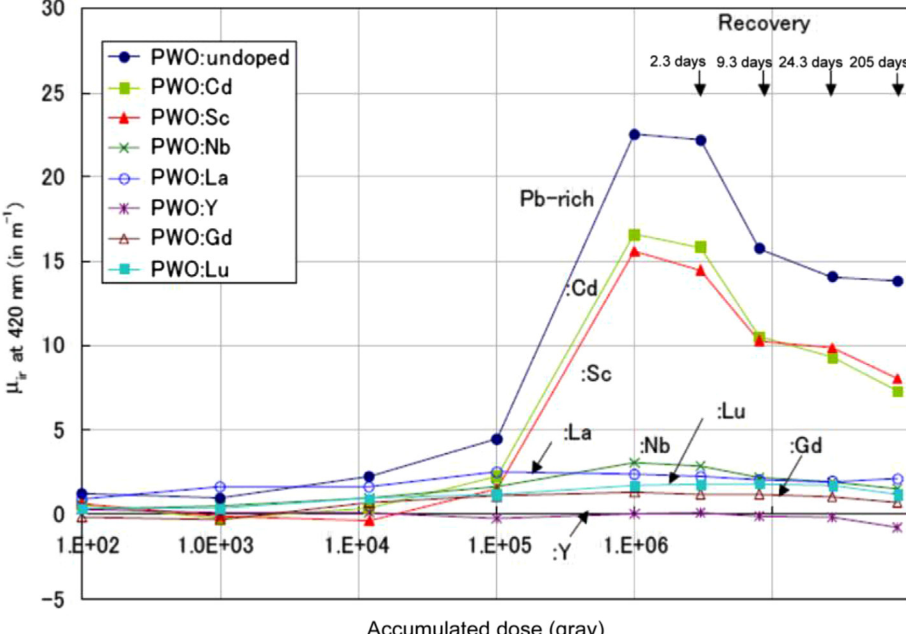

FIGURE 4.25 Radiation damages of trivalent ion-doped PWO. *After Ref. [68] with permission of the publisher.*

A CMS collaborative project began in 1994 for the search of the high energy particle by LHC of CERN. Lecoq reports the development of the PWO crystal and its application for EM calorimeter [66]. The crystals made by Bogorodisk Techno-Chemical Plant were used for the CMS experiment. The 80,000 crystals weigh 90 tons and have a 23-cm length, 2.5 × 2.5-cm^2 cross-sectional area, and 11-m^3 volume. From 1998 to 2007, 61,000 and 2000 PWO crystals were being produced by the CZ and Bridgman methods, respectively, for the CMS electromagnetic calorimeter. Figure 4.26 shows CZ-grown PWO ingots and two CMS barrel crystals.

4.5.4 Gadolinium Silicate

Gadolinium silicate or GSO (Gd_2SiO_5) is denser than NaI:Tl, faster, and emits more light than BGO, hard for radiation damage, not hygroscopic, and nonradioactive. Among all scintillator crystals, GSO has a good balance of every scintillator property. GSO was discovered by Takagi and Fukazawa in 1983 [70]. It was initially used to detect oil well loggings due to its good performance in high temperature [68]. It was then employed for PET detectors because of its good energy resolution [69].

GSO is the only congruent material among the three compounds in a Gd_2O_3–SiO_2 pseudobinary system. For this reason, a single crystal GSO can be grown by the standard CZ method. The starting materials include Gd_2O_3, SiO_2, and CeO_2 with purity of 99.99% or more. The iridium (Ir) crucible is induction heated to melt the starting materials at a controlled temperature of about 1950 °C in a nitrogen or oxygen-containing atmosphere [70]. The crystal is pulled slowly upward at a rate of 1–3 mm/h with a seed rotation rate of 30–50 per minute. After the growth, the crystal boule is cut off from the melt and gradually cooled. However, it has been difficult to grow even a small crack-free single crystal GSO.

Figure 4.27(A) and (B) shows typical cracks in single crystal GSO. In a GSO crystal boule, we typically observe cracks on the (100) cleavage plane (Figure 4.27(A)) and on the

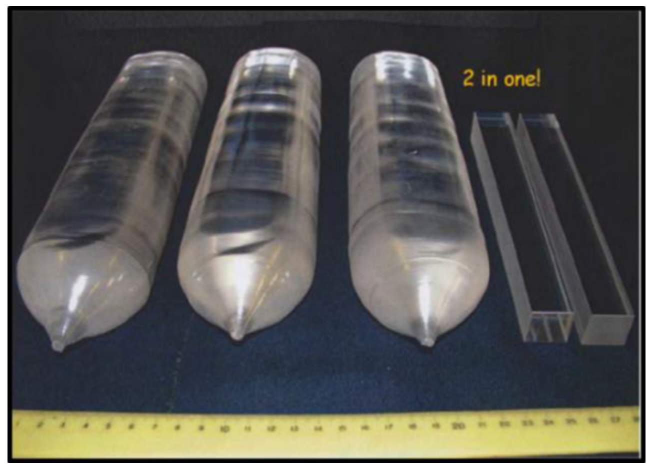

FIGURE 4.26 Ingots of PWO crystal with 65-mm diameter and two CMS barrel crystals cut per ingot. *After Ref. [69] with permission of the publisher.*

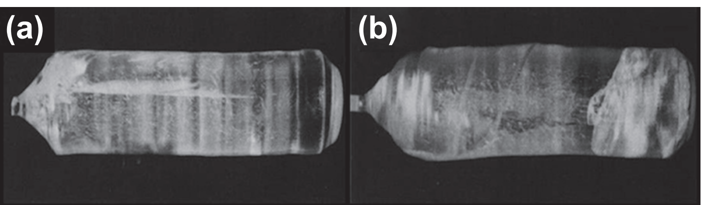

FIGURE 4.27 Typical (a) cleavage and (b) noncleavage cracks in single crystal GSOs. *After Ref. [71] with permission of the publisher.*

noncleavage plane close to (010) (Figure 4.27(B)) [73]. These cracks are related to an anisotropic crystal structure of GSO. GSO has a monoclinic symmetry with $P2_1/c$ space group and has a (100) cleavage plane as shown in Figure 4.28(A) [74]. Figure 4.28(B) shows the thermal expansion coefficients of GSO along different crystallographic planes [74]. The coefficient of thermal expansion changes greatly with direction. The coefficient of the [010] axis is two or three times as large as that along the other axes. These anisotropic properties of the thermal expansion and cleavage are assumed to be the main reasons for the existence of cracks.

In clearly identifying the causes of the cracks, we measured the fracture strength and anisotropic elastic constants and calculated the thermal stress distribution in the boule during growth. The analyses led to the conclusion that possible causes for cracking are the stresses induced during the process:

1. Thermal stresses generated in the processes of "cutting off" and "cooling down";
2. Stress due to the anisotropic thermal expansion in accidentally formed polycrystal; and,
3. Residual stress due to defects in crystal boule created during crystal growth.

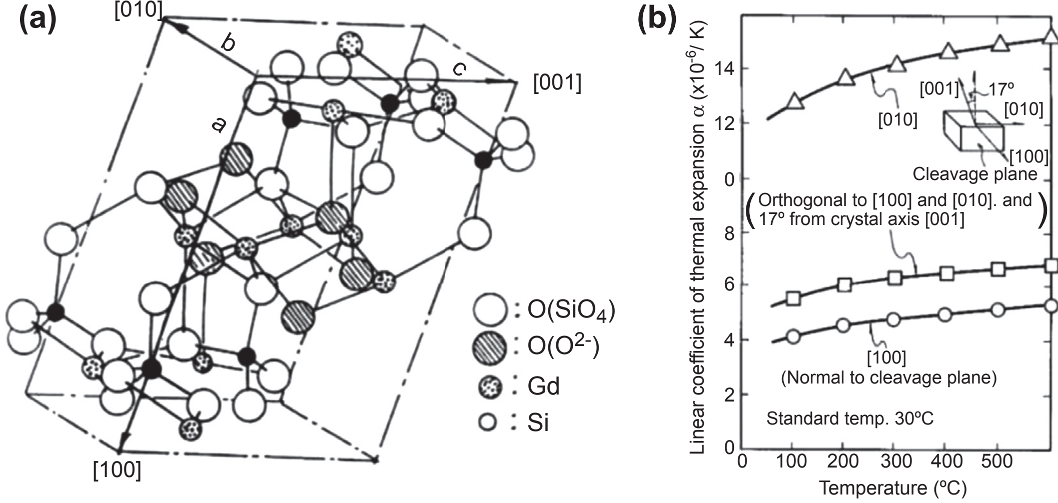

FIGURE 4.28 (a) Unit cell crystal structure and (b) thermal expansion coefficients of GSO. *After Ref. [72] with permission of the publisher.*

To eliminate causes (1) and (2), we reduced the temperature gradient in the growth furnace. As a result, the natural convection of the melt decreased, which suppressed the accidental polycrystalline formation. In realizing the temperature gradient reduction during the crystal growth and cooling process, we used numerical simulation to design the growth chamber with optimal thermal condition to obtain large GSO single crystals without cracks. The calculated temperature distribution in the furnace is shown in Figure 4.29. The optimal cooling condition, which can prevent cracks, was also calculated from the simulation results [74].

Growth conditions such as pulling rate, rotation rate, and gas atmosphere in the furnace were optimized for getting defect-free large GSO crystals with uniform scintillation performance. By applying the above techniques, we could enlarge the GSO crystal without cracks. We are finally able to grow large GSO single crystals with 105-mm diameter and 290-mm length weighing 19.5 kg as shown in Figure 4.30. The volume of the GSO crystal corresponded to about 80% of melted raw material in the crucible.

Ce concentrations of GSO boule with 0.5 mol% Ce, 0.95 mol% Ce, and 1.5 mol% Ce were measured by means of inductively coupled plasma (ICP) atomic emission spectroscopy [71]. The solidification fraction (g) and Ce concentrations were fitted to the Scheil equation:

$$C_S/C_0 = k(1-g)^{k-1} \tag{4.6}$$

where C_S is the Ce concentration at g in the crystal, C_0 is the Ce concentration in the initial melt, and k is the effective distribution coefficient of Ce in GSO, and was determined by the curve fitting. The k value decreased with the increasing of Ce

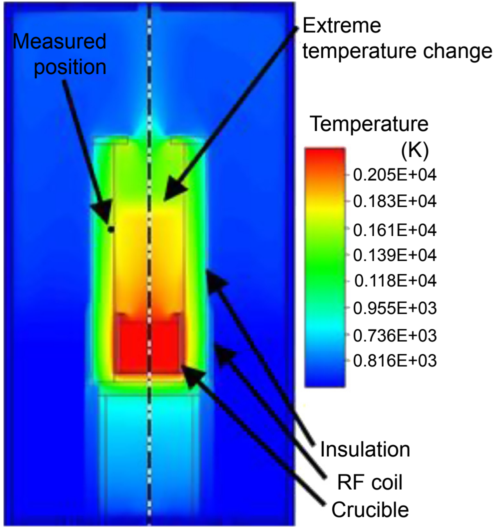

FIGURE 4.29 Numeral simulation results for the temperature distribution inside the GSO growth furnace. *After Ref. [75] with permission of the publisher.*

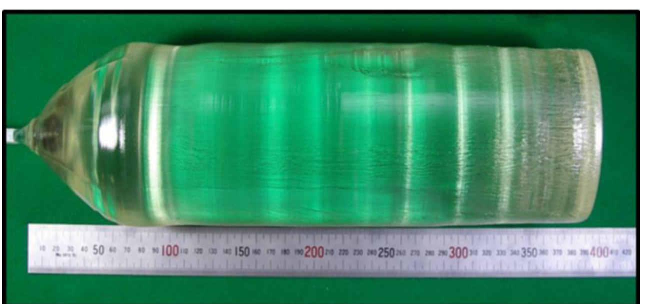

FIGURE 4.30 Large GSO single crystal with 105-mm diameter and 290-mm length. *After Ref. [75] with permission of the publisher.*

concentration, resulting in the concentration variation in the crystal. The variation, however, is small enough to give a good longitudinal uniformity in scintillation performance.

4.5.5 Lutetium and Other Silicates

Cerium-doped lutetium silicate has a 75% light output compared to NaI:Tl, a decay time of 42 ns, and a density of 7.4 g/cm^3. LSO was discovered by Melcher and Schweitzer in 1992 [76]. Due to its good timing resolution for coincidence, LSO is used for PET detectors, especially in time of flight (TOF) PET [75,77]. The only limitation for LSO is the background signal originating from the admixture of the radioactive ^{176}Lu isotope with a 2.6% natural abundance [76]. Modified LSO crystals such as LGSO ($Lu_{2-x}Gd_xSiO_5$:Ce) and LYSO ($Lu_{2-x}Y_xGd_xSiO_5$:Ce) are also applied to TOF-PET due to good timing resolution with fast decay and high light output [78,79]. These Lu-based crystals are also grown by Czochralski method [80,81]. The background noise from ^{176}Lu in these specific scintillators may not be a problem in PET application because of the coincidence detection for γ-ray in PET detectors.

LSO has a monoclinic structure with space group C2/c like other rare earth silicates such as GSO. LSO has a melting point of around 2100 °C. Since Ce-doped LSO has a significant good scintillation performance [72], it is used for detectors in PET, especially in TOF-PET.

LSO-like crystals such as LGSO and LYSO have almost the same melting point of around 2100 °C and can be grown by the typical CZ method [80,81]. Figure 4.31 shows an LGSO single crystal with 90-mm diameter and 300-mm length for PET application.

4.5.6 Scintillator Applications

4.5.6.1 X-ray Computer Tomography

When X-ray computer tomography (CT) was developed by Hounsfield et al. in 1972 [41], NaI:Tl was used in the detector. BGO [43] and CsI:Tl coupled to PMT were then used in order to remove the image quality deterioration caused by afterglow. To achieve better spatial resolution and higher speed, a multichannel detector array composed of CWO

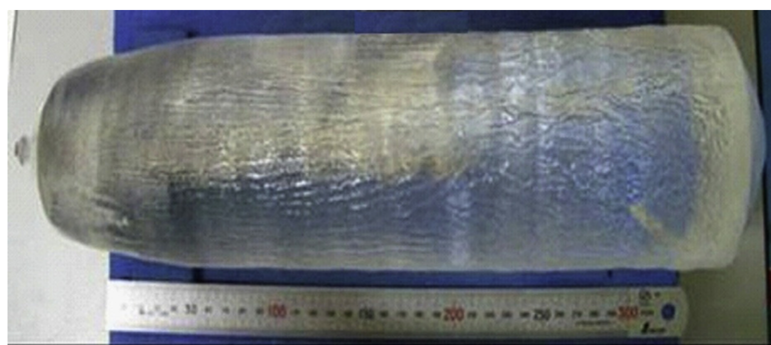

FIGURE 4.31 Large LGSO single crystal with 90-mm diameter and 300-mm length.

and PD was implemented in the detectors [42]. Ceramics scintillators, such as europium (Eu)- and praseodymium (Pr)-doped yttrium oxide (Y_2O_3) and gadolinium oxide (Gd_2O_3) and Pr- and Ce-doped gadolinium oxysulfide (Gd_2O_2S), are mainly used as detectors for recent X-ray CTs [55].

4.5.6.2 Positron Emission Tomography

PET, which can detect a small cancer tumor a few millimeters (mm) in size, is a diagnostic imaging technique different from X-ray CT and magnetic resonance imaging (MRI). A medical reagent labeled with positron-emitting tracer such as ^{11}C, ^{13}N, ^{15}O, and ^{18}F are injected into the patient. The reagent collects at the cancer tumor while emitting positrons. The positron will then combine with an electron from the surroundings and convert to two γ-rays flying off at 180° from each other. In the PET equipment, the human body is located in the middle of a cylindrical array of γ-ray detectors. We can assume that the tracer is collinear with the centers of the two γ-ray detectors in coincidence. The lines of response connecting the coincidence detectors are used in the image reconstruction. Scintillator crystals are used as radiation detectors in PET.

The original PET with NaI:Tl detectors was used in nuclear medicine, for example, by Ter-Pogossian et al., in 1975 [42]. Upon the availability of dense BGO in late 1970s, more advanced PET used BGO crystals [50]. PET technology made rapid progress when PET diagnosis was covered by insurance plans in the 1990s, especially in the United States. High performance PET demands high performance scintillation detectors. A large scintillation light output and short decay time are desired to improve the PET imaging resolution. Dense and fast scintillators are also prerequisites for increased sensitivity. A usual PET is loaded with several tens of thousands of detector pieces, which must be mass produced with uniform and stable performance.

4.5.6.3 High Energy Physics

NaI:Tl has been used for a long time in nuclear physics experiments. NaI:Tl single crystals were used with sizes up to 50 cm in both diameter and depth, and then in crystal. NaI:Tl and BGO have been used as active shielding materials in Compton-suppressed

spectrometers that use Ge semiconductor detectors in in-beam γ-ray spectroscopy. Recent information linked to the discovery of the Higgs particle by CERN announced that a CMS detector equipped with around 80,000 PWO scintillators contributed to said discovery [62].

4.5.6.4 Other Applications

Applications for PET include environment monitors for radiation, X-ray baggage detectors, nondestructive X-ray inspection machines for industrial goods, oil well logging, survey meters, radiation detectors for oil exploration, and neutron detectors, etc. implement many kinds of scintillators.

4.6 Summary and Outlook

Large and high quality oxide and fluoride crystals have been produced by the CZ growth method. The availability of these crystals offers many practical applications not only in the semiconductor and optoelectronics industries but also in medicine and other research fields. For example, sapphire is used as a substrate, CaF_2 as an optical material, large fluorides as UV and VUV light sources, and germinates, tungstates, and silicates, as scintillators and detectors. The development of large crystal technology and high purity material synthesis such as the CZ method makes it possible to improve oxide and fluoride crystal production. Challenges, though, are still present in this specific growth method. Efforts to increase the quantity output, to reduce the thermal stress, to maintain sample homogeneity, and to remove scattering centers and voids are being studied. Additional investigations on high purity growth mechanisms and on high temperature material physics are also anticipated. With the demand of these oxides and fluorides, similar materials are also expected to be grown using the CZ technique. Possible laser and magnetic refrigeration materials such as garnets can be further studied. VUV fluorescent materials such as potassium magnesium fluoride ($KMgF_3$) and barium lithium fluoride ($BaLiF_3$) are also currently under investigation. Recently developed fast and large light output Ce-doped chloride and bromide scintillators can possibly be grown by CZ method like Ce-doped garnets [82]. CZ crystal growth technology, which is not only limited to oxides and fluorides, is expected to advance in the coming years.

References

[1] Nassau K. J Cryst Growth 1969;5:338.

[2] Harris DC. A peek into the history of sapphire crystal growth. Proc SPIE 2003;5078:1.

[3] LaBelle Jr HE. J Cryst Growth 1980;50:8.

[4] Akselrod MS, Bruni FJ. J Cryst Growth 2012;360:134.

[5] Li J, Su X, Mujilatu NA, Yang H, Li J, Yu Y, et al. Rare Met 2006;25:260.

[6] Richard Scherdtferger C, Ullal S, Shetty R, Filgate J, Dhanaraj G. J Cryst Growth 2014;393:123.

[7] Miyagawa C, Kobayashi T, Taishi T, Hoshikawa K. J Cryst Growth 2013;372:95.

[8] Stockbarger DC. J Opt Soc Am 1949;39:731.

[9] Jasper H, Boom H, Uitterdijk T, Modderman T, Mulkens J, Stoeldraijer J, et al. In: 3rd international symposium on 157 nm Lithography; 2002.

[10] Burnett JH, Levine ZH, Shirley EL. Phys Rev 2001;B 64:241102.

[11] Shiraishi N, Kido K, Nagatsuka J, Ohmura Y, Aoki T, Nishikawa J, et al. In: 4th international symposium on 157 nm lithography; 2003.

[12] Nassau K. J Appl Phys 1961;32:1820.

[13] Ko JM, Tozawa S, Yoshikawa A, Inaba K, Shishido T, Oba T, et al. J Cryst Growth 2001;222:243.

[14] Yonezawa T, Matsuo K, Nakayama J, Kawamoto Y. J Cryst Growth 2003;258:385.

[15] Nassau K. The physics and chemistry of color. New York: Wiley; 1983.184.

[16] Gektin A, Goriletskiy V, Zaslavskiy B. Continuous growth of large halifde scintillation crystals. In: Scheel HJ, Capper P, editors. Crystal growth technology – from fundamentals and simulation to large-scale production. Weinheim: Wiley-VCH; 2008. p. 353.

[17] Ogino H, Miyazaki N, Mabuchi T, Nawata T. J Cryst Growth 2008;310:221.

[18] Sarukura N, Dubinskii MA, Liu Z, Semashko VV, Naumov AK, Korableva SL, et al. IEEE J Sel Top Opt Microelectron 1995;1:792.

[19] Dubinskii MA, Semashko VV, Naumov AK, Abdulsabirov RY, Korableva SL. In: Pinto AA, Fan TY, editors. OSA proc. Advanced solid state lasers, vol. 15. Washington, D.C: Optical Society of America; 1993. p. 195.

[20] Dubinskii MA, Semashko VV, Naumov AK, Abdulsabirov RY, Korableva SL. J Mod Opt 1993;40:1.

[21] Dubinskii MA, Abdulsabirov RY, Korableva SL, Naumov AK, Semashko VV. In: Int. quantum electronics conf. Washington, D.C: Optical Society of America; 1992. Paper FrL2.

[22] Dubinskii MA, Abdulsabirov RY, Korableva SL, Naumov AK, Semashko VV. Laser Phys 1994;4:480.

[23] Belt RF, Uhrin R. J Cryst Growth 1991;109:340.

[24] Shimamura K, Mujilatu N, Nakano K, Baldochi SL, Liu Z, Ohtake H, et al. J Cryst Growth 1999;197:896.

[25] Shimamura K, Baldochi SL, Mujilatu N, Nakano K, Liu Z, Sarukura N, et al. J Cryst Growth 2000;211:302.

[26] Ranieri IM, Shimamura K, Nakano K, Fujita T, Liu Z, Sarukura N, et al. J Cryst Growth 2000;217:151.

[27] Shimamura K, Fujita T, Sato H, Bensalah A, Sarukura N, Fukuda T. Jpn J Appl Phys 2000;39:6807.

[28] Bensalah A, Shimamura K, Fujita T, Sato H, Nikl M, Fukuda T. J Alloys Compd 2003;348:258.

[29] Ono S, Suzuki Y, Kozeki T, Murakami H, Ohtake H, Sarukura N, et al. Appl Opt 2002;41(36):7556.

[30] Shimamura K, Sato H, Bensalah A, Machida H, Sarukura N, Fukuda T. Opt Mat 2002;19:109.

[31] Kozeki T, Suzuki Y, Sakai M, Ohtake H, Sarukura N, Liu Z, et al. J Cryst Growth 2001;229:501.

[32] Shimamura K, Sato H, Bensalah A, Sudesh V, Machida H, Sarukura N, et al. Res Technol 2001;36(8–10):801.

[33] Liu Z, Shimamura K, Nakano K, Fukuda T, Kozeki T, Ohtake H, et al. Jpn J Appl Phys 2000;39:L466.

[34] Liu Z, Izumida S, Ohtake H, Sarukura N, Shimamura K, Mujilatu N, et al. Jpn J Appl Phys 1998;37:L1318.

[35] Wechsler BA, Sumida DV. In: Weber MJ, editor. CRC handbook of laser science & technology, supplement 2: optical materials. Florida, USA: CRC Press, Inc.; 1995. p. 607. Sect. 16.

[36] Liu Z, Shimamura K, Nakano K, Mujilatu N, Fukuda T, Kozeki T, et al. Jpn J Appl Phys 2000;39:L88.

[37] Liu Z, Kozeki T, Suzuki Y, Sarukura N, Shimamura K, Fukuda T, et al. Opt Lett 2001;26(5):301.

[38] Sarukura N, Watanabe M, Endoh A, Watanabe S. Opt Lett 1988;13(11):996.

[39] Hofstadter R. Phy. Rev 1948;74:100.

[40] Hofstadter R. Phy. Rev 1949;75:796.

[41] Hounsfield GN. Brit. J Radiol 1973;46:1016.

[42] Ter-Pogossian MM, Phelps ME, Hoffman EJ, Mullani NA. Radiology 1975;114:89.

[43] Ishii M, Kobayashi M. Prog Cryst Growth Charact 1991;23:245.

[44] De Notaristefani F, Lecoq P, Schneegans M. In: Proc. of the crystal 2000 international workshop, "Heavy scintillators for scientific and industrial applications" (Chamonix, France, 1992). Git-sur-Yvette Cedex, France: Frontieres; 1993.

[45] Globus M, Grinyov B, Kim JK. Scintillators for modern and traditional applications. Ukraine, Kharkov: Institute for Single Crystals; 2005.

[46] Gektin A, Goriletsky V, Zaslavsky B. In: Scheel H, Capper P, editors. Crystal growth technology. Weinheim: Wiley-VHC; 2008. p. 353.

[47] Gektin A. In: Capper P, Rudolph P, editors. Crystal growth technology. Weinheim: Wiley-VHC; 2010. p. 299.

[48] Weber MJ, Monchamp RR. J Appl Phys 1973;44:5495.

[49] Nester OH, Huang CY. IEEE Trans Nucl Sci 1975;22:68.

[50] Nikl M, Vedda A, Laguta VA. In: Dhanaraj G, Byrappa K, Prasad V, Dudley M, editors. Springer handbook of Crystal growth. Berlin: Springer; 2010. p. 1663.

[51] Nitsche R. J Appl Phys 1965;36:2358.

[52] Cho ZH, Faruki MR. J Nucl Med 1977;18:846.

[53] Dickinson SK, Hilton RH, Lipson HG. Mat Res Bull 1972;7:178.

[54] Kaminsky AA, Sarkisov SE, Butaeva TI, Denisenko GA, Hermont B, Bohm J, et al. Phy Stat Sol (a) 1979;56:725.

[55] Chongfan H, Shiji F, Jingying L, Quanshun S, Dinghong S, Tiangun Z. Prog Cryst Growth Charact 1985;11:253.

[56] Allegretti F, Borgia B, Riva R, Denotaristefani F, Pizzini s. J Cryst Growth 1989;94:373.

[57] Kroger FA. Some aspects of the luminescence of solids. Amsterdam: Elsevier Publ. Co.; 1948. p.107.

[58] Gillette RH. Rev Sci Insr 1950;21:294.

[59] Vasiliev YaV, Akhmetshin RR, Borovlev YuA, Grigoriev DN, Gusev VA, Shlegel VN, et al. Nucl Instr Meth. 1996;379:533.

[60] Grabmaier BC, Rossner W, Berthold T. In: Dorenbos P, Van Eijk CWE, editors. Proc. Of the international conference on inorganic scintillators and their applications, "SCINT 95". Delft, The Netherlands: Delft University Press; 1995. p. 29.

[61] Kinloch DR, Novak W, Raby P, Toepke I. IEEE Trans Nucl Sci 1994;41:752.

[62] Robertson DS, Young IM, Telfer JR. J Mat Sci 1979;14:2967.

[63] Oi T, Takagi K, Fukazawa F. Appl Phys Lett 1980;36:278.

[64] Derenzo SE, Moses WW, Perera JLRCC, Litton LE. IEEE Trans Nucl Sci 1990;37:203.

[65] Kobayashi M, Ishii M, Usuki Y, Yahagi H, Ref. [43], p. 375.

[66] Nagornaya L, Ryzhikov V, Ref. [43], p. 367.

[67] Auffray E. IEEE Trans Nucl Sci 2008;55:1314.
[68] Kobayashi M, Usuki Y, Ishii M, Senguttuvan N, Tanji K, chiba M, et al. Meth A 1999;434:412.
[69] Lecoq P. Nucl Instr Meth A 2005;537:15.
[70] Takagi K, Fukazawa T. Appl Phys Lett 1983;42:43.
[71] Kurata Y, Kurashige K, Ishibashi H, Susa K. IEEE Trans Nucl Sci 1995;42:1038.
[72] Utsu T, Akiyama S. J Cryst Growth 1991;109:385.
[73] Roscoe BA, Grau JA, Manente RA, Melcher CL, Peterson CA, Schweitzer JS, et al. IEEE Trans Nucl Sci 1992;39:1412.
[74] Surti S, Karp JS, Freifelder R, Liu F. IEEE Trans Nucl Sci 2000;47:1030.
[75] Kurashige K, Gunji A, Kamada M, Shimura N, Ishibashi H, Yoshida K, et al. IEEE Trans Nucl Sci 2004;51:742.
[76] Melcher CL, Schweitzer JS. IEEE Trans Nucl Sci 1992;39:502.
[77] Ishibashi H, Kurashige K, Kurata Y, Susa K, Kobayashi M, Tanaka M, et al. IEEE Trans Nucl Sci 1998; 45:518.
[78] Moses WW. IEEE Trans Nucl Sci 2003;50:1325.
[79] Aykac M, Bauer F, Williams CL, Loope M, Schmand M. IEEE Trans Nucl Sci 2006;53:1084.
[80] McIntosh B, Stout DB, Goertzen AL. IEEE Trans Nucl Sci 2011;58:682.
[81] Shimizu S, Pepin CM, Lecomte R. IEEE Trans Nucl Sci 2010;57:1512.
[82] Kamada K, Prusa P, Nikl M, Blazek K, Endo T, Tsutsumi K, et al. IEEE Trans Nucl Sci 2014;61:293.
[83] Yole Developpement, “Sapphire Market” Report, 2011 (http://www.yole.fr/).

Czochralski and Flux Growth of Crystals for Lasers and Nonlinear Optics

Jiyang Wang[1], Guochun Zhang[2], Haohai Yu[1], Yan Wang[3], Chuantian Chen[2]

[1]STATE KEY LABORATORY OF CRYSTAL MATERIALS, SHANDONG UNIVERSITY, JINAN, CHINA;
[2]BEIJING CENTER FOR CRYSTAL RESEARCH AND DEVELOPMENT, KEY LABORATORY OF FUNCTIONAL CRYSTALS AND LASER TECHNOLOGY, TECHNICAL INSTITUTE OF PHYSICS AND CHEMISTRY, CAS, BEIJING, CHINA;
[3]FUJIAN RESEARCH INSTITUTE OF MATTER STRUCTURES, CAS, FUZHOU, CHINA

CHAPTER OUTLINE

5.1 Laser Crystals Grown by the Czochralski Method 170
5.1.1 Introduction 170
5.1.2 Tm- and Ho-Doped GGG Laser Crystals 171
5.1.2.1 Crystal Growth 171
5.1.2.2 Selected Laser Properties of Tm and Ho and Co-Doped GGG Crystals 176
5.1.3 Vanadate Crystals Grown by the CZ Method 178
5.1.3.1 Crystal Growth and Quality 179
5.1.3.2 Mechanism of Bulk Spiral Formation during Growth 180
5.1.3.3 Basic Properties of Vanadate Family of Laser Crystals 187
5.2 Nonlinear Optical Borate Crystals Grown by the Flux Method 187
5.2.1 Introduction 187
5.2.2 Growth of Bulk Borate NLO Crystals 188
5.2.2.1 Low-Temperature Phase of Barium Metaborate (β-BaB_2O_4, or BBO) 188
5.2.2.2 LiB_3O_5 Family of Crystals 192
5.2.2.3 Potassium Beryllium Borate Fluoride ($KBe_2BO_3F_2$, or KBBF) 199
5.2.2.4 Bismuth Triborate (BiB_3O_6, or BiBO) 201
5.3 Conclusion 202
Acknowledgments 203
References 203

Handbook of Crystal Growth. http://dx.doi.org/10.1016/B978-0-444-63303-3.00005-5
Copyright © 2015 Elsevier B.V. All rights reserved.

5.1 Laser Crystals Grown by the Czochralski Method

5.1.1 Introduction

Since the first report of the successful construction of a Cr:ruby crystal laser in 1960 [1], lasers have undergone extensive development for over half a century. Laser materials are the basis of the creation of many different kinds of modern lasers. Among these, laser crystals are an important factor in the manufacture of highly efficient, all-solid-state lasers that are widely used in different fields, especially in high-tech industries and, more recently, in modern daily life. Investigation into detailed laser technology and suitable gain materials is crucial for fostering the development and application of lasers. Currently, continuous-wave (cw), Q switching, and mode locking are well-developed laser technologies for the generation of cw, short, and ultrashort pulsed lasers, respectively. In gain materials, gas, liquid, and solid materials have been widely investigated, aiming at different applications, and crystals with a complete lattice play the most important role. Laser crystals are mainly composed of a host material with the addition of active ions. The laser action arises from the stimulated emission by the active ions, and their emission properties are mainly determined by the electronic structure and partly modulated by the crystalline field of the host material [2].

Until now, sapphire (Al_2O_3), YAG, and vanadate-based crystals [3] have been the most prominent hosts, because they have superior chemical and physical properties, including a suitable crystalline field for active ions and thermal mechanisms. The Nd:YAG crystal has been widely developed and fully commercialized. For Al_2O_3-based crystals, titanium–sapphire (Ti:sapphire) can be used as the tunable laser medium. Lasers based on Ti:sapphire were first constructed in 1982 [4]. A Ti:sapphire laser can usually be operated most efficiently at wavelengths near 800 nm while being pumped by another laser with a wavelength of 514–532 nm. The laser is tunable from 650 to 1100 nm and can generate ultrashort pulses. The growth and the properties of Ti:sapphire crystals have been widely studied and summarized [5]. Benefiting from the development of laser diodes at the end of the 20th century [3,6], vanadate-based crystals have come to represent an important series of gain materials. Nd:YVO_4 is the most prevalent and has been commercialized to produce low- and even moderate-power lasers at wavelengths of 0.9, 1.06, and 1.3 μm. These crystals possess a large emission cross-section and a short fluorescence lifetime, both of which are favorable for constructing highly efficient lasers. $Gd_3Ga_5O_{12}$ (GGG) is an analog crystal of YAG, and there are several advantages in using GGG to serve as a host material [7].

Laser emission at 1.0 μm is normally obtained with Nd:YAG and Nd:YVO_4 crystals. In recent years, a series of novel vanadate-based crystals were developed, including Nd^{3+}- and Yb^{3+}-doped crystals. The 2.0 μm wavelength lasers have applications in optical communications, coherent laser radars, detection of pollutants, and medical equipment [1–3,6,7–9]. Therefore, in recent years, increasing interest has focused on the Tm^{3+} and Ho^{3+} ions as activators for solid-state lasers operating at 2.0 μm [10–15]. In this section,

the crystal growth and properties of GGG- and YVO_4-based laser crystals at lasing wavelengths of 1.0 and 2.0 μm are summarized.

5.1.2 Tm- and Ho-Doped GGG Laser Crystals

Using Tm^{3+} and Ho^{3+} as activators in a host material produces a laser that can emit radiation near the 2.0 μm region. Due to the efficient energy transfer between the Tm $^3F_4$ and Ho $^5I_7$ manifolds, Tm-sensitized Ho materials can be used to produce laser action around 2.0 μm. For this job, GGG was chosen for the following reasons: First, GGG can be grown with a flat solid–liquid interface, which leads to crystals of high optical quality that are free of the so-called core. An entire flat cross-section of the interface crystal can be used to process large slabs for use in high-power lasers. Second, GGG crystals can be grown at a high pulling rate (up to 5 mm/h) with high quality. Third, the crystal has a high density and a large specific heat, both of which are favorable for avoiding thermal effects in a solid-state laser.

The crystal structure of GGG belongs to the cubic garnet structure with space group O_h^{10}-Ia3d. The cell parameters are $a = 12.38$ Å, and $Z = 8$ [16]. Most of the Tm^{3+} and Ho^{3+} ions substitute for Gd^{3+} at the dodecahedral D_2 sites, but a small fraction can occupy the octahedral Ga^{3+} sites in crystals grown at high temperature [17]. This particular crystal has relatively wide phase homogeneity, suitable hardness, high specific heat, and good chemical stability, and it is moisture free. Because it melts congruently, a large single crystal can be obtained by the Czochralski (CZ) method. Moreover, the crystal provides a suitable crystal field environment for rare-earth active ions and thus can provide good spectral and laser properties. The lower phonon energy, compared with that of YAG, makes GGG a good laser matrix at the 2 μm wavelength.

5.1.2.1 Crystal Growth

A GGG single crystal was grown by using the CZ method for the first time in 1978. Brandle obtained a GGG crystal with a 3 in diameter and a low defect density [18]. Over the next decade, Nd:GGG crystals with diameters of 25 ∼ 30 and 70 mm were obtained using the temperature gradient technique. Using the CZ method, crystals with a diameter of 130 mm were grown by Asadian et al. in 2010 [19], as shown in Figure 5.1. Now, even larger GGG crystals have been grown in China: For example, a group at Shandong University has grown GGG crystals with a diameter of 190 mm that exhibit good optical quality.

In this work, a crystal growth procedure designed for growing high-quality Tm^{3+}- and Ho^{3+}-doped GGG crystals is detailed as follows: First, the polycrystalline materials used as precursors are obtained by solid-state reaction. The initial chemicals used are Ga_2O_3 (5N), Gd_2O_3 (5N), Cr_2O_3 (5N), Ho_2O_3 (5N), and Tm_2O_3 (99.95%) powders. They are mixed in molar ratio in an agate mortar according to the stoichiometric formula with 1∼2 wt.% excess of Ga_2O_3. They are then pressed into tablets and sintered to obtain a single-phase powder. Second, crystal growth is performed in an iridium (Ir) crucible that is

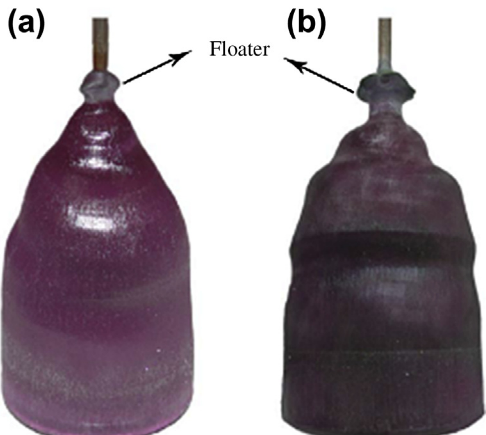

FIGURE 5.1 Crystals obtained by the Czochralski (CZ) method. Crystal (a): 0.8 at.% Nd, 130 × 75 mm length and diameter; crystal (b): 2.0 at.% Nd, 130 × 75 mm length and diameter [18]. *With permission of Elsevier.*

Φ55 × 35 mm in size along with a $N_2 + 2$ vol.% O_2 atmosphere. The heating instrument is a 2 kHz radiofrequency furnace, and the temperature controller is a Eurotherm 818 Controller/Programmer with a precision of ±0.5 °C. During crystal growth, the Ir rod is rotated at a rate of 12.0–20.0 rpm, and the pulling rate is 1.50–2.00 mm/h. Finally, when the growth process is completed, the crystal is drawn out of the melt and cooled down to room temperature at a rate of 12.0–30.0 °C/h.

There are nevertheless many problems encountered in GGG crystal growth, which greatly reduce crystal quality and size. The first problem is the decomposition of GGG and the rapid evaporation of Ga_2O_3, which takes place at temperatures above 1970 K, as illustrated in Figure 5.2. The evaporation of Ga_2O_3 leads to asymmetric composition of the crystal, and it can result in cracking. Also, Ga_2O_3 can react with the Ir crucible to produce IrO_2 and Ir, as well as $Gd_{2y}Ga_{10}O_{15-2x+3y}$, which makes the crystal quality even worse.

If the seed is located exactly at the center of the temperature field, the iridium oxide can easily adhere to the seed and to the shoulder of the crystal, and will thus cause asymmetric growth of the shoulder. If the seed location does not properly correlate with the temperature field, the crystal will first grow around the iridium oxide rather than at the point where the seed is located. This is because iridium oxide is always located at the center of the temperature field. Moreover, the heat radiation ability of iridium oxide is much higher than that of the melt, which means that the temperature at the location of the iridium oxide can be much lower than that of the seed.

In short, the evaporation of Ga_2O_3 and its reaction with the Ir crucible reduce crystal quality, and the existence of iridium oxide makes seed insertion and shoulder extension very difficult, resulting in many defects inside the crystal. In order to inhibit this complication, an extra 1 ∼ 2 wt.% of Ga_2O_3 is added into the initial composition. The best solid-state reaction temperature to avoid this complication was found to be 1350 °C.

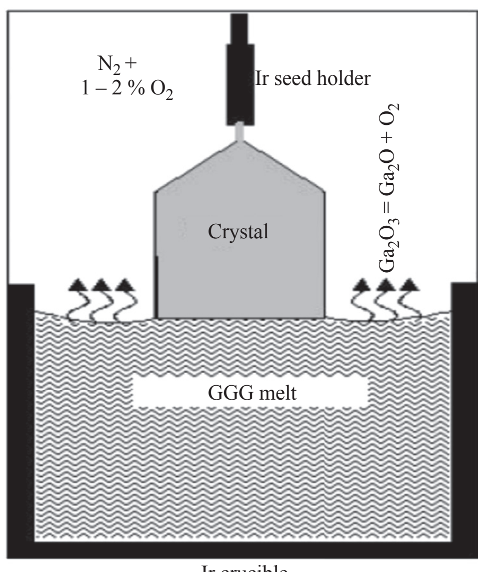

FIGURE 5.2 Sketch diagram of $Gd_3Ga_5O_{12}$ (GGG) crystal growth setup.

Considering the problem of Ga_2O_3 decomposition in the melt, a growth atmosphere of $N_2 + 2$ vol.% O_2 or 98% $Ar_2 + 2\%$ O_2 was adopted. Both of these atmospheres can inhibit the evaporation of Ga_2O_3 to some degree. However, the addition of oxygen to the atmosphere can also result in an increase of Ir metal and its oxide on the melt surface. Therefore, the amount of oxygen used in the growth atmosphere should be limited appropriately. The partial pressure of O_2 must be very low at low temperatures to suppress Ir oxidation, but more oxygen is required to prevent Ga_2O_3 decomposition at high temperatures.

The second problem is the formation of defects, such as cracks, deposits, cavities, and inclusions in the crystal. Using the scanning electron microscope (SEM) technique, the existence of Ir particles in the GGG crystal can be confirmed, including agglomerates, heterogeneous inclusions, and inappropriate particle distribution. The size of some particles in the crystal can reach up to 30 μm.

There are two kinds of dislocations: one is the isolated line dislocation that arises from the strain at the seed–crystal junction and/or the appearance of a concave growth interface [20]; the other is a major dislocation with closed loops and helices that appears in the bulk crystal, which is normally associated with large inclusions [21,22]. It was found that the number of Ir inclusions can be restrained by increasing the amount of oxygen near the melting point of the material.

It was also discovered that other complex components exist at different inclusion sites, such as $[Gd(Nd)]_4Ga_2O_9$, $[Gd(Nd)]_3GaO_6$, and $[Gd(Nd)]GaO_3$, as demonstrated by SEM and energy spectrum measurements. It was shown that some of the inclusions in

Nd:GGG also consist of the volatile flux Ga_2O_3, which enters the crystal through the solid–liquid interface during the growth process.

The third problem is how to optimize the growth conditions, such as crucible size, growth rate, post process heating, rotation rate, temperature procedure, and so on. In order to obtain optimized growth conditions, some important factors must be considered, such as composition variation, dissociation reactions that occur during the growth process, and maintaining a flat crystal–melt interface with different crucible sizes.

Some important practical observations were summarized in the description of the crystal growth of GGG. For example, an excessively large rotation rate is the main reason for hollow boule growth and nonconcentricity of the heating winding. In addition, both unduly large temperature gradients and inappropriately large shoulder-extension angles will lead to cracking.

After overcoming the above problems, and by using the furnace for GGG growth shown in Figure 5.3, we obtained high-quality Tm- and Ho-doped GGG crystals such as the as-grown Tm-doped GGG crystal shown in Figure 5.4. Figure 5.5 presents the X-ray diffraction results of the Tm- and Ho-doped GGG crystals, confirming the phase purity of the grown crystals.

The concentration of rare-earth ions in the crystals was measured by an inductively coupled plasma–atomic emission spectrum apparatus. The average concentrations and segregation coefficients *K* of the Tm and Ho dopant ions in the crystals are listed in Table 5.1.

The thermal expansion coefficient of the Tm- and Ho-doped GGG crystals were measured by a Diatometer 402 PC over the temperature range of 100–800 °C. The sample was kept in a fused silica sample holder and heated at a rate of 10 °C/min in air. The

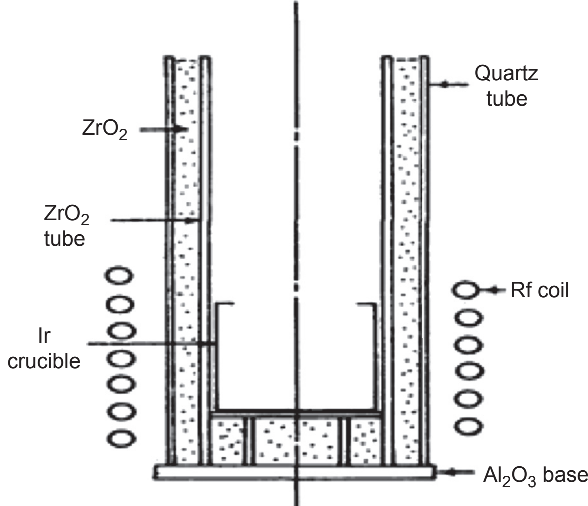

FIGURE 5.3 Sketch of furnace for $Gd_3Ga_5O_{12}$ growth.

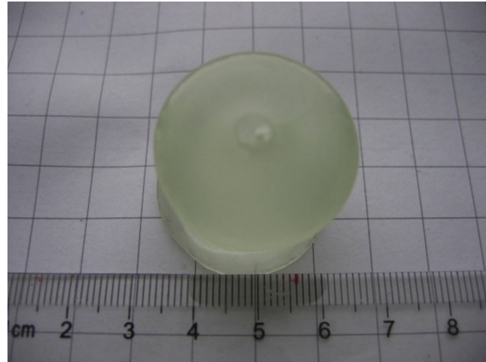

FIGURE 5.4 As-grown Tm:GGG crystal.

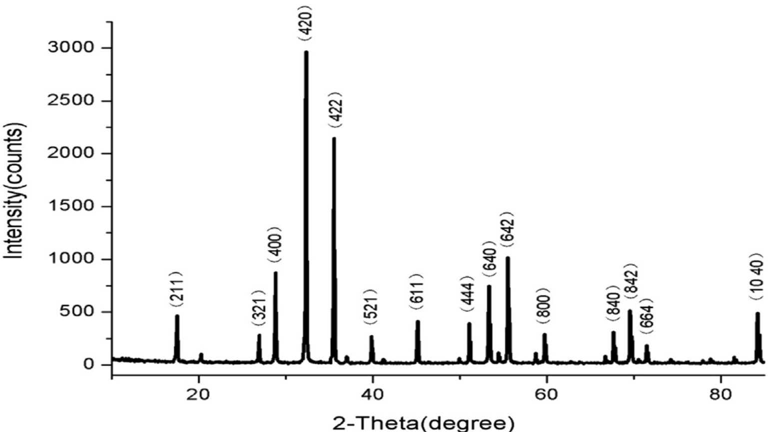

FIGURE 5.5 X-ray diffraction of Tm- and Ho-doped $Gd_3Ga_5O_{12}$ crystals.

Table 5.1 Ions' Concentration and Segregation Coefficient of the Dopant in Crystals, *K*

Crystals	N_0 (at. %)	N_c (10^{20} ions/cm)	K
Tm^{3+}:GGG	2	2.83	1.12
Ho^{3+}:GGG	2	2.59	1.05
Tm^{3+}/Ho^{3+}:GGG	6 (Tm)	8.23 (Tm)	1.11 (Tm)
	0.4 (Ho)	0.53 (Ho)	1.08 (Ho)

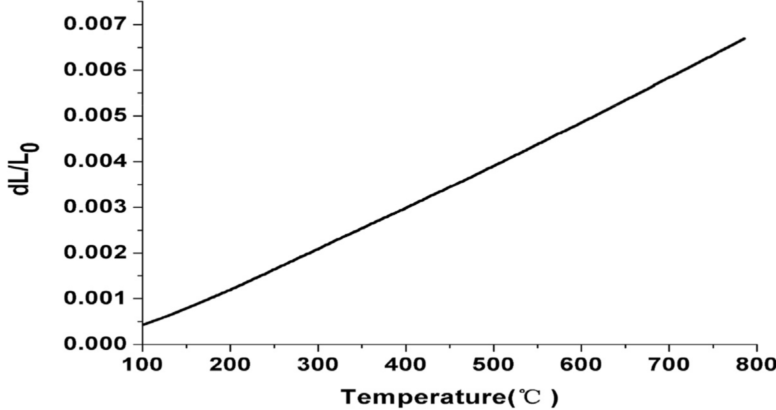

FIGURE 5.6 Thermal expansion of the Tm- and Ho-doped $Gd_3Ga_5O_{12}$ crystals. *With permission of Elsevier.*

dependence of the linear expansion versus temperature is shown in Figure 5.6. The linear thermal expansion coefficient was determined to be 9.005×10^{-6} 1/K.

5.1.2.2 Selected Laser Properties of Tm and Ho and Co-Doped GGG Crystals

Figure 5.7 shows the room temperature absorption spectrum of a 2 at.% Tm^{3+}:GGG crystal. The spectrum consists of six resolved bands associated with the transitions from the $^3H_6$ ground state to the $^3F_4$, $^3H_5$, $^3H_4$, $^3F_3 + {}^3F_2$, $^1G_4$, and $^1D_2$ excited states. The absorption centered at 788 nm, which is suitable for pumping by a commercial GaAlAs laser diode, has an absorption coefficient of 4.03 1/cm and a 14 nm full width at half maximum (FWHM). The corresponding absorption cross-section is 0.357×10^{-20} cm^2, which is comparable to those of Tm^{3+}:YVO_4 (2.5×10^{-20} cm^2) [23] and Tm^{3+}:YAG (0.75×10^{-20} cm^2) [24].

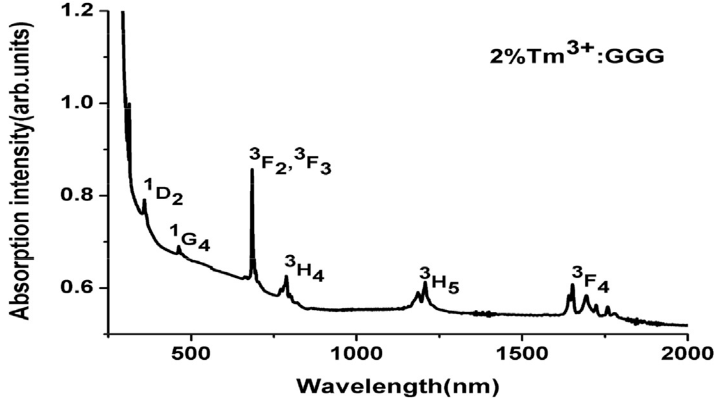

FIGURE 5.7 Room temperature absorption spectrum of Tm^{3+}:GGG crystal. *With permission of Elsevier.*

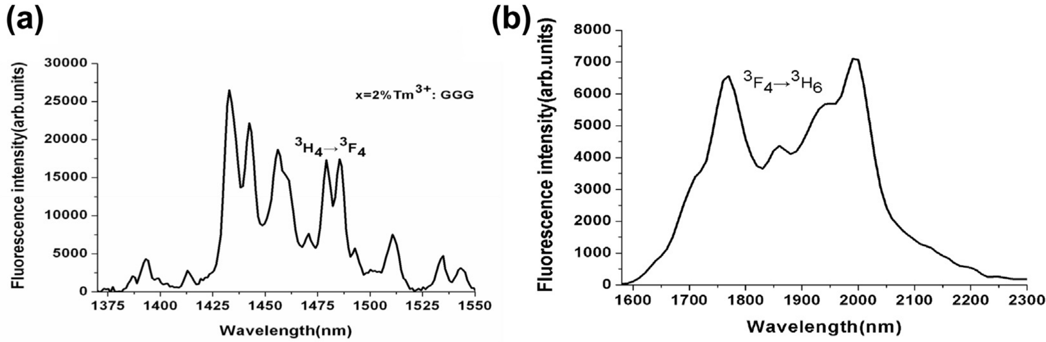

FIGURE 5.8 Emission spectra excited by 684 nm: (a) 1350–1550 nm; (b) 1580–2300 nm. *With permission of Elsevier.*

Table 5.2 Comparison of the Emission Cross-sections and Lifetimes of Tm-Doped Crystals

Crystals	σ_{em} ($^3F_4 \rightarrow {}^3H_6$) ($\times 10^{-21}$ cm^2)	τ_r [$^3F_4$ (ms)]	References
2%Tm^{3+}:GGG	1.05	20.25	This work
5%Tm^{3+}:YVO_4	1.60	0.8	[24]
1% Tm^{3+}:YAG	0.22	8.5	[23]
0.1% Tm^{3+}:LaF_3	0.25	11	[23]
1% Tm^{3+}:$LiYF_4$	0.33	13	[23]

The room temperature emission spectra excited at 684 nm are shown in Figure 5.8. The intense emission peaks belong to the transitions from $^3H_4 \rightarrow {}^3F_4$ of the Tm^{3+} ions. A comparison of the emission cross-sections of the $^3F_4 \rightarrow {}^3H_6$ transitions and the lifetimes of the $^3F_4$ state in Tm^{3+}-doped crystals is given in Table 5.2.

The same methods were used for measuring the room temperature absorption spectra of Ho^{3+}:GGG. There are 10 absorption bands centered at 335, 346, 365, 387, 419, 454, 538, 637, 1132, and 1918 nm, which correspond to the transitions of Ho^{3+} from the ground state $^5I_8$ to the excited states $^3K_6 + {}^3F_4 + {}^3H_4 + {}^3G_4$, $^3L_9 + {}^3G_3$, $^3H_6 + {}^3G_2 + {}^3H_5$, $^3K_7 + {}^5G_4$,$^3G_5$($^5G_3$), $^5F_1 + {}^5G_6 + {}^3K_8 + {}^5F_2 + {}^5F_3$, $^5S_2 + {}^5F_4$, $^5F_5$, $^5I_6$, and $^5I_7$, respectively [25,26]. The strongest peak is located at 538 nm, which is favorable for pumping by a visible light source.

The room temperature emission spectrum of Ho^{3+}:GGG excited at 538 nm shows that the intense emission peak at 2080 nm belongs to the transition $^5I_7 \rightarrow {}^5I_8$ of the Ho^{3+} ion. The emission cross-section curve for the $^5I_7 \rightarrow {}^5I_8$ transition gives a maximum emission cross-section at 2080 nm that is about 5.08×10^{-21} cm^2, and that is comparable to that of Ho^{3+}:$LiYF_4$ (3.9×10^{-21} cm^2) [27] and Ho^{3+}:YAG(4.5×10^{-21} cm^2) [28].

The absorption spectrum of the Tm^{3+}- Ho^{3+}-co-doped GGG crystal shows a relatively broad and strong absorption band at about 800 nm corresponding to the

$^3H_6 \rightarrow {^3H_4}$ (Tm^{3+}) transition, suitable for AlGaAs diode pumping. The absorption cross-section and the FWHM for this absorption band are 3.53×10^{-21} cm^2 and 13 nm, respectively. The fluorescence spectra, ranging from 1580 to 2300 nm for the $^3F_4 \rightarrow {^3H_6}$ (Tm) and $^5I_7 \rightarrow {^5I_8}$ (Ho) transitions, were also obtained for the Tm:GGG and Ho:GGG crystals.

Some of the parameters that are important to the performance of a 2.0 μm Tm–Ho laser are the energy transfer efficiency of (Tm) $^3F_4 \rightarrow$ (Ho) $^5I_7$ and of the back transfer process, both of which can be easily obtained from the absorption and emission cross-sections by the Forster–Dexter (F-D) theory [29,30]. After making the calculations, we find that the values of the Tm → Ho and Ho → Tm energy transfer coefficients are comparable to those observed in other hosts, such as Tm, Ho:YAG, and Tm, Ho:YLF crystals [31], and the ratio between the back transfer Ho → Tm coefficient and that of the Tm → Ho energy transfer process is higher than that of Tm, Ho co-doped YAG, and YLF crystals [31]. A high value of this ratio is important when constructing an efficient 2.0 μm Ho laser. The calculated efficiencies of the energy transfers Tm → Ho and Ho → Tm are 63.1% and 46.6%, respectively. The results show that these crystals may be viable candidates for use as a tunable infrared laser material at 2.0 μm.

5.1.3 Vanadate Crystals Grown by the CZ Method

In 1966, O'Conner reported the successful performance of the first pulsed Nd:YVO_4 laser at a temperature of 90 K. It was pumped with three flashlamps [8]. Bagdasarov et al. described the spectral and room temperature stimulated emission of the Nd:YVO_4 crystal in 1968 [32,33]. However, difficulty with vanadate crystal growth prevented the realization of any laser applications. Until 1973, it had been proposed that important advances in the growth of Nd:YVO_4 would boost its use in lasers [34]. In 1976, Yaney and DeShazer studied the spectrum anisotropy of the Nd:YVO_4 laser states [35]. Since then, the behavior of Nd:YVO_4 has become fully understood in its role as an excellent gain material in the efficient application of lasers. Since the end of the 20th century, as laser diodes became better developed, Nd:YVO_4 technology has been greatly improved, and the size and quality of the available crystals satisfied laser requirements [36,37], thus advancing the commercialization of Nd:YVO_4.

In order to explore the vanadate family of crystals, other vanadate crystals, including $GdVO_4$, $LuVO_4$, $LaVO_4$, and their mixed crystals, have been grown and investigated. In general, $GdVO_4$ has the highest thermal conductivity [38], $LuVO_4$ possesses the largest emission cross-section [39], $LaVO_4$ has the lowest symmetry and strongest anisotropy [40], and the mixed crystals can exhibit a large variation in the internal crystal field, thus inhomogeneously broadening the spectrum [41,42]. The recently developed vanadate crystals also exhibit novel laser physics, such as the enhancement of passively Q-switched pulse energy, bistability of the output power, and stimulated Raman effects generated by a large third-order nonlinearity $\chi^{(3)}$ [43–45].

5.1.3.1 Crystal Growth and Quality

The quality of the polycrystalline materials used as precursors determines the quality of the resulting single crystal and dictates any possible applications. In general, the vanadate polycrystalline precursor materials were synthesized by the liquid phase reaction method. For Nd:YVO_4, polycrystalline $NdVO_4$ and YVO_4 were prepared and synthesized with V_2O_5, Nd_2O_3, and Lu_2O_3, all of which have 99.99% purity [36]. The V_2O_5 was dissolved into hot high-purity ammonia. By chemical reaction, NH_4VO_3 was formed and was used as the precursor. Nd_2O_3 and Lu_2O_3 were dissolved into hot high-purity nitric acid (HNO_3), and $Nd(NO_3)_3$ and $Lu(NO_3)_3$ were obtained. By mixing the solutions of NH_4VO_3 with $Nd(NO_3)_3$ and $Y(NO_3)_3$, polycrystalline $NdVO_4$ and YVO_4 were synthesized. The purity of the polycrystalline materials can be improved by getting rid of some of the impurities in V_2O_5, Lu_2O_3, and Nd_2O_3. By mixing $NdVO_4$ and YVO_4 together with the expected final Nd^{3+} concentration in the crystal, the raw materials for Nd:YVO_4 were prepared.

All of the vanadate crystals have a melting temperature of about 1800 °C, and there is no phase change below the melting temperature. This property indicates that the vanadate crystals can be grown by the CZ method [46] with an Ir crucible. The vanadate crystals belong to the $ZrSiO_4$ structure with space group I41/amd. As an example, the crystal structure of YVO_4 observed along the *a*-axis is shown in Figure 5.9, from which we observe that in a unit cell, there are four layers of ions in the *c*-direction when taking VO_4^{3-} as a single ion. There are only two layers of ions along the *a*- or *b*- direction [47], and therefore the vanadate crystals possess a strong physical anisotropy according to the Neumann principle.

Considering the similarity in the melting temperatures, structures, and growth habits, all of the vanadate crystal can be grown with the same growth process and equipment

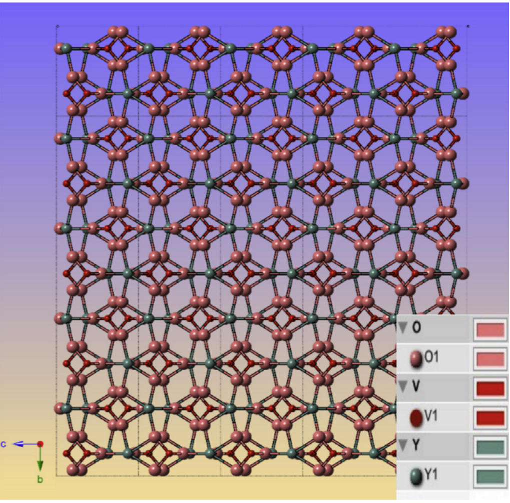

FIGURE 5.9 Structure of YVO_4 observed from an *a*-axis.

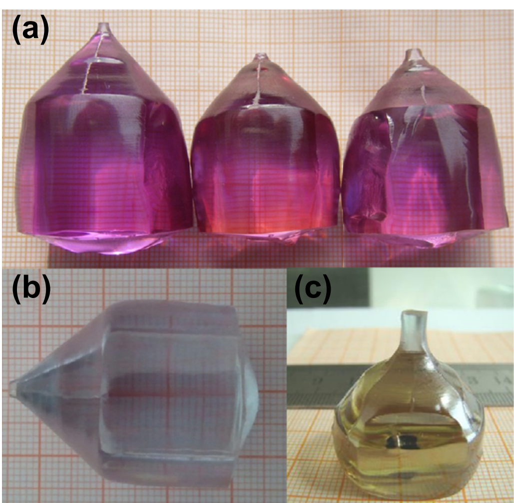

FIGURE 5.10 Vanadate single-crystal boules. (a) As-grown Nd:YVO_4 crystal with a doping concentration of 1 at.%. (b) As-grown Nd:$GdVO_4$ crystal with a doping concentration of 0.5 at.%. (c) As-grown Nd:$LuVO_4$ crystal with a doping concentration of 2 at.%.

that were previously reported [42,47]. In our experiments, the temperature control apparatus is a Eurotherm 818 Controller/Programmer with a precision of ±0.5 °C. The crawling distance of the pulling apparatus is less than 1 mm. The Ir crucible is 5.6 cm in diameter and 4 cm in height. The growth atmosphere was $N_2 + O_2$ (2%). The pulling rate was set at 1–2 mm/h after a certain value of the diameter was reached, and the rotation rate was 10–30 rpm during growth. After completion of the growth, the crystal was cooled to room temperature at a speed of 18–20 °C/h. Images of Nd:YVO_4, Nd:$GdVO_4$, and Nd:$LuVO_4$ crystal boules with doping concentrations of 1, 0.5, and 2 at.% grown by the CZ method are presented in Figure 5.10(a)–(c), respectively. The effective segregation (*es*) coefficient of Nd^{3+} ions in YVO_4, $GdVO_4$, and $LuVO_4$ was measured to be 0.63, 0.78, and 0.91, respectively [39,48,49,50]. For mixed vanadate crystals, the *es* coefficient of Nd ions in $Gd_xY_{1-x}VO_4$ and $Lu_xGd_{1-x}VO_4$ crystals is linear with the fractional x values [51,52], and can be expressed as: $es = 0.78x + 0.63(1 - x) = 0.63 + 0.15x$ and $es = 0.78x + 0.91(1 - x) = 0.91 - 0.13x$, respectively. The lattice constants of mixed crystals are also influenced by the cation radius and increase with the value of x, since the largest radius is that of Lu^{3+} and smallest radius that of Y^{3+}. In the case of doping concentration, in the early work, the maximum Nd^{3+} doping concentration in vanadate crystals that could be used as an efficient laser material was 3.2 at.%. However, concentration quenching and optical losses constrained efficient laser radiation generation when the Nd^{3+} doping concentration was larger than 2 at.% [53,54].

5.1.3.2 *Mechanism of Bulk Spiral Formation during Growth*

Bulk spiral formation is a challenging problem commonly present in the CZ growth of bulk oxide crystals. Compared to the growth of conventional tetragonal orthovanadate

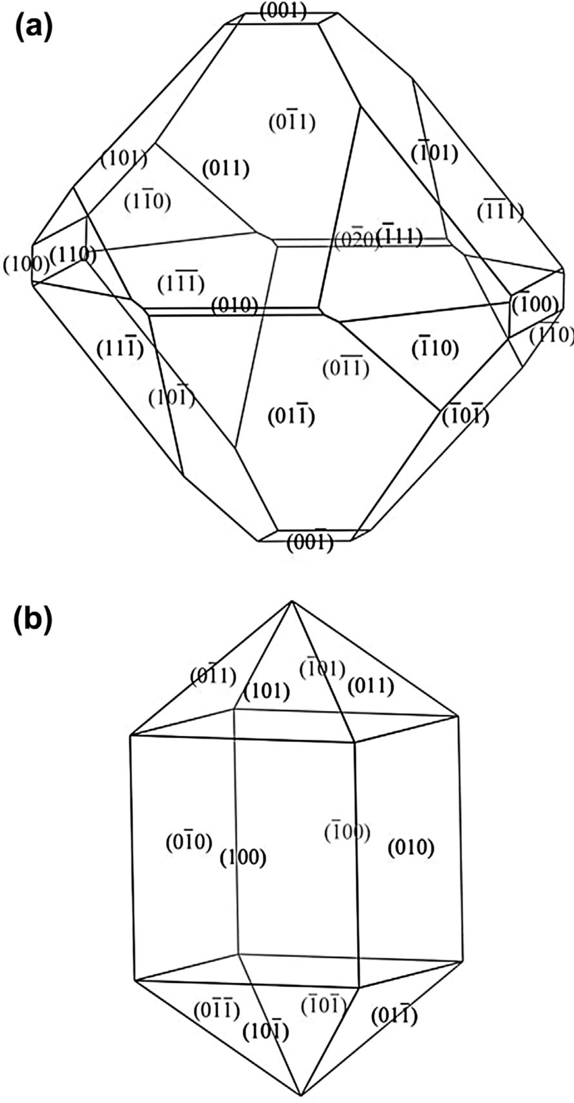

FIGURE 5.11 Theoretical growth morphology of lanthanide orthovanadates: (a) $LaVO_4$; (b) YVO_4.

single crystals, much stronger bulk spiral growth is observed in the growth of monoclinic crystals, accompanied by degradation of the structural symmetry [40,55]. This phenomenon is highly detrimental not only to growing large long crystals, but also to obtaining-high quality single crystals for practical laser applications because of the concomitant growth striations. It is well known that selecting seeds with a proper orientation during crystal growth helps overcome the energy barrier to nucleation and makes it easier to obtain large and flaw-free single crystals [55]. In this section, the spiral

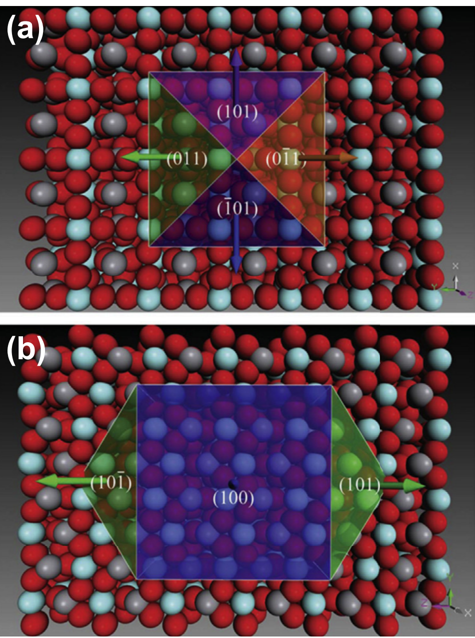

FIGURE 5.12 Schematic structure of ideal atomic-level crystal–melt interfaces and growth velocities of tetragonal YVO_4 single crystals (viewed bottom-up): (a) [001]; (b) [100].

growth and seed direction selection of monoclinic $LaVO_4$ and tetragonal YVO_4 are presented and compared with each other.

A morphological analysis of monoclinic $LaVO_4$ and tetragonal YVO_4 is shown in Figure 5.11(a) and (b). The structure of the ideal atomic level crystal–melt surface of YVO_4 for seed direction [001] is shown in Figure 5.12(a). It can be seen clearly that the interface consists of four equivalent faces with perfect C_{4v} symmetry. If growth proceeds along the [100] direction, a large portion of the ideal crystal–melt interface is occupied by the (100) face and thus has only C_{2v} symmetry, as Figure 5.12(b) shows. At the same time, there are two small faces, (101) and (10$\bar{1}$), at the interface that have a larger growth velocity than (100). Such a tendency causes the crystal to develop more in the radial direction than in the axial direction. Thus, in growth along the [001] direction, the crystal readily exhibits its original I4/mmm symmetry, whereas in growth along the [100] direction, the crystal presents a cylindrical form as a result of the rotation. If we grow the crystal perpendicular to the {101} face, which is roughly at an angle of 48° away from the axial direction, the interface will have no symmetry at all. Such an orientation means there is a large departure from the rotation direction and corresponds to certain bulk footing growth. From the aforementioned analysis, it can be deduced that, in the CZ growth of YVO_4, growth along the [001] direction is the best choice for the largest utilization ratio with the best quality, because such growth affords the most symmetric

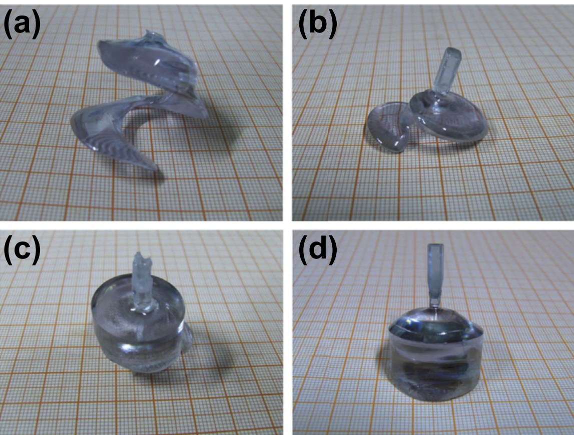

FIGURE 5.13 Actual growth morphology of $LaVO_4$ for different seed orientations: (a) arbitrary orientation (oriented at an angle of about 10°with the [98] direction); (b) perpendicular to $(10\bar{1})$; (c) perpendicular to (001); (d) perpendicular to $(00\bar{1})$.

crystal–melt interface (C_{4v}). The next most favorable direction is along [100] with C_{2v} symmetry, and the worst is perpendicular to the (011) surface.

For $LaVO_4$, the symmetry is much lower. The loops of bulk spiral growth in $LaVO_4$, which are typical representatives of hydrodynamic instability, can clearly be seen in Figure 5.13(a), where they have been grown near the [010] direction. Figure 5.13(b) shows that the growth can even be stopped by severe footing growth shortly after the shouldering process begins when using the $(10\bar{1})$ plane as the seeding surface, whereas the bulk spiral formation is heavily reduced in growth perpendicular to the (001) and (001) faces, as Figure 5.13(c) and (d) shows. (Only one slight footing can be found in the (001) case, an occurrence that we believe can safely be avoided by improving the growth operation.) From Figure 5.13, it can be concluded easily that the degree of bulk spiral formation decreases in the following sequence: $(10\bar{1})$, arbitrary crystal face, and (001) or $(00\bar{1})$.

The ideal atomic-level structure of a $LaVO_4$ crystal–melt interface that makes use of the (001) seed surface during CZ growth is sketched in Figure 5.14(a). The interface is composed of seven faces: the (001) face; the four main surrounding faces (011), $(0\bar{1}1)$, (101), and $(\bar{1}01)$; and two small faces $(\bar{1}\bar{1}1)$ and $(\bar{1}11)$. The growth velocity of each face is marked with an arrow. Because the $LaVO_4$ structure belongs to point group 2/m, this interface should be of m-symmetry. The surface area percentages for $(\bar{1}01)$, (011), $(0\bar{1}1)$, and (101) are 9.00, 9.86, 9.86, and 9.03%, respectively. However, the surface area percentage for $(\bar{1}11)$ and $(\bar{1}\bar{1}1)$ is only 3.56% each. Thus, the four main faces, $(\bar{1}01)$, (011), $(0\bar{1}1)$, and (101), take up more than 84% of the crystal–melt interface area by rough estimation. It can be concluded that the surface area of the $(\bar{1}01)$ face is very close to that of the (101) face and that both of them have a large surface area at the interface. Thus, the interface should have roughly a C_{2v} symmetry. Moreover, it can be seen from the yellow contour line indicated in Figure 5.14(a) that the symmetry of the interface increases from nearly C_{2v} to C_{4v} as the total area of the interface shrinks.

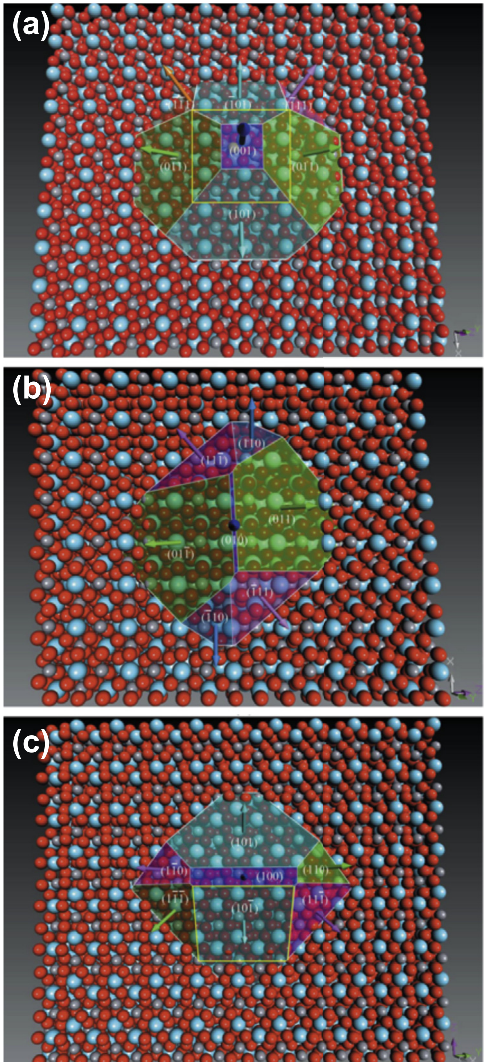

FIGURE 5.14 Schematic structure of ideal atomic-level crystal–melt interfaces and growth velocities of monoclinic $LaVO_4$ single crystals (viewed bottom-up): (a) perpendicular to (001) (the yellow contour line indicates that with the shrinkage of the total area of the crystal–melt interface, the symmetry of the interface improves from nearly C_{2v} to C_{4v}); (b) along [010]; (c) perpendicular to (100) (the intersected (101) face is shown as the area enclosed in the yellow contour line).

As Figure 5.14(b) depicts, near the small-area seed surface (010), there are two large equivalent surfaces, (011) and $(0\bar{1}1)$, and two midsized equivalent surfaces, $(1\bar{1}1)$ and $(\bar{1}11)$. The surface area percentages for the sets are 9.61 and 7.12%, respectively. Only C_2 symmetry exists at the interface, which conforms to the point group $2/m$ of $LaVO_4$. Growth using seed surface (100) is shown in Figure 5.14(c). This figure illustrates that the

ideal interfacial structure consists of two large surfaces, (101) and $(10\bar{1})$, and four midsized surfaces, $(\bar{1}10)$, (110), (111), and $(\bar{1}\bar{1}1)$. Similar to Figure 5.14(a), the interface has *m*-symmetry. Although the surface areas of the (101) and $(10\bar{1})$ surfaces are nearly equivalent, as mentioned in this chapter, the (101) surface at the interface has been intersected by the atomic plane and its surface area is greatly reduced, as indicated by a yellow line in Figure 5.14(c). Moreover, the ratio of areas between the (110) and $(1\bar{1}1)$ surfaces is 2.3:1, so the major difference lies in the absence of axial symmetry at the interface.

All energy calculations were conducted without consideration of the polar surface of the slice. In the F faces, only {011} and {101} can have a polar surface near the boundary of the growth slice. If we subtract the energies resulting from the polar surface, the attachment energies of {011} and {101} are −127.41 and −123.41 J/mol, respectively [56]. These values are similar to the value of −122.71 J/mol for the {101} surface. The growth rate along the seed surface (001) has C_{4v} symmetry and is thus much more energetically favored. Combining these results with the actual growth morphology depicted in Figure 5.12, it can be concluded that the facet patterns being formed on the crystallization front according to the atomic emission (AE) model play an important role in the mechanism of instability of thermo-hydrodynamic origin. The ideal interface with C_2 symmetry corresponds to bulk spiral growth, and an ideal interface with no axial symmetry corresponds to severe footing growth. In the case of an interface with rough C_{4v} symmetry exhibiting C_4 axial symmetry, no bulk spiral growth occurs. Therefore, a more regular morphology and a larger size with fewer defects render the crystals grown using seeds with (001) and $(00\bar{1})$ faces easier to orient and cut, giving a higher utilization ratio. Furthermore, it can be concluded that the more axially symmetric the structure of the ideal crystal–melt interface is, the smaller is the chance of bulk spiral formation. Given that the bulk growth velocity deviates from the axial orientation, bulk spiral growth should take place. It can be deduced that, in the initial stage of crystal growth where many S and K faces with large growth velocity and relatively small A_{hkl} (the surface area of a crystal form {hkl} at the ideal interface) are present [57], the bulk growth velocity near the crystal–melt interface is a rate-controlled process and remains roughly axially symmetric. Shortly after the onset of the crystal diameter extension process, stable F faces appear and come to dominate the crystallization front. From the AE model, for F faces the growth rate R_{hkl} is proportional to the attachment energy and the interfacial area A_{hkl} varies greatly as compared to the corresponding attachment energy. This shows that the volume change per unit time is directly related to the interfacial area A_{hkl}, so the axial symmetry of the interface breaks down along some seed orientations. Once the interfacial structure loses its axial symmetry, then the crystallization front will have an inclination to grow away from the rotation axis because of the anisotropy of the growth velocity at the interface. When the rotation of the crystal is maintained, under the action of the inertial centrifugal force, this process will continue to deteriorate in that it will even stimulate a stirring effect that can trigger instability of thermo-hydrodynamic origin, as Figure 5.13 shows. The length

Table 5.3 Basic Properties of the Neodymium-Doped Single Vanadate Crystals

Crystal / Parameter	$Nd:YVO_4$	$Nd:GdVO_4$	$Nd:LuVO_4$
Cell parameters	a = b = 0.7118 nm, c = 0.6293 nm	a = b = 0.7211 nm, c = 0.6350 nm	a = b = 0.70243 nm, c = 0.62316 nm
Melting point		1810 °C	
Moh's hardness	4.6–5		
Density	4.22 g/cm^3	5.48 g/cm^3	6.233 g/cm^3
Thermal-Optical Coefficient			
dn_0/dt	8.5×10^{-6}/°C	4.7×10^{-6}/°C	
dn_e/dt	3.0×10^{-6}/°C		
Thermal Conductivity			
a-axis	5.1 W/mK	10.1 W/mK	7.96 W/mK
c-axis	5.23 W/mK	11.4 W/mK	9.77 W/mK
Absorption peak	808.6 nm 879 nm	808.4 nm 879.8 nm	807 nm 880 nm
Width of absorption peak (FWHM) at 808 nm	1.3 nm (π) 1.8 nm (σ)	1.6 nm (π) 2.2 nm (σ)	1.5 nm (π) ~2 nm (σ)
Absorption cross-section at 808 nm ($\times 10^{-19}$ cm^2)	6 (π) 1.2 (σ)	5.36 (π) 1.23 (σ)	6.9 (π) ~1.6 (σ)
Emission peak	1064 nm 914 nm 1342 nm	1063 nm 912 nm 1342 nm	1066 nm 916 nm 1343 nm
Width of emission peak (FWHM) at 1064 nm	1.5 nm (π) 3 nm (σ)	1.6 nm (π) 2.4 nm (σ)	1.6 nm (π) 3.4 nm (σ)
Efficient emission cross-section ($\times 10^{-19}$ cm^2)	~0.4 (π 914 nm) ~0.5 (σ 914 nm) 13.5 (π 1064 nm) 6.5 (σ 1064 nm) ~1.5 (π 1342 nm) ~0.9 (σ 1342 nm)	6.6 (π 914 nm) 5.6 (σ 914 nm) 7.6 (π 1064 nm) 1.2 (σ 1064 nm) 1.8 (π 1342 nm) 0.8 (σ 1342 nm)	~7 (π 916 nm) ~7 (σ 916 nm) 14.6 (π 1064 nm) 3.24 (σ 1064 nm) 1.5 (π 1342 nm) 1.9 (σ 1342 nm)
Fluorescence lifetime	91 μs	90 μs	82 μs
Sellmeier equation	$n_0^2 = 3.77834 + 0.069736/(\lambda^2 - 0.04724)$ $-0.01081133\lambda^2$ $n_e^2 = 4.59905 + 0.110534/(\lambda^2 - 0.04813)$ $-0.0122676\lambda^2$	$n_0^2 = 3.8714 + 0.0604/(\lambda^2 - 0.06119)$ $-0.03961\lambda^2$ $n_e^2 = 4.7331 + 0.1054/(\lambda^2 - 0.06112)$ $-0.02409\lambda^2$	

FWHM, full width at half maximum

Table 5.4 Basic Properties of the Nd:$Lu_xGd_{1-x}VO_4$ Mixed Crystals

Crystal / Parameter	X	0.14	0.32	0.50	0.61	0.70	0.80
Cell parameters	*a* (nm)	0.7161	0.7149	0.7108	0.7072	0.7070	0.7044
	c (nm)	0.6312	0.6311	0.6296	0.6265	0.6258	0.6240
Melting point				1800 °C			
Thermal conductivity (W/m K)	*a*-axis	6.7	5.9	4.8	4.9	4.8	5.7
	c-axis	7.3	6.3	5.4	5.4	5.5	6.6
Experimental fluorescence lifetime (μs)		101	107	118	114	110	108
π emission cross-section ($\times 10^{-19}$ cm^2)	1.06 μm	6.73	5.23	4.03	4.25	5.11	5.23
	1.34 μm	1.67	1.55	1.35	1.48	1.69	1.47

of crystal grown before instability can be used as an indicator of how easily the instability can be triggered by the shape of the crystallization front. Bulk spiral and footing growth will thus begin to emerge.

5.1.3.3 Basic Properties of Vanadate Family of Laser Crystals

Based on the Neumann principle, the anisotropic structure of the vanadate crystals determines their anisotropic physical properties, including spectra, thermal properties, mechanical properties, and so on. The basic physical properties related to laser applications of Nd^{3+}-doped vanadate crystals, including single and mixed crystals, have been summarized in Tables 5.3 and 5.4, respectively, which determine their possible laser applications.

5.2 Nonlinear Optical Borate Crystals Grown by the Flux Method

5.2.1 Introduction

Nonlinear optical (NLO) crystals are key materials in the development of laser science and technology because these are almost the only materials that can change the frequency of a laser beam and modulate it in both amplitude and phase. It can be said that lasers would not be in such wide use in modern science and technology without NLO crystals. The borate compounds like NLO have many outstanding advantages, such as a relatively large second harmonic generation coefficient, a wide transparency spectral range on the ultraviolet (UV) side, a high damage threshold, and so on. Since the discovery of β-BaB_2O_4 (BBO), more than 20 borate NLO crystals have been discovered up to the present, including LiB_3O_5 (LBO), CsB_3O_5 (CBO), $CsLiB_6O_{10}$ (CLBO), $KBe_2BO_3F_2$ (KBBF), BiB_3O_6 (BIBO), and others, all of which have important applications, particularly

in the laser industry [58]. Among them, BBO, LBO, and KBBF melt incongruently and have to be obtained by flux growth. Although CBO, CLBO, and BIBO can be grown from the stoichiometric melt, flux growth is still thought to be the optimal choice.

The key factor for successful flux growth lies in choosing an ideal flux. Theoretically, it is always possible to find a suitable flux and the most convenient crystallization conditions to obtain any material. In the practical growth process, an ideal flux candidate can only be identified by experimentally investigating the phase diagram of the desired compound, the solubility curve of the crystallizing phase in the chosen flux, the viscosity and volatility of the growth solution, and so on. Flux growth can be carried out either through spontaneous nucleation or crystallization on a seed. Supersaturation can be achieved through slow cooling, flux evaporation, and vertical temperature gradient transport methods. According to the growth habit of the materials required and the physicochemical properties of the growth system, several techniques of crystallization on a seed have been developed: top-seeded solution growth (TSSG), flux pulling growth, immersion-seeded solution growth (ISSG), the accelerated crucible rotation technique (ACRT), the heat field rotation method (HFRM), and so on [59]. In this section, a brief overview of flux growth techniques for bulk borate NLO crystals is presented.

5.2.2 Growth of Bulk Borate NLO Crystals

5.2.2.1 Low-Temperature Phase of Barium Metaborate (β-BaB_2O_4, or BBO)

BaB_2O_4 was first synthesized in 1874 through the fusion reaction of NaB_2O_4 and $BaCl_2$ [60]. It has two known phases, α and β, which historically were considered to be the high-temperature and the low-temperature phases of BaB_2O_4, respectively. The low-temperature phase of β-BaB_2O_4 is traditionally denoted as BBO. BBO was first recognized as having a centrally symmetric structure C2/c (C_{2h}^6) by Hubner [61], which was later refined to $R3C$ (C_{3v}^6) by Liebertz et al. [62], and confirmed by Froehlich [63] and Eimerl [64]. The melting point of BaB_2O_4 is $1095 \pm 5\,°C$, and the α–β phase transition temperature is $925 \pm 5\,°C$ [65]. Therefore, it is recommended to preferably grow the crystal from a flux solution.

A number of different techniques had previously been developed over the last 30 years. The CZ method starting from a stoichiometric BaB_2O_4 melt has also been used to grow BBO [66–69]. Compared to the flux method, the CZ method is free of a solvent acting as an impurity and affords a faster growth rate. However, in this case, crystallization occurs under non-equilibrium conditions with large temperature gradients, thus causing the development of mechanical strain and cracking of the crystal. In addition, the crystal quality strongly depends on the procedure employed for the preparation of the starting materials, and it is difficult to control crystal morphology and grow large crystals. This method has not received wide application so far. Some other techniques have also been developed, such as crystal growth under an argon atmosphere [70], an external electric potential [71], the laser-heated pedestal growth method [72], the traveling solvent-zone melting method [73], the ISSG technique [74], and TSSG technique

[75–82]. Among these techniques, only the TSSG method with or without pulling has been successfully applied to the preparation of large BBO single crystals.

In the TSSG method, the choice of flux is a vital step. Until now, there have been a number of fluxes used to grow BBO, such as B_2O_3, Li_2O, Na_2O, K_2O, $Na_2B_4O_7$, $Na_2B_2O_4$, $K_2B_2O_4$, NaCl, $BaCl_2$, NaF, KF, BaF_2, CaF_2, Na_2O–B_2O_3, Na_2O–NaCl, Na_2O–BaO, Na_2O–NaF, NaCl–NaF, Na_2SO_4, and so on. The most favorable fluxes for growing BBO crystals are Na_2O and NaF.

The phase diagram of the BaB_2O_4–Na_2O system was first studied by Huang and Liang in 1981 [75]. In the BaB_2O_4–Na_2O pseudo-binary system, BaB_2O_4 forms a eutectic with $Na_2O.BaB_2O_4$ ($Na_2BaB_2O_5$) at 755 °C. There is a large temperature interval from 925 °C to 755 °C for the growth of BBO crystals, which allows them to be grown from a 20–32 mol.% Na_2O solution. The phase diagram of the BaB_2O_4–NaF pseudo-binary system was first researched in 1996 by Roth et al. who reported a simple eutectic point at a composition of 61 mol.% NaF and a temperature of 754 °C. The liquidus temperature of the 31 mol.% NaF solution is about 925 °C, which corresponds to the α–β phase transition temperature of BBO [83]. But, in 1998, Kim et al. suggested that a eutectic point may exist at a composition between 45 and 50 mol.% NaF [84]. Therefore, BBO should be grown from a 31 to 45 mol.% NaF solution.

Compared with the BBO–Na_2O system, the BBO–NaF system has two main advantages. One is the essential viscosity reduction; that is, the viscosity of the latter is 15% below that of the former at comparable temperatures, a property that could make natural convection dominant over forced convection and result in vertical growth dominating radial growth. Thus, by maintaining the same diameter, the grown crystal is thicker. On the other hand, the liquidus curve of the latter is smoother than that of the former, which implies a higher crystal yield over an almost equal theoretical crystallization temperature range. Typical growth results show that the temperature must be reduced from 925 to 835 °C in order to grow a 100 g BBO crystal from 350 g solution with 22 mol.% Na_2O; whereas for a 350 g solution with 31 mol.% NaF, the same BBO crystal can be obtained by cooling from 925 to only 875 °C. Therefore, larger BBO crystals can be grown from the BBO–NaF solution before its viscosity increases to a level that inhibits mass transport and leads to the onset of constitutional supercooling. Although the volatility of BBO–NaF solutions is almost an order of magnitude higher than that of BBO–Na_2O solutions, the average escape of 6 mg of solution per hour (mainly NaF) does not considerably affect the crystal growth process and can be corrected by adjusting the cooling rate during growth. Adding Na_2O to the BBO–NaF system also reduces the volatility of the solution to less than 1% during the entire growth process [81].

Seed orientation has an important effect not only on the growth rate and quality, but also on the shape of the BBO crystals. Crystals grown along the *a*- or *b*- axis, or other directions that deviate significantly from the *c*-axis, usually crack spontaneously along the (0001) cleavage planes during cooling due to anisotropy in the thermal expansion coefficient ($\alpha_a = 4.3 \times 10^{-6}/°C$, $\alpha_c = 44.9 \times 10^{-6}/°C$ for BBO) [85]. Therefore, the

preferred seeding direction was found to be with the crystallographic *c*-axis normal to the solution surface.

The main problem with BBO crystals grown by the traditional TSSG method without pulling is that they grow in the shape of a convex lens with a large diameter and a small thickness, especially at the crystal edges. This shape makes it difficult to produce elements with large size in the desired direction of propagation of a laser beam. In order to grow a large specimen along the *c*-axis, the TSSG method with pulling, that is, the flux pulling method, was developed in the early 1990s. By using this technique with Na_2O flux, Tang [86] and Bosenber [87] grew ϕ 46 × 18 mm and ϕ 84 × 18 mm BBO crystals, respectively. Compared to the traditional TSSG method, the major advantages of the flux pulling method are as follows: (1) the crystal can be grown at a higher growth rate; (2) thick crystals can be obtained in smaller crucibles; and (3) seed failure, in which the crystal grows so big that it touches the crucible wall, is prevented. Presently, the flux pulling method is the best known growth method for BBO crystals.

The key to the flux pulling method lies in reasonably synchronizing the pulling rate, rotation rate, and cooling rate, so as to effectively control the radial growth and avoid growing crystals that touch the crucible wall, as well as obtaining a stable growth interface. In 2000, Wang et al. [88] investigated the range of stable growth conditions of BBO crystals from the BBO–Na_2O system by the flux pulling method. An empirical expression describing the process resulted as $\Delta T = 0.00225 \nu R_s^2 \text{ m x }^2/G$, where ΔT is the cooling amount in one day (°C/d), ν is the pulling rate (cm/day), R_s is the radius of the crystal (cm), m is the slope of the liquidus curve in the BBO–Na_2O phase diagram, x is the concentration of Na_2O within the 24–32 mol.% range, and G is the total molar amount of solution (BBO + Na_2O). For the BBO–NaF system, Zhang et al. [89] also gave an empirical expression: $\Delta T = 0.00159 \nu R_s^2 \text{ mx}^2/G$, where m is the slope of the liquidus curve in the BBO–NaF phase diagram, x is the concentration of NaF within the 31–45 mol.% range, G is the total molar amount of solution (BBO + NaF), and the other variables are the same. Based on the above analysis and experiments, the suitable pulling rates, rotation rates, and cooling rates are in the range of 0.5–1.0 mm/day, 4–8 rpm, and 0.5–2.0 °C/day, respectively.

Temperature gradients are also an important factor in the flux pulling growth process. A sufficiently large axial gradient in the solution is helpful for inducing the natural convection required both for rigorous mixing of the liquid and for maintaining the coldest spot to be at the center of the solution surface, resulting in high-quality crystals. A suitable radial gradient is favorable for controlling the diameter of the crystal. A typical value for the axial temperature gradient has been estimated to be 10–20 °C/cm for the growth of BBO crystals.

Whether Na_2O or NaF flux is used, and whether a flux growth process with pulling or without pulling is employed, success can be gained in growing BBO crystals. However, there are some problematic features associated with the growth process. Beyond a certain diameter of the growing crystal, the temperature gradient decreases near the crystallization front, and the free convection flow in the solution around the crystal in

the centripetal direction is opposed by a counter flow of forced convection due to the rotation of the crystal. The interaction between these two flows below the crystal leads to temperature instability, and hence a disturbance of the growth interface, which ultimately results in cellular growth and large channel-type inclusions [90]. In order to improve growth stability, some additives, such as Nd_2O_3 or NaCl, and mixed Na_2O–NaF flux, were tried [91], but no stabilizing effect was observed. Inclusions are generally linked to unstable growth conditions, and a standard method of improving growth stability is mechanical stirring of the solution. However, none of the conventional stirring techniques, including forced stirring, uniform crucible rotation, accelerated crucible rotation, and uniform boule rotation, produced any substantial change in the quality of the BBO crystals [92,93].

In recent years, efforts to improve the optical quality and to increase the size of crystals grown along the *c*-axis have not ceased, but rather have focused on reinvestigating the BBO–Na_2O and BBO–NaF systems, and on developing new techniques. Fedorov et al. reinvestigated the region of primary BBO crystallization in the BaO–B_2O_3–Na_2O ternary system, which extends from 30 to 42.5 mol.% $NaBaBO_3$ [94]. BBO crystals grown in the BaB_2O_4–$NaBaBO_3$ system are of very high optical quality with no scattering centers, a result that can be connected to the reduction of Na concentration in the initial high-temperature solution. The $NaBaBO_3$ solvent is superior to the commonly used Na_2O solvent [95,96]. Up to now, BBO crystals of up to ϕ (65–75) $\times$ (35–40) mm have been grown in a crucible 100 mm in diameter using this solvent [97].

In 2009, the phase equilibrium diagram of the BaB_2O_4–NaF system was reinvestigated by Bekker et al. [98]. The results indicated that there is an additional compound $Ba_2Na_3(B_3O_6)_2F$ in this system and that the BaB_2O_4–NaF section cannot be considered as quasibinary. BBO crystals can be obtained from a 31–45 mol.% NaF solution. A typical as-grown BBO boule grown from the BBO–NaF system weighs about 0.8 kg, and is $\sim$55 mm in length in the *Z*-direction at the center and $\sim$50 mm long at the periphery, as shown in Figure 5.15. Constitutional undercooling and corresponding cellular growth were not observed, and absorption has been found to be extremely low, at $<$2 ppm/cm at 1064 nm and $<$900 ppm/cm at 532 nm [99].

Based on using the flux pulling method and the BaB_2O_4–NaF phase system, Kokh et al. further suggested that the HFRM be used. The growth furnace developed consists of the appropriate commutation of the heating elements with vertically aligned elements distributed around the crucible along with a thermal regulation system, which creates stationary and rotating heat fields of variable symmetry with different amplitude and frequency characteristics. The change in symmetry and the rotation of the thermal field create nonuniform and cyclically changing external thermal fields, which considerably intensify the stirring, both in the bulk flux region and in the vicinity of the crystallization front. HFRM provides a chance to intensify the convection and control the heat–mass transfer, and thus it creates a vibrational temperature regime in the crystal growth zone. Thus, the thickness of the diffuse layer at the crystallization front decreases and

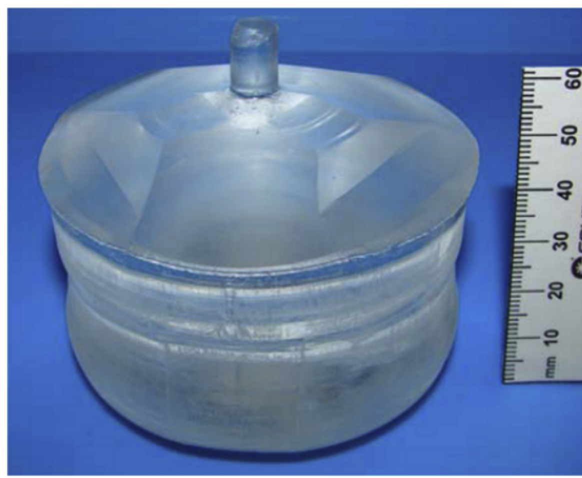

FIGURE 5.15 Barium metaborate crystal grown by top-seeded solution growth with pulling from NaF flux.

concentration supercooling is delayed, making it possible to grow large BBO single crystals with a circular cross-section and high structural quality. A high-quality BBO crystal of about 400 g in weight has been grown in a two-zone growth station with three heating sectors in each zone [100–102].

Another method used to improve the quality of BBO crystals grown in BBO–Na_2O solution is continuous feeding during growth by adding pure BBO. This provides the possibility of isothermal growth at a suitable temperature. Gradual depletion of the solution during growth was constantly compensated by manual addition of pure BBO through an alumina tube that transferred the feed material to a small platinum crucible that was partially immersed in the melt and whose bottom was punched, allowing for slow dissolution of the feedstock [103].

5.2.2.2 *LiB_3O_5 Family of Crystals*

The LiB_3O_5 family of crystals includes three known NLO crystals, LiB_3O_5 (LBO), CsB_3O_5 (CBO), and $CsLiB_6O_{10}$ (CLBO), which crystallize in space group $Pna2_1$ (C_{2v}^9) [104], $P2_12_12_1$ (D_2^4) [105], and [106], respectively. Each of the crystal structures is built up of a continuous network of B_3O_7 groups with Li^+ or Cs^+ cations located in the interstices of the network.

5.2.2.2.1 LITHIUM TRIBORATE (LIB_3O_5, OR LBO)

The LBO compound was first reported by Mazzeti and Carli [107], and later by Rollet and Bouaziz [108] in 1955. Later, the phase diagram of the Li_2O–B_2O_3 pseudo-binary system was reported by Sastry et al. in 1958 [109]. Since LBO melts incongruently at 834 ± 4 °C and dissociates to $Li_2O.2B_2O_3$ and $Li_2O.4B_2O_3$ at 595 ± 20 °C, LBO single crystals can be grown only by the flux method. Naturally, the use of B_2O_3 as self-flux was first applied for growing LBO crystals [110]. In 1990, Zhao et al. grew an LBO crystal of dimensions

$35 \times 30 \times 15$ mm^3 by a modified flux or flux pulling method, and they found that no decomposition or phase transition was observed in the crystal when it was cooled from 834 °C to room temperature [111].

Afterward, many researchers worked on growing larger LBO crystals of high optical quality by the TSSG technique from an excess B_2O_3 solution. Other related investigations, including on the nucleation thermodynamics of the Li_2O–B_2O_3 system, the physical properties of the LBO–B_2O_3 melt, the surface stability of the LBO crystal, critical growth parameters, post–growth thermal treatment, crystal morphology, and crystal defects, have also been carried out, and some important results have been obtained [112–122].

First, the most suitable composition region for the growth of LBO crystals in the Li_2O–B_2O_3 system is from 72 to 82 wt.% LBO in solution, in which the viscosity has a relatively low value and varies only slightly with concentration. If the concentration is lower than 72 wt.%, mass transport is rather difficult because of the high viscosity, and the growth of crystals without inclusions is practically impossible. At concentrations higher than 82 wt.%, the initial value of supersaturation is high and drives the crystallization process too fast and hard for a successful outcome.

Second, a small temperature gradient in the crystallization zone allows for better control of the cooling rate, while in the upper part of the growth chamber it reduces cracking when the crystal is lifted out of solution. However, growth in solution with an insufficiently high temperature gradient results in the appearance of large inclusions of fluxed melt and an oxygen nonstoichiometry in the crystal. These defects are caused by the presence of a concentration gradient in the fluxed melt, which cannot readily be removed via the usual diffusion process due to its high viscosity. As the axial and radial thermal gradients increase near the crystallization front, the fluxed melt becomes more homogeneous, and the optical quality of the crystal improves.

Third, seeding in a direction normal to wide developed faces is thought to enlarge the diameter of the crystal. The diameter of an LBO crystal grown from the seed normal to the (011) face was larger than that of a crystal grown by seeding in the <001> direction, and the thickness of the crystals was almost the same under the same growth conditions. Generally, forced convection in the solution is affected by the ratio of the crystal to crucible diameter. As the diameter of the growing crystal increases, forced convection in the solution increases. Thus, the rotation of a crystal grown by seeding normal to the (011) face produces stronger forced convection in the solution, which in turn increases crystal yield.

Additionally, the surface of LBO crystals grown under an ambient atmosphere gradually decomposes to form a millimeter-thick, optically opaque, white polycrystalline $Li_3B_7O_{12}$ layer, covering the surface of the growing crystal. Upon cooling, severe cracking occurs on the crystal surface adjacent to this layer. Under a dry nitrogen atmosphere, the formation of this layer and the subsequent cracking can effectively be avoided.

Unfortunately, B_2O_3 excess solutions form three-dimensional networks, mainly consisting of randomly oriented boroxol rings interconnected by B–O–B bridges, which

result in a very high viscosity. This leads to the appearance of growth defects, such as inclusions, inhomogeneous distribution of uncontrolled impurities, and non-stoichiometry of composition. So, in order to greatly reduce the entrapment of the parent phase and the formation of inclusions in the growing crystal, the growth rate in the excess B_2O_3 solution must be very low. This makes it very difficult to control the growth process and to obtain crystals of large size and good quality in a short time. To lower the viscosity of the melt, some additives are used, for example the alkali oxides, LiF, KF, NaCl, and MoO_3 [123–125]. The results show that the additives can effectively reduce the concentration of bridging boron–oxygen atom groups and significantly decrease the viscosity of the Li_2O–B_2O_3 system. To date, the addition of MoO_3 as a flux is the most successful example.

The first attempt to study the LBO–MoO_3 binary system in the interval between 44 and 74 wt.% of MoO_3 was made by Parfeniuk et al. [126]. The eutectic composition corresponds to 61.5 wt.% of MoO_3 and melts at 611 °C. Parfeniuk also suggested a finite element mathematical model, which is used to calculate the thermal fields and fluid flow in the melt containing the flux MoO_3 during TSSG crystal growth. The calculated results show that the most effective means of producing fluid flow in this system is by crucible rotation, which makes the MoO_3 flux move away from the interface. The results of the calculations were experimentally confirmed by the growth of LBO in the Li_2O–B_2O_3–MoO_3 system [127].

The principal advantage of MoO_3-based flux is the much lower viscosity of the melt in the temperature range that is suitable for LBO growth, compared to that produced by B_2O_3 flux. The application of MoO_3 as the flux introduces a key growth technique for obtaining large, high-quality LBO crystals. After 1996, the Li_2O–B_2O_3–MoO_3 and sB_2O_3–$Li_2O.B_2O_3$–$Li_2O.MoO_3$–MoO_3 systems were investigated in detail [128–130]. At the same time, new growth techniques were also developed, which enabled the large size and good optical quality of LBO crystals to be a common feature. In 2004, Kokh et al. used a precision heating furnace with high-symmetry heat fields to grow LBO crystals from the Li_2O–B_2O_3–MoO_3 system by the TSSG method with pulling, and the grown crystal enabled them to fabricate elements of various orientation with dimensions of $30 \times 30 \times (20–30)\ mm^3$ [131]. In the same year, Pylneva et al. introduced a thermal field configuration technique, and the crystal obtained was up to $105 \times 100 \times 75\ mm^3$ in size and 570 g in weight [132]. In 2005, Kokh et al. grew a 429 g LBO crystal by using the heat field symmetry control technique [133]. With the development of the heat field symmetry control technique and by using the Kyropoulos method, a facility for growing LBO single crystals from the Li_2O–MoO_3 flux system was established at the Institute of Geology and Mineralogy, Russian Academy of Sciences. It has successfully grown high-quality and large LBO crystals with weights in excess of 1.3 kg [134,135]. Recently, on the basis of combining the ACRT and the TSSG method, Hu's group successfully grew LBO crystals along a near phase-matching angle direction in LBO–MoO_3 solution, and an LBO crystal close to 2 kg was obtained [136], as shown in Figure 5.16. To date, the largest LBO single crystal grown, with a size of

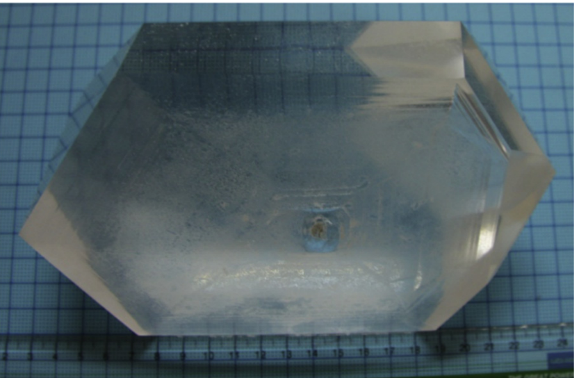

FIGURE 5.16 Large lithium triborate crystal.

$285 \times 160 \times 110\ mm^3$ and a weight of 4798 g, was successfully obtained from the improved Li_2O–MoO_3 flux system [137].

In summary, the applications of MoO_3 flux and new techniques, such as heat field symmetry control and ACRT, have brought considerable progress in LBO growth technology. In the future, LBO devices of large aperture (>20 cm) may be achieved and used in wide-aperture laser systems.

5.2.2.2.2 CESIUM TRIBORATE (CsB_3O_5, or CBO)

The phase diagram of the Cs_2O–B_2O_3 binary system was first reported in Ref. [138]. There are four crystal phases in the range from 7 to 26 mol.% of Cs_2O, including $Cs_2O \cdot 9B_2O_3$, $Cs_2O \cdot 5B_2O_3$, $Cs_2O \cdot 4B_2O_3$, and $Cs_2O \cdot 3B_2O_3$. Some researchers later reinvestigated the phase relationships in the binary system Cs_2O–B_2O_3, and Penin et al. presented a complete Cs_2O–B_2O_3 phase diagram, which indicates that CsB_3O_5 (CBO) melts congruently at 835 °C [139–141].

Since CBO melts congruently and the crystallization of the CBO phase was confirmed to take place in the composition range from 67 to 81 mol.% B_2O_3, several growth techniques can be used to grow CBO single crystals. In 1993, transparent single crystals of CBO of centimeter size were successfully grown from a stoichiometric melt for the first time [142]. During the period 1997–1999, the Kyropoulos method and the CZ method were also applied to growing CBO crystals. The sizes obtained were up to $40 \times 25 \times 25\ mm^3$ and $\phi 20 \times 30$ mm, respectively [143,144]. However, since Cs_2O is more volatile than B_2O_3, especially in the case of large-temperature gradients (60 °C/cm in the vertical direction) for the CZ method, the former melt composition deviates from the stoichiometry of CBO. Excess Cs_2O evaporation gives rise to an undesirable supersaturated region near the solution surface, and the high viscosity limits mixing and mass transport in the solution. These problems lead to unstable growth (spontaneous nucleation, inclusions, hopper growth, etc.), so it is difficult to obtain high-quality and large CBO crystals fr.om a stoichiometric melt.

Cs_2O-enriched melts acting as self-flux were widely used in order to make up for the evaporation of Cs_2O and to decrease the viscosity of the solution. In 1999, Kagebayashi et al. grew CBO crystals from an 8.9 mol.% Cs_2O-enriched melt by the Kyropoulos technique using a five-zone resistance-heated furnace. The as-grown crystal, which has high optical homogeneity and is free of cracks and inclusions, was up to $45 \times 41 \times 44\ mm^3$ in size [145]. In 2003, Kitano et al. grew CBO crystals from a 28.6 mol.% Cs_2O-enriched melt employing a modified TSSG technique, in which an additional propeller was used to stir the solution so that a more uniform melt state was achieved. This technique decreased inclusions that cause light scattering in the as-grown CBO crystals [146]. In 2005, Saji et al. investigated the growth conditions in solutions having various compositions of Cs_2O and B_2O_3 by using the TSSG method, and they suggested that CBO crystals free from scattering centers could be dependably obtained only if the solution composition is lower than 72 mol.% B_2O_3 [141]. However, the growth of large CBO crystals from this solution composition is quite difficult because of the high evaporation and low growth rate. At the same time, a $65 \times 44 \times 49\ mm^3$ CBO single crystal was grown from a 3–5 mol.% Cs_2O-enriched melt by means of the ISSG method [147]. A three-zone resistance-heated furnace was adopted, as shown in Figure 5.17, in order to get a suitable temperature distribution in the axial direction so that the temperature of the solution surface was about 1 °C higher than that at 10 mm beneath it

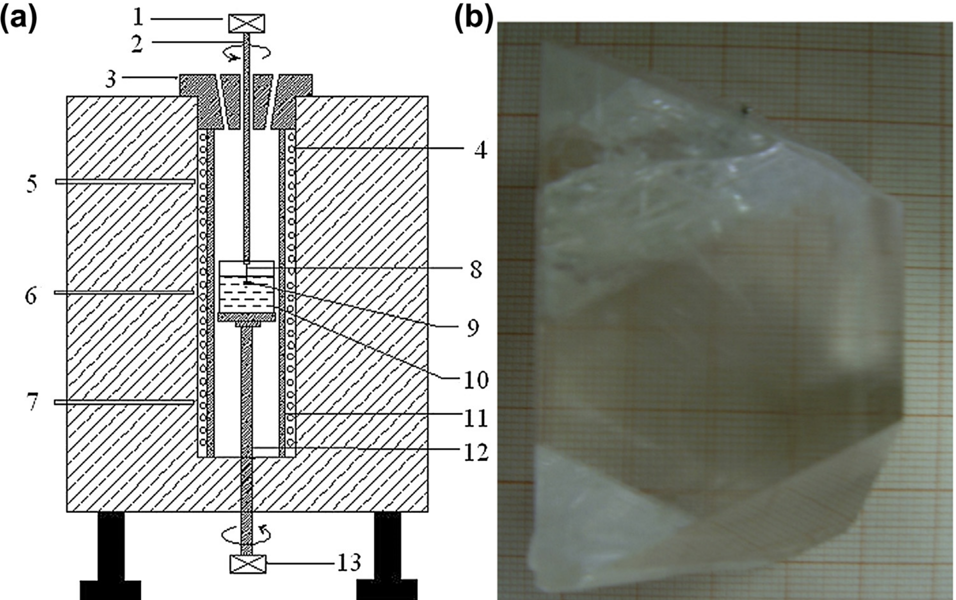

FIGURE 5.17 (a) Sketch of immersion-seeded growth equipment (1: seed rotator; 2: seed holder; 3: lip of furnace; 4: resistance heater; 5,6,7: thermal couple; 8: Pt wire; 9: seed; 10: Pt crucible; 11: Al_2O_3 tube; 12: crucible base; 13: crucible rotator and lifting); (b) immersion-seeded grown crystal.

(seeding place). Thus, any volatiles depositing on the seed rod and on the furnace lip drop down onto the solution surface and dissolve gradually without nucleating and growing. However, since Pt wire was wrapped on the grown crystal, cracking at the upper end of the crystal was unavoidable.

Although much effort has been devoted to obtaining high-quality CBO crystals, as-grown CBO crystals often contain a high density of optical scattering centers. Saji et al. proposed that the origin of the scattering centers is the CBO phase particles that nucleate during the cooling process after crystal growth. They successfully eliminated the scattering centers by heating the as-grown crystals at 815–820 °C for 2 h and subsequently quenching them at a cooling rate of about 60 °C/min [148]. In 2008, Rajesh et al. suggested that additional phase precipitation occurring near the critical 650 °C region during the slow cooling process could be the reason for the formation of scattering centers in CBO crystals. Although the scattering centers are reduced by post-growth quenching, the treated CBO crystals exhibit a green luminescence when illuminated with a deep UV laser. The green luminescence is caused by cesium vacancies that are created by the dissolution of scattering centers in the solid solution at high temperatures. The off-stoichiometric as-grown crystals can be returned to the stoichiometric composition by the vapor transport equilibration process in the presence of a cesium-rich atmosphere, so that the scattering centers and green luminescence are removed [149,150].

In order to lower the growth temperature and decrease the volatilization of Cs_2O, in recent years, many fluxes, such as NaF, V_2O_5, and MoO_3, have been applied to grow CBO crystals. Chen et al. successfully grew a CBO crystal by the TSSG method using NaF as a flux [151]. In the CBO–NaF system, there is a single eutectic point, and the eutectic composition corresponds to 40 mol.% NaF at a temperature of 690.5 °C. The addition of NaF can reduce the number of scattering centers, and the composition of 10 mol.% NaF in the CBO–NaF system was considered to be preferable for CBO growth. In 2010, Pylneva et al. investigated the CBO–V_2O_5 and CBO–MoO_3 systems. A transparent $15 \times 18 \times 15\ mm^3$ CBO single crystal with no visual defects was grown from ternary Cs_2O–B_2O_3–MoO_3 using the TSSG method [152]. Recently, a CBO crystal free of scattering centers of dimensions $47 \times 45 \times 41\ mm^3$ was successfully grown from the Cs_2O–B_2O_3–MoO_3 ternary system by the TSSG method [153], and the largest CBO crystal obtained is up to $70 \times 50 \times 49\ mm^3$ in size and 410 g in weight, as shown in Figure 5.18. The optical absorption of as-grown crystals at the critical wavelengths of 1064 and 532 nm was at the same level as in commercially available LBO crystals [154].

5.2.2.2.3 CESIUM LITHIUM BORATE ($CsLiB_6O_{10}$, OR CLBO)

The phase diagram of the ($Cs_2O + Li_2O$)–(B_2O_3) binary system was first reported by Mori et al., and CLBO was found to melt congruently at 848 °C [155]. After the phase equilibria in the Cs_2O–Li_2O–B_2O_3 system were reinvestigated, it was established that CLBO melts congruently at 859 ± 2 °C [156]. Therefore, CLBO can be grown from the stoichiometric melt by means of the top-seeded Kyropoulos method. Presently, using a [001] crystal

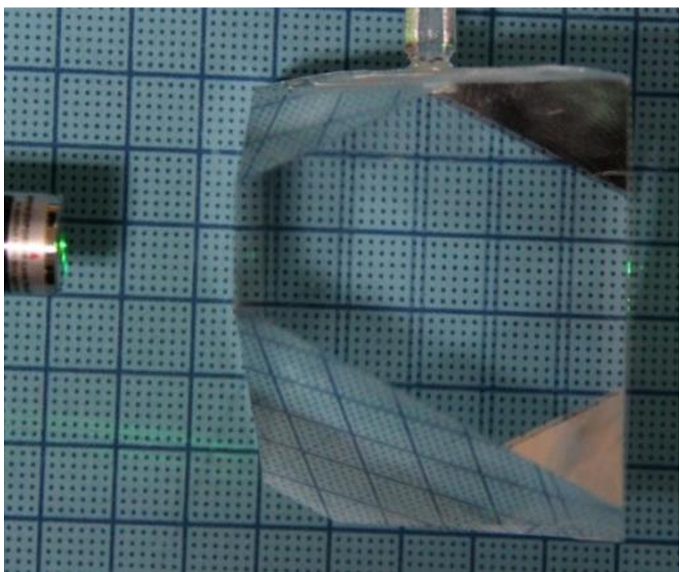

FIGURE 5.18 Cesium triborate crystal grown by top-seeded solution growth in a Cs_2O–B_2O_3–MoO_3 system.

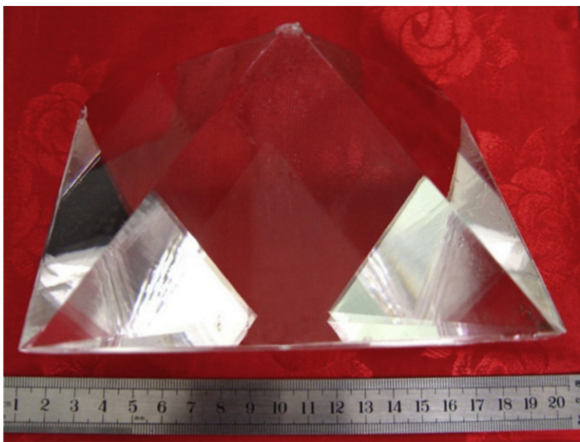

FIGURE 5.19 Cesium lithium triborate crystal grown from a stoichiometric melt.

seed, the maximum size of a CLBO crystal grown from the stoichiometric melt was as large as $146 \times 132 \times 118\ mm^3$ and 1800 g in weight after 30 days of growth [157], as shown in Figure 5.19. CLBO crystals can be also grown from fluxes that are either poor or rich in B_2O_3. Since the B_2O_3-enriched solutions have high viscosity, a self-fluxed solution poor in B_2O_3 (Cs_2CO_3:Li_2CO_3:B_2O_3 with a molar ratio of 1:1:5.5) was used to grow the CLBO crystals. Using an *a*-axis seed crystal, a large CLBO crystal with dimensions of $14 \times 11 \times 11\ cm^3$ was grown in 12 days. The crystal also exhibited easily distinguishable facets similar to those of crystals grown from the stoichiometric melt [158].

In order to obtain CLBO with a high bulk laser-induced damage threshold (LIDT), Sasaki et al. developed a new growth apparatus based on an effective solution-stirring (SS) technique that combines a propeller and crucible rotation to thoroughly stir the solution [159]. Rotating the crucible with a static propeller effectively induces forced convection despite the high viscosity of the solution. A $12 \times 6 \times 5\ cm^3$ CLBO crystal was grown by the above SS technique in 16 days. Prior to crystal growth, the preparation method for the growth materials was also improved. After dissolving the starting materials in pure water, the precursor was obtained by evaporating the solvent. Then, the precursor was sintered in air at 800 °C for 24 h. This process yielded a completely crystalline single phase of CLBO. By combining the SS-TSSG and the mixing-in-aqueous-solution techniques, the grown crystals possessed an approximately 2.3-fold higher bulk LIDT for UV light than those grown by the conventional method, and they exhibited superior water resistance due to the lower defect density [160]. In 2010, Kawamura et al. investigated CLBO growth from a stoichiometric melt by the SS-TSSG method in a dry atmosphere. The growth furnace was filled by flowing Ar gas, which reduced the humidity in the furnace to below 5% relative humidity at room temperature. The results showed that growth in a dry atmosphere prevents water vapor from entering the CLBO solution, and growth from a stoichiometric melt prevents water from being included in the growing crystal [161]. In addition, the LIDT of the CLBO crystal was also effectively improved by doping. A newly developed Al-doped CLBO crystal ($85 \times 53 \times 46\ mm^3$, 199 g) with little light scattering exhibits about a two times higher threshold (40–50 MW/cm^2) than that of the conventional undoped crystal (20–30 MW/cm^2) [162].

Besides reduced B_2O_3, $LiCsMoO_4$ and NaF were also applied as fluxes to grow CLBO crystals. Since the addition of MoO_3 decreases viscosity and improves intermixing in the melt, $LiCsMoO_4$ can be considered as efficient solvent for the growth of CLBO single crystals. A $60 \times 40 \times 20\ mm^3$ CLBO crystal grown using $LiCsMoO_4$ as the flux was found to be free of cracks, bubbles, and inclusions [163]. In addition, the heat field rotation technique was applied to grow a CLBO crystal from the CLBO–$LiCsMoO_4$ system [164]. When NaF was used as the flux, the solution viscosity decreased and the growth temperature also decreased with increased NaF content. The decrease in growth temperature reduces the volatilization of Cs in the solution, but on the other hand it increases the solution viscosity. Using the TSSG method, a CLBO crystal with dimensions of $54 \times 51 \times 32\ mm^3$ was grown from the NaF flux system [165].

5.2.2.3 Potassium Beryllium Borate Fluoride ($KBe_2BO_3F_2$, or KBBF)

KBBF was first synthesized in the KBF_4–BeO system in 1968 [166]. Solov'eva et al. reported in 1970 that the space structure of the crystal is C121 (C_2^1) [167]. However, optical observation by polarization microscopy and Laue X-ray photographs clearly shows that the crystal has a triangular or hexagonal axis. In 1995, the designated space group was revised to be R32 (D_3^7) [168]. KBBF has triangular $(BO_3)^{3-}$ groups and tetrahedral $(BeO_3F)^{5-}$ anionic groups as fundamental building units, where a triangular $(BO_3)^{3-}$ group connects two neighboring $(BeO_3F)^{5-}$ tetrahedra together to form into an infinite

planar framework $(Be_2BO_3F_2)\infty$ along the *a–b* plane with all $(BO_3)^{3-}$ triangles parallel and F atoms above or below the plane. Moreover, owing to the large distance and weak K–F interactions between neighboring $(Be_2BO_3F_2)$ layers along the *c*-axis, the crystals exhibit a layer growth habit, which makes it difficult to grow thick crystals along the *c*-axis.

KBBF single crystals must be grown using the flux method because the material quickly volatilizes and decomposes above 820 °C before melting at 1100 °C. A number of solvent systems were tested, including KBF_4–BeO–B_2O_3–K_2CO_3, KBF_4–BeO–B_2O_3, KBBF–KF–B_2O_3, KBBF–KF, KBBF–KCl, KBBF–M_2O–MoO_3 (M = Li, Na, K), KBBF–PbO–PbF_2, KBBF–PbO–PbF_2–B_2O_3, KBBF–$K_2Mo_2O_7$–MoO_3, and KBBF–$K_2W_2O_7$ [169,170]. The experimental results show that the first three systems are suitable for KBBF crystal growth.

In 1993, the first KBBF single crystal with dimensions of $20 \times 10 \times 1.0\ mm^3$ was grown from the KBF_4–BeO–B_2O_3 system by the flux method. In 2001, Tang et al. investigated the KBF_4–BeO–B_2O_3 and KBBF–KF–B_2O_3 systems, and transparent single crystals ($10 \times 10 \times 1\ mm^3$) were grown.

The main problems encountered in KBBF growth are (1) an undesirable plate-like growth habit (thin (001) platelets), which is attributable to the sheet structure of KBBF. Since the interactive force between adjacent sheets is the weak K–F electrostatic force and the axial ratio reaches $c/a = 4.234$, the growth rate along the *c*-axis is so slow that crystals grown along this direction are generally very thin. (2) Uncontrolled nucleation, in which many new nuclei are formed, grow parallel to the (001) face, and subsequently intersect each other, resulting in a tendency for the crystal to trap flux. (3) Volatilization of the solution, toxicity of beryllium compounds, and low growth reproducibility. Due to these difficulties, only KBBF single crystals with up to 2 mm in thickness along the *c*-axis could be grown by the spontaneous nucleation method before 2003 [171]. Moreover, up to now, many attempts to grow large sized KBBF crystals along the *c*-axis by the seeding technique have been unsuccessful due to the low energy barrier for spontaneous nucleation in the flux system.

To increase the size and further improve the quality of the crystals grown by the spontaneous nucleation growth technique, a new growth project was started at the beginning of the 2000s. First, the region of KBBF primary crystallization was investigated, which is located in the pseudo-ternary system KF:B_2O_3:(3BeO:BeF_2). Second, in order to control or restrict nucleation at one spot or over a narrow region where the crystal starts to grow, and as a consequence to obtain thicker bulk KBBF crystals oriented along the *z*-axis, the localized spontaneous nucleation technique was developed [172]. It consists of a special temperature distribution, restriction of the nucleation site, and cyclic temperature oscillation. Aided by a crucible cooler at the base center, and after ensuring that the base of the crucible is cooler than at any other place in the melt, nucleation then occurs at the center of the crucible bottom.

By using the above-mentioned new technology, the efficiency of growing large and thick KBBF crystals is greatly improved. Unavoidably, many as-grown KBBF crystals are adhered to by some small crystals that spontaneously nucleate in the later period of

growth. A bulk KBBF crystal with a transparent area of $50 \times 40\ mm^2$ and thickness of about 3.7 mm oriented along the *c*-axis was obtained after removing these attached crystals. The as-grown KBBF crystals possess hexagonal or near-hexagonal trigonal symmetry, which mainly consists of two sets of tabular facets (0001).

5.2.2.4 Bismuth Triborate (BiB_3O_6, or BiBO)

The phase diagram for the system Bi_2O_3–B_2O_3 was first investigated in 1962 and refined in 1999, which led to the discovery of four BiB_3O_6 polymorphs [173,174]. The bismuth triborate polymorph investigated as an NLO crystal is α-BiB_3O_6 (hereafter denoted as BIBO) [175]. The first BIBO crystals were obtained in 1982 [176], but optimal conditions for single crystal growth were only extensively investigated after its excellent NLO properties were discovered. BIBO melts congruently at 708 °C and occurs only in a small region of composition from about 72.5 to 77.5 mol.% B_2O_3. In 1999, Becker et al. grew a BIBO single crystal with dimensions of $20 \times 20 \times 30\ mm^3$ from a stoichiometric melt using the TSSG method. In the process of growth, the following parameters are especially notable [177–180]:

1. *Composition of the melt*: Melt with a stoichiometric composition of 75 mol.% B_2O_3 tends to form glass and has a high viscosity, which limits the mixing and mass transport in the melt and leads to the growth of parasitic crystals under conditions close to equilibrium. Although an excess of Bi_2O_3 in the melt can lower the viscosity, it leads to formation of $Bi_3B_5O_{12}$ so that BIBO has to be grown from a stoichiometric melt. However, since B_2O_3 evaporates from the melt during the growth process, an excess of 1 mol.% B_2O_3 was added to the melt, which had no effect on the optical quality of the crystals.
2. *Preparation of the melt*: Due to the value of the specific gravity of Bi_2O_3, the top part of the melt is enriched in boron, whereas the bottom part is enriched in bismuth. It is imperative to synthesize BIBO powder by the solid-state reaction technique to avoid a separation of the melting components and the deposition of Bi_2O_3 at the base of the crucible during the melting of B_2O_3. A reaction temperature of 700 °C held over 24 h proved to be sufficient to obtain a homogeneous BIBO melt. A clear, transparent, and homogeneous melt was also achieved by mixing the Bi_2O_3 and B_2O_3 powders, heating to 800 °C, and stirring for 96 h.
3. *Cooling and rotation rates*: In general, the stoichiometric melt was supercooled by 3–4 °C by lowering the furnace temperature at a rate of 6 K/h to the desired temperature, followed by a dwell time of 24 h. The supercooling by 10 °C led to the spontaneous growth of parasitic crystals at the edges of the growing crystal. A cooling rate of 0.1 °C/day was applied. The crystals grown with this temperature regime show sharp edges between their well-developed morphological faces. Since rotation in a high-viscosity melt gives rise to additional stresses in a growing crystal and may result in the destruction of the seed, no seed rotation or a minimal rotation rate of 3–4 rpm was applied in practice.

4. *Seed direction*: Because of the low symmetry of the BIBO crystal, the growth anisotropy was very strong, and the crystal morphology and quality depended crucially on seed orientation. In view of the technological factors, the optimal direction of crystal growth is that with zero thermal expansion. For BIBO, the coefficient of thermal expansion along the crystallographic direction $[\bar{1}01]$ is close to zero. Therefore, the optimal seed orientation was found to be $[\bar{1}01]$.
5. *Temperature gradients:* A resistive-heating furnace was specially designed for maintaining a very even temperature gradient in both the axial and the radial directions, and it was divided into three independently powered and controlled zones so that temperature fluctuations in the crucible zone were limited to only 2 °C per 200 mm along the furnace axis.

Under the optimal conditions discussed here, a high-optical-quality BIBO crystal with dimensions of $30 \times 30 \times 40\ mm^3$ and a weight of 120 g was successfully grown from high-temperature solutions by the TSSG method.

5.3 Conclusion

In summary, as required by laser development, Tm^{3+} and Ho^{3+} as activators in laser hosts can produce lasers that radiate near the 2.0 μm region. Due to efficient energy transfer between the Tm $^3F_4$ and Ho $^5I_7$ manifolds, Tm-sensitized Ho materials are used to produce laser action around 2.0 μm. Ho-doped, Tm-doped, and co-doped GGG crystals have been grown. The growth conditions and the spectroscopic properties of the materials have been summarized. Having been chosen due to the excellent laser performance of the vanadates, a series of vanadate laser crystals were successfully grown by the CZ method. The actual formation of bulk spiral growth during the CZ process is very complicated and cannot be simply ascribed to one factor or another. It reflects an interaction between the internal crystal structure and the exterior environment that controls the growth process. However, because a highly axially symmetric crystal–melt interface consisting of large facets with similar growth velocities is much more preferable according to morphological analysis, the use of an appropriate seed crystal is advisable and thus can greatly reduce the chance of bulk spiral formation. It is beneficial to follow the prescribed procedure for the selection of seed crystals in CZ growth of low-symmetry oxide crystals, a process that in the past has usually been achieved by trial and error.

Based on the traditional TSSG method, significant progress has been made in the growth of bulk borate NLO single crystals by applying new fluxes combined with other new techniques, such as flux pulling for BBO, heat field rotation for BBO and CLBO, accelerated crucible rotation for LBO, seed submersion for CBO, SS for CLBO, and localized spontaneous nucleation for KBBF. However, there are still other difficulties that affect the growth of large, high-quality single crystals. For example, so far, KBBF crystals grown by the spontaneous nucleation method have not been obtained that are greater than 4 mm along the *c*-axis, and thus they cannot be used to fabricate optical devices for

frequency conversion. Therefore, much effort still remains to be exerted to grow large, high-optical-quality single crystals, including searching for more suitable fluxes, investigating the physical and chemical properties of growth systems, developing new techniques, surveying crystal defects, and so on.

Acknowledgments

The authors express their thanks to Prof. Dr R. Boughton for careful manuscript revision, and to Prof. P. Rudolph for very fruitful discussions. These works were supported by National Science Foundation of China (51372139, 51132008, and 61078076) and 973 2010CB833103.

References

[1] Maiman TH. Nature 1960;187:493.

[2] Weber MJ, Myers JD, Blackburn DH. J Appl Phys 1981;52:2944.

[3] Koechner W. Solid-state lasers. 5th ed. Springer; 2002.

[4] Moulton PF. J Opt Soc B 1986;3:125.

[5] Li H, Xu J. Crystal growth of laser host fluorides and oxides. Handbook of crystal growth. Springer; 2010. p. 479–503.

[6] Fields RA, Birnbaum M, Fincher CL. Appl Phys Lett 1987;51:1885.

[7] Zhang QL, Yin ST, Wang AH, Xiao JZ. Chin J Quan Elect 2002;19:481.

[8] O'Conno JR. Appl Phys Lett 1966;9:407.

[9] Bagdasarov Kh S, Bogomolova GA, Kaminskii AA, Popov VI. Sov Phys Dokl 1968;13:516.

[10] Bagdasarov Kh S, Kaminskii AA, Krylov VS, Popov VI. Phys Stat Sol 1968;1–3:27.

[11] Kaminskii AA, Bodretsova AI, Levikov SI. Sov Phys Tech Phys 1969;14:396.

[12] Kaminskii AA, Bogomolova GA, Li L. Inorg Mater 1969;5:573.

[13] Kaminskii AA. Sov Phys JETP 1969;29:46.

[14] Kaminskii AA. Phys Stat Sol (A) 1970;1:573.

[15] Kaminskii AA, Sarkisov SÉ, Bagdasarov Kh S. Inorg Mater 1973;9:457.

[16] Sawada H. J Solid State Chem 1997;132:300.

[17] Lupei A, Lupei V, Grecu S, Tiseanu C, Boulon G. J Appl Phys 1994;75:4652.

[18] Brandle CD. J Appl Phys 1978;49:1855.

[19] Asadian M, Hajiesmaeilbaigi F, Mirzaei N, Saeedi H, Khodaei Y, Enayati Sh. J Cryst Growth 2010; 312:1645.

[20] Cockayne B, Roslington JM. J Mater Sci 1973;8:601.

[21] Stacy WT. J Cryst Growth 1974;24/25:137.

[22] Zhao G, Li T, Xu J. J Cryst Growth 2002;237–239:720.

[23] Ohta K, Saito H, Obara M. J Appl Phys 1993;73:3149.

[24] Fan TY, Huber G, Byer RL, Mitzscherlich P. IEEE J Quantum Electron 1988;24:924.

[25] Payne SA, Chase LL, Smith LK, Kway WL, Krupke WF. IEEE J Quantum Electron 1992;28:2619.

[26] Rustad G, Stenersen K. IEEE J Quantum Electron 1996;32:1645.

[27] Karayianis N, Wortman DE, Jenssen HP. J Phys Chem Solids 1976;37:675.

[28] Johnson LF, Geusic JE, Van Uitert LG. Appl Phys Lett 1966;8:200.

[29] Forster T. Ann Phys 1948;6:55.

[30] Dexter DL. J Chem Phys 1953;21:21836.

[31] Walsh BM, Barnes NP, Bartolo BDi. J Lumin 1997;75:89.

[32] Bagdasarov Kh S, Bogomolova GA, Kaminskii AA, Popov VI. Sov Phys Dokl 1968;13:516.

[33] Bagdasarov Kh S, Kaminskii AA, Krylov VS, Popov VI. Phys Stat Sol 1968;27:1.

[34] McKnight HG, Rothrock LR. Technical Report No. ECOM 0022F, U.S. Army ECOM Contract No. DAAB07-72-C-0022; April, 1973.

[35] Yaney PP, DeShazer LG. J Opt Soc Am 1976;66:1405.

[36] Li GS, Wu XQ, Wei M, Zhu YM, Yu ZS, Teng S, et al. J Synth Cryst 1999;28:27.

[37] Wei M, Li GS, Zhu YM, Wu XQ, Yu ZS, Teng S. J Synth Cryst 1998;27:178.

[38] Studenikin PA, Zagumennyi AI, Zavartsev YD, Popov PA, Shcherbakov IA. Quantum Electron 1995;25:1162.

[39] Maunier C, Doualan JL, Moncorge R, Speghini A, Bettinelli M, Cavalli E. J Opt Soc Am B 2002;19:1794.

[40] Cong H, Zhang H, Sun S, Yu Y, Yu W, Yu H, et al. J Appl Cryst 2010;43:308.

[41] Liu JH, Meng XL, Shao ZS, Jiang MH, Ozygus B, Ding A, et al. Appl Phys Lett 2003;83:1289.

[42] Yu HH, Zhang HJ, Wang ZP, Wang JY, Yu YG, Shao ZS, et al. Opt Lett 2007;32:2152.

[43] Liu J. IEEE J Quantum Electron 2011;47:100.

[44] Kaminskii AA, Ueda K, Eichler HJ, Kuwano Y, Kouta H, Bagaev SN, et al. Opt Commun 2001;194:201.

[45] Kaminskii AA, Lux O, Rhee H, Eichler HJ, Ueda K, Yoneda H, et al. Laser Phys Lett 2012;9:879.

[46] Rubin JJ, Van Uitert LG. J Appl Phys 1966;37:2920.

[47] Zhang HJ, Zhu L, Meng XL, Yang ZH, Wang CQ, Yu WT, et al. Cryst Res Technol 1999;34:1011.

[48] Zagumennyi AI, Ostroumov VG, Shcherbakov IA, Jensen T, Meyen JP, Huber G. Sov J Quantum Electron 1992;22(12):1071.

[49] Zhang HJ, Meng XL, Zhu L, Zhang HZ, Wang P, Dawes J, et al. Cryst Res Technol 1998;33:801.

[50] Zhang H, Kong H, Zhao S, Jiu J, Wang J, Wang Z, et al. J Cryst Growth 2003;256:292.

[51] Yu Y, Wang J, Zhang H, Yu H, Wang Z, Jiang M, et al. J Opt Soc Am B 2008;25:995.

[52] Yu HH, Zhang HJ, Wang ZP, Wang JY, Yu YG, Cheng XF, et al. J Appl Phys 2007;101:113109.

[53] Wang ZP, Sun X, Xu XG, Sun LK, Sun SJ, Meng XL, et al (in Chinese) Chin J Quantum Electron 2000;18:104.

[54] Lupei V, Pavel N, Taira T. Opt Commun 2002;201:431.

[55] Zhang LZ. [Ph.D. thesis]. People's Republic of China: Fujian Institute of Research on the Structure of Matter, Chinese Academy of Science; 2005.

[56] Hartman P. In: Sunagawa I, editor. Morphology of crystals, part A. Tokyo: Terra Scientific Publishing; 1987. p. 269–319.

[57] Hurle DTJ, Rudolph P. In: Feigelson RS, editor. 50 years progress in crystal growth. Amsterdam: Elsevier; 2004. p. 119.

[58] Chen C, Sasaki T, Li R, Wu Y, Lin Z, Mori Y, et al. Nonlinear optical borate crystals. KG, Germany: Wiley-VCH Verlag GmbH & Co; 2012.

[59] Elwell D, Scheel HJ. Crystal growth from high temperature solution. London: Academic Press; 1975.

[60] Benedikt R. Ber Deut Chem Ges 1874;7:700.

[61] Hubner KH. Neues Jahrb Mineral Monatsh 1969;111:335.

[62] Liebertz J, Stähr S. Z Kristallogr 1983;165 91.

[63] Froehlich R. Z Kristallogr 1984;168 109.

[64] Eimerl D, Davis L, Velsko S, Graham EK. J Appl Phys 1987;62:1968.

[65] Chen CT, Wu BC, Jiang AD, You GM. Sci Sin 1985;18:235.

[66] Ltoh K, Marumo F, Kuwano Y. J Cryst Growth 1990;106:728.

[67] Kouta H, Kuwano Y, Ito K, Marumo F. J Cryst Growth 1991;114:676.

[68] Kouta H, Imoto S, Kuwano Y. J Cryst Growth 1993;128:938.

[69] Kouta H, Kuwano Y. J Cryst Growth 1996;166:497.

[70] Sabharwal SC, Sangeeta. J Cryst Growth 2001;222:427.

[71] Tyurikov VI, Tsvetkov EG. J Cryst Growth 2002;237-239:403.

[72] Tang DY, Route RK, Felgelson RS. J Cryst Growth 1988;91:81.

[73] Hengel RO, Fischer F. J Cryst Growth 1991;114:656.

[74] Bordui PF, Calvert GD, Blachman R. J Cryst Growth 1993;129(1–2):371.

[75] Huang QZ, Liang JG. Acta Phys Sin 1981;30(4):559.

[76] Wang GF, Huang QZ. Acta Phys Sin 1985;34(4):562.

[77] Jiang AD, Cheng F, Lin Q, Cheng ZS, Zheng Y. J Cryst Growth 1986;79:963.

[78] Cheng LK, Bosenberg W, Tang CL. J Cryst Growth 1988;89:553.

[79] Gualtieri DM, Chai BHT. J Cryst Growth 1989;97:613.

[80] Huang QZ, Liang JK. J Cryst Growth 1989;97:720.

[81] Oseledchik YS, Osadchuk VV, Prosvirnin AL, Selevich AF. J Cryst Growth 1993;131:199.

[82] Chen TB, Guo XB, Zhen Y, Lin JJ. J Synth Cryst 1997;26(1):44.

[83] Roth M, Perlov D. J Cryst Growth 1996;169:734.

[84] Kim HG, Kang JK, Park SJ. Opt Mater 1998;9:356.

[85] Tang DY, Zeng WR, Zhao QL. J Cryst Growth 1992;123:445.

[86] Tang DY, Lin ST, Dai GQ, Lin Q, Zeng WR, Zhao QL, et al. J Synth Cryst 1990;19:21.

[87] Bosenberg WR, Lane RJ, Tang CL. J Cryst Growth 1991;108:394.

[88] Wang BG, Lu ZP, Voigt A. Cryst Res Technol 2000;35(10):1141.

[89] Zhang GC. Growth and properties of several optic-electric function crystals [Postdoctoral thesis]. Technical Institute of Physics and Chemistry, Chinese Academy of Sciences; 2004.

[90] Nikolov V, Peshev P, Khubanov K. J Solid State Chem 1992;97:36.

[91] Solé R, Nikolov V, Pujol MC, Gavaldà J, Ruíz X, Massons J, et al. J Cryst Growth 1999;207:104.

[92] Kokh A. J Cryst Growth 1998;191:774.

[93] Kokh AE, Kononova NG. J Cryst Growth 1999;198/199:161.

[94] Fedorov PP, Kokh AE, Kononova NG, Bekker TB. J Cryst Growth 2008;310:1943.

[95] Tsvetkov EG, Tyurikov VI, Khranenko GG. J Cryst Growth 2002;237–239:658.
[96] Kokh AE, Kononova PP, Fedorov NG, Bekker TB, Kuznetsov SV. Inorg Mater 2005;41:60.
[97] Tsvetkov EG, Khranenko GG, Solntsev VP. J Cryst Growth 2005;275:e2123.
[98] Bekker TB, Kokh AE, Kononova NG, Fedorov PP, Kuznetsov SV. Growth Des 2009;9:4061.
[99] Perlov D, Livneh S, Czechowicz P, Goldgirsh A, Loiacono D. Cryst Res Technol 2011;46(7):651.
[100] Kokh AE, Kononova NG, Mokruchnikov PW. J Cryst Growth 2000;216:359.
[101] Kokh AE, Popov VN, Bekker TB, Kononova NG, Kokh KA, Mokrushnikov PV. J Cryst Growth 2005;275:e669.
[102] Kokh AE, Kononova NG, Bekker TB, Vlezko VA, Mokrushnikov PV, Popov VN. Crystallogr Rep 2005;50:160.
[103] Perlov D, Roth M. J Cryst Growth 1994;137:123.
[104] König H, Hoppe R, Anorg Z. Allg Chem 1978;439(1):71.
[105] Krogh-Moe J. Acta Crystallogr 1974;B30:1178.
[106] Sasaki T, Mori Y, Kuroda I, Nakajima S, Yamaguchi K, Watanabe S, et al. Acta Crystallogr 1995;C51:2222.
[107] Mazzeti C, Carli FD. Gazz Chim Ital 1926;56:19.
[108] Rollet AP, Bouaziz R. Comp Rend 1955;240:2417.
[109] Sastry BSR, Hummel FA. J Am Ceram Soc 1958;41(1):7.
[110] Chen CT, Wu YC, Jiang AD, Wu BC, You GM, Li RK, et al. J Opt Soc Am B 1989;6(4):616.
[111] Zhao SQ, Huang CE, Zhang HW. J Cryst Growth 1990;99:805.
[112] Ukachi T, Lane RJ, Bosenberg WR, Tang CL. J Opt Soc Am B 1992;9(7):1128.
[113] Brück E, Raymakers RJ, Route RK, FeigeIson RS. J Cryst Growth 1993;128(1–4):933.
[114] Markgraf SA, Furukawa Y, Sato M. J Cryst Growth 1994;140(3–4):343.
[115] Shumov DP, Nikolov VS, Nenov AT. J Cryst Growth 1994;144(3–4):218.
[116] Guretskii SA, Ges AP, Zhigunov DI, Ignatenko AA, Kalanda NA, Kurnevich LA, et al. J Cryst Growth 1995;156:410.
[117] Shumov DP, Nenov AT, Nihtianova DD. J Cryst Growth 1996;169(3):519.
[118] Nihtianova DD, Shumov DP, Macicek JJ, Nenov AT. J Cryst Growth 1996;169(3):527.
[119] Zhong WZ, Tang DY. J Cryst Growth 1996;166:91.
[120] Hu XB, Jiang SS, Huang XR, Zeng W, Liu WJ, Chen CT, et al. J Cryst Growth 1996;163:266.
[121] Kim HG, Kang JK, Lee SH, Chung SJ. J Cryst Growth 1998;187:455.
[122] Dhanaraj G, Byrappa K, Prasad V, Dudley M, editors. Springer handbook of crystal growth. Germany: Springer-Verlag Berlin Heidelberg; 2010.
[123] Hao ZW, Ma XM. J Synth Cryst 2002;31(2):124.
[124] Kim JW, Yoon CS, Gallagher HG. J Cryst Growth 2001;222:760.
[125] Liu HB, Shen GQ, Wang XQ, Wei JZ, Shen DZ. Prog Cryst Growth Charact 2000;40:235.
[126] Parfeniuk C, Samarasekera IV, Weinberg F. J Cryst Growth 1996;158:514.
[127] Parfeniuk C, Samarasekera IV, Weinberg F, Edel J, Fjeldsted K, B. Lent. J Cryst Growth 1996;158:523.
[128] Pylneva NA, Kononova NG, Yurkin AM, Bazarova GG, Danilov VI. J Cryst Growth 1999;198/199:546.

[129] Pylneva N, Kosyakov V, Yurkin A, Bazarova G, Atuchin V, Kolesnikov A, et al. Cryst Res Technol 2001;36(12):1377.

[130] Kosyakov VI, Pylneva NA, Bazarova ZG, Yurkin AM. Mater Res Bull 2001;36:573.

[131] Kokh AE, Kononova NG. Abstract of the 14th international conference on crystal growth (ICCG-14); 2004. P593, Grenoble, France.

[132] Pylneva NA, Tsirkina NL, Rozkov AF, Pylneva LL, Vratskih VF. Abstract of the 14th international conference on crystal growth (ICCG-14); 2004. P561, Grenoble, France.

[133] Kokh AE, Kononova NG. Abstracts of the 3rd Asian conference on crystal growth and crystal technology (CGCT-3); 2005. Beijing China. CD-edition, http://www.cgct-3.cn.

[134] Kokh AE, Vlezko VA, Kokh KA. Instrum Exp Tech 2009;52(5):747.

[135] Kokh AE, Kononova N, Mennerat G, Villeval P, Durst S, Lupinski D, et al. J Cryst Growth 2010;312:1774.

[136] Hu ZG, Zhao Y, Yue YC, Yu XS. J Cryst Growth 2011;335:133.

[137] Hu ZG. Large size LBO crystal for high power laser, Abstract of the 6th international symposium on lasers, scintillators and non-linear optical materials (ISLNOM-6); October 20–23, 2013. P32, Shanghai, China.

[138] Krogh-Moe J. Ark Kemi 1958;12(26):247.

[139] Kaplun AB, B Meshalkin A. J Cryst Growth 2000;209:890.

[140] Penin N, Touboul M, Nowogrocki G. J Cryst Growth 2003;256:334.

[141] Saji T, Hisaminato N, Nishioka M, Yoshimura M, Mori Y, Sasaki T. J Cryst Growth 2005;274:183.

[142] Wu YC, Sasaki T, Nakai N, Yokotani A, Tang HG, Chen CT. Appl Phys Lett 1993;62(21):2614.

[143] Fu PZ, Wang JX, Hu ZG, Wu YC, Yin ST, Xu ZY. J Synth Cryst 1999;28(3):215.

[144] Wu YC. In: Proceedings of international symposium on laser and nonlinear optical Materials; 1997. p. 120.

[145] Kagebayashi Y, Mori Y, Sasaki T. Bull Mater Sci 1999;22(6):971.

[146] Kitano H, Matsui T, Sato K, Ushiyama N, Yoshimura M, Mori Y, et al. Opt Lett 2003;28(4):263.

[147] Chang F, Fu PZ, Wu YC, Chen GJ, Xu ZJ, Chen CT. J Cryst Growth 2005;277:298.

[148] Saji T, Yoshimura M, Hisaminato N, Mori Y, Sasaki T, Katsura T, et al. Jpn J Appl Phys 2005;44(14):L422.

[149] Rajesh D, Yoshimura M, Shimatani H, Mori Y, Jayavel R, Sasaki T. Cryst Growth Des 2008;8(10):3713.

[150] Rajesh D, Eiro T, Yoshimura M, Mori Y, Jayavel R, Sasaki T. J Cryst Growth 2008;310:1950.

[151] Chen GJ, Wu YC, Fu PZ. Chin J Struct Chem 2007;26(9):1047.

[152] Pylneva NA, Pylneva LL, Meshalkin AB, Kosyakov VI, Kaplun AB. The 16th international conference on crystal growth (ICCG16); August 8–13, 2010. Beijing, China.

[153] Liu SS, Zhang GC, Feng K, Wu YC. J Cryst Growth 2013;364:46.

[154] Liu SS, Zhang GC, Li XM, Yang F, Bo Y, Fu PZ, et al. Cryst Eng Comm 2012;14:4738.

[155] Mori Y, Kuroda I, Nakajima S, Taguchi A, Sasaki T, Nakai S. J Cryst Growth 1995;156:307.

[156] Kaplun AB, Meshalkin AB. J Cryst Growth 2001;229:248–51.

[157] Yuan X, Shen GQ, Wang XQ, Shen DZ, Wang GL, Xu ZY. J Cryst Growth 2006;293:97.

[158] Mori Y, Kuroda I, Nakajima S, Sasaki T, Nakai S. Appl Phys Lett 1995;67:1818.

[159] Sasaki T, Mori Y, Yoshimura M. Opt Mater 2003;23:343.

[160] Nishioka M, Kanoh A, Yoshimura M, Mori Y, Sasaki T. J Cryst Growth 2005;279:76.

[161] Kawamura T, Yoshimura M, Shimizu Y, Nishioka M, Fukushima Y, Kaneda Y, et al. J Cryst Growth 2010;312:1118.

[162] Mori Y, Yoshimura M, Sasaki T, Takahashi Y. Abstract of the 6th international symposium on lasers, scintillators and non-linear optical materials (ISLNOM-6); October 20–23, 2013. P31, Shanghai, China.

[163] Py1neva NA, Kononovaa NG, Yurkina AM, Kokh AE, Bazarovab GG, Danilova VI, et al. Part of the SPIE conference on laser material crystal growth and nonlinear materials and devices. SPIE 1999; 3610:148.

[164] Kokh AE, Kononova NG. Solid-state Electron 2000;44:819.

[165] Yu XS, Hu ZG. J Cryst Growth 2010;312:2415.

[166] Batsanova LR, Egorov VA, Nikolaev AV. Dokl A N SSSR 1968;178:1317.

[167] Solovéva LP, Bakakin VV. Sov Phys Crystallogr 1970;15:802.

[168] Mei LF, Huang XY, Wang YB, Wu QJ, Wu BC, Chen CT. Z Fuer Kristallogr 1995;210:93.

[169] Mei LF, He CZ, Chen CT. J Cryst Growth 1993;132(3–4):609.

[170] Tang DY, Xia Y, Wu BC, Chen CT. J Cryst Growth 2001;222:125.

[171] Wang JY, Zhang CQ, Liu YG, Hu Z, Jiang MH, Chen CT, et al. J Mater Res 2003;18(10):2478.

[172] Wang XY, Yan X, Luo SY, Chen CT. J Cryst Growth 2011;318:610.

[173] Levin EM, McDaniel CL. J Am Ceram Soc 1962;45(8):355.

[174] Cong RH, Zhu JL, Wang YX, Yang T, Liao FH, Jin CQ, et al. Cryst Eng Commun 2009;11:1971.

[175] Becker P, Liebertz J, Bohatý L. J Cryst Growth 1999;203:149.

[176] Liebertz J. Z Kristallogr 1982;158:319.

[177] Teng B, Wang JY, Wang ZP, Jiang HD, Hu XB, Song RB, et al. J Cryst Growth 2001;224:280.

[178] Teng B, Wang JY, Wang ZP, Hu XB, Jiang HD, Liu H, et al. J Cryst Growth 2001;233:282.

[179] Teng B, Wang JY, Dong SM, Hu XB, Wang ZP. J Cryst Growth 2005;275:e615.

[180] Egorysheva AV, Skorikov VM. Inorg Mater 2009;45(13):1461.

6

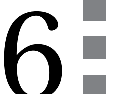

Growth Measures to Achieve Bulk Single Crystals of Transparent Semiconducting and Conducting Oxides

Zbigniew Galazka

LEIBNIZ INSTITUTE FOR CRYSTAL GROWTH, BERLIN, GERMANY

CHAPTER OUTLINE

6.1 Introduction **209**
6.2 Basics of TSO Thermodynamics **210**
6.3 Growth Techniques **212**
6.3.1 β-Ga_2O_3 212
6.3.2 ZnO 218
6.3.3 In_2O_3 223
6.3.4 SnO_2 228
6.4 Basic Electrical and Optical Properties of Bulk TSO Crystals **230**
6.5 Summary **235**
References **236**

6.1 Introduction

The exploration of oxides from the perspective of semiconductor science and technology offers exciting opportunities for uncovering new physics as well as developing novel devices with unprecedented performance and functionality. A number of binary and ternary oxides, such as β-Ga_2O_3, ZnO, In_2O_3, SnO_2, SnO, $BaSnO_3$ and $CuAlO_2$, are considered to be new wide band-gap electronic materials with continuously increasing exploration and development activities at the academic and industrial levels. Because such oxides exhibit both transparency in the visible spectrum, even down to deep ultraviolet wavelength region (DUV), and conducting behavior at the same time, they have been or can be used in a wide spectrum of electronic (particularly optoelectronic)

Handbook of Crystal Growth. http://dx.doi.org/10.1016/B978-0-444-63303-3.00006-7
Copyright © 2015 Elsevier B.V. All rights reserved.

applications. When the oxides are moderately doped, they behave as nondegenerate semiconductors and are called transparent semiconducting oxides (TSOs). The TSOs are used as DUV photodetectors [1], photodiodes [2,3], transparent thin-film transistors [3–9], light-emitting diodes [3,10–14], high-voltage transistors [15–17], Schottky diodes [3,18,19], spintronics [20], high-temperature gas sensors [21–23] and scintillators [24,25]. When the TSOs are prepared as polycrystalline or amorphous thin films, they can be highly doped, resulting in degenerate semiconductors with metallic-like conductivities; in this case, they are called transparent conducting oxides (TCOs). Such oxides are typically used as transparent electrodes for solar cells, in flat-panel displays and touch screens [26–30], and in energy-efficient windows [31,32].

Although various thin-film technologies (e.g., sputtering, pulsed laser deposition, molecular beam epitaxy, metal-organic chemical vapor deposition) can be easily applied to most of the TSOs and TCOs, truly bulk single crystals of such compounds are rarely obtained due to their high melting points and instabilities at high temperatures. Growing bulk single crystals of the TSOs and TCOs is a great challenge from both scientific and technological point of view. The availability of bulk TSOs/TCOs single crystals is a driving force for the development of novel electronic devices. In the case of the bulk single crystals, after a certain number of attempts in the 1960s, there was a long period in which the TSOs were forgotten to some extent. In the twenty-first century, the TSOs have been rediscovered and new compounds are being discovered, such as wide band-gap oxide semiconductors. This has resulted in rapid progress in state-of-the-art growth techniques for epitaxial films and bulk crystals, as well as a better understanding of the properties and mechanisms that control conductivity.

This chapter focuses on the growth and fundamental properties of selected TSO compounds (β-Ga_2O_3, ZnO, In_2O_3, and SnO_2), which have already been grown in the form of truly bulk single crystals. It discusses the origin of growth difficulties, different growth techniques (including gas phase, solution, and melt), and the basic quality and properties characterizing this class of materials. The materials described herein show semiconducting behavior; therefore, the discussion includes TSOs.

6.2 Basics of TSO Thermodynamics

A major problem in growing truly bulk single crystals from most of the TSOs, especially from the melt, is their thermochemical instability at elevated temperatures. In combination with high melting points (>1800 °C), this leads to strong decomposition and evaporation prior to melting. To minimize the decomposition of such compounds, a high oxygen partial pressure is required. Figure 6.1 shows the minimum oxygen partial pressures required for the stabilization of β-Ga_2O_3, ZnO, In_2O_3, and SnO_2 versus temperature [33]. Above each solid line, a corresponding compound exists in the solid phase, but in practice the required oxygen partial pressure must be higher than the minimum value by a factor of at least 10^4 to minimize decomposition.

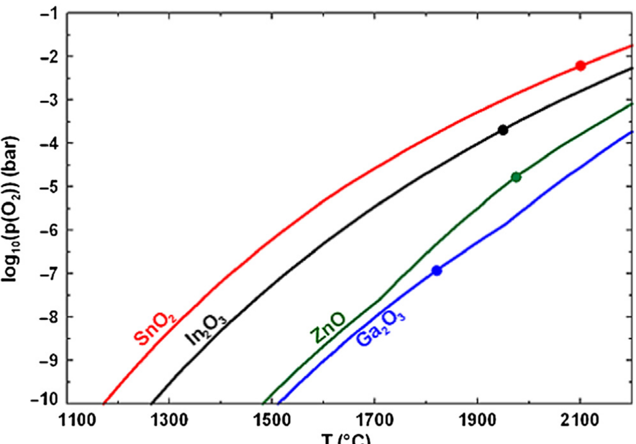

FIGURE 6.1 Stability plot showing the minimum oxygen partial pressure required for the stabilization of selected TSOs. The melting points of the corresponding TSOs are indicated by solid circles. TSO, transparent semiconducting oxide.

After scaling the minimum oxygen partial pressure at the melting points of the TSOs to that of β-Ga_2O_3, as shown in Table 6.1, it is easy to understand the difficulties in growing bulk single crystals of TSOs, especially from the melt (see Section 6.3).

At such high temperatures, the only metal crucible for melt growth techniques that can withstand small oxygen concentration is iridium or its alloys. Iridium easily oxidizes at low and moderate temperatures (roughly 600–1200 °C), but it is substantially intact at high temperatures. To avoid intensive oxidizing of iridium, instead of using an admixture of O_2 (up to ~2%) and a neutral atmosphere (e.g., N_2, Ar), a CO_2-containing growth atmosphere as a nonlinear oxygen source has been found to be a good solution for ZnO [69], β-Ga_2O_3 [70], and In_2O_3 [71]. CO_2 decomposes into $CO + {}^1/_2\ O_2$, thus providing more oxygen with increasing temperatures. In this way, a higher oxygen partial pressure could be provided at high temperatures (2–5%) while minimizing oxidation of the iridium crucible (and other metal components). Moreover, by applying an overpressure along with CO_2, a further increase of oxygen partial pressure and a lower decomposition rate could be achieved for ZnO [55] and β-Ga_2O_3 [70]. More details on using such dynamic, self-adjusting growth atmospheres can be found in Refs [72–74].

Table 6.1 Minimum Oxygen Partial Pressure Required for the Stabilization of Selected Transparent Semiconducting Oxide (TSO) Compounds at Their Melting Points

TSO	β-Ga_2O_3	ZnO	In_2O_3	SnO_2
Melting point (°C)	1820	1975	1950	>2100
Relative oxygen partial pressure	1	~100	~1000	~50,000

Values were normalized with respect to β-Ga_2O_3 (FactSage calculations).

The result of the decomposition of the TSOs are different volatile species, namely oxygen, metal monoxides and suboxides (GaO, Ga_2O, InO, In_2O, SnO), and free metals (Ga, Zn, In, Sn). The most volatile species (i.e., those having the highest partial pressure) are oxygen and Zn, SnO, In_2O, Ga_2O for β-Ga_2O_3, ZnO, In_2O_3, and SnO_2, respectively. Oxygen from CO_2 at atmospheric pressure is sufficient to decrease Ga_2O partial pressure to a level that enables the growth of Ga_2O_3 single crystals by the Czochralski method. This is, however, not the case for other TSO compounds. Other approaches have been found for growing crystals from the melt, such as CO_2 overpressure (in the case of ZnO) and a new crystal growth method using electromagnetic levitation (in the case of In_2O_3).

6.3 Growth Techniques

This section summarizes the growth techniques for obtaining bulk single crystals of β-Ga_2O_3, ZnO, In_2O_3, and SnO_2. The basic structural and physical properties of the TSOs are presented in Table 6.2. The bulk growth techniques are also discussed in more detail.

6.3.1 β-Ga_2O_3

Ga_2O_3 has five polymorphic phases: α, β, γ, δ, and ε. At high temperatures (>900 °C), only the β-phase is stable; therefore from the melt (melting point = 1820 °C), only the β-phase can be grown. For details on the polymorphic phases of Ga_2O_3, including their structure and transition temperatures, see Ref. [75]. When β-Ga_2O_3 is grown from the melt, it does

Table 6.2 Structural and Basic Physical Properties along with Growth Techniques for Selected TSOs

	β-Ga_2O_3	**ZnO**	**In_2O_3**	**SnO_2**
Structure	Monoclinic a = 12.214 Å b = 3.037 Å c = 5.798 Å β = 103.83°	Hexagonal (wurtzite) a = b = 3.250 Å c = 5.205 Å	Cubic (bixbyite) a = b = c = 10.117 Å	Tetragonal (rutile) a = b = 4.74 Å c = 3.18 Å
Melting point (°C)	1820	1975	1950	>2100
Density (g/cm^3)	6.00	5.61	7.12	6.95
Melt growth techniques	**1.** Verneuil **2.** OFZ **3.** EFG **4.** Czochralski	**1.** Cold crucible **2.** Bridgman	**1.** LASSCGM	–
Other bulk growth techniques	**1.** CVT **2.** Flux	**1.** CVT **2.** PVT **3.** Flux **4.** Hydrothermal	**1.** CVT **2.** PVT **3.** Flux	**1.** CVT **2.** PVT **3.** Flux

CVT, chemical vapor transport; PVT, physical vapor transport; OFZ, optical floating zone; EFG, edge-defined film-fed growth; TSO, transparent semiconducting oxide; LASSCGM, levitation-assisted self-seeding crystal growth method (for details on this novel growth technique, see Section 6.3.3).

not undergo any phase transition; this is also the case for postgrowth heat treatments. The single phase of β-Ga_2O_3 has been confirmed by X-ray powder diffraction and differential thermal analysis. Details of the crystal structure of β-Ga_2O_3 can be found in Ref. [76].

Although β-Ga_2O_3 undergoes quite intense decomposition at its melting point (1820 °C) at limited oxygen partial pressure (several percent), it is still the most stable compound as compared with other discussed TSOs. The growth techniques for obtaining bulk crystals can be divided into three groups (see also Table 6.2): growth from the gas phase (chemical vapor transport (CVT)), solution (flux), and melt (Verneuil, optical floating zone (OFZ), edge-defined film-fed growth (EFG), Czochralski).

Small β-Ga_2O_3 crystals were reported by Pajaczkowska et al. for the *CVT method*, in which the transport gas was N-H-Cl system [77]. The crystal coloration, from colorless through yellow and green-blue to blue, was found to be a function of growth temperature from below 1100 K to above 1200 K for the CVT method.

Small platelets or needle-shaped β-Ga_2O_3 crystals were obtained by the *flux method* from PbF_2 (98 wt%)–$PbSO_4$ (2 wt%) [78], Bi_2O_3 (90.8 wt%)–V_2O_5 (9.2 wt%) [79], and Bi_2O_3 (41 wt%)–B_2O_3 (59 wt%) [80] fluxes. Katz et al. [78] equilibrated the flux in a Pt crucible for 0.5–2 days at 1225 °C, then cooled at 4 K/h to 872 °C and air-quenched. The crystals were removed with dilute HNO_3; they had a size of 3–10 mm in length and a weight below 0.2 g. The Pb-impurity concentration was found to be at the level of 0.07–0.2 wt%. Garton et al. [79] obtained colorless β-Ga_2O_3 crystal plates up to 6 mm long and 1 mm thick. The initial temperature of a Pt crucible with the flux was 1300 °C; a slow cooling was performed to 900 °C, below which the flux was then quenched. Chani et al. [80] heated up a Pt crucible containing the flux to 1300 °C for 12 h, then kept it at that temperature for 5 h; afterwards it was cooled down to 1120 °C for 0.5 h, 600 °C for 24 h, and then to room temperature for 10 h. The crystals were removed from the flux by dilute HNO_3. The obtained crystals were bright green needles or platelets. The main disadvantages of that method are a small crystal size, high contamination by flux elements, and twinning.

The first reports on bulk β-Ga_2O_3 grown from the melt date back to 1960s, when the first bulk single crystals were grown by the *Verneuil* (or flame fusion) *method* [34,81–83]. Chase [81] used flow rates of 14 L/min for outer H_2, 1 L/min for inner O_2, and 7.5 L/min for outer O_2, which produced slightly oxygen-rich conditions that were found to be favorable. The crystals had dimensions of about 1 and 2.5 cm for diameter and length, respectively. Lorenz et al. [34] pointed out that crystals grown under oxidizing conditions were colorless, whereas those grown under reducing conditions were light blue. Harwig et al. [82,83] reported that β-Ga_2O_3 crystals doped with Mg were colorless, whereas those doped with Zr were light blue. The major problem for this technique is laminar twinning, which results from the high-temperature gradients present in the growth method.

Due to possibility of using high oxygen concentration in a growth chamber, the crucible-free *OFZ method* was successfully applied to growth β-Ga_2O_3 single crystals from the melt [12,31,35–38,40,84,85]. That method uses a sintered feed rod of Ga_2O_3 with a seed rod located underneath. A tip of the feed rod is molten by a light beam generated

by high-power lamps and focused by mirrors. Molten Ga_2O_3 contacts the seed and crystallizes thereon. By counterrotating the feed and seed rods and moving both downwards, the feed rod is gradually converted into a single crystal. In the OFZ furnace, Ueda et al. [35] used 3.5-kW halogen lamps, a growth rate of 15 mm/h, and a rotation of the sintered feed and seed rods of 17 rpm. The growth atmosphere was a varying mixture of $N_2 + O_2$ at a total flow rate of 0.2 m^3/h. When grown in pure O_2, the crystals were colorless and they became pale blue with increasing N_2 flow. The colorless crystals were electrical insulators, whereas the blue ones were semiconductors. When doped with Sn, β-Ga_2O_3 crystals were blue even when grown in pure O_2.

Tomm et al. [31] reported the growth of undoped, as well as Ge- and Ti-doped, β-Ga_2O_3 single crystals by the OFZ technique. The crystals were grown either in air or in pure oxygen, with a growth rate of 5 mm/h and counterrotation of feed and seed rods. The undoped and Ge-doped crystals were colorless, whereas those doped with Ti were pale purple. Shimamura and Villora [12] and Villora et al. [37,38] applied pulling and rotation rates of the feed and seed rods of 1–5 mm/h and 20 rpm, respectively; the atmosphere consisted of $N_2 + O_2$ with flow rates of 250 mL/min for both N_2 and O_2. The crystals were grown along <100>, <010>, and <001> axes. The crystal diameter was typically approximately 5–8 mm and the length was 50 mm, although 1-in diameter crystals were demonstrated as well, as shown in Figure 6.2. The rocking curve of the (400) peak of large β-Ga_2O_3 by the OFZ in Ref. [37] shows a very broad full width at half maximum (FWHM) over 300 arcsec and additional peaks, suggesting the presence of twins. Zhang et al. [84,85] used four halogen lamps, a growth rate of 5–10 mm/h, a rotation rate of 15 rpm, and air as the growth atmosphere with a flow of 0.2 m^3/h. The crystals were colorless with diameters of 6 mm and lengths of 20 mm. The FWHM of the rocking curve was about 100 arcsec. The crystals doped with 5 mol% of Sn were blue, whereas those with 10 mol% of Sn were deep blue. Ohira et al. [40] described the following conditions for the OFZ method: growth rate of 7.5–15 mm/h, counterrotation for the feed and seed rods of 20 rpm, and a growth atmosphere of dry air. The crystals were doped with 500 ppm of Sn.

Due to the particularities of the OFZ method (i.e., small cross-sectional area of the light beam) crystals with small diameters could be grown. Additionally, the temperature

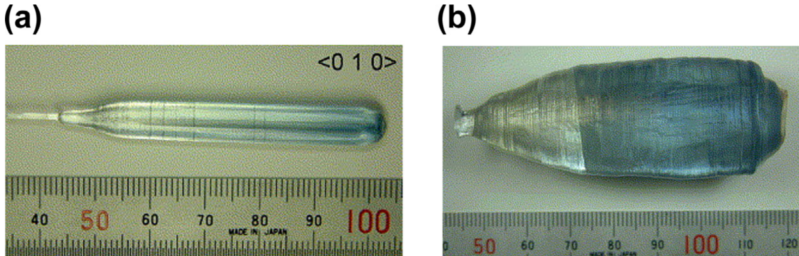

FIGURE 6.2 β-Ga_2O_3 single crystals obtained by the OFZ method: (a) about 6 mm in diameter and (b) 25 mm in diameter. OFZ, optical floating zone. *Reprinted from Ref. [37] with permission from Elsevier, Copyright 2004.*

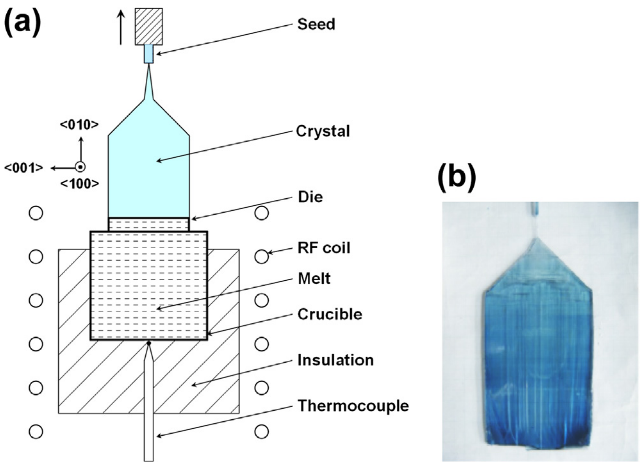

FIGURE 6.3 (a) Sketch of the EFG configuration. *(Based on Ref. [86].)* (b) β-Ga_2O_3 single crystal obtained by the EFG method, with a vertical cross-section of 2 × 3 in and thickness of 3 mm. EFG, edge-defined film-fed growth. *Reprinted from Ref. [86] with permission from Japan Society of Applied Physics and the author's consent (Hideo Aida), Copyright 2008.*

gradients in the vicinity of the growth interface are rather large, which, in combination with two strong cleavage planes and the twinning tendency, may deteriorate the structural quality of the grown crystals.

Another approach for growing bulk β-Ga_2O_3 single crystals from the melt involves the *EFG method* by Aida et al. [86]. That method (see Figure 6.3(a)) uses an inductively heated iridium crucible containing molten Ga_2O_3 and a die located on the top of the crucible with well-defined slits. The melt is transported to the top of the die by capillary forces, where a crystal seed is contacted and pulled up. The temperature gradients above the die allow for crystallization of the melt on the crystal seed to form a single crystal ribbon. The reported dimensions for the crystal ribbons were 3, 50, and 70 mm for the thickness, width, and length, respectively [86]. The crystals were blue in color. The etch pits density (EPD) and the rocking curve were reported to be $0.9–4 \cdot 10^5/cm^2$ and 75–160 arcsec, respectively [86]. An example of bulk β-Ga_2O_3 single crystals (vertical cross-section of 2 × 3 in, thickness of 3 mm) obtained by the EFG method is shown in Figure 6.3(b).

For mass production, a large crystal volume and high crystal quality is required. These conditions are typically satisfied by the *Czochralski method*, if a crystal can be grown by that technique. The possibility of growing β-Ga_2O_3 single crystals by the Czochralski method was first demonstrated by Tomm et al. [87] with the use of a dynamic, self-adjusting growth atmosphere consisting of 90% Ar and 10% CO_2. The crystals were transparent but bluish. The crystal diameter and length were 10 and 20 mm, respectively. A comprehensive study on Czochralski growth of β-Ga_2O_3 single crystals was performed by Galazka et al. [70]. In the Czochralski method (as shown in Figure 6.4), the Ga_2O_3 starting material is molten in an inductively heated iridium crucible. Next, a Ga_2O_3 crystal seed is brought into a contact with the melt. Then, after obtaining thermal equilibrium between the seed and the melt, the seed is slowly pulled up (typically 1–3 mm/h) while

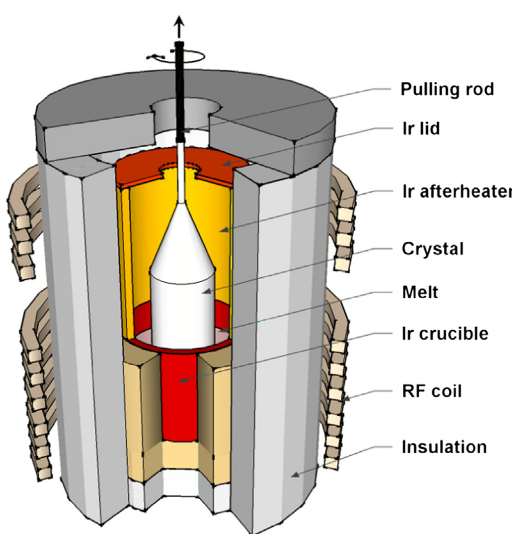

FIGURE 6.4 Sketch of a Czochralski growth furnace.

rotating (5–20 rpm). A seed diameter is slowly increased to a desired cylinder diameter, which is then grown to a predefined length. After that, the crystal is separated from the melt and slowly cooled down to room temperature (typically >15 h). The crystal diameter is controlled automatically by a PID (Proportional, Integral, Derivative) controller that reacts on mass changes and adequately regulates the temperature of the melt. The iridium crucible with possible iridium afterheater and a suitable thermal insulation all around the crucible constitute a Czochralski growth furnace. The growth furnace is placed inside a growth chamber, which in this case can withstand a high overpressure up to 20 bar, with the possibility of supplying a variety of growth atmospheres, such as oxidizing (O_2, CO_2), neutral (Ar, N_2), reducing (H_2, CO), and any combination thereof.

To grow β-Ga_2O_3 single crystals by the Czochralski method, only an oxidizing atmosphere should be used, keeping in mind that Ir components easily oxidize at low and moderate temperatures. The oxygen partial pressure in the growth chamber (provided by any manner) affects the decomposition rate of Ga_2O_3 and thus its stoichiometry; this in turn (rather indirectly) influences electrical and optical properties of the obtained crystals and, as a consequence, the crystal coloration. Other factors also have a high impact on crystal properties, quality, and overall appearance, such as the initial stoichiometry of the starting material, temperature gradients, type of atmosphere, and intentional doping (or unintentional impurities), because they all influence the growth behavior and the Ga_2O_3 stoichiometry. Table 6.3 summarizes the different atmospheres used to grow β-Ga_2O_3 single crystals by the Czochralski method and the resulting oxygen partial pressure along with the crystal appearance. The crystal surface is typically rough for low oxygen partial pressures (<0.02 bar) and smooth and shiny for higher oxygen partial pressures (see Figures 6.5(a) and 6.5(b)).

Table 6.3 Influence of the Different Growth Atmospheres and Dopants on Crystal Coloration and Quality Using the Czochralski Method

	$p(O_2)$ at Melting Point (atm)	Crystal Coloration	Crystal Quality	Note
10% CO_2 + 90% Ar (1 bar)	3.6×10^{-3}	Dark blue	Average	Tendency to spiral formation; high evaporation rate
50% CO_2 + 50% Ar (1 bar)	8.0×10^{-3}	Colorless to blue	Good	Moderate evaporation rate
100% CO_2 (1 bar)	1.2×10^{-2}	Light gray to blue	Good	Traces of C in the crystals
100% CO_2 (7 bar)	4.4×10^{-2}	Gray	Very good	Higher concentration of C in the crystal
2% O_2 + 98% Ar (1 bar)	2.0×10^{-2}	Blue	Average	High Ir oxidation.
Dopants at 100% CO_2 (1 bar)				
Sn^{4+} 800 ppm in the crystal	1.2×10^{-2}	Dark blue	Not good	Only very small crystal can be grown
Mg^{2+} 6–30 ppm in the crystal	1.2×10^{-2}	Yellowish	Very good	Stable growth

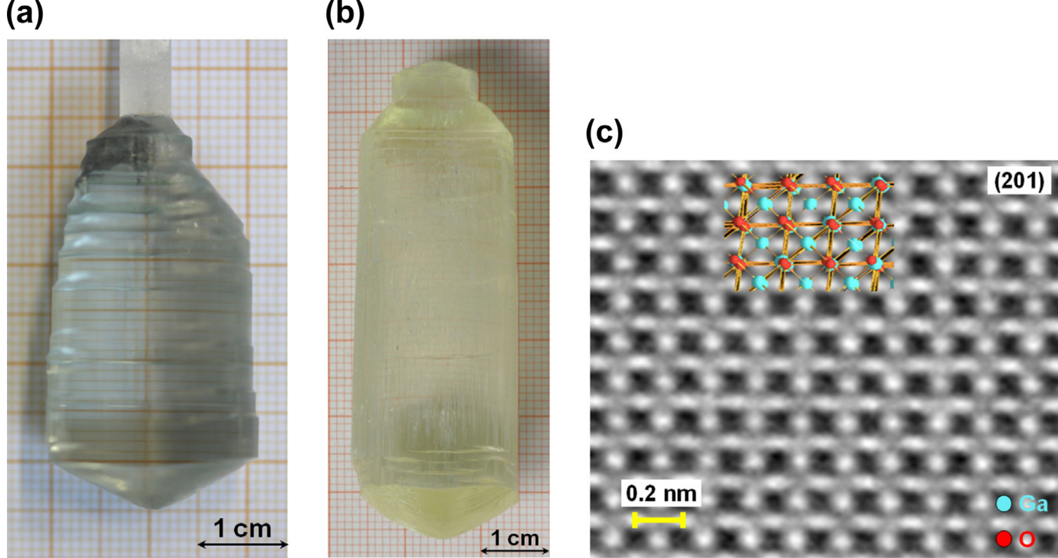

FIGURE 6.5 Selected β-Ga_2O_3 single crystals obtained by the Czochralski method under 100% CO_2: (a) undoped, 7 bar. *(Adapted from Ref. [70].)* (b) doped with Mg, 1 bar; and (c) high-resolution TEM image. *(Adapted from Ref. [70].)* TEM, transmission electron microscopy.

Figure 6.5 shows examples of undoped and Mg-doped β-Ga_2O_3 single crystals grown by the Czochralski method (see figure caption). Typically the crystal diameter and length are 20–22 mm and 2–3 in, respectively (crystal volume 15–25 cm^3). As the result of such advanced research, high-volume (2-in diameter) single crystals of β-Ga_2O_3 have been demonstrated by Galazka et al. [41] with use of the Czochralski method.

β-Ga_2O_3 has two strong cleavage planes parallel to the {100} and {001} planes; therefore, all the crystals were grown along <010> direction, parallel to both cleavage planes. Growing β-Ga_2O_3 crystals by the Czochralski method perpendicular to the cleavage planes is not advisable; in this case, a crystal hanging on a thin seed may break it very easily with a mass increase and/or due to thermal stresses. However, it is possible to grow the crystals by the Czochralski method with other orientations, deviating from the <100> and <001> directions to some extent. Small-diameter crystals along <100> and <001> directions were obtained by the OFZ method [37]; the Ga_2O_3 melt solidifies on the seed in accordance to the gravity vector, not opposite as in the case of the Czochralski method. Despite the two strong cleavage planes, it is possible to fabricate large, twin-free wafers of β-Ga_2O_3 obtained by the OFZ, EFG, and Czochralski methods.

The crystal quality of the β-Ga_2O_3 single crystals obtained by the Czochralski method is good. A typical value for the FWHM of the rocking curve of the (400) peak is around or much below 100 arcsec. Dislocations are parallel to the cleavage plane (100); therefore, they are not readily visible on (100) wafers, but they can be revealed in the crystal volume by laser scattering tomography [41]. Although the two cleavage planes make crystal fabrication difficult, it is a perfect situation for crystal investigation because extremely thin samples can be easily cleaved from the bulk crystals, which are very useful for spectroscopic and optical studies. An example of a high-resolution transmission electron microscopy (TEM) image is shown in Figure 6.5(c). It was possible to exfoliate just several atomic layers so that they present a real as-grown crystal structure that is not affected by any mechanical or chemical treatment. The exfoliated β-Ga_2O_3 is therefore a perfect model for investigating point defects.

6.3.2 ZnO

ZnO is the most investigated TSO material, with the longest research and development history. First reports on ZnO growth date back to the 1930s [88]. ZnO single crystals were grown from the vapor phase (physical vapor transport (PVT), CVT), solution (flux, top-seeded solution growth, hydrothermal methods), and melt (pressurized cold crucible, Bridgman method). The chemical, structural, and physical properties of ZnO are summarized in Ref. [88].

The *PVT method* uses the evaporation of ZnO starting material and its sublimation. In this process, Zn evaporates as a result of decomposition, which next oxidizes at lower temperatures to form ZnO. Typical growth conditions used by Helbig [48] for the PVT included a temperature at the growth zone of 1600 °C and a gas mixture of H_2 (2 L/h), N_2 (80 L/h) and O_2 (0.5–2 L/h). The crystals were up to 7 mm in diameter and up to 40 mm long. The crystals were also doped with a variety of elements, including Li, Na, Cu, Ga, In, and Mn.

Small bulk ZnO single crystals were also grown by the *CVT method* with different approaches using a variety of chemical transport agents. For example, variants of the

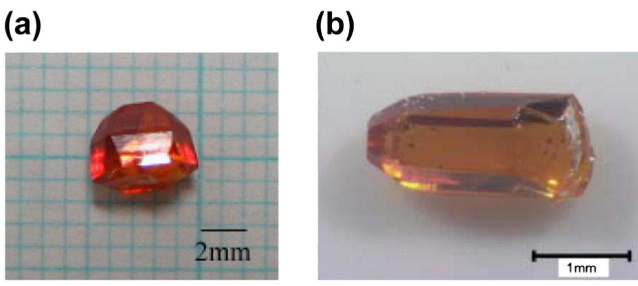

FIGURE 6.6 ZnO crystals grown by the CVT method: (a) *(Reprinted from Ref. [89] with permission from Elsevier, Copyright 2009.)*; and (b) *(Reprinted from Ref. [92] with permission from Elsevier, Copyright 2007.)* CVT, chemical vapor transport.

CVT method include the cold-wall CVT by Abe et al. [42], contactless CVT by Grasza et al. [43], and seeded CVT by Hong et al. [89]. The transport agents used in this growth method included H_2 [90], C [89,91], $CO_2 + Zn$ [92], $H_2 + C + H_2O$ or $N_2 + C + H_2O$ [93], $C + CO_2$ or Ar [44], $Ar + H_2O + CO_2$ [42], $C + CH_4$ [45], C + Cl [46], and many others (see e.g., Ref. [44]). Typically, quartz or graphite-covered quartz ampoules are used; the source temperature is smaller than 1200 °C and the crystallization takes place in the cooler region of the ampoule (e.g., by about 50 K). The growth rate is very small, usually less than 2 mm/day. The crystal size is typically a only a few millimeters and the crystal coloration varies depending on growth conditions; it changes from colorless, through yellowish or brownish to red, which is likely associated with a deviation from the stoichiometry. The crystallinity of the CVT-grown ZnO can be very good, as 30 and 44 arcsec of the FWHM of the rocking curves were reported [46,89]. Figure 6.6 shows examples of CVT-grown ZnO single crystals.

Another approach for ZnO growth proposed by Santailler et al. [47] is chemically assisted CVT, which is a combination of the CVT and PVT methods. It uses the evaporation of a ZnO starting material in the presence of a CO transport gas and sublimation on a crystal substrate (seed) of sapphire being covered with ZnO. By this method, high-purity single crystals of 46-mm diameter and 8-mm thickness were obtained, with a high growth rate of 0.4 mm/h. The growth temperature was between 800 and 1200 °C.

Bulk ZnO single crystals were grown form different *fluxes*, such as $V_2O_5 + B_2O_3$ and $V_2O_5 + MoO_3$ by Kunihiko et al. [94], PbF_2 by Li et al. [95], and hydrous KOH and NaOH by Ushio et al. [96]. In the first case [94], the top-seeded solution growth was used with the following compositions: (1) 76–80 mol% ZnO and 20–24 mol% $V_2O_5 + B_2O_3$ and (2) 52 mol% ZnO and 48 mol% $V_2O_5 + MoO_3$. The flux was molten within an inductively heated Pt crucible. By this method, polycrystals were obtained with maximum single crystal grains of $10 \times 5 \times 2$ mm^3. The crystal coloration was pale yellow to brown. The obtained crystals contained a very high concentration of flux elements, between 0.6 and 1.7 wt%. In the second case [95], the composition of 22% ZnO and 78% of PbF_2, a Pt crucible, a furnace temperature of 1100 °C, and oxygen flow were used. The obtained crystals were up to 25 mm in diameter and 5–8 mm thick. The crystals, however, suffered from Pb and F impurities at the levels of 390 and 40 ppm, respectively. In the third case

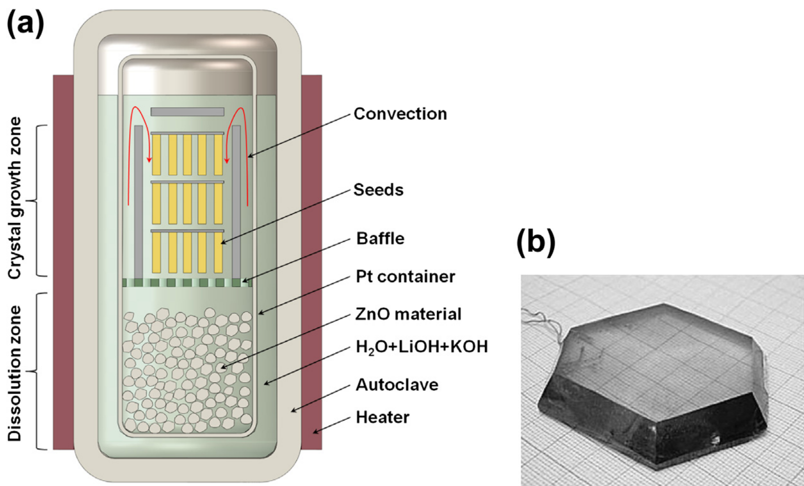

FIGURE 6.7 (a) Sketch of a hydrothermal growth system. *(Based on Ref. [51].)* (b) A 2-in size ZnO single crystal obtained by the hydrothermal method. *Reprinted from Ref. [102] with permission from Elsevier, Copyright 2008.*

[96], needle-shaped crystals were obtained with a size of 0.5–1 mm in diameter up to 18 mm long, with a crystal coloration from white through brown to black, depending on the growth temperature (450–900 °C) and time.

The most successful technique for growing large ZnO single crystals of high quality is the *hydrothermal method* described by various authors, including Croxall et al., Sakagami, Sekiguchi et al., Dem'yanets et al., Ohshima et al., Maeda et al., Dhanaraj et al., Ehrentraut et al., Wang et al., and Zuo et al. [49–53,97–103]. This method, shown schematically in Figure 6.7(a), is conducted in autoclaves made of steel with a platinum, silver, or titanium-alloy liner to isolate the growth environment from the autoclave containing an aqua alkaline solution of KOH and NaOH (mineralizer). The interior of the autoclave is divided into dissolution and growth zones by a baffle with an opening. In the bottom dissolution zone high purity ZnO powder is dissolved within the solution, while in the upper growth zone a number of ZnO crystal seeds are located. A temperature difference between both zones (lower in the growth zone by 8–80 K) initiates convection, which transports ZnO from the dissolution zone to the growth zone, where ZnO crystallizes on the seeds. The typical temperature in the dissolution zone is between 270 and 400 °C, while the pressure is in the range of 100–1400 atm. The growth rate is very low, below 1 mm/day, but on the other hand many crystals can be grown simultaneously in one single run, which takes usually several weeks. Exemplary hardware parameters and growth conditions described by Dem'yanets and Lyutin in Ref. [102] are as follows:

1. Diameter and height of the inner container of the autoclave of 280 and 1000 mm, respectively
2. Outer heaters disposed outside the autoclave wall and inner heaters disposed between the inner container and autoclave walls

3. The baffle located in the middle of the container height
4. 96–100 crystal seeds in the form of plates parallel to the (0001) face
5. Solution composition of KOH (3.5 mol%) + LiOH (0.5–1 mol%) + NH_4OH (0.5–1 mol%)
6. Solution temperature and pressure of 330–360 °C and 30–40 MPa, respectively
7. Temperature difference between the growth and dissolution zones of 8–15 K
8. Growth rate of 0.15–0.2 mm/day.

As large as 3-in diameter ZnO single crystals were reported by Ehrentraut et al. [101] and Dem'yanets and Lyutin [102], although the thickness is smaller (up to 15 mm). An example of a 2-in diameter ZnO single crystal is shown in Figure 6.7(b). Different crystal coloration was reported: colorless, green, pale green, or pale yellow, depending on the growth conditions. The structural quality of hydrothermally grown ZnO crystals is very good, for example, Maeda et al. [51] reported the following values: a FWHM of the rocking curve of 18 arcsec and an EPD less than $80/cm^2$. Also, the impurity level from the alkaline solvents is very low—0.9 and 0.3 ppm for Li and K, respectively—although other impurities might be still present.

The high instability of ZnO at high temperatures and high melting point (1975 °C) makes the growth of ZnO single crystals from the melt challenging. So far, only two growth techniques from the melt have successfully been applied for ZnO: the pressurized cold crucible [54,104,105] and the Bridgman [55,69,106–109] methods.

In the *pressurized cold crucible method* by Nause [104] and Nause and Nemeth [105], the interior of ZnO starting material is melted directly by a radio-frequency (RF) induction heating under overpressure (between 1 and 100 atm) of oxygen to minimize the decomposition of ZnO. The outer part of the ZnO starting material is cooled by a water-cooled segmented Cu crucible; therefore, it forms a self-created crucible for the molten ZnO. During cooling down by lowering the crucible away from the heater, the ZnO melt crystalizes randomly (no crystal seed) with a number of single crystal blocks being formed, from which single crystal parts or wafers can be fabricated, as shown in Figure 6.8. A crystal size of 2 in, EPD of $10^4/cm^2$, and FWHM of the rocking curve of 49 arcsec were reported [105].

Growth of ZnO single crystals from a melt contained in an inductively heated *iridium crucible* was first reported by Schulz et al. [69], who used the vertical Bridgman method (Figure 6.9(a)). The bottom part of the crucible is conically shaped, with a small cylindrical tip to accommodate a ZnO crystal seed. To minimize the decomposition of ZnO and avoid oxidation of iridium, a CO_2 growth atmosphere was used under an overpressure of 5–20 bars. A slow cool-down of the crucible at a rate of 25 K/h at well-defined axial temperature gradients of approximately 10 K/h cause crystallization of ZnO melt starting from the seed in the upward direction at a rate of several millimeters per hour [55,69]. The growth direction was [0001]. A direct contact of the crystal with the crucible wall and the possible expansion of ZnO solid during cooling [106] may cause small cracks at the crystal periphery. The crystals were removed from the Ir crucibles by

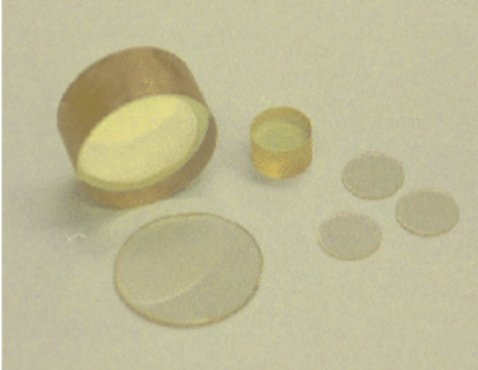

FIGURE 6.8 Bulk ZnO single crystals and wafers obtained from the melt by the cold crucible method. *Reprinted from Ref. [105] with permission from IOP publishing and author's consent (Catherine Nause and Bill Nemeth), Copyright 2005.*

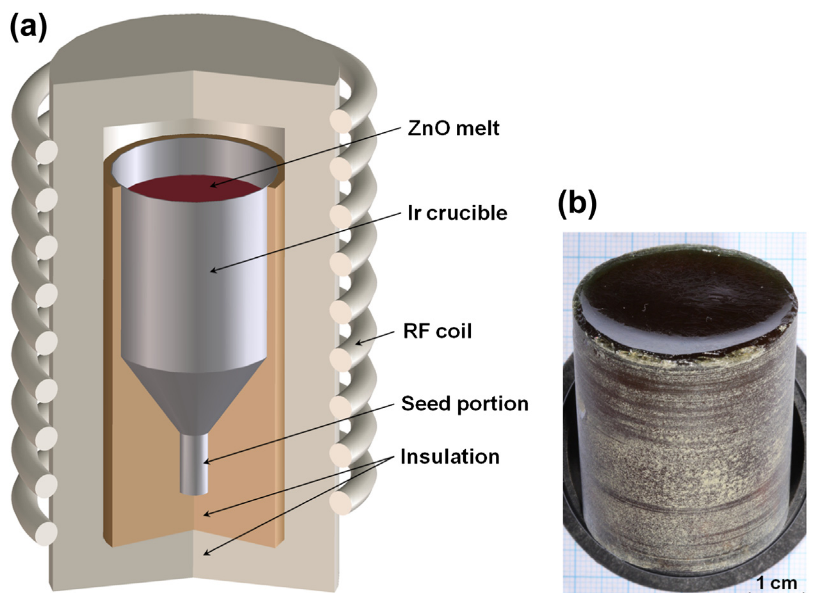

FIGURE 6.9 (a) Sketch of a vertical Bridgman growth furnace. (b) ZnO single crystal obtained by the Bridgman method. *Photograph courtesy of Detlev Schulz, IKZ, Berlin, Germany.*

a core-drill. In this way, single crystals of 33 mm in diameter and 2 in long were obtained (Figure 6.9(b)), from which epi-ready wafers could be prepared. As-grown ZnO crystals are typically red to orange or pale green due to the presence of Zn particles [110] produced during the ZnO decomposition at high temperatures. The crystals become pale yellow or colorless and transparent after annealing in an oxidizing atmosphere at

900–1100 °C for several hours. The impurity concentration in ZnO crystals grown by the Bridgman method is typically smaller than that in ZnO crystals obtained by the hydrothermal method when high-purity ZnO starting material (5N) is used [108]. The FWHM of the rocking curve was reported to be as low as 22 arcsec [69]. Doping ZnO with Mg at concentration up to 4 mol% deteriorates crystal quality [109] with increasing Mg concentration. The measured equilibrium distribution coefficient of Mg in the ZnO melt is 1.32–1.4. Despite the high Mg concentration, the ZnO crystals remain semiconducting. Also, the coloration of Mg:ZnO is almost the same as that of undoped ZnO.

6.3.3 In_2O_3

In_2O_3 is much more unstable than β-Ga_2O_3 and ZnO (see Table 6.1) at high temperatures; therefore, it could not be grown from the melt by the current state-of-the-art growth techniques. This is why only very small bulk In_2O_3 single crystals were grown from the gas phase by CVT [56,57,111] and its variant called vapor phase reaction [58,59,112], from the flux [61,62,113,114], and by electrolysis [60]. Galazka et al. [63,71,115,116] introduced a novel crystal growth method for obtaining truly bulk In_2O_3 single crystals from the melt.

For the *CVT* method, De Wit [56] used HCl vapor (at 0.02 bar) as the transport agent inside a sealed quartz ampoule containing the powdered In_2O_3 starting material. The part of the ampoule with In_2O_3 was heated up to 950 °C, while the growth took place at a cooler region of the ampoule at 680–720 °C, with a growth rate of 4 mg/h. Small green octahedral crystals (1 mm^3) were obtained after several days of growth. In the case of I_2 and Cl_2 agents, there was no chemical transport and the crystals could not be grown. Nitsche [111] demonstrated the successful growth of In_2O_3 crystals with the use of $I_2 + S_2$ as transport agents. The obtained crystals were light green and $3 \times 3 \times 3$ mm^3 in size. The same transport agents and a sealed quartz ampoule were used by Scherer et al. [57] to grow green single crystals of size $3 \times 3 \times 1$ mm^3. Another vapor phase growth of In_2O_3 was proposed in Refs [58,59,112]. In the case of the vapor phase reaction, the starting material to be transported is provided in the gas phase; in classic CVT, it is provided in the solid phase.

In the case of the *vapor phase reaction*, Weiher [58] proposed a mixture of metallic In and carbon, which were placed in a porcelain crucible and heated at 1000 °C for 24 h in air. In this way, pale yellow, needle-shaped crystals of $0.5 \times 0.5 \times 5$ mm^3 in size were grown. According to Shimada [112], In_2O_3 powder mixed with SnO_2 and graphite powders was heated at 960–1100 °C for 3–6 h in N_2. Due to the reaction of In_2O_3 and SnO_2 with graphite, gaseous In_2O and SnO were formed, which next reacted together to form In_2O_3 solid and Sn liquid. In this way, green or yellowish green needle-shaped crystals were obtained, with a size of $0.1 \times 0.1 \times 10$ mm^3. In another approach reported by Shimada [59], a system of graphite/In_2O_3, graphite/In, graphite/In_2O_3/In, and In_2O_3/In was used in a closed porcelain crucible, which upon heating to 960–1200 °C provided In_2O or In vapor, which next reacted with oxygen from air to form In_2O_3 single crystals.

The best results were obtained for a graphite/In_2O_3 system at 1000 °C, which produced yellow needle-shaped crystals of $0.5 \times 0.5 \times 8$ mm^3 in size.

The *flux method* was first applied to the growth of In_2O_3 crystals by Remeika and Spencer [61]. The In_2O_3 starting material was placed along with the flux consisting of PbO and B_2O_3 into a Pt crucible with a Pt cover and melted at 1200 °C. After holding the flux for 4 h, the temperature was lowered at the rate of 10 K/h. At approximately 500 °C, the crucible with the flux was removed from the furnace and cooled down naturally. Next, the crucible was immersed in a solution of HNO_3 and H_2O, which dissolved the flux and released unaffected crystals. The obtained crystals were prismatic platelets of size $10 \times 10 \times 1$ mm^3, whereas the color was slightly yellow-green. The same flux was used by Chase [113,114], but the temperature was higher (1250 °C), the cooling rate was slower (2.3–4 K/h), and the crucible was removed from the furnace at 900 °C. The obtained crystals were black and contaminated with flux elements, with a size of $5 \times 5 \times 3$ mm^3. However, doping In_2O_3 with Mg at 0.16 and 0.23 wt% produced green and yellow colors, respectively, whereas the size was $2 \times 2 \times 1$ mm^3. Chase [114] used PbO–B_2O_3 flux with the following proportions: $In_2O_3 = 5$ mol%, PbO = 75 mol%, and $B_2O_3 = 20$ mol%. The growth was conducted in a Pt crucible, where the flux was held at 1250 °C for 4–10 h and then cooled down to 900 °C, with a cooling rate of 2.3–10 K/h. The crystals were removed by 20% HNO_3. Many defects in the crystals were reported: dislocations, striations, and trapped flux elements. Very similar growth conditions to those of Ref. [61] for flux-grown In_2O_3 were reported recently by Hagleitner et al. [62]. The obtained crystals intentionally doped with Mg (about 1380 ppm) were yellow thin platelets composed of crystal domains of approximately 2×2 mm^2 in size (Figure 6.10). The crystals were highly contaminated with Pb (~4300 ppm), Pt (~155 ppm), and other impurities.

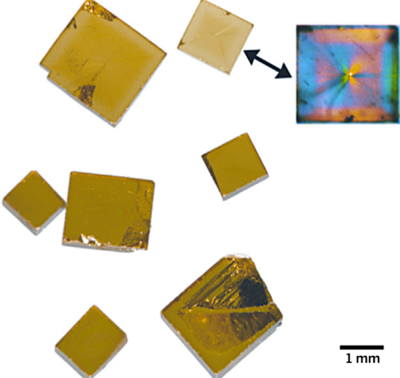

FIGURE 6.10 Small bulk In_2O_3 single crystals obtained by the flux method, with a front size of about 2×2 mm^2. *Reprinted from Ref. [62] with permission from the American physical society and author's consent (Lynn A. Boatner), Copyright 2012.*

In_2O_3 crystals grown by *molten salt electrolysis* were reported by Teweldemedhin et al. [60], using a mixture of In_2O_3-Li_2MoO_4-MoO_3 in the form of a fine powder placed into a porcelain or alumina crucible. Electrolysis was carried out at a temperature of 1113 K by passing a constant current of 35 mA for about 6 days. The crystals were grown on a platinum cathode of 0.5×2 cm size. The anode used was a platinum foil. The crystal color ranged from dark green to green yellow.

Such small In_2O_3 crystals obtained by the previously mentioned techniques are suitable for many research studies, but they are not sufficient for practical applications, such as substrates for homo- and heteroepitaxy. Moreover, because such crystals were grown at low temperatures (<1250 °C; i.e., far away from the melting point, which is about 1950 °C), the crystal properties may be different from crystals grown at higher temperatures.

Galazka et al. [71] reported truly bulk In_2O_3 single crystals (>1-in diameter) grown from the melt for the first time, as obtained by a novel crystal growth technique called the *levitation-assisted self-seeding crystal growth method* (LASSCGM) [115,116]. This approach uses In_2O_3 decomposition as a driving force for the melting and crystallization process instead of stabilizing of In_2O_3 at high temperatures (problem inversion). In terms of In_2O_3 crystal growth from the melt, the principle idea was to convert the initially insulating or semiconducting In_2O_3 starting material, which was placed in an iridium crucible, into an electrical conductor in the liquid phase. Electromagnetic levitation of the molten In_2O_3 was used inside the iridium crucible, which was heated inductively by an RF coil. To induce an eddy current inside the In_2O_3 starting material, the crucible wall thickness must be smaller than the penetration depth of the electromagnetic field. The conversion of the insulating/semiconducting starting material into the conducting state is performed via controlled decomposition by providing a limited oxygen concentration (still at the level of 2–6%, typically obtained by decomposition of CO_2 used as the growth atmosphere). During the decomposition, all possible species are formed in the gas phase, including metallic indium—a fraction of which remains in the liquid phase of molten In_2O_3, giving rise to the electrical conductivity.

It is to be noted that the liquid indium in the In_2O_3 melt has high chemical activity and tends to form a eutectic system with the iridium crucible, and the electromagnetic levitation separates, at least partly, liquid In_2O_3 from the crucible wall. Additionally, the crucible requires a cover of a special design, which has one or more openings with a total cross-sectional area equal to 5–15% of the crucible's cross-sectional area. This is to effectively evacuate gaseous decomposition products and ensure low-temperature gradients inside the crucible. If the crucible is fully or partly open, melting may not be completed. On the other hand, if the crucible if fully enclosed, decomposition products may build up an overpressure, leading to an explosion at a certain point. Finally, to obtain a single crystal, a seed is required, which cannot be provided externally. In this method, a seed is self-created by levitating a portion of the melt and thus forming a liquid neck between the two liquid regions of In_2O_3, which act as a seed during the solidification process.

The principle of the LASSCGM is shown in Figure 6.11. Initially (Figure 6.11(a)), the In_2O_3 starting material inside the Ir crucible is heated up normally by heat conduction and radiation from the crucible wall, which in turn is heated up inductively by an RF coil. At high temperatures, roughly above 1800 °C (Figure 6.11(b)), the decomposition rate of In_2O_3 is quite high and it becomes conducting, especially near the hottest region of the crucible, where a weak eddy current is induced inside In_2O_3. When approaching the melting point, which is around 1950 °C (Figure 6.11(c)), the decomposition rate is very high and In_2O_3 becomes more conducting. As a result, the eddy current is induced in a larger area of In_2O_3 in the vicinity of the crucible wall, which speeds up melting of the In_2O_3 starting material. The electrical conductivity of molten In_2O_3 is higher (due to advanced decomposition) and the eddy current flowing through it induces a magnetic field. This opposes the magnetic field from the coil to such an extent that it overcomes gravity forces and rises a portion of the melt inside the crucible, depending on the mutual crucible-coil position and their configurations, the design of the evacuation openings in the lid and the top thermal insulation, and the amount of the starting material. The neck thickness can be controlled by several ways, such as the geometrical

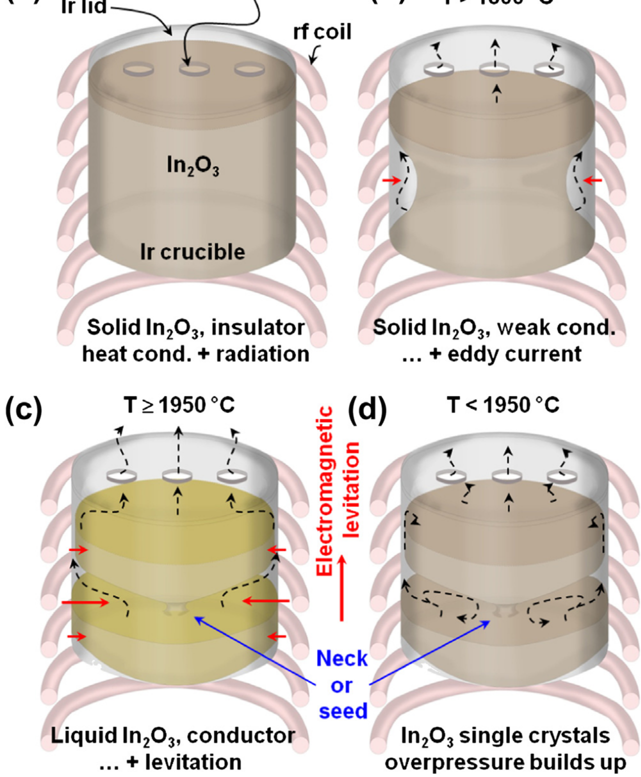

FIGURE 6.11 Successive stages of the LASSCGM: (a) In_2O_3 at the initial stage, before heating up; (b) In_2O_3 before melting; (c) In_2O_3 in the liquid phase; and (d) In_2O_3 single crystals after crystallization. Dashed arrows indicate decomposition products, whereas horizontal solid arrows indicate an eddy current. LASSCGM, levitation-assisted self-seeding crystal growth method. *Reprinted from Ref. [116] with permission from Elsevier, Copyright 2014.*

design of the growth furnace (including the coil, crucible, and the lid), soaking/overheating time, and the amount of the starting material. After reaching the final temperature point, the furnace must be cooled down very quickly, at least to the solidification point, because the decomposition rate of the liquid In_2O_3 is about as high as 20 wt% per hour. During solidification, two single crystals are formed on the opposite sides of the seed (Figure 6.11(d)). If the liquid neck is broken before solidification, single crystals will not form, only polycrystals.

Because there is no visual access to the interior of the crucible, all important information is gathered by external monitoring devices, such as a pyrometer/thermocouple for temperature, mass spectrometer/gas analyzer for oxygen concentration, and a balance for mass losses from the crucible. For more technical and scientific details on LASSCGM, including different furnace configurations, see Refs [115,116].

Figure 6.12(a) shows an exemplary In_2O_3 single crystal obtained from the LASSCGM. The crystal thickness is between 5 and 15 mm, whereas the diameter corresponds to the inner crucible diameter (in this case, ~40 mm). The dark coloration of the as-grown crystal is due to the presence of metallic indium particles [116,117], which are responsible for light extinction (absorption and scattering). After annealing in the presence of oxygen at a temperature of >700 °C for at least several hours, In nano-particles are oxidized and the crystals become yellowish and fully transparent (Figure 6.12(b)).

Even though the crystals were obtained at such extreme conditions, their structural quality is quite good. The FWHM of the rocking curve could be as low as 28 arcsec, whereas the EPD is typically between 5×10^4 and $3 \times 10^5/cm^2$, although there are large areas of very low EPD ($<10^4$) [63]. Figure 6.12(c) shows a high-resolution TEM image of a defect-free (111) plane of cubic In_2O_3. The hexagonal pattern of the (111) plane fits very well to the c-plane of hexagonal InN (lattice mismatch = 1%), and high quality InN has already been grown on melt-grown In_2O_3 substrates by plasma-assisted molecular beam epitaxy (PAMBE) [118]. The main detected impurities (by inductively coupled plasma–optical emission spectroscopy) include the following (in wt ppm): Fe = 16, Al = 11, Ca = 8, Ti = 8, Cr = 5, Co = 3, Ni = 1.6, Cu < 2, and Zr < 1.3 [63].

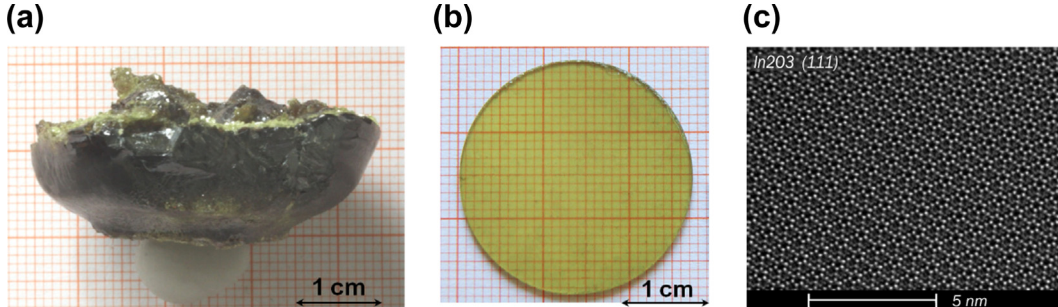

FIGURE 6.12 (a) Bulk In_2O_3 single crystal obtained by the LASSCGM. (b) In_2O_3 wafer after annealing in an oxidizing atmosphere; *(Adapted from Ref. [116] with permission from Elsevier, Copyright 2014.)* (c) High-resolution TEM image of the (111) plane. LASSCGM, levitation-assisted self-seeding crystal growth method; TEM, transmission electron microscopy. *Reprinted from Ref. [71] with permission from Elsevier, Copyright 2013.*

6.3.4 SnO_2

As shown in Figure 6.1 and Table 6.1, SnO_2 is the most unstable compound at high temperatures as compared with the previously discussed materials. Growing SnO_2 from the melt is not possible using the current state-of-the-art growth techniques. So far, SnO_2 single crystals have been grown from the gas phase and flux only.

Matsumoto et al. [119] applied the *CVT method* to obtain SnO_2 crystals with use of iodine and sulfur transport agents. SnO_2 powder, prepared by heating hydrous stannic oxide at 800 °C, was placed in a silica ampoule together with iodine and sulfur, which was then evacuated to 10^{-6}–10^{-7} bar, sealed off, and heated in an electric furnace. The temperature of the hotter furnace part varied between 700 and 1180 °C, whereas the cooler part was lower by 100, 200, or 300 K. The transport time was typically 2 or 3 days, and cooling to room temperature was a half-day. The obtained crystals were dark and were a maximum of 2 mm in size. The dark coloration was partly removed by annealing in oxygen at 1000 °C for 1 week. Fonstad et al. [64,120] applied the vapor phase reaction method. To produce SnO_2 crystals, gaseous stannic chloride, hydrogen, and oxygen reacted inside a quartz tube at 1250 °C and 0.01 bar pressure.

Another growth from the vapor phase includes the *PVT* [65–67,121–123], which involves the decomposition of SnO_2 into SnO and oxygen at high temperatures (vaporization zone) and reoxidation of SnO to SnO_2 at lower temperatures (growth zone). Marley et al. [65,121] used an alumina ceramic muffle tube furnace with a vaporization zone held at 1650 °C and a longer zone with a temperature gradient of 20 K/in, where crystal growth occurred on a removable mullite tube. Different growth atmospheres (or carrier gases) were tested, such as neutral gases, oxygen, and oxygen in combination with either argon, nitrogen or helium. N_2 and Ar led to a rapid growth (due to the high decomposition rate) and produced low-quality crystals. On the other hand, O_2 led to very small growth rates and very small crystals. A combination of O_2 and N_2 or Ar produced crystals of $25 \times 2 \times 2$ mm^3 in size (24 h growth), but they contained large voids. The best results were obtained for an $O_2 + He$ growth atmosphere. The crystals were colorless with a size of $30 \times 4 \times 2$ mm^3, and they were free of gross imperfections. The growth habit of the crystals was found to be dependent on the crystallization temperature: between 1620 and 1570 °C, rods were formed; between 1570 and 1460 °C, twinned plates were formed; and between 1460 and 1300 °C, needles were formed. The EPD on the {100} faces of quenched and slowly cooled-down crystals was as high as 10^8 cm^2; on {110} faces, it was 10^2–10^3 cm^2; and in the interior of the crystals after cleaving, it was 0–10^2 cm^2 [124]. The crystals were also annealed at different conditions (air, O_2, Ar, also quenched) and doped with Sb (300 ppm). Reed et al. [122] grew the crystals in the presence of tin metal in order to lower the operating temperature by lowering the oxygen partial pressure and increasing the SnO partial pressure being formed by oxidizing tin metal. This allowed the growth to be performed in a quartz tube. The crystals were up to 30 mm long and up to 5 mm across. A number of impurities (Si, Mg, Cr, Al, Cu, and Ca) were found in nominally undoped crystals. SnO_2 crystals were also intentionally doped

with Cr, Nb, Mn, and Co. Summit et al. [123] used the same setup as in Ref. [121]. When the crystals were cooled down rapidly, they became brown. Doping with Sb made the SnO_2 crystals blue. Thiel et al. [66] applied an alumina furnace and a N_2 growth atmosphere with a small admixture of H_2. The furnace temperature was 1450 °C. The average crystal size was $3 \times 3 \times 15$ mm, whereas the maximum size was $7 \times 7 \times 20$ mm^3. Most of the crystals were colorless, but some of them were pink or violet. The crystals had a relatively high EPD, were twinned, and some of them were hollow. The main impurities detected in the crystals at a level above 10 ppm were Na, Fe, Si, and Ca.

Galazka et al. [67] applied the *PVT method* with an iridium crucible containing the SnO_2 starting material, which was covered by a ring-shaped seed holder acting as a nest for a circular sapphire or rutile crystal seed (or substrate). The crucible was placed inside thermal insulation and was heated up inductively. The furnace for that PVT method is schematically shown in Figure 6.13(a). The source of the oxygen was CO_2, which provided a variable oxygen concentration versus temperature. Figure 6.14 shows the relationship between oxygen, the partial pressure from CO_2, and SnO partial pressure resulting from the decomposition of SnO_2 versus temperature. At oxygen-rich conditions the crystals were orange or pink-orange and electrical insulators; at approximately the same oxygen and SnO partial pressures, the crystals were brownish; while at SnO-rich conditions, the crystals were dark violet to almost black (for high SnO partial pressure). In the latter two cases, the crystals were semiconductors. The brownish crystals turned pink or colorless by annealing in the presence of oxygen at temperatures of at least 1000 °C for at least several hours. For these specific growth conditions, the best results were obtained for a substrate temperature between approximately 1480 and 1580 °C and a source temperature that was higher by 100–130 K when using CO_2 growth atmosphere at atmospheric pressure. The optimum growth rate was 0.5–0.6 g/h.

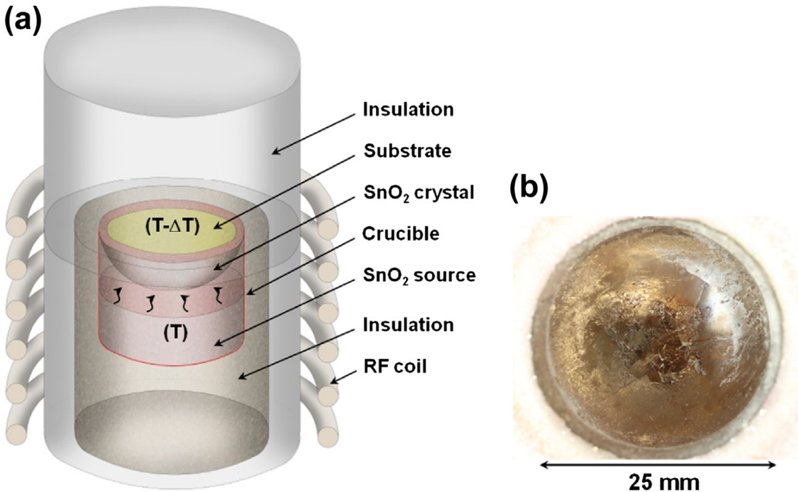

FIGURE 6.13 (a) Sketch of a PVT growth furnace. (b) Bulk SnO_2 single crystal of 1-in diameter grown by the PVT method on an R-plane sapphire substrate. PVT, physical vapor transport. *Reprinted from Ref. [67].*

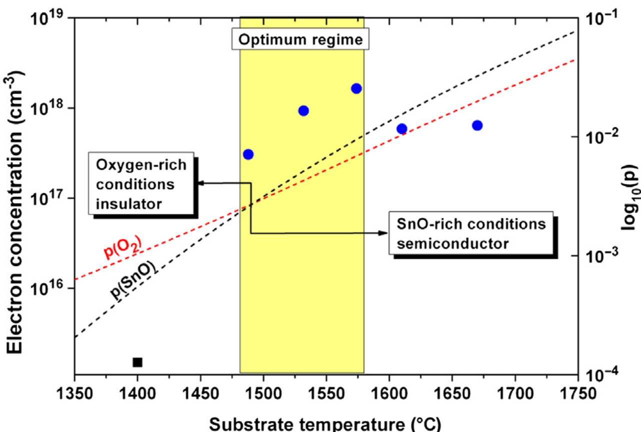

FIGURE 6.14 Relationship between free electron concentration and growth conditions: substrate temperature and p(SnO)/p(O_2) partial pressure. The black square at 1400 °C indicates the insulating state. *Reprinted from Ref. [67].*

In this way, large SnO_2 single crystals were obtained, 25 mm in diameter and 10–15 mm thick (Figure 6.13(b)), from which substrates for epitaxy could be fabricated. The FWHM of the rocking curve of the (200) peak was around 35 arcsec. The impurity level in the grown crystals was very low; the highest content was 10 wt ppm for Al and Si. Fe was below 5 wt ppm, while Cu, Ca, Mg, and Zr were below 1 wt ppm.

The *flux method* to grow SnO_2 crystals was first applied by Kunkle et al. [68]. The growth was carried out from Cu_2O flux (2 parts Cu_2O to 1 part SnO_2 by volume) in a platinum crucible placed in a muffle furnace. The temperature at the base of the crucible was 1250 °C, while at the top it was 100 K lower. The growth time was 1 week, after which the furnace was switched off and it was cooled down to room temperature naturally. The crystals were separated from the flux by HCl. The crystals were typically needles, with a 1-mm^2 cross-section and 10–15 mm in length. The crystals were contaminated with Cu (0.002 wt%) and Si (0.02 wt%). The same flux was applied by Kawamura et al. [125] with the use of a seed and Cr dopant. The growth was performed at 1290 °C. The use of Zn_2SnO_4 containing B_2O_3–V_2O_5 flux by Shimada et al. [126] resulted in needle-shaped SnO_2 crystals of pale brown to brown coloration. The same authors [127] also used Bi_2O_3–V_2O_5 flux. The growth runs were performed in a Pt crucible that was soaked at 1300 °C for 20 h and then cooled down to 900–1000 °C at the rate of 5 K/h. The crystals were removed from the flux by HNO_3. The obtained SnO_2 crystals were needles or small plates with pale red coloration.

6.4 Basic Electrical and Optical Properties of Bulk TSO Crystals

In addition to the availability of bulk crystals, an important criterion for the practical application of the TSOs are suitable properties. In the case of this class of electronic materials, the main properties include, among other ones, electrical properties

(conduction type, free carrier concentration/resistivity, and free carrier mobility) and transparency in the visible/ultraviolet spectrum. In other words, the TSOs/TCOs have, in addition to electrical properties, wide bandgaps that offer a number of applications, as summarized in the introduction section.

Table 6.4 lists the basic electrical properties of bulk TSO single crystals obtained by different growth techniques. Not all data are available for all of these methods. All the TSOs listed here are naturally n-type semiconductors or electrical insulators depending on growth conditions, dopants/impurities, and/or postgrowth heat treatments. Even the same material may have quite different properties as a result of various growth techniques, which allow for different oxygen partial pressures (stoichiometry control) and certain impurity levels (donor/acceptor control). Usually, the TSOs grown from the gas phase (CVT, PVT) are semiconductors, likely due to stoichiometry deviation. Solution techniques (hydrothermal, flux) provide relatively high concentrations of impurity elements, which may act as compensating acceptors; therefore, the resulting crystals are usually insulators or semi-insulators. In the case of the TSOs grown from the melt using crucible-free techniques (Verneuil, OFZ, cold crucible), it is possible to provide a high oxygen partial pressure; therefore, the electrical conductivity may span a wide spectrum depending on oxygen concentration. Finally, in the case of melt-grown techniques using Ir crucibles (Czochralski, Bridgman, LASSCGM), the oxygen concentration is limited and the obtained undoped crystals are always semiconductors. Another factor affecting electrical properties of the bulk TSO single crystals are intentional dopants. Generally, elements substituting cations and having higher valences act as donors, whereas those with lower valences act as acceptors. For example, doping β-Ga_2O_3 with Si or Sn increases its electrical conductivity, whereas it decreases with Mg doping. In the case of ZnO, Li decreases the conductivity, while In and Sc increase it. Sb in SnO_2 increases the conductivity. Also, nonmetal impurities (H, F, N, P) affect the electrical conductivity of the TSOs, especially hydrogen, which is omnipresent. It has been theoretically [128–132] and experimentally [63,133,134] demonstrated that hydrogen introduces shallow donors in the previously discussed TSOs; therefore, it increases their electrical conductivity.

One of the issues with n-type TSOs is obtaining p-type conductivity. Despite the enormous efforts undertaken, especially in the case of ZnO films, reliable p-type conductivity has not been achieved. It was reported that the acceptor dopants N, P, As, and Sb turn ZnO into p-type [135–140]; however, it was not found to be stable. ZnO reverted into n-type or mixed p- and n-type states naturally or when subjected to annealing or light exposure. p-type conductivity of N:SnO_2 films was also reported [141]. Even with the difficulties in obtaining p-type conductivity, the TSOs have still high potential for unipolar devices, such as Schotky diodes, field effect transistors.

Electrical conductivities may be modified by postgrowth heat treatments. Typically, annealing in the presence of oxygen at temperatures of 700–1400 °C for at least several hours decreases the electrical conductivity, even from a semiconducting state to an insulating state (β-Ga_2O_3 on the surface and SnO_2 in the bulk). On the other hand, annealing in reducing conditions (in the presence of hydrogen) below 700 °C (above

Table 6.4 Summary of the Fundamental Electrical Properties at Room Temperature of the Bulk TSO Single Crystals Obtained by Different Growth Methods

Growth Technique	Typical Carrier Concentration (cm^{-3})	Typical Resistivity (Ωcm)	Typical Carrier Mobility ($cm^2/V/s$)	Note	References
β-Ga_2O_3					
Verneuil	–	>10^6	–	AG: oxidizing atm	[34]
	10^{18}	0.04	80	AG: reducing atm	
OFZ	–	0.026–10^9	–	AG: depending on O_2	[35]
	–	1.04	–	AG, DP: Sn = 0.05 mol%, O_2	[35]
	5.2×10^{18}	0.026–0.454	2.6–46	AG: <010>, <001>	[36]
	4×10^{17}–7×10^{17}	0.08–0.19	78–98	AG: <100>, <010>, <001>	[37]
	1×10^{16}–1×10^{18}	0.02–33.3	–	AG, DP: Si = 10^{-5}–0.2 mol%	[38]
	–	6×10^{11}	–	AG, DP: Mg = 4–20 × $10^{18}/cm^3$	[39]
	0.98–1.15 × 10^{18}	0.065–0.079	80–83	AG, AN: O_2, 1100 °C, 3 h, DP: Sn = 500 ppm,	[40]
EFG	4.9×10^{18}	93	0.014	AG, DP: Si	[39]
Czochralski	4×10^{16}–2×10^{18}	0.1–1.0	120–150	AG	[41]
	1×10^{19}	0.012	49	AG, DP: Sn = 800 ppm	
	–	Insulator	–	AG, DP: Mg = 6–30 ppm	
ZnO					
CVT	7×10^{16}–2×10^{17}	0.2–0.5	150–190	AG	[42]
	–	1–100	–	AG	[43]
	–	10–1000	–	AG, DP: Cr, Cu, As	[43]
	9×10^{15}–1×10^{18}	0.4–5.8	14–120	AG	[44]
	1×10^{18}	50	183	AG	[45]
	3×10^{19}	–	–	AG	[46]
	7×10^{15}–2×10^{17}	–	107–182	AG, AN: O_2, 1100 °C, 1 h	[47]
PVT	–	10–100	220	AG	[48]
	–	10^{-3}–10^{11}	–	DP: Li, Na, Cu, Ga, In, Mn	

Hydrothermal	–	10^4–10^7	–	AG, AN: 650–750 °C	[49]
	–	1.3×10^0–4.6×10^9	–	AG, DP: Li = 1.7–150 ppm	[50]
	8×10^{13}	380	200	AG	[51]
	1.1×10^{19}	0.015	–	AG, DP: In = 150–175 ppm	[52]
	1×10^{18}	0.056	121	AG, DP: Sc = 8–12 ppm	[53]
Cold crucible	8.4×10^{16}	0.49	150	AG	[54]
Bridgman	5×10^{17}	0.08	153	AG	[55]
	1.7–1.8×10^{17}	0.19	180–187	AN: O_2, 900–1000 °C	
In_2O_3					
CVT	–	4×10^4	–	AG	[56]
	1.3×10^{19}	0.0085	66	AG	[57]
Vapor phase	5×10^{17}–1.1×10^{18}	0.02–0.2	160	AG	[58]
reaction	–	0.055	–	AG	[59]
Salt electrolysis	–	10^{-2}–10^{-4}	–	AG	[60]
Flux	–	2.2	–	AG, IM: Pb	[61]
	10^{12}	2×10^5	–	IM (ppm): Pb = 4307, Mg = 1388, Pt = 155, also (<50) Zr, Sn, Sb, Nd, Bi	[62]
LASSCGM	1×10^{18}–4×10^{18}	0.01–0.03	140–170	AG	[63]
	1.2×10^{17}–2×10^{18}	0.03–0.70	80–190	AN: O_2, 400–1400 °C	
	2.4×10^{18}–5.9×10^{19}	0.003–0.02	40–130	AN: H_2 + Ar, 200–600 °C	
SnO_2					
CVT	8.5×10^{15}–2.2×10^{18}	–	150–260	AG	[64]
PVT	$\sim 1 \times 10^{16}$–2×10^{18}	~0.02–10	50–150	AG, AN: O_2, 1165–1390 °C, 62–282 h	[65]
	$\sim 8 \times 10^{18}$	~0.01	–	AG, DP: Sb = 300 ppm	[65]
	–	10–10^3	–	AG	[66]
	3×10^{17}–2×10^{18}	0.03–0.11	125–202	AG	[67]
	–	Insulator	–	AN: O_2, 1000–1400 °C, >5 h	[67]
Flux	–	10^9–10^{10}	–	AG, IM (wt%): Cu = 0.002, Si = 0.02	[68]

AG, as-grown; AN, annealed; DP, doped; IM, impurities; atm, atmosphere; OFZ, optical floating zone; EFG, edge-defined film-fed growth; CVT, chemical vapor transport; PVT, physical vapor transport; TSO, transparent semiconducting oxide; LASSCGM, levitation-assisted self-seeding crystal growth method.

which strong decomposition proceeds) for at least several hours typically increases the electrical conductivity of the TSOs.

As demonstrated in Table 6.4, the bulk TSO single crystals show either insulating, semi-insulating, semiconducting, or degenerate semiconducting states, but not a conducting state in the sense of typical metallic conductivity, which requires a free electron concentration at the level of 10^{20}–$10^{21}/cm^3$, such as $Sn:In_2O_3$ (ITO) and Al:ZnO (AZO) [30]. The highest obtained free electron concentration in bulk TSO crystals was at a level just above 10^{19} cm^3. TCOs with a very-high free electron concentration are typically used as transparent electrodes, such as in photovoltaics; however, for such applications, thin films or layers are used, which are typically amorphous or polycrystalline materials. It is to be noted that such high free carrier density causes a high absorption in bulk single crystals, not only in the near-infrared spectrum (NIR), but also in the visible spectrum. However, even limited transparency in the visible spectrum decreases energy losses of the operating devices with such electrodes, especially when thin films are used.

The discussed TSOs have fundamental optical gaps ranging from 2.8 for In_2O_3, through 3.2 for ZnO and 3.5 for SnO_2, to 4.8 eV for β-Ga_2O_3. Such wide bandgaps make these materials transparent down to 440, 330, 250, and 260 nm, respectively. Figure 6.15 shows

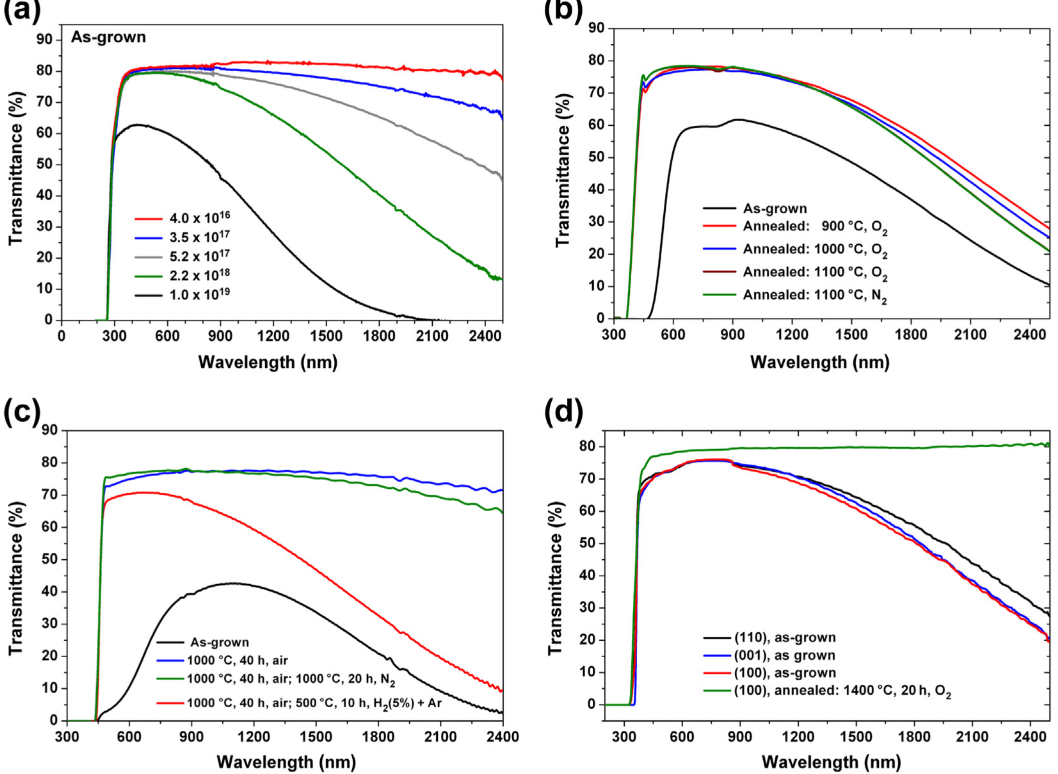

FIGURE 6.15 Transmittance spectra of bulk single crystals: (a) β-Ga_2O_3 by Czochralski; (b) ZnO by Bridgman; (c) In_2O_3 by LASSCGM. *(Adapted from Ref. [63].)* and (d) SnO_2 by PVT. *(Adapted from Ref. [67].)* Sample thickness = 0.5 mm. LASSCGM, levitation-assisted self-seeding crystal growth method.

the transmittance spectra for bulk single crystals of β-Ga_2O_3 (Figure 6.15(a)), ZnO (Figure 6.15(b)), In_2O_3 (Figure 6.15(c)), and SnO_2 (Figure 6.15(d)), as obtained by the Czochralski, Bridgman, LASSCGM, and PVT methods, respectively. The common feature of the transmittance spectra is a very steep absorption edge of as-grown and/or annealed crystals, whereas the high absorption of as-grown ZnO and In_2O_3 crystals (Figure 6.15(b) and (c)) in the visible spectrum is due to the presence of metallic particles (Zn and In, respectively) being responsible for light extinction. Such metallic particles are the result of the advanced decomposition of ZnO and In_2O_3 at high temperatures due to an insufficient oxygen partial pressure. Postgrowth annealing in an oxidizing atmosphere oxidizes the metallic particles and makes these materials fully transparent in the visible/ultraviolet spectrum, with a steep absorption edge. In the case of β-Ga_2O_3 and SnO_2, annealing does not affect essentially the onset of the absorption edge but may improve the transmittance in the visible spectrum when the crystals initially have moderate or high electron concentrations ($>10^{17}/cm^3$). Moreover, β-Ga_2O_3 and SnO_2 show dichroism, which is a polarization dependent absorption of the near edge (not shown in the plots).

The absorption of the TSO crystals at the NIR, and in some cases in the visible spectrum, is due to the free carrier absorption, which is directly proportional to the carrier density in cube and wavelength in square. This phenomenon is well demonstrated in the case of β-Ga_2O_3 shown in Figure 6.15(a), where the transmittance spectra indicate as-grown single crystals having different free electron concentrations. For small and moderate free electron concentrations, the crystals are substantially fully transparent in both the visible and NIR spectra; however, with an increase of that parameter, the crystals become less transparent in the NIR and even in the red part of the visible spectrum. This explains the change of the crystal coloration from colorless to blue and dark blue for electron concentrations above 10^{17} and 10^{18} $/cm^3$, respectively. Insulating or semi-insulating TSOs exhibit full transparency in both the visible and NIR spectra (see annealed SnO_2 in Figure 6.15(d)). In other words, the transmittance spectra of undoped crystals are an indication of the presence of free carriers in the TSOs.

6.5 Summary

The TSOs/TCOs are the subject of very intensive research activities, not only in exploring their existing properties but also their potential applications, as the result of a unique combination of conductivity and transparency in the visible/DUV spectra. To cover a wide spectrum of applications, bulk single crystals are typically required, in the same manner as silicon drives most of the electronic industry. A common feature of the TSOs/TCOs is their instability at high temperatures, which drastically limits the possibility of obtaining truly bulk single crystals, especially from the melt. The intensive research, understanding, and new findings of the field of bulk crystal growth opens the door for a future of increased crystal volume, suitability for industrial applications, and new compounds in the form of bulk single crystals. A number of various oxide compounds show semiconducting behavior.

In addition to n-type conductivity, which is the most common polarity of the bulk oxide crystals, there is also an intensive search for p-type TSOs. It has already been demonstrated for thin films of Cu-based oxides, such as $CuAlO_2$, $CuGaO_2$, $CuInO_2$, and $SrCu_2O_2$, exhibit p-type conductivity. Another p-type semiconducting oxide is SnO. These compounds constitute a potential field for development of p-type bulk TSO single crystals, which provide a complementary polarity with potential expansion of applications of this class of electronic materials.

References

[1] Oshima T, Okuno T, Fujita S. Jpn J Appl Phys 2007;46:7217.

[2] Suzuki R, Nakagomi S, Kokubun Y. Appl Phys Lett 2011;98:131114.

[3] Özgür Ü, Alivov Ya I, Liu C, Teke A, Reshchikov MA, Doğan S, et al. J Appl Phys 2005;98:041301.

[4] Presley RE, Munsee CL, Park C-H, Hong D, Wager JF, Keszler DA. J Phys D Appl Phys 2004;37:2810.

[5] Matsuzaki K, Hiramatsu H, Nomura K, Yanagi H, Kamiya T, Hirano M, et al. Thin Solid Films 2006;496:37.

[6] Izyumskaya N, Avrutin V, Özgür Ü, Alivov YI, Morkoç H. Phys Status Solidi B 2007;244:1439.

[7] Grundmann M, Frenzel H, Lajn A, Lorenz M, Schein F, von Wenckstern H. Phys Status Solidi A 2010;207:1437.

[8] Yuan Z, Zhu X, Wang X, Cai X, Zhang B, Qiu D, et al. Thin Solid Films 2011;519:3254.

[9] Fortunato E, Barquinha P, Martins R. Adv Mater 2012;24:2945.

[10] Hosono H, Ohta H, Orita M, Ueda K, Hirano M. Vacuum 2002;66:419.

[11] Ohira S, Yoshioka M, Sugawara T, Nakajima K, Shishido T. Thin Solid Films 2006;496:53.

[12] Shimamura K, Villora EG. J Fluor Chem 2011;132:1040.

[13] Chen L-C, Tien C-H, Liao W-C. J Phys D Appl Phys 2011;44:165101.

[14] Li Y, Yin W, Deng R, Chen R, Chen J, Yan Q, et al. NPG Asia Mater 2012;4:e30.

[15] Higashiwaki M, Sasaki K, Kuramata A, Masui T, Yamakoshi S. Appl Phys Lett 2012;100:013504.

[16] Sasaki K, Higashiwaki M, Kuramata A, Masui T, Yamakoshi S. J Cryst Growth 2013;378:591.

[17] Hwang WS, Verma A, Peelaers H, Protasenko V, Rouvimov S, Xing H, et al. Appl Phys Lett 2014;104:203111.

[18] Brillson LJ, Lu Y. J Appl Phys 2011;109:121301.

[19] Mohamed M, Irmscher K, Janowitz C, Galazka Z, Manzke R, Fornari R. Appl Phys Lett 2012;101:132106.

[20] Ogale SB, Choudhary RJ, Buban JP, Lofland SE, Shinde SR, Kale SN, et al. Phys Rev Lett 2003;91:077205.

[21] Bartic M, Baban C-I, Suzuki H, Ogita M, Isai M. J Am Ceram Soc 2007;90:2879.

[22] Kannan S, Steinebach H, Rieth L, Solzbacher F. Sens Actuators B 2010;148:126.

[23] Tischner A, Maier T, Stepper C, Köck A. Sens Actuators B 2008;134:796.

[24] Tanaka M, Nishikino M, Yamatani H, Nagashima K, Kimura T, Furukawa Y, et al. Appl Phys Lett 2007;91:231117.

[25] Kano M, Wakamiya A, Sakai K, Yamanoi K, Cadatal-Raduban M, Nakazato T, et al. J Cryst Growth 2011;318:788.

[26] Diniz ASAC. Renew Energy 2011;36:1153.

[27] Kim SI, Cho SH, Choi SR, Oh MC, Jang JH, Song PK. Thin Solid Films 2009;517:4061.

[28] Murty NS, Jawalekar SR. Thin Solid Films 1983;108:277.

[29] Kikuchi N, Kusano E, Kishio E, Kinbara A. Vacuum 2002;66:365.

[30] Minami T. Semicond Sci Technol 2005;20:S35.

[31] Tomm Y, Ko JM, Yoshikawa A, Fukuda T. Sol Energy Mater Sol Cells 2001;66:369.

[32] Hamberg I, Granqvist CG. J Appl Phys 1986;60:R123.

[33] Klimm D, Schulz D, Ganschow S, Galazka Z, Uecker R. MRS Proc 2012;1394.

[34] Lorenz MR, Woods JF, Gambino RJ. J Phys Chem Solids 1967;28:403.

[35] Ueda N, Hosono H, Waseda R, Kawazoe H. Appl Phys Lett 1997;70:3561.

[36] Ueda N, Hosono H, Waseda R, Kawazoe H. Appl Phys Lett 1997;71:933.

[37] Villora EG, Shimamura K, Yoshikawa Y, Aoki K, Ichinose N. J Cryst Growth 2004;270:420.

[38] Víllora EG, Shimamura K, Yoshikawa Y, Ujiie T, Aoki K. Appl Phys Lett 2008;92:202120.

[39] Onuma T, Fujioka S, Yamaguchi T, Higashiwaki M, Sasaki K, Masui T, et al. Appl Phys Lett 2013;103:041910.

[40] Ohira S, Suzuki N, Arai N, Tanaka M, Sugawara T, Nakajima K, et al. Thin Solid Films 2008;516:5763.

[41] Galazka Z, Irmscher K, Uecker R, Bertram R, Pietsch M, Kwasniewski A, et al. J Cryst Growth 2014;404:184.

[42] Abe K, Banno Y, Sasayama T, Koizumi K. Jpn J Appl Phys 2009;48:021101.

[43] Grasza K, Mycielski A. Phys Status Solidi C 2005;2:1115.

[44] Tena-Zaera R, Martínez-Tomás C, Gómez- García CJ, Muñoz-Sanjosé V. Cryst Res Technol 2006;41:742.

[45] Hassani S, Tromson-Carli A, Lusson A, Didier G, Triboulet R. Phys Status Solidi B 2002;229:835.

[46] Ntep J-M, Said Hassani S, Lusson A, Tromson-Carli A, Ballutaud D, Didier G, et al. J Cryst Growth 1999;207:30.

[47] Santailler J-L, Audoin C, Chichignoud G, Obrecht R, Kaouache B, Marotel P, et al. J Cryst Growth 2010;312:3417.

[48] Helbig R. J Cryst Growth 1972;15:25.

[49] Croxall DF, Ward RCC, Wallace CA, Kell RC. J Cryst Growth 1974;22:117.

[50] Sakagami N. J Cryst Growth 1990;99:905.

[51] Maeda K, Sato M, Niikura I, Fukuda T. Semicond Sci Technol 2005;20:S49.

[52] Wang B, Callahan MJ, Xu C, Bouthillette LO, Giles NC, Bliss DF. J Cryst Growth 2007;304:73.

[53] Zuo Y-B, Lu F-H, Zhang C-L, Hang Y, Zhou W-N, Huo H-D, et al. J Cryst Growth 2011;318:513.

[54] Reynolds DC, Litton CW, Look DC, Hoelscher JE, Claflin B, Collins TC, et al. J Appl Phys 2004;95:4802.

[55] Schulz D, Ganschow S, Klimm D, Struve K. J Cryst Growth 2008;310:1832.

[56] De Wit JHW. J Cryst Growth 1972;12:183.

[57] Scherer V, Janowitz C, Krapf A, Dwelk H, Braun D, Manzke R. Appl Phys Lett 2012;100:212108.

[58] Weiher RL. J Appl Phys 1962;33:2834.

[59] Shimada S, Sato O, Tsunashima A, Kodaira K, Matsushita T. J Cryst Growth 1987;80:366.

[60] Teweldemedhin ZS, Ramanujachary KV, Greenblatt M. J Solid State Chem 1990;86:109.

[61] Remeika JP, Spencer EG. J Appl Phys 1964;35:2803.

[62] Hagleitner DR, Menhart M, Jacobson P, Blomberg S, Schulte K, Lundgren E, et al. Phys Rev B 2012;85:115441.

[63] Galazka Z, Irmscher K, Pietsch M, Schulz T, Uecker R, Klimm D, et al. CrystEngComm 2013;15:2220.

[64] Fonstad CG, Rediker RH. J Appl Phys 1971;42:2911.

[65] Marley JA, Dockerty RC. Phys Rev 1965;140:A 304.

[66] Thiel B, Helbig R. J Cryst Growth 1976;32:259.

[67] Galazka Z, Uecker R, Klimm D, Irmscher K, Pietsch M, Schewski R, et al. Phys Status Solidi A 2014;211:66.

[68] Kunkle HF, Kohnke EE. J Appl Phys 1965;36:1489.

[69] Schulz D, Ganschow S, Klimm D, Neubert M, Rossberg M, Schmidbauer M, et al. J Cryst Growth 2006;296:27.

[70] Galazka Z, Uecker R, Irmscher K, Albrecht M, Klimm D, Pietsch M, et al. Cryst Res Technol 2010;45:1229.

[71] Galazka Z, Uecker R, Irmscher K, Schulz D, Klimm D, Albrecht M, et al. J Cryst Growth 2013;362:349.

[72] Klimm D, Ganschow S, Schulz D, Bertram R, Uecker R, Reiche P, et al. J Cryst Growth 2009;311:534.

[73] Klimm D, Bertram R, Galazka Z, Ganschow S, Schulz D, Uecker R. Cryst Res Technol 2012;47:247.

[74] Ganschow S, Schulz D, Klimm D, Bertram R, Uecker R. Cryst Res Technol 2010;45:1219.

[75] Roy R, Hill VG, Osborn EF. J Am Ceram Soc 1952;74:719.

[76] Åhman J, Svensson G, Albertsson JA. Acta Cryst 1996;C52:1336.

[77] Pajaczkowska A, Juskowiak H. J Cryst Growth 1986;79:421.

[78] Katz G, Roy R. J Am Ceram Soc 1966;49:168.

[79] Garton G, Smith SH, Wanklyn BM. J Cryst Growth 1972;13/14:588.

[80] Chani VI, Inoue K, Shimamura K, Sugiyama K, Fukuda T. J Cryst Growth 1993;132:335.

[81] Chase AB. J Am Ceram Soc 1964;47:470.

[82] Harwig T, Wubs GJ, Dirksen GJ. Solid State Commun 1976;18:1223.

[83] Harwig T, Schoonman J. J Solid State Chem 1978;23:205.

[84] Zhang J, Li B, Xia C, Pei G, Deng Q, Yang Z, et al. J Phys Chem Solids 2006;67:2448.

[85] Zhang J, Xia C, Deng Q, Yang Z, Xu W, Shi H, et al. J Phys Chem Solids 2006;67:1656.

[86] Aida H, Nishiguchi K, Takeda H, Aota N, Sunakawa K, Yaguchi Y. Jpn J Appl Phys 2008;47:8506.

[87] Tomm Y, Reiche P, Klimm D, Fukuda T. J Cryst Growth 2000;220:510.

[88] Klimm D, Schulz D, Ganschow S. Compr Semicond Sci Technol 2011;3:302.

[89] Hong S-H, Mikami M, Mimura K, Uchikoshi M, Yasuo A, Abe S, et al. J Cryst Growth 2009;311:3609.

[90] Grasza K, Skupiński P, Mycielski A, Łusakowska E, Domukhovski V. J Cryst Growth 2008;310:1823.

[91] Mikami M, Sato T, Wang JiF, Masa Y, Isshiki M. J Cryst Growth 2006;286:213.

[92] Mikami M, Hong S-H, Sato T, Abe S, Wang JiF, Masumoto K, et al. J Cryst Growth 2007;304:37.

[93] Mycielski A, Kowalczyk L, Szadkowski A, Chwalisz B, Wysmołek A, Stepniewski R, et al. J Alloys Compd 2004;371:150.

[94] Kunihiko O, Hajime S, Satoshi K. J Cryst Growth 2002;237/239:509.

[95] Li X, Xu J, Jin M, Wu X, Qian G, Li X. Cryst Res Technol 2007;42:221.

[96] Ushio M, Sumiyoshi Y. J Mater Sci 1993;28:218.

[97] Sekiguchi T, Miyashita S, Obara K, Shishido T, Sakagami N. J Cryst Growth 2000;214/215:72.

[98] Dem'yanets LN, Kostomarov DV. Ann Chim Sci Mat 2001;26:193.

[99] Ohshima E, Ogino H, Niikura I, Maeda K, Sato M, Ito M, et al. J Cryst Growth 2004;260:166.

[100] Dhanaraj G, Dudley M, Bliss D, Callahan M, Harris M. J Cryst Growth 2006;297:74.

[101] Ehrentraut D, Sato H, Kagamitani Y, Sato H, Yoshikawa A, Fukuda T. Prog Cryst Growth Charact Mater 2006;52:280.

[102] Dem'yanets LN, Lyutin VI. J Cryst Growth 2008;310:993.

[103] Dem'yanets LN, Zakalyukin RM, Mavrin BN. Inorg Mater 2011;47:649.

[104] Nause JE. III-Vs Rev 1999;12:28.

[105] Nause J, Nemeth B. Semicond Sci Technol 2005;20:S45.

[106] Klimm D, Ganschow S, Schulz D, Fornari R. J Cryst Growth 2008;310:3009.

[107] Jacobs K, Schulz D, Klimm D, Ganschow S. Solid State Sci 2010;12:307.

[108] Schulz D, Ganschow S, Klimm D. Mater Res Soc Symp Proc 2010;1201:H06.

[109] Schulz D, Bertram R, Klimm D, Schulz T, Thiede E. J Cryst Growth 2011;334:118.

[110] Irmscher K, Albrecht M, Heimbrodt B, Naumann M, Remmele T, Schulz D, et al. Phys Status Solidi C 2009;6:2658.

[111] Nitsche R. J Phys Chem Solids 1967;(Suppl. 1):215.

[112] Shimada S, MacKenzie KJD. J Cryst Growth 1981;55:453.

[113] Chase AB, Tippins HH. J Appl Phys 1967;38:2469.

[114] Chase AB. J Am Ceram Soc 1968;51:507.

[115] Galazka Z, Uecker R, Fornari R, patent application No. PCT/EP2012/057447 (publication No. WO 2013/159808 A1), entitled : Method and apparatus for growing indium oxide (In_2O_3) single crystals and indium oxide (In_2O_3) single crystal; 2012.

[116] Galazka Z, Uecker R, Fornari R. J Cryst Growth 2014;388:61.

[117] Albrecht M, Schewski R, Irmscher K, Galazka Z, Markurt T, Naumann M, et al. J Appl Phys 2014;115:053504.

[118] Sadofev YJ, Cho O, Brandt M, Ramsteiner R, Calarco H, Riechert SC, et al. Appl Phys Lett 2012;101:172102.

[119] Matsumoto K, Kaneko S, Takagi K. J Cryst Growth 1977;40:291.

[120] Fonstad CG, Linz A, Rediker RH. J Electrochem Soc 1969;116:1269.

[121] Marley JA, MacAvoy TC. J Appl Phys 1961;32:2504–5.

[122] Reed TB, Roddy JT, Mariano AN. J Appl Phys 1962;33:1014.

[123] Summit R, Borrelli NF. J Phys Chem Solids 1965;26:921.

[124] Koffyberg FP. J Appl Phys 1965;36:844.

[125] Kawamura F, Takahashi T, Yasui I, Sunagawa I. J Cryst Growth 2001;233:259.

[126] Shimada S, Kodaira K, Matsushita T. Chem Lett 1976;5:235.

[127] Shimada S, Kodaira K, Matsushita T. J Cryst Growth 1982;59:662.

[128] Van de Walle CG. Phys B 2006;376–377:1.

[129] Janotti A, Van de Walle CG. Nat Mater 2007;6:44.

[130] Singh AK, Janotti A, Scheffler M, Van de Walle CG. Phys Rev Lett 2008;101:055502.

[131] King PDC, Lichti RL, Celebi YG, Gil JM, Vilão RC, Alberto HV, et al. Phys Rev B 2009;80:081201.

[132] Varley JB, Weber JR, Janotti A, Van de Walle CG. Appl Phys Lett 2010;97:142106.

[133] Fleischer M, Giber J, Meixner H. Appl Phys A 1992;54:560.

[134] Thomas DG, Lander JJ. J Chem Phys 1956;25:1136.

[135] Barnes M, Olson K, Wolden CA. Appl Phys Lett 2005;86:112112.

[136] Tsukazaki A, Ohtomo A, Onuma T, Ohtani M, Makino T, Sumiya M, et al. Nat Mater 2005;4:42.

[137] Krtschil A, Dadgar A, Oleynik N, Bläsing J, Diez A, Krost A. Appl Phys Lett 2005;87:262105.

[138] Claflin B, Look DC, Park SJ, Cantwell G. J Cryst Growth 2006;287:16.

[139] Grasza K, Mycielski A, Domagała J, Domukhovski V, Paszkowicz W, Sakowska H, et al. Phys Status Solidi C 2006;3:793.

[140] Maksimov O. Rev Adv Mater Sci 2010;24:26.

[141] Pan SS, Wang S, Zhang YX, Luo YY, Kong FY, Xu SC, et al. Appl Phys A 2012;109:267.

7 Floating Zone Growth of Silicon

Andris Muiznieks[1,†], Janis Virbulis[1], Anke Lüdge[2], Helge Riemann[2], Nico Werner[2]

[1]DEPARTMENT OF PHYSICS, UNIVERSITY OF LATVIA, RIGA, LATVIA;
[2]LEIBNIZ INSTITUTE FOR CRYSTAL GROWTH, BERLIN, GERMANY;
[†]DECEASED 5 APRIL 2013

CHAPTER OUTLINE

Preface **242**
7.1 Basics of the Floating Zone Silicon Crystal Growth **243**
7.1.1 History: From Zone Melting Purification to the Crucible-free Silicon Crystal Growth 243
7.1.2 Fundamentals of the FZ Technology 245
7.1.2.1 FZ Setup 245
7.1.2.2 Main Steps of the FZ Process 246
7.1.3 Crucial FZ Details 249
7.1.3.1 Origin and Analysis of Failures 249
7.1.3.2 Rotation and Pull Rates 250
7.1.3.3 Stability of the Molten Zone and Growth Angle 251
7.1.3.4 The Feed Rod 251
7.1.3.5 Induction Coil and Arcing 252
7.1.4 FZ Crystal Morphology: Ridges and Orientation 253
7.1.4.1 Growth Habitus 253
7.1.5 Doping Techniques and Impurity Distribution 253
7.1.6 Recent Development 254
7.2 Automation of the Floating Zone Process Using Model-Based Control **255**
7.2.1 Motivation 255
7.2.2 Description of the Measurement System 256
7.2.3 Modeling of the Floating Zone Process 257
7.2.4 Choice of Reference and Manipulated Variables 258
7.2.4.1 Creating the Thin Neck 258
7.2.4.2 Growing the Crystal Cone 258
7.2.4.3 Growing the Cylinder 259

Handbook of Crystal Growth. http://dx.doi.org/10.1016/B978-0-444-63303-3.00007-9
Copyright © 2015 Elsevier B.V. All rights reserved.

7.2.5 Regulated Growth of the Avogadro Crystal ... 259
7.3 Mathematical Modeling of the Floating Zone Silicon Growth ... 260
7.3.1 Introduction ... 260
7.3.2 Historical Overview ... 262
7.3.3 Mathematical Models ... 263
7.3.3.1 Electromagnetic Field ... 263
7.3.3.2 Temperature Field ... 264
7.3.3.3 Melt Flow ... 265
7.3.3.4 Impurity Distribution ... 265
7.3.3.5 Shape of Interfaces ... 266
7.3.3.6 Thermomechanical Stress ... 266
7.3.3.7 Transient Modeling ... 267
7.3.4 Exemplary Results ... 267
7.3.4.1 Electromagnetic Field ... 268
7.3.4.2 Temperature Field ... 269
7.3.4.3 Melt Flow and Impurity Distribution ... 270
7.3.4.4 Shape of Interfaces ... 272
7.3.4.5 Stress ... 274
7.3.4.6 Transient Modeling ... 275
7.3.5 Summary, Conclusions, and Outlook ... 276
References ... 277

Preface

This chapter has been decisively influenced by Andris Muiznieks (*August 1,1961–April 5, 2013) from University of Latvia, Riga. He was a brilliant scientist who investigated and understood floating zone (FZ) silicon growth more deeply and in detail than nearly everyone else. As a genuine physicist and a skilled numerical expert, he logically explained, simulated, and predicted a variety of processes of silicon growth for the first time without actually carrying them out. He was delighted to become the lead author of this chapter and to summarize his work of more than 20 years on FZ silicon.

Shortly after beginning his work on this chapter, Andris died on April 5, 2013, at the age of 51. It was totally unexpected and inconceivable. Our scientific community not only lost a good friend but also a great scientist. Janis Virbulis, his longtime friend and colleague, then assumed the position of lead author of the chapter, which has now been written in honor and memory of Andris's life work.

We confine ourselves to discussing FZ crystals that have technical relevance. Therefore, only the inductively heated crystal growth with the needle-eye method is described in detail. For other types such as optically heated crystal growth of silicon or FZ applications to other materials, the reader is referred to [1].

We start with an historical sketch and phenomenological description of the FZ technique, which is followed by a conception of predictive automation on a simplified dynamic model, and finished with the comprehensive numerical modeling of the FZ process.

7.1 Basics of the Floating Zone Silicon Crystal Growth

7.1.1 History: From Zone Melting Purification to the Crucible-free Silicon Crystal Growth

Zone melting is a technique that was mainly applied for purifying congruently melting substances in a physical way. Originally, a narrow heater generates a molten zone in the solid substance being in a horizontal boat-like crucible made of a material that must not pollute that substance. If the molten zone is continuously shifted through the material in the boat by the relative movement between boat and heater, impurities are partly gathered in the molten zone due to their almost increased solubility in the liquid state according to the segregation coefficient k:

$$k = c_s/c_l \tag{7.1}$$

where c_s and c_l are the solubilities in the solid and in the liquid state, respectively.

In that way, impurities are traveling with the molten zone to one end of the rod where they are deposited in the last solidifying material. As a result, most material of the rod becomes purer at the cost of the end part. Multiple zone melting enables high purity grades as needed for semiconductors. Unfortunately, horizontal zone melting fails for silicon, the most important semiconductor, because any material for the boat including quartz markedly reacts with the silicon melt, and silicon adheres mostly at the boat causing cracks during cooling down due to different thermal contraction.

However, amazingly large and rather pure silicon single crystals can be grown directly from the melt in a quartz crucible bowl after the well-established Czochralski (CZ) method, but CZ silicon does not fit all needs for some important electronic devices because the eroding crucible introduces oxygen into the silicon forming SiO_x precipitates and thermal donors. Other specific impurities are carbon and B, Al, Fe, etc., which limit resistivity and carrier lifetime of the material.

In order to overcome these drawbacks, the crucible-free FZ method was invented in the early 1950s [1,2], as a contactless vertical zone melting technique. Starting with a seed crystal, the FZ process becomes a crucible-free crystal growth method, which is widely technically used [3]. Silicon suits this method very well, because the “floating” molten zone is neatly stabilized by the strong surface tension and is located between the vertically positioned growing crystal at the bottom and the melting silicon feed rod at the top. It is commonly generated by the contactless inductive heating via the RF (c. 3 MHz) magnetic field of a one-turn induction coil. The zone “floats” upward due to the relative movement between the heating coil and the silicon rods. The induction coil and the RF generator are fixed and crystal and rod are moved downward while rotating.

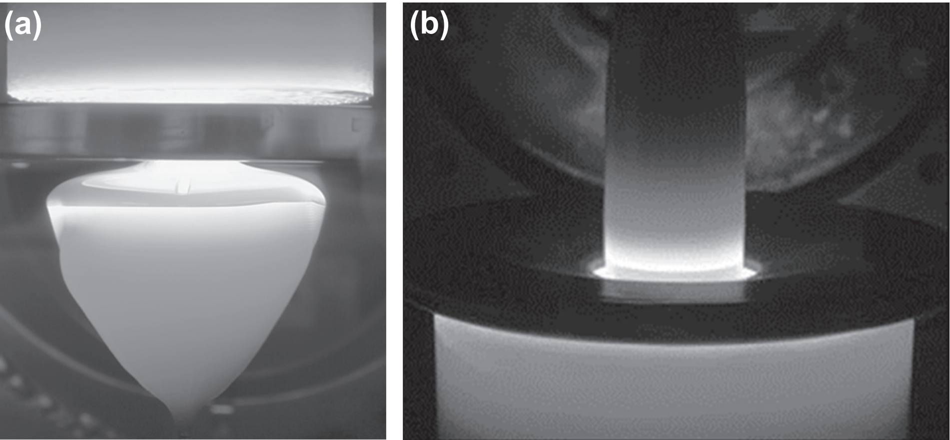

FIGURE 7.1 Floating zone (a) and pedestal (b) crystal growth [4].

Radiative heating, instead of inductive, was also investigated, especially in space experiments, but it is only feasible if the crystal diameter is below c. 30 mm [4].

The FZ process also works if the feed rod is placed on the bottom as a pedestal and the crystal is pulled upward. This pedestal growth method is inherently more stable, but the diameter of the crystal is markedly smaller than that of the feed rod and of the inductor hole as shown in Figure 7.1(b). This method also has industrial relevance as a technique for producing the slim rods needed as filaments for the Siemens process.

Both, FZ and CZ silicon crystals can be grown in a dislocation-free structure after eliminating all dislocations by the thin-neck method after Dash [5]. The dislocation-free growth is absolutely necessary for single crystals with a diameter of more than c. 40 mm in order to avoid the rapidly increasing multiplication of any new dislocations due to the higher thermal stress, resulting very quickly in polycrystallinity. The diameter of FZ silicon is currently limited to 200 mm (Figure 7.2), mainly by high voltage breakthroughs at the “pancake inductor” [6]. In contrast to this, CZ silicon crystals can be grown with greater diameter of up to 450 mm.

FZ and CZ silicon complement each other. Compared with CZ silicon, typical impurity concentrations of FZ silicon are two to three orders of magnitude smaller and electric resistivities of up to 30 kOhm cm and carrier lifetimes τ of about 8000 µs are achievable. Especially the very low oxygen concentration prevents any oxide precipitation in thermal processing, which is important for high voltage applications. The worldwide production of FZ silicon continuously rises, but not as fast as that for CZ, so, the percentage of the FZ silicon production has dropped from 20% in the 1980s to about 5% nowadays.

However, FZ silicon is essential and indispensable for high power electronics as well as for innovative devices. The main objectives of the present research on FZ silicon are innovative concepts for crystal diameters beyond 200 mm, FZ crystal growth directly

FIGURE 7.2 A silicon monocrystal with 200-mm diameter grown at Siltronic AG using the floating zone process. *Photo: Siltronic AG.*

from much cheaper Si feedstock, e.g., fluid bed granulate and a cost reduction of FZ silicon for PV application.

7.1.2 Fundamentals of the FZ Technology

7.1.2.1 FZ Setup

The essential components of an FZ crystal puller are the vacuum-tight growth chamber containing the protection gas atmosphere, and the upper pulling shaft and the lower one, which can independently vertically translate and rotate. The former carries the feed rod mount and the latter the seed mount. The heart of the puller is the induction coil (Figure 7.3), which is connected to the coaxial RF power feedthrough as well as to the cooling water supply. State of the art is a flat, one-turn pancake induction coil, which has to enclose the molten zone but avoid any contact with it. Several geometric items of the

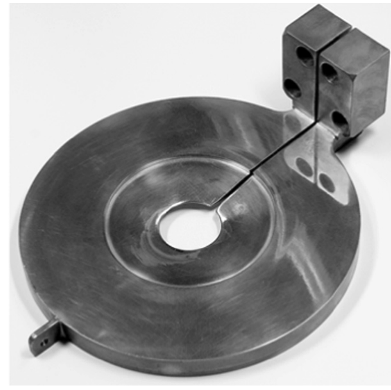

FIGURE 7.3 Induction coil suitable for growing floating zone crystals.

inductor, like slots, diameters, and angles, define shape and structure of the RF magnetic field and, finally, the distribution of the induced thermal power and the electrodynamic forces on the melt surface. The induction coil significantly determines yield and success of the FZ crystal growth.

Auxiliary installations in the setup are heat reflection shields, a feed rod preheating system, a mechanical supporting system for big crystals, and the supplies for vacuum and protecting gas with controlled gas composition, a dosing apparatus for the doping gas and measuring devices for diameters, and zone height required for automatic process control.

7.1.2.2 Main Steps of the FZ Process

After assembling the shaped and cleaned silicon feed rod and the oriented seed crystal of pencil shape in their mounts, Figure 7.4(b) and (c) 4 and 7, the growth chamber will be closed, evacuated, and commonly filled with high purity argon as protecting gas. Preheating the conical lower end of the feed rod to above 450 °C raises the intrinsic electric conductivity so that the RF field of the coil can inductively heat up the cone tip above the melting point (1413 °C), generating a big hanging melt drop held by adhesion and surface tension.

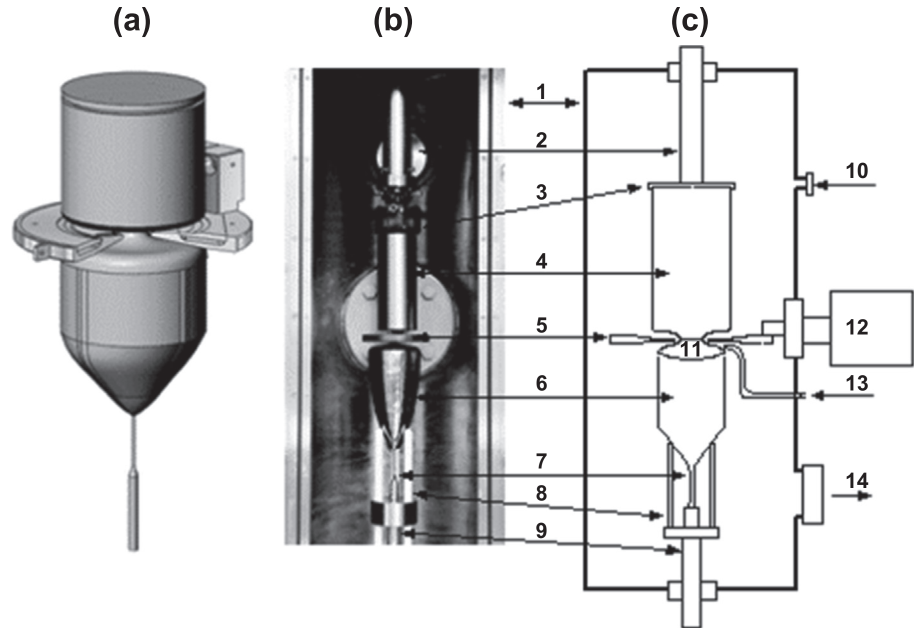

FIGURE 7.4 Setup of a floating zone puller [4] (a) three-dimensional scheme, (b) model setup of the chamber, (c) cross-section through a growth chamber. 1, growth chamber; 2, upper spindle; 3, rod holder; 4, feed rod; 5, induction coil; 6, growing crystal; 7, seed with thin neck; 8, crystal support; 9, lower spindle; 10, gas inlet; 11, molten zone; 12, RF generator; 13, doping gas supply; 14, pump.

The seed crystal is moved upward until it is close below the drop where it heats up for some time for reducing the temperature difference in relation to the melt. Then it is further moved up until it dips into the melt drop from the bottom, whereby the seed melts back a bit and the seed-melt interface smoothes. The oriented crystallization is initiated by lowering the RF power and pulling down the seed with a rate of 6–12 mm/min. Doing this, the drop is shrunk and stretched and the monocrystalline thin neck of 2–3 mm thickness grows initially with the high dislocation density of the seed generated by the thermal shock from before. In this phase, a tiny flat melt zone is establishing, and the so-called thin neck can grow under very low thermomechanical stress unable to initiate further dislocation gliding and multiplication. Because, practically, all dislocation lines deviate from the growth axis, they leave the thin neck, which becomes dislocation-free after a few centimeters of growth length. This technique, as shown in Figure 7.5, was originally invented by Dash for CZ silicon growth [5] and works pretty certainly for several crystal orientations but generally not for the <110> direction because it is the preferred orientation of dislocation lines in silicon.

If the crystal neck is dislocation-free and the growth is not seriously disturbed, the crystal will stay in that state even if the diameter increases because of the very high generation energy of dislocations in contrast to that of dislocation multiplication. Therefore, both the inductor current and the speed of the upper feed rod can be gradually increased in order to raise the melt flow and to increase the molten zone, resulting in a steadily rising diameter of the crystal obtaining a conical shape, see Figure 7.1(a). This has to be done smoothly and steadily especially regarding the shape of the free melt meniscus at the crystallization interface because of the danger of spilling out of the melt or of a thermally induced loss of the dislocation-free structure.

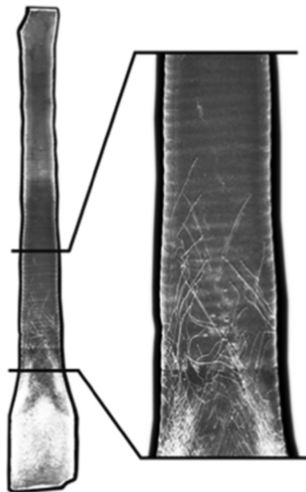

FIGURE 7.5 X-ray topogram of a <111> thin neck (5 mm × 40 mm) with vanishing dislocations, enlargement on the right: no further dislocations after about 20 mm [4].

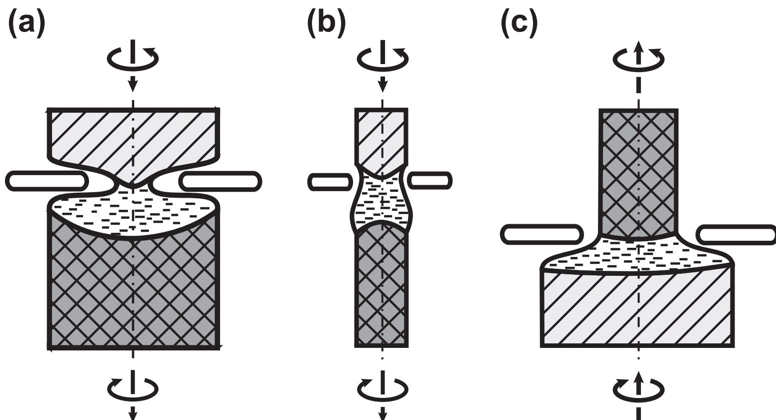

FIGURE 7.6 Floating zone needle-eye technique (a), non-needle-eye crystal growth for small diameters (b) and pedestal crystal growth (c) [4].

A distinctive feature of the FZ method was invented with the needle-eye technique (Figure 7.6), which allows overcoming the dilemma of the limited capillary stability of a molten zone that becomes unstable if its height exceeds a critical value of c. 17 mm for silicon [4]. Using the needle-eye technique, the molten zone forms a narrow neck of c. 20 mm diameter, which is fed through and enclosed by the inner hole of the inducting coil as shown in Figure 7.6(a) in comparison to the non-needle eye technique (b) with which only small diameters can be reached.

In that way, the height of the zone can be held below the critical value because the relevant diameter of the neck of the zone can stay small and almost independent on the crystal diameter. Moreover, the crystal diameter can exceed the diameter of the feed rod in contrast to the pedestal technique, where the diameters of pedestal or inductor hole, whichever is greater, cannot be exceeded.

If the growing FZ crystal is approaching the target diameter, the transient growth process has to be changed to an almost stationary one with constant diameter and pulling rate. The gain of the induced power has to be carefully stopped and the feed rate has to be balanced regarding the target diameter. This is accompanied with distinct changes of the melt meniscus shape and the thermal stress field and is the most critical phase of the FZ process.

The subsequent growth of the cylindrical part is almost stationary. Only the changing lengths of crystal and feed rod require slight corrections of the RF power during the whole process.

If the desired crystal length is grown or the feed is coming to its end, the process will be finished by lowering the inductor power and subsequently stopping the feed rod. The shrinking molten zone finally divides due to the move of the crystal carrying the remaining melt, which is gradually solidifying.

At the end of the process, the heating field fades and the crystal cools down mostly accompanied by stress-induced generation of new dislocations in the vicinity of the upper "tail."

7.1.3 Crucial FZ Details

7.1.3.1 Origin and Analysis of Failures

The growth of dislocation-free silicon FZ crystals is rather sophisticated especially in view of large-diameter crystals. FZ runs can fail accidentally by, for example, dust particles in the growth surroundings, ground vibrations, or structural anomalies of the feed rod, or, systematically, by inconvenient growth conditions like wrongly chosen RF power, pull or rotation values, and inappropriate design or adjustment of the inducting coil that can cause inapplicable temperature and stress anomalies in the crystal or electrodynamic forces destabilizing the melt zone. It is quite advantageous that the FZ process can be well visually observed. However, it is almost impossible to clarify the real reasons of failures because most in situ measurements are impossible. Therefore, structural and electrical diagnostics of the grown crystal are essential for process evaluation and optimization.

The crystallization interface as a distinct isothermal face, in particular its deflection, gives information about the temperature and stress fields' overall growth phases, and its shape is generally used for the validation of numerical models. This can be determined from the striation pattern in the grown crystal, which can be well detected on axially cut samples by evaluation of the doping or rather the resistivity distribution using the lateral photovoltage scanning (LPS) method [7] (Figure 7.7). Here, a scanning laser focus generates a small voltage signal between opposite sample rims corresponding to the lateral gradient of the doping concentration. Besides the interface curve, the LPS plot contains information about resistivity fluctuations originated by crystal rotation as well as by the time-dependent melt flow field responsible for the radial resistivity profile and its variations.

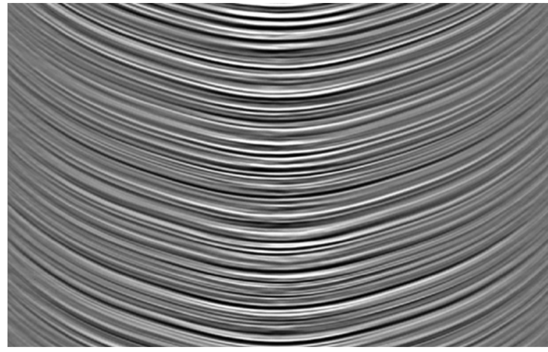

FIGURE 7.7 Lateral photovoltage scanning plot of an axially cut sample from a silicon single crystal showing solid liquid interface curves and resistivity variations.

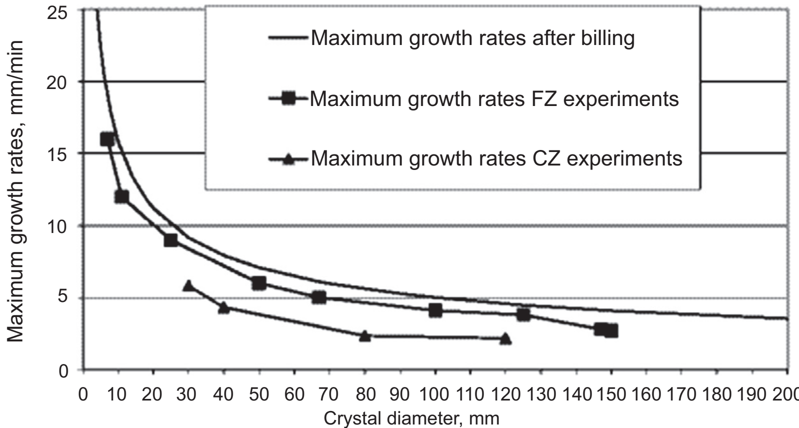

FIGURE 7.8 Maximum growth rates for floating zone silicon compared to Czochralski silicon and the theoretical limit calculated by Billig [9]. *From Ref.[8].*

7.1.3.2 Rotation and Pull Rates

FZ crystals grow in relatively cold surroundings causing high temperature gradients at the crystallization front. Therefore, compared with the CZ process, higher pull rates are possible. Figure 7.8 shows experimentally determined values of the maximum pull rates for dislocation-free FZ crystals depending on the diameter [8].With their FZ technique, the authors reached pull rates of about 75% (CZ: c. 50%) of the thermotechnically determined upper limit calculated by Billig [9] for crystal diameters of 10–150 mm corresponding to the maximum pull rates for a dislocation-free FZ growth of 17 mm/min to 3 mm/min, respectively.

The necessary feed rate is determined by the silicon mass balance as crystal pull rate multiplied by the squared ratio of the diameters of crystal and feed. However, there are limitations. On one hand, a high feeding rate lets the distance shrink between the induction coil and the melting front of the feed rod that could touch each other; on the other hand, too low melting rates cause a rough melting front, and, as a consequence, skin-effect related silicon “noses” are formed that cannot be inductively removed as shown in Figure 7.9. This and other effects limit the relative deviation between the diameters of crystal and feed rod empirically to c. ±25%.

Generally, feed and crystal rotate in order to improve the thermal symmetry, but furthermore, the rotation affects the process.

If the feed rod rotates with c. 2–4/min, “noses” can appear. Therefore, lower rotation rates are preferred.

On one hand, high crystal rotation rates lower the radial resistivity variation (RRV) and the deflection of the growth interface by homogenizing the dopant concentration as well as the temperature in the melt; on the other hand, the centrifugal forces act against the surface tension and destabilize the melt meniscus and following crystal morphology. This double bind can be overcome if the comparably fast crystal rotation

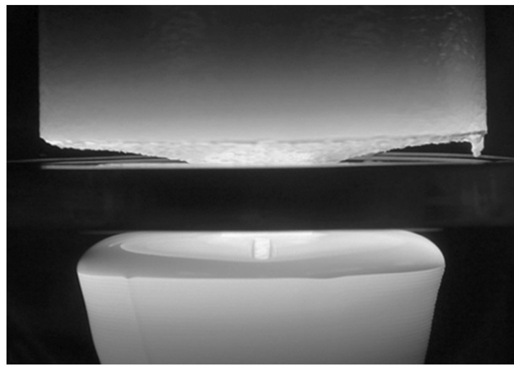

FIGURE 7.9 Formation of a "nose" that cannot be molten inductively and can lead to a process crash.

is periodically reversed. Specially designed schemes of rotation modulation are patented [10].

7.1.3.3 Stability of the Molten Zone and Growth Angle

For a successful FZ growth, the molten zone must be in equilibrium of all acting forces originated mainly by surface tension, electrodynamics, inertia, and gravity. Furthermore, the equilibrium has to be dynamically stable, i.e., it has to steadily come back to the equilibrium by itself after mechanical deviations. The isostatic melt pressure corresponding to the degree of filling of the molten zone in relation to its diameter and height is most relevant for the stability, but hardly measurable, and will be discussed in the next sections. Instability of the zone is generally followed either by spilling out of the melt (too much melt) or by zone separation (too little melt).

Visible indications of an upcoming loss of the zone stability is the melt neck diameter in relation to the zone height, e.g., the vertical distance between upper and lower interface lines and the meniscus shape or rather the angle between the melt meniscus and the crystal surface at the crystallization interface. For a safe crystal growth, this angle appears to be relevant to avoid deviations of the so-called growth angle.

However, even a stable molten zone does not ensure a successful dislocation-free growth. The time-depending thermomechanical shear stress in the crystal must generally be limited, but cannot be quantitatively specified today.

If the crystal grows stationary with a constant diameter, the angle between the tangents to the melt surface and the crystal surface at the position of the crystallization interface is commonly not zero and depends only on material parameters. It was experimentally determined for several substances from photographs of melt zones. This growth angle for silicon was recently determined to be $11.5° \pm 1.9°$ [11].

7.1.3.4 The Feed Rod

The almost cylindrical silicon feed rod, which has to be controlled molten inductively, is commonly produced after the so-called Siemens process by pyrolytic deposition of

either trichlor silane $SiHCl_3$ or mono silane SiH_4 on electrically heated silicon filaments (slim rods). Sometimes, feed rods are used that were solidified from the melt after techniques like CZ, directional solidification, continuous crystallization, or previous FZ purification runs.

The purity of the feed rod influences the purity of the grown FZ crystal, which is generally improved by segregation. Especially transition metals with segregation coefficients $k \ll 1$ are effectively depleted, whereas the important dopants boron ($k = 0.8$) and phosphorus ($k = 0.36$) are rather evenly distributed, which facilitates axially homogenous doping techniques.

The crystalline structure of the feed rod is not implicitly important, but thermal and electrical properties should be homogeneous, at least free of anomalies like cavities, cracks, and resistant microinclusions like SiO_2 or SiC.

The surface roughness of the rod should approximately be below 1 mm. If necessary, it can be ground. Normally, the feed rod needs to be shaped for the FZ process by grinding a cone on one end as well as mounting grooves on the other end. Before assembling, the feed rod must be carefully cleaned by etching off a few microns from the surface with a mixture of nitric and hydrofluoric acid followed by rinsing with ultra pure water.

7.1.3.5 Induction Coil and Arcing

Of course, all other items of the FZ setup positioned near the hot zone must also be cleaned carefully. Especially the surfaces of the induction coil made of copper or silver should be brightly polished and freshly cleaned in an ultrasonic bath.

The coil is electrically and mechanically connected with the RF power generator outside the growth chamber via the coaxial feedthrough, even supplying the coil with water. It is a very sensitive component because, here, the highest voltages occur and surface damage or pollution could initiate electrical breakthrough.

However, most critical for electrical breakthrough or arcing is the slit of the inductor. In fact, this is not the region of maximum RF voltage but of the highest electric field strength due to the narrow gap, which has to be minimized in order to reduce a heating peak under the slit causing local stress near the growth interface. Arcing and stress anomalies are the worst drawbacks against increasing the crystal diameter. Unfortunately, most approaches to prevent that arcing lead to double binds:

- Reduction of the electric field strength by widening the slot is coupled with increasing deviations of the thermal symmetry, causing dislocations.
- Increased pressure of the growth atmosphere accelerates the convective cooling of the crystal, causing hazardous thermal stress and the risk of crystal cracking or at least dislocation generation.
- A lower working frequency corresponds to lower RF voltages at the coil but increases the Lorenz forces driving the melt convection [12]. Additionally, the enlarged skin depth disturbs the melting of the feed rod.

- Adding traces of nitrogen increases the electric strength of the argon atmosphere, but too much nitrogen causes silicon nitride precipitates.

7.1.4 FZ Crystal Morphology: Ridges and Orientation

7.1.4.1 Growth Habitus

Indeed, the crystal anisotropy of silicon concerning the most material parameters is not negligible but comparably weak due to the fully covalent bonds and the high symmetry of the face-centered cubic lattice, but FZ silicon crystals grow under thermal conditions, which are not homogeneous but of almost rotational symmetry that dominate their habitus. Both the axisymmetric temperature gradient and the surface tension tend to form a circular crystal cross-section and a cylindrical shape, which is not completely perfect in reality. If the radial temperature gradient is too weak combined with an imperfect thermal symmetry, e.g., due to inductor issues, the growth interface easily becomes inclined, which deforms the melt meniscus and causes eccentric crystal growth. The interaction with the rotation then affects a corkscrew-like habitus, being a fatal risk for the crystal.

Additionally, typical ridges appear along specific cylinder surface lines according to the respective crystallographic growth direction because the temperature of solidification slightly depends on the local orientation of the curved crystallization front. As a result, the radial crystallization rate differs when generating those ridges. Watching the ridges, the crystal grower can directly realize the crystal orientation and the loss of the dislocation-free structure.

In case of the <100> growth direction, four equal ridges appear mutually twisted by an angle of 90° according to the fourfold axial symmetry. These ridges are commonly weak and do not disturb the thermal symmetry. On the other hand the threefold <111> direction corresponds to three larger ridges twisted by 120° and three weaker ones in between. The <111> ridges often transform to different bulges causing eccentric distortions of the temperature and stress fields (see Figure 7.1(a)).

Other orientation-related peculiarities are based on different angles between crystal axis and the main planes for dislocation gliding and cleavage, which are influencing the probability of dislocation generation and crystal bursting during FZ growth, respectively.

For these reasons, <111> FZ crystals can currently be grown with a maximum diameter of 150 mm, whereas <100> crystals reach 200 mm.

7.1.5 Doping Techniques and Impurity Distribution

The classical doping method for FZ silicon is the use of pre-doped feed rods produced after the Siemens process (see Section 7.1.3.4) using intentionally doped slim rods that define the resistivity and the conduction type of the resulting FZ crystal. This method is rather simple and axially homogeneous but not flexible.

Presently, FZ crystals are mostly doped in situ by a controlled gas stream containing traces of gaseous compounds of the doping elements (PH_3 or B_2H_4), which is blown

directly onto the molten zone, where the compound decomposes and the remaining dopants P or B dissolve and spread homogeneously by melt convection. However, the doping concentration varies radially because the melt flow field influences the thickness of the diffusion layer close to the crystallization interface.

For dopants with small segregation coefficients $k \ll 1$ like Ga, In, or Al, a piece of highly pre-doped silicon ("doping pill") can be put in a small radial hole that has been drilled into the feed rod. When molten, the pill will dope the melt. During the FZ growth, the doping concentration in melt and crystal will stay almost constant because a tiny but constant fraction of the dopant will be dissolved in the crystal.

Doping with oxygen from the gas phase is not effective because mainly gaseous SiO evaporates, but by contacting the melt surface with a slice of fused silica (SiO_2), oxygen (but no carbon) is introduced according to the contact area similar to the CZ process [13].

7.1.6 Recent Development

FZ silicon has some benefits in comparison to CZ silicon. It features some superior material parameters, and the FZ process saves energy and avoids consumables like crucible, heaters, and thermal insulation. However, its field of application is restricted mainly by the expensive high quality feed rods and the limitation of the diameters of the Siemens feed rods and the FZ crystals.

Recently, a novel crystal growth concept was investigated with the goal to grow cost-reduced crystals of FZ quality by replacing the feed rod with continuously fed fluid bed granulate, which is produced by the Siemens process with excellent purity and only a fraction of the effort necessary for polysilicon rods. For this granulate FZ (gFZ) method, the German company Siltronic AG applied several patents [14] concerning the process principle and special induction coils as shown in Figure 7.10. The Si granulate is

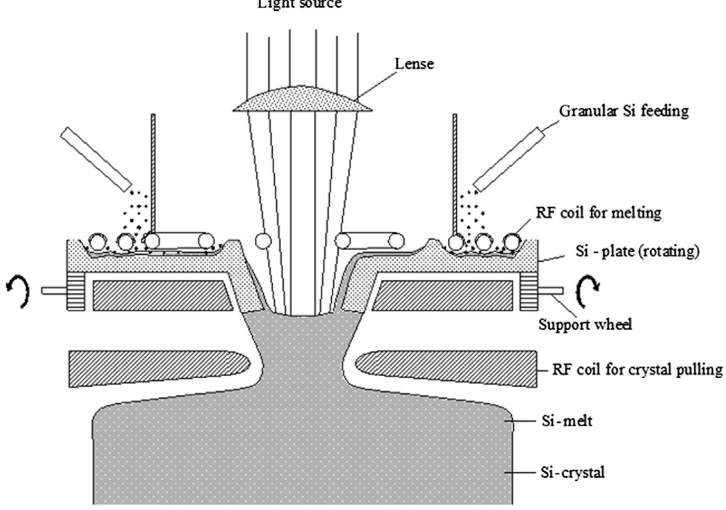

FIGURE 7.10 Principle of the granulate floating zone method. *After [14].*

continuously supplied to a plate made of silicon being heated by a sophisticated inductor, which simultaneously melts the granulate and sustains a tubular opening in the center of the silicon plate, where the melt can pass down by forming a hanging neck as a bridge to the melt lake on top of the growing gFZ crystal. This silicon plate must be cooled from the bottom to protect it against distortion. As a consequence, a second independent inductor is installed on top of that Si melt lake in the gap under the cooled Si plate. This lower induction coil has to maintain the thermal field for the crystal, which grows like in the FZ process. If the gFZ method is matured, silicon crystals of FZ quality can be produced with reduced costs and could compete even against CZ silicon particularly for high efficiency solar modules.

Another new attempt also targets PV application: the growth of FZ crystals with quadratic cross-section (qFZ) [15]. In principle, the qFz crystal grows without rotation in a heating field of fourfold symmetry provided by a special inducting coil [16]. The feasibility of that concept was demonstrated for a 100 mm × 100 mm cross-section. Because solar cells are quadratic, the waste of silicon is reduced if the crystal is quadratic. Furthermore, the needed RF voltage mainly depends on the crystal cross-section, larger squares can be grown before arcing occurs.

Electric breakthrough at the coil slit is still the most crucial drawback for the FZ development toward diameters beyond 200 mm. The application of lower working frequencies resulting in an approximately linearly decreasing voltage could be promising, but negative side effects might be difficult to overcome.

A detailed understanding of the gas-discharge processes under the specific FZ conditions appears as the key for substantial progress. It is presently not well understood why the RF breakthrough voltage only weakly increases with increasing pressure of the growth atmosphere and not linearly as predicted by the Paschen rule [17]. Especially the impact of the gas temperature in the vicinity of the cooled coil, where the temperature difference to the melt is more than 1000 K over a few mm distance, should be investigated in detail.

7.2 Automation of the Floating Zone Process Using Model-Based Control

7.2.1 Motivation

For increasing the yield of dislocation-free monocrystals, attempts are being made to make the FZ process automatic. The large silicon crystals of up to 200 mm diameter, as grown in the modern industrial FZ production, require sophisticated process conditions. Even for experienced operators, it is difficult to keep the small window of suitable growth conditions by manual growth. Therefore, automatic growth control is a key issue in production of monocrystalline silicon with respect to yield, quality, and reproducibility. It is essential to produce crystals with equal properties by keeping identical processing conditions.

In the 1980s, in the FZ industry, the application of automatic control, mainly PID controllers, was targeted [18–20]. Reference values are crystal diameter and axial height of the molten zone. The process is monitored with an imaging device, and geometric quantities are measured from the obtained video camera images. The controller parameters are set up separately for each setup in every process phase due to the changing dynamics during the process. If the process environment is modified (new machine components, new crystal diameter), the PID controller has to be set up again. The better way is a model-based controller that gives a widely flexible handling of different machine components, different inductor types, and different target diameters. Also, the changing dynamics of the process can be directly handled by model-based automation if a suitable mathematical model is available. In 1996, the German company Wacker Siltronic AG published an idea to control growth processes, for instance, CZ and FZ, by a prediction control method (see [21,22]). The patents do not provide a model description, they include the idea of predictive control by using online and offline simulation. Due to the complex dynamics, it is necessary to use a nonlinear model for controlling the crystal growth of large-diameter crystals. In this section, a nonlinear model predictive control (NMPC) is presented to control the process as developed in the Leibniz Institute for Crystal Growth (IKZ) by Werner [23].

7.2.2 Description of the Measurement System

The growth chamber has an optical access to the FZ process through a quartz window, so that the geometrical quantities of feed rod, molten zone, and crystal can be obtained by visual image processing. Figure 7.11 shows a sketch of the geometrical quantities calculated from measurements. The identification of the quantities is based on the idea of edge detection, a mathematical method to identify points in a digital image. The points are characterized by a sharp change of the image brightness [24]. The crystal radius R_C is directly measured at the line of crystallization (solid–liquid interface). The lower zone height h_C is the distance between the lower edge of the inductor and the line of crystallization. The volume of the molten zone consists of a visible and a hidden part.

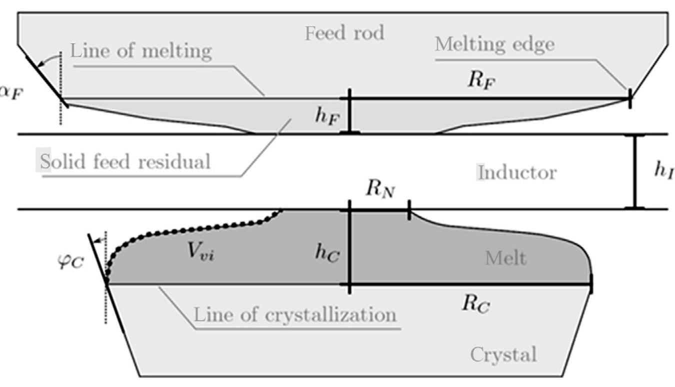

FIGURE 7.11 Geometrical quantities calculated from measurements: visible melt volume V_{vi}, crystal radius R_C, crystal angle φ_C, feed radius R_F, feed angle α_F, upper zone height h_F, lower zone height h_C, height of the inductor h_I, radius of the melt neck R_N.

The visible melt volume V_{vi} is calculated from the outer contour of the molten zone assuming rotational symmetry. The volume V_{bo} of the melt bowl is covered by the crystal surface and arises due to the radial temperature gradient in the crystal. An approximation of V_{bo} based on LPS is given in Ref. [23]. Instead of the real melt neck, which is covered by the inductor, an approximated R_N is measured directly below the inductor. The upper zone height h_F is the distance between the upper edge of the inductor and the line of melting. The solid part below the line of melting is the feed residual. The feed rod is shaped at the lower end, so, it is required to measure radius R_F and angle α_F of the feed rod. The distance between the lines of melting and crystallization is the height of the full zone h_G.

The melting rate v_{Me} and the crystallization rate v_{Cr} are not directly measurable and have to be identified using an estimator. The melting rate $v_{Me} = -\dot{L}_F$ is defined as negative derivative of the feed rod length L_F (distance between line of melting and feed holder). A positive melting rate v_{Me} means a decreasing feed length. The crystallization rate $v_{Cr} = \dot{L}_C$ is the derivative of the crystal length L_C (distance between line of crystallization and crystal holder). In the literature, the crystallization rate is also denoted as the growth rate.

7.2.3 Modeling of the Floating Zone Process

The goal is to get a set of nonlinear differential equations of first order with respect to time, which predicts the fundamental behavior of the process dynamics without expensive and time-consuming calculations. The model based on physical conservation laws and details are given in Ref. [23]. The model describes the dynamical behavior in the mathematical form

$$\dot{\underline{x}}(t) = f\left(t, \underline{x}(t), \underline{u}(t), \underline{\Theta}\right) \quad \text{with} \quad \underline{x}(0) = \underline{x}_0. \tag{7.2}$$

For a given initial state $\underline{x}_0$ and a given sequence of inputs $\underline{u}(t)$, the future development of the state vector $\underline{x}(t)$ can be calculated by using a numerical integration of the state derivatives $\dot{\underline{x}}(t)$. The elements of the parameter vector $\underline{\Theta}$ represent the model parameters. The state vector $\underline{x}(t)$ includes the components: radius of feed R_F and crystal R_C, height of upper zone h_F and lower zone h_C, angle at feed α_F and crystal φ_C, volume of visible melt V_{vi}, radius of melt neck R_N, crystallization rate v_{Cr}, melting rate v_{Me}, and inductor power P_{ind}. The input vector $\underline{u}(t)$ includes the three components: generator power P_{gen}, pull rate of feed v_F, and crystal v_C. The following differential equations are involved:

$$\frac{d}{dt}(R_F) = v_{Me} \cdot \tan(\alpha_F), \tag{7.3}$$

$$\frac{d}{dt}(R_C) = v_{Cr} \cdot \tan(\varphi_C), \tag{7.4}$$

$$\frac{d}{dt}(h_F) = v_{Me} - v_F, \tag{7.5}$$

$$\frac{d}{dt}(h_C) = v_C - v_{Cr}, \tag{7.6}$$

$$\frac{d}{dt}(\alpha_F) = 0, \tag{7.7}$$

$$\frac{d}{dt}(\varphi_C) = \frac{\Delta\varphi_C}{\Delta V_{vi}}\dot{V}_{vi} + \frac{\Delta\varphi_C}{\Delta R_C}\dot{R}_C + \frac{\Delta\varphi_C}{\Delta h_C}\dot{h}_C + \frac{\Delta\varphi_C}{\Delta R_N}\dot{R}_N, \tag{7.8}$$

$$\frac{d}{dt}(V_{vi}) = \frac{\rho_S}{\rho_M}\left(\pi R_F^2 v_{M\acute{e}} - \pi R_C^2 v_{Cr} - \dot{V}_{fr}\right) - \frac{\rho_M - \rho_S}{\rho_M}\dot{V}_{bo}, \tag{7.9}$$

$$\frac{d}{dt}(R_N) = n_h\left(\dot{h}_F + \dot{h}_C\right), \tag{7.10}$$

$$\frac{d}{dt}(P_{ind}) = \frac{1}{\tau_p}\left(K_p \cdot P_{gen} - P_{ind}\right), \tag{7.11}$$

$$\frac{d}{dt}(v_{Me}) = \frac{d}{dt}\left(\frac{p_F - P_{F,loss} + q_0\rho_S\dot{V}_{fr}}{q_0\rho_S\pi R_F^2}\right), \tag{7.12}$$

$$\frac{d}{dt}(v_{Cr}) = \frac{d}{dt}\left(\frac{p_{C,loss} - P_C + q_0\rho_S\dot{V}_{bo}}{q_0\rho_S\pi R_C^2}\right). \tag{7.13}$$

where ρ_M is the density of the melt, ρ_S is the solid density, $\dot{V}_{fr}$ is the derivative of the volume of the feed residual, $\dot{V}_{bo}$ is the derivative of the volume of the melt bowl, q_0 is the latent heat. The variables n_h, K_p, τ_p are model parameter. The terms $P_{F,loss}$ and $P_{C,loss}$ describe the power loss of feed rod and crystal due to radiation. The power introduced into feed rod P_F and crystal P_C are modeled as functions of inductor power P_{ind}, corresponding radii R_F and R_C, corresponding zone heights h_F and h_C, and further model parameters. A detailed description is given in Ref. [23].

7.2.4 Choice of Reference and Manipulated Variables

It is essential to set up suitable reference and control variables to fulfill the requirements of the FZ process. In the presented automation concept, the considered control variables are the heater power of the inductor and the pull rates of feed and crystal.

7.2.4.1 Creating the Thin Neck

This is the start of growing a crystal. Feed and crystal are moved downward to create the thin neck. The crystal diameter of 5–6 mm, resulting from the diameter of the seed, has to be reduced down to 2–3 mm and kept constant until the end of that phase where all dislocations have to grow out. For creating the thin neck, the references are zone height and crystal diameter as functions of time.

7.2.4.2 Growing the Crystal Cone

The crystal diameter has to be increased by producing and keeping a melt overhang by adjusting heater power and pull rate of the feed rod. In this phase, a constant or slowly changing pull rate of the crystal is used to ensure the dislocation-free growth. The observation of the melt neck is important to satisfy the limits due to the inductor hole.

To overcome measuring problems of the melt neck, the zone height h_G is applied as an auxiliary quantity within the automation. The reference of the zone height has to be designed for a suitable melt neck. The complete crystal, starting from the cone, can be defined as a function of the crystal length L_C for achieving a reproducible crystal shape.

7.2.4.3 Growing the Cylinder

Here, the crystal diameter is held constant. This is managed by constant heater power and constant pull rates of feed and crystal. The process is self-regulating and in a stable state during this phase. At the end of the process, the heater power has to be adjusted slightly to keep the height of the molten zone. Here, the heat transport of the feed rod is affected due to its length reduction.

7.2.5 Regulated Growth of the Avogadro Crystal

As an example of applying this control method, the regulated growth of a crystal with a special shape, the so-called Avogadro crystal, is shown. The crystal is used in an approach to determine the Avogadro constant by "counting" the atoms of a 1 kg monocrystalline sphere of ^{28}Si isotope. Details of the physical background are given in the reviews [25–27]. Two silicon spheres have to be obtained from one grown crystal. Due to the high costs of the material, a regulation is applied to grow a crystal with

FIGURE 7.12 Image of the grown Avogadro crystal using regulation. The image was taken by Turschner at the Leibniz Institute for Crystal Growth (IKZ).

minimum material waste. So, there is no cylindrical part in the crystal. The diameter has to be decreased after finishing the cone and increased again up to the full diameter. A regulation is needed to fulfill this reference of the shape. For this experiment, a common feed rod of polycrystalline silicon is used instead of the expensive ^{28}Si material. The automation starts at a crystal diameter D_C of 42 mm. Figure 7.12 shows the image of an “Avogadro crystal”. The advantage of applying the model predictive control, instead of the previously used PID control, is that this shaped crystal can be grown at other FZ machines without a new parameter identification.

7.3 Mathematical Modeling of the Floating Zone Silicon Growth

7.3.1 Introduction

The numerical simulation of the FZ process is mainly carried out to understand the physics of the process and to support its development. The simulation considers the most important physical effects that connect the process parameters to quality, shape, and yield of the grown crystals and to the ability to grow the crystal at all. Nowadays, models of the FZ process can predict the effects quantitatively and are successfully used in the process development.

This section describes the needle-eye FZ process from the modeling point of view, gives an overview of the modeling history, outlines the state-of-the-art model system, and presents modeling results characterizing the most important findings and the effects of process parameters.

Due to the absence of a crucible, all melt interfaces are determined by the machine setup, process parameters, and the process history, but not by a predefined geometry of the crucible. This requires a global model for the calculation of the interface shapes considering the electromagnetic (EM), thermal, and flow fields.

The RF inductor (Figure 7.13) induces the EM field into the Si material at all surfaces that are in contact with the process gas, mainly in the feed rod and in the melt. As a result, the feed rod is molten and the so-called open melting front 2 is formed. A part of the induced heat is radiated away from the open melting front directly and the rest is conducted through the feed rod to its cylindrical surface 1 and radiated away there. The heat sources at the free melt surface 4 keep the zone molten, compensating the radiation heat loss and ensuring some heat flux and thermal gradient at the crystallization interface 6 and melting interface 3. The induced Lorenz forces influence the shape of the free melt surface and contribute to the convection in the molten zone. Aside from the EM forces, the shape of the free surface is determined by the hydrostatic pressure and the surface tension. The free surface contacts the crystal at exterior triple point (ETP) and the poly rod at internal triple point (ITP). The shape of the crystallization interface is determined mainly by the heat flux from the melt and by the radiation on the crystal surface 5, which is sometimes reduced using a reflector.

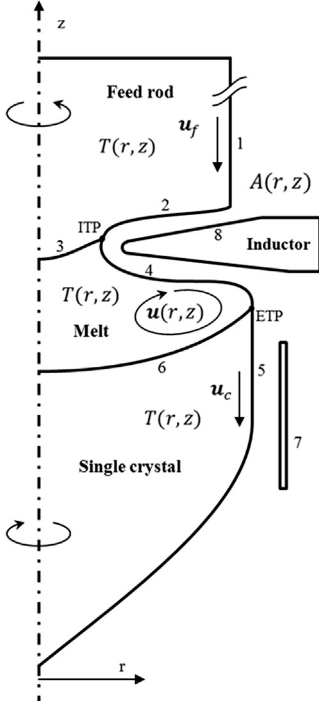

FIGURE 7.13 Schematics of the floating zone model. 1, cylindrical surface of feed rod; 2, open melting front; 3, melting front; 4, free melt surface; 5, cylindrical crystal surface; 6, crystallization interface; 7, reflector; after [28].

The EM and temperature fields are strongly coupled with the interface shapes and a change of some process parameter will influence all of them, see Figure 7.14. Therefore the modeling of particular processes without the use of a global model is questionable and should be handled with care, if some a priori shapes are used, also experimentally obtained ones.

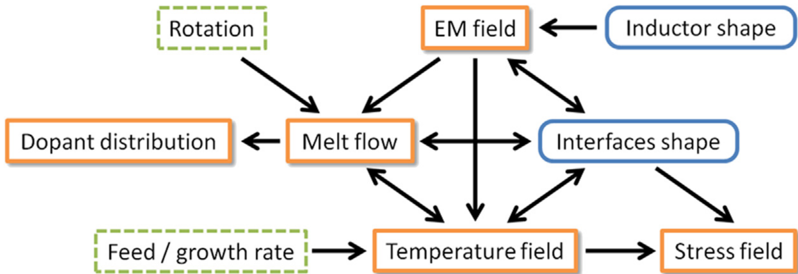

FIGURE 7.14 Schematic of the coupling between the modeled physical fields (solid rectangles), the interface shapes (rounded rectangles), and the influence of process parameters (dashed rectangles).

7.3.2 Historical Overview

The first article on modeling of the needle-eye FZ growth process was published in 1983 by Mühlbauer et al. [28]. The current distribution at the free melt surface and the electromagnetically driven flow in the melt were calculated assuming a predefined interface. Later articles in the early 1990s were also devoted to the modeling of the EM field [29]. The shape of free surface and distribution of electric current for predefined triple points were calculated by Lie et al. in Ref. [30] and the melt motion under the influence of a strong axial magnetic field in Ref. [31]. The 3D distribution of the EM field was calculated by Mühlbauer et al. in Refs [32,33]. Despite a considerable asymmetry as shown in these articles, axisymmetric 2D models were widely used to reduce the computational effort. The effect of the inductor slits on the current distribution is considered in 2D models in a simple [34] and advanced way [35].

The first global 2D model considering the EM, temperature, and transient fluid flow fields as well as the interface shapes was published by Mühlbauer et al. [29] and investigated in detail in Ref. [34]. Riemann et al. calculated the shapes of the free surface and the crystallization interface, and the thermal stress in the crystal [36]. Mühlbauer et al. extended the model [34] and calculated transient dopant transport in the melt [37] and compared the calculated resistivity distributions with experiments [38,39]. The influence of different additional magnetic fields on the resistivity distribution is studied by Raming et al. in [40–42].

Other global models were developed in the late 1990s. Togawa et al. [43] calculated the interface shapes, heat transfer, a transient melt flow including dopant transport, and the resistivity distribution. This model is improved with implemented radiation view factors by Guo et al. [44]. Larsen et al. [45] calculated interface shapes, heat transfer, and point defect dynamics in 4″ and 0.8″ crystals. The dopant transport for 4″ processes is modeled in Ref. [46].

Muiznieks et al. [47] showed that the thermal stress in 4″ FZ crystals is higher than in 300 mm CZ crystals and investigated the dislocation generation induced by thermal stress.

The model [34] is reconsidered, rewritten, and extended by the view factor radiation and the variable liquid film thickness on the open melting front by Ratnieks et al. [48,49]. Next model extension by Rudevics et al. [50–52] allows calculating the FZ process in a transient way, the growth of starting and end cones, as well as the control of the crystal diameter using PID algorithm.

A coupled 3D model for the EM, temperature, melt flow, and dopant concentration fields was developed for the first time by Ratnieks et al. [53]. Here and in further studies [54–56] the generation of the rotational striations in the crystal were shown. The paper [57] shows that the resistivity fluctuations due to convection are at least by one order of magnitude higher than those due to the changes of the local growth velocity.

The 3D resistivity distribution is investigated under the impact of rotating [58–60] and steady axial [59] magnetic fields.

A model for the simulation of an EM field, heat transfer, melt flow, and thermal stress was developed and presented in the PhD theses of Assaker [61] and Bioul [62].

Rudevics et al. [63] presented a nonsymmetric 3D model calculating EM and temperature fields as well as the free melt surface and crystallization interface based exclusively on boundary element method (BEM).

3D modeling of the free melt surface and crystallization interface during the growth of square-shaped FZ crystals is presented in Ref. [64].

Menzel [65] uses the measured interface shapes to calculate the 3D EM field of different frequencies using the commercial code SINGULA and applying these results for the calculation of 2D fluid flow using the commercial code ANSYS-CFX.

Wünscher et al. [66] and Menzel [12] applied COMSOL for 3D and 2.5D modeling of EM, temperature, and stress fields as well as the shapes of free surface, melting, and crystallization interfaces for 4″ and 5″ process.

The effect of gas flow on the cooling of the crystal is considered by applying a heat transfer coefficient in Refs [12,46].

7.3.3 Mathematical Models

The models described here build the core system necessary to satisfy the interests of crystal growers developing the process regarding increased quality and yield requirements. The models are macroscopic, i.e., they consider the material with continuum properties and do not describe the atomistic scale of crystal growth. However, the calculated quantities can be further used to analyze the processes on micro and atomistic scales [67].

The conditions near the molten zone during the growth remain very similar for a long time, therefore, mainly the quasi-steady approach is used (the non-steady model is described in Section 7.3.3.7).

The crystal, poly rod, and the melting and crystallization interfaces are assumed axisymmetric in all models because the rotation averages the influence of the nonsymmetric one-turn inductor (except for growth of square-shaped crystals [64]).

The schematic of main influences coupling the modeled physical fields, the interface shapes, and the process parameters is shown in Figure 7.14. The interface shapes depend on the EM, temperature, and melt flow fields, and vice versa. Therefore, any modeling study of one of the particular fields demands the coupled modeling of the interface shape. The following sections describe first the particular models assuming fixed interfaces, and Section 7.3.3.5 reports on the coupling procedure in more detail. Afterward the specifics of transient modeling are described.

7.3.3.1 Electromagnetic Field

The EM field heats up and melts the polycrystalline rod as well as maintains the molten zone from which the crystal is grown. As the EM field distributes with the speed of light and its frequency is several orders higher than the time scale of the thermal and mass

transport processes, all other fields and interfaces can be assumed to be fixed during the calculation of the EM field. At the typical frequency of 3 MHz the EM field penetrates into the thin skin layer of 1.3 mm in solid Si, 0.27 mm in molten Si, and 0.04 mm into the Ag inductor. The rest of the conducting bodies are free from the EM field. Using Maxwell's equations in quasi-static approximation, where the displacement current is neglected [68] in the formulation of the magnetic vector potential the Laplace equation in a nonconducting space is

$$\Delta A = 0. \tag{7.14}$$

Assuming that all currents can be described by surface currents, the boundary condition (BC) for the vector potential on Si surfaces is

$$A = 0 \tag{7.15}$$

and on the inductor surface it is defined by the applied voltage [34]. The distribution of currents is searched to fulfill Eqn (7.15). It is solved using BEM, therefore only surface meshes in 3D space are necessary. The result is the distribution of the effective surface current density j_S. For more detail on the 2D case and the 2D slit model see Ref. [35], and for the 3D case formulation see Ref. [33]. From the surface current density j_S the normal EM pressure for the calculation of the free surface shape, the tangential EM surface force for the melt convection, and the Joulean heat sources for the temperature field can be calculated [35].

7.3.3.2 Temperature Field

Due to inductive heating, the highest temperature in the FZ system is in the melt. Therefore, the temperature for the crystal and the melt ambient is lower than in the CZ system and the temperature gradients are higher. The heat transport is characterized by Joulean heat sources at Si surfaces, by conduction in a poly rod and a crystal, and by conduction and convection in the melt as well as radiation in the gas.

The temperature transport equation in solids using the quasi-stationary approach is

$$\rho c_p \boldsymbol{u}_c grad\ T = div(\lambda_s(T) grad\ T) \tag{7.16}$$

where $\boldsymbol{u_c}$ is the vertical pull rate of the feed or the crystal with respect to the laboratory reference system. The interfaces' shape is assumed to be fixed during the calculation of the temperature field. Surface heat sources are not included in Eqn (16) but are considered in the BC. The temperature on the melting, crystallization, and free melting front is set to melting temperature T_0. On Si–gas interfaces the heat flow BC is set to

$$\lambda_S(T)\frac{\partial T}{\partial n} = q^{EM} - q^{rad}, \tag{7.17}$$

where q^{EM} are the Joulean heat sources and q^{rad} are the radiation heat losses described in the next section. Heat transfer is modeled by finite element method (FEM). The calculated temperature fields are used for the calculation of interface shapes and the thermal stress.

The radiation in ambient gas is the main heat transfer mechanism from the hot crystal, melt, and poly rod surfaces to the cold recipient and inductor, the conduction and convection effects in the gas are less important [12]. The simplest assumption is the radiation to predefined ambient temperature T_a

$$q^{rad} = \varepsilon \sigma_{SB} \left(T^4 - T_a^4 \right). \tag{7.18}$$

Lower ambient temperature for crystal and poly rod and higher for melt and open melting front are applied [34].

Later the radiation heat exchange is calculated more precisely using view factors describing the gray diffuse radiation exchange in transparent media; see Ref. [44] for differences between the results using constant ambient temperature and view factors. Details about the calculation of view factors can be found in Ref. [35]. The calculation of view factors is a time-consuming operation in the 3D [63] and also in the 2D axisymmetric case [69] and is often optimized at the expense of precision [35].

7.3.3.3 Melt Flow

The melt flow in the FZ process is laminar but nonstationary [28]. The continuity equation for an incompressible fluid and the Navier–Stokes equation using the Boussinesq approximation including the external force, e.g., due to an applied steady or low frequency magnetic field, are solved. Marangoni forces due to the temperature dependence of surface tension and EM forces caused by the RF inductor are included in the BC on the free melt surface [35], and Ref. [70] shows that it is allowable. The rotation of the crystal and the poly rod causes forced convection and the corresponding velocities are also included in the BC.

The temperature distribution in the melt is described by the heat transfer equation and is coupled to the Navier–Stokes equation. Joulean heat sources are included in the BC similarly as in the solid parts.

In the 2D case model equations can be rewritten in the vorticity-stream function $(\omega - \psi)$ formulation and can be solved using FEM as described in detail in Refs [34,35]. Three dimensional laminar unsteady model equations are solved based on the OpenFOAM libraries [71,72].

7.3.3.4 Impurity Distribution

Concentrations of impurities (dopants) in the Si melt are small, therefore, they have no influence on the flow. The conservation equation of dilute species C is

$$\frac{\partial C}{\partial t} + (\boldsymbol{u} \nabla) C = D \Delta C \tag{7.19}$$

where D is the diffusion coefficient of dopants in molten Si. The segregation BC is set at the crystallization interface [73]. If the doping is realized from the feed rod, the concentration C at the melting front is set equal to the concentration of the dopants in the feed rod [40,41,46] and zero flux is set to the free melt surface [37]. In the case of doping from

gas, the concentration is set to zero on the feed rod and is normalized to 1 at the free surface [74] or constant flux is set at the free surface [46]. The different conditions at the free surface are used because the precise transport of dopants in the gas is not modeled.

7.3.3.5 Shape of Interfaces

The shapes of melting and crystallization interfaces are defined by the balance of heat fluxes. The BC for temperature is set to $T = T_0$ during the calculation of the temperature field in each part (poly rod, melt, crystal). The difference of the calculated heat fluxes on both sides must be equal to the latent heat for given feed and pull rates, i.e., fulfill the Stefan condition [75]. Each point of the melting (M) or crystallization (C) interface is moved by their normal velocity according to the laboratory reference system

$$v_n^{M,C}(t) = \frac{\lambda_S}{\rho_S Q}\frac{\partial T(t)}{\partial n}\bigg|_S - \frac{\lambda_S}{\rho_S Q}\frac{\partial T(t)}{\partial n}\bigg|_L - V^{M,C}(t)n_z^{M,C}(t) \tag{7.20}$$

where V^M is the feed rate of the poly rod and V^C is the pull rate of the crystal. The indices S and L depict the solid and liquid side of the interface. The shape of the interface is found when the velocity is zero.

On the open melting front the temperature is also assumed to be $T = T_0$, although the thin liquid film with a thickness around 0.2 mm has a slightly higher temperature [35]. The velocity of the open melting front (O) movement is

$$v_n^O(t) = \frac{\lambda_S}{\rho_S Q}\frac{\partial T(t)}{\partial n}\bigg|_S - \frac{q^{rad} - q^{EM}}{\rho_S Q} - V^M(t)n_z^O(t). \tag{7.21}$$

The shape of the interface is found and the velocity of the open melting front is zero if EM heat sources are balanced by radiation, heat conduction in the poly rod, and latent heat.

The shape of the free melt surface is calculated as a balance of normal stress considering the surface tension and hydrostatic and EM pressure

$$p_0 - \rho_l g z - \gamma\left(\frac{\cos\phi}{\mathrm{r}} + \frac{1}{R'}\right) - p^{EM} = 0 \tag{7.22}$$

where R' is the radius of curvature in the (r,z) plane, ϕ is the angle with the vertical, and p_0 is the reference gauge pressure. For fixed ETP and ITP positions and a given p_0, the shape of the free surface can be determined minimizing the imbalance of Eqn (22). The value of p_0 is unknown and can be chosen in order to satisfy the Si growth angle and keep the diameter of the crystal constant. Special attention should be paid to the modeling of ETP and ITP where conditions for all encountering interfaces must be satisfied [35].

7.3.3.6 Thermomechanical Stress

The relation between stress and strain tensors (Hooke's law) in isotropic case for small linear displacements is

$$\sigma_{ij} = \frac{E}{1+v}\left(\varepsilon_{ij} + \frac{v}{1-2v}\varepsilon_{kk}\delta_{ij}\right) - \frac{E\alpha t}{1-2v}\delta_{ij} \tag{7.23}$$

where for Si the Young modulus $E = 1.56 \times 10^{11}$ N/m^2, Poisson's ratio $\upsilon = 0.25$, and coefficient of thermal expansion $\alpha = 3.2 \times 10^{-6}$ $1/K$ [47]. Considering that the crystal is in equilibrium state

$$\sigma_{ji,j} = 0 \tag{7.24}$$

and strain–displacement relation

$$\varepsilon_{ij} = \frac{1}{2}(u_{i,j} + u_{j,i}) \tag{7.25}$$

the displacements $\boldsymbol{u}$ can be found solving the Eqn (24) and fixing the displacement at some point as BC. The second invariant of stress tensor, called von Mises stress [12], is often used for the analysis as a scalar measure, which is representative for the generation of dislocations.

7.3.3.7 Transient Modeling

The transient model described in Ref. [50] is based on the steady state model [48] but does not account for the convective heat transfer in the melt. The movement at any position of the melting (M) or crystallization (C) interface is defined by their normal velocity in the laboratory reference system in Eqn (20) and the movement of the open melting front (O) in Eqn (21). Knowing these velocities, the calculation of the new positions of the interfaces after a time step Δt is a straightforward task. The volumes of molten and crystallized Si during each time step are calculated as sums over all elements considering the volume change due to feed and pull rates and the volume change due to changed interface positions.

The difference between molten and crystallized volumes is the change of the melt volume ΔV_{melt} As the starting point (ETP) and endpoint (ITP) of the free surface are known (their movements and positions are calculated to fulfill the thermal conditions, as in the quasi-steady model), the new shape of the free surface is calculated iteratively so that the difference between the new and old surface shapes is equal to ΔV_{melt}. The result of the changed free surface is a new melt angle at the ETP, which determines the change of the crystal diameter in the next time step.

The process control based on the PID algorithm is implemented in the FZoneT software to ensure the growth of the crystal with a predefined shape [52]. The inductor current and the feed rate are adjusted according to the deviation between the actual and desired values for the position of the crystal radius and zone height. The process control is described in more detail in Section 7.2 and in Vol. 2b, Section 10.

7.3.4 Exemplary Results

All results demonstrated in this section are calculated with software included in the program complex FZone [48,49] or in predecessor models [28,34] and are closely related to the work of Prof. Muiznieks.

7.3.4.1 Electromagnetic Field

The results of EM field calculations are taken from Ref. [55] and are carried out for the geometry corresponding to the 4″ process at the IKZ. All surfaces are assumed axisymmetric, but the inductor is nonsymmetric with its current suppliers having a 1-mm-wide slit between them. The shapes of the open melting front and the free melt surface are taken from the global simulation, i.e., they are calculated using a coupled algorithm also including the 2D calculation of EM pressure and EM heat sources. The surfaces are meshed into triangular boundary elements (Figure 7.15(a)), and the distribution of the surface current density is calculated according to the model described in Section 7.3.3.1. The current on Si surfaces flows almost azimuthally, but in the region of the inductor slit, the current is shifted to the vertical surfaces of feed rod and crystal. The density of EM heat sources on the free surface shows a distinct minimum under the slit at the central part of the free surface (Figure 7.15(b)). The 3D current distribution can be analyzed directly to optimize the inductor shape or used as an input for 3D melt flow simulations. 3D EM field modeling with subsequent azimuthally averaging of heat sources is often used for more precise calculations of 2D interface shapes using the FZone software. The averaging is justifiable due to rotation of crystal and feed rod.

In spite of the distinct nonsymmetry of the current distribution, 2D modeling of the EM field was a standard procedure in early models [28] and is frequently used during the calculation of interface shapes in order to reduce the computation time nowadays [51,52]. The simple model for the consideration of a narrow inductor slit in 2D reduces the EM field in the central part and increases it in the outer part of Si, making the differences between 2D and 3D even smaller. This effect can be seen in the 2D EM field calculation shown in Figure 7.16, where a part of the field lines goes through the inductor (in a truly 2D case, all lines must go between inductor and the Si surfaces).

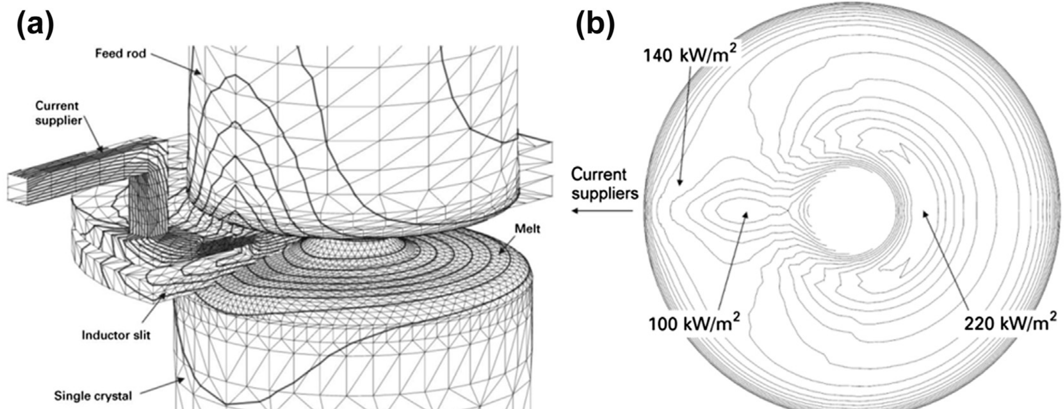

FIGURE 7.15 Results of 3D electromagnetic field simulation. View of the model geometry with only half of the inductor shown, triangular boundary elements, and calculated lines of the electric current stream function (a); Joulean power density q_{EM} on the free surface of the melt (b) [55].

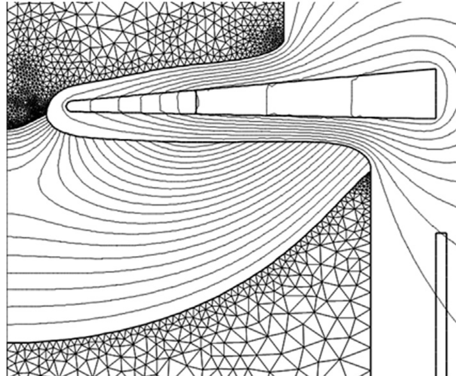

FIGURE 7.16 2D results showing isolines of magnetic vector potential A, isolines of temperature in the melt with step 2.9 K, and finite element mesh in poly rod and crystal [35].

7.3.4.2 Temperature Field

The calculated temperature field for three different stages of 4″ crystal growth with $v_G = 3.3$ mm/min and without a reflector is shown in Figure 7.17 [28]. The interface shapes are a result of the coupled EM and temperature field simulation (the influence of melt flow is not considered here) as described in Section 7.3.3.5. The temperature decreases faster along the vertical axis if the crystal or poly rod is longer due to a larger surface through which the heat can be radiated away. In the case of a short crystal, the crystallization interface has larger deflection and is located closer to the crystal surface to provide larger heat flux to the hotter crystal surface with high radiation.

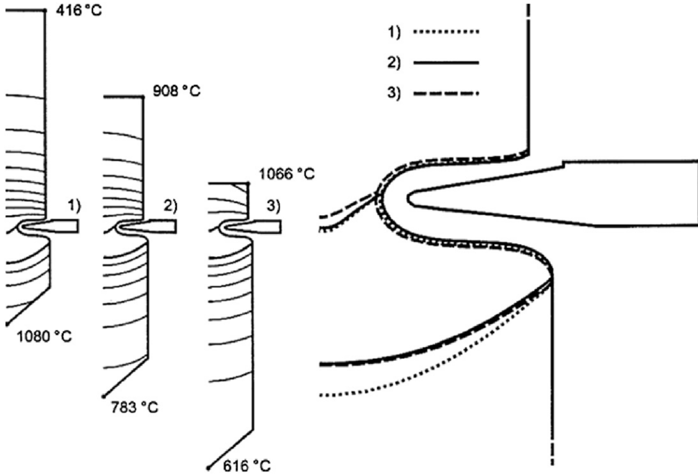

FIGURE 7.17 Temperature field (isolines with step 100 K) and shape of interfaces for three different stages of 4″ crystal growth. *From Ref. [28].*

7.3.4.3 Melt Flow and Impurity Distribution

The forces responsible for the melt convection are buoyancy, Marangoni and EM forces. The buoyancy causes downward flow along the cold interfaces and upward flow in the hot region between them. The Marangoni forces cause flow at the free surface toward the interfaces. EM forces at the free surface are directed toward the position of maximum electric current and are opposite to the Marangoni forces.

The results of transient 2D melt flow in the 4″ process for three subsequent time moments with the time step of 2 s are shown in Figure 7.18 [28]. The stream function of meridional flow with two typical vortices (left), the isolines of azimuthal velocity (center), and the isolines of temperature (right) show oscillations, especially near the axis of symmetry. However, the flow is still in laminar regime. Due to the low Prandtl number of 0.013, the temperature field is not strongly influenced by the melt flow—the distribution is similar to one without flow (Figure 7.16).

The meridional convection is reduced when the rotation rate of crystal increases [34]. Nonuniform rotation of crystal causes large vertical gradients of azimuthal velocity at the crystallization interface, which results in meridional forces with a mean value directed toward the center [34].

The inductor with slits creates a nonsymmetric distribution of Joulean sources and EM forces (Figure 7.16) and, as a result, a 3D melt flow. The results of 3D flow simulation for 4″ process is shown in Figure 7.19 [55]. Both velocity (a) and temperature (b, c) distributions show certain nonsymmetry. The resulting dopant distribution at the

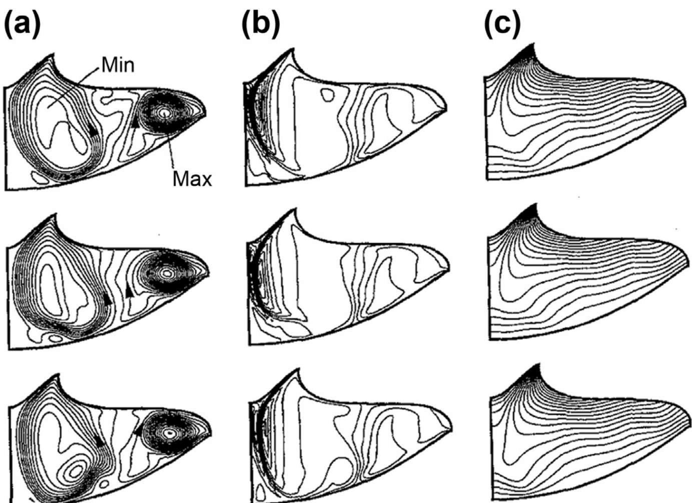

FIGURE 7.18 2D axisymmetric model. Streamlines (a), isolines of azimuthal velocity (b), and isotherms (c) for the three subsequent time moments with the time step of 2 s. *From Ref. [28].*

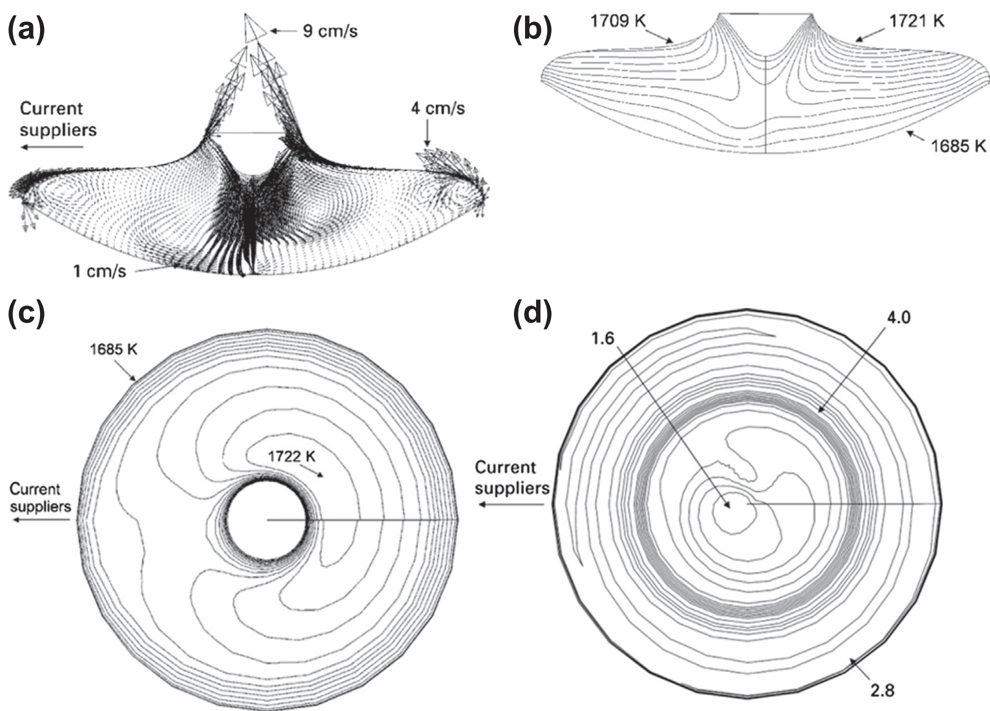

FIGURE 7.19 Results of 3D melt flow simulation for 4″ process. Velocity arrows in vertical cross-section parallel to inductor slit (a), isolines of temperature in the same cross-section (b), isolines of temperature on the free melt surface (c), and dopant concentration at the crystallization interface (d). *From Ref. [55].*

crystallization interface is nonsymmetric as well (Figure 7.19(d)), and this causes the resistivity striations in a rotating crystal.

The influence of different types of magnetic fields on the melt flow and RRV in grown crystal is demonstrated using 2D simulation of 4″ process corresponding to the IKZ facility in Figure 7.20 (from Ref. [41]). For each case, a representative time instant of the stream function of the meridional velocity and several radial resistivity profiles are shown for a time period of 50 s according to an axial length of 2.8 mm in the grown crystal. The mean value of RRV of the standard case (a) is shown in other RRV distributions (b)–(d). The reduction of the frequency of the RF inductor increases the EM forces causing more intense convection and more uniform RRV distribution with increased microscopic fluctuations (Figure 7.20(b)). A magnetic field rotating in the direction of crystal rotation with a frequency of 50 Hz and an intensity of 1 mT also creates slightly more uniform RRV distributions and increased microscopic fluctuations (Figure 7.20(c)). The application of a vertical steady magnetic field of 50 mT suppresses the microscopic oscillation of resistivity but makes the RRV less homogeneous (Figure 7.20(d)).

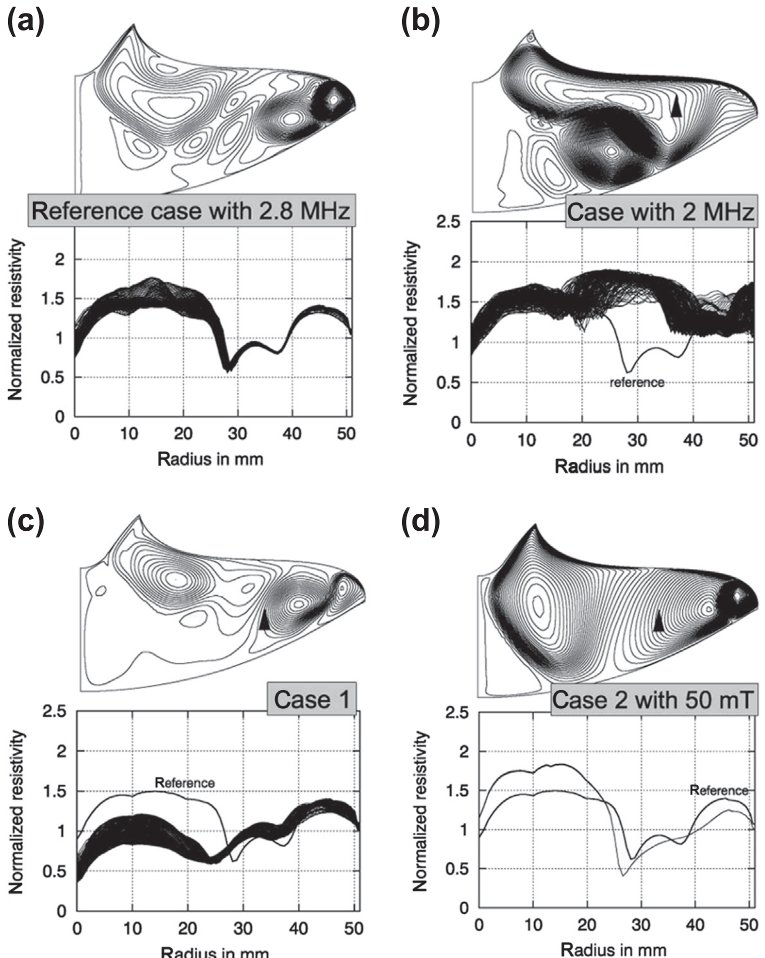

FIGURE 7.20 Stream function of meridional velocity and normalized radial resistivity distribution for basic reference case (a), with reduced frequency (b), with rotating magnetic field (c), and with vertical steady magnetic field (d). *From Ref. [41].*

7.3.4.4 Shape of Interfaces

The interface shapes are important for the quality of the crystal and crucial for the feasibility of the process, therefore, the dependencies of system geometry and process parameters are of utmost importance. Presented studies are carried out without consideration of melt flow, which was analyzed separately in Section 7.3.4.3.

The effect of the growth rate for an 8″ crystal is shown in Figure 7.21(a) for a constant zone height [35]. At higher pull rate, the deflection of the crystallization interface is larger and the open melting front is located closer to the inductor where higher Joulean heat sources are used to compensate the larger latent heat for melting the feed rod with higher feed rate. The deflection of the melting interface gets larger with an increased feed

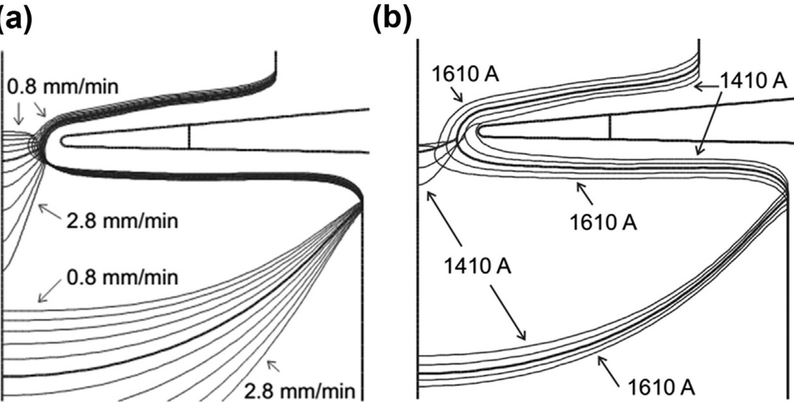

FIGURE 7.21 Phase boundaries at different crystal pull rates from 0.8 till 2.8 mm/min with a step of 0.2 mm/min (a) and for different inductor currents (zone heights) with 50 A step (b) for an 8″ crystal. *From Ref. [35].*

rate and would approach the crystallization interface when further increasing the feed rate.

The interface shapes at different inductor currents for the 8″ system are shown in Figure 7.21(b). The main effect of increasing the inductor current is the increase of zone height and decrease of the neck diameter. The variation of the inductor current for a given inductor geometry is limited by the neck diameter—at large current values the neck is too thin and will break, but for too small current values the neck approaches the inductor surface (it will result in voltage breakdown at a certain distance before touching the inductor).

The importance of the shape of the inductor is demonstrated in Figure 7.22 for 4″ process [34]. If the thickness of the inductor is halved, the process is no longer possible as the part of the melting front has a slope directed outward and the molten Si cannot flow toward the molten zone (Figure 7.22(a)). Increasing the inner diameter of this configuration by 10% assures the melt flow into the molten zone again (Figure 7.22(b)). It can also be seen that the inner diameter of the inductor strongly influences the diameter of the neck and the deflection of the crystallization interface.

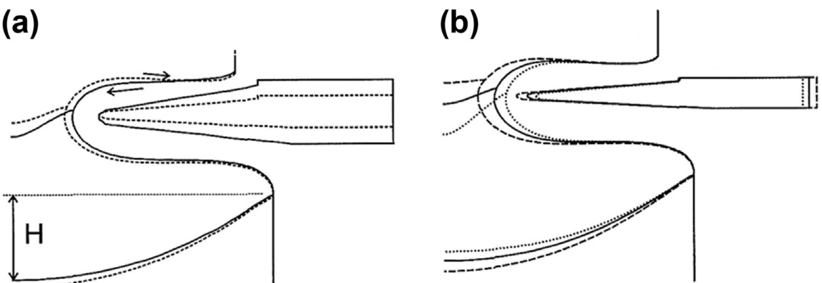

FIGURE 7.22 Phase boundaries for various inductor shapes: different heights (a) and different diameters of central hole (b). *From Ref. [34].*

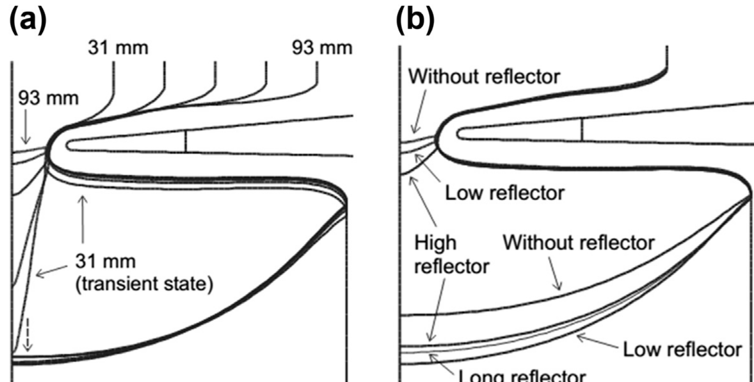

FIGURE 7.23 Phase interfaces for the 8″ process with different radii of the feed rod (a) and with different positions of the reflector (b). *From Ref. [35].*

The interface shapes for the 8″ process with different diameters of the feed rod are shown in Figure 7.23(a) [35]. The smaller the feed rod diameter, the larger the feed push rate VF and the deeper the deflection of the melting interface. A too small diameter of the feed rod (r = 31 mm in Figure 7.23(a)) makes the growth impossible because a solid bridge is built between the polycrystalline feed and the growing monocrystal.

The effect of the reflector placed around the upper part of the crystal in order to reduce the thermal stress is demonstrated in Figure 7.23(b) [35]. The "low" position of the reflector is shown in Figure 7.16 and in the "high" position the top of the reflector is placed in face of the ETP. In the presence of the reflector, fewer EM heat sources are needed, therefore, the current in the inductor is reduced (from 1600 to 1510 A for reflector in "low" position). Consequently, the maximum temperature difference in the melt is reduced by 13 K and the temperature gradients in melt and crystal are also reduced. As the main part of the heat flux in the crystal is the latent heat, which is not reduced, the position of the interface at the crystal axis is shifted down toward the region without a reflector to be able to radiate away this amount of heat. Correspondingly, at the "high" position of the reflector, the increase of deflection is not so pronounced.

The consideration of the effect of the melt flow for 8″ crystal results in a smaller deflection of the crystallization interface and a better agreement with the experimental shape [35].

7.3.4.5 Stress

In Figure 7.24 the results for the 4″ crystal with a length of 200 mm corresponding to the IKZ laboratory system are shown with and without reflector [47]. The reflector with a diameter of 140 mm and a height of 40 mm is located 20 mm below the triple point position. The reflector does not deform the temperature field considerably and the minimal temperature at the cone bottom changes slightly. A maximum value of the von Mises stress is on the symmetry axis at the growth interface, and a lower maximum is at

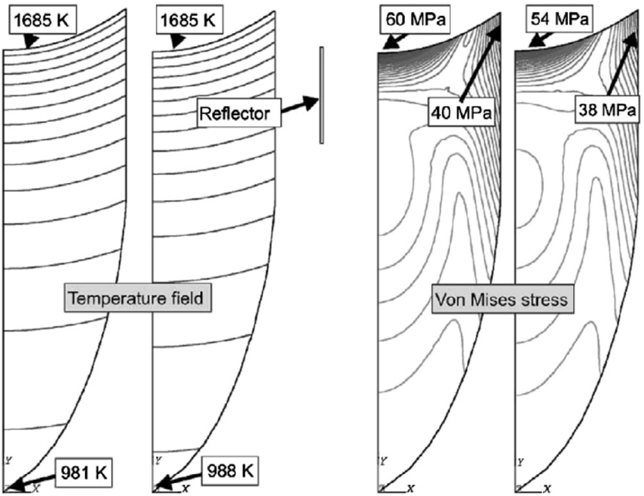

FIGURE 7.24 Temperature field with step 50 K and von Mises stress with step 2 MPa for a 4″ crystal without (left) and with reflector (right). *From Ref. [47].*

the rim of the crystal near the growth interface. The reflector reduces the stress in the center by 6 MPa and at the rim by 2 MPa. It is also shown in Ref. [47] that both maxima increase with increasing the crystal diameter and, especially, when increasing the deflection of the crystallization interface.

7.3.4.6 Transient Modeling

The response of the FZ system to the jumps of the inductor current and the feed rod velocity, which are typical process control parameters, are shown as an example of a transient model result and are compared with experiments [51]. The simulation starts from the equilibrium state calculated using the quasi-steady model, and the curves of the inductor current I_0 and the feed rate v_F, as shown in Figure 7.25(a), are applied.

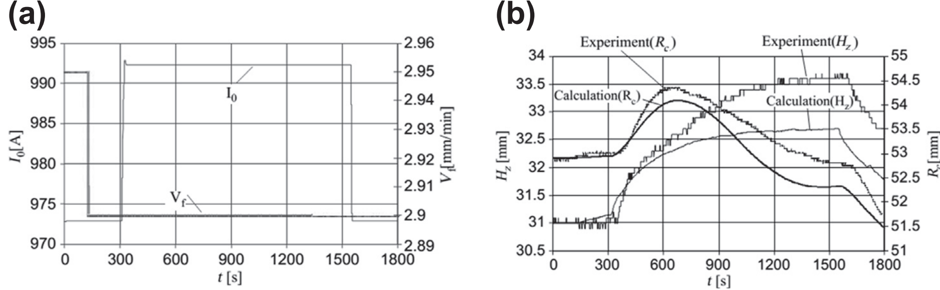

FIGURE 7.25 Step-like time dependencies of the feed rod push rate and the inductor current (a) and crystal radius and zone height response (b) during the experiment and calculation [51].

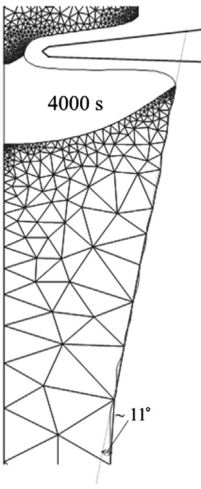

FIGURE 7.26 A numerically calculated process with automatic regulation for v_F and I_0 that ensures the crystal growth with the given slope angle of 11°, phase boundaries and finite element method mesh 4000 s from the start [52].

Figure 7.25(b) shows the calculated and measured time dependencies for crystal radius and zone height. Size and location of the calculated crystal radius response are similar to the experimental data. The shapes of the curves agree particularly well. The dependencies of the zone height in calculation and experiment show good agreement, too.

To ensure the crystal growth with a constant slope, the automatic regulation based on the PID algorithm for I_0 and V_F is implemented in FZoneT. During regulation, I_0 and V_F are adjusted depending on the deviation of the actual and desired values for the slope of the crystal surface and zone height. The constants in the PID algorithm are chosen according to the gathered experiences from calculations with V_F and I_0 jumps. The calculation sample in Figure 7.26 shows the modeled crystal growth process with a desired slope angle of approximately 11° [52].

7.3.5 Summary, Conclusions, and Outlook

Extensive development of coupled multiphysical numerical models during the last 20 years resulted in an effective specialized program packages allowing numerical investigation of numerous aspects of the floating zone process in great detail. The effect of system geometry and process parameters on the shape of interfaces, melt flow, temperature, stress, and dopant distribution is well understood. However, the connection of the calculated macroscopic distributions to dislocation rate and fractures of FZ crystals is still a subject of future investigation. Although the basic effects can be shown using the axisymmetric 2D models, the 3D modeling provides essential improvements of precision mandatory for the simulation-aided process development. The first demonstrations of transient modeling showed a large potential for deeper investigation and

optimization of the starting and ending phases of the FZ process as well the use for process control and stability analysis. Many 3D aspects are still not modeled—deviations from the round crystal shape due to ridges, the nonsymmetric and nonuniform melting of the feed rod. The requirements for larger diameters and higher quality crystals will desire challenging technical solutions and then new models have to fulfill those.

References

[1] Theuerer HC. US Patent No. 3060123; 1952.

[2] Keck PH, Golay MJE. Phys Rev 1953;89:1297.

[3] Zulehner W. Mater Sci Eng B 2000;73:7.

[4] Lüdge A, Riemann H, Wünscher M, Behr G, Löser W, Muiznieks A, et al. In: Duffar T, editor. Crystal growth processes based on capillarity. Wiley-Blackwell; 2010. p. 203.

[5] Dash WC. J Appl Phys 1958;29:705.

[6] von Ammon W. In: Müller G, Metois JJ, Rudolph P, editors. Crystal growth – from fundamentals to technology. Elsevier B.V.; 2004. p. 239.

[7] Lüdge A, Riemann H. Inst Phys Conf Ser No 160 1997:145.

[8] Lüdge A, Riemann H, Hallmann B, Wawra H, Jensen L, Larsen TL, et al. High purity silicon VII. Electrochem Soc Proc 2002;20:75.

[9] Billig E. Proc R Soc Lond A 1955;229:346. Nr. 1178.

[10] Keller W, Barowski G, Kramer H. German Patent No. DE2626756; 1977.

[11] Wünscher M. [Thesis]. Berlin: Technische Universität; 2011.

[12] Menzel R. [Thesis]. Berlin: Technische Universität; 2013.

[13] von Ammon W, Ehlert A, Hensel W. Electrochem Soc PV 1993;36:93.

[14] von Ammon W. US Patent application US 2003/0145781A1.

[15] Riemann H, Lüdge A. In: Nakajima K, Usami N, editors. Crystal growth of silicon for solar cells. Springer; 2009. p. 41.

[16] Abrosimov N, Luedge A, Muiznieks A, Riemann H. Patent DE 102005016776 A1.

[17] Paschen F. Wied Ann Phys 1889;37:69.

[18] Ikeda Y, Ohara N, Suzuki K, Watanabe M. US Patent 4,866,230; 1987.

[19] Ohhara N, Taguchi K, Watanabe M. US Patent 4,876,438; 1988.

[20] Taguchi K, Watanabe M. US Patent 4,931,945; 1988.

[21] Dornberger E, von Ammon W, Ölkrug H, F. Wasmeier. DE Patent 69601424 T2; 1996.

[22] Dornberger E, von Ammon W, Ölkrug H, Wasmeier F. US Patent 5,868,831; 1997.

[23] Werner N. [Thesis]. Berlin: Technische Universität: 2014.

[24] Ziou D, Tabbone S. Int J Pattern Recognit Image Anal 1998;8:537.

[25] Becker P, Friedrich H, Fujii K, Giardini W, Mana G, Picard A, et al. Meas Sci Technol 2009;20.

[26] Becker P, Schiel D. Int J Mass Spectrom 2013:219.

[27] Borys M, Gläser M, Mecke M. Measurement 2007;40:785.

[28] Mühlbauer A, Erdmann W, Keller W. J Cryst Growth 1983;64:529.

[29] Mühlbauer A, Muižnieks A, Virbulis J, Lüdge A, Riemann H. J Cryst Growth 1995;151:66.

[30] Lie KH, Walker JS, Riahi DN. J Cryst Growth 1990;100:450.

[31] Lie KH, Walker JS, Riahi DN. J Cryst Growth 1991;109:167.

[32] Mühlbauer A, Muižnieks A, Jakowitsch A, Virbulis J. Latv J Phys Technol Sci 1992;4.

[33] Mühlbauer A, Muižnieks A, Jakowitsch A, Virbulis J. Arch für Elektrotechnik 1993;76:161.

[34] Virbulis J. [Thesis]. Rīga: University of Latvia; 1997.

[35] Ratnieks G. [Thesis]. Rīga: University of Latvia; 2007.

[36] Riemann H, Lüdge A, Böttcher K, Rost H-J, Hallmann B, Schröder W, et al. J Electrochem Soc 1995; 142(3):1007.

[37] Mühlbauer A, Muižnieks A, Virbulis J. J Cryst Growth 1997;180:372.

[38] Mühlbauer A, Muižnieks A, Raming G, Riemann H, Lüdge A. J Cryst Growth 1999;198/199:107.

[39] Mühlbauer A, Muižnieks A, Raming G. Cryst Res Technol 1999;34:217.

[40] Raming G, Muižnieks A, Mühlbauer A. Proc. international colloquium “modelling of material processing”, Rīga; May 1999. 24.

[41] Raming G, Muiznieks A, Muhlbauer A. J Cryst Growth 2001;230:108.

[42] Raming G. [Thesis]. Hannover: Institut für Elektrowärme, Universität Hannover; 2000.

[43] Togawa S, Nishi Y, Kobayashi M. Electrochem Soc Proc 1998;98(13):67.

[44] Guo Z, Maruyama S, Togawa S. J Cryst Growth 1998;194:321.

[45] Larsen TL, Jensen L, Lüdge A, Riemann H, Lemke H. J Cryst Growth 2001;230(1–2):300.

[46] Larsen L. [Thesis]. Technical University of Denmark; 2000.

[47] Muižnieks A, Raming G, Mühlbauer A, Virbulis J, Hanna B, von Ammon W. J Cryst Growth 2001; 230(1–2):305.

[48] Ratnieks G, Muižnieks A, Mühlbauer A. J Cryst Growth 2003;255(3–4):227.

[49] Ratnieks G, Muižnieks A, Mühlbauer A. Proc. international colloquium “modelling of electromagnetic processing” Hanover; March 2003. 205.

[50] Rudevičs A, Muižnieks A, Ratnieks G, Mühlbauer A, Wetzel Th. J Cryst Growth 2004;266:54.

[51] Rudevičs A, Muižnieks A, Riemann H, Lüdge A, Ratnieks G, von Ammon W. J Cryst Growth 2005; 275:561.

[52] Rudevičs A, Muižnieks A, Ratnieks G. Proc. joint 15th Riga and 6th PAMIR conference on fundamental and applied MHD, Rīga, vol. 2; June 2005. 229.

[53] Ratnieks G, Muižnieks A, Raming G, Mühlbauer A, Buligins L. Proc. international colloquium “modelling of material processing” Rīga; May 1999. 30.

[54] Ratnieks G, Muižnieks A, Buligins L, Raming G, Mühlbauer A. Magnetohydrodynamics 1999;35(3): 278.

[55] Ratnieks G, Muižnieks A, Buligins L, Raming G, Mühlbauer A, Lüdge A, et al. J Cryst Growth 2000; 216:204.

[56] Ratnieks G, Muižnieks A, Mühlbauer A, Raming G. J Cryst Growth 2001;230:48.

[57] Lacis K, Muiznieks A, Jekabsons N, Rudevics A, Nacke B. Magnetohydrodynamics 2009;45(4):549.

[58] Lācis K, Muižnieks A, Ratnieks G. Magnetohydrodynamics 2005;41(2):147.

[59] Lācis K, Muižnieks A, Rudevičs A, Sabanskis A. Magnetohydrodynamics 2010;46(2):199.

[60] Muižnieks A, Lācis K, Rudevičs A, Lācis U, Sabanskis A, Plāte M. Magnetohydrodynamics 2010; 46(4):475.

[61] Assaker R. [Thesis]. Belgium: Universite Catholique de Louvain; 1998.

[62] Bioul F. [Thesis]. Belgium: Universite Catholique de Louvain; 2007.

[63] Rudevičs A, Muižnieks A, Ratnieks G, Riemann H. Magnetohydrodynamics 2005;41(2):123.

[64] Muižnieks A, Rudevičs A, .Lācis K, Riemann H, Lüdge A, Schulze FW, et al. Magnetohydrodynamics 2007;43(2):269.

[65] Menzel R, Rost A, Luedge A, Riemann H. Cryst Res Technol 2011;46(10):1003. http://dx.doi.org/10.1002/crat.201100230.

[66] Wünscher M, Menzel R, Riemann H, Lüdge A. J Cryst Growth 2014;385:100.

[67] Barinovs G, Sabanskis A, Muiznieks A. J Cryst Growth. http://dx.doi.org/10.1016/j.jcrysgro.2013.12.019.

[68] Jackson JD. Classical electrodynamics. New York: John Wiley & Sons; 1998.

[69] Dupret F, Nicodème P, Ryckmans Y, Wouters P, Crochet MJ. Int J Heat Mass Transf 1990;33(9):1849.

[70] Dadzis K, Muižnieks A, Rudevičs A, Ratnieks G. Magnetohydrodynamics 2005;41(2):105.

[71] Rudevics A, Lacis K, Muiznieks A, Jekabsons N, Nacke B. Proc. international scientific colloquium “modelling for electromagnetic processing” Hannover; October 2008.

[72] Open source library OpenFOAM. http://www.opencfd.co.uk/openfoam.

[73] Muiznieks A, Lacis K, Nacke B. Magnetohydrodynamics 2007;43(3):377.

[74] Surovovs K, Muiznieks A, Sabanskis A, Virbulis J. J Cryst Growth. http://dx.doi.org/10.1016/j.jcrysgro.2013.12.066.

[75] Stefan J. Sitzungsber Wiener Akad Math Naturwiss Abt 1889;98:473.

8 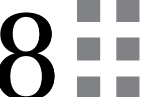

Floating Zone Growth of Oxides and Metallic Alloys

CHAPTER OUTLINE

Acknowledgments **282**

8.1 Optical Floating Zone—Complementary Crystal Growth Technique for New Classes of Oxide Materials **283**

8.1.1 Introduction **283**

8.1.2 Optical Floating Zone Technique **288**

8.1.2.1 Experimental Setup 288

8.1.2.2 Ceramic Rod Preparation 290

8.1.2.3 Growth Conditions 291

8.1.2.4 Temperature Distribution in the Zone 292

8.1.2.5 Rotation 294

8.1.2.6 Overpressure and Growth Atmosphere 296

8.1.2.7 Crystal Growth Termination and Cooling 298

8.1.3 Conditions for Stable Growth of Congruently and Incongruently Melting Oxides **298**

8.1.4 Constitutional Supercooling and Crystallization Front Stability **300**

8.1.5 Selected Examples of Crystal Characterization **301**

8.1.6 Concluding Remarks **305**

Acknowledgments **306**

References **306**

8.2 Floating-Zone Single Crystal Growth of Intermetallic Compounds Using a Two-phase RF Inductor **313**

8.2.1 Introduction **313**

8.2.2 Two-phase Inductor and Its Basic Characteristics **315**

8.2.3 Single Crystal Growth of Intermetallic Compounds **318**

8.2.3.1 Ruthenium Aluminides 318

8.2.3.2 Titanium Aluminides 319

8.2.3.3 Manganese Silicides 321

8.2.3.4 Titanium Niobium 323

8.2.4 Conclusions **326**

Acknowledgments **326**

References **326**

Handbook of Crystal Growth. http://dx.doi.org/10.1016/B978-0-444-63303-3.00008-0

Copyright © 2015 Elsevier B.V. All rights reserved.

In Chapter 7, the floating zone (FZ) method exclusively for silicon was discussed. This chapter demonstrates much broader applicability of FZ for different materials. It relates to application of the optical floating zone (OFZ) technique for growing crystals of congruently and incongruently melting oxides (Part I) and to the work done on RF floating zone crystallizing complex, intermetalic compounds (Part II).

Whereas the basic concept, which goes back to Pfann (1952) and von Emeis (1954), is similar for all the FZ methods, the details are significantly different, allowing this versatile method to serve successfully different crystal growing communities—from space research to research for new materials to manufacture of defect-free semiconductors.

Acknowledgments

The authors are very grateful to BIMR for financial support, Dr Bruce Gaulin for continuous support and encouragement and Tim Munsie for helpful suggestions.

The financial support of the Deutsche Forschungsgemeinschaft within the Collaborative Research Centre SFB 609 “Electromagnetic flow control in metallurgy, crystal growth and electrochemistry” is gratefully acknowledged.

8.1 Optical Floating Zone—Complementary Crystal Growth Technique for New Classes of Oxide Materials

Hanna A. Dąbkowska, Antoni B. Dąbkowski

BROCKHOUSE INSTITUTE FOR MATERIALS RESEARCH, MCMASTER UNIVERSITY, HAMILTON, ON, CANADA

8.1.1 Introduction

Over the past 60 years, artificially grown single crystals have become a key material in the field of computer components fabrication, optics, optoelectronics, and scintillator materials [1,2]. For advanced investigation of physical and chemical properties of new oxides it is crucial to have good quality single crystals, since in polycrystalline samples the properties of grain boundaries often show themselves dominant over the properties of the bulk material [3]. Growing large, high quality single crystals of many oxides is possible by methods like the Czochralski, Bridgman, Verneuil, or slow cooling techniques [1,2], but in the search for new materials, the optical floating zone (OFZ) has many advantages over the other methods, allowing for growth of crystals of various newly designed nonconventional oxides and their solid solutions. This crucibleless technique, environment friendly and relatively inexpensive, where halogen lamps (or high pressure discharge tubes) are used as an energy source, established itself as a powerful research tool [1,4–7]. It is complementary to the conventional oxide crystal growth methods from melt or solution as it extends the range of materials that can be crystallized in different (reducing, neutralizing, and oxidizing) atmospheres and at elevated pressures.

A brief history of how the molten zone techniques developed is presented in [8] and [9].

The demand for high quality crystals of ferrites for microwave applications promoted the introduction of halogen lamps and, later, more powerful xenon arc lamps as heat sources. The first “optical” apparatus, sometimes called an image furnace, for growth of ferrites was developed by groups of Akashi [4] and Shindo [5].

With a growing number of OFZ furnaces around the world, this technique has gained popularity for fast growth of oxides that were too difficult to grow using other techniques. Complex high temperature superconductors like $Bi_2Sr_2CaCu_2O_n$ [10,11] or new refractory, high melting, magnetic materials like $SrRE_2O_4$ [12] are good examples of this.

Crystals grown by the optical floating zone techniques are of high quality, usually not bigger than a few mm in diameter and a few cm in length. The majority of them are grown for research purposes. High quality crystals as large as 1 in in diameter have been reported (as an example, β-Ga_2O_3 [13]), but the only oxides ever grown by this technique specifically for industrial applications are $Y_3Fe_5O_{12}$ [4,5,14] and TiO_2 [15,16].

In this review, the advantages and disadvantages of the OFZ technique for the growth of crystals of congruently and incongruently melting oxides and their solid solutions are discussed. For incongruently melting materials the variety of the OFZ technique, called the traveling solvent floating zone (TSFZ) technique, is used. In this case, compositions of liquid and solid are different and continuously changing during crystal growth process. Because the volume of molten material in the zone is small compared with the obtained crystal volume, a practical steady state ("nearly steady state") can be achieved relatively easily. Furthermore, solid solution crystals with relatively uniform chemical composition can also be prepared. This is beneficial for crystallization of incongruently melting materials and for doped materials with a dopant distribution coefficient different than one, as well as for materials in which the congruently melting composition is a nonstoichiometric one. The later effect is observed mainly when either cation substitution or vacancies are possible. Discussion of composition evolution in conservative (like crucible) vs nonconservative (like traveling zone) techniques can be found in crystal growth textbooks [17,18].

The floating zone technique, when supported by characterization methods such as differential thermal analysis (DTA) and/or X-ray diffraction. is also an effective way for the construction and investigation of phase diagrams [19].

The strongest advantages of the optical floating zone technique come from the facts that no crucible is used and that both congruently and incongruently melting materials can be grown in the same furnace. This allows obtaining large-sized crystals that were not previously achievable with other crystal growth methods. A relatively high thermal gradient on the crystallization front, characteristic for this method, decreases the danger of constitutional supercooling (see Section 8.1.4) and enable faster growth of incongruently crystallizing materials (see Section 8.1.3). It is also important to note that, depending on the type of lamps used and their power, oxides with melting temperatures as high as 2500 °C can be grown.

There are limitations to the growth of crystals by the OFZ method. It is not suitable for materials with a high vapor pressure, a low surface tension, or a high viscosity. One has to deal with heating instabilities and low heating penetration depth. It is difficult to obtain large crystals of materials that undergo a phase transition during cooling, but even then, small, good quality samples of new materials can be obtained.

The list of oxide materials grown by OFZ and TSFZ methods presented in Table 8.1.1 is extensive and included (at the time of publication) most of the oxide crystals grown by these methods that have been reported. The occurrence of the most common macroscopic and microscopic defects, which often strongly influence crystal properties and applications, is also briefly discussed.

Table 8.1.1 Oxide Crystals Grown by Optical Floating Zone Technique and Traveling Solvent Optical Floating Zone Technique

	Growth			
Material	**Rate, mm/h**	**Atmosphere**	**Rotation, rpm**	**References and Comments**
Al_2O_3	10–1500	Air	0–200	[20,21]
$BaCo_2Si_2O_7$	1	Air	20–30	[22]
$BaAl_xFe_{12-x}O_{19}$	6	40–70 atm O_2	10–30	[23]
$BaFe_{12}O_{19}$	6	40–70 atm O_2		[14,23]
$BaTiO_3$	1	O_2/Ar 1:1	20	[24]
$Ba_{1-x}Sr_xTiO_3$	1–2	O_2	30	[25]
$x = 0.03$	10–20			[26]
$Ba_3Cr_2O_8$	1–20	Ar	30	[27]
$Bi_2Sr_2CaCu_2O_n$	0.2–0.35	O_2	20–30	[28–33]
$Bi_2Sr_2CaCu_2O_n$:Y	0.5	1 atm air	10	[34]
$Bi_2Sr_2CaCu_2O_n$:Li	0.5			[35]
$Bi_2Sr_2Ca_2Cu_3O_{10}$	0.05	O_2/4Ar	10	[36]
$Bi_2Sr_2CuO_6$	1.5			[37,38]
$Bi_{12}TiO_{20}$	0.25	O_2 flow	35–45	[39]
$Ca_{12}Al_{14}O_{33}$	0.3			[40]
$CaAl_2O_4$	4	Ar-O_2, Ar, Ar-H_2	21	[41]
$Ca_2Al_2SiO_7$	3		25	[42,43]
α $CaCr_2O_4$				[44]
Ca_2CuO_3	1	1 atm O_2	20–30	[45]
$CaCu_3Ti_4O_{12}$	6	O_2	30	[46]
Ca_2FeMoO_6	60	0.25–0.5 atm N_2		[47]
$Ca_2Fe_2O_5$	1–2	O_2, 1–2 atm		[48]
$Ca_{0.5}La_{0.5}MnO_3$	1–10	Air, O_2		[49–51]
$Ca_2MgSi_2O_7$	2–3	Air, O_2	30–45	[43]
$CaTiSiO_5$	0.5–12	Air		[52]
Ca_2RuO_4, $Ca_{2-x}La_xRuO_4$	20	9Ar:1O_2 10 atm		[53]
$Ca_{2-x}Sr_xRuO_4$	20	9Ar:1O_2 10 atm		[54]
$CaYAlO_4$	3–5	Ar, O_2, N_2, air, O_2/N_2	15–20	[55]
$Ca_{2+x}Y_{2-x}Cu_5O_{10}$	0.5	O_2	15	[56]
$CdCu_3Ti_4O_{12}$	6	O_2	30	[57]
$Ce_2Fe_2O_5$	1			[48]
$CoFe_2O_4$	10	O_2 40 atm	40	[58]
$Co_{1-x}Zn_xFe_2O_4$	10	O_2 50–70 atm	40	[58]
$CoNb_2O_6$	1–3	20%Ar O_2		[59]
$CoTiO_3$	5	O_2	20	[22]
$Co_3(VO_4)_2$	0.5–3	Air	20–30	[60,61]
$(Co_{1-x}Mg_x)_3V_2O_8$	2	Air	30	[62]
CoV_2O_4	30	Ar	25	[63]
CuO	10	3.5–5.5 MPa O_2	30.7	[64]
$CuGeO_3$	1–10	1 atm O_2	30	[52,65,66]
β-$CuNb_2O_6$	1–3	Air		[67]

(*Continued*)

Table 8.1.1 Oxide Crystals Grown by Optical Floating Zone Technique and Traveling Solvent Optical Floating Zone Technique—cont'd

Material	Growth			References and Comments
	Rate, mm/h	Atmosphere	Rotation, rpm	
alpha-Fe_2O_3	0.15–0.2	8 bar	18	[68]
Fe_3O_4	6	CO_2	20–30	[7]
$FeNb_2O_6$	1–3	20%Ar O_2	0–40	[59]
FeV_2O_4	30	Ar	25	[63,69]
Ga_2O_3	5–10	Air, Ar	15–30	[13] Volatile
$GeCo_2O_4$	15–30	Air		[70] Evaporation, low viscosity
$GeNi_2O_4$	40	1 MPa, O_2		[70] Evaporation, low viscosity
$Gd_3Fe_5O_{12}$	1.5	70 atm O_2		[24]
$Gd_2Si_2O_7$	2	N_2	6	[71]
$Ho_3Al_5O_{12}$	10	Ar	10–20	[72] Growth on seed
$Ho_3Ga_5O_{12}$	10	Ar	10–20	[72] Growth on seed
La_2CuO_4	0.5–1	O_2	25–30	[65,73]
$La_{2-x}Sr_xCuO_4$	1–15	O_2, air	40	[74–79]
$La_{2-x}Ba_xCuO_4$	0.5–0.7	10^{-2} atm O_2	30	[73,74,79–85]
$(La_{1-x}Ca_x)_2CaCu_2O_{6+\delta}$	0.35–1	10 atm O_2		[86]
$La_{14-x}Ca_xCu_{24}O_{41}$	1–1.5	13 atm O_2	40	[87]
$LaCoO_3$	20	O_2		[88,89]
$LaFeO_3$, $YFeO_3$	20	O_2		[90]
$LaMnO_3$	10	Air		[90]
$La_{0.8}Sr_{0.2}MnO_3$	3–10	Air, Ar/O_2	15–50	[50,51,91–93]
$La_{1.5}Sr_{1.75}Mn_2O_7$	3–7	Ar 30%O_2 6–8 × 10^5 Pa	40	[94]
La_2NiO_4	20	O_2	30–50	[95]
$La_{2-x}Sr_xNiO_{4+\delta}$	3–5	5–7 atm Ar:O_2	40	[96]
$LaTiO_3$	50	Ar/30%H_2		[90]
$LaVO_4$:Nd	10	Air	5.4	[96]
$LiNbO_3$	9			[97–99]
Li_3VO_4, β(II)-Li_3VO_4	0.5–1	Ar, O_2, air		[100,101]
$LuFe_2O_4$	1	Air, CO_2/CO = 5/2 2 bar		[102,103]
$LuGaCoO_4$	1–20	Ar, O_2, air	30	[22]
$LuFeCoO_4$		CO_2/CO		[102]
$MgAl_2O_4$	7	Air	10–30	[22]
$MgFe_2O_4$	5	50 atm O_2		[24]
Mg_2SiO_4:Cr		Ar/O_2 300 cc/min		[104]
$MgTi_2O_4$	1–5	O_2	30	[105]
$Mg_3(VO_4)_2$	0.5	O_2/N_2, O_2	16–18	[106]
MgV_2O_4	2	H_2/Ar_2	50	[107]
$MnNb_2O_6$	1–3	20%Ar O_2	0–40	[59]
MnV_2O_4	30	Ar	25	[63]
Na_xCoO_2	2	O_2		[108–110]

Table 8.1.1 Oxide Crystals Grown by Optical Floating Zone Technique and Traveling Solvent Optical Floating Zone Technique—cont'd

Material	Growth			References and Comments
	Rate, mm/h	Atmosphere	Rotation, rpm	
Nd_2CuO_4, $Nd_{1.85}Ce_{0.15}Cu_{4-\delta}$	0.5–0.7	O_2 flow, O_2/Ar, 8 atm O_2	30	[78,111]
$Nd_{9.33}(SiO_4)O_2$	2–5	N_2 1 L/min	50–80	[112,113]
$Nd_{0.7}Sr_{0.3}MnO_3$	2.5–10	Air/O_2		[51]
$Nd_{1+x}Sr_{2-x}Mn_2O_7$	2–8	Air	25–30	[114]
$NdTiO_3$, $Nd_{1-x}TiO_3$	25	95Ar 5H_2	15	[115]
$NiAl_2O_4$	2.5–10	1–3 atm O_2	5–40	[116]
$NiFe_2O_4$	10	O_2 30 atm	40	[58]
$Ni_{1-x}Zn_xFe_2O_4$	10	O_2 50–70 atm	40	[58]
$NiNb_2O_6$	1–3	20%Ar O_2	0–40	[59]
$Ni_3(VO_4)_2$	0.5–3	Air	20–30	[61]
$Pr_{1+x}Sr_{2-x}Mn_2O_7$	2–8	Air	25–30	[114]
$Pr_2CaMn_2O_7$	2,5–8	90%Ar10% O_2 5 bar	16	[117]
$Pb_2V_3O_9$	0.5	Ar, 5 L/min	5	[118]
$RE_3Ga_5O_{12}$	10	Air		[24]
$REBaNiO_5$	1	O_2		[119]
$REBa_2Cu_3O_{7-y}$ (RE = Y,La,Pr,Nd,Sm)	0.4–1	10^{-2} atm O_2	25	[120]
$REFeO_3$	3–10	70 atm O_2		[24]
$REMnO_3$	6	Ar 6–8 atm + 1–5% O_2	40	[90,93,121]
$RE_2Ti_2O_7$	5–20	Ar, O_2	10–20	[96,122–126]
$REVO_4$:Er, Ho, Tm	5–20	Ar/7%H_2, O_2	20–30	[90,96,127–129]
$SrAl_2O_4$	4	Ar-O_2, Ar, Ar-H_2	21	[41]
$Sr_2CuO_2Cl_2$	5	Ar, Ar/O_2	30	[130]
$Sr_3Cr_2O_8$	4 or 20	Ar		[131]
$SrCuO_2$	0.5–2	1 atm O_2		[65,132,133]
Sr_2CuO_3	1	1 atm O_2		[65,132]
$SrCu_2(BO_3)_2$, $SrCu_2(BO_3)_2$:Mg, La, Na	0.2–0.5	O_2	10–20	[134–137] Low surface tension
$Sr_{14}Cu_{24}O_{41}$	1	500 kPa		[22,52,65,132,137,138]
$Sr_{14-x}Ca_xCu_{24}O_{41}$	0–8.2	13 atm		[139]
$SrFe_{12}O_{19}$	6	50 atm O_2		[24]
$Nd_{9.33}(SiO_4)_6O_2$ $Sr_2Nd_8(SiO_4)_6O_2$	2–5	N_2 1 L/min	50–80	[112] Core
$Sr_3Fe_2O_{7-x}$	1–5	0.2–3 bar O_2	10–15	[140]
$SrRE_2O_4$	1–10	Ar 2 L/min	20–30	[12,141]
Sr_2RhO_4	10	10 bar O_2	10–30	[142]
Sr_2RuO_4, Sr_2RuO_4:Ti	25–45	2Ar:1O_2		[143–145] Volatile
$Sr_3Ru_2O_7$	15–20	1Ar:9O_2		[145,146] Volatile
$SrTiO_3$, $SrTiO_3$:La	15	15 atm	20–30	[24,147,148]

(*Continued*)

Table 8.1.1 Oxide Crystals Grown by Optical Floating Zone Technique and Traveling Solvent Optical Floating Zone Technique—cont'd

Material	Growth			References and Comments
	Rate, mm/h	Atmosphere	Rotation, rpm	
$SrZrO_3$	5–65	Air	3–25	[149] Evaporation
$TbMnO_3$		CO/CO_2, 1:5		[150]
$Tb_{0.9}Dy_{0.1}BaCo_2O_{5+\delta}$	0.2–2	Ar 2% O_2	15	[151]
TiO_2	5	Air, O_2	30	[16,24,152] ZrO_2 added
$Y_3Al_5O_{12}$	5	Air		[24,26,153]
$Yb_3Al_5O_{12}$	10	Ar	10–20	
$YCrO_3$	20	Ar		[90]
$Y_3Fe_5O_{12}$	1.5–3	15–30 atm O_2	10–30	[7,24,154–156]
$Y_3Fe_{5-x}Al_xO_{12}$	6	O_2		[5,7,153]
$Y_3Fe_{5-x}Ga_xO_{12}$	1.5–3	20–30 atm O_2		[5,24] Dop. AlGa
YFe_2O_4	<2	$CO_2/H_2 = 0.8$ $CO_2/CO = 0.4$	30	[157]
$Y_2Mo_2O_7$	30	Ar	25	[158]
$YTiO_3$	50	Ar/30%H_2		[90]
YVO_4:Er, Ho, Tm	5–20	Ar/7%H_2, O_2	20–30	[90,127,128]
$YbCoGaO_4$	1.7	Air	15–30	[159]
$Yb_3Ga_5O_{12}$	10	Ar + 4%O_2	10–20	[72]
$YbFeMgO_4$		Air		[102]
ZnO	0.5–1	Air	20	[160]

RE = rare earth, Bold = TSFZ (Traveling Solvent Optical Floating Zone).

8.1.2 Optical Floating Zone Technique

8.1.2.1 Experimental Setup

Several types of optical floating zone furnaces are commercially available, in two- and four-ellipsoidal mirror configurations. These furnaces use either incandescent tungsten halogen bulbs or xenon arc lamps as an energy source, which is an efficient way of heating, thanks to the fact that most of oxides easily absorb infrared energy. Furthermore, infrared laser diodes heating is an emerging technology applied in the new OFZ systems, with different optical design [165]. More information about commercially available furnaces can be found in references [6,7,9,14,161] as well as on various manufacturers' Web sites [162–165].

All modern image furnaces are equipped with video cameras, allowing for the in situ observation of crystal growth process. There are also options that allow for remote control of the furnace via the Internet. This is helpful for adjusting growth conditions during lengthy experiments.

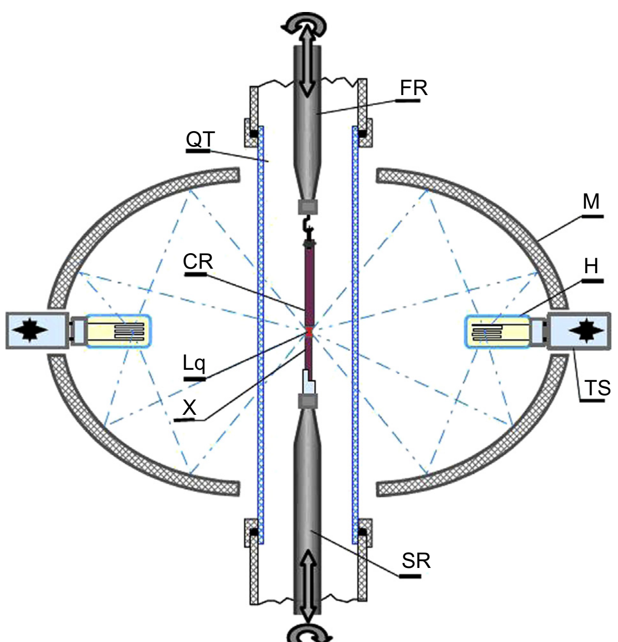

FIGURE 8.1.1 The schematic drawing of the optical floating zone. M, elliptical mirror; H, halogen tungsten lamp; TS, x-y-z micrometer translation stage for filament adjustment; QT, vitreous silica tube (quartz glass); FR, upper translation/rotation rod; CR, ceramic "feed rod"; Lq, liquid bridge "floating zone"; X, "seed rod" and crystal; SR, lower translation/rotation rod.

The schematic drawing of the optical floating zone is presented in Figure 8.1.1. In a typical crystal growth process, two ceramic rods are mounted in such a way that their tips meet at the common focal point of the ellipsoidal mirrors. Rods are inside a fused silica tube, which allows control of the growth atmosphere. Either halogen or xenon lamps sit in the other focal point of each mirror. Any crystal growth process performed by the OFZ starts by melting the tips of these rods, bringing them together and establishing a liquid bridge commonly called the "floating zone" between the bottom (seed) rod and the top (feed) rod. After the zone is created, it travels upward, either by moving the seed-and-feed setup downward or by moving the mirrors upward. During this translation, the melt cools down and the material crystallizes on top of the seed rod. Many grains form at the beginning of the process. Eventually, the grain with higher radial component of growth velocity continues to grow.

The stability of the growth process depends on the quality of the material and on the shape of the starting rod as well as on the alignment of both seed and feed rods. The seed rod is rigidly fixed to the lower shaft. The feed rod may be moved up and down independently, and it can either be attached rigidly to the top holder or it can hang loosely from a hook. Rigid mounting of the top rod requires high quality ceramics, manufactured straight and with a high density. It also requires a very precise alignment. It is advisable to start the growth on a crystalline and oriented seed as this facilitates the beginning of crystallization and can control the crystal orientation. Growing on a crystalline seed also prevents the absorption of liquid from the molten zone into a porous

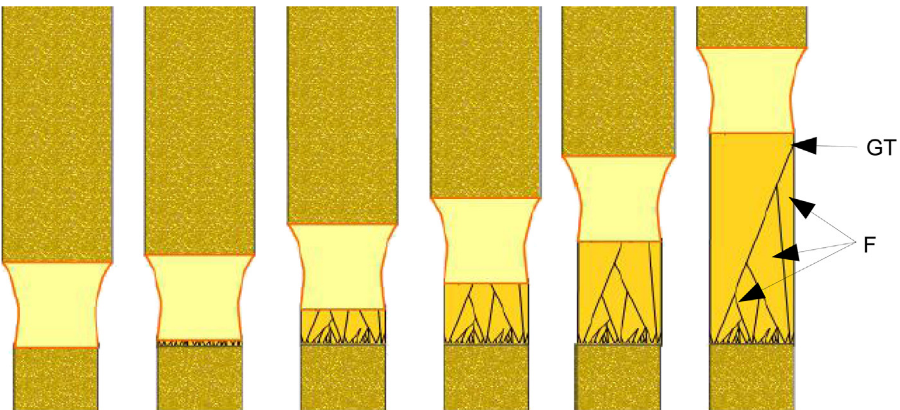

FIGURE 8.1.2 Schematic of stages of nucleation on ceramic rods and grains expansion. Individual grains can exhibit facets (F) on the crystal lateral side. After last secondary grain termination (GT), single crystal continues to grow.

seed rod. In practice, the appropriately oriented seed is rarely available. Crystals of new materials are grown, as a rule, on ceramic seeds obtained by a time-consuming grain segregation process (Figure 8.1.2).

8.1.2.2 Ceramic Rod Preparation

Preparation of feed rods for OFZ crystal growth requires grinders, mortars, a press for ceramic rod preparation, as well as furnaces with controlled atmosphere and long isothermal plateau for uniform rod sintering.

The first step of rod preparation is a typical ceramic synthesis. A batch of oxide constituents is weighed accordingly to the stoichiometry of the reaction. To assure proper composition, preannealing of starting reagents is recommended. This step is especially important for oxides that are known to be hygroscopic or can form hydrates or carbonates. It is critical to choose an appropriate annealing temperature and time, especially if decomposition change of oxidation state in the starting material can be expected. Multiple syntheses with a regrinding of the oxide mixture is a more effective way of producing uniform ceramics than simply a long thermal annealing. Mechanical ball milling is a convenient and reproducible way of homogenizing and decreasing grain size of the powders. The quality of the preprepared ceramics should be assessed by X-ray powder diffraction in case a single phase starting material is required. The annealed material is then reground and shaped as a rod, typically 8–10 mm in diameter and 100–150 mm long by either cold or hot pressing in dies of special design. The applied pressure has to be experimentally selected to avoid “overpressing” of material (tablet or rod breakup into shell-like flakes) and to avoid damage to the die. A very convenient and “clean” technique to perform cold pressing is the isostatic method (“hydrostatic pressing”), described below. The powder is loaded and compacted uniformly into a cylindrical rubber balloon, 5–8 mm in diameter and 150–200 mm long. After evacuating air and

sealing the balloon, it is placed in a hydrostatic chamber filled with hydraulic media and pressurized with pressure in the range of 800–2500 bar. A tiny amount of glycerol, polyvinyl alcohol, or similar additive mixed well with powder can be used to reduce internal friction during pressing, allowing the production of denser, less porous ceramic rods. The pressed, fragile rod is carefully separated from the balloon and sintered at a temperature and atmosphere specific to each compound.

The ratio of (measured) rod density to the crystallographic density depends on the material properties and on the quality of preparation, varying from under 60% to above 90%. If the rod density is low, it is suggested to proceed with premelt (a very fast growth process conducted in the same furnace) before performing the final crystal growth. This procedure was found to be especially important for slower grown, incongruently melting compounds like $SrCu_2(BO_3)_2$ [134,135] or $Bi_2Sr_2CaCu_2O_{8+\delta}$ [28]. Attention must be paid to evaporation losses during synthesis. Inhomogeneous evaporation can be eventually compensated for in the sintering step by adding an appropriate amount of the evaporating compound, above the expected stoichiometry, which will be discussed later (Section 8.1.2.7).

8.1.2.3 Growth Conditions

The stability of the growth process and the quality of the obtained crystal depend strongly on the stability of the molten floating zone. Following are the general prerequisites to stable growth:

1. stability of power (modern equipment is capable of stabilizing the power supplied to the halogen lamp with relative accuracy 10^{-4} or better);
2. stability of feed and seed rod shafts translations (the rate of shafts translation is electronically controlled with similar accuracy);
3. stability of the gas flow and gas pressure (is important for constant temperature distribution within the growth chamber as even small fluctuations can cause significant process disruption and have to be avoided);
4. high homogeneity of a well-shaped, uniformly dense ceramic rod; such a rod is acting as the source of crystallizing material, and important aspects of its synthesis were mentioned in Section 8.1.2.2.

Variations in shape and/or density of the feed rod rapidly change the volume of molten zone, potentially even causing its collapse. Nonuniformity of feed rod ceramics seriously impacts the zone, introducing gas bubbles and interrupting the crystal growth process [15,20,21].

During the crystal growth process, the translation rate (pulling rate) of lower rod with regard to the lamps is often referred to as a growth speed (rate), although this definition is not actually precise. The distance between rods is controlled by adjusting translation rate of the feed rod. This directly controls the size and volume of the molten zone, adjusting crystallization and dissolution rates and avoiding instabilities, which can be

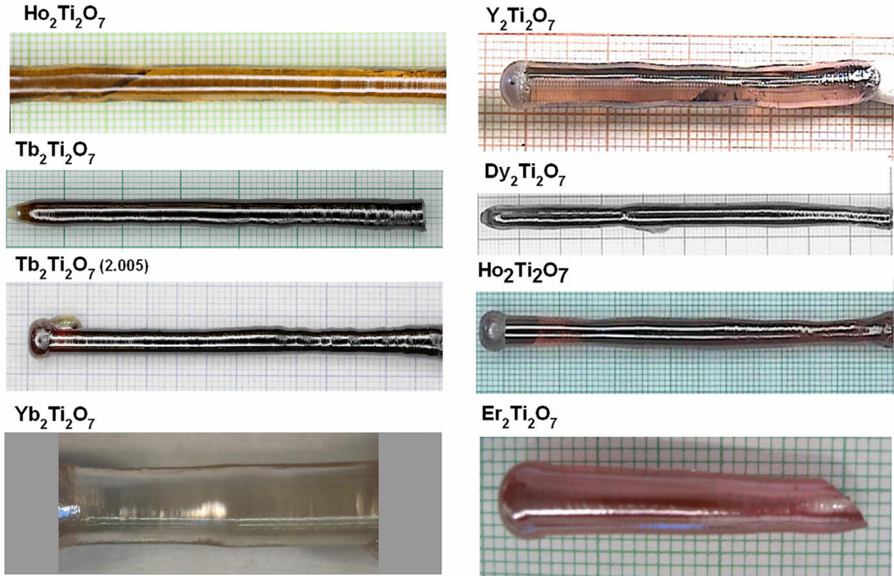

FIGURE 8.1.3 Rare earth titanates with pyrochlore structure. These materials melt congruently and pulling rate was 2–9 mm/h. *Pictures courtesy of Marjerrison CA, Morningstar A, Munsie TJS, Ross K, Couchman M.*

catastrophic to the crystal growth process. The power settings of the lamps is being monitored at the same time, to ensure long-term zone stability. Rotation rates of rods are usually kept stable (see Section 8.1.2.6).

Congruently melting crystals can be grown faster, with rates typically from 1 to 20 mm/h (e.g., $RE_2Ti_2O_7$ – Figure 8.1.3). In the case of doped or incongruently melting crystals, where transport and, as a result, growth rate are limited by phenomena in the diffusion layer, stable growth and sustainability of the zone can only be achieved at much lower growth rate, typically between 0.1 and 2 mm/h. Classical problems of diffusion layer, constitutional supercooling, and crystallization front stability are discussed in most of textbooks in the field of crystal growth; see for example [1,2]. Materials that evaporate have to be grown very quickly, sometimes in the range of 20–50 mm/h. This usually has a negative effect on the quality of the crystal (e.g., Sr_2RhO_4 [142]).

The small volume of liquid in the zone makes the stability of this crystal growth method susceptible to even small fluctuations of power or short time oscillations of the gas pressure. Together with a very high thermal gradient at the liquid/solid interface this causes difficulties in achieving and maintaining a flat crystallization front and a stable growth rate. These issues result in many defects and growth instabilities [9,97,166].

8.1.2.4 Temperature Distribution in the Zone

Growth rate, controlled by the supercooling on the crystallization front, should be coordinated with pulling rate. Figure 8.1.4 presents some typical problems encountered

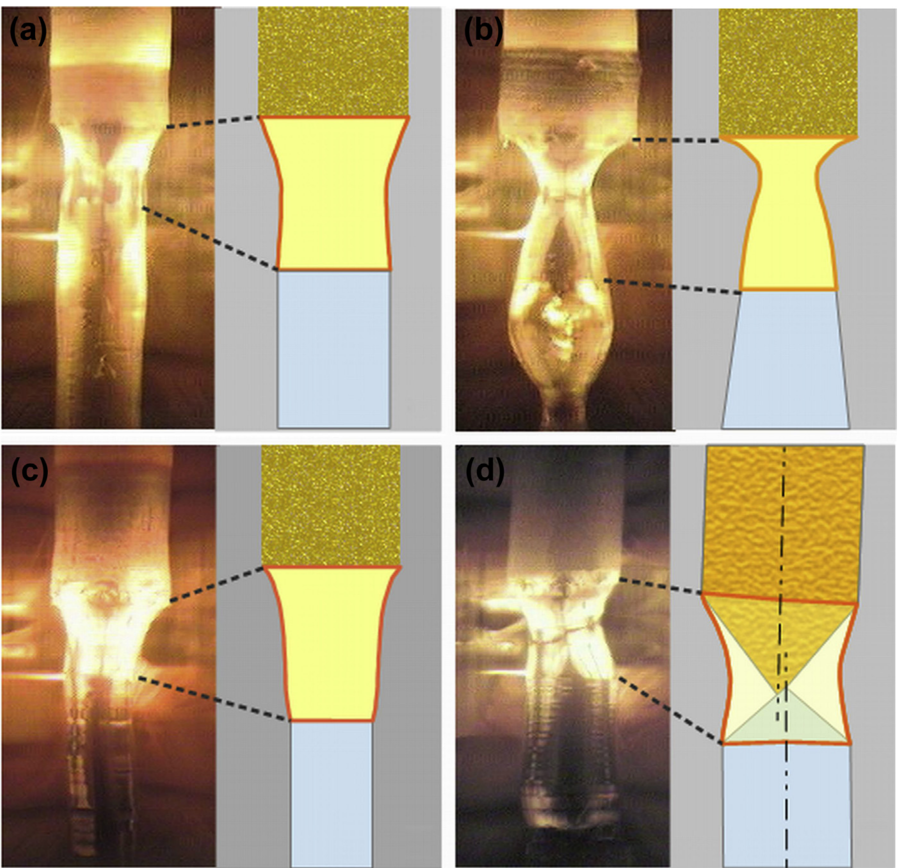

FIGURE 8.1.4 Shapes of the liquid zone for $Dy_2Ti_2O_7$: (a) Good conditions; (b) Zone overheated; growth too slow or not enough feeding; (c) Too much feeding, temperature not high enough; (d) Zone not hot enough, growth too fast.

during the growth and suggests how to deal with them. These are suggestions only, as each material is unique, even within the same family of compounds. Too slow growth (lower supercooling, caused by overheating), increases the length of liquid bridge (Figure 8.1.4(b)), which can lead to its collapse. Too fast growth (high supercooling, usually when zone is not hot enough) will lead to instabilities of crystallization front, decreasing crystal quality. Even further, such conditions can close the space between rods (Figure 8.1.4(d)). Temperature distribution in the vicinity of crystallization front is a key parameter that cannot be measure directly. Adjusting the output power of the lamps directly controls the zone maximum temperature and temperature gradients but the results of the adjustments are observed with a delay and, preemptive efforts of operator are in essence rather intuitive.

Heat transport in this growth system is very complex, and advance modeling is required to treat it quantitatively. Energy is delivered to the molten zone in the form of

light with maximum intensity depending on the temperature of the tungsten filament in the halogen lamp, in the 1–2 μm wavelength range, and it is emitted out from liquid and crystal in a longer wavelengths. Additionally, heat is dissipated by surrounding gas and by conduction of solids. The temperature distribution in the liquid bridge and the growing crystal depends on the thermal conductivity and spectral properties of both molten material and crystal, but also—to a smaller extent—of ceramic feed rod. Dramatic changes in the temperature distribution after doping $Y_3Al_5O_{12}$ with Nd (that has a strong absorption band in the near infrared (NIR) region), have been well documented for the Czochralski growth method [2], and similar effects are observed in the OFZ experiments.

There has been an intensive effort in modeling the silicon growth process [167], but only a few attempts were made to assess the interface shape, heat, and fluid flow inside the oxide molten zone [98,99].

The recent, and probably the most advanced 3-D modeling reported by Lan [168] presents the temperature distribution and the pattern of convection cells in the molten zone (rotation is not considered). Using as an example congruently melting $Y_3Al_5O_{12}$, grown in a typical double elliptical mirror system, and applying melt parameters experimentally measured by Fratello and Brandle [169], Lan concluded that the overheating, a condition where the temperature is above the melting point of the material, is higher than 600°, with azimuthal differences of more than 400° in the plane of lamps. A thermal gradient near the liquid/crystal interface is also very high, in the range of 1500 degrees per centimeter.

Very high thermal gradients cause fast convection flows, even with the small volume of the liquid zone (typically ~0.4 cm^3). The results of Lan's modeling suggest that the liquid velocity in the zone is in the range of few cm/s. In order to do more targeted modeling, the experimental values of material properties such as the surface tension, wetting angle, melt viscosity, and material density, as well as emissivity factor and thermal conductivity of the melt and of the crystal are required. To obtain a complete picture of the system changes of these properties with temperature should be understood as well. As these variables are not yet measured for the majority of oxides, primarily due to experimental challenges inherent with the necessarily high temperatures involved, it is not yet feasible to directly compare modeling and experimental results.

Other modeling attempts investigate detailed lamp irradiation [98] and analysis of thermal flows [99]. As expected, the external heating, either optical, including laser, or radio frequency (RF), causes significant overheating of the liquid zone surface. The length of the zone depends on the power used [170]. High temperature gradients within the zone lead to strong buoyancy as well as to noticeable Marangoni convection (Figure 8.1.5).

8.1.2.5 Rotation

During growth, the rods rotate either in the same or in the opposite directions with experimentally established rates. Rotation of the molten zone not only averages the

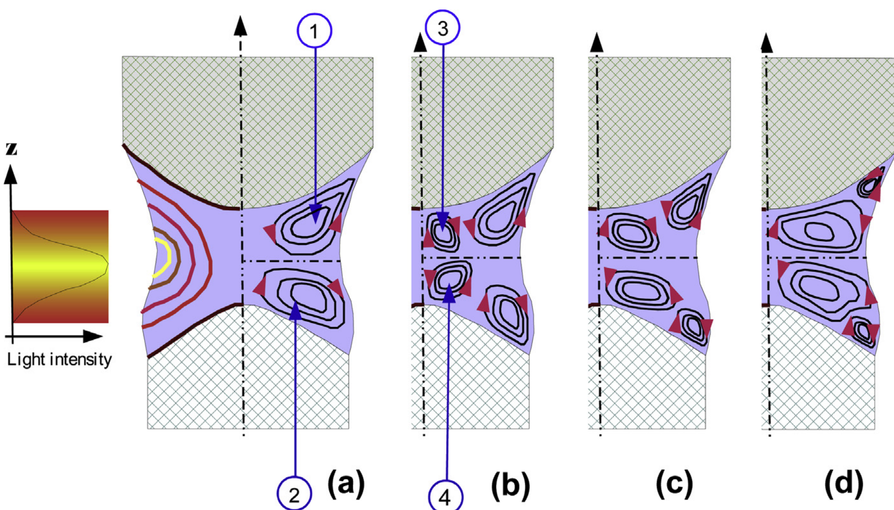

FIGURE 8.1.5 Influence of rotation on Marangoni, buoyancy, and centrifugal convections. (1) Upper cell: buoyancy and Marangoni convections combined, acting in the same direction, stronger. (2) Lower combine buoyancy and Marangoni cell, acting in opposite direction, weaker. (3) Upper and (4) Lower centrifugal convection. (a) Low or no rotation. (b) Counter-rotation low, centrifugal convection low, buoyancy and Marangoni decreased (c) Counter-rotation medium. Centrifugal mixing of liquid decreases thermal gradient in liquid. Buoyancy and Marangoni convection decrease further; crystallization and dissolution fronts can be flatter (not shown on the picture) (d) Counter-rotation high. Centrifugal mixing decreases thermal gradient in liquid. Buoyancy and Marangoni convections marginal. Crystallization and dissolution fronts can be flat or concave (not shown on the picture). *Visualization only, based on [29,168].*

temperature and therefore decreases the thermal gradient but also influences convection patterns in the liquid, allowing for control of the shape of the crystallization front. Convection patterns in the molten zone for rotating or counter-rotating rods are very complicated. To explain them, the existence of upper and lower convection cells has been suggested. A schematic explanation of convection flows in the molten zone and their influence by rotation is shown in Figure 8.1.5. Because the flows on the convection cells' interface should be collinear, one can expect a limited liquid exchange and, for incongruently melting materials, upper and lower cells having distinctively different chemical compositions.

The rate of rotation of a seed rod is important as it is responsible for the pattern of forced convection flows within the zone. As a result, rotation is responsible for mixing of material, the shape of crystallization front (the solid–liquid interface), and for the thickness of the diffusion layer on the crystallization front. The thickness of the diffusion layer limits transport on the crystallization interface and, from a practical point of view, the critical growth rate. Exceeding the critical rate can cause various defects. The rotation speed is optimized experimentally for each material and varies from 0 to 50 rpm. Figure 8.1.6 shows crystals of a solid solution of $Er_{1.95}Y_{0.05}Ti_2O_7$ [122], grown with different rotation conditions. In this case, the quality of the grown crystal was the best when there was no rotation of the feed rod.

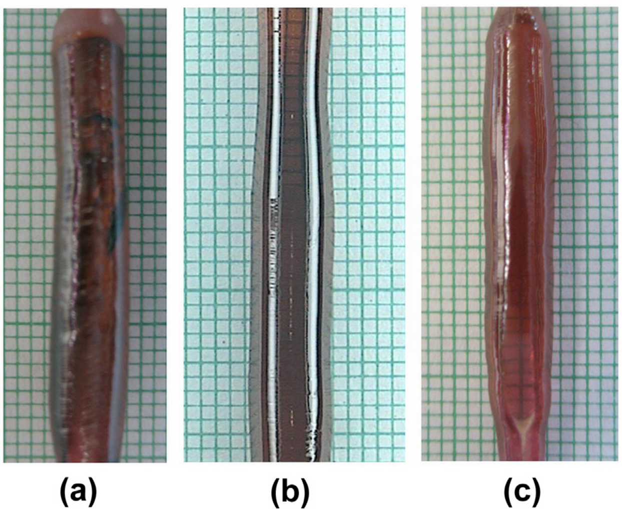

FIGURE 8.1.6 Influence of rotation on quality of transparent crystals of solid solution $Er_{1.95}Y_{0.05}Ti_2O_7$ (a) no seed rotation, quality poor (b) no feed rotation, the best quality (c) counter rotation, quality fine. *Pictures courtesy of Murray P.*

8.1.2.6 Overpressure and Growth Atmosphere

In the OFZ setup, crystals of oxides can be grown in either inert, oxidizing, or reducing atmospheres, depending on the purpose of the experiment. The high flexibility in controlling partial pressure of oxygen PO_2 allows for stabilization of required oxidation state of cations in the grown crystal. In Figure 8.1.7, the results of growths that started from the same rods, V_2O_5:$Lu_2O_3 = 1$:1 mol, but were performed in different growth atmospheres are shown. It was relatively easy to obtain different kinds of crystals, stabilizing different

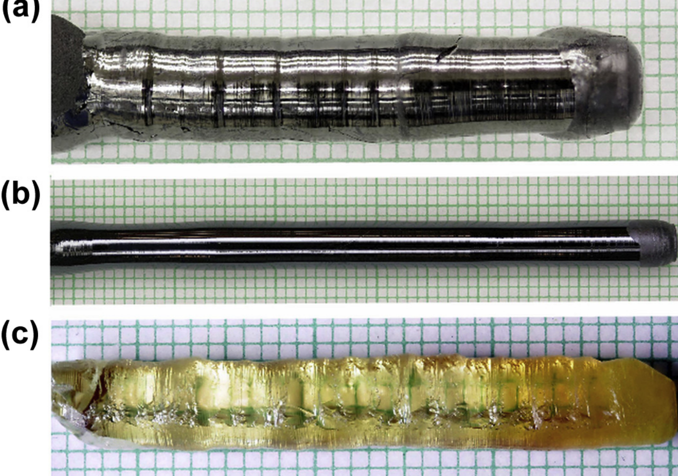

FIGURE 8.1.7 Lutetium vanadates grown at different oxidizing conditions: (a) $LuVO_3$ [V^{+3}] 5%H_2/Ar 1 atm abs (b) $Lu_2V_2O_7$ [V^{+4}] Ar, 5N5 1 atm abs (c) $LuVO_4$ [V^{+5}] O_2 1 atm abs. *Pictures courtesy Marjerrison C.*

oxidation states of vanadium ions: $LuVO_4$ [V^{+5}] in oxygen, $Lu_2V_2O_7$ [V^{+4}] in slightly reducing, and $LuVO_3$ [V^{+3}] in reducing atmosphere. Similar study on Na_xCoO_2 shows influence of PO_2 on Co_3O_4 precipitation and on total pressure on evaporation [108].

The OFZ method offers the potential for application of highly oxidizing conditions at elevated temperatures, which is a condition very difficult or impossible to achieve using other crystal growth techniques.

One has to be aware of the fact that changing the oxygen pressure influences the delicate oxygen balance in the grown crystal. This is very visible in high temperature superconductors such as $Bi_2Sr_2CaCu_2O_{8+\delta}$ (BSCCO) [11,171], frustrated rare earth pyrochlores, such as $RE_2Ti_2O_7$ [123,124], or multiferroics, such as $REMnO_3$ [121,172]. Furnaces capable of working at $PO_2 = 70$ bars or higher enabled growth of technically important ferrites and multiferroics [14,23,58]. Also, as oxides of metals have different vapor pressures for different oxidation states, the proper choice of PO_2 helps control the evaporation and can help to stabilize the required oxidation state of the components as shown in the case of the material decomposing at high temperatures, such as La_2CuO_4 [65] or Sr_2RuO_4 [143].

If the desired material contains a volatile component, then applying an elevated pressure of inert gas can slow down diffusion of vapors (e.g., CuO) from the liquid zone as the diffusion coefficient is inversely proportional to the gas pressure. Additionally, using a gas with higher molecular mass, such as argon, can also decrease the diffusion coefficient (e.g., [173]):

$$D_{1,2} \propto \frac{1}{P} * \sqrt{\frac{1}{M_1} + \frac{1}{M_2}} \tag{8.1.1}$$

where $D_{1,2}$ is the interdiffusion coefficient of the volatile compound within vapor (1) and surrounding (inert) gas (2), M_1 and M_2 the molecular mass of vapor and gas, respectively, and P the total pressure.

With increasing gas pressure, the temperature of the sample decreases, due to a larger heat exchange with the atmosphere, and a higher lamp power is needed to conserve the molten zone. It is sometimes incorrectly interpreted that this is because of an "increase" of the melting point of material due to higher external pressure. Faster heat exchange at higher gas pressure creates also a larger temperature gradient in the crystal—this can cause more cracks in many materials.

The presence of bubbles is one of the major causes of unexpected and unwanted growth terminations. They appear in the zone usually at higher applied pressure and can be caused either by gas trapped in the voids in ceramic feed rods or by partial decomposition of oxides in the highest temperature region of liquid.

Solubility of oxygen in molten oxides creates liquid that contains significantly more oxygen than expected for the highest oxidation state of the ions involved. In general, little is known about the composition of most of molten oxides, but this effect is documented in the case of Fe–O system where excess of oxygen is very significant at elevated PO_2 [174]. As the excessive oxygen cannot be accommodated in the crystal structure, it may

create either a bubble on the melt–crystal interface or it will gather in the upper part of ceramic rod.

If the techniques described above are not adequate to prevent excessive decomposition or evaporation from the melt, then the experimentally established additional amount of evaporating constituent has to be added to the starting rod. Adding about 1–3% of CuO to a $La_{2-x}Me_xCuO_4$ rod, where Me = Ba or Sr [138,175], or about 15% of RuO_2 to Sr_2RuO_4 [144], proved to be a useful approach.

8.1.2.7 Crystal Growth Termination and Cooling

As most of the heat is supplied to the crystal via the liquid zone, growth termination generates a difficult to avoid "thermal shock" to the crystal. To lower this shock, the tip of an as-grown crystal should be left in the hot zone during the cooling process. The rate of lamp cooling should be related to the pulling rate (often referred to as a growth rate), as switching off the lamps rapidly will likely result in cracks in crystals.

To estimate cooling rate, a simple formula can be used:

$$CR = \frac{P_{melt} \cdot \nabla_i T \cdot v_g}{M_p} \tag{8.1.2}$$

with CR (%/h) – maximum cooling rate (halogen dimming rate), P_{melt} (%) – lamp power at the melting point, $\nabla_i T$(°K/mm) – temperature gradient in the upper part of crystal, 50 °K/mm – a crude approx., v_g (mm/h) – pulling rate, M_p (°C) – melting point.

Note, Eqn (8.1.2) is valid for lamp power controllers calibrated in % of maximum power. For instance, if a material with $M_p = 1500\,°C$ is melted at $P_{melt} = 75\%$ of maximum power and the crystal was pulled with a rate $v_g = 2$ mm/h, a cooling rate 5%/h should be taking place over a time period of minimum 15 h.

Furthermore, postannealing of a grown crystal can reduce internal stress and often will lower defect density. The choice of atmosphere (PO_2) and a choice of chemically inert substrate used for supporting the crystal in this process are both important if the crystal quality is to be improved [1,2].

8.1.3 Conditions for Stable Growth of Congruently and Incongruently Melting Oxides

One of the important preconditions for successful growth is the knowledge of the related phase diagram [176]. If it is not available (as in the case of new crystals), a differential thermal analysis (DTA) should be routinely performed on all the considered materials to establish their melting properties. For many new materials it is not possible, as DTA apparatus rated above 1500 °C is not commonly available and analysis at elevated temperatures is often limited by a lack of an appropriate crucible material. In such a case, the melting properties are necessarily determined during a preliminary growth

experiment. Depending on the assessed properties, either direct crystallization or the TSFZ approach can then be attempted.

For congruently melting oxides, the material composition of the ceramic rod, the grown crystal, and the liquid melt is the same. The crystal growth process in this case is relatively fast, and the growth rates vary from 1 to as high as 50 mm/h, where the higher speeds are more likely to be used in the case of evaporating materials [143]. The rotation rates should be high enough to assure flat or slightly convex crystallization front and dissolution front in the feed. Too low rotation rate makes these fronts too convex—in extreme case rods can touch one another. Too high rotation rate can cause concave, unstable interface. Additionally, rotation rate controls thickness of diffusion layer (see Section 8.1.2.5).

When an incongruently melting material is being grown (see Table 8.1.1), one has to use a solvent, also known as a flux, to make crystallization possible [176]. The composition of the flux can be suggested on the basis of information from the appropriate phase diagram [177]. The flux pellet is synthesized and mounted between the feed and the seed rods. As the temperature increases, the flux pellet melts and the rods are joined via a liquid bridge. At this point, the temperature has to be carefully adjusted again to allow for homogenization. Once this is done, the growth can proceed. Dissolving the feed rod in the liquid of the zone steadily restores the amount of material solidifying from the zone on the seed rod. This type of growth should be slow, owing to the slow mass transport through the diffusion layer at the solid–liquid interface. This mode of operation is called traveling solvent floating zone.

The volume of the flux pellet is low, so, even if its components have a low vapor pressure, the evaporation and dispersion of flux between the grains of the initially multigrain crystallizing material usually make the flux bridge short lived.

The “self-flux” approach proved often to be more reliable. In this case the zone is created by melting the ceramic rod, with a composition identical to the composition of required crystal, or sometimes a composition corrected for evaporation as described in Section 8.1.2.7 Careful adjustment of the temperature and the pulling rate is required until the evolution of the composition of liquid zone stabilizes the growth of required material. In the case of a very common peritectic transition, the crystal growth starts with the precipitation of the high temperature primary phase (A) on the seed rod (Figure 8.1.8). The zone composition then changes toward and beyond the peritectic liquid composition, until a nearly steady state is established and crystallization of the required phase begins. If the zone is quenched at this point, it is possible to analyze the composition of the self-flux [9,86,105].

If the composition of self-flux is established, pellet of such composition can be used to speed-up the process of achieving nearly steady state and creating a molten zone. This is important for complex oxides that require the growth rate as slow as 0.1–0.2 mm/h like $Bi_2Sr_2Ca_2Cu_3O_{10}$ [36] or $SrCu_2(BO_3)_2$ [135].

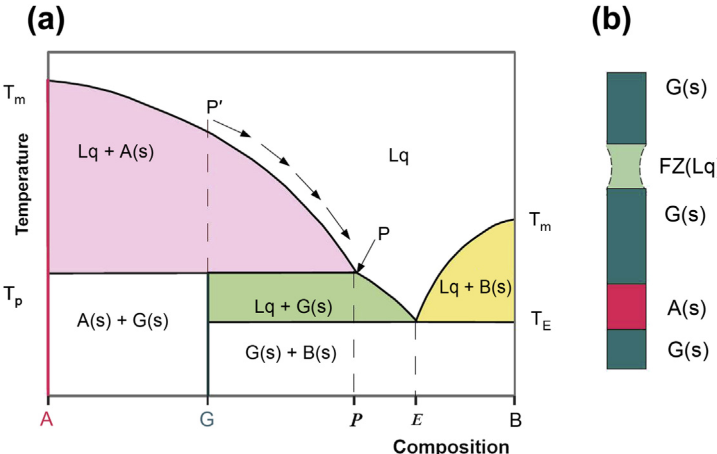

FIGURE 8.1.8 Evolution of growth process for incongruently melting compound G (a) Phase diagram (generic diagram, no solid solubility assumed) "A" and "B" are forming compound "G," T_m – melting points T_P, T_E – temperatures of peritectic and eutectic transformation, *P* – composition of liquid at peritectic point *E* – eutectic composition. (b) Evolution of composition – phases present during advanced crystal growth. (1) G(s) supporting ceramic rod "seed-rod" (2) A(S) compound A crystallizing from molten zone with composition richer in A than peritectic composition *P* depleting FZ (liquid) of compound A. (3) G(S) steady crystallization of compound G (4) FZ (lq) Floating zone – subperitectic liquid richer in B than peritectic composition *P* (5) G(s) polycrystalline "feed rod."

8.1.4 Constitutional Supercooling and Crystallization Front Stability

In most materials the congruently melting composition is usually not a stoichiometric one. In such a case, the evolution of the zone composition helps to produce crystals with desired close-to-stoichiometric composition. Similarly, using OFZ method doped crystals with more uniform distribution can be obtained even if dopant distribution coefficient $\neq 1$. In the case of a peritectic type of melting of binary (or more complex) oxides incongruently crystallizing crystal can be produced. In all these cases, the composition of liquid and solid crystallizing from this liquid (being in equilibrium) have to be different. Convection in conjunction with mechanical mixing stirs the majority of the volume of the liquid phase; this volume has a relatively uniform composition. The layer of liquid in the vicinity of the crystallization front is nearly stagnant. This layer is depleted of the species that are incorporated into the crystal and enriched in the species rejected from the solid state. In contrast to the volume of the well-stirred convection cell, the mass transport in this stagnant layer is mostly driven by diffusion, hence it is referred to as a "diffusion layer," and a significant gradient of chemical species concentration is observed. For distribution coefficients $k \neq 1$ ($k >> 1$ or $k << 1$) this effect is more pronounced, especially if a peritectic-type transition takes place. As a result of this concentration gradient, the solidus temperature decreases toward the solid–liquid interface. For a lower thermal gradient in the diffusion layer, a part of this layer can be

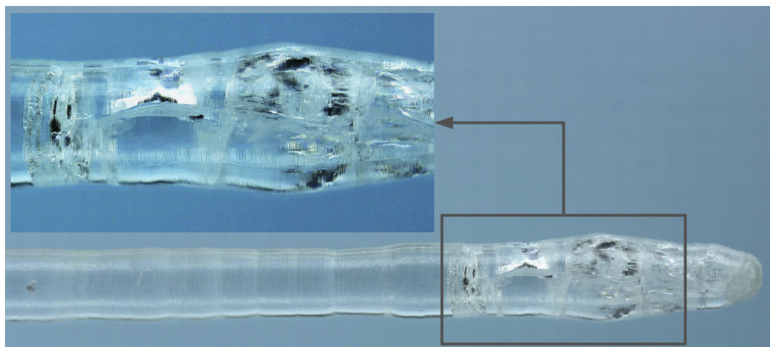

FIGURE 8.1.9 $Yb_3Ga_5O_{12}$ – insert shows top of the crystal with cracks caused by too high thermal gradient caused by high cooling rate. *Picture courtesy D'Ortensio RM.*

supercooled more than the liquid adjoining to the solid/liquid interface. This effect is referred to as constitutional supercooling [2,177] and for the case of OFZ it is discussed in [9].

As the growth rate of the crystal is proportional to the degree of supercooling, any positive fluctuation in the growth rate will lead to a further increase in the degree of supercooling and force rapid crystallization deeper into the supercooled liquid. The regions of the neighboring liquid will become even more depleted of crystal constituency, and locally the solidus temperature will be considerably lower. This effect (negated to some extent by release of latent heat of crystallization) causes a crystallization front instability. Numerous defects are caused by these instabilities. In more severe cases, solute-rich channels, known as flux tubes, form with the general direction parallel to the crystallization direction, which is not necessarily the pulling direction. Note that both convex and concave crystallization fronts have been observed in OFZ experiments [9,116].

To avoid constitutional supercooling, the growth rate of the crystal should be decreased leading to a reduced concentration gradient due to back diffusion of the enriched element into the melt. Higher thermal gradients on the solid/liquid interface and a faster seed rod rotation can also be suggested as remedies. Unfortunately, these actions result in an even larger temperature gradient in the already grown crystal, which can result in cracking during growth (Figure 8.1.9) [86]. Significant thermal and mechanical stresses limit the size and quality of crystals that can be obtained by the OFZ method. These problems are reduced if an afterheater is applied [14,25,58,100,116,147].

8.1.5 Selected Examples of Crystal Characterization

Defects occurring in the OFZ grown oxides are caused by high temperature gradient or by presence of flux [9]. An excellent discussion of defects found in oxide crystals grown from high and low temperature solutions is given by Rudolph [178,179] and Klapper [180]. Following are some examples of defects present in OFZ crystals.

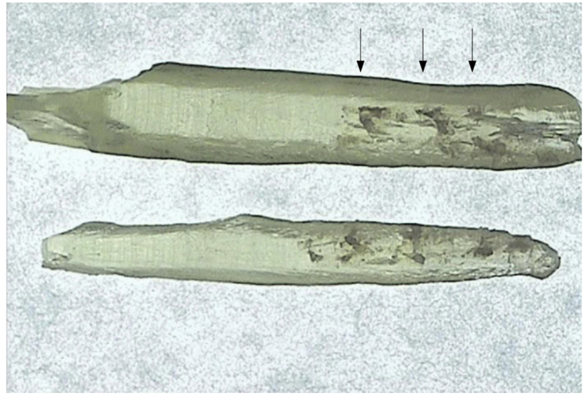

FIGURE 8.1.10 Impurity precipitations in $SrDy_2O_4$. Each precipitation path was triggered by nearly catastrophic instability of molten zone and caused by rapid and significant variations in the growth rate. As the crystal was transparent, it was possible to observe the consequences of the manual, stressful attempts to restore stability. Purity of starting materials was lower than 3N, melting point $>2000\,^{\circ}C$. *Picture courtesy of Medina T.*

Impurities often distribute homogeneously through the crystal—typically substituting atoms on particular crystallographic position. If the specific atoms are introduced on purpose, they are called *dopants*. The influence of convection on dopants segregation is discussed theoretically in [97,181]. Both dopants and impurities can strongly influence material properties [136]. Impurities, combining together, form *inclusions* of a foreign phase (Figure 8.1.10). This effect can be limited if high purity starting materials (4N and better) are used.

Inclusions in the form of precipitates and flux tubes are found in many relatively good OFZ crystals (e.g., in YVO_4 [127,128] or in $(La_xSr_{2-x})CuO_4$ [74]). They are created by instabilities in the crystallization front, leading to a noticeable amount of particles nucleating in the molten zone. Sometimes slower growth or changing of growth atmosphere is all that is needed to eliminate these precipitations (e.g., Al_2O_3 in $NiAl_2O_4$ [116] or carbonates and BiO_x phase in BSCCO [29]). In other cases, a slight change in composition of the starting rod helps correct for evaporation of the volatile component from the molten zone (e.g., Mg_2TiO_4 grown from ceramic rod with Mg:Ti as 2:1.01 [105]). Crystal quality can be further improved with the rotation adjusted to maintain flat crystallization front. Dense feed rods and slower growths in the case of TiO_2 have been suggested [15,166] for reducing the number of dislocation promoting inclusions.

Vacancies of both cations and anions are observed in many oxide crystals. They influence physical properties (like transport or magnetic) of the grown crystal, but their presence is difficult to evaluate.

Characteristic for OFZ crystals, *cracks* (see Figures 8.1.3 and 8.1.9) are caused by mechanical stress during cooling in the time of the growth (e.g., $(La_{1-x}Ca_x)_2CaCu_2O_{6+\delta}$) [86]. They can be limited either with the use of an afterheater (see Section 8.1.4) or with defocusing the lamps [26]. Slower growth (although not always feasible) and very slow cooling of a grown rod sometimes limit cracking of the crystal, and so does optimizing the growth atmosphere. Some severe cracks are the result of phase transitions during cooling (e.g., $CaTiSiO_5$) [9,52].

Gas bubbles are trapped inside of the crystals grown by the OFZ method as the shape of solid–liquid interface causes the bubbles to expand in the core region of the crystals (extreme case was reported for $CoTiO_3$) [9]. This often catastrophic effect (see Section 8.1.2.6) is caused by either solubility of O_2 in the liquid phase or by partial decomposition of oxides in the zone. In the last case it can be—to some extent—controlled by adjusting partial oxygen pressure (PO_2) as described for Al_2O_3 [20,21] and Li_3VO_4 [101].

Eutectic solidification is sometimes observed for preliminary experiments of incongruently melting materials grown with high growth rates (e.g., Sr_2RuO_4, $Sr_3Ru_2O_7$) [182]. Lowering growth speed is not possible in the case of highly volatile RuO_2, which limits the chance of obtaining single crystalline phase [145].

Striations are caused by fluctuations of temperature of the liquid near the crystallization front, originating from convection flows. Temperature fluctuations cause fluctuations of growth rate, which result in changes of chemical composition (as an effective segregation coefficient depends on the growth rate). Striations may be used as indicators of the shape of the solid–liquid interface [7,128].

In the case of transparent materials, observation of as-grown crystal using various microscopic techniques (transmission, polarized light, phase contrast, confocal microscopy, light scattering, and similar techniques) can deliver meaningful information about the quality of crystal grown. Surface features observed on nontransparent crystals can also deliver information about crystal quality. A distinctive *facet* on as-grown crystal (often indication of single grain) is very informative as the quality of a facet is a sign of overall crystal quality. Facets are the result of growth rate anisotropy and formally are considered to be a defect in the sense of “ideal” crystal. Multiple and incoherent facets are often observed on a lateral surface as a result of grain evolution, and they are more visible at the beginning of nonseeded crystallization—before a boule becomes a single crystal. For materials with high growth rate anisotropy (especially for crystals with layered crystallographic structures like $CuGeO_3$ [65,183] or $Bi_2Sr_2CaCu_2O_n$), instability of the crystallization front results in growth of boule that separates into thin crystalline plates [28] typically visible on lateral or cross-section surfaces. The majority of the crystals grown by OFZ technique do not show distinctive facets. Usually crystals are round or growth rate anisotropy is manifested as an oblong cross-section. Facets on the crystallization front (not visible directly on the grown crystal) can be a source of defects, for example, of core effect. If the striations are observed in the crystal (typically in the cross-section parallel to the growth axis) they are indicating the shape of crystallization front (see also Section 8.1.6). Detailed optical analysis of (especially opaque) crystal requires the boule to be cut and polished.

Accurate values of crystallographic lattice parameters can then be determined by X-ray powder diffraction on pulverized sample [184]. In the case of solid solutions or nonstoichiometric compounds, this method provides vital information about composition, oxidation state, and other chemical properties of the material.

For high quality crystals, information about mosaic spread, grains, and twinning in a more quantitative manner can be obtained by pole-figures analysis, rocking curve measurements, or X-ray topography [1,180].

The Laue method utilizing systems with area detectors and specialized software [185,186] is an excellent approach to orient crystal before cutting.

Model experimental work on defect characterization using STEM, EELS, and TEM techniques on cleaved $Bi_2Sr_2CaCu_2O_{8+\delta}$ crystals grown very slowly (0.21 mm/h) by the TSFZ method has been published by Zhu et al. [30]. Similar work in the future will likely answer many questions about microscopic defects. High angle annular dark field – scanning transmission electron microscopy (HAADF-STEM) imaging can also be used to characterize some growth defects in obtained crystals. An example of such work revealing stacking faults in BSCCO is presented in Figure 8.1.11. Whereas these techniques provide interesting information about the internal properties of a grown oxide on the atomic level, there is no possibility to use this information as feedback to modify growth conditions and improve the overall quality of the grown crystal. It is important to stress here that the information about grain boundaries, stacking faults, and intergrowth of layers of different phases can only be obtained in a useful sense by electron microscopic methods, if the investigated material is a crystal of a high quality.

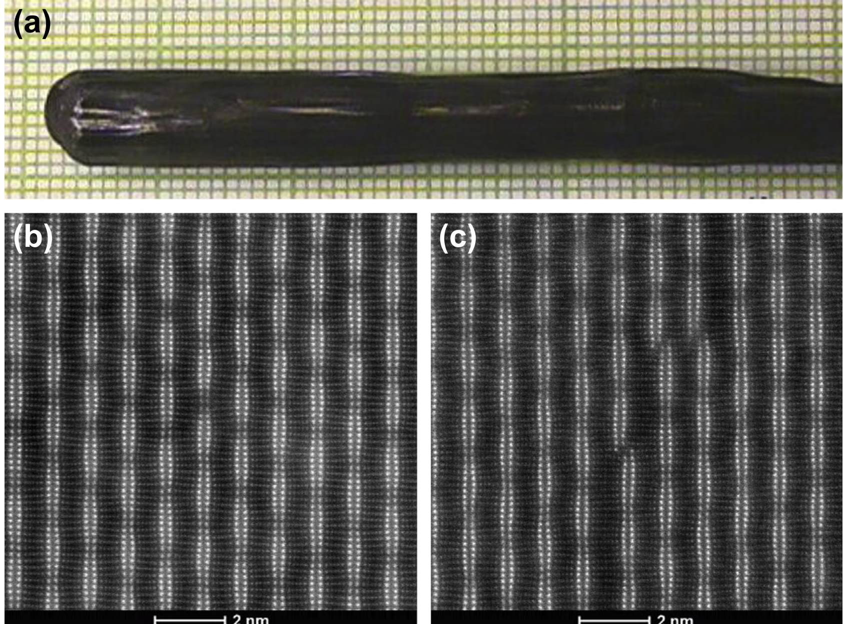

FIGURE 8.1.11 (a) Single crystal of incongruently $Bi_2Sr_2CaCu_2O_{8+\delta}$ (BSCCO) grown at puling rate 0.2 mm/h (b) Perfect region of BSCCO crystal (c) Stacking fault visible on STEM image [96]. *Picture courtesy of Couillard M.*

Energy dispersive X-ray analysis (EDAX) and electron probe microanalysis (EPMA, electron microprobe) with good standards can confirm the exact chemical formula of crystals and solid solutions grown in different conditions.

Both X-ray and electron diffraction supply very valuable surface information. Neutron diffraction techniques, if available, provide information about the entire volume of a crystal, due to low absorption of neutrons in the majority of materials. They provide an excellent confirmation of the total crystal quality, as all the substantial grains present in the as-grown crystal can be detected. This is especially important in the case of non-transparent crystals where the assessment of the total quality of boule can be performed without the labor-intensive and destructive process of crystal cutting followed by subsequent surface preparation. Neutron rocking curves (FWHM) measured on as-grown boule (Figure 8.1.12) opens new ways of crystal quality assessment [96].

8.1.6 Concluding Remarks

More and more complex crystals are grown by the optical floating zone and traveling solvent floating zone techniques due to the fact that these methods produce high quality, relatively large and uniform crystals of oxides inexpensively and without contaminating the environment, without any crucible, and in selected atmosphere and pressure. Obtained crystals are investigated accordingly to their physical properties and predicted applications. These unique magnetic, electrical, and optical properties and their changes with different dopants and/or growth conditions are now the main purpose of growing crystals of oxides by OFZ and TSFZ methods. Some crystals are new and have never been grown before. Others have already been studied, but larger or better quality samples are

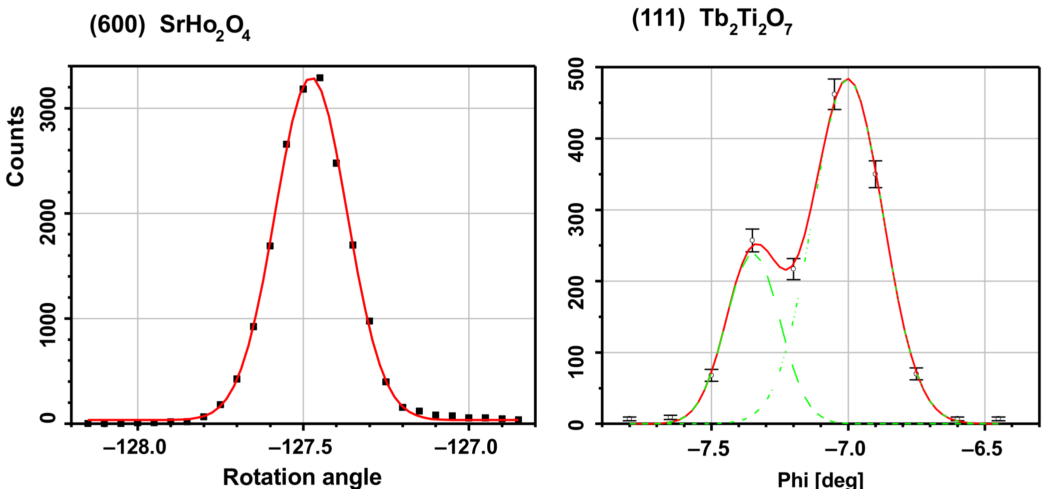

FIGURE 8.1.12 Neutron rocking curve (600) reflection of $SrHo_2O_4$ (one grain crystal) and (111) reflection of $Tb_2Ti_2O_7$ (two grains detected). *Pictures courtesy of Pole A. and Fritsch K.*

now needed. These two methods also provide a relatively easy and consistent way of crystallizing solid solutions of oxides, modifying their properties according to future applications.

It would be very beneficial for scientific development of the OFZ methods if more modeling for different oxides is performed. Then it will be possible to connect growth features with the applied change of growth conditions. To develop this field of research, the properties of molten oxides at high temperature have to be assessed. More information about thermodynamic properties (including phase diagrams) for the systems of interest will also be beneficial.

There is also the crucial but nearly untouched problem of automation of this crystal growth. The automatic diameter control systems have proven to be very useful in the Czochralski crystal growth (see Chapter 28 of Volume IIB) and it is also successfully applied to the floating zone process with RF heating (see Chapter 7 of Volume IIA). Unless such progress happens for the optical floating zone method, the process control and crystal quality rely only on the experience and skills of a crystal grower.

As the crystal growth process has to be refined in multiple experiments, close collaboration between the grower and all the crystal users is essential.

Acknowledgments

The authors are very grateful to BIMR for financial support, Dr Bruce Gaulin for continuous support and encouragement and Tim Munsie for helpful suggestions.

The financial support of the Deutsche Forschungsgemeinschaft within the Collaborative Research Centre SFB 609 “Electromagnetic flow control in metallurgy, crystal growth and electrochemistry” is gratefully acknowledged.

References

[1] Springer handbook of crystal growth, defects and characterization. Berlin: Springer-Verlag; 2010.

[2] Hurle DTJ. Crystal pulling from the melt. Berlin: Springer-Verlag; 1993.

[3] Ferrarelli MC, Sinclair DC, West AR, Dabkowska HA, Dabkowski A, Luke GM. J Mater Chem 2009; 19:5916.

[4] Akashi T, Matumi K, Okada T, Mizutani T. IEEE Trans Mag 1969;Mag-5:285.

[5] Shindo I, Li N, Kitamura K, Kimura S. J Cryst Growth 1979;46:307.

[6] Croll A. Ger Assoc Cryst Growth (DGKK) Newsl 1997;65:13.

[7] Kimura S, Kitamura K. J Am Ceram Soc 1992;75:1140.

[8] Mühlbauer A. International Scientific Colloquium “Modelling for material processing” Riga; June 8–9, 2006.

[9] Dabkowska Hanna A, Dabkowska Antoni B. Crystal growth of oxides by optical floating zone technique. In: Springer handbook of crystal growth, defects and characterization. Berlin Heidelberg New York Tokyo: Springer-Verlag; 2010. p. 367.

[10] Revcolevschi A, Jegoudez J. Prog Mater Sci 1997;42:321.

[11] Gu GD, Egi T, Koshizuka N, Miles PA, Russell GJ, Kenned SJ. Phys C 1996;263:180.

[12] Balakrishnan G, Hayes TJ, Petrenko OA, Paul DMc K. J Phys Condens Matter 2009;21:012202.

[13] Villora EG, Shimamura K, Yoshikawa Y, Aoki K, Ichinose N. J Cryst Growth 2004;270:420.

[14] Balbashov AM, Egorov SK. J Cryst Growth 1981;52:498.

[15] Koohpayeh SM, Fort D, Abell JS. J Cryst Growth 2005;282:190.

[16] Higuchi M, Kodaira K. J Cryst Growth 1992;123:495.

[17] Tiller WA. In: The art and science of growing crystals. New York London: John Wiley&Sons, Inc.; 1963 [chapter 15].

[18] Shah JS. In: Crystal growth. International series on the science of the solid state. 2nd ed., vol. 16. Pergamon Press Oxford, New York Toronto, Sydney Paris Frankfurt; 1980 [chapter 8].

[19] Shindo I. J Cryst Growth 1980;50:839.

[20] Saito M. J Cryst Growth 1986;74:385.

[21] Saito M. J Cryst Growth 1985;71:664.

[22] Dabkowska HA, to be published.

[23] Pavlova SG, Balbashov AM, Rybina LN. J Cryst Growth 2012;351:161.

[24] Furukawa J, Tsukamoto T. Jpn J Appl Phys 1991;30:2391.

[25] Subramanian R, Higuchi M, Dieckman R. J Cryst Growth 1994;143:311.

[26] Chen J-C, Chin G-H. J Cryst Growth 1995;154:98.

[27] Aczel AA, Dabkowska HA, Provencher PR, Luke GM. J Cryst Growth 2008;310:870.

[28] Gu GD, Takamuku K, Koshizuka N, Tanaka S. J Cryst Growth 1994;137:472.

[29] Maljuk A, Liang B, Lin CT, Emelchenko GA. Phys C 2001;335:140.

[30] Zhu Y, Niewczas M, Couillard M, Botton GA. Ultramicroscopy 2006;106:1076.

[31] Balakrishnan G, Paul DMc K, Lees MR. Phys B 1994;194–196:2197.

[32] Murugakoothan P, Jayavel R, Rao CRV, Subramanian C, Ramasamy P. Mater Chem Phys 1992;31:281.

[33] Huang Y, Wang B-L, Hong M-Y, Wu M-K. Phys C 1994;235–240:525.

[34] Takamuku K, Ikeda K, Takata T, Miyatake T, Tomeno I, Gotoh S, et al. Phys C 1991;185–189:451.

[35] Horiuchi T, Kitahama K, Kawai T, Kawai S, Hontsu S, Ogura K, et al. Phys C 1991;185–189:629.

[36] Fujii T, Watanabe T, Matsuda A. J Cryst Growth 2001;223:175.

[37] Liang B, Maljuk A, Lin CT. Phys C 2001;361:156.

[38] Matsumoto M, Shirafuji J, Kitahama K, Kawai S, Shigaki I, Kawate Y. Phys C 1991;185–189:455.

[39] Miyazawa S, Tabata T. J Cryst Growth 1998;191:512.

[40] Watauchi S, Tanaka I, Hayashi K, Hirano M, Hosono H. J Cryst Growth 2002;237–239:801.

[41] Katsumata T, Nabae T, Sasajima K, Matsuzawa T. J Cryst Growth 1998;83:361.

[42] Britos N, Lejus A-M, Viana B, Vivien D. Eur J Solid State Inorg Chem 1995;32:415.

[43] Li N, Shindo I. J Cryst Growth 1979;46:569.

[44] Toth S, Lake B, Hradil K, Guidi ST, Rule KC, Stone MB, et al. Phys Rev Lett 2012;109:127203.

[45] Wada J, Wakimoto S, Hosoya S, Yamada K, Endoh Y. Phys C 1997;244:193.

[46] Kim YJ, Wakimoto S, Shapiro SM, Gehring PM, Ramirez AP. Solid State Commun 2002;121:625.

[47] Barbosa LB, Ardila DR, Andreeta JP. J Cryst Growth 2003;254:378.

[48] Maljuk A, Strempfer J, Lin CT. J Cryst Growth 2003;258:435.

[49] Belevtsev BI, Naugle DG, Rathnayaka KDD, Parasiris A, Fink-Finowicki J. Phys B Condens Matter 2005;355:341.

[50] Tomioka Y, Asamitsu A, Tokura Y. Phys Rev B 2000;63:024421.

[51] Kloc Ch, Cheong S-W, Matl P. J Cryst Growth 1998;191:294.

[52] Tanaka I, Obuchi T, Kojima H. J Cryst Growth 1988;87:169.

[53] Fukazawa H, Nakatsuji S, Maeno Y. Phys B 2000;281:613.

[54] Nakatsuji S, Maeno Y. J Solid State Chem 2001;156:26.

[55] Wanyan W, Yan X, Wu X, Zhang Z, Hu B, Zhou J. J Cryst Growth 2000;219:56.

[56] Oka K, Yamaguchi H, Ito T. J Cryst Growth 2001;229:419.

[57] Homes CC, Vogt T, Shapiro SM, Wakimoto S, Subramanian MA, Ramirez AP. Phys Rev B 2003;67:092106.

[58] Balbashov AM, Rybina LN, Fetisov YK, Meshcheryakov VF, Srinivasan G. J Cryst Growth 2005;275:E733.

[59] Prabhakaran D, Wondre FR, Boothroyd AT. J Cryst Growth 2003;250:72.

[60] Balakrishnan G, Petrenko OA, Lees MR, Paul DMK. J Phys Condens Matter 2004;16:L347.

[61] Laverock J, Chen B, Preston ARH, Smith KE. Phys Rev B 2013;87:125133.

[62] Fritsch K, Ramazanoglu M, Dabkowska HA, Gaulin BD. J Cryst Growth 2011;327:205.

[63] Kismarahardja A, Brooks JS, Zhou HD, Choi ES, Matsubayashi K, Uwatoko Y. Phys Rev B 2013;87:054432.

[64] Behr G, Löser W, Apostu M-O, Gruner W, Hücker M, Schramm L, et al. Cryst Res Technol 2005;40:21.

[65] Revcolevschi A, Ammerahl U, Dhalenne G. J Cryst Growth 1999;198/199:593.

[66] Dhalenne G, Revcolevschi A, Rouchaud JC, Fedoroff M. Mater Res Bull 1997;32:939.

[67] Islam ATMN, Pieper O, Lake B, Siemensmeyer K. Cryst Growth Des 2011;11:154.

[68] Chiaramonti AN, Pless JD, Liu L, Smit JP, Lanier CH, Poeppelmeier KR, et al. Cryst Growth Des 2004;4:749.

[69] MacDougall GJ, Garlea VO, Aczel AA, Zhou DH, Nagler SE. Phys Rev B 2012;86:060414.

[70] Hara S, Yoshida Y, Ikeda SI, Shirakawa N, Crawford MK, Takase K, et al. J Cryst Growth 2005;283:185.

[71] Kawamura S, Kaneko JH, Higuchi M, Haruna J, Saeki S, Fujita F, et al. IEEE Trans Nucl Sci 2009;56:328.

[72] Kimura H, Tanahashi R, Maiwa K, Morinaga R, Sato Kimura TJ. J Cryst Growth 2009;311:522.

[73] Yan XL, Zhou JF, Niu XJ, Chen XL, Tu QY, Wu X. J Cryst Growth 2002;242:161.

[74] Zhang K, Mogilevsky R, Hinks DG, Mitchell J, Schultz AJ, Wang Y, et al. J Cryst Growth 1996;169:73.

[75] Trouilleux L, Dhalenne G, Revcolevschi A, Monod P. J Cryst Growth 1988;91:268.

[76] Tanaka I, Kojima H. Nature 1985;337:21.

[77] Tanaka I, Yamane K, Kojima H. J Cryst Growth 1989;96:711.

[78] Balbashov AM, Shulyatev DA, Panova GKh, Khlopkin MN, Chernoplekov NA, Shikov AA, et al. Phys C 1996;256:371.

[79] Kojima H, Yamamoto Y, Mori Y, Khan MKR, Tanabe H, Tanaka I. Phys C 1997;293:14.

[80] Adachi T, Noji T, Koike Y. Phys Rev B 2001;64:144524.

[81] Ito T, Oka K. Phys C 1994;231:305.

[82] Ito T, Oka K. Phys C 1994;235:549.

[83] Yu JD, Yanagida JD, Takashima H, Inaguma Y, Itoh M, Nakamura T. Phys C 1993;209:442.

[84] Jia LS, Yan XL, Zhou JF, Chen XL. Phys C 2003;385:483.

[85] Tanaka I, Kojima H. In: The international workshop on superconductivity, Honolulu; 1992. pp. 146–9.

[86] Gu GD, Hucker M, Kim YJ, Tranquada JM, Dabkowska H, Luke GM, et al. J Phys Chem Solids 2006; 67:431.

[87] Ammerahl U, Revcolevschi A. J Cryst Growth 1999;197:825.

[88] Zobel C, Kriener M, Bruns D, Baier J, Grüninger M, Lorenz T, et al. Phys Rev B 2002;66:020402.

[89] Aleshkevych P, Baran M, Barilo SN, Fink-Finowicki J, Szymczak H. J Phys Condens Matter 2004;16: L179.

[90] Arima Taka-hisa, Tokura Y. J Phys Soc Jpn 1995;64:2488.

[91] De Leon-Guevara AM, Berthet P, Berthon J, Millot F, Revcolevschi A. J Alloys Compd 1997; 262–263:163.

[92] Urushibara A, Moritomo Y, Arima T, Asamitsu A, Kido G, Tokura Y. Phys Rev B 1995;51:14103.

[93] Prabhakaran D, Coldea AI, Boothroyd AT, Blundell S. J Cryst Growth 2002;237:806.

[94] Prabhakaran D, Boothroyd AT. J Mater Sci Mater Electron 2003;14:587.

[95] Ido T, Magoshi K, Eisaki H, Uchida S. Phys Rev B 1991;44:12094.

[96] Yomogida S, Higuchi M, Ogawa T, Wada S, Takahashi J. J Cryst Growth 2012;359:20.

[97] Chen CJ, Lee Y-C, Hu C. J Cryst Growth 1996;166:151.

[98] Chen JC, Wu H-K. J Heat Mass Transf 1996;39:3707.

[99] Chen CJ, Chieh H. J Cryst Growth 1995;149:87.

[100] Itoyama W, Iishi K, Sakata S. J Cryst Growth 1996;158:534.

[101] Sakata S, Itoyama W, Fujii I, Iishi K. J Cryst Growth 1994;135:555.

[102] Iida J, Takekawa S, Kimizuka N. J Cryst Growth 1990;102:398.

[103] Lafuerza S, Garcıa J, Subıas G, Blasco J, Conder K, Pomjakushina E. Phys Rev B 2013;88:085130.

[104] Mass JL, Burlitch JM, Markgraf SA, Higuchi M, Dieckmann R, Barber DB, et al. J Cryst Growth 1996; 165:250.

[105] Shindo I, Kimura S, Kitamura K. J Mater Sci 1979;14:1901.

[106] Pless JD, Erdman N, Ko D, Marks LD, Stair PC, Poeppelmeier KR. Cryst Growth Des 2003;3:615.

[107] Higuchi M, Geray RF, Dieckmann R, Park DG, Burlitch JM, Barber DB, et al. J Cryst Growth 1995; 148:140.

[108] Prabhakaran D, Boothroyd AT, Coldea R, Charnley NR. J Cryst Growth 2004;271:74.

[109] Chen DP, Chen HC, Maljuk A, Kulakov A, Zhang H, Lemmens P, Lin CT. Phys Rev B 2004;70: 024506.

[110] Lin CT, Chen DP, Lemmens P, Zhang XN, Maljuk A, Zhang PX. J Cryst Growth 2005;275:606.

[111] Jia LS, Yan XL, Chen XL. J Cryst Growth 2003;254:437.

[112] Higuch M, Kodaira K, Nakayama S. J Cryst Growth 1999;207:298.

[113] Masubuchia Y, Higuchia M, Katasea H, Takeda T, Kikkawaa Shinichi, Kodairaa Kohei, et al. Solid State Ionics 2004;166:213.

[114] Balakrishnan G, Lees MR, Paul DM. J Phys Condens Matter 1997;9:L471.

[115] Sefat AS, Greedan JE, Luke GM, Niewczas M, Garrett JD, Dabkowska H, et al. Phys Rev B 2006;74: 104419.

[116] Kojima H, Watanabe M, Tanaka I. J Cryst Growth 1995;155:70.

[117] Deng G, Thiyagarajanc R, Mohan Radheepc D, Pomjakushinaa E, Medardea M, Krzton-Maziopa A, et al. J Cryst Growth 2012;353:25.

[118] Conner BS, Zhou HD, Balicas L, Wiebe CR, Whalen J, Siegrist T. J Cryst Growth 2011;321:120.

[119] Popova MN, Klimin SA, Higel P, Dhalenne G. Phys Lett A 2006;354:487.

[120] Ito T, Oka K. Phys C 1994;235:355.

[121] Ivanov V, Mukhin A, Glushkov V, Balbashov A. JETP Lett 2013;97:28.

[122] Bryan C, Whitman CA, Johnson MB, Murray P, Bourque A, Dabkowska HA, et al. Phys Rev B 2012; 86:054303.

[123] Ross KA, Proen Th, Dabkowska HA, Quilliam JA, Yaraskavitch LR, Kycia JB, et al. Phys Rev B 2012; 86:74424.

[124] Gardner JS, Gaulin BD, Paul DMc K. J Cryst Growth 1998;191:740.

[125] Revell HM, Yaraskavitch LR, Mason JD, Ross KA, Noad HML, Dabkowska HA, et al. Nat Phys 2013; 9:34.

[126] Li QJ, Xu LM, Fan C, Zhang FB, Lv YY, Ni B, et al. J Cryst Growth 2013;377:96.

[127] Yan X-l, Wu X, Zhou J-F, Zhang Z, Wang J. J Cryst Growth 2000;220:543.

[128] Nakamura S, Agata T, Ogawa T, Wada S, Higuchi M. Opt Rev 2013;20:390.

[129] Yan X-l, Wu X, Zhou J-F, Zhang Z, Wang J, Xiao M, et al. J Cryst Growth 2000;212:204.

[130] Hien NT, Franse JJM, Pothuizen JJM, Menovsky AA. J Cryst Growth 1997;171:102.

[131] Islam ATMN, Quintero-Castro D, Lake B, Siemensmeyer K, Kiefer K, Skourski Y, et al. Cryst Growth Des 2010;10:465.

[132] Revcolevschi A, Vietkine A, Moudden H. Phys C 1997;282–287:493.

[133] Ohashi N, Fujiwara K, Tsurumi T, Fukunaga O. J Cryst Growth 1998;186:128.

[134] Kageyama H, Onizuka K, Yamauchi T, Ueda Y. J Cryst Growth 1999;206:65.

[135] Dabkowska HA, Dabkowski AB, Luke GM, Dunsiger SR, Haravifard S, Cecchinel M, et al. J Cryst Growth 2007;306:123.

[136] Aczel AA, MacDougall GJ, Rodriguez JA, Luke GM, Russo PL, Savici AT, et al. Phys Rev B 2007;76: 214427.

[137] Dabkowska HA, Gaulin BD. J Optoelectron Adv Mater 2007;9:1215.

[138] Dunsiger SR, Zhao Y, Gaulin BD, Qiu Y, Bourges P, Sidis Y, et al. Phys Rev B 2008;78:092507.

[139] Ammerahl U, Dhalenne G, Revcolevschi A, Berthon J, Moudden H. J Cryst Growth 1998;193:55.

[140] Maljuk A, Strempfer J, Ulrich C, Sofin M, Capogna L, Lin CT, et al. J Cryst Growth 2004;273:207.

[141] Quintero-Castro DL, Lake B, Reehuis M, Niazi A, Ryll H, Islam ATMN, et al. Phys Rev B 2012;86: 064203.

[142] Dabkowska HA, Mortimer K, to be published.

[143] Mao ZQ, Maeno Y, Fukazawa H. Mater Res Bull 2000;35:1813.

[144] Maeno Y, Hashimoto H, Yoshida K, Nishizaki S, Fujita T, Bednorz JG, et al. Nature 1994;372:532–4.

[145] Fittipaldi R, Vecchione A, Fusanobori S, Takizawa K, Yaguchi H, Hooper J, et al. J Cryst Growth 2006;282:152.

[146] Perry RS, Maeno Y. J Cryst Growth 2006;271:134.

[147] Nabokin PI, Souptel D, Balbashov AM. J Cryst Growth 2003;250:397.

[148] Uematsu K, Sakurai O, Mizutani N, Kato M. J Mater Sci 1984;19:3671.

[149] Souptel D, Behr G, Balbashov AM. J Cryst Growth 2002;236:583.

[150] Balakrishnan G, Geetha T. Solid state physics. AIP Conference Proceedings, 1512, vol. 57; 2012. 1320.

[151] Stingaciu M, Pomjakushina E, Grimmer H, Trottmann M, Conder K. J Cryst Growth 2008;310: 1239–44.

[152] Higuchi M, Hatta K, Takahashi J, Kodaira K, Kaneda H, Saito J. J Cryst Growth 2000;208:501.

[153] Sugimoto A, Nob Y, Yamagish K. J Cryst Growth 1994;140:349.

[154] Balbashov AM, Tsvetkova AA, Chervonenkis AYa. Neorg Mater 1975;11:108.

[155] Kitamura K, Kimura S, Miyazawa Y, Mori Y, Kamada O. J Cryst Growth 1983;62:351.

[156] Abernethy LL, Ramsey Jr TH, Roaa JW. J Appl Phys 1961;32 sup:376S.

[157] Shindo I, Kimizuka N, Kimura S. Mater Res Bull 1976;11:637.

[158] Silverstein HJ, Fritsch K, Flicker F, Hallas AM, Gardner JS, Qiu Y, Ehlers G, Savici AT, Yamani Z, Ross KA, Gaulin BD, Gingras MJP, Paddison JAM, Foyevtsova K, Valenti R, Hawthorne F, Wiebe CR, Zhou HD. Physical Review B 2014;89:054433.

[159] Dabkowska HA, Dabkowski A, Luke GM, Gaulin BD. J Cryst Growth 2002;234:411.

[160] Oka K, Shibata H, Kashiwaya S. J Cryst Growth 2002;237:509.

[161] Kitamura K, Shindo I, Kimura S. J Cryst Growth 1979;46:277.

[162] Scientific Instruments Dresden (SciDre) GmbH www.scidre.com.

[163] Mizutani T, Matsumi K, Makino H, Yamamoto T, Kato T. NEC Res Dev 1974;33:86. NEC now: CANON MACHINERY Inc. 85 Minami Yamada-cho Kusatsu-city Shiga pref. 525–8511 Japan.

[164] Balbashov A, Moscow Power Engineering Institute Technical University, 14 Krasnokazarmennaya, Moscow, 111250, Russia.

[165] Shindo I, Crystal System Inc, 9633 Kobuchisawa, Yamanashi 408 Japan, http://www.crystalsys.co.jp/english/product05_e.htm.

[166] Koohpayeh SM, Fort D, Abell JS. Prog Cryst Growth Charact Mater 2008;54:121.

[167] Rudevics A, Muiznieks A, Radnieks G. In: Proc. joint 15th Riga and 6th, int. conf. on fundamental and applied MHD, vol. 2; 2005. p. 229.

[168] Lan CW. J Cryst Growth 2003;247:597.

[169] Fratello VJ, Brandle CD. J Cryst Growth 1993;128:1006.

[170] Singh DK, Helton JS, Chu S, Han TH, Bonnoit CJ, Chang S, et al. Phys Rev B 2008;78:20405.

[171] Dabkowska HA, Gaulin BD. In: Crystal growth of technologically important electronic materials, vol. 341. Allied Publishers PVT Ltd.; 2003.

[172] Balakrishnan G. Solid state physics. AIP Conference Proceedings, vol. 57; 2012. 1520.

[173] Chen NH, Othmer DF. J Chem Eng Data 1962;7:37.

[174] SteinbergA TA, Kurtz J, Wilson DB. Combust Flame 1998;113:27.

[175] Wagman JJ, van Gastel G, Ross KA, Yamani Z, Zhao Y, Qiu Y, et al. Phys Rev B 2013;88:014412.

[176] Elwell D, Scheel HJ. Crystal growth from high-temperature solutions. Academic Press; 1975.

[177] Levin EM, Robins CR, McMurdie HF. Phase diagrams for ceramists; 1964 (American Ceramical Society, Columbus, Ohio, 1964 and the next volumes); electronic version of this data-base is

available online, http://phase.ceramics.org/Publicstore/IPUser.aspx. by American Ceramic Society and NIST.

[178] Rudolph P. Stoichiometry related growth phenomena and methods of controlling. In: Crystal growth of technologically important electronic materials. Allied Publishers PVT Ltd.; 2003. p. 407.

[179] Rudolph P. Defect formation during crystal growth from the melt. In: Springer handbook of crystal growth. 1st ed. Berlin: Springer; 2010. p. 159.

[180] Klapper H. Reconstruction of the growth history of crystals by analysis of growth defects. In: Crystal growth of technologically important electronic materials. Allied Publishers PVT Ltd; 2003. p. 603.

[181] Winkler C, Amberg G, Carlberg T. J Cryst Growth 2000;210:573.

[182] Fittipaldi R, Sisti D, Vecchione A, Pace S. Cryst Growth Des 2007;7:2495–9.

[183] Watauchi S, Wakihara M, Tanaka I. J Cryst Growth 2001;229:423.

[184] Structure determination from powder diffraction data. In: David WIF, Shankland K, McCusker LB, Baerlocher Ch, editors. IUCr monographs on crystallography. IUCr Oxford Science Publication; 2002.

[185] "OrientExpress" is a part of LMGP suite for Windows by J. Laugier and B. Bochu (Laboratoire des Materiaux et du Génie Physique de l'Ecole Supérieure de Physique de Grenoble, http://www.inpg.fr/LMGP/). Program can be downloaded from the LMGP Crystallography software suite website at: http://www.ccp14.ac.uk/ccp/web-mirrors/lmgp-laugier-bochu/.

[186] "CLIP" The Cologne Laue Indexation Program by O. Schumann, http://clip.berlios.de/.

8.2 Floating-Zone Single Crystal Growth of Intermetallic Compounds Using a Two-phase RF Inductor

Regina Hermann[1], Janis Priede[2], Gunter Gerbeth[3]
[1]*LEIBNIZ INSTITUTE FOR SOLID STATE AND MATERIALS RESEARCH, DRESDEN, GERMANY;* [2]*APPLIED MATHEMATICS RESEARCH CENTER, COVENTRY UNIVERSITY, UK;* [3]*HELMHOLTZ-ZENTRUM DRESDEN-ROSSENDORF, DRESDEN, GERMANY*

8.2.1 Introduction

Chapter 7 discussed the high importance of crucible-free floating zone (FZ) for silicon, and Part I of this chapter demonstrated its versatility for dielectric crystals. Here, in Part II of this chapter, the favorable applicability for intermetallic compounds will be shown.

Especially the crystal growth of intermetallic compounds requires the application of the floating zone technique because of their high melting points and reactivity to oxygen. The term *intermetallics* was introduced by William Hume-Rothery in 1955 [1] for solid state phases involving metals. Examples for such phases are Laves phases, rare-earth compounds, silicides, and many others. A recent description of properties and emerging applications of intermetallics can be found, e.g., in [2]. Recently, much interest has been concentrated on the single crystal growth of multicomponent intermetallics, such as rare-earth-transition compounds. Silicides and borocarbides have been grown by the floating-zone method to study their magnetic, electric, and transport properties, as well as superconductivity [3–5]. The use of standard radio frequency (RF) floating zone for the growth of high melting point compounds is often problematic due to strong heat radiation from the surface and melt convection, which give rise to a nonuniform solid–liquid interface being concave toward the solid phase parts at the crystal rim. In that case, complex multicomponent intermetallic compounds are particularly difficult to produce as single crystals over the whole cross-section. Especially in demand are high precision single crystals of novel materials with interesting properties. The growth of single crystals of such intermetallic compounds by floating zone requires a well-designed electromagnetic control of heat and mass transfer, which, in turn, determines the shape of the solid–liquid interface [6]. To obtain single crystals, a convex to the melt growth interface is usually desirable [7]. As it is well known, the growth of defect-free single crystals is strongly affected by the heat transfer and the melt flow [8,9]

(see also Chapters 20 and 21 in Volume IIB). This is also valid for FZ characterized by high temperature gradients and forcible buoyancy and Marangoni convections within the melt zone. Thus, much research is concentrated on the application of rotating [10,11] as well as static magnetic fields [12] in order to reduce the convection-driven temperature fluctuations and isotherm curvatures causing harmful dopant fluctuations. In the floating zone process with RF heating, the electromagnetic force is one of the major mechanisms driving the melt flow. This force is directed against the phase gradient of the AC magnetic field [13]. The standard single-phase inductor, which is shown in Figure 8.2.1 (top), generates an AC phase gradient directed almost normally to the free surface of the melt with the maximum of the force at about mid-height of the floating zone [14]. Such a force usually drives a radially inward jet of hot melt at the middle of the floating zone. At the center of the floating zone, the radial jet splits into two nearly symmetric axial jets, which further stream toward both solid–liquid interfaces. The hot axial jet impinging at the center of the growth interface renders it concave, promoting polycrystalline growth.

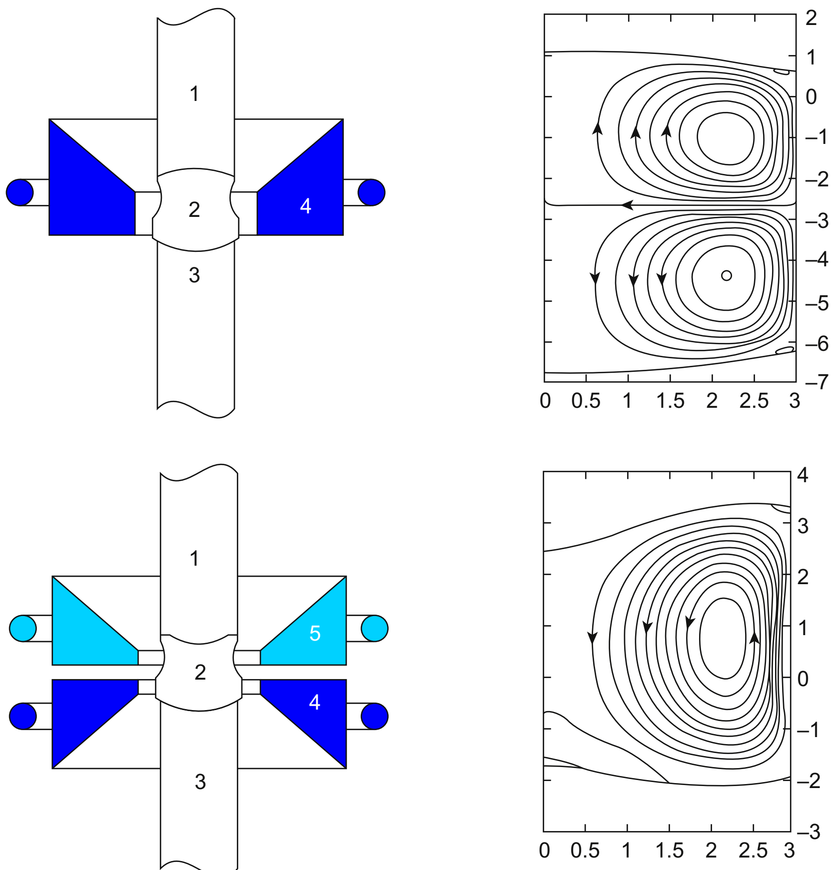

FIGURE 8.2.1 Schematic view of the floating-zone setup (on left) and the basic structure of electromagnetically driven melt flow (on right) for a standard single-phase inductor (top) and a two-phase inductor (bottom) containing crystal (1), molten zone (2), feed rod (3), primary coil (4), and secondary coil (5).

Favorable growth conditions require a flow directed away from the solidification front at the axis of symmetry and against the front at the free surface of the floating zone. Such a flow can be generated by an electromagnetic force directed along the free surface toward the solidification front. To obtain such an electromagnetic force directed along the floating zone, a phase gradient of the AC magnetic field in the respective direction is required. This phase gradient can be produced by using a two-phase magnetic field instead of the standard single-phase one. Recently, such a two-phase inductor was developed, shown in Figure 8.2.1 (bottom), which reverses the direction of the electromagnetically driven melt flow so that the solidification front becomes mostly convex [15,16]. In this chapter, the design of the two-phase inductor is presented, together with its basic features and experimental results concerning the growth of a number of industrially relevant single crystals.

8.2.2 Two-phase Inductor and Its Basic Characteristics

Figure 8.2.2 (top) shows a two-phase inductor. The inductor consists of a primary coil (1), which is connected to an RF power generator, and a secondary coil (2), which is short-circuited through capacitor and resistor as shown in the principal electric scheme in Figure 8.2.2 (bottom). The capacitor is tuned to have a resonance in the secondary circuit, which results in a 90° phase lag of the secondary current relative to the primary one. The resistor, in turn, is tuned to balance the secondary and primary current amplitudes. Thus, a component of the magnetic field is created that travels toward the coil with the phase lag dragging the melt with it. As a result, the outer layers of the hot melt are driven toward the periphery of the solidification front, while the cooled down melt returns in the center [17].

To verify and optimize the design of the two-phase inductor, both numerical and physical modeling were used. Numerical simulation of the melt flow and the temperature distribution in it was carried out using the commercial code FLUENT. This allowed us to take into account all relevant effects including buoyancy, Marangoni convection, electromagnetic forces, heat diffusion, crystal and feed rotation, and the boundary conditions at the solid–liquid interface. As seen in Figure 8.2.3, the EM force generates a meridional flow directed upward along the free surface of the floating zone, which produces the desired, mostly convex solid–liquid interface.

Important parameters that determine the intensity of melt pumping are the gap between the coils, as well as the capacitance and the resistance of the secondary circuit. The strongest pumping effect is achieved at 90° phase shift between the coil currents. This is reflected by the variation of the dimensionless Reynolds number from 917 at 0° phase shift to 1160 at 60° phase shift and 1210 at 90° phase shift, with other parameters kept constant (see Figure 8.2.3). Note that the 0° phase shift generates the usual double-vortex flow pattern that is characteristic for the standard single-phase FZ process. The EM field, which is defined by the complex azimuthal component of the magnetic vector potential, was computed by the boundary integral method [18].

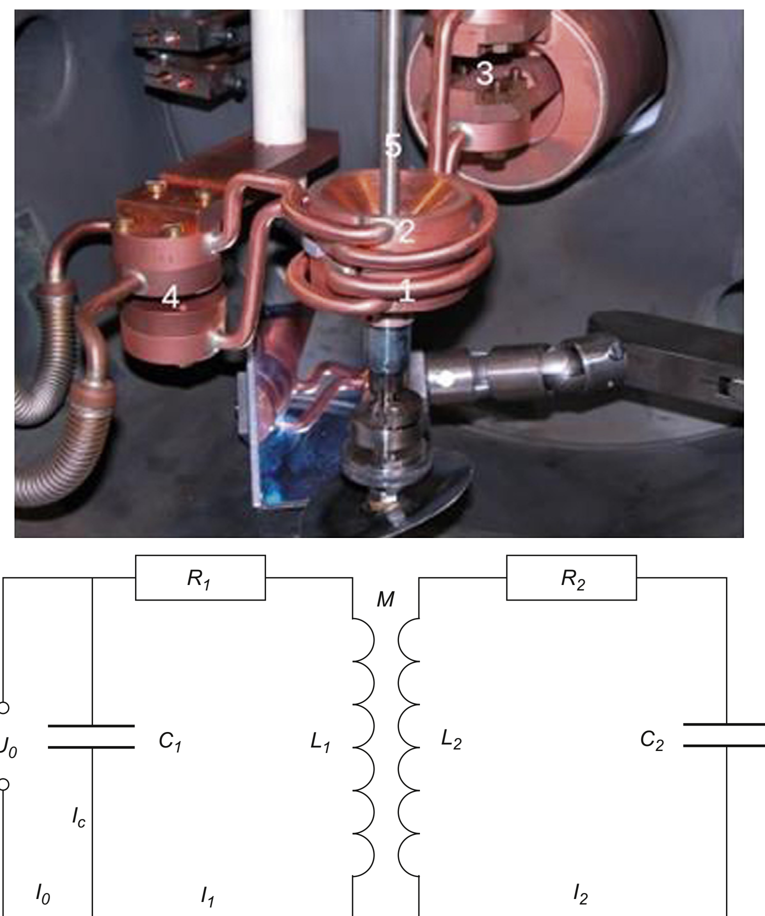

FIGURE 8.2.2 Photograph of a two-phase inductor (top) and its basic electric scheme (bottom). The inductor containing a nickel rod of 6 mm in diameter (5) consists of a primary (bottom) coil ($1,L_1$), which is connected to an RF generator through terminals (3), and a secondary (top) coil ($2,L_2$), which is short-circuited thorough a remote adjustable capacitor (C_2) connected to terminals (4).

The action of the two-phase inductor was verified also by means of physical modeling. The velocity distribution in a eutectic GaInSn melt filled in a cylindrical cavity and placed into a two-phase inductor was measured using both ultrasonic Doppler velocimetry and local potential probes. The phase shift was varied using independent power supplies for each of the two coils. This allowed us to observe the transition from a typical double to single toroidal vortex flow structure as the phase shift between the currents in two coils was gradually increased from 0° to 90° [19]. Figure 8.2.4 shows a good agreement between experimentally measured and numerically computed velocity distributions driven by the two-phase inductor in the eutectic GaInSn melt.

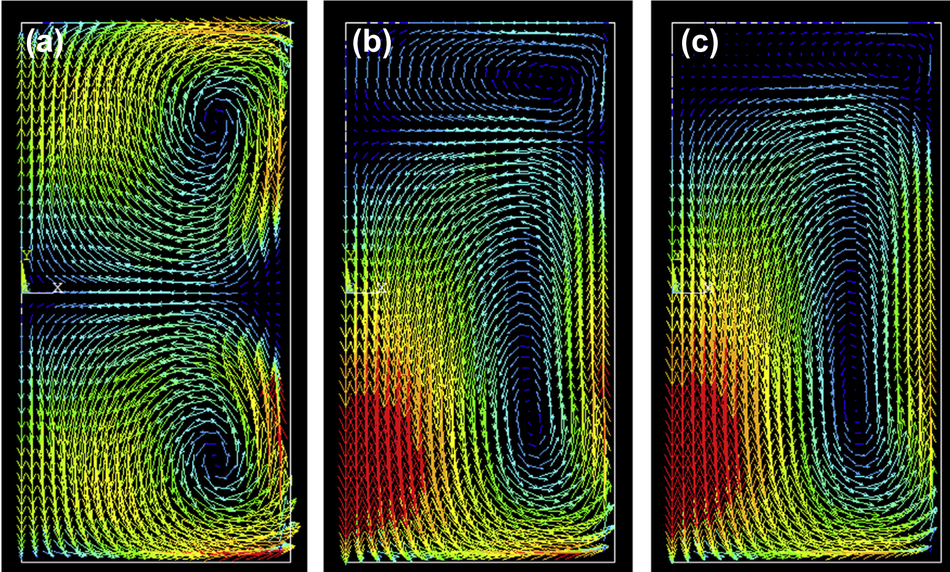

FIGURE 8.2.3 Velocity distributions in the melt at various phase shifts between the currents in primary and secondary coils: (a) 0° (Re = 917), (b) 60° (Re = 1160), (c) 90° (Re = 1210); the Reynolds number in the brackets characterizes the magnitude of the flow.

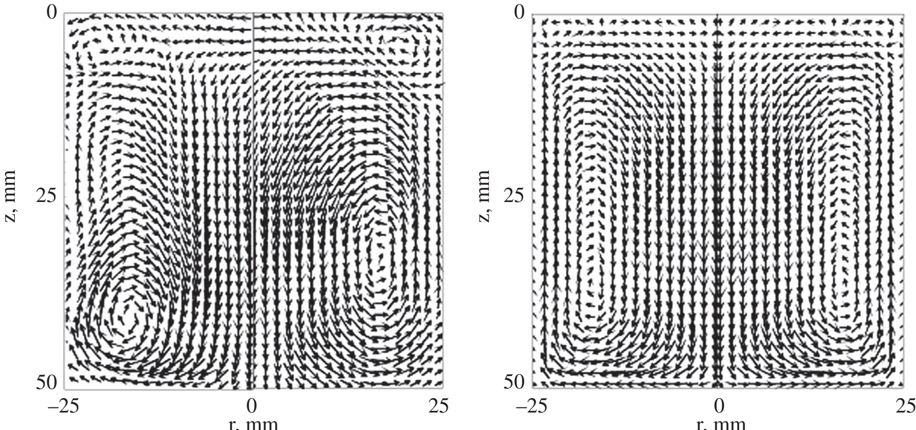

FIGURE 8.2.4 Velocity distributions in the GaInSn eutectic melt measured by the potential probe (left) and computed numerically (right) for equal effective currents of I = 350 A alternating with 400 Hz frequency and a 90° phase shift between the two coils.

8.2.3 Single Crystal Growth of Intermetallic Compounds

8.2.3.1 Ruthenium Aluminides

Ruthenium aluminide is an interesting candidate for future applications because of its extraordinary thermodynamic, mechanical, and chemical properties. There have been recent reports of the synthesis of B2-RuAl coatings on mild steel [20], phase formation during annealing of Ru/Al multilayers [21], and compositional and grain size effects on the interdiffusional behavior in the single-phase RuAl intermetallic compound [22]. The intermetallic compound RuAl exhibits a high melting point (about 2323 K), high temperature strength, good corrosion resistance, and even good room temperature ductility [23,24]. Particularly single-phase RuAl shows extraordinary resistance against oxidation at high temperature, making RuAl a potential material for high temperature applications in aggressive environments. But due to the high difference in melting points and a great enthalpy from the reaction between Ru and Al, homogeneous RuAl is difficult to prepare either by melting or by powder metallurgy processes [25]. Therefore, intense research activities are focused on processing and alloying to improve the mechanical properties and the oxidation resistance of RuAl [26–29]. For the first time, single-phase crystals of RuAl alloys with near stoichiometric composition were grown by the authors' magnetic field controlled floating zone technique with the two-phase stirrer system.

The aim of this work was twofold: synthesis and growth of RuAl single crystals and the study of composition effects on resistivity and microhardness. For this reason, experiments were performed using single crystal as well as polycrystalline single-phase and multiphase material. The master alloy preparation and the subsequent crystal growth proved to be rather complicated. Only small rods, with maximum 2.5 cm length, could be cast. The RuAl single-phase master alloy was, therefore, done by powder metallurgy using reactive sintering and reactive hot pressing. Due to the strong Al loss during crystal growth, the master alloys were prepared with an Al excess of 1 and 2 at%, respectively, from pure Ru (99.95%) and pure Al (99.9965%). The growth rate for the RuAl-single crystal growth was chosen to 30 mm/h to reduce the strong Al loss that limits finally the growth experiment. Because the intermetallic RuAl compound is a congruent melting material, relative high growth rates can be applied. The whole crystal rod can be divided into two parts. The initial part of the crystal is characterized by growing of large grains leading to single crystal after some millimeters. Strong Al evaporation during crystal growth leads furthermore to the transformation to dual phase microstructure.

Figure 8.2.5 shows the X-ray Laue back-scattering pattern of the final single crystal of a $Ru_{51,25}Al_{48,75}$ (at%) alloy (a). In contrast, Figure 8.2.5(b) maps the transformation to dual phase microstructure after rather high aluminum loss. According to the binary RuAl phase diagram [30], the second phase is attributed to the eutectic $Ru_{70}Al_{30}$ composition. The resistivity in dependence on the temperature (273–4.2 K) and the microhardness (Vickers hardness) were measured at different alloy compositions on single-phase and

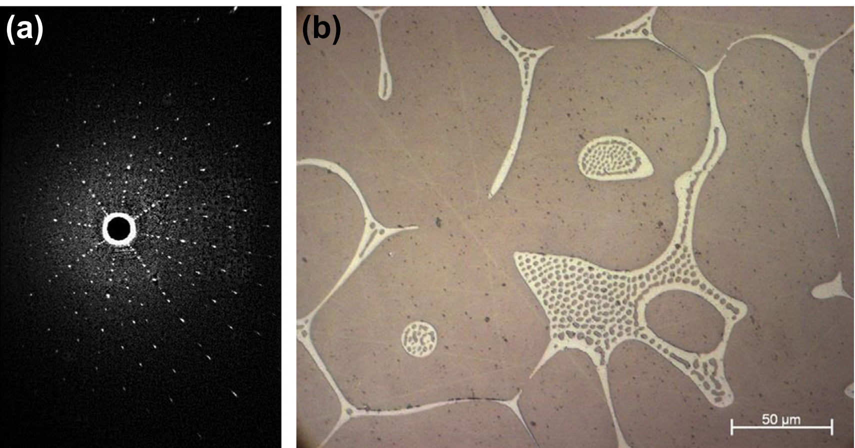

FIGURE 8.2.5 (a) X-ray Laue back-scattering pattern of the final single crystal of a $Ru_{51,25}Al_{48,75}$ (at%) alloy, (b) SEM micrograph: transformation to dual-phase microstructure.

dual-phase regions of selected samples. The resistivity decreases linearly up to 70 K and runs to a saturation value at 4.2 K. The dependence of the reciprocal residual resistance ratio on the composition of RuAl alloy is very sensitive to composition fluctuations and shows a maximum value of 6.7 close to the stoichiometric composition. In contrast, the Vickers hardness decreases up to a minimum close to the stoichiometric composition on the hypertectic composition region and raises on the hypotectic composition side again. Hence, the maximum of the reciprocal residual resistance ratio coincides with the minimum of the Vickers hardness [31].

8.2.3.2 Titanium Aluminides

TiAl intermetallic alloys have been developed as potential materials for high temperature applications because of their excellent chemical and physical properties such as low density, high modulus, and corrosion resistance at high temperatures. These characteristics are attractive for applications in aerospace and automotive industries as well as for chemical and biomedical applications [32,33]. However, their low ductility at room temperature but also microscopic factors such as volume fraction of the apparent phases, the distribution of orientations, and the microscopic structure strongly affect the mechanical properties and limit their application [34–38].

Ti-Al alloys can be classified into equiaxed single-phase γ-TiAl, fully lamellar microstructures consisting of lamellar grains composed of alternate α_2 and γ-plates, and the mixture of equiaxed γ-phase and lamellar $(\gamma + \alpha_2)$ phase (duplex microstructure) [34,35]. γ-TiAl is very reactive to oxygen, which dissolves interstitially, leading to hardness increase and alloy brittleness. To improve the properties of gamma-TiAl alloys, the influence of alloying elements has been extensively studied. Small chromium additions lead to increased ductility, whereas niobium is used to improve oxidation resistance [39,40]. A representative number of samples of titanium aluminides (40–60 at% Ti) were

grown by the magnetic field controlled floating zone technique (two-phase stirrer) [15], part of them with Nb additions. The master alloys were prepared from pure (99.99%, Alfa Aesar) Ti and Al in a cold crucible induction furnace under argon atmosphere and cast to rods with 6 mm diameter and 60 mm length. The growth rate for crystal growth was chosen to 10 mm/h. Necessary for the parameter configuration of the two-phase stirrer, the thermophysical properties, such as electrical conductivity, thermal conductivity, and viscosity were firstly investigated since there are no data available in the literature for this material [41,42]. With the knowledge of these material parameters, the systematic growth of high precision crystals is feasible because an optimized, well-defined melt convection can be adjusted by the two-phase stirrer action.

The nature of the crystal growth process under optimum conditions leads to fast selection of grains. Figure 8.2.6(a) shows the optical micrograph of a longitudinal cut through a $Ti_{45}Al_{55}$ alloy processed at optimum 90° phase shift between the coils. Clearly visible here, the grains grow rapidly out resulting finally in a dominating single crystal. Figure 8.2.6(b) displays the cross-section of a $Ti_{46}Al_{46}Nb_8$ alloy with fully lamellar microstructure (three large grains), respectively.

To study the reactivity to oxygen of these alloys, the oxygen content of binary TiAl and ternary TiAlNb single crystals and polycrystalline alloys was quantified using secondary ion mass spectrometry (SIMS). Hereby, Cs+ primary ions were applied for sputtering, which exhibit a high sensitivity for oxygen determination. The absolute concentration was determined using oxygen-implanted reference samples. As a result, the ternary alloy contains generally less oxygen. Additionally performed microhardness measurements yielded in higher Vickers hardness for the binary TiAl alloy compared to the ternary TiAlNb crystal. As a conclusion, the Nb elemental addition combined with the positive impact against oxygen adsorption increases the ductility of the ternary alloy [43].

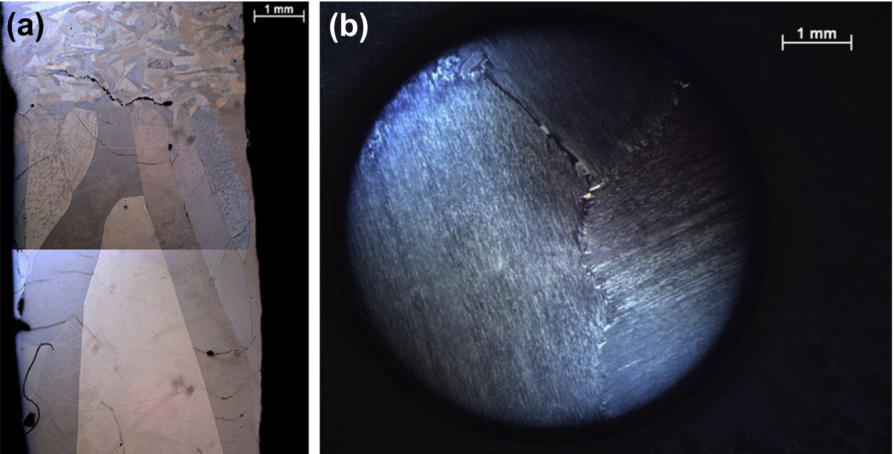

FIGURE 8.2.6 Optical micrograph (a) of a longitudinal cut through a $Ti_{45}Al_{55}$ alloy showing rapid growing out of grains from inner to outer part of the rod, (b) a cross-section of a $Ti_{46}Al_{46}Nb_8$ alloy with fully lamellar microstructure.

8.2.3.3 Manganese Silicides

The magnetic two-phase stirrer system was furthermore applied to the crystal growth of the Heusler compound Mn_3Si. For the first time, single-phase crystals of this Heusler compound could be obtained. This compound is known as an itinerant antiferromagnet with an incommensurate spin-density wave [44,45]. It is assumed that its unusual magnetic behavior, in particular an extraordinary stability of the itinerant antiferromagnetism in high fields [46], is related to a half metallic electron structure [47]. Neutron scattering experiments and measurements of the magnetic susceptibility show that Mn_3Si orders as an antiferromagnet below 23 K [44,48]. The interesting Mn_3Si phase forms via peritectic reaction from liquid and the properitectic Mn_5Si_3 phase. It is therefore complicated to grow single crystals with Mn_3Si composition, as, e.g., also described in [45,49]. The difficulty to produce single-phase crystals becomes also apparent in [50], where the authors detected surface structures (white lines of some μm thickness) on all polished surfaces of the Mn_3Si crystals. Because no evidence for compositional variations with the used method could be found, the authors assumed crystal defects like line dislocations or small angle grain boundaries. Concerning the magnetic properties, the authors observed furthermore quantitatively large differences between the samples.

We expected that these differences have their origin in the presence of a second phase. The origin of the white lines with micro-cuts cleared up using a focused ion beam (FIB) technique revealing their three-dimensional sheet-like shape and composition. This investigation indicated the precipitates to be the Mn_5Si_2 phase. To achieve more composition accuracy of the very thin line phase, a sample was annealed at 800 °C for 72 h (within the corresponding temperature region of the phase formation) and subsequently fast cooled to increase thickness and volume fraction of these precipitates. On the other hand, to obtain real single-phase crystals of the Mn_3Si phase, samples were annealed at 1000 °C for 72 h, well above the formation of the Mn_5Si_2 phase in order to dissolve the precipitates but also the residual properitectic Mn_5Si_3 phase. Master alloys with the composition $Mn_{75}Si_{25}$ (at%) were prepared from pure Mn (99.99%, ChemPur) and Si (99.999%). The growth rate for crystal growth was chosen to 10 mm/h.

Figure 8.2.7 compares SEM micrographs of cross sections at different growth stages. Large grains grow rapidly from start to finish of the crystal growth. The SEM micrograph of Figure 8.2.7(a) shows single-phase Mn_3Si grains surrounded by a second phase. This phase, located at the grain boundaries, was clearly identified by EDX as the properitectic Mn_5Si_3 phase. With proceeding crystal growth, precipitates (white lines, see Figure 8.2.7(b)) form in the Mn_3Si crystals arising from peritectoid solid state transformations. The volume fraction of the precipitates increased continuously from 1.6 ± 0.9 vol% after 1.5 cm growth to 11 ± 3 vol% after 4 cm growth. Figure 8.2.7(b) shows a tilted SEM view (45°) on a FIB cut through a platelet stack formation revealing the three-dimensional sheet-like shape of the precipitates. On the other hand, the elevated annealing led to complete dissolving of Mn_5Si_2 precipitates and residual properitectic Mn_5Si_3 phase, respectively. For the first time, single-phase crystals of the Heusler

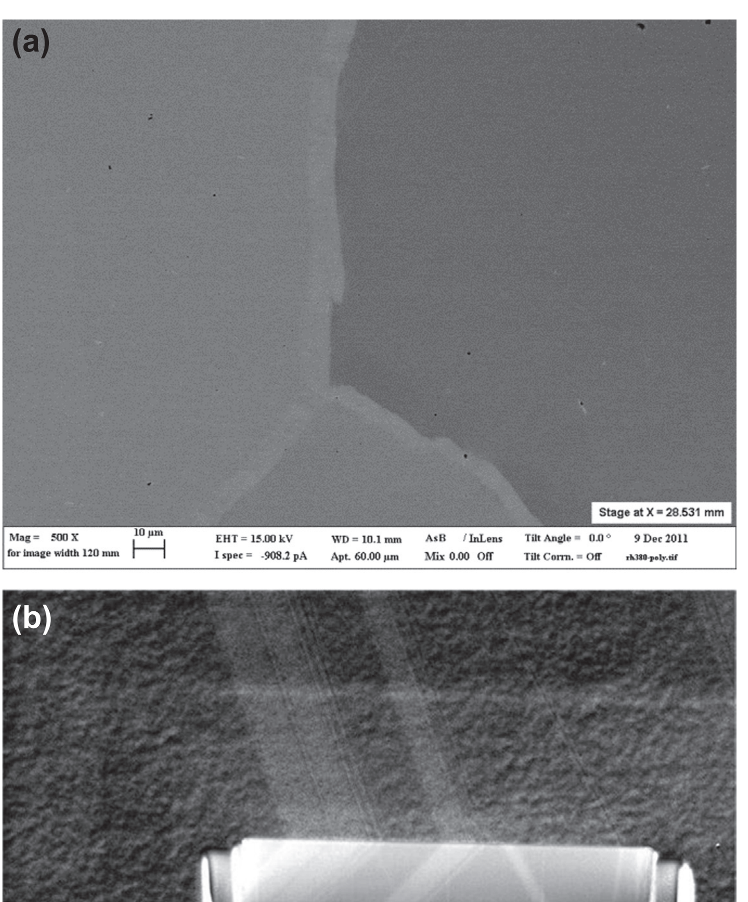

FIGURE 8.2.7 SEM micrographs of different cross-sections of as-grown Mn_3Si alloy. (a) start region, (b) tilted SEM view (45°) on a FIB cut through platelet stacks.

compound Mn_3Si could be prepared using the magnetic field controlled RF floating zone technique with two-phase stirrer system. (Single phase hereby means no detection of second-phase precipitations using high resolution SEM or X-ray powder diffraction.)

Thus, the present investigation cleared up the solidification and phase transformation of the peritectic solidifying Heusler compound Mn_3Si. Confirmed by the binary MnSi phase diagram, it could be shown that in fact it is not possible to prevent the

precipitation formation via peritectoid reaction during crystal growth. But the advantage of the strong mixing due to the two-phase stirrer application and the high growth rate allows the growth of large crystal sections with low volume fraction of precipitations that can be dissolved with adequate subsequent annealing. It is important to note that the elucidation of the second phase is essential due to their influence on material properties such as magnetic and transport properties.

For measurements of the temperature dependence of magnetization and specific heat, the grown crystals were oriented and cut to samples with the crystallographic orientations [100] and [110] normal to a plane. The measured magnetization curves display maxima that correspond to the Néel temperature T_N, indicating the phase transition to antiferromagnetic order at 23 K. The hysteresis loops exhibit small permanent magnetic moments even above the ordering temperature of the majority magnetic Mn_3Si phase. It can be assumed that this ferromagnetic hysteresis, superimposed to the paramagnetic or antiferromagnetic behavior of the Mn_3Si phase, is related to a very small residual amount of the impurity Mn_5Si_2 precipitates, but not to the majority helix magnetic phase Mn_3Si. The remanent moments determined from the volume fractions of the precipitation phase are between 0.1 and 3 μB/Mn atom [51,52]. Furthermore, the microhardness (Vickers hardness) were measured on the two main phases, whereby the peritectic Mn_3Si phase possesses distinct lower Vickers hardness (average value 644) than the residual properitectic Mn_5Si_3 phase (average value 906).

8.2.3.4 Titanium Niobium

The magnetic system was furthermore applied to crystal growth of the very recently studied biocompatible β-type (bcc phase) TiNb alloys. These titanium-based alloys belong to the materials currently used for biomedical applications. They exhibit high corrosion resistance and excellent biocompatibility [53–56]. This material is favored as the ultimate choice for orthopedic implants due to the combination of high strength and low Young's modulus [54–59]. The strength of the titanium alloys is close to that of stainless steel, but the density is about half the value of steel. The Young's modulus should be comparable to that of bone because this is an essential condition for implants to minimize stress-shielding [60] and to serve for a long period without failure [57]. The value of the bone modulus varies between 4 and 30 GPa [57] depending on the type of bone and on the direction of measurement. Second generation biomedical Ti-based alloys with β-phase stabilizers (Mo, Nb, Ta, V) possess Young's moduli between 85 and 55 GPa [57]. The development of biocompatible alloys with lower modulus is actually of high priority in materials science and biomedical research. Only a few studies have been done on single-crystalline materials for biomedical application probably due to their limited availability. Elastic constants of TiNb β-phase single-crystal alloys were investigated by [61,62]. Tane et al. [63] studied β-Ti-Nb-Ta-Zr single crystals with high elastic anisotropy and low Young's modulus in [100] direction. Lee et al. [64] presented the plastic deformation behavior of a Ti-Mo-Zr-Al single crystal. Takesue et al. [65]

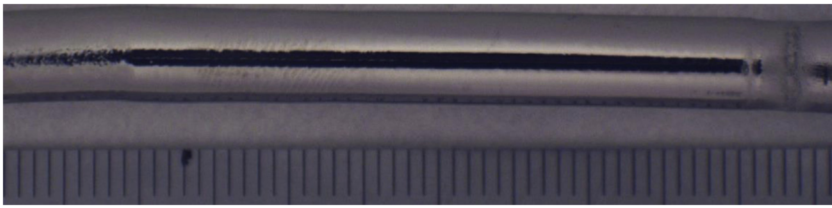

FIGURE 8.2.8 Photo of the grown crystalline rod of $Ti_{70}Nb_{30}$ alloy. Left – start of growth, right – final zone.

investigated the elastic properties of a typical β-type Ti-Nb-Ta-Zr-O single-crystal gum metal. Zhang et al. [66] prepared and characterized Ti-Nb-Zr-Sn single crystals.

Here, the crystal growth of TiNb is reported with focus on the elastic properties of β-$Ti_{70}Nb_{30}$ (at%) single crystals. Figure 8.2.8 shows a photo of as-grown TiNb crystals. The surface appears very shiny obviously indicating single crystallinity over the full cross-section. The orientation of the grown crystals was determined from X-ray Laue back scattering and additionally proved with the space-resolved electron back-scatter diffraction (EBSD). The growth rates for crystal growth were chosen to 10 and 15 mm/h, respectively.

The ultrasonic sound velocity measurement technique was used to determine the elastic constants. The acoustic velocities of both the titanium single crystals and a polycrystalline alloy were measured at room temperature, whereby the elastic waves were propagated between the parallel pairs of the orientated crystal planes. These velocities in the longitudinal and shear mode, respectively, can be written in terms of elastic coefficients using the measured density. The three independent elastic constants of a cubic crystal are C11, C12, and C44. Additionally, the bulk modulus B and the shear moduli G110, G100, and G111 for the [110], [100], and the [111] direction, respectively, were determined, identified by means of the connections $B = (C11 + 2C12)/3$, $G110 = (C11 - C12)/2$, $G110 = C44$, $G111 = 3C44(C11 - C12)/(C11 - C12 + 4\ C44)$. The anisotropy factor calculates from $A = C44/G110$.

The Young's moduli, E, of the crystals show pronounced anisotropy. The values for the different directions were determined to E100 = 39.5 GPa, E110 = 68.7 GPa, and E111 = 91.0 GPa, respectively. The effective Young's modulus, E*, of the polycrystal is $E^* = (65.5 \pm 0.5)$ GPa. The lowest Young's modulus, E100 of 39.5 GPa, is approximately half of the Young's modulus of the [111] direction and closely to that of cortical bone. This relatively high anisotropy resulting in low E100 can give advantages in suppression of stress-shielding in bone. Therefore, in accordance with the conclusions drawn by Tane et al. [63], single crystals with [100] orientation or textured polycrystals with the preferred [100] orientation are promising candidates for biomedical implants in humans [67]. Comparison of the present results with recently published data and on the extrapolation to low Nb content of about 20 at% shows that the preparation of TiNb-based alloys with E100 of 20–30 GPa should be possible, which would match the modulus of bone [68]. Therefore, TiNb single crystals with 25 and 20 at% Nb were grown and investigated, respectively.

Despite high rates of success in medical applications, there remain serious problems, for example, the rate of revision surgery for orthopedic implants. One important fact is the surface modification of the TiNb biomaterial such as the formation of oxidic

nanotubes to improve the healing phase in the human body. This can be done using mechanical, chemical, and physical methods [69]. Because only a few studies on single crystals of materials for biomedical application have been published in the literature concerning the crystal orientation dependence in electrochemical and cell biological experiments, the hereby obtained oriented crystals were subjected to surface modification. Electrochemical anodic oxidation is a technique for the preparation of oxide layers on metals. Oxidic nanotubes were formed on the surfaces of $Ti_{70}Nb_{30}$ single crystals, and the influence of the grain orientation was investigated [70]. The formation mechanism of oxidic nanotubes performed in 0.25 M NH_4F + 1 M $(NH_4)2SO_4$ at room temperature depends strongly on the electrolyte, potential, and temperature. The potential was adjusted from 0 to 20 V with a rate of 50 mV/s and the holding time of the high level potential was 1 h. Figure 8.2.9 shows SEM micrographs of nanotubes

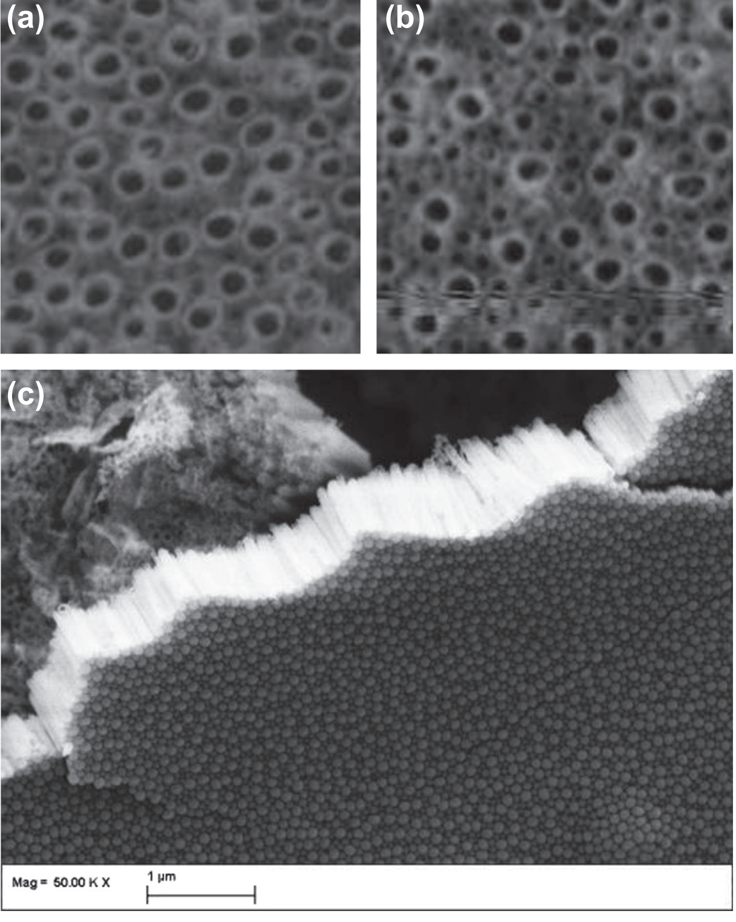

FIGURE 8.2.9 SEM micrographs of nanotubes grown on $Ti_{70}Nb_{30}$ single crystals. (a) parallel to the [100] direction, (b) parallel to the [101] direction, and (c) side view on a flake imaging the nanotube length of about 1 μm. The photo area in (a) and (b) is 1 μm^2.

grown on $Ti_{70}Nb_{30}$ single crystals (a) parallel to the [100] direction, (b) parallel to the [101] direction, and (c) a side view on a flake imaging the nanotube length of about 1 μm. The nanotubes grown along the [100] direction display a close-packed configuration with diameters of about 100 nm. The nanotubes grown along the [101] direction show a distinct different feature, whereas the nanotube structure is a mixture of tubes with large diameters of about 70–80 nm and tubes with small diameters of about 30–40 nm. The origin of the orientation dependence of the nanotube growth is unclear so far and requires further investigation. But the size of the nanotubes and the morphology is very important because the healing process of an implant in a human body depends on it. It is already reported that a porosity of the surface with nanotube diameter between 70 and 100 nm improves the bioactivity [71]. The growth of nanotubes on material with preferred [100] orientation therefore seems to be an interesting approach.

8.2.4 Conclusions

The floating-zone crystal growth using a two-phase RF inductor is a novel technique capable of producing single crystals of complex intermetallic compounds. The two-phase inductor not only melts the material but also stirs it in such a way as to maintain a convex toward the liquid phase solidification front. This is essential for the growth of bulk single crystals. When the current in the secondary coil is adjusted to have nearly the same amplitude and about a 90° phase lag relative to the current in the primary coil, a component of the magnetic field is generated that travels toward the secondary coil. This traveling magnetic field drags the hot outer layer of the melt with it toward the periphery of the solidification front, while the cooled down melt returns in the center. This results in the formation of the desired convex solidification front, which, in turn, facilitates the growth of single crystal over the whole cross-section of the solidified material. The operation of this two-phase inductor was demonstrated by growing single crystals of industrially relevant RuAl and TiAl intermetallic compounds. Recently, the crystals of antiferromagnetic Heusler MnSi compounds and biocompatible TiNb alloys [72] were grown by this method.

Acknowledgments

The financial support of the Deutsche Forschungsgemeinschaft within the Collaborative Research Centre SFB 609 “Electromagnetic flow control in metallurgy, crystal growth and electrochemistry” is gratefully acknowledged.

References

[1] Hume-Rothery W. Electrons, atoms, metals and alloys. New York: Philosoph. Library; 1955.

[2] Sauthoff G. Intermetallics. Weinheim: Wiley-VCH; 1995.

[3] Tanaka T, Bannai E, Kawai S, Yamane T. J Cryst Growth 1975;30:193.

[4] Takeya H, Habuta E, Kawano-Furukawa H, Ooba T, Hirata K. J Magn Magn Mater 2001;226–230(Part 1):269.

[5] Behr G, Löser W, Graw G, Bitterlich H, Freudenberger J, Fink J, et al. J Cryst Growth 1999;198–199(Part 1):642.

[6] Hermann R, Behr G, Gerbeth G, Priede J, Uhlemann H, Fischer F, et al. J Cryst Growth 2005;275:e1533.

[7] Rudolph P. In: Springer handbook of crystal growth. 1st ed. Berlin: Springer; 2010. p. 159.

[8] Morthland T, Walker J. Int J Heat Mass Transfer 1997;40:3283.

[9] Tanasawa I, Munakata T. J Cryst Growth 1999;206:27.

[10] Dold P, Cröll A, Lichtensteiger M, Kaiser T, Benz K. J Cryst Growth 2001;23:95.

[11] Ma N, Walker J, Lüdge A, Riemann H. J Cryst Growth 2001;230:118.

[12] Cröll A, Benz K. Prog Cryst Growth Charact Mater 1999;38:133.

[13] Hermann R, Priede J, Behr G, Gerbeth G, Schultz L. J Cryst Growth 2001;223:577.

[14] Bohm J, Lüdge A, Schröder W. In: Handbook of crystal growth, Amsterdam, North-Holland, p. 213.

[15] Priede J, Gerbeth G, Hermann R, Behr G, Schultz L, Uhlemann HJ. German Patent DE10328859B4, 2007.

[16] Hermann R, Gerbeth G, Priede J, Krauze A, Behr G, Büchner B. J Mater Sci 2010;45(8):2228.

[17] Rudolph P. J Cryst Growth 2008;310:1298.

[18] Priede J, Gerbeth G. IEEE Trans Magn 2006;42(2):301.

[19] Pedcenko A, Bojarevičs A, Priede J, Gerbeth G, Hermann R. Exp Fluids 2013;54:1558.

[20] Bax B, Pauly C, Leibenguth P, Woll K, Mücklich F. Surf Coat Technol 2012;206(19–20):3931.

[21] Zotov N, Woll K, Mücklich F. Intermetallics 2010;18(8):1507.

[22] Woll K, Holzapfel C, Mücklich F. Intermetallics 2010;18(4):553.

[23] Fleischer R. Metall Trans 1993;24:227.

[24] Wolff I. JOM 1997;49:34.

[25] Wolff IM, Sauthoff G. Metall Trans A 1996;27:2642.

[26] Gobran H, Liu K, Heger D, Mücklich F. Scr Mater 2003;49:1097.

[27] Liu K, Mücklich F, Birringer R. Intermetallics 2001;9:81.

[28] Reynolds T, Johnson D. In: George EP, Inui H, Mills MJ, Eggeler G, editors. Mater res soc symp proc, MRS, Pittsburgh, PA; 2003. BB5.341.

[29] Mücklich F, Ilíc N. Intermetallics 2005;13(1):5.

[30] Gobran H, Heger D, Mücklich F. Z für Met 2005;96:7.

[31] Hermann R, Vinzelberg H, Behr G, Woll K, M. F, Büchner B. J Cryst Growth 2008;310(18):4286.

[32] Clemens H. Z Met 1995;86(12):814.

[33] Dimiduk DM. Mater Sci Eng A 1999;263:281.

[34] Dudzinski D, Zhao L, Beddoes J, Wallace W. Scr Mater 1996;35:367.

[35] Kim Y-W. Mater Sci Eng A 1995;192/193:519.

[36] Parthasarathy TA, Keller M, Mendiratta MG. Scr Mater 1998;38:1025.

[37] Karthikeyan S, Viswanathan GB, Gouma PI, Vasudevan VK, Kim Y-W, Mills MJ. Mater Sci Eng A 2002;329–331:321.

[38] Boehlert CJ, Dimiduk DM, Hemker KJ. Scr Mater 2002;46:259.

[39] Lamirand M, Bonnentien J-L, Gúerin S, Chevalier J-P, Ferrière G. Scr Mater 2007;56(5):325.

[40] Kawabata T, Tamura T, Izumi O. Metall Trans A 1993;24:141.

[41] Plevachuk Y, Sklyarchuk V, Hermann R, Gerbeth G. Int J Mater Res (formerly Z Met) 2011; 102:3.

[42] Plevachuk Y, Sklyarchuk V, Hermann R, Gerbeth G. Int J Mater Res 2008;99(3):261.

[43] Oswald S, Hermann R, Schmidt B. Mater Sci Eng A 2009;516:54.

[44] Tomiyoshi S, Watanabe H. J Phys Soc Jpn 1975;39:295.

[45] Tomiyoshi S, Cowley E, Onodera H. Phys Rev B 2006;73:024416.

[46] Pfleiderer C, Boeuf J, Löhneysen H. Phys Rev B 2002;65:172404.

[47] Pfleiderer C. Phys B 2003;329–333:1085.

[48] Kalishevich G, Vereshagin Y, Gel'd P. Sov Phys Solid State 1974;16:1151.

[49] Neubauer A, Boeuf J, Bauer A, Russ B, Löhneysen H, Pfleiderer C. Rev Sci Instrum 2011;82: 013902.

[50] Neubauer A, [Ph.D. thesis]. Technische Universität München; 2011.

[51] Hermann R, Wendrock H, Rodan S, Rößler UK, Blum CGF, Wurmehl S, et al. J Cryst Growth 2013; 363:1.

[52] Steckel F, Rodan S, Hermann R, Blum CGF, Wurmehl S, Büchner B, et al. arXiv:1309.1636; 2013.

[53] Black J. Biological performance of materials: fundamentals on Biocompatibility. Boca Raton (FL): CRC Press; 2006.

[54] Niinomi MJ. Mech Behav Biomed Mater 2008;1:30.

[55] Kanetka H, Hosoda H, Shimizu Y, Kudo T, Zhang Y, Kano M, et al. Mater Trans 2010;50:1944.

[56] Miura K, Yamada N, Hanada S, Jung T-K, Itoi E. Acta Biomater 2011;7:2320.

[57] Geehta M, Singh A, Asokamani R, Gogia A. Prog Mater Sci 2009;54:397.

[58] Al-Zain Y, Kim H, Koyano T, Hosoda H, Nam T, Miyazaki S. Acta Mater 2011;59:1464.

[59] Henriques V, Galvani E, Petroni S, Paula M, Lemos T. J Mater Sci 2010;45:5844.

[60] Bundy K, Williams C, Luedemann R. Biomaterials 1991;12:627.

[61] Reid C, Routbort J, Maynard R. J Appl Phys 1973;44:1398.

[62] Jeong H, Yoo Y, Lee Y, Park J. J Appl Phys 2010;108:063515.

[63] Tane M, Akita S, Nakano T, Hagihara K, Umakoshi Y, Niinomi M, et al. Acta Mater 2008;56: 2856.

[64] Lee S, Hagihara K, Oh M, Nakano T. J Phys Conf Ser 2009;165:012086.

[65] Takesue N, Shimizu Y, Yano T, Hara M, Kuramoto S. J Cryst Growth 2009;311:3319.

[66] Zhang Y, Li S, Obbard E, Wang H, Wang S, Hao Y, et al. Acta Mater 2011;59:3081.

[67] Hermann R, Hermann H, Calin M, Büchner B, Eckert J. Scr Mater 2012;66:198.

[68] Hanada S, Ozaki T, Takahashi E, Watanabe S, Yoshimi K, Abumiya T. Mater Sci Forum 2003; 426–432:3103.

[69] Liu X, Chu P, Ding C. Mater Sci Eng 2004;47:49.

[70] Hermann R, Uhlemann M, Wendrock H, Gerbeth G, Büchner B. J Cryst Growth 2011;318: 1048.

[71] Oh S, Brammer K, Li Y, Teng D, Engler A, Chien S, et al. PNAS 2009;106:2130.

[72] Hermann R, Gerbeth G, Priede J. The European Physical Journal, EPJ ST, Gerbeth G, Eckert K, Odenbach S, editors 2013; 220, p. 227.

Vertical Bridgman Growth of Binary Compound Semiconductors

Manfred Jurisch[1], Stefan Eichler[1], Martin Bruder[2]

[1]FREIBERGER COMPOUND MATERIALS, FREIBERG, GERMANY;
[2]AIM INFRAROT MODULE GMBH, 74072 HEILBRONN, GERMANY

CHAPTER OUTLINE

9.1 Introduction ... 332
9.2 Equipment (Design and Engineering Issues) ... 336
9.2.1 Basics ... 336
9.2.2 Specifics ... 338
9.2.2.1 General ... 338
9.2.2.2 Flow Control by Electromagnetic Fields ... 341
9.2.2.3 Submerged Heater ... 343
9.2.2.4 Flow Control by Vibrations ... 344
9.2.3 Optimization and Control of VB/VGF-Growth ... 345
9.3 Growth of Binary Compound Semiconductors ... 346
9.3.1 Synthesis ... 346
9.3.2 Liquid Encapsulation ... 347
9.3.3 Crucibles ... 348
9.3.4 Facets and Local Interface Shape ... 349
9.3.5 Doping and Segregation ... 352
9.3.6 Crystal Defects ... 356
9.3.6.1 Point Defects ... 356
9.3.6.2 Dislocations ... 356
9.3.6.3 Twins ... 359
9.3.6.4 Precipitates and Inclusions ... 362
9.4 Conclusions ... 365
References ... 365

Handbook of Crystal Growth. http://dx.doi.org/10.1016/B978-0-444-63303-3.00009-2
Copyright © 2015 Elsevier B.V. All rights reserved.

9.1 Introduction

The binary inorganic compound semiconductors that are relevant to solid-state electronics are commonly classified according to the position of their constituents in the periodic table of elements as II-VI, III-V, and IV-IV compounds, representatives of which are CdTe, GaAs, and SiC. The IV-VIs (e.g., PbTe) and I-VIIs (e.g., CuCl), which are also semiconductors, are of less commercial interest and are omitted from the discussion here. However, they have found some applications, such as PbTe for infrared detectors and in thermoelectricity [1–3] or metal halides in electro-optic light modulators [4,5]. In Table 9.1, relevant data for some compound semiconductors considered in this chapter are compiled and compared with that of silicon [6–15].

A common feature of III-V and II-VI compound semiconductors (with the exception of the III-nitrides) is congruent melting at moderate temperatures, with the compounds dividing the phase diagram into two eutectic partial diagrams. This basically allows the melt growth of single crystals. However, although the liquid state of the elemental and III-V compound semiconductors is metal-like [16], the melt of the II-VIs is characterized by a noticeable long-range order, resulting in serious problems of melt growth of crystals [14,17]. This is related to the greater iconicity of the latter compared to the III-V semiconductors (see Table 9.1).

The melting temperature of the III-nitrides and SiC are not well established. They decompose at high temperatures and cannot be grown from the melt using Bridgman techniques; instead, mostly vapor transport or solution growth is used. Therefore, they will not be considered in this chapter.

In the early 1950s, Welker [18–20] invented the III-Vs, studied the properties of GaAs and its kin, and recognized that the III-V compounds could be a material to compete silicon. At that time, the II-VI compound semiconductors were already known. Today, it has become obvious that, despite of some possible overlapping in application, compound semiconductors are powerful supplementations to silicon due to a number of unique physical properties, which allow for special and superior functionality of electronic devices. All III-V and II-VI compounds (with the exception of GaP) are direct semiconductors, whereas silicon has an indirect transition.

Due to a higher efficiency to emission of light, these compounds are suited for optoelectronic devices such as laser diodes, light-emitting diodes, light sensors, and solar cells. Furthermore, the mutual solubility of the compounds allows for a bandgap tailoring and, therefore, to achieve a spectral range from infrared to ultraviolet. In addition the adaptation of the lattice constants of substrate, epitaxially grown layers are possible, such as in the system $Cd_{1y}Zn_yTe$ substrate –$Hg_{1-x}Cd_xTe$ layer; for every x in the range of $0 < x < 1$, a y can be determined such that the misfit is minimal. In addition, lattice constants can be adapted easily in multilayer systems. The larger bandgap and the higher electron mobility of GaAs and InP allow devices to operate at higher temperatures, which has led to their adoption in both high-speed digital and high-frequency analog devices. Doping to obtain n- and p-conductivity in the range of 10^{-3} to

Table 9.1 Properties of Compound Semiconductors

Property	Si	GaAs	InP	GaP	InSb	ZnSe	CdTe
Crystal structure/space group	$Fd3m$	$F\bar{4}3m$	$F\bar{4}3m$	$F\bar{4}3m$	$F\bar{4}3m$	$F\bar{4}3m$	$F\bar{4}3m$
Bandgap (eV)	1.12 indirect	1.43 direct	1.35 direct	2.26 Indirect	0.17 direct	2.82 direct	1.56 direct
Electron mobility at 300 K (cm^2/ Vs)	1450	8500	5400	160 (250)	(77000)	500	1100
Hole mobility at 300 K (cm^2/Vs)	600	400	200	75 (150)	850	30	100
Saturation velocity at 300 K (10^7 cm/s)	1	2.1	2.3	2	(9.8)		
Breakdown voltage at 300 K (10^6 V/cm)	0.3	0.4	0.5	≈ 1	(10^{-3})		
Melting point T_m (°C)	1420	1239	1062	1457	527	1515	1092
Decomposition pressure at T_m (bar)	1E-7	2.2	27.5	32	2.3E-5	4	0.7
Linear thermal expansion coefficient α (10^{-6}/K) at 300 K	2.6	5.73	4.60	4.65	5.37	7.8	4.8
Latent heat of fusion L (kJ/mol)	50.7	96.7	62.7	122.3	48.7	51,9	50.1
Thermal conductivity at T_m λ_s (W/cmK)	0.223	0.071	0.091	0.08	0.0474	0.2	0.009
Thermal conductivity of melt at T_m λ_m (W/cmK)	0.64	0.178	0.228		0.123		0.018
Thermal diffusivity of melt κ_m (cm^2/s)	0.264	0.072	0.103		0.068		0.0475
Density/solid–liquid $\rho(T_m)$ (g/cm^3)	2.29/2.42	5.17/5.72	4.71/5.05	4.138/	5.76/6.48	5.26/	6.2/5.64
Kinematic viscosity v (cm^2/s)	0.0028	0.0048	0.0016		0.0037		0.0041
Prandtl number $Pr = v/\kappa$	0.011	0.068	0.015		0.054		0.086
Critical resolved shear stress τ near T_m (MPa)	9 ($T_m - 200$ K)	0.3–0.5 ($T_m - 200$ K)	0.6 ($T_m - 330$) K	4.1 ($T_m - 670$) K	0.25 (T_m)		0.2 ($\approx T_m$)
Ionicity	0	0.310	0.421	0.327	0.321	0.630	0.717
Stacking fault energy (mJ/m^2)	100	55 ± 5	17 ± 3	41 ± 4	38 ± 4	13 ± 1.5	10 ± 1.5

10^{-1} Ωcm is easily accessible. Even semi-insulating behavior characterized by an electrical resistivity greater than 10^6 Ωcm can be adjusted by pinning the Fermi level at midgap donors or acceptors. Nevertheless, their market volume is and will be considerably less than that of silicon-based technologies.

The fabrication of electronic devices inevitably needs single crystals and wafers, which have to meet customers' continuously increasing high quality standards at affordable costs. Quality requirements include large-diameter and long crystals, high physical and chemical (compositional) perfection, uniformity of structural and physical properties, low strain, and high reproducibility and reliability from wafer to wafer and from crystal to crystal. State-of-the-art device technology uses epitaxial growth of ternary or quaternary layers on top of the wafer. Therefore, the structural properties and the surface perfection are very important quality criteria. To address this challenge, the crystal grower and wafer manufacturer have continuously to develop technologies that constantly reduce production costs and improve the environmental friendliness of every technological step.

In contrast to elemental semiconductors, compounds possibly exhibit a homogeneity range. However, knowledge about the existence and extent of a homogeneity range relative to the stoichiometric composition is limited and not commonly accepted in every case. Some data on the maximal width of selected compounds are given elsewhere [14,21]. Likewise, the composition and the partial pressure of the components at the congruent melting point are still under discussion. Typically, the homogeneity range contracts with decreasing temperature. Therefore, precipitation of a degraded eutectic can occur during cooling down from growth temperature. This is well known for GaAs, GaP, ZnSe, CdTe, and PbTe. Deviation from stoichiometry and its change with temperature is related to (charged or uncharged) native defects (vacancies, interstitials, antisite defects). These native point defects will influence carrier inventory and carrier mobility. They can interact with dopants, form complexes, and thus again affect the physical properties of the material.

Arsenides, phosphides, and tellurides have a substantially higher decomposition pressure in the melt at or near to the congruently melting compound compared to silicon (see Table 9.1). This can lead to a loss of the II, V, or VI group component from the melt or the crystal and to a deviation from the stoichiometric composition, which causes changes of the defect content and physical properties. Therefore, adequate measures have to be taken to control the volatile component and prevent it from escaping.

Crystals could be grown by direct solidification of a melt with a composition exactly corresponding to the melting point of the compound. However, this composition is hardly precisely known and cannot be adjusted exactly under technological conditions. Therefore, crystal growth is practically always carried out from a melt, the composition of which deviates from that of the congruently melting compound. This possibly results in macro- and microsegregation of the components and even breakdown of the solid/liquid interface due to constitutional supercooling.

The thermal conductivities of the compound semiconductors in the solid and liquid state are significantly smaller compared to silicon. That is, the transport of heat at solidification is lower, leading to a lower growth rate. At the same time, the Prandtl numbers ($Pr = \nu/\kappa$, with ν and κ being the kinematic viscosity and thermal conductivity, respectively) of the melts are small, indicating that convection in the melt has limited influence on the temperature field. The opposite applies for the diffusive transport of species, which is substantially influenced by convection in the melt and described by the Schmidt number being much greater than 1 ($Sc = \nu/D$, with D being the diffusion coefficient in the melt).

The classic Bridgman methods modified to meet the special requirements of the III-V and II-VI compounds have been used to grow single crystals for quite some time. These methods are suitable for an upscaling of the diameter and the length of crystals. The growth of crystals in crucibles has some advantages and drawbacks. The temperature fields of Bridgman techniques are less nonlinear as compared to the Czochralski method, in particular for the liquid encapsulated Czochralski technique. Therefore, thermal stresses in the crystals are lower, resulting in a lower dislocation density in comparison to Czochralski grown crystals. On the other hand, it is practically impossible to observe the outer contour of the solid/liquid interface during Bridgman growth. Another problem in Bridgman growth is the wetting of the melt and the crystal to the crucible wall, which promotes twinning and polycrystallization as well as stresses (see Section 9.3.3).

At the beginning of the 1990s, when the market for GaAs and InP wafers significantly rose, the Czochralski method was mainly used for crystal growth. After the recession in the early twenty-first century, the demand for wafers with a higher structural perfection increased above the ordinary because of the switch from ion implant devices (i.e., MESFET – MEtal-Semiconductor Field Effect Transistor) to epitaxial grown structures (e.g., for HEMT's – High-Electron-Mobility Transistor, HBT's – Heterojunction Bipolar Transistor, and BiFET's – Bipolar Field-Effect Transistors). This demand could be better fulfilled by the Bridgman method, with a vertical arrangement of the crucible resulting in circular single crystals. Therefore, in recent years, the ratio between Czochralski and Bridgman originating wafers has changed in favor of the latter, now being approximately 10:90. In that time, the horizontal Bridgman methods (HB- Horizontal Bridgman, HGF – Horizontal Gradient Freezing), which are also appropriate for the growth of crystals with higher structural perfection, lost their meaning as they produced D-shaped crystals and required more effort to manufacture circular wafers. In addition, the diameter of the wafers could not easily be increased above 50 mm.

In the following section, the substantial progress made in the development of the vertical Bridgman method in recent decades will be considered. It has now reached maturity and is used for mass production of single crystalline III-V and II-VI compounds [22–25]. However, it should be mentioned that the Bridgman method has also been successfully applied to the growth of a plurality of other single crystals, such as ZnO, CaF_2 [26,27], or ternary compounds such as $ZnGeP_2$ [28].

This chapter tries to continue the review by E. M. Monberg in the first edition [29], who together with W. A. Gault and J. E. Clemans are the pioneers having brought forward

the vertical Bridgman methods for single crystal growth of III-V-compounds [30,31]. The method was first commercialized by American Xtal Technology [24] in the late 1980s. A comprehensive but dense description of all the methods used for single crystal growth of III-V and II-VI compound semiconductors in the past can be found in the monograph by Oda [8]. M. Tatsumi and K. Fujita [32] reported the situation of the “melt growth of GaAs single crystals” up to 1998. Chapters devoted to Bridgman growth of III-Vs can be also found in Refs [33–40] and to the II-VIs in Refs [41–43].

Section 9.2 summarizes the progress made in the hardware of Bridgman growth, including control of the growth process and some remarks to modeling. Section 9.3 deals with the results of single crystal growth of III-Vs and II-VIs, respectively. Finally, Section 9.4 indicates some issues to be solved in the future.

No attempt could be made to cover the huge number of relevant publications (See [8]). Instead, this chapter tries to give only relevant examples.

9.2 Equipment (Design and Engineering Issues)

9.2.1 Basics

Both versions of the method of crystal growth in a crucible (or boat) are used to grow compound semiconductor single crystals: the classical vertical Bridgman–Stockbarger method (abbreviated here as VB) characterized by a downward or upward displacement of crucible or furnace, respectively, and the growth in a stationary crucible by vertical gradient freezing (abbreviated as VGF), sometimes also called the Tammann-Ströber method [44]. Schematic representations of the hot zones of the methods are given in Figure 9.1. The hot zone of a VB apparatus consists usually of two cylindrical furnaces possibly composed of several separate resistance heaters with a temperature above and below the melting point of the substance to be crystallized, supplying/extracting heat mainly radially inward/outward and inducing radial temperature gradients. An insulation member or a booster heater separates the furnaces and defines the position and shape of the solid/liquid interface and the temperature gradients in the melt and the

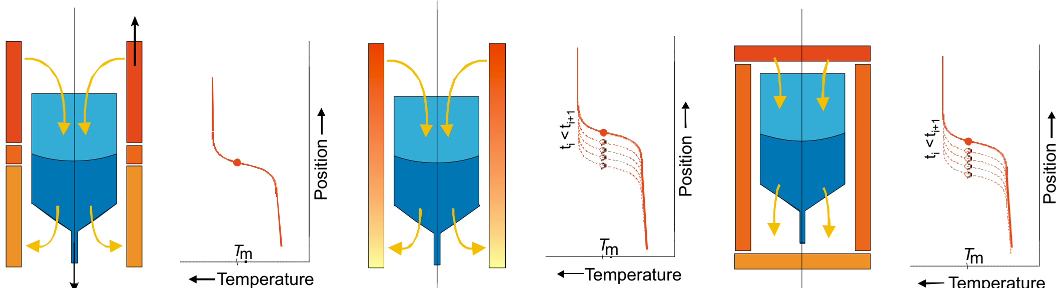

FIGURE 9.1 Hot zones of VB (left) and vertical gradient freezing (VGF) (middle and right). *(Reproduced in part from [45], with kind permission from Springer Science and Business Media.)*

crystal, which are typically on the order of magnitude of 5 K/cm. The crucible rests on a support pad cooled at its lower part in order to facilitate an axial heat flow. Seeded and unseeded growth for III-V and II-VI compounds is used. To prevent or to reduce radial/azimuthal inhomogeneities of the temperature field, the crucible can be rotated with constant or alternating rotation rate. The displacement rate of the crucible or the furnace is often held constant and is related to the growth rate, but does not necessarily agree with it along the entire charge. It amounts to approximately 1 mm/h for the growth of $Cd_{1-x}Zn_xTe$ and 3–5 mm/h for GaAs, GaP, and InP, respectively. This also applies to the position and the shape of the interface. The reasons are end effects caused by the radial/axial heating and cooling and their dependence on the relative position of crucible and furnaces. An upscaling of the hot zone is possible to grow long single crystals with aspect ratios of $H/R > 3$ (where H is the length and R is the radius of the crystal).

The growth process is followed by a controlled cooling to room temperature in which the cooling rate is determined such that thermal stress is below the critical shear stress for dislocation multiplication and glide processes.

VGF of a charge in a stationary crucible is achieved by a cylindrical furnace composed of a plurality of separate heaters, the temperature of which is to be controlled so as to generate a T-field moving along the charge with a controlled rate. The connecting terminals of the heaters are disposed at different azimuthal positions to avoid temperature inhomogeneities. Up to 23 separate heaters have been used in such VGF equipment [46]. In industrial crystal growth equipment, the number of heaters is less for reasons of cost, stability, and reliability. An upscaling is possible. The aspect ratio seems to be limited to $H/R < 2$ because of difficulties to keep the phase boundary deflection low for longer crystals. Temperature gradients and growth rates are similar to those of VB growth.

Instead of heating the charge from the side only, directional solidification can also be performed by a system consisting of a top and a bottom heater and one or more mantle heaters in between, as described by Rampsberger and Melvin [47] and adapted to the growth of GaAs single crystals by Sonnenberg and Küssel [48]. It better approximates the required axial heat transfer. More than one charged crucible can be arranged in the hot zone and converted to single crystals (see Section 9.2.2.1). Another possibility to create a preferably axially directed temperature field is the application of a submerged heater (see Section 9.2.2.3).

The hot zones described above are either incorporated in a water-cooled pressure vessel (cold wall) or the heater system is arranged outside of the reactor (hot wall). Depending on the melting temperature and gas pressure of the substance to be grown, both constructions have advantages and disadvantages. The active heaters are screened from the vessel wall or the surroundings by a sophisticated system of passive insulation, which together with liners, crucible support, etc., produce as a whole the required temperature field and control the heat fluxes around the crucible with the charge. The temperature of the heaters and the seed well is followed by thermocouples and regulated and/or controlled by closed loop systems. Evacuation and refilling with inert gas of the vessel or reactor are provided.

The so-called heat exchanger method (HEM) is a further version of the growth methods in a stationary crucible. A seed crystal is placed on the bottom of the crucible and connected with a heat-conducting rod (the heat exchanger), which prevents the seed from melting. Solidification takes place by reduction of the heating power and/or increase of the cooling efficiency. This method is used to produce large sapphire single crystals [49], for example, but it has not achieved acceptance for crystal growth of compound semiconductors.

9.2.2 Specifics

9.2.2.1 General

As mentioned, the high vapor pressure of the V-component of some of the III-V compounds (see Table 9.1) requires measures to prevent decomposition during crystal growth. This can be done either by liquid encapsulation of the molten presynthesized charge or by solidification of the charge under the equilibrium pressure of the V-component.

In the liquid encapsulation VB (LEVB) or liquid encapsulation VGF (LEVGF) method, high-purity boron oxide (B_2O_3) with well-defined water content (see Section 9.3.2) is added to the pyrolytic boron nitride (pBN) crucible with the charge. Other encapsulants, such as $BaCl_2$ or $CaCl_2$, have also been applied, but boron oxide has been proven to be most successful, mainly because boron is an isoelectric impurity in most III-V compounds. During heating, the initially solid boron oxide gradually softens; at around 600 °C, the viscosity is small enough to completely cover the charge. At the same time, an inert gas pressure is established in the vessel, overcompensating for the vapor pressure of the molten charge. Boron oxide is not at all inert. Instead, chemical reactions with the charge and the surrounding gas atmosphere have to be considered. This can be used to some degree to influence the impurity content of the compound and, more importantly, for doping. This will be briefly discussed in Sections 9.3.3 and 9.3.5.

Crystal growth under the equilibrium pressure of the compound requires a closed reactor/ampoule consisting of two compartments connected with each other. One compartment contains the charge, whereas the other contains the component to be evaporated in elemental form. During heating and crystal growth, the charge and receiver are held at different temperatures in order to establish a partial pressure of the evaporating component corresponding to the decomposition pressure of the charge. In addition, this allows some degree of control of the III/V or II/VI ratio, respectively, by the temperature of the receiver—that is, the composition of the compound if there is a homogeneity range [50]. Obviously, this arrangement can also be used to synthesize the compounds from the components followed by crystal growth. An outer pressure has to be established to approximately correspond to the equilibrium pressure inside to prevent damage of the reactor/ampoule. Due to its good workability, fused silica is mainly used for the reactor/ampoule. However, the application of quartz limits both the temperature of the compound to be grown and the mass of the inserted charge.

For the growth of $Cd_{1-x}Zn_xTe$ and ZnTe crystals, the unseeded vertical Bridgman growth process in quartz crucibles is used [51].

A plurality of embodiments of VB and VGF crystal growth apparatuses for compound semiconductors have been reported in the patent and technical literature, but little is known about the inwards of equipment actually used for mass production in the industry. Two examples are given here, with the viewpoint that the cost of equipment as a crucial factor in crystal growth should be as low as possible.

In a series of granted patents, Hashio et al. [52] disclosed a furnace system arranged outside of a reactor in the air atmosphere, which can be used for VB/VGF as well as Czochralski growth of single crystals of GaAs, InAs, CdTe, and the like. Even synthesis by the injection method should be possible. The main feature of the equipment is a reactor tube having at least one open end. The tube consists by way of example of silicon carbide, silicon nitride, aluminum nitride, aluminum oxide, or a composite of these or other refractory materials. If necessary, it can be covered by an oxidation resistant or an airtight layer. Specially designed flanges are attached to the open ends to seal the reactor tube. The sealing portion of the flanges is water-cooled or shielded against the furnace by a heat insulator. The lower flange exhibits a lead through for a moveable shaft carrying a crucible support and the crucible. An exhaust tube and an inlet tube in the upper flange allow for evacuation of the reactor tube and refilling it with inert or process (e.g., doping) gas. The apparatus has a Kanthal heater, which is divided in several zones depending on the applied method and equipped with thermocouples to control their temperatures. The described apparatus has several advantages: the cost of the reusable reactor tube is lower than that of a water-cooled stainless steel high-pressure vessel, which is necessary if carbon heaters are used. Furthermore, the interior of the reactor can be carbon free, which simplifies the carbon doping of GaAs, for example (see Section 9.3.5). In principle, the length of the crystals that can be grown is not limited, although it depends on the length of the furnace and crucible. The maximum pressure in the reactor tube seems to be limited to 2 bar. Because auxiliary elements, such as insulators, are not applied, the impurity content in the hot zone should be low. Low service and maintenance costs are to be expected. A cost reduction of about 20% compared to VB growth in a pressure vessel has been reported [52].

Another approach to reduce production costs determined in addition to the costs of the production equipment by the operational capacity and the crystal growth rate is the simultaneous growth of several crystals [53–55]. For example, Eichler et al. [56] disclosed a Tammann-Ströber–like apparatus for the LEVGF-growth of III-V-crystals. The cylindrical hot zone is assembled of planar top and bottom heaters and a mantle heater possibly composed of several heating elements in between. CFC-heating elements characterized by superior heat conductivity and embedded in a graphite carrier for heat equalization and graphite heating elements are applied for the planar and mantel heaters, respectively. The dimensions of the planar heaters overlap the mantel heater(s). Several crucibles of the same dimensions are coaxially arranged around the axis of the hot zone, resting in cone-shaped support members on the bottom heater. In the center

of the hot zone, a further crucible or an additional heater has been arranged. The seed position in the seed wells is for all crucibles at the same relative height. Crystal growth is performed by lowering the temperature of the bottom heater while the mantle heater is kept at a temperature close to the melting point. The diameter of the complete arrangement is much larger than its height. The latter one is generally scaled with the length of the crucibles. The hot zone resides in a vacuum-tied pressure vessel.

Obviously, due to the arrangement of the crucibles outside the axis of the hot zone, the cylindrical symmetry in each of the crucibles has been broken, which could lead to unacceptable radial/azimuthal inhomogeneities in the grown crystals. However, this breakdown of symmetry could be compensated for to an acceptable degree by filling the clearances between the crucibles by means of specific material bodies, the heat conduction properties of which are adapted to that of the freezing substance. Graphite, ceramics, and fiber materials (graphite felts and laminates) with adjusted density were used. As a result, the radial temperature gradient with regard to the central axis of the hot zone was suppressed. In addition, the axial temperature distribution could be properly designed by utilization of the anisotropic heat conductivity of fiber materials. As a side effect, the convection in the gas phase, which has to be considered at pressures higher than several bars, was likewise reduced by the fillers.

The described VGF method has been successfully used for the growth of $9 \times 3''\varnothing$, 7×100 mm∅, 3×150 mm∅, and 3×200 mm∅ GaAs single crystals. Also, 4×100 mm∅ InP (flat bottom) and GaP crystals have been successfully grown.

For both methods discussed, an upper limit of the growth rate v exists, which is determined by the heat balance at the solid/liquid interface. Neglecting the heat transport in the melt to the interface, it follows:

$$v/\mathrm{grad}T_s \leq \lambda_s/L\rho_s$$

with the latent heat of fusion L, the thermal conductivity λ_s, the temperature gradient $\mathrm{grad}T_s$ and the density of the crystal ρ_s.

Inserting for $\lambda_s/L\rho_s = 5.4 \times 10^{-5}$, 4.5×10^{-5} and 2.0×10^{-5} cm^2/ks for Si, InP, and GaAs, respectively, and assuming (typical) $\mathrm{grad}T_s = 5$ K/cm, the upper limits of growth rate are 9.7, 8.1, and 3.6 mm/h. It furthermore follows that changes of the temperature gradient in the crystal will lead to corresponding changes of the maximum growth rate.

Due to the combined axial and radial/lateral heat flow in the crystal and the melt, the melting point isotherm—that is, the solid/liquid interface in case of rough growth - is typically not flat but curved. In addition, the thermal field often deviates from an exact cylindrical symmetry; that is, the interface is not rotationally symmetric. Its shape is formed in such a way that the effective local heat flux is always perpendicular to the corresponding element of the interface. More specifically, for III-V compounds, it is concave toward the crystal with an increasing curvature near the crucible wall [57,58]. The latter is a consequence of the low thermal conductivity of the crystal relative to the higher axial conductivity of the exclusively used pBN crucible wall (see Section 9.2.3). The interface deflection increases with growth rate. A concavely curved interface is

known to deteriorate the structural (stresses, dislocations, spontaneous nucleation at the crucible wall) and chemical perfection (macroscopic segregation) of the crystal [59]. A slightly convex shape would significantly reduce these problems. Therefore, efforts have been reported to flatten the shape of the interface up to the three-phase junction at the crucible wall by equipment-oriented optimization of the furnace profile in the gradient zone by localized radiant heating [58] and by a control of convection in the melt.

In contrast, for $Cd_{1-x}Zn_xTe$ growth in quartz ampoules, a strongly convex-shaped phase boundary is found at the beginning of the growth, followed by slightly convex-shaped phase boundary in the middle and a flat phase boundary at the end of the growth. This is due to the similar heat conductivities of fused silica and II-VI compounds.

Several possibilities to influence convective flows and thus interface shape by external force fields have been studied in the past [60], including flow control by electromagnetic fields, submerged or booster heaters, and excitation of vibrations. However, to the author's knowledge nothing is known about the application of these possibilities in industrial VB/VGF crystal growth for III-V compounds.

9.2.2.2 Flow Control by Electromagnetic Fields

A widely used means to externally influence the natural convection and the T-field in VB growth is crucible rotation, but it is rarely applied in VGF growth.

The melts of compound semiconductors are electrical conductors. Therefore, steady as well as alternating (pulsating, rotating, and traveling) magnetic fields, also in combination, are basically suited to actively influence the hydrodynamics and heat/mass transfer directly in the bulk of the melt as well as near the solid/liquid interface. Two objectives are pursued: damping of stationary or nonstationary natural convection and excitation of controlled stationary fluid flow, such as to override and/or stabilize natural convection, to symmetrize the thermal field of the heater, and to flatten the solid/liquid interface near the crucible wall. However, the Prandtl numbers of semiconductor melts are small (see Table 9.1), so a forced flow should be strong enough to contribute to the overall heat transfer in the melt and, therefore, to influence the interface shape and interface position. On the other hand, large driving forces result in unwanted flow instabilities; therefore, a compromise has to be found. In particular, nonstationary flow is appropriate for stirring a melt, such as to homogenize dopant distribution. The topic is thoroughly considered by D. Vizman in this volume. Reviews treating the application of magnetic fields in crystal growth of compound semiconductors can also be found in Refs [61–65].

Concerning the application of static magnetic fields in VB/VGF growth of compound semiconductors, only a few experimental and numerical results have been reported; for example, see Refs [66–73]. Much more attention has been paid to numerical and, to a lesser extent, to experimental, III-V related studies of alternating magnetic field in Bridgman-like configurations.

Rotating magnetic fields (RMF) have been reviewed in Refs [63,65,74]. For example, the growth of 2-inch Si-doped GaAs single crystals by the vapor pressure–controlled VGF method with and without an RMF should be mentioned. Details of the growth trials are given in Ref. [75].

Schwesig et al. [76] (in agreement with [77]) concluded that alternating magnetic fields do not allow minimization of the concave shape of the interface around the triple junction at the crucible wall if the axial thermal conductivity of the crucible material used is higher compared to the grown crystal. This is the case in growing III-V-crystals in pBN crucibles. It can be avoided by a localized radial heating at the gradient zone [58].

Among time-dependent magnetic fields, the traveling magnetic fields (TMF), possibly in connection with a steady magnetic field [78], is the most flexible means to influence hydrodynamics in electrically conducting melts [79]. The TMF drives directly either an upward or downward meridional (axial and radial) melt flow without exciting an unnecessary azimuthal flow as an RMF.

In laboratory trials, the AC magnet is often arranged outside the growth chamber. This has the disadvantage that, due to the field loss in the space between the magnet and the crucible caused by the chamber wall, screens, and heaters, stronger magnets must be used in order to exploit the entire potential of a TMF [64]. This especially applies for the growth of III-V and II-VI compounds with high vapor pressures, requiring very compact chambers with water-cooled walls. As a result, only approximately one-tenth of the magnet energy is indeed invested in the crucible. The positioning of the AC magnet inside the growth chamber would be a solution.

This idea has been advanced by the group of P. Rudolph using the earlier approaches of Keiki [80], Grimes [81], von Ammon et al. [82], and Mühe et al. [83]. Details can be found in Ref. [64]. As a result, the so-called internal heater-magnet module (HMM) has been developed and built, including power supply and control systems. In the meantime, the HMM has been tested in VB/VGF growth of GaAs and Ge-single crystals [84,85], as well as for directional solidification of solar silicon [86–88]. It also has been refined for applications in a multicrucible VGF puller, as outlined in Figure 9.2 [89]. In crystal growth, the main objective has been the control of the solid/liquid interface shape under laminar flow conditions, whereas most attention has been directed on an efficient stirring of the melt during solidification of mc-silicon.

A cylindrical traveling magnetic field with an induction of $B = 1-10$ mT, a frequency $f = (10,600)$ Hz, and phase shifts $|\Phi_I| = 5-120°$ can be generated [85]. By varying the frequency of the ACs, the penetration depth (skin effect) of the magnetic field is determined—that is, the thickness of the melt layer where a Lorentz force acts. In addition, a direct current is supplied to the heater coils, which (together with the superimposed AC) allow for melting of the charge and also generate a steady axial magnetic field. In this connection, the ratio of the AC and DC is chosen to produce the required traveling magnetic and temperature fields. If necessary, this ratio can be changed during crystal growth. However, due to the contribution of the AC to the thermal field, there is a

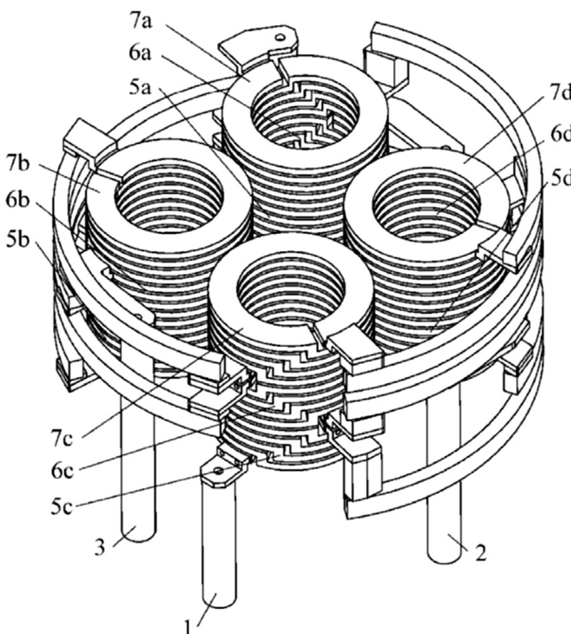

FIGURE 9.2 Internal heater-magnet module (HMM) for application of several crucibles. 1–3 are the connections; 5a–5d, 6a–6d, and 7a–7d are the interconnected upper, middle, and lower HMM's. *(From patent DE10 2012 204 313 B3, courtesy of N. Dropka et al./IKZ Berlin 2012.)*

limitation for inducing Lorentz force. The temperature gradient is adjusted by bottom and top heaters according to Refs [38,48].

Numerical results of the influence of HMM-generated TMF on the interface shape for materials with rather different physical properties (e.g., Ge, Si, CdTe, BeF_2, and YAG) were published by N. Dropka et al. [90]. It was demonstrated that basically for all materials, a beneficial influence of the TMF on the solid/liquid interface deflection can be obtained when the process parameter's frequency, phase shift, and AC current were properly chosen. However, it has to be considered that with decreasing electrical conductivity, higher frequencies and higher currents are necessary, which enhances the share of AC relative to DC heating and, therefore, could sets limits for the TMF [91]. In all cases tested, a downward TMF increased the convexity of the central interface due to a downward heat transport at the side wall of the crucible. The application of two or more frequencies makes it possible to influence the waveform of the TMF and thus to tailor the radial and axial components of the Lorentz force. In addition, up and down waves can be combined [88,91]. These findings could broaden the applicability of TMF.

9.2.2.3 Submerged Heater

Ostrogorsky [92–94] introduced the modification of the bottom-seeded VB/VGF method in which a (resting or rotating) flat disc-shaped heater or baffle is submerged into the melt. This submerged heater method is practically identical to the so-called axial heat processing method (AHP) described in a patent application by Golyshev and Gonik [95].

The submerged heater/baffle is encased to prevent contact to the melt, using preferably the same material as the crucible (e.g., silica, graphite). It separates the melt into an upper and lower zone. The temperature of the submerged heater is held above the melting temperature of the material to be solidified. Together with the axial temperature gradient, this temperature difference determines the position of the solid/liquid interface below the heater, typically 3−10 mm away [96]. As the crystal grows upwards, the crucible or the submerged heater is slowly lowered or raised, respectively. During growth, the lower melt is continuously replenished with melt of constant composition from above the heater through an annular gap of approximately 0.3−0.5 mm [94,96] between crucible and heater, at which the gap should prevent back diffusion of solute. The influence of nonvanishing back diffusion has been considered in Ref. [97].

The shape of the solid/liquid interface can be controlled by the temperature of guarding heaters surrounding the crucible [98]. A circular disk with high heat conductivity and possibly a shaped surface [99] below the submerged heater further improves the uniformity und symmetry of the T-field in the lower zone. Radial temperature differences as low as 0.5 K were measured in growth experiments of Ga-doped Ge and Te-doped InSb [100]. Further details are given in Refs [94,95].

Due to the reduced height and the small radial temperature difference of the melt under the heater, the axial and radial Rayleigh numbers of the enclosed melt are reduced by a factor of 10^3–10^4 compared to VB/VGF without the submerged heater [100]. Therefore, a submerged heater has nearly the same effect on the reduction of the Ra number as a decrease of the gravitational acceleration under microgravity conditions.

Except for a short transition range, the distribution of dopants reaches steady state with the initial melt concentration, clearly indicating diffusion-controlled axial segregation. The radial solute distribution in the crystals was found to be quite uniform, which proves a nearly convection-free segregation and/or flat solid/liquid interface.

The submerged heater/baffle can also be rotated for stirring and homogenization in the lower zone. Instead, the same effect can be reached by a small axial/radial DC electric current in the melt flowing between a central electrode in the axis of the heater/baffle and the crucible wall and in the presence of an axial magnetic field. The corresponding axial and radial solute distributions have been numerically investigated for different stages during growth and different process parameters in a number of papers by Bliss et al. [71–73,101–103].

The stirring effect described above is qualitatively similar to that of the application of a rotating magnetic field. A comparison of both methods has been made in Ref. [102].

9.2.2.4 Flow Control by Vibrations

A further possibility to influence the heat and mass transfer in the melt, the shape of the interface, and possibly also the interface kinetics is the application of various vibrational techniques [60,104–107], which are considered in detail by P. Capper and E. Zahrikov in this volume. These include the well-known *accelerated crucible rotation technique* (ACRT, [108,109]), the *angular vibration technique* (AVT, [110–112]), the *axial vibration*

control (AVC, [113,114]), the *coupled vibrational stirring* of the ampoule (CVS, [115]), and *ultrasonic vibrations* [116,117]. Vibrational techniques are basically applicable to all methods of crystal growth from the melt, the floating zone technique, Czochralski, and the VB/VGF method. They are characterized by the cycle time τ and acceleration/deceleration rate in ACRT; angular frequency f (O(f) $\approx$ 1 Hz) and angular amplitude $b = \alpha/2\pi$ (O(b) $\approx$ 0.04) in AVT; axial frequency f of crystal or submerged body and amplitude A (O(A) $\approx$ 10–100 μm) in AVS; frequency, amplitudes, and the phase shift of the sloshing motion of the crucible in CVS; and frequencies in the range of 0.15–10 MHz in the case of ultrasonic vibrations. A detailed analysis shows that each of the techniques mentioned above creates an individual type of flow in the melt and, correspondingly, the induced flow is controlled differently in each method [105].

With the exception of ACRT, these methods are not yet applied for crystal growth outside laboratories. In the 1080s and 1990s, the applicability of ACRT to the VB growth of II-VI compounds (CdHgTe, CdTe, $Cd_{1-x}Zn_xTe$) was thoroughly investigated in a series of experimental studies by Capper et al. [118–124]. II-VI compounds are difficult to grow with satisfying yield, size, and crystal quality (grain boundaries, twins, and dislocation density). The topic is reviewed in Refs. [41,42,118].

The formation of a stable Ekman layer is very important to maintain a flat solid–liquid interface [124]; it allows for a faster stable growth rate [122], improves macrocrystallinity [123], and results in better radial and axial homogeneity [122,123]. The segregation behavior of important elements in $Cd_xHg_{1-x}Te$ crystals grown by VB without and with application of ACRT have been compared [121]. Distribution coefficients were found to be lower in ACRT material.

9.2.3 Optimization and Control of VB/VGF-Growth

For the development and the optimization of hot zones of VB/VGF devices, thermal modeling is widely used. In addition to all-purpose software packages, such as ANSYS and FIDAP, adapted software such as Crysvun or Crysmas [125], CGSIM [126], and FEMAGSoft [127] can be used. All mechanisms of heat transport (conduction, radiation, convection in the fluid phases) as well as effects at interfaces (latent heat of fusion, facets, supercooling) are regarded in two dimensional (2D) and three-dimensional (3D) time-dependent models. Numerical modeling of heat transfer, flow dynamics, and the influence of external fields in crystal growth are covered in detail in the chapters by Derby, Yeckel, and Kakimoto in this book; therefore, these topics will not be explored in depth here.

The temperature of the heaters is controlled by thermocouples, the stability of which depends on the growth conditions. For temperatures below 1100 °C, Ni/NiCr thermocouples (type K) are convenient; for higher temperatures, Pt/PtRh and W/WRe thermocouples have to be applied. In addition to the high temperatures, the ambient atmosphere (CO, As, P, etc.) possibly also limits the lifetime and reliability of thermocouples. So, for example, W/WRe-thermocouples degrade in the course of GaAs crystal

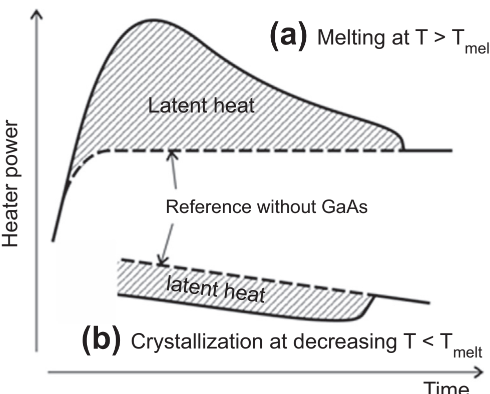

FIGURE 9.3 Time evolution of heater power during melting (a) and crystallization (b) at constant or decreasing temperatures, respectively.

growth in a cold-wall system up to 20 K. For this reason in multiheater arrangements, the power of most of the heaters is controlled; the exception is the main heater, in which a relative graduation of the corresponding thermocouple situated distant from the charge can be performed by using the phase transition at melting of the charge. As an example, the evolution of the power at a constant set point of temperature $T_{set} > T_{melt}$ during melting as well as during crystallization at decreasing temperature of 25 kg GaAs is depicted in Figure 9.3. It is compared with the behavior of a graphite block under identical conditions replacing the charge The area between the two power curves characterizes the latent heat of the solid/liquid phase transition. The time τ, the melting of the charge, requires increases with decreasing temperature T_{set} of the control thermocouple. An analysis of the hyperbolic dependence $\tau(T_{set})$ yields a $T_{set,\ melt}$ corresponding to the melting temperature of the charge, which can also be used to define the superheating of the melt. In a similar way, the thermocouple at seed position can be graduated and different thermocouples can be compared with each other to ensure a "copy exact" of the growth process from run to run and from furnace to furnace.

9.3 Growth of Binary Compound Semiconductors

9.3.1 Synthesis

Crystal growth precedes synthesis of the compounds from the constituents. Under industrial conditions, it is commonly performed in separate equipment. Composition close to the stoichiometric one, high purity, and shape of the ingot adapted to the growth crucible are the main demands that have to be fulfilled. The application of high-purity constituents ("7 N") and possibly an etching before charging the crucibles are mandatory. Depending mainly on the thermochemical properties of the constituents, one of the following methods is used: horizontal/vertical gradient freeze, injection synthesis, or high-pressure direct synthesis.

The synthesis of antimonides (InSb, GaSb) can easily be performed by a melting together the constituents with an excess of antimony in a pretreated horizontal or vertical boat made from fused silica, pBN, and graphite, respectively, followed by directional solidification. Due to gravity segregation, mechanical stirring could be necessary.

Selenides and tellurides (e.g., $Cd_{1-x}Zn_xTe$) are synthesized in quartz ampoules. After evacuation and sealing off, the charge is heated in an encapsulated furnace to initiate the exothermic reaction, then homogenized and directionally solidified. The resulting ingot is ready for crystal growth. Due to deviation of the congruent melting point toward the Te-rich side of the phase projection, a Cd excess must be added in order to ensure near-stoichiometric composition.

The high-pressure method using a pressure vessel has been commonly used to synthesize GaAs, InP, and GaP from the components under a boron oxide encapsulate in a PBN crucible and an appropriate argon or nitrogen overpressure [128–130]. After a homogenization period slightly above the melting temperature, the charge is directionally solidified. Reactions between charge, encapsulation, and ambient atmosphere have to be considered. An ingot slightly rich in the V-component is preferred for subsequent crystal growth.

Alternatively, the injection method developed by A.G. Fisher [131] has been applied for the synthesis of InP and GaP. Red phosphorus is controlled sublimated in a separate compartment and reacted with molten gallium and indium in a pBN crucible covered by boron oxide encapsulant. A more complex system for in-situ injection synthesis and magnetic field–supported LEC (Liquid Encapsulated Czochralski) growth of InP single crystals in a two-step process has been developed by Bliss et al. [39].

9.3.2 Liquid Encapsulation

Boron oxide has turned out to be best suited to fully encapsulate the charge for synthesis and growth of arsenides and phosphides. Two objectives are pursued: prevention of decomposition due to the high partial pressure of the V component and formation of a separating layer between crucible and charge [132].

Boron oxide is produced from high-purity boric acid by a high-temperature treatment in vacuum. It contains chemically bounded water, the content of which can be adjusted and is usually between 200 and 3000 ppmw depending on the application. The water content is part of the “oxygen pool” of the system and is essential for synthesis as well as crystal growth. The overall content of metallic impurities relevant for compensation is below 1 ppmw.

Boron oxide cannot be regarded as an inert cover, but instead is part of a reaction system. To ensure reliable and reproducible synthesis and growth with well-determined properties, a comprehensive chemical analysis of the rather complex reaction system would be necessary, comprising on one side the III/V-ratio (stoichiometry) and on the other side the behavior of impurities (gettering) and dopants with possible consequences for the properties of the III-V compounds but also for surface tensions at three phase boundaries, for example (see Section 3.3).

Several attempts have been made to formulate the most important chemical reactions between boron oxide and the other phases of the system to find the technological control parameters relevant for the system. However, as indicated by Oates and Wenzl [133], this approach is less successful because of the great number of components/species and interrelated reactions in the system. Instead, the concept of minimization of the Gibbs free energy of the global or of a partial system is more appropriate. This analysis can be performed by the complex software ChemSage [134,135] and its successor FactSage. Other program packages with similar capabilities are available on the market, such as Thermo-Calc [136] or HSC Chemistry [137].

The basics of the ChemSage package and the general procedures are described in Ref. [138]. An example of chemical modeling applied to different questions in the GaAs-encapsulant system is given in Ref. [139].

9.3.3 Crucibles

Crucibles for synthesis and growth of compound semiconductors have to fulfill several physical/chemical and technological requirements: high-temperature thermal and mechanical stability allowing repeatable use without deterioration of the product's quality or safety risks, no wetting, no interaction between crucible wall and melt/crystal leading potentially to contamination or structural defects near the surface or in the bulk of crystals, reproducible and homogeneous properties, reliable production of crucibles to ensure similar synthesis and growth procedures from charge to charge, and, finally, low production costs. Pyrolytic boron nitride (pBN) was proven to be the best for the synthesis and growth of Ga- and In-arsenides and phosphides, even for industrial use. GaSb and InSb and the selenides/tellurides, respectively, can be grown in pretreated fused silica crucible.

Freestanding crucibles of pBN are reproducibly produced by the chemical vapor deposition (CVD) process on a graphite mandrel at temperatures between 1450 and 2300 °C in a hot wall furnace [140,141] using boron trichloride (BCl_3) and ammonia (NH_3). pBN is a fine-grained anisotropic high-temperature ceramic with a layered hexagonal structure similar to graphite but with a different step sequence in the c-direction (AAA in pBN, ABAB in graphite). In the CVD process, the c-axis is parallel to the growth direction, resulting in a pronounced texture of the material. Properties and the morphology/grain structure of pBN can be influenced by the deposition conditions [141].

The VB/VGF of III-V compounds is critically sensitive to crucible preparation [142]. It determines not only the lifetime of a crucible as a cost factor but also the structural quality of the crystal. Before first use of the crucible and after each run, pBN crucibles are usually heat treated at 900–1200 °C for several hours in air, an oxygen/nitrogen mixture, or pure oxygen, to form a boron oxide layer mainly on the inner wall, which is in contact with the III-V melt/crystal. The thickness of the boron oxide coating is approximately 10–15 μm. Coating the crucible with boron oxide, together with additional B_2O_3 placed

between seed and ingot and on top of the ingot, leads to full encapsulation of the material after melting. According to Duffar et al. [143], liquid boron oxide spreads over pBN with a wetting angle of $59^\circ \pm 2^\circ$. Wetting of pBN by B_2O_3 appears to increase with its water content [144].

Special attention has been directed to the process of oxidation in order to ensure a homogeneous layer of constant thickness and constant properties [144,145] on selected parts of the crucible wall, including the seed well. Instead of oxidizing pBN itself, a boron-containing compound can be coated first and then oxidized [146].

After cooling a charged crucible to room temperature, the boron oxide layer solidifies; hence, the crucible and ingot are fixed to each other. The pBN crucible, therefore, is delaminated by removing the ingot, which reduces its lifetime. Surface sites where the ingot adhered to the crucible tend to produce chips and/or defects in the ingot. In addition, due to its much higher coefficient of expansion compared to III-V compounds, shrinkage of the crucible places stress on the crystal, possibly resulting in slip lines. Coating the crucible instead with boron oxide by pBN powder in dry state or by slurry and subsequent heat treatment has been proposed to prevent these effects [147,148]. Coating of the seed has an additional advantage: a gap between crucible and seed can be avoided, which otherwise would be infiltrated by melt and could cause spurious nucleation at crucible wall and polycrystallization or twin generation [148].

Qualitatively, it is commonly accepted that the appearance of near-surface defects in liquid encapsulated VB/VGF growth of semiconductors is related to the local wetting behavior in the region of the three-phase junction line (TPL) and its local and temporal change.

Under special conditions, a detachment of the growing crystal from the crucible can be achieved. Further details will be considered by T. Duffar in this volume.

9.3.4 Facets and Local Interface Shape

The macroscopic shape and position of the solid/liquid interface in the course of crystal growth is determined by the time-dependent heat transport in the entire system, slightly modified by impulse and mass transport. It has been already discussed in Section 9.2.

On the other hand, the phase transition occurs on an atomic scale and is governed by the atomic structure of the interface and the related atomic mechanisms of growth. According to the two-level lattice model of K. A. Jackson [149], the transition from an atomically smooth to a rough solid/liquid interface can be evaluated by the Jackson factor $\alpha = \frac{\Delta S}{k}\xi_{hkl}$ wherein ΔS, k, and $\xi_{hkl} = \eta/Z$ are the melting entropy, the Boltzmann constant, and a factor, respectively, calculated from the number of bonds of first coordination of growth units in the plane $\{hkl\}$ divided by the number of bonds of growth units in the crystal. Corresponding data for some III-V compounds are given in Table 9.2 in comparison to silicon. The interface will be rough for $\alpha < 2$ and smooth for $\alpha > 2$. Later refinements of the Jackson model and Monte Carlo simulations of surface roughening, including a driving force $\Delta\mu$ for crystallization, have specified the critical factor to be

Table 9.2 Jackson Factor of Some III-V-Compounds

Material	L/kT_m	η/Z (100)	η/Z (111)	$\alpha\{100\}$	$\alpha\{111\}$
Si	3.6	$^1/_2$	$^3/_4$	1.8	2.7
GaAs	7.4	$^1/_2$	$^3/_4$	3.7	5.6
InP	5.6	$^1/_2$	$^3/_4$	2.8	4.2
GaP	8.5	$^1/_2$	$^3/_4$	4.3	6.4
InSb	7.1	$^1/_2$	$^3/_4$	3.5	5.3
CdTe	4.4	$^1/_2$	$^3/_4$	2.2	3.3

$\alpha_c \approx 3.2$ for $\Delta\mu = 0$ (thermodynamic equilibrium) and increasing α_c for increasing $\beta = \Delta\mu/kT$ (kinetic roughening) [150]. It follows from Table 9.2 that the most closely packed {111} planes can be expected as atomically smooth facets, with the lowest specific solid/liquid interface energy in melt growth of compound semiconductors.

In Figure 9.4, a Lang topogram of a {110}-oriented longitudinal slice is shown from the cone-shaped part of Si-doped <100>-grown GaAs crystal. It is used to illustrate the main characteristics of facets, which qualitatively also apply to other III-V compounds. This has been done because facets are certainly a prerequisite of twinning (Section 9.3.6.3).

A region of facetted growth near the surface of the cone can easily be recognized by some straight lines—*kinetic* striations according to [151]. The extension of facets is typically several millimeters, measured on longitudinal cuts containing the growth axis. Apart from the faceted region, slightly concavely curved *thermal* striations mark instantaneous positions of the atomically rough solid/liquid interface. These regions differ from each other by the growth mechanism. It should be mentioned that the observation of thermal striations in the Si-doped crystal points to a nonstationary convection in the melt, despite low Grashof-numbers.

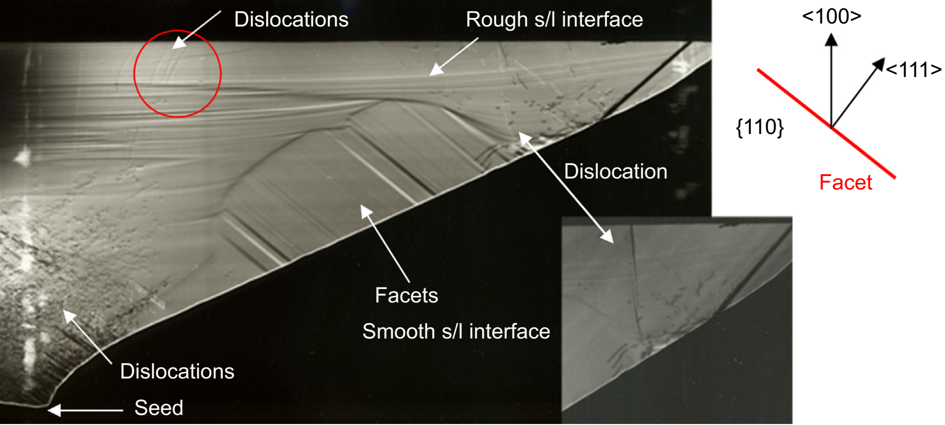

FIGURE 9.4 Lang topogram, with Insert: $\vec{g} = (\bar{2}0\bar{2})$. *(Courtesy of V. Alex/IKZ Berlin, 2002.)*

The growth rate for a rough interface is approximately given by $V \approx \beta^T \Delta T$, with β^T and ΔT being the kinetic coefficient and the supercooling driving growth, respectively [152]. With an estimation of $\beta^T \approx 20$ mm/sK for silicon [152] and a typical growth rate of V = 5 mm/min, a characteristic supercooling $\Delta T \approx 0.004$ K is obtained. With respect to the smaller growth rate of compound semiconductors, even lower supercooling has to be assumed. Therefore, the solid/liquid interface agrees with the melting point isotherm during growth and, thus, thermal striations can be regarded as demarcations of the instantaneous position of an interface.

On the other hand, the displacement of a faceted region perpendicular to the facet requires a repeated 2D nucleation followed by rapid spread of steps parallel to the facet. The velocity V_{step} is determined by a kinetic coefficient of step movement, the step orientation, and local undercooling [152]. This implies a supercooled region ∝ in front to the facet. The growth rate V depends on supercooling ΔT according to $lnV \propto -1/\Delta T$. The 2D nucleation occurs at a site with maximum supercooling, probably near the TPL. The spreading of steps is stopped as soon as $\Delta T = 0$ is reached. Latent heat is released during displacement, which is dissipated in the crystal or the undercooled melt in front of the facet and is controlled by the overall T-field around the interface. Therefore, growth could occur intermittently, leading to kinetic striations (See below). Facet areas are almost dislocation free.

If dislocations cross the facet, nucleation is no longer necessary and $V \propto \Delta T^2$ is fulfilled for small supercooling, assuming movement of approximately straight steps with V_{step} distant from each other. With increasing supercooling or higher density of threading dislocations, the distance between steps decreases and the thermal fields of steps superpose, resulting in $V \propto \Delta T$. Again, a supercooled region exists in front of the interface, which should depend on type and number of threading dislocations. But at high enough density of crossing dislocations, facets will vanish. The maximum supercooling in areas with threading dislocations is surely smaller compared to dislocation-free areas, where the 2D nucleation mechanism works. Correspondingly, the length of facets grown by the 2D mechanism will be larger. In general, the length of facets is in inversely proportional to the T-gradient in the melt and proportional to the supercooling. It fluctuates with T-fluctuations in the melt.

As also visible in Figure 9.4, faceted growth can be abruptly terminated. Dislocations seen in the insert, which was taken by the $(\bar{2}0\bar{2})$ reflex and/or another defects initiated at the TPL, are obviously responsible for this sudden breakdown. The subsequent growth occurs very rapidly with a rough interface, in which the deliberated latent heat obviously led a local remelting. This is indicated by some shaping of the faceted region and the black line representing a thermal striation. After that, faceted growth can start again. As observed by Chen et al. [152,153], twins were generated at the position where the size of facets varied drastically.

The time-dependent movement of a melt/crystal interfaces consisting of rough and faceted parts in large-scale melt–growth systems has been modeled by Weinstein and Brandon [154,155], applying the above mentioned relationships for rough and smooth

interfaces. The change of the growth mechanism in the faceted region from 2D nucleation to dislocation interface kinetics leads to sudden decreases of the size of a facet.

The critical supercooling for 2D growth can be experimentally determined by measuring the length of facets and the T-gradients in the melt and the crystal. It amounts up to about 3 K for GaAs. The supercooling in front of a facet with a threading dislocation is significantly smaller. The incorporation of dopants/impurities is different in atomically rough and smooth sections of solid–liquid interfaces at growth rates typical for VB/VGF of III-V compounds. It can be concluded that both, growth mechanism dependent fluctuations of the lengths of facets and terminations of faceted growth are controlled by the local conditions at the TPL.

The c-axis of III-V and II-VI compounds is polar; therefore, $\{111\}_A$ and $\{111\}_B$ facets have to be distinguished. By measuring the length of facets on two longitudinal {110} sections parallel to the axis but perpendicular to each other, it has been found for GaAs that on the average $\{111\}_B$ facets are longer by about 20% than $\{111\}_A$ facets [156]. In addition, Amon et al. [156] observed that the length of facets decreases with increasing distance from the seed region. However, facets also occur in the seed well soon after the seeding procedure. They are important for the structural properties of the grown crystals [157].

Furthermore, larger aperture angles of the conical part of the crucible cause smaller facet lengths. Doping will influence faceted growth as well. Therefore, heavy Si-doping enhances the asymmetry of facet length.

9.3.5 Doping and Segregation

Macrosegregation at crystal growth from the melt is detailed by A. Ostrogorsky and M. Glicksmann in this volume.

It has been already emphasized in Section 9.3.2 that liquid encapsulated VB/VGF growth of III-arsenides and III-phosphides occurs in a thermodynamic system, in which dependence on the constituents being involved has to be regarded as a closed, partially open, or open system. It follows that not only the III/V-ratio is influenced during growth, but the distribution of dopants also can no longer be described by distribution functions, assuming conservation of constituents in the melt. Three examples (tellurium, silicon, and carbon doping of GaAs) will be discussed in the following for illustration.

The simplest case is the closed system. The dopant is homogenously dissolved in the melt; no thermochemical reactions have to be considered. The dopant distribution in the crystal is described by the Scheil equation $c_{solid} = k\, c_0\, (1-g)^{k-1}$, with the effective distribution coefficient k, the initial dopant concentration c_0 , and the solidified fraction g. Examples for this behavior are Te-doping of GaAs ($k = 0.04$) and Zn-distribution in $Cd_{1-x}Zn_xTe$ ($k = 1.25$).

Silicon doping of GaAs in liquid encapsulated VB/VGF growth is an example for doping in a partially open system. Due to the exchange reaction $2B_2O_3 + 3Si \rightleftharpoons 3SiO_2 + 4B$, silicon added to the melt will be partly incorporated into boron oxide,

whereas boron pollutes the melt [158]. This reaction takes place during the entire growth process; that is, the boron content increases continuously from seed to tail of the crystals. Boron is mainly substituted isoelectrically for the gallium site, but at higher concentrations it also occupies arsenic sites, which gives a double acceptor. In addition, a B_{As}–Si_{Ga} complex is formed [158], which is also an acceptor. As a consequence, the carrier concentration in the grown crystal—that is, the doping efficiency $\eta = \frac{n}{N_{Si}}$, with n and N_{Si} being the carrier concentration and Si concentration, respectively—will be reduced twice, by the reduced concentration of Si donors and by compensating boron-related acceptors. The compensating defects limit the achievable charge carrier concentration of Si-doped GaAs to approximately $3 \times 10^{18}/cm^3$ at a doping level of $8 \times 10^{18}/cm^3$. The boron content of the crystals usually increases with the Si concentration and is slightly higher than the latter [159–161]. It is also higher compared to LEC-grown Si-doped GaAs crystals due to the higher temperature of the boron oxide in LEVB/VGF growth. In addition, the incorporation of boron in GaAs leads to contraction of the lattice, which is unwanted for the subsequent epitaxy.

As a first approach, SiO_2 is usually added to boron oxide to enhance the Si chemical activity and to reduce the exchange reaction. Another possibility is the application of a B_2O_3/SiO_2-mixture to prepare the inner wall of pBN crucibles to enhance their lifetime, but also for doping with silicon [148].

Still another solution, called "retarded doping," is disclosed in Ref. [162]. The main feature of the proposed process consists of adding the predetermined amount of doping material to adjust the desired electrical conductivity of the semiconductor single crystal not completely prior to solidification but only partly, with the addition of the remaining part after partial solidification has occurred in the tapered portion below the transition to the cylindrical portion of the crucible. For this, the dopant is added in a suitable form, which enables it to pass the coverage completely in the added amount. The solidification process can be interrupted for a certain time period to permit dissolution and homogenization of the melt. The required homogenization time after the second addition of the dopant depends on the time since the start of solidification. The first added part of the dopant should be below the critical concentration to avoid defect formation and twinning in the seeding period (about $4 \times 10^{18}/cm^3$ for Si in GaAs). In the second step, the crystallization in the cylindrical portion of the crucible, a concentration higher than the critical concentration is added. As a result, a silicon concentration that is 2.5 times higher and a boron concentration that is lower by a factor of 2–3 in the cylindrical part of the crystal are observed. Due to the reduced boron concentration in the crystal, the carrier mobility is higher compared to conventionally doped crystals. A side effect of the proposed procedure is an enhanced yield because defect formation in the conical part can be reduced due to the reduced dopant concentration.

Carbon doping of GaAs [163] is an example of crystal growth in an open system. The response to a step-like increase of carbon potential in the gas phase on the axial carbon distribution in a GaAs crystal initially grown at constant carbon potential is shown in Figure 9.5. The carbon potential in the gas phase was stepwise increased at $g = 0.5$.

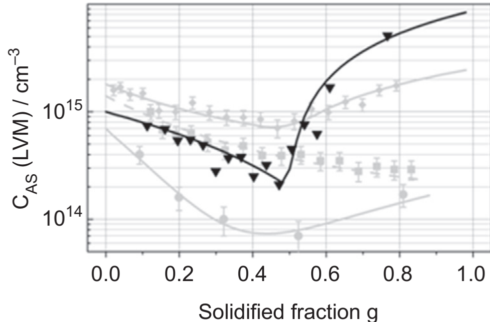

FIGURE 9.5 Comparison of measured (dots) and calculated (solid lines) axial carbon distributions in vertical gradient freezing (VGF) GaAs crystals grown under conditions of an open system. *(Localized Vibrational Mode spectroscopy)*

Due to an equilibrium distribution of *C* in GaAs ($k_C = 2.0$ [164]), the *C* concentration continuously decreased up to g = 0.5. As soon as the C potential in the gas phase is raised, a transient region occurs, where the carbon content increases without reaching a new equilibrium state. This indicates the possibility to establish a control procedure for compensation of axial carbon macrosegregation. Essential relationships can be clarified by thermochemical modeling of equilibrium; however, to understand transient behavior, a transport model is required, as outlined in Figure 9.6 [165]. According to this model, carbon is supplied to or extracted from the melt by decomposition or formation of CO at

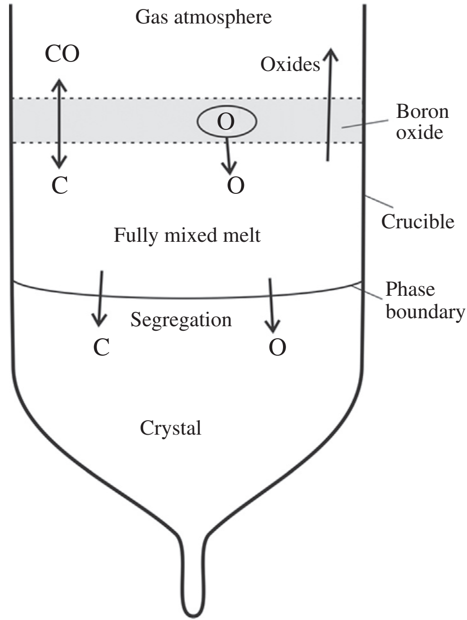

FIGURE 9.6 Advanced transport and segregation model.

the boron oxide/GaAs melt interface, with the assumption of a preset CO partial pressure in the gas phase and diffusional transport in boron oxide. Carbon in the GaAs melt is incorporated into the growing crystal according to the equilibrium distribution coefficient, but it can react with dissolved oxygen in the melt. The dissolved oxygen content in the melt is determined by an incorporation of oxygen from the B_2O_3 melt and an extraction due to oxidation of As and Ga at the GaAs/B_2O_3 interface and evaporation of Ga_2O at the surface of the encapsulant.

Furthermore, system-related parameters, such as the area and thickness of the boron oxide layer and its transport properties [165], are included. The elementary processes included in the model are schematically illustrated in Figure 9.6.

Transport in the GaAs melt is assumed to be quick enough in order to neglect concentration differences in the melt. Assuming further a planar solid/liquid interface, the balance of carbon and oxygen in liquid GaAs can be expressed by expanding the well-known Scheil equation as follows:

$$\frac{dN_m^{\mathrm{C}}}{dt} = -\frac{dN_s^{\mathrm{C}}}{dt} + \frac{dN_{\mathrm{B_2O_3}}^{\mathrm{C}}}{dt} - \frac{dN_R^{\mathrm{C}}}{dt};$$

$$\frac{dN_m^{\mathrm{O}}}{dt} = -\frac{dN_s^{\mathrm{O}}}{dt} - \frac{dN_{\mathrm{B_2O_3}}^{\mathrm{O}}}{dt} - \frac{dN_R^{\mathrm{O}}}{dt} + \frac{dN_{res}^{\mathrm{O}}}{dt}.$$

In these equations, m is GaAs melt, s is GaAs, B_2O_3 is the boron oxide, and R is the ambient.

The first terms on the right-hand sides describe the incorporation of carbon and oxygen into the growing crystal (usual Scheil equation); the second terms show an effective transport of carbon (CO) and oxygen (Ga_2O)-containing species through boron oxide (index B_2O_3), including reaction kinetics at the phase boundaries; and the third terms (index R) show a decrease of carbon and oxygen in the GaAs melt due to a chemical reaction and transport of carbon oxide into boron oxide and surrounding gas phase. The last term in the balance equation of oxygen takes into consideration that boron oxide can serve as a reservoir for oxygen due to the heterogeneous reaction of nitrogen with boron oxide. Further details can be found in Ref. [165].

The system of differential equations given above has been numerically solved and applied to analyze the axial C-distributions in 150 mm∅ GaAs crystals under various CO partial pressures. Results are represented in Figure 9.5. Except for the initial concentrations of carbon and oxygen in the melt, which were fitted, the different experimentally obtained carbon distributions could be described by the developed C–O model using a single set of parameters quite well. Based on this, a control procedure has been developed using a predetermined function $p_{CO} = f(g)$ at a preset oxygen chemical potential to ensure nearly constant axial carbon concentration. The procedure works equally for VGF and LEC growth. Solely, the enhanced transport of carbon oxides in the boron oxide melt has to be regarded due to stronger (natural and forced) convection compared to VGF.

Due to the time-dependent natural (VGF) flow in the melt, microsegregation occurs during growth, resulting in thermal and kinetic striations [151] with a distance up to

several millimeters for Si-doped crystals. All in all, striations do not influence the application of semiconducting GaAs wafers.

9.3.6 Crystal Defects

9.3.6.1 Point Defects

Theoretically, a plurality of intrinsic point defects exists in compound semiconductors [166]. Besides vacancies and interstitials, there are also antisite defects and complexes consisting of impurities/dopants and intrinsic point defects. In thermodynamic equilibrium at the growth temperature, those point defects dominate, the Gibbs free energy of which is minimal under the constraint of electrical neutrality and composition (chemical potential). If the point defect concentration is low ($<10^{-4}$), then it depends on the formation enthalpy only, according to $\propto e^{-h_f/k_bT}$. Under these conditions, the contribution of configurational and vibrational entropy can be neglected [167]. The enthalpy of formation of point defects is essentially determined by the chemical potential of the carriers (Fermi level) [168]. Written for GaAs, the enthalpy of formation of a defect is given by:

$$h^f = e_0^f + q\mu_e - \frac{1}{2}(n_{\mathrm{Ga}} - n_{\mathrm{As}})\Delta\mu_{\mathrm{GaAs}} - \sum n_{dot}\Delta\mu_{dot}$$

where e_0^f is the formation energy independent of chemical potentials; q is the elementary charge; μ_e is the chemical potential of electron (Fermi energy); ($n_{\mathrm{Ga}}- n_{\mathrm{As}}$) is the deviation from stoichiometric composition; $\Delta\mu_{\mathrm{GaAs}}$ is the chemical potential of GaAs; n_{dot} is the number of dopant atoms; and $\Delta\mu_{dot}$ is the chemical potential of the dopant.

It is obvious that electrically charged defects influence the position of the Fermi level and, therefore, the formation enthalpy and the concentration of all other electrically charged defects. This behavior is called the Fermi-level effect. Tan, Gösele, and Yu have developed a thermodynamic model of the Fermi-level effect in compound semiconductors, in particular for GaAs [169,170]. They concluded that at thermodynamic equilibrium, the most dopants will be compensated by intrinsic point defects or point defect complexes. Kretzer [160] described the doping efficiency at room temperature as a nonequilibrium state. The formation of compensating defects is suppressed by kinetic effects below a certain freezing temperature. For example, in n-type GaAs, the freezing takes place between 650 and 750 °C.

9.3.6.2 Dislocations

In addition to point defects and the related electrical and optical properties (doping, carrier concentration, mobility, local and global homogeneity) of compound semiconductors, their structural perfection—that is, the density and distribution of one-, two- and three-dimensional lattice defects—are equally important properties, influencing the performance and reliability of electronic devices. For a more detailed coverage of the subject, the reader may consult the reviews by Hurle [21], Rudolph [13,166], Klapper [171], Völkl [172], and H. Klapper and P. Rudolph in this volume.

The density and distribution of dislocations and the related residual stress fields in melt-grown crystals are caused by thermoplastic relaxation of thermally and, to a much lower extent, constitutionally induced stress during crystal growth [173]. Thermoplastic relaxation is controlled by (material-dependent) dislocation dynamics—conservative glide and nonconservative (thermal and/or stress-induced diffusional climb) motion of dislocations, multiplication of dislocations by interaction, and their rearrangement. Dislocations are introduced from the dislocated seed crystal, initiated at outer surfaces or internal phase boundaries, and generated at different kinds of multiplication mechanisms. Homogeneous nucleation of dislocations is insignificant. The thermal stress field for this part is unambiguously related to the time-dependent temperature field, including its local and temporal fluctuations during growth and cooling. An empirical optimization of temperature fields in growth equipment with respect to lowering stress and controlling dislocations is very time-consuming. Therefore, numerical simulation techniques have been developed to predict the dislocation density and distribution, to study the influence of growth parameters and doping/impurities, and to tailor the T field. Numerical modeling will be treated by Miyazaki in this volume.

The dislocation density (ρ) is commonly equated with the etch pit density (epd) determined on a plane cut of the crystal after a dislocation sensitive etching. Usually, 100% area mappings are automatically enumerated and evaluated statistically. An example of an epd mapping of a 150-mm diameter semi-insulating GaAs crystal is represented in Figure 9.7. The inset shows the typical cellular arrangement of the dislocations. Typical data of dislocation densities for <100>-oriented III-V compounds are presented in Table 9.3. The dislocation density increases with increasing diameter because of the larger nonlinearity of temperature fields. A slight W-shaped pattern is observed, with a minimum typically around R/2. The distribution in the <100>-direction is somewhat different from <110>, with higher densities at the periphery around <100>.

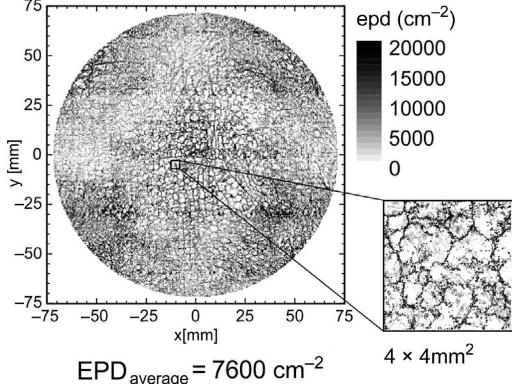

FIGURE 9.7 The epd-mapping of a 150-mm GaAs wafer (standard KOH etching).

Table 9.3 Average epd of Liquid Encapsulation Vertical Gradient Freezing (LEVGF) Grown III-V-Compound Semiconductor crystals (FCM)

Diameter (mm)	Undoped GaAs (cm^{-2})	Si-Doped GaAs (cm^{-2})	Fe-Doped InP (cm^{-2})	S-Doped GaP (cm^{-2})
100	$<5 \times 10^3$	<100	$<3 \times 10^3$	$<3 \times 10^3$
150	$<10 \times 10^3$	<300		
200	$(8–15) \times 10^3$			

The dislocation density of $Cd_{1-y}Zn_yTe$ substrates measured on $\{111\}_A$ or $\{111\}_B$ planes has been found to vary in the range of $2 \times 10^4/cm^2$ –$1 \times 10^5/cm^2$ [174]. A lattice hardening effect of Zn is suspected to lead to a lower dislocation density in comparison with pure CdTe [51].

Independent of the growth method and the diameter of the crystals, the majority of dislocations in undoped, C-, Te-, and B-free Si-doped GaAs form an irregular cellular pattern consisting of tangled walls with high dislocation density and a nearly dislocation-free interior. Dislocation cells occur also in GaP, CdTe, $Cd_{1-x}Zn_xTe$, PbTe, but obviously not in InP.

The disorientation angles between cells caused by the dislocation walls are very small (around 10 arcsec). The patterns turn out to be very stable to a postgrowth annealing, indicating that they were formed immediately behind the growth front at high temperatures. The mean cell diameter is inversely proportional to the average epd [13] and reaches >2 mm for epd $<5 \times 10^3/cm^2$. With decreasing dislocation density, the cell walls disintegrate into fragments. From laser scattering studies [175,176], it could be concluded that cells have a globular shape, ruling out constitutional supercooling as a reason for dislocation cell structures.

No cells were found in crystals grown from a nearly stoichiometric melt [177] or in Si/B- or In-doped GaAs [177]. The latter is due to a dopant-dependent lattice hardening, resulting in very low density of dislocations, which moreover are distributed inhomogeneously. A detailed analysis of the corresponding pattern for Si-doped GaAs is published in Ref. [178].

A Burgers vector analysis performed by Schlossmacher and Urban [179] has demonstrated that 70–80% of dislocations forming the cell walls are 30° and 60° dislocations in the glide set and 7–11% are screw dislocations. Therefore, glide processes play an important role in the formation of cells. On the other hand, the disappearance of cells in nearly stoichiometric GaAs has been interpreted by an influence of point defects (i.e., nonconservative climb and cross-glide processes on cell formation) [13]. The concentration of structural point defects realizing the off-stoichiometry is reduced to thermally activated point defects in stoichiometric GaAs only.

The origins of cell pattering in III-V compound semiconductors with emphasis of undoped GaAs have been thoroughly investigated by Rudolph [13,166,177,180]. It has

been concluded that the cell structure is due to simultaneous deformation, recovery, and polygonization (sometimes called dynamic polygonization) in a zone near behind the solid/liquid interface.

In addition to statistically distributed dislocations and dislocation organized in a cell structure, localized dislocation bunches (clusters, tangles), lineages, and slip lines are other peculiar structural defects found occasionally on wafers of melt-grown III-V and II-VI compounds.

9.3.6.3 Twins

Twinning on {111} facets during liquid encapsulated VB/VGF growth of III-V and II-VI compound semiconductors is a recurrent problem that reduces the yield of single crystalline material in industrial production. The topic has been reviewed by Bliss [39] with regard to magnetic liquid encapsulated Kyropoulos growth of InP, but the knowledge presented there is also of relevance for VB/VGF growth of III-V compound semiconductors.

Twin formation in III-V compounds takes place during faceted growth only. The formation of twins has been empirically related to several growth parameters, such as temperature gradient, temperature fluctuations, the shape of the solid/liquid interface, deviation from stoichiometry, purity of the raw materials, doping, irregularities/fluctuations of the facet evolution, and the cone angle of the crystal ([156,181,182] and references therein). Stress-induced mechanical twinning in crystal growth seems to be without relevance. By optimization of the supposed (but among the community of crystal growers, often differently weighted) influencing factors, the probability of twinning can be reduced, although it cannot be converted to zero.

Twins in III-V and II-VI materials were identified to be rotation twins [183,184]; inversion twins are energetically unfavorable. Two kinds of twins are distinguished: bulk (or standard) twins, which proceed through the crystal, and patch twins, which grow out and are therefore benign with regard to wafer yield. Both types are generated on <110> ride lines. In addition, bulk twin lamellas of diverse thickness are observed occurring by two successive rotations about the normal of the facet. There is a clear preference of twinning on $\{111\}_B$-planes [39,156], in contrast to an earlier study [183], which did not find differences for the generation of twins on $\{111\}_A$ or $\{111\}_B$. Twinning preferentially occurs in the shoulder region of crystals, but it is not at all limited to it (Figure 9.8). As twinning changes the stacking sequence in the <111>-direction, the incidence of twinning increases with decreasing stacking fault energy. Therefore, it is more pronounced in the growth of In- than of Ga-containing compounds and even more in II-VI compound semiconductors (see Table 9.1). There is a pronounced influence of doping elements on the incidence of twins. So, for example, Si in GaAs and S in InP enhance the probability of twinning. According to Klapper [171], the nucleation and generation of twins can also be initiated by inclusions.

The understanding of twin formation has been significantly advanced from a pioneering work by Hurle [181,184]. He proposed a mechanism considering twinning as a

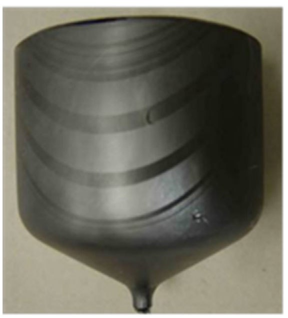

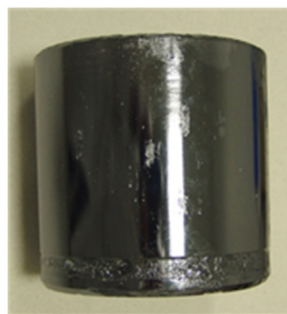

FIGURE 9.8 Heavily twinned 4-inch liquid encapsulation vertical gradient freezing (LEVGF) IP crystal and twin-free crystals grown in a standard and a flat bottom crucible, respectively.

thermodynamic process and analyzed the conditions under which this process occurs. It is applicable for low dislocation densities only, as dislocations reduce or even suppress facet formation at the solid/liquid interface (see Section 9.3.4.). The proposed mechanism is based on the theoretical results of Voronkov [185], who investigated the displacement of a facet parallel to its normal by lateral step motion near the solid/liquid/ambient three-phase boundary (TPB).

In short, following D.T.J. Hurle [181], a step will only be absorbed (and, correspondingly, emitted) by the TPB if the energy associated with this is lower than the energy of the step distant from the TPB. This energy change is caused by the change of the geometry upon absorption of the step. However, this means that a facet will be anchored at TPB only under certain conditions. Identifying the angle between the facet and the extension of the crystal surface by ν (Figure 9.9), it is $\nu_{\min} < \nu < \nu_{\max}$ with material dependent critical values. The angle $\nu_{\min}$ is given by $\nu_{\min} = \Phi^\circ - \Theta_L^\Phi$, with the wetting angle Φ° of the facet and the growth angle Θ_L^Φ. Θ_L^Φ is to be replaced by $\Theta_L^\Phi(111)$ when an external facet extends to the TPB. The calculation of the upper limit $\nu_{\max}$

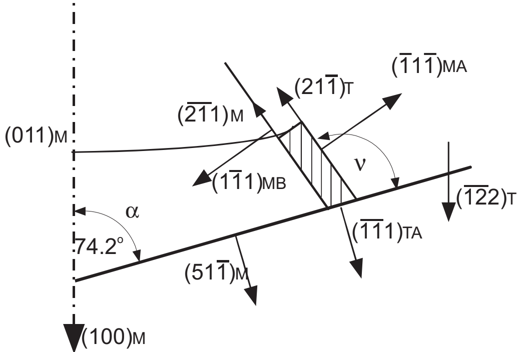

FIGURE 9.9 Schematic representation of the orientation relationship between matrix (M) and twin (T) at the three-phase boundary (TPB). *(Adapted from [184].)*

requires data for the interface energies at the TPB in contact to the liquid boron oxide encapsulant, which are only partly available (i.e., estimation is necessary). For example, Hurle [181] obtained for GaAs and InP $\upsilon_{min} = 30$ and 31° and $\upsilon_{max} = 104$ and 112°, respectively, with the latter value corrected in Ref. [184].

Inside $\upsilon_{min} < \upsilon < \upsilon_{max}$, the formation of a nucleus attached to the TPB is energetically more favorably than of a circular nucleus distant from it. The formation free energy of a truncated nucleus in twin orientation would be enhanced by the amount of the twin energy (stacking fault energy) compared to a correctly oriented nucleus. But when a {111} riser is generated at the TPB by the twin operation, this energy could be reduced due to the fact that the {111} plane has the lowest surface free energy among all other planes, with an appropriate size of the nucleus. This would require a certain critical supercooling in front of the TPB. Under these conditions, a nucleus in twin orientation is thermodynamically stable [181]. The critical supercooling above which a twinned nucleus could exists was estimated for GaAs and InP to be $\Delta T = 47$ K and 15 K, respectively (Table 9.1 in [181]). Compared to the undercooling for the growth of a facetted region estimated in Section 9.3.4 on the basis of a mean length of the facets and axial T-gradient ($\Delta T \approx 3$ K for GaAs), the estimated critical supercooling is very high and twinning should not be expected. But, according to Ref. [184], this could be caused by an overestimation of the twin energy at the melting point, which was taken to be half of the stacking fault energy measured at temperature $0.65T_m$ [186], but it is probably lower.

Now, the critical cone angle of the crystal at a given seed orientation can be defined by the condition that the external surface of the growing crystal is so oriented that its extension leads to a {111} segment by the twin operation. This is outlined in Figure 9.9. The {511} surface segment parallel to the surface of the crystal is converted to a {111} plane by 180° rotation around the surface normal (normal vector) of a {111} facet. The rotary matrix D corresponding to the orientations in Figure 9.9 is also given:

$$D([\bar{1}1\bar{1}], 180^\circ) = \frac{1}{3}\begin{pmatrix} -1 & -2 & 2 \\ -2 & -1 & -2 \\ 2 & -2 & -1 \end{pmatrix}$$

The cone angles α for which the {111} riser of the twinned nucleus forms an extension of the crystal surface amounts to 74.2° for <100>, 51.1° for <111>, and 15.8° for <110> crystal orientation, respectively [181,184].

Chung et al. [184] performed X-ray measurements of the orientation on the cone surface along a <110> ride line, both immediately before and on the twinned region (visible by different reflectance) and also on a {110}-oriented longitudinal cut of a LEC-grown InP crystal. Besides proving that the twin under study was clearly nucleated in a region where an edge facet intersected the external surface, it could be also proven that a {511} orientation of the segment before the twinned region as well as a {111} orientation of the twin is in agreement with the predictions of the theory. In addition, twin lamella have been found on the same crystal that exhibited $\{110\}_T$ facets on the external shoulder surface and a $\{114\}_M$ orientation of the segments immediately before

the twin (relative to the growth direction). This orientation relationship is also consistent with a 180° rotation twin. The corresponding critical growth angle is $\alpha = 70.5°$. At a cone angle of 35.3°, parts of the crystal surface correspond to low index outer {111} planes and twin formation should be prevented, or at most lead to less harmful patch twins [181].

Based on his model, Hurle has proposed the following conditions as a guideline to avoid twinning: damp temperature fluctuations, avoidance of growth angles at and around 70.5° and 74.2° (for <100>-growth; e.g., by application of crucibles with flat bottom and seeds with the diameter of the crystals to be grown), growth of crystals with an excess of group-V-constituent, avoidance of solutes increasing the surface tension of the solvent melt, suppression or influence of formation of edge facets (e.g., by increasing of the dislocation density; reduction of necessary supercooling).

To prove the prediction of Hurle's model that above the roughly estimated value $\upsilon_{max} \approx 104°$ a {111} edge facet would detach from the TPB and the proposed mechanism of twin formation would fail, Amon et al. [156] have grown GaAs crystals by the LEVGF in a crucible (among others) with a cone angel $\alpha = 72°$. The angle υ is related to α by $\upsilon = \alpha + 35.3°$ (i.e., $\upsilon > \upsilon_{max}$ was fulfilled). Both (110) and $(1\bar{1}0)$ longitudinal cuts were investigated, which could reveal $\{111\}_{As}$ and $\{111\}_{Ga}$ edge facets. Almost no $\{111\}_{Ga}$ facets were found. Conversely, on the (110) oriented cut, $\{111\}_{As}$ facets existed, but they detached from the TPB in accordance with the model and were replaced by $\{111\}_{Ga}$ facets at the rim of the crystal. Therefore, it was concluded that twinning would still be possible. Twins formed in this connection are patch twins growing finally out. It has been pointed out that the length of the edge facets declines with increasing cone angle, which should allow for the control of the length of facets.

Growth trials under production conditions with optimized T-fields have shown that the probability of twinning in LEVGF growth of undoped and S-doped InP could be significantly reduced by the transition from conical to flat bottom crucibles [187] (see also Fig. 9.8). In contrast no significantly lower incidence of twin formation has been observed in VB growth of $Cd_{1-x}Zn_xTe$.

The incidence of bulk twins or twin lamellas in II-VI material is used for the manufacturing of {111} oriented substrates. It also corresponds to the experience of crystal growers that even care and attention to the conditions formulated by Hurle [181] cannot reliably guarantee twin-free growth of group III-V compounds. Additional influencing factors (possibly of stochastic nature) not considered in the thermodynamic model are estimated (see Ref. [188] and the comments of Hurle and Dudley [189]).

9.3.6.4 Precipitates and Inclusions

Some of the binary compounds (e.g., GaAs, GaP, $Cd_{1-x}Zn_xTe$) exhibit a homogeneity range with retrograde solubility. No reliable information is available for InP. Inside the homogeneity range, the deviation from stoichiometric composition is fixed as established at the solid–liquid interface. Native point defects are realized by deviations from stoichiometry [190].

As soon as the retrograde solubility line is reached during cooling, nucleation and growth of precipitates takes place, connected with a change of the III/V-ratio and corresponding changes of the native defect inventory. Size, density, distribution, and precipitated volume fraction of precipitates follow the relationships of nonstationary nucleation and Ostwald ripening. That is, they are related to the nucleation sites available (homogeneous and heterogeneous nucleation), the supersaturation (supercooling), the temperature, and resting time below the solubility limit, which determine the average diffusion length of defects and a (defect and locally dependent) effective temperature, below which the defect state is frozen-in. The interplay of precipitation and deviation from stoichiometry is the basis for a certain control of concentration and distribution of native defects by heat treatment of the boules under mass-conserving conditions (defect engineering). Therefore, boule annealing first applied by Rumsby et al. [191] to improve the uniformity and to reduce residual stress of LEC-grown GaAs single crystals in 1982 is nowadays a common technological step in the production line of wafers. Depending on the objective, different time-temperature procedures have been published. Further reading can be found in Ref. [192].

Precipitates heterogeneously nucleated at dislocations (decoration precipitates [DP]) and homogeneously distant from dislocations (matrix precipitates [MP]) are observed in GaAs. The density of DPs in undoped GaAs is roughly in the range of 10^8–$10^{10}/cm^3$, with their sizes ranging from 10 nm to about 200 nm. MPs are smaller than DPs; their density is about one order of magnitude smaller compared to DPs. They are observed when the average diffusion length of native defects is smaller than the average distance between heterogeneous nucleation sites. DPs are also observed in VGF-grown undoped and S-doped GaP and in Fe-doped InP.

Precipitates in $Cd_{1-x}Zn_xTe$ crystals grown with a small excess of Cd are homogeneously distributed. Their size has been estimated by to be about 200 nm. The annealing under Cd-atmosphere leads to a displacement of the size distribution to smaller particles. $Cd_{1-x}Zn_xTe$ serves as substrate material for HgCdTe-based infrared detector arrays. As illumination of the detectors takes place from the backside, the influence of the precipitates on transparency has been shown to be negligible.

In addition to a boule annealing, single wafers can be heat treated under reduced V chemical potential defined by an appropriate pressure. This wafer annealing allows the extraction of arsenic, for example, from a near surface region and, therefore, reduction of the size distribution of As precipitates. As soon as the As precipitates are totally dissolved, the native defect inventory will be changed, allowing control of the electrical properties of GaAs. Wafer annealing of semi-insulating GaAs is thoroughly discussed in the literature; see, for example, [192,193].

Different from precipitates, inclusions of constituents, as well as of foreign particles, are formed by a capture mechanism at the solid–liquid interface [152]. One of several preconditions for trapping is a segregation of constituents of the compound to be grown. Tellurium as well as cadmium inclusions have been observed in VB-grown $Cd_{1-x}Zn_xTe$ crystals [14], which influence energy resolution and the efficiency of radiation detectors

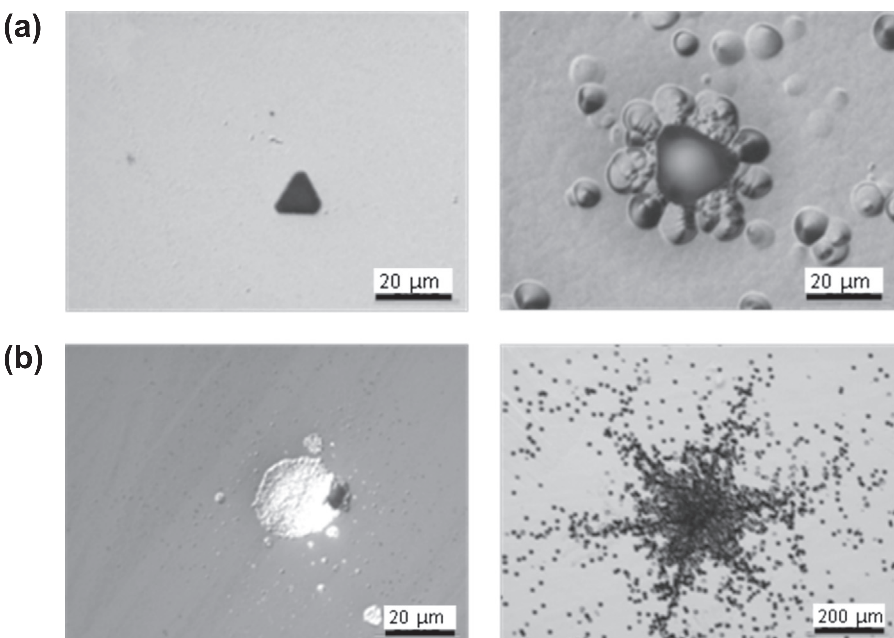

FIGURE 9.10 (a): Tellurium inclusion on a CdZnTe substrate surface (left) and after dislocation etching (right). (b): Cadmium inclusions on a CdZnTe substrate surface (left) and after dislocation etching (right).

based on substrates of this compound [194]. Examples are represented in Figure 9.10(a) and (b).

The size and density of Te inclusions are in the range of 3–20 μm and 10^3–10^4 cm^{-3}, respectively. A slightly increased dislocation density has been found around Te inclusions [195]. Inclusions with a size <15 μm are typically overgrown in the liquid phase epitaxy process to produce the (Hg,Cd)Te-detector layer. Larger inclusions induce holes in the epilayer and have to be avoided.

Cadmium inclusions are typically smaller than 5 μm, but they induce a star-shaped strain area of 50 μm, up to 200 μm in size. The space between the "stars" is free of infrared visible disturbances. If the size and density of the stars is low, normally the substrate surface is free of cadmium inclusions. In the case of a high density of stars with dimensions of 200 μm, cadmium inclusions occur on the substrate surface up to a size of 15 μm. Due to the high density of dislocations around the inclusion, they lead to macrodefects in the epitaxial layer.

An annealing of the grown crystals or the sliced substrates under defined atmospheres of cadmium or tellurium can influence the properties of the grown material [174,196]. Therefore, the size of Te inclusions is reduced in substrates annealed in the temperature range of 660 and 800 °C for 12–50 h under a Cd atmosphere [196] accompanied by an improvement of the IR-transmittance at 10 μm from 10% to over 60%. However, the formation of CdTe at the site of the former Te inclusion increased the local

number of dislocations dramatically. For crystals containing Cd inclusions, a Te annealing at 700 °C for 24 h eliminates most of the Cd inclusions, but a final annealing under Cd overpressure is necessary to obtain the same transmittance as in the grown crystals.

9.4 Conclusions

At present, the Bridgman methods dominate the crystal growth of binary III-V and II-VI compound semiconductors with melting temperatures below 2000 K and decomposition pressures below some 10 bar. Scalability, maturity for mass production, and especially superior quality of crystals and wafers/substrates appropriate for device manufacturing has promoted the predominance opposite to the Czochralski method.

From a commercial point of view, the development in crystal growth of the corresponding arsenides, phosphides, antimonides, and tellurides in recent years was characterized by efforts to make the production more efficient, to meet on one side the requirements of the device manufacturers with regard to price and quality of substrates and on the other side the demanding yield and cost targets of the producers.

Significant cost reductions could be reached by increasing the charge size and yield of crystal growth and improving the reliability with which the customer-specific properties of the wafers could be obtained. Caused by constantly high prices of the required high-purity constituents, recycling has become an essential factor in cost reduction. This also applies to auxiliary materials such as crucibles.

A prerequisite, therefore, was the development and operation of unified, cost-effective, but versatile pullers and highly flexible growth technologies. This implied detailed knowledge about the influence of hardware tolerances and growth parameters on the global and local temperature field in the growth region. Computer simulation was (and is) extensively used to acquire the respective knowledge. Analogously, progress was made in understanding of the growth process, the thermochemical reactions taking place during growth, and the relationships between growth conditions and defect formation and properties of crystals.

In the future, the application of external forces to influence melt convection and the shape of the solid/liquid interface are expected to bring further benefits for the economy of crystal growth and quality of grown crystals.

References

[1] Gille P, Mühlberg M, Parthier L, Rudolph P. Cryst Res Technol 1984;19:881.

[2] Piccioni G, Formisano V, Bellussi G. Nuovo Cimento 1992;C15:1121.

[3] Xu J. Proc ICT; 2001.

[4] Inoue T, Kuriyama M, Komatsu H. J Cryst Growth 1991;112:531.

[5] Kondo S, Inoue T. J Lumin. 2010;130:191.

[6] Ioffe Physico-Technical Institute. 26 Polytekhnicheskaya, St. Petersburg 194021, Russian Federation. http://www.ioffe.ru/SVA/NSM/.

[7] Yu PY, Cardona M. Fundamentals of semiconductors: physics and material properties. Berlin: Springer; 2004.

[8] Oda O. Compound semiconductor bulk materials and characterization. New Jersey: World Scientific; 2007.

[9] Palmer Semiconductor Associates. Deran House, Gulworthy, Tavistock., Devon PL19–8JA, UK. http://www.semiconductors.co.uk.

[10] Regel AP, Glasov VM. Periodischeskij zakoni fizicheskije svoistva elektronnikh resplavov. Moskva: Izdatelstvo Nauka:21978.

[11] Vurgaftman I, Meyer JR, Ram-Mohan LR. J Appl Phys 2001;89:5815.

[12] Jordan AS. J Cryst Growth 1985;71:559.

[13] Rudolph P. Cryst Res Technol 2005;40:7.

[14] Rudolph P. Prog Cryst Growth Ch 1994;29:275.

[15] Phillips JC, Lucovsky G. Bonds and bands in semiconductors. New York: Momentum Press,LLC; 2010.

[16] Tsuchiya Y, Hiskabe M. J Non-Cryst Solids 2007;353:3000.

[17] Derby JJ, Zhang N, Yeckel A. J Cryst Growth 2013;379:28.

[18] Welker H. DE970420. 1951.

[19] Welker H. Z. Naturforschg 1952;7a:744.

[20] Welker H. Z. Naturforschg 2013;8a:248.

[21] Hurle DTJ, Rudolph P. J Cryst Growth 2004;264:550.

[22] Sumitomo Electric Industries Ltd–Compound Semiconductor. http://global-sei.com/sc/index.en.html.

[23] Freiberger Compound Materials GmbH. Am Junger Löwe Schacht 5, D-09599 Freiberg, Germany. http://www.fcm-germany.com.

[24] AXT Inc., China, Beijing Tongmei xtal technology, 4 Eastern second Street, industrial development zone, Zhangjiawan Ind. Development zone, Tongzhou District, Beijing, China 101113. http://www.axt.com/site/index.php?q=node/1.

[25] AIM INFRAROT-MODULE GmbH, D-74072 Heilbronn, Theresienstr. 2, Germany. http://www.aim-ir.com.

[26] Jacobs C, Schulz D, Klimm D, Ganschow St. Solid State Sci 2010;12:307.

[27] Fedorov PP, Osiko VV. Crystal growth of fluorides. In: Capper P, editor. Bulk crystal growth of electronic, optical & optoelectronic materials. Chichester: John Wiley & Sons Ltd; 2005. p. 339.

[28] Shen L, Wang B, Wu D, Jiao Z. J Cryst Growth 2013;383:79.

[29] Monberg EM. Bridgman and related growth techniques. In: Hurle DTJ, editor. Handbook of crystal growth. Amsterdam: North-Holland; 1994. p. 51.

[30] Gault WA, Monberg EM, Clemans JE. J Cryst Growth 1986;74:491.

[31] Monberg EM, Gault WA, Simchock F, Dominguez F. J Cryst Growth 1987;83:174.

[32] Tatsumi M, Fujita K. Melt growth of GaAs single crystals. In: Isshiki M, editor. Recent development of bulk crystal growth. Trivandrum-695008, India: Research Signpost; 1998. p. 47.

[33] Asahi T, Kainosho K, Kohiro K, Noda N, Sato K, Oda O. Growth of III-V and II-VI single crystals by the vertical gradient-freeze method. In: Scheel HJ, Fukuda T, editors. Crystal growth technology. Chichester: Wiley & Sons Ltd; 2004. p. 323.

[34] Kawase T, Tatsumi M, Nishida Y. Growth technology of III-V single crystals for production. In: Scheel HJ, Fukuda T, editors. Crystal growth technology. Chichester: Wiley & Sons Ltd; 2004. p. 349.

[35] Brozel MR, Grant IR. Growth of gallium arsenide. In: Capper P, editor. Bulk crystal growth of electronic, optical & optoelectronic materials. Chichester: John Wiley & Sons Ltd; 2005. p. 43.

[36] Grant IR. Indium phosphide crystal growth. In: Capper P, editor. Bulk crystal growth of electronic, optical & optoelectronic materials. Chichester: John Wiley & Sons Ltd; 2005. p. 121.

[37] Micklethwaite W. Bulk growth of InSb and related ternary Alloys. In: Capper P, editor. Bulk crystal growth of electronic, optical & optoelectronic materials. Chichester: John Wiley & Sons Ltd; 2005. p. 149.

[38] Eichler St, Börner F, Bünger T, Jurisch M, Köhler A, Kretzer U, et al. Recent progress in GaAs growth technologies at Freiberger. In: Scheel HJ, Capper P, editors. Crystal growth technology - from fundamentals and simulation to large-scale production. Weinheim: Wiley-VCH; 2008. p. 231.

[39] Bliss DF. Indium phosphide: crystal growth and defect control by applying steady magnetic fields. In: Dhanaraj G, Byrappa K, Prasad V, Dudley M, editors. Springer handbook of crystal growth. Heidelberg: Springer Verlag; 2010. p. 205.

[40] Dutta PS. Growth and characterization of antimony-based narrow-bandgap III–V semiconductor crystals for infrared detector applications. In: Dhanaraj G, Byrappa K, Prasad V, Dudley M, editors. Springer handbook of crystal growth. Heidelberg: Springer Verlag; 2010. p. 281.

[41] Triboulet R. CdTe and CdZnTe growth. In: Scheel HJ, Fukuda T, editors. Crystal growth technology. Chichester: Wiley & Sons Ltd; 2004. p. 373.

[42] Capper P. Bulk growth of cadmium mercury telluride (CMT). In: Capper P, editor. Bulk crystal growth of electronic, optical & optoelectronic materials. Chichester: John Wiley & Sons Ltd; 2005.

[43] Hirano R, Kurita H. Bulk growth of CdZnTe/CdTe crystals. In: Capper P, editor. Bulk crystal growth of electronic, optical & optoelectronic materials. Chichester: John Wiley & Sons Ltd; 2005. p. 241.

[44] Wilke KTh, Bohm J. Kristallzüchtung. Thun-Frankfurt/Main: Verlag Harri Deutsch; 1988.

[45] Jurisch M, Jacobs H, Flade T. Supplementing silicon–the compound semiconductors. In: Siffert P, Krimmel E, editors. Silicon. Heidelberg: Springer Verlag; 2004. p. 423.

[46] Monberg EM, Brown H, Bonner CE. J Cryst Growth 1989;94:109.

[47] Ramsperger HC, Melvin EH. J Opt Soc Am 1927;15:359.

[48] Sonnenberg K, Küssel E. III-Vs Rev 1997;10:30.

[49] Khattak CP, Schmid F. J Cryst Growth 2001;225:572.

[50] Frank Ch, Hein K, Hannig C, Gärtner G. Cryst Res Technol 1996;31:753.

[51] Bruder M, Schwarz HJ, Schmitt R, Maier H, Möller MO. J Cryst Growth 1990;101:266.

[52] Hashio K, Sawada S, Tatsumi M. US6,254,677B1, 3-7-2001.

[53] Robinson M, Cripe DM. US3,796,552, 12-3-1974.

[54] Ferrand B, Grange Y. EP0130865B1, 15-3-1989.

[55] Yang P, Liao J, Shen B, Shao P, Ni H, Yin Z. J Cryst Growth 2002;236:589.

[56] Eichler St, Bünger T, Butter M, Rühmann M, Scheffer-Czygan M. US2008/0311417A1, 18-12-2008.

[57] Jasinski T, Witt AF. J Cryst Growth 1985;71:295.

[58] Koai K, Sonnenberg K, Wenzl H. J Cryst Growth 1994;137:59.

[59] Shibata M, Suzuki T, Kuma S. J Cryst Growth 1993;128:439.

[60] Rudolph P, Kakimoto K. MRS Bull 2009;34:251.

[61] Hurle DTJ, Series RW. Use of magnetic fields in melt growth. In: Hurle DTJ, editor. Handbook of crystal growth. Amsterdam: North Holland; 1994. p. 259.

[62] Gelfgat YuM, Krumin J, Abricka M. Prog Cryst Growth Ch. 1999:59.

[63] Dold P, Benz KW. Prog Cryst Growth Ch 1999;38:39.

[64] Rudolph P. J Cryst Growth 2008;310:1298.

[65] Gerbeth G, Eckert K, Odenbach S. Eur Phys J Spec Top 2013;220:1.

[66] Park YJ, Kim EK, Son MH, Min SK. J Cryst Growth 1995;156:487.

[67] Park YJ, Min SK. US5,769,944, 23-6-1998.

[68] Gelfgat AYu, Bar-Yoseph PZ, Solan A. J Cryst Growth 2001;230:63.

[69] Gelfgat AYu, Bar-Yoseph PZ, Solan A. J Cryst Growth 2000;220:316.

[70] Mößner R, Gerbeth G. J Cryst Growth 1999;197:341.

[71] Wang X, Ma N, Bliss DF, Iseler GW. Int J Eng Sci 2005;43:908.

[72] Wang X, Ma N, Bliss DF, Iseler GW. J Thermophys Heat Tr 2005;19:95.

[73] Ma N, Bliss DF, Iseler GW. J Cryst Growth 2003;259:26.

[74] Gelfgat YuM. J Cryst Growth 1999;198–199:165.

[75] Pätzold O, Grants I, Wunderwald U, Jenkner K, Cröll A, Gerbeth G. J Cryst Growth 2002;245:237.

[76] Schwesig P, Hainke M, Friedrich J, Müller G. J Cryst Growth 2004;266:224.

[77] Sorkin MZ, Zabelina MP, Gelfgat YuM, Fryazinov IV. Magnetohydrodynamics 1992;28:149.

[78] Lantzsch R. VGF-Kristallzüchtung unter dem Einfluss externer Magentfelder (in German) [Thesis]. TU Bergakad Freiberg; 2009.

[79] Gelfgat YuA, Abricka M, Krumins J. Magnetohydrodynamics 2001;37:337.

[80] Keiki W. JP59–063779, 1984.

[81] Grimes HM, Hariri FA. US5, 571, 320, 1996.

[82] Von Amon W, Virbulis J, Tomzig E, Gelfgat Yu, Gorbunov L. DE10102126A1, 22-8-2002.

[83] Mühe A, Altekrüger B, Vonhoff A. DE10349339A1, 16-6-2005.

[84] Frank-Rotsch Ch, Jockel D, Ziem M, Rudolph P. J Cryst Growth 2008;310:1505.

[85] Frank-Rotsch Ch, Rudolph P. J Cryst Growth 2009;311:2294.

[86] Kudla Ch, Blumenau AT, Büllesfeld F, Dropka N, Frank-Rotsch Ch, Kiessling FM, et al. J Cryst Growth 2013;365:54.

[87] Kiessling FM, Büllesfeld F, Dropka N, Frank-Rotsch Ch, Müller M, Rudolph P. J Cryst Growth 2012; 360:81.

[88] Dropka N, Miller W, Rehse U, Rudolph P, Büllesfeld F, Sahr U, et al. J Cryst Growth 2011;318:275.

[89] Dropka N, Frank-Rotsch Ch, Ziem M, Lange RP. DE10 2012 204 313B3, 2013.

[90] Dropka N, Frank-Rotsch Ch, Miller W, Rudolph P. J Cryst Growth 2012;338:208.

[91] Yeckel A, Derby JJ. J Cryst Growth 2013;364:133.

[92] Ostrogorsky AG. J Cryst Growth 1990;104:233.

[93] Ostrogorsky AG. Meas Sci Technol 1990;1:463.

[94] Ostrogorsky AG. US5,047,113 B, 10-9-1991.

[95] Golyshev VD, Gornik MA. SU1800854 A1, 20–6-1996.

[96] Ostrogorsky AG, Muller G. J Cryst Growth 1994;137:64.

[97] Dario A, Sicim HO, Balikci E. J Cryst Growth 2011;337:65.

[98] Meyer S, Ostrogorsky AG. J Cryst Growth 1996;166:700.

[99] Vogel MJ, Ostrogorsky AG. Acta Astronaut 2001;48:93.

[100] Ostrogorsky AG, Sell HJ, Scharl S, Muller G. J Cryst Growth 1993;128:201.

[101] Holmes AM, Wang X, Ma N, Bliss DF, Iseler GW. Int J Heat Fluid Fl 2005;26:792.

[102] Wang X, Ma N, Bliss DF, Iseler GW, Becla P. J Cryst Growth 2006;287:270.

[103] Wang X, Ma N, Bliss DF, Iseler GW. Int J Heat Mass Tr 2006;49:3429.

[104] Gershuni GZ, Lyubimov DV. Thermal vibration convection. New York: Wiley; 1998.

[105] Zharikov EV. Advanced technologies of crystal growth from melt using vibrational influence. In: Capper P, Rudolph P, editors. Crystal growth technology. Semiconductors and dielectrics. Weinheim: Wiley-VCH Verlag GmbH & Co. KGaA; 2010. p. 41.

[106] Zharikov EV. J Cryst Growth 2012;360:146.

[107] Ubbenjans B, Frank-Rotsch Ch, Virbulis J, Nacke B, Rudolph P. Cryst Res Technol 2012;47:279.

[108] Scheel HJ, Schulz-Dubois EO. J Cryst Growth 1971;8:304.

[109] Scheel HJ. J Cryst Growth 1972;13/14:560.

[110] Yu WC, Chen ZB, Hsu WT, Roux B, Lyubimova TP, Lan CW. J Cryst Growth 2004;271:474.

[111] Yu WC, Chen ZB, Hsu WT, Roux B, Lyubimova TP, Lan CW. Int J Heat Mass Tr 2007;50:58.

[112] Liu YC, Yu WC, Roux B, Lyubimova TP, Lan CW. Chem Eng Sci 2006;61:7766.

[113] Zharikov E, Prihod́ko LV, Storozev NR. J Cryst Growth 1990;99:910.

[114] Avetissov ICh, Sukhanova EA, Khomyakov AV, Zinovjev AY, Kostikov VA, Zharikov E. J Cryst Growth 2011;318:528.

[115] Liu W-S, Wolf MS, Elwell D, Feigelson RS. J Cryst Growth 1987;82:589.

[116] Kozhemyakin GN. J Cryst Growth 2003;257:237.

[117] Kozhemyakin GN, Kolodyazhnaya LG. J Cryst Growth 1995;147:200.

[118] Brice JC, Capper P, Jones CL, Gosney JJG. Prog Cryst Growth Ch 1986;13:197.

[119] Capper P, Harris JE, ÓKeefe E, Jones CL, Ard CK, Mackett P, et al. Mat Sci Eng B-Solid 1993;16:29.

[120] Capper P, Gosney JJG, Jones CL. J Cryst Growth 1984;70:356.

[121] Capper P, Gale IG, Grainger F, Roberts JA, Jones CL, Gosney JJG, et al. J Cryst Growth 1988;92:1.

[122] Capper P, Coates WG, Jones CL, Gosney JJG, Kenworthy I, Ard CK. J Cryst Growth 1990;102:848.

[123] Capper P, Coates WG, Jones CL, Gosney JJG, Ard CK, Kenworthy I. J Cryst Growth 1987;83:69.

[124] Capper P, Brice JC, Jones CL, Coates WG, Gosney JJG, Ard CK, et al. J Cryst Growth 1988;89:171.

[125] CGL Fraunhofer IISB, Fraunhofer-Institut für Integrierte Systeme und Bauelementetechnologie IISB, Schottkystr. 10, 91058 Erlangen, Deutschland. http://www.iisb.fraunhofer.de/de/abteilungen/kristallzuechtung.html.

[126] STR Group, Inc., STR group, Inc., Engels av. 27, P.O. Box 89, 194156, St.-Petersburg, Russia. http://www.semitech.us/products/CGSim/.

[127] FEMAGSoft S.A., Centre Monnet, Avenue Jean Monnet 1, B-1348 Louvain-la-neuve, Belgium. http://www.femagsoft.com.

[128] Ware RM, US4,265,661, 5-5-1981.

[129] Guadalupi G, Danieli F, Meregalli L. CA2326056, 14-10-2008.

[130] Terashima K, Watanabe M. EP0196854B1, 10-11-1993.

[131] Fischer AG. J Electrochem Soc 1970;117:41C.

[132] Hoshikawa K, Nakanishi H, Kohda H, Sasaura M. J Cryst Growth 1989;94:643.

[133] Oates WA, Wenzl H. J Cryst Growth 1998;191:303.

[134] Eriksson G, Hack K. Metall Trans 1990;B 21:1013.

[135] GTT Technologies GmbH, Herzogenrath, Germany. http://gtt.mch.rwth-aachen.de/gtt-web/software/gtt-thermodynamic-software-family.

[136] Thermo-Calc Software, Norra Stationsgatan 93, SE-113 64 Stockholm, Sweden. http://www.thermocalc.com/start/.

[137] Chemical Software Ltd., Gateways, Kings Cross Lane, South Nutfield, Surrey, RH1 5NS UK. http://www.hsc-chemistry.net/contact.htm.

[138] Buhrig E, Jurisch M, Korb J, Pätzold O. Thermodynamic modeling of crystal growth processes. In: Capper P, Rudolph P, editors. Crystal growth technology, semiconductors and dielectrics. Weinheim: Wiley-VCH Verlag Gmbh & Co KGaA; 2010. p. 41.

[139] Korb J, Flade T, Jurisch M, Köhler A, Reinhold Th, Weinert B. J Cryst Growth 1999;198– M199:343.

[140] Basch M. US3,152,006, 6-10-1964.

[141] Moore AW. J Cryst Growth 1990;106:6.

[142] Mullin JB. J Cryst Growth 2004;264:578.

[143] Duffar T, Boiton P, Dusserre P, Abadie J. J Cryst Growth 1997;179:397.

[144] Bourret ED, Merk EC. J Cryst Growth 1991;110:395.

[145] Clemans JE, Monberg EM. US4,923,561, 8-5-1990.

[146] Kawase T. US5,584,929, 12-12-1996.

[147] Kremer RE, Francomano DM. US4,999,082, 12-3-1991.

[148] Kawase T, Tatsumi M, Wakayama Y. EP0744476B1, 2-8-2000.

[149] Jackson KA. Interface structure. In: Doremus RH, Roberts RW, Turnbull D, editors. Growth and perfection of crystals. New York, New York: Wiley; 1958. p. 319.

[150] Markov IV. Crystal growth for beginners. Singapore: World Scientific Publishing Co. Pte. Ltd; 2003.

[151] Scheel HJ. J Cryst Growth 2006;287:214.

[152] Chernov AA. Prozessy kristallisazii (in Russian). In: Chernov AA, Givargizov EI, Bagdasarov ChS, Kusnezov VA, Demjanez LN, Lobatschev AN, editors. Sovremennaja kristallografija (in Russian). Moskva: Izdatelstvo Nauka; 1980. p. 7.

[153] Chen TP, Guo YD, Huang TS, Chen LJ. J Cryst Growth 1990;103:243.

[154] Weinstein O, Brandon S. J Cryst Growth 2004;268:299.

[155] Weinstein O, Brandon S. J Cryst Growth 2004;270:232.

[156] Amon J, Dumke F, Müller G. J Cryst Growth 1998;187:1.

[157] Rasp M, Birkmann B, Müller G. J Cryst Growth 2001;222:88.

[158] Hannig C, Schwichtenberg G, Buhrig E, Gärtner G. Mat Sci Eng B-Solid 1999;66:97.

[159] Birkmann B, Weingärtner R, Wellmann P, Wiedemann B, Müller G. J Cryst Growth 2002;237–239:345.

[160] Kretzer U. Punktdefekte und elektrische Kompensation in Galliumarsenid-Einkristallen (in German) [Thesis]. Technische Universität Chemnitz; 2007.

[161] Bassignana IC, Macquistan DA, Hillier GC, Streater R, Beckett D, Majeed A, et al. J Cryst Growth 1997;178:445.

[162] Kretzer U, Eichler St, Bünger T. US7,410,540B2, 12-8-2008.

[163] Bünger T, Stenzenberger J, Börner F, Kretzer U, Eichler St, Jurisch M, et al. Manuf Technol 2003. http://csmantech.org/Digests/2003/2003PDF/3-5.pdf.

[164] Sato N, Kakimoto M, Kadota Y. 6th conference on Semiinsulating III-V Materials; 1990.

[165] Eichler St, Seidl A, Börner F, Kretzer U, Weinert B. J Cryst Growth 2003;247:69.

[166] Rudolph P. Defect formation during crystal growth from the melt. In: Dhanaraj G, Byrappa K, Prasad V, Dudley M, editors. Springer handbook of crystal growth. Heidelberg: Springer Verlag; 2010. p. 159.

[167] Zhang SB, Northrup JE. Phys Rev Lett 1991;67:2339.

[168] Northrup JE, Zhang SB. Phys Rev 1993;B 47:6791.

[169] Tan TY, Gösele UM, Yu S. Critical Rev Solid State Mater Sci 1991;17:47.

[170] Tan TY, You HM, Gösele UM. Appl Phys a: Mater Sci Process 1993;56:249.

[171] Klapper H. Generation and propagation of defects during crystal growth. In: Dhanaraj G, Byrappa K, Prasad V, Dudley M, editors. Springer handbook of crystal growth. Heidelberg: Springer Verlag; 2010. p. 93.

[172] Völkl J. Stress in the cooling crystal. In: Hurle DTJ, editor. Handbook of crystal growth. Amsterdam: North-Holland; 1994. p. 821.

[173] Jordan AS, VonNeida AR, Caruso R. J Cryst Growth 1986;76:243.

[174] Figgemeier H, Bruder M, Mahlein K-M, Wollrab R, Ziegler J. J Electron. Mater 2003;32:588.

[175] Naumann M, Rudolph P, Neubert M, Donecker J. J Cryst Growth 2001;231:22.

[176] Naumann M, Donecker J, Neubert M. J Cryst Growth 2000;210:203.

[177] Rudolph P, Frank-Rotsch Ch, Juda U, Kiessling FM. Mater Sci Eng 2005;400–401:170.

[178] Birkmann B, Stenzenberger J, Jurisch M, Härtwig J, Alex V, Müller G. J Cryst Growth 2005;276:335.

[179] Schlossmacher P, Urban K, Rüfer H. J Appl Phys 1992;71:620.

[180] Rudolph P, Frank-Rotsch Ch, Juda U, Naumann M, Neubert M. J Cryst Growth 2004;265:331.

[181] Hurle DTJ. J Cryst Growth 1995;147:239.

[182] Shibata M, Sasaki Y, Inada T, Kuma S. J Cryst Growth 1990;102:557.

[183] Chen TP, Chen FR, Chuang YC, Guo YD, Peng JG, Huang TS, et al. J Cryst Growth 1992;118:109.

[184] Chung H, Dudley M, Larson DJ, Hurle DTJ, Bliss DF, Prasad V. J Cryst Growth 1998;187:9.

[185] Voronkov VV. Kristallografija 1974;19:922.

[186] Gottschalk H, Patzer G, Alexander H. Phys Stat sol(a) 1978;45:207.

[187] Schwesig P. Zum Einfluss der Prozessparameter auf die Bildung von Kristalldefekten bei der Züchtung von 2″ InP Einkrstallen mit dem vertikalen Gradient-Freeze Verfahren (in German) [Thesis]. Univ Nürnb; 2009.

[188] Neubert M, Kwasniewski A, Fornari R. J Cryst Growth 2008;310:5270.

[189] Hurle DTJ, Dudley M. J Cryst Growth 2010;312:1659.

[190] Wenzl H, Oates WA, Mika K. Defect thermodynamics and phase diagrams in compound crystal growth processes. In: Hurle DTJ, editor. Handbook of crystal growth. Amsterdam: North-Holland; 1993. p. 103.

[191] Rumsby D, Ware R, Smith B, Tyberg M, Brozel MR, Foulkes EJ. In: IC Symposium; 1983.

[192] Oda O, Yamamoto H, Kainosho K, Imaizumi T, Okazaki H. Recent developments of bulk III-V materials: annealing and defect control. IOP Publishing Ltd; 1994.

[193] Oda O, Yamamoto H, Seiwa M, Kano G, Mori M, Shimakura H, et al. Semicond Sci Technol 1992;7:A215.

[194] Bolotnikov AE, Camarda GS, Cui Y, Yang G, Hossain A, Kim K, et al. J Cryst Growth 2013;379:46.

[195] Kim K-H, Bolotnikov AE, Camarda GS, Franc J, Fochuk P, James RB. J Cryst Growth 2014;390:1.

[196] Belas E, Bugar M, Grill R, Horodysky P, Fes R, Franc J, et al. J Electron Mater 2007;36:1025.

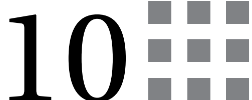

10 Multicrystalline Silicon Crystal Growth for Photovoltaic Applications

Chung-wen Lan[1], Chuck Hsu[2], Kazuo Nakajima[3]

[1]DEPARTMENT OF CHEMICAL ENGINEERING, NATIONAL TAIWAN UNIVERSITY, TAIPEI, TAIWAN; [2]SINO-AMERICAN SILICON PRODUCTIONS INC., HSIN-CHU, TAIWAN; [3]GRADUATE SCHOOL OF ENERGY SCIENCE, KYOTO UNIVERSITY, YOSHIDA, SAKYO-KU, KYOTO, JAPAN

CHAPTER OUTLINE

10.1 Introduction **374**
10.2 Ingot Growth Methods **374**
10.2.1 Casting and Directional Solidification 374
10.2.2 Crucible and Coating 377
10.2.3 Impurities and Defects 379
10.2.3.1 Oxygen, Nitrogen, and Their Precipitates 381
10.2.3.2 Carbon and Silicon Carbide Precipitates 381
10.2.3.3 Transition Metals 382
10.2.3.4 Dislocations and Their Clusters 383
10.3 Hot-zone Design **385**
10.3.1 Control of Growth Front 386
10.3.2 Growth Rate 387
10.3.3 Thermal Stress 388
10.3.4 Convection and Segregation 388
10.3.5 Control of Impurities 389
10.4 Nucleation and Grain Control **391**
10.4.1 Dendritic Casting Method 392
10.4.2 High-Performance mc-Si 397
10.4.3 Mono-like Casting 403
10.5 Conclusions **406**
References **406**

Handbook of Crystal Growth. http://dx.doi.org/10.1016/B978-0-444-63303-3.00010-9
Copyright © 2015 Elsevier B.V. All rights reserved.

10.1 Introduction

Because of the rapid development of the photovoltaic (PV) industry, in recent years, multicrystalline silicon (mc-Si) used for solar cells has become the largest commodity in crystal growth industry. Since 2012, more than 120,000 tons of mc-Si have been produced annually, and the market share of mc-Si solar cells has been greater than 60% [1]. Especially, due to the low cost and high production throughput, the directional solidification (DS) method for the growth of mc-Si ingots has attracted much attention. There are also ribbon growth methods for mc-Si, but their market share is too small to be discussed here.

Because silicon is the absorber for solar cells, its quality plays a crucial role in the conversion efficiency. However, the DS grown mc-Si from the nitride-coated quartz crucible contains many defects, such as randomly oriented grain boundaries, dislocations, inclusions, and impurities. These defects, especially dislocations, are the recombination centers for the light-generated electrons and holes and therefore are harmful to solar cell performance. On the other hand, how to grow mc-Si with good quality and low cost is not a trivial task. The interplays of the hot-zone design, nucleation, crystal growth, segregation, and species transport are very complicated, but they are crucial to crystal quality and thus the solar cell efficiency, as well as the production yield and cost.

10.2 Ingot Growth Methods

10.2.1 Casting and Directional Solidification

Typical mc-Si is grown inside a quartz crucible by the casting or DS method [2]. For casting, silicon is melted first and then poured into the crucible for solidification, but for DS, silicon is melted and solidified in the same crucible. The casting method has been used by some companies like Deutsche Solar GmbH and Kyocera Solar Power Inc. for many years. However, since equipment companies, such as GT Advanced Technologies Inc. (GTAT) stepped into the PV business, DS has been widely adopted. For example, up to 2012 GTAT has delivered more than 3100 furnaces worldwide, particularly in China and Taiwan.

The designs of DS furnaces used in production are all very similar. Figure 10.1 summarizes the three most typical designs. The first one in Figure 10.1(a), which has been adopted by GTAT (http://www.gtat.com/) as discussed, is solidifies the crystal by elevating the insulation basket; this allows the graphite heat exchanger block to cool by radiation to the low-temperature ambient. The second design shown in Figure 10.1(b) lowers the insulation block beneath the heat exchanger block. The advantage of the second design is the insulation during melt down stage could be better if the insulation block can be closer to the heat exchanger block. The second design has been adopted by Zhejiang Jinggong New Energy Inc. (http://www.jgsolar.com/). The third design in Figure 10.1(c) uses top and bottom heaters, and the cooling is initiated by removing the lower thermal shield, i.e., the cooling device. This design has been adopted by ALD

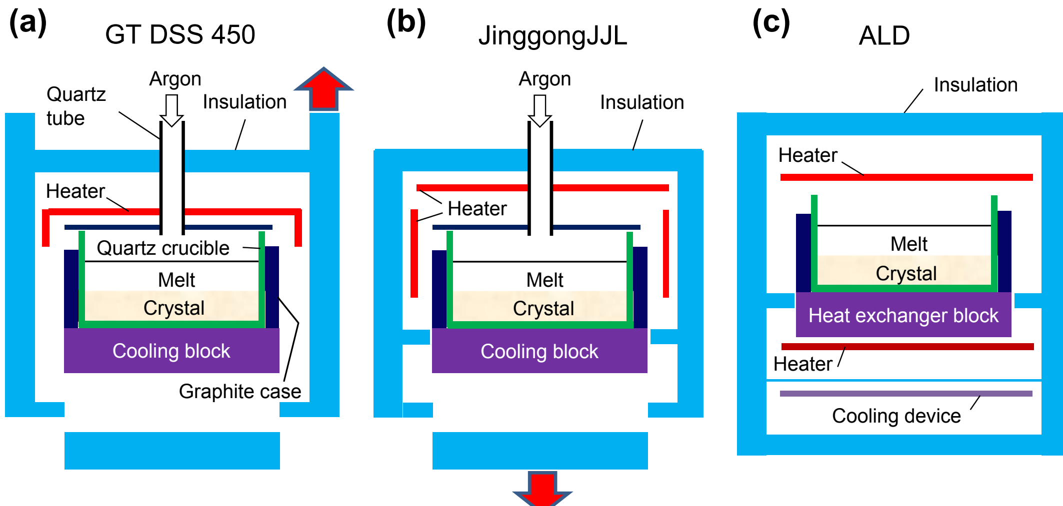

FIGURE 10.1 Three different directional solidification furnace designs. (a) GT DSS 450; (b) JJL; (c) ALD.

Vacuum Technologies Inc. (http://web.ald-vt.de/cms/). Another interesting design is to consider an active cooling device by using circulated argon gas. The argon gas is pumped into the graphite heat exchanger block to remove the heat from the crucible, and then pumped out for cooling by using a water-cooled heat exchanger. The maximum argon flow rate could be higher than 10,000 slpm. This design was proposed by Li et al. [3] and has been implemented by Zhejiang Jingsheng Mechanical & Electrical Co. (http://www.jsjd.cc/). This active cooling is particularly useful for seeded growth in preserving the seeds. The argon nozzles could also be placed at the corners of the graphite block to prevent the seeds from completely melting.

In a typical production procedure, solar-grade (SoG) polysilicon, as well as the doping material, is loaded in a quartz crucible, which is placed inside a graphite case, and then covered with a graphite plate. The cover plate, as shown in Figure 10.1(a), is important in the control of impurities, particularly carbon. The hole at the center of the cover is used for flushing argon to carry away SiO evaporated from the melt, preventing the back diffusion of CO from the graphite parts. As the graphite case is placed upon the graphite cooling block, the furnace is closed, vacuumed, and purged with argon for crystal growth. Up to now, all the available mc-Si in the market are boron-doped, i.e., p-type. The resistivity of the wafers ranges from about 2 Ω-cm (bottom) to 1 Ω-cm (top).

Although many companies are using similar furnaces for production, the detailed hot zone and process parameters have been modified, from the defaulted ones, for process optimization and improvement. Nevertheless, the growth cycle is pretty much about the same. Figure 10.2 shows typical parameter profiles for an ingot growth cycle in a GT DSS 240 furnace [4]. Besides using a smaller crucible, its hot zone is similar to GT DSS 450 shown in Figure 10.1(a), but without the top heater. The silicon charge for DSS 240 is

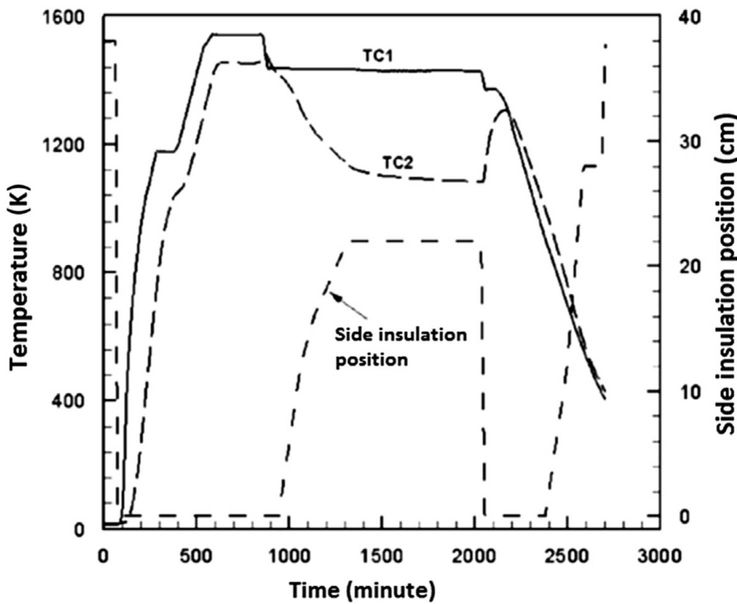

FIGURE 10.2 Process parameters for 240 kg multicrystalline silicon ingot growth. *Ref. [4] with permission of Elsevier.*

about 240 kg and the crucible size is about 69 × 69 × 46 cm; the grown ingot height is 24 cm. The ingot could be sliced into 4 × 4 blocks, i.e., the so-called G4 size, for wafering. In general, two thermocouples (TC1 and TC2) are used in the furnace, and TC1 is used for power control, which is installed next to the graphite heater near the melt surface. TC2 is installed vertically at the center of the heat-exchange block. As shown, during melting stage, the power output is high so that TC1 is rapidly increased to a temperature setting higher than the melting point of silicon (1410 °C). As TC2 reaches a temperature near the melting point, i.e., about complete melting, the power output is reduced and adjusted for stabilization. To start the growth, the insulation basket is moved upward and TC1 setting is slightly reduced; the growth rate is controlled at around 1–2 cm/h. After the insulation reaches the maximum position, TC1 is further reduced to complete the solidification. The melt around four corners is the last portion to be solidified. When the ingot is solidified completely, the insulation is lowered down again for annealing. At this stage, TC2 increases and reaches the setting of TC1, making the whole ingot temperature uniform. As the temperature is below 800 °C, the insulation is moved upward again to accelerate the cooling process. The growth cycle for 450 kg (G5) is similar. The whole growth cycle takes about 60–70 h including the melting (about 20 h), crystal growth (30–40 h), annealing, and cooling down. The annealing stage helps the relaxation of thermal stress and dislocations. As the temperature is below 800 °C, silicon becomes brittle. Hence, if the ingot is cooled too fast, the elastic thermal stress could cause ingot breakage.

After growth, the crucible is taken out. The crucible can break due to the irreversible phase change of β- to α-cristobalite at around 275 °C, which is accompanied with 2–7% of volume change during the phase transformation. The ingot is then cut into blocks by wire or band saws. As will be discussed later, the ingot in contact with the coating has lower minority lifetime, the so-called “red zone” in carrier lifetime measurements about 3 cm, needs to be cut off, and so as the top surface that solidifies the last. Therefore, the best yield of G5 growth is about 70%; the larger the ingot the higher the yield. These bricks are then sliced into wafers, about 180–200 μ in thickness, by wire saws (see Chapter 18, Vol. IIa).

The safety of the ingot growth is important and cannot be ignored. Some protections for melt leakage must be considered. The most typical one is to use a sensor for leakage detection; as the leakage occurs, the power is shut down immediately. In addition, more insulation felt is added at the bottom of chamber for better protection; some designs also move the water cooling away from the lowest part of the chamber. The thermocouple well for TC2 is often blocked and a safety valve for pressure relief may also be considered.

10.2.2 Crucible and Coating

In the growth of mc-Si, fused silica crucibles are widely used. The major reasons for choosing fused silica are: (1) high purity and low contamination to silicon; (2) good mechanical strength and high thermal shock resistance; (3) high softening point; and (4) good insulation. The quality of the grown mc-Si is affected by the crucible significantly, particularly its metal contents [5]. Typically, the crucible has 100% of the glassy structure. However, during ingot production the crucible is experiencing a long thermal cycle, and the phase transition could occur. As the temperature is greater than 1200 °C, the crucible creeps rapidly and shrinks slightly due to sintering. At this stage, the stress inside the crucible could be easily relaxed [6]. During the melting down stage, as the temperature is higher than 1450 °C, devitrification accelerates, and a substantial amount of β-cristobalite phase is formed. At this stage, the crucible becomes more rigid, and the creeping deformation is low. On the other hand, during the cooling down stage, the phase transformation from β- to α-cristobalite occurs at around 275 °C, leading to a significant volume change, and this often causes crucible breakage.

When silicon solidifies, it sticks to the silica crucible without coating. As silicon cools down, due to its larger thermal expansion coefficient than silica, it shrinks, and the sticking stress can cause ingot cracks. In order to resolve the problem, silicon nitride (α or β-Si_3N_4) coating has been adopted. The purity of silicon nitride affects the lifetime of the grown ingot significantly; additional acid leaching was found useful in reducing some contaminants [5,7]. In order to have a uniform coating, the particle size and distribution, as well as surface properties, of silicon nitride need to be carefully controlled. Table 10.1 lists the typical impurity contents of the major impurities in the crucible and the coating materials [7,8]; some impurity levels in SoG silicon are also added for comparison [9]. As shown, the purity of silicon nitride is much higher than silica.

Table 10.1 Impurity Concentrations in Crucible, Si_3N_4, and SoG Silicon [7–9]

Element	Crucible	High Purity Crucible	Si_3N_4	High Purity Si_3N_4	SoG Si
B				<10	<0.05
P				<6	<0.1
Al	<1500	<160	<34	<21	<0.05
Fe	<100	<5	<30	<15	<0.05
Ca	<89		<1		–
Ti	<110	<2	<25	<1	–
Ni	<1	<0.2	<1	<1	<0.01
Mn	<2	<0.2	<0.2	<0.2	
O			<16	<1	<5
C					<5

SoG, solar grade.

Nevertheless, the contamination from the coating material is still significant. Buonassisi et al. [10] did an extensive study of the impurities in silicon from the coating material, and they showed a strong correlation. Their data indicated that the impurities and impurity-rich particles in the coating may dissolve into silicon melt and crystal forming point defects and precipitates, as well as microdefects. Metal silicides, typically 30–60 nm in diameter, from Fe, Cu, Ni, and Co having highest solubilities and diffusivities in silicon, appeared mainly along the grain boundaries. Also, impurity-rich particles could form inclusions during ingot growth, especially near the edges, bottom, and top of the ingots.

In production, silicon nitride coating and calcination are also important. The sticking problem due to poor coating often causes ingot breakage after growth. This significantly reduces the production yield. The use of robots for crucible coating should be helpful in keeping a good coating quality. At a normal condition, silicon melt does not wet the nitrite-coated crucible. However, the wetting angle is affected by oxygen content and time; the higher the oxygen content, the larger the wetting angle [11]. Also, increasing the firing time increased the oxygen content. A wetting angle of around 100° was achieved with oxygen contents higher than 14 wt%. In comparison, at oxygen levels around 2 wt%, the angles amounts to ~60° [11]. The wetting process of silicon melt with the nitride coating layer has been studied in detail recently by Drevet et al. [12]. They observed that the melt infiltration was the main mechanism for sticking; however, the silicon monoxide (SiO) generated during the melt/silica reaction could stop or reduce the infiltration. Nevertheless, at the melt/crucible/gas tri-junction line, the escape of SiO to the gas allowed the infiltration to proceed, and this might explain why the most common sticking appears along the tri-junction line, i.e., the contact line of the melt surface and the crucible.

Some crucible companies also provide ready-to-use crucibles with an already coated nitride layer. However, in addition to the higher price, the breakage of crucibles or ingots for using the ready-to-use crucibles often causes controversy between the crucible

suppliers and users. To increase the adhesion of the coating layer, silica could be added, but this also increases oxygen content, which might reduce the minority lifetime of the grown ingot. On the other hand, reusable crucibles have also attracted much attention for a long time. Saito et al. [13] used a graphite mold, coated with SiC or Si_3N_4, with some success; more than 10 ingots could be grown in a small crucible (5 cm in diameter). A graphite mold made of graphite sheets coated with silicon oxynitride was also considered [14]. Similarly, GTAT [15] also proposed a multipart reusable graphite crucible for the growth of large ingots. In addition to the powder releasing agent, molten salts, such as CaF_2 and MgF_2 [16], and liquid precursors [17] have also been considered. Silicon nitride crucibles have also been proposed [18–20]. However, so far no matured products are available in the market for production.

10.2.3 Impurities and Defects

Impurities in mc-Si are usually much more than that in the Czochralski (Cz)-grown silicon (see Chapter 2, Vol. IIa). The major reasons, as discussed previously, are caused by the less pure crucible/coating materials and silicon feedstock for low cost. The performance of mc-Si solar cells is limited by the impurities and defects, which reduce the minority carrier lifetime. Nitrogen and oxygen come directly from the nitride coating and the silica crucible. The infiltration of silicon melt can also react with the silica crucible forming SiO. Carbon is normally from the gas phase; the graphite parts react with SiO and H_2O forming CO and CO_2, and they diffuse back to the melt. The supersaturation of these light elements further drives the formation of the precipitates of oxide, nitride, and carbide. Metals, such as iron, aluminum, copper, nickel, and chromium, are also mainly from crucible/coating materials; some might be from silicon feedstock. Because these impurities, as well as their precipitates, also interact with the extended defects, such as dislocations and grain boundaries, during crystal growth and cell processing, their interplays with the solar cell performance are very complicated. The extended defects usually getter and store the majority of the mobile metallic impurities, leaving rather few active metals in the intragrains [21–25]. Some of these active metals are extremely detrimental to minority lifetime and need to be controlled carefully during crystal growth. During the cell processing step, the $POCl_3$ diffusion could quickly remove the fast-diffusion metals through gettering. However, precipitates, particularly at grain boundaries, are less affected by gettering and thus are a limiting factor for the gettering efficacy [26,27].

In general, the segregation of impurities pretty much follows the traditional segregation behavior of direction solidification, i.e., the Scheil equation, as follows:

$$C_s = k_0 C_0 (1 - f)^{k_0 - 1},$$

where C_s is the impurity concentration in the solid, k_0 the equilibrium segregation coefficient, C_0 the initial impurity concentration in the melt, and f the solidification fraction. Sometimes, the Scheil equation is used to determine the segregation of the impurity. The fitted value is often called the effective segregation coefficient, k_{eff}, which

accounts for the effect of the growth rate, convection, and diffusion. In reality, the detailed segregation of impurities requires detailed global simulation coupling with the heat and mass transfer, as well as gas and melt convection [28]. Nevertheless, the Scheil equation is often adequate in the prediction of impurity segregation, except for the fast-diffusion species near the crucial wall and the top ingot surface, about 2–3 cm, due to solid state diffusion. Table 10.2 gives the typical k_{eff} or k_0 values for some impurities. The diffusivity, solubility, and the capture cross-section for minority carriers of some impurities are also given in the table for reference [29–33]. It should be noted that the Scheil equation is not applicable if the impurity forms precipitates or evaporate during solidification. Moreover, because of the extended defects, the interactions of the impurities with them make the microsegregation quite complicated. The segregation of impurities to grain boundaries is particularly important, but the gettering behavior also depends on the boundary types. The noncoherent grain boundaries or the grain boundaries with high coincidence site lattice (CSL) indices, i.e., Σ values, could easily getter the rapid diffusion species such as Fe, Ni, and Cu. This makes the grain boundaries electrically active as the recombination center. On the other hand, for Σ3 grain boundaries (twins), typically they are not associated with the impurities [34–36]. Hence, they are electrically inactive. Nevertheless, Σ3 grain boundaries could also be electrically active containing fast-diffusing metals if they are decorated by dislocations [25]. Moreover, the small angle gran boundaries were also observed having better gettering capability than the large angle grain boundaries [37]. Fortunately, grain boundaries are less important for DS mc-Si because of the relatively large grains in the centimeter range; the fraction of grain boundaries in a wafer is very small. On the other hand, the slower-diffusing metals (e.g., Ca, Cr, Mn, Mo, Ti, Zn) are often presented in large inclusions up to several microns within the grains, typically in an oxidized chemical state. These inclusions are distributed near the crucible wall and the top surface of the ingot [23].

Table 10.2 Diffusivity, Solubility, Segregation Coefficient, and Carrier Cross-section of Impurities

Species	Diffusivity at 850 K [25] or 1685 K (cm^2/s)	Solubility at 1685 K ($atoms/cm^3$)	Effective or Equilibrium Segregation Coefficient (k_{eff} or k_0) [26,29,30]	Cross-section (σ_n/σ_p) (cm^2) [26]
Fe	1.2×10^{-6}	1.2×10^{13}	1.5×10^{-5}	$\sigma_{nFei} = 4 \times 10^{-14}$/ $\sigma_{pFei} = 7 \times 10^{-17}$
Cr	3.6×10^{-7}	1.7×10^{12}	3.1×10^{-6}	$\sigma_{nCrB} = 4.5 \times 10^{-15}$/ $\sigma_{pCrB} = 1.1 \times 10^{-14}$
Ni	1.6×10^{-5}	3.5×10^{16}	8×10^{-4}	
Cu	8.0×10^{-5}	1.1×10^{17}		
Ti	7.6×10^{-11}	$1–7 \times 10^{10}$	3.5×10^{-5}	$\sigma_{nTidd} = 1.5 \times 10^{-15}$/ $\sigma_{pTidd} = 3.7 \times 10^{-17}$
C	3.5×10^{-4} [32]	5×10^{18} [37]	0.07 [29]	
N	4.1×10^{-4} [32]	2.2×10^{18} [31]	7×10^{-4} [30]	
O	3.6×10^{-4} [32]	5.7×10^{18} [33]	1.25 [30]	

10.2.3.1 Oxygen, Nitrogen, and Their Precipitates

During crystal growth, significant oxygen and nitrogen are dissolved in silicon melt from segregation coefficient of oxygen (1.25) is greater than 1 the coating/crucible materials, and they also react with silicon forming silicon dioxide and silicon nitride precipitates. The oxygen in the boron-doped Cz-grown silicon is responsible for the light-induced degradation (LID) due to the boron–oxygen pairs [38]. Although the oxygen content in mc-Si, being less than 10 ppma, is much lower than that in Cz silicon, some LID could still be observed in commercial p-type mc-Si cells, particularly using the wafers from the upgraded metallurgical silicon (UMG) feedstock. As the oxygen content was less than 3 ppma, no significant LID was observed [39]. The equilibrium oxygen concentrations in contact with a quartz crucible with and without silicon nitride have been estimated by Matsuo et al. [40]. According to their thermodynamic calculation, the oxygen in mc-Si is about half of that in the Cz silicon. Because the segregation coefficient of oxygen (k_0=1.25 [33]) is greater than 1 and the decreasing melt/crucible contact area, while SiO evaporation is about the same, its concentration decreases along the ingot growth direction. The dissolved oxygen, usually the interstitial oxygen (Oi), could be measured by Fourier transformed infrared (FTIR) spectroscopy. The oxygen in mc-Si is present in either the interstitial atom or silicon oxide, and they are often gettered by the extended defects forming precipitates [41]. Nevertheless, oxygen seldom reaches a high concentration in the melt, so that large SiO_2 precipitates in mc-Si are few.

Because of the nitride coating and the much lower segregation of nitrogen, about 7×10^{-4}, the nitrogen content in the melt often exceeds its solubility limit (about 128 ppma). Once silicon nitride supersaturates and nucleates, due to the much larger diffusivity in the melt, large Si_3N_4 precipitates could grow in the form of long filaments, needles, or tubes up to several mm [41]. On the other hand, nitride particles could also come off from the powdery coating. By controlling the melt convection, one can reduce the nitrogen accumulation at the interface, and this is also helpful in reducing the precipitates or inclusions [42,43].

10.2.3.2 Carbon and Silicon Carbide Precipitates

Carbon forms defects that are less electrically active, but they are important because they form SiC precipitates that cause wire breakage during slicing and shunting in solar cells. SiC precipitates are usually n-type, and they form local heterojunction at Si/SiC interfaces [2]. SiC precipitates in mc-Si ingots after crystal growth could be easily visualized by infrared transmission imaging; the precipitates appear as dark contrast [42]. The segregation of carbon plays a crucial role in the formation of SiC precipitates. As carbon is supersaturated in silicon melt to a certain degree, SiC nucleates and grow. This happens within the diffusion boundary layer at the propagating melt–solid interface, even when strong convection is missing. The relatively low solubility limit of C in Si of $\sim$100 ppma can then be easily exceeded. Very often Si_3N_4 particles or filaments could be the nucleation sites of the precipitates. SiC precipitates could grow up to several mm, and the rod- and planar-like strictures have been observed [44]. The solubility limit of

carbon in the solid is about 7 ppma; $k_0 \sim 0.07$ [42,45]. It has been shown that carbon in silicon melt is mainly from the gas phase due to the reaction of graphite parts with SiO or water forming CO. Using a nongraphite cover and purging with argon could minimize the back diffusion of CO and reduce carbon [46]. The formation of SiC precipitates is rather sensitive to crystal growth rate. Figure 10.3 shows two segregation curves of carbon in a small-scale (10 cm in diameter) silicon growth [42]. As shown, if the growth rate was low, the segregation curve behavior followed the numerical prediction assuming a planar growth front; the IR transmission image of the ingot was also clear without significant SiC precipitates in the ingot. However, at the high growth rate, the initial boundary layer was built up. As SiC precipitated, which could be seen from the dark area of the IR image of the ingot, the interstitial carbon concentration decreased, and the simulation failed to describe the segregation behavior.

Although carbon is less harmful to the minority lifetime, it could enhance oxygen precipitates that have more influence on the solar cell efficiency [41]. Moreover, some effects on the B–O pairs in the degradation of lifetime were also observed [47,48].

10.2.3.3 Transition Metals

The effects of transition metals on the solar cell efficiency have been investigated for years. In general, with different metallic impurities purposely added into the feedstock for ingot growth, the solar cell performances using the contaminated wafers could be evaluated. A good summary was given by Coletti et al. [26,49]. They found that the metal impurity with the highest impact is Ti, followed by Cu, Cr, Ni, and Fe; the impact of the former is two orders of magnitude more sensitive than the group of the latter [49]. In addition, the sensitivity of the impurity level depends on the capture cross-section ratio. The reduction of the impurity impact is more visible for impurities with a larger capture cross-section ratio like Fe. The capture cross-section ratio is also different for different

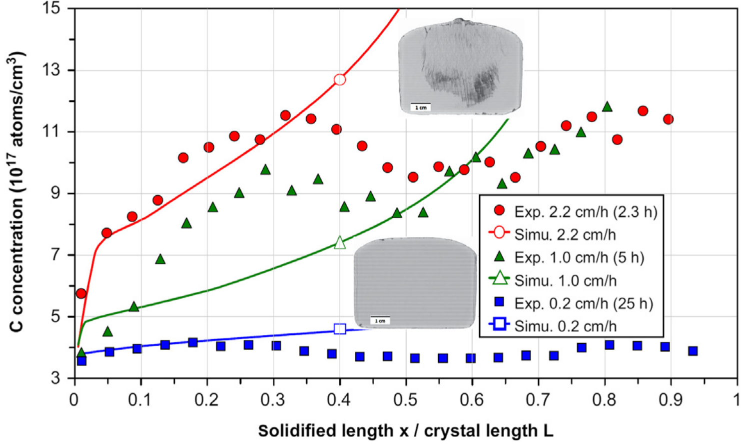

FIGURE 10.3 Measured (FTIR) and calculated axial carbon concentration in 10^{17} atoms/cm^3 in the center of a solid silicon ingot for different growth rates R = 0.2, 1.0, and 2.2 cm/h. *Ref. [42] with permission of Elsevier.*

minority carriers, as listed in Table 10.2, and in general n-type materials have a better impurity tolerance [50]. Cr is a special case for n-type silicon. Its cross-section value is $2 \times 10^{-14}\,cm^2$ that is much larger than that in p-type material ($4 \times 10^{-15}\,cm^2$). Fortunately, Cr is quite volatile at high temperature (above 1205 °C) and could be easily removed during solidification ($k_{eff} \sim 10^{-6}$) [51]. Moreover, gettering during cell processing (around 700–850 °C) is useful. However, a too high temperature greater than 950 °C, such as in the boron diffusion process for n-type cells, could be harmful due to the dissolution of silicides [52,53]. So far, the efficiency of n-type mc-Si solar cells is far less than that of p-type, and this could be due to the less efficient emitter formation that requires high temperature.

10.2.3.4 Dislocations and Their Clusters

Dislocations and their clusters are active recombination centers for mc-Si solar cells. A large portion of dislocations in mc-Si is generated by plastic deformation at higher temperature (>800 °C) to release thermal stress. Dislocations multiply rapidly under stress and easily form clusters during solidification, and the dislocation bundles could extend over a few centimeters. Hence, the crystal quality deteriorates quickly with the ingot height. Figure 10.4(a) shows a cross-section lifetime mapping of an ingot (600 kg); the ingot was grown from the default hot zone in a GT DSS-650 growth station. Because dislocations were bounded by grain boundaries, and metals aggregated at the grain boundaries as well, the lifetime distributions followed the grain structures closely. Therefore, from the lifetime mapping, the grains grew inward near the crucible wall,

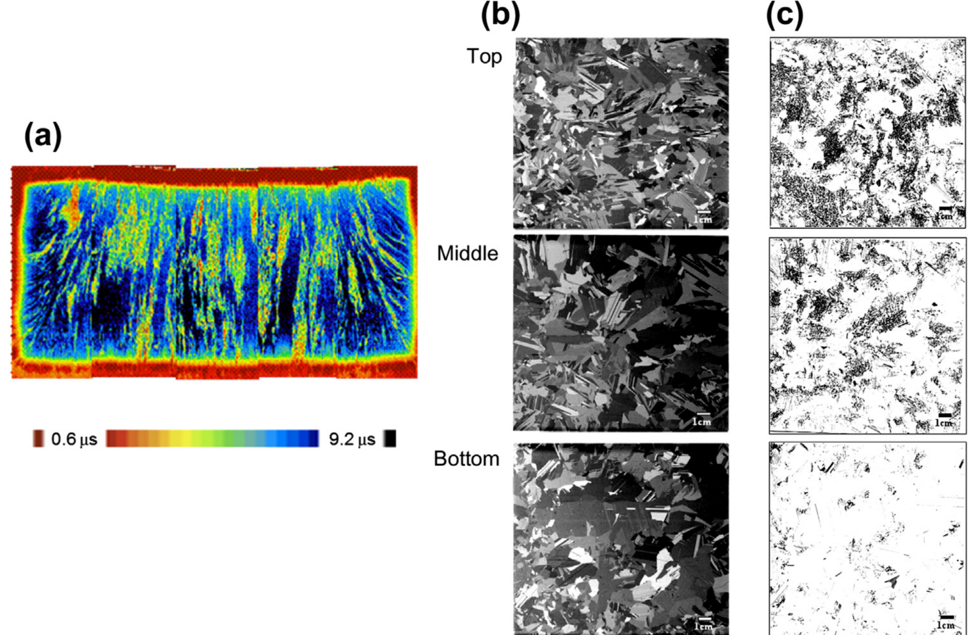

FIGURE 10.4 (a) Lifetime; (b) grains; and (c) etched pit density distributions at different positions of an ingot from the default hot zone. *Ref. [67] with permission of Wiley & Sons.*

especially near the top of the ingot. From this lifetime mapping, it is clear that the solidification front was concave, and the lifetime decreased rapidly as the grains grew more. The grain structure from the middle of the ingots is displayed in Figure 10.4(b); as shown, the grain size decreased, and near the top of the ingot, equiaxed grains appeared as a result of the grain collision. More importantly, as shown in Figure 10.4(c), the etched pit density (EPD) revealed by acid etching increased rapidly from the bottom to the top of the ingot. The effect of EPD on the minority carrier lifetime was investigated by Arafune et al. [54]. Similar results were also reported by Mouller et al., as shown in Figure 10.5 [2], but on the effect of EPD on the internal quantum efficiency. As shown, the efficiency decreases with the increasing dislocations. Also, the impact of dislocations increases with the increasing recombination strength Γ; $\Gamma = V_D/D$, where V_D is the dislocation recombination velocity and D the diffusivity of minority carriers. In other words, a better passivated cell is less vulnerable to the defect density.

To control dislocations, understanding their formation kinetics is necessary. In mc-Si, most of dislocations nucleate at grain boundaries [55,56] or generate from particles, such as SiC and Si_3N_4 [57], due to the lattice distorted stress concentration around them. As solidification proceeds, dislocation density increases due to plastic deformation under thermal stress. Meanwhile, the thermal stress is relaxed. Because of high temperature, recovery is also possible. The photo luminescence (PL) images of the wafers could also reveal similar information. Figure 10.6 shows the PL images of the wafers at different growth stages; the dark areas indicate high defect density, i.e., dislocations. As shown, the PL is darkened from the grain boundaries, as indicated by an arrow at t_1, due to the appearance of dislocations. As the growth proceeds, they grow inward to the grains. Interestingly, some dark areas disappear afterward (as indicated by the arrow at time t_3). This rearrangement of dislocations, or recovery, made the PL signals lighter, which in

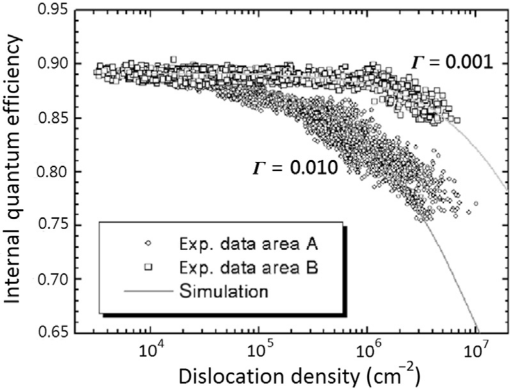

FIGURE 10.5 Internal quantum efficiency as a function of dislocation density for different recombination strengths $G = V_D/D$, where V_D is the recombination velocity and D the diffusivity of minority carriers. *Ref. [2] with permission of Elsevier.*

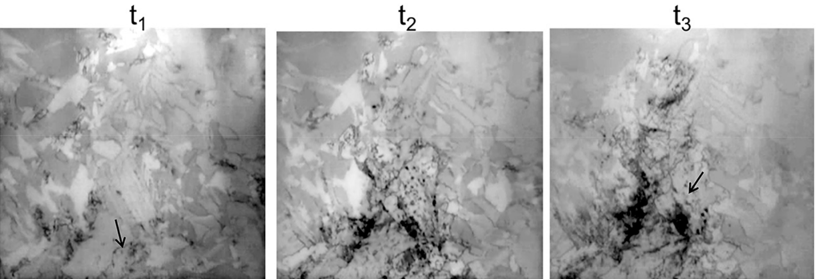

FIGURE 10.6 Development of defects revealed by PL at different times. The arrow at t_1 indicates the nucleation of defects from the grain boundary and that at t_3 indicates the region with reduced defects.

turn increases the minority carrier lifetime. Because the growth period in production is rather long, about 60–70 h, unlike the fast-cooled ribbons, the further wafer annealing has little effect on dislocations, both on their density and structures [58–60]. By using electron backscatter diffraction and infrared microscopy, Schmid et al. [60] observed that {111} and {211} planes were involved in plastic deformation and recovery processes during growth, respectively.

Reducing the nucleation sources of dislocations and the thermal stress is useful in reducing dislocations. The control of initial grain nucleation and growth behaviors by high undercooling for more twin formations has been proposed, but mainly for small ingots [61–63]. For larger ingots, some success has also been reported [2,64,65]. By using a very different concept, Lan et al. [66] and Yang et al. [67] made a great success in reducing the defect propagation rate by having small and uniform grains at the nucleation stage through an incubation layer, which will be discussed shortly. This approach has been adopted widely by industry for the growth of the so-called high performance mc-Si. On the other hand, reducing thermal stress generation through hot-zone design is often necessary. Because the yield stress at high temperature ($>1000\,°C$) is only about 9 MPa [68–70] for multiplication, the thermal stress in the furnace could be easily higher than this value [71–73]. Therefore, the multiplication of dislocations, as a result of plastic deformation, for releasing thermal stress is inevitable during ingot growth. Germanium doping was also found useful in reducing dislocation density through the solution hardening mechanism or the pinning effect [74].

10.3 Hot-zone Design

The hot zone in the DS furnace is very important in practice. The power consumption, initial undercooling, growth front shape, growth speed, thermal stress, and segregations are all affected by the hot zone. Computer modeling has become a powerful tool for hot-zone design, and one could easily get a better understanding of the process and come out with an improved design, as well as suitable growth parameters, in a short period of time.

10.3.1 Control of Growth Front

The first step to grow a good ingot, as a common practice of crystal growth, is to control the solidification front. Again, this could be achieved through the hot-zone design. A flat or slightly convex growth front is usually favored for grain growth and stress reduction. To do this, the control of heat flow is important. As discussed by Yeh et al. [63], the most efficient way in the small furnace is crucible insulation. A similar concept could be adopted by using the so-called adiabatic zone, as shown in Figure 10.7(b) [67], where the default hot zone is shown in Figure 10.7(a) for comparison. This concept is not new and has been used in the vertical Bridgman crystal growth for years; a convex interface could be obtained by adjusting its relative interface position with the adiabatic zone [75]. Recently, Chen and Dai [76] modified the hot zone by adding similar side blocks, and the simulated results with a more convex interface and less power consumption were also verified by experiments. Similar insulation partition was also considered by Wei et al. [4] for mc-Si and Ma et al. [77] for mono-like ingot growth. The simulated thermal fields using commercial software CrysMas [78] for the default (without the adiabatic zone) and the improved (with the adiabatic zone) hot zones for Figure 10.7(a) and (b) are shown in Figure 10.8(a) and (b), respectively. The gran structures of the ingots grown from the hot zones are also shown at the top of the simulated results. As shown, the interface was very concave with the default hot zone. On the contrary, after a proper hot-zone modification using the adiabatic zone, by reducing the heat loss from the crucible wall, a flat growth front could be obtained for the whole growth period. Similar effort has also been used in

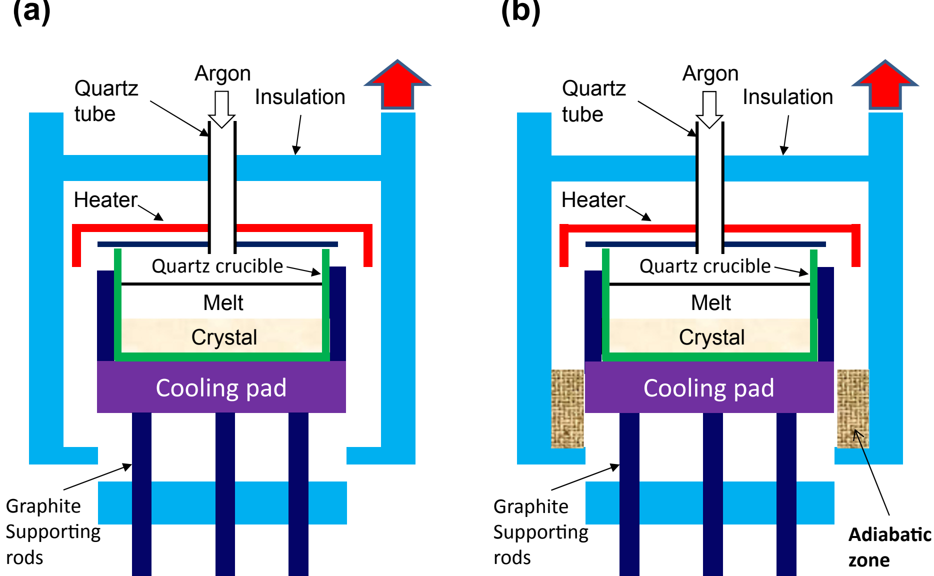

FIGURE 10.7 (a) Default hot zone; (b) modified hot zone. *Ref. [67] with permission of Wiley & Sons.*

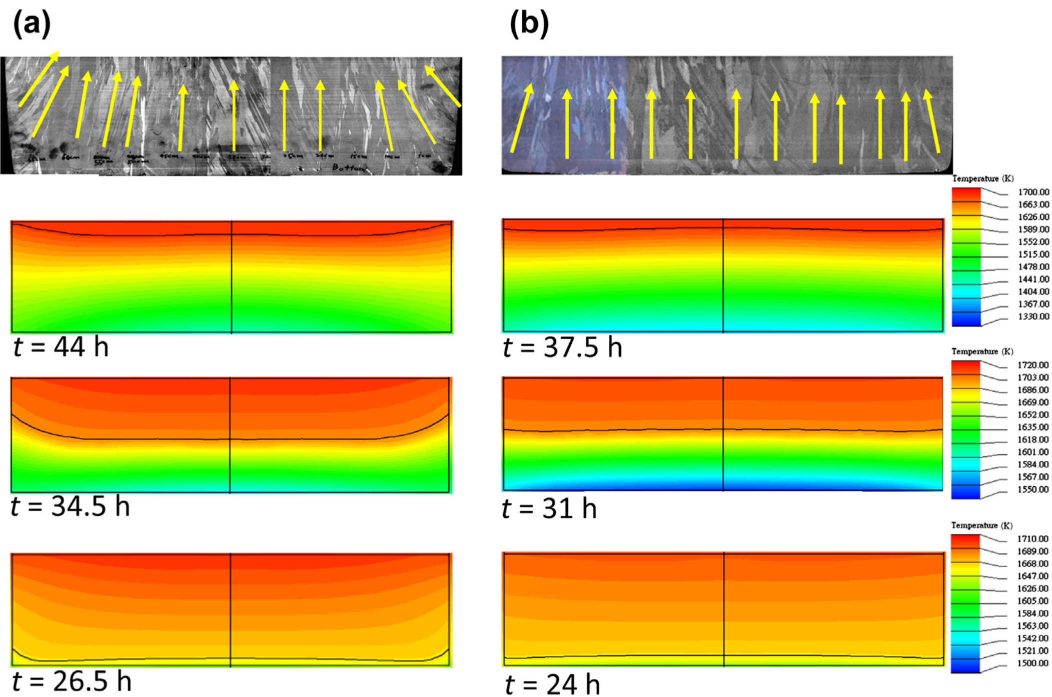

FIGURE 10.8 Calculated thermal fields and the interface shape for (a) the default hot zone; (b) the modified hot zone; the grain structures from different hot zones are shown at the top. *Ref. [67] with permission of Wiley & Sons.*

the 600-kg hot-zone design [67]. With the improved hot zone, the columnar grains grew vertically, and the equiaxed grains near the top were significantly reduced [64].

The control of the interface is particularly important for seeded growth. Nowadays, a precise control down to 1 cm is possible without over melting at the corners. By using an insulated crucible susceptor, Ding et al. [79] have shown that a flat back melting could be obtained. Because the back melting could be precisely controlled for the flat interface, the cost of monocrystalline seeds for mono-like ingot growth could be greatly saved.

10.3.2 Growth Rate

To shorten the growth cycle, a faster growth rate is preferred. However, if the solidification speed is too high, constitutional supercooling could occur that causes the formation of inclusions, such as SiC, in the grown ingot [42], as discussed for Figure 10.3. The crystals grown from higher speeds were also found to have more dislocations [57]. The solidification speed also affects the interface shape. As the solidification speed increases, the interface becomes more concave due to the release of heat of fusion. The concave interface shape could also generate larger thermal stress in the ingot [71,72]. Keeping a constant growth rate might be useful in getting crystals with a uniform

quality. For example, Nara et al. [80] could obtain a high quality ingot by keeping a constant growth rate, where the growth rate was monitored by the interface position measured by a quartz rod dipping into the melt. However, this approach is not convenient. Estimating the interface position from the melt level monitored by a laser, taking account of the melt/crystal density difference, was proposed recently, and the result was promising [81].

Moreover, the accumulation of impurities near the solidification interface is affected by the growth speed, and an interrupted growth could let the impurities diffuse back into the melt. With this concept, the so-called successive relaxation of undercooling by interrupted growth was proposed by Arafune et al. [82]. The grown crystal by using this method had a better lifetime than the one without the interrupted growth.

10.3.3 Thermal Stress

To reduce dislocation density, reducing the thermal stress is also necessary. The calculation of thermal stress for mc-Si so far still assumes silicon to be isotropic. With this assumption, the constitutive equation for thermoelastic solid is based on Hook's law, i.e., $\sigma_{ij} = c_{ij}\varepsilon_{ij}^{e}$, where σ_{ij} is the stress, c_{ij} the elastic constant tensor, and ε_{ij}^{e} the elastic stress considering the elastic and thermal strains. The calculations based on stress-free and no-slip (with the crucible constrain) boundary conditions give very different thermal stress distributions. In the calculation by Fang et al. [72], the maximum von Miss stress is about 40 MPa without the crucible constrain, but it increases to 180 MPa with the crucible constrain for an ingot growth in a G5 furnace. The maximum stress regions are located at the surface, the interface, and the bottom of the ingot. As the thermal stress is built up, both elastic and plastic deformations occur. However, to consider the plastic deformation, usually the Hassen–Alexander–Sumino model (HAS model) is considered for silicon [71]. So far, the simulated results are all based on the growth in the [100] direction, and this is not realistic for mc-Si. How the grain orientation and size affect the stress distribution and the dislocation density is still not yet understood. This is particularly difficult because silicon is an anisotropic material. The stress concentration caused by the anisotropic thermal expansion among grains cannot be calculated without the detailed information of the grain growth.

10.3.4 Convection and Segregation

Convections in the melt and gas phase are important in mc-Si growth. The segregation of impurities, such as metals and light elements, as well as their precipitates, are strongly affected by convections. In general, due to the thermally stabilized configuration, the buoyancy flow in the DS growth is weak if the growth front does not deform much, even though the melt volume is large in production. In addition, due to the upper free surface, Marangoni convection could also be important near the end of growth. Nevertheless, the horizontal thermal gradient in production is rather low, and the Marangoni flow is not very strong. As a result, the growth front shape is usually not affected much by the

flows; however, the carbon and oxygen segregations could be affected significantly. In the numerical simulations by Teng et al. [83], the melt convection mainly consists of upper and lower vortices coupled with each other; the lower ones are induced by the buoyancy force caused by the concave interface, while the upper ones are induced by the Marangoni effect. At the initial stage, the lower flow cells are stronger and the carbon accumulates more near the center of the interface. However, near the end the growth, carbon accumulates more near the crucible wall due to the Marangoni flow. On the other hand, the control of melt flow by the buoyancy and Marangoni forces through the hot-zone design might not be very effective because the melt mixing is not adequate. Another way is to enhance the convection by the use of external forces.

The use of external forces has been widely adopted to enhance the mixing in the melt growth [84]. For vertical DS, vibrations [85], rotation rate variations [86], and magnetic forces [84,87–91] are often used. Among these techniques, the traveling magnetic fields (TMF) have been shown promising. The grown ingot of up to 640 kg with TMF showed very homogeneous IR transmission and few inclusions. Dislocation densities were relatively low, resulting in overall high minority carrier lifetimes [89]. The use of a heater-magnet module (HMM), simultaneously generating heat and TMF within the heating coils, is particularly convenient and effective. A snapshot of the 3D convection due to TMF is given in Figure 10.9(a). Because the induced flow by TMF is downward near the crucible rim, the solidification front was bent toward convexity. With the enhanced mixing, the precipitates in the grown crystal could be reduced significantly, as the comparison shown in Figure 10.9(b). Different frequencies in different TMF directions could also be considered to reduce the convection near the crucible wall. This is particularly useful in stabilizing the crucible coating [90]. Dropka et al. [91] further compared four different nonsteady magnetic stirrings, including traveling (TMF), rotating (RMF), alternating (AMF), and carousel magnetic fields (CMF), during unidirectional solidification of large rectangular silicon melts of 700 kg. They found that the CMF configuration outperformed others in terms of stirring efficiency.

10.3.5 Control of Impurities

The global species transport in the furnace is also important [40]. In general, SiO evaporated from the melt could react with graphite parts as the following:

$$SiO_{(g)} + 2C_{(s)} = 2CO_{(g)} + SiC_{(s)}.$$

In addition, CO could transport back to the melt with the following reaction:

$$CO_{(g)} = C_{(m)} + O_{(m)}.$$

In some furnaces, the carbon solubility limit in the melt could be already exceeded during melting down resulting in significant SiC precipitates at the beginning [92]. Furthermore, the reaction of the silica crucible and the graphite susceptor could also occur [46], i.e.,

$$SiO_{2(s)} + C_{(s)} = SiO_{(g)} + CO_{(g)}.$$

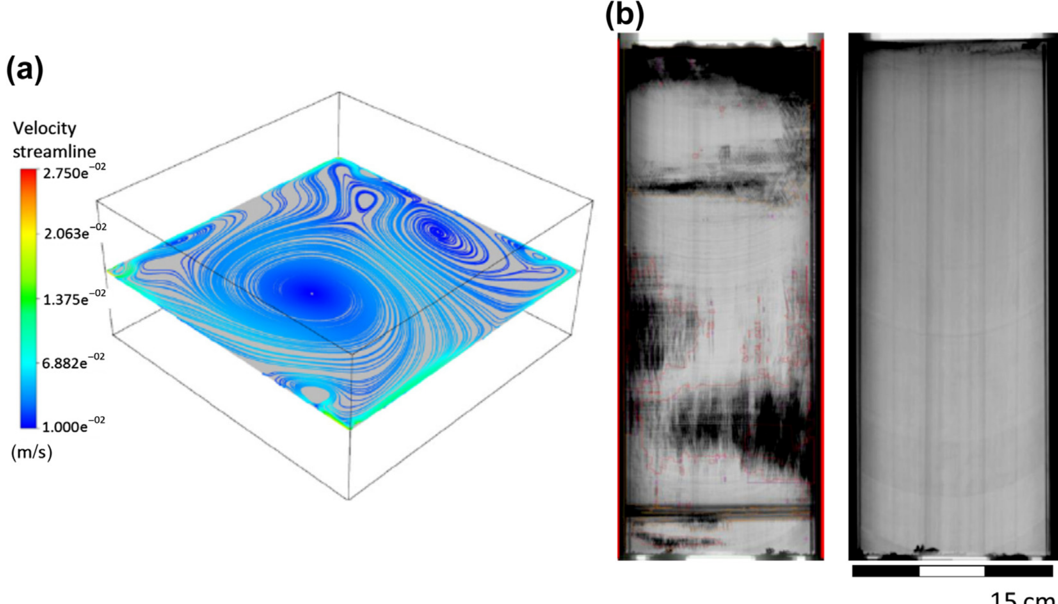

FIGURE 10.9 (a) The flow field with traveling magnetic fields (TMF); (b) comparison of IR transmission images of bricks from the center of two ingots without (left) and with TMF. *Ref. [89] with permission of Elsevier.*

The use of gas flushing unit [93] and crucible cover [46] could effectively reduce the carbon incorporation in the melt as well as in the grown crystal. If gas flushing is considered for the case with the cover, the oxygen content near the top of the ingot could be reduced as well due to the better evaporation of SiO [46,94]. Rabbe et al. [45] have demonstrated that low carbon content could be achieved if the graphite components in the hot zone were replaced by other materials. In a typical production hot zone, the initial oxygen content is around 5–10 ppma, decreasing with height, depending on the coating material, while the carbon content is about 7 ppma, increasing with height. In addition, the furnace pressure could affect the oxygen concentration. In a recent simulation by Teng et al. [95], increasing furnace pressure reduced the evaporation of SiO, leading to a higher oxygen concentration in the grown crystal.

In addition to C and O, the transport of metal impurities from the crucible to the melt is also crucial. The segregation of metal impurities, such as iron, coupling with the melt convective transport and solid state diffusion, is important. Although the segregation coefficient of iron is very small, $k_{eff} = 1.5 \times 10^{-5}$ (Table 10.2), due to the high diffusivity of the interstitial iron, contamination continues from the crucible and the coating during crystal growth. Even at the end of crystal growth, back diffusion from the top surface is also significant. As the crystal is cooled down, iron silicide precipitates at extended defects, and they may dissolve into interstitial iron in the cell processing as well if the

temperature is higher than 900 °C. The solubility limit for interstitial iron is about 2×10^{13} cm^{-3} at 870 °C. Therefore, it was also reported that significant precipitation will occur in a temperature range of 400–800 °C [96,97]. The transport phenomena and the reaction kinetics of the impurities are also affected by the hot-zone design. Some simulations for iron distribution have also been carried out, e.g., by Liu et al. [28]. Due to the long solidification time, additional solid state segregation occurs inside the grains and the extended defects, especially at the edges of the ingot, i.e., the red zone. Therefore, a shorter growth time and a lower overheating are recommended to reduce the red zone [98].

Another interesting example of iron segregation and solid state diffusion is the high-low-high distribution of the minority lifetime in the mono-like ingot. During the melting-down stage, iron is dissolved from the crucible/coating into the melt, and the seed in contact with the melt is contaminated quickly and further during back melting. Meanwhile, as solidification starts, iron segregates and the solid state diffusion continues leading to such a high-low-high iron distribution. Gao et al. [99] have illustrated this through numerical simulation. Yu et al. [100] also proposed a simple diffusion model considering the high undercooling at the beginning. The high growth rate due to the undercooling causes the trapping of the iron-rich boundary layer. Therefore, the second peak, as a result of iron trapping, occurs at a height above the initial solid/liquid interface.

10.4 Nucleation and Grain Control

For obtaining high quality mc-Si using silica crucibles, the control of purity, structure, crystal defects, and thermal stress is necessary. Mc-Si has many grains with different orientations and different sizes, as well as many grain boundaries with different characteristics, and they significantly affect the crystal quality and thus the conversion efficiency of solar cells [101–103]. Particularly, the grain orientations, the grain boundaries, and the dislocation density are closely related, and they play a crucial role on the wafer properties [104–106]. Grain boundaries could also lead to different mechanical and electrical characteristics under different orientations [107,108]. For example, the $\Sigma 3$ grain boundary offers a larger resistance to the cutting stress and facilitates ultra-thin wafer slicing. Also, it is electrically inactive, even in contaminated samples, so that it does not act as recombination centers for electrons and holes [109]. The fraction of grain boundaries for DS mc-Si is low, so that their effect on the overall wafer lifetime is not very significant. Nevertheless, they play a crucial role in impurity gettering and dislocation kinetics; the stress field is affected as well. In addition, the dislocation density is usually much lower for the grains containing twins or in certain orientations [104]. Therefore, in order to obtain high quality mc-Si for high efficiency solar cells, it is important to obtain mc-Si that has grains with the favored orientations and proper sizes, as well as grain boundaries with preferred characteristics. Therefore, the nucleation and grain control are crucial.

In the early days of the DS for mc-Si, getting large grains to reduce grain boundaries was regarded as the most straightforward approach to increase crystal quality and solar cell efficiency [110]. A careful control of initial nucleation by slow cooling and grain competition through growth rate and the growth front shape are believed to be crucial [111]. Indeed, some remain correct, but some may be doubtful. For example, a flat or slightly convex growth front is still believed to be beneficial to reduce the parasitic nucleation from the crucible wall, as well as the thermal stress as we discussed. However, the low supercooling in the nucleation stage and the low growth rate during grain growth might not be always positive. Recent results showed that higher initial cooling induced dendritic growth that could lead to larger grains with better quality [61–63,112].

In addition, the effect of coating materials on nucleation and growth has also been studied, but the results are not conclusive. Brynjulfsen and Arnberg [113] studied silicon nucleation on the Si_3N_4-coated SiO_2 substrate and found that there were no significant differences in nucleation undercooling for various coatings. Tsai et al. [114] further investigated the grain structures from Si_3N_4-coated crucibles with different firing conditions, and the results were scattered. However, through a large-scale experimental study, no significant difference on the ingot lifetime was found by elongating the firing time from 4 to 8 h at 1100 °C. The use of notched crucibles, as a self-seeded growth, was proposed [115], and the results were promising. The evolution of grain orientations from a small notch of 6 mm in diameter was quite dramatic, from the <110> to <112> grains in a few mm.

10.4.1 Dendritic Casting Method

The dendritic casting method was originally developed at Tohoku University, e.g., Fujiwara et al. [61]. To understand the crystal growth mechanism for the control of grain orientation and grain size, an in situ observation system was developed to directly monitor the growing interface of Si crystals at temperatures above 1400 °C through a silica window with a microscope [116]. Using this in situ observation system, they found that with proper supercooling conditions, a thin Si dendritic crystal grew along the bottom of the crucible at the initial stage, and then Si multicrystals grew on the upper surface of the thin Si crystal [61,102]. There has been a long history of fundamental studies on the growth of Si dendritic crystals, the so-called faceted dendrites, since the first report by Billig in 1955 [117]. It has been shown that more than two parallel twins exist at the center of a faceted dendrite [118–123]. Such parallel twins are known to play an important role in the growth of a dendrite. A dendritic crystal appeared from the growing interface consisting of many steps with the {111} facets when the supercooling of the melt occurred above 10 °C. The growth direction of the dendritic crystal was exactly parallel to the {111} facets. The orientation of dendritic crystals depended on supercooling of the Si melt [122,123]. When the supercooling took place at temperatures above 10 °C, the preferred orientation of the dendritic crystals was <112> or <110>. These dendritic crystals had two parallel twins with Σ3 grain boundaries, and the Σ3

grain boundaries had the same {111} facets. Therefore, the upper surface of the dendritic crystals was fixed to {110} or {112}, and the growth direction of the twins was exactly the same as that of the dendritic crystal.

In the conventional casting method, nucleation occurs at random points on the bottom of the crucible, and many grains with random orientations grow from these nucleation sites. Grains with preferred orientations remained at the end. The structure of mc-Si grown by this method could not be controlled at all. On the other hand, using dendritic crystals grown along the bottom of the crucible, the grain orientation and grain size of grown mc-Si could be controlled. Figure 10.10(a) shows the concept of the dendritic casting method for controlling the grain orientation and the grain size [61,102]. At first, dendritic crystals with the upper surface in the <110> or <112> direction are grown along the bottom of the crucible using the proper supercooling conditions. Then, Si multicrystals are grown on the upper surface of the dendritic crystals. Using the dendritic crystals, as shown in Figure 10.10(b), Si multicrystals that have larger grains with the same <112> orientation could be grown, compared to conventional mc-Si that have smaller grains with random orientations. However, dendritic crystals usually appeared with a random distribution and a random direction at the bottom of ingots [65]. It was confirmed that the initial thickness of the dendrite crystals just after their

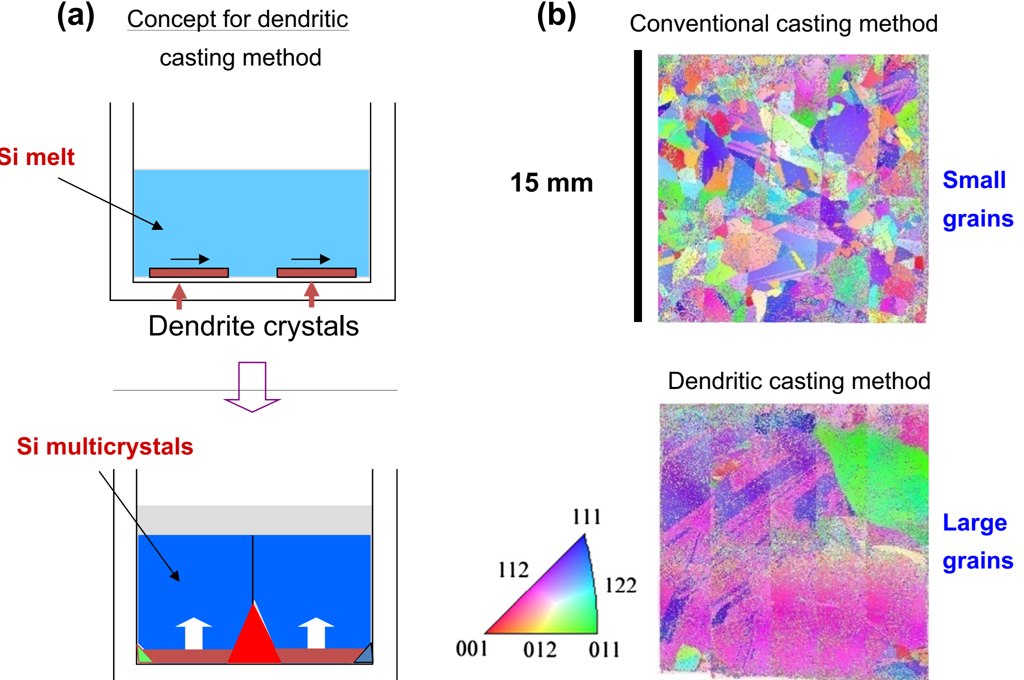

FIGURE 10.10 (a) Concept of dendritic casting method; (b) grain orientation and grain size of two different casting methods. *Refs [61,102] with permission of Elsevier.*

lateral growth was only 2 mm. Therefore, the structure of the bottom of the Si ingot was affected by the dendritic crystals, while the structure of the center and top of the Si ingot was not affected by dendritic crystals. The minority-carrier diffusion length was higher than 150 μm all over the Si wafer. The distribution of the minority-carrier diffusion length of the Si ingot was not affected by the dendritic crystals.

Figure 10.11 shows a schematic illustration of the relationship between random grain boundaries and dislocations during crystal growth using the conventional casting method and the dendritic casting method [56,105,124–126]. Usually, dislocations are generated from random grain boundaries during crystal growth. If random grain boundaries are reduced especially at the initial stage of the growth, dislocations are also reduced in the Si multicrystals. Obviously, the mc-Si grown by the dendritic casting method had few random grain boundaries because the grain size was large. Therefore, the dendritic casting method was effective in suppressing dislocations that could significantly increase the efficiency of solar cells.

The driving force behind the generation of dislocations is stress, and the origin of dislocations is random grain boundaries. Stress is naturally reduced by the introduction of dislocations or through arrangement of grains during crystal growth. Therefore, structural control is necessary to obtain appropriately large grains to reduce stress and dislocations, as well as random grain boundaries, and to increase coherent grain boundaries. In order to confirm how and where dislocations are generated from a random grain boundary during crystal growth, a Si crystal was grown on a special seed

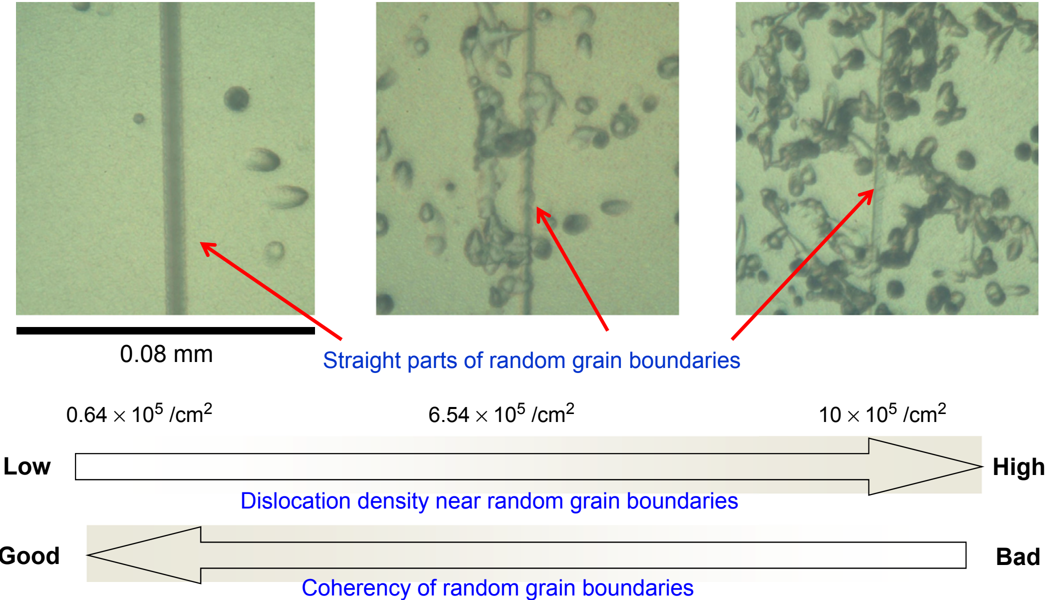

FIGURE 10.11 Relationship between the coherency of random grain boundaries and the dislocation density. *Refs [56,105,126] with permission of AIP.*

crystal with artificially manipulated grain boundaries made by several single crystal sheets with different orientations [56]. It was found that dislocations were generated from this particular random grain boundary during crystal growth, and they appeared on only one side of the boundary. In Figure 10.11, the straight lines correspond to parts of random grain boundaries. As the coherency of random grain boundaries increased, the dislocation density near the random grain boundaries became lower. However, from the viewpoint of stress reduction in mc-Si, a proper density of the random grain boundary should be maintained by controlling the grain size.

Figure 10.12 shows the effect of the angle between dendritic crystals with different orientations. The effects on the shear stress and dislocation density were studied [105,124]. When the angle was zero, the dendritic crystals were arranged completely parallel to each other. The shear stress increased as the angle became larger, and the dislocation density increased as the angle became larger in spite of the orientation of the dendritic crystals. Therefore, the dislocation density could be drastically reduced by controlling the arrangement of dendritic crystals to be completely parallel to each other.

To control the arrangement of the dendritic crystals grown along the bottom of the ingots, it was necessary to intentionally create nucleation sites at the bottom of the crucibles. A method of controlling thermal conductivity under crucibles was proposed by Nakajima et al. [65] to control these nucleation sites. To obtain a highly supercooled section, graphite plates with high and low thermal conductivities were combined into one plate. It was then set between the crucible and the holder and the plate could

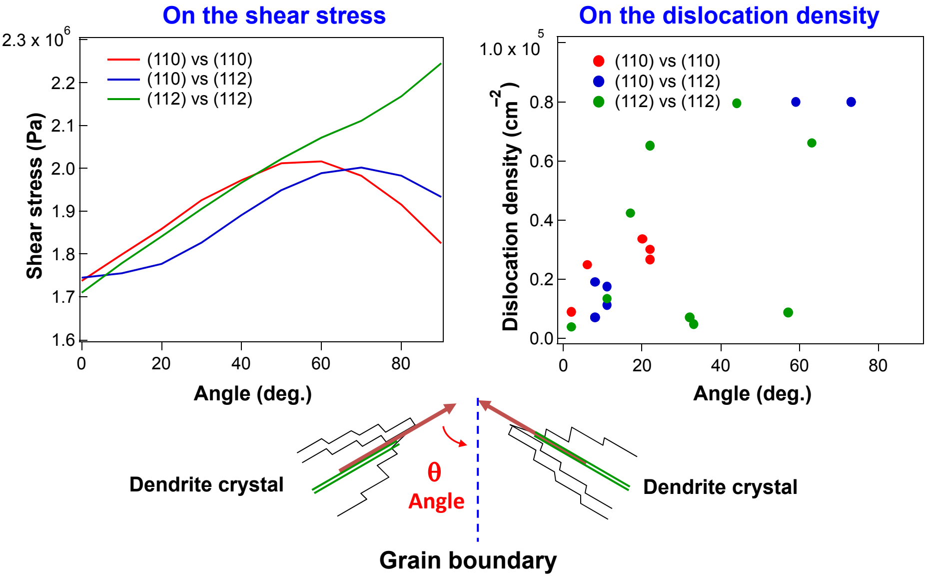

FIGURE 10.12 Effect of the angle between dendritic crystals with different orientations. *Refs [56,105,124–126] with permission of AIP.*

completely cover the bottom surface of the crucible. Dendritic crystals first grew from the highly supercooled section, followed by Si multicrystals growing on the upper surface of the dendritic crystals. Figure 10.13 shows the distribution of dendritic crystals grown along the bottom of an ingot with a diameter of 30 cm. The line-shaped highly cooled section was made from a graphite plate with a high thermal conductivity. It was located 30 mm from the edge of the plate. In Figure 10.13, the red lines show the dendritic crystals that appeared first, and the light blue lines show the dendritic crystals that appeared later by branching off from the initial dendritic crystals. Most of the dendritic crystals that appeared first were generated from the line-shaped, highly supercooled section. They were distributed and arranged such that they were fairly parallel to each other. There were just a few dendritic crystals that appeared from the edge of the ingot because the highly supercooled part in the Si melt acted as a strong nucleation site of the dendritic crystals. The distribution of most of the dendritic crystals that appeared first was well controlled within an angle of $\pm 60°$. In the wafers grown by the dendritic casting method, at a distance of 0.1 cm from the bottom of the ingot, dendritic crystals grew along the bottom of the ingot. At 0.3 cm, grains grew corresponding to the distribution of dendritic crystals. The initial thickness of the dendritic crystals just after their lateral growth was only 0.2 cm.

Recently, Dai-ichi Kiden Corporation (KDN) has manufactured a pilot furnace to produce ingots with controlled crystal structures on an industrial scale. Figure 10.14 shows an example of the conversion efficiency of solar cells using 180 μm-thick wafers grown by KDN using the dendritic casting method without controlling the arrangement of the dendritic crystals. The percentage was obtained using 3000 wafers selected from every part of an ingot with a mass of 420 kg. The peak efficiency was 17.2%. The solar cells prepared from 92% of the total wafers showed conversion efficiencies above 16.5%. The solar cells prepared from 60% of the total wafers showed conversion efficiencies above 17%. The peak value could be higher by controlling the gas flow and the arrangement of the dendritic crystals. The distribution of the minority carrier lifetime

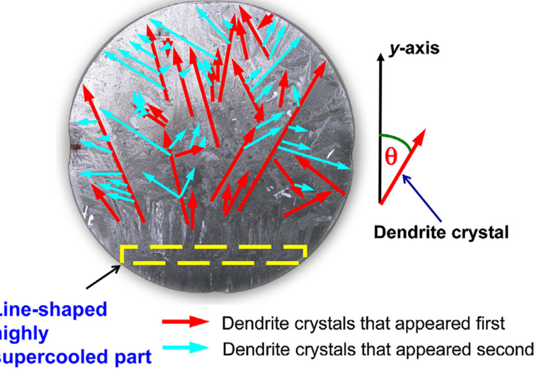

FIGURE 10.13 Distribution of dendritic crystals grown at the bottom of an Si ingot with a diameter of 30 cm. The red arrows show the dendritic crystals that appeared first, and the light blue arrows show the dendritic crystals that appeared later. The distribution was obtained using the circular graphite plate with the line-shaped, highly cooled section. *Ref. [65] with permission of Elsevier.*

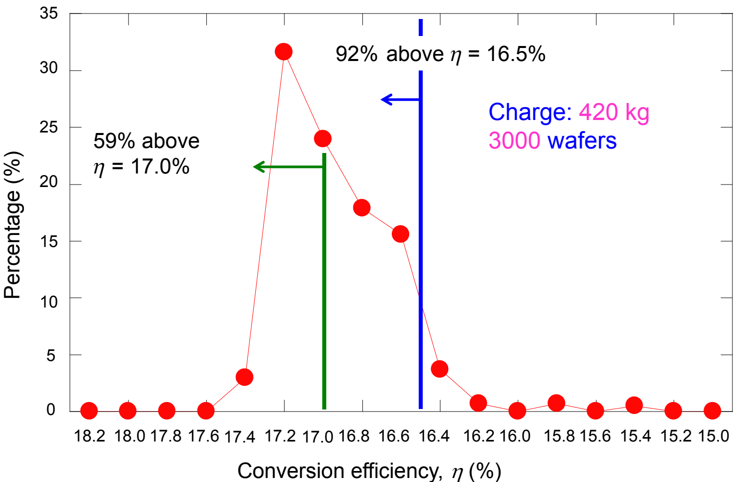

FIGURE 10.14 Conversion efficiencies of solar cells using 180-µm-thick wafers grown by Dai-ichi Kiden Corporation using the dendritic casting method without controlling the arrangement of dendritic crystals [123].

was also very uniform in the cross-section of the same ingot, but the upper half part of the ingot should still be improved by controlling the gas flow and the arrangement of the dendritic crystals.

10.4.2 High-Performance mc-Si

As the dendritic casting method was proposed [61,102], tremendous effort was spent to control the initial undercooling [64]. Using the elevation rate of the insulation was found to be the easiest way without modifying the hardware. Further enhancement of the initial cooling rate was also considered by modifying the heat exchange block, and one example using argon cooling was discussed by Li et al. [3]. The use of argon cooling recently was implemented in G6 furnaces (JSH800) by Jingsheng Inc. However, due to the poor thermal conductivity of silica, the thermal resistance through the crucible bottom was high. Therefore, without the extensive modification of the available furnaces, the use of initial cooling for grain control, unfortunately, was found rather difficult and unstable for production. Figure 10.15 shows three typical grain structures and brick lifetime mappings usually observed by controlling the initial undercooling [67]. In general, if the initial undercooling was low, due to less nucleation sites, the grown grains were reasonably large, but not uniform. On the other hand, if the initial cooling rate was high enough, dendritic grains could be obtained, as discussed previously [61,102]. An interesting observation was found that there was a small window for uniform grains, but they were relatively small. In fact, based on the nucleation theory, the nucleation rate increases with the increasing melt undercooling. More nucleation sites could appear with the increasing undercooling as well. However, if the undercooling is high enough, say more than 10 K for the dendritic growth, the fast-growing dendrites, preferred in the

<110> or <112> direction, overgrow the others, and lead to larger grains. Unfortunately, keeping a large undercooling was not easy even with a rapid cooling in a small crucible. In a recent paper by Brynjulfsen et al. [127], four experiments were carried out with a similar growth setting. One growth had an undercooling of about 10 K, but the other three did not have a significant undercooling for the high crucible pulling rate up to 300 cm/h. The transition, from the nucleation to growth-controlled modes, was not clear. However, for the cooling rate that could be used in the current production facility, the grain structure control was found rather difficult [128].

Interestingly, as shown in Figure 10.15, the lifetime mapping of the brick having small uniform grains turned out to have the best uniformity. The wafers with small initial grains had higher solar cell efficiency as well. Their dislocation clusters near the top of the ingot were found much less than the others. The product from this generation of technology was referred to as the A++ wafers first released by SAS, while the one based on the high undercooling with the dendritic grains was referred to as the A+ wafers. The growth yield of A++ ingots from the uniform grains controlled by undercooling was not high. However, once an ingot with good grain structures was obtained, it could be reused as seeds for a new growth. Though more troublesome, this increased the production yield significantly. The cell efficiency was improved from 16.8% to 17.1% from the A+ to A++ wafers [64]. Although the performance of A++ wafers was reasonably good, the

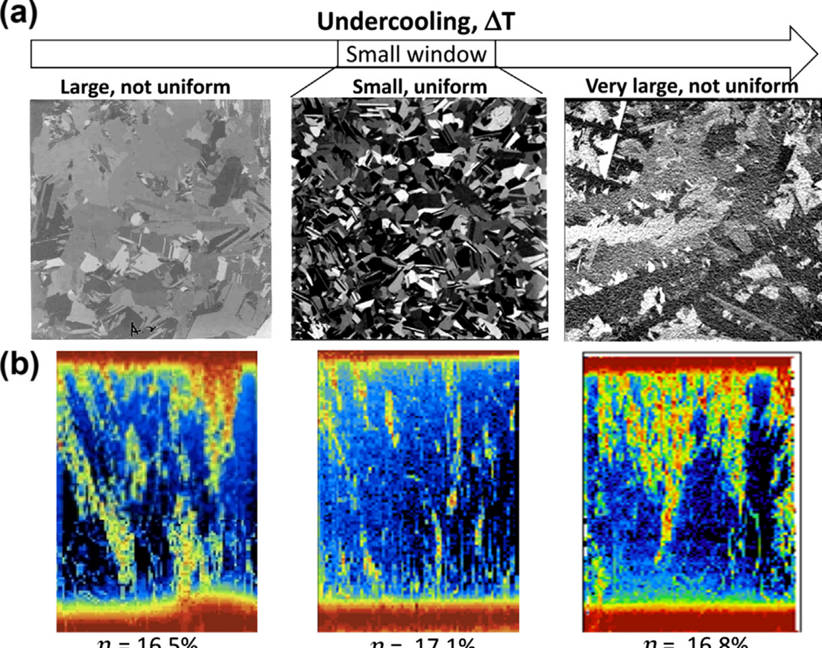

FIGURE 10.15 (a) Three typical grain structures and (b) lifetime mappings from different undercooling; the average solar cell efficiencies from the ingots are shown at the bottom. *Ref. [67] with permission of Wiley & Sons.*

seed selection was troublesome. Also, similar to the dendritic casting method, the Σ3 grain boundaries or twins were dominant.

Apparently, the initial grain size played a crucial role in the defect formation. The seeded growth from small silicon chips and chucks was reported by Lan et al. [129]. As shown in Figure 10.16, the etched defects were significantly lower for the grains grown from the small seeds. By controlling the initial small grains using small silicon chips or beads as the seeds, the ingot with uniform grains and low defects could be easily obtained. The product from this generation was referred to as A3+ wafers, and the product was first released in the late 2011 by SAS. The wafers from the whole ingot, except the red zone and the top ingot surface, were used for solar cell fabrication. The distributions of solar cell efficiency from A+ and A+++ wafers are summarized in Figure 10.17. As shown, the average efficiency for A+++ was about 17.4%, which was about 0.6% more than that for A+. The solar cells based on A+++ wafers had high open-circuit voltage (V_{oc}) ranging from 630 to 633 mV and high shunting resistance R_{sh} (266 Ω). With the improvement of ingot growth and the use of high purity coating and crucibles, the current efficiency has been increased to 17.8% based on the same growth concept in mid-2012; the product was referred as A4+ wafers. The portion of poor performance (<17%) was less than 1%. The major advantage of this current technology is that the production yield for high quality ingots is very high. Moreover, with the passivated emitter and rear cell (PERC) using a plasma-enhanced chemical vapor deposition (PECVD) aluminum oxide layer, the average efficiency could be increased to over 18.5% [129]. In late 2013, the average efficiency for using the standard cell process was improved to more than 18% due to the use of better silver paste for metallization.

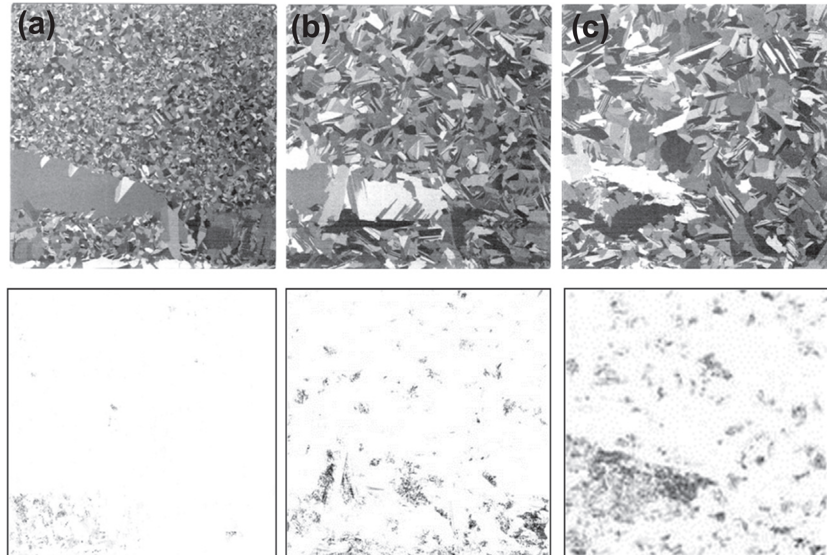

FIGURE 10.16 Grain structures (upper) and etched defects from seed crystals with different sizes: (a) bottom; (b) middle; (c) top of the ingots [129].

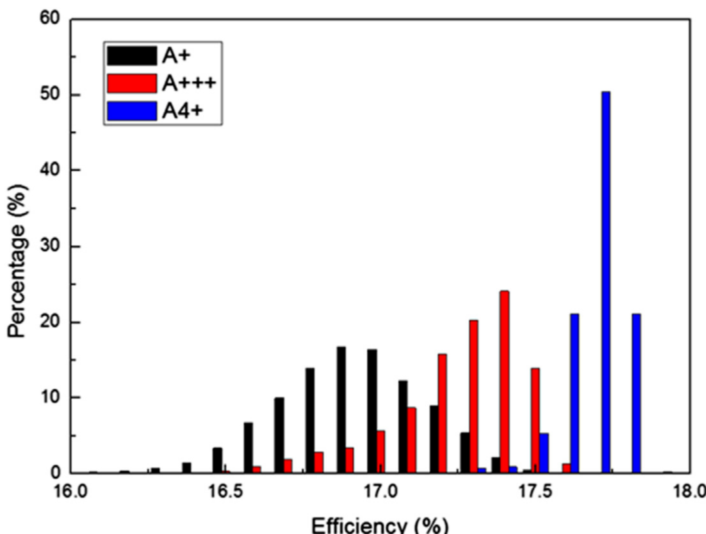

FIGURE 10.17 Comparison of efficiency distribution of solar cells from A+, A+++, and A4+ wafers. *Ref. [67] with permission of Wiley & Sons.*

Due to the high cell performance of the wafers from this growth technology, the name of "high-performance mc-Si" has been widely used by the PV industry since 2012.

Figure 10.18 shows the PL images of the A+++ wafers from the center brick. As shown in Figure 10.18(a), in the early stage, dislocation clusters were localized in intragrains, and often disappeared when those grains were overgrown by others. Accordingly, the defect multiplication was easily terminated. However, near the later stage of the growth in Figure 10.18(b), where the grains became larger, more defects were induced. Again, they tended to be localized in smaller grains surrounded by the large grains. Because the stress was concentrated again in the small defective grains, the stress could be greatly relaxed. As a result, the massive multiplication in the big grains was much less as compared with that in the conventional growth [66,67]. Nevertheless, more dislocations were also observed in bigger grains at the latter stage, and they were more vulnerable to the propagation of dislocations because less grain boundaries were available to stop them. It needs to be pointed out that the thermal stress during solidification was inevitable, and particularly silicon expanded as it solidified. The generation of dislocations during plastic deformation was an effective way for stress relaxation. The sacrifice of small defective grains seemed to be critical in this technology, and interestingly enough, the small defective grains could easily be overgrown by healthy grains.

The development of grain orientation is shown in Figure 10.19(a). As shown, the grains in {112} seemed to be dominant; {113}, {111}, and {315} grains were also present in large portions. The reason for having more {112} grains was not clear, but {112} grains have the smallest interfacial energy next to {111}. Because we did not find dendrite grains in the wafers, the {112} orientation was not originated from the dendrite growth mechanism [61–64,102]. Interestingly, in the study of the grain development in notched

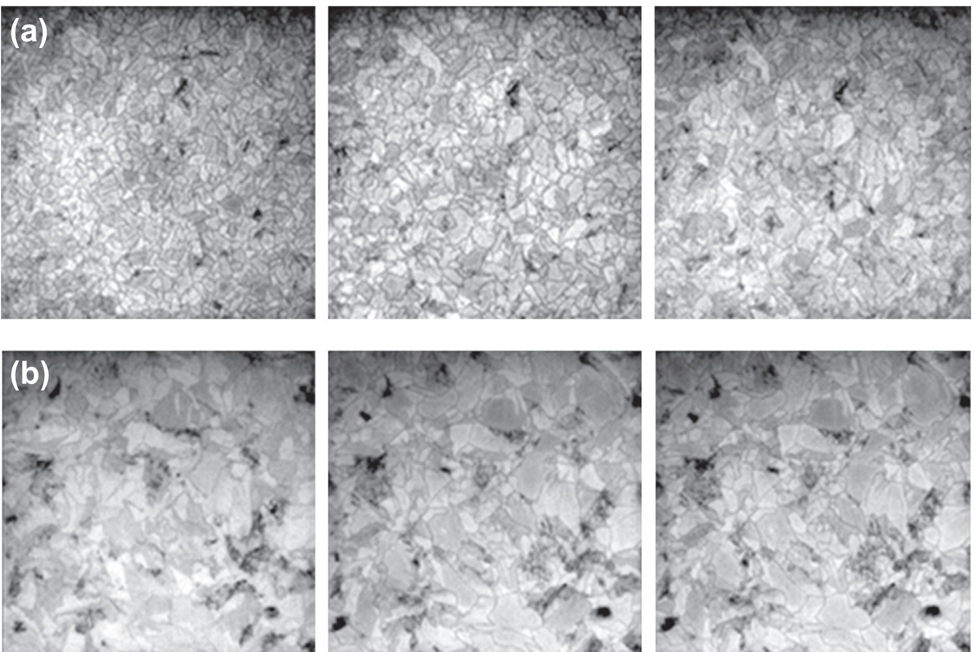

FIGURE 10.18 PL images of the wafers. (a) Initial stage (within the first 10 cm); (b) later stage (in the last 10 cm); the sequence of the development of grains and defects at different heights is shown from the left to right.
Ref. [67] with permission of Wiley & Sons.

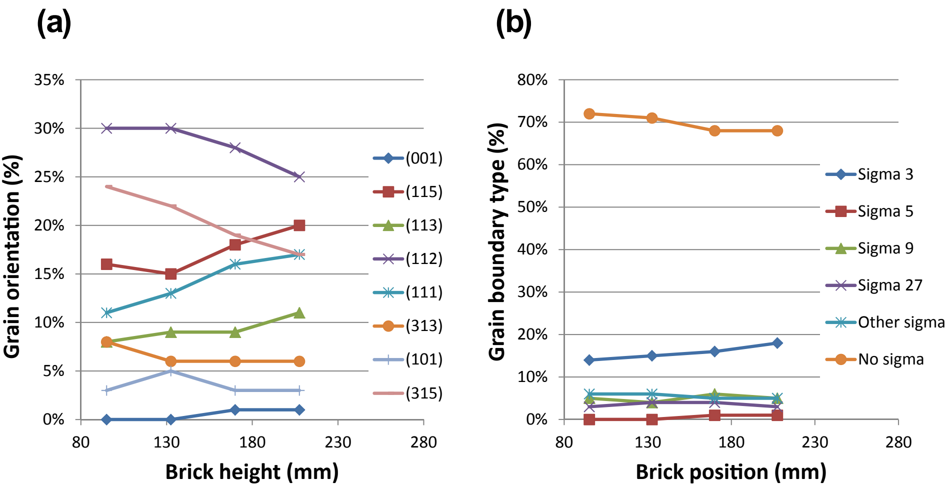

FIGURE 10.19 Development of (a) grain orientations and (b) grain boundary types. *Ref. [67] with permission of Wiley & Sons.*

crucibles, Li et al. [3] also observed the rapid transition from {110} to {112} orientations in the small notch. The increase of {111} grains might also indicate the reduction of interfacial energy during solidification. On the other hand, the twin formation from {111} facets also played a crucial role in the grain competition by forming new grains and twin boundaries [130,131]. Recently, Wong et al. [132] carried out ingot growth from silicon beads with random orientations at different crucible pulling speeds, and the detailed grain selection mechanisms were discussed.

Moreover, due to the random nucleation from the small seeds, the percentage of non-sigma random grain boundaries was over 70% at the beginning, as shown in Figure 10.19(b). In the conventional casting process, the percentage is usually lower than 50%. Especially for the dendritic casting method, the percentage of the random grain boundaries could be less than 30%; more than 80% of Σ3 twin boundaries were found as well in a small-scale DS furnace by Yeh et al. [63]. Nevertheless, as shown in Figure 10.19(b), as the mc-Si grew with height, more Σ3 twin boundaries were generated in consuming the random grain boundaries. Again, as discussed by Nadri et al. [131], twin nucleation from {111} facets was the mechanism for new grains, and this also led to the increase of the Σ3 twin boundaries. Wong et al. [132] also observed that as a new grain, which could be a low or high energy grain, appeared, it was accompanied by twin boundaries. If a high energy grain was bounded by noncoherent grain boundaries, it tended to be overgrown by the low energy grains, and the associated noncoherent grain boundaries disappeared. Therefore, the reduction of noncoherent grain boundaries was due to grain competition that favors low energy grains, while the increase of the twin boundaries was due to twin formation from {111} facets. However, due to the twin formation, the high energy grains could also be generated, so that they would not disappear completely.

Because of the noncoherent nature of the random grain boundaries, the thermal stress might be better relaxed. Although there was no clear evidence of the grain boundary slip, no residual stress was found in the noncoherent grain boundaries of mc-Si wafers, but residual stress existed at the Σ3 grain boundaries [133]. Hoshikawa et al. [134] also designed a nice experiment using polycrystalline seeds for Cz crystal growth, and they found that dislocations and subgrain boundaries appeared easily from the semicoherent grain boundaries. The noncoherent grain boundaries did not have significant internal energy for defect generation.

The technology for high performance mc-Si has been widely adopted in production. The grain structures of the wafers from most companies are all very similar, such as S2 and S3 wafers from GCL [135], M3 wafers from LDK, A2+ from RenaSolar, HP3 from Nexlon, A4+ from GET, etc. They had uniform and fine grains in the portion near the bottom ingot. The high performance mc-Si wafers give the solar cells not only the high efficiency but also the narrow distribution in the performance. In a recent report from JA Solar [136], the lifetime mappings of the ingots grown by traditional DS, split mono-seeded, and the small-chip seeded growth were compared. As shown in Figure 10.20, the high performance mc-Si had the most uniform lifetime distribution. Nevertheless,

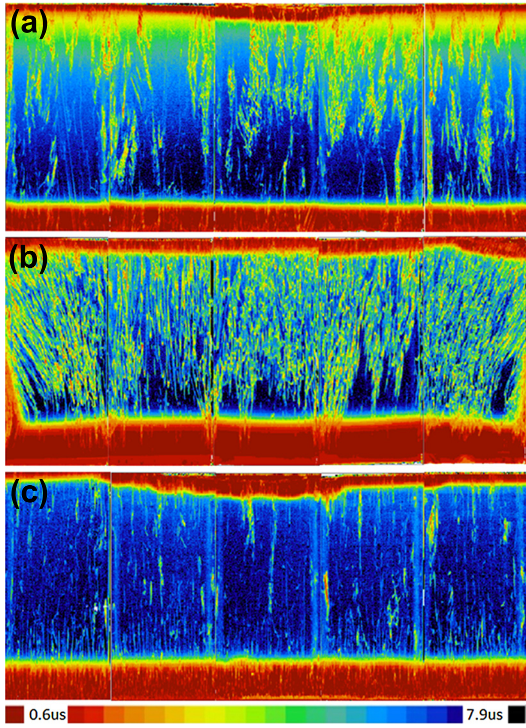

FIGURE 10.20 Comparison of the lifetime mappings from ingots grown by (a) traditional method; (b) split mono-seeded method; (c) chip-seeded method. *Ref. [136] with permission of Prof. Xinming Huang.*

both seeded growths had a much thicker red zone (>5 cm) at the bottom, and this decreased the production yield. The propagation of the defects from the seed joints, as shown in Figure 10.20(b), was a serious issue in production. According to their report, they had shifted all the production to high performance mc-Si due to the robustness of the technology, as well as the uniformity and the good quality of the wafers. The use of nucleation other than silicon seeds was also reported to reduce the red zone [129], and the small and uniform grains could also be obtained at the initial stage of the growth.

10.4.3 Mono-like Casting

In addition to mc-Si, monocrystalline Si ingots could also be grown with monocrystalline seeds, i.e., the so-called mono-like or quasi-mono casting. In fact, at the beginning of the development of DS growth for silicon ingots, seeded growth was considered [137,138]. The main reason that this technology did not continue was that the quality of the ingot was not as good as the mc-Si ingot grown without seeds. The seeded growth was brought into attention again by BP Solar in 2007 using split seeds [139,140], and the product with the similar name, either mono-like, cast-mono, or quasi-mono, has been adopted by industry quickly since then. The major issues are: (1) nucleation from the crucible wall

and the joints of split seeds; (2) the generation and multiplication of dislocation from the seeds, especially from the joints of split seeds, as discussed for Figure 10.20(b); and (3) seed cost. The first issue has been better understood, and nowadays 90% of the ingot could remain almost monocrystalline. The third issue is been mitigated by the better control of the interface shape and the back melting, so that the seed thickness could be greatly reduced to 1–3 cm. Furthermore, to save the cost, the seeds could be recycled for a couple times without much affecting the ingot quality. However, the second issue is much more troublesome. Although some ideas in the patent literature have been proposed to overcome the problems using different seeding concepts, the control of dislocation multiplication is still difficult. Recently, Jouini et al. [141] have reported some nice results for n-type mono-like ingots. Figure 10.21(a) shows the arrangement of the {100} seeds in their G5 experiment. As shown, in addition to the central 5×5 seeds, there are also some extra seeds near the edge. These seeds could be used to accommodate the red zone or the grains nucleated from the wall. Recently, Kutsukake et al. [142] arranged the orientation of the extra seeds to have the {310} $\Sigma5$ grain boundaries within central seeds, and they could suppress the inward growth of the grains from the crucible wall. The appearance of the grown crystal by Jouini's group is shown in Figure 10.21(b), and the seed print could be clearly seen from the top surface. Moreover, if defects existed in the edges of the seeds, as shown on the left of Figure 10.21(c), they could easily multiply upward. However, for the nondislocated grain boundaries, as shown on the right figure, no defect propagation was observed. Again, the bottom red zone, the same as that in Figure 10.20(b), was also thick. The best part of the ingot, near the middle height, was used for making heterojunction solar cells, and cell efficiency of 21.57% was achieved [141].

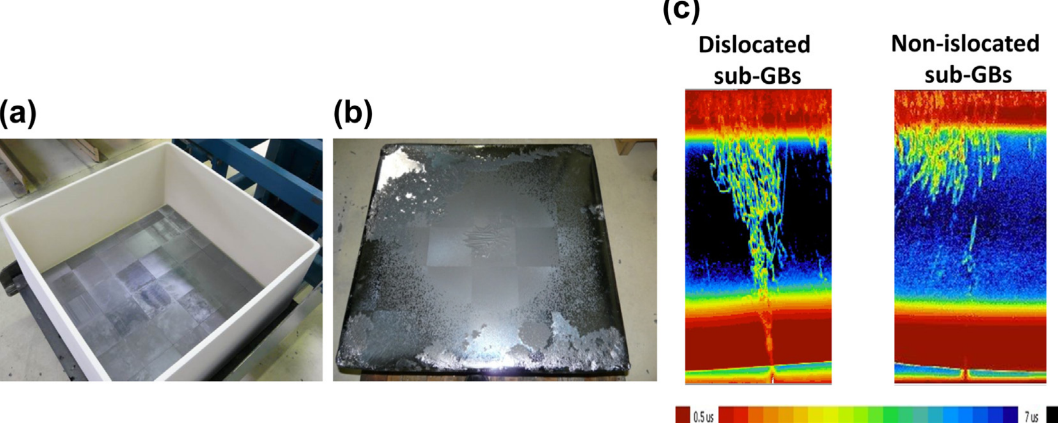

FIGURE 10.21 (a) Arrangement of {100} seeds (5×5) at the bottom of the crucible; (b) as grown mono-like ingot; (c) two different lifetime mappings of the block from the dislocated subgrain boundaries (left) and nondislocated subgrain boundaries originated from the junction of the seeds. *Ref. [141] with permission of Dr. A. Jouini.*

Recently, Trempa et al. [143] reported a systematic study to understand the new grain formation from the crucible wall and the junction of split seeds. They used seeds with orientation varied between <100>, <111>, and <110>; in some cases, split seeds was considered. They showed that the nucleation at the crystal periphery as well as the gap between the split seeds depends on the seed orientation. The typical <100> direction turned out to be the most difficult one. The twin nucleation at the {111} facets was used to explain the formation of misoriented grains, as illustrated in Figure 10.22(a). As shown in the figure, as the undercooling DT at the edge is high enough for nucleation, the layer L, which could be oriented or misoriented, grows until it reaches the melt/solid interface. The process repeats until the undercooling is not enough for nucleation. This growth mode, the so-called Frank–van der Merwe growth [144], is quite rapid as compared to the normal growth rate of the facet. For example, if the growth is in <100> direction, the twins are nucleated from the crucible wall at $\alpha = \beta = 45°$; β is the orientation angle of the facet with respect to the temperature gradient, and $\alpha = 90^{\circ} - \beta$. Then, the twin orientation is {221}, which is consistent with the calculations by Wilhelm [145] for the first-order twinning on {111}. Figure 10.22(b) is an example of new grain formation from the crucible wall for the growth from a {100} seed. To avoid the stress from the crucible or the twining from the crucible, a top-seeded growth, the so-called noncontact crucible method, was also proposed [146–148]. This method is rather similar to the Kyropoulos method, typically used in sapphire growth. High quality silicon ingots with low oxygen

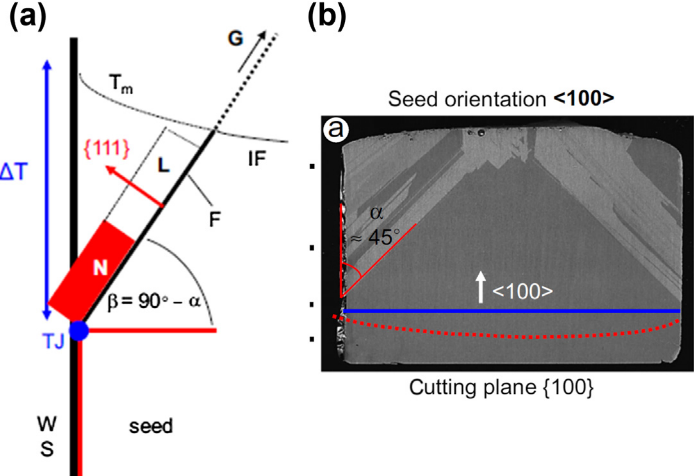

FIGURE 10.22 (a) Sketch of a seed edge near the crucible wall W or another seed crystal S with a {111} facets plane (bold line F) oriented at an angle to the horizontal *x* direction. TJ is the position of the triple junction melt–seed–crucible wall or melt–seed–seed. A two-dimensional nucleus N is formed at the lower edge of the {111} facet where the supercooling DT is maximum (at TJ). The size of the nucleus N is blown up in the figure as help for the eye. The nucleus N grows in direction of the arrow G, thus completing the layer L until it reaches the melting point isotherm T_m (dotted line). The melting point isotherm T_m is identical to the interface IF where the original seed grows with an on-facetted interface; (b) Scan image revealing the <100> grain orientation of the vertical cut at {100}. *Ref. [143] with permission of Elsevier.*

content, due to low thermal gradients (week flow) and noncoated crucibles, were reported with a diameter up to 30 cm. With sufficiently low radial thermal gradients, square-shaped ingots with {110} side faces were also grown [149].

Since 2010, a few companies have jumped into the production of mono-like ingots. However, because of the higher seed cost and the longer cycle time due to dipping for the back melting of the seeds, the production cost for mono-like ingots is higher. In addition, the distribution of the solar cell efficiency made from the mono-like wafers is also wider. Hence, the market penetration of mono-like wafers is not much. Although some promising results have been reported as just discussed, the success in mass production with good quality is very limited. Particularly, after the development of high performance mc-Si since 2011 [66,67], the market share of the mono-like product became very small.

10.5 Conclusions

Due to the low cost production and high throughput of the mc-Si grown by the DS method, the solar cells based on mc-Si have become the mainstream in recent years. The crystal quality has improved significantly over the years through the basic understanding of crystal growth. The most important two factors are impurities and dislocations. We have discussed how the impurities, as well as their precipitates, and the dislocations affect the lifetime time and the solar cell performance. How to control them has also been discussed. Although the high performance mc-Si technology is emerging and becoming the mainstream in mass production, other crystal growth technologies are still in progress. A promising one is the mono-like technology, either using the bottom- or top-seeded approach. However, the control of growth defects, particularly the dislocation clusters, remains the key issue. On the other hand, further reduction of the impurities is also necessary to increase the ingot lifetime, but this would rely more on the effort from the crucible and silicon nitride suppliers. Moreover, using cheaper UMG or SoG silicon as the feedstock could be an effective way for cost reduction. However, the balance between cost and quality is necessary.

References

[1] Winneker C. Global Market Outlook for Photovoltaics until 2016. EPIA report 2012.

[2] Mouller HJ, Funke E, Rinio M, Scholz S. Thin Solid Film 2005;487:179.

[3] Li TF, Huang HC, Tsai HW, Lan A, Hsu C, Lan CW. J Cryst Growth 2012;340:202.

[4] Wei J, Zhang H, Zheng L, Wang C, Zhao B. Sol Energy Mater Sol Cells 2009;93:1531.

[5] Kvande R, Arnberg L, Martin C. J Cryst Growth 2009;311:765.

[6] Martin C, Rancoule G, Dupuy L, Mabrut M. 2CV4.43 2012.

[7] Olsen E, Øvrelid EJ. Prog Photovolt Res Appl 2008;16:93.

[8] Degoulange J, Martin C, Arnberg L, Ndzogha C, Pihan E, Dubois S. CSSC-6, 1261 2012.

[9] Coletti G, Macdonald D, Yang D. Chapter 3. In: Pizzini S, editor. Advanced silicon materials for photovoltaic applications. John Wiley & Son; 2012. p. 79.

[10] Buonassisi T, Istratov AA, Pickett MD, Rakotoniaina J-P, Breitenstein O, Marcus MA, et al. J Cryst Growth 2006;287:402.

[11] Brynjulfsen I, Bakken A, Tangstad M, Arnberg L. J Cryst Growth 2010;312:2404.

[12] Drevet B, Pajani O, Eustathopoulos N. Sol Energy Mater Sol Cells 2010;94:425.

[13] Saito T, Shimura A, Ichikawa S. Sol Energy Mater 1983;9:337.

[14] Prakash P, Singh PK, Singh SN, Kishore R, Das BK. J Cryst Growth 1994;144:41.

[15] Parthasarathy SR, Wan Y, Chartier S, Talbott JA, Gupta KP. US Patent 7,540,919 B2 (1009).

[16] Minster O, Granter J, Potard C, Eustathopoulos N. J Cryst Growth 1987;82:155.

[17] Huguet C, Brizé V, Bailly S, Lignier H, Flahaut E, Drevet B, et al. 26th European Photovoltaic Solar Energy Conference and Exhibition, Hamburg, Germany; 2011.

[18] Khattak CP, Schmid F. US Patent 0211496 A1 2004.

[19] Julsrud S, Naas TL. WO Patent 148987 A1 2007.

[20] Roligheten R, Rian G, Julsrud S. WO Patent 48986 A1 2007.

[21] Buonassisi T, Istratov AA, Heuer M, Marcus MA, Jonczyk R, Isenberg J, et al. J Appl Phys 2005;97:74901.

[22] Buonassisi T, Marcus MA, Istratov AA, Heuer M, Ciszek TF, Lai B, et al. J Appl Phys 2005;97:63503.

[23] Buonassisi T, Istratov A, Marcus MA, Lai B, Cai Z, Heald SM, et al. Nat Mater 2005;4:676.

[24] Buonassisi T, Istratov AA, Pickett MD, Heuer M, Kalejs JP, Hahn G, et al. Prog Photovolt Res Appl 2006;14:513.

[25] Buonassisi T, Istratov AA, Pickett MD, Marcus MA, Ciszek TF, Webe ER. Appl Phys Lett 2006;89:042102.

[26] Coletti G, Bronsveld PCP, Hahn G, Warta W, Macdonald D, Ceccaroli B, et al. Adv Funct Mater 2011;21:879.

[27] Fenning DP, Hofstetter J, Bertoni MI, Coletti G, Lai B, del Canizo C, et al. J Appl Phys 2013;113:044521.

[28] Liu L, Nakano S, Kakimoto K. J Cryst Growth 2006;292:515.

[29] Nozaki T, Yatsurugi Y, Akiyama N. J Electrochem Soc 1970;117:1566.

[30] Yatsurugi Y, Akiyama N, Endo Y, Nozaki T. J Electrochem Soc 1973;120(7):975.

[31] Endo Y, Yatsurugi Y, Terai Y, Nozaki T. J Electrochem Soc 1979;126(8):1422.

[32] Engh TA, Simensen CJ. Principles of metal refining. Oxford University Press; 1992.

[33] Reimann C, Trempa M, Jung T, Friedrich J, Muller G. J Cryst Growth 2010;312:878.

[34] Ihlal A, Rizk R, Hardouin Duparc OBM. J Appl Phys 1996;80:2665.

[35] Chen J, Sekiguchi T, Yang D, Yin F, Kido K, Tsurekawa S. J Appl Phys 2004;96:5490.

[36] Chen J, Yang D, Zhenqiang X, Sekiguchi T. J Appl Phys 2005;97:033701.

[37] Chen J, Sekiguchi T. Jpn J Appl Phys 2007;46:6489.

[38] Schmidt J, Aberle AG, Heze R. Proceedings of 26th IEEE Photovoltaic Specialists Conference, 13; 1997.

[39] Saitoh T, Wang X, Hashigami H, Abe T, Igarashi T, Glunz S, et al. Sol Energy Mater Sol Cells 2001;65:277.

[40] Matsuo H, Ganesh RB, Nakano S, Liu LJ, Kangawa Y, Arafune K, et al. J Cryst Growth 2008;310:2204.

[41] Moller HJ, Long L, Werner M, Yang D. Phys Stat Sol (A) 1999;171:175.

[42] Trempa M, Reimann C, Friedrich J, Mueller G. J Cryst Growth 2010;312:1517.

[43] Trempa M, Reimann C, Friedrich J, Muller G. J Cryst Growth 2010;312:1510.

[44] Mouller HJ, Kaden T, Scholz S, Wurzner S. Appl Phys A Mater Sci Process 2009;96:207.

[45] Raabe L, Patzold O, Kupka I, Ehrig J, Wurzner S, Stelte M. J Cryst Growth 2011;318:234.

[46] Gao B, Nakano S, Kakimoto K. J Cryst Growth 2011;318:255.

[47] Coletti G, Mulder CL, Galbiati G, Geerligs LJ. Proceedings of the 21st EU-PVSEC, Dresdon, 1515; 2006.

[48] Yu X, Yang DR, Ma X, Li L, Que Q. Semicond Sci Technol 2003;18:399.

[49] Coletti G. Prog Photovolt Res Appl 2013;21:1163.

[50] MacDonald D, Geerligs JL. Proceedings of the 19th European photovoltaic solar Energy Conference, Paris, France; 2004. p. 492.

[51] Martinuzzi S, Warchol F, Dubois, Enjalbert N. Mater Sci Eng B 2009;159–160:253.

[52] Bentzen A, Holt A. Mater Sci Eng B 2009;159–160:228.

[53] Coletti G, Kvande R, Mihailetchi VD, Geerligs LJ, Arnberg L, Øvrelid EJ. J Appl Phys 2008;104: 104913.

[54] Arafune K, Sasaki T, Wakabayashi F, Terada Y, Ohshita Y, Yamaguchi M. Phys B 2006;376–377:236.

[55] Ryningen B, Stokkan G, Kivambe M, Ervik T, Lohne O. Acta Mater 2011;7703.

[56] Takahashi I, Usami N, Kutsukake K, Stokkan G, Morishita K, Nakajima K. J Cryst Growth 2010; 312:897.

[57] Schmid E, Würzner S, Funke C, Galindo V, Pätzold O, Stelter M. J Cryst Growth 2012;359:77.

[58] Stokkan G, Rosario C, Berg M, Lohne O. High temperature annealing of dislocations in multicrystalline silicon for solar cells. In: Rugescu R, editor. Solar power. InTech; 2009.

[59] Ervik T, Kivambe M, Stokkan G, Ryningen B, Lohne O. Acta Mater 2012;60:6762.

[60] Schmid E, Funke C, Behm T, Patzold O, Berek H, Stelter M. J Cryst Growth 2013.

[61] Fujiwara K, Pan W, Sawada K, Tokairin M, Usami N, Nose Y, et al. J Cryst Growth 2006;292:282.

[62] Wang TY, Hsu SL, Fei CC, Yei KM, Hsu WC, Lan CW. J Cryst Growth 2009;311:263.

[63] Yeh KM, Hseih CK, Hsu WC, Lan CW. Prog Photovolt Res Appl 2010;18:265.

[64] Lan CW, Lan WC, Li TF, Yu A, Yang YM, Hsu C, et al. J Cryst Growth 2012;360:68.

[65] Nakajima K, Kutsukake K, Fujiwara K, Morishita K, Ono S. J Cryst Growth 2011;319:13.

[66] Lan CW, Yang YM, Yu A, Hsu B, Yang A. The 27th European Photovoltaic Solar Energy Conference (27th EU PVSEC), Frankfurt; September 24–28, 2012.

[67] Yang YM, Yu A, Hsu B, Hsu WC, Yang A, Lan CW. Prog Photovolt Res Appl 2013. http://dx.doi.org/10.1002/p.p.2437. Wiley online library.

[68] Tsai CT. J Cryst Growth 1991;113:499.

[69] Miyazaki N, Okuyama SJ. J Cryst Growth 1998;183:81.

[70] Rabier J, Pizzagalli L, Demenet JL. In: Hirth JP, Kubin L, editors. Dislocations in solids, vol. 16. The Netherlands: North-Holland; 2010. p. 47.

[71] Chen X, Nakano S, Kakimoto K. J Cryst Growth 2010;312:3261.

[72] Fang HS, Wang S, Zhou L, Zhou NG, Lin MH. J Cryst Growth 2012;346:5.

[73] Fang H, Zhang Q, Pan Y, Wang S, Zhou N, Zhou L, et al. J Thermal Stresses 2013;36:947.

[74] Bellmann MP, Kaden T, Kressner-Kiel D, Friedl J, Muoller HJ, Arnberg L. J Cryst Growth 2011;325:1.
[75] Lan CW, Ting CC. J Cryst Growth 1995;149:175.
[76] Chen L, Dai B. J Cryst Growth 2012;354:86.
[77] Ma W, Zhong G, Sun L, Yu Q, Huang X, Liu L. Sol Energy Mater Sol Cells 2012;100:231.
[78] CrysMas: user manual and tutorial. Crystal growth laboratory, Fraunhofer IISB; 2011.
[79] Ding C, Huang M, Zhong G, Ming L, Huang X. J Cryst Growth 2014;387:73.
[80] Nara S, Sekiguchi T. J Chen Eur Phys J AP 2004;27:389.
[81] Jouini A, Fortin G, Pihan E, Amaral V, Camel D, Jay F, et al. The 27th European Photovoltaic Solar Energy Conference (27th EU PVSEC), Frankfurt; September 24–28, 2012.
[82] Arafune K, Ohishi E, Sai H, Ohshita Y, Yamaguchi M. J Cryst Growth 2007;308:5.
[83] Teng Y-Y, Chen J-C, Lu C-W, Chen C-Y. J Cryst Growth 2010;312:1282.
[84] Rudolph P, Kakimoto K. MRS Bull 2009;34(4):251.
[85] Zharikov EV. In: Capper P, Rudolph P, editors. Crystal growth technology: semiconductors and dielectrics. Weinheim: Wiley-VCH; 2010. p. 41.
[86] Bellmann P, Meese EA, Arnberg L. J Cryst Growth 2011;318:239.
[87] Grants I, Gerbeth G. J Cryst Growth 2008;310:3699.
[88] Frank-Rotsch Ch, Rudolph P. J Cryst Growth 2009;311:2294.
[89] Kudla Ch, Lumenau AT, Ullesfeld F, Ropka N, Frank-Rotsch Ch, Kiessling F, et al. J Cryst Growth 2013;365:54.
[90] Dropka N, Miller W, Rehse U, Rudolph P, Buellesfeld F, Sahr U, et al. J Cryst Growth 2011;318:275.
[91] Dropka N, Frank-Rotsch C, Rudolph P. J Cryst Growth 2013;365:64.
[92] Bellmann MP, Panjwani B, Syvertsen M, Meese EA. J Cryst Growth 2013;369:47.
[93] Reimann C, Friedrich J, Dietrich M, WO Patent 100694A1 2009.
[94] Gao B, Chen XJ, Nakano S, Kakimoto K. J Cryst Growth 2010;312:1572.
[95] Teng Y-Y, Chen JC, Lu C-W, Chen H-I, Hsu C, Chen C-Y. J Cryst Growth 2011;318:224.
[96] Istratov AA, Hieslmair H, Weber ER. Appl Phys A Mater Sci Process 1999;69:13.
[97] Ramappa DA, Henley WB. J Electrochem Soc 1997;144:4353.
[98] Martinuzzi S, Perichaud I, Palais O. Sol Energy Mater Sol Cells 2007;91:1172.
[99] Gao B, Nakano S, Kakimoto K. Cryst Growth Des 2012;12:522.
[100] Yu X, Gu X, Yuan S, Guo K, Yang D. Scr Mater 2013;68:655.
[101] Yang K, Schwuttke GH, Ciszek TF. J Cryst Growth 1980;50:301.
[102] Fujiwara K, Pan W, Usami N, Sawada K, Tokairin M, Nose Y, et al. Acta Mater 2006;54:3191.
[103] Wang HY, Usami N, Fujiwara K, Kutsukake K, Nakajima K. Acta Mater 2009;57:3268.
[104] Stokkan G. Acta Mater 2010;58:3223.
[105] Usami N, Yokoyama R, Takahashi I, Kutsukake K, Fujiwara K, Nakajima K. J Appl Phys 2010;107:013511.
[106] Würzner S, Helbig Funke RC, Möller HJ. J Appl Phys 2010;108:083516.
[107] Martinelli G, Kibizov R. Appl Phys Lett 1993;62:3262.
[108] Endrös AL. Mono- and tri-crystalline Si for PV production. Sol Energy Mater Sol Cells 2002;72:109.
[109] Chen J, Sekiguchi T, Xie R, Ahmet P, Chikyo T, Yang D, et al. Scr Mater 2005;52:1211.

[110] Khattak CP, Schmid F. In: Khattak CP, Ravi KV, editors. Silicon processing for photovoltaics II. Elsevier Science Publishers; 1987. p. 153.

[111] Koch W, Endrös AL, Franke D, Haßler C, Kalejs JP, Moller HJ. In: Luque A, Hegedus S, editors. Handbook of photovoltaic science and engineering. John Wiley & Sons; 2003. p. 205.

[112] Sabatino M, Juel M, Arnberg L, Syvertsen M, Traneli G. Trans Indian Inst Met 2009;62:511.

[113] Brynjulfsen I, Arnberg L. J Cryst Growth 2011;331:64.

[114] Tsai HW, Yang M, Hsu C, Lan CW. J Cryst Growth 2013;363:242.

[115] Li TF, Yeh KM, Hsu WC, Lan CW. J Cryst Growth 2011;318:219–23.

[116] Fujiwara K, Obinata Y, Ujihara T, Usami N, Sazaki G, Nakajima K. J Cryst Growth 2004;262:124.

[117] Billig E. Proc R Soc A 1955;229:346.

[118] Wagner RS. Acta Metal 1960;8:57.

[119] Hamilton DR, Seidensticke RG. J Appl Phys 1960;31:1165.

[120] Hamilton DR, Seidensticker RG. J Appl Phys 1963;34:1450.

[121] Leung KK, Kui HW. J Appl Phys 1994;75:1216.

[122] Nagashio K, Kuribayashi K. Acta Mater 2005;53:3021.

[123] Fujiwara K, Maeda K, Usami N, Sazaki G, Nose Y, Nakajima K. Scr Mater 2007;57:81.

[124] Nakajima K, Kutsukake K, Fujiwara K, Usami N, Ono S, Yamasaki I. High efficiency solar cells using small size ingots with 30 cmφ by controlling the distribution and orientation of dendrite crystals grown along the bottom of the ingots. In: Proceedings of the 35th IEEE Photovoltaic Specialists Conference; 2010. pp. 817–9.

[125] Nakajima K, Kutsukake K, Fujiwara K, Usami N, Ono S, Yamasaki I. Proceedings of the 25th European Photovoltaic Solar Energy Conference and Exhibition (25th EU PVSEC), The 5th World Conference on Photovoltaic Energy Conversion (WCPEC-5), 1299;2010.

[126] Nakajima K, Usami N, Fujiwara K, Kutsukake K, Okamoto S. Proceedings of 24th European Photovoltaic Solar Energy Conference; 2009. 1219–1221.

[127] Brynjulfsen I, Arnberg L, Autruffe A. J Cryst Growth 2012;361:206.

[128] Zhang H, Zheng L, Ma X, Zhao B, Wang C, Xu F. J Cryst Growth 2011;318:283.

[129] Lan CW, Yang YM, Yu A, Hsu B, Hsu WC, Yang A. The 7th International Conference on Crystalline Silicon Solar Cells, Fukuoka, Japan; October 22–25, 2013.

[130] Voronkov VV. Sov Phys Crystallogr 1975;19:573.

[131] Nadri A, Duterrail-Couvat Y, Duffar T. The 7th Internal Workshop on Modeling in Crystal Growth, Taipei; October 29–31, 2012.

[132] Wong YT, Hsu B, Lan CW. J Cryst Growth 2013;387:10.

[133] Chen J, Chen B, Sekiguchi T, Fukuzawa M, Yamada M. Appl Phys Lett 2008;93:112105.

[134] Hoshikawa T, Taishi T, Huang X, Uda S, Yamatani M, Shirasawa K, et al. J Cryst Growth 2007;307: 466.

[135] Tang X, Francis LA, Gong L, Wang F, Raskin JP, Flandre D, et al. Sol Energy Mater Sol Cells 2013; 117:225.

[136] Huang X, Huang M, Ding C, Zhu D, Min H. The 7th International Conference on Crystalline Silicon Solar Cells, Fukuoka, Japan; October 22–25, 2013.

[137] Helmreich D. In: Ravi KV, O'Mara B, editors. Proceedings of the Symposium on Electronic and Optical Properties of Polycrystalline or Impure Semiconductors and Novel Silicon Growth Methods, St. Louis. Pennington: Electrochemical Society; 1980.

[138] Khattak CP, Schmid F, Hunt LP. NASA Technical Report. In: Silicon ingot casting phase 3 and 4; 1982.

[139] Stoddard N, BP Corp., WO Patent 084936 A2 2007.

[140] Stoddard N, Wu B, Witting I, Wagener M, Park Y, Rozgonyi G, et al. Solid State Phenom 2008;1:131.

[141] Jouini A, Jay F, Amaral V, Pihan E, Veschetti Y. The 7th International Conference on Crystalline Silicon Solar Cells, Fukuoka, Japan; October 22–25, 2013.

[142] Kutsukake K, Usami N, Ohno Y, Tokumoto Y, Yonenaga I. Appl Phys Express 2013;6:025505.

[143] Trempa M, Reimann C, Friedrich J, Mueller G, Oriwol D. J Cryst Growth 2012;351:131.

[144] Frank FC, van der Merwe JH. Proc R Soc Lond A 1949;198:205.

[145] Wilhelm F. J Appl Crystallogr 1971;4:521.

[146] Nakajima K, Murai R, Morishita K, Kutsukake K, Usami N. J Cryst Growth 2012;344:6.

[147] Nakajima K, Morishita K, Murai R, Kutsukake K. J Cryst Growth 2012;355:38.

[148] Nakajima K, Murai R, Morishita K, Kutsukake K. J Cryst Growth 2013;372:121.

[149] Nakajima K, Murai R, Morishita K. Jpn J Appl Phys 2014;53:025501.

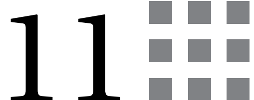

The Unidirectional Crystallization of Metals and Alloys (Turbine Blades)

Krzysztof Kubiak, Dariusz Szeliga, Jan Sieniawski, Arkadiusz Onyszko

THE FACULTY OF MECHANICAL ENGINEERING AND AERONAUTICS, DEPARTMENT OF MATERIALS SCIENCE, RZESZOW UNIVERSITY OF TECHNOLOGY, RZESZOW, POLISH, POLAND

CHAPTER OUTLINE

11.1 Introduction ... 414
11.2 DS Castings Manufacturing ... 415
11.2.1 DS Casting Manufacturing Methods ... 415
11.2.1.1 Power Down Method ... 415
11.2.1.2 Bridgman Method – High Rate Solidification ... 416
11.2.1.3 LMC Method ... 418
11.2.1.4 GCC Method ... 418
11.2.2 Manufacture of SC Castings ... 418
11.2.2.1 Grains Selector ... 418
11.2.2.2 Solidification from the Seed ... 420
11.2.3 Parameters for Manufacture of Directional Solidification Castings ... 421
11.3 Nickel-based Superalloys and Heat Treatment Process ... 423
11.4 Methodology for Manufacture of Ceramic Shell Molds for Directional Solidification Casting ... 425
11.4.1 Ceramic Materials for Molds and Their Production Methods ... 425
11.4.1.1 Zirconium Silicate ... 425
11.4.1.2 Aluminosilicates and Mullite ... 427
11.4.1.3 Corundum ... 428
11.4.1.4 Zirconium Dioxide ... 429
11.4.1.5 Binder ... 429
11.4.2 Manufacturing of Elements and Wax Model Assemblies ... 430
11.4.3 Manufacturing of Ceramic Shell Molds ... 431
11.4.4 Ceramic Shell Mold Investigation Methods ... 434
11.5 Investigation Methods for Directional Solidification Castings ... 435
11.5.1 Testing of Mechanical Properties ... 435

Handbook of Crystal Growth. http://dx.doi.org/10.1016/B978-0-444-63303-3.00011-0
Copyright © 2015 Elsevier B.V. All rights reserved.

11.5.2 Macro and Microstructure Investigation 436
11.5.3 Porosity Investigation 442
11.5.4 Determination of Crystal Perfection and Crystallographic Orientation (Laue and XRD Methods) 444
11.6 Numerical Modeling of Thermal and Solidification Processes for Directional Solidification Castings 447
11.6.1 Analytical Thermal Analysis of Directionally Solidified Casting 448
11.6.2 Numerical Modeling of Temperature Field 451
11.6.3 Numerical Modeling of Nucleation and Grain Growth 452
11.7 Summary 454
References 455

11.1 Introduction

Trends in development of aircraft turbine engines seek to increase their economy (reduced specific fuel consumption) and specific thrust (power), by increasing the exhaust gas temperature before the turbine and the airflow through the engine. Performance and development of aircraft engines turbines and industrial gas turbines (IGT) are strongly associated with new heat resistant materials, especially nickel, cobalt, and titanium-based superalloys, and additionally with protective layers and thermal barrier coatings. The maximum allowed temperature of the turbine exhaust gas inlet depends on the microstructure and properties of the materials used for components of aircraft engine turbine hot parts, particularly of the high pressure turbine blades. Due to aircraft engines' safe operation, they are subject to special requirements in the manufacturing process and quality control. Research carried out in many laboratories is designed to increase mechanical properties, creep, fatigue, fracture, and corrosion resistance of turbine blades at high temperature.

These requirements are met by directionally solidified (DS) castings of nickel-based superalloys. Their microstructure and properties depend mainly on chemical composition, the conditions of solidification process, and the heat treatment. Formation of columnar grains is performed thanks to heat flow control and mechanism of competitive grain growth along the height of the casting. Single crystal (SC) castings can be achieved thanks to specially designed ceramic molds and by using the starter and grains selector. Eliminating wide-angle grain boundaries in the casting results in significant improvement in creep resistance. Nowadays, more and more attempts are being made to replace the DS casting by a SC casting, especially in large castings of IGT elements. Nickel-based superalloy SC castings used in aircraft engine turbines and IGT are produced by Bridgman – high rate solidification (HRS) and liquid metal cooling (LMC) methods.

For manufacturing of nickel-based superalloy SC castings it is necessary to establish the critical pulling rate. This value and the method of casting are crucial to the

temperature gradient and cooling rate, which determine the shape of the solidification front and thus the microstructure of the casting. An increase in cooling rate reduces the distance between the primary and secondary dendrite arm spacing, fragmentation of the γ/γ' eutectic and the γ' phases, which reduces dendritic microsegregation and the time and cost of further heat treatment process. Temperature gradient and the alloy chemical composition influence the type and amount of defects (freckle defects, strain grains, high and low angle boundaries) especially in large-size castings. The increase in the temperature gradient along the axis of the casting reduces the size of mushy zone and tendency to create freckles, spurious grains, and shrinkage porosity.

11.2 DS Castings Manufacturing

11.2.1 DS Casting Manufacturing Methods

Manufacturing of castings by directional solidification method is based on the movement of ceramic mold, filled with molten metal, and at a certain speed, from the heating zone to the cooling area. In this way, positive value of the temperature gradient and a movement of the continuous solidification front along the height of the casting can be both achieved. The positive temperature gradient in the casting can be obtained by various methods. All available ones are based on control of the heat flow in the casting. Direct flow of heat is achieved by the application of intense cooling of the mold located below the heating zone [1].

Since the early 1980s, three main methods have been developed that are used on the industrial scale for manufacturing of directional solidified nickel-based superalloy castings of aircraft engine and gas turbine hot components. Depending on the cooling mode, the following methods are used: Bridgman, LMC, and to a lesser extent gas cooling casting (GCC).

11.2.1.1 Power Down Method

The power down method is based on the progressive reduction of the temperature in the furnace heating zones. This method does not require the displacement of the mold with molten metal from the heating furnace (Figure 11.1) [2]. The ceramic mold is placed in the heating furnace on a water-cooled copper chill plate and heated to the desired temperature. Further, obtaining an equal temperature throughout the whole volume of the mold, it is filled with liquid metal. Directional heat flow is possible by the use of a chill plate, heating furnace, and the ceramic mold gradual temperature control. Temperature control is carried out by using two independent heating zones (heaters). After the pouring process, the lower heating zone is switched off. The liquid metal, on contact with the chill plate, begins the process of solidification. Under the impact of the chill plate, high value temperature gradient forms in the casting. Columnar grains grow into a parallel direction with reference to the flow of the heat. After some time from the start of the solidification process, steady heat flow conditions are formed in the casting.

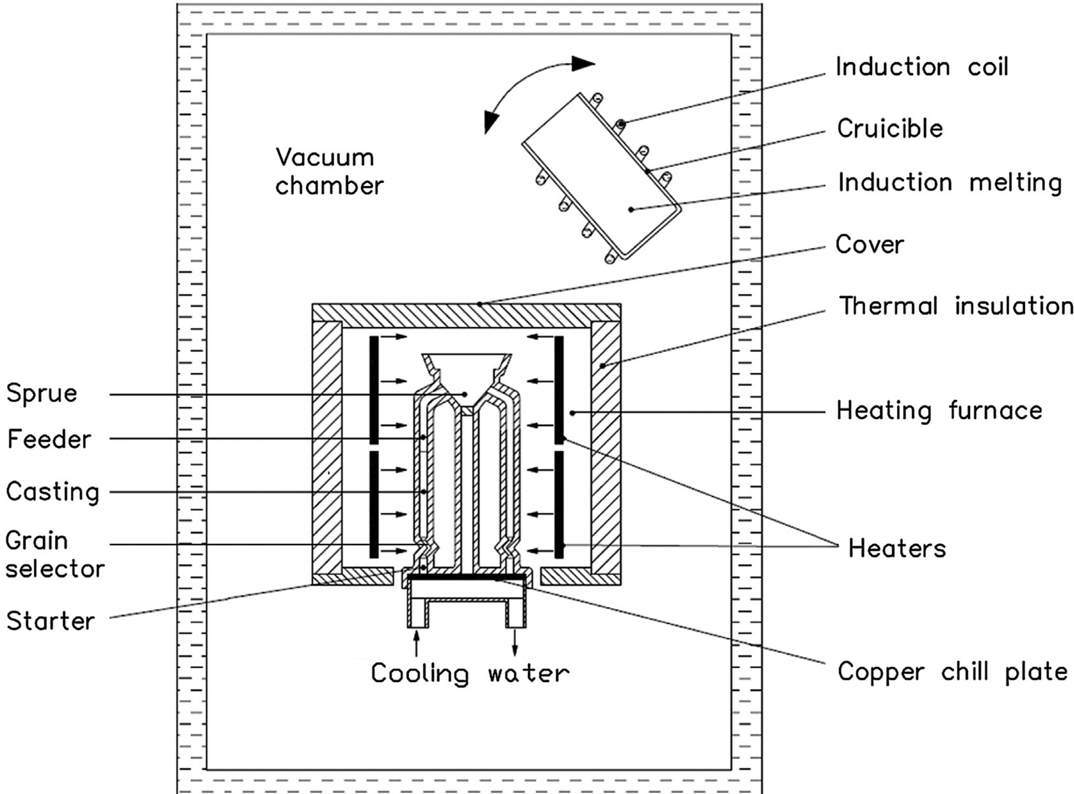

FIGURE 11.1 Schematic diagram of the directional solidification of nickel-based superalloy castings using the power down method.

Directional grain growth is then completed. When the temperature of the second heating zone is lowered, the further solidification process is possible. In this way the solidification front and further solidification process moves continuously. The described method was also used for the directional solidification of SC castings.

11.2.1.2 Bridgman Method – High Rate Solidification

The Bridgman method is characterized by the radiation heating and cooling of the ceramic mold and casting (Figure 11.2(a)). Initially, it was used only for a directional solidification of the castings on the laboratory scale. However, with the development of aircraft engines, it has been adapted for the industrial castings manufacturing process [3]. For this purpose, the device providing directional heat flow and castings directional solidification is used.

The ceramic mold is placed on a copper chill plate. The chill plate and the mold are both moved to the heating furnace by means of the lift. There, the heating takes place until the entire volume of the ceramic mold shows constant temperature value in time. The heating temperature of the ceramic mold depends on many factors, and in the industrial production process of SC casting it is mainly about 1500 °C. Increasing the

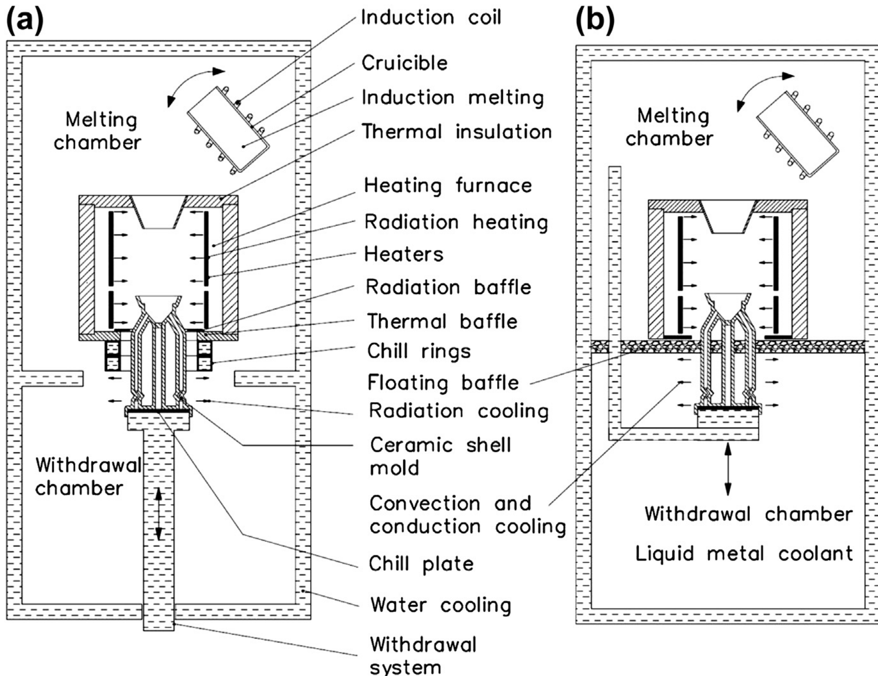

FIGURE 11.2 Schematic diagram of directional solidification of casting by: (a) a Bridgman, (b) LMC method.

temperature of the mold leads to an increase in the temperature gradient at the solidification front. A further increase in temperature depends on the material of ceramic molds. When the value is too high, excessive shrinkage and stress occur.

Induction melting of nickel superalloy ingot begins in the final ceramic mold annealing step. The melting process is conducted in a vacuum. After melting of the charge in a ceramic crucible, filling of the ceramic mold with molten metal begins. The liquid metal fills the starter, selector, and the blade casting cavity. This kind of solution allows the control of ceramic mold casting speed and the movement of impurities out of the casting. Sprue particulate filter is placed on the liquid metal supply system to the casting. The ceramic mold, filled with molten metal, is now moved with the set speed from the furnace to the cooling zone. Pulling speed of the ceramic mold is a fundamental parameter of the manufacturing of DS castings. For SC castings directionally solidified with Bridgman method, ceramic mold pulling speed is usually in the range of 2–4 mm/min [4].

In order to reduce the heat loss and increase the temperature gradient, radiation baffle can be applied. It is usually a plate-shaped graphite ring, placed on the thermal insulation compartment. It significantly affects the temperature distribution in the ceramic mold during its heating and annealing stages. Additionally, it enables an equal distribution of temperature, which affects the shape solid–liquid interface. The cooling rate of the casting and the mold is higher in comparison with the results obtained without the use of thermal baffle [4].

11.2.1.3 LMC Method

Preparation of SC castings using the LMC method proceeds in a similar manner as Bridgman method (Figure 11.2(b)). Instead of chill ring, under the heating furnace, there is a reservoir of liquid metal. Heating of the ceramic mold is conducted in a heating furnace using the heat radiation. Ceramic mold filled with liquid metal is moved with set speed from the heating furnace to the tank with coolant bath. Between the ceramic mold and the coolant, high intensity heat transfer by convection occurs. Solidification front is formed at a certain distance from the surface of the coolant bath. Thus, above the coolant bath level, ceramic mold is cooled by radiation. Coolant convective motion is caused by mechanical mixing. A liquid metal used for cooling is usually Al or Sn. These metals are characterized by a low melting point, high thermal conductivity, high evaporation in a vacuum temperature, the lack of toxicity, and low price [5]. The melt is continuously stirred and maintained at a constant temperature. In order to increase the temperature gradient and the withdrawal speed, ceramic spheres arranged on the metal bath are used as a floating baffle.

Spherical shape provides a precise fit to the ceramic mold, which reduces the distance between the solidification front and the coolant bath level. The use of such a solution and the Sn coolant leads to an increase in the temperature gradient in the casting to about 90 K/cm for large blades [6]. The use of liquid Al and no floating thermal baffle allows obtaining the temperature gradient in the range of 40–50 K/mm [7].

11.2.1.4 GCC Method

In order to conduct an effective process cooling and reduce the number of defects in large castings, the GCC method was developed [8]. Using GCC, heat is removed from the casting through the mold as a result of the gas flowing over the intense convection and thermal radiation. In this method, the ceramic mold is heated in a heating furnace. After filling the mold with molten metal, it is moved into the area where intensive convection cooling by the cooling gas occurs.

The gas stream, disposed under the thermal baffle, is directed through the nozzles to the surface of ceramic mold. Ar, He, or a mixture of both is used as the cooling gas. The amount of removed heat depends on the gas stream steering angle on the surface of the ceramic mold. In case of the multiple component ceramic molds, the GCC and the Bridgman methods do not use their full potential due to the presence of gaps between components. Studies show the desirability of a GCC method for manufacturing of single crystal and columnar grains castings.

11.2.2 Manufacture of SC Castings

11.2.2.1 Grains Selector

Two different techniques, grain selector or seed, are frequently used for manufacturing of SC castings of nickel-based superalloys with predetermined applied crystallographic orientation (Figure 11.3).

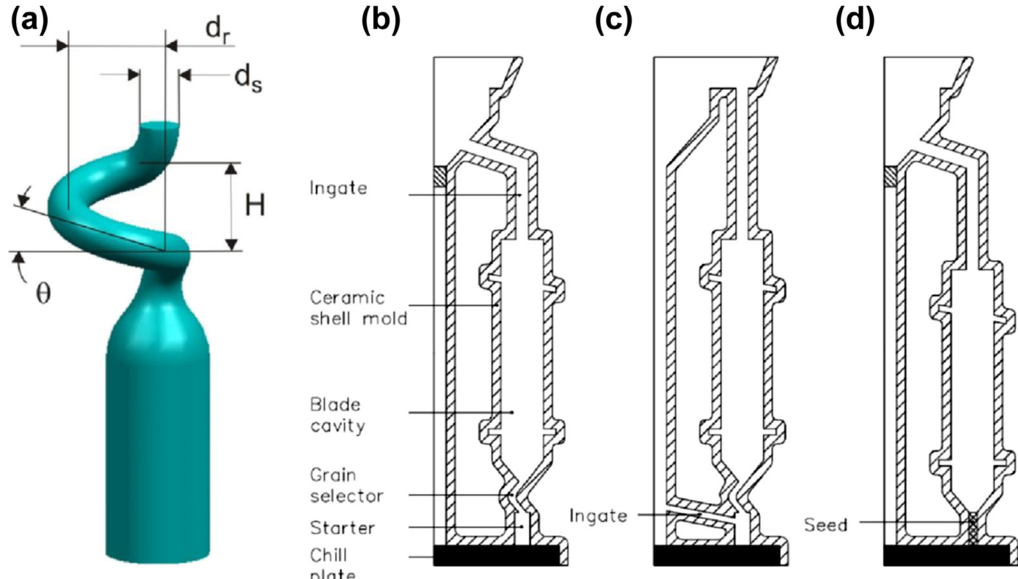

FIGURE 11.3 Starter and spiral grain selector (a). placement of the selector (b, c), the seed (d), and upper (b, d) and lower (c) blade cavity feeding system, where: takeoff angles – θ, wire diameter – d_s, spiral rotation diameter – d_r, the pitch length – H.

The use of a grain selector can provide growth of one grain in a casting in a particular direction close to [001] axis. The shape of selector has been changing with the development of technology of SC castings. Grain selectors are used in the restrictor, angled and spiral shapes [9]. Currently, the most commonly used is a spiral grain selector (Figure 11.3(a)).

In the industrial manufacturing process, single grain is obtained in the casting process, in the lower region of the ceramic mold, by using a selector that is connected to the starter block located on the chill plate. The starter block is usually made in the shape of a cylinder, with a height of 20–30 mm and a diameter of 10–20 mm. Shape and dimensions of the selector and the starter both have a large influence on obtaining single grains with the correct crystal orientation and on the cost of the manufacturing process. The solidification process in the selector is closely linked to the number of grains per unit area in the upper part of the starters block. The main aim of the starter is to produce the smallest possible number of columnar grains at the input to the selector while maintaining the lowest yaw angle of crystallographic orientation from the [001] axis.

Columnar grains are formed, arranged parallel to the direction of the heat flow. The number of grains is largest in the area with the highest undercooling value (contact of the chill plate with the casting) and decreases with increasing distance from the casting base [10]. With the increase in the starter height, a proportion of grains with unfavorable crystallographic orientation decreases. At a height of approximately

20–30 mm, grains deviation angle does not exceed 20° and is in the largest proportion of 5–10° [11]. The use of grain starter with a height greater than 30 mm does not result in a significant reduction in the number of grains and the deviation angle. However, reducing the height of the blade casting occurs, and as a consequence, there is an increase in the manufacturing costs. Thus, in industrial production starter of 20–30 mm height is used.

Further solidification occurs in the grains selector. Grains are automatically selected until only one remains. The selection of grains in the selector is random and has little to do with a temperature distribution. The growth of dendrites, from the starter to the selector, leads to them being blocked by the wall of the ceramic mold. Secondary dendrite growth begins in the free volume of the selector [12]. Next, further blocking by neighboring dendrites or the surface of the mold occurs. As a result, only one of the starter grains continues to grow in the selector, with an orientation not necessarily close to the [001] crystallographic direction.

In the design process of spiral grain selectors, the following geometrical parameters are included: takeoff angles – θ, wire diameter – d_s, spiral rotation diameter – d_r, and the pitch length – H. The most commonly used spiral selectors are of single or at most double the period. It has been found that a small value of the takeoff angle leads to an increase in the efficiency of the selector [13]. The increase in the takeoff angle leads to a formation of one grain at a higher level. In practice, the angle is chosen in the range of 20°–30°. Too low of its value increases efficiency but complicates manufacturing of spiral wax models. It has been concluded that the use of a selector reduces the number of grains but does not affect the angle of [001] deviation [11]. For larger values of the takeoff angle, the temperature gradient begins to have a greater impact on the solidification front and grain selection. Selection of grain orientation in the selector is random. Wire diameter, spiral rotation diameter have lesser impact on the selection process of grains in the selector. However, reduction of the wire diameter leads to the blockage of grains by the ceramic mold's internal surface [13].

11.2.2.2 Solidification from the Seed

Application of a starter and selector allows the solidification of casting grains of crystallographic orientation close to [001] axis. Often, in the SC castings, the crystallographic orientation other than [001] is required [14]. It was noted that the manufacturing of castings of orientation near to [111] further improves creep resistance. Nickel-based superalloy SC castings of predetermined crystallographic orientation are manufactured using casting seed (Figure 11.3(d)). The method is used to control the orientation of the SC casting produced on industrial and on laboratory scale [15].

Single crystal seed at a specific crystallographic orientation, height, and a diameter is placed inside the ceramic mold at a chill plate. The ceramic mold is heated to a predetermined temperature. The impact of the chill plate causes a large axial temperature gradient in the lower area of the ceramic mold and positioned seed. Knowledge of the temperature gradient in this area allows specifying the height of the seed.

At a fixed height, the seed transforms to a mushy zone—the range between the solidus and liquidus temperature. Annealed ceramic mold is being filled with a liquid metal. The process of solidification of molten metal begins as a result of contact with the upper surface of the molten seed. The growth of dendrites in the melt with crystallographic orientation of the seed takes place. Further directional solidification process is possible by withdrawing ceramic mold at a certain speed from the heating furnace. Heat flow begins to dominate on the crystallographic orientation. Liquid metal, when exposed to the contact with the seed, can continue to grow directly to the blade casting.

11.2.3 Parameters for Manufacture of Directional Solidification Castings

Manufacture of DS castings of nickel-based superalloys requires an accurate defining of process parameters, especially critical speed of mold withdrawal. The solidification rate and the method of casting are crucial to the temperature gradient and the cooling rate in accordance with the equation:

$$v = \frac{v_c}{G} \tag{11.1}$$

where: v – solidification rate, v_c – cooling rate, G – temperature gradient in mushy zone.

Directional heat dissipation causes the movement of isotherms along the height of the casting. Isotherms between the liquidus and solidus temperatures determine the shape of the solid–liquid interface, which may be: convex, flat, concave, or inclined (depending on the values of the transverse and axial temperature gradients). It was found that the transverse temperature gradient affects the dendrites' growth direction in DS castings. Thus, the shape of the solid–liquid interface affects the direction of the solidification and the formation of columnar grain boundaries relative to the axis of symmetry of the casting [16]. The shape of the solid–liquid interface is especially important in the transition area between the blades root and the air foil. Typically, it has a concave shape for the standard speed of mold withdrawal from the heating zone [12]. The end of the platform, the most distant part of the air foil, reaches the liquidus temperature much sooner than the central part of it. Thus, in this area favorable conditions for strain grains solidification are formed [16]. Castings solidified with a flat shape of the solid–liquid interface are characterized by good mechanical properties. This is particularly difficult to obtain for the castings of large size and with complex shapes.

The value of the axial temperature gradient in the mushy zone has a large impact on the microstructure of DS castings. It determines geometric parameters of cellular-dendritic construction through solidification, and affects the shape of solidification front (flat, cellular, cellular-dendritic) in castings of nickel-based superalloys [17–19] (Figure 11.4). To manufacture the casting with a flat solidification front one must meet the following relation [18]:

$$\frac{G}{v} \leq \frac{\Delta T_o}{D} \tag{11.2}$$

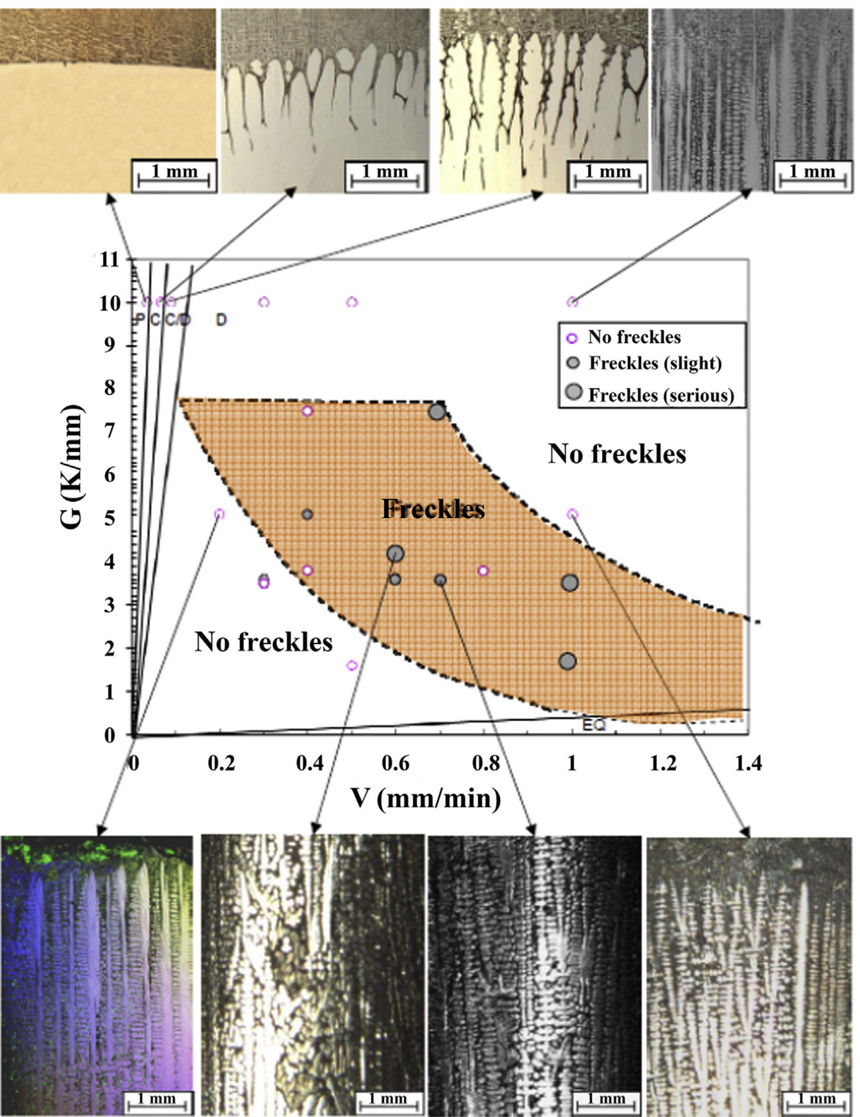

FIGURE 11.4 Freckle formation in superalloy CMSX-4 under different solidification conditions. The diagram excludes the planar (P), cellular (C), cellular to dendritic (C/D), and equiaxed (EQ) zones from freckle formation. Besides, the columnar dendritic zone is also divided into three zones, in the middle of which freckle occurrence is possible (marked "Freckles") [19].

where: G – temperature gradient on the solidification front or in the mushy zone, D – diffusion coefficient in the liquid phase, ΔT_o – equilibrium solidification range. Based on the analysis of the equation 11.2 it was stated that the solidification front shape and the microstructure of the casting are affected by the furnace (G, v) and the alloy (ΔT_o, D) parameters.

The increase in solidification rate from planar front state (at constant temperature gradient) leads to solutal supercooling. The planar front is changed into a cellular one. Further increase of the solidification rate and reduction of the temperature gradient lead to the development of the secondary dendrite arms on the cells' surface. A cellular-dendritic solidification front is formed. Solidification of the casting at high speed and with low temperature gradient leads to nucleation and growth of equiaxed grains in front of the solidification front [19].

Single crystal nickel-based superalloy castings manufactured in industrial conditions solidify with cellular-dendritic solidification front. Obtained microstructure consists of the cellular dendrites, with arms of the first, second, or third kind. In the interdendritic spaces, a eutectic solidifies. The most important parameter of the microstructure, gained with cellular-dendritic solidification front, is the primary dendrite arm spacing (PDAS), described by the equation [17]:

$$\lambda = \frac{4.3(\Delta T_o \cdot D \cdot \Gamma)^{0.25}}{k^{0.25}} v^{-0.5} \cdot G^{-0.5} \tag{11.3}$$

where: k – partition coefficient. PDAS decreases with an increasing temperature gradient and solidification rate. The smallest cooling rate and the greatest distance between the arms of the first kind are obtained in castings manufactured by the Bridgman method. The increase in the cooling rate in the LMC method leads to a reduction of distance between the dendrite arms of the first kind [20].

11.3 Nickel-based Superalloys and Heat Treatment Process

The basic operations of nickel-based superalloy heat treatment are: homogenizing, annealing, and precipitation hardening (supersaturation and aging) (Table 11.1) [21,22].

Both operations are aimed at reducing microsegregation of chemical composition (homogenizing annealing) and a γ' phase precipitation of similar size in the dendritic areas and γ/γ' eutectic (precipitation hardening), and thereby increase the mechanical properties, particularly creep resistance (Table 11.2).

Heat-treatment operations carried out under protective gas atmosphere (usually Ar) and high temperature are difficult, especially in industrial practice, because they require very precise temperature control. γ' phase precipitates, which are a component of γ/γ' eutectic, are not allowed to melt. During the solutioning process, nucleation and growth of secondary phase γ' precipitates occur, in which the embryos are initially of spherical and then cubic shapes. Solutioned castings are usually subjected to two or three phases of aging process. The first aging temperature is usually 1050–1150 °C, depending on the alloy chemical composition and expected casting operation temperature. The microstructure after the first aging process consists of cubic γ' phase and secondary precipitates separated by γ phase, in which tertiary, spherical γ' phase nanoparticles may appear (Figure 11.5) [28].

Table 11.1 Heat Treatment of Selected Nickel-Based Superalloys

Alloy (Source)	Heat Treatment Type	Heat Treatment Parameters
PWA 1483 [22]	Solutioning	1260 C/1 h
	Aging	1090 C/4 h
CMSX-11B [23]	Solutioning	1204/2 h; 1227/2 h; 1249/3 h; 1260/6 h; vg = 1 K/min
	Aging	1120/5 h; 870/24 h; 760/30 h
SRR 99 [23]	Solutioning	1270/0.5 h; 1280/1 h; 1300/0.5 h; 1305/0.5 h; vg = 1 K/min
	Aging	1080/4 h; 870/16 h
CMSX-6 [23]	Solutioning	1127/2 h; 1238/2 h; 1271/2 h; 1277/3 h 1280/2 h vg = 1 K/min
	Aging	1080/4 h; 870/16 h
CMSX-4 [24,25]	Solutioning	1277/4 h; 1287/2 h; 1296/3 h; 1304/3 h; 1313/2 h; 1316/2 h; 1318/2 h; GFC
	Aging	1140/6 h AC; 871/20 h AC
CMSX-2 [25]	Solutioning	1250/0.25; 1276/2; 1296/3; GFC
	Aging	1080/4 GFC; 870/4 h AC
CMSX-10 [26]	Solutioning	1350/1 h; 1353/3 h; 1356/1 h; 1359/1 h; 1362/1 h; 1365/10 h; GFC
	Aging	1152/6 h GFC + 871/24 h GFC + 760/30 h GFC
CMSX-486 [27]	Solutioning	1238/1 h; 1243/1 h; 1249/1 h AC/GFC
	Aging	1080/4 h AC/GFC; 871/20 h AC

Table 11.2 Heat-Treatment Effect on CMSX-486 Alloy Mechanical Properties [27]

Test Condition	HT Condition	Life, h	Time to 1% Creep	Time to 2% Creep	Elong.%	RA %
982 °C/248 MPa	Partial sol'n	168.1	51.7	74.8	39.7	47.0
	Double age	172.0	56.4	80.9	35.4	45.1
	As cast+	143.0	48.0	66.3	35.7	48.1
	Double age	138.3	42.9	61.0	46.1	47.0
1038 °C/172 MPa	Partial sol'n	114.3	39.4	59.8	28.4	52.5
	Double age					
	As cast+	119.2	39.5	57.8	41.7	49.2
	Double age	110.9	37.3	56.1	16.1	17.2
1093 °C/83 MPa	Partial sol'n	472.0	218.7	315.9	33.9	36.1
	Double age	474.2	145.8	289.1	35.2	43.4
	As cast+	643.9	357.7	462.1	33.0	37.0
	Double age	673.9	360.2	495.5	25.4	40.0

Partial solution: 1238 °C/1 h + 1243 °C/1 h + 1249 °C/1 h AC/GFC.
Double age: 1080 °C/4 h AC/GFC + 871 °C/20 h AC.

In the single crystal nickel-based superalloy castings γ/γ' eutectic can appear. Due to high brittleness it is an undesirable phase microstructure component that negatively affects mechanical properties of the alloy. There is a tendency for complete elimination of this phase [28]. In the second-generation single crystal superalloys, one can observe small clusters of rhenium atoms with a diameter less than 1 nm in the microstructure.

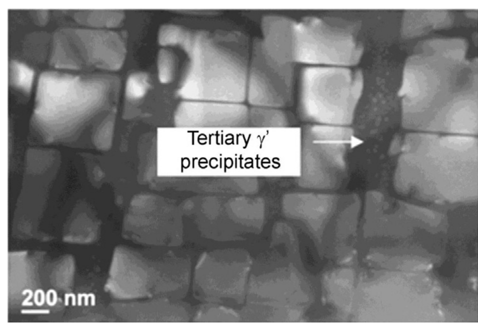

FIGURE 11.5 Microstructure of the CMSX-4 alloy casting after the first aging phase – tertiary γ' phase precipitates in the γ phase channels. Dark field in (001) γ' reflection [28].

They play an important role in the improvement of creep strength. Rhenium clusters are strong obstacles to the dislocation movement, compared with the individual atoms of additives dissolved in the γ phase matrix [29].

Microstructure of single crystal CMSX-4 superalloy is heterogeneous. Dendritic areas can be observed, in which γ/γ' eutectic and γ' phase separation of different morphology occurs (Figure 11.6(a)) [30].

After the precipitation hardening process, interdendritic areas with wider γ matrix channels remain in the microstructure (Figure 11.6(b)). γ' phase precipitates are of regular shape, similar to a cube (Figure 11.6(c)), and with the average diameter of $D = 700$ nm. Relative volume of the γ' phase particles is $V_V = 72\%$. Inside these areas and in their vicinity, separation of small globular (Figure 11.6(d)) or lamellar-shaped (Figure 11.6(e)) carbides can be found. Heat treatment has significantly reduced the relative volume of γ/γ' eutectic (Figure 11.6(f)) [30].

11.4 Methodology for Manufacture of Ceramic Shell Molds for Directional Solidification Casting

11.4.1 Ceramic Materials for Molds and Their Production Methods

A proper selection of ceramic materials for disposable molds is a key issue. The most commonly used are oxides or their compounds in the form of powders (meals) (Table 11.3) [31,32]. Depending on the application of ceramic mixtures for the first or subsequent layers, there are different property requirements.

11.4.1.1 Zirconium Silicate

The largest deposits of natural $ZrSiO_4$ are found in Australia, South Africa, India, and the United States. It has a tetragonal structure. Silicate powder is white or pale yellow. Its density is 4.56 g/cm^3 and does not depend on the temperature. It is characterized by a low coefficient of linear thermal expansion (1.06×10^{-6}–1.10×10^{-6} 1/K) and thermal conductivity (Figure 11.7). Additionally, it has no phase transition and is low wettable by

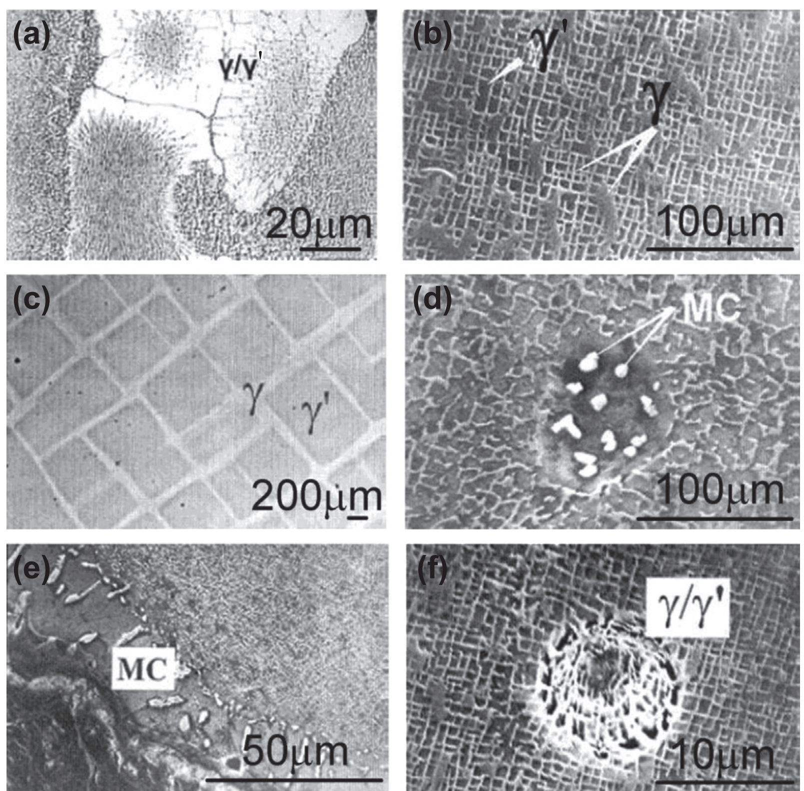

FIGURE 11.6 Microstructure of CMSX-4 nickel-based superalloy: (a) as cast, large γ/γ' eutectic areas, (b) cubic γ' phase separation in the γ matrix, (c) γ' phase of regular similar to a cube shape separation, γ matrix channels, (d) globular particles of MC carbides, (e) lamellar separation of MC carbides, (f) γ/γ' eutectic [30].

liquid alloys. Zirconium silicate contains 67.2% ZrO_2 and 32.8% SiO_2. The zirconia powders used in investment casting of nickel superalloys also consist of 1–1.5 wt% of HfO_2, and additionally Al_2O_3, Fe_2O_3, TiO_2, MnO, CaO, MgO, P_2O_5, and Cr_2O_3 in the amount of 3 wt%. $ZrSiO_4$. Dissociation temperature is 1285–2550 °C, depending on the degree of purity—the lower the content of impurities, the lower the dissociation temperature [33,34]. Zirconium silicate is used in the form of powders with # 325 (average particle size of 10 μm) and # 200 (average particle size of 25 μm) gradation as a liquid ceramic matrix used in the first mold layer. Zirconium silicate powders are manufactured by grinding method, which gives the particles an irregular shape with sharp edges along the cleavage planes. Commercial powders consist of two fractions: fine and coarse; the latter arises from forming of the coarse units from fine-grained fraction. Powdered zirconium silicate meals are used with the binders based on colloidal silica matrix both in acidic and alkaline reaction.

Table 11.3 Required Properties of Ceramic Materials According to the Application for the First Layer (Model One) and the Structural Layers for Ceramic Molds

Requirements According to the Layer Type	
First Layer (Model One)	**Structural Layer**
1. No (or small) reactivity with liquid alloy **2.** Chemical stability at high temperature (1500 °C) and at high vacuum (10^{-4} Tr) **3.** High susceptibility for smooth surfaces coating **4.** Erosion resistance **5.** No allotropic transformation Materials: **a.** $ZrSiO_4$ – increasing price, easy to form, deteriorating material purity (mineral) **b.** Al_2O_3 – best compromise between price and technological properties **c.** ZrO_2 – high price, technological difficulties with manufacturing of molding mixtures **d.** Y_2O_3 – very high price	**1.** High strength in raw state, at high temperature (up to 1500 °C) and high vacuum (10–4 Tr) **2.** Creep resistance **3.** Easy to shape and knock out the casting **4.** No allotropic transformation **5.** Low cost Materials: Aluminosilicates (42–47% Al_2O_3) Aluminosilicates (60% Al_2O_3) Mullite (72% Al_2O_3) Al_2O_3

11.4.1.2 Aluminosilicates and Mullite

Aluminosilicates are obtained directly from the aluminosilicate rocks or as synthetic materials. These oxides have the general formula: $mAl_2O_3 \cdot nSiO$, e.g., andalusite, sillimanite, disthene, kaolinite, topaz, and mullite. Natural aluminosilicate powders used in investment casting are supplied with various Al_2O_3 content, such as 42–47% (e.g., Molochite) and 60% (e.g., Remasil, Mulgrain), and with gradation in the range of 325#−120#. The higher the content of Al_2O_3 in the powder, the higher its resistance to temperature. Most common contaminants in aluminosilicate powder are: Fe_2O_3, TiO_2,

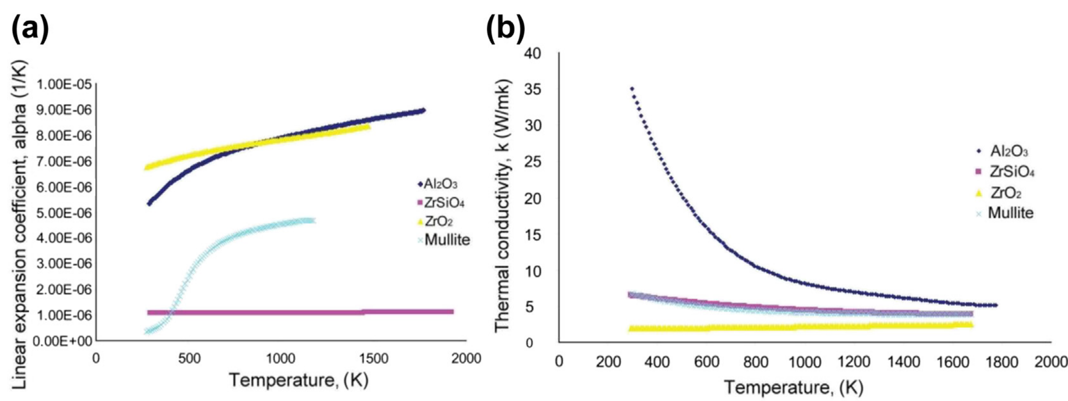

FIGURE 11.7 Temperature effect on: (a) linear thermal expansion coefficient, (b) thermal conductivity of selected ceramic materials.

Table 11.4 Chemical Composition of Synthetic Mullite Powders used in Ceramic Mixtures Matrix and Stucco for Structural Layers of Ceramic Molds

Component	Mullite 0.07 mm	Mullite 0.12 mm	Mullite 0.25–0.50 mm	Mullite 0.5–1.0 mm
	wt% Content			
Al_2O_3	76.86	75.04	74.99	73.03
SiO_2	22.80	24.50	24.50	26.70
Na_2O	0.30	0.36	0.40	0.22
CaO	0.045	0.037	0.029	0.042
Fe_2O_3	0.0335	0.0370	0.0283	0.0375
Ga_2O_3	0.009	0.0113	0.009	0.015

and ZrO_2, while the content of CaO, MgO, K_2O, P_2O_5, and Cr_2O_3 is very small. An important advantage of aluminosilicate powders is their availability and low price of about 0.5 €/kg.

Mullite $3Al_2O_3 \cdot 2SiO_2$ is a mineral that is rarely found in nature (known deposits on the Isle of Mull, Scotland). For industrial purposes, synthetic mullite is used almost exclusively (sintered or melted) with particle sizes up to: 0.07, 0.12, 0.25–0.5, 0.5–1.0 mm (Table 11.4) and of white color. The raw material is milled and fractionated for a suitable grain size matrix of the ceramic powders and stucco. The melting point of mullite is 1810 °C and density is 3.05 g/cm^3, which does not depend on the temperature. It is characterized by high resistance to creep and thermal shock due to a low coefficient of thermal expansion and a low thermal conductivity (Figure 11.7). Synthetic mullite is characterized by a high chemical purity—total content of impurities does not exceed 0.5 wt% (Table 11.4). The price is high (about 2.5 €/kg), thus it is used for ceramic molds for casting turbine blades with a DS or SC microstructure.

11.4.1.3 Corundum

Corundum (α-Al_2O_3) is the most thermodynamically stable allotropic form of alumina. It crystallizes in a hexagonal structure. In the investment casting of aircraft components only synthetic corundum is used (sintered or melted). The powdered corundum is colorless or white. Its density is 3.9 g/cm^3, and it does not depend on temperature. On the other hand, the linear coefficient of thermal expansion, specific heat, and thermal conductivity strongly depend on the temperature. Melting point of corundum is 2050 °C. It has a very good resistance to metal oxides and the alkaline and acid solutions, even in high temperature. Synthetic corundum also features high chemical purity of min. 99.5 wt% Al_2O_3 [34,35]. The most common impurities are SiO_2, Fe_2O_3, CaO, MgO, K_2O, Na_2O, and TiO_2. Its grains are irregular in shape with sharp edges. Corundum is most often used as a matrix for model layer and its stucco. For liquid ceramic mixture, the matrix is most commonly made of powders with gradations of 200# and 325# (particle sizes: 15–45 μm), while the stucco is of 80# and 100#

(above 250 μm particle size). Current prices (1.5 €/kg) cause it to be used widely for manufacturing of ceramic molds.

11.4.1.4 Zirconium Dioxide

Zirconium dioxide is obtained from natural zirconium silicate ($ZrSiO_4$) containing about 66.9 wt% ZrO_2 and baddeleyite, containing 96–99 wt% ZrO_2. It appears in three allotropic forms: regular, tetragonal, and monoclinic. Monoclinic structure of zirconium dioxide is stable below 1170 °C. A phase transition occurs at 1170 °C, which results in a change into tetragonal structure, while phase transition at 2370 °C results in a regular phase structure. Due to a phase change, volume change of ZrO_2 by about 3–4% occurs, which can result in cracks of ceramic mold layers or cause dimensional changes of castings. Therefore, it is necessary to add oxides (CaO, MgO, CeO_2, Y_2O_3) stabilizing tetragonal and regular structure. Addition of 7.9 wt% CaO, 5.86 wt% MgO, and 13.75 wt% Y_2O_3 allows obtaining fully stabilized ZrO_2 (FSZ – fully stabilized zirconia) with regular structure type (not used with ceramic molds due to very high prices). For mold ceramic mixtures and stucco, partially stabilized ZrO_2 (PES – partially stabilized zirconia) powders are used containing 3–6 mol% MgO and Y_2O_3. At room temperature they consist of a regular phase structure with monoclinic or/and tetragonal phase inclusions. Partially stabilized ZrO_2 has a high chemical resistance, high melting point (2715 °C), and the lowest thermal conductivity compared to other ceramic materials used (Figure 11.7). The disadvantage of ZrO_2 PES is its high price of about 11 €/kg and its high density of 6 g/cm^3 that has a tendency to cause sediment and thus make it difficult to prepare stable molding mixture.

11.4.1.5 Binder

For manufacturing of molds, ceramic mixture binders based on ethyl silicate or colloidal silica are used. Ethyl silicate is a liquid with a characteristic odor, yellow or light brown color, and with density that is close to the density of water (it is now rarely used due to environmental requirements). Colloidal silica is a hydrosol of orthosilicic acid, diffused in water. SiO_2 particles in the sol are spherical, and their size ranges from several to several tens of nanometers. Binder based on colloidal silica is subjected to the process of stabilization and modification with sodium, alginate, alumina, or polymers such as latex or polyvinyl alcohol, which allows maintenance of an adequate charge on the surface of SiO_2 nanoparticles and gives adequate strength and "flexibility" of binder after gelation (in hardened state). The stability of the binder is ensured by maintaining an appropriate pH, usually strongly basic, by introduction of a solution of sodium or ammonium hydroxide. Basic properties of the binders on the basis of colloidal silica, prior to preparation of the ceramic mixture, are: solid fraction content, wettability, viscosity and density, the binding capacity, temperature sensitivity, and pH. The advantages of binders based on colloidal silica are: long life (the period of technological usefulness), good wettability of wax surface, sufficient strength during the entire technological process, and ease of preparation in terms of foundry. The disadvantages are: a relatively long drying and curing time of successive ceramic layers compared to binders based on ethyl silicate.

11.4.2 Manufacturing of Elements and Wax Model Assemblies

The investment casting process consists of: manufacturing of wax models of gating system components and castings, preparing a wax model set, manufacturing of ceramic mold, pouring alloy, mold removal, and finishing of casting [36]. Manufacturing of cast models is therefore the first essential step in this process. Waxes used in investment casting are a complex mixture of various components: natural waxes, synthetic waxes, polymers, resins, fillers, and other additives that improve their properties [37,38]. The most common fillers are: cross-linked acrylic acid, cross-linked polystyrene, isophthalic acid, terephthalic acid, bisphenol, and water [39].

In general, for the preparation of wax model set, two types of waxes are implemented. Components of the gating system are made of wax with the softening and melting temperature of about 10 °C lower than the corresponding temperature of the wax used for the casting models (Table 11.5).

In commercial practice, wax elements are produced by specialized injection molding machines and metal matrices. Construction of the matrix is dependent on the geometry of the model. Dies for manufacturing of turbine blades with uncomplicated geometry consist of two parts, while for blades of complex geometry, the number of elements of the matrix increases. The matrix is provided with pushing elements to facilitate taking out the finished model. In order to increase efficiency, one can also apply multipocket dies.

While making wax models, it is necessary to:

1. stabilize the temperature of the wax in: (a) a tank (about 70–85 °C), (b) cylinder (about 65–75 °C), (c) injector supply lines (about 67–75 °C),
2. adjust the pressure (about 0.3–0.35 MPa), injection time (depending on the size of the model—the larger the size, the longer injection time—up to about 25 s), and matrix hold time (depending on the geometry and dimensions of the model, usually about 1 min).

In the prototype series or laboratory tests, wax models are often made by rapid tooling (RT) method, including vacuum casting. For this aim, rapid prototyping methods are used for manufacturing of castings models and then wax models in silicon molds.

Table 11.5 Properties and Applications of Casting Waxes

Wax Type	Color	Application	Melting Temperature (°C)	Mold Temperature Before Pouring, (°C)	Average Mold Annealing Time, (h)	Filling of the Mold
B405	Red	Model set	130	85	2.1	Good
RECLM	Brown	Model set	130	85	2.1	Good
Blue wax RECLM+	Grey-blue	Model set	130	85	2.1	Good
A7FR/60	Light green	Casting model	140	90	2.1	Poor
KC4017B	Dark green	Blades	140	90	2.1	Medium

Prototypes of components of the model set are carried out in silicone molds by gravity casting at atmospheric pressure or under reduced pressure (vacuum), and by injection [29]. The silicon molds can be used for casting of polyester, epoxy, polyurethane resins, and casting wax. Preparation of individual wax casting models, such as blades by vacuum casting method, creates conditions for improving process efficiency through the use of: cheap material on the model (wax casting), material that is easy to dewax from the mold (without using nonstandard operations), finishing of the pattern model (superfinish and polishing) before preparation of silicone matrix, and silicone molds with high dimensional stability. Prepared wax models are combined in wax model sets. For this purpose, specialized assembly devices are used, which ensure a required accuracy. Combining of models is performed by connecting elements together and melting their mutual parts (usually with small soldering irons). Wax model sets are submitted to several water cleaning and degreasing operations (e.g., Trisol 60 Plus Wax Pattern Cleaner and Blyson etchant).

11.4.3 Manufacturing of Ceramic Shell Molds

In industrial practice, there are several masses, which are known as molding system. It usually consists of three ceramic mixtures, named the first, second, and further ceramic layers. They have different chemical compositions and different rheological properties. The main ceramic mold layer forms a first layer, so-called model layer, which is in contact with the liquid alloy. It should be thermally stabile and should not react with liquid metal. The main parameter that characterizes the first layer is its thickness. It should be thick enough so that the stucco grains would not able to break it. Stucco grains breaking through a first layer may be “frozen” in the cast (nonmetallic inclusions). Too thick a layer does not provide sufficient strength and is susceptible to infiltration by the liquid metal (ceramic accretions on the surface of the casting) (Figure 11.8). Additionally, the first layer should evenly cover the wax model, which is difficult, e.g., at the edges with small radius. In comparison with the first molding layer, the second can be made of a mixture of lower viscosity and larger powder particle size. This allows a better “connection” between the model layer and structural layers (Figure 11.9).

Manufacturing of ceramic mixtures should include:

1. the proper sequence of components input (binder, wetting, and antifoaming agents, ceramic powders) dosed in small portions, from the largest to the smallest particle sizes,
   a. impacts on the rheological properties of the mixture and the time to achieve the desired performance: minimum mixing time is approximately 30 min for each added component.
2. parameter verification at minimum 12 h after the mixture execution (Table 11.6).

Aging of ceramic mixtures based on colloidal silica is caused by permanent changes in the structure occurring as a result of the binder sol–gel transition. Although binders

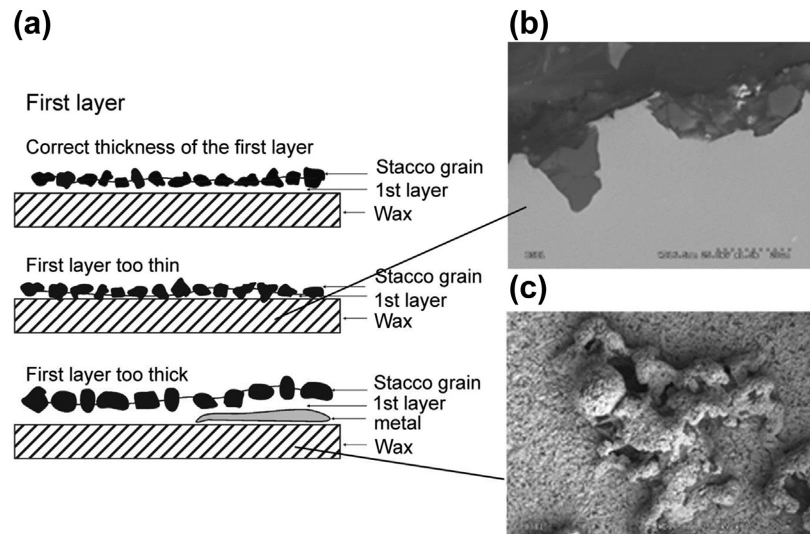

FIGURE 11.8 Defects arising from improper thickness of the first layer: (a) construction scheme of the defects mechanism, (b) ceramic grains in the casting, (c) the surface of the casting with ceramic "accretions."

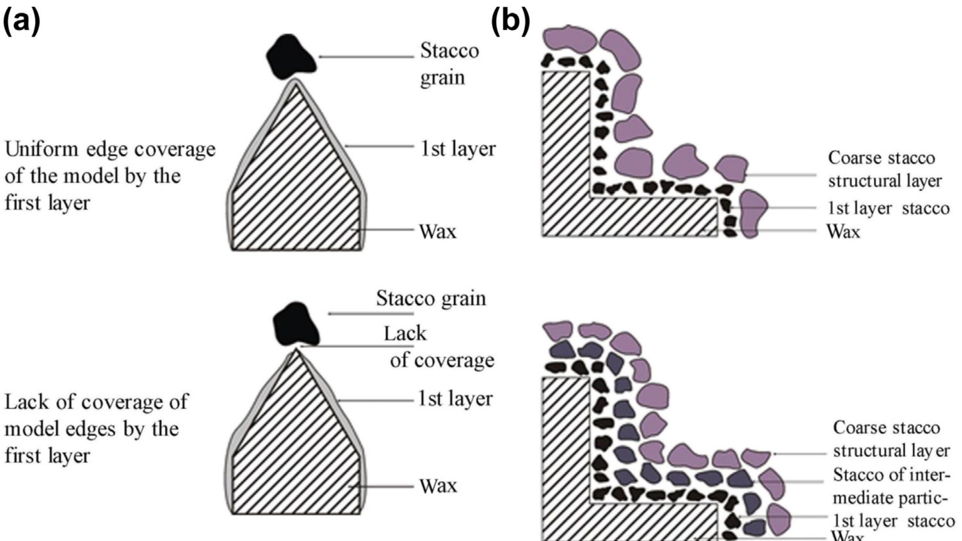

FIGURE 11.9 Effects of the first layer covering the edges of wax mold. (a) and powder grain size of the stucco (b) on the quality of the ceramic mold.

of this type are stable for at least one year (some even for few years), SiO_2 particles can be easily pushed out of balance by changing pH or by contaminating the mixture. They then merge into the three-dimensional network, resulting in the change of mixture parameters (in the worst-case scenario the mixture becomes gelatinous). Sol–gel

Table 11.6 Technological Parameters of Molding Mixtures Based on Silica Binders and Corundum and Mullite Matrices

Layer Type	Viscosity (s) Zahn/ Ford Cup	Temperature (°C)	pH	Binder Solid Content (%)
First	25–40	22–24	9.0–9.5	26–30
Second	10–11	22–24	9.0–9.5	20–25
Structural	11–12	22–24	9.0–9.5	20–25

transition may be very slow or very quick (in extreme cases, in less than 1 s). Often the mixture is enriched with various organic additives (rheology modifiers or polymers) that can cause the presence of various microorganisms that accelerate the aging process. The level of bacteria and fungi amount should be regularly checked and controlled by performing inoculation tests. For control purposes, commercially available preparations and antimicrobial chemicals are used. Mixture properties should be monitored at least once a day at a fixed time, and the results archived. Ceramic molds (such as for casting of aircraft engines turbine blades) are manufactured on the basis of wax model set using the "stucco" method. It involves the application of a number of ceramic layers (approximately 5–15), depending on the weight and dimensions of the casting. Mold layers are prepared by dipping the wax model set in the molding mixture and then covering it (sprinkling it) with ceramic powder (Table 11.7).

The process of ceramic mold manufacturing can be highly automatized. In large foundries there are specialized assemblies for automatic immersing of wax models in the liquid ceramic mixtures, the ceramic powder coating, and drying. Drying of the mold is a very important operation, during which the curing of ceramic layers occurs. Inadequate drying time and humidity can cause cracks, delamination, and collapse of the ceramic layer during dewaxing in an autoclave, and thus, the formation of defects in castings geometry. This is a result of differences in the thermal expansion coefficient of wax and molding material (Figure 11.10).

Table 11.7 The Type and Granularity of Ceramic Mixtures and Stucco Materials

	Slurry			
Type	**Binder**	**Ceramic Powder**	**Share (%)**	**Stucco**
First layer	Colloidal silica	Fused alumina 325#	30	Fused alumina 100#
		Fused alumina 200#	45	
Second layer	Colloidal silica	Fused alumina 325#	35	Fused mullite 0.125–0.250 mm
		Fused alumina 325#	35	
Backup	Colloidal silica	Fused mullite 0.07 mm	30	Fused mullite 0.250–0.500 mm
		Fused mullite 0.125–0.250 mm	45	

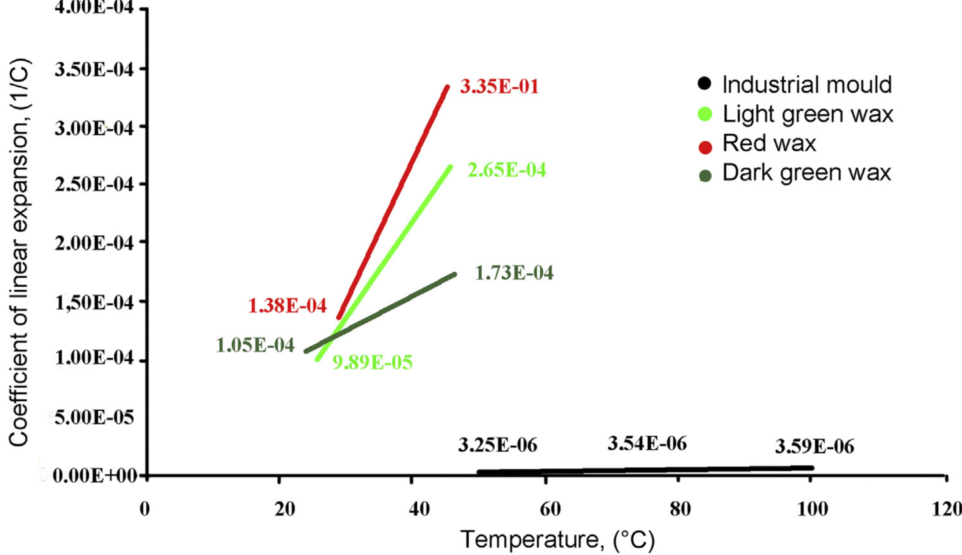

FIGURE 11.10 Temperature effect on linear coefficient of thermal expansion of modeling waxes and ceramic molds.

Gravimetric, thermal, current, and ultrasound methods are used to determine the drying parameters. After application of the required number of layers and drying of the mold, wax removal is performed: in hot air, in boiling water, or in an autoclave. In foundries that manufacture aircraft engine turbine components, currently an autoclave method of dewaxing is used. In the autoclave chamber the ceramic molds are subjected to a shock treatment with overheated steam. Overheated steam temperature depends on the pressure and is usually in the range from 110 to 160 °C. The pressure levels that are used come in the range from 0.2 to 0.8 MPa. Processing time varies from a few to tens of minutes. After the dewaxing operation, molds are washed in water and subjected to the annealing process (700–1500 °C) to burn residual wax and obtain the required mechanical properties.

11.4.4 Ceramic Shell Mold Investigation Methods

The quality of ceramic molds is determined by:

1. observation of mold microstructure (LM, SEM, X-ray tomography)
2. study of mold mechanical properties (three-point bending test, static tensile test at elevated temperature)
3. investigation of thermophysical properties (thermal conductivity, heat capacity, linear coefficient of thermal expansion)
4. investigation of the density and porosity (mercury porosimetry).

11.5 Investigation Methods for Directional Solidification Castings

11.5.1 Testing of Mechanical Properties

Development of alloys for castings with directional orientation of grains is related to the patent of directional solidification method that was filed in 1966 by F. L. Ver Snyder, who at the time was an employee of Pratt & Whitney [40]. Since the early seventies of the last century, their chemical composition underwent numerous changes (Table 11.8).

Single crystal alloying began in the early 1980s. As a result of changes in chemical composition, an increase in mechanical properties in high temperature has been achieved by increasing the relative volume of the γ' phase [42]. Nowadays, there are ongoing attempts to find practical application of the fifth-generation alloys (Table 11.9).

Producers are looking for a compromise between creep resistance, density (about 8.5–9 g/cm^3) and high production costs [43,44]. Nickel-based superalloys for castings with directional arrangement of grains (DS) or SC microstructure are submitted to typical mechanical properties tests: static tensile test at room temperature or raised temperature, hardness measurement, impact resistance test, and the creep resistance test. The results of castings creep resistance are of particular importance due to their usage for aircraft engine turbine blades. Creep resistance is significantly dependent on the orientation of [001] γ' direction with respect to casting main axis (Figure 11.11).

In the aerospace industry it is assumed that it should not be greater than 15°. Creep resistance of single-crystal nickel-based superalloys is greater in comparison with polycrystalline structured ones with equiaxed (EQ) and columnar (DS) grains [46].

Unique mechanical properties of single crystal nickel-based superalloys at high temperature are caused by: precipitation hardening by the second phase γ' particles and solution strengthening of matrix with alloying elements. Titanium, niobium, and tantalum improve solution strengthening of γ' phase precipitates, while chromium, molybdenum, and tungsten improve the matrix γ phase. High total content of alloying

Table 11.8 Chemical Composition of Nickel-Based Superalloys for DS Casting [41]

	Chemical Composition, (wt%)												
Name	**C**	**Cr**	**Co**	**Mo**	**W**	**Nb**	**Ta**	**Ti**	**Al**	**B**	**Zr**	**Hf**	**Re**
MAR M 200 + Hf	0.14	9.00	10.00	–	12.00	1.00	–	2.00	5.00	0.015	–	0.80–1.90	–
MAR M 002	0.15	9.00	10.00	–	10.00	–	2.50	1.50	5.50	0.015	0.05	1.50	–
MAR M247	0.16	8.20	10.00	0.60	10.00	–	3.00	1.00	5.50	0.015	0.05	1.50	–
PWA 1426	0.10	6.50	12.00	2.00	6.00	–	4.00	–	6.00	0.015	0.03	1.50	3.00
Rene'142	0.12	6.80	12.00	2.00	5.00	–	6.00	–	6.20	0.015	0.02	1.50	3.00
CM186LC	0.07	6.00	9.00	0.50	8.00	–	3.00	0.70	5.70	0.015	0.005	1.40	3.00
CM247LC	0.07	8.00	9.00	0.50	10.00	–	3.20	0.70	5.60	0.015	0.01	1.40	–
Rene'80H	0.16	14.00	9.00	4.00	4.00	–	–	4.70	3.00	0.015	0.01	0.80	–
GTD 111M	0.10	14.00	9.50	1.60	3.80	–	2.80	4.90	3.00	0.012	–	–	–

Table 11.9 Chemical Composition of Single Crystal Nickel-Based Superalloys [41]

		Chemical Composition, (wt%)										
Generation	**Name**	**Cr**	**Co**	**Mo**	**Re**	**Ru**	**W**	**Al**	**Ti**	**Ta**	**Hf**	**Other**
I	Nasair 100	9.0		1.0			10.5	5.75	1.2	3.3		
	SRR99	8.0	5.0				10.0	5.5	2.2	3.0		
	RR 2000	10.0	15.0	3.0				5.5		4.0		1.0 V
	Rene N4	9.0	8.0	2.0			6.0	3.7	4.2	4.0		0.5 Nb
	AM 1	7.8	6.5	2.0			5.7	5.2	1.0	7.9		
	AM 3	8.0	5.5	2.25			5.0	6.0	2.0	3.5		
	CMSX-2	8.0	4.6	0.6	–	–	8.0	5.6	2.0	6.0	–	
	CMSX-6	9.8	5.0	3.0	–	–	–	4.8	4.7	2.0	0.1	
	PWA 1480	10.0	5.0	–	–	–	4.0	5.0	1.5	12.0	–	
	TMS-6	9.2					8.7	5.3		10.4		
	TMS-12	6.6					12.8	5.2		7.7		
II	CMSX-4	6.5	9.0	0.6	3.0	–	6.0	5.6	1.0	6.5	0.1	
	PWA 1484	5.0	10.0	2.0	3.0	–	6.0	5.6	–	8.7	0.1	
	Rene N5	7.0	8.0	2.0	3.0		5.0	6.2		7.0	0.2	
	MC 2	8.0	5.0	2.0			8.0	5.0	1.5	6.0		
	TMS-82+	4.9	7.8	1.9	2.4		8.7	5.3	0.5	6.0	0.1	
III	CMSX-10	2.0	3.0	0.4	6.0	–	5.0	5.7	0.2	8.0	0.03	0.1 Nb
	TMS 75	3.0	12.0	2.0	5.0		6.0	6.0		6	0.1	
	Rene N6	4.2	12.5	1.4	5.4		6.0	5.75		7.2	0.15	0.05C; 0.004B; 0.01Y
IV	MC-NG	4.0	max0.2	1.0	4.0	4.0	5.0	6.0	0.5	5.0	0.1	0.03C
	MX 4	2.0	16.5	2.0	5.95	3.0	6.0	5.5		8.25	0.15	
	PWA 1497	2.0	16.5	2.0	5.9	3.0	6.0	5.5	–	8.2	0.1	0.004B
	TMS 138	2.9	5.9	2.9	4.9	2.0	5.9	5.9	–	5.6	0.1	
	TMS 162	2.9	5.8	3.9	4.9	6.0	5.8	5.8	–	5.6	0.1	
V	TMS 173	2.8	5.6	2.8	6.9	5.0	5.6	5.6	–	5.6	0.1	

elements (W + Re + Ta), which allow the formation of precipitates, causes nickel-based superalloys to be characterized by high creep resistance [42].

11.5.2 Macro and Microstructure Investigation

The macrostructure should be determined in the relevant areas of directionally solidified and SC castings (areas of research should be established together with the consignee of the product). Macrostructure studies should be carried out at a magnification of max. 15x, after proper preparation of the sample surface and its corresponding chemical etching.

Based on the macrostructure observations, the distance between the arms of the primary and secondary dendrites can be determined using the following methods: (1) count method, (2) secant method, (3) measuring the distance to four nearest neighbors,

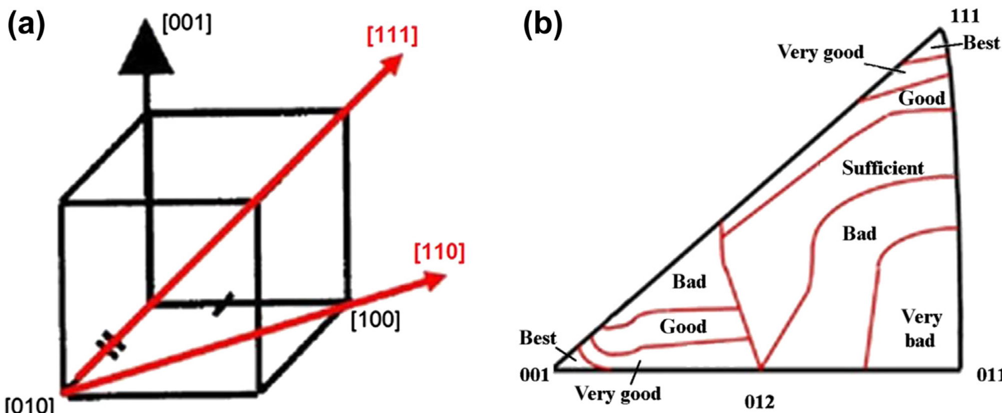

FIGURE 11.11 Relationship between crystal orientation and creep resistance of single crystal nickel-based superalloy CMSX-4: (a) spatial position of crystal axes, (b) creep resistance – inverse pole figure map [45].

(4) measuring the distance from six nearest neighbors, and (5) dendrite cross-section gravity center method. The best method is to measure the distance to the four nearest neighbors (dendrites), as it provides results not significantly different when compared to the counting method, which is recommended in the literature, and it allows the calculation of the variation coefficient characterized by varying the distance between the arms of primary dendrites [47].

The basic components of the single crystal nickel-based superalloy microstructure are: γ phase (matrix), γ' phase (hardening phase), $\gamma + \gamma'$ eutectic mixture, carbides, and topologically close-packed (TCP) phases (Figure 11.12) [28,43,44,47,48].

γ phase is a solid solution (face center cubic structure of lattice parameter: $a_0 = 0.352$ nm) of alloying elements (Cr, Co, Mo, W) in nickel.

γ' phase of regular body center cubic structure $L1_2$ is present in the form of precipitates and is coherent with the matrix. Lattice parameters are: Ni_3Al – $a_0 = 0.3561$ nm,

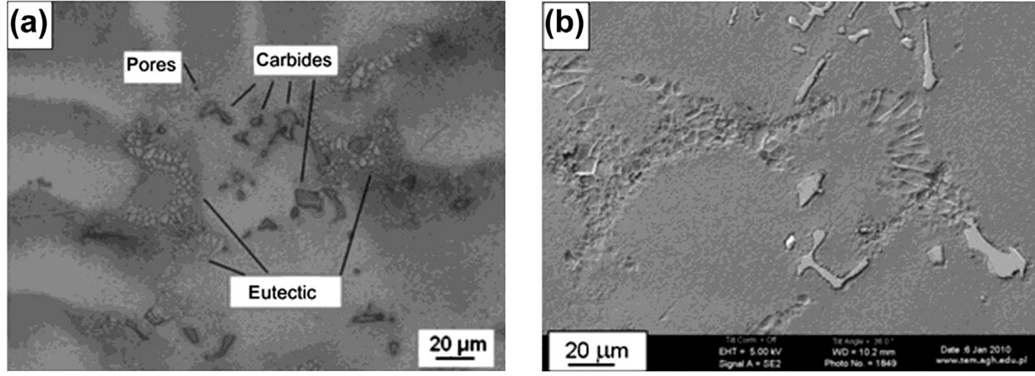

FIGURE 11.12 Microstructure of CM186LC alloy in interdendritic area. (a) LM, (b) SEM [48].

$Ni_3(Al_0,5Ti_{0.5})$ – $a_0 = 0.3568$ nm. γ' phase crystals strengthen the matrix, increasing the tensile strength with temperature rising, while maintaining ductility. Its relative volume ranges from a few to about 75% depending on chemical composition and heat treatment of the alloy.

Carbides present in the nickel-based superalloys are primary carbides of MC type. They have strong impact on material hardening. Carbon (0.05–0.2 wt%) forms carbides with major alloying elements (Cr, Mo, W, Nb). During the heat treatment as a result of conversion of MC carbides, complex structures are being formed: $M_{23}C_6$ and M_6C. Lattice parameters are: MC (regular structure) – $a_0 = 0.340–0470$ nm, $M_{23}C_6$ (regular complex structure) – $a_0 = 1050–1070$ nm, M_6C (regular complex structure) – $a_0 = 1085–1175$ nm.

TCP phase (secondary phase) is formed in nickel-based superalloys in the heat-treatment process or after a long period of operation at raised temperature. It causes reduction in the strengthening of matrix (by reducing the content of Mo and W in the matrix), reduction of heat resistance (by binding Cr and Co), and lower plasticity. In DS and SC nickel-based superalloys the following TCP phase types can appear: δ (tetragonal structure) – $a_0 = 0.912$ nm, $c_0 = 0.472$ nm; P (rhombohedral structure) – $a_0 = 1.690$ nm, $b_0 = 0.471$ nm, $c_0 = 0.904$ nm μ (rhombohedral structure) – $a_0 = 0.473$ nm, $c_0 = 2.554$ nm, $\alpha = 120°$, R (rhombohedral structure) – $a_0 = 1.093$ nm, $c_0 = 1.934$ nm, $\alpha = 120°$.

$\gamma + \gamma'$ eutectic mixture is characterized by high brittleness, which reduces mechanical properties of the alloy—conventionally this phase is eliminated by the heat-treatment process.

In nickel-based superalloys, operated at raised temperature and under the influence of stress, the phenomenon known as rafting can occur. It means that γ/γ' phases approach each other and connect/bond creating γ' phase precipitates (Figure 11.13) [28,48]. Depending on the direction of stress that is given, one can distinguish:

1. N rafting – causes formation of γ' plate-shaped phase in a direction perpendicular to the direction of tensile (in the γ/γ' negative network mismatch superalloys) or compressive (in the γ/γ' positive network mismatch superalloys) stresses,
2. P rafting – causes formation of γ' plate-shaped phase in a direction parallel to the direction of tensile (in the γ/γ' negative network mismatch superalloys) or compressive (in the γ/γ' positive network mismatch superalloys) stress.

Rafting phenomenon is an effect of stresses at high temperature, the difference on the lattice parameters, the modulus of elasticity and chemical composition of the γ/γ' phases, and the movement of γ/γ' phase boundaries [28,48,49].

In SC and DS castings, the following typical defects may occur: nonmetallic inclusions, porosity, TCP phases, shrinkage porosity, hot cracks, and strip folds (wrinkles); and also the defects that are unique to this kind of casting, including freckles, strain grains, wide-angle grain boundaries, slivers zebra grains, and recrystallized grains [44,50,51] (Figure 11.14).

Improper orientation of crystal grains (grain orientation deviation from the axis of casting) is a defect that disqualifies the casting.

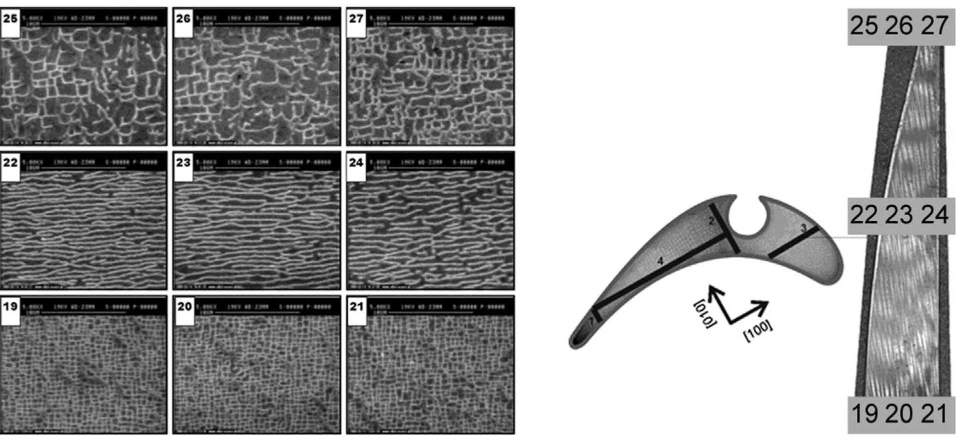

FIGURE 11.13 Microstructure of CMSX-4 alloy blade at a section parallel to the (010) plane, SEM [28].

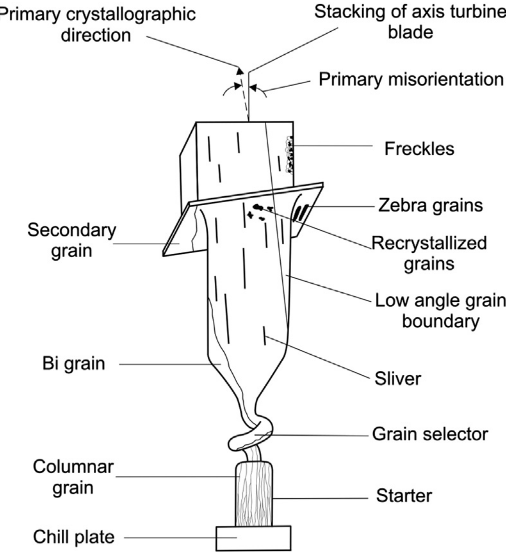

FIGURE 11.14 SC and DS casting defects scheme.

Nonmetallic inclusions may be present both on the surface and inside the castings. They arise as a result of: improper metallurgical purity of master heat, interactions between the liquid metal and the mold or crucible material, and thermal decomposition of chemical reactions on liquid alloy—ceramic mold and liquid alloy—crucible interfaces. The most common nonmetallic inclusions in nickel-based superalloy precision castings are: ZrO_2, SiO_2, HfO_2, HfC, and TiC. Nonmetallic inclusions in the casting surface can be detected using fluorescence method. An exact identification is possible by means of transmission (TEM + EDS) and scanning electron microscopy (SEM + EDS + EBSD).

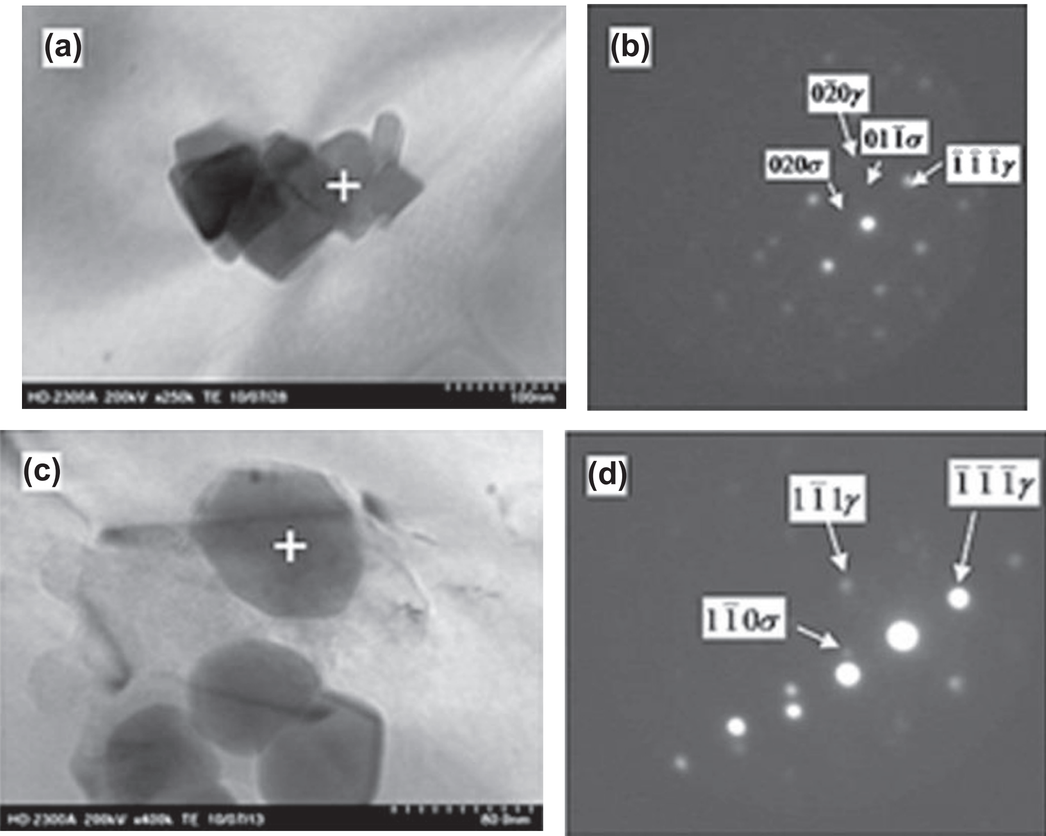

FIGURE 11.15 TCP phase identification in CMSX-4 superalloy after thermal exposure: (a, c) STEM images and (b, d) electron diffraction patterns of σ phase [52].

TCP phases are formed in nickel-based superalloys through prolonged annealing at high temperature (during improper heat treatment or operation). The most common phases of this type are: σ, μ, and P (needle-shaped or globular morphology), which are rich in chromium, molybdenum, and tungsten (Figure 11.15) [52,53]. They are characterized by high hardness and brittleness, thereby their presence decreases properties of the nickel-based superalloys, especially at raised temperature. Identifying the TCP phases is done by means of transmission microscopy (TEM + EDS), scanning electron microscopy (SEM + EDS + EBSD), and diffractometry.

Freckles are equiaxed grains forming chains, arranged parallel to the direction of gravity, enriched in alloying elements segregating to the liquid phase (Ti, Ta, Al, Nb) [54]. The length of chains varies from a few to a few hundred, and their width reaches maximum few millimeters. They usually appear in the interdendritic areas, mostly on the surface of the casting. Around the freckles, areas of higher relative volume of carbides, eutectic, and porosity occur.

The criteria for formation of freckles has been divided into three categories: the criterion of cooling rate (known as the G-R criteria) (Figure 11.4), Fleming criterion, and the criterion of the Rayleigh number [54–58].

The main cause of freckles formation is a large alloying elements segregation to the solid phase (W, Re) causing the liquid metal density inversion in the interdendritic areas, the emergence of buoyant forces [55–57], and additional effects of: thermal shadow, edge shadow, cross-section changes, and crystallographic orientation changes [54,56,58]. Susceptibility of the alloy to form freckles is determined by factor F (freckling index) [44]:

$$F = C_{Ta} + 1.5C_{Hf} + 0.5C_{Mo} - 0.5C_{Ti}/C_W + 1.2C_{Re}$$

where: C_{Ta}, C_{Hf}, C_{Mo}, C_{Ti}, C_W, and C_{Re} are the contents (wt%) of alloying elements. If $F > 1$, the probability of freckles is small.

Strain grains are columnar grains appearing in single-crystal castings due to improper nucleation and grain selection in the selector. It is assumed that these are the result of growth of secondary and tertiary dendrite arms [59]. Elimination of strain grains requires proper selection of the alloy chemical composition, geometry of nucleus and the selector, and solidification conditions, mainly a temperature gradient in the mushy zone and the single-crystal casting withdrawal rate.

High angle boundaries (HAB) and low angle boundaries (LAB) are formed in directionally solidified and SC castings as a result of incorrect direction of heat transfer during solidification, mold impurities, and too low temperature gradient [60]. Contact between dendrites of different orientation relating to the direction of casting solidification causes the formation of high or low angle grain boundaries. In industrial practice, SC castings, that have experienced high angle grain boundaries are not used because they significantly reduce the casting (turbine blades) work time at raised temperature.

Slivers are characterized by high elongation and similar orientation in the direction of solidification (Figure 11.16(a)) [61]. It is assumed that they are formed as a result of nucleation in other defects (f. e. freckles) or nonmetallic inclusions. It was found that the

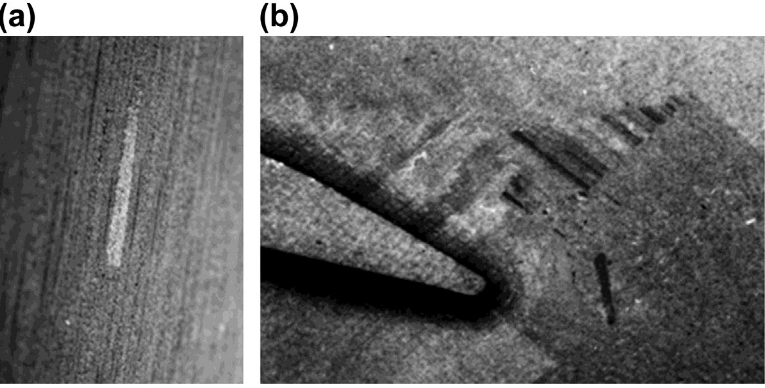

FIGURE 11.16 Sliver (a) [61], zebra grains (b) [62] on the surface of CMSX-4 nickel-based superalloy casting.

cause of silvers formation can be: (1) too long time of holding molten metal in the ceramic mold, causing the reaction of an alloy with the mold and the increase of the content of nonmetallic inclusions in the casting, and (2) increase of carbon content in nickel-based superalloys to about 0.15 wt% [63].

Zebra grains are formed during growth of dendrites in supercooled casting area (especially in the dovetail blade root) and their fragmentation caused by recalescence. They are generally perpendicular to the direction of solidification and are characterized by a band or globular morphology (Figure 11.16(b)).

Wrinkles are formed on the casting surface in the form of characteristic irregularities as a result of liquid metal (especially Hf) reaction with a ceramic mold [44,51]. Their formation can be prevented by increasing alloy metallurgical purity and shortening the metal-mold reaction time.

11.5.3 Porosity Investigation

Porosity is a microstructure defect. It is a presence of pores (open or closed spaces) in the casting. It significantly reduces the mechanical properties of the casting—particularly the fatigue strength, creep resistance, impact strength, elongation, and tensile strength [64,65]. Therefore, an evaluation of porosity in precision castings of nickel-based superalloys (in particular turbine blades) is one of the most important performance criteria. Currently, each of engine manufacturer uses their own methods and procedures for assessing the porosity (comparative and quantitative X-ray tomography) [65,66]. It was found [67] that methodological factors affecting the results of porosity evaluation are:

1. proper cutting of test samples,
2. correct execution of test samples (grinding and polishing),
3. appropriate selection of the pores output image transformations into binary measurement images (Gutter Shadow Correction and decimal-to-binary conversion),
4. estimating the required number of measurements required to obtain reproducible results,
5. assessment of heterogeneity in size, shape, and distribution of pores.

The porosity in the turbine blades and vane segments is divided into:

1. gas porosity – arising as a result of evolution of dissolved gases (Figure 11.17(a)),
2. shrinkage porosity – formed as a result of the lack of feed in interdendritic areas and shrinkage during solidification (Figure 11.17(b)).

Shrinkage porosity occurs due to molten metal supply to the solidifying areas cutoff by reducing the interdendritic areas, or by solidification of large-sized primary carbides blocking the flow in the interdendritic areas (mainly in DS casting method) [67,68]. The relative shrinkage pores volume increases when the casting temperature and a cooling rate raise, and a coefficient of contraction of the alloy is bigger/higher. The intensity of

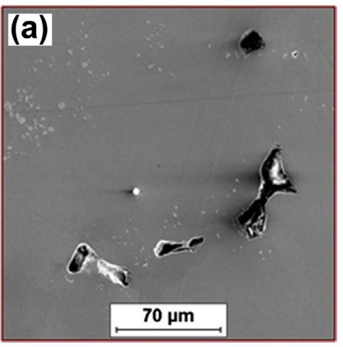

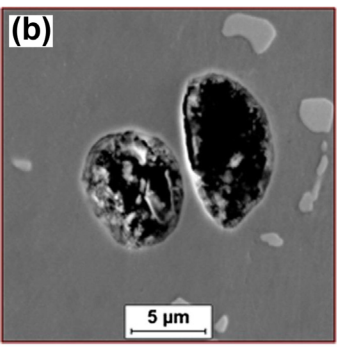

FIGURE 11.17 Shrinkage (a) and gas (b) porosity in René142 DS nickel-based superalloy turbine blade casting [67].

gases emission, which causes the formation of gas pores, increases with lowering of the melted metal solidification temperature (by reducing the solubility of H_2, N_2, and O_2 in the alloy). Depending on the rate of coagulation and gas content in the alloy, gas pores have different morphology and distribution [69,70].

In addition to gas and shrinkage porosity, in nickel-based superalloy castings, two different types of porosity, resulting from the homogenization annealing, can occur [70,71]:

1. type H porosity – caused by different diffusion coefficients of alloying elements favoring dendritic segregation and thus formation of excess vacancies and Kirkendall–Frenkel voids, which coalesce into the H-type pores (occurring in low-angle grain boundaries),
2. type D porosity – caused by creeping process during the operation, which leads to vacancies, voids, and following pores (having characteristic rectangular shape).

Relative volume, morphology, size, and distribution of pores in the single crystal and DS castings depend on:

1. chemical composition of the alloy – the difference between liquidus and solidus temperature and purity of the master heat,
2. phenomena occurring during solidification – order of phases solidification, casting shrinkage and the type of phase transitions,
3. melting and casting parameters – superheating and pouring temperature, mold temperature, solidification and cooling rate, the type and purity of crucibles, mold withdrawal rate from the heating zone, and temperature gradient in the mesh zone,
4. reactions on the liquid metal – ceramic mold interface,
5. geometry and shape of the casting and the gating system – the liquid metal transporting method, size and geometry of the channels, and casting walls thickness.

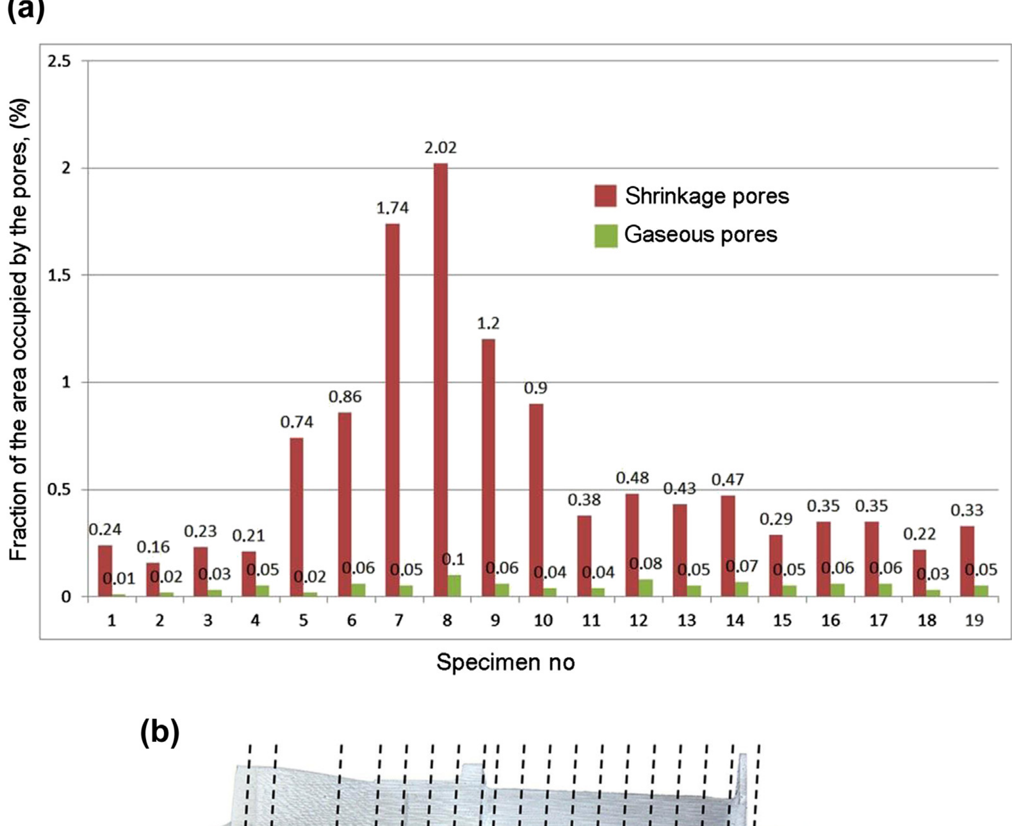

FIGURE 11.18 Diagram of sampling to asses porosity, (a) porosity in various areas (b) of single crystal blade castings made of the CMSX-4 superalloy [67].

To evaluate the porosity of DS and SC castings, the most commonly used are the quantitative metallography parameters; Assessment of DS and SC castings porosity is carried out on a larger number of samples (Figure 11.18) to determine representative and critical areas depending on the geometry [67,71].

11.5.4 Determination of Crystal Perfection and Crystallographic Orientation (Laue and XRD Methods)

The basic method to define an orientation of SC castings is Laue method. It provides information about the structure of an area with a diameter of about 1.5 mm. Laue diffraction is obtained from polished and chemically etched surface with the usage of,

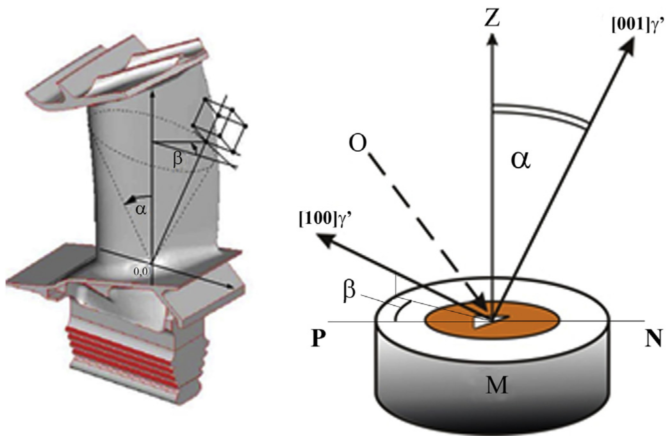

FIGURE 11.19 Crystallographic orientation determining diagram: α – [001] γ′ direction angle deviation from blade's Z axis, β – the angle between projection of the [100] γ′ direction on the test cross-section surface S and the longer side (PN) of the dovetail blade root cross-section, M – thermosetting mass matrix, in which the sample is mounted, O – Laue diffraction area.

e.g., Mo lamp (Kα = 0.0709 nm, with a power of approximately 50 MW and backscattered radiation geometry) (Figure 11.19). Areas of samples for determining the orientation depend on customer requirements (Figure 11.20) [72,73].

Cross-section orientation is determined by Laue reflection method using back-scattered rays. The images show reflection of two pairs of orthogonal strips (A1 ⊥ A2, B1 ⊥ B2) corresponding to the symmetry of regular structure (Figure 11.21). In single crystal nickel-based superalloys, the highest relative volume has Ni_3Al phase (γ′) with a regular structure (Laue diffractions come from this phase). Laue diffraction indexing is performed adopting the lattice parameter of investigated phase. β angle is defined between the B2–B2 belt and the T axis. It is assumed that β angle has a positive value when the B2–B2 belt is above the T axis and negative when it is below. When performing diffraction, T axis should be horizontal and parallel to the AB reference line (for blade cross-section: C1–C3 in Figure 11.21), while for the blade's dovetail root cross-sections (C4 and C5 in Figure 11.21), parallel to the PN reference line.

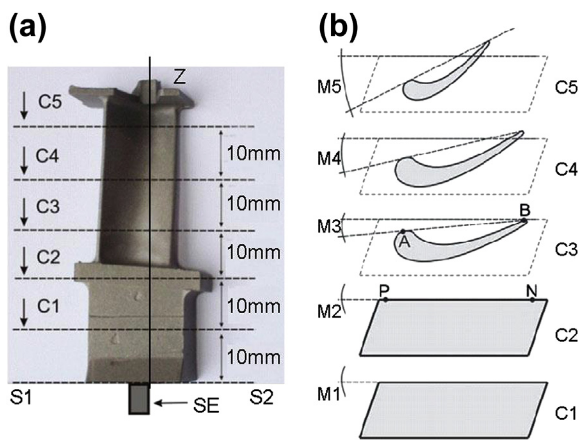

FIGURE 11.20 Sampling scheme for the single crystal blade orientation testing: (a) C1, C2, C3, C4, C5 – cross-sectional planes. Arrows indicate the areas of cross-sections examined. SE – grains selector, Z – blade main axis (solidification direction) perpendicular to S1–S2 plane, (b) the angular corrections M scheme for determination of β angle (view from C1, C2, C3, C4 and C5 arrows directions), AB – reference line.

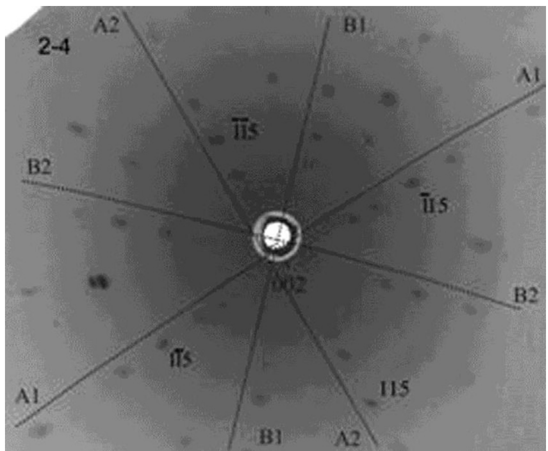

FIGURE 11.21 Laue diffraction image from C2 area (Figure 11.20) for CMSX-4 blades dovetail root withdrawn with a speed of 2 mm/min.

Crystal orientation can be also determined on the basis of observations with scanning electron microscope equipped with an EBSD detector and appropriate software: Twist (Diffraction Data Creator), Flamenco (Phase ID), Mambo (Inverse Pole Figures), Tango (Mapping) and Salsa (Orientation Distribution Functions). Crystal orientation of single crystal blades depends on manufacturing conditions and area of testing (Figure 11.22). Both Laue and EBSD methods for determining single crystal fineness are destructive methods (require cutting of the casting and testing samples preparation).

Automatic diffractometer for the investigation of crystal orientation distribution on the surface of SC casting has been designed and manufactured by the EGF Berlin company and the Department of Materials Science of Rzeszow University of Technology.

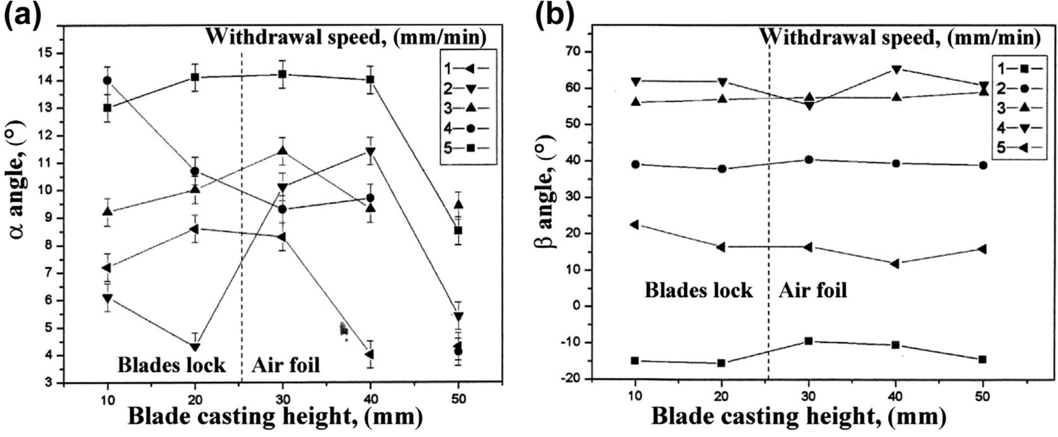

FIGURE 11.22 Effect of single crystal CMSX-4 alloy blade withdrawal rate on. (a) α and (b) β angles determined by Laue method.

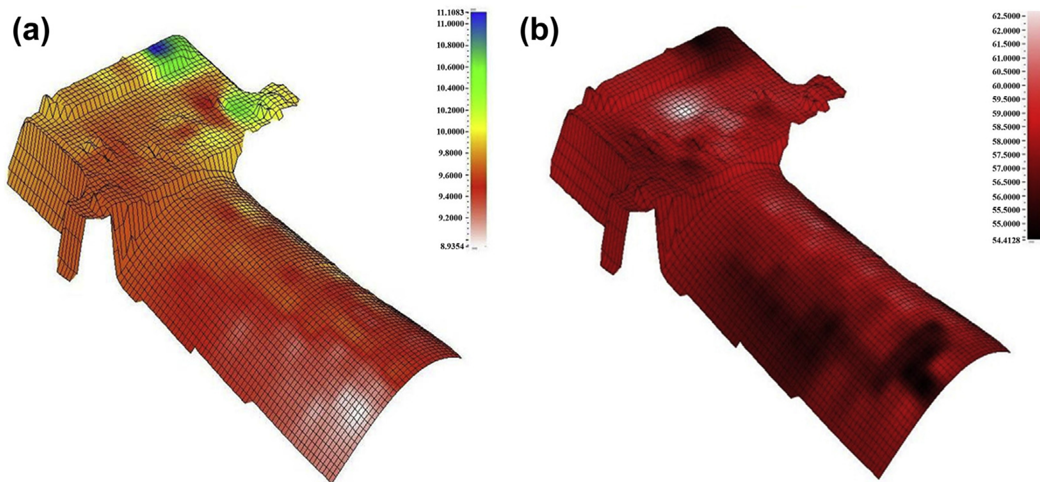

FIGURE 11.23 Single crystal CMSX-4 superalloy blade surface distribution of the: (a) α angle, (b) β angle.

It has many advantages over traditional Laue diffractometer: about 100 times shorter measurement time, detector and measurement data processing computer linkage, and the ability to determine crystal orientation in any three-dimensional area of the casting (Figure 11.23).

11.6 Numerical Modeling of Thermal and Solidification Processes for Directional Solidification Castings

Numerical modeling of the solidification process of macro-, micro-, meso- and nano-structure of the castings is carried out with the use of professional commercial and proprietary software. Macrostructure modeling is based on defining the temperature field in the volume of the casting, usually by using finite elements and finite difference methods. Micro- and mesostructure is modeled with the use of cellular automata and the phase-field method [74]. These methods allow determination of grains and dendritic microstructures and solve many problems connected with their solidification.

Numerical modeling of directional solidification on an industrial scale is generally conducted in micro- and macroscale with the use of the Bridgman and the LMC methods, using commercial software [75]. Thus, in the next section, modeling of the temperature field and solidification of columnar grains will be discussed. Numerical simulation can accurately and quickly optimize the manufacturing process of DS castings: temperature of the furnace heaters, liquid metal, and the mold. The obtained forecasted temperature distribution is a base to determine important process parameters, such as temperature gradient, cooling rate, solidification velocity, and curvature of

the mushy zone. Their analysis allows selection of suitable arrangement of the blades in a model set and determination of the shape of the radiation and thermal baffle, and the choice of the most important parameter, the ceramic mold withdrawal rate from the heating to the cooling zone.

11.6.1 Analytical Thermal Analysis of Directionally Solidified Casting

The basis for modeling of directional solidification process is to determine the change in casting temperature over time, taking into account evolved solidification heat by numerical solving of the heat conduction equation [76]:

$$\rho c \frac{\partial T}{\partial t} = \frac{\partial}{\partial x}\left(\lambda \frac{\partial T}{\partial x}\right) + \frac{\partial}{\partial y}\left(\lambda \frac{\partial T}{\partial y}\right) + \frac{\partial}{\partial z}\left(\lambda \frac{\partial T}{\partial z}\right) + \rho L \frac{\partial f}{\partial t} \tag{11.4}$$

where: ρ – density, c_v – specific heat, λ – thermal conductivity, L – latent heat of fusion, f – solid fraction. The presented version of the equation does not take into account convection heat transfer. The left side of Eqn (11.4) takes into account the heat accumulated by the material. However, the components of the right side of this equation take into account the thermal conductivity, and the last factor is a phase transition heat (latent heat of solidification). Numerical solution of the equation allows approximation of the temperature distribution of the alloy in the liquid–solid state (mushy zone), the temperature change in the mold and the casting, temperature at the beginning and the end of solidification, and forecasting of casting defects.

Solution of the heat flow equation requires establishment of appropriate boundary conditions. Thus, an important step in numerical modeling of directional heat flow and solidification is the adoption of appropriate boundary and initial conditions in the casting, mold, and their surroundings, geometric models, and thermophysical parameters of materials. In order to improve their characterization, and adoption of appropriate values, the heat flow during the process of directional solidification on an industrial scale will be discussed.

DS casting is divided into three areas regarding the state of aggregation. In the area of the heating furnace impact, the ceramic mold is filled with an alloy in the liquid state at a temperature above the liquidus level (Figure 11.24(a)). Below the heating furnace, chill rings affect the ceramic mold. Along this height, the temperature is lower than the solidus and the alloy is in a solid state. Between the heating and cooling areas there is a thermal baffle. At the height of thermal baffle the ceramic mold is under the impact of temperature gradient. The alloy is in the liquidus–solidus temperature range, and it is in the mushy zone. In the directional solidification, the direction of heat flow is parallel to the temperature gradient in mushy zone. The heat is accumulated in the liquid melt and generated in mushy zone (latent heat of solidification) and by solidification is removed from the casting by conduction.

In the casting, heat flow is carried out to the chill plate and outside the mold (Figure 11.24(b)). In the lower part of the ceramic mold, at a height of about 30 mm, a heat flow perpendicular to the surface of the chill plate dominates. Mold displacement,

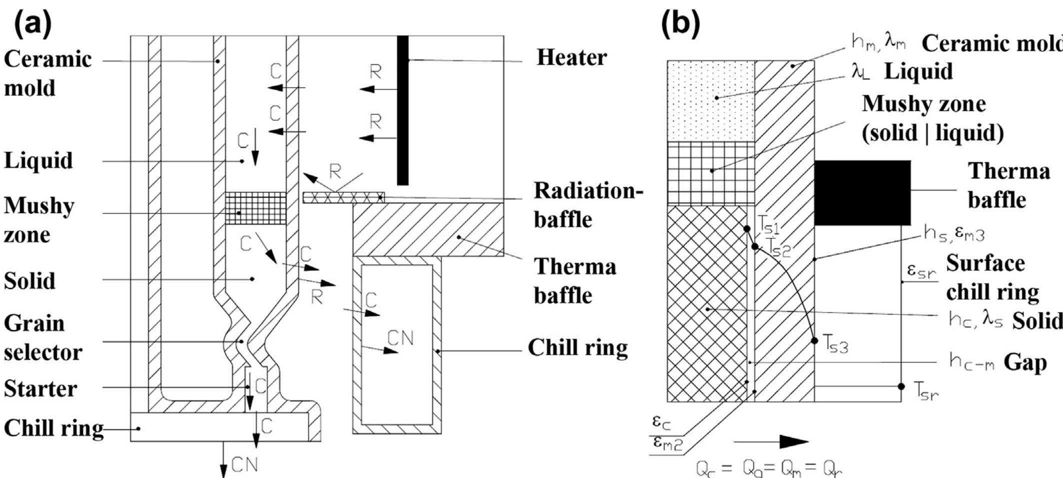

FIGURE 11.24 (a) Heat flow scheme during directional solidification of the casting, C – conduction, CN – convection, R – radiation, ε_c – the emissivity of the casting, ε_{m2} – the emissivity of the inner surface of the mold, ε_m – emissivity of the outer surface of the mold, T_{ch} – surroundings temperature, T_{s3} – temperature of the outer surface of the mold, T_{s1} – casting surface temperature, T_{s2} – the temperature of the inner surface of the mold, h_{c-m} – casting-mold interface heat transfer coefficient, h_m – mold heat transfer coefficient, h_s – radiation or convection heat transfer coefficient from the mold surface, λ_S, λ_L – thermal conductivity coefficient, respectively, in solid and liquid phase, (b) schematic distribution of the temperature and heat flow between the casting and the surroundings of the ceramic mold.

with reference to the heating element, reduces the impact of the chill plate on the casting. The cooling effect on the surface of the mold increases and the radial flow of heat in the casting begins to dominate.

As a result of the solidification process and the casting shrinkage, a gap between the casting and the mold, as well as between the casting and the chill plate, occurs [77]. It is assumed that a heat exchange between the unconnected surfaces of the two materials occurs via radiation. The process of heat transfer between the mold and the casting is characterized by the casting-mold interface heat transfer coefficient h_{c-m} and defined by the equation [78]:

$$h_{c-m} = \frac{q}{T_{s1} - T_{s2}}, \mathrm{W/m^2/K} \tag{11.5}$$

where: T_{s1} – casting surface temperature, T_{s2} – the temperature of the inner surface of the mold, q – heat flux.

A gap is also formed between the casting and the chill plate due to a contact of molten metal and its rapid solidification. A chill-casting interface heat transfer coefficient of the resulting gap (h_{c-p}) may have a huge impact on the solidification process of columnar grains in the starter, and thus, on the crystal structure of SC casting.

During the directional solidification process modeling, one should take into account the gap that is formed between the ceramic mold and the cooling plate. The heat flow

between these elements is characterized by the mold-chill interface heat transfer coefficient (h_{m-p}). Its value affects the forecasted temperature distribution in the area where the cooling plate affects the casting.

The phenomenon of heat transfer between two materials, at an imperfect surface contact, is described by boundary condition of the fourth kind [79]. Assuming a one-way heat flow, this condition is described by the relation:

$$\lambda_I \frac{\partial T_I}{\partial x} = h_g(T_{Is} - T_{IIs}) = \lambda_{II} \frac{\partial T_{II}}{\partial x} \tag{11.6}$$

where: T_{Is} – 1st material surface temperature, T_{IIs} – 2nd material surface temperature, T_I – 1st material temperature, T_{II} – 2nd material temperature, λ_I, λ_{II} – material thermal conductivity coefficients, h_g – interface heat transfer coefficient.

Subsequently, the heat flow is discharged through a mold layer. In ceramic molds the heat flow, being a result of thermal conduction, dominates. The mold heat transfer coefficient h_m depends on the mold thickness and thermal conductivity, as shown in the equation:

$$h_m = \frac{\lambda_m}{l_m}, \mathrm{Wm^{-2}K^{-1}} \tag{11.7}$$

where: λ_m– thermal conductivity coefficient of the mold, l_m – mold thickness.

The methods used in the manufacture of single crystal nickel-based superalloy castings differ mainly in the cooling method of the ceramic mold. Between the mold and its surroundings, usually two types of heat transfer occur: convection and radiation. However, one type of heat transfer takes precedence over the other. Intensity of mold cooling depends on the contribution of different ways of implementing the heat exchange. Radiative cooling of the mold dominates in the manufacturing of SC castings by the Bridgman method. Radiation heat transfer coefficient h_{s-r} of the ceramic mold to the environment takes the form:

$$h_{s-r} = \sigma \cdot \varepsilon_m \cdot (T_{s3} + T_{ch}) \cdot \left(T_{s3}^2 + T_{ch}^2\right), \mathrm{Wm^{-2}K^{-1}} \tag{11.8}$$

where: σ – Boltzmann constant.

Heat, absorbed from the surface of the mold and the starter, is dissipated to the chill rings and the chill plate. Next, heat is absorbed by water, in a convective process from the inner surfaces of the cooling elements. Both the rings and the chill plate are intensively cooled by water and have a large influence on the temperature distribution in the mold and the casting. Hence, the phenomenon of intensive cooling should be taken into a consideration when modeling the directional solidification casting, taking into account the convection heat transfer coefficient of the inner surface of the cooling elements.

The problem of heat transfer from the surface of the material (barrier) to the surrounding fluid is described by the boundary conditions of the third kind [79]. Assuming a one-way heat flow, this condition is described by the following relation:

$$\lambda_I \frac{\partial T_I}{\partial x} = h_{s-c}(T_{sI} - T_{sr}) \tag{11.9}$$

where: h_{s-c} – convection heat transfer coefficient from the surface of the barrier, T_{sI} – barrier surface temperature, T_{sr} – liquid temperature.

11.6.2 Numerical Modeling of Temperature Field

In this section, an exemplary numerical modeling of temperature field in DS will be carried out using specialized software. It was assumed that the directional solidification process is carried out using the Bridgman method, on an industrial scale.

To carry out the modeling, it is necessary to implement a digital recording of a geometrical model set and the model of the furnace (heating furnace, melting and withdrawal chamber) (Figure 11.25). A model set consists of eight rods with a diameter of 12.5 mm each, ingate, and the pouring cup. A model of the heating furnace consists of two heaters with a diameter of 300 mm, a graphite thermal insulation, and a radiation baffle having an inner diameter of 220 mm and a thickness of 2.5 mm. For creating the mentioned models, the actual size of the installation of a vacuum furnace for manufacturing of castings by the Bridgman method was taken into account. Chill rings with an internal diameter of 250 mm are placed below the heating furnace. The inner surface of the cooling and melting chambers of the furnace (surroundings) have been considered in the studied model.

An axial symmetry that was assumed for the analysis of the system can decrease the time of numerical calculations. Therefore, for the modeling one-fourth of the real system was taken into account. A developed geometrical pattern of the model set, the heating furnace, and the inner surface of the melting and cooling chambers was a basis for

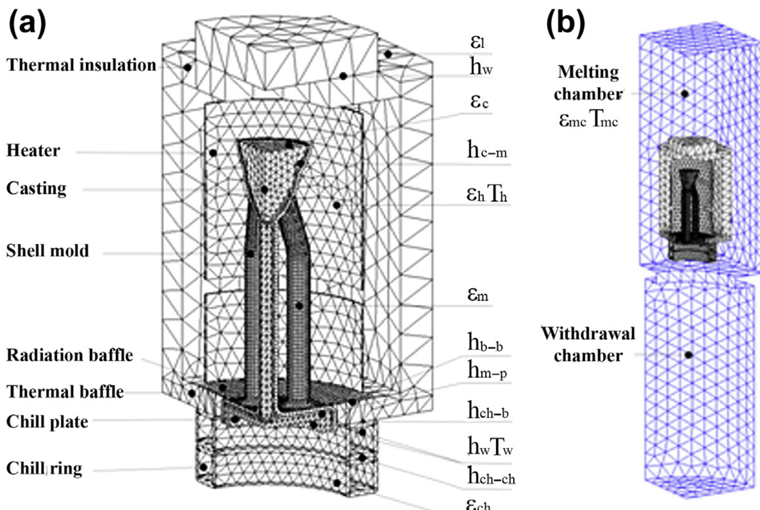

FIGURE 11.25 Finite element mesh on a geometrical model of the heating furnace. (a), the inner surface area of the melting and withdrawal chamber (b), and the place of the appropriate boundary conditions adopted (ProCAST software).

generating a finite element mesh. Next, the prepared model set was a basis for generating the ceramic mold layer with a thickness of 10 mm.

Geometric model materials have been defined and the thermophysical properties have been adopted. For thermal insulation, heaters, and thermal and radiation baffle, graphite was used. And for the chill rings and the chill plate, copper was adopted. The castings were made of CMSX-4 nickel-based superalloy. For the spatial context material—the inner surface of the melting and withdrawal chambers—steel was assumed.

Numerical simulation of the casting solidification process requires an establishment of boundary and initial conditions that reflect the actual heat exchange process (Figure 11.25). The boundary conditions of the first kind were assumed—the temperature on the inner surface of the melting and withdrawal chamber – T_{mc}, also heaters surface – T_h. The boundary conditions of the third kind were adopted at the inner surface of the chill rings and chill plate intensively cooled with water. An appropriate value of the water temperature – T_w and convection heat transfer coefficient of the inner surface of the rings and chill plate – h_w were assumed.

The boundary conditions of the fourth kind were assumed for the interface of two materials. The values of the interface heat transfer coefficient for contact has been defined for the following pairs: casting-ceramic mold (h_{c-m}), casting-chill plate (h_{c-p}), ceramic mold-chill plate (h_{m-p}), thermal insulation-insulation (h_{i-i}), chill ring-thermal baffle (h_{ch-b}), chill ring-chill ring (h_{ch-ch}), thermal baffle-radiation baffle – h_{b-b}.

In the simulation, it was assumed that the solidification process occurs in a vacuum. Thus, the heat exchange between the surfaces of the heating elements of the furnace, the inner surface of the surroundings, and the ceramic mold occurs through a thermal radiation. Value of the surface emissivity coefficient was assumed for: ceramic mold – ε_m, thermal insulation, radiation and thermal baffle (graphite) – ε_i, heaters – ε_h, chill rings – ε_{ch} and surface surroundings (melting and withdrawal chamber) – ε_{mc}, casting – ε_c.

The initial conditions (temperature) were adopted for insulation of the heating furnace, thermal and radiation baffle, ceramic mold, heaters, rings, and the chill plate. The mold after annealing was poured with liquid metal and withdrawn at a speed of 3 mm/min from the heating furnace to the cooling zone of the furnace (Figure 11.26).

11.6.3 Numerical Modeling of Nucleation and Grain Growth

Simulation of macro- and microstructure of the entire volume of the casting in a short calculation time is possible thanks to the use of the cellular automaton finite element (CAFÉ) numerical method. The CAFÉ module employs the cellular automata method (CA) and the finite element method (FEM) for simulation [80]. The differential equations, which describe the temperature field and characterize the flow of liquid metal, were solved by applying the FEM. The simulation of the grains nucleation and growth process, combined with the influence of temperature field, is based on the calculations using the CA method. The model space is discretized with finite element mesh, however, in the

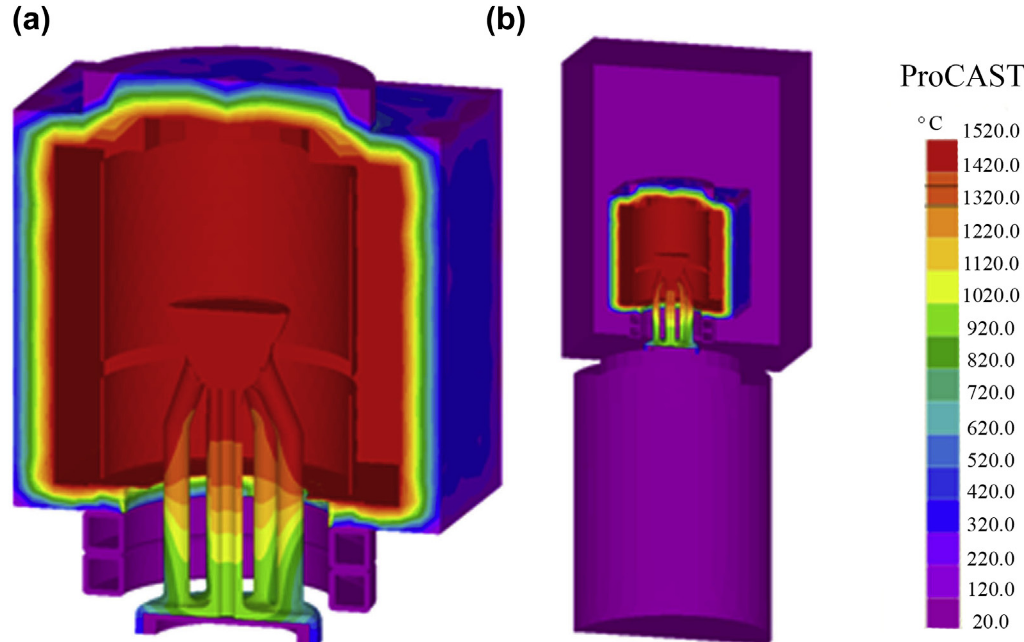

FIGURE 11.26 Temperature distribution in the heating furnace and the mold after relocation to a distance of 150 mm (a), and inner surface of the melting and withdrawal chambers (b) (ProCAST software).

area, which was selected for microstructure modeling, the additional, regular CA mesh was created. The CA mesh covered at least the specified part of the finite element mesh.

CAFÉ method allows prediction of the morphology (shape and size) and the amount of equiaxed grains in the casting [81], as well as a relation between the equiaxed and columnar layers in the ingot [82]. It is employed for the simulation of the directional solidification process of the castings manufactured with use of the Bridgman and LMC methods.

Numerical simulation of the nucleation process is usually carried out with the use of normal statistical (Gaussian) distribution, which takes into account the dependence of the number of grains on the degree of undercooling of liquid metal [80]:

$$\frac{dn}{d(\Delta T)} = \frac{n_{max}}{\Delta T_{\sigma} \cdot \sqrt{2\pi}} \exp\left(-\frac{1}{2}\left(\frac{\Delta T - \Delta T_N}{\Delta T_{\sigma}}\right)^2 \right) \tag{11.10}$$

where: ΔT – current value of undercooling, K, ΔT_N – mean value of Gaussian distribution, K, ΔT_{σ} – mean value of undercooling (Gaussian distribution), K, n_{max} – the maximum amount of substrata that enables the grain nucleation (surface nucleation, m^{-2}; bulk nucleation, m^{-3}).

Growth of grains in the process of solidification is caused by undercooling of the liquid metal. Dendrite tip growth rate (grain growth) depends on the degree of

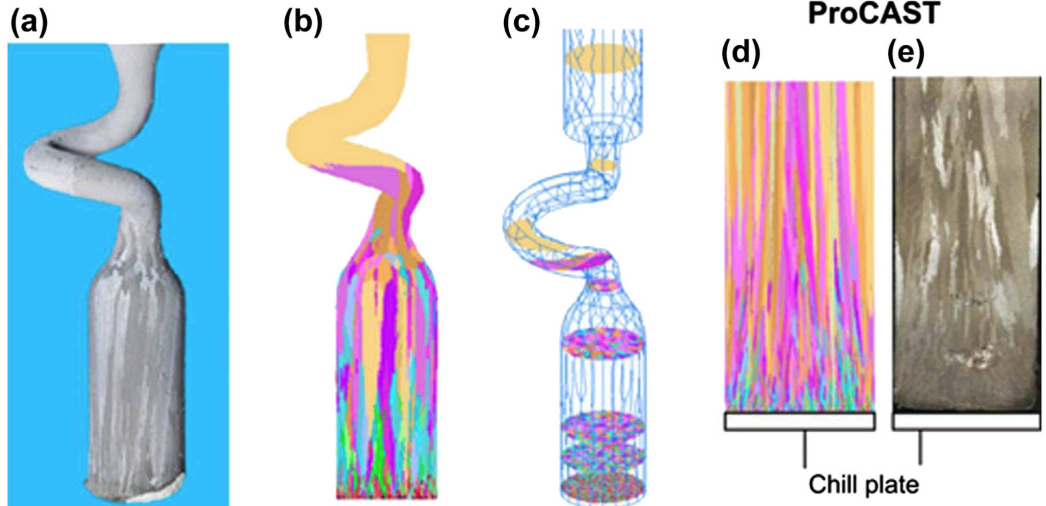

FIGURE 11.27 Real (a, e) and predicted (b, c, d) columnar grains macrostructure:, (b), (c) starter and grain selector, (d) area of chill plate impact.

undercooling and can be described by the Kurz–Giovanola–Trivedi (KGT) model [8], according to the equation:

$$v(\Delta T) = a_2 \cdot \Delta T^2 + a_3 \cdot \Delta T^3 \tag{11.11}$$

The values of parameters a_2 and a_3 of Eqn (11.8) for the adopted KGT model take into account the properties of the alloy admitted in the study.

Figure 11.27 presents an example of numerical modeling of the columnar grain growth process and grain selection in the starter and selector, in directionally solidified SC casting by the Bridgman method.

11.7 Summary

Nowadays, single crystal superalloys of fifth generation are available, which can operate up to about 1000 °C. The National Research Institute for Metals (NIMS) in Japan leads researches on development of chemical composition and the heat treatment of sixth-generation superalloys, for which the predicted operating temperature will be up to about 1500 °C [83]. Increased interest in SC castings of nickel-based superalloy applicability for IGT encourages research on new methods for manufacturing of large-size castings, in which the tendency for formation of defects and the cost of producing by a standard Bridgman method are increased [8]. Thus, there has been the development of the liquid metal cooling method, and attempts are being made to implement new methods such as gas cooling casting and thin shell casting in industrial production [19]. These methods allow the temperature gradient and the solidification rate to increase,

thereby reducing the distance between the dendrites' arms, shortening the heat treatment time and the number of defects in castings. The development of LMC method is mainly based on development of new floating baffle [84], cooling bath, ceramic molds, and process parameters (pulling rate, mold temperature) [85]. Significant reduction in ceramic mold thickness and use of gas cooling in TSC method allow an increase in heat transfer coefficient and the cooling rate and thus improvement of the quality and reduced cost of manufactured casting.

References

[1] Lacaze J, Hazotte A. Textures Microstruct 1990;13:1.

[2] Versnyder FI, Shank ME. Mater Sci Eng 1970;6(4):213.

[3] Elliott AJ, Pollock TM. Metall Mater Trans 2007;38 A:871.

[4] Szeliga D, Kubiak K, Jarczyk G. Int J Metalcast 2013;7(3):17.

[5] Lohmüller P, Esser P, Großmann J, Hordler M, Preuhs J, Singer RF. Superalloys 2000. Miner Met Mater Soc 2000:181.

[6] Elliott AJ, Tin S, King WT, Huang S-C, Gigliotti MFX, Pollock TM. Metall Mater Trans 2004;35 A(10):3221.

[7] Kermanpur A, Varahram N, Davami P, Rappaz M. Metall Mater Trans 2000;31 B(6):1293.

[8] Konter M, Kats E, Hofman N. Superalloys 2000. Miner Met Mater Soc 2000:189.

[9] Dai HJ, D'Souza N, Dong HB. Metall Mater Trans 2011;42 A:3430.

[10] Chmiela B, Szeliga D, Sozańska M, Jarczyk G, Cwajna J. Pract Metallogr 2013;(8):548.

[11] Gao SF, Liu L, Wang N, Zhao XB, Zhang J, Fu HZ. Metall Mater Trans 2012;43 A(10):3767.

[12] Ma D, Lu H, Bührig-Polaczek A. IOP Conf Ser Mater Sci Eng 2011;27:012036.

[13] Dai HJ, Dong HB, D'Souza N, Gebelin J-C, Reed RC. Numerical modeling. Metall Mater Trans 2011;42 A:3439.

[14] Xinbao Z, Lin L, Zhuhuan Y, Weiguo Z, Hengzhi F. Mater Charact 2010;61(1):7.

[15] Toloraiya VN, Orekhov NG, Kablov EN. Met Sci Heat Treat 2002;44(7–8):279.

[16] Meyer ter Vehn M, Dedecke D, Paul U, Sahm PR. Superalloys 2000. Miner Met Mater Soc 1996:471.

[17] Xiping G, Hengzhi F, Jiahua S. Metall Mater Trans 1997;28 A(4):997.

[18] Dantzing V, Rappaz M. Solidification. EPFL Press; 2009.

[19] Ma D, Wu Q, Hollad A, Bührig-Polaczek A. Mater Sci Eng 2011;27(1).

[20] Brundidge CL, Miller JD, Pollock TM. Metall Mater Trans 2011;42 A:2723.

[21] Sims CT, Stoloff NS, Hagel WC. Superalloys II. New York: J.Willey & Sons; 1987.

[22] Caron P, Lavigne O. J Aerosp Lab 2011;3(1).

[23] Burgel R, Portella PD, Preuhs J. Proceedings of superalloys. Miner Met Mater Soc 2000:229.

[24] Wilson BC, Hickman JA, Fuchs GE. JOM 2003:35.

[25] Okazaki M, Hiura T, Suzuki T. Proceedings of superalloys. Miner Met Mater Soc 2000:505.

[26] Othani R, Tada N, Shibata M, Taniyama S. Fatigue Fracture Eng Mater Struct 2001;24(12):867.

[27] Harris K, Wahl JB. Proceedings of superalloys. Miner Met Mater Soc 2004:45.

[28] Dubiel B. Microstructural changes during Creep of Single-Crystalline Nickel-based Superalloys. AGH University of Science and Technology Press; 2011 [in polish].

[29] Budzik G, Matysiak H. Arch Foundry Eng 2010;1:399.

[30] Biel M, Dubiel B, Czyrska-Filemonowicz A. Hut Wiadomości Hut 2002;69(4):144 [in polish)].

[31] Ferenc J, Michalski J, Matysiak H, Sikorski K, Kurzydłowski KJ. J Eng Manuf 2009;223(B11):1417.

[32] Patnaik P. Handbook of inorganic chemicals. McGraw-Hill Professional Publishing; 2002.

[33] Pavlik S, Holland HJ, Payzant EA. J Am Ceram Soc 2001;84:2930.

[34] Kasprzyk-Hordern B. Adv Colloid Interface Sci 2004;110:19.

[35] Corundum, c 2001-2005 Mineral Data Publishing, version 1.

[36] Beeley PR, Smart RF. Investment casting. UK: The University Press Cambridge; 1995.

[37] Wax Castylene B405 Red – characteristic card.

[38] Wax A7-FR/60 – characteristic card.

[39] Niles JC. Incast 2003; 3:16.

[40] Ver Snyder FL, Guard RW. Trans Am Soc Met 1960;52:485.

[41] www.c-mgroup.com.

[42] Napolitano RE, Schaefer R. J Mater Sci 2000;35:1641.

[43] Pollock TM, Tin S. J Propuls Power 2006;22:361.

[44] Reed RC. The superalloys fundamentals and applications. Cambridge University Press; 2006. ISBN-978-0-521-85904.

[45] Caron P, Khan T. Aerosp Sci Technol 1999;3:513.

[46] Muttasim Z. Turbomach Int 2008;9–10:38.

[47] Szczotok A, Richter J, Cwajna J. Mater Charact 2009;60:1114.

[48] Poirier DR. Permeability for flow of interdendritic liquid in columnardendritic alloys. Metall Trans 1987;B18:245.

[49] Nabarro FRN, Cress CM, Kotschy P. Acta Mater 1996;44:3189.

[50] Ohasi T, Hidaka K, Imano S. Acta Mater 1997;45:1801.

[51] Donachie MJ, Donachie SJ. Superalloys. A technical guide. ASM; 2002.

[52] Chmiela B, Sozańska M, Rodak K. Solid State Phenom 2012;186:58.

[53] Long F, Yoo YS, Jo CY, Seo SM, Song YS, Song YS, et al. Mater Sci Eng A 2009;527:361.

[54] Ma D, Zhou B, Bührig-Polaczek A. Adv Mater Res 2011;278:428.

[55] Tin S, Pollock TM. J Mater Sci 2003;39:7199.

[56] Ma D, Wu Q, Bührig-Polaczek A. Metall Mater Trans B 2011. http://dx.doi.org/10.1007/s11663-011-9608-0.

[57] Auburtin P, Wang T, Cockroft SL, Mitchell A. Metall Mater Trans B 2000;31B:801.

[58] Ma D, Mathes M, Zhou B, Bührig-Polaczek A. Adv Mater Res 2011;278:114.

[59] Zhou YZ, Volek A, Green NR. Acta Mater 2008;56:2631.

[60] D‘Souza N, Newell M, Devendra K, Jennings PA, Ardakani MG, Shollock BA. Mater Sci Eng A 2005;413–414:567.

[61] Jarczyk G. ALD Vacuum Technologies GmBH Hanau, unpublished data.

[62] Preuhs J. Precicast Switzerland, unpublished data.

[63] Al-Jarba KA, Fuchs GE. Mater Sci Eng A 2004;373:255.

[64] Cormier J, Villechaise P, Milhet X. Mater Sci Eng 2009;A501:61.

[65] Roskosz S, Staszewski M, Cwajna J, Borla K, Sarek D. Proc. of 9th Eu. congress on stereology and image analysis and 7th Int. conf on stereology and image analysis in materials science stermat 2005 p. 211.

[66] Jaroszewicz J, Matysiak H, Michalski J, Matuszewski K, Kubiak K, Kurzydłowski KJ. Adv Mater Res 2011;27:66.

[67] Roskosz S. Wydawnictwa Politechniki Ślaskiej, Gliwice 2011 [in polish].

[68] Flemings MC. Soldification processing. Mc Graw Hill; 1974.

[69] Monroe R. AFS Trans 2005;4:205.

[70] Bokstein BS, Epishin AI, Link T, Esin VA, Rodin AO, Svetlov IL. Scr Mat 2007;57:801.

[71] Link T, Epishin A, Haibel A, http://www.extremat.org/ib/site/publication/downloads/Paper%20Link%20.pdf.

[72] Onyszko A, Bogdanowicz W, Kubiak K, Sieniawski J. Solid State Phenom 2010;163:260.

[73] Bogdanowicz W, Albrecht R, Sieniawski J, Kubiak K, Onyszko A. Solid State Phenom 2012;186:135.

[74] Gurgul D, Burbelko A. Arch Metall Mater 2010;55(1):53.

[75] Miller JD, Pollock TM. Metall Mater Trans 2012;43 A(7):2414.

[76] Weihong Z, Gongnan X, Dan Z. Therm Fluid Sci 2010;34(8):1068.

[77] Dong Yieri, Bu Kun, Dou Yangquing, Zhang Dinghua. J Mater Process Technol 2011;211:2123.

[78] Konrad CH, Brunner M, Kyrgyzbaev K, Volkl R, Glatzel U. J Mater Process Technol 2011;211(2):181.

[79] Mochnacki B, Suchy JS. PFTA Cracow 1995.

[80] Gandin Ch-A, Rappaz M. Acta Metall Mater 1994;42 A(7):2233.

[81] Szeliga D, Kubiak K, Burbelko A, Cygan R, Ziaja W. Solid State Phenom 2013;197:83.

[82] Burbelko A, Falkus J, Kapturkiewicz W, Sołek K, Drożdż P, Wróbel M. Arch Metall Mater 2012; 57(1):379.

[83] http://sakimori.nims.go.jp/topics/hightemp_e.pdf.

[84] Miller JD, Pollock TM. Metall Mater Trans A 2014;45(1):411.

[85] Yu A, Bondarenko E, Kablov N. Metal Sci Heat Treat 2002;44(7–8):288.

Crystal Growth by Traveling Heater Method

Robert Triboulet

CNRS/GEMAC, VERSAILLES CEDEX, FRANCE

CHAPTER OUTLINE

12.1 Introduction 460
12.1.1 THM Principle 460
12.1.2 THM Advantages and Issues 461
12.1.2.1 Advantages 461
12.1.2.2 Issues 462
12.2 Technology 462
12.2.1 Mode of Zone Heating 462
12.2.1.1 Electrical Resistance Heating 462
12.2.1.2 RF Heating 464
12.2.1.3 Optical Heating 465
12.2.2 Pulling Systems 467
12.2.3 Feed Material 468
12.3 Versatile THM 468
12.4 Materials Grown by THM 475
12.5 Segregation, Purification 475
12.5.1 Segregation 475
12.5.2 Purification 479
12.5.3 Inclusions and Precipitates 482
12.6 Mass and Heat Transport, Simulation and Modeling 485
12.7 Single Crystal Growth by THM 492
12.7.1 Seeding 492
12.7.2 Microgravity Growth 493
12.7.3 THM Growth Under Magnetic Fields 493
12.7.3.1 Static Magnetic Fields 493
12.7.3.2 Rotating Magnetic Fields 494
12.7.4 Forced Convection Regimes 496

Handbook of Crystal Growth. http://dx.doi.org/10.1016/B978-0-444-63303-3.00012-2
Copyright © 2015 Elsevier B.V. All rights reserved.

12.7.4.1 Centrifuge 496
12.7.4.2 Accelerated Crucible Rotation Technique 497
12.7.5 THM + Solid State Recrystallization 498
12.8 Conclusions 499
Acknowledgments 499
References 499

12.1 Introduction

12.1.1 THM Principle

Following the introduction by Pfann from 1955 [1] of the temperature gradient zone melting (TGZM), a rather similar technique, traveling solvent method (TSM), was proposed and described by Mlavsky and Weinstein [2]. In this technique, the migration of a solvent zone through the solid source material is induced by a thermal gradient according to the scheme of Figure 12.1.

The traveling heater method (THM) has been the most popular form of traveling solvent techniques for the last decades. It combines zone melting and growth from solutions. In THM, as described by Wolf and Mlavsky [3], a molten zone is made to migrate through a solid homogeneous source material by the slow movement of the ampoule relative to the heater as shown in Figure 12.2.

THM is some kind of continuous liquid phase epitaxy in which a typical configuration consists of a seed, which plays the role of a substrate, at the bottom of an ampoule, a saturated solvent zone surmounted by a polycrystalline source material. The solvent zone dissolves the source material at its hot upper interface and deposits, in near equilibrium conditions, a material of nearly the same composition at the lower interface which is colder than the upper interface because of the movement of the heater. Matter transport from the source to the growing crystal occurs by convection and diffusion

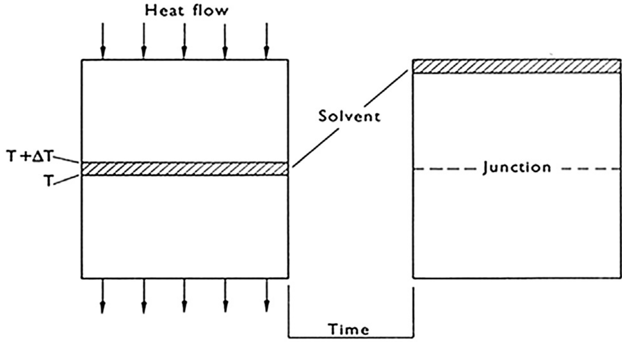

FIGURE 12.1 Schematic principle of the traveling solvent method. *From Ref. [3].*

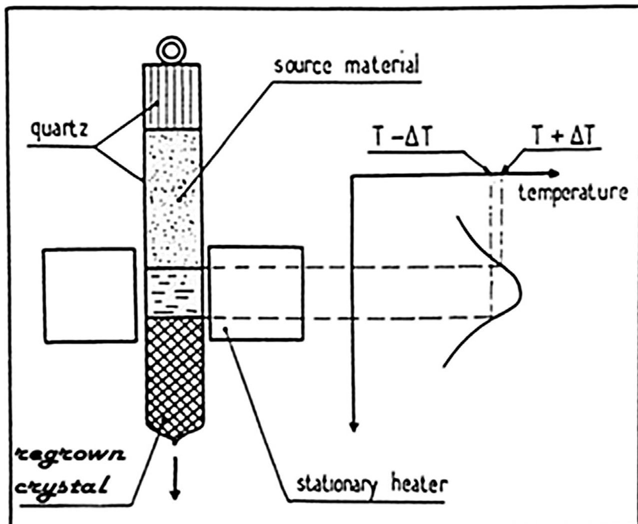

FIGURE 12.2 Traveling heater method principle.

across the solvent zone under the influence of the temperature gradient resulting from the movement of the ampoule relative to the heater.

12.1.2 THM Advantages and Issues

12.1.2.1 Advantages

- After an eventual initial transient period at the onset of a run, a steady state is established during which the constant growth temperature leads to a constant composition of the regrown solid.
- Growth occurs at a temperature lower than the maximum solidus temperature of the material, with all the classical advantages of low temperature growth, i.e., less contamination from the container, less vapor or decomposition pressures, more perfect crystals as a result of less generation and propagation of dislocations.
- The growth of compounds melting noncongruently or exhibiting a first-order phase transition below their melting point is made possible by THM. As an example, pre-transition phenomena were found by Ivanov [4] to occur below the melting point of CdTe, making it very suitable for the growth of this compound by THM.
- Very efficient "zone refining"purification occurs by THM, as will be shown in Section 12.5.
- THM requires only rather simple and low-cost equipment.
- Most of the time, only liquid/solid equilibrium takes place in THM.
- THM offers a very appropriate configuration for seeded growth.
- Finally, as will be shown in Section 12.3, several variants of THM, offering attractive possibilities, have been devised and experimented, making it a versatile technique.

12.1.2.2 Issues

- As a result of a steep temperature gradient at the growth interface, an uncontrolled thermosolutal convective flow in the solvent zone makes uncertain the growth of single crystals by THM, as will be discussed in Section 12.6.
- Constitutional supercooling within the solvent zone can occur at low temperature and results in interface instability. It has been shown [3] that the growth rate had not exceed a critical growth rate, which lies surprisingly for most of the materials within the range 1–7.5 mm/day.
- THM growth rates, significantly lower than those of melt growth techniques, are considered as a severe drawback in the industrial crystal growth by THM.
- Inclusions and precipitates form frequently in THM grown materials presenting a wide homogeneity range with its consequential retrograde solidus shape, as a result of growth temperatures lower than the congruent melting point of such materials.
- THM technology turns out to be rather tricky.
- In the case of the growth of alloys, a large segregation effect can be observed, which will be treated in Section 12.5.

12.2 Technology

As noted above, THM is a tricky technology requiring the control of numerous technological parameters, radiant heating, ampoule diameter and thickness of its walls, adjustment of the source material in the ampoule, pulling system, temperature stability, ground stability, etc.

Among them, a significant prerequisite is an appropriate temperature profile of the growth furnace. It has to possess a sharp temperature peak producing a narrow molten zone (roughly of length close to the ampoule diameter) and a sharp temperature gradient at the growth interface to prevent constitutional supercooling.

Different types of solvent zone heaters were used, either with electrical resistance heating (RH) or radio frequency heating (RF) or optical heating.

12.2.1 Mode of Zone Heating

12.2.1.1 Electrical Resistance Heating

The control of temperature using RH, the most used way of heating in the THM growth of a lot of materials, is simple and rigorous.

A typical RH THM furnace scheme was proposed in Ref. [5] (Figure 12.3).

The insulator thickness was calculated and experimentally determined to obtain an isothermal plane at the lower side of the heating element (nickel ring), where the growth interface was positioned (depending on the initial solvent amount) according to the scheme of Figure 12.4. This picture shows that the intersection of lateral and axial thermal temperature profiles is situated at the lower side of the heating ring. Thermal stability is essential to prevent the growth of parasitic nuclei. A calculation shows that a

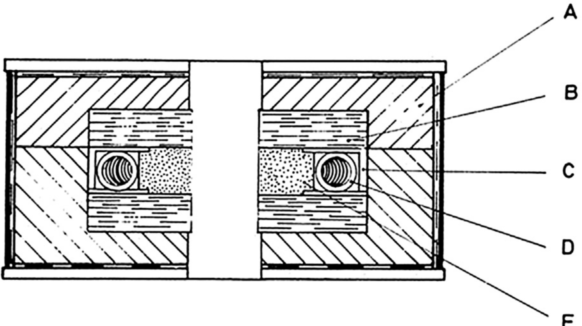

FIGURE 12.3 Traveling heater method furnace (schematic): (A) cement, (B) Pyronap, (C) stainless steel, (D) Thermocoax, (E) nickel.

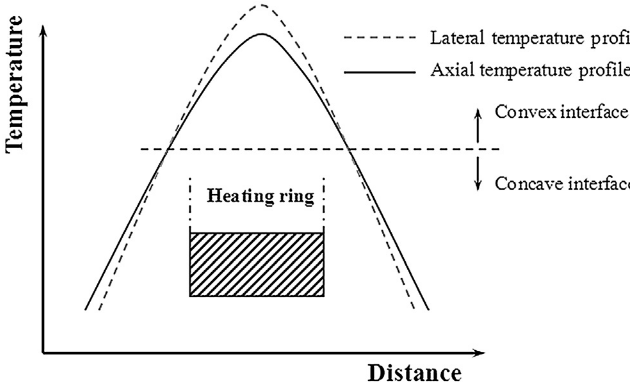

FIGURE 12.4 Axial and radial temperature profiles. *From Ref. [5].*

thermal stability of ±1 °C per hour is insufficient for the instantaneous rate, due to the thermal perturbation, to remain negligible compared to the critical rate. Stability at least ±0.1 °C per hour is necessary, which implies a highly stable regulator, high inertia furnace, stabilized network, and air-conditioned environment.

In some cases, the solvent heater was surrounded by lateral heaters in order to obtain a temperature distribution controlling the partial pressure of a volatile component. This is the case of a five-zone furnace (Figure 12.5) and a three-zone furnace, respectively, proposed by Schmitz et al. [6] and Colombo et al. [7], dedicated to the control of the Hg vapor pressure in the THM growth of (HgCd)Te. Mochizuki et al. [8] used, in addition, a mercury reservoir chamber supplying mercury to the Te solvent through a small gap beside a CdTe feed in order to form a (Hg,Cd)Te alloy, according to the scheme of Figure 12.6. Furthermore, a lower lateral furnace can allow controlling the postgrowth cooling-down of the ingot.

In order to obtain an interface as flat as possible, in the growth of $CaCO_3$ by THM with $LiCO_3$ as a solvent, a platinum heating strip embedded in the molten zone was used by Brissot and Belin [9], as shown in Figure 12.7, according to the submerged heater method proposed by Ostrogorsky [10].

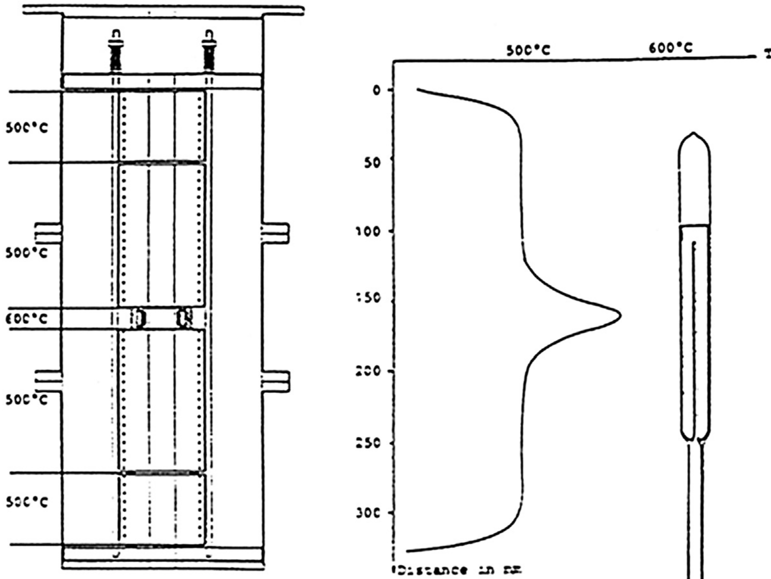

FIGURE 12.5 Five zone furnace and its temperature distribution. *From Ref. [6].*

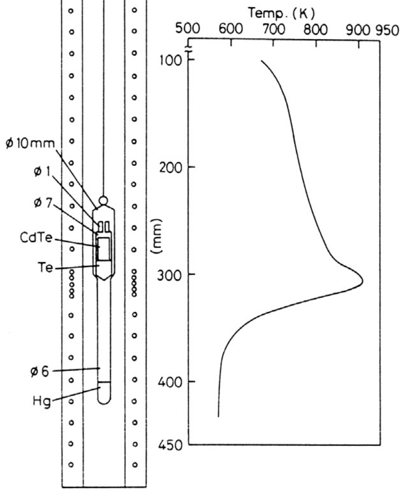

FIGURE 12.6 Schematic construction of traveling heater method using a mercury reservoir. *From Ref. [8].*

12.2.1.2 RF Heating

In the case of a solvent with a higher electrical conductivity in comparison to that of the material, RF heating can be more advantageous than resistance heating. But temperature control is more difficult in the case of RF heating and can be at the origin of temperature and growth fluctuations.

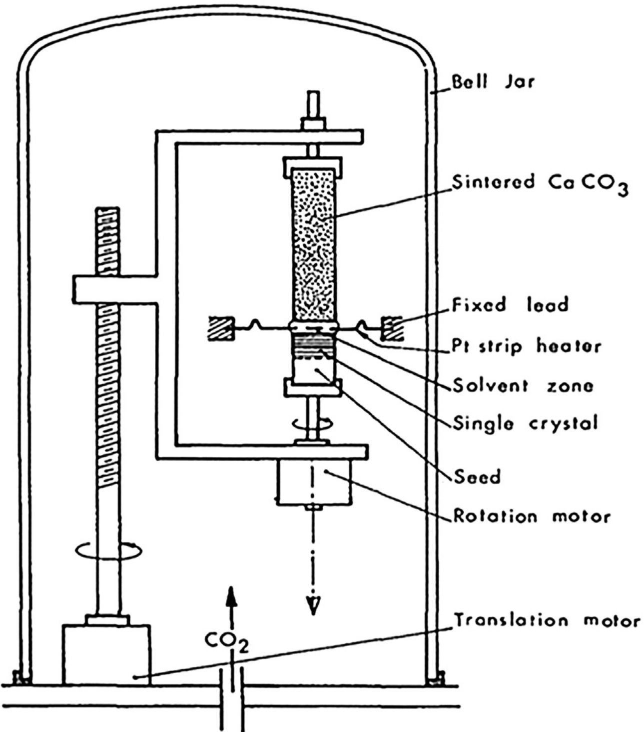

FIGURE 12.7 Diagram of the apparatus used to grow calcite. *From Ref. [9].*

RF heating is more generally preferred in the high temperature range, for instance for the THM growth of SiC with Si as a solvent, using direct coupling [11] (Figure 12.8) or of ZnO [12] with PbF_2 as a solvent using coupling to a sealed Pt crucible or to a circumferential Pt susceptor.

12.2.1.3 Optical Heating

Optical heating, using infrared focusing heaters such as elliptical mirror furnaces, was proposed and used as well by several authors, mainly in the case of crystal growth in space. In such a case, several considerations make it clear that focused radiation from a suitable source would be the most effective way to produce small gaseous or liquid zones. Such optical furnaces present several significant advantages: small size and low weight; low energy consumption; no environmental problems by heat, radiation, gasses, or RF signals; and great flexibility [12].

Several kinds of elliptical mirror furnaces were proposed. In mono-ellipsoid furnaces, the necessarily large filament of the halogen lamp turns out to decrease the furnace performance because of its worse focusing properties. Furthermore, the temperature distribution along the periphery of the molten zone is highly asymmetric leading to nonplanar solid–liquid interfaces. Multi-ellipsoid arrangements, with several lamps,

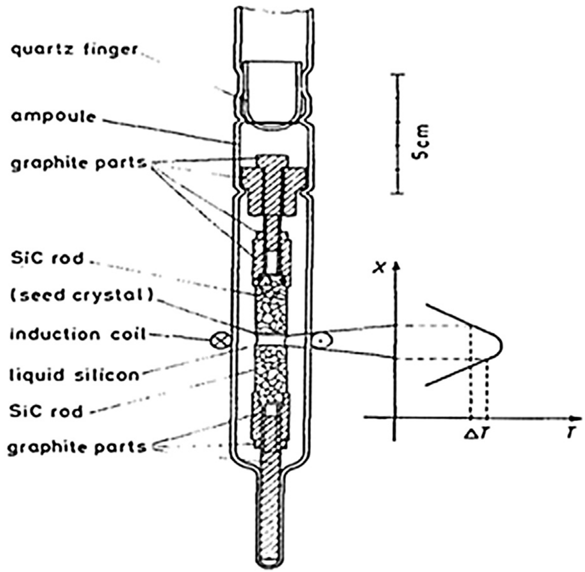

FIGURE 12.8 Sealed tube arrangement for the traveling heater method growth of SiC. *From Ref. [11].*

consisting of two or more ellipsoids, were proposed by Eyer et al. [12] in order to improve thermal symmetry. From a computer simulation, the authors advocate the double-ellipsoid arrangement over mono- and multi-ellipsoid configurations. The scheme of such a double-ellipsoid crystal growth furnace is pictured in Figure 12.9.

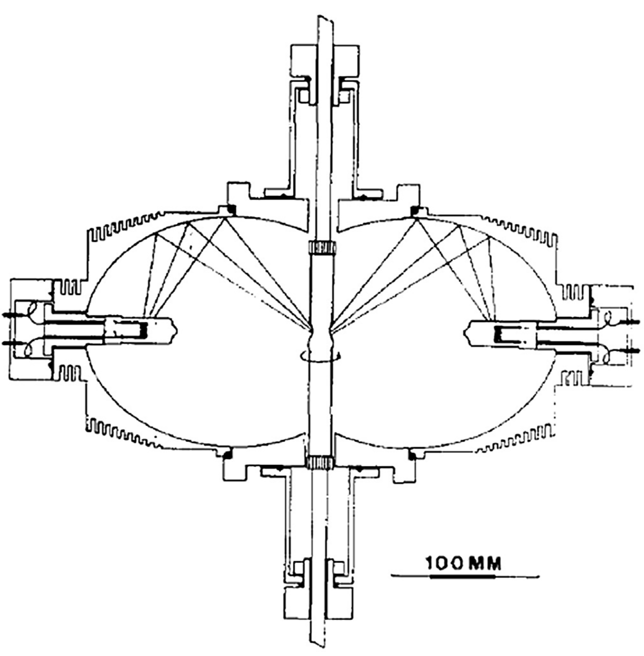

FIGURE 12.9 Double-ellipsoid crystal growth furnace. *From Ref. [12].*

It turns out finally that an issue of such furnaces remains the difficulty of obtaining solid/liquid interfaces of appropriate shape.

12.2.2 Pulling Systems

Two kinds of arrangements are used as a pulling system: either traveling down the ampoule in a stationary heater or moving up the heater along a stationary ampoule.

A lot of mechanical pulling systems were used, basically constituted of a worn screw whose rotation is activated by a motor associated with speed reducers. Mechanical vibrations generated by such systems can be responsible for spurious nucleation.

A sophisticated gas-bearing system that permits producing separate and adjustable rotation and translation vibration-free motions without any mechanical motor was proposed by Tranchart and Bach [13] (Figure 12.10). A silica tube (1) containing the growing crystal is fastened to a perfectly ground Pyrex tube (2), resting on the bottom of a methylmethacrylate floater (3). A thrust bearing (4) is the only mechanical contact of the apparatus. The floater is inside the principal vessel (5) partially filled with water. A brass chamber (6), rigidly attached to vessel 5, is placed in the space between Pyrex tube and floater. Compressed air, at a pressure of 1–1.2 bars, is let into the chamber by the tube (7) and released through small holes drilled in the chamber wall toward both the tube and the chamber, allowing Pyrex tube and floater to be auto centered with respect to the chamber by this gas-bearing system. Rotation of the Pyrex tube is given by means of a tangential air flow coming through hole (8). Vertical translation motion is obtained by evaporating water from vessel (9), which is connected to the principal vessel (5).

Such simpler systems use for the vertical translation motion either the evaporation of water or the progressive emptying of a liquid, like oil, through a valve [14].

Steadiness and quality of the vertical translation motions can be precisely controlled using differential transformers.

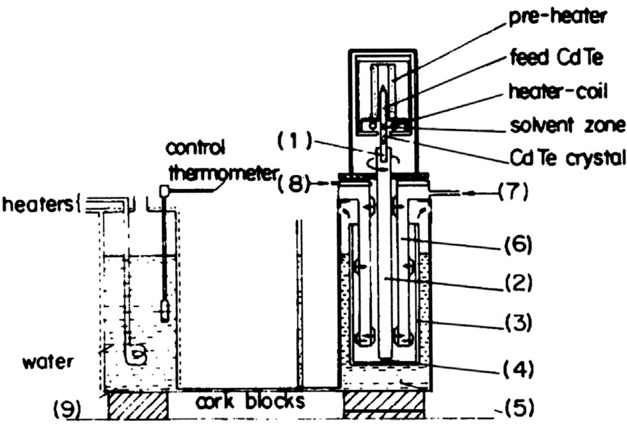

FIGURE 12.10 Principle of the gas-bearing system. *From Ref. [13].*

12.2.3 Feed Material

One of the more severe issues of THM growth is the availability of feed material of the required composition and dimensions, furthermore homogeneous and compact.

The fabrication of suitable feed material turns out to be one of the most significant problems to overcome, on which has to be focused a major part of the efforts when experimenting with the THM growth of any material.

The source material has to be as dense as possible. Otherwise, a gap will rapidly appear between solvent zone and source material, which will come uncoupled from it, the growing crystal being denser than the feed material. The length of the grown crystals is then restricted. Such a situation occurs, for instance, when powder, even compressed, is used as a source material.

The fabrication of the feed material dedicated to the growth of peritectic compound turns out to be a particularly severe issue. In the growth of $CdIn_2Te_4$ by THM, for instance, a balance between the compositions of feed material and of solvent zone was shown necessary to compensate from some Cd deficiency in the growing crystals, according to Launay and Lestournelle [15].

In all cases, the mechanical fit of the source material cylinder into a calibrated silica tube has to be excellent, with a tolerance of less than 100 μm, reckoning in the material thermal expansion.

Some complex source material arrangements will be presented in the next section, illustrating the versatility of THM.

12.3 Versatile THM

Numerous variants of the classical THM, as defined in Section 12.1.1, were proposed.

Although in most cases a vertical arrangement is used, horizontal THM was also implemented by Benz and Müller [16] for the growth of GaSb and InSb using, respectively, Ga and In as a solvent and by Gille et al. [17] for the growth of $Hg_{1-x}Cd_xTe$ with ampoule rotation necessary to crystallize the whole cylindrical cross-section of the ingot with respect to the partially filled solution zone (Figure 12.11). Note that horizontal THM needs a complex experimental equipment without presenting a definite advantage over vertical THM with ampoule rotation which is much easier to implement.

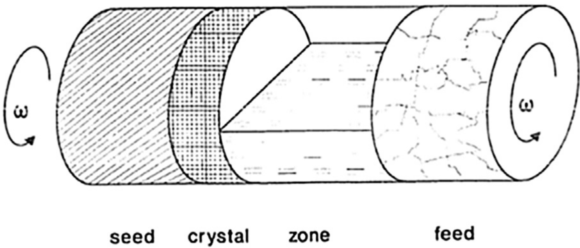

FIGURE 12.11 Schematic representation of a horizontal traveling heater method crystal growth arrangement. *From Ref. [17].*

The following picture, Figure 12.12, displays different THM configurations and arrangements illustrated here in the CdTe, ZnTe, and (Cd,Zn)Te cases.

First of all, the direction of charge travel could be inversed beside the traditional one, i.e., raising the ampoule rather than lowering it, with the potential advantage of a crystallization beginning from a free interface. Upward motion was used as well in a floating zone configuration for the THM growth of SiC [11].

Homosolvents, such as tellurium or cadmium [18] in the CdTe case again, or Ga and In for the growth of GaSb an InSb [16], are preferentially used when the main goal is purity.

Heterosolvents are used if the compound to be grown is not sufficiently soluble in one of its components in an accessible temperature range, which is very frequently the case. The main drawback of heterosolvents is the unavoidable presence of solvent precipitates and inclusions in the grown crystals. On the other hand, heterosolvents turn out to be useful when searching for intentional doping. As an example, such solvents as In [19] and $CdCl_2$ [20] were used in the CdTe case for n-type doping or to get semi-insulating crystals.

An original growth technique called sublimation traveling heater method (STHM), in which the solvent zone is replaced by an empty space having approximately the same dimensions, was devised by Triboulet et al. [21,22]. In the case of CdTe, STHM allowed overcoming two intrinsic drawbacks of classical THM using tellurium as a solvent, which are: (1) the unavoidable Te precipitates related to the retrograde solidus line on the tellurium-rich side, and (2) the necessity to compensate for a large concentration of off-stoichiometry intrinsic defects, if a high resistivity is needed. Note nevertheless that the maximum congruent sublimation temperature of CdTe lies slightly on the Te-rich side.

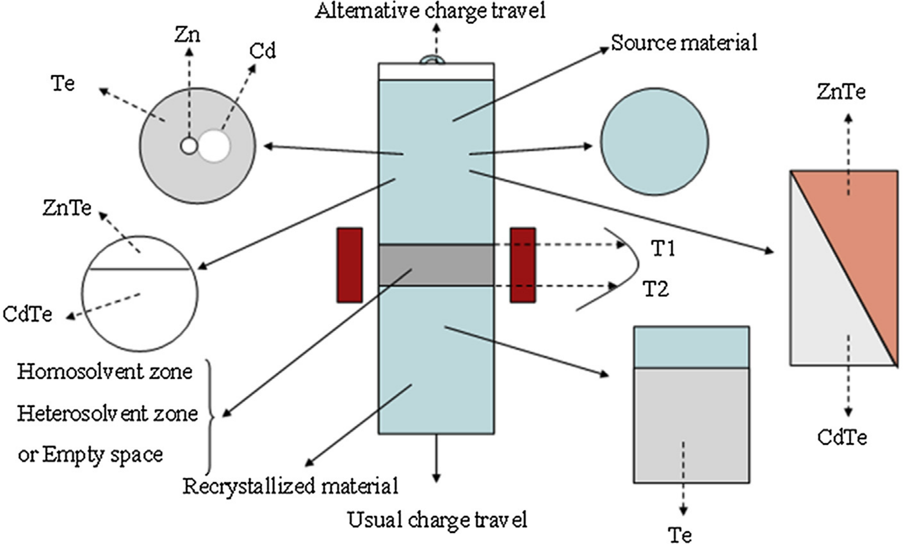

FIGURE 12.12 Different possible traveling heater method configurations and arrangements.

This method was then again successfully applied to CdTe for halogen doping [23], and extended by Taguchi et al. to such compounds as ZnTe, which showed excellent luminescent properties [24], and ZnSe [25].

For all these materials, the growth occurred in the same temperature range as in classical THM, 800–1000 °C for CdTe, at pulling rates equivalent to those used for classical THM with Te solvent, i.e., 2–5 mm/day, 785–800 °C for ZnTe, 3 mm/day, and 900 °C for ZnSe, 1 mm/day.

In the “classical” STHM technique as implemented above, the pressure regime in the empty space was not well defined—the system has two degrees of freedom and is not completely determined by fixing only the temperature. As a consequence, the electronic properties of crystals grown under these conditions were found to change depending on factors such as the volume of the empty space, the distance between the source

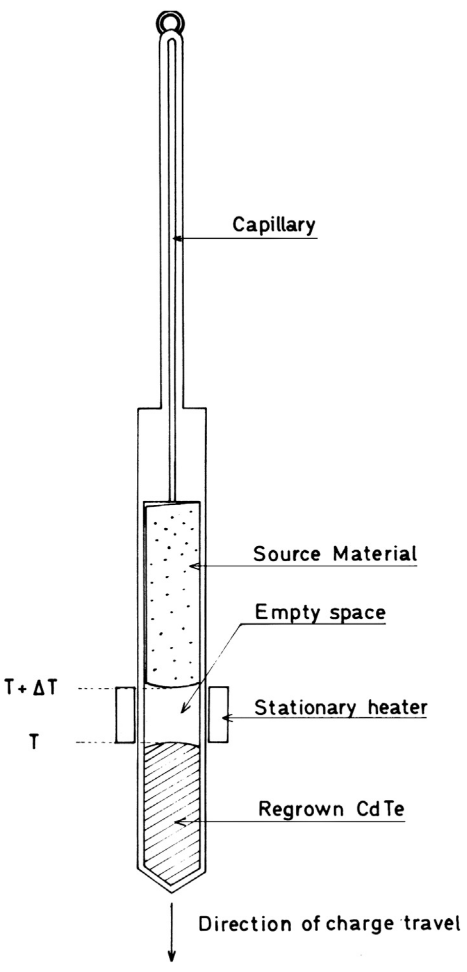

FIGURE 12.13 Principle of sublimation traveling heater method with capillary. *From Ref. [22].*

material and the tube walls, etc. That is why STHM was modified and made more sophisticated according to the scheme of Figure 12.13. The sublimation chamber was connected to a capillary tube whose upper end stays at room temperature. This connection is ensured by a small void along a generating line of the ingot, the section of this passage corresponding to the internal section of the capillary. In such an arrangement, the total pressure P_T in the chamber tends to the minimum one P_{min} corresponding to a congruent sublimation. Under such conditions a CdTe ingot presenting a resistivity as high as 10^7 cm was obtained without doping, which was not possible to reach without a capillary.

While all the previous variants concern the solvent zone, several variants related to the source material were proposed as well, as illustrated again in Figure 12.12.

With the goal of growing (Hg,Cd)Te, (MCT), crystals of uniform composition, a geometry in which the feed material is a cylinder constituted of two cylindrical segments (Figure 12.14)—one in CdTe and the other one in HgTe—whose cross-sections are in a ratio corresponding to the desired alloy composition [26], was proved to be successful for the growth of large diameter crystals (up to 40 mm) [26–28]. This configuration was proven to be efficient as well in the case of (Cd,Zn)Te (CZT), using two cylindrical segments, one in CdTe and the other one in ZnTe [29].

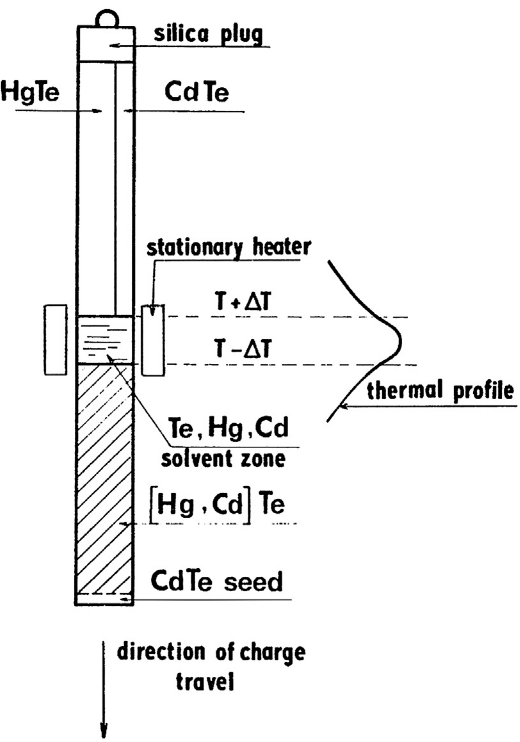

FIGURE 12.14 Principle of the traveling heater method growth of (Hg,Cd)Te using as a feed material for a cylinder made of two cylindrical segments, one HgTe, the other one CdTe. *From Ref. [27].*

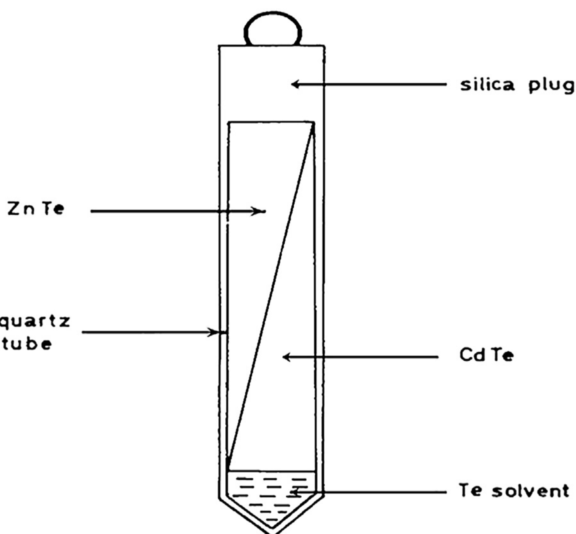

FIGURE 12.15 Sectional view of an ampoule dedicated to the growth of $Cd_{1-x}Zn_xTe$ alloys of graded composition. *From Ref. [31].*

With the goal of growing graded composition alloys, the source material was made of two beveled cylinders—one in HgTe and the other one in CdTe in the case of MCT [30], one in CdTe and the other one in ZnTe in the case of CZT [31], one in ZnTe and the other one in HgTe in the case of MZT [32]—reconstituting a perfect cylinder, as pictured in Figure 12.15 in the case of CZT. The complete series of $Hg_{1-x}Cd_xTe$ [30], $Cd_{1-x}Zn_xTe$ [31], and $Hg_{1-x}Zn_xTe$ [32] alloys, from $x = 0$ to $x = 1$, were prepared by a single THM pass, allowing to study the physical properties of the crystals as a function of composition over the whole composition range.

A method of synthesis, growth, and purification, called “cold traveling heater method” (CTHM), was first devised for CdTe and ZnTe by Triboulet et al. [33,34] before being extended to other materials.

In CTHM and in the case of CdTe and ZnTe, a Te solvent zone migrates through a composite source material constituted of a Cd (or Zn) rod of appropriate diameter surrounded with Te pieces and powders, as shown schematically in Figure 12.16 in the CdTe case. The crossing of the solvent zone through this charge, at a temperature lower than the melting point of the compound, induces the fractional synthesis of the compound in Te solution, its growth, and also its purification. Synthesis, growth, and purification are thus achieved at low temperature, at the same time, in a simple and inexpensive furnace, in contrast to other processes.

CTHM was indeed developed for mass production of large diameter CdTe ingots [35]. This technique was shown to be extendable to ternary and even sometimes quaternary alloys. CZT ingots of excellent uniformity were grown by CTHM using both a Cd and a Zn rod surrounded by tellurium (Figure 12.17).

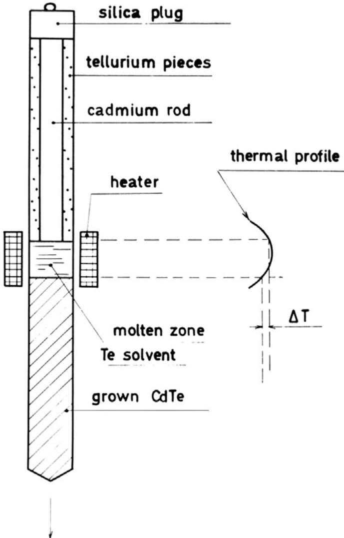

FIGURE 12.16 Principle of cold traveling heater method. *From Ref. [33].*

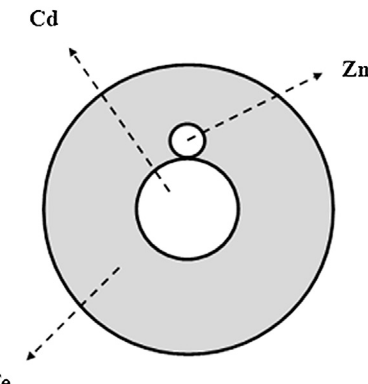

FIGURE 12.17 CZT feed material cross-section for THM synthesis and growth.

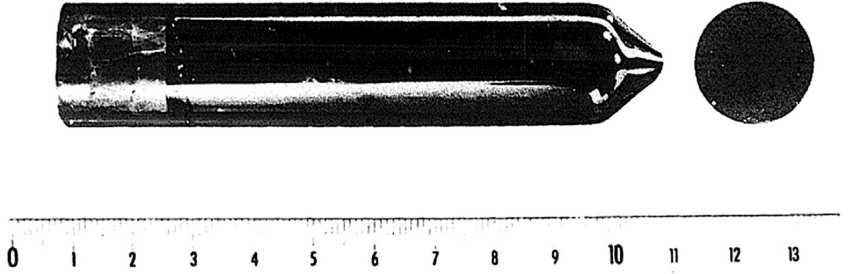

FIGURE 12.18 HgTe ingot grown by traveling heater method at 500 °C from mercury and tellurium. *From Ref. [36].*

A slightly modified CTHM process was devised by Triboulet et al. [36] for the growth of HgTe ingots (Figure 12.18) in which the feed material is a mixture, in stoichiometric proportions, of tellurium, in a fragmentary or powder form, and mercury.

CTHM was shown further to be extendable to HgSe [38], according to a process similar to the HgTe one.

With the aim of using the zone refining effect of THM, a multipass traveling heater method (MTHM) was devised by Triboulet et al. [22] and applied to the purification of CdTe. Rather than using as a source material for a subsequent THM pass an ingot obtained from a first THM run and so on, with the contamination resulting from several handlings of the ingot, in MTHM the successive runs occur in the same ampoule, according to the principle pictured in Figure 12.19. The starting Te-solvent consists of a tellurium column of several cm in length, a certain fraction of which is taken up at each pass; this arrangement allows one to carry out several passes in the same ampoule without any handling of the material, and with the aid of a single THM furnace. The efficiency of MTHM will be emphasized in Section 12.5. The authors stated that this method was not limited to CdTe and tellurium but was of general interest and could be applied to all compounds for which THM can be achieved with one of their components as a solvent.

Finally, THM offers the possibility of growing materials presenting a compact fine grain size structure suitable for the growth of single crystals by solid state recrystallization (SSR). This possibility has not been very much explored so far, but for the growth of CdTe single crystals [34].

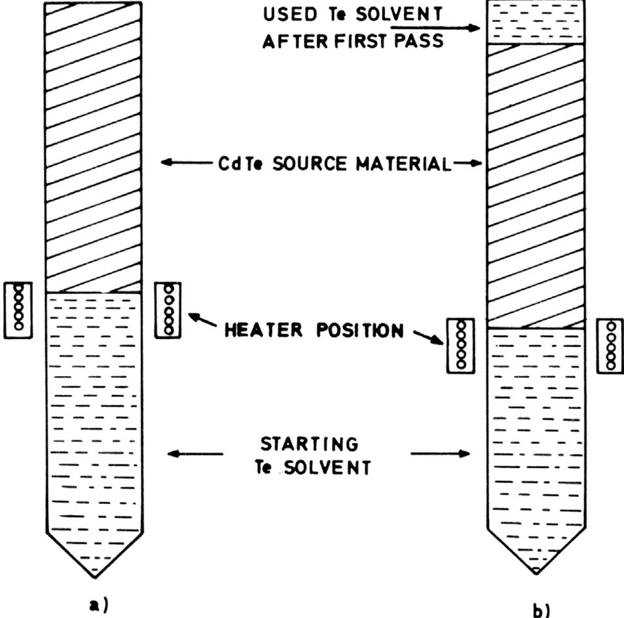

FIGURE 12.19 Principle of multipass traveling heater method. *From Ref. [22].*

12.4 Materials Grown by THM

An additional expression of the versatility of THM is the great variety of materials grown by this technique. They are listed in the following table, which includes the solvent used, the mode of heating, and the growth rate.

12.5 Segregation, Purification

12.5.1 Segregation

Segregation issues arise when it comes to producing homogeneous ingots not only for the numerous alloys grown by THM, as seen in Table 12.1, but furthermore to achieving uniform doping.

The axial segregation in growing pseudobinary alloys was particularly studied by Gille [136]. The Pfann's segregation function (12.1) [137], with c_s being the concentration of solute, c_0 the mean concentration in the charge, k the distribution coefficient of the solute in the material, z the distance from the beginning of the charge, l the zone length,

$$c_s(z) = c_0[1 - (1 - k)\exp(-kz/l)] \tag{12.1}$$

remains valid to account for the composition distribution in a mixed crystal $A_{1\text{-}x}B_xC$ grown from either (A,B)-rich or C-rich solution zone in a THM or related technique configuration, but is written as:

$$x_s(z) = x_0 - \left(x_0 - x_L^0 k\right)\exp\left(-kz/l_{eff}\right)$$

with x_L^0 being the mole fraction of the starting molten zone, x_0 the mole fraction of the source material, k the segregation coefficient, z the axial position, l_{eff} the effective zone length. Beside the classical Pfann's expression, the atomic concentrations c are replaced by the mole fractions x, and the molten zone length 1 by an effective zone length l_{eff}, which is the length that the liquid zone $(A_{1\text{-}xL}B_{xL})_{1\text{-}yL}C_{yL}$ would have if it has the same atomic fraction as the solid (i.e., $A_{1\text{-}xL}B_{xL}C$). The expressions of the effective zone lengths are given for both C-rich and (A,B)-rich solution zones [136].

A good illustration of this approach was related to the THM growth of the $Hg_{0.8}Cd_{0.2}Te$ alloys as achieved industrially [27,95]. The axial composition profile of Cd is characterized by what is called an initial transition induction period, where the composition changes from Cd-rich values before the desired concentration, which is that of the source material, is then asymptotically reached, as seen in Figure 12.20.

The variation of $(1 - x_s/x_0)$ on a logarithmic scale versus z for this ingot, as displayed in Figure 12.21, is linear, in agreement with Eqn (12.1) with a slope $(-k/l_{eff})$. From the intersection with $z = 0$, the segregation coefficient is determined to be $k \sim 3.2$, compared with the value of ~2.5 found in the pseudobinary CdTe-HgTe system [27]. An effective zone length $l_{eff} \sim 6$ mm follows, to be compared with an actual zone length of about 15 mm.

Table 12.1 Experimental data on Materials grown by THM

Material	Solvent	Growth Rate (mm/day)	T_G (°C)	Heating Mode	Type of THM	Ref.
$AgGaS_2$	$PbCl_2$, AgBr	1.5–3	750	Optical		[39]
As	Tl	0.5	457	traveling heater method		[40]
$Bi_{1-x}Sb_x$	Bi	4	~550	RH		[41]
$(Bi_xSb_{1-x})_2Te_3$	(Bi,Te) or (Bi,Sb,Te)	4		RH		[42]
$Bi_2Te_{2.55}Se_{0.45}$	Bi,Te,Se	4–8	580	RH		[43]
$CaCO_3$	$CaCO_3$–Li_2CO_3	5	700–800	RH		[9]
$CdCr_2Se_4$	$CdCl_2$	≤1.5		RH		[44]
$CdIn_2Te_4$	In_2Te_3–CdTe	30–200	800	RH	Horizontal zone	[45]
	In_2Te_3–CdTe	1.5–3	700–800	RH	leveling	[15]
CdTe	Te	≤5–7.5		RH		[46–48]
–	–	2.5	820	RH		[49]
–	–	≤10	800	Opt.		[50]
–	–	4	750	RF-RH		[51]
–	Cd	1	1000	RH		[18]
–	Te	3–5	700–750	RH	MTHM	[22]
–		5	800–1000	RH	STHM	[22]
–		2	815	Opt.	STHM	[22]
–	Te			RH	Repetition effect	[53]
–	Te	2.5	780	RH	CTHM	[33]
–	Te	3–7		RH	Ø 100 mm	[157]
CdTe,$CdTe_{0.9}Se_{0.1}$	Te			Opt.	μg, rot. magn. field	[52]
(Cd,Mn)Te	Te	2–2.5	700–750	RH		[107]
(Cd,Zn)Te	Te	2–3.6	850	RH		[34]
–	–	3–5		RH	Static magn. field	[54,55]
–	–	4–10	700–800	Opt.		[56]
–	–	3	750–850	RH		[57]
–	–		762	RH	1g and μg	[58–60]
$Cu(Ga,In)Se_2$	In					[61]
$CuAlSe_2$	In	5	1090	RH		[62]
CuCl	KCl	0.2–0.25	386	RH		[63,64]
$CuGaS_2$	CuI	4–5	1100	RF		[65]
$CuGaSe_2$	In	4	870–980	RH		[66,67]
$CuInS_2$	In	3–4	800	RH		[68,69]
	In		860–900	RH		[70,71]
$CuInSe_2$	In	1.5–5	780–790			[72]
–	–	1–1.5	650–700			[73]
–	–	4	750	RH		[74]
–	Cu-40%In	4	770	RH		[75,76]
(Ga,Al)As	Al–Ga	≤3–5		RH		[44]

Table 12.1 Experimental data on Materials grown by THM—cont'd

Material	Solvent	Growth Rate (mm/day)	T_G (°C)	Heating Mode	Type of THM	Ref.
–	Ga		1100	RH	CTHM	[82,77]
(Ga,Al)Sb	Ga or Sb	0.8 to 1.44	550–630	Opt.	TLZ	[78–80]
(Ga,In)As	In	0.25	1020–1050	RH		[84]
(Ga,In)P	In	0.5–1.5	900	Opt.		[81]
(Ga,In)Sb		2	600	RH		[77,82,83]
GaAs	Ga	≤5		RH		[85]
–	–	1–2	850–870	Opt.		[86]
–	–	1–1.5	980	RH		[77,87,88]
GaP	Ga	4	1160	RF		[89]
–	Ga	6	1000–1100	RF		[90]
Ga(As,P)	Ga	≤5 to 6	900	RF		[91]
GaSb	Ga	14–20		RH		[92]
–	Ga	2.5 ± 0.5	500–560	RH		[16,93]
Ga_2Te_3	Ga–Te		792	RH		[94]
(Hg,Cd)Te	Te	1–2.5	500–700	RH		[27,95,96,98,100]
–	–		800–875	RH		[97]
–	–	<3		RH	Hg reservoir	[8]
–	–	8.5	500 ± 10	RH	ACRT	[99]
–	–	5	510 ± 20	RH	Horizontal THM	[17]
–	–	3.5	650–670	RH	Rot. magn. field	[101]
–	–	4.8–7.2		RH		[102]
(Hg,Mn)Te	Te	2	600	RH	CTHM	[37]
–	–	2	590	RH		[103]
(Hg,Zn)Te	Te	2–2.5	700	RH		[104–107]
–	–	5	500–650	RH-RF	Controlled P_{Hg}	[91]
$Hg_{1-x-y}Cd_xMn_yTe$	Te			RH		[109]
HgSe	Se	2.5	670	RH	CTHM	[38]
HgTe	Te	2–3	400–500	RH		[36,110]
InP	In	2	850	Opt.	1g and μg	[93,111–113]
InSb	In	2.5 ± 0.5	400	RH	Horizontal THM	[16]
InSe	In	2.5	590	RH		[114]
MnTe	Te	2.5	800	RH		[115]
Naphtalene	Benzoic acid			RH		[158]
(Pb,Mn)Te	Te		600	RH		[109]
$Pb(Ti,Zr)O_3$	Borate flux	≤1		RF		[117]
(Pb,Sn)Te	Te				1g and μg	[118]
$(Pb,Sr)TiO_3$	Borate flux	0.1–10	1060–1100	RF		[116]
PbTe	Te or Pb	2–3	500–750	RH		[119]
–	Te	1.5	550	RH		[120–123]
–	Te	2.7–8	650	RH		[124]
–	Pb					[125]
–	Pb	∼5	640–800	RH		[159]
Si	Au–Si	200–400		RF		[126]

Continued

Table 12.1 Experimental data on Materials grown by THM—cont'd

Material	Solvent	Growth Rate (mm/day)	T_G (°C)	Heating Mode	Type of THM	Ref.
SiC	Si	~9	1800	RF	Upward motion	[11,127]
Tl_2S	Tl-S solution	0.3	450	RH		[128]
$TlInS_2$				RH		[14]
$Y_3Fe_5O_{12}$	Y_2O_3–Fe_2O_3	30–150		RF	Floating zone	[129]
–	Y_2O_3–Fe_2O_3 15:85	24–36		Opt.	TSFZ	[130]
–	Y_2O_3-rich melts	<24	~1500	Opt.	TSFZ	[131]
ZnO	PbF_2	≤3		RF		[132]
ZnSe	In	1–2.5	1100–1150	RH		[133]
–	$PbCl_2$	1	900	RH		[133]
–		3	785–800		STHM	[24]
–	SnSe	0.4 and 1.4	950–1050	RH		[134]
ZnTe	Te	7	850–950	RH		[5]
–	–	2.5	780	RH	CTHM	[33]
–	–	3	950	RH		[33]
–	–	3.7	955–975	RH		[135]

THM, traveling heater method; RH, resistance heating; MTHM, multipass traveling heater method; STHM, sublimation traveling heater method; CTHM, cold traveling heater method; ACRT, accelerated crucible rotation technique.

In order to avoid the initial transient induction period during which the composition changes asymptotically from Cd-rich to the desired value, the solvent zone composition (x_L0) has to be adjusted to x_0/k to yield the desired composition from the onset of the growth [27,138]. However, the original liquid zone composition was shown to depend on several unknown parameters. It depends not only on the growth temperature but also

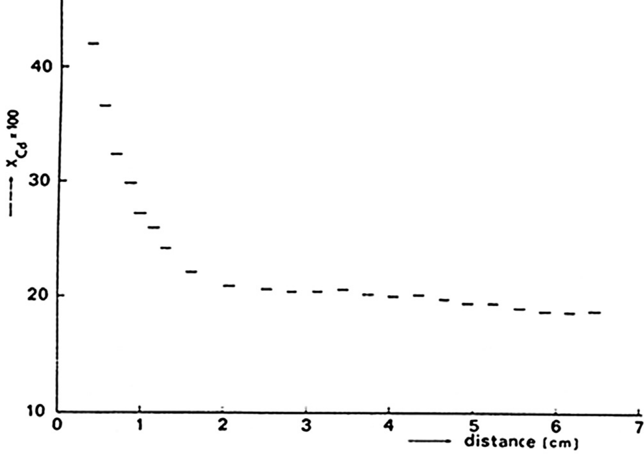

FIGURE 12.20 Composition profile of a traveling heater method grown $Hg_{0.8}Cd_{0.2}Te$ ingot using Te as a solvent. *From Ref. [27].*

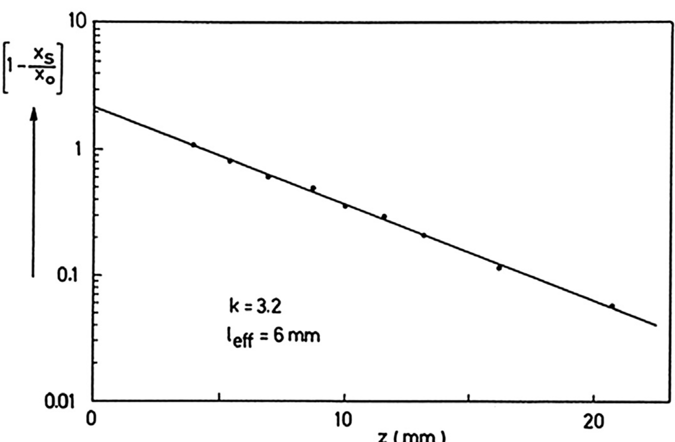

FIGURE 12.21 Logarithmic representation of the axial distribution x_s in the (Hg,Cd)Te ingot whose composition is given in Figure 12.20.

on the temperature gradient within the zone, which itself is related to the traveling rate. That is why it is usual to determine this composition from chemical analysis measurements performed after quenching a solvent zone picked up when some stationary state is reached after the initial transient induction period.

Equation (12.1) is valid in the case of a solute of mean concentration c_0 in the charge. However, the distribution coefficient of different impurities have been shown to be lower in the liquid solvent than in the solid charge, and, more generally, segregation can become more effective with decreasing temperature [139].

Very weak segregation was found when using Cold THM, which was shown suitable for the growth of homogeneous ingots. As an example, homogeneous 2-inch diameter $Cd_{1-x}Zn_xTe$ ingots, with $x_{Zn} = 0.04$ and $x_{Zn} = 0.20$, were grown by El Mokri et al. [34] by this technique whose principle is described in Section 12.3. Both Cd and Zn rods, of appropriate diameter to obtain the desired composition, surrounded with pieces and powders of Te, were used as a source material. The longitudinal composition profile, measured by electron microprobe analysis, of a $Cd_{0.96}Zn_{0.04}Te$ ingot, is depicted in Figure 12.22. The radial homogeneity was found better than 0.1% over a 2-inch diameter slice (Figure 12.23).

12.5.2 Purification

A very extensive study on the purification process by solution zone passages was achieved by Nicolau [140,141], one on the Process' Theory, the second on the Process' Practice. The author suggests the name traveling heater zone refining (THZR), rather than THM, considering THM was essentially a purification process. He concludes that the purification is particularly advantageous when the solute forms either eutectics or solid solutions with the impurities, since they permit the subunity segregation coefficient to be as far as possible from unity. Furthermore, he recommends selecting a crystallization temperature as close as possible to the solvent boiling temperature.

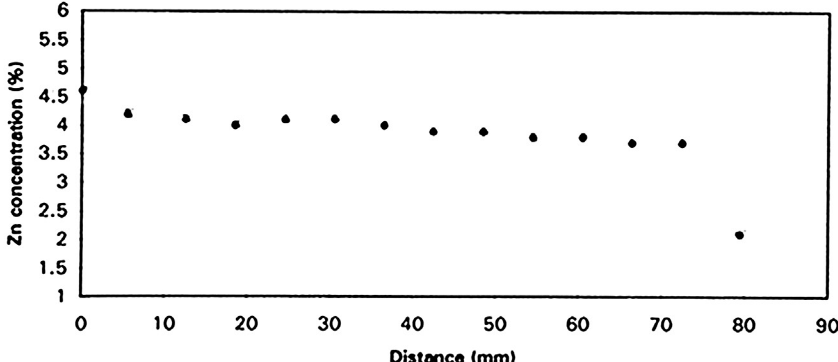

FIGURE 12.22 Longitudinal composition profile of a $Cd_{0.96}Zn_{0.04}Te$ ingot grown by cold traveling heater method. *From Ref. [34].*

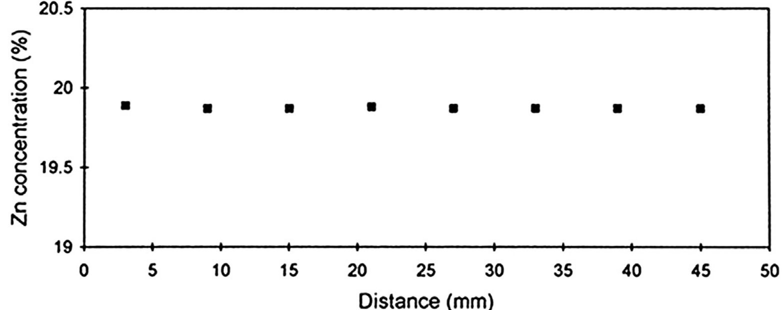

FIGURE 12.23 Radial composition profile of a $Cd_{0.8}Zn_{0.2}Te$ ingot grown by cold traveling heater method. *From Ref. [34].*

Furthermore, while classical zone refining needs more than one pass to be effective, a THM single pass is already very efficient because the solvent acts as an extracting medium.

Purification by THM was mostly emphasized in the case of tellurides and sometimes pointed out as well for various other compounds.

- The passage of a single Te-rich zone through a CdTe ingot by THM was reported to lead to a significant reduction of Mg, Si, Ca, Fe, Cu, and Ag [46,142] and B, Na, S, Cl, Y, Zr, Pd, Ag, and In [143].
- THM purification using Te as a solvent was reported as well to be very efficient in the growth of ZnTe ingots from electrical measurements displaying very high mobilities of holes at low temperature [5]. By comparison, ZnTe crystals grown by CTHM, as described in Section 12.3, a technique in which the material never sees its melting point, were shown to have lower RT carrier concentrations, in the range 7.6×10^{14}–$3 \times 10^{15}/cm^3$, and a mobility of holes reaching 7180 cm^2/V s at 81 K, which is the highest mobility ever reported at this temperature for ZnTe [33].

- The purification of the (Cd,Mn)Te ternary alloys by THM using Te as a solvent is particularly illustrative because of the poor purity of the metallurgical Mn used for the Bridgman-grown ingots as a source [108], as illustrated in the following Table 12.2.
- The electrical characteristics of THM-grown HgTe samples correspond to intrinsic mercury telluride with a concentration in electrically active residual impurities of about $2 \times 10^{15}/cm^3$ [36].
- The removal of iodine from PbTe crystals grown by the iodine method was shown very effective by THM [123]. The electronic properties of THM-grown PbTe crystals were stated as well to demonstrate their very high purity level as expected from the low growth temperature and purification achievable by THM processing [124].
- The better purity of THM grown InSe crystals in comparison to those grown by Bridgman was demonstrated from their electrical properties and their photo-electrochemical behavior [115]. It is shown that at every temperature, the carrier concentration is smaller by one order of magnitude in the THM-grown InSe in contrast to crystals obtained from Bridgman growth.

Table 12.2 Emission Spectroscopy Analysis of Elements (in ppm) detected in a Bridgman ingot and in the THM Ingot using it as a source material

Elements	Bridgman	THM
Ca	50	4
Fe	100	3
Mo	100	0.3
V	100	0.1
Cr	20	
Mg	20	
As	50	0.1
Na	20	
Cu	5	3
Sn	20	0.3
B	50	0.1
Be	1	
Al	50	4
Pb	10	
Ti	50	0.1
Li	1	0.1
K	1	
Sb	10	0.1
Ni	50	3
Co	50	0.1

THM, traveling heater method.
Source: From Ref. [108].

- Photoluminescence results, proving the efficiency of the THM zone refining effect for lithium in ZnSe crystals grown by THM using $PbCl_2$ as a solvent, was reported [133].
- From measurements of the free exciton intensity of $CuInSe_2$ crystals grown by THM using Cu-In alloys as a solvent, it was found that the nonradiative recombination centers decreased from the bottom to the top end of the crystal, likely indicating a segregation of impurities as a result of the THM process [76].

Several means were used to improve the purification of tellurides, when using tellurium as a solvent. A very simple one is the repetition effect, i.e., using as source material for a subsequent THM run an ingot obtained from a first THM pass [53,143]. By repeating the THM process [53], the dark electrical conductivity of the crystals due to a deep level dropped about two orders of magnitude, and an extremely low conductivity sample of 10^{-8} to $10^{-9}\,\Omega^{-1}\,cm^{-1}$ was obtained. Through these results, the authors deduced that the repetition of THM runs is still effective for reducing the impurities through Te solvent.

To overcome the drawback of contamination occurring from successive handlings of the ingots, multipass THM process, as described briefly in Section 12.3, was devised [22], which is an extension of classical zone melting (refining) to solution growth, according to the scheme of Figure 12.20. Higher purity and a better structural perfection of a crystal obtained by multipass THM compared to a single pass one was demonstrated from a photoluminescence study.

12.5.3 Inclusions and Precipitates

The devices made from semiconductors require chemically and electrically homogeneous crystals free from extraneous second-phase microparticles. Such structural defects were shown to adversely affect the structural quality and electrical performance of crystals. Furthermore, such microparticles were shown not only to be a source of dislocations, cracks, and holes [144] but also to gather the impurities originating from various sources, starting elements, containers used during crystal growth, and eventual contamination during material preparation prior to growth [145]. The THM growth temperature is often far below the melting point of the compounds. As a result, in the frequent case of compounds presenting a solidus of retrograde shape, the crystals grown by THM turn out to be off-stoichiometric. The component in excess can lead to the formation of precipitates or inclusions, or both, depending on the growth conditions used, mainly on the growth rate. That is why precipitation and formation of inclusions has been extensively studied and frequently mentioned for several materials, mainly in the case of tellurides.

According to Rudolph et al. [146], the difference between an inclusion and a precipitate was shown as depending upon their size and their mode of formation; inclusions are considered to be usually much larger than precipitates, which are nucleated during cooling down in the as-grown crystal. The authors correlated size, density, and axial distribution of inclusions and precipitates to the nonstoichiometry of the melt.

In an AB compound, inclusions result from A- or B-rich melts, due to morphological instabilities at the crystallization interface. A or B inclusions form by entrapment of A or B droplets from the A- or B-rich diffusion layer. Large droplets of the A- or B-rich compound are captured from the diffusion layer at the interface's front. Their size and morphology depend on the experimental conditions.

A mechanism of inclusion formation during crystal growth by the traveling heater method was proposed by Barz and Gille [144] after an investigation of Te inclusions in $Cd_{1-x}Zn_xTe$ crystals grown from Te-rich solution zones. They gave an explanation of the mechanism of their formation by interpreting the composition changes of the matrix surrounding them. They stated also that the shape of the inclusions, which contain a very high fraction of Te, was due to the structure of the crystal matrix, because the actual Te inclusion was accommodated in the space left during the included droplet crystallization process.

Schwarz and Benz [147] studied the thermal field influence on the formation of Te inclusions in CdTe grown by THM. They found that hexagonal polygons tend to form under small gradients, whereas triangular-shaped inclusions occur under larger temperature gradients. The occurrence of elongated inclusions parallel to the growth front was explained by temperature fluctuations at the crystal-solution phase boundary. It was stated as well that the shape of the Te inclusions visible after growth strongly depended on radial and axial temperature distribution during cooling after a growth experiment.

In the framework of the growth of GaSb and InSb crystals by the vertical and horizontal THM, Benz and Müller [16] demonstrated that the horizontal THM had the advantage of a free surface, and also that it led to stable growth conditions that resulted in inclusion-free GaSb and InSb single crystals due to the more effective melt mixing in horizontal arrangement where additionally Marangoni convection does act. They determined the maximum growth rates for inclusion-free crystals of both compounds to be obtained.

In a study of the growth and interface of 2-inch diameter (Cd,Zn)Te ingots grown by THM, Roy et al. [55] investigated both macroscopic and microscopic morphology of the growth interface for large diameter CZT ingots grown by THM technique using Te as the solvent. They stated that the microscopic morphology of the growth interface was responsible for Te inclusions in the grown crystals (Figure 12.24). They showed as well that after optimization of the growth parameters, a reasonably flat/slightly convex interface could be obtained, which eventually reduced the Te inclusion density in the grown ingots. Nevertheless, this study of the growth interface was achieved in the last-to-freeze region of the ingots that were said to be cooled down, either slowly or rapidly, after completion of the growth process, and then after exhaustion of the source material. It means that the morphology of such an interface does not likely reflect the morphology of the interface at midpoint because the convective flows in the solvent zone are very likely different in both cases, respectively.

Te inclusions are indeed likely due to morphological instabilities at the crystallization interface as a result of factors such as constitutional supercooling, grain boundaries and

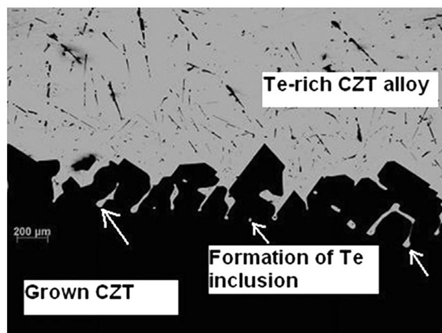

FIGURE 12.24 Magnified portion of a growth interface. CZT, CdZnTe. *From Ref. [55].*

twins intersecting the interface, and poor control of the process's temperature, as stressed by Ndap [148].

Post and Krämer [39] compared the transparency of melt-grown and THM-grown $AgGaS_2$ crystals. Melt-grown crystals showed inclusions of $AgGa_{20}S_{31}$, which lowered the transparency, while flux-grown $AgGaS_2$ were clear but showed well-shaped "negative crystals" of solvent inclusions. The authors suggested this may be due to the lower THM growth temperature, where only near-stoichiometric $AgGaS_2$ is stable so that no inclusions of $Ag_2Ga_{20}S_{31}$ can form during cooling.

In a TEM investigation of precipitates in $Hg_{0.8}Cd_{0.2}Te$ grown by the traveling heater method from Te-rich conditions, Kiessling and Leipner [149] identified the precipitates observed as being mercury vacancy loops found at a density of about 10^{15} cm^{-3}. These defects were found to completely disappear by annealing under mercury-saturated conditions.

In the growth of YIG crystals by traveling solvent floating zone, Kimura et al. [130] pointed out that precipitation of foreign phases occurred in the crystals for excessive growth rates and imprecise control of the solvent zone composition.

In order to get rid of the excess component second-phase microparticles, which were shown to adversely affect the electrical performance of crystals, different strategies were used.

As shown in [55], the optimization of the THM growth parameters can lead to a flat/convex, microscopically smooth interface reducing inclusions in the grown ingots.

Furthermore, postgrowth processes were commonly developed. They involve annealing in a controlled atmosphere, usually of the deficient component, or under vacuum. This may be done either on the whole ingot during its cooling down after growth [150–154], however with low efficiently because of short diffusion lengths within the large solid boule, or on wafers cut from the ingots, either under uniform temperature conditions [154] or by thermomigration [153].

The removal of second-phase particles during the postgrowth annealing process is usually accompanied with the release of impurities they contained. Further purification of postgrowth annealed crystals is therefore a logical step within this process [148].

12.6 Mass and Heat Transport, Simulation and Modeling

Although growing crystals is a skill that can only be mastered well after attempting numerous crystallizations, numerical simulation can be of great aid for the crystal grower in the determination of the growth conditions and also to explain growth difficulties. Progress in crystal growth is clearly accelerated by the careful application of computational models.

In the early studies related to matter transport in a THM configuration, only diffusion was taken into account. Such an approach allowed determining the diffusion constant within solution zone and the subsequent maximum growth rates [3].

It was shown further from experimental studies that matter transport in the solvent zone occurred both by diffusion and convection and that natural convection was even expected to be the most effective and dominant mechanism of matter transport. That is why the convenient growth rates are always above those calculated from a purely diffusive matter transport mechanism.

In an investigation of the axial temperature distribution in the solution zone at THM growth of CdTe, Schwenkenbecher and Rudolph [47] estimated the Rayleigh number of the THM zone and found it was substantially higher than the critical Rayleigh number. That is why the authors assumed that concentration-driven convection made the main contribution to the overall convection.

Wald and Bell [155], comparing the calculated temperature profiles for convection-free solvent zones to the actual temperature profiles, concluded that natural convection was an effective mechanism of material transport in THM growth of CdTe from Te solution. They evaluated the material transport coefficient M defined by the equation $F = M\ dC/dx$, where F is the flux of Cd across the liquid zone and dC/dx is the concentration gradient in the zone. M was found about 25 times larger than the extrapolated value of the self-diffusion coefficient of liquid Te or the diffusion coefficient of Cu in liquid Te at 700 °C. The authors concluded that concentration-driven convection was the main process of convection in the THM growth of CdTe, which possesses an especially favorable combination of properties for natural convection to occur.

Following the work of Cherepanova [160], El Mokri et al. [34] adapted to their configuration a quasi-diffusive one-dimensional model (diffusion of (Cd,Zn)Te in a (Cd,Zn)Te:Te mixture). They found the solutal Rayleigh number larger than the thermal one, confirming that solutal convection was the dominant mechanism in THM growth.

Again in the case of the CdTe THM growth, Ye et al. [156] studied the effect of natural convection on growth rate and growth uniformity. The authors developed a thermosolutal convection model that accounted for the influence of both thermal and solute convections on heat and mass transfer, as well as growth rate in the process. Their computations were carried out with the assumption of a quasi-steady state condition for temperature, concentration, and convective flow fields in the ampoule. The simulation results showed that the heat transfer in the liquid zone was dominated by heat

conduction and was not affected significantly by fluid flow. However, fluid flow was found to play an important role in influencing concentration distribution in the liquid zone. This study quantitatively showed as well that the growth rate was greatly enhanced by convective mass transfer in the liquid. The uniform growth, necessary to produce a planar interface, was related to the convective state leading to radial uniformity in concentration gradient along the growing interface. The authors concluded that this must be obtained from reduced natural convection near the interface. For this, the heater thermal gradient should be small and the asymmetry should be large so that the natural convection is moderated in the interface region. Since convective mass transfer enhances growth rate, forced convection to create uniform growth was stated by the authors to be desirable.

In the THM growth of naphthalene, Chang and Wilcox [158] attributed interface breakdown to variations in temperature gradient along the interface and to convection currents in the zone that cause solute variations along the interface.

The influence of gravitation on the processes of heat and mass transfer in the THM growth of PbTe was studied by Cherepanova et al. [160,161] through the resolution of a two-dimensional hydrodynamic thermodiffusive problem. The authors stressed the importance of free convection, which removes constitutional supercooling occurring in the absence of gravitation at the growing interface and leads to greater morphological stability of a growing crystal face. They noted that their results were of rather general character and could be used to forecast the processes under microgravity conditions.

Langbein [162] developed the equations describing heat and particle flow during crystal growth by THM, for which analytical solutions were obtained in all crystal and solvent regions. The author showed that the heat flow enforced by the travel rate causes the temperature gradient in the feed crystal to become steeper than that in the growing crystal. The position and temperature of the dissolving and of the growing interfaces are fixed by the particle flow. Effects of convection are: a leveling of the temperature in the solvent, an increase in the temperatures at the dissolving and the growing interfaces, and an extension of the solvent zone. Unstable convection causes temperature fluctuations at the dissolving and the growing interfaces and thus favors supercooling of the growing interface. Zero gravity avoids convection and further, heat and particle flow stabilize mutually and suppress supercooling. Note that this last conclusion does not agree with Cherepanova's.

Using a thermodynamically rational mathematical model, Dost et al. [163] set out a numerical simulation for the growth of $Ga_xIn_{1-x}Sb$ by the traveling heater method. The momentum equations including the solutal and thermal buoyancy terms, the mass transport equations in terms of the mole fraction of components, the interface mass conservation equations, and the phase equilibrium equations were presented for a two-dimensional axisymmetric growth cell configuration. The field equations were solved numerically by an adaptive finite element procedure as the interfaces between the solid and liquid phases change in time. The fully implicit time integration technique was adopted to solve the transient equations, and the resulting nonlinear algebraic equations

were solved by the Newton–Raphson method. Numerical results showed that the furnace thermal profile, the thermal as well as solutal convection in the liquid solution, have significant effects on the growth process.

A finite element, quasi-steady state thermal model using Newton's iteration scheme was developed by Chang et al. [164] to simulate the growth of (Hg,Cd)Te by THM. The ampoule region was incorporated in the thermal model and formed the basis to compare the simulation results to experimental measurements. Sensitivities studies were carried out to explore the change of interface shape due to variations of thermophysical parameters, physical dimensions of the system, thermal boundary profile, and crystal growth conditions. The effects of the ampoule wall—silica thermal conductivity and silica wall thickness—were investigated as well, both experimentally [7] and by modeling. Figure 12.25 displays the calculated isotherms as a function of the silica wall

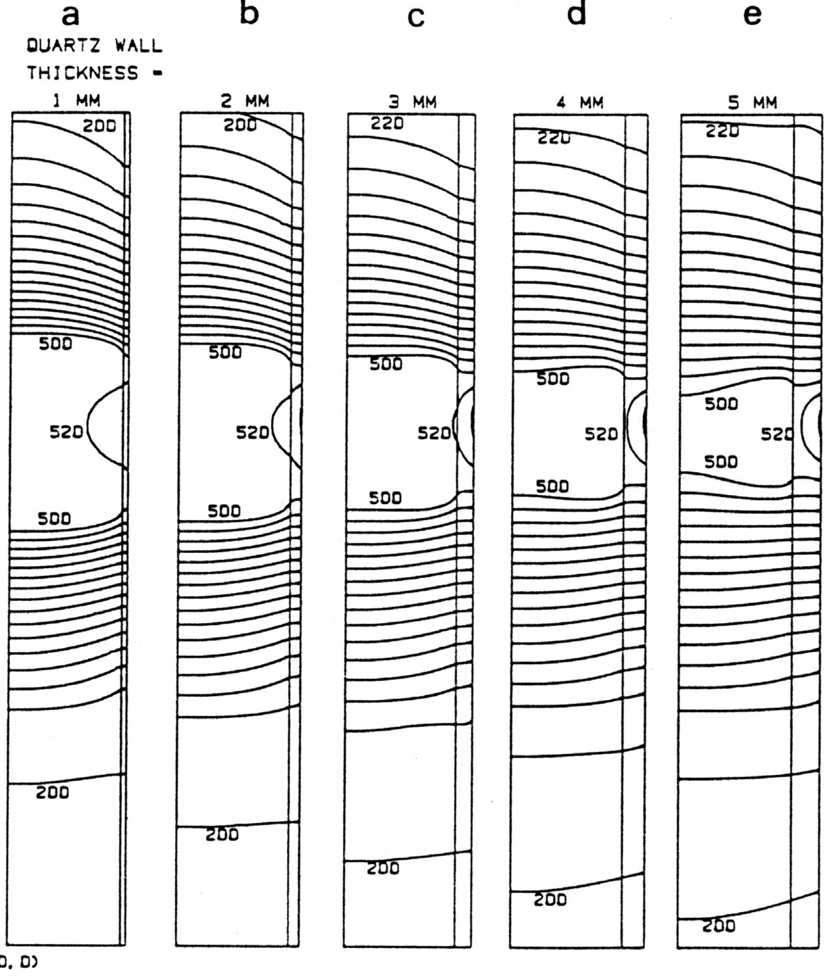

FIGURE 12.25 Calculated isotherms as a function of quartz wall thickness. *From Ref. [164].*

thickness. It was found that the interface shape was always concave, with respect to the solid, at the solvent/crystal/quartz three-phase contact point whether the macroscopic interface shape would be convex or concave. This was attributed to the higher quartz thermal conductivity with respect to that of MCT. By reducing the thermal conductivity of the ampoule, for instance by using ampoules with thicker walls, this local concavity could be removed. The temperature field was shown to depend substantially on variations in physical properties of the materials used for MCT growth such as, grown crystals, solvent, and feed material. The interface shape was shown to depend on MCT thermal conductivity, k_{MCT}, which varies with x, the Cd concentration. The lowest k_{MCT} has the most concave interface shape, the largest solvent volume, and the highest interface thermal gradient. For increasing solvent thermal conductivity k_{sol}, the trends of interface shape, solvent volume, and thermal gradient in the vicinity of the growing interface were shown to be the reverse of those for the k_{MCT}. The lower the k_{sol}, the less concave the interface shape, the less the volume of the solvent, and the lower the interfacial thermal gradient. The isotherms have also been calculated for various solvent liquidus temperatures T_M. The interface shape becomes less concave and the solvent volume decreases as T_M gets higher. The solvent volume was found to be a linear function of T_M. Marked changes in interface shape and solvent volume were found as a function of position along the ingot. As growth proceeds, the interface evolves from a convex shape to a concave one, and, at the same time, the solvent volume increases. An increase of the peak of the surrounding temperature from 600 to 710 °C was shown to generate a change in interface shape from convex to concave and an increase of the solvent volume of 100%. It was also shown that the higher the growth rate the more concave the interface shape becomes. An accurate estimate of the volume of the loaded zone was shown to be critical. Finally, a good agreement was found between experimental and calculated interface shape, demonstrating the validity of the predictions. For appropriate thermal and thermodynamic conditions, as a result of the simulation, slightly macroscopic convex interface shapes can be achieved and MCT single crystals were grown.

The influence of convection and heat and mass transfer on the shape and position of melt/solid interfaces, and on radial composition segregation, was analyzed numerically by Apanovich and Ljumkis [165] for the THM growth of a binary alloy in a vertical transparent ampoule. The results are presented for crystal and melt with thermophysical properties similar to $Cd_xHg_{1-x}Te$, with the assumption that the pseudobinary CdTe-HgTe phase diagram was true. The two-dimensional axisymmetric heat transfer equation, hydrodynamical equation, and convective diffusion equation were included in the mathematical model. The rates of crystal growth and dissolution were supposed to be proportional to the compositional supercooling in the melt near the interfaces. It was shown, for the conditions when convection was absent, that the interfaces were asymmetrically positioned, respectively, to the heater's centerline. Intensive convection made their position more symmetrical, but the length of the liquid zone greater. The flow pattern in the melt appeared to be more influenced by solutal gravitational convection than by thermal

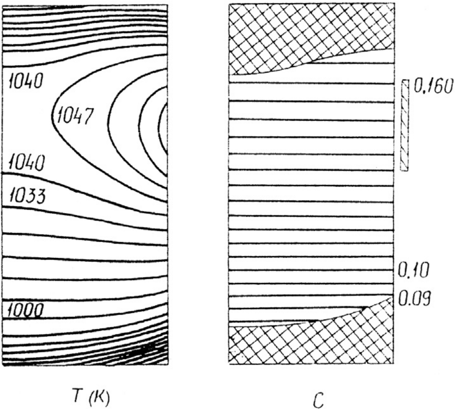

FIGURE 12.26 Isotherms and contours of constant concentration; heater moves with v = 0.5 mm/h, zero gravity condition g = 0. *From Ref. [165].*

convection. The nonlinear dependence of the melt density on the temperature and composition were used in the model. The concentration and temperature fields are shown in Figure 12.26 in the absence of convection in the melt, compared to the concentration, flow, and temperature fields displayed in Figure 12.27 under earth gravity conditions. Under earth gravity conditions, an intensive counterclockwise vortex with maximal velocity 0.55 cm/s is formed in the molten zone. In comparison to the case where convection is absent (Figure 12.26, g = 0), the length of the zone is about 1.5 times greater and almost symmetrically placed relative to the heater.

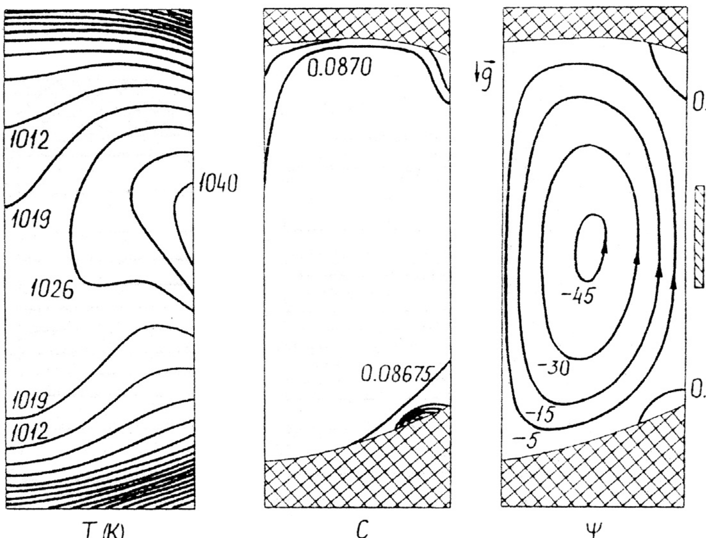

FIGURE 12.27 Isotherms, contours of constant concentration and thermal convection flow field, g = 9.81 m/s^2, heater moves with v = 0.5 mm/h. *From Ref. [165].*

Including the governing equations of continuity, momentum, mass transport, and heat transfer in their model, and applying different thermal boundary conditions and a crucible rotation, Dost and Liu [166] obtained the optimum growth conditions for a desired interface shape in the THM growth of CdTe single crystals. The simulation results show that by controlling the heat removal at the bottom of the crucible, a flatter (or slightly convex toward the crystal) growth interface could be maintained throughout the growth process (Figure 12.28). A crucible rotation rate of 5 rpm seemed optimal for a favorable growth interface shape (Figure 12.29).

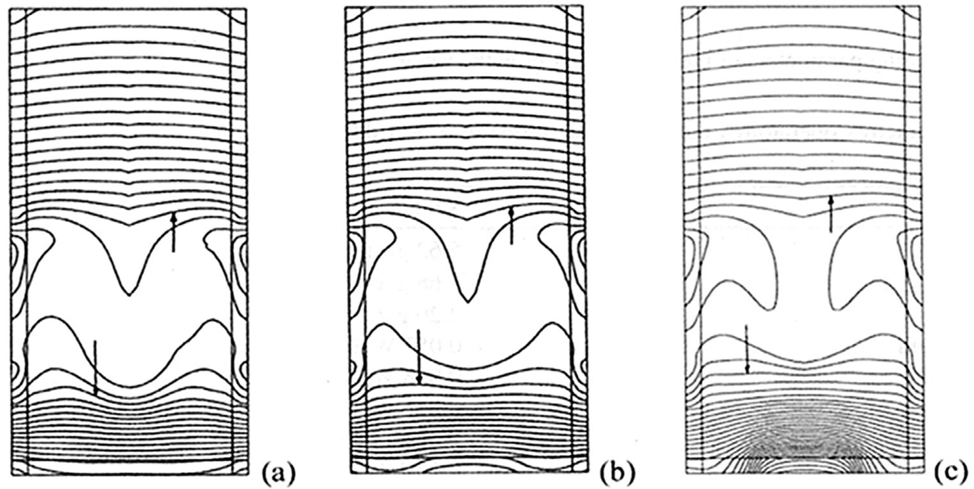

FIGURE 12.28 The evolution of the thermal field (at t = 10 min growth time): (a) no heat removal; (b) small heat removal (c) large heat removal. *From Ref. [166].*

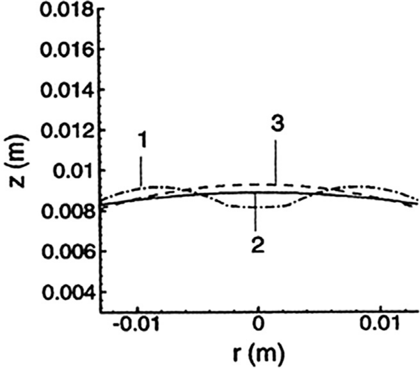

FIGURE 12.29 Change of growth interface shape under various ampoule rotation rates: (1) 3 rpm, (2) 5 rpm, and (3) 7 rpm. *From Ref. [166].*

Martinez-Tomas et al. [110] made use of the commercial computational code FLUENT to solve the governing equations of fluid flow, heat transfer, and mass transport in the frame of a quasi-steady state model in a numerical simulation of the THM growth of HgTe. The simulation was made by using a three-level strategy allowing the reduction of the computational effort. This numerical study permitted to put forward some ineffectiveness for the heat evacuation at certain positions of the growth run, closely related to the thermal properties of the whole system and particularly of HgTe, as a plausible explanation of the presence of defects in the form of thin Te-rich layers.

A theoretical model describing the growth of ternary mixed crystals by THM under steady growth conditions was presented by Sell and Müller [167]. The model used the one-dimensional time-dependent equations of species diffusion without convection with the two moving free boundaries of the solution zone determined via consideration of the phase diagram. Numerical solutions were presented for the growth of $Ga_xIn_{1-x}As$ crystals, using a feed of $x = 0.8$. Assuming steady experimental boundary conditions, these solutions showed that mixed crystals normally grow with an inhomogeneous composition in the initial transient. Modeling using different lengths of the solvent zone showed that smaller zones were advantageous with respect to the homogeneity (Figure 12.30). The authors stated as well that it should be possible to grow more homogeneous crystals under conditions of enhanced gravity in a centrifuge.

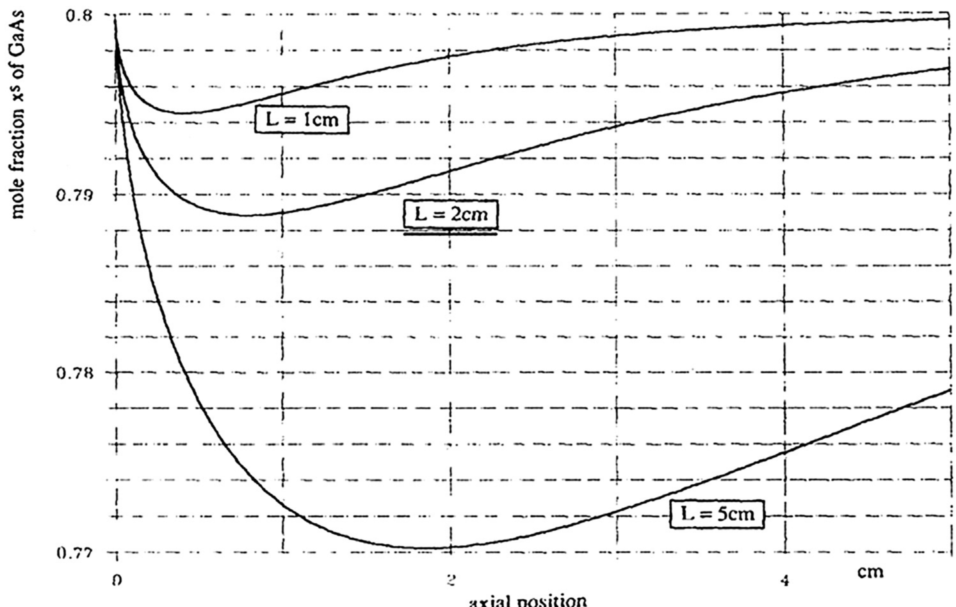

FIGURE 12.30 Different numerical results show the variation of the homogeneity as function of the initial zone length in the traveling heater method growth of $GaxIn_{1-x}As$. *From Ref. [167].*

12.7 Single Crystal Growth by THM

Single crystal materials are finding more use in industrial applications every day. That is why considerable efforts were devoted to the THM growth of single crystals, which are of particular interest to industry for many applications such as electronic, optical, or electro-optical devices.

It turns out, as discussed in the previous section, that natural convection is an effective intrinsic mechanism of matter transport in THM. Due to high temperature gradients used in THM, strong convective flows develop in the liquid zone. The thermal as well as solutal convection in the liquid solution have significant effects on the growth process. The detrimental effects of free-convection currents in the zone causing solute variations along the interface were stressed. Temperature fluctuations and flow turbulences may adversely affect the quality and reproducibility of the grown crystals. Heterogeneity in the fluid or instability of the growth interface will alter the composition and quality of the solid product. It was therefore stated desirable to minimize these effects by suppressing the natural convection in the liquid solution and replacing it by a controllable forced convection regime, or growing crystals under a pure diffusion regime either under zero gravity conditions or under magnetic field.

12.7.1 Seeding

Spontaneous nucleation is a rare and an unusual event. No other step in crystallization requires as much energy as the formation of a nucleus. In the experiment that uses a seed, this difficult kinetic barrier to spontaneous nucleation is bypassed.

Some uncontrollable parameters generally prevent the seedless THM growth of single crystals. Furthermore, the seedless grown crystals can be of random orientation. Seeding, technologically very easy in a THM configuration, will facilitate the most appropriate crystallographic direction to achieve optimum microstructure and uniformity. Seeding is then mentioned in most of the reports dealing with the growth of single crystals by THM.

Seeding requires:

- The convenient choice of the seed material, which can be different from the one to be grown.
- The determination of a convenient crystallographic plane and eventually of its polarity.
- An appropriate cutting and polishing technology.
- Finally, a last surface treatment, generally a chemical one.
- A satisfactory positioning in the crucible.

All the technologic details of seeding are generally not extensively reported.

12.7.2 Microgravity Growth

As well summarized by Benz and Fiederle [168], crystal growth under microgravity in space drastically reduces buoyancy convection. Heat and mass transport become dominated by diffusion. Furthermore, gravity causes hydrostatic pressure in melts, which in turn influences the shape of a liquid surface, while under microgravity the liquid shape, and then the shape of the liquid zones, depends only on the surface tension. Also, the wetting behavior of the melt on solid surfaces, such as seeds, crucibles, or technical parts, is modified by the absence of gravity. As a consequence, liquid menisci are formed and dramatically influence the crystal growth.

Long-term THM growth experiments of $Al_xGa_{1-x}Sb$ under microgravity during the EURECA-1 mission using the automatic mirror furnace (AMF) were achieved by Danilewsky et al. [80]. The space-grown samples showed an improved microscopic homogeneity, compared to the 1 g reference crystals, indicating the absence of time-dependent convection. The authors concluded that microgravity offers the opportunity to grow homogeneous crystals in regard to the dopant, as well as the composition distribution.

Most frustrating was the fact that due to missing convection under μg conditions many more solvent inclusions appeared [52], because a considerable diffusion boundary was generated.

Note that the microgravity conditions can presently only be used as a tool for studying the fundamentals of crystal growth and finding better growth conditions on earth. Industrial production of crystals in space can only be thought of in the far future.

12.7.3 THM Growth Under Magnetic Fields

While static magnetic fields can suppress thermal convection by simulating a microgravity environment, rotating fields could improve homogeneity and axisymmetry in the solution zone.

12.7.3.1 Static Magnetic Fields

Most of the studies dealing with the influence of a static magnetic field in THM are numerical simulations.

A three-dimensional numerical simulation for the THM growth of CdTe single crystals under an applied (vertical) static magnetic field was carried out by Liu et al. [169]. A suitable applied magnetic field was very beneficial, as it suppressed the convection and led to more uniform concentrations and temperature distributions, as well as flatter growth interfaces for a prolonged and stable growth. Numerical results showed that the transport structures in the liquid solution exhibited three distinct behaviors at different field intensity levels. There was a critical magnetic field level, about 8.0 kG, below which the applied magnetic field was very beneficial. It appeared that the field

intensity of 8.0 kG was the optimum level for which the convection was suppressed to a minimum and the growth interface was the flattest. At the higher field levels, between 8.0 and 12.0 kG, the transport structures exhibited transitional behavior. The concentration distribution was different, and the growth interface and isotherms became convex toward the solution, losing their flatness. At higher field levels, the computed flow and temperature fields indicated unstable transport structures in growth experiments.

In agreement with this article, Kumar et al. [170] presented, as well, a 3D numerical simulation study for the THM growth of CdTe single crystal under strong static vertical magnetic fields. In spite of the initially assumed axisymmetric boundary conditions, three-dimensional transport structures developed as soon as the growth process began. There was an optimum magnetic field level for which the growth interface became slightly concave toward the liquid zone, giving rise to a favorable condition for growth of crystals with a uniform composition and fewer inclusions. The optimum magnetic field level observed in this study agrees with those reported in the literature. However, the computed transport structures became more suppressed and smoother with the increasing magnetic field level, and were stable and did not become stronger even above this optimum magnetic field level, up to 15 kG. Application of the magnetic field suppressed the flow velocity in the solution, and the magnitude of the maximum flow velocity decreased monotonically with increasing the magnetic field intensity. This observation was due to a novel numerical treatment presented in the study. The authors suggested that the results of their study could be important for crystal growers in designing their THM setups.

In a study of the THM growth of (Cd,Zn)Te single crystals on CdTe substrate from Te solution under a uniform static magnetic induction of 3T, Wang et al. [56] showed in their experimental results that applying a 3T magnetic induction improved the morphology of the growth interface in the crystal. The authors attributed this improvement to the damping effect of the Lorentz force in Te solution, and that improvement of growth interface was beneficial to improve crystal microstructure of (Cd,Zn)Te.

12.7.3.2 Rotating Magnetic Fields

The influence of rotating magnetic fields (RMF) on flow pattern and compositional uniformity in the solution zone of a THM system for growth of CdTe was numerically investigated by Ghaddar et al. [49], under space and ground processing conditions. It was shown that under μg conditions, application of RMF could be used to overwhelm residual buoyancy-induced convection and to control the uniformity of solution-zone composition at the growth front without appreciable modification of the growth interface shape. In contrast, in the high-g regime, application of RMF was observed, for the field strengths studied, to increase the convexity of the growth interface (Figure 12.31) and deteriorate the compositional uniformity at growth interface. Whereas it is conceivable that at higher field strengths interfacial compositional uniformity should be improved, high flow velocities and the multicellular flow structure presented in the

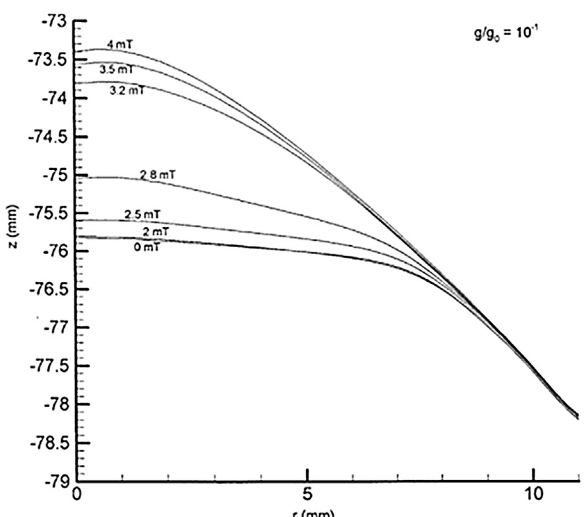

FIGURE 12.31 Growth interface shapes for different rotating magnetic fields strengths at $g/g_0 = 10^{-1}$. *From Ref. [49].*

solution zone were likely to lead to unsteady flow conditions and associated deleterious effects on the quality of grown crystal. This scaling analysis provided a generalized framework for analysis of the relative influence of RMF and gravity on convection in the solution zone.

A numerical simulation study was carried out by Dost et al. [171] for the growth of CdTe crystals by THM, in order to examine the effects of applied stationary and rotating magnetic fields, and also small nonuniformities in the stationary magnetic field. In this simulation, a strong stationary field was applied to suppress the natural convection in the solution zone, and a small but rotating magnetic field was considered for better mixing in the horizontal plane. The spatial distribution of the stationary field was considered to be almost uniform before the furnace and the growth system were lowered into the magnet opening. However, the field uniformity may be altered by the presence of the growth system. In order to determine the effect of such field nonuniformities, small magnetic body force components were considered in the model. Results showed that higher stationary field levels were better in suppressing convection in the solution, but enhanced the compositional nonuniformity in the solution. Small but unintentional nonuniformities in the stationary magnetic field also enhanced compositional nonuniformity. A rotating magnetic field, on the other hand, was beneficial for mixing in the horizontal plane, and reduced the compositional nonuniformity in the solution. Mixing was enhanced at higher rotating magnetic field frequencies.

As for static magnetic fields, a very few experimental studies have tackled the influence of RMF on the quality of crystals grown by THM.

Single (Cd,Hg)Te crystals with diameter of 25 mm were grown by seedless THM within an RMF of 2–6 mT by Senchenkov et al. [101]. RMF was used as an effective tool

for controlling the heat and mass transport. The adequate choice of the magnetic induction value allowed to obtain the required growing interface shape and to grow large diameter crystals with the appropriate radial homogeneity of the composition that met the requirements of the industry.

CdTe and $CdTe_{0.9}Se_{0.1}$ crystals were grown by Salk et al. [172] by THM under μg conditions. A forced convection regime was produced by a B = 2 mT rotating magnetic field. The equations describing the rotating magnetic field were derived for μg conditions and small Hartmann numbers. The rotating magnetic field generated a stable steady flow in the Te zone, essentially improving the radial and axial distribution of μτ products.

A series of THM growth runs based on 32 mm diameter CdTe ingots with and without use of a rotating magnetic field was completed by Sowinska et al. [173]. From a detailed characterization of the grown crystals as well as of the detectors produced, the conclusion of the authors was that there was a weak impact of the use of RMF on the quality of the crystals and on the performances of the nuclear detectors. Note furthermore that the use of magnetic fields in the THM growth at industrial scale is not actually conceivable because of its very costly and complex impact on the experiments.

12.7.4 Forced Convection Regimes

12.7.4.1 Centrifuge

After stressing the big disadvantage of low growth rates of some mm/day for the technical fabrication of large bulk crystal by THM, Müller and Neumann [92] were able to grow GaSb crystals by horizontal THM in a centrifuge at growth rates nearly one order of magnitude faster than at normal earth gravity (Figure 12.32). This strong increase in the growth rate was explained by an enhancement of convection in the solution zone.

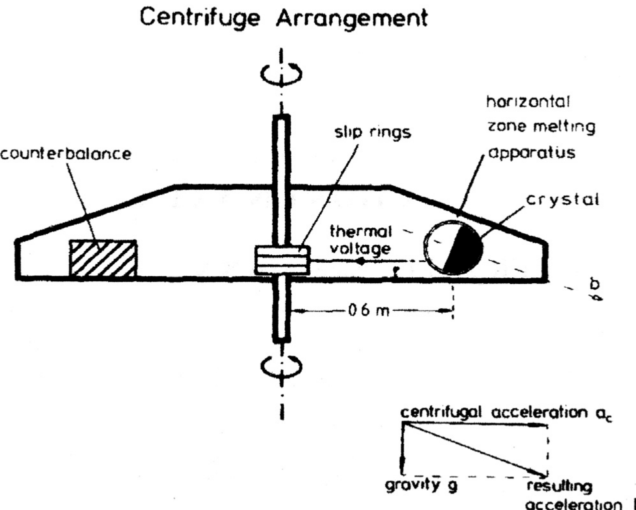

FIGURE 12.32 Centrifuge arrangement for the horizontal traveling heater method. *From Ref. [92].*

12.7.4.2 Accelerated Crucible Rotation Technique

The ACRT was developed initially by Scheel et al. [174] for the solution growth of garnets at high temperatures. ACRT was initially modeled by Schulz-Dubois [175] and is discussed in detail in Chapter 24 of the Handbook, Vol. IIB. An improvement of the size of the crystals by a factor of 1000 over growth without ACRT was obtained by the authors. Natural convection being the most effective and dominant mechanism of matter transport in CdTe THM growth, it makes ACRT very promising for creating a forced convection regime that will dominate the hydrodynamic scene and will be easily controlled, contrary to natural convection. One can expect ACRT to be particularly efficient in the case of large diameters where the "supercooling amount" is quite large [99] and should impose excessively low growth rates.

Wald and Bell [155] suggested that forced convection using ACRT might be employed because it is reproducible and amenable to control. They performed a series of THM experiments for the crystal growth of CdTe from a Te solution, observing the effect of rotation speed, cycle time, growth rate, and temperature on the crystallinity and the number of voids or inclusions. They found that the ACRT was capable of doubling the maximum growth rate for which inclusion-free crystals could be obtained.

Note that the efficiency of their ACRT-assisted experiments was penalized by the small diameter of 1 cm of the container used.

Using containers of 5-cm diameter and solvent zones of 3-cm long for the THM growth of $Cd_{0.8}Zn_{0.2}Te$ crystals, El Mokri et al. [34] found, using ACRT, a very significant enlargement in the grain size of the grown crystals associated with a substantial increase in the growth rate.

The growth of $Hg_{1-x}Cd_xTe$ single crystals by THM using ACRT was proven to be possible by Bloedner and Gille [99]. They showed that the growth rate could be increased by extending the region of convective mixing toward the interfaces, as predicted by theoretical considerations. An effective way of stirring the solution zone in front of the interfaces was achieved by the use of cycles that satisfy the conditions to enhance the Ekman flow. The density of tellurium inclusions did not increase markedly with increasing growth rates up to 8.5 mm/day. The microscopic and macroscopic homogeneity were not degraded relative to crystals grown without ACRT at much lower rates.

The same group [48] proved ACRT and horizontal rotation around the ampoule axis to be effective techniques to enhance convective flow within Te-rich solution zones in THM growth of $Hg_{1-x}Cd_xTe$ and $Cd_{1-x}Zn_xTe$. Forced convection close to the growing interface was found to markedly increase the growth rate. Rates as high as 12 mm/day, with ACRT and with the horizontal rotation technique, were used without degrading the structural perfection.

A numerical study of ACRT-forced convection in the THM growth of CdTe was carried out by Barz et al. [176]. Comparison between calculations with or without including the thermally driven convection showed that the flow is dominated by the

forced convection. Therefore, attempts were made to optimize the ACRT regimes by detailed investigations of the forced convection. It was found that when the rotation changes from spin-up to spin-down and vice versa, the mixing in the zone is weak. To overcome this problem, an ACRT regime was recommended, which maintains the Ekman flow in the radially outward direction and suppresses it in the opposite one and is, therefore, expected to improve the material transport in the zone in a way allowing the maximum growth rate to increase. The authors stated as well that if the ampoule rotated with a constant rotation rate ($\omega = 30$ rpm), the combined convection and, therefore, the mixing was much weaker than without rotation. This was due to the suppression of natural convection by the centrifugal forces arising from the rotation, and only one vortex is observed in the entire solution zone.

12.7.5 THM + Solid State Recrystallization

In the solid state recrystallization (SSR), strains are intentionally introduced in a polycrystalline source and then released by high temperature thermal annealing. The structure tends toward the state of lower potential energy, which is the single crystal, through the motion of dislocations and grain boundaries. Furthermore, it avoids the uncontrolled effects of the earth gravity field. A growth quasi-contactless with the crucible walls can be achieved as in microgravity experiments.

As pointed out in Section 12.4, a significant asset of THM is the possibility of obtaining, with suitable growth parameters, a compact material presenting a regular fine-grain-size structure well adapted to the subsequent growth of single crystals by SSR. This possibility has not been much exploited so far, except by El Mokri et al. [34] in the case of CdTe. Starting from a polycrystalline CdTe ingot grown by THM, using growth parameters not still optimized to get an actually fine grain structure, a significant increase in the grain size was obtained after an SSR heat treatment. Several parameters, including initial structure, heating time, SSR temperature and time, and vapor pressure need to be adjusted. Later on, better SSR conditions were found for the growth of CdTe to get ingots totally as single crystals [177].

To summarize this section, it is well understood that industrial production of crystals grown by THM under microgravity conditions could only be thought of in a far future. Only weak effects have been obtained using magnetic fields for the THM growth of single crystals. Furthermore, the limitations of the use of magnetic fields are the cost and complexity of the setup. THM coupled to SSR allows to get rid of the uncontrolled effects of the earth's gravity field and a quasi-contactless growth beside the crucible walls, as in microgravity experiments. It offers promising possibilities that have not yet been thoroughly investigated. Considering the fact that ACRT allows to (1) create an easy-to-control forced convection regime that dominates the hydrodynamic scene, and (2) significantly increase the growth rate, it appears to be an effective alternative to both magnetic fields and microgravity conditions.

12.8 Conclusions

For the past decades, the traveling heater method has proven to be a very versatile and powerful technique for the growth of numerous materials and, sometimes, for their synthesis as well. It showed some decisive advantages over melt growth or vapor growth for peritectic compounds, some solid solutions, or incongruently evaporating materials. It offers a convenient arrangement for the seeded growth of single crystals. It benefits from all the classic advantages of low temperature growth, i.e., less contamination from the container, less vapor or decomposition pressures, higher critical shear stress, lower dislocation mobility, more perfect crystals as a result of less generation, and propagation of dislocations. Various attractive variants of THM have been devised and experimented, making it a very versatile technique. THM has been enriched with numerous computational models that have helped it to become a mature technique. Furthermore, its development occurred not only at the level of basic research in the laboratory, but also at that of the industry. It appeared as well as a good tool for fundamental studies on the crystal growth. In existence for almost 60 years, THM remains a topical and still modern technique of crystal growth. As an example, the best CdTe and (Cd,Zn)Te nuclear detectors brought to the market are industrially produced from THM grown crystals.

Acknowledgments

The author is pleased to thank Dr. Jean-Olivier Ndap for valuable discussions.

References

[1] Pfann WG. J Met 1955;7:961.

[2] Mlavsky AI, Weinstein M. J Appl Phys 1958;34:2885.

[3] Wolf GA, Mlavsky AI. In: Goodman CHL, editor. Crystal growth, theory and techniques, vol. 1. New York: Plenum Press London; 1974.

[4] Ivanov YM. J Cryst Growth 1996;161:12.

[5] Triboulet R, Didier G. J Cryst Growth 1975;28:29.

[6] Schmitz J, Walcher H, Baars J. SPIE Proc Mater Technol IR Detectors 1986;659:137.

[7] Colombo L, Chang RR, Chang CJ, Baird BA. J Vac Sci Technol 1988;A6:2795.

[8] Mochizuki K, Masumoto K, Iwanaga H. J Cryst Growth 1990;99:722.

[9] Brissot JJ, Belin C. J Cryst Growth 1971;8:213.

[10] Ostrogorsky AG. J Cryst Growth 1990;104:233.

[11] Gillessen K, von Münch W. J Cryst Growth 1973;19:263.

[12] Eyer A, Nitsche R, Zimmermann H. J Cryst Growth 1979;47:219.

[13] Tranchart JC, Bach P. J Cryst Growth 1976;32:8.

[14] Gamal GA. Phys Status Solidi (A) 1996;158:441.

[15] Launay J-C, Lestournelle F. J Cryst Growth 1992;121:202.
[16] Benz KW, Müller G. J Cryst Growth 1979;46:35.
[17] Gille P, Presia M, Bloedner RU, Puhlmann N. J Cryst Growth 1993;130:188.
[18] Triboulet R, Legros R, Heurtel A, Sieber B, Didier G, Imhoff D. J Cryst Growth 1985;72:90.
[19] Wald FV. Phys Status Solidi (A) 1976;38:253.
[20] Tai H, Hori S. J Jpn Inst Met 1976;40:722.
[21] Triboulet R. Rev Phys Appl 1977;12:123.
[22] Triboulet R, Marfaing Y. J Cryst Growth 1981;51:89.
[23] Laasch M, Schwarz R, Rudolph P, Benz KW. J Cryst Growth 1994;141:81.
[24] Taguchi T, Fujita S, Inuishi Y. J Cryst Growth 1978;45:204.
[25] Taguchi T, Kusao T, Hiraki A. J Cryst Growth 1985;72:46.
[26] Royer M, Jean B, Durand A, Triboulet R. Patent no 88 04 370 (1988).
[27] Triboulet R, Nguyen-Duy T, Durand A. J Vat Sci Technol 1985;A3:95.
[28] Kim KM, Hahn SR, Noh SK, Park HL, Chung CH. J Mater Sci Lett 1987;6:1205.
[29] Triboulet R. Unpublished work.
[30] Triboulet R, Neu G. J Cryst Growth 1985;72:258.
[31] Triboulet R, Neu G. J Cryst Growth 1983;65:262.
[32] Triboulet R. Prog Cryst Growth Charact 1994;29:85.
[33] Triboulet R, Pham Van K, Didier G. J Cryst Growth 1990;101:216.
[34] El Mokri A, Triboulet R, Lusson A, Tromson-Carli A, Didier G. J Cryst Growth 1994;138:168.
[35] Audet N, Cossette M. J Electron Mater 2005;34:683.
[36] Triboulet R, Triboulet D, Didier G. J Cryst Growth 1977;38:82.
[37] Reig C, Gomez-Garcıa CJ, Munoz-Sanjose V. J Cryst Growth 2001;223:357.
[38] Reig C, Paranchych YS, Munoz-Sanjose V. Cryst Growth Des A 2002;2:91.
[39] Post E, Krämer V. J Cryst Growth 1993;129:485.
[40] Tester JW, Reid RC, Wolf GA. Mat Res Bull 1971;6:1265.
[41] Lenoir B, Demouge A, Perrin D, Scherrer H, Scherrer S, Cassart M, et al. J Phys Chem Solids 1995;56:99.
[42] Caillat T, Carle M, Pierrat P, Scherrer H, Scherrer S. J Phys Chem Solids 1992;53:1121.
[43] Lahalle-Gravier C, Scherrer H, Scherrer S. J Phys Chem Solids 1996;57:1713.
[44] Hemmat N, Lamport CB, Menna AA, Wolf GA. Proc ACCG Conf Cryst Growth 1979:79.
[45] Mason DR, Cook JS. J Appl Phys 1961;32:475.
[46] Bell RO, Hemmat N, Wald F. Phys Stat Sol (A) 1970;1:375.
[47] Schwenkenbecher K, Rudolph P. Cryst Res Technol 1985;20:1609.
[48] Bloedner RU, Presia M, Gille P. Adv Mater Opt Electron 1994;3:233.
[49] Ghaddar CK, Lee CK, Motakef S, Gillies DC. J Cryst Growth 1999;205:97.
[50] Schoenholz R, Dian R, Nitsche R. J Cryst Growth 1985;72:72.
[51] Soji T, Onabe H, Hiratate Y. Nucl Instrum Methods Phys Res 1992;A322:324.
[52] Salk M, Lexow B, Benz KW, Matioukhin DG, Gelfgat YM, Sorkin MZ, et al. Microgravity Sci Technol 1993;6:88.

[53] Mochizuki K, Masumoto K. Mater Lett 1986;4:298.

[54] Roy UN, Gueorguiev A, Weiller S, Stein J. J Cryst Growth 2009;312:33.

[55] Roy UN, Weiler S, Stein J. J Cryst Growth 2010;312:2840.

[56] Wang Y, Kudo K, Inatomi Y, Ji R, Motegi T. J Cryst Growth 2005;275:e1551.

[57] Taguchi T. Phys Status Solidi A Appl Res 1983;77:K115.

[58] Rudolph P, Engel A, Schentke I, Grochocki A. J Cryst Growth 1995;147:297.

[59] Chen H, Awadalla SA, Mackenzie J, Redden R, Bindley G, Bolotnikov AE, et al. IEEE Trans Nucl Sci 2007;54:811.

[60] Chen H, Awadalla SA, Iniewski K, Lu PH, Harris F, Mackenzie J, et al. J Appl Phys 2008;103:014903.

[61] Miyake H, Haginoya T, Sugiyama K. Sol Energy Mater Sol Cells 1998;50:51.

[62] Shim Y, Horikawa S, Kikuno Y, Yamamoto N. J Cryst Growth 2002;234:190.

[63] Perner B. J Cryst Growth 1969;6:86.

[64] Kvapil J, Perner B. J Cryst Growth 1971;8:162.

[65] Miyake H, Hata M, Hamamura Y, Sugiyama K. J Cryst Growth 1994;144:236.

[66] Sugiyama K, Kato H, Miyake H. J Cryst Growth 1989;98:610.

[67] Miyake H, Tajima M, Sugiyama K. J Cryst Growth 1992;125:381.

[68] Hsu HJ. J Appl Phys 1986;59:2538.

[69] Hsu HJ, Yang MH, Tang RS, Hsu TM, Hwang HL. J Cryst Growth 1984;70:427.

[70] Shirakata S, Miyake H. J Phys Chem Solids 2003;64:2021.

[71] Hsu HJ, Sun CY, Hwang HL. Electron Lett A 1984;20:376.

[72] Lyahovitskaya V, Richter S, Frolow F, Kaplan L, Manassen Y, Gartsman K, et al. J Cryst Growth 1999;197:177.

[73] Baldus A, Benz KW. J Cryst Growth 1993;130:37.

[74] Miyake H, Sugiyama K. J Cryst Growth 1992;125:548.

[75] Shirakata S, Miyake H. Phys Stat Sol A Appl Mater Sci 2006;203:2897.

[76] Yoshimi M, Noda Y. Mater Trans-JIM 1996;37:473.

[77] Yip VFS, Wilcox WR. Mater Res Bull 1976;11:895.

[78] Bischopink G, Benz KW. J Cryst Growth 1993;128:470.

[79] Meyer BK, Bischopink G, Benz KW, Schöner A, Pensl G. J Cryst Growth 1993;128:475.

[80] Danilewsky AN, Lauer S, Bischopink G. Cryst Res Technol 1996;A31:11.

[81] Bischopink G, Benz KW. J Cryst Growth 1989;97:245.

[82] Yip VES, Wilcox WR. Bull Am Phys Soc 1972;17:1185.

[83] Meric RA, Dost S, Lent B, Redden RF. Intern J Appl Electromag Mech 1999;10:505.

[84] Kinoshitaa K, Katoa H, Iwaib M, Tsurub T, Muramatsub Y, Yoda S. J Cryst Growth 2001;225:59.

[85] Hemmat N, Lamport CB, Menna AA, Wolf GA. Proc Mater Eng Sci Div Biennial Conf Am Inst Eng 1970:112.

[86] Weishart H, Danilewsky AN, Benz KW, Bauser E. J Cryst Growth 1993;131:17.

[87] Yip VES, Changand Ct, Wilcox WR. J Cryst Growth 1975;29:69.

[88] Yip VES, Wilcox WR. Mater Res Bull 1976;11:895.

[89] Plaskett TS, Blum SE, Foster LM. J Electrochem Soc 1967;114:1304.

[90] Broder JD, Wolff GA. J Electrochem Soc 1963;110:1150.
[91] Wolff GA, LaBelle HE, Das BN. TMS-AIME 1968;242:436.
[92] Müller G, Neumann G. J Cryst Growth 1983;63:58.
[93] Danilewsky AN, Benz KW, Nishinaga T. J Cryst Growth 1990;99:1281.
[94] Gamal GA, Abdalrahman MM, Ashraf MI, Eman HJ. J Phys Chem Solids 2005;66:1.
[95] Durand A, Dessus JL, Nguyen Duy T. Proc SPIE Int Soc Opt Eng 1986;587:68.
[96] Kim KM, Hahn SR, Noh SK, Park HL, Chung CH. J Cryst Growth 1988;86:673.
[97] Genzel C, Gille P, Hähnert I, Kiessling FM, Rudolph P. J Cryst Growth 1990;101:232.
[98] Gille P, Kiessling FM, Burkert M. J Cryst Growth 1991;114:77.
[99] Bloedner RU, Gille P. J Cryst Growth 1993;130:181.
[100] Weiss E, Benory E, Kedar E, Juravel Y, Frenkel A. J Cryst Growth 1996;166:745.
[101] Senchenkov AS, Barmin IV, Tomson AS, Krapukhin VV. J Cryst Growth 1999;197:552.
[102] Ueda R, Ohtsuki O, Shinohara K, Ueda Y. J Cryst Growth 1972;13/14:668.
[103] Gille P, Rössner, Puhlmann N. Semicond Sci Technol A 1995;10:353.
[104] Triboulet R, Lasbley A, Toulouse B, Granger R. J Cryst Growth 1986;79:695.
[105] Triboulet R. J Cryst Growth 1990;86:79.
[106] Wu CC, Chu DY, Sun CY, Yang TR. Mater Chem Phys 1995;40:7.
[107] Sasaki T, Taguchi T, Hiraki A. Jpn J Appl Phys A 1988;27:L913.
[108] Triboulet R, Heurtel A, Rioux J. J Cryst Growth 1990;101:131.
[109] Triboulet R. In: Averous M, Balkanski M, editors. Semimagnetic semiconductors and diluted magnetic semiconductors. Plenum Press; 1991. p. 23.
[110] Martinez-Tomas MC, Munoz-Sanjose V, Reig C. J Cryst Growth 2002;243:463.
[111] Danilewsky AN, Benz KW. J Cryst Growth 1989;97:571.
[112] Danilewsky AN, Okamoto Y, Benz KW. Jpn J A Phy A 1992;31:2195.
[113] Danilewsky AN, Meinhardt J, Benz KW. Cryst Res Technol A 1996;31:139.
[114] Triboulet R, Levy-Clément C, Theys B, Chevy A. J Cryst Growth 1986;79:984.
[115] Reig C, Munoz V, Gomez C, Ferrera Ch, Segura A. J Cryst Growth 2001;223:349.
[116] diBenedetto B, Mlavsky AI. Am Ceram Soc Bull 1968;44:436.
[117] diBenedetto B, Cronan CJ. J Am Ceram Soc 1971;51:364.
[118] Harr M, Dornhaus R, Brütz G. Scientific results of the German Spacelab Mission D1. 1987. p. 283.
[119] Triboulet R, Didier G, Lasbley A, Morales F, Toulouse B, Pelletier CM, et al. Phys Narrow Gap Semicond Lect Notes Phys 1982;152:54.
[120] Gille P, Rudolph P. J Cryst Growth 1983;64:613.
[121] Winkler M, Genzel C, Parthier L. Cryst Res Technol 1984;19:613.
[122] Gille P, Muhlberg M, Parthier L, Rudolph P. Cryst Res Technol 1984;19:881.
[123] Assenov R, Polychroniadis EK. J Cryst Growth 1991;112:227.
[124] Munoz V, Lasbley A, Klotz S, Triboulet R. J Cryst Growth 1999;196:71.
[125] Kazakov P, Rachmatov I. Space technology and material science. Moscow: Nauka; 1982. 143 [in Russian].
[126] Hein CC. US Patent No. 2,747,971 1956.

[127] Wolff GA, Das BN, Lamport CB, Mlavsky AI, Trickett EA. Mat Res Bull 1969;4:S67.

[128] Gamal GA, Zied M, Abou M, Gerges MK, Galal EM. Jpn J Appl Phys 2003;42(9A):5480.

[129] Abernethy LL, Ramsey TH, Ross JW. J Appl Phys 1961;32:376S.

[130] Kimura S, Shindo I. J Cryst Growth 1977;41:192.

[131] Kimura S, Kitamura K, Shindo I. J Cryst Growth 1983;65:543.

[132] Wolff GA, LaBelle HE. J Am Ceram Soc 1965;48:441.

[133] Triboulet R, Rabago F, Legros R, Lozykovski H. J Cryst Growth 1982;59:172.

[134] Dohnke I, Mühlberg M, Neumann W. J Cryst Growth 1999;198/199:287.

[135] Su C-H, Volz MP, Gillies DC, Szofran FR, Lehoczky SL, Dudley M, et al. J Cryst Growth 1993;128:627.

[136] Gille P. Cryst Res Technol 1988;23:481.

[137] Pfann WG. Trans Met Soc AIME 1952;194:747.

[138] Gille P, Rudolph P. Cryst Res Technol 1984;19:K61.

[139] Zanio K. Semiconductors and semimetals, vol. 13. Academic Press; 1978.

[140] Nicolau IF. J Mat Sci 1970;5:623.

[141] Nicolau IF. J Mat Sci 1971;6:1049.

[142] Bell RO, Hemmat N, Wald F. IEEE Trans Nucl Sci 1970;17:241.

[143] Triboulet R, Marfaing Y, Siffert P, Cornet A. J Appl Phys 1974;45:2759.

[144] Barz RU, Gille P. J Cryst Growth 1995;149:196.

[145] Yang G, Bolotnikov AE, Cui Y, Camarda GS, Hossain A, James RB. J Cryst Growth 2008;311:99.

[146] Rudolph P, Neubert M, Mühlberg M. J Cryst Growth 1993;128:582.

[147] Schwarz R, Benz KW. J Cryst Growth 1994;144:150.

[148] Ndap J-O. In: Triboulet R, Siffert P, editors. CdTe and related compounds; physics, defects, hetero- and nano-structures, crystal growth, surfaces and applications. Elsevier; 2010.

[149] Kiessling F-M, Leipner HS. J Cryst Growth 1993;128:599.

[150] Bruder M, Schwarz H-J, Schmitt R, Maier H, Möeller M-O. J Cryst Growth 1990;101:266.

[151] Ivanov YM, Artemov VV, Kanevsky VM, Polyakov AN, Chudakov VS, Pashaev EM, et al. Eur Phys J Appl Phys 2004;27:371.

[152] Trivedi SB, Wiedemeier H. J Electrochem Soc 1987;134:3199.

[153] Vydyanath HR, Ellsworth JA, Parkinson JB, Kennedy JJ, Dean B, Johnson CJ, et al. J Electron Mat 1993;22:1073.

[154] Belas E, Bugár M, Grill R, Horodyský P, Feš R, Franc J, et al. J Electron Mater 2007;36:1025.

[155] Wald FV, Bell RO. J Cryst Growth 1975;30:29.

[156] Ye X, Tabarrok B, Walsh D. J Cryst Growth 1996;169:704.

[157] Funaki M, Shiraki H, Mito Y, Ohno R. Mater Res Soc Proc 2009;1164:3.

[158] Chang CE, Wilcox WR. J Cryst Growth 1974;21:182.

[159] Kazarov JP. Coll Abstr II USSR Conf Hydrodyn Heat Mass Trans Perm 1981;16.

[160] Cherepanova TA. Cryst Res Technol 1982;17:735.

[161] Cherepanova TA, Iljukhin VV, Cherepanov VY. Cryst Res Technol 1982;17.

[162] Langbein D. Rev Phys Appl 1977;12:129.

[163] Dost S, Meric RA, Lent B. Trans Can Soc Mech Eng 2000;24:95.

[164] Chang CJ, Baird B, Liao PK, Chang R, Colombo L. J Cryst Growth 1989;98:595.

[165] Apanovich YV, Ljumkis ED. J Cryst Growth 1991;110:839.

[166] Dost S, Liu YC. C R Mec 2007;335:323.

[167] Sell HE, Müller G. J Cryst Growth 1989;97:194.

[168] Benz KW, Fiederle M. In: Triboulet R, Siffert P, editors. CdTe and related compounds; physics, defects, hetero- and nano-structures, crystal growth, surfaces and applications. Elsevier; 2010.

[169] Liu Y, Dost S, Lent B, Redden RF. J Cryst Growth 2003;254:285.

[170] Kumar V, Dost S, Durst F. Appl Math Model 2007;31:589.

[171] Dost S, Liu Y, Lent B, Redden RF. Int J Appl Electromagn Mech 2003;17:271.

[172] Salk M, Fiederle M, Benz KW, Senchenkov AS, Egorov AV, Matioukhin DG. J Cryst Growth 1994;138:161.

[173] Sowinska M, Fauler A, Hennard G, Fiederle M, Siffert P. Oral communication in the E-MRS Fall Meeting, September 2013, Symposium entitled CdTe and Cd-rich ternary tellurides: growth and characterization, physics of defects and impurities, surfaces and applications.

[174] Scheel HJ. J Cryst Growth 1972;13/14:560.

[175] Schulz-Dubois EO. J Cryst Growth 1972;12:81.

[176] Barz RU, Sabhapathy P, Salcudean M. J Cryst Growth 1997;180:566.

[177] Hassani S, Lusson A, Tromson-Carli A, Triboulet R. J Cryst Growth 2003;249:121.

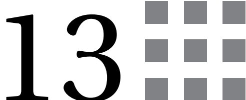

Growth of Bulk Nitrides from a Na Flux

Yusuke Mori[1], Mamoru Imade[1], Mihoko Maruyama[1], Masashi Yoshimura[1], Hisanori Yamane[2], Fumio Kawamura[3], Takahiro Kawamura[4]

[1]OSAKA UNIVERSITY, SUITA, OSAKA, JAPAN; [2]TOHOKU UNIVERSITY, AOBA-KU, SENDAI, MIYAGI, JAPAN; [3]NATIONAL INSTITUTE FOR MATERIALS SCIENCE, TSUKUBA, IBARAKI, JAPAN; [4]MIE UNIVERSITY, TSU, MIE, JAPAN

CHAPTER OUTLINE

13.1 Introduction **505**
13.1.1 The Discovery of GaN Crystal Growth Using a Na Flux 506
13.2 Growth Conditions and Mechanism of the Na Flux Method **507**
13.2.1 Growth Conditions of GaN Crystal by the Na Flux Method 507
13.2.2 The Effects of Na in the Ga-Na Solution 509
13.2.3 An Investigation on the Mechanism of Nitrogen Dissolution in the Na Flux Method 513
13.3 Nucleation Control **515**
13.3.1 Discovery of Carbon Doping for Nucleation Control 515
13.3.2 Mechanism of Carbon Doping 518
13.4 LPE Growth of GaN by the Na Flux Method **520**
13.4.1 Dislocation Behavior during LPE Growth of GaN by the Na Flux Method 520
13.4.2 Characterization of GaN Crystal Grown by the Na Flux Method 524
13.5 Point Seed and Coalescence Growth Technique **525**
13.5.1 Na-flux Point Seed Technique 525
13.5.2 Coalescence Growth Technique 527
13.6 Summary **531**
References **531**

13.1 Introduction

Blue light-emitting diodes (LEDs) were first realized using a buffer layer deposited at a low temperature [1] and *p*-type GaN crystals [2], both of which were developed by

Handbook of Crystal Growth. http://dx.doi.org/10.1016/B978-0-444-63303-3.00013-4
Copyright © 2015 Elsevier B.V. All rights reserved.

Akasaki, Amano and their colleagues. After these discoveries, GaN-based semiconductors have been used for not only blue LEDs but also semiconductor lasers and electronic devices such as high frequency power devices. High quality and low cost bulk crystals are needed in the field of GaN in order to enhance device performances.

High pressure solution growth (HPSG) method [3–5] has been developed to realize high quality bulk GaN crystals for many years (the details will be described in Chapter 15 by M. Bockowski). With this method, it is possible to grow high quality GaN crystals. However a high pressure and a high temperature condition (e.g., 10,000 atm and 1500 °C) needed for HPSG method has difficulty to achieve mass production of GaN crystals. Under such circumstances, in 1997, Yamane et al. [6] have reported the Na flux method by which GaN crystal can be grown in a Ga-Na mixed solution at relatively low pressure of nitrogen (gas) atmosphere (<50 atm) and at a lower temperature range of 700–900 °C compared with the high pressure solution growth method. The Na flux method has a significant advantage in synthesizing high quality GaN crystal through spontaneous nucleation process with very simple equipment. It had been, however, difficult to grow GaN crystals of a large size with a moderate growth rate at the beginning stage of the research because of the difficulty in controlling the nucleation. Through studies thereafter, growth of high quality GaN crystals with large diameter of larger than 2 in has been made possible by coalescence of GaN crystals from many isolated small seeds. Significant advance has been achieved in the 18 years since the Na flux method was discovered.

In this chapter, while looking back on the history of research and development of the Na flux method from its discovery until now, the latest results will discussed.

13.1.1 The Discovery of GaN Crystal Growth Using a Na Flux

From 1994 to 1995, H. Yamane synthesized single crystals of new ternary nitrides containing alkaline earth metals by using the Na flux metal to clarify their crystal structures at the research laboratory of F. J. DiSalvo at Cornell University (Ithaca, NY). Since nitrogen (N or N_2) is barely capable of dissolving into a Na melt, the first task was to introduce nitrogen into the melt by adding Zn, which forms a nitridometallate anion group, and a new nitride synthesis was carried out using the Ba-Zn-N system. Na and other metal materials were cut out in a glove box under an Ar-gas atmosphere. They were weighed along with NaN_3 as a nitrogen source and a Na source, accommodated in an Nb tube, and the Nb tube was sealed by arc welding. Further, the welded Nb tube was vacuum encapsulated in a quartz glass tube to prevent oxidation. After it was heated in an electric furnace, growth of single crystals was attempted by slow cooling over several days. The size needed as a single crystal was about 1 mm or less, with which X-ray crystal structural analysis can be performed. In most cases, the synthesized new nitride single crystals were unstable in air and they were covered with Na. The Na was dissolved and removed in liquid ammonia. With the method above, ternary nitrides Sr_2ZnN_2, Ba_2ZnN_2, $Ba_3Ga_2N_4$, and $Ba_5Si_2N_6$, an oxynitride $Ba_3ZnN_2O_2$, and a compound $Ba_3Ge_2N_2$ including

nitridometallate anions and Zintl anions, that is, six new materials in total, were synthesized, and their crystal structures were clarified by the single-crystal X-ray diffraction method.

Through the searching a series of new materials, it was found that the use of Na is very effective for synthesizing some ternary nitrides. In the course of understanding their reaction processes, I became interested in the effect of Na on synthesizing binary nitrides. Therefore, using Ga and Si materials, which were used for synthesizing the ternary nitrides $Ba_3Ga_2N_4$ and $Ba_5Si_2N_6$, preparation of the single crystals of binary nitrides was attempted by adding Na and NaN_3. In this technique, Na was removed from the product material using liquid ammonia in the same way as for the ternary nitrides. After removal of Na, very small transparent pieces like glass were found by observation with the naked eye. When the operation was performed to remove Na with liquid ammonia, the edge of the Nb tube was cut, and the part containing the product material was put into a glass container. In rare cases, the Nb tube collided with the glass container during stirring and the broken pieces sometimes contaminated the material. Just to make sure, the condition of the material was observed with a stereoscopic microscope from outside the glass container and hexangular-plate-shaped single crystals were found. Then, the container was put into a glove box under an Ar-gas atmosphere in the same way as when handling a nitride that is unstable in air. After being placed on an X-ray sample holder, the sample was covered by a Mylar film for preventing oxidation during measurement, and the X-ray diffraction pattern was measured. (It was found later that since GaN is stable in air, the Mylar film is not necessary.) As a result of analyzing the pattern, the product material was found to be GaN [6,7].

13.2 Growth Conditions and Mechanism of the Na Flux Method

13.2.1 Growth Conditions of GaN Crystal by the Na Flux Method

First, the growth conditions of GaN crystals by the Na flux method will be reported [6]. The starting materials used are Ga (99.9999% purity) and NaN_3 (99.9% purity). Thermal decomposition of NaN_3 at 300 °C provides highly purified N_2 and Na: $2NaN_3 \rightarrow 2Na + 3N_2$. NaN_3 (0.117 g (1.8 mmol) or 0.234 g (3.6 mmol)) and Ga from 0.035 to 1.116 g (0.5–16.0 mmol) is weighed under N_2 atmosphere and sealed in a stainless steel tube (SUS 316, 7.5 mm inner diameter, 9.5 mm outer diameter, and 100 mm inside length). The starting material is heated to 600–800 °C for 24–96 h. The results of XRD on the products obtained by heating at 600–800 °C for 24 h are shown in Figure 13.1 against the $r\text{Na} = \text{Na}/(\text{Ga} + \text{Na})$ molar ratio of the starting mixtures. The maximum N_2 pressure calculated from the amount of NaN_3 is given in Figure 13.1. The actual N_2 pressure was probably lower due to the formation of GaN. The broken lines at $r\text{Na} = 0.25$ in the figure indicate a Ga:N = 1:1 M ratio. Intermetallic compounds of Ga_4Na and/or $Ga_{13}Na_7$ and Ga

are contained in the samples prepared at the conditions marked with solid circles and shaded circles. The Ga was probably formed from the decomposition of these intermetallic compounds during handling in air. No Na-Ga-N ternary nitrides were found. In both cases of $NaN_3 = 3.6$ and 1.8 mmol, GaN was produced at the high *r*Na molar ratios.

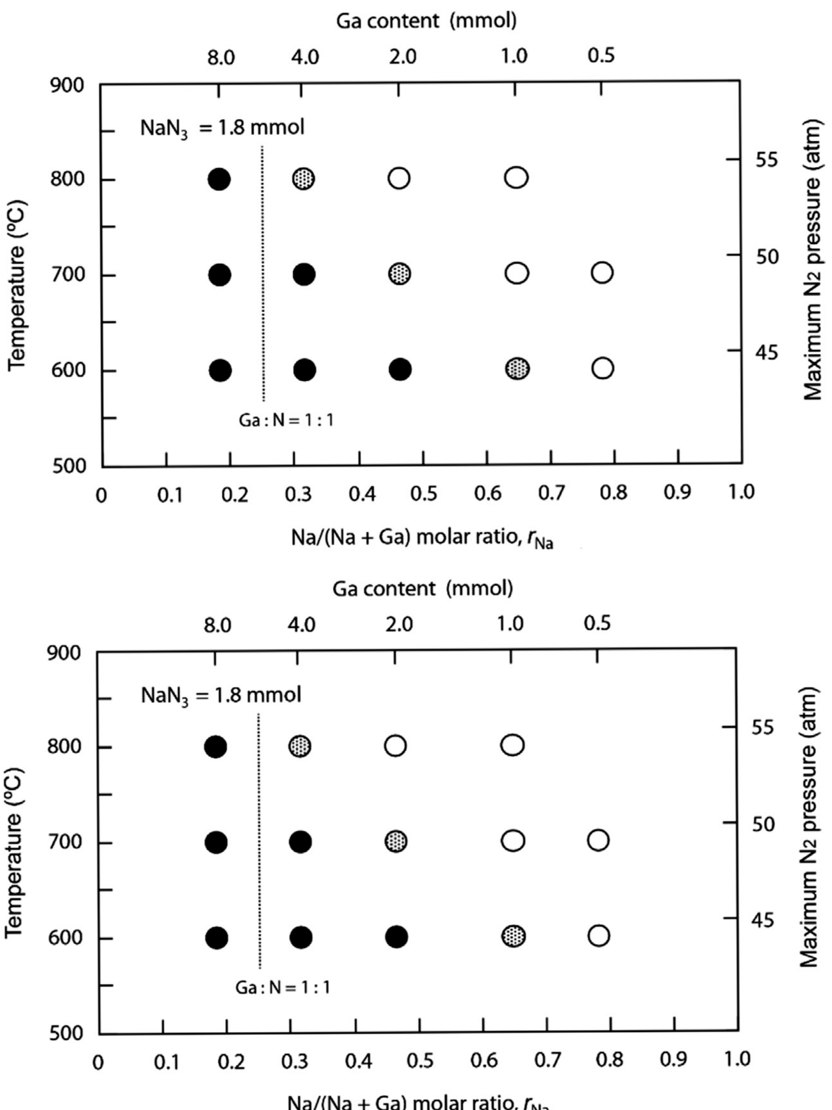

FIGURE 13.1 Experimental conditions and products obtained by heating for 24 h and by washing Na with alcohol: (solid circle) Na-Ga compounds, (shaded circle) Ga-Na compounds, and GaN, (open circle) GaN. N_2 pressures calculated from the NaN_3 contents are maximum limits, and actual pressures in the stainless steel tube reactor should be lower than those because of the formation of GaN. SC indicates that the sample contains GaN single crystals with a size over 0.1 mm.

The region in which GaN was formed spreads toward smaller *r*Na with increasing temperature. The yields of the GaN decreased with increasing *r*Na and were from 10 to 60 mol % against the initial Ga at $NaN_3 = 3.6$ mmol and 0.1–10% at $NaN_3 = 1.8$ mmol. From these results follows that the Na flux method has a high potential to be a practical method for growing GaN crystals.

13.2.2 The Effects of Na in the Ga-Na Solution

The principle of generation of supersaturation with the Na flux method is basically the same as that in the high pressure solution growth (HPSG) method. While in the HPSG method ultra-high pressure nitrogen gas is dissolved in a Ga melt, in the Na flux method, nitrogen gas is dissolved in a Ga-Na binary melt to grow a GaN single crystal. Although these methods are analogous, the temperature and pressure required for crystal growth are quite different. The growth conditions generally adopted in the Na flux method are approximately 800 °C and about 30 atm.

It has been known that the solubility of nitrogen in a Na melt is as small as approximately 7×10^{-9} at. % at 600 °C under 1 atm as shown in Table 13.1, which is smaller than the solubility of nitrogen in a Ga melt. However, as a result of actual measurement of the solubility of nitrogen in a Ga-Na binary melt, significant increase in nitrogen solubility was confirmed. That is, although the Na melt in itself does not have the ability to dissolve the nitrogen, forming the Ga-Na binary melt promotes the nitrogen dissolution, resulting in the changes shown by arrows in Figure 13.2, followed by GaN

Table 13.1 Solubility of Nitrogen to Na Single Melt

Temperature (°C)	Solubility (at.%)
450	1.552×10^{-9}
500	2.751×10^{-9}
550	4.549×10^{-9}
600	7.102×10^{-9}

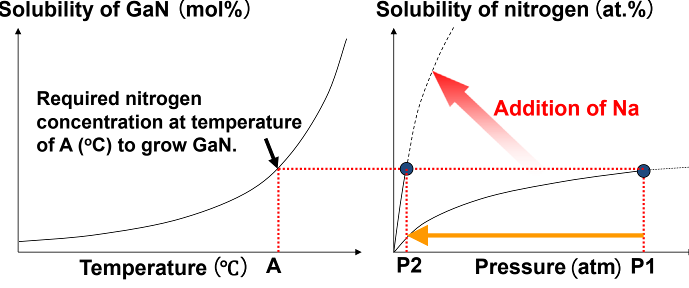

FIGURE 13.2 Changes in pressure of nitrogen required for growth of GaN crystal when assuming that solubility of nitrogen increases by adding Na to Ga.

single crystals that can easily grow. The graph on the left in Figure 13.2 shows solubility of GaN into a Ga melt. The graph on the right in Figure 13.2 shows the relation between the pressure of nitrogen and the solubility of nitrogen at temperature A. When the solubility of nitrogen in the right figure exceeds the solubility of GaN in the left figure as pressure increases, GaN can grow. It is assumed that by adding Na to a Ga melt, the solubility of nitrogen changes as per the dotted line in Figure 13.2 ([8]). If the solubility of solid GaN does not change by addition of Na to the Ga melt, the pressure required for the concentration of nitrogen in the liquid to reach the solubility of GaN at temperature A significantly reduces from P1 to P2.

A next issue is why nitrogen becomes easily dissolved by adding Na, which is less able to dissolve nitrogen than Ga. The solubility of nitrogen into a Fe melt is shown in Figure 13.3 as a similar example. Figure 13.3 shows the relation between the added elements to iron and change in the solubility of nitrogen. It is found that the solubility of nitrogen significantly depends on the added elements. While carbon greatly decreases solubility of nitrogen, adding a small amount of vanadium drastically increases solubility of nitrogen. These kinds of phenomena are not rare, and considering the dissolution process of gas into solution is important to understand them.

The nitrogen concentration in a liquid should be treated based on the data of equilibrium value when we discuss the mechanism of nitrogen dissolution in the Na flux method. However, to claim equilibrium of a liquid is practically impossible, even when the concentration of nitrogen in the liquid is quite low after a certain time period, because the real dissolution rate is determined by the kinetics of dissolution processes. The processes involved in dissolution of gas until reaching equilibrium are shown as follows (the numbers correspond to those of Figure 13.4).

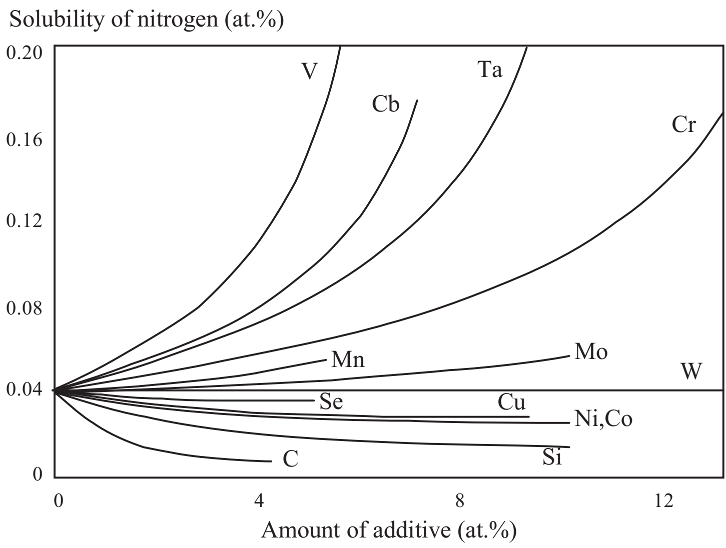

FIGURE 13.3 Changes in solubility of nitrogen when each element is added to iron melt.

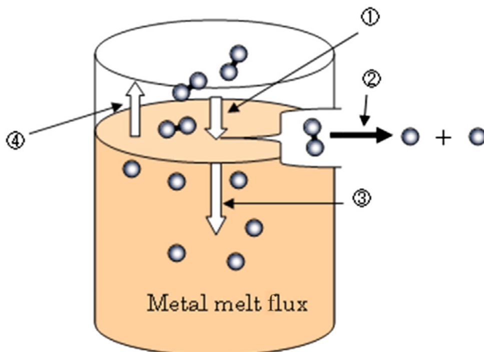

FIGURE 13.4 Factors that determine equilibrium concentration of nitrogen in alloy liquid.

① Process of N_2 gas diffusion to gas–liquid interface
② Process of dissociation from N_2 to 2N
③ Process of dissolved nitrogen transport from gas–liquid interface into the liquid
④ Process of nitrogen desorption from liquid to atmospheric environment

Increasing pressure of a gas accelerates the process of ①, resulting in the increase in the nitrogen concentration at the gas–liquid interface. The next process is dissociation of N_2 to 2N (②), and in the case that the liquid is the metal-melt to which nitrogen dissolves, this process plays an important role at decision of the nitrogen dissolution rate because molecules of a gaseous species commonly dissolve after dissociation in a metal-melt. When this process is slow, the gas dissolves only slightly. If the process ③ (diffusion of nitrogen in liquid) progresses slowly, the dissociation of nitrogen molecules occurs with sluggish pace regardless of how large the ability of nitrogen dissociation because the nitrogen concentration at gas–liquid interface quickly reaches saturation. The case where the process ② is slower than process ③ is called "surface reaction control." On the other hand, when the rate of process ③ (gaseous species dissolved at the gas–liquid interface is transported into a liquid) is slower than process ②, the case is called "volume diffusion control." Although, process ② and ③ affect the nitrogen concentration and the period for reaching the equilibrium concentration, the value of equilibrium concentration also strongly depends on the rate of process ④. Even in the case where both the process of ② and ③ sluggishly progress, if the rate of process ④ is also slow, equilibrium concentration in the liquid becomes high at some point in time. In this case, since all processes progress slowly, the concentration in the liquid is low after a certain time period, which often misleads us to conclude that the gas is hardly dissolved. However, it should be noted that it is not the equilibrium value.

The discussion mentioned above is applicable to the Na flux method without any change, and has the key to clarify the strangeness that the addition of Na to Ga-melt causes incredible increase in nitrogen solubility. When some additive changes the equilibrium concentration of nitrogen, a certain part of these processes (①, ②, ③, and ④) should be affected by additive. Needless to say, the process in which molecules of a gas

are transported to the surface of the liquid (process ①) is not affected by addition of additive to the melt. Since the viscosity of a liquid usually rarely changes greatly by adding a small amount of additive, the process ③ is assumed not to be changed. Then, remaining possibilities are twofold: the process ② in which molecules of a gas are dissociated at gas–liquid interface or a process ④ in which the gas dissolved in a liquid is escaped from the liquid is affected by additive.

It is known that nitrogen is dissolved in the form of a N^{3-} ion in almost all metal-melt systems [8]. Nitrogen undergoes the process of disassociation and reduction until coming into stable state in the liquid. It had been reported that high temperature Na has a function to dissociate and reduce the valence of nitrogen [9]. Thus, the Na added in the Ga-melt greatly affects the process ②. The disassociation of gaseous molecules at gas–liquid interface is activated, then the equilibrium concentration increases. This is a main mechanism how Na increases the solubility of nitrogen in solution (Ga-Na binary melt) in the case of the Na flux method.

The right figure in Figure 13.5 shows the relation between pressure versus solubility of nitrogen at each temperature. "Growth region" represents the region in which GaN can grow at each temperature. Solubility of nitrogen to the Ga-Na melt at the temperature above 600 °C is shown. At the temperature less than 600 °C, solubility of nitrogen is too small to be expressed on this graph. In general, such a rise in the solubility of nitrogen will not occur only by increasing temperature. Therefore, it is considered to represent that chemical reaction such as disassociation and reduction by Na is activated at the temperature above 600 °C [10].

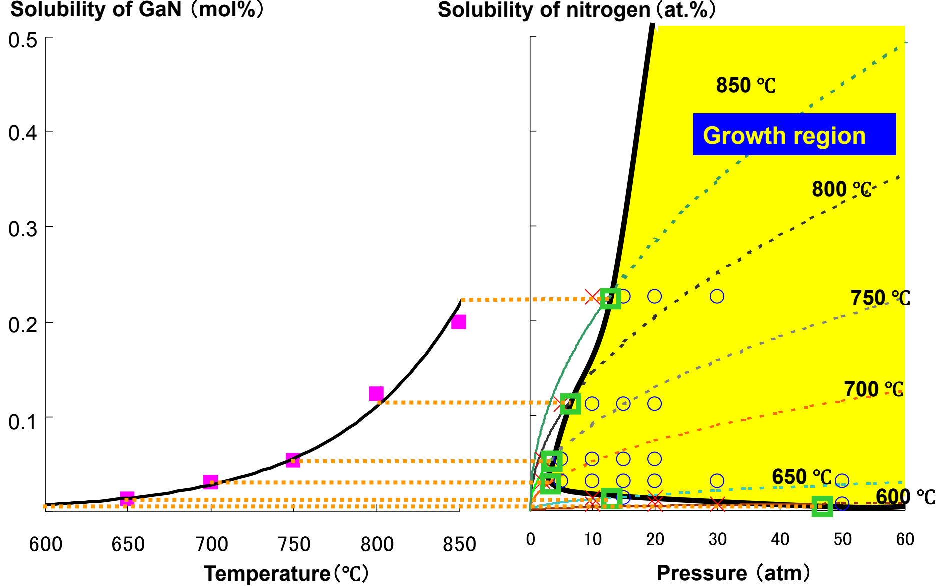

FIGURE 13.5 Summary of solubility of nitrogen in Ga-Na melt (27:73 mol) and the region where GaN crystal can be grown.

The "growth region" of GaN can be drawn by connecting the points where the equilibrium value of the solubility of nitrogen exceeds the solubility of a solid GaN at each temperature. When temperature rises and reaches approximately 700 °C, the pressure at which GaN can be produced decreases down to about 5 atm at the minimum. It is found that when the temperature is increased more than 700 °C, the pressure required for producing the GaN crystal increases again. This is because in the high temperature region, increase in the solubility of a gas with increase in temperature becomes slower compared with increase in solubility of solid GaN [10].

13.2.3 An Investigation on the Mechanism of Nitrogen Dissolution in the Na Flux Method

As mentioned above, the role of Na in the Na flux method was experimentally revealed. In this session, theoretical investigation on the role of Na is introduced. The N solubility in $Ga_{0.27}Na_{0.73}$ alloy is order of 10^{-2} at. % at 1073 K [11], while the one in Ga metal is almost zero below 1273 K [4] and N_2 is known to be insoluble in pure Na metal [12]. Moreover, the N solubility depends strongly on the Ga_xNa_{1-x} composition [13]. From the GaN yield, it is concluded that the N solubility is very low for Ga_xNa_{1-x} liquid alloys over $x = 0.5$, while it is drastically enhanced as x decreases to 0.1. The mechanism that explains those experimental facts is desired to be clarified. First-principles theoretical calculations have been employed to clarify the roles of Ga and Na and the origin for the strong dependence of the GaN yield on the flux composition.

The calculations can be carried out using a density functional theory program package "simulation tool for atom technology" (STATE). A generalized gradient approximation for the exchange-correlation functional is employed. Ultrasoft pseudopotentials can be employed for the N 2p state, while norm-conserving pseudopotentials can be used for other states. These techniques are described in detail elsewhere [14,15].

First, the calculation results of Ga_xNa_{1-x} liquid structures with and without one N atom are shown. The total number of atoms in the supercell is 100, and the cell parameters are determined from the experimental densities [16]. Each liquid structure is obtained by cooling slowly from 4000 to 1073 K and equilibrated at 1073 K for 1.5 ps. The extra 1 ps is used for the sampling of the atomic trajectory. A notable difference is found in terms of aggregation of Ga atoms. In $Ga_{0.8}Na_{0.2}$ alloy, Ga and Na atoms tend to segregate, and N is located at the interface of Ga- and Na-rich domains. Ga coordination number around N is 4, and N–Ga bond length is about 0.2 nm. On the other hand, isolated Ga atoms and small clusters consisting of a few Ga atoms are seen in $Ga_{0.2}Na_{0.8}$ alloy. N is coordinated by one Ga atom, and the N–Ga bond length is about 0.18 nm, which is shorter than the one in $Ga_{0.8}Na_{0.2}$ alloy. The segregation of Ga and Na can be explained by the concept of Zintl phase [17,18], where p-block elements form polyhedral clusters or network in alkali metals.

Next, a calculation of the N solubility in Ga_xNa_{1-x} alloy crystals is shown. Ga_xNa_{1-x} crystals are employed, whose structures have characteristic features seen in liquid

simulations, because it is hard to use a realistic liquid model. To estimate the solubility, the excess grand potential of both cases, $\Delta\Omega_{diss}^{ex}$, are defined as follows [19]:

$$\Delta\Omega_{diss}^{ex} \equiv E^{tot}(N + alloy) - E^{tot}(alloy) - (1/2)\mu_{N_2(g)} + n^{rep}\mu_{metal(s)} - T\Delta S^{ex}, \quad (13.1)$$

where E^{tot} is the total energy of the supercell, n^{rep} is the number of metal atoms replaced with N, μ_{N_2} and $\mu_{metal(s)}$ are the chemical potentials of gas phase N_2 and metal atoms, respectively, and ΔS^{ex} is the excess entropy in which only N vibration is taken into account. $\Delta\Omega_{diss}^{ex}$ for Ga, Ga_4Na, and Na with some atoms replaced with Ga and Na crystals are calculated. As a Ga-rich host, Ga_4Na is chosen because it has an ordered phase with sandwich structure of Ga and thin Na layers, as seen in the liquid $Ga_{0.8}Na_{0.2}$. As a Na-rich host, diluted limit of Ga_xNa_{1-x} alloy is calculated: Na crystal with some Na atoms replaced by Ga. Assuming that N always makes bonds with Ga atoms in liquid Na-rich alloys, the substitutional sites for metal atoms were restricted only to the first neighboring sites of N atom. The chemical potential of Ga and Na metals is approximated by their respective elemental bulk energies. For N_2, the total energy of a single molecule is calculated using a cubic supercell with a side of 30 bohr, and the entropy is estimated from the gas phase N_2 at 3.0 MPa and 1073 K, a typical condition for the Na flux method. The solubility of N, x_N, can be obtained purely from the results of first-principles calculations by

$$x_N = N_{site} \exp\left(-\Delta\Omega_{diss}^{ex}/k_B T\right), \quad (13.2)$$

where N_{site} is the number of sites where N is incorporated in the lattice, k_B is Boltzmann constant, and T is temperature.

The N solubility calculated from $\Delta\Omega_{diss}^{ex}$ at $T = 1073$ K is shown in Figure 13.6 as a function of the Ga fraction along with the experimental values. The calculated N

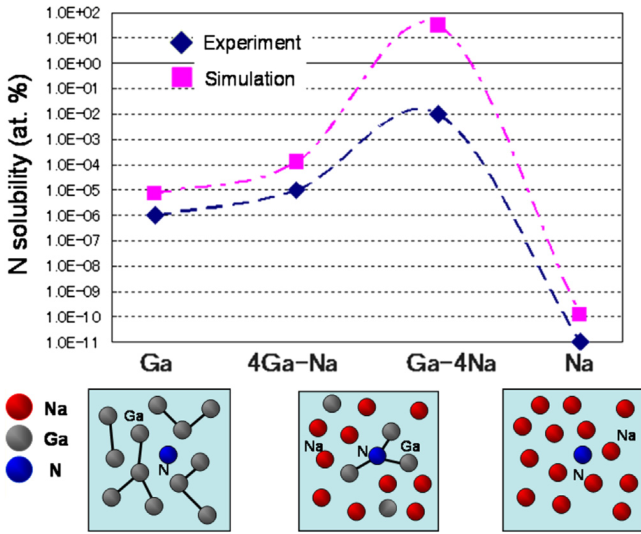

FIGURE 13.6 Dependences of solubility of nitrogen on ratio of Ga to Na obtained by first-principles calculation and experimentally, and schematics of bonding states of elements.

solubility agrees semiquantitatively well with the experimental results. The N solubility starts to decrease, and its proportionality with Ga fraction is broken somewhere below the Ga fraction of 0.27. This is probably related with Ga aggregation behavior appearing with increase in the Ga fraction. The calculated N solubility agrees quantitatively well with the experiments. It turned out that when the Ga concentration in Ga_xNa_{1-x} alloy is low, isolated Ga atoms or small clusters in Na interact weakly with Na, and therefore, they are rather active and can make strong bonds with dissolved N, enhancing the N solubility in Na-rich alloys.

13.3 Nucleation Control

13.3.1 Discovery of Carbon Doping for Nucleation Control

Although the Na flux method has a big advantage of synthesizing GaN crystal, it had been difficult to grow large size crystal by the spontaneous nucleation. In order to make a large diameter GaN crystal, the seed substrate fabricated by the metal organic chemical vapor deposition (MOCVD) method has been utilized. In the Na flux method, the spontaneous nucleation tends to occur near gas–liquid interface because the concentration of the nitrogen in this region is higher compared to that at the bottom of the solution (Figure 13.7). It was the problem that the polycrystalline GaN crystal nucleated spontaneously would grow rapidly compared with the GaN crystal grown on seed substrate located on the bottom of solution.

Preventing unfavorable nucleation is common issue in the solution growth, because crystal quality and growth rate are limited by spontaneous nucleation at undesired sites. The doping of carbon into solution can greatly suppress spontaneous nucleation on any area other than the substrate [20].

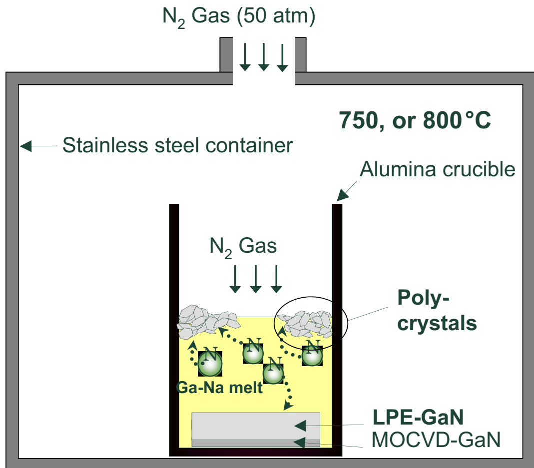

FIGURE 13.7 Schematic illustration of the growth of LPE and polycrystals in a stainless steel tube.

Figure 13.8 shows the dependence of the yields of polycrystals and the growth increment of LPE on the amount of carbon at 750 and 800 °C. The yields are calculated as the amounts of metal-Ga consumed in the growth of GaN. The total yield was almost 100% in all attempts. It is noteworthy that almost all Ga is consumed for the growth of polycrystals in the case of a nonadditive system at both temperatures. At 800 °C, when the amount of carbon exceeded 1 at%, the generation of polycrystals is completely eliminated. In the case of growth at 750 °C, 3 at% is needed to completely eliminate polycrystals, even though the addition of carbon consistently reduces the generation of polycrystals.

The supersaturation occurring at 750 °C can be estimated to be higher than that at 800 °C if the applied pressure is the same at 50 atm. This seems to be the reason why more carbon was necessary to completely eliminate the polycrystals at 750 °C. Thereafter, the carbon content incorporated in LPE crystals grown with and without carbon were measured (Figure 13.9). The carbon content is almost the same in both samples, regardless of carbon concentrations in the solution, and the concentrations are fairly low ($<10^{17}cm^{-3}$). This result indicates that a certain amount of carbon existed in the solution as contamination, even in the nonadditive system. The distribution coefficient of carbon against GaN crystal is probably quite low in a Ga-Na melt system, which may be the reason why the amount of carbon taken into the crystal is the same in both cases because the carbon concentrations reaches saturation in the crystals even in the nonadditive system.

It was also found that increasing the carbon amount in the growth solution caused the change of the morphology of the grown GaN crystal from platelet shape to prismatic shape [21,22]. Although the reason of this phenomenon is not well understood, carbon in

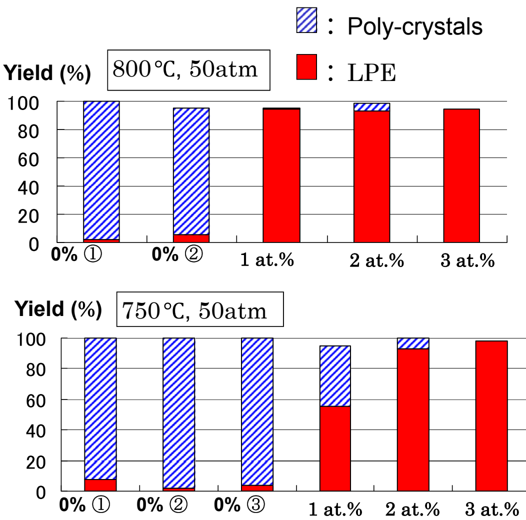

FIGURE 13.8 Yield of LPE–GaN and polycrystals in the growth with and without a carbon additive at 750 and 800 °C.

the solution seems to affect the solubility of GaN. The dependence of the growth rate on Ga/Na ratio and the concentration of carbon in the solution are shown in Figure 13.10. The growth rate becomes faster for lower Ga ratio to Na, except 27% Ga with 0% carbon case. This tendency may be explained roughly by the result of the first-principles calculations of liquid structures of GaNa alloys as shown in Section 13.2.3. It is interesting that increase of carbon in the solution enhances the growth of GaN at lower concentrations and tends to suppress the GaN growth at higher concentrations. At lower Ga ratio to Na, growth mode of GaN crystal tends to be two dimensional, resulting in a flat

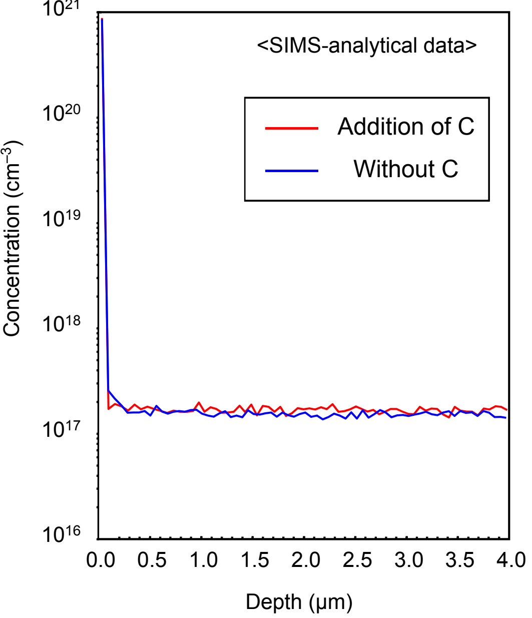

FIGURE 13.9 Carbon concentrations incorporated into the LPE crystals grown in a pure system and a carbon-added system measured by SIMS.

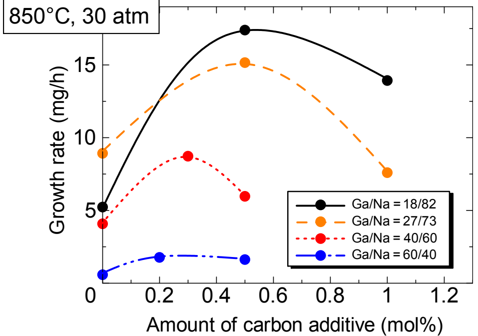

FIGURE 13.10 Growth rate of GaN crystal as a function of carbon amount at various Ga/Na ratios.

surface. On the other hand, growth mode becomes three dimensional for higher Ga ratio to Na resulting in formation of $\{10\bar{1}1\}$ facets. The formation of $\{10\bar{1}1\}$ facets is important for reduction of dislocation density at the initial stage, the solution with higher Ga ratio is useful to grow high quality GaN crystal on low-quality seed substrate (the details are shown in Section 13.4.1). On the other hand, the growth condition with the lower Ga ratio would become important for the growth of GaN crystal with higher growth rate. The control of Ga/Na ratio during the growth would be an important technique for growth of boule-sized bulk GaN crystals through long-term growth.

13.3.2 Mechanism of Carbon Doping

The mechanism of suppressing the spontaneous nucleation by the carbon doping mentioned above was studied by using first-principles molecular dynamics simulation [23]. For the simulation, "Simulation Tool for Atom TEchnology (STATE)-Senri [24]" is used, which is a first-principles molecular dynamics program developed at Osaka University and the National Institute of Advanced Industrial Science and Technology (the same program of Section 13.2.3). This program was also used for analyzing the process of epitaxial growth of GaN [25] and the solubility of nitrogen into a Ga-Na melt [26,27].

In Na flux GaN growth, since solution of nitrogen into Ga-Na melts significantly affects growth amount and growth rate, spontaneous nucleation has to be studied focusing on a phenomenon associated with nitrogen atoms. In addition, since the presence of CN^- ions is detected in Na after crystal growth, it is considered that the presence of CN^- ions affects the suppression of the spontaneous nucleation. Using a first-principles molecular dynamics simulation, the melt structure around a nitrogen atom was investigated for the two cases of Ga-Na melts with and without carbon doping.

Figure 13.11(a) and (b) show results of the melt simulations at 1073 K using a calculation model without carbon (number of atoms: Ga 27, Na 100, N 1) and with

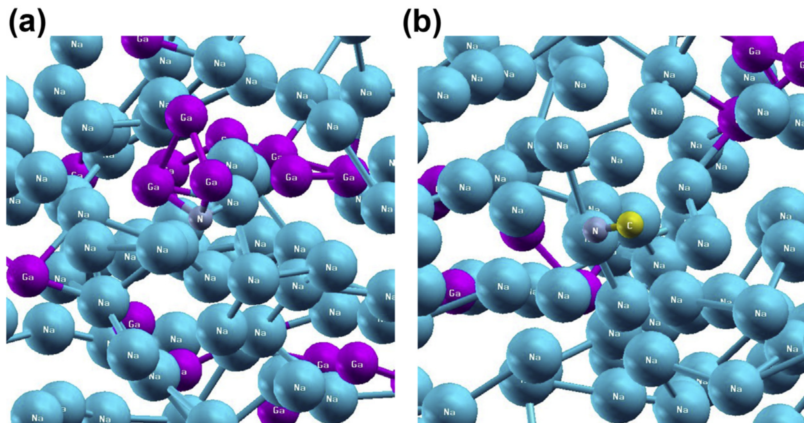

FIGURE 13.11 Snapshots of atomic coordinates in the Na-Ga melts: (a) without C addition and (b) with C addition models.

carbon (number of atoms: Ga 26, Na 100, N 1, C 1), respectively. It is found in Figure 13.11(a) that a nitrogen atom bonded to two gallium atoms. On the other hand, in Figure 13.11(b), a nitrogen atom bonded to a carbon atom and Ga-N bonding was not observed. In order to investigate bonding state of each atom in detail, two-body correlation functions were obtained from time-series data of atomic coordinate. Figure 13.12(a) and (b) show the two-body correlation functions corresponding to calculation models without carbon and with carbon, respectively. In Figure 13.12(a), the peak of Ga-N bonding appears at approximately 1.9 Å, which is almost equal to 1.94 Å that is a Ga-N bond distance calculated from the lattice constant of the Ga-N crystal. In Figure 13.12(b), although the peak of C-N bonding appears at approximately 1.2 Å, no peak of Ga-N bonding is observed. From these results, it is found that when there are carbon atoms in Ga-Na melts, the C-N bond is more stable than the Ga-N bond. In order to investigate the C-N bonding state from the viewpoint of bond energy, C-N bond energy was calculated under various conditions using the Blue Moon method [28]. As a result, it is found that the presence of gallium atoms affects the C-N bond energy. The C-N bond energy was estimated to be approximately 3.0 eV in the case of using a calculation model containing gallium atoms (number of atoms: Ga 10, Na 42, N 1, C 1), and approximately 6.3 eV in the case of using a calculation model containing no gallium atom (number of atoms: Na 52, N 1, C 1) (refer to Figure 13.13). Since both values are larger than Ga-N bond energy (2.26 eV [29]), it was confirmed that C-N bond is more stable than Ga-N bond in Ga-Na melts from the viewpoint of bond energy. As a result of the simulations, it was verified that when carbon is added in the Ga-Na melt, a carbon atom bonds to a nitrogen atom to form a CN^- ion. Accordingly, it is suggested that the generation of the spontaneous nucleation is suppressed not by the effect of a single carbon atom but by the effect of the CN^- ion by the first-principles molecular dynamics simulation.

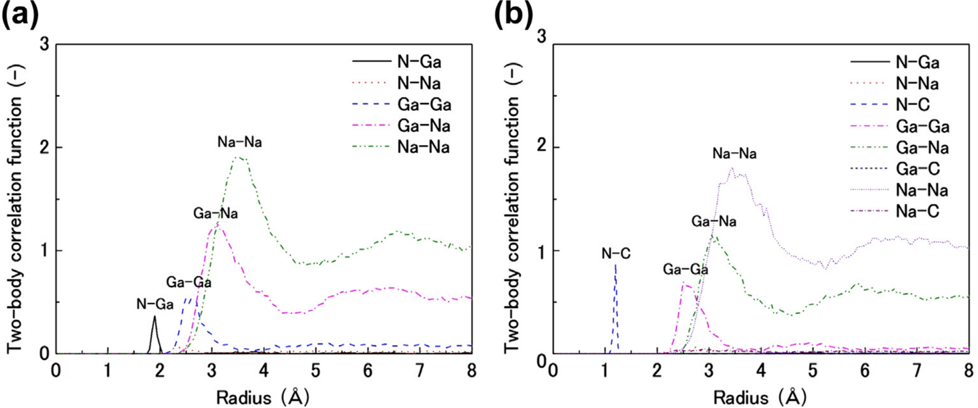

FIGURE 13.12 Two-body correlation functions of the Na-Ga metals: (a) without C addition and (b) with C addition models.

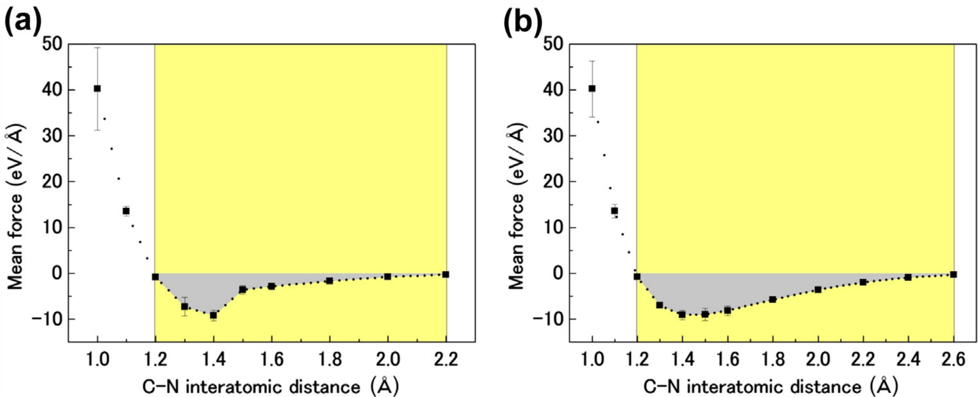

FIGURE 13.13 Mean forces of C–N bond: (a) with Ga model and (b) without Ga model. Mean force indicates the atomic forces needed to maintain the interatomic distance. The C–N interatomic distance at which the value of mean force is zero equals to a stable bond length. The gray area in the figures corresponds to the C–N bond energy.

13.4 LPE Growth of GaN by the Na Flux Method

13.4.1 Dislocation Behavior during LPE Growth of GaN by the Na Flux Method

The suppression of spontaneous nucleation of GaN by carbon doping makes it possible to grow GaN crystal only on a seed crystal. The MOCVD method and HVPE method can prepare larger diameter seed crystals. Although various techniques for dislocation reduction in a GaN crystal have already been reported for MOCVD and HVPE methods, such as the epitaxial lateral over growth (ELO) method, the crystallinity is not yet enough at this moment ([30,31] and refer to Chapter 16).

On the other hand, the Na flux method can make it possible to grow a large GaN single crystal with a low dislocation density (on the order of 10^4 cm^{-2} on MOCVD-GaN thin film, which has a high dislocation density on the order of 10^7–10^8 cm^{-2} [32–34]). Transmission electron microscopy (TEM) observation around the interface between MOCVD-GaN and LPE-GaN revealed that the drastic decrease in the dislocation density occurs in the initial stage of LPE growth. TEM investigations of dislocations and scanning electron microscopy (SEM) observations have revealed the dislocation reduction mechanism during LPE growth. A GaN single-crystal sample for TEM observation was prepared by applying the LPE technique to the Na flux method [34]. LPE-GaN was grown on MOCVD-GaN thin film fabricated on a sapphire (0001) substrate. For TEM observations, a portion around the interface between LPE GaN and MOCVD-GaN was quarried out, and then the sample was thinned to 200 nm using a focused ion beam (FIB) to investigate dislocation behavior by TEM (Hitachi H-800, accelerated voltage: 200 kV) as shown in Figure 13.14. To observe all kinds of dislocations (Burgers vector b = <0001>, b = 1/3<11$\bar{2}$0>, and b = 1/3<11$\bar{2}$3>) in the crystal, a reflection vector of 11$\bar{2}$2 was adopted, and then TEM images were captured by bright-field imaging under the Bragg

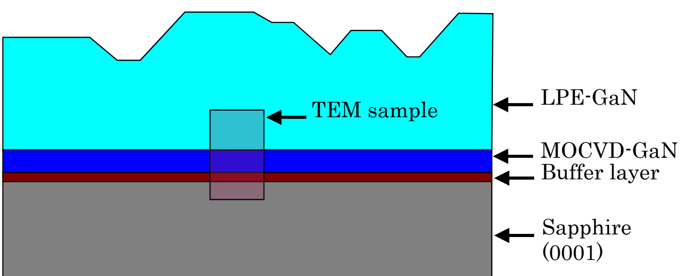

FIGURE 13.14 Schematic illustration of an LPE sample for TEM observation.

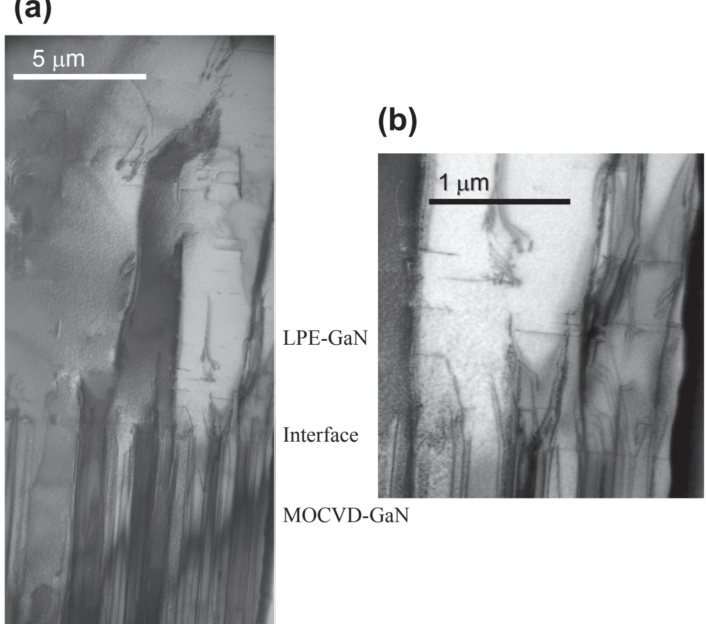

FIGURE 13.15 (a) TEM [$1\bar{1}00$] photograph taken around the interface between MOCVD-GaN and LPE-GaN. (b) Enlarged view of TEM [$1\bar{1}00$] photograph around the interface between MOCVD-GaN and LPE-GaN.

condition. The direction of incident electron beam was approximately [$1\bar{1}00$]. Figure 13.15(a) shows a TEM [$1\bar{1}00$] image near the interface between LPE-GaN and MOCVD-GaN. After LPE growth started, almost all dislocations taking over from the MOCVD-GaN disappeared within 2 μm. It was confirmed that almost all dislocations were bent at the initial LPE growth stage and were then concentrated as shown in Figure 13.15(b). Although some bent dislocations may move outside the sample, TEM observations suggest that a number of dislocations should be drastically reduced.

Figure 13.16 shows an SEM image taken at each stage of LPE growth. At the stage of a few mm thickness, many small facets bounded by {$10\bar{1}1$} formed across the whole surface of MOCVD-GaN (0001). Thereafter, the number of facets decreased as thickness increased and a (0001) face started to develop. Then, at the stable growth stage, GaN (0001) developed across the whole surface. In the Na flux method, a distinctive

phenomenon in which the GaN $\{10\bar{1}1\}$ face forms easily at low supersaturation and then at higher supersaturation, and GaN (0001) preferentially develops has already been reported [35]. This phenomenon corresponds to our LPE growth regarding the preferentially developed change in the face index.

Dislocation reduction process caused by the change in the face preferentially develops and coalescence of facets is summarized in Figure 13.17 [36]. Dislocations existing at positions A and C propagate along the c-axis, while those at the staircase structures (positions B) propagate along the development of the stair edge, resulting in oblique propagation from the c-axis. By following the bold line in the figure, the propagation of the dislocations is explained as follows. Type A dislocations are aggregated to Type B ones as the LPE growth progresses, followed by their aggregation to Type C, and eventually back to Type B. Although the transformation of the dislocations from Type B to Type C and subsequently back from Type C to Type B occurred naturally, transformations into Type A were not

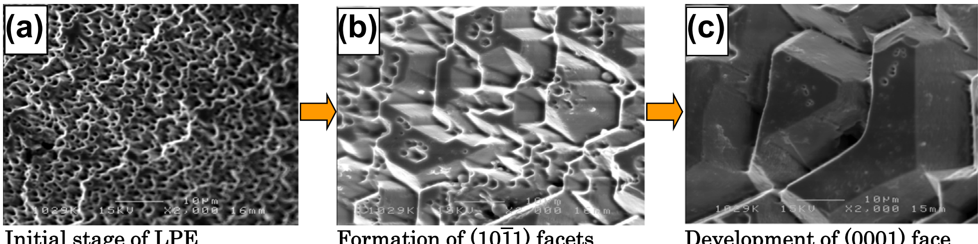

FIGURE 13.16 Changes in surface morphology of LPE-GaN grown using the Na flux method: (a) "Initial stage of LPE (thickness: approximately 1–2 mm)"; (b) "Formation of $(10\bar{1}1)$ facets (thickness: a few mm)"; (c) stable growth of large facets with coalescence (thickness: several tens of mm).

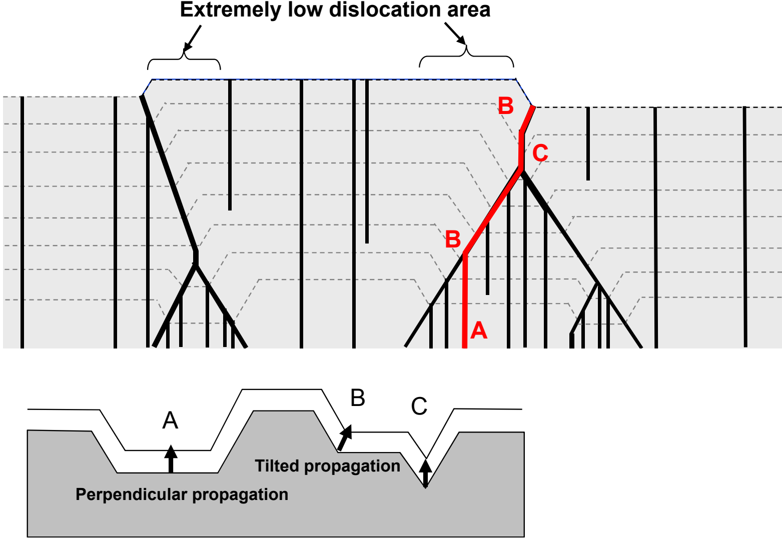

FIGURE 13.17 The dislocation reduction process after the middle stage of the LPE.

allowed after extinction of the concave portions. Therefore, the dislocation types transformed in the order of A, B, C, B, C, B…, reducing the number of dislocations. Ultimately, almost all dislocations were categorized as Type B.

In the Na flux method, stirring the solution during crystal growth is effective to improve crystal quality [37]. The morphology of GaN crystals got better, and the yields of GaN crystals were also increased by stirring techniques [38]. There are many methods for stirring solutions. For example, solution flow in a growth crucible placed in the chamber can be introduced by the seesaw motion of the chamber. The seesaw motion provides flow with well-defined pattern and can increase flow velocity up to 2 cm/s, a 30 times increase from that without motion. The flatness and uniformity of the grown GaN surface depends on the flow velocity and flow uniformity on the growing surface. Although the growth condition is not optimized yet, we could grow 2 ∼ 4-in-diameter GaN crystals on HVPE substrate with high uniformity without cracks as shown in Figure 13.18 [37]. Recently, 6-in-diameter GaN crystal could be grown as shown in Figure 13.19.

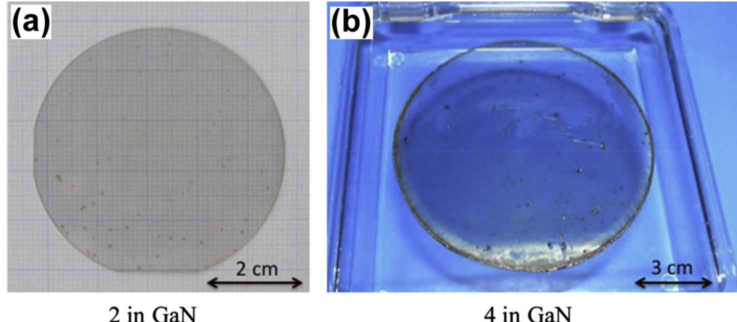

FIGURE 13.18 (a) 2-in and (b) 4-in GaN crystals grown on HVPE-GaN seed crystals.

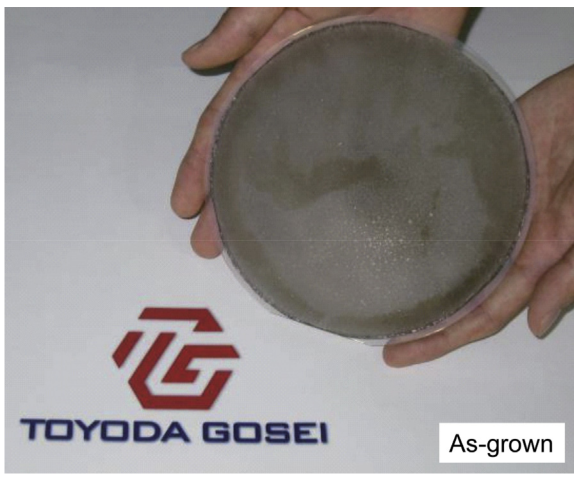

FIGURE 13.19 First 6-in GaN crystal grown by the Na flux method.

13.4.2 Characterization of GaN Crystal Grown by the Na Flux Method

In the Na flux method, because the dislocations can be automatically decreased during growth, high quality GaN crystals can be grown even on the large diameter and poor quality GaN thin film prepared by a vapor-phase growth method. Optical and electrical characteristics of GaN crystals grown by the method are introduced [22]. Figure 13.20 shows the photograph of a typical GaN crystal grown by the Na flux method on HVPE substrate. Both sides of the crystal were polished to the thickness of 750 μm to remove the HVPE substrate. The transmission spectrum of the GaN crystal is shown in Figure 13.21. The absorption edge of the GaN crystal at 372 nm and no absorption peak were observed in this range. In the case of a typical non-doped GaN crystal, average dislocation density of +c-face is $7.3 \times 10^5/cm^2$ and that of −c-face is $1.7 \times 10^6/cm^2$. Crystal quality of the non-doped GaN crystal was estimated by the full width at half maximum (FWHM) value of the (0002) face, and it is 47.6 arcsec.

Tables 13.2 and 13.3 summarize the electrical characteristics and the results of analyzing the impurities in GaN crystals grown by the Na flux method, respectively. GaN crystal grown by the Na flux method showed relatively low resistivity around sub Ω cm without any intentional doping. The mobility of the unintentionally doped sample was 930 cm^2/Vs. The residual carrier concentration of the GaN crystal was $\sim 4 \times 10^{16}/cm^3$ attributed to unintentionally doped oxygen ($\sim 3 \times 10^{16}/cm^3$) and/or nitrogen defect. Such unfavorable incorporation of oxygen into GaN crystal is much lower compared to a GaN crystal grown by ammonothermal method ($>10^{19}/cm^3$). The resistivity of GaN crystal could be reduced by Ge doping and the lower resistivity of 10^{-3} Ω cm was obtained at Ge concentration of $3 \times 10^{18}/cm^3$ with the mobility of 250 cm^2/Vs. It was found that Zn doping could increase resistivity of the GaN crystal and the higher resistivity of 10^8 Ω cm was obtained at Zn concentration of $\sim 10^{19}/cm^3$. The secondary ion mass

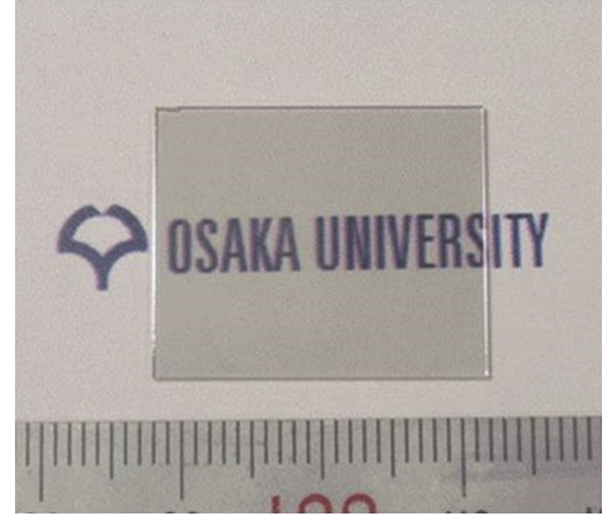

FIGURE 13.20 Photograph of the GaN crystal grown by the Na flux LPE method on HVPE-GaN seed crystals. Both sides of the crystal were polished to the thickness of 750 μm to remove the seed crystals.

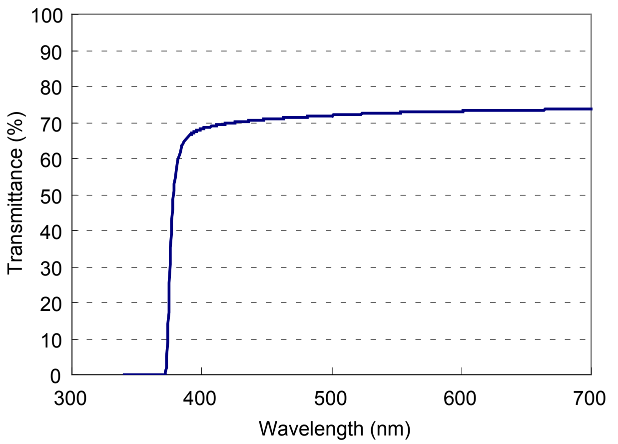

FIGURE 13.21 The typical transmission spectrum of the GaN crystal.

Table 13.2 Electrical Property of GaN Crystal Grown by the Na Flux Method

	Carrier Concentration	Resistivity (Ω cm)	Mobility (cm^2/Vs)
Non-doped GaN	$\sim 4 \times 10^{16}/cm^3$	~ 0.2	930
Ge doping	$\sim 6 \times 10^{17}/cm^3$	$\sim 10^{-2}$	430
	$\sim 3 \times 10^{18}/cm^3$	$\sim 10^{-3}$	250
Zn doping	(Zn concentration) $\sim 10^{19}/cm^3$	~ 108	–

Table 13.3 Impurities in the GaN Crystal Grown by the Na Flux Method

Element	Detection Limits (per cm^3)	Results (per cm^3)
Na	3E + 14	Below detection limit
C	2E + 16	<E + 17
Si	1E + 15	Below detection limit
O	3E + 16	3E + 16
Ca	2E + 14	1E + 16 (from Na)
Al	1E + 16	Below detection limit

spectroscopy measurement revealed that the Na and carbon additives are not incorporated in the grown crystal.

13.5 Point Seed and Coalescence Growth Technique

13.5.1 Na-flux Point Seed Technique

The LPE growth by the Na-flux method was found to be successful in reducing the dislocation density from $\sim 10^8\ cm^{-2}$ in a seed to $10^4 \sim 10^6$ in grown 2-in GaN crystals [21,39]. Unfortunately, however, despite the amount of effort that has been placed into

growing perfect GaN bulk crystals, these dislocation densities are still high. In 2012, Na-flux point seed technique (SPST) was developed to grow perfect GaN crystals [38,40,41]. Brief overviews of SPST and structural properties of typical GaN crystals grown by this technique are shown in the following.

As illustrated in Figure 13.22(a), the GaN point seed is produced by freely mounting a 430-μm-thick sapphire plate containing a small hole (0.5–1.5 mm in diameter) on a 10-μm-thick (001) GaN seed layer grown on a (001) sapphire substrate. GaN crystals can be grown on the GaN point seed through a hole in the Na flux as shown in Figure 13.22(b). This configuration suppresses dislocation propagation in the early growth stage. Details of the dislocation termination mechanism are given in Ref. [40].

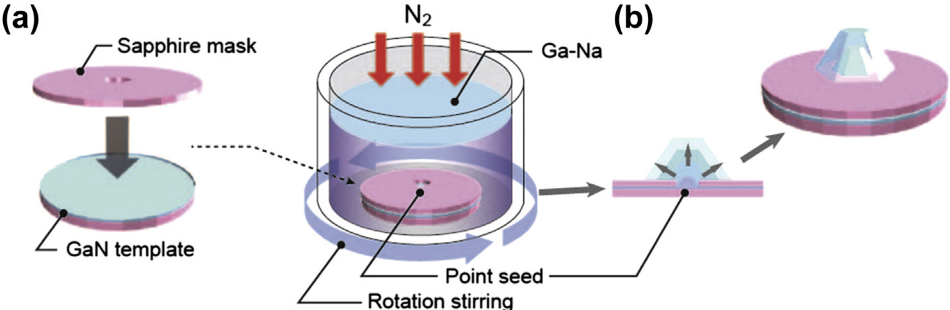

FIGURE 13.22 Schematic illustration of experimental setup. (a) Configuration of GaN point seed. The GaN point seed was produced by freely mounting a sapphire with a small hole on a GaN template and placing it in a crucible with a diameter of *f* 80 mm. The nitrogen source gas was pressurized during growth. The solution was stirred by intermittently rotating the crucible. (b) Illustration of crystal growing on the point seed. The crystal grows through the small hole in the sapphire wafer.

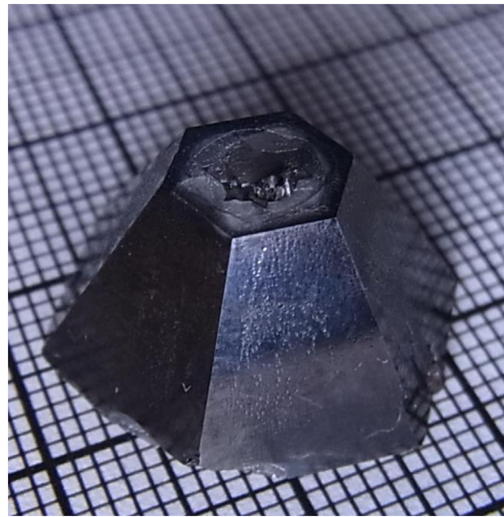

FIGURE 13.23 Optical photographs of bulk GaN crystal. Pyramid-shaped, well-facetted GaN single crystals could be grown on the point seed for growth period of 400 h.

Figure 13.23 is a photograph of a typical bulk GaN crystal grown by SPST (SPST-GaN). Up to now, well-facetted bulk GaN crystals have been obtained, with diameters of up to 2.1 cm and heights of up to 1.2 cm, corresponding to growth rates of 52 μm/h in both a-directions and 30 μm/h in the c-direction. A number of c- and m-face wafers could be sliced from SPST-GaN crystals, and these wafers are almost free from dislocations over the entire area from results of panchromatic cathodoluminescence mapping measurements as shown in Figure 13.24(a) and (b).

The synchrotron X-ray beam produced at the BL24XU beamline at the SPring-8 facility was used for evaluating the structural perfection of these wafers. Details concerning the optical system are given in Ref. [42]. The small angular divergence of 0.7 arcsec can be achieved by this system, and it enables detection of minute strains even in almost perfect crystals. The square symbols in Figure 13.25 represent the experimentally measured 006 GaN X-ray rocking curve for the c-face GaN wafer. The FWHM value was 2.1 arcsec, which is almost the same as that of the simulated curve (FWHM: 2.0 arcsec, red curve in Figure 13.25), indicating that the wafer has almost perfect structure.

13.5.2 Coalescence Growth Technique

In 2013, coalescence growth, which is a technique to effectively enlarge the diameter of GaN crystals by coalescing GaN crystals grown from many isolated point seeds, was developed [43–45]. Schematic illustration of the coalescence growth process is shown in Figure 13.26. A multipoint-seed-GaN substrate (MPS-GaN sub.) was produced by patterning a 10-μm-thick (0001) GaN layer that was grown on a (0001) sapphire substrate by MOVPE. Point seeds were arranged in a hexagonal pattern so that the coalescence direction corresponded to the a-direction of the GaN. The diameter of each point seed

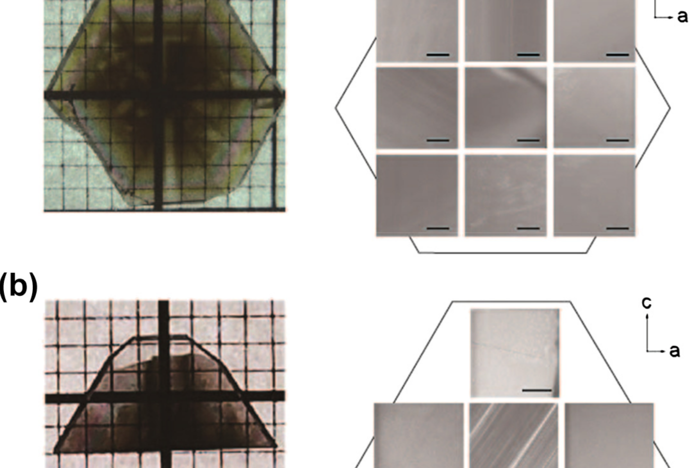

FIGURE 13.24 Photographs and panchromatic CL images of the (a) c-face and (b) m-face GaN wafers sliced from the bulk GaN single crystal. No dark spots associated with dislocations appear in any of the images.

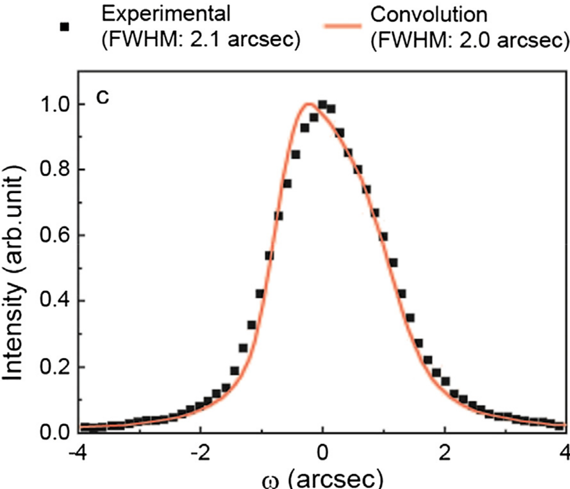

FIGURE 13.25 Experimental X-ray rocking curve (dotted) of the c-face wafer measured at Spring-8 facility. Red curve shows the calculated XRC obtained by convoluting X-ray beam and theoretical 006 GaN. The experimental XRC and its FWHM (2.1 arcsec) are in good agreement with the calculated XRC (2.0 arcsec), indicating that the crystal structure is almost perfect.

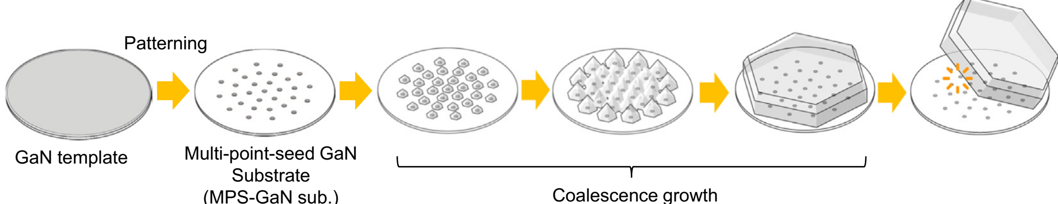

FIGURE 13.26 A multipoint-seed-GaN substrate (MPS-GaN sub.) was produced by patterning a 10-mm-thick (0001) GaN layer that was grown on a (0001) sapphire substrate by MOVPE. High quality GaN crystals grown on each point seed easily coalesce and unify in the Na flux. After the coalescence growth, coalesced GaN naturally separated from the sapphire substrate.

and the distance between the centers of the neighboring point seeds ranged from 0.25 to 1 mm and from 0.20 to 1 mm, respectively. High quality GaN crystals grown on each point seed easily coalesce and unify in the Na flux.

Figure 13.27 shows a photograph of a typical coalesced 2-in GaN crystal obtained by this technique. The sapphire substrate separated naturally from the MPS-GaN sub. The XRC profiles of 002 GaN and 102 GaN in Figure 13.28 showed that the FWHM values were 27.7–30.6 arcsec and 13.3–15.8 arcsec at 002 and 102 diffraction, respectively, indicating that crystallinity is satisfactory and homogeneous across the entire surface of the sample. The dislocation density was estimated by the etch-decoration technique. In general, etch pits resulting from etching in a NaOH-KOH solution are considered to come from dislocations [41–44,46,47]. Figure 13.29(a) is an illustration of coalescing crystals grown from each point seed. Figure 13.29(b) and (c) show SEM images after NaOH-KOH etching at

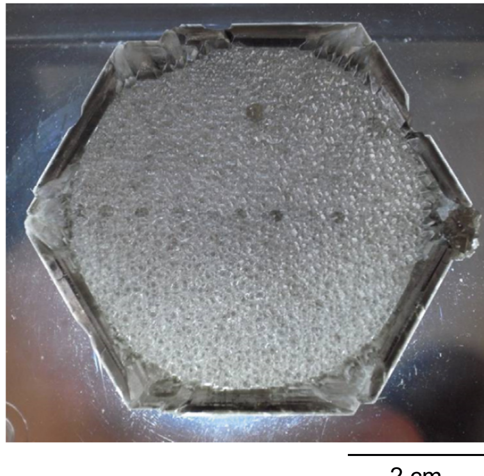

FIGURE 13.27 Photograph of the 2-in GaN crystal grown by the coalescence growth. GaN crystals grown from many point seeds coalesced and unified. The sapphire substrate separated naturally from the MPS-GaN sub.

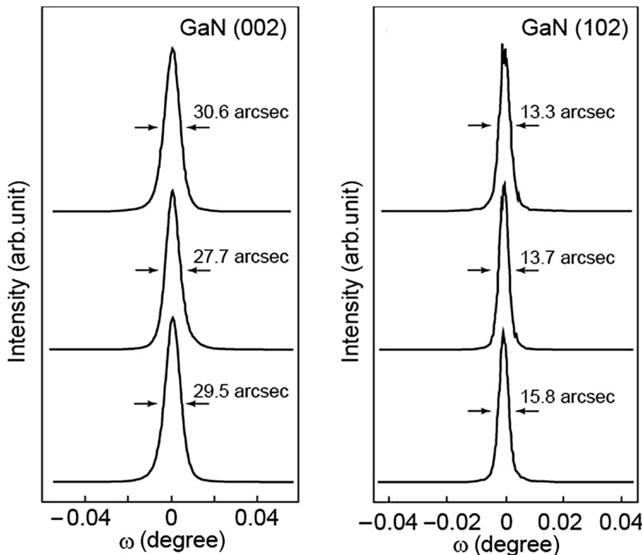

FIGURE 13.28 XRC measurement results of coalesced crystal. Mapping profiles of the 002 GaN XRC and 102 GaN XRC.

450 °C for 20 min, which were taken close to the coalescence boundary and away from the coalescence boundary, respectively. Note that Figure 13.29(b) and (c) are focused on the regions that etch pits (white arrows in Figure 13.29(b) and (c)) exist, and no other etch pits existed in the area of 500 × 500 μm, indicating that dislocation density is on the order of 10^2 cm^{-2} both at and away from the coalescence boundary. The mechanism is still unclear and research for clarifying it is in progress.

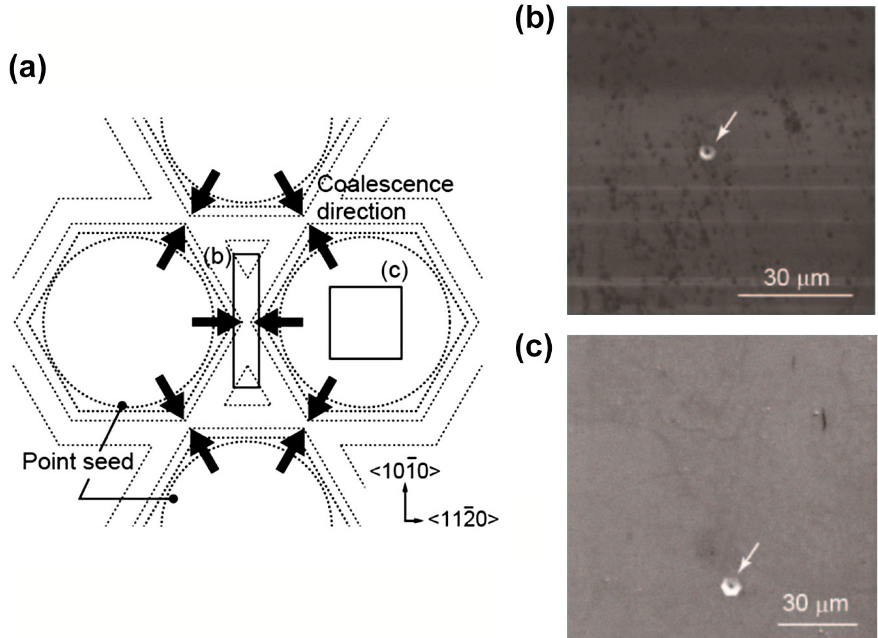

FIGURE 13.29 (a) Illustration of coalescing crystals grown from each point seed and surface SEM image of the coalesced GaN after CMP and NaOH-KOH etching at 450 °C for 20 min (a) at the coalescence region and (b) away from the coalescence region. Dislocation density is on the order of 10^2 cm^{-2} both at the coalescence boundary and away from the coalescence boundary.

The radius of lattice curvature can be calculated from the shift of peak top angle of 002 GaN XRCs. Figure 13.30 illustrates the results of mapping the XRC peak top angles of the GaN template (solid circles), MPS-GaN sub. (open circles), and coalesced GaN crystal after separation from the sapphire (solid square). The radius of curvature corresponds to the inverse of the slope of the line in Figure 13.30. The results showed that the GaN template had large curvature with a radius of lattice curvature of 4.4 m, but the MPS-GaN sub. and the coalesced GaN crystal both had very little curvature, with radii of lattice curvature above 100 m (measuring limit of X-ray diffractometer). From this transition in radius of lattice curvature, the coalescence growth is predicted to proceed according to the following process. First, the GaN template bends greatly due to the difference between the thermal expansion coefficients of the GaN layer and the sapphire substrate. However, the strain caused by the difference in thermal expansion coefficients is released due to the GaN layer separating in the PS shape as a result of the patterning, and the curvature disappears. The Na flux coalescence growth occurs on this low-curvature MPS-GaN sub. and a low-curvature coalesced GaN crystal grows. It would appear that distortion occurs as temperature starts to fall after Na-flux growth due to the difference in thermal expansion coefficients between the coalesced crystal and the sapphire, but separation occurs immediately in the multipoint-seed areas and so the distortion

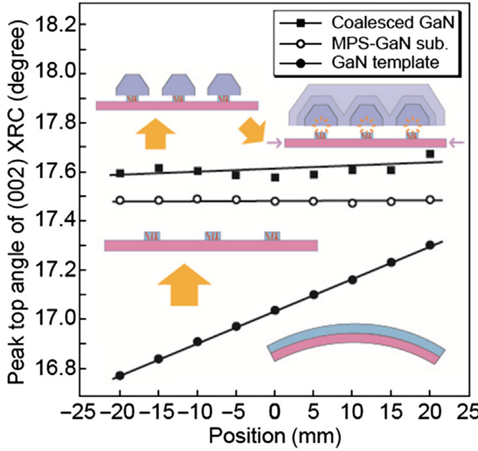

FIGURE 13.30 Dependence of peak top angle of the XRC on the measurement point. The inverse of slope of a line represents the radius of lattice curvature. The solid circles, open circles, and solid squares represent the shift in XRC peak top angle of the GaN template, the MPS-GaN sub., and the coalesced GaN crystal after separation from the sapphire substrate, respectively.

disappears. This appears to happen as a result of high detachability of the coalesced GaN crystal and the sapphire substrate.

13.6 Summary

In this chapter, growth of GaN crystals by the Na flux method was introduced. Though only 18 years have passed since the Na flux method was discovered, significant results were reported. Experimental conditions for the growth of GaN single crystals with high quality were optimized over several years. The optimized condition realized the growth of 2∼4-in-diameter GaN crystals on HVPE substrate with high uniformity without cracks. These crystals have good optical properties (doping of Ge, Zn, Ba, Sr, Ca, and Li can change the properties), and relatively low dislocation density (10^4–10^6 cm^{-2}). SPST has been developed since 2012 for further reduction of dislocations of GaN crystals. SPST realized centimeter-sized GaN crystals with almost no dislocations, and the crystal quality was next to a perfect structure of GaN. Coalescence growth technique enables enlarging diameter of GaN crystals with high perfection. The coalesced GaN substrates have large radius of curvatures. The Na flux method with these new techniques opened a new door to the realization of low cost and high performance GaN-based electronic devices.

References

[1] Amano H, Sawaki N, Akasaki I, Toyoda Y. Appl Phys Lett 1986;48:353.

[2] Amano H, Kito M, Hiramatsu K, Akasaki I. Jpn J Appl Phys 1989;28:L2112.

[3] Porowski S. J Cryst Growth 1996;166:583.

[4] Porowski S, Grzegory I. J Cryst Growth 1997;178:174.

[5] Karpinski J, Jun J, Porowski S. J Cryst Growth 1984;66:1.

[6] Yamane H, Shimada M, Clarke SJ, DiSalvo FJ. Chem. Matter. 1997;9:413.

[7] Yamane H. J Ceram Soc Jpn 2009;117:7.

[8] Shimoo T, Kimura H, Kawai M. J Jpn Inst Met (in Japanese) 1971;35.

[9] Morita Z, Iwanaga Y, Hamada S, Adachi A. Iron Steel Inst Jpn (in Japanese) 1973;2.

[10] Kawamura F, Morishita M, Omae K, Yoshimura M, Mori Y, Sasaki T. J Mater Sci Mater Electron 2005;16:29.

[11] Morishita M, Kawamura F, Kawahara M, Yoshimura M, Mori Y, Sasaki T. J Cryst Growth 2005;284:91.

[12] Hubberstey P. In: Proceedings of the international conference organized by the British Nuclear Energy Society. London: Nottingham University; 1973.

[13] Morishita M. Applied electro-physics. Osaka University; 2007.

[14] Morikawa Y, Ishii H, Seki K. Phys Rev B 2004;69:041403.

[15] Yanagisawa S, Morikawa Y. Chem Phys Lett 2006;420:523.

[16] Kinzoku Databook. 4th ed. Tokyo: Maruzen; 2004.

[17] Zintl E, Woltersdorf G. Z Elektrochem. Angew Phys Chem 1935;41:876.

[18] Klemm W, Busmann E, Anorg Z. Allg Chem 1963;319:297.

[19] Darken LS, Gurry RW. Physical chemistry of metals. New York: McGraw-Hill Book Company, Inc; 1953.

[20] Kawamura F, Morishita M, Tanpo M, Imade M, Yoshimura M, Kitaoka Y, et al. J Cryst Growth 2008; 310:3946.

[21] Imade M, Hirabayashi Y, Konishi Y, Ukegawa H, Miyoshi N, Yoshimura M, et al. Appl Phys Express 2010;3:075501.

[22] Mori Y, Kitaoka Y, Imade M, Kawamura F, Miyoshi N, Yoshimura M, et al. Physica Status Solidi (a) 2010;207:1283.

[23] Kawamura T, Imabayashi H, Yamada Y, Maruyama M, Imade M, Yoshimura M, et al. Jpn J Appl Phys 2013;52:08JA04.

[24] Morikawa Y. Phys Rev B 1995;51:14802.

[25] Ishii A. Appl Surf Sci 2003;216:447.

[26] Kawahara M, Kawamura F, Yoshimura M, Mori Y, Sasaki T, Yanagisawa S, et al. J Cryst Growth 2007; 303:34.

[27] Kawahara M, Kawamura F, Yoshimura M, Mori Y, Sasaki T, Yanagisawa S, et al. J Appl Phys 2007; 101:066106.

[28] Sprik M, Ciccotti G. J Chem Phys 1998;109:7737.

[29] Nord J, Albe K, Erhart P, Nordlund K. J Phys Condens Matter 2003;15:5649.

[30] Usui A, Sunakawa H, Sakai A, Yamaguchi AA. Jpn J Appl Phys 1997;36:L899.

[31] Hiramatsu K, Nishiyama K, Onishi M, Mizutani H, Narukawa M, Motogaito A, et al. J Cryst Growth 2000;221:11.

[32] Kawamura F, Iwahashi T, Omae K, Morishita M, Yoshimura M, Mori Y, et al. Jpn J Appl Phys 2003; 42:L4.

[33] Kawamura F, Iwahashi T, Morishita M, Omae K, Yoshimura M, Mori Y, et al. Jpn J Appl Phys 2003; 42:L729.

[34] Morishita M, Kawamura F, Kawahara M, Yoshimura M, Mori Y, Sasaki T. J Cryst Growth 2004;270:402.

[35] Aoki M, Yamane H, Shimada M, Sarayama S, DiSalvo FJ. Mater Lett 2002;56:660.

[36] Kawamura F, Morishita M, Miyoshi N, Imade M, Yoshimura M, Kitaoka Y, et al. J Cryst Growth 2009; 311:4647.

[37] Mori Y, Imade M, Murakami K, Takazawa H, Imabayashi H, Todoroki Y, et al. J Cryst Growth 2012; 350:72.

[38] Murakami K, Matsuo D, Imabayashi H, Takazawa H, Todoroki Y, Kitamoto A, et al. Jpn J Appl Phys 2013;52:08JA03.

[39] Kawamura F, Tanpo M, Miyoshi N, Imade M, Yoshimura M, Mori Y, et al. J Cryst Growth 2009;311: 3019.

[40] Imade M, Murakami K, Matsuo D, Imabayashi H, Takazawa H, Todoroki Y, et al. Cryst Growth Des 2012;12:3799.

[41] Imade M, Maruyama M, Yoshimura M, Mori Y. Jpn J Appl Phys 2014;53:05FA06.

[42] Takeda S, Yokoyama K, Tsusaka Y, Kagoshima Y, Matsui J, Ogura A. J Synchrotron Radiat 2006;13: 373.

[43] Imanishi M, Murakami K, Imabayashi H, Takazawa H, Todoroki Y, Matsuo D, et al. Appl Phys Express 2012;5:095501.

[44] Imanishi M, Murakami K, Imabayashi H, Takazawa H, Todoroki Y, Matsuo D, et al. Physica Status Solidi (c) 2013;10:400.

[45] Imade M, Imanishi M, Todoroki Y, Imabayashi H, Matsuo D, Murakami K, et al. Appl Phys Express 2014;7:035503.

[46] Imade M, Imanishi M, Todoroki Y, Imabayashi H, Matsuo D, Murakami K, et al. Appl. Phys. Express 2014;7:035503.

[47] Weyher JL. Superlattices Microstruct 2006;40:279.

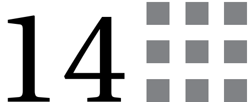

14 Hydrothermal Growth of Crystals—Design and Processing

Kullaiah Byrappa[1], Namratha Keerthiraj[1], Shayan M. Byrappa[2]

[1]CENTER FOR MATERIALS SCIENCE AND TECHNOLOGY, UNIVERSITY OF MYSORE, MYSORE, KARNATAKA, INDIA; [2]DEPARTMENT OF MATERIALS SCIENCE AND ENGINEERING, STONY BROOK UNIVERSITY, STATE UNIVERSITY OF NEW YORK AT STONY BROOK, STONY BROOK, NY, USA

CHAPTER OUTLINE

14.1 Introduction **536**
14.2 History of Hydrothermal Growth of Crystals and Current Trends in Hydrothermal Research **538**
14.3 Intelligent Engineering of the Hydrothermal Processes **542**
14.3.1 Physicochemical and Hydrodynamic Principles of the Hydrothermal Design and Processing of Crystals 542
14.3.2 Basic Principles of Phase Formation under Hydrothermal Conditions 543
14.3.3 Solution, Solubility, Kinetics of Crystallization, Experimental Investigations of Solubility 544
14.3.4 Thermodynamic Calculations for the Intelligent Engineering of Crystals 547
14.4 Apparatus **548**
14.4.1 Morey Autoclave 549
14.4.2 Tuttle–Roy Cold-Cone Seal Autoclaves 551
14.4.3 General Purpose Autoclaves 551
14.5 Hydrothermal Processing of Some Selected Crystals **553**
14.5.1 Quartz 553
14.5.2 Aluminum and Gallium Berlinites 556
14.5.3 Potassium Titanyl Phosphate 558
14.5.4 Calcite 560
14.5.5 Corundum, Ruby, Emerald 561
14.5.6 Rare Earth Vanadates 563
14.5.7 Native Elements, Simple Oxides, and Sulfides 563
14.5.8 Complex Coordinated Crystals 565
14.6 Hydrothermal Growth of Fine to Nanocrystals **566**
14.7 Conclusions **571**
References **571**

Handbook of Crystal Growth. http://dx.doi.org/10.1016/B978-0-444-63303-3.00014-6
Copyright © 2015 Elsevier B.V. All rights reserved.

14.1 Introduction

The term *hydrothermal* was first introduced by British geologist Sir Roderick Murchison (1792–1871) purely in a geological sense to describe the action of water at elevated temperature and pressure in bringing about changes in the earths's crust leading to the formation of various rocks and minerals [1]. However, in recent years the hydrothermal technique has been most popular, garnering interest from scientists and technologists of different disciplines, particularly since the 1990s [2]. It is well known that the largest single crystal formed in nature (a beryl crystal of >1000 kg) and some of the largest quantities of single crystals created by man in one experimental run (quartz crystals of nearly 5000 kg at the Toyo Communication Co. Ltd. Japan) are both of hydrothermal origin [3,4]. The hydrothermal method is very important for its technological efficiency in developing bigger, purer, and dislocation-free single crystals. The method has been widely accepted since the 1960s, and practically all inorganic species, starting from native elements to the most complex oxides, hydroxides, silicates, germanates, phosphates, nitrides, and others have been obtained by this method both in the bulk crystal form to fine, ultrafine, and nanocrystal form, which is popularly called polyscale crystal form [5]. Today the technique has advanced significantly and researchers have clear knowledge about the hydrothermal system, including the chemistry of the hydrothermal solutions, the reaction mechanism, and the evaluation of the kinetics and phase relations in a given system, much before the actual experiments. Therefore, it has been more relevant in recent years to address the hydrothermal growth of crystals as design and processing of crystals. Besides, the multifunctional organic-inorganic hybrid structures, metal-organic framework materials, and surfactant-directed structures with molecularly ordered inorganic frameworks are designed and processed with great application potential from catalysis, sensing, gas storage, nonlinear optics, magnetism, ferroelectricity, luminescence, etc. using hydrothermal technique. Accordingly, there are thousands of reports in the literature using hydrothermal design, hydrothermal processing, and hydrothermal fabrication, hydrothermal cooking, as popular terminologies [4–14]. The term *hydrothermal* refers to any homogeneous (nanocrystals processing) or heterogeneous (bulk single to small crystals processing) reaction in the presence of aqueous or nonaqueous solvents above room temperature and at pressure greater than 1 atm in a closed system [15]. Similarly, there are several other terms such as *solvothermal*, *glycothermal*, *alcothermal*, *ammonothermal*, *lyothermal*, and *carbonothermal*, depending upon the type of solvent used in such chemical reactions [6,16,17]. In recent years, the additional energy into the hydrothermal process like hydrothermal-electrochemical, hydrothermal-mechanochemical, hydrothermal-microwave, hydrothermal-sonar, hydrothermal-sol-gel, hydrothermal-biomolecular, etc., makes the process extremely effective and the fastest. It also leads us to a new concept like chemistry at the speed of light [2,15]. However, this new process is only suitable for the preparation of fine to nanosize crystals and thin films with high crystallinity and desired properties. Also capping agents, organic molecules, surfactants, etc. are commonly being used to achieve growth in the desired crystallographic direction and to

stunt the crystal growth in the undesired directions under hydrothermal conditions. Such developments have made the technique user friendly to fabricate the functional products with in situ control over their growth. Table 14.1 gives different terminologies under hydrothermal and related processes involved. However, in this chapter, the authors use the broader term *hydrothermal* throughout the text and other terms only when such an occasion arises.

In general, under hydrothermal conditions, the reactants that are otherwise difficult to dissolve go into solution as complexes under the action of mineralizers or solvents, hence, one can expect the conditions of chemical transport reactions. Therefore, some workers even define hydrothermal reactions as special cases of chemical transport reactions. Owing to the specific physical properties, particularly the high solvation power, high compressibility, and mass transport of these solvents, one can also expect the occurrence of different types of reactions like:

1. Synthesis of new phases or stabilization of new complexes.
2. Crystal growth of several inorganic compounds.
3. Preparation of finely divided materials and microcrystallites with well-defined size and morphology for specific applications.
4. In situ fabrication of crystals with desired size, shape, and dispersibility in case of nanocrystals and nanoparticles.
5. Leaching of ores in metal extraction.
6. Decomposition, alteration, corrosion, etching.

The hydrothermal method has several advantages over the conventional crystal growth techniques as far as the purity, homogeneity, crystal symmetry, metastable phases formation, reproducibility, lower crystallization temperature, singe-step process, simple equipment, lower energy requirements, fast reaction times, desired polymorphic modifications, growth of ultra-low solubility materials, etc., are concerned. For example,

Table 14.1 Different Terminologies under Novel Solution Routes

Conventional Hydrothermal	Solvothermal	Supercritical Hydrothermal	Related Terminologies	Multienergy Hydrothermal
Aqueous solvent Refers to conditions above the atmospheric temperature and pressure. Suitable for high quality bulk, fine nanocrystals.	Nonaqueous solvents Low to high temperature conditions. Suitable for good quality bulk, fine nanocrystals.	Critical to supercritical conditions Both aqueous and nonaqueous solvents Suitable for fine and nanocrystals. Rapid.	Ammonothermal, glycothermal, lyothermal, alcothermal, carbonothermal, etc. depending upon the specific solvent used. Spray pyrolysis. Suitable for fine to nanocrystals and thin films.	Hydrothermal in combination with extra energy like microwave, electrochemical, sonar, mechanochemical, biomolecular, sol-gel, etc. Extremely efficient for thin films, fine to nanocrystals. Epitaxy, etc. Very fast processsing.

it is the only method employed successfully to produce large size single crystals of α-quartz on an industrial scale. Similarly, for compounds with elements in oxidation states that are difficult to obtain (especially transitional metal compounds) by other ordinary methods, they can be well synthesized under hydrothermal conditions, for example, ferromagnetic chromium (IV) oxide. The synthesis of metastable phases like sub iodides of tellurium (Te_2I) can be carried out more easily under hydrothermal conditions [18]. The authors have limited the scope of this chapter to some of the key parameters, which provide basics of hydrothermal method, and its principles and theoretical aspects involved, so that the young researchers who have no prior knowledge of hydrothermal technique can successfully carry out experiments keeping in mind the safety measures to be adopted. The reader can find more detailed information in [19].

14.2 History of Hydrothermal Growth of Crystals and Current Trends in Hydrothermal Research

The history of hydrothermal processing of crystals has been earlier reviewed by Byrappa [2–5,15,17,19]. In 1839, the German chemist Robert Bunsen held aqueous solutions in thick-walled glass tubes at temperatures above 200 °C and at pressures above 100 bar [20]. The first publication on hydrothermal research appeared in 1845 reporting the successful synthesis of tiny quartz crystals upon transformation of freshly precipitated silicic acid in Papin's digester by Schafthaul [1,21].

The majority of the early hydrothermal experiments carried out during the 1840s to early 1900s were discarded as failures due to the lack of sophisticated electron microscopic techniques available during that time to observe small-sized resultant products. The experiments were concluded by stating that the solubility was not suitable for growing crystals. Thus the whole focus was on the processing of bulk crystals [22]. Until the works of Giorgio Spezia in 1900, hydrothermal technology did not gain much importance in the growth of bulk crystals, as the products in a majority of the cases were very fine grained without any X-ray data [23]. With the introduction of steel autoclaves and suitable metal linings, attempts were initiated to reach higher pressure–temperature conditions to obtain other compounds and purer phases. However, no attention was paid to the chemistry of the solvent, the frequent appearance of the metastable phases, solubility relations, kinetics, phase equilibria, and related phenomena, which complicated the earlier studies.

The greatest contribution in the nineteenth century was by de Sénarmont. He used glass tubes containing gel, SiO_2 and H_2O, HC1, or CO_2, enclosed in steel tubes, and heated at 200−300 °C and synthesized mineral silicates, carbonates, sulfates, sulfides, and fluorides. With the introduction of steel autoclaves and noble metal linings, the tendency to reach higher pressure–temperature conditions began. Hanny (1880) claimed to have synthesized artificial diamond by the hydrothermal technique [24]. Similarly, Moissan (1893) also claimed to have synthesized diamond artificially as large as 0.5 mm

from charcoal [25]. Though the success of these experiments was treated as dubious, they certainly provided a further stimulus for the development of high pressure techniques. Toward the end of nineteenth century, Spezia from the Torino Academy of Science began his classical work on the seeded growth of quartz. He concluded that pressure alone has no influence on the solubility of quartz [26]. Perhaps the first North American published work on hydrothermal research was by Barus (1898), who essentially worked on the impregnation of glass with water to such an extent that it melted below 200 °C by using steel autoclaves [27]. Following this, Allen published his classical work on the growth of quartz crystals of 2-mm long using steel autoclaves provided with copper sealing. The first commercialization of the hydrothermal technique took place in the early twentieth century to leach bauxite, which is an ore of aluminum, through Bayer's process. The credit goes to pioneers like Tammann and Boeke who studied the carbonate and silicate reactions at higher pressure and temperature conditions with CO_2 pressure. Perhaps this is the beginning of the solvothermal research, although the term *solvothermal* was introduced by French chemists in 1971 [28].

There followed the development of the test tube–type pressure vessels by Tuttle, later modified by Rustum Roy. These test tube–type pressure vessels are one of the most versatile autoclaves today used worldwide, which are also popularly known as batch reactors, that could hold temperatures up to 1150 °C at lower pressures and pressure up to 10 kbar at lower temperatures (the modified TZM autoclaves).

When Brazil imposed an embargo on the supply of high purity quartz that was a strategic material for telecommunications purposes during World War II, many countries like the United States, the United Kingdom, Germany, and the former Soviet Union got into hydrothermal growth of large quartz crystals. Nacken grew large crystals of emerald, quartz, beryl, and corundum (Figure 14.1(a)) [29]. During 1950, Nacken published his work on quartz that today remains a classic [29,31]. Walker produced bulk

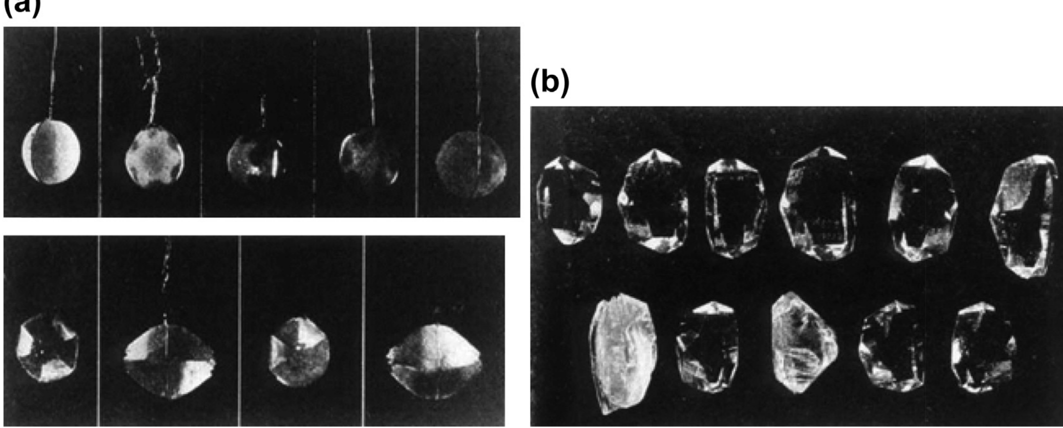

FIGURE 14.1 (a) The first man-made large size crystals of quartz, obtained by Nacken [29]; (b) Quartz crystals obtained by Walker [30].

single crystals of quartz during the 1950s at AT and T Bell Labs., USA [30]. Japan is now the largest producer of commercial quartz in the world. Japan alone produces >50% of world's annual production; it has the largest autoclaves in the world [3]. Figure 14.1(b) shows the quartz crystals obtained by Walker during 1950s [30]; and Figure 14.2 shows the production of quartz crystals in the world's largest autoclave located at the Toyo Communication Co. Ltd., Tokyo, Japan [3].

During the 1970s, there was a quest for the search and the growth of hitherto unknown compounds of photo-semiconductors, ferromagnets, lasers, piezo- and ferroelectrics, and, in this regard, hydrothermal technology attracted a great attention. During the early 1980s, a new sealing for the autoclave was designed, *Grey-Loc* sealing, which facilitates the construction of the very large size autoclaves with a volume of 5000 L [3].

Toward the end of the 1970s, on the whole the hydrothermal field experienced a declining trend and unanimously decided that the technique is not suitable for the growth of large crystals other than quartz. The Nobel Symposium organized by the Swedish Academy of Sciences, during September 17–21, 1979, on "The Chemistry and Geochemistry of Solutions at High Temperatures and Pressures" is remembered as an eye opener. The presence of pioneers in the field of hydrothermal physical chemistry like Franck, Seward, Helgeson, Pitzer, and so on drew the attention of hydrothermal crystal growers, and a new trend was set to look into the hydrothermal solvent chemistry and

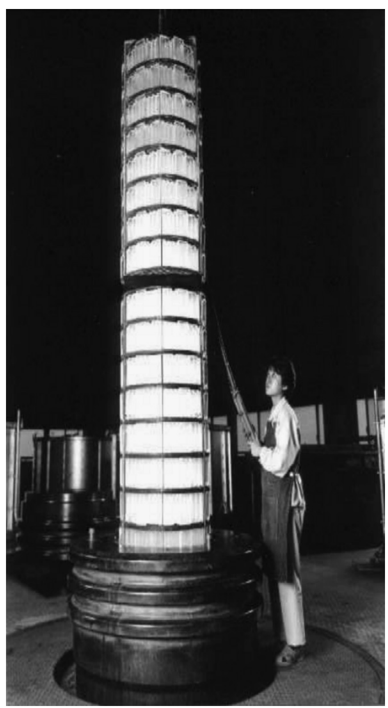

FIGURE 14.2 Production of quartz crystals in the world's largest autoclave. *Photograph courtesy S. Taki, Japan [3].*

the physical chemistry of the hydrothermal systems [32–35]. Following this, Japan organized the first ever International Hydrothermal Symposium held in April 1982, which was attended largely by specialists from different branches of science including physical chemistry, inorganic chemistry, solid state physics, materials scientists, organic chemists, hydrometallurgists, hydrothermal engineers, etc. This is the dawn of modern hydrothermal research. Tables 14.2 and 14.3 give the decade-wise development and the current trend in hydrothermal research.

Table 14.2 Evolution of Hydrothermal Technique of with Time

Period	Focus	Equipment	Remarks
1850–1900	Mineral synthesis, imitation of natural conditions	Simple reactors, glass reactors, digestors	Lower growth rate, tiny particles, geological interest
1900–1940	Mineral synthesis, improvement in PT conditions, German domination	Morey autoclaves, flat closures	Lower growth rate, silicates, carbonates, Germany, Russia, France, USA, geological interest
1940–1950	Large-size and large-scale production of quartz, and beginning of zeolites, clays, and micas	Test-tube type (cold-cone-sealed), welded closure modified Bridgman type	Cold-cone-seal type autoclaves made revolution, *PVT* diagrams systems
1950–1960	Phase diagrams for natural systems	Morey, Tuttle–Roy, welded closures, modified Bridgman	The dawn of modern hydrothermal research
1960–1970	Synthesis of technological materials, new inorganic compounds without natural analogs	New designs from USSR, commercialization of the autoclaves, improved sealing, larger size of the autoclaves	Russian School dominated, Japanese labs appeared
1970–1980	A variety of new materials synthesis, ceramic processing in a bigger way, advanced materials	New designs, improved PT conditions, Grey-Loc sealing, large autoclaves	Appearance of many hydrothermal labs in several countries
1980–1990	Decline in interest on hydrothermal research. Importance of the technique in materials science, physical chemistry of hydrothermal solutions		Japan organized 1st Int. Conf. Hydrothermal Reactions, beginning of the entry of physical chemists
>1990	Diversification of hydrothermal technique, age of solvothermal, physical chemistry of hydrothermal solutions	Design of new reactors to suit the specific applications: batch reactors, flow reactors, and so on	Entry of organic chemists, environmental scientists, fall in Russian domination and beginning of the Japanese domination
>2000	Nanoparticles processing for nanotechnology, nanobiotechnology, rapid processing of particles, multienergy processing of materials, modeling of hydrothermal processes	Design of new flow reactors, instant hydrothermal systems, multienergy processing systems and so ons	Entry of biologists, beginning of Chinese domination

Table 14.3 Current Trends in Hydrothermal Growth of Crystals

Compound	Earlier Work	Author
$Li_2B_4O_7$	T = 500–700 °C	T = 240 °C
	P = 500–1500 bar	$P \leq 100$ bar
$Li_3B_5O_8(OH)_2$	T = 450 °C	T = 240 °C
	P = 1000 bar	P = 80 bar
$NaR(WO_4)_2$	T = 700–900 °C	T = 200 °C
R = La,Ce,Nd	P = 2000–3000 bar	$P \leq 100$ bar
$R{:}MVO_4$	Melting point >1800 °C	T = 100 °C
R = Nd,Eu,Tm; M = Y,Gd		$P \leq 30$ bar
$LaPO_4$	Synthesized at >1200 °C	T < 120 °C
		P < 40 bar
Diamond	T > 1000 °C	T < 800 °C
	$P \leq 3$ kbar	P = 10 kbar

14.3 Intelligent Engineering of the Hydrothermal Processes

The intelligent engineering of the hydrothermal processes of formation of crystals has replaced the conventional empirical approach of crystal growth. It involves several parameters of physicochemical and hydrodynamic factors like phase formation, solutions, solubility, kinetics of crystallization, and thermodynamic calculations. This is also popularly known as thermochemical modeling.

14.3.1 Physicochemical and Hydrodynamic Principles of the Hydrothermal Design and Processing of Crystals

There are two aspects involved:

1. The physicochemical studies on various aqueous solutions studied within a wide range of pressure temperature conditions.
2. The physical chemistry of the hydrothermal growth of crystals.

However, the correlation of the two works has not been done with enough accuracy.

Ezersky et al. studied the hydrodynamics under hydrothermal conditions using a shadowgraph technique [36,37]. This facilitated understanding of the spatiotemporal structure of hydrothermal waves in Marangoni convection. However, a lot more experimental and theoretical developments are needed to clarify and complete the description of the hydrothermal waves.

The growth of single crystals on a seed is represented by the sum of macro- and microprocesses occurring between the interface boundary of the solution and the crystal. The composition and concentration of the solution, temperature and pressure, hydrodynamic conditions, and surface contact of the phases are some of the basic physicochemical

parameters that determine the regime and rate of dissolution of the nutrient, mass transport, and possibility of the formation of new phases. Balitsky and Bublikova have studied the physicochemical foundation of malachite synthesis [38]. Similarly, Kuznetsov has reviewed the physical chemistry of hydrothermal crystal growth and the crystallization of some A_2B_6 crystals [39]. Further, Popolitov has reviewed the physical chemistry of the hydrothermal growth of tellurium dioxide crystals [40]. The reader can find more valuable information in the book *Hydrothermal Growth of Crystals* [3]. These studies along with the pioneering works by Hegleson, Pitzer, Frank, Seeward, Kaufman, etc. set a new trend for thermochemical computation leading to the intelligent engineering of materials through the generation of stability field diagrams for a variety of systems followed by their experimental validation. In addition, these studies helped significantly to understand the flow pattern, velocity distributions, and temperature contours for autoclaves with (varying percent opening) and without baffles. There are several numerical modeling of heat transfer processes and flow fields, for example, beryl, $AlPO_4$, and $GaPO_4$, which have yielded much insight into the flow pattern under hydrothermal conditions. Even the influence of a rotating solid crystal or a seed crystal inside the autoclave has been considered in such numerical modeling. In spite of the fact that considerable progress has been achieved in the numerical flow pattern, there is an incomplete picture overall with respect to the flow dynamics. A lot more experimental and theoretical investigations are needed to clarify and complete the description of the hydrothermal flow dynamics.

14.3.2 Basic Principles of Phase Formation under Hydrothermal Conditions

A *phase* is defined as a part of the system that is homogeneous throughout and is physically separable from other phases by distinct boundaries. Phase relationships are conveniently represented by means of phase diagrams. Phase diagrams and the phase rules apply only to systems at equilibrium. These data are extremely important to any crystal grower for successful growth of crystals. Gibbs deducted a quantitative relationship for phase rule:

$$F = C - P + 2$$

where $F =$ degrees of freedom, $C =$ number of components, $P =$ number of phases.

The above relation holds true if pressure, temperature, and composition are the only variables. If other variables such as magnetic, electric, or gravitational fields are considered, the numerical value 2 on the right-hand side of the equation will increase by the number of new variables considered. However, in recent years, the phase relationship under nonequilibrium conditions is gaining momentum especially with respect to the crystallization of metastable phases.

The hydrothermal method is considered as one of the best methods to study phase relationships and for constructing *PTX* diagrams. The present chapter is restricted only to some basic systems and popular nonconventional phase diagrams.

Among the binary systems, the H_2O–CO_2 system is important with regard to the role of H_2O and CO_2 vapor pressures in native mineral formation and in the hydrothermal

synthesis of inorganic compounds [41,42]. The nonconventional phase diagrams plotted for equilibrium conditions are popular, especially among Russian workers. These diagrams are popularly known as *composition diagrams* or *NC* diagrams, where N is the nutrient composition and C is the concentration of the solvent mineralizer. Hundreds of phase diagrams of compositions are available, especially in the Russian literature. Similarly, temperature versus concentration diagrams (TC diagrams) are also popular for some of the systems because the variation in temperature of the system can lead to the formation of various polymorphic modifications and several other phases that are not normally observed in NC diagrams. These nonconventional diagrams are relatively easy to obtain and are highly useful for the growth of single crystals as they clearly depict the growth conditions [43]. Similarly, the components can be represented for example, in a ternary system as a triangle. This type of phase diagram occurs for hundreds of compounds and they give in general the phase boundaries and the phase formation within a given system under fixed PT conditions, and help to select the conditions for crystal growth.

14.3.3 Solution, Solubility, Kinetics of Crystallization, Experimental Investigations of Solubility

A hydrothermal solution is generally considered as a thermodynamically ideal one; the real hydrothermal solutions differ from ideal solutions and their understanding requires knowledge of specific hydrothermal process and its important characteristics such as the solubility of the starting materials, quantity of the phases, their composition, output of the phases, kinetics, and growth mechanism of single crystals.

The following conditions are adopted in selecting the most suitable mineralizers:

1. Congruence of the dissolution of the test compounds.
2. A fairly sharp change in the solubility of the compounds with changing temperature or pressure.
3. A specific quantitative value of the absolute solubility of the compound being crystallized.
4. The formation of readily soluble mobile complexes in the solution.
5. A specific redox potential of the medium ensuring the existence of ions of the required valence.

Additionally, the solvent should have the desired viscosity, insignificant toxicity, and very weak corrosion activity with respect to the apparatus.

Therefore, it is necessary to understand the basic principles, which insist upon the understanding of the properties of water, including density, dielectric constant, and ion product, varying greatly around the critical point of water and result in a specific reaction atmosphere [44]. The experimental *P-V-T* behavior of water has been reviewed and summarized by several workers [45–48]. Due to the variation in the properties of water, phase behavior changes greatly around the critical point. Since supercritical water is of high density steam, light gases like oxygen or hydrogen from a homogeneous phase with

supercritical water. The organic compounds and water are not miscible at a low temperature range, but form a homogeneous phase at higher temperatures, which is because of the reduced dielectric constant of water. Several chemical changes arise from changes in ionic dissociation of the solution. Therefore, it is better to understand the characteristics of the pure water under hydrothermal conditions; especially the hydrogen ions show an influence on the solubility of various compounds under hydrothermal conditions. Several reports have appeared in the literature on such studies. The reader can find additional valuable information in [19].

Thermodynamic principles enable us to design a reaction to yield phase-pure phases. Without this, it is impossible to distinguish a process that is being controlled by thermodynamics versus kinetics. Several models have been proposed in order to understand the hydrothermal synthesis of a variety of compounds like ABO_4 ($A =$ alkaline earth elements, $B =$ Ti, Zr, Hf), HAp, sulfides of gold, silver, iron, copper, and so on [49–55]. Thermodynamic studies yield rich information on the behavior of solutions with varying pressure–temperature conditions.

An understanding of theory and the experimental results on the hydrothermal physical chemistry is essential to the crystal grower. It has been demonstrated for many cases that the mineralizer solutions (typically 1 M NaOH, Na_2CO_3, NH_4F, K_2HPO_4, etc.) are close to the properties of water. For 1 M NaOH at room temperature, $\eta_{\mathrm{solution}}/\eta_{\mathrm{H_2O}} = 1.25$, one can expect that the viscosity of hydrothermal solutions can be as much as two orders of magnitude lower than “ordinary” solutions [56]. The mobility of molecules and ions in the supercritical range is much higher than under normal conditions. In addition, electrolytes, which are completely dissociated under normal conditions, tend to associate with rising temperature [57].

The *PVT* data for water up to 1000 °C and 10 kbar is known accurately enough (within 1% error) [58–60]. At very high *PT* conditions (1000 °C and 100 kbar), water is completely dissociated into H_3O^+ and OH^-, behaving like a molten salt, and has a higher density of the order of $1.7-1.9\ \mathrm{g/cm^3}$.

In the hydrothermal growth of crystals, the *PVT* diagram (Figure 14.3) of water proposed by Kennedy is very important [61]. Usually, in most routine hydrothermal experiments, the pressure prevailing under the working conditions is determined by the degree of filling and the temperature. The critical temperatures are not known for the usually complex solutions at hand; hence, one cannot distinguish between sub- and supercritical systems for reactions below 800 °C.

Fundamental understanding of kinetics of crystallization under hydrothermal conditions was lacking until recently. Insight into this would enable us to understand how to control the formation of solution species, solid phases and the rate of their formation. In this respect, the recent progress in the area of time-resolved hydrothermal synthesis for tomographic energy dispersive diffraction imaging (TEDDI) using synchrotron beam and neutron beam has contributed significantly to the understanding of the intermediate phases and, in turn, the hydrothermal mechanism of formation of various inorganic phases and their kinetics [62,63]. In combination with the thermodynamics of the

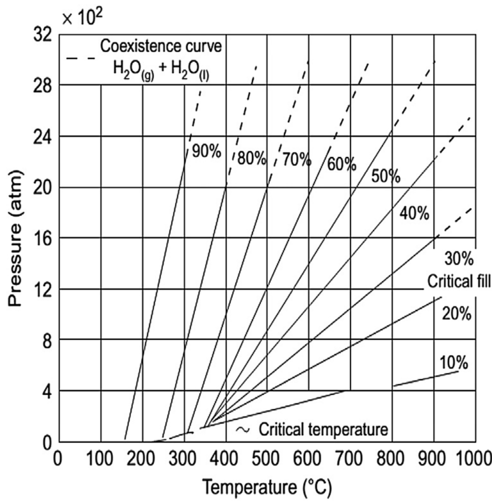

FIGURE 14.3 PVT diagram of water [61].

reaction system, one can precisely understand various parameters related to the hydrothermal synthesis of a desired phase [64].

The fundamental role of temperature, pressure, precursor, and time on crystallization kinetics of perovskite oxides has been studied in detail [64]. Similarly, the kinetics in the HAp system has been studied [65].

Following is information on the solubility of two representative compounds viz. quartz and berlinite because they both have contrasting solubility data.

Solubility of quartz: The first systematic study of the solubility of quartz was carried out by Spezia, which opened up the trend for the growth of bulk crystals overall using the hydrothermal method [26]. The solubility of quartz in pure water was found to be too less for crystal growth (0.1–0.3 wt%), but the solubility could be markedly increased by the addition of OH^-, Cl^-, F^-, Br^-, I^-, and acid media, which act as mineralizers. Alkaline additions, such as NaOH, Na_2CO_3, KOH, and K_2CO_3 are all effective as mineralizers in this pressure and temperature range. Laudise and Ballman have measured the solubility of quartz in 0.5 M NaOH as a function of temperature [66] and even today the classical work carried out Laudise and his group remains the standard as far as the quartz growth under hydrothermal conditions is considered. Figure 14.4(a) shows the solubility curve for quartz in 0.5 M NaOH as a function of temperature and % fill [66].

Solubility of berlinite: The solubility of berlinite was first determined by Jahn and Kordes in orthophosphoric acid above 300 °C and it was found positive [67]. Subsequently, Stanley reported a negative solubility for berlinite in 6.1 M H_3PO_4 [68]. The solubility of $AlPO_4$ varies widely with the type of solvent used. The authors [69] have studied the solubility of $AlPO_4$in some new solvents like HCOOH, NH_4Cl, Na_2CO_3,

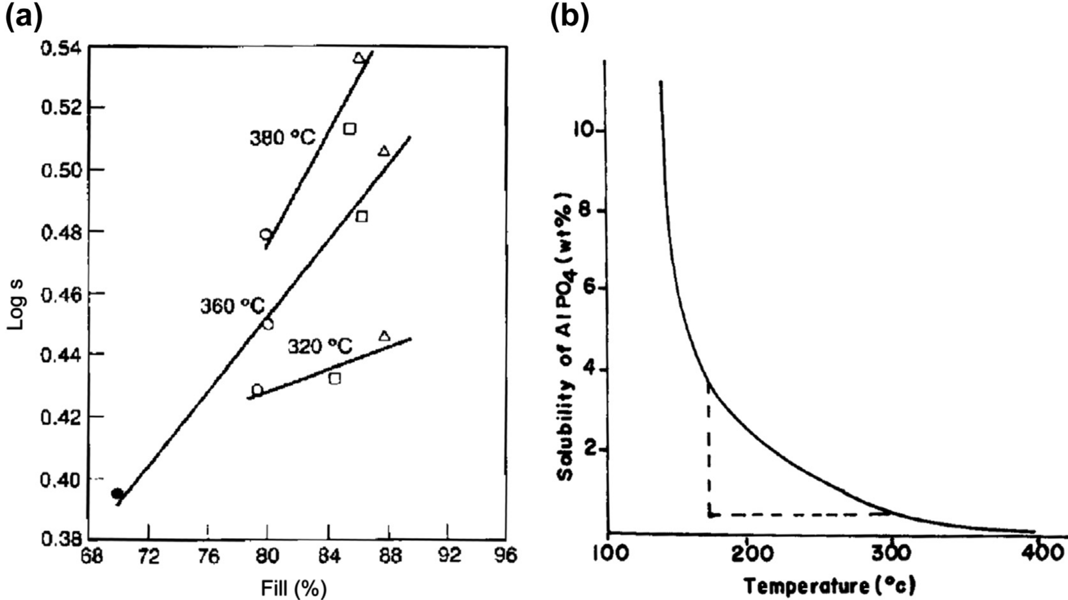

FIGURE 14.4 Solubility of quartz with pressure (a); solubility of berlinite with temperature (b).

$NH_4H_2PO_4$, NaF, KF, LiF, etc. The solubility of $AlPO_4$ (in wt%) as a function of temperature and at a pressure of 2 Kpsi, in 2 M HCOOH solution is shown in Figure 14.4(b) [69].

14.3.4 Thermodynamic Calculations for the Intelligent Engineering of Crystals

Edisonian trial-and-error approach for designing hydrothermal experiments has become a part of the history of this field. Thermodynamic modeling has been successfully used for the synthesis of a wide range of metal oxides, hydroxyapatite, PZT family of materials, etc. Usually any thermodynamic model requires the following information for all species in the solution: the standard Gibbs energies ΔG_f^o and enthalpies ΔH_f^o of formation, entropies S_o at a reference temperature (298.15 K), and the partial molar volumes V_o and heat capacities C_p^o as functions of temperature. Equilibrium equations for all the species in the solution are set up. The model considers all the activity coefficients of aqueous species, for example, the data bank from OLI Systems Inc. [70], and in the absence of thermodynamic values, estimation methods are used to obtain such values [65,71,72].

Figure 14.5 shows the stability field diagram for $CaO–P_2O_5–NH_4NO_3–H_2O$ system at 200 °C as a function of precursor concentration and pH [65].

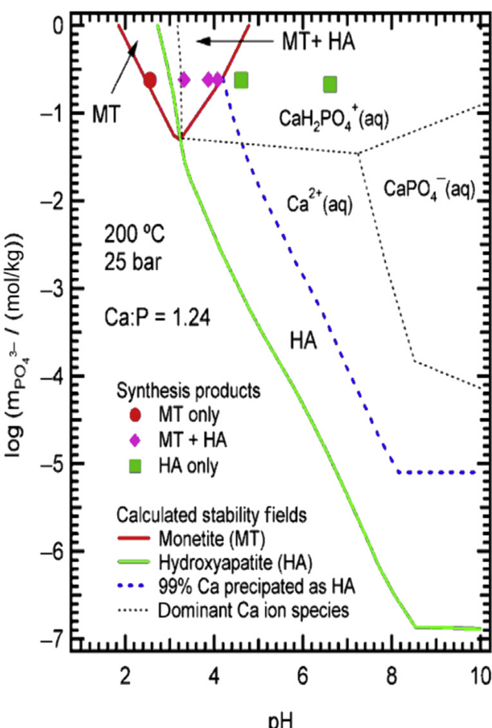

FIGURE 14.5 Calculated stability field diagram for the hydroxyapatite system at 200 °C and 25 bar with Ca: P ratio at 1.24 [65].

14.4 Apparatus

Crystal growth or materials processing under hydrothermal conditions requires a pressure vessel capable of containing highly corrosive solvent at high temperature and pressure over a long period of time. Ideal hydrothermal autoclave should have the following characteristics:

1. Inertness to acids, bases, and oxidizing agents.
2. Easy to assemble and dissemble.
3. A sufficient length to obtain a desired temperature gradient.
4. Leakproof with unlimited capabilities to the required temperature and pressure.
5. Rugged enough to bear high pressure and temperature experiments for long duration, so that no machining or treatment is needed after each experimental run.

The most commonly used autoclaves in hydrothermal research are listed in Table 14.4 [73]. The majority of these autoclaves are externally heated pressure vessels and their pressure–temperature range cannot be extended further due to lack of suitable refractory alloys. However, internally heated pressure vessels are now commercially available up to 10 kbar and 1400 °C. The list given in Table 14.4 does not include some of

Table 14.4 Autoclaves [73]

Type	Characteristic Data
Pyrex tube 5-mm i.d. 2-mm wall thickness	6 bar at 250 °C
Quartz tube 5-mm i.d. 2-mm wall thickness	6 bar at 300 °C
Flat plate seal, Morey type	400 bar at 400 °C
Welded Walker–Buehler closure 2600 bar at 350 °C	2 kbar at 480 °C
Delta ring, unsupported area	2.3 kbar at 400 °C
Modified Bridgman, unsupported area	3.7 kbar at 500 °C
Full Bridgman, unsupported area	3.7 kbar at 750 °C
Cold-cone seal, Tuttle–Roy type (batch reactors)	5 kbar at 750 °C
Piston cylinder	40 kbar, 1000 °C
Belt apparatus	100 kbar, $>$1500 °C
Opposed anvil	200 kbar, $>$1500 °C
Opposed diamond anvil	Up to 500 kbar, $>$2000 °C
Continuous flow reactors	2 kbar at 600 °C

the recent designs and modifications or upgrades as their applications are restricted to specific studies. In addition, the last four autoclaves are useful for the preparation of nanocrystals and powders under extreme conditions.

The most successful materials are corrosion resistant, high strength alloys, such as 300 series (austenitic) stainless steel, iron, nickel, cobalt-based super alloys, and titanium and its alloys. In recent years, Hastelloy is the most preferred material worldwide. Some crystals like quartz can be grown readily within the autoclave without any lining, liners, or cans as silica and NaOH form an acmite layer that protectively coats the ground vessel. In contrast, the growth of berlinite crystals requires a Teflon lining or beakers because phosphorus is highly corrosive; it can even corrode platinum if used for a long time. Depending upon the hydrothermal medium, the outer liner is made up of copper, nickel, silver, graphite, titanium, etc.

The internal assembly of the liner depends upon the solubility of the compound to be processed under hydrothermal conditions. For example, quartz and berlinite have contrasting solubility, and accordingly their processing requires equally contrasting experimental setup as shown in Figure 14.6 [66,69].

Several advanced electronic tools are available today for the measurement of temperature and pressure conditions within the autoclave assembly. Similarly, pressure gauges are available with auto cut-off devices to prevent the reactor explosion. More specific information on a wide range of autoclaves designs may be found in [19].

14.4.1 Morey Autoclave

The Morey autoclave has a simple sealing gasket and a volume of generally 25–100 mL [75]. The usual dimensions of a Morey autoclave are 10–20 cm length and 2.5-cm inner diameter (Figure 14.7(a)). The autoclave generates an autogenous pressure depending on the degree of filling, the fluid, and the temperature. The autoclave is limited to ~450 °C

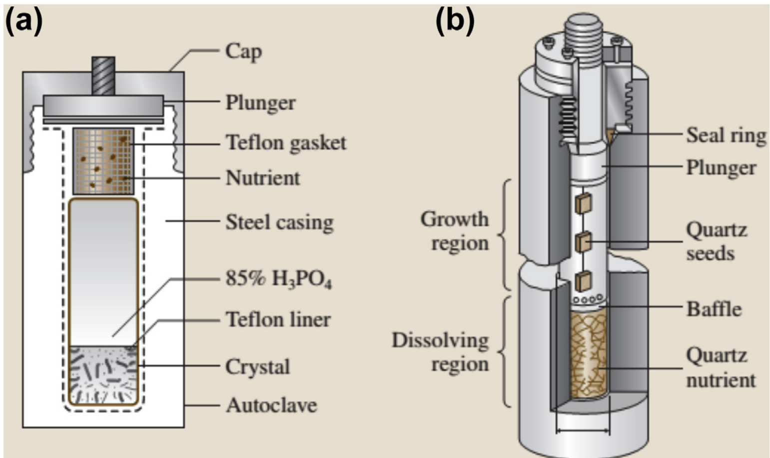

FIGURE 14.6 The internal liner assembly: (a) Berlinite with negative temperature coefficient of solubility has the seed crystals (growth zone) at the bottom and nutrient (dissolution zone) at the top [69]; (b) Quartz with positive temperature coefficient of solubility has the nutrient (dissolution zone) at the bottom and the seed crystals (growth zone) in the top [74].

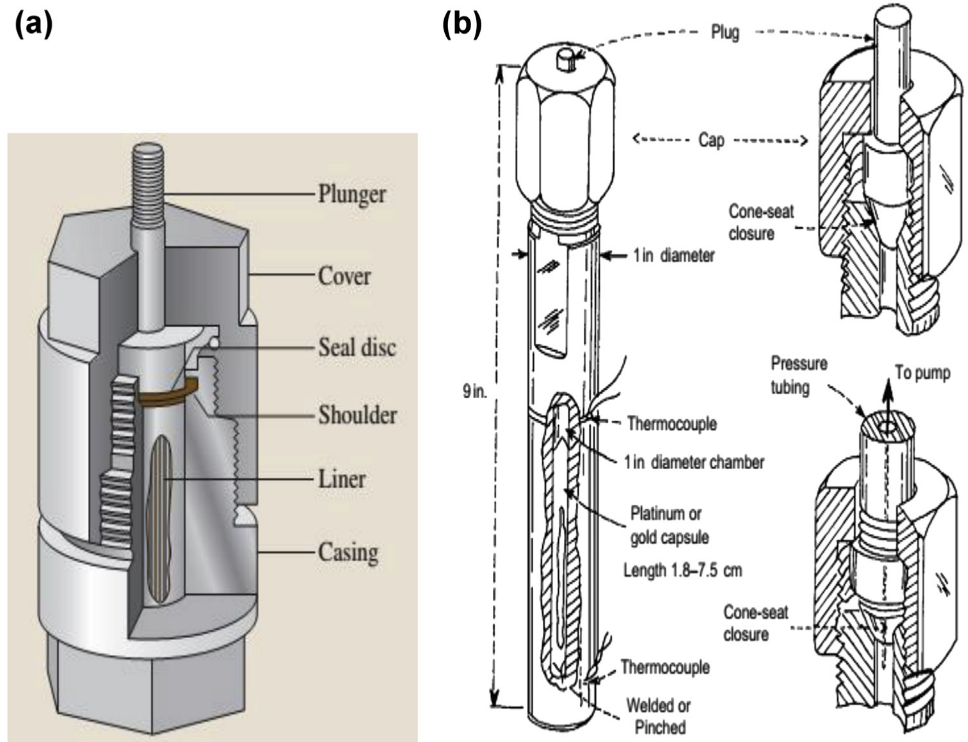

FIGURE 14.7 Schematic cross-section of Morey autoclaves (a) and Tuttle autoclaves (b).

and 2 kbar in routine use. A thermocouple is inserted in the well close to the sample and the vessel is placed inside a suitable furnace so that the entire Morey autoclave and closure lie within the element of the furnace. At the end of the run, the vessel is quenched in a jet of air followed by dipping in water and the closure seal is broken.

14.4.2 Tuttle–Roy Cold-Cone Seal Autoclaves

The open end and autoclave seal outside the furnace gave the term *cold-cone seal* (although in the real sense the seal is far from being cold) to this most popularly used autoclave (Figure 14.7(b)). Pressure is transmitted to the sample, which is contained in a sealed capsule, through a hole in the closure. The capsules are normally made up of noble metals (platinum, gold, or silver). These vessels may be operated closure up, closure down, or horizontally. The ratio of the vessel diameter to the wall diameter determines the strength of the vessel. In most standard Tuttle vessels this ratio is 4%. Using Stellite 25, experiments can be carried out at 900 °C and 1 kbar or 750 °C and 3 kbar for long-term use (from hours to weeks). Roy and Tuttle actually made many hydrothermal experimental runs for several months in the late 1950s. Moreover, the reaction could be "quenched" by lowering the furnace quickly and surrounding the bomb with a container of water. These autoclaves are highly useful for the hydrothermal researchers to carry out phase equilibria studies, solubility, high temperature–pressure synthesis, nanocrystal synthesis, etc. Today they are also called *batch reactors* by several researchers and are popularly used for nanomaterial synthesis. The advent of new materials, particularly molybdenum-based alloys, has extended the temperature capabilities of cold-seal vessels to about 1150 °C at a pressure above 4 kbar (the so-called TZM vessels). The prospects of new refractory alloys extending up to this range are encouraging. These cold-seal vessels are safe, inexpensive, simple, and operationally routine. Unlike the Morey type of autoclaves, in the Tuttle cold-seal vessel, the pressure is built up by an external pump and the pressure medium is usually distilled water with a little glycol added to inhibit corrosion.

14.4.3 General Purpose Autoclaves

For the synthesis of crystals under hydrothermal conditions, very simple general purpose autoclaves are typically used; they are commercially available from many sources. Usually these autoclaves are provided with Teflon liners. Some modifications can be provided to create a temperature gradient within the autoclave. Figure 14.8(a) shows the general purpose autoclave.

Many other designs are available today to meet specific requirements, like stirred autoclaves (Figure 14.8(b)), which are very useful to stir the mixture during the hydrothermal synthesis and also to extract the contents inside the reactor during the experiments, and also to pump in the desired gas into the reactor at any given time. The internal pressure can be directly read. The products can be quenched readily with the circulation of chilled water through the cooling coils running inside the autoclave. These

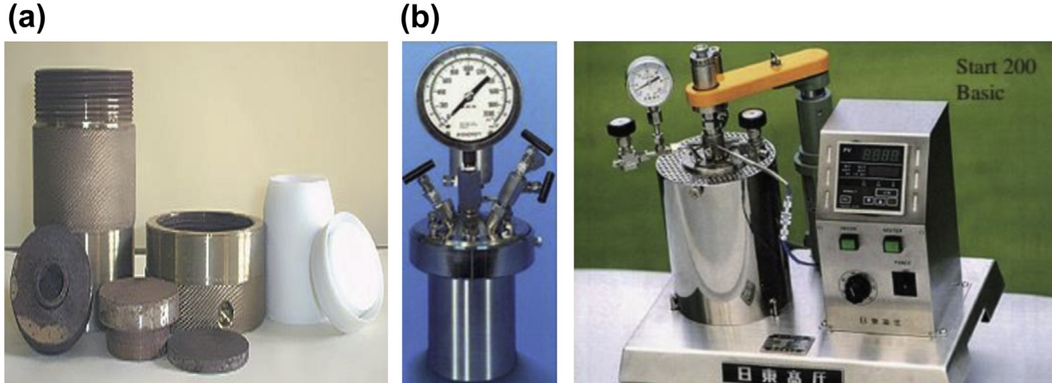

FIGURE 14.8 General purpose autoclaves (a); and commercially available stirred reactors (b).

additional advantages have helped greatly to more precisely understand the hydrothermal crystallization mechanism, kinetics, and metastable phases.

In the last two decades, the use of continuous flow reactors has become very popular to synthesize small micron-sized crystals to nanocrystals with a high degree of control over the shape and size of the crystals. These reactors operate at or above the supercritical conditions of the solvents. The method is also popularly known as the supercritical fluid technology (SCF). It has also emerged as an alternate to most of the existing techniques for designing and crystallizing new drug molecules.

There are many more reactor designs for special purposes such as rocking autoclaves, PVT apparatus, multichamber autoclaves, fluid-sampling autoclaves, microautoclaves, autoclaves for visual examination, hydrothermal hot pressing, vertical autoclaves, continuous flow reactors, hydrothermal electrochemical autoclaves, autoclaves for solubility measurements, autoclaves for kinetic study, pendulum autoclave, horizontal autoclaves for controlled diffusion study, and so on. Among these, novel designs for the in situ time-resolved hydrothermal synthesis for TEDDI using synchrotron beam and similarly in situ time-resolved neutron diffraction analyses of hydrothermal synthesis are very prominent ones [63].

The addition of external energy sources like sonar, mechanical energy, microwave, and magnetic field has contributed to the enhanced reaction kinetics in the processing of a variety of compounds. Such processes are popular in materials science as multienergy processing. The reader can get more information on these novel autoclaves designs from [19].

Safety and maintenance of the autoclaves is the prime factor one has to bear in mind while carrying out experiments under hydrothermal conditions. It is estimated that for a 100 cm^3 vessel at 20,000 psi, the stored energy is about 15,000 ft-1b. Figure 14.9 shows ruptured autoclaves because of pressure surge.

The hydrothermal solutions—either acidic or alkaline—at high temperatures are hazardous to human beings if the autoclave explodes. Therefore, the vessels should have rupture discs calibrated to burst above a given pressure. Such rupture discs are

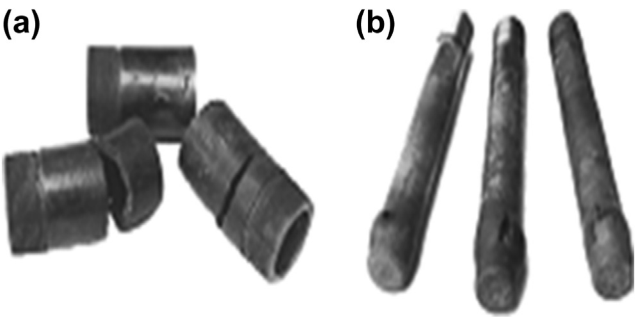

FIGURE 14.9 (a) Stainless steel acid digestion bombs; (b) Stellite Tuttle cold-cone-sealed autoclaves ruptured due to pressure surge. *Courtesy K. Byrappa.*

commercially available for various ranges of bursting pressure. The most important arrangement is that provision should be made for venting the live volatiles out in the event of rupture. Proper shielding of the autoclave should be given to divert the corrosive volatiles away from personnel.

After each run, the autoclave should be properly treated before using it for the next run. The autoclave threads should be maintained carefully and are always painted with an appropriate pipe thread lubricant to reduce friction and prevent seizing of the autoclaves at high temperature.

14.5 Hydrothermal Processing of Some Selected Crystals

With thousands of existing publications on the hydrothermal processing of crystals, it is impossible to discuss every material in detail. Therefore, the scope of this section is restricted to only the processing of some selected crystals of technological importance.

14.5.1 Quartz

Quartz is one of the technologically most important materials, existing in over 22 polymorphic modifications, of which only α-quartz is piezoelectric and is stable below 573 °C. Only hydrothermal technique is suitable to produce this polymorph in the laboratory conditions. In fact, researchers directly relate the progress of quartz growth with the evolution of hydrothermal technology. Therefore, crystal growth of quartz serves as the best tutorial for beginners in hydrothermal research. The principal source of electronic-grade natural quartz is Brazil. Today, the electronics industries are largely inclined to use synthetic quartz. The production of high quality defect-free quartz has a great potential market among all the electronic materials. Japan alone produces more than 50% of the world production, followed by the United States and China. Recently, several Japanese companies including Kyocera, Shin-Etsu, and Asahi Glass Co. have started producing quartz for highly specialized applications. The total cost involved in the production of quartz is over 1.2 billion US dollars. Thus quartz takes the first place in value and quantity of single-crystal piezoelectric materials produced. Much of the

research related to quartz today is confined to the industries. Major research activity was initiated at the AT & T Bell Labs, and the most important contributions to quartz growth came from the workers like Ballman, Laudise, Kolb, and Shtenberg, during the 1970s. High quality quartz crystals have been obtained in NaCl and KCl solutions, NaOH and Na_2CO_3 solutions (10%) [76,77]. In the growth of α-quartz, available nutrient material such as small particle size α-quartz, silica glass, high quality silica sand, or silica gel is placed in a liner made up of iron or silver with a suitable baffle and a frame holding the seed plates. A mineralizer solution with a definite molarity is poured into the liner to make the required percent fill. The increased solubility in the presence of mineralizer increases the supersaturation without spontaneous nucleation and consequently allows more rapid growth rates on the seeds.

The optimum growth conditions for synthesis of quartz based on the work in Bell Laboratories are [74]:

Dissolution temperature	425 °C
Growth temperature	375 °C
Pressure	15,000–25,000 psi
Mineralizer concentration	0.5–1.0 M NaOH
Temperature gradient (ΔT)	50 °C
% fill	78–85%
Growth rate in (0001)	1.0–1.25 mm/day

The quality of the grown crystals is also a function of the seed orientation and its quality. Strained seeds generally produce strained growth regions. The growth of quartz crystals has been understood precisely with reference to the growth temperature, temperature gradient, percent of fill, solubility, percent of baffle open, orientation and nature of seed, and type of nutrient. Also many kinetic studies have been carried out [74]. Figure 14.10 shows the growth rate of quartz as a function of seed orientation [74]. The solubility of quartz has been studied with temperature, growth rate as a function of seed orientation, and growth rate as a function of percent of fill. Figure 14.11 shows quartz crystals obtained by hydrothermal method.

Most of the recent research on quartz growth is for improved resonator performance, which requires the growth of high quality and low dislocation quartz. In the last two decades, the main objective among quartz crystal growers has been to improve Q, which in turn leads to the production of a low concentration of physicochemical and structural defects. Martin and Armington have studied the effect of growth rate on the aluminum content at low growth rates [78]. Both Al^{3+} and H^{+} are the most deleterious impurities in quartz used for frequency and timing applications, and they also vary the growth rates. Sweeping is one of the most popularly used techniques in recent years to enhance the performance of quartz resonators. Sweeping reduces the formation of etch tunnels. The effect of sweeping is to remove lithium and sodium deposited interstitially in the lattice during growth.

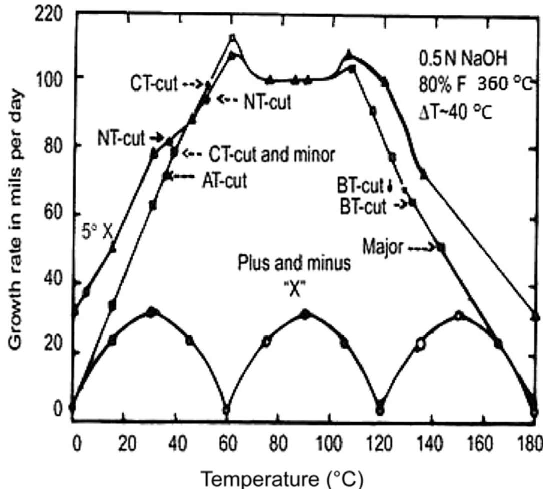

FIGURE 14.10 Growth rate of quartz as a function of seed orientation [74].

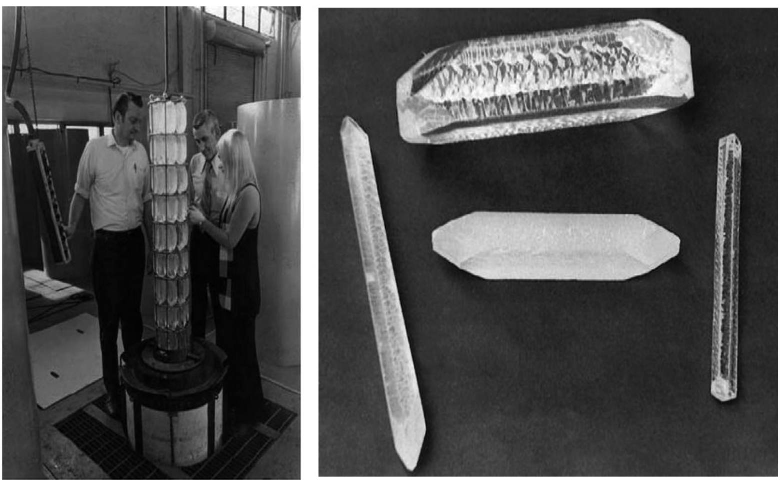

FIGURE 14.11 Quartz crystals obtained at AT & T Bell Labs during 1970s. *Courtesy R. A. Laudise.*

The preparation of quartz for other applications like photomask substrates for lithography, poly-Si TFT-LCD, high purity and high precision polishing devices is a new trend in science. For example, Shin-Etsu Chemical, Japan; Asahi Glass Co, Japan; NDK America, USA; and APC International Ltd., USA, are engaged in such research and development. Whereas companies like Sawyer Research Inc., G. E., Philips, and Toyo Communication are engaged in bulk crystals of quartz for oscillators, frequency devices, etc.

Another important area in the growth of quartz is colored quartz crystals for lapidary applications. Some of the high quality synthetic colored quartz crystals with popular amethyst, citrine, emerald, and ruby colors are frequently used as their replacements for

the natural gemstones and with quartz crystals clear adamantine luster is used as special windows and ceramics. These colored quartz crystals are also called poor man's gemstones. Throughout history, quartz has been the common chameleon of gemstones. Purple to violet amethyst and yellow to orange citrine are jewelry staples with increasing popularity. The credit for hydrothermal growth of gem-quality colored quartz goes to pioneers like Tsinobar, Nassau, and Balitsky. Purple-colored quartz has been synthesized under the following conditions [79]:

Growth temperature	400–450 °C
ΔT	25–50 °C
Pressure	800–1300 kg/cm^2
Solvent	10 wt% NaCl; 10 wt% KCl
Dopant	Fe in the form of a metal; α-Fe_2O_3 in the form of a powder
Vessel	Platinum lined (16.5 ml)
Irradiation	(2–15) $\times$ 10^6 Roentgen (^{60}Co)

Faint-pink-colored quartz can be obtained in the presence of iron and titanium ions. The type and concentration of impurity ions used by the industries producing these colored quartz crystals commercially are not exactly known. Readers can find more extensive information on this subject in [79–81].

14.5.2 Aluminum and Gallium Berlinites

Berlinite is isostructural and isoelectronic with quartz and replaces quartz in electronic devices because its large mechanical coupling factors are greater than α-quartz, and its resonant frequency is nearly independent of temperature for certain orientations [82–84]. Table 14.5 gives a tentative comparison of some piezoelectric characteristics of berlinites with quartz in the AT cut.

The main problem connected with the growth of berlinite is the negative temperature coefficient of solubility, which insists on some special growth conditions, because of the lower solubility at higher temperatures and higher solubility at lower temperatures. One of the principal problems in the growth of $AlPO_4$ crystals is the growth rate relationship in H_3PO_4 and the lack of good solubility data at the constant fill conditions [85]. The first successful growth of berlinite crystals was by John and Kordes [67], followed by Stanely [68]. Stanley carried out the experiments in a sealed borosilicate glass vessel placed in a low pressure environment. However, the importance of berlinite only came to light in

Table 14.5 Comparison of Some Piezoelectric Characteristics

Parameter	Quartz	Berlinite	Gallium Berlinite
Coupling coefficient, K%[a]	8.5	11.0	>16.0
Surtension coefficient, Q[a] (Overvoltage coefficient)	3.10^6	10^6	>5.10^4
$\alpha-\beta$ phase transition, °C	573	584	No

[a]AT cut.

1976 when Chang and Barsch [82] studied the piezoelectric properties of berlinite and reported large mechanical coupling constants and that its resonant frequency was nearly independent of temperature for certain orientations. The growth of gallium berlinite began only during the late 1980s, when the growth of aluminum berlinite was at its peak [86,87]. The solubility of gallium berlinite resembles that of aluminum berlinite.

Berlinite growth has to be carried out at a temperature above 150 °C and below 300 °C because of the reverse solubility. It is quite interesting to note that in contrast to aluminum berlinite, gallium berlinite has no phase transition, and, therefore, some researchers have even synthesized $GaPO_4$ using flux method [87]. However, the quality of these flux-grown gallium berlinite crystals is quite inferior compared to hydrothermally grown crystals. Several versions of the hydrothermal growth of berlinite single crystals have been tried to suit the solubility. Initially small crystals of berlinites are obtained through spontaneous nucleation, and, in turn, this product is used as the nutrient for the seeded growth. However, there are some important modifications suggested from time to time in the growth of berlinite crystals:

1. Crystal growth by slow heating method
2. Crystal growth by composite gradient method
3. Crystal growth by temperature gradient method
4. Growth on seeds

The crystal growth with reverse temperature gradient is much more versatile for these compounds in general. Here the nutrient (either crystalline powder or fine grains of $AlPO_4$ usually obtained from the slow heating method) is kept in a gasket at the upper portion of the autoclave, which is cooler than the bottom of the liner that is kept at slightly higher temperature and it forms the crystallization zone (Figure 14.6(a)).

The crystal growth on seeds uses the spontaneously nucleated seeds and the oriented seeds cut from grown crystals usually mounted on a platinum frame placed in the bottom (hotter) region of an autoclave, and the nutrient (~60 mesh particle size prepared by other methods) is placed above in a platinum gasket in the upper region (or in a Teflon gasket) (Figure 14.6(a)).

The typical experimental conditions in the growth of aluminum berlinite used are given below:

Growth temperature	240 °C
Pressure	15–35 MPa
Solvents	Mixed acid mineralizers
Nutrient	Powdered nutrient, preferably aluminum phosphate glass
Filling	80%
ΔT	$5 < T < 30$ °C
Growth rate	0.35–0.50 mm/day in H_3PO_4
	0.35–0.45 mm/day in HCl
	0.25–0.35 mm/day in HNO_3
	0.2–0.3 mm/day in H_2SO_4

Similarly, the growth conditions for gallium berlinite are:

Experimental temperature	280 °C
Experimental pressure	8 MPa
Mineralizer (pH = 3–4 under ambient conditions)	$H_3PO_4 + H_2SO_4$

Figure 14.12 shows the characteristic photographs of berlinite crystals.

Although the growth of berlinite is not very popular, there are some groups still working on improving the growth conditions to obtain larger size crystals and use of other seed crystals like langasite, or aluminum berlinite for the growth of gallium berlinite crystals. If the researchers increase the size of the grown crystals at least by one-fourth the value of the quartz under hydrothermal conditions, then $GaPO_4$ would be the best piezoelectric material to replace quartz in the twenty-first century.

14.5.3 Potassium Titanyl Phosphate

Potassium titanyl phosphate, $KTiOPO_4$ (KTP) is one of the best nonlinear optical materials increasingly being used commercially for the second harmonic generation (SHG)

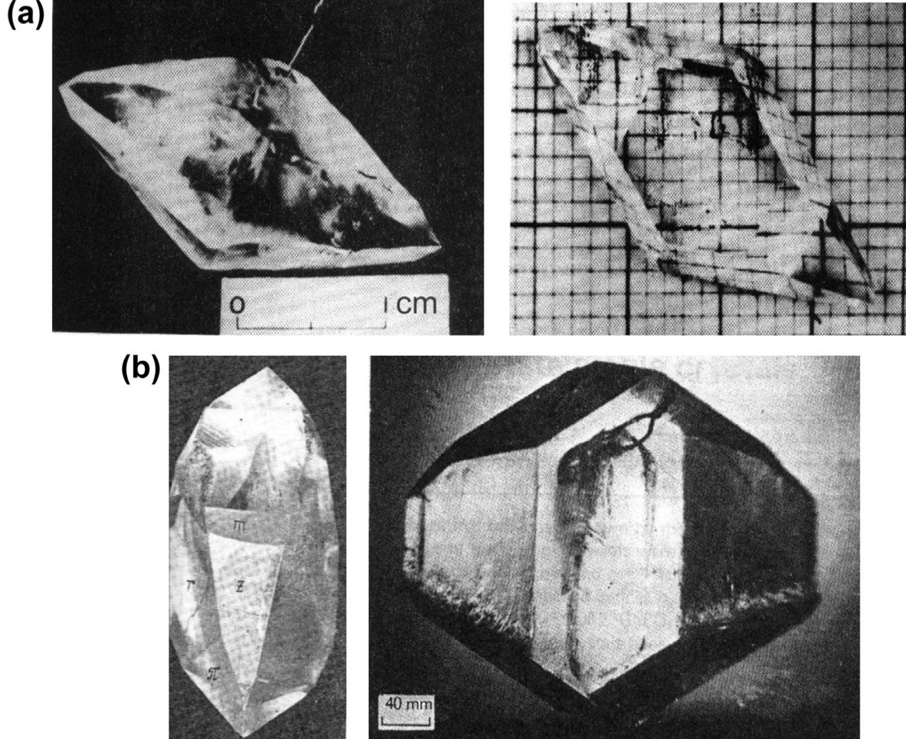

FIGURE 14.12 Hydrothermally grown: (a) aluminum berlinite crystals *(Courtesy Y. Toudic.)*; (b) $GaPO_4$ crystals. *Courtesy L. N. Demianets.*

and parametric oscillation since its discovery and introduction in 1976 [88]. KTP crystals are mechanically, chemically, and thermally stable and nonhygroscopic with high nonlinear optical coefficients and high conversion efficiency. It belongs to the family of compounds that have the formula unit $MTiOXO_4$, where M = K, Rb, Tl, NH_4, or Cs (partial) and X = P or As. All members belong to the orthorhombic space group, $P_{na21,}$ point group, mm2, with the following lattice cell parameters: a = 12.814, b = 6.404, c = 10.616 Å, V = 371.115 $Å^3$.

KTP decomposes before melting at 1148 °C. Thus, incongruent melting and glass formation make it impossible to grow KTP crystals directly from the melt. Similarly, growth from aqueous solution at low temperature (less than 300 °C) is impossible because of the low solubility of KTP. Therefore, large single crystals of KTP can be grown by both high temperature and pressure hydrothermal and flux techniques. There are several problems with reference to the quality of the crystals grown by the flux method. When pure phosphate self-fluxes is used, the main problem is the high melt viscosity. It has a tendency to spuriously nucleate and also to leave behind major structural defects and the inclusions of the solvents in the crystals. In fact, when the authors [88,89] synthesized KTP by the hydrothermal method, the pressure–temperature conditions were quite high (P = 1.5–3 kbar, T = 650° to 700 °C). The crystal size was not more than a few millimeters since the experiments were carried out in small platinum or gold capsules. Liu et al. have reported the growth and properties of hydrothermally grown KTP [90,91]. They prepared nutrient by the reaction of KH_2PO_4 and TiO_2 at 1250 °C. The hydrothermal “flux” was 1.5 KH_2PO_4, 1.0 TiO_2 in Ag^- or Au^- lined autoclaves at a pressure of 24−28 kpsi (1.66–1.93 kbar) and 520−560 °C in a gradient of 30−70 °C. Growth rate on (011) was 0.2−1.8 mm/week. The use of solvothermal technique along with the organic additives and surfactant has brought down the pressure–temperature conditions for KTP growth. It has renewed interest in KTP crystal growth. Laudise et al. have carried out PVT measurements on 2 M K_2HPO_4 and 2 M K_2HPO_4 saturated with KTP [92]. Zhang et al. succeeded in growing KTP crystals with high damage threshold by hydrothermal method [93]. Usually the flux grown small crystals of KTP are used as the nutrient material.

Belt and coworkers from Airtron Division of Litton Systems have increased the autoclave volume further and developed the low temperature hydrothermal process in 5-liter systems. These large autoclaves have produced the largest KTP single crystals available in the world (Figure 14.13(a and b)). These crystals are typically 4 × 5 × 8 cm and easily provide finished parallelepipeds of 1−1.5 cm^2 apertures and up to 2-cm long when material is extracted from either side of a seed [94]. Figure 14.13(b) shows a high quality KTP crystal obtained by Zhang et al. under hydrothermal conditions [93]. The darkening of KTP crystals caused by the oxygen deficiency can be overcome by adding an oxidizing agent like 1–5 wt% of H_2O_2 into the mineralizer solution.

Similarly, potassium titanyl arsenate (KTA) is another important nonlinear optical crystal belonging to this family of KTP, and some researchers have proved this to be superior to KTP. The crystal growth methods are analogous to those used for KTP [95]. In

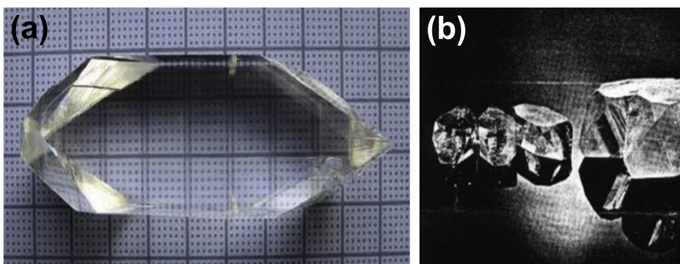

FIGURE 14.13 Hydrothermally grown KTP crystal (a) *(Photo courtesy C. L. Zhang.)*; KTP crystals grown using 5-L capacity autoclaves (b). *Courtesy R. F. Belt.*

recent years, the growth of small size and nanosize crystals of KTP is an attractive field in the area of biolabels.

14.5.4 Calcite

Calcite is one of the most well-studied materials. Optically clear calcite is called Iceland spar, and it exists in at least five modifications. The two polymorphs commonly found in nature are calcite and aragonite. In addition, there are two synthetic forms known only at high pressures: calcite II and calcite III. Vaterite (γ-$CaCO_3$) is a metastable hexagonal form that crystallizes at ordinary temperatures and pressures [96]. Several growth techniques have been employed to grow large single crystals of calcite, but most of these techniques encounter problems owing to the thermal stress, CO_2 dissociation, and metal ions contamination. Hence, hydrothermal remains one of the most promising techniques for growing calcite and other carbonates with the advantage of suppressing the dissociation of CO_2 and yielding high quality crystals in a homogeneous ambient at relatively low temperatures [97]. Many researchers have tried to grow calcite single crystals at relatively low temperatures since calcite crystals dissociate to form CaO and CO_2 above 900 °C under atmospheric pressure. Varieties of solvents have been used for hydrothermal growth of calcite, but none of them has succeeded in growing large single crystals. The solubility of calcite is very interesting. It has been studied in water under various CO_2 pressures [98,99]. Ikornikova [99] has carried out an extensive work on the growth of calcite covering aspects like solubility, designing of apparatus, growth kinetics, and growth mechanism.

For hydrothermal crystal growth of calcite, several inorganic solvents like NaCl, LiCl, $CaCl_2$, $NaNO_3$, $Ca(NO_3)_2$, NH_4NO_3, K_2CO_3, and carbonic acid have been employed as mineralizers. The growth conditions vary from 150 °C and 15 MPa to 600 °C and 200 MPa. No one has used organic salt solutions to grow calcite crystals under hydrothermal conditions, and also solvothermal growth of bulk single crystals of calcite is not popular. The authors [100] have studied the effect of pH and increase of carbon number in alkyl group of the ammonium monocarboxylate solvents on the growth of calcite and also the effect of dopant metals on the dislocation density of calcite crystals. Solubility of calcite can be both positive and negative for increasing CO_2 pressure and increasing temperatures, respectively.

Kinloch et al. have obtained calcite single crystals in large autoclaves provided with cylindrical silver and platinum liners using the following experimental conditions [101]:

Nutrient	45 kg of optical grade crystals of Mexican origin
Seeds	Natural calcite crystals cutting rhombohedra with 10–20 cm^2 surfaces and 1–2 cm thick
Solvent	6 M K_2CO_3
Nutrient temperature	435–445 °C
Seed temperature range	410–425 °C
% fill	86% (1.72 kbar)
Baffle opening	8%
Temperature gradient	5–10 °C
Experimental duration	30–50 days
Growth rate obtained	50 μm/day/face for {1011} face

Much of the recent work on the growth of calcite single crystals is being carried out under moderate to lower temperatures (200–150 °C) using several new solvents like ammonium nitrate, ammonium acetate, and so on in autoclaves provided with Teflon liners. A considerable amount of progress has been achieved in the single crystal growth of calcite with reference to the solubility, growth rate, reaction kinetics, seed orientation, morphology, surface morphology, optical and laser quality, and so on. The rhombohedral face (1011) is the fastest growing face. Hence, natural calcite crystals cleaved at (1011) plane are used generally as seed crystals. This provides good quality calcite crystals obtained with a temperature gradient of 15 °C and growth temperature of 235 °C, with a growth rate of 57 μm/day. Figure 14.14 shows the hydrothermally grown calcite crystals.

14.5.5 Corundum, Ruby, Emerald

Corundum, Al_2O_3, is one of the most sought after materials in recent years for various applications, both in bulk and nanosize. It is stable under hydrothermal conditions at

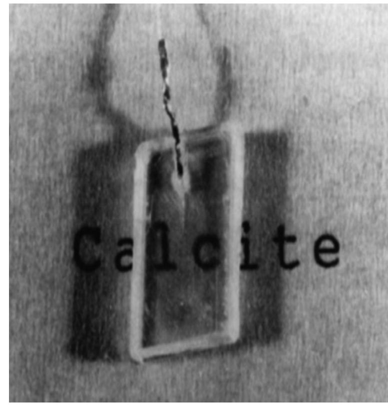

FIGURE 14.14 Calcite crystals obtained hydrothermally. *Courtesy Hirano.*

T > 400 °C [102,103] and is soluble in alkali and carbonate solutions. The hydrothermal growth of corundum is achieved using a metastable-phase technique because of a very low solubility. Gibbsite ($Al(OH)_3$) is used as a nutrient, α-Al_2O_3 as a seed, and an alkaline solution as a solvent. A more rapid growth rate is obtained in KOH or K_2CO_3 solution than in NaOH or Na_2CO_3 solution. The lower the pH level in the solution, the thicker the growth layer, along the c-axis. Kashkurov et al. have studied the growth of large corundum crystals at pressures up to 2000 atm and at temperature up to 550 °C in alkali solutions of various concentrations; crystals weighing up to 1 kg were prepared by hydrothermal technique, and the imperfect state of these crystals was apparently associated with internal stresses and the mosaic structure of seed crystals that were prepared by Verneuil technique [104].

The ideal experimental conditions for the growth of good quality corundum crystals are:

Temperature	480 °C
Pressure	1.33 kbar
Mineralizer	4 M K_2CO_3
% fill	85%
ΔT	30 °C

The rise in temperature gives higher growth rate in the temperature interval 400–500 °C.

The solvothermal growth of crystals especially for the micron size crystals of alpha-alumina is very popular for various applications, and the growth can be achieved under much lower temperature and pressure in simple stainless steel autoclaves, using glycol based solvents.

Ruby and sapphire crystals are the colored varieties of corundum and are grown using the hydrothermal method popularly in carbonate solutions using the appropriate dopants to the similar experimental conditions as that of corundum crystal growth. Probably sapphire is the second material after quartz to be grown in any size by hydrothermal method, because of a wide range of applications, especially as substrate materials for other crystals. The solubility of sapphire and ruby are the same as that of corundum and it increases with temperature. However, when the concentration of these components in the nutrient is higher, >1.6% in 10% Na_2CO_3, solution crystals practically do not grow.

Monchamp et al. have carried out very large-scale growth of sapphire and ruby with considerable success [105]. Emerald is one of the important crystals being grown by hydrothermal technique, because of its beauty and rarity, and as a most popular gemstone. The presence of Cr^{3+} in beryl gives a green color emerald. The bluish-green variety of the same is known as aquamarine. Accordingly, beryl crystals that are greenish-yellow to iron-yellow and honey-yellow are called golden beryl. The rose-colored variety is called morganite or vorobyevite. Alkali metals are usually present in beryl as impurities. Although several researchers have attempted the growth of emerald since the late nineteenth century, the best work came from Nacken during the 1930s and

1940s. Subsequently, the hydrothermal growth of emerald was commercialized by Lechleitner of Innsbruck, Austria, during the 1960s and 1970s [106,107] and marketed under the names Emerita and Symerald. In addition, the Linde Division of the Union Carbide Corporation in 1965 commercially produced and marketed synthetic emerald. Emerald is typically grown under pressure of 10,000–20,000 psi at temperatures of 500–600 °C resulting from a 62% fill in the autoclave. A small temperature gradient of 10–12 °C is employed. Usually acidic solution or fluorine bearing solutions are used as solvents. This produces a growth rate of 0.33 mm/day. The emerald produced by Biron Mineral (Pvt.) Ltd., Australia, is very popular currently and its growth conditions remain classified.

14.5.6 Rare Earth Vanadates

Rare earth vanadates are known as multifunctional materials with attractive properties like highly efficient laser-diode pumped microlasers, efficient phosphors, polarizer materials, and low threshold laser hosts, magnetic, and bioimaging capabilities [108–111]. The major problem in the growth of rare earth vanadates is the presence of oxygen deficiencies/imperfections (color centers and inclusions) and additional phases. YVO_4 melts congruently [111] and vanadium oxides vaporize incongruently, causing changes in Y/V ratio and oxygen stoichiometry in the melt. The instability of pentavalent vanadium at higher temperatures and the loss of oxygen through surface encrustation by the reaction of the melt with the crucible material further complicate the growth processes. In order to overcome most of the difficulties encountered in the melt and high temperature solution techniques, the hydrothermal technique has been proposed as an alternate [112,113]. The experiments are usually carried out in the temperature range 240–400 °C, and the pressure from 40 bar to 1 kbar. The solubility of rare earth vanadates is found to be negative. It increases with the concentration of the solvent. Both acid and basic mineralizers are used in the growth of these vanadates. However, the acid mineralizers are more effective, especially the mixed acid mineralizers ($HCl + HNO_3$ in a particular molar ratio).

Byrappa et al. [112,113] have extensively studied the morphology tuning through selective doping and experimental design. The presintered YVO_4 nutrient, and an oxidizing agent like hydrogen peroxide, yield better results. Figure 14.15 shows characteristic photographs of Nd:YVO_4 crystals.

14.5.7 Native Elements, Simple Oxides, and Sulfides

The hydrothermal technique is especially suitable for obtaining pure and high quality crystals of several elements. Interest in the synthesis of these elements has rejuvenated, particularly after the discovery of noble metals in seafloor hydrothermal mineralization [114,115]. Gold, silver, iridium, palladium, platinum, etc. have been reported in hydrothermal mineralization from two mid-oceanic ridges: Juan de Fuca and Mid-Atlantic at 26°N [115]. In fact, this has also led to the development of a new branch of science called

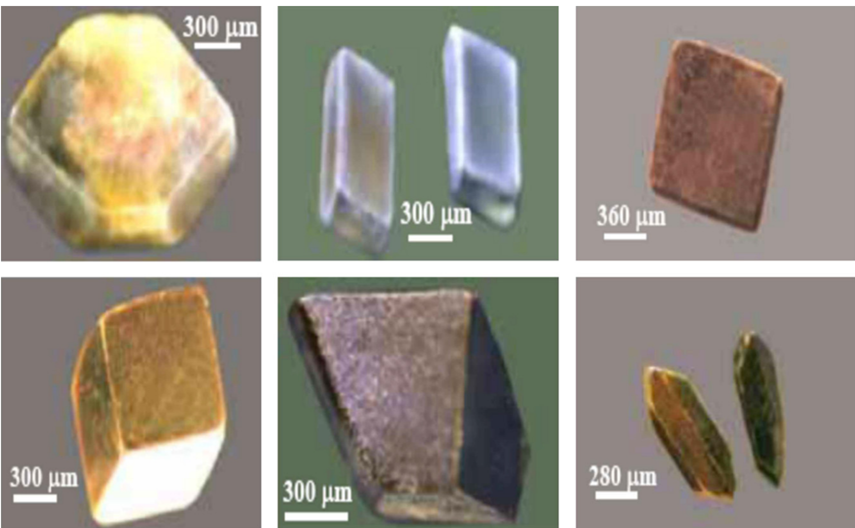

FIGURE 14.15 Characteristic photographs of Nd: YVO_4 crystals. *Courtesy K. Byrappa.*

geomicrobiology, and biologists have begun to synthesize nanoparticles of several metals, particularly gold, silver, copper, and so on combining the hydrothermal solution medium and the bacterial activity based on the nature-inspired processes. The hydrothermal synthesis of noble metals takes place through two types of reactions:

$$2Me(s) + 2(OH)^{-}(1) \rightarrow 2MeO_x(1) + H_2\uparrow$$
$$2Me(s) + 2(HI)(1) \rightarrow 2MeL(1) + H_2\uparrow$$

where L = acid anion (ligand).

The first reaction is characteristic of alkali solutions and the second reaction is characteristic of acids. In both cases, hydrogen helps in establishing equilibrium. As a result of this, the desired metal crystallizes. If the temperature gradient is maintained in the autoclave, the reaction route is determined by the Eh of metals from temperatures. Therefore, in one case, the crystallization of native metal crystals takes place in the hotter zone, and in the other case, in the cooler zone. It is possible to obtain the entire series of metals as single crystals when an oxidizing agent like halogenide is used [116].

Hydrothermal technique is highly suitable for the growth of oxides of various metals in polyscale. TiO_2, ZrO_2, HfO_2, Cu_2O, BeO, Bi_2O_3, In_2O_3, $A1_2O_3$, ZnO, Fe_2O_3, etc. have been obtained by the hydrothermal method. Some of these carry great significance as synthetic gemstones, and some as technological materials both in nanosize and bulk size. Here, we describe the hydrothermal growth of ZnO as it is one of the most studied materials in recent years. It is well known as *n*-type wide band gap semiconductor with unique mechanical, electrical, and optical properties. ZnO is also used in UV light emitting diodes and UV lasers operating at room temperature and display devices [117–119]. Moreover, ZnO quantum dots with very low toxicity, high photostability, and that are biofriendly and biodegradable have been demonstrated.

The hydrothermal technique is found to be the most suitable one for the growth of ZnO crystals. Seeded crystal growth of zincite has been carried out using NaOH and KOH solutions and, similarly, aqueous solutions of chlorides. The most useful solvent is 2–10 M KOH, in which the growth takes place within a wide temperature interval 200–500 °C and $P = 150$–600 atm. Lobachev et al. have studied the solubility of zincite in detail [117].

Sakagami has obtained high purity zincite crystals by hydrothermal method under partial pressure of oxygen in platinum-lined autoclaves using the following conditions [119]:

Growth temperature	370–400 °C
Temperature difference	10–15 °C
Total pressure	700–1000 kg/cm
Partial pressure	10–30 kg/cm
Solvent	KOH 3.0 M + LiOH 1.5 M
Oxidizer	H_2O_2 0.1–0.3 M
Nutrient	ZnO sinter
Lining tube	Point (0.3 mm thickness)
Growth run	15–20 days/run

Ehrentraut et al. [120] have successfully grown large size single crystals of ZnO using hydrothermal method. These authors used the crystal growth mechanism of ZnO proposed by earlier workers [121]. Almost 100 specimens of 2-in size have been grown on mainly (0001) and (1010) oriented seeds. All crystals developed excellent facets, and the average crystal thickness was about 1 cm in the <0001> direction (Figure 14.16(a)). A ZnO crystal of 3-in diameter and a wafer processed from it are shown in Figure 14.16(b and c), respectively. These are the largest ZnO single crystals grown by hydrothermal method.

Hydrothermal growth of other oxides of Ti, Zr, Hf, Fe, Te, Mn, In, and mixed oxides of aluminates, antimonites, antimonates, garnets, ferrites, and also some complex oxides has been reported extensively in the literature [3,19].

14.5.8 Complex Coordinated Crystals

The complex coordinated crystals include silicates, phosphates, vanadates, arsenates, molybdates, tungstates, fluorides, sulfates, selenides, borates, and so on, with a great variety of cations starting from alkali, alkaline-earth, transitional, to rare earth metals. The number of all such compounds exceeds several hundred owing to their academic and technological interest, and here it is impossible to discuss each compound. Instead, we offer a broad outline of the hydrothermal growth of these complex coordinated crystals, especially rare earth silicates, germanates, phosphates, and fluorides because of their academic and technological importance. Many of these compounds were found to be new phases with unique physical properties. These rare earth silicates, germinates, phosphates, fluorides, and borates exhibit very interesting mixed framework structures, and the alkali ion if present can serve as a mobile charge carrier. Most of these mixed framework structures are prepared under alkali-rich environment under higher

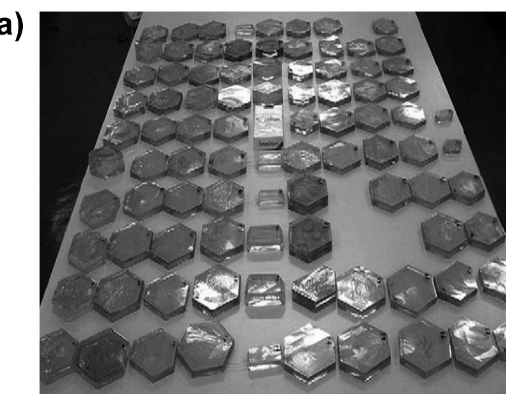

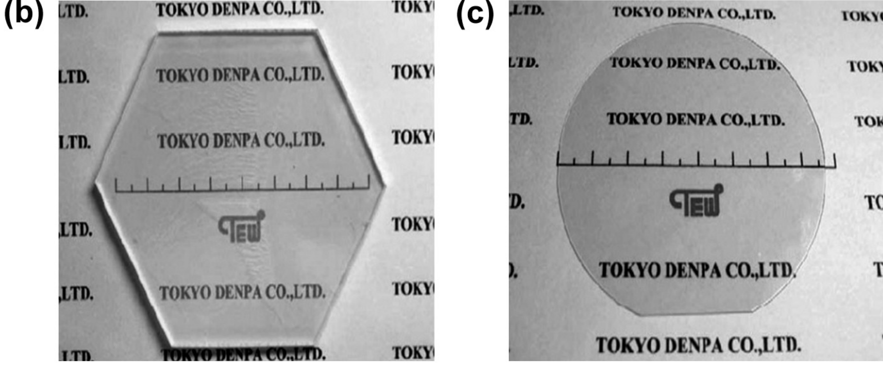

FIGURE 14.16 ZnO crystals of size 2 in produced in one growth run. (a) *(Courtesy D. Ehrentraut.)* View down c-axis of (a) 3-in ZnO crystal and (b) 3-in (0001) ZnO wafer (b,c). Scale bar is 80 mm. *Courtesy D. Ehrentraut.*

pressure–temperature conditions. The thermal and chemical stability of these compounds is very high, and hence requires highly acid or basic conditions to prepare these compounds. All the information related to the phase equilibria, kinetics, and properties of these compounds has been discussed in the literature. The growth of these crystals was extremely popular from the 1960s to 1980s. Demyanets, Dimitrova, Litvin, Byrappa, etc. have carried out extensive studies on these compounds, and a good review of these works is found in Refs [3,122–124].

The solvothermal growth of nitrides is very popular, and this topic is discussed separately in this book.

14.6 Hydrothermal Growth of Fine to Nanocrystals

The growth of fine to nanocrystals is not new to hydrothermal research. The earliest research on hydrothermal work mostly yielded small size products that were discarded as failures. When Barrer reported the hydrothermal synthesis of fine particles of zeolites in the 1940s, this opened up a new branch of science, viz. molecular sieve technology.

Hydrothermal research during the 1990s marked the beginning of work on the processing of fine to ultrafine crystals with controlled size and morphology. Today, this has become as one of the most efficient methods in preparative chemistry for advanced materials like fine to nanocrystals with a controlled size and shape. Currently, the annual market value of electronic ceramics is over a billion dollars, and the market for nanocrystals is a trillion-dollar industry as per National Science Foundation (NSF) prediction.

Of all the ceramics, the PZT family of ceramics has been studied extensively using the hydrothermal technique. Since the early 1980s, several thousands of reports have appeared on the preparation of these ceramics. Thermodynamic calculation and kinetics of these systems have been studied extensively. A great variety of precursors and also the solvents have been attempted in the processing of these fine crystals. Similarly, fine film formation of these on an appropriate substrate has been accomplished by several researchers [125,126] for a wide variety of technological applications such as electronics, optoelectronics, catalysis, ceramics, magnetic data storage, biomedical applications, biophotonics, etc. On the whole, the twenty-first century hydrothermal technology is more inclined toward nanotechnology owing to its advantages in obtaining high quality, monodispersed, homogeneous nanocrystals with a controlled size and shape, besides the lower PT conditions of the synthesis, simple apparatus, short experimental duration and lower cost of production. The greatest advantage is that the nanocrystals with desired surface chemistry can be achieved onto the nanocrystals in situ with the help of surface modifiers and capping agents. Almost all the groups of advanced nanocrystals like metals, metal oxides, and semiconductors including the II-VI and III-V compounds, silicates, sulfides, hydroxides, tungstates, titanates, carbon, zeolites, etc. have been processed by hydrothermal technique.

Figures 14.17(a–d) show the designer fine crystals of PZT, $LiMn_2O_4$, $PbTiO_3$, and $BaTiO_3$ prepared under hydrothermal conditions.

Gersten has extensively reviewed the processing parameters of the synthesis of fine ferroelectric perovskite crystals by the hydrothermal method [72,127]. Accordingly, the first step in the growth of these fine particles is the thermodynamic verification of the correct processing conditions for the reaction of the desired product.

Figure 14.18 shows the TEM images of nanoparticles synthesized under supercritical hydrothermal conditions [6]. The nanoparticles obtained without modifier are aggregated and do not disperse in the aqueous solvents. Also the particle size is larger compared to the modified particles. It seems that because of redissolving of nanoparticles at very high and low pH, Ostwald repining occurs. Therefore, in surface modification, pH of the medium, isolectric point (iep) and another important parameter, viz. dissociation constant (pKa) of the modifiers are very important. At pH below pKa, the modifier does not dissociate. Moreover, below iep, the surface of metal oxide nanoparticles is surrounded by positive charges (major) and hydroxylic groups (minor). Under these conditions no chemical reaction occurs between the modifier and the metal oxide nanoparticle surface; only through a strong hydrogen bond can the modifier attach to the nanoparticle surface. In contrast, at higher pH than pKa, dissociation of modifier

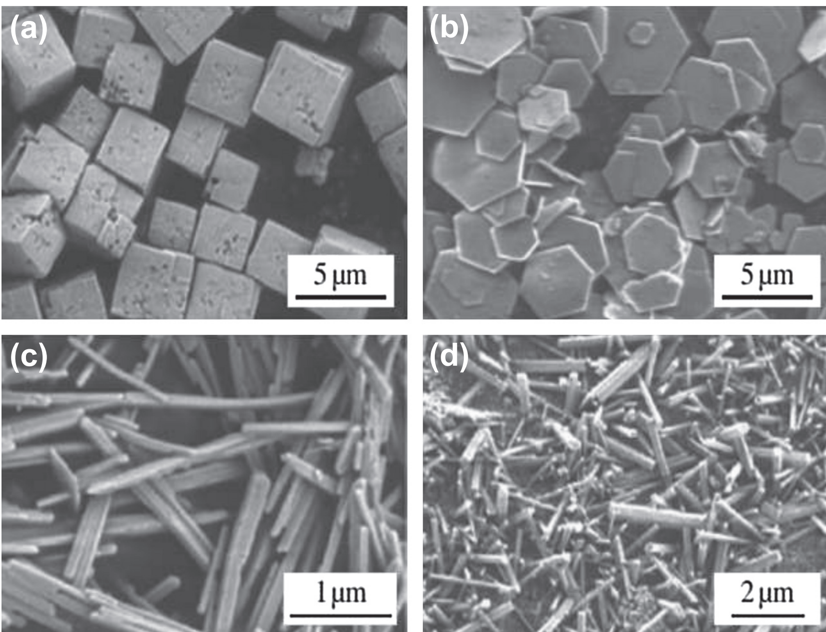

FIGURE 14.17 Hydrothermally synthesized fine crystals: (a) PZT; (b) $LiMn_2O_4$; (c) $PbTiO_3$; (d) $BaTiO_3$. *Courtesy Richard E. Riman.*

takes place and results in chemical reaction between dissociated part of modifier and OH_2^+ from the particle surface. Thus, by dehydration reaction the modifier attaches to the surface of the particles. By considering the chemical reactions, mass balances, charge balance in the actual system, pH and the modifier can be fixed for most of the systems. Figure 14.19 shows the mechanism involved in the in situ surface modification of the metal oxide nanocrystals under hydrothermal conditions.

There are thousands of reports on the hydrothermal synthesis of noble metal nanoparticles, magnetic metals, metal oxides including corundum or alpha-alumina, etc. under mild hydrothermal and solvothermal conditions. Also there is large number of publications on the supercritical water technology for a wide range of nanocrystal processing within a short period of time.

Hydrothermal synthesis of sulfides of various divalent, trivalent, and pentavalent metals forms an important group of materials for a variety of technological applications. They popularly form II-VI, III-VI, V-VI groups of semiconductors that are being studied extensively with respect to their different morphologies and particle size, which, in turn, greatly influence their properties. There are several hundreds of reports on these sulfides such as CdS, PbS, ZnS, CuS, NiS, NiS_2, NiS_7, Bi_2S_3, $AgIn_5S_8$, MoS, FeS_2, InS, Ag_2S, and so on, prepared through hydrothermal or solvothermal routes with or without capping agents/surfactants/additives to alter their morphologies and sizes as desired. Some of the II-VI group of nanocrystals form the core–shell structures and quantum dots for a variety of applications including in the biomedical field.

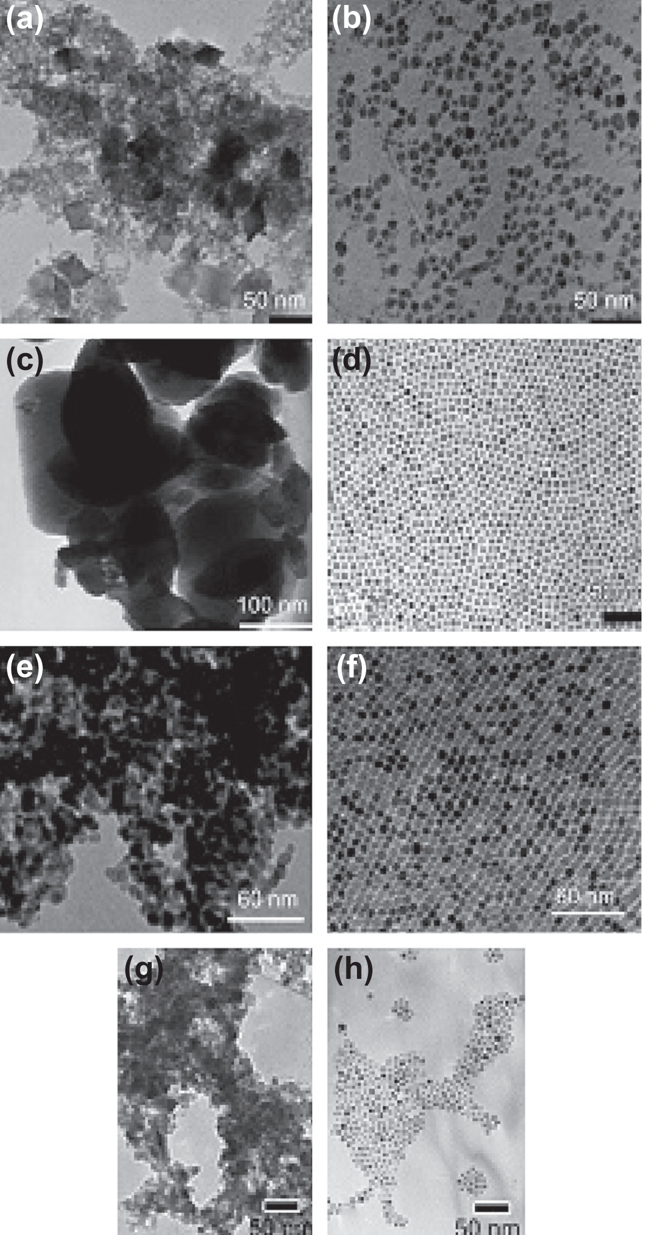

FIGURE 14.18 TEM images of nanocrystals synthesized under supercritical hydrothermal conditions: (a) Fe_2O_3 (without modifier); (b) Fe_2O_3 (with modifier); (c) Co_3O_4 (without modifier); (d) Co_3O_4 (with modifier); (e) CeO_2 (without modifier); (f) CeO_2 (with modifier); (g) TiO_2 (without modifier); and (h) TiO_2 (with modifier) [6]. *Courtesy K. Byrappa and T. Adschiri.*

Within nanocrystal synthesis, the synthesis of diamond nanocrystals under supercritical hydrothermal conditions is very interesting because these crystals form in the laboratory at pressure/temperature much lower than in the nature. Usually metal carbides are used as the source of carbon and several organic compounds are used as

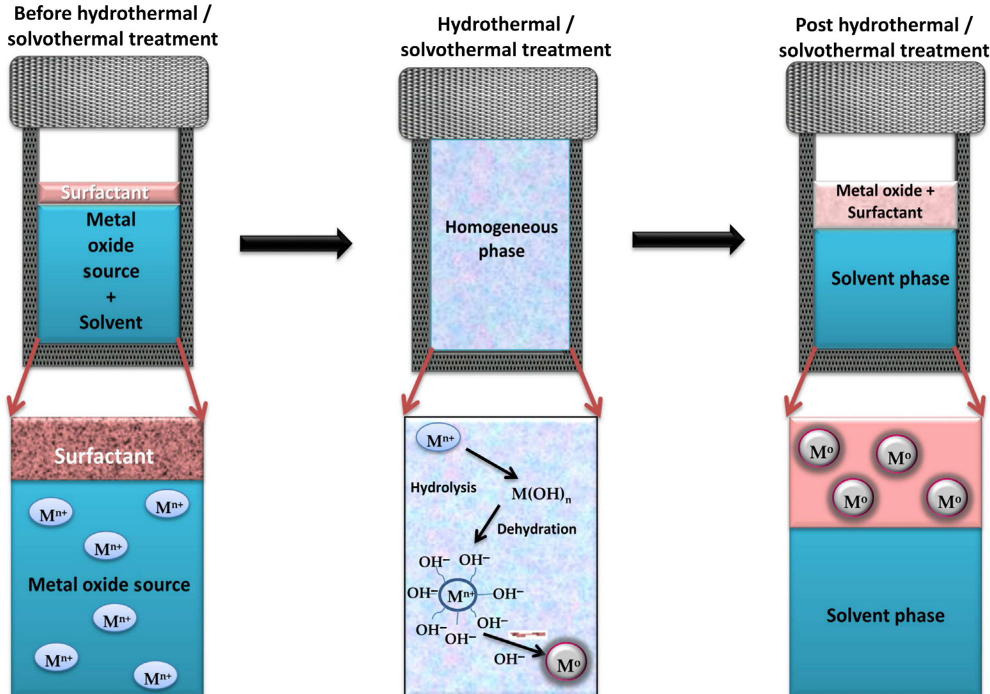

FIGURE 14.19 Mechanism involved in the in situ surface modification of the metal oxide nanocrystals under hydrothermal conditions. *Courtesy K. Byrappa.*

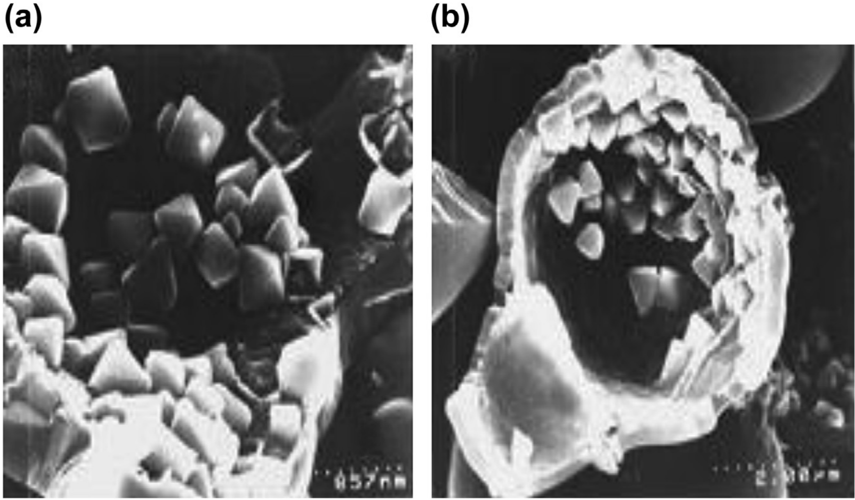

FIGURE 14.20 SEM images of diamond nanocrystals with well-developed octahedral facets adhered to the inner walls of the broken spherical particles [129]. a) under higher magnification; b) under lower magnification.

solvents and additives instead of water in diamond synthesis, and these organics decompose into various C–O–H fluids such as CO, OH, CO_2, and C_1H_x radicals. These fluids play a significant role in creating a highly reducing environment in the system and also assist in the dissociation of silicon carbide and precipitation of carbon phase [128,129]. Figure 14.20 shows SEM images of diamond nanocrystals with well-developed octahedral facets adhered to the inner walls of the broken spherical particles.

There are hundreds of reports on the hydrothermal preparation of nanocrystals of $AlPO_4$, ferrites, phosphors like Eu:$Y_2Sn_2O_7$, Nd:$YAlO_3$, GaN, GaP, vanadates, fluorides, carbonates, garnets, hydroxides, etc. using both hydrothermal and solvothermal routes.

14.7 Conclusions

The hydrothermal technique has evolved as one of the most efficient crystal growth methods. The importance of the technique in the preparation of GaN, ZnO, and AlN has been realized in recent years. The thermodynamic modeling and also the solution chemistry of the hydrothermal media have greatly contributed to the drastic reduction in the PT conditions of the growth of crystals. The application of additional energy such as microwave, sonar, mechanochemical, electrochemical, biomolecules, stirring, etc. take us to a different field like chemistry at the speed of light, because of the increased growth kinetics.. The organic molecules, capping agents, and surfactants assist in the in situ fabrication of crystals with desired surface charge to the crystal surface; in addition, the properties of the crystal surface can be altered to either hydrophobic or hydrophilic. This area of in situ crystal growth process is fast growing and makes the hydrothermal technique one of the most efficient in crystal growth.

References

[1] Sir Roderick Murchison (1840s), (cited by S. Somiya).

[2] Byrappa K. Hydrothermal processing of advanced materials. In: Kirk-othmer encyclopedia of chemical technology. London: John Wiley & Sons; 2005.

[3] Byrappa K, editor. Hydrothermal growth of crystals. Progress crystal growth characterization of materials, vol. 21; 1990.

[4] Byrappa K, Adschiri T. Prog Cryst Growth Charact Mater 2007;53:117.

[5] Byrappa K. In: Dhanaraj G, Byrappa K, Prasad V, Dudley M, editors. Springer handbook of crystal growth. Germany: Springer-Verlag; 2010.

[6] Byrappa K, Ceram J. Soc Jpn 2009:117.

[7] Tuitemwong PELE, Fung DVC, Tuitemwong K. J Food Process Preserv 1993;17. 153A175.

[8] Liu Y, Ren L, Qi X, Wang Y, Liu X, Zhong J. RSC Adv 2014;4:8772.

[9] Byrappa K, Yoshimura M, editors. Special ed.: J Mater Sci; 2006. p. 41.

[10] Byrappa K, Adschiri T, editors. Special ed.: J Mater Sci; 2008. p. 43.

[11] Hedin N, Graf R, Christiansen SC, Gervais C, Hayward RC, Eckert J, et al. J Am Chem Soc 2004;126: 9425.

[12] Hulvey Z, Ayala E, Furman JD, Forster PM, Cheetham AK. Cryst Growth Des 2009;9:4759.

[13] Zou C, Zhang Z, Xu X, Gong Q, Li J, Wu CD. J Am Chem Soc 2012;87:134.

[14] Kreno LE, Leong K, Farha OK, Allendorf M, Van Duyne RP, Hupp JT. Chem Rev 2012;112:1105.

[15] Yoshimura M, Byrappa K. J Mat Sci 2008;43:2085.

[16] Roy R. Fifty-year perspective on hydrothermal research. In: Proc workshop on solvothermal and hydrothermal reacts. Japan: Sun Mess Kogawa; January 22–24, 1996. 1.1–1.20.

[17] Byrappa K, Yoshimura M. Handbook of hydrothermal technology. 1st ed. NY (USA): William Andrew & Sons; 2001.

[18] Byrappa K. In: Hurle DTJ, editor. Handbook of crystal growth, vol. 2. The Netherlands: Elsevier Science Publishers BV; 1994. p. 465.

[19] Byrappa K, Yoshimura M. Handbook of hydrothermal technology. 2nd ed. USA: Elsevier; 2013.

[20] Bunsen R. The growth of single crystals (1839), (cited by Laudise RA). Englewood Cliffs (NJ): Prentice-Hall; 1970. p. 278–281.

[21] Schafthaul KFE. Gelehrte Anzeigen Bayer Akad 1845;20(557). p. 561, 569, 575, 593.

[22] Byrappa K. In: Capper Peter, editor. Bulk crystal growth of electronic, optical and optoelectronic materials. John Wiley and Sons; 2005. p. 387.

[23] Spezia G. Sull accresimento del Quarzo. Atti Accad Sci Torino 1900;35:95.

[24] Hannay JB. Proc R Soc Lond 1880;30:178.

[25] Moissan R. (cited by A.D. Edgar). Experimental petrology, basic principles and techniques, vol. 5. Oxford (UK): Clarendon Press; 1973.

[26] Spezia G. Atti Accad Sci Torino 1905;40:254.

[27] Barus C. Am J Sci 1898;6:270.

[28] Demazeau G, Marbeuf A, Pouchard M, Hagenmuller P. Sur une Serie de Compose's Oxygenes du Nickel Trivalent Derive's de la Perovskite. J Solid State Chem 1971;3:582.

[29] Nacken R. Artificial quartz crystals, etc; 1946. U.S. Office of Technical Services Report PB.

[30] Walker AC. Ind Eng Chem 1953;36:250.

[31] Nassau K. J Cryst Growth 1976;35:211.

[32] Franck EU. In: Rickard DT, Wickman FE, editors. Chemistry and geochemistry of solutions at high temperatures and pressures. Proc. noble symp, vol. 13/14. New York: Pergamon Press; September 1979. pp. 65–88.

[33] Seward TM. In: Rickard DT, Wickman FE, editors. Chemistry and geochemistry of solutions at high temperatures and pressures. Proc. noble symp, vol. 13/14. New York: Pergamon Press; September 1979. pp. 113–32.

[34] Helgeson HC. In: Rickard DT, Wickman FE, editors. Chemistry and geochemistry of solutions at high temperatures and pressures. Proc. noble symp, vol. 13/14. New York: Pergamon Press; September 1979. pp. 133–78.

[35] Pitzer KS. In: Rickard DT, Wickman FE, editors. Chemistry and geochemistry of solutions at high temperatures and pressures. Proc. noble symp, vol. 13/14. New York: Pergamon Press; September 1979. pp. 249–72.

[36] Ezersky AB, Garcimartin A, Burguete J, Mancini HL, Perez-Garcia C. Phys Rev E 1993;47:1126.

[37] Ezersky AB, Garcimartin A, Mancini HL, Perez-Garcia C. Phys Rev E 1995;48:4414.

[38] Balitsky VS, Bublikova TM. Hydrothermal growth of crystals. Prog Cryst Growth Charact Mater 1990;21:139.

[39] Kuznetsov VA. Hydrothermal growth of crystals. Prog Cryst Growth Charact Mater 1990;21:163.

[40] Popolitov VI. Hydrothermal growth of crystals. Prog Cryst Growth Charact Mater 1991;21:255.

[41] Zakirov IV. Experimental investigations of PVT relations in the H2O–CO2 system [Ph.D. thesis]. Moscow: Moscow State University; 1987.

[42] Spycher N, Pruess K, Ennis-King J. Geochim et Cosmochim Acta 2003;67:3015.

[43] Ilijushin GD, Demianets LN, Iljukhin VV, Belov NV. Dokl Akad Nauk USSR (In Russian) 1983;217: 1133.

[44] Deidler K. Kinetics of organic reactions M. p. 237. Moscow: Mir; 1966.

[45] Uematsu M, Franck EU, Phys J. Chem Ref Data 1980;9:1291.

[46] Kennedy GC, Holser WT. In: Clark Jr SP, editor. Handbook of physical constants. Washington (DC): Geological Society of America; 1966. pp. 371–83.

[47] Koster H, Franck EU. Ber Bunsenges 1969;73:716.

[48] Todheide K. In: Franks F, editor. Water a comprehensive treatise, vol. 1. New York: Plenum Press; 1972. pp. 463–514.

[49] Anderson GM, Castet S, Schoot J, Mesmer RE. Geochim Cosmochim Acta 1991;55:1769.

[50] Franck EU. Pure Appl Chem 1981;53:1401.

[51] Riman RE, Lencka MM, McCandlish LE, Gersten BL, Andrenko A, Cho SB. In: Palmer DA, Wesolowski DJ, editors. Proc. 5th int. symp. hydrothermal reactions; July 20–24, 1997. pp. 74–8. Gatlinburg (Tennessee, USA).

[52] Lencka MM, Riman RE. Chem Mater 1993;5:61.

[53] Lencka MM, Riman RE. Chem Mater 1995;7:18.

[54] Byrappa K, Riman RE. In: Yanagisawa K, Feng Q, editors. Proc. joint ISHR-6 and ICSTR-4. Kochi (Japan): Nishimura Tosha-Do Ltd; 2000. p.389.

[55] Seward TM. Metal complex formation in aqueous solutions at elevated temperatures and pressures. Proc Nobel Symp Phys Chem Earth 1981;13/14:132.

[56] Helgeson HC. Prediction of the thermodynamic properties of electrolytes at high pressures and temperatures. Proc Nobel Symp Phys Chem Earth 1981;13/14:177.

[57] Weast RC, editor. Handbook of physics and chemistry, D261. 64th ed. Boca Raton (FL): CRC Press; 1983.

[58] Haman SD. Phys Chem Earth 1981;13/14:89.

[59] Todheide K. Ber. Bunsenges, Hydrothermal solutions. Phys Chem 1982;86:1005.

[60] Frank EU. Properties of water. Int Corros Conf Ser 1973;109:45.

[61] Kennedy GC. Am J Sci 1950;248:540.

[62] Bernstein S, Fehr KT. Prog Cryst Growth Charact Mater 2011;58:84.

[63] Middelkoop V, Jacques SD, O'Brien MG, Beale AM, Barnes P. J Mat Sci 2008;43:2222.

[64] Lencka MM, Andrenko A, Riman RE. J Am Ceram Soc 1995;78:2609.

[65] Riman RE, Suchanek WL, Byrappa K, Chen CW, Shuk P, Oakes CS. Solid State Ionics 2002;151:393.

[66] Laudise RA, Ballman AA. J Phys Chem 1961;65:1396.

[67] John VM, Kordes S. Chem Earth 1953;70:75.

[68] Stanely JM. Ind Eng Chem 1954;468:1684.

[69] Byrappa K, Venkatachalapathy V, Puttaraju B. J Mater Sci 1984;19:2855.

[70] Environmental and corrosion simulation program (ESP/CSP) version 6.7. Morris Plains (NJ): OLI Systems, Inc.; 2010.

[71] Eckert Jr JO, Hung-Houston CC, Gersten BL, Lencka MM, Riman RE. J Am Ceram Soc 1996;79:2929.

[72] Gersten BL. Influences of the A and B site cation species in the kinetics of hydrothermal synthesis of ABO_3 perovskite-type materials [Ph.D. thesis]. Rutgers University, NJ, USA; 1999.

[73] Rabenau A. Angew Chem (Engl Ed) 1985;24:1026.

[74] Laudise RA. The growth of single crystals. New Jersey (NY, USA): Prentice-Hall Inc.; 1973. p. 286.

[75] Morey GW, Niggli P. J Am Chem Soc 1913;35:1086.

[76] Laudise RA, Nielsen JW. Solid State Phys 1961;12:149.

[77] Lafon F, Demazean G. J Phys IV 4[C_2] 1994;177.

[78] Martin JJ, Armington AF. J Cryst Growth 1983;62:203.

[79] Balitskii VS, Lisinstina EE. Synthetic analogues and imitation of natural gemstones. Moscow: Nedra; 1981.

[80] Nassau K. Gemstone enhancement. 2nd ed. Boston (Mass): Butterworths; 1984. 1994.

[81] Murakami Y, Chiashi S, Miyauchi Y, Hu M, Ogura M, Okubo T, et al. Chem Phys Lett 2004;385:298.

[82] Chang ZP, Barsch GR. IEEE Trans Sonics Ultrason 1976;23:127.

[83] Jacobs K, Hofmann P, Klimm D, Reichow J, Schneider M. J Solid State Chem 2000;14:180–8.

[84] Kolb ED, Laudise RA. J Cryst Growth 1978:43.

[85] Prud'homme N, Cachau-Herreillat D, Papet P, Cambon O. J Cryst Growth 2006;286:102.

[86] Balitsky DV, Philippot E, Papet Ph, Balitsky VS, Pey F. J Cryst Growth 2005;275:887.

[87] Beaurain M, Armand P, Papet P. J Cryst Growth 2006;294:396.

[88] Zumsteg FC, Bierlein JD, Gier TE. J Appl Phys 1976;47:4980.

[89] US Patent, 3, 949, 323, Bierlein JD, Assigned to E. I. Du Pont de Nemours and Company. April 6, 1976.

[90] Liu YS, Drafall L, Dentz D, Belt R. Nonlinear optical phase-matching properties of KTiOPO4 (KTP). G.E. Tech. Inf. Series Rep. No. 82 CR DO16. Schenectady (New York): General Electric Company; 1982.

[91] Liu YS, Dentz D, Belt R. Opt Lett 1984:76.

[92] Laudise RA, Sunder WA, Belt RF, Gashurov G. J Cryst Growth 1990:102.

[93] Zhang ZL, Hu ZG, Huang LX, Zhou WN, Lu Z, Zhang G, et al. J Cryst Growth 2008;310:2010.

[94] Belt RF, Iradi T. Hydrothermal growth produces large KTP nonlinear crystals. Laser Focus World November 1993:155–62.

[95] Masse R, Grenier JC. Bull Soc Fr Mineral Crist 1971;94:437.

[96] Deer WA, Howie RA, Zussman J. An introduction to the rock-forming minerals. England: Longman Group Limited; 1966. p. 473.

[97] Hirano S, Kikuta K. J Cryst Growth 1989;94:113.

[98] Gorai M, Syuutou K. In: Tikaku Ganseki Koukutsu. Japan: Kyuyitsu Publishing House; 1981. p. 123.

[99] Ikornikova N Yu. Hydrothermal synthesis of crystals in chloride systems (in russian). Moscow (Russia): Nauka; 1975. 1–222.

[100] Yanagisawa K, Feng Q, loku K, Yamasaki N. J Cryst Growth 1996;163:285.

[101] Kinloch DR, Belt RF, Puttbach RC. J Cryst Growth 1974;24/25:610.

[102] Barus RL, Laudise RA, Shields RM. J Phys Chem 1963;67:835.

[103] Yamaguchi G, Yanagida H, Sojma S. Bull Soc Chem Jpn 1962;35:1789.

[104] Kashkurov KF, Nikitichev PI, Osipov VV, Sizova LD, Simonov AV. Sov Phys Crystallogr 1968;12:837.

[105] Monchamp RR, Puttbach RC, Nielson JW. J Cryst Growth 1968;2:178.

[106] Anderson BW. Gem testing. 8th ed. London (UK): Butterworths; 1971.

[107] Liddicoat Jr RT. Handbook of gem identification. 10th ed. Los Angeles (USA): Gemmological Institute of America; 1975.

[108] Chakoumakos BC, Abraham MM, Batner LA. J Solid State Chem 1994;109:197.

[109] Prasad M, Pandit A, Ansari TH, Singh RA, Wanklyn BM. Phys Lett 1989;A138:61.

[110] Chai BHT, Loutts G, Chang XX, Hong P, Bass M, Shcherbakov IA, et al. Advanced solid state lasers, technical digest, vol. 20. Washington (DC): Optical Society of America; 1994. 41.

[111] Byrappa K, Rai KML, Nirmala B, Yoshimura M. Mater Sci Forum 1999;506:315.

[112] Byrappa K, Chandrashekar CK, Rai KML, Basavalingu B, Soga K. J Mater Sci 2006;41:1415.

[113] Byrappa K, Chandrashekar CK, Lokanatha Rai KM, Ananda S, Yoshimura M. J Cryst Growth 2007;306:94.

[114] Crocket JH. Can Mineral 1990;28:639.

[115] Hannington MD, Peter JM, Scott SD. Econ Geol 1986;81:1867.

[116] Laudise RA, Nielsen JW. In: Seitz F, Turnbull D, editors. Solid state physics, vol. XII. New York: Academic; 1961.

[117] Lobachev AN, Kuzmina IP, Shaldin YuV. In: Crystal growth from high temperature aqueous solution. Moscow (Russia): Nauka; 1977. p. 158.

[118] Namratha K, Byrappa K. Prog Cryst Growth Charact Mater 2012;58:14.

[119] Sakagami N. J Cryst Growth 1990;99:905.

[120] Ehrentraut D, Sato H, Kagamitani Y, Sato H, Yoshikawa A, Fukuda T. Prog Cryst Growth Charact Mater 2006;52:280.

[121] Demianets LN, Kostomarov DV. Ann Chim Sci Mat 2001;26:193.

[122] Byrappa K. Prog Cryst Growth Charact 1986;3:163.

[123] Dimitrova OV [Ph.D. thesis]. Moscow: Moscow State University; 1977.

[124] Demianets LN, Lobachev AN, Emelchenko GA. Germanates of rare earth elements. Moscow: Nauka; 1980.

[125] Kajiyoshi K, Tomono K, Hamaji Y, Kasanami T, Yoshimura M. J Am Ceram Soc 1995;78:1521.

[126] Cho WS, Yashima M, Kakihana M, Kudo A, Sakata T, Yoshimura M. J Am Ceram Soc 1997;80:765.

[127] Gersten B. In: Byrappa K, Ohachi T, editors. Handbook of crystal growth technology. USA and Germany: William Andrew Publications and Springer; 2003. p. 299.

[128] Roy R, Ravichandran D, Ravindranathan P, Badzian A. J Mater Res 1996;11:1164.

[129] Basavalingu B, Byrappa K, Yoshimura M, Madhusudan P, Dayananda AS. J Mat Sci 2006;41:1465.

High-Pressure, High-Temperature Solution Growth and Ammonothermal Synthesis of Gallium Nitride Crystals

Dirk Ehrentraut

SORAA, INC., GOLETA, CA, USA

Michal Bockowski

INSTITUTE OF HIGH PRESSURE PHYSICS POLISH ACADEMY OF SCIENCES AND TOPGAN LTD., WARSAW, POLAND

CHAPTER OUTLINE

15.1 Introduction 578
15.2 High Nitrogen Pressure Solution Growth Method 579
15.2.1 Method and Experimental Setup 579
15.2.2 Thermodynamic and Kinetic Aspects 581
15.2.3 Spontaneous Crystallization 584
15.2.4 Seeded Growth 585
15.2.4.1 LPE Growth: Single Seed Configuration 585
15.2.4.2 LPE Growth: The Multifeed Seed Configuration 587
15.2.5 Perspective for HNPS Growth Method 594
15.3 Ammonothermal Growth of GaN 595
15.3.1 Historical Development of Ammonothermal Growth Techniques 595
15.3.2 Ammonothermal Growth Method 600
15.3.3 Chemistry of the Ammonothermal Solution 602
15.3.4 Solubility in Ammonothermal Growth 604
15.3.5 Growth Rates and Morphology 607
15.3.6 Doping under Ammonothermal Conditions 608
15.3.7 Properties of Ammonothermal GaN 610
15.3.8 Prospects and Future Developments for Ammonothermal GaN 613
15.4 Overall Summary with an Outlook into the Future 613
References 614

Handbook of Crystal Growth. http://dx.doi.org/10.1016/B978-0-444-63303-3.00015-8

Copyright © 2015 Elsevier B.V. All rights reserved.

15.1 Introduction

Gallium nitride (GaN)-based devices, such as light-emitting diodes (LEDs) and high electron mobility transistors (HEMTs), are mainly built on foreign substrates such as sapphire (α-Al_2O_3), silicon (Si), and silicon carbide (SiC). High-quality, free-standing (F-S), and large-size GaN substrates are far from being a commodity, as is the case for Si (>300 mm available), α-Al_2O_3 (150 mm), or SiC (150 mm); only 2-inch (50-mm) wafers with high defect densities (typically around $1 \times 10^6\ cm^{-2}$ and up) are being sold, at relatively high prices. Therefore, the nitride crystal growth community is looking for technologies to produce large-size, cost-efficient GaN substrates. For example, laser diodes (LDs), ultraviolet (UV), and blue and green LDs are exclusively built on a GaN foundation. The wafers have to be 2 inches or larger in diameter with a high structural integrity (structurally flat; i.e., low bow and threading dislocation density) and a free carrier concentration that is higher than $2 \times 10^{18}\ cm^{-3}$ to achieve appropriate electrical contacts with the epitaxial LD structure. For electronic applications, the GaN substrates should be at least 4 inches in diameter and be available at different levels of carrier concentrations, from n-type to semi-insulating types.

The growth of GaN bulk crystals has proven to be difficult. Gallium nitride compound melts at an extremely high temperature of 2493 K. The nitrogen (N_2) pressure necessary for congruent melting of GaN is 6 GPa [1]. Thus, it is currently impossible to crystallize GaN just from the melt using the Czochralski or Bridgman method. Therefore, other techniques requiring lower pressure and temperature, such as crystallization from vapor phase and from the solution, are being developed.

Hydride vapor phase epitaxy (HVPE) is currently the most common approach for manufacturing the vast majority of commercially available GaN substrates [2–5]. This technique has a relatively fast growth rate of up to 200 μm per hour, but it suffers from a phenomenon known as parasitic nucleation. The HVPE method involves crystallization at ambient pressure with GaN deposited on a foreign substrate through the reaction of ammonia (NH_3) with gallium chloride at temperatures of about 1300 K. Etching, laser lift-off, and self lift-off techniques can be used to remove the GaN from the foreign substrate to yield free-standing 2-, 4-, or even 6-inch GaN substrates. Deposition on a foreign substrate enables the growth of large-diameter GaN crystals, but these suffer from lattice bowing. This stems from significant differences between the lattice constant and thermal expansion coefficient of the foreign substrate and the nitride film. The bowing radii of crystallographic planes can be below 10 m. This relatively low number means that there is little benefit in using HVPE-grown GaN as a seed for subsequent crystallization runs.

The largest GaN crystallized from the solution is 3 inches, as obtained in the laboratory [6], but only 1-inch substrates are commercially available [7]. Crystallization from the solution is possible by employing supercritical ammonia (sc–NH_3; ammonothermal method) or using a solution with gallium (Ga) or gallium-sodium mixtures (sodium flux method). Each of these methods requires pressure that is far higher than atmospheric.

The role of pressure, its absolute value, and the medium that establishes it (N_2 or NH_3) is absolutely different for each of the growth methods. In the ammonothermal growth, high pressure allows one to obtain supercritical ammonia, which leads to sufficient solubility of GaN in the supercritical ammonia-based solution. The ammonothermal approach is analogous to the hydrothermal crystallization of quartz (α-SiO_2) [8] or zinc oxide (ZnO) [9], although supercritical ammonia is used in place of water. The supercritical state is generated by heating up the closed vessel, which contains ammonia, a mineralizer to enhance solubility of GaN in NH_3, a source for GaN, and any furniture and flow-guiding devices. The mass transport is governed by forced convection, which is the result of a temperature gradient between the crystal growth and feedstock zone.

In turn, in the sodium flux method, the high pressure of nitrogen ensures the supersaturation in the flux, because its value is higher than the equilibrium value for considered phases of the flux [10]. The growth proceeds at a constant temperature. The mass transport is governed by convection caused by mechanical stirring of the flux.

For the case of growth from gallium solution at high pressure, the high nitrogen pressure allows one to increase the range for the thermodynamic stability of GaN. Therefore, crystallization at high temperatures ($\sim$1800 K) becomes possible. The method is called high nitrogen pressure solution growth (HNPS). In this case, supersaturation is created by the presence of temperature gradient in the solution, and the mass transport is governed by forced convection. It makes this method more similar to the ammonothermal method than to a classic flux method. Although the range of applied temperatures and their gradients, as well as thermodynamic properties, are very different, the growth rate and structural quality of crystals obtained is similar. Thus, in this chapter, the two high-pressure growth methods will be described in detail: the ammonothermal technique and growth from gallium solution under high nitrogen pressure. The chapter starts with the description of the HNPS growth method. The second part deals with the ammonothermal technique to crystallize bulk GaN crystals.

15.2 High Nitrogen Pressure Solution Growth Method

15.2.1 Method and Experimental Setup

The HNPS growth method is a temperature gradient method based on a direct reaction between gallium and nitrogen at a high temperature (up to 2000 K) and a high nitrogen pressure (up to 1 GPa). Nitrogen molecules dissociate on the gallium surface and dissolve in the metal. Therefore, crystals are grown from the solution of atomic nitrogen in liquid gallium. Supersaturation, the driving force of the crystallization process, is created by the application of temperature gradient along the liquid gallium. Thus, the HNPS method consists of three stages: (1) dissociative adsorption of nitrogen on liquid metal surface, (2) dissolution and transport of nitrogen atoms from the hot end of the solution to the cooler one, and (3) the crystallization process.

Due to the temperature gradient in the system, the atomic nitrogen is transported from the hot end of the solution to the cooler part. It has been shown that the convection mechanism plays a dominant role in the transport phenomenon [11–13]. The nitrogen in the solution is uniformly distributed due to the convection flow. Thus, the solution at the cold part must be supersaturated. This means that the excess nitrogen concentration related to the equilibrium value for a given temperature exists at the cold part of the liquid metal. Hence, only in this zone does GaN crystal growth take place. The gallium nitride crystals can be grown spontaneously from the wall of the crucible; then, they are distributed randomly in the supersaturated cold zone of the solution. For a seeded crystallization, GaN or foreign seeds have to be immersed in the gallium at supersaturated zone of the solution. The schematic illustration of the HNPS method (spontaneous growth) is presented in Figure 15.1.

Typical crystal growth experiment is when the metal (Ga) placed in the crucible (graphite or boron nitride, BN) is heated in the furnace inside the high pressure reactor with a constant rate to given axial and/or radial temperature profiles [14]. Then, the system is annealed at these conditions under high nitrogen pressure (1 GPa or less) for 100–500 h. After that, the furnace is cooled down at a constant rate, the system is decompressed, and the metal with GaN crystals inside is removed. The charge from the crucible is etched with boiling HNO_3/HCl acid solution to extract the crystals. Vertically positioned, technological gas pressure chambers (reactors) of internal diameters up to 10 cm are used, allowing crucibles with working volumes up to 150 cm^3 [14]. The multizone cylindrical graphite furnaces, capable of reaching a maximum temperature of 2073 K, are placed inside the gas pressure reactors. To register the temperature during the crystal growth experiments, PtRh6%–PtRh30% thermocouples are used. They are

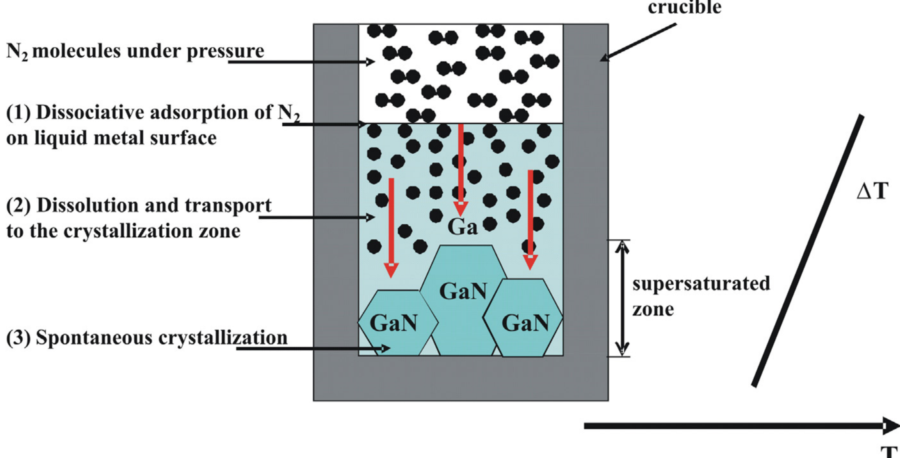

FIGURE 15.1 Schematic illustration of the crystallization process in a temperature gradient by the high pressure solution growth (HNPS) method. A spontaneous crystallization is shown; three basic stages of the method are marked.

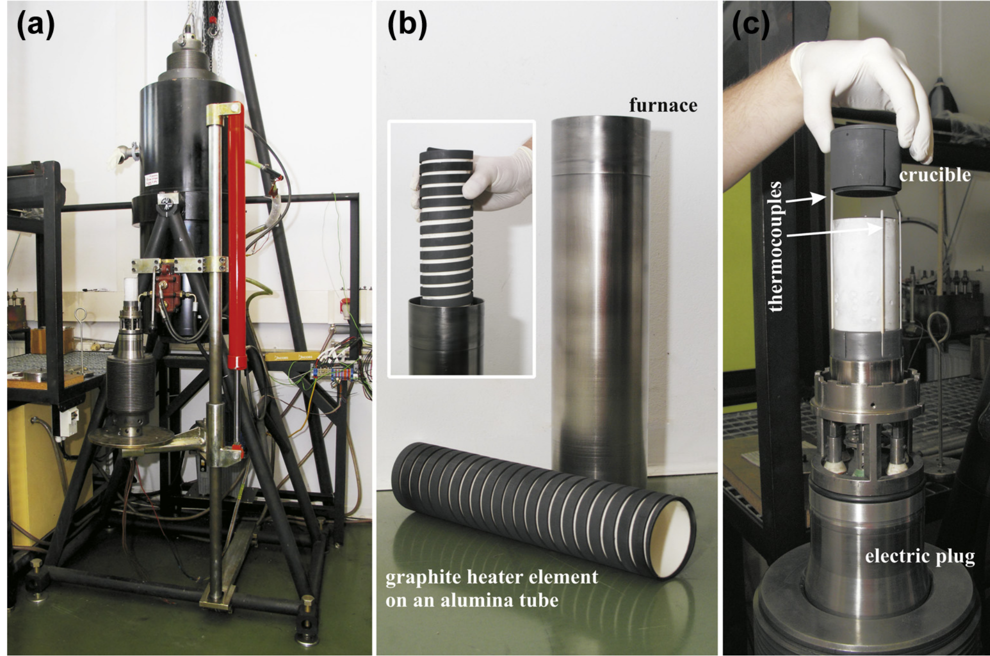

FIGURE 15.2 Experimental system for crystal growth of GaN at high nitrogen pressure. (a) High-pressure chamber. (b) Furnace; graphite heater element is also shown. (c) Crucible, with a set of thermocouple and electric plug.

arranged along the furnace and coupled with the input power control electronic systems. The pressure is measured by Manganin gauges positioned in the low temperature zone of the reactors. The pressure and temperature are stabilized with an accuracy of 1 MPa and 0.1 K, respectively. One of the typical experimental systems for crystal growth of GaN at high nitrogen pressure is shown in Figure 15.2.

During the crystallization process, the pressure and the temperature in the whole gallium sample correspond to the nitride stability range. Thus, the highest measured temperature is lower than the equilibrium temperature for a given nitrogen pressure at three-phase Ga–N_2–GaN equilibrium conditions.

15.2.2 Thermodynamic and Kinetic Aspects

The equilibrium p_{N2}–T conditions for GaN have been determined by Karpinski et al. [15] by a direct synthesis and decomposition experiments performer by both: gas-pressure technique (for pressures up to 2 GPa) and high-pressure anvil technique (up to 7 GPa). The curve derived from these data is shown in Figure 15.3(a). Figure 15.3(b), on the other hand, shows the N solubility data resulting from the annealing of Ga in N_2 atmosphere at the three-phase Ga–N_2–GaN equilibrium conditions for the temperature range from 1573 to 1850 K. It should be noted that even the highest available temperature of 1850 K is quite far from the melting temperature of GaN. Therefore, the nitrogen concentrations

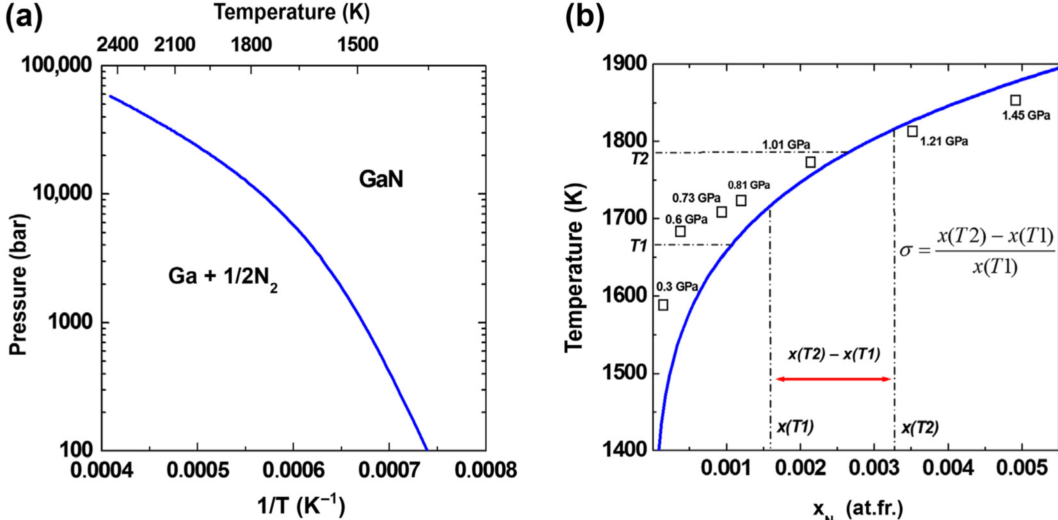

FIGURE 15.3 (a) *p-T* equilibrium curve for GaN [15]. (b) Liquidus curve for Ga–GaN system [16]. Determination of the relative supersaturation in the solution is presented.

are not high at less than 1% [16,17]. The solid line, shown in Figure 15.3(b), has been calculated in the ideal solution approximation. This curve allows one to determine the maximum of the relative supersaturation reached in the solution. Under standard growth conditions, the relative supersaturation can be expressed as:

$$\sigma = \frac{x(T2) - x(T1)}{x(T1)} \tag{15.1}$$

where σ represents the relative supersaturation and $x(T2) - x(T1)$ is the difference between equilibrium nitrogen concentrations at the hot and cold zones of the solution. Determination of σ is also schematically presented in Figure 15.3(b).

The analysis of thermodynamics properties of GaN and the system of its constituents explains the role of the use of high pressure. This analysis was performed by I. Grzegory and S. Porowski [16,18]. Because gallium nitride is a strongly bonded compound (with bonding energy of 9.12 eV per atom pair), the free energy of the crystal is very low in relation to the reference state of free N and Ga atoms. The N_2 molecule is also strongly bonded (4.9 eV per atom). Therefore, the free energy G of GaN constituents in their normal states becomes close to the crystal's. This is illustrated in Figure 15.4, in which the free energy of GaN (blue curve) and the free energy of the system of its constituents Ga+1/2N_2 (red and green curves) are shown as a function of temperature and N_2 pressure. With an increase of the temperature, Gibbs free energy of the constituents decreases faster than the free energy of the crystal. Therefore, at higher temperatures, the nitride becomes thermodynamically unstable. The crossing of $G(T)$ curves determines the equilibrium temperature where GaN coexists with its constituents at a given N_2 pressure. Two points are shown: for nitrogen pressure of

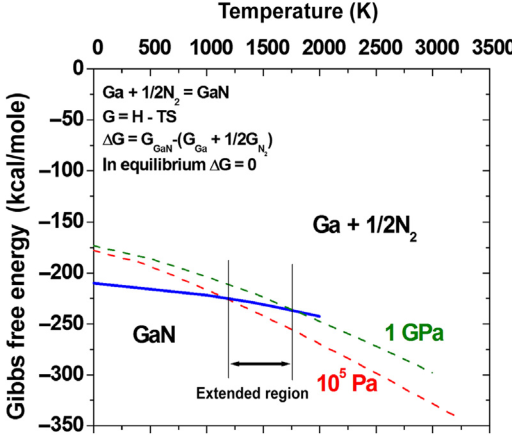

FIGURE 15.4 Gibbs free energy of GaN and its constituents. Extension of the stability range due to an increase of nitrogen pressure is shown.

10^5 Pa and 1 GPa. It can be noticed that the application of pressure increases the free energy of the constituents to a much higher degree than the Gibbs free energy of the crystal. Then, the equilibrium point shifts to the higher temperatures and the GaN stability range extends. This extension allows the growth of GaN crystals from solution in liquid Ga.

It should be noted that the nitrogen pressure is also important for the kinetics of the GaN synthesis. The synthesis of GaN from its constituents is possible due to dissociative chemisorption of N_2 molecules on the Ga surface, as was proven by Krukowski et al. [19] by density functional theory calculations. The nitrogen molecule dissociates on the Ga surface only if it overcomes the potential barrier of about 3.5 eV. If the molecule has enough energy to overcome the potential barrier, it comes closer to the gallium surface and dissociates into two atoms, forming new bonds with the metal. The potential barrier is lower than the bonding energy in the nitrogen molecule. However, its value of 3.5 eV seems to be quite high. Therefore, the density of the interacting gas (and thus its pressure) is of crucial importance. It should be mentioned that for oxygen interacting with gallium, there is no potential barrier [13]. Thus, one can always expect the oxygen atoms in liquid gallium. This fact is very important for the properties of GaN crystals grown by the HNPS method, which will be shown later.

The high potential barrier for nitrogen dissociation on the liquid gallium surface also suggests that this dissociation process is kinetically controlled, even for relatively high temperatures. Determining the rate of dissociation at 2 GPa, Krukowski et al. [19] showed that the rate of dissociation is not very fast for gallium nitride. For an effective synthesis (10 mg cm^{-2} during 100 h), the temperature ought to be higher than 1500 K. Comparing this last result with the equilibrium p_{N2}–T curve for GaN (see Figure 15.3(a)), it may be concluded that only the application of the high nitrogen pressure allows the synthesis of gallium nitride from its constituents.

15.2.3 Spontaneous Crystallization

Crystallization without seeds in the solution is called a spontaneous crystallization. The dominating morphological form of GaN crystals grown by the spontaneous method is a hexagonal platelet (see Figure 15.5(a)). However, at a relatively high supersaturation, needles become the dominating morphological form. The crystals in the form of hexagonal platelets grow slowly at a rate lower than 0.1 mm h^{-1} into $[10\bar{1}0]$ directions (perpendicular to the c-axis) [18,20]. They are single crystals, slightly gray or transparent, very often with flat mirror-like faces. The maximum lateral size of the platelets is 3 cm^2, whereas the thickness is approximately 150 μm. The tendency for unstable growth is stronger for one of the polar (0001) faces of the platelets. The morphological features such as macrosteps, periodic inclusions of solvent, or cellular growth structures are observed on this side. The opposite surface is mirror-like and often atomically flat. For crystals grown without intentional doping, the unstable surface always corresponds to the Ga-polar (0001) surface of GaN.

As mentioned above, the second possible form of pressure grown crystals is a needle (see Figure 15.5(b)). The needles are elongated into the c-direction, with a diameter of about 1 mm and up to 10 mm in length [20]. The GaN needles are strongly unstable crystals. They are dark due to the presence of microdefects, such as dislocation loops and gallium inclusions, which are the result of a fast and unstable growth in the c-direction. These crystals are often hollow inside. However, they have very well developed faces of orientations that are different from the [0001] ones, which provides an opportunity to check the growth behavior in these directions using the needles as the seeds [21].

The HNPS-GaN crystals (both platelets and needles) are strongly n-type, with uniform free electron concentration of about 5×10^{19} cm^{-3} (metallic conductivity) and carrier mobility of about 60 $cm^2\,V^{-1}\,s^{-1}$ [22]. The high free carrier concentration is due to oxygen. It was shown that the level of the oxygen impurity in the GaN crystals was exactly the same as the level of the free carrier concentration. These free carriers can be fully eliminated by Mg acceptor added into the growth solution [23]. High concentration of the gallium vacancies was found in the conductive crystals in contrast to the

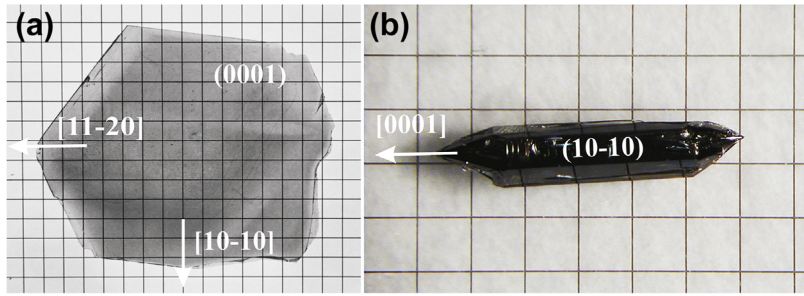

FIGURE 15.5 Two habits of GaN crystals grown by the HNPS method. (a) Platelet, for which nonpolar growth directions and polar facets are marked. Grid: 1 mm. (b) Needle, for which the growth direction [0001] and well-developed nonpolar facets $(10\bar{1}0)$ are presented. Grid: 1 mm.

Mg-doped samples, where the vacancies were not observed. The presence of the native point defects in the crystals was checked by positron annihilation measurements [24]. The difference in the PL spectra of the conductive (strong yellow emission) and Mg-doped crystals (no yellow emission, but blue Mg-related signal) revealed that the gallium vacancies are involved in strong yellow luminescence in GaN.

The structure of the spontaneously pressure-grown GaN crystals was studied by X-ray diffraction (XRD) [25]. The crystallinity depends on the size of the crystal. The full width at half maximum (FWHM) for the (002) reflection is of the order of 50 arcsec for 1- to 3-mm large crystals. For larger platelets, the X-ray rocking curve (XRC) often split into a few peaks showing the presence of low angle boundaries separating grains of a few millimeters in size. In order to determine dislocation densities in GaN crystals, the defect selective etching (DSE) method has been developed [26]. It has been proved that etching in molten KOH–NaOH eutectic (at 723 K) reveals dislocations in GaN pressure-grown single crystals. The etch pit density in HNPS-GaN, estimated by counting the etch pits in a given area, is very low, of the order of $10^2\ cm^{-2}$.

15.2.4 Seeded Growth

The main disadvantages of spontaneous crystallization by the HNPS method are small size and poor reproducibility of the size, as well as the distribution of GaN crystals in the crucible. Better control of the last two parameters has been achieved by growth with seed crystals introduced intentionally into the solution. A technique called directional crystallization or liquid phase epitaxy in the HNPS method is described below. Two configurations are presented: with one seed applied and its consequence with many seeds used—a relatively new approach proposed in 2010 by I. Grzegory, named multi-feed seed (MFS).

15.2.4.1 LPE Growth: Single Seed Configuration

The LPE technique—deposition of GaN on the substrate to force the growth in a particular direction—was examined with a few kinds of substrates, including HNPS-GaN, HVPE-GaN, SiC, sapphire, and sapphire/GaN MOCVD (Metal Organic Chemical Vapor Deposition) templates [27–30]. A typical experimental configuration—a crucible with a baffle plate positioned close to the seed, as well as axial and radial temperature distributions—is shown in Figure 15.6. The baffle plate allowed one to obtain a macroscopically flat crystallization front on the substrate and consequently maintain a flat GaN surface during a long crystallization run. The crystallization without the baffle always led to a nonuniform crystallization front and thereby formation of the growth hillock at the center of the substrate.

The LPE experiments have shown that the polarity of the GaN seed surface has been determined and controlled by the Ga solution and its impurities. For growth without intentional doping, the crystallization process is perturbed when the nitrogen polar surface $(000\bar{1})$ of the GaN substrate is exposed to liquid gallium. Then, the presence of

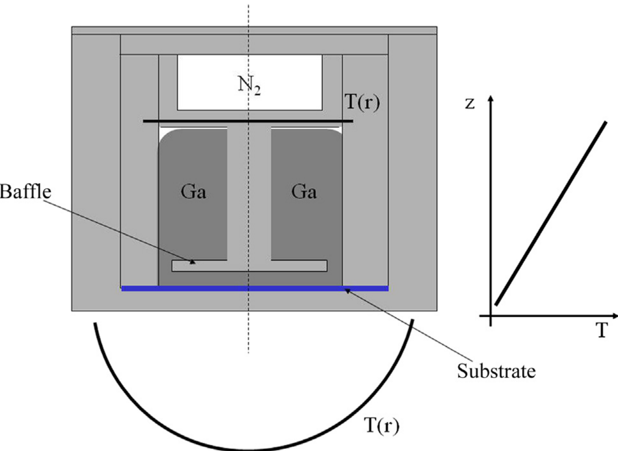

FIGURE 15.6 Scheme of the experimental LPE configuration with the baffle plate. The axial and radial temperature distributions are marked.

several growth centers is observed. The simultaneous nucleation and growth of randomly oriented crystals have also been noticed. In turn, on the gallium polar surface (0001), the growth mode has been stable and proceeded by the steps propagation from the center of the sample to its sides. An average growth rate, determined by a comparison of a seed's weight before and after the experiment, is of the order of 1 $\mu m\,h^{-1}$. The new deposited material has always been n-type with metallic conductivity ($\sim 5 \times 10^{19}\,cm^{-3}$). On the other hand, for crystallization of highly resistive GaN (in the Ga:Mg solution), the new material has been grown by a stable way on the $(000\bar{1})$ surface of the seed. The growth rate, however, has also been on the order of 1 $\mu m\,h^{-1}$.

The average dislocation density in GaN crystallized on the HNPS-GaN has always been as low as $10^2\,cm^{-2}$. The dislocation density in the pressure-grown material on sapphire/GaN templates has been on the order of $5 \times 10^7\,cm^{-2}$ for layers thicker than 40 μm. Lower defect density can be obtained when HVPE-GaN is used as a substrate. Then, the dislocation density in the starting material has been on the order of $5 \times 10^6\,cm^{-2}$, since HVPE-GaN was grown before on a MOCVD-GaN/sapphire template (for details, see Section 15.2.4.2.1). For 40-μm-thick GaN layers, the defect density has been $5 \times 10^6\,cm^{-2}$. For layers thicker than 250 μm, the etch pit density has attained $1 \times 10^6\,cm^{-2}$.

Two factors were proven to be responsible for GaN growth in the c-direction. These factors do not depend on the experimental configurations or the kind of the substrates. For a short time ($\sim$30 h), the growth rate is governed mainly by nitrogen transport to the crystallization zone, and the observed average growth rate can reach 10 $\mu m\,h^{-1}$. After a longer time ($\sim$100 h), the surface kinetic factor becomes more important and the average growth rate decreases to 1 $\mu m\,h^{-1}$ [28]. The analysis of the GaN mass crystallized at configuration with and without seed confirmed that the growth rate on the seed is governed by surface kinetics. The GaN mass crystallized at the bottom of the crucible without a seed was bigger than the mass crystallized on the seed (with no parasitic

growth observed) under the same experimental conditions. Thus, not all the nitrogen atoms from the solution reaching the seed surface were adsorbed there [29].

The finite element calculation has been used for modeling the convective transport in the solution during the LPE process in a positive temperature gradient configuration, as presented in Figure 15.6 [14,29,30]. The radial temperature distribution at the bottom of the crucible was approximated as parabolic and the vertical temperature distribution as linear. The radial temperature distribution on the crucible's top was estimated as a constant (see Figure 15.6). Assuming the flow in gallium to be laminar, the convectional flow velocity in the metal, and the temperature distribution in the liquid, in the seed, and in the crucible wall were determined. The maximum velocity for the convectional flow above the baffle was on the order of 1 mm s^{-1} when using temperature gradients. Under the baffle, the convection was very weak; the maximum flow velocities in two rolls reached 0.2 mm s^{-1}. Thus, the nitrogen was transported to the baffle by a relatively strong convection. Then, the N atoms were dispersed on the baffle. However, by the sides (opening areas), they were supplied below the baffle to the seed region, where their velocity was low. Thus, by a very weak convection process, they were transported to the seed. It seems that, due to a very low convectional flow velocity, the growth could be macroscopically stable; however, the rate was as slow as 1 μm h^{-1}.

15.2.4.2 LPE Growth: The Multifeed Seed Configuration

Recently, the MFS configuration in the HNPS growth method has been proposed and developed [31–36]. This configuration is based on the conversion of free-standing HVPE-GaN crystals to free-standing, pressure-grown HNPS-GaN of a much higher quality than the seeds. The great strength of this approach is that it yields several GaN crystals from one run. Furthermore, the crystals satisfy all criteria for being substrates. Production of this material begins by positioning several (0001) or $(000\bar{1})$-oriented HVPE-GaN seeds in a vertical stack, separated by liquid gallium or liquid gallium doped with magnesium, respectively (see Figure 15.7). The lowest seed is placed above the bottom of the crucible and the distance between individual seeds can be varied. Under nitrogen pressures of typically 1 GPa and at temperatures in the range of 1593–1773 K, an axial temperature gradient (from 5 to 30 K cm^{-1}) is applied along the crucible, leading to an overgrowth of seeds on their upper surface and their dissolution from the opposite side. Due to the dissolution process, atomic nitrogen is supplied into the metal solution and is transported to the underlying crystal. In other words, each seed is overgrown and dissolved at the same time, but at slightly different temperatures, varying by a few degrees. Therefore, they are feeds and seeds at the same time, and the liquid gallium discs (sometimes doped by magnesium) play the role of traveling zones.

After the growth run (typically 400 h), the crystals are cut by a drill pipe to round forms with a diameter of 16 mm, 20 mm, 1 inch, or 1.5 inches; then, their (0001) surface is mechanically and mechanochemically polished to the epi-ready state. The HNPS growth in the MFS configuration results in a stable and macroscopically flat crystallization. This is probably associated with an appropriate convective or diffusive transport

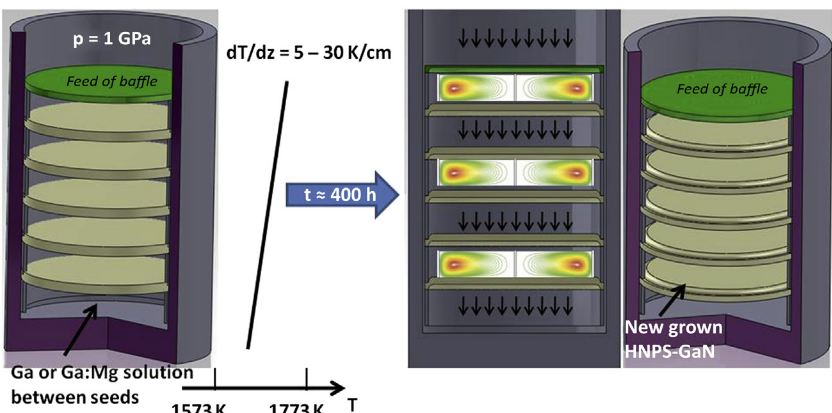

FIGURE 15.7 Scheme of the MFS configuration, showing a section of the crucible. The free-standing HVPE-GaN substrates are positioned vertically. Liquid gallium discs (in some cases doped with magnesium) are between them. Due to the temperature gradient applied at the bottom sides of HVPE-GaN, crystals are dissolved in liquid gallium supplying atomic nitrogen to the solution. Nitrogen is then transported in the liquid gallium by convection or diffusion to the underlying seed, where the crystallization takes place.

(flow) in the solution. In the MFS configuration, the gallium solution is divided by the HVPE-GaN seeds positioned in a vertical stack. The flow between the seeds has to be stable because the upper crystals work like baffles for the lower crystals (see subsection above). They not only supply nitrogen to the solution but also stabilize the flow. They introduce an order to the Ga–N solution and uniform the nitrogen concentration field at the crystals growing surfaces. This phenomenon allows one to obtain a flat crystallization front and a flat growth of GaN during a long period of time.

15.2.4.2.1 HVPE-GAN SEEDS

The seeds for the HNPS-MFS growth, the HVPE-GaN crystals, are prepared in a home-made horizontal quartz HVPE reactor. Free-standing (F-S) HVPE-GaN crystals that are 2 inches and up to 1 mm thick are obtained using MOCVD-GaN/sapphire templates as seeds; for details, see Refs. [37–39]. For some high-pressure experiments, the smaller crystals are cut from them. The surfaces (0001) and $(000\bar{1})$ of all F-S HVPE-GaN crystals are prepared to the epi-ready state by a combination of mechanical and mechanochemical polishing. The typical properties of the F-S HVPE-GaN crystals used as seeds for the HNPS-MFS crystallization runs are as follows: (1) free carrier concentration from 2×10^{16} to 10^{17}, with a mobility of the order of 1000 $cm^2\,V^{-1}\,s^{-1}$; (2) threading dislocation density of the order of 5×10^6; and (3) an absolute value of the bowing radius from 1 to 5 m.

Using ammonothermally grown GaN as a seed, one can obtain high-quality F-S HVPE-GaN [40]. Smooth GaN layers up to 2.5 mm thick (crystallized with a stable growth rate of 240 $\mu m\,h^{-1}$) and of an excellent crystalline quality, without cracks, and with low threading dislocation density ($5 \times 10^4\,cm^{-2}$) have been grown and then sliced from the ammono-GaN seed wafers (see Figure 15.8(a) and (b), respectively). The structural

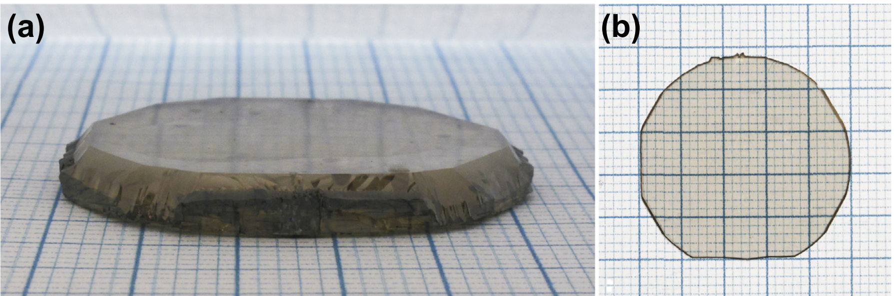

FIGURE 15.8 (a) HVPE-GaN grown on Am-GaN seed (as grown crystal). (b) F-S HVPE-GaN sliced from the Am-GaN seed after mechanical polishing; grid: 1 mm.

properties of the F-S HVPE-GaN do not differ from the structural properties of the ammono-GaN seeds. Additionally, this is a high-purity material. According to the SIMS (Secondary Ion Mass Spectrometry) analysis, the oxygen and carbon content is below $10^{16}\ \mathrm{cm}^{-3}$. The only Si impurity is of the order of $3 \times 10^{16}\ \mathrm{cm}^{-3}$. Thus, from the physical properties point of view, this HVPE-GaN is of a much higher quality than the one obtained using MOCVD-GaN/sapphire templates as seeds.

15.2.4.2.2 CONDUCTIVE (N-TYPE) HNPS-MFS-GAN CRYSTALS

The HNPS crystallization in gallium without an intentional doping always leads to the n-type HNPS-GaN crystals (see Section 15.2.3). During growth in the MFS configuration, three types of morphology are observed: hillocks, hillocks and macrosteps (mixed), and macrosteps. They are all presented in Figure 15.9. The presence of these three modes of growth depends on the supersaturation at the growing crystal surface. In turn, the supersaturation mainly depends on the growth temperature, the temperature gradient applied, and the distance between seeds. Because the growth temperature and gallium heights are fixed, the morphology of the grown crystal surface depends only on the temperature gradient applied. Obviously, changing the temperature gradient varies the growth temperatures, but it can be assumed that the system is still in a comparable temperature region. The supersaturation is also associated with the mechanism of transport for the nitrogen in the liquid gallium solution. The nitrogen can be transported by diffusion or convection from the upper to the lower seed.

For the smallest temperature gradient ($\sim 5\ \mathrm{K\ cm}^{-1}$)—and thus for low supersaturation—the hillock growth mode is observed. In this case, the growth rate is not higher than $1\ \mu\mathrm{m\ h}^{-1}$. It was suggested [34] that for the hillocks growth mode the diffusion of nitrogen in gallium plays a dominant role as a transport mechanism. The hillocks growth mode has been observed only for very low convectional velocities in gallium, on the order of $1 \times 10^{-4}\ \mathrm{m\ s}^{-1}$ or less. Such small values of the calculated convectional velocities indicate a diffusive transport in the solution. Additionally, the hillocks are always correlated with screw and mixed dislocations in the pressure grown material, which can be clearly seen in Figure 15.9(b). One can observe the as-grown surface

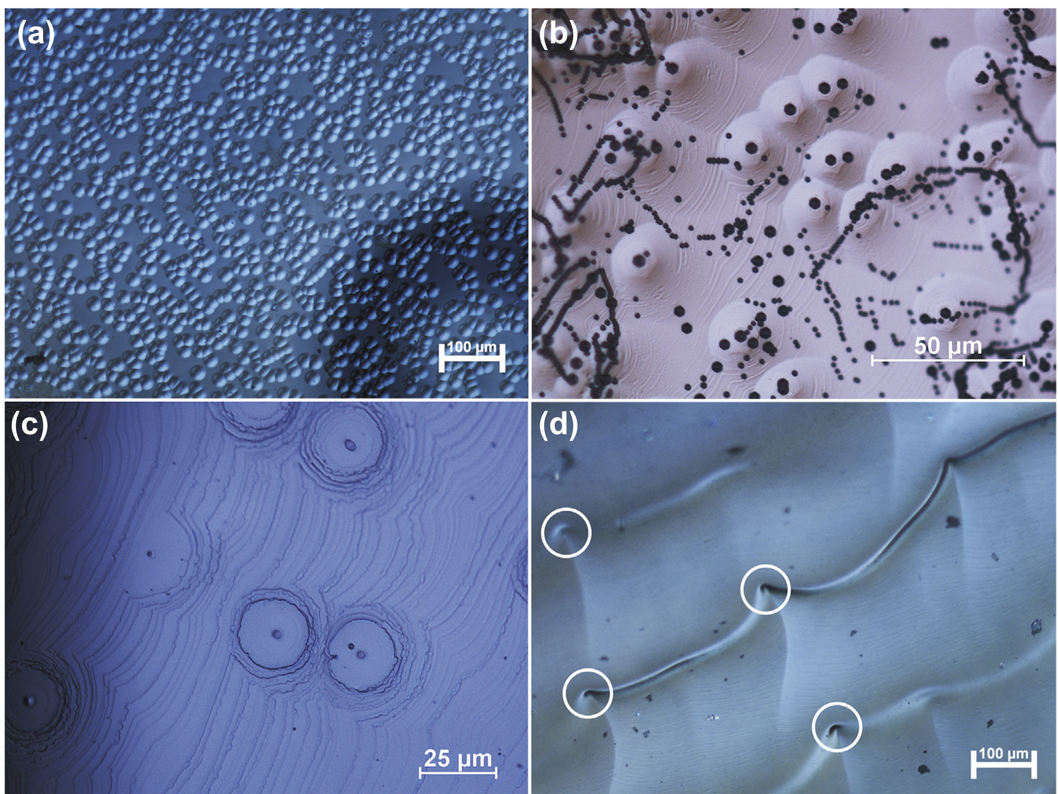

FIGURE 15.9 Three types of morphology of the HNPS-MFS-GaN crystals. (a) Hillocks. (b) As-grown surface with hillocks etched in molten KOH/NaOH solution at 723 K. Large hexagonal etch pits are positioned on the top of the each hillock, which is proof that hillocks are correlated with screw and/or mixed dislocation in the HNPS-MFS-GaN. (c) Hillocks and macrosteps together. (d) Macrosteps with flounces and step bunching effect. Favorable places for formation of voids and inclusions of solvent in the HNPS-MFS-GaN are marked by circles.

etched in molten KOH/NaOH solution at relatively high temperatures (723 K). The large hexagonal etch pits, associated with the screw and/or mixed dislocations, are positioned on the top of each hillock. It should be noted that the hillock's density is always strictly the same as screw and mixed dislocation density in the HNPS-MFS-GaN, about $5 \times 10^5\ cm^{-2}$. The crystals are grown slowly by steps propagating from the hillocks' centers, which are formed on the screw and mixed dislocations. If the supersaturation is increased—thus, for a bigger temperature gradient ($\geq 5\ K\ cm^{-1}$)—the mixed growth mode appears. The convection in liquid gallium solution starts. For some convection flow, the macrosteps coexist with hillocks on the growing crystal surface (see Figure 15.9(c)). Then, the average growth rate is $2\ \mu m\ h^{-1}$. For higher supersaturations (i.e., a bigger temperature gradient), the convectional velocity increases, the hillocks disappear, and only the macrosteps are detected (see Figure 15.9(d)), which begin to play a dominant role on the growing crystal surface.

Then, the growth rate can reach 5 μm h^{-1}. However, stronger convective flow disturbs the macrosteps' propagation. It leads to the step bunching effect and macroscopically unstable growth, with formation of voids and gallium inclusions in the HNPS-MFS-GaN.

The deposition of HNPS-GaN layers and dissolution of HVPE-GaN can improve the structural quality of the obtained crystals [32]. The XRCs are narrower and the lattice bowing radii increase. For the (002) reflection, the FWHM of the HNPS-MFS-GaN can be equal to 100 arcsec. The absolute value of the bowing radius can be increased from 2 to 20 m. Obviously, the formation of the HNPS-GaN layer on the HVPE-GaN substrate significantly changes the bowing radius of the crystal if only the HVPE-GaN and the HNPS-MFS-GaN are elastically strained. Almost total dissolution of the HVPE-GaN substrate helps to release the stress in the HNPS-MFS-GaN [32,33]. Therefore, the bowing radius of the HNPS-GaN crystal increases in comparison to the seed. As is shown in Figure 15.10, due to the difference in the *a* lattice constant between the HVPE-GaN and the HNPS-MFS-GaN, the pressure grown material is under compressive strain and the HVPE-GaN seed is under tensile strain during the crystallization process. The HVPE-GaN, however, dissolves from its $(000\bar{1})$ surface. On the other hand, the HNPS-MFS-GaN becomes thicker and thicker. Thus, the compressive strain for the HNPS-MFS-GaN has to be decreased in time so the pressure grown crystal can be structurally flatter.

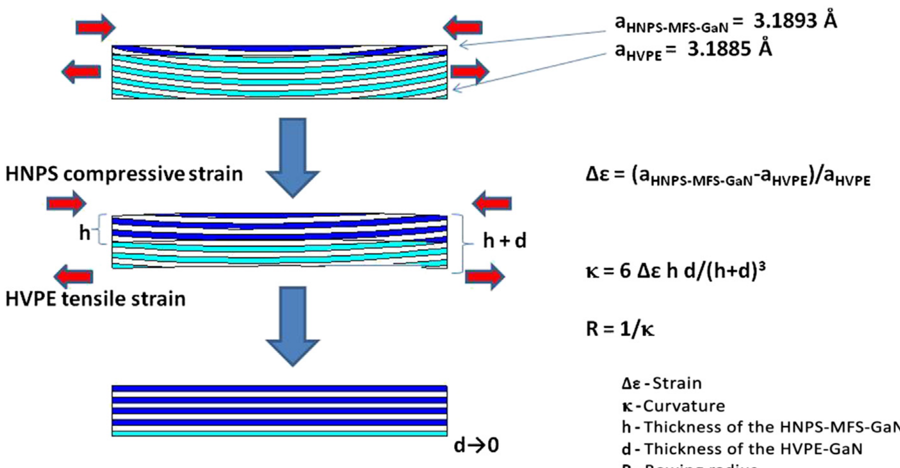

FIGURE 15.10 Scheme of the time evolution of the growing HNPS-MFS-GaN crystal. Due to the difference in the "a" lattice constant of the HNPS-MFS-GaN and the HVPE-GaN seed, the pressure grown material is under compressive strain and the HVPE-GaN seed is under tensile strain. If the HNPS-MFS-GaN and the HVPE-GaN are elastically strained, the bowing radius of the final crystal can be increased according to the Stoney-Clyne formula [41] presented in the figure.

The average etch pit density for the HNPS-MFS-GaN is of the order of 1×10^6 cm^{-2}. The growth of several hundred microns of the HNPS-MFS-GaN allows a reduction of the threading dislocation density by a factor of five. The high-pressure material of lower defect density was never grown using the HVPE-GaN seeds grown before on MOCVD-GaN/sapphire templates (see Section 15.2.4.2.1).

The free carrier concentration for the HNPS-MFS-GaN crystals is always higher than 10^{19} cm^{-3}; its value depends on the growth temperature. The dependence between the free carrier concentration in the crystals and the growth temperature is presented in Figure 15.11. With an increase of the growth temperature from 1593 to 1723 K, the carrier concentration in the HNPS-MFS-GaN increases. Then, for a higher temperature (higher than 1723 K), it is saturated, reaching a constant value on the order of 5×10^{19} cm^{-3}. As was confirmed by SIMS analysis, this high free electron concentration in HNPS-MFS-GaN is associated with a high oxygen concentration in the material. The level of the oxygen impurity in the crystals is just the same as the level of the free carrier concentration. Lower oxygen concentration is noted for a lower growth temperature. The oxygen atoms in the HNPS-MFS-GaN crystals have to originate from the liquid gallium. An increase of the oxygen content in the GaN crystals with an increase of the growth temperature is probably due to a higher solubility of the oxygen in the liquid gallium at high temperature and high pressure. For the highest temperatures, an oxygen solubility limit in liquid gallium can be observed. Therefore, the oxygen concentration and also free carrier concentration in the HNPS-MFS-GaN crystals do not increase any more.

As mentioned, the (0001) surface of the HNPS-MFS-GaN could be prepared to the epi-ready state by mechanical and mechanochemical polishing (and then appropriate

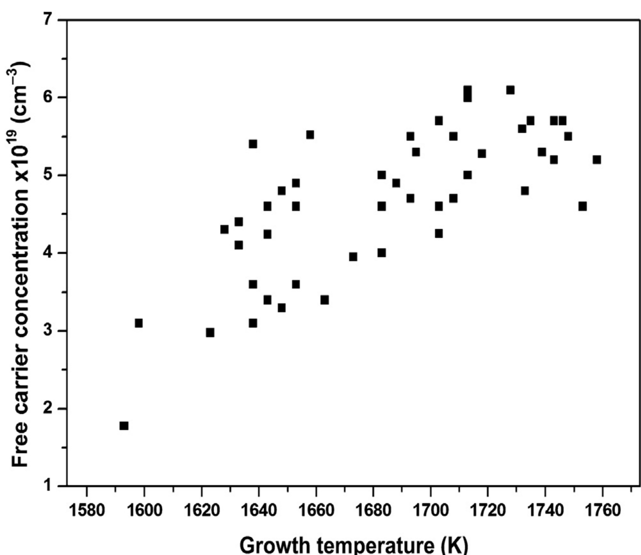

FIGURE 15.11 Free carrier concentration as a function of the growth temperature. At temperatures up to 1713 K, free carrier concentration increases; then, it reaches a constant value of approximately 5×10^{19} cm^{-3}.

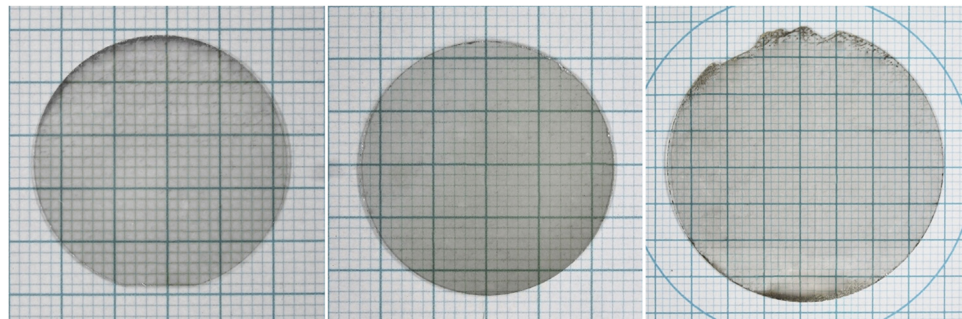

FIGURE 15.12 One-inch and 1.5-inch n-type HNPS-MFS-GaN (plasmonic) substrates. Grid: 1 mm.

cleaning). The substrates for making laser diodes (from 16 mm up to 1.5 inch in diameter) can be prepared (see Figure 15.12). They are called plasmonic substrates due to their extremely high free carrier concentration. The plasmonic GaN substrate has the advantage of increasing the refractive index contrast between substrate and epitaxial laser diode structure, suppressing optical mode leakage into the substrate and optimizing the optical mode in the active region. This approach is superior to using a conventional GaN substrate (with a free electron concentration on the order of 5×10^{18} cm^{-3} or less) and adding a thick AlGaN layer or an AlGaN super lattice beneath the active region to prevent light propagating from there into the substrate. Going down this more common route, the strain increases in the epi-structure, leading to macroscopic bowing, cracking, and the creation of misfit dislocations [42,43]. The laser diodes made on HNPS-MFS-GaN substrates (by MOCVD technology), emitted at 390–420 nm, had typical threshold voltages of 4.5 V at 2.5 kA cm^{-2} and lifetimes of up to 5000 h [44]. Defect-selective etching revealed that the dislocation density in the laser diode was below 5×10^{6} cm^{-2}, about one-fifth of that value in the substrate.

The HNPS-MFS-GaN crystals have been also used for preparing undulated substrates (with locally controlled miscut) [45]. Laser diodes made on them emitted from 400 to 410 nm at a threshold voltage of 5.5 V and 4 kA cm^{-2}.

15.2.4.2.3 SEMI-INSULATING HNPS-MFS-GAN:MG CRYSTALS

As shown previously, HNPS crystallization in gallium without an intentional doping always leads to the n-type HNPS-GaN crystals. The free carriers can be fully eliminated by Mg acceptor added into the growth solution. For HNPS-MFS-GaN crystallization in the solution of Ga:Mg (up to 1 at% of Mg in the solution), the typical morphology observed is the macrosteps propagation. The growth rate varies from 1 to 2 μm h^{-1}. The gallium inclusions or voids in the material are not observed. The addition of Mg to the Ga solution would likely drastically change a few properties of the solution, mainly its viscosity. Some changes in the composition of the solution can prevent formation of the voids and inclusions while maintaining a relatively high growth rate. It should be mentioned that the XRC FWHM and the bowing radii of the HNPS-MFS-GaN:Mg crystals

are not changed significantly compared to the HVPE-GaN seeds. The *a* lattice constant of the HNPS-MFS-GaN:Mg is the same as for the F-S HVPE-GaN seed [35,46]. There is no difference in strains for these two layers. The F-S HVPE-GaN seed is structurally reproduced by the high-pressure material. Thus, it looks to be the opposite for intentionally undoped crystals (see Figure 15.10). Because the (0001) surface of the examined material is situated close to the HVPE-GaN seed, the average etch pit density for HNPS-MFS-GaN:Mg is always on the order of 5×10^6–10^7 cm^{-2} (like in the HVPE-GaN seed).

The SIMS analysis showed that the magnesium concentration in HNPS-MFS-GaN:Mg crystals is strictly the same as oxygen concentration. Thus, the magnesium impurity compensates for oxygen donors in the pressure-grown material. Therefore, these crystals are semi-insulating at room temperature, as well as higher (107–1173 K) temperatures, and its electrical properties are very stable against annealing and time. Resistivity at the room temperature was estimated to be 10^{15}–10^{16} Ω cm for crystals grown at higher temperatures (1693–1723 K) and 10^{11}–10^{12} Ω cm for crystals grown at lower temperatures (1653–1693 K). For the same magnesium concentration in the solution (and probably in the crystals), the resistivity depends on the growth temperatures. It is lower for crystals grown at low temperatures. It seems that it is again associated with the oxygen concentration in the solution and in the crystals (see Section 15.2.4.2.2 and Figure 15.11).

The biggest disadvantage of HNPS-MFS-GaN:Mg crystals are the precipitates of small magnesium oxide crystallites. They are mainly formed at the interface between F-S HVPE-GaN seed and new, pressure-grown material. Some of them also exist in the volume of HNPS-MFS-GaN:Mg crystal. It seems that the affinity of oxygen to magnesium is so high that during crystallization process, especially at the beginning of the growth, the formation of MgO crystals takes place. Then, these crystals are overgrown by the HNPS-MFS-GaN:Mg. Unfortunately, during the preparation of HNPS-MFS-GaN:Mg substrates, MgO crystals or voids after them can create some large pits in the nitride material. However, despite this, some parts of the HNPS-MFS-GaN:Mg crystal surfaces were prepared to the epi-ready state. A 2D GaN/AlGaN structure was built by MBE technology. At 295 K, the mobility in the 2D GaN/AlGaN structure was 2100 $cm^2 V^{-1} s^{-1}$ with carrier concentration n_{2DEG} of 5×10^{12} cm^{-2} [47].

15.2.5 Perspective for HNPS Growth Method

The HNPS-MFS configuration involves the conversion of free-standing HVPE-GaN crystals to free-standing HNPS-MFS-GaN. These crystals have a much higher quality than the seed material. The free-standing HNPS-MFS-GaN crystals can be strongly n-type (GaN:O) or semi-insulating (GaN:Mg). They can also be prepared as substrates for the laser diodes (plasmonic substrates) or for the high electron mobility transistors (semi-insulating substrates), respectively. One way to improve the structural quality of HNPS-MFS-GaN is to use high-quality HVPE-GaN crystals as seeds. It has been shown that ammonothermally grown GaN (as a seed) allows one to obtain high-quality F-S

HVPE-GaN (see Section 15.2.4.2.1). Because doping in HVPE technology is still a big challenge, the use of new F-S HVPE-GaN crystals as seed for the HNPS growth method seems to be an interesting approach for producing high-quality n-type and semi-insulating GaN crystals.

On the other hand, to improve the HNPS growth method, a higher growth rate in the MFS configuration may be needed. We believe that some changes in the metallic solution properties should be carried out. Their purpose is to increase the nitrogen solubility in the liquid gallium, as well as convectional velocities in the solution. As presented previously, the convectional velocities in gallium solution are at the level of a millimeter per second. In the ammonothermal and sodium flux growth methods, these velocities are at least one order of magnitude faster [48,49]. Certainly, the slow convection flow in the gallium solution is due to the high density of gallium ($\rho = 5.6\ \mathrm{g\,cm^{-3}}$). By adding sodium or lithium impurities into the Ga metal, one may obtain a solution (or a flux) of a lower density with an increase in the nitrogen solubility. Another possibility may be mechanical stirring of the solution, which is applied in the sodium flux GaN growth [50].

15.3 Ammonothermal Growth of GaN

15.3.1 Historical Development of Ammonothermal Growth Techniques

Supercritical ammonia has been used as a solvent in high-pressure autoclaves to synthesize new complex nitrides [51] and nano- and micro-crystalline AlN and GaN [52–55]. The latter results were encouraging enough to have some groups challenging the bulk crystal growth of GaN as a prospective candidate for a future bulk crystal growth technology on an industrial scale. Similarly, the low-temperature phase of quartz has been mass produced using the hydrothermal technique (with water as the solvent host) for many decades; industrial scale was demonstrated in the 1950s (e.g., see Refs [56,57] and Chapter 14 by Byrappa et al. in this volume). The largest hydrothermal autoclaves in operation have geometrical dimensions of 14 m inner length and 0.65 m inner diameter [9]. Interestingly, the feedstock to grow hydrothermal quartz is naturally occuring quartz; however, this is not possible for GaN because GaN is not abundant on Earth. Therefore, GaN feedstock has to be synthesized prior to the ammonothermal crystal growth of GaN using GaN as feedstock. The first publications reporting ammonothermal crystal growth of GaN were released starting in the mid-1990s; this number increased around the year 2000. Ammonothermal growth of the isostructural aluminum nitride (AlN) was reported earlier in 1990 by Peters [52], who grew small crystals up to 1 mm in size using potassium amide (KNH_2) dissolved in super critical ammonia at $T = 773$–873 K and $p = 200$ MPa.

Free-standing millimeter-sized GaN crystals were grown by Ketchum and Kolis ($0.5 \times 0.2 \times 0.1\ \mathrm{mm^3}$) [58]. Callahan et al. used polycrystalline as well as single-crystalline

HVPE-GaN (thick films) [59]; Wang et al. grew crystals up to $10 \times 10 \times 1\ mm^3$ at growth rates $\leq 2\ \mu m\ h^{-1}$ [60]. Dwilinski et al. and Hashimoto et al. reported efforts in ammonothermal technology using basic mineralizer (also referred to as ammono-basic). Purdy et al., Yoshikawa et al., and Kagamitani and Ehrentraut et al. worked with acidic mineralizers (also referred to as ammono-acidic) to synthesize free-standing hexagonal GaN crystals and homoepitaxial films [61,62,77].

Table 15.1 summarizes some of the important achievements to crystallize self-nucleated GaN under different ammonothermal conditions. Temperature and pressure stretch from relatively modest, subcritical conditions to as high as $T = 1273$ K and $p = 2000$ MPa. In addition, a mineralizer seems necessary to grow larger size crystals. The mineralizer (a term borrowed from geochemistry) enables chemical reactions of a desired phase by forming intermediates (see Section 15.4). Basic mineralizers with an NH_2^- group (e.g., KNH_2) and acidic mineralizers with an NH_4^+ group (e.g., NH_4Cl) are suitable candidates.

Ehrentraut et al. have worked to find an optimized acidic mineralizer to achieve a high yield of hexagonal GaN in order to be able to control the rate for dissolving the GaN precursor until re-crystallization on the GaN seed [78]. Mixed mineralizers have been studied, such as $\geq$80 mol% NH_4Cl/$\leq$20 mol% NH_4Br or $\geq$80 mol% NH_4Cl/$\leq$20 mol% NH_4I, which proved successful in terms of crystal yield and phase stability. The crystal yield, defined as the ratio of re-crystallized GaN feedstock to dissolved, increases with increasing acidity from NH_4Cl to NH_4I (see Figure 15.13). It was found that there is a limit to the acidity, above which cubic phase GaN is dominant over the hexagonal phase of GaN.

Results on the successful fabrication of sizable ammonothermally grown GaN crystals were published by a number of groups around the mid-2000s [59,60,62,74,81,82] (Table 15.2).

The next natural milestone was the growth of 2-inch large bulk GaN crystals, which would eventually result in the first 2-inch wafers fabricated by an ammonothermal crystal growth technology. A GaN crystal of more than 1-inch nucleated under ammono-basic conditions on an HVPE-grown GaN seed was published by a group from the University of California Santa Barbara in 2005 [94]. The first successful demonstration of 2-inch ammonothermal GaN was published by a group from Tohoku University in collaboration with Mitsubishi Chemical Corp [94]. Figure 15.14(a) shows a nearly 2-inch GaN crystal, the first to be ever grown under acidic ammonothermal conditions [88]. An HVPE crystal served as seed crystal in this case and the thickness of ammonothermal GaN was less than 1 mm in total for the Ga and N-polar face together. Ammono S.A. is now routinely growing bulk crystals in a basic ammonothermal regimen, with more than 70 two-inch crystals produced in a single run, from which up to 2-inch large (0001) wafers are prepared and commercially available [7,83]. Figures 15.14(b) and (c) depict a 2×1 inch bulk crystal of ~1 cm in thickness and a 1-inch (0001) bulk crystal to prepare 1-inch $(10\bar{1}0)$ wafers, respectively, as grown under ammono-basic conditions by Ammono. Soraa, Inc. reported the successful growth of 2-inch GaN crystals under

Table 15.1 Synthesis of Self-Nucleated GaN Crystals under Different Ammonothermal Conditions

Gallium Source	Mineralizer	Temperature (K)	Pressure (MPa)	a (Å)	c (Å)	Phase, Crystal Size; Remarks	References
Ga	$LiNH_2$	≤823	100–500	3.1877	5.183	*h*-GaN, few μm	[63]
	$NaNH_2$			3.1885	5.1842	*h*-GaN, few μm	[64]
Ga	Li	623	~150	3.2012(6)	5.208(2)	*h*-GaN, 32 nm	[65]
		623		3.1974(4)	5.197(1)	*h*-GaN, 50 nm	
		673		3.1885(2)	5.1845(5)	*h*-GaN, 73 nm	
Ga	$CsNH_2$	703		3.197	5.195	*h*-GaN, 4.5 nm	[66]
GaN	5.4 mol $KNH_2 \pm 0.1$ mol KI	673	Maximum 240	3.182(5)	5.178(3)	*h*-GaN	[58]
GaN	Amides (KNH_2 $NaNH_2$)	573–898	100–300	/	/	*h*-GaN; lattice parameters obtained from GaN nucleated on HVPE-GaN seed	[67,68]
Ga	NH_2NH_3Cl[a]	923	200	/	/	*h*-GaN, few μm	[69]
	NaN3	673–1073	100			*h*-GaN, few μm	
$[H_2GaNH_2]_3$[b]	None	423–723	12	/	/	*h*/*c*-GaN, 17 nm	[70]
Ga_2O_3	None	1273 & 1373	Quasi open	3.185(1)	5.179(1)	*h*-GaN, 200 nm	[71]
Ga_2O_3 + Ga	None	1373	system	3.1978(2)	5.199(1)	*h*-GaN	
Ga	None		(NH_3 flow)	3.176(1)	5.164(1)	*h*-GaN; yielded	
				3.1419(1)	5.105(1)	two phases: N-poor and stoichiometric *h*-GaN	
$Ga(NH)_{3/2}$	NH_4Cl						[72]
	NH_4Br						
	NH_4I						
GaN	NH_4Cl + LiCl	748–758	47% Fill			*h*-GaN, 800 μm	[55,73]
	NH_4Br + LiBr	767	55% Fill			95% *c*-GaN, 75 μm	
	NH_4I + CuI	764	54% Fill			*c*-GaN, 50 μm	
GaN	NH_4F	873–1273	500–2000	/	/	*h*-GaN, few mm	[74]
GaN	NH_4F	923	80–150	/	/	*h*-GaN, 5 mm	[75]
GaN	NH_4Cl	973–993	≤150	/	/	*h*-GaN, few mm	[76]
Ga	NH_4Cl	773	135	3.196(1)	5.192(1)	*h*-GaN; top[c]	[77]
				3.189(1)	5.185(1)	*h*-GaN; bottom[c]	
GaN	NH_4Cl	773	120	3.191(1)	5.189(1)	*h*-GaN; top	
GaN + Ga	NH_4Cl	823	120–130	3.1948	5.1929	*h*-GaN; top	[78]
	NH_4Cl	743	93	3.1975	5.2006	*h*-GaN; top	
	NH_4Cl	743	81	3.1944	5.2016	*h*-GaN; top	
	NH_4Cl	683	109	3.1928	5.192	*h*/*c*-GaN; top	

Continued

Table 15.1 Synthesis of Self-Nucleated GaN Crystals under Different Ammonothermal Conditions—cont'd

Gallium Source	Mineralizer	Temperature (K)	Pressure (MPa)	a (Å)	c (Å)	Phase, Crystal Size; Remarks	References
	NH_4Br	823	136	3.1947	5.1909	*h*/*c*-GaN; top	
	NH_4Br	773	127	3.1921	5.1901	*h*/*c*-GaN; top	
	NH_4Br	723	113	3.1925	5.1968	*h*/*c*-GaN; top	
	NH_4Br	673	96	3.1894	5.2040	*h*/*c*-GaN; top	
	NH_4I	823	128	3.1919	5.1970	*h*/*c*-GaN; top	
	NH_4I	773	121	3.1856	5.2294	*h*/*c*-GaN; top	
	NH_4I	723	110	3.1900	5.2011	*h*/*c*-GaN; top	
	NH_4I	673	97	3.1887	5.1955	*h*/*c*-GaN + Ga_2O_3; top	
Ga	NH_4Cl	773	/	3.1889	5.1981	*h*/*c*-GaN, sub-μm	[79]
		673	/	3.1899	5.1839	*h*-GaN, sub-μm	
	NH_4Br	773	/	3.1881	5.2063	*h*/*c*-GaN, sub-μm	
		673	/	None	None	No GaN phase	
	NH_4I	773	/	3.1886	5.1998	*h*/*c*-GaN, sub-μm	
		673	/	None	None	No GaN phase	
Ga	$ZnCl_2$	693–813	110	/	/	*h*-GaN, about 100 μm	[80]

[a]Hydrazine hydrochloride.
[b]Cyclotrigallazane.
[c]Location within the autoclave where solid state phase crystallized.

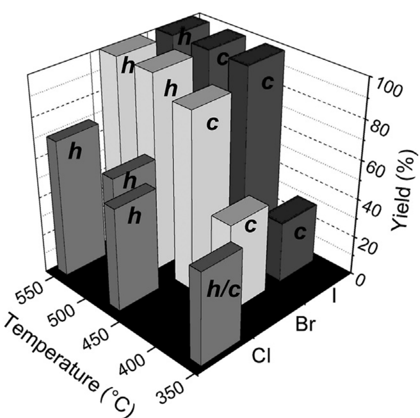

FIGURE 15.13 Temperature dependence of yield of self-nucleated GaN synthesized under different acidities of the mineralizer NH_4X with X = Cl, Br, and I as observed from 96-h growth cycles. The purely hexagonal (*h*) and cubic (*c*) GaN phases were identified by means of powder X-ray diffraction. *(Reprinted from Ref. [78], with permission.)*

Table 15.2 Seeded GaN Crystal Growth under Ammono-Basic and -Acidic Conditions

Mineralizer	Temperature (K)	Pressure (MPa)	Growth Rate ($\mu m\ h^{-1}$)	XRC FWHM (arcsec) (002)	(100)	(201)	a (Å)	c (Å)	Crystal Size; Remarks	References
Basic	773–873	100–300			15	19	3.1897	5.1861	26 × 26 mm^2, (1–100)	[82–87]
					21	17	3.18908(10)	5.18517(10)	26 × 26 mm^2, (20–21)	
				16			3.189(2)	5.185(2)	1″ (0001); narrow slit opening of 0.1 × 0.1 mm^2	
									2″ (0001)	
Basic									Tadao (large size)	[87]
NH_4Cl									2″, (0001)	[88]
KNH_2 and $NaNH_2$	823–873	(60–85% fill)	0.5 (0001), (000–1); 1	100		90	/	/	~1 cm^2,	[89,90]
Basic	823–873	100–400 (55–70% fill)	14.3 (0001)	527 (Ga) 163 (N)		189 (Ga) 136 (N)			1″ x 0.5″ x 0.5″, (0001) starting from (11–22) seed crystal	[91,92]
			1.2 (10–10)			152				
						131				
			4.8 (10–11)			372				
						104				
			22.7 (11–22)			171				
						186				
Acidic	923–1023	100–600	10–30 routinely, highest >40		25	28	/	/	Maximum 2″ (0001), 0.5–2 mm thick	[93]
				21[a]		25[a]				
				178		90				
$ZnCl_2$	693–813	110	0.6	411			/	/	~60 μm thick, each Ga and N face	[80]
Acidic	873–1273	500–2000 (70–95% fill)					/	/	11 × 13 mm^2, 0.15–1 mm thick	[74]
NH_4F	823–923	80–150	10–12.5	28.6	28.9		/	/	7 × 3 × 3 mm, along c-axis	[75]
NH_4Cl	993	Maximum 150	3–5	26[a] (Ga)			/	/	0.5 cm^2, 1.2 mm thick	[76]
				30 (Ga)	43					
				48 (Ga)					0.5 cm^2, 3 mm thick	
				29 (N)					0.5 cm^2, 3 mm thick	

[a]FWHM for laterally grown c-plane.

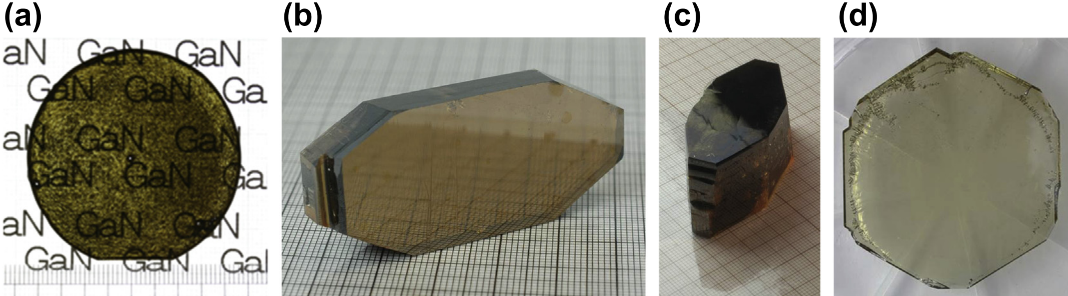

FIGURE 15.14 (a) The first nearly 2-inch large GaN crystal grown by ammono-acidic technique. (b) A 2×1 inch GaN crystal grown under ammono-basic conditions. *(Courtesy of Ammono S.A.)* (c) A 1-inch-thick (0001) bulk GaN crystal used to prepare 1-inch $(10\bar{1}0)$ wafers grown under ammono-basic conditions. *(Courtesy of Ammono S.A.)* (d) A 2-inch crystal grown using the SCoRA reactor. *(Courtesy of Soraa, Inc.)*

ammono-acidic conditions [95]. A 2-inch GaN crystal grown under ammono-acidic conditions using the SCoRA (scalable compact rapid ammonothermal) technique (see Section 15.3.2) is shown in Figure 15.14(d) [96].

15.3.2 Ammonothermal Growth Method

The core hardware for ammonothermal crystal growth is a closed vessel to generate sufficient pressure, as in the classic hydrothermal growth of quartz. This vessel is heated externally. All constituents required to run the growth process are enclosed in this vessel: solvent (NH_3, mineralizer), solute (also referred to as feedstock; mostly solid GaN), GaN seed crystals (to promote epitaxial nucleation and subsequently growth), and any devices needed to control the fluid transport and to keep seed crystals in place.

The ammonothermal vessel encounters multiple challenges. The chemical environment is very corrosive, whether basic or acidic in nature. The fluid embraces the mineralizer dissolved in ammonia and takes on its supercritical state far below typical growth conditions at $T > 673$ K and $p < 100$ MPa (see Table 15.2). Likewise, many other crystal growth techniques from the solution, satisfying rates to grow high-quality crystals, are achieved at higher temperatures due to the thermal activation needed to enable the building units to settle in the right crystal lattice site.

Until recently, only the classic autoclave design has been employed to develop an ammonothermal growth technology (see Figure 15.15(a)). This autoclave is composed of a thick steel tube, which is permanently closed at its bottom part and has a lid as its top part. This lid must be sealed perfectly to generate a closed system. The entire autoclave is heated from the outside. The steel walls will experience the entire heat, traveling from the heater inside the autoclave, and pressure, directed from inside the autoclave toward its inner walls. The choice of steel alloy is of highest importance for the autoclave to withstand the chemically harsh conditions at high temperatures and pressure over a long period of time. Corrosion-resistant Ni-based alloys (e.g., alloy 625, Rene 41, Nimonic 90) are thus used as the material of choice.

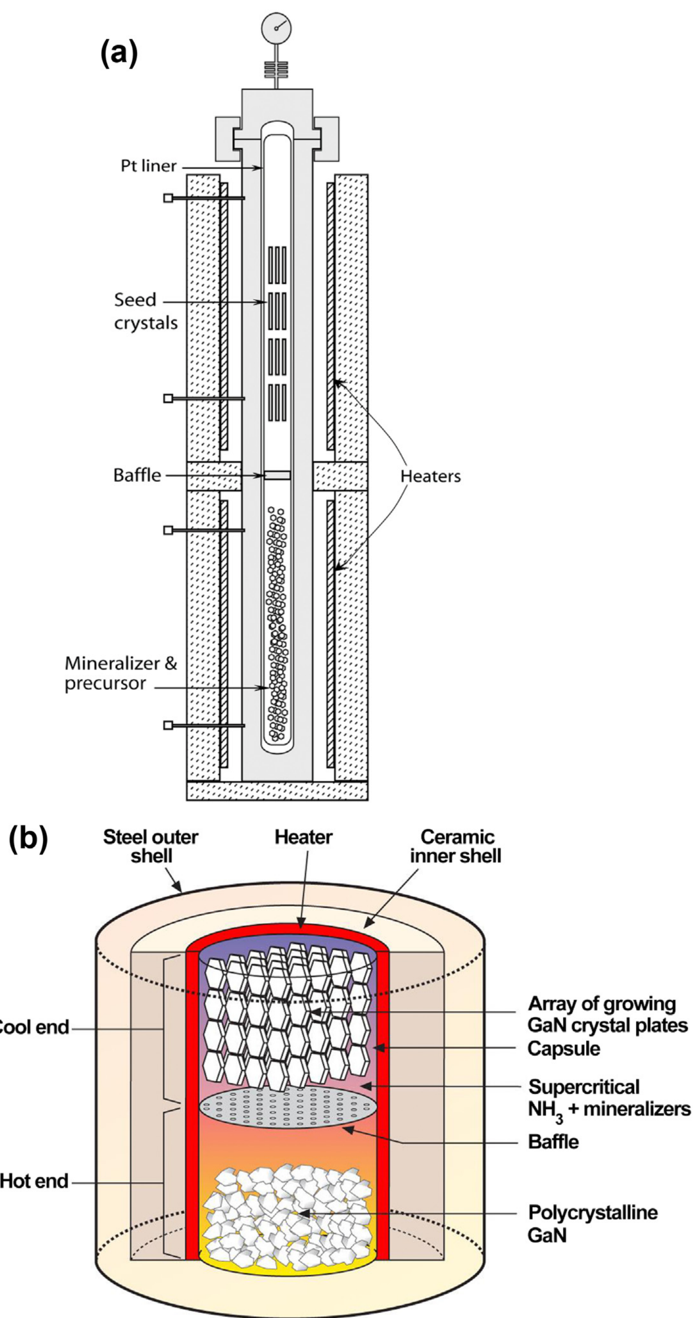

FIGURE 15.15 (a) Typical autoclaves for production (cross-sectional view). (b) A schematic showing the principle of a SCoRA reactor.

To grow high-purity GaN crystals, it seems necessary to use a protective inner layer (sometimes referred to as inner liner), which can be made out of precious metals such as silver (Ag), gold (Au), platinum (Pt), or alloys thereof to increase mechanical stability. Alternative to an inner layer tightly fit to the inner wall, a capsule made out of precious metal can also be used (Figure 15.15(a)). Counterpressure must be applied to the volume, defined as the difference of the volume of the autoclave minus that of the closed capsule, to avoid strong deformation of the latter.

An alternative design has been developed by Soraa, who demonstrated a novel ammonothermal approach for the growth of high-quality, true bulk GaN crystals at a greatly reduced cost. Soraa's approach, known as SCoRA (scalable compact rapid ammonothermal), uses internal heating to circumvent the material-property limitations of conventional ammonothermal reactors (Figure 15.15(b)). Raw material, including seed crystals, polycrystalline GaN nutrient, a mineralizer, and ammonia, are placed inside a capsule and sealed. The capsule is surrounded successively by a heater, a ceramic shell providing structural support and thermal insulation, and an externally cooled steel outer shell that provides mechanical confinement. The use of steel rather than a nickel-based superalloy for the pressure apparatus greatly reduces the cost, including both raw material and machining costs, and enables forging to much larger volumes. The low thermal conductivity of the ceramic enables the steel shell to remain below 473 K, even at an operating temperature of 1023 K, maintaining high creep resistance. The SCoRA reactor has demonstrated capability for temperatures and pressures as high as 1023 K and 600 MPa, respectively, enabling higher growth rates than conventional ammonothermal techniques; it is less expensive and more scalable than conventional autoclaves fabricated from nickel-based superalloys. The configuration shown in Figure 15.15(a) is appropriate for a mineralizer with a positive solubility coefficient as well as those showing retrograde solubility; in the latter case, seeds will be hung in the lower fraction and the nutrient in the upper fraction of the vessel.

Generally, several methods may be used to fill the growth chamber with ammonia. In the high-pressure injection system, ammonia is injected into the vessel by a high-pressure injection syringe. However, dirt and oil in the cylinder can mix in the container, thus polluting the system. A better method is to process under low temperatures to conduct so-called cooling introduction, which is at least suitable for small vessels. The latter is vacuum-pumped and cooled below the boiling point T_b of NH_3 (under atmospheric pressure, $T_b = 239.8$ K, melting point $T_m = 195.45$ K). Then, ammonia is flushed in via a controlled method using a mass flow controller. The ammonia in the autoclave takes over its liquid state. Typical fill ranges are around 40–80 vol% of NH_3. Finally, the growth cycle can begin by heating up the vessel in the desired way.

15.3.3 Chemistry of the Ammonothermal Solution

Ammonia is a relatively weak solvent for ionic substances. The dielectric constant ε, which is a measure of the energy of solvation compared to the lattice energy, $\varepsilon = 16.5$, is

smaller for NH_3 when compared to H_2O, $\varepsilon = 80$. Consequently, the formation of low-crystallinity phases is therefore preferred. A way to partly overcome this problem is to conduct the reaction at much higher pressures, which leads to an increase of ε at higher density of the solvent [51]. However, the solubility of GaN in sc–NH_3 has been observed to be much too small to dissolve a measurable amount of GaN [84], so that enhancing the solubility of GaN by using a mineralizer must be adopted in order to process under reasonable p-T conditions at high growth rate.

There has been substantial interest in the past to find ways of synthesizing GaN by solvothermal reactions. Table 15.1 gives an overview of some of the methods that successfully crystallized self-nucleated GaN under different ammonothermal conditions. As can be seen, inorganic acidic and basic and even some metal-organic reactions have been explored.

Currently, both the inorganic ammono-basic and ammono-acidic paths are regarded as promising methods of bulk crystal growth of gallium nitride. The metal-organic paths turned out to be inefficient (thermal stability of the precursors, potentially low growth rates due to low thermal activation energy) and very costly (precursor cost, handling).

In general, there are several contributors impacting the growth rate. First is the polarity, which is the electrical charge and density of complex ions able to attach to the crystal surface before decomposition of the same to add a building block (Ga and or N, in case of GaN) to the surface. The second contribution comes from the concentration of growth species draw from the solution in front of the growing face of a crystal. In same context, the transport rate to replenish consumed complex ions is important and determining if slower than the decomposition rate and successive growth step. Known from the HVPE of GaN on foreign substrate (sapphire in this case) is that the limit for the kinetic stability of the growth rate of wurtzite GaN was not yet reached at $v_{gr} = 150\ \mu m\ h^{-1}$ for (0001) GaN [97], nor was it at higher $v_{gr} = 240\ \mu m\ h^{-1}$ for the HVPE growth on practically strain-free ammonothermal seed crystals [40]. Both numbers are much higher compared to the highest reported growth rate for ammonothermal (0001) GaN with $v_{gr} = 40\ \mu m\ h^{-1}$ [98].

Unlike relatively simple, well-understood systems (e.g., NaCl dissolving in H_2O, resulting in a solution consisting of metal aquo complexes of the formula $[Na(H_2O)_8]^+$ and strongly solvated chloride ions, with each being surrounded by an average of six molecules of H_2O [99]), the understanding of ammonothermal chemistry (i.e., which intermediates are present and at what concentration at a given high pressure and temperature) is very low.

A number of phases with potential relevance to the ammonothermal chemistry under growth conditions within the acidic system Ga–N–H–X with X = I, Br, Cl, F and a basic system Me–Ga–N–H with Me = Li, Na, K are known, such as $[Ga(NH_3)]F_3$, $[Ga(NH_3)_5Cl]Cl_2$, $KGa(NH_2)_4$, etc.; see Refs [65,66,91,99–106].

Pentaaminechlorogallium (III) dichloride, $[Ga(NH_3)_5Cl]Cl_2$, has been proposed to be an effective precursor for the growth of GaN. It has been synthesized at 840 K [101],

suggesting that it might be thermally stable under conditions applied for the ammonothermal growth of GaN when using NH_4Cl as mineralizer. The building blocks are cationic $[Ga(NH_3)_5Cl]^{2+}$ octahedra surrounded by distorted cubes of chlorine anions. The latter can relatively easily disconnect from the cationic octahedra in a given environment so that the double positively charged $[Ga(NH_3)_5Cl]^{2+}$ might be present in sc–NH_3 with NH_4Cl dissolved. This, in turn, might explain the higher growth rate of the $(000\bar{1})$ face in comparison to the (0001) face; a positively charged growth species such as $[Ga(NH_3)_5Cl]^{2+}$ is likely to be attracted by the negatively charged$(000\bar{1})$ face rather than the positively charged (0001) face. It had been noted earlier [107] that a major process seems to govern the chemical equilibrium because the Arrhenius plot from the solubility chart unambiguously revealed a linear slope (see Section 15.3.4).

Roos et al. studied the thermal decomposition of ammonothermally synthesized $(NH_4)_3GaF_6$ under elevated NH_3 pressure using powder XRD. $Ga(NH_3)F_3$ and $Ga(NH_3)_2F_3$ were obtained in the ranges $T = 493$–503 K and $T = 513$–533 K, respectively, and GaN was obtained at $T \geq 613$ K [104]. To continue with the fluorine system, several potential intermediates are known [99,101–104]; however, precise data on thermal stability within the p-T range of interest for the ammonothermal growth is not known; neither is it clear whether or not there are other species present. The same can be said for the other halogenides as well as for the metal ions in the ammono-basic systems.

The use of a quasi-transparent reactor with the chance to employ a probe to investigate chemical reactions seems to be an attractive option; however, a serious drawback is the corrosive nature of the chemistry in use as well as high p-T conditions required to successfully run an ammonothermal reaction leading to the crystal growth of GaN at suited high rates and quality. A first step toward gaining some understanding was the construction of a quasi-transparent high-pressure high-temperature ammonothermal cell for UV/VIS transmission spectroscopy [107]. There, a light beam passing the cell through sapphire windows is the probe to monitor changes in the chemical environment inside the cell upon modifiyng the temperature. A typical spectra recorded from the system GaN–NH_4Cl–NH_3 at various temperatures shows a steady decrease of the total intensity for $558\ K \leq T \leq 679\ K$.

15.3.4 Solubility in Ammonothermal Growth

The necessity for a solubility-enhancing specimen (i.e., a mineralizer) has an impact on the solubility of GaN in that the mineralizer will add to the complexity of species present in the solution. Two different types of mineralizers are found to be suited to this process: the acidic and the basic mineralizer. Table 15.1 provides an overview on some earlier work employing a wide range of acidic, basic, and neutral salts for their potential as mineralizers. Downselected and commonly used mineralizers in ammonothermal crystal growth runs are $NaNH_2$ and KNH_2 as basic mineralizers and NH_4X with X = F, Cl, I. Other alkali metals (group I elements of the periodic table of elements) such as rubidium (Rb) and cesium (Cs) have not proven to be superior to either $NaNH_2$ or KNH_2.

Lithium (Li) has a very small ionic radius; hence, it has potential to diffuse into the wurtzite GaN structure and also might form stable nitrides. Adding hydrogen (H) to the NH_2^- anionic group would simply form NH_3; thus, no mineralizer effect will be observed. Francium (Fr) is highly radioactive with a very short half-life; therefore, Fr is out of consideration. Alkaline earth metals are known to form stable nitrides and will therefore incorporate into the GaN crystal structure.

Moving over to the acidic mineralizers, bromine (Br) has been found to have a much lesser effect on the solubility of GaN than fluorine, chlorine, or iodine. The latter is the largest of the four group-VII elements of relevance; astatine (At) is radioactive with a half-life time of 8.5 days and is a product of the decay of Fr. An advantage of the acidic mineralizer NH_4Cl over basic mineralizers, such as KNH_2 or $NaNH_2$, is the high solubility in NH_3 already at room temperature, where 124 g NH_4Cl ($T = 297.95$ K), 3.6 g KNH_2 ($T = 298.15$ K), and 0.163 g $NaNH_2$ ($T = 293.15$ K) per 100 g NH_3 were reported [108]. This suggests that a larger amount of GaN could be dissolvable in NH_3 containing an acidic mineralizer in comparison to a basic mineralizer. Also, the reaction between NH_3 saturated with the mineralizers and Ga-containing feedstock might commence at relatively low temperatures.

The solubility of GaN under ammono-acidic conditions using NH_4X with X = Cl, Br, I has been studied by groups from Tohoku University in Sendai, Japan [109,110]. A high-pressure cell with a volume of 10 mL was used at pressures around 100 MPa [107]. Experiments were conducted for 120 h under isothermal conditions to avoid transport and successive recrystallization of the dissolved GaN. Polycrystalline HVPE GaN has been used as precursor. Figure 15.16 shows the solubility of GaN in NH_4Cl-containing NH_3. It becomes clear that an increase of the concentration of NH_4Cl as well as temperature results in an increase of GaN in the solution. Also shown in Figure 15.16 is the solubility of the isostructural AlN under similar T and molar ratio NH_4Cl/NH_3 of about 0.032. AlN shows a somewhat higher solubility than the GaN.

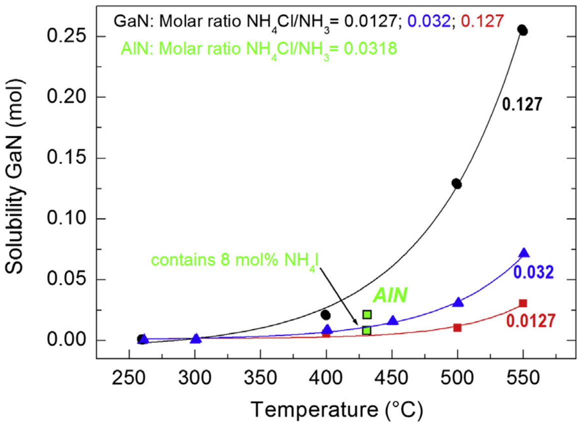

FIGURE 15.16 Solubility of GaN and some AlN in ammono-acidic solutions. *(Reprinted from Ref. [78] with permission.)*

Increasing the acidity of the solution by adding NH_4I lowers the solubility of AlN. Derived from the single exponential growth of the concentration of GaN for $523K \leq T \leq 873$ K, we have calculated the energy of formation $\Delta H_F = 15.9$ kcal mol^{-1} [107]. It was found that this value is independent from the concentration of mineralizer in NH_3 and will provide a tool to calculate the overall energy needed to control the solubility of GaN, thus controlling the growth of GaN under acidic ammonothermal conditions for a given system.

It is well established that the acidic mineralizer NH_4X (X = Cl, Br, I) shows an increase in the acidity with increasing ionic radius of the halogen; that is, the ligands X determine the concentration of free NH_2^- in the solution. The increasing acidity, on the other hand, goes along with an increasing fraction of self-nucleated cubic GaN, space group F4$\overline{3}$ m, as evidenced by powder XRD [78]. However, this is strictly true only for the growth of GaN without providing a seed crystal of hexagonal GaN. Adding a wurtzite-type GaN seed crystals at growth conditions otherwise producing cubic GaN upon self-nucleation has yielded 100% hexagonal-phase GaN. As a side note, the company of oxygen in the system at high levels at $>10^{18}$ cm^{-3} causes the formation of crystalline gallium oxide (Ga_2O_3, space group R$\overline{3}$ c) as precipitates if unseeded growth was performed. A hailed effect of increased acidity is the increase of the yield of GaN, indicated by the quantity of used up GaN precursor, as shown in Figure 15.13 [78].

Although employing NH_4Cl does not substantially change the yield over increased temperatures from 633 K to 823 K, the effect that the mineralizers NH_4Br and NH_4I have is clearly seen: the yield is increased at $T \geq 723$ K. Also seen in Figure 15.13 is that phase stability to the favor of the hexagonal phase is better achievable at $T \geq 773$ K when NH_4Br and NH_4I are used, which is in agreement to work reported by Purdy et al. [61].

Because the dissolution of GaN occurs in two principal steps, as has been discussed in Section 15.4, the solubility of GaN is governed by the stability range of the intermediates that have been formed in a given chemistry. Temperature, pressure, and the initial concentration of the mineralizer in the ammonia host will therefore affect the solubility of GaN. For example, it was believed until recently that NH_4Cl as a mineralizer will result in a positive gradient for the solubility. With higher T, more GaN can be dissolved. However, Yoshida et al. [76] described their observations of changing solubility behavior. The solubility changed from a positive to those with a negative coefficient (also known as retrograde solubility) at $T > 923$ K and $p \sim 110$ MPa. Crystal growth is now enabled in the hotter zone of the vessel. This is the first such observation from any acidic ammonothermal system.

Much less data are available for the ammono-basic crystal of GaN. Wang and Callahan have reported that the most favorable conditions for the growth of GaN under basic ammonothermal conditions with either purely KNH_2 or mixed $KNH_2 + KN_3$ as mineralizers are at $T \sim 823$ K in the hot zone where the crystals are growing and $p = 172$–310 MPa with the NH_3 fill at >60% [91].

Hashimoto et al. [111] estimated the solubility of GaN in NH_3 with $NaNH_2$ as mineralizer by measuring the weight loss of polycrystalline GaN after immersing and

soaking in the supercritical solution, followed by a sudden release of the solution. They also reported a change of the solubility from a positive to a negative gradient at $T \sim 873$ K.

15.3.5 Growth Rates and Morphology

Unsurprisingly, the growth rate weighs heavily on the overall economy of a crystal growth process, strongly determining the price of wafers cut from the grown crystals. Generally, the growth of a single crystal from a solution is a much slower process than growth from the melt; reasons for that have been discussed extensively in the literature (e.g., Ref. [112]). However, the growth of a large number of crystals in parallel in the same vessel during a growth cycle—as is common practice for the case of hydrothermal growth of quartz [113], where more than 1000 crystals are growing at the same time in one autoclave—gives the ammonothermal technique huge leverage over methods where a single or a small number of GaN crystals are produced in parallel.

The growth rate as determined from experiments is a function of the concentration of the mineralizer, the absolute temperature, and temperature gradient between dissolution and growth zone in the vessel. A growth rate exceeding 2 $\mu m\, h^{-1}$ for long-term growth cycles requires $\geq$1 mol% NH_4Cl per 1 M NH_3; higher growth rates close to 4 $\mu m\, h^{-1}$ were achieved in experiments [88]. A stable growth rate around 4 $\mu m\, h^{-1}$ could already be satisfying for a mass-production of GaN by the ammonothermal route, but it requires the use of large-size vessels containing hundreds of GaN seed crystals per single growth cycle [60].

Growth rates for crystals produced in solution systems are typically slower than those from the melt: in cases of some flux growth, a $v_{max} = 72$–180 $\mu m\, h^{-1}$ was reported [114]. In the production of large-size hydrothermal α-SiO_2 and ZnO crystals, typical growth rates of 20–40 $\mu m\, h^{-1}$ and 10–15 $\mu m\, h^{-1}$ were observed for the (0001) planes to manufacture large-size and low-defect crystals, respectively [9].

Interestingly, the growth rates of GaN obtained for the acidic and basic ammonothermal systems are very similar. This becomes clear from Table 15.2, in which growth rates are listed for ammonothermal GaN yielded under different ammono-acidic and basic conditions.

In Figure 15.17, Bao et al. have summarized the growth rate under different ammonoacidic conditions as function of system pressure [75]. The highest rates of $v_{gr} = 12\ \mu m\, h^{-1}$ and 9 $\mu m\, h^{-1}$ were achieved for growth on m- and c-plane seeds, respectively, when employing NH_4F as mineralizer.

Ammonothermal GaN crystals exhibit a number of well-known surface morphologies. Figure 15.18 shows a large size (0001) GaN crystal with a few hillocks. The source for the hillocks typically are threading dislocations, with the Burgers vector directing toward the growth direction of the respective crystallographic plane.

Pimputkar et al. conducted some detailed studies on the morphology of GaN grown on $(10\bar{1}0)$ seed crystals [93]. Mounds, actually depicting hillocks, were found for on-axis growth on $(10\bar{1}0)$ seed crystals. This changed with increased off-orientation toward

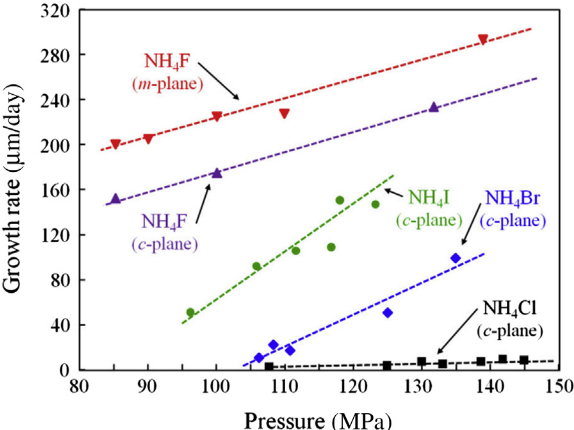

FIGURE 15.17 v_{gr} vs pressure for ammono-acidic growth conditions. *(Reprinted from Ref. [75] with permission.)*

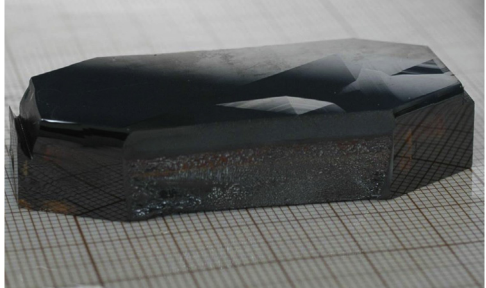

FIGURE 15.18 A 55-mm long (0001) GaN crystal exhibiting a few hillocks. *(Courtesy of Ammono S.A.; reprinted with permission).*

$\{11\bar{2}0\}$, and large steps or slate-like morphology has been observed. If the off-axis tilt was $\geq 20°$, tetrahedrally shaped pyramids were found to cover the surface. Figure 15.19 shows the cross-sectional view of a grown GaN crystal on an off-oriented seed. A tapered growth is noted. The resulting grown crystal face is composed of microfacets toward $(000\bar{1})$.

15.3.6 Doping under Ammonothermal Conditions

Doping under high pressure from a liquid solution, which is in its supercritical state in the case of the ammonothermal technique, and consequently crystal growth near the thermodynamic equilibrium, has several limitations. The building blocks (Ga and N atoms to form the host GaN and a doping atom) are transported to a growing facet as part of an intermediate phase (also referred to as metastable phase in crystal growth), which is dissolved in the solvent. The concentration c of such intermediate dissolved in the hosting solvent depends on the concentration of mineralizer, system pressure p, and temperature T. The thermodynamic stability of the dopant-containing intermediate in any case is different from the one delivering the building blocks to form the host GaN.

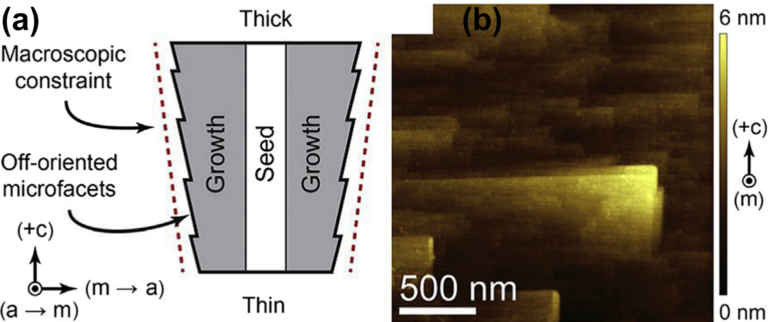

FIGURE 15.19 (a) Schematic of the cross-sectional view of a grown crystal on an off-oriented seed, showing the resulting growth front being composed by off-oriented microfacets toward $(000\bar{1})$. (b) AFM (Atomic Force Microscopy) scan of a newly formed surface on a 5° off-oriented seed crystal. *(Reprinted from Ref. [93] with permission.)*

Given the above considerations, the bandwidth for doping of GaN will be rather limited. The control of dopant concentrations will hardly be comparable to vapor phase growth methods, such as MOCVD, where the growth occurs far away from the thermodynamic equilibrium compared to the ammonothermal growth of GaN.

To control doping levels in a crystal, it is necessary to reduce the levels of relevant impurities—that is, those contributing to modification of the Fermi level, acting as donor or acceptor. Table 15.3 gives the impurity levels reported for GaN grown under ammono-basic and acidic chemistry in comparison to ultra-pure HVPE-grown GaN.

An early attempt to get oxygen by introducing rare-earth (RE) ions in the solution was reported by Dwilinski et al. [64]. It was suggested that these RE ions do form stable oxygen-containing phases, which are not incorporated into the GaN wurtzite lattice. It could, however, be the case that the concentration of these undisclosed RE ions was below the detection limit for PL.

Zajac et al. [118] grew GaN doped with manganese (Mn), iron (Fe), chromium (Cr), and zinc (Zn) under ammono-basic conditions. Metal precursors were used to add to the

Table 15.3 Impurity Levels in Unintentionally Doped Ammonothermal GaN Crystals Grown under Ammono-Basic and Acidic Conditions in Comparison to Ultra-Pure HVPE-Grown GaN [75,89,91,115–117]

Element	Ammono-Basic (atoms cm^{-3})	Ammono-Acidic (atoms cm^{-3})	HVPE (atoms cm^{-3})
Si	$\leq 3.5 \times 10^{18}$–1×10^{19}	9×10^{14}–10^{19}	1.5×10^{17}
O	10^{17}–10^{19}	8×10^{18}–10^{20}	$<7 \times 10^{15}$
Fe	$\leq 2 \times 10^{17}$	10^{17}–10^{20}	$<1 \times 10^{15}$
Ni	$<8 \times 10^{15}$	10^{17}–10^{20}	$<3 \times 10^{15}$
Cr	/	10^{15}–10^{18}	2.2×10^{14}
K	$\leq 10^{20}$	/	/
Pt	$<5 \times 10^{16}$	$\leq 10^{16}$	/

chemistry, but $CrBr_3$ was found to be more suited for doping Cr. GaN:Zn yielded an intense blue emission, peaking around 3.3 eV. Manganese can be doped at <1%, whereas Fe (0.03%) and Cr (<0.02%) turned out to be less efficient as dopants.

Initially thought to capture residual oxygen (O) in the ammonothermal solution, doping with erbium (Er) has been reported by Adekore et al. [119]. Erbium concentrations of $1 \times 10^{17}\,cm^{-3}$ and $1 \times 10^{18}\,cm^{-3}$ in the N- and Ga-polar sectors, respectively, have been observed. Photoluminescence spectra were recorded at $T = 15$ K, revealing a strong band edge emission around 3.495 eV from the Ga-polar face due to free exciton (FE) and at 3.475 eV due to neutral donor bound exciton (D^0X) from the N-polar face; donor acceptor pair (DAP) and its corresponding longitudinal optical phonon replica occurred at 3.277 and 3.185 eV, respectively.

The control of electrical conductivity in ammonothermal GaN can be done by incorporating oxygen, a practice applied to HVPE GaN, where doping levels of $2 \times 10^{19}\,cm^{-3}$ have been achieved for n-type material. Highly resistive substrates have a concentration of donors and acceptors of about $10^{19}\,cm^{-3}$ [116]. There have not been more reports published on the in-situ doping of ammonothermal GaN, but this will certainly change in the future as more sources for ammonothermal GaN wafers arise.

15.3.7 Properties of Ammonothermal GaN

The crystallinity of ammonothermal GaN as measured by XRC is already exceeding that of any GaN grown by any other method. FWHM of 16 arcsec for the symmetric (002) reflection and 17 arcsec for the asymmetric (201) reflection are routinely observed on material from Ammono S.A. (see Table 15.2).

A yellow coloration is typically seen for ammonothermal GaN, apparently independent from the chemistry in GaN grown under ammono–acidic or basic conditions. Little is known as to what the cause for such coloration in ammonothermal GaN is, and consequently how to reduce or even avoid it.

Based on the principal impurities O, H, and C in their crystals, with impurity leveling in the $10^{18}\,cm^{-3}$ range under ammono–acidic conditions, D'Evelyn et al. [74] suggested that H-related defects may be a major cause for optical absorption (α) tailing from the band edge into the near-UV and violet range of the spectrum of light. Fourier-transform infrared spectroscopy (FTIR) was measured on as-grown, polished samples, and a series of sharp features centering around 3175 cm^{-1} was observed. Hydrogen can bind to Ga vacancies (V_{Ga}) and N-H bonds can be formed by capping dangling bonds on some or all of the 4 N atoms surrounding the V_{Ga} (i.e., $V_{Ga}H_n$ with $n = 1, 2, 3,$ or 4). High-temperature annealing as a possible path to improve optical transmission has not been reported yet.

Table 15.4 summarizes data on the optical absorption of the two main growth sectors (0001) and ($000\bar{1}$), which constitutes the two basal planes of wurtzite GaN. The difference in the surface energy between each plane explains the different α due to variances in the nature and concentration of impurities. There seems to be no crucial dependence

Table 15.4 Optical Absorption of Ammonothermal (0001) and $(000\bar{1})$ GaN Grown under Ammono-Basic and -Acidic Conditions

Basic/Acidic Mineralizer	α450 (cm^{-1})		α_{400} (cm^{-1})		References
	(0001)	(000–1)	(0001)	(000–1)	
Basic	5	7.5	10	15	[92]
Basic	~1.6		~5 (O ~ 10^{18} cm^{-3})		[116]
Acidic	<1		<4		[96]
Basic	3.8		/		[117]

in α from the chemistry of the growth environment, although more data must be gathered to make a definitive statement.

Jiang et al. measured the optical absorption coefficient α of free-standing GaN grown by the SCoRA technique at room temperature [96]. Figure 15.20 shows some representative graphs for (0001) GaN samples. Both end faces were polished to optical grade. The progress achieved over a short period of time is demonstrated by comparing results obtained from characteristic specimens grown during the years 2011 and 2013 in comparison to a commercial epi-ready HVPE-GaN wafer. At the wavelength important for blue emitters, $\Lambda = 450$ nm, the recent SCoRA GaN shows α of approximately 0.75 cm^{-1}, which is smaller than for the HVPE sample (i.e., $\alpha \sim 1.5$ cm^{-1}). At $\Lambda = 410$ nm, the absorption coefficient for the SCoRA and the HVPE sample is equal at $\alpha \sim 2$ cm^{-1}. This demonstrates that optimized ammonothermal crystal growth technology is suited to manufacture GaN that meets the specifications required for fabricating LED structures. The average dislocation density for the SCoRA sample has been measured at 7×10^4–1×10^6 cm^{-2}, as revealed by counting etch pits compared to the mid 10^6 cm^{-2}

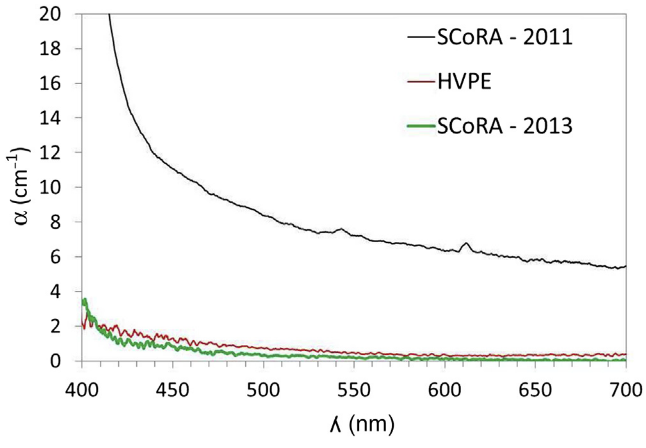

FIGURE 15.20 Optical absorption coefficient of ammonothermal and HVPE GaN.

range for the HVPE wafer. The lowest dislocation density has been reported for ammonothermal GaN crystals grown by Ammono S.A.

Letts et al. [117] reported on experiments in ammono-basic chemistry where Na_2O was deliberately added as a source for oxygen. Increasing the concentration of Na_2O clearly led to increased α. Under best growth conditions, $\alpha \sim 5\,cm^{-1}$ for the oxygen concentration of $1 \times 10^{19}\,cm^{-3}$ ($Na_2O = 0$) but increased to $\alpha > 100\,cm^{-1}$ upon adding 1.1% Na_2O.

To reduce the impurity levels in growing crystals, the entire chain for handling and preparation of an ammonothermal crystal growth experiment must use high-purity ingredients in an oxygen-free atmosphere in a glove box, extensively vacuuming the autoclave before filling with NH_3, and so forth. Figure 15.21 shows a transparent (0001) GaN crystal grown under improved ammono–basic conditions [90].

The thermal conductivity in ammonothermal GaN crystals produced under ammono-basic conditions decreases with increasing oxygen content from $220\,W\,m^{-1}K^{-1}$ (O level: $10^{17}\,cm^{-3}$) to $170\,W\,m^{-1}K^{-1}$ (O level: $10^{19}\,cm^{-3}$) and is $140\,W\,m^{-1}K^{-1}$ for SI-GaN [116].

TopGaN and IHPP PAS have demonstrated high-power laser diode devices, both single-emitter laser diodes and laser diode arrays, fabricated on ammonothermally grown GaN crystals from Ammono S.A [120]. The laser diodes structures were grown by metaloorganic chemical vapor deposition (MOCVD) and molecular beam epitaxy (MBE) methods. The single-emitter laser diodes emitted at 395–450 nm with a typical threshold voltage of 4.5 V at $2.5\,kA\,cm^{-2}$. For the sixteen-emitter laser diode array, the maximum optical power demonstrated was 4 W at 6 A. The operation current density was around $18\,kA\,cm^{-2}$. It offers the possibility of obtaining a lifetime exceeding 5000 h. These results indicate the great potential of nitride laser arrays manufactured on ammonothermally grown GaN substrates for making very high-optical-power emitters for large television and movie projectors.

FIGURE 15.21 A transparent GaN crystal grown under ammono-basic conditions. *(Reprinted from Ref. [90] with permission.)*

15.3.8 Prospects and Future Developments for Ammonothermal GaN

Given the few research groups involved, also in comparison to the development of HVPE technology, for example, the ammonothermal bulk growth technique for GaN has come a long way since the first attempts commenced in the 1990s. Although limited, ammonothermal GaN wafers and substrates are now commercially available. Figure 15.22 shows a 2-inch (0001) wafer manufactured by Ammono S.A [7].

It is within expectation that GaN epi-ready wafers fabricated from ammonothermal GaN boules will enter the market for electronic and opto-electronic substrates in the near future; however, it is speculative to say at what quantity this will happen. Although the high structural integrity of ammonothermal GaN crystals is now a widely accepted fact, some issues to be resolved remain: (1) defined doping to yield n-type and semi-insulating electric conductivity; (2) scaling the hardware to enable the growth of a large quantity of GaN boules from which to fabricate 4-inch, 6-inch, and even larger size wafers in the future; and (3) a stable high growth rate to permit for optimized and economic growth cycles.

15.4 Overall Summary with an Outlook into the Future

It has been shown that crystals grown by HNPS and ammonothermal methods are of high structural quality, each of which grown under completely different temperature-pressure ranges. They have uniform and unique properties, which allow their use as substrates for building laser diodes and other electronic devices. The main disadvantage of HNPS is a low growth rate, which slows down the progress toward cost-efficient mass production. The ammonothermal technique has already demonstrated growth rates

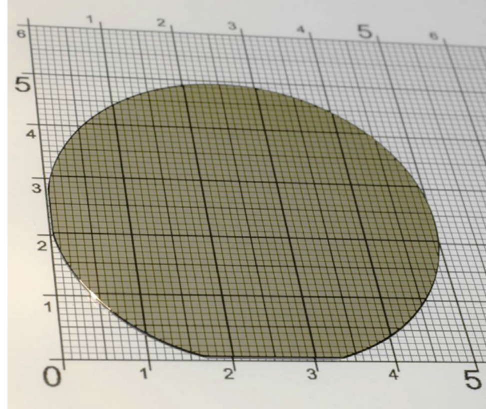

FIGURE 15.22 A 2-inch wafer grown under ammono-basic conditions. *(Courtesy of Ammono S.A. Reprinted with permission).*

large enough to be economical. An important factor for the development of the discussed methods is the need for lattice-matched, low-stress native seed crystals on which to nucleate and grow high-quality GaN. It was shown that GaN crystals grown by the same methods (and in case of the HPNS method, even by the HVPE technology) can be used.

Looking into GaN crystal manufacturing, in the case of using crystals grown by the same method as seeds, access to high-quality substrates to grow device structures initially is very limited. All high-quality crystals might be used to multiply the number of existing crystals to generate a sufficient amount of seed crystal for production. When using foreign seeds, such as HVPE-GaN, which are commercially available already, the quality of the seeds decides the quality of the material to be grown on them. It should be noted that the structural quality of commercial HVPE-GaN is still not very high (high defect density, low bowing radius). The third factor impacting the technology relates to scalability. High pressure is used for both methods discussed in this chapter; consequently, high-pressure containing vessels are required to operate at high temperatures. As was shown, up to 2-inch bulk crystals were demonstrated (although in case of the ammonothermal technique, it is expected that crystals larger than 2 inches might be demonstrated soon). This might be more challenging for the HNPS technique.

Next, it was demonstrated that the combination of HNPS and HVPE or ammonothermal and HVPE method provides an opportunity to obtain high-quality GaN crystals by the HNPS method. This could be a new, repeatable, and scalable route toward the growth of high-quality GaN. A great challenge, however, is to solve the question on how to increase the lateral size of this new material.

Finally, with several enterprises currently working toward a viable ammonothermal growth technology, it seems imminent that the ammonothermal technique could occupy a big share of the total market for GaN substrates. The best GaN substrates in terms of stress and lattice perfection are ammonothermally grown; the first demonstration of highly transparent material, comparable to best-in-class HVPE GaN, is another point of strength for the ammonothermal GaN. Finally, it must be proven that ammonothermal and HNP-grown GaN substrates can compete with the available HVPE substrates in terms of cost.

References

[1] Utsumi W, Saitoh H, Kaneko H, Watanuki T, Aoki K, Shimomura O. Nat Mater 2003;2:735.

[2] Koukitu A, Kumagai Y. In: Ehrentraut D, Meissner E, Bockowski M, editors. Technology of gallium nitride crystal growth. Heidelberg: Springer-Verlag; 2010, ISBN 978-3-642-04828-9. p. 31.

[3] Motoki K. SEI Tech Rev April 2010;70:28.

[4] Oshima Y, Yoshida T, Eri T, Watanabe K, Shibata M, Mishima T. In: Ehrentraut D, Meissner E, Bockowski M, editors. Technology of gallium nitride crystal growth. Heidelberg: Springer-Verlag; 2010, ISBN 978-3-642-04828-9. p. 79.

[5] Geng H, Sunakawa H, Sumi N, Yamamoto K, Yamaguchi AA, Usui A. J Cryst Growth 2012;350:44.

[6] Mori Y, Imade M, Murakami K, Takazawa H, Imabayashi H, Todoroki Y, et al. J Cryst Growth 2012;350:72.

[7] www.ammono.com.

[8] Byrappa K. In: Capper P, editor. Bulk crystal growth of electronic, optical and optoelectronic materials. John Wiley & Sons; 2005. pp. 387–406.

[9] Ehrentraut D, Sato H, Kagamitani Y, Sato H, Yoshikawa A, Fukuda T. Prog Cryst Growth Charact Mater 2006;52:280.

[10] Kawamura F, Morishita M, Tanpo M, Imade M, Yoshimura M, Kitaoka Y, et al. J Cryst Growth 2008;310:3946.

[11] Grzegory I, Bockowsk M, Lucznik B, Krukowski S, Romanowski Z, Wroblewski M, et al. J Cryst Growth 2002;246:177.

[12] Porowski S, Bockowski M, Lucznik B, Wroblewski M, Krukowski S, Grzegory I, et al. In: III-V nitrides book series MRS symposium proceedings, vol. 449; 1997. p. 35.

[13] Krukowski S, Bockowski M, Lucznik B, Grzegory I, Porowski S, Suski T, et al. J Phys Condens Mater 2001;13:8881.

[14] Bockowski M, Strak P, Grzegory I, Porowski S. High pressure solution growth of gallium nitride. In: Ehrentraut D, Meissner E, Bockowski M, editors. Technology of gallium nitride crystal growth. Springer series in materials science, 133. Springer; 2010. p. 207.

[15] Karpinski J, Jun J, Porowski S. J Cryst Growth 1984;66:1.

[16] Porowski S, Grzegory I. J Cryst Growth 1997;178:174.

[17] Grzegory I, Bockowski M, Jun J, Figurny P. High Pres Res 1991;7-8:248.

[18] Grzegory I, Bockowski M, Porowski S. In: Capper P, editor. Bulk crystal growth of electronic, optical and optoelectronic materials. Wiley&Sons; 2005. p. 173.

[19] Krukowski S, Romanowski Z, Grzegory I, Porowski S. J Cryst Growth 1999;189/190:159.

[20] Bockowski M, Grzegory I, Kamler G, Lucznik B, Krukowski S, Wroblewski M, et al. J Cryst Growth 2007;305:414.

[21] Grzegory I, Teisseyre H, Lucznik B, Pastuszka B, Bockowski M, Porowski S [chapter 3]. In: Paskova T, editor. Nitrides with nonpolar surfaces. New York: Wiley; 2007. pp. 53–71.

[22] Perlin P, Camassel J, Knap W, Talercio T, Chervin JC, Suski T, et al. Appl Phys Lett 1995;67:2524.

[23] Litwin-Staszewska E, Suski T, Piotrzkowski R, Grzegory I, Bockowski M, Robert JL, et al. J Appl Phys 2001;89:7960.

[24] Saarinen K, Laine T, Kuisma S, Hautojarvi P, Dobrzynski L, Baranowski JM, et al. Phys Rev Lett 1997;79:3030.

[25] Leszczynski M, Grzegory I, Teisseyre H, Suski T, Bockowski M, Jun J, et al. J Cryst Growth 1996;169:235.

[26] Weyher LJ, Brown PD, Rouviere J-L, Wosinski T, Zauner AR, Grzegory I. J Cryst Growth 2000;210:151.

[27] Bockowski M, Grzegory I, Krukowski S, Lucznik B, Wroblewski M, Kamler G, et al. J Cryst Growth 2004;270:409.

[28] Bockowski M, Grzegory I, Krukowski S, Lucznik B, Wroblewski M, Kamler G, et al. J Cryst Growth 2005;274:55.

[29] Bockowski M, Strak P, Kempisty P, Grzegory I, Krukowski S, Lucznik B, et al. J Cryst Growth 2007;307:259.

[30] Bockowski M, Strak P, Grzegory I, Lucznik B, Porowski S. J Cryst Growth 2008;310:3924.

[31] Bockowski M, Grzegory I, Łucznik B, Sochacki T, Krysko M, Kamler G, et al. Sci China Tech Sci 2011;54:42.

[32] Bockowski M, Grzegory I, Łucznik B, Sochacki T, Kryśko M, Strak P, et al. Phys Stat Solidi A 2011;208:1507.

[33] Bockowski M, Łucznik B, Sochacki T, Sadovyi B, Nowak G, Litwin-Staszewska E, et al. Phys Stat Solidi C 2012;9:453.

[34] Bockowski M, Grzegory I, Łucznik B, Sochacki T, Nowak G, Sadovyi B, et al. J Cryst Growth 2012;350:5.

[35] Grzegory I, Bockowski M, Lucznik B, Weyher JL, Litwin-Staszewska E, Konczewicz L, et al. J Cryst Growth 2012;350:50.

[36] Bockowski M, Lucznik B, Sochacki T, Amilusik M, Litwin-Staszewska E, Piotrzkowski R, et al. Proc SPIE 2013;8625:862509. pp.1-11.

[37] Lucznik B, Pastuszka B, Kamler G, Grzegory I, Porowski S. In: Ehrentraut D, Meissner E, Bockowski M, editors. Technology of gallium nitride crystal growth. Heidelberg: Springer-Verlag; 2010, ISBN 978-3-642-04828-9. pp. 61–78.

[38] Lucznik B, Sochacki T, Sarzynski M, Krysko M, Dziecielewski I, Grzegory I, et al. Phys Stat Solidi C 2011;8:2117.

[39] Amilusik M, Sochacki T, Lucznik B, Bockowski M, Sadovyi B, Presz A, et al. J Cryst Growth 2013;380:99.

[40] Sochacki T, Bryan Z, Amilusik M, Collazo R, Lucznik B, Weyher JL, et al. Appl Phys Exp 2013;6:075504.

[41] Clyne TW. Encyclopedia of material science and technology. Elsevier; 2001.

[42] Gorczyca I, Suski T, Christensen NE, Svane A. Appl Phys Lett 2010;96:101907.

[43] Sarzynski M, Krysko M, Targowski G, Czernecki R, Sarzynska A, Libura A, et al. Appl Phys Lett 2006;88:121124.

[44] Perlin P, Czyszanowski T, Marona L, Grzanka S, Kafar A, Stanczyk S, et al. Proc SPIE 2012;8262:826216.

[45] Sarzynski M, Suski T, Staszczak G, Khachapuridze A, Domagala J, Czernecki R, et al. Appl Phys Express 2012;5:021001.

[46] Krysko M, Sarzynski M, Domagala J, Grzegory I, Lucznik B, Kamler G, et al. J Alloys Comp 2005;401:261.

[47] Skierbiszewski C. Private communication.

[48] Masuda Y, Suzuki A, Mikawa Y, Kagamitani Y, Ishiguro T, Yokoyama C, et al. Int J Heat Mass Transf 2010;53:940.

[49] Kashiwagia D, Gejo R, Kangawa Y, Liu L, Kawamura F, Mori Y, et al. J Cryst Growth 2008;310:1790.

[50] Morishita M, Kawamura F, Kawahara M, Yoshimura M, Mori Y, Sasaki T. J Cryst Growth 2005;284:91.

[51] Jacobs H, Schmidt D. High-pressure ammonolysys in solid-state chemistry. In: Kaldis E, editor. Current Topics in materials Science, vol. 8. Amsterdam: North-Holland; 1982. p. 379.

[52] Peters D. J Cryst Growth 1990;104:411.

[53] Dwilinski R, Wysmolek A, Baranowski J, Kaminska M, Doradzinski R, Garczynski J, et al. Acta Phys Pol 1995;88:833.

[54] Kolis JW, Wilcenski S, Laudise RA. Mater Res Soc Symp Proc 1998;495:367.

[55] Purdy AP. Chem Mater 1999;11:1648.

[56] Brown CS, Kell RC, Thomas LA, Wooster Nora, Wooster WA. Nature 1951;167:940.

[57] Walker AC. J Am Ceram Soc 1953;36:250.

[58] Ketchum DR, Kolis JW. J Cryst Growth 2001;222:431.

[59] Callahan MJ, Wang B, Bouthillette LO, Wang S-Q, Kolis JW, Bliss DF. Mater Res Soc Symp Proc 2004;798. Y2.10.1.

[60] Wang B, Callahan MJ, Rakes KD, Bouthillette LO, Wang S-Q, Bliss DF, et al. J Cryst Growth 2006; 287:376.

[61] Purdy AP, Jouet RJ, George CF. Cryst Growth Des 2002;2:141.

[62] Kagamitani Y, Ehrentraut D, Yoshikawa A, Hoshino N, Fukuda T, Kawabata S, et al. Jpn J Appl Phys 2006;45:4018.

[63] Dwilinski R, Doradzinski J, Garczynski J, Sierzputowski L, Palczewska M, Wysmolek A, et al. MRS Internet J Nitride Semicond Res 1998;3:1.

[64] Dwilinski R, Doradzinski R, Garczynski J, Sierzputowski L, Baranowski JM, Kaminska M. Mater Sci Eng 1997;B50:46.

[65] Lan YC, Chen XL, Xu YP, Cao YG, Huang F. Mater Res Bull 2000;35:2325.

[66] Lin W, Huang J, Chen D, Lin Z, Li W, Huang J, et al. J Nanosci Nanotechnol 2010;9:5741.

[67] Callahan MJ, Wang BG, Rakes K, Bliss D, Bouthillette LO, Suscavage M, et al. J Mater Sci 2006;41: 1399.

[68] Wang B, Callahan MJ, Rakes KD, Bouthillette LO, Wang S-Q, Bliss DF, et al. J Cryst Growth 2006; 287:367.

[69] Demazeau G, Goglio G, Denis A, Largeteau A. J Phys Condens Matter 2002;14:11085.

[70] Jegier JJ, McKernan S, Purdy AP, Gladfelter WL. Chem Mater 2000;12:1003.

[71] Schwenzer B, Hu J, Seshadri R, Keller S, DenBaars SP, Mishra UK. Chem Mater 2004;16:5088.

[72] Jason Jouet R, Purdy AP, Wells RL, Janik JF. J Clust Sci 2002;13:469.

[73] Purdy A. J Cryst Growth 2005;281:355.

[74] D'Evelyn MP, Hong HC, Park D-S, Lu H, Kaminsky E, Melkote RR, et al. J Cryst Growth 2007;300:11.

[75] Bao Q, Saito M, Hazu K, Furusawa K, Kagamitani Y, Kayano R, et al. Cryst Growth Des 2013;13: 4158.

[76] Yoshida K, Aoki K, Fukuda T. J Cryst Growth 2014;393:93. http://dx.doi.org/org/10.1016/j.jcrysgro.2013.09.010.

[77] Yoshikawa A, Ohshima E, Fukuda T, Tsuji H, Oshima K. J Cryst Growth 2004;260:67.

[78] Ehrentraut D, Hoshino N, Kagamitani Y, Yoshikawa A, Fukuda T, Itoh H, et al. J Mater Chem 2007; 17:886.

[79] Wu Y-Shiang, Chang W-Ku, Lai H-Yu. J Cryst Growth 2008;310:2800.

[80] Yokoyama C, Hashimoto T, Bao Q, Kagamitani Y, Qiao K. Cryst Eng Comm 2011;13:5306.

[81] Hashimoto T, Fujito K, Wu F, Haskell BA, Fini PT, Speck JS, et al. Jpn J Appl Phys 2005;44:L797.

[82] Dwilinski R, Doradzinski R, Garczynski J, Sierzputowski LP, Puchalski A, Kanbara Y, et al. J Cryst Growth 2008;310:3911.

[83] Stevenson R. IEEE Spectr 2010;47:40.

[84] Ehrentraut D. Private communication.

[85] Kucharski R, Zajac M, Doradzinski R, Rudzinski M, Kudrawiec R, Dwilinski R. Semicond Sci Technol 2013;27:024007.

[86] Gogova D, Petrov PP, Buegler M, Wagner MR, Nenstiel C, Callsen G, et al. J Appl Phys 2013;113:203513.

[87] Dwilinski R, Doradzinski R, Garczynski J, Sierzputowski LP, Puchalski A, Kanbara Y, et al. J Cryst Growth 2009;311:3015.

[88] Ehrentraut D, Kagamitani K, Fukuda T, Orito F, Kawabata S, Katano K, et al. J Cryst Growth 2008;310:3902.

[89] Bliss D, Wang B, Suscavage M, Lancto R, Swider S, Eikenberry W, et al. J Cryst Growth 2010;312:1069.

[90] Wang B, Bliss D, Suscavage M, Swider S, Lancto R, Lynch C, et al. J Cryst Growth 2011;318:1030.

[91] Wang B, Callahan MJ. Cryst Growth Des 2006;6:1227.

[92] Pimputkar S. Ammonothermal growth of gallium nitride [Ph.D. thesis]. University of California Santa Barbara; 2012.

[93] Pimputkar S, Kawabata S, Speck JS, Nakamura S. J Cryst Growth 2013;368:67.

[94] Hashimoto T, Fujito K, Saito M, Speck JS, Nakamura S. Jpn J Appl Phys 2005;44:L1570.

[95] Stevenson R. Compd Semicond 2013;19:27.

[96] Jiang W, Ehrentraut D, Downey BC, Kamber DS, Pakalapati RT, Yoo H. J Cryst Growth 2014;403:18. http://dx.doi.org/org/10.1016/j.jcrysgro.2014.06.002.

[97] Henning Ch, Richter E, Weyers M, Tränkle G. J Cryst Growth 2008;310:911.

[98] Ehrentraut D, Pakalapati RT, Kamber DS, Jiang W, Pocius DW, Downey BC, et al. Jpn J Appl Phys 2013;52:08JA01.

[99] Lincoln SF, Richens DT, Sykes AG. Metal aqua ions, reference module in chemistry, molecular sciences and chemical engineering, from comprehensive coordination chemistry II, Editors-in-Chief: McCleverty JA, Meyer TJ. Oxford; 2003. p. 515–555, http://dx.doi.org/org/10.1016/B0-08-043748-6/01055-0.

[100] Zhang S, Hintze F, Schnick W, Niewa R. Eur J Inorg Chem 2013:5387.

[101] Yamane H, Mikawa Y, Yokoyama C. Acta Cryst E 2007;63:i59.

[102] Roos M, Meyer G, Anorg Z. Allg Chem 1999;625:1129.

[103] Roos M, Meyer G, Anorg Z. Allg Chem 1999;625:1839.

[104] Roos M, Wittrock J, Meyer G, Fritz S, Strähle J, Anorg Z. Allg Chem 2000;626:1179.

[105] Roos M, Meyer G, Anorg Z. Allg Chem 1999;625:1843.

[106] Goglio G, Denis A, Gaudin E, Labrugère C, Foy D, Largeteau A. Z Naturforsch 2008;63b:730.

[107] Ehrentraut D, Kagamitani Y, Yokoyama C, Fukuda T. J Cryst Growth 2008;310:891.

[108] Nicholls D. Inorganic chemistry in liquid ammonia. Monograph 17. In: Clark RJH, editor. Topics in inorganic and general chemistry. Amsterdam: Elsevier; 1979.

[109] Tomida D, Kuroda K, Hoshino N, Suzuki K, Kagamitani Y, Ishiguro T, et al. J Cryst Growth 2010;312:3161.

[110] Ehrentraut D, Kagamitani Y. In: Ehrentraut D, Meissner E, Bockowski M, editors. Technology of gallium nitride crystal growth. Heidelberg: Springer-Verlag; 2010, ISBN 978-3-642-04828-9. p. 189.

[111] Hashimoto T, Saito M, Fujito K, Wu F, Speck JS, Nakamura S. J Cryst Growth 2007;305:311.

[112] Chernov AA. In: Modern Crystallography III: crystal growth. Springer series in solid-state sciences, vol.36. Berlin, Heidelberg, New York, Tokyo: Springer-Verlag; 1984.

[113] Byrappa K, Yoshimura M. In: Handbook of hydrothermal technology – technology for crystal growth and materials processing. Park Ridge, New Jersey: Noyes Publications; 2001.

[114] Scheel HJ, Elwell D. J Cryst Growth 1972;12:153.

[115] Fujito K, Kubo S, Fujimura I. MRS Bull 2009;34:313.

[116] Dwilinski R, Doradzinski R, Zajac M, Iwinska M, Kucharski R, Krupka J, et al. Progress on purity of conductive and highly resistive GaN substrates obtained by ammonothermal method, workshop abstracts, 8th international workshop on bulk nitride semiconductors; 2013. Kloster Seeon, Germany.

[117] Letts E, Hashimoto H, Hoff S, Key D, Male K. Development of GaN wafers for solid-state lighting via the ammonothermal method, workshop abstracts, 8th international workshop on bulk nitride semiconductors; 2013. Kloster Seeon, Germany.

[118] Zajac M, Gosk J, Grzanka E, Stelmakh S, Palczewska M, Wysmolek A, et al. J Alloys Comp 2008;456:324.

[119] Adekore BT, Callahan MJ, Bouthillette L, Dalmau R, Sitar Z. J Cryst Growth 2007;308:71.

[120] Perlin P, Marona L, Holz K, Wisniewski P, Suski T, Leszczynski M, et al. Appl Phys Express 2011;4:062103.

16

Vapor Transport Growth of Wide Bandgap Materials

Matthias Bickermann[1,2], Tania Paskova[3]

[1]LEIBNIZ INSTITUTE FOR CRYSTAL GROWTH, BERLIN, GERMANY;
[2]INSTITUTE FOR CHEMISTRY, TECHNICAL UNIVERSITY BERLIN, BERLIN, GERMANY;
[3]DEPARTMENT OF ELECTRICAL AND COMPUTER ENGINEERING, NORTH CAROLINA STATE UNIVERSITY, RALEIGH, NC, USA

CHAPTER OUTLINE

16.1 Introduction ... 622

16.2 High Temperature Sublimation Growth of Wide Bandgap Materials (SiC and AlN)... 623

16.2.1 Brief History and Applications of Bulk SiC and AlN Growth ... 623

16.2.2 Crystal Growth by High Temperature Dissociative Sublimation (PVT Method) ... 625

16.2.2.1 Growth Conditions ... 625

16.2.2.2 Considerations from Growth Theory ... 627

16.2.2.3 Dissociative Sublimation and Rate-Limiting Species ... 628

16.2.2.4 Crystal Habit and Anisotropic Growth ... 630

16.2.3 Technology of High Temperature Sublimation (PVT) Growth ... 631

16.2.3.1 Growth Setup and Process ... 631

16.2.3.2 Hot-Zone Materials ... 633

16.2.3.3 Seeded Growth and Crystal Enlargement ... 634

16.2.3.4 Doping ... 636

16.2.4 Structural Defects in PVT-Grown SiC and AlN Bulk Crystals ... 638

16.3 HVPE of Nitride Semiconductors (AlN, GaN, InN, and Ternary Alloys) ... 641

16.3.1 Thermodynamic Analysis of HVPE Growth of Compound and Ternary Nitride Growth ... 641

16.3.2 Growth Kinetics ... 645

16.3.3 Laboratory and Industrial Setups ... 647

16.3.4 Growth on Foreign Substrates ... 649

16.3.4.1 Substrates and Buffers ... 649

16.3.4.2 Template Growth ... 650

16.3.4.2 Quasi-Bulk Single-Wafer Growth ... 651

16.3.3.3 Bulk Growth ... 654

Handbook of Crystal Growth. http://dx.doi.org/10.1016/B978-0-444-63303-3.00016-X
Copyright © 2015 Elsevier B.V. All rights reserved.

16.3.5 Homoepitaxial Seeded Growth ... 654
16.3.6 Growth Related Properties ... 656
16.3.6.1 Residual Impurities and Native Defects ... 656
16.3.6.2 Doping ... 657
16.3.6.3 Structural Defects ... 659
16.4 Conclusion ... **661**
Acknowledgements ... **661**
References ... **661**

16.1 Introduction

Novel semiconductor materials show bandgap energies greater than 3 eV, which exceeds the classical definition of a semiconductor. Nevertheless, they can be doped (i.e., made *n*-type or *p*-type conducting) by introducing neighboring elements from the periodical table, in a way conventional semiconductors are. Out of these wide bandgap materials, gallium nitride (GaN) caused the solid state lighting revolution in optoelectronics and enabled the fabrication of blue laser diodes, silicon carbide (SiC) is about to take high shares in high power electronics, and aluminum nitride (AlN) is a promising material for UV optoelectronics. Other materials are also expected to find their applications, but are not in the scope of this work.

SiC, AlN, and GaN have in common that they crystallize in close-packed structures with strong, partly ionic bonding. As a consequence, these materials exhibit a very high thermal stability (e.g., melting point) and mechanical strength. The latter ensures their unique applicability for devices operating in a harsh environment, but also presents serious challenges to grow them as bulk single crystals. In the case of SiC, formation of different polytypes (modifications with different stacking sequences of the Si-C bilayers along the hexagonal *c*-axis direction) further complicates crystal growth. Providing conditions for melt growth is impossible or at least extremely difficult because the materials dissociate before they melt, and there is hardly any crucible material available that sustains against the molten compounds.

Unfortunately, most wide bandgap materials are not easily grown from solution either. For example, the solubility of nitrogen in liquid gallium is extremely low at atmospheric pressure and temperatures of GaN stability. It increases with pressure and temperature but is still limited to about 1 at.% even at pressures up to 2.0 GPa and temperatures of about 1600 °C. Thus, to overcome limitations of solubility and the challenges of melting conditions, alternative approaches have been developed, such as solvothermal growth, flux-mediated growth, or vapor transport growth. In fact, today vapor transport by sublimation or hydride vapor phase epitaxy (HVPE) is the common technique to produce bulk crystals of the most prominent and advanced wide bandgap semiconductor materials, SiC, AlN, and GaN.

16.2 High Temperature Sublimation Growth of Wide Bandgap Materials (SiC and AlN)

16.2.1 Brief History and Applications of Bulk SiC and AlN Growth

Today, bulk SiC and AlN crystals are almost exclusively grown by physical vapor transport (PVT). In this method, sublimation is used to facilitate the transport, mediated, e.g., by a concentration gradient that is induced by a temperature gradient, from the hotter source to the colder growth area, where the species recondense to form a crystal. While there are significant differences in growth technology, many common features allow for a unified discussion of growth of bulk SiC and AlN by PVT. Note that alternative growth methods like high temperature hot-wall chemical vapor deposition (HT-CVD) [1a,1b] and high temperature solution/flux growth [2], as well as PVT variations using a gas inlet [3], liquid precursors [4], or the sandwich sublimation method [5a,5b] are also investigated for bulk growth, but currently remain at a research level due to unresolved restrictions in crystal size, growth rate, or yield.

The first industrial synthesis of bulk SiC was performed around 1890 by E. G. Acheson [6] to utilize its hardness as an abrasive powder. In 1955, J. A. Lely [7] developed laboratory furnaces that replicated an isolated Acheson druse by heating a cave formed by SiC powder feedstock, either carefully arranged or stabilized by a porous graphite cylinder, within a graphite crucible (Figure 16.1(a)). At around 2600 °C in an argon atmosphere of about 1 bar, the SiC sublimates and SiC crystals nucleate and grow attached to the inner walls. The technological breakthrough was paved around 1976 when Yu. M. Tairov and V. F. Tsvetkov [11a,11b,12a,12b] modified the Lely-type growth process by separating the growth room into a (hotter) source and a (colder) growth area and mounting a SiC seed in the growth area. The seed crystal sets up the orientation, the initial diameter, and in most cases also the polytype of the growing crystal. The seeding also enables steady improvement of crystal quality and diameter by repeated growth on seeds prepared from previously grown crystals. Vodakov (1974) invented carburized Ta crucibles for SiC growth [13], and Ziegler (1983) employed an alternate

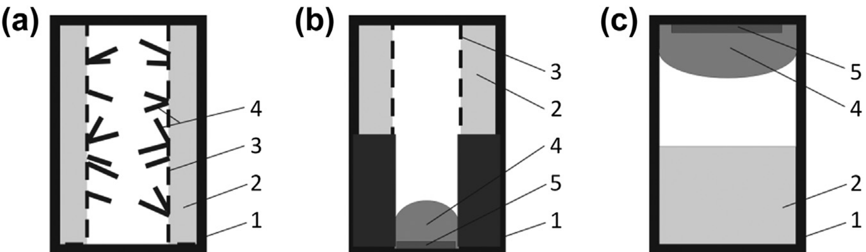

FIGURE 16.1 Schematic cross-section drawings of hot zone setups used for SiC bulk crystal growth. (a) Lely setup [7], (b) Ziegler setup [8a,8b,9], (c) modified PVT setup as typically used today [10], 1: graphite crucible, 2: SiC source material, 3: optional porous graphite cylinder, 4: growing SiC crystal(s), 5: SiC seed.

setup design with seed-down configuration [8a,8b], which was later used by Barrett et al. [9] (Figure 16.1(b)), but both were superseded during the 1990s by the design now commonly used [10] (Figure 16.1(c)).

In the 1980s, SiC substrates were first used to produce blue light emitting diodes (LEDs) [8], however, with low efficiency, as SiC is an indirect semiconductor. Later on, SiC was used as substrate material for InGaN/GaN LEDs. At the same time, SiC was successfully reconsidered as a promising material for high power electronics [14,15]. The crystal diameter steadily evolved, with 2-in, 4-in, and 6-in SiC substrates available commercially in 1999, 2005, and 2013, respectively [16]. While power electronics based on 4H-SiC is now established, and semi-insulating 4H-SiC substrates are used in GHz electronics, 6H-SiC as substrate for GaN-based optoelectronics was widely replaced by more cost-effective sapphire and silicon. Consequently, the focus in bulk SiC growth shifted from 6H-SiC to 4H-SiC. A part of SiC bulk production is used for gemstone manufacture [17].

The first serious attempts to grow bulk AlN single crystals dates to the 1960s [18,19]. AlN powder, sometimes also liquid Al, was used as source material in an atmosphere of nitrogen at temperatures exceeding 1700 °C. The experiments were conducted in carbon-containing setups (Figure 16.2(a)), which, however, led to highly contaminated crystals. In 1976, G. A. Slack and T. F. McNelly achieved mm-sized AlN single crystals with high purity [20,22a,22b] by using a type of Piper–Polich [23] growth technique, in which a sealed tungsten crucible was moved through a hot zone of an inductively heated furnace (Figure 16.2(b)). However, research on growth of large-area AlN bulk single crystals only started in the late 1990s with the advent of wide bandgap semiconductor research. Single-crystalline AlN is considered a preferential substrate material for UV optoelectronic applications (LEDs, lasers, and sensors), where devices contain epilayers of group III-nitride alloys with high Al content [24]. After some preliminary concepts [21] (Figure 16.2(c)), the successful SiC crucible design (Figure 16.1(c)) was widely adopted for AlN bulk growth, while using tungsten or tantalum carbide as hot-zone materials

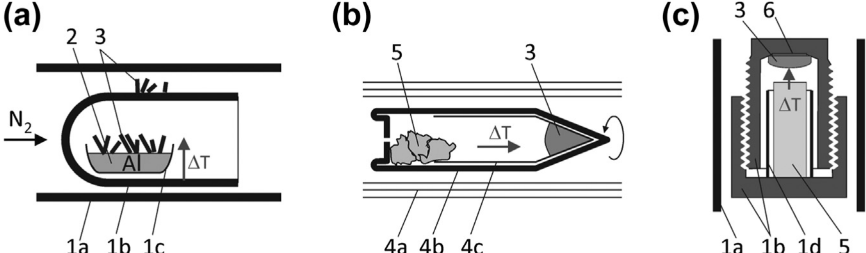

FIGURE 16.2 Schematic cross-sections of growth setups historically used for AlN bulk crystal growth. (a) graphite-based setup after Pastrnak et al. [19], (b) tungsten-based setup after Slack [20], (c) graphite-based setup for seeding on SiC after Balkas at el. [21]. 1: graphite parts (a heater, b tube/crucible, c boat, d sleeve); 2: liquid Al; 3: growing AlN crystal(s); 4: tungsten or rhenium parts (a heat shields, b rotating welded crucible with leak hole, c inner liner); 5: AlN source material; 6: SiC seed.

(see below). As of today, a few companies and research groups have demonstrated AlN single crystals of up to 2-in diameter. But worldwide AlN wafer production is still very small as compared to SiC.

16.2.2 Crystal Growth by High Temperature Dissociative Sublimation (PVT Method)

16.2.2.1 Growth Conditions

Several phase diagrams based on calculations and experimental data exist for the Si-C [25,26] and the Al-N [22a,22b,27] system; SiC (different polytypes are usually not accounted for [11a,11b,28].) and AlN are the only binary compounds in those systems. At about 2830 °C, SiC undergoes peritectic decomposition into solid C and a Si-based liquid containing about 13 at.% of carbon (Figure 16.3). In the interesting temperature range ($T > 660$ °C), AlN is in equilibrium with liquid Al or gaseous N_2. A liquid is expected to form at the decomposition point, whose composition however remains unclear. In any case, formation of a liquid at a given pressure represents the upper limit for crystal growth, as it will inevitably destroy the growing crystal or the setup.

Figure 16.4 shows calculated temperature-dependent partial pressures of gaseous species involved in the decomposition [22a,22b,29–31]; the occurrence of different species in the gas phase will be discussed later on. Assuming that the total partial pressure of growth species has to be at least 1 mbar to facilitate bulk growth by PVT, reasonable growth rates for SiC bulk growth can be achieved only at temperatures exceeding 2100 °C [28]. In contrast, the Al partial pressure over AlN provides sufficient evaporation for mass transport already at 1600 °C, but due to insufficient surface adatom

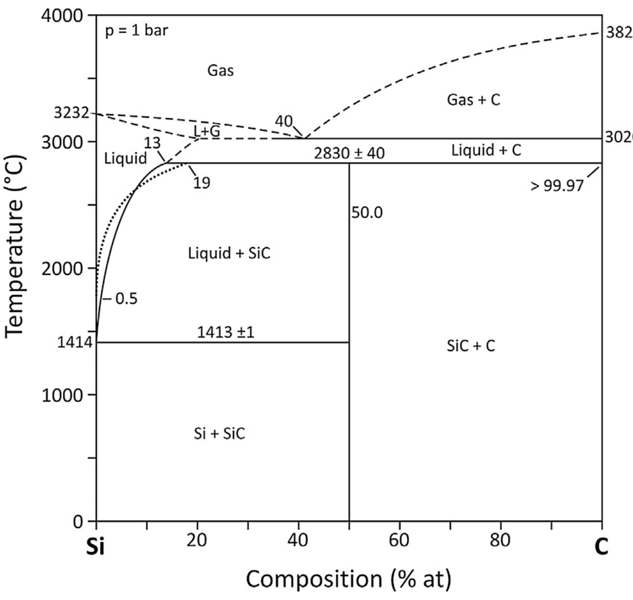

FIGURE 16.3 Phase diagram of the SiC-System (p = 1 bar) after Kleykamp et al. [26] (solid and slashed lines) and after Scace and Slack [25] (dotted line).

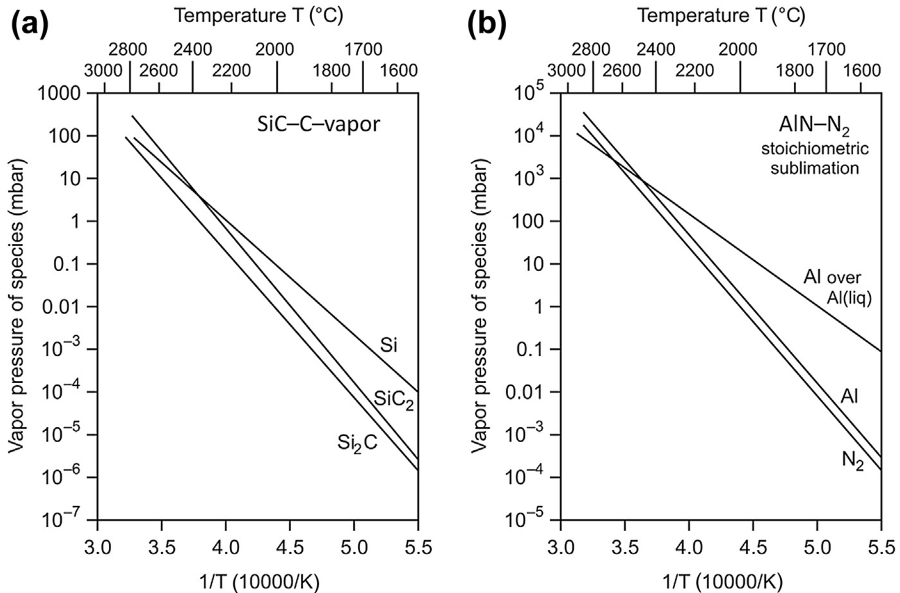

FIGURE 16.4 Calculated partial pressures for (a) SiC under C-rich conditions after Lilov [29], and (b) AlN under N-rich conditions after Slack and NcNelly [22a,22b] (note the different ordinate).

mobility and N_2 chemical activity, only very thin needles form [30]. Higher temperatures are beneficial for increasing both growth rate and surface kinetics, i.e., helping the atoms to properly arrange themselves at the surface.

Sublimation into vacuum is possible but leads to high deposition rates and polycrystalline growth due to lack of growth control. Transport and deposition during growth is regulated by buffering, i.e., using an additional “inert gas.” For SiC, mostly argon is employed; AlN is grown with N_2 “in excess.” To control and set p_{sys} during growth, the crucible has to be semi-open. The inert gas is introduced in the outer setup area at a controlled flow rate, and excess gas is pumped to exhaust. This implies that also a fraction of vapor species evades the crucible during growth, which influences the gas phase composition in the hot zone and may alter growth conditions.

The process windows for stable growth of SiC or AlN depend on the polytype and growth orientation (polarity). 4H-SiC single crystals are reported to grow at temperatures below 2300 °C. The temperature limit for 4H-SiC growth is associated with the stoichiometry in the gas phase [11a,11b,28]; reasonable growth rates can still be achieved by lowering the pressure to $p_{sys} = 5$ mbar [32]. In contrast, 6H-SiC boules are grown at 2300–2500 °C and $p_{sys} = 5$–50 mbar [33]. The reported growth temperatures vary, probably due to differences in pyrometer measurement. Formation of polytypes is also sensitive to stoichiometry and abundance of impurities in the gas phase [11a,11b], and to polarity of the growth surface. Growth of 4H-SiC is only stable on C-polar or non-polar planes, while it converts to 6H or 15R during growth on Si-polar SiC basal planes [33,34].

6H-SiC [35] and 15R-SiC [36] are grown with better structural quality and lower risk of polytype inclusions on the Si-polar basal plane. This is attributed to different surface energies of the crystal planes, leading to different surface kinetics and morphology (see below). AlN bulk growth is performed at temperatures ranging from 2000 to 2300 °C. Higher temperatures and supersaturations seem to stabilize N-polar growth [37], but influence of impurities is also under discussion. Typically, p_{sys} is chosen in the range of 300–900 mbar, while the dependence of pressure on growth rate is not as sensitive as in the case of SiC [31,38].

Understanding of sublimation growth of SiC and AlN remains limited due to unavoidable presence of impurities at the high temperatures employed for crystal growth. They may significantly change growth behavior via impurity-assisted transport of growth species [39,40], or by acting as surfactants, altering kinetic barriers at the growth surface [41,42]. As a consequence, preparation of highest purity starting materials is not only mandatory to control semiconductor properties of the grown crystals, but it is also necessary for stable and reproducible crystal growth.

16.2.2.2 Considerations from Growth Theory

Under thermodynamic equilibrium, the pressure, p, and the temperature, T, where a solid-to-gas phase transition of a single component occurs are linked by the Clausius–Clapeyron equation:

$$dp/dT = \Delta H/(T \cdot \Delta V), \tag{16.1}$$

where ΔH is the sublimation enthalpy (619 kJ/mol for SiC [43] and 630 kJ/mol for AlN [44]), $\Delta V = V_{gas} - V_{solid} \approx V_{gas} = RT/p$ is the ideal gas volume (as $V_{gas} >> V_{solid}$), and R is the universal gas constant. The equation can then be rewritten as [44]:

$$dp/dT = (\Delta H/R) \cdot \left(p/T^2\right). \tag{16.2}$$

Applying a temperature difference $\Delta T = T_{source} - T_{seed}$ between the hotter sublimation (source) and the colder recondensation (seed) area, a term describing the pressure ratio can be found by integration:

$$\sigma = \ln\left(p_{source}/p_{seed}\right) = (\Delta H/R) \cdot (1/T_{seed} - 1/T_{source}). \tag{16.3}$$

σ is called relative supersaturation, because the change in chemical potential $\Delta\mu = -RT_{seed} \cdot \ln\ (p_{source}/p_{seed})$ represents the driving force for transport and crystal growth. It can be approximated for small values by $\sigma \approx p_{source}/p_{seed} - 1$.

The sublimation of the source material is endothermic and depends on the surface area, in particular, on the form and grain size of the feedstock. The recondensation is accompanied by release of latent heat. The species flow, which is induced by a difference $\Delta p_\nu = \left|p_\nu^* - p_\nu\right|$ between the actual (supersaturated or supercooled) and the equilibrium partial pressure at the source or seed area, respectively, can be described by the Hertz–Knudsen equation:

$$J_\nu = \alpha_\nu \cdot (2\pi m R T_\nu)^{-1/2} \cdot \Delta p_\nu (\nu = \text{seed, source}) \tag{16.4}$$

where $\alpha_v = 0\ldots1$ are the (effective) sublimation/condensation coefficients, which account for the surface reactions and kinetic barriers, and m is the molar mass of the transported species. Typically, $\alpha_{source} \leq \alpha_{seed}$ due to the source material properties [45]. Note that in a multicomponent system, it is sufficient to determine the flow of the rate-limiting species (see below) as it has the lowest supersaturation in the system, while all the other species are provided in excess. In SiC growth, α_{source} is often set to unity [46]. In AlN growth, $\alpha_{source} = 1$ for Al species, while the dissociation of N_2 at the growth interface is considered to yield values in the range of $\alpha_{seed} = 2\ldots5\cdot10^{-3}$ [47,48].

Natural convection is most probably absent in currently used growth geometries, as Grashof numbers are typically below 100 even in 4-in diameter growth cells [49,50]. Similarly, Stefan flow is not considered a significant transport mechanism for SiC and AlN sublimation growth as the inert gas concentration is several times higher than the concentration of growth species [46]. As a consequence, the mass transport in the gas phase is dominated by diffusion (Fick's law):

$$J_{transp} = -D\cdot(dc/dx) = D\cdot(dc/dT)\cdot(\Delta T/L) \approx D/RT\cdot(dp/dT)\cdot(\Delta T/L), \tag{16.5}$$

where $D \propto T^{1.8}/p_{sys}$ is the binary diffusion coefficient from kinetic gas theory, $c \approx RT\cdot p$ is the concentration, and $p = e^{-\Delta G/RT}$ (see Figure 16.4) is the partial pressure of the rate-limiting species, x is the coordinate between source and seed area, and L is the source-to-seed distance. The last expression is obtained assuming an ideal gas and neglecting higher-order terms [44]. With Eqn (16.2), one yields:

$$J_{transp} \propto (\Delta T/L)\cdot e^{-\Delta G/RT}\Big/\left(T^{1.2}\cdot p_{sys}\right). \tag{16.6}$$

The parameters governing the mass transport are thus T, p_{sys}, and $\Delta T/L$. If the limiting step for bulk growth is indeed mass transport, i.e., sublimation or recondensation kinetics are considerably faster than diffusion in the vapor phase, the growth rate is $R_G = J_{transp}\, m/\rho$ where m is the mass and ρ the density of the growth-limiting vapor species. The experimentally achievable growth rate is lower due to volatile species leaving the semi-open crucible and reacting with the crucible materials. The growth rate increases with increasing temperature gradient and temperature (due to the exponential term), and with decreasing total pressure, as $R_G \propto 1/p_{sys}$ [44,46]. Note, however, that often only a relatively low growth rate (typically lower than 200 μm/h) will allow for single-crystalline growth without deterioration of structural quality. This is achieved by applying low axial gradients of 2–10 K/cm [51] in case of AlN growth and 5–30 K/cm [10] in case of SiC growth, which restricts the supersaturation to values in the range of 10–50%.

16.2.2.3 Dissociative Sublimation and Rate-Limiting Species

The sublimation of SiC and AlN is dissociative. Chemical reactions are involved in the dissociation of the feedstock and the reassembling of the gaseous species when they get attached to the crystal. The main species in the vapor phase, calculated or identified by high temperature mass spectrometry [22a,22b,47,52,53] are shown in Figure 16.4. Other

species appear at much lower concentrations, and their relevance for crystal growth is negligible. Neglecting any influence of impurities, sublimation and recondensation will occur according to the following simplified reactions [22a,22b,54]:

$$6SiC(s) \rightleftharpoons 2SiC_2(g) + Si_2C(g) + 2Si(g) + C(s), \quad \text{and} \tag{16.7}$$

$$2AlN(s) \rightleftharpoons 2Al(g) + N_2(g). \tag{16.8}$$

Note that Eqn (16.7) only formally obeys a quantitative relation. The growing crystal enforces stoichiometry, as the existence range of the solid compounds SiC or AlN is confined [10], but the composition in the gas phase clearly deviates from stoichiometry.

SiC dissociates incongruently, leaving solid carbon behind, which accumulates in the source zone. The gas phase is Si rich; it can be derived from Figure 16.4 that the relevant ratio of atoms [29a,29b,29c],

$$N_{Si}/N_C = \left(2 \cdot p_{Si_2C} + p_{SiC_2} + p_{Si}\right) \Big/ \left(p_{Si_2C} + 2 \cdot p_{SiC_2}\right), \tag{16.9}$$

is in the order of 5…10 at growth temperature. On the other hand, the volatile Si partly reacts with the graphite crucible to form SiC_2 and Si_2C, and some Si is lost due to evasion from the crucible. As a consequence, the Si excess in the vapor phase depends on the growth setup and conditions, including the temperature gradient. Growth of SiC in semi-open graphite crucibles is considered to eventually happen in a C-rich regime (SiC-C-vapor equilibrium) with the danger of decomposing/graphitizing the source and—in extreme cases—the growing crystal. In contrast, growth at low temperatures or in Ta crucibles might be better described in a Si-rich regime (SiC-Si-vapor equilibrium).

AlN is grown with N_2 in excess, and

$$N_{Al} \Big/ N_{N_2} = p_{Al} \Big/ 2 \cdot p_{N_2} \approx 0.1. \tag{16.10}$$

While excess N_2 doesn't necessarily lead to N-rich growth conditions, this is the commonly assumed growth regime for AlN growth (AlN-N_2 system). The chemical activity of N_2 is most probably governed by kinetics of the surface reaction [30]

$$Al(ads) + N_2(ads) \rightleftharpoons AlN(s) + N(ads). \tag{16.11}$$

Additionally, nitrogen could be dissociated by reaction with impurities (e.g., cyanogen formation).

Consideration of a Si-rich and C-rich (or, in the case of AlN, Al-rich and N-rich) thermodynamic system leads to different border cases with different partial pressures of the species in the vapor phase. As a consequence, the rate-limiting species in a diffusion-limited regime depend on both temperature and the border case under review. In case of SiC-C-vapor equilibrium, according to Lilov [29a,29b,29c] the rate-limiting reactions and equilibrium constants are

$$SiC(s) \rightleftharpoons Si(g) + C(s) \quad \text{with} \quad K_1 = p_{Si}, \text{ and} \tag{16.12}$$

$$2SiC(s) \rightleftharpoons SiC_2(g) + Si(g) \quad \text{with} \quad K_2 = p_{Si} \cdot p_{SiC_2}. \tag{16.13}$$

The first reaction leads to carbon accumulation in the SiC source. It is calculated to become unfeasible at $T > 2270\ ^\circ C$, but graphitization of the source appears also at higher

temperatures. The vapor pressure of silicon is larger than that of SiC_2 at $T < 2270\,^\circ C$, less than that of SiC_2 at $T > 2630\,^\circ C$, and equal in between [29a,29b,29c]. Thus, at $T < 2270\,^\circ C$, SiC_2 is the rate-limiting species with $\sigma = (p^*_{SiC_2} \cdot p^*_{Si})/K_2 - 1$. For $T > 2270\,^\circ C$, Si is considered as rate-limiting species with $\sigma = p^*_{Si}/K_1 - 1$. Above $2630\,^\circ C$, SiC starts to dissociate in the condensed phase, accompanied by formation of liquid silicon, if no carbon source is available. For AlN growth, most recent reports see Al transport as the rate-limiting step [30], with $K = p_{Al} \cdot p^{0.5}_{N_2}$. As N_2 is provided in excess and thus $p_{sys} \approx p_{N_2}$, Eqn (16.6) changes to [44,55].

$$J_{transp} \propto (\Delta T/L) \cdot e^{-\Delta G/RT} \Big/ \left(T^{1.2} \cdot p^{1.5}_{sys}\right). \quad (16.14)$$

Detailed models have been elaborated for SiC and AlN bulk growth, including, e.g., release of latent heat, advective flows, growth kinetics, and possible reactions during dissociative sublimation [56]. During the last decade, numerical modeling has become a standard tool also in SiC and AlN sublimation growth. Even the evolution of the growth interface and the formation of dislocations can be predicted from the heat and mass transfer data [57]. However, different results are obtained from the models due to different assumptions on the material properties at growth temperature, the dissociative reactions, the rate-limiting step, mass and heat transfer mechanisms, and effective sublimation/condensation coefficients.

16.2.2.4 Crystal Habit and Anisotropic Growth

Growth rate and growth mode strongly depend on the crystallographic orientation of the growth interface. The differences are caused by different surface energies and kinetics. As an example, the surface energies of SiC are $2.2\ J/m^2$ and $0.3\ J/m^2$ for the Si-polar and the C-polar basal plane, respectively [58]. Impurities in the gas phase may act as surfactant on particular facets [42]. Also, faceted and non-faceted areas show significant differences. As shown in Figure 16.5, SiC generally forms platelets, thus growth is slowest on both basal plane facets [30]. Dual-seed experiments remained ambiguous about

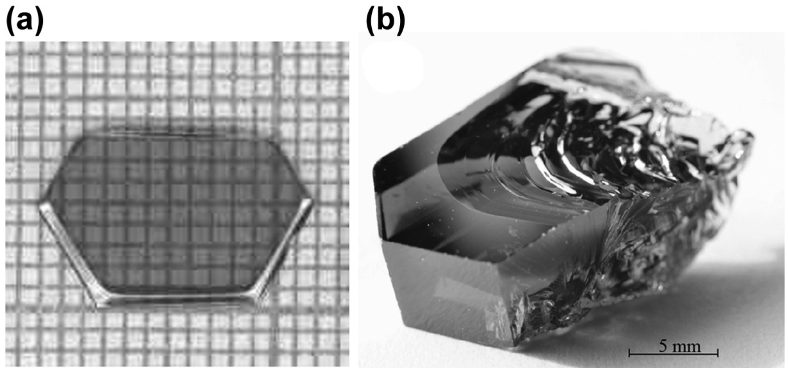

FIGURE 16.5 Spontaneously nucleated single crystals. (a) SiC platelet grown in a Lely furnace (on mm-sized grid), courtesy Heikki Helava/Nitride Crystals, Inc. [61]; (b) AlN crystal grown at $T = 2200\,^\circ C$ [60].

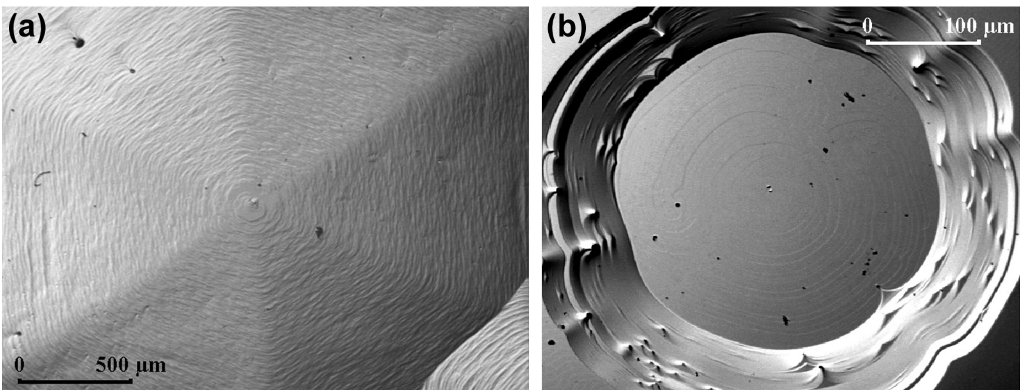

FIGURE 16.6 Spiral growth and step bunching on basal planes of SiC (optical microscopy images): (a) C-polar face, (b) Si-polar face.

growth rate dependence on polarity [33,62]. In contrast, the growth rate of AlN is slowest on the prismatic facets for all but the highest growth temperatures, thus the crystal habit changes from needles to almost equiaxed (isometric) crystals [30,60] with increasing temperature. Furthermore, AlN generally shows a stronger tendency to form pyramidal facets on the metal-polar side [59].

On the basal planes of SiC and AlN crystals, the dominant growth mechanism is in spiral growth, where a spiral originates from threading screw dislocations [63], thereby also preserving the SiC polytype during growth [64]. Step bunching is regularly observed on such surfaces, with the step height and terrace width depending on the supersaturation [65], surface inclination in respect to the basal plane [66], stoichiometry, impurities in the vapor phase, polytype, and polarity [37]. Due to the different surface energy, the spirals form hexagonal hillocks on the C-polar face and round plateaus on the Si-face of SiC [67], see Figure 16.6. Both types of morphologies have also been identified on basal plane AlN surfaces [68]. Crystals grown with an off-orientation or with very low density of dislocations are expected to grow in a step-flow mode.

16.2.3 Technology of High Temperature Sublimation (PVT) Growth

16.2.3.1 Growth Setup and Process

The hot zone of today's typically used vertical "modified PVT" setup consists of a cylindrical crucible with removable upper lid, surrounding susceptor, and thermal insulation (Figure 16.7). The crucible has to be porous or semi-open to allow for gas and pressure exchange with the environment, often provided already by the nonideal closure between the lid and the crucible. It is filled with source material—AlN or SiC as powder, sintered bodies, or lumps from previous growth experiments—to 50–80% of its total height.

Electrical power is used to heat the crucible either by induction (at 8–20 kHz frequency) or by resistive heating. The use of a susceptor is advantageous in that it remits

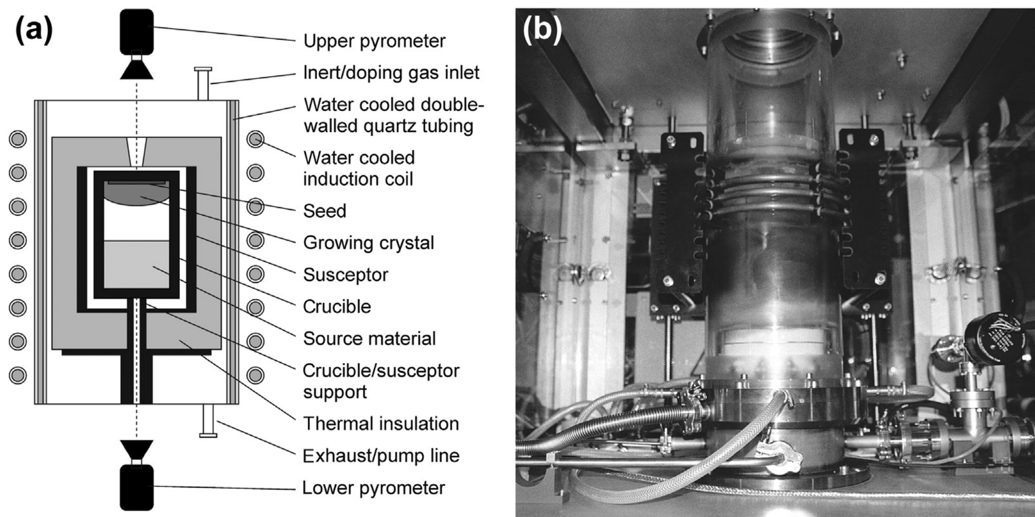

FIGURE 16.7 (a) Schematic and (b) photograph of a typical PVT growth setup.

the heat to the crucible via radiation, providing a more homogeneous temperature field in the growth cell. The setup is located inside a water-cooled growth vessel that provides the gas-tight enclosure, a loading port, and connections for pyrometer access and gas inlet/outlet as shown in Figure 16.7. The common vessel type consists of cylindrical double-walled quartz glass tubing with stainless steel flanges. As an alternative, the vessel can be made of stainless steel with the coil located inside the water-cooled vessel.

In order to provide the necessary purity, SiC or AlN source material is either synthesized directly from pure elements or prepared by purification of commercially available ceramic powder material. The latter can be achieved by high temperature processes, e.g., carbothermal reduction, sintering, or sublimation [22a,22b,71]. The knowledge of efficient purification is considered an important proprietary part of growth technology. After proper purification, the concentration of lightweight impurities (boron, carbon, oxygen, nitrogen) and trace metals should be clearly below 100 ppm and below 1 ppm, respectively.

The growth procedure typically includes the following steps: The hot zone is assembled and loaded into the reactor. Then the vessel is purged with inert gas. For high purity demands, a high vacuum ($<1\cdot10^{-5}$ mbar) preheating stage at moderate (1000–1200 °C) temperatures is used to remove moisture, adsorbed gases, and volatile impurities. The vessel is then filled with inert gas, and the growth cell is heated to growth temperature. During this stage, an elevated pressure may be chosen to suppress initial feedstock sublimation, as surface mobility of the species is still insufficient for single-crystal growth. Alternatively, the axial temperature gradient in the growth cell is

inverted, i.e., the seed is kept at a higher temperature than the source material to prevent early growth and to clean the seed surface. This is performed by moving the coil relative to the crucible [72]. If the growth temperature is reached, the gas flows are adjusted, gaseous dopants (e.g., nitrogen in SiC growth) are added, and a soft growth start is performed by reverting the temperature gradient or by slowly reducing the pressure to the finally desired value [11a,11b,12a,12b].

Maintaining the temperature gradients at the growth interface during growth is crucial in order to obtain crystals with high chemical and structural homogeneity. If the crystal length is small compared to the crucible dimensions, constant heating might be applied, but typically, a decrease of ΔT and thus R_G with growth time is observed [73]. Thus, the heater power is controlled by constant temperature monitoring. Corrections to the temperature field to account for the moving growth interface, the partial degradation of insulation materials, or the progressing feedstock consumption might also be achieved by a gradual change in heater position [74] or by separate control of several heaters. Considering the typical growth rates of 50–500 μm/h, it takes several days to grow 10–30 mm thick crystals. Mass transport yields exceeding 80% are possible if the evaporation losses through the semi-open crucible are kept at a low level [10]. Finally, the end of growth is initiated by decreasing the heater power, inverting the gradient again, or increasing the pressure. A controlled cooling is demanded to mitigate strain-induced defect formation.

16.2.3.2 Hot-Zone Materials

Due to their different chemical nature and materials compatibility, the choice of materials for the inner setup parts differs strongly for SiC and AlN bulk growth. In the case of SiC growth, all parts are made of high purity graphite/carbon, so no foreign chemical elements are introduced. The susceptor, the crucible support, and the crucible itself are machined from dense graphite parts (porosity 2–5% vol). Thermal insulation is provided by assembled parts of carbon-bonded carbon fiber (CBCF), carbon felt, or pressed exfoliated graphite. The porous nature of these materials effectively prevents generation of Joule's heat at induction frequencies of 8–20 kHz, chosen to match the intrusion depth of dense graphite to heat the susceptor homogeneously. The carbon purity is crucial; in former times, nominally undoped SiC crystals were *p*-type due to contamination with boron from the crucible and thermal insulation materials [33].

For AlN growth, requirements of refractory behavior and chemical inertness in regard to Al vapor strongly limits materials availability. A lot of work was dedicated to finding a chemically stable and suitable crucible material [75–78]. Graphite and boron nitride are stable up to temperatures of about 2000 °C, but lead to considerable contamination of the crystal with carbon or boron, respectively [42,77]. Coatings tend to crack and spall off due to differences in thermal expansion and chemical attack. Today, only tantalum carbide (TaC) and tungsten (W) are used as crucible materials in different combinations as described below. A few more materials have been evaluated (Re, TaN, HfN, TaB_2), but are not currently used.

Tungsten is long-term stable against Al vapor in the presence of excess N_2, and chemical erosion is negligible up to temperatures of about 2250 °C [20]. However, tungsten will react with oxygen, carbon, and silicon. The presence of SiC seeds as well as the use of a graphite susceptor or insulation parts is possible in such setups if not in direct contact, but the crucible lifetime will be seriously reduced. In contrast, TaC is chemically stable under AlN growth conditions at temperatures well exceeding 2300 °C. TaC elements are electrically conductive and compatible with graphite (for susceptor and insulation elements), tungsten (for an inner crucible), and SiC (as seeds), even if in direct contact. Long-term stability is generally limited by cracking due to internal grain growth [75] or decarburization. To prevent structural failure, they may be enclosed in graphite cylinders, which also act as a susceptor [79]. As a variant, carburized tantalum crucibles can be employed [80]. Such parts have no open porosity, and their mechanical stability under temperature cycling is excellent. However, especially if used in conjunction with graphite parts, such crucibles continue to carburize and finally become brittle, in particular at growth temperatures exceeding 2100 °C.

16.2.3.3 Seeded Growth and Crystal Enlargement

Both SiC and AlN growth are best performed on polar basal plane (c-plane) surfaces, because these planes possess isotropic in-plane properties. In SiC bulk growth, the demand of slightly offcut (2–8°) substrates for epitaxy [81] has led to optimized bulk growth using these offcut surface planes. On the other hand, growth in off orientations leads to formation of stacking faults [82]. Growth in other crystallographic directions is accompanied by an even higher density of structural defects, caused by propagation of basal plane dislocations and by crystal anisotropy, which leads to orientation-dependent growth mechanisms on the growth surface [83a,83b,84]. Thus, industrial production of boules remains focused on homoepitaxial seeds with basal plane surface. Wafers cut from the grown crystal are used as seeds in subsequent growth runs. A sample SiC crystal is shown in Figure 16.8(a).

In this regard, AlN growth is still in its infancy, and some groups still prepare their seeds out of freestanding single crystals that spontaneously nucleated on crucible parts in a Lely-type process, using conditions close to equilibrium and low nucleation density [59,85]. Such freestanding crystals, cf. Figure 16.5(b), are virtually unstrained and show the highest structural perfection, i.e., dislocation densities below $100/cm^2$ without any micropipes or volume defects [60]. Single crystals with a size of up to $15 \times 15 \times 10\ mm^3$ have been obtained. However, this process is not very reproducible; the yield of large and well-formed crystals is low and presumably depends on impurity contamination.

AlN crystals can also be grown on SiC seeds (Figure 16.8(b)), which are commercially available at industrial relevant sizes. AlN always grows Al-polar on polar SiC planes. However, the maximal crystal thickness is restricted to about 5 mm due to gradual deterioration of the structural quality. Still, the grown AlN layer can be separated from the SiC seed and used as a seed in subsequent AlN bulk growth [68,86]. The fundamental disadvantage is the partial decomposition of SiC in the presence of Al vapor already at

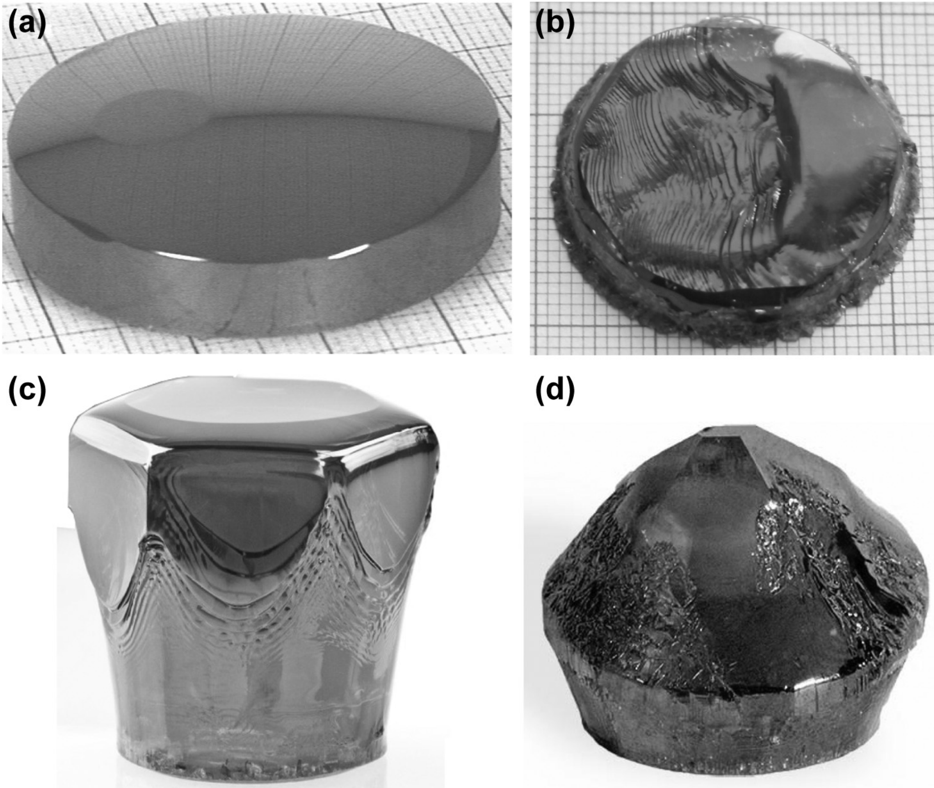

FIGURE 16.8 Bulk single crystals of SiC and AlN grown on seeds. (a) 4H-SiC bulk crystal (on mm grid) grown at the IKZ Berlin; (b) Al-polar AlN crystal grown on an SiC seed (on mm grid), courtesy R. R. Sumathi/LMU Munich [68]; (c) 1-in diameter AlN single crystal grown on the N-polar basal plane, courtesy Z. Sitar/Hexatech, Inc. [69]; (d) 1-in diameter AlN single crystal grown on the Al-polar basal plane, courtesy B. M. Epelbaum/CrystAl-N GmbH [70].

temperatures below 2000 °C. As a consequence, the AlN crystal is contaminated with up to several atomic percent of silicon [87]. Additionally, the mismatch of lattice parameters and thermal expansion coefficients between AlN and SiC lead to partial stress relaxation at the SiC/AlN interface, resulting in formation of tilted domains and the risk of crack formation.

Seed fixation is a critical issue in high temperature sublimation growth. Due to the differences in thermal expansion [78], a rigid interface between seed and crucible lid will cause strain and lead to crack formation or even seed separation during the heating-up stage. In contrast, pores or gaps between the seed and the lid lead to seed backside evaporation—material from the seed sublimes toward the colder crucible lid to close the pore or gap. As a consequence, voids travel through the seed and eventually through the growing crystal (negative crystal growth) and locally degrade the crystal quality [88,89]. Seed backside plating [90] is a possible means to mitigate both backside evaporation and cracking.

In case of SiC, chemical attachment to the lid is often performed using molten sugar [88]. During the heating-up stage in crystal growth, the glue decomposes into carbon and punctually bonds with the graphite lid. AlN seeds may be fixed in a similar way by AlN ceramic cement, which cures in air and also forms pores during sintering at growth temperatures. In the case of mechanical fixation, the seed is partially covered by a fixation rim. Finally, the seed can be fixed on the lid by heating the assembly in upside-down configuration until it is sublimated to the lid by sintering and surface sublimation.

A parasitic growth adjacent to the growing crystal leads to strain and crystal cracking during cooling due to anisotropic thermal expansion. Parasitic grains may induce structural defects, disturbance of structural quality, or even partial overgrowth of the main crystal [91]. In particular, a cylindrical or conical "growth channel" is proposed in order to close the space adjacent to the growing crystal and to provide for single-crystalline enlargement [92]. Another strategy is to facilitate freestanding growth by increasing the temperature adjacent to the seed area. Using tailored temperature fields, detached growth in a growth channel is possible [93].

The ideal interface shape in seeded sublimation growth is slightly convex, to allow the step flow from a single growth center (e.g., a screw dislocation to enable spiral growth) to spread across the whole surface area. The interface shape, and thus the local growth rate, during growth of SiC can be determined in situ by digital X-ray imaging [94]. Another method is to analyze colored striations in the crystal after growth. They are introduced by subjecting the growing crystal to periodic changes of dopant supply, e.g., introducing N_2 gas along with the Ar flow in SiC growth [95]. Finally, different facets feature a different incorporation of impurities and thus may show different optical properties (e.g., coloration, luminescence). The resulting crystal zones, i.e., volume parts that were grown on the respective facets, can be compared and analyzed after growth [60,95,96]. In the same way, polycrystalline areas can be reliably detected.

In sublimation growth, crystal enlargement is very challenging, and in order to grow a single crystal of a particular diameter, the seed must have roughly the same diameter. In principle, the ratio of normal and lateral growth rates can to some extent be influenced by the thermal gradients near the growth interface [95] or by the presence of impurities [42]. However, lateral growth is accompanied by formation of dislocations that may polygonize, form lineages and low-angle grain boundaries (LAGBs) [97–99]. Thus, the enlarged area typically shows a high defect density. Another problem in particular in regard to AlN bulk growth is that the enlargement decreases significantly as the crystal sides become faceted (Figure 16.8(c)). In the case of Al-polar AlN growth (e.g., on SiC seeds), the formation of pyramidal side facets even leads to an effective diameter decrease during growth (Figure 16.8(d)) [100]. As a rule of thumb for both SiC and AlN, the low-defect single-crystalline diameter can be increased by only about 1 mm in one growth run.

16.2.3.4 Doping

SiC bulk crystals are typically doped with nitrogen for *n*-type and with aluminum for *p*-type electrical behavior. Semi-insulating SiC crystals are obtained by doping with

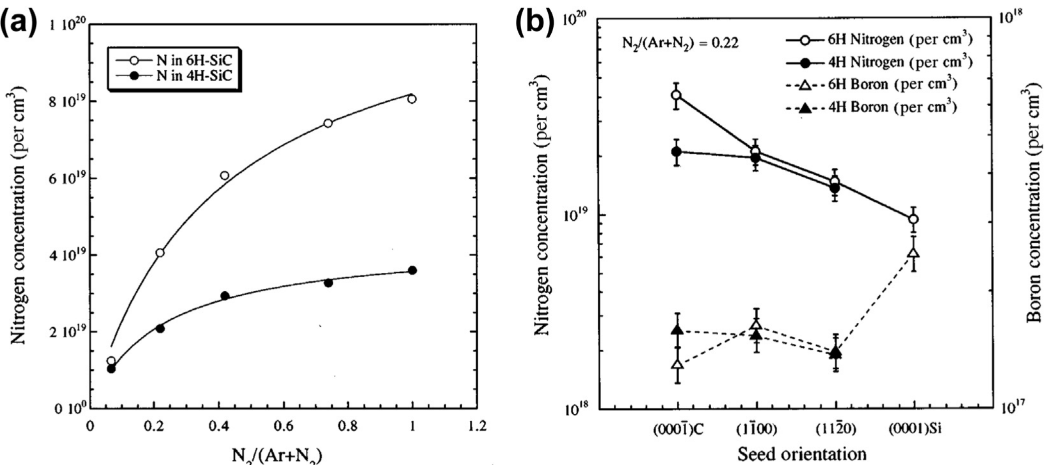

FIGURE 16.9 (a) N_2 partial pressure dependence of the nitrogen concentration in 6H- and 4H-SiC crystals grown on C-face basal planes of SiC. The solid lines are best-fitted theoretical curves using a Langmuir isotherm type equation. (b) Seed orientation dependence of the impurity incorporation during growth of 6H- and 4H-SiC crystals. *Reprinted with permission from [107]. Copyright 1998, American Institute of Physics.*

vanadium [101]; co-doping with boron or aluminum is used to compensate residual nitrogen, i.e., to pin the Fermi level to the more mid-gap $V^{4+/5+}$ transition energy instead of the $V^{3+/4+}$ level [102,103]. Semi-insulating SiC can also be prepared by providing high purity conditions where intrinsic defects with their deep levels in the bandgap govern the electrical behavior [104,105]. Note that for any dopant or impurity, the ionization levels in the bandgap, and thus the electrical and optical behavior of the crystals, depend on the polytype [106].

Nitrogen doping is provided by adding N_2 to the inert gas (argon) at ratios of N_2/Ar ranging from 0.01 to 1. As shown in Figure 16.9(a), the concentration of nitrogen in the crystal C_N at a given N_2 partial pressure p follows a Langmuir isotherm:

$$C_N \propto (K \cdot p)/(1 + K \cdot p), \tag{16.15}$$

where K is a kinetic coefficient [107]. While at low N_2/Ar ratios C_N goes linear with p, it saturates at higher N_2/Ar ratios at levels of high $10^{19}/cm^3$. C_N decreases with increasing growth temperature, because the partial pressure of species involved in SiC growth increases. Figure 16.9(b) shows that the nitrogen incorporation decreases from the C-polar to the Si-polar basal plane, with rhombohedral and prismatic planes in between. A gradual dependence of the polytype on the C-polar basal plane is attributed to a preferential incorporation of nitrogen on hexagonal lattice sites [107]. Unfaceted vicinal areas, which appear on the SiC crystals adjacent to the basal plane facet, feature different nitrogen incorporation with respect to the faceted area due to different step-flow conditions.

If added to the source material, aluminum, boron, and vanadium form carbides that are volatile at growth temperatures. Thus, their incorporation into the crystal strongly decreases during growth [108]. While the partial pressure of B_4C is sufficiently low to

provide for a virtually constant boron incorporation when added to the source material [109], vanadium should be better provided as a dense VC-SiC sublimation product whose vanadium supply is kinetically limited [102]. Constant aluminum incorporation can be facilitated by supply of gaseous trimethylaluminum (TMAl) or by a reservoir located at a colder place, from which Al-containing species are brought into the growth chamber by a carrier gas flow [110]. The effective segregation coefficient at the growth interface in the quasi-open system is about unity for nitrogen and boron, but only about 0.005 for vanadium [111]. The dependence of boron and aluminum incorporation on the facet orientation is reversed to that of nitrogen [107], cf. Figure 16.9(b). Also, incorporation increases with increasing growth temperature. Al and B doping is possible up to concentrations of several $10^{20}/cm^3$, limited by deterioration of the structural quality of the crystals [109], while incorporation of vanadium is limited by its solubility to $3 \cdot 10^{17}/cm^3$ [102].

Regarding AlN, incorporation of silicon is used to produce *n*-type epitaxial layers [112], but reports about doping during bulk growth are still rare [113]. At the time of writing, the efforts to influence electrical and optical properties of bulk AlN crystals are still focused on reducing contamination from both feedstock and setup materials, rather than on controlled doping.

16.2.4 Structural Defects in PVT-Grown SiC and AlN Bulk Crystals

Apart from structural defects being inherited from the seed or caused by backside evaporation due to improper seed fixation, a number of defects originate at the seed surface or form during initial stages of growth when the growth conditions are not yet stable [114]. Defect formation during further growth is caused by growth instabilities, such as local variations of the supersaturation at the growth interface, and promoted by high temperatures and gradients, low pressures, and high growth rates. In the seeded growth of SiC, continuous optimization of growth conditions have led to a formidable decrease of structural defects in the crystals, while size and wafer yield of the crystals have increased concurrently [115]. As of today, commercially available SiC wafer of production grade have at least 95% of useable surface area free of macroscopic defects such as micropipes, inclusions, and LAGBs. However, efforts to eliminate structural defects continue, in particular, in regard to the border areas of crystals during diameter enlargement. Again, seeded AlN growth is much less mature and the defect density in the crystals is considerably higher.

Dislocations in bulk crystals may form during growth by penetration from the seed crystal or adjacent parasitic grains into the bulk or by nucleation at other defects [115]. Due to annihilation processes, the dislocation density in the crystals generally decreases with increasing distance from the seed. Dislocations entering the crystal from the sides tend to polygonize and form lineages and LAGBs [98,99]. Thermal stress during cooling leads to formation of glide bands consisting of straight rows of basal plane dislocations [99].

Micropipes are considered as most detrimental defects in SiC crystals in regard to device applications, while they are hardly observed in nitride crystals. According to F. C. Frank [116], it is energetically profitable for dislocations with burgers vectors with their length exceeding about two unit cell heights [117] to form hollow cores, as the strain energy exceeds the necessary surface energy to form the core. While roughly running normal to the basal plane (i.e., in growth direction), they are also influenced by the thermal field and thus typically slightly bent outward in crystals grown with a convex growth interface. Their density is clearly lower on the faceted basal plane compared to vicinal unfaceted areas. Another type of hollow core is formed when voids originating from improper seed fixation travel through the seed and the crystal, leaving behind a deteriorated resublimated area that is not completely closed [73].

Generally, the polytype information of SiC crystals is inherited by spiral growth even on basal plane surfaces. However, areas with a different polytype in SiC crystals (polytype inclusions, Figure 16.10(a)) can nucleate at the crystal sides or at macrosteps on the

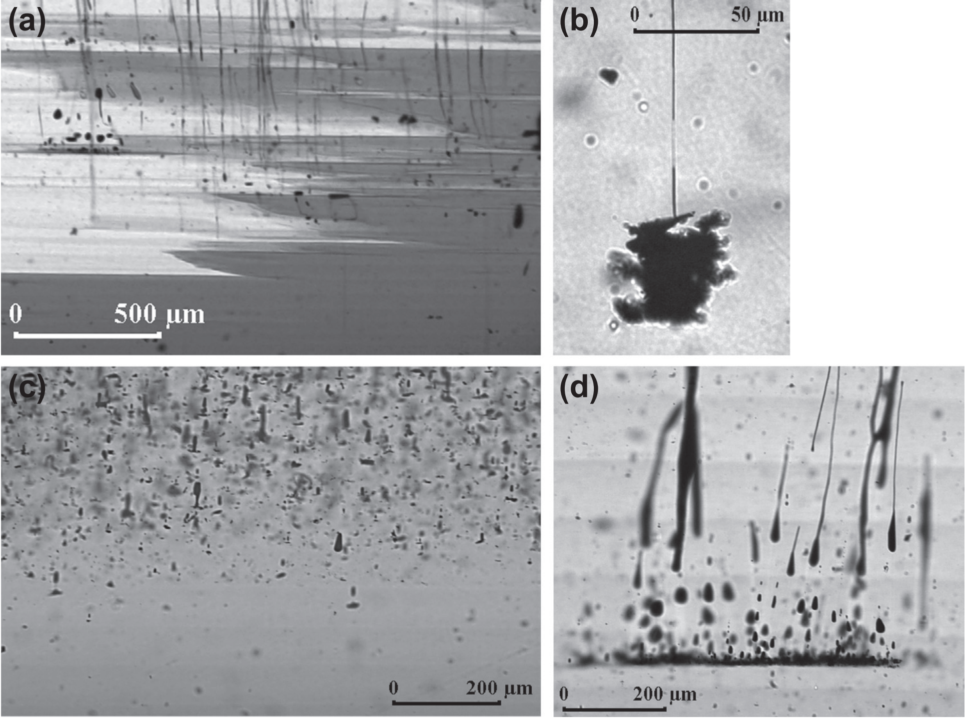

FIGURE 16.10 Structural defects in SiC observed in longitudinal cuts by optical transmission microscopy (growth direction is upward): (a) polytype instability with partial change from 4H-SiC (dark) to 15R-SiC (bright), many hollow defects and even silicon droplets nucleate at the polytype inclusion boundary. *(Reprinted from [118] with permission of ELSEVIER S.A.)*; (b) carbon precipitate with nucleating micropipe. *(Reprinted from [73] with permission of ELSEVIER BV.)*; (c) clusters of carbon inclusions form presumably after a gradual change of growth conditions; (d) "silicon droplet" formation. *(Reprinted from [118] with permission of ELSEVIER S.A.)*

surface. The former can be hindered to grow into the boule by providing a convex growth interface [32]. But growth of 4H-SiC without polytype inclusions remains a technological challenge due to the narrow growth window and the low stacking fault energy on the C-polar face [119]. The 4H polytype can be stabilized by providing more stoichiometric (carbon-rich) [11a,11b] or nitrogen-rich (highly doped) [41] conditions in the gas phase. Both carbon and nitrogen have been evidenced to change the step-flow properties and thus mitigate the formation of macrosteps [107]. On the other hand, several groups have reported that adding silicon to the source material might stabilize the 6H-SiC polytype [11,34] and mitigate formation of carbon inclusions [93], but excess silicon shortly evades from the crucible during growth.

Different types of carbon particles can appear in SiC crystals. Bigger inclusions are typically tens of microns in size and have an irregular surface (Figure 16.10(b)). They come as isolated defects or clustered in some volume fraction. Most probably they are graphitized feedstock particles, or particles that get detached from the crucible walls after attack by the silicon-rich vapor [73]. Smaller, more round carbon particles appear always in clusters (Figure 16.10(c)). They are generally attributed to local surface graphitization during growth, caused, e.g., by pressure reduction [120] or nonoptimized growth conditions [121]. It is assumed that local surface graphitization is correlated to the step flow and bunching. A more occasionally observed type of defect in SiC, which—from its form in longitudinal cuts—indicates that the growth interface was suddenly damaged in areas spanning over several 100 μm, is attributed to “silicon droplet” formation [73,118]. The defect is eventually overgrown, but the region above such a silicon droplet remains highly defective (Figure 16.10(d)).

Inclusions as well as macrosteps act as stress concentrators and may emit a number of dislocations or even micropipes that penetrate through the growing crystal [73,122]. As a consequence, the dislocation density in the crystals is typically inhomogeneous and their local density varies from $10^2/cm^2$ to $10^6/cm^2$. In SiC, basal plane dislocations can easily split into Shockley-type partial dislocations, which form stacking faults in between them [119]. Migration of these partial dislocations under high electric fields during SiC device operation is a serious problem for high power applications [123], but such dislocations can be converted into threading dislocations in subsequent SiC epitaxy [124].

A mosaic structure is often observed in AlN and SiC crystals. It consists of subgrains bound by LAGBs that are slightly tilted against each other and eventually form a cellular structure [125]. Several growth centers appearing at initial stages of growth may lead to tilted domains after coalescence [97]. A mosaic structure of the seed is inherited in the growing crystal. Additionally, lattice plane bending is observed in the crystals, as the lateral thermal gradient at the growth interface during growth leads to a continuous shift in crystallographic orientation after cooling down [126]. Finally, inversion domains can be observed in particular in nominally Al-polar AlN crystals grown on SiC seeds [89,127]. While their behavior during growth is similar to polytype inclusions in SiC, they are fenced by a dislocation wall.

16.3 HVPE of Nitride Semiconductors (AlN, GaN, InN, and Ternary Alloys)

In the 1990s, the need for nitride lattice-matched substrates had become apparent, and HVPE has attracted significant attention as a promising technique to produce thick nitride layers on foreign substrates that could be subsequently separated and used as quasi-bulk substrates. This became possible by the availability of high purity source materials, improved heteronucleation schemes, as well as by taking advantage of the high growth rate typical for this method and relatively inexpensive process [128–132].

16.3.1 Thermodynamic Analysis of HVPE Growth of Compound and Ternary Nitride Growth

The HVPE growth of epitaxial nitride-based materials is generally accomplished by reaction of a group-III metal chloride with NH_3. The general overall reaction for the HVPE growth of III-nitrides is given by [131]:

$$M^{III}Cl(g) + NH_3 \Leftrightarrow M^{III}N(s) + xHCl(g) + \frac{(3-x)}{2}H_2(g) \tag{16.16}$$

where M^{III} is the Ga, Al, or In species. An accurate thermodynamic analysis of the HVPE growth process requires a detailed understanding of the chemical reaction pathway. The HVPE reactors for growing III-nitrides consist of two main zones: source zone and growth zone. The chemistry of the both zones is quite complex, but generally the source zone enables the formation of chloride gas of group-III metals (Al, Ga, In) and the growth zone provides the necessary conditions for growth of the nitride (AlN, GaN, InN) binary material.

Thermodynamic analysis on the metal chloride formation can predict the preferred molecular form of the metal chlorides and identify a suitable carrier gas. The elemental metals Ga, Al, and In are liquids at the source zone temperature. When HCl flows over the liquid metal, there are several reactions that occur simultaneously, forming three gaseous metal chloride species: $M^{III}Cl$, $M^{III}Cl_2$, and $M^{III}Cl_3$ [132]:

$$M^{III}(l) + HCl(g) \Leftrightarrow M^{III}Cl(g) + {}^1\!/\!_2\, H_2(g) \tag{16.17}$$

$$M^{III}(l) + 2HCl(g) \Leftrightarrow M^{III}Cl_2(g) + H_2(g) \tag{16.18}$$

$$M^{III}(l) + 3HCl(g) \Leftrightarrow M^{III}Cl_3(g) + {}^3\!/\!_2\, H_2(g) \tag{16.19}$$

$$2M^{III}Cl_3(g) \Leftrightarrow \left(M^{III}Cl_3\right)_2(g) \tag{16.20}$$

where l = liquid, g = gas, s = solid. The equilibrium partial pressures of the gaseous species in the source zone versus temperature can be estimated by thermodynamic calculations [133–135]. Figure 16.11 shows in a comparative way the partial pressure for the gaseous species for Ga-, Al- and In-source zones as a function of temperature in inert N_2 atmosphere.

FIGURE 16.11 Equilibrium partial pressures of gaseous species over group-III metals placed in the source as a function of temperature calculated for: (a) Ga, (b) Al, (c) In source zones. *Courtesy of Yoshinao Kumagai.*

In case of AlN growth, when HCl reacts with Al liquid metal, three gaseous aluminum chloride species that may be formed: AlCl, $AlCl_2$, and $AlCl_3$. The dimer of $AlCl_3$, Al_2Cl_6, is not considered because at temperatures higher than 800 °C, the dimer molecule dissociates into two molecules of $AlCl_3$ [136]. Over the high temperature range typically used in the HVPE AlN growth, the equilibrium partial pressure of $AlCl_3$ is about eight and four orders of magnitude higher than the partial pressures of AlCl and $AlCl_2$, respectively. Several HVPE AlN growth experiments observed that $AlCl_3$ was the dominant aluminum chloride gaseous species [137–139].

$$Al(l) + 3HCl(g) \Leftrightarrow AlCl(g) + {}^{3}\!/_{2}\,H_2(g) \quad (16.21)$$

$$Ga(l) + HCl(g) \Leftrightarrow GaCl(g) + {}^{1}\!/_{2}\,H_2(g) \quad (16.22)$$

$$In(l) + HCl(g) \Leftrightarrow InCl(g) + {}^{1}\!/_{2}\,H_2(g) \quad (16.23)$$

In case of GaN growth, the thermodynamic analysis predicts that the partial pressure of GaCl is about four and eight orders of magnitude higher than the partial pressures of $GaCl_2$ and $GaCl_3$, respectively, over the temperature range of 800–1000 °C, and experimental data confirmed the prediction that only gallium chloride species were formed at these high temperatures [140]. Furthermore, experiments in wide temperature ranges also confirmed that only GaCl was stable at temperatures above 600 °C [141–143].

In the case of InN growth, there are three gaseous indium chloride species that may be produced as well: InCl, $InCl_2$, and $InCl_3$. The thermodynamic study of the equilibrium between In metal and HCl shows that the partial pressure of InCl and $InCl_2$ is about four

to ten orders of magnitude higher than the partial pressures of $InCl_3$ [144], yet they are not involved in the growth of InN owing to their low reactivity with NH_3 [132], and thus leaving the only option of decreasing the source temperature below 500 °C to allow sufficient formation of $InCl_3$ species.

From the source zone, the metal chlorides flow to the deposition zone, and the dominating species react with NH_3 to synthesize GaN, AlN, and InN films, respectively:

$$AlCl_3(g) + NH_3(g) \Leftrightarrow AlN(s) + 3HCl(g) \tag{16.24}$$

$$GaCl(g) + NH_3(g) \Leftrightarrow GaN(s) + HCl(g) + H_2(g) \tag{16.25}$$

$$InCl_3(g) + NH_3(g) \Leftrightarrow InN(s) + 3HCl(g) \tag{16.26}$$

Thermodynamic analysis of the HVPE growth zones has been reported in multiple publications for GaN [145], AlN [146], and InN [144], analyzing the influence of different growth parameters. Among the three nitrides, AlN formation has the largest thermodynamic driving force. Experimental observations have shown severe gas phase reactions leading to the formation of AlN powder, such that the reactant gases become depleted of $AlCl_3$, resulting in a low growth rate [147,148]. The free energy dependence shows that GaN and InN formation reactions have a positive free energy of reaction; however, film growth is favored since the deposition zone is highly supersaturated by the metal chlorides and NH_3. The thermodynamic driving force for film growth, $\Delta G_{T,\text{driving force}}$, is given by [131]:

$$\Delta G_{T,\text{driving force}} = \Delta G_T^0 + RT\ln\left(\frac{(P_{HCl})^n (P_{H_2})^m}{P_{MCl} \cdot P_{NH_3}}\right) \tag{16.27}$$

where T is the growth temperature, ΔG_T^0 is the Gibbs free energy of layer formation at the growth temperature, R is the ideal gas constant, n is the stoichiometric coefficient of HCl ($n = 1$ for GaN, $n = 3$ for AlN and InN), m is the stoichiometric coefficient of H_2 ($m = 1$ for GaN, $m = 0$ for AlN and InN), and $M^{III}Cl$ is the metal chlorides (i.e., GaCl, $AlCl_3$, or $InCl_3$). When the deposition zone is highly supersaturated with the reactants, the second term on the right hand side of Eq (16.27) becomes a large negative number so that even though ΔG_T^0 is positive, the overall growth driving force is negative and, thus, thermodynamically favored.

The thermodynamic analysis also shows that InN formation is thermodynamically favored at higher temperatures, however, a rapid dissociation of InN film has been reported at temperatures above 500 °C [149]. In $In_xGa_{1-x}N$ alloy growth, experimental observations revealed a preferential incorporation of the GaN component into the alloy and that the epitaxial layer became GaN-rich with increasing growth temperature [144,150]. In fact, the InN mole fraction in the alloy was very low for films grown at higher temperatures. Changes in growth temperature lead to opposite trends in AlN and GaN growth. While the GaN formation reaction is exothermic and becomes more favored as the temperature decreases, the AlN formation reaction is endothermic and becomes more favored as the growth temperature increases. The difference in the

temperature dependence of the growth reaction is attributed to the greater stability of $AlCl_3$ over GaCl [139]. Thus, the optimum growth temperature of AlN should be higher than the optimum growth temperature of GaN. Experimental observations have indicated that the optimum growth temperature of AlN is around 1250 °C [151]. In fact, HVPE $Al_xGa_{1-x}N$ films have been grown over the entire alloy composition range [139,152,153], due to the fact that AlN is completely miscible in GaN over the entire composition range. The mole fraction of $AlCl_3$ molecules in the gas phase has been observed to be proportional to the mole fraction of AlN molecules in the film. The optimum growth temperature for $Al_xGa_{1-x}N$ is predicted to increase proportionally with AlN concentration. Melnik et al. reported that the quality of HVPE $Al_xGa_{1-x}N$ film decreased with increasing AlN concentration when the growths were performed at a single temperature [153].

The main formation mechanism of nitrides is given by Eqns (16.24–16.26) is accompanied by decomposition in the sense that the reactions may be reversed (etching of the growing crystal) and also thermal decomposition may take place:

$$M^{III}N(s) + HCl(g) \rightarrow M^{III}Cl(g) + \tfrac{1}{2}N_2(g) + \tfrac{1}{2}H_2(g) \tag{16.28}$$

$$M^{III}N(s) \rightarrow M^{III}(l) + \tfrac{1}{2}N_2(g) \tag{16.29}$$

However, in the temperature ranges typically used for the HVPE nitride growth (750–1200 °C) reactions 30 and 31 are practically negligible.

The main gaseous species involved in the HVPE growth of $M^{III}N$ are $M^{III}Cl$, $M^{III}Cl_2$, and $M^{III}Cl_3$, HCl, NH_3, H_2, and the carrier gas. Thermodynamic functions of the material, the enthalpy $H(T)$, entropy $S(T)$, and specific heat $C_p(T)$, of all the species involved in the growth have been theoretically calculated [154] for the standard pressure of 1 atm and arbitrary temperature using a polynomial approximation of the Gibbs free energy. Detailed thermodynamic calculations of HVPE growth of GaN have been published by several authors [140,155–157]. Based on their analysis, several important features can be pointed out, which make the GaN growth different from the growth of other III-V materials, and should be taken into account for successful HVPE $M^{III}N$ growth: (1) An inert ambient atmosphere is preferred and is more effective for the $M^{III}N$ growth than hydrogen atmosphere, the latter being widely used for other III-V systems, like GaAs; (2) In HVPE-GaN growth, NH_3 should be used as the source of the group V element rather than a nitrogen halide (NCl_3), which is highly explosive. Moreover, the thermal dissociation of NH_3 results in the formation of N_2 molecules, which are extremely stable and nonreactive at the temperatures used, while the thermal dissociation of $AsCl_3$, in GaAs growth, results in the formation of As_2 and As_4 molecules, which typically remain volatile and chemically reactive in the next step of the growth reaction; (3) Another problem comes from the fact that the $M^{III}N$ reaction tends to create huge amounts of byproducts such as NH_3Cl and $M^{III}Cl_3 \cdot NH_3$, leading to a massive condensation of these reaction species on the reactor walls. This fact makes the development of last-running process for very thick samples quite challenging.

16.3.2 Growth Kinetics

The kinetics of the HVPE nitride process and growth mechanisms occurring at the solid/vapor interface was predominantly studied for HVPE growth of GaN on sapphire substrate. The growth was simulated based on several models [157,158] for the surface process involving the following steps: (1) adsorption of NH_3 molecules, (2) adsorption of N atoms coming from ammonia decomposition, (3) adsorption of GaCl molecules on the N atoms forming NGaCl, and (4) decomposition of the NGaCl via different desorption mechanisms (Figure 16.12). Two of them were suggested in analogy with the GaAs model: desorption forming HCl and desorption forming $GaCl_3$ [158]. One more $GaCl_2$ desorption mechanism was suggested based on specific experimental observations for the GaN growth [159]. Statistical treatment of the dynamic equilibrium between the adsorbed and gas phase species allowed explicit expressions of the growth rates via the different pathways.

An optimum HVPE growth process requires a good selection of the reactor geometry and operating conditions, to ensure a minimization of undesired parasitic reactions and to provide a uniform reactant distribution across the substrate. Although, temperature distributions for specific reactor designs and geometry have been simulated using different software models [160], the optimization of HVPE growth is predominantly done by empirical studies of external parameters such as temperature, flow rates of active gases, and substrate orientation.

There are several detailed kinetics considerations published in the literature [161–165] even in the initial stages of development of the technique. The regularities established in the fundamental dependence of growth rate upon the temperature generally agree among different researchers, although the reported details are partly in contradiction to each other. These studies have identified regions with a different character, illustrated in Figure 16.13(a).

The *low-temperature region*: The exponential dependence of the growth rate in the low temperature region is a characteristic of kinetically controlled growth and may be attributed to the surface reaction, adsorption, and surface diffusion. The monotonic

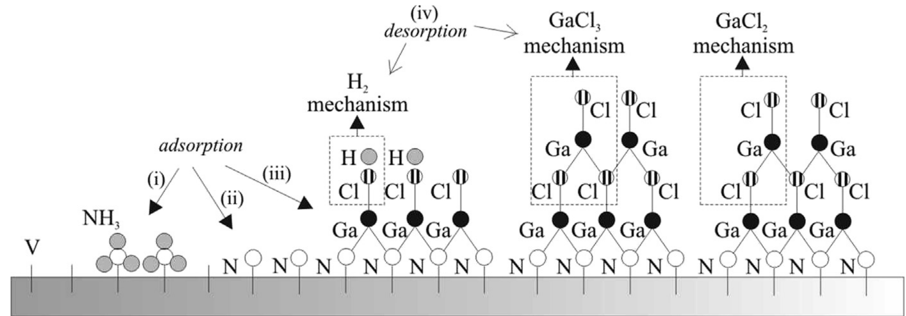

FIGURE 16.12 Schematic drawing of possible reaction steps: three possible adsorption (i – NH_3 adsorption, ii – N adsorption, iii– GaCl adsorption) and three possible desorption (H_2 desorption [158], $GaCl_3$ desorption [158], and $GaCl_2$ desorption [159]) mechanisms of the surface growth process of HVPE growth of GaN.

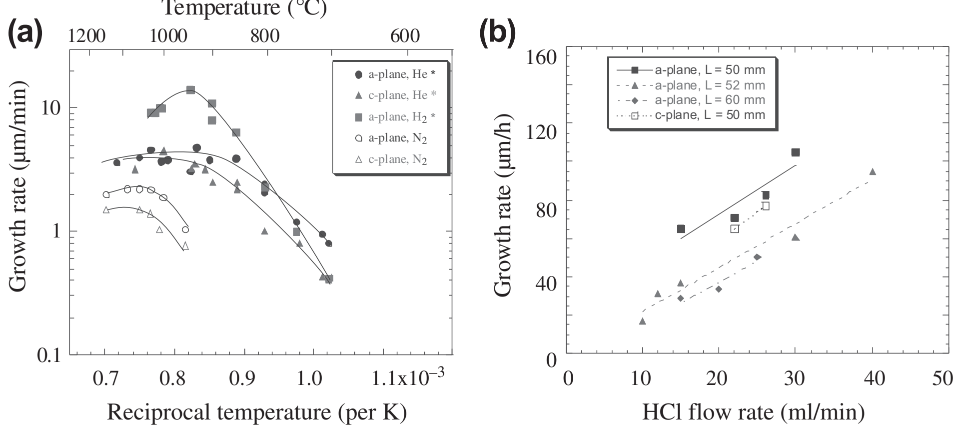

FIGURE 16.13 (a) Growth temperature dependence of the GaN growth rate. *Seifert et al. [155]. (b) The dependence of GaN growth rate on the HCl flow rate. The growth temperature was 1080 °C. The distance between the NH_3 outlet and the substrate is given in the inset, as well as the sapphire orientation.

increase of the growth rate with substrate temperature leads to a calculation of the activation energy of the epitaxial GaN growth from the Arrhenius plot. The reported values in the literature vary between 0.9 and 1.6 eV (21 and 37 kcal/mol), and the magnitude of the value suggests that the main rate-determining step in this low temperature region is related to the surface reaction [162,163]. A thermodynamic calculation of the equilibrium partial pressures in this region allowed speculations of a dominant mechanism for surface processes in different ambient [157,161].

The *high-temperature region* has been the subject of extensive experimental studies because of the larger practical interest and better material quality ensured. The growth rate reaches its maximum value at a temperature that varies in wide range of 950–1080 °C, according to different reports [162,163,166]. The difference in the temperature value for maximum growth rate may be attributed to differences in reactor design and growth conditions. At the temperature of 1080 °C, the dependence of GaN growth rate on HCl flow rate is shown in Figure 16.13(b). The growth rate increases linearly as a function of both HCl flow rate and GaCl partial pressure [163,164]. This fact combined with the weak temperature dependence of the growth rate in the higher growth temperature region indicates that the growth rate is limited by the transport of the gallium-containing species to the growth surface.

While the HCl flow rate appeared to be the key growth parameters, other parameters such as the NH_3 flow rate or the substrate orientation do not seem to affect the growth rate in a critical way, although they can affect the layer quality to a large extent. The weak growth rate dependence on NH_3 flow rate is reasonable since the concentration typically used in GaN HVPE is far larger than that of HCl, in order to suppress GaN dissociation. Also, the different carrier gases used were found to have noticeable effect in the range of low growth temperatures. Namely, the growth rate in case of using hydrogen was higher

than that in inert gas carrier gas for the temperature interval from 800 to 1050 °C. It was concluded that it was indicative of a growth rate–limiting surface reaction involving hydrogen [167]. The growth rate–determining steps in the high temperature region, which are typically thought to be related to enhanced gas-phase prereactions leading to a depletion of the chemical reactants at the substrate surface and/or enhanced etching of the growth surface, are likely to involve the hydrogen as a critical component controlling the process chemistry. There are also some experimental findings showing that additional HCl gas intentionally introduced downstream of the Ga boat can change the Cl/Ga ratio at the growth surface and thus enhance the lateral/vertical growth ratio, resulting in both a decrease of growth rate and an improvement of film quality.

16.3.3 Laboratory and Industrial Setups

The HVPE technique uses a hot-wall reactor due to the relatively low vapor pressure of the metal chloride at low temperature, aiming to avoid the condensation of the metal chloride molecules on unheated surfaces. Typically, the HVPE growth of the nitride layers is carried out in reactors based on the first concept reported over 30 years ago [128]. There are many different modifications, which can be summarized into two groups: horizontal and vertical reactor design [129–132].

In general, the HVPE reactor requires two temperature zones to enable the two chemical reactions in the standard HVPE growth of binary nitrides. However, most laboratory and all industrial reactors have more reactor zones, typically up to five temperature zones (Figure 16.14(a)). This allows larger flexibility, providing either more stable temperature control in the two main zones and/or allowing a doping or a second

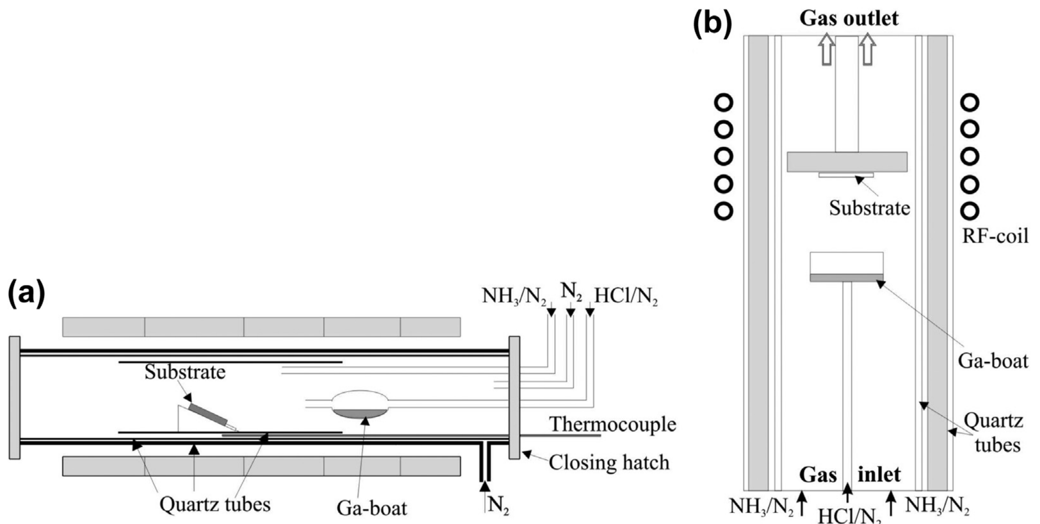

FIGURE 16.14 Schematic drawings of: (a) horizontal and (b) vertical HVPE reactors.

metal boat in case of growing nitride ternary alloys. The area of the liquid metal source is preferred to be as large as possible, depending on the reactor geometry, in order to achieve a large reactive surface area for efficient chloride production [168]. The second zone may be used for other metallic sources as In or Al, or for dopants when needed. In the third zone, kept at higher temperatures, the chloride and NH_3 are introduced and mixed. The substrate holder is placed in the fourth region of the reactor. We note that the reported substrate temperatures vary considerably, from 950 °C [169] up to 1150 °C [170], but some of the high quality GaN films, for example, were achieved at 1050–1080 °C [171]. The most common method of heating is a resistive one, although also RF heating is quite popular for some of the reactor zones. The horizontal reactors utilize a substrate holder that has a variety of designs and is situated either parallel or inclined or perpendicular to the gas flow direction. In most reported reactor designs, the active gases are delivered to the mixing point through separated parallel quartz liners. An alternative is the coaxial arrangement of the gas inlet tubes [161] to achieve a better mixing of the reaction gases prior the deposition and to improve the uniformity of the layers.

In the vertical design, the reactants are typically introduced through the top. The substrate is held flat on a susceptor that is perpendicular to the gas flow direction. The vertical reactor design usually facilitates easier substrate rotation during the growth to improve the film uniformity. An alternative modification is an inverted vertical reactor [130,132,171] where the process gases are supplied through the bottom inlet flange, while the top flange can be lifted for loading and unloading of substrates (Figure 16.14(b)). In this configuration the substrates are placed in the upper part where the gases are mixed. The inverted reactor keeps all advantages of the vertical design and also provides the possibility of raising the substrate holder, maintaining constant distance to the gas mixing point in case of long boule growth. An additional advantage of the inverted vertical reactor is the minimization of solid particle contamination of the growing surface.

The III-nitride HVPE growth is strongly thermodynamically favored, as compared to other III-V material systems grown using HVPE, which leads to undesirable homogeneous gas phase reactions and problems with extraneous wall deposition, especially in AlN growth [172]. This leads to severe gas phase depletion effects and difficulties in keeping constant growth rate over long growth runs and along consequent runs. The remaining portions of the NH_3 and HCl gases, which have not been consumed completely in the growth zone, proceed in the downstream of the reactor, where they react and form ammonium chloride (NH_4Cl), which leaves the process furnace in a vapor form but readily condenses to a heavy powder below $\sim$300 °C. Along with the $GaCl_3$ and the $GaCl_3$:NH_3 adduct, a large amount of NH_4Cl can eventually condense along the exhaust lines and complicate the system maintenance. Additional complications arise in AlN growth because $AlCl_3$ reacts with the quartz reactor wall at high temperatures [173]. The chemical reaction with the quartz wall can be mitigated by using a reactor liner and Al boat that are made from less reactive materials, such as alumina (Al_2O_3).

Most of the advanced laboratory and commercial reactors are reported with optimized laminar flow patterns in order to avoid the turbulence at the wafer edge and to achieve the necessary growth rate uniformity across a large wafer diameter and respectively uniform material properties [171–173]. The flow patterns are influenced by reactor geometry, the heat transfer, the flow boundary conditions, the choice of carrier gas, and all the gas velocities. A commercial software, for example, Hydride Epitaxial GaN Simulator (HEpiGANS) [174] is now developed, accounting for heat transfer by conduction, convection, and radiation, and species transport via convection, multicomponent diffusion, and thermodiffusion. The modeling of gas patterns is particularly useful to optimize the gas velocities in order to reduce the recirculation due to natural convection in vertical reactors and to avoid turbulent flows with vortex pattern in the middle of the wafer.

16.3.4 Growth on Foreign Substrates

16.3.4.1 Substrates and Buffers

In addition to the most commonly used sapphire substrates, several other substrates, such as sapphire (Al_2O_3), 6H-SiC, GaAs, Si, and some oxide substrates such as MgO, ZnO, TiO_2, $MgAl_2O_4$, and $LiGaO_2$ have been successfully used. Some characteristics are summarized in Table 16.1 [175], showing a significant lattice parameter and thermal expansion coefficient mismatch, for instance, of about 14% and 34%, respectively, for GaN on sapphire.

HVPE GaN, AlN, AlGaN, and AlInN layers grown directly on foreign substrates have varied from being highly transparent to brown. The surface morphology of thick layers is typically rough, consisting of hexagonal-shaped islands and often marked by hexagonal pits. The mosaicity and/or cracks are also typical in such layers. In order to mitigate the

Table 16.1 Characteristics of the Most Popular Substrates Used for HVPE Growth of GaN and AlN Substrates [175]

	Crystal Structure	Lattice Parameter a (A)	Lattice Parameter c (A)	TEC $\alpha \times 10^{-6}$/K	Substrate Separation
AlN	Wurtzite	0.31106	0.49795	$\alpha_a = 5.3$; $\alpha_c = 4.2$	
GaN	Wurtzite	0.31885	0.5185	$\alpha_a = 5.59$, $\alpha_c = 7.75$	
Sapphire	Rhombohedral	0.4765	1.2982	$\alpha_a = 5.0$; $\alpha_c = 9.03$	Laser liftoff self-separation
SiC	Wurtzite (6H)	0.30806	1.51173	$\alpha_a = 4.46$, $\alpha_c = 4.16$	Reactive ion etching
GaAs	Zincblende	0.56536		6.03	Chemical etching
Si	Diamond	0.543102		2.616	Chemical etching
MgO	Rock salt	0.421		8.0	
ZnO	Wurtzite	0.32496	0.5265	$\alpha_a = 6.5$; $\alpha_c = 3.0$	
$MgAl_2O_4$	Spinel	0.8083		7.45	
$\gamma LiAlO_2$	Tetragonal	0.5169	0.6267	$\alpha_{100} = 6.5$; $\alpha_{001} = 14.9$	Self-separation
$LiGaO_2$	Orthorhombic	0.5402/0.6372	0.5007	$\alpha_{100} = 6$; $\alpha_{010} = 9$	Chemical etching

large mismatch and some of the above drawbacks, specific pretreatments, buffers, and nucleation schemes have been developed. The most popular pretreatment was the so-called nitridation of the sapphire substrates, performed in 10–30% NH_3 atmosphere at the growth temperature for 5–30 min, which led to a noticeable improvement of the material properties [176,177]. Later on, alternative surface treatments of the foreign substrate were developed by GaCl gas [178] or a combination of the nitridation and the GaCl treatments [179].

Another widely used approach of growing nitrides by HVPE is by employing buffer layers. In contrast to the MOCVD nitride technology, the early work on low temperature GaN buffers in the same chamber was not successful in the HVPE technology, although some recent advances of the low temperature buffers resulted in good quality material [180]. Alternatively, buffers of different nature, deposited by different techniques, mostly reactive sputtering, have been proposed and demonstrated to ensure significant improvement of the crystal quality of the layers with thickness up to several tens of micrometers without cracks. The ZnO buffer was first suggested as a buffer for HVPE growth of thick GaN films [170]. Alternative buffers grown at high growth temperature were later suggested [181] and successfully employed in the HVPE growth to avoid the highly defective region at the interface containing columnar structures in case of direct growth on sapphire. Reactively sputtered thin AlN buffer with thickness of about 1 μm have been proven to ensure smooth epilayer surface and low defect density GaN material [182,183]. The use of MOCVD templates for GaN growth on sapphire has been firstly shown in MBE growth of thin GaN layers. Later on, it was successfully employed in the HVPE-GaN growth [184] and is currently used by many research groups.

It is important to note that the growth process (including nucleation scheme, the growth rate, and growth recipes), as well as the material properties resulting from using different foreign substrates and optimizations are very different for growth of thin films with thickness from 1 to 50 μm (often called templates), for thick films in the range of 100–2000 μm, and for boule growth with thickness more than several millimeters, the latter two being of interest for substrate applications after removing the foreign substrate.

16.3.4.2 Template Growth

Templates is the term typically used for layers deposited and remaining on foreign substrates (usually sapphire), with thickness in the range of 1–50 μm. This HVPE growth has been demonstrated practically for all binary and ternary nitrides, but it was particularly developed for GaN and AlN, which can be used for direct growth of device structures. The advantages of this approach in the device growth are based on the fact that these "template substrates" eliminate the need for the low temperature buffer growth step and, even more important, the dislocation density in these layers is noticeably reduced down to 10^8–$10^7/cm^2$, depending on the thickness. This ensures lower defect density and higher structural quality in the subsequently grown multilayer device structures.

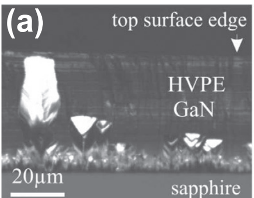

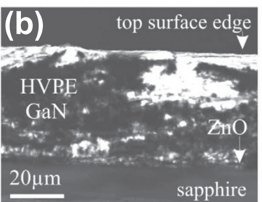

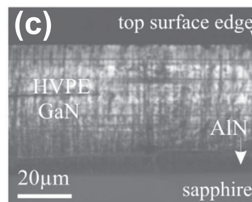

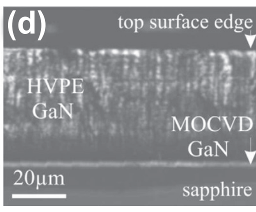

FIGURE 16.15 Panchromatic CL image in cross-section of thick HVPE-GaN layer grown (a) directly on sapphire, showing three specific growth zones—the highly disordered interface region, the columnar region, and the good quality region; (b) with ZnO buffer; (c) with reactive sputtered AlN buffer; and (d) with Si-doped MOVPE-GaN template.

The HVPE templates typically employ high temperature buffers deposited by other techniques, such as reactive sputtered ZnO and AlN or more often MOCVD-grown GaN. The ZnO is known to be one of the most effective buffers for growth of thick GaN layers of very good quality, but thick large-area crack-free layers suitable for quasi-substrate applications have not been demonstrated by using this buffer. Similar nucleation and layer quality improvements (Figure 16.15) have been observed by using reactive sputtered AlN and MOCVD-GaN templates with optimized ratio of the layer and buffer thicknesses [179,181–185].

Figure 16.15(a) shows panchromatic cathodoluminescence (CL) image of HVPE-GaN layers grown without buffer, revealing three distinctive regions [130]: (1) the interface region shows a greatly reduced radiative efficiency attributed to a very high degree of structural imperfections; (2) In the second zone clearly defined columns can be seen, often referred to as columnar defective region, with some of the columns protruding through the entire layer thickness, characterized with nonuniform emission attributed to nonuniform impurity incorporation; (3) the upper zone, extending over several tens of micrometers in thickness, is generally of good quality with more uniform radiative emission. Figure 16.15(b–d) show CL images of HVPE-grown GaN layers, employing reactive sputtered ZnO, AlN, and MOCVD-GaN buffers, respectively. The results show that the growth on these buffers helps to: (1) eliminate the large-scale structural defects at the sapphire/GaN interface; (2) reduce the concentration and nonuniform distribution of residual carriers; (3) partially relieve the compressive stress in the HVPE-GaN layers [130]. It is important to note that all the templates can provide good buffers for growth of thick HVPE-GaN layers with very good structural and optical characteristics, although it is difficult to grow films with sufficient thickness (larger than 50 μm) without cracks.

16.3.4.2 Quasi-Bulk Single-Wafer Growth

The growth of quasi-bulk single wafer for substrate applications needs to ensure layer thickness of at least a few hundreds of micrometers without cracks. A weak interface region between the substrate and nitride layer is also needed in order to allow easier delamination process for producing a freestanding nitride layer. This growth method is developed for GaN thick layers, while the AlN thick layer growth is still in its infancy. There are two main approaches for growth of single-wafer GaN substrate: the first one is

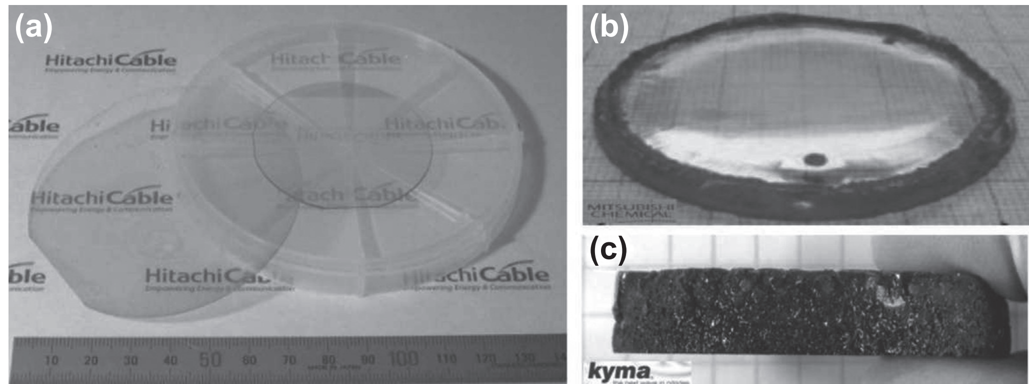

FIGURE 16.16 (a) Large 3″ GaN substrates announced by Hitachi Cable (CompoundSemiconductor.net) and currently the largest 2″ GaN boules reported by Mitsubishi Chemical (b) and Kyma Technologies (c). *After Ref. [190].*

producing GaN layers with a thickness in the range of 150–400 μm often with ELOG templates in order to achieve low defect density material in the lateral regions, and the second one is producing layers with thickness of 1–2 mm in order to achieve low defect density due to thickness increase. There are also several approaches for separation of the thick GaN layer from the substrate, depending on the thickness achieved and the buffer used. The most popular is the self-separation, which can be achieved by the so-called void-assisted separation, which in turn requires a special buffer. Such a buffer could be reactively sputtered TiN, as suggested by Japanese researchers in 2002 [186]. This approach was developed and successfully implemented for substrate manufacturing by Hitachi Cable, which announced production of crack-free 3-in freestanding GaN wafer (Figure 16.16(a)) [187,188]. Another high temperature reactively sputtered AlN buffer [189,190] was also found to be effective in suppressing defect formation in the GaN nucleation region, reducing tensile stress during GaN growth by forming a weak “pitted” interface that leads to optimized structural properties and allows self-separation of the films during cooldown.

Crack-free thick HVPE-GaN layers with thicknesses of about 300–500 μm have been demonstrated by using multiple-step technology processes such as epitaxial lateral overgrowth (ELOG) [191,192], two-step epitaxial lateral overgrowth (2S-ELOG) [193,194], or Pendeo epitaxy [194,195]. This growth procedure consists principally of an HVPE growth on a thin MOCVD-grown GaN layer. The MOCVD growth was performed using the conventional two-step procedure, consisting of a 20-nm-thick low temperature buffer layer and a high temperature main layer. A SiO_2 layer was then deposited by chemical vapor deposition and window stripes with a period of about 7 μm were opened using conventional photolithographic techniques. Alternatives of using W [196] and SiN [197] masks instead of SiO_2, or using GaAs [198], $LiGaO_2$ [199], or $LiAlO_2$ [200] substrates instead of sapphire have also been demonstrated. In addition, in order to further reduce the dislocation density, the ELOG approach can be performed by the so-called two-step

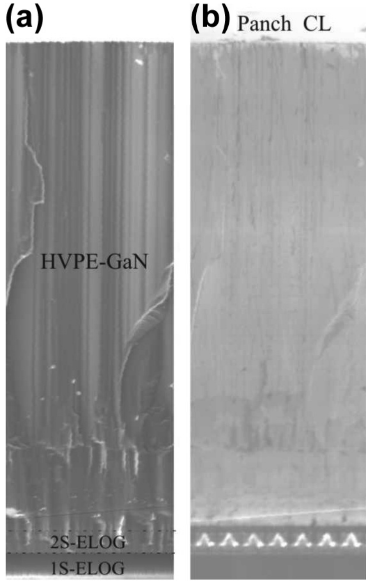

FIGURE 16.17 (a) A secondary electron image and (b) a panchromatic CL image in a cross-section of an HVPE-GaN layer grown on 2S-ELOG template.

approach (2S-ELOG), which can employ either a second layer of mask usually with shifted period with respect to the first mask, or it can employ a change of the growth parameters, usually a reduced growth temperature during the second stage [193]. In spite of complicated defect, strain, and emission distribution in the early stages of the growth, a more uniform main part of the film is followed (as shown in the panchromatic CL image in Figure 16.17(b)). A common feature for the growth on such templates is the formation of voids (Figure 16.17(a)) in the coalescence areas, found to partially release the strain. This allows an increase of the critical thickness for crack appearance, and in some cases leads to self-separation of the film.

These types of thick layers can be separated from the substrates by different methods, depending on the type of the substrate used and the nucleation scheme. The easiest substrate removal is through a chemical etching as is often done in the case of GaAs or $LiGaO_2$ substrate. This approach is now routinely used at Sumitomo Electric Industries Ltd for removing the initial GaAs substrate. In case of transparent sapphire substrates, a laser-induced liftoff process was developed in order to separate the GaN from the sapphire using pulsed UV laser beams. The process works by irradiating the sapphire/GaN interface with intense laser pulses just at the absorption edge of GaN. It leads to a fast and strong local heating, which causes thermal decomposition in the interface region of the film, yielding metallic Ga and nitrogen gas evaporation. This approach was particularly developed for 2S-ELOG buffer and successfully use in wafers production by Lumilog Ltd. [193].

16.3.3.3 Bulk Growth

The bulk growth is the most preferable and economical pathway to produce substrates with the necessary quality, size, and cost. At this time, however, GaN boule growth is still in early stages of development, and no mature technology is available yet due to several growth-related issues. The most critical challenges are related to maintaining stable growth conditions in the HVPE reactors during long growth runs. Wall deposition and secondary reaction products lead to reactor clocks, which can be handled by a proper pressure balance, or to a depletion of the growth efficiency, which can be mitigated by modulation epitaxy. Another issue is related to growth cracks, provoking lateral growth and polycrystalline inclusions, which limit the growth duration and the boule thickness. Mitsubishi Chemical Co. reported a successful growth of 2-in boules up to 6–10 mm thick (Figure 16.16(b)) [201]. Two-inch boule growth ranging from 2.5 mm up to 10 mm has been reported by ATMI Inc. [202], Ferdinand-Braun-Institute [203], and Kyma Technologies Inc. Figure 16.16(c) [187], respectively. Different buffers and high growth rates up to 300 μm/h are likely to be used by the different groups.

The boule growth approach is also the technique of choice for producing substrates with surface orientation different from the (0001) for growth of device structures on crystallographic planes that exhibit lower or no polarization (the so-called nonpolar and semipolar planes). This is so far accomplished by slicing nonpolar or semipolar substrates perpendicularly or inclined with respect to the as-grown c-plane surface of the boules.

16.3.5 Homoepitaxial Seeded Growth

Another approach that recently attracted significant attention is the so-called seeded growth by the HVPE process. This approach aims at combining the high growth rate and higher crystalline quality achievable by the homoepitaxial regrowth employing GaN seeds instead of using sapphire to avoid the initial highly defective interface region. Several alternatives of seeded growth have been elaborated recently by research from Unipress. Namely, seeds produced either by high pressure solution growth (HPSG), HVPE, or ammonothermal growth methods have been used for regrowth by HVPE. Figure 16.18(a–c) show optical images of the three types of seeds and the HVPE regrown wafers (Figure 16.18(d–f)), respectively.

The first type of seeded growth was reported first due to the early availability of high quality HPSG crystals, although of small form factor (Figure 16.18(a,d)). The main challenge of this seeded growth was the expansion of the seed crystal [204,205]. In HVPE growth of GaN, crystal expansion can be controlled through physical-chemical gradients and concentrations, which result in stabilization of crystal planes under the appropriate growth conditions. For in-plane expansion, size expansion will depend on the anisotropy of the growth rates for different crystallographic planes. Growth parameters, such as temperature, pressure, growth rate (source species flux), or the ratio between the nitrogen and the gallium species, can influence the stabilization of one crystal plane over another. Additionally, the geometric configuration of the seed in the system may

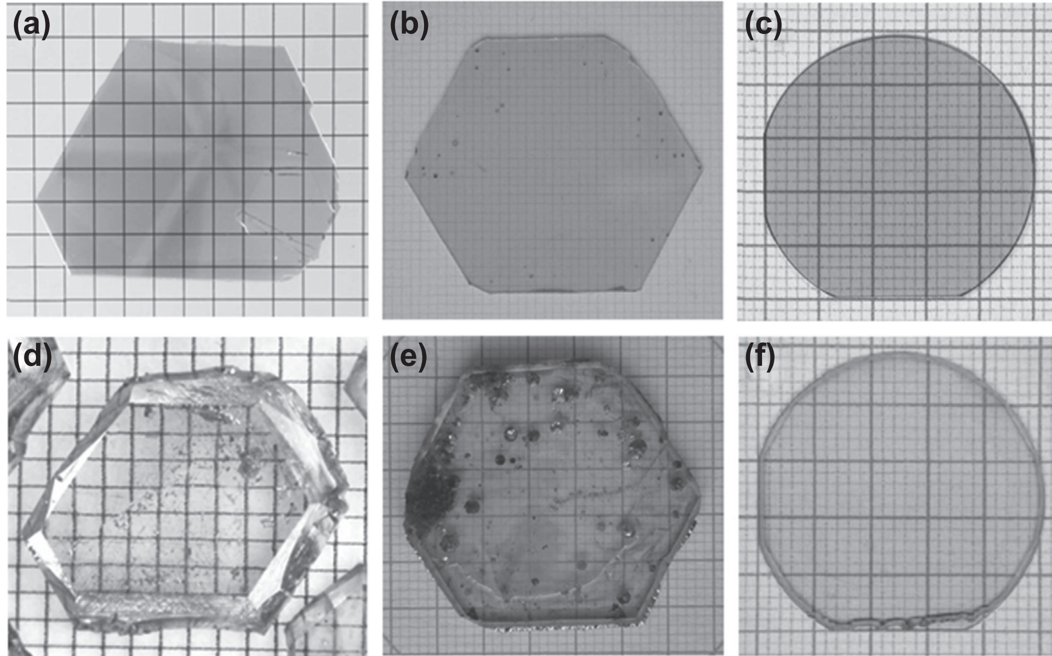

FIGURE 16.18 Optical images of GaN seeds grown by: (a) high pressure solution growth, (b) HVPE, (c) ammonothermal methods, and (D, E, F) HVPE-grown GaN on the respective seeds shown above. *Courtesy of Bolesław Łucznik.*

contribute to the flux of the growth species from additional sources, such as surface migration. As shown in the ELOG growth of GaN [197,198], inclined crystalline facets can be formed under certain growth conditions that give undesirable crystalline morphologies. An important part of the growth process development is to identify growth parameters that give a planar (as opposed to prismatic – Figure 16.18(d)) crystal, and then find the way to extend the growth in directions normal to those edge planes. One issue that has been observed with seed expansion is the variation in impurity content and carrier concentration. The physical and electrical properties of GaN grown by HVPE are very sensitive to the orientation of the crystallization front. This could present a challenge for bulk growth, particularly for undoped and semi-insulating material, where a low background concentration of shallow impurities, such as oxygen, is desired.

With the availability of larger wafers, produced by HVPE, the regrowth by HVPE was optimized and proven successful in maintaining the seed wafers' size during the HVPE-seeded growth, as shown in Figure 16.18(b,e) [206]. Even the very early HVPE regrowth on HVPE freestanding crystal showed that the material produced during regrowth possesses significantly improved structural characteristics. In particular, the dislocation density was found to be noticeably reduced. The analysis of the defect density in the regrown HVPE-GaN with different thicknesses has shown that the trend of decreasing the defect density with increasing thickness remains [207]. The high purity of

the crystals and the high optical quality have been proven reproducible. In particular, the low temperature photoluminescence (PL) spectra of the regrown GaN films showed comparable narrow ($\sim$2 meV) exciton peaks as in the PL spectrum of the seed. However, based on different studies performed by variety of techniques, such as X-ray diffraction, PL, Raman scattering spectroscopies [206,207], it is clear that both the residual strain and curvature (radius of about 10 m in the best case) of the seed was reproduced, which remains the main undesirable characteristic of these materials.

The most recent availability of low dislocation-density wafers grown by ammonothermal method open a new possibility for homoepitaxial seeded growth (Figure 16.18(c,f)). The HVPE-seeded growth on such seeds has also been proven successful in reproducing the seed characteristics in regard to very low curvature (radius close to 100 m) and low dislocation density (in the angle of $10^4/\text{cm}^2$) [208]. Moreover, in contrast to the ammonothermal seed characteristics, the HVPE-GaN wafer grown on ammonothermal seed possessed high purity and transparency, which are typical characteristics for the HVPE growth. Thus, the combination of the two methods seems to enable the advantages of both in the regrown material.

16.3.6 Growth Related Properties

16.3.6.1 Residual Impurities and Native Defects

The HVPE-grown nitrides, including GaN, AlN, and AlGaN, have generally been reported with high purity, low density of background impurity, vacancy and deep-level complexes, and with high transparency. The lowest unintentional free carrier concentration in bulk GaN material was reported in HVPE material to be in the range of 8×10^{15}–$2 \times 10^{16}/\text{cm}^3$ and was explained by the presence of oxygen and silicon impurities, being unavoidable in the nitride materials grown by HVPE. There are numerous reports about the origin of the residual impurities in HVPE-grown nitrides, as well as for their distribution. The interface region, close to the substrate, is typically characterized by high defect density of impurities, predominantly oxygen (Figure 16.19(a)) and vacancies (Figure 16.19(b)), which quickly decrease with increasing the layer thickness and overall leads to thickness improvement of material properties [210]. This trend, however, is typical for growth along the [0001] c-direction, and contradicts the flat thickness distribution of the V_{Ga}-O_N pair defects observed in the GaN growth along nonpolar directions, as seen in Figure 16.19(b) for a-plane GaN on sapphire [209]. This general trend of the point defects decreasing is more complicated, particularly in the interface region for material grown without buffers, possessing columnar interface structure, and in materials grown on ELOG-type of buffer. The material with columnar interface structure may dramatically affect the Hall effect results, indicating highly conductive or even degenerate materials in some cases, which was explained by the high concentration of the interface connected to the contacts via the columnar structure (Figure 16.15(a)) and thus bypassing the high quality low impurity concentration part of the layers. The impurity distribution in the ELOG part is even more complicated, as seen

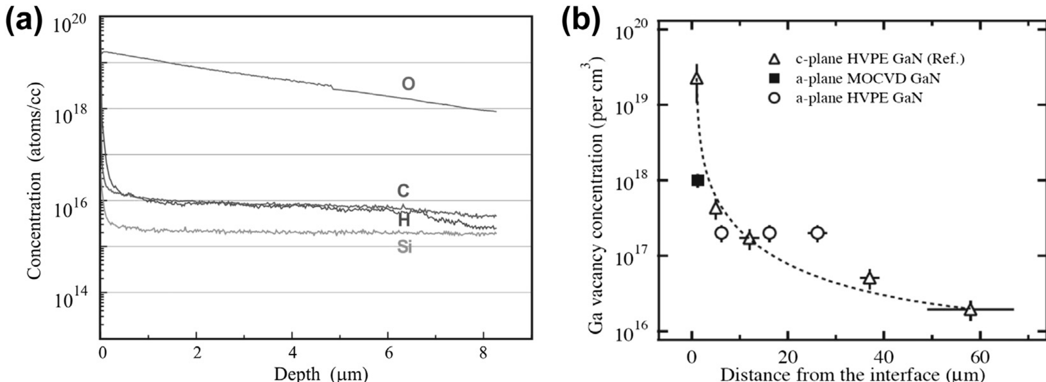

FIGURE 16.19 Ga vacancy defect distributions: (a) along the film thickness in polar and in nonpolar GaN heteroepitaxial layers grown by HVPE in the near interface region (60 μm) close to the substrate interface; (b) across a nonpolar bar sliced from a 2-in boule across the boule center—the experimental data depicted from the spots indicated in the inset. *After Ref. [209].*

in the CL images (Figure 16.17), although it is more regular and controllably distributed in the coalescent part, while the larger main part of the layer remains generally uniform and not affected by the interface impurities.

The presence of the interface layer with high density of point defects in most of the heteroepitaxial nitride and the near-surface accumulation layer often observed in InN layers provoked a need for using a two-layer model [211] for analysis of the Hall effect data in all cases of HVPE template layers. The bulk nitrides, however, do not require a consideration of this interface layer due to its self-separation removal or polishing away. The Hall effect data of bulk GaN grown by HVPE revealed high mobility, i.e., $1280/cm^2/Vs$ for free carrier concentration of $1.23 \times 10^{16}/cm^3$ at room temperature, close to the theoretical predictions [212].

16.3.6.2 Doping

Although all intentionally undoped GaN material grown by HVPE method possesses *n*-type conductivity, *p*-type and semi-insulating materials are also available by adding different impurities.

Intentional *n*-type doping can be achieved by O and Si doping introduced by gaseous or solid sources. Typical gaseous Si dopant precursors for HVPE growth include silane, disilane, and dichloresilane. Alternatively, Si doping can be achieved in HVPE by exposing Si to the HCl gas to form $SiCl_x$, which then transports to and reacts with the growing film. HVPE-grown bulk GaN doped with Si by using SiH_4 source was reported to result in material with carrier concentration in the range of 1.3×10^{16}–$8.3 \times 10^{18}/cm^3$ while maintaining high crystalline and optical quality [213]. Alternative doping with oxygen, using gaseous source of high quality was also reported to achieve carrier concentration up to $8.5 \times 10^{18}/cm^3$. Temperature dependence of Hall carrier concentration and mobility of two such representative samples doped with Si ($n = 7.3 \times 10^{16}/cm^3$) and O ($n = 2 \times 10^{17}/cm^3$) are shown in

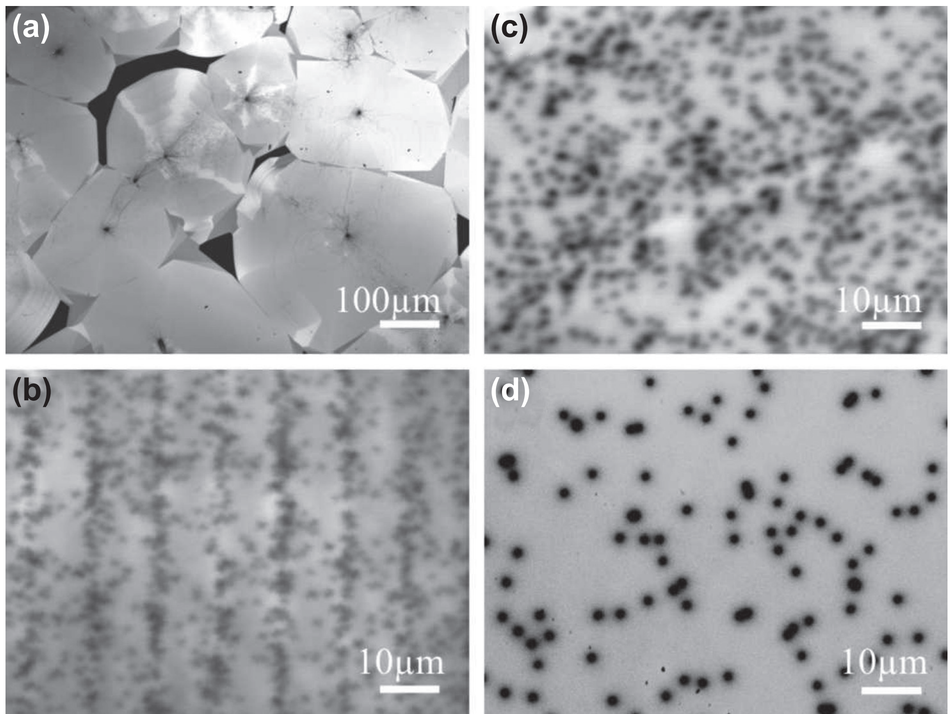

FIGURE 16.20 Panchromatic CL images visualizing in-plane dislocation distribution in GaN layer grown by HVPE on: (a) GaAs substrate using ELOG technique with hexagonal mask openings; (b) sapphire substrate using ELOG technique with striped mask; and on sapphire substrate using high temperature AlN buffer with thickness of about 150 μm (c) and 700 μm (d).

Figure 16.20(a,b), respectively, showing similar trends as the ones for undoped material with the offset related to the higher free carrier concentrations.

P-type doping of GaN bulk material was reported by HVPE techniques as well. Today Mg is the element proven to be the most efficient and controllable in achieving *p*-type conductivity. Despite that, high hole concentrations are challenging due to Mg high thermal activation energy of 150–200 meV [214], however, resulting in only a few percent of the Mg acceptor ionization at room temperature. Additionally, postgrowth annealing is required for removing the hydrogen passivation of the Mg dopant. Other elements such as Zn and Cd have also been used but with even less activation efficiency due to their larger thermal activation energy and much less activation achievable at room temperature. The doping with Mg in HVPE was done by either using a separate temperature zone and source bath or by mixing the Mg in the Ga source. The HCl gas, reacting with Mg can form MgCl, which is transported to the growth zone [215]. The role of H carrier gas was reported in a controversial way. Although one would expect that it is preferable to use inert carrier gas to avoid Mg-H passivation, the experimental results have shown preferable behavior of the passivation during growth to prevent the

incorporation of residual donor impurities [216]. Thus, despite the technological breakthroughs in growing *p*-type GaN by HVPE, the reports are very limited and the exact governing mechanisms remain unclear.

Semi-insulating GaN bulk substrates are currently only possible by doping with compensating elements. The most promising approach suggested so far in HVPE growth is doping with Fe using metalorganic source. The HVPE-growth GaN with varying Fe concentration for semi-insulating substrate application has been demonstrated, and such bulk wafers are available on the market. The material was reported with sufficiently high resistivity (larger than 10^6 Ωcm). Despite the fact that the reports on this topic are relatively limited, and the compensation mechanism is not yet fully understood, the growth of semi-insulating GaN with high quality was proven successful.

The doping of HVPE-grown bulk GaN technique was proven capable of maintaining good crystalline quality and excellent optical properties. The structural quality of non-intentionally doped (n−), Si-doped (n+), O-doped (n+), and Fe-doped (semi-insulating) GaN was studied by a variety of techniques, consistently revealing high crystalline quality, small lattice curvature, and low defect density [213]. The results are also suggestive of the relative independence of structural quality on the doping parameters within the moderate doping levels typically needed [217]. It is important to note that the doping has a noticeable effect on the lattice parameters, especially in the case of semi-insulating material doped with Fe. A precise analysis of the doping effect, however, requires a series of low defect density bulk material grown with controllable doping concentration and accounting for the background impurities and native point defects, such as Ga vacancies, despite the fact that the method produced the lowest density of native point defects as compared to all other bulk nitride techniques.

16.3.6.3 Structural Defects

The microstructure, particularly the dislocation density and distribution, represent especially important characteristics of HVPE-grown nitride template and substrates. There are two primary approaches toward decreasing the dislocation density in HVPE-GaN: ELOG-type approaches and greater GaN thickness (boule type), as mentioned earlier. The ELOG approaches can provide areas of very low defect density, where the lateral growth mode dominates. Depending on the mask geometry, these low-defect density areas could have different shape and size as visualized by panchromatic CL imaging in Figure 16.20(a,b) for hexagonal and stripe openings, respectively. Usually the devices have been placed on top of these areas.

Increasing thickness of the HVPE-GaN layer is another way of decreasing dislocation density. Panchromatic CL images (Figure 16.20(c,d)) visualize the dislocation density decrease down to 10^7–10^8/cm^2 in a ~150-μm-thick film (Figure 16.20(c)) and 10^6–10^7/cm^2 in a ~700-μm-thick film (Figure 16.20(d)). This effect was also visualized in transmission electron microscopy (TEM) cross-section image taken from the interface region of an HVPE-GaN layer grown on sapphire with reactive sputtered AlN buffer (Figure 16.21(a)). The AlN buffer comprises well-defined, slightly misoriented domains

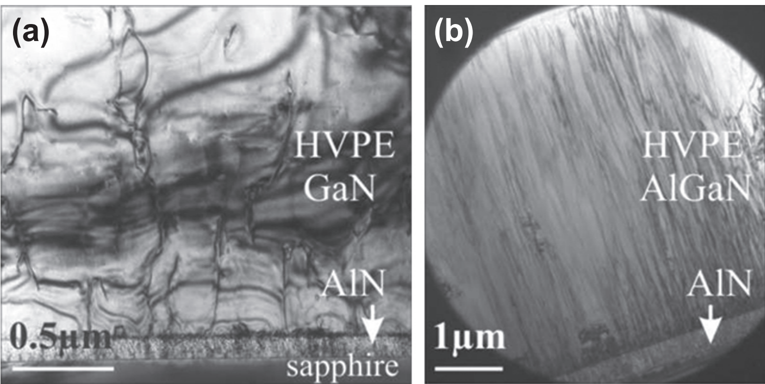

FIGURE 16.21 TEM images of: (a) HVPE-grown GaN and (b) HVPE-grown AlGaN *(Courtesy of Zuzanna Liliental-Weber)* layers, using reactive sputtered AlN buffers and showing similar decrease of dislocation density along the growth direction in both materials.

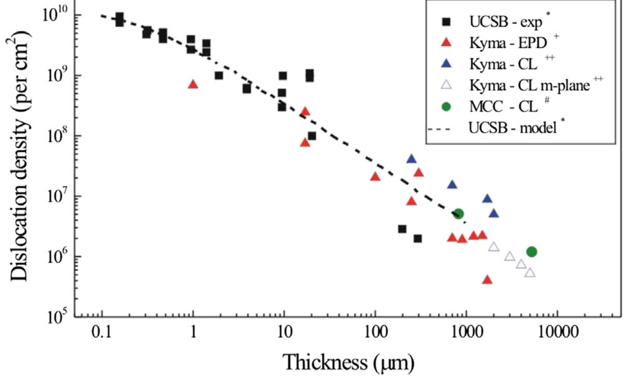

FIGURE 16.22 Combined graph of experimental data and theoretical expectations for dislocation density as a function of the GaN layer thickness. *Mathis et al. [218]; +Hanser et al.[219]; ++Paskova et al. [187]; #Fujimori et al. [220].

[178] and accommodates most of the misfit defects usually generated in the interface region. One can see a reduction of the threading dislocation along the sample thickness, which was consistently shown in a number of publications. This effect is observed for all the nitrides heteroepitaxially grown by HVPE. For example, one representative TEM image of a ternary AlGaN layer grown by HVPE on sapphire substrate with reactive sputtered AlN buffer with a thickness of about 6 μm is shown in Figure 16.21(b), showing a similar trend of dislocation reduction with thickness down to $8 \times 10^8/cm^2$ in the near surface region.

The decrease of dislocation density with increasing film thickness was reported for all nitride materials and explained either by annihilation of mixed dislocations with opposite Burger's vectors [218] and/or by point defect–assisted dislocation climb. Figure 16.22 summarizes results obtained by different characterization techniques

[218–222]. TEM is the most reliable approach to differentiate and estimate the dislocation type and density, however, the technique approaches its sensitivity limit for densities around $10^5/cm^2$. Complementary studies by CL topography reveal [219,220] a different dark contrast usually interpreted as due to nonradiative recombination, with strong contrast for screw and mixed dislocations and a quite weak contrast for edge dislocations [216]. Alternative techniques used are atomic force microscopy and different etching procedures, revealing large pits related to dislocations of screw type and small pits related to edge type dislocations [222]. The graph shows a monotonic decrease of dislocation density with GaN layer thickness over several orders of magnitude, consistent with the theoretical model.

16.4 Conclusion

In this chapter the current status of vapor transport bulk growth of wide bandgap semiconductors, focusing on SiC, AlN, and GaN, was summarized. Remarkable development has been demonstrated during the last 10 years regarding understanding of the growth mechanisms and reactor optimizations. The crystal quality has been significantly improved, but much remains to be done, especially for the bulk nitrides. Growth-related defect density and doping control are the most critical current challenges that remain to be resolved in order to achieve the full potential of the bulk wide bandgap semiconductors.

Acknowledgements

T. Paskova acknowledges NSF support by DMR-1207075 and CBET-1336464 projects. M. Bickermann acknowledges DFG support by BI781/5-1, 6-1, and 8-1 projects, and BMBF support during Berlin WideBaSe project 03WKBT05A.

References

[1] [a] Kordina O, Hallin C, Ellison A, Bakin AS, Ivanov IG, Henry A, et al. Appl Phys Lett 1996;69:1456;
[b] Kordina O, Hallin C, Henry A, Bergman JP, Ivanov IG, Ellison A, et al. Phys Status Solidi B 1997;202:321.

[2] Hofmann DH, Müller MH. Mater Sci Eng B 1999;61–62:29.

[3] Wellmann P, Desperrier P, Mueller R, Straubinger T, Winnacker A, Baillet F, et al. J Cryst Growth 2005;275:e555.

[4] Schlesser R, Sitar Z. J Cryst Growth 2002;234:349.

[5] [a] Vodakov YuA, Mokhov EN, Ramm MG, . Roenkov AD. Krist Tech 1979;14:729;
[b] Mokhov EN, Shulpina IL, Tregubova AS, Vodakov YuA. Krist Tech 1981;16:879.

[6] [a] Acheson EG. Great Britain Patent 1890;17911;
[b] United States Patent 1893;492767.

[7] [a] Lely JA. Ber Dt Keram Ges 1955;8:229 [in German];
[b] United States Patent 1958;2854364.

[8] [a] Ziegler G, Lanig P, Theis D, Weyrich C. IEEE Trans Electron Devices 1983;ED-30:277;
[b] Ziegler G. German Patent 3230727 (1984).

[9] Barrett DL, Seidensticker RG, Gaida W, Hopkins RH, Choyke WJ. J Cryst Growth 1991;109:17.

[10] Tairov YuM. Mater Sci Eng B 1995;29:83.

[11] [a] Tairov YuM, Tsvetkov VF. Prog Cryst Growth Charact 1983;7:111;
[b] Tairov YuM, Tsvetkov VF. Cryst Growth Prop Appl 1984;10:1 [Springer].

[12] [a] Tairov YuM, Tsvetkov VF. J Cryst Growth 1978;43:209;
[b] Tairov YuM, Tsvetkov VF. J Cryst Growth 1981;52:146.

[13] Vodakov YuA, Roenkov AD, Ramm MG, Mokhov EN, Makarov YuN. Phys Status Solidi B 1997;202:177.

[14] Davis RF, Sitar Z, Williams BE, Kong HS, Kim HJ, Palmour JW, et al. Mater Sci Eng B 1988;1:77.

[15] Carter Jr CH, Tsvetkov VRF, Glass RC, Henshall D, Brady M, Müller StG, et al. Mater Sci Eng B 1999;61–62:1.

[16] Cree Inc., 4600 Silicon Drive, Durham, NC 27703–8475, USA, http://www.cree.com/.

[17] Charles & Colvard Ltd., 300 Perimeter Park Drive, Suite A, Morrisville, NC 27560, USA, http://www.charlesandcolvard.com/.

[18] Slack GA. MRS Symp Proc 1998;512:35.

[19] Pastrnak J, Roskovcova L. Phys Status Solidi 1964;7:331 [in German].

[20] Slack GA. Aluminum nitride crystal growth. U.S. Air Force Office of Scientific Research; 1979. DTIC document ADA085932, http://www.dtic.mil.

[21] Balkas CM, Sitar Z, Zheleva T, Bergman L, Nemanich R, Davis RF. J Cryst Growth 1997;179:363.

[22] [a] Slack GA, McNelly TF. J Cryst Growth 1976;34:263;
[b] Slack GA, McNelly TF. J Crystal Growth 1977;42:560.

[23] Piper WW, Polich SJ. J Appl Phys 1961;32:1278.

[24] Kneissl M, Kolbe T, Chua C, Kueller V, Lobo N, Stellmach J, et al. Semicond Sci Technol 2011;26:014036.

[25] Scace RI, Slack GA. J Chem Phys 1959;30:1551.

[26] Kleykamp H, Schumacher G. Ber Bunsenges Phys Chem 1993;97:799.

[27] Siang-Chung L. Mater Sci Lett 1997;16:759.

[28] Knippenberg WF. Philips Res Rep 1963;18:161.

[29] [a] Lilov SK. Cryst Res Technol 1993;28:503;
[b] Lilov SK. Diam Relat Mater 1995;4:1331;
[c] Lilov SK. Mater Sci Eng B 1993;21:65.

[30] Epelbaum BM, Bickermann M, Nagata S, Heimann P, Filip O, Winnacker A. J Cryst Growth 2007;305:317.

[31] Epelbaum BM, Bickermann M, Winnacker A. Mater Sci Forum 2004;457–460:1537.

[32] Straubinger TL, Bickermann M, Hofmann D, Weingärtner R, Wellmann PJ, Winnacker A. Mater Sci Forum 2001;353–356:25.

[33] Augustine G, Hobgood HMcD, Balakrishna V, Dunne G, Hopkins RH. Phys Status Solidi B 1997;202:137.

[34] Stein RA, Lanig P, Leibenzeder S. Mater Sci Eng B 1992;11:69.

[35] Snyder DW, Heydemann VD, Everson WJ, Barrett DL. Mater Sci Forum 2000;338–342:9.

[36] Schulze N, Barrett D, Weidner M, Pensl G. Mater Sci Forum 2000;338–342:111.

[37] Herro ZG, Zhuang D, Schlesser R, Collazo R, Sitar Z. J Cryst Growth 2006;286:205.

[38] Segal AS, Karpov SYu, Makarov YuN, Mokhov EN, Roenkov AD, Ramm MG, et al. J Cryst Growth 2000;211:68.

[39] Jacquier C, Ferro G, Cauwet F, Monteil Y. Mater Sci Forum 2002;389–393:307.

[40] Karpov SYu, Kulik AV, Przhevalskii IN, Ramm MS, Vodakov YuN. Phys Status Solidi C 2003;0:1989.

[41] Rost H-J, Doerschel J, Irmscher K, Roßberg M, Schulz D, Siche D. J Cryst Growth 2005;275:e451.

[42] Albrecht M, Wollweber J, Rossberg M, Schmidbauer M, Hartmann C, Fornari R. Appl Phys Lett 2006;88:211904.

[43] Kroko LJ. J Electrochem Soc 1966;113:801.

[44] Noveski V, Schlesser R, Mahajan S, Beaudoin S, Sitar Z. J Cryst Growth 2004;264:369.

[45] Schönherr E. Cryst Growth Prop Appl 1980;2:51 [Springer].

[46] Ma R, Zhang H, Prasad V, Dudley M. Cryst Growth Des 2002;2:213.

[47] Dreger LH, Dadape VV, Margrave JL. J Phys Chem 1962;66:1556.

[48] Hoch M, Ramakrishnan D. J Electrochem Soc 1971;118:1204.

[49] Chen Q-S, Zhang H, Prasad V, Balkas CM, Yushin NK. J Heat Transfer 2001;123:1098.

[50] Lilov SK, Yanchev IY. Cryst Res Technol 1993;28:495.

[51] Mokhov EN, Smirnov SN, Segal AS, Bazarevskiy D, Makarov YuN, Ramm MG, et al. Mater Sci Forum 2004;457–460:1545.

[52] Drowart J, De Maria G, Inghram MG. J Chem Phys 1958;29:1015.

[53] Sadowski H, Helbig R. J Electrochem Soc 1998;145:3556.

[54] Tairov YuM, Tsvetkov VF, Lilov SK, Safaraliev GK. J Cryst Growth 1976;36:147.

[55] Karpov SYu, Zimina DV, Makarov YuN, Mokhov EN, Roenkov AD, Ramm MG, et al. Phys Status Solidi A 1999;176:435.

[56] Chen Q-S, Prasad V, Zhang H, Dudley M. In: Byrappa K, Ohachi T, editors. Crystal growth technology. New York: William Andrew; 2003, ISBN 978-0-8155-1453-4 [chapter 7].

[57] Selder M, Kadinski L, Durst F, Hofmann D. J Cryst Growth 2001;226:501.

[58] Okamoto A, Sugiyama N, Tani T, Kamiya N. Mater Sci Forum 1998;264–267:21.

[59] Epelbaum BM, Seitz C, Magerl A, Bickermann M, Winnacker A. J Cryst Growth 2004;265:577–81.

[60] Hartmann C, Wollweber J, Dittmar A, Irmscher K, Kwasniewski A, Langhans F, et al. Jpn J Appl Phys 2013;52:08JA06.

[61] Nitride Crystals Inc., 181 E Industry Ct., Suite B, Deer Park, NY 11729, USA, http://www.nitride-crystals.com/.

[62] Heydemann VD, Schulze N, Barrett DL, Pensl G. Appl Phys Lett 1996;69:3728.

[63] Giocondi J, Rohrer GS, Skowronski M, Balakrishna V, Augustine G, et al. J Cryst Growth 1997;181:351.

[64] Frank FC. Philos Mag 1951;42:1014.

[65] Burton WK, Cabrera N, Frank FC. Philos Trans R Soc Lond Ser A 1951;243:299.

[66] Herro ZG, Epelbaum BM, Weingärtner R, Bickermann M, Masri P, Winnacker A. J Cryst Growth 2004;270:113.

[67] Ohtani N, Katsuno M, Aigo T, Fujimoto T, Tsuge H, Yashiro H, et al. J Cryst Growth 2000;210:613.

[68] Sumathi RR. CrystEngComm 2013;15:2232.

[69] Hexatech Inc., 991 Aviation Pkwy, Suite 800, Morrisville, NC 27560, USA, http://www.hexatechinc.com/.

[70] CrystAl-N GmbH, Dr.-Mack-Str. 77, 91762 Fürth, Germany, http://www.crystal-n.com/.

[71] Bickermann M, Epelbaum BM, Winnacker A. J Cryst Growth 2004;269:432.

[72] Madar R, Anikin M, Chourou K, Labeau M, Pons M, Blanquet E, et al. Diam Relat Mater 1997;6:1249.

[73] Hofmann D, Bickermann M, Eckstein R, Kölbl M, Müller StG, Schmitt E, et al. J Cryst Growth 1999;198/199:1005.

[74] Straubinger TL, Bickermann M, Grau M, Hofmann D, Kadinski L, Müller SG, et al. Mater Sci Forum 2000;338–342:39.

[75] Schlesser R, Dalmau R, Zhuang D, Collazo R, Sitar Z. J Cryst Growth 2005;281:75.

[76] Dalmau R, Raghothamachar B, Dudley M, Schlesser R, Sitar Z. MRS Symp Proc 2004;798:Y2.9.

[77] Liu B, Edgar JH, Gu Z, Zhuang D, Raghothamachar B, Dudley M, et al. MRS Internet J Nitride Semicond Res 2004;9:6.

[78] Slack GA, Whitlock J, Morgan K, Schowalter LJ. MRS Symp Proc 2004;798:Y10.74.

[79] Makarov YuN, Avdeev OV, Barash IS, Bazarevskiy DS, Chemekova TYu, Mokhov EN, et al. J Cryst Growth 2008;310:881.

[80] Hartmann C, Wollweber J, Albrecht M, Rasin I. Phys Status Solidi C 2006;3:1608.

[81] Matsunami H, Kimoto T. Mater Sci Eng R 1997;20:125.

[82] Siche D, Albrecht M, Rost H-J, Sendzik A. Mater Sci Forum 2007;556–557:21.

[83] [a] Takahashi J, Ohtani N. Phys Status Solidi B 1997;202:163;
[b] Takahashi J, Ohtani N, Katsuno N, Shinoyama S. J Cryst Growth 1997;181:229.

[84] Filip O, Epelbaum B, Li J, Bickermann M, Xu X, Winnacker A. Mater Sci Forum 2009;600–603:23.

[85] Raghothamachar B, Bai J, Dudley M, Dalmau R, Zhuang D, Herro Z, et al. J Cryst Growth 2006;287:349.

[86] Sumathi RR, Gille P. Jpn J Appl Phys 2013;52:08JA02.

[87] Bickermann M, Filip O, Epelbaum BM, Heimann P, Feneberg M, Neuschl B, et al. J Cryst Growth 2012;339:13.

[88] Sanchez EK, Kuhr T, Heydemann D, Snyder W, Rohrer S, Skowronski M. J Electron Mater 2000;29:347.

[89] Filip O, Epelbaum BM, Bickermann M, Heimann P, Winnacker A. J Cryst Growth 2011;318:427.

[90] Helava H, Mokhov EN, Avdeev OA, Ramm MG, Litvin DP, Vasiliev AV, et al. Mater Sci Forum 2013;740–742:85.

[91] Anikin M, Chourou K, Pons M, Bluet JM, Madar R, Grosse P, et al. Mater Sci Eng B 1999;61–62:73.

[92] Bahng W, Kitou Y, Nishizawa S, Yamaguchi H, Nasir Khan M, Oyanagi N, et al. J Cryst Growth 2000;209:767.

[93] Rost H-J, Siche D, Dolle J, Eiserbeck W, Müller T, Schulz D, et al. Mater Sci Eng B 1999;61–62:68.

[94] Wellmann PJ, Bickermann M, Hofmann D, Kadinski L, Selder M, Straubinger T, et al. J Cryst Growth 2000;216:263.

[95] Herro ZG, Epelbaum BM, Bickermann M, Masri P, Winnacker A. J Cryst Growth 2004;262:105.

[96] Bickermann M, Heimann P, Epelbaum BM. Phys Status Solidi C 2006;3:1902.

[97] Ha S, Nuhfer NT, De Graef M, Rohrer GS, Skowronski M. Mater Sci Forum 2000;469–472:477.

[98] Bondokov RT, Morgan KE, Shetty R, Liu W, Slack GA, Goorsky M, et al. MRS Symp Proc 2006;892: FF30-03.

[99] Dalmau R, Moody B, Xie J, Collazo R, Sitar Z. Phys Status Solidi A 2011;208:1545.

[100] Bickermann M, Epelbaum BM, Filip O, Tautz B, Heimann P, Winnacker A. Phys Status Solidi C 2012;9:449.

[101] Hobgood HMcD, Glass RC, Augustine G, Hopkins RH, Jenny J, Skrowonski M, et al. Appl Phys Lett 1995;66:1364.

[102] Bickermann M, Weingärtner R, Winnacker A. J Cryst Growth 2003;254:390.

[103] Rasp M, Straubinger ThL, Schmitt E, Bickermann M, Reshanov S, Sadowski H. Mater Sci Forum 2003;433–436:55.

[104] Mitchel WC, Saxler A, Perrin R, Goldstein J, Smith SR, Evwaraye AO, et al. Mater Sci Forum 2000; 338–342:21.

[105] Carter Jr. CH, Brady M, Tsvetkov VF, United States Patent 6218680 (2001).

[106] Pensl G, Choyke WJ. Physica B 1993;185:264.

[107] Ohtani N, Katsuno M, Takahashi J, Yashiro H, Kanaya M. J Appl Phys 1998;83:4487.

[108] Schulze N, Gajowski J, Semmelroth K, Laube M, Pensl G. Mater Sci Forum 2001;353–356:45.

[109] Bickermann M, Epelbaum BM, Hofmann D, Straubinger TL, Weingärtner R, Winnacker A. J Cryst Growth 2001;233:211.

[110] Straubinger TL, Bickermann M, Weingärtner R, Wellmann PJ, Winnacker A. J Cryst Growth 2002; 240:117.

[111] Glass RC, Augustine G, Balakrishna V, Hobgood HMcD, Hopkins RH, Jenny J, et al. Inst Phys Conf Ser 1996;142:37.

[112] Taniyasu Y, Kasu M, Makimoto T. Appl Phys Lett 2004;85:4672.

[113] Schulz T, Irmscher K, Albrecht M, Hartmann C, Wollweber J, Fornari R. Phys Status Solidi RRL 2007;1:147.

[114] Chen Y, Dhanaraj G, Vetter W, Ma R, Dudley M. Mater Sci Forum 2007;556–557:231.

[115] Schmitt E, Straubinger T, Rasp M, Weber A-D. Superlattices Microstruct 2006;40:320.

[116] Frank FC. Acta Crystallogr 1951;4:497.

[117] Si W, Dudley M, Glass R, Tsvetkov V, Carter Jr CH. Mater Sci Forum 1998;264–268:429.

[118] Hofmann D, Schmitt E, Bickermann M, Kölbl M, Wellmann PJ, Winnacker A. Mater Sci Eng B 1999; 61–62:48.

[119] Hong MH, Samant AV, Pirouz P. Mater Sci Forum 2000;338–243:513.

[120] Kitou Y, Bahng W, Nishizawa S, Nishino S, Arai K. Mater Sci Forum 2000;338–242:83.

[121] Rost H-J, Dolle J, Doerschel J, Siche D, Schulz D, Wollweber J. J Cryst Growth 2001;225:317.

[122] Dudley M, Huang XR, Huang W, Powell A, Wang S, Neudeck P, et al. Appl Phys Lett 1999;75:784.

[123] Lendenmann H, Dahlquist F, Bergman JP, Bleichner H, Hallin C. Mater Sci Forum 2002;389–393: 1259.

[124] Ha S, Mieszkowski P, Skowronski M, Rowland LB. J Cryst Growth 2002;244:257.

[125] Bickermann M, Schimmel S, Epelbaum BM, Filip O, Heimann P, Nagata S, et al. Phys Status Solidi C 2011;8:2235.

[126] Seitz C, Herro ZG, Epelbaum BM, Hock R, Magerl A. J Appl Cryst 2006;39:17.

[127] Dalmau R, Schlesser R, Sitar Z. Phys Status Solidi C 2005;2:2036.

[128] Maruska HP, Tjetjen JJ. Appl Phys Lett 1969;15:327.

[129] Molnar RG. In: Pankove J, Moustakas TD, editors. Galium nitride (GaN) II. Semiconductors and semimetals, vol. 57. London: Academic Press; 1999 [chapter 1].

[130] Paskova T, Monemar B. In: Manasreh O, editor. III-nitride semiconductors: growth. NY: Taylor & Francis Group; 2002. pp. 175–236 [chapter 10].

[131] Dwikusuma F, Kuech TF. In: Paskova T, Monemar B, editors. Nitrides as seen by technology. Research Signpost; 2002 [chapter 3].

[132] Hemmingsson C, Monemar B, Kumagai Y, Koukitu A. In: Dhanaraj G, Byrappa K, Prasad V, Dudley M, editors. Handbook of crystal growth. Berlin: Springer-Verlag; 2008.

[133] Cadoret R, Trasoidaine A. J Phys Condens Matter 2001;13:6893.

[134] Koukitu A, Hama S, Taki T, Seki H. Jpn J Appl Phys 1998;37:762.

[135] Kumagai Y, Yamane T, Miyaji T, Murakami H, Kangawa Y, Koukitu A. Phys Status Solidi C 2003;0: 2498.

[136] Nickel KG, Riedel R, Petzow G. J Am Ceram Soc 1989;72:1804.

[137] Efimov AN, Lebedev AO, Tsaregorodtsev AM. Tech Phys Lett 1998;24:810.

[138] Bugge F, Efimov AN, Pichugin IG, Tsaregorodtsev AM, Chernov MA. Cryst Res Technol 1987;22:65.

[139] Kumagai Y, Takemoto K, Kikuchi J, Hasegawa T, Murakami H, Koukitu A. Phys Status Solidi B 2006; 243:1431.

[140] Ban VS. J Electrochem Soc 1972;119:761.

[141] Ilegems M. J Cryst Growth 1972;13/14:360.

[142] Huang JS, Kuznetsov AV, Lee SS, Kim HS, Choi JG, Chong PJ. J Cryst Growth 1994;142:5.

[143] Tsuchiya H, Okahisa T, Hasegawa F, Okumura H, Yoshida S. Jpn J Appl Phys 1994;33:1747.

[144] Kumagai Y, Adachi H, Otake A, Higashikawa Y, Togashi R, Murakami H, et al. Phys Status Solidi C 2010;7:2022.

[145] Kumagai Y, Takemoto K, Hasegawa T, Koukitu A, Seki H. J Cryst Growth 2001;231:57.

[146] Kumagai Y, Yamane T, Koukitu A. J Cryst Growth 2005;281:62.

[147] Lebedev AO, Melnik YV, Tsaregorodtsev AM. Inst Phys Conf Ser 1994;137:405.

[148] Kumagai Y, Takemoto K, Koukitu A, Seki H. J Cryst Growth 2001;222:118.

[149] Trainor JW, Rose K. J Electron Mater 1974;3:821.

[150] Sato Y, Sato S. Jpn J Appl Phys 1997;36:4295.

[151] Noreika AJ, Ing DW. J Appl Phys 1968;39:5578.

[152] Tsaregorodtsev AM, Efimov AN, Pikhtin AN, Pichugin IG. Inst Phys Conf Ser 1997;155:243.

[153] Melnik Y, Nikolaev A, Stepanov S, Kikitina I, Vassilevski K, Ankudinov A, et al. Mater Sci Forum 1998;264–268:1121.

[154] Przhevalskii IN, Yu S, Karpov S, Makarov YN. MRS Internet J Nitride Semicond Res 1998;3. art 30.

[155] Seifert W, Franzheld R, Butter E, Sobotta H, Reide V. Cryst Res Technol 1983;18:383.

[156] Koukitu A, Hama S, Taki T, Seki H. Jpn J Appl Phys 1998;37:762.

[157] Aujol E, Napierala J, Trassoudain A, Gil-Lafon E, Cadoret R. J Cryst Growth 2001;222:538.

[158] Cadoret R. J Cryst Growth 1999;205:123.

[159] Trassaudaine A, Aujol E, Cadoret R, Paskova T, Monemar B. Mater Res Soc Symp Proc 2001:G.3.2.

[160] Segal AS, Kondratyev AV, Karpov S Yu, Martin D, Wagner V, Ilegems M. J Cryst Growth 2004;270:384.

[161] Safvi SR, Perkins NR, Horton MN, Thon A, Zhi D, Kuech TF. Mater Res Soc Symp Proc 1996;423:227.

[162] Shintani A, Minagawa S. J Cryst Growth 1974;22:1.

[163] Liu SS, Stevenson DA. J Electrochem Soc 1978;125:1161.

[164] Paskova T, Svedberg E, Henry A, Ivanov IG, Yakimova R, Monemar B. Phys Scr T 1999;79:67.

[165] Luzcnik B, Invited talk at the IW on Bulk Nitride Semiconductors VII (IWBNS-7), September 30–October 5, 2013, Kloster Seeon, Germany.

[166] Molnar RJ, Nichols KB, Maki P, Brown ER, Melngailis I. Mater Res Soc Symp Proc 1995;378:479.

[167] Dam CEC, Hageman PR, Larsen PK. J Cryst Growth 2006;205:123.

[168] Fremunt R, Cerny P, Kohout J, Rosicka V, Burger A. Cryst Res Technol 1981;16:1257.

[169] Ohki Y, Toyoda Y, Kobayasi H, Akasaki I. Inst Phys 1982:479.

[170] Molnar RJ, Gotz W, Romano LT, Johnson JM. J Cryst Growth 1997;178:147.

[171] Richter E, Henning C, Weyers M, Habel F, Tsay J-D, Liu W-D, et al. J Cryst Growth 2005;277:6.

[172] Kumagai Y, Takemoto K, Kikuchi Y, Hasegawa T, Murakami H, Koukitu A. Phys Status Solidi B 2006;243:1431.

[173] Wang WN, Stepanov SI, UK Patent GB 2 415 707, Vertical hydride vapor epitaxy deposition using a homogenising diaphragm.

[174] Semiconductor technology Research, http://www.str-soft.com/products/cvdsim/HVPE/, www.semitech.us.

[175] Liu L, Edgar J. Mater Sci Eng B 2002;37:61.

[176] Grandjean N, Leroux M, Laugt M, Massies J. Appl Phys Lett 1997;71:1240.

[177] Molnar RJ, Aggarwal R, Liau ZL, Brown ER, Melngailis I. Mater Res Soc Symp Proc 1996;395:189.

[178] Naniwae K, Itoh S, Amano H, Itoh K, Hiramatsu K. J. Crystal Growth 1990;99:381.

[179] Molnar RJ, Maki P, Aggarwal R, Liau ZL, Brown ER, Melngailis I, Götz W, Romano LT, Johnson NM. Mater. Res. Sos. Symp. Proc 1998;423:221.

[180] Hemmingsson C, Pozina G. Journal of Crystal Growth 2013;366:61.

[181] Paskova T, Birch J, Tungasmita S, Beccard R, Heuken M, Svedberg E, Runesson P, Goldys EM, Monemar B. Physica Status Solidi A 1999;176:415.

[182] Paskova T, Valcheva E, Birch J, Tungasmita S, Persson P, Paskov PP, Evtimova S, Abrashev M, Monemar B. Journal of Crystal Growth 2001;230:381.

[183] Valcheva E, Paskova T, Tungasmita S, Persson P, Birch J, Svedberg E, Hultman L, Monemar B. Applied Physics Letters 2002;76:1860.

[184] Paskova T, Tungasmita S, Valcheva E, Svedberg E, Arnaudov B, Evtimova S, Persson P, Henry A, Beccard R, Heuken M, Monemar B. Materials Research Society International Journal Nitride Semiconductor Research 2000;5S1:W3.14.

[185] Valcheva E, Paskova T, Birch J, Tungasmita S, Person POA, Hultman L, Monemar B. J Appl Phys 2001;90:6011.

[186] Oshima Y, Eri T, Sunakawa H, Usui A. Physica Status Solidi A 2002;194:554.

[187] [Online]. Available, http://www.hitachi-able.co.jp/en/products/news/20030213t.html; 2007.

[188] [Online]. Available, http://www.sei.co.jp/; 2007.

[189] Hanser D, Liu L, Preble EA, Thomas D, Williams M. Materials Research Society Symposium Proceedings 2004;798:Y2.1.1.

[190] Paskova T, Evans K. IEEE. J. Sel Topics Quantum Electronics 2009;15:1041.

[191] Kawaguchi Y, Nambu S, Sone H, Yamagichi M, Miyake H, Hiramatsu K, Sawaki N, Iyechika Y, Maeda T. Mater. Res. Sos. Symp. Proc. 1996;537:G.4.1.

[192] Usui A, Sunakawa H, Sakai A, Yamaguchi AA. Japanese Journal of Applied Physics 1997;36:L899.

[193] Gibart P, Beaumont B, Vennegues P. In: Ruterana P, Albrecht M, Neugebauer J, editors. Nitride Semiconductors, Handbook on Materials and Devices; 2003. ch. X, Wiley-VCH, Berlin.

[194] Paskova T, Valcheva E, Paskov PP, Monemar B, Rockowski AM, Davis RF, Beaumont B, Gibart P. Diamond and Related Materials 2004;13:1125.

[195] Zheleva Tz, Smith SA, Thomson DB, Linthicum KJ, Rajagopal P, Davis RP. J Electron Mater 1999;28: L5.

[196] Sone H, Nambu S, Kawaguchi Y, Yamaguchi M, Miyake H, Hiramatsu K, et al. Jpn J Appl Phys 1999; 38:L356.

[197] Davis RF, Roskowski AM, Preble EA, Speck JS, Heying B, Freitas JA, et al. Proc IEEE 2002;90:993.

[198] Motoki K, Okahisa T, Nakahata S, Matsumoto N, Kimura H, Kasai H, et al. J Cryst Growth 2002; 237–239:912.

[199] Kryliouk O, Reed M, Dann T, Anderson T, Chai B. Mater Sci Eng B 1999;66:26.

[200] Richter E, Hnnig C, Zeimer U, Weyers M, Tranke G, Reiche P, et al. Phys Status Solidi C 2006;3: 1439.

[201] Fujito K, Kiyomi K, Mochizuki T, Oota H, Namita H, Nagao S, et al. Phys Status Solidi A 2008;5: 1056.

[202] Vaudo RP, Xu X, Loria C, Salant AD, Flynn JS, Brandes JR. Phys Status Solidi A 2002;194:494.

[203] Weyers M, Richter E, Hennig C, Hagedorn S, Wernicke T, Trankle G. Proc SPIE 2008;6910:691001.1.

[204] Lucznik B, Pasturszka B, Grzegory I, Bockowski M, Kamler G, Litwin-Staszewska E, et al. J Cryst Growth 2005;281:38.

[205] Grzegory I, Łucznik B, Boćkowski M, Pastuszka B, Kryśko M, Kamler G, et al. Proc SPIE 2006;6121: 612107.

[206] Lucznik B, Pasturszka B, Kamler G, Grzegory I, Porowski S. In: Ehrentraut D, Meissner E, Bockowski M, editors. Technology of gallium nitride crystal growth. Springer series in materials science, vol. 133. Springler; 2009 [chapter 3].

[207] Paskova T, Paskov PP, Birch J, Valcheva E, Abrashev M, Tungasmita S, et al. Proc IWN2000, Nagoya Jpn IPAP Conf Ser 2000;C1:19–22.

[208] Sochalski T, Bryan Z, Amilusik M, Collazo R, Lucznik B, Weyher JL, Nowak G, Sadovyi B, Kamler G, Kucharski R, Zajac M, Doradzinski R, Dwilinski R, Grzegory I, Bockowski M, Sitar Z. Appl Phys Express 2013:6:075504.

[209] Tuomisto F, Saarinen K, Paskova T, Monemar B, Bockowski M, Suski T. J Appl Phys 2006;99: 066105.

[210] Oila J, Kivioja J, Ranki V, Saarinen K, Look DC, Molnar RJ, et al. Appl Phys Lett 2003;82:3433.

[211] Look DC, Reynolds DC, Hemsky JW, Sizelove JR, Jones RL, Molnar RJ. Phys Rev Lett 1997;79:2273.

[212] Look DC, Sicelove JR. Appl Phys Lett 2001;79:1133.

[213] Paskova T, Preble EA, Hanser AD, Evans KR, Kröger R, Paskov PP, et al. Phys Status Solidi C 2009;6: S344.

[214] Goetz W, Kern RS, Chen CH, Liu H, Steigerwald DA, Fletcher RM. Mater Sci Eng B 1999;59:211.

[215] Usikov A, Kovalenko O, Ivantsov V, Sukhoveev V, Dmitriev V, Shmidt N, et al. Mater Res Soc Symp Proc 2005;831:453.

[216] Neugebauer J, Van der Walle CG. Phys Rev Lett 1995;75:4452.

[217] Van der Walle CJ. Phys Rev B 2003;68:165209.

[218] Mathis SK, Romanov AE, Chen LF, Beltz GE, Pompe W, Speck JS. Phys Status Solidi A 2000;179:125.

[219] Hanser D, Liu L, Preble EA, Thomas D, Williams M. Mater Res Soc Symp Proc 2004;798:Y2.1.1.

[220] Fujimori T, Plenary talk at Int Workshop on nitride semiconductors, October 6–10, 2008, Montreux, Switzerland.

[221] Hino T, Tomiya S, Miyajima T, Yanashima K, Hashimoto S, Ikeda M. Appl Phys Lett 2000;76:3421.

[222] Weyher JL, Macht L, Kamber G, Borysiuk J, Grzegory I. Phys Status Solidi C 2003;0:821.

17

Crystal Growth of Diamond

Yuri N. Palyanov[1,2], Igor N. Kupriyanov[1,2], Alexander F. Khokhryakov[1,2], Victor G. Ralchenko[3]

[1]V.S. SOBOLEV INSTITUTE OF GEOLOGY AND MINERALOGY, SIBERIAN BRANCH OF THE RUSSIAN ACADEMY OF SCIENCES, NOVOSIBIRSK, RUSSIA; [2]NOVOSIBIRSK STATE UNIVERSITY, NOVOSIBIRSK, RUSSIA; [3]PROKHOROV GENERAL PHYSICS INSTITUTE, RUSSIAN ACADEMY OF SCIENCES, MOSCOW, RUSSIA

CHAPTER OUTLINE

17.1 Introduction 672
17.2 High Pressure Crystal Growth of Diamond 674
17.2.1 Methods of High Pressure Diamond Synthesis and Growth 674
17.2.1.1 Diamond Synthesis with Metallic Catalysts 674
17.2.1.2 Temperature Gradient Growth Method 675
17.2.2 High Pressure Equipment 675
17.2.2.1 Belt-Type Apparatus 675
17.2.2.2 Toroid-Type Apparatus 676
17.2.2.3 Multi-Anvil Apparatus 676
17.2.2.4 High Pressure Cell for Diamond Growth 678
17.2.3 High Pressure Growth of Main Types of Diamond 678
17.2.3.1 Diamond Classification 678
17.2.3.2 Nitrogen-Containing Type I Diamond 679
17.2.3.3 Nitrogen-free Type IIa Diamond 683
17.2.3.4 Boron-Doped Type IIb Diamond 684
17.2.4 Morphology of HPHT Diamond Crystals 685
17.2.5 Extended Defects in HPHT Diamond Crystals 686
17.2.6 Diamond Crystallization in Non-metallic Systems 688
17.2.6.1 Carbonate-Silicate Systems 688
17.2.6.2 Sulfide-Carbon and Sulfur-Carbon Systems 689
17.2.6.3 C–O–H System 690
17.2.6.4 Diamond Formation through Redox Reactions 690
17.2.6.5 Phosphorus-Carbon System 691
17.2.7 Ultra-High Pressure Synthesis of Bulk Diamond 691

Handbook of Crystal Growth. http://dx.doi.org/10.1016/B978-0-444-63303-3.00017-1
Copyright © 2015 Elsevier B.V. All rights reserved.

17.3 Growth of Diamond from Gas Phase **691**
17.3.1 Introduction 691
17.3.2 Principles of Chemical Vapor Deposition 692
17.3.3 Gas Activation Methods 694
17.3.3.1 Hot Filament CVD 695
17.3.3.2 DC Plasma CVD 695
17.3.3.3 DC Arc-Jet CVD 695
17.3.3.4 Microwave Plasma CVD 696
17.3.4 Epitaxial Growth and Treatment 698
17.3.4.1 High Speed Growth 698
17.3.4.2 Lift-Off Process 699
17.3.4.3 Mosaic Structures 700
17.3.4.4 Postgrowth Treatment 700
17.3.4.5 Doping 701
17.4 Applications **701**
17.4.1 HPHT Diamond Specialties 701
17.4.2 CVD Diamond Specialties 703
17.5 Conclusions **704**
References **705**

17.1 Introduction

Diamond possesses a remarkable range of extreme and outstanding properties superior to other materials. The large band gap, high mobility and saturated velocity of charge carriers, optical transparency in wide spectral range, the highest thermal conductivity, extreme mechanical properties, and resilience to harsh environments rank diamond among the top advanced materials whose development would lead to a major breakthrough in twenty-first-century materials science and engineering. Besides its importance as the strategic future electronic material, diamond has been the classical model object of fundamental research in solid state physics, chemistry, and engineering. It is difficult to overestimate the significance of diamond in the earth sciences, where it serves as an invaluable source of information about the earth interiors. But perhaps the greatest impact that diamond casts upon human civilization is associated with its special role as the gemstone. For centuries it has been treasured for its exquisite beauty and rarity, and it remains a symbol of wealth and prestige.

The history of attempts that have been made to synthesize diamond dates back to the beginning of the nineteenth century when diamond was proved to be an allotrope of carbon. It was not however until the beginning of the twentieth century that the necessity of high pressures to convert graphite to diamond was recognized. Thermodynamic

calculations of Rossini and Jessup [1], Leipunskii [2], and Berman and Simon [3] on the diamond–graphite equilibrium line together with the development of high pressure experimental techniques [4,5] were the important steps that finally led to the successful synthesis of diamond reported by the General Electric (GE) team in 1955 [6,7]. It was approximately at the same time that the possibility of diamond synthesis from the vapor phase was demonstrated [8,9]. Since then, diamond synthesis has become a mature technology as the man-made diamond became a realm for scientists and engineers.

The purpose of this chapter is to give a brief review of the state of the art of bulk diamond growth, the main methods and equipment used for bulk diamond growth, current understanding of the effect of growth conditions on the properties of diamond, and achievements in single crystal growth using high pressure high temperature (HPHT) and chemical vapor deposition (CVD) approaches.

Methods of conversion of various forms of carbon to diamond can be divided into two broad categories depending on whether diamond is thermodynamically stable or not at the synthesis conditions (Figure 17.1). At low pressure in the graphite stable field of the phase diagram diamond may be synthesized using a host of chemical and physical vapor deposition techniques [10]. The state of the art of bulk diamond growth using CVD methods will be considered in Section 17.3. At high pressure in the field of diamond stability, synthesis techniques may be split into the methods of direct graphite-to-diamond conversion, and methods of catalytic diamond synthesis and growth. Due to extreme pressure-temperature (P-T) conditions required for the direct conversion of graphite to diamond, initially only very small polycrystalline diamonds could be produced by this method [11]. Recently, substantial progress in ultra-high pressure techniques has been made [12]; a brief account of the achievements in bulk diamond

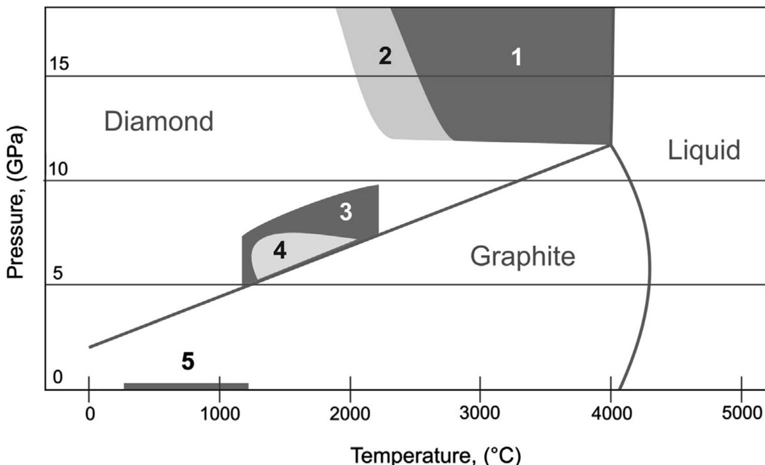

FIGURE 17.1 P-T phase diagram for carbon. Fields of diamond synthesis by various methods are denoted. Direct conversion from graphite under (1) shock-wave compression and (2) static pressure; catalytic synthesis and growth with (3) nonmetallic and (4) metallic solvents; (5) growth via chemical vapor deposition.

synthesis via direct conversion will be discussed in Section 17.2.7. The catalytic synthesis and growth of diamond at high pressures and high temperatures can be achieved using metallic and nonmetallic solvent-catalysts, which will be the major focus of this chapter.

17.2 High Pressure Crystal Growth of Diamond

17.2.1 Methods of High Pressure Diamond Synthesis and Growth

17.2.1.1 Diamond Synthesis with Metallic Catalysts

High pressure synthesis with the metal solvent-catalysts is currently the most elaborated and well-studied process used for manufacturing single crystal diamonds [13]. The group VIII transition metals Fe, Co, and Ni together with Mn, Cr, Ta, and Nb aid to decrease the P-T parameters of the graphite-to-diamond phase transition and are commonly used both in their elemental form and in alloy combinations as the solvent-catalysts [6,7]. Under synthesis conditions, typically 1300–1500 °C and 5–6 GPa, the metal bath is in a molten state and the driving force for diamond crystallization derives from the difference in the solubility of metastable graphite (Figure 17.2, point N) and stable diamond (point M) in the melt at a constant temperature. Several models have been proposed to account for the role of the solvent-catalyst, including pure solvent, pure catalytic, and solvent-catalyst approaches [13,14]. In this method, sometimes called film growth (FG), diamond crystallizes via the diffusion of carbon or carbon species through the surrounding film of metal melt, 0.01–0.1 mm thick. Diamond crystals up to 1 mm in size can be produced by this method. The HPHT diamond synthesis with metal solvent-catalysts is currently the dominant manufacturing process for industrial diamond for abrasive and cutting applications.

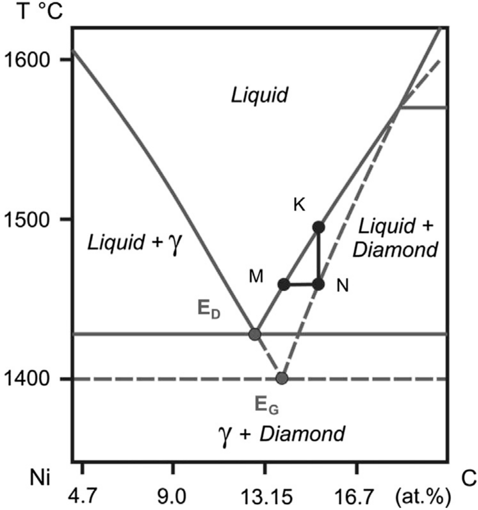

FIGURE 17.2 A fragment of nickel–carbon phase diagram at 5.4 GPa. γ – solid solution of carbon in nickel, E_G – metastable graphite-γ eutectic, E_D – stable diamond-γ eutectic. Points K, M, N are explained in the text. *Adapted with permission from Ref. [15]. Copyright 1967, AIP Publishing LLC.*

17.2.1.2 Temperature Gradient Growth Method

The temperature gradient growth (TGG) method is in fact a variety of the widely used method of crystal growth from solution in melt. For growing diamond, this method was originally developed and applied by the GE scientists, who first produced large diamond crystals weighting about one metric carat (200 mg, 5–6 mm across) in the early 1970s [16,17]. Since fine diamond powder or compact serve as the source of carbon, this method is also referred to as the reconstitution technique. The driving force for crystallization, under diamond stable conditions, is the difference in diamond solubility in the hotter source zone (point K in Figure 17.2) and the cooler crystallization zone (point M), where diamond seed(s) is(are) located. The solvent-catalysts are generally the same as those used for spontaneous diamond synthesis. The solvents are selected in order to have a broad field of the liquid–diamond equilibrium with respect to both temperature and system composition at pressures of about 6 GPa. The ternary systems have as a rule some advantages compared to the constituting binary systems. For instance, the Fe-Ni-C system shows a decreased field of stability of iron carbide, Fe_3C, and increased field of the liquid + diamond equilibrium. For this system, there is a wide region of ternary melts and extended field of diamond crystallization. The temperature difference between the carbon source and the seeded region, which defines the growth rate and is typically 20–50 °C, is set through high pressure cell design. Since its introduction in 1970s, the temperature gradient growth method has been adopted and further developed by the De Beers Diamond Research Laboratory (UK, South Africa) and Sumitomo Electric Industries (Japan), who, along with GE, became the major producers of HPHT synthetic diamonds.

17.2.2 High Pressure Equipment

The progress in bulk diamond growth is essentially connected with the development of high pressure techniques capable of creating relevant pressures (5–6 GPa) and temperatures (1350–1500 °C) and maintaining them stable over the period of 50–100 h and longer. There are several types of high pressure apparatus that are now routinely used for diamond growth by the temperature gradient growth method.

17.2.2.1 Belt-Type Apparatus

The basic construction of the belt-type apparatus was developed by Tracy Hall [18] (Figure 17.3). A modification of this apparatus, called flat belt (FB), was later developed by Japanese scientists [19]. A powerful press (up to 300 MN) and efficient massive support of the anvils and belt matrix enable the creation of necessary pressures in the reaction volume of several hundred cubic centimeters. The effective thermal isolation of the high pressure cell and cooling system enable growth cycles of more than 10 days long. It is the belt-type apparatus with which the pioneering works on the synthesis of diamond [6,7] and diamond growth by the temperature gradient growth method [16,17] were accomplished. De Beers and Sumitomo, using belt-type equipment, have made substantial progress in growing diamond crystals [20].

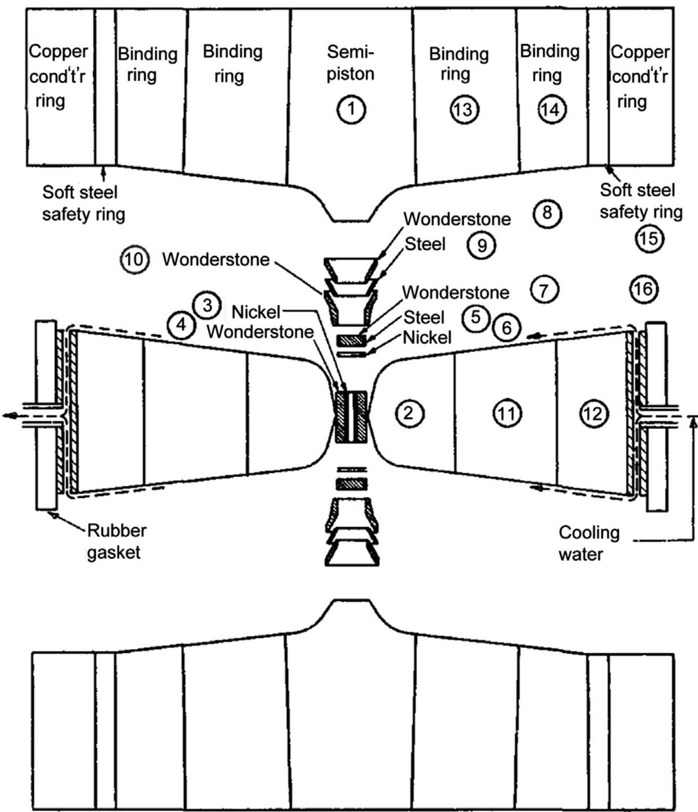

FIGURE 17.3 The belt-type high temperature, high pressure apparatus. "Exploded" assembly. *Reprinted with permission from Ref. [18]. Copyright 1960, AIP Publishing LLC.*

17.2.2.2 Toroid-Type Apparatus

Apparatus of this type are based on the concept of the Bridgman anvils. The history of the development of this high pressure equipment, and its capabilities and applications, have been reviewed by Khvostansev et al. [21]. A relatively simple and technologically feasible technique called *chechevitsa* (lentil) was developed in the 1960s at the Institute of High Pressure Physics of the Russian Academy of Science and was widely used in the USSR for industrial production of abrasive synthetic diamonds. Further development of this technique led to the invention of the toroid apparatus (Figure 17.4) [22]. It operates on the principle of uniaxial compression and enables pressure and temperature conditions of diamond synthesis in the reaction volume of about 10 cubic centimeters. With subsequent modifications, this equipment has been successfully applied for growing large diamond crystals [23–26].

17.2.2.3 Multi-Anvil Apparatus

One of the first apparatus of this type was developed by Von Platen [27]. Later a series of multi-anvil apparatus capable of producing pressures up to 30 GPa were developed in

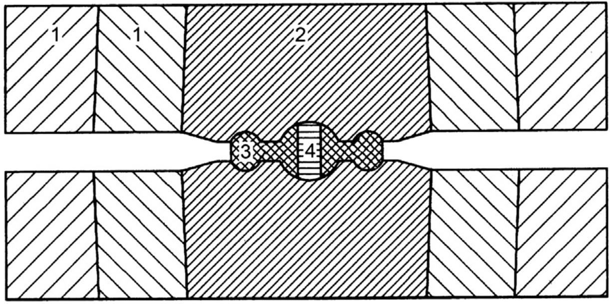

FIGURE 17.4 The toroid-type apparatus. 1 – hardened steel; 2 – WC-Co hard alloy; 3 – lithographic stone; 4 – sample and heater. *Redrawn with permission from Ref. [22].*

Japan. Kawai [28] proposed several modifications of one- and two-stage multi-anvil devices, which created the basis for the progress in multi-anvil techniques. Recently, a comprehensive review of this type of high pressure equipment has been made by Lieberman [29].

At the Institute of Geology and Geophysics, Siberian Branch of the Academy of Sciences, USSR work on the development of multi-anvil apparatus began in the 1970s. Initially an apparatus of "split-cube" type was developed [30]. The next step was the development and construction of a series of multi-anvil apparatus of "split-sphere" type [31,32]. In this apparatus, a block of anvils is placed in a split casing with a spherical inner cavity, which is locked with a flange. The hydrostatic pressure is created by oil injected by a pump into the space between semispheres and rubber membranes covering the anvil block (Figure 17.5). Using this equipment, which became known by Russian abbreviation BARS, first synthetic diamonds weighting about one carat were produced in Russia [33]. At present a modernized BARS apparatus with a two-stage anvil block of 8-6 scheme and a tetragonal high pressure cell is used for diamond growth by the TGG method [34]. An efficient system of water cooling of the outer and inner anvils enables stable growth cycles of a hundred hours long.

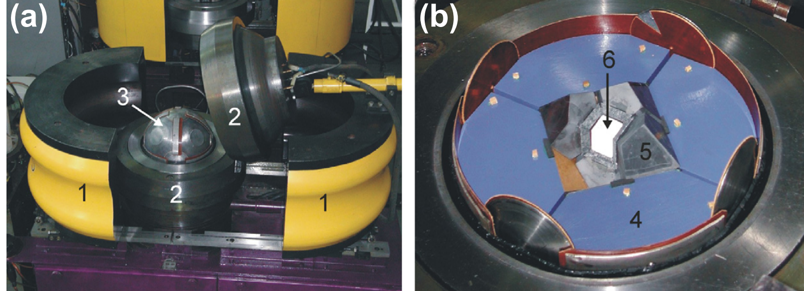

FIGURE 17.5 High pressure apparatus of the split-sphere type (BARS): (A) general view, (B) split-sphere multi-anvil block. 1 – clamps, 2 – assembly with semisphere cavities, 3 – multi-anvil block (diameter 300 mm), 4 – steel anvils, 5 – tungsten carbide anvils, 6 – high-pressure cell. *Reprinted with permission from Ref. [34]. Copyright 2010, American Chemical Society.*

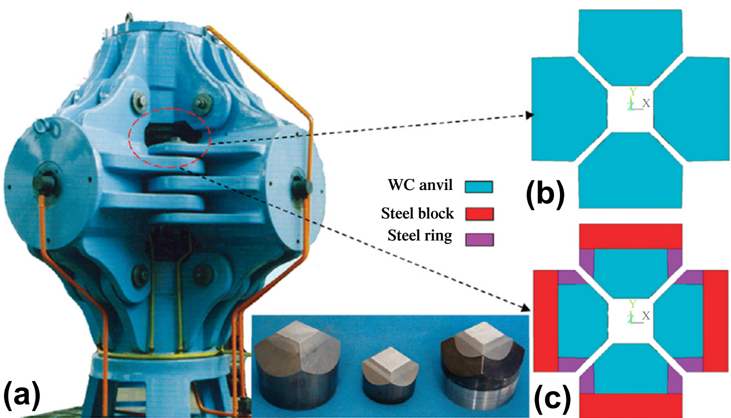

FIGURE 17.6 Optical photo of the CHPA. (A), the cross-section of the multi-anvil assembly for traditional anvils (B), and the cross-section of the multi-anvil assembly for hybrid anvils (C). The inset shows the optical photo of anvils. *Reprinted with permission from Ref. [35]. Copyright 2011, American Chemical Society.*

Recently, significant progress has been achieved by Chinese scientists in the development of the cubic high pressure apparatus (CHPA) and its adaption to the growth of diamond by TGG method (Figure 17.6) [35]. This is a one-stage apparatus with hybrid anvils based on the original design of Tracy Hall. Han et al. [35] presented a review of the results on the growth of various types of gem quality, relatively large single crystal diamond using CHPA apparatus.

17.2.2.4 High Pressure Cell for Diamond Growth

Although the configuration and design of the high pressure cells used in the above apparatus are rather different, the schemes of the crystallization chambers are similar in principle. As an example, the scheme of the high pressure cell used for diamond growth on the BARS apparatus is shown in Figure 17.7.

17.2.3 High Pressure Growth of Main Types of Diamond

17.2.3.1 Diamond Classification

Most of the physical properties of diamond are significantly affected by impurities present in diamond crystals as point defects. The dominant impurity in both natural and synthetic diamonds is nitrogen, which may be present in the diamond in various structural forms. The classification of diamond is based on the concentration and aggregation stage of nitrogen. Depending on nitrogen concentration, diamonds are divided into type I, nitrogen-containing, and type II, containing less than c. 1 ppm of nitrogen. Type I diamonds are further subdivided into type Ib, containing nitrogen impurity in the form of single substitutional atoms (C-centers), and type Ia, containing aggregated nitrogen forms (A- and B-centers). An overwhelming majority (~98%) of natural diamonds correspond to type Ia with maximum nitrogen concentrations up to 3000–5000 ppm. Most synthetic

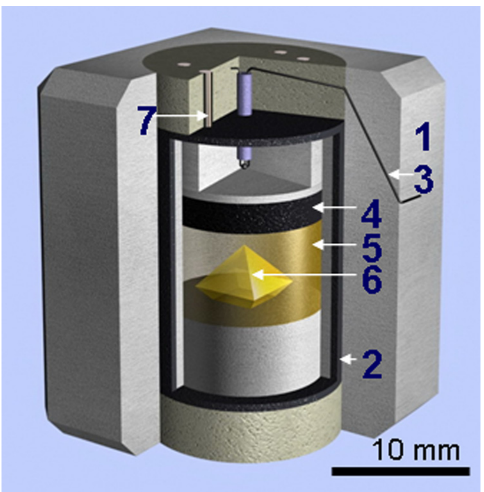

FIGURE 17.7 High pressure cell used for diamond growth with BARS equipment at the IGM SB RAS. 1 – ZrO_2 container, 2 – graphite heater, 3 – thermocouple, 4 – graphite (source of carbon), 5 – metal solvent-catalyst, 6 – growing diamond crystal, 7 – electric supply. *Adapted with permission from Ref. [34]. Copyright 2010, American Chemical Society.*

diamonds correspond to type Ib with nitrogen concentrations typically in the range 100–300 ppm. The formation of the aggregated forms of nitrogen is known to proceed through thermally activated migration of nitrogen atoms in the diamond lattice and their aggregation [36,37]. Type II diamonds are also subdivided into two different classes: type IIa diamond is relatively free from extrinsic impurities, while type IIb diamond has boron as the major impurity. Type IIb diamonds are semiconductors with *p*-type conductivity.

17.2.3.2 Nitrogen-Containing Type I Diamond

The isolated substitutional nitrogen (C-centers), which is the dominant form of nitrogen impurity in synthetic diamonds, behaves as a deep donor, with an ionization energy of around 1.7 eV. The photoionization of nitrogen donors gives rise to continuum absorption at wavelength shorter than about 600 nm, which is responsible for typical yellow or brown coloration of type Ib diamonds. The A-form nitrogen (a pair of nitrogen atoms in neighboring substitutional positions) is less common but also important for synthetic diamonds. The A-centers form a very deep donor level ($\sim$4 eV) and produce no absorption in the visible range, making type IaA diamond colorless.

The incorporation of nitrogen in diamond crystals shows a distinct growth sector dependence. Synthetic diamonds grow with a cubo-octahedral morphology, often modified by minor {113} and {110} faces. Under standard growth condition, 1300–1450 °C and 5.5 GPa, nitrogen concentrations are the highest in the {111} growth sectors, typically 100–300 ppm for diamonds grown using Fe-Co and Fe-Ni solvent-catalysts. The average nitrogen concentration in the {100} is generally two or more times lower than that for the {111} sectors. It was shown that at comparatively low growth temperatures, cubic growth

sectors may predominate and contain higher nitrogen concentrations than the {111} sectors [38]. However, it is thought that the low growth temperature is not the only prerequisite for growth of cubic diamond, and some other factors such as chemical composition or oxidation state of the growth system should be considered. Nitrogen concentrations in the minor growth sectors, that is {110} and {113}, are about an order of magnitude lower compared with the {111} and {100} sectors. Within a given growth sector, nitrogen also demonstrates inhomogeneous distribution caused by both local variations and long-term changes in the growth conditions. These variations are not necessarily due to the extrinsic factors such as insufficient stability of the input power or applied pressure, but can be related to some intrinsic features of diamond growth such as convective flows in the metal melt or effects of accumulation and diffusive relaxation of impurities at the growth front. The pronounced growth sector dependence of nitrogen distribution is evidence that its incorporation in the growing diamond is nonequilibrium and governed mainly by the growth kinetics and surface processes. The sources of nitrogen in synthetic diamond are the nitrogen impurities in the solvent metal and carbon source material, as well as the atmospheric nitrogen in the pore space in the high pressure cell components. It was shown that when using reaction mixtures pretreated at a high temperature and a high vacuum it was possible to grow diamond crystals with substantially reduced nitrogen concentrations [39]. The nitrogen take-up is also affected by the nitrogen solubility of the metal solvent-catalyst; the higher the solubility, the lower the amount of free nitrogen that may incorporate into the diamond. The solubility effect is thought to be responsible for decreasing nitrogen concentrations in diamonds grown using metals with a higher deficiency in d-shell electrons, e.g., iron, and/or at relatively high temperatures [40,41]. The growth rate is also reported to affect the concentration of nitrogen in diamond [42,43]. In general, higher growth rates promote higher nitrogen concentrations in the grown crystals. Considering the effect of the growth temperature, another important phenomenon, which is related to the process of nitrogen aggregation, should be taken into account. It has been found [44–48] that diamonds grown using nickel or cobalt-based solvent-catalysts at temperatures of about 1450–1500 °C and higher show a significant portion of nitrogen in the aggregated form, as the A-centers, and correspond to the mixed Ib + IaA type. The A-centers in as-grown diamonds tend to dominate in the inner regions of a crystal. Although temperatures of about 1500 °C are less than those typically used in the annealing experiments (1700–2000 °C) [37], given the high duration of the growth runs, typically several tens of hours, it is reasonable that the inner parts of a crystal underwent annealing during the growth.

As noted above, there is an essential difference between natural and synthetic diamonds in respect of both predominant form of nitrogen impurity and typical nitrogen concentrations. The first one can now be well explained by the prolonged annealing of natural diamonds during their residence in the earth's mantle. The second one is less clear, but obviously due to the difference in the growth environments. There have been several studies addressing the question of how much nitrogen can be incorporated in synthetic diamonds. Kanda et al. [49] synthesized diamonds from nonmetallic

solvent-catalysts such as Na_2CO_3 and Na_2SO_4 and found that they may contain 1200 to 1900 atomic ppm of nitrogen atoms. Borzdov et al. [50] studied diamond crystallization in the Fe_3N-C system at 7 GPa and 1550–1850 °C and found that at temperatures of 1700 °C and higher iron nitride acted as the solvent-catalyst for diamond synthesis. Infrared absorption measurements revealed that the crystallized diamonds contained very high amount of nitrogen, up to 3300 ppm. This apparently is the highest value reported so far for synthetic diamonds and close to the maximum concentrations found in natural diamonds. The special role of the nature of the solvent-catalyst in the processes of nitrogen incorporation in diamond was demonstrated in studies on diamond crystallization using nonmetallic solvent-catalysts. It has been shown that diamonds synthesized from such solvents may contain high nitrogen concentrations even if no nitrogen was deliberately added to the growth system. For instance, diamonds produced using sulfur [51], sulfides [52], and carbonates [53] as the solvents, or in complex carbonate-oxide-sulfide systems [54] were found to contain 1000–1500 ppm of nitrogen. Several studies were performed on diamond synthesis using metal solvent-catalysts with various nitrogen additives, NaN_3, $Ba(N_3)_2$, and P_3N_5 [55–57]. Diamond crystals up to 0.5 mm in size were synthesized in these works via the spontaneous crystallization at 5.0–6.3 GPa and 1250–1550 °C. These crystals contained up to about 2000 ppm of nitrogen mainly in the single substitutional C-form and had specific green color. The effect of nitrogen impurity on diamond crystal growth was studied recently in detail by Palyanov et al. [34]. The experiments were performed at 5.5 GPa and 1400 °C for 65 h in the FeNiC system with different concentrations of Fe_3N and $CaCN_2$ additives. The temperature gradient growth method on seed crystals was applied. It was found that an increase in nitrogen concentration in metal melts results in an increase in the concentration of nitrogen impurity in diamonds up to about 1100 ppm. As nitrogen concentration increased, the crystals attained a specific green coloration. Optical absorption measurements made for these crystals showed a specific broad absorption band with maximum at around 660 nm, whose intensity increased with nitrogen concentration. In combination with the absorption related to C-centers, this band gave rise to the greenish component in the color of nitrogen-doped diamonds. The nature of the 660-nm absorption band is not clear at the moment.

It is generally believed that due to small covalent radius of the sp3-configured carbon atom and the rigidity of the diamond lattice, only light elements like H, B, and N can incorporate into diamond as point defects. Therefore, it comes as a surprise that transition metals Ni and Co were identified to be able to enter the diamond lattice in the atomically dispersed form. The first indication on the possibility of nickel incorporation into the diamond came from the results of Loubser and Van Ryneveld [58]. They detected a specific electron paramagnetic resonance (EPR) center (W8 center) in polycrystalline synthetic diamonds made with Fe-Ni solvent/catalyst, which was absent for diamonds grown without nickel. The involvement of nickel in the W8 center was confirmed by observing hyperfine splitting from ^{61}Ni [59], and the center was associated with negatively charged substitutional nickel [60]. Later it was found that diamonds grown using

nickel-containing solvent-catalysts show a number of specific optical absorption and luminescence bands, which were assigned to Ni-related centers [61]. Collins et al. [62] observed that the relative intensities of the different nickel-related absorption bands depend on the composition of the nickel-containing solvent-catalyst and that all the optical features attributed to nickel are confined exclusively to the octahedral growth sectors of diamond. The concentration of nickel impurity in diamond may reach several tens ppm, but in most cases it is less than 1 ppm [63]. A rich variety of optical and paramagnetic centers were found in synthetic diamonds grown with Ni or Co solvents and annealed at temperatures where nitrogen atoms are mobile ($\geq$1500 °C). Nickel- and cobalt-related defect centers in synthetic diamonds have been extensively studied in numerous experimental and theoretical studies, resulting in relatively good understanding of these defects (see reviews [61,63] and references given therein).

An important aspect of nickel and cobalt impurities in synthetic diamond is their influence on the kinetics of the aggregation of nitrogen from single substitutional C-form to the paired A-form. Fisher and Lawson [64] and Kiflawi et al. [65] found that the presence of Ni- or Co-related defects significantly enhanced the process of the aggregation of nitrogen, and that the aggregation did not follow second-order kinetics. It has been proposed that the enhancement is achieved either by the release of vacancies from Ni-vacancy or Co-vacancy complexes, which in turn assist in the migration of nitrogen, or through the release of carbon interstitials that in turn release highly mobile nitrogen interstitials.

Nitrogen-containing type Ib or mixed type Ib + IaA synthetic diamonds are currently the major commercially available product. For this material, growth rates as high as 15 mg/h have been achieved [66], but more commonly high quality inclusion-free diamond crystal are grown at rates within 3–6 mg/h. Typical diamond crystals produced with BARS technique are shown in Figure 17.8. The record synthetic diamond crystal produced by HPHT method weights 34.80 ct and was grown by the De Beers Diamond Research Laboratory for research purposes in 1992.

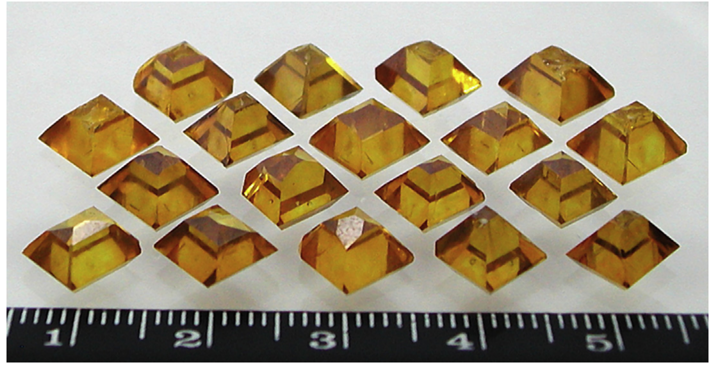

FIGURE 17.8 Typical diamond crystals produced at the IGM SB RAS using BARS equipment.

17.2.3.3 Nitrogen-free Type IIa Diamond

Diamond crystals with very low content of impurities, first of all nitrogen, are of key importance for many existent or prospective applications of diamond. The most commonly used approach to reduce the amount of nitrogen in the grown crystals relies on the addition to the growth system of elements with a high affinity to nitrogen [16,17]. These elements, typically Ti, Al, and Zr, act as nitrogen getters by forming stable or transient nitrides. The realization of this relatively simple idea to grow large, high quality diamond faces has, however, had a number of obstacles. The presence of nitrogen getters strongly affects the properties of the growth system. The growing diamond crystals tend to entrap metallic inclusions, thought to be due to a decrease in the solubility of carbon in the melt and/or prevention of carbon transport in the melt. Consequently, to produce high quality type IIa diamonds without metallic inclusions, the growth rate had to be decreased to less than 1.5 mg/h, requiring several hundreds of hours to grow 1-2 ct crystals [16]. Comprehensive investigations into the growth of type IIa diamonds were reported by Sumiya et al. [66,67] and Burns et al. [41]. It has been demonstrated that with an adequate selection of the solvent-catalyst composition, type and amount of nitrogen getter and additives suppressing the formation of carbides, and with prolonged maintenance of a high precision temperature control, high quality type IIa diamonds weighting 7-8 ct ($\sim$10 mm across) can be produced at growth rates as high as 6–7 mg/h [67]. Recently, successful synthesis of large type IIa diamond crystals measuring up to 12 mm in diameter ($\sim$10 ct) has been reported [68]. These crystals (Figure 17.9) contain less than 0.1 ppm of nitrogen and are free from dislocations and stacking faults in areas as large as $5 \times 5\ mm^2$.

It should be noted that for diamond crystal growth as a whole and for growth of type IIa diamonds in particular, it turns out that the optimal growth conditions developed by one group may not work as well or even be easily adopted with other diamond-growing groups. Although the general principles and approaches are common, each group has to invent its own "receipt" to get the best results. This is partly due to the different high pressure cell designs and materials of the cell components used by different groups. Typical conditions employed for growing type IIa diamonds can be summarized as

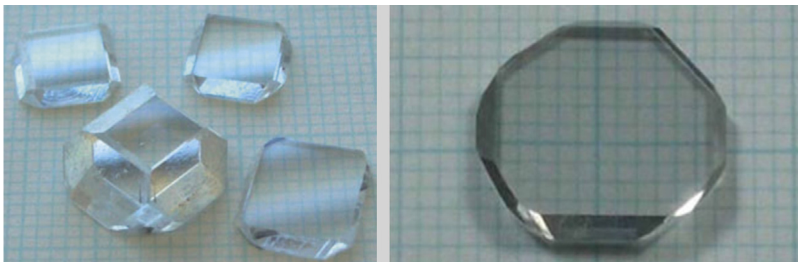

FIGURE 17.9 Large synthetic type IIa diamond crystals. Right: the largest diamond plate prepared from a large crystal of 12-mm diameter. *Reprinted with permission from Ref. [68]. Copyright 2012, The Japan Society of Applied Physics.*

follows. A Co-Fe alloy, typically in 40/60 proportion, or pure iron is used as the solvent-catalysts, with Ni being excluded due to its ability to enter diamond lattice. Ti and Al in amounts up to 2 and 3 wt%, respectively, are used as the nitrogen getters. Cu in amounts 1–3 wt% may be added to suppress the formation of carbides. Growth temperatures are within 1320–1500 °C at 5.5–6 GPa. However, the presence of getter components has the effect of reducing the range of temperatures in which well-formed diamond crystals will grow. At too low a temperature there is a competing process of precipitation of carbides and resorption of the diamond crystals. If the temperature is too high, the crystals tend to entrap metallic inclusions [66–69].

17.2.3.4 Boron-Doped Type IIb Diamond

Boron is an important impurity in diamond. So far, it is the only element that forms in the diamond lattice an acceptor state shallow enough ($E_a = 0.37$ eV) to produce *p*-type conductivity and which can be incorporated with high reproducibility and high enough concentration to be useful for electronic applications. Besides, recent discovery of superconductivity in heavily boron-doped diamonds [70] sparked new interest to this material. Diamonds containing uncompensated boron acceptors are extremely rare in nature and are highly prized especially for their blue color. It suffices to mention the famous 45 ct Hope Diamond or 35 ct Blue Wittelsbach-Graff Diamond.

Optical and electrical properties of boron-doped diamonds as well as the procedures of boron doping have been comprehensively studied in numerous works, resulting in a plethora of data concerning boron impurity in diamond (for details, see reviews [71,72] and references given therein). Type IIb diamonds have a characteristic infrared absorption consisting of a series of relatively sharp zero-phonon peaks at 2455, 2802 and 2928/cm, which are due to bound-hole transitions, a photoionization continuum, starting at around 3000/cm, and boron-induced one-phonon absorption band peaking at 1290/cm. The photoionization continuum extends into the visible part of the spectrum and produces the characteristic blue color of type IIb diamonds.

To produce boron-doped *p*-type semiconducting diamond, the incorporation of nitrogen impurities should be effectively suppressed. This implies that the general approach to the growth of type IIb diamonds is basically the same as for the type IIa diamonds, but with the addition of boron or boron-containing compounds to the growth system. In most cases, Fe-Al-C or Co-Fe-Ti/Al-C system compositions are used. As with nitrogen, the rate of boron incorporation in different types of growth sectors is markedly different. Burns et al. [73] studied the growth sector dependence of boron uptake in synthetic diamond for various amounts of added boron and various solvent/catalysts. Most effectively boron incorporates into the {111} growth sectors, but since the concentration of nitrogen is also highest for the {111} sectors of diamonds grown both with and without nitrogen getters, the amount of boron additive necessary to produce uncompensated acceptors is the highest for the {111} sectors. Boron concentrations as high as $>10^{20}/cm^3$ are reported for synthetic diamonds [71]. For low doping levels, Sumiya and Satoh [66] showed that approximately 1–2% of boron present in the carbon source

may be included in the grown diamond. Blank et al. [25] demonstrated that the concentration of boron incorporated in the {100} and {111} growth sectors increases with increasing growth temperature.

17.2.4 Morphology of HPHT Diamond Crystals

The morphology of synthetic diamond is determined by the major {111} and {100} faces and minor {311} and {110} faces. The relative development of these faces is influenced by the P-T conditions, growth system composition, and growth rate. With increasing temperature at a constant pressure, the crystal habit changes from cubic to octahedral. Depending on the solvent-catalyst composition and growth conditions, diamond crystal of higher quality is produced either at medium temperatures where cubes and cuboctahedrons are stable [66,74] or at higher temperatures where the stable form is octahedron [47,75,76]. The morphology is influenced by the growth rate. As the growth rate decreases, the relative development of minor faces {110} and {113} increases [46]. The composition of the solvent-catalyst and the presence of impurities also significantly influence the morphology of diamond crystals. Palyanov et al. [34] found that with increasing nitrogen concentration in the Fe-Ni solvent, the rate of diamond crystal growth decreases and the morphology of the crystals changes in the sequence: $\{111\} > \{100\},\{311\},\{110\} \rightarrow \{111\} > \{100\},\{311\} \rightarrow \{111\} >> \{100\}$. With further increases in nitrogen concentration in the melt, the stage of single crystal growth is followed by the formation of block crystals and then crystal aggregates with intense polysynthetic microtwinning. Diamond crystals grown with the addition of nitrogen getters frequently exhibit rather complicated habit due to significant development of the {113}, {110} and sometimes {115} or {117} faces [16,41,73]. The abundance of these otherwise minor faces may be a combined effect of a reduced nitrogen activity in the melt and a low growth rate, typical of nitrogen-gettered diamonds.

The influence of boron impurities on the morphology of diamond crystals in most detail was considered in [25]. Diamond crystals were grown in Fe-Al-C system at 1440 °C. It was found that increasing the added amount of boron leads to the morphology variation of the grown crystal. Undoped and lightly doped crystals were covered by the dominant {100} and {111} faces and minor {113} and {110} faces. As the amount of boron increased, the {111} faces became dominant, {113} and {110} faces became more prominent, and minor {115} facets were present. At 1.2 wt% of boron added, the habit became octahedral, and at 3.3 wt% skeleton crystals or clusters grew.

Of particular interest is the effect of surface-active impurities, which do not enter diamond structure but significantly affect the processes of diamond crystallization. For instance, the special role of H_2O impurity inducing drastic changes in diamond morphology and growth of crystals with dodecahedral habit was originally established in the 1980s [77,78] and confirmed recently [79]. In other work, the influence of H_2O additive on the growth and morphology of the diamond has been systematically studied [80]. It is found that the impurity adsorption effect leads to growth inhibition followed by

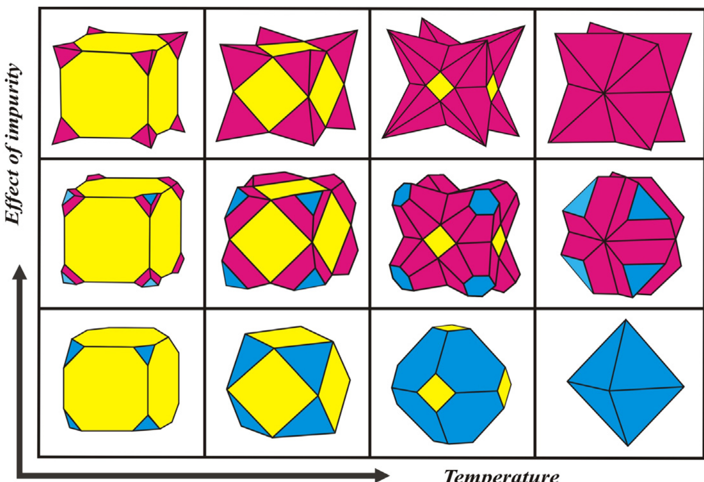

FIGURE 17.10 General scheme of the effects of crystallization temperature and impurity adsorption on diamond crystal habit. The {100} faces are shown by light gray (yellow), {111} faces – dark gray (blue), and side surfaces of the {111} pyramids – gray (red) colors. *Reprinted with permission from Ref. [80]. Copyright 2013 American Chemical Society.*

complete blocking of growth of the {100} faces. At these conditions, the {111} faces continue to grow but reduce in area due to the inhibition of the ends of the {111} growth layers. As a result, a rich morphological diversity of antiskeletal diamond crystals is produced, whose growth and design are determined by the impurity adsorption effect and crystallization temperature (Figure 17.10).

17.2.5 Extended Defects in HPHT Diamond Crystals

Along with impurities and point defects, diamond crystals may contain various extended defects, such as dislocations, stacking faults, and microtwins, which affect crystalline perfection. The control over these defects is essential for growing high quality diamond crystals. Extended defects in diamond have been investigated using a suite of X-ray diffraction methods [81–83]. Khokhryakov and Palyanov [84,85] demonstrated that selective etching in KNO_3 or $NaNO_3$ melts at 700–750 °C can be used as an effective method to study dislocations in synthetic diamond crystals. From the established correlation between the etch pits and dislocations emerging on the {111} faces, the types of dislocation can be identified [76].

It is known that dislocations are unevenly distributed in the diamond crystals. The highest densities of dislocations are typical for the {111} growth sectors (Figure 17.11). Dislocations are less common in the {100} growth sectors and can entirely be absent in {100} sectors of type IIa diamonds (Figure 17.11(d)) [68,69,86]. The density of dislocations in the {111} growth sectors varies from 10 to $10^6/cm^2$ depending on the growth temperature, rate of crystal growth, and nitrogen impurity concentration [34,46,47,76,83].

The influence of the growth rate on the density of dislocations and planar defects in diamond crystals grown in the NiFe-C system has been reported [46]. It is shown that the dislocation density in the {111} growth sectors increases from about 10 to

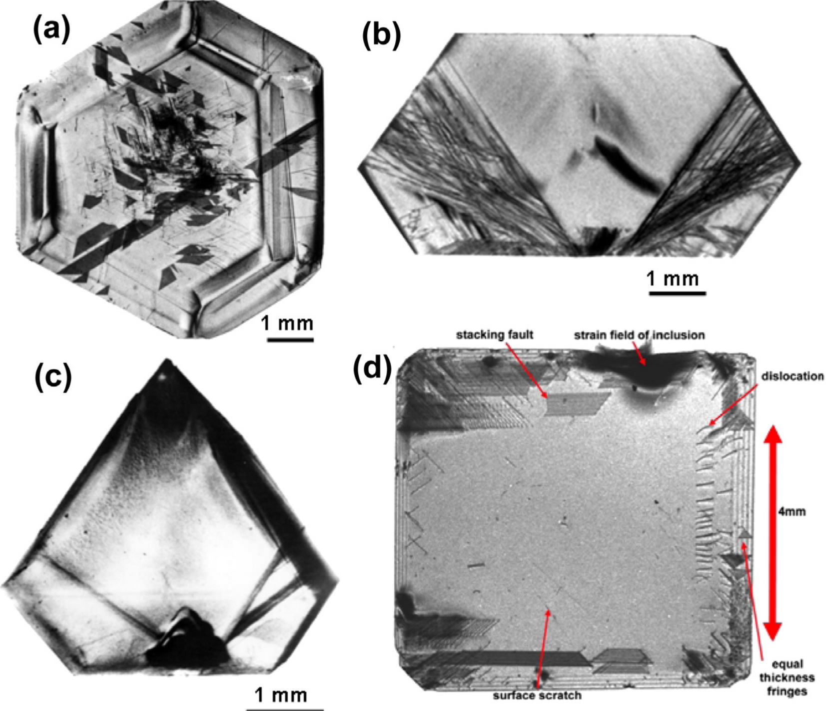

FIGURE 17.11 X-ray topographs of (a,b) ordinary and (c,d) high quality synthetic diamond crystals. *Topographs (a) and (c) are reprinted from Ref. [87]; topograph (d) is reprinted with permission from Ref. [69]. Copyright 2009, The IOP Publishing LTD.*

$10^4/cm^2$ as the growth rate increased from 0.8 to 9.9 mg/h. The influence of nitrogen impurities on the dislocation structure of diamond crystals is reported in refs. [34,88]. It is established that the density of dislocations increases from 80 to $100/cm^2$ to $4.0 \times 10^3/cm^2$ as the nitrogen content in crystals increases from 1 to 10 ppm to 600 ppm.

Dislocations are known to form in diamond crystal bundles and fans. Most dislocations extend from the seed crystal and can be inherited from the seed or arise during the regeneration of the surface of the seed crystal [46,76,83,89]. The use of seed crystals of high crystalline perfection allows growing large type IIa diamond crystals with low content of linear defects [68,86]. Inclusions of foreign phases are another source of dislocation. Synthetic diamond crystals may contain relatively large metallic inclusions and polyphase microinclusions, the so-called "pin-point" inclusions [90]. These inclusions cause significant stress in the diamond [91] and therefore can also be a source of dislocation.

Nitrogen-containing synthetic diamond crystals with very low content of extended defects were grown at high growth temperatures (1600 °C) and low growth rates (0.8–1.5 mg/h) [47,87]. These octahedral crystals contained single dislocations and

stacking faults, which are located in the bottom part of the crystals. Most of the crystal volume is free of defects, as revealed by X-ray topography (Figure 17.11(c)).

Planar defects in {111} planes include microtwins and stacking faults in synthetic diamond. Planar defects in {111} planes revealed in synthetic diamonds by X-ray topography are supposed to be stacking faults [82,83,86]. Stacking faults often have a shape of a triangle, trapezoid, or another polygon (Figure 17.11(b)). They also form V-shaped defects and tetrahedral stacking faults. It is established then that the density and size of stacking faults to a great extent depend on the growth rate [46,87]. Large stacking faults and low dislocation density characterize diamonds grown at low growth rate. With increasing growth rate, the sizes of stacking faults decrease.

17.2.6 Diamond Crystallization in Non-metallic Systems

HPHT diamond crystallization aided by nonmetallic solvent-catalysts has been actively studied since the 1990s. The main objectives of these studies are connected with the fundamental aspects of diamond nucleation and growth, modeling natural diamond-forming processes, as well as with the development of new routes of synthesizing diamond crystals with specific and unusual properties.

Modern concepts and models of diamond genesis are based on quite different viewpoints suggesting a wide range of P-T conditions for this process in the upper and lower mantle. For example, it is supposed that silicate, sulfide, metal, and carbonate melts can be favorable media for diamond crystallization. Given the complicated multicomponent compositions of natural environments, it is very important to understand which components are directly responsible for diamond formation.

17.2.6.1 Carbonate-Silicate Systems

At the beginning of the 1990s, the first report appeared about the synthesis of diamond in carbonate–carbon systems at 7.7 GPa pressure and 2000 °C or higher temperatures [92]. First data on diamond synthesis in carbonate–silicate melt (kimberlite) at 7–7.7 GPa and 1800–2200 °C were reported by Arima et al. [93]. Subsequent studies revealed the kinetic character of diamond nucleation and growth and showed the possibility of decreasing P-T parameters of diamond crystallization in the carbonate–silicate melts [53,94,95]. It was established that the processes of diamond crystallization, namely film growth and temperature gradient growth, described by Kanda and Fukunaga [40] for metal–carbon systems, are also typical for diamond crystallization in nonmetallic systems [53,96]. As opposed to the metal–carbon systems, diamond crystallization in nonmetallic systems is characterized by a substantial induction period, whose duration depends on P-T parameters and composition of the crystallization medium [95,97].

Given the significance of silicate systems, the interaction of dry alkaline silicate melt with graphite was studied [98]. No diamond nucleation was observed; even on the seed crystals no traces of growth or dissolution were revealed at 7 GPa and 1750 °C. These

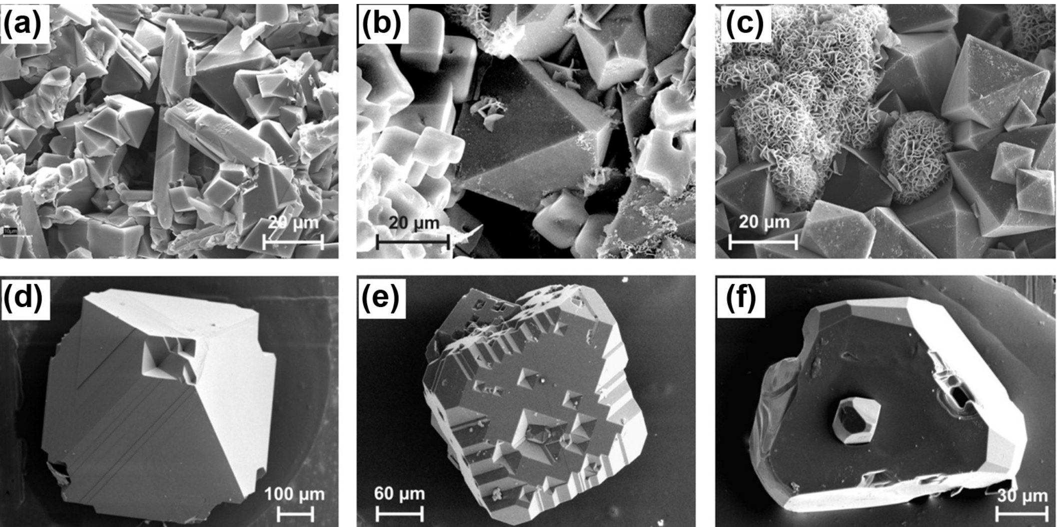

FIGURE 17.12 SEM micrographs of diamond and quench phases from runs in (a) Mg_2SiO_4-H_2O-C (b) KCl-H_2O-C and (c) H_2O-C systems [95]; a seed diamond crystal after the experiment in the $(Fe,Ni)_9S_8$-C systems (d) [52]; diamond crystals synthesized in (e) S-C system *(Adapted with permission from Ref. [51]. Copyright 2009 American Chemical Society.)*. and (f) P-C system. *Adapted with permission from Ref. [110]. Copyright 2011, American Chemical Society.*

media became diamond forming [98,99] only when carbonates or water were added. These results are in good agreement with data on micro- and nanoinclusions in natural diamonds [100–104].

Diamond crystallization has been studied in different subsystems modeling natural diamond-forming environments [93–95,105,106]. The general tendency for carbonate-silicate melts consists in decreasing the degree of graphite-to-diamond conversion with increasing silicate content in the crystallization medium. Water has been shown to play a special role in diamond crystallization in modeling media [99,107,108]. Experiments demonstrate that the degree of the graphite-to-diamond conversion is a function of the concentration of water, which controls both the kinetics of diamond nucleation and the intensity of carbon mass transfer in the water containing silicate, carbonate, and chloride systems (Figure 17.12(a,b,c)). The minimal P, T parameters of diamond nucleation were established for alkaline carbonate–fluid (H_2O, CO_2) systems at 5.7 GPa and 1150 °C [109].

17.2.6.2 Sulfide-Carbon and Sulfur-Carbon Systems

Sulfide minerals are the commonest among inclusions observed in natural diamond [111,112] that led to the development of a concept of an essential role of sulfides in the natural diamond formation processes [113]. To test the sulfide model of diamond genesis and determine the boundary conditions of its applicability, interaction of sulfide melt with graphite over a broad range of pressures and temperatures was studied [55]. The minimal P-T parameters for spontaneous diamond nucleation in sulfide melts are 7.5 GPa and 1600 °C. The stable growth form of diamond in sulfide melts is octahedron

and does not depend on the P-T parameters (Figure 17.12(d)). Studies on diamond crystallization in the sulfur-carbon (S-C) system are also of importance for understanding the conditions of natural diamond formation [114]. It is established that the minimal P-T conditions of spontaneous nucleation of diamond in the S-C system are determined by both temperature and pressure [51]. In the S-C system, with an increase in crystallization temperature, the morphology of diamond crystals changes gradually from cubic habit to octahedral habit (Figure 17.12(e)).

Thus, based on the experimental data obtained, the sulfide model for natural diamond genesis at 5–6 GPa and 900–1400 °C seems unlikely. In the system Ni–Fe–S–C, the melt reactivity (in terms of their capability for diamond formation) follows the sequence: metal >> sulfur > sulfide.

17.2.6.3 C–O–H System

The C–O–H system represents a particular interest. It can be to some extent considered as an analog of the crystallization media of CVD diamond, and a simplified model of the mantle diamond-forming fluid. Diamond crystallization in the system H_2O–C at 7.7 GPa and 2000–2200 °C was first reported by Yamaoka et al. [115]. Subsequently, systematic studies of spontaneous crystallization and growth of diamond on seed crystals in C–O–H fluid were performed [116–119]. As follows from results of these studies, diamond crystallization in the C–O–H system is preceded by a long induction period, during which no crystals form. Summarizing, it can be concluded that in oxidized fluids (CO_2; CO_2–H_2O; H_2O), the intensity of spontaneous nucleation, the rate of diamond growth on seed crystals, and the degree of graphite–diamond transformation are considerably higher than those in reduced fluids (H_2O–CH_4; CH_4–H_2).

17.2.6.4 Diamond Formation through Redox Reactions

Many models of diamond genesis suggest diamond formation through redox reaction, with carbon-bearing minerals and fluids being the carbon source. The first successful experiments on diamond crystallization with carbonates as the carbon source were reported in 2002 [120,121]. Arima et al. [120] synthesized diamond as a result of reaction between dolomite ($CaMg(CO_3)_2$) and silicon or silicon carbide. Another mechanism, which has higher relevance to natural conditions, was demonstrated by Palyanov et al. [121,122]. In this case, carbon dioxide was first released in the reaction $3MgCO_3 + 2SiO_2 + Al_2SiO_5 = Mg_3Al_2Si_3O_{12}$ (pyrope) $+ 3CO_2$ and then reacted with hydrogen following the reaction $CO_2 + 2H_2 = C + 2H_2O$. As a result, diamond was produced from carbon of initial carbonates in association with silicate phases, which are typical satellites of natural diamonds.

Marx [123] proposed that diamond could form via the reaction $2FeS + CO_2 = 2FeO + S_2 + C$. First study along this line is the experimental investigation of magnesite reduction in the presence of an eutectic-composition $Fe_{70}S_{28}O_2$ melt [124]. As a result of carbonate reduction by Fe^0-rich sulfide melt, metastable graphite was produced in the experiments. Subsequent studies [54] show that the interaction in the $MgCO_3$–SiO_2–Al_2O_3–FeS system proceeds via the reactions of decarbonation and

reduction of CO_2 to elemental carbon, resulting in the formation of an association of Mg, Fe silicates, sulfides, and graphite or diamond.

17.2.6.5 Phosphorus-Carbon System

Doping of diamond with phosphorus to produce n-type conductivity is a challenging task tackled mainly by CVD diamond growers. At HPHT conditions, the synthesis of P-doped diamonds was realized only from carbon solution in phosphorus melt [125]. Recently the range of P-T conditions of diamond crystallization in the P-C systems has been substantially extended [110]. Nucleation and growth of diamond, as well as the degree of the graphite-to-diamond conversion, are shown to be determined by the temperature, pressure, and kinetics of the processes. The morphology of the crystals is determined by the relative development of the {111}, {310}, and {911} faces (Figure 17.12f). Depending on the synthesis temperature, crystallized diamonds have pale blue to very dark blue color, which as confirmed by spectroscopic measurements is due to photoionization of phosphorus donors. Along with single substitutional phosphorus, a number of new phosphorus-nitrogen centers were revealed in these crystals by electron paramagnetic resonance [126].

17.2.7 Ultra-High Pressure Synthesis of Bulk Diamond

Diamond synthesis via the direct phase transition of the hexagonal graphite structure to the cubic diamond structure at static pressures in excess of 13 GPa and temperatures of about 2500–3000 °C was demonstrated in the early 1960s [11]. It was not, however, until the beginning of the 2000s that bulk polycrystalline diamond could be produced by this method. Scientists from the Geodynamics Research Center of Ehime University in collaboration with Sumitomo have made substantial progress in the development of ultra-high pressure multi-anvil techniques with large reaction volumes. In experiments at 15–25 GPa and 2000–2700 °C for up to 2–3 h, centimeter-sized high purity nanopolycrystalline diamond samples have been produced (Figure 17.13(a)). The produced polycrystalline diamond has a very fine mixed texture of a homogeneous fine structure with particle size of 10–20 nm and a lamellar structure. This new material has extremely high hardness and possesses great potentials for various technical and scientific applications [127,128] (Figure 17.13(b,c)).

17.3 Growth of Diamond from Gas Phase

17.3.1 Introduction

Diamond synthesis by chemical vapor deposition takes place in essentially metastable conditions, not favored by thermodynamics, but rather driven by kinetics. The first attempts to realize the CVD process on diamond seeds (on crystals or powder) at low pressures more than 50 years ago used methane and CO [8] or CBr_4 and CI_4 [9]. However, the growth rate in the early work was extremely low, for example, under thermal decomposition of methane–hydrogen mixtures, the growth rate on submicron-scale diamond single crystals was less than 20 nm/h [130,131]; this made the method

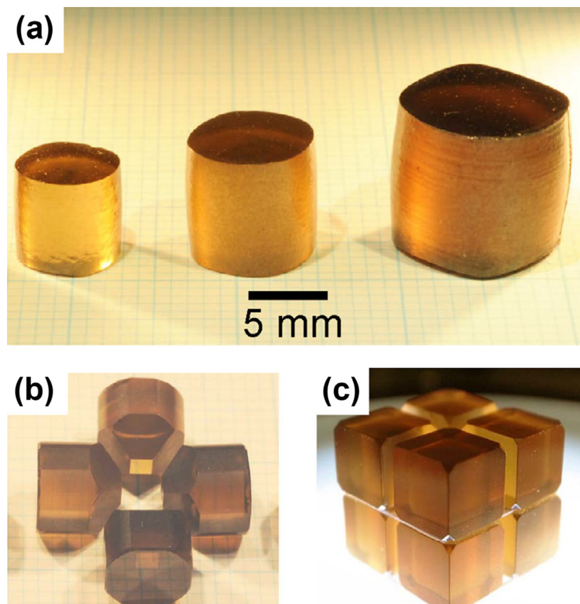

FIGURE 17.13 (a) Nanopolycrystalline diamond (NPD) rods produced by direct conversion from graphite. These NPD rods are cut with pulsed laser to various shapes, including anvils for a small cubic cell (b) and for a KAWAI cell (c). *Reprinted from Ref. [128].*

unpractical at that time. Only when the importance of atomic hydrogen in the gas phase was recognized were the high growth rates, of several microns per hour, obtained [132–134]. The atomic hydrogen stabilizes the diamond surface via H-termination and selectively etches graphite that might be co-deposited along with diamond. Historical aspects on early development of the CVD methods to produce diamond can be found in a number of reviews [10,135–137]. Since the early 1990s, CVD diamond synthesis has become an established technology, and a variety of diamond products, in particular, based on nanocrystalline coatings, polycrystalline thin films and wafers, and single crystals, are now produced commercially, yet in volume much less than compared to HPHT diamonds. The advantages of CVD diamond are: (1) large area deposition (polycrystalline wafers with diameter larger than 150 mm and thickness above 2 mm are already demonstrated); (2) very high purity, better than for natural or HPHT diamonds); (3) simple precursors (CH_4, H_2); (4) possibility to obtain both thin and thick (hundreds microns) films; and (5) direct growth of shaped films using an appropriate template as the substrate. The present state of the art of CVD diamond technology is described in a number of reviews and books [129,136,138–143].

17.3.2 Principles of Chemical Vapor Deposition

The CVD process is based on activation of a small amount (a small percent) of a hydrocarbon, typically, methane, in a mixture with hydrogen H_2 to form an appropriate composition of atomic hydrogen H and C_xH_y radicals, which are transported by diffusion

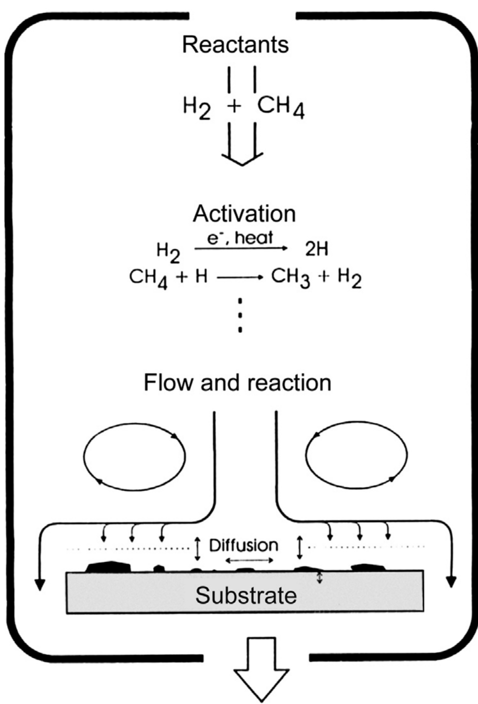

FIGURE 17.14 A schematic showing diamond CVD process: flow of precursors (reactants) into the reactor, thermal or plasma activation of the reactants, gas phase reactions and transport of species to the substrate, and surface reactions to form diamond. *Reproduced with permission from Ref. [129].*

and convection to the growing diamond surface and participate in surface chemical reactions to build up the diamond structure (Figure 17.14). The process goes at pressures from a few Torr to several hundred Torr, while the substrate temperature varies in the range of 700–1000 °C. Other carbon precursors like CO, CO_2, ethanol, or halocarbons are rarely used [144]. Noble gases like Ar can be added in significant percentage to modify plasma parameters, while small amounts of O_2 or N_2 are added to change both plasma and surface chemistry.

Theoretical considerations [145–148] revealed that behind the successful, but very simplified, idea of selective etching of co-deposited graphite by hydrogen during diamond deposition, much more complex reactions take place. A sequence of events to incorporate a C atom to form a new bridge C–C on the surface, the elementary step of the growth process, includes a chain of reactions, H and CH_3 radicals playing the key roles. A significant part of the growing diamond surface is terminated by adsorbed hydrogen atoms at any moment, thus the diamond lattice is stabilized. Hydrogen atom desorption leaves free C bond–active site, the H desorption and absorption being in a kinetic equilibrium. Then the CH_3 radical attaches to the active site. Actually, in the gas phase many more species are present, for instance, besides CH_3 stable hydrocarbon molecules

like CH_4, C_2H_2 and C_2H_6 are detected [149]. In the case of microwave plasma CVD modeling performed by Lombardi et al. [150] a total of 28 species and 131 reactions were taken into account. Kinetic Monte Carlo simulation [147] revealed the important role of surface migration of the species, which enhances the growth rate and contributes to the surface roughness of growing diamond. A summary of recent achievements in understanding of CVD growth process of diamond is given in ref. [140].

Natural or HPHT diamond substrates are used for epitaxial growth of CVD diamond films and crystals. On foreign substrates the spontaneous nucleation of diamond is difficult [151], therefore the substrate surface should be preliminarily seeded with fine diamond particles that serve as diamond nucleation centers. The seeding with nanodiamond particles, such as nanodiamonds of detonation synthesis (size less than 10 nm), is most effective as it results in very high nucleation density of 10^{10}–$10^{11}/cm^2$ [152,153] that allows formation of a continuous polycrystalline thin diamond film in the early stage of the process, when individual epitaxially growing particles merge. Another approach to stimulate the nucleation is a bias-enhanced nucleation (BEN), when a bias voltage is applied to the substrate in the first stage of growth to accelerate carbon ions in discharge, which produce sp3-bonded clusters on the surface upon the bombardment [154]. The formed nuclei give rise to polycrystalline, but highly oriented diamond films with thickness up to 30 μm on Si substrate [155].

For heteroepitaxial growth (without seeding), the lattice mismatch between diamond and substrate must be as small as possible. The heteroepitaxy has been confirmed in experiments on diamond deposition on c-BN (its cubic lattice constant is only 1.3% larger than for diamond) [156,157], the growth proceeds better on (111) plane of c-BN. However, since the size of c-BN crystals is typically less than 1 mm, these substrates seem to be unpractical for large SC diamond synthesis. High quality heteroepitaxial films have been grown on single crystal iridium layers deposited on (100) MgO or (100) $SrTiO_3$ substrates, and also on Si wafers with thin yttria-stabilized zirconia (YSZ) interlayer and BEN substrate pretreatment in microwave plasma [158]. The lattice constant for Ir $a = 0.3840$ nm is 7.6% larger than for diamond ($a = 0.3567$ nm). The mosaicity of 45 μm thick (100)-oriented diamond film deposited on Ir/YSZ/Si(001) substrate was rather low, 0.27° for the tilt (FWHM) as determined from rocking curves [158]. This approach promises the epitaxial growth on large area (~10 cm^2) wafers [159]. Recently [160], a heteroepitaxial diamond film on multilayer Ir/YSZ/Si substrate as thick as 300 μm for use as high energy particle detector has been reported.

17.3.3 Gas Activation Methods

More than 10 variants of diamond deposition techniques, differing in the methods of gas excitation, have been developed. The most common are microwave plasma-assisted CVD [161,162], hot filament [133,163], DC plasma [164,165], and DC arc-jet CVD [166,167], while oxygen–acetylene flame [168,169] or laser plasma jet [170] are more rarely used.

17.3.3.1 Hot Filament CVD

The simplest way to activate a mixture of hydrogen and methane (~0.5–2 vol %) is to place a refractory filament heated to ≈2000 °C near the substrate heated to 700–1000 °C, as introduced by Matsumoto [133]. The vapor pressure is typically 15–50 Torr, and the filament–substrate distance is 4–10 mm. The commonly used filament materials are W, Ta, and Re. The hot filament (HF) technique provides rather low growth rate of ~1 μm/h and is preferably used for thin film deposition. The drawback of the HF scheme is that the filament material is sputtered and incorporates into the growing film in significant amount. The contamination with W of up to ~0.1% is found in the films [171], and such material cannot be used for active electronic applications. The filament deformation and embrittlement due to carburization require its periodical replacement. The HF CVD advantages are simple apparatus and ease of scaling up. Using a multifilament system, the deposition of boron-doped diamond films as well as tribiological coatings on substrates up to $50 \times 100\ cm^2$ size has been reported [163].

17.3.3.2 DC Plasma CVD

Deposition in a direct current (DC) arc plasma [152,165,172,173] provides high growth rates, up to tens of microns per hour; however, the growing film is typically contaminated with electrode sputtering products. The substrate serves as anode, while the cathode can be made of glassy carbon, TiC or Mo. Ternary mixtures of CH_4, H_2, and Ar enable the synthesis of nanocrystalline films in a broad range of methane concentrations [164]. The substrate diameter can be increased using a multicathode discharge; as an example, Lee et al. [173] developed a seven-cathode system to produce 100-mm-diameter polycrystalline diamond wafers with uniform thickness (800–900 μm) at deposition rate of 10 μm/h.

17.3.3.3 DC Arc-Jet CVD

In a DC arc plasma jet reactor, a gas heated by the DC discharge in a cylindrical channel expands through a nozzle to form a high velocity jet with the core temperature of up to 40,000 °C, which far exceeds the temperature attained in microwave plasma and hot filament activation systems. Since the growth rate increases with gas temperature as deduced by Bachmann et al. [144] from comparison of different CVD systems, the high growth rates are expected for this method. Ohtake and Yoshikawa [174] achieved growth rates over 900 μm/h (this value still remains unsurpassed by any other CVD technique) and about 8% conversion of carbon from methane to diamond, but the deposition area was as small as several square millimeters. The gas mixture consists of argon with admixtures of methane and hydrogen. The consumption of gas is high, 10–30 l/min, so the gas cost may contribute significantly to the growth process cost. The commercial-scale production of diamond wafers up to 175 mm in diameter using DC arc-jet technology is known from the 1990s [175]. To increase the deposition area and reduce the production cost, an increase of the reactor power is required. A representative example of this approach is a 100-kW DC

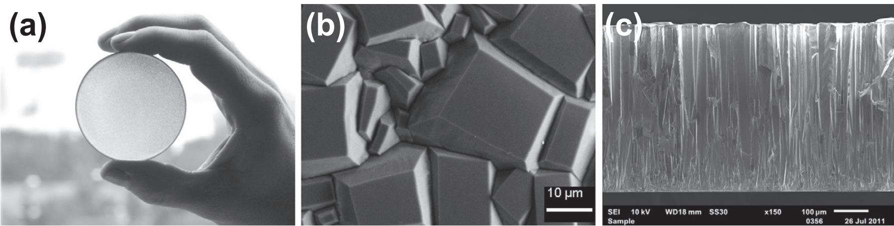

FIGURE 17.15 Unpolished free-standing optical quality polycrystalline diamond wafer of 57-mm diameter, 0.5-mm thickness (a); growth surface (b) and cross-section (c) of 0.5 thick "black" diamond wafer. Note columnar structure seen on fractured surface.

arc-jet system developed by Lu et al. [176], in which the gas mixture is recirculated in the system for more efficient precursor gas utilization. The contamination from the electrodes is again difficult to avoid, so the produced polycrystalline material can be of optical quality for IR range at best. Only recently has the DC arc-jet technique been used for SC diamond growth [177].

17.3.3.4 Microwave Plasma CVD

Microwave plasma deposition (MPCVD) is the most widespread method for diamond synthesis [143,178] due to several advantages. The microwave plasma is "sterile" in a sense that there is no electrode sputtering as in other types of discharge. This minimizes contamination of the growing diamond with the reactor material and allows growth of the most pure optical- and electronic-grade diamond. The MPCVD reactors are able to work continuously for the several hundred hours that are needed to produce thick (of the order of 1 mm and more) polycrystalline films or large single crystals. As a rule, the polycrystalline diamond is deposited on a Si substrate, and thick film can be separated from the substrate to obtain the free-standing diamond wafer. The as-grown 0.5-mm-thick transparent polycrystalline wafer, and SEM images of the grain structure of an opaque (black) diamond, both produced by MPCVD, are shown in Figure 17.15. The microwave power is generated by a magnetron operated at 2.45 GHz or 915 MHz. The plasma is ignited in a resonator in proximity to the substrate at pressures ~100 Torr, but that can approach 300–400 Torr. The plasma ball diameter is approximately a half the radiation wavelength, that is $\lambda/2 \approx 6.1$ cm at 2.45 GHz. The gas temperature in the plasma at 100 Torr and 5 kW input MW power is about 2800 K [179], increasing with pressure.

Microwave plasma–assisted deposition of diamond films was first reported in 1983 by Kamo et al. [134]. Since then, a number of MPCVD system designs were proposed that enhance growth rate, improve uniformity and quality of the film, reduce contamination, and make the control process easier, some reactors being produced commercially [180]. As an example, a cross-sectional view of the MPCVD reactor developed by Asmussen et al. [181] to grow SC diamond at pressures up to 160 Torr is displayed in Figure 17.16. The reactor consists of a cylindrical resonant cavity applicator that selects the

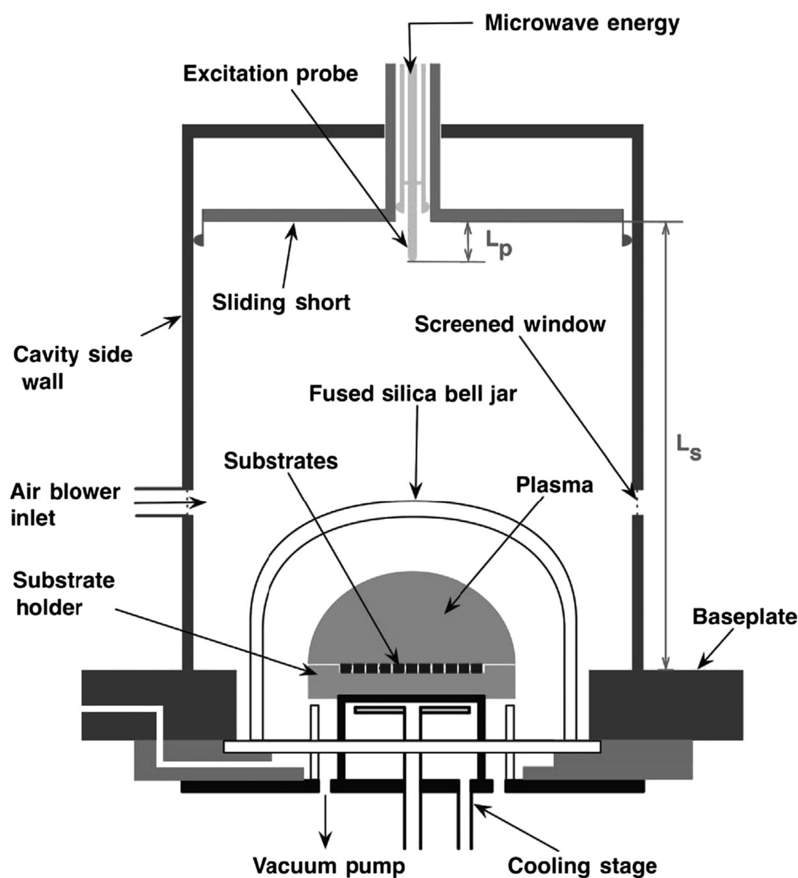

FIGURE 17.16 Cross-sectional view of the microwave CVD reactor operated at 915 MHz to deposit diamond on multiple substrates. *Reprinted with permission from Ref. [181]. Copyright 2008, AIP Publishing LLC.*

electromagnetic mode excitation (TM013 mode), positions and shapes the microwave discharge, which is confined inside a fused silica bell jar. The system is operated at 915 MHz excitation frequency to provide deposition over a 6- to 8-inch-diameter surface area. High purity feed gases, H_2 (99.9995%) and CH_4 (99.999%), were employed. Particularly, at 11.5 kW power and pressure of 125 Torr, the average growth rate of ~18 μm/h for single crystals was reported.

The original resonator design in the form of an ellipsoidal cavity was proposed by Füner et al. [182] who placed the microwave antenna at one focus of the ellipsoidal chamber and the substrate at another focus, where the microwave radiation is concentrated. Optical-quality and boron-doped polycrystalline diamond wafers grown in such a system were demonstrated [183].

An interesting idea to excite the plasma by shorter waves—millimeter waves, rather than by microwaves—was realized by Vikharev et al. [184], who deposited polycrystalline

diamond films on 60- to 90-mm-diameter substrates using for plasma excitation a 10 kW gyrotron operating at a frequency of 30 GHz. Later they demonstrated a pilot CVD reactor with a 15 kW, 28 GHz gyrotron source with almost flat plasma, extending over 100 mm substrate, and the growth rate of 10–15 μm/h. It is believed that the CVD systems equipped with a gyrotron can be easier scaled up in power in comparison with conventional magnetron-based reactors.

17.3.4 Epitaxial Growth and Treatment

17.3.4.1 High Speed Growth

With a few exceptions, only MPCVD technique is used for synthesis of high quality single crystals. Yan et al. [185] from Carnegie Institution of Washington were the first who reported high growth rates for SC diamond, up to 150 μm/h, two orders of magnitude higher than for polycrystalline diamond films. This was a result of combination of three factors: enhanced microwave power density due to pressure increase from conventional ~100–160 Torr, high percentage of methane (12% CH_4/H_2), and adding nitrogen (3% N_2/CH_4). Smooth transparent, yellow-tint, CVD diamond on (100) HPHT diamond seed, enlarging both the thickness and area of the crystal, were produced. The epitaxy on (100) face results in fewer defects compared with deposition on facets with other orientations. Later the same group further improved the growth technology by going to even higher pressures. Single crystals of diamond up to 18 mm in thickness have been grown by MPCVD at gas pressures of up to 350 Torr, and the growth rate as high as 165 μm/h has been achieved for brown crystals at 310 Torr and high power density (and nitrogen doping) [186]. Colorless crystals were produced at growth rate 50–70 μm/h without N_2 addition; in gas, the brilliant cut, and polished single crystals become transparent (Figure 17.17) [187].

FIGURE 17.17 The picture on the right shows a 2.4-carat single-crystal CVD diamond compared with 0.25-carat CVD diamond. On the left, example of the evolution of CVD diamond single crystal starting with crystal 13.5-carat block (a) to the 2.3-carat cut gem anvil (d). *Reprinted with permission from Ref. [187]. Copyright 2012, Wiley-VCH Verlag GmbH & Co. KGaA.*

Theoretical calculations predict a continuous increase in growth rate with pressure at least up to 200 Torr [188,189]. It was speculated that the growth rate for SC CVD diamond could be increased to ~1 mm/h under pressure above 1 atm, if the problem of plasma stability would be solved. Recently, a microwave plasma jet CVD technique operated at atmospheric pressure in argon-hydrogen-methane mixtures has been demonstrated for deposition of SC diamond [190], however, the growth rate was low (~5 μm/h) even at very high power density ~10^3 W/cm^3, possibly because of nonoptimal other deposition parameters.

The addition of N_2 even at concentrations as low as a few ppm in the gas phase strongly increases the crystal growth rates on <100> orientations by a catalytic effect [191]. The 10 ppm of N_2 improves growth rate by more than a factor of two, the free-standing CVD diamond remaining uncolored, optical grade [143]. For this reason, the synthesis of millimeter-thick crystals is often performed with addition of several hundreds of ppm of N_2 [143,186,192]. However, nitrogen in diamond deteriorates the electronic properties, thus any source of nitrogen impurity, in the feed gas or from a leakage in the reactor, should be eliminated in order to have N content at the level of few ppb in the crystal, if electronic application is assumed.

To make the process economically viable, the multiple substrate deposition in one run is preferable; this is possible since the plasma area exceeds the single substrate size. The simultaneous synthesis of SC diamonds over 70 diamond seeds has been realized by Asmussen et al. [181], who reported to add 1.8–2.5 mm of diamond material to each of the seed crystals for 145 h of deposition time by MPCVD. Mass production of single crystals is commercialized using growth on the multiple seeds [193]. The lateral size of the SC CVD diamond typically is restricted by dimensions of the seed crystal and rarely exceeds 5–6 mm. However, by appropriate choice of the growth parameters, a significant, more than a factor of two, enlargement of the top (001) face area can be achieved, the development of unwanted facets being suppressed [194].

17.3.4.2 Lift-Off Process

The produced homoepitaxially grown CVD diamond layer is separated from the substrate by laser sawing to allow repeated use of the substrate. However, a significant cutting loss (>0.3 mm in thickness) can be expected for slicing such a bulk diamond into wafers. More economical but more complex is a lift-off process based on ion implantation. The liftoff technique to remove thin sheets of diamond from bulk crystals, originally introduced by Parikh et al. [195], consists of three steps: (1) carbon ion implantation to form a buried, well-defined damaged layer below the surface, (2) graphitization of this layer by annealing in vacuum, and (3) etching of the damaged layer in an acid solution. This process lifts off the diamond foil of submicron scale thickness above the graphite layer. It was demonstrated later [196] that the liftoff after homoepitaxial growth of diamond film on implanted layer can separate a diamond film with thickness less than 100 μm. Mokuno et al. [197] used an improved liftoff process to make large (10 × 10 mm) and thick (>0.2 mm) single crystal diamond plates. Then, the

substrate could be used as a seed for more than three times without polishing the surface.

17.3.4.3 Mosaic Structures

Since the availability of large area SC diamond seeds is limited and costly, an idea to grow quasi-SC structures with increased size, so-called “mosaics”, was suggested [198]. The approach involves assembling together a number of precisely cut, polished, and crystallographically oriented seed crystals of single-crystalline diamond plates. On top of this mosaic, a closed single-crystalline diamond layer is grown to fuse the seeds. The gap between adjacent diamond plates is completely filled with CVD diamond. In their experiment Janssen and Giling [198] used hot filament CVD to overgrow two natural type IIa diamond seed crystals with (100) orientation. The seeds were well aligned within 0.2° in each of three perpendicular directions, with the gap between the crystals less than 1 μm and the height difference less than 3 μm. However, defects, particularly dislocations, and even cracks due to tensile stress buildup, formed within junctions. Similar mosaic structures based on type IIa natural diamond seeds have been produced also by the acetylene-oxygen combustion flame technique [199], and MPCVD [200]. Kobashi et al. [201] used 16 pieces of Ib-type (100) oriented diamond, each $4 \times 4\ mm^2$ in size, to deposit by MPCVD 1-mm-thick single crystal CVD diamond layer of total area 2.5 cm^2; however, again high internal stress and macroscopic defects remained problematic. A further improvement in diamond mosaic technique has been made by Yamada et al. [202] who introduced identical *clone* seed substrates to minimize their differences in off angle, purity, dimensions, and structure. They succeeded in production of 1×1 inch freestanding mosaic wafers using identical seed crystals from the liftoff process [197], with almost invisible junctions between the clone plates.

17.3.4.4 Postgrowth Treatment

Annealing of SC diamonds at very high pressures (above 5 GPa) and temperatures (above ~1800 °C) can cause significant changes in their color by affecting certain optically active defects and their absorptions in the visible spectrum. The HPHT treatment is used to enhance the optical properties both of natural and synthetic HPHT diamonds [203], mostly for jewelry industry demand. The SC CVD diamonds also have been treated in a similar way to improve optical and/or mechanical properties. The crystals annealed at 2000 °C and 5–7 GPa for 10 min using a belt-type apparatus transformed into transparent colorless material [204], while the hardness can be enhanced by ≈ 50% (up to ~160 GPa as measured with a Vickers indenter on the {100} faces under low load). A similar hardness enhancement has been reported for polycrystalline CVD diamond rods imbedded in a diamond-SiC composite matrix and sintered at HPHT conditions [205].

Recently, a low pressure/high temperature (LPHT) annealing has been applied to improve transparency [206] and intrinsic hardness of SC CVD diamond without appreciable loss in fracture toughness [207]. The crystals were annealed in a hydrogen

environment by using microwave plasma technique for periods of time ranging from a fraction of minute (2100–2200 °C) to a few hours (1400–1600 °C) at pressures <300 Torr. The observed decrease in optical absorption after the LPHT annealing by factors of two to six was ascribed to changes in defect structure associated with hydrogen incorporation during CVD growth (typically hydrogen, rather than nitrogen is the most abundant impurity in CVD diamond, especially in polycrystalline films [208]). It is important to note that this LPHT method is applicable in the same CVD reactor as used for synthesis, and is not constrained by the size of the crystals. The treatment time is limited by necessity to avoid significant etching of the diamond by active atomic hydrogen in the plasma. The combination of high growth rate regimes with a subsequent LPHT annealing makes the CVD diamond process a more economically viable technique.

17.3.4.5 Doping

Since the intrinsic (undoped) diamond has very high electrical resistivity (10^{13}–10^{14} Ohm cm at room temperature) a doping is needed to provide *p*-type or *n*-type conductivity required for electronic and electrochemical applications. Until now only boron doping [209], giving *p*-type conductivity with activation energy $E_a = 0.37$ eV, and phosphorus doping [210] resulting in *n*-type material with $E_a = 0.59$ eV, have been realized reliably. Hall mobility of holes at 300 K as high as 1890 cm^2V/s was measured for 10 μm thick homoepitaxial B-doped films at low, $2.5 \cdot 10^{16}/cm^3$ boron content [211]. The B-doping from gas phase upon diamond growth gives better electrical characteristics than ion implantation due to absence of damage (even after annealing) produced by the ion irradiation. The most common boron precursors used are diborane (B_2H_6) and trimethylboron $B(CH_3)_3$ added to conventional H_2–CH_4 mixture, while other boron sources such as ethanol/trimethyl borate/hydrogen mixtures [212] or boron trichloride [213] are used more rarely. At high B concentration ($>3 \cdot 10^{20}/cm^3$) in diamond a metallic-type conductivity is observed; moreover, at even higher B content ($8 \cdot 10^{21}/cm^3$) the superconductivity has been revealed in homoepitaxial diamond films [214], with onset of superconductivity at 11.4 K and zero resistance at 8.4 K.

17.4 Applications

17.4.1 HPHT Diamond Specialties

The traditional applications of diamond as a material with extreme mechanical properties apparently remain the main large-scale niche for bulk synthetic diamonds. The development of a mass-production process of diamond crystals by the temperature gradient method enabled the commercialization of type Ib diamonds of one to two carats (5–7 mm across) for industrial applications. Both Sumitomo Electric and Element Six (formerly De Beers Industrial Diamond Division) offer a wide range of HPHT diamond products, which can be used as cutting tools for nonferrous and nonmetallic

materials, dressers for wheel dressing, a variety of specialty knives, burnishing tools, wear parts, and wire drawing dies.

Diamond anvil cell (DAC) devices are the principal tool in modern ultra-high pressure research [215]. It has been demonstrated that synthetic diamonds can effectively be used for this application [216,217]. Pressures in the range 250–300 GPa were successfully generated using high-quality type Ib synthetic diamonds produced by De Beers [216]. Due to limited range of optical transmission, type Ib diamond anvils are mainly used with X-ray diffraction techniques. For spectroscopic studies, e.g., Raman scattering or FTIR absorption, diamond anvils based on synthetic type IIa diamonds are used. Sumiya et al. [217] demonstrated that synthetic type IIa diamond anvils can generate pressures of up to 200 GPa with good reproducibility and without emitting any luminescence.

Synthetic diamond attains an increasing importance as a material of X-ray optical components, such as filters, phase plates, beam splitters, and monochromators, to be used in third- and fourth-generation X-ray sources, producing highly collimated X-ray beams of very high power and brilliance [69,87,218–220]. With the unprecedented heat loads imposed in these sources on the X-ray optical elements, diamond—due to its superb thermal and mechanical properties and low X-ray absorption coefficient, and thanks to substantial progress in growing large type IIa diamonds with high crystalline perfection—became the material of choice for these very demanding applications. Currently, diamond monochromators, phase plates, and other elements are routinely used at the major synchrotron radiation facilities, such as the European Synchrotron Radiation Facility (ESRF, France), Advanced Photon Source (APS, USA) and Super Photon Ring (Spring-8, Japan). Recently, high quality type IIa diamond crystals have been identified as indispensable for the realization of X-ray free-electron laser oscillators (XFELOs), next-generation hard-X-ray sources of the highest average and peak brightness and extremely narrow bandwidth [221–223]. The targets for further development of the type IIa diamond are size, crystal perfection, and also surface quality.

At the early stages of production of bulk synthetic diamonds there was great skepticism that they might potentially enter the jewelry market, mainly due to very high costs involved in growing gem-quality diamonds. None of the major synthetic diamond producers made practical steps towards jewelry applications. Small experimental batches of faceted synthetic diamonds were produced exclusively for research purposes to establish their gemological properties and identification criteria [45,224–227]. Nevertheless, with progress in diamond growth capabilities, since the early 1990s reports on synthetic diamonds seen in the gem trade have started to appear. Unfortunately, the synthetic origin of these diamonds was not always properly disclosed, which created immense concern to the jewelry community and was bad publicity for synthetic diamond as the gemstone. During the last decade several companies (e.g., Gemesis Corporation, Chatham Created Gems, Advanced Optical Technologies Corporation, and others) appeared that produce and/or distribute synthetic diamond gems with explicit disclosure of their origin.

HPHT synthetic diamonds are now used in many other applications. There are commercially available compression cells and attenuated total reflection (ATR) prisms made from type IIa diamonds for FT-IR spectroscopy. They are traditionally used as heat sinks for microwave diodes and semiconductor laser diodes [228]. Low cost substrates made from synthetic type Ib diamond are readily available that have significantly contributed to the progress in epitaxial CVD diamond growth. A present, diamond substrates of lager sizes and higher quality are required. Several electronic applications of HPHT diamonds, such as radiation detectors and dosimeters [229–232], have been demonstrated.

17.4.2 CVD Diamond Specialties

In view of very high purity achieved in CVD diamond it is requested for high-tech applications, primarily in optics and electronics, exploiting the best quality grades of this material. The SC CVD diamond is used in detectors and monitors of X-rays [233], beta particles [234], neutrons [235], UV light [236], and in dosimeters in radiotherapy [237] to combine good electronic properties and radiation hardness. Because diamond can be locally graphitized by laser or ion beams, graphite electrodes (strips or pillars) can be formed on the diamond surface [238] or in bulk [234,239] to make all-carbon devices, such as radiation detectors.

A number of active high power high frequency electronic devices based on doped diamond have been developed [141], including field-effect transistor (FET) with boron-doped conducting channel, or metal-semiconductor FET (MESFET) on the H-terminated diamond surface [240]. The latter device is possible due to the discovery that the hydrogen surface termination causes a 2D hole channel (hole concentration of around $10^{13}/cm^2$ and activation energy of a few meV only) to form in the diamond layer several nanometers below the surface. The best results reported for such MESFETs are: output power density of 2.1 Wm/m at 1 GHz [241], $f_T = 45$ GHz (gain cutoff frequency) and $f_{max} = 120$ GHz (max frequency for operation) [242].

Recently, CVD diamond attracted high interest as the medium for Raman lasers, or Raman shift converters [243,244] utilizing the effect of stimulated Raman scattering (SRS). The advantages of diamond as SRS material are large Raman frequency 1332/cm (larger than for other Raman crystals (<1100/cm)), high SRS gain, wide transparency window and high thermal conductivity, which greatly reduces thermal gradient within the crystal. Using the pumping at $\lambda = 1064$ nm, the radiation is shifted to 1300–1500 nm range, which is interesting for medical applications and communications. A pulsed Raman laser at 1193 nm based on SC CVD diamond 8 mm long with a record output average power of 24.5 W under cryogenic operation at 77 K is reported [245]. Also, a continuous-wave (cw) operation of a diamond Raman laser at 1240 nm with power 10.1 W and 33% conversion efficiency was also demonstrated [246]. More details on the rapidly developing technique of diamond Raman lasers can be found in a recent comprehensive review [247]. Other laser applications include doped dielectric and

semiconductor disk lasers with diamond plate to effectively dissipate the heat absorbed in the gain crystal [248].

There are a number of applications for SC CVD diamond beyond optical and electronic ones. With the increase in size and quality and the decrease in production costs, the CVD diamond is attracting interest in the jewelry field. The SC CVD diamonds used as anvil cells can generate ultrahigh pressures up to 200 GPa in studies of properties of materials at high pressures [249], thus being a good alternative to traditional natural or HPHT diamond anvils. Since the diamond is a biocompatible material, its surface is a good platform for covalent attachment of biomolecules such as DNA [250], growth of neurons [251], and other processes on biofunctionalized surfaces. The list of applications will be extended if thick polycrystalline diamond films are also considered [139].

17.5 Conclusions

It is evident that since the early reports on successful laboratory synthesis of diamond, the field of the man-made diamond has tremendously advanced, now reaching the stage of commercial production of single crystal diamond of relatively large sizes and high crystalline quality. Given the extreme pressure and temperature conditions required for HPHT diamond growth, the success achieved for this method deserves special esteem. The largest diamond crystal grown by the HPHT method weights 34.80 ct (7 g, ~2 cm across) and high purity type IIa crystals with low dislocation content can now be produced up to 1 cm size. Much work has been done to understand the influence of the growth conditions, such as pressure and temperature, composition of the solvent-catalyst, doping and nondoping impurities, etc., on the growth and properties of diamond. This, together with the continuing developments in high pressure equipment and technologies, has enabled the use of synthetic diamond in a number of advanced technical and industrial applications. An improvement in crystal quality, cost reduction, and increase in crystal size and yield are apparent challenges for further work on HPHT diamond growth. Also noteworthy are the achievements in diamond synthesis with new nonmetallic solvent-catalysts. These studies have notably expanded the range of diamond-forming media and made a significant contribution to our understanding of natural diamond genesis. Although diamonds synthesized in these nontraditional systems are still within submillimeter range, the ongoing search and exploration of new diamond growth systems are of great promise.

Even more outstanding is the progress achieved during last 10–15 years in CVD diamond technology. It has made possible the growth of large, high quality diamond single crystals with high deposition rates. CVD diamonds may boast higher purity than that of the best natural diamonds or those grown by HPHT processes. In particular, nitrogen content as low as 5 ppb or even less is achieved, which introduced the term "IIIa diamond" for this category of material. While certain problems like *n*-type doping or dislocation-free diamond growth remain to be solved, the CVD diamonds are already

in use in a range of applications, from optics and electronics to lasers and fine mechanics. There is no doubt that further scientific and technological advances in CVD diamond growth will markedly expand the range of applications exploiting the unique properties of diamond.

References

[1] Rossini FD, Jessup RS. J Nut Bur Std 1938;C21:491.

[2] Leipunskii OI. Uspekhi Khimii 1939;8:1519.

[3] Berman R, Simon F. Zeirs Elektrochm 1955;59:333.

[4] Bridgman PW. Phys Rev 1935;48:825.

[5] Bridgman PW. J Chem Phys 1947;12:92.

[6] Bundy FP, Hall HT, Strong HM, Wentorf Jr RH. Nature 1955;176:51.

[7] Bovenkerk HP, Bundy FP, Hall HT, Strong HM, Wentorf Jr RH. Nature 1959;184:1094.

[8] Eversole WG, US Patent No 3030187. Synthesis of diamond. 1960, filed 23.07.1958.

[9] Spitsyn BV, Deryagin BV, USSR Patent No 339134. A technique of diamond growth on diamond's face. 1980, filed 10.07.1956.

[10] Spitsyn BV. In: Hurle DTJ, editor. Handbook of crystal growth, vol. 3a. Elsevier; 1994. p. 401–56.

[11] Bundy FP. J Chem Phys 1963;38:631.

[12] Irifune T, Kurio A, Sakamoto S, Inoue T, Sumiya H. Nature 2003;421:806.

[13] Wedlake RJ. In: Field JE, editor. The properties of diamond. London: Academic Press; 1979. p. 501–35.

[14] Muncke G. In: Field JE, editor. The properties of diamond. London: Academic Press; 1979. p. 473–99.

[15] Strong HM, Hanneman RE. J Chem Phys 1967;46:3668.

[16] Strong HM, Chrenko RM. J Phys Chem 1971;75:1838.

[17] Wentorf RH. J Phys Chem 1971;75:1833.

[18] Hall HT. Rev Sci Inst 1960;31:125.

[19] Fukunaga O, Yamaoka S, Endo T, Akaishi M, Kanda H. In: Timmerhaus KD, Barber MS, editors. High-pressure science and technology, vol. 1. New York: Plenum Pub. Co.; 1979. p. 846–52.

[20] Burns RC, Davies GJ. In: Field JE, editor. The properties of natural and synthetic diamond. London: Academic Press; 1992. p. 395–422.

[21] Khvostantsev LG, Slesarev VN, Brazhkin VV. High Press Res 2004;24:371.

[22] Institute for High Pressure Physics RAS, www.hppi.troitsk.ru

[23] Novikov N, Nachalnaya TA, Ivakhnenko SA, Zanevsky OA, Belousov IS, Malogolovets VG, et al. Diam Relat Mater 2003;12:1990.

[24] Lysakovskii VV, Ivakhnenko SA. J Superhard Mater 2009;31:7.

[25] Blank VD, Kuznesov MS, Nosukhin SA, Terentiev SA, Denisov VN. Diam Relat Mater 2007;16:800.

[26] Polyakov SN, Denisov VN, Kuzmin NV, Kuznetsov MS, Martyushov SY, Nosukhin SA, et al. Diam Relat Mater 2011;20:726.

[27] von Platen B. In: Wentorf RH, editor. Modern very high pressure techniques. Washington: Butterworths; 1962. p. 118–36.

[28] Kawai N. Proc Jpn Acad 1966;42:385.

[29] Liebermann RC. High Press Res 2011;31:493.

[30] Ran EN, Malinovskii IYu. Novosibirsk. In: Experimental studies in mineralogy (1974–1975); 1975. p. 149–54 (in Russian).

[31] Malinovsky IYu, Shurin YaI, Run EN, Godovikov AA, Kalinin AA, Doroshev AM. Abstr. Conf. Phase transfomation at high pressure and tempperatures: applications of geophysical and petrological problems, Misasa, Japan; 1989. p.12.

[32] Malinovskii IYu, Palyanov YuN, Shurin YaI, Doroshev AM, Kalinin AA, Borzdov YuM. In: Kvaskov BV, editor. Prospects of application of diamond in electronics. Energoizdat; 1991. p. 35–6 (in Russian).

[33] Palyanov YuN, Malinovskii IYu, Borzdov YuM, Khokhryakov AF, Chepurov AI, Godovikov AA, et al. Dokl Akad Nauk USSR 1990;315(5):1221 (in Russian).

[34] Palyanov YuN, Borzdov YM, Khokhryakov AF, Kupriyanov IN, Sokol AG. Cryst Growth Des 2010;10: 3169.

[35] Han QG, Liu B, Hu MH, Li ZC, Jia XP, Li MZ, et al. Cryst Growth Des 2011;11:1000.

[36] Chrenko RM, Tuft RE, Strong HM. Nature 1977;270:141.

[37] Evans T. In: Field JE, editor. The properties of natural and synthetic diamond. London: Academic Press; 1992. p. 259–90.

[38] Satoh S, Sumiya H, Tsuji K, Yazu S. In: Saito S, Fukunaga O, Yoshikawa M, editors. Science and technology of new diamond. Tokyo: KTK Scientific Publishers/Terra Scientific Publishing; 1990. p. 351–5.

[39] Stromann CVH, Tshisikawe F, Hansen JO, Burns RC, US Patent Application 20100028246, filed on 9.12.2004, published on February 4, 2010.

[40] Kanda H, Fukunaga O. In: Akimoto S, Manghnani MH, editors. Advances in earth and planetary science, high pressure research in geophysics, vol. 12. Dordrecht: Reidel; 1982. p. 525.

[41] Burns RC, Hansen JO, Spits RA, Sibanda M, Welbourn CM, Welch DL. Diam Relat Mater 1999;8:1433.

[42] Kiflawi I, Kanda H, Lawson SC. Diam Relat Mater 2002;11:204.

[43] Babich YV, Feigelson BN, Fisher D, Yelisseyev AP, Nadolinny VA, Baker JM. Diam Relat Mater 2000;9:893.

[44] Kanda H, Yamaoka S. Diam Relat Mater 1993;2:1420.

[45] Shigley JE, Fritsch E, Koivula JI, Sobolev NV, Malinovsky IY, Pal'yanov YuN. Gems Gemol 1993;29:228.

[46] Pal'yanov YuN, Khokhryakov AF, Borzdov YuM, Sokol AG, Gusev VA, Rylov GM, et al. Geol i Geofiz 1997;38:882.

[47] Pal'yanov YuN, Borzdov YuM, Sokol AG, Khokhryakov AF, Gusev VA, Rylov GM, et al. Diam Relat Mater 1998;7:916.

[48] Yelisseyev A, Babich Yu, Nadolinny V, Fisher D, Feigelson B. Diam Relat Mater 2002;11:22.

[49] Kanda H, Akaishi M, Yamaoka S. Diam Relat Mater 1999;8:1441.

[50] Borzdov Y, Pal'yanov Y, Kupriyanov I, Gusev V, Khokhryakov A, Sokol A, et al. Diam Relat Mater 2002;11:1863.

[51] Palyanov YN, Kupriyanov IN, Borzdov YM, Sokol AG, Khokhryakov AF. Cryst Growth Des 2009;9:2922.

[52] Palyanov YN, Borzdov YM, Khokhryakov AF, Kupriyanov IN, Sobolev NV. Earth planet. Sci Lett 2006;250:269.

[53] Pal'yanov YuN, Sokol AG, Sobolev NV. Russ Geol Geophys 2005;46:1271.

[54] Palyanov YuN, Borzdov YuM, Bataleva YuV, Sokol AG, Palyanova GA, Kupriyanov IN. Earth planet. Sci Lett 2007;260:242.

[55] Liang ZZ, Jia X, Ma HA, Zang CY, Zhu PW, Guan QF, et al. Diam Relat Mater 2005;14:1932.

[56] Yu RZ, Ma HA, Liang ZZ, Liu WQ, Zheng YJ, Jia X. Diam Relat Mater 2008;17:180.

[57] Zhang Z-F, Jia X-P, Liu X-B, Hu M-H, Li Y, Yan B-M, et al. Chin Phys 2012;B 21:038103.

[58] Loubser JHN, Van Ryneveld WP. Nature 1966;211:517.

[59] Samoilovich MI, Bezrukov GN, Butuzov VP. JETP Lett 1971;14:370.

[60] Isoya J, Kanda H, Norris JR, Tang J, Bowman MK. Phys Rev 1990;B 41:3905.

[61] Collins AT. Diam Relat Mater 2000;9:417.

[62] Collins AT, Kanda H, Burns RC. Philos Mag 1990;B 61:797.

[63] Yelisseyev A, Kanda H. New Diam Front Carbon Technol 2007;17:127.

[64] Fisher D, Lawson SC. Diam Relat Mater 1998;7:299.

[65] Kiflawi I, Kanda H, Mainwood A. Diam Relat Mater 1998;7:327.

[66] Sumiya H, Toda N, Satoh S. J Cryst Growth 2002;237-239:1281.

[67] Sumiya H, Satoh S. Diam Relat Mater 1996;5:1359.

[68] Sumiya H, Tamasaki K. Jpn J Appl Phys 2012;51:090102.

[69] Burns RC, Chumakov AI, Connell SH, Dube D, Godfried HP, Hansen JO, et al. J Phys Condens Matter 2009;21:364224.

[70] Ekimov EA, Sidorov VA, Bauer ED, Mel'nik NN, Curro NJ, Thompson JD, et al. Nature 2004;428:542.

[71] Collins AT. Mat Res Symp Proc 1986;162:3.

[72] Thonke K. Semicond Sci Technol 2003;18:S20.

[73] Burns RC, Cvetcovic V, Dodge CN, Evans DJF, Rooney M-LT, Spear PM, et al. J Cryst Growth 1990;104:257.

[74] Sumiya H, Toda N, Satoh S. SEI Tech Rev 2005;60:10.

[75] Abbaschian R, Zhu H, Clarke C. Diam Relat Mater 2005;14:1916.

[76] Khokhryakov AF, Palyanov YN, Kupriyanov IN, Borzdov YM, Sokol AG, Härtwig J, et al. J Cryst Growth 2011;317:32.

[77] Kanda H, Ohsawa T, Fukunaga O, Sunagawa I. In: Sunagawa I, editor. Morphology and growth unit of crystals. Tokyo: Terra Sci. Pub. Co.; 1989. p. 531–42.

[78] Pal'yanov YuN, Chepurov AI, Khokhryakov AF. Mineral Zh 1985;6:50 (in Russian).

[79] Palyanov YuN, Borzdov YM, Kupriyanov IN, Khokhryakov AF. Cryst Growth Des 2012;12:5571.

[80] Palyanov YuN, Khokhryakov AF, Borzdov YM, Kupriyanov IN. Cryst Growth Des 2013;13:5411.

[81] Wood GS, Lang AR. J Cryst Growth 1975;28:215.

[82] Wierzchowski W, Moore M, Makepeace APW, Yacoot A. J Cryst Growth 1991;144:209.

[83] Lang AR, Moore M, Walmsley JC. In: Field JE, editor. The properties of natural and synthetic diamond. London: Academic Press; 1992. p. 215–58.

[84] Khokhryakov AF, Palyanov YuN. J Cryst Growth 2006;293:469.

[85] Khokhryakov AF, Palyanov YuN. J Cryst Growth 2007;306:458.

[86] Sumiya H, Noda N, Nishibayashi Y, Satoh S. J Cryst Growth 1997;178:485.

[87] Pal'yanov YuN, Borzdov YuM, Gusev VA, Sokol AG, Khokhryakov AF, Rylov GM, et al. Nucl Instrum Methods A 2000;446:178.

[88] Khokhryakov AF, Palyanov YN, Kupriyanov IN, Borzdov YM, Sokol AG. J Cryst Growth 2014;386:162.

[89] Tamasaku K, Ueda T, Miwa D, Ishikawa T. J Phys D Appl Phys 2005;38:A61.

[90] Lang AR, Vincent R, Burton NC, Makepeace APW. J Appl Cryst 1995;28:690.

[91] Kowalski G, Moore M, Gledhill G, Maričić Z. Diam Relat Mater 1996;5:1254.

[92] Akaishi M, Kanda H, Yamaoka S. J Cryst Growth 1990;104:578.

[93] Arima M, Nakayama K, Akaishi M, Yamaoka S, Kanda H. Geology 1993;21:968.

[94] Shatskii AF, Borzdov YuM, Sokol AG, Pal'yanov YuN. Geol i Geofiz 2002;43:940.

[95] Palyanov YuN, Sokol AG. Lithos 2009;112S:690.

[96] Pal'yanov YuN, Sokol AG, Borzdov YuM, Sobolev NV. Russ Geol Geophys 1998;39:1768.

[97] Pal'yanov YuN, Sokol AG, Borzdov YuM, Khokhryakov AF. Lithos 2002;60:145.

[98] Borzdov YuM, Sokol AG, Pal'yanov YuN, Kalinin AA, Sobolev NV. Dokl Acad Nauk 1999;366:530.

[99] Sokol AG, Borzdov YM, Khokhryakov AF, Pal'yanov YN, Sobolev NV. Dokl Acad Nauk 1999;368:99.

[100] Zedgenizov DA, Kagi H, Shatsky VS, Sobolev NV. Mineral Mag 2004;68:61.

[101] Klein-BenDavid O, Izraeli ES, Hauri E, Navon O. Lithos 2004;77:243.

[102] Logvinova AM, Wirth R, Fedorova EN, Sobolev NV. Eur J Mineral 2008;20:317.

[103] Dobrzhinetskaya LF, Wirth R, Green HW. PNAS 2007;104:9128.

[104] Hwang SL, Shen P, Chu HT, Yui TF, Liou JG, Sobolev NV, et al. Earth planet. Sci Lett 2005;231:295.

[105] Litvin YuA, Litvin VYu, Kadik AA. Geochem Int 2008;46:531.

[106] Bureau H, Langenhorst F, Auzende A-L, Frost DJ, Estève I, Siebert J. Geochim Cosmochim Acta 2012;77:202.

[107] Sokol AG, Pal'yanov YN. Contrib Mineral Petrol 2008;155:33.

[108] Fagan AJ, Luth RW. Contrib Mineral Petrol 2011;161:229.

[109] Pal'yanov YN, Sokol AG, Borzdov YM, Khokhryakov AF, Sobolev NV. Nature 1999;400:417.

[110] Palyanov YuN, Kupriyanov IN, Sokol AG, Khokhryakov AF, Borzdov YuM. Cryst Growth Des 2011;11:2599.

[111] Sobolev NV. The deep-seated inclusions in kimberlites and the problem of the composition of the upper mantle. Washington: American Geophysics Union; 1977. p. 304.

[112] Taylor LA, Anand M. Chem Erde 2004;64:1.

[113] Bulanova GP. J Geochem Explor 1995;53:1.

[114] Haggerty SE. Nature 1986;320:34.

[115] Yamaoka S, Akaishi M, Kanda H, Osawa T. J Cryst Growth 1992;125:375.

[116] Akaishi M, Kumar MSD, Kanda H, Yamaoka S. Diam Relat Mater 2000;9:1945.

[117] Sokol AG, Pal'yanov YuN, Pal'yanova GA, Khokhryakov AF, Borzdov YuM. Diam Relat Mater 2001;10:2131.

[118] Yamaoka S, Kumar MSD, Kanda H, Akaishi M. J Cryst Growth 2002;234:5.

[119] Sokol AG, Pal'yanov YN. Geochem Int 2004;42:1018.

[120] Arima M, Kozai Y, Akaishi M. Geology 2002;30:691.

[121] Pal'yanov YN, Sokol AG, Borzdov YM, Khokhryakov AF, Sobolev NV. Am Mineral 2002:1009.

[122] Pal'yanov YN, Sokol AG, Tomilenko AA, Sobolev NV. Eur J Mineral 2005;17:207.

[123] Marx PC. Mineral Mag 1972;38:636.

[124] Gunn SC, Luth RW. Am Mineral 2006;91:1110.

[125] Akaishi M, Kanda H, Yamaoka S. Science 1993;259:1592.

[126] Nadolinny VA, Palyanov YuN, Kupriyanov IN, Newton MJ, Kryukov E, Sokol AG. Appl Magn Reson 2012;42:179.

[127] Nakamoto Y, Sakata M, Sumiya H, Shimizu K, Irifune T, Matsuoka T, et al. Rev Sci Instrum 2011;82:066104.

[128] Irifune T, Isobe F, Shinmei T. Phys Earth Planet Inter 2014;228:255.

[129] Butler JE, Windischmann H. MRS Bull (USA) 1998;23:22.

[130] Chauhan SP, Angus JC, Gardner NC. J Appl Phys 1976;47:4746.

[131] Deryagin BV, Fedoseev DV. Russ Chem Rev 1970;39:783.

[132] Spitsyn BV, Bouilov LL, Derjaguin BV. J Cryst Growth 1981;52:219.

[133] Matsumoto S, Sato Y, Tsutsumi M, Setaka N. J Mater Sci 1982;17:3106.

[134] Kamo M, Sato Y, Matsumoto S, Setaka N. J Cryst Growth 1983;62:642.

[135] Angus JC, Hayman CC. Science 1988;241:913.

[136] Varnin VP, Laptev VA, Ralchenko VG. Inorg Mater 2006;42(Suppl. 1):S1.

[137] DeVries RC. Ann Rev Mater Sci 1987;17:161.

[138] May PW. Philos Trans R Soc 2000;A 358:473.

[139] Balmer RS, Brandon JR, Clewes CL, Dhillon HK, Dodson JM, Friel I, et al. J Phys Condens Matter 2009;21:364221.

[140] Butler JE, Mankelevich YA, Cheesman A, Ma J, Ashfold MNR. J Phys Condens Matter 2009;21:364201.

[141] Sussmann RS, editor. CVD diamond for electronic devices and sensors. John Wiley & Sons; 2009.

[142] Mildren RP, Rabeau JR, editors. Optical engineering of diamond. Weinheim: Wiley-VCH Verlag; 2013.

[143] Tallaire A, Achard J, Silva F, Brinza O, Gicquel A. Compt Rend Phys 2013;14:169.

[144] Bachmann PK, Leers D, Lydtin H. Diam Relat Mater 1991;1:1.

[145] Butler JE, Woodin RL. Philos Trans R Soc Lond Ser A 1993;342:209.

[146] Harris SJ, Goodwin DG. J Phys Chem 1993;97:23.

[147] Netto A, Frenklach M. Diam Relat Mater 2005;14:1630.

[148] Goodwin DG, Butler JE. In: Prelas MA, et al., editors. Handbook of industrial diamonds and diamond films. New York: Marcel Dekker; 1997. p. 527–81.

[149] Lombardi G, Hassouni K, Stancu GD, Mechold L, Röpcke J, Gicquel A. Plasma sources. Sci Technol 2005;14:440.

[150] Lombardi G, Hassouni K, Stancu GD, Mechold L, Röpcke J, Gicquel A. J Appl Phys 2005;98:053303.

[151] Das D, Singh RN. Int Mater Rev 2007;52:29.

[152] Smolin AA, Ralchenko VG, Pimenov SM, Kononenko TV, Loubnin EN. Appl Phys Lett 1993;62:3449.

[153] Daenen M, Williams OA, D'Haen J, Haenen K, Nesladek M. Phys Status Solidi A 2006;203:3005.

[154] Yugo S, Semoto K, Hoshina K, Kimura T, Nakai H. Diam Relat Mater 1995;4:903.

[155] Jiang X, Fryda M, Jia CL. Diam Relat Mater 2000;9:1640.

[156] Kobashi K. Diamond films: chemical vapor deposition for oriented and heteroepitaxial growth. Elsevier; 2005.

[157] Nistor L, Buschmann V, Ralchenko V, Dinca G, Vlasov I, Van Landuyt J, et al. Diam Relat Mater 2000;9:269.

[158] Gsell S, Bauer T, Goldfub J, Schreck M, Stritzker B. Appl Phys Lett 2004;84:4541.

[159] Fischer M, Gsell S, Schreck M, Brescia R, Stritzker B. Diam Relat Mater 2008;17:1035.

[160] Berdermann E, Pomorski M, De Boer W, Ciobanu M, Dunst S, Grah C, et al. Diam Relat Mater 2010;19:358.

[161] Bachmann PK. In: Prelas MA, et al., editors. Handbook of industrial diamonds and diamond films. New York: Marcel Dekker; 1997. p. 821–50.

[162] Ralchenko VG, Smolin AA, Konov VI, Sergeichev KF, Sychov IA, Vlasov II, et al. Diam Relat Mater 1997;6:417.

[163] Schäfer L, Höfer M, Kröger R. Thin Solid Films 2006;515:1017.

[164] Konov VI, Smolin AA, Ralchenko VG, Pimenov SM, Obraztsova ED, Loubnin EN, et al. Diam Relat Mater 1995;4:1073.

[165] Obraztsov AN, Kopylov PG, Chuvilin AL, Savenko NV. Diam Relat Mater 2009;18:1289.

[166] Kurihara K, Sasaki K, Kawarada M, Koshino N. Appl Phys Lett 1988;52:437.

[167] Pereverzev VG, Pozharov AS, Konov VI, Ralchenko VG, Brecht H, Metev S, et al. Diam Relat Mater 2000;9:373.

[168] Ravi KV. Diam Relat Mater 1995;4:243.

[169] Takeuchi S, Murakawa M. Thin Solid Films 2000;377/378:290.

[170] Bolshakov AP, Konov VI, Prokhorov AM, Uglov SA, Dausinger F. Diam Relat Mater 2001;10:1559.

[171] Gheeraert E, Deneuville A, Brunel M, Oberlin JC. Diam Relat Mater 1992;1:504.

[172] Nesladek M. Diam Relat Mater 1993;2:357.

[173] Lee JK, Eun KY, Baik YJ, Cheon HJ, Rhyu JW, Shin TJ, et al. Diam Relat Mater 2002;11:463.

[174] Ohtake N, Yoshikawa M. J Electrochem Soc 1990;137:717.

[175] Gray KJ, Windishmann H. Diam Relat Mater 1999;8:903.

[176] Lu FX, Zhong GF, Sun JG, Fu YL, Tang WZ, Wang JJ, et al. Diam Relat Mater 1998;7:737.

[177] Hei LF, Liu J, Li CM, Song JH, Tang WZ, Lu FX. Diam Relat Mater 2012;30:77.

[178] Sevillano E. Microwave-plasma deposition of diamond. In: Low-pressure synthetic diamond. Berlin: Springer; 1998. p. 11–39.

[179] Gritsinin SI, Kossyi IA, Malykh NI, Ralchenko VG, Sergeichev KF, Silakov VP, et al. J Phys D Appl Phys 1998;31:2942.

[180] SEKI Technotron Corp., http://www.sekitech.com.

[181] Asmussen J, Grotjohn TA, Schuelke T, Becker MF, Yaran MK, King DJ, et al. Appl Phys Lett 2008;93:031502.

[182] Füner M, Wild C, Koidl P. Appl Phys Lett 1998;72:1149.

[183] Wörner E, Pleuler E, Wild C, Koidl P. Diam Relat Mater 2003;12:744.

[184] Vikharev AL, Gorbachev AM, Kozlov AV, Radishev DB, Muchnikov AB. Diam Relat Mater 2008;17:1055.

[185] Yan CS, Vohra YK, Mao HK, Hemley RJ. Proc Natl Acad Sci 2002;99:12523.

[186] Liang Q, Chin CY, Lai J, Yan CS, Meng Y, Mao HK, et al. Appl Phys Lett 2009;94:024103.

[187] Meng YF, Yan CS, Krasnicki S, Liang Q, Lai J, Shu H, et al. Phys Status Solidi A 2012;209:101.

[188] Mankelevich YA, May PW. Diam Relat Mater 2008;17:1021.

[189] Silva F, Achard J, Brinza O, Bonnin X, Hassouni K, Anthonis A, et al. Diam Relat Mater 2009;18:683.

[190] Sergeichev KF, Lukina NA. Plasma Phys Rep 2011;37:1225.

[191] Frauenheim T, Jungnickel G, Sitch P, Kaukonen M, Weich F, Widany J, et al. Diam Relat Mater 1998;7:348.

[192] Wang WY, Moses T, Linares RC, Shigley JE, Hall M, Butler JE. Gems Gemol 2003;39:268.

[193] McMahon MW. Finer points. No. 3; 2013. 8.

[194] De Sio A, Di Fraia M, Antonelli M, Menk RH, Cautero G, Carrato S, et al. Diam Relat Mater 2013;34:36.

[195] Parikh NR, Hunn JD, McGucken E, Swanson ML, White CW, Rudder RA, et al. Appl Phys Lett 1992;61:3124.

[196] Marchywka M, Pehrsson PE, Vestyck DJ, Moses D. Appl Phys Lett 1993;63:3521.

[197] Mokuno Y, Chayahara A, Yamada H. Diam Relat Mater 2008;17:415.

[198] Janssen G, Giling LJ. Diam Relat Mater 1995;4:1025.

[199] Schermer JJ, de Theije FK, Giling LJ. J Cryst Growth 1996;165:387.

[200] Findeling-Dufour C, Gicquel A, Chiron R. Diam Relat Mater 1998;7:986.

[201] Kobashi K, Nishibayashi Y, Yokoya Y, Ando Y, Tachibana T, Kawakami N, et al. Diam Relat Mater 2003;12:233.

[202] Yamada H, Chayahara A, Mokuno Y, Umezawa H, Shikata SI, Fujimori N. Appl Phys Express 2010;3:051301.

[203] Shigley JE. Elements 2005;1:101.

[204] Yan CS, Mao HK, Li W, Qian J, Zhao Y, Hemley RJ. Phys Status Solidi A 2004;201:R24.

[205] Shul'zhenko AA, Ashkinazi EE, Sokolov AN, Gargin VG, Ral'chenko VG, Konov VI, et al. J Superhard Mater 2010;32:293.

[206] Meng YF, Yan CS, Lai J, Krasnicki S, Shu H, Yu T, et al. Proc Natl Acad Sci 2008;105:17620.

[207] Liang Q, Yan CS, Meng Y, Lai J, Krasnicki S, Mao HK, et al. J Phys Condens Matter 2009;21:364215.

[208] Sukhadolau AV, Ivakin EV, Ralchenko VG, Khomich AV, Vlasov AV, Popovich AF. Diam Relat Mater 2005;14:589.

[209] Deneuville A. In: Nebel CE, Ristein J, editors. Thin film diamond I. Amsterdam: Elsevier; 2003. p. 183–238.

[210] Koizumi S. In: Nebel CE, Ristein J, editors. Thin film diamond I. Amsterdam: Elsevier; 2003. p. 239–59.

[211] Barjon J, Chikoidze E, Jomard F, Dumont Y, Pinault-Thaury MA, Issaoui R, et al. Phys Status Solidi A 2012;209:1750.

[212] Belousov ME, Mankelevich YA, Minakov PV, Rakhimov AT, Suetin NV, Khmelnitskiy RA, et al. Chem Vap Dep 2012;18:302.

[213] Jackman RB, Baral B, Kingsley CR, Foord JS. Diam Relat Mater 1996;5:378.

[214] Takano Y, Takenouchi T, Ishii S, Ueda S, Okutsu T, Sakaguchi I, et al. Diam Relat Mater 2007;16:911.

[215] Mao HK, Bell PM. Science 1978;200:1145.

[216] Ruoff AL, Vohra YK. Appl Phys Lett 1989;55:232.

[217] Sumiya H, Nakamoto Y, Matsuoka T, Shimizu K, Ohishi Y. High Press Res 2008;28:217.

[218] Freund AK. Opt Eng 1995;34(2):432.

[219] Freund AK, Hoszowska J, Sellschop JPF, Burns RC, Rebak M. Nucl Instrum Methods A 2001;467–468:384.

[220] Sumiya H, Satoh S, Yazu S. Rev High Press Sci Technol 1998;7:960.

[221] Shvyd'ko YuV, Stoupin S, Cunsolo A, Said AH, Huang X. Nat Phys 2010;6:196.

[222] Shvyd'ko YuV, Stoupin S, Blank V, Terentyev S. Nat Photonics 2011;5:539.

[223] Amann J, Berg W, Blank V, Decker FJ, Ding Y, Emma P, et al. Nat Photonics 2012;6:693.

[224] Koivula JI, Fryer CW. Gems Gemol 1984;20:146.

[225] Shigley JE, Fritsch E, Stockton CM, Koivula JI, Fryer CW, Kane RE. Gems Gemol 1986;22:192.

[226] Shigley JE, Fritsch E, Stockton CM, Koivula JI, Fryer CW, Kane RE, et al. Gems Gemol 1987;23:187.

[227] Rooney M-LT, Welbourn CM, Shigley JE, Fritsch E, Reinitz I. Gems Gemol 1993;29:38.

[228] Seal M, Field JE, editors. The properties of natural and synthetic diamond. London: Academic Press; 1992. p. 607–36.

[229] Nam TL, Karfunkel U, Keddy RJ, Every AG. Radiat Eff Defects Solids 1991;116:233.

[230] Kaneko J, Katagiri M. Nucl Instrum Methods A 1996;383:547.

[231] Marczewska B, Kupriyanov I, Pal'yanov Yu, Nowak T, Olko P, Rebisz M, et al. Diam Relat Mater 2007;16:191.

[232] Benabdesselam M, Iacconi P, Gheeraert E, Kanda H, Lapraz D, Briand D. Rad Prot Dosim 2001;100:329.

[233] Morse J, Salomé M, Berdermann E, Pomorski M, Cunningham W, Grant J. Diam Relat Mater 2007;16:1049.

[234] Kononenko T, Bolshakov A, Ralchenko V, Konov V, Allegrini P, Pacilli M, et al. Appl Phys A 2014;114:297.

[235] Angelone M, Aielli G, Almaviva S, Cardarelli R, Lattanzi D, Marinelli M, et al. IEEE Trans Nucl Sci 2009;56:2275.

[236] De Sio A, Achard J, Tallaire A, Sussman RS, Collins AT, Silva F, et al. Appl Phys Lett 2005;86:213504.

[237] Balducci A, Garino Y, Giudice AL, Manfredotti C, Marinelli M, Pucella G, et al. Diam Relat Mater 2006;15:797.

[238] Pacilli M, Allegrini P, Conte G, Spiriti E, Ralchenko VG, Komlenok MS, et al. J Instrum 2013;8:C10013.

[239] Caylar B, Pomorski M, Bergonzo P. Appl Phys Lett 2013;103:043504.

[240] Conte G, Giovine E, Bolshakov A, Ralchenko V, Konov V. Nanotechnology 2012;23:025201.

[241] Kasu M, Ueda K, Yamauchi Y, Tallaire A, Makimoto T. Diam Relat Mater 2007;16:1010.

[242] Ueda K, Kasu M, Yamauchi Y, Makimoto M, Schwitters M, Twitchen DJ, et al. IEEE Electron Device Lett 2006;27:570.

[243] Kaminskii AA, Ralchenko VG, Konov VI. Laser Phys Lett 2006;3:171.

[244] Kaminskii AA, Hemley RJ, Lai J, Yan CS, Mao HK, Ralchenko VG, et al. Laser Phys Lett 2007;4:350.

[245] Feve JPM, Shortoff KE, Bohn MJ, Brasseur JK. Opt Express 2011;19:913.

[246] Kitzler O, McKay A, Mildren RP. Opt Lett 2012;37:2790.

[247] Mildren RP, Sabella A, Kitzler O, Spence DJ, McKay AM. In: Mildren RP, Rabeau JR, editors. Optical engineering of diamond. Weinheim: Wiley-VCH; 2013. p. 239–76.

[248] Millar P, Kemp AJ, Burns D. Opt Lett 2009;34:782.

[249] Mao WL, Mao HK, Yan CS, Shu J, Hu J, Hemley RJ. Appl Phys Lett 2003;83:5190.

[250] Yang W, Auciello O, Butler JE, Cai W, Carlisle JA, Gerbi JE, et al. Nat Mater 2002;1:253.

[251] Specht CG, Williams OA, Jackman RB, Schoepfer R. Biomaterials 2004;25:4073.

18 Wafer Processing

Hans-Joachim Möller[1,2]

[1]FRAUNHOFER TECHNOLOGY CENTER FOR SEMICONDUCTOR MATERIALS, FREIBERG, GERMANY; [2]TECHNICAL UNIVERSITY BERGAKADEMIE FREIBERG, INSTITUTE FOR EXPERIMENTAL PHYSICS, FREIBERG, GERMANY

CHAPTER OUTLINE

18.1 Introduction **716**
18.1.1 Overview 716
18.1.2 Economic Issues and Future Development 717
18.2 Multi-wire Sawing Process **718**
18.2.1 Technologies 718
18.2.1.1 Slurry-based Sawing 718
18.2.1.2 Fixed Abrasive Sawing 721
18.2.2 Process Investigations for Mono- and Multicrystalline Silicon 722
18.2.2.1 Slurry-based Sawing 723
18.2.2.2 Fixed Abrasive Sawing 728
18.2.3 Wafering of Other Materials 729
18.2.3.1 Electronic Grade Silicon 729
18.2.3.2 Compound and Dielectric Materials 729
18.3 Determination of Wafer Properties **730**
18.3.1 Surface Properties 731
18.3.1.1 Thickness, TTV, Roughness 731
18.3.1.2 Single Indentation Tests 733
18.3.1.3 Fracture Behavior 737
18.4 Basic Sawing Mechanisms **738**
18.4.1 Slurry-based Sawing 738
18.4.1.1 Material Removal Rate 740
18.4.1.2 Elastohydrodynamic Behavior of Slurry and Wire 742
18.4.1.3 Roughness and Subsurface Damage 744
18.5 Alternative Slicing Technologies **745**
18.5.1 Ion Implantation Technologies 745
18.5.2 Other Wafering Technologies 746
18.5.2.1 Layer Transfer Process from Porous Silicon 746
18.5.2.2 Laser Chemical Processing 747

Handbook of Crystal Growth. http://dx.doi.org/10.1016/B978-0-444-63303-3.00018-3
Copyright © 2015 Elsevier B.V. All rights reserved.

18.6 Grinding, Lapping, and Polishing **748**
18.6.1 Mechanical Machining 748
18.6.2 Plasma Chemical and Elastic Emission Machining 749
18.6.2.1 Plasma Chemical Vaporization Machining 749
18.6.2.2 Elastic Emission Machining 750
18.7 Conclusions and Outlook **750**
References **751**

18.1 Introduction

18.1.1 Overview

Artificially grown crystals usually have to be cut after growth so they can be used for electronic, optical, or other applications. The requirements on the size, the quality of the cut surfaces, and the slicing cost vary, however, considerably depending on the material and the application. Hard and brittle materials such as ceramics and semiconductors are mainly cut by sawing techniques. In all cases one needs abrasive materials for the process, which are harder than the material that has to be cut. Typical abrasive materials are diamond, silicon carbide, or boron nitride powders, but other materials have also been used. Cost and availability considerations decide which abrasive material is best suited.

In many cases crystals have to be sliced into wafers. Diamond-coated blades, ribbons, or wheels are available methods and first applied here. Particularly inner diameter (ID) saws were for a long time the dominant slicing machines because they allowed cutting large crystals with high accuracy and good surface quality. These methods are still used today for certain applications, where cutting speed is less important.

The increasing demand for a higher productivity led to the development of the multi-wire sawing technique. It was first used as the main wafer slicing technique for large multi- and monocrystalline silicon crystals in the photovoltaic industry. In the 2000s, the technology was also introduced into the microelectronic industry. The technique allows the cutting of thousands of wafers in one step. The advantages are a high yield in production and a good wafer quality. Through the continuous improvement of the technology, increasingly thinner wafers with less kerf loss can be cut today, which reduces the inevitable loss of expensive crystal material.

Considering the production volume of crystals in the photovoltaic and microelectronic industry, silicon is the dominant material. The advances in the multi-wire sawing technique were therefore mainly developed for this material, but the technical and scientific findings are applicable to other materials as well. The basic mechanism in all cases is the mechanical interaction of individual abrasive particles with the crystal surface. These micromechanical processes cause the material removal, but also lead to

an inevitable damage of the surface. The improvements of the sawing techniques became possible by the development of a deeper understanding of these micromechanical interactions. The following sections will mainly focus on the multi-wire sawing of silicon, but many results are also valid for other materials. The same basic micromechanical mechanisms also occur in grinding, lapping, and polishing processes, therefore the fundamental findings can also be applied to these techniques.

18.1.2 Economic Issues and Future Development

The mass market in the photovoltaic industry drives the development of the multi-wire technology [1–3]. About 80% of today's solar cell production is based on silicon bulk crystals and therefore requires the fabrication of wafers [4]. Considering that the production of wafers for solar cells has a cost share of about 15% of the final module cost [5], the cost pressure on the wafer fabrication is high. One of the reasons is that wire sawing needs expensive supply materials and is still accompanied by a substantial loss of high quality crystal material. Significant advances have already been made with the result that the module prices have dropped by 20% every year, which is typical for a growing and upscaling industry [6]. The goal for the next years is to reduce the cost below 0.5 €/W_p. Cost reduction of wafer processing is also an issue in the microelectronic industry, but the requirements on the process are different for each material.

In the photovoltaic industry one can expect that the wafer thickness will be reduced further in the future. The current wafer thickness is around 180 μm, but a reduction eventually down to 100 μm is predicted, because one can obtain more wafers from expensive silicon crystals [7]. Simultaneously, one has to reduce the wire diameters and the kerf loss. With deceasing thickness the wafer stability becomes an issue, because silicon is very fragile and can break more easily in the processing steps. This reduces the production yield.

In the microelectronic industry the wafers are generally larger and thicker. Here the surface flatness and quality and the loss of the expensive semiconductor material through wafer processing are the main problems. A more uniform wafer surface after sawing requires less material removal in the subsequent grinding, lapping, and polishing processes.

The multi-wire sawing process depends on many variable parameters, which makes it difficult to optimize the process in view of throughput, material losses, reduction of supply materials, and wafer surface quality. Most of the progress has been made by experience and improved machine technology. Further progress needs, however, a more basic knowledge about the microscopic details of the sawing process in order to slice crystals in a controlled way. In the following discussion, the principles of the multi-wire sawing process will be described as far as they are understood today. Most of the results are obtained for silicon, but the basic principles are also valid when sawing other brittle materials such as compound semiconductors or ceramics.

18.2 Multi-wire Sawing Process

18.2.1 Technologies

Worldwide only very few companies have developed multi-wire saws, which can fulfill the current requirements of the industry. The companies with the greatest market share are located in Switzerland, Japan, and the United States. Multi-wire saws are high precision machines, which have tolerances in the cutting area of a few micrometers.

The principle of a multi-wire saw is shown in Figure 18.1. A single wire is supplied by a spool, wound several hundred times around two to four wire guide rollers (depending on the machine type and the manufacturer) and picked up on the other side by another spool. Depending on the wire guide arrangement, one to four ingots can be cut at the same time. The wires are made from steel and have a thickness of 100–130 μm. The wire guide rollers have grooves, which guide the wires and keep them at a defined distance. The groove distance, the wire diameter, and the abrasive particle size determine the final thickness of the wafers.

The machines are loaded with ingots of a length between 300 and 1000 mm. Since today's mono- and multicrystals have dimensions, which do not fit into sawing machines, they first have to be cut into an appropriate shape. This is done first by special band, ID or wire saws, where the side and end parts of the crystals are removed.

18.2.1.1 Slurry-based Sawing

Today's dominant sawing technique uses saws, where the cutting is achieved by free-floating abrasive particles, which are suspended in a carrier fluid (loose abrasive sawing). The suspension or slurry is supplied through nozzles on the wire web and carried by the wires into the sawing channel. The crystals (ingots or bricks) that have to be cut into wafers are pushed through the wire web until the cut is finished. The motion can be either up- or downward into the wire web, depending on the machine type. This so-called slurry or loose abrasive sawing technique is applied worldwide in the photovoltaic and microelectronic industry [8].

The general requirement for the abrasive material is that it must be harder than the material that has to be cut. However, the crystal structure, the particle microstructure, and the outer shape of the particles can also be relevant properties. The abrasive powders for sawing applications have typical grain sizes between 3 and 20 μm. Table 18.1

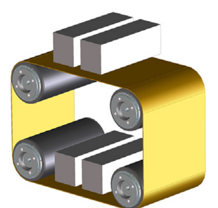
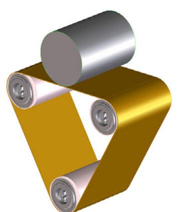
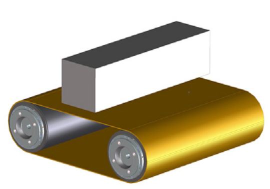

FIGURE 18.1 Principle of different wire guide arrangements of multi-wire saws.

Table 18.1 Crystal Structures, Vickers and Mohs Hardness values of Common Abrasive Powders

Material	Crystal Structure	Vickers Hardness (GPa)	Mohs Hardness	Ref.
β-C	Cubic (diamond)	75–100	10	[9]
β-BN	Cubic	45–50		[10]
β-B	Rhombohedral	30	9.3	[11]
B_4C	Rhombohedral	30–32	9.3–9.5	[12]
SiC	Cubic	26–28	>9	[9]
TiN	Cubic	21	8–9	[13]
Al_2O_3	Trigonal (sapphire)	20–21	9–9.5	[9]
Si_3N_4	Hexagonal	14–17	7.5–8	[14]
SiO_2	Trigonal	10	7	[15]
Si	Cubic	9–13	6.5–7.4	[16]
GaAs	Cubic	7.5	4–5	[17]

For comparison the corresponding data of silicon and gallium arsenide are included.

summarizes properties of some hard abrasive powders that can be used for sawing, grinding, or lapping applications.

SiC is the most commonly used abrasive today. Table 18.2 shows some typical parameters of SiC powders. The volume fraction of solid SiC particles in the carrier fluid can vary between 18% and 25%. Most of the commercial slurries are based on polyethylenglycol (PEG) carrier fluids. Others fluids such as monoethylenglycole (MEG), diethylenglycole (DEG), or dipropylenglycole (DPG) are also used. Further alternatives are water with some additives to improve the transport properties for the abrasive particles and oil. In fact, oil has been the main fluid in previous years and is still partly used in some Asian countries. Water-based slurries are currently under investigation, because they can be cheaper. The problems that have to be solved here

Table 18.2 Size Specifications of Commercial SiC Powders and Viscosities of Carrier Fluids at 20 °C

Grit	D50 (μm)	D97 (μm)	D3 (μm)	Fluid	Viscosity (Pa s)
F 2000	1.2	0.3	3.5	PEG 200	0.07
F 1500	2.0	0.4	5.0	PEG 300	0.09
F 1200	3.0	0.5	7.0	Oil	0.06–0.2
F 1000	4.5	0.8	10	Water	0.001
F 800	6.5	1.0	14		
F 600	9.3	1.0	19		
F 500	12.8	1.0	25		
F 400	17.3	1.0	32		

D50 mass median diameter, 3% of the SiC particles smaller than D97 and larger than D3.

are the lower transport properties and unwanted chemical reactions with the silicon, which leads to the production of hydrogen or the formation of silicates on the wafer surface.

Both fluids and abrasive particles deteriorate after some cuts. It is, however, possible to recycle the fluid and the SiC and mix a new slurry with additions of virgin SiC. Since recycling of the slurry and cleaning of the wafers is cheaper for PEG than for oil, this slurry is mainly used in industry today.

The main purpose of the slurry is to transport the abrasive particles into the sawing channel. Since material is continuously removed through the interaction of the SiC particles with the silicon and wire surface, the slurry is enriched with fine-grained debris of silicon and iron. The abrasive action of the SiC depends on many factors such as wire speed, force between wire and crystal, the solid fraction of SiC in the suspension, the viscosity of the suspension, and the size distribution and shape of SiC particles. The viscosity of the slurry depends on the temperature and the solid fraction of particles and changes because of the continuous abrasion of silicon and iron from the wire. A kerf loss around 120–160 μm per wafer with 180 μm thickness is typical today.

In today's industrial machines the wires move in one direction with a speed between 10 and 20 m/s. Therefore, in a standard cutting process between 300 and 500 km of wire are used. The wires are used only once, but the slurry can be used 2–4 times and is then recycled. The cutting speeds are around 0.3–0.5 mm/min, which yields a total cutting time of about 8–13 h for a standard ingot cross-section of $156 \times 156\ mm^2$.

Modern machines can cut several ingots simultaneously and yield between 2000 and 5000 wafers in one run. Currently, wafers with a thickness of about 180 μm are cut. The thickness varies, however, along the direction of the wire motion and is higher at the wire outlet. This is due to the unidirectional motion of the wire and changes of the sawing activity along the wire channel. The change of the wafer thickness should be, however, less than 15 μm (specified by the total thickness variation parameter; TTV) for high quality wafers.

The objective of efficient sawing is to slice with a high throughput, a minimum loss of slurry and silicon, and a high quality of the resulting wafers. The control of the process is very complex, since many parameters can be varied and may have an impact on the wafer quality and yield. The optimization of the sawing is therefore a difficult task. Important are the control of wire speed, wire tension, cutting speed, and other machine parameters, but also of parameters concerning the composition and properties of the abrasive SiC powders and the carrier fluids [18–21].

Currently, two improvements of the sawing technology are being tested: the use of structured steel wires and the use of wires that are coated with diamond particles (fixed abrasive wires). In the first case, the wires have small kinks at certain distances, which improves the transport of slurry into and through the sawing channel. In the second case, the cutting is achieved by the fixed abrasive diamond particles on the wire. The advantage in both cases is that the cutting speed can be increased.

18.2.1.2 Fixed Abrasive Sawing

Most of the industrial multi-wire saws today can also be used with fixed abrasive wires. The technique itself has been applied for a long time to cut hard materials such as sapphire crystals. The slurry is replaced here by a coolant such as water.

Recent developments have shown that fixed abrasive wires can also be used to cut silicon wafers [22–27]. The requirements on the wafer quality in the photovoltaic industry are, however, different compared for instance to sapphire. Wafers and wires have to be much thinner to reduce the loss of expensive silicon material. The quality of the wafer surface, such as roughness, TTV, and subsurface damage, has to be high and at least comparable to conventionally sawn wafers. Furthermore, there must be a cost advantage. Since the diamond-coated wires are at present (2013) still more than 50 times more expensive (about 70–100 €/km), one has to reduce cost by higher sawing speeds and multiple use of the wires. The goal here is a cost reduction of more than 20% and at least maintenance of the present wafer qualities. Up to now the technology has not been introduced into the high volume production PV market. An exception is in Japan, where fixed abrasive sawing already has a market share.

Although the fixed abrasive sawing technique is certainly not optimized, estimations of the cost have been made for the Japanese market [28]. Based on current parameters for monocrystalline silicon (in 2012) the cost of consumables per wafer are 0.07 €/wafer, which is still higher compared to 0.05 €/wafer for a slurry-sawn wafer. An introduction of the technology in mass production is not expected before the year 2020.

Figure 18.2 shows the surface of such a wire with fixed diamond particles. There are three techniques to fix the particles on the surface: resin bonding, electroplating bonding, and blazing. Only the first two are currently considered. Resin bonding is cheaper to manufacture, but the particles are less strongly bonded. Therefore, the wires cannot be loaded too much, which reduces the performance. In the electroplating technique, the particles are embedded in a nickel coating layer, which gives a stronger bond, but at the expense of the cost. One can expect, however, that a mass production of such wires will reduce the wire cost substantially.

In fixed abrasive sawing the machines are operated in an oscillating (pilgrim) mode, where the wire is moved back and forth. Typically, the wire runs for several hundred meters in one direction before it is stopped and the motion direction is reversed. In each cycle a few meters of new wire are added in one direction.

Since higher cutting speeds can be achieved (>1 mm/min) the cutting times can be reduced to 2–3 h. The wire consumption is about 5 km per cut and thus very much reduced. Many of the current industrial saws allow high wire and cutting speeds. The

FIGURE 18.2 Steel wire coated with diamond particles.

sawing machines therefore require almost no modifications to operate with the diamond-coated wires. Recent results indicate that better wafer qualities can be achieved for lower wire bows. This can be achieved by a higher wire tension or a shorter distance between the wire guide rollers. Dedicated fixed abrasive wire saws have already been developed, which incorporate these improvements.

The competitiveness of the fixed abrasive technique depends on the cost per wafer. In recent years the cost of the wires could already be reduced, but other factors are also important. During sawing the wafer surface is damaged, as will be discussed in the next section in detail. This reduces the mechanical stability of the wafers, which is important for the following processing steps of the wafers, such as cleaning, solar cell processing, and module manufacturing. With increasing cutting speeds the wafers become more instable and the wafer yield is reduced.

Experience so far indicates that fixed abrasive sawing is able to cut monocrystalline ingots into wafers of standard thickness of 180 μm. The wafer surface quality is good but may require an adjustment of the following etching processes for texturization and further solar cell processes. The results also show that sawing multicrystalline wafers works less well [29]. The wafer surface quality is lower and wafer breakage more frequent. The reasons for these differences between mono- and multicrystalline silicon will be discussed in the next section. Such a difference between the two materials is not observed for slurry-based sawing.

Consideration of the industrial development of wafers of less than 100 μm may be required in the future. At present, such thin wafers cannot be handled in the downstream process of solar cell and module fabrication. Thinner wafers require adopted solar cell designs, because they absorb less light. Such processes have not been implemented into the standard production chain. In addition, the following industrial processing steps, which require mechanical handling of the wafers, are even more prone to breakage because of the lower fracture toughness. Therefore, it is still uncertain whether multicrystalline silicon can be sawn on an industrial scale with this technique.

18.2.2 Process Investigations for Mono- and Multicrystalline Silicon

Industrial multi-wire saws allow one to record machine parameters during the entire process, such as wire and cutting speed, wire tension, power consumption, slurry flow, temperature, etc. More detailed information can be obtained from measurements of the forces on the wires, the resulting wire bow, and the temperature variation along sawing channel. This requires the installation of special diagnostic tools into sawing machines. Furthermore, it is important to analyze the as-cut wafer surfaces, the wire surfaces, and the slurry properties. Quantitative force measurements have been carried out on single wires as well as with many wires. In the latter case one has to consider that the wire properties may change from the first to the last wire due to wire wear [30–33]. Typically, one measures the forces perpendicular to the wire, in the direction of ingot motion, and parallel to the wire. The latter gives the friction force of the sawing process. Due to the

friction, the temperature increases along the sawing channel. Measurements have shown that the temperatures close to the exit region can increase up to 80 °C [34]. These variations are important to know since the viscosity of the slurry depends exponentially on the temperature.

18.2.2.1 Slurry-based Sawing

18.2.2.1.1 FORCE IN INGOT FEED DIRECTION

Figure 18.3 shows the applied vertical total force on a single wire as a function of the ratio of feed velocity over the nth power of the wire velocities. For $n = 1125$, a straight line is obtained. The sawing rate can thus be summarized by the equation

$$v_s = v_{so} v^n F_{tot} \tag{18.1}$$

where v is the wire velocity and F_{tot} the total force on the wire. This equation is known as the Preston equation (for $n = 1$) and is used for material removal processes such as lapping and polishing [35–37]. Some investigations indicate, however, that the velocity exponent for sawing may be slightly higher, being $n \approx 1.1$–1.3, but such measurements are often not precise enough to yield an exact value. In some measurements one has also observed that the material removal starts above a certain threshold value of about 0.0–0.03 N per wire. This has been explained with a minimum load on the abrasive particle that is required for the chipping mechanism to operate.

The prefactor v_{so}, the Preston coefficient, depends on many factors such as wire tension, slurry viscosity, temperature, SiC concentration, etc. It is therefore difficult to make quantitative predictions about the sawing process when these factors change. A more detailed investigation of the underlying sawing mechanism, as discussed in the next section, will give a better physical description of this prefactor.

18.2.2.1.2 FRICTION FORCES

The friction force in wire direction is depicted in Figure 18.4. It increases both with the feed (a) and the wire velocity (b) [38]. An important feature is that there is friction even

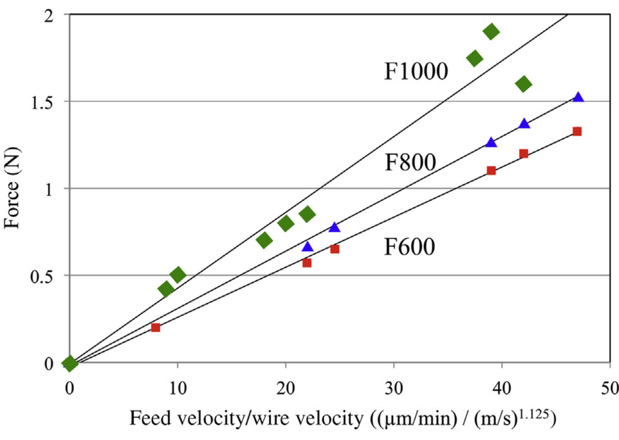

FIGURE 18.3 Force per wire in cutting direction (ingot feed motion) as a function of the ratio of feed velocity/(wire velocity)^n for different grit sizes ($n = 1.125$) [31,32].

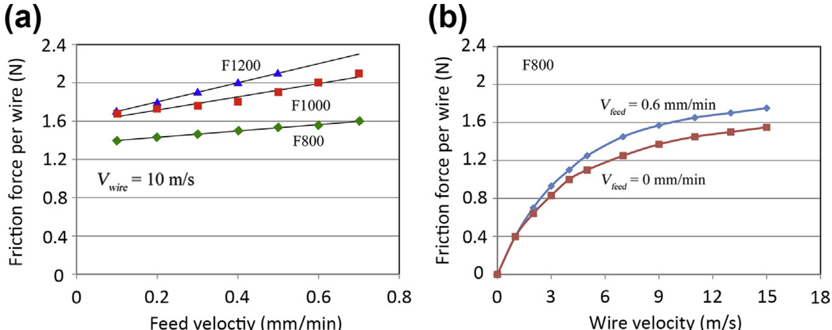

FIGURE 18.4 Force measurements parallel to a single wire as a function of the feed (a) and wire velocity (b) for different grit sizes (PEG 200 and a SiC volume fraction of 23%).

without sawing (for zero feed velocity). This indicates that the friction force is less determined by the interaction of the SiC particles with the wire and crystal surfaces but mainly by friction processes inside of the slurry. These can be the interactions between particles, the internal friction in the fluid, and the interaction forces between particles and fluid. Therefore, it is not surprising that the particle size is also important, as can be seen in Figure 18.4. In general the friction forces increase for finer grit sizes. It has also been observed that there is a slight dependence on the shape of the size distribution. Bulkier particles lead to more friction.

The friction is responsible for the temperature increase along the sawing channel. Since the viscosity is exponentially dependent on the temperature (see next section), there is a substantial change of the viscosity along the sawing channel. All factors that affect the friction force thus also have an impact on the viscosity.

Sawing experience shows that small changes of the slurry temperature can have a significant influence on the sawing result. Therefore, good control and stabilization of the slurry temperature is very important in the sawing process. The ramifications of the slurry temperature on the wire sawing process will be discussed in Section 3.2.2.

18.2.2.1.3 DEPENDENCE ON SLURRY PROPERTIES

Many experimental results show that the slurry properties play an important role in the sawing process. It is, however, difficult to understand the various dependences because of the complexity of the interactions. The slurry has to transport the abrasive particles into the sawing channel and to remove the silicon and iron debris (from the steel wire) out of the sawing channel [39,40]. Figure 18.5 shows that there is an influence of the slurry viscosity on the force per wire in the table feed and wire direction. In both cases the forces increase with the viscosity (measured at room temperature and with suspended SiC powder). These and many other measurements, where viscosity effects have been investigated, are, however, difficult to analyze. One of the problems is the correct determination of the viscosity. At present no reliable conditions have been defined for such measurements.

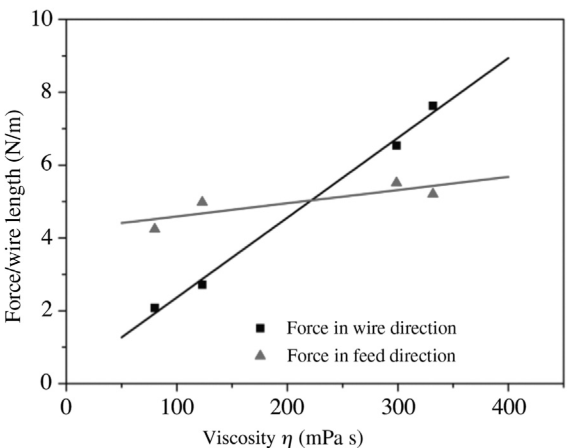

FIGURE 18.5 Dependence of friction and feed forces per wire on the slurry viscosity.

Standard practice is to take measurements with conventional viscometers, which determine the viscosity for shear velocities, which are, however, about a factor of a thousand smaller than the ones that occur in the sawing channel. Recent measurements at these high shear rates indicate that the viscosity decreases a little, but systematic measurements are currently not available [41,42].

A second factor that has to be considered is the change of the carrier fluid viscosity with the volume fraction of solid material, which is suspended in the fluid. This is depicted in Figure 18.6 for different slurries with SiC loading. The general trend is that with increasing volume fraction the viscosity increases. One can also see that a smaller grit size increases the viscosity as well. In general, the dependence on the solid volume fraction ϕ can be approximated by the Krieger–Dougherty relationship

$$\eta = \eta_o (1 - \phi/\phi_o)^{-q} \tag{18.2}$$

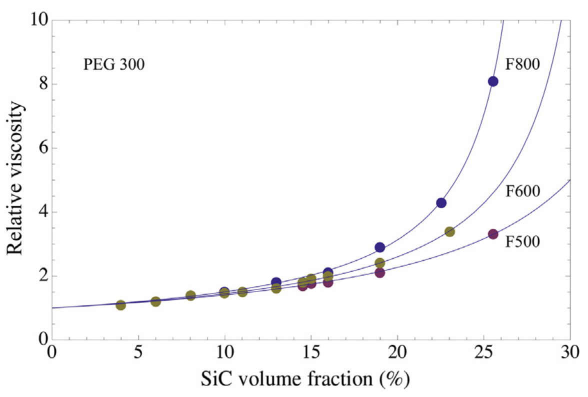

FIGURE 18.6 Relative viscosity as a function of the volume fraction of SiC in a PEG 300 carrier fluid for different grit size distributions.

if appropriate parameters are selected for ϕ_o and q. η_o is the viscosity of the carrier fluid [43]. The experimental data given here yield values for $q \approx 1$.

During sawing the solid volume fraction in the fluid changes in the sawing channel because of the removed silicon and the wear of the wire. The debris is finer than the average SiC grain size. Therefore, one can expect an increase in the viscosity due to the increased volume and the contribution of finer particles. Because of the temperature changes in the sawing channel, one also has to consider the temperature dependence of the viscosity. Generally the viscosity decreases with increasing temperature T according to an Arrhenius law $\eta_o = \eta_{oo} e^{Q/RT}$, where Q is an activation energy and R the universal gas constant [44].

Carrier fluids from different suppliers can have quite different activation energies, because the composition of the main carrier fluids, polyethylenglycol or oil, and the basic molecules can be modified to some extent.

The viscosity at the entry and exit of the sawing channel differs and can decrease by a factor of 3–4, when the temperature increases from 20 °C to 60–80 °C. Today experimental results are compared using the original slurry viscosity measured at room temperature. No procedures exist how to take into account the various factors that cause viscosity changes along the sawing channel, or how to determine a relevant viscosity value correctly. Since the influence of the slurry on the sawing performance is a key factor, further research is required to better understand the role of the slurry in the sawing process (see Section 18.4.1).

18.2.2.1.4 WIRE TENSION

Control of the wire tension is very essential in the sawing process, both to prevent wire breakage and to guarantee stable sawing conditions. The sawing machines therefore have sophisticated control mechanisms. The wire tension is kept constant before and behind the wire web, mostly at a value of 20–25 N. Changes of the wire tensions between the wire guide rollers in the cutting area cannot be controlled. Recent investigations have shown that the wire tension is actually reduced from the first to the last wire in the web due to two effects [32,33]. During the first 50 mm in the wire web the wire is plastically deformed by about 0.25%. It could be shown that this is due to the repeated chipping events and/or sticking at SiC precipitates in the silicon crystal, which momentarily hinder the motion of the wire at this position and stretch it beyond the elastic limit. This effect saturates after some time since the material hardens due to the plastic deformation. The second reason is the wire wear, which reduces the diameter of the wire continuously up to about 10%. A total reduction of the tension by about 25% has been measured over an ingot length of 220 mm.

In production the cutting speed has to be reduced and adjusted to the performance of the worst wires, but this wastes the potential of the wire at the beginning of the cut. Possible countermeasures are to change the diameter of the wire guide rollers parallel to the ingot so that the free length of the wire between the wire guides is reduced. This is, however, not yet standard practice in industrial production.

18.2.2.1.5 WAFER THICKNESS, WIRE DIAMETER, AND PARTICLE SIZE DISTRIBUTION

The expected future reduction of wafer thickness will also require a reduction of the kerf loss by using thinner wires. It has been demonstrated that one can slice 100-μm-thick wafers with 80-μm wires and probably even less [45,46]. Such investigations also have shown that one has to adjust the mean size of the abrasive particle. The results given in Figure 18.7 indicate that there is an optimum average grit size for each wire diameter [47].

Finer grain diameters result in a reduced sawing velocity and higher forces on the wire. If the resulting stress exceeds the fracture strength the wire will break. Commercial steel wires have fracture stresses around 4 GPa and can bear forces around 40–50 N. Calculations of the wire stresses as a function of the total applied forces, which have been obtained from experimental results, show that for thinner wires and finer grit sizes one approaches the fracture stress of wires [48]. Because of this limit for commercial wires, one cannot increase the cutting velocity too much. At present it appears that F600 or F800 are already the best choices, so that it is not clear how much the wafer thickness and the kerf will actually be reduced in the future. At present one cannot saw 100-μm wafers with wires of 100 μm or less under production conditions, where one needs a high yield.

18.2.2.1.6 SAW MARKS

Experimental results as well as the experiences from industrial sawing experience show that the sawing process can become unstable under certain conditions. This instability leads to the occurrence of deep grooves on the wafer surface. They are commonly called outlet grooves or saw marks (Figure 18.8). Such wafers cannot be processed further and therefore reduce the production yield.

A typical feature of saw marks is that they are mainly observed at the wafer side, where the wire leaves the sawing channel during cutting. They occur randomly and do

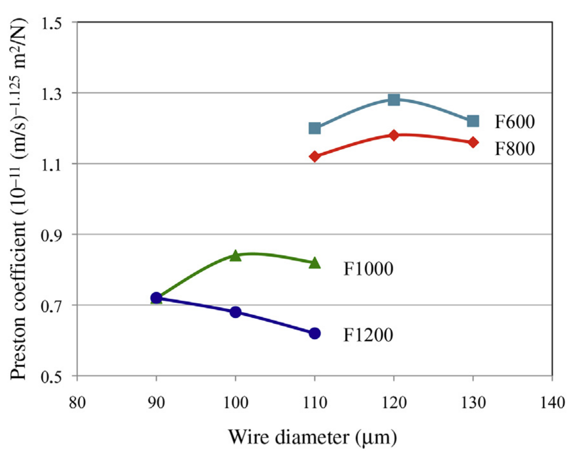

FIGURE 18.7 Preston coefficient as a function of the wire diameter for different grit sizes [47].

FIGURE 18.8 Part of an as-sawn silicon wafer surface showing saw marks.

not affect all wafers in one batch. Because of the statistical nature of their occurrence, one needs a large number of wafers to determine the conditions under which saw marks occur. Such data are available in an industrial production process, where thousands of wafers are cut, but systematic data have not been published. There are indications that a high sawing velocity v_s, a low SiC load, and high slurry temperatures enhance the probability for the occurrence of saw marks [49,50].

In the industrial process sawing conditions have to be chosen where saw marks can be avoided. The drawback is that in particular higher sawing speeds cannot be reached, which reduces the productivity. Recently an improvement of the slurry-based sawing could be achieved by the use of structured wires. These are wires that contain periodic kinks. This can improve the slurry transport in the sawing channel, so that higher sawing speeds (by about 20%) become possible.

Considering the observed dependencies one can assume that a homogenous slurry transport along the entire sawing channel is important for a stable process and a good wafer quality. A possible explanation, which has recently been proposed, will be given in Section 4.2.1.

18.2.2.2 Fixed Abrasive Sawing

The experimental results with fixed abrasive wires are at present not as detailed as the slurry-based experiences [24,51–54]. Systematic measurements of forces and temperatures have not yet been carried out. So far one has tried to optimize the process with respect to low wire wear, a longer lifetime of the wire, higher sawing speeds, or an improvement of the wafer surface quality.

Wire breakage is a serious problem because of the high wire cost. Diamond-coated wires are more prone to wire breakage due to the protruding particles on the surface. The wire can get stuck in the sawing channel or during winding-up in the spools. One has to find sawing conditions under which that problem can be reduced. Wire wear is also important because diamond particles can break out, which reduces sawing performance. The loss of abrasive particles determines the number of cycles in the oscillating mode for which a wire can be used. This problem may become less so when improved wires become available in the future.

During typical sawing conditions about 300–800 m of wire are used in one direction before the wire motion is reversed. The backwards movement is shorter by about a few meters so that in each cycle a fresh wire segment is added. The deceleration and acceleration phases have to kept short but depend on the machine type. Deceleration times down to 2 s are feasible today, but one can expect that improved machine types will be constructed in the future, when the technique becomes more established. The cutting times of a standard silicon ingot can be reduced today by approximately a factor of two. Another aspect that has to be taken into account is the wafer quality, which will be discussed next.

18.2.3 Wafering of Other Materials

18.2.3.1 Electronic Grade Silicon

The multi-wire sawing technique has also been introduced to saw monocrystalline wafers for the microelectronic industry. Today 300 mm wafers with a thickness of about 650 μm are the standard size. The requirements on the sawing process are different from those for the solar cell wafers. Whereas cutting speed and fracture stability are less demanding requirements, the planarity over the entire wafer surface is very important. Although the processing steps of grinding, lapping, and polishing produce the final surface quality with planarities in the nanometer range, the sawing step also has to be very precise. Thickness variations that occur here require higher efforts in the following steps to remove them and are therefore expensive.

The wafers are cut in the oscillating mode, which avoids the wedge shape of the slurry-sawn wafer. The adjustments of the wire speed, tension, and other parameters already enable the production of high quality wafer surfaces. A problem that remains, however, is when the wires first cut into the crystal. It has been observed that the wafers often show a shallow bump of a few micrometers at the rim of the surface there, which has to be later removed. It is assumed that the wires move sideways before they cut into the material and straighten out afterward during cutting. The reason for the sideward motion is not quite clear, but may have to do with some irregularities on the crystal surface. The precise control of the wire motion through the crystal is the most demanding requirement when cutting monocrystalline wafers [55].

18.2.3.2 Compound and Dielectric Materials

When considering production volumes, gallium arsenide, silicon carbide, and sapphire are the most important compound materials. They are used either as monocrystalline bulk materials or as substrates for the deposition of thin semiconductor films. Typical applications are lasers, light-emitting diodes, high frequency integrated circuits, or solar cells. In all cases, a very high surface quality is an essential requirement for the further processing steps.

Multi-wire sawing has also been introduced with these materials, but has to be adapted. Whereas silicon carbide and sapphire are very hard materials, gallium arsenide

has a hardness lower than that for silicon (see Table 18.1). In the first case, diamond powders or wires with fixed diamond particles have to be applied. Cutting is slow and requires high forces. The surfaces are therefore highly damaged and require further grinding, lapping, and polishing processes to achieve a damage-free surface.

In contrast, gallium arsenide can be cut very efficiently with conventional SiC slurries. However, a particular problem can occur here for cuts along (111) oriented surfaces. In this case the two opposite surfaces along the cut are crystallographically different because they terminate either with a gallium or an arsenic atom. When applying a constant force on the wire, as is the case in a sawing machine, the amount of material that is removed differs on both sides. The wire will experience a sideward motion due to the stronger material removal on the softer surface during the cutting. The effect can be suppressed by using certain crystallographic orientations, for which the micro-mechanical processes on both side are equal [56].

Very hard materials such as sapphire, silicon carbide, or in the future gallium nitride require harder abrasives such as diamond or boron nitride powders to slice wafers. So far the interest has been to slice these materials efficiently without paying too much attention to the wafer surface. The final quality of the surfaces is achieved by the subsequent grinding, lapping, and polishing steps. The required surface quality is determined by the application for which the wafers are determined. Sapphire and SiC wafers for instance are used as substrates for the fabrication of light-emitting diodes. This requires high quality surfaces, which can only be achieved by a final polishing step. If, however, sapphire wafers are used as cover glasses for watches and mobile phones, the previous steps also have to be fast and efficient to reduce cost. In general, wafers can be sliced both by the fixed abrasive and loose abrasive method using diamond powders.

18.3 Determination of Wafer Properties

The detailed evaluation of the sawing process requires a careful analysis of the wafer surface quality. For instance, for the solar cell process it is preferable to have wafers with uniform thicknesses and low surface damage. The thickness variation of a wafer is thus an important specification parameter for a wafer. The wafer surface damage can be described by the roughness and subsurface damage, which consists of microcracks mainly perpendicular to the surface and usually between 2 and 20 μm in length. The microcracks are generated by indenting the abrasive particles. They extend from the wafer surface into the volume and directly determine the wafer stability. These cracks depend on the shape, size, and indenting force of particles, wire load, and wire speed.

This damage has to be removed before further processing. For solar cell applications this is done by etching. Experience shows that the etching process depends on the as-sawn surface profile. It requires, for instance, adjustments if the wafer are sawn by with fixed abrasive wires, because they have a different surface profile. For microelectronic applications, planar and defect-free surfaces are required (see Section 18.6).

18.3.1 Surface Properties

18.3.1.1 Thickness, TTV, Roughness

The surface profiles of wafers sawn with loose abrasives (slurry) and fixed abrasives (diamond-coated wires) are completely different (Figure 18.9). In the first case, a uniform surface profile, consisting of statistically distributed shallow pits, occurs (Figure 18.9(a)); whereas in the second case the surface profile shows mainly parallel grooves (Figure 18.9(b)). The depths and distances of the grooves depend on the sawing conditions. This already indicates that the underlying material removal process differs in both cases [52,57–60].

Although the slurry-sawn wafer surfaces appear rather uniform, measurements show that the wafers are thinner at the side where the wire has entered the sawing channel. The thickness difference can be about 10–40 μm depending on the sawing conditions. Correspondingly, the channel or kerf width decreases. This indicates that the material removal process varies along the wire motion. Similar variations can also been seen in the surface roughness and, as shown in the next section, in the microcrack length. From wire inlet to wire outlet the roughness decreases. The absolute values depend on the grit size, the slurry viscosity, and to some extent on the feed rate and the wire velocity.

An important industrial parameter for the wafer characterization is the total thickness variation. It is an average of thickness measurements at five positions on the wafer, four at the corners and one in the middle. High quality wafers have a TTV below 15 μm. It has been shown to be independent of the wafer thickness and to be related to the mechanism of material removal in the sawing channel [12,13]. Considering that the thickness of the wafers will decrease further in the future, the percentage of the TTV compared to the whole thickness of the wafer rises to unacceptable values if the TTV is not reduced as well. It is therefore important to understand the processes that determine the TTV. Two major factors have been identified so far: the size distribution of the abrasive particles and the slurry viscosity. The role of the slurry transport is less obvious and has long been underestimated. Recent investigations [61] have proven, however, that there is a linear

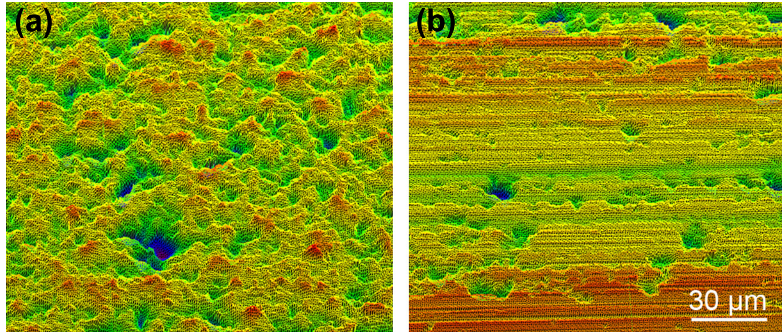

FIGURE 18.9 Surface height profile of a slurry-sawn wafer (a) and of fixed abrasive sawn wafer (b), measured by confocal optical microscopy.

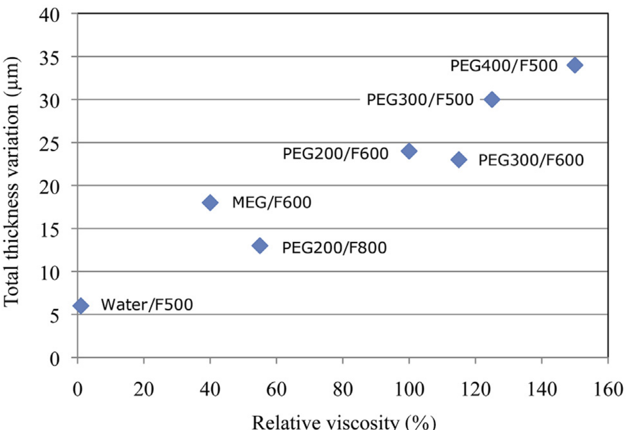

FIGURE 18.10 Total thickness variation (TTV) versus relative dynamic viscosity for different slurries with PEG 200/F600 as a reference slurry [61].

dependence of the TTV on the slurry viscosity (Figure 18.10). The mechanisms behind this behavior will be discussed in Section 18.3.

18.3.1.1.1 SUBSURFACE DAMAGE

The most reliable technique to determine the subsurface damage is the direct observation of the microcracks. This can be done by scanning electron microscopy on cross-sections of the wafer (Figure 18.11) or by optical microscopy on beveled, polished surfaces, which are slightly etched (Figure 18.12). For slurry-sawn wafers the microcrack depth decreases toward the wire outlet and is strongly influenced by the size distribution of SiC sawing particles. Finer grit sizes reduce the damage depth [58]. These results correspond to the roughness.

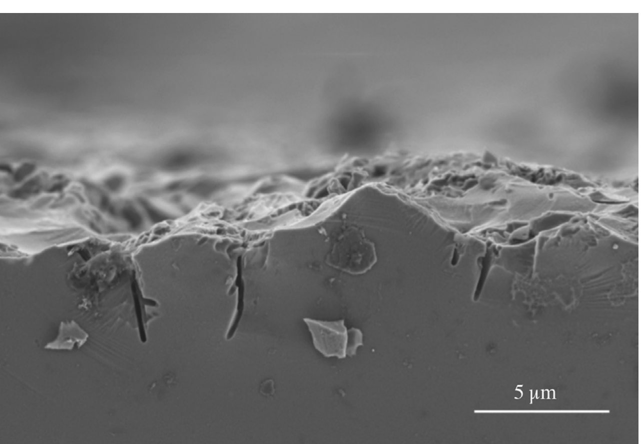

FIGURE 18.11 SEM image of microcracks at a cross-section of a slurry-sawn wafer.

FIGURE 18.12 Optical microscope image of an etched, beveled wafer surface after fixed abrasive sawing. The microcracks are aligned along the wire motion direction.

Roughness and crack depth are therefore both dependent on the position at the wafer surface. They change in the same way because both parameters originate from the same indentation process during wire sawing. Microcracks also occur on wafers sawn with fixed abrasives, but their distribution and sizes differ [52]. The cracks are aligned along the direction of the sawing grooves and show a distinct pattern, which is repeated periodically.

A further difference is that the surface can become amorphous locally. This has been observed by Raman spectroscopy. The extension of the amorphous regions depends on the sawing conditions [62]. No systematic investigations exist so far about the extension of these regions. It is also still unknown how and under which conditions the crystalline-to-amorphous transformation of silicon occurs. Single scratching experiments as described in the next section may give some indications about these transformation processes.

The amorphization of the surface can have an impact on the etching behavior. Since this is an important processing step before solar cell fabrication, it may be difficult then to produce a uniform, textured surface.

18.3.1.2 Single Indentation Tests

18.3.1.2.1 LOOSE ABRASIVE SAWING

There is general agreement today that in the slurry-based sawing, free-floating abrasive particles in the sawing channel remove material by rolling and indenting into the silicon crystal surface. The same interactions are known from lapping processes and similar dependencies can be derived here. The coarser particles are in direct contact with the wire and the silicon surface. The wire is pushed against the particles and indents these particles in the silicon surface. The particles below the wire are mainly responsible for the material removal process, and the particles at the side of the sawing channel determine the damage on the wafer surface.

The individual particle interaction processes have been studied by indentation experiments with a microhardness tester. A geometrically defined sapphire or diamond tip is indented under load into a silicon surface. The resulting damage pattern and the extension of the cracks is then determined. From the large number of results that have

been published for silicon [63–74], the following sequence of events can be deduced (Figure 18.13).

At low loads a plastic zone forms first. The diameter a depends on the applied load F and can be described by the following equation:

$$a = \left(\frac{\alpha}{4H \tan[\varphi]^2} F \right)^{1/2} \tag{18.3}$$

H is the hardness of the material, φ the angle of the indentation tip, and α a geometry factor. If the load is increased, the material breaks and different types of crack systems can occur depending on the crystal orientation and the tip geometry. So-called median and/or radial cracks directly under the load tip extend vertically into the surface. The force dependence of the median crack length is given by

$$c = \left(\frac{\beta}{K_c} F \right)^{2/3} \tag{18.4}$$

K_c is the fracture toughness of the material and β a geometry factor. For the Vickers indenter the parameter $\alpha = 2$, for a Knoop indenter $\alpha = 4/\pi$, while the best fit value $\beta = 1/7$ varies considerably in published data. Measurements for monocrystalline silicon at room temperature yield $H = 10.6$ GPa [49,50] and $K_{IC} = 0.75$ MPa $m^{1/2}$ in large-grained polycrystalline silicon [72,73].

When the load is removed, the stress difference between the plastic zone and the crystalline silicon leads to the formation of lateral cracks. When they reach the surface, a piece of material is removed (chipping). This process is responsible for the material removal in the sawing process. The volume of the chipped material has been determined experimentally and depends on the applied load by a power law with an exponent $n = 2.2$

$$V_o = \gamma F^n \tag{18.5}$$

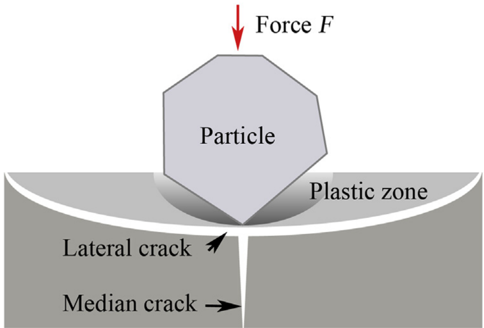

FIGURE 18.13 Indentation of a single particle into the surface. Under the action of the normal force, a plastic zone and cracks are formed. The extension of the lateral cracks and the depth of the plastic zone determine the chipped volume.

γ is a geometry factor [74]. Since the formation of the median cracks occurs before the chipping, these cracks partially remain in the crystal surface at the side of the sawing channel. They form the saw damage of the as-sawn wafers [75–80].

18.3.1.2.2 FIXED ABRASIVE SAWING

Much less is currently known about the single indentation process of particles for the fixed abrasive sawing. There is general agreement that material removal occurs by scratching the diamond particles over the crystal surface. Although this is known from grinding processes on ductile materials, not much is known about the microscopic details for silicon. Recent experimental scratching tests with a single particle tip on a monocrystalline (111) silicon surface have given the following results. Figure 18.14 shows a typical scratch pattern after such a test. It resembles the patterns that are observed on as-sawn wafers (Figure 18.12). An important feature is the periodicity, which has been explained by a periodic sequence of several microscopic events [51,52].

In the first step, the scratching tip is indented into the surface by the back force of the bowed wire. Since the tip is also pulled by the wire in wire motion direction, the resulting force faces obliquely into the bulk. The stress that builds up has not been calculated so far, but one can assume that it consist of tensile stresses behind the tip and compressive stress components in front of the tip (Figure 18.15). The stresses depend on the tip shape and the orientation of the crystal. This could be confirmed by the experimental results. The stresses eventually will lead to cracking. Usually one can expect a crack directly in

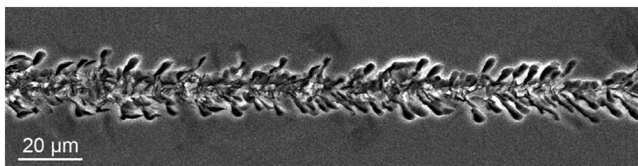

FIGURE 18.14 Single scratch test showing periodic crack patterns on the surface.

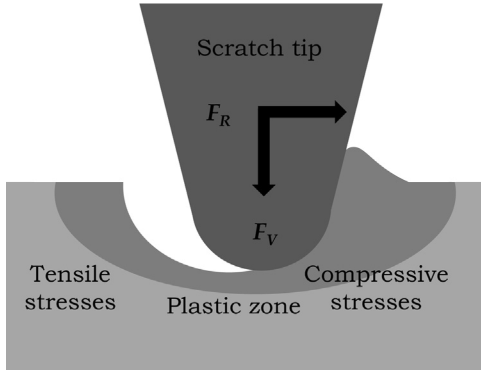

FIGURE 18.15 Schematic diagram of the forces and stresses at a scratching tip.

front of the moving direction and several cracks to sides. Because of the oblique force, some cracks will chip material away mainly in front of the tip. Once the material breaks, the tip can move a certain distance before it is blocked again. Then the process of stress buildup and breakage repeats.

The lengths of the cracks depend on the applied forces both in wire direction and in the vertical (indentation) direction. Quantitative measurements yielded a crack length dependence on the applied forces given in Figure 18.16. A slight dependence on the crystal orientation was also observed [52].

Recent measurements of the crack length distribution in multicrystalline silicon also showed a correlation with the grain orientation [35]. This result may give an explanation for the observed difference of the lower stability of multicrystalline wafers compared to monocrystalline silicon after fixed abrasive sawing. If one assumes that there are always unfavorable grain orientations, which yield deeper cracks, these “weaker” cracks determine the overall fracture stability of the wafer (see next section).

The single scratch tests also show that in some areas a transformation of the crystalline silicon into an amorphous phase can occur. The conditions under which this happens are, however, not yet clear. Single Vickers indentations experiments have shown that in the regions of very high stresses in the plastic zone, phase transformations of the silicon can occur. Several phase changes have been observed by Raman spectroscopy, in particular a metallic high pressure phase [81–86]. Under loading at 11.8 GPa, an endothermic transformation to metallic silicon (Si II and III) occurs, which transforms back partly into microcrystalline or amorphous silicon upon unloading. In the metallic state, the silicon can plastically deform and material can be removed by processes known for ductile metals. These regions are probably very thin and are removed when the material is further stressed and breaks (Figure 18.13).

In the scratching mode, highly strained regions occur in front (compressed region) and behind (tensile region) the indenting tip. Since chipping occurs mainly in front of the tip, any phase changes that occur here will be removed. But phase changes behind

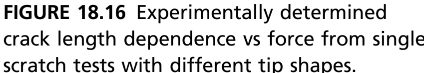

FIGURE 18.16 Experimentally determined crack length dependence vs force from single scratch tests with different tip shapes.

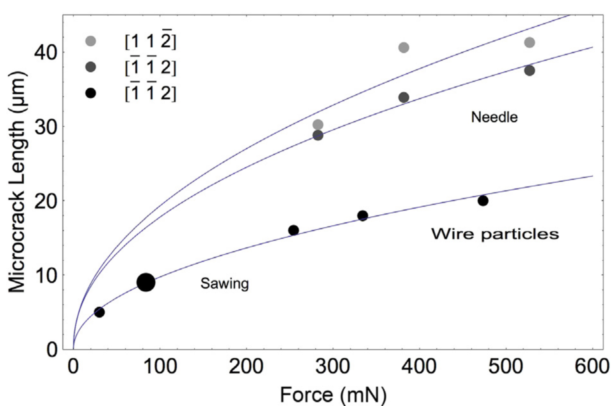

the moving tip could remain. This may explain why one can observe, for instance, amorphous regions on the surface after sawing.

18.3.1.3 Fracture Behavior

The microcracks in the wafer surface are directly responsible for the mechanical fracture stability of the wafer. The "weakest link," which is the longest crack in a wafer, will cause mechanical failure when the wafer is loaded with stresses exceeding the fracture strength of that crack. When deforming different wafers in a batch of comparable wafers, the fracture stresses will vary because of the statistical distribution of the cracks. Statistical considerations based on the Poisson distribution of crack lengths result in a Weibull distribution of fracture stresses

$$F(\sigma) = 1 - e^{-(\sigma/\sigma_o)^m} \tag{18.6}$$

Here, $F(\sigma)$ is the failure probability for a stress σ, σ_0 is the characteristic fracture stress, where 63% of all wafers are broken, and m is the Weibull parameter, which characterizes the width of the fracture stress distribution.

Different fracture tests are available today depending on which part of the wafer has to be characterized [87–91]. The most widely used tests are the biaxial fracture and the four line bending test. They differ in the way stress is applied across the wafer surface and the edges. In the biaxial fracture test, a force is applied locally in the center of the wafer surface and thus determines the fracture properties in that region. In the four line bending test, both the surface and two opposite edges are stressed. It is used to characterize the mechanical stability of the overall wafer, including the wafer edges.

In practice, the force–displacement curves are measured up to fracture. Wafer bending tests lead to high deflections of the specimens, particularly, when the wafer thicknesses become smaller than 150 μm. Generally, finite element calculations are required to determine the corresponding stresses from measured force–displacement curves. Usually at least 30 wafers of equal properties should be tested for a statistically significant Weibull analysis.

Figure 18.17 shows the biaxial fracture test results for batches of wafers sawn with two different SiC grit size distributions. One can see that the measured fracture stresses are

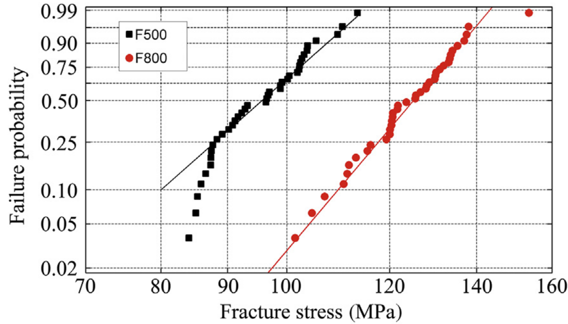

FIGURE 18.17 Weibull plots for wafers sawn with different SiC grit sizes.

lower for powders with larger average grain sizes (F500 vs F800). The removal of the microcracks in the damaged layer by etching increases the fracture strength by a factor of 3–5.

As-sawn wafers are rather fragile and can easily break during handling in the following processing steps. Less wafer saw damage is therefore essential to increase the yield in production, particular when the wafer thickness is reduced.

18.4 Basic Sawing Mechanisms

Slurry-based sawing has been optimized for many years now by practical experience. A further fine-tuning of the process is possible. This requires, however, a good understanding of the basic mechanisms. Great progress has been made here over the years [87–105]. The description of loose abrasive process is based on the individual process of the interaction of a single particle with the crystal surface and the resulting microfracture processes. The main ideas will be outlined in the following section.

18.4.1 Slurry-based Sawing

Under normal sawing conditions, the space between the wire and the crystal surface is filled with fluid and abrasive particles (slurry). Experimental investigations with a high speed camera indicate that the wire is in direct contact with the largest particles. They determine the distance between the wire and crystal surface. The smaller particles are floating freely (Figure 18.18). SiC particles are facetted and contain sharp edges and tips, which can exert very high local pressures (Figure 18.19). The microscopic material removal process is explained by the interaction of rolling SiC particles that are randomly indented into the crystal surface until small silicon pieces are chipped away. This "rolling–indenting grain" model forms the physical basis of the wire sawing process. The same mechanism also occurs in lapping brittle material surfaces with loose abrasive particles [35–37].

During sawing, the crystal is pushed against the wires with a constant forward (feed) velocity. Only the larger particles, which are in direct contact, participate in the material removal process. With increasing feed velocity, the total force F_{tot} on the wire increases and more and more particles are indented. Since the wire is elastic, it will bow out under

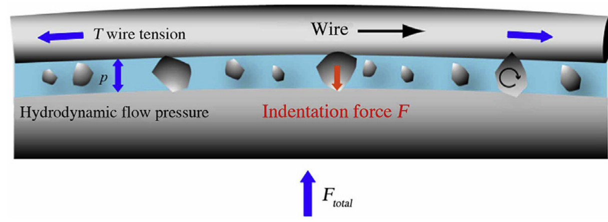

FIGURE 18.18 Schematic diagram of the sawing channel. It shows the main forces that are assumed in the model (cutting direction upward here).

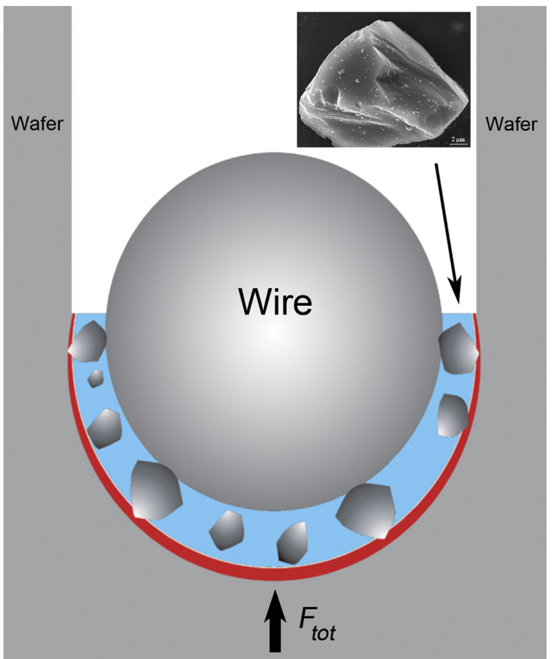

FIGURE 18.19 Schematic diagram of the cross-section of the sawing channel. Insert shows SEM image of a SiC particle.

the force like a string. The resulting wire curvature adjusts to achieve an overall constant feed velocity.

The forces vary below the wire depending on the local conditions in the sawing channel. Considering the cross-section view, the resulting force perpendicular to the wire surface, which pushes the particles into the surface, also varies along the contact area (Figure 18.19). The forces are maximal directly below the wire and decrease toward the side faces. The cutting process at the side and the applied force there is important because it determines the final surface quality of the sliced wafers.

Furthermore, the fast-moving slurry builds up a hydrodynamic pressure, which may exert additional force on the wire. The hydrodynamic pressure decreases to the side of the channel, because it is zero at the free slurry surface. Particles in the channel will be pushed sideward, because of the pressure difference at their surface, and eventually be removed from the sawing channel when they reach the free slurry surface. Since the pressure difference depends on the particle size, one can expect a rearrangement of the particle size distribution by the removal of larger particles from the sawing channel below the wire. In fact, several results have been reported that show that the size distribution varies along the sawing channel. This aspect will be discussed in more detail in Section 18.3.2.1.

All processes together determine the local forces on the indenting particles. The individual process of the interaction of a single particle with the surface has been studied

by microindentation experiments as discussed in Section 18.2.4.2. The main process for material removal during sawing is the formation of lateral cracks and the chipping of material. The median and radial cracks partly remain. This crack system is part of the saw damage that has to be removed for further processing of the wafers. Combining the rolling-indenting process of free abrasive grains with the fracture mechanics of brittle materials, a quantitative description of the material removal process could be derived. For a detailed review of the basic ideas, see references [97–99].

18.4.1.1 Material Removal Rate

During sawing the feed velocity of the ingot is equal to the material removal rate or velocity v_s. Under steady state conditions it must be constant at any point below the wire. The material removal rate can be calculated from the number of indentation events m per contact area A_{tot} and time Δt multiplied by the volume of material V_o that is removed in a single event

$$v_s = \frac{mV_o}{A_{tot}\Delta t} \tag{18.7}$$

The material volume V_o that can be removed in a single event is determined by the extension of the lateral cracks below the indentation of a single grain (Figure 18.13). It depends on the applied normal force F_p on the particle according to Eqn [18.5].

The laminar velocity profile in the slurry between wire and crystal surface leads to a rotation of the particles. If a rolling grain makes one indentation per cycle, the average time interval for a single indentation event is given by $\Delta t = 2\ d_p/v$, where v is the wire velocity and d_p the particle diameter, which is determined by the largest particles in the size distribution.

The experimental results show that wire distance, particle size distribution, the temperature, and other parameters vary along the sawing channel. Therefore, it is necessary to consider the local situation. Each wire segment exerts a force F_n on the particles, which depends on the local curvature and the wire tension. For a rigid wire segment of length Δx, the resulting average force on a single particle F_p is given by $F_n = mF_p$, where m is the number of all the particles in contact under the segment. Combining the equations yields for the local sawing rate the fundamental relationship that forms the basis for the following theoretical description:

$$v_s = v_{so}^{*} v m \frac{(F_n/m)^n}{d_p r_w \Delta x} \tag{18.8}$$

where the prefactor v_{so} summarizes material and geometry parameters. The contact area below the wire has been expressed by $A_{tot} = \pi\ r_w\ \Delta x$ here with the wire radius r_w. The remaining problem that has to be solved is to determine the number m of indenting grains in the slurry, and the average force F_n per wire segment.

The number m of particles in contact and the average force F_n are calculated from the grain size distribution. Commercial, virgin SiC particle sizes can be described rather well by a Gaussian distribution. In general, the size distribution will differ from this form,

particularly when slurry is transported along the sawing channel and particles are lost or break. It is useful therefore to assume a general size distribution, which shall be expressed by $g(l) = n_o\, g_o(l)$, where $g_o(l)$ is the normalized distribution and n_o the total number of all particles in the contact volume below the wire segment (Figure 18.20).

For a wire segment at a distance h to the crystal surface, all grains with a size $l > h$ are in direct contact. The contact number m is calculated from

$$m = n_o \int_{h}^{h_{\max}} g_o(l)dl \tag{18.9}$$

where $h_{\max}$ is the maximum distance where just one particle is in contact in the contact area.

If a force F_n is applied, the distance h decreases and more grains come into contact with the surface. Neglecting the indentation in the wire, the force F_n is equal to the force on all particles $F_n = F_{np}$, which are actually indented into the crystal surface

$$F_{np} = n_o \int_{h}^{h_{\max}} F_{ind}(l-h)g_o(l)dl \tag{18.10}$$

$F_{ind}\,(x)$ is the force law, which applies when a single particle is indented by a distance x into a surface. It depends on the elastic, plastic, and fracture behavior of the material. For sharp Vickers indentations and a brittle material F_{ind} as a function of the indentation depth, $x = l - h$ could be given by Eqn [18.3], but other force laws have been derived as well depending on the shape of the indented grains.

Combining the equations, one calculates the average force $F_p = F_{np}/m$ on a single particle for a given size distribution $g_o(l)$. The result is shown in Figure 18.21 for the Gaussian distribution as a function of the wire distance h and different opening angles of the indenting particle tip.

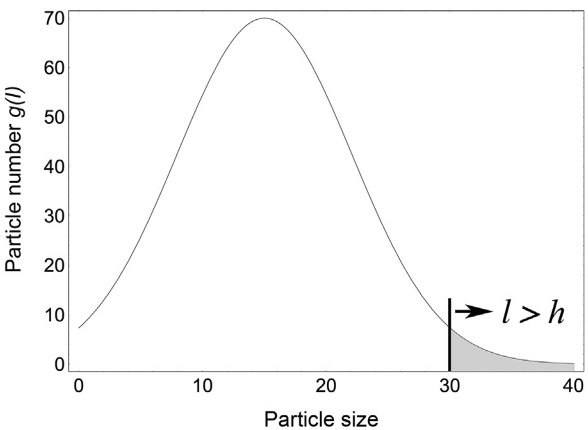

FIGURE 18.20 Schematic particle size distribution $g(l)$. Grains with a diameter $l > h_o$ are in contact both with wire and crystal surface. The total number m of particles in contact is proportional to the shaded area.

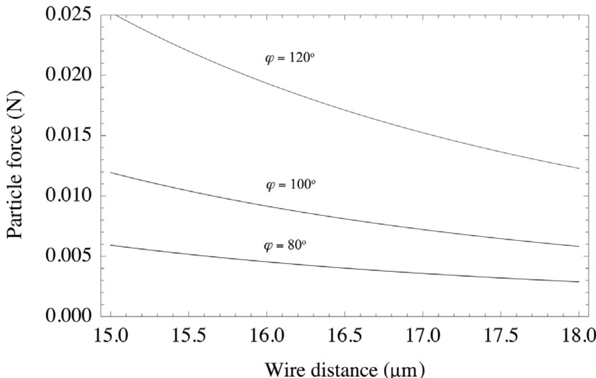

FIGURE 18.21 Average normal force on a single particle $F_p = F_{np}/m$ as a function of the wire-crystal distance for different opening angles of the indenting particle tip.

An important result is that F_p remains almost constant for sharp tips, when the wire distance decreases. Only the number m of indented particles increases. For constant F_p one can simplify Eqn [18.3] then for a wire segment of length l_o

$$v_s = v_{so} v F_n \quad v_{so} = \frac{v_{so}^* F_p^{n-1}}{d_p r_w l_o} \tag{18.11}$$

This is the well-known Preston equation, where the sawing rate is proportional to the wire velocity and the applied force for the entire wire segment in the sawing channel. It has been derived here from a microscopic description of the basic particle-interaction process with the material. The prefactor changes when the wire distance varies along the sawing channel.

The experimental observations have shown, however, that this equation is not sufficient to describe all possible sawing conditions. Particularly it does not take into account the observed dependencies on slurry properties such as the viscosity. An extension of the model has been proposed and is summarized in the next section.

18.4.1.2 Elastohydrodynamic Behavior of Slurry and Wire

Taking into account slurry properties, one has to consider the hydrodynamic behavior of the slurry in the sawing channel [89–93,97,98]. The slurry consists of the fluid and a high volume concentration of particles. In the following, the simplification is made that one has a single-phase system, where the viscosity is changed by the addition of the abrasive powder. The viscosity changes can be described by Eqn [18.2]. Because of the narrow sawing channel, one can assume a laminar flow of the slurry. A similar situation occurs in lubrication and polishing processes, where many fundamental aspects could be derived from experimental and theoretical results [100–113]. An important aspect is that a hydrodynamic pressure can build up in the slurry and if high enough deform the wire elastically in response to the pressure (Figure 18.18). Some consequences can be derived from a one-dimensional treatment of the hydrodynamic slurry transport below a flexible

wire. The starting point to describe the slurry flow directly below the wire is the Reynolds equation

$$\frac{\partial p}{\partial x} = 6 \ v \ \eta \frac{h - h_o}{h^3} \tag{18.12}$$

where x is the coordinate along the wire, $h(x)$ the distance between wire and crystal surface, v the wire velocity, h the slurry viscosity, $p(x)$ the hydrodynamic slurry pressure, and h_o is a constant that has to be derived from boundary condition. A two-dimensional approach has recently been developed [114] that also allows to describe the pressure dependence over the cross-section of the sawing channel (see Figure 18.19).

The hydrodynamic pressure in the slurry p exerts forces on the wire, which will then deform elastically. It has been shown that one has to take into account the elastic response of the wire to obtain numerical results, which are in agreement with experimental observations [18,114]. A significant hydrodynamic pressure can push the wire away from the ingot surface and increase the wire distance h. This reduces the sawing rate since the force on a single particle is reduced and fewer particles are in contact, see Eqn [18.6]. Numerical results show that this is particularly the case in the exit region of the sawing channel, when p becomes large (Figure 18.22).

Furthermore, one can see in Figure 18.22 that negative pressure values can occur in the exit region when the sawing velocity is increased. This means that the slurry flow becomes discontinuous here. It has recently been suggested that such a slurry behavior may lead to an instability of the wire motion and be the reason for the occurrence of saw marks [114].

Based on this assumption one can use the calculations to determine the parameters that lead to high and negative pressures in the exit regions. Figure 18.23 shows in a feed vs wire velocity diagram calculated borderlines, which separate the parameter regions, where stable and unstable wire motion occurs. Important parameters for the position of the border lines are the SiC volume concentration and the fraction of silicon, which

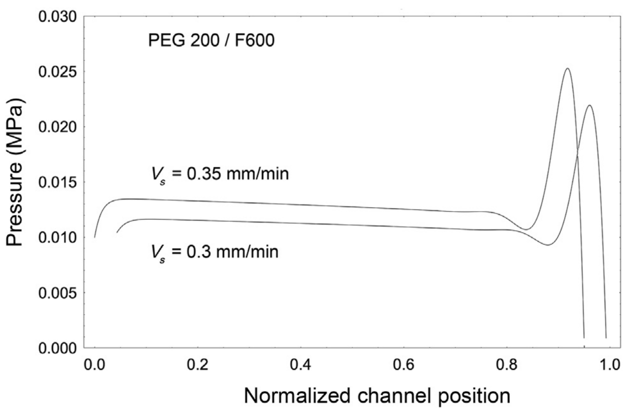

FIGURE 18.22 Calculated hydrodynamic pressure p in the slurry film along the wire length for two different feed velocities [114].

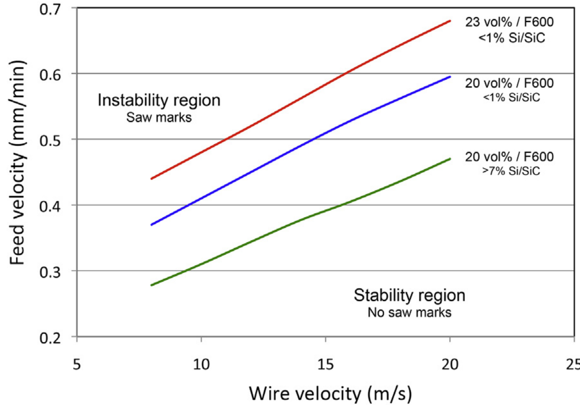

FIGURE 18.23 Feed velocity versus wire velocity diagram showing stability regions of wire motion for different SiC and silicon volume concentrations.

accumulates during sawing in the slurry. The results also depend on the initial viscosity of the slurry. The calculation results are in qualitative agreement with experimental observations and can be used to define guidelines for process windows.

The parameter range for the wire and feed velocities, which is used in industrial production, is between 10 and 18 m/s and 0.3–0.6 mm/min, respectively. Normally one saws with a fixed feed and wire velocity, which determines a point in the diagram. Only values below the corresponding borderline are in the stability region. From the industrial perspective of high productivity and low cost, one will choose a high sawing rate, a low wire velocity, and a low SiC concentration. One can see from the diagram that these are conflicting requirements, which limit suitable sets of parameters.

If one chooses parameters close to the borderline, small changes in the sawing parameters can easily lead to a shift from the stable to the unstable regime. It is therefore necessary to control the specifications of parameters such as the SiC load, the silicon concentration, or the grit size distribution quite tightly.

18.4.1.3 Roughness and Subsurface Damage

Saw mark–free wafers are a prerequisite for further processing. The quality of these wafers is then specified by other parameters. The commercially important parameter is the TTV of the wafers, which is basically determined by the difference in thickness and the roughness values at the wire inlet and outlet side. Good wafers have a TTV $< 15\ \mu m$ for wafers with a thickness of $180\ \mu m$. If saw marks occur, the TTV can increase up to $60\ \mu m$ because of the additional grooves. It is assumed that a strong increase of the TTV and the occurrence of saw marks are related to the same process, namely the instability of wire motion near the exit region of the sawing channel, as described in the previous section.

If one saws with parameters in the stability region, the TTV correlates mainly with the roughness. The dependence of the roughness on feed and wire velocity and other factors has been investigated experimentally quite extensively (see Section 2.4.1). Considering

the micromechanical particle-crystal interaction model, the roughness and the micro-crack depth depend on the forces acting on each particle. Reduced forces will decrease both roughness and microcrack depth. For instance, smaller grit sizes lead to smaller particle forces and a reduced roughness. The observed decrease of the roughness can be explained by the loss of larger particles along the sawing channel.

The roughness also correlates with the microcrack depth. They are important because they mainly determine the fracture behavior of a wafer. Therefore, sawing conditions, which change the overall forces in the process, also have an impact on the wafer stability. The previous numerical calculations are in good agreement with the observed roughness and microcrack results and can be used to predict which parameters are significant here [114].

18.5 Alternative Slicing Technologies

Although multi-wire sawing is the dominant and mature wafering technology, it certainly has the inherent drawback that valuable silicon and supply materials are wasted by the process. There will probably also be limitations when wafers with a thickness below 100 μm are produced in the future. Therefore, many attempts have been used to develop alternative "kerfless" technologies, which avoid these shortcomings. Since the 1980s, over 20 variants of kerfless wafering have been proposed, but few have demonstrated a lasting potential to be competitive in cost and quality [115].

The most direct route is the production of wafers directly from a silicon melt. The most advanced techniques are the "edge-defined film-fed growth—EFG" technique [116], the "string ribbon" method [117], the "ribbon growth on substrate—RGS" method [118], and the Direct Wafer™ technology [119]. All liquid-phase approaches have shown great difficulty in achieving good absorber yield and quality for standard wafers much below 200 μm. At the same time, the wire saw process has undergone impressive evolutionary improvements in the important areas of yield, quality, kerf loss, productivity, and thickness reduction. As a result, the kerfless material efficiency advantage becomes moot if the next-generation wire saw processes yield stronger, high efficiency 120–150 μm wafers. This is why these liquid-phase wafering methods have either been terminated in commercial production or have never started.

Kerfless technologies, which can overcome the quality problem, start from solid monocrystalline silicon. The basic principle is to separate many thin wafers consecutively from a high quality silicon monocrystal. The technologies differ in the separation process, which has to be fast, cheap, kerfless, and without loss of material quality. Two of the more advanced methods shall be described next.

18.5.1 Ion Implantation Technologies

The process technology that uses ion implantation methods is a cyclic, two-step process: first, a high energy proton beam (or other ions) is directed on the top surface of a CZ

silicon ingot. Such a wafering process (direct film transfer, DFT) has been developed by the company Silicon Genesis. Although it has not yet reached the industrial production stage, the technique appears to have some potential for an alternative wafering method [120–126].

The process consists of several steps. Initially a DC electrostatic linear accelerator produces a proton beam with energies of 2–4 MeV. The protons are implanted in a thin layer at a controlled depth under the surface of the silicon. The proton beam has both high current and high energy and therefore carries a very high power. This heat load into the silicon bricks can reach many tens or even hundreds of kilowatts and has to be removed by cooling the bricks efficiently, since the silicon temperature is a critical part of the wafering process. After the implant step, the silicon is induced to fracture, or cleave, in a highly controlled manner, along the cleave plane defined by the implanted ions. A single wafer of silicon is released and the process is repeated on the newly exposed surface of the brick. The use of cleaving, rather than sawing, eliminates the waste due to kerf.

One cleaving method uses a high surface thermal flux, which generates a thermoelastic stress within the patterned brick implant layer. If the stress exceeds the required fracture strength, a thin silicon layer can be cleaved from the brick with high yield.

An alternate cleaving approach applies external energy to the silicon with lower net thermal budget. The method involves the formation of an initiation area followed by a propagation pattern. A small area at a brick corner (mm^2 to cm^2) is implanted with a relatively higher dose and thermally pulse treated to initiate a starting crack. This crack occurs at an edge area of the cleave plane and is designed to avoid generating cleave artifacts. A second energy source is used to propagate the cleave front from this small initiation area through the brick to fully detach the film. The key technology in achieving high throughput is the development and use of advanced controlled propagation to limit the cleave plane dose requirement. Recently wafers with a thickness drawn to 20 μm have been reported [127].

The light ion implant avoids damaging the bulk silicon, while the low energy (threshold) cleave process creates only surfaces with low defect density. Both factors contribute to maintain the high lifetime of the silicon crystal and high mechanical strength. Bulk lifetimes up to 0.5 ms have been reported. Roughness of the cleaved wafers is generally less than 1 μm. The process has also been verified to be capable of repeatedly detaching films from an ingot without surface preparation between successive detachments. The films continue to have repeatable roughness and total thickness variation (TTV $<$1–2%) without any interim polishing or other surface modification steps.

18.5.2 Other Wafering Technologies

18.5.2.1 Layer Transfer Process from Porous Silicon

A further decrease of the wafer thickness down to 10–80 μm requires new methods. Liftoff techniques as developed for the microelectronic device technology have the

potential to fulfill such an objective. The basic principle is the following. A high quality thin silicon film is grown on a sacrificial layer, which can be separated and transferred to a low cost substrate. Latest developments use double porous silicon layers [128–135]. On top is a layer of a low porosity for further growth of a high quality epitaxial film and below is a high porosity layer for separation (Figure 18.24).

The porous silicon is formed by electrochemical etching of a highly doped monocrystalline silicon crystal. Experimentally, different techniques have been explored over the years. Typically vertical trenches are electrochemically etched with an HF-based solution into the surface of highly doped monocrystalline polished substrate. They are transformed into spherical voids by annealing at around 1100 °C in a hydrogen atmosphere [136–140]. The formation of a perfect detachable film requires a specific aspect ratio and pitch. Today, it is possible to form porous silicon layers with a desired void structure. Typically, the top layer is 1–3 μm thick with a porosity of 20–30%. This seed layer permits the subsequent growth of a high quality epitaxial silicon film.

The bottom layer has an initial porosity in the 60–75% range and a thickness of about 0.2–0.3 μm. After annealing, several large buried plate-shaped voids form, which allow the further detachment of the epilayer. The separation process is done mechanically by breaking the small supporting pillars in the separation layer. This requires an initiation crack at the edges of the film, for instance, by laser scribing. Depending on the thickness of the epitaxial film, it can either be used as free-standing foil or, if thinner, has to be transferred to a supporting substrate.

Solar cells have been fabricated in the epitaxial foil with efficiencies up to 15% and have the potential for efficiencies up to 18%. Despite a number of convincing lab-based solar cell showcases, there has thus far been no breakthrough of this technology at the (semi)-industrial level.

18.5.2.2 Laser Chemical Processing

The idea to slice an ingot into wafers by a laser beam is intriguing and has been pursued for some time. The challenge is to cut through an entire brick with a diameter of currently 156 mm, with a kerf loss below 100 μm, and a surface damage below 10 μm. A technology that is in principle capable to achieve these goals is the laser chemical processing method [141]. The principle is to use a water jet–guided laser beam. A very thin liquid jet stream (width 30–80 μm) is generated in a nozzle that has a transparent

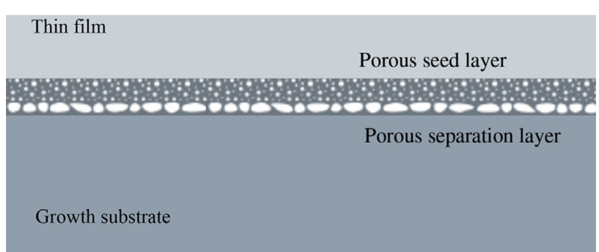

FIGURE 18.24 Schematic layer sequence of an epitaxial film grown on a double porous silicon layer.

window on top. The laser beam is focused into the jet stream and guided via total internal reflection. The material removal occurs by heating or evaporation and can be enhanced by adding etching solutions. This also offers the possibility to remove any surface damage directly.

First experimental results with a high power infrared Nd:YAG laser have shown that up to 7 cm of cutting depth could be reached [142]. The addition of a 10% KOH solution enhanced the cutting speed by almost an order of magnitude compared to multi-wire sawing. However, this initial speed could not be maintained at larger cutting depths. Furthermore, it turned out that the parallelization of the technique with hundreds of laser beams is a technological challenge.

Other clear technological advantages have not be found, so the technology has not been pursued further in the past years as an alternative technology to the multi-wire sawing process.

18.6 Grinding, Lapping, and Polishing

For most applications the as-cut surfaces of the sawn wafers need further treatments to achieve required surface qualities. In general, one has to remove the subsurface saw damage consisting of microcracks, dislocations, and deformed or phase-transformed layers. Furthermore, the wafer surfaces are usually specified regarding roughness, texture, and planarity. This can be achieved by additional mechanical surface treatments, namely grinding, lapping, and polishing and/or etching procedures.

Whereas wafers for solar cell applications are only etched to remove the saw damage, wafers for microelectronic applications require very high surface qualities, which can only be achieved by a sequence of mechanical surface treatments and etching steps. For each procedure, particularly in the microelectronic industry, special grinding, lapping, and polishing machines and processes have been developed.

18.6.1 Mechanical Machining

The first step is grinding to obtain a planar surface and homogeneous wafer thickness. A novel and powerful technology for precision-machining monocrystalline silicon wafers is double-disk grinding (DDG). Here both sides of the wafer are ground simultaneously between two opposite grinding wheels on collinear spindle axes. It is a chuck-less process, in which the workpiece is machined in “free-floating” water beds. The resulting wafer shape differs from those known from (chuck-mounted) single-side grinding or double-sided batch lapping, which are conventionally used in mechanical wafer shaping. With DDG an extreme degree of planarity can be achieved, which the fabrication of microelectronic devices with minimum lateral feature dimensions of 90 nm and below demands today [143]. Problems that have to be solved here are the occurrence of a center dip (“navel”) and edge thickness roll-off in the micrometer range.

The grinding wheels have fixed abrasive particles. The micromechanical processes of material removal are thus similar to the fixed abrasive wire saw mechanisms. The following lapping and polishing steps with wafers on rotating chucks are slurry based with loose abrasive particles. Diamond and SiO_2 particles (silica) are mainly used here. The grain sizes are generally finer compared to the loose abrasive sawing process, but the micromechanical mechanisms are essentially the same. Therefore, many of the previously described features apply here also.

Very high surface qualities can be achieved with the chemomechanical polishing (CMP) process, which combines the application of pressure in combination with chemical etching of the surface [144,145]. Typical CMP tools consist of a rotating and extremely flat plate, which is covered by a pad. The wafer is mounted upside down in a carrier. Both the plate and the carrier are rotated and the carrier is kept oscillating as well. A downward force is applied to the carrier, pushing it against the pad. Typically, the pads have a roughness of 50 μm and contact is made by asperities, typically the high points on the wafer. Therefore, the mechanical properties of the wafer itself must also be considered. If the wafer has a slightly bowed structure, the pressure will be greater on the edges than it would on the center, which causes nonuniform polishing. In order to compensate for the wafer bow, pressure can be applied to the wafer's backside, which, in turn, will equalize the center-edge differences. The pads used in the CMP tool are often stacks of soft and hard materials that conform to the wafer topography to some extent. Generally, these pads are made from porous polymeric materials with a pore size between 30 and 50 μm. They are consumed in the process and must be regularly reconditioned. The polymer pad structure applies locally mechanical pressure and the fluid in the pores supplies the etchant. The right combination of pressure and etchant supply is essential. In most cases the pads are very much proprietary and are usually referred to by their trademark names rather than their chemical or other properties.

18.6.2 Plasma Chemical and Elastic Emission Machining

18.6.2.1 Plasma Chemical Vaporization Machining

Plasma chemical vaporization machining (PCVM) is a gas-phase chemical etching method in which reactive species in an atmospheric-pressure plasma are used [146]. Using different types of electrodes one can slice wafers or pattern, shape or polish surfaces. PCVM has a high removal rate equivalent to those of conventional machining methods such as grinding and lapping. This is because the radial density of an atmospheric-pressure plasma is much higher than that of a normal low pressure plasma. Since the plasma is localized in the area of high electric fields, it can have a high spatial resolution depending on the shape of the electrodes. Furthermore, because of the short mean free path at atmospheric pressure, the ion energy of the plasma is so small that there is little damage to the processed surfaces.

The major application of the method is in polishing high quality smooth and flat surfaces. A cylindrical electrode is rotated in the plasma and moved over the wafer

surface. The reactive gas is supplied to a narrow region between cylinder and surface and enables high speed machining. The etching rate depends on the crystal surface orientation and also varies when the surface contains microcracks or pits. Therefore, with this method one can only obtain smooth surfaces with no damage for monocrystalline or amorphous surfaces. The technique is thus suitable to improve already high quality surfaces. Such surfaces are not only required for microelectronic applications but also for total reflection mirrors with a very high uniformity. Results have been obtained for silicon [147], silicon dioxide on insulator (SOI) [148], and silicon carbide wafers [149]. For instance, for silicon after the removal of a 6 μm thick layer by PCVM polishing with a gas mixture of helium, carbon tetra fluoride, and oxygen (98.9:0.1:0.1) a roughness $R_a = 0.11$ nm could be achieved.

18.6.2.2 Elastic Emission Machining

A further improvement of already very smooth silicon surfaces can be achieved by the elastic emission machining (EEM) method [150]. Such surfaces are required for total reflection mirrors for steering synchrotron hard X-rays, imaging optics for extreme ultraviolet lithography, and substrates for future nanoscale devices. EEM is applied where conventional mechanical polishing methods reach their limits. The technique utilizes chemical reactions between solid surfaces. In practice one uses fine powder particles whose surfaces are reactive to the target material. For silicon surfaces this effect has been demonstrated with amorphous silicon dioxide powders with a mean diameter of 2 μm, which is uniformly mixed in ultrapure water. When the particles come into contact with the silicon surface, there is a notable probability that the atoms on the surface will adhere to the powder particles and be removed. Since atoms at bumps on the surface have a higher probability to come into contact than atoms in pits, the overall effect is the smoothening of the surface. Removal rates of 2 nm/min could be obtained by this method.

18.7 Conclusions and Outlook

Wafer manufacturing today is based on mechanical processing steps: sawing, grinding, lapping, and polishing. The main developments have been generated in the microelectronic and photovoltaic industries. Each of these steps has been continuously improved, in particular because the requirements on the wafer qualities and on cost reduction have increased over the last decades. To meet these goals it became necessary to investigate the fundamental micromechanical processes. This scientific approach has reached a high level of understanding, which continues to allow further improvement of the processing steps.

In the photovoltaic industry, wafers will eventually become even thinner to save costs. The mechanical stability will therefore remain the main issue since thinner wafers become more fragile and more difficult to handle. In addition, the surface properties

such as thickness variations, impurity contamination, or the etching behavior are important issues. In the microelectronic industry, wafer flatness is the main issue, particularly as wafers become larger.

The continuous improvement of manufacturing machines, processes, and the understanding of the basic mechanisms will lead to further developments. In addition, in the photovoltaic industry with its mass production of wafers, one can expect more automation of different processing steps to reduce costs. The limits of today's wafer processing techniques have certainly not been reached.

This also makes it difficult to develop alternative wafering technologies. Many attempts have been tried using lasers, plasmas, or smart cut technologies based on ion implantation, electrochemical etching, or heat pulses. In some cases it could be shown that one can produce wafers successfully. However, in comparison with the established wafering processes, these techniques are either too expensive or do not yield the wafer qualities that are required today. Therefore, none of these techniques has reached the industrial production level. Some of these alternative processes may, however, become of interest again when the requirements on the wafers, such as a low thicknesses, can no longer be achieved by mechanical processing.

References

[1] Martínez-Duart JM, Hernández-Moro J. J Nanophot 2013;7(1):24.

[2] Waldau AJ. Renew Sustain Energy Rev 2007;11(7):1414.

[3] Wüstenhagen R, Bilharz M. Energy Policy 2006;34(13):1681.

[4] Report Navigant Consulting Solar PV market forecast; 2012.

[5] International technology roadmap for photovoltaic. SEMI Europe Photovoltaics Group; 2012.

[6] Global market outlook, Report of European photovoltaic industry association; 2012.

[7] International Technology Roadmap for Photovoltaic, Report SEMI PV Group; 2012.

[8] Endrös A, Franke D, Häßler C, Kaleis J, Koch W, Möller HJ. In: Luque A, Hegedus S, editors. Handbook of photovoltaic engineering. Wiley-VCH; 2002. p. 1254.

[9] Tillmann W. Int J Refract Metals Hard Mater 2000;18:301.

[10] Tillman W, Nebel J. Metall 2006;11:729.

[11] Solozhenko V, Kurakevych O, Oganov A. J Superhard Mater 2008;30:428.

[12] Marx C. In: Diamantwerkzeuge und ihr Einsatz in Flachbohrungen; 1967. Report Fa. Christensen Diamond Products GmbH, Celle, Germany.

[13] Münster A. Angew Chem 1957;69(7):281.

[14] Gilman J. Chemistry and physics of mechanical hardness. Wiley & Sons; 2009.

[15] Iler RK. The chemistry of silica. Wiley & Sons; 1979.

[16] Rybicki G. J Mater Res 1997;12(1):59.

[17] Hjort K. J Micromech Microeng 1994;4(1):564.

[18] Möller HJ. Phys Stat Sol (A) 2006;203(4):659.

[19] Nasch PM, Schneeberger S. In: Proc. 20th European PVSEC; 2005. 1139.

[20] Bidiville A, Wasmer K, Michler J, Nasch PM, Van der Meer M, Ballif C. Prog Photovolt Res Appl 2010;18:563.

[21] Heppner D, Sueldia R, Daridon A, Nasch PM, Yin M. In: Proc. 20th European PVSEC; 2005. 949.

[22] Aoyama T, Kondo Y, Asai H, Takato H, Sakata I. In: Proc. 25th Europ. PVSEC; 2009. 1965.

[23] Provent E, Brize V, Drevet B, Coustier F, Flahaut E. In: Proc. 24th Europ. PVSEC; 2010. 2429.

[24] Proventa E, Brize V, Dreveta B, Coustier F, Flahaut E. In: Proc. 26th Europ. PVSEC; 2012. 1965.

[25] Bidiville A, Wasmer K, Kraft R, Ballif C. In: Proc. 24th Europ. PVSEC; 2009. 1400.

[26] Bye J-I, Jensen SA, Aalen F, Rohr C, Nielsen Ø, Gaumann B, et al. In: Proc. 24th Europ. PVSEC; 2009. 1269.

[27] Lombardi I, Fragiacomo G, Zehetmeier C, Bye J-I, Nielsen Ø, Rohr C, et al. In: Proceeding 24th European PVSEC; 2009. 1256.

[28] Solar battery technologies – present market situation and future perspective, vol. 2. Japan: Fuji Keizai Co; 2012.

[29] Buchwald R, Fröhlich K, Würzner S, Lehmann T, Sunder K, Möller HJ. Energy Proc 2013;38:901.

[30] Rietzschel R, Wagner T, Funke C, Möller HJ. In: Proc. 23rd European PVSEC; 2008. 1301.

[31] Anspach O, Lawerenz A. Photovoltaics international. 6th ed. 2010. 36.

[32] Meißner D, Schönfelder St, Hurka B, Zeh J, Sunder K, Köpge R, et al. Energy Proc 2013;38.

[33] Meißner D, Hurka B, Zeh J, Köpge R, Wagner T, Möller HJ, et al. In: Proc. 6th int. conf. crystalline silicon for solar cells; 2012.

[34] Johnsen L, Gastinger K, Bjerkan L, Rietzschel R, Möller HJ. In: Proc. 24th Europ. PVSEC; 2009. 1248.

[35] Buijs M, Korpel-van Houten K. Wear 1993;162:954.

[36] Buijs M, Korpel-van Houten K. Wear 1993;166:237.

[37] Buijs M, Korpel-van Houten K. J Mater Sci 1993;28:3014.

[38] Rietzschel R, Senf A, Seelmann-Eggebert HP, Kaminski S, Wagner T, Funke C, et al. In: Proc. 25th Europ. PVSEC; 2010. 1596.

[39] Kaminski S, Wagner T, Rietzschel R, Fütterer W, Funke C, Möller HJ. In: Proc. 25th Europ. PVSEC; 2010. 1315.

[40] Retsch S, Jentsch S, Möller HJ. In: Proc. 27th European PVSEC; 2012. 947.

[41] Anspach O, Schulze F-W. In: Proc, 22nd European PVSEC; 2007. 912.

[42] Hurka B, Anspach O. In: Proc. 26th Europ. PVSEC; 2011. 1977.

[43] Struble LJ, Sun GK. Flow and microstructure of dense suspensions. In: Struble, Zukoski, Maitland, editors. Materials Research Society (MRS), Symposia Proc., Pittsburgh MRS, vol. 289; 1993. p. 173.

[44] Doolittle AK. J Appl Phys 1951;22(8):1031.

[45] Kaminski S, Rietzschel R, Wagner T, Funke C, Möller HJ. In: Proc. 24th Europ. PVSEC; 2009. 1299.

[46] Beesley JG, Schönholzer U. In: Proc. 22nd Europ. PVSEC; 2007. 956.

[47] Meißner D, Hurka B, Rietzschel R, Möller H-J, Anspach O. In: Proc. 27th EU PVSEC; 2012. 1076.

[48] Wagner T, Möller HJ. In: Proc. 23th Europ. PVSEC; 2008. 1315.

[49] Park JE, Dibiase N. In: Proc. 27th Europ. Europ. PVSEC; 2012. 957.

[50] Möller HJ, Retsch S, Rietzschel R. In: 28th Europ. PVSEC; 2013.

[51] Möller HJ, Buchwald R, Winstanley S. In: Proc. 6th int. conf. crystalline silicon for solar cells; 2012.

[52] Buchwald R, Fröhlich K, Würzner S, Lehmann T, Sunder K, Möller HJ. In: Proc. 28th EU PVSEC; 2013.

[53] Kondo Y, Watanabe N, Ide D, Matsuki T, Takato H, Sakata I. In: Proc. 23rd Europ. PVSEC; 2008. 1297.

[54] Bidiville A, Heiber J, Wasmer K, Habegger S, Assi F. In: Proc. Proc. 25th Europ. PVSEC; 2010. 1673.

[55] Tilli M. Handbook of silicon based MEMS materials and Technologies. Elsevier; 2010. p. 71.

[56] Baliff C. In: Fundamentals of nanoindentation and nanotribology III. Mat. Research Soc.; 2005. p. 259.

[57] Wagner T, Behm T, Rietzschel R, Kaminski S, Funke C, Möller HJ. In: Proc. 25th Europ. Europ. PVSEC; 2010. 1267.

[58] Funke C, Kiriyenko O, Sciurova O, Möller HJ. In: Proc. 20th Europ. PVSEC; 2005. 1128.

[59] Funke C, Sciurova O, Möller HJ, Stephan M, Fröhlich KJ, Seifert C, et al. In: Proc. 19th Europ. Europ. PVSEC; 2010. 1226.

[60] Bidiville A, Wasmer K, Michler J, Ballif C, Van der Meer3 M, Nasch PM. In: Proc. 13rd Europ. PVSEC; 2010. 1311.

[61] Anspach O, Stabel A, Lawerenz A, Riesner S, Porytskyy R, Schulze F-W. In: Proc. 23rd Europ. PVSEC; 2008. 923.

[62] Bidiville, Wasmer K, Kraft R, Ballif C. In: Proc. 24th EU PVSEC; 2009. 1400.

[63] Evans AG, Marshall DB. In: Fundamentals of friction and wear. Metals Park, OH: ASM; 1981. p. 441.

[64] Malkin S, Ritter JE. ASME J Eng Ind 1989;111:167.

[65] Lawn B. Fracture of brittle solids. Cambridge University Press; 1993.

[66] Lawn B, Evans A. J Mater Sci 1977;12:2195.

[67] Evans AG, Charles EA. J Am Cer Soc 1976;59(7):371.

[68] Lankford J, Davidson D. J Mater Sci 1979;14:1662.

[69] Hagan J. J Mater Sci 1979;14:2975.

[70] Feltham P, Banerjee R. J Mater Sci 1992;27:1626.

[71] Li H, Bradt R. J Mater Sci 1996;31:1065.

[72] Chen CP, Leipold M. J Am Cer. Soc 1980;59:342.

[73] Anstis GR, Chantikul P, Lawn BR, Marshall DB. J Am Cer Soc 1981;64(9):533.

[74] Möller HJ, Funke C. In: Möller HJ, Roewer G, editors. Freiberger Forschungshefte B, TU Bergakademie Freiberg; 2003. p. 230.

[75] Chauhan R, Ahn Y, Chandrasekar S, Farris T. Wear 1993;166:246.

[76] Verspui M, de With G, van der Varst P, Buijs M. Wear 1995;188:102.

[77] Larsen-Basse J. Wear 1993;166:93.

[78] Hamblin M, Stachowiak G. Wear 1995;190:237.

[79] Poon C, Bushan B. Wear 1995;190:76.

[80] Misra A, Finnie I. Wear 1981;65:359.

[81] Gogots Y, Baek C, Kirscht F. Semicond Sci Technol 1999;14:936.

[82] Weppelmann E, Field J, Swain M. J Mater Res 1993;8:246.

[83] Jang J, Lance MJ, Wen S. Acta Mater 2005;53:1759.

[84] Gassilloud R, Ballif C, Gasser P, Buerki G, Michle J. Phys Stat Sol (A) 2005;202(15):2858.

[85] Domnich V, Gogotsi Y. Rev Adv Mater Sci 2002;3:1.

[86] Kailer, Gogotsi YG, Nickel KG. J Appl Phys 1997;81(7):3057.

[87] Funke C, Sciurova O, Fütterer W, Möller HJ. In: Proc. 21st Europ. PVSEC; 2006. 171.

[88] Funke C, Wolf S, Stoyan D. J Sol Energy 2009;131(1):011012–21.

[89] Funke C, Kullig E, Kuna M, Möller HJ. Adv Eng Mater 2004;6:594.

[90] Orellana Pérez T, Schmid C, Riepe St, Möller HJ, Reber St. In: Proc. 24th Europ. PVSEC; 2009. 1228.

[91] Retsch S, Budnitzki M, Wagner Th, Möller HJ. In: Proc. 26th Europ. PVSEC; 2011. 1973.

[92] Sahoo RK, Prasad V, Kao I, Talbott J, Gupta K. ASME J Electron Packag 1998;120:131.

[93] Li J, Kao I, Prasad V. In: Proc. ASME – IMECE. Dallas: ASME Press; 1997. p. 439.

[94] Yang F, Kao J. ASME J Electron Packag 1999;121:191.

[95] Bhagavat M, Prasad V, Kao I. J Tribol 2000;122:394.

[96] Wei S, Kao I. Trans Int J Vib Sound 2000;231:1383.

[97] Yang F, Kao I. ASME J Electron Packag 2001;123:254.

[98] Kao I, Wei S, Chiang P. In: Proc. of NSF design & manufact. grant. conf.; 1997. 239.

[99] Philips K, Crimes GM, Wilshaw TR. Wear 1977;41:327.

[100] Jeynes C. Phil Mag 1983;48 A:178.

[101] Wei S, Kao I. In: Proc. manufact. eng. div. - IMECE. ASME Press; 1998. 813.

[102] Möller HJ. Adv Eng Mater 2004;6:501.

[103] Möller HJ. Crystal sawing technology. In: Scheel HJ, Capper P, editors. Crystal growth technology. Weinheim: Wiley - VCH; 2008. p. 457.

[104] Behm Th, Fütterer W, Funke C, Kaminski S, Möller HJ, Rietzschel R, et al. Photovoltaics Int 2011; 11:38.

[105] Hamrock BJ. In: Fundamentals of fluid film lubrication, NASA Reference Publication 1225. New York: McGraw-Hill; 1991.

[106] Gane N, Pfalzer PF, Tabor D. Proc R Soc Lond Ser A 1974;340:495.

[107] Gohar R. In: Horwood E, editor. Elastohydrodynamics, series in mech. engineering; 1988.

[108] Rohde S, Oh K. Proc R Soc Lond Ser A 1975;343:315.

[109] Su Y-T, Wang S-Y, Hsiau J-S. Wear 1995;188:77.

[110] Su Y-T, Horng C-C, Hwang Y-D, Guo W-K. Wear 1996;199:89.

[111] Kasai T, Doy TK. Jpn J Tribol 1992;37(5):539.

[112] Siekman G. Wear 1987;117:359.

[113] Cook LM. J Non-Cryst Solids 1990;120:152.

[114] Möller HJ, Retsch S, Rietzschel R. In: Proc. 28th Europ. PVSEC; 2013.

[115] Henley F. In: 35th IEEE PVSC; 2010. 387.

[116] Wald FV. Crystals 5. Berlin: Springer; 1981. p. 147.

[117] Ciszek TF. Crystals 5. Berlin: Springer; 1981. p. 183.

[118] Lange H, Schwirtlich I. J Cryst Growth 1990;104:108.

[119] Henley F, Lamm A, Kang S, Liu Z, Tian L. In: 23rd Europ. PVSEC; 2008.

[120] Mueller A, Cherradi N, Nasch PM. In: Proc. 3rd world conference on photovoltaic energy conversion; 2003.

[121] Nasch PM, Cherradi N, Mueller A. In: Proc. 19th Europ. PVSEC; 2004. p. 357.

[122] Henley F, Brailove A, Lamm A, Heerwagen T, Sauar E, Nese M, et al. In: 23rd Europ. photovoltaic solar energy conference; 2008. 2017.

[123] Henley F, Kang S, Liu Z, Tian L, Lamm A. In: 34th IEEE PVSC; 2009. 56.

[124] Henley F, Lamm A, Kang S, Liu Z, Tian L. In: 24th Europ. PVSEC; 2009. 1090.

[125] Brailove A, Kang S, Fujisaka A, Henley F. In: 25th Europ. Europ. PVSEC; 2010. 1613.

[126] Fujisaka A, Kang S, Tian L, Chow Y, Belyaev A. Photovoltaics world; 2011. p. 21.

[127] Brendel R. Physica Status Solidi 2003;197(2):497.

[128] Reuter M. Sol Energy Mater Sol Cells 2008;93(6):704.

[129] Petermann JH. J Prog Photovoltaics Res Appl 2012;20:1.

[130] Depauw V, Qiu Y, Van Nieuwenhuysen K, Gordon I, Poortmans J. In: 25th Europ. PVSEC; 2010. 2843.

[131] Depauw V, Qiu Y, Van Nieuwenhuysen K, Gordon I, Poortmans J. J Prog Photovoltaics Res Appl 2010;18:102.

[132] Ghannam MY, Alomar A, Poortmans J, Mertens R. In: 26th Europ. PVSEC; 2011. 2821.

[133] Van Nieuwenhuysen K, Depauw V, Martini R, Govaerts J, Debucquoy M, Radhakrishnan HS, et al. In: 27th Europ. PVSEC; 2012. 2471.

[134] Depauw V, Gordon I, Beaucarne G, Poortmans J, Mertens R, Celis J-P. J Appl Phys 2009;106:033516.

[135] Depauw V, Gordon I, Beaucarne G, Poortmans J, Mertens R, Celis J-P. Mat Sci Eng 2009; B159(160):286.

[136] Usenko AY, Carr WN, Chen B. J Mater Sci Mater Electron 2003;14:305.

[137] Johnson NM, Ponce FA, Street RA, Nemanich RJ. Phys Rev B 1987;35:4166.

[138] Hourahine B, Jones R, Oberg S, Briddon PR. Mater Sci Eng 1999;B58:24.

[139] Deak P, Snyder LC. Solids 1989;111:77.

[140] Weldon MK. J Vac Sci Tech 1997;B 15:1065.

[141] Kray D, Fell A, Hopman S, Mayer K, Mesec M, Glunz SW, et al. In: 22nd Europ. PVSEC; 2007. 1227.

[142] Hopman S, Fell A, Mayer K, Mesec M, Willeke GP, Kray D. In: 23rd Europ. PVSEC; 2008. 1131.

[143] Pietsch GJ, Kerstan M. Precis Eng 2005;29(2):189.

[144] Wolf S. Silicon processing for the VLSI era, vol. IV; 2002. 313.

[145] Pietsch GJ, Higashi GS, Chabal YJ. Appl Phys Lett 1994;64:3115.

[146] Sano Y, Yamamura K, Mimura H, Yamauchi K, Mori Y. In: Scheel H, editor. Crystal growth technolgy. Weinheim: Wiley VCH; 2008. p. 475.

[147] Yamamura K, Sano Y, Shibahara M, Mimura H, Yamauchi K, Endo K, et al. Jpn J Appl Phys 2006;45: 8270.

[148] Mori Y, Yamamura K, Sano Y. Rev Sci Instrum 2004;75:942.

[149] Mori Y, Yamamura K, Sano Y. Jpn J Appl Phys 2006;45:8277.

[150] Mori Y, Yamamura K, Endo K. Prec Eng 1987;9:123.

19

Capillarity and Shape Stability in Crystal Growth from the Melt

Thierry Duffar

SIMaP-EPM, SAINT MARTIN D'HÈRES, FRANCE

CHAPTER OUTLINE

19.1 Introduction ... 758

19.1.1 Drawbacks of Growing a Crystal in a Crucible ... 758

19.1.2 Capillarity-Driven Processes ... 760

19.2 Fundamentals of Capillarity for the Crystal Grower ... 761

19.2.1 Surface and Cohesion Energies ... 761

19.2.2 Marangoni Convection ... 762

19.2.3 Young–Laplace Equation ... 764

19.2.4 Growth Angle ... 764

19.2.5 Wetting Angle ... 766

19.2.6 Catching and Horizontal Conditions ... 768

19.3 Solutions of the Young–Laplace Equation ... 769

19.3.1 Nonlinearity of the Young–Laplace Equation ... 769

19.3.2 Axisymmetric and Two-Dimensional Formulations ... 769

19.3.3 Approximations and Meniscus Shape in the Czochralski Configuration ... 770

19.3.4 Numerical Integration: The Runge-Kutta Algorithm ... 772

19.3.5 Application to the Floating Zone Process ... 773

19.3.6 Usefulness of Meniscus Shape: Ribbon Thickness in the Pendant Drop Growth and Micro-Pulling-Down Methods ... 773

19.4 Shape Stability Analysis ... 776

19.4.1 Static Stability ... 776

19.4.2 Importance of Heat Transfer and Growth Rate in Shape Stability ... 777

19.4.3 Capillary Stability and Applications to Dewetting under Microgravity ... 779

19.4.4 Dynamic Stability: The Classical Lyapunov Approach and Applications to the Verneuil Process ... 782

19.4.5 Practical Stability with Bounded Time Limits and Applications to Dewetting Growth ... 785

Handbook of Crystal Growth. http://dx.doi.org/10.1016/B978-0-444-63303-3.00019-5
Copyright © 2015 Elsevier B.V. All rights reserved.

19.5 Conclusions **788**
Acknowledgment **788**
Nomenclature **788**
References **789**

19.1 Introduction

Capillarity deals with liquid surfaces. At first sight, the concept has little to do with crystals and crystal growth. However, unlike cast metallic alloys, crystals are generally not directly grown by melting and solidification in a crucible because interaction of the grown crystal with the crucible severely impairs crystal quality. Most crystal growth processes involve a liquid surface from which the crystal is pulled without contact with any solid part. As a consequence, the crystal shape is controlled by the liquid surface and then by capillarity. This chapter introduces these crucibleless growth techniques, some of which are extensively covered in other chapters of this handbook, such as the Czochralski (See Chapters 2–5, Volume IIA) and floating zone (See Chapters 7–8, Volume IIA) processes.

This chapter gives an introduction to the basic concepts of capillarity, including the typical growth angle, which is a material-dependent physical property involved in the analysis of capillarity-controlled processes. Capillarity parameters (surface energy, wetting, and growth angles) that are typical of various crystal classes will be given, as well as tools to solve capillarity problems. Of course, the main issue in these techniques concerns the control of the shape of the crystal, which is freely growing from the melt. It appears that some processes are stable from this point of view, and thus do not need a specific shape-control loop. Some other processes are unstable and thus necessitate sophisticated regulation equipment and software, as comprehensively explained in Chapter 28 of Volume IIB for all melt processes, such as Czochralski, floating zone, vertical directed crystallization, and Kyropoulos. This chapter describes stability analyses and applications of the principal growth techniques not extensively covered in other chapters of this handbook, such as the dewetting, shaping, and Verneuil processes. The detached Bridgman (dewetting) process is also treated here from the automation point of view. For more detailed treatment of all of these matters, the reader is referred to a book on crystal growth processes based on capillarity that was edited by the author [1].

19.1.1 Drawbacks of Growing a Crystal in a Crucible

All processes that cast crystals in a crucible are derived from the Bridgman technique [2], in which the material to be crystallized is molten in a crucible placed in an appropriate furnace and then slowly solidified (see Chapter 9, Volume IIA for more details). A single crystal seed, which should be only partially molten, is generally placed at the cold part of

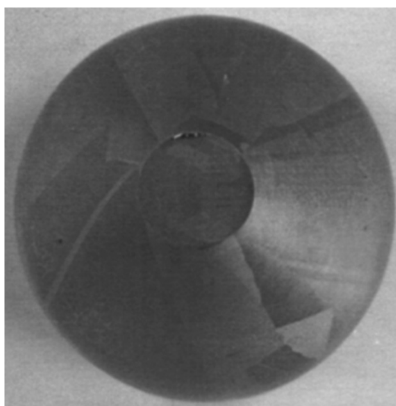

FIGURE 19.1 Spurious nucleation of grains at the bottom of a 2-in GaSb crystal grown by the Bridgman technique: bottom (left) and side (right) views.

the crucible or, alternatively, this part is designed as a thin capillary with the hope that only one seed grain will nucleate there inside. Obviously, a great advantage of this technique is that the shape of the crystal is imposed by the shape of the crucible. However, this advantage most often turns out to be a drawback because the material-crucible contact generates defects in the grown crystal:

1. The liquid is contaminated by the crucible, which leads to unintentional doping or contamination of the crystal.
2. The solid–liquid–crucible triple line is the location of spurious nucleation, which produces twins or grains (Figure 19.1).
3. Crucible contact affects the heat fluxes (which causes a curvature of the solid–liquid interface [3]), the source of radial chemical segregation, and thermoelastic stresses in the solid.
4. There is always sticking of the crystal on the crucible. During cooling, differential dilatation creates stresses in the crystal with a succession of thermo-mechanical features, including elastic deformation, plasticity (which gives dislocation generation and residual stresses [4,5]), detachment from the crucible if the elastic energy passes the adhesion energy and, in the worst case, crucible or crystal breakage. Figure 19.2 shows the increase of dislocation density along the conical part of a GaSb crystal obtained by the Bridgman technique. The density of dislocations increases until subgrain boundaries are formed and grains appear, as can be seen on the crystal at the periphery of the conical part.

Most of these problems can be solved by the full encapsulation technique, in which a liquid encapsulant separates the liquid and the crystal from the crucible. Analysis showed that this mechanism occurs when the liquid encapsulant totally wets (i.e., the wetting angle is practically 0°) both the crucible and the solidifying material [7]. This

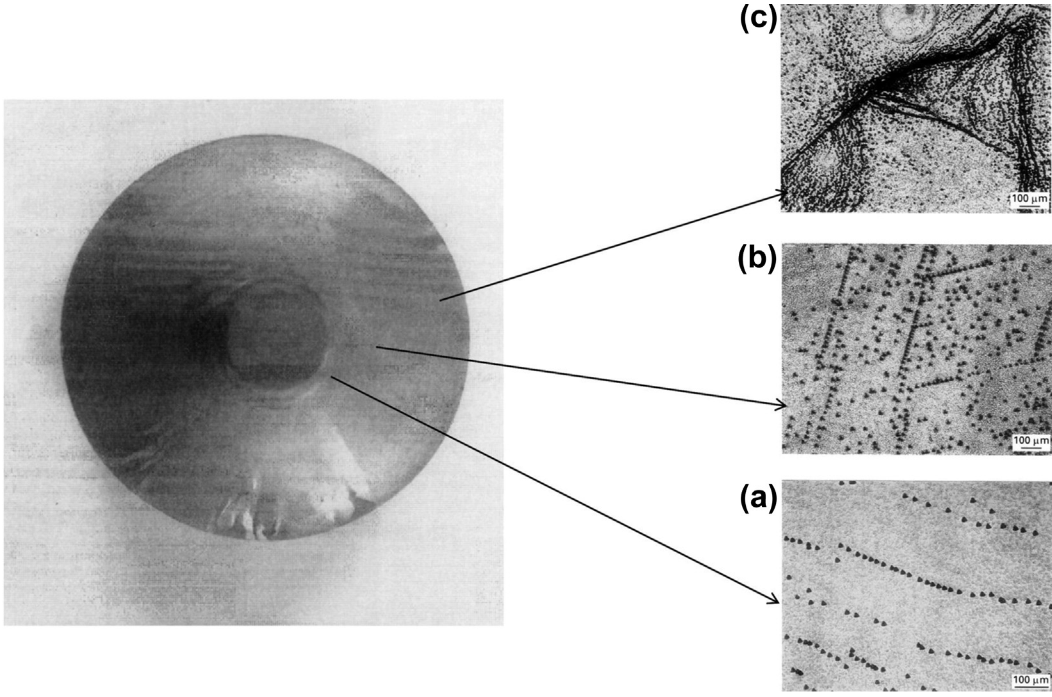

FIGURE 19.2 Evolution of dislocation etch pit density (right) at successive places (a, b, c) after growth of the conical part of a 2-in GaSb crystal grown by the Bridgman technique, seen from the bottom on the left. *Adapted from Ref. [6] with permission of Elsevier.*

makes it difficult to find an appropriate encapsulant that should have the following characteristics [7,8]:

1. Have a low vapor pressure at the melting point of the material
2. Be less dense than the liquid
3. Be insoluble in the liquid
4. Be nonreactive and uncontaminated by the liquid
5. Have a melting point below the one of the solidified material
6. Be chemically inert toward the solid
7. Wet both crucible and solidified material as well as possible
8. Have a high viscosity

Such a large amount of conditions explain why the only practically used encapsulant is B_2O_3 in the case of III-V semiconductor Bridgman grown in SiO_2 or BN crucibles.

19.1.2 Capillarity-Driven Processes

Crucibleless techniques have been developed from the very beginning of crystal growth from the melt, even before Bridgman introduced his technique. Those inventors seemed to think that freely grown crystals would be of better quality. In chronological

order, the principal techniques are the Verneuil process [9], the Czochralski process [10], and the Floating Zone process [11]. Numerous variants were also introduced, the most important of which (from the capillarity point of view) introduced a "shaper" in order to control the shape of the melt and consequently of the crystal: Gomperz used a floating ring in the Czochralski process to stabilize the diameter of the pulled crystalline rod [12], which led to many shaping techniques, such as Stepanov, edge-defined film-fed growth (EFG), micro-pulling down, and so on. Some techniques do not use any crucible at all, with the liquid being just constrained by the capillary forces, whereas others use a crucible and a shaper that are in contact with the melt, with a risk of pollution. Also, in certain processes, the crystal is pulled upwards, whereas in others it is pulled downwards. Figure 19.3 classifies the most important of these technologies. It can be seen that they all are derived from each other, with some technological changes in between.

Due to the absence of crucible contact, most drawbacks listed for Bridgman growth are avoided. However, in all cases, the solidification occurs on a liquid meniscus, which has a shape controlled by capillary forces. Furthermore, the relationship between the meniscus shape and the crystal shape is not immediately obvious or unique, so the stability of the growth process has to be studied. This chapter will introduce these concepts and describe some examples.

19.2 Fundamentals of Capillarity for the Crystal Grower

19.2.1 Surface and Cohesion Energies

Inside a condensed phase (a solid or liquid), there are interactions between atoms that are generally attractive, which gives cohesion to this phase. Atoms situated at the surface, under vacuum, lack half of these interactions, and their energetic state is different compared to the bulk atoms (Figure 19.4). This is the origin of the surface energy of the liquid or the solid. Cutting the material into two pieces creates two equal surfaces, so that the cohesion energy is twice the surface energy:

$$W_{coh,s} = 2\gamma_{sv} \text{ and } W_{coh,l} = 2\gamma_{lv}. \tag{19.1}$$

When the solid and liquid surfaces are put in contact, a solid–liquid interface is created with a characteristic surface energy, γ_{sl}. Because the liquid–solid interactions are not directly related to the liquid–vacuum and solid–vacuum situations, γ_{sl} is not the sum of γ_{sv} and γ_{lv}. The work of adhesion is the deviation from this equality and reflects the interactions between the atoms in the solid and liquid phases; it is defined as [13]:

$$W_a = \gamma_{sv} + \gamma_{lv} - \gamma_{sl}. \tag{19.2}$$

These quantities correspond to the energy per surface unit and are expressed in J/m^2. They can also be found, in some papers, as N/m, because they also represent the force that should be applied, per unit length on a line perpendicular to the surface, in order to

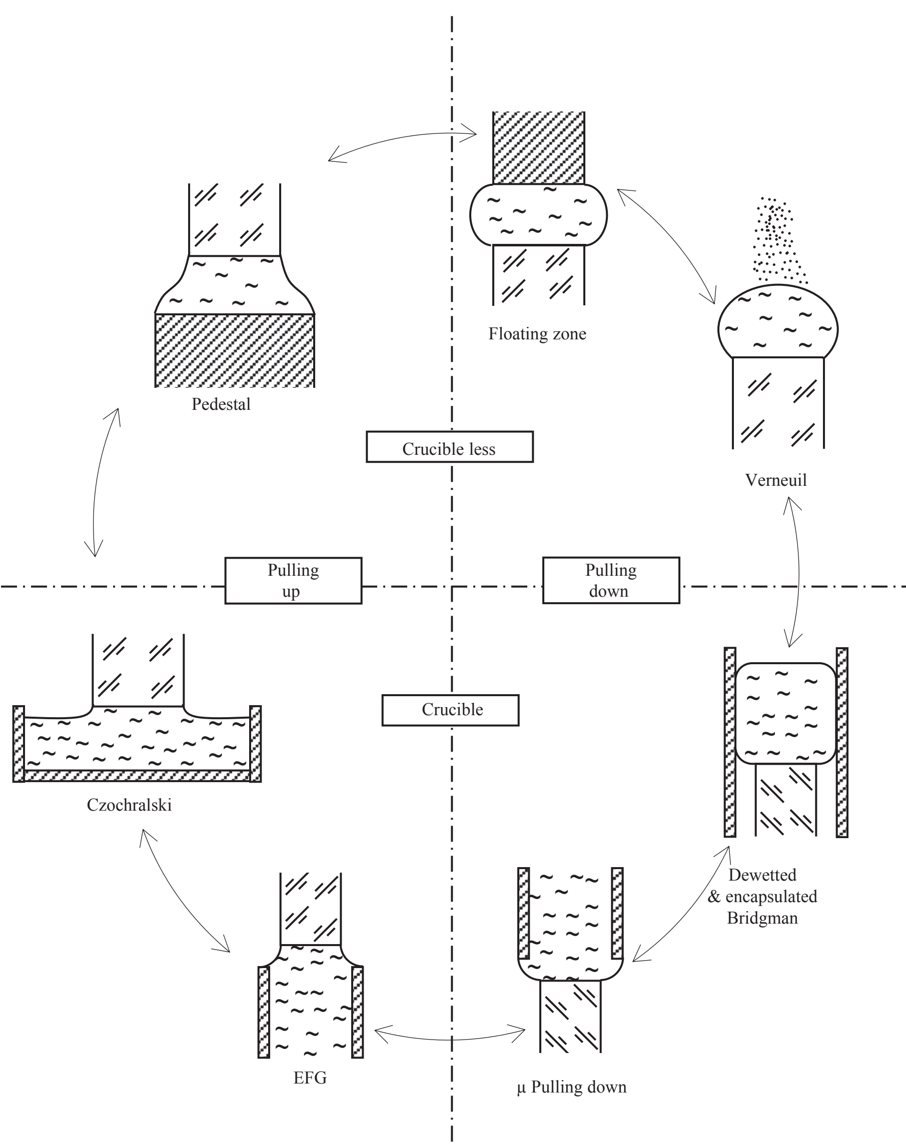

FIGURE 19.3 Classification of crystal growth techniques in which the crystal grows from the melt without contact with a crucible. *Reprinted from Ref. [1], with permission of Wiley-Blackwell.*

increase this surface. Table 19.1 gives the values of the surface energy of various liquids of interest to the crystal grower.

19.2.2 Marangoni Convection

Another issue concerning capillarity and crystal growth is the occurrence of thermocapillary convection, named after Carlo Giuseppe Matteo Marangoni (for more details, see

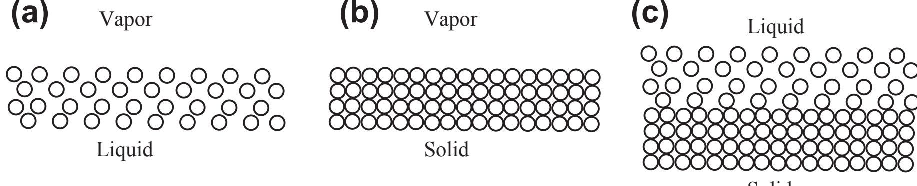

FIGURE 19.4 Atomic interactions: (a) in the liquid and at its surface; (b) in the solid and at its surface; (c) between a solid and a liquid.

Table 19.1 Surface Energy of Various Materials

Compound	T_m (°C)	γ_{lv} (mJ/m^2)
Ge	937	587 − 0.105 ($T - T_m$)
Si	1412	827 − 0.48 ($T - T_m$)
		749 − 0.15 ($T - T_m$)
GaSb	711	453 − 0.14 ($T - T_m$)
InSb	530	434 − 0.08 ($T - T_m$)
CdTe	1092	181 − 0.16 ($T - T_m$)
$Pb_{0.8}Sn_{0.2}Te$	$T_L = 905$	230 − 0.17 (T − 905 °C)
GaAs	1238	465 − 0.96 ($T - T_m$)
Al_2O_3	2047	630 at T_m
SiO_2	1720	307 at T_m
CaF_2	1418	387 at T_m
BaF_2	1290	253 at T_m
LiF	848	236 at T_m
NaF	992	186 at T_m
CsI	621	72 at T_m
NaI	660	86 at T_m
$LiNbO_3$	1250	192 at 1300 °C

Extracted from Chapter 1 of Ref. [1] with permission of Wiley-Blackwell.

Chapter 22, Volume IIB). Because atomic interactions are thermodynamic variables, they change with temperature and the surface energies as well. This variation is the origin of the Marangoni convective effect. As can be seen in Table 19.1, surface energy decreases with temperature so that the atoms at the hot areas on the surface tend to move toward the cold side in order to decrease the overall energy of the surface. This creates a countercurrent in the liquid below the surface. Because the meniscus joins the hot bulk liquid to the colder liquid–solid interface, temperature gradients and thus Marangoni convection are unavoidable. Heat diffusivity tends to decrease the temperature differences and viscosity to damp the fluid motion. Therefore, the relative strength of thermocapillary convection is estimated by the Marangoni number:

$$Ma = -\frac{\partial \gamma_{lv}}{\partial T}\frac{L\Delta T}{\nu \rho_l D_{th}}. \tag{19.3}$$

Another cause of surface energy variation is chemical composition. As explained in Chapter 25, Volume IIB, solute rejection during solidification creates a composition gradient in the liquid at the solid–liquid interface and then on the meniscus, such that solutocapillary and thermocapillary convections always exist jointly. A solutal Marangoni number is defined similarly:

$$Ma_{ch} = -\frac{\partial \gamma_{lv}}{\partial c} \frac{L\Delta c}{\nu \rho_l D}. \tag{19.4}$$

These numbers are useful because they show the critical values between different fluid flow regimes. For example, floating zone is subject to intense Marangoni flows because steep temperature gradients exist on the liquid surface. Studies have shown that below $Ma = 10$, the flow is steady axi-symmetric, then becomes three-dimensional steady until 10^2, then periodic up to 10^4, and finally turbulent above 10^4.

Such flows strongly affect the heat and solute transfer in the vicinity of the growth front and then have a marked effect on the crystal quality. For more detail, the reader is referred to Chapter 22 in Volume IIB, where Marangoni convection is extensively covered.

19.2.3 Young–Laplace Equation

Bending a surface increases its area and then its energy. As a consequence, a bended surface has a tendency to come back to a flat state; it is therefore necessary to apply a force per surface unit (i.e., pressure) to keep the surface bent. Laplace [14] has shown that the pressure difference between the two sides of a bent surface is proportional to its curvature:

$$\Delta p = \gamma_{lv} \left(\frac{1}{r_1} + \frac{1}{r_2} \right), \tag{19.5}$$

where r_1 and r_2 are the two radii of curvature of the surface at the point of interest (Figure 19.5). This equation, also known as the Young–Laplace equation, is a second-order differential equation giving z as function of (x, y) (see Figure 19.5) that is used to compute the shape of the meniscus in the capillarity-related crystal growth processes. Unfortunately, it is strongly nonlinear and some approximations (or specific analytical or numerical methods) should be used in order to get a solution. In order to solve the differential equation, boundary conditions are needed—the growth and wetting angles. These are discussed in more detail in the next sections.

19.2.4 Growth Angle

In the crystal growth processes based on capillarity, there is a crystal–liquid–vapor triple line on the crystal side of the meniscus, which is at equilibrium at the melting point. It follows that the surface energies, or surface forces, equilibrate on this line. This leads to the Herring relationship [15], which, in the isotropic approximation, reads:

$$\gamma_{lv} \cdot \boldsymbol{t}_{lv} + \gamma_{ls} \cdot \boldsymbol{t}_{ls} + \gamma_{sv} \cdot \boldsymbol{t}_{sv} = 0. \tag{19.6}$$

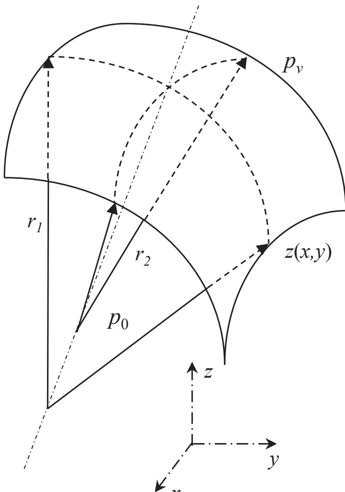

FIGURE 19.5 Radii of curvature of a bended surface.

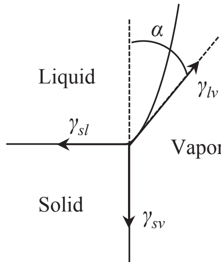

FIGURE 19.6 Definition of the growth angle, α, from the equilibrium of the capillary forces.

This equilibrium defines the growth angle between the liquid–vapor surface and the crystal–vapor surface (Figure 19.6), which is a thermodynamic parameter characteristic of each material. It is quite difficult to measure, either from pictures taken during crystal growth or from the interpretation of the shape of solidified droplets. These measurement methods, their accuracy, and relevant hypotheses, as well as the assumption that the growth angle remains constant during growth, are discussed in detail by Brandon and Virozub in Chapter 1 of Ref. [1].

The growth angle is of critical importance for a correct understanding of the phenomena involved in the crystal shaping process. As can be seen in the case of Czochralski pulling in Figure 19.7, neglecting this angle will cause the crystal diameter to decrease continuously.

Table 19.2 gives the values of growth angles for materials of interest, selected from the more comprehensive table given in reference [1]. Metals generally show a nonmeasurable growth angle (Cu, Ga, Au) because the atomic interactions at the

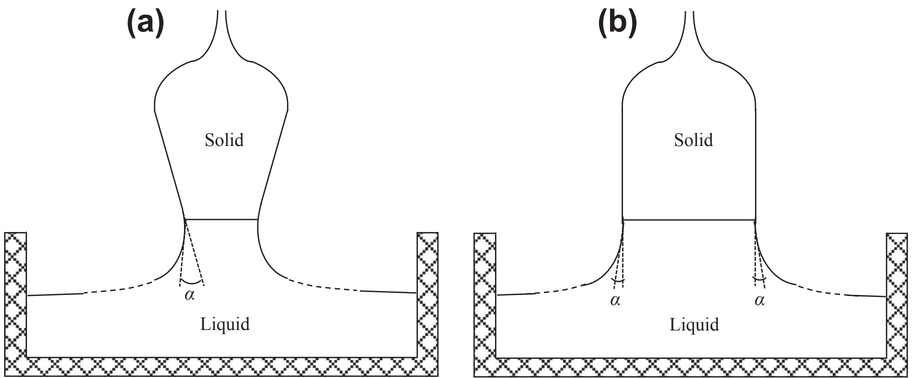

FIGURE 19.7 Importance of the growth angle in the Czochralski process. (a) Not taking into account the growth angle leads to radius decrease. (b) Growth angle should be satisfied for a constant diameter growth.

Table 19.2 Selected Values of Growth Angles (α) for Commonly Grown Crystals

Material	α (°)
Si	12 ± 1
Ge	13 ± 1
InSb	25 ± 1
$LiNbO_3$	0
$NaNO_2$	7 ± 1
LiF	19 ± 2
Sapphire	17 ± 2
GaP (111)	9.8 ± 0.5
InP (111)	7.0 ± 0.5
GaSb	29 ± 2
GaAs	16

solid–liquid interface are of the metallic type and not very different from the bulk interactions—except for the case of W, for which a growth angle of 20° has been measured [16].

19.2.5 Wetting Angle

On the side of the meniscus surface opposite to the crystal, the melt is anchored on a solid surface, such as crucible or shaper material. The boundary condition there corresponds to the wetting angle of the liquid on the solid surface, as defined in Figure 19.8. This angle is generally measured by the sessile drop method, which consists of an analysis of the shape of a molten drop on a flat substrate and also gives the surface energy of the melt.

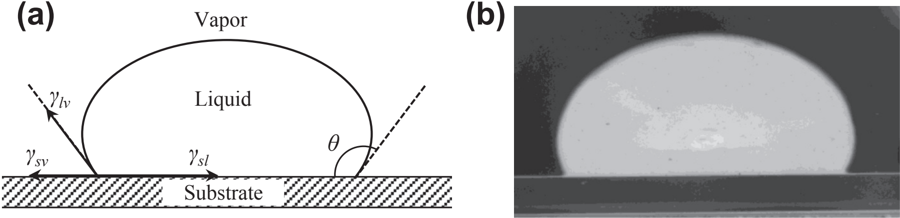

FIGURE 19.8 Sessile drop used for the measurement of γ_{lv} and wetting angle θ. (a) Force equilibrium, (b) Photograph obtained of GaSb on a sapphire substrate at 820 °C ($\theta = 110°$).

Figure 19.8 gives the geometric relation (which is the projection of Eqn (19.6) on the substrate surface):

$$\gamma_{lv} \cos\theta + \gamma_{sv} = \gamma_{sl}. \tag{19.7}$$

Generally, γ_{sv} and γ_{sl} are unknown. However, Eqn (19.2) gives the adhesion energy from the two measurable parameters (γ_{lv} and θ):

$$W_a = \gamma_{LV}\,(1 + \cos\theta). \tag{19.8}$$

Wetting at the high temperatures encountered in crystal growth often involves chemical reactivity or roughness issues that make the analysis complex. The interested reader is referred to [17] for a comprehensive treatment of this topic. Table 19.3 gives the standard values of wetting angles for common semiconductor–crucible couples of interest in crystal growth [1]. The wetting angle is also important in the case of molten oxides because they are often pulled by EFG or micro-pulling-down methods. Values are only known for sapphire: 7° on W, 15° on Mo, 40° on Nb, and 40° on Ta [18].

Table 19.3 Typical Values of Wetting Angles for Molten Semiconductors on Classical Crucible Materials

Molten Material	Substrate	Wetting Angle (°)
Ge	Graphite	135
Si		15
III-V		120–150
CdTe		104
Ge	BN	140
Si		110
III-V		130–150
CdTe		132
Ge	SiO_2	155
Si		85
III-V		110–140
CdTe		83

19.2.6 Catching and Horizontal Conditions

A particular behavior occurs on sharp edges. Figure 19.9 shows the advancement of a drop-solid-vapor triple line when the drop volume increases, on a surface limited by sharp edges. When the volume is small (Figure 19.9(a) and (b)), the wetting angle is satisfied on the horizontal surface. When it is large, the wetting angle is satisfied on the vertical surface (Figure 19.9(e); not taking into account gravity). In between (Figures 19.9(c) and (d)), the situation is sometimes referred as the "catching condition" because the meniscus seems to be caught on the sharp edge that limits the surface; therefore, a known position is fixed for the meniscus boundary. In fact, the edge is not sharp at the microscopic scale and a wetting angle exists, as shown on the enlarged drawings. It has been demonstrated [19] that the wetting condition can be approximated by a catching condition when the radius of curvature of the solid edge is less than $0.1a$, with a being the capillary length of the liquid (see Table 19.4 for typical values):

$$a = \sqrt{\frac{\gamma_{lv}}{\rho_l g}}. \tag{19.9}$$

This parameter is important in capillarity problems, as it compares the surface energy to the gravitational energy. When the typical size of the system is smaller than a, gravity effects can be neglected. In the reverse case, gravitational forces are preponderant.

The last case of the boundary condition is encountered only in the Czochralski growth process. Provided that the crucible diameter is significantly larger than the crystal diameter, it can be considered that the meniscus extends to an infinite radius, where it vanishes on the horizontal surface of the liquid.

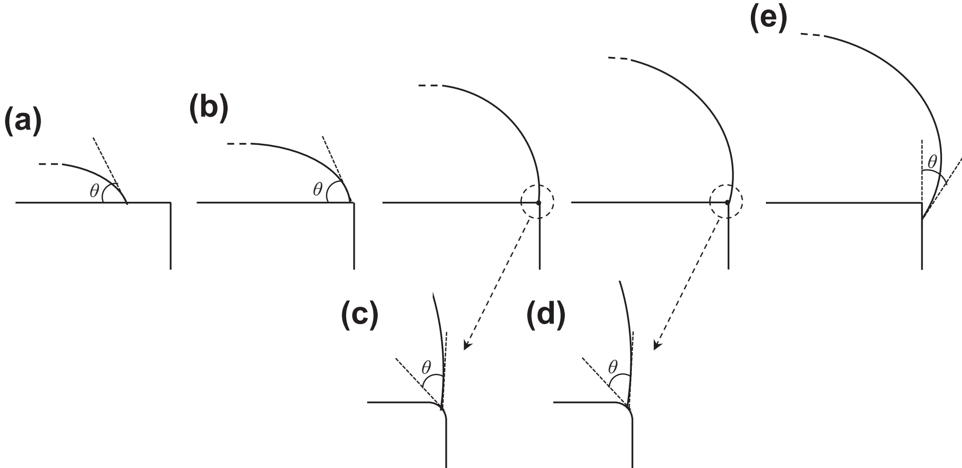

FIGURE 19.9 Wetting (a, b, and e) and catching (c and d) conditions for a meniscus close to a sharp edge.

Table 19.4 Maximal Zone Length and Capillary Length for Various Materials

Material	ρ_l (kg/m^3)	γ_{lv} (N/m)	a (mm)	L_{Max} (mm)
Si	2580	0.88	5.9	17
Co	7750	1.87	5	14
Mo	9099	2.25	5	14
Cu	8000	1.30	4.1	12
Ge	5490	0.62	3.4	10
GaAs	5400	0.45	2.9	8
GaSb	6030	0.47	2.8	8
Al_2O_3	3980	0.65	4	11
Pb	10,670	0.46	2.1	6

19.3 Solutions of the Young–Laplace Equation

19.3.1 Nonlinearity of the Young–Laplace Equation

Equation (19.3) looks rather simple. However, developing the curvature radii in a general three-dimensional $z(x, y)$ function that represents the meniscus surface leads to the following equation (with reference to Figure 19.5):

$$\gamma_{lv}\frac{\left[1+\left(\frac{dz}{dy}\right)^2\right]\frac{\partial^2 z}{\partial x^2}-2\frac{\partial z}{\partial x}\frac{\partial z}{\partial y}\frac{\partial^2 z}{\partial x\partial y}+\left[1+\left(\frac{dz}{dx}\right)^2\right]\frac{\partial^2 z}{\partial y^2}}{\left[1+\left(\frac{\partial z}{\partial x}\right)^2+\left(\frac{\partial z}{\partial y}\right)^2\right]^{\frac{3}{2}}}=\pm\left(p_0-p_v-\rho_l g z\right), \tag{19.10}$$

where other pressure terms (e.g., centrifugal in case of rotation, electromagnetic) can be added on the right side. The positive or negative sign is conventional and is generally chosen in agreement with the physical problem. On the mathematical point of view, it depends on the choice of the reference frame, which is also arbitrary.

Due to its strongly nonlinear form, no analytical solution of the problem exists in the general case. On the contrary, it has been proven that each case should be solved independently, and that generally the equation and associated wetting or catching boundary conditions can only be solved by numerical integration [20]. In several cases corresponding to crystal growth capillary problems, solutions have been found by approximating the problem to two-dimensional (2D) or axisymmetric configurations.

19.3.2 Axisymmetric and Two-Dimensional Formulations

Most crystal growth processes produce cylindrical crystals and can be represented in an axisymmetric configuration where the meniscus shape corresponds to a $z(r)$ function. By introducing the angle Φ between the tangent to the meniscus and the

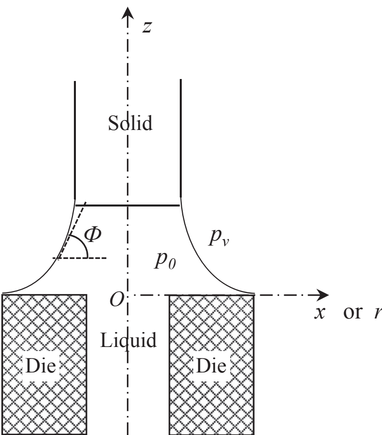

FIGURE 19.10 Axisymmetric (r-axis) and 2D (x-axis) configurations of the meniscus in the EFG process.

horizontal axis (see Figure 19.10), the differential equation can be replaced by a more convenient form:

$$\begin{cases} \dfrac{dz}{dr} = \pm \tan \Phi \\ \dfrac{d\Phi}{dr} = \pm \dfrac{p_0 - p_v - \rho_l g z}{\gamma_{lv} \cos \Phi} - \dfrac{1}{r} \tan \Phi \end{cases}. \tag{19.11}$$

Pulling planar sheets (ribbons) by the EFG or micro-pulling-down methods (see Figure 19.3) gives another simplification of the Young–Laplace equation. By considering the flat sheet side, the curvature radius of which is infinite, a 2D configuration is obtained, in which the meniscus shape is represented by a $z(x)$ function. Of course, border effects, occurring at the edges of the sheet, are therefore neglected. These edges can be studied with the approximation that they are two half-axisymmetric menisci; however, the connection with the flat edge remains an issue [21]. Also introducing the angle Φ gives the 2D formulation of the Young–Laplace equation:

$$\begin{cases} \dfrac{dz}{dx} = \pm \tan \Phi \\ \dfrac{d\Phi}{dx} = \pm \dfrac{p_0 - p_v - \rho_l g z}{\gamma_{lv} \cos \Phi} \end{cases}. \tag{19.12}$$

19.3.3 Approximations and Meniscus Shape in the Czochralski Configuration

Besides the solutions of the Young–Laplace equation obtained by numerical integration, which will be described in the next section, approximated solutions have been proposed.

A first approximation is valid when the dimension of the meniscus is much lower than the capillary length a (Eqn (19.9)). In this case, the gravitational force is negligible compared to the capillary force and the Young–Laplace equation reduces to:

$$\left(\frac{1}{r_1}+\frac{1}{r_2}\right)=\frac{p_0-p_v}{\gamma_{lv}}=Ct. \tag{19.13}$$

This means that the curvature is constant and the meniscus is a portion of a sphere. Calculations are considerably simplified in this case; an example will be shown in Section 19.3.6.

Approximations are also necessary in the case of axisymmetric Czochralski pulling—a particular case in which the meniscus can be considered as extending to infinity, provided that the crucible diameter is significantly larger than the crystal diameter. By the way, due to this boundary condition extending to infinity, numerical integration of the meniscus shape is not possible.

In this technique, the meniscus height, h (Figure 19.11) is mainly controlled by heat transfer—that is, by the heating power delivered to the crucible, by the growth rate (which releases latent heat), and by the cooling of the crystal to its surroundings. As explained in Chapter 28 of Volume IIB, control of the crystal diameter often involves the weight of the hanging crystal, to which the meniscus is attached. Therefore, exact knowledge of meniscus height and shape is mandatory to get good control. As detailed in Ref. [22], several equations have been proposed in order to give accurate enough analytic approximations. By expanding the second curvature radius in the Taylor series, Tsivinski [23] has obtained the following expression for the meniscus height as function of the crystal radius r_c:

$$h(r_c)=-\frac{\cos\alpha}{2r_c}\frac{\gamma_{lv}}{\rho_l g}+\sqrt{\left(\frac{\cos\alpha}{2r_c}\frac{\gamma_{lv}}{\rho_l g}\right)^2+\frac{2\gamma_{lv}}{\rho_l g}(1-\sin\alpha)}. \tag{19.14}$$

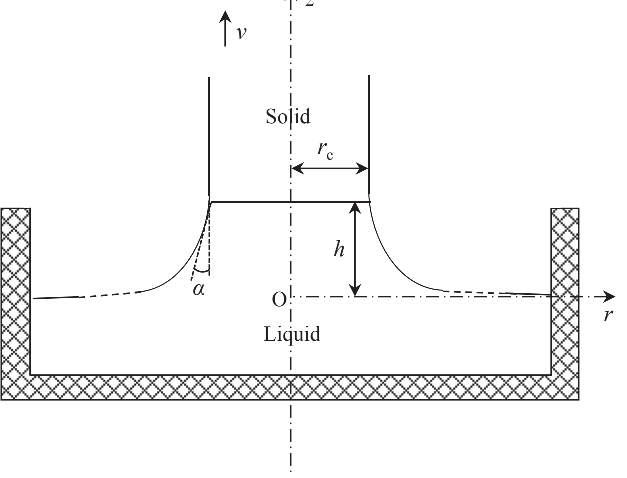

FIGURE 19.11 Capillarity configuration of the Czochralski process.

From this, Hurle obtained an analytical expression of the meniscus shape [24]:

$$\begin{cases} r(z) = r_c + \sqrt{\frac{2}{A} - h^2} - \sqrt{\frac{2}{A} - z^2} - \frac{1}{\sqrt{2A}} ln\left(\frac{z}{h}\frac{\sqrt{2}+\sqrt{2-Ah^2}}{\sqrt{2}+\sqrt{2-Az^2}}\right) \\ A = \frac{1}{2}\left(\frac{\cos\alpha}{r_c h} + \frac{\rho_l g}{\gamma_{lv}}\right) \end{cases}. \quad (19.15)$$

Another expression, based on Bessel functions, has also been proposed in Ref. [24]:

$$h(r_c) = \sqrt{\frac{2\gamma_{lv}}{\rho_l g}}\sqrt{\frac{1-\sin\alpha}{1+\frac{1}{r_c}\sqrt{\frac{\gamma_{lv}}{\rho_l g}}}}, \quad (19.16)$$

with an associated equation for the meniscus shape. A comparison shows that the error between Eqns (19.14) and (19.16) is on the order of 10^{-4} for small cylindrical crystals and decreases for higher diameters [22]. Mika and Uelhoff [25] proposed another approximated solution for the meniscus shape, which is analytical far from the crystal and numerical close to it. The accuracy, compared to the solutions above, is on the same order.

In summary, it is impossible to find an analytical or numerical solution of the meniscus problem in the Czochralski case, but approximations exist that are accurate enough for practical use.

19.3.4 Numerical Integration: The Runge-Kutta Algorithm

Integration of the Young–Laplace equation is currently performed numerically, especially for the axisymmetric and 2D cases in Eqns (19.11) and (19.12). Looking at those equations reveals that we are facing a classical "artillery problem": finding $y(x)$ by knowing the initial point and the derivative $f = \frac{dy}{dx}(x,y)$.

This is solved numerically with help from the Runge-Kutta method. This is an iterative step-by-step method that uses Taylor series expansion of the derivative in order to approximate the location of the further point on the trajectory, knowing the location of the current point. Special care is given to the truncation error because it propagates and amplifies when the calculation goes on. This leads to several types of this method; the most commonly used is the fourth-order Runge-Kutta method, abbreviated as RK4. The interval $x_0 - x_N$ on which the equation should be integrated is divided in N steps. At each step, the next point y_i is calculated from the current point y_{i-1} as:

$$\begin{cases} y_i = y_{i-1} + \frac{1}{6}(k_1 + 2k_2 + 2k_3 + k_4) \\ h = \frac{x_N - x_0}{N} \\ k_1 = hf(x_{i-1}, y_{i-1}) \\ k_2 = hf\left(x_{i-1} + \frac{1}{2}, y_{i-1} + \frac{k_1}{2}\right) \\ k_3 = hf\left(x_{i-1} + \frac{1}{2}, y_{i-1} + \frac{k_2}{2}\right) \\ k_4 = hf(x_{i-1} + h, y_{i-1} + k_3) \end{cases}, \quad (19.17)$$

in which k_i are estimations of the slope of the function in the interval x_{i-1}–x_i.

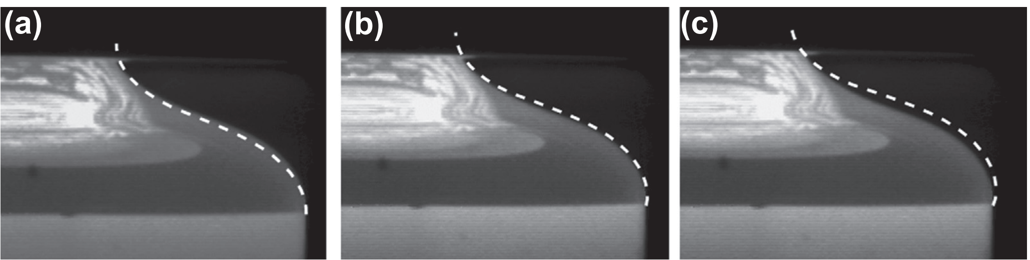

FIGURE 19.12 Calculation of the shape of the meniscus in the Si floating zone process and comparison with a photograph. The difference between the three figures is the starting angle: a = 0°, b = 11° (Si growth angle), and c = 20°. *From Ref. [28] with permission of Wiley-Blackwell.*

Application to the capillary problem needs to solve two equations simultaneously, such as $z(r)$ and $\Phi(r)$ in the case of Eqn (19.8). This is not a particular problem because z_{i-1} and Φ_{i-1} are known at each step. The method is simple and robust, and several ready-to-use programs are available on the internet, such as the code provided by Ref. [26] or the online method available in Ref. [27].

19.3.5 Application to the Floating Zone Process

Application of the RK4 algorithm to the shape of the meniscus in floating zone pulling of silicon is addressed in Chapter 7 in Volume IIA and is shown in Figure 19.12 [28]. This case is special from the pressure point of view. The reference pressure in the melt is unknown, and then the curve should be numerically forced to pass by an experimental point (the top of the meniscus in these figures). Also, additional pressure, due to the electromagnetic force applied by the induction coil on the molten Si, should be added to the Young–Laplace equation:

$$\begin{cases} \dfrac{dz}{dr} = \pm \tan \Phi \\ \dfrac{d\Phi}{dr} = \pm \dfrac{p_0 - p_v - \rho_l g z - \dfrac{B^2(r)}{2\mu}}{\gamma_{lv} \cos \Phi} - \dfrac{1}{r} \tan \Phi \end{cases} . \tag{19.18}$$

The calculation begins at the solid–liquid–vapor triple line (between the clear solid and darker liquid zones, at the lower right side) and proceeds upwards. It can be seen that the growth angle, (i.e., the initial meniscus direction) should be carefully introduced in the simulation in order to get an accurate meniscus shape.

19.3.6 Usefulness of Meniscus Shape: Ribbon Thickness in the Pendant Drop Growth and Micro-Pulling-Down Methods

Single crystal thin plates (e.g., photovoltaic substrates, sapphire ribbons) and fibers (e.g., lasers, scintillators, waveguides, nonlinear optics, harmonic generation) have many potential applications. Due to their large surface-to-volume ratio, they cannot easily be

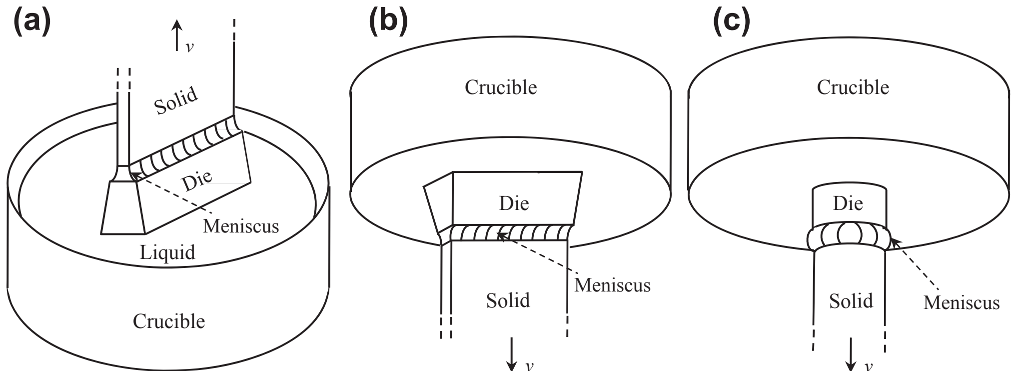

FIGURE 19.13 Processes of pulling single crystals from shaping dies. (a) Pulling a plate upward by the EFG or Stepanov method. (b) Pulling a plate downwards by the pendant drop growth method. (c) Pulling a fiber downwards by the micro-pulling-down method.

grown in crucibles that interact very much with the surface and then, for such shapes, with the whole bulk material. Several capillary-driven processes have been developed in order to pull these crystals in the appropriate shape. Some are based on the floating zone, which melts and moves part of an existing small-diameter rod in order to get a fiber, called a microfloating zone; a variant is the laser-heated floating zone. Other methods use shaping dies in order to fix the meniscus, and thus the crystal shape; they are generally known as "shaping processes." Two main variants are commonly used (Figure 19.13): pulling upwards (Stepanov or EFG methods) and pulling downwards from a hole at the bottom of a crucible.

Apparently, the first idea of pulling a shaped crystal from a hole at the bottom of a crucible was from Rupprecht [29]. Ricard [30] added a shaping die and called the technique the pendant drop growth (PDG) method, which he developed for some years; a few sapphire plates were produced in the 1980s by the RSA Company on this basis.

The full maturity of this idea and the great success that it has nowadays, with companies producing single crystal fibers on a daily basis, is due without any doubt to its development by Fukuda's laboratory in Japan in the 1980s and 1990s, under the name of the micro-pulling-down method (μ-PD) [31]. Several hundreds of papers are devoted to theoretical studies and practical pulling of uncountable varieties of crystal fibers by the μ-PD method. All of these aspects are reviewed in the excellent book edited by Fukuda, Rudolph, and Uda [32].

This section essentially presents some unpublished results of my PhD thesis, prepared in Ricard's laboratory [33]. It is focused on the problem of finding the crystal size when only the die size is known; this clearly involves a computation of the meniscus shape. Figure 19.14 presents the geometry of the problem.

Pulling a ribbon will be considered and referred as PDG pulling because this technique has been applied only to the growth of Si or sapphire sheets. The μ-PD method will be reserved for the pulling of rods and fibers, to which it is essentially applied. A ribbon

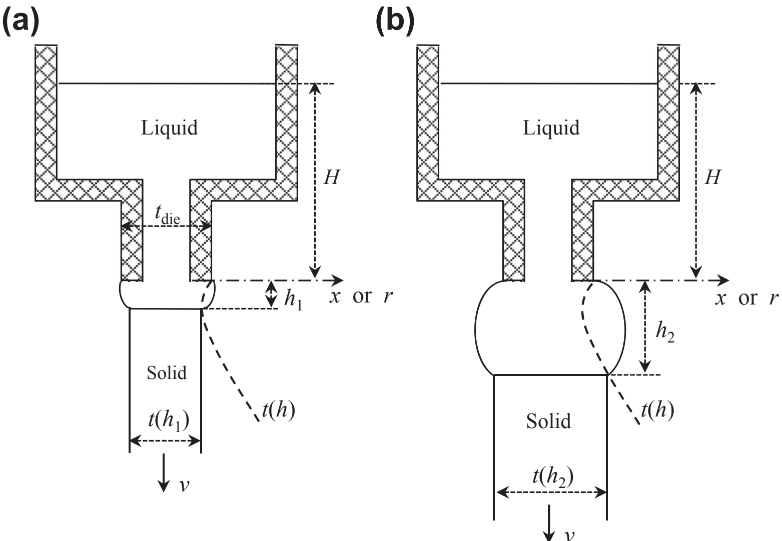

FIGURE 19.14 Geometry of the PDG method: cross-section of two plates of different thicknesses obtained from the same die (a) Minimal thickness configuration; (b) possible configuration for a thicker plate.

can be divided in flat faces that control its thickness and to hemi-circular sides that control its width; it can be considered as two half-rods pertaining to the μ-PD problem (however, the exact connection between the curved sides and the flat faces remains a difficult capillary problem). The main parameter of interest for a ribbon is its thickness, especially in the case of Si sheets for photovoltaic cell applications. The flat ribbon face and corresponding meniscus present an infinite radius of curvature. Therefore, the Young–Laplace equation (Eqn (19.5)) can be written as follows, with respect to the notation of Figure 19.14:

$$\frac{\Delta p}{\gamma_{lv}} = \frac{1}{r_1} = \frac{\rho_l g}{\gamma_{lv}}(H - z(x)). \tag{19.19}$$

It should be noted that, for high pulling rates, the hydrostatic pressure should be decreased by the pressure loss due to the liquid flow in the capillary die. This equation allows one to compute the meniscus shape, $z(x)$, which, for a given material, depends only on the liquid height in the crucible. The boundary condition is:

$$z(x_{die}) = 0. \tag{19.20}$$

An analytical solution exists [34], but it is quite complicated to use in this particular case. Hopefully, the meniscus height, h, in the PDG method is less than 1 mm, which is much lower than the capillary length (see Table 19.4), so that the term $z(x)$ can be neglected in Eqn (19.19) and the meniscus can be approximated by an arc of circumference of constant radius r_1. A comparison with analytical solutions shows that the error is less than 1% in the case of Si, as well as alumina, for menisci lower than 1 mm.

The crystal half-thickness is given by the location on the meniscus where

$$\begin{cases} z(x) = h \\ \dfrac{dz(x)}{dx} = \tan\left(\dfrac{\pi}{2} - \alpha\right) \end{cases}. \tag{19.21}$$

The constant radius approximation allows a simple computation of the ribbon thickness:

$$t = t_{die} + 2r_1 \cos \alpha - 2\sqrt{r_1^2 - (h - r_1 \sin \alpha)^2}. \tag{19.22}$$

This relation $t(h)$ is represented by the dashed line on Figure 19.14. It can be seen that the ribbon thickness depends on the meniscus height, which is given by the position of the melting isotherm and controlled by the heat transfer in the process, as will be discussed in Section 19.4.2. A minimal thickness exists on the position h_1 on the figure. For longer menisci, thicker ribbons can be obtained; however, attention should be paid to the fact that a high meniscus can be unstable and flow down (see Section 19.4.1). Of course, when the meniscus height approaches the capillary length, Eqn (19.22) is not valid anymore and a more complex analytical expression should be used.

This figure is very important to find the relationship between the die thickness, the crystal size, and the heat transfer (i.e., the meniscus height). Therefore, the general method to find the crystal size in the shaping processes is always the same:

1. Design the die.
2. Compute the meniscus shape, analytically, numerically, or with some approximation.
3. Find the place where the meniscus tangent makes an angle α with the vertical axis.
4. This place is the location of the solid–liquid–vapor triple line and gives the crystal size.

This approach has been used for the EFG [34] and μ-PD methods [35], with good agreement with experiments.

19.4 Shape Stability Analysis

In capillary-based crystal growth techniques, the crystal size and shape is only controlled by the liquid meniscus, which is free to deform and move in any direction. Therefore, there is no reason that the crystal dimensions will remain constant throughout the growth process. This section addresses the various stability analyses that have been developed in order to study in which conditions the crystal shape is stable or unstable. Small perturbations of mechanical or thermal origin occur throughout the growth process. The question is to know in which cases the system comes back spontaneously to a steady state (stable growth) or, on the contrary, deviates from the expected dimensions.

19.4.1 Static Stability

A first question concerns the existence of the meniscus and is referred as "static stability." Not all menisci, while obeying the Young–Laplace equation (Eqn (19.5)), can exist in

practice because any small mechanical vibration will cause the liquid to flow down. The total energy of the liquid is the sum of a potential term and a surface term [36]:

$$E = \iint\limits_{domain} \left(\frac{1}{2} \rho_l g z^2(x,y) + \gamma_{lv} \sqrt{1 + \left(\frac{\partial z}{\partial x}\right)^2 y + \left(\frac{\partial z}{\partial y}\right)^2 x} \right) dS. \tag{19.23}$$

The equilibrium state comes from the minimization of this energy, with the constraint of keeping the liquid volume constant. It can be demonstrated that surfaces obeying the Young–Laplace equation satisfy this minimum criterion. However, the energy, at constant volume, presents minima and maxima; only minima are statically stable. The static stability analysis is classically performed by perturbation analysis. From a practical point of view, in crystal growth processes, menisci present a very small height and there is no problem of static stability (e.g., Figure 19.3). It is only in the case of the floating zone process that the height of the molten zone becomes dangerously high.

Stability of liquid bridges in the floating zone configuration has been extensively studied, essentially by the perturbation analysis of Eqn (19.23). For small-diameter rods(<2–3 cm, depending on the material), the maximum stable zone length varies linearly with the diameter, to which it is approximately equal. For larger diameters, the maximum height of the zone is independent of the diameter:

$$L_{Max} = C\sqrt{\frac{\gamma_{lv}}{\rho_l g}}, \tag{19.24}$$

where the constant C varies between 2.62 and 3.18, depending on the solution approach [37]. It is amazing to remark that equating the mass of the liquid zone to the surface forces acting on the two triple lines gives the same result:

$$\rho_l g \pi \frac{d^2}{4} L = \gamma_{lv} 2\pi d \quad \Rightarrow \quad L = 2.82\sqrt{\frac{\gamma_{lv}}{\rho_l g}} = 2.82a, \tag{19.25}$$

in the case where the length equals the diameter—that is, for the maximal stable length. Table 19.4 gives the maximum length for various materials, as well as the capillary length, a parameter to which it is closely related (see Eqn (19.9)). Silicon is the easiest material to grow by the floating zone technique, which is indeed the case industrially. However, it should be noted that the electromagnetic field delivered by the heating coil generates an electromagnetic pressure, which contributes significantly to the stabilization of the liquid zone. It can also be seen that heavy metals are good candidates as well because their surface energy is high, whereas some lighter materials can only be grown with small zones.

19.4.2 Importance of Heat Transfer and Growth Rate in Shape Stability

The shape of the crystal is controlled by the meniscus shape and by the position of the solid–liquid–vapor triple line, which is the place where the meniscus ends on the

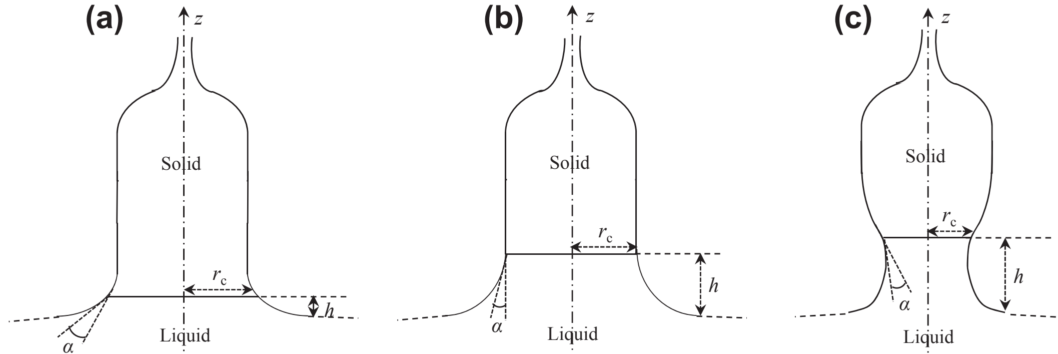

FIGURE 19.15 Variation of the Czochralski crystal diameter from the steady state (b) when the meniscus height decreases (a) or increases (c).

growing crystal surface. This triple line corresponds to the solidification isotherm. Its temperature may depend on local chemical composition, curvature, or solid–liquid interface morphology (e.g., rough, faceted) however only a constant melting point will be considered here.

Heat transfer conditions evolve all along the crystal pulling because geometry changes and liquid is replaced by the crystal, which has different thermal properties. Therefore, the solid–liquid interface moves in the frame of the setup and then the meniscus height changes. Obviously, this impacts the crystal shape: Figure 19.15 shows how variations of the meniscus height affect the diameter of a crystal grown by the Czochralski process.

For a given fluctuation of temperature dT, the variation of meniscus height depends on the temperature gradient:

$$dh = \frac{dT}{\nabla T}, \tag{19.26}$$

and then, in order to keep low fluctuations of size, large temperature gradients are preferred for capillary growth processes. However, higher temperature gradients can generate higher mechanical stresses in the crystal, and then dislocations and other defects.

On the other hand, the speed at which dimensions change is proportional to the growth rate (see Figure 19.16):

$$\frac{\partial r_c}{\partial t} = v\tan(\alpha_0 - \alpha) \approx v(\alpha_0 - \alpha). \tag{19.27}$$

Growth rate and temperature gradient are intimately linked. This is due to the release of latent heat by the solidification process, which should be taken into account in the heat balance at the interface:

$$\lambda_l \nabla T_l^i + \rho_l \Delta H_m v = \lambda_s \nabla T_s^i. \tag{19.28}$$

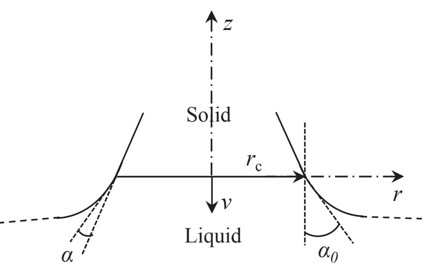

FIGURE 19.16 Variation of crystal radius as function of the meniscus angle to the vertical.

This balance is the most important equation in solidification because it links the temperature field to the growth conditions. The temperature field affects the solid–liquid interface curvature, convection in the liquid, chemical segregation in the crystal, mechanical stresses and dislocations, and point defect density. It is also intensively used in the stability analysis of the crystal growth processes because it affects the meniscus height and the crystal shape through Eqns (19.26) and (19.27).

19.4.3 Capillary Stability and Applications to Dewetting under Microgravity

The simplest approach in dynamic stability concerns cases where capillarity (meniscus shape; i.e., Eqn (19.10)) and heat transfer (heat balance at the solid–liquid interface, Eqn (19.28)) are uncoupled. This means that perturbations of crystal and meniscus shapes do not significantly affect heat transfer in the process, and vice versa. Generally speaking, this is not true in crystal growth processes; however, capillary stability is a simple, first-order way to look at dimensional stability, and it is useful as a pedagogic introduction to growth stability. It should generally be completed by more complex analyses, to be introduced here, because it can lead to wrong conclusions when it is not applicable.

In such cases, stability of the crystal shape is controlled by capillarity only—hence the name "capillary stability." Figure 19.17 shows the two configurations that may occur, depending on the shape of the meniscus, in the example of μ-PD of a rod. The rationale can be extended to any crystal growth process driven by capillarity. The situation on the left corresponds to the case where the pressure in the meniscus is higher than the ambient gas pressure, generally because of the hydrostatic pressure due to the liquid in the above crucible. The situation on the right shows a lower pressure in the meniscus than in the surrounding gas; this is generally due to the viscosity of the melt or a very small capillary channel in the die, which create a large pressure drop so that the solid–liquid interface acts as a piston that pumps the melt out of the crucible.

If heat transfer and capillarity are uncoupled (which is generally *not* the case in μ-PD, but is supposed here for the sake of demonstration), capillary stability analysis applies. Looking at the left configuration in Figure 19.17, the vertical situation in the middle corresponds to a crystal growing with a constant radius. The key parameter is the growth

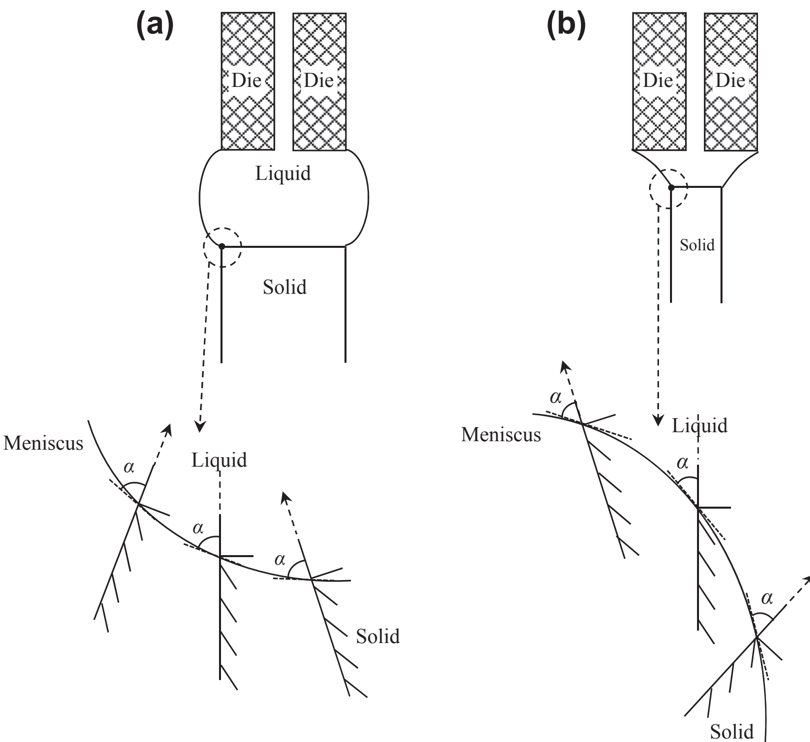

FIGURE 19.17 Capillary stability in relation to meniscus curvature. (a) Concave meniscus seen from the melt; stable configuration. (b) Convex meniscus seen from the melt; unstable configuration.

angle α, which is always conserved between the crystal and meniscus surfaces. For this reason, it can be seen that any perturbation that causes the crystal radius to decrease (to the right) or increase (to the left) will be followed by, respectively, an increase or decrease (arrows) of the radius, leading back to the initial radius. Clearly, the system is stable toward any dimensional perturbation. On the contrary, the situation on the right leads to the inverse conclusion: the system is unstable toward any dimensional perturbation, which is always amplified.

The difference between the two configurations is the curvature of the solid–liquid interface. The application of capillary stability leads to the following conclusions:

1. If the meniscus surface is concave at the solid–liquid–gas triple line, seen from the melt, then the growth is stable.
2. If the meniscus surface is convex at the solid–liquid–gas triple line, seen from the melt, then the growth is unstable.

Capillary stability analysis is restricted to a few situations, which require that the meniscus shape does not depend on the position of the solid–liquid interface. This is seldom the case because of hydrostatic pressure. However, under microgravity

conditions, the gravity force disappears and capillary stability can be applied. This is the case for the dewetting phenomenon, which was discovered after Bridgman crystal growth experiments under microgravity conditions. Most of such experiments revealed that the semiconductor crystal grew free of any contact with the crucible, with a gap of several tenths of micrometers in between. This peculiar phenomenon was initially classified under detachment results, which also include bubbles and crystal necking (for a review of this topic, see Ref. [38]). Later on, an explanation of the phenomenon, restricted under the term of “dewetting,” was proposed based on the spontaneous existence of a liquid meniscus between the crucible and the solid–liquid interface [39]. More precisely, the occurrence of dewetting was linked to the conjunction of a high wetting angle of the liquid on the crucible wall, a nonzero growth angle, and the absence of gravity (i.e., of hydrostatic pressure).

This situation is presented in Figure 19.18. The model is based on the assumption that the liquid–crucible–vapor triple line moves upwards at the same speed than the crystal–liquid–vapor triple line, which is the growth rate. A striking point in these experiments is the fact that the crucible–crystal gap, as measured during postflight sample analysis, was found to be extremely constant all along the crystal length—for example, 70 ± 5 μm on 5-cm length for the gap between a GaInSb crystal and an open boron nitride crucible [40]. The natural stability of the process was then obvious and has been studied in Ref. [41]. Referring to Figure 19.18, the difference of pressure between the vapor phase and the liquid is controlled by the shape of the hot liquid-free surface. Because gravity is very small (on the order of 10^{-5} m/s^2 in a spacecraft), the capillary length is of the order of meters. Gravity effects are negligible at the

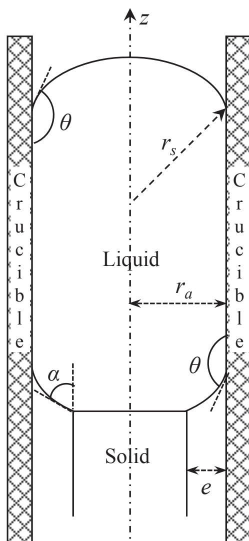

FIGURE 19.18 Configuration of the dewetting phenomenon under microgravity conditions.

scale of the experiment (some centimeters) and the Young–Laplace equation reduces to Eqn (19.13).

Due to the axisymmetry of the system, it follows that the two radii of curvature are equal and the hot meniscus is a spherical cap of radius r_s. In many of these microgravity experiments, the crucible is an open tube so that the gas pressure is the same at the cold and hot sides of the melt. It follows that the lower meniscus, which joins the crucible to the crystal, is also part of a spherical surface with the same radius (the case where a pressure difference exists is treated in the original paper). Simple geometrical considerations then give the gap thickness:

$$e = r_a \frac{\cos\alpha + \cos\theta}{\cos\theta}, \tag{19.29}$$

which is independent of the meniscus height and then of the solid–liquid interface movement driven by heat transfer in the process. Therefore, the stability problem reduces to capillary stability and, because the meniscus is concave seen from the melt, the process is spontaneously stable. This explains why so many Bridgman solidification experiments under microgravity conditions have shown dewetting, especially those devoted to semiconductor growth; for these materials, the growth angle is nonzero (Table 19.2) and contact angles on commonly used crucibles (e.g., graphite, silica, boron nitride) are large (Table 19.3).

19.4.4 Dynamic Stability: The Classical Lyapunov Approach and Applications to the Verneuil Process

Capillary stability can only be applied when the capillarity problem is disconnected from the other phenomena involved in the crystal growth process. This is generally not the case, and more sophisticated analyses are needed. Stability is classically studied in the first-order linear approximation known as the Lyapunov method. Its application to various crystal growth processes has essentially been performed by Tatarchenko in numerous papers, which are reviewed in details in his book [42].

The Lyapunov method first considers the number n of degrees of freedom, $X_{i=1,n}$, of the process. For example, the Czochralski process has two degrees of freedom—the meniscus height, h, and the crystal radius, r_c—as can be seen in Figure 19.15. It is their variations that might cause instability of the system. These variables are linked by physical equations that describe the process. In the Czochralski case, the two equations are the Young–Laplace equation in Eqn (19.11) and the heat balance at the solid–liquid interface in Eqn (19.28). Therefore, it is possible to link the variation of one degree of freedom as a function of the variations of the other degrees of freedom. In the general form, this is written as a system of n equations:

$$\frac{dXi}{dt} = f_i\left(X_1, \ldots, X_n, \frac{dX_1}{dt}, \ldots, \frac{dX_n}{dt}, t\right) \quad i = 1, \ldots, n. \tag{19.30}$$

In the stationary state, the variables have values X_i^0, which satisfy Eqn (19.30) and then:

$$f_i\left(X_1^0, \ldots, X_n^0, t\right) = 0 \quad i = 1, \ldots, n \tag{19.31}$$

Any variation of the variable X_i from its stationary value is noted as $\delta X_i = X_i - X_i^0$. Linearization of Eqn (19.30) gives their evolutions as function of the other degrees of freedom:

$$\frac{d\delta X_i}{dt} = \sum_{k=1}^{n} \frac{\partial f_i}{\partial X_k} \delta X_k \quad i = 1, \ldots, n. \tag{19.32}$$

In his thesis [43], Lyapunov demonstrated that solutions of Eqn (19.30) are stable if they are stable for the set of n (Eqn (19.32)). This occurs when the roots S of the following characteristic equation have negative values:

$$det\left(\frac{\partial f_i}{\partial X_k} - S \cdot \delta_{ik}\right) = 0 \quad i = 1, \ldots, n, \tag{19.33}$$

If at least one root has a real positive value, the equilibrium is unstable. As a matter of example, this method will be applied to the analysis of the stability of the Verneuil process [44].

Verneuil developed the first technology for growing artificial crystals at the very end of the nineteenth century in order to study the physical properties of sapphire, ruby, and related gemstones [9]. In this process, alumina powder flows continuously through a hydrogen-oxygen flame, where it melts and forms small droplets. The molten alumina droplets fall on the liquid meniscus, which feeds the growing crystal. Nowadays, this process is used for the industrial production of various crystals, mainly colored or white sapphire and spinels. Several thousands of setups, very close to Verneuil's original design [45], are operated daily. The process has been applied to several hundred materials [46], changing the heating system to arcs, lasers, plasma torches, or electron beams when an oxidizing flame could not be used. This is reviewed elsewhere [47].

This process is characterized by three degrees of freedom (see Figure 19.19):

1. The position of the liquid–vapor interface in the furnace, l
2. The meniscus height, h
3. The crystal radius, r_c

Linearization of the set of Eqn (19.32) gives:

$$\begin{cases} \dfrac{d\delta r_c}{dt} = A_{rr}\delta r_c + A_{rl}\delta l + A_{rh}\delta h \\[2ex] \dfrac{d\delta l}{dt} = A_{lr}\delta r_c + A_{ll}\delta l + A_{lh}\delta h \\[2ex] \dfrac{d\delta h}{dt} = A_{hr}\delta r_c + A_{hl}\delta l + A_{hh}\delta h \end{cases}, \tag{19.34}$$

where the A_{ij} coefficients should be found from physical laws.

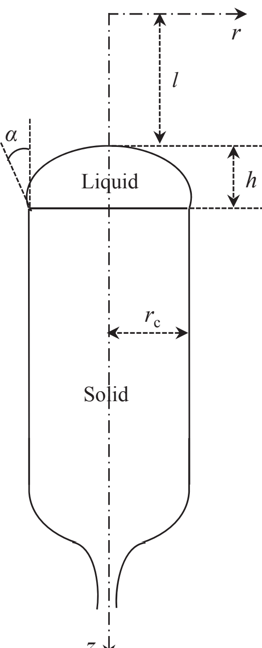

FIGURE 19.19 Geometry of the Verneuil process.

1. $A_{rl} = 0$ because the meniscus shape and angle α_0 are not dependent on the free surface position.
2. A_{rh} and A_{rr} depend on the Young–Laplace equation through Eqn (19.27). For small crystals (diameter smaller than capillary length), the following is found [44]:

$$A_{rr} = -\upsilon r_c \cos \alpha_0 < 0 \quad A_{rh} = -\upsilon r_c \frac{\cos \alpha_0}{1 + \sin \alpha_0} > 0. \tag{19.35}$$

   For larger crystals, numerical integration should be used, but the signs of the coefficients remain the same.
3. Variations of the melt position, l, come from the mass balance:

$$\frac{dl}{dt} = \frac{-W}{\pi \rho_l r_c^2} + \upsilon, \tag{19.36}$$

   where W is the mass flow of material droplets fed to the meniscus, with W_0 being its steady-state value. Linearization gives:

$$A_{lr} = \frac{2W_0}{\pi \rho_l r_c^3} > 0 \quad A_{ll} = 0 \quad A_{lh} = 0. \tag{19.37}$$

4. Variation of the meniscus height, h, depends on the heat balance at the solid–liquid interface (Eqn (19.28)). The heat transfer in the Verneuil process is quite complicated because heat is produced by combustion and numerical simulation is

needed to get accurate heat flux values [48]. By using some simplifying assumptions [44], one obtains:

$$\begin{cases} A_{hr} = \dfrac{1}{\Delta H_m}\left(\lambda_l\left(T_m - T_{gas}\right)\xi^2\dfrac{h}{r_c} + \dfrac{Q\xi h^2}{2r_c}\right) - A_{lr} > 0 \\ A_{hl} = \dfrac{1}{\Delta H_m}\dfrac{dQ}{dl} \\ A_{hh} - \dfrac{1}{\Delta H_m}\left(\lambda_l\left(T_m - T_{gas}\right)\xi^2 + Q\xi^2 h\right) \end{cases}, \tag{19.38}$$

where dQ/dl is the change of heat, provided by the flame to the meniscus surface when this surface moves, and ξ represents the heat exchange between the crystal and its surroundings. They are both dependent on the furnace design only.

For this 3-degree of freedom system, the stability condition, Eqn (19.33), can be written as

$$\begin{cases} A_{rr} + A_{hh} < 0 \\ A_{rh}A_{lr}A_{hr} < 0 \\ -(A_{rr} + A_{hh})(A_{hh}A_{rr} - A_{rh}A_{hr}) + A_{rh}A_{lr}A_{hr} > 0 \end{cases}. \tag{19.39}$$

Analysis of the signs and relative values of the A_{ih} gives the following results:

1. If the crystal radius is smaller than the capillary length, the process is stable if $dQ/dl < 0$ and is relatively small: the provided heat should decrease when the crystal recedes from the torch (this depends on the position of the meniscus in the flame) and this variation should be small. In practice, this means that the solidification front should be positioned a little bit below the maximal temperature in the flame.
2. If the crystal radius is larger, the process is unstable. For example, in the case of sapphire ($a = 3.8$ mm), the growth is totally stable when the crystal diameter is lower than 8–10 mm, but it becomes unstable for larger diameters. This is a common industrial experience.

It should be noted that unstable growth does not mean that growth is impossible; it means that the process will need some control, which, in the case of Verneuil process, is performed by an operator who changes the mass flow W_0 from time to time. Figure 19.20 shows two sapphire crystals grown by the Verneuil process—one with bad control by the operator, which shows that the process is not inherently stable, and the other one with good periodical control.

19.4.5 Practical Stability with Bounded Time Limits and Applications to Dewetting Growth

As described in the last section, dynamic stability studies the absolute stability of the process—that is, if any perturbation will disappear or amplify. However, it does not take into account the time scale for the perturbation damping or amplification. In practice, there are cases where the system may be stable in the sense of Lyapunov, but it may be

FIGURE 19.20 Two 40-mm diameter sapphire crystals grown by the Verneuil process, with (right) and without (left) efficient process control. The white aspect is due to a nitride layer that appears on the boule surface, due to air reaction at a temperature lower than the melting point.

useless because the region of stability is too small or the recovering time is too long. On the contrary, the system may be unstable in the sense of Lyapunov, but it may oscillate sufficiently close to a state whose performance is acceptable. Practical stability is a mathematical concept allowing the analysis of these more complicated cases, including the dynamics of a system in the presence of unexpected perturbations [49]. This method introduces an interval in which fluctuations of the crystal shape are acceptable for practical applications and a time scale corresponding to the growth duration. Then, the objective is to find which external perturbation amplitude maintains the crystal size in the acceptable interval during the growth duration.

A perturbing input is introduced in the system of equations describing the crystal growth process. These equations are the same than those used for the Lyapunov analysis, but the system is modeled in terms of time evolution. As a matter of example, the stability of the dewetting growth process on the ground will be studied.

As explained in Section 19.4.3, the dewetting phenomenon has been discovered after growth experiments under microgravity conditions. Its occurrence has been related to the existence of a meniscus between the crucible and the solid–liquid interface, which slides along the crucible wall at the same velocity as the growth rate. Characterizations have shown that the absence of crystal–crucible contact gives crystals with a much better quality: fewer dislocations and stresses, no spurious grain or twin nucleation, and a less curved solid–liquid interface. In an attempt to get same advantages, the dewetting

process has been imagined, allowing getting detached crystals on the ground as well [50,51]. The idea is to allow the existence of a meniscus by counterbalancing the hydrostatic pressure of the liquid by a gas pressure applied on the cold side of the melt. Figure 19.18 is still valid; however, the pressure at the cold side of the melt is higher than at the hot side, and the top and bottom liquid free surfaces are not portions of spheres because the gravity effect is not negligible. The dewetting process has been successfully applied to the growth of many IV, III-V, and II-VI semiconductors. (See Chapter 6 in Ref. [1] for a comprehensive review on the dewetting process.)

Several studies of the stability of dewetting have been reported, all based on the Lyapunov approach [50,52,53]. For the crystal grower, the stability of the dewetting process means that the crystal side should never get in contact with the crucible wall and the crystal diameter should remain larger than a minimal value given a priori. There are two degrees of freedom of the system, the crystal radius r_c and the meniscus height h, and they are linked by the Young–Laplace and heat balance Eqns (19.11) and (19.28). The practical stability of this system has been studied with respect to fluctuations of the gas pressure at the cold side, which controls the process [54] as introduced in these two equations. The main result of the study is that the process is stable when the sum of the wetting angle and growth angle is higher than 180°. In this case, the range of acceptable gas pressure fluctuations can be calculated from the process parameters. Figure 19.21 shows the result of the analysis in the case of the growth of 2-in GaAs crystals in BN crucibles. On the left side, the applied pressure difference (between the cold side and hot side) is shown: it decreases all along the growth process because the hydrostatic pressure decreases with the liquid height, and fluctuations of given amplitude A are superimposed. The resulting changes in the crystal radius are shown on the right side. For a low amplitude, the crystal radius remains inside the prescribed limits (horizontal dotted

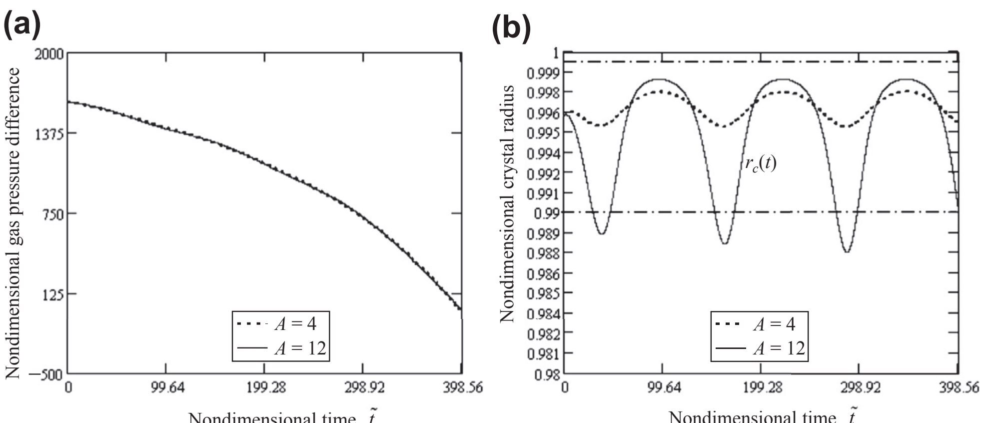

FIGURE 19.21 (a) Variations in the gas pressure difference. (b) Crystal radius showing practical stability of the system for acceptable pressure fluctuations ($A = 4$) and its instability for larger pressure fluctuations ($A = 12$). *From Ref. [54], with permission of Elsevier.*

lines), whereas it extends outside these limits for a larger amplitude. It is possible to maintain the crystal radius within ±500 μm provided that the gas pressure fluctuations are less than 300 Pa.

This study demonstrates that the practical stability approach is of high interest, not only to study the stability of the process but also to gain knowledge about the system's response to fluctuations in terms of frequency, time scales, and amplitudes.

19.5 Conclusions

Crystals are generally grown from the melt without crucible contact, so capillarity is the main phenomenon that controls the crystal shape. This chapter has been designed as a guide on the various aspects of capillarity that are of interest to the crystal grower. The reader was introduced to the basic concepts and the most sophisticated stability analyses for more and more complex phenomena. The main crystal growth techniques were presented as examples throughout the text. Few, but important, concepts drive the capillary shaping of crystals: surface energy, the Young–Laplace equation, and the growth angle. The main difficulty concerns in the strong nonlinearity of the Young–Laplace equation, which can be solved only on a case-by-case basis.

Because crystals grow from liquid, a moving medium, their shape stability is a serious problem. It has been shown that, thanks to the stabilizing effect of heat transfer, some processes are always self-stabilizing and thus do not require any control system. However, other processes are not stable at all, or are stable only under given conditions or crystal sizes. The fact that a process is not stable does not mean that crystal growth is impossible; it just means that an external control system, more or less complicated, will be needed in order to grow the crystal. From a practical point of view, an unstable process can be useful if the associated fluctuations remain inside acceptable values, at least at the time scale of the growth.

In conclusion, capillarity-driven crystal growth processes are very efficient for getting crystals with few defects, but this area needs further research, especially for any newly introduced process.

Acknowledgment

The author thanks Dr Simona Epure for her help in drawing many figures and critical reading of the text.

Nomenclature

a	capillary length
c	chemical composition, constant
d	diameter
e	gap thickness
g	gravitational acceleration
h	meniscus height

$\boldsymbol{p}$	pressure
$\boldsymbol{p_0}$	reference pressure in the melt
$\boldsymbol{p_v}$	vapor (gas) pressure
$\boldsymbol{r}$	radial coordinate, radius
$\boldsymbol{r_c}$	crystal radius
$\boldsymbol{r_a}$	ampoule/crucible radius
$\boldsymbol{t}$	time, also ribbon thickness
$\boldsymbol{v}$	solid–liquid interface velocity (growth rate)
$\boldsymbol{x, y, z}$	axis
$\boldsymbol{A}$	amplitude, also Lyapunov coefficients
$\boldsymbol{B}$	magnetic field
$\boldsymbol{C}$	a constant
$\boldsymbol{D}$	diffusion coefficient
$\boldsymbol{D_{th}}$	heat diffusivity
$\boldsymbol{L}$	characteristic dimension of the liquid
$\boldsymbol{Ma}$	Marangoni number
$\boldsymbol{Q}$	Heat introduced in the system
$\boldsymbol{T}$	temperature
$\boldsymbol{W}$	mass flow
$\boldsymbol{W_{coh}, W_a}$	Cohesion energy, adhesion energy
$\boldsymbol{\alpha}$	growth angle
$\boldsymbol{\alpha_0}$	angle between the tangent to the meniscus and the vertical axis
$\boldsymbol{\gamma}$	surface energy (solid–liquid, liquid–vapor…)
$\boldsymbol{\delta}$	variation of a degree of freedom from its stationary value
$\boldsymbol{\delta_{ik}}$	Kronecker symbol
$\boldsymbol{\theta}$	wetting angle (Young, or apparent…)
$\boldsymbol{\nu}$	kinematic viscosity
$\boldsymbol{\lambda}$	thermal conductivity
$\boldsymbol{\rho}$	density
$\boldsymbol{\mu}$	permeability
$\boldsymbol{\Phi}$	angle between the tangent to the meniscus and the horizontal axis;
$\boldsymbol{\Delta H_m}$	latent heat of melting
$\boldsymbol{\nabla}$	gradient operator

Subscripts

a	adhesion
ch	chemical, solutal
i	at the s/l interface
l	liquid
m	melting
s	solid
t	time
0	reference
v	vapor

vectors are represented in bold

References

[1] Duffar T, editor. Crystal growth processes based on capillarity: Czochralski, floating zone, shaping and crucible techniques. J. Wiley-Blackwell; 2010, ISBN 978-0-470-71244-3.

[2] Bridgman PW. Proc Am Acad Arts Sci 1925;20:305.

[3] Stelian C, Duffar T, Santailler JL, Barvinschi F, Nicoara I. Cryst Res Technol 2001;36:663.

[4] Gallien B, Sylla L, Bengulescu M, Barvinschi F, Duffar T. CrystEngComm 2013;15:2329.

[5] Gallien B, Duffar T. J Cryst Growth, available online July 31, 2013, http://dx.doi.org/10.1016/j.jcrysgro.2013.05.044.

[6] Boiton P, Giacometti N, Duffar T, Santailler JL, Dusserre P, Nabot JP. J Cryst Growth 1999;206:159.

[7] Duffar T, Gourbil JM, Boiton P, Dusserre P, Eustathopoulos N. J Cryst Growth 1997;179:356.

[8] Metz EPA, Miller RC, Mazelsky R. J Appl Phys 1962;33:2016.

[9] Verneuil A. Comptes Rendus (Paris) 1902;135:791.

[10] Czochralski J. Z Phys Chem 1918;92:219.

[11] Theuerer HC. US Patent n° 3060123 V; 1952.

[12] Gomperz EV. Z Phys 1922;8:184.

[13] Dupré A. Théorie mécanique de la chaleur [chapter IX]. Paris: Gauthier-Villard; 1869.

[14] Laplace PS. Traité de mécanique céleste, vol. 4. Paris: chez Courrier; 1805.

[15] Herring C. In: Kingston WE, editor. The physics of powder metallurgy. New York: Mc Graw-hill; 1951. p. 143.

[16] Glebovsky VG, Semenov VN, Lomeyko VV. J Cryst Growth 1989;98:487.

[17] Eustathopoulos N, Drevet B, Nicholas M. Wettability at high temperature. oxford: Pergamon; 1999.

[18] Kosokitov IV, Tseitlin E, Chaikin P, Mel'nikova A. Sbornik-Moskovskii Institut Stali i splavov 1968;49:125.

[19] Tatarchenko VA, Nabot JP, Duffar T, Tatarchenko EV, Roux B, Uspenski VS. J Cryst Growth 1997;180:615.

[20] Clanet C, Quere D. J Fluid Mech 2002;460:131.

[21] Despréaux S, Duffar T, Witomski P. J Cryst Growth 2000;209:983.

[22] Braescu L, Epure S, Duffar T. In: Duffar T, editor. Crystal growth processes based on capillarity: Czochralski, floating zone, shaping and crucible techniques. J. Wiley-Blackwell; 2010, ISBN 978-0-470-71244-3 [chapter 8].

[23] Tsivinski SV. Inzheherno Fiz Zhur 1962;5:59.

[24] Hurle DTJ. J Cryst Growth 1983;63:13.

[25] Mika K, Uelhoff W. J Cryst Growth 1975;30:9.

[26] Wang Q, http://web.mit.edu/qiqi/www/code/rungekutta/rungekutta.py.html; 2009.

[27] http://www.mathstools.com/section/main/runge_kutta_calculator.

[28] Lüdge A, Riemann H, Wünscher M, Behr G, Löser W, Muiznieks A, Cröll A. In: Duffar T, editor. Crystal growth processes based on capillarity: Czochralski, floating zone, shaping and crucible techniques. J. Wiley-Blackwell; 2010, ISBN 978-0-470-71244-3 [chapter 4].

[29] Rupprecht J. US patent 3393054A; 1968.

[30] Ricard J. French Pattern 2.321.326; 1975.

[31] Mimura Y, Okamura Y, Komazawa Y, Ota C. Jpn J Appl Phys 1980;19:L269.

[32] Fukuda T, Rudoloph P, Uda S, editors. Fiber crystal growth from the melt. Berlin: Springer; 2004.

[33] Duffar T. [Ph.D. thesis]. Institut National Polytechnique de Grenoble; 1982.

[34] Tatarchenko VA. J Cryst Growth 1977;37:272.

[35] Schäfer N, Yamada T, Shimamura K, Koh HJ, Fukuda T. J Cryst Growth 1996;166:675.

[36] Landau L, Lifchitz E. Physique Théorique : Mécanique des fluides. French translation. 2nd ed. Moscow: Mir; 1989.

[37] Bohm J, Lüdge A, Schröder W. In: Hurle DTJ, editor. Handbook of crystal growth, vol. 2a. Amsterdam: Elsevier Science; 1994.

[38] Wilcox WR, Regel LL. Microgravity Sci Technol 1998;XI(4):152.

[39] Duffar T, Boiton P, Dusserre P, Abadie J. J Cryst Growth 1997;179:397.

[40] Duhanian N, Marin C, Duffar T, Abadie J, Chaudet M, Dieguez E. Microgravity Sci Technol 1997; XI(4):187.

[41] Duffar T, Epure S. Cryst Res Technol 2010;45:1209.

[42] Tatarchenko VA. Shaped crystal growth. In: Moreau R, editor. Fluid mechanics and its applications, vol. 20. Dordrecht: Kluwer Academic Publishers; 1993.

[43] Lyapunov A. The general problem of the stability of motion. [Ph.D. thesis]. CRC Press; 1992: translated in English for the 100th anniversary of his thesis defense in 1892.

[44] Borodin VA, Brener A, Steriopolo TA, Tatarchenko VA. Cryst Res Technol 1982;17:1187.

[45] Verneuil A. Ann Chim Phys 1904;8-3:20.

[46] Ueltzen M. J Cryst Growth 1993;132:315.

[47] Scheel HJ, Lytvynov L. In: Scheel HJ, Capper P, editors. Crystal growth technology. Wiley; 2008. p. 415.

[48] Barvinschi F, Santailler JL, Duffar T, Le Gal H. J Cryst Growth 1999;198–199:239.

[49] Balint S, Epure S, Duffar T, Braescu L. J Eng Math 2012;75:191.

[50] Duffar T, Dusserre P, Picca F, Lacroix S, Giacometti N. J Cryst Growth 2000;211:434.

[51] Duffar T, Dusserre P, Giacometti N. J Cryst Growth 2001;223:69.

[52] Bizet L, Duffar T. Cryst Res Technol 2004;39:491.

[53] Epure S, Duffar T, Braescu L. J Cryst Growth 2010;312:1416.

[54] Epure S, Duffar T. J Cryst Growth 2012;360:25.

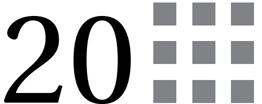

Heat Transfer Analysis and Design for Bulk Crystal Growth: Perspectives on the Bridgman Method

Jeffrey J. Derby, Andrew Yeckel

DEPARTMENT OF CHEMICAL ENGINEERING AND MATERIALS SCIENCE, UNIVERSITY OF MINNESOTA, MINNEAPOLIS, MN, USA

CHAPTER OUTLINE

20.1 Introduction **794**
20.2 Historical Perspective: Experimental Practice **796**
20.3 Heat Transfer Fundamentals **799**
20.3.1 The Energy Equation 800
20.3.2 Boundary Conditions 803
20.4 Heat Transfer in Melt Crystal Growth **805**
20.4.1 Phase-Change Interface 805
20.4.2 Radiation Heat Transfer 808
20.4.2.1 Surface Radiation 809
20.4.2.2 Internal Radiation 812
20.4.3 Furnace Heat Transfer 814
20.5 Historical Perspective: Theoretical Developments **817**
20.6 Research Vignette: Bridgman Growth of Cadmium Zinc Telluride **820**
20.6.1 Motivation 820
20.6.2 Heat Transfer Analysis 822
20.6.2.1 Ampoule Support and Cold Finger 822
20.6.2.2 Crucible Configuration and Stage of Growth 825
20.6.3 Experimental Validation 828
20.6.4 Bell-Curve Furnace Profile 829
20.6.5 Summary 832

Handbook of Crystal Growth. http://dx.doi.org/10.1016/B978-0-444-63303-3.00020-1
Copyright © 2015 Elsevier B.V. All rights reserved.

20.7 Final Remarks 833
Acknowledgments 834
References 834

20.1 Introduction

Growth from the melt is the most important means of producing large, single crystals of semiconductor and optical materials used in the manufacture of electronic and photonic systems. Important examples of such materials are silicon, gallium arsenide, and sapphire, which are grown as single-crystalline boules that are then sliced and polished into wafers and subsequently employed as substrates for the fabrication of devices. Many other crystalline materials are produced from the melt or from liquids [1,2]. Indeed, for commercial production of bulk crystalline material, growth from a liquid is inherently advantageous due to the greater mass processing rates that are attained, compared to the growth of crystalline layers from a vapor phase. In large part, this is simply due to the much higher density of a condensed liquid phase, from which the solid crystal grows, compared to the low density of a gaseous phase, especially the near-vacuum conditions employed in molecular beam epitaxial processes.

A single-component material can be solidified simply by translating a molten sample from above its melting point to a temperature below its melting point. This process can be represented as a path along the thermodynamic phase diagram for the material, typically at constant pressure, from the liquid phase to the solid phase. The same principles apply to the growth of a multiple-component material. Namely, the process must enact a path along the phase diagram that brings the material from a liquid state to a solid state. Again, this path is typically carried out at constant pressure; however, compositional effects are typically important in the growth of a multiple-component solid [3]. If the path from liquid to solid is isothermal, following a path of changing composition, the process is typically referred to as *solution growth* [4]. Often, such methods are employed to grow a single-component material from a solvent of a different material and can be used as a means of purification [5]. If the process is driven along a path of changing temperature, the process is often called a *flux growth method* [6] and, although this process is driven by temperature changes, there is typically a pronounced compositional change from the liquid to solid.

While characterizing these growth processes as paths along thermodynamic phase diagrams is enlightening, the actual mechanics of enacting these paths is complicated by phenomena that arise from nonequilibrium effects. The first overall challenge is the need to move heat and mass through space and time in a suitable manner, which is governed by process design and transport phenomena. This chapter will focus on heat transfer, perhaps the most important aspect of transport phenomena in melt crystal growth. Another challenge is presented by the dynamics of phase change, namely solidification kinetics, a topic of much importance that will be briefly discussed, as it relates to

understanding heat transfer and solidification. Finally, the establishment of conditions to promote the growth of a single crystal of sufficiently high quality must be considered in our practical path along the phase diagram. Aside from avoiding morphological instabilities during growth (an important and fascinating topic that will not be considered here), attaining this goal of a large, single crystal without too many defects is incompletely understood [7], and just a few words are offered below.

While forming a crystalline solid is energetically favored in the liquid-to-solid phase change, it is hardly an assured outcome in a large-scale crystal growth process. The goal to attain a single crystal of specific crystallographic orientation can be achieved by initiating solidification from a single-crystal "seed" of sufficient quality, which is usually accomplished via clever engineering design to partially melt a captive seed crystal (as in Bridgman methods) or to gently introduce a seed by touching to a melt surface (as in meniscus-defined systems, such as Czochralski or edge-defined film-fed methods). The minimization of structural defects during crystal during growth involves heat transfer to a large extent. For example, native point defects (vacancies and interstitials) arise, move, and interact to produce microdefects, such as voids that are created via the condensation of excess vacancies and dislocation loops formed by excess interstitials. These atomic-scale processes are strongly activated by temperature, leading to important interactions between growth rates and thermal gradients during growth [8]. Line defects, namely dislocations, are multiplied by thermal stresses during growth and cool-down [9], and their number density can be reduced by minimization of these stresses. Furthermore, dislocations can organize into mosaic-like networks during melt crystal growth, leading to the formation of ordered cellular structures with low-angle grain boundaries [10]. Finally, new grain formation during growth is poorly understood, except that it is known that interactions between the solidification interface and a solid wall can be deleterious. Further comments on this issue will be provided in the research vignette presented later.

What follows is a chapter devoted to heat transfer during the melt growth of large, or bulk, crystals. Heat transfer is the macroscopic mechanism by which our manifestations of equipment and processes will impact the conditions that drive atomic-level crystallization processes. The premise of the following discussion is that heat transfer in melt growth systems is the most significant aspect of their operation and the primary determinant of the properties of the crystalline phase that is produced. This premise must be modified for other crystal growth processes, particularly those with driving forces that arise from chemical potential differences, such as classical solution growth and chemical vapor deposition. Nevertheless, the ideas presented here may still be of importance in these systems.

To provide some focus in the very broad topic of heat transfer in crystal growth, we will emphasize the Bridgman processes. Below, we first present a brief historical overview to provide some perspective on how heat transfer in crystal growth systems has evolved. We follow with a discussion of the fundamentals of heat transfer in crystal growth, along with the mathematical description of heat transfer and its implementation in crystal growth models. A quick review of prior literature of heat transfer in Bridgman

crystal growth is followed by a research vignette on our evolving understanding of a specific growth system. We close with a brief summary and discussion of directions for future research in this area.

20.2 Historical Perspective: Experimental Practice

As alluded to in the previous section, the general idea behind melt growth is quite simple. One somehow moves a sample from higher temperature to lower temperature, crossing the melting point in the process. The details of how this is accomplished, however, can be quite involved, and there are many different methods that have been developed for growth, most of which are addressed by other chapters in this handbook. Indeed, successful crystal growth from the melt requires much more than simply melting and cooling, as illustrated nicely by the following brief history of the Bridgman crystal growth process.

The crystal growth community holds Percy Williams Bridgman in high regard for receiving the 1946 Nobel Prize in Physics. However, Bridgman did not win this prize for the crystal growth method named after him but, according to the Nobel Committee, "for the invention of an apparatus to produce extremely high pressures, and for the discoveries he made therewith in the field of high pressure physics." Rather, in a biographical memoir, Kemble and Birch [11] noted that "Bridgman's mastery of laboratory techniques was also applied to the preparation of samples… A method of growing large single crystals of metals which has been widely used by later workers was described more or less in passing…"

Bridgman's landmark publication from 1925 [12] described the process as follows: "The general method is that of slow solidification from the melt. A tubular electric furnace, in a vertical position, is maintained at a temperature above the melting point of the metal in question. The metal in the molten condition in a suitable mold of glass or quartz tubing is slowly lowered through the bottom of the furnace into the air of the room or into a cooling bath of oil." Thus, Bridgman enabled the path along the phase diagram corresponding to melt growth using the key idea of directional solidification via ampoule[1] translation through a furnace. His method is depicted schematically in Figure 20.1(a). Incidentally, Bridgman also elucidated important ideas concerning the initiation of the growth of a single crystal, a process that he referred to as *inoculation*, which today we refer to as *seeding*.

Bridgman's process was relatively uncontrolled from a heat transfer point of view. He felt that the temperature level of the furnace was relatively unimportant, as long as it was above the melting point, arguing that very slow growth rates rendered it "not a matter of much importance." He also felt that furnace regulation was not an issue, claiming "Slow

[1]Bridgman referred to the charge being held in a *mold*. More modern accounts typically describe the charge as contained within a *crucible*, which may further be sealed within an *ampoule*. In this chapter, we beg the reader's indulgence as we alternatively describe the charge as being contained within either a crucible or an ampoule. While our usage is imprecise, we believe the meaning will always be clear.

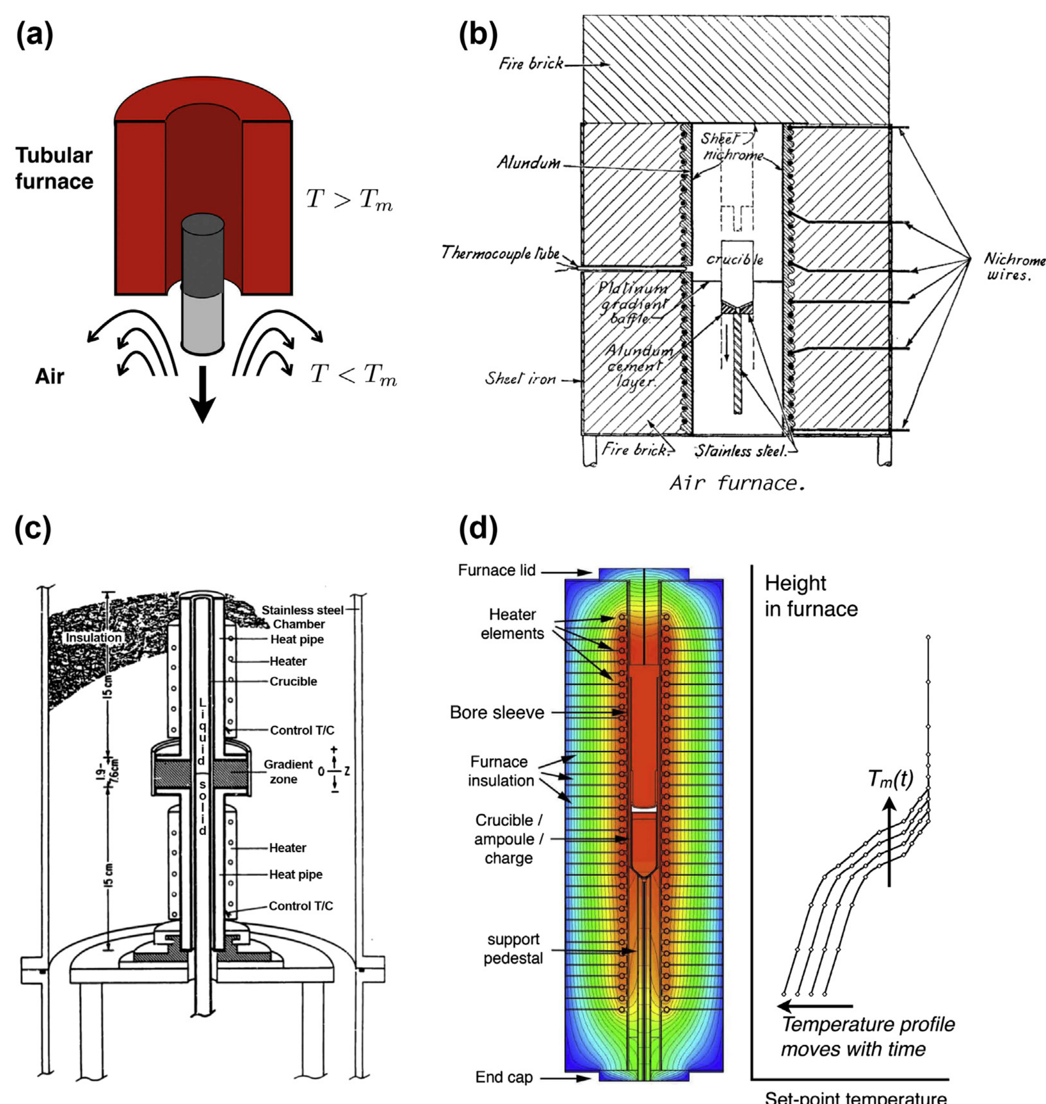

FIGURE 20.1 (a) Bridgman's device for growing large, single crystals featured an ampoule pulled from a heated furnace directly into ambient surroundings. (b) Stockbarger's multiple zone furnace was a "radical change in technique" that provided for higher gradients and more control (*adapted from [13]*). (c) The heat-pipe, Bridgman-Stockbarger furnace of Wang and Witt was designed to provide extremely well-specified thermal boundary conditions (*adapted from [14]*). (d) Depiction of a modern, electrodynamic gradient freeze furnace for crystal growth. This system is equivalent to a Bridgman configuration; however, the movement of the solidification interface through the charge is achieved by power changes that, in time, move the location of the melting point of the material upward in the furnace, shown by $T_m(t)$ on right.

fluctuations of temperature are not of much importance, and rapid changes are eliminated by the thermal inertia of the furnace." However, Bridgman did realize that problems could arise in his system, noting that "It is important that air drafts be kept from the emerging mold, as otherwise new centers of solidification may be started."

Stockbarger [13] recognized that more controlled conditions were needed to successfully grow other materials. He was faced in 1936 with the rather formidable task of growing single crystals of lithium fluoride, a material with a much higher melting point than the metals grown by Bridgman. In the words of Stockbarger, this problem called for "a radical change in technique" that was "solved by modifying the well-known Bridgman scheme… employing two such furnaces…" so that "freezing occurs in the high gradient region between the furnaces." The resultant apparatus is diagrammed in Figure 20.1(b). Stockbarger realized that simply pulling a sample from a high-temperature furnace into the surrounding room was not always sufficient for crystal growth. His work clearly demonstrated that temperature gradients that impact the rate of heat transfer, i.e., kinetics, can be as important as temperature levels that determine stable phase, i.e., thermodynamics. The use of multiple heating zones persists to this day in melt crystal growth, and, while it is probably more fitting to refer to this process as the Bridgman–Stockbarger method, our modern penchants for first above all and linguistic brevity compel us to refer to this process simply as Bridgman growth.

In succeeding decades, there were many important advances in understanding the details of heat transfer in crystal growth processes. Notable progress in both understanding and practice were put forth throughout the 1970s and 1980s by August Witt and his coworkers, who were among the first to unambiguously identify the effects of heat and mass transfer dynamics in crystal growth systems [15–21]. Particularly significant was the research of Wang and Witt [14], who refined the notion of Stockbarger's zones via the development of the heat-pipe furnace, shown in Figure 20.1(c). This furnace employed two high-temperature heat pipes separated by an insulator, a design that attempts to achieve the idealized thermal conditions of two constant-temperature regions spanning the melting point and connected by a linear profile. The motivation for their work was eloquently summarized as follows by Wang [14]: "In spite of the widespread use of the vertical Bridgman and Bridgman–Stockbarger techniques for the production of single crystals, process optimization has been restricted to empirical approaches… The application of thermal modeling, a potentially powerful means to this effect, is complicated by the existence of ill-defined thermal boundary conditions, which, moreover, are subject to change during growth because of end effects related to the charge size and geometry."

Equivalent to the Bridgman method is the gradient freeze method, where the thermal environment in the furnace is changed in a time-dependent manner to effectively translate the profile along the charge.[2] This system has an advantage of no

[2]While Bridgman and others moved an ampoule through a furnace, the same effect can be achieved by physically moving the furnace past a stationary ampoule or by moving the temperature profile within the furnace by changing power inputs. This is most easily accomplished in a gradient freeze system by simply powering down the furnace over time.

moving parts; the translation of the temperature field is accomplished by changing the heat input within the furnace over time. A refined approach to the gradient freeze technique is the electrodynamic gradient freeze (EDG) system, represented schematically in Figure 20.1(d). EDG employs dynamic computer control of individual heating zones to impose a specific temperature schedule for growth. Interestingly, such an approach provides an almost unlimited number of thermal profiles to drive crystal growth. However, to the knowledge of the authors, only very simple profiles have been used with these furnaces, such as classical profiles of linear, connected temperature segments.

There are several compelling ideas in this history of Bridgman growth that continue to resonate. First is the idea, promoted most strongly by Witt and coworkers, that crystal growth optimization can be accomplished by the suitable design and operation of the process. In particular, furnace design sets the thermal boundary conditions that ultimately control growth in a deterministic manner. Second is the above assertion by Wang [14] and others that process optimization will be enabled by thermal modeling, which is needed due to the inherent complexity of heat transfer in melt growth systems. Finally, a natural outcome of the first two assertions is that, in terms of the thermal field, there is a desired growth state for the system that an optimized process will achieve and maintain throughout the entire growth of the crystal. We will expand on these ideas in the results shown in Section 20.6, but first we need to discuss the basics of heat transfer.

20.3 Heat Transfer Fundamentals

The notion of temperature as a measure of hot and cold has been long established. However, the mechanisms responsible for temperature change, namely by the transfer of heat, remained rather murky for centuries. For example, in the eighteenth century it was posited that heat consisted of a fluid called *caloric* that flowed from hotter to colder bodies. The view of heat as caloric matter was replaced in the mid-nineteenth century by the mechanical theory of heat, of which Tyndall [22] states, “The supporters of this theory do not believe heat to be matter, but an accident or condition of matter; namely, a motion of its ultimate particles.”

This led to the important concept that both heat and work are forms of energy that are unified via the first law of thermodynamics, which details the exact inventory of exchanges among various forms of energy (internal, kinetic, potential, etc.) and changes in heat and work. Thermodynamics catalogs the final and initial states of systems with exquisite rigor, while transport attempts to track how changes occur over space and time. Specifically, heat transfer focuses on how thermal energy is transferred through a system, as measured by the state variable temperature.

The following sections outline the development of the fundamental conservation equations that can be written for energy in terms of a body’s temperature. More detail and rigor can be found in many textbooks that cover transport phenomena and

heat transfer, such as the classic texts by Arpaci [23,24], Bird et al. [25], and Siegel and Howell [26]. The following sections discuss relevant concepts for melt crystal growth.

20.3.1 The Energy Equation

Temperature is one of the fundamental measures of the state of matter. Heat is a form of energy that is intimately related to temperature. For example, heat always flows from a higher temperature to a lower one, thus temperature difference is the driving force for heat transfer. From a classical thermodynamic perspective, heat is never thought of as being stored within a body; rather, it exists only as energy in transit from one body to another. Thus, when energy is added to a body, it is stored as internal energy, which is physically manifested via kinetic and potential energy of atoms.

If we consider a control volume fixed in space inside a material, we can do an accounting of energy changes within this closed system (i.e., no mass is flowing through the control volume). The first law of thermodynamics is written as

$$dU = dW + dQ, \tag{20.1}$$

where dU is the differential change in internal energy, dW is the differential work performed on or by this system, and dQ is a differential flow of heat into or out of the volume. If the volume is fixed in size, there is no work performed and we can simplify the first law to relate changes in internal energy directly to flows of heat

$$dU = dQ. \tag{20.2}$$

We relate the internal energy of this system to its temperature via

$$dU = \rho V C_v dT, \tag{20.3}$$

where ρ is the density of the material, V is the volume of the element, C_v is the heat capacity of the material at constant volume, and dT is the differential change in temperature.

Next, we consider an exchange of heat between the control volume and its external environment over time. Without making any specific assumptions on the mechanism of heat transfer, we can quantify the amount of heat exchanged as

$$dQ = hA(T - T_0)dt, \tag{20.4}$$

where h is a heat transfer coefficient that represents the rate of heat flow per temperature driving force, A is the area across which heat flows, T_0 is the temperature representative of the external environment, and dt is a differential in time.

Substituting Eqns (20.3) and (20.4) into our expression for the first law of thermodynamics, Eqn (20.2), we get

$$\rho V C_v dT = hA(T - T_0)dt, \tag{20.5}$$

which can be rearranged to

$$\rho C_v \frac{dT}{dt} = h\frac{A}{V}(T - T_0). \tag{20.6}$$

This is a first-order, ordinary differential equation that relates the temperature of a body to heat flows into or out of it, but this is about as far as we can go with only our knowledge of thermodynamics.

The next level of analysis considers that the temperature is not constant through the body of interest; that, in fact, it is a field, $T(\mathbf{x},t)$, that depends on both position, $\mathbf{x}$, and time, t. We also introduce a phenomenological concept known as *conduction*, which states that energy can be carried by a conductive heat flux that is proportional to the gradient of the temperature field. This mechanism is represented by Fourier's first law, which we write in vector form as

$$\mathbf{q} = -\kappa \nabla T, \tag{20.7}$$

where $\mathbf{q}$ is a heat flux vector, κ is the thermal conductivity, and $\nabla \equiv \frac{\partial}{\partial x}\mathbf{e}_x + \frac{\partial}{\partial y}\mathbf{e}_y + \frac{\partial}{\partial z}\mathbf{e}_z$ is an operator written in terms of partial derivatives and unit coordinate vectors (here, in terms of Cartesian coordinates). The negative sign in front of the right-hand side indicates that heat always flows "downhill," from higher to lower temperatures. A more geometrically precise interpretation of this downhill flow of heat is that its direction is given by the negative gradient of the temperature field, namely $-\nabla T$, which is a vector that points in the direction of steepest descent of temperature. This direction is perpendicular to surfaces of constant temperature, commonly referred to as *isotherms*.

Summing the conductive heat fluxes over all surfaces of a control volume, and taking the limit as the control volume shrinks to zero, leads to an expression involving the divergence of the heat flux, $\nabla \cdot \mathbf{q}$. This provides a differential balance of energy that holds at every point within the body. The mechanics of this derivation are often referred to as performing a shell balance over a differential volume [25]. Then the equation for heat transfer through a solid is written as

$$\rho C_v \frac{\partial T}{\partial t} - \nabla \cdot (\kappa \nabla T) = 0, \tag{20.8}$$

which is a parabolic partial differential equation that describes the temperature distribution within the body. Interactions of the body with its exterior must now be separately specified via boundary conditions, which are discussed in the next section.

If the control volume in the body of interest contains a fluid that can flow, the analysis becomes quite involved, since we must now account for kinetic energy and work effects that can be brought about via changes in the velocity and density of the fluid. We refer the interested reader to classical sources, such as Bird et al. [25], for more rigor. We instead choose to present only the outcome of the more specific case of an incompressible fluid (i.e., one with a density independent of pressure and temperature) under conditions where viscous dissipation (the conversion of work done by the fluid into heat)

is negligible. Both of these assumptions are quite valid for crystal growth systems from liquids.[3] Under these conditions, the energy balance equation is given by the following expression:

$$\rho C_p \frac{\partial T}{\partial t} + \rho C_p \mathbf{v} \cdot \nabla T = \kappa \nabla^2 T, \tag{20.9}$$

where $\mathbf{v}$ represents the velocity field of the fluid.

Some comments on this celebrated equation are in order. First are issues concerning rigor; for example, the careful reader will notice that we replaced the heat capacity at constant volume, C_v, with the more conveniently measured heat capacity at constant pressure, C_p, in the left-hand side of the energy equation. These terms arise from the change in internal energy of the medium and, as indicated in Eqn (20.3), are appropriately expressed in terms of C_v for the constant-volume element used in our original derivation. However, if the medium is indeed incompressible, which is an extremely good approximation for all liquids and solids, $C_v = C_p$ and the substitution is warranted. Next, the conductive transport term on the right-hand side of the equation has been simplified from Eqn (20.8) by assuming a constant thermal conductivity, κ. Finally, the above equation considers that there is no source of heat in the medium (such as a chemical reaction or electric current flow, as is produced by induction heating, for example).

We also note that dimensional analysis can be quite illuminating to identify heat transfer mechanisms that are important in specific situations. For example, we can estimate the rate of heat transfer by convection as $\approx \rho C_p v \Delta T$, where v is a representative fluid velocity and ΔT is an estimate of a temperature difference over a characteristic length L. Similarly, we estimate the rate of conduction as $\approx \kappa \Delta T / L$. Comparing the ratio of convective to conductive heat transfer in a system, we arrive at a dimensionless group known as the *Peclet number*:

$$Pe \equiv \frac{vL}{\alpha}, \tag{20.10}$$

where $\alpha = \kappa / \rho C_p$ is the thermal diffusivity of the fluid. For $Pe \gg 1$, conductive heat transfer dominates convective heat transfer, whereas for $Pe \ll 1$, the converse is true.

Another expression for the Peclet number is

$$Pe \equiv RePr, \tag{20.11}$$

where $Re = vL/\nu$, with ν denoting kinematic viscosity, is the dimensionless *Reynolds number*, which is a measure of the intensity of the flow,[4] and $Pr = \nu / \alpha$ is the

[3]Describing heat transfer in gas-phase systems requires only a slight modification of the equation for energy to account for the compressibility of gas. We will not discuss this here, but standard sources can be consulted.

[4]The Reynolds number, named after the renowned fluid mechanician Osborne Reynolds, measures the ratio of inertial to viscous forces in a fluid flow. As the Reynolds number becomes larger, inertia becomes more important and the flow becomes more complicated. At a critical value of *Re*, a laminar flow loses stability and becomes turbulent.

dimensionless *Prandtl number*. The Prandtl number is a ratio of physical properties and is constant for any specific system. For a given flow intensity, the magnitude of the Prandtl number thus indicates the general importance of convective heat transfer. Typically, molten metals and semiconductors have very small characteristic Prandtl numbers of $Pr \approx 0.01$, while nonmetallic melts and fluxes, such as inorganic oxide and nearly all organic materials, often have $Pr \approx 1-100$ or higher. Remember, however, that flows vary dramatically from system to system; in large-scale semiconductor systems, convective heat transfer can be significant, while in small-scale oxide systems, convective heat transfer can be negligible. For a more extensive discussion on dimensionless groups in crystal growth, the interested reader is referred to [27–29].

Our final comments concern language, which is typically less than precise in the heat transfer literature. The first term of Eqn (20.9) represents changes in internal energy over time. In common usage, this is often referred to as the accumulation of *sensible heat* in the system, a term that reflects a curious disregard for the rigors of thermodynamics (remember that heat is not stored within a body but represents a form of energy transported between bodies). Similarly, the second term of the energy equation, involving the velocity, $\mathbf{v}$, refers to a phenomenon called *convection* or *advection*, depending upon the discipline. This term is typically considered to describe heat that is transported by flow, rather than the more formally correct thermodynamic concept of internal energy being transported via the motion of material.

20.3.2 Boundary Conditions

The energy conservation equations of the previous section, Eqns (20.8) and (20.9), are valid throughout the media of interest, provided that the proper physical properties (density, heat capacity, and thermal conductivity) are used in conjunction with the equations. However, any mathematical model of a system that we develop must be finite in its extent, and we must therefore define external boundaries that are artificial.[5] From a purely mathematical perspective, integrating the spatial derivatives in the energy equation, Eqn (20.8) or Eqn (20.9), gives rise to unspecified integration constants, and *boundary conditions* need to be applied along the spatial boundaries of the domain. From a physical perspective, all boundary conditions arise from nature.[6]

Of course, all crystal growth systems used in practice consist of many different media and domains, notably the solid ampoule containing melt (liquid) and crystal (solid), as well as all furnace components. The simplest types of boundary conditions are those that are written to connect adjacent domains. First, the temperature field must be continuous between any two domains, thus

$$T_i = T_j, \quad \text{along the interface between } i \text{ and } j, \tag{20.12}$$

[5]These model boundaries are artificial in the sense that we typically define the outer boundaries to mark the end of our interest in the world, rather than the any real end to the world.

[6]I must attribute the statement, "All boundary conditions arise from nature" to Neal R. Amundson, one of the pioneers of mathematical modeling applied to chemical engineering systems; see,e.g., [30–32].

must be applied at the shared boundary, where i and j represent adjacent domains. Second, energy must also be conserved across a material domain boundary, leading to

$$\mathbf{n}_i \cdot \mathbf{q}_i + \mathbf{n}_j \cdot \mathbf{q}_j = 0, \quad \text{along the interface between } i \text{ and } j, \tag{20.13}$$

where $\mathbf{q}$ denotes the heat flux vector and $\mathbf{n}$ denotes a unit vector that is oriented in a direction which is normal to the interface shape and pointing outward from the domain of interest. There is no materials transport across most common boundaries, in which case conduction is the only active heat transfer mechanism. We can thus apply Eqn (20.7) on both sides of the boundary and modify Eqn (20.13) to write

$$\mathbf{n} \cdot \kappa_i \nabla T_i = \mathbf{n} \cdot \kappa_j \nabla T_i \quad \text{along the interface between } i \text{ and } j, \tag{20.14}$$

where we also used the geometrical fact that $\mathbf{n}_i = -\mathbf{n}_j$ to simply use $\mathbf{n}$, a unit vector normal to the interface, in the above expression. These fundamental relations must hold across all interfaces.[7]

For the external boundaries of a model, boundary conditions can be imposed to supply information about either the actual temperature of the boundary or heat fluxes across it. If the actual temperature along a boundary is known (which is rarely the case), a Dirichlet condition, or boundary condition of the first kind, can be supplied as

$$T_i = f(\mathbf{x}), \quad \text{along boundary of domain } i, \tag{20.15}$$

where $f(\mathbf{x})$ denotes a specified temperature distribution (the simplest case is just a constant value). Otherwise, one can describe the heat flux across the boundary. A Neumann condition, or boundary condition of the second kind, specifies the heat flux as a constant (this case is also somewhat idealized, although it is often a more realistic representation than the Dirichlet condition)

$$-\mathbf{n} \cdot \kappa_i \nabla T_i = g(\mathbf{x}), \quad \text{along boundary of domain } i, \tag{20.16}$$

where $\mathbf{n}$ is an outward-pointing unit vector normal to the surface and $g(\mathbf{x})$ denotes a heat flux. In some cases, the particular choice of $g(\mathbf{x}) = 0$, which represents the case of no heat flow across a perfectly insulated surface, is a reasonable approximation to reality. However, the most realistic approximation to describing heat transfer from an external boundary is the Robin condition, or boundary condition of the third kind, which takes the form of

$$-\mathbf{n} \cdot \kappa_i \nabla T_i = h(T_i - T_e), \quad \text{along boundary of domain } i, \tag{20.17}$$

where h is a suitable heat transfer coefficient and T_e is a suitable external temperature. The right-hand side of this equation is also referred to as Newton's law of cooling, and

[7]There is, however, an interesting and sometimes vexing effect that can arise when two solid surfaces are not in intimate thermal contact. Due to microscopic voids that are present between imperfectly smooth surfaces in contact, there is an additional resistance to thermal transport across the boundary. A suitable factor can be applied at such boundaries for more quantitative computations. Our experience for melt crystal growth systems has shown that, even when temperature fields are well predicted by a thermal model, quantitative closure of the overall heat balance over the system may be off by as much as a factor of two, if these contact resistance effects are ignored.

reflects the tendency of a heated body to cool at a rate linearly proportional to the temperature difference between it and its environment. The heat transfer coefficient accounts for both conduction into and natural convective cooling by the surrounding medium. In this case, it is important to employ a heat transfer coefficient and external temperature that reasonably represent the system. There is a large body of heat transfer literature addressing how such quantities can be estimated; see, e.g., [24,25,33]. In high-temperature systems, such as most melt crystal growth processes, thermal radiation is extremely important, and the above boundary conditions must be appropriately modified. This introduces significant challenges for heat transfer analysis, to such a great degree that radiation heat transfer will be separately discussed in Section 20.4.2.

Additional comments are warranted on the preceding sections. The underlying energy equations, Eqns (20.8) and (20.9), are quite rigorous and extremely reliable for describing heat transfer in physical systems. Realistic outcomes are virtually guaranteed if the needed physical properties are known and solutions to the equation can be found with sufficient accuracy. However, the appropriate choice of boundary conditions to apply to crystal growth models is more of an art than most practitioners are willing to admit. Boundary conditions must represent the net heating needed to attain temperatures above the melting point of the material to be grown, while simultaneously representing the cooling needed to enable the phase change, via the removal of latent heat, and promote crystal growth. Poor choices for thermal boundary conditions can lead to models that are perfectly well specified in a mathematical sense but totally unrealistic in their physical predictions. Finally, there are two issues of particular importance for melt crystal growth models: The first is proper representation of phase change physics and heat effects, and the second is faithful representation of furnace heat transfer, which involves radiation heat transfer and geometrical complexity. These issues and more are discussed next.

20.4 Heat Transfer in Melt Crystal Growth

Melt crystal growth presents special challenges beyond the general understanding of heat transfer. First, the change of phase from liquid to solid is accompanied by changes in energy that affect heat flow. Second, most materials of interest are characterized by melting temperatures that are high enough so that thermal radiation becomes important. Finally, the complicated configuration of high-temperature furnaces must be addressed to assess crystal growth performance. These issues are discussed, in turn, in the following sections.

20.4.1 Phase-Change Interface

The representation of a crystal growth process as the enactment of a path along a thermodynamic phase diagram is too simple in depicting the actual mechanisms at play during phase change in the course of crystal growth. In particular, it must be emphasized

that crystal growth is not an equilibrium process. Indeed, there must be some driving force to locally induce a liquid to solidify, and this driving force must be tailored over space and time to be consistent with the growth of a single, macroscopically large crystal. Thus, there are dynamic aspects, or kinetics, associated with phase change and crystal growth. Somewhat paradoxically, it is useful to understand these nonequilibrium effects by returning to thermodynamic fundamentals.

The formation of a crystalline solid from a fluid is a first-order phase transformation, accompanied by discontinuous changes in enthalpy, entropy, and specific volume. Under equilibrium conditions, the Gibbs free energy is continuous from the solid to the fluid phases. However, as emphasized above, crystal growth occurs under nonequilibrium conditions, when the thermodynamically stable crystal phase coexists with a thermodynamically metastable phase, typically a supersaturated or supercooled fluid. The driving force for transition to the stable, crystalline phase is the difference in Gibbs free energy between the two phases. Thus, all crystal growth processes are designed to set up and maintain a driving force, $\Delta G = G_2 - G_1$, for crystallization, where G_i denotes the Gibbs free energy associated with each phase. This driving force manifests itself in the form of an undercooling in temperature in melt growth, $\Delta T = T_m - T_i$, where T_m is the melting temperature of the material under thermodynamic equilibrium and T_i is the actual temperature along the interface (which is the temperature of both the liquid and solid in contact).

For melt crystal growth, we may posit a kinetic relationship between the normal growth velocity of the interface, V_n, and undercooling as

$$V_n = \beta(\theta, \Delta T)\,(T_m - T_i), \tag{20.18}$$

where $\beta(\theta,\Delta T)$ denotes a kinetic coefficient. In general, the equilibrium melting temperature, T_m, depends upon the energetics associated with the shape of the solid–liquid interface, and

$$T_m = T_{m,0} - \gamma \mathcal{H}, \tag{20.19}$$

where $T_{m,0}$ is the melting temperature of a planar interface, γ is a coefficient of surface energy, and $\mathcal{H}$ depicts the local mean curvature of the solid–liquid interface. This dependence is widely known as the Gibbs–Thomson effect.

The kinetic coefficient in the above expression is a function of both crystallographic orientation, θ, and the amount of undercooling at the interface, ΔT. We refer the motivated reader to a series of papers by Brandon et al. [34–38] for an excellent overview of these effects and an elegant mathematical representation for this coefficient. We present a brief summary below.

The orientational dependence of β arises from the fundamental mechanisms responsible for crystal growth. In particular, if the growth direction is very nearly perpendicular to a plane of symmetry of the crystal, a *singular* face, or *facet*, may arise. Growth via additional layers of atoms to the facet is typically slow and requires a significant amount of undercooling. Thus, the kinetic coefficient along a facet is very small. However, such facets are not always present during melt growth. Understanding how

and when they arise was first explained in a model of interface thermodynamics by Jackson [39,40] that gives rise to an effect known as *interface roughening*.

Jackson argued that there is an energetic driving force to add atoms from the liquid to the crystal surface, as they form new bonds to the surface and to each other. However, if there is a large change in entropy between the crystal and fluid phases, the Gibbs free energy is lowest when there are just a few extra atoms on the surface or a few atoms missing in the plane below. Under these conditions, the surface is smooth and the crystal exhibits a faceted shape during growth. On the other hand, if the change in entropy between phases is small enough, as is common for the melt growth of most metals and semiconductors, then the Gibbs free energy of the surface is minimized when half of the available surface sites are filled, resulting in a "rough" interface. The many atomic gaps in this rough surface allow the easy addition of atoms from the liquid phase, so that the kinetic coefficient becomes very large and the kinetics of phase change are very fast.

The dependence of the kinetic coefficient, β, on undercooling, ΔT, comes from a phenomenon known as *kinetic roughening* [41]. If the driving force for crystallization is sufficiently high, two-dimensional (2D) nucleation of new layers on a crystal surface can occur fast and often enough to make the surface atomically rough, even when the interface is near to a singular orientation that would favor faceting at low undercoolings. This phenomenon is observed in vapor and molecular beam growth, but is much less likely to be observed during melt growth, because of the very high undercooling that would typically be required.

Fortunately, many melt growth systems are well described by the case of the atomically rough solid–liquid interface. Under these conditions, the kinetic coefficient becomes so large that we may divide Eqn (20.18) by β and take the limit as $\beta \to \infty$ to achieve the surprisingly simple result of

$$T_i = T_m, \quad \text{along the solid} - \text{liquid interface.} \tag{20.20}$$

Furthermore, in many large-scale growth systems, the interface curvature is gentle enough so that $\mathcal{H}$ is small, Gibbs–Thomson effects are unimportant, and the melting temperature is a constant, with $T_m = T_{m,0}$.[8] This result has been referred to as the *isotherm condition*, referring to the location of the solid–liquid interface lying along the melting point isotherm of the system. Interestingly, this condition is the same as that which would arise if the liquid and solid were truly at equilibrium; however, one should remember that this is not the case and that the isotherm condition represents the mathematical limit of fast phase-change kinetics.

Returning to heat transfer, we can interpret the solid–liquid interface as separating the two domains that represent liquid and solid, thus the boundary conditions discussed earlier, Eqns (20.12) and (20.13), must hold. First, continuity of the temperature field is

[8]To be more rigorous, we should note that the melting temperature will also depend upon the composition of the liquid, as represented by the phase diagram of a multi-component system. Such composition-dependent effects can be extremely important in crystal growth, for example, leading to morphological instability via constitutional supercooling; however, we will not discuss such effects here.

automatically satisfied by the isotherm condition, Eqn (20.20). Interestingly, a mathematical interpretation of this condition leads to the specification of two constraints, namely that the solid and liquid are at the same temperature and that this particular temperature is given by the melting point. This apparent over-specification of conditions is not a paradox. One condition (continuity of temperature across the interface) is applied as a boundary condition for heat transfer, while the other (isotherm condition) provides information to locate the position and shape of the interface. The significance of this for heat transfer is that there is a strong nonlinear coupling between the shape of the solidification interface and the form of the heat flows near it. This effect can give rise to multiple steady states, particularly in meniscus-defined growth systems; see, e.g., [42–51]. A particularly dramatic manifestation, known as *interface flipping*, occurs in Czochralski growth of oxide crystals, where increasing crystal rotation can drive convective heat flows that invert a deeply convex interface to an almost flat shape nearly instantaneously at a critical rotation rate [52,53]. Because two nonlinear states with different interface shapes can exist within a range of rotation rates, hysteresis effects can be exhibited if the rotation is decreased for the flat-interface state.

The second condition, Eqn (20.13), represents an energy balance and takes on a special form across the phase change interface. Under conditions of constant temperature and pressure, the change in molecular configuration between a liquid and a solid changes the potential energy of the system, thus releasing heat upon solidification and absorbing an equivalent amount of heat upon melting. This is known as the heat of transformation, more commonly referred to as *latent heat*. Writing the energy balance across a solidification interface takes on the following form:

$$\mathbf{n} \cdot \left(-\kappa_\ell \nabla T_\ell + \kappa_s \nabla T_s \right) = \rho_\ell \Delta H_f \mathbf{n} \cdot \mathbf{V}_g, \quad \text{along the solid} - \text{liquid interface}, \tag{20.21}$$

where the subscripts ℓ and s refer to liquid and solid domains, respectively, ΔH_f is the latent heat of fusion per unit mass, and $\mathbf{V}_g$ is the velocity of the phase change interface, measured in a frame of reference that is stationary with respect to the solid, often casually referred to as the growth rate of the crystal. In many crystal growth systems, the latent heat of solidification is large enough to significantly affect heat transfer near the interface and distort its shape. We will return to this important issue in ensuing discussions about the design of heat transfer toward controlling interface shape during Bridgman growth.

20.4.2 Radiation Heat Transfer

Energy is transported by radiation, and the rate of radiative energy transfer is proportional to a body's absolute temperature raised to the fourth power. This form of heat transfer is often very important in melt crystal growth systems due to the very high melting points typical of many classical electronic and photonic materials. Thermal radiation most typically involves only heat fluxes from surfaces, and we first address how to approximate these fluxes in a heat transfer analysis using an approach referred to as *enclosure analysis*. However, some materials exhibit enough transparency to infrared

radiation at high temperatures to permit the transport of energy via radiation through the medium itself, an effect known as *internal radiation*. Our discussion of these complicated phenomena is necessarily brief, and the motivated reader is referred to classic texts on radiation heat transfer, such as Siegel and Howell [26], Sparrow and Cess [54], and Modest [55] for more rigorous presentations.

20.4.2.1 Surface Radiation

Let us first consider an opaque body at a high temperature. The Stefan–Boltzmann law states that q_b^e, the total emitted energy from a black surface into a vacuum,[9] is given by

$$q_b^e = \sigma T^4, \tag{20.22}$$

where σ is the Stefan–Boltzmann constant and T is the absolute temperature of the surface. A black surface is a perfect absorber and emitter of radiation, and a more realistic approximation is that of a nonblack surface, for which the Stefan–Boltzmann law is modified as

$$q^e = \varepsilon\sigma T^4, \tag{20.23}$$

where $\varepsilon \leq 1$ is the emissivity of the surface. For a real surface, the emissivity is a function of temperature, radiation wavelength, and direction, but a useful approximation is that of a *diffuse-gray* surface, where ε is taken to be constant.

A very simple boundary condition representing heat transfer from a hot surface can be obtained from the Robin condition, Eqn (20.17), by adding an approximation for radiative surface flux as follows:

$$-\mathbf{n} \cdot \kappa \nabla T = h(T - T_e) + \varepsilon\sigma(T^4 - T_e^4), \tag{20.24}$$

where the variable T must represent absolute temperature in this equation. While the nonlinear aspects of radiation are represented via the added fourth-order term, the above expression is ambiguous about the definition of the external temperature T_e, which is often prescribed as a known function of position to describe furnace heating and cooling in system models. In reality, radiation heat transfer can be greatly complicated by the relative orientation of system surfaces, their properties, and the effects of multiple reflections from those surfaces. A more realistic accounting for these effects, in particular a more rigorous interpretation of T_e in Eqn (20.24), will be subsequently addressed.

Nevertheless, the above expression can be gainfully employed in crystal growth models if sufficient care is exercised. Again, this is somewhat of an art and involves good engineering judgment. For example, a useful scaling analysis can be derived from a nondimensionalization of Eqn (20.24), which is rewritten as

$$-\mathbf{n} \cdot \nabla\theta = Bi(\theta - \theta_e) + Ra(\theta^4 - \theta_e^4), \tag{20.25}$$

[9] If the surface emits into a transparent material, the refractive index of this phase, n, must be included to yield $q_b^e = \sigma n^2 T^4$. For a gas, $n \approx 1$ and can be ignored; however, the effect of n is likely significant for condensed phases of solids and liquids.

where $\theta \equiv T/T_m$ is a dimensionless absolute temperature scaled by the melting point, $Bi \equiv hL/\kappa$ is the dimensionless Biot number (with L as a characteristic length for the system), and $Ra \equiv \varepsilon\sigma T_m^3 L/\kappa$ is the dimensionless radiation number. A Taylor series approximation yields $\theta^4 - \theta_e^4 \approx 4\theta_e^3(\theta - \theta_e)$, and we can rewrite the prior equation as

$$-\mathbf{n}\cdot\nabla\theta \approx Bi(\theta - \theta_e) + 4\theta_e^3 Ra(\theta - \theta_e).$$

Thus, for the same driving force, $\theta - \theta_e$, the ratio $4\theta_e^3 Ra/Bi$ represents an estimate of the comparative ratio of radiative to convective heat exchange. For high-temperature melt growth systems, we expect that $\theta_e \approx 1$, so this radiation-to-convection ratio is about $4Ra/Bi = 4\varepsilon\sigma T_m^3/h$, a number that grows with the cube of the absolute melting temperature, indicating the dominance of radiation over convection at high temperatures. For the melt growth of silicon, $T_m = 1{,}683$ K, $\varepsilon_\ell \approx 0.2$, and $\varepsilon_s \approx 0.8$, and a reasonable heat transfer coefficient is $h = 10\ \mathrm{W/m^2K}$, giving a ratio of $4Ra/Bi \approx$ 20–88, showing the predominant effect of radiation transfer from surfaces in silicon melt growth systems.

The thermal modeling of crystal growth systems often requires a more accurate and realistic accounting of thermal radiation than is allowed by the simple formulas presented above. One of the best approaches is called *enclosure analysis*, in which all surfaces of a system are considered to form an enclosure made up by M surfaces, with each surface characterized by a temperature distribution, $T_k(\mathbf{r}_k)$, and a diffuse-gray emissivity, ε_k. This surface will radiate thermal energy at a rate given by the Stefan–Boltzmann law, Eqn (20.23), but it will also receive incoming thermal radiation that is emitted from other surfaces in the enclosure. Further complicating the situation, a portion of the radiant energy arriving at all surfaces will be diffusely reflected according to the reflectivity of the surface, which is equal to $\tilde{\rho}_k = 1 - \varepsilon_k$ for surface k.

For the sake of brevity, we skip the derivation and present the outcome:

$$q_k(\mathbf{r}_k) = \varepsilon_k\sigma T_k^4(\mathbf{r}_k) + \frac{\varepsilon_k}{\pi}\sum_{j=1}^{M}\int_{\omega_j}\left[\frac{\tilde{\rho}_j}{\varepsilon_j}q_j(\mathbf{r}_j) - \sigma T_j^4(\mathbf{r}_j)\right]\cos\psi_{kj}\,d\omega_j, \tag{20.26}$$

where T_i and q_i represent the absolute temperature and net radiant flux, respectively, at any point $\mathbf{r}_i$ along surface i in the enclosure (subscript i refers to either k or j in the above equation), and the integral is performed over the solid angle subtended by surface dj on dk, denoted by $d\omega_j$. The geometrical factor ψ_{kj} is the angle between the inward normal at the point $\mathbf{r}_k$ and the incident radiation from another point $\mathbf{r}_j$ in the enclosure. See, e.g., [26], for more details. Significantly, this expression is rigorously correct for the case of surfaces that are gray and diffuse, i.e., the gray radiant properties are independent of wavelength and diffuse properties do not depend on direction. Although real surfaces rarely exhibit true diffuse-gray behavior, analyses based on this approximation often yield very good descriptions of enclosure heat transfer; see, e.g., Schornhorst and Viskanta [56].

While Eqn (20.26) can be applied and evaluated directly to account for radiant fluxes in a heat transfer analysis [57–59], a simpler approach assumes that the temperature and radiant heat flux over each surface are constant, which allows the integrals in Eqn (20.26)

to be evaluated independently using only geometric information of the enclosure surfaces. Their evaluation over all pairs of surfaces results in view factors F_{kj}, which are defined as

$$F_{kj} = \frac{1}{\pi A_k} \int_{A_k} \int_{\omega_j} \cos\psi_{kj} d\omega_j dA_k, \tag{20.27}$$

where A_k is the area of surface k. This evaluation results in a much simpler expression for the flux from each surface:

$$q_k = \varepsilon_k \sigma T_k^4 + \varepsilon_k \sum_{j=1}^{M} \left[\frac{\tilde{\rho}_j}{\varepsilon_j} q_j - \sigma T_j^4 \right] F_{kj}. \tag{20.28}$$

The direct implementation of the above equation in a heat transfer analysis is termed Poljak's method [60]. However, this expression is awkward to implement within a boundary condition such as Eqn (20.24) because of the summation involving surface fluxes on the right-hand side.

Noting that Eqn (20.28) is simply a set of linear equations, Gebhart [61,62] proposed a simple way of rearranging them in a more convenient form. In Gebhart's method, the net radiant heat flux on surface k is given as

$$q_k = \varepsilon_k \sigma T_k^4 - \frac{1}{A_k} \sum_{j=1}^{M} \varepsilon_j \sigma A_j T_j^4 G_{jk}, \tag{20.29}$$

where the Gebhart factor G_{jk} represents the fraction of energy leaving surface j which is absorbed by surface k.

A total of M^2 Gebhart factors for the enclosure are calculated by solving the following M linear equations a total of M times. For each surface k, the Gebhart factors $\{G_{jk}, j = 1,\ldots,M\}$ are calculated from

$$\mathbf{A}\mathbf{G}_k = \mathbf{b}_k, \quad \text{for } k = 1, \ldots, M, \tag{20.30}$$

where

$$\mathbf{A} \equiv \begin{bmatrix} (F_{11}\tilde{\rho}_1 - 1) & F_{12}\tilde{\rho}_2 & \cdots & F_{1M}\tilde{\rho}_M \\ F_{21}\tilde{\rho}_1 & (F_{22}\tilde{\rho}_2 - 1) & \cdots & F_{2M}\tilde{\rho}_M \\ \vdots & \vdots & \ddots & \vdots \\ F_{M1}\tilde{\rho}_1 & F_{M2}\tilde{\rho}_2 & \cdots & (F_{MM}\tilde{\rho}_M - 1) \end{bmatrix},$$

$$\mathbf{G}_k^T \equiv \left[G_{1k}, G_{2k}, \ldots, G_{Mk} \right],$$

$$\mathbf{b}_k^T \equiv \left[-F_{1k}\varepsilon_k, -F_{2k}\varepsilon_k, \ldots, -F_{Mk}\varepsilon_k \right].$$

Thus, we finally write a realistic heat transfer boundary condition for surface i including an approximation to thermal radiation using

$$-\mathbf{n} \cdot \kappa_i \nabla T_i = h(T_i - T_a) + \varepsilon\sigma\left(T_i^4 - T_R^4\right), \tag{20.31}$$

where T_a represents a suitable choice of the ambient temperature to account for convective cooling of the surface, and T_R is an effective sink temperature for radiation

that is provided by Gebhart's analysis as

$$T_R \equiv \left(\frac{1}{\varepsilon_k A_k} \sum_{j=1}^{M} \varepsilon_j A_j T_j^4 G_{jk} \right)^{1/4}. \tag{20.32}$$

Note that Eqn (20.31) is identical to Eqn (20.24) except that T_e in the radiation term has been replaced by the more rigorously defined T_R given here, and T_e in the convective term of Eqn (20.24) has been replaced by the ambient temperature T_a, which will not, in general, be the same as T_R.

We provide a few final comments on surface radiation, which is predominant in virtually all melt crystal growth systems. A general rule of thumb, estimated using the previous expression for $4Ra/Bi$, is that radiative cooling will be comparable to convective cooling at approximately 400°C and will quickly dominate as temperatures rise. A simple accounting for radiation heat transfer effects can be implemented using Eqn (20.24) with careful consideration of its limitations and potential consequences. However, a more realistic approach, such as enclosure theory with Gebhart's method, is needed to predict radiation heat transfer with quantitative precision. Compared to the ease of applying Eqn (20.24), methods based on enclosure theory are considerably more complicated in their formulation and costly in their implementation. For example, there is often considerable expense in the computation of accurate view factors, and the strongly nonlinear coupling among all surface temperatures in the enclosure can make solution of the heat transfer problem difficult. Finally, even using classical enclosure analysis, the assumption of constant surface fluxes and temperatures can result in low accuracy if too few surfaces are defined in the enclosure; however, accuracy can be improved by using more surfaces or by employing higher order approximations to the surface temperatures and heat fluxes [57,58].

20.4.2.2 Internal Radiation

Internal radiation refers to energy transport via radiation emitted and absorbed within a participating medium. Such media are termed *semitransparent*, since they are neither opaque nor transparent, and both absorption and emission processes are important. This process is quite complex due to its nonlinear dependence on the temperature field and its potentially long-range interaction with system geometry. Internal radiation is important during the growth of crystalline materials that melt at high temperatures and are transparent to some extent within portions of the infrared spectrum. In particular, internal radiation is significant during the melt growth of many oxide crystals, such as yttrium aluminum garnet (YAG), gadolinium gallium garnet (GGG), and sapphire (Al_2O_3). We refer the interested reader to more specific examples in the early work of Brandon and coworkers [63–68] and the more recent work of Yuferev and coworkers [69–74]. Some salient aspects of internal radiation are outlined in the following discussion.

The most straightforward approach to representing internal radiation in an analysis of heat transfer is to modify the heat flux vector as follows:

$$\mathbf{q} = -\kappa \nabla T + \mathbf{q}_R, \tag{20.33}$$

where $\mathbf{q}$ is the total heat flux vector, κ is the thermal conductivity, T is temperature, and $\mathbf{q}_R$ represents the energy flux associated with internal radiation[10]. The energy equation thus takes on the form

$$\rho C_v \frac{\partial T}{\partial t} - \nabla(\kappa \nabla T) - \nabla \cdot \mathbf{q}_R = 0, \tag{20.34}$$

where components of the radiative flux vector are given by

$$\mathbf{q}_R \cdot \mathbf{e}_x = \int_{\Omega=0}^{4\pi} i'(\Omega)\cos(\theta)d\Omega. \tag{20.35}$$

Here, $\mathbf{e}_x$ is a unit vector defining a direction, $i'(\Omega)$ is the radiation intensity directed along the solid angle Ω, and θ represents an angle defined with respect to $i'(\Omega)$ and a surface perpendicular to the vector $\mathbf{e}_x$.

The radiation intensity at any point within the medium, $i'(\Omega)$, arises from a balance of locally emitted radiation and radiation received from the surroundings. In a gray, absorbing and emitting medium, with no scattering and with uniform optical properties, the radiation intensity is given by the integrated form of the equation of radiation transfer [26]

$$i'(\Omega) = i'(\Omega, 0)\exp[-a\, l(\Omega)] + \frac{a}{\pi}\int_0^l n^2 \sigma T^4(l^*)\exp\left[-a\left(l - l^*\right)\right]dl^*, \tag{20.36}$$

where l is the distance from the domain boundaries along the solid angle Ω, a is the optical absorption coefficient, n is the refractive index of the medium, and l^* is a dummy variable of integration. The first term on the right-hand side of Eqn (20.36) accounts for radiative intensity $i'(\Omega,0)$ that is emitted from the system boundaries and received at the point within the medium, and the second term comprises incoming radiation emitted from the intervening media between the point at which i' is evaluated and the boundaries.

Solving for the radiation intensity is particularly challenging, requiring accurate integration of nonlinear integrals over all solid angles. The rigorous representation of internal radiation via Eqns (20.35) and (20.36) converts the partial differential energy Eqn (20.8) into the integro-differential Eqn (20.34). Brandon and Derby [63,64,66] solved this integro-differential equation directly using a finite element method; however, this approach was very demanding from formulation and computational perspectives [75,76]. Yuferev and coworkers [69,70] have developed approximation methods to reduce the computational load and have also extended their formulations to more rigorously represent boundary conditions between media of different refractive indices [71–73].

[10]In this and succeeding equations, we consider only transport through a solid and ignore convective terms. Internal radiation is typically more important in solids than in fluids. Gases are usually quite transparent, though absorption and scattering can be important in atmospheric heat transfer occurring over long length scales, and liquids are typically quite opaque, since molecular vibrations and rotations absorb strongly in the infrared.

Simpler approaches to account for internal radiation are based on consideration of the mean free path of a photon within a medium, which is given by the inverse of the absorption coefficient, a, and a characteristic length scale, L, that is representative of the physical extent of the medium. The ratio of these two length scales is termed the *optical thickness* of the medium and is given by $\tau = aL$. If $\tau \ll 1$, the medium is termed to be optically thin. In this case, the medium is very nearly transparent, radiation transport is dominated by surface exchanges, and enclosure analysis (discussed in the prior section) can be applied. This approach has been employed in prior crystal growth analyses to good effect [52,53,65].

If $\tau \gg 1$, the medium is termed to be optically thick, and radiation transport can be approximated as a diffusion-like process. The Rosseland diffusion approach [26,77] represents the heat flux in an optically thick medium via a temperature-dependent thermal conductivity,

$$\kappa_T = \kappa + \frac{16 n^2 \sigma T^3}{3a}, \tag{20.37}$$

which is simply substituted into the conductive term of the heat transfer equation for analysis. In this limit, a useful dimensionless group can be derived, known as the conduction-to-radiation parameter, given by

$$N = \frac{\kappa a}{4 n^2 \sigma T_0^3}, \tag{20.38}$$

where T_0 is a characteristic temperature of the system, which is well represented by T_m in a melt crystal growth process. As may be surmised from its name, this dimensionless parameter is a measure of the relative importance of conductive heat transfer with respect to radiant transport in an optically thick medium. While simple, the Rosseland diffusion approximation breaks down within a distance of a^{-1} from the boundaries of the medium (at this length scale, the system is no longer optically thick), thus the specification of boundary conditions can be problematic. Therefore, a better approach is the P_1 approximation, also known as the differential and Milne–Eddington approximations [26], where a finite set of moments are employed to reduce the integral terms of the radiation transfer equation to differential terms. While slightly more complicated to implement than the Rosseland approach, it can yield more meaningful results [78].

Finally, the above approaches considered that the medium is gray, meaning that all properties are independent of wavelength. Some materials exhibit strong absorbance across a range of infrared wavelengths. One such material is quartz, which is commonly employed in crystal growth systems. A reasonable approach for representing internal radiation transport through such materials is called the *band approximation*, where the medium is assumed to exhibit a combination of transparent and opaque behaviors [79–85].

20.4.3 Furnace Heat Transfer

This section specifically addresses the technological challenges to understanding and modeling heat transfer in the high-temperature furnaces required for melt crystal

growth. There are tremendous practical challenges for the design and operation of such furnaces. Mechanical design and construction must account for cycling between room temperature and the high temperatures required for growth. Degradation of components is accelerated by chemical interactions at sustained high temperatures. Diagnostic measurements, such as the accurate monitoring of temperature, become extremely challenging in this harsh environment. These issues and more are important, and are well beyond the expertise of the authors of this chapter.

Heat transfer in a real crystal growth furnace is complicated by intricate geometries, multiple materials with differing thermal properties, contact resistance among solid elements, gaseous convection, and the predominance of thermal radiation. Nevertheless, from a theoretical perspective, furnace heat transfer is rather straightforward. Thermal models of high-temperature furnaces can be readily assembled using radiation enclosure analysis coupled with multidomain conduction. However, the effort required for such analyses is daunting. For these models, the representation of geometry and the computation of accurate radiation view factors are typically the greatest challenges.

Adding to this picture, it requires an inordinate amount of effort to include a rigorous representation of the combined heat transfer and solidification occurring inside the ampoule combined with detailed modeling of heat transfer in a crystal growth furnace. Thus, more pragmatic approaches are often used. A common strategy is to consider only heat transfer within the domains of crystal, melt, and containing ampoule, and apply boundary conditions to represent the furnace. This strategy is represented by the specification of the external temperature profile, T_e, in Eqns (20.17) and (20.24), which represents heat exchange between ampoule and furnace. A more rigorous approach is to perform a radiation enclosure analysis to compute an effective external temperature due to radiation, T_R, as expressed in Eqn (20.31); however, such a model is still somewhat idealized if all surfaces associated with the furnace are prescribed as isothermal. Nevertheless, these approaches, applied with good engineering judgment and a modicum of care (such as measuring a thermal profile through the system and performing validation steps) can be useful in analyzing the behavior of a crystal growth system.

Such simple strategies to represent furnace heat transfer have obvious flaws. Most notably, they neglect important interactions between the furnace and the load represented by the ampoule and crystallizing contents. As a result, such idealized models are not likely to be accurate enough for experimental validation, equipment optimization, or model predictive control. A more quantitative analysis requires integrating global (furnace-scale) heat transfer and local phenomena (growth within the ampoule). This can be achieved within a monolithic model of the entire system [57,81,82,86] or via the coupling of these different effects via a modular approach. Monolithic models for crystal growth processes require intensive and coordinated programming efforts, are typically system specific, and are often difficult to maintain and modify. Modular approaches, whereby different models and solvers are used together, can optimally employ software tools that are well suited to the tasks at hand. In particular, an obvious approach for crystal growth modeling is to couple a global furnace model with a local crystal growth model.

There have been prior efforts to couple global and local models to describe melt crystal growth processes [87–90]. However, these models employed a one-way coupling—furnace heat transfer is computed with a coarse-scale representation of the melt and crystal, and then temperature boundary conditions are supplied to the local model. One-way coupling ignores the change in the furnace heat load caused by such local factors as melt convection and latent heat generation at the solid–liquid interface. If this load is very small, as may be the case if the thermal mass of the furnace is very large, this approach may be adequate. However, a more rigorous approach requires a true coupling of the codes and an efficient means to iterate back and forth toward a self-consistent solution.

We have made progress in developing fully coupled models that compute steady states of complicated crystal growth systems. Such an approach couples a sophisticated furnace modeling code, CrysMAS [80–82,91], with our finite element code, Cats2D, which has been developed in-house to model transport and solidification phenomena. Our efforts in this area are described in [92–95]. The development of such coupled models is an active and important area of crystal growth research.

Before leaving this discussion of furnace heat transfer, we note that there are two major designs for heating in crystal growth systems. The simpler approach is to employ electrical resistive heating. Here, an electrical current, either direct or alternating, is passed through a resistive element to generate volumetric heating via the Joule effect, with a resulting heat generation rate of $Q = J^2R$, where J is the current density and R is the electrical resistance of the element. The resistive element attains a very high temperature, and thermal radiation transfers heat to the crystal growth charge across the typically open bore of the furnace, which may be partially evacuated or filled with a gas.

A more complicated but more direct manner of heating is induction heating, which passes an alternating current through a coil that generates time-harmonic electric and magnetic fields. These fields, in turn, drive an alternating current in a nearby susceptor, which is often a metallic crucible. The current in the susceptor then gives rise to Joule heating. This technique can deliver energy directly to system components that need to be heated, bypassing the radiant transfer step of purely resistive heaters. Thus, induction heating is often effective for attaining conditions needed for the growth of very high melting-point materials, such as oxides. Its disadvantage is that the heating distribution can be quite inhomogeneous due to two effects. First, the susceptor is heated unevenly, since the majority of heat is deposited into a thin layer, characterized by a penetration depth, δ, which scales as $\delta \sim \sqrt{2/\mu_0 \sigma_E \omega}$ where μ_0 is the free space permeability, σ_E is the electrical conductivity of the susceptor, and ω is the frequency of alternating current through the coil. Second, geometrical discontinuities of the susceptor, such as sharp edges or corners, lead to a bending of the electromagnetic fields that can strongly focus heating. Gresho and Derby [96] were among the first to analyze induction heating in crystal growth systems; similar approaches have been widely applied by others [97–102].

20.5 Historical Perspective: Theoretical Developments

Having presented a general discussion of the most important elements of heat transfer in crystal growth systems, it is time to return to the specifics of heat transfer in Bridgman crystal growth. Section 20.2 put forth a brief history of the experimental development of this process. In the following, we present a very brief synopsis of theoretical developments that have brought us to our present state of understanding of heat transfer in the Bridgman crystal growth method.

Wilcox and coworkers were among the first to analyze heat transfer and its effects in Bridgman crystal growth [103–106]. Chang and Wilcox [103] performed an idealized 2D analysis of the system. Although rudimentary, their analysis was one of the first to point out the importance of heat flows on interface shape. For example, the drawing on the left of Figure 20.2, adapted from [103], illustrates the wholly correct notion that, due to the solid–liquid interface lying along the melting point isotherm, heat must flow in a direction normal to it. Thus, the arrows indicate the heat flows that must accompany convex, planar, and concave interfaces. In addition to the ever-present axial flow of heat from the hot melt to the cool crystal, they argued that heat must be flowing radially into the ampoule from the exterior to support a convex shape, and that heat flowing out of the system to the exterior would be consistent with a concave interface. Following this logic, Chang and Wilcox suggested that introducing an adiabatic zone between isothermal hot and the cold zones in the furnace would minimize radial heat exchange and promote the evolution of a flat solidification interface. This was later substantiated

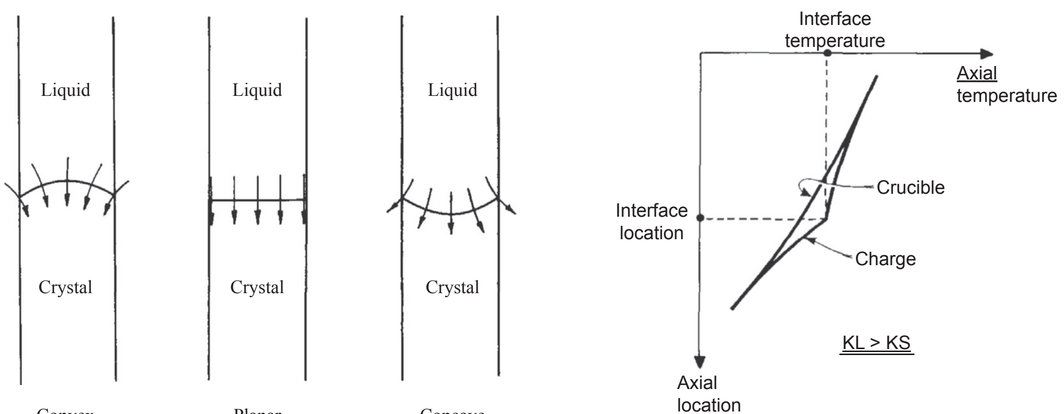

FIGURE 20.2 Left: A very early, but still insightful, outcome of heat transfer analysis of the Bridgman process by Chang and Wilcox [103] shows the flow of heat, indicated by arrows, that must accompany certain interface shapes. As indicated in the rightmost image, a convex interface shape can only occur if heat is entering radially into the system near the interface. Right: Later analyses by Jasinski and Witt [20] showed the significant effect of heat transfer through the crucible on the shape of the solid–liquid interface. This "interface effect" leads to an outward radial flow of heat near the interface when the thermal conductivity of the liquid is greater than that of the solid, thus promoting concave interface shapes.

by numerical calculations of Fu and Wilcox [105]. Indeed, these analyses provided motivation for the development of the heat-pipe furnace of Wang and Witt [14], described in Section 20.2, which featured isothermal zones connected by an insulating gradient zone.

However, there are two important effects that were not accounted for in these simple analyses of interface shape. First, the release of latent heat along the solidification interface must also be removed during growth. The shortest path for this extra heat to flow from the interface is toward the cooler exterior surrounding the ampoule, so concave interface shapes are reinforced by latent heat effects. Paradoxically, one of the greatest heat transfer challenges in melt crystal growth systems is removing the comparatively small amount of latent heat generated at the interface during growth rather than adding the large amount of heat needed to melt the material at high temperature.

Second, the effect of heat transfer through the ampoule or crucible is very important for setting interface shape. In several insightful analyses, Jasinski, Rohsenow, and Witt [17,18,20] showed the significant influence of ampoule thermal mass on the thermal field and, most importantly, the *interface effect*, where the thermal conductivity mismatch among melt, crystal, and ampoule results in significant interface deflection at the ampoule wall. In the typical case for semiconductors, with the liquid thermal conductivity being greater than that of the solid ($k_L > k_S$), they argued that the axial temperature gradient at the interface must be discontinuous, whereas the gradient is constant though the ampoule wall, as depicted by the right-hand image of Figure 20.2. Thus, the temperature within the charge must be greater than the temperature in the ampoule at the same axial position, driving an outward radial heat flow and giving rise to the concave interface shape that must accompany it (as shown in the image on the left of Figure 20.2). In [20], Jasinksi and Witt state, “To the authors’ knowledge, all published results concerning interface shapes for Bridgman grown semiconductor crystals indicate the establishment of a similar (concave) interface shape.” Incidentally, the interface effect is reversed for the case of the conductivity of the solid being greater than that of the liquid ($k_S > k_L$), in which case the temperature within the charge must be less than in the ampoule, thus promoting a convex interface shape.

Our focus on heat transfer and interface shape is motivated by the generally held belief that interface shape is one of the most important factors affecting crystal quality in bulk growth processes. In particular, an interface shape that is convex with respect to the crystal has been postulated to minimize the potential for defects that may arise from deleterious ampoule wall interactions, such as dislocations, grains, or twins, to propagate toward the bulk crystal [1,107]. The general argument asserts that the solid grows by the attachment of atoms to the interface from the liquid, and that this material addition only can result in macroscopic growth in a direction that is normal (i.e., perpendicular) to the shape of the solid–liquid interface. Thus, a concave interface will allow a defect, such as a new grain, to persist and grow toward the center of the crystal, while a convex interface shape forces the defect to grow outward toward the ampoule wall, where it may

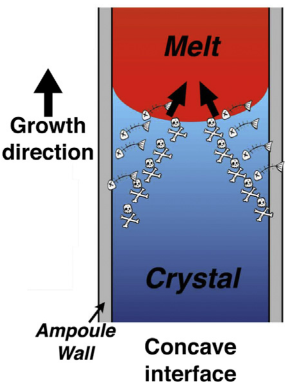

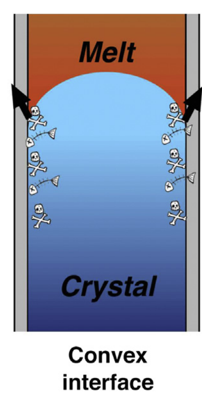

FIGURE 20.3 Schematic depiction of how the solidification interface shape may affect the propagation of deleterious wall interactions during growth. The solid phase grows by the addition of material in a direction normal to the shape of the solid–liquid interface. A concave interface (left) will propagate defects toward the interior, while the preferred, convex interface (right) isolates defects along the ampoule wall, maintaining the quality of the bulk of the crystal.

be annihilated. This mechanism is depicted, rather whimsically, by the cartoons presented in Figure 20.3.

While this general argument is qualitative, it has been rigorously shown that twins, which are high-symmetry grains, can arise from certain macroscopic solid–liquid interface shapes. Specifically, in an insightful analysis, Hurle [108,109] derived conditions under which twinning would be likely to occur during the growth of III-V crystals. He argued that the energetics associated with different angles formed at the three-phase boundary; i.e., the solid–liquid interface, as it meets a surrounding gas or a solid ampoule wall, would dictate the probability of nucleating a twin. Amon et al. [110] performed a series of growth experiments using the vertical gradient freeze technique with different ampoule shapes, and confirmed Hurle's theory. Namely, twin formation was prevented if certain interface shapes were avoided during growth. There is also rather convincing evidence of the benefits of a convex interface shape in the growth of cadmium zinc telluride, as will be discussed in the following section.

Returning to historical advances in our understanding of heat transfer in Bridgman systems, Naumann [111,112] developed 1D and 2D analytical models of heat transfer in Bridgman crystal growth. He studied the effects of varying the different operating parameters (e.g., adiabatic zone length and ampoule pull rate) on the axial gradients in the system as well as on the melting point isotherm shape and position. In addition, both Naumann [111] and Jasinski et al. [17], using 1D models, clarified the role of finite-length ampoule end effects on heat transfer, and defined minimum lengths of the hot and cold zones for which an infinite ampoule assumption is valid.

Large-scale, computer-aided analysis of coupled heat transfer and melt convection during the vertical Bridgman growth of single crystals was pioneered by Brown and coworkers [113–119]. In particular, Adornato and Brown [114] studied the effect of different furnace profiles and ampoule materials, and compared their predictions to the growth experiments conducted by Wang and Witt [14]. In significant work of the same time frame, Crochet et al. [79] solved a 2D, quasi-steady-state, finite element model of coupled heat transfer and melt flow during the Bridgman growth of InP. They included

intricate details of the furnace and ampoule in their model and compared their results to experimental temperature profiles.

There have been a great many studies of heat transfer in melt crystal growth since these early days, indeed too many to summarize here. In most respects, the community has reached a high level in its ability to analyze heat transfer in crystal growth systems. What is more important now is to posit how we can improve crystal growth by the synthesis and design of new approaches to heat transfer. Toward such a goal, we discuss next what we feel is an enlightening story of our path toward understanding the interactions between heat transfer and interface shape in the Bridgman crystal growth of a specific material.

20.6 Research Vignette: Bridgman Growth of Cadmium Zinc Telluride

The following describes prior and ongoing research that has advanced our understanding of heat transfer in the Bridgman growth of cadmium zinc telluride (CZT). We believe that the ideas put forth in this vignette will be useful for improving this and other materials grown by the Bridgman method.

20.6.1 Motivation

Cadmium telluride (CdTe) and its alloy, cadmium zinc telluride ($Cd_{1-x}Zn_xTe$, hereafter referred to as CZT), are wide-bandgap, II-VI semiconductors that are used in the fabrication of high-performance sensors for infrared and gamma radiation. Compositions of interest are typically $x = 0.04$ for infrared applications and $x = 0.10$ for gamma detectors. Although the great potential of such sensors has long been known, it has been very difficult to reproducibly grow crystals of sufficiently high quality [120–123], particularly for gamma radiation detector applications. Among the many challenges are compositional inhomogeneity with respect to zinc, high levels of dislocations, loss of single-crystallinity via the emergence of new grains, and the formation of large, tellurium-rich, second-phase particles during growth.

Heat transfer during the melt growth of CZT is complicated by a number of factors. First, its melting point temperature is quite high, with $T_m = 1365$ K, so radiative heat transfer will be the dominant mode of heat exchange between the furnace and the ampoule and crucible containing melt and crystal. Within the melt, a high viscosity and low thermal conductivity [121,124] lead to a Prandtl number of $Pr \approx 0.4$, much higher than the typical value of $Pr \approx 0.01$ for most semiconductor crystals. As a result, convective heat transfer in the melt is very important under typical growth conditions, and there is strong coupling between heat and momentum transport. The thermal conductivity of the crystal is 20–30% lower than that of the melt. This and a high latent heat of fusion readily lead to a solidification interface that is concave with respect to the melt [18,20,125–127]. Finally, the low thermal conductivity of the solid also tends to

increase thermal gradients and associated thermal stresses within the crystal during growth. Under such conditions, dislocation multiplication mechanisms are active, and the material is plagued by high densities of dislocations.

We have applied computational modeling to better understand the growth characteristics of CZT. Our initial studies focused on infrared detector material grown by both vertical [59,126–130] and horizontal [131–133] Bridgman techniques. We also modeled atomistic phenomena of the liquid phase of CdTe and CZT via ab initio methods [124,134–136] and found unusual behaviors, such as a semiconducting character of the melt and long-range tellurium structuring. Yeckel and Derby [137,138] studied the influences of transient flows driven by the accelerated crucible rotation technique (ACRT) on zinc segregation; in [139], they considered the effects of a submerged heater on shaping the interface during CZT growth. Yeckel et al. [140] considered 3D effects during small-scale, low-gradient CZT growth. Lun et al. [141] found that axial gradients could be manipulated to affect flow intensity and interface shape, and later assessed an idealized, closed-loop control strategy for interface shape control [142]. Stelian et al. [143,144] and Yeckel et al. [46,145,146] analyzed the detached Bridgman process applied to CZT growth. Pandy et al. [147] and Gasperino et al. [148–150] studied electrodynamic gradient freeze (EDG) furnaces during the growth of cadmium zinc telluride crystals. More recently, Zhang et al. [151–153] analyzed segregation effects and interface shape control in EDG growth of CZT.

Through this odyssey of modeling and analysis, we have learned much about the general characteristics of CZT growth. However, in the following discussion, we choose to focus on just one aspect, namely the shape of the solid–liquid interface. As mentioned previously, controlling the shape of the solid–liquid interface has long been desired for improving crystalline quality in melt crystal growth processes. This may be particularly important in the melt growth of CZT, since this material exhibits a propensity to lose its single-crystal character via the generation of new grains during growth [120,121,154]. The emergence of new grains is particularly damaging, since it directly impacts the single-crystal yield, which is rarely better than 4% [155] for commercial Bridgman growth of CZT for radiation detector applications.

Understanding of grain emergence during CZT growth is lacking; however, new grains are postulated to arise via events occurring at the junction of the solidification interface and the crucible wall, similar to the mechanism of twin formation explained by Hurle [108,109]. Following the arguments put forth in the previous section, a convex interface shape may act to isolate those new grains along the periphery and prevent their growth inward. Indeed, there is experimental evidence that convex interface shapes do give rise to better quality CZT and that concave shapes can be harmful. For example, Shiraki et al. [156] and Roy et al. [157] observed that locally concave interface shapes in CZT growth in the traveling heater method are directly correlated with the unwanted formation of new grains. Further, in important recent papers, Carcelén et al. [158] and Crocco et al. [159] demonstrated how changes in pedestal heat transfer, which ostensibly promoted a convex interface shape during the first stages of growth, resulted in a

dramatic reduction in the number of grains in the grown ingot. We will discuss the results of these recent experimental studies in Section 20.6.3.

We believe that achieving a predominantly convex interface shape is essential to reduce the propensity for new grain formation during CZT growth. However, the challenge is then to design a Bridgman system in which the inherent tendency to grow with a concave interface is overcome. This is the focus of the ensuing discussion.

20.6.2 Heat Transfer Analysis

20.6.2.1 Ampoule Support and Cold Finger

Kuppurao and Derby [59] examined how the design of the ampoule support influences the solid–liquid interface shape during the early stages of CZT growth. They considered the vertical Bridgman growth process used by Johnson Matthey Electronics, Inc. (The general characteristics of this system were analyzed previously in [126–128].) This system featured a CZT charge contained in a 7.5-cm diameter cylindrical ampoule with a conical tip, grown at rates of 1 mm/h. The ampoule was fabricated from quartz and lined with a thin coating of pyrolitic boron nitride (PBN). The ampoule was contained in a vertical gradient furnace, and solidification proceeded from the bottom of the ampoule as the furnace was translated upward.

The model employed here extended the original formulations used in [126–128] to include an ampoule support, as shown schematically in Figure 20.4(a). The support was considered to be fabricated from blocks of solid graphite or mullite, either as a single material or in composite form, with a “cold finger” consisting of a solid core of highly conductive material embedded within a less-conductive block. Heat transfer was computed within the ampoule and support, and solidification and flow were modeled for the crystal and melt. Heat exchange with the furnace was represented using the simple condition represented by Eqn (20.24), where T_e was specified to represent the general characteristics of the furnace bore temperature; see [160] for details. While the form of the furnace temperature profile remained unchanged for all simulations, its axial position (corresponding to furnace position) was changed for each configuration. Different support compositions gave rise to varying thermal resistances and heat loads through the system; repositioning the furnace allowed the interface to be placed at nearly the same location in the ampoule for each design, thus simplifying interface shape comparison. Physical properties needed for these simulations can be found in [126–128,160]. The finite element method was applied for solution of all governing equations, and a sample mesh for these computations, resulting in a mathematical system of 18,320 total unknowns, is shown in Figure 20.4(b).

Figure 20.4(c)–(e) show, respectively, the overall temperature field for supports of solid mullite, solid graphite, and the composite design including the cold finger. Let us first examine the nature of heat transfer through these different supports. As indicated by the shape and spacing of the isotherms, heat flow is relatively uniform and mostly directed axially downward through both single-material supports. The lower-conductivity mullite

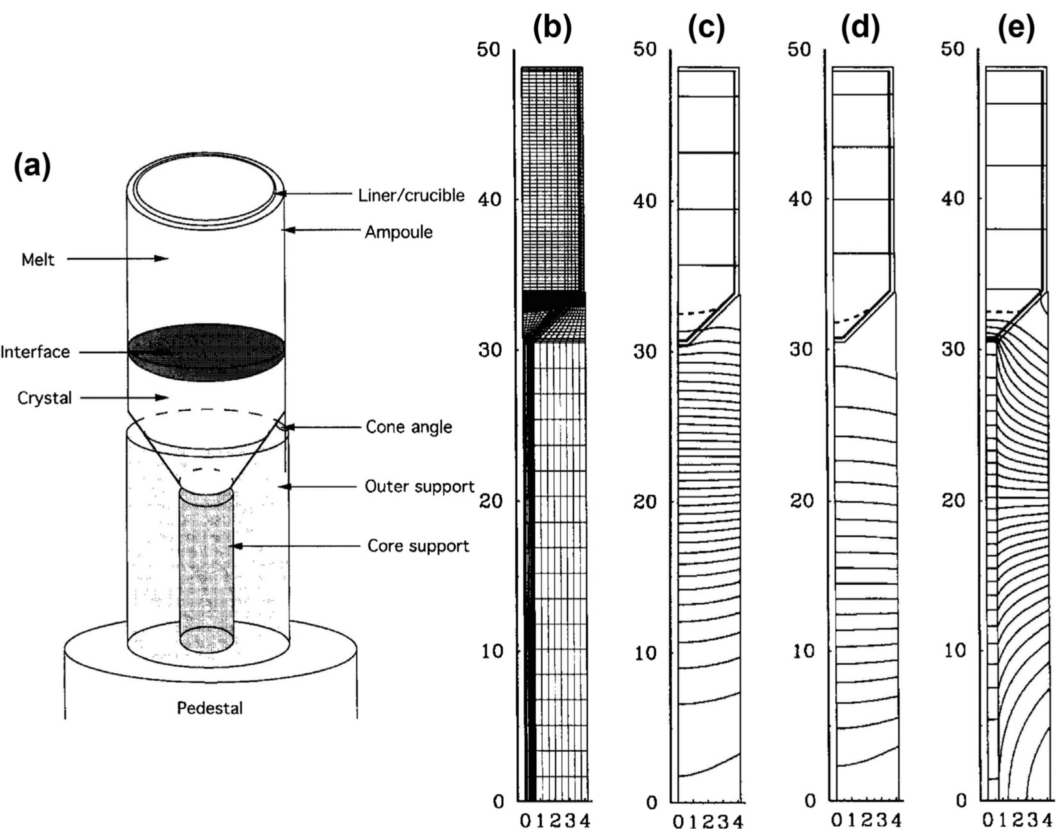

FIGURE 20.4 Computations of heat transfer during CZT Bridgman growth for various ampoule support designs. (a) Schematic indicating system configuration. (b) Sample finite element mesh used in computations. Overall temperature fields, shown by equally-spaced isotherms, for supports fabricated from (c) solid mullite, (d) solid graphite, and (e) mullite with graphite core, or "cold finger." *Adapted from Ref. [59].*

support, shown in Figure 20.4(c), is more insulating and supports larger axial gradients than the more conductive graphite support, shown in Figure 20.4(d). Figure 20.4(e) shows the very different heat transfer that arises with the composite support. Strikingly, the high-conductivity core, i.e., the cold finger, promotes a sizable heat flow that is nearly purely axial, while significant radial gradients are exhibited in the more insulating mullite that surrounds it. In the upper portion of the mullite, heat is flowing downward and radially inward. The outcome is a channeling of heat to the cold finger, where it is conducted downward to the cooler portions of the furnace.

The effect of these different heat transfer behaviors on the contents of the ampoule are shown in Figure 20.5, where streamlines of melt convection are indicated on the left and equally spaced isotherms are displayed on the right for the three cases; additionally, the solid–liquid interface is indicated by dashed lines. Figure 20.5(a) shows the case when the support is fabricated entirely from mullite. Concentrating on heat transfer, we

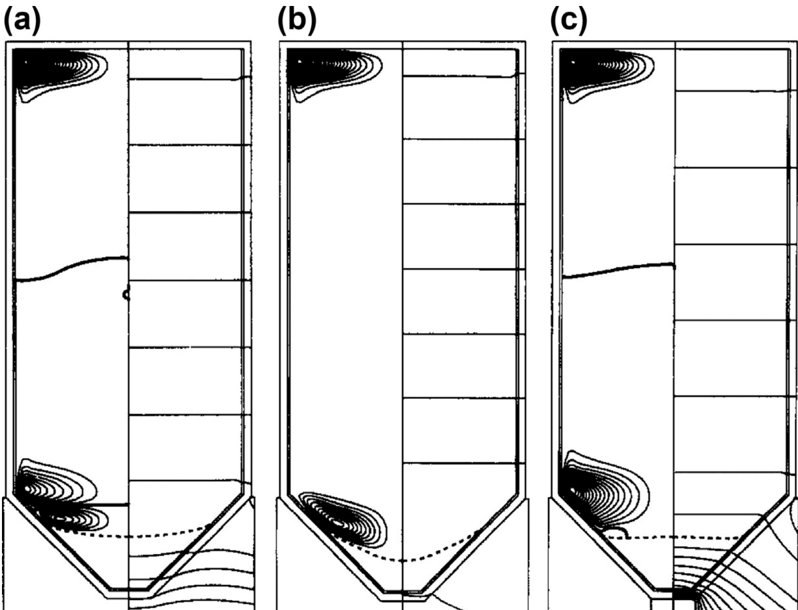

FIGURE 20.5 Streamlines for melt flow are shown on the left, and equally-spaced isotherms are shown on the right for the different ampoule supports. Solid-liquid interface is indicated by the dashed line. Case of (a) mullite support, (b) graphite support, and (c) cold finger, mullite support with graphite core. *Adapted from Ref. [59].*

observe that the isotherms in the support curve downward as they intersect the ampoule, indicating outward radial heat fluxes. Consistent with this outward flow of heat, the solid–liquid interface takes on a concave shape. The case for a support made of graphite, whose thermal conductivity is 40 times higher than that of mullite, is shown in Figure 20.5(b). The high conductivity promotes a larger heat flow through the graphite support, both axially and radially, making the solid–liquid interface even more concave than the case of the mullite support.

The case of the cold finger, with an outer support made of low-conductivity mullite and a core fabricated of high-conductivity graphite, is shown in Figure 20.5(c). The outcome for this ampoule support differs dramatically from the two prior configurations. Here, the isotherms in the mullite intersect with the ampoule at nearly right angles, and the corresponding heat flows downward and inward, almost parallel to the ampoule wall. There is virtually no heat flowing normal to the ampoule wall, and, due to the conical shape of the ampoule, the exterior temperature along a uniform axial height is higher than that within the charge. Hence, heat flows into the ampoule and the interface shape is convex. This effect depends on both the conical shape of the ampoule and, importantly, the presence of the cold finger under the center of the ampoule. This is shown by the shape of the isotherms in the crystal, which indicate a focusing of heat flow into the cold finger. This support design thus achieves a convex interface shape until the crystal grows out of the cone region of the ampoule.

The above outcomes illustrate that the delicate balance between both axial and radial heat flows is important for shaping the solid–liquid interface. For example, changing the support material from solid mullite to the more thermally conductive graphite promotes greater axial heat fluxes through the system, yet it also promotes significantly higher radial flows than the less-conductive mullite support. Hence, the use of an isotropic material for the fabrication of the support does not result in any significant alteration of thermal environment in the cone region, nor does it improve the shape of the interface. It is evident that the cold finger design increases axial heat flow while simultaneously decreasing radial heat fluxes. The net result is heat flow into the charge near the interface, thus bringing about its convex shape.

This idea of locally influencing heat transfer and interface shape by appropriate thermal design has been put forth previously in melt crystal growth systems. For example, Schmid and Viechnicki [161,162] developed the Heat Exchanger Method for growth of sapphire and other materials, which relies on a gas-cooled heat exchanger, effectively equivalent to a cold finger, placed at the bottom center of a crucible to remove heat and drive crystal growth. Similar ideas have been employed in the past for the growth of II-VI semiconductors. Kyle [163] used a metal support as a heat sink below the tip of the ampoule in a vertical Bridgman system to grow CdTe. Zanio [164] used an actively cooled, stainless steel cold finger below a flat-bottomed quartz ampoule to grow CdTe from Te-rich solution. Jones et al. [165] used water-cooled jets to cool the tip of a Bridgman ampoule during the growth of mercury cadmium telluride (HgCdTe). Monberg et al. [166] achieved twin-free growth of indium phosphide by the use of radiation channels through their ampoule support to promote favorable interface shapes. Nevertheless, the calculations of Kuppurao and Derby [59], discussed above, were among the first to clearly show how the design of the support structure and ampoule could significantly influence heat transfer and solid–liquid interface shape.

20.6.2.2 Crucible Configuration and Stage of Growth

More detailed computations of Bridgman CZT growth were later performed by Gasperino et al. [148–150]. Desiring to more faithfully represent furnace heat transfer, they employed the crystal growth simulation software CrysMAS, developed by the Crystal Growth Laboratory of the Fraunhofer Institute of Integrated Systems and Device Technology (IISB) in Erlangen, Germany [91]. This package is capable of predicting high-temperature heat transfer within complex crystal growth furnaces. Radiant heat transfer is represented using an enclosure method, and heat transfer, fluid flow, and phase change within the crucible are computed. Furnace set point temperatures can be explicitly specified, and the heater powers are solved as unknowns in an inverse calculation.

Gasperino et al. [148–150] constructed a model of a modern EDG furnace with 18 controlled heating zones, and considered growth behavior in two different crucibles—one composed of graphite and one of pyrolytic boron nitride (PBN). These furnaces were employed for CZT crystal growth by Dr. Mary Bliss of Pacific Northwest National

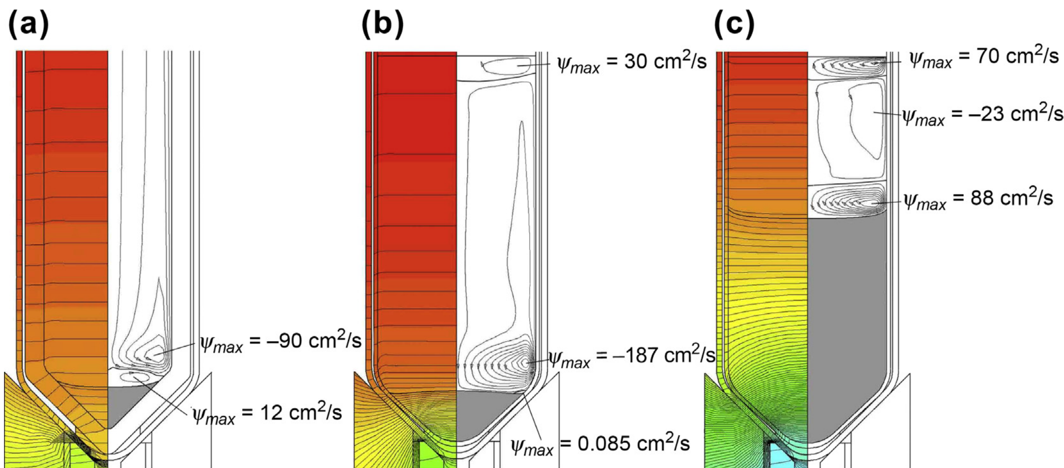

FIGURE 20.6 Detailed heat transfer calculations of CZT Bridgman growth clarify the effects of crucible design and the limitations of a cold finger on shape of solid–liquid interface. Isotherms are shown on left, streamlines are indicated on right, and crystal is shown in gray. (a) Graphite crucible negates the effect of the cold finger and produces a concave interface. (b) PBN crucible with cold finger results in a convex interface during initial growth. (c) However, growth out of the cone region and away from the influence of the cold finger results in a concave interface. *Adapted from Ref. [150].*

Laboratory (PNNL) and Prof. Kelvin Lynn of Washington State University (WSU). Each crucible rests inside a fused-silica ampoule, which is supported by a highly conductive silicon carbide (SiC) cold finger that extends to the bottom of the furnace. A complete listing of physical properties for these computations is available in [167].

Figure 20.6 shows three important cases from these analyses. The first two compare the system with the graphite crucible to that of the PBN crucible at similar stages during growth. The system with the graphite crucible exhibits a strongly concave interface shape in early stages of growth, as indicated by the calculation shown in Figure 20.6(a). Figure 20.6(b) shows the case of the PBN crucible early during growth, where heat transfer through the cone region promotes an interface shape that is convex, consistent with the results of Kuppurao and Derby [59], discussed in the prior section. However, when growth proceeds beyond the cone region of either ampoule, such as shown for the PBN system in Figure 20.6(c), heat transfer more typical of Bridgman systems leads to the classical concave shape of the solid–liquid interface.

To better understand the heat transfer conditions during the early growth stage, we examine heat flows in Figure 20.7 for the graphite and PBN system states corresponding to Figure 20.6(a) and (b). Heat flux vectors are plotted as a qualitative representation of the magnitude and direction of heat flows normal to the inner crucible wall (white arrows) and parallel to the crucible wall (black arrows). In general, heat flows through the walls are between two to four orders of magnitude larger than heat flows across the inner wall of the crucible, so the white arrows normal to the crucible wall have been exaggerated in scale relative to the black arrows parallel to the wall.

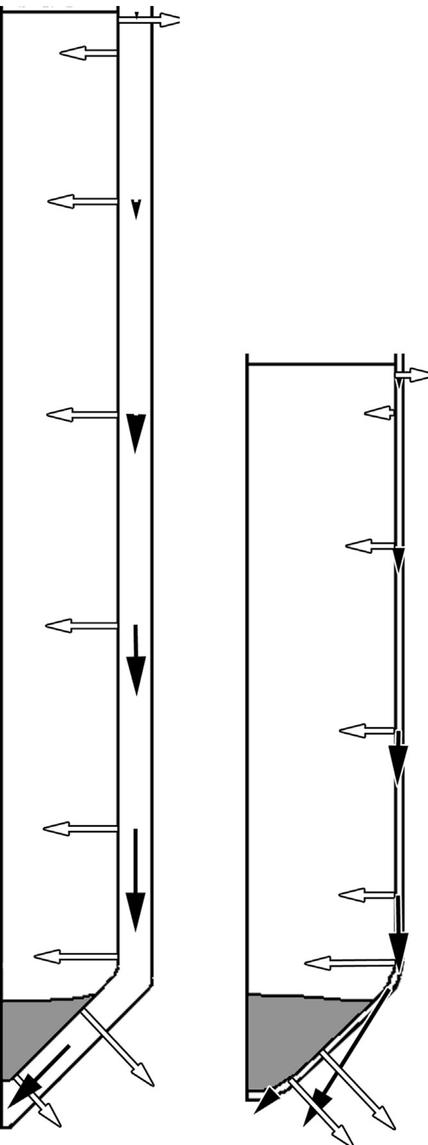

FIGURE 20.7 Vector plots of heat flows normal to the crucible inner wall inner (white) and within and parallel to the crucible wall (black). Centerline is on the left, and the crystal is shaded in gray. Cases show the graphite (left) and PBN (right) crucibles. Vectors are logarithmically scaled and represent heat flow magnitudes at their point of origin. The vectors in the wall of the PBN crucible are exaggerated by a factor of four relative those in the graphite crucible. Heat flows within the wall are much greater than those normal to the wall, and their vectors are scaled differently. *Adapted from Ref. [150].*

Thermal energy is exchanged between the ampoule and the furnace inner bore primarily via radiation (these fluxes are not shown). Heat is then conducted into the crucible wall, where it conducts both axially downward and radially into or out of the charge. Above the solid–liquid interface, most of the heat received from the furnace is simply conducted downward through the crucible wall, but some heat flows inward, keeping temperatures above the melting point. Below the solid–liquid interface, heat is conducted outward from the charge.

The flow of heat through the bottom of the graphite crucible is approximately seven times greater than that flowing through the bottom of the PBN crucible. Thus, the influence of the cold finger on the charge contained by the graphite crucible is far less than its effect on the contents of the PBN crucible. Notice that comparatively more heat is flowing out of the crystal near the bottom tip of the crucible in the PBN system, as indicated by the length of the two white vectors emanating from the crystal in the cone region of the crucible for each case. Thus, the use of a cold finger alone does not guarantee a convex interface shape. In particular, poor crucible design, as represented here by the graphite case that features thick, highly conductive walls, can produce heat flows that overwhelm the beneficial effects provide by the cold finger.

20.6.3 Experimental Validation

In a series of noteworthy experiments, researchers under the direction of Prof. Ernesto Diéguez, of the Autonomous University of Madrid, designed and constructed a Bridgman furnace for the growth of CZT, citing the influence of ideas put forth in the analyses of Kuppurao and Derby [59] and Gasperino et al. [148–150]. In particular, their furnace featured a PBN crucible supported by a composite pedestal featuring a cold finger, comprising a highly conductive thermal core of SiC surrounded by insulation; see the photographs in Figure 20.8(a). This furnace and subsequent growth experiments are documented in [158,159,168].

Of special interest are the experiments by Crocco et al. [159], who grew CZT under identical conditions, changing only the contact between the ampoule and the cold finger in different runs. When the cold finger in the growth furnace of Crocco et al. was withdrawn from the tip of the ampoule, growth likely occurred with a concave interface similar to that shown previously in Figure 20.6(a). The experimental outcome, as indicated by the slice taken from grown crystal shown in Figure 20.8(b), was a boule with many grains. When the cold finger was put into contact with the ampoule for another growth run under the same conditions, heat transfer similar to that shown in Figure 20.6(b) took place, and initial growth likely occurred with a convex interface shape. Under these conditions, the grown crystal displayed just two grains, as shown in Figure 20.8(c). Thus, the convex interface in this growth experiment promoted better crystallinity by preventing the growth of spurious grains.

However, the cold finger did not completely solve the problem of CZT crystallinity. The photos in Figure 20.8(d), on the far right, show a slice from the boule of the growth run

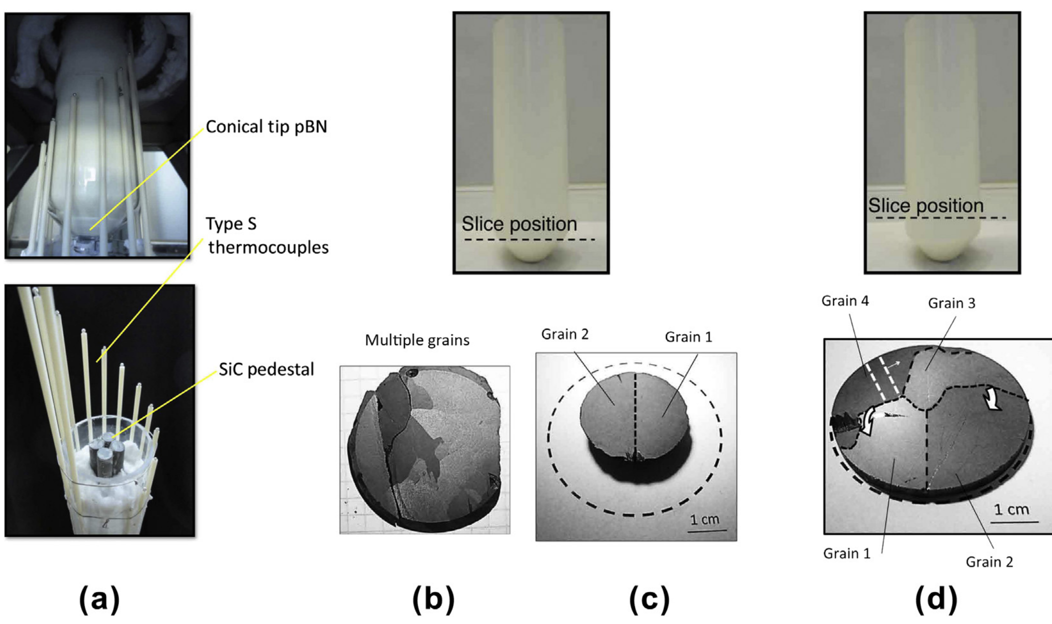

FIGURE 20.8 (a) Photographs of the PBN crucible (above) and insulated ampoule support with SiC cold finger (below) from the Bridgman growth system of Crocco et al. [159,168]. Results for the growth of CZT under different conditions are shown from the cone region of crucible (above) in (b) without touching the cold finger and (c) with cold finger contact. (d) The two-grain crystal of (c) is shown after subsequent growth in cylindrical region of crucible (above). *Images adapted from Ref. [168].*

conducted with the cold finger (namely the same run that had only two grains early on) but at a later time than that shown in Figure 20.8(c). At this later time, growth has proceeded beyond the cone region and into the cylindrical region of the crucible. Now the material contained many more grains. The corresponding computation for heat transfer, represented by Figure 20.8(c), shows that, even with the cold finger, later growth switches to a concave interface shape, with the resultant propensity toward spurious grains.

These experiments were repeated and conclusively showed the tendencies discussed above, namely that the PBN crucible with a cold finger would reliably reduce the number of grains during the initial growth of CZT. However, this exciting outcome was tempered by the realization that the advantage of fewer grains was often lost as growth proceeded higher into the crucible. These results emphasize the need to initially establish a convex interface and then maintain it throughout the entire growth run. We address the feasibility of this idea in the next section.

20.6.4 Bell-Curve Furnace Profile

Our goal is to design heat transfer conditions to achieve a convex solid–liquid interface shape during all growth stages of a Bridgman system. We showed above that convex interface shapes are possible during the initial stages of growth by using a suitable

ampoule support with a cold finger. However, the beneficial effect of the cold finger on interface shape is lost after the crystal emerges from the conical region of the crucible. The vexing question is then how to promote a convex shape at later times, as the interface grows through the cylindrical portion of the crucible.

If we revisit the very basic ideas put forth by Chang and Wilcox [103] and shown previously in Figure 20.2, a convex interface can only arise if radial heat flow is directed inward near the solid–liquid interface. Jasinski and Witt [20] arrived at a similar conclusion and predicted that "adverse interface curvature [concave shapes] may be favorably affected [i.e., converted to convex]… by heating the crucible near the interface." Likewise, if we return to the heat flux vectors shown previously in Figure 20.7, we note that the radial heat flux into the melt (shown by the white vectors) for the PBN case is substantially increased near the solid–liquid interface, compared to radial fluxes that decrease further up the crucible wall. This is quite different from the radial heat fluxes for the graphite crucible, which are nearly uniform along the entire inner wall.

The strategy suggested by all of these observations is to manipulate furnace heat transfer, using thermal profiles different from classical approaches, to actively push heat into the charge above the interface. Implementing such a strategy should be feasible, considering the flexibility provided by modern, multiple-zone gradient freeze furnaces. The challenge, then, is synthesizing a heating profile that will do the job.

Zhang et al. [153,169] approached this idea by designing a "bell-curve" furnace temperature profile[11] to preferentially direct heat into the system near the solidification interface. This idea was tested via CrysMAS computations for the same CZT EDG system modeled by Gasperino et al. [150], and discussed above, with the PBN crucible and SiC cold finger. Figure 20.9(a) shows the temperature along the outer surface of the ampoule plotted as a function of dimensionless distance along the furnace axis, where $z = 0$ denotes the bottom tip of the crucible and $z = 1$ corresponds to the crucible height. The dashed line indicates the outcome from a classical furnace design comprising two simple linear temperature segments, while the solid line shows the curved temperature distribution from the application of the bell-curve profile. The corresponding CrysMAS predictions for the quasi-steady thermal field, melt flow structure, and solidification interface shape are presented as Figures 20.9(b) and (c) for the traditional and bell-curve profiles, respectively.

Growth under the traditional furnace profile results in a state, shown in Figure 20.9(b), that is typical of nearly all classical Bridgman semiconductor crystal growth systems and features a solid–liquid interface that is concave with respect to the crystal. Quite differently, the system employing the bell-curve furnace profile, shown in Figure 20.9(c), exhibits dramatically different thermal and melt flow fields and, significantly, a solidification interface shape that is primarily convex with respect to the crystal. Only a very small portion of the interface near the crucible wall is flattened due to the

[11]This profile consists of linear segment that is connected to a parabolic segment that resembles a shallow bell curve. The segments connect below the melting temperature, thus providing for additional heat input to the ampoule and charge near the axial location of the solid–liquid interface.

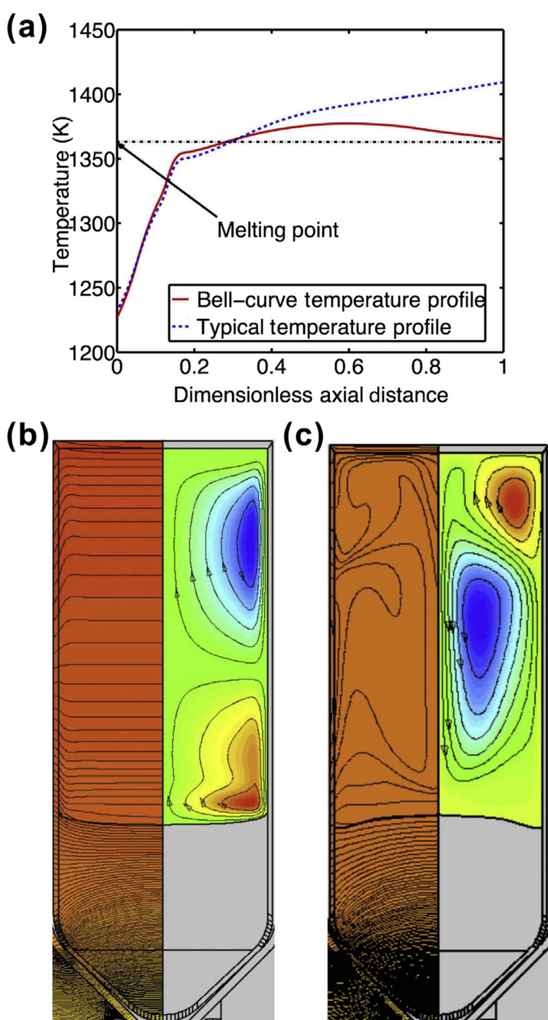

FIGURE 20.9 (a) Temperature profiles along the outer surface of the ampoule are plotted as functions of dimensionless axial distance for a traditional, piecewise-linear furnace profile and the bell-curve profile. (b) State obtained using the traditional furnace profile shows a concave interface. (c) State obtained using the bell-curve furnace profile shows a convex interface. Isotherms are shown on the left and melt flow streamlines on the right. *Adapted from Ref. [153].*

interface effect [20], which is caused by the different thermal conductivities of the solid and liquid. Clearly, this modified furnace profile is able to achieve a convex solid–liquid interface well outside of the conical part of the crucible.

While the basic idea of the bell-curve profile is rather simple, its successful implementation will be much more challenging. In particular, Zhang et al. [153] showed that the bell-curve profile must be dynamically changed to account for geometrical effects, i.e., the "end effects" identified in past analyses [17,111] and experiments [19],that arise

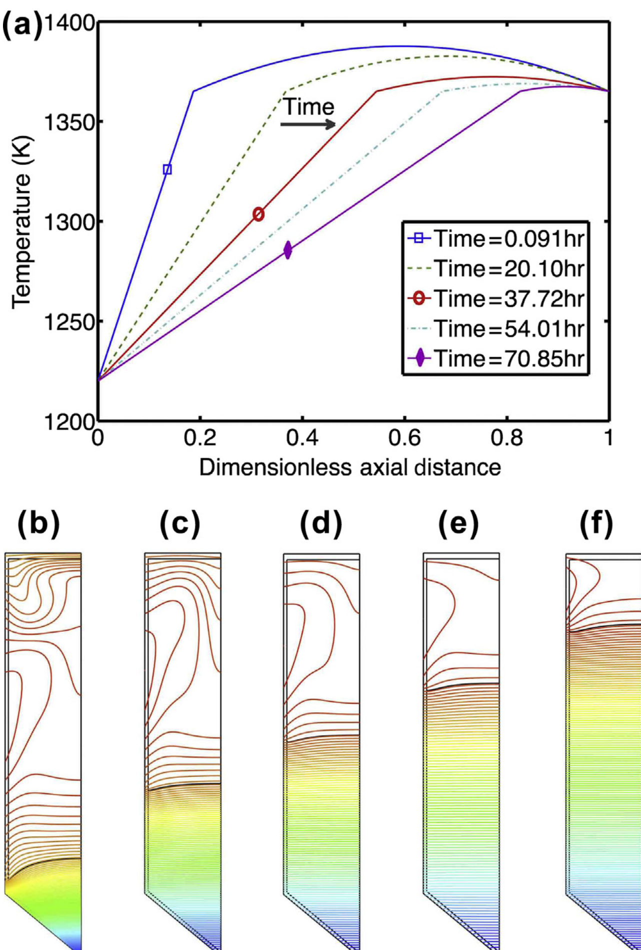

FIGURE 20.10 (a) Bell-curve temperature profile with variable peak temperature that is changed dynamically to keep the interface shape with constantly convex deflection. (b)–(f) The thermal field and interface shapes predicted by a transient simulation are shown at times corresponding to the furnace profiles above (right edge denotes centerline). *Adapted from Ref. [153].*

in different stages of growth. Figure 20.10(a) shows a series of different profiles employed in [153] to simulate a dynamic growth run. These profiles were computed using a control strategy that dynamically adapted the bell-curve profile to keep a constant interface deflection. The lower series of plots, labeled as (b)–(f), show the temperature field and solidification interface at times corresponding to the above profiles. Notably, a convex interface shape is maintained throughout the entire growth run.

20.6.5 Summary

We believe that this vignette illustrates the considerable potential to more fully utilize our understanding of heat transfer and the power of sophisticated modeling approaches to improve crystal growth processes. In the early discussions of this section, we have shown that a cold finger, along with suitable ampoule and crucible design, can lead to

convex interface shapes during the initial growth of CZT [59,150], thus promoting growth with fewer grains. This beneficial outcome has been demonstrated in the experiments of Crocco et al. [159,168]. While appealingly simply, this approach is effective only during the first stages of growth while the interface remains influenced by the cold finger and in the conical section of the crucible.

To achieve the benefits of convex interface shapes during the entire growth run, a more active approach is needed. We have put forth the idea of the bell-curve furnace profile to achieve convex interfaces beyond the cone region of the crucible and a strategy to dynamically adapt this profile during growth to maintain the convex shape of the interface. With a sufficiently accurate thermal model, this approach may be employed to generate a series of dynamic set points for the heaters in a suitable multizone furnace toward achieving the benefits of convex interfaces. We are awaiting future experimental validation of this strategy.

20.7 Final Remarks

Heat transfer is extremely important in melt crystal growth processes, since it sets the conditions by which the crystal grows and evolves. In addition, since heat transfer can be engineered via equipment design and process operation, it is one of the few macroscopic means to directly influence the inherently atomistic phenomena governing phase change and structural perfection. Thus, the purposeful design of heat transfer during crystal growth represents perhaps the best opportunity to improve current and future outcomes.

There are several prerequisites to enable the optimization of heat transfer in crystal growth processes. In general, a broad knowledge of heat transfer is required. Fortunately, as we hope to have shown in this chapter, the understanding of heat transfer in crystal growth processes is arguably complete, although certain aspects, such as thermal radiation within enclosures and participating media, remain quite challenging. A reasonably detailed understanding of how thermal conditions affect growth and perfection is also needed. Regarding this point, the crystal growth community is making significant strides toward connecting processing conditions to growth mechanisms and defect formation, and we can confidently leverage many ideas to improve crystal growth results. However, our understanding is still imperfect and there is much to learn. Finally, quantitative tools are needed that will allow us to go well beyond our intuitive notions and experiential perceptions of heat transfer in these processes. Indeed, sophisticated computational models for heat transfer have been developed that are able to rigorously analyze the many phenomena that interact in a crystal growth process.

Bridgman was the first to develop a workable method to move a sample in space and time, traversing a path from liquid to solid on the thermodynamic phase diagram, to achieve crystal growth. Stockbarger advanced a radical change in technique by establishing exquisite control of heat transfer and thermal gradients. Witt and his contemporaries rationalized that well-defined thermal boundary conditions would promote

deterministic outcomes for growth and postulated that thermal modeling would provide the tools necessary to improve these outcomes. Today, nearly nine decades after Bridgman's pioneering work, we believe that our understanding is deep enough and our tools powerful enough to start achieving these aspirations.

We argue that future advances in melt crystal growth will be enabled by the skillful deployment of computational models (in which heat transfer is rigorously represented) in conjunction with experimental validation and inquiry to truly close the loop between materials quality and process development. Such model-based strategies for crystal growth promise better results and higher yields than obtained via past approaches that have relied primarily on empiricism and hands-on experience. Indeed, this future becomes even brighter as our fundamental understanding of crystal growth mechanisms broadens and our tools for analysis, design, control, and optimization become more powerful.

Acknowledgments

The author would like to acknowledge prior and current support of many organizations including the Alexander von Humboldt Foundation, the Graduate School of the University of Minnesota, the Israeli-US Binational Science Foundation, the Minnesota Supercomputer Institute, the Petroleum Research Fund, the United States Department of Energy, the United States Department of Homeland Security, the United States National Aeronautics and Space Administration, and the United States National Science Foundation. Any opinions, findings, and conclusions or recommendations expressed in this material are those of the authors and do not necessarily reflect the position or policy of the United States Government, and no official endorsement should be inferred. The authors would like to acknowledge the significant input from prior analyses conducted by David Gasperino, Satheesh Kuppurao, and Nan Zhang and the seminal experimental work of Ernesto Diéguez and his colleagues, particularly Jerome Crocco, that were highlighted in the research vignette. Finally, JJD would like to express his supreme gratitude to the many talented graduate students with whom he has enjoyed working over the years.

References

[1] Brice JC. Crystal growth processes. New York: Halsted Press; 1986.

[2] Scheel HJ, Fukuda T. Crystal growth technology. John Wiley & Sons, Ltd.; 2003.

[3] Rudolph P. Non-stoichiometry related defects at the melt growth of semiconductor compound crystals – a review. Cryst Res Technol 2003;38(7–8):542–54.

[4] Davey R, Garside J. From molecules to crystallizers: an introduction to crystallization. Oxford (UK): Oxford University Press; 2000.

[5] Myerson A. The handbook of industrial crystallization. 2nd ed. Stoneham (MA): Butterworth-Heinemann; 2001.

[6] Elwell D, Scheel HJ. Crystal growth from high-temperature solutions. Academic Press; 1975.

[7] Hurle DTJ, Rudolph P. A brief history of defect formation, segregation, faceting, and twinning in melt-grown semiconductors. J Cryst Growth 2004;264(4):550–64.

[8] Sinno T, Dornberger E, von Ammon W, Brown RA, Dupret F. Defect engineering of Czochralski single-crystal silicon. Material Sci Eng Reports 2000;28:149–98.

[9] Völkl J. Stress in the cooling crystal. In: Hurle D, editor. Handbook of crystal growth, Vol. 2b; 1994. p. 821–74. North-Holland, Amsterdam.

[10] Rudolph P. Dislocation cell structures in melt-grown semiconductor compound crystals. Cryst Res Technol 2005;40(1/2):7–20.

[11] Kemble EC, Birch F. Percy Williams Bridgman, 1882–1961. A Biographical Memoir. National Academy of Sciences; 1970.

[12] Bridgman PW. Certain physical properties of single crystals of tungsten, antimony, bismuth, tellurium, cadmium, zinc, and tin. Proc Am Acad Arts Sci 1925;60(6):305–83.

[13] Stockbarger DC. The production of large single crystals of lithium fluoride. Rev Sci Instrum 1936;7:133.

[14] Wang CA. Crystal growth and segregation in verical Bridgman configuration [Ph.D. thesis]. Massachusetts Institute of Technology, 1984.

[15] Kim KM, Witt AF, Gatos HC. Crystal growth from the melt under destabilizing thermal gradients. J Electrochem Soc 1972;119:1218–26.

[16] Kim KM, Witt AF, Lichtensteiger M, Gatos HC. Quantitative analysis of the effects of destabilizing vertical thermal gradients on crystal growth and segregation: Ga-doped Ge. J Electrochem Soc 1978;125:475–80.

[17] Jasinski T, Rohsenow WM, Witt AF. Heat transfer analysis of the Bridgman-Stockbarger configuration for crystal growth: I. Analytical treatment of the axial temperature profile. J Cryst Growth 1983;61:339–54.

[18] Jasinski T, Rohsenow WM, Witt AF. Heat transfer analysis of the Bridgman-Stockbarger configuration for crystal growth: II. Analytical treatment of radial temperature variations. J Cryst Growth 1984;67:173–84.

[19] Wang CA, Witt AF, Carruthers JR. Analysis of crystal growth characteristics in a conventional vertical Bridgman configuration. J Cryst Growth 1984;66:299–308.

[20] Jasinski T, Witt AF. On control of the crystal melt interface shape during growth in a vertical Bridgman configuration. J Cryst Growth 1985;71:295–304.

[21] Wargo MJ, Witt AF. Real time thermal imaging for analysis and control of crystal growth by the Czochralski technique. J Cryst Growth 1992;116(1–2):213–24. http://dx.doi.org/10.1016/0022-0248(92)90131-2. http://www.sciencedirect.com/science/article/pii/0022024892901312.

[22] Tyndall J. Heat considered as a mode of motion: being a course of twelve lectures delivered at the royal institution of great britain in the season of 1862. New York: D. Appleton and Company; 1865.

[23] Arpaci VS. Conduction heat transfer. Addison-Wesley; 1966.

[24] Arpaci VS. Convection heat transfer. Prentice-Hall; 1984.

[25] Bird RB, Stewart WE, Lightfoot EN. Transport phenomena. New York: John Wiley & Sons; 1960.

[26] Siegel R, Howell JR. Thermal radiation heat transfer. 2nd ed. New York: McGraw-Hill; 1981.

[27] Brown RA. Theory of transport processes in single crystal growth from the melt. AIChE J 1988;34: 881–910.

[28] Derby JJ. Theoretical modeling of Czochralski crystal growth. MRS Bull 1988;XIII:29.

[29] Derby JJ. Modeling and bulk crystal growth processes: what is to be learned? In: Wang M, Tsukamoto K, Wu D, editors. Selected topics on crystal growth: 14th international summer school on crystal growth, AIP Conference Proceedings 1270, Melville, New York. AIP Publishing; 2010. p. 221–46.

[30] Amundson NR. The mathematical understanding of chemical engineering systems: selected papers of Neal R. Amundson. New York: Pergamon Press; 1980.

[31] Aris R. Mathematical modeling: a chemical engineer's perspective. Academic Press; 1999.

[32] Ramkrishna D. The Neal Amundson era. Rapid evolution of chemical engineering science. AIChE J 2013;59:3147–57.

[33] Schlichting H, Gersten K. Boundary layer theory. 8th ed. Springer-Verlag; 2004.

[34] Weinstein O, Brandon S. Dynamics of partially faceted melt/crystal interfaces I: computational approach and single step–source calculations. J Cryst Growth 2004;268(1–2):299–319. http://dx.doi.org/10.1016/j.jcrysgro.2004.04.108. http://www.sciencedirect.com/science/article/pii/S0022024804005470.

[35] Weinstein O, Brandon S. Dynamics of partially faceted melt/crystal interfaces II: multiple step–source calculations. J Cryst Growth 2004;270(1–2):232–49. http://dx.doi.org/10.1016/j.jcrysgro.2004.06.002. http://www.sciencedirect.com/science/article/pii/S0022024804007158.

[36] Weinstein O, Brandon S. Dynamics of partially faceted melt-crystal interfaces III: three-dimensional computational approach and calculations. J Cryst Growth 2005;284:235–53.

[37] Weinstein O, Brandon S. Erratum to: dynamics of partially faceted melt/crystal interfaces I: computational approach and single step-source calculations. J Cryst Growth 2005;276(1–2):332. http://dx.doi.org/10.1016/j.jcrysgro.2004.11.424. http://www.sciencedirect.com/science/article/pii/S0022024804019475.

[38] Weinstein O, Virozub A, Brandon S. Estimation of surface energy effects in partially faceted melt/crystal interfaces during directional growth of single crystals from their melt. J Cryst Growth 2007;306(2):480–90. http://dx.doi.org/10.1016/j.jcrysgro.2007.05.040. http://www.sciencedirect.com/science/article/pii/S0022024807005271.

[39] Jackson KA. Constitutional supercooling surface roughening. J Cryst Growth 2004;264:519–29.

[40] Jackson KA. Mechanism of growth, in: liquid metals and solidification. Am Soc Met 1958:174–86.

[41] Jackson KA. The present state of the theory of crystal growth from the melt. J Cryst Growth 1974;24–25(0):130–6. http://dx.doi.org/10.1016/0022-0248(74)90290-5. http://www.sciencedirect.com/science/article/pii/0022024874902905.

[42] Ettouney HM, Brown RA, Kalejs JP. Analysis of operating limits in edge-defined film-fed crystal growth. J Cryst Growth 1983;62:230–46.

[43] Thomas PD, Ettouney HM, Brown RA. A thermal-capillary mechanism for a growth rate limit in edge-defined film-fed growth silicon sheets. J Cryst Growth 1986;76:339–51.

[44] Derby JJ, Atherton LJ, Gresho PM. An integrated process model for the growth of oxide crystals by the Czochralski method. J Cryst Growth 1989;97:792–826.

[45] Yeckel A, Salinger AG, Derby JJ. Theoretical analysis and design considerations for float-zone refinement of electronic grade silicon sheets. J Cryst Growth 1995;152:51.

[46] Yeckel A, Derby JJ. Existence, stability, and nonlinear dynamics of detached Bridgman growth states under zero gravity. J Cryst Growth 2011;314:310–23.

[47] Samanta G, Yeckel A, Daggolu P, Fang H, Bourret-Courchesne ED, Derby JJ. Analysis of limits for sapphire growth in a micro-pulling-down system. J Cryst Growth 2011;335(1):148–59. http://dx.doi.org/10.1016/j.jcrysgro.2011.09.015. http://www.sciencedirect.com/science/article/pii/S0022024811007585.

[48] Samanta G, Yeckel A, Bourret-Courchesne ED, Derby JJ. Parametric sensitivity and temporal dynamics of sapphire crystal growth via the micro-pulling-down method. J Cryst Growth 2012;359(0):99–106. http://dx.doi.org/10.1016/j.jcrysgro.2012.08.037. http://www.sciencedirect.com/science/article/pii/S0022024812006008.

[49] Daggolu P, Yeckel A, Bleil C, Derby JJ. Thermal-capillary analysis of the horizontal ribbon growth of silicon crystals. J Cryst Growth 2012;355:129–39.

[50] Daggolu P, Yeckel A, Bleil C, Derby JJ. Stability limits for the horizontal ribbon growth of silicon crystals. J Cryst Growth 2013;363:132–40.

[51] Yeckel A, Feigelson RS, Derby JJ. Analysis of scintillator crystal production via the edge-defined film-fed growth method. In: Fiederle M, Burger A, Franks L, James RB, editors. Hard X-Ray, Gamma-Ray, and neutron detector physics XV, Vol. 8852; 2013. SPIE.

[52] Xiao Q, Derby JJ. The role of internal radiation and melt convection in Czochralski oxide growth: deep interfaces, interface inversion, and spiraling. J Cryst Growth 1993;128:188–94.

[53] Xiao Q, Derby JJ. Heat transfer and interface inversion during the Czochralski growth of yttrium aluminum garnet and gadolinium gallium garnet. J Cryst Growth 1994;139:147.

[54] Sparrow EM, Cess RD. Radiation heat transfer. Brooks Pub. Co.; 1966.

[55] Modest MF. Radiative heat transfer. Academic Press; 2013.

[56] Schornhorst JR, Viskanta R. An experimental examination of the commonly used methods of radiant heat transfer analysis. J Heat Transf 1968;90:429–36.

[57] Dupret F, Nicodème P, Ryckmans Y, Wouters P, Crochet MJ. Global modelling of heat transfer in crystal growth furnaces. Int J Heat Mass Transf 1990;33:1849–71.

[58] Kuppurao S, Derby JJ. Finite element formulations for accurate calculation of radiant heat transfer in diffuse-gray enclosures. Numer Heat Transf Part B: Fundam 1993;24:431–54.

[59] Kuppurao S, Derby JJ. Designing thermal environments to promote convex interface shapes during the vertical Bridgman growth of cadmium zinc telluride. J Cryst Growth 1997;172:350–60.

[60] Poljak G. Analysis of heat interchange by radiation between diffuse surfaces. Tech Phys USSR 1935;1:555–90.

[61] Gebhart B. Unified treatment for thermal radiation transfer processes — gray, diffuse radiators and absorbers. Tech. Rep. 57-A-34. ASME; 1957.

[62] Gebhart B. Heat Transfer. New York: McGraw-Hill; 1971.

[63] Brandon S, Derby JJ. Internal radiative transport in the vertical Bridgman growth of semi-transparent crystals. J Cryst Growth 1991;110:481–500.

[64] Brandon S, Derby JJ. A finite element method for internal radiative heat transfer and its application to analysis of the growth of semitransparent crystals. In: Fiveland W, Crosbie A, Smith A, Smith T, editors. Fundamentals of radiation heat transfer, Vol. 160. ASME Heat Transfer Division; 1991. p. 1–16.

[65] Brandon S, Derby JJ. Heat transfer in vertical Bridgman growth of oxides: effects of conduction, convection, and internal radiation. J Cryst Growth 1992;121:473–94.

[66] Brandon S, Derby JJ. A finite element method for conduction, internal radiation, and solidification in a finite axisymmetric enclosure. Int J Num. Meth. Heat Fluid Flow 1992;2:299–333.

[67] Brandon S, Gazit D, Horowitz A. Interface shapes and thermal fields during the gradient solidification method growth of sapphire single crystals. J Cryst Growth 1996;167:190–207.

[68] Virozub A, Brandon S. Radiative heat transport during the vertical Bridgman growth of oxide single crystals: slabs versus cylinders. J Cryst Growth 1998;193(4):592–6. http://dx.doi.org/10.1016/S0022-0248(98)00554-5. http://www.sciencedirect.com/science/article/B6TJ6-3V7899C-1V/2/874a9070f7eb7a24a22a6f39847386db.

[69] Rukolaine SA, Yuferev VS. Discrete ordinates quadrature schemes based on the angular interpolation of radiation intensity. J Quant Spectrosc Radiat Transf 2001;69(3):257–75. http://dx.doi.org/10.1016/S0022-4073(00)00079-0. http://www.sciencedirect.com/science/article/pii/S0022407300000790.

[70] Rukolaine SA, Vasilyev MG, Yuferev VS, Galyukov AO. Numerical solution of axisymmetric radiative transfer problems in arbitrary domains using the characteristic method. J Quant

Spectrosc Radiat Transf 2002;73(2–5):205–17. http://dx.doi.org/10.1016/S0022-4073(01)00204-7. http://www.sciencedirect.com/science/article/pii/S0022407301002047.

[71] Yuferev VS, Budenkova ON, Vasiliev MG, Rukolaine SA, Shlegel VN, Vasiliev YV, et al. Variations of solid–liquid interface in the BGO low thermal gradients Cz growth for diffuse and specular crystal side surface. J Cryst Growth 2003;253(1–4):383–97. http://dx.doi.org/10.1016/S0022-0248(03)01110-2. http://www.sciencedirect.com/science/article/pii/S0022024803011102.

[72] Rukolaine SA, Vasilyev MG, Yuferev VS, Mamedov VM. A numerical scheme for the solution of axisymmetric radiative transfer problems in irregular domains filled by media with opaque and transparent diffuse and specular boundaries. J Quant Spectrosc Radiat Transf 2004;84(4):371–82. http://dx.doi.org/10.1016/S0022-4073(03)00256-5. http://www.sciencedirect.com/science/article/pii/S0022407303002565.

[73] Budenkova ON, Vasilyev MG, Rukolaine SA, Yuferev VS. Radiative heat transfer in axisymmetric domains of complex shape with fresnel boundaries. J Quant Spectrosc Radiat Transf 2004;84(4):451–63. http://dx.doi.org/10.1016/S0022-4073(03)00262-0. http://www.sciencedirect.com/science/article/pii/S0022407303002620.

[74] Budenkova O, Vasiliev M, Yuferev V, Kalaev V. Effect of internal radiation on the solid–liquid interface shape in low and high thermal gradient Czochralski oxide growth. J Cryst Growth 2007;303(1):156–60. http://dx.doi.org/10.1016/j.jcrysgro.2006.12.055. http://www.sciencedirect.com/science/article/pii/S0022024806016241.

[75] Salinger AG, Brandon S, Aris R, Derby JJ. Buoyancy-driven flows of a radiatively participating fluid in a vertical cylinder heated from below. Proc R Soc Lond A 1993;442(1915):313–41.

[76] Derby JJ, Brandon S, Salinger AG, Xiao Q. Large-scale numerical analysis of materials processing systems: high-temperature crystal growth and molten glass flows. Comput Methods Appl Mech Eng 1994;112(1–4):69–89. http://dx.doi.org/10.1016/0045-7825(94)90019-1. http://www.sciencedirect.com/science/article/pii/0045782594900191.

[77] Rosseland S. Theoretical astrophysics; atomic theory and the analysis of stellar atmospheres and envelopes. Oxford: Clarendon Press; 1936.

[78] Derby JJ, Brandon S, Salinger AG. The diffusion and P_1 approximation for modeling buoyant flow of an optically thick fluid. Int J Heat Mass Transf 1998;41:1405–15.

[79] Crochet MJ, Dupret F, Ryckmans Y, Geyling FT, Monberg EM. Numerical simulation of crystal growth in a vertical Bridgman furnace. J Cryst Growth 1989;97:173.

[80] Kurz MRH. Development of CrysVUn++, a software system for numerical modelling and control of industrial growth processes [Ph.D. thesis]. Universität Erlangen - Nürnberg, 1998.

[81] Kurz M, Pusztai A, Müller G. Development of a new powerful computer code CrysVUN++ especially designed for fast simulation of bulk crystal growth processes. J Cryst Growth 1999;198/199:101–6.

[82] Backofen R, Kurz M, Müller G. Process modeling of the industrial VGF growth process using the software package CrysVUN++. J Cryst Growth 2000;211:202–6.

[83] Nunes EM, Modi V, Naraghi MHN. Radiative transfer in arbitrarily-shaped axisymmetric enclosures with anisotropic scattering media. Int J Heat Mass Transf 2000;43(18):3275–85. http://dx.doi.org/10.1016/S0017-9310(99)00384-1. http://www.sciencedirect.com/science/article/pii/S0017931099003841.

[84] Nunes EM, Naraghi MHN, Zhang H, Prasad V. A volume radiation heat transfer model for Czochralski crystal growth processes. J Cryst Growth 2002;236(4):596–608. http://dx.doi.org/10.1016/S0022-0248(02)00826-6. http://www.sciencedirect.com/science/article/pii/S0022024802008266.

[85] Galazka HWZ, Schwabe D. Influence of internal radiation on the heat transfer during growth of YAG single crystals by the Czochralski method. Cryst Res Technol 2003;38(10):859–67.

[86] Liu L, Kakimoto K. Partly three-dimensional global modeling of a silicon Czochralski furnace: principles, formulation and implementation of the model. Int J Heat Mass Transf 2005;48: 4481–91.

[87] Baumgartl J, Bune A, Koai K, Müller G, Seidl A. Global simulation of heat transport, including melt convection in a Czochralski crystal growth process - combined finite element/finite volume approach. Mater Sci Eng A 1993;A173:9–13.

[88] Ouyang H, Shyy W. Multi-zone simulation of the Bridgman growth process of β-NiAl crystal. Int J Heat Mass Transf 1996;39(10):2039–51.

[89] Ouyang H, Shyy W. Numerical simulation of CdTe vertical Bridgman growth. J Cryst Growth 1997; 173:352–66.

[90] Tomás CM, Mućoz V. CdTe crystal growth process by the Bridgman method: numerical simulation. J Cryst Growth 2001;222:435–51.

[91] Fainberg J, Vizman D, Friedrich J, Müller G. A new hybrid method for the global modeling of convection in cz crystal growth configurations. J Cryst Growth 2007;303(1):124–34.

[92] Yeckel A, Pandy A, Derby JJ. Fixed-point convergence of modular, steady-state heat transfer models coupling multiple scales and phenomena for melt-crystal growth. Int J Numer Methods Eng 2006;67:1768–89.

[93] Derby JJ, Lun L, Yeckel A. Strategies for the coupling of global and local crystal growth models. J Cryst Growth 2007;303:114–23.

[94] Yeckel A, Lun L, Derby JJ. An approximate block Newton method for coupled iterations of nonlinear solvers: theory and conjugate heat transfer applications. J Comput Phys 2009;228:8566–88.

[95] Yeckel A, Lun L, Derby JJ. Multi-scale crystal growth computations via an approximate block Newton method. J Cryst Growth 2010;312:1463–7.

[96] Gresho PM, Derby JJ. A finite element model for induction heating of a metal crucible. J Cryst Growth 1987;85:40–8.

[97] Rajendran S, Chao CC, Hill DP, Kalejs JP, Overbye V. Magnetic and thermal field model of EFG system. J Cryst Growth 1991;109(1–4):82–7. http://dx.doi.org/10.1016/0022-0248(91)90160-7. http://www.sciencedirect.com/science/article/pii/0022024891901607.

[98] Chen QS, Gao P, Hu WR. Effects of induction heating on temperature distribution and growth rate in large-size sic growth system. J Cryst Growth 2004;266(1–3):320–6. http://dx.doi.org/10.1016/j.jcrysgro.2004.02.061. http://www.sciencedirect.com/science/article/pii/S0022024804002362.

[99] Sun D, Wang C, Zhang H, Mackintosh B, Yates D, Kalejs J. A multi-block method and multi-grid technique for large diameter EFG silicon tube growth. J Cryst Growth 2004;266(1–3):167–74. http://dx.doi.org/10.1016/j.jcrysgro.2004.02.042. http://www.sciencedirect.com/science/article/pii/S002202480400212X.

[100] Tavakkoli MH, Wilke H. Numerical study of induction heating and heat transfer in a real Czochralski system. J Cryst Growth 2005;275(1–2):e85–9. http://dx.doi.org/10.1016/j.jcrysgro.2004.10.128. http://www.sciencedirect.com/science/article/pii/S0022024804014496.

[101] Tavakoli MH, Mohammadi-Manesh E, Ojaghi A. Influence of crucible geometry and position on the induction heating process in crystal growth systems. J Cryst Growth 2009;311(17):4281–8. http://dx.doi.org/10.1016/j.jcrysgro.2009.07.013. http://www.sciencedirect.com/science/article/pii/S002202480900685X.

[102] Zhang H, Zheng L, Fang H. Hot zone design for controlled growth to mitigate cracking in laser crystal growth. J Cryst Growth 2011;318(1):695–9. http://dx.doi.org/10.1016/j.jcrysgro.2010.11.130. http://www.sciencedirect.com/science/article/pii/S0022024810011115.

[103] Chang CE, Wilcox WR. Control of interface shape in the vertical Bridgman-Stockbarger technique. J Cryst Growth 1974;21(1):135–40. http://dx.doi.org/10.1016/0022-0248(74)90161-4. http://www.sciencedirect.com/science/article/pii/0022024874901614.

[104] Sen S, Wilcox WR. Infuence of crucible on interface shape, position and sensitivity in the vertical Bridgman-Stockbarger technique. J Cryst Growth 1975;28:26–40.

[105] Fu T-W, Wilcox WR. Influence of insulation on stability of interface shape and position in the vertical Bridgman-Stockbarger technique. J Cryst Growth 1980;48:416–24.

[106] Fu T-W, Wilcox WR. Rate of change of transients in Bridgman-Stockbarger growth. J Cryst Growth 1981;51:557–67.

[107] Tiller WA. Principles of solidification. In: Gilman JJ, editor. The art and science of growing crystals. John Wiley & Sons, Inc; 1963. p. 276.

[108] Hurle DTJ. A mechanism for twin formation during Czochralski and encapsulated vertical Bridgman growth of III–V compound semiconductors. J Cryst Growth 1995;147:239–50.

[109] Chung H, Dudley M, Larson DJ, Hurle DTJ, Bliss DF, Prasad V. The mechanism of growth-twin formation in zincblende crystals: new insights from a study of magnetic liquid encapsulated Czochralski-grown InP single crystals. J Cryst Growth 1998;187:9.

[110] Amon J, Dumke F, Müller G. Influence of the crucible shape on the formation of facets and twins in the growth of GaAs by the vertical gradient freeze technique. J Cryst Growth 1998;187(1):1–8. http://www.sciencedirect.com/science/article/B6TJ6-3VWG46G-V/1/b453af2b44286b693b4dcbad614a5a27.

[111] Naumann RJ. An analytical approach to thermal modeling of Bridgman-type crystal growth: I. one-dimensional analysis. J Cryst Growth 1982;58(3):554–68. http://dx.doi.org/10.1016/0022-0248(82)90143-9. http://www.sciencedirect.com/science/article/pii/0022024882901439.

[112] Naumann RJ. An analytical approach to the thermal modeling of Bridgman-type crystal growth II. Two-dimensional analysis. J Cryst Growth 1982;58:569–84.

[113] Chang CJ, Brown RA. Radial segregation induced by natural convection and melt/solid interface shape in vertical Bridgman growth. J Cryst Growth 1983;63:343.

[114] Adornato PM, Brown RA. Convection and segregation in directional solidification of dilute and non-dilute binary alloys: effects of ampoule and furnace design. J Cryst Growth 1987;80:155–90.

[115] Adornato PM, Brown RA. Petrov-Galerkin methods for natural convection in directional solidification of binary alloys. Int J Num Meth Fluids 1987;7:761.

[116] Kim DH, Adornato PM, Brown RA. Effect of vertical magnetic field on convection and segregation in vertical Bridgman crystal growth. J Cryst Growth 1988;89:339.

[117] Kim DH, Brown RA. Models for convection and segregation in the growth of HgCdTe by the vertical Bridgman method. J Cryst Growth 1989;96:609.

[118] Kim DH, Brown RA. Modelling of the dynamics of HgCdTe growth by the vertical Bridgman method. J Cryst Growth 1991;114. 441–434.

[119] Brown RA, Kim DH. Modeling of directional solidification: from Scheil to detailed numerical simulation. J Cryst Growth 1991;109:50–65.

[120] Rudolph P. Fundamental studies on Bridgman growth of CdTe. Prog Cryst Growth Charact Mater 1994;29:275–81.

[121] Rudolph P. Melt growth of II-VI compound single crystals. In: Isshiki M, editor. Recent development of bulk Crystal growth. Trivandrum, India: Research Signpost; 1998.

[122] Triboulet R. CdTe and CdZnTe growth. In: Scheel HJ, Fukuda T, editors. Crystal growth technology. John Wiley & Sons, Ltd. Sons Ltd; 2003. p. 373–406. Chapter 17.

[123] Triboulet R. Fundamentals of the CdTe and CdZnTe bulk growth. Phys Status Solidi C 2005;2: 1556–65.

[124] Godlevsky VV, Derby JJ, Chelikowsky JR. *Ab initio* molecular dynamics simulations of liquid CdTe and GaAs: semiconducting versus metallic behavior. Phys Rev Lett 1998;81:4959–62.

[125] Naumann RJ, Lehoczky SL. Effect of variable thermal conductivity on isotherms in Bridgman growth. J Cryst Growth 1983;61:707–10.

[126] Kuppurao S, Brandon S, Derby JJ. Modeling the vertical Bridgman growth of cadmium zinc telluride. I. Quasi-steady analysis of heat transfer and convection. J Cryst Growth 1995;155:93.

[127] Kuppurao S, Brandon S, Derby JJ. Modeling the vertical Bridgman growth of cadmium zinc telluride. II. Transient analysis of zinc segregation. J Cryst Growth 1995;155:103.

[128] Kuppurao S, Brandon S, Derby JJ. Analysis of interrupted growth strategies for cadmium telluride in an unseeded vertical Bridgman system. J Cryst Growth 1996;158:459–70.

[129] Xiao Q, Kuppurao S, Yeckel A, Derby JJ. On the effects of ampoule tilting during vertical Bridgman growth: three-dimensional computations via a massively parallel, finite element model. J Cryst Growth 1996;167:292–304.

[130] Lun L, Yeckel A, Daoutidis P, Derby JJ. Decreasing lateral segregation in cadmium zinc telluride via ampoule tilting during vertical Bridgman growth. J Cryst Growth 2006;291:348–57.

[131] Edwards K, Derby JJ. Understanding horizontal Bridgman shelf growth of cadmium zinc telluride: I. heat and momentum transfer. J Cryst Growth 1997;179:120–32.

[132] Edwards K, Derby JJ. Understanding horizontal Bridgman shelf growth of cadmium telluride and cadmium zinc telluride: II. Thermoelastic stresses. J Cryst Growth 1997;179:133.

[133] Edwards K, Brandon S, Derby JJ. Transient effects during the horizontal Bridgman growth of cadmium zinc telluride. J Cryst Growth 1999;206:37–50.

[134] Godlevsky VV, Jain M, Derby JJ, Chelikowsky JR. First-principles calculations of liquid CdTe at temperatures above and below the melting point. Phys Rev B 1999;60(12):8640–9. http://dx.doi.org/10.1103/PhysRevB.60.8640.

[135] Chelikowsky JR, Derby JJ, Godlevsky VV, Jain M, Raty JY. *Ab initio* simulations of liquid semiconductors using the pseudopotential-density functional method. J Phys Condens Matter 2001;13:R817–54.

[136] Ko E, Alemany M, Derby JJ, Chelikowsky JR. *Ab initio* simulations of non-stoichiometric Cd_xTe_{1-x} liquids. J Chem Phys 2005;123:084508.

[137] Yeckel A, Derby JJ. Effect of accelerated crucible rotation on melt composition in high-pressure vertical Bridgman growth of cadmium zinc telluride. J Cryst Growth 2000;209:734.

[138] Yeckel A, Derby JJ. Buoyancy and rotation in small-scale vertical Bridgman growth of cadmium zinc telluride using accelerated crucible rotation. J Cryst Growth 2001;233:599–608.

[139] Yeckel A, Derby JJ. Feasibility study of cadmium zinc telluride growth using submerged heater in a vertical Bridgman system. J Electron Mater 2004;33:488–97.

[140] Yeckel A, Compèrere G, Pandy A, Derby JJ. Three dimensional imperfections in a model vertical Bridgman growth system for cadmium zinc telluride. J Cryst Growth 2004;263:629–44.

[141] Lun L, Yeckel A, Reed M, Szeles C, Daoutidis P, Derby JJ. On the effects of furnace gradients on interface shape during the growth of cadmium zinc telluride in EDG furnaces. J Cryst Growth 2006; 290:35–43.

[142] Lun L, Yeckel A, Derby JJ, Daoutidis P. Control of interface shape of cadmium zinc telluride grown via an electrodynamic gradient freeze furnace. In: Proceedings of IEEE 2007 Mediterranean Conference on control and Automation (MED '07). Athens, Greece: IEEE Xplore; 2007. p. 1–6.

[143] Stelian C, Yeckel A, Derby JJ. Influence of thermal phenomena on crystal reattachment during dewetted Bridgman growth. J Cryst Growth 2009;311(8):2572–9.

[144] Stelian C, Volz MP, Derby JJ. On favorable thermal fields for detached Bridgman growth. J Cryst Growth 2009;311:3337–46.

[145] Yeckel A, Derby JJ. Stabilizing detached Bridgman melt crystal growth: proportional-integral feedback control. J Cryst Growth 2012;356:33–45.

[146] Yeckel A, Derby JJ. Stabilizing detached Bridgman melt crystal growth: model-based nonlinear feedback control. J Cryst Growth 2012;361:16–24.

[147] Pandy A, Yeckel A, Reed M, Szeles C, Hainke M, Müller G, et al. Analysis of the growth of cadmium zinc telluride in an electrodynamic gradient freeze furnace via a self-consistent, multi-scale numerical model. J Cryst Growth 2005;276:133–47.

[148] Derby JJ, Gasperino D. Computational models for crystal growth of radiation detector materials: growth of CZT by the EDG method. In: Perry D, Burger A, Franks L, Schieber M, editors. Nuclear radiation Detection materials. Materials research Society Symposium Proceedings, vol. 1038. MRS (Materials Research Society); 2008. 1038–O05–O09.

[149] Derby JJ, Gasperino D, Zhang N, Yeckel A. Modeling the crystal growth of cadmium zinc telluride: accomplishments and future challenges. In: Perry D, Burger A, Franks L, Schieber M, editors. Nuclear radiation Detection materials — 2009. Materials research Society Symposium Proceedings, vol. 1164. MRS (Materials Research Society); 2009. 1164–L05–L02.

[150] Gasperino D, Bliss M, Jones K, Lynn K, Derby JJ. On crucible effects during the growth of cadmium zinc telluride in an electrodynamic gradient freeze furnace. J Cryst Growth 2009;311: 2327–35.

[151] Zhang N, Yeckel A, Burger A, Cui Y, Lynn K, Derby JJ. Anomalous segregation during electrodynamic gradient freeze growth of cadmium zinc telluride. J Cryst Growth 2011;325:10–9.

[152] Zhang N, Yeckel A, Derby JJ. Segregation and interface shape control during electrodynamic gradient freeze (EDG) growth of cadmium zinc telluride (CZT). Proc Hard X-Ray, Gamma-Ray, Neutron Detect Phys XIII, SPIE Opt Eng + Applications 2011;8142:41.

[153] Zhang N, Yeckel A, Derby JJ. Maintaining convex interface shapes during electrodynamic gradient freeze growth of cadmium zinc telluride using a dynamic, bell-curve furnace profile. J Crystal Growth 2012;355:113–21.

[154] Rudolph P, Koh HJ, Schafer N, Fukuda T. The crystal perfection depends on the superheating of the mother phase too – experimental facts and speculations on the "melt structure" of semiconductor compounds. J Crystal Growth 1996;166:578–82.

[155] C. Szeles, personal communication; 2013.

[156] Shiraki H, Funaki M, Ando Y, Tachibana A, Kominami S, Ohno R. THM growth and characterization of 100 mm diameter CdTe single crystals. In: Nuclear science Symposium Conference Record, 2008. NSS '08. IEEE Xplore; 2008. p. 126–32.

[157] Roy UN, Weiler S, Stein J. Growth and interface study of 2 in diameter CdZnTe by THM technique. J Crystal Growth 2010;312(19):2840–5.

[158] Carcelén V, Kim KH, Camarda GS, Bolotnikov AE, Hossain A, Yang G, et al. Pt coldfinger improves quality of Bridgman-grown $Cd_{0.9}Zn_{0.1}Te$:Bi crystals. J Crystal Growth 2012;338:1–5.

[159] Crocco J, Bensalah H, Zheng Q, Carcelén V, Diéguez E. Influence of SiC pedestal in the growth of 50 mm CZT by vertical gradient freeze method. J. Crystal Growth 2012;360:92–4.

[160] Kuppurao S. Analysis of transport processes during the growth of single crystal by the vertical Bridgman method [Ph.D. thesis]. University of Minnesota, 1995.

[161] Viechnicki D, Schmid F. Growth of large monocrystals of Al_2O_3 by a gradient furnace technique. J Crystal Growth 1971;11(3):345–7.

[162] Viechnicki D, Schmid F. Crystal growth using the heat exchanger method (HEM). J Crystal Growth 1974;26(1):162–4.

[163] Kyle NR. Growth of semi-insulating cadmium telluride. J Electrochem Soc 1971;118:1790–7.

[164] Zanio K. Cadmium telluride. In: Willardson R, Beer A, editors. Semiconductors and Semimetals, Vol. 13. New York: Academic Press; 1978.

[165] Jones CL, Capper P, Gosney JJ, Kenworthy I. Thermal modelling of Bridgman crystal growth. J Crystal Growth 1984;69:281–90.

[166] Monberg EM, Gault WA, Simchock F, Dominguez F. Vertical gradient freeze growth of large diameter, low defect density indium phosphide. J Crystal Growth 1987;83(2):174–83. http://dx.doi.org/10.1016/0022-0248(87)90004-2. http://www.sciencedirect.com/science/article/pii/0022024887900042.

[167] Gasperino DJ. Modeling of transport processes during solution, melt and Colloidal Crystal growth [Ph.D. thesis]. University of Minnesota, 2008.

[168] Crocco J. 2 inch CdZnTe single crystals for security applications [Ph.D. thesis]. Universidad Autónoma de Madrid, 2012.

[169] Zhang N. Modeling and control of transport processes during melt crystal growth [Ph.D. thesis]. University of Minnesota, 2012.

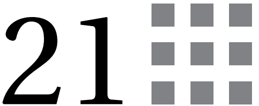

Fluid Dynamics: Modeling and Analysis

Koichi Kakimoto, Bing Gao

RESEARCH INSTITUTE FOR APPLIED MECHANICS, KYUSHU UNIVERSITY, KASUGA, FUKUOKA, JAPAN

CHAPTER OUTLINE

21.1 Introduction **846**
21.2 Diffusion **846**
21.3 Natural and Forced Convections **848**
21.3.1 Computation 848
21.3.2 Crystal and Crucible Rotations 849
21.3.3 Gravitational Effects 850
21.3.4 Centrifugal Effects 852
21.3.5 Convective–Diffusive Transport 854
21.4 External Fields **855**
21.4.1 Static Magnetic Fields 855
21.4.2 Dynamic Magnetic Fields 858
21.4.3 Electromagnetic Fields 858
21.4.4 Vibrational Effects 859
21.5 Flow Instability **860**
21.5.1 The Rayleigh–Bénard Instability 860
21.5.2 Baroclinic Instability 862
21.5.3 Turbulence 862
21.6 Impurity Transfer **864**
21.6.1 Boundary Layer 864
21.6.2 Mass Transfer in Gases 865
21.6.3 Mass Transfer between Gas and Melt 866
21.7 Summary **868**
References **869**

Handbook of Crystal Growth. http://dx.doi.org/10.1016/B978-0-444-63303-3.00021-3
Copyright © 2015 Elsevier B.V. All rights reserved.

21.1 Introduction

"Crystallization building blocks," such as atoms or molecules, present in fluid-starting media (gas, melt, or solution) must be transported over macroscopic distances before being assembled into crystalline solids. Mass transport proceeds by diffusion, buoyancy-driven convection, surface-tension-driven convection, and forced convection (rotation, acceleration, vibration, magnetic field applied mixing). If the transport is faster or slower than the aggregation kinetics, the rate of crystal growth is limited by interfacial kinetics or macroscopic mass transport, respectively. The rate of atomistic incorporation from a melt is typically much faster than the convective mass transport velocity, whereas diffusion is still slower. Hence, crystallization from a melt is generally controlled by mass transport. In contrast, growth from solution or vapor is kinetically controllable because the attachment kinetics can be inhibited by desorption or release of transport agents. However, the density of the mother phase and hence the supply of "crystal building blocks" at the interface is lower than in melts and must be frequently encouraged by enhanced evaporation (of gases) or artificial mixing (of liquids).

Mass and heat transport are closely coupled. For instance, convection assumes that the transported fluid volume units have the same density. However, gravitational sedimentation may lead to temperature and density gradients, with resulting thermal and solute volume expansion. Such mass transport processes are treated in the present chapter. Heat transport was covered in Chapter 20 of the present volume.

Mass can be transported by natural or buoyancy-driven convection, surface tension effects, or Marangoni convection. In addition, it can be artificially evoked by magnetic or mechanical (vibrational) fields. This chapter focuses on naturally generated flows in crystal growth arrangements. To facilitate the discussion, Marangoni convection, magnetic field influences, and mechanically induced stirring are briefly introduced. These topics are detailed in subsequent chapters (Chapters 22, 23 and 24 of this volume, respectively).

21.2 Diffusion

Heat and mass transport through fluids occurs by diffusion and convection. Diffusion occurs by atomic-scale random walk processes [1]. Essentially, a single atom cannot remain stationary in time. However, as shown below, the statistically random motions of atoms give rise to deterministic diffusion at macroscopic scales.

Fick's first law states that mass flux (J) is proportional to the spatial concentration gradient [1]:

$$J = -D\frac{\partial c}{\partial x}, \tag{21.1}$$

where D is the diffusion constant, and x and c denote the volume and mass concentrations of the diffusing substance, respectively. According to Eqn (21.1), no flux exists in a homogenized sample. Therefore, diffusion is driven by a chemical potential gradient originating from the concentration gradient.

Figure 21.1 plots the incoming and outgoing mass flux in a square of length Δx. The incoming flux J_1 is given by

$$J_1 = J_2 - \Delta x \frac{\partial J}{\partial x}. \tag{21.2}$$

The mass concentration within this region depends on the incoming (J_1) and outgoing (J_2) fluxes, which alter over time. The net mass increase is given by

$$(J_1 - J_2) = \Delta x \frac{\partial c}{\partial t} = -\Delta x \frac{\partial J}{\partial x}, \tag{21.3}$$

where t denotes time. When the diffusion constant is constant, substitution of Eqn (21.1) into Eqn (21.3) gives Fick's second law [1]:

$$\frac{\partial c}{\partial t} = -D\nabla^2 c, \tag{21.4}$$

In steady state, Eqn (21.4) further reduces to

$$0 = -D\nabla^2 c \tag{21.5}$$

Thermodiffusion is induced by spatial difference of the chemical potential and can be determined from spatial temperature gradients. The thermodiffusion flux is contributed

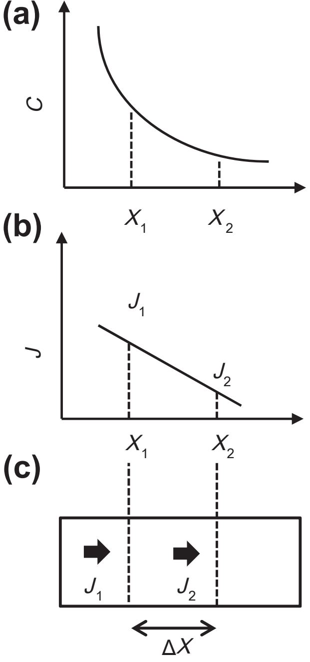

FIGURE 21.1 (a) Concentration distribution, (b) flux (c) incoming and outgoing flux.

by both simple and thermal diffusion, governed by the first and second terms, respectively, in the right-hand side of Eqn (21.6)

$$J = -D_0\left(\frac{\partial T}{\partial x} + \beta\frac{dT}{dx}\right), \tag{21.6}$$

where D_0 is the thermodiffusion coefficient, β is a constant, and T is the temperature. If a large temperature gradient develops in a furnace, thermal diffusion dominates the transport process. Assuming irreversible thermodynamics [1], the constant β is expressed as

$$\beta_1 = \frac{DQc}{RT^2}, \tag{21.7}$$

where Q and R are the mass transfer heat and the gas constant, respectively. Q is empirically derived from experiment. D is the diffusion constant given in Eqn (21.1).

Another diffusive process, electromigration, is driven by differences in electronic chemical potential:

$$J = -D_1\left(\frac{\partial V}{\partial x} + \gamma\frac{\partial V}{\partial x}\right), \tag{21.8}$$

where D_1 is the diffusion constant of electromigration, γ is a constant, and V is the electric voltage. The constant γ is analogous to β in Eqn (21.6). In Eqn (21.8), diffusion occurs via collisions with charged particles such as electrons and ions.

Diffusion plays an important role in crystallization processes, even when convection is weak or absent. For instance, diffusion occurs near solid–melt interfaces when a segregated region is enriched by a foreign component (dopant, impurity, mixed atoms), generating a diffusion boundary layer (see Chapter 25, this volume). Furthermore, transport through solids is dominated by the diffusion of intrinsic and extrinsic atoms through the solidified crystal volume. Such diffusion considerably affects the chemical homogeneity of the as-grown crystals during the cooling process.

21.3 Natural and Forced Convections

21.3.1 Computation

To evolve the governing equations of crystal growth, such as mass, momentum, and energy conservation, the crystal, crucible, and melt are simulated on grids. Figure 21.2 shows the CZ furnace components (Figure 21.2(a)) configured on a two-dimensional (2D) (Figure 21.2(b)) and three-dimensional (3D) (Figure 21.2(c)) grid. The grid systems are designed for global calculation of radiative, conductive, and convective heat transfer in the furnace. The governing equations of mass, momentum, and energy transfer are typically discretized by finite element and finite volume methods. Temperature and species concentrations in actual furnaces sometimes require huge grids or meshes (up to several tens of millions of nodes) to adequately express the boundary layers of temperature, velocity, and mass.

21.3.2 Crystal and Crucible Rotations

To homogenize the radial temperature distribution, crystals are usually rotated as they grow from the melt. Crystal rotation also homogenizes the radial distribution of dopants and impurities. Finally, rotation generates shear forces, which effectively reduce the

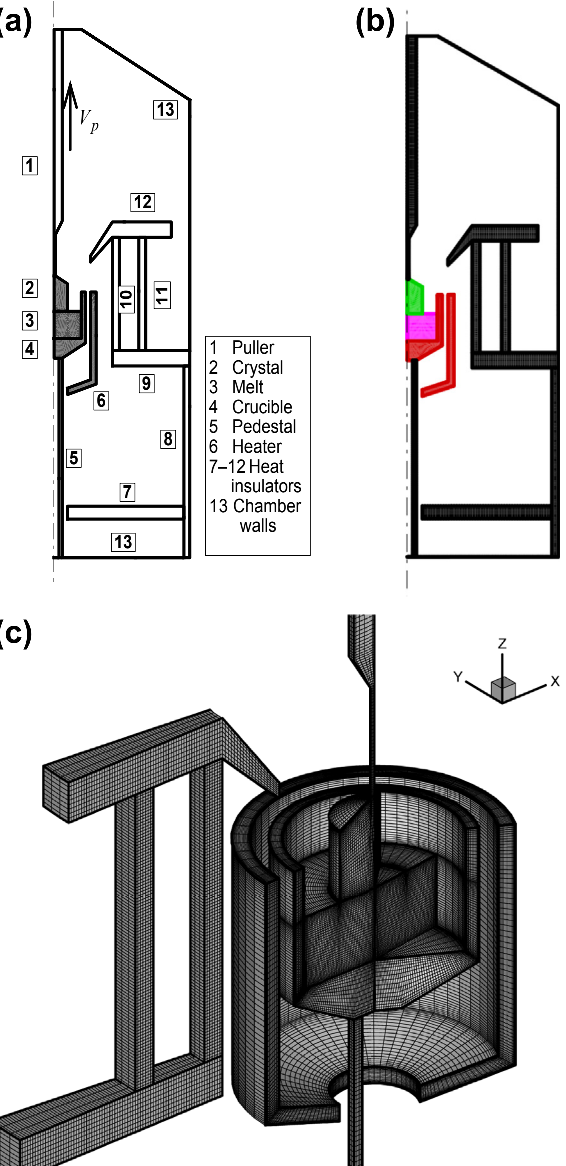

FIGURE 21.2 Typical grids of 2D and 3D configuration of CZ furnace. Furnace components (a), grid in 2D (b) and grid in 3D (c). *After Ref. [2] with permission from Elsevier.*

diffusion boundary layer at the growing interface. Consequently, when the segregation coefficients are below unity, fewer impurities are incorporated into the growing crystal. Figure 21.3 shows the velocity distributions in a crucible during temperature-independent Czochralski (CZ) growth of silicon [3]. This configuration contains the melt and a silicon crystal. The rotation rates of the crystal (ω_S) and crucible (ω_C) in Figure 21.3 are listed in Table 21.1 [3].

In Figure 21.3(a), no external or internal forces exist in the melt and no flow develops. Figure 21.3(b) plots the velocity profile when the crystal rotates at relatively low velocity. This profile is attributable to the small viscosity of the silicon melt, which cannot effectively diffuse the momentum generated by the rotating crystal to the melt through the crystal–melt interface. The distributions in Figure 21.3(c) and (d) are similarly induced by crucible rotation, which exerts a large effect on melt convection.

21.3.3 Gravitational Effects

Crystal growth is largely driven by temperature distribution between source and seed crystal. The temperature distribution stimulates natural convection under gravitational acceleration, which enhances heat and mass transfer in the system. The two main types

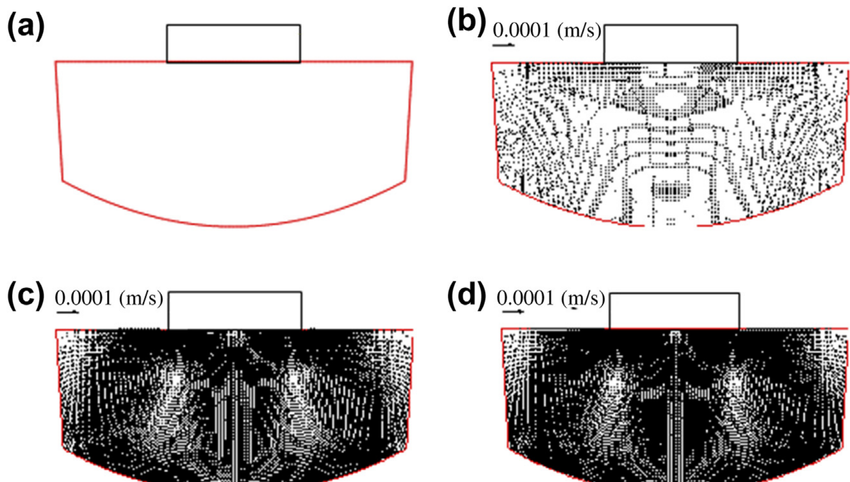

FIGURE 21.3 Velocity profiles of Czochralski growth of silicon without temperature effect. *After Ref. [3] with permission from Springer.*

Table 21.1 Rotation Rates of Crystal (ω_S) and Crucible (ω_C)

Figure 21.3	(a)	(b)	(c)	(d)
ω_S (rpm)	0	−3	0	−3
ω_C (rpm)	0	0	10	10

of temperature gradients, formed parallel to Figure 21.4(a) and (b) and perpendicular to (Figure 21.4(c)) gravitational acceleration, occur with equal probability. Although the flow pattern is identical in Figure 21.4(a) and (b), directions of the convection differ between the two panels. Below some critical temperature difference, convection is suppressed by the balance between thermal diffusion and the viscous force of the melt. A small temperature difference between the top and bottom of the melt is sufficient to induce convection. Convection strength is determined by the thermal Rayleigh number (Ra_T) [4]:

$$Ra_T = \frac{g\beta\Delta T}{\nu\kappa} = \frac{\text{convective heat transfer}}{\text{diffusive heat transfer}} \tag{21.9}$$

where g, β, and ΔT are the gravitational acceleration, volume expansion coefficient of the melt, and temperature difference between the seed and source, respectively. ν and κ denote the viscosity and thermal conductivity of the melt, respectively. Two systems with the same thermal Rayleigh number may develop different convection patterns. Heat and mass transfer in the melt also depends on the system configuration and temperature distribution along the walls.

The flow is governed by the Navier–Stokes momentum equation, which accounts for the Coriolis and centrifugal force terms in the rotating coordinate system:

$$\frac{\partial u}{dt} = -u\nabla u - 2(\Omega k) \times u + (\Omega k) \times (\Omega k) \times r + \frac{1}{\rho}\nabla p + \mu/\rho\Delta u + g\beta(T - T_0), \tag{21.10}$$

where u and r are the relative rotational velocity and position vectors, respectively, Ω denotes the crucible rotation rate, and k is a unit vector in the z-direction. The pressure and viscosity of the melt are denoted by p and μ, respectively, and g, β, and T_0 are the gravitational acceleration, volume expansion coefficient, and the specific-mass reference temperature, respectively.

To evolve convection in a 2D configuration, the equations of mass conservation (21.11), momentum (21.12–21.14), and energy (21.15) for the thermal flow of the melt in the crucible must be solved. Natural convection can be solved by the Boussinesq approximation. The NS equations are given by

$$\frac{1}{r}\frac{\partial}{\partial r}(ru_r) + \frac{1}{r}\frac{\partial u_\phi}{\partial \phi} + \frac{\partial u_z}{\partial z} = 0 \tag{21.11}$$

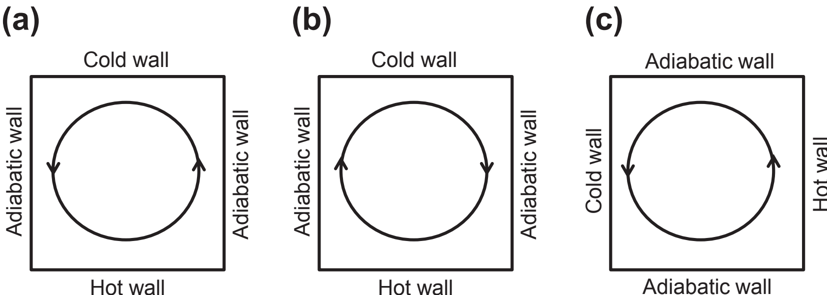

FIGURE 21.4 Thermal configuration of growth system: (a), (b) bottom heating, (c) side heating.

$$\frac{du_r}{dt} - \frac{u_\phi^2}{r} = -\frac{1}{\rho}\frac{\partial p}{\partial r} + \nu\left(\nabla^2 u_r - \frac{u_r}{r^2} - \frac{2}{r^2}\frac{\partial u_\phi}{\partial \phi}\right) \tag{21.12}$$

$$\frac{du_\phi}{dt} + \frac{u_r u_\phi}{r} = -\frac{1}{\rho}\frac{1}{r}\frac{\partial p}{\partial \phi} + \nu\left(\nabla^2 u_\phi + \frac{2}{r^2}\frac{\partial u_r}{\partial \phi} - \frac{u_\phi}{r^2}\right) \tag{21.13}$$

$$\frac{du_z}{dt} = -\frac{1}{\rho}\frac{\partial p}{\partial r} - g\beta(T - T_m) + \nu\nabla^2 u_z \tag{21.14}$$

$$\frac{dT}{dt} = \frac{\lambda}{\rho C_p}\nabla^2 T \tag{21.15}$$

$$\frac{d}{dt} = \frac{\partial}{\partial t} + u_r\frac{\partial}{\partial r} + \frac{(u_\phi - u_G)}{r}\frac{\partial}{\partial \phi} + u_z\frac{\partial}{\partial z} \tag{21.16}$$

$$\nabla^2 = \frac{\partial^2}{\partial r^2} + \frac{1}{r}\frac{\partial}{\partial r} + \frac{1}{r^2}\frac{\partial^2}{\partial \phi^2} + \frac{\partial^2}{\partial z^2}, \tag{21.17}$$

where r, ϕ, and z are the radius, azimuthal angle, and height, respectively, in cylindrical coordinates. The velocity components in the r, ϕ, and z directions are u_r, u_ϕ, and u_z, respectively. p and T are the pressure and temperature of the melt, respectively. The other parameters are the thermal expansion coefficient β, kinematic viscosity ν, melt density ρ, specific heat capacity C_p, thermal conductivity λ, and gravitational acceleration g. u_G is the grid velocity in the ϕ direction, which equals the crucible rotation rate.

21.3.4 Centrifugal Effects

Figure 21.5 shows the temperature and velocity profiles under the conditions listed in Table 21.2 [3]. At small melt viscosity, crystal rotation exerts little effect on convection in the melt, and the profiles of Figure 21.5 (a) and (b) are almost identical. In Figure 21.5 (c) and (d), the velocities are small and the temperature profiles resemble those of dominant conduction. The small velocity is attributable to angular momentum conservation in the rotating melt, which is related to the Coriolis force.

The second and third terms on the right-hand side of Eqn (21.10) express the Coriolis force and centrifugal acceleration, respectively. The centrifugal acceleration vector (a_{cen}) is given by

$$a_{cen} = \Omega^2 r = L^2/r^3, \tag{21.18}$$

where L is the angular momentum of the melt. The velocity profiles for various rotation rates of the crystal and crucible are shown in Figure 21.5.

When a small volume element instantaneously moves from position r to r' ($= r + \Delta r$), angular momentum conservation generates an excess force given by

$$\Delta a_{cen} = L^2\left(1/r^3 - 1/r'^3\right). \tag{21.19}$$

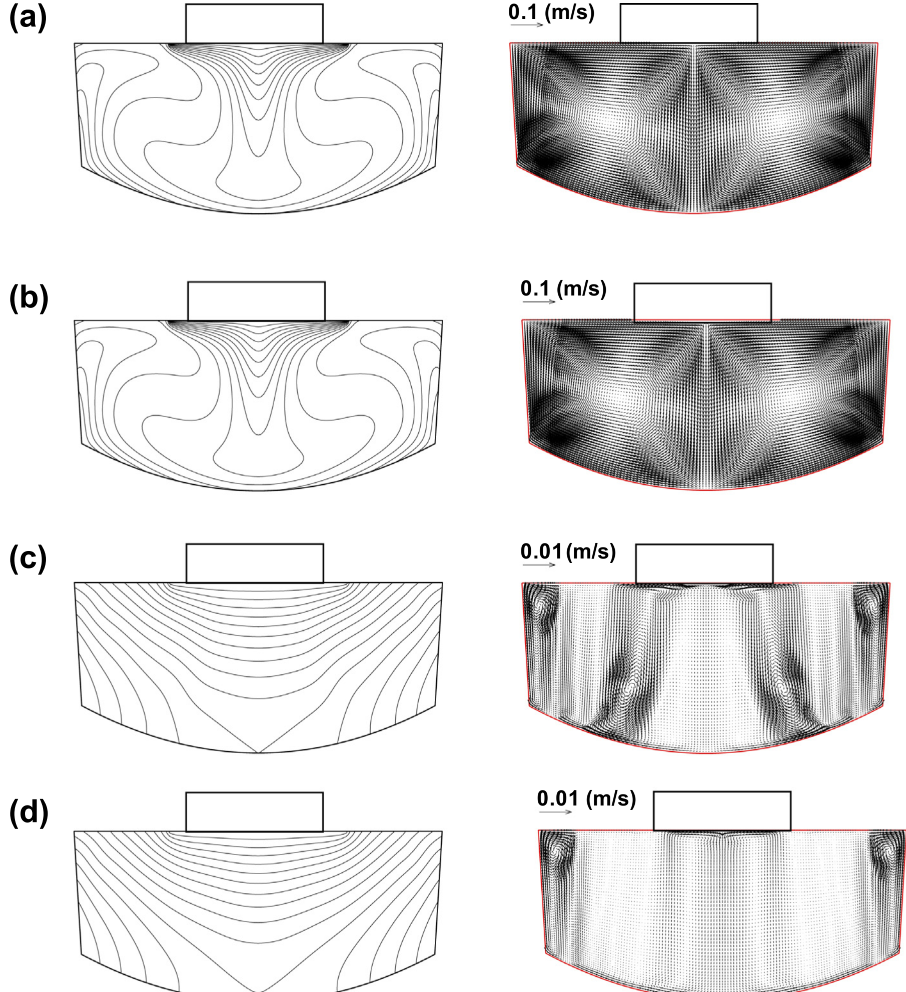

FIGURE 21.5 Temperature (left) and velocity profiles (right) of Czochralski growth with effect of temperature. Temperature difference between contours is $\Delta T = 5$ K. *After Ref. [3] with permission from Springer.*

Table 21.2 Rotation Rates of Crystal (ω_s) and Crucible (ω_c)

Figure 21.5	(a)	(b)	(c)	(d)
ω_s (rpm)	0	−3	0	−3
ω_c (rpm)	0	0	10	10

Consequently, the centrifugal force always opposes the direction of outward movement. Therefore, melt motion in the radial direction is suppressed by the crucible rotation. As the crucible rotation rate increases, the radial temperature gradient in the melt enlarges.

21.3.5 Convective–Diffusive Transport

Solids and liquids can also diffuse by directional solidification. Figure 21.6 shows the configuration and dimensions of a small unidirectional-solidification furnace for producing multicrystalline silicon [5]. The melt, crystal, crucible, and pedestal are labeled 1, 2, 3, 4, 5, and 6, respectively. Thermal shields are labeled 7–10. Three heaters (11, 12, and 13) are affixed to the furnace. Conductive heat transfer in all solid components, radiative heat exchange between the diffusive surfaces in the unidirectional-solidification furnace, and the Navier–Stokes equations for the melt flow in the crucible are coupled and iteratively solved by a finite volume method in a transient condition [5]. The iron distributions in the silicon melt and solidified silicon ingot are determined from the thermal field and melt flow in the crucible. Segregation of impurities at the melt–solid interface is also considered.

Figure 21.7 shows the iron concentration gradients in a solidified silicon ingot that had been cooled for 1 h [5]. The figure shows a vertical cross-section of the iron concentration in the crystal. The iron concentration scale of Figure 21.7 should be multiplied

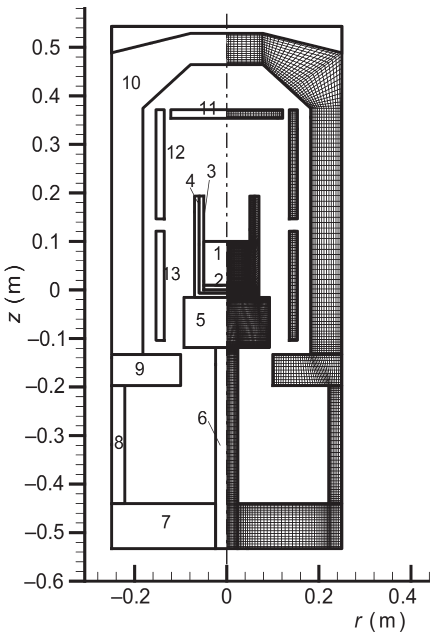

FIGURE 21.6 Configuration and computation grid of a casting furnace. The melt, a crystal, a crucible, and a pedestal are denoted as 1, 2, 3, 4, 5, and 6, respectively. Thermal shields are labeled as 7 to 11. Numbers 12 and 13 show multi heater. *After Ref. [5] with permission from Elsevier.*

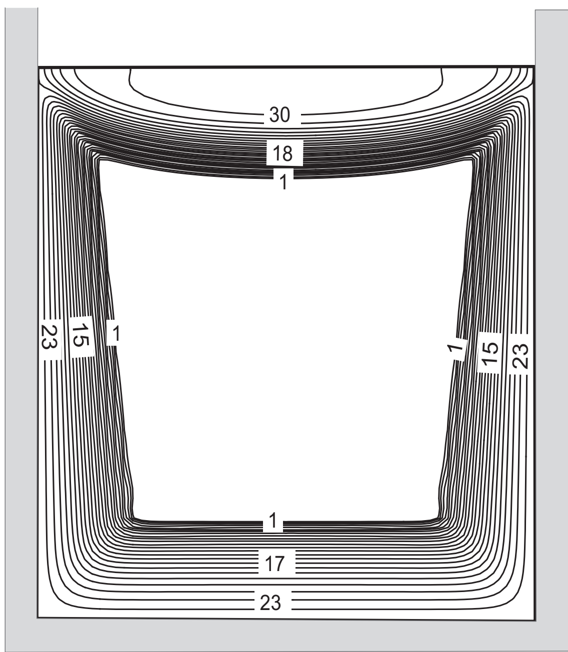

FIGURE 21.7 Distribution of iron concentration in a solidified silicon ingot after the solidification process. The scale of iron concentration should be multiplied by 1×10^{10}/cm^3. The periphery of the crystal contains order of 1×10^{15}/cm^3. *After Ref. [5] with permission from Elsevier.*

by 1×10^{10}/cm^3. Therefore, the iron concentration at the periphery of the crystal is of the order of 1×10^{15}/cm^3. Iron concentration was high at the top of the melt where iron had segregated, and in the vicinity of the crucible walls where iron had diffused during the solidification/cooling process. These distributions arise from the small activation energy of iron diffusion in solid silicon. Iron concentration was low in the central region of the solidified ingot (see Figure 21.7), indicating that diffusion occurred after the solidification/cooling process.

21.4 External Fields

21.4.1 Static Magnetic Fields

When electrically conducting materials (such as metals and semiconductor melts) intercept static magnetic fields, they are subjected to a Lorentz force. The Lorentz force results from the balance between the electrical current generated by the melt flow and the electric field in the metallic melt. This force exerts a damping effect on the melt velocity. It can also change unsteady or turbulent flows to steady flows, and suppress temperature fluctuations with subsequent reduction of growth velocity fluctuations and striation formation within the growing crystal. In the typical CZ method used for silicon growth, the force density of natural convection is of the order of 100 N/m^3 [6]. To suppress the convection induced by static magnetic fields, forces of the same magnitude

should be applied to the melt. These conditions are satisfied by magnetic fields of the order of 10–40 mT. Magnetic fields of these magnitudes are typically applied in the industrial-scale production of silicon crystals. The effects of magnetic fields on the melt motion are detailed in Chapter 23.

Three configurations of magnetic fields are currently adopted. In the axial magnetic field, the melt axis is aligned parallel to the field generated by a single axisymmetric coil. In the transverse magnetic field, the magnetic field lines run perpendicular to the axis of symmetry of the system. In the cusp-shaped magnetic field, two coils powered in opposite directions generate circular field lines, usually retaining the center of the system field free. Panels (a), (b), and (c) of Figure 21.8 show the vertical (VMCZ, axial, longitudinal), transverse (TMCZ, horizontal), and cusp-shaped (CMCZ) static magnetic fields, respectively, that typify the CZ method. Radial and/or azimuthal melt motions react with a vertically applied magnetic field, whereas vertical melt flows do not.

Notably, transverse magnetic fields can disrupt the symmetry of the system, converting axisymmetric flow fields into nonaxisymmetric 3D flow field structures. In turn, symmetry breaking disrupts the chemical homogeneity of the growing crystal, with

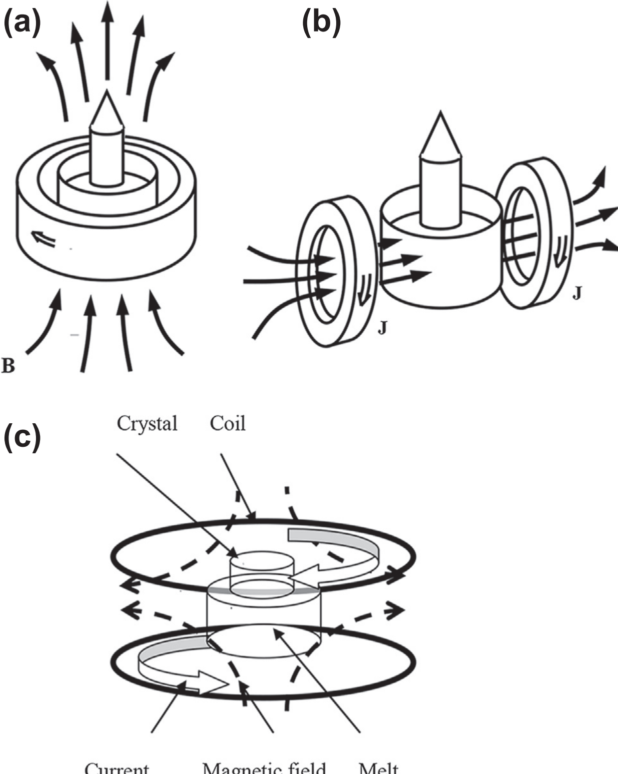

FIGURE 21.8 Schematic of VMCZ (a), TMCZ (b), and CMCZ (c). *After Ref. [3] with permission from Springer.*

consequent deformation of the crystal. However, transverse magnetic fields can be combined with crystal and or crucible rotation to generate an azimuthal Lorentz force, which behaves as a rotating magnetic field (RMF) [7] and realizes homogeneous impurity distributions in the grown crystal.

Hoshi et al. [8] and Suzuki et al. [9] successfully reduced the growth striations of oxygen in silicon crystals by applying steady magnetic fields during CZ growth. The transverse magnetic fields suppressed fluctuations in the melt flow and furnace temperatures, and homogeneous crystals could be grown. Furthermore, this technique reduced the oxygen concentration in the crystals, indicating effective defect removal. The silicon crystals in charge-coupled devices (CCD), which are still used in modern cameras, are grown by this method. Because defects degrade the image characteristics of CCDs, this method remains extremely important for the Internet community. Large-diameter silicon crystals (300 mm) are mass produced by the CZ method in huge crucibles with several hundred kilograms of feedstock material. Under these conditions, magnetic fields that dampen convection streams and turbulences within the melt have proven essential for dislocation-free growth. Silicon crystals of 450 mm diameter grown under magnetic fields will be commercially available in the near future.

Unlike transverse magnetic fields, cusp-shaped magnetic fields can maintain axisymmetry [10,11]. Magnetic fields are also used during oxide crystal growth. Oxide melts are partially ionized into anions and cations, whose motions generate Lorentz forces. Because both positively and negatively charged ions are subjected to Lorentz forces, the melt motion is determined by summing the momenta of all ions. Jing et al. analyzed the effects of magnetic field on $LiNbO_3$ in terms of the effective lifetime of the ion collisions [12]. Miyazawa et al. grew $LiNbO_3$ and TiO_2 crystals in TMCZ magnetic fields [13]. According to their calculations and experiments, Lorentz forces were produced by coupling between the motion of ions and current-free vertical magnetic fields in the melt. These Lorentz forces accelerated the azimuthal motion in the vertical magnetic field. However, these researchers accounted only for the currents produced by the flow of ions in the melt. Because the electric conductivity of the oxide melt is smaller than that of the semiconductor melt, the melt flow must be effectively controlled by large magnetic fields. Semiconductor melts provide almost four electrons per atom, and their electrical conductivity is increased by the large electron concentration. On the other hand, the effect of the Lorentz force is reduced by the low ionization ratio of the oxides.

Magnetic fields do not always suppress temperature fluctuations. Chandrasekhar conducted a series of mercury experiments under a magnetic field [14], and reported that the temperature oscillation amplitude reduces with increasing magnetic field. Axial and cusp-shaped magnetic fields, being axisymmetric themselves, are assumed to preserve axisymmetry of the growth system. Growth in transverse magnetic fields, which is subjected to symmetry breaking, should be simulated by 3D global modeling. However, calculating the 3D convection, radiative heat transfer, and the view factor is computationally time consuming and resource intensive. Ozoe and Iwamoto [15], Krauze et al.

[16], Liu and Kakimoto [17], Kalaev [18], and Vizman et al. [19] have developed 3D codes to model such convective and radiative heat transfers.

21.4.2 Dynamic Magnetic Fields

Dynamic magnetic fields are of practical interest in crystal growth because they consume less power than static fields, enable effective melt mixing, and effectively suppress fluctuations in the growth system when applied at small magnitudes. Therefore, low-strength dynamic magnetic fields are an attractive option for controlling melt flows.

The electric field associated with a dynamic magnetic field is given by Eqns (21.20) and (21.21). Faraday's equation (Eqn (21.21)) is expressed as a vector potential in Eqn (21.22).

$$E = -\nabla\Phi - \frac{\partial A}{\partial t} \tag{21.20}$$

$$\nabla \times E = -\frac{\partial B}{\partial t}, \tag{21.21}$$

$$\nabla \times A = B \tag{21.22}$$

The electric current and Lorentz force in a melt are given, respectively, by

$$J = \sigma_e\left(- \nabla\Phi - \frac{\partial A}{\partial t} + v \times B\right). \tag{21.23}$$

$$F = \sigma_e\left(- \nabla\Phi - \frac{\partial A}{\partial t} + v \times B\right) \times B. \tag{21.24}$$

The Lorentz force involves the electric field, velocity field, and time evolution of the vector potential, corresponding to the second term on the right-hand side of Eqn (21.24). This latter term plays an important role in Lorentz force-driven melt convection because the magnetic field density varies with time in an RMF. From Eqn (21.24), we obtain

$$\nabla \cdot \left(- \nabla\Phi - \frac{\partial A}{\partial t} + v \times B\right) = 0. \tag{21.25}$$

Therefore, the electric potential in the melt is given by

$$\nabla^2\Phi = -\frac{\partial}{\partial t}(\nabla \cdot A) + \nabla \cdot (v \times B). \tag{21.26}$$

Because the electric potential creates the above-mentioned electric current and Lorentz forces in the melt, the flow structure can be controlled by the Lorentz force calculated by Eqn (21.24).

21.4.3 Electromagnetic Fields

To homogenize the radial and axial oxygen and dopant distributions, Watanabe et al. [20] proposed the electromagnetic CZ (EMCZ) method, where the melt is azimuthally rotated by an electromagnetic force whereas the crucible is stopped. This method

modifies the heat and mass transfer in the melt, effectively engineering the shape of the melt–crystal interface. The oxygen content of silicon crystals must be controlled when manufacturing electronic devices such as integrated and large-scale integrated circuits. Equivalently, we must control the distribution and concentration of oxygen in silicon crystals grown by the CZ method. Melt convection, and hence oxygen concentration, can be controlled by applying electric current and magnetic fields. Therefore, various magnetic field configurations have been investigated and applied. However, magnetic fields cause several recognized problems such as high oxygen concentration, radially inhomogeneous oxygen distribution in grown crystals, and long-term instability of the melt flow [21,22]. The EMCZ process developed by Watanabe et al. [23] prevents such inhomogeneities and instabilities by adopting static magnetic fields and static electric currents. They experimentally investigated the concentration and distribution of oxygen in silicon crystals grown by the EMCZ method using a vertical and a cusp-shaped magnetic field. Kakimoto et al. [24,25] investigated heat and oxygen transfer in the silicon melt in an EMCZ system with transverse magnetic fields (EMCZ-TMF), which has great potential for controlling the melt flow and oxygen transport.

The 3D global model proposed by Liu and Kakimoto [2] is applicable to EMCZ with a transverse magnetic field configuration, as shown in Figure 21.9 [2]. The temperature distribution in the melt of this system is shown in Figure 21.10 [2]. The additional electromagnetic force enhances heat and mass transfer in the melt with a potential for modifying the shape of the solid–melt interface.

21.4.4 Vibrational Effects

How mechanical waves are generated and transduced, and their influence on convection and component distribution in the melt, is discussed in Chapter 24. Here, we state that the diffusion boundary layer can be effectively destroyed by Schlichting vortexes. In general, mechanical vibration induces convection in most processes that grow crystals

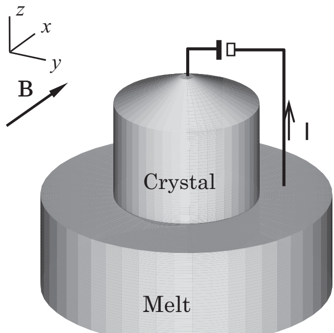

FIGURE 21.9 Spatial arrangement of transverse magnetic field and electrodes. External applied magnetic field and electric current circuit. *After Ref. [26] with permission from Elsevier.*

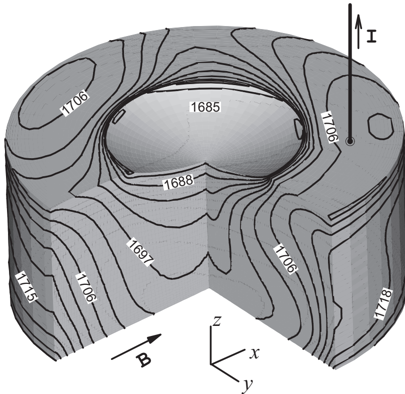

FIGURE 21.10 Temperature and oxygen distributions in melt. (a) Three-dimensional temperature distribution in melt. Isotherms plotted every 3 K. *After Ref. [26] with permission from Elsevier.*

from melt or solution. Furthermore, unlike magnetic field applications, the material is not required to couple to the electrical conductivity and, therefore, can be more freely selected. Mechanical vibration induces convection in both semiconductor and dielectric substance melts. A potential limiting factor is the mechanical integration of the system in the growth chamber. The vibrational device must be rigidly connected to the seed or melt, and the vibrational amplitude and frequency must be appropriate for the crystal weight and the stacking fault energy of the material.

Many studies have focused on enhancing heat and mass transfer ahead of the solid–liquid interface [27,28] and on homogenizing the melt [29,30]. Besides improving the growth process, researchers have applied vibrations to interface demarcation [31] and to thermophysical data (viscosity and surface tension) measurements [32]. The underlying physics is rather challenging and the mechanisms by which vibrations induce flow in the melt (i.e., Schlichting flow, volume flow, and flow induced by propagating surface waves) are varied and contentious.

21.5 Flow Instability

21.5.1 The Rayleigh–Bénard Instability

The driving force of crystallization must first be triggered by a temperature distribution. However, temperature distributions enhance the Rayleigh–Bénard instability, as shown in Figure 21.11 [33]. As the flow velocity increases, the flow structure generally evolves in space and time. Such a structure exhibits a time-independent spatial periodicity at the initial stage of instability. The structure becomes more time dependent as the temperature difference increases. Finally, the structure establishes turbulence, which is characterized by large spatial and temporal dependency.

Instabilities in CZ melts can arise from various sources [33]. Among these, the vertical temperature profile near the free surface, coupled with density and surface

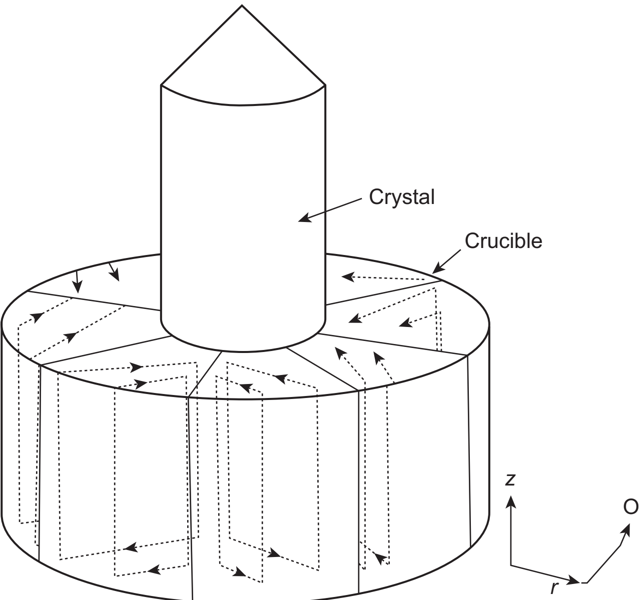

FIGURE 21.11 Schematic diagram for spoke pattern in silicon melt. *After Ref. [33] with permission from Elsevier.*

tension differences, is considered largely responsible for the spoke patterns observed on oxide melts [34,35]. As heat is lost from the free surface, the surface temperature becomes lower than the bulk temperature, and a vertical temperature gradient is established. If the temperature difference between the top and bottom of the unstable layer exceeds some critical value, an asymmetric pattern is formed by natural convection [34] (known as the Rayleigh–Bénard instability) or by surface-tension driven flow [36] (the Marangoni–Bénard instability). Both instabilities are schematized on the vertical plane in Figure 21.12. The surface temperature profile is modified by small

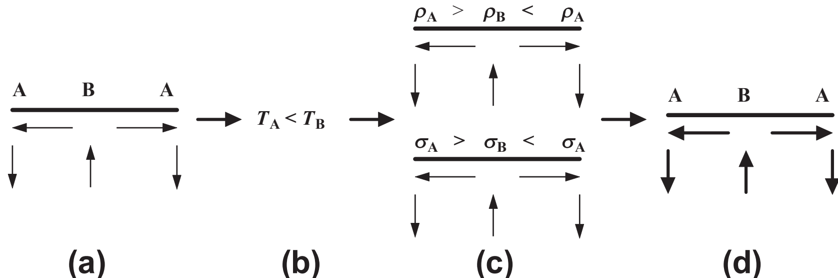

FIGURE 21.12 Roll structure stabilization. (a) Fluctuations occur near free surface. (b) Temperature in region B increases. (c) Temperature differences cause different surface tensions or density and fluid flow in the same direction as initial fluctuation. (d) Fluctuations change to a stable roll flow pattern.

fluctuations in the fluid flow. Because the temperature is higher at the bottom than at the surface, the temperature of region B becomes higher than that of region A, reducing the surface tension (σ) or density (ρ) in that region (note that both the temperature coefficient of the surface tension and the thermal expansion coefficient (β) are negative). This density or surface tension differential induces a fluid flow in the direction of the initial fluctuations, promoting and stabilizing them (see Figure 21.12(c)). Therefore, a roll-type flow pattern appears in the melt. These two types of convection (i.e., natural and Marangoni convection) are usually simultaneous. Consequently, the extent of symmetry breaking by either the Bénard or the Marangoni–Bénard convection in the melt of CZ systems is almost impossible to determine by numerical methods.

21.5.2 Baroclinic Instability

In crystal growth processes, the temperature and impurity distributions are usually homogenized by rotating the crystal or crucible. Crucible rotation enhances the Coriolis force, which is based on momentum conservation. The temperature distribution in the crucible establishes coexisting gravitational and Coriolis force–driven convection. When the Coriolis force exceeds the force of natural convection, the flow becomes dominated by horizontal vortices, a condition known as baroclinic instability. Baroclinic instability is responsible for the transition boundary between axisymmetric and nonaxisymmetric flow, which is almost uniquely identified in a phase diagram of thermal Rossby number (Ro_T) versus the Taylor number (Ta) as shown in Figure 21.13. This phase diagram was proposed by Fowlis and Hide [37,38], who observed the transition in water and water–glycerol mixture contained in a rotating annulus. The thermal Rossby number and the Taylor number are, respectively, given by [39–41]

$$Ro_T = \frac{g\beta \Delta T h}{\omega^2 r^2}, \tag{21.27}$$

$$Ta = \frac{4r^5\omega^2}{h\nu^2}, \tag{21.28}$$

where g, β, and ν are the gravitational acceleration, volume expansion coefficient, and kinematic viscosity, respectively. This instability assumes that a temperature distribution exists in a rotating system. Therefore, growth can be controlled by controlling the temperature distribution and rotation rate.

21.5.3 Turbulence

Flow can be laminar (time dependent or independent) or turbulent. In a large low-viscosity system, such as CZ silicon, the flow is easily changed from laminar to turbulent. Turbulence also appears when many oscillating modes intercept in oxide systems. Several models of turbulent flow have been proposed. The Smagorinsky model [42] describes turbulent convection and transport in large-diameter crucibles.

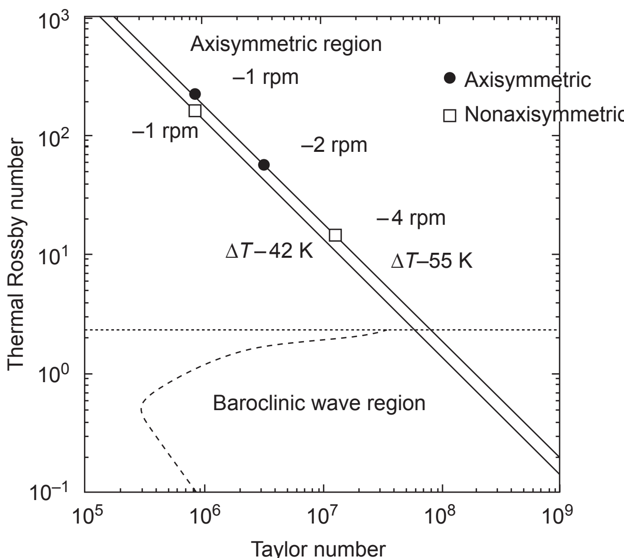

FIGURE 21.13 Flow mode phase diagram showing transition from axisymmetric to nonaxisymmetric flow: (●, □) experimental results [40], (———) transition boundary after Fowlis and Hide [37], Edys's linear boroclinic model [38]. *After Ref. [37] with permission from Elsevier.*

The transient governing equations of velocity and temperature in a Si melt are given by

$$\frac{\partial(\rho_{Si}u_i)}{\partial x_i} = 0, \tag{21.29}$$

$$\frac{\partial(\rho_{Si}u_i)}{\partial t} + \frac{\partial(\rho_{Si}u_i u_j)}{\partial x_j} = -\frac{\partial p}{\partial x_i} + \mu_{eff}\frac{\partial}{\partial x_j}\left(\frac{\partial u_i}{\partial x_j} + \frac{\partial u_j}{\partial x_i}\right) + \rho_{Si}g_i\beta_T(T - T_{ref}), \tag{21.30}$$

$$\frac{\partial(\rho_{Si}T)}{\partial t} + \frac{\partial(\rho_{Si}u_i T)}{\partial x_i} = \frac{\lambda_{eff}}{c_{pSi}}\frac{\partial^2 T}{\partial x_i^2} + \frac{\rho_{Si}L}{c_{pSi}}\frac{\partial f_S(T)}{\partial t}, \tag{21.31}$$

where ρ_{Si} and c_{pSi} are the density and specific heat of silicon, respectively. The last term in Eqn (21.30) accounts for the buoyancy effect. β_T is the thermal expansion coefficient of the melt. The effective eddy viscosity and effective thermal diffusivity are defined as $\mu_{eff} = \mu + \mu_t$ and $\lambda_{eff} = \lambda + \mu_t/Pr_t$, respectively.

The eddy-viscosity model of melt turbulence is given by [43]

$$\mu_t = 2\rho_{Si}(C_S\Delta)^2\sqrt{2S_{ij}S_{ij}}, \tag{21.32}$$

where C_S is the Smagorinsky constant (equal to 1), and the filter width Δ is defined as $\Delta = (Volume)^{1/3}$. The strain rate tensor is expressed as $S_{ij} = (\partial u_i/\partial x_j + \partial u_j/\partial x_i)/2$.

Given the complexity of turbulent phenomena, the understanding and control of turbulence is a major challenge in fluid dynamics. If properly controlled, future research may realize large crystals grown from turbulent melts to homogenize impurity and temperature distributions.

21.6 Impurity Transfer

21.6.1 Boundary Layer

Near the growth interface, the velocity u, concentration c, and temperature T frequently follow an exponential distribution, with boundary layer thicknesses of δ_V, δ_C, and δ_T, respectively. The thickness of the velocity boundary layer δ_V manifests from momentum transfer through the viscous melt material near the interface. Therefore, the flow velocity parallel to the interface continuously changes from its bulk fluid value u_∞ to stagnation $u_0 = 0$. The segregation effect creates a concentration boundary layer δ_C, through which the solid–liquid interface rejects or accumulates components (solvent, impurities, dopants) depending on whether the segregation coefficient k_0 is less than or greater than 1, respectively. Because the developing concentration gradient generates diffusive flow, this zone is commonly called the diffusion boundary layer (Figure 21.14(a)). Finally, the thermal boundary layer δ_T describes the transition from the fluid bulk temperature T_∞ to the solid interface temperature T_0. Governed by the thermal conductivity through the interface, δ_T relates the thermal diffusion to the convective heat transport.

The boundary layer thicknesses depend on the diffusivities of momentum, mass, and temperature, which differ among systems. Therefore, Figure 21.14 is not universally representative of these thicknesses [44]. The most fundamental boundary thickness is the velocity boundary layer δ_H, to which δ_C and δ_T are related by

$$\delta_D \approx \delta_H \left(\frac{D}{\nu}\right)^{1/3} = \delta_H Sc^{-1/3}, \tag{21.33}$$

$$\delta_T \approx \delta_H \left(\frac{a}{\nu}\right)^{1/3} = \delta_H Pr^{-1/3}. \tag{21.34}$$

Here, D, ν, and a are the mass diffusivity, kinematic viscosity, and thermal diffusivity, respectively. The Schmidt number, $Sc = \nu / D$, is the mass transport ratio of momentum diffusivity to mass diffusivity. The Prandtl number, $Pr = \nu / a$, defines the heat transfer ratio of momentum diffusivity to thermal diffusivity.

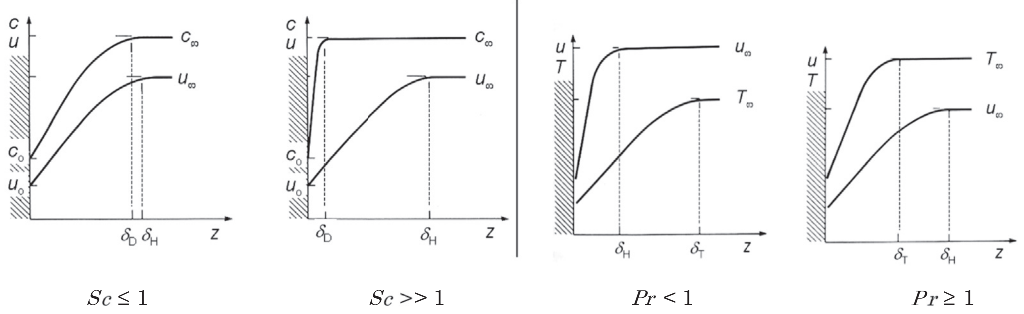

FIGURE 21.14 Schematic comparison between concentration c, velocity u, and temperature T distributions at the fluid–solid interface in gases ($Sc \leq 1$), liquids ($Sc >> 1$), liquid metals and semiconductors ($Pr < 1$), and aqueous solutions and molten oxides ($Pr \geq 1$). *Adapted from Proc. ISSCG in Dalian.*

Figure 21.14 has some practical consequences for crystal growth. Liquid metals are characterized by low Prandtl numbers ($Pr < 1$), implying low viscosity and high thermal conductivity. Therefore, in metallic melts, heat transport is conductive rather than convective, and the thermal boundary layer δ_T extends farther into the fluid than the velocity transition region δ_H. In contrast, in molten oxides and aqueous solutions with typically low thermal conductivity ($Pr > 1$), δ_H is broader than δ_T. Unlike metal fluids, in which the temperature field introduced by the heating furnace remains largely unaffected by convection, the temperature distribution in the melt (i.e., the temperature gradient near the interface) is markedly influenced by the mass flow mode. In multicomponent melts (fluxes), $Sc >> 1$, whereas in gases, $0.1 \leq Sc \leq 1$. Thus, in gases, δ_D and δ_H extend by approximately the same distance, whereas in liquids, δ_H is much wider than δ_D. In front of the gas–liquid interface (the region of highest concentration gradient), the flow velocity is reduced to relatively small values that barely influence the concentration profile.

21.6.2 Mass Transfer in Gases

Silicon carbide (SiC) is a promising semiconductor material for electronic and opto-electronic devices operating at high power, high temperature, high frequency, and under intense radiation, owing to its stable chemical and thermal properties [45,46]. Bulk SiC crystals are commonly grown by the physical vapor transport (PVT) method, as shown in Figure 21.15. At present, commercial use of SiC is limited by problems related to SiC

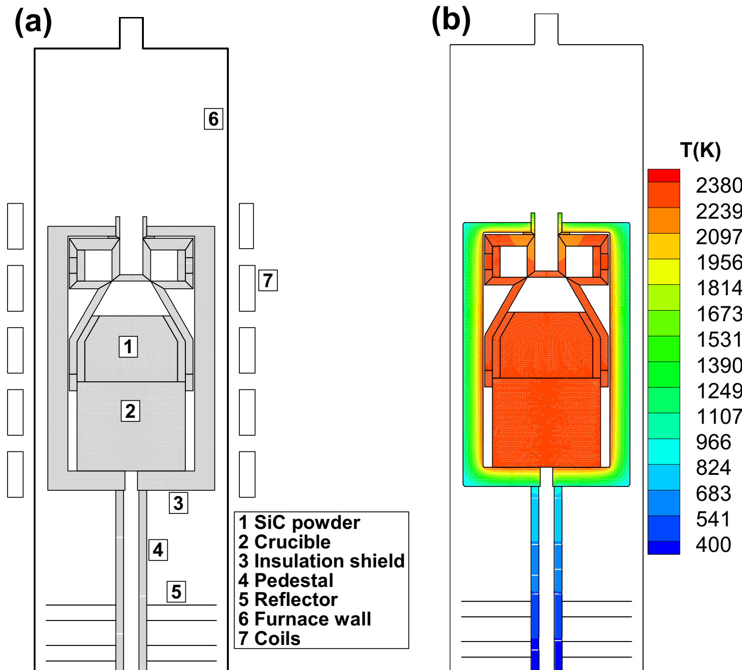

FIGURE 21.15 Typical furnace structure (a) and temperature distribution (b) of PVT method. *After Ref. [47] with permission from Elsevier.*

growth. A major outstanding issue is crystal size. Large crystals tend to be of inferior quality. Manufacture of large high-quality crystals requires an understanding of the gas flow in large furnaces. First, the large Grashof number—the ratio between gravitational and viscous forces—in a large furnace enhances the buoyancy effect. Consequently, the flow pattern might change from well-known diffusion-dominated flow to convection-dominated flow. To accurately predict the flow pattern, the incompressible solver based on the Boussinesq approximation should be replaced with a fully compressible flow solver. The Boussinesq approximation introduces substantial error, and may even yield a qualitatively different solution, if the temperature difference a crystal and a wall exceeds 15 K [48]. Second, a low-pressure system in a large furnace can beneficially increase the growth rate. When the pressure of the species and the argon gas are of similar order of magnitude, the fluid density, velocity, pressure, temperature, viscosity, and conductivity in the Navier–Stokes equations are equally contributed by both molecules.

The faces of the source and seed crystal are coated by a thin Knudsen layer, whose phase is between a solid and a vapor [49]. Within the two thin Knudsen layers, the vapor fluxes and the mass sublimation and deposition fluxes at the seed and source faces are exactly determined by the Hertz–Knudsen equation. Conceptually, the relationships between gas and solid may be treated as a kinetic jump of the vapor pressure at the Knudsen layer [49]. For example, at the seed face, the molar deposition flux is given by

$$\begin{aligned} &(\chi_i V - D_i \nabla \chi_i) \cdot \overrightarrow{n} = \frac{1}{\sqrt{2\pi M_i \Re T}} \left(p_i - p_i^* \right), \quad i = 1, 2, 3, \\ &(\chi_4 V - D_i \nabla \chi_4) \cdot \overrightarrow{n} = 0, \end{aligned} \tag{21.35}$$

where χ_i is the molar concentration of species i, V is the Stefan velocity, $\overrightarrow{n}$ is the unit normal vector to the surface, which specifies the direction of molar flux, M_i is the molecular weight of species i, $\Re$ is the universal gas constant, and p_i^* is the equilibrium pressure of species i. The indexes 1, 2, 3, and 4 represent SiC_2, Si, Si_2C, and Ar, respectively. Thus, a thin Knudsen layer-like boundary forms during melt growth and the solution growth method.

21.6.3 Mass Transfer between Gas and Melt

This subsection discusses the crystallization of silicon ingots for photovoltaic applications. In the fabrication method, impurities are largely controlled by the gas–melt flow relationships. Multicrystalline silicon is widely used in the photovoltaic industry because of its low production cost and its relatively high conversion efficiency when made into solar cells. The unidirectional solidification method is a cost-effective technique for the large-scale production of multicrystalline silicon material. Similar to the CZ method, unidirectional solidification is associated with the transport of impurities [50]. Carbon is one of the main impurities in multicrystalline silicon. If the carbon concentration exceeds 10^{16} atom/cm^3, it markedly affects oxygen precipitation during thermal annealing

of crystals and during device processing of wafers cut from these crystals [51–57]. Oxygen precipitates provide intrinsic gettering sites for impurities and affect the mechanical strength of the wafer [51,58,59]. When the concentration of carbon exceeds its solubility limit in silicon, it precipitates out as silicon carbide (SiC) particles, potentially causing severe ohmic shunts in solar cells and the nucleation of new grains in silicon ingots [60]. Carbon, oxygen, and SiC particles in solidified silicon ingots can significantly decrease the conversion efficiency of solar cells. Therefore, the carbon concentration must be effectively controlled to obtain high-quality crystals. Crystals with low carbon concentration have been experimentally grown in a unidirectional solidification furnace. The improved furnace design was then validated in global simulations of coupled oxygen and carbon transports within the furnace.

The basic configurations of unidirectional solidification furnaces are well known [61–65]. The graphite components, which source most of the carbon in the grown crystals, include the crucible, heat shields, heaters, and pedestal. The basic processes of carbon incorporation into a crystal are shown in Figure 21.16. First, the silica (SiO_2) crucible dissolves, releasing oxygen and silicon atoms into the melt. Second, the dissolved oxygen atoms are transported to the gas–melt interface and evaporate as SiO gas. The SiO gas is then removed by the argon gas flow and reacts with all of the graphite components to produce gas-phase CO. The resultant CO returns to the melt surface by diffusion or convection and dissolves in the melt. Finally, C and O atoms are assembled into the crystal [51].

The mechanism of carbon incorporation was fully elucidated in a global simulation of coupled oxygen and carbon transport within the unidirectional solidification furnace. The argon gas flow above the melt is shown in Figure 21.17. The simulated inlet flow rate was 0.8 L/min, the inlet static temperature was 350 K, and the outlet

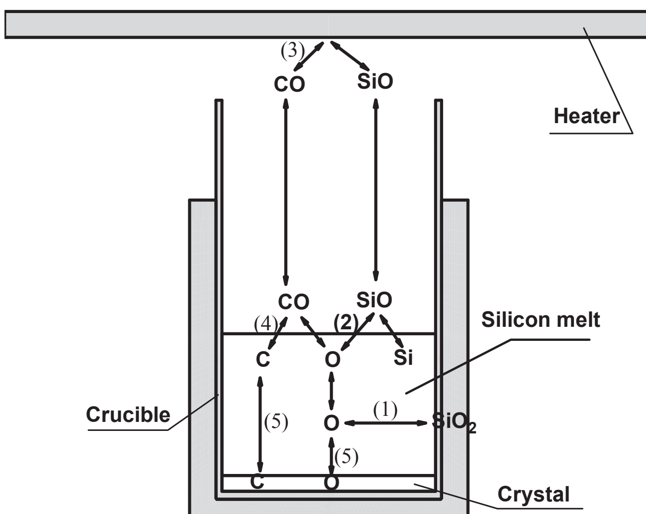

FIGURE 21.16 The basic processes of oxygen and carbon incorporation into a crystal. *After Ref. [66] with permission from Elsevier.*

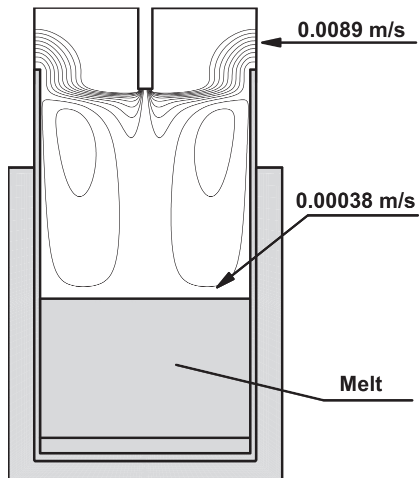

FIGURE 21.17 Gas flow field above the crucible for flow rate of 0.8 L/min and pressure of 0.1 atm. *After Ref. [66] with permission from Elsevier.*

static pressure was 0.1 atm. A recirculation flow establishes above the melt surface and a main convection flow passes through the top of the crucible. The upper convection flow hinders the back diffusion of CO from the crucible exterior into the melt. Therefore, if the upper convection flow is increased and the recirculation flow eliminated, CO transportation into the melt might be dramatically reduced. From Figure 21.17, CO reenters the melt mainly by diffusion flux through the area AB. Significant reduction of the diffusion area will reduce the CO flux into the melt. To reduce carbon or oxygen in a grown crystal, we must optimize the flows of gas and the melt during crystal growth.

21.7 Summary

Melt convection plays an important role in all crystal growth processes. The melt flow transports mass and heat, and may considerably affect the crystal growth conditions. For instance, convection may introduce undesired temperature fluctuations and inhomogeneous impurity and dopant incorporation, but may also dampen or stir the fluid phase, which improves the crystal quality. Understanding and controlling convection remain major challenges for industrial crystal production. Convection is also highly important in epitaxial processes, as discussed in Volume III. Engineering the melt flow is essential for increasing the production yield of grown materials. Especially, the flow structure and strength can be enhanced by external forces such as magnetic fields. Steady and unsteady Lorentz forces become important in large melt masses. These measures have greatly benefitted the production of standard crystals such as silicon and semiconductor compounds, and are applicable to new materials that will be developed in future information and energy-saving technologies.

References

[1] Shewmon PG. Diffusion in solids. McGraw-Hill; 1963. p. 2.

[2] Liu LJ, Kakimoto K. Int J Heat Mass Transfer 2005;48:4481.

[3] Kakimoto K. Czochralski, silicon single crystals for semiconductor and solar cell applications. Springer; 2010. 231.

[4] Mueller G, Ostrogorski A. Handbook of crystal growth. Growth mechanism and dynamics, vol. 2b. North Holland; 1994. 738.

[5] Liu L, Nakano S, Kakimoto K. J Cryst Growth 2006;292:515.

[6] Rudolph P, Kakimoto K. MRS Bull 2009;34:1.

[7] Akamatsu M, Kakimoto K, Ozoe H. J Mater Process Manuf Sci 1997;5:329.

[8] Hoshi K, Suzuki T, Okubo Y, Isawa N. Extended abstracts electrochem. soc. Spring Meeting V01. 80-1. Pennington (NJ): Electrochemical Society; 1980. 811.

[9] Suzuki T, Isawa N, Okubo Y, Hoshi K. In: Huff HR, Kriegler RJ, Takeishi Y, editors. Semiconductor silicon 1981. Pennington (NJ): Electrochemical Society; 1981. p. 213.

[10] Hirata H, Hoshikawa K. J Cryst Growth 1989;98:777.

[11] Series RW. J Cryst Growth 1989;7:92.

[12] Jing CJ, Imaishi N, Yasuhiro S, Sato T. Int J Heat Mass Transfer 2000;43:4347.

[13] Miyazawa Y, Morita S, Sekiwa H. J Cryst Growth 1996;166:286.

[14] Chandrasekhar S. Hydrodynamic and hydromagnetic stability. Clarendon, Oxford; 1961.

[15] Ozoe H, Iwamoto M. J Cryst Growth 1994;142:236.

[16] Krauze A, Muiznieks A, Muhlbauer A, Wetzel Th, Ammon W v. J Cryst Growth 2004;262:157.

[17] Liu L, Kakimoto K. Int J Heat Mass Transfer 2005;48:4481. 4492.

[18] Kalaev VV. J Cryst Growth 2007;303:203.

[19] Vizman D, Watanabe M, Friedrich J, Müller G. J Cryst Growth 2007;303:221.

[20] Watanabe M, Eguchi M, Wang W, Hibiya T, Kuragaki SS. J Cryst Growth 2002;237:1657.

[21] Hoshi K, Isawa N, Suzuki T, Ohkubo Y. J Electrochem Soc 1985;132:693.

[22] Watanabe M, Eguchi M, Hibiya T. J Cryst Growth 1998;193:402.

[23] Watanabe M, Eguchi M, Hibiya T. Jpn J Appl Phys 1999;38:L10.

[24] Kakimoto K, Tashiro A, Shinozaki T, Ishii H, Hashimoto Y. J Cryst Growth 2002;243:55.

[25] Kakimoto K, Shinozaki T, Hashimoto Y. Int J Mater Product Technol 2005;22:84.

[26] Liu L, Nakano S, Kakimoto K. J Cryst Growth 2007;299:48.

[27] Verezub NA, Zharikov EV, Kalitin SP, Lavrishchev SV, Myal'dun AZ, Pain YM. Crystallogr Rep 1996; 41(6):1056.

[28] Grugel NR, Lee CP, Anilkumar AV, Wang TG, Shen XF, Croell A, et al. Adv Space Res 1999;24:1195.

[29] Feigelson RS, Zharikov EV. NASA microgravity materials science conference. Tuntsville (AL); 2000. 222.

[30] Liu W–S, Wolf MF, Elwell DE, Feigelson RS. J Cryst Growth 1987;82:589.

[31] Carruthers JR, Witt AF. Cryst growth Charact 1976;32:13.

[32] Mollot DJ, Tsamopoulos J, Chen T-Y, Ashgriz N. J Fluid Mech 1993;255:411.

[33] Yi K-W, Kakimoto K, Eguchi M, Watanabe M, Shyo T, Hibiya T. J Cryst Growth 1994;144:20.

[34] Ristorcelli JR, Lumley JL. J Cryst Growth 1992;116:447.

[35] Jones ADW. J Cryst Growth 1983;63:70.

[36] Miller DC, Pernell TL. J Cryst Growth 1982;57 (1992) 447.

[37] Fowlis WW, Hide R. J Atmos Sci 1965;31:541.

[38] Hide R, Mason PJ. Adv Phys 1975;4:47.

[39] Morita O. Phase Transitions 1990;28:213.

[40] Watanabe M, Eguchi M, Kakimoto K, Baros Y, Hibiya T. J Cryst Growth 1993;128:288.

[41] Eady ET. Tellus 1949;1:33.

[42] Smagorinsky. Mon Weather Rev 1963;91:99.

[43] Liu LJ, Liu X, Wang Y. Int J Heat Mass Transfer 2012;55:53.

[44] Rudolph P. Transport phenomena of crystal growth-heat and mass transfer. 107 Selected Topics on Crystal Growth AIP Conf Proc 2010.

[45] Wang XL, Cai D, Zhang H. Int J Heat Mass Transfer 2007;50:1221.

[46] Wang XL, Cai D, Zhang H. J Cryst Growth 2007;305:122.

[47] Chen XJ, Liu LJ, Tezuka H, Usuki Y, Kakimoto K. J Cryst Growth 2008;310:1810.

[48] Buckle U, Peric M. Numer Heat Transfer Part A 1992;21:101.

[49] Segal AS, Vorob'ev AN, Karpov S Yu, Makarov Yu N, Mokhov EN, Ramm MG, et al. Mater Sci Eng B 1999;61–62:40.

[50] Matsuo H, Ganesh RB, Nakano S, Liu LJ, Kangawa Y, Arafune K, Ohshita Y, Yamaguchi M, Kakimoto K. J Cryst Growth 2008;310:2204.

[51] Bornside DE, Brown RA. J Electrochem Soc 1995;142:2790.

[52] Fukuda T, Koizuka M, Ohsawa A. J Electrochem Soc 1994;141:2216.

[53] Sun Q, Yao KH, Lagowski J, Gatos HC. J Appl Phys 1990;67:4313.

[54] Ogino M. Appl Phys Lett 1982;41:847.

[55] Kolbesen BO. Aggregation phenomena of point defects in silicon. In: Sirtl E, Goorissen J, editors. The electrochemical society proceedings series, vol. 83–4; 1983. pp. 155–75.

[56] Goesele U. Oxygen, carbon, hydrogen and nitrogen in crystalline silicon. In: Mikkelsen Jr JC, Peaton SP, Corbett JW, Pennycook SJ, editors. Mater. Res. Soc. Symp. Proc. Pittsburgh (PA): MRS; 1986. p. 419.

[57] Shimura F. In: Semiconductor silicon crystal technology. New York: Academic Press; 1989. p. 148.

[58] Abe T. Silicon materials. In: Einspruch NG, Huff H, editors. VLSI electronics, microstructure science series, vol. 12. New York: Academic Press, Inc.; 1985. p. 3.

[59] Goesele U, Tan TY. Appl Phys 1982;A 28:79.

[60] Bauer J, Breitenstein O, Rakotoniaina JP. In: Proceedings of 21st EUPVSEC, September, Dresden, Germany; 2006. p. 1115. p. 3.

[61] Liu LJ, Nakano S, Kakimoto K. J Cryst Growth 2007;303:165.

[62] Miyazawa H, Liu LJ, Hisamatsu S, Kakimoto K. J Cryst Growth 2008;310:1034.

[63] Chen XJ, Nakano S, Liu LJ, Kakimoto K. J Cryst Growth 2008;310:4330.

[64] Nakano S, Liu LJ, Chen XJ, Matsuo H, Kakimoto K. J Cryst Growth 2009;311:1051.

[65] Gao B, Nakano S, Kakimoto K. J Electrochem Soc 2010;157:H153.

[66] Gao B, Chen XJ, Nakano S, Kakimoto K. J Cryst Growth 2010;312:1572.

22 The Role of Marangoni Convection in Crystal Growth

Takao Tsukada

DEPARTMENT OF CHEMICAL ENGINEERING, TOHOKU UNIVERSITY, SENDAI, JAPAN

CHAPTER OUTLINE

22.1 Introduction 871
22.2 Surface Tension of Molten Materials 873
22.2.1 Surface Tension of Molten Silicon 873
22.2.2 Surface Tension of Other Molten Semiconductors 877
22.2.3 Surface Tension of Molten Oxides 878
22.3 Marangoni Convection 878
22.3.1 Thermo-Solutocapillary Convection 878
22.3.2 Marangoni–Benard Instability 882
22.3.3 Hydrothermal Wave 884
22.4 Marangoni Convection in Crystal Growth 886
22.4.1 CZ Crystal Growth System 886
22.4.1.1 Silicon Crystal Growth 886
22.4.1.2 Oxide Crystal Growth 888
22.4.2 FZ Crystal Growth System 892
22.4.3 Bridgman, Edge-defined Film-fed, and Other Crystal Growth Systems 897
22.4.3.1 Horizontal Bridgman 898
22.4.3.2 Other Methods 902
22.5 Concluding Remarks 904
References 904

22.1 Introduction

Surface tension acts at the liquid/gas interface (usually called “surface”), and the force tends to minimize the surface area, i.e., surface energy. Therefore, in the absence of other forces, including gravity force, the floating quiescent liquid volume takes a perfectly spherical shape.

Handbook of Crystal Growth. http://dx.doi.org/10.1016/B978-0-444-63303-3.00022-5
Copyright © 2015 Elsevier B.V. All rights reserved.

From a microscale viewpoint, the unbalanced forces of intermolecular attraction at the liquid surface result in the attracted forces into the bulk liquid because the attraction of the underlying molecules is greater than the attraction by the vapor or other gas molecules on the other side of the surface. This inward attraction force causes the surface contraction and gives rise to a force in the plane of the surface, namely surface tension. Surface tension of water is larger than that of organic liquids, and, furthermore, surface tension of molten metals and semiconductors is approximately five or ten times as large as that of water. This is due to the differences of intermolecular forces; the hydrogen bond and metallic bond exist between water molecules and between metal atoms as the attractive forces, respectively, although the force between organic molecules is only van der Waals force.

The surface tension of common liquids decreases with temperature. Therefore, the surface tension–induced shear stress acts from a region of higher temperature to that of lower temperature along the liquid surface when a temperature gradient exists on the surface as shown in Figure 22.1. Considering the force balance across an infinitesimal length dx on the surface, the following equation for the shear stress along the surface τ is obtained if the viscous force from the gas phase can be negligibly small.

$$\tau dx = -\mu\left(\frac{\partial u}{\partial z}\right)dx = -d\gamma = -\left(\frac{\partial \gamma}{\partial T}\right)\left(\frac{\partial T}{\partial x}\right)dx \tag{22.1}$$

Here, T, u, γ, $(\partial\gamma/\partial T)$ and μ are temperature, x-component of velocity, surface tension, temperature coefficient of surface tension and liquid viscosity, respectively. The shear stress due to the surface tension gradient in Eqn (22.1) drives the flow in the liquid. This phenomenon is called the Marangoni effect, and the induced flow is Marangoni flow (convection), named after the Italian physicist Carlo Giuseppe Matteo Marangoni (1840–1925). Since the surface tension gradient is caused not only by difference in temperature but also by that in concentration of surface active solute C or surface adsorption of surfactant Γ, Eqn (22.1) is generally rewritten as follows:

$$\tau dx = -\left(\frac{\partial \gamma}{\partial T}\right)\left(\frac{\partial T}{\partial x}\right)dx - \left(\frac{\partial \gamma}{\partial C}\right)\left(\frac{\partial C}{\partial x}\right)dx - \left(\frac{\partial \gamma}{\partial \Gamma}\right)\left(\frac{\partial \Gamma}{\partial x}\right)dx \tag{22.2}$$

In every crystal growth process with the melt-free surface, e.g., the Czochralski (CZ) growth, floating-zone (FZ) growth, horizontal Bridgman (HB) growth, edge-defined film-fed growth (EFG), and also solution or flux growth techniques, the surface

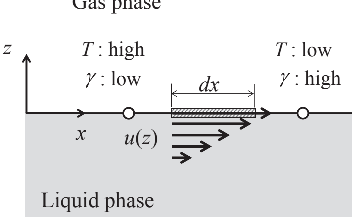

FIGURE 22.1 Schematic diagram of Marangoni flow.

tension–driven Marangoni convection occurs because the temperature gradient and also concentration gradient in the mixed materials should exist along the melt or solution surface (the following concentrate on melt growth only, but all fundamentals are applicable for solution and flux growth, too).

Melt convection, e.g., buoyancy convection or forced convection due to crystal or crucible rotation in the CZ growth, affects heat and mass transfer in the melt and crystal, and consequently, the spatial homogeneity of impurities or dopants and formation of microdefects in semiconductor crystals, and also melt/crystal interface inversion and crack formation in oxide crystals. Marangoni convection in the melt should also exhibit similar effects with regard to the crystal quality. Some pioneers of Marangoni convection research in the field of crystal growth include Chang and Wilcox [1,2], Chang et al. [3], Clark and Wilcox [4], for numerical simulation research; Chun and Wuest [5,6], Schwabe et al. [8], Schwabe and Scharmann[9], Schwabe [10], for experimental research; these researchers have carried out a large number of experiments with real or model materials and numerical simulations for Marangoni convection. The opportunity to conduct scientific experiments in a microgravity environment triggered intensive studies on Marangoni flow in low and high Prandtl number liquids, because the Marangoni flow is a typical gravity-independent phenomenon but is often obscured by buoyancy convection on the ground whose direction is generally the same as that of Marangoni convection.

In this chapter, firstly, the measured values of surface tension and its temperature coefficient of molten semiconductors and oxides that are key thermophysical properties in numerical simulations and discussions on Marangoni convection will be introduced in Section 22.2, and then general considerations of the Marangoni effect, i.e., thermo- and solutocapillary flows, Marangoni–Benard convection and hydrothermal wave, will be described in Section 22.3. Finally, the Marangoni convection in important melt growth techniques, such as Czochralski, floating-zone, horizontal Bridgman growth, and others will be discussed in detail in Section 22.4.

22.2 Surface Tension of Molten Materials

22.2.1 Surface Tension of Molten Silicon

Figure 22.2 shows the temperature dependences of surface tension of molten silicon [12]. The thin lines in the figure are the surface tensions collected in the paper by Keene [13], who, in 1987, reviewed the studies on the surface tension of molten silicon based on 26 previous papers; the thick lines are the data measured after Keene's review plus the data by Yuan et al. [12]. From the figure, it is found that there are considerable variations in the measured data of surface tension, and, moreover, the maximum variation in its temperature coefficient might be more than one digit. Although Keene [13] pointed out that the reason why some surface tensions of the thin lines in Figure 22.2 are relatively lower than the others might be due to the presence of oxygen in molten silicon acting as

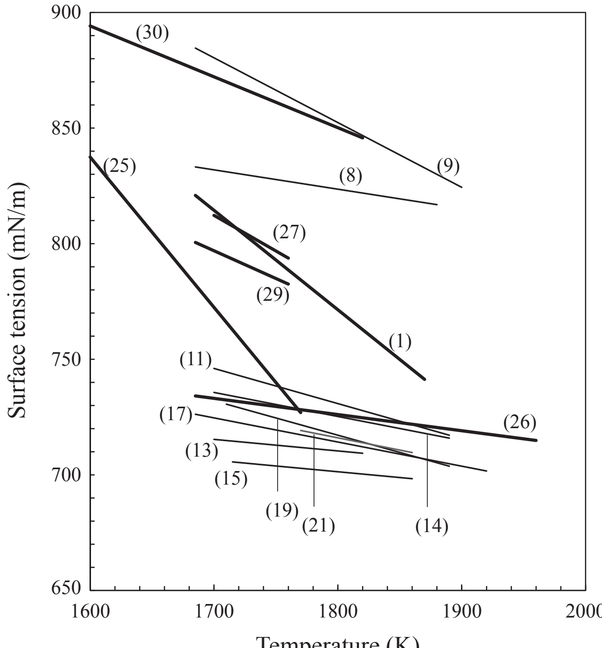

FIGURE 22.2 Surface tension of molten silicon measured by various researchers. The reference number given in each line corresponds to that used in Yuan et al. [12]. *(From Ref. [12].)*

a contaminant, there was no study in which the effect of oxygen on surface tension of molten silicon was quantitatively investigated before his review.

Mukai et al. [14,15] investigated the effects of temperature and oxygen partial pressure in argon atmosphere P_{O_2} on surface tension of molten silicon using a sessile droplet method. Figures 22.3 and 22.4 show the measured results of surface tension and its temperature coefficient of molten silicon, respectively. The dotted lines in the figures correspond to the following equations fitted to the measured data:

(Surface tension)

$$\gamma = 831 - 29.5 \ln\left(1 + 3.88 \times 10^{10} P_{O_2}^{1/2}\right) \quad \text{at } 1693\text{ K} \tag{22.3}$$

$$\gamma = 814 - 30.1 \ln\left(1 + 3.06 \times 10^{10} P_{O_2}^{1/2}\right) \quad \text{at } 1723\text{ K} \tag{22.4}$$

$$\gamma = 793 - 30.6 \ln\left(1 + 2.47 \times 10^{10} P_{O_2}^{1/2}\right) \quad \text{at } 1753\text{ K} \tag{22.5}$$

$$\gamma = 774 - 31.0 \ln\left(1 + 1.01 \times 10^{10} P_{O_2}^{1/2}\right) \quad \text{at } 1773\text{ K} \tag{22.6}$$

(Temperature coefficient of surface tension)

$$\begin{aligned} &d\gamma/dT = -0.90 + 0.370 \ln\left(1 + 6.62 \times 10^{10} P_{O_2}^{1/2}\right) - 0.387 \ln\left(1 + 8.22 \times 10^{9} P_{O_2}^{1/2}\right) \\ &(1693\text{ K} < T < 1773\text{ K}, \quad P_{O_2} < P_{O_2,sat}) \end{aligned} \tag{22.7}$$

Here, $P_{O_2,sat}$ is the equilibrium oxygen partial pressure at which SiO_2 can be formed at the molten silicon surface. These results suggest that the surface tension and its

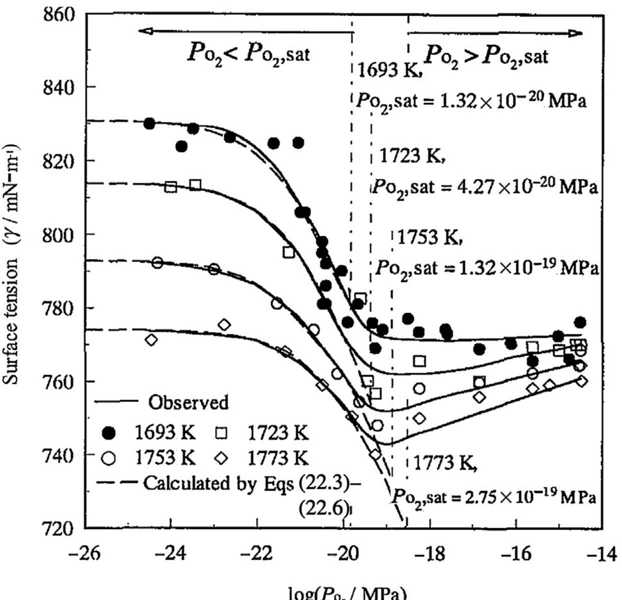

FIGURE 22.3 Surface tension of molten silicon as a function of logarithmic oxygen partial pressure in argon. *(From Ref. [15].)*

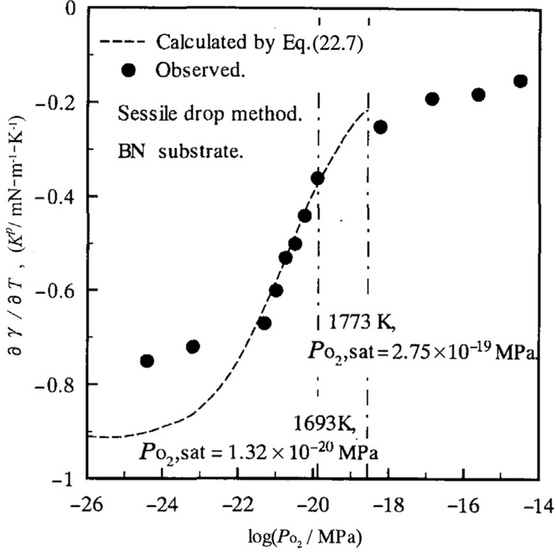

FIGURE 22.4 Relation between the temperature coefficient of surface tension and the oxygen partial pressure. *(From Ref. [15].)*

temperature coefficient strongly depend on the oxygen partial pressure in the atmosphere; in other words, control of partial pressure is important for the measurement of surface tension. Comparing the values in Keene's review with the measured values by Mukai et al. [15], it can be inferred that low surface tension of approximately 700 mN/m in Figure 22.2 might be measured at oxygen partial pressure higher than $P_{O_2,sat}$ and the melt surface might be oxidized.

Recently, a droplet oscillation method using an electromagnetic levitator has been proposed as a method to precisely measure surface tension of molten materials [16,17]. This containerless method, by which surface tension can be determined from the oscillatory frequency of electromagnetically levitated droplet shape, has the following advantages: (1) the contamination from the container to hold a sample is completely avoidable, (2) measurement at high temperature is possible because of preventing the reaction with container wall, (3) measurement under undercooling conditions is possible without inhomogeneous nucleation at container wall, and (4) control of surrounding atmosphere is easy. Since these advantages allow the measurement to be performed in a wide range of temperature including undercooling condition, measurement uncertainties of surface tension and its temperature coefficient can be reduced. Although a droplet oscillation method with an electrostatic levitator has been also used to measure the surface tension of molten silicon [18,19], this measurement method must be operated only in low pressure to prevent electric discharge.

Figure 22.5 shows the relationship between temperature and surface tension of molten silicon measured with an electromagnetic levitator [16], considering the dependence of oxygen partial pressure in surrounding atmosphere, P_{O_2}. In the figure, the values measured by Mukai et al. [15] are also shown. Increasing P_{O_2}, the surface tension

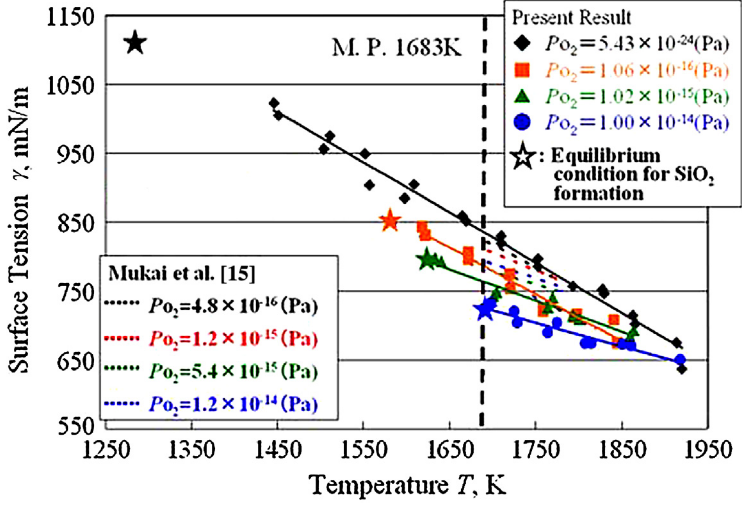

FIGURE 22.5 Surface tension of molten silicon measured by electromagnetically levitation technique. *(From Ref. [16].)*

decreases due to the adsorption of surface active element, namely oxygen, and the absolute value of its temperature coefficient also decreases gradually. These trends are almost the same as those by Mukai et al. [15], although the absolute value is different. From the figure, it is found that the degree of undercooling becomes smaller, and, consequently, the temperature range to measure the surface tension becomes narrow as P_{O_2} increases. This is due to the increase in the equilibrium temperature of SiO_2–O_2 system with P_{O_2}. The star plots in the figure are the calculated equilibrium temperatures for each $P_{O_2,sat}$ at which SiO_2 is generated at the melt surface, and coincide with the minimum temperatures to measure the surface tension except for $P_{O_2} = 5.43 \times 10^{-24}$ Pa. The measurement certainty of surface tension in Figure 22.5 was approximately 5%.

Since adsorption of surface active element, oxygen on the surface of molten metals, is always an exothermic process, at highly increased temperatures the oxygen molecules desorb, and consequently the surface tension should approach the value of pure (oxygen free) molten metals. Considering the temperature dependence of surface tension itself is negative as well, it can be inferred that the surface tension of molten materials under an oxygen atmosphere takes its maximum value at a certain temperature. Recently, it was demonstrated by experiments using an electromagnetic levitator that the temperature dependence of surface tension of molten materials such as iron and silver is boomerang shaped [20,21]. In the case of molten silicon, however, the temperature dependence of surface tension is only negative as shown in Figure 22.5 because the surface is covered by stable SiO_2 film at high P_{O_2}.

22.2.2 Surface Tension of Other Molten Semiconductors

Besides molten silicon, the surface tension measurements of molten germanium and Si_xGe_{1-x} have also been performed. Rhim and Ishikawa [22] measured the surface tension of molten germanium by an oscillating drop method with an electrostatic levitation technique in a temperature range of 1160–1430 K in a vacuum, and indicated the temperature dependence $\gamma = 583 - 0.08(T - 1211)$ mN/m (measurement uncertainty: <2%). Kaiser et al. [23] also carried out the surface tension measurement of molten germanium by a sessile drop method and obtained the temperature dependence $\gamma = 591 - 0.08(T - 1211)$ mN/m.

For molten Si_xGe_{1-x}, the concentration (x) dependence of surface tension has been investigated as well as the temperature dependence. Cröll et al. [24] measured the surface tension of molten Si_xGe_{1-x} by a sessile drop method and obtained the concentration coefficient of surface tension, $+2.2 \times 10^{-3}$ N/(m.at%Si) for $0.02 < x < 0.13$. In addition, they revealed that the average temperature coefficient of Si_xGe_{1-x} in this concentration range was -0.07×10^{-3} N/(mK), which was almost the same as that of pure molten germanium. Recently, Chathoth et al. [25] measured a unique concentration dependence of molten Si_xGe_{1-x} surface tension by using an electromagnetic levitation technique in microgravity environment. Here, the surface tension of molten Si_xGe_{1-x} took a minimum at approximately $x = 0.25$ for liquidus temperature, although this experimental fact has already been predicted by a molecular dynamics simulation [26].

For molten compound semiconductor GaAs, Shetty et al. [27] measured the surface tension as a function of As concentration in a temperature range of 1513–1553 K by using a sessile drop method, and proposed the following temperature and concentration dependences of surface tension $\gamma = -0.96T - 10000\rho + 1670$ mN/m (ρ = the amount of excess As in ampoule (g)/vapor space in ampoule (cm^3)). Similarly, Rupp and Müller [28] measured the temperature dependence of the surface tension of GaAs by a sessile drop method under As vapor pressure controlled in a temperature range of 1370–1610 K, and obtained, for instance, $\gamma = 401$ mN/m and $d\gamma/dT = -0.18$ mN/(mK) at the melting point 1511 K, respectively. Including the above surface tensions of molten GaAs, the surface tensions of molten compound semiconductors measured before 1992 were reviewed by Nakamura and Hibiya [29].

22.2.3 Surface Tension of Molten Oxides

Comparing with surface tension of molten semiconductors described above, the amount of data for the surface tension of molten oxides is limited. Shigematsu et al. [30] measured the surface tension of molten $LiNbO_3$ by the du Nouy ring method in a temperature range of 1250–1340 K. The measurement error was ± 0.03 N/m, and the temperature coefficient of surface tension of molten $LiNbO_3$ was -3×10^{-4} N/(mK). Tokizaki et al. [31] investigated the effect of additional impurity, MgO, on the surface tension of congruent $LiNbO_3$ in a temperature range of 1250–1450 K, and revealed that the temperature dependences at 0 and 5 mol% MgO were $400.4 - 7.98 \times 10^{-2}T$ mN/m and $491.8 - 1.75 \times 10^{-1}T$ mN/m, respectively. Recently, Nagasaka and Kobayashi [32] have developed a new noncontact method for measuring the surface tension of molten oxides in which the propagation of thermally exited capillary wave with nanometer-order amplitude, namely ripplon, was detected by a surface laser–light scattering (SLLS) apparatus, and revealed the temperature dependence of surface tension of molten $LiNbO_3$ in Ar gas and dry air atmospheres, i.e., $\gamma(\mathrm{Ar}) = 311.7 - 0.0736(T - 1526)$ mN/m (measurement uncertainty: $\pm 2.6\%$) and $\gamma(\mathrm{air}) = 296.4 - 0.1642(T - 1526)$ mN/m (measurement uncertainty: $\pm 1.9\%$), respectively.

22.3 Marangoni Convection

22.3.1 Thermo-Solutocapillary Convection

Consider the steady, two-dimensional flow and thermal fields in a thin liquid layer of depth d and width L as shown in Figure 22.6, where the bottom of the layer is adiabatic and the temperatures on the left and right sides are T_H and T_C ($<T_H$), respectively. When the temperature distribution in x-direction along the surface of the layer is linear, the distribution of surface tension in x-direction $\gamma(x)$ is given as follows:

$$\gamma(x) = \gamma(T_H) - \left(\frac{\partial \gamma}{\partial T}\right)\left\{\frac{(T_H - T_C)x}{L}\right\}. \tag{22.8}$$

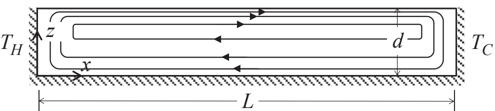

FIGURE 22.6 Thin liquid layer.

Here, it is assumed that the flow in the layer is governed by the Stokes equation without external forces, which neglects the nonlinear inertial term. Considering that the fluid motion in x-direction is dominant and the z-component of velocity is negligibly small in the region far away from both sides of the layer, the momentum and energy equations for x-component of velocity u and T there are given by the following equations.

$$\mu\left(\frac{\partial^2 u}{\partial z^2}\right) = 0, \tag{22.9}$$

$$u\left(\frac{dT}{dx}\right) = \kappa\left(\frac{\partial^2 T}{\partial z^2}\right) \tag{22.10}$$

where κ and μ are thermal diffusivity and viscosity, respectively, and dT/dx is the longitudinal temperature gradient on the surface. If the volume of the liquid layer is finite, the circular flow that satisfies the mass balance expressed by Eqn (22.11) appears in the layer, as shown in Figure 22.6.

$$\int_0^d u dz = 0 \tag{22.11}$$

Solving Eqns (22.9) and (22.10) under the constraint condition of Eqn (22.11) and the following boundary conditions,

$$\text{At wall surface } (z = 0)\text{: } u = 0, \tag{22.12}$$

$$\text{At wall surface } (z = 0)\text{: } \frac{\partial T}{\partial z} = 0 \tag{22.13}$$

$$\text{At liquid surface } (z = d)\text{: } \mu\left(\frac{\partial u}{\partial z}\right) = \left(\frac{\partial \gamma}{\partial T}\right)\left(\frac{dT}{dx}\right), \tag{22.14}$$

$$\text{At liquid surface } (z = d)\text{: } \frac{\partial T}{\partial z} = 0 \tag{22.15}$$

the equations for x-component of velocity u and temperature T are obtained as follows:

$$u = \frac{1}{4\mu d}\left(\frac{\partial \gamma}{\partial T}\right)\left(\frac{dT}{dx}\right)(3z^2 - 2zd) = \frac{1}{\mu}\left(\frac{\partial \gamma}{\partial T}\right)\left(\frac{dT}{dx}\right)z + \frac{3}{4\mu d}\left(\frac{\partial \gamma}{\partial T}\right)\left(\frac{dT}{dx}\right)z(z-2d) \tag{22.16}$$

$$T = \frac{1}{16\mu\kappa d}\left(\frac{\partial \gamma}{\partial T}\right)\left(\frac{dT}{dx}\right)^2\left(z^4 - \frac{4}{3}dz^3 + \frac{1}{3}d^4\right) \tag{22.17}$$

Figure 22.7 shows the distribution of u and T in Eqns (22.16) and (22.17). Also, the surface velocity of the liquid layer, i.e., the maximum velocity in Eqn (22.16), u_{max}, is a quarter of the surface velocity without the reverse flow, i.e., the first term of the u in Eqn (22.16).

$$u_{\text{max}} = \frac{d}{4\mu}\left(\frac{\partial \gamma}{\partial T}\right)\left(\frac{dT}{dx}\right) \tag{22.18}$$

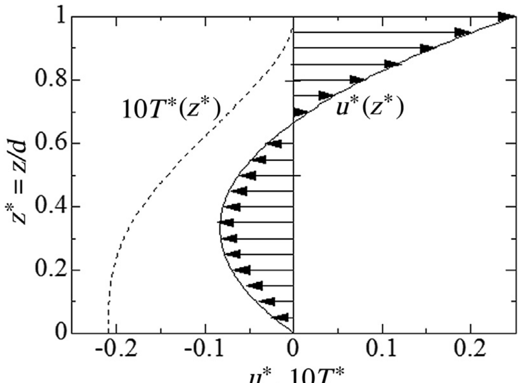

FIGURE 22.7 Marangoni flow pattern and temperature distribution in a thin liquid layer,

$$\text{where}\begin{cases} u^* = \dfrac{\mu}{(\partial\gamma/\partial T)(dT/dx)d}u = \dfrac{1}{4}\left(3z^{*2} - 2z^*\right) \\ T^* = \dfrac{\mu\kappa}{(\partial\gamma/\partial T)(dT/dx)^2 d^3}T = \dfrac{1}{16}\left(z^{*4} - \dfrac{4}{3}z^{*3} + \dfrac{1}{3}\right) \end{cases}$$

Note that the simple one-dimensional distributions expressed by Eqns (22.16) and (22.17) are applicable only at the central region in the liquid layer with sufficiently large aspect ratio L/d, and that the two-dimensional velocity distributions of return flow definitely appear near both sides of the layer as shown in Figure 22.6.

The flow induced by surface tension gradient due to the temperature distribution along the surface of a thin layer, such as expressed by Eqn (22.16) or shown in Figure 22.7, is Marangoni convection introduced in Section 22.1, and also called thermocapillary convection. Besides, the similar convection induced by the concentration gradient of solute along the surface of a solution is called solutocapillary convection. The thermo- and solutocapillary convections are characterized by the following Marangoni numbers, *Ma*, respectively:

$$\text{Thermocapillary Marangoni number}: \quad Ma = \frac{\left|\frac{\partial\gamma}{\partial T}\right|\left(\frac{\Delta T}{L}\right)d^2}{\mu\kappa} \tag{22.19}$$

$$\text{Solutocapillary Marangoni number}: \quad Ma = \frac{\left|\frac{\partial\gamma}{\partial C}\right|\left(\frac{\Delta C}{L}\right)d^2}{\mu D}. \tag{22.20}$$

Here, $\partial\gamma/\partial T$ and $\partial\gamma/\partial C$ are the temperature and concentration coefficients of surface tension, ΔT and ΔC are the temperature and concentration differences, D is diffusion coefficient, and L or d is the characteristic length, e.g., width and depth of the layer in Figure 22.6, respectively. In some cases, the following Reynolds numbers Re_γ are used instead of Ma:

$$\text{Thermocapillary Reynolds number}: \quad Re_\gamma = \frac{Ma}{Pr} = \frac{\left|\frac{\partial\gamma}{\partial T}\right|\left(\frac{\Delta T}{L}\right)d^2}{\mu\nu} \tag{22.21}$$

$$\text{Solutocapillary Reynolds number}: \quad Re_{\gamma} = \frac{Ma}{Sc} = \frac{\left|\frac{\partial \gamma}{\partial C}\right| \left(\frac{\Delta C}{L}\right) d^2}{\mu \nu}. \tag{22.22}$$

Here, Pr $(=\nu/\kappa)$ and Sc $(=\nu/D)$ are the Prandtl and Schmidt numbers, and ν is kinematic viscosity.

Figure 22.8 shows the numerical results of the changes in the pattern of two-dimensional Marangoni convection in a liquid layer with low Prandtl number $Pr = 0.01$ for increasing values of Ma, where the cold and hot sides are on the left and on the right of each layer, and additionally both upper and lower boundaries are adiabatic [33]. For small Ma, the flow in the layer is simply unicellular and reveals a parallel flow state in the central region of the layer with the exception of an upwind region close to the hot sidewall in which the flow is accelerated and a downwind region close to the cold sidewall in which the flow is decelerated. As Ma increases, however, the circulation flow near the cold sidewall develops and the secondary cell appears in the overall circulation.

In the case of a thick liquid layer, buoyancy (Rayleigh) convection is also induced due to density variations in the layer as well as Marangoni convection if a horizontal

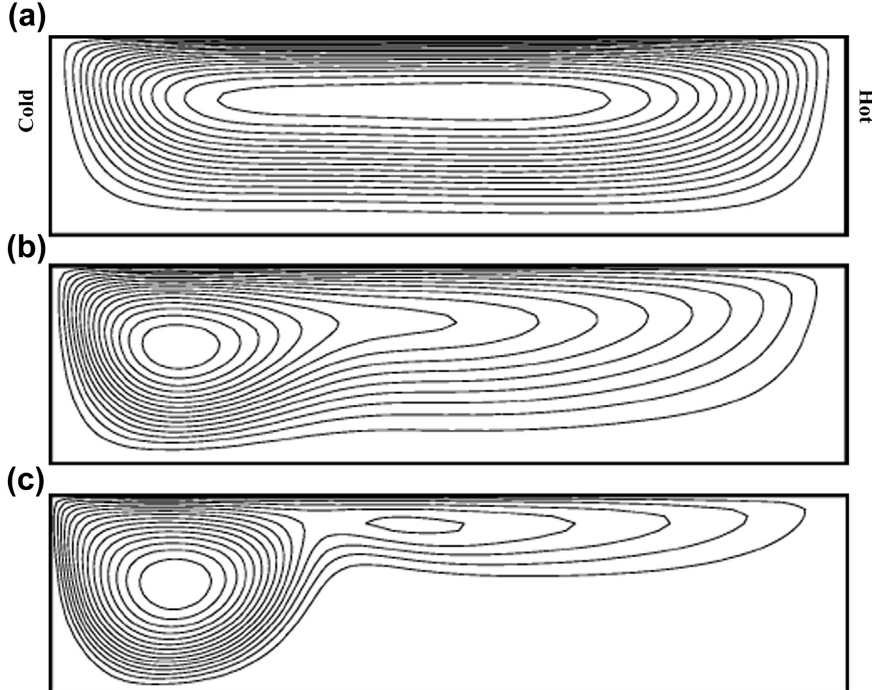

FIGURE 22.8 Structure of Marangoni convection in two-dimensional liquid layer for $Pr = 0.01$ and $L/d = 4$: $Ma =$ (a) 10, (b) 100, and (c) 1000. *(From Ref. [33].)*

temperature gradient exists in the layer. The buoyancy convection can be characterized by the following Rayleigh number Ra or Grashof number Gr:

$$Ra = \frac{\beta_T g(\Delta T/L)d^4}{\mu\kappa} = Gr \cdot Pr, \tag{22.23}$$

where β_T is volumetric expansion coefficient of the layer and g is gravitational acceleration. Considering the ratio of Rayleigh number to Marangoni number, i.e., the dynamic Bond number defined by

$$Bo_d = \frac{Ra}{Ma} = \frac{\beta_T g d^2}{|\partial\gamma/\partial T|} \tag{22.24}$$

it is found that buoyancy convection weakens rapidly if the depth of liquid layer d or the gravitational acceleration g decreases.

22.3.2 Marangoni–Benard Instability

Benard [34] carried out an experiment in which a horizontal liquid thin layer was heated from the bottom. When the heating rate is small, the liquid layer is quiescent, and heat transfers from the bottom to the top surface across the layer by conduction, being lost to the surroundings. In contrast, when the heating rate increases and the temperature difference across the layer exceeds a critical value, convection with aesthetic hexagonal patterns appears in the layer as shown in Figure 22.9 [35]. Here, the fluid streams up at the center of the hexagonal cell and flows down at the cell edges, and, moreover, it was found by the interferometric observations of surface deformation that the center of the cell is concave, whereas the cell edge is convex. Such convection is called the Marangoni–Benard convection induced by the Marangoni instability. The Marangoni

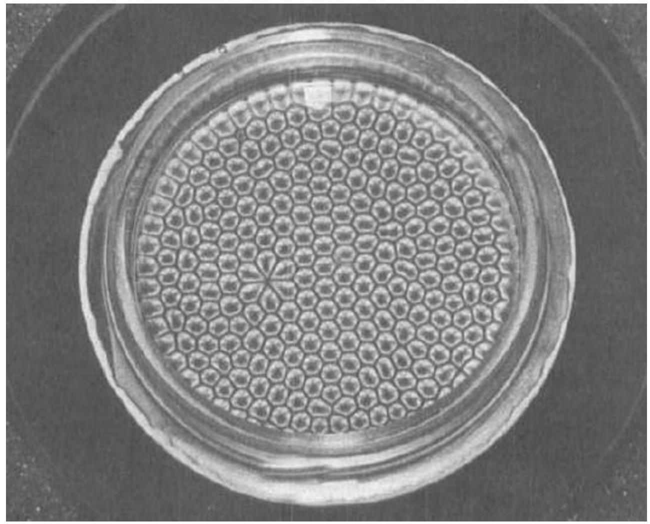

FIGURE 22.9 Marangoni–Benard convection in a thin liquid layer. *(From Ref. [35].)*

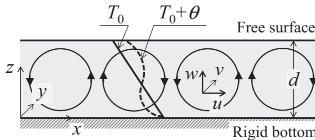

FIGURE 22.10 Schematic diagram of Marangoni instability, where u, v, w, and θ are the perturbations of velocity components and temperature.

number Ma^{MB}, in this case is defined by $|\partial\gamma/\partial T|\Delta Td/\mu\kappa$ using the temperature gradient across the layer ($\Delta T/d$) in Eqn (22.19). Although the thermocapillary or Marangoni convection in the previous section is absolutely induced if only a small horizontal temperature gradient exists along the surface of liquid layer, there is a critical value of temperature gradient across the layer that can initiate the Marangoni–Benard convection. Such a critical value, namely, the critical Marangoni number Ma_c^{MB}, can be found by the linear stability analysis of the Marangoni instability [36]. In the analysis, the instability of the basic state, where a liquid layer with a finite depth d is quiescent and a linear temperature profile $T_0(z)$ is applied across the layer as shown in Figure 22.10, with respect to infinitesimal perturbations of velocity and temperature is examined. When the force induced by the surface tension gradient due to the perturbations overcomes the frictional viscous damping, we expect that the basic state is destabilized and then patterned convection occurs as shown in Figure 22.10. According to the results of the analysis, Ma_c^{MB} varies depending on the boundary conditions at the bottom surface and Bi (defined by hd/k with thermal conductivity k and heat transfer coefficient h) at the liquid surface. For instance, when the bottom of the layer is solid and its temperature is fixed, and moreover the surface of the layer is adiabatic, $Ma_c^{MB} = 80$. In contrast, when both the rigid bottom and top of the layer are adiabatic, $Ma_c^{MB} = 48$. As Ma^{MB} increases, moreover, a new secondary pattern emerges, where the regularly assembled hexagons are replaced by a flow with another type of topology [37–39].

The linear stability analysis for a combination of the Rayleigh and Marangoni instabilities in a liquid layer heated from the bottom was carried out by Nield [40], who demonstrated that the onset condition of motion by the mixed effect could be predicted by the following correlation:

$$\frac{Ma^{MB}}{Ma_c^{MB}} + \frac{Ra}{Ra_c} \cong 1. \tag{22.25}$$

Here, Ra_c is a critical value of Ra for the onset of buoyancy-driven convection, i.e., $Ra_c = 669$ for a liquid layer with adiabatic surface and constant temperature bottom. At and above Ra_c, the buoyancy force overcomes the frictional viscous damping, and then the roll-patterned convection appears in the layer. Since Ma scales linearly with the depth of the layer d, whereas Ra exhibits a cubic dependence on d, the Marangoni instability becomes more dominant as d decreases.

22.3.3 Hydrothermal Wave

The thermocapillary convection (Marangoni flow) is driven by temperature-induced surface tension variations along the surface of a thin liquid layer as shown in Figure 22.6. When the temperature gradient along the liquid surface is relatively small, a two-dimensional surface flow directs from the hot side to the cold side, and a return flow appears at the bottom of the layer. However, this steady flow becomes unstable under a large temperature gradient. Smith and Davis [41] carried out a linear stability analysis of thermocapillary flow in an infinitely extended liquid layer with a depth d subjected to a constant horizontal temperature gradient (dT^0/dx) and with adiabatic bottom solid surface and free surface in the absence of gravity force, i.e., the flow and temperature distributions in this case are expressed by Eqns (22.16) and (22.17) and Figure 22.7. This two-dimensional flow becomes unstable when the temperature gradient, or Marangoni number Ma^{HTW} $(=|\partial\gamma/\partial T|(dT^0/dx)d^2/\mu\kappa)$, exceeds a certain threshold value. At and above the critical Marangoni number Ma_c^{HTW}, which is completely different from a critical Marangoni number Ma_c^{MB} for the onset of Marangoni–Benard convection in section 22.3.2, there appears a bunch of traveling oblique hydrothermal waves (HTWs), i.e., a group of roll cells propagates from colder region to hotter region. The propagation direction (wave vector of the HTWs) makes an angle θ with respect to the temperature gradient as shown in Figure 22.11. The figure also shows θ and Ma_c^{HTW} as a function of Pr. For low Pr liquids, the propagation direction is nearly perpendicular to the basic flow, while, for high Pr liquids, the waves propagate almost in the upstream direction.

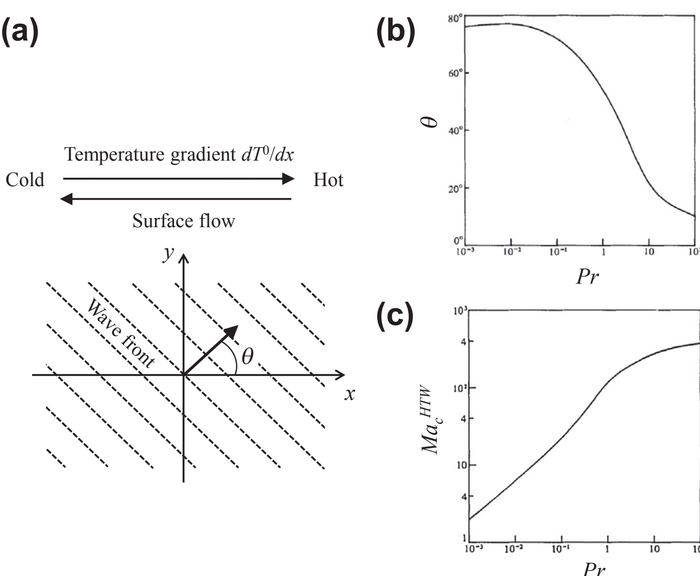

FIGURE 22.11 (a) Schematic of HTWs propagation from top view. (b), (c) Effect of Pr on propagation angle θ and critical Marangoni number. *(From Ref. [41].)*

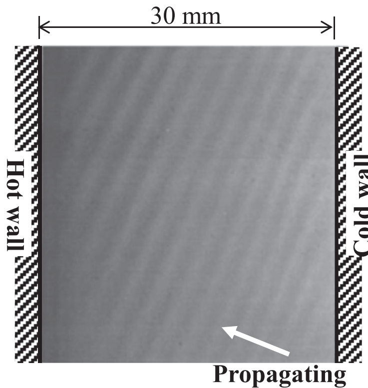

FIGURE 22.12 Instantaneous thermograph of HTWs on a 1.0-mm-deep layer viewed from above. *(From Ref. [42].)*

After the work of Smith and Davis [41], the HTWs have been confirmed by the experiments using thin rectangular pools of silicone oils with different Prandtl numbers as well as numerical simulations. Figure 22.12 shows an instantaneous infrared thermograph on the free surface of 1 cSt silicone oil layer ($Pr = 13.9$) with a depth of 1 mm [42]. The thermal waves are obliquely propagating from the cold wall to the hot wall as the theory of Smith and Davis predicts. Figure 22.13 shows a numerical results of flow field in a layer for $Pr = 10.3$, $Ma^{HTW} = 1000$, and aspect ratio $As = L/d = 10$ (L: width of the layer) [43]. It is found that, in the region outside the vicinity of the hot wall, secondary multicellular vortices are superimposed upon the basic return flow. The secondary vortices travel toward the hot wall, rotating in the same direction as the basic return flow, and cause the oblique thermal wave to propagate over the free surface as shown in Figure 22.12. In addition, it was revealed by the linear stability analysis of an infinitely extended liquid layer that a critical Marangoni number for the onset of the HTWs becomes larger in the presence of buoyancy force in liquid pool of $Pr = 13.9$ fluid [44] and increases with the heat transfer rate from liquid ($Pr < 1.0$) free surface to the surroundings [45].

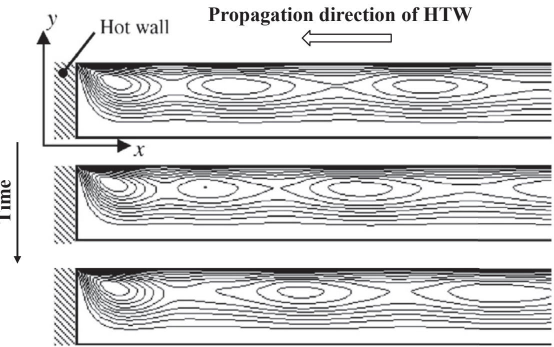

FIGURE 22.13 Instantaneous streamlines in the liquid layer near the hot wall at three instants. Time is increasing from the top to bottom. *(From Ref. [43].)*

However, the HTWs theory by Smith and Davis [41], in which the thermocapillary flow in an infinitely extended liquid layer was assumed as the basic state, is not directly applicable to the flow in liquid layer with finite extent, such as Figure 22.6, because the existence of the heat transfer walls significantly changes the base state from Figure 22.7 and the spatial structure of disturbances. The experimental and numerical results of the HTWs in Figures 22.12 and 22.13, strictly speaking, are influenced by both sidewalls. For instance, there is a steady vortex near the hot wall and thermal boundary layers beside the hot and cold walls. Because of the steep temperature changes in the thermal boundary layers in high Pr liquid pools, the actual temperature gradient along the surface is much smaller than the apparent gradient $\Delta T/L$ where ΔT is the temperature difference between the heat transfer walls. In a deep liquid layer in the presence of gravity, a steady vortex appearing near the heated side of the layer becomes stronger and its shape changes to ellipsoid as ΔT increases, and, consequently, the transition from two-dimensional steady flow to three-dimensional steady flow occurs due to the elliptic instability [46]. Since there is no thermal boundary layer in a low Pr liquid layer with finite extent, the surface flow is accelerated over the entire surface due to the Marangoni effect, and a strong vortex flow appears near the cold wall as shown in Figure 22.8(c). Consequently, the oscillatory flow similar to the HTWs arises due to the centrifugal instability in the vortex flow [47]. Such a variety of hydrodynamic instabilities modify the stability limit of two-dimensional steady thermocapillary flow in finite liquid layers.

22.4 Marangoni Convection in Crystal Growth

22.4.1 CZ Crystal Growth System

22.4.1.1 Silicon Crystal Growth

As mentioned in section 22.2.1, surface tension of molten silicon decreases with temperature. Therefore, the surface tension-induced shear stress, whose direction is from a region of higher temperature near the crucible to that of lower temperature near the crystal, gives rise to the thermocapillary (Marangoni) convection in the Czochralski (CZ) silicon melt. However, in addition to thermocapillary force, the flow in the CZ melt is also governed by the interaction of various driving forces for fluid flow, namely buoyant force, centrifugal force, and Coriolis force. For instance, the ratio of the buoyancy to thermocapillary forces (Bo_d) in a practical silicon CZ crucible is not small, but it might be difficult to evaluate the contribution of thermocapillary force on the melt flow since these two forces act in the same direction to drive the flow. Additionally, today's semiconductor industry requires large crystals grown in large crucibles, and, consequently, the magnitudes of these interacting forces increase and the melt flow becomes three dimensional, time dependent, and even turbulent accompanying with velocity and temperature fluctuations.

Recent numerical studies [48–51] investigated the contribution of Marangoni effect to the turbulent melt flow in a relatively large CZ crucible based on the "bulk-flow model"

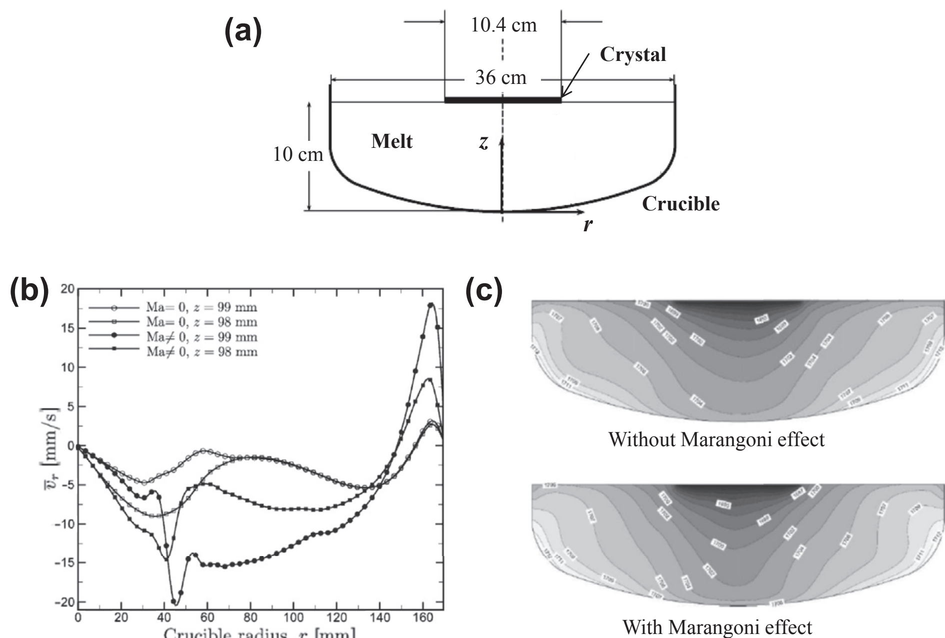

FIGURE 22.14 Effect of Marangoni convection on velocity and thermal fields in the CZ silicon melt. *(From Ref. [48].)* (a) Geometry of the CZ crucible model, (b) Azimuthal-and-time-averaged radial velocities at different heights with and without Marangoni effect, (c) Time-averaged isotherms on a vertical plane with and without Marangoni effect.

that considers only the flow and thermal fields in the crucible. These simulations used a direct numerical simulation (DNS) or a large-eddy simulation (LES). Figure 22.14 shows the calculated flow and thermal fields in the CZ silicon melt with and without Marangoni effect by using the DNS [48]. Here, the crystal diameter ($2R_s$) is 10.4 cm, the crucible diameter ($2R_c$) 36 cm, and the maximum melt depth (H_c) 10 cm, as shown in Figure 22.14 (a). The crystal and crucible are rotated in opposite directions at 20 and 2 rpm, respectively, and Gr $(=g\beta_T H_c^3 \Delta T_{\max}/\nu^2) = 4.1 \times 10^8$, Ma $(=|\partial\gamma/\partial T| Pr \Delta T_{hor}(R_c - R_s)/\rho\nu^2$; ΔT_{hor} : horizontal temperature difference$) = 1.2 \times 10^5$ and Re $(=\Omega_c R_c^2/\nu$; Ω_c : crystal rotation rate$) = 3176$. The azimuthal-and-time-averaged radial velocity distributions below the melt-free surface in (b) indicate that the Marangoni effect enhances the inward radial velocity on the melt surface except near the sidewall of the crucible. The calculated time-averaged thermal field on a vertical plane through the crucible axis in (c) demonstrated that the regions underneath and around the crystal become cooler, but the temperature of the melt-free surface increases and the radial temperature gradients along the surface become smaller owing to the enhanced flow induced by the Marangoni effect. In addition, the net radial mass flow rate near the crystal enhanced by surface tension–driven flow brings about better mixing, and thus influences the temperature fluctuations and turbulent kinematic energy in the melt. Similar numerical simulations

of CZ silicon melt flow considering the Marangoni effect have been carried out in the absence of crystal [49] or varying the Marangoni number to take into account the dependence of surface tension on the oxygen partial pressure in the atmosphere [51]. The Marangoni flow also influences the spatial and temporal distributions of impurities through the velocity and temperature fluctuations, particularly near the edge or underneath the pulling crystal, and, consequently, the quality of the crystal, e.g., microsegregations.

22.4.1.2 Oxide Crystal Growth

It is well known that so-called spoke patterns are observed on the melt surface in the CZ crystal growth of oxides as shown in Figure 22.15 [52], and similar patterns were also reported in silicon CZ systems [53,54]. There have been several discussions concerning the mechanism of spoke pattern formation in the oxide melt. Miller and Pernell [55,56] carefully observed the spoke patterns in a mimic garnet melt, i.e., water in an open cylindrical container, and provided Figure 22.16 as an illustration of the flow near the surface. They speculated that the Marangoni effect could be the possible cause of the pattern. Moreover, Shigematsu et al. [30] and Morita et al. [57] observed the spoke and network patterns in $LiNbO_3$ melt and also in Ti-doped Al_2O_3 melt, and supported the Marangoni (thermocapillary and/or solutocapillary) effect as the prime cause of spoke patterns. In contrast, Jones [58,59] observed a similar pattern on the water surface in a cylindrical container mimicking the CZ crucible, and attributed its cause to buoyancy-driven instability. However, it might be difficult to identify the mechanism of spoke patterns only through the experiments, because the buoyancy and Marangoni convections coexist in the melt at least under the terrestrial condition, and there is no method to visualize the flow and temperature fields in the real oxide melt.

Jing et al. [60,61] have demonstrated the mechanism of the spoke patterns on the melt surface for the first time by numerical simulations based on the bulk-flow model.

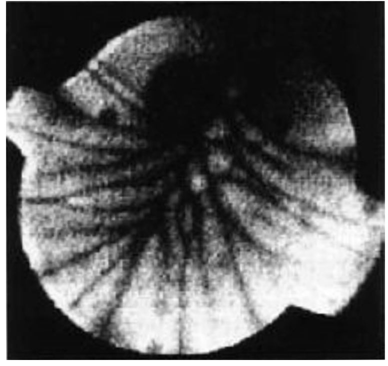

FIGURE 22.15 Spoke patterns observed on the $LiNbO_3$ melt surface without the crystal. *(From Ref. [52].)*

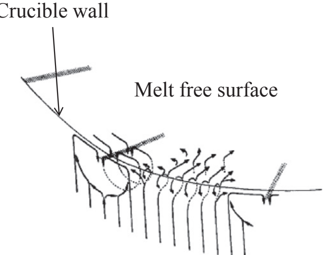

FIGURE 22.16 Schematic illustrating the geometry of the flow in the surface region. *(From Ref. [56].)*

Figure 22.17 shows the top and meridional views of the calculated velocity vectors and isotherms in the $LiNbO_3$ melt ($Pr = 13.6$) without the crystal in the absence of Marangoni convection [60]. Here, the crucible sidewall is heated at a constant heat flux, the bottom is assumed to be adiabatic, and heat loss from the melt surface to the ambient is considered to be due to radiation alone. Under a condition of Gr $(=g\beta_T T_m R_c^3/\nu^2) = 2.62 \times 10^5$ and $Re_\gamma = 0$, a steady, axisymmetric flow due to the buoyancy is generated in the melt. In contrast, when the Marangoni effect is taken into account, the flow and

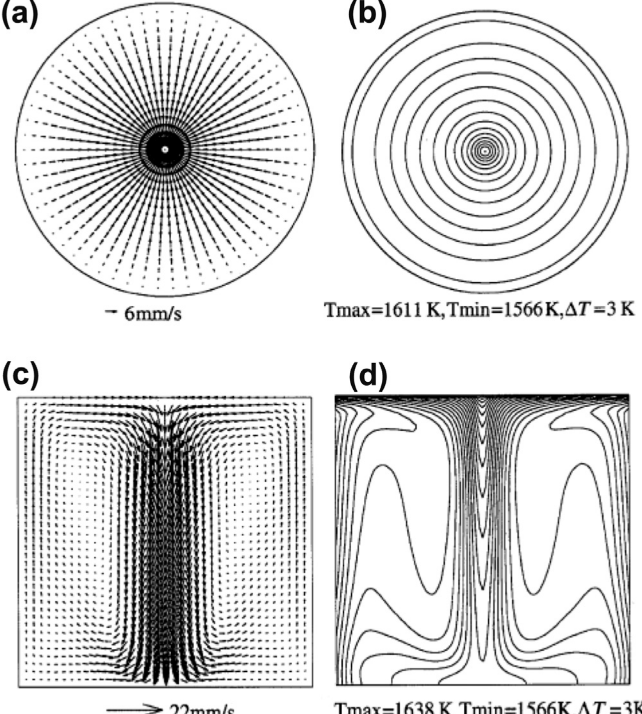

FIGURE 22.17 The top views (a and b) and the meridional views (c and d) of the velocity vectors and isotherms of the axisymmetric, steady convection without Marangoni effect. *(From Ref. [60].)*

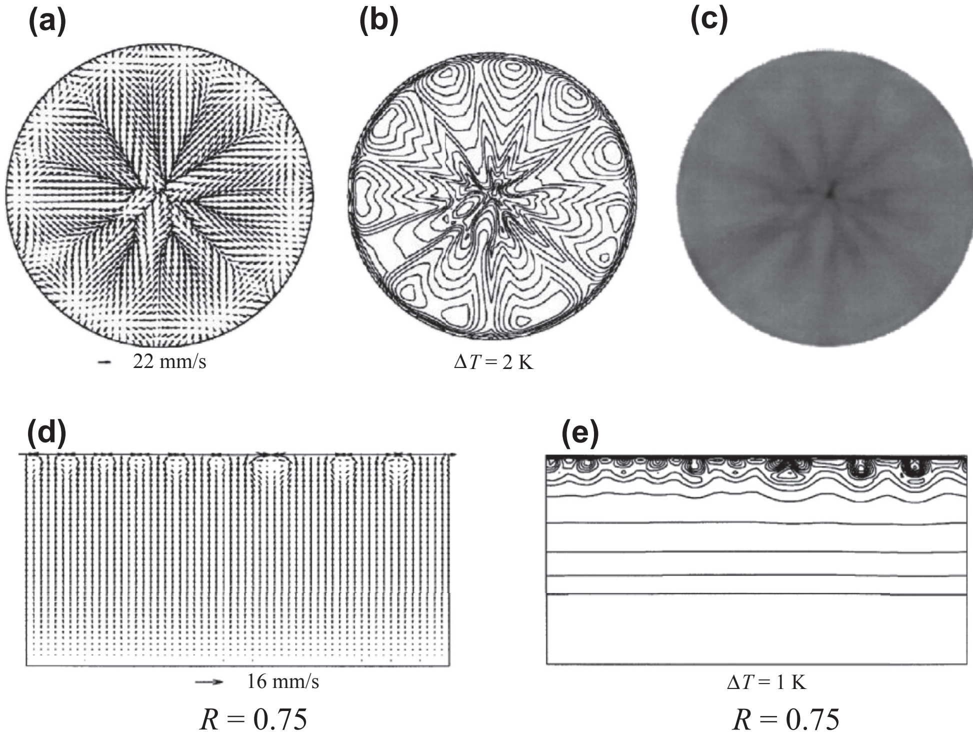

FIGURE 22.18 The calculated flow and thermal fields in the $LiNbO_3$ melt in the presence of the Marangoni effect. (a) Surface velocity vectors, (b) surface isotherms, (c) visualized gray-scale surface temperature, (d) circumference view of velocity vectors, and (e) circumference view of isotherms (R: radial distance scaled with R_c). *(From Ref. [60].)*

temperature fields become three-dimensional and time-dependent, as shown in Figure 22.18, where Re_γ $(=|\partial\gamma/\partial T|T_m R_c/\rho\nu^2) = 2.32 \times 10^4$. The azimuthal velocities emerge and converge at several spoke-like lines (Figure 22.18(a)), and the surface temperature pattern (Figure 22.18(c)) is similar to the observed pattern of Figure 22.15. The converging lines in Figure 22.18(a) coincide with the dark lines on Figure 22.18(c) where the surface temperature is lower than the other parts on the surface. In addition, it is found that the secondary flow is generated in the upper corner where the hot melt ascends to the melt surface, flows on the surface toward the crucible wall, and descends along the wall. However, such three-dimensional flow structures appear just below the melt surface, and the flow and temperature fields become nearly axisymmetric in the lower region, as shown in the circumference views of Figure 22.18(d) and (e), which also show the generations of many longitudinal roll cells (extending their axes in a radial direction) beneath the melt surface. These numerically simulated flow structures in the surface region coincide with those in Figure 22.16. When the crystal is touched on the melt surface, a regular spoke pattern shown in Figure 22.19 is generated on the melt surface [61], but the flow and temperature distributions in the lower melt zone are

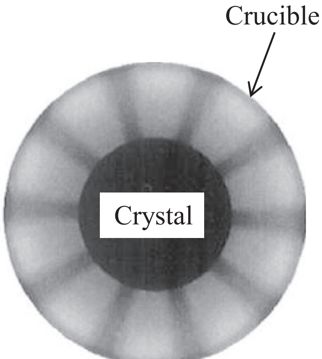

FIGURE 22.19 Spoke pattern on the melt surface with the crystal. *(From Ref. [61].)*

almost axisymmetric, like those shown in Figure 22.18. The numerical results including Figures 22.17–22.19 suggest that the spoke patterns are caused by the Marangoni–Benard instability in a thin thermal boundary layer just below the melt surface. However, the polygonal roll cells in a quiescent layer (Figure 22.9) are elongated by the radial flow in the melt. Also, the reason why the spoke patterns appear on the surface of oxide melt so often and stable might be due to relatively high *Pr* numbers of oxide, which cause the steep temperature change in the thin thermal boundary layers below the melt surface, and, consequently, the layers are easily destabilized by the Marangoni instability. However, when the transmittance of oxide melt increases and the temperature gradient in the melt becomes small, the Marangoni instability is suppressed and the spoke pattern might disappear [62].

Besides the spoke patterns, wave patterns have been also seen experimentally on the free surface of some oxide melts accompanying with crystal rotation. Jones [63] carried out cold-model experiments to investigate the hydrodynamics of oxide melt of $Pr < 10$, using an aqueous solution of glycerol, and pointed out that the wave patterns observed on the free surface are caused by the interaction between buoyancy-driven convection and forced convection caused by the crystal rotation, that is, the baroclinic instability [64,65]. Figure 22.20 compares the wavy temperature patterns on the surface of $LiNbO_3$ melt in a CZ crucible [66] without and with the Marangoni effect, where the radius of the crucible was 100 mm, the height of the crucible was 100 mm, and the radius of the crystal was 50 mm. As the boundary conditions, the crucible sidewall was heated at a constant heat flux, the bottom was assumed to be adiabatic, and radiative heat loss from the melt surface to the ambient was considered. Figure 22.20(a) is the three-folded wave pattern on the surface when the Marangoni effect is neglected. If the Marangoni effect is taken into account, the wave patterns disappeared because the Marangoni effect enhances the inward radial flow, and confines the outward flow driven by the rotating crystal under the crystal (Figure 22.20(b)). If the crystal rotation rate exceeds 40 rpm, the border of these two flows is pushed out of the crystal radius as shown in Figure 22.20(c)

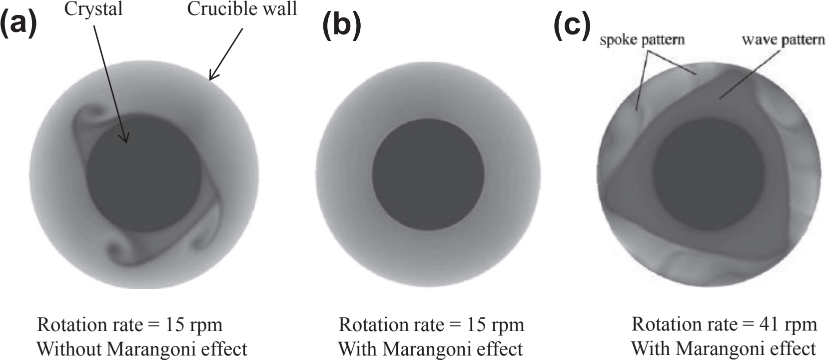

FIGURE 22.20 Snapshots of surface wave patterns. *(From Ref. [66].)*

for the crystal rotation rate of 41 rpm. Here, the wave and spoke patterns coexist, and the triangular-shaped pattern on the free melt surface rotates at approximately 1 rpm. The mechanism for the spoke pattern in Figure 22.20(c) is identical to that in Figure 22.19. When the crystal rotation rate exceeds a certain critical value, the centrifugal effect of the rotating crystal suppressed the horizontal Marangoni effect and, therefore, enabled the spoke pattern to appear. The cause of the wave pattern is considered to be due to the baroclinic instability. As the crystal rotation rate is further increased, e.g., 45 rpm, such wave-spoke pattern disappears and the rotation-driven flow becomes dominant.

22.4.2 FZ Crystal Growth System

The flow in a floating-zone (FZ) melt is essentially driven by the Marangoni effect caused by the surface tension gradients along the melt surface. Although buoyancy is the major driving force of melt flow in the CZ systems, its effect is less significant in FZ systems because the volume of the FZ molten zone is rather small due to the shape instability of the zone. The detailed experimental and numerical investigations of Marangoni convection in the real FZ crystal growth system might be difficult because the geometry of the zone such as the height and melt/crystal interface shape depends on the solidification conditions and is not known a priori. Therefore, many studies on Marangoni convection in the FZ system have been performed for simple liquid bridges, such as the "half-zone" or "full-zone" as shown in Figure 22.21 [33].

When the temperature difference ΔT between the upper and lower disks of a half-zone liquid bridge is relatively small, an axisymmetric stationary Marangoni flow appears in the bridge. However, this axisymmetric flow is destabilized and becomes three-dimensional and oscillatory as ΔT increases. Figure 22.22 shows the schematic diagram of flow transitions in half-zone liquid bridges [67]. For low *Pr* liquids, two-step flow transitions occur, while the axisymmetric flow directly changes to three-dimensional oscillatory flows for high *Pr* liquids. Under much larger ΔT the flow in the liquid bridge becomes chaotic and may become turbulent at further larger ΔT. In addition, the linear stability analysis [68] suggested that the nature of the instability of

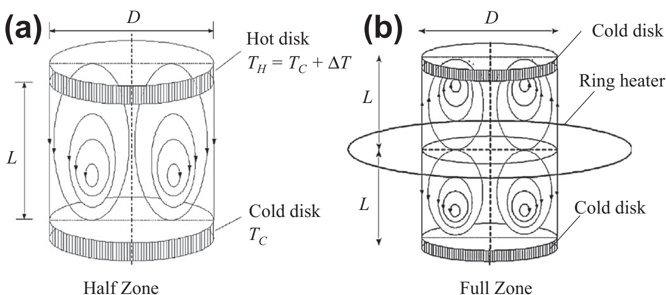

FIGURE 22.21 Geometrical models of the FZ technique and related boundary conditions. *(From Ref. [33].)*

Marangoni flow in liquid bridges of low *Pr* fluid is hydrodynamic and hydrothermal in high *Pr* liquid bridge. In this section, Marangoni convection in the FZ system only for low *Pr* will be discussed.

The existence of oscillatory Marangoni flow (convection) in low *Pr* liquids was confirmed for the first time through the FZ silicon crystal growth experiment under microgravity condition [69], in which the micro striations in the grown crystal were considered to be caused by the oscillatory Marangoni flows in the molten zone, although the oscillatory Marangoni flow in the silicon FZ melt and its influence to striation formed in the crystal have already been discussed by Chang and Wilcox [1]. Thereafter, many theoretical works on the Marangoni convection in the FZ melts have been carried out using a half- or full-zone model. Rupp et al. [70] performed three-dimensional time-dependent numerical simulations for liquid bridges with a half-zone configuration for GaAs and other liquids, and indicated that the Marangoni flow becomes oscillatory via two-step flow transitions as shown in Figure 22.22; the first transition occurs at a critical Marangoni number Ma_{c1}^{LB}(or a critical Reynolds number $Re_{\gamma c1}^{LB} (= Ma_{c1}^{LB}/Pr)$) from an axisymmetric steady flow to a three-dimensional steady flow, and then, at a larger temperature difference, i.e., Ma_{c2}^{LB} or $Re_{\gamma c2}^{LB}$, the second transition to a three-dimensional oscillatory flow takes place. According to such a numerical knowledge, the

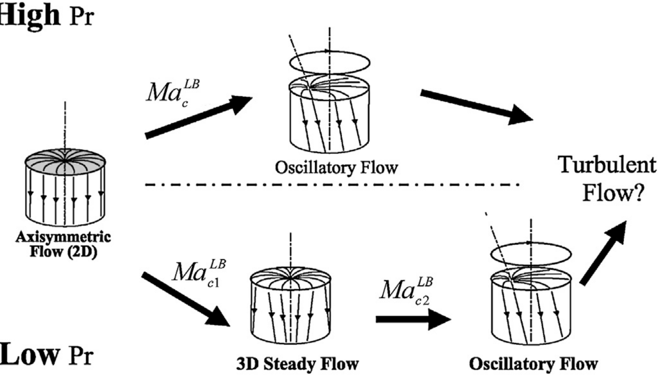

FIGURE 22.22 Schematic diagram of flow transitions in half-zone liquid bridges. *(From Ref. [67].)*

experimentally determined critical Marangoni number [69] under microgravity condition might be larger than true Ma_{c2}^{LB}.

Imaishi et al. [71] have carried out a series of numerical simulations to understand the general feature of oscillatory Marangoni convection in half-zone liquid bridges, for wide range of Prandtl number ($Pr = 0$, 0.01, 0.02) and aspect ratio A_S ($=2L/d = 0.6-2.2$, d and L: diameter and length of liquid bridge), and obtained a Re_γ ($=|\partial\gamma/\partial T|\Delta Td/2\mu\nu$) vs A_s stability map of Marangoni convection in cylindrical liquid bridges under microgravity as shown in Figure 22.23. Here, numerals beside keys in the figure represent the modes, the azimuthal wave number, and the tempo-spatial oscillation behaviors. A numeral in parenthesis (m) near the $Re_{\gamma c1}^{LB}$ key represents the azimuthal wave number m of steady three-dimensional flow. Also, ($m+1$) near the $Re_{\gamma c2}^{LB}$ key represents an oscillation mode that is characterized by a superposition of $m=1$ type oscillating three-dimensional disturbance over a steady three-dimensional flow pattern of m (in case of Figure 22.24(a), $m=2$). (mT) represents a torsional (twisting) oscillation of the pattern of m in the azimuthal direction (Figure 22.24(b) is (2T)). And, (mR) corresponds to a mere rotation of the pattern of m around the liquid bridge's axis. The numerical simulations for much realistic bridge geometry by Li et al. [72], in which a half-zone liquid bridge of molten tin was held between two supporting rods of smaller thermal conductivity than the liquid bridge and under ramped temperature difference, revealed that Ma_{c1}^{LB} and Ma_{c2}^{LB} fall close to, but slightly larger than, those in Figure 22.23.

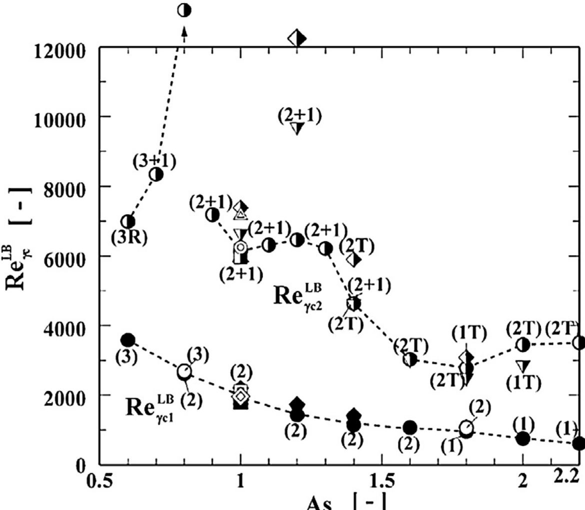

FIGURE 22.23 Stability map for Marangoni flow in half-zone liquid bridges of low *Pr* Liquids. Numeral beside each key represents *m* and the mode of oscillation. Present work: for $Pr = 0$: ○ and ● $Re_{\gamma c1}^{LB}$, ◑: $Re_{\gamma c2}^{LB}$; for $Pr = 0.01$ ▼: $Re_{\gamma c1}^{LB}$, ▽: $Re_{\gamma c2}^{LB}$; for $Pr = 0.02$ ◆: $Re_{\gamma c1}^{LB}$, ◇: $Re_{\gamma c2}^{LB}$. Ref. (*): for $Pr = 0$ ■: $Re_{\gamma c1}^{LB}$, ◨: $Re_{\gamma c2}^{LB}$; for $Pr = 0.02$ ▣: $Re_{\gamma c1}^{LB}$, △: $Re_{\gamma c2}^{LB}$. Ref. (**): for $Pr = 0$ ▲: $Re_{\gamma c1}^{LB}$, ◭: $Re_{\gamma c2}^{LB}$; for $Pr = 0.01$ ◈: $Re_{\gamma c1}^{LB}$, ◎: $Re_{\gamma c2}^{LB}$. Refs. (*) and (**) correspond to Refs. [15] and [17] used in Imaishi et al. [71], respectively. *(From Ref. [71].)*

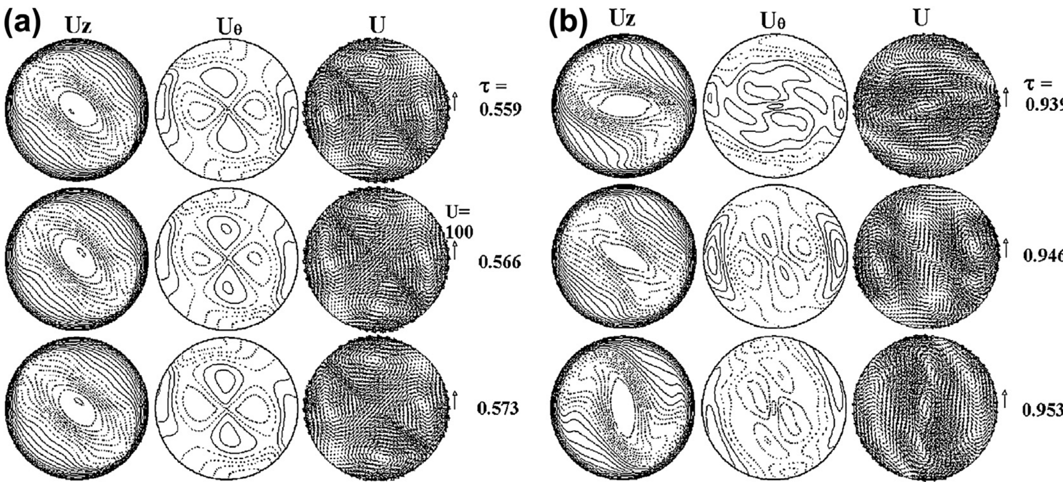

FIGURE 22.24 Snapshots of velocity distributions on $Z = 0.7$ cut over a half-period of oscillations, where U_z and U_θ are axial and azimuthal components of velocity vectors U, respectively. (a) Oscillations in (2 + 1) mode, (b) oscillations in (2*T*) mode. *(From Ref. [71].)*

The above numerical simulations were conducted to investigate Marangoni convection in a liquid bridge with a cylindrical surface. In a real FZ crystal growth system, however, the free surface of the molten zone is deformed, caused by gravity, liquid volume, and electromagnetic force. The surface deformation may affect the stability of the Marangoni-driven melt flow in the liquid bridge [73–75]. According to Lappa's numerical study [75], in which a full-zone liquid bridge heated by a ring heater, positioned around the equatorial plane of the bridge, under microgravity was considered, the azimuthal wave number m is a function of the volume factor S (=the volume of the liquid bridge/$(\pi d^2 L/4)$), as well as the aspect ratio A_S, as shown in Table 22.1. For the case $A_S = 1.0$, m increases if the volume is decreased with respect to the condition $S = 1.0$. For $A_S = 1.5$, m increases with increasing S. The table also indicates that critical

Table 22.1 Critical azimuthal wave number and Marangoni number vs the volume of the liquid zone

A_S	S	m	Ma_{c1}^{LB}
1.0	0.80	4	48.08
1.0	0.85	3	34.59
1.0	1.0	2	12.41
1.0	1.2	2	6.85
1.0	1.3	2	10.87
1.5	1.0	1	10.15
1.5	1.2	1	1.454
1.5	1.4	2	11.53

(From Ref. [75]).

Marangoni number Ma_{c1}^{LB} depends on S, and, in the range investigated, the percent variation of the critical Marangoni number varies as much as 10 times.

Although numerical simulations of the Marangoni flows in simple half-zone or full-zone bridges provide the detailed information of hydrodynamics and flow instability in low Pr liquids, more practical information for real silicon FZ furnace operations, such as the effect of operation conditions on the melt flow, heat and mass transfer, and the melt/crystal interface shapes, cannot be obtained by the simplified models. Lan and Chian [76] have conducted three-dimensional simulations for the FZ growth of silicon with 8-mm diameter in an ellipsoid mirror furnace under microgravity condition, considering simultaneously the time-dependent Marangoni flow, heat transfer, and moving melt/crystal interfaces. The full-zone calculations including the feeding and growth interfaces indicated that the bifurcation behavior is similar, but the primary bifurcation was found to be subcritical and the three-dimensional onefold flow mode was dominant. It was also found that significant growth rate fluctuations and back melting occurred for a typical growth condition, and that the severe back melting may be related to the angular waves. For the floating-zone crystal growth with the needle-eye technique to produce high-quality silicon single crystals with large diameters ($\geq$100 mm), also, a three-dimensional quasi-steady state numerical simulation was carried out, considering the buoyancy, Marangoni and electromagnetic forces as the driving forces of the melt flows [77]. Figure 22.25 shows the calculated distributions of temperature, velocity, and dopant concentration in the molten zone. The maximum

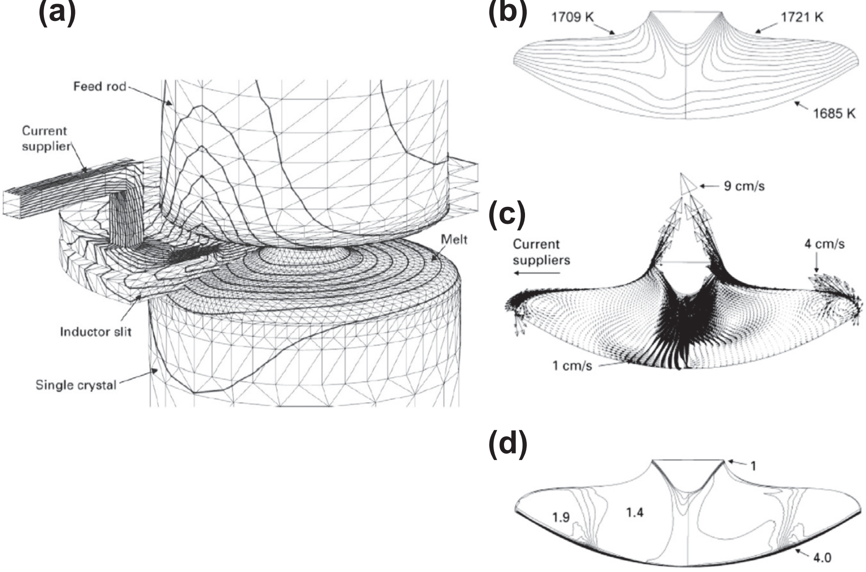

FIGURE 22.25 Temperature, velocity, and dopant concentration fields in the FZ melt. *(From [77].)* (a) 3D view of the EM model for the FZ-growth system, (b) temperature field in the melt, (c) velocity field in the melt, (d) dopant concentration field in the melt.

velocity appears at the free surface near the melting interface due to a steep temperature gradient and, consequently, a strong Marangoni force at this location. The calculated three-dimensional dopant concentration field succeeded to explain the variations of resistivity in a longitudinal cut of the grown crystal.

Along with these numerical simulations, many experimental studies on the Marangoni flows in the FZ crystal growth system have been carried out. Cröll et al. [78] have determined experimentally the second critical Marangoni number Ma_{c2}^{LB} for oscillatory convection in a silicon FZ furnace. P-doped silicon rods of 10 mm in diameter, whose surface was coated with thin film of SiO_2 with an annular opening distance $L = 0.5$–3 mm, were zone melted and recrystallized in a double-ellipsoid mirror furnace under microgravity condition as shown in Figure 22.26. The critical Marangoni number for the onset of oscillatory flow was determined as $Ma_{c2}^{LB}(=|\partial\gamma/\partial T|\Delta TL/\mu\kappa)$, where ΔT is the temperature difference over the slot when striation-free crystal is grown there. The results suggested that Ma_{c2}^{LB} is approximately 200 for $A_S \approx 0.3$.

Time-dependent Marangoni convection in the FZ molten zone, and the consequent growth rate fluctuations and dopant striation formations in the crystal, could be controlled or suppressed by applying static magnetic fields [79–81], where the Lorentz force acting on the flow components perpendicular to the magnetic field can damp the flow in electrically conducting liquids. Dold et al. [80] carried out silicon floating-zone experiments using P- and Sb-doped crystals of 8-mm diameter and zones of 10–12 mm length in a mirror furnace under static axial magnetic fields with the strength up to 500 mT. Although the crystals grown without magnetic field showed irregular microscopic striation patterns implying a broad frequency range of the melt convection, nearly striation-free crystals could be obtained above 240 mT, as shown in Figure 22.27. However, it is found from the figure that, at the same time, radial unsteadiness of the dopant concentration, which can be explained by remaining Marangoni flow near the free melt surface and a quiescent melt core, appears. This radial inhomogeneity was forced to the edge of the crystal as the magnetic fields increased.

In addition, according to the dependence of surface tension on the oxygen partial pressure in the atmosphere as mentioned in Section 22.2.1, the Marangoni flow in molten silicon during the FZ crystal growth can be also affected by the oxygen partial pressure [82,83]. More information on FZ and related convection features can be also obtained from Chapter 7 in Vol. IIA.

22.4.3 Bridgman, Edge-defined Film-fed, and Other Crystal Growth Systems

In this section, the Marangoni flow in the crystal growth systems with the different configurations from the CZ and FZ crystal growth processes, such as the Bridgman, edge-defined film-fed growth (EFG), and micro-pulling down crystal growth processes, will be discussed.

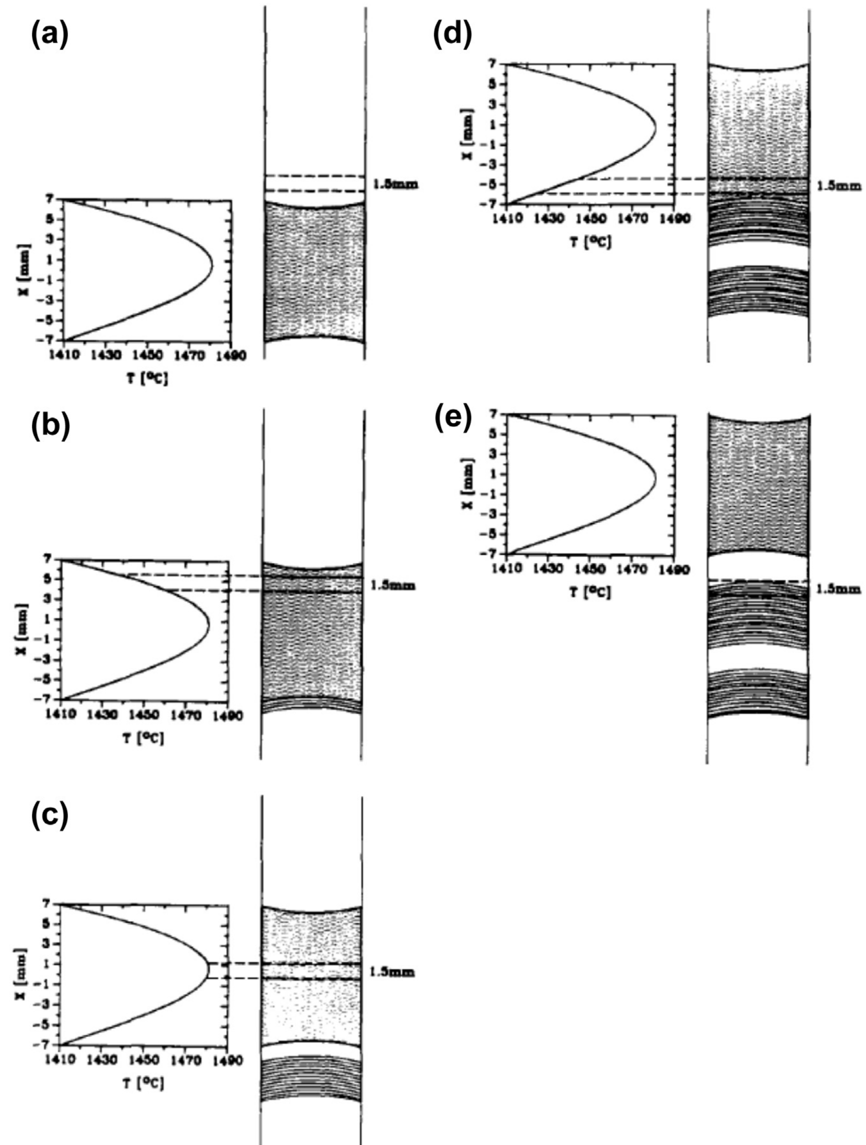

FIGURE 22.26 Sequence of striation formation during floating-zone growth of Si with a partially free melt surface. *(From Ref. [78].)*

22.4.3.1 Horizontal Bridgman

In Section 22.3.1, the Marangoni flow in a liquid layer was discussed. When the lower temperature T_C in Figure 22.6 coincides with the melting point temperature T_m, the figure corresponds to the configuration of the horizontal Bridgman (HB) crystal growth with an open boat. Because of the presence of a relatively large free melt surface at HB,

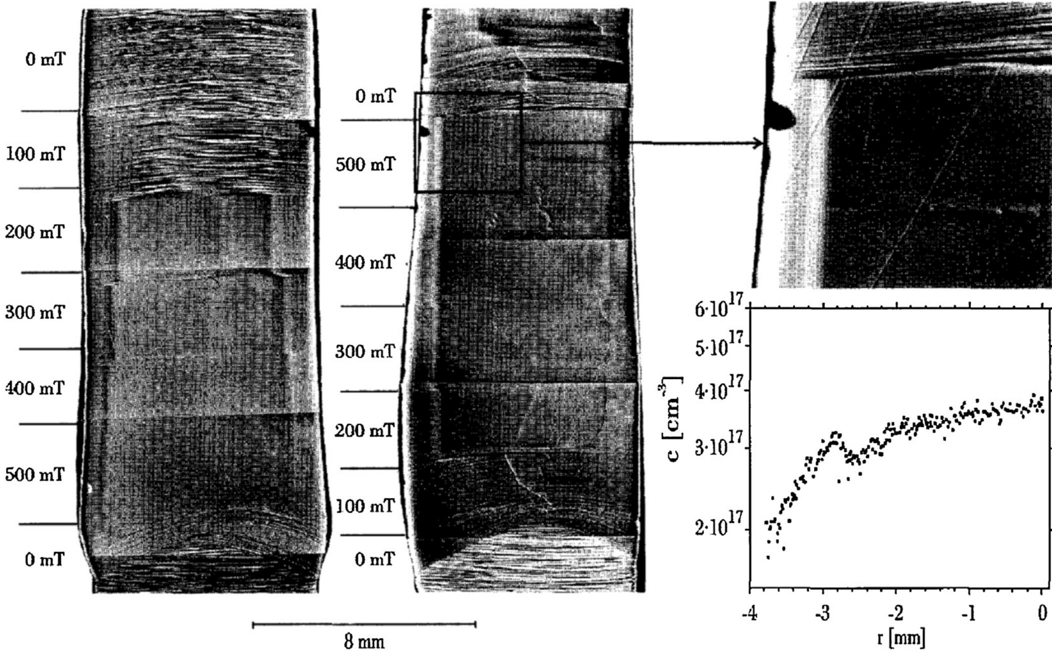

FIGURE 22.27 Radial dopant segregation in dependence on the magnetic field strength and radial distribution of dopant concentration. *(From Ref. [80].)*

the properties of the crystals, such as the melt/crystal interface shape and dopant concentration in the crystals, and, consequently, the qualities of the grown crystals, might be affected by the Marangoni flow very intensively.

Lan et al. [84] observed the flow patterns in the melt, heating profiles, and melt/crystal interface shape during the crystal growth of $NaNO_3$ using an HB furnace, where the crucible was made of a half of a Pyrex glass tube. The inner diameter (ID) and outer diameter (OD) of the body part were 2.8 and 3.2 cm, respectively, and the length was 12 cm, while the seeding part had ID = 0.8 cm, OD = 1.2 cm, and length = 1.5 cm. In addition, they carried out three-dimensional numerical simulations for the same system as that in experiments to understand the flow and heat transfer in the HB system in detail. Figure 22.28 shows the typical experimental and numerical results of a snapshot at given melt surface area for flow patterns and isotherms at the midplane of the melt. Clearly, the velocity at the surface appears to be higher due to the Marangoni effect, and two flow cells are induced at both ends of the melt, although the coexisting buoyancy force enhances the Marangoni convection. Due to the vigorous convection, temperature was quite uniform in the bulk melt, and the thermal gradients were restricted in front of the melt/crystal interface, inducing a major flow cell there. From the distortion of the isotherms, it is found that the hot melt at the top surface is pushed toward the melt/crystal interface. Since molten $NaNO_3$ is a relatively high *Pr* material, the convective heat

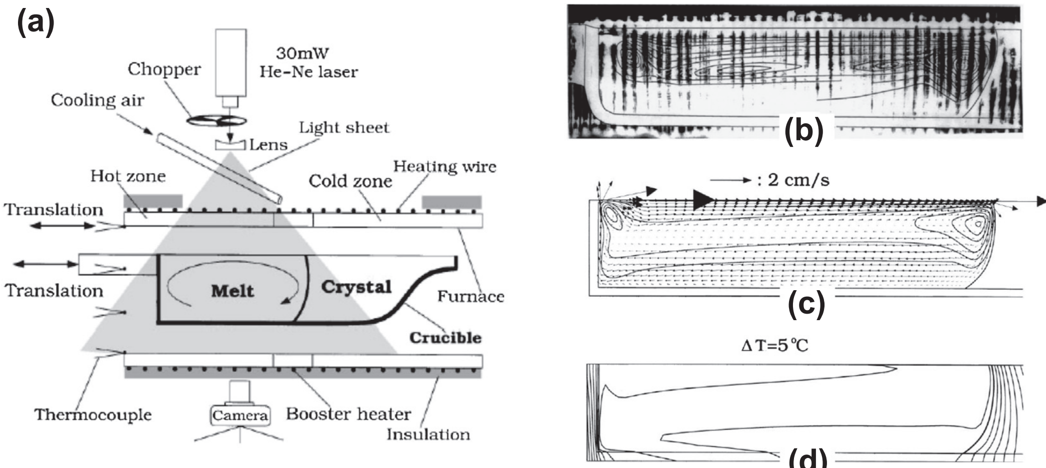

FIGURE 22.28 (a) Schematic diagram of experimental setup for HB crystal growth, (b) observed melt flow pattern, (c) calculated melt flow pattern, and (d) calculated isotherms in the furnace. *(From Ref. [84].)*

transfer is dominant in the melt, and, consequently, the interface shape is significantly affected by the flow and becomes highly concave. The top view of the simulated interface is also very concave, because the divergent flow near the interface due to the Marangoni force further sharpens the interface shape near the crucible and deteriorates the growth. Similar simulations were also performed for the HB growth of GaAs crystals from its low *Pr* melt [85].

For the HB growth system of crystals with mixed compositions, such as Ge_xSi_{1-x} and GaSb-InSb systems, the effect of solutocapillary convection must be considered as well as the thermocapillary convection. According to Cröll *et al.* [86], such mixed convection is explained below. The following are, of course, applicable for other growth systems, such as the CZ or FZ crystal growth. Considering both temperature and concentration gradients in z-direction along the HB free melt surface, Eqn (22.2) gives the following equation for the surface tension gradient near the melt/crystal interface of a growing crystal:

$$\frac{\partial \gamma}{\partial z} = \frac{\partial \gamma}{\partial T}\frac{\partial T}{\partial z} + \frac{\partial \gamma}{\partial C}\frac{\partial C}{\partial z}. \tag{22.26}$$

If $\partial\gamma/\partial C \neq 0$ and the segregation coefficient $k \neq 1$, the segregation during crystal growth causes a concentration gradient and, consequently, a surface tension gradient along the melt-free surface close to the melt/crystal interface. Thermocapillary convection does not change as long as the temperature gradient along the surface is maintained, whereas solutocapillary convection changes through the buildup or reduction of solute in front of the interface. Here, assuming that the growth process is in a steady state and the growth rate is at the limit of constitutional supercooling, i.e., the concentration gradient $\partial C/\partial z$

can be substituted by$(dC_L/dT)\cdot(\partial T/\partial z)$ with the liquidus slope dT/dC_L, Eqn (22.26) is rewritten by Eqn (22.27):

$$\frac{\partial \gamma}{\partial z} = \left(\frac{dC_L}{dT}\frac{\partial \gamma}{\partial C} + \frac{\partial \gamma}{\partial T}\right)\frac{\partial T}{\partial z}. \tag{22.27}$$

The direction and intensity of the surface tension-driven convection is governed by the contribution of $\partial\gamma/\partial T$ for the thermocapillary-driven part versus that of $(dC_L/dT)\cdot(\partial\gamma/\partial C)$ for the solutocapillary-driven part. In principle, although four different combinations are possible, only the following two cases are of practical importance because $\partial\gamma/\partial T$ is usually negative:

$\partial\gamma/\partial T < 0$, $(dC_L/dT)\cdot(\partial\gamma/\partial C) < 0$: normal thermo- and solutocapillary forces,
$\partial\gamma/\partial T < 0$, $(dC_L/dT)\cdot(\partial\gamma/\partial C) > 0$: normal thermo- and inverse solutocapillary forces, where normal force directs toward the melt/crystal interface and inverse force directs away from the interface. Opposing forces, as in Case 2, can cause additional instabilities. In addition to purely hydrodynamic flow instabilities that influence the crystal composition through oscillations of the temperature field and boundary layer thickness, there is also a possible instability from the mutual coupling between the flow and the segregation induced by crystal growth itself. Solutocapillary convection must be considered especially for mixed crystals like Ge_xSi_{1-x}, crystals grown from non-stoichiometric melts or from solutions.

Cröll et al. [86] carried out the directional solidification experiments of Ge_xSi_{1-x} mixtures of different compositions between 3% and 9% Si under microgravity condition during a parabolic flight campaign, where the samples of 2–3 mm in depth poured in a SiC-coated graphite crucible (inside dimensions $15 \times 30\ mm^2$) were heated by a double-ellipsoid mirror furnace whose two lamps were focused onto one end of the crucible. Figure 22.29 shows the three different experimental stages with a schematic view of the convective flow and the position of tracers put to visualize the flow direction of the solutocapillary flows: (a) the sample is completely melted by equally heating from both sides, and the cold spot is in the crucible center leading to two opposing thermocapillary convective rolls, (b) completely molten sample is reduced heating from the right side, and consequently the cold spot moves near the crucible wall, leading to a much reduced thermocapillary convective roll on the right, and (c) solidification starts from the right side, and solutocapillary flow caused by the concentration gradient along the surface due to segregation pushes the tracers away from the melt/crystal interface, where solutocapillary convection opposes thermocapillary convection in the Ge_xSi_{1-x} system since Si, having the higher surface tension, is preferentially incorporated into the crystal during growth. In microgravity experiments, solutocapillary flow with initial flow rates in excess of 5.5 cm/s at the onset of crystallization was measured. A slight dependence of the flow velocity on the initial Si content has been found. Experiments on the ground showed the same effect but with smaller speeds; this difference was explained by the additional action of solutal-buoyancy convection. Arafune et al. [87] have also carried

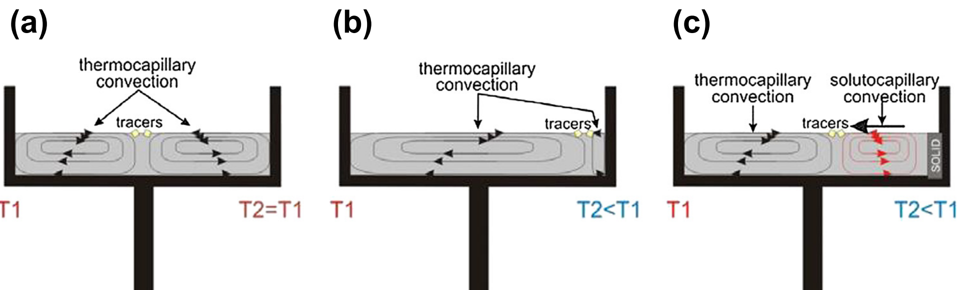

FIGURE 22.29 Three different experiment stages with a schematic view of the convective flow and the tracer position. *(From Ref. [86].)*

out the HB growth experiments of InSb crystals to investigate the effect of solutocapillary convection on the melt/crystal interface shape, in addition to the effects of temperature gradient, cooling rate, and Sb composition of the initial melt.

In contrast, at the vertical Bridgman (VB) method, the seed crystal, growing crystal, and melt are arranged about each other in an adjusted container, and thus the melt and crystal completely contact the inner wall of the container during the growth process. Such contact between crystal and dissimilar container material may cause mechanical stress and chemical contamination. As a consequence, defects are generated at the periphery of the growing crystal. Marangoni convection mostly does not occur because of a small free-melt surface on top only. (Note, here only the classical Bridgman geometries with diameters of some cm are considered. Of course, at vertical directional solidification of very large silicon ingots for photovoltaics, the Marangoni convection plays again a certain role; see Chapter 10 in Vol. IIA). To relax the contact problem with container wall nowadays the detached nonwetting Bridgman mode is under investigation, at which a crystal solidifies from its melt without contacting the container wall as shown in Figure 22.30(a). Such arrangement remembers the meniscus-defined crystal growth, such as CZ, but being favored due to the much lower thermal stresses caused by characteristic small thermal gradients. However, here the Marangoni convection must be considered, which is induced at the free meniscus-like melt surface between interface and container wall as shown in Figure 22.30(b). Of course, this effect is only weak because of the small temperature variations along the small meniscus, and might be neglected [88,89].

22.4.3.2 Other Methods

In the EFG method using the die with one or more capillary channels, a melt meniscus is formed on the die rising by capillary action. A seed crystal is put in contact with the melt meniscus and pulled up so that the single crystal with a cross-section controlled by the die geometry can grow. In the EFG method, since the ratio of the surface area to the volume of molten zone is relatively large, Marangoni convection must dominate the flow in the molten zone. It has been reported that the gaseous inclusions and their locations

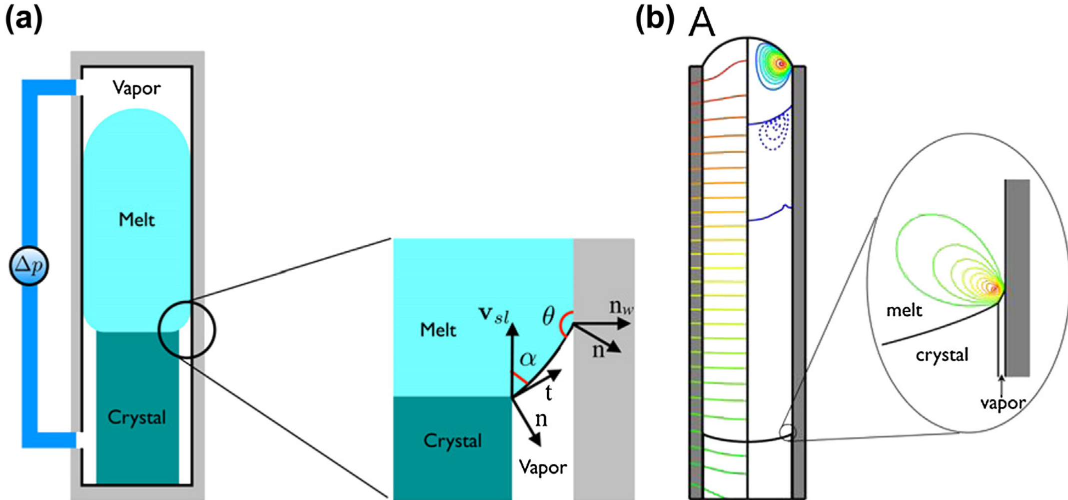

FIGURE 22.30 (a) Schematic diagram of detached Bridgman growth with a pressure regulator, (b) isotherms (on the left) in the furnace and streamlines in the melt (on the right). *(From Ref. [89].)*

in the rod sapphire crystals [90,91] or the dopant distributions in single crystal fibers of Nd:YAG and Nd:$LiNbO_3$ [92] were affected by the Marangoni flow in the melt meniscus.

In the micro-pulling down process whose ratio of free surface to volume of the melt is large, Marangoni convection might also dominate the flow in the melt [93–95]. Figure 22.31 shows the numerical results of temperature and flow fields in the micro-pulling down crystal growth furnace [95], where the sapphire fiber crystal

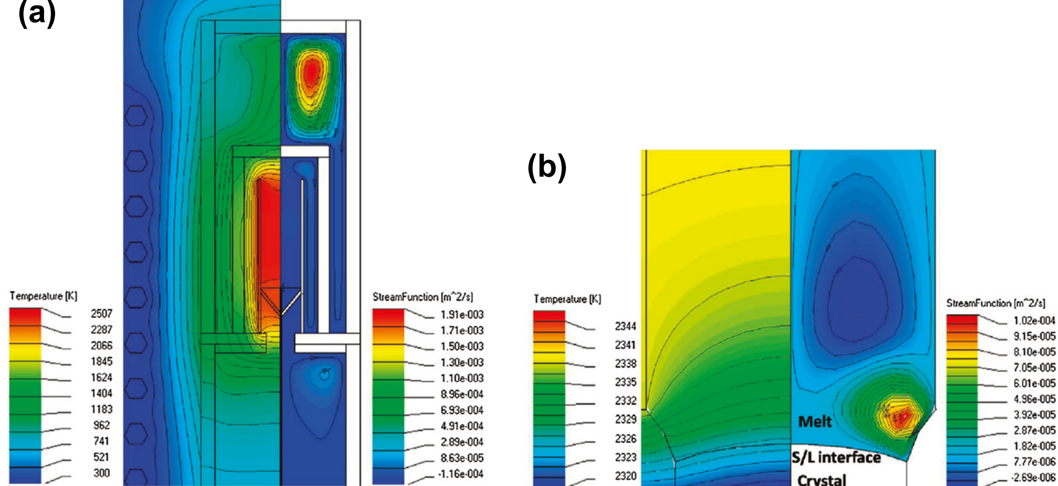

FIGURE 22.31 Temperature (on the left) and stream function (on the right) distributions: (a) in the entire furnace for micro-pulling down crystal growth process and (b) in the molten zone. *(From Ref. [95].)*

is grown at a pulling rate of 0.6 mm/s from the iridium crucible with 46-mm length and 16-mm diameter. From the figure (b), the Marangoni convection appears in the molten zone, and the melt flows from hot to cold regions (from the crucible to the crystal near the triple point of the melt/crystal/gas phase) and penetrates into the capillary from the meniscus. A weak buoyancy convection roll is also generated above the Marangoni convection as shown in Figure 22.31(b).

22.5 Concluding Remarks

In crystal growth methods from the melt with free melt surfaces, preferentially such as CZ or FZ, the always existing temperature gradients along the surfaces induce surface-tension variations that generate thermocapillary or Marangoni convection. When mixed compositions (or fluxes and solutions) are presented, the solutocapillary convection occurs additionally to the thermocapillary convection. Since melt convection affects heat and mass transport to the growing crystal and also the heat penetration mode within the crystal itself, the spatial, structural and chemical homogeneity, i.e., the distributions of stress, impurity and dopant, in the crystal depend on melt convection mode. As a result, microdefects such as melt/crystal interface oscillations, striations within the growing crystals, and crack formation, even in oxide crystals, appear. Thus, it is of importance to analyze and know the contribution of the Marangoni convection in combination with buoyancy-driven and forced convections.

In this chapter, first, the values of surface tension and its temperature coefficients of molten materials measured by various methods were introduced. As it is well known, these parameters are one of indispensable thermophysical properties used as input data in numerical simulations for design and optimization of crystal growth processes. Then, the characteristics of thermo- and solutocapillary flows, Marangoni–Benard instability and hydrothermal wave instability have been described. Finally, the role of Marangoni convection in CZ, FZ, HB, and other growth arrangements were demonstrated.

References

[1] Chang CE, Wilcox WR. J Cryst Growth 1975;28:8.
[2] Chang CE, Wilcox WR. Int J Heat Mass Transf 1976;19:355.
[3] Chang CE, Wilcox WR, Lefever RA. Mat Res Bull 1979;14:527.
[4] Clark PA, Wilcox WR. J Cryst Growth 1980;50:461.
[5] Chun CH, Wuest H. Acta Astronaut 1978;5:681.
[6] Chun CH, Wuest H. Acta Astronaut 1979;6:1073.
[7] Chun CH, Wuest H, Flugwiss Z. Weltraumforsch 1982;6:316.
[8] Schwabe D, Scharmann A, Presser F, Oeder R. J Cryst Growth 1978;43:305.
[9] Schwabe D, Scharmann A. J Cryst Growth 1979;46:125.
[10] Schwabe D. Physicochem Hydrodyn 1981;2:263.

[11] Schwabe D, Scharmann A, Presser F, Oeder R. Acta Astronaut 1982;9:183.
[12] Yuan ZF, Mukai K, Huang WL. Langmuir 2002;18:2054.
[13] Keene BJ. Surf Interface Anal 1987;10:367.
[14] Mukai K, Yuan ZF. Mater Trans JIM 2000;41:331.
[15] Mukai K, Yuan ZF, Nogi K, Hibiya T. ISIJ Int 2000;40:S148.
[16] Hibiya T, Morohoshi K, Ozawa S. J Mater Sci 2010;45:1986.
[17] Ozawa S, Koda T, Adachi M, Morohoshi K, Watanabe M, Hibiya T. J Appl Phys 2009;106:034907.
[18] Rhim WK, Ohsaka K. J Cryst Growth 2000;208:313.
[19] Zhou Z, Mukherjee S, Rhim WK. J Cryst Growth 2003;257:350.
[20] Ozawa S, Morohoshi K, Hibiya T, Fukuyama H. J Appl Phys 2010;107:014910.
[21] Ozawa S, Suzuki S, Hibiya T, Fukuyama H. J Appl Phys 2010;109:014902.
[22] Rhim W-K, Ishikawa T. Int J Thermophys 2000;21:429.
[23] Kaiser N, Cröll A, Szofran FR, Cobb SD, Benz KW. J Cryst Growth 2001;231:448.
[24] Cröll A, Salk N, Szofran FR, Cobb SD, Volz MP. J Cryst Growth 2002;242:45.
[25] Chathoth SM, Damaschke B, Samwer K, Schneider S. Appl Phys Lett 2008;93:071902.
[26] Yu W, Stroud D. Phys Rev B 1997;56:12243.
[27] Shetty R, Balasubramanian R, Wilcox WR. J Cryst Growth 1990;100:58.
[28] Rupp R, Müller G. J Cryst Growth 1991;113:131.
[29] Nakamura S, Hibiya T. Int J Thermophy 1992;13:1061.
[30] Shigematsu K, Anzai Y, Morita S, Yamada M, Yokoyama H. Jpn J Appl Phys 1987;26:1988.
[31] Tokizaki E, Terashima K, Kimura S. J Cryst Growth 1992;123:121.
[32] Nagasaka Y, Kobayashi Y. J Cryst Growth 2007;307:51.
[33] Lappa M. Cryst Res Technol 2005;40:531.
[34] Benard H. Rev Gen Sci Pure Appl 1900;11:1261.
[35] Koschmieder EL. Adv Chem Phys 1974;26:177.
[36] Pearson JRA. J Fluid Mech 1958;4:489.
[37] Eckert K, Bestehorn M, Thess A. J Fluid Mech 1998;356:155.
[38] Thess A, Bestehorn M. Phys Rev E 1995;52:6358.
[39] Boeck T, Thess A. J Fluid Mech 1999;399:251.
[40] Nield DA. J Fluid Mech 1964;19:341.
[41] Smith MK, Davis SH. J Fluid Mech 1983;132:119.
[42] Riley RJ, Neitzel GP. J Fluid Mech 1998;359:143.
[43] Kawamura H, Tagaya E, Hoshino Y. Int J Heat Mass Transf 2007;50:1263.
[44] Chan CL, Chen CF. J Fluid Mech 2010;647:91.
[45] Priede J, Gerbeth G. Phys Fluids 1997;9:1621.
[46] Kuhlmann C, Albensoeder S. Phys Rev E 2008;77:036303.
[47] Kuhlmann HC, Schoisswohl U. J Fluid Mech 2010;644:509.
[48] Kumar V, Biswas G, Brenner G, Durst F. Int J Heat Mass Transf 2003;46:1641.
[49] Kumar V, Basu B, Enger S, Brenner G, Durst F. J Cryst Growth 2003;253:142.

[50] Kumar V, Basu B, Enger S, Brenner G, Durst F. J Cryst Growth 2003;255:27.

[51] Cen X, Zhan J, Li YS. Cryst Res Technol 2011;46:14.

[52] Miyazawa Y. unpublished data.

[53] Yi KW, Kakimoto K, Eguchi M, Watanabe M, Shyo T, Hibiya T. J Cryst Growth 1994;144:20.

[54] Azami T, Nakamura S, Eguchi M, Hibiya T. J Cryst Growth 2001;233:99.

[55] Miller DC, Pernell TL. J Cryst Growth 1981;53:523.

[56] Miller DC, Pernell TL. J Cryst Growth 1982;58:253.

[57] Morita S, Sekiwa H, Toshima H, Miyazawa Y. J Ceram Soc Jpn 1993;101:108.

[58] Jones ADW. J Cryst Growth 1983;63:70.

[59] Jones ADW. Phys Fluids 1985;28:31.

[60] Jing CJ, Imaishi N, Yasuhiro S, Miyazawa Y. J Cryst Growth 1999;200:204.

[61] Jing CJ, Imaishi N, Sato T, Miyazawa Y. J Cryst Growth 2000;216:372.

[62] Jing CJ, Hayashi A, Kobayashi M, Tsukada T, Hozawa M, Imaishi N, et al. J Cryst Growth 2003;259:367.

[63] Jones ADW. J Cryst Growth 1989;94:421.

[64] Brandle CD. J Cryst Growth 1982;57:65.

[65] Seidi A, McCord G, Müller G, Leister H-J. J Cryst Growth 1994;137:326.

[66] Jing CJ, Tsukada T, Hozawa M, Shimamura K, Ichinose N, Shishido T. J Cryst Growth 2004;265:505.

[67] Matsumoto S. J Jpn Soc Microgravity Appl 2004;21:300.

[68] Wanschura M, Shevtsova VM, Kuhlmann HC, Rath HJ. Phys Fluids 1995;7:912.

[69] Eyer A, Leiste H, Nitsche R. J Cryst Growth 1985;71:173.

[70] Rupp R, Müller G, Neumann G. J Cryst Growth 1989;97:34.

[71] Imaishi N, Yasuhiro S, Akiyama Y, Yoda S. J Cryst Growth 2001;230:164.

[72] Li K, Xun B, Imaishi N, Yoda S, Hu WR. Int J Heat Fluid Flow 2008;29:1190.

[73] Chen Q-S, Hu W-R, Prasad V. J Cryst Growth 1999;203:261.

[74] Nienhuser CH, Kuhlmann HC. J Fluid Mech 2002;458:35.

[75] Lappa M. Comput Fluids 2005;34:743.

[76] Lan CW, Chian JH. J Cryst Growth 2001;230:172.

[77] Ratnieks G, Muiznieks A, Buligins L, Raming G, Muhlbauer A, Ludge A, et al. J Cryst Growth 2000;216:204.

[78] Cröll A, Müller-Sebert W, Nitsche R. Mat Res Bull 1989;24:995.

[79] Cröll A, Dold P, Benz KW. J Cryst Growth 1994;137:95.

[80] Dold P, Cröll A, Benz KW. J Cryst Growth 1998;183:545.

[81] Cröll A, Szofran FR, Dold P, Benz KW, Lehoczky SL. J Cryst Growth 1998;183:554.

[82] Hibiya T, Asai Y, Sumiji M, Kojima T. Cryst Res Technol 2003;38:619.

[83] Sumiji M, Azami T, Hibiya T. Jpn J Appl Phys 2003;42:6243.

[84] Lan CW, Su MC, Liang MC. J Cryst Growth 2000;208:717.

[85] Liang MC, Lan CW. J Cryst Growth 1997;180:587.

[86] Cröll A, Mitric A, Aniol O, Schütt S, Simon P. Cryst Res Technol 2009;44:1101.

[87] Arafune K, Kodera K, Kinoshita A, Hirata A. J Cryst Growth 2003;249:429.
[88] Stelian C, Yeckel A, Derby JJ. J Cryst Growth 2009;311:2572.
[89] Yeckel A, Derby JJ. J Cryst Growth 2011;314:310.
[90] Nicoara I, Vizman D, Friedrich J. J Cryst Growth 2000;218:74.
[91] Bunoiu OM, Duffar Th, Nicoara I. Prog Cryst Growth Charact 2010;56:123.
[92] Braescu L, Duffar T. J Cryst Growth 2008;310:484.
[93] Lan CW, Uda S, Fukuda T. J Cryst Growth 1998;193:552.
[94] Epelbaum BM, Schierning G, Winnacker A. J Cryst Growth 2005;275:e867.
[95] Fang HS, Yan ZW, Bourret-Courchesne ED. Cryst Growth & Des 2011;11:121.

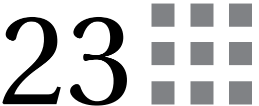

Flow Control by Magnetic Fields during Crystal Growth from Melt

Daniel Vizman

FACULTY OF PHYSICS, DEPARTMENT OF PHYSICS, WEST UNIVERSITY OF TIMISOARA, TIMISOARA, ROMANIA

CHAPTER OUTLINE

23.1 Introduction **910**
23.2 Selected Fundamentals of Magnetohydrodynamics **911**
23.3 Effects of Steady Magnetic Fields **914**
23.3.1 Axial Magnetic Field 914
23.3.1.1 Czochralski Method 914
23.3.1.2 Bridgman Methods and Vertical Gradient Freeze 917
23.3.1.3 Floating Zone 918
23.3.2 Transverse Magnetic Field 919
23.3.2.1 Czochralski Method 920
23.3.2.2 Bridgman Methods and Vertical Gradient Freeze 922
23.3.2.3 Floating Zone 923
23.3.3 Cusp-Shaped Magnetic Field 923
23.3.3.1 Czochralski Method 924
23.3.3.2 Floating Zone 927
23.4 Effects of Nonsteady Magnetic Fields **928**
23.4.1 Rotating Magnetic Field 928
23.4.1.1 Czochralski Method 929
23.4.1.2 Bridgman Methods and Vertical Gradient Freeze 930
23.4.1.3 Floating Zone and Traveling Heater Method 931
23.4.2 Alternating Magnetic Field 932
23.4.3 Traveling Magnetic Field 934
23.4.3.1 Czochralski Method 936
23.4.3.2 Bridgman Methods and Vertical Gradient Freeze 937
23.4.3.3 Directional Solidification 938
23.5 Combined Action of Various Types of Magnetic Fields and Electric Currents **941**
23.6 Conclusions and Outlook **943**
References **945**

Handbook of Crystal Growth. http://dx.doi.org/10.1016/B978-0-444-63303-3.00023-7
Copyright © 2015 Elsevier B.V. All rights reserved.

23.1 Introduction

Research carried out over many years has clearly demonstrated that the control of melt convection plays a key role in the optimization of semiconductor bulk crystal growth processes in order to increase their quality. With increasing crystal dimensions, the control of melt convection becomes a crucial issue for process optimization. Over time, two main strategies have been developed for the control of melt convection:

- Mechanical control: mainly by crucible or/and crystal rotation
- The use of magnetic fields in metal and semiconducting melts with a relatively high electrical conductivity or in the oxides melts with a high-enough ionic conductivity

These strategies usually go in two directions. The first strategy is damping the convective perturbations and turbulence, mainly generated by natural convection. These fluctuations can have a strong influence on the growth rate, interface shape, and nucleation, which play an important role in the crystal quality. The other strategy is melt mixing, which is used mainly for the growth of doped crystals in order to homogenize the dopant distribution; this approach is for the control of the diffusion boundary layer or to enhance the evaporation of unwanted components (e.g., SiO in silicon melts).

Recent decades have proven that magnetic fields are a powerful tool to use as an external force to control the convection in an electrically conducting melt. In the early 1980s, the Czochralski (CZ) method for the industrial growth of silicon crystals developed faster than the floating zone technique, mainly because applying magnetic fields allowed the growth of low-oxygen crystals that had similar properties to the floating-zone grown crystals (Ammon et al. [1]).

Depending on the applications, steady-state magnetic fields (e.g., vertical, transverse, cusp-shaped) or time-dependent magnetic fields (e.g., rotating, alternating, traveling) can be used. Sometimes, to compensate for some nonbeneficial effects, a superposition of different types of magnetic fields can be taken into account.

This chapter aims to provide an up-to-date review of the main contributions in the application of different types of magnetic fields in the growth process of semiconductor bulk single crystals. The next section reviews the physical description of the heat and mass transfer in magnetohydrodynamic flows that are relevant for the crystal growth processes. Section 23.3 is devoted to the steady magnetic field, whereas Section 23.4 focuses on the nonsteady magnetic fields. Section 23.5 presents combinations of different types of magnetic fields and electrical currents.

There are also important applications of magnetic field for dielectric materials with ionic melt characteristics, such as metal-organic chemical vapor deposition of YBCO films [2], solution growth of $CaCO_3$ and $CaSO_4$ [3], crystallization of Fe_3O_4 nanoparticles [4], and protein crystallization [5–7].The author would like to acknowledge other review works (Series and Hurle [8], Kakimoto [9], Ozoe et al. [10], Rudolph and Kakimoto [11],

Dold and Benz [12], Bliss [13], and Rudolph [14]) on the applications of magnetic fields in crystal growth processes. These authors made considerable efforts to synthesize the research done in the field at their time.

23.2 Selected Fundamentals of Magnetohydrodynamics

Melt flow plays a key role in all bulk crystal growth methods, having a strong effect on growth rates, solid–liquid (S-L) interface shape, chemical composition of the crystal, and defect formation. For electrically conducting melts, magnetic fields are an additional useful instrument to influence the melt convection. To understand the characteristics of the melt convection in a magnetic field, one should have a deep understanding of the physical phenomena that occur in a crystal growth process at the system scale: magnetohydrodynamics, heat, and mass transport. Conservation laws of mass, momentum, and energy, which govern these phenomena, are described by a set of partial differential equations.

Conservation of momentum and continuity are given by the Navier–Stokes equations for an incompressible fluid placed in a magnetic field:

$$\rho\left(\frac{\partial \vec{u}}{\partial t} + (\vec{u}\cdot\nabla)\vec{u}\right) = -\nabla p + \mu\nabla^2\vec{u} - \rho_{ref}\vec{g}\left[\beta\left(T - T_{ref}\right) + \beta_s\left(c - c_{ref}\right)\right] + \vec{F}_L \tag{23.1}$$

$$\nabla\cdot\vec{u} = 0 \tag{23.2}$$

where $\vec{u}$ is the velocity vector, p is the pressure, T is the temperature, c is the molar concentration, t is the time, μ is the viscosity, $\vec{g}$ is the gravitational vector, and ρ_{ref} is the density at a reference temperature T_{ref} and reference concentration c_{ref}. $\vec{F}_L$ is the inductive force due to the motion of a conducting liquid in a magnetic field, computed as the sum of the Lorentz forces acting on all the fluid's charged particles in a unit volume.

Conservation of energy is given by:

$$\rho C_p\left(\frac{\partial T}{\partial t} + (\vec{u}\cdot\nabla)T\right) = \lambda\nabla^2 T \tag{23.3}$$

where C_p is the heat capacity and λ is the thermal conductivity.

Conservation of mass is given by:

$$\frac{\partial c}{\partial t} + (\vec{u}\cdot\nabla)c = D\nabla^2 c \tag{23.4}$$

where D is the diffusion coefficient of the species.

The equation for the resulting Lorentz force is:

$$\vec{F}_L = \vec{j}\times\vec{B} \tag{23.5}$$

where $\vec{j}$ is the current density and $\vec{B}$ is the magnetic induction.

The basic mechanism of magnetohydrodynamics is dynamic: when currents are induced by a motion of a conducting fluid through a magnetic field, a Lorentz force will act on the fluid and modify its motion. The motion modifies the field and the field, in turn, reacts back and modifies the motion. This makes the theory highly nonlinear.

In a classical approximation, the magnetic field is described by the magnetic induction equation:

$$\frac{\partial \vec{B}}{\partial t} = -\frac{1}{\mu \sigma_{el}} \left(\nabla^2 \vec{B} \right) + \left(\nabla \times \left(\vec{u} \times \vec{B} \right) \right) \tag{23.6}$$

together with the Ohm's law:

$$\vec{j} = \sigma_{el} \left(\vec{E} + \left(\vec{u} \times \vec{B} \right) \right) \tag{23.7}$$

where σ_{el} is the electrical conductivity and $\vec{E}$ is the intensity of the electrical field.

In the case of steady magnetic fields, a scalar electric potential can be introduced to describe the electric field:

$$\vec{E} = \nabla \Phi \tag{23.8}$$

Considering Eqn (23.7) and the continuity equation $\nabla \vec{j} = 0$, a differential equation for scalar electric potential can be derived:

$$\Delta \Phi = \nabla \left(\vec{u} \times \vec{B} \right) \tag{23.9}$$

The nondimensional Lorentz force in the case of steady magnetic fields can be characterized by the Hartmann number, describing the ratio of electromagnetic to viscous forces:

$$Ha = BR \sqrt{\frac{\sigma}{\rho \nu}} \tag{23.10}$$

where R is the characteristic length (usually the radius in a cylindrical geometry), ρ is the density, and ν is the kinematic viscosity.

In the case of nonsteady magnetic fields, under typical conditions for crystal growth processes, the movement of the melt has only negligible influence on the induced current $\vec{j}$, so that, neglecting $\vec{u} \times \vec{B}$ in Eqn (23.7), Eqn (23.6) yields:

$$\frac{\partial \vec{B}}{\partial t} = -\frac{1}{\mu \sigma_{el}} \left(\nabla^2 \vec{B} \right) \tag{23.11}$$

Therefore, in the case of dynamic fields, the Lorentz force is independent of the melt flow velocity, which makes it easier to avoid instabilities of the convection pattern compared to some of the static field configurations.

The electric field and current density can be described with the vector potential $(\vec{A}(\vec{B} = \nabla \times \vec{A}))$:

$$\vec{E} = -\frac{\partial \vec{A}}{\partial t}; \quad \vec{j} = -\sigma \frac{\partial \vec{A}}{\partial t} \tag{23.12}$$

A nonsteady magnetic field applied externally to a melt will change if the electrical conductivity of the melt is sufficiently high and is able to expel the magnetic field. This well-known skin effect can be characterized by the skin depth:

$$\delta = \sqrt{\frac{1}{\mu\sigma\omega}} \tag{23.13}$$

where μ is the magnetic permeability, σ is the electrical conductivity, and ω is the angular frequency of the applied magnetic field.

If $\delta >> D$ (D-characteristic size of the melt), the magnetic field distribution is changed by the melt, which means that the field penetrates over the melt volume without any changes. If $\delta << D$, the magnetic field penetrates only slightly into the melt because the field lines are expelled due to the high electrical conductivity of the melt.

Note that an increase in frequency decreases the skin depth of the magnetic field. Thus, high frequency concentrates the force into a narrower layer near the ampoule wall. This effect is important for many semiconducting melts (e.g., Si, Ge) for which δ is in the range of 1–5 cm. However, it is less significant in poorly conducting melts (e.g., cadmium zinc telluride), for which δ is in the range of 10–50 cm, depending on the frequency [15].

The driving force of a rotating magnetic field is usually scaled by the nondimensional Taylor number (sometimes referred as the magnetic Taylor number), which represents an expression for the ratio of the electromagnetic force to the viscous force:

$$Ta = \frac{\sigma\omega B^2 R^4}{2\rho\upsilon^2} \tag{23.14}$$

In the case of a traveling magnetic field (TMF), a dimensionless force number F can be introduced to characterize the relative influence of the magnetic field on the melt [15]:

$$F = \frac{\sigma\omega k B^2 R^5}{4\rho\upsilon^2} \tag{23.15}$$

where $k = \frac{2\pi}{\lambda_{TMF}}$ denotes the wave number of TMF.

In the case of steady magnetic fields, a simplified analysis of the main melt flow driving mechanisms and forces in the CZ method, as performed by Muižnieks et al. [16], showed that the lowest limit of the magnetic induction needed to obtain a significant influence of a static magnetic field on the melt flow is just 28 mT. This is enough to generate a force density of 150 N/m^2, which is a characteristic value for a buoyancy force density in a silicon melt with a 40 K temperature difference.

Experiments performed by Miyazawa [17] revealed that high-intensity magnetic fields (usually 8–10 times higher than for semiconductor melts) can also have a strong influence on the flow of oxide melts. It is believed that, in this case, the Lorentz force is generated by both positive and negative ions, which can occur in the melt instead of free electrons, as it does in the semiconducting melts.

23.3 Effects of Steady Magnetic Fields

The first crystal growth experiments in a horizontal boat under magnetic fields were done by Pfann and Hagelbarger [18]. Ten years later, in 1966, Utech and Flemings [19] and independently Chedzey and Hurle [20] demonstrated the first successful use of steady magnetic fields to damp the melt convection and thereby improve the microscopic homogeneity of the crystal in a Bridgman boat for tellurium-doped indium antimonide crystal growth. Since then, three types of steady magnetic fields—axial (vertical) magnetic field (VMF), horizontal (transverse) magnetic field (HMF), and cusp-shaped magnetic field (CMF)—have received attention in almost all bulk crystal growth methods for semiconductor materials.

Steady magnetic fields produce no movement in a static melt. They can just influence an existing melt flow generated by other forces, such as buoyancy, centrifugal, Marangoni, or solutal. From a technological point of view, one of the main problems in working with the steady magnetic fields is the generation of high-intensity magnetic fields (200–500 mT or even higher). To obtain the necessary field strength, special magnets should be designed—large enough to contain the entire growth chamber and strong enough to produce the magnetic field over a volume with a diameter sometimes larger than 1 m. Nowadays, superconducting magnets, which are smaller and consume much less energy, can be used.

23.3.1 Axial Magnetic Field

The VMF is produced with a magnet (resistive or superconducting) large enough to contain the growth chamber (Figure 23.1). The Lorentz force generated by the magnetic field and flow velocity ($\vec{F}_L = (\vec{v} \times \vec{B}) \times \vec{B}$) typically damps the melt motion. VMF has no influence on the vertical (axial) component of the velocity ($\vec{v}_{||}$), but breaks the flow perpendicular to the magnetic field direction ($\vec{v}_{\perp}$) due to the Lorentz force ($\vec{F}_{L\perp}$), which points opposite to the $\vec{v}_{\perp}$ velocity component (Figure 23.2). Therefore, because the Lorentz force does not directly oppose gravitational force but suppresses the recirculation, local instabilities can occur in the melt. The influence of VMF on the melt flow was investigated in bulk crystal growth methods such as Czochralski, vertical Bridgman (VB), horizontal Bridgman (HB), vertical gradient freeze (VGF), and floating zone (FZ). In the following sections, the details of each of these methods are analyzed.

23.3.1.1 Czochralski Method

Melt convection in the CZ method is one of the most complex convections among the growth methods from the melt. General descriptions of possible Czochralski flow patterns and instabilities were presented by Müller [21] and Ristocelli and Lumley [22]. Characteristic for the melt convection in the CZ method are high-amplitude temperature fluctuations in the melt, especially near the S–L interface [23,24]. Therefore, the control of temperature fluctuations is one of the major issues in the optimization of the CZ method, which can be addressed by the use of magnetic fields.

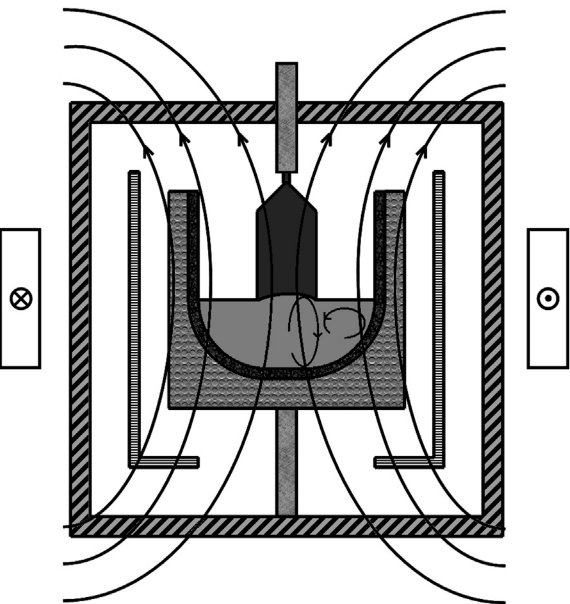

FIGURE 23.1 Schematic representation of a vertical magnetic field configuration.

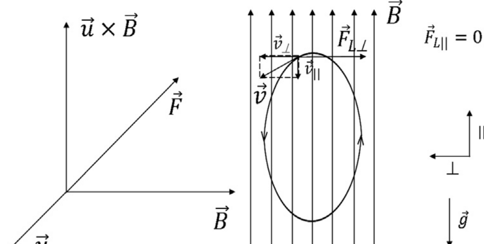

FIGURE 23.2 Principle of flow damping.

As already mentioned, the main effect of a VMF applied in a CZ configuration will be to slow down the melt convection. Consequently, all other parameters related to melt convection can be influenced by the magnetic field. In this section, the influence of the VMF on the most important growth parameters is presented:

Temperature field and fluctuations. Solid–liquid interface shape and temperature gradients near the S–L interface are strongly related to the thermal stress and consequently with dislocation formation in the crystal. Temperature gradient (G) in the crystal plays also an important role (through the V/G parameter and V-pulling rate) in the growing point defects mechanism [25]. Melt convection is strongly related to the temperature field (both distribution and temperature fluctuations) and S–L interface shape. Therefore, by manipulating the melt convection, both temperature field and interface shape can be controlled. Because of its damping effect, VMF will prevent the hot melt

from traveling from the crucible wall to the center of the melt. Thus, in order to maintain the same interface deflection, the temperature difference in the melt will increase and the crucible temperature will be higher [26]. The S–L interface shape in the presence of a VMF was studied by Virbulis et al. [27] using a complex numerical model; the results showed good agreement with the experimental results.

The main effect of the melt convection suppression is the decrease of temperature fluctuations. A VMF of 400 mT was found to almost totally suppress the temperature fluctuations in a 152-mm diameter CZ silicon melt [28]. The same effect was also found in a Liquid Encapsulated Czochralski (LEC) GaAs growth by Terashima et al. [29]. They reported that a magnetic field of 100 mT generated by a superconducting magnet strongly suppressed the temperature fluctuations.

Dopant distribution. Besides the effect of damping the temperature fluctuations, the static magnetic fields have an important effect on the boundary layer at the S–L interface, which, according to the Burton–Prime–Slichter (BPS) theory [30], affects the axial uniformity of the impurities incorporated into the growing crystal. By damping the entire melt flow, VMF will have as an effect a decrease of melt mixing near the growth interface. Hence, the diffusion boundary layer will increase and, in accordance with the BPS theory, the axial uniformity will increase too. Extensive boundary-layer models for segregation in a CZ growth under VMF were developed by Hurle and Series [31], Kobayashi [32], and Riley [33]. Experimental studies have been performed to validate the theoretical results. Thus, Series et al. [34] have demonstrated experimentally that the effective segregation coefficient (k_{eff}) of phosphorus and carbon in silicon approaches unity as the field increases over 200 mT. The same effect was demonstrated theoretically by Kobayashi [32]. Ravishankar et al. [35] proved that the effective segregation coefficient of gallium in silicon increases with the increase of the VMF intensity and that the values are in very good agreement with the Hurle and Series [31] theory.

The analysis of dopant incorporation in a CZ silicon crystal can indirectly confirm the effect of inhibition of melt flow in the presence of a VMF. Kim and Smetana [28], using a high-sensitivity striation etching, have shown that most of the 152-mm diameter crystal was free of striations for a relatively high magnetic induction of $B > 400$ mT. Ravishankar et al. [35] also proved that the benefit of a VMF is the elimination of random striations associated with natural convection in the melt, which improved the macroscale uniformity. However, VMF did not remove the rotational striations that are caused by small temperature asymmetries of the hot zone.

Performing experiments on oxygen incorporation in silicon by the CZ method with a VMF, Series [36] and Ravishankar et al. [35] have demonstrated that the axial uniformity of oxygen increases with an increase of the magnetic field induction, while the radial uniformity deteriorates. The deterioration of the radial uniformity is due to the damping of the radial flow, which generates nonmixing cells in the melt near the S–L interface; thus, the diffusion boundary layer in front of the crystal becomes perturbed radially [8].

The level of oxygen concentration is another critical issue for the quality of the silicon crystals. The oxygen source is the silica crucible through the following reaction:

$SiO_2(s) \rightarrow Si(m) + 2O(m)$. In the absence of the magnetic field, the oxygen is transported by the melt convection mainly to the melt–gas interface, where the reaction $Si(m) + O(m) \rightarrow SiO(g)$ takes place. Evaporation of SiO(g) occurs at the gas–melt interface and the remaining oxygen gets incorporated into the crystal. Marangoni convection has a favorable influence on the SiO evaporation.

As we have seen, VMF strongly damps the melt convection and Marangoni flow. Consequently, less oxygen is transported by convection from the crucible to the free surface and less SiO will evaporate. Thus, the oxygen concentration near the crucible wall and in the melt will increase.

Doing experiments in a 4 in diameter puller with a 500-mT superconducting axial field magnet, Ravishankar et al. [35] demonstrated that the oxygen concentration increases with the magnetic field strength and is much higher in comparison with cases that have no magnetic field. For a weak magnetic field (<100 mT), when a thermal dominant regime is still present in the melt, a decrease of oxygen concentration was demonstrated numerically [37] and experimentally [36,38]. The oxygen distribution is also affected by the other growth parameters, such as crucible and crystal rotation rates. Therefore, in order to find the optimum combination of parameters, complex numerical models are necessary [37,39].

Hofmann et al. [40] and Ozawa et al. [41] have shown that a controlled variation of the magnetic field during the growth process can produce a homogeneous impurity distribution along the growth axis of a Fe-doped InP crystal grown by LEC.

23.3.1.2 Bridgman Methods and Vertical Gradient Freeze

In VB, HB, and VGF configurations, the melt convection is basically driven by two different sources: buoyancy and surface tensions. Although the HB technique has side heating (i.e., the temperature gradient is perpendicular to the gravitational force direction), a variety of flow structures can occur [42,43]. The effect of a VMF (parallel to the gravitational force direction) was less investigated in HB than in a transverse one (see Section 23.3.2). The first experimental work in a HB configuration was performed by Utech and Flemings [19], who showed that a VMF damps the temperature fluctuations in the melt and the dopant striations are eliminated in tellurium-doped indium antimonide crystals. A relatively high intensity of a VMF (up to 1.35 T) has been found to have a moderate effect on the axial segregation in HB growth of a dilute metallic alloy.

VB/VGF configurations are characterized by the heating of the melt from above in an axial temperature gradient, which is favorable for a hydrodynamically stable flow. By numerical simulations, Kim et al. [44] have shown that the radial segregation is set by the flow structure near the S–L interface, whereas axial segregation is influenced by solute mixing throughout the melt. The VMF preserves the axisymmetry of the forces in the melt and thus the radial compositional profiles are expected to remain axisymmetric.

Because of a more stable convection, the potential of a VMF field to suppress the melt convection in a VB/VGF configuration is higher than for the CZ method. This was demonstrated by Matthiesen et al. [45], who grew a 1.5-cm germanium crystal using a

VMF of 3 T. The solute distribution in the crystal was similar to diffusion-controlled growth, leading to the conclusion that the melt convection was suppressed. Also, for the VGF growth of GaAs single crystals lightly doped with indium, the application of a 150 mT VMF was enough to suppress the Marangoni flow and to obtain low-defect and nearly striation-free single crystals [46]. Becla et al. [47] have observed a dramatic improving influence on radial homogeneity in a VB growth of HgMnTe under a 300-mT VMF.

Extensive simulation efforts have been made to investigate the effects of VMF in VB/VGF crystal growth: from two-dimensional models [44,48,49] to more complex three-dimensional (3D) models [50]. All these models have shown the potential of the VMF to suppress the buoyancy convection and to achieve a diffusion control limit. Thus, the axial segregation can be minimized and the radial segregation can be optimized as well. VMFs were also used in space experiments to suppress the g-jitter effects, as has been demonstrated by Baumgartl and Müller [51] and Duffar et al. [52].

23.3.1.3 Floating Zone

Because of the small dimensions of the melt, it is expected that the Marangoni convection will play a more important role in the FZ method than in the CZ case. A complex investigation of these processes, using a 3D numerical model, was performed by Mühlbauer et al. [53] and Rudevics et al. [54].

Technologically, the most relevant quality parameter of FZ silicon crystals is a homogeneous resistivity profile, in both the axial and radial directions [1]. The main source for the inhomogeneous resistivity (dopant) distribution is the time-dependent flow (mainly dominated by Marangoni convection) in the melt during the growth process [55]. Therefore, the most important effect of the VMF—the damping of the convection in the melt—is also of high interest here. The pioneering work of applying a VMF in the FZ technique was done by De Leon et al. [56] and Robertson and O'Connor [57]. To avoid the effects generated by the radiofrequency field and the counterrotation employed in the industrial FZ process, Dold et al. [55] performed experiments in a FZ-mirror configuration for small-diameter (8 mm) doped silicon crystals; they demonstrated that a weak magnetic field <500 mT can damp the flow instabilities and the striation patterns are more regular. However, a deterioration of the radial segregation occurs and residual striations can be found at the crystal periphery. A possible explanation for this behavior is that, under a VMF, the melt flow separates into two areas: a static central region and a thin boundary layer strongly mixed by thermocapillary convection. This explanation is also supported by numerical modeling [58,59]. It was also observed that, due to the reduced flow velocity, less heat is transported along the free surface and the S–L interface; thus, the isotherms became flatter.

By increasing the VMF strength (from 500 mT to a few T), the outer boundary layer is strongly reduced and the thermocapillary convection can be totally suppressed (Cröll et al. [60]), leading to a striation-free crystal. Sometimes, however, at high VMF, oscillatory dopant striations occurred. This effect is due to thermoelectromagnetic

convection caused by the interaction of thermoelectric currents (generated by the Seebeck effect) with the magnetic fields [60], which produce a Lorentz force. Because of the axial orientation of the magnetic field, the generated Lorentz force leads to an azimuthal flow, which is consistent with the striation patterns observed in experiments [61].

A VMF applied in a needle-eye FZ configuration was investigated by Lie et al. [62]. Using a more complex model that takes into account also the electromagnetic body force and the Joule heat generated by the alternating electric current density (which is induced by the needle-eye induction coil), they found that the melt flow is also divided into two major regions—the outer and the inner core regions. The flow due to electromagnetic pumping involves a balance between the averaged electromagnetic body force due to the alternating currents and the constant electromagnetic body force due to the VMF and the direct azimuthal electric currents. Besides applications in silicon growth, some experiments in the GaAs FZ growth were performed by Herrmann et al. [63], who showed that a VMF can dampen the Marangoni convection under microgravity conditions.

23.3.2 Transverse Magnetic Field

A transverse (or horizontal) magnetic field, because of its orientation perpendicular on the gravitational force and on the crystal growth direction, is much easier to produce using an external system of coils than a VMF (Figure 23.3). In comparison with the VMF, an HMF destroys the axial symmetry of the melt flow. It strongly dampens the vertical flow (which is now perpendicular to the field direction) and has no effect on the melt, which flows mainly along the HMF direction. The HMF is used on a large scale in CZ applications. There are also some reports on its application in VB, HB, VGF, and FZ techniques.

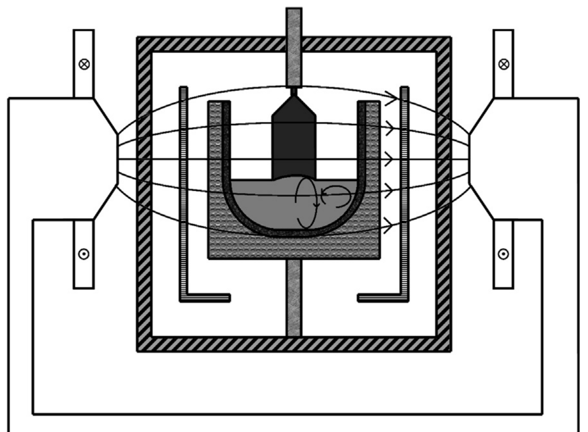

FIGURE 23.3 Schematic representation of a horizontal magnetic field configuration.

23.3.2.1 Czochralski Method

The first application of an HMF in the CZ method was carried out by Witt et al. [64]. They reported a strong decrease of the amplitude of temperature fluctuations in CZ growth of InSb when an HMF of 4000 Oe was applied. In the industrial CZ growth of silicon, HMF was first used in 1980 [65,66]. In the LEC growth of GaAs, Terashima and Fukuda [67] were the first to apply an HMF in the growth process. To understand the beneficial influences of the HMF on the growth process, the main effects of the HMF on the melt flow will be summarized in the following:

Temperature field and fluctuations. The experiments performed by Hoshi et al. [65] have shown that an applied HMF of 400 mT in a 5 cm diameter silicon CZ puller can dampen 10 times the temperature fluctuations in the melt and, consequently, a dislocation-free boron-doped silicon crystal was grown. A comparison between the influences of a VMF and an HMF was performed by Ravishankar et al. [35]; they found that, in a CZ silicon melt, the temperature fluctuations become negligibly small under the influence of a VMF or HMF of 150 mT. However, the cooling produced, as measured by the temperature change at the center of the melt, is much higher for the VMF than for the HMF. Thus, the VMF is effective in suppressing radial flow, whereas HMF favors the suppression of vertical flows in the melt. In LEC growth of GaAs, Terrashima and Fukuda [67] also reported a strong decrease of temperature fluctuations (from 18 to 0.1 K) when an HMF of 125 mT was applied.

Because of its orientation, HMF has a breaking influence on the melt flow and temperature field. Therefore, without three-dimensional numerical modeling and model experiments, it is very difficult to describe and understand these influences. All numerical models developed over time [26,68–75] showed that the main buoyant vortex is suppressed in the vertical cross-section parallel to the HMF (Figure 23.4(c)), whereas this vortex is very strong in the perpendicular cross-section (Figure 23.4(d)). In the middle horizontal cross-section (Figure 23.4(b)), the temperature field and the electrical potential are distorted in the direction of the HMF. The distorted direction at the free surface of the melt (Figure 23.4(a)) is rotated from the HMF direction because of the crystal rotation. In general, one can imagine the melt flow pattern as two vortex tubes along the HMF. The electrical potential, which generates a part of the Lorentz force $\overrightarrow{F}_L = \sigma(-\nabla\varphi + \overrightarrow{v} \times \overrightarrow{B}) \times \overrightarrow{B}$, is antisymmetrical to the plane parallel to the magnetic field.

A complex qualitative explanation of the melt flow pattern was given by Krauze et al. [76]. They showed that the electric field $\overrightarrow{E}_{vB} = \overrightarrow{v} \times \overrightarrow{B}$ and the potential electric field $\overrightarrow{E}_{\varphi} = -\nabla\varphi$ fully compensate for each other near the walls in the plane perpendicular to the magnetic field and partially compensate in the area under the crystal (Figure 23.5).

Dopant distribution. Ravishankar et al. [35] demonstrated that the effective segregation coefficient (k_{eff}) of phosphorous in a CZ silicon growth remains unchanged and the microscale dopant uniformity across the crystal improved dramatically in the case of an HMF of 150 mT in comparison to the VMF. The same result—a decrease of impurity

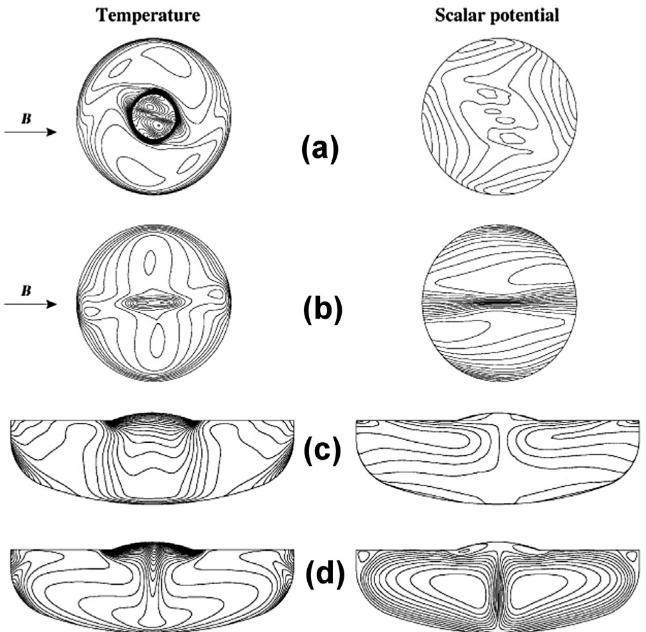

FIGURE 23.4 Temperature distribution and distribution of the scalar electrical potential for an applied horizontal magnetic field with $B = 128$ mT in a 100 mm silicon Cz configuration. (a) Horizontal cross-section close to the free surface of the melt. (b) Horizontal cross-section at half of the melt height. (c) Vertical cross-section parallel to the external field lines. (d) Vertical cross-section perpendicular to the external field lines. The spacing of the isotherms is 2.2 K. *From Ref. [26], with permission from Elsevier.*

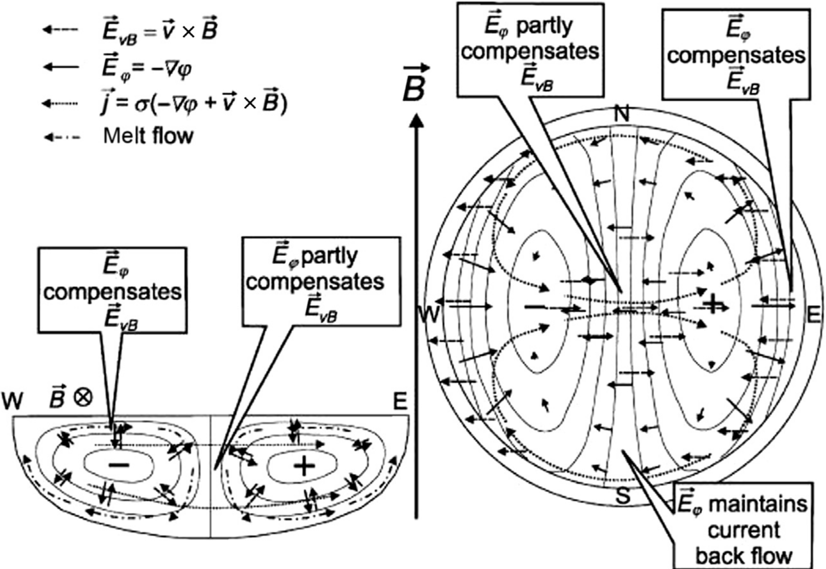

FIGURE 23.5 The qualitative explanation of the horizontal direct current magnetic field–induced electric field and current density distribution (cases with motionless crystal and crucible). *From Ref. [76], with permission from Elsevier.*

fluctuations along the crystal in the presence of a 400-mT HMF—was also obtained by Iino et al. [77] in a 200-mm CZ silicon growth configuration.

Analyzing the carbon and boron distribution in the LEC growth of GaAs, Terashima et al. [78] obtained a decrease of their concentration when an HMF field was applied. This decrease was correlated with a decrease in the amplitude of temperature fluctuations. The axial distribution of carbon was found to be much more uniform in the presence of an HMF of approximately 130 mT, which suggests an increase in the carbon segregation coefficient toward unity.

In one of the first theoretical studies on the influence of HMF on the distribution of the solute in a crystal, Kobayashi [32] demonstrated that the forced convection due to the rotating crystal is not affected by the magnetic field and that the effective distribution coefficient will approach, with an increase of the HMF, the value given by the BPS theory obtained from the value of the equilibrium distribution coefficient as a result of the suppression of thermal convection. In contrast, a VMF suppresses the forced convection and generates an effective distribution coefficient close to unity with an increase of the VMF intensity.

The influence of the HMF on oxygen distribution was analyzed by Ravishankar et al. [35] and Iino et al. [77]. It was demonstrated that the oxygen concentration decreases with an increase of the HMF strength to 150 mT and remains almost unchanged for higher values. This behavior can be a consequence of the melt flow, which prevents the oxygen-rich melt in the crucible bottom from reaching the S–L interface, as well as of the Marangoni convection, which is not damped as in the case of VMF and increases the evaporation loss of SiO.

Numerical models can give a more complex view of the oxygen distribution under an HMF. Kakimoto and Ozoe [71] have shown the limit of the BPS theory due to the intrinsic inhomogeneity of oxygen distribution in the melt under HMF. The main reason is the oxygen evaporation—it generates an inhomogeneous distribution of oxygen on the surface in contrast with boron and phosphorus, which are distributed almost homogeneously at the top of the melt and at the S–L interface. Collet et al. [75] developed a complex numerical model to analyze the inhomogeneities generated by the real for of the HMF.

23.3.2.2 Bridgman Methods and Vertical Gradient Freeze

Utech and Flemings [19] found that, similar to VMF, an HMF oriented along the crucible axis also dampens the temperature fluctuations in the melt and eliminates the dopant striations in HB growth of tellurium-doped indium antimonide crystals.

By applying an HMF in the VB growth of indium antimonide, Kim [79] showed that the random temperature fluctuations in the melt turn into periodic oscillations for an HMF intensity between 92 and 142 mT and are completely suppressed for an HMF above 170 mT. In the last case, a striation-free crystal growth was achieved.

Sen et al. [80] used an HMF in a VB configuration for the growth of indium–gallium antimonide. They show that an HMF of 400 mT produced a strong decrease in the

density of grain boundaries and of twin boundaries; they correlated these effects with the reduction of temperature fluctuations. In the VB growth of HgCdTe under an HMF in the range of 200–500 mT, Su et al. [81] showed an abrupt decrease in the mole fraction of CdTe when the magnetic field was applied.

Lan et al. [50] developed a three-dimensional numerical model to study the influence of an HMF on the flow and segregation in a VB setup for gallium-doped germanium. They demonstrated that the damping by HMF is more effective than by VMF and that the axial segregation can be pushed to the diffusion-controlled limit much more easily in the case of HMF. On the other hand, the radial solute segregation is large and highly asymmetric due to the nonuniform local dopant mixing caused by the melt flow. In a further study, Lan and Yeh [82] proposed an ampoule rotation together with the application of an HMF in order to improve the dopant nonuniformity. Today, HMF is rarely used in Bridgman or VGF configurations and is less investigated in comparison with a VMF.

23.3.2.3 Floating Zone

Kimura et al. [83] were the first to study the effects of an HMF on the FZ melting of gallium-doped silicon. They found that an HMF of 180 mT causes a significant reduction in fluid motion and the striation pattern is rendered more regular and orderly. In another study, Robertson and O'Connor [84] showed that a higher HMF of 550 mT has a strong effect on the growth interface shape, the Ga distribution, and the crystal morphology. The striation etch pattern reveals a reduction in the concavity of the growth interface when the HMF is present and the crystal is rotated. For nonrotating crystals, the HMF breaks the symmetry and the cross-section of the crystal has an elliptical form, with the major axis aligned along the magnetic field direction. Oscillations in dopant concentrations have been observed and the effective segregation coefficient of the gallium was found to increase in the presence of the HMF as a consequence of the increase of the diffusion boundary layer thickness.

Similar effects were seen in FZ growth of GaAs (6-mm diameter) [63] with the striations suppressed under an HMF of 60 mT. In a microgravity GaAs FZ experiment, Herrmann and Müller [85] employed an HMF configuration to damp the thermocapillary convection. Although the HMF used was nonuniform due to the equipment constraints, a significant reduction of the amplitude of the concentration fluctuations was found.

23.3.3 Cusp-Shaped Magnetic Field

VMF and HMF have both favorable and unfavorable effects on the melt convection in different crystal growth methods. Although VMF and HMF significantly damp the melt flow, they have also undesirable effects: VMF degrades the uniformity of the radial dopant distribution and HMF breaks the geometrical symmetry of the melt flow. A CMF, which is generated by a pair of Helmholtz coils operated in opposed current mode

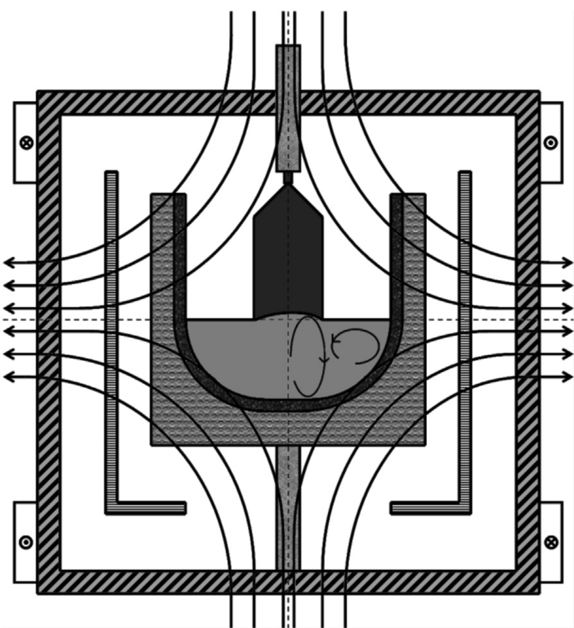

FIGURE 23.6 Schematic representation of a cusp magnetic field configuration.

(Figure 23.6), was designed to damp undesirable flows while minimizing the damping of desirable flows. Such a field configuration uses the advantage of an HMF to preserve a radial flow in the S–L interface plane while using the advantage of a VMF to dampen the turbulent convection in a large fraction of the melt. It is axially symmetric and perpendicular to the whole melt–crucible interface and it decreases the boundary layer at the crucible wall. In fact, there is a zone under the crystal free of magnetic field, while the crucible walls are exposed to large field strengths. In comparison to the VMF and HMF, which have just one control parameter (the field strength), the CMF can be operated with two control parameters—the strength and the relative position of the CMF center to the S–L interface.

The maximal intensity of the CMF used in applications is in the range of tens of mT, in comparison to the intensities of VMF and HMF, which are in the range of hundreds of mT. The CMF is used mainly in CZ applications. There are also some reports on applications in the FZ technique.

23.3.3.1 Czochralski Method

The first application of a CMF in a CZ configuration was reported independently by Hirata and Hoshikawa [86] and Series [87]. They showed the potential of the CMF to realize localized control of thermal convection at the melt–crucible interface, independent of that at the free melt surface. The S–L interface was located in the symmetry plane between the two coils and was maintained in this position by continuously moving the

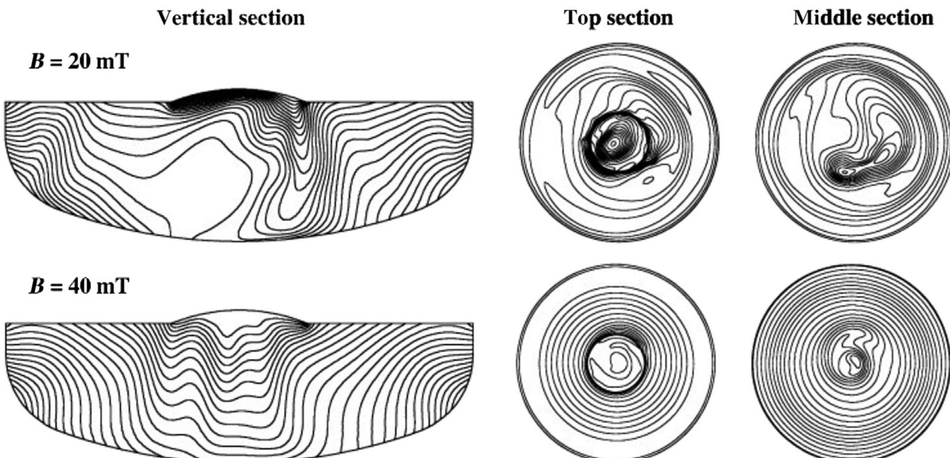

FIGURE 23.7 Isotherms in a vertical section and two horizontal sections placed at the free surface of the melt (top section) and at half height of the melt (middle section), for two magnetic field intensities. Isotherms step is 1.5 K. *From Ref. [91], with permission from Elsevier.*

crucible upwards to compensate for the decrease of the melt height by the crystal growth. The main effects of the CMF on the melt flow are summarized in this section.

Temperature field and fluctuations. The mechanism by which the CMF configuration affects the melt flow was investigated both by numerical modeling and experimental investigations [27,88–93]. All of these contributions showed that the stabilizing effect on the flow and temperature field near the crucible wall (where the applied field is the highest) is stronger than under the crystal. This effect can be clearly seen in Figure 23.7, where the calculated temperature field for two intensities of the magnetic field at a fixed time in a vertical section and two horizontal sections are presented. The stabilizing effect is stronger with the increase of the magnetic field. Experimental measurements and numerical simulations performed by Hirata and Hoshikawa [89] for the CZ growth of silicon crystals showed that, in a crucible with a 15 cm diameter, the amplitude of the temperature fluctuations under the crystal decreases significantly when a CMF field is applied (from 2.8 K with no magnetic field to 0.5 K). Performing measurements and numerical simulations in a larger crucible with a diameter of 36 cm, Vizman et al. [91] found that under the crystal remains a higher amplitude of temperature fluctuations, of about 10 K, when a CMF is applied. This can be because the zone under the crystal is less influenced by the magnetic field. The same effect was found numerically by Savolainen et al. [92] in a 50 cm diameter crucible. Liu et al. [93] carried out a numerical comparison between HMF and CMF and found that, due to the different damping mechanisms, a CMF provides a stronger suppression effect of thermal instabilities than an HMF, for the same magnetic field intensity.

Watanabe et al. [94] investigated the temperature fluctuations under the crystal in a small crucible (7 cm in diameter) for different positions of the CMF center relative to the

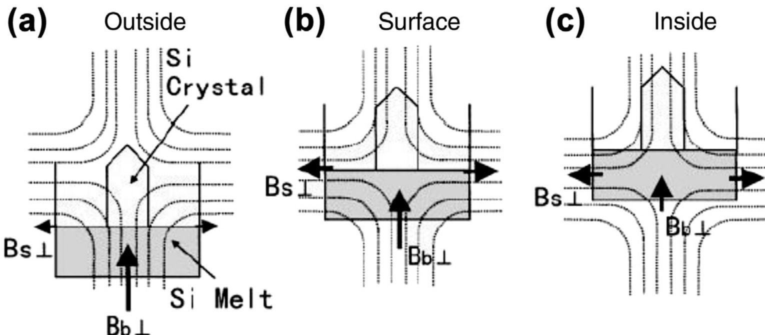

FIGURE 23.8 The CMF configurations: (a) the center of the CMF positioned 20 mm above the melt-free surface (outside), (b) the center of the CMF positioned at the melt-free surface (surface), and (c) the center of the CMF positioned 20 mm below the melt-free surface. *From Ref. [94], with permission from Elsevier.*

S–L interface (outside, surface, and inside; see Figure 23.8). They found a significant amplitude of temperature fluctuations below the crystal for the outside and surface CMFs, but almost no fluctuations for the inside CMFs configuration. Contrary to this result, in a much larger crucible of 50 cm diameter, Savolainen et al. [92] showed by numerical modeling that there is no significant difference between surface and inside CMF configurations.

Dopant distribution. Because CMF has a minimum influence on the melt convection near the S–L interface, Series [87] demonstrated experimentally that the axial phosphorus and carbon incorporation in the crystals was similar to the nonmagnetic crystals. The radial uniformity of the dopants was much higher in comparison with VMF crystals.

Hirata and Hoshikawa [86] found that the nonrotational dopant striations were reduced by the CMF and rotational striations were not detected, probably due to the axially symmetric damping of the melt convection. This is superior to the conventional HMF or VMF, in which nonrotational striations are reduced but rotational striations are often increased.

Oxygen incorporation is another area where CMF plays a beneficial role. Hirata and Hoshikawa [95] analyzed the oxygen distribution in the silicon crystals grown by the CZ method under a CMF and found the following characteristics:

- The axial homogeneity of oxygen concentration is improved by the CMF in comparison with no magnetic CZ, similar to that obtained in the HMF case.
- The radial homogeneity improved also in comparison to the case with no magnetic field, as an effect of the damping of the thermal convection and the centripetal flow at the free surface.
- Oxygen concentration decreases steadily with the increase of the CMF strength due to the damping of the convection adjacent to the melt–crucible interface, whereas those adjacent to the free surface do not change as much. Thus, the crucible dissolution (which is the oxygen source) decreases relative to the rate of oxygen evaporation at the melt free surface.

- The oxygen concentration in the crystal can be controlled by the field strength at constant, high crystal, and crucible rotation rates. This is very different from the HMF or VMF cases, which require changing the crucible or crystal rotation rates for oxygen concentration control.

Sim et al. [96] demonstrated that the growth of large single silicon crystals of 200 mm in diameter with extremely low oxygen concentration and with a radial gradient less than 2% is possible with the CZ method under CMF. The influence of the relative position of the CMF center to the S–L interface on the oxygen distribution was investigated by Watanabe et al. [94]. They found that the growth striations, which were related to the fluctuations of the oxygen concentration, were clearly visible for the outside and surface CMF configurations but were not observed for the inside configuration (Figure 23.9). Numerical models have also been developed to understand the oxygen transport in CZ silicon growth under a CMF [90,97].

23.3.3.2 Floating Zone

No experimental data are available in the literature for the application of a CMF in FZ growth. Based on numerical modeling, Morthland and Walker [98] suggested that a CMF can influence the radial distribution of dopants, creating large field strength near the S–L interface and a small angle between the local field vector and the normal at each point on the free surface.

Lan [58] showed that, because the coils are quite far from the sample, extremely large currents are required to generate a sufficient field strength in the melt, comparable with a VMF. Unexpectedly, the weak flow in the core region affects the dopant redistribution and results in an even larger radial segregation in comparison with VMF or CZ growth. In a further study, Lan and Liang [99] investigated a superposition of CMF, a rotation of the

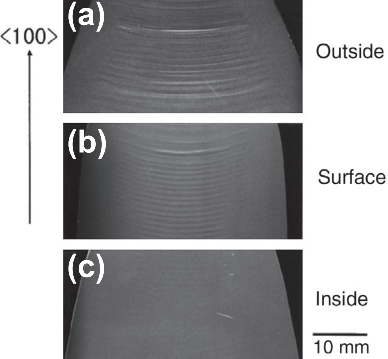

FIGURE 23.9 Growth striations in the grown crystals taken by the X-ray topograph method: (a) for the outside CMF configuration, (b) for the surface CMF configuration, and (c) for the inside CMF configuration. *From Ref. [94], with permission from Elsevier.*

feed rod, and a counterrotation of the crystal. They found that the mixing in the core region seems to be better and, as a result, the dopant uniformity is improved.

23.4 Effects of Nonsteady Magnetic Fields

The interest in the application of nonsteady magnetic fields in crystal growth of single crystals has increased in recent decades, mainly because of their potential to influence heat and mass transfer through the well-defined flow generated by relatively low nonsteady induction forces. A simplified analysis performed by Rudolph and Kakimoto [11] estimated that the required magnetic induction necessary to counteract a buoyancy force density of $150/\mathrm{Nm}^3$ is $B \approx \sqrt{150/\sigma\pi f L} = 1.4\ \mathrm{mT}$ for the frequency $f = 50\ \mathrm{Hz}$ and characteristic length $L = 0.4$ m. This value is almost one order of magnitude lower than in the case of steady magnetic fields (see Section 23.2). From a technological point of view, this means smaller size and lower costs for the magnets. The main types of nonsteady magnetic fields used in crystal growth are alternating magnetic field (AMF), rotating magnetic field (RMF), and traveling magnetic field (TMF). Sometimes, nonsteady magnetic fields are used in combination with steady magnetic fields.

An RMF was first used by Pfann and Dorsi [100] in the zone melting process. Mullin and Hulme [101] were the first to use an AMF in a zone-refining process; they obtained an enhanced purification rate due to the force melt mixing.

23.4.1 Rotating Magnetic Field

An RMF is basically generated by a three-phase asynchronous electrical engine (sketched in Figure 23.10) and induces currents in a conducting melt. The wires of the winding forming three coils are integrated into slots of the iron sheet package. Connecting these coils to a three-phase power supply yields a rotating transversal magnetic field in the horizontal plane (Figure 23.10).

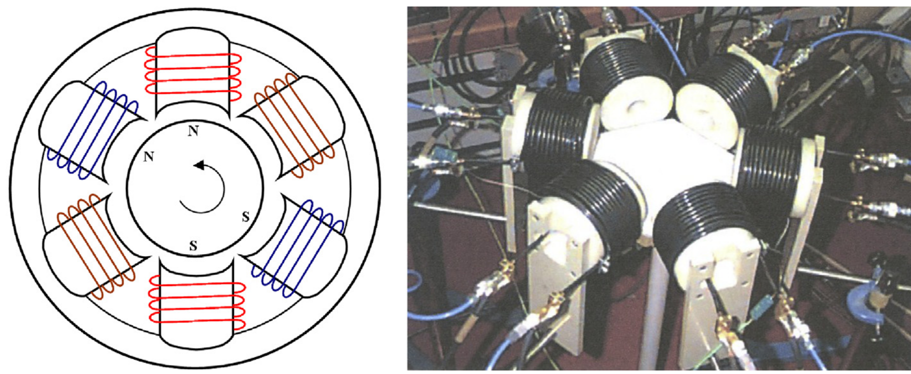

FIGURE 23.10 Sketch of the stator of an asynchronous electric engine. *Photo from the thesis of P. Dold.*

Applied to a melt, an RMF induces an azimuthal electromagnetic force, which generates mainly an azimuthal flow. A secondary meridional flow also arises due to the imbalance of the centrifugal force and the radial pressure gradient in the boundary layer in the vicinity of the horizontal container walls. This imbalance is known as Ekman pumping [102], and the rate of this secondary flow is about one order of magnitude smaller than the primary, azimuthal flow [12].

In a survey on RMF applications in the process of bulk single crystal growth, Gelfgat [103] distinguished four flow regimes that sequentially occur in the melt under an RMF:

- Small values of an RMF induce a laminar flow regime with a structural symmetry of the azimuthal and meridional flows.
- A further increase in the field induction generates a stationary nonlinear flow regime.
- If the RMF induction is higher than a critical value, an oscillating flow regime occurs in the melt. It is strongly nonlinear and nonstationary.
- A further increase of the RMF induction generates a quasi-stationary stable flow regime in the melt.

Complex stability analysis of the interaction between the natural convection and RMF were carried out by Friedrich et al. [104], Kaiser and Benz [105], and Grants and Gerbeth [106].

Many model experiments have been developed over time in order to get a fundamental understanding of the effect of an RMF on the melt flow and to evaluate the numerical models. In these experiments, different low Prandl number fluids were used: mercury [102,107], gallium [108–110], or InGaSn [111]. Dold and Benz [109] and Friedrich et al. [104] investigated the stable and the unstable Benard configuration and showed that RMF can be used to significantly dampen the temperature fluctuations caused by time-dependent, buoyancy-driven forces. A more complete review on these experiments and on other RMF applications can be found in Ref. [12]. The effect of an RMF on the growth process was studied in bulk crystal growth methods, such as VB, HB, VGF, CZ, and FZ, as discussed in the following sections.

23.4.1.1 Czochralski Method

The first application of an RMF in a CZ configuration was reported by Shaskow and Shushlebina [112]. They showed that the convective temperature fluctuations in the melt were reduced and the dopant inhomogeneities decreased when an RMF was applied. Later, just a few real growth experiments were reported in literature. Hoshikawa et al. [113] have grown a 100 mm diameter boron-doped silicon crystal with a CZ puller, where the graphite heaters were connected to a three-phase current source. Their results show that a low-oxygen-content silicon crystal can be obtained when the rotation of the crucible, the seed crystal, and the melt rotation imposed by RMF are in the same direction. Zhou and Huang [114] and Spitzer [115] numerically investigated a similar configuration and qualitatively obtained the same effect. Kakimoto [116] demonstrated

that the secondary flow in a meridional plane enhances heat and impurity transfer from the crucible wall to the S–L interface.

Another growth experiment was performed by Brückner and Schwerdtfeger [117]. They developed a modified Czochralski technique to pull single crystals without mechanical rotation of the crystal and of the crucible by bringing forth the controlled convection in the melt solely by RMF. Crystals of copper, germanium, and silicon were grown successfully with this technique.

Grants and Gerbeth [118] experimentally studied the phenomenon of temperature field stabilization by an RMF in a simplified physical low-temperature model of a medium-size Czochralski facility, with a 140 mm diameter crucible filled with gallium melt. The stabilization occurs as the result of a flow transition from a large-scale buoyancy driven to a small-scale magnetically driven turbulence. The amplitude of temperature fluctuations at the side wall was suppressed by a factor of five immediately after the flow transition and decreased further as the strength of the RMF increased. The fluctuation damping was even more pronounced in the core of the flow, where a factor of 50 may be reached. They also found that the stabilizing effect disappears in a high-frequency RMF. Based on these results and using a scale-up evaluation, Grants and Gerbeth [118] estimated that an RMF with an amplitude of 0.95 mT at 50 Hz frequency is sufficient for a significant suppression of the temperature fluctuations in an LEC GaAs crucible with a diameter of 300 mm.

23.4.1.2 Bridgman Methods and Vertical Gradient Freeze

RMF was successfully applied for the first time in gallium-doped germanium crystal growth experiments by Dold and Benz [119] in the VB technique and by Friedrich et al. [120] in the VGF technique. Both groups reported a change in the S–L interface curvature, from concave to a slight W-shape when an RMF is applied, due to the secondary convective motion. The axial macrosegregation did not seem to be influenced by the RMF because of a totally mixed regime. Friedrich et al. [120] also observed an increase of the radial dopant homogeneity. This behavior can be understood as an effect of the increased flow velocity in the vicinity of the interface, which led to a better mixing of the melt. Applying an RMF of 2 mT/50 Hz, Dold and Benz [119] found that the dopant striations due to the buoyancy convection are strongly reduced.

Si-doped GaAs crystal of 50 mm in diameter under an RMF were grown by Pätzold et al. [121]. Under the forced flow, a significant reduction of the bending of the concave interface was obtained and a W-shaped interface was observed at an aspect ratio of approximately 1.5. Lyubimova et al. [122] performed numerical modeling for VB-grown GaAs and also showed that higher magnetic field intensity results in the S–L interface shape change from concave to W-shaped.

RMF influence on the VB growth of gallium-doped germanium crystals was investigated by Volz et al. [123]. The RMF also has a marked effect on the interface shape in this case, changing it from concave to nearly flat as the RMF strength is increased. It was also shown that time-dependent flow instabilities occur when the critical magnetic Taylor

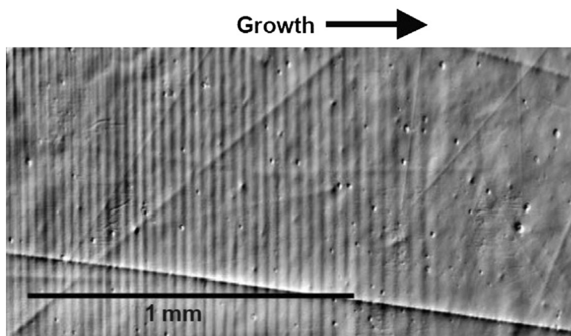

FIGURE 23.11 Transition from unstable to stable flow in VB growth of Ga-doped Ge for a critical Taylor number of 6×10^4. *From Ref. [123], with permission from Elsevier.*

number is exceeded; this can be observed by noting the appearance of striations in the grown crystals (Figure 23.11). In a similar experiment, Bellmann et al. [124] found that the accumulation of the Ga solute near the center of the melt during growth under natural buoyancy is reduced by the electromagnetically induced flow.

Using numerical simulations to study the VGF growth of 2-in InP crystals, Schwesig et al. [125] suggested that an RMF offers no possibility to minimize the strong concave curvature of the interface very close to the crucible wall. By means of numerical modeling, Wang et al. [126] found that, in VGF submerged heater growth, RMF seems to be not as efficient as a combination of an axial magnetic field and an electrical current. Bellmann et al. [127] performed a global numerical study of Ga segregation in the VGF growth of Ga-doped Ge under the influence of an RMF. Galindo et al. [128] built a low-temperature flow experiment using a GaInSn alloy and a numerical model to study the complex fluctuation flow patterns in a combined VGF-type buoyancy and RMF flow.

23.4.1.3 Floating Zone and Traveling Heater Method

Because of the high velocity in the melt of approximately 15 cm/s [105], a higher intensity of the RMF is needed in the FZ process to counteract the Marangoni convection compared to the buoyancy convection in VB/VGF. Using an RMF field of $B = 7.5$ mT/50 Hz, Dold et al. [129] obtained an FZ silicon crystal of 14 mm in diameter with substantially reduced dopant inhomogeneities. Their main results were as follows:

- The intensity of the dopant nonuniformities is strongly reduced by the RMF.
- The fluctuations of the dopant concentration are reduced under the influence of the RMF.
- Axial macrosegregation decreased upon application of the magnetic field.
- A symmetrization of the S–L interface shape was observed in the RMF growth and the interface curvature is slightly flatter.

The effect of the intensity reduction of the dopant striations, which are caused by time-dependent Marangoni convection with increasing RMF, was also observed by Fischer et al. [110] in FZ-GaAs. Higher diameter equipment, relevant for industrial Si-FZ,

have not been experimentally investigated in literature. Raming et al. [130] numerically investigated an Si-FZ configuration of 100 mm diameter and suggest that an RMF can lead to just a slightly improved (more homogeneous) macroscopic radial resistivity profile, whereas microscopic axial resistivity oscillations will increase. Liu et al. [131] have applied RMF in the FZ growth of oxide crystals ($Bi_{12}SiO_{20}$) and reported that an applied RMF of 25 mT/50 Hz is efficient enough to control the oxide melt flow during the growth process, and the quality of as-grown BSO single crystals is obviously improved. This effect was explained as being generated by the Lorentz force, which is created by an interaction between the magnetic field and electric current in the melt due to the ionic electrical conductivity of the oxide melt.

A linear stability analysis for the thermocapillary convection in the floating zone process with an RMF was performed by Walker et al. [132]. Other numerical investigations of the melt flow in the FZ were performed by Ma et al. [133] and Yao et al. [134].

Beneficial effects of RMF were also observed in the traveling heater method growth of CdTe and (Hg, Cd)Te crystals by Salk et al. [135] and Senchenkov et al. [136], who performed RMF experiments in an ampoule designed for the PHOTON 7 mission, both in gravity and microgravity conditions. It was observed that RMF generates a stable steady flow in the Te-zone, improving the radial and axial distribution of the Te inclusions.

23.4.2 Alternating Magnetic Field

From a technical point of view, an AMF can be achieved more simply than an RMF or a TMF, by only a single coil. Only a few reports can be found in the literature on the application of AMF in crystal growth processes, much less and not as systematic as in the case of RMF or TMF.

The first low-temperature model experiment relevant for a CZ configuration was developed by Wetzel et al. [137]. They used eutectic InGaSn as a model melt in a 20-in standard CZ crucible. The equipment was supplied with two types of AMF inductors: a bottom AMF and a side AMF (see Figure 23.12). A numerical approach was validated against the experimental results and used in the flow analysis. It was found that the AMF generated by the side inductor causes a two-vortex structure in the outer melt region, but it leaves the inner region underneath the crystal almost unaffected. Because of the increased mixing, a lowered temperature and a widening of the isotherms in the outer region toward the crucible wall were observed. In the case of the AMF generated by the bottom inductor, a flow cell was observed in the outer region near the crucible wall, which was rotating opposite to the original buoyancy-driven convection. As in the case with an AMF side inductor, there was a significant decrease in the temperatures in the outer melt region. The same behavior was obtained numerically by Virbulis et al. [27] in a real silicon CZ puller for a 200 mm crystal and 24-in crucible.

Mercier and Nishizawa [138] numerically studied the influence of the AMF on the solution growth of SiC from silicon melts. Due to a higher temperature difference in the

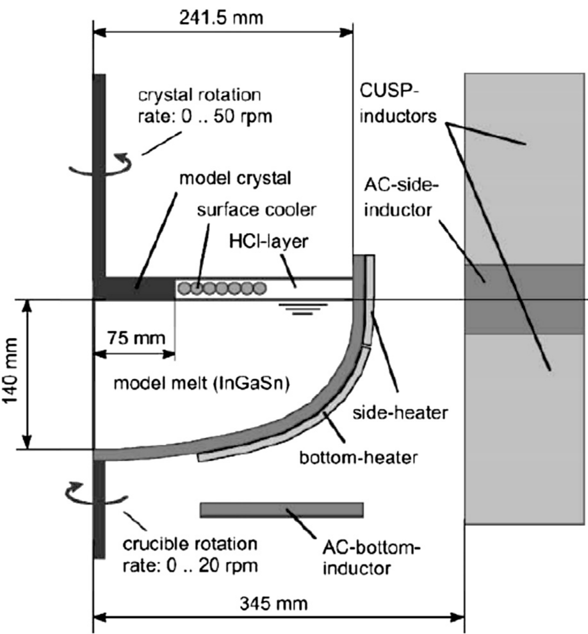

FIGURE 23.12 Laboratory CZ setup: main parts and dimensions. *From Ref. [137], with permission from Elsevier.*

melt, the buoyancy force density is almost seven times higher than in a classical CZ. Therefore, even a higher Lorentz force generated by an AMF cannot totally control the melt convection. However, at high Lorentz force density, a bottom inductor, located below the melt, was seen to generate a more efficient pattern for the enhancement of the carbon transport from the dissolution area to the crystal growth front in comparison to a side inductor.

For an FZ configuration, Raming et al. [130] demonstrated by numerical modeling that an additional low-frequency AMF can lead to a more forced convection in the molten zone, therefore resulting in better mixing of the dopant concentration field. This leads to a more homogeneous macroscopic radial resistivity profile, whereas axial microscopic resistivity oscillations may increase too.

A more systematic study was carried out to investigate the influence of an AMF on the VB growth of (Ga, In)Sb by numerical modeling [139,140] and growth experiments [141]. From transient numerical analysis, it was found that the axial and radial segregation can be maintained at lower values during the whole growth process if the magnetic field intensity is progressively increased during the solidification. In this case, the interface deflection was also maintained at reasonably constant values. In the growth experiment [141], a polycrystalline, crack-free, and nondestabilized (Ga,In)Sb ingot was obtained under a 2 mT AMF. The results indicated that the S–L interface deflection decreases with the increase of AMF and that the radial segregation was almost constant along the ingot, which confirm efficient mixing of the melt near the S–L interface. In a later study, Mitric

and Duffar [142] proposed a theoretical model to estimate the optimal parameters of the AMF to overcome the solutal effect. Based on the analytical estimations, a magnetic field of 3 mT and 5000 Hz has been found to be optimal for efficient mixing. Although the AMF seems to be very efficient for effective mixing (as it is also in metallurgy), more growth experiments are necessary to prove if AMF is favorable for crystal growth.

23.4.3 Traveling Magnetic Field

Lately, melt flow control by means of TMF has been one of the most active research directions in the optimization of crystal growth processes from melt. The TMF coil system consists of a number of coils, which are arranged vertically one over the other (Figure 23.13). The coil system is fed by an electrical current characterized by amplitude, frequency, and phase shift. The resulting magnetic field travels either upward or downward. The magnetic induction B can be described as a wave model with wavelength $\lambda = 2\pi/k = nh$ (with k being the wave number, n being the number of coils, and h being the distance between coils). A conventional TMF arrangement consists of three coils in a delta connection. More variability can be achieved when the coils are coupled in a star connection. In this case, each coil can be supplied separately, and frequency and phase shift can be varied over a wide range [14].

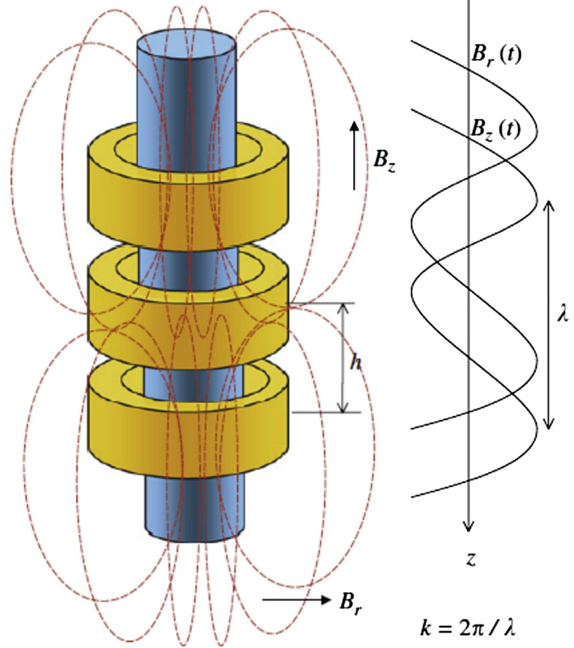

FIGURE 23.13 The principle of a traveling magnetic field using three axially parallel coils. Bz and Br are the axial and radial magnetic field components, respectively. $\lambda = 2\pi/k = nh$ is the magnetic wavelength, where n is the number of coils, h is the distance between coils; and k is the wave number. *From Ref. [14], with permission from Elsevier.*

The advantage of a TMF is the creation of a Lorentz force, which acts as a body force in the direction of gravity and directly induces a meridional flow. The generated Lorentz force can be adjusted not only to counteract the buoyancy force but also to create conditions similar to varying levels of gravity. Because of the melt aspect ratio variation (due to the solidification), the critical magnetic Taylor number, indicating the transition from stationary to time-dependent flows, also varies. Normally, the critical magnetic Taylor number increases with a decrease in the aspect ratio.

The first theoretical and experimental studies on TMF were reported by Gelfgat et al. [143] and Ramachandran et al. [144]. Complex stability analysis of the thermally stratified melt flow under TMF has been carried out by Grants and Gerbeth [15], Gelfgat [145], and Grants et al. [146].

The design of magnet configuration is one of the most important issues to make the control of melt flow by magnetic fields attractive for industrial applications. Usually, the magnets are positioned outside the growth chamber; therefore, they should produce a much higher induction force than the one actually needed for convection control. A significant economical effect can be achieved when the magnetic field generator is placed close to the melt. A promising idea for industrial applications is to couple the generation of heat and the magnetic field in a so-called internal heater-magnet module. Such a configuration was first used by Hoshikawa et al. [113] to produce an RMF in a CZ silicon growth experiment.

A novel special configuration of a heater-magnet module based on a hole-cylindrical body with an upwards-winding slit for the generation of TMF was proposed by Rudolph [14] and Klein et al. [147] (Figure 23.14). This idea was successfully implemented in different types of industrial-scale crystal growth configurations: LEC growth of 3-in GaAs crystals [148], VGF growth of 4-in Ge crystals [149], and G5 multicrystalline Si crystallizer of 640 kg Si-ingots [150].

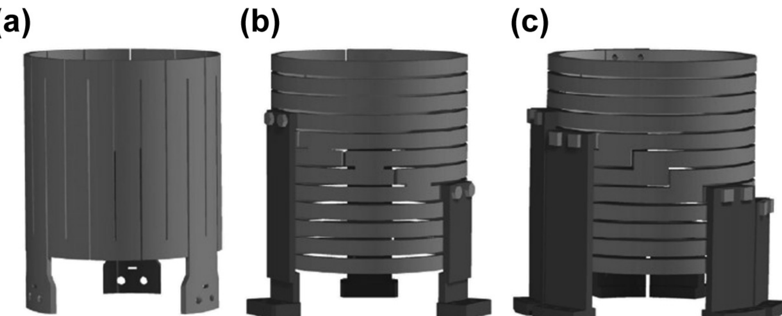

FIGURE 23.14 Layouts of three graphite heaters for LEC growth of semiconductor compounds without (a) and with TMF (b and c). The nearly identical dimensions facilitate the replacement in one and the same puller vessel. (a) Conventional "picket fence" (meander) heater fed by three-phase current in delta connection. (b and c) Magnet-heater modules with staircase-shaped current path, subdivided in three sections for TMF generation by feeding with three-phase current of given phase shift in delta (b) and star connection (c). *From Ref. [14], with permission from Elsevier.*

In the following sections, details of the use and the effect of TMF are discussed for the different crystal growth methods from melt.

23.4.3.1 Czochralski Method

The first attempt to use a TMF in a CZ method was made by Wetzel [151] in 2001. Since then, the influence of a TMF on CZ growth was studied mainly through numerical modeling and model experiments. One of the few reports on experimental results in the CZ growth of large silicon crystals was made by Tomzig et al. [152]. They showed that a nearly ideal uniform oxygen distribution along the grown crystals can be obtained, even better than under RMF and AMF conditions (see Figure 23.15).

Temperature fluctuations in a CZ-like configuration were studied both numerically and experimentally by Krauze et al. [76] in a model experiment in which an InGaSn eutectic with a 10.5 °C melting point was used. It was demonstrated that the corresponding electromagnetic force distributions do not depend on the velocity distributions in the melt and cause an intense and well-defined melt flow. Temperature fluctuations in the outer crucible region and radial temperature difference in the melt decrease with an increase of magnetic field intensity. This effect is stronger for TMF-down in comparison with TMF-up. In a later paper, Krauze et al. [153] presented and validated an improved numerical model based on an LES turbulence model.

More complex numerical models were used to study the influence of a TMF generated by a magnet-heater module. Klein et al. [147] performed numerical simulations in an LEC configuration with a 4-kg GaAs melt. They showed that TMF generated by a magnet-heater module significantly reduces the temperature oscillations with low

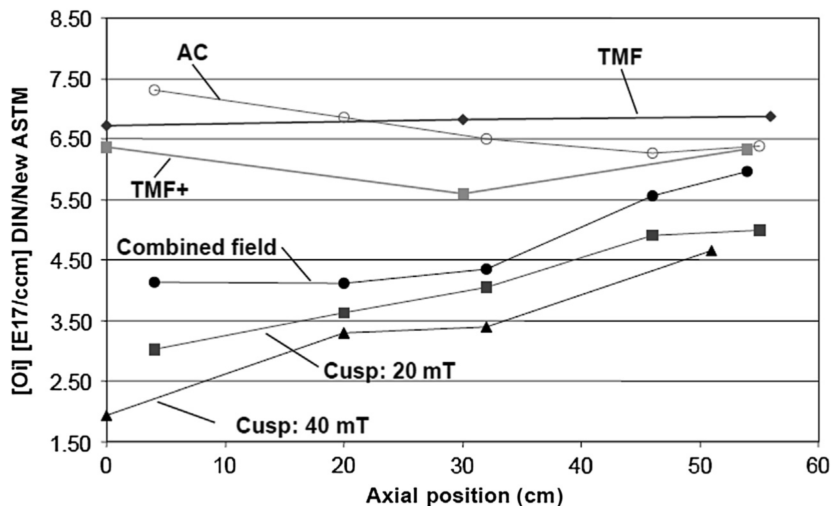

FIGURE 23.15 Axial oxygen concentration of 300-mm crystals grown with different magnetic fields: (a) AC: 6 mT, (b) TMF: 5 mT, (c) TMF+: 5 mT, (d) Combined field: cusp 20 mT/AC 6 mT, (e) Cusp 20 mT, (f) Cusp 40 mT. *From Ref. [152], with permission of Elsevier.*

frequency, contrary to a configuration with an external coil, where only a small positive effect could be shown [154]. The asymmetry effects induced by the magnet-heater design were investigated by Kasjanow et al. [155]. It was concluded that, for an LEC setup, these effects can be effectively graduated by crucible and crystal rotations. The first semi-insulating GaAs crystal grown by the LEC method using a TMF generated in a magnet-heater module was reported by Rudolph et al. [148].

The following correlations between as-grown crystal qualities and TMF parameters have been observed:

- A slight reduction of the peripheral interface concavity at low field frequencies
- A damping of nonsteady convection perturbations by stabilizing the stream stationarity within the melt, especially when high field frequencies are applied
- A lowering of the dislocation density by radial temperature leveling with a decrease of thermal stress, especially at low field frequency
- Enhanced transport of oxygen and boron releasing from boric oxide layer by TMF-induced high-speed vortices toward growing crystal, which increases the O and B incorporation but reduces the As content

For photovoltaic applications, Rudolph et al. [156] proposed a new pulling technology in a CZ puller for the growth of silicon crystals with both quadratic cross-sections and relatively low as-grown oxygen content. A stable low radial temperature gradient in the melt, in the range of 1–2 K/cm, was obtained by applying a special double TMF mode generated in a graphite magnet-heater ensemble consisting of three side coils around the crucible and two consecutive spirals below the crucible bottom. As a result, a silicon single crystal with a near-quadratic cross-section of $91 \times 91\ \mathrm{mm}^2$ and length up to 100 mm was obtained. Miller et al. [157] performed 3D simulations of the melt flow in the configuration described above; they showed that the TMF as used in the experiments causes a strong vortex with a heat transport from the crucible's bottom to the crystal. This heat transport stabilizes the low-temperature gradient along the free surface and the stable growth of the silicon crystal with {110} facets becomes possible.

23.4.3.2 Bridgman Methods and Vertical Gradient Freeze

Taking into account two criteria for the optimization of VGF growth process—a nearly flat S–L interface and a minimization of the von Mises stress—Schwesig et al. [125] demonstrated by numerical analysis that a downward-oriented TMF has a beneficial influence on the quality of a 2-in InP crystal in contrast to an upward-oriented TMF. In the case of TMF-down, the deflection of the S–L interface as well as the maximum flow velocity is decreasing at small values of magnetic induction (<5 mT). At higher values of magnetic induction, the maximum flow velocity is increasing again and a W-shaped interface is observed. Time-dependent flow occurs at about 8 mT for all investigated aspect ratios. The von Mises stress at the S–L interface decreases significantly with increasing magnetic induction. Similar results were obtained by Lyubimova et al. [122] for GaAs and Yesilyurt et al. [158] for Ge crystals grown by the VB method.

A model experiment close to the conditions used for VGF crystal growth was developed by Lantzsch et al. [159]. The melt flow was analyzed in dependence on a dimensionless shielding parameter, defined as $S = 2\pi\mu_0\sigma f R^2$ (with σ being electrical conductivity, f being frequency, and R being the radius). For $S > 10$, the flow velocity was shown to decrease significantly, whereas almost no influence was found for a smaller shielding parameter. A more detailed analysis of this flow sensitivity is presented in Galindo et al. [160] and Niemietz et al. [161].

By numerical modeling, Frank-Rotsch et al. [162] studied the influence of a TMF generated by a magnet-heater module on the interface shape in an industrial-size VGF growth of a 4-in Ge crystal. It was found that a favorable interface with a slightly convex part in the central region was obtained by applying a downward-directed TMF with a drastically reduced frequency of 20 Hz. The optimal parameters predicted by numerical simulation were used to optimize a real growth experiment. As a result, for the first time, 4-in Ge single crystals were grown using the VGF technique in a TMF generated in a heater-magnet module [149]. Striations were also minimized by effective damping of the convection-driven temperature fluctuations.

Dropka et al. [163] numerically demonstrated that, due to the larger skin depths of the materials with lower electrical conductivity, a much larger current amplitude or a much higher frequency are necessary to generate a Lorentz force of desired intensity and distribution. A rigorous numerical model developed by Yeckel and Derby [164] has shown that TMF is only slightly effective at controlling the interface shape in an industrial-scale VGF of cadmium zinc telluride growth. This is because buoyancy overwhelms the Lorentz force throughout the melt for typical currents and frequencies of existing TMF systems.

Based on numerical modeling, Dropka and Frank-Rotsch [165] proposed a novel electromagnetic stirring approach using pulse-downward TMF generated by a magnet-heater module for a complete suppression of the instability in temperature distribution caused by asymmetry in furnace design. A downward TMF in an accelerated VGF growth of 4-in GaAs was used to improve the interface deflection toward a convex morphology during the fast growth [166].

23.4.3.3 Directional Solidification

The quality of the silicon ingot obtained by the directional solidification (DS) method is strongly dependent on the growth parameters that control the melt flow and interface shape. An active control of the melt flow is possible using magnetic fields and TMF is a strong candidate. This gives the crystal grower additional process parameters, such as the inductor current and the direction of the TMF. A deep understanding of the influence of the growth and process parameters on the crystallization interface is crucial for the optimization of the ingot quality. To understand the basic features of the melt flow in a DS-like configuration under a TMF, Dadzis et al. [167] developed a low-temperature model experiment and 3D time-dependent flow simulations. They reported that in a $10 \times 10\ \mathrm{cm}^2$ crucible with GaInSn isothermal melt, an applied TMF generates a typical

toroidal flow structure with some extension into the melt corners. It was also shown that the flow structure is sensitive to the TMF geometry, melt height, and melt axis shift. A horizontal vortex was found to dominate the central part of the melt for smaller melt heights. In a later study, Dadzis et al. [168] investigated the same configuration but imposed an axial temperature gradient. It was reported that transitions from the flow regime dominated by the Lorentz force (high velocity and melt mixing) to the regime where the Lorentz force is balanced by the buoyancy forces (low velocity and melt mixing) may occur; these may have a critical characteristic in which the flow velocity drops and the temperature difference increases rapidly.

Dropka et al. [169], using 3D modeling, studied the influence of the TMF generated by a magnet-heater module on the silicon melt flow in an industrial-size crucible of $70 \times 70 \times 20\ cm^3$. It was shown that different field configurations (TMF-up or TMF-down) have a significant influence on the flow structure, and they can both damp and enhance the mixing (Figure 23.16). In a later study, Dropka et al. [170] investigated the mixing efficiency of a double-frequency TMF, generated within a magnet-heater module around a rectangular container with molten silicon. The double-frequency electromagnetic stirring is performed with a summary TMF composed of two oppositely directed longitudinally traveling fields with different strengths, frequencies, and

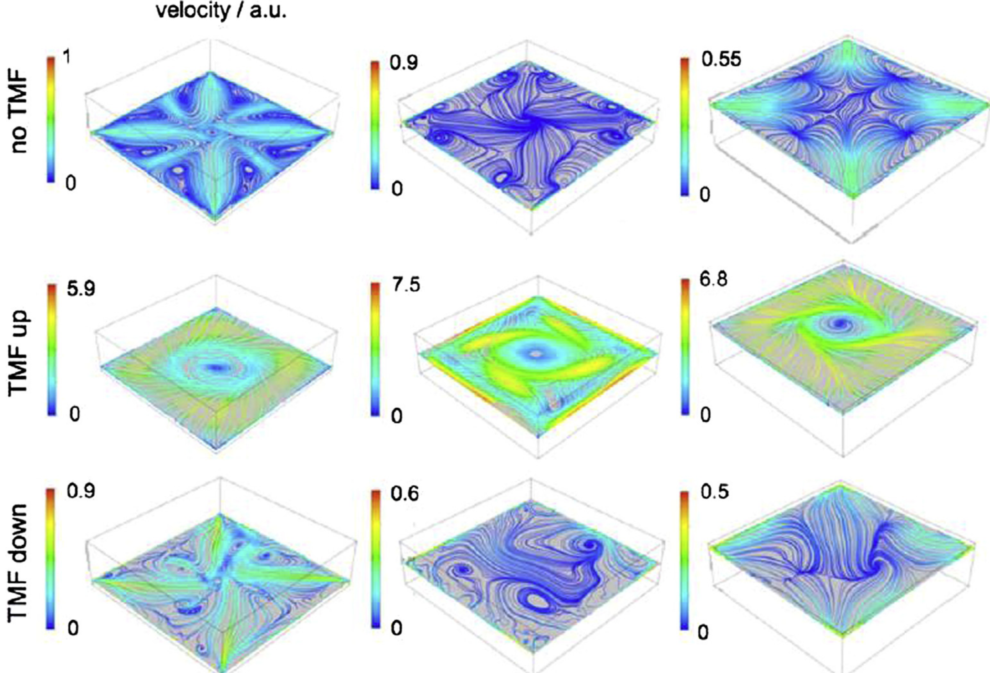

FIGURE 23.16 Velocity streamlines at different cross-sections in the melt: without TMF (*top*), TMF down (*middle*), and TMF up (*bottom*). Streamlines are the representation of the velocity field projected on the plane. *From Ref. [169], with permission from Elsevier.*

phase shifts. Such variations produce variable skin depths and horizontal velocity profiles. It was demonstrated numerically that, in comparison to the buoyancy-driven natural convection and single-frequency TMF, at double-frequency TMF mode the flow in the bulk volume is intensified without the generation of hazardous velocities in the peripheral region. This is beneficial for the melt mixing and general process purity. The same numerical model was used by Dropka et al. [171] to evaluate the efficiency of a novel electromagnetic stirring approach using a carousel magnetic field generated by a bottom magnet-heater module consisting of several spiral coils arranged horizontally around the vertical axis. It was found that, in comparison to the conventional sidewise electromagnetic stirring, the flow maximum is shifted from the peripheral region toward the melt bulk, increasing the stirring within the central region and thus decreasing the diffusion boundary thickness more effectively and uniformly.

Multicrystalline silicon ($22 \times 22 \times 13$ cm^3) grown under a TMF field generated by a magnet-heater module has been reported by Kießling et al. [172] (Figure 23.17(a)). It was demonstrated that TMFs can be used to influence the melt convection, reduce the thickness of the diffusion boundary layer, and adjust the shape and morphology of the S–L growth interface. The influence of the TMF orientation on the S–L interface shape was also analyzed. It was found that a TMF-up configuration generates a concave curvature of the S–L interface, whereas a TMF-down configuration generates a convex one

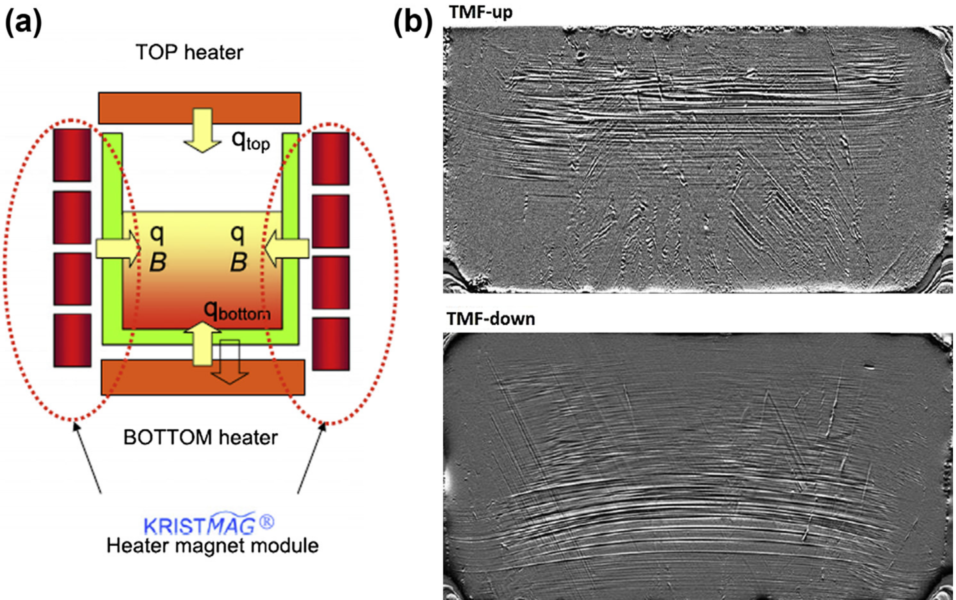

FIGURE 23.17 (a) Sketch of the DS growth arrangement for Si, showing top and bottom heaters and four coils of the side heater to produce TMFs. (b) Images of the S–L interface revealed from striation morphology analysis by lateral photo-voltage scanning on vertical cuts shows a concave curvature at the rim as a result of an applied TMF-up and a convex shape as a result of an applied TMF-down. *After Ref. [172], with permission from Elsevier.*

(Figure 23.17(b)). The same qualitative results were obtained in numerical simulations performed by Dadzis et al. [173] and Vizman et al. [174].

Kudla et al. [150] reported the successful growth of a G5 multicrystalline silicon (640 kg) in an industrial-scale crystallizer equipped with a magnet-heater module for the TMF generation. Effective melt mixing and precise control of the interface shape have been achieved using TMF, which resulted in a very homogeneous infrared (IR) transmission without second-phase inclusions in most of the solidified volume. Dislocation densities were relatively low and bunching was only rarely observed, resulting in overall high carrier lifetimes.

23.5 Combined Action of Various Types of Magnetic Fields and Electric Currents

Sometimes, more types of actions should be taken in the process of melt control to optimize the quality of the grown crystals, such as a reduction of temperature fluctuations combined with better mixing. A combination of a steady magnetic field (to damp the flow) and a nonsteady magnetic field (to impose a forced convection) could be imagined to fulfill such a task and to offer a larger variety of control parameters for the contactless optimization of heat and mass transfer.

The first application of the combined action of VMF and RMF was reported by Yamashita et al. [175] to lower the oxygen concentration in Czochralski silicon. In a theoretical study, Mößner and Gerbeth [176] analyzed the stability thresholds of RMF and buoyancy-driven flows, also by additionally superimposing a VMF. Because of the stabilizing effect of the VMF, the critical magnetic Taylor number (from where the flow became instable) was found to increase strongly when VMF is superimposed on the RMF. A similar combination between RMF and VMF was studied by means of numerical simulations by Yildiz and Dost [177] in the liquid-phase diffusion growth process of 12 mm SiGe single crystals. Under the effect of the combined magnetic fields (0.3 T VMF and 5 mT/10 Hz RMF), the growth process became diffusion dominant and the S–L interface was almost flat.

The stability analysis of a Rayleigh-Benard flow under the combined action of an RMF and CMF in a gallium melt was carried out by Grants et al. [178]. It was demonstrated that the CMF just sharpened the transition diagram in terms of the fluctuation amplitude, while the transition in terms of the structure change was not influenced too much by the CMF.

Galindo et al. [179] numerically investigated the influence of the combined action of an AMF field and VMF or CMF on the melt flow in a 4-in Si-CZ growth process. It was shown that the VMF and CMF damp the flow and, at the same time, the main action of the AMF was to generate a reversed flow direction at the melt free surface (from the crystal to the crucible) and to improve the oxygen distribution. A better overall damping effect was found for the CMF because it provided no preferred direction to the flow field.

Tomzig et al. [152] reported the successful growth of 300 mm silicon crystals by the CZ method under the combined action of AMF and CMF. They showed that the oxygen

content can be very effectively adjusted between the highest (in the case of AMF) and the lowest (in the case of CMF) oxygen level (Figure 23.15). The increase of the oxygen in the growing crystal in the case of AMF was explained due to the direct transport of the SiO from the hot wall to the S–L interface without SiO reduction due to evaporation. The experiments had additionally shown that the application of AMF reduces the crucible wall temperature, which is favorable for the silica crucible lifetime, with strong implications for cost reduction.

A special method for the melt control in CZ systems was proposed by Watanabe et al. [180]. The so-called electromagnetic Czochralski method (EMCZ) combines a VMF and a static electric current passing through the melt from the growing crystal to an electrode attached to the melt surface (Figure 23.18). Because the main path of the electrical current is directed in the radial direction, the electromagnetic force ($\vec{F} = \vec{I} \times \vec{B}$) is therefore generated in the azimuthal direction; consequently, the melt is rotated.

Silicon crystals with 30 mm diameters were grown using the EMCZ method by Watanabe et al. [181]. A low crystal rotation (~1 rpm) and no crucible rotation were considered. Melt rotation rates from 0 to more than 105 rpm were obtained with $I = 0$–8 A and $B = 0$–0.1 T. A continuous change in the oxygen concentration and the homogenization of the oxygen distribution along the radial direction were obtained due to the reduction of the diffusion layer, both at the melt–crucible interface and at the crystal–melt interface, by forced flow caused by the electromagnetic force. The influence of the electrode design (the number of electrodes and position) was numerically investigated by Kakimoto et al. [182] in the same configuration.

Watanabe et al. [181] reported the growth of a 200 mm silicon crystal by the EMCZ method. Two configurations were used—electric current + VMF and electric current + CMF—with the symmetry plane placed under the S–L interface (inside configuration). The crystals grown with CMF-EMCZ method have a higher oxygen concentration and a more homogeneous oxygen distribution than the crystals grown by VMF-EMCZ. This result means that, for large-diameter crystals, the melt rotation under VMF was not effectively mixing the oxygen in the melt and that the VMF was strong

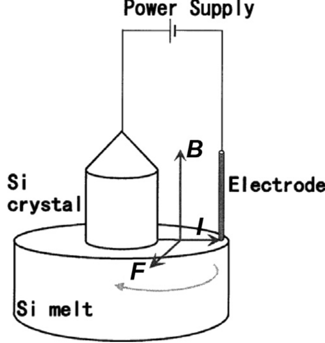

FIGURE 23.18 The principle of the EMCZ method. *From Ref. [180], with permission from Elsevier.*

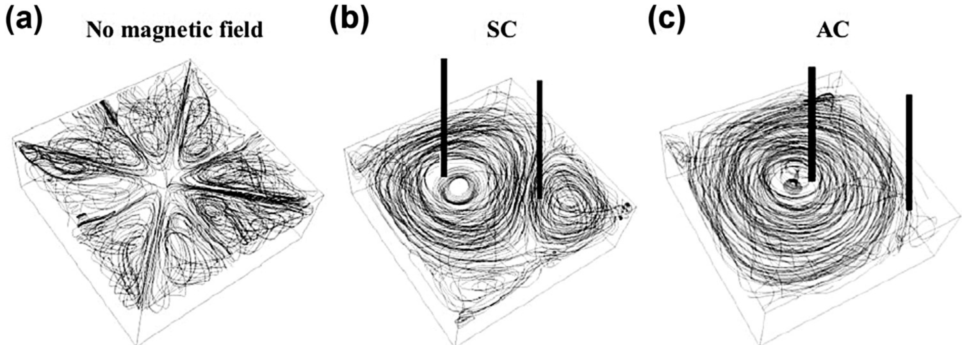

FIGURE 23.19 Particle tracking with no magnetic fields (a), for a symmetric configuration (b), and for an asymmetric configuration (c). $I = 10$ A; $B = 10$ mT. Particle tracking plots are shown in a zone 10 cm above the S–L interface. *From Ref. [185], with permission from Elsevier.*

enough to reduce the melt flow just below the S–L interface. On the contrary, CMF has a lower influence on the flow below the S–L interface and seems to be a better option for large-diameter crystals. Numerical simulations performed by Vizman et al. [183] showed that the S–L interface shape of 200-mm diameter Si crystals is greatly modified to a concave shape as a result of the temperature distribution at the interface by the controlled melt flow induced by electromagnetic force. The interface deflection was higher for the EMCZ configuration with CMF than with VMF. Point defect behavior in Si crystals grown by EMCZ method was investigated by Kim et al. [184]. The results indicate that in comparison to a simple CMF-CZ configuration, in the case of a CMF-EMCZ configuration the increased heat transfer due to electromagnetic force makes the interface concave and the pulling speed at which OSF (oxygen-induced stacking fault) is formed in the crystal increases.

Based on numerical modeling, Vizman and Tanasie [185] proposed a combination of electric current and VMF for melt stirring in a directional solidification method of multicrystalline silicon. They have shown that an electric current (2–10 A) that passed through two electrodes placed at the melt surface and a VMF of 10 mT can efficiently stir a melt with a size of $68 \times 68 \times 68$ cm^3. Melt flow configuration was found to depend strongly on the position of the electrodes on the melt surface; thus, it changes from a two-vortex type for a symmetrical configuration (with the electrodes placed symmetric from the central point) to a one-vortex type for the asymmetric configuration (with one electrode placed at the center point; see Figure 23.19).

23.6 Conclusions and Outlook

The discussions presented in this chapter have shown that magnetic fields offer the crystal grower a large variety of control possibilities for contactless optimization of heat and mass transfer processes from growth equipments. There is already a huge research

Table 23.1 Summary of the Effects of Magnetic Field Applications in Crystal Growth Processes

Type of Magnetic Field	Beneficial Effects	Detrimental Effects
VMF	**1.** Damp thermal convection **2.** Eliminate temperature fluctuations **3.** Increase effective segregation coefficient **4.** Eliminate growth-striae (dopant bands) in the crystal **5.** Increase axial uniformity of oxygen (CZ-Si) **6.** Increase radial uniformity of dopants (VB)	**1.** Local instabilities can occur in the melt **2.** Increase temperature difference in the melt (CZ-Si) **3.** Increase the level of oxygen and deteriorate its radial uniformity (CZ-Si) **4.** Deteriorate radial uniformity of dopants (FZ)
HMF	**1.** Damp vertical flow **2.** Eliminate temperature fluctuations **3.** Eliminate growth-striae (dopant bands) in the crystal **4.** Decrease the level of oxygen (CZ-Si)	**1.** Destroy the axial symmetry of the melt flow **2.** Deteriorate the symmetry of dopant distribution (VB) **3.** Elliptical form of the crystal in FZ with no crystal rotation
CMF	**1.** Damp thermal convection **2.** Eliminate temperature fluctuations **3.** Smaller magnetic field intensity (in comparison with VMF and HMF) **4.** Reduce nonrotational dopant striations (CZ) **5.** Increase axial and radial uniformity of oxygen (CZ-Si) **6.** Decrease the level of oxygen (CZ-Si)	**1.** Higher amplitude of temperature fluctuations near the S–L interface possible
RMF	**1.** Generate stable steady azimuthal flow **2.** Eliminate temperature fluctuations **3.** Decrease dopant inhomogeneities **4.** Reduce dopant striations to a high degree (VB)	**1.** Weak meridional mixing **2.** W-interface shape possible (VB)
TMF	**1.** Lorentz force in the direction of gravity **2.** Generate a meridional flow **3.** Eliminate temperature fluctuations **4.** Uniform oxygen distribution (CZ-Si) **5.** Lowering the dislocation density (LEC-GaAs) **6.** Coils placed close to the melt	**1.** Limited effect in the central region of large-scale melts due to the skin effect
AMF	**1.** Efficient mixing in the melt **2.** Lower axial and radial segregation (VB-(Ga,In)Sb)	**1.** No influence on the melt flow underneath the crystal for large CZ melt

base in this field, a large body of literature, and an important number of applications in crystal growth industry. A short summary of the beneficial and detrimental effects of the application of magnetic fields in crystal growth processes is presented in Table 23.1.

Because of their versatility and lower costs for the magnets, nonsteady magnetic fields have been intensively studied in recent years. With development of the experiments on laboratory scale and more realistic computer models, industrial crystal growth applications of magnetic fields will become more based on a detailed analysis rather than intuition. In the coming years, the research suggesting new magnetic field designs

or beneficial modifications to the existing configurations will likely be concretized in industrial applications. This success will depend on the degree of fulfillment of the industry's cardinal demands, such as increased process output, improved crystal quality, and reduced costs.

References

[1] von Ammon W, Gelfgat Yu, Gorbunov L, Muehlbauer A, Muižnieks A, Makarov Y, et al. Application of magnetic fields in industrial growth of silicon single crystals. In: Proc. of the 15th Riga and 6th PAMIR conference on fundamental and applied MHD; 2005. p. 41.

[2] Ma Y, Watanabe K, Awaji S, Motokawa M. Appl Phys Lett 2000;77:3633.

[3] Mwaba MS, Gu J, Gorliz MR. J Cryst Growth 2007;303:381.

[4] Wang J, Zhang K, Peng Z, Chen Q. J Cryst Growth 2004;266:500.

[5] Sazaki G, Yoshida E, Komatsu H, Nakada T, Miyashita S, Watanabe K. J Cryst Growth 1997;173: 231–4.

[6] Ataka M, Katoh E, Wakayama NI. J Cryst Growth 1997;173:592–6.

[7] Moreno A, Quiroz-Garcia B, Yokaichiya F, Stojanoff V, Rudolph P. Cryst Res Technol 2007;42:231.

[8] Series RW, Hurle DTJ, North-Holland. Use of a magnetic field in melt growth. In: Hurle DTJ, editor. Handbook of crystal growth, vol. 2a. Elsevier; 1994. p. 259.

[9] Kakimoto K. In: Scheel HJ, Fukuda T, editors. Crystal growth technology. Wiley; 2003. p. 139.

[10] Ozoe H, Szmyd J, Tagawa T. In: Molokov Sergeĭ, Moreau R, Moffat HK, editors. Magnetohydrodynamics: historical evolution and trends. Springer; 2007. p. 375.

[11] Rudolph P, Kakimoto K. MRS Bull 2009;34:251.

[12] Dold P, Benz KW. Prog Cryst Growth Charact Mater 1999;38:39.

[13] Bliss D. In: Dhanaraj G, Byrappa K, Prasad V, Dudley M, editors. Springer handbook of crystal growth. Springer; 2010. p. 205.

[14] Rudolph P. J Cryst Growth 2008;310:1298.

[15] Grants I, Gerbeth G. J Cryst Growth 2004;269:630.

[16] Muižnieks A, Krauze A, Nacke B. J Cryst Growth 2007;303:211.

[17] Miyazawa Y. Prog Cryst Growth Charact Mater 1999;38:261.

[18] Pfann WG, Hagelbarger DW. J Appl Phys 1956;27:12.

[19] Utech HP, Flemings MC. J Appl Phys 1966;37:2021.

[20] Chedzey HA, Hurle DTJ. Nature 1966;210:933.

[21] Müller G. J Cryst Growth 1993;128:26.

[22] Ristocelli JR, Lumley JL. J Cryst Growth 1992;116:447.

[23] Gräbner O, Mühe A, Müller G, Tomzig E, Virbulis J, von Ammon W. Mater Sci Eng B 2000;73:130.

[24] Vizman D, Gräbner O, Müller G. J Cryst Growth 2001;233:687.

[25] Voronkov VV. J Cryst Growth 1982;59:625.

[26] Vizman D, Friedrich J, Müller G. J Cryst Growth 2001;230:73.

[27] Virbulis J, Wetzel Th, Muižnieks A, Hanna B, Dornberger E, Tomzig E, et al. J Cryst Growth 2001; 230:92.

[28] Kim KM, Smetana P. J Appl Phys 1985;58:2731.

[29] Terashima K, Katsumata T, Orito F, Fukuda T. Jpn J Appl Phys 1984;23:L302.

[30] Burton JA, Prim RC, Slitcher WP. J Chem Phys 1953;21:1987.

[31] Hurle DTJ, Series RW. J Cryst Growth 1985;73:1.

[32] Kobayashi S. J Cryst Growth 1986;75:301.

[33] Riley N. J Cryst Growth 1987;85:417.

[34] Series RW, Hurle DTJ, Barraclough KG. J Appl Math 1985;35:195.

[35] Ravishankar PS, Braggins TT, Thomas RN. J Cryst Growth 1990;104:617.

[36] Series RW. J Cryst Growth 1989;97:85.

[37] Kobayashi N. J Cryst Growth 1991;108:240.

[38] Salnick ZA. J Cryst Growth 1992;121:775.

[39] Kakimoto K, Yi K, Eguchi M. J Cryst Growth 1996;163:238.

[40] Hofmann D, Mosel F, Müler G. In: Grossman G, Lebedo L, editors. Proc. Of the 5th conf. on semi-insulating III-V materials, Malmo (1988). Bristol (UK): Hilger; 1988. p. 429.

[41] Ozawa S, Kimura T, Kobayashi J, Fukuda T. Appl Phys Lett 1987;50:329.

[42] Hurle DTJ, Jakeman E, Johnson CP. J Fluid Mech 1974;64:565.

[43] Kuhl R, Wilke H. In: Vol. 41 of Congress of the International Astronautical Federation. Dresden (GDR): IAF; 1990. 90–398.

[44] Kim DH, Adornato PM, Brown RA. J Cryst Growth 1988;89:339.

[45] Matthiesen DH, Wargo MJ, Motakef S, Karlsonn DJ, Nakos JS, Witt AF. J Cryst Growth 1987;85:557.

[46] Park YJ, Min SK, Hahn SH, Yoon JK. J Cryst Growth 1995;154:10.

[47] Becla P, Han J-C, Motakef S. J Cryst Growth 1992;121:394.

[48] Yao M, Chait A, Fripp AL, Debnam WJ. J Cryst Growth 1997;173:467.

[49] Ma N, Walker JS. J Cryst Growth 2000;208:757.

[50] Lan CW, Lee IF, Yeh BC. J Cryst Growth 2003;254:503.

[51] Baumgartl J, Müller G. J Cryst Growth 1996;169:582.

[52] Duffar Th, Nabot J Ph, Barat C, Favier JJ, Cambon G. Microgravity Sci Technol 1993;6:74.

[53] Mühlbauer A, Muižnieks A, Virbulis J, Lüdge A, Riemann H. J Cryst Growth 1995;151:66.

[54] Rudevics A, Muižnieks A, Riemann H, Luedge A, Ratnieks G, von Ammon W. J Cryst Growth 2005;275:e561.

[55] Dold P, Cröll A, Benz KW. J Cryst Growth 1998;183:545.

[56] De Leon N, Guldberg J, Salling J. J Cryst Growth 1981;55:406.

[57] Robertson Jr GD, O'Connor D. J Cryst Growth 1986;76:111.

[58] Lan CW. J Cryst Growth 1996;169:269.

[59] Kaiser Th, Benz KW. J Cryst Growth 1998;183:564.

[60] Cröll A, Szofran FR, Dold P, Benz KW, Lehoczky SL. J Cryst Growth 1998;183:554.

[61] Cröll A, Benz KW. Prog Cryst Growth Charact Mater 1999;38:7.

[62] Lie KH, Walker JS, Riahi DN. J Cryst Growth 1991;109:167.

[63] Herrmann FM, Baumgartl J, Feulner T, Müller G. In: Proc. VIIIth Europ. symp. on materials and fluid sciences in microgravity. Brussels: ESA SP–333; 1992. p. 57.

[64] Witt AF, Herman CJ, Gatos HC. J Mater Sci 1970;5:822.

[65] Hoshi K, Suzuki T, Okubo Y, Isawa N. In: Extended Abstracts Electrochem. Soc., vol. 80-1. Pennington (NJ): Electrochemical Society; 1980. p. 811.

[66] Hoshi K, Isawa N, Suzuki T. OYOBUTURI (in Japanese) 1984;53:38.

[67] Terashima K, Fukuda T. J Cryst Growth 1983;63:423.

[68] Mihelčić M, Wingerath K. J Cryst Growth 1987;82:318.

[69] Oshima M, Taniguchi N, Kobayashi T. J Cryst Growth 1994;137:48.

[70] Ozoe H, Iwamoto M. J Cryst Growth 1994;142:236.

[71] Kakimoto K, Ozoe H. J Cryst Growth 2000;212:429.

[72] Ivanov NG, Korsakov AB, Smirnov EM, Khodosevitch KV, Kalaev VV, Makarov Yu N, et al. J Cryst Growth 2003;250:183.

[73] Liu L, Kakimoto K. J Cryst Growth 2005;275:e1521.

[74] Kalaev VV. J Cryst Growth 2007;303:203.

[75] Collet Y, Magotte O, Van den Bogaert N, Rolinsky R, Loix F, Jacot M, et al. J Cryst Growth 2012; 360:18.

[76] Krauze A, Muižnieks A, Mühlbauer A, Wetzel Th, von Ammon W. J Cryst Growth 2004;262:157.

[77] Iino E, Takano K, Kimura M, Yamagishi H. Mater Sci Eng B 1996;36:142.

[78] Terashima K, Nishio J, Okada A, Washizuka S, Watanabe M. J Cryst Growth 1986;79:463.

[79] Kim KM. J Electrochem Soc 1982;129:427.

[80] Sen S, Lefever RA, Wilcox WR. J Cryst Growth 1978;43:526.

[81] Su C-H, Lehoczky SL, Szofran FR. J Cryst Growth 1991;109:385.

[82] Lan CW, Yeh BC. J Cryst Growth 2004;266:200.

[83] Kimura H, Harvey MF, O'Connor DJ, Robertson GD, Valley GC. J Cryst Growth 1983;62:523.

[84] Robertson Jr GD, O'Connor DJ. J Cryst Growth 1986;76:100.

[85] Herrmann FM, Müller G. J Cryst Growth 1995;156:350.

[86] Hirata H, Hoshikawa K. J Cryst Growth 1989;96:747.

[87] Series RW. J Cryst Growth 1989;97:92.

[88] Hicks TW, Organ AE, Riley N. J Cryst Growth 1989;94:213.

[89] Hirata H, Hoshikawa K. J Cryst Growth 1992;125:181.

[90] Kakimoto K, Eguchi M, Ozoe H. J Cryst Growth 1997;180:442.

[91] Vizman D, Gräbner O, Müller G. J Cryst Growth 2002;236:545.

[92] Savolainen V, Heikonen J, Ruokolainen J, Anttila O, Laakso M, Paloheimo J. J Cryst Growth 2002; 243:243.

[93] Liu X, Liu L, Li Z, Wang Y. J Cryst Growth 2012;360:38.

[94] Watanabe M, Eguchi M, Hibiya T. J Cryst Growth 1998;193:402.

[95] Hirata H, Hoshikawa K. J Cryst Growth 1989;98:777.

[96] Sim B-C, Lee I-K, Kim K-H, Lee H-W. J Cryst Growth 2005;275:455.

[97] Won YC, Kakimoto K, Ozoe H. J Cryst Growth 2001;233:622.

[98] Morthland TE, Walker JS. J Cryst Growth 1996;158:471.

[99] Lan CW, Liang MC. J Cryst Growth 1997;180:381.

[100] Pfann WG, Dorsi D. Rev Sci Instrum 1957;28:720.
[101] Mullin JB, Hulme KF. J Electron Control 1958;4:170.
[102] Davidson PA, Boyson F. Appl Sci Res 1987;44:241.
[103] Gelfgat Yu M. J Cryst Growth 1999;198–199:165.
[104] Friedrich J, Lee YS, Fischer B, Kupfer C, Vizman D, Müller G. Phys Fluids 1999;11:853.
[105] Kaiser Th, Benz KW. Phys Fluids 1998;10:1104.
[106] Grants I, Gerbeth G. J Fluid Mech 2002;463:229.
[107] Robinson T, Larsson K. J Fluid Mech 1973;60:641.
[108] Volz MP, Mazuruk K. Exp Fluids 1996;20:454.
[109] Dold P, Benz KW. Cryst Res Technol 1995;30:1135.
[110] Fischer B, Friedrich J, Weimann H, Müller G. J Cryst Growth 1999;198–199:170.
[111] Barz RU, Gerbeth G, Wunderwald U, Buhrig E, Gelfgat Yu M. J Cryst Growth 1997;180:410.
[112] Shaskow YM, Shushlebina NY. Fiz Khim Obrab Mater 1972;1:34.
[113] Hoshikawa K, Kohda H, Hirata H, Nakanishi H. Jpn J Appl Phys 1980;19:L33.
[114] Zhou X, Huang H. J Cryst Growth 2012;340:166.
[115] Spitzer K-H. Prog Cryst Growth Charact Mater 1999;38:59.
[116] Kakimoto K. J Cryst Growth 2002;237–239:1785.
[117] Brückner F-U, Schwerdtfeger K. J Cryst Growth 1994;139:351.
[118] Grants I, Gerbeth G. J Cryst Growth 2007;308:290.
[119] Dold P, Benz KW. Cryst Res Technol 1997;32:51.
[120] Friedrich J, Kupfer C, Fischer B, Müller G. In: Fluid mechanics and its applications. The Netherlands: Kluwer; 1998.
[121] Pätzold O, Grants I, Wunderwald U, Jenkner K, Cröll A, Gerbeth G. J Cryst Growth 2002;245:237.
[122] Lyubimova TP, Croell A, Dold P, Khlybov OA, Fayzrakhmanova IS. J Cryst Growth 2004;266:404.
[123] Volz MP, Walker JS, Schweizer M, Cobb SD, Szofran FR. J Cryst Growth 2005;282:305.
[124] Bellmann MP, Pätzold O, Gärtner G, Möller HJ, Stelter M. J Cryst Growth 2009;311:1471.
[125] Schwesig P, Hainke M, Friedrich J, Müller G. J Cryst Growth 2004;266:224.
[126] Wang X, Ma N, Bliss DF, Iseler GW, Becla P. J Cryst Growth 2006;287:270.
[127] Bellmann MP, Pätzold O, Wunderwald U, Stelter M, Möller HJ. J Cryst Growth 2007;303:250.
[128] Galindo V, Niemietz K, Pätzold O, Gerbeth G. J Cryst Growth 2012;360:30.
[129] Dold P, Cröll A, Lichtensteiger M, Kaiser Th, Benz KW. J Cryst Growth 2001;231:95.
[130] Raming G, Muižnieks A, Mühlbauer A. J Cryst Growth 2001;230:108.
[131] Liu Y, Ai F, Pan XH, Zhang Y, Zhou YF, Feng CD. J Cryst Growth 2010;312:1622.
[132] Walker JS, Martin Witkowski L, Houchens BC. J Cryst Growth 2003;252:413.
[133] Ma N, Walker JS, Lüdge A, Riemann H. J Cryst Growth 2001;230:118.
[134] Yao L, Zeng Z, Li X, Chen J, Zhang Y, Mizuseki H, et al. J Cryst Growth 2011;316:177.
[135] Salk M, Fiederle M, Benz KW, Senchenkov AS, Egorov AV, Matioukhin DG. J Cryst Growth 1994;138:161.
[136] Senchenkov AS, Barmin IV, Tomson AS, Krapukhin VV. J Cryst Growth 1999;197:552.

[137] Wetzel Th, Muižnieks A, Mühlbauer A, Gelfgat Y, Gorbunov L, Virbulis J, et al. J Cryst Growth 2001;230:81.

[138] Mercier F, Nishizawa S. J Cryst Growth 2011;318:385.

[139] Stelian C, Delannoy Y, Fautrelle Y, Duffar Th. J Cryst Growth 2004;266:207.

[140] Stelian C, Delannoy Y, Fautrelle Y, Duffar Th. J Cryst Growth 2005;275:e1571.

[141] Mitric A, Duffar Th, Diaz-Guerra C, Corregidor V, Alves LC, Garniera C, et al. J Cryst Growth 2006;287:224.

[142] Mitric A, Duffar Th. J Cryst Growth 2008;310:1511.

[143] Gelfgat Y, Krümins Yu, Abricka M. Magnetohydrodyn 1999;35:1.

[144] Ramachandran N, Mazuruk K, Volz MP. J Jpn Soc Microgravity Appl 2000;17:98.

[145] Gelfgat A Yu. J Cryst Growth 2005;279:276.

[146] Grants I, Klyukin A, Gerbeth G. J Cryst Growth 2009;311:4255.

[147] Klein O, Lechner Ch, Druet P-É, Philip P, Sprekels J, Frank-Rotsch Ch, et al. J Cryst Growth 2008;310:1523.

[148] Rudolph P, Czupalla M, Lux B. J Cryst Growth 2009;311:4543.

[149] Frank-Rotsch Ch, Rudolph P. J Cryst Growth 2009;311:2294.

[150] Kudla Ch, Blumenau AT, Büllesfeld F, Dropka N, Frank-Rotsch Ch, Kießling F, et al. J Cryst Growth 2013;365:54.

[151] Wetzel Th. Fortschritt-Berichte. VDI Reihe 9, No. 328. Dusseldorf: VDI Verlag; 2001.

[152] Tomzig E, Virbulis J, Ammon WV, Gelfgat Y, Gorbunov L. Mater Sci Semicond Process 2003;5:347.

[153] Krauze A, Jēkabsons N, Muižnieks A, Sabanskis A, Lācis U. J Cryst Growth 2010;312:3225.

[154] Lechner Ch, Klein O, Druet P-E. J Cryst Growth 2007;303:161.

[155] Kasjanow H, Nacke B, Eichler St, Jockel D, Frank-Rotsch Ch, Lange P, et al. J Cryst Growth 2008;310:1540.

[156] Rudolph P, Czupalla M, Lux B, Kirscht F, Frank-Rotsch Ch, Miller W, et al. J Cryst Growth 2011;318:249.

[157] Miller W, Frank-Rotsch Ch, Rudolph P. J Cryst Growth 2011;318:244.

[158] Yesilyurt S, Motakef S, Grugel R, Mazuruk K. J Cryst Growth 2004;263:80.

[159] Lantzsch R, Galindo V, Grants I, Zhang C, Pätzold O, Gerbeth G, et al. J Cryst Growth 2007;305:249.

[160] Galindo V, Grants I, Lantzsch R, Pätzold O, Gerbeth G. J Cryst Growth 2007;303:258.

[161] Niemietz K, Galindo V, Pätzold O, Gerbeth G, Stelter M. J Cryst Growth 2011;318:150.

[162] Frank-Rotsch Ch, Jockel D, Ziem M, Rudolph P. J Cryst Growth 2008;310:1505.

[163] Dropka N, Frank-Rotsch Ch, Miller W, Rudolph P. J Cryst Growth 2012;338:208.

[164] Yeckel A, Derby JJ. J Cryst Growth 2013;364:133.

[165] Dropka N, Frank-Rotsch Ch. J Cryst Growth 2014;386:146.

[166] Dropka N, Frank-Rotsch Ch. J Cryst Growth 2013;367:1.

[167] Dadzis K, Ehrig J, Niemietz K, Pätzold O, Wunderwald U, Friedrich J. J Cryst Growth 2011;333:7.

[168] Dadzis K, Niemietz K, Pätzold O, Wunderwald U, Friedrich J. J Cryst Growth 2013;372:145.

[169] Dropka N, Miller W, Menzel R, Rehse U. J Cryst Growth 2010;312:1407.

[170] Dropka N, Miller W, Rehse U, Rudolph P, Büllesfeld F, Sahr U, et al. J Cryst Growth 2011;318:275.

[171] Dropka N, Frank-Rotsch Ch, Rudolph P. J Cryst Growth 2013;365:64.
[172] Kießling F-M, Büllesfeld F, Dropka N, Frank-Rotsch Ch, Müller M, Rudolph P. J Cryst Growth 2012;360:81.
[173] Dadzis K, Vizman D, Friedrich J. J Cryst Growth 2013;367:77.
[174] Vizman D, Dadzis K, Friedrich J. J Cryst Growth 2013;381:169.
[175] Yamashita K, Kobayashi S, Aoki T, Kawata Y, Shiraiwa T. Semiconductor fabrication: technology and metrology. American Society for Testing Materials; 1989. 7.
[176] Mößner R, Gerbeth G. J Cryst Growth 1999;197:341.
[177] Yildiz E, Dost S. J Cryst Growth 2007;303:279.
[178] Grants I, Pedchenko A, Gerbeth G. Phys Fluids 2006;18. Art. No 124104.
[179] Galindo V, Gerbeth G, von Ammon W, Tomzig E, Virbulis J. Energy Convers Manage 2002;43:309.
[180] Watanabe M, Eguchi M, Hibiya T. Mater Sci Semicond Process 1999;38:L10.
[181] Watanabe M, Eguchi M, Wang W, Hibiya T, Kuragaki S. J Cryst Growth 2002;237–239:1657.
[182] Kakimoto K, Tashiro A, Shinozaki T, Ishii H, Hashimoto Y. J Cryst Growth 2002;243:55.
[183] Vizman D, Watanabe M, Friedrich J, Müller G. J Cryst Growth 2007;303:221.
[184] Kim K-H, Sim B-C, Choi I-S, Lee H-W. J Cryst Growth 2007;299:206.
[185] Vizman D, Tanasie C. J Cryst Growth 2013;372:1.

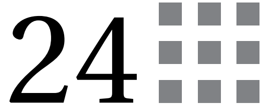

24 Oscillatory-Driven Fluid Flow Control during Crystal Growth from the Melt

Peter Capper[1], Evgeny Zharikov[2]

[1]SELEX ES, SOUTHAMPTON, UK; [2]D. MENDELEYEV UNIVERSITY OF CHEMICAL TECHNOLOGY OF RUSSIA, MOSCOW, RUSSIA

CHAPTER OUTLINE

24.1 Introduction **952**
24.2 Constant-Speed Rotation in Melts **953**
24.3 Accelerated Crucible Rotation Technique **955**
24.3.1 Introduction and Theory 955
24.3.2 CMT Growth 959
24.3.3 High-*x* CMT Material 960
24.3.4 ACRT in the Growth of CdTe/$Cd_{1-x}Zn_xTe$ 964
24.3.5 ACRT in Group-IV Growth 967
24.3.6 ACRT in Other Material Systems 968
24.4 Axial Vibration Control **968**
24.4.1 Physical Nature of the Phenomenon 969
24.4.2 Effects of AVC on Crystal Growth from the Melt 971
24.4.3 Application of AVC in Crystal Growth Methods 973
24.4.4 Crystal Materials Grown by the AVC Technique 980
24.5 Other Types of Oscillatory Techniques **981**
24.5.1 Ultrasonic Vibration 981
24.5.2 Coupled Vibrational Stirring 982
24.6 Conclusions and Outlook **983**
References **988**

Handbook of Crystal Growth. http://dx.doi.org/10.1016/B978-0-444-63303-3.00024-9
Copyright © 2015 Elsevier B.V. All rights reserved.

24.1 Introduction

Despite the progress made in recent decades in the various epitaxial growth techniques, bulk crystals are still used actively in numerous electronic and photonic applications, as well as passively as epitaxial substrates, for example [1–3]. In these bulk growth activities, although the basic growth mechanisms have been explained, there is still a growing need to improve the size and quality of crystals while reducing production costs. Rudolph and Kakimoto [4] have outlined various means of controlling the uniformity and stability of crystal growth from the melt by complementing internal parameters (e.g., temperature field, pressure, growth velocity) by external influences (e.g., mechanical, electrical, and mechanical fields). Stirring during crystal growth can often be essential to enhance solute transport through the growth fluid, to homogenize the solute concentration in the fluid and solid, and to reduce the thickness of the solute diffusion boundary layer (in order to prevent constitutional supercooling and hence the morphological instability of the crystal). Why are the properties of the crystal not markedly affected by the periodic disturbances applied to growth fluids? The answer lies in a comparison of the time scales involved. Movement of solute species in melt growth is normally on the order of hundreds of centimeters per second. With growth rates in the region of 10^{-2} cm/s and induced fluctuations in the region of centimeters per second, solute movement dominates. In addition, if the characteristic ratio of D/δ^2 (with D being the diffusion coefficient and δ the boundary layer thickness) is less than the frequency of any hydrodynamic changes and their related temperature oscillations, then mass diffusivity cannot follow the thermal changes.

Consideration of fluctuation effects in directional crystallization showed [5] that, after a single disturbance at the growth interface, the steady-state composition is reached within a time:

$$t \approx 2\delta^2/D,$$

where δ is the boundary layer thickness and D is the diffusion coefficient. Taking typical values of $\delta = 10^{-4}$ m and $D = 10^{-8}$ m^2/s, we obtain a time on the order of 1 s. This means that the solutal transient of the growing interface is quite slow, and the interface acts as a "low-pass filter" [6] preventing the influence of growth rate perturbations or temperature oscillations with certain frequencies. The frequency limit from the above estimation is approximately 1 Hz. The same value can also be obtained from the analysis presented in Ref. [7]. According to estimates in [8], the critical value could be approximately 10 Hz. Below this limit (a few hertz), any fluctuations are dangerous. On the contrary, higher-frequency perturbations, including those typical for AVC values, should be damped.

Table 24.1 shows a summary of both steady and unsteady force fields that have been applied to crystal growth systems over the years. Although other areas will be covered in various chapters throughout this handbook, this chapter focuses on nonsteady mechanical means of affecting crystal growth, including the accelerated crucible rotation technique (ACRT) and various forms of vibration. After a short section covering other

Table 24.1 External Parameters that Influence Melt Flow Dynamics

Force Field	Mechanical (*g*)	Thermal (T)	Electrical (*E*)	Magnetic (*B*)
Steady	RCC, μg, multi-g	TFR	DC	SMF
Nonsteady	ACRT, AVC, CVS, USV	TFR	AC	RMF, TMF, AMF

Note: RCC, rotation of crucible and/or crystal; μ*g*, microgravity; multi-g = centrifugation, TFR, thermal field rotation; *E*, electric field; *B*, magnetic induction; DC, direct current; AC, accelerated current; ACRT, accelerated crucible technique; AVC, axial vibrational control; CVS, coupled vibrational stirring; USV, ultrasonic vibration; SMF, steady magnetic field; RMF, rotating magnetic field; TMF, traveling magnetic field; AMF, alternating (pulsed) magnetic field.
Adapted from Rudolph and Kakimoto [4].

mechanical means of melt mixing, the subsequent three main sections will discuss the topics of ACRT, axial vibrational control (AVC), and other vibration techniques.

Oscillatory techniques offer the means to control melt transport conditions in non-electroconductive melts that cannot be controlled using magnetic fields (see Chapter 23 in Volume IIB). That is, they have an effect on any fluid and open up possibilities to govern the crystal growth of not only semiconductors but also dielectrics, salts, etc.

24.2 Constant-Speed Rotation in Melts

A study of the relative importance of the rotation rate and thermal stability was conducted by Rossby [9]. By plotting the Rayleigh number ($\mathrm{Ra} = g\alpha\Delta T h^3(\nu\kappa)^{-1}$, where g is the gravitational constant, α is the volume expansion coefficient, ΔT is the temperature difference, h is the melt height, ν is the melt viscosity, and $\kappa = \lambda C_\mathrm{p}^{-1}\rho^{-1}$, where λ is the heat conductivity and C_p is the heat capacity) against the Taylor number ($\mathrm{Ta} = 4\omega^2 h^4(\nu)^{-2}$, where ω is the rotation rate). Two regions can be identified on such a plot characterized by stable laminar and irregular turbulent flow, respectively. Typical values are $\mathrm{Ra} = 10^5$ at $\mathrm{Ta} = 10^7$ and $\mathrm{Ra} = 10^6$ at $\mathrm{Ta} = 10^9$. These criteria set practical limits on the rotation rates and melt depths of certain important growth systems, particularly as scale-up is considered.

Constant-speed rotation of either the crystal or crucible, or both, have been used for many years in all of the major bulk crystal growth techniques, such as Czochralski, Bridgman, vertical gradient freeze, and high- and low-temperature solution techniques [1,4]. Crystal characteristics that are influenced by constant-speed rotation include uniformity in both the radial and axial directions, segregation of matrix elements (in ternary compounds), striations (growth-induced inhomogeneities parallel to the growth interface), and secondary phases, to name only a few. Striations have several underlying causes, such as temperature fluctuations due to convective oscillations or nonsymmetry, hydrodynamic variations, and surface macrosteps (see the review by Scheel [10]). In each material system, a particular cause of striations is often found; for example, in Czochralski-grown silicon, striations are linked to the crystal rotation rate (see Chapter 2 in Volume IIA). Various means have been attempted to reduce striations, such as growth

under microgravity conditions [11] or centrifugation [12]. Eidelman et al. [13], used forced convection, via counterrotating crystals and crucibles, in small melt volumes in Czochralski growth to produce 700 mm/550 kg halide scintillator crystals. Scheel [10] described more than six types of melt flow below a Czochralski crystal that need to be considered or overcome to control melt mixing. Double crucibles can alleviate some of these problems, albeit with some practical difficulties. Scheel proposed an alternative of a solid ring located coaxial with and below the crystal to separate the flows from the melt fraction inside the ring and produce a quasi-stationary region below the crystal. Ostrogorsky and Muller [14] suggested a submerged heater in vertical Bridgman, where a thin melt and stabilizing the temperature gradient should minimize striations. By applying rotation to the baffle in this technique, Dutta and Ostrogorsky [15] were able to improve compositional homogeneity and reduce chemical stresses in grown $In_{1-x}Ga_xSb$ crystals.

Study of the rotation of the crystal or a special rotating stirrer in crystallization from melt has attracted renewed attention regarding the large volumes of metal alloy and semiconductor melts, such as silicon melt. Electromagnetic control of melt flow can have a limited effect on heat and mass transfer in the central area of large-scale Si ingots grown from the melt due to skin-depth issues [16,17]. Numerical studies of directional solidification of multicrystalline silicon with use of a rotating stirrer in the melt have been performed by Dumitrica et al. [18]. They demonstrated the promise of mechanical stirring to control the melt convection in directional solidification of large-scale silicon ingots; in particular, a strong increase of both melt convection and solid–liquid interface deflection was found.

Thermal field rotation is a new method of governing heat and mass transfer in a liquid phase, as proposed by Kokh and coworkers [19–22]. They organized a traveling heat wave propagating along the crucible wall by alternate switching of the vertical heating elements located around the crucible. As a result, the rotation of a nonuniform and cyclically changing heat field appeared on the crucible wall, producing the contactless generation of azimuthal flows in the melt. The outside impact decreased the role of the centrifugal force in melt motion, smoothed away the convection instability, and eliminated completely the melt disturbance as a result of the absence of mechanical rotation of the crystal/crucible. The authors found that changing the heating from an axisymmetric to a nonsymmetric, nonstationary configuration resulted in an increase in the convective flow and thus led to an increase of the melt uniformity because the convective cell occupies almost the entire melt domain. Curie's symmetry principle must play a significant role in crystal growth technology assisted with heat field rotation. Thus, by setting up a certain symmetry of the external thermal field in accordance with Curie's principle, one may expect the attainment of possible symmetrization of the convective flows in the system. The governing heat and mass transfer by rotation of the heat field was successfully realized by the authors in Czochralski, Bridgman, top-seeded solution growth, Kyropoulos, and some other growth techniques.

24.3 Accelerated Crucible Rotation Technique

24.3.1 Introduction and Theory

ACRT has been used extensively in the past to help melt homogenization in high-temperature solution growth of garnets and to improve crystal size by reducing the boundary layer thickness, as well as to prevent unwanted second-phase material from forming. In this section, we present a further example of the use of ACRT—that of cadmium mercury telluride (CMT, $Cd_xHg_{1-x}Te$), which is still the pre-eminent infrared material, despite the difficulties associated with its production and subsequent processing. By varying the x value, the material can be made to cover all of the important infrared (IR) ranges of interest (i.e., 1–3, 3–5, and 8–14 μm). Bridgman growth takes place in simple two-zone furnaces, with the pure elements contained in thick-walled, high-purity silica ampoules. The thick ampoule walls are needed to contain the high (up to ∼70 atm) mercury vapor pressures within the ampoules. It was found to be necessary to purify both the mercury and the tellurium on site before use to obtain the required electrical properties. There is marked segregation of the matrix elements in standard Bridgman growth that is both a disadvantage and an advantage [23]. Its disadvantage is that the yield of material in terms of composition for the most commonly required regions is low. The advantage is that all regions of interest can be produced in the same crystal, to some extent. A further advantage is that segregation of impurities also occurs, which leads to low background donor levels in Bridgman material. The other main disadvantages of the standard Bridgman technique are that the material is nonuniform in composition in the radial direction and the growth direction, resulting in low yields, and there are numerous grain and subgrain boundaries.

Limits on controlling melt mixing in the Bridgman process necessitated a means of stirring melts contained in sealed, pressurized ampoules. The ACRT of Scheel [24] was used because it had been seen to increase the size of crystals, eliminate unwanted phases, and increase stable growth rates in high-temperature solution growth of a range of crystals. The first reported use of ACRT in CMT Bridgman growth was given by Capper and Gosney [25]. These effects were developed and discussed in more detail in later papers (see Refs [26–28] for reviews) and are outlined here.

The following three processes are fast by comparison with buoyancy-driven convection and occur on acceleration/deceleration:

1. Transient Couette flow, which occurs on rapid deceleration (spin-down), particularly in tall containers. Liquid adjacent to the container walls decelerates faster than liquid in the bulk and centrifugal forces drive the inner portions of liquid toward the wall. Horizontal vortices form in counterrotating pairs. This only occurs beyond a critical rotation rate, given by a value of 270 for the dimensionless Reynolds number:

$$\mathrm{Re} = R^2 \Delta\Omega_c \sigma / \eta \tag{24.1}$$

where $\Delta\Omega_c$ is the step change in rotation rate (rpm), such that $\Delta\Omega_c \times 2\pi/60$ rad/s; R is the container radius (cm); σ is the fluid density (g/cm^3); and η is the dynamic viscosity of fluid (g/cm/s).

2. Spiral shearing flow, which occurs on both spin-down and spin-up, and is again caused by fluid at the walls changing its velocity faster than liquid in the bulk. It is characterized by the thickness, d, of a layer close to the wall where the rotation rate is half its initial value, and by τ_1, the time taken by the central part of the fluid to reduce to this level:

$$d = R(E\Omega_o t)^{0.5} \approx (\eta t/\sigma)^{0.5} \tag{24.2}$$

$$\tau_1 = 0.1(E\Omega_o)^{-1} \approx 0.1\sigma R^2/\eta \tag{24.3}$$

where t is the time after the container stops rotating (s), Ω_o is the maximum rotation rate (rpm), and E is the Ekman number ($\eta/\Omega_o R^2\sigma$). Spin-up/spin-down times should be $<\tau_1$ to maximize stirring.

The number of spiral arms is given by:

$$N = \Omega_o \sigma R^2 / 16\pi\eta \tag{24.4}$$

with separation,

$$\Delta r = 4\pi\eta/\sigma\Omega_o r \tag{24.5}$$

where r is the radius of the point in question. Δr should be kept at 0.01–0.1 cm to ensure diffusion can act as the mixing process.

3. Ekman flow, which occurs above a solid boundary placed perpendicular to the axis of rotation. During spin-up, fluid adjacent to the boundary is forced to the side walls and returns diffusely and more slowly through the bulk, with the reverse occurring on spin-down.

The Ekman layer thickness is given by:

$$d_E = (\eta/\Omega_o\sigma)^{0.5} \tag{24.6}$$

with a maximum radial fluid velocity of:

$$V = \Omega_o R \tag{24.7}$$

and a maximum vertical fluid velocity of:

$$W = (\eta\Omega_o/\sigma)^{0.5} \tag{24.8}$$

The flow decreases within a time:

$$\tau_E = R(\sigma/\eta\Omega_o)^{0.5} \tag{24.9}$$

Figure 24.1 shows the ACRT rotation sequence used and Figure 24.2 depicts the various flows as seen in water simulation trials using a flat-based ampoule to simulate a crystal–melt interface [26]. All three predicted flow patterns were seen and showed qualitative agreement with the parameters given in Eqns (24.2)–(24.9). The most vigorous stirring arose due to Ekman flow for distances of $\sim R$ to $2R$ from the container base (Ekman volume), particularly when a flat-based container was used.

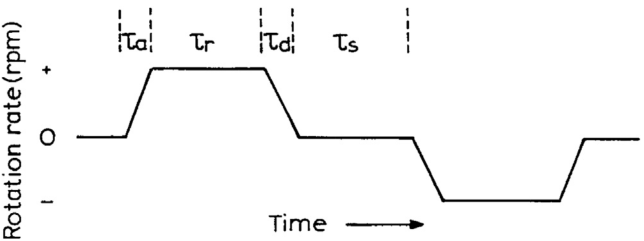

FIGURE 24.1 ACRT rotation sequence. *Reprinted from Capper et al. [26], copyright (1988) reproduced with permission from the Minerals, Metals and Materials Society.*

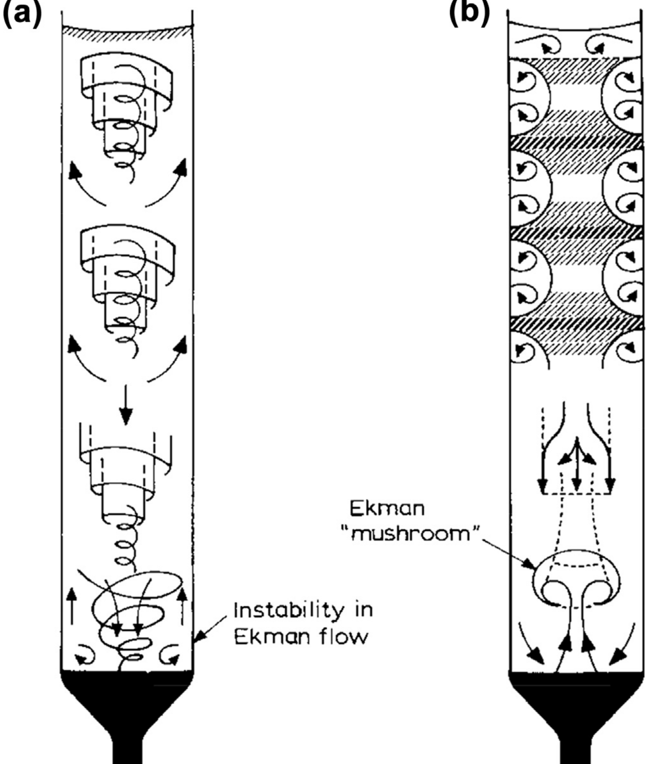

FIGURE 24.2 Flows in a flat-based container during (a) spin-up and (b) spin-down. *Reprinted from Capper et al. [26], copyright (1988) reproduced with permission from The Minerals, Metals and Materials Society.*

Brice et al. [28] summarized the models developed for flows induced by ACRT by identifying three distinct flow regimes as the acceleration/deceleration rate increases. For small accelerations, axially symmetric fluid flows increase the symmetry of heat and mass flows. Moderate accelerations produce axial and radial fluid flows at the base of the column (R to $2R$) that stir the fluid in this region only. Large accelerations give rise to unstable asymmetric flows. The system is characterized by the Reynolds number. Table 24.2 lists the critical Reynolds numbers and the corresponding rotation rates for

Table 24.2 Critical Reynolds number (Re_c) and Corresponding Critical Rotation Rates for ACRT in 13-, 20-, 50-, and 75-mm Diameter Ampoules

		Critical rotation rates (rpm)			
Event	**Re_c**	**13 mm**	**20 mm**	**50 mm**	**75 mm**
Ekman flow starts	15	≥2	~1	0.1	0.05
Ekman flow fully developed	70	10	4	0.6	0.25
Couette flow unstable	270	38	16	2.4	1.1
Ekman flow unstable	500	69	30	4.5	2.1

$v = \eta/\sigma = 0.006$, kinematic viscosity in cm^2/s.
Adapted from Capper et al. [29,30] with permission from Elsevier.

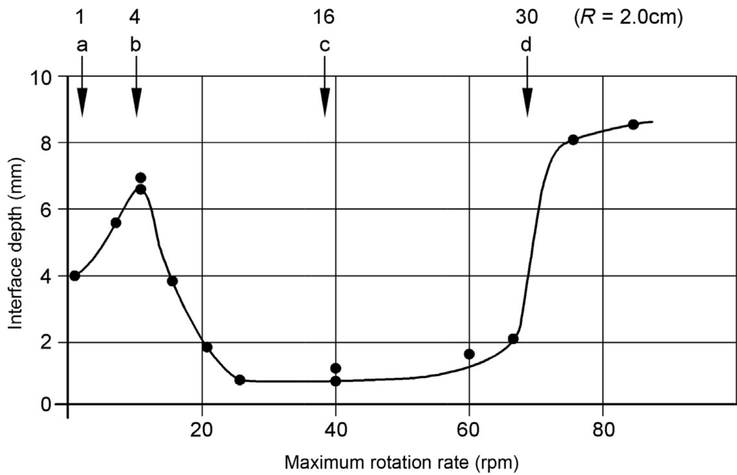

FIGURE 24.3 Interface depths in quenched crystals versus maximum ACRT rotation rates for 13-mm diameter crystals, with rotation values for 20-mm crystals superimposed at the top. *Adapted from Capper et al. [30], copyright (1988) reproduced with permission from Elsevier Science.*

the values of R (0.65 cm) and η/σ (0.006 cm^2/s) typical of CMT melts. These values of Re_c are superimposed onto the interface depth (from crystal quenching studies) versus the rotation plot of Figure 24.3 [30], together with other diameters typical of later CMT growth (20, 50, and 75 mm) and CdTe growth (50 and 75 mm). For points (a) and (b), Ekman flow is delayed because the ampoule base is not perpendicular to the rotation axis in the conical-based ampoules used for growth. Once Ekman flow is fully established, the interface depth decreases to a minimum. Couette instabilities are predicted to occur at point (c) and were seen in the simulations, although they do not affect the interface depth because they only occur in the upper regions of the liquid not near to the solid–liquid interface. As the Reynolds number increases further, Ekman flow will become unstable at point (d), and the interface depth consequently increases. Too

Table 24.3 ACRT Parameters

Parameter	Figure/Equation	Aim
1. Acceleration/deceleration time, τ_a, τ_d	Figure 24.1	τ_a, $\tau_d << \tau_E$ (to maximise use of Ekman flow)
2. Ekman time, τ_E	Equation (24.9)	$\tau_E >> \tau_a$, τ_d
3. Ekman layer thickness, d_E	Equation (24.6)	$d_E < 0.05$ cm
4. Vertical/horizontal fluid velocities, W, V	Equations (24.7) and (24.8)	$V\tau_E$, $W\tau_E > R$ (to pass Ekman volume through Ekman layer)
5. Separation of spiral arms, Δr	Equation (24.5)	$\Delta r < 0.1$–0.001 cm (to enable homogenization via diffusion)
6. Run/stop times, τ_a, τ_d	Figure 24.1	τ_a, $\tau_d << \tau_E$ (to maximize use of Ekman flow)
7. Reynolds number, Re	Equation (24.1)	Re < 500 (for stable Ekman flow)

Reprinted from Capper et al. [23], with permission from Elsevier.

much melt mixing can be introduced by certain ACRT conditions, which leads to deterioration in crystal properties.

Table 24.3 details the various ACRT parameters and the desired magnitudes of these to ensure a high level of controlled melt mixing. Bidirectional rotation is employed and rapid acceleration/deceleration (in 1–2 s) is easily achieved at any rotation rate. The Ekman layer thickness d_E, from earlier flux growth, should be <0.05 cm, which necessitates rotation rates >20 rpm. Horizontal and vertical flow velocities, V and W, are $>> R/\tau_E$ for all rotation rates, ensuring that the Ekman volume passes through the Ekman layer at each ACRT cycle. Rotation rates of >20 rpm will ensure that Δr is within the preferred range of 0.1–0.01 cm to homogenize the fluid body by diffusion. Both run (at maximum rate) and stop times, τ_r and τ_s, can be set to values close to the Ekman time, τ_E, to ensure mixing occurs for as long as possible and that decaying Ekman flow is minimized.

24.3.2 CMT Growth

The major effect of ACRT is to stir the melt during growth and produce flatter solid–-liquid interfaces. In turn, the radial and axial compositional uniformity of the material are improved, normally by a factor of at least ten-fold, and the grain and subgrain densities are reduced somewhat. The increase in uniformity enables larger-diameter material to be produced (up from 13 to 50 mm in our case). Assessment of the material includes wavelength mapping of both radially cut slices and axially cut planks; the latter gives useful information on the shape and change in the solid–liquid interface as growth proceeds. Images taken with an IR camera and a blackbody source revealed features in slices, such as cracks, inclusions of second phase, and swirl patterns; the origin of the latter is as yet unknown. We are currently routinely growing 20-mm diameter, 200-mm long crystals of ~0.5 kg weight with good uniformity of composition and good electrical properties for first-generation photoconductive IR detector programs that require low carrier concentration n-type material. Compositions produced range from x of ~0.93 (~0.91 μm) through to $x = 0.0$ (i.e., HgTe)—the latter in the tail ends of the crystals.

Application of ACRT opened up a large number of possible parameter combinations [23,29,31–34]. Quenching studies of crystals grown under a wide variety of conditions showed interface depths of ≈1 mm for $x = 0.12$ and 0.19 start crystals, unlike the values of 1 and 4 mm, respectively, seen in equivalent standard Bridgman crystals. Increasing the maximum rotation rate produced the interface depths shown in Figure 24.3. The preferred region in which to operate is clearly $25 < \Omega_o < 60$ rpm for a 13-mm diameter crystal. As growth rate increased, interface depth changed much less than in Bridgman growth, suggesting that faster stable growth rates are possible with ACRT. From the simulation studies, it was apparent that a small stagnant region occurred in the tip of a conical-based ampoule. Quenching studies in flat-based ampoules revealed not only a flat interface but also that the slow-grown material, produced prior to quenching, was single crystal. These studies demonstrated the power of Ekman stirring and the importance of initiating the growth of a single crystal grain.

In the early days of ACRT development, various rotation sequences and start compositions were investigated using 13-mm diameter crystals and x uniformity and crystal structure determined [23]. After comparing results, $x = 0.19$ was chosen as the preferred start composition. For these crystals grown with short run and stop times (8 and 1 s), there was a region (several centimeters long) of $x = 0.21$ material with axial and radial x uniformity of ±0.002. A similar Bridgman crystal would produce <0.8 cm of similar x material with considerably larger radial x variations; that is, ACRT gives a five- to ten-fold increase in potentially usable material. See Figure 24.4 for a schematic of the Bridgman grower used [35].

24.3.3 High-*x* CMT Material

This section focuses on the work undertaken to produce near-IR material, for which higher starting x values are used. The assessment of the near-IR material has included wavelength mapping of radially cut slices and images taken with an IR camera to reveal features in slices, cracks, and inclusions of second-phase and swirl patterns; the origin of the latter is unknown. This work is being undertaken to improve our basic understanding of the properties of CMT in the near-IR region and to investigate the suitability of the material for use in various IR optical applications.

Figure 24.5(a) shows the pseudobinary phase diagram of the HgTe-CdTe system (Yu and Brebrick [36]). This demonstrates the fundamental problem in the near-equilibrium growth of CMT by melt growth methods, i.e., the wide separation between the liquidus and the solidus. However, this is actually a benefit when we are trying to produce higher x material. Because the starting x is increased, the first-to-freeze material also increases in x, although not at quite the same rate due to the relative curvatures of the liquidus and solidus. The initial goal was to produce material of x ∼0.7, corresponding to ∼1.3- to 1.4-μm cut-off wavelength. Figure 24.5(a) shows that this necessitates using starting x values of 0.33–0.35. Figure 24.5(b) shows the pressure–temperature phase diagram for various x values [36]. The region above the P^{o}_{Hg} line is essentially Hg vapor, with solid of

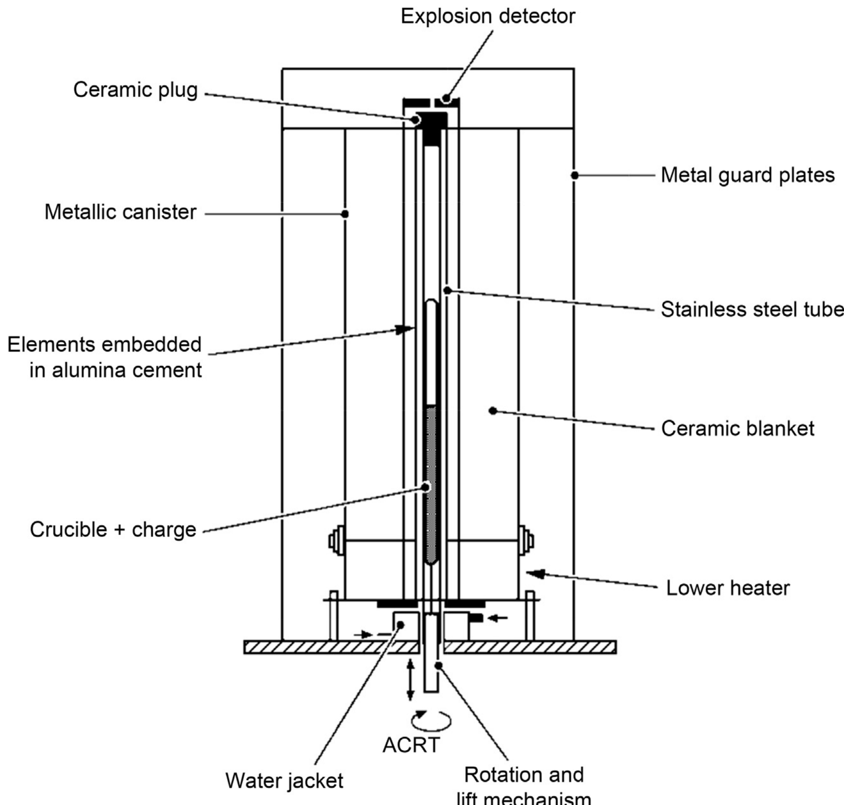

FIGURE 24.4 Bridgman/ACRT growth apparatus. *Reprinted from Capper et al. [35], copyright (1979) reproduced with permission from Elsevier Science.*

the indicated x values existing in the loops on the lower right and liquid to the left of the loops. This amply demonstrates how the maximum growth temperature and hence the Hg vapor pressure increases as x increases.

The loading procedure for these high-x crystals was as for the earlier crystals. We have had to develop the seal-off procedure to reduce the possibility of explosions due to the high pressures. This entailed ensuring that the wall thickness remained at the 7-mm value of the ampoule body and ensuring that there were no re-entrant angles in the seal-off area. By making the internal surface of the seal-off smooth, we have greatly reduced the occurrence of explosions and have successfully grown at temperatures $>950\,^{\circ}C$—approximately $130\,^{\circ}C$ above "standard" growth temperatures used before in this system.

Start compositions of $x = 0.19–0.8$ have been used and the melts were homogenized by melting/rocking as for standard charges. The growth process remained essentially unchanged for these high-x crystals [32,37]. Slices were cut (at >1-mm thickness) from the resulting crystals using a diamond peripheral-wheel cutting machine and then

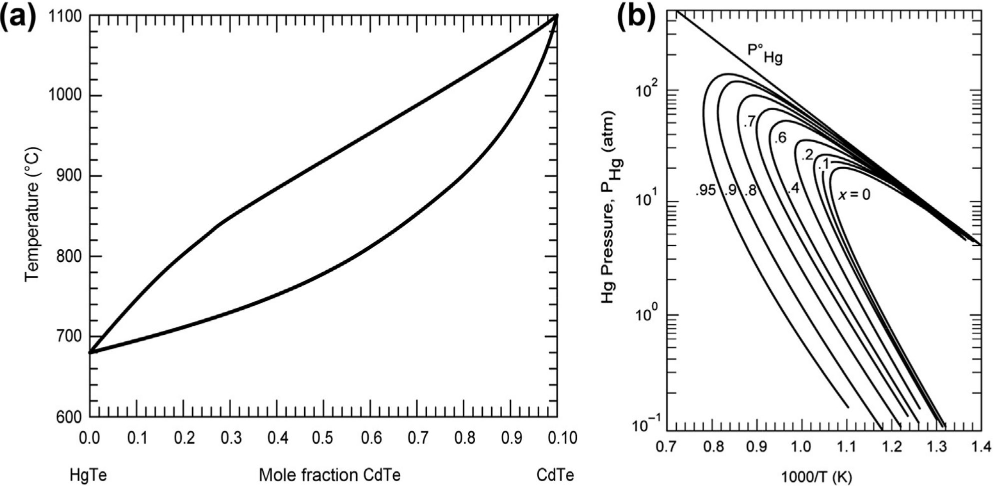

FIGURE 24.5 (a) Pseudobinary phase diagram for HgTe-CdTe system (L = liquid, S = solid). (b) Pressure–temperature diagram for CMT. *Reprinted from Yu and Brebrick [36], copyright (1994) reproduced with permission from IEE.*

polished and assessed for x uniformity with infrared transmission (IRT) measurements, as well as the mid-IR camera system.

Figure 24.1 shows the ACRT sequence that was also used for these high-x crystals. Standard bidirectional rotation is still employed with rapid acceleration/deceleration (in 1–2 s). From considerations of the simple model (Table 24.2), it was seen that maximum rotation rates for these 20-mm diameter crystals should be between 4 and 30 rpm. Also for these crystals, short run and stop times (8 and 1 s, respectively) were used as for standard crystals. To maximize the Ekman stirring—that is, to increase the vertical and horizontal flow velocities (to values of $> R/\tau_E$)—we chose to use 25 rpm as the maximum rate. This rotation rate also ensures that the spiral separation is $\sim$0.03 cm at its maximum value, which ensures full mixing by diffusion between the spiral arms (see Eqn (24.5)).

Another assessment tool that is used for these high-x crystals is that of IR imaging. By placing a blackbody on one side of the slice (polished on both sides to $\sim$1 mm thickness) and a midwave camera system (CEDIP) on the other, images can be taken that reveal IR-absorbing defects. (This camera system uses an OSPREY detector manufactured at Selex ES from liquid phase epitaxial [LPE] material). This is a rapid, noncontact assessment method that can be used for all slices with cut-off wavelengths less than that of the camera system's detector.

Highly uniform, extremely high-x value material has been produced using these techniques. Figure 24.6 shows the uniformity map and IR transmission image of the shortest-wavelength 20-mm slice grown to date.

A second aim of this work was to scale-up growth using ACRT to maintain x uniformity. Several 40-, 50-, and 70-mm diameter crystals have been grown. Figure 24.7

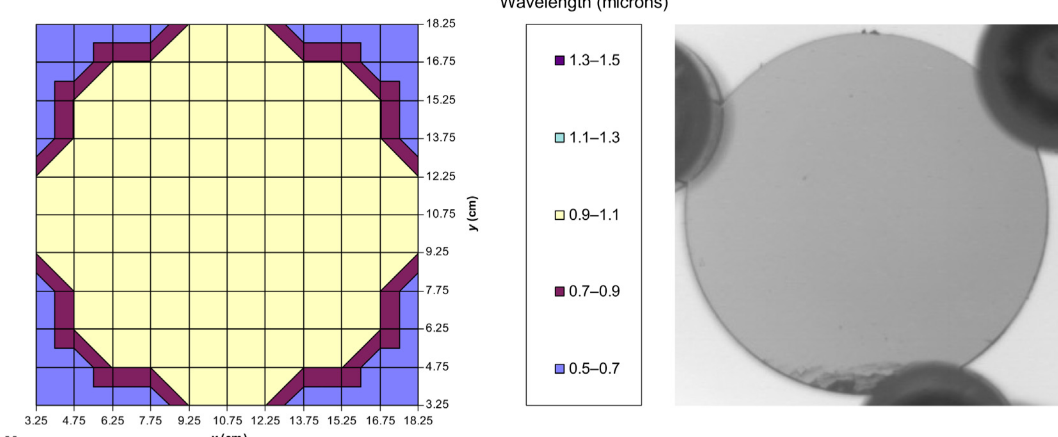

FIGURE 24.6 Radial distribution of wavelength (in μm at room temperature—0.91 μm ≡ x ~0.93) in 20-mm diameter slice. *Courtesy of Selex ES.*

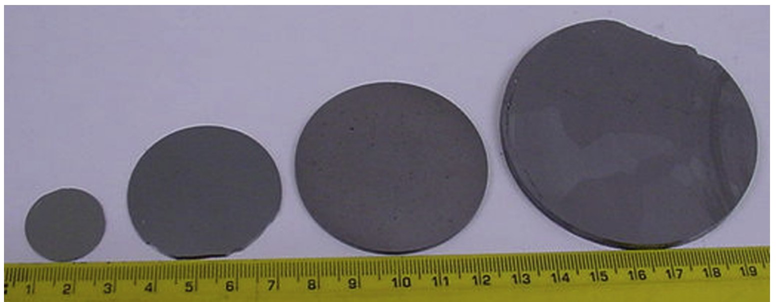

FIGURE 24.7 Comparison of 20-, 40-, 50- and 70-mm CMT slices. *Courtesy of Selex ES.*

shows slices from 20-, 40-, 50-, and 70-mm diameter crystals. The 70-mm crystal is the largest diameter CMT crystal grown anywhere, to this author's knowledge. In tandem with increasing diameter, the weight of crystals was also increased to maintain the number of usable slices. The largest weight currently used for 50-mm diameter crystals is ~2 kg. The highest x value seen in these 50-mm crystals (from a 30% start) is ~1.5 μm (x ~0.67). Figure 24.8 shows the wavelength uniformity of this slice, together with the IR image of the adjacent slice, where a central area (~36 × 36 mm in size) can be seen to be clear of defects or grain boundaries. Figure 24.8 also shows the overall size of this 50-mm diameter crystal.

In the preferred case of short cycle times, outlined above, Gray et al. [38], have confirmed the observations in our quenched crystals that no striations should be present.

Liu et al. [39], have modeled the ACRT process in small-diameter CMT with a rotation sequence very similar to that described above. They showed that the optimum conditions

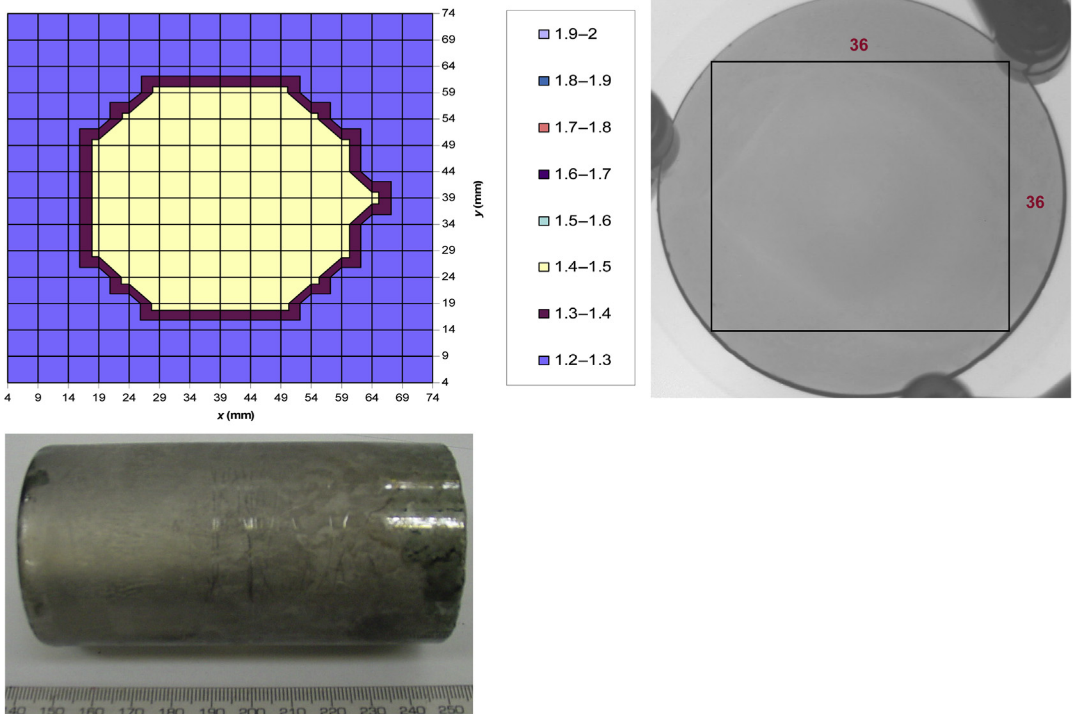

FIGURE 24.8 Radial distribution of wavelength (in μm at room temperature) in 50-mm diameter high-x slice from 30% start. *Courtesy of Selex ES.*

for flows, temperature, solute distribution, and interface depth were ~45 rpm with a total time of ~36 s, which are very close to the values of 40 rpm and ~33 s mentioned above. Jie [40] also modeled this system and found that the interface position shifted by up to 80 mm during growth with an axial temperature gradient of 10 K/cm, which has implications for the compositional control. Increasing growth rate caused this shift to occur more rapidly, but by the same overall extent, when no ACRT was used; however, with ACRT, this interface shift occurred independently of the growth rate and eventually reached ~100 mm in the last-to-freeze region. Thus, there was a need to vary the lowering rate during the growth process to keep the actual growth rate constant.

Bloedner and Gille [41] used ACRT in traveling heater method (THM) growth of 16-mm diameter CMT using various sequences. They were able to achieve marked improvement in growth rate, with no increase in second-phase precipitates or evidence of striations (more details on ACRT THM are given in Chapter 12 of Volume IIA).

24.3.4 ACRT in the Growth of CdTe/$Cd_{1-x}Zn_xTe$

The first use of ACRT in the growth of CdTe was by Wald and Bell [42]. The growth of larger-diameter, 50-mm material with ACRT was described by Capper et al. [43]. This

size was chosen to produce suitable grain sizes for 20×30 mm liquid-phase epitaxy substrate production for the subsequent growth of CMT layers. It was anticipated from earlier work on ACRT growth of CMT [23] that larger grain sizes would be produced. On studying the parameter values in Table 24.3 for the larger-diameter case (i.e., 50-mm), two distinct ACRT combinations of parameters were recognized: the combinations that maximize flows (items 1–6 in Table 24.3) and the combination that maintains stable Ekman flow (item 7 in Table 24.3). With $R = 25$ mm, combinations of 40 rpm with 15 s run/stop times and 4 rpm with 50 s run/stop times corresponded to the two regimes. Experimentally, it was found that crystals grown under the first regime consisted of many grains, yielding no usable substrates. This strongly suggested that stable Ekman flow was required to produce large grains. To confirm whether rotation rates <5 rpm were absolutely necessary, a crystal was grown with 10 rpm and 12 run/stop times. A weighing error caused this crystal to produce polycrystalline growth, but an interesting feature was seen on the top of the crystal, where the segregated liquid cadmium was quenched during ACRT stirring. Figure 24.9 shows what appear to be spirals on the acid-etched top surface. The spiral separation was $\sim$0.1 cm near the periphery, increasing to $\sim$0.5 cm near the center, as predicted from Eqn (24.5), and the number of spiral arms was in qualitative agreement with Eqn (24.4). This provided the first direct evidence that such ACRT flows exist in these high-temperature melts. When crystals were grown using 4 rpm with 50 s run/stop times, a single grain was seen to run the entire length of the 7-cm crystal, albeit with some edge grains, too. This suggests that ACRT did indeed increase the overall grain structure (see Figure 24.10).

Figure 24.10 shows the result of using a necked ampoule base in ACRT growth. It was concluded by comparison with other crystals that the constriction reduces the number of grains propagating through to the full-diameter region. At this point, Ekman flow dominates and, if stable, should minimize the nucleation of secondary grains.

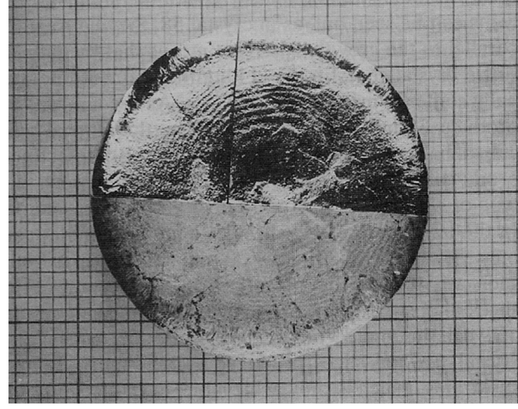

FIGURE 24.9 “Sprials” caused by ACRT on frozen Cd on top of CdTe crystal. *Reprinted from Capper et al. [43], copyright (1993) reproduced with permission from Elsevier.*

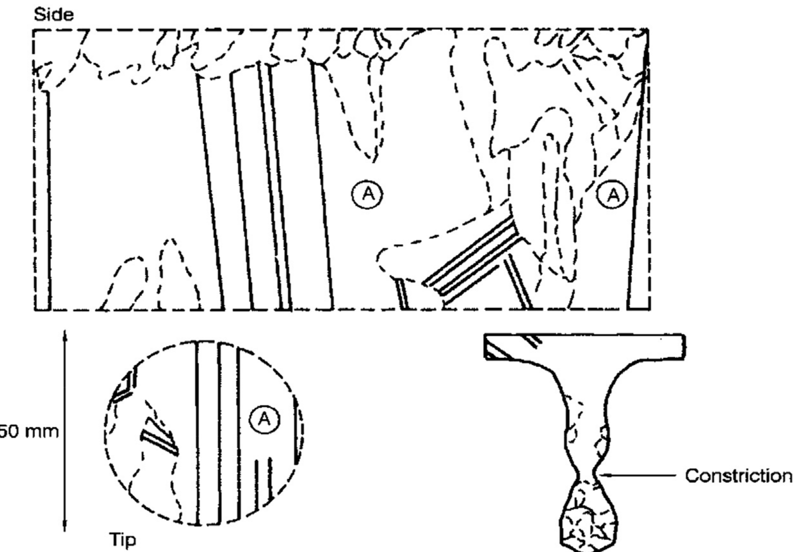

FIGURE 24.10 Grain map of CdTe crystal using ACRT and a constriction in the first-to-freeze region. *Reprinted from Capper et al. [43], copyright (1993) reproduced with permission from Elsevier.*

Figure 24.10 shows that this is successful because grain A is present over ~75% of the area. The cut in the central section shows that grain A occupies ~75% of the crystal volume. Several twins propagate through the length of the crystal, but these lie roughly parallel to the growth axis. This results in the largest single crystal (111) slices being potentially ~65 × 50 mm in size. As the aim of the work was generally to produce 30 × 20 mm slices; this crystal was cut in half to maximize the potential number of substrates. Obviously both sections could, and indeed did, produce 30 × 20 mm slices. Several slices from this crystal produced two 30 × 20 mm substrates. This is only achievable in 50-mm diameter crystals if the (111) twins lie nearly parallel to the growth axis. Sliding-boat Te-rich LPE growth (see Chapter 10 in Ref. [3]) requires regular, rectangular, or square, substrates, so having the (111) direction parallel to the growth axis is an obvious advantage.

Application of ACRT was also found to reduce the level of second-phase Te precipitates, strain (as measured by X-ray diffraction curve widths), and etch pit densities in CdTe (these were also equivalent to the then-current literature values). Chemical analysis of the Zn distribution in CdTe/$Cd_{1-x}Zn_xTe$ (CZT) crystals showed that ACRT moved the segregation coefficient much closer to unity, meaning that more of the ACRT crystal had a Zn level for lattice matching to the CMT to be grown on it (see Figure 24.11). The near maximum transmission value, at 750/cm, showed that the impurity levels in these ACRT crystals was also extremely low due to the enhanced segregation caused by ACRT melt mixing. Finally, substrates from some of these ACRT crystals were used to produce LPE layers of CMT with acceptable properties for use in IR detector manufacturing.

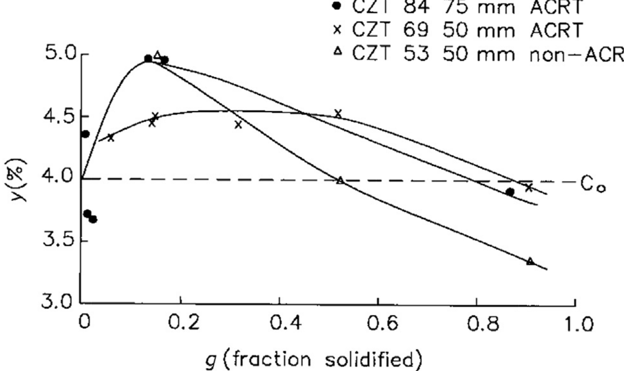

FIGURE 24.11 Segregation of Zn in non-ACRT and ACRT crystals of CdZnTe. *Reprinted from Capper et al. [23], copyright (1994) reproduced with permission from Elsevier.*

Wang et al. [44] studied the effects of ACRT on impurity behavior in vertical Bridgman-grown CZT. Segregation coefficients of several impurities were determined; however, because the one ACRT crystal was more heavily doped, no meaningful comparisons with non-ACRT crystals could be made. Wang et al. [45], studied the effects of ACRT and seeding in 60-mm diameter CZT crystals. They found that seeding clearly improved crystallinity and dislocation densities compared with ACRT growth but that ACRT improved the Zn distribution; that is, it reduced the segregation coefficient closer to unity and produced a similar improvement in impurity (In) behavior, mirroring that seen by Capper et al. [43]. However, this study [45] only compared one seeded crystal with one ACRT crystal, grown under otherwise identical conditions.

Jie et al. [46] used ACRT in their growth of 5-mm diameter $Hg_{1-x}Mn_xTe$ and modeled the Mn distribution. The segregation coefficient was found to vary with axial position.

24.3.5 ACRT in Group-IV Growth

There have been several reports of the extension of ACRT to the growth of group-IV elements and compounds. Bairava Ganesh et al. [47,48] used ACRT to induce striations in mc-Si used for photovoltaics to determine the growth rate during unidirectional solidification. A growth rate of ∼0.4 mm/min was found in 50-mm sized samples. It was noted that the carbon concentration was more homogeneously distributed with ACRT and there was also a reduction in the number of impurity precipitates. Belleman et al. [49] used transient simulation of mc-Si with ACRT over a 10-h growth time. For 12.5-cm diameter, 10-cm high crystals, a rotation rate of ∼1 rpm and an Ekman time of 600 s were used. It was found that ACRT increased the radial segregation of impurities, which perhaps is not too surprising at such low rotation rates and for such large samples.

ACRT becomes even important for crucible-free floating zone (FZ) growth of oxygen-free large-diameter (200 mm) silicon crystals [50,51]. To overcome the difficulty of growth front break out in the radial direction, especially at large diameters, the growing crystal is periodically rotated through a sequence of rotation angles. The direction of

rotation is changed, after each rotation, by a rotation angle belonging to the sequence. As a result, the diameter constancy is controlled markedly.

Kusunoki et al. [52] used ACRT in their Si-Ti solvent growth of SiC for use as substrates for the LPE growth of SiC layers. ACRT allowed growth rates to be increased up to 200 μm/h, enabling growth of 5-mm thick substrates. This is another example of ACRT as an "enabling" technique to produce something normal melt growth cannot readily produce to further progress production of a key material, in this case SiC. The resultant LPE layers had high quality, low impurity levels, and good electrical properties.

Seki et al. [53] employed ACRT in their top-seeded solution growth of SiC for high-power electronics applications. In 12-mm diameter crystals, a 30-rpm rotation rate was used to produce the desired 3C polytype for higher electron mobilities, at the expense of the undesirable 6H polytype.

24.3.6 ACRT in Other Material Systems

Several other materials systems have seen benefits from the addition of ACRT to the growth process. Distanov et al. [54] used unidirectional ACRT, with maximum rotation rates between 20 and 60 rpm, to grow good-quality Ag_3AsS_3. These crystals were used in nonlinear optics applications.

Lui et al. [55] found that ACRT suppressed constitutional supercooling in the growth of succinonitrile in acetone at room temperature, and hence morphological instabilities. Near the interface, the forced convection from ACRT was seen to be dominant. This same group [56] used both simulations and visualization techniques to look at the effects of various ACRT sequences. They found that the trapezoidal sequence is best because it maintains a controlled amount of melt mixing throughout the ACRT cycle, in agreement with the conclusions outlined in Section 24.3.2.

Uda et al. [57] used ACRT to grow 50-mm diameter crystals of langasite ($La_3Ga_5SiO_{14}$) for piezoelectric applications. Employing rotation rates of 0–25 rpm reduced the occurrence of undesirable secondary phases of lanthanum gallate and gallium oxide.

Kim et al. [58] and Dutta [59] used ACRT to increase melt stirring in their growth of antimony-based quaternary compounds because it is easily adapted for larger sizes and for sealed crucibles. They also noted that ACRT can be used in shallow melts where baffles/stirrers are not easily incorporated. To reduce constitutional supercooling, they needed to reduce the growth, but this proved to be uneconomical; hence, ACRT was used to increase the growth rate, by a factor of three in this case. In their (Ga,In)Sb ternary system, ACRT was also found to reduce crystal cracking.

24.4 Axial Vibration Control

The vibrational technique AVC applies axial low-frequency (tens of hertz) and small-amplitude (tens to hundreds of micrometers) vibration to the growth system [60,61]. The technique of applying vibration is realized either by vibration of the growing crystal

or by oscillation of a special submerged inert body/baffle, which is located near the crystal–melt interface and oscillates, inducing vibrational convection flows. Applying the vibration to the growth container/ampoule was experimentally and theoretically investigated for the Bridgman technique [62,63] and for the vertical zone-melting process [64,65].

The first studies of the influence of axial low-frequency vibrations on crystal growth from the melt appeared in the 1950s and 1960s [66–70]. Since that time, a number of papers on this subject have been published. The positive effects were found to occur to a different extent for a wide region of intensity/amplitude and frequency of vibration. The influence of vibrations on crystal growth in the ultrasonic (from tens of kHz to several MHz), acoustic (usually tens to hundreds of Hz), and even subsonic ranges (from 0.5 to 5 Hz) has been investigated. The displacement amplitudes are usually confined to several micrometers for ultrasound [71] and reach 10–25 mm in experiments on the influence of infrasound [72,73]. A detailed list of published papers can be found in reviews [74,75]. Data on the favorable influence of vibrations on various crystal properties have been obtained. However, those pioneering studies of vibrations were nonsystematic and casual: one author published usually no more than one or two papers. This situation is understandable and explicable because the mechanisms were unknown and really efficient use of axial vibration in crystal growth was very difficult to perform.

24.4.1 Physical Nature of the Phenomenon

The application of axial low-frequency vibration to the submerged body produces stable symmetric vibrational flows in the bulk liquid. This was shown by the primary numerical modeling of this phenomenon carried out by Avdonin et al. [76] and Zharikov et al. [77], both in 1989. The body with a dihedral rectangular edge executed linear harmonic vibrations in a stationary infinite liquid. The solution reveals the existence of a stationary average flow characterized by two areas of circulation, with opposite direction of motion flowing from the vibrating body edge (Figure 24.12). The average flow induced by oscillations of a solid body immersed in a liquid arises due to nonlinear effects. The physical nature of this phenomenon lies in the formation of a nonstationary boundary layer near the body surface and its periodic break-off, which causes the stationary movement in the liquid.

According to numerical simulation of vibration in the Czochralski process performed by Lyubimov et al. [79], the average AVC flow represented by two toroidal vortices of comparable intensity and specific directions could transform along with an increase of the vibration frequency into regular Schlichting flow when an external vortex occupies most of the flow area. The critical frequency for flow transition from AVC-type to Schlichting flow depends on the radius of curvature of the vibrating body edge: the smaller the radius, the larger the critical frequency. Lyubimov et al. [79] demonstrated this correlation by the corresponding diagram for some fixed value of vibration amplitude. A numerical study [80] has shown that, in the case of a vibrating disk located under

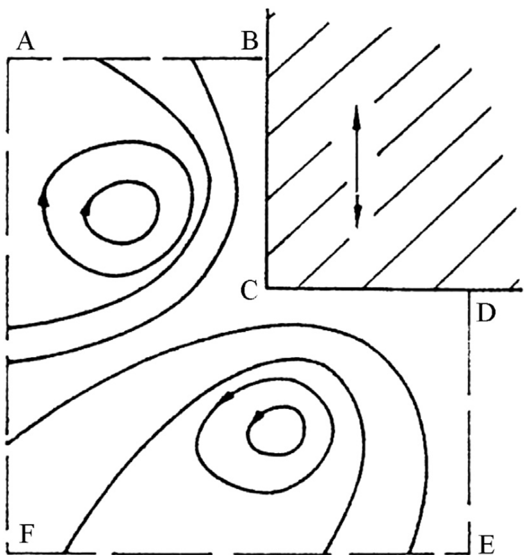

FIGURE 24.12 Fluid motion under vibration of a dihedral rectangular edge. *Adapted from Zharikov et al. [78].*

a solid–liquid interface (see below), the vibrational efficiency is determined not only by the sharpness of the oscillating disk edge but also by the ratio of an edge radius to a cylindrical disk thickness. Another mechanism leading to similar transformation of the flow pattern is given by Zharikov [81]. This is connected with the penetration depth of the solid–liquid interface regarding the position of the free surface of the liquid.

For a comparison of the various vibration regimes, the nondimensional vibrational Reynolds number is used:

$$\mathrm{Re_v} = \frac{2\pi fAR}{\nu} \tag{24.10}$$

An alternative is its variation, the pulsating Reynolds number:

$$\mathrm{Re_p} = \frac{2\pi fA^2}{\nu} \tag{24.11}$$

Another parameter characterizing the vibration regimes is vibrational acceleration, which is useful for analysis of parametric dependences and comparison of experimental data related to the same material within a series of experiments:

$$I_a = (2\pi f)^2 A\ [\mathrm{m/s^2}] \tag{24.12}$$

In Eqns (24.10)–(24.12), f is the vibration frequency, A is the vibrational amplitude, ν is the kinematic viscosity, and R is the vibrating body radius.

Bulk fluid flows of vibrational convection initiated by oscillations with low-frequency and small-scale amplitude is a specific type of stationary flow in the fluid. It differs from known fluid flow, which is evident from a comparison with acoustic flows [82] and Schlichting flow [83]. The phenomenon of vibrational convection cannot be explained by

the theory of acoustic flow because the characteristic dimension of the vortices in such currents is similar to or greater than the wavelength of the sound [82]. In contrast, the typical wavelengths for the vibrations under study are about 10 m, whereas the characteristic dimensions of the circulation, as a rule, are three orders of magnitude less. Steady-state convective flow generated by vibrations is established at lower amplitudes than the Schlichting flow. The appearance of small-scale vortices near the edge of the vibrating body is a significant difference from ordinary flows within the boundary layer.

The influence of low-frequency and small-amplitude axial vibration on crystal growth from a liquid phase is not confined to formation of bulk flows shown in Figure 24.12. Various new effects of vibration were discovered during the subsequent studies [74,75,80,81], as discussed in the following sections. Although the effects were observed in the case of particular vibration-assisted growth configurations, there are reasons to believe that these effects have a common character.

24.4.2 Effects of AVC on Crystal Growth from the Melt

Axial vibrational control allows one to efficiently govern the heat and mass transfer as well as the growth kinetics during crystallization from the melt. The introduction of axial vibration with frequency of tens to hundreds of hertz and amplitude up to hundreds of micrometers into a liquid phase provides the growth of high-quality crystals with high growth rates, under the control of stoichiometry and dopant distribution. AVC can noticeably alter both the composition and dopant segregation/distribution in the crystal. Such behavior was shown for both the Czochralski and Bridgman methods. AVC provides leveling of both dopant concentration and stoichiometry along and across the crystal [84–87]. The AVC-assisted Bridgman method under controlled pressure technique allowed the growth of CdTe and PbTe crystals with the required nonstoichiometry, which was constant along the crystal length [86,88,89].

The numerical modeling performed by Fedyushkin et al. [90,91], Fedyushkin and Bourago [92], and Avetisov et al. [93] has shown that vibrations can reduce the thickness of boundary layers at solid–liquid interfaces [90,91], which is of critical importance when growing single crystals. Using vibrational agitation of the melt, one can change the value of the temperature gradient at the interface—that is, one can change the kinetics and rate of crystal growth. The boundary layer thickness depends on the amplitude, the frequency, and the Prandtl (Pr) number of the melt. The melts with large Pr numbers, such as oxides and salts, are controlled by low-frequency vibration very efficiently. The influence on melts with small Prandtl numbers will be essential with an increase of the amplitude and the frequency of vibration (with increase of the vibrational Reynolds number Re_V).

A change of the hydrodynamic situation and temperature conditions near the interface provides the possibility to control the shape of crystallization front. Simulations demonstrated that the shape of the crystal–melt interface is strongly dependent on vibrational parameters [93]. Experimentally, the flattening of the solid–liquid interface

was obtained for growth of $NaNO_3$ crystals by both AVC-assisted Czochralski [74,80,94] and Bridgman [86] methods.

In a series of papers, Avetisov et al. [80,86,88,94–96] demonstrated that the Bridgman and Czochralski configurations significantly improved structural perfection of crystals (decrease of dislocation density, crystal mosaicity, and point-defect concentration) grown under AVC conditions compared to nonvibrational crystals. This is connected mostly with changes at the solid–liquid interface and nearby arising due to the vibrational influence. There are the changes of boundary layers thickness and temperature gradients values, as well as changes of the melt structure near the interface such as destruction of clusters, initiation of reconstructive processes, etc.

Crystal growth under axial vibration results in a substantial increase of the maximum allowable growth rate. It was shown [86] that the growth rate of $NaNO_3$ crystals grown by the Bridgman method under vibration of a submerged baffle with frequency 50 Hz and amplitude 0.2 mm could be increased from 2 mm/h to 10 mm/h without loss of crystal quality. Along with increasing of the vibration amplitude at fixed frequency (50 Hz), the dislocation density in $NaNO_3$ crystals grown by the AVC-assisted Bridgman technique decreased down to unit values (Figure 24.13(b)).

The AVC-grown crystals by the Czochralski method were characterized as dislocation free at pulling rates less than 10 mm/h and vibrational frequency higher than 10 Hz (Figure 24.13(a)). The reason for the significant decrease of dislocation density and substantial enhancement of growth rate along with maintenance of crystal quality could be attributed to a reduction of the diffusion layer thickness at the crystallization front and an increase in the diffusion rate, as well as to the influence of the vibrational force on heat and mass transfer at the interface and the influence on precrystallization phenomena, which stimulate the destruction of clusters in the liquid at the boundary layer. It should be noted that the latter behavior is more pronounced for strongly associated

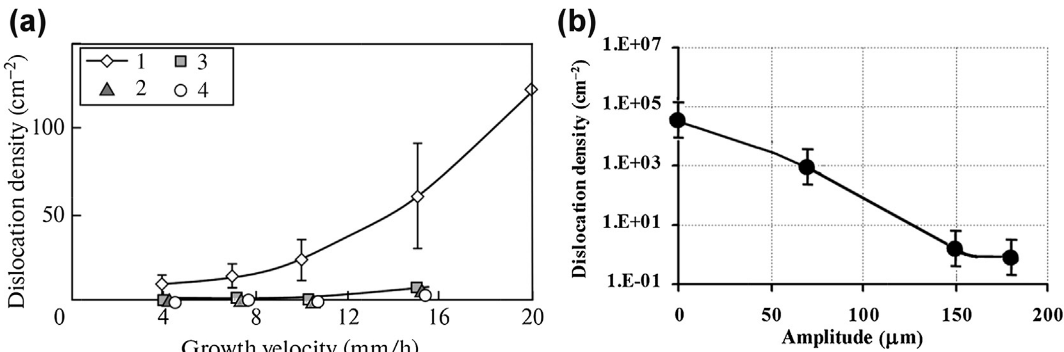

FIGURE 24.13 Dislocation density in $NaNO_3$ single crystals grown under vibration (a) by Czochralski method (type II) versus growth rate with amplitude 1 mm and different frequencies (1) 0; (2) 10 Hz; (3) 17 Hz; (4) 25 Hz. *(Adapted from Avetissov et al. [95].)* (b) by the Bridgman method versus amplitude at oscillation frequency 50 Hz *(Adapted from Avetissov et al. [86].)*.

melts of compounds with high ionicity, such as fluorides, oxides, silicates, and some A^2B^6 semiconductors.

Reducing of the diffusion layer together with destruction of clusters at the interface result in an increase of the diffusion speed of melt species and their easier incorporation into a growing crystal. This leads to enhancement of the growth rate and building of a more perfect crystal. An additional contribution to the decrease of the dislocation density could give the energy of vibration itself, which plays a role of external force stimulating the motion of dislocations and their further annihilation.

Improvements of the structural perfection of crystals grown under the AVC impact was confirmed for $NaNO_3$ by studies of the Raman spectra and measurements of X-ray rocking curves [80,95]. In the case of $Bi_{12}SiO_{20}$ crystals grown under low-frequency vibration by Zhang et al. [97], the extension of the short-wavelength spectral absorption edge and corresponding narrowing of X-ray rocking curves in a certain range of vibration amplitudes that appear also as evidence of improvement of crystal perfection was demonstrated.

There are many documentary pieces of evidence about melt clusterization, polymerization processes in the melts, and precrystallization phenomena (see, e.g., Refs [98–101]). Actually, the energy of motion of an oscillating body, together with induced heat and mass flows through their impact on boundary layers and bulk melts, could lead to structural reconstruction of melt, especially close to the crystallization front [78].

Direct measurements of the heat of crystallization of $NaNO_3$ and CdTe melts subjected to agitation by low-frequency vibration using the oscillating baffle submerged in the melt (AVC-assisted Bridgman configuration) demonstrated [96] up to a 30% increase compared to the melt without agitation. This can be explained as a real influence of low-frequency vibration on the microstructure of the melt. The calculation made by the authors of this paper led them to the conclusion that low-frequency vibration of the solid baffle can partially destroy the existing clusters in the melt, which is especially the case for the associated melts, such as oxide, silicate, and borate melts.

24.4.3 Application of AVC in Crystal Growth Methods

AVC can easily be adapted to many methods of crystal growth from a fluid medium (melt or solution). Application of AVC to different techniques of crystal growth from the melt was presented elsewhere [81,102]. By now, it is realized with regard to Czochralski, top-seeded solution growth, vertical Bridgman (VGF), zone melting, and floating zone methods, which will be discussed in more detail. The most comprehensive work has been done for AVC-assisted Czochralski (AVC-Cz) and Bridgman (AVC-Br) techniques. Accordingly, the majority of this section discusses these two important melt growth methods assisted with controlled vibrational influence.

Of particular interest is the use of controlled low-frequency vibration for crystal growth experiments in space. For acceleration magnitudes of 10^{-4} g and less, flows generated by controlled vibration can be used to suppress undesirable convective effects

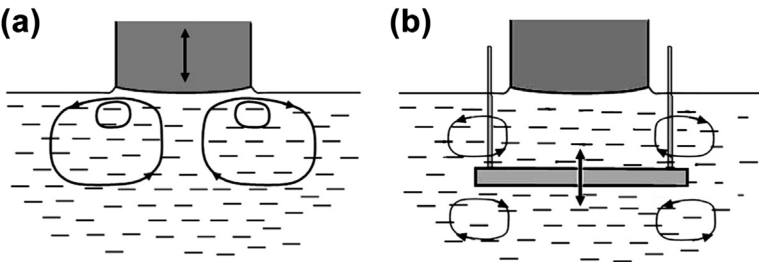

FIGURE 24.14 Vibrational flows in AVC-assisted Czochralski method. AVC-Cz type I: vibration of crystal (a). AVC-Cz type II: vibration of submerged baffle (b). *Adapted from Zharikov [102].*

caused by "g-jitter." The convective heat flow component caused by the controlled vibration can be of the same order of magnitude or larger than the conductive heat-transfer mode. The first experimental confirmation of AVC promise to control the fluid flows in space and create the new efficient technologies of crystal growth in microgravity was done on the Mir space station by Zharikov et al. [103].

AVC-assisted Czochralski I method. In the Czochralski configuration (type I), the crystal itself plays the role of a vibrating body, which is contacting the surface of melt and produces intensive vibrational flows in the bulk melt (Figure 24.14(a)). The advantage of this kind of vibrational impact, in comparison to other flow initiation strategies, is that it exerts a great influence on transport processes in immediate proximity to the solid–liquid interface. In Figure 24.15, the size of vibrational vortices and flow velocity for AVC-Cz (type I) are plotted versus the vibration amplitude. It is seen that the size of the vortex linearly depends on the vibration amplitude (Figure 24.15(a)). The average linear flow velocity in the vortex strongly increases along with the amplitude of vibration and also increases with the viscosity of the liquid (Figure 24.15(a)).

Experimental studies of interaction between vibrational and thermal convections in the Czochralski configuration showed that vibration could efficiently compete with the natural convection flows because the direction of melt motion in vibrational vortices is opposite to that of thermal convection. Along with an increase of the vibrational Reynolds number, the vortices of vibrational convection suppress the thermal convective flows and spread to the crucible wall, occupying more and more space until the whole volume of the crucible becomes occupied only by vibrational flow [61].

AVC flows allow efficient suppression of the temperature oscillations at the interface arising due to irregular thermogravitational convection flow [104]. As was shown by Avetisov et al. [80], the application of low-frequency vibration to the submerged disk in the Czochralski configuration type II (see Figure 24.14(b)) produces a decrease in the thermoconvectional fluctuations of temperature near the solid–liquid interface from 8 K for conventional Cz to 0.2 K.

The suppression of the thermal convective flows leads to smoothing of compositional fluctuations in doped crystals [84,90,91]. Experiments on AVC-assisted high-temperature Czochralski growth of yttrium-scandium-gallium garnet doped by erbium and

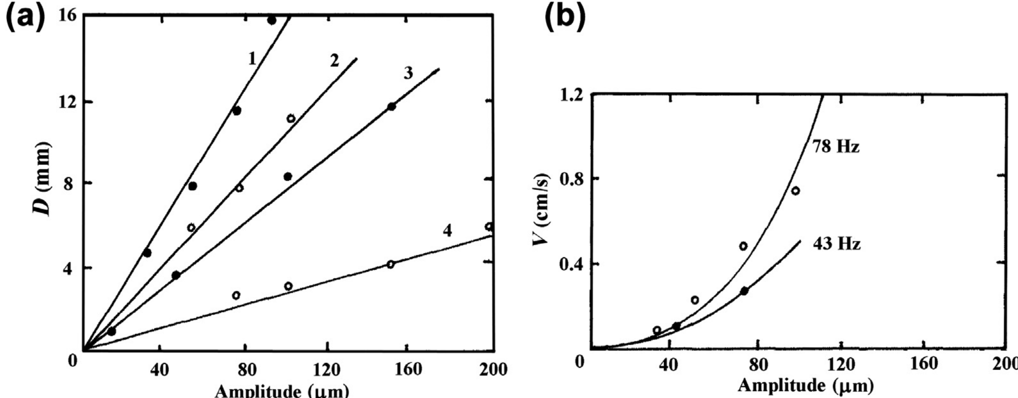

FIGURE 24.15 The size of vibrational vortices (a) and flow velocity (b) for AVC-Cz (type I) upon the vibration amplitude. *Adapted from Zharikov et al. [61].*

chromium ions Er,Cr:YSGG (melting point 1910 °C) showed [84] noticeable weakening of striations.

The simultaneous interplay of the vibration, thermal convection, and rotation for the Czochralski configuration was investigated by numerical calculations [92] for the case of opposite rotations of the crystal and the crucible. It was shown that interaction of these three factors leads to the appearance of flows with a complex structure consisting of two domains. For the particular parameters of calculations ($A = 100$ μm, $f = 50$ Hz, Gr = 214,610, Pr = 5.43), it was found that the flow structure in the external domain is caused by the thermal convection; in the internal domain, the flow pattern is formed by both the vibration and rotation. Conflict between the vibration and the rotation takes place. The preliminary results of these calculations suggest that this conflict could lead to homogeneity alterations of the temperature field. Further parametric investigation of this triple interaction is necessary to get a proper view of the complex phenomenon.

Intensive axial low-frequency vibration applied to a vibrating body in the Czochralski configuration produces not only bulk flow but also complex surface flow (Figure 24.16). It is polyharmonic motion that includes two different but closely related flows [106]. The first of these is a standing surface wave that expands from the vibrating crystal to the crucible wall. The other type of flow superimposed on this wave appears as large vortices, similar to cells—the dimension of which is several times greater than the length of the surface wave. In Figure 24.16(a), one can see only surface vertical cells; however, along with an increase of vibrational Reynolds number Re_V in addition to them, the standing surface wave appears (Figure 24.16(b)). The wavelength of the standing wave, the number of vibrational vortices, and the velocity of the liquid motion in them are controlled by the vibration parameters (see Figure 24.16(c)). For instance, in the case presented in Figure 24.16(b), the number of surface vortices is eight and the velocity of surface flow $V = 2.2$ cm/s.

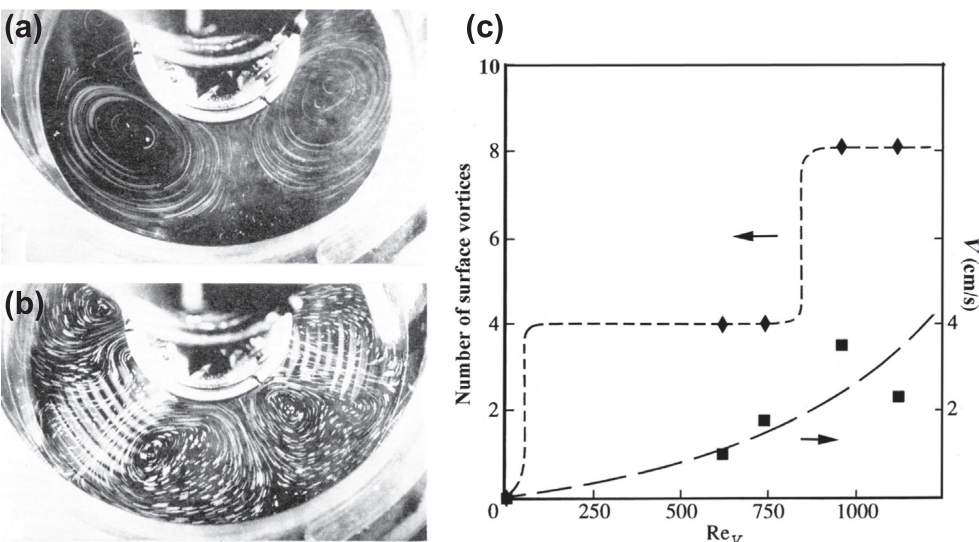

FIGURE 24.16 Surface flows in Czochralski configuration under vibration of crystal (AVC-Cz type I). *Left:* (a) and (b) change of flow pattern as a function of vibrational Reynolds number. *Right:* (c) number of surface vortices (rhombohedra) and flow velocity depending on vibrational Reynolds number. *From Verezub et al. [105].*

The surface vortices could be involved in a slow motion around the crucible axis in a ring gap between the vibrating crystal and the crucible wall. An additional effect produces the crucible rotation, which creates a shearing perturbation. This leads to a reduction of a number of surface vortices by their association into pairs [105].

The numerical calculations of interaction between the low-frequency vibration ($A = 100$ μm, $f = 50$ Hz) and the Marangoni convection (Mn = 500) showed [92] that the vibration allows one to weaken the influence of the thermocapillary Marangoni convection in Czochralski crystal growth. The vibration makes the temperature distribution at the free surface more homogeneous, reducing the thermal gradients along the melt surface. The growth of crystals in low-temperature gradients is preferable because it results in a better quality; in addition, it was already successfully demonstrated, for instance, in the case of sapphire growth by Kyropoulos and HEM (Heat Exchanger Method) or, in the case of BGO crystals, grown by a low-thermal gradient Czochralski technique (for a review, see Ref. [102]). On the other hand, if it is necessary to increase the radial gradients in the system for some reason, it can be done by well-known regular technological measures, holding the neutralization of the surface-tension-driven flow by forced surface vibrational flow.

The action of thermocapillary convection on crystal growth processes is generally considered to be undesirable. It significantly affects the crystal growth for the free-surface fluids, especially in reduced-gravity environments. However, even under normal gravity, the thermocapillary effect can be very important in the overall transport pattern. It is more pronounced for high Prandtl fluids, such as oxide melts; however, the

results indicate (e.g., Ref. [107]) that also in low-Pr melts, the thermocapillary impact is important and may significantly affect the quality of the crystal by influencing the turbulent transport of heat and mass near the growing crystal. Thermocapillary convection is shown [108] to have an influence on various solidification parameters, such as the shape of the solid–liquid interface and the solute segregation. It was demonstrated for both Czochralski and float zone processes that thermocapillary convection becomes unstable (oscillatory) at high enough Marangoni numbers, which gives rise to temperature oscillation in the melt [109,110], thus generating impurity striations in growing crystal. Therefore, it is necessary to take into consideration a contribution of Marangoni tension in directional solidification processes [111]. A review of various numerical and experimental studies of the surface-tension-driven flow in crystal growth melts can be found in Refs [112,113].

The action of thermocapillary convection on crystal growth and the transition to unsteady behavior is hard to control [114]. In particular, the observations of Azami et al. [115] indicate that the surface flow, and its instability pattern, of the CZ melt cannot be fully suppressed by a magnetic field. Hence, the phenomenon of the complex surface flow formation due to axial low-frequency vibration gives a unique opportunity to control/compensate for undesirable surface flows caused by both thermocapillary and thermoconcentration Marangoni convections [106].

AVC-assisted Czochralski-II method. Another scheme of AVC introduction in the Czochralski configuration has been proposed [95]. According to this scheme, the forced flows in the melt are generated by axial oscillations of a disk submerged under the crystal (see Figure 24.14). The vibrational flows are directed from the disc toward the crystal and the bottom of crucible. In the area between the disc and crystal, the direction of forced vibroconvective flows is opposite to the direction of thermoconvection flows and facilitates melt mixing in the entire volume of the crucible.

The experiments carried out according to the new version of AVC-assisted Czochralski were performed by growth of $NaNO_3$ crystals and $NaNO_3$-$LiNO_3$ solid solutions, as well as by physical modeling using water–glycerin mixtures with viscosities from 1 to 100 cP [80,87,93–95,116]. It was found that this new scheme allows stable symmetrical vibrational bulk flows to be obtained within the entire range of viscosities.

The vibrating disk is fabricated from the same inert material as the crucible. For instance, in physical modeling experiments with water–glycerin solutions, the quartz glass was used for both disk and crucible fabrication. The same material was used during the growth of nitrate crystals of different compositions. For growth of larger $NaNO_3$ and $NaNO_3$-$LiNO_3$ crystals from 1000-cm^3 crucibles, the disk was fabricated from alumina, which made it possible to prepare more sophisticated baffle configurations [116].

AVC-assisted Bridgman method. The insertion of a submerged body, which is located in the melt near the solid–liquid interface and subjected to low-frequency vibration, induces macroscopic vibrational convection flows, as in the Czochralski case

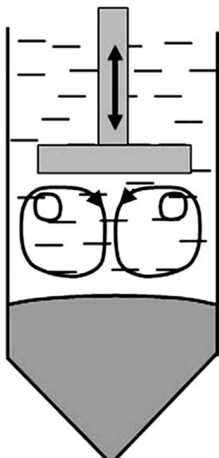

FIGURE 24.17 Vibrational flows in AVC-assisted Bridgman/VGF method. *Adapted from Zharikov [102].*

(Figure 24.17). For growth of PbTe [85] and CdTe [89] by the Bridgman technique from evacuated closed ampoules, the specific unit for the excitation of low-frequency vibration was constructed [88]. It contains a system of external permanent magnets, providing a free suspension of the internal permanent magnet as well as the electromagnet, which provided vibrations of the latter magnet with a specified frequency and amplitude. In this case, both the reactor and baffle were made from graphite.

Flow from the vibrating baffle down to a crystal causes efficient stirring in the melt, produces a displacement of the crystal–melt interface, and changes its shape. Manipulation of the amplitude–frequency input can be used to obtain a practically flat crystal–melt interface.

Numerical simulation of CdTe growth by the axial vibration control technique in the Bridgman configuration [89] showed that switching on the disk oscillation causes an increase in the temperature gradient between the disk and the crystal–melt interface. The flow velocity also increases by one order of magnitude compared to the non-vibrating regime.

Physical modeling on water–glycerin mixtures showed [117] that an increase of the vibrational intensity (Re_V) as well as the diameter of the vibrating disk resulted in more intensive vibrational flow. The change in diameter of the vibrating baffle considerably altered the flow pattern in the melt [118]. The normalized difference between the cross-sectional area of the ampoule and the cross-sectional area of the vibrator is used as a geometrical parameter:

$$S_k = \frac{D^2}{d^2} - 1 \tag{24.13}$$

where D is the internal diameter of the ampoule and d is the diameter of the vibrating body.

The application of vibrating disks of different shapes in the AVC-assisted Bridgman method have been investigated by physical modeling of transparent model liquids [117] and by numerical simulation [89]. In the case of vibration of the whole ampoule in the Bridgman method, the mechanism of the resultant vibrational convection differs from vibration of a body with sharp edges in a fluid. The closed-ampoule translational vibration under isothermal conditions does not result in any flow. The liquid in this case behaves as a rigid body. The vibrations of an ampoule with a free liquid surface can produce rather intensive flows, but usually they are limited by the surface and cannot exert much influence directly on the crystallization front.

In the presence of an axial temperature gradient when the fluid density is nonuniform, fluid motion known as thermovibrational convection may ensue. However, the magnitude of this motion strongly depends on the orientation of the vibrational direction with respect to the local density gradients. Fedoseyev and Alexander [119] showed that the inclined oriented direction of vibration in relation to the ampoule axis enhances the intensity of convection flows. It was shown that axial vibration of the ampoule is the least efficient and the maximum observed effect corresponds to an angle of 90°.

Several papers discuss low-frequency vibration axially applied to the ampoule in vertical Bridgman growth [62,97,120,121]. No notable effect of vibration on microstructure, compositional profile, interface shape, etc. was found by Caram et al. [121] or Yuan et al. [62] for such a configuration of experiment. Feigelson and Borshchevsky [120], who grew CdTe crystals, and Zhang et al. [97], who studied the growth of $Bi_{12}SiO_{20}$, have shown that low-frequency axial vibration applied to the growth ampoule could produce a perceptible effect. These papers demonstrated the improvement of crystal perfection by a decrease in dislocation density [120] and by control of X-ray rocking curves and short-wavelength spectral absorption edge of the grown crystals [97].

AVC-assisted floating zone method. The controlled vibration induces a flow that streams away from the vibrating end wall along the zone surface, returning through the bulk [122]. Because this flow has a direction opposite to the adjacent thermocapillary flow in the floating zone, it can compensate for this undesirable convection. As a result, the vibration end of the solid–liquid interface becomes flatter, indicating the presence of more uniform axial temperature gradients and flat isotherms near the interface.

Several authors have investigated the use of axial vibration in the floating zone method by experimental studies and by numerical simulation [79,122–125]. It was found that vibration produced a notable influence on the heat transport and on the interface curvature. Grugel et al. [123] and Shen et al. [122] observed a flattening of the interface accompanied by a reduction of radial temperature gradients, as well as a change in the eutectic microstructure of $NaNO_3$-$Ba(NO_3)_2$ upon application of the vibration.

AVC-assisted zone melting method. Oscillations in this method were applied to the ampoule (container) in both the vertical [64] and horizontal [126] versions. The mechanisms of initiation and development of vibrational flow in this method are more complicated than in the case of ampoule vibration in the Bridgman method or in the case

of the AVC-assisted floating zone method due to the larger number of boundaries where the density is changing, which may create the complicated interplay of the forced flows. In the horizontal version, an additional contribution makes the free surface of liquid.

Experiments on the growth of $NaNO_3$ crystals by a horizontal zone melting process [126] showed that vibration considerably suppresses the temperature oscillations in the melt and allows the shape of the solid–liquid interface to be governed and made flatter. Strutynska [64] found that vibration significantly affected the hydrodynamics, heat and mass transfer, the distribution of impurities, and kinetics of growth of the investigated Bi_2Te_3-based thermoelectric materials. Owing to the vibration effect on the melt, the distribution of impurities becomes more uniform, and the radial and axial homogeneities of materials are increased. According to measurements, the material homogeneity with regard to Seebeck coefficient improved by a factor of 2—and in respect to electric conductivity, by a factor of 3.

The effects of axial vibration on the heat flow, the growth rate, and the interface shapes have been studied numerically for vertical zone melting [65]. It was found that the low-frequency axial vibration can be effective for the control of melt flows and the growth interface. Nevertheless, to prevent crystal growth from periodic remelting, the author recommends frequencies higher than 10 Hz.

24.4.4 Crystal Materials Grown by the AVC Technique

Up to now the AVC-assisted crystal growth by Czochralski method has been realized for $NaNO_3$, $NaNO_3$–$LiNO_3$ solid-solutions [61,95], and some complex oxides with garnet structure (particularly Er,Cr:$Y_3Sc_2Ga_3O_{12}$), as discussed above. Pankrath et al. [127] reported the successful growth of $K(Ta_{1-x}Nb_x)O_3$ solid solutions with composition $0.30 < x < 1$, by applying the AVC technique with a vibration frequency of 50 Hz and an amplitude of 0.5 mm to the Czochralski configuration using the top-seed-solution growth method. These vibration parameters were considered optimal, allowing the striation-free $K(Ta_{1-x}Nb_x)O_3$ samples to be obtained.

AVC-assisted crystal growth by the Bridgman method has been realized for both low melting point and high melting point dielectric and semiconductor materials [86,88,97,128,129]. In particular, the AVC-Br technique was adapted for growth of $NaNO_3$, AgBr, AgBrCl, $Bi_{12}SiO_{20}$, PbTe, and CdTe crystals and the corresponding equipment for crystal growth was fabricated, including an AVC-assisted computer-controlled transparent furnace for growth of low melting point compounds [128] and a high-temperature sealed furnace for crystallization of decomposing materials [88].

Crystal growth of Bi_2Te_3-Bi_2Se_3 and Bi_2Te_3-Sb_2Te_3 solid solutions by an AVC-assisted vertical zone melting technique has been reported [64]. It was shown that vibration of the ampoule during the growth contributes to leveling of the crystallization front and mixing of melt components. Owing to the vibration effect on the melt, the distribution of impurities became more uniform, and the radial and axial homogeneities of materials were increased.

24.5 Other Types of Oscillatory Techniques

24.5.1 Ultrasonic Vibration

Imaging of convection in a Czochralski configuration under ultrasound waves was studied in model liquids using the crystallizing naphthalene–camphor eutectics [130], water–glycerol mixture [131] and distilled water [132]. In one study [133], water–glycerol mixture and acetone were using as model liquids. Ultrasound was introduced into the model liquid from a piezotransducer through a waveguide from the top [130] or to the crucible bottom [132–134]. When the melt agitation was organized from the top, the initiated acoustic flows were directed downwards from the vibrating surface. With bottom insertion of ultrasound, an upward flow formed in the liquid from the center of the crucible bottom toward the crystal model has been found. Hayakawa et al. [134] introduced ultrasonic vibrations (USV) of 10 kHz and 60 W. The velocity of flows caused by ultrasonic vibration was very high compared with that of both the forced and thermal convections due to rotation and buoyancy, respectively. According to Ref. [134], because the ultrasonic vibrations have a thermal effect, they can reduce the region of a supercooled melt. As a result, the shift and reduction of the facet region occurs under the ultrasonic vibrations.

Kozhemyakin and coworkers [132,133] used the higher-energy ultrasound with frequencies in the MHz range with an ultrasound intensity up to 0.3 W/cm^2, which was smaller than the cavitation threshold. They found that instead of the fluid flow, the standing wave forms after a few seconds in the central part of the bulk liquid by the diameter of waveguide between the crucible bottom and the solid–liquid interface. The distances between the standing wave antinodes were around 1 mm, which corresponded to half the wavelength of the ultrasound. They prevented the motion of convective flows in the region of standing waves. At the same time, in the periphery of the liquid, stable rotating vortices exist that stir the peripheral area of liquid. As a result, nonuniform heat and mass transfer conditions form in the melt.

In the regime of an ultrasonic standing wave, the heat sources are localized in an area of maximal shift and they are periodically distributed along the axis of the ultrasound resonator. The crystal growth rate will be modulated, which leads to the formation of striations in the crystal with a space period equal to half the wavelength of the ultrasound. According to Ref. [135], the striations in the central part of $Ga_{0.03}In_{0.97}Sb$ single crystals vanish when ultrasound at a frequency in the MHz range is applied.

A number of studies were concerned with the influence of ultrasound on the distribution of doping impurities in the crystal growth of compound semiconductors, dielectrics, and on the crystallization of various metallic alloys [131,136–139]. A reduction of the diffusion layer thickness, enhancement of the temperature gradient at the interface, and intensification of the zone refinement purification was found by Abramov et al. [140] when ultrasound (frequency 19.7 kHz, power up to 60 W) was applied to naphthalene growth by zone melting.

Numerical calculation of the influence of ultrasonics on the VGF process applied centrally from the topside of the crucible [141] demonstrated that using an ultrasonic frequency of 581 kHz produces Schlichting flow inside the hydrodynamic boundary layer, which helps to remove the harmful diffusion boundary layer, for instance, as the authors underlined, during directional solidification of silicon ingots for photovoltaics. The use of USV in the VGF growth of germanium crystals in addition to a double-frequency traveling magnetic field [142] showed the increase of the melt mixing within the diffusion boundary layer by intense Schlichting curling. As a result, the morphological interface stability can be enhanced and the axial carrier distribution approached the theoretical curve of complete melt mixing.

A novel approach to application of ultrasound to the Czochralski growth system has been proposed by Kozhemyakin [143]. In addition to ultrasonic waves introduced in parallel to the pulling axis from the crucible bottom, ultrasound with another frequency was entered into the melt perpendicular to the growth direction under the solid–liquid interface from the sidewall of the crucible. The author emphasizes that all previous experiments with axially directed ultrasonic waves were unsuccessful in getting striation-free single crystals. On the contrary, with the introduction of ultrasound in two orthogonal directions at frequencies differing by factor of 2 (0.71 MHz parallel and 1.44 MHz perpendicular to the pulling axis), the striations in grown InSb crystals with a convex solid–liquid interface were totally eliminated.

A few papers have been published on the influence of ultrasound on bubble entrapment by the growing crystals and their optical quality [142,144]. Vyshnevskiy et al. [139] investigated the bubble formation in sapphire and Ti:sapphire crystals grown by Czochralski in an ultrasonic field. It was found that the effect of ultrasound on the bubble entrapment from the melt by the growing crystal depends on the ultrasonic frequency. The reduction of the rate of bubble entrapment by the growing crystal by a factor of 2–2.5 was achieved by using ultrasound with frequency 350–400 kHz.

24.5.2 Coupled Vibrational Stirring

Liu et al. [145] developed a method for rapidly stirring liquids called coupled vibrational stirring (CVS), which appeared to be useful in crystal growth applications; in particular, it could be applied to the vertical Bridgman growth. CVS involves the application of orthogonally coupled low-frequency vibrations to the growth ampoule in the x–y plane and produces strong flows emanating from the free fluid surface. Because CVS flows are generated at the free surface of the liquid and propagate downward, a velocity gradient develops, with the fastest flows near the surface. Both the velocity profile and the depth of flows are highly dependent on fluid viscosity, vibrational frequency, and crucible diameter [146].

The CVS technique was applied to several real crystal growth systems. In the transparent $CsCdCl_3$ Bridgman melt system [145], the solid–liquid interface position was found to be a function of the vibrational frequency. Liu et al. [147] showed that

CVS-induced flows improved the initial grain selection and chemical homogeneity of Bridgman-grown CdTe crystals, but with some degradation in crystalline quality. DeMattei and Feigelson [148] examined the effects of CVS on temperature profiles during the growth of $PbBr_2$. The application of CVS flattened the temperature gradient in the melt; however, at the same time, the temperature gradient at the interface was dramatically increased as a result of CVS flows.

Feigelson and Zharikov [149] and Zawilski et al. [150] used three different systems to investigate the impact of CVS-generated flows in a Bridgman growth environment. In addition to water/glycerin solutions, which were used as a physical modeling system to study fluid flow, CVS was applied to two growth systems—namely, sodium nitrate ($NaNO_3$) and lead magnesium niobate–lead titanate (PMNT) with the general formula $(1-x)$ $PbMg_{1/3}Nb_{2/3}O_3$—$x PbTiO_3$. Zawilski et al. [150] showed that the crystal–melt interface position is a function of vibrational frequency and a continuous frequency ramp is necessary to reduce the growth rate fluctuations. CVS was found to be useful in manipulating the growth interface shape of $NaNO_3$ at high growth rates. A flatter interface curvature was obtained at high growth rates (>10 mm/h) in the presence of CVS flows. In the PMNT system, the use of a continuous vibrational frequency ramp during growth was shown to produce improved growth control.

24.6 Conclusions and Outlook

This chapter has described several nonsteady mechanical means of stirring melts to influence the growth of crystals of various types. The two main themes have been forced stirring by the accelerated crucible rotation technique and various forms of vibrational control, and the theoretical bases of these two types of stirring have been outlined, as summarized in Table 24.4. In the former case of stirring by ACRT, major improvements in compositional uniformity, compositional ranging, size of crystals produced, segregation of both matrix and impurity elements, grain size, and overall crystal quality are seen in the important II–VI compounds of cadmium mercury telluride and cadmium zinc telluride used in infrared detectors and optical components and in epitaxial substrates, respectively. More recently, ACRT has also been applied to a range of elemental (e.g., silicon) and compound materials (e.g., silicon carbide, Ag_3AsS_3, langasite ($La_3Ga_5SiO_{14}$), and Sb-based quaternaries), with improved properties seen in the majority of cases.

Another technique of mass-transfer control in crystal growth is axial vibrational control, which uses the introduction of low-frequency and small-amplitude axial vibration into liquid phase either by a submerged inert solid body or by the crystal itself. AVC produces a specific type of stationary flow in the fluid that results in a number of positive effects in crystal growth and affords improved crystal perfection. AVC-assisted melt crystal growth has now been realized in several growth techniques and for a number of oxides, salts, and semiconductors. AVC has not as yet been as broadly or industrially applied as ACRT. Nevertheless, the low-frequency axial vibration technique

Table 24.4 Crystals Grown by Oscillatory Techniques (Exemplary, Not Exhaustive)

Crystal	Growth Technique	Oscillatory Technique	Oscillation Parameters	Effect on Crystal Quality and Properties	References
CMT	Vertical Bridgman	ACRT	Various depending on crystal diameter	Improved radial and axial compositional uniformity, reduced number of grains, improved segregation of impurities	[33,34]
CMT	THM	ACRT	Various	Increased growth rates	[41]
CdTe	THM	ACRT	Various	Increased growth rates	[42]
CZT	Vertical Bridgman	ACRT	Various depending on crystal diameter	Reduction in number of grains, improved segregation of Zn, reduced Te precipitates, reduced strain and etch pit densities	[43]
CZT	Vertical Bridgman	ACRT	Added seeding	Reduction in number of grains, improved segregation of Zn, reduced etch pit densities	[44]
mc-Si	DS	ACRT	Induced striations for monitoring purposes	Improved segregation of C, reduced precipitates	[47,48]
mc-Si	DS	ACRT	Used 1 rpm and 600 s Ekman time	Improved radial distribution of impurities	[49]
Si	FZ	ACRT		Improved diameter control	[50,51]
SiC	Solvent growth	ACRT		Higher growth rates	[52]
SiC	Top-seeded solution growth	ACRT		Enabled polytype selection	[53]
Ag_2AsS_3		ACRT	20–60 rpm	Improved crystal quality	[54]
Succinonitrile		ACRT		Reduced constitutional supercooling and hence morphological instabilities	[55]
$La_3Ga_5SiO_{14}$		ACRT	0–25 rpm	Reduced unwanted phases	[57]
Sb-based quaternaries	Vertical Bridgman	ACRT	Various depending on crystal diameter	Improved growth rates and reduced crystal cracking	[58,59]
KCl NaCl LiF	Czochralski	AVC-Cz I	$f = 2$–20 Hz	• Faceting of lateral surface of crystals in accordance with crystallography direction (roughly square or rectangular shape)	[66]

$CsCdCl_3$	Vertical Bridgman	CVS	$f = 0.8–5$ Hz	• Interface position shifting downward with increased frequency • Small influence on interface shape	[145]
AgClBr AgBrI doped by Tl AgClBrI doped by Tl	Vertical Bridgman	AVC-Br	$f = 15–100$ Hz $A \leq 1.5$ mm	• Control of interface shape • Improved crystal quality	[151]
$PbBr_2$ doped by Ag	Vertical Bridgman, VGF	CVS	$f = 7.1$ Hz	• Increase of growth rate	[148]
$NaNO_3$	Czochralski	AVC-Cz I AVC-Cz II	$f = 10–200$ Hz $A = 0.01–1.0$ mm	• Control of interface shape • Reduction of dopant striation • Improved structural uniformity	[77,94]
	Vertical Bridgman	AVC-Br	$f = 10–100$ Hz $A = 75$ μm–1.2 mm	• Strong reduction in dislocation density • Flattening the interface shape control the impurity distribution	[152]
	Vertical Bridgman	CVS	$f = 5.5–6.3$ Hz	• Interface position change with increased frequency	[146]
$NaNO_3$—18 wt% $Ba(NO_3)_2$ Eutectics	Floating zone	Vibration of one of the supporting end-walls	$f = 1.0–1.5$ kHz $A = 10–20$ μm	• Elimination of radial temperature gradients • Suppression of thermocapillary convection • Flattening interface • Improved structural uniformity	[122]
Ge	Czochralski	AVC-Cz I	$f = 2–20$ Hz	• Faceting of lateral surface of crystals in accordance with crystallography direction (roughly square or rectangular shape)	[66]
	Vertical Bridgman	Container vibration	$f = 0.5–200$ Hz $A \leq 5 \times 10^{-1} g_o$	• No effect registered	[153]
	VGF	USV applied axially from the top	f (in the kHz-MHz range)	• Enhanced morphological interface stability • Improved axial carrier distribution	[142]
Si doped by Sb ($2 \times 10^{18}/cm^3$)	Floating zone under microgravity (Maxus-4 flight)	Vibration of one of the supporting end-walls	$f = 3.95$ kHz $A = 1.1$ μm	• Reduction of dopant striation • Interface flattening	[154]

Continued

Table 24.4 Crystals Grown by Oscillatory Techniques (Exemplary, Not Exhaustive)—cont'd

Crystal	Growth Technique	Oscillatory Technique	Oscillation Parameters	Effect on Crystal Quality and Properties	References
GaAs	Vertical Bridgman	Container vibration	$f = 100$ Hz	• Improved crystallinity	[155]
	Czochralski (LEC)	USV applied axially from the crucible bottom	$f = 150$ kHz	• Reduced striation • Improved As distribution	[138]
InSb: Te	Czochralski	AVC-Cz I	$f = 50$ Hz	• Improved crystallinity	[70]
	Czochralski	USV applied axially from the crucible bottom	$f = 10$ kHz P = 150 W	• Improved dopant distribution • Elimination of facet regions	[156]
	Czochralski	USV applied axially from the crucible bottom	$f = 0.15$–10 MHz	• Reduced striations	[138]
	Czochralski	USV applied in two orthogonal directions: parallel and perpendicular to pulling axis	$f_1 = 0.71$ MHz (parallel to pulling axis from crucible bottom) $f_2 = 1.25$; 1.44 and 2.0 MHz (perpendicular to pulling axis from crucible sidewall)	• Striation-free crystals (with 1.44 MHz US perpendicular to pulling axis)	[143]
InSb–GaSb	Czochralski	AVC-Cz I	$f = 100$ Hz $A = 0.1$–0.14 mm	• Improved homogeneity • Enhanced by several times growth rate	[68]
	Czochralski	USV applied axially from the crucible bottom	$f = 10$ kHz P = 150 W	• Improved crystallinity (increased with increase USV output power)	[157]
	Czochralski	USV applied axially from the crucible bottom	$f = 0.69$–1.44 MHz	• Significant decrease of striation • Increase of carrier mobility more than 40%	[158]
	Vertical Bridgman	Container vibration	$f = 20$ Hz $A = 0.5$ mm	• Small change of interface shape • No radial composition variation observed	[62]
CdTe	Vertical zone melting	Container vibration	$f = 0.3$–3.5 Hz $A = 2$–5 mm	• Reduced number of grains • Growth of large single crystals	[157]

	Vertical Bridgman	Container vibration	$f < 1000$ Hz A < 0.1 mm	• Reduced dislocation density	[120]
	Vertical Bridgman	CVS	$f = 5.5$ Hz E = 3.2 mm $T_m = 8$ s	• Improved grain structure • More uniform free carrier	[147]
	Vertical Bridgman	AVC-Br	$f \leq 150$ Hz $A = 0.02$–1.0 mm	• Maintenance of constant nonstoichiometry along the crystal	[89]
Bi-Sb (5 at%)	Czochralski	USV applied axially from the crucible bottom	$f = 0.15$–10 MHz	• Reduced striations	[138]
Bi_2Te_3–Bi_2Se_3 Bi_2Te_3–Sb_2Se_3	Zone melting	Container vibration	$f = 50$–100 Hz $A = 100$–150 μm	• Improved radial and axial homogeneity	[64]
Al_2O_3 Al_2O_3 doped by Ti^{3+} (0.07 wt%)	Czochralski	USV applied axially from the crucible bottom	$f = 100$–400 kHz $P = (2–5) \times 10^4$ Pa $I = (0.5–2.0) \times 10^{-2}$ W/cm^2	• Reducing the pores density in crystal by factor 2–2.5 due to bubbles rejection from growth interface	[139]
$(1-x)$ $PbMg_{1/3}Nb_{2/3}$—x $PbTiO_3$ (PMNT)	Vertical Bridgman	CVS	$f = 6.3$ Hz Gradually decreased	• No improvement of crystal quality	[150]
$K(Ta_{1-x}Nb_x)O_3)$ $0.30 \leq x \leq 1$	TSGG	AVC-Cz I	$f = 50$ Hz $A = 0.3$ mm	• Striation-free crystals	[127]
$Y_3Sc_2Ga_3O_{12}$:Er,Cr	Czochralski	AVC-Cz I	$f = 50$ Hz $A = 17$–35 μm	• Controlled alteration of interface shape • 2-fold reduced striation	[84]
$B_{12}SiO_{20}$	Vertical Bridgman	Container vibration	$f = 50$ Hz $A = 50$–100 μm	• 2-fold decrease in dislocation density • 10% increase of optical transmission	[159]

Notes: A is amplitude of vibration, ACRT is accelerated crucible rotation technique, AVC is axial vibrational control technique, Br is Bridgman technique, Cz is Czochralski technique, CVS is coupled vibrational stirring technique, DS is directed solidification, E is axial eccentricity, f is frequency of vibration, FZ is floating zone method, I is intensity of ultrasound, LEC is liquid encapsulated Czochralski technique, LF is low frequency, mc is multicrystalline, P is acoustic pressure, T_m is total mixing time, THM is traveling heater method, TSGG is top-seeded solution growth technique, USV is ultrasonic vibration, VGF is vertical gradient freeze technique.

and the AVC-assisted melt growth are challenging new ways to grow high-quality crystals.

Two additional oscillatory techniques were described in this chapter more briefly: coupled vibrational stirring and ultrasonic action on melt crystal growth. CVS was applied to the vertical Bridgman growth of several different compounds and found to be useful in producing efficient stirring of fluids, as well as manipulating the temperature gradients in the melt and growth interface shape. The application of ultrasonic vibrations to crystallization processes demonstrates a large variety of different effects, and this has been studied for many years. New findings on the ultrasonic influence of melt crystal growth promise the efficiency of its application to improve the crystal perfection, especially by elimination of growth striations.

References

[1] Capper P, editor. Bulk crystal growth of electronic, optical and optoelectronic materials. Chichester: Wiley; 2005.

[2] Scheel HJ, Capper P, editors. Crystal growth technology. Weinheim: Wiley-VCH; 2008.

[3] Capper P, Rudolph P, editors. Crystal growth technology. Weinheim: Wiley-VCH; 2010.

[4] Rudolph P, Kakimoto K. Mater Res Soc Bull 2009;34:1.

[5] Rosenberger F. Fundamentals of crystal growth I. macroscopic equilibrium and transport concepts. New York: Springer Verlag, Berlin, Heidelberg; 1979.

[6] Hurle DTJ, Rudolph P. J Cryst Growth 2004;264:550.

[7] Haddad FZ, Garandet JP, Henry D, Ben Hadid H. J Cryst Growth 1999;204:213.

[8] Hurle DTJ, Jakeman EJ. Cryst Growth 1969;5:227.

[9] Rossby C-G. J Fluid Mech 1969;36(2):309.

[10] Scheel HJ. J Cryst Growth 2006;287:214.

[11] Duffar T. In: Capper P, editor. Bulk crystal growth of electronic, optical and optoelectronic materials. Chichester: Wiley; 2005 [chapter 17].

[12] Regel LL, Wilcox WR. Processing by centrifugation. Germany: Springer, Heidelberg; 2001.

[13] Eidelman LG, Goriletsky VI, Nemenov VA, Protsenko VG, Radkevich AV. Cryst Res Technol 1985;20:167.

[14] Ostrogorsky AG, Muller G. J Cryst Growth 1994;137:64.

[15] Dutta PS, Ostrogorsky AG. J Cryst Growth 1998;194:1.

[16] Dropka N, Miller W, Rehse U, Rudolph P, Büllesfeld F, Sahr U, et al. J Cryst Growth 2011;318:275.

[17] Cramer A, Eckert S, Galindo V, Gerbeth G, Willers B, Witke W. J Mater Sci 2004;39(24):7285.

[18] Dumitrica S, Vizman D, Garandet J-P, Popescu A. J Cryst Growth 2012;360:76.

[19] Kokh AE, Kononova NG. Solid State Electron 2000;44:819.

[20] Kokh AE, Kononova NG, Bekker TB, Vlezko VA, Mokrushnikov PV, Popov VN. Crystallogr Rep 2005;50:160 [translated from Kristallografiya 50 (2005) 169].

[21] Kokh AE, Vlezko V, Kokh K, Kononova N, Villeval Ph, Lupinski D. J Cryst Growth 2012;360:158.

[22] Kokh KA, Popov VN, Kokh AE, Krasin BA, Nepomnyaschikh AI. J Cryst Growth 2007;303:253.

[23] Capper P. Prog Cryst Growth Charact 1994;28:1.

[24] Scheel HJ. J Cryst Growth 1972;13/14:560.

[25] Capper P, Gosney JJG. UK Patent 8 115 911 May, 1981.

[26] Capper P, Gosney JJG, Jones CL, Pearce EJ. J Electron Mater 1986;15:361.

[27] Capper P, Gosney JJG, Jones CL, Kenworthy I. J Electron Mater 1986;15:371.

[28] Brice JC, Capper P, Jones CL, Gosney JJG. Prog Cryst Growth Charact 1986;13:197.

[29] Capper P. Prog Cryst Growth Charact 1989;19:259.

[30] Capper P, Brice JC, Jones CL, Coates WG, Gosney JJG, Ard CK, Kenworthy I. J Cryst Growth 1988; 89:171.

[31] Capper P, Coates WGC, Jones CL, Gosney JJG, Kenworthy I, Ard CK. J Cryst Growth 1990;102:858.

[32] Capper P, Maxey CD, Butler C, Grist M, Price J. J Cryst Growth 2005;275:259.

[33] Capper P. In: Kasap S, Capper P, editors. Handbook of electronic and optoelectronic materials. Springer, Heidelberg; 2006. p. 303.

[34] Coates WGC, Capper P, Jones CL, Gosney JJG, Ard CK, Kenworthy I, Clark A. J Cryst Growth 1989; 94:959.

[35] Capper P, Harris JE, Nicholson D, Cole D. J Cryst Growth 1979;46:575.

[36] Yu T-C, Brebrick RF. Properties of narrow gap cadmium-based compounds. In: Capper P, editor. EMIS datareview series No. 10. London: IEE; 1994. p. 55.

[37] Capper P, Maxey CD, Butler C, Grist M, Price J. J Mater Sci Mater Electron 2004;15:721.

[38] Gray RT, Larrousse MF, Wilcox WR. J Cryst Growth 1988;92:530.

[39] Liu X, Jie W, Zhou Y. J Cryst Growth 2000;209:751.

[40] Jie W. J Cryst Growth 2000;219:379.

[41] Bloedner RU, Gille P. J Cryst Growth 1993;130:181.

[42] Wald FV, Bell RO. J Cryst Growth 1975;30:29.

[43] Capper P, Harris JE, O'Keefe E, Jones CL, Ard CK, Mackett P, et al. Mater Sci Eng 1993;B16:29.

[44] Wang T, Jie W, Zhang J, Yang G, Zeng D, Xu Y, et al. J Cryst Growth 2007;304:313.

[45] Wang T, Jie W, Xu Y, Zha G-q, Fu L. Trans Nonferrous Met Soc China 2009;19:s622.

[46] Jie W, Li Y, Liu X. J Cryst Growth 1999;205:510.

[47] Bairava Ganesh R, Matsuo H, Kangawa Y, Arafune K, Ohshita Y, Yamaguchi M, et al. Cryst Growth Des 2008;8:2525.

[48] Bairava Ganesh R, Matsuo H, Kawamura T, Kangawa Y, Arafune K, Ohshita Y, et al. J Cryst Growth 2008;310:2697.

[49] Belleman MP, Meese EA, Arnberg L. J Cryst Growth 2011;318:239.

[50] Altmannshofer L, Grundner M Virbulis J. Patent DE 10137856, 2001.

[51] Altmannshofer L, Grundner M Virbulis J. Patent US 6,840,998, 2002.

[52] Kusunoki K, Kamei K, Yashiro N, Hattori R. Mater Sci Forum 2009;615–617:137.

[53] Seki K, Kogawa S, Ujihara T, Chaudouet P, Chaussende D, Takeda Y. J Cryst Growth 2011;335:94.

[54] Distanov VE, Nenashev BG, Kirdyashkin AG, Serboulenko MG. J Cryst Growth 2002;235:457.

[55] Lui YC, Roux B, Lan CW. Int J Heat Mass Transfer 2007;50:5031.

[56] Lui YC, Roux B, Lan CW. J Cryst Growth 2007;304:236.

[57] Uda S, Wang S-Q, Kimura H, Huang X. In: Scheel HJ, Capper P, editors. Crystal growth technology. Weinheim: Wiley-VCH; 2008 [chapter 15].

[58] Kim HJ, Chandola A, Bhat R, Dutta PS. J Cryst Growth 2006;289:450.

[59] Dutta P. In: Scheel HJ, Capper P, editors. Crystal growth technology. Weinheim: Wiley-VCH; 2008 [chapter 12].

[60] Zharikov EV, Prihod'ko LV, Storozhev NR. The phenomenon of formation of steady-state fluid flow under solid body vibration. Preprint No. 18 General Phys Inst Acad Sci USSR Moscow 1989:1 [in Russian].

[61] Zharikov EV, Prihod'ko LV, Storozhev NR. J Cryst Growth 1990;99:910.

[62] Yuan W, Banan M, Regel LL, Wilcox WR. J Cryst Growth 1995;151:235.

[63] Uspenskii V, Favier JJ. Int J Heat Mass Transfer 1994;37:691.

[64] Strutynska LT. J Thermoelectr 2012;4:53.

[65] Lan CW. Int J Heat Mass Transfer 2000;43:1987.

[66] Izergin AP, Pavlenko YuS, Stroitelev SA. Izv Vyssh Uchebn Zaved Fiz 1959;(1):107.

[67] Langenecker B, Frandsen WH. Philos Mag 1962;7:2079.

[68] Nikitina GV, Romanenko VN, Tuchkevich VS. In: Crystallization and phase transitions. Minsk: Izd. Acad. Sci. USSR; 1962. pp. 379–85 [in Russian].

[69] Kirgintsev AN, Avvakumov EG. Sov Phys Crystallogr 1965;10:449.

[70] Witt AF, Gatos HC. J Electrochem Soc 1967;114(4):413.

[71] Agranat BA, Dubrovin MN, Khavskii NN. Akusticheskij Zhurnal 1976;22:141 [in Russian].

[72] Petrov TG. Method of growing single crystals. USSR Pat. No. 136,057, 1960, [in Russian].

[73] Ship V, Vanichek V. In: Shubnikov AV, Sheftal NN, editors. Growth of crystals. New York: Consultants Bureau; 1962. p. 191.

[74] Zharikov EV, Prikhod'ko LV, Storozhev NR. Vibrational convection during the growth of crystals. In: Givargizov EI, Grinberg SA, editors. Growth of crystals, vol. 19. New York: Consultants Bureau; 1993. p. 71.

[75] Myal'dun AZ, Prostomolotov AI, Tolochko NK, Verezub NA, Zharikov EV. Vibrational control of Czochralski crystal growth. In: Givargizov EI, Melnikova AM, editors. Growth of crystals, vol. 21. New York: Kluwer Academic Publishers; 2002. p. 181.

[76] Avdonin NA, Kalis Kh E, Zharikov EV, Storozhev NR. Appl Prob Math Phys Latv St Inst Riga 1989:4.

[77] Zharikov EV, Prikhod'ko LV, Storozhev NR. Cryst Res Technol 1989;24(8):761.

[78] Zharikov EV, Zavartsev YuD, Laptev VV, Samoilova SN. Cryst Res Technol 1989;24(8):751.

[79] Lyubimov DV, Lyubimova TP, Meradji S, Roux B. J Cryst Growth 1997;180:648.

[80] Avetissov ICh, Sukhanova EA, Orlova GYu, Belogorokhov IA, Zharikov EV. J Cryst Growth 2012;360:167.

[81] Zharikov EV. Advanced technologies of crystal growth from melt using vibrational influence. In: Capper P, Rudolph P, editors. Crystal growth technology. Semiconductors and dielectrics. Weinheim: Wiley-VCH Verlag; 2010. p. 41.

[82] Nyborg WL. Acoustic streaming. In: Mason WP, editor. Physical acoustics, IIB. New York: Academic Press; 1965.

[83] Schlichting G. Boundary-layer theory. 7th ed. New York: McGraw-Hill; 1979.

[84] Verezub NA, Zharikov EV, Kalitin SP, Lavrishchev SV, Myaldun AZ, Papin Yu M, et al. Crystallography 1996;41(6):1056.

[85] Fedyushkin AI, Bourago NG, Polezhaev VI, Zharikov EV. Proc. 2nd Pan Pacific Basin workshop on microgravity sciences. USA: Pasadena; 2001. paper CG-1065.

[86] Avetissov ICh, Zinovjev AYu, Romanenkov MV, Romanenkova LV, Zharikov EV. New achievements in materials science. In: Proc. II France–Russia seminar, Moscow; November 10–12, 2005. p. 48. Moscow.

[87] Avetissov ICh, Sadovskii AP, Sukhanova EA, Zharikov EV. J Cryst Growth 2011;318:979.

[88] Avetissov ICh, Mel'kov A Yu, Zinov'ev A Yu, Zharikov EV. Crystallogr Rep 2005;50(1):S124.

[89] Avetissov ICh, Sukhanova EA, Khomyakov AV, Zinovjev AYu, Kostikov VA, Zharikov EV. J Cryst Growth 2011;318:528.

[90] Fedyushkin AI, Bourago NG, Polezhaev VI, Zharikov EV. Proc. VII Russian symp. mechanics of microgravity. Moscow: IPM RAS; 2001 [in Russian], p. 365.

[91] Fedyushkin AI, Bourago N, Polezhaev V, Zharikov E. J Cryst Growth 2005;275:e1557.

[92] Fedyushkin AI, Bourago NG. Proc. 2nd Pan Pacific Basin workshop on microgravity sciences. USA: Pasadena; 2001. paper CG-1072.

[93] Avetissov ICh, Sukhanova EA, Sadovskii AP, Kostikov VA, Zharikov EV. J Cryst Growth 2010;312:1429.

[94] Avetissov ICh, Sadovskii AP, Sukhanova EA, Zharikov EV, Belogorokhov AI, Levonovich BN. J Cryst Growth 2010;312:1104.

[95] Avetissov ICh, Zharikov EV, Zinovjev A Yu, Sadovskii AP. Dokl Phys 2009;54:410.

[96] Avetissov ICh, Sadovskii A, Belov S, Khomyakov A, Rekunov K, Kostikov V, et al. CrystEngComm 2013;15:2213.

[97] Zhang Y, Liu Y, Jiang W, Pan XH, Jin WQ, Ai F, et al. Cryst Res Technol 2009:248.

[98] Ubbelhode AR. Melting and crystal structure. Oxford: Clarendon Press; 1965.

[99] Rudolph P, Koh HJ, Schäfer N, Fukuda T. J Cryst Growth 1996;166:578.

[100] Chelikowsky JR, Derby J, V Godlevsky V, Jain M, Raty JY. J Phys Condens Matter 2001;13:R817.

[101] Ginkin V, Kartavykh A, Zabudko M. J Cryst Growth 2004;270(3–4):329.

[102] Zharikov EV. J Cryst Growth 2012;360:146.

[103] Zharikov EV, Avetisov ICh, Lazarenko TA, Chigrai AA, Levtov VL, Novikov VA, et al. Experimental study of vibrational convection in a fluid on orbital complex "Mir". In: Proc. VII Rus. symp. "Mechanics of weightlessness. Outputs and prospects of fundamental studies of gravitationally sensitive systems", Moscow; 2001. p. 137 [in Russian].

[104] Verezub NA, Zharikov EV, Myaldun AZ, Prostomolotov AI. Crystallogr Rep 1996;41:335.

[105] Verezub NA, Zharikov EV, Myaldun AZ, Prostomolotov AI, Tolochko NK. Crystallogr Rep 1996;41:151.

[106] Verezub NA, Zharikov EV, Myaldun AZ, Prostomolotov AI. Dokl Acad Sci 1996;350:474.

[107] Kumar V, Biswas G, Brenner G, Durst F. Int J Heat Mass Transfer 2003;46:1641.

[108] Sampath R, Zabaras N. J Comput Phys 2001;168:384.

[109] Schwabe D, Scharmann A. J Cryst Growth 1981;52:435.

[110] Hong Y, Jin W-Q, Pan X-H. Chin Phys Lett 2004;21:1986.

[111] Li Z, Liu L, Nan X, Kakimoto K. J Cryst Growth 2012;346:40.

[112] Schwabe D. Surface-tension-driven flow in crystal growth melts. In: Freyhardt HC, editor. Crystals: growth, properties and applications, vol. 11. Berlin: Springer-Verlag; 1988. p. 75.

[113] Kuhlmann HC. Thermocapillary convection in models of crystal growth. New York: Springer-Verlag; 1999. p. 172.

[114] Mueller G, Ostrogorsky A. Convection in melt growth. In: Hurle DTJ, editor. Handbook of crystal growth, bulk crystal growth, vol. 2b. North-Holland, Amsterdam; 1993. p. 711 [chapter 13].

[115] Azami T, Nakamura S, Eguchi M, Hibiya T. J Cryst Growth 2001;233:99.

[116] Avetissov ICh, Sadovskii AP, Belov SN, Khan CK, Mozhevitina EN, Sukhanova EK, et al. J Cryst Growth 2014. http://dx.doi.org/10.1016/j.jcrysgro.2013.12.060i.

[117] Bushmakin OA, Verezub NA, Zharikov EV, Myal'dun AZ, Prostomolotov AI. Fluid Dyn 1997;32(N3):366.

[118] Zharikov EV, Myaldun AZ, Prostomolotov AI, Skorenko AV, Verezub NA. In: Gershuni GZ, Alexander I, editors. Vibrational effects in fluid dynamics. Perm State Univ; 2000. p. 1.

[119] Fedoseyev AI, Alexander JID. J Cryst Growth 2000;211:34.

[120] Feigelson RS Borshchevsky A. Method of growing single crystal cadmium telluride. US Patent 4,465,545, August 14, 1984.

[121] Caram R, Banan M, Wilcox WR. J Cryst Growth 1991;114:249.

[122] Shen XF, Anilkumar AV, Grugel RN, Wang TG. J Cryst Growth 1996;165:438.

[123] Grugel RN, Shen XF, Anilkumar AV, Wang TG. J Cryst Growth 1994;142:209.

[124] Dold P, Benz KW, Croell A, Roux B, Lyubimov D, Lyubimova T, et al. Acta Astronaut 2001;48:639.

[125] Lyubimova TP, Scuridin RV, Croell A, Dold P. Cryst Res Technol 2003;38:635.

[126] Verezub NA, Myaldun AZ, Prostomolotov AI, Milvidskii MG. Heat and mass transfer processes and growth of single crystals and thin-film structures. In: Proc II Russian symp. Obninsk; September 22–24, 1997. p. 110.

[127] Pankrath R, Doeppner K, Kuper C, Hesse H. XI-th Int Conf Cryst Growth 1995:131. The Hague, The Netherlands, Abstracts.

[128] Avetissov ICh, Zharikov EV, Zinov'ev A Yu, Mel'kov A Yu. Instrum Exp Tech 2004;47:554.

[129] Korsakov AS, Zhukova LV, Zharikov EV, Vrublevsky DS, Korsakov VS. Tsvetnye Met 2010;1:69 [in Russian].

[130] Abramov OV, Astashkin YuS, Stepanov VS. Akusticheskij Zhurnal 1979;25(2):180 [in Russian].

[131] Hayakawa Y, Kumagawa M. Cryst Res Technol 1983;20(1):3.

[132] Kozhemyakin GN. J Cryst Growth 2003;257:237.

[133] Kozhemyakin GN, Nemets LV. Crystallogr Rep 2009;54(4):707.

[134] Hayakawa Y, Sone Y, Ishino F, Kumagawa M. Jpn J Appl Phys 1983;22:206.

[135] Zolkina LV, Kozhemyakin GN. Funct Mater 2005;12(4):714.

[136] Abramov OV. Ultrasonics 1987;25:73.

[137] Jia S, Nastac L. Chem Mater Eng 2013;1:69.

[138] Kozhemyakin GN. Crystallogr Rep 2004;49(2):318.

[139] Vyshnevskiy SD, Kryvonosov EV, Lytvynov LA. Inorg Mater 2009;45(9):1009.

[140] Abramov OV, Teumin II, Filonenko VA, Eskin GI. Akusticheskij Zhurnal 1967;13(2):161 [in Russian].

[141] Ubbenjans B, Frank-Rotsch Ch, Virbulis J, Nacke B, Rudolph P. Cryst Res Technol 2012;47(3):279.

[142] Frank-Rotsch Ch, Juda U, Ubbenjans B, Rudolph P. J Cryst Growth 2012;352:16.

[143] Kozhemyakin GN. J Cryst Growth 2012;360:35.

[144] Kumagawa M, Tsuruta T, Nishida N, Ohtsuki J, Takahashi K, Adachi S, et al. Cryst Res Technol 1994;29(8):1037.

[145] Liu W-S, Wolf JF, Elwell DF, Feigelson RS. J Cryst Growth 1987;82:589.

[146] Zawilski KT, Custodio MCC, DeMattei RC, Feigelson RS. J Cryst Growth 2003;258:211.

[147] Liu YC, Shiau J-J, Feigelson RS, Route RK. J Cryst Growth 1990;102:807.

[148] DeMattei RC, Feigelson RS. J Cryst Growth 1993;128:1062.

[149] Feigelson RS, Zharikov EV. Investigation of crystal growth of dielectric materials by the Bridgman technique using vibrational control. Final Technical Report for NASA contract # NAG 8-1457-06; 2002.

[150] Zawilski KT, Custodio MCC, DeMattei RC, Feigelson RS. J Cryst Growth 2005;282:236.

[151] Korsakov A, Zhukova L, Korsakova E, Zharikov E. J Cryst Growth 2014;386:94.

[152] Barmin IV, Senchenkov AS, Avetisov ICh, Zharikov EV. J Cryst Growth 2005;275(1–2):e1487.

[153] Strelov VI, Zakharov BG, Sidorov VS, Ananyev PA. J Cryst Growth 2002;241:74.

[154] Croell A, Dold P, Kerat U, Lyubimova T. Proc. 16th ESA symp., ESA SP-530, St. Gallen, Switzerland; June 2–5, 2003. p. 123.

[155] Borshchevskii AS, Tretjakov DN. Kristall Tech 1968;34:69.

[156] Kumagawa M, Oka H, Quang N, Hayakawa Y. Jpn J Appl Phys 1980;19:753.

[157] Woodbury HH, Lewandowski RS. J Cryst Growth 1971;10:6.

[158] Kozhemyakin GN, Zolkina LV, Rom MA. Crystallogr Rep 2008;53:1236.

[159] Zhang Y, Liu Y, Jiang W, Pan XH, Jin WQ, Ai F. J Cryst Growth 2008;310:5432.

Segregation and Component Distribution

Aleks G. Ostrogorsky[1,*], Martin E. Glicksman[2]

[1]MECHANICAL & AEROSPACE ENGINEERING DEPARTMENT, ILLINOIS INSTITUTE OF TECHNOLOGY, CHICAGO, IL, USA; [2]MECHANICAL & AEROSPACE ENGINEERING DEPARTMENT, FLORIDA INSTITUTE OF TECHNOLOGY, MELBOURNE, FL, USA

*RESEARCH ON SEGREGATION WAS PARTIALLY SUPPORTED BY NASA.

CHAPTER OUTLINE

25.1 Introduction 997
25.2 Segregation Coefficients 998
25.2.1 Segregation under Local Equilibrium 998
25.2.2 Nonequilibrium and the Fourier Number 999
25.2.3 Nonequilibrium in the melt 999
25.2.4 Effective Segregation Coefficient, k_{eff} 1000
25.3 Limit Theories: "Perfect Mixing" and "No-Mixing" 1001
25.3.1 Perfect Mixing 1001
25.3.2 "No-Mixing," Diffusion-Controlled Segregation 1003
25.3.2.1 Initial Transient 1003
25.3.2.2 Steady State Segregation 1004
25.3.2.3 Final Transient 1004
25.4 Convective Heat and Mass Transfer 1005
25.4.1 Flow Patterns in Crystal Growth 1005
25.4.1.1 One-Dimensional Perpendicular Convection 1005
25.4.1.2 Two- and Three-Dimensional Flow Patterns 1006
25.4.1.3 Perpendicular Convection 1006
25.4.1.4 Lateral Convection 1006
25.4.2 Convection Flux, j 1006
25.4.2.1 Fick's First Law 1007
25.4.2.2 Film Thickness Formulation 1008
25.4.2.3 Mass Transfer Convection Coefficient 1009
25.4.3 Phenomenological Approach and Correlations for Nusselt Numbers 1009
25.4.4 Classification of Melt Convection 1010
25.4.4.1 Forced Convection 1011

Handbook of Crystal Growth. http://dx.doi.org/10.1016/B978-0-444-63303-3.00025-0
Copyright © 2015 Elsevier B.V. All rights reserved.

25.4.4.2 Natural Convection 1011
25.4.4.3 Convection Driven by Freezing 1011
25.4.4.4 Thermocapillary Convection 1012
25.4.4.5 Mixed Convection 1012
25.5 Segregation Theories Based on Solute Layer Thickness 1012
25.5.1 BPS Theory 1012
25.5.2 Wilson–Garandet's Model: Forced Convection Alone 1014
25.5.3 Models Considering Natural Convection and/or Lateral Melt Convection 1015
25.6 Segregation Model with Nusselt Numbers and Mixed Convection 1016
25.6.1 Combined Mass Transfer Coefficient 1016
25.6.2 Phenomenological Approach to Determine the Combined Mass Transfer Coefficient 1017
25.6.3 Effective Segregation Coefficient, k_{eff}, as Function of Combined Nusselt Number 1018
25.7 Correlations for Nusselt Numbers 1018
25.7.1 Correlations for Disk-Driven Forced Convection 1018
25.7.1.1 Exact Similarity Solution for Laminar Flow and Sc $\rightarrow \infty$ 1018
25.7.1.2 Empirical Correlations, Laminar Flow 1019
25.7.1.3 Empirical Correlations, Turbulent Flows 1020
25.7.2 Empirical Correlations for Natural Convection 1021
25.7.2.1 Vertical Walls 1021
25.7.2.2 Horizontal Disks 1022
25.7.2.3 Rayleigh–Bénard Convection 1023
25.8 Directional Solidification: Segregation without Forced Convection 1023
25.8.1 Segregation Under Vanishing Natural Convection ($Gr \rightarrow 0$) 1024
25.8.1.1 Diffusion Coefficients Extracted under Minimum Convection 1027
25.8.2 Bottom-seeded VB Growth 1028
25.9 CZ Process: Segregation Controlled by Mixed Convection 1029
25.9.1 Segregation under Steady Forced (Negligible Natural) Convection 1029
25.9.1.1 Diffusion Coefficients of Impurities in Germanium 1029
25.9.2 CZ Process with Mixed Convection $Re^2 \approx Gr$ 1031
25.9.2.1 Diffusion Coefficients of Impurities in Silicon 1031
25.9.2.2 CZ Growth of Large Crystals at Low Rotation Rates 1032
25.10 Zone Melting 1034
25.10.1 Introduction 1034
25.10.2 Single-Pass ZM, "Perfect" Mixing 1037
25.10.3 Effective Segregation Coefficient in Zone Purification 1038
25.10.4 Single-Pass ZM, "Partial" Mixing 1038
25.10.5 Multipass ZM 1039

25.11 Lateral Segregation **1039**
25.11.1 Curved Solid–Liquid Interface 1039
25.11.2 Convection 1040
25.11.3 Nonequilibrium Segregation 1043
25.11.4 Local Nusselt Numbers 1044
25.12 Microsegregation **1044**
25.12.1 Doping Striations 1045
25.13 Summary **1045**
References **1046**

25.1 Introduction

Fluid flow during crystal growth generally enhances mass transfer by transporting melt with high solute concentration near the solid–liquid interface and replacing it with fluid having a lower bulk-melt concentration. Segregation and component distribution—two critical aspects for achieving successful crystal growth—are consequently controlled by melt convection.

Melt flows are governed by a well-known set of nonlinear partial differential equations, the Navier–Stokes equations, which are rarely solvable by analytic techniques. As a result, classic chemical segregation theories usually consider only limiting cases of zero melt velocity (diffusive mixing) or "infinite" melt velocity (perfect mixing). Sixty years ago, the seminal Burton, Prim, and Slichter (BPS) theory was developed to consider how finite levels of melt convection accompanying crystal growth affect segregation [1,2]. The influence of convection was captured through an "effective" segregation coefficient, k_{eff}, which was modeled by postulating a supposed "stagnant solute layer" at the crystal–melt interface of thickness δ. The "stagnant" layer thickness, δ, was estimated in BPS theory using an analytical solution of the governing hydrodynamic equations developed by Cochran and Levich [3–5], describing forced laminar convection near a rotating disk.

All effective segregation coefficient models for crystal growth, until recently, were based on a solute boundary layer thickness, δ, developed in laminar flow, thus ignoring the complicating, but important, effects of turbulence and unavoidable buoyancy-induced (natural) convection. The Cochran–Levich solution remains as the only equation for estimating δ in wide use today by crystal growers.

The effective segregation coefficient, k_{eff}, is controlled by the rate of solute transfer from the interface, i.e., by the solute flux, j, transported from the advancing crystal–melt interface. Convection fluxes in general (viz., heat and mass transfer rates) are usually calculated in engineering by appealing to empirical correlations developed from laboratory experiments, rather than from fundamental theoretical estimates. The use of empirical correlations is a widely accepted practice in many engineering applications

and has become necessary for most industrial crystal growth applications, as melt flows in bulk crystal growth are often turbulent. This statement remains especially true for low Prandtl number fluids, such as the semiconductor and metallic melts.

In this chapter we focus on reviewing the recently proposed combined convection (CC) model, which relates the effective segregation coefficient ($k_{eff,CC}$) to the solute convection flux. The solute flux is calculated using a phenomenological approach, a method that takes advantage of empirical correlations established for laminar or turbulent flows, combining, as needed, both natural (buoyancy-induced) and forced (extrinsically driven) convection to represent solute segregation under realistic crystal growth conditions. This phenomenological approach is well justified, considering the overall complexity and diversity of melt flows during crystal growth.

More specifically, the chapter focuses on solute segregation encountered in several industrially important crystal growth processes based on three fundamentally different configurations: Czochralski (CZ), directional solidification (DS), and zone melting (ZM). We emphasize the benefits of forced convection relative to natural convection, which is unavoidable, unsteady, and difficult to control.

25.2 Segregation Coefficients

In monocomponent (unary) systems, and in congruently melting multicomponent systems, redistribution of components, segregation leading to local changes in composition, does not occur during freezing. Segregation, or component redistribution, otherwise always occurs in noncongruent systems. Of particular interest to crystal growers is the segregation of impurities and dopants[1] occurring in melt-grown semiconductor crystals, which include directional solidification/crystal growth, and purification achieved by zone refining.

25.2.1 Segregation under Local Equilibrium

Phase diagrams provide the equilibrium concentrations established locally at the interface in the solid and liquid phases. Their ratio is used to define the equilibrium segregation coefficient, k_0, conventionally defined as,

$$k_0 = \frac{C_s(x=0)}{C_L(x=0)} = \frac{C_s}{C_0}, \tag{25.1}$$

where x is the distance away from the interface. C_S and C_0 are the solute concentrations in the solid and in the liquid phase measured, respectively, at the crystal–melt interface, i.e., $x = 0$. The liquidus and solidus lines on the binary phase diagram remain straight for ideal and dilute solutions, and, if straight, yield a value for k_0 that is independent of concentration and temperature. Otherwise, k_0 is defined as the changing ratio of C_S to C_0 across any solid–liquid tie line.

[1]Intentionally added impurity atoms to control electronic properties.

The equilibrium segregation coefficient, k_0, is a fundamental thermodynamic property of a binary solid–liquid system and not a function of the crystal growth process parameters or hydrodynamic melt properties; k_0 appears in a great number of mathematical macrosegregation expressions involving redistribution of the solute during crystal growth [6]. Two cases of chemical segregation are encountered, depending on the binary system: (1) $k_0 < 1$, where solutes are rejected at the interface into the melt phase, and (2) $k_0 > 1$, where solutes are preferentially absorbed into the crystalline phase. The former is more common than the latter, but both situations occur. For brevity of the mathematical presentations in this chapter, and without loss of generality, we shall proceed by discussing segregation for the more common case of $k_0 < 1$.

25.2.2 Nonequilibrium and the Fourier Number

Full thermodynamic equilibrium during crystal growth is seldom, if ever, attained within the developing solid. The reason that achieving full equilibrium throughout the solid phase during crystal growth is so difficult in practice is that atomic diffusion in the solid is too slow a process to allow extensive homogenization within a growing crystal. The time needed for homogenization by atomic diffusion in the solid sets a time scale that can be calculated using the dimensionless Fourier number, defined as

$$Fo = \frac{Dt}{L^2},$$

where L (cm) is a characteristic length, and t (s) is time. In the case of mass transfer, $D(\text{cm}^2/\text{s})$ is the diffusion coefficient, or chemical diffusivity. In the case of heat transfer, $Fo = \alpha t/L^2$, where thermal diffusivity $\alpha(\text{cm}^2/\text{s})$ replaces chemical diffusivity, D. The Fourier number is the dimensionless "characteristic" time for the occurrence of a diffusion transient over the length scale, L. Thus, the time needed to achieve homogenization by diffusion is, $t \gg L^2/D$.

Typical values of diffusion coefficients of dopants and impurities in crystalline silicon close to its melting point, T_m, are circa $D = 10^{-10}$ cm^2/s. Thus, for a 1-cm-long Si crystal, near 1400 °C, $t \gg 10^{10}$ s, or about 10^5 days! Even short-range microscopic fluctuations in the dopant concentration will remain "frozen" in the solid (where $L \approx 1\ \mu\text{m} = 10^{-4}$ cm) often due to crystal rotation during growth and unsteady or turbulent melt convection. At room temperature, near 300 K, dopant diffusivities in Si drop to circa 10^{-50} cm^2/s, a value so small that for practical purposes is effectively zero. It is assumed in this chapter, moreover, that diffusion does not occur within the solid over the typical time scales considered here for crystal growth, and that whatever segregation does occur during crystal growth remains unaltered in the product phase. Clearly, long-term annealing at elevated temperature of a crystalline solid can reduce its as-grown segregation level.

25.2.3 Nonequilibrium in the melt

Melt equilibrium at or near a crystal–melt interface is disturbed by segregation. Solute additions and impurities are usually rejected during crystal growth at the crystal–melt

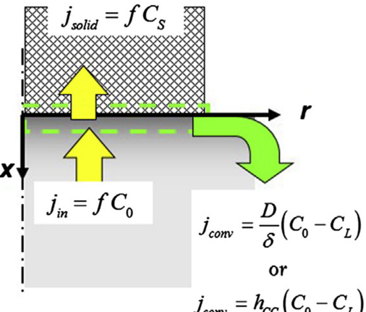

FIGURE 25.1 Lateral convection caries solute way from the interface. Convective flux j_{conv} is calculated using the film thickness or combined convection (CC) coefficient formulation.

interface, or, less frequently, preferentially absorbed into the growing solid. As a result, a concentration or solute boundary layer having some thickness, δ, develops ahead of the interface. The concentration of impurities, $C_L(x)$, within this boundary layer changes from its initial equilibrium value, $C_L(0) = C_0$ at the interface, to a lower, or higher, value $C_L(\delta) = C_L$ in the bulk melt, depending, of course, on the value of k_0 relative to unity.

Figure 25.1 shows the solute fluxes acting at a growing crystal–melt interface. During steady state solidification at some specified freezing rate, f (cm/s), all solute rejected at the moving interface must be transported away by lateral melt convection. The mass transfer, specified by a convective mass transfer coefficient, h, relates the convective flux, j_{conv}, to the local concentration difference from the equilibrium value, C_0. The mass transfer coefficient, h, for CZ crystal growth, accounts for the net influences of "combined" convection, which include: (1) forced convection, (2) natural convection, and (3) perpendicular convection.

The actual thickness of the solute layer, δ, that develops is controlled by the state of melt convection. Without the presence of any convection, for a typical crystal growth rate of $f = 0.3$–3 cm/h, and assuming $D = 10^{-4}\text{cm}^2/\text{s}$, a purely diffusive boundary layer develops, where the thickness $\delta = D/f \approx 0.1 - 1$ cm. In the presence of melt convection, however, δ is reduced to $\delta < 0.1$ mm.

25.2.4 Effective Segregation Coefficient, k_{eff}

In the presence of melt convection, one may still relate the solid to the liquid solute concentrations by an "effective" segregation coefficient, defined as,

$$k_{eff} = \frac{C_s}{C_L} = \frac{C_s(x = 0)}{C_L(x > \delta)}. \tag{25.2}$$

Thus, C_L represents the melt concentration just beyond the outer limit of the solute boundary layer, $C_L(x > \delta)$. Sufficiently vigorous convection reduces the layer thickness, δ, and, in principle, as the convection intensity becomes "infinitely" strong, a limit is approached as $\delta \to 0$, namely, $k_{eff} \to k_0$.

The governing mathematical statement for conservation of solute atoms in a convecting melt is the convection–diffusion equation,

$$\frac{\partial C}{\partial t} + \overrightarrow{v} \cdot \vec{\nabla} C = D\nabla^2 C. \tag{25.3}$$

This general equation couples mass transfer to melt flow, via the fluid velocity vector, $\overrightarrow{v}$. Melt flow itself, however, is governed by a set of hydrodynamic, nonlinear, partial differential equations, called the Navier–Stokes equations (N–S). Only a few analytical "similarity"[2] solutions to the N–S equations exist [7]. The following list of important similarity solutions, and their sources, provides useful insights into interfacial convection, which lead to all the basic forms of axial and radial segregation that will be considered later in this chapter. These include:

1. Laminar flow and convection near a rotating disk, by von Karman/Cochran [3,5] and Levich [4].[3]
2. Laminar forced flow and convection along flat plates (Blasius and Polhausen [8,9]), (see Section 25.11.2).
3. Laminar natural convection along a vertical plate (Polhausen and Ostrach solution [9,10]).

For any other configuration (excepting laminar, one-dimensional flows in pipes and ducts), one must rely on empirical correlations rather than on exact analytical solutions to the N–S.

25.3 Limit Theories: "Perfect Mixing" and "No-Mixing"

Figure 25.2 depicts the concentration of solute after normal freezing (i.e., plane-front directional solidification) for a system with $k_0 < 1$, taken to two important limiting cases: (1) "perfect mixing" in the melt, and (2) "no mixing" (diffusion only). It is assumed further that the solute distribution depends only on the axial distance from the interface, x. Lateral segregation is temporarily ignored but included in remarks in Section 25.11.

25.3.1 Perfect Mixing

G. Gulliver (1921) [11] and E. Scheil (1942) [12] independently solved the mass conservation problem of interfacial segregation under local equilibrium. Both investigators

[2]In fluid mechanics, a similarity solution is a mathematical solution of the velocity profile within a boundary layer that is self-similar, i.e., appearing to be identical, save for a uniform size-scale factor, or magnification. Such self-similar solutions allow a temporary reduction in the number of independent variables.

[3]The similarity solution for laminar ow near a rotating disk was obtained by von Karman in 1921 [5] and Cochran in 1934 [3]. Levich [4] in turn solved for the concentration field in a fluid driven by a rotating disk, which he coupled to the hydrodynamic velocity field. It provides the foundation of BPS theory and several subsequent models for the effective distribution coeffcient, k_{eff}. (See, for example, Section 25.5.)

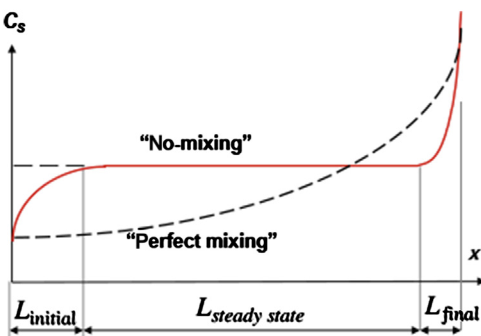

FIGURE 25.2 Limiting profiles of axial component distribution: dashed line is "perfect mixing." Full line is "no mixing." All actual segregation profiles controlled by convection fall between the limiting profiles.

assumed, (1) perfect mixing in the liquid phase to maintain a homogeneous melt, and (2) no subsequent diffusion in the solid phase. The Gulliver–Scheil solution gives a one-dimensional segregation curve containing only one system-based parameter, the equilibrium segregation coefficient, k_0, which is available for many binary systems in either tabular form and/or in graphical form on the equilibrium phase diagrams, or computed using thermochemical data. The Gulliver–Scheil segregation distribution for perfect mixing in the melt, as a function of the fraction of the molten charge solidified, f_S, is given by

$$\frac{C_S}{C_L^i} = k_0(1 - f_S)^{(k_0 - 1)}, \tag{25.4}$$

where C_L^i is initial dopant concentration in the melt. Independent of the geometry, the fraction solidified, f_S, may be expressed as the volumetric ratio

$$f_S = \frac{V_S}{V_S + V_L}.$$

For the case of parallelepipeds with a charge of length L, $f_S = x/L$, where x indicates the length solidified. Melt equilibrium due to perfect mixing becomes realistically approximated when crystals are grown at a slow rate from well-stirred melts, e.g., the situation closely met in CZ growth of large-diameter crystals. The actual concentration profiles achieved in the solid will depend on details of the melt convection and the freezing rate. If the growth rate of a crystal is not extremely slow, one must employ an effective segregation coefficient, where k_{eff} becomes a fitting parameter in the Gulliver–Scheil equation, namely,

$$\frac{C_S}{C_L^i} = k_{eff}(1 - f_S)^{(k_{eff} - 1)}. \tag{25.5}$$

The effective segregation coefficient can be measured by conducting a normal freezing experiment and applying Eqn (25.5) to the segregation data. Simple mold geometries should be used to facilitate measuring the fraction solidified. Note that the measured k_{eff}

includes the complicated influences of melt convection, interface stability, and freezing speed. Solute concentration, C_S, relative to the initial concentration, C_L^i, is measured for several values of the fraction solidified, f_S. Equation (25.5) can be written as [13],

$$\log_{10}\left(\frac{C_S}{C_L^i}\right) = \log_{10} k_{eff} + (k_{eff} - 1)\log_{10}[1 - f_S], \tag{25.6}$$

and plotted log–log. Both the ordinate intercepts of the lines and their slopes provide independent estimates for k_{eff}.

25.3.2 "No-Mixing," Diffusion-Controlled Segregation

A suction flow normal to the interface is unavoidable when growing any material from the melt. Suction flow is a one-dimensional, perpendicular melt motion[4] driven by freezing. This generally weak flow is caused by the crystallization growth rate, f, and the small mass density difference between the growing crystal and its melt. The perpendicular flow velocity at the interface is

$$V_{perp.} = f\left(\frac{\rho_S}{\rho_L}\right), \tag{25.7}$$

where f is the crystal growth rate and ρ_S and ρ_L are, respectively, the mass densities of the solid and liquid phases. Solute is transported by the suction flow toward the interface, where segregation occurs. As a result, a solute boundary layer develops having some thickness δ.

The key assumptions used are: (1) uniform initial dopant concentration in the melt C_L^i; (2) constant growth rate, f; and (3) during the initial transient, the remaining melt length, L, is larger than δ. The crystal grown under diffusion-controlled segregation will develop three distinct regions: (1) initial transient, (2) steady state segregation, and (3) final transient, see Figure 25.2.

25.3.2.1 Initial Transient

During the initial transient, a crystal's concentration increases until $C_S = C_L^i = k_0 C_0$. Tiller et al. [14] derived an approximate solution for the initial transient region by assuming that the concentration profile at the interface is described by the following differential equation,

$$D\frac{d^2C}{dx^2} + f\frac{dC}{dx} = 0 \tag{25.8}$$

The same differential equation is employed in the BPS segregation model published later the same year. Solution of Eqn (25.8) yields a solute concentration profile in the stagnant liquid near the interface, of the following exponential form,

[4] In fluid mechanics, the flow perpendicular to a porous interface is known as "uniform suction flow." Its effect is to stabilize the boundary layers by reducing their thickness. (See Schlichting [7].)

$$\frac{C_S(x)}{C_L^i} = k_0 + (1 - k_0)\left[1 - e^{-k_0 \frac{xf}{D}}\right] \tag{25.9}$$

Tiller's Eqn (25.9), results in about 30% error for profiles measured in Te-doped InSb ($k_0 = 0.5$) and in 78% Zn-doped InSb ($k_0 = 2.9$) [15]. It is hard to justify using Eqn (25.9) in view of the exact solution, published later by Smith et al. (1955 [16]), who found

$$\frac{C_S(\chi, k_0)}{C_L^i} = \underbrace{\frac{1}{2}\left(1 + erf\sqrt{\chi}\right)}_{F_1(\chi)} + \underbrace{\left(k_0 - \frac{1}{2}\right) \mathrm{e}^{-4k_0(1-k_0)\chi} erfc\left[(2k_0 - 1)\sqrt{\chi}\right]}_{F_2(k_0,\chi)} \tag{25.10}$$

with

$$\chi \equiv \frac{xf}{4D},$$

where x is the axial distance from the starting seed. For:

1. $k_0 \approx 0.5$, $F_2(k_0,\chi) = 0$, the transient portion ends at $C_S/C_L^i = 0.99$, or $L_{initial} \approx 11(D/f)$.
2. $0.5 < k_0 < \infty$, $F_2(k_0,\chi) < 0$, the transient portion of the crystal decreases.
3. $k_0 > 0.5$, $F_2(k_0,\chi) > 0$, the transient portion of the crystal lengthens.

An ideal, uniform, axial, and radial composition can be achieved in practice only for crystal growth under steady state diffusion-controlled segregation. Binary systems with $0.5 < k_0 < \infty$, and grown at higher growth rates, are especially amenable to diffusion-controlled growth, because the initial transient remains relatively short, producing a usefully long homogeneous section of the crystal.

For example, in 2002 during the SUBSA investigation aboard the International Space Station (ISS), four Te-doped InSb crystals ($k_0 = 0.5$) [17] and three Zn-doped InSb crystals ($k_0 = 2.9$) [18] were grown under microgravity conditions. The growth rate was $f = 0.5$ (cm/hr). The initial transient length was $L_{\text{transient}} = 0.93$ cm and 0.7 cm, respectively, for Te and Zn, with the time scale of the initial transients of $\tau_{trans} \approx 1\ h$. The diffusion coefficients were determined to be: for Te, $D = 1.0 \times 10^{-4}$ cm^2/s and for Zn, $D = 1.2 \times 10^{-4}$ cm^2/s. When identical crystal growth was carried out terrestrially, by contrast, natural convection precluded significant diffusion-limited solute buildup at the interface, so that the initial transients lasted only several seconds, and their length became negligible [19].

25.3.2.2 Steady State Segregation

Steady state segregation, where a homogeneous composition is obtained, initiates when $x > L_{trans}$, so that $k_{eff} = 1$. The concentration of solute incorporated into the crystal exactly equals the initial melt concentration, $C_S = C_L^i$, thus allowing a time-invariant solute balance and achieving steady state growth.

25.3.2.3 Final Transient

Final transient segregation begins when the solute boundary layer traveling ahead of the advancing interface approaches the end of the melt. Thus, one finds that

the final transient is brief, the affected length of crystal is relatively short, and is approximately equal to the thickness of the steady state solute boundary layer. Thus,

$$L_{final} \approx D/f.$$

Usually batch crystal growth processes are terminated for other reasons before the final transient occurs.

25.4 Convective Heat and Mass Transfer

Melt convection during crystal growth is complicated by the fact that it combines advection—the macroscopic transport of solute coupled to fluid motion—with diffusion, the microscopic random motions of individual atoms or molecules. Convection phenomena are further classified “natural” or “forced,” “laminar” or “turbulent.” Natural convection is driven by body forces, such as gravity interacting with density gradients within the melt, and is usually unavoidable under terrestrial crystal growth conditions. In forced convection, fluid is driven by an external source, e.g., crystal rotation, moving magnetic fields, or crucible rotation.

Bulk fluid flow enhances mass transfer by carrying the fluid near the interface, which has a higher solute concentration, C_0, and replacing it with fresh fluid having a lower concentration $C_L \ll C_0$. Convection, as explained earlier, can drastically reduce the time and distance over which the initial transient occurs during crystal growth. In the presence of vigorous melt convection, such transients, even for small k_0 values, might last only a few seconds [19]. Quasi-steady state crystal growth occurs when the solute flux rejected at the interface, $j_{rej.} = f(C_0 - C_S)$, is transported away by convective melt motion and its mass flux, j_{conv}.

25.4.1 Flow Patterns in Crystal Growth

25.4.1.1 One-Dimensional Perpendicular Convection

Perpendicular convection, driven by the growth rate, f, is the only one-dimensional advective process always occurring during melt growth. It is, of course, unavoidable, but weak, and has a low associated velocity, usually $\leq$30 μm/s. This weak suction flow, under terrestrial crystal growth conditions, is normally overwhelmed by natural convection, which achieves much higher velocities, typically about 10 mm/s.

Numerical simulations have convincingly demonstrated that some level of natural convection will always be present, even at gravity levels as small as $10^{-5}g_0$, where $g_0 = 9.81$ (m/s^2) is the average gravitational acceleration on earth (see Section 25.8.1). Numerous melt growth experiments conducted in various orbiting laboratories support this finding. Thus, a one-dimensional flow model is realistic *only under controlled microgravity conditions*, where the buoyancy-driven fluid flow velocity components, $\{u,v,w\}$, are negligible compared to f.

25.4.1.2 Two- and Three-Dimensional Flow Patterns

The steady state continuity equations for incompressible fluid flow are

$$\frac{\partial u}{\partial x}+\frac{\partial v}{\partial y}=0 \ \text{(rectangular coordinates)} \tag{25.11}$$

$$\frac{\partial u}{\partial r}+\frac{u}{r}+\frac{\partial w}{\partial z}=0 \ \text{(cylindrical coordinates)} \tag{25.12}$$

These equations state that one-dimensional flows are possible if, and only if, components u and v are either constant or zero. One-dimensional flows are observed only in pipes or ducts, where $u=\text{const.}$ and $v=0$. Convection occurring in a melt can never result in a one-dimensional flow.

Typical flow patterns occurring near a growing crystal growth interface are depicted in Figure 25.3. Crystal growth configurations for (1) CZ, (2) vertical Bridgman (VB), and (3) horizontal Bridgman (HB) are shown. Note especially that perpendicular flows carry rejected impurities toward the interface, whereas lateral flows transport solute along the interface and eventually back into the bulk melt.

25.4.1.3 Perpendicular Convection

In the z-direction, the flow velocity is $v_z=f+w$. As $z\to 0$, the term f dominates, because the velocity component $w\to 0$. Outside of the solute layer, $w \gg f$.

25.4.1.4 Lateral Convection

Melts typically flow tangentially along the solid–liquid interface and thus transport away latent heat and rejected solute laterally, as indicated schematically in Figures 25.1 and 25.3 [20]. The melt velocity component along the crystal–melt interface in either the x- or r-direction is u.

The intrinsic importance of lateral flow on component redistribution is emphasized in segregation models for k_{eff} developed by Yen and Tiller [21] and by Mueller and Ostrogorsky [20,22]. The key issue stressed in both of these models is that all solute that is not absorbed into the interface would be transported laterally, not axially. Again, it is stressed that solutes cannot “escape” axially, by simply diffusing back into the bulk melt. This situation becomes evident from the limiting case of “no-mixing,” where component $w=0$ (see Eqn (25.10)), and since the solute cannot escape, one finds that $k_{eff}=1$.

25.4.2 Convection Flux, j

A key goal of convection mass transfer theory is to determine the magnitude of the convection flux, j (cm/s). Despite the complexities and nonlinearity of convection, the associated mass flux, j, is observed to be proportional to its driving force, which is proportional to the solute concentration difference. Convection mass fluxes can be calculated using three approaches: (1) Fick’s first law, (2) static layer thickness, or (3) convection coefficients.

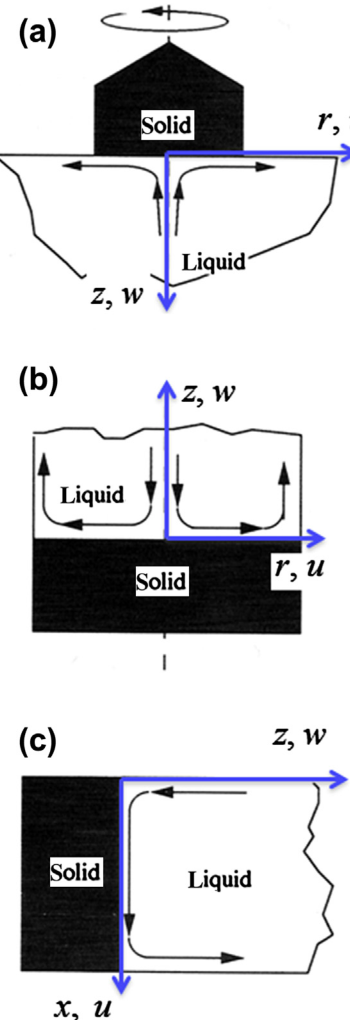

FIGURE 25.3 Schematic of flow patterns near the growth interface. (a), (b) axisymmetric flows, and (c) nonaxisymmetric flows.

25.4.2.1 Fick's First Law

At the crystal–melt interface, the hydrodynamic no-slip condition[5] requires zero tangential fluid velocity. Thus, at $x = 0$, transport occurs solely by diffusion, so in one dimension the mass flux is

$$j \equiv -D \left. \frac{dC_L}{dx} \right|_{x=0} \tag{25.13}$$

[5]Fluid "sticks" to the solid.

25.4.2.2 Film Thickness Formulation

If one assumes that diffusion occurs through a fictitious "film" or stagnant layer, the mass flux may be written as,

$$j \approx D\left(\frac{C_0 - C_L}{\delta_{static}}\right). \tag{25.14}$$

Equation (25.14) is an approximation of Fick's first law, where the gradient, $dC_L/dx|_{x=0}$, is replaced by the ratio of concentration difference to layer thickness, δ_{static}. A fictitious layer with thickness δ_{static} lacks a physically realistic foundation, so that the main limitation of Eqn (25.14) is that the nonexistent distance, δ_{static}, which does not, in principle, exist, also cannot be calculated. A film-thickness-based formulation becomes meaningful, and useful, provided that the concentration gradient, $dC_L/dx|_{x=0}$, is known, or estimated, from the appropriate analytical solution of a hydrodynamic boundary layer equation. Then, such a gradient-defined layer thickness may be set equal to the concentration difference divided by the concentration gradient in the following manner,

$$\delta_{grad} \equiv \frac{\Delta C}{dC_L/dx|_{x=0}} = D\left(\frac{\Delta C}{j}\right). \tag{25.15}$$

As is shown in Figure 25.4, such a gradient-defined layer thickness, δ^{grad}, may be obtained by extending a tangent at $x = 0$ (dashed line) to the actual concentration profile normal to the interface [19]. One finds that $\Delta C/\delta^{grad} = dC_L/dx|_{x=0}$. Equation (25.15) was, in fact, employed by Levich to calculate δ^{grad}, which provided the foundational fluid mechanical aspect of the BPS model. See Eqn (25.25).

For convection driven by a rotating infinite disk, the actual thicknesses of the velocity and solute boundary layers are, respectively [3,4],

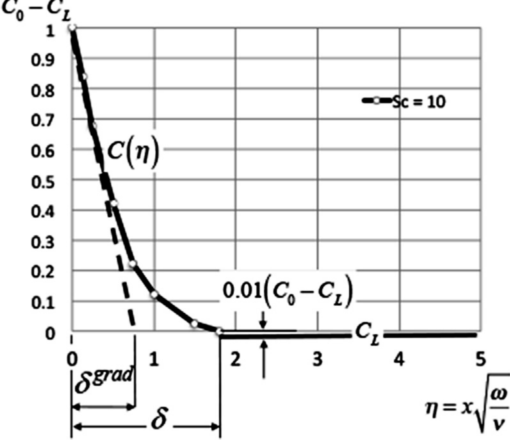

FIGURE 25.4 Actual and gradient thickness of solute boundary layer. η is dimensionless distance from the interface [7,8]. Note that $\delta \approx 2.5\delta^{grad}$.

$$\delta_\nu \approx 4\left(\frac{\nu}{\omega}\right)^{1/2},$$

and

$$\delta = \delta_\nu Sc^{-1/3} \approx 4D^{1/3}\nu^{1/6}\omega^{-1/2}. \tag{25.16}$$

25.4.2.3 Mass Transfer Convection Coefficient

Newton's law of cooling [8,9] defines the convective heat transfer coefficient, h^{HT}, based on the ratio of the heat flux, q, to the temperature difference, $T_0 - T_L$, namely,

$$h^{HT} = \frac{q}{T_0 - T_L}$$

where T_0 and T_L are, respectively, the temperature at the interface, $x = 0$, and within the bulk liquid. By analogy,[6] a comparable mass transfer coefficient can be similarly defined as,

$$h = \frac{j}{C_0 - C_L}, \tag{25.17}$$

where j is mass flux. Combining Fick's first law Eqn (25.13) with Eqn (25.17) defines the corresponding mass transfer coefficient as

$$h \equiv \frac{j}{C_0 - C_L} = \frac{-D\frac{dC}{dx}\Big|_{x=0}}{C_0 - C_L}. \tag{25.18}$$

An exact value for h is readily obtained if the concentration gradient, $\frac{dC}{dx}\Big|_{x=0}$, is obtained from the appropriate analytical fluid flow solution.

25.4.3 Phenomenological Approach and Correlations for Nusselt Numbers

As noted earlier, Navier–Stokes equations are usually not solvable excepting the cases of laminar flow along flat plates or rotating disks. Furthermore, the accuracy of such simplified solutions applied to crystal growth problems is often limited by the very assumptions that made the analytical solutions possible. For example, the Cochran–Levich solution, valid when the Schmidt number $Sc \to \infty$, still admits a 17% error when $Sc = 10$ (see Section 25.7.1.2). Therefore, in engineering practice one must adopt phenomenological approaches and rely instead on empirical rate/flux relationships that are based on laboratory experiments. The phenomenological mass transfer coefficient, h, is then determined by measuring the flux j. See again Eqn (25.18).

In order to reduce the number of independent variables, such phenomenological correlations are always given in dimensionless form. The dimensionless heat and mass

[6]This analogy is based on the observation that a temperature gradient is the driving potential for heat transfer, whereas the concentration gradient in a mixture is the driving potential for mass transfer.

transfer coefficients are called Nusselt numbers [8,9],[7] and these quantities can be calculated from the corresponding ratios of the thermal and diffusive fluxes under both hydrodynamic and static conditions,

$$Nu^{HT} \equiv \frac{h^{HT} L}{k} = \frac{h^{HT} \Delta T}{\frac{k}{L} \Delta T} = \frac{q_{convection}}{q_{diffusion}},$$

and

$$Nu \equiv \frac{hL}{D} = \frac{h \Delta C}{\frac{D}{L} \Delta C} = \frac{j_{convection}}{j_{diffusion}}, \tag{25.19}$$

where k is the thermal conductivity, and L is the characteristic length of the interface. Thus, the common physical interpretation of a Nusselt number, Nu, in heat and mass transfer is that it scales the ratio of a convective flux, $j_{convection}$, to the corresponding diffusive flux, $j_{diffusion}$, which is the flux expected under identical conditions in the same fluid held, hypothetically, stagnant.

The main advantage of using a convective-coefficient (i.e., Nusselt number) formulation relative to using the solute layer thickness is that numerous empirical correlations exist for Nusselt numbers that were developed for various flow configurations, including, especially, turbulent natural convection in liquid metals.

25.4.4 Classification of Melt Convection

Convection, as mentioned earlier, can be natural or forced, depending on how the flow is driven. It is well established [8,9] that the ratio of the Grashof number, Gr, to the Reynolds number squared, Re^2, captures the relative strengths of buoyancy-to-inertial forces acting on an element of fluid,

$$\frac{Gr}{Re^2} \sim \left(\frac{Buoyancy}{Inertia}\right).$$

where,

$$\mathrm{Re} = \frac{VR}{\nu} = \frac{\omega R^2}{\nu},$$

and R is the crystal radius and ω is its rotation rate. Buoyancy can arise from gradients in either temperature, due to thermal expansion, or from gradients in composition, due to mass density changes with composition. The latter effect is usually more significant than the former whenever a solute is present of significantly different atomic weight from the solvent,

$$Gr = \frac{g \Delta\rho/\rho L^3}{\nu^2} = \frac{g\beta \Delta T L^3}{\nu^2} + \frac{g\beta_C \Delta T L^3}{\nu^2}.$$

Here, $g = 9.81$ (m/s^2) is the average terrestrial gravitational acceleration, β and β_C are the corresponding temperature and concentration expansion coefficients of the melt, and ν (cm^2/s) is the kinematic viscosity of the melt.

[7]The corresponding dimensionless mass transfer coeffcient is also called the Sherwood number, Sh.

Three distinguished limits may be considered for natural convection during crystal growth:

1. $Gr/Re^2 < 0.1$, natural convection is negligible.
2. $0.1 < Gr/Re^2 < 10$, neither is negligible.
3. $Gr/Re^2 > 10$, forced convection is negligible.

Natural convection for melt growth processes conducted terrestrially may only be ignored in small-diameter CZ melts, crystallizing at high rotational rates.[8]

25.4.4.1 Forced Convection

Fluid flow, when driven by some external source, allows the Reynolds number of the flow, Re, to be calculated. Using forced convection it becomes easier to maintain a crystal growth process at a steady rate, and, moreover, employing forced flow also allows enhanced heat and/or mass transfer to occur, to achieve faster crystal growth rates. Techniques that have proven successful for achieving forced-flow crystal growth from the melt include: crystal rotation, or crucible rotation; accelerated crucible rotation technique (ACRT) [23]; application of external magnetic fields with conducting melts [24]; and insertion of oscillating baffles [25]. The Nusselt number, for forced convection mass transfer, may be expressed as,

$$Nu = \frac{h_{FC}L}{D} = F(Re^n, Sc^m). \tag{25.20}$$

where $n = 1/2$ for laminar flow and $n = 0.8$ for turbulent flow; $m = 1/3$.

25.4.4.2 Natural Convection

Natural convection is driven by buoyancy forces due to mass density differences $\Delta\rho$, caused by temperature differences, ΔT, and or concentration differences, ΔC. The Nusselt number, for natural convection mass transfer, may be expressed as,

$$Nu_{NC} = \frac{h_{NC}L}{D} = F\left(Gr^n, Sc^m, \mathrm{Pr}^k\right), \tag{25.21}$$

where $n = 1/4$ for laminar flow, and $n = 1/3$ for turbulent flow; $m = 1/3$.

25.4.4.3 Convection Driven by Freezing

Perpendicular or suction flows, due to crystallization, may also be classified as "forced convection," since the interface velocity, f, is known. Such perpendicular flows on earth can reduce the solute layer thickness and, as a result, increase the concentration gradient at the interface; whereas in space experiments, where natural convection tends to be weak, perpendicular flows control segregation. The Péclet number, expressible as the product of the Reynolds and Schmidt numbers, is dimensionless interface velocity,

[8]Burton et al. [1,2] conducted experiments at 57, 144, 575, and 1440 rpm. Hence, natural convection was negligible.

$$Pe_f = \frac{fL}{D} = Re_f \cdot Sc \tag{25.22}$$

25.4.4.4 Thermocapillary Convection

Thermocapillary (Marangoni) convection is driven by surface tension gradients. Thermocapillary convection is unavoidable when free melt surfaces are present during crystal growth. On earth, with the presence of strong buoyancy forces, thermocapillary convection is usually less important then either forced or natural convection. The chief exception occurs where thermocapillary convection can actually dominate the flow state in microgravity crystal growth and in floating zone crystal growth. Its specific influences on solute segregation will not be elaborated any further.

25.4.4.5 Mixed Convection

Mixed convection is the term describing various combinations of forced and natural convection [8,9]. See Section 25.6.2.

25.5 Segregation Theories Based on Solute Layer Thickness

Next we consider several theories of solute segregation, where the effective segregation coefficient is a function of the solute boundary layer thickness, i.e., $k_{eff} = F(\delta)$. The following definitions are used in modern crystal growth literature, see Figure 25.4:

1. Physical film thickness.
2. Gradient of tangential film thickness, δ_{grad}, defined by Eqn (25.15). The profile $C_L(x)$ is linear.
3. Fictitious stagnant film thickness, δ_{exp}. See BPS theory below.

25.5.1 BPS Theory

A seminal paper concerning solute segregation during melt crystal growth by BPS appeared in 1953 [1,2]. This theory was the first attempt to introduce melt convection as a factor influencing solute segregation during unidirectional crystal growth. BPS theory provides a one-dimensional solute segregation model, which consequently ignores any associated transport of solute in directions lateral to the crystal–melt interface. As pointed out earlier in this chapter, such an approach is physically incorrect, as melt convection is not realistically unidirectional and always moves some of the fluid laterally along the crystal–melt interface. By restricting convection to one-dimensional steady state incompressible flow, Eqn (25.3) reduces to

$$D\frac{d^2C}{dz^2} - V_z\frac{dC}{dz} = 0. \tag{25.23}$$

Here velocity $V_z = w + f$, is just the sum of the normal fluid velocity, w,[9] and the interface speed, f. Next, BPS assumes that within the "stagnant layer," δ, the normal flow velocity merely matches the interface speed, f. Equation (25.23), subject to that assumption, becomes identical to Tiller's expression, Eqn (25.8), the solution to which yields an exponential concentration profile in the melt adjacent to the advancing interface,

$$\frac{C_L(x) - C_S}{C_0 - C_S} = e^{-\frac{f}{D}x}. \tag{25.24}$$

BPS then truncates the full exponential solute concentration profile by introducing a fictitious stagnant layer thickness, $x = \delta$, claiming further that $C_L(\delta) = C_L$, a condition introduced into Eqn (25.24), which provides the outer matching condition for the concentration field where the stagnant boundary layer ends and the outer perfectly mixed melt begins. Next, introducing $k_0 = C_S/C_0$, BPS obtains its "effective segregation coefficient,"

$$k_{eff} = \frac{C_S}{C_L} = \frac{k_0}{k_0 + (1 - k_0)e^{-\Delta}}, \tag{25.25}$$

expressed by a dimensionless exponent $\Delta = -f\delta_{\text{exp}}/D$. The term δ_{exp} is the thickness of the exponentially decaying solute profile, which supposedly develops within the putative "stagnant film" given by Eqn (25.24). Now the quantity δ_{exp} may be determined from Levich's similarity solution to the hydrodynamic equations governing convection, namely,

$$\delta_{FC}^{grad} = 1.61\, D^{1/3}\nu^{1/6}\omega^{-1/2} \tag{25.26}$$

The subscript FC in Eqn (25.26) denotes that the layer thickness, δ_{FC}^{grad}, is actually controlled by forced convection alone. The superscript *grad* in Eqn (25.26) reminds the reader that the solute layer thickness, δ_{FC}^{grad}, is not based on the physical solute concentration profile δ, given by Eqn (25.16), but rather on the linear profile illustrated in Figure 25.4.

Why does replacing the exponential profile thickness, δ_{exp}, with one determined from the linear solute layer thickness estimate, δ_{FC}^{grad}, work so well? The answer to this question is that Eqn (25.25) is actually applicable only to CZ crystal growth, and specifically where the dimensionless exponent is small, i.e., where $\Delta \ll 1$,[10] so that a one-term expansion remains accurate, and

$$e^{-\Delta} \approx 1 - \Delta$$

Therefore, one obtains

$$k_{eff} = \frac{k_0}{k_0 + (1 - k_0)e^{-\Delta}} \approx \frac{k_0}{1 - (1 - k_0)\Delta} \tag{25.27}$$

[9]According to Cochran, $w = 0.51w^{3/2}\nu^{-1/2}x^2$ valid for $x < \sqrt{\nu/w}$.
[10]δ_{grad} will be small because of the intense forced convection.

The above connection was first noted by Lynne Wilson, who remarked, “We feel that the right answer has been obtained for the wrong reason” [26]. It is interesting to note that in the classic 1965 book, in the section “Partial Stirring,” J.C. Brice derived the relation,

$$k_{eff} = \frac{k_0}{1 - (1 - k_0) f \frac{\delta^{grad}}{D}},$$

and proceeds to present the BPS model, see p. 81 in [27]. In conclusion, Eqn (25.26) is a similarity solution for the solute segregation in CZ crystal growth, the validity for which is limited by the following five assumptions used in its derivation:

1. Melt flow is characterized as laminar, symmetric, and rotating;
2. The disk (growing crystal face) is infinitely large and impermeable, so δ is not a function of f;
3. The Schmidt number for the melt is large, $Sc \to \infty$; See Section 25.7.1.
4. Buoyancy forces are negligible compared to forces applied by the crystal face;
5. Solute transfer is one-dimensional.

In conclusion, Eqn (25.26) is applicable only to laminar melt flows occurring in small-diameter CZ melts where $Re^2 \gg Gr$.

The physical basis for, and the mathematical consistency of, BPS segregation theory has been challenged since 1970. BPS predictions for the segregation, in fact, could neither be validated nor refuted, because the diffusion coefficients for solutes D—key melt parameter—were not known precisely enough (see Section 25.9).

25.5.2 Wilson–Garandet’s Model: Forced Convection Alone

Wilson (1978) [26] and Garandet et al. (1993) [30] recognized the shortcomings of stagnant layer segregation models. Their model also considers forced convection acting alone but eliminates the questionable assumption of a stagnant solute layer. Lateral melt convection along the crystal–melt interface is again ignored, so melt flow again is assumed to be one-dimensional. The Wilson–Garandet formula for the effective segregation coefficient is the *linearized* BPS estimate, Eqn (25.27),

$$k_{eff} = \frac{k_0}{1 - (1 - k_0)\Delta}. \tag{25.28}$$

But dimensionless solute layer thickness, Δ, is instead defined by the following definite integral,

$$\Delta = \frac{f\delta}{D} = \int_0^\infty \exp\left(-z - Bz^3\right) dz, \tag{25.29}$$

where the constant in the integrand of Eqn (25.29) is defined as, $B = 0.17 f^{-3} \omega^{3/2} \nu^{-1/2} D^2$. The integration variable, z, designates the perpendicular distance from the interface [1,3,4]. This model is exact, but again its validity remains limited in scope by the five

assumptions concerning the similarity solution (listed in Section 25.5.1, BPS theory). Hence the Wilson–Garandet formula provides a solid estimate for k_{eff}, providing that the CZ crystal is rotating rapidly [31], so natural convection may be ignored.

25.5.3 Models Considering Natural Convection and/or Lateral Melt Convection

Camel and Favier (1984) [32], chose an order-of-magnitude analysis to extract scaling laws that delineate longitudinal solute segregation in HB crystal growth. In contrast to the BPS and Wilson–Garandet forced-convection models, Favier and Camel analyzed the influences of natural convection on solute segregation. Natural convection, as discussed earlier in this Chapter, ensures lateral melt flow along an advancing crystal–melt interface.

Yen and Tiller [21] also pointed out that in BPS's one-dimensional analysis of only an axial normal flow component was considered. Neither buoyancy-driven natural convection nor lateral convection was considered, although in many instances it may be the dominant flow mode. Yen and Tiller instead incorporated the important effects of lateral melt convection into their solute redistribution analysis by introducing an "effective" solute source/sink term in the solute transport equation, as

$$D\frac{d^2C}{dz^2} - V_z\frac{dC}{dz} - \dot{q} = 0. \tag{25.30}$$

Ostrogorsky and Mueller [20,22] derived a correlation for the effective segregation coefficient using integral boundary layer analysis, Figure 25.5. Their segregation model for k_{eff} becomes a function of the actual/physical thickness of the solute layer, δ, given by Eqn (25.16). Natural convection was considered using scaling arguments. This

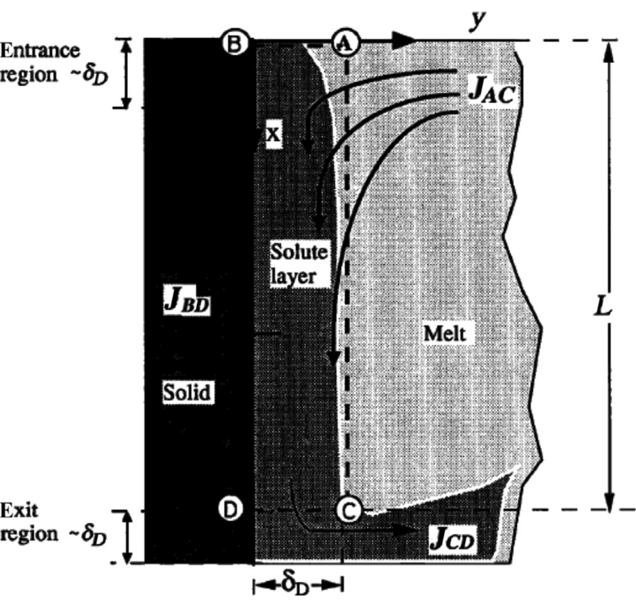

FIGURE 25.5 Schematic of lateral convection, from Ostrogorsky and Mueller [20].

segregation model provides a criterion for the maximum convective velocity that allows diffusion-controlled segregation. Interestingly, this criterion suggests that diffusion-controlled segregation of a binary system with a low value for the equilibrium segregation coefficient ($k_0 \ll 0.1$) might, in fact, not be possible even in an ideal microgravity environment.

In conclusion, the solute segregation models developed by Camel and Favier (1984) [32], Yen and Tiller [21], and Ostrogorsky and Mueller [20] include the important melt flow feature of lateral melt convection. Without the presence of some lateral melt convection, solute transport away from the crystal–melt interface would cease, and k_{eff} would become equal to unity.

25.6 Segregation Model with Nusselt Numbers and Mixed Convection

The application of forced melt convection during bulk crystal growth proves to be advantageous from several standpoints. Initially, forced convection was incorporated only in CZ, using crystal rotation, and similarly in float zone (FZ) processing. As the advantages of forced melt convection and the disadvantages of natural melt convection became clearer, novel adaptations involving forced melt flow were implemented for Bridgman/Vertical Gradient Freeze (VGF) crystal growth. These innovations included the use of traveling magnetic fields [24] (see Vol. IIb, Chapter 23), forced mechanical vibrations, and rotating/oscillating immersed baffles [25] (see Vol. IIb, Chapter 24). The melt convection during crystal growth resulting from the application of these techniques usually produces a mix of natural and forced convection, and perpendicular suction flow. Such complex flow states will be referred to as “combined convection.”

25.6.1 Combined Mass Transfer Coefficient

Mass conservation at steady state in the presence of combined melt convection requires that the solute flux rejected at the crystal–melt interface, j_{rej}, is transported away into the bulk melt by a combined convective flux, j_{CC} [33]. See again Figure 25.1. Expressions for the rejected mass flux and the combined convective flux are, respectively,

$$j_{rej.} = f\left(C_0 - C_S\right),$$

and

$$j_{CC} = h_{CC}(C_0 - C_L),$$

where h_{CC} is the “combined” mass transfer coefficient. Referring again to Figure 25.1, solute mass conservation requires their balance, specifically,

$$f(C_0 - C_S) = h_{CC}(C_0 - C_L).$$

Rearranging the above mass balance, and substituting the equilibrium segregation coefficient, k_0, yields the relationship for the effective segregation coefficient for combined melt convection, $k_{eff,CC}$, as [33],

$$k_{eff,CC} = \frac{C_S}{C_L} = \frac{k_0}{1 - (1 - k_0)\frac{f}{h_{CC}}}. \tag{25.31}$$

Equation (25.31) is a statement of mass conservation, and, as such, is exact, recognizing, of course, that practical applications of Eqn (25.31) require a suitable correlation linking the crystal growth rate, f, with the combined mass transfer coefficient, h_{CC}.

25.6.2 Phenomenological Approach to Determine the Combined Mass Transfer Coefficient

In order to take advantage of existing empirical correlations for the mass transfer coefficient for forced and natural melt convection, h_{CC} is modeled as follows.

1. *"Mixed" convection:* Based on extensive heat transfer data, it is common practice to correlate combined or mixed natural and forced convection by the following formula,

$$h_{mix} = \left(h_{FC}^m \pm h_{NC}^m\right)^{1/m}. \tag{25.32}$$

The value of the exponent, m, varies between 3 and 4, depending on the flow configuration. The value $m = 3$ correlates data obtained from vertical surfaces. Values for m that fall between 3.5 and 4 are used to correlate flow data from horizontal surfaces [8,9]. The sign within Eqn (25.32) is selected as positive when forced and natural convection reinforced, i.e., act in the same direction, thereby enhancing the overall mixed flow state. The sign in Eqn (25.32) is selected as negative when forced and buoyant convection oppose each other, leading to a weakened mixed flow state. For processes where $Gr \gg Re^2$, e.g., Bridgman crystal growth, one allows $h_{mix} = h_{NC}$. For processes where $Re^2 \gg Gr$, one chooses $h_{mix} = h_{FC}$.

2. *Perpendicular flows can reinforce mixed convection:* Perpendicular (suction) flow $f(\rho_S/\rho_L)$ can reinforce mixed convection, and for situations where $f/h > 0.1$, it should not be ignored. As correlations for interfaces with suction flow are not currently available, it has been suggested to use an effective combined convection coefficient, h_{CC}, of the following form [33],

$$h_{CC} = h_{mix}\left[1 + \left(\frac{f}{h_{mix}}\right)^n\right]^{1/n} = \left[h_{mix}^n + f^n\right]^{1/\mathrm{n}}, \tag{25.33}$$

where n is an arbitrary exponent. This mathematical form is selected because Churchill and Usagi [34] established that such a correlation is remarkably successful in correlating rates of heat, mass, and momentum transfer. According to reference [35], $n = 1.4$.

Combining Eqns (25.32) and (25.33) gives the combined convection mass transfer coefficient as,

$$h_{CC} = \left[\left(h_{FC}^{m} \pm h_{NC}^{m} \right)^{n/m} + f^{n} \right]^{1/n} \tag{25.34}$$

Note, once again that typically, $h_{mix} \gg f$. Perpendicular convection becomes important primarily in reduced gravity situations, where $h_{mix} = h_{NC}$ is small.

25.6.3 Effective Segregation Coefficient, k_{eff}, as Function of Combined Nusselt Number

Empirical correlations for mass transport coefficients are conveniently given in terms of a CC Nusselt number, Nu_{CC}. Thus, one can rewrite Eqns (25.31) and (25.34) in terms of dimensionless parameters,

$$k_{eff,CC} = \frac{k_0}{1 - (1 - k_0) Pe_f / Nu_{CC}}, \tag{25.35}$$

and

$$Nu_{CC} = \left[Nu_{mix}^{n} + Pe_f^{n} \right]^{1/n} = \left[\left(Nu_{FC}^{m} \pm Nu_{NC}^{m} \right)^{n/m} + Pe_f^{n} \right]^{1/n}, \tag{25.36}$$

where $Pe_f = fL/D$, see Eqn (25.22). Nu_{NC} and Nu_{FC} are given by empirical correlations found for pure forced convection and pure natural convection. See below.

25.7 Correlations for Nusselt Numbers

Numerous established correlations are available for natural convection and convection driven by rotating disks. To our knowledge, there are no correlations relating Nusselt numbers to the magnetic Taylor number or to other parameters characterizing moving magnetic fields.

25.7.1 Correlations for Disk-Driven Forced Convection

Many correlations for laminar and turbulent flows are given in the 1963 monograph by L.A. Dorfman [36], and in the recent monograph *Convective Heat and Mass Transfer in Rotating Disk Systems* by Igor V. Shevchuk (2009) [28]. The key correlations for convection occurring in CZ melts are listed in [31].

25.7.1.1 Exact Similarity Solution for Laminar Flow and Sc → ∞

Levich's similarity solution for the mass flux is expressed as

$$j = 0.62 D^{2/3} \nu^{-1/6} \omega^{1/2} (C_0 - C_L). \tag{25.37}$$

Levich specified neither the mass transfer convection coefficient, h, nor the Nusselt number, Nu, both of which are obviously based on the mass flux,

$$h = 0.62D^{2/3}\nu^{-1/6}\omega^{1/2} = 0.62D\sqrt{\frac{\omega}{\nu}}Sc^{1/3}. \tag{25.38}$$

and,

$$Nu_{FC} = \frac{hR}{D} = 0.62Re^{1/2}Sc^{1/3}(Sc \to \infty). \tag{25.39}$$

25.7.1.2 Empirical Correlations, Laminar Flow

Doped semiconductor melts, Si and Ge, have Schmidt numbers in the range $10 \le Sc \le 100$ [31]. The Nusselt number correlations for this important range are:

$$Nu_{FC} = 0.485Re^{1/2}Sc^{0.373}(5 \le Sc \le 100), \tag{25.40}$$

as proposed by Ostrogorsky [31], and

$$Nu_{FC} = \frac{0.62045 \cdot Re^{1/2}Sc^{1/3}}{(1 + 0.298Sc^{-1/3} + 0.14514Sc^{-2/3})}(2 \le Sc \le \infty), \tag{25.41}$$

as proposed by Newman [37]. In Figure 25.6, the above forced convection Nusselt number correlations, Nu_{FC}, are plotted as a function of the Schmidt number. The curve labeled "Exact," is the numerical solution of the governing equations. Levich's "exact" solution Eqn (25.39), which requires $Sc \to \infty$, shows a 7% error at $Sc = 100$ and a 17%

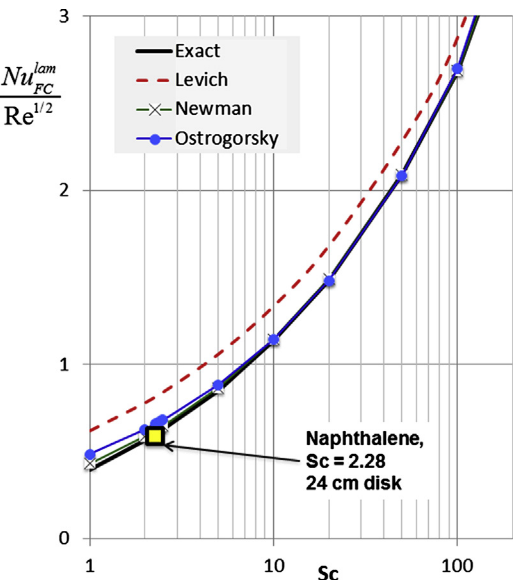

FIGURE 25.6 Exact numerical solution from [28], and correlations for Nusselt numbers, divided by $Re^{1/2}$, for laminar flow versus Schmidt numbers, Sc. *Data point is from Chen et al.; see [29].*

disparity at $Sc = 10$ [31]. The correlation Eqn (25.40), indicates less than 1% error, for $10 \leq Sc \leq 100$ and less than 4% error for $5 \leq Sc \leq 500$ [31]. The correlation, Eqn (25.41), even more impressively provides less than 4% error for the range $2 \leq Sc \leq \infty$ [31].

It is also encouraging to see near perfect agreement with the experimental data point, obtained using a 24-cm-diameter disk and evaporating naphthalene at a Schmidt number $Sc = 2.28$.

25.7.1.3 Empirical Correlations, Turbulent Flows

Melt convection in CZ crystal growth is turbulent from the combined action of strong centrifugal and buoyancy forces. Yet CZ melt flow should be laminar based on the Reynolds numbers alone, excepting growth of large CZ Si crystals at high rates of rotation. For flat disks, the lamellar–turbulent transition occurs at $Re \approx 8.8 \times 10^4$, with flow reaching a fully turbulent state at $Re \approx 3.2 \times 10^5$ [38]. By contrast, a 20-cm-diameter Si crystal rotating at 30 RPM has a Reynolds number of $Re \approx 100{,}000$.

Numerous correlations for turbulent flow driven by a rotating disk can be found in reference [28]. Here we present the two correlations by Dossenbach: (1) for fully turbulent flow, $Re > 300{,}000$,

$$\overline{Nu^{turb}} = 0.0108 Re^{0.87} Sc^{1/3}, \tag{25.42}$$

and (2) transition from laminar to turbulent flow, valid for $Re_{tr} < Re < 1.8 \times 10^6$ (see Figure 25.7) [28],

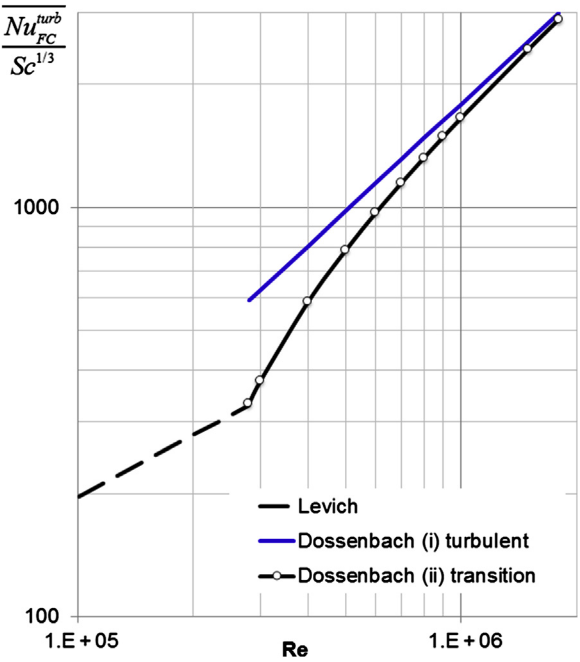

FIGURE 25.7 Average Nussel number divided by $Sc^{1/3}$ as a function of Re, for turbulent flow, from [31].

$$\overline{Nu^{tr}} = \frac{Sc^{1/3}}{Re^{0.5}}\left[0.62Re_{tr} + 0.0108\left(Re^{1.37} - Re_{tr}^{1.37}\right)\right]. \tag{25.43}$$

The transition occurs at $Re_{tr} = 278{,}000$.

25.7.2 Empirical Correlations for Natural Convection

The general form of a Nusselt number correlation for natural convection is given by Eqn (25.20). The majority of these correlations were developed using heat transfer data,[11] but by analogy also hold for mass transfer, provided that mass transfer does not alter the fluid velocity. When $Sc \gg Pr$, a heat transfer correlation may be transformed into a mass transfer correlation by using the following substitution [39,40]:

$$\text{For } Pr/Sc \rightarrow 0, Nu^{HT} \rightarrow Nu, \text{ and } Gr \cdot Pr \rightarrow Gr \cdot Sc \cdot Le^{1/3} \tag{25.44}$$

where $Le = Sc/Pr = \alpha/D$ is the Lewis number. For silicon melts, $Pr = 0.014$, and for silicon melts doped by B, P, or As, $Sc \approx 15$ [31]. Thus, for this semiconductor melt $Sc \gg Pr$ and $Le \approx 1070$.

Natural convection in large CZ melts is complex, as it depends on the solid–liquid interface diameter, *d*, the overall melt geometry, vertical and horizontal thermal gradients, etc. Here we consider well-established correlations developed for natural convection in liquid metals and applicable to semiconductor crystal growth.

25.7.2.1 Vertical Walls

A vertical solid–liquid interface, oriented parallel to gravity, is typical of the crystal growth configuration for both HB growth and horizontal zone refining. This configuration is also relevant to CZ crystal growth, because vertical heated crucible walls drive natural melt convection. Churchill and Chu's [39] empirical correlation was tested against experimental heat or mass transfer data. Their correlation may be expressed as,

$$Nu_L^{HT} = \frac{h^{HT}L}{\lambda} = \left\{0.825 + \frac{0.387(Gr_L Pr)^{1/6}}{\left[1 + (0.492/Pr)^{9/16}\right]^{8/27}}\right\}^2.$$

It is valid for any Prandtl number, *Pr*, and the range of Rayleigh numbers, $0.1 \le Ra_L \le 10^{12}$. *L* is the wall length, and $Ra_L = Gr_L Pr$. For the case of mass transfer, substitution of Eqn (25.44) gives the result,

$$Nu_L = \frac{hL}{D} = \left\{0.825 + \frac{0.387(Gr_L Sc)^{1/6} Le^{1/18}}{\left[1 + (0.492/\mathrm{Pr})^{9/16}\right]^{8/27}}\right\}^2. \tag{25.45}$$

where *Le* is Lewis number.

[11]Convection heat transfer experiments are more precise and easier to conduct than are convection mass transfer experiments.

Masliyah and Nguyen's [41] correlation was developed from mass transfer experiments, using the binary system 2-bromopyridine in water. The Nusselt number correlation they found is

$$N_L = \frac{hL}{D} = 0.258(Gr_L \cdot Sc)^{0.289}. \qquad (25.46)$$

This correlation was tested for $2 \times 10^{12} \le Gr_L Sc \le 10^{13}$. For 2-bromopyridine in water, $Pr = 6.7$, $Sc = 2500$, and $Le = 373$. This system is roughly comparable to the Lewis number for doped silicon melt, $Le = Sc/Pr = 1070$. For comparison, Nusselt versus Grashof number correlations Eqns (25.45) and (25.46) based on a vertical wall are given in Figure 25.8, along with the Ostrach's similarity solution for laminar flow [10] and Sparrow and Greg's correlation, see [44].

25.7.2.2 Horizontal Disks

The solid–liquid interface can be modeled as a downward-facing cooled disk for both CZ and Kyropoulos crystal growth processes, which feature relatively large melt volumes and small crystals. McDonald and Connolly [43] carried out experiments with a cooled, horizontal, downward-facing circular plate ($d = 20$ cm) immersed in a tank of liquid sodium metal. Experiments were carried out over the Grashof number range $6 \times 10^8 \le Gr \le 5 \times 10^9$. Those investigators found the Nusselt number correlation for heat transfer as

$$Nu_d^{HT} = \frac{h^{HT} d}{\lambda} = 0.262\left[Gr_d \cdot Pr^2\right]^{0.35}.$$

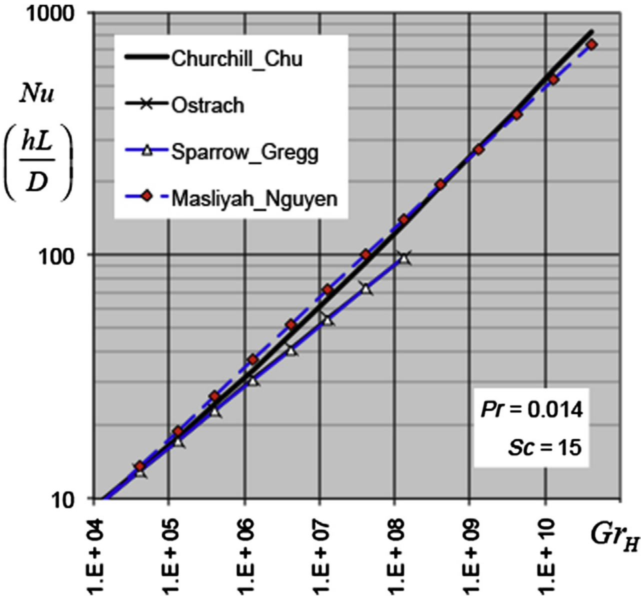

FIGURE 25.8 Comparison of mass transfer correlations for vertical walls. $Sc = 15$ is typical for impurities in silicon [44].

The Nusselt number correlation for the case of mass transfer was similarly found to be [44],

$$Nu_d = \frac{hd}{D} = 0.262[Gr_d \cdot Sc \cdot Pr]^{0.35} Le^{0.35/3}. \tag{25.47}$$

Reference [44] illustrates the excellent agreement between the above correlations with key correlations for heat and mass transfer.

25.7.2.3 Rayleigh–Bénard Convection

Rayleigh-Bénard convection between a cooled interface and the heated crucible bottom may be used for large-diameter Kyropoulos or CZ crystal growth. The Globe–Dropkin correlation [45] was tested for the parameter ranges $3 \times 10^5 \le Gr \cdot Pr \le 7 \times 10^9$ and $0.02 \le Pr \le 8750$, where for heat transfer,

$$Nu_L^{HT} = \frac{h^{HT} L}{\lambda} = 0.069(Gr_L \cdot Pr)^{1/3} Pr^{0.074},$$

and for mass transfer,

$$Nu_L = \frac{hL}{D} = 0.069(Gr_L \cdot Sc)^{1/3} Le^{1/9} Pr^{0.074}. \tag{25.48}$$

Reference [44] illustrates the good agreement between the above correlations and several other well-established correlations for liquid metals.

25.8 Directional Solidification: Segregation without Forced Convection

Natural convection is almost always unsteady in semiconductor melts. It is turbulent for $Gr > 10^9$. The level of unsteady convection depends both on the melt size and radial temperature gradients, as well as on the interfaces shape, etc.—all of which continually change during growth. Unsteady convection yields significant fluctuations in growth rate, leading to compositional inhomogeneities and misoriented nucleation and growth [24].

Radial inhomogeneity during directional crystal growth is high compared to CZ growth. Research on this topic focused initially on minimizing natural convection, by application of axial and transverse magnetic fields, insertion of baffles and other flow restrictors, etc. Numerical modeling conducted in the 1980s [46,47], however, eventually revealed that the highest lateral segregation usually occurs when the melt flow velocity is low. Lateral segregation during HB crystal growth reaches a maximum when the Grashof number $Gr_H \approx 10^3$ [46]. See also Section 25.11.2. Reduction of natural convection through the use static magnets or melt baffles helps to prevent turbulence but does not necessarily yield significant improvements of either crystalline and chemical perfection of the crystals so grown. This disappointing fact remains true even for directional solidification conducted in microgravity. Therefore, research conducted during the past decade focused mainly on introducing strong, controllable, forced convection rather than attempting to actually minimize levels of natural convection.

In conclusion, one finds that natural convection is an unavoidable phenomenon; moreover, it is virtually impossible to eliminate natural convection entirely, given that the flow direction and magnitude of its velocity are extremely difficult to control. As a result, both macroscopic and microscopic component redistributions are notably inferior (less well controlled) when compared to those obtained via the CZ growth process. In those instances where directional solidification is carried out without forced convection, the effective segregation coefficient simplifies because $Nu_{mix} = Nu_{NC}$. Thus,

$$k_{eff,NC} = \frac{k_0}{1 - (1 - k_0)Pe_f \Big/ \left[Nu_{NC}^{1.4} + Pe_f^{1.4}\right]^{1/1.4}}. \tag{25.49}$$

where $Pe_f = fL/D$, see Eqn (25.22). The correlation found for Nu_{NC} may be selected on the basis of the orientation of the crystal–melt interface; $k_{eff,NC}$, is expected to vary as the melt size changes. Thus, Eqn (25.49) provides only a first-order model of the segregation process.

It appears that future improvements of directional crystal growth will rely more heavily on schemes that use forced convection-dominated processes, where, $Re^2 > Gr$, rather than reduction of natural convection.

25.8.1 Segregation Under Vanishing Natural Convection ($Gr \to 0$)

DS experiments carried out in orbital laboratories during the 1970s and 1980s were focused on achieving diffusion-controlled solute segregation (see Section 25.3.2). In addition, magnetic fields reaching 3 T were applied in an effort to diminish natural convection [48].

Diffusion-controlled solute segregation occurs when the advective flux, $j_{advection}$, via bulk melt motion, becomes insignificant compared to the diffusion flux, so their ratio, $j_{advection}/j_{diffusion} \to 0$. As noted earlier, however, diffusion-controlled solute segregation acting alone should result in an ideal uniform axial and lateral segregation [49]. To reduce the distorting influence of natural convection, one must reduce the buoyancy forces. On orbiting platforms, the quasi-static gravitational acceleration is routinely reduced by factors of about 10^{-5} or less. The Grashof number is commensurately reduced, since $Gr \approx g\Delta TL^3$, as neither the melt's viscosity, ν, nor its thermal expansion coefficient, β, can be altered. Therefore, the goal of pioneering microgravity experiments conducted in near-Earth orbit[12] was to approach to as a high degree as possible the ideal diffusion-controlled segregation. At that early time for microgravity experiments, the "gap" between theory and experiments was attributed to "gravity-induced convection effects" [49,50]. It was expected that reducing the gravitational acceleration (and the Grashof number) by a factor of roughly 10^{-5} or less should also reduce buoyancy forces to the point that the convective mass flux would be negligible compared to the diffusion flux.

[12]As occurred during the Skylab [49] and Apollo-Soyuz missions.

To the contrary, it actually turned out that nearly every segregation experiment conducted in orbital (low-gravity) environments was disturbed by convection driven by buoyancy and/or surface tension (Marangoni) forces. Steady state segregation was achieved only during the Skylab mission by growing Te-doped InSb [49] and, again more recently, Te- and Zn-doped InSb [17,18]. Yet, the Ga-doped Ge crystal growth experiments, conducted during the Apollo–Soyuz mission [50], clearly revealed appreciable convective influences on the measured solute segregation. This unexpected result can be explained now by using the CC model given by Eqn (25.49).

In microgravity conditions, the most pervasive influence altering a diffusion-limited segregation pattern arises from accelerations acting parallel to the interface [22], as would be the terrestrial situation for the HB configuration. See Figure 25.9, where a horizontal temperature difference, ΔT, drives convection. The solid–liquid interface is the vertical cooled wall (see Section 25.7.2.1).

When applying the Nusselt number correlations to extremely low flow velocities, one should consider the following correction. All such correlations are developed for solid (impermeable) walls, where for "zero" flow velocity $j_{advection} = 0$ and $Nu = 1$,

$$Nu \equiv \frac{j_{convection}}{j_{diffusion}} = \frac{j_{advection} + j_{diffusion}}{j_{diffusion}} = 1 \tag{25.50}$$

During crystal growth, however, the crystal–melt interface acts as a porous boundary. Without the presence of some advection, solute cannot be transported by diffusing against the perpendicular flow velocity (i.e., $j_{diffusion} = 0$). Thus, one should use the so-called "excess" Nusselt number [31], namely, the amount by which the Nusselt number exceeds unity,

$$Nu^{excess} \equiv \frac{j_{advection}}{j_{diffusion}} = \frac{j_{convection} - j_{diffusion}}{j_{diffusion}} = Nu - 1 \tag{25.51}$$

Using the excess Nusselt number only becomes a significant correction in microgravity environments, since on Earth, typically $Nu^{excess} \approx Nu$.

Figure 25.10 shows $k_{eff,NC}$ calculated using Eqn (25.49), for Ga-doped Ge crystal growth experiments, conducted during the Apollo–Soyuz mission [50]. $Nu_{NC}^{excess} = Nu - 1$ was calculated using

1. Churchill and Chu's Eqn (25.45);
2. Ostrach's similarity solution [9,10];
3. Masliyah and Nguyen's Eqn (25.46).

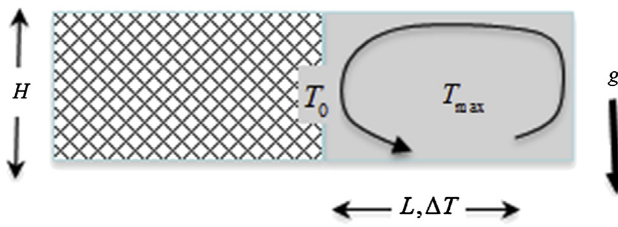

FIGURE 25.9 Schematic of horizontal Bridgman (HB) process: characteristic lengths and temperature differences.

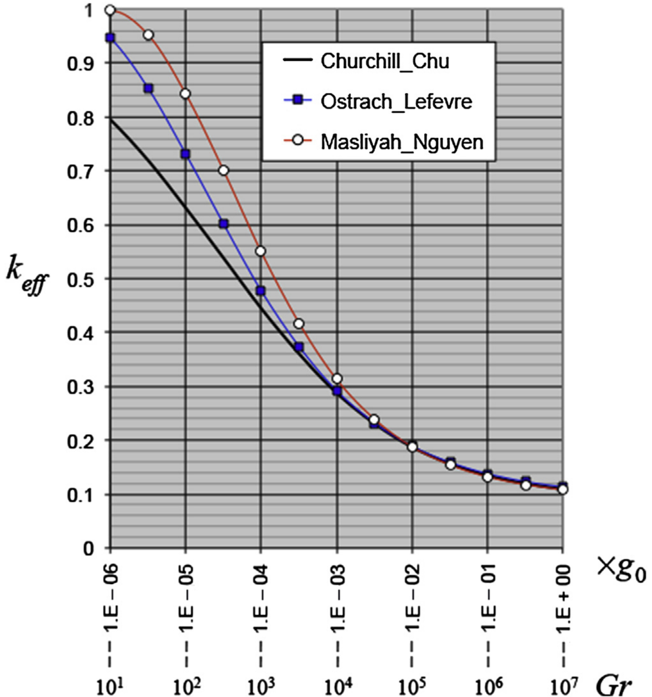

FIGURE 25.10 k_{eff} for $10^{-6}g_0 < g < g_0$ ($g_0 = 981$ cm/s^2) calculated using Eqn (25.49) for parameters used by Witt et al. [50]. Nu_{NC} was calculated using Eqn (25.45), Eqn (25.46), and Ostrach's similarity solution for laminar flow [8,9].

Overall, the agreement found among these correlations is solid for $Gr > 10^4$, see Figure 25.10. Churchill and Chu's correlation has been tested for $GrPr > 0.1$ (or $Gr > 10$ since $Pr \approx 0.01$). Therefore, it should be accurate down to $10^{-6}g_0$. Ostrach's similarity solution is valid only for laminar "boundary-layer" flow, or typically $Gr > 10^4$. For ground-based experiments, all three correlations give $k_{eff} \approx 0.11$, whereas Witt et al. reported $k_{eff} \approx 0.099$.

At $10^{-5}g_0$, Eqn (25.49), with Churchill and Chu's correlation, gives $k_{eff,NC} \approx 0.63$, whereas from the segregation profiles reported by Witt et al.[13] one calculates $k_{eff} \approx 0.6$ [50].

Figure 25.11 illustrates the effect of the crystal growth rate. The solute boundary layer is thinner at high growth rates and, therefore, is less sensitive to convection. For the case of Ga-doped Ge, grown at $10^{-6}g_0$, growth rate $f \approx 10$ (cm/hr) would yield $k_{eff} \approx 0.95$. By contrast, $f \approx 1$ (cm/hr) would yield $k_{eff} \approx 0.5$. Thus, diffusion-controlled segregation becomes infeasible at low growth rates, under conditions, for example, that are needed to grow semiconductor alloy crystals.

Figure 25.12 focuses on the significance of the equilibrium segregation coefficient k_0. It shows clearly that diffusion-controlled melt growth on orbital platforms becomes practical only with systems having moderate to high k_0-values ($0.5 \le k_0 \le \infty$). This fact

[13]The initial dopant concentration in the melt was $C_L^i = 1.78 \times 10^{19}$ cm^{-3}. Accordingly, the first to freeze section had a concentration $C_s(0) = k_0 C_L^i = 1.55 \times 10^{18}$ cm^{-3}. The highest concentration achieved in the solid was at 2 cm, where $C_s = 1.1 \times 10^{18}$ cm^{-3}.

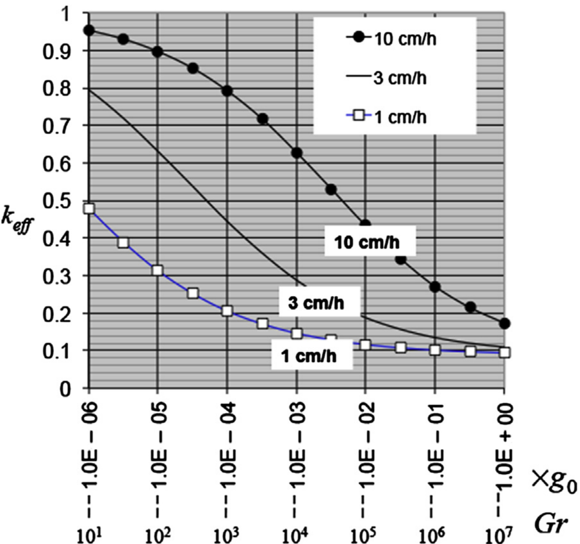

FIGURE 25.11 $k_{eff,NC}$ as a function of growth rate f (cm/h) and gravity level, calculated for parameters used by Witt et al. [50].

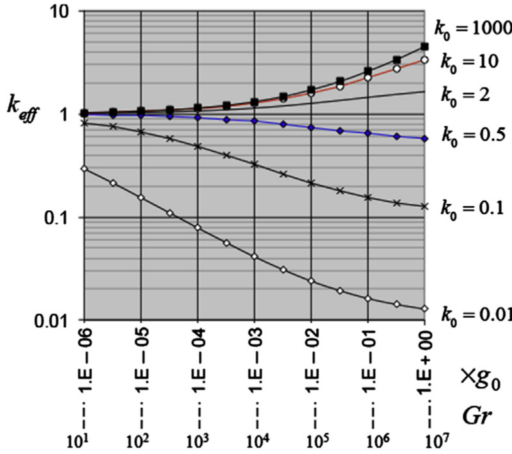

FIGURE 25.12 $k_{eff,NC}$ as a function of k_0 and gravity level, calculated for parameters used by Witt et al. [50].

was not recognized in the 1970s and 1980s, and futile attempts were made to grow Sn-doped InSb ($k_0 = 0.057$) [49] or Sb-doped Ge ($k_0 = 0.003$) [50–52]. In low gravity, systems with $k_0 = 10$ to 1000 yield nearly the same k_{eff}-values.

25.8.1.1 Diffusion Coefficients Extracted under Minimum Convection

Solute segregation developed under diffusion-controlled conditions provides a suitable setting for estimating the diffusion coefficients of dopants and impurities in

semiconductor melts. Yet published data based on this approach often reveal that minute levels of unpredictable, unsteady convection "boost" mass transfer, yielding inflated values of the "effective" diffusion coefficients. Examples of this convective interference are Ga-doped Ge, the reported values for which are $D = 1.7 \times 10^{-4}$ cm^2/s (microgravity experiments [50]), $D = 2.1 \times 10^{-4}$ cm^2/s (shear cell data, [53]), $D = 1.5 \times 10^{-4}$ cm^2/s (3 T axial magnetic field, [48]), and $D = 1.2 \times 10^{-4}$ cm^2/s (5 T axial magnetic field, [54]).

Dutta and Ostrogorsky [54] provide a table that lists some diffusion coefficients obtained under diffusion-controlled, or nearly diffusion-controlled, conditions. They reported $D = 0.8 \times 10^{-4}$ cm^2/s using a submerged heater/baffle—which acted as a flow restrictor—in a 20-zone Mellen furnace. The advantage of using a submerged baffle under terrestrial conditions, relative to the microgravity environment, is that buoyancy forces are steady and point in the direction that opposes convection.

It is interesting to note that the lowest value observed for the diffusion coefficient of Ga-doped Ge was obtained by analyzing CZ segregation data, as described in Section 25.9 below.

25.8.2 Bottom-seeded VB Growth

Crystal growth using bottom-seeded VB has the melt radially heated and, in cases where large-diameter crucibles are required, supplemental heat is added from above. The vertical temperature gradient is stabilizing. However, convection is driven by horizontal temperature gradients. The velocity field depends on the curvature of the interface, horizontal and vertical ΔTs, melt height, crucible material, and other melt parameters. Given the overall complexity of the melt flow, it is advantageous to study segregation and component distribution using three-dimensional numerical modeling techniques, which are capable of including the many interacting parameters that are involved. This is especially true when dealing with molten Si contained in large square crucibles for photovoltaic applications, where melt sizes can reach 1000 kg.

In VB, both crystalline and chemical perfection are often improved by imposing forced convection. This approach, using melt flow control, has been well established through the use of the accelerated crucible rotation technique (ACRT) [23]. Attempts were also made to apply "dominating" forced convection by introducing vibration (see Vol. IIB, Chapter 24) or an oscillating submerged baffle [25]. During the past decade, however, the application of moving magnetic fields (MF) has emerged as the best practice for imposing forced convection during directional solidification. Examples of such moving magnetic fields include traveling MF [24], rotating MF [55], alternating MF, etc. Each of these magnetic field flow-control methods has resulted in a significant improvement in lateral homogeneity, interface shape and symmetry, and crystalline perfection. For further details on the use of moving magnetic fields to stimulate forced convection, see Vol. IIB, Chapter 23, or the excellent review by Rudolph [24].

25.9 CZ Process: Segregation Controlled by Mixed Convection

In Section 25.8 we concluded that natural convection tends to be unsteady, difficult to account for, and thus generally undesirable during crystal growth. Forced convection, by contrast, typically used in CZ growth, is desirable. We proceed by focusing next on solute segregation controlled by forced convection.

25.9.1 Segregation under Steady Forced (Negligible Natural) Convection

The diffusion coefficients of most impurities in semiconductor melts are low, so that even a minute level of convection can alter the diffusion-mediated distribution of impurities in the melt. As noted in Section 25.8.1, weak buoyancy-driven flows have arisen and disturbed numerous microgravity experiments, inflating the apparent values of the diffusivity. This situation remains true even for those measurements conducted in fine capillaries and shear cells. Shear cell measurements, in fact, are usually conducted at a temperature well above the system's melting point,[14] whereas for the purposes of segregation modeling, one would like instead to know the value for the diffusion coefficient in the solute boundary layer at a temperature that is close to the melting point.

Applying a specific amount of laminar forced convection is a good alternative approach, compared to the more difficult and less reliable options of eliminating convection in microgravity. For example, in small CZ melts, the velocity field remains steady and easy to account for. Thus, one concludes that the most reliable approach used to determine the diffusion coefficient is from analysis of the segregation profiles obtained in small CZ systems, provided that melt viscosity is reasonably well known.

25.9.1.1 Diffusion Coefficients of Impurities in Germanium

In 1953, Burton et al. [1,2] reported CZ growth of germanium crystals at various growth rates f and rotation rates ω. To minimize the influence of natural convection, extremely high crystal rotation rates were used: 57, 144, 575, and 1440 RPM, corresponding to $Re^2/Gr = 16$, 110, 1600, and 11,000, respectively.

As the diffusion coefficients of Ga and Sb in molten Ge were not known at that time, Burton et al. [2] applied their segregation data to calculate the apparent diffusivities, rather than to verify the BPS model. Using incorrect viscosity, $\nu = 0.0025\ \text{cm}^2/\text{s}$, Burton et al. reported that for gallium, $D_{Ga} = 0.75 \times 10^{-4}\ \text{cm}^2/\text{s}$. Kodera [56] used $\nu = 0.0055\ \text{cm}^2/\text{s}$, and got $D_{Ga} = 1.03 \times 10^{-4}\ \text{cm}^2/\text{s}$.

[14] The data indicate that close to the melting point viscosity significantly increases. Based on the Stokes–Einstein equation, viscosity varies reciprocally with diffusivity.

Table 25.1 Recommended Values of Diffusion Coefficients in Molten Germanium

Dopant	k_0	D (cm^2/s)	Reference for Data	Reference for Calculation
B	17	2.7×10^{-4}	Bridges [58]	[33]
Ga	0.087	0.67×10^{-4}	Burton et al. [2]	Equation (25.52)
Sb	0.003	0.5×10^{-4}	Burton et al. [2]	Equation (25.52)

Table 25.1 contains the diffusion coefficients, recalculated using combined Eqns (25.35), (25.36), (25.40), (25.42), and (25.45) listed below as:

$$k_{eff,CC} = \frac{k_0}{1-(1-k_0)Pe_f \Big/ \left[\left(Nu_{FC}^{3.5} \pm Nu_{NC}^{3.5}\right)^{1.4/3.5} + Pe_f^{1.4}\right]^{1/1.4}} = k_{measured} \tag{25.52}$$

where $Pe_f = fR/D$ and

$$Nu_{FC} = 0.485\left(\frac{\omega R^2}{\nu}\right)\left(\frac{\nu}{D}\right)^{0.373} \textit{laminar flow} \tag{25.52.1}$$

$$\overline{Nu^{turb}} = 0.0108\left(\frac{\omega R^2}{\nu}\right)^{0.87}\left(\frac{\nu}{D}\right)^{1/3} \textit{turbulent flow} \tag{25.52.2}$$

$$Nu_{NC} = \left\{0.825 + \frac{0.387(Gr_L Sc)^{1/6} Le^{1/18}}{\left[1+(0.492/\mathrm{Pr})^{9/16}\right]^{8/27}}\right\}^2 \tag{25.52.3}$$

$k_{measured}$ is the experimentally determined value of $k_{eff,CC}$. Natural convection was ignored by setting $Nu_{NC} = 0$. For Ga-doped Ge, $k_0 = 0.087$ and $\nu = 0.00135$ cm^2/s. The crystal radius was $R = 1$ cm.

The diffusion coefficients given in Table 25.1 were calculated by iterating on D, to fit $k_{measured}$ for all growth rates, and rotation rates [31,33]. Assuming laminar flow, the diffusion coefficient $D = 0.67 \times 10^{-4}$ cm^2/s gave a solid fit to the data, at 57, 144, and 575 RPM. At 1440 RPM, the Reynolds number, $Re = 1.2 \times 10^5$, was sufficiently high to assume turbulent flow, see Section 25.7.1.3. Thus, for 1440 RPM, the correlation Eqn (25.52.2), gave a good fit to $k_{measured} \approx 0.09$[15] at $f = 70$ μm/s.

In conclusion, small CZ systems, subject to $Re_R^2 \gg Gr$, are suitable for measuring the diffusion coefficients of impurities because:

- Forced convection can be characterized more precisely than natural convection.
- k_{eff} depends only on f, R, ω, ν, k_0, and D. Typically, f, ω, and R are known. Thus, if k_0 and ν are known, D can be calculated from k_{eff}.
- The segregation data reflect realistic diffusion conditions in the solute layer at the interface, such as temperature, viscosity, and potential association, or clustering, in compound semiconductors.

[15] $k_{measured} \approx k_0 = 0087$ indicates nearly perfect mixing, caused by turbulent flow.

25.9.2 CZ Process with Mixed Convection $Re^2 \approx Gr$

Intense mixed convection, with $0.1 \leq Re_R^2/Gr \leq 10$, is typical for the CZ process; k_{eff} is close to k_0, unless extremely high pulling rates are used. Laminar forced convection, driven by crystal rotation, yields no lateral segregation. However, natural convection, crucible rotation, and turbulence all disturb the laminar flow driven by the crystal and cause lateral and microsegregation.

25.9.2.1 Diffusion Coefficients of Impurities in Silicon

The widely used diffusion coefficients of impurities in molten silicon have all been obtained from CZ segregation data, published by Turkovskii (1962 [57]) and Kodera (1963 [56]). Both authors used the BPS model to extract diffusion coefficients, although, in contrast to Burton et al. [2], their experiments were performed at relatively modest rotation rates.

The crystal radius R was not reported by Turkovskii or Kodera. This was possible because the BPS model does not account for crystal/melt size. R is not included in Eqns (25.25) or (25.26). Infinite rotating crystal and melt are assumed.

Turkovskii grew Al-, P-, and As-doped silicon crystals at 10, 12, and 60 RPM [57]. The diffusion coefficients obtained at 10 or 12 RPM were consistently higher than the coefficients obtained at 60 RPM. For example, for Al-doped Si, $D_{Al}^{12RPM} = 3.26 \times 10^{-5} \text{cm}^2/\text{s}$, whereas $D_{Al}^{60RPM} = 1.31 \times 10^{-5} \text{cm}^2/\text{s}$.

Kodera [56] grew doped silicon crystals at 5 to 200 RPM. Unfortunately, erroneous kinematic viscosity, $\nu = 0.0106 \times 10^{-4}$ cm^2/s, was used in the BPS model, whereas the established value is $\nu = 0.0035 \times 10^{-4}$ cm^2/s. Furthermore, a single “RPM-averaged” diffusion coefficient was reported for each dopant. For example, for phosphorus doping, $D_P = (5.1 \pm 1.7) \times 10^{-4}$ cm^2/s.

Kodera’s data were revisited, by fitting the BPS model, for each RPM, without averaging [31]. Again, Kodera obtained diffusion coefficients at 5 and 10 RPM that were consistently higher than his values at higher rotation rates. For example, for phosphorus, at 5 RPM, $D_P^{5RPM} = 9.4 \times 10^{-4} \text{cm}^2/\text{s}$, and at 55 RPM, $D_P^{55RPM} = 3.9 \times 10^{-4} \text{cm}^2/\text{s}$. For details, see Figure 3 in reference [31].

In 1968, Shaskov and Gurevich used the capillary-reservoir method for diffusivity measurement and reported drastically different D values [42], see Table 25.2.

Assuming R = 1.5 cm, 12 RPM corresponds to $Re_R = 942$ and $Re_R^2/Gr \sim 0.2$. Thus, one must conclude that natural convection increased the apparent transport rate of impurities and elevated the apparent diffusivity. The data obtained at 5 to 12 RPM should not have been used in Eqn (25.26), where the velocity filed and the solute layer thickness δ are controlled by the crystal rotation rate ω. For $Gr \gg Re_R^2$, δ is controlled by the Grashof and Prandtl numbers (i.e., ΔT, L, β, g, etc.), and not by the Reynolds number (i.e., ω).

Equation (25.52) was applied to Turkovskii and Kodera’s segregation data, see [31]. As shown in Figure 25.13, by using just a single value of D, one can fit the $k_{measured}$ at

Table 25.2 Values of Diffusion Coefficients in Molten Silicon Calculated Using Eqn (25.52)

Dopant	Tetrahedral Covalent Radius A	k_0	D (cm^2/s) Shaskov and Gurevich	D (cm^2/s) Eqn (25.52)	References for Data
B	0.88	0.8	3.3×10^{-4}	1.7×10^{-4}	[56]
P	1.1	0.3	2.7×10^{-4}	2.1×10^{-4}	[56,57]
As	1.18	0.35		2.2×10^{-4}	[56,57]
Ga	1.26	0.008	0.66×10^{-4}	1.3×10^{-4}	[56]
Al	1.26	0.002		0.13×10^{-4}	[57]
Sb	1.36	0.023	1.4×10^{-4}	0.7×10^{-4}	[56]
In	1.44	0.0004	0.17×10^{-4}		see [31]

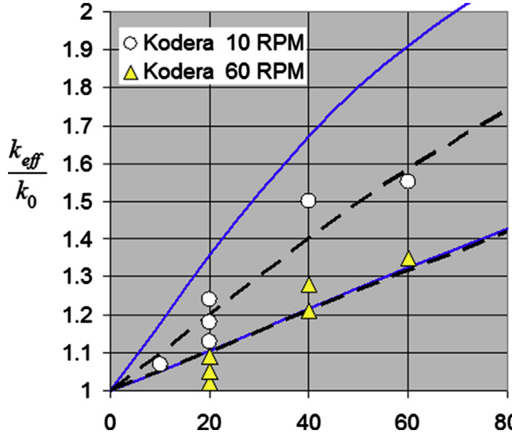

FIGURE 25.13 Symbols are data reproduced from Kodera, for P-doped Si. Dashed lines are Eqn (25.52) for "mixed" convection; one value of D (recorded in Table 25.2) fits data at 10 and 60 RPM. Full lines: natural convection is ignored ($Nu_{NC} = 0$). Full and dashed lines overlap for 60 RPM, where $Re^2 \gg Gr$.

10 RPM and 60 RPM, for $0 < f < 70$ µm/s. To illustrate the significance of natural convection at 10 RPM, these calculations were repeated assuming $Nu_{NC} = 0$ (full lines).

The calculated D values are listed in Table 25.2 along with the capillary-reservoir diffusivity measurements by Shaskov and Gurevich [42].

25.9.2.2 CZ Growth of Large Crystals at Low Rotation Rates

In the commercial production of large-diameter electronic grade Si crystals, the crystal rotation rate is typically less than 15 RPM, which corresponds to a Reynolds number of $Re_R = \omega R^2/\nu \approx 10^5$, assuming crystal diameter $d = 20$ cm.

Melt mass varies from 80 to 200 kg, with the corresponding Grashof numbers, $Gr \sim 10^{10}$, so that $Re_R^2 \sim Gr$. Natural convection is driven by (1) hot, vertical, crucible

walls and (2) the crystal–melt interface, which acts as a "cooled horizontal disk." Both oppose the forced flow driven by the rotating crystal. Furthermore, crucible rotation is also driving forced convection. The resulting "combined-convection" is so complex that numerical three-dimensional modeling provides the only reliable approach to optimize the distribution of impurities in the resulting crystal.

We proceed to reduce the number of parameters by ignoring crucible rotation. Without crucible rotation, we consider combined crystal- and buoyancy-driven convection.

Figure 25.14 illustrates the relative importance of forced and natural convection on k_{eff}. Melt height H was kept constant and equal to the crystal diameter, $d = H = 20$ cm. Natural convection was modeled as a "cooled horizontal disk" using Eqn (25.47) for Nu_{NC}. The cooler crystal–melt interface induces downward buoyancy forces, opposing forced convection, hence a minus sign is used in Eqn (25.52). The characteristic temperature difference is $\Delta T_{max} = 5\,°C$. The corresponding Grashof number is $Gr = 5.8 \times 10^8$. Rotation rates of 1, 3, 5, 10, and 30 RPM yield corresponding Re_R^2/Gr parameters of 0.02, 0.19, 0.53, 2.1, and 19.

The Nusselt numbers for forced convection were then calculated using Eqn (25.40) for rotation rates of 1–15 RPM. For 30 RPM, Eqn (25.42) was applied to determine Nu_{FC}.

The dashed line in Figure 25.14 represents Eqn (25.52), plotted for 0 RPM. The full line at 1 RPM overlaps with this dashed line, as forced convection is negligible ($Re_R^2 \approx 0.02 Gr$). For 1, 3, and 5 RPM, the flow direction is downward, because $Gr_d > Re_R^2$. At 5 RPM, convection is weakest, and k_{eff} is highest, because the centrifugal rotation forces are nearly balanced by buoyancy.

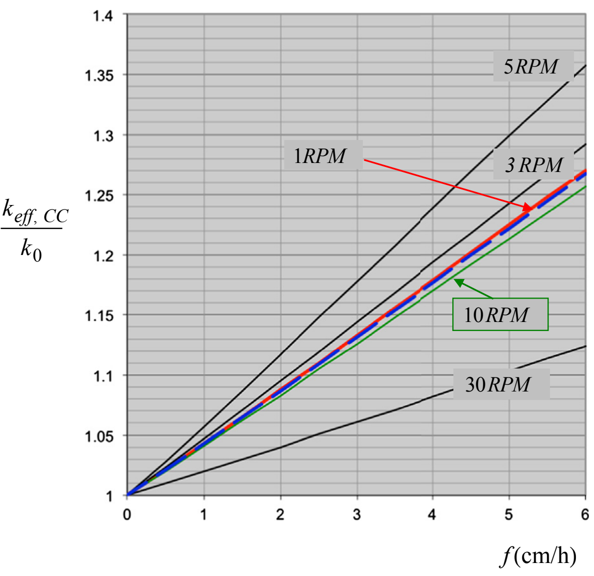

FIGURE 25.14 Segregation controlled by combined convection (CC), forced, natural, and perpendicular. k_{eff} was calculated using Eqn (25.52). Interface acts as horizontal cooled disk. Buoyancy forces act downward "opposing" forced convection, hence "−" sign is used in Eqn (25.52).

At 6 to 7 RPM, the flow changes direction and reverses for 10 and 30 RPM. This flow transition is known to cause abrupt interface shape changes in oxide CZ crystal growth, as the crystal radius and the Reynolds number both increase during the so-called "shouldering" stage early in the process [59]. Carruthers suggested that the transient flow state occurs when $Gr \approx Re^2$, a condition that occurs when buoyancy and rotational forces are equivalent [59].

25.10 Zone Melting

25.10.1 Introduction

The process of ZM for achieving single crystallinity was first reported by E. N. da C. Andrade and R. Roscoe in 1937, in their now-classic paper on single crystal plasticity [19]. In 1952, zone refining was applied for the first time by W.G. Pfann in the purification of germanium to allow the demonstration at Bell Laboratories of transistor switching [13]. A decade later, H.C. Theurer extended Pfann's method to silicon, using a clever adaptation called the "float-zone" (FZ) method, used for ultrapurification and single crystal growth.

Several books have been devoted to the fundamental theory and practice of zone refining, beginning with Pfann's classic monograph on this process and its variants [13], updated in the recent textbook/monograph *Principles of Solidification* by M.E. Glicksman [6], which presents the state of the art, including recent experiments and other contributions that consider the effective distribution coefficient, k_{eff}, as a function of the solute layer thickness, δ [60,61].

Only a relatively short zone of the total charge is melted at any given time in ZM. Typically, zone length, Z, is about 10% of the total ingot length, L, so that $Z \sim \frac{L}{10}$. See Figure 25.15. The purposes of zone refining processes are to: (1) maximize the crystal purity and the amount of material so purified, thus reducing recycle and waste, and (2) minimize the time required to perform the process. One must manage to have $k_{eff} \ll 1$ and also move the molten zones at a reasonably high rate, f.

Zone refining often requires multiple passes, or "stages," using, where possible, multiple molten zones through long charges. The total process may entail weeks to complete. In the interest of reducing process time, one is compelled to employ a relatively brisk zone translation rate, f, although it is well known that increasing the growth rate also elevates the value of k_{eff}. As k_{eff} approaches unity, an individual zone pass becomes less efficient and wastes time and material.

Figure 25.16, reproduced from Pfann [13], uses BPS segregation theory to illustrate the effect of the "normalized" growth rate, $f\delta/D$, on the value of δ. It is evident that two limits exist:

1. $k_{eff} \to k_0$, for $f\delta/D \to 0$, whereas
2. $k_{eff} \to 1$, for $f\delta/D > 5$.

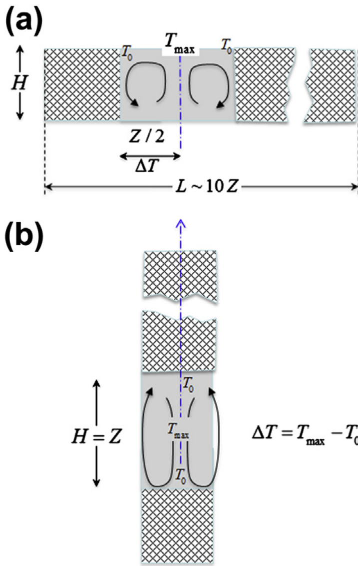

FIGURE 25.15 Characteristic lengths and temperature differences in (a) horizontal and (b) vertical zone melting (ZM).

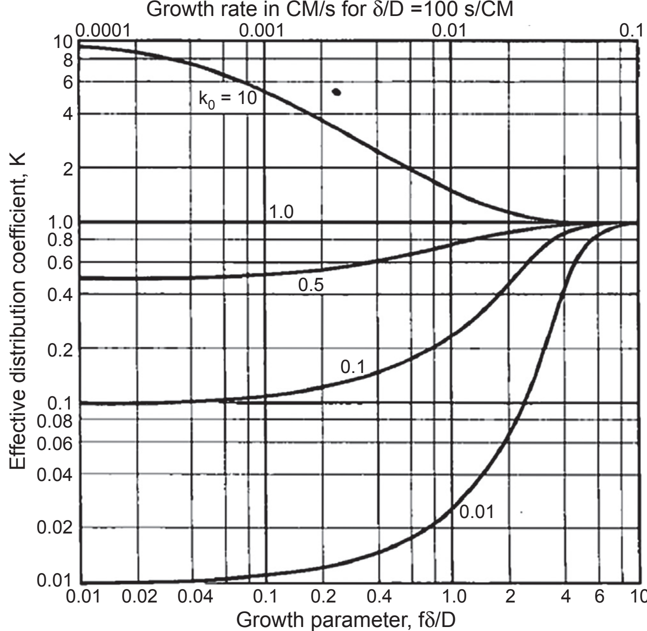

FIGURE 25.16 Dependence of k_{eff} on normalized growth rate *f*δ*/D* for several values of k_0. *From Pfann's book [13]. Note that top abscissa is* f *(cm/s) for* δ/D = *100 (s/cm).*

Thus, one observes that excessive growth rates lead to severely reduced macrosegregation and little net purification. Moreover, if the zone speed is set too high, constitutional supercooling will occur, leading to interface instability and microsegregation, which also results in the formation of undesirable microstructures such as cells and dendrites, where $k_{eff} \approx 1$, and impurities are simply retrapped locally among the last portions of the microstructure to freeze.

A serious drawback to using Figure 25.16 is that the solute boundary layer thickness, δ, is fictitious and, as a result, remains unknown. Crystal growers cannot determine the growth rate, f (cm/hr), needed to attain a desired value for the effective distribution coefficient, k_{eff} in the zone. One notes that the Cochran/Levich Eqn (25.26) is applicable to the case of *rotating* crystals, which may not be appropriate to zone purification. Furthermore, in Eqn (25.26), δ is not a function of growth rate, which is physically incorrect.

Figure 25.17 shows the dependence of k_{eff} on the zone speed, f (cm/hr). The curves were plotted using Eqn (25.49), where k_{eff} is a function of the Nusselt number, which is calculated using Eqn (25.45). Assuming that the value of the equilibrium segregation coefficient, k_0, is known, one may choose both an "appropriate" zone speed, f, and k_{eff}. Again, achieving efficient zone refining requires, (1) maintaining a small k_{eff}, which minimizes the number of passes to attain a desired level of purity, and (2) a relatively high f, to minimize the total transit time for a zone through the total charge. Additional details for implementing zone purification are provided below.

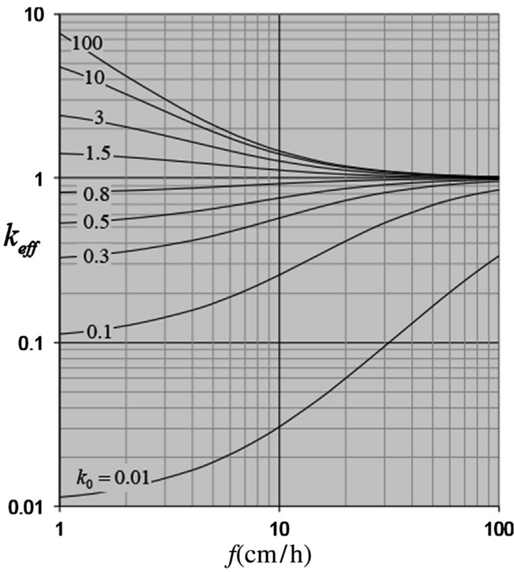

FIGURE 25.17 Dependence of k_{eff} on growth rate f (cm/h), calculated using Eqn (25.49) with Eqn (25.45). For horizontal zone melting (ZM), molten germanium properties ($Pr = 0.01$), $H = 2.5$ cm and $\Delta T = 20$ K $Gr \approx 10^7$

A brief review of macrosegregation theory for single-pass zone refining is given next. The zone speed and the number of passes (stages) are the two most important parameters that a crystal grower needs to determine before attempting zone purification.

25.10.2 Single-Pass ZM, "Perfect" Mixing

If the molten zone is assumed to remain under "perfect" mixing, where $k_{eff} = k_0$, then the concentration of impurities throughout the melt is uniform. This limiting condition can, in fact, be approached, provided that the zone speed is kept extremely low, e.g., $f \ll 1$ cm/hr. See Figure 25.16. This condition, although ideal, is of little practical interest in zone refining. Were such a slow zone speed established, the resulting axial concentration profile takes the exponential form [6,13]:

$$\frac{C_S(x)}{C_L^i} = 1 - (1 - k_0)e^{-k_0\frac{x}{Z}}, \quad \text{for } 0 \le x \le (L - Z) \tag{25.53}$$

where C_L^i denotes the initial solute concentration in the charge, which is assumed to be uniform. It is advantageous that the zone be kept as short as practicable, however, to achieve both efficient, per pass, purification along with minimal charge loss. For the last zone length to freeze, the mass balance calculation shows that

$$\frac{C_S(x)}{C_L^i} = \left[1 - (1 - k_0)e^{-k_0\frac{L-Z}{Z}}\right]\left(\frac{1-x}{Z}\right)^{k_0-1} \quad \text{for } (L-Z) \le x \le L$$

As the melt volume is kept as small as possible, compared to that in ordinary directional freezing, one finds that the concentration of rejected impurities in the zone, $C_{zone}(x)$, builds up rapidly. Again, in the limit of perfect mixing, the concentration in the solid will be $C_S(x) = k_0 C_{zone}(x)$. Figure 25.18 shows for $k_0 = 0.1$ and $Z = L/10$, the variation of

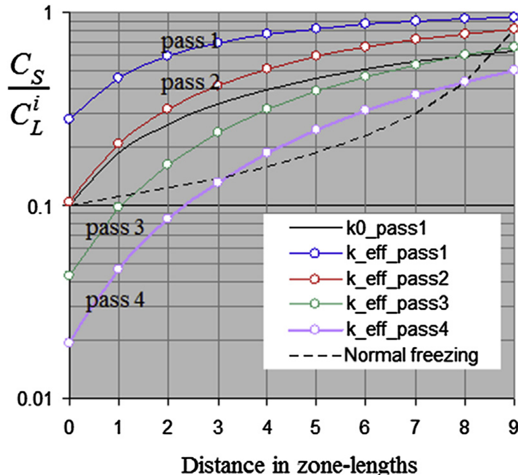

FIGURE 25.18 Relative impurity concentration versus distance, scaled in zone lengths, for multipass zone melting (ZM). Dashed line is normal freezing with $k_0 = 0.1$. Full line is one pass with k_0. Lines with circles are passes one to four with $k_{eff} = 0.28$.

relative impurity concentration, C_S/C_L^i, versus distance in zone lengths. The solid line is the profile expected after a single "slow" passage, as described by Eqn (25.53). The purification obtained from a single zone pass is actually inferior to that obtained from just Gulliver–Scheil segregation, Eqn (25.4) (dashed line). The benefits of zone refining only become evident after applying multiple passes.

25.10.3 Effective Segregation Coefficient in Zone Purification

The effective segregation coefficient is not a function of the fraction solidified because the zone length, Z, and the melt temperature do not change significantly during the process but rather rise slowly ($k_0 < 1$) with increasing purity. The Grashof number and the related Nusselt number characterizing flows in the zone also remain approximately constant throughout a pass, in contrast to what is expected in normal freezing. Figure 25.15 shows the characteristic length and ΔT for two common configurations: (1) horizontal boat, and (2) vertical ampoule.

In the absence of any forced convection, perhaps induced by induction heating or moving magnetic fields, k_{eff} can be calculated using Eqn (25.49). The correlation for Nu_{NC}, may be selected on the basis of the orientation of the crystal–melt interface. For example, in Figure 25.17, this was done using Eqn (25.45), assuming a horizontal boat configuration, a charge with germanium melt properties, a melt height $H = 2.5$ cm, a maximum superheat of $\Delta T = 20$ K, and a diffusivity, $D = 10^{-4}$ cm^2/s. The dimensionless parameters are: $Gr \approx 10^7$, $Pr = 0.01$, $Sc = 13$.

25.10.4 Single-Pass ZM, "Partial" Mixing

The zone speed chosen in practical zone refining is often high, typically exceeding several cm/hr (e.g., $f = 5$ cm/hr). Neglecting the brief initial transient near the beginning of the charge under convection-controlled segregation, one obtains a realistic $C_S(x)$ profile[16] by simply replacing k_0 with k_{eff} in Eqn (25.53),

$$\frac{C_S(x)}{C_L^i} = 1 - (1 - k_{eff})e^{-k_{eff}\frac{x}{Z}}, \quad \text{for } 0 \le x \le (L - Z). \tag{25.54}$$

To keep purification efficient, $1 - k_{eff}$ should stay large, and close to $1 - k_0$. As a rough estimate for k_{eff} one may use

$$1 - k_{eff} = 0.8(1 - k_0). \tag{25.55}$$

According to Figure 25.17, for $f = 1$ cm/hr, the effective segregation coefficient is $k_{eff} \approx k_0 = 0.1$. For $k_0 = 0.1$, Eqn (25.55) "suggests" $k_{eff} = 0.28$, which corresponds to zone speed of $f = 11$ cm/hr (the intersection of the horizontal $k_{eff} = 0.28$ line with the $k_0 = 0.1$ contour at a zone speed of $f = 11$ cm/hr). Thus, 11 passes with $k_{eff} = 0.28$ can be performed in the same time needed to run one pass with $k_{eff} \approx 0.1$ at a speed of 1 cm/h.

[16]In the literature, such profiles are labeled as "partial" mixing [19].

25.10.5 Multipass ZM

Obtaining a profile after the second pass and the subsequent passes becomes difficult, and one must resort to numerical methods, as the solute distribution in the charge is no longer uniform. A manageable expression for calculating multipass zone refining was presented by Milliken, based on a simplification of Lord's expression for the solute distribution [13], namely,

$$\frac{C_n(a)}{C_L^i} = 1 - (1 - k_{eff})[n - \Sigma(n)]e^{-k_{eff}a} \tag{25.56}$$

where the summation for n-passes in Eqn (25.56) is given by

$$\Sigma(n) = \sum_{s=1}^{n-1} (n-s)k_{eff}^{s-1}e^{-sk_{eff}}\frac{(s+a)^{s-2}}{s!}\{a(s-1) + (1 - k_{eff}a)(s+a)\}$$

Here a is the distance expressed in zone lengths, Z [13]. Equation (25.56) was used to plot zone passes one to four in Figure 25.18, using a value of $k_{eff} = 0.28$. It is evident from this calculation that three zone passes performed at a zone speed of $f \approx 11$ cm/h, with $k_{eff} = 0.28$, yield better multipass purification than does a single slower pass at $f \approx 1$ cm/h with a lower $k_{eff} = 0.1$. Furthermore, three passes at a zone speed of $f \approx 11$ cm/h can be performed in about 30% of the time needed for a single pass at 1 cm/h.

25.11 Lateral Segregation

Lateral segregation usually results in the nonuniform distribution of impurities in the y-direction,[17] perpendicular to the growth direction, x. This segregation has several causes including the fact that sections of a wafer cut perpendicular to the x-axis were actually grown at slightly different fractions solidified, f_S. Also, as convection causes some variation in the solute concentration in the melt, near-equilibrium segregation results in an uneven concentration in the solid. Finally, if nonequilibrium effects occur at the interface, say near a facet, the concentration at the interface would be controlled by interface kinetics.

25.11.1 Curved Solid–Liquid Interface

Solid–liquid interfaces are rarely ever macroscopically planar. As a result, a wafer cut perpendicular to the crystal axis contains regions grown at different times, i.e., at slightly different fraction solidified, f_S, so axial segregation, which invariably occurs in crystal growth processes, causes different concentrations in different areas across the wafer, which appear as lateral segregation.

Figure 25.19 illustrates the position of an advancing curved interface at different times. An impurity having $k_0 < 1$ will have a lower concentration at t_1 compared to t_2. The wafer cut along the horizontal plane A–A will have sections crystallized at different

[17] The radial, r-direction, is used for the cylindrical coordinate system.

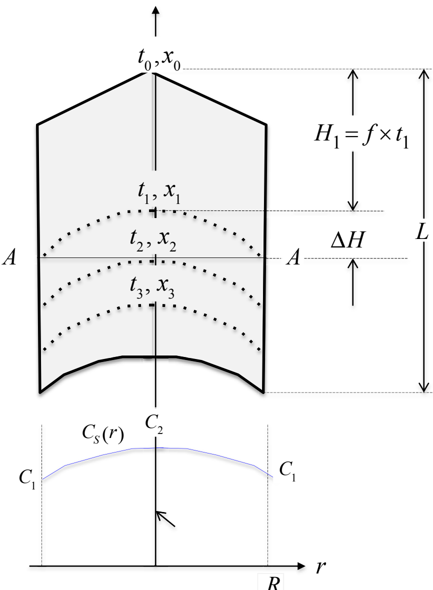

FIGURE 25.19 Lateral segregation caused by curved interface for normal freezing. Schematic and C_S, for an impurity distribution with $k_0 < 1$.

times, with different fractions solidified. Specifically, the periphery grew at t_1, f_{S1}, whereas the center grew at t_2, f_{S2}. Hence, based on Gulliver–Scheil Eqn (25.5), one expects a higher solute concentration at t_2, f_{S2}, as indicated in the U-shaped profile.

Axial segregation can be avoided in principle by attaining strict steady state, diffusion-controlled segregation, and/or by using melt replenishment. In this regard, the submerged heater method has been quite effective, as shown in Figure 25.20.

25.11.2 Convection

Lateral flows along the interface in the y-direction sweep and carry away the impurities rejected at the interface. The analytical solutions discussed below are essential for understanding lateral segregation caused by convection.

(a) Radial segregation in CZ-grown crystals

The von Karman/Cochran/Levich solution [3–5] for laminar flow and concentration field near an infinite rotating disk indicate that, ideally, the solute layer thickness δ and concentration at the liquid phase at interface C_0 should not change in the radial direction. Therefore, there should be no lateral segregation in CZ-grown crystals. Experimental evidence reveals to the contrary that lateral segregation does occur. The possible reasons for this include:

1. Buoyancy-induced natural convection opposes and alters CZ-forced convection.
2. Crucible rotation “disturbs” the Cochran–Levich flow.

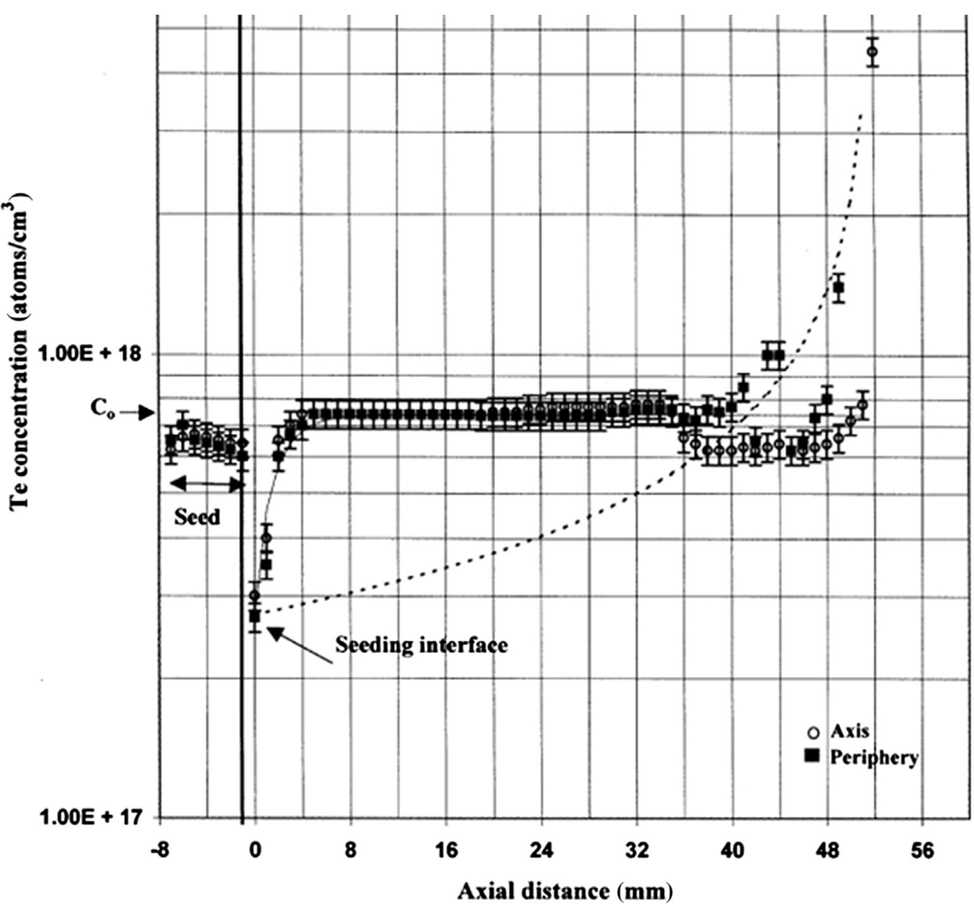

FIGURE 25.20 Te concentration in GaSb crystal, grown using the *SH* method, in multizone Mellen furnace. Open circles represent Te concentration along the axis; the filled squares are obtained along the edge of the crystal. Dashed line is the theoretically calculated profile for complete mixing using. From [62].

3. Crystal and melt are, of course, always finite in extent.

4. The velocity boundary layer thickness in turbulent flow is [63],

$$\delta_\nu(r) = 0.526\left(\frac{\nu}{\omega}\right)^{\frac{1}{5}} r^{\frac{3}{5}}. \tag{25.57}$$

Using Eqn (25.16), the solute layer thickness increases, leading to lateral segregation,

$$\delta(r) \sim r^{\frac{3}{5}} Sc^{-\frac{1}{3}}$$

(b) Convection along a flat plate and Bridgman growth

The similarity solutions developed by Blasius and Polhausen [9] illustrate how boundary layers and concentration profiles develop with flows directed along a

solid–liquid interface. Their solutions hold for laminar flow providing that the interface remains reasonably flat. For a constant bulk flow velocity, U, along the interface in the y-direction, the similarity solutions show that layer width is given by

$$\delta(y) = 5yRe_y^{-\frac{1}{2}}Sc^{-\frac{1}{3}} = 5D^{\frac{1}{3}}\nu^{\frac{1}{6}}\sqrt{\frac{y}{U}}, \tag{25.58}$$

where $Re_y \equiv Uy/\nu$. The gradient in layer thickness, $\delta(y)$, is therefore

$$\frac{d\delta}{dy} \sim \frac{1}{\sqrt{Uy}} \sim \frac{1}{\sqrt{Re_y}}. \tag{25.59}$$

By using Eqn (25.13), $\delta = \frac{D}{j}(C_0 - C_L)$, one obtains

$$\frac{dC_0}{dy} = \propto \frac{1}{\sqrt{Re_y}}. \tag{25.60}$$

Thus, dC_0/dy, is high at low Re. Equation (25.60) provides the theoretical underpinning for the observations that lateral segregation strengthens at low flow Re and Gr numbers.

The third fundamental similarity solution is given by Ostrach [9,10]. He found that in buoyancy-driven laminar flow along a vertical wall, the boundary layer thickness varies inversely with the fourth root of the Grashof number,

$$\delta(y) \sim \frac{y}{Gr^{1/4}} \tag{25.61}$$

$$\frac{\partial\delta}{\partial y} \propto \frac{1}{Gr_y^{1/4}} \tag{25.62}$$

Equations (25.60) and (25.61) are consistent as $Re_y \sim \sqrt{Gr_y}$. Thus, in natural convection, lateral segregation is weak at high Gr_y numbers,

$$\frac{dC_S}{dy} \propto \frac{1}{Gr_y^{1/4}} \tag{25.63}$$

Similarity solutions are applicable only to laminar boundary layer flow, where $10^3 \leq Gr_y \leq 10^9$. Below $Gr \approx 10^3$, lateral nonuniformity of the solute concentration is reduced by diffusion.

The pioneering modeling papers on segregation in Ga-doped Ge, by Polezhaiev [46] and Brown et al. [47,64], confirm that in HB growth ΔC_{max} occurs at $10^3 \leq Gr_H \leq 10^4$ [46], where the subscript H designates melt height. In the VB configuration, the maximum value for ΔC_{max} occurs for $Ra_L = Gr_L Pr \sim 10^8$ [64]. Adoranto and Brown's Grashof number, $Gr_L \sim 10^6$, appears to be much higher, because it is based on the melt height, L, and *not* on the interface size, d. The aspect ratio was $L/d \approx 6$, giving a Grashof number $Gr_d \sim 10^3$, which is a value in good agreement with the similarity solution. The value of $Gr_d \sim 10^3$ shown in Figure 25.10 corresponds to a low gravity level reduced to a value of about $10^{-4}g_0$.

Figure 25.21 shows the uniform radial segregation obtained by using an oscillating baffle in the VB configuration. Radial uniformity in this case remains exceptionally good because the melt is constantly homogenized by intense mixing.

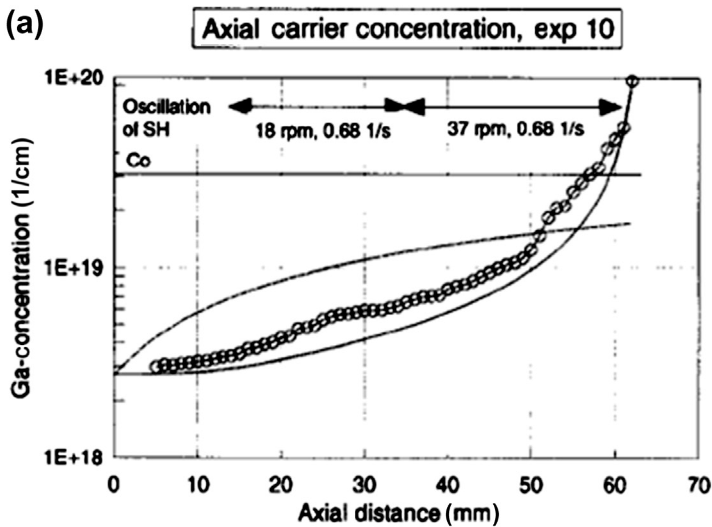

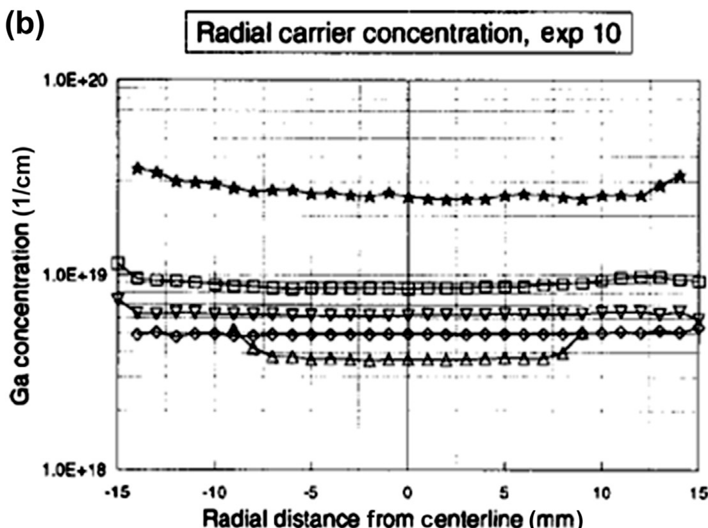

FIGURE 25.21 (a) Axial and (b) radial concentration of Ga in Ge crystal grown using the SH method, in multizone Mellen furnace. (b) Lines with symbols correspond to different axial locations, spaced by 10 mm. The line with stars in last-to-freeze portion ($x = 55$ mm) and SH if out from the melt [25].

25.11.3 Nonequilibrium Segregation

The linear, local equilibrium relation given by Eqn (25.1) would no longer apply when the concentration in the solid at the crystal–melt interface is controlled by (nonequilibrium) interface kinetics. Such nonequilibrium segregation occurs, more prevalently, at faceted interfaces, where stronger interfacial supercooling necessarily develops to allow higher lateral growth rates. In addition, the effective segregation coefficient can also depend on the crystallographic orientation of the interface. This

circumstance becomes evident when the solid–liquid interface is nonplanar, and the crystal grows on and off its facet orientations. For example, in the case of Te-doped InSb, the effective distribution coefficient that equals to the equilibrium one, $k_0 = 0.5$, along its atomically rough interface increases to 4.2 on the facet orientations [65]. The interested reader concerned with such nonequilibrium segregation is encouraged to review the detailed arguments by Rosenberger [19] and the chapter "Dendritic Growth" by Glicksman [6].

Incorporation of ionized (electronically active) impurities in semiconductors, according to reference [65], may also be influenced by the position of the Fermi level (see Vol. IIB, Chapter 27).

25.11.4 Local Nusselt Numbers

Convection is a two-dimensional process where diffusion occurs normal to the interface, while advection carries away the solute laterally. Some analytical solutions and empirical correlations provide the local Nusselt numbers, $Nu(y)$ for plates, and $Nu(r)$[18] for rotating disks. These data can also be used to quantify lateral segregation. For example, Ostrach's local Nusselt number[19] for heat transfer on vertical plates is

$$Nu^{HT}(y) = \left(\frac{Gr_y}{4}\right)^{1/4} \frac{0.75Pr^{1/2}}{(0.609 + 1.221Pr^{1/2} + 1.238Pr)^{1/4}}. \tag{25.64}$$

For mass transfer, substitution of Eqn (25.44) into Eqn (25.64) gives the result,

$$Nu(y) = \frac{hy}{D} = \left(\frac{Gr_y ScLe^{1/3}}{4}\right)^{1/4} \frac{0.75Pr^{1/2}}{(0.609 + 1.221Pr^{1/2} + 1.238Pr)^{1/4}}. \tag{25.65}$$

The average Nusselt number $\overline{Nu_L}$, is defined as the lateral integral average

$$\overline{Nu_L} = \frac{1}{L}\int Nu(y)dy. \tag{25.66}$$

From Eqns (25.65) and (25.66), the average Nusselt number becomes simply

$$\overline{Nu_L} = (4/3)Nu(L) \tag{25.67}$$

25.12 Microsegregation

The length scale of microsegregation and related inhomogeneities range from 1 μm to 1 mm. Generally, microscopic segregation can be classified as either fluctuations in dopant concentration, called striations, or inhomogeneities caused by interface breakdown.

[18] In fluid mechanics and heat transfer, x-direction is parallel to the solid surface, hence $Nu(x)$.
[19] Including LeFevre's interpolation formula for various Pr, see [9].

25.12.1 Doping Striations

The most common microscopic inhomogeneities found in melt-grown semiconductor crystals are fluctuations in the dopant concentration. These fluctuations are revealed by etching techniques and are usually referred to as doping striations. Doping striations result from process fluctuations that are usually caused by one or more of the following factors:

1. unsteady convection causing brief variations in melt temperature;
2. unsteady convection causing fluctuations in dopant concentration in the solute layer;
3. variations in the furnace translation rate or crystal pull rate;
4. temperature fluctuations in the furnace related to the thermal control system;
5. vibrations affecting convection at the interface;
6. crystal rotation in the furnace, which is never perfectly symmetric, causes wobble and rotational striations.

The topics of microsegregation and the formation of microscopic crystalline imperfections are covered in greater detail in chapters by Mueller [65], Rosenberger [19], Glicksman [6], and Rudolph [66].

25.13 Summary

This chapter focuses on solute segregation and component distribution encountered in CZ, DS, and ZM processes.

The influence of melt convection on segregation was first considered in the 1953 BPS theory, where (1) the effective segregation coefficient, k_{eff}, is defined as a function of the solute layer thickness δ, and (2) δ is calculated using the analytical solution by Cochran and Levich, for forced laminar convection near a rotating disk. The complicating, but important, effects of turbulence and buoyancy-induced convection were ignored.[20] Yet, the BPS equation, relating k_{eff} to δ, is possibly the most widely used equation by practical crystal growers.

Considerable attention is given to the recently proposed combined convection (CC) segregation model,[21] where the influence of convection is captured via the Nusselt number, as a ”replacement” for δ. In short, (1) the effective segregation coefficient $k_{eff,CC}$ is defined as function of the relevant Nusselt numbers, for forced (Nu_{FC}) and natural (Nu_{NC}) convection, and (2) the Nusselt numbers are calculated using the well-established empirical correlations, developed in laboratory mass transfer experiments, under realistic conditions, including three-dimensional buoyancy-driven flows, turbulence, etc. This phenomenological approach is advantageous, considering the overall complexity and diversity of melt flows during crystal growth.

[20] Unsteady and turbulent ows are not solvable by analytical techniques.
[21] The term combined convection (CC) is used to designate the mixed natural and forced convection.

We emphasize the fact that natural (buoyancy-driven) convection is present in all crystal growth processes. It is unavoidable, unsteady, and difficult to control. In contrast, forced (extrinsically driven) convection is beneficial. Natural convection can be ignored only in CZ experiments, conducted at a sufficiently high rotation rate ω (i.e., for $Re^2 \gg Gr$).

References

[1] Prim RC, Burton JA, Slichter WP. J Chem Phys 1953;21:1987–91.

[2] Prim RC, Burton JA, Slichter WP. J Chem Phys 1953;21:1991–6.

[3] Cochran WG. Proc Camb Phil Soc 1934;30(4):365.

[4] Levich VG. Physicochemical hydrodynamics. Englewood Cliffs (NJ, Berlin): Springer Finance. Prentice-Hall; 1961.

[5] von Karman T. Uber laminare und turbulente reibung. ZAMM 1921;1(4):233–5.

[6] Glicksman ME. Principles of solidification. Springer Verlag; 2011.

[7] Schlichting H. Boundary layer theory. New York: McGraw-Hill; 1968.

[8] Cengel YA, Ghajar AJ. Heat and mass Transfer. McGraw Hill; 2007.

[9] Incropera FP, DeWitt DP. Introduction to heat transfer. New York: Willey; 1990.

[10] Ostrach S. NACA Rep 1953;1111.

[11] Gulliver GH. Metallic alloys: their structure and constitution. London: Charles Griffin and Co.; 1922.

[12] Scheil E. Z Metall 1942;34:70.

[13] Pfann WG. Zone refining. Wiley series on the science and technology of materials. Wiley; 1966.

[14] Tiller WA, Jackson KA, Rutterand JW, Chalmers B. Acta Metall 1953;1:428–37.

[15] Churilov A, Ostrogorsky AG. AIAA J Thermophys Heat Transf 2005;19:542–8.

[16] Smith VG, Tiller WA, Rutter JW. Can J Phys 1955;33:723–45.

[17] Ostrogorsky AG, Marin C, Churilov A, Volz M, Bonner WA, Duffar T. J Cryst Growth 2008;310:364–71.

[18] Ostrogorsky AG, Marin C, Volz M, Duffar T. J Cryst Growth 2009;311:3243–8.

[19] Rosenberger F. Fundamentals of crystal growth, I. Berlin: Springer; 1979.

[20] Ostrogorsky AG, Mueller G. J Cryst Growth 1992;121:587–98.

[21] Yen CT, Tiller WA. J Cryst Growth 1992;118:259–67.

[22] Ostrogorsky AG, Mueller G. J Cryst Growth 1993;128:207–12.

[23] Scheel HJ. J Cryst Growth 1972;13–14:560–5.

[24] Rudolph P. J Cryst Growth 2008;310:1298–306.

[25] Meyer S, Ostrogorsky AG. J Cryst Growth 1997;171:566–76.

[26] Wilson LO. J Cryst Growth 1978;44:247–50.

[27] Brice JC. The growth of crystals from the melt. Amsterdam: North Holland, Publishing Co.; 1965.

[28] Shevchuk IV. Convective heat and mass transfer in rotating disk systems. Springer Verlag; 2009.

[29] Chen YM, Lee WT, Wu SJ. Heat Mass Transf 1998;34:195–201.

[30] Garandet JP, Favier JJ, Camel D. J Cryst Growth 1993;130:113–22.

[31] Ostrogorsky AG. J Cryst Growth 2013;380:43–50.

[32] Camel D, Favier JJ. J Cryst Growth 1984;67:42–56.

[33] Ostrogorsky AG. J Cryst Growth 2012;348:97–105.

[34] Churchill SW, Usagi R. AIChE J 1972;18:1121–8.

[35] Ostrogorsky AG. J Serbian Soc Comput Mech 2012;6:97–107.

[36] Dorfman LA. Hydrodynamic resistance and heat loss of rotating solids. Oliver & Boyd; 1963.

[37] Newman JS. Electrochemical systems. Englewood Cliffs (NJ): Prentice-Hall; 1981.

[38] White F. Viscous fluid flow. McGraw-Hill, Inc.; 1991.

[39] Churchill SW, Chu HS. Int J Heat Mass Transf 1975;18:1323–9.

[40] Lightfoot EN. Chem Eng Sci 1968;23:93.

[41] Masliyah JH, Nguyen T. Int J Heat Mass Transf 1975;18:1443–7.

[42] Shaskov YuM, Gurevich VM. Russ J Phys Chem 1968;24:1082–3.

[43] McDonald JS, Connolly TJ. Nucl Sci Eng 1960;8:369–77.

[44] Ostrogorsky, A.G. J Cryst Growth, submitted.

[45] Globe S, Dropkin D. J Heat Transf 1959;81:24–8.

[46] Nikitin SA, Polezhaev VI, Fedyushkin AI. J Cryst Growth 1981;52:471.

[47] Chang CJ, Brown RA. J Cryst Growth 1983;63:343.

[48] Matthiesen D, Wargo MJ, Motakef S, Carlson DJ, Nakos JS, Witt AF. J Cryst Growth 1987;85:557.

[49] Witt AF, Gatos HC, Lichtensteiger M, Avine MC, Herman CJ. J Electrochem Soc 1975;122:276–83.

[50] Witt AF, Gatos HC, Lichtensteiger M, Herman CJ. J Electrochem Soc 1978;125:1832–40.

[51] Yue JT, Voltmer FW. J Cryst Growth 1975;29:329–41.

[52] Zemskov VS, Shulpina IL, Titkov AN, Belokurova IN, Guseva NB, Safarov VI. Sov Phys Solid State 1979;21:576.

[53] Bourret E, Favier JJ, Bourrel O. J Electrochem Soc 1981;128:2438.

[54] Dutta PS, Ostrogorsky AG. J Cryst Growth 2000;217:360–5.

[55] Fischer B, Friedrich J, Weimann H, Muller G. J Cryst Growth 1999;198/199:170–5.

[56] Kodera H. Jpn J Appl Phys 1963;2:212.

[57] Turkovskii BM. Russ J Phys Chem 1962;36:983–5.

[58] Bridges HE. J Appl Phys 1956;27:746–51.

[59] Carruthers JR. J Cryst Growth 1976;36:212–4.

[60] Ghosh K, Mani VN, Dhar S. J Cryst Growth 2009;312:1521.

[61] Cheung N, Bertazzoli R, Garcia A. J Cryst Growth 2008;310:1274.

[62] Dutta PS, Ostrogorsky AG. J Cryst Growth 1999;197:749–54.

[63] Hartnett JP, Tsai SH, Jantscher HN. J Heat Transf 1965;87:362–8.

[64] Adornato PM, Brown RA. J Cryst Growth 1987;80:155–90.

[65] Mueller G. Convection and inhomogeneities in crystal growth from the melt, vol. 12. Berlin: Springer; 1988.

[66] Rudolph P. Chapter defect formation during the crystal growth from melt. In: Dhanaraj G, Byrappa K, Prasad V, Dudley M, editors. Handbook of crystal growth. Springer Verlag; 2010. p. 153–202.

Thermal Stress and Dislocations in Bulk Crystal Growth

Noriyuki Miyazaki[1,2]

[1]KYOTO UNIVERSITY, KYOTO, JAPAN;
[2]KYUSHU UNIVERSITY, FUKUTSU-SHI, FUKUOKA, JAPAN

CHAPTER OUTLINE

26.1 Overview **1050**
26.2 Thermal Stress in Bulk Single Crystals **1050**
26.2.1 Introduction 1050
26.2.2 Methodology for Calculating Thermal Stress 1051
26.2.2.1 Elastic Constant Matrix 1051
26.2.2.2 Thermal Strain Vector 1058
26.2.2.3 Finite Element Formulation 1059
26.2.3 Several Examples of Thermal Stress Analysis 1060
26.2.3.1 Effect of Crystal Anisotropy on Thermal Stress for Cubic Bulk Single Crystals (Si, GaAs, and InP) 1060
26.2.3.2 Thermal Stress Analysis of Lithium Niobate Bulk Single Crystal 1063
26.2.3.3 Thermal Stress Analysis of Lead Molybdate Bulk Single Crystal 1065
26.2.4 Cracking of Bulk Single Crystal Caused by Thermal Stress 1069
26.3 Dislocations in Bulk Single Crystals **1074**
26.3.1 Introduction 1074
26.3.2 Qualitative Estimation of Dislocation Density 1074
26.3.3 Quantitative Estimation of Dislocation Density: Haasen-Alexander-Sumino Model 1075
26.3.3.1 HAS Model for the Uniaxial Stress State 1076
26.3.3.2 HAS Model for a Multiaxial Stress State under Isotropic Assumption 1077
26.3.3.3 HAS Model for a Multiaxial Stress State under Consideration of Crystal Anisotropy 1078
26.3.3.4 Several Applications of the HAS Model to the Quantitative Estimation of Dislocation Density 1079
26.3.4 Modified HAS Models 1083
26.3.4.1 Consideration of Immobilization of Mobile Dislocations and High-Temperature Recovery Mechanisms 1083

Handbook of Crystal Growth. http://dx.doi.org/10.1016/B978-0-444-63303-3.00026-2
Copyright © 2015 Elsevier B.V. All rights reserved.

26.3.4.2 Consideration of Dislocation Annihilation 1084
26.3.4.3 Consideration of Different Types of Dislocations 1085
26.3.4.4 Consideration of the Immobilization of Mobile Dislocations 1086
26.4 Summary **1089**
References **1090**

26.1 Overview

Various single crystals, such as semiconductor single crystals (e.g., Si, GaAs, InP) and oxide single crystals (e.g., $LiNbO_3$, $LiTaO_3$, Al_2O_3) are used as materials for electronic/optical devices. Their bulk single crystals are usually manufactured using melt growth methods, such as the Czochralski (CZ) method, Bridgman (BR) method, and floating zone (FZ) method. Because the melt growth of a bulk single crystal is carried out under severe and complex thermal conditions, large thermal stress is induced in a bulk single crystal during the growth process. Such thermal stress causes the multiplication of dislocations that affect the performance of electronic/optical devices. In the case of oxide single crystals, even cracking may result. Single crystals with cracking cannot be used as materials for devices due to their reduced productivity. Solid mechanics and material strength studies on the melt growth of bulk single crystals are important for understanding and solving problems related to the generation and multiplication of dislocations and the cracking of single crystals.

As for the melt growth of bulk single crystals, attention has been paid to heat transfer problems in a crystal growth furnace, and several review papers have been published to date [1–6] (see also Chapter 20 in Vol. IIB). From the viewpoint of crystal quality, studies of solid mechanics and material strength are important for controlling the dislocation density and cracking of a crystal during the growth process in situ. Only a few review papers [7–9] have been published concerning the solid mechanics and material strength in the manufacturing process of single crystals. In this chapter, we focus on thermally generated stress and associated effects during the melt growth processes of bulk single crystals.

26.2 Thermal Stress in Bulk Single Crystals

26.2.1 Introduction

Dislocations generated during growth process within the growing crystals affect the performance of devices. Sometimes, even macrocracking occurs in single crystals. Dislocations and macrocracking can be caused by thermal stress during crystal growth. Therefore, the first step for the estimation of dislocation density and cracking of a crystal is to calculate the thermal stress in the crystal.

Crystal anisotropy should be considered in the thermal stress analysis of single crystals. Because single crystals have crystal anisotropy in elastic constants and thermal

expansion coefficients, three-dimensional analysis is required in thermal stress analysis, even though a crystal shape is axisymmetric. Single crystals were assumed to be isotropic in all thermal stress analyses performed through the late 1980s [10–13]. Then, Lambropoulos [14,15] and Miyazaki et al. [16–18] performed their pioneering three-dimensional finite element analyses including crystal anisotropy. Without consideration of crystal anisotropy, one cannot obtain the effect of the crystal growth direction on thermal stress within the crystal.

In thermal stress analysis, the elastic constant matrices and thermal strain/thermal expansion coefficient vectors are needed for the respective crystal systems. They are provided in Nye's textbook [19]. These elastic constant matrices and a thermal strain/thermal expansion coefficient vectors for each crystal system are given in the crystallographic coordinate system, a Cartesian coordinate system based on the unit cell of the single crystal. The values for an analysis coordinate system, a Cartesian coordinate system in the analysis space, can be obtained by using tensor transformation.

Only the cubic crystals, such as Si, GaAs, and InP, were dealt with Lambropoulos' works [14,15] and the earlier works by Miyazaki et al. [16–18]. Later, Miyazaki et al. developed three-dimensional finite element codes for trigonal single crystals [20] and monoclinic single crystals [21]. In addition to these three kinds of single crystals, they have also developed three-dimensional finite element codes for tetragonal single crystals [22] and orthorhombic single crystals [23]. Most important single crystals for electronic/optical devices are included in these five kinds.

In this section, the method for three-dimensional finite element thermal stress analysis, including crystal anisotropy, is presented for various kinds of single crystals. Several numerical examples of thermal stress analyses are given to discuss the relationship between crystal quality and thermal stress, depending on the crystal growth directions. Quantitative evaluations of the critical stress for crystal cracking are also shown here based on the thermal stress analysis of experimental data on crystal cracking induced by thermal stress.

26.2.2 Methodology for Calculating Thermal Stress

In the thermal stress analysis of a single crystal, we should consider crystal anisotropy in the elastic constants and thermal expansion coefficients. We can obtain those for arbitrary crystal growth directions using the tensor transformation technique. The details are shown here.

26.2.2.1 Elastic Constant Matrix

The stress–strain relation of single crystals is given as

$$\sigma_{ij} = C_{ijkl}\varepsilon^{e}_{kl} \tag{26.1}$$

where σ_{ij} and ε^{e}_{kl} are the stress tensor and elastic strain tensor, respectively, and C_{ijkl} denotes the elastic constant tensor. According to Nye [19], the vector components of

stress σ_i and elastic strain ε_i are related to their correspondent tensor components σ_{ij} and ε_{ij} as follows:

$$\begin{bmatrix} \sigma_{11} & \sigma_{12} & \sigma_{13} \\ \sigma_{21} & \sigma_{22} & \sigma_{23} \\ \sigma_{31} & \sigma_{32} & \sigma_{33} \end{bmatrix} \Rightarrow \begin{bmatrix} \sigma_1 & \sigma_6 & \sigma_5 \\ \sigma_6 & \sigma_2 & \sigma_4 \\ \sigma_5 & \sigma_4 & \sigma_3 \end{bmatrix}, \begin{bmatrix} \varepsilon_{11} & \varepsilon_{12} & \varepsilon_{13} \\ \varepsilon_{21} & \varepsilon_{22} & \varepsilon_{23} \\ \varepsilon_{31} & \varepsilon_{32} & \varepsilon_{33} \end{bmatrix} \Rightarrow \begin{bmatrix} \varepsilon_1 & \varepsilon_6/2 & \varepsilon_5/2 \\ \varepsilon_6/2 & \varepsilon_2 & \varepsilon_4/2 \\ \varepsilon_5/2 & \varepsilon_4/2 & \varepsilon_3 \end{bmatrix} \tag{26.2}$$

Then, the stress–strain relation is given by the matrix notation as follows:

$$\sigma_i = C_{ij}\varepsilon_j^e \tag{26.3}$$

where C_{ij} is the component of the elastic constant matrix. The details of the elastic constant tensor or elastic constant matrix are shown hereafter.

26.2.2.1.1 CUBIC SINGLE CRYSTAL

Let us consider the Cartesian coordinates X_1, X_2, and X_3 that coincide with the crystallographic axes, as shown in Figure 26.1. In case of cubic single crystals such as Si, GaAs, and InP, there exist three elastic constants: C_{11}, C_{12}, and C_{44}. The elastic constant matrix is given by [19]

$$[C_{ij}] = \begin{bmatrix} C_{11} & C_{12} & C_{12} & 0 & 0 & 0 \\ & C_{11} & C_{12} & 0 & 0 & 0 \\ & & C_{11} & 0 & 0 & 0 \\ & & & C_{44} & 0 & 0 \\ & \text{Sym.} & & & C_{44} & 0 \\ & & & & & C_{44} \end{bmatrix} \tag{26.4}$$

Now, let us consider a right-handed Cartesian coordinate system $X_1' - X_2' - X_3'$ (shown in Figure 26.2), where the X_3'-axis coincides with the growth direction of a single crystal, and the X_1'-axis is in the $X_1 - X_2$ plane and normal to the X_3'-axis. Hereafter, we call $X_1' - X_2' - X_3'$ the *analysis coordinate system*. By the standard tensor transformation,

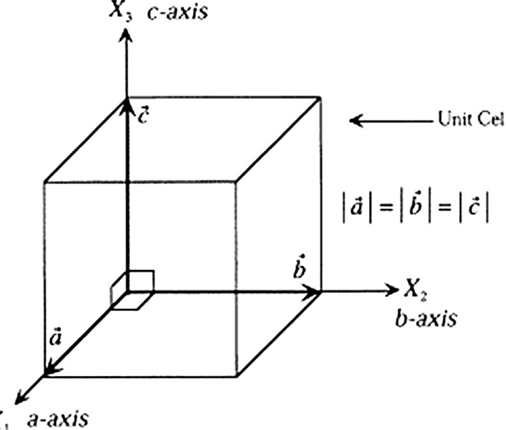

FIGURE 26.1 Coordinate system for cubic crystals. *From Ref. [22] with permission of Elsevier Science.*

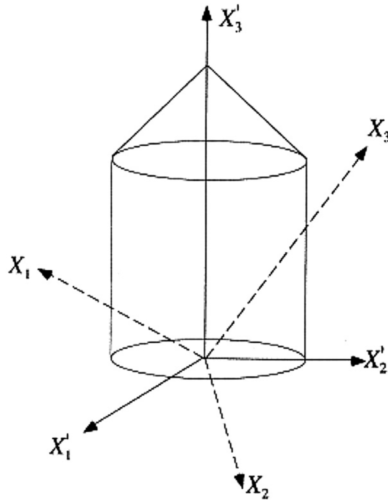

FIGURE 26.2 Analysis coordinate system. *From Ref. [22] with permission of Elsevier Science.*

the elastic constant tensor C'_{ijkl} associated with the $X'_1 - X'_2 - X'_3$ system is related to C_{ijkl} of the $X_1 - X_2 - X_3$ system as follows:

$$\begin{aligned} C'_{ijkl} &= a_{im}a_{jn}a_{ko}a_{lp}C_{mnop} \\ &= C_{11}\left(a_{i1}a_{j1}a_{k1}a_{l1} + a_{i2}a_{j2}a_{k2}a_{l2} + a_{i3}a_{j3}a_{k3}a_{l3}\right) + C_{12}\left\{\left(a_{i1}a_{j1}a_{k2}a_{l2} + a_{i2}a_{j2}a_{k1}a_{l1}\right)\right. \\ &\quad + \left(a_{i1}a_{j1}a_{k3}a_{l3} + a_{i3}a_{j3}a_{k1}a_{l1}\right) + \left.\left(a_{i2}a_{j2}a_{k3}a_{l3} + a_{i3}a_{j3}a_{k2}a_{l2}\right)\right\} \\ &\quad + C_{44}\left\{\left(a_{i2}a_{j3}a_{k2}a_{l3} + a_{i2}a_{j3}a_{k3}a_{l2} + a_{i3}a_{j2}a_{k2}a_{l3} + a_{i3}a_{j2}a_{k3}a_{l2}\right)\right. \\ &\quad + \left(a_{i1}a_{j3}a_{k1}a_{l3} + a_{i1}a_{j3}a_{k3}a_{l1} + a_{i3}a_{j1}a_{k1}a_{l3} + a_{i3}a_{j1}a_{k3}a_{l1}\right) \\ &\quad + \left.\left(a_{i1}a_{j2}a_{k1}a_{l2} + a_{i1}a_{j2}a_{k2}a_{l1} + a_{i2}a_{j1}a_{k1}a_{l2} + a_{i2}a_{j1}a_{k2}a_{l1}\right)\right\} \end{aligned} \tag{26.5}$$

where a_{ij} is the direction cosine of the X'_i-axis and X_j-axis.

We can use the relationship between the indices of tensor and those of matrix shown in Table 26.1 to change the tensor component C_{ijkl} or C'_{ijkl} into the matrix component C_{ij} or C'_{ij}. Finally, the stress–strain relation in the $X'_1 - X'_2 - X'_3$ system can be written as follows:

$$\sigma'_i = C'_{ij}\left(\varepsilon^e_j\right)' \tag{26.6}$$

Table 26.1 Relationship between Tensor Indices and Matrix Indices

Tensor	11	22	33	23, 32	31, 13	12, 21
Matrix	1	2	3	4	5	6

26.2.2.1.2 TRIGONAL SINGLE CRYSTAL

Lithium niobate (LN, $LiNbO_3$) and lithium tantalate (LT, $LiTaO_3$) single crystals with a trigonal class $3m$ lattice have threefold symmetry around the c-axis, as shown in Figure 26.3. When a right-handed Cartesian coordinate system $X_1 - X_2 - X_3$ is taken in such a way that the X_1- and X_3-axes coincide with the crystallographic a- and c-axes, respectively, as shown in Figure 26.3, the elastic constant matrix is written as follows, using six independent constants [19]:

$$[C_{ij}] = \begin{bmatrix} C_{11} & C_{12} & C_{13} & C_{14} & 0 & 0 \\ & C_{11} & C_{13} & -C_{14} & 0 & 0 \\ & & C_{33} & 0 & 0 & 0 \\ & & & C_{44} & 0 & 0 \\ & \text{Sym.} & & & C_{44} & C_{14} \\ & & & & & C_{66} \end{bmatrix} \qquad (26.7)$$

$$C_{66} = \frac{1}{2}(C_{11} - C_{12})$$

If we consider the analysis coordinate system $X_1 - X_2 - X_3$ as shown in Figure 26.2, the elastic constant tensor C'_{ijkl} associated with the $X'_1 - X'_2 - X'_3$ system is related to C_{ijkl} of the $X_1 - X_2 - X_3$ system as follows:

$$\begin{aligned} C'_{ijkl} &= a_{im}a_{jn}a_{ko}a_{lp}C_{mnop} \\ &= C_{11}\{a_{i1}a_{j1}a_{k1}a_{l1} + a_{i2}a_{j2}a_{k2}a_{l2} + (a_{i1}a_{j2} + a_{i2}a_{j1})(a_{k1}a_{l2} + a_{k2}a_{l1})/2\} \\ &\quad + C_{12}\{a_{i1}a_{j1}a_{k2}a_{l2} + a_{i2}a_{j2}a_{k1}a_{l1} - (a_{i1}a_{j2} + a_{i2}a_{j1})(a_{k1}a_{l2} + a_{k2}a_{l1})/2\} \\ &\quad + C_{13}\{(a_{i1}a_{j1} + a_{i2}a_{j2})a_{k3}a_{l3} + a_{i3}a_{j3}(a_{k1}a_{l1} + a_{k2}a_{l2})\} \\ &\quad + C_{14}\{(a_{i1}a_{j1} - a_{i2}a_{j2})(a_{k2}a_{l3} + a_{k3}a_{l2}) + (a_{i2}a_{j3} + a_{i3}a_{j2})(a_{k1}a_{l1} - a_{k2}a_{l2}) \\ &\quad + (a_{i1}a_{j3} + a_{i3}a_{j1})(a_{k1}a_{l2} + a_{k2}a_{l1}) + (a_{i1}a_{j2} + a_{i2}a_{j1})(a_{k1}a_{l3} + a_{k3}a_{l1})\} \\ &\quad + C_{33}a_{i3}a_{j3}a_{k3}a_{l3} \\ &\quad + C_{44}\{(a_{i2}a_{j3} + a_{i3}a_{j2})(a_{k2}a_{l3} + a_{k3}a_{l2}) + (a_{i1}a_{j3} + a_{i3}a_{j1})(a_{k1}a_{l3} + a_{k3}a_{l1})\} \end{aligned} \qquad (26.8)$$

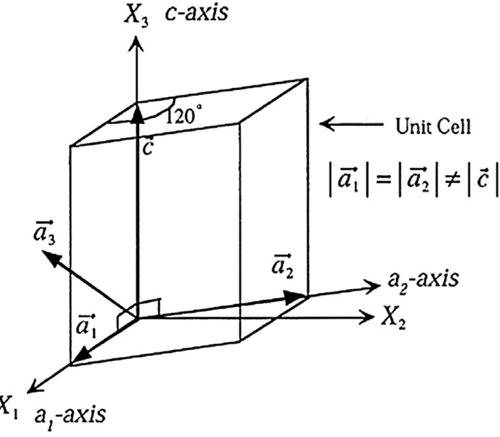

FIGURE 26.3 Coordinate system for a trigonal crystal. *From Ref. [22] with permission of Elsevier Science.*

26.2.2.1.3 MONOCLINIC SINGLE CRYSTAL

A gadolinium orthosilicate (GSO, Gd_2SiO_5) single crystal with a monoclinic lattice has a crystallographic a-axis inclining from the b–c plane ($\alpha = 17.5°$ for the GSO single crystal), as shown in Figure 26.4. When a right-handed Cartesian coordinate system $X_1 - X_2 - X_3$ is taken in such a way that the X_2- and X_3-axes coincide with the crystallographic b- and c-axes, respectively, as shown in Figure 26.4, the elastic constant matrix is written as follows, using 13 independent constants [19]:

$$[C_{ij}] = \begin{bmatrix} C_{11} & C_{12} & C_{13} & 0 & C_{15} & 0 \\ & C_{22} & C_{23} & 0 & C_{25} & 0 \\ & & C_{33} & 0 & C_{35} & 0 \\ & & & C_{44} & 0 & C_{46} \\ & \text{Sym.} & & & C_{55} & 0 \\ & & & & & C_{66} \end{bmatrix} \tag{26.9}$$

If we consider the analysis coordinate system $X_1' - X_2' - X_3'$ as shown in Figure 26.2, the elastic constant tensor C'_{ijkl} associated with the $X_1' - X_2' - X_3'$ system is related to C_{ijkl} of the $X_1 - X_2 - X_3$ system as follows:

$$\begin{aligned} C'_{ijkl} &= a_{im}a_{jn}a_{ko}a_{lp}C_{mnop} \\ &= C_{11}a_{i1}a_{j1}a_{k1}a_{l1} + C_{12}\left(a_{i1}a_{j1}a_{k2}a_{l2} + a_{i2}a_{j2}a_{k1}a_{l1}\right) + C_{13}\left(a_{i1}a_{j1}a_{k3}a_{l3} + a_{i3}a_{j3}a_{k1}a_{l1}\right) \\ &\quad + C_{15}\left\{a_{i1}a_{j1}\left(a_{k1}a_{l3} + a_{k3}a_{l1}\right) + \left(a_{i1}a_{j3} + a_{i3}a_{j1}\right)a_{k1}a_{l1}\right\} + C_{22}a_{i2}a_{j2}a_{k2}a_{l2} \\ &\quad + C_{23}\left(a_{i2}a_{j2}a_{k3}a_{l3} + a_{i3}a_{j3}a_{k2}a_{l2}\right) + C_{25}\left\{a_{i2}a_{j2}\left(a_{k1}a_{l3} + a_{k3}a_{l1}\right) + \left(a_{i1}a_{j3} + a_{i3}a_{j1}\right)a_{k2}a_{l2}\right\} \\ &\quad + C_{33}a_{i3}a_{j3}a_{k3}a_{l3} + C_{35}\left\{a_{i3}a_{j3}\left(a_{k1}a_{l3} + a_{k3}a_{l1}\right) + \left(a_{i1}a_{j3} + a_{i3}a_{j1}\right)a_{k3}a_{l3}\right\} \\ &\quad + C_{44}\left(a_{i2}a_{j3} + a_{i3}a_{j2}\right)\left(a_{k2}a_{l3} + a_{k3}a_{l2}\right) + C_{46}\left\{\left(a_{i1}a_{j2} + a_{i2}a_{j1}\right)\left(a_{k2}a_{l3} + a_{k3}a_{l2}\right)\right. \\ &\quad \left. + \left(a_{i2}a_{j3} + a_{i3}a_{j2}\right)\left(a_{k1}a_{l2} + a_{k2}a_{l1}\right)\right\} + C_{55}\left(a_{i1}a_{j3} + a_{i3}a_{j1}\right)\left(a_{k1}a_{l3} + a_{k3}a_{l1}\right) \\ &\quad + C_{66}\left(a_{i1}a_{j2} + a_{i2}a_{j1}\right)\left(a_{k1}a_{l2} + a_{k2}a_{l1}\right) \end{aligned} \tag{26.10}$$

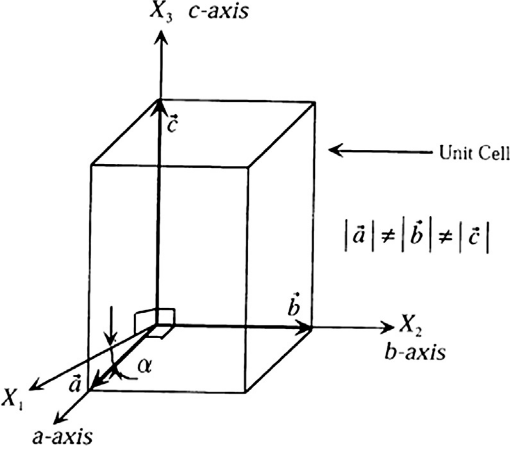

FIGURE 26.4 Coordinate system for a monoclinic crystal. *From Ref. [22] with permission of Elsevier Science.*

26.2.2.1.4 TETRAGONAL SINGLE CRYSTAL

In the case of tetragonal single crystals such as lead molybdate (PMO, $PbMoO_4$), the Cartesian coordinates X_1, X_2, and X_3 are taken in such a way that they coincide with the crystallographic *a*-, *b*-, and *c*-axes, respectively, as shown in Figure 26.5. Then, the elastic constant matrix in the $X_1 - X_2 - X_3$ coordinate system is given as follows, using seven independent elastic constants [19]:

$$[C_{ij}] = \begin{bmatrix} C_{11} & C_{12} & C_{13} & 0 & 0 & C_{16} \\ & C_{11} & C_{13} & 0 & 0 & -C_{16} \\ & & C_{33} & 0 & 0 & 0 \\ & & & C_{44} & 0 & 0 \\ & \text{Sym.} & & & C_{44} & 0 \\ & & & & & C_{66} \end{bmatrix} \tag{26.11}$$

If we consider the analysis coordinate system $X_1' - X_2' - X_3'$ as shown in Figure 26.2, the elastic constant tensor C'_{ijkl} associated with the $X_1' - X_2' - X_3'$ system is related to C_{ijkl} of the $X_1 - X_2 - X_3$ system as follows:

$$\begin{aligned} C'_{ijkl} &= a_{im}a_{jn}a_{ko}a_{lp}C_{mnop} \\ &= C_{11}(a_{i1}a_{j1}a_{k1}a_{l1} + a_{i2}a_{j2}a_{k2}a_{l2}) + C_{12}(a_{i1}a_{j1}a_{k2}a_{l2} + a_{i2}a_{j2}a_{k1}a_{l1}) \\ &\quad + C_{13}\{(a_{i1}a_{j1} + a_{i2}a_{j2})a_{k3}a_{l3} + a_{i3}a_{j3}(a_{k1}a_{l1} + a_{k2}a_{l2})\} \\ &\quad + C_{16}\{(a_{i1}a_{j1} - a_{i2}a_{j2})(a_{k1}a_{l2} + a_{k2}a_{l1}) + (a_{i1}a_{j2} + a_{i2}a_{j1})(a_{k1}a_{l1} - a_{k2}a_{l2})\} \\ &\quad + C_{33}a_{i3}a_{j3}a_{k3}a_{l3} + C_{44}\{(a_{i1}a_{j3} + a_{i3}a_{j1})(a_{k1}a_{l3} + a_{k3}a_{l1}) + (a_{i2}a_{j3} + a_{i3}a_{j2})(a_{k2}a_{l3} + a_{k3}a_{l2})\} \\ &\quad + C_{66}(a_{i1}a_{j2} + a_{i2}a_{j1})(a_{k1}a_{l2} + a_{k2}a_{l1}) \end{aligned} \tag{26.12}$$

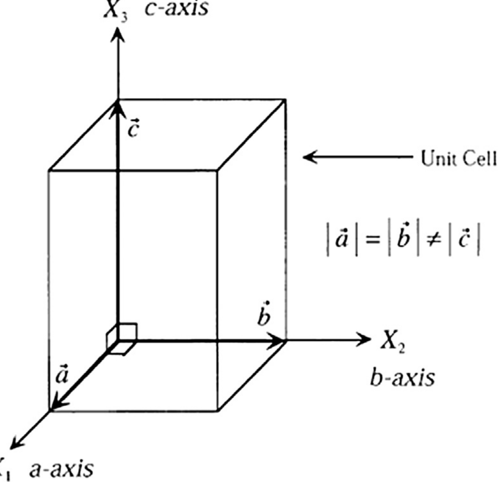

FIGURE 26.5 Coordinate system for a tetragonal crystal. *From Ref. [22] with permission of Elsevier Science.*

26.2.2.1.5 ORTHORHOMBIC SINGLE CRYSTAL

In the case of orthorhombic single crystals, such as alexandrite (Cr-doped BAO, $BeAl_2O_4$: Cr), the Cartesian coordinates X_1, X_2, and X_3 are taken in such a way that they coincide with the crystallographic *a*-, *b*-, and *c*-axis, respectively, as shown in Figure 26.6. Then, the elastic constant matrix in the $X_1 - X_2 - X_3$ coordinate system is given as follows, using nine independent elastic constants [19]:

$$[C_{ij}] = \begin{bmatrix} C_{11} & C_{12} & C_{13} & 0 & 0 & 0 \\ & C_{22} & C_{23} & 0 & 0 & 0 \\ & & C_{33} & 0 & 0 & 0 \\ & & & C_{44} & 0 & 0 \\ & \text{Sym.} & & & C_{55} & 0 \\ & & & & & C_{66} \end{bmatrix} \tag{26.13}$$

If we consider the analysis coordinate system $X_1' - X_2' - X_3'$ as shown in Figure 26.2, the elastic constant tensor C'_{ijkl} associated with the $X_1' - X_2' - X_3'$ system is related to C_{ijkl} of the $X_1 - X_2 - X_3$ system as follows:

$$\begin{aligned} C'_{ijkl} &= a_{im}a_{jn}a_{ko}a_{lp}C_{mnop} \\ &= C_{11}a_{i1}a_{j1}a_{k1}a_{l1} + C_{12}\left(a_{i1}a_{j1}a_{k2}a_{l2} + a_{i2}a_{j2}a_{k1}a_{l1}\right) + C_{13}\left(a_{i1}a_{j1}a_{k3}a_{l3} + a_{i3}a_{j3}a_{k1}a_{l1}\right) \\ &\quad + C_{22}a_{i2}a_{j2}a_{k2}a_{l2} + C_{23}\left(a_{i2}a_{j2}a_{k3}a_{l3} + a_{i3}a_{j3}a_{k2}a_{l2}\right) + C_{33}a_{i3}a_{j3}a_{k3}a_{l3} \\ &\quad + C_{44}\left(a_{i2}a_{j3} + a_{i3}a_{j2}\right)\left(a_{k2}a_{l3} + a_{k3}a_{l2}\right) + C_{55}\left(a_{i1}a_{j3} + a_{i3}a_{j1}\right)\left(a_{k1}a_{l3} + a_{k3}a_{l1}\right) \\ &\quad + C_{66}\left(a_{i1}a_{j2} + a_{i2}a_{j1}\right)\left(a_{k1}a_{l2} + a_{k2}a_{l1}\right) \end{aligned} \tag{26.14}$$

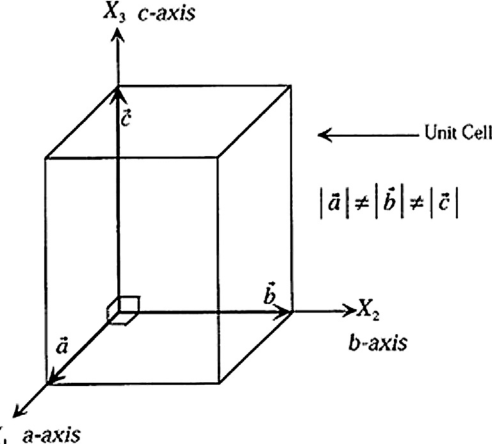

FIGURE 26.6 Coordinate system for an orthorhombic crystal. *From Ref. [22] with permission of Elsevier Science.*

26.2.2.2 Thermal Strain Vector

The thermal strain tensor ε_{ij}^t is given as follows:

$$\varepsilon_{ij}^t = \int \alpha_{ij} dT \tag{26.15}$$

where α_{ij} is the thermal expansion coefficient tensor and T denotes temperature.

26.2.2.2.1 CUBIC SINGLE CRYSTAL

For a cubic single crystal, Eqn (26.15) in the $X_1 - X_2 - X_3$ system shown in Figure 26.1 can be written by only one thermal expansion coefficient α_1 as follows [19]:

$$\begin{Bmatrix} \varepsilon_1^t \\ \varepsilon_2^t \\ \varepsilon_3^t \\ \varepsilon_4^t \\ \varepsilon_5^t \\ \varepsilon_6^t \end{Bmatrix} = \begin{Bmatrix} \int \alpha_{11}\,\mathrm{d}T \\ \int \alpha_{22}\,\mathrm{d}T \\ \int \alpha_{33}\,\mathrm{d}T \\ 2\int \alpha_{23}\,\mathrm{d}T \\ 2\int \alpha_{31}\,\mathrm{d}T \\ 2\int \alpha_{12}\,\mathrm{d}T \end{Bmatrix} = \begin{Bmatrix} \int \alpha_1\,\mathrm{d}T \\ \int \alpha_1\,\mathrm{d}T \\ \int \alpha_1\,\mathrm{d}T \\ 0 \\ 0 \\ 0 \end{Bmatrix} \tag{26.16}$$

where ε_i^t and α_i are the components of the thermal strain vector and those of the thermal expansion coefficient vector, respectively. Using the standard tensor transformation, we obtain the thermal expansion coefficient tensor α'_{ij} in the analysis coordinate system $X'_1 - X'_2 - X'_3$ shown in Figure 26.2 as follows:

$$\alpha'_{ij} = a_{ik}a_{jl}\alpha_{kl} = \alpha_{11}\left(a_{i1}a_{j1} + a_{i2}a_{j2} + a_{i3}a_{j3}\right) = \alpha_1\left(a_{i1}a_{j1} + a_{i2}a_{j2} + a_{i3}a_{j3}\right) \tag{26.17}$$

We can use the relationship between the indices of tensor and those of matrix shown in Table 26.1 to change the tensor components α_{ij} or α'_{ij} into the vector components α_i or α'_i. Finally, we obtain a matrix form of thermal strain in the $X'_1 - X'_2 - X'_3$ system shown in Figure 26.2 from the following relation:

$$\left(\varepsilon_{ij}^t\right)' = \int \alpha'_{ij} dT \tag{26.18}$$

26.2.2.2.2 TRIGONAL SINGLE CRYSTAL

For a trigonal single crystal, Eqns (26.15) or (26.16) in the $X_1 - X_2 - X_3$ system shown in Figure 26.3 can be written with two independent thermal expansion coefficients α_1 and α_3 [19] by substituting α_{ij} with

$$\alpha_{11} = \alpha_{22} = \alpha_1,\ \ \alpha_{33} = \alpha_3,\ \ \alpha_{23} = \alpha_{32} = 0,\ \ \alpha_{31} = \alpha_{13} = 0,\ \ \alpha_{12} = \alpha_{21} = 0 \tag{26.19}$$

Then, we obtain the thermal expansion coefficient tensor in the analysis coordinate system $X'_1 - X'_2 - X'_3$ shown in Figure 26.2 as follows:

$$\alpha'_{ij} = a_{ik}a_{jl}\alpha_{kl} = \alpha_{11}\left(a_{i1}a_{j1} + a_{i2}a_{j2}\right) + \alpha_{33}a_{i3}a_{j3} = \alpha_1\left(a_{i1}a_{j1} + a_{i2}a_{j2}\right) + \alpha_3 a_{i3}a_{j3} \tag{26.20}$$

26.2.2.2.3 MONOCLINIC SINGLE CRYSTAL

For a monoclinic single crystal, Eqns (26.15) or (26.16) in the $X_1 - X_2 - X_3$ system shown in Figure 26.4 can be written with four independent thermal expansion coefficients α_1, α_2, α_3 and α_5 [19] by substituting α_{ij} with

$$\alpha_{11} = \alpha_1, \ \ \alpha_{22} = \alpha_2, \ \ \alpha_{33} = \alpha_3, \ \ \alpha_{23} = \alpha_{32} = 0, \ \ \alpha_{31} = \alpha_{13} = \alpha_5, \ \ \alpha_{12} = \alpha_{21} = 0 \tag{26.21}$$

Then, we obtain the thermal expansion coefficient tensor in the analysis coordinate system $X_1' - X_2' - X_3'$ shown in Figure 26.2 as follows:

$$\begin{aligned} \alpha'_{ij} &= a_{ik}a_{jl}\alpha_{kl} = \alpha_{11}a_{i1}a_{j1} + \alpha_{22}a_{i2}a_{j2} + \alpha_{33}a_{i3}a_{j3} + \alpha_{31}a_{i3}a_{j1} + \alpha_{13}a_{i1}a_{j3} \\ &= \alpha_1 a_{i1}a_{j1} + \alpha_2 a_{i2}a_{j2} + \alpha_3 a_{i3}a_{j3} + \alpha_5\left(a_{i3}a_j + a_{i1}a_{j3}\right) \end{aligned} \tag{26.22}$$

26.2.2.2.4 TETRAGONAL SINGLE CRYSTAL

For a tetragonal single crystal, Eqns (26.15) or (26.16) in the $X_1 - X_2 - X_3$ system shown in Figure 26.5 can be written with two independent thermal expansion coefficients α_1 and α_3 [19] by substituting α_{ij} with

$$\alpha_{11} = \alpha_{22} = \alpha_1, \ \ \alpha_{33} = \alpha_3, \ \ \alpha_{23} = \alpha_{32} = 0, \ \ \alpha_{31} = \alpha_{13} = 0, \ \ \alpha_{12} = \alpha_{21} = 0 \tag{26.23}$$

Then, we obtain the thermal expansion coefficient tensor in the analysis coordinate system $X_1' - X_2' - X_3'$ shown in Figure 26.2 as follows:

$$\alpha'_{ij} = a_{ik}a_{jl}\alpha_{kl} = \alpha_{11}\left(a_{i1}a_{j1} + a_{i2}\alpha_{j2}\right) + \alpha_{33}a_{i3}a_{j3} = \alpha_1\left(a_{i1}a_{j1} + a_{i2}a_{j2}\right) + \alpha_3 a_{i3}a_{j3} \tag{26.24}$$

26.2.2.2.5 ORTHORHOMBIC SINGLE CRYSTAL

For a monoclinic single crystal, Eqn (26.15) or (26.16) in the $X_1 - X_2 - X_3$ system shown in Figure 26.6 can be written with three independent thermal expansion coefficients α_1, α_2, and α_3 [19] by substituting α_{ij} with

$$\alpha_{11} = \alpha_1, \ \ \alpha_{22} = \alpha_2, \ \ \alpha_{33} = \alpha_3, \ \ \alpha_{23} = \alpha_{32} = 0, \ \ \alpha_{31} = \alpha_{13} = \alpha_5, \ \ \alpha_{12} = \alpha_{21} = 0 \tag{26.25}$$

Using the standard tensor transformation, we obtain the thermal expansion coefficient tensor in the analysis coordinate system $X_1' - X_2' - X_3'$ shown in Figure 26.2 as follows:

$$\alpha'_{ij} = a_{ik}a_{jl}\alpha_{kl} = \alpha_{11}a_{i1}a_{j1} + \alpha_{22}a_{i2}a_{j2} + \alpha_{33}a_{i3}a_{j3} = \alpha_1 a_{i1}a_{j1} + \alpha_2 a_{i2}a_{j2} + \alpha_3 a_{i3}a_{j3} \tag{26.26}$$

26.2.2.3 Finite Element Formulation

From Eqn (26.6), we can obtain the final form of the stress–strain relation for a thermoelastic problem in the analysis coordinate system $X_1' - X_2' - X_3'$, assuming that the total strain ε'_j is a sum of the elastic strain $(\varepsilon^e_i)'$ and the thermal strain $(\varepsilon^t_i)'$:

$$\sigma'_i = C'_{ij}\left(\varepsilon'_j - \left(\varepsilon^t_j\right)'\right) \tag{26.27}$$

It is very easy to obtain a finite element equilibrium equation using a standard formulation for the finite element method. The components of elastic constant matrix for the respective crystal systems are given in Eqns (26.5), (26.8), (26.10), (26.12), and (26.14). The components of a thermal expansion coefficient vector for the respective crystal systems are given in Eqns (26.17), (26.20), (26.22), (26.24), and (26.26).

26.2.3 Several Examples of Thermal Stress Analysis

26.2.3.1 Effect of Crystal Anisotropy on Thermal Stress for Cubic Bulk Single Crystals (Si, GaAs, and InP)

Thermal stress analyses of Si, GaAs, and InP bulk single crystals during crystal growth are performed for the [001] and [111] growth directions, taking account of the elastic anisotropy [24]. Considering that cubic single crystals have 12 slip systems, Jordan et al. [25] proposed the following parameter σ_{tot}, which can be calculated from the results of thermal stress analysis:

$$\sigma_{tot} = \sum_{n=1}^{12} \left| \sigma_{RS}^{(n)} \right| \tag{26.28}$$

where $\sigma_{RS}^{(n)}$ denotes the resolved shear stress of nth slip system. This parameter can be used as a measure for thermal stress effective for glide strains.

The material properties required for a thermal stress analysis are the elastic constants C_{11}, C_{12}, and C_{44} (dyn/cm^2), and the thermal expansion coefficient $\alpha_1^{(1/\mathrm{K})}$. The following were employed in the present analyses:

Si single crystal [26]:

$$\begin{gathered} C_{11} = 16.564 \times 10^{11} \exp\left(-9.4 \times 10^{-5}(T - 298.15)\right) \\ C_{12} = 6.394 \times 10^{11} \exp\left(-9.8 \times 10^{-5}(T - 298.15)\right) \\ C_{44} = 7.951 \times 10^{11} \exp\left(-8.3 \times 10^{-5}(T - 298.15)\right) \\ \alpha_1 = 3.725 \times 10^{-6}\left(1.0 - \exp\left(-5.88 \times 10^{-3}(T - 124.0)\right)\right) + 5.84 \times 10^{-10} T \end{gathered}$$

GaAs single crystal [27]:

$$\begin{gathered} C_{11} = 12.16 \times 10^{11} - 1.39 \times 10^{8} T \\ C_{12} = 5.43 \times 10^{11} - 5.76 \times 10^{7} T \\ C_{44} = 6.18 \times 10^{11} - 7.01 \times 10^{7} T \\ \alpha_1 = 4.68 \times 10^{-6} + 3.82 \times 10^{-9} T \end{gathered}$$

InP single crystal [28]:

$$\begin{gathered} C_{11} = 10.76 \times 10^{11} - 1.397 \times 10^{8} T \\ C_{12} = 6.080 \times 10^{11} - 8.344 \times 10^{7} T \\ C_{44} = 4.233 \times 10^{11} - 4.035 \times 10^{7} T \\ \alpha_1 = 4.869 \times 10^{-6} - 5.164 \times 10^{-9} T + 6.048 \times 10^{-12} T^2 \end{gathered}$$

The unit of temperature T is K. The melting points of Si, GaAs, and InP are respectively 1685, 1511 and 1335 K.

The isotropic analysis was also carried out for comparison with the anisotropic analysis. In the isotropic analysis, Young's modulus E and Poisson's ratio ν in the {111} plane [29] were used in the same way as in Jordan et al.'s analysis [25].

Thermal stress analyses were performed for bulk single crystals, which have a cylindrical shape of 5 cm in diameter and 5 cm in height. Figure 26.7 shows the temperature distribution used in the thermal stress analysis of a GaAs single crystal. This temperature distribution was obtained from a heat conduction analysis during CZ growth by Jordan et al. [25]. The temperature distributions in Si and InP single crystals are so determined that the temperature difference from the solid–liquid interface, the temperature at which is the melting point of each crystal, is the same as that of a GaAs single crystal shown in Figure 26.7.

Figure 26.8 shows the contour lines of σ_{tot} in the cross-section at 2.474 cm above the solid–liquid interface in case of the [001] growth direction of a Si bulk single crystal. The results of both the isotropic analysis and the anisotropic analysis are given in this figure. The distribution patterns of σ_{tot} obtained from the anisotropic analysis are similar to those obtained from the isotropic analysis, but the isotropic analysis provides larger σ_{tot} values than the anisotropic analysis. Similar results are obtained for GaAs and InP single crystals in case of the [001] growth direction. As can be seen in Figure 26.8, the contour

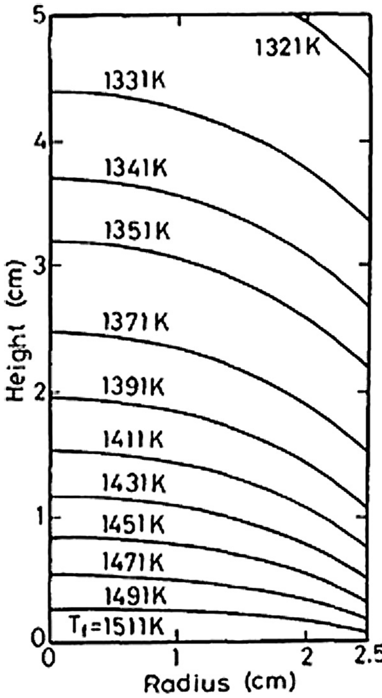

FIGURE 26.7 Temperature distribution used in the thermal stress analysis of a GaAs bulk single crystal. *From Ref. [24] with permission of Japan Society of Mechanical Engineers.*

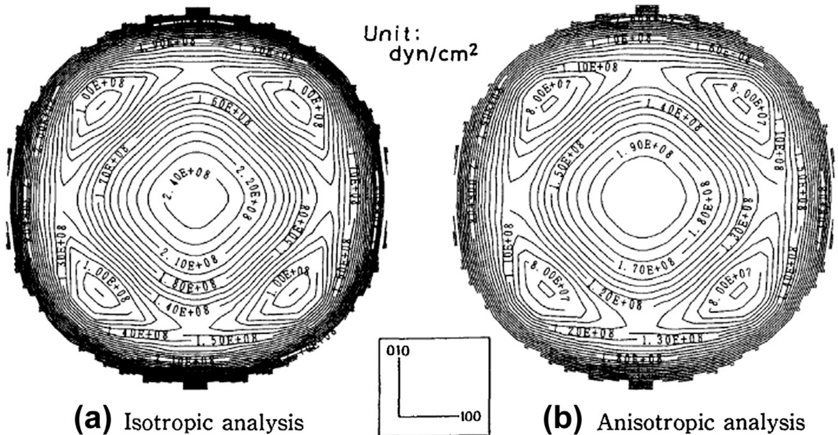

FIGURE 26.8 Contour lines of σ_{tot} in the cross-section at 2.474 cm above the solid–liquid interface in the [001] growth direction of a Si bulk single crystal. (a) Isotropic analysis and (b) Anisotropic analysis. *From Ref. [24] with permission of Japan Society of Mechanical Engineers.*

lines are dense near the side wall. In Table 26.2, the value of σ_{tot} at the side wall is compared between the isotropic analysis and the anisotropic analysis for the respective bulk single crystals in case of the [001] growth direction. In Table 26.2, the parameter A denotes a measure of elastic anisotropy defined as

$$A = 2C_{44}/(C_{11} - C_{12}) \tag{26.29}$$

The parameter A is equal to unity for elastically isotropic materials. It is found from the table that the difference between the isotropic analysis and the anisotropic analysis increases with increase of A.

Figure 26.9 shows the contour lines of σ_{tot} in the case of cross-section at 2.474 cm above the solid–liquid interface in case of the [111] growth direction of an InP bulk single crystal. The results of both the isotropic analysis and the anisotropic analysis are given in the figure. We can see the difference in the distribution patterns of σ_{tot} rather than its value.

Table 26.2 σ_{tot} at the Side Wall

		(dyn/cm²)		
	A	iso.	aniso.	iso./aniso.
Si	1.58	5.4×10^8	4.6×10^8	1.17
GaAs	1.86	8.0×10^8	6.4×10^8	1.25
InP	1.88	4.9×10^8	3.7×10^8	1.32

iso. : Result of isotropic analysis.
aniso. : Result of anisotropic analysis.

From Ref. [24] with permission of Japan Society of Mechanical Engineers.

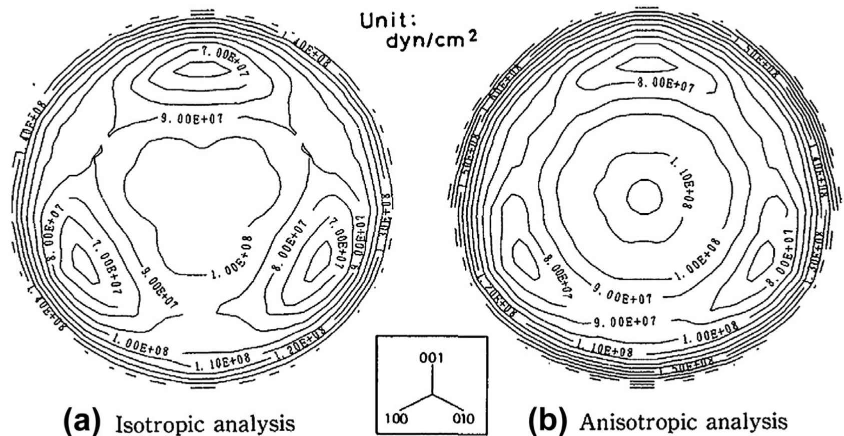

FIGURE 26.9 Contour lines of σ_{tot} in the cross-section at 2.474 cm above the solid–liquid interface in the [111] growth direction of an InP bulk single crystal. (a) Isotropic analysis and (b) Anisotropic analysis. *From Ref. [24] with permission of Japan Society of Mechanical Engineers.*

26.2.3.2 Thermal Stress Analysis of Lithium Niobate Bulk Single Crystal

Trigonal single crystals, such as lithium niobate (LN, $LiNbO_3$) and lithium tantalite (LT, $LiTaO_3$) are important for surface acoustic wave (SAW) and photonic devices. Cracking of the crystals sometimes occurs during the CZ growth, especially during cooling down. Because the cracking can be avoided by adjusting the thermal conditions of the CZ furnace, this defect is supposed to be caused by thermal stress [30,31]. Thus, it is essential to calculate the thermal stress during the growth for the quantitative assessment of cracking. Here, the results of thermal stress analyses for an LN bulk single crystal during the CZ growth are shown for different growth directions by using a three-dimensional finite element computer program [20]. Crystal anisotropy in the elastic constants and thermal expansion coefficients was considered in the analysis.

Thermal stress analyses of LN bulk single crystals of 1-inch diameter were performed using the temperature distribution calculated from a global analysis of heat transfer in an inductively heated CZ furnace [32]. The temperature distribution and crystal shape are shown in Figure 26.10, in which contour lines are so drawn as to divide the difference between the maximum temperature and the minimum one into 20 equal portions. Here, the maximum temperature corresponds to the temperature at the interface between the crystal and the melt (i.e., the melting point of LN: 1526.15 K), and the minimum one corresponds to the temperature at the top of a bulk single crystal (i.e., 1112.08 K). The temperature-dependent elastic constants C_{ij} [33] and thermal expansion coefficients α_i [34] are given as follows:

$$C_{11} = 2.030 \times 10^{12}\left(1.0 - 1.74 \times 10^{-4}(T - 298.15)\right)$$
$$C_{12} = 0.573 \times 10^{12}\left(1.0 - 2.52 \times 10^{-4}(T - 298.15)\right)$$
$$C_{13} = 0.752 \times 10^{12}\left(1.0 - 1.59 \times 10^{-4}(T - 298.15)\right)$$
$$C_{14} = 0.085 \times 10^{12}\left(1.0 - 2.14 \times 10^{-4}(T - 298.15)\right)$$
$$C_{33} = 2.424 \times 10^{12}\left(1.0 - 1.53 \times 10^{-4}(T - 298.15)\right)$$

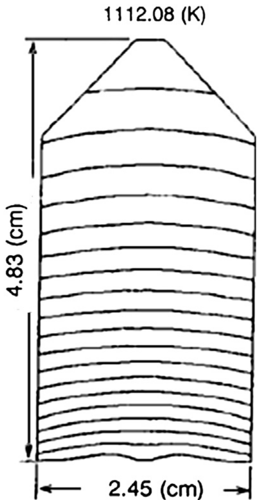

FIGURE 26.10 Temperature distribution and crystal shape of an LN bulk single crystal obtained from a global analysis of heat transfer in an inductively heated CZ furnace [32]. *From Ref. [20] with permission of Elsevier Science.*

$$C_{44} = 0.595 \times 10^{12}\left(1.0 - 2.04 \times 10^{-4}(T - 298.15)\right)$$
$$\alpha_1 = -2.8540 \times 10^{-6} + 2 \times 2.2573 \times 10^{-8}T - 3 \times 6.3438 \times 10^{-12}T^2$$
$$\alpha_3 = -1.0666 \times 10^{-6} + 2 \times 8.8951 \times 10^{-9}T - 3 \times 5.6895 \times 10^{-12}T^2$$

Three-dimensional finite element thermal stress analyses of LN bulk single crystals were carried out for both a-axis growth and c-axis growth. The von Mises equivalent stress $\sqrt{3J_2'}$, where J_2' is the second invariant of the deviatoric stress, and the maximum principal stress σ_1 ($\sigma_1 \geq \sigma_2 \geq \sigma_3$) were calculated from the results of thermal stress analyses. The stresses $\sqrt{3J_2'}$ and σ_1 were adopted as a measure for ductile failure or slip and a measure for brittle failure, respectively. The maximum values of $\sqrt{3J_2'}$ and σ_1 are as follows:

$\sqrt{3J_2'}$: 75.1 MPa for the a-axis growth and 59.3 MPa for the c-axis growth
σ_1: 72.2 MPa for the a-axis growth and 40.6 MPa for the c-axis growth

It is found from the above results that $\sqrt{3J_2'}$ and σ_1 are much larger for the a-axis growth than for the c-axis growth. This fact indicates that a-axis growth cracks easier than c-axis growth, which is consistent with the experience of LT crystal growth [31].

Figures 26.11 and 26.12 show the contour lines of $\sqrt{3J_2'}$ and σ_1 for the case of a-axis growth and c-axis growth, respectively. In these figures, a quarter of the crystal is eliminated to show the internal part clearly; the numeral 1 indicates the minimum and the numeral 9 indicates the maximum. The differences in stress distribution are shown in Figures 26.11 and 26.12 according to the crystal growth directions. For a-axis growth, the maximum values of stresses $\sqrt{3J_2'}$ and σ_1 occur either at the crystal–melt interface or at the outer surface of the crystal, and the lower-stress region spreads widely in the internal part of the bulk single crystal. On the other hand, the bulk single crystal grown in

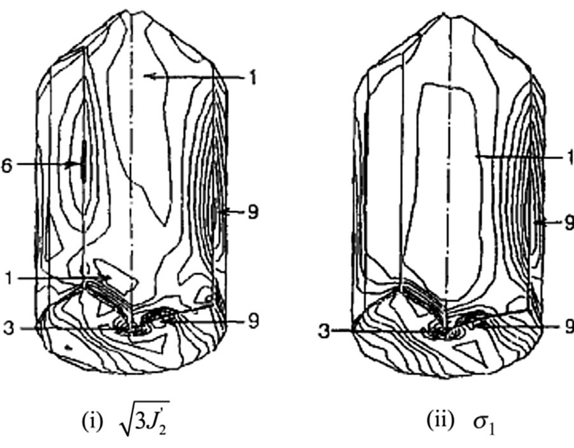

FIGURE 26.11 Stress distributions in an LN bulk single crystal grown in the *a*-axis. *From Ref. [20] with permission of Elsevier Science.*

the *c*-axis has a higher stress region in the internal part of the crystal in addition to the outer surface of the crystal. This fact indicates that one can obtain a bulk single crystal of high quality using *a*-axis growth, which has lower dislocation density than a bulk single crystal grown in the *c*-axis, if one can grow a bulk single crystal without macrocracking.

26.2.3.3 Thermal Stress Analysis of Lead Molybdate Bulk Single Crystal

A lead molybdate ($PbMoO_4$, hereafter abbreviated as PMO) single crystal has a tetragonal crystal structure and is used in acousto-optic light detectors and modulators. Its bulk single crystal is usually manufactured by the CZ growth technique. Several experimental studies have been performed on the relationship between the growth direction of the PMO bulk single crystal and crystal quality [35–42]. Thermal stress analyses of a PMO bulk single crystal were performed to discuss the formation of macrocracking and subgrains.

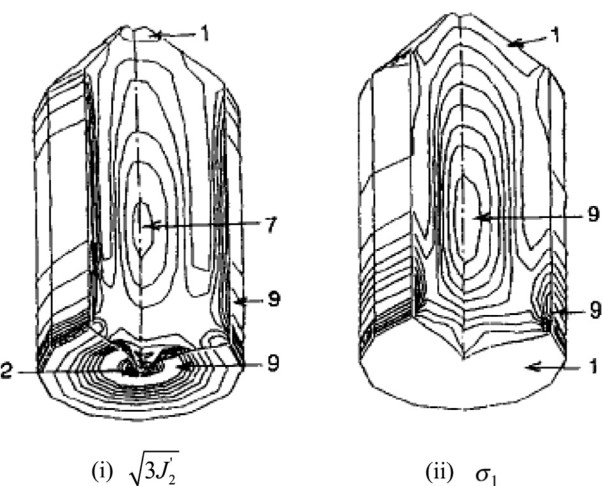

FIGURE 26.12 Stress distributions in an LN bulk single crystal grown in the *c*-axis. *From Ref. [20] with permission of Elsevier Science.*

Table 26.3 Elastic Constants and Thermal Expansion Coefficients of PMO Single Crystals

C_{ij} and α_i	Value	Unit
C_{11}	1.092×10^{12}	[dyn/cm^2]
C_{12}	0.683×10^{12}	[dyn/cm^2]
C_{13}	0.528×10^{12}	[dyn/cm^2]
C_{16}	0.136×10^{12}	[dyn/cm^2]
C_{33}	0.917×10^{12}	[dyn/cm^2]
C_{44}	0.267×10^{12}	[dyn/cm^2]
C_{66}	0.337×10^{12}	[dyn/cm^2]
α_1	10×10^{-6}	[1/K]
α_3	25×10^{-6}	[1/K]

10^7 dyn/cm^2 = 1 MPa

Three-dimensional finite element thermal stress analyses of a PMO bulk single crystal with a cylindrical shape of 5 cm in diameter and 5 cm in height were carried out for various growth directions including the *a*-, *b*-, and *c*-axis directions to discuss the relationship between the thermal stress and the crystal quality obtained from the experiments [22,43]. The temperature distribution used in thermal stress analysis is similar to Figure 26.7 for GaAs single crystals [25]. That is, the temperature difference from the crystal–melt interface is the same as that of a GaAs single crystal shown in Figure 26.7, and the temperature at the crystal–melt interface is the melting point of a PMO single crystal, 1343 K. The elastic constants and thermal expansion coefficients of a PMO single crystal are summarized in Table 26.3 [44].

The maximum principal stress σ_1 and the von Mises equivalent stress $\sqrt{3J_2'}$ were calculated from the results of thermal stress analyses. The maximum values of σ_1 and

Table 26.4 The Maximum Values of σ_1 and $\sqrt{3J_2'}$ in a PMO Bulk Single Crystal for Various Growth Directions

Growth Direction	σ_1(MPa)	$\sqrt{3J_2'}$(MPa)
a (90-0)	36.5	41.7
b (90-90)	36.5	41.7
c (0-0)	19.7	17.3
30-0	27.3	28.3
30-30	26.7	26.3
30-60	27.4	28.4
30-90	27.3	28.4
60-0	35.2	38.3
60-30	36.6	42.2
60-60	34.8	37.8
60-90	35.2	38.3
90-30	41.7	53.9
90-60	35.8	40.2

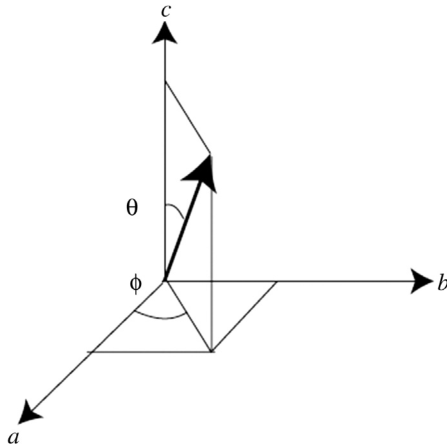

FIGURE 26.13 Notation of angles defining crystal growth direction. *From Ref. [43] with permission of Elsevier.*

$\sqrt{3J_2'}$ for the respective growth directions are summarized in Table 26.4, in which the growth direction is defined as $\theta-\varphi$ by the combination of the angle θ and φ, shown in Figure 26.13. The contour lines of σ_1 and $\sqrt{3J_2'}$ for *a*-, *b*-, and *c*-axis growth directions are shown in Figure 26.14. Due to crystallographic equivalence, the *a*-axis growth provides exactly the same results as the *b*-axis growth, and the stress distributions for *c*-axis growth are perfectly axisymmetric. It is also found from the figure that the stresses are higher in the peripheral region than in the internal region. This fact conforms to the experimental result obtained by Loiacono et al. [36] showing that the subgrain density is maximized at the outer surface of a bulk single crystal. The results of *a*-, *b*-, and *c*-axis growth directions in Table 26.4 show that the *a*- and *b*-axis growth directions provide larger stress values than the *c*-axis growth direction. As Bonner and Zydzik [35] pointed out, large stress is induced in the crystals grown on the *a*- and *b*-axis as a result of an unequal radial coefficient of expansion in the plane normal to the growth direction. Therefore, they are excessively strained after crystal growth and often shatter from the heat of a hand and always with attempted annealing.

Macrocracking and subgrains are the main concerns in the quality of PMO bulk single crystals. As for macrocracking, Bonner and Zydzik [35] concluded from their experimental study that the best orientation for crack-free growth is about 30° off the *c*-axis. Takano et al. mentioned in their paper [37] that the *c*-axis or near *c*-axis growth direction produces large crack-free crystals. Sabharwal et al. [42] found from their experimental study that the growth axis lying between 20° and 30° off the *c*-axis yields crack-free crystals. On the other hand, according to the experiments done by Zeng [41], the most suitable growth orientation for crack-free crystal is [100]. The following are the experimental results concerning the relationship between subgrains and growth direction. A study on the x-ray characterization of PMO single crystals performed by Loiacono et al. [36] showed that crystals grown in the *a*-axis direction had higher quality than those

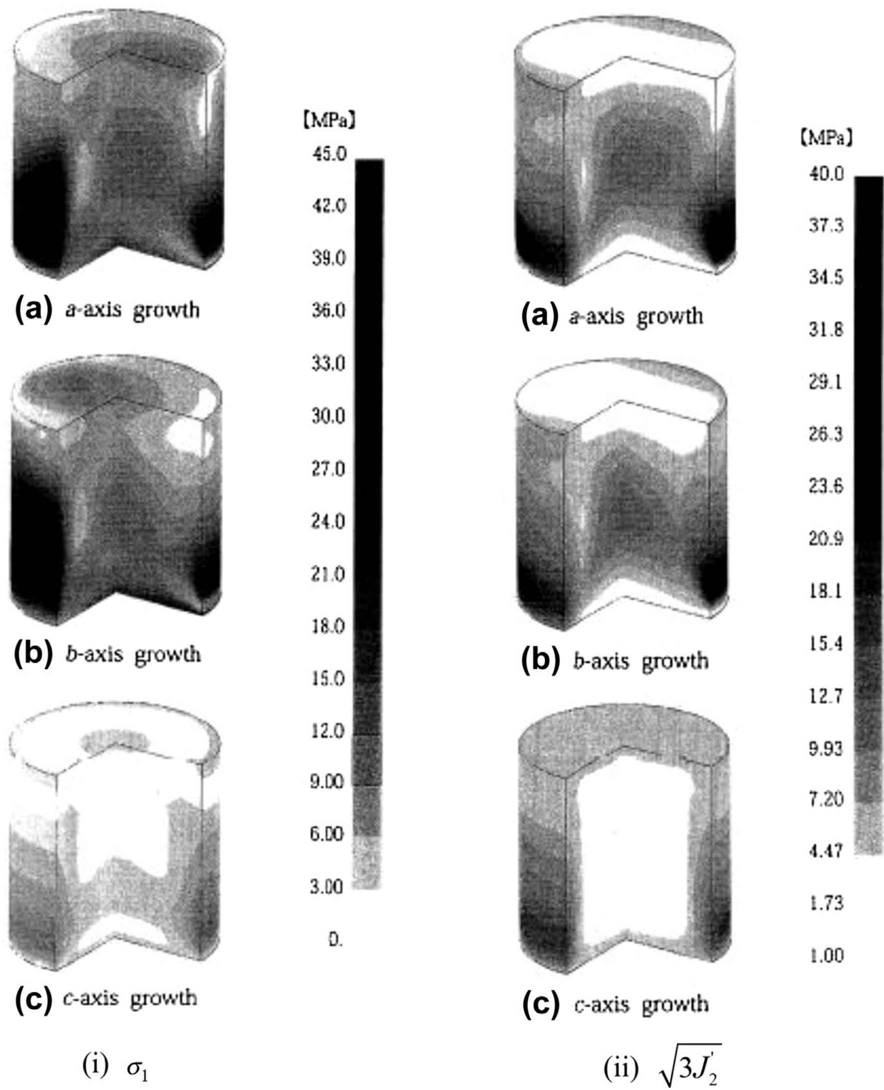

FIGURE 26.14 Stress distributions in a PMO bulk single crystal for various growth directions. *From Ref. [22] with permission of Elsevier Science.*

grown in the *c*-axis direction. Takano et al. [37] carried out PMO crystal growth for the various growth directions, concluding that high-quality single crystals without subgrains are obtained by using orientations inclined more than 30° from the *c*-axis in the intermediate planes between the *a*-*c* plane and the *b*-*c* plane. Based on these results, PMO crystals are usually grown either in the *a*-axis direction [38,39] or in the [110] direction [40], but no definite conclusion has been derived so far on the relationship between subgrains and growth direction.

As shown in Table 26.4, thermal stress is lowest in case of the *c*-axis growth and relatively small in cases of growth directions 30° off the *c*-axis (i.e., the 30-0, 30-30, 30-60, and 30-90 growth directions). This fact validates the experimental results that the *c*-axis or near *c*-axis growth direction produce large crack-free crystals, as pointed out by Bonner and Zydzik [35], Takano et al. [37], and Sabharwal et al. [42], but it does not comply with the experimental results on subgrain distribution in the PMO single crystal obtained by Loiacono et al. [36] and Takano et al. [37]. Loiacono et al. [36] presumed that the thermal conductivity of the *a*-axis direction is much larger than that of the *c*-axis direction by comparing the quality of the *a*-axis grown crystal with that of *c*-axis grown crystal, but no experimental data are available for such anisotropy in the thermal conductivity of the PMO single crystal at elevated temperatures. It may be therefore concluded that subgrains are not related to thermal stress during the growth process [45].

26.2.4 Cracking of Bulk Single Crystal Caused by Thermal Stress

A Ce-doped gadolinium orthosilicate (GSO) single crystal is classified as a monoclinic class 2/*m* single crystal. It is used as a scintillator material [46,47]. GSO bulk single crystals are manufactured by the CZ growth technique. Cracking is one of the biggest problems in GSO single crystal growth [48]. Here, quantitative estimation of the cracking of GSO single crystals is presented based on thermal stress tests and three-point bending tests [49]. The results of failure data obtained from the thermal stress tests are related to those of three-point bending tests.

Figure 26.15 shows the apparatus for thermal stress tests. Figure 26.16 shows a cylindrical test specimen of 50 mm in diameter and 10 mm in thickness used in thermal stress tests. The (100) cleavage plane is depicted in the figure. As shown in Figure 26.15, a test specimen was heated up to approximately 470 K in a silicone oil bath. Then, thermal stress was applied by pouring silicone oil at room temperature into a heated oil bath. Cracking occurred during cooling due to thermal stress. The surface temperatures were

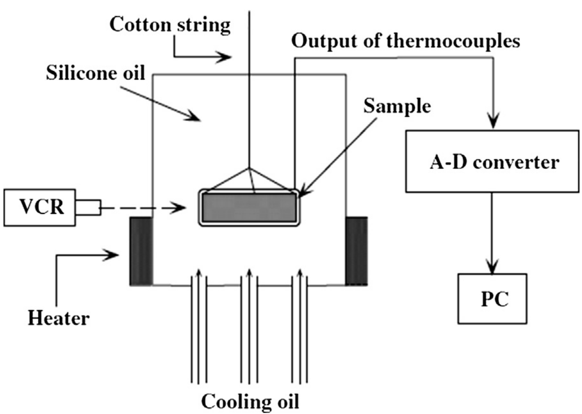

FIGURE 26.15 Apparatus for thermal stress test. *From Ref. [49] with permission of Tech Science Press.*

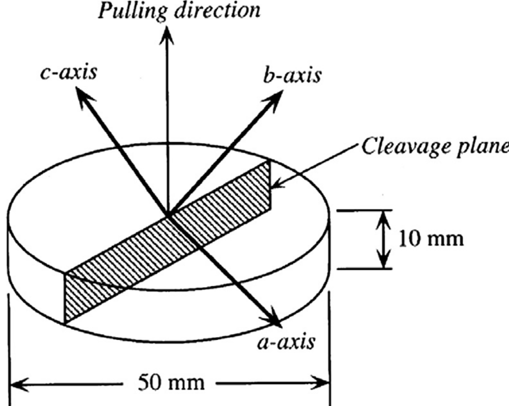

FIGURE 26.16 GSO test specimen for thermal stress tests and cleavage plane. *From Ref. [49] with permission of Tech Science Press.*

measured using thermocouples attached on the surface of the test specimen. The time when the cracking occurred was identified by a video recording. The finite element method was applied both to the heat conduction analysis and to the thermal stress analysis. The density ρ, specific heat C_p, and thermal conductivity λ of a GSO single crystal are required for the heat conduction analysis. The following material properties were used in the heat conduction analysis:

$$\rho = 6.71 \times 10^3 \mathrm{kg/m^3}, C_p = 350\mathrm{J/(kg \cdot K)}, \lambda = 2.98\mathrm{W/(m \cdot K)}$$

The values of C_p and λ were measured by Hitachi Chemical Co. by the laser flash method. The elastic constants C_{ij} and thermal expansion coefficients α_i of the GSO single crystal were reported by Kurashige et al. [50], as summarized in Table 26.5. The detailed method for thermal stress analysis of GSO single crystals is given in Ref. [21].

The thermal stress at the time of cracking obtained from the analysis was converted into the von Mises equivalent stress $\sqrt{3J_2'}$, the maximum principal stress σ_1, the normal stress σ_n acting on the (100) cleavage plane, and the shear stress σ_s acting on the (100) cleavage plane. Figure 26.17 shows an example of the distributions of these stresses at the time of cracking. The cracking shown in Figure 26.18 was observed in all of the test specimens in the thermal stress tests. The crack surface is confirmed to be the (100) cleavage plane by X-ray diffraction. Among the four kinds of stress shown in Figure 26.17, the stress σ_n can be used to explain the cracking phenomenon. It is found from Figure 26.17(c) that σ_n is at the maximum at the side surface of the test specimen where the (100) cleavage intersects. Therefore, the crack runs along the (100) cleavage plane. Among the four kinds of stress evaluated for the cracking, it was concluded that the maximum value of σ_n dominates the cracking induced by thermal stress.

Three-point bending tests were also performed to examine the relationship between the critical stress for cracking induced by thermal stress and the three-point bending strength. The details of the three-point bending tests are given in Ref. [51]. Test

Table 26.5 Elastic Constants and Thermal Expansion Coefficients of GSO Single Crystals

C_{ij} and α_i	Value	Unit
C_{11}	2.23×10^{12}	[dyn/cm^2]
C_{12}	1.08×10^{12}	[dyn/cm^2]
C_{13}	0.985×10^{12}	[dyn/cm^2]
C_{15}	0.084×10^{12}	[dyn/cm^2]
C_{22}	1.50×10^{12}	[dyn/cm^2]
C_{23}	1.02×10^{12}	[dyn/cm^2]
C_{25}	0.333×10^{12}	[dyn/cm^2]
C_{33}	2.51×10^{12}	[dyn/cm^2]
C_{35}	-0.06×10^{12}	[dyn/cm^2]
C_{44}	0.788×10^{12}	[dyn/cm^2]
C_{46}	-0.066×10^{12}	[dyn/cm^2]
C_{55}	0.688×10^{12}	[dyn/cm^2]
C_{66}	0.827×10^{12}	[dyn/cm^2]
α_1	4.8×10^{-6}	[1/K]
α_2	14.0×10^{-6}	[1/K]
α_3	6.4×10^{-6}	[1/K]

10^7 dyn/cm^2 = 1 MPa

specimens are 4.5×4.5 mm in cross-section and 50 mm in length. The GSO single crystal has a (100) cleavage plane and a [001] slip direction in the (100) cleavage plane. As shown in Figure 26.19, six cases of three-point bending tests were performed at a temperature of 470 K—the same temperature as silicone oil in the thermal stress test. The average value of the three-point bending strength σ_b for each case is given in Table 26.6. Because Case 2 has the lowest three-point bending strength and complete cleavage fracture was observed both in Case 2 and in the thermal stress test specimens, the three-point bending strength for Case 2 should be compared with the critical stress for the cracking induced by thermal stress.

Weibull plots of the failure data obtained from the thermal stress tests and the three-point bending tests are shown in Figure 26.20 where the cumulative failure probability F is related to the stress σ_n for the thermal stress tests and the stress σ_b for the three-point bending tests. Both sets of failure data show good linearity and obey the Weibull distributions. According to the weakest link model of the Weibull distribution, a larger specimen has lower failure stress. This is why the failure data of the thermal stress tests scatter at lower stress than those of the three-point bending tests. Furthermore, the slopes of both lines are almost the same, which indicates that the Weibull distribution of the thermal stress tests can be estimated from that of the three-point bending test by correcting a size effect. A return period T_r (defined by $T_r = L_1/L_2$, where L_1 and L_2 are respectively the effective lengths for a thermal stress test specimen and a three-point bending test specimen) is used for the correction of a size effect. In thermal stress

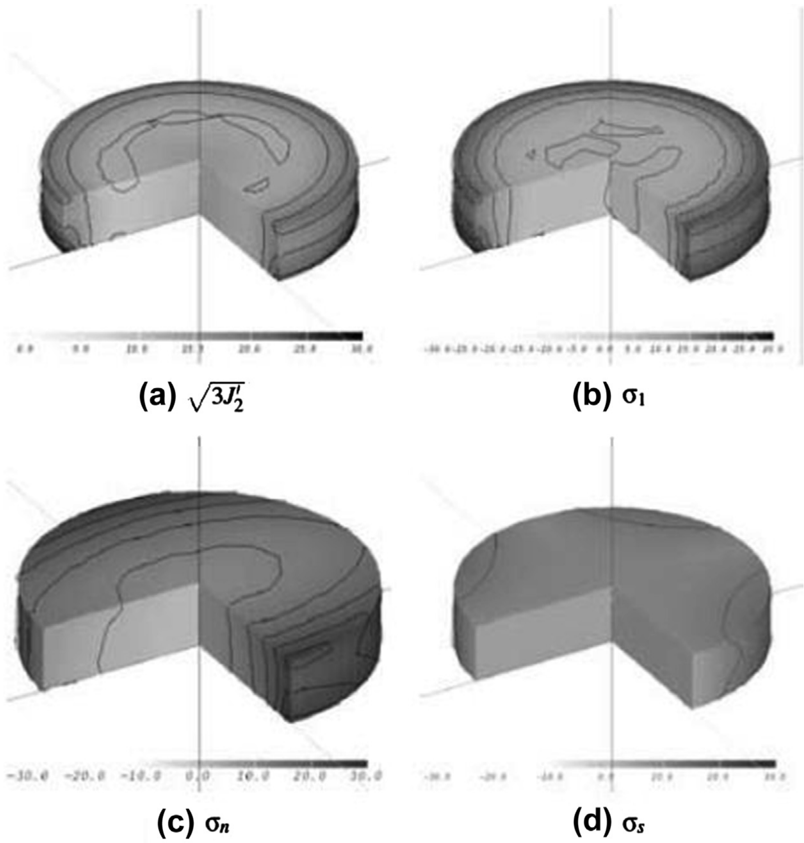

FIGURE 26.17 Distributions of stresses in a GSO test specimen at the time of cracking obtained from thermal stress analysis (unit: MPa, $\Delta\sigma = 5$ MPa). *From Ref. [49] with permission of Tech Science Press.*

FIGURE 26.18 Cracking of a GSO test specimen observed in a thermal stress test. *From Ref. [49] with permission of Tech Science Press.*

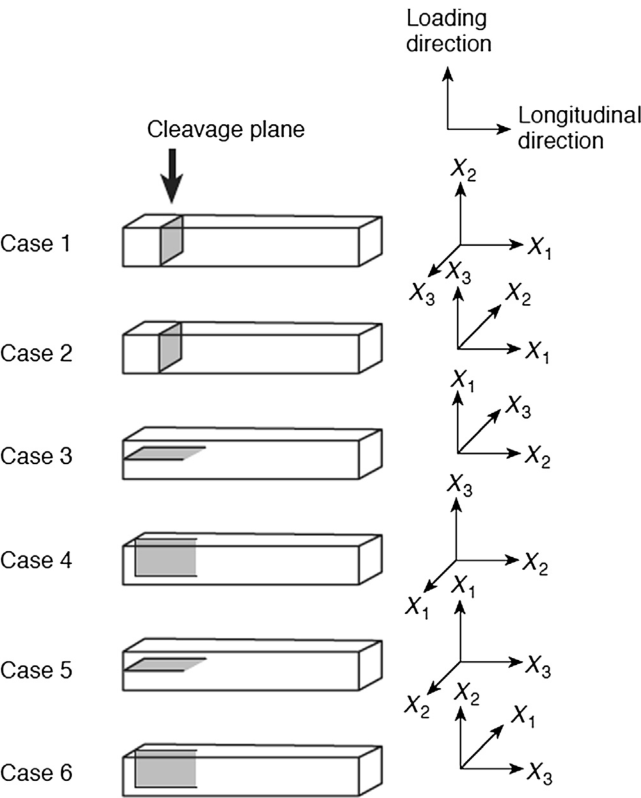

FIGURE 26.19 Schematic diagrams of test conditions for three-point bending tests of a GSO single crystal. *From Ref. [49] with permission of Tech Science Press.*

tests, the origin of cracking is located at the side surface of the cylindrical specimen where σ_n is the maximum, as shown in Figure 26.17(c), so the double thickness of the test specimen, 20 mm, was chosen as L_1. On the other hand, the length of the three-point bending specimen just under the loading location, which is subjected to the maximum tensile stress caused by the bending moment, is chosen as L_2. So, L_2 is equal to 4.5 mm. The broken line in Figure 26.20 is the Weibull distribution estimated from the three-point bending data using the return period. The estimated Weibull distribution agrees very well with that of the thermal stress tests. Miyazaki et al. also performed cracking experiments of the LN single crystal [52] and LT single crystal [53] under thermal loading conditions.

Table 26.6 Average Value of Three Point Bending Strength for a GSO Single Crystal

Case	**1**	**2**	**3**	**4**	**5**	**6**
Average σ_b[MPa]	102.5	44.34	151.2	157.3	—	618.2

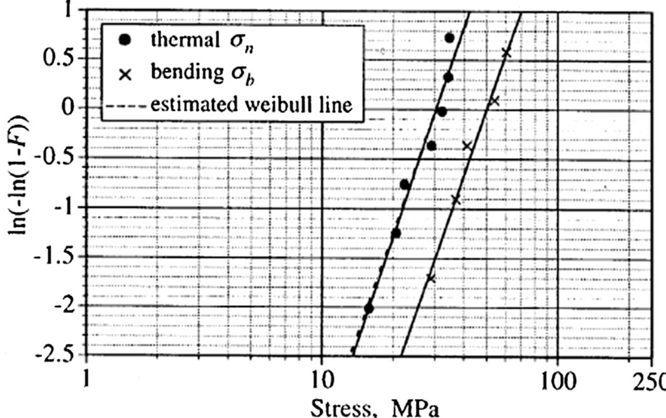

FIGURE 26.20 Weibull plots for failure stresses of a GSO single crystal obtained from thermal stress tests and the three-point bending tests. *From Ref. [49] with permission of Tech Science Press.*

26.3 Dislocations in Bulk Single Crystals

26.3.1 Introduction

Single crystals for electronic and optical devices (e.g., Si, Ge, GaAs, InP, CdTe) are manufactured by the Czochralski (CZ), floating zone (FZ) and vertical gradient freeze (VGF) methods, for example. As crystal growth is carried out under thermal gradients, large thermal stress is induced in a crystal by nonlinear thermal gradients during the growth process. Such thermal stress causes the multiplication of dislocations that affect the performance of devices. In particular, GaAs and InP single crystals have low critical resolved shear stress, and it is easy to multiply dislocations due to thermal stress during the growth process. Therefore, it is important to reduce the dislocations as low as possible. After crystal growth, compound semiconductor single crystals, such as GaAs and InP, are annealed to improve their electrical properties. One of the technical problems of ingot annealing is the increase of the dislocation density caused by thermal stress during ingot annealing. Computer simulations of dislocation density play a major role in determining the process conditions of crystal growth and crystal annealing. Quantitative methods for dislocation density estimation are presented here, as well as a qualitative method.

26.3.2 Qualitative Estimation of Dislocation Density

The main objective of thermal stress analysis of the crystal growth process is to clarify the relationship between defects such as dislocations and thermal stress. For this purpose, Jordan et al. [25] proposed a parameter for the qualitative estimation of dislocation density σ_{ex}. They assumed that dislocation density is proportional to the

amount of slip or glide strain, which is also proportional to the excess shear stress $\sigma_e^{(n)}$ defined by

$$\begin{aligned} \sigma_e^{(n)} &= \left|\sigma_{RS}^{(n)}\right| - \sigma_{CRS}, \quad \text{when} \quad \left|\sigma_{RS}^{(n)}\right| > \sigma_{CRS} \\ &= 0, \quad \text{when} \quad \left|\sigma_{RS}^{(n)}\right| \leq \sigma_{CRS} \end{aligned} \tag{26.30}$$

where the subscript (n) denotes the nth slip system, $\sigma_{RS}^{(n)}$ is the resolved shear stress for the nth slip system calculated from the stress transformation from the analysis coordinate system to the slip system, and σ_{CRS} is the critical resolved shear stress. Considering that cubic single crystals such as Si, GaAs, and InP single crystals have 12 equivalent slip systems {111}<110>, the total excess shear stress is

$$\sigma_{ex} = \sum_{n=1}^{12} \sigma_e^{(n)} \tag{26.31}$$

A positive value of σ_{ex} means that dislocations occur in the crystal. The nondimensional parameter σ_{mex} [18,54] can be also used as a measure for the qualitative estimation of dislocation density:

$$\sigma_{mex} = \frac{\sigma_{tot}}{12\sigma_{CRS}} \tag{26.32}$$

where

$$\sigma_{tot} = \sum_{n=1}^{12} \left|\sigma_{RS}^{(n)}\right| \tag{26.33}$$

When σ_{mex} is larger than the unity, the average resolved shear stress ($\sigma_{tot}/12$) is larger than the critical resolved shear stress. It is concluded that dislocations occur in such a case.

Qualitative estimation of dislocation density was performed by Jordan et al. [25] for the first time. They used the parameter σ_{ex} calculated from the results of the isotropic thermal stress analysis of a GaAs bulk single crystal during crystal growth. After that, they also performed the analyses for InP and Si crystals, in addition to GaAs crystals [55,56]. Quantitative methods for dislocation density estimation described later need creep or viscoplastic constitutive equations as a function of the dislocation density. On the other hand, the qualitative method for dislocation density estimation described here requires only elastic constants, thermal expansion coefficients, the slip system, and critical resolved shear stress. Therefore, this method can be applied to various kinds of single crystals, such as SiC [57] and AlN [58] crystals grown by the sublimitation technique.

26.3.3 Quantitative Estimation of Dislocation Density: Haasen-Alexander-Sumino Model

The quantitative estimation of the dislocation density provides more useful information on the quality of a single crystal than the qualitative estimation. In the quantitative

estimation, the Haasen-Alexander-Sumino (HAS) model [59,60] is used as the constitutive equation relating time-dependent inelastic strain (i.e., creep strain or viscoplastic strain) with dislocation density. Quantitative dislocation density analysis during the crystal growth process using the HAS model was performed by Dillion et al. [61] for the first time, followed by several papers [62,63]. All of these papers dealt with the growth of an Si ribbon. Afterward, several papers were published concerning the dislocation density analyses of compound semiconductor single crystals, such as GaAs and InP grown by the CZ method and the vertical Bridgman method. Some of them [64–66] do not deal with a multiaxial stress state exactly; others [67–70] are quasistatic finite element analyses that assume a constant growth rate and constant radius of a bulk single crystal, and they give only steady-state values of dislocation density. The quasistatic method is only a simple model of the actual growth process, in which the growth rate and radial of a bulk single crystal are dynamically changed. Miyazaki et al. [71–73] developed a computer code for the transient simulation of dislocation density during crystal growth. In this computer code, axisymmetric finite element modeling is used, together with the HAS model for creep constitutive equations. It provides the space and time variations of dislocation density in a bulk single crystal.

Here, we provide methods for the quantitative estimation of dislocation density using the HAS model. In particular, we show a method for expanding the HAS model to a multiaxial stress state that is necessary for finite element analysis. Furthermore, we present another HAS model for a multiaxial stress state that takes into account crystal anisotropy in elastic constants and specific slip directions. Such constitutive equations enable the exact three-dimensional finite element analysis of quantitative dislocation density estimation. Then, the results of finite element analyses are shown for two kinds of quantitative dislocation density problems: dislocation density estimation during the crystal growth process and the ingot annealing process.

26.3.3.1 HAS Model for the Uniaxial Stress State

Time-dependent creep deformation is induced in a bulk single crystal under elevated temperatures during the crystal growth process. The creep constitutive equations for single crystals based on a dislocation kinetics model is known as the HAS model [59,60], in which the creep strain rate is related to the dislocation density. In this model, the creep strain rate $\mathrm{d}\varepsilon^c/\mathrm{d}t$ and the mobile dislocation density rate $\mathrm{d}N_m/\mathrm{d}t$ are given as follows for a uniaxial stress state:

$$\mathrm{d}\varepsilon^c/\mathrm{d}t = \phi N_m v b \tag{26.34}$$

$$\mathrm{d}N_m/\mathrm{d}t = \delta N_m v \tag{26.35}$$

where ε^c is the creep strain, t is the time, N_m is the density of mobile dislocation, and b is the magnitude of the Burgers vector. Hereafter, the superscript or subscript c indicates creep. ϕ is a geometric factor on the order of 1 relating the creep shear strain γ^c and the axial creep strain ε^c as $\varepsilon^c = \phi\gamma^c$. Equation (26.34) is obtained from the Orowan relation

$$\mathrm{d}\gamma^c/\mathrm{d}t = N_m v b \tag{26.36}$$

together with $\varepsilon^c = \phi\gamma^c$. The dislocation velocity v and the parameter δ that characterizes the multiplication rate in the above model are assumed to be

$$v = k_o(\tau_{eff})^p \exp(-Q/kT) \tag{26.37}$$

$$\delta = K(\tau_{eff})^\lambda \tag{26.38}$$

Here, τ_{eff} is the effective resolved shear stress and is given by

$$\tau_{eff} = \left\langle \tau_a - D\sqrt{N_m} - \tau_d \right\rangle \tag{26.39}$$

In the above equations, τ_a is externally applied shear stress on the active slip system or resolved shear stress; $D\sqrt{N_m}$ is the back-stress on a given dislocation due to the neighboring ones, which resists its movement through interaction; τ_d is the back-stress caused by the interaction between dislocations and impurity atoms; D is the strain hardening factor; Q is the Peierls potential; k is the Boltzmann constant; k_0, K, and λ are the material constants; and T is the absolute temperature. The value of $\langle x \rangle$ denotes $\langle x \rangle = x$ if $x > 0$ and 0 if $x \leq 0$. The parameters for creep constitutive equations are determined in such a way that the stress–strain curves under constant strain-rate test conditions obtained by solving Eqns (26.34) and (26.35) numerically agree well with experimentally obtained stress–strain curves around the upper and lower yielding points. The parameters are identified for Ge, Si, InSb, InP, GaAs, and so on [64–66,74]. Among them, the values of Si, InP, and GaAs are given later.

26.3.3.2 HAS Model for a Multiaxial Stress State under Isotropic Assumption

When we use the HAS model in a dislocation density analysis, we must expand Eqn (26.34) to a multiaxial stress state. Such an expansion can be done by assuming that a single crystal is isotropic, neglecting crystal anisotropy [75]. According to isotropic creep theory, the multiaxial creep strain rate $\mathrm{d}\varepsilon_{ij}^c/\mathrm{d}t$ is given by

$$\frac{\mathrm{d}\varepsilon_{ij}^c}{\mathrm{d}t} = \frac{3\mathrm{d}\varepsilon^c/\mathrm{d}t}{2\overline{\sigma}} S_{ij} \tag{26.40}$$

where S_{ij} is the deviatoric stress and $\overline{\sigma}$ is the equivalent stress defined by the second invariant of the deviatoric stress J_2' as follows:

$$\overline{\sigma} = \sqrt{3J_2'} \tag{26.41}$$

The following relationships hold for the simple shear characterized by the shear stress τ and the creep shear strain increment $\mathrm{d}\gamma^c$:

$$\overline{\sigma} = \sqrt{3}\tau \tag{26.42}$$

$$\mathrm{d}\varepsilon^c = \mathrm{d}\gamma^c/\sqrt{3} \tag{26.43}$$

Substituting Eqns (26.41) and (26.43) into Eqn (26.40), we obtain

$$\frac{\mathrm{d}\varepsilon_{ij}^c}{\mathrm{d}t} = \frac{\mathrm{d}\gamma^c/dt}{2\sqrt{J_2'}} S_{ij} \tag{26.44}$$

From Eqns (26.36) and (26.37), Eqn (26.44) becomes

$$\frac{\mathrm{d}\varepsilon_{ij}^{c}}{\mathrm{d}t} = fS_{ij} \tag{26.45}$$

$$f = \frac{bk_o N_m \left(\tau'_{eff}\right)^p \exp(-Q/kT)}{2\sqrt{J'_2}} \tag{26.46}$$

where

$$\tau'_{eff} = \left\langle \sqrt{J'_2} - D\sqrt{N_m} - \tau_d \right\rangle \tag{26.47}$$

It is found from Eqns (26.41) and (26.42) that $\sqrt{J'_2}$ represents the equivalent shear stress. The rate of dislocation density is represented by

$$\mathrm{d}N_m/\mathrm{d}t = Kk_o N_m \left(\tau'_{eff}\right)^{p+\lambda} \exp(-Q/kT) \tag{26.48}$$

If we use the creep constitutive equations given by Eqns (26.45) and (26.48), we can perform dislocation density analysis under an isotropic assumption neglecting crystal anisotropy.

26.3.3.3 HAS Model for a Multiaxial Stress State under Consideration of Crystal Anisotropy

Single crystals have crystal anisotropy in elastic constants and specific slip directions. Exact consideration of crystal anisotropy requires a three-dimensional analysis even for an axisymmetric solid. Great amounts of computational time would be necessary for the three-dimensional analysis of dislocation density during crystal growth. Therefore, several attempts have been made to avoid three-dimensional analysis by introducing approximate methods for dealing with the crystal anisotropy. Tsai et al. [68–70] proposed such a method in the framework of a quasistatic analysis. They applied the axisymmetric finite element method to the thermal stress analysis of a cylindrical single crystal, neglecting the crystal anisotropy in the elastic constants, then estimated the dislocation density using the resolved shear stress calculated from the results of the thermal stress analysis. Although their method considers the specific slip directions of a single crystal, it does not deal with the coupled phenomenon of dislocation multiplication and stress relaxation. Miyazaki et al. [76,77] proposed another approximate method for taking account of the crystal anisotropy of cubic single crystals, such as Si, GaAs, and InP. In their method, the effects of elastic constants and slip directions are approximately taken into account by averaging Young's modulus, Poisson's ratio, and the resolved shear stress along the azimuthal direction. Axisymmetric finite element method can be applied to quantitative estimation of the dislocation density by using such an averaging technique together with the HAS model for a creep constitutive equation. This approximate method is able to deal with the coupled phenomenon of dislocation multiplication and stress relaxation.

A full three-dimensional finite element analysis of dislocation density has become possible due to the rapid progress of computer performance [78,79]. Miyazaki and

Sakaguchi [78] expanded the HAS model to a multiaxial stress state based on the theory of crystal plasticity [80], as follows:

$$\frac{d\varepsilon_{ij}^c}{dt} = \sum_{n=1}^{N} f^{(n)} P_{ij}^{(n)} \tag{26.49}$$

$$f^{(n)} = bk_0 N_m \left(\tau_{eff}^{(n)}\right)^p \exp(-Q/kT) \tag{26.50}$$

$$P_{ij}^{(n)} = \frac{1}{2} \frac{\sigma_{RS}^{(n)}}{\left|\sigma_{RS}^{(n)}\right|} \left(\nu_i^{(n)} b_j^{(n)} + \nu_j^{(n)} b_i^{(n)}\right) \tag{26.51}$$

$$dN_m^{(n)}/dt = Kk_0 N_m \left(\tau_{eff}^{(n)}\right)^{p+\lambda} \exp(-Q/kT) \tag{26.52}$$

$$\tau_{eff}^{(n)} = \left\langle \left|\sigma_{RS}^{(n)}\right| - D\sqrt{N_m} - \tau_d \right\rangle \tag{26.53}$$

where the superscript (n) represents the nth slip system, N is the total number of slip systems, $\sigma_{RS}^{(n)}$ is the resolved shear system for the nth slip system, and ν_i and b_i denote the components of the unit vectors normal to the slip plane and parallel to the slip direction, respectively. Then, the total dislocation density N_m is given as follows:

$$N_m = \sum_{n=1}^{N} N_m^{(n)} \tag{26.54}$$

N should be 12 for a cubic single crystal such as Si, GaAs, or InP.

26.3.3.4 Several Applications of the HAS Model to the Quantitative Estimation of Dislocation Density

26.3.3.4.1 BULK SINGLE CRYSTAL GROWTH PROCESS

Miyazaki et al. [71–73] developed a computer code for a transient simulation of dislocation density during the bulk single crystal growth process, using the creep constitutive equations in Eqns (26.45)–(26.48). In a dislocation density analysis, one needs the parameters of the HAS model shown in Table 26.7. For Si, GaAs, and InP single crystals, the parameters in the HAS model are completely identified for Si, GaAs, and InP [74], as shown in Table 26.8. In this computer code, an axisymmetric finite element analysis is performed by neglecting crystal anisotropy. This computer code can be used as a postprocessor of a global heat transfer code for a bulk single crystal growth system. Such a global heat transfer code provides shape and temperature distributions of a bulk single crystal during the growth process in the time sequence. Figure 26.21 shows the temperature distributions and crystal shapes of a GaAs bulk single crystal with an 8-inch diameter for several times after the CZ growth starts, as are obtained from a global heat transfer code. The results of the global heat transfer analysis are provided at discrete times, and they may be insufficient for a dislocation density analysis. Therefore, we divide a time step between two adjacent times for the global heat transfer analysis into several substeps to deal with the growth process as

Table 26.7 Parameters in the HAS Model

Parameter	Description	Unit
N_m	Density of moving dislocation	$1/cm^2$
b	Magnitude of burgers vector	cm
Q	Peierls potential	eV
k	Boltzmann constant	8.617×10^{-5}ev/K
T	Absolute temperature	K
K	Material constant	cm/dyn
D	Strain hardening factor	dyn/cm
k_0	Material constant	$cm^{2p+1}/dyn^p s$
τ_d	Drag-stress	dyn/cm^2
P	Material constant	–
λ	Material constant	1.0

Table 26.8 Material Properties in the HAS Model for Si, GaAs, and InP Single Crystals

	T_m	b	Q	p	D	K	k_0
Si	1685	3.8×10^{-8}	2.2	1.1	4.3×10^3	3.1×10^{-7}	6.815×10^{-3}
GaAs	1511	4.0×10^{-8}	1.5	1.7	3.1×10^3	7.0×10^{-6}	3.59×10^{-8}
InP	1331	4.0×10^{-8}	1.0	1.4	3.0×10^3	1.2×10^{-5}	5.57×10^{-8}

Tm: melting point (K). Units of other material properties are shown in Table 26.7.

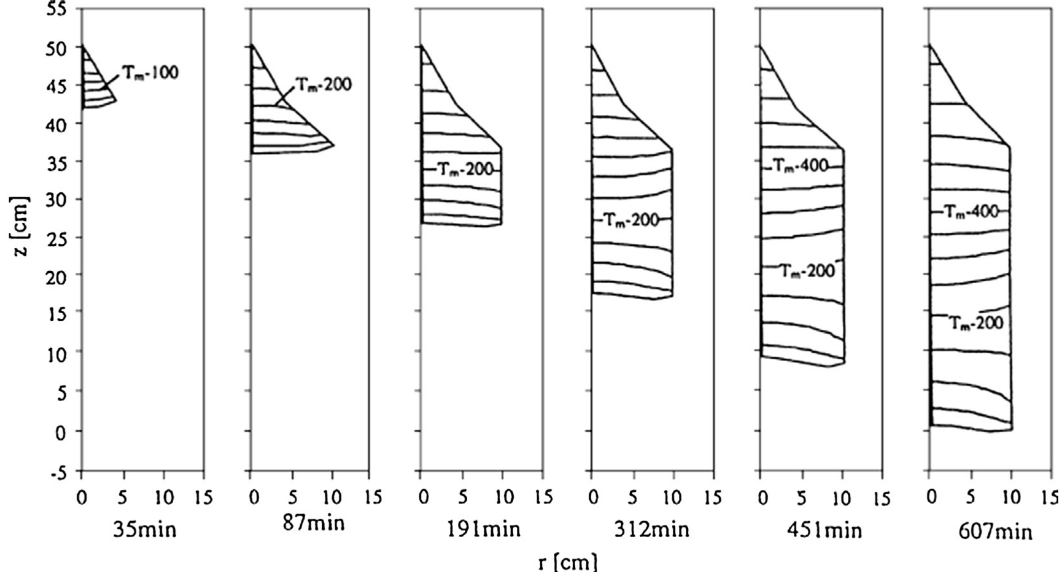

FIGURE 26.21 Temperature distributions and crystal shapes for a GaAs bulk single crystal at several times after the CZ growth starts. *From Ref. [71] with permission of Elsevier Science.*

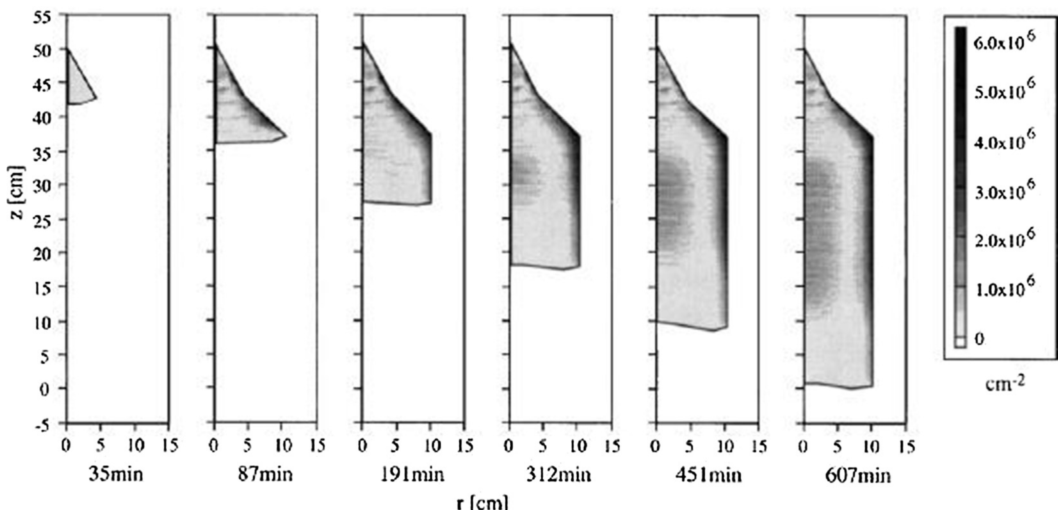

FIGURE 26.22 Dislocation density distributions in a GaAs bulk single crystal at several times after the CZ growth starts. *From Ref. [71] with permission of Elsevier Science.*

continuously as possible. The shape of the crystal–melt interface and the temperature in the crystal at an arbitrary substep are determined by linear interpolation of the results at two adjacent times for the global heat transfer analysis. The incremental form of a finite element equilibrium equation for a creep problem given as follows is solved at the time step in each substep:

$$\mathbf{K}\Delta\mathbf{U} = \Delta\mathbf{F}_t + \Delta\mathbf{F}_C \tag{26.55}$$

where $\mathbf{K}$, $\Delta\mathbf{U}$, $\Delta\mathbf{F}_t$ and $\Delta\mathbf{F}_c$ denote the stiffness matrix, the incremental nodal displacement vector, the incremental load vector due to thermal strain, and the incremental load vector due to creep strain, respectively, and $\Delta\mathbf{F}_c$ is a function of the HAS-type creep strain rate given by Eqn (26.45). Solving Eqn (26.55) at each time step and integrating Eqn (26.48), we can obtain variables such as displacement, strain, stress, and dislocation density.

Figure 26.22 shows the dislocation density distributions for a GaAs bulk single crystal of 8-inch diameter for several times after the CZ growth starts. High dislocation density appears at the central and peripheral regions of the bulk single crystal. The results indicate a W-type dislocation density distribution across the diameter that can be observed from the etch pit density in actual single crystals [81].

26.3.3.4.2 INGOT ANNEALING PROCESS

As an example of the application of a full three-dimensional dislocation density analysis using Eqns (26.49)–(26.53), we show the results of a dislocation density analysis of the GaAs ingot annealing process [82]. Ingot annealing of a GaAs bulk single crystal is an indispensable process to homogenize the electric characteristics of an as-grown single

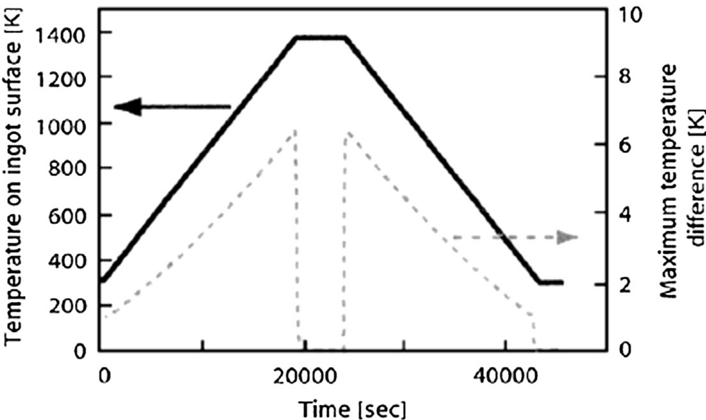

FIGURE 26.23 Time variations of the temperature on a GaAs ingot surface (solid line) and the maximum temperature difference in a GaAs ingot (dashed line) obtained from the transient heat conduction analysis. *From Ref. [82] with permission of Elsevier Science.*

crystal. One of the technical problems of GaAs ingot annealing is the increase of dislocation density due to the thermal stress induced during its annealing. A GaAs cylindrical ingot with a 101.6 mm diameter and 81.0 mm height is considered here. The solid line in Figure 26.23 shows the time variation of temperature on the GaAs ingot surface, and the dashed line in Figure 26.23 shows the time variation of the maximum temperature difference in the ingot obtained from the transient heat conduction analysis. The temperature difference in the ingot induces thermal stress, by which dislocation multiplication is caused during ingot annealing. The dislocation density analyses were performed for the ingot grown in the [001] direction and that grown in the [111] direction. Figure 26.24 shows the distributions of dislocation density at the cross-section of 56.7 mm distant from the bottom of ingot. We can find the difference of the maximum dislocation density between the [001]-grown ingot and the [111]-grown ingot. As for the distribution patterns of dislocation density, the result of the [001]-grown ingot shows fourfold symmetry and that of the [111]-grown ingot shows threefold symmetry. Such differences can be obtained from three-dimensional analyses considering the crystal anisotropy.

In addition to the above research, Miyazaki et al. carried out dislocation density analyses during the annealing of a GaAs ingot using axisymmetric modeling under the isotropic assumption of the GaAs crystal [83]. They also compared the results of dislocation density among three kinds of creep constitutive equations [84]: (1) the HAS model for a multiaxial stress state under isotropic assumption, (2) the HAS model for a multiaxial stress state under approximate consideration of crystal anisotropy, and (3) the HAS model for a multiaxial stress state under exact consideration of crystal anisotropy, the details of which were already described in this section. Kouno et al. [85]. compared the experimental results of dislocation density with analysis results.

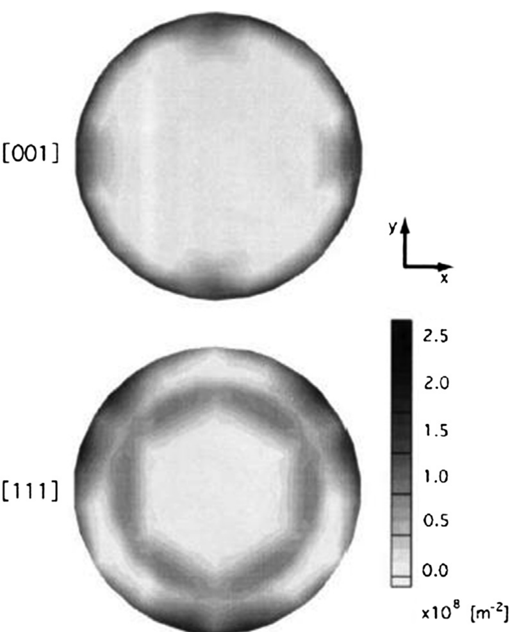

FIGURE 26.24 Distributions of dislocation density at the cross-section of 56.7 mm distant from the bottom of a GaAs ingot after annealing. *From Ref. [82] with permission of Elsevier Science.*

26.3.4 Modified HAS Models

26.3.4.1 Consideration of Immobilization of Mobile Dislocations and High-Temperature Recovery Mechanisms

Moosbrugger [86,87] proposed a modified HAS model to take account of high-temperature recovery mechanisms as well as immobilization of mobile dislocations. In his model, the rate of immobile dislocation density $\mathrm{d}N_i^{(\alpha)}/\mathrm{d}t$ on slip system α is given as

$$\mathrm{d}N_i^{(\alpha)}/\mathrm{d}t = \sum_{\alpha \neq \beta} f_1^{(\alpha\beta)} N^{(\beta)} \left(\mathrm{d}p^{(\alpha)}/\mathrm{d}t\right) - w(T) N_i^{(\alpha)} \tag{26.56}$$

$$\mathrm{d}N_m^{(\alpha)}/\mathrm{d}t = \mathrm{d}N^{(\alpha)}/\mathrm{d}t - \mathrm{d}N_i^{(\alpha)}/\mathrm{d}t \tag{26.57}$$

where N is the total dislocation density, N_m is the mobile dislocation density, and $\mathrm{d}p^{(\alpha)}/\mathrm{d}t = \left|\mathrm{d}\gamma_c^{(\alpha)}/\mathrm{d}t\right|$. In Eqn (26.56), the first term represents the immobilization rate with dislocations on slip system α by interactions with the system β. The matrix $f_1^{(\alpha,\beta)}$ is meant to reflect various relative strengths of types of slip system interactions in immobilizing dislocations, following the suggestion of Basani and Wu [88]. The second term in Eqn (26.56) allows for "remobilization" of dislocations by a recovery mechanism such as dislocation climb, in which $w(T)$ is the temperature-dependent empirical recovery function. Moosbrugger [86,87] determined empirical model constants and temperature-dependent functions in his modified HAS model for CdTe, using trial-and-error fitting of the experimental data.

26.3.4.2 Consideration of Dislocation Annihilation

The original HAS model shown in Section 26.3.3.1 allows only for dislocation multiplication and for no dislocation annihilation by the interaction of dislocations with opposite Burgers vectors. Gondet et al. [79] proposed a model to take account of dislocation annihilation. They give the effective shear stress as follows, taking account of the dislocation density in each glide plane:

$$\tau_{eff}^{i} = \left\langle \left|\sigma_{RS}^{(i)}\right| - \frac{Gb}{\beta}\sqrt{N_i} - \frac{Gb}{\beta^*}\sum_{j\neq i}\sqrt{N_j} \right\rangle \tag{26.58}$$

where the superscript (i) and the subscript i denote the glide system under consideration, and j is the other glide system. G is the shear modulus, and β and β^* are constants reflecting the intensity of the interaction.

Gondet et al. [79] give the dislocation multiplication rate as

$$\mathrm{d}N_i^+/\mathrm{d}t = \left(K + K^*\sum_{j\neq i}N_j\right)N_i v_i \tau_{eff}^{(i)} \tag{26.59}$$

The first term proportional to N_i accounts for self-multiplication—that is, multiplication on a pinning point created by double cross-slip of the dislocation, for instance. The second term proportional to N_iN_j accounts for dislocation sources on pinning points resulting from intersections between dislocation systems i and j.

Two dislocations gliding in the same system but with opposite signs are likely to annihilate each other. Considering that the phenomenon depends on the dislocation density and velocity, Gondet et al. [79] proposed the following relationship for the dislocation annihilation rate:

$$\mathrm{d}N_i^-/\mathrm{d}t = A_o N_i^2 v_i^2 \tag{26.60}$$

where A_0 is the annihilation parameter, the value of which is adjusted in order to get a satisfactory agreement with experimental results. Annihilation is important near the solid–liquid interface of a growing single crystal, which is subjected to high temperatures. Then, the total dislocation density rate becomes

$$\mathrm{d}N_i/\mathrm{d}t = \mathrm{d}N_i^+/\mathrm{d}t - \mathrm{d}N_i^-/\mathrm{d}t = \left(K + K^*\sum_{j\neq i}N_j\right)N_i v_i \tau_{eff}^{(i)} - A_0 N_i^2 v_i^2 \tag{26.61}$$

According to Orowan's law, the creep shear strain rate is given as follows, considering that annihilated dislocations participated in plasticity before annihilation:

$$\frac{\mathrm{d}\gamma^c}{\mathrm{d}t} = \left(N_i + \frac{\mathrm{d}N_i^+}{\mathrm{d}t}\Delta t\right) b v_i \tag{26.62}$$

For an InP single crystal, Gondet et al. gave the values of β and K based on Ref. [64] and those of β^* and K^* based on Ref. [89]. They also determined the value of the annihilation parameter A_0 from the dislocation density analysis [79]. Table 26.9 summarizes the values of parameters used for the dislocation interaction model.

Table 26.9 Parameters Used in the Dislocation Interaction Model for InP Single Crystal

β	β^*	K	K^*	A_0
3.3	2.2	1.2×10^{-2}m/N	10^{-12} m^3/N	5×10^{-7}s

Gondet et al. [79] performed a three-dimensional dislocation density analysis for the growth process of an InP bulk single crystal using the modified HAS model mentioned above. In the creep constitutive equations proposed by Gondet et al., the annihilation term is given by Eqn (26.60) together with the annihilation parameter A_0. They did not provide a reason why the annihilation term is expressed by Eqn (26.60). In addition, the parameter A_0 has only meaning as an adjustment parameter and no physical meaning.

26.3.4.3 Consideration of Different Types of Dislocations

As shown in Figure 26.25, the dislocations in the diamond structure of single crystals, such as Si, GaAs, InP, and InSb, belong mostly to the closely packed (111) system of glide planes with $<110>$ directions. They are screw dislocations, α dislocations, and β dislocations with different mobilities, respectively denoted by S, α and β (Figure 26.25). Kalan and Marniatty [90], Lohonka et al. [91], and Pendurti et al. [92] considered these three kinds of dislocations. According to Ref. [92], the creep shear strain rate $\mathrm{d}\gamma^c/\mathrm{d}t$ is given as follows by extending the Orowan equation:

$$\mathrm{d}\gamma^c/\mathrm{d}t = (N_\alpha v_\alpha + N_\beta v_\beta + N_S v_S)b \tag{26.63}$$

where N_α, N_β, and N_S are respectively the densities of α, β and S dislocations in the (111) plane with the Burgers vector in the $[\bar{1}10]$ direction; v_α, v_β, and v_S are the corresponding velocities; and b is the magnitude of the Burgers vector. According to Ref. [92], $\mathrm{d}\gamma^c/\mathrm{d}t$ is given as follows:

$$\mathrm{d}\gamma^c/\mathrm{d}t = 2N_S v_S b \tag{26.64}$$

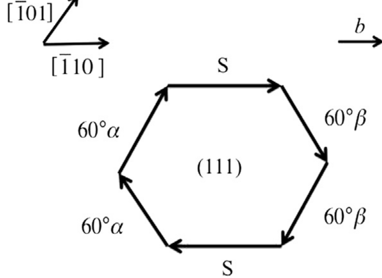

FIGURE 26.25 Geometry of a hexagonal dislocation loop on the (111) plane for a diamond structure of single crystals.

A similar treatment was first proposed by Steinhardt and Haasen [93] and used by Yonenaga et al. [94].

Extension of the multiaxial stress state can be done based on the theory of crystal plasticity [80]:

$$\frac{d\varepsilon_{ij}^{c}}{dt} = \sum_{n=1}^{12} 2N_S^{(n)} v_S^{(n)} P_{ij}^{(n)} \tag{26.65}$$

where P_{ij} was given by Eqn (26.51), and the superscript (n) represents the nth slip system.

As for a dislocation multiplication law, Pendurti et al. [92] considered multislip systems and proposed the following equation based on Sumino and Yonenaga's research [89]:

$$\frac{dN_S^{(i)}}{dt} = KN_S^{(i)} v_f^{(i)} \tau_{eff}^{(i)} + K^* N_S^{(i)} v_f^{(i)} \tau_{eff}^{(i)} \sum_{f \neq i} f_{ij} N_S^{(i)} \tag{26.66}$$

where the superscript (i) denotes the ith slip system, and $v_f^{(i)}$ is the velocity of the fastest dislocation. Almost the same equation was proposed by Kalan and Maniatty [90]. In the right-hand side of Eqn (26.66), the first term represents an increase in dislocation due to the glide on the slip plane, and the second term represents the formation of jogs on screw dislocation. f_{ij} in Eqn (26.66) is related to the formation of jogs. The value of f_{ij} is 1 when a jog is formed on a screw dislocation of the system i cut by a forest dislocation of system j; otherwise, it is 0. The complete table for the value of f_{ij} is given in Ref. [92]. $\tau_{eff}^{(i)}$ is the effective shear stress necessary for dislocation motion in the ith slip system, as given by

$$\tau_{eff}^{(i)} = \left\langle \left| \sigma_{RS}^{(i)} \right| - \frac{Gb}{\beta} \sqrt{N_S^{(i)}} - \frac{Gb}{\beta^*} \sum_{j \neq i} g_{ij} \sqrt{N_S^{(i)}} \right\rangle \tag{26.67}$$

This equation is essentially the same as Eqn (26.58). The second term on the right-hand side is the self-hardening term, while the third term represents the cross-hardening term together with the parameter g_{ij}, depending on the type of interaction between the dislocations of different slip systems. The values of g_{ij} and other parameters such as K, K^*, β, and β^* for an InP single crystal are calculated from shear stress–shear strain curves experimentally obtained under the constant shear strain rate [92]. Pendurti et al. performed a dislocation density analysis for the high-pressure CZ growth of an InP single crystal, using these parameters; the results are shown in Figure 26.26 [95]. Kalan and Maniatty [90] determined the material parameters for an InP single crystal based on the experimental data. Lohonka et al. [91] obtained the stress–strain curves not only for an InP single crystal but also for GaAs and InSb single crystals by using a modified HAS model that they developed.

26.3.4.4 Consideration of the Immobilization of Mobile Dislocations

In the creep constitutive equations for Si proposed by Gao et al. [96], all material parameters are identified by the experimental data obtained by Cochard et al. [97], and no adjustment parameter, such as A_0 in Eqn (26.60) of Gondet et al.'s research [79], is

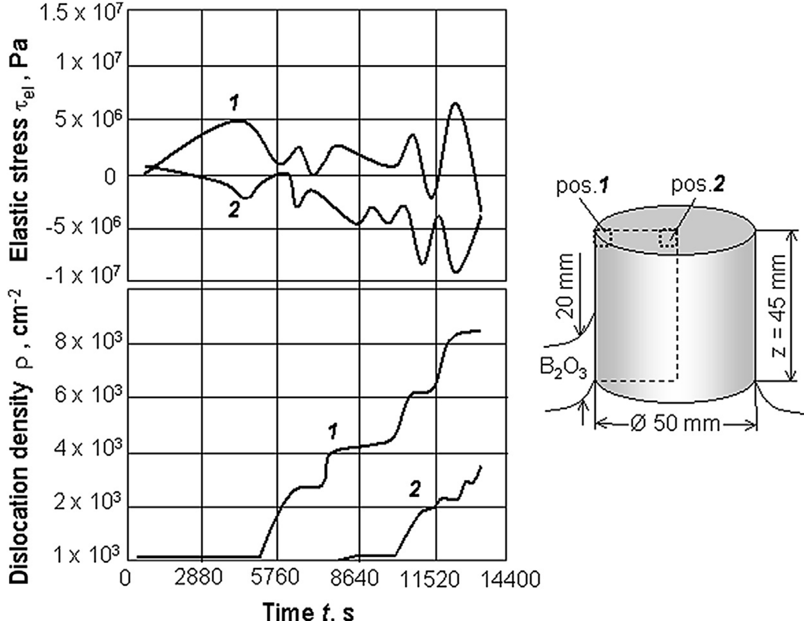

FIGURE 26.26 Sketched stress and dislocation density development with time along a CZ InP crystal considering the boric oxide encapsulation layer. *From Ref. [95] with permission of Springer.*

needed in the creep constitutive equations. In addition, they take account of multislip systems, immobilization of mobile dislocations, the jog formation between different slip systems and its influence on dislocation generation, and the internal stress due to short-range interactions from the total dislocation density.

Here, we summarize the creep constitutive equation for an Si single crystal proposed by Gao et al. The creep strain rate $\mathrm{d}\varepsilon_c^{(\alpha)}/\mathrm{d}t$ is given by the Orowan relationship:

$$\mathrm{d}\varepsilon_c^{(\alpha)}/\mathrm{d}t = N_m^{(\alpha)} v^{(\alpha)} b \tag{26.68}$$

where the subscript m denotes the mobile dislocation, the superscript (α) is the slip system, b is the magnitude of the Burgers vector, N is the dislocation density, and v is the velocity of dislocation. The rate of the mobile dislocation density $\mathrm{d}N_m^{(\alpha)}/\mathrm{d}t$ in the slip direction α is given by

$$\mathrm{d}N_m^{(\alpha)}/\mathrm{d}t = KN_m^{(\alpha)} v^{(\alpha)} \tau_{eff}^{(\alpha)} + K^* N_m^{(\alpha)} v^{(\alpha)} \tau_{eff}^{(\alpha)} \sum_{\beta \neq \alpha} f_{\alpha\beta} N_m^{(\beta)} - 2r_c N_m^{(\alpha)} N_m^{(\alpha)} v^{(\alpha)} \tag{26.69}$$

The above equation is an extension of Eqn (26.66), as proposed by Pendurti et al. [92]. That is, the first and second terms of the right-hand side in Eqn (26.69) are the same as those in Eqn (26.66), and the third term represents the sink for the mobile dislocation (i.e., immobilization). According to Ref. [97], the immobilization rate $\mathrm{d}N_i^{(\alpha)}/\mathrm{d}t$ can be expressed as

$$dN_i^{(\alpha)}/dt = 2r_c N_m^{(\alpha)} N_m^{(\alpha)} v^{(\alpha)} \tag{26.70}$$

The dislocation velocity v is given by

$$v^{(\alpha)} = v_0\left(\tau_{eff}^{(\alpha)}\Big/\tau_0\right)^m \exp\left(-U\Big/kT\right) \tag{26.71}$$

where $v_0 = 500$ m/s, $\tau_0 = 1$ MPa, $m = 1$, and $U = 2.2$ eV for an Si single crystal [97]. The values of K, K^*, and r_c are given as follows [97]:

$$K(T) = 7.6 \times 10^{-1} \exp(-0.72/kT)(\mathrm{m/N}), \quad K^* = 8.0 \times 10^{-15}\mathrm{m}^3/\mathrm{N},$$
$$r_c(T) = 7.2 \times 10^{-3} \exp(-1.48/kT)(\mathrm{m}) \tag{26.72}$$

The effective shear stress necessary for dislocation motion is given by

$$\tau_{eff}^{(\alpha)} = \left\langle\left|\sigma_{RS}^{(\alpha)}\right| - \tau_i^{(\alpha)} - \tau_b^{(\alpha)}\right\rangle \tag{26.73}$$

where $\tau_i^{(\alpha)}$ is the stress required to overcome short-range obstacles, and $\tau_b^{(\alpha)}$ is the internal long-range elastic stress generated by mobile dislocation. They are given by [97]

$$\tau_i^{(\alpha)} = Gb\sqrt{\sum_\beta a_{\alpha\beta}\left(N_m^{(\beta)} + N_i^{(\beta)}\right)} \tag{26.74}$$

$$\tau_b^{(\alpha)} = Gb\sum_\beta A_{\alpha\beta}\sqrt{N_m^{(\beta)}} \tag{26.75}$$

where the coefficients $A_{\alpha\beta}$ and $a_{\alpha\beta}$ are summarized in Table 26.10. Then, the total dislocation density and the multiaxial creep strain rate $\mathrm{d}\varepsilon_{ij}^c/\mathrm{d}t$ is expressed by

$$N_m = \sum_{\alpha=1}^{12} N_m^{(\alpha)} \tag{26.76}$$

$$\frac{\mathrm{d}\varepsilon_{ij}^c}{\mathrm{d}t} = \sum_{\alpha=1}^{12} P_{ij}\frac{\mathrm{d}\varepsilon_c^{(\alpha)}}{\mathrm{d}t} \tag{26.77}$$

where P_{ij} is already given by Eqn (26.51).

Using the above-mentioned constitutive equations, Gao et al. [96] performed dislocation density analyses of seed cast-grown Si single crystals in the [001] and [111] growth directions to study the effective reduction of dislocation by controlling the cooling process.

Table 26.10 Long-Range Interaction Coefficients $A_{\alpha\beta}$ and Short-Range Interaction Coefficients $a_{\alpha\beta}$ for Si Single Crystal

Interaction	Self	Coplanar	Collinear	Hirth Locks	Lomer Locks	Glissile Junction
$A_{\alpha\beta}$	0.21	1/16	1/20	1/12	1/12	1/12
$a_{\alpha\beta}$	0.09	0.09	0.41	0.06	0.12	0.12

26.4 Summary

The research activities related to the solid mechanics and mechanical strength of the crystal growth process and crystal annealing process are reviewed in this chapter. Although single crystals are the basic materials supporting the present advanced technologies and such research activities play an important role in manufacturing high-quality single crystals, only a few researchers have been involved in such research activities. It is hoped that more researchers will take part in such research activities.

The finite element method is a powerful tool for the stress analysis of solids. It can be applied not only to elastic thermal stress problems of single crystals, taking account of anisotropy in elastic constants and thermal expansion coefficients, but also to nonlinear analysis such as dislocation density problems, in which the rate of creep strain or viscoplastic strain is related to dislocation density. The finite element method is one of the numerical methods for boundary value problems of partial differential equations, and it provides very accurate solutions if an appropriate finite element modeling is used.

To make progress in research, we need the material properties and deformation behaviors of single crystals at very high temperatures near the melting point. We need material properties near the melting point in cases of thermal stress and dislocation density analyses during crystal growth. Although a large research project called Kimura Metamelt [98] was organized by the Japan Science and Technology Agency to measure the various properties of the Si melt and oxide melts, no research project has been performed to clarify the mechanical behaviors of single crystals under elevated temperatures near the melting point. Even for elastic constants and thermal expansion coefficients of single crystals, we have no experimental data near the melting point. We have to extrapolate the measured data to the melting point to get the material properties near the melting point. It is much more difficult to get stress–strain curves under constant strain rates at elevated temperatures near the melting point, which are required to formulate constitutive equations for creep.

We are expecting both experimental and numerical research concerning the mechanical behaviors of single crystals at elevated temperatures. Atomistic simulation techniques, such as the first-principle calculation and molecular dynamics method, for example, are promising tools for obtaining the mechanical behaviors of single crystals at elevated temperatures. Simulation techniques based on computational mechanics, such as the finite element method, will provide more useful information to establish the manufacturing process of high-quality single crystals, if the mechanical behaviors of single crystals at elevated temperatures are properly represented by material properties, such as elastic constants, thermal expansion coefficients, and creep constitutive equations.

References

[1] Brown RA. AIChE J 1988;34:881.

[2] Kakimoto K. J Appl Phys 1995;77:1827.

[3] Rudolph P, Jurisch M. J Cryst Growth 1999;198–199:325.

[4] Müller G. J Cryst Growth 2002;237–239:1628.

[5] Müller G, Friedlich J. J Cryst Growth 2004;266:1.

[6] Lan CW. Chem Eng Sci 2004;59:1437.

[7] Miyazaki N. J Cryst Growth 2007;300:452.

[8] Miyazaki N. J Cryst Growth 2007;303:302.

[9] Prasad V, Pendurti S. In: Dhanaraj G, Byrappa K, Prasad V, Dudley M, editors. Springer handbook of crystal growth. Springer, Heidelberg; 2010. p. 1335.

[10] Jordan AS, Von Neida AR, Caruso R. J Cryst Growth 1984;70:555.

[11] Kobayashi N, Iwaki T. J Cryst Growth 1985;73:96.

[12] Dupret F, Nicodeme P, Ryckmans Y. J Cryst Growth 1989;97:162.

[13] Tsukada T, Hozawa M, Imaishi N. J Chem Eng Jpn 1990;23:186.

[14] Lambropoulos JC. J Cryst Growth 1987;84:349.

[15] Lambropoulos JC. J Mater Res 1988;3:531.

[16] Miyazaki N, Hagihara S, Munakata T. J Cryst Growth 1990;106:149.

[17] Miyazaki N, Uchida H, Hagihara S, Munakata T, Fukuda T. J Cryst Growth 1991;113:227.

[18] Miyazaki N, Uchida H, Munakata T, Fujioka K, Sugino Y. J Cryst Growth 1992;125:102.

[19] Nye JF. Physical properties of crystals. Oxford: Clarendon Press; 1957.

[20] Miyazaki N, Uchida H, Tsukada T, Fukuda T. J Cryst Growth 1996;162:83.

[21] Miyazaki N, Tamura T, Kurashige K, Ishibashi H, Susa K. J Cryst Growth 1997;182:73.

[22] Miyazaki N. J Cryst Growth 2002;236:455.

[23] Miyazaki N, Imahase D. Simulation 2001;20:274 [in Japanese].

[24] Miyazaki N, Uchida H, Munakata T, Fukuda T. JSME Int J Ser A 1994;37:124.

[25] Jordan AS, Caruso R, Von Neida AR. Bell Syst Tech J 1980;59:593.

[26] INSPEC. Properties of silicon, EMIS datareview series, No.4. The Institute of Electrical Engineers; 1988. 14.

[27] Jordan AS. J Cryst Growth 1980;49:631.

[28] Jordan AS. J Cryst Growth 1985;71:559.

[29] Brantley WA. J Appl Phys 1973;44:534.

[30] Brandle CD, Miller DC. J Cryst Growth 1974;24–25:432.

[31] Brice JC. J Cryst Growth 1977;42:427.

[32] Tsukada T, Hozawa M, Imaishi N. J Chem Eng Jpn 1994;27:25.

[33] Smith RT, Welsh FS. J Appl Phys 1971;42:2219.

[34] Gallagher PK, O'Bryan HM. J Am Ceram Soc 1985;68:147.

[35] Bonner WA, Zydzik GJ. J Cryst Growth 1970;7:65.

[36] Loiacono GM, Balascio JF, Bonner R, Savage A. J Cryst Growth 1974;21:1.

[37] Takano S, Easashi S, Mori K, Namikata T. J Cryst Growth 1974;24–25:437.

[38] Lim LC, Tan LK, Zeng HC. J Cryst Growth 1996;167:686.

[39] Senguttuvan N, Moorthy Babu S, Subramanian C. Mater Sci Eng 1997;B47:269.

[40] Senguttuvan N, Moorthy Babu S, Dhanasekaran R. Mater Chem Phys 1997;49:120.

[41] Zeng HC. J Cryst Growth 1997;171:136.

[42] Sabharwal SC, Sangeeta, Desai DG. Cryst Growth Des 2006;6:58.

[43] Miyazaki N, Matuura Y, Imahase D. J Cryst Growth 2006;289:659.

[44] Coquin GA, Pinnow DA, Warner AW. J Appl Phys 1971;42:2162.

[45] Rudolph P. Cryst Res Technol 2005;40:7.

[46] Takagi K, Fukazawa T. Appl Phys Lett 1983;42:43.

[47] Ishibashi H, Shimizu K, Susa K, Kubota S. IEEE Transactions Nucl Sci 1989;36:170.

[48] Ishibashi H, Kurata Y, Kurashige K, Susa K. Proc Int Workshop Heavy Scintillators Sci Industrial Appl Crystal 2000;1993:389.

[49] Miyazaki N, Tamura T, Yamamoto K. CMES-Computer Model Eng Sci 2000;1:99.

[50] Kurashige K, Kurata Y, Ishibashi H, Susa K. Jpn J Appl Phys 1997;36:2242.

[51] Miyazaki N, Tamura T, Yamamoto K, Kurashige K, Ishibashi H, Susa K. J Mater Sci Lett 1998;17:935.

[52] Miyazaki N, Hattori A, Uchida H. J Mater Sci Mater Electron 1997;8:133.

[53] Miyazaki N, Koizumi K. J Mater Sci 2006;41:6313.

[54] Matakef S, Witt AF. J Cryst Growth 1987;80:37.

[55] Jordan AS, Caruso R, Von Neida AR, Nielsen JW. J Appl Phys 1981;52:3331.

[56] Jordan AS, Von Neida AR, Caruso R. J Cryst Growth 1986;76:243.

[57] Zhmakin IA, Kulik AV, Karpov S Yu, Demina SE, Ramm MS, Makarov Yu N. Diam Relat Mater 2000;9:446.

[58] Wu B, Ma R, Zhang H, Dudley M, Schlesser R, Sitar Z. J Cryst Growth 2003;253:326.

[59] Alexander H, Haasen P. Solid State Phys 1969;22:27.

[60] Suezawa M, Sumino K, Yonenaga I. Phys Status Solidi (a) 1979;51:217.

[61] Dillon Jr OW, Tsai CT, De Angelis RJ. J Appl Phys 1986;60:1784.

[62] Tsai CT, Dillon Jr OW. Int J Solids Struct 1987;23:387.

[63] Tsai CT, Dillon Jr OW, De Angelis RJ. J Cryst Growth 1987;82:695.

[64] Völkl J, Müller G. J Cryst Growth 1989;97:136.

[65] Maroudas D, Brown RA. J Cryst Growth 1991;108:399.

[66] Motakef S, Kelly KW, Koai K. J Cryst Growth 1991;113:279.

[67] Tsai CT. J Cryst Growth 1991;113:499.

[68] Tsai CT, Gulluoglu AN, Harley CS. J Appl Phys 1993;73:1650.

[69] Tsai CT, Subramanyam N. Model Simul Mater Sci 1995;3:93.

[70] Zhu XA, Tsai CT. J Appl Phys 2000;88:2295.

[71] Miyazaki N, Okuyama S. J Cryst Growth 1998;183:81.

[72] Miyazaki N, Kuroda Y. Metals Mater 1998;4:883.

[73] Miyazaki N, Kuroda Y. J Cryst Growth 1999;196:62.

[74] Lambropoulos JC, Wu CH. J Mater Res 1996;11:2163.

[75] Tsai CT, Dillon Jr OW, De Agelis RJ. J Eng Mater Technol 1990;112:183.

[76] Miyazaki N, Kuroda Y. JSME Int J Ser A 1999;42:485.

[77] Miyazaki N, Kuroda Y, Sakaguchi M. J Cryst Growth 2000;218:221.

[78] Miyazaki N, Sakaguchi M. Transactions JSME, Ser A 2002;68:21 [in Japanese].

[79] Gondet S, Duffar T, Louchet F, Theodore F, Van Den Bogaert N, Santailler JL. J Cryst Growth 2003;252:92.

[80] Asaro RJ. J Appl Mech 1983;50:921.

[81] Barrett DL, McGuigan S, Hobgood HM, Eldridge GW, Thomas RN. J Cryst Growth 1984;70:174.

[82] Miyazaki N, Kutsukake H, Kumamoto A. J Cryst Growth 2002;243:47.

[83] Miyazaki N, Yamamoto S, Kutsukake H. J Cryst Growth 2000;216:6.

[84] Miyazaki N, Kumamoto A, Harada C. J Cryst Growth 2004;271:358.

[85] Kouno J, Yosida H, Kawase T, Sawada S, Nakai R, Tatsumi M. SEI Tech Rev 2001;158:65 [in Japanese].

[86] Moosbrugger JC. Int J Plasticity 1995;11:799.

[87] Moosbrugger JC, Levy A. Metallurgical Mater Transactions A 1995;26A:2687.

[88] Bassani JL, Wu TY. Proc Royal Soc A 1991;435:21.

[89] Sumino K, Yonenaga I. Phys Status Solidi (a) 1993;138:573.

[90] Kalan RJ, Mainiatty AM. J Cryst Growth 2001;233:645.

[91] Lohonka R, Vanderschaeve G, Kratochvil J. Mater Sci Eng 2002;A337:50.

[92] Pendurti S, Prasad V, Zhang H. Model Simulations Mater Sci Eng 2005;13:249.

[93] Steinhardt H, Haasen P. Phys Status Solidi (a) 1978;49:93.

[94] Yonenaga I, Onose U, Sumino K. J Mater Res 1987;2:252.

[95] Rudolph P. In: Dhanaraj G, Byrappa K, Prasad V, Dudley M, editors. Handbook of Crystal growth. Berlin: Springer; 2010. p. 159.

[96] Gao B, Nakano S, Harada H, Miyaura Y, Kakimoto K. Cryst Growth & Des 2013;13:2661.

[97] Cochad J, Yonenaga I, Gouttebroze S, M'Hamdi M, Zhang ZL. J Appl Phys 2010;107:033512.

[98] http://www.jst.go.jp/erato/en/research_areas/completed/kyd_P.html.

27

Defect Generation and Interaction during Crystal Growth

Helmut Klapper[1], Peter Rudolph[2]

[1]INSTITUTE OF CRYSTALLOGRAPHY, RWTH AACHEN UNIVERSITY, AACHEN, GERMANY;
[2]CRYSTAL TECHNOLOGY CONSULTING, SCHÖNEFELD, GERMANY

CHAPTER OUTLINE

27.1 Introduction **1094**
27.2 Point Defects **1096**
27.2.1 Native Point Defect Thermodynamics 1096
27.2.2 Point Defect Dynamics 1098
27.2.3 Extrinsic Point Defect Incorporation 1100
27.2.4 Native and Extrinsic Point Defect Interaction (Complex Formation) 1101
27.2.5 Point Defect Engineering 1103
27.3 Dislocations **1105**
27.3.1 Growth Dislocations and Postgrowth Dislocations 1105
27.3.2 Sources of Growth Dislocations 1105
27.3.3 Propagation of Growth Dislocations 1106
27.3.3.1 Characteristic Configurations, Theory of Preferred Direction 1106
27.3.3.2 Verification of the Minimum Energy Approach and Examples 1110
27.3.4 Postgrowth Dislocations 1111
27.3.5 Dislocation Dynamics (Patterning, Cell Structures, Clustering) 1111
27.3.6 Dislocation Engineering 1119
27.4 Grain Boundaries **1121**
27.4.1 Dynamic Polygonization-Low-Angle Grain Boundaries 1121
27.4.2 Large-Angle Grain Boundaries-Polycrystallinity 1123
27.5 Foreign Phase Particles **1125**
27.5.1 Precipitates (Retrograde Solidus, Defect Decoration) 1125
27.5.2 Solvent Inclusions 1126
27.5.2.1 Faceting ("Capping") of Rounded Surfaces 1126
27.5.2.2 Fluctuation of Growth Conditions (Growth Accidents) 1128
27.5.3 Melt Growth Inclusions 1129
27.5.4 Structural Consequences of Second-Phase Particles 1129

Handbook of Crystal Growth. http://dx.doi.org/10.1016/B978-0-444-63303-3.00027-4
Copyright © 2015 Elsevier B.V. All rights reserved.

27.6 Faceting and Twinning **1130**
27.6.1 Faceting during Growth 1130
27.6.2 Growth Twins and Postgrowth Twins 1131
27.6.4 Measures to Avoid Twinning 1135
27.7 Concluding Remarks **1136**
References **1136**

27.1 Introduction

The quality of single crystals (and the devices made from them) is very sensitive to atomistic and structural deficiencies generated during the crystal growth process. This is one of the main challenges for crystal growers to determine the conditions for the control, minimization, or even prevention of deficiencies.

Most of the important defect-forming mechanisms are well understood, as summarized by Hurle and Rudolph [1]. Today, an enormous body of knowledge exists about the defect genesis in as-grown crystals, supported by demanding theoretical fundamentals and computational modeling. As a result, the present state of technology makes it possible to produce crystals of remarkably high quality, with tailored parameters that fit the demands of the device industry quite well. However, not all problems have been solved. This chapter includes still-open questions and investigates the optimal measures of defect engineering.

The international standard crystal lattice defects (in short, defects) are usually classified according to their dimensions, as described in the following sections (e.g., Ref. [2]).

Zero-dimensional defects

Zero-dimensional defects are *point defects*, often called by the unpopular name *atomic size defects*, which include the intrinsic defect types *vacancies*, *interstitials*, and, in compounds, *antisites*. If extrinsic atoms are introduced unintentionally (as residual *impurities*) or intentionally (as *dopants*), they occupy interstitial or substitutional (lattice) positions. At growth temperatures, the point defects are isolated and usually electrically charged. The charge state of point defects can lead to their interaction with electrically active dopants, creating *point defect complexes*.

One-dimensional defects

One-dimensional defects include all kinds of *dislocations*, such as perfect screw and edge dislocations, mixed dislocations, partial dislocations (always in connection with a stacking fault), and dislocation loops. In crystals growing under low- or zero-temperature gradients and in their brittle state (e.g., from solutions), dislocations usually originate from inclusions and propagate with the growing face. In crystals growing at

high temperatures and under temperature gradients in their plastic state (e.g., from melts), the propagation and interaction of dislocations over mesoscopic distances are the subjects of *dislocation dynamics*.

Two-dimensional defects

Two-dimensional defects are grain boundaries, stacking faults, phase boundaries, facets, and twins. A *low-angle grain boundary* structure is formed by the mechanism of dynamic polygonization (DP) and belongs conventionally still to a single crystalline state. In contrast, *large-angle grain boundary* structures are formed by polycrystalline growth due to spontaneous or foreign nucleation processes. *Facets* are formed along atomically smooth planes, indicating the tendency of high-quality crystals to form polyhedra. *Growth twins* originate from a false stacking sequence, especially when the two-dimensional nucleus on a growing facet is disoriented.

Three-dimensional defects

Three-dimensional defects include second-phase particles (*precipitates*), intrinsic vacancy conglomerates (*microvoids*), and foreign particles (*inclusions*). It is important to differentiate between precipitates and inclusions, which are often mixed up in the literature. Precipitates and microvoids are formed by supersaturation-driven condensation of intrinsic point defects (i.e., interstitials and vacancies, respectively), whereas inclusions are melt-solution droplets, gas bubbles, and foreign microparticles incorporated at the growing melt–solid interface, especially when the melt composition is deviated from the congruent melting point or contaminations are presented.

Defects have deleterious effects on the performance, reliability, and degradation behavior of devices. Following the early classification of Pick [3], defects influence the following:

- Structural properties (vacancies and interstitials may change the lattice constant; grains affect the single crystallinity)
- Chemical properties (defects participate in chemical reactions; their redistribution causes composition inhomogeneities)
- Electronic properties (defects occupy a specific state in the band structure)
- Scattering properties, or the defect interaction with particles (phonons, photons of any energy, electrons, positrons, etc.)

As can be seen, the interaction processes are many-sided and require broad interdisciplinary research with direct correlation to advanced technical progress. In fact, a large part of the world's technological progress depends on the control and manipulation of defects in crystals, particularly in the semiconductor, optical, and biotechnology industries. An enormous number of monographs and publications deal with this subject. In this chapter, however, only selected examples of defect impacts are discussed.

27.2 Point Defects

27.2.1 Native Point Defect Thermodynamics

In growing crystals at all temperatures above absolute zero, the total concentration of native (intrinsic) point defects (consisting of vacancies, self-interstitials, and, in the case of compounds, antisite defects) strive toward a thermodynamic minimum that does not reach zero. In other words, point defects are always present. This is also due to the increase of configurational entropy, leading to the decrease of total Gibbs free energy. Realistically, at low temperatures, such as 300 K, the equilibrium is rarely obtained. This is primarily due to the decreasing point defect diffusivity in the course of cooling down of the as-grown crystals, freezing the superior equilibrium concentration at much higher temperatures. Thus, it is not possible to grow an absolutely perfect (point defect-free) crystal. In reality, only an "optimal" crystalline state can be obtained, not an "ideal" one.

Neglecting the effects of volume change, defect interaction, and local vibration state around the defect, at constant pressure the change of the Gibbs potential caused by adding, for example, n vacancies (Schottky defects) can be written as

$$\Delta G = H_d - S_d T \tag{27.1}$$

where $H_d = nE_d$ is the internal energy of n defects, having a total defect formation energy E_d, and $S_d = k \ln W = k \ln(N!)/[n!(N-n)!]$ is the accompanying change of configuration entropy. W is the number of ways in which N atoms and n point defects can be arranged, and k is the Boltzmann constant. After substitution and application of Stirling's approximation $[\ln N! \approx N \ln N, \ln n! \approx n \ln n, \ln(N-n)! \approx (N-n)\ln(N-n)]$ for multi-particle systems such as a crystal, Eqn (27.1) becomes

$$\Delta G = nE_d - kT[N \ln N - n \ln n - (N-n)\ln(N-n)]. \tag{27.2}$$

Setting the first derivative of Eqn (27.2) $\partial\Delta G/\partial n = 0$, which equals the energetic minimum defect concentration n_{min}, and considering $N >> n$, the "perfection limit" of the crystal is

$$n_{min} = N \exp(-E_d/kT), \tag{27.3}$$

increasing exponentially with T.

Figure 27.1 shows the realistic (Schottky) point-defect excess against the thermodynamic minimum when a restricted mobility (diffusivity) is considered.

In the case of formation of vacancy-interstitial complexes (Frenkel defects), the value of $n_{min}^{(F)}$ is somewhat modified and yields $\sqrt{N_{is}N}\exp(-E_d^{(F)}/kT)$, with N_{is} being the total number of interstitial positions (depending on the given crystal structure) and $E_d^{(F)}$ being the formation energy of a Frenkel defect. More fundamental details are given in Kröger's compendium [4].

The typical energies of isolated neutral point defects E_d are in the region between 1 and 5 eV. Usually at high temperatures, point defects are electrically charged and therefore show a certain affinity to complex formation with other point defects or

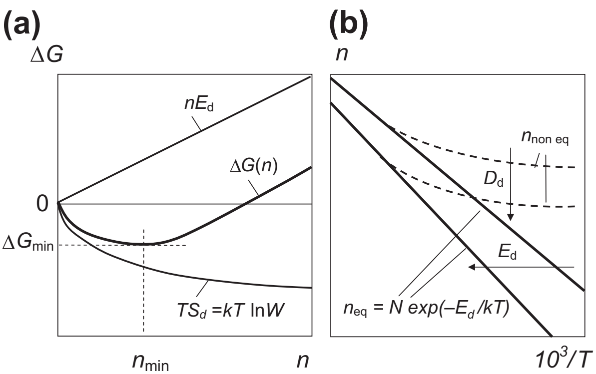

FIGURE 27.1 (a) Sketched equilibrium point defect (Schottky) concentration n_{min} at a given temperature T, obtained by superposition of defect enthalpy $H_d = nE_d$ and configurational entropy $S_d = k \ln W$ using Eqns (27.1)–(27.3). (b) Two equilibrium defect concentrations n_{eq} of various defect energies E_d vs reciprocal temperature $10^3/T$ following Eqn (27.3). The dashed lines show the nonequilibrium ("frozen") curves obtained in reality due to decreasing defect diffusivity D_d with decreasing T.

present impurities. Depending on the crystal structure and temperature, their diffusivities vary near the crystal melting points between 10^{-5} and 10^{-4} cm^2/s. Note that the values given in the literature, mostly obtained by numeric modeling such as quantum Monte Carlo or density functional theory, can differ substantially. The reason for this includes the specification of point defect configuration, such as the number and arrangements of neighboring atoms, and also the careful examination of electron density (as reported for silicon [5]).

The intrinsic point defect situation is best known in high-purity silicon crystals growing from the melt. This has been intensively studied by Voronkov [6]. It was found that there are remarkably low concentrations of both vacancies and interstitials in the order of 5×10^{14} cm^{-3} at melt temperature T_m and very high diffusivities of 3×10^{-4} and 5×10^{-4} cm^2/s, respectively. At the growing interface, vacancy and interstitial fluxes take place, which are both directed into the crystal. Although one flux component is driven by the propagating growth interface (i.e., the crystallization (pulling) velocity v), the second one is driven by a temperature-dependent vacancy-interstitial recombination behind the interface, which creates a concentration gradient with Fickian diffusion flow and is proportional to the temperature gradient G_T. At high crystallization rates, the first component dominates, leading to a higher vacancy flow into the crystal. This is due to their lower formation energy (~4.0 eV) than that of self-interstitials (~4.8 eV). In contrast, at low crystallization velocities, the diffusion is dominant and leads to an excess of interstitials due to their larger diffusivity than vacancies. The type and concentration of "surviving" point defects is controlled by the v/G_T ratio, which is for Czochralski growth larger in the crystal core than in the peripheral regions, thus leading to different vacancy and interstitial excesses in both regions. The critical transition ratio for which vacancy and self-interstitial fluxes are equal and the recombination is optimal is $v/G_T = 1.34 \times 10^{-3}$ cm^2/K/min, as summarized by von Ammon [7]. A given native point defect content belongs to each crystalline phase like a "solute component" in a system of ideal mixing. When the defect solubility is exceeded, the dominant point defects begin to conglomerate, forming defects of higher order, such as microvoids, due to vacancy

condensation and precipitates due to interstitial fusion. Usually, such defects are generated during the cooling-down process because of the retrograde behavior of the existing solubility limits. For instance, in vacancy-rich silicon crystals, characteristic microvoids with dimensions of 100 nm are formed [8].

Compared with elementary materials (metals, Ge, Si), in compound crystals (e.g., alloys, $A_{II}B_{IV}$, $A_{III}B_{V}$, dielectric and organic compounds) additional antisite defects and a characteristic phase region (called the existence or homogeneity region) are present. Depending on the temperature and atomic interaction energies, the solubility of point defects of the given excess component (e.g., A or B interstitials in AB, respectively) deviates more or less from that of the stoichiometric composition (AB). Then, at a given T, the deviation δ of the concentrations of the present native point defects in each sublattice can be estimated as follows [4,9]:

$$\delta = \delta A - \delta B = \{[A_i] - [V_A] + 2[A_B] - 2[B_A]\} - \{[B_i] - [V_B] + 2[B_A] - 2[A_B]\} \quad (27.4)$$

with $[A_i]$, $[B_i]$, $[V_A]$, $[V_B]$, $[A_B]$, and $[B_A]$ being the interstitial, vacancy, and antisite contents, respectively.

As can be seen from Figure 27.2, the shape and maximum width of the phase extent are material-specific features from concentrations of 10^{-5} (e.g., InP [10], Figure 27.2(a)) up to several mole fractions (e.g., $LiNbO_3$ [11], Figure 27.2(d)). Due to the retrograde behavior of the solidus curves, the crystals pass during cooling through a process of excess point defect condensation, which may generate second-phase particles (see Section 27.5.1). Note that there are compounds in which the homogeneity region is located off the stoichiometric composition, making it quasi-impossible to grow second-phase free crystals (e.g., SnTe [12], Figure 27.2(c)). Even for GaAs, thermochemical calculations [13] confirmed the earlier and newer growth observations [14] showing that the phase extent is deviated exclusively toward the arsenic-rich side (Figure 27.2(a)).

Thus, nonstoichiometric point defects play a role because the crystallization path starts always usually at the boundary (solidus) of the existence region but not at exact stoichiometry. This is also the case in solution growth dealing mostly with compounds. However, compared with melt growth, the situation is much more advantageous due to its considerably smaller extent at low temperatures. In this way, for growth from solutions or fluxes, the crystal composition approaches stoichiometry with a much smaller content of native point defects.

27.2.2 Point Defect Dynamics

Principally, the energetic interplay between point defect types, the applied temperature field consisting of gradients and fluctuations, crystallization rate, differing growth kinetics along various crystal planes, and out-diffusion through the crystal surface under real growth conditions cause marked deviations from the thermodynamic equilibrium. As already mentioned, the related point defect dynamics have been well studied in silicon crystals [6]. In semiconductor and oxide compound crystals, however, these

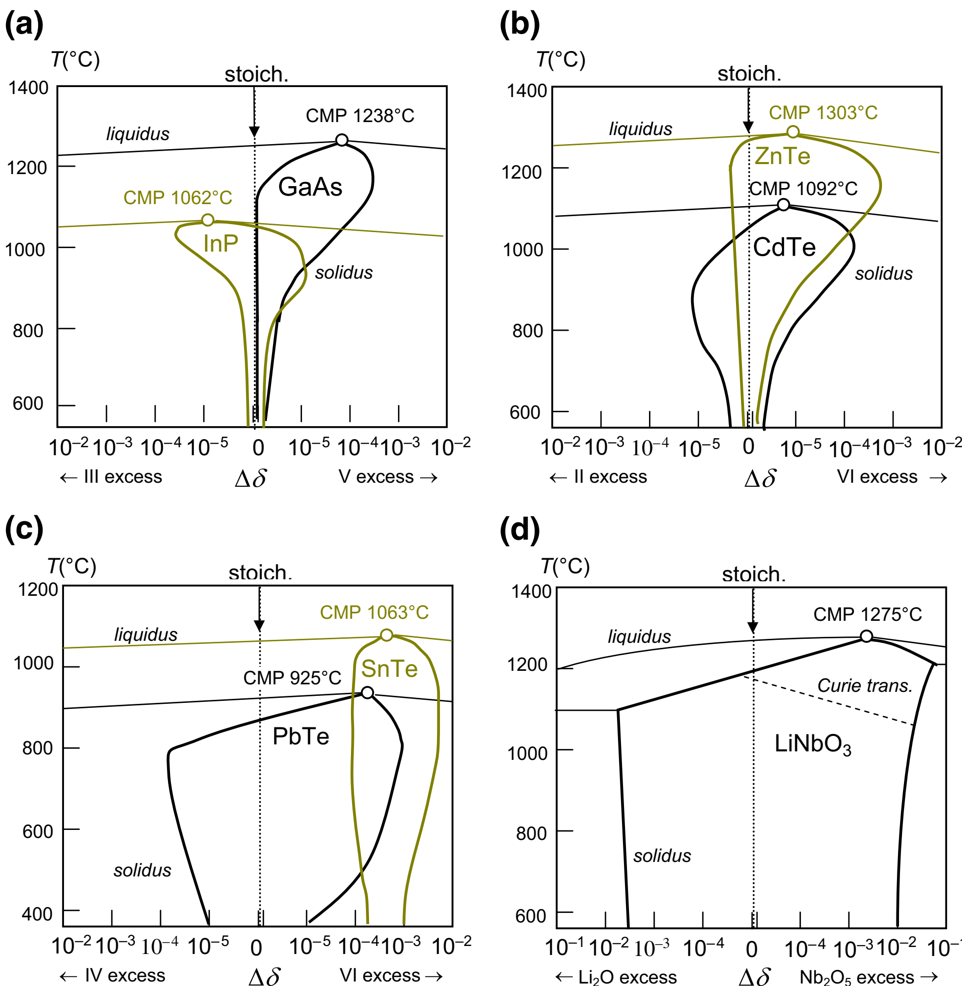

FIGURE 27.2 Selected phase projections of various compounds showing the diverseness of shape and deviation of the existence region $\Delta\delta$ from stoichiometry and temperature. (a) GaAs and InP; ZnTe and CdTe; SnTe and PbTe; CMP, congruent melting point [10–15].

processes are not nearly as well understood. One reason is that the presence of dislocations acting as effective point defect getters hampers point defect analysis in its pure form. Furthermore, as follows from Eqn (27.4), the situation in multicomponent materials is complicated due to the presence of equivalent defect types and antisites in each sublattice. For instance, it has been established that As_{Ga} antisites in GaAs crystals, known as neutral EL2 defects with the charged states $EL2^{+}$ and $EL2^{2+}$, do not appear at the growth temperature but form during the cooling-down process only. In materials grown from a near-congruent composition (i.e., slightly As-rich melt), the As_i content removes the $[V_{Ga}]$ by producing As_{Ga} as soon as the lowering temperature evokes

supersaturation [9]. A nearly identical mechanism takes place in CdTe. In cooling Te-saturated samples, the antisite Te_{Cd} is formed and may become important as singly- and doubly-ionized midgap donors $Te_{Cd}^{1+,2+}$ that are responsible for the compensation of the shallow native acceptor $V_{Cd}^{1-,2-}$ [16].

For estimation of the defect trapping kinetics along a propagating melt-solid interface, one first must clarify whether the front moves by atomically rough or smooth morphology [17]. Although metals show atomically rough interfaces, dielectrics crystallize mostly with atomically smooth interfaces; the semiconductor materials stand in between. Semiconductors with diamond, zinc blende, and wurtzite structures grow from the melt along most directions by the atomically rough mode. However, they tend to form atomically smooth interfaces on their most closely packed {111} planes. On atomically rough interfaces, atoms can be added singly without the need for nucleation—that is, at a very low chemical potential difference between solid and liquid phases. As a result, possible defect sites are added to the crystal under quasi-equilibrium conditions. On the contrary, for atomically smooth planes, much higher supercooling is required in order to initiate two-dimensional nucleation followed by layer-by-layer growth. In such a case, vacancies, interstitials, and foreign atoms can be overgrown very rapidly; hence, they can be incorporated in metastable states in much higher concentrations than equilibrium if their diffusion-back rate into the melt is not high enough [18,19].

One can assume that the fluid phase provides sufficient imperfections due to its "structural" instability and disordered character. According to Motooka's molecular dynamics simulations [20], point defects can be formed directly at the interface due to the density misfit between the liquid and solid phases.

The same situation takes place when extrinsic point defects (foreign atoms, such as impurities) are presented. On atomically smooth planes, they can be made quasi-metastable by enhanced concentrations due to the high-speed lateral layer-by-layer overgrowth that downplays the effect of segregation.

27.2.3 Extrinsic Point Defect Incorporation

As was introduced in Section 27.1, the term *extrinsic point defect* describes unintentionally and intentionally present foreign atoms such as residual impurities and dopants, respectively. They occupy interstitial or substitutional (lattice) positions. When growing crystals with dopant concentrations below the solubility limits, the matrix contributes one component in the phase diagram and the solute contributes another. Thus, the system can be considered as binary. The equilibrium between the chemical potentials of the species involved in the liquid (i.e., solvent) i and solid phases $\mu_{il}(x,T) = \mu_{is}(x,T)$ yields

$$\mu_{is}^{o} + kT \ln x_{is}\gamma_{is} = \mu_{il}^{o} + kT \ln x_{il}\gamma_{il} \tag{27.5}$$

where μ^{o} is the standard potential and γ is the interaction activity between i and atoms or molecules of the matrix. Setting $\mu_{il}^{o} - \mu_{is}^{o} = \Delta\mu_{i}^{o} = \Delta h_{i}^{o} - \Delta s_{i}^{o}T$ and $s_{i}^{o} = h_{i}^{o}/T_{mi}$, with

h_i^o, s_B^o as the intensive standards enthalpy and entropy, respectively; T_{mi} as melting point of the dopant; and $\Delta h^o_{Mis,l} = kT \ln \gamma_{is,l}$ as the mixing enthalpy, the transformed Eqn (27.5) becomes [21]

$$\frac{x_{is}}{x_{il}} = k_o = \exp\left[-\frac{\Delta h_i^o}{k}\left(\frac{1}{T} - \frac{1}{T_{mi}}\right) + \frac{\Delta h_{Mil} - \Delta h_{Mis}}{kT}\right] \tag{27.6}$$

with $k_o = x_{is}/x_{il}$ being the (thermodynamic) equilibrium distribution (or segregation) coefficient, which can be assumed as a constant for residual impurity or low dopant concentrations if the solidus and liquidus curves allow their linearization.

The homogeneous redistribution of dopants (and also impurities) along the growing crystal proves to be a great challenge for the crystal grower. The deviation of the equilibrium distribution coefficient k_o (Eqn (27.6)) from unity causes segregation phenomena during melt and solution growth, which can be treated in terms of an effective segregation coefficient $k_{eff} = x_{is}/x_{il}^{(\infty)}$, with $x_{il}^{(\infty)}$ being the mole fraction of the dopant or impurity in the fluid far away from the crystallizing interface. During the solidification process, the solute is rejected ($k_o < 1$) or preferentially absorbed ($k_o > 1$) by the propagating solid–liquid interface, forming an enriched or depleted solute boundary layer in front of it. The width δ_s of this boundary layer is determined by the growth rate R and by the diffusive and convective species transport in the melt, which is very often difficult to predict. A very popular model that is commonly used in melt growth was introduced by Burton, Prim, and Slichter (BPS) [22] for the steady state of segregation:

$$k_{eff} = \frac{k_o}{k_o + (1 - k_o)\exp(-R\delta_s/D)} \tag{27.7}$$

Thus, when characteristic convective fluctuations in the melt cause related R oscillations, the k_{eff} varies accordingly. As a result, mesoscopic transversal impurity or dopant inhomogeneities ("striations") are generated. More details, especially on quantification of the δ_s value depending on the melt convection regime, are given by Müller and Ostrogorsky [23] and also in this volume by Ostrogorsky and Glicksman (see Chapter 25).

27.2.4 Native and Extrinsic Point Defect Interaction (Complex Formation)

Impurities and dopants are incorporated on lattice sites or interstitial positions. In compounds, depending on their position in the periodic table, the foreign atoms may occupy one or both sublattice sites. In general, their incorporation efficiency is affected by the present intrinsic point defects, which at growth temperatures can be isolated and are usually electrically charged [9]. (Note that in undoped silicon, the self-interstitials are assumed to be electrically neutral but negatively charged in n-doped Si and positively charged in p-doped Si [24]—an often-observed phenomenon in many materials.) Generally, the charge state of point defects depends on the Fermi position

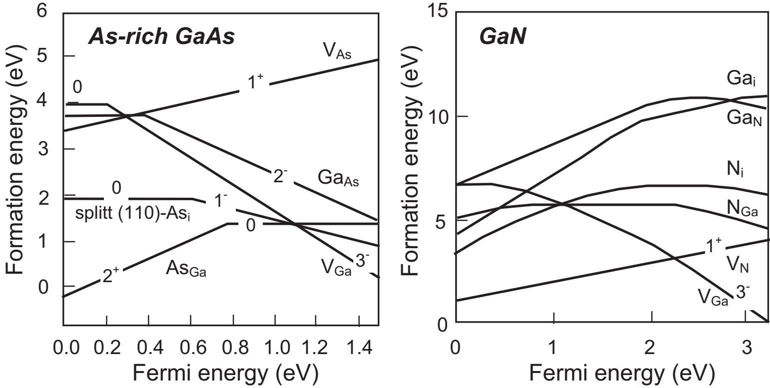

FIGURE 27.3 Dependence of native point defect formation energies and ionization levels of native point defects on the Fermi energy in As-rich GaAs [27] and GaN [28]. Ionization levels are added.

leading to their complex interaction with electrically active dopants. As a result, the dopant solubility can be markedly influenced and, controversially, doping can affect the native point defect solubility and also the formation energy. This phenomenon has been well known for a long time in numerous melt-grown semiconductor compounds, such as GaAs doped with Te and Si [25], CdTe doped with Ag and Cu [26], and GaN. As can be seen from Figure 27.3, in GaN the native V_{Ga} and V_N defects show the lowest formation energies, leading at n-doping to the highest presence of the acceptor-type V_{Ga} [29]. However, p-type GaN is difficult to obtain because of its highest concentration of the shallow donator V_N with the lowest formation energy in such material [28].

The influence of the electron or hole concentration generated by the ionized impurities and dopants X^z on the charge state of the native point defects is called the Fermi level effect [27], whereby the degree of ionization z depends on the position of the Fermi level [30] (Figure 27.3). For instance, the charge state of the Ga vacancy in GaAs changes from neutral V_{Ga}^{o} in p-type material over double-negatively-charged V_{Ga}^{2-} in the midgap to a triple-negatively-charged V_{Ga}^{3-} in n-type material that affects the compensation level and enhances the *complex formation* probability as well. An example of a complex reaction in the common form is

$$\left(V_A^{3-} + 3h\right) + \left(X_B^{+} + e\right) \leftrightarrow \left(V_A X_B\right)^{2-} + 2h \tag{27.8}$$

This can be found in the form of $[Te_{As}V_{Ga}]^{2-}$ or $[Si_{Ga}V_{Ga}]^{-}$ in GaAs crystals or in the form of neutral $[V_{Ga}O_N]$ complex in GaN stabilizing the V_{Ga} presence during the cooling-down process [29].

Thus, nonstoichiometry in compound crystals influences the incorporation efficiency of impurities and dopants as well. Larger deviations from stoichiometric composition during growth lead to higher possibilities of vacancy generation within the compositionally impoverished sublattice. As a result, the incorporation density of atoms at the

growing interface occupying these vacant sites increases with nonstoichiometry. This was demonstrated by Rudolph et al. [26], who grew CdTe crystals by a vapor pressure–controlled Bridgman method from different melt compositions containing silver as the dopant. At near-stoichiometric growth conditions, the concentration of Ag^{o}_{Cd} is drastically reduced down to 2×10^{13} cm^{-3}. Compared to that, a Te excess of 5×10^{17} cm^{-3} leads to an incorporation of Ag atoms on V_{Cd} sites of about one order of magnitude higher concentration.

27.2.5 Point Defect Engineering

To ensure specified electrical and optical qualities of single crystals and devices made from them, the control of native point defects plays an important technological role, especially if harmful secondary reactions are evoked by point imperfections, such as precipitation and microvoid generation. From an experimental point of view, there are two possible ways of defect mastering: (1) in situ control during the crystal growth process and/or (2) postannealing of the as-grown crystal bulk or pieces (wafers) cut from them.

In the case of dislocation-free crystals, a quasi-homogeneous point defect interplay without catalytic effects takes place. As a result, the relatively high supersaturation promotes vacancy and/or interstitial condensations within the cooling crystal volume, escalating to unfavorable micro- and meso-conglomerations. As discussed in Section 27.2.1, in silicon at high pulling rates, vacancies are incorporated in excess and condense during cooling down to form octahedral voids of $\sim$100 nm [8]. At low pulling rates, interstitials are in excess, forming a network of dislocation loops [7]. The balance between the number of vacancies and interstitials is the controlling factor. Based on these experimental observations, three ways to achieve microdefect-free silicon have been investigated [31]:

- Keep the growth conditions within the defect-free regime, which is approximately $\pm$10% of the critical ratio $v/G_T = 1.34 \times 10^{-3}$ cm^2 $K^{-1}min^{-1}$, where v is the growth velocity and G_T is the temperature gradient at the interface. However, such a small tolerance permits only very low pulling velocities of about 0.5 mm/min and extended cooling times.
- Keep a maximum pulling rate with fast cooling followed by a wafer annealing process to reduce the microvoids.
- Use a "flash wafer" step, where a thin active Si layer of 0.5 μm is deposited onto the wafer surfaces, which combines the maximum pull rate and fast cooling with low-cost treatment.

The in situ control of native point defects in compound crystals is coupled with the feasibility of accurate composition control during the growth process and, therefore, with the exact knowledge of the phase diagrams. When the T-x shape of the homogeneity region is better known, the in situ control can be more accurately

adjusted. The application of a temperature-fixed vapor source of the volatile component during the horizontal Bridgman (HB) method without covering of the melt is well known [32]. In this technique, there is direct contact of the vapor phase with the crystallizing melt-solid phase region, which guarantees near-phase equilibrium conditions during the whole growth run. Also, the vertical Bridgman (VB) and vertical gradient freeze (VGF) techniques were introduced by using an extra source for the vapor phase control [33] (see also Volume IIA, Chapter 9). A certain transport transient of the vapor species has to be considered due to the complete covering of the crystallization front by the melt column. As a result, the equilibrium temperatures for the vapor pressure source can somewhat differ between the techniques. Vapor-pressure-controlled HB, VB, and VGF have been successfully used to grow near-stoichiometric compound semiconductors, such as CdTe [34] and GaAs crystals—the latter even without boric oxide encapsulation of the melt surface [35]. If highly purified material is used, high-resistivity CdTe crystals could be obtained [36], caused by intrinsic defect annihilation and compensation. However, ensuring a stable intrinsic semi-insulating state of high reproducibility over the whole crystal length is very complicated due to native point defect segregation. A well-controlled source temperature program that is well fitted with the growth rate would be required. Compensation doping, such as that realized in CdTe [37], may be more promising. At present, however, the stoichiometry is still tuned in cut wafers by postgrowth annealing when required for a given application [38,39].

Much less practicable is the in situ control of stoichiometry in the Czochralski growth of semiconductor compounds. For this, a modified technique without encapsulant is required to influence the melt composition by partial pressure of the volatile element. For instance, the in situ control of stoichiometry was achieved in GaAs by the vapor-pressure-controlled Czochralski (VCz) technique [40] without boric oxide encapsulation [41] (see Volume IIA, Chapter 3). It was demonstrated that near-stoichiometric growth conditions with a Ga-rich melt reduce both the As_{Ga} antisite and V_{Ga} concentrations [41].

Currently, for dielectric compounds, Czochralski growth experiments with precise in situ vapor pressure control are still rare. This is primarily due to the much higher growth temperatures and chemical aggressiveness of oxygen or fluorine, which make it difficult and expensive to insert a chemically resistant and gastight inner growth chamber with an extra source. However, some activities have been described. For instance, high-quality composition-controlled $Bi_{12}GeO_{20}$ (BGO) crystals were grown in an inner chamber made of platinum [42]. A related patent [43] describes the control of stoichiometry during Czochralski growth of $PbMoO_4$ crystals, with markedly improved optical transmission using an MoO_3 evaporation source within a bell covering around the pulling crystal.

For the control of intentionally introduced extrinsic point defects (dopants), the engineering is directed on their homogeneous or linear-gradient distribution, as described in detail in the Volume IIb, Chapter 25.

27.3 Dislocations

27.3.1 Growth Dislocations and Postgrowth Dislocations

Dislocations are generated during crystal growth via plastic deformation and by the condensation of self-interstitials and vacancies. In the study of crystal growth defects, it is useful to distinguish between two categories of dislocations [44,45]:

1. Dislocations that are connected with the growth front and proceed with it during growth (i.e., growth dislocations, grown-in dislocations).
2. Dislocations that are generated behind the growth front, either during the growth run or during cooling down to room temperature (i.e., postgrowth dislocations), later during processing, or by improper handling.

The final arrangement of dislocations in a crystal at room temperature results from growth dislocations, postgrowth dislocations, and the movement, multiplication, and reactions of both after growth. Crystals grown at low temperatures with low- or zero-temperature gradients (e.g., from aqueous solution) and in their brittle state usually contain dislocations in their original “as-grown” configuration; in crystals grown at high temperatures, the original dislocation configurations may be drastically altered by dislocation movement, dislocation multiplication, and dislocation reactions. These processes, which may occur during the growth run (behind the growth front), are induced by thermal stress due to inhomogeneous temperature fields and—particularly in crystals grown at very high temperatures—by the absorption of interstitials and vacancies (“dislocation climb”) during cooling. They usually occur in crystals grown from melt because these are always plastic in a more or less extended temperature range below the melting point; thus, they allow the movement of dislocations even under low critical stress. Dislocation arrangements, which are described in Sections 27.3.5 and 27.3.6, result from these processes. Detailed summaries on dislocation multiplication by thermomechanical stress during the growth of crystals from the melt are given by Völkl [46] and Prasad and Pendurti [47].

27.3.2 Sources of Growth Dislocations

For topological reasons, dislocation lines cannot start or end in the interior of a perfect crystal. They either form closed loops, start from external and internal surfaces (e.g., grain boundaries), or start from defects with a break of the crystal lattice. In crystal growth, such defects may arise from all kinds of inclusions (e.g., foreign particles, liquid inclusions, bubbles, solute precipitates). When inclusions are overgrown and “closed” by growth layers, lattice closure errors may occur. These errors are the origin of growth dislocations that are connected to the growth front and propagate with it during further growth [44,45].

It is a common observation that inclusions are the source of growth dislocations. Examples are shown in Figures 27.4, 27.5 and 27.9(a). The appearance of dislocations

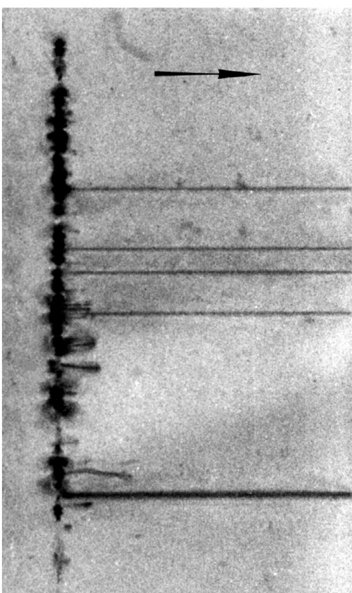

FIGURE 27.4 Liquid (zonal) inclusions in solution-grown potassium alum (water), triggered on a (110) face by an intentionally introduced re-dissolution due to a temporary increase of solution by 1 °C. The original temperature (~40 °C) was restored until a slight rounding of crystal edges had appeared. Arrow *n*: growth direction. A few edge dislocations originate from the inclusions. A section ($6 \times 12\ mm^2$) of an X-ray topograph of a 0.9-mm thick (100) plate is shown. Diffraction vector is $\mathbf{g}(2\bar{2}0)$; MoKα radiation. *With permission from Springer Science + Business Media.*

"behind" an inclusion (viewed in the direction of growth) is correlated with its size: small inclusions emit only few dislocations or are often dislocation free. Large inclusions (>50 μm) usually emit bundles of dislocations.

The generation of growth dislocations by foreign particle inclusions has been experimentally studied on crystals growing in aqueous solution (potassium alum) and in supercooled melt (benzophenone $(C_6H_5)_2CO$, $T_m = 48$ °C; salol $C_{13}H_{10}O_3$, $T_m = 42$ °C) [48]. Similar studies were reported by Forty [49], who presented a rich collection of photographs of growth spirals and other surface patterns on growth faces of various crystals.

27.3.3 Propagation of Growth Dislocations

27.3.3.1 Characteristic Configurations, Theory of Preferred Direction

As summarized in the reviews by Klapper [44,45,50], a dislocation line ending on a growth face will proceed with it. Its direction depends on the shape and the orientation of the growth face and on its Burgers vector. A crystal growing on planar (habit) face consists of growth sectors belonging to different growth faces (different growth directions **n**; see Section 27.6.1). This leads under ideal conditions (i.e., stress-free growth) to a characteristic configuration of growth dislocations, which is illustrated in Figure 27.6. The dislocations start from inclusions and propagate as straight lines with

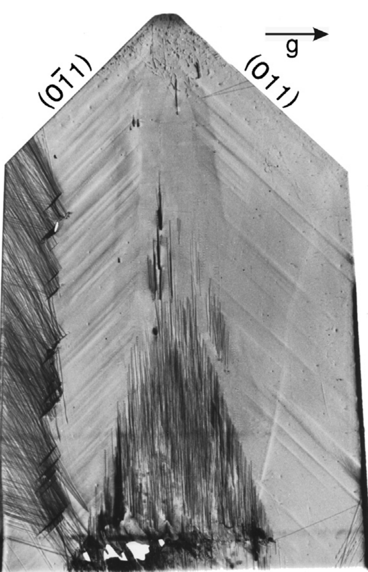

FIGURE 27.5 X-ray diffraction topograph of a (100) plate (approximately 1.5-mm thick, 50-mm long), cut from the rear side of a potassium dihydrogen phosphate crystal rotated through the solution. Due to a closed wake of solution with reduced supersaturation behind the $(0\bar{1}1)$ growth face, liquid inclusions were repeatedly formed. They are the origin of numerous dislocations, which grow out at the side because the prism face is practically not growing. The dislocations in the triangular region above the capping zone belong to one of the growth sectors (101) or (101). At their top ends, they emerge out of the plate *t. With permission from Springer Science + Business Media [45].*

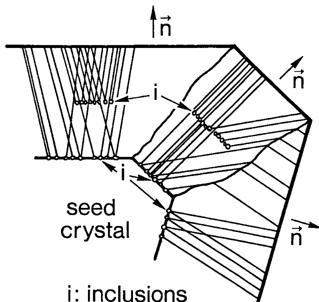

FIGURE 27.6 Typical geometry of growth dislocations in crystals grown on habit faces. The different preferred directions of dislocations lines within one growth sector result from different Burgers vectors. These directions abruptly change their directions when they penetrate a growth-sector boundary, where, during growth, the dislocation outcrops shift over the edge from one face to the other. *After Klapper [44,45], with permission from Springer Science + Business Media [45].*

directions $\mathbf{l}$, which are usually close to, and frequently parallel to, the growth direction of the sector in which they lie. They usually exhibit sharply defined, often noncrystallographic preferred directions $\mathbf{l_o}$, which depend on the growth direction $\mathbf{n}$ and on the Burgers vector $\mathbf{b}$: $\mathbf{l_o} = \mathbf{l_o}(\mathbf{n}, \mathbf{b})$. The dependence of the preferred direction $\mathbf{l_o}$ on the growth

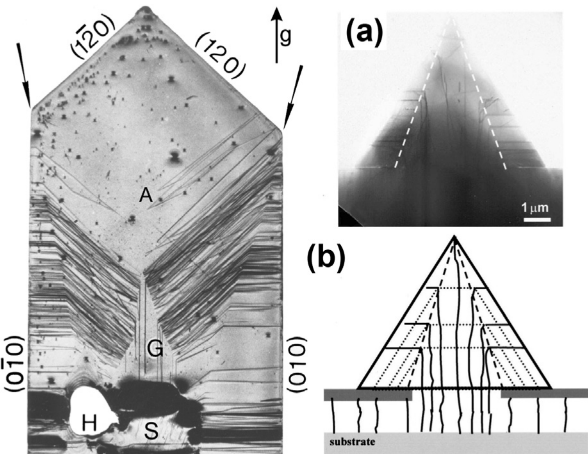

FIGURE 27.7 *Left*: This section of a (001) plate (horizontal width about 15 mm, thickness 1.5 mm) was cut out of a salol crystal (orthorhombic) grown from supercooled melt. The dislocation lines change their preferred directions when they penetrate the boundaries (arrows) from the {120} into the {010} growth sectors. S: seed crystal, H: hole due to a gas bubble, G: grown-out (100) sector, A: dislocation pairs (with opposite Burgers vectors of their components) originating from tiny inclusions, dots: surface damages. *With permission from Springer Science + Business Media [45].*) *Right*: (a) transmission electron micrograph of the dislocation arrangement in GaN grown on a sapphire substrate by MOVPE epitaxial lateral overgrowth (ELO) through the window (width 3 μm) of a mask, viewed along direction [10$\bar{1}$0]. (b) Sketch of growth features and dislocation arrangement. Dotted lines shapes of the GaN crystal with faces {11$\bar{2}$2} and (0001) in successive stages of ELO-growth; dashed lines (white in (a)): boundary between the (0001) and the neighbored {11$\bar{2}$2} growth sectors. The basal (0001) face has the higher growth velocity and, thus, finally vanishes from the crystal shape. The dislocations (full lines), proceeding through the mask window and ending on the basal plane, are bent by 90° into the horizontal direction when penetrating the boundary to the neighbored {11$\bar{2}$2} sectors. *Courtesy of Vennéguès et al. [60]; reproduced with permission from [60], copyright (2000), AIP Publishing LLC.*

direction **n** becomes conspicuously apparent when the dislocations penetrate growth-sector boundaries, which implies an abrupt change of the growth direction. As a result, the dislocation lines undergo an abrupt change of their preferred direction $\mathbf{l_o}$. Examples are shown in Figure 27.7.

This preferred direction of growth dislocations is explained by two approaches:

1. The *minimum-energy theorem* (Figure 27.8(a)): The dislocation lines adopt a direction **l** (unit vector), for which its energy within any growth layer is a minimum. For a growth layer of unit thickness $d = 1$, this can be expressed as $E/\cos\alpha = $ minimum, with $E = E(\mathbf{l}, \mathbf{b}, c_{ij})$ being the elastic energy (strain energy) per unit length of the dislocation line (c_{ij} are the elastic constants of the crystal) and α being the angle between **n** and **l**. The factor $1/\cos\alpha$ accounts for the length of the dislocation line in the layer [44,50,52].
2. The *zero-force theorem* (Figure 27.8(b)): A dislocation line emerging at the surface experiences a force dF, which depends on the angle α between the dislocation direction **l** and the surface normal **n**. At the surface, this force is infinitely large. According to Lothe [51], there exists always a direction $\mathbf{l_o}$ for which this force is

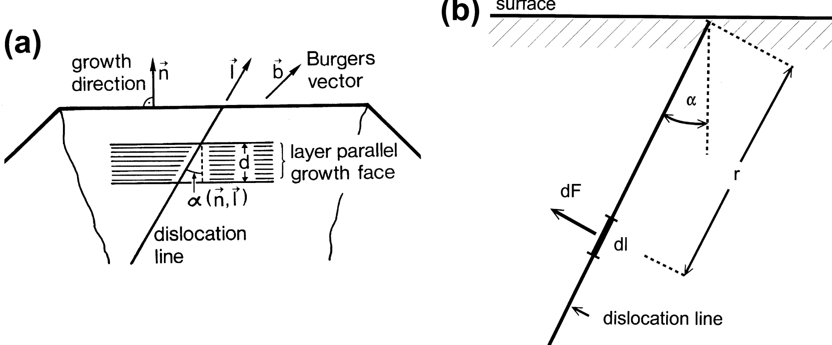

FIGURE 27.8 (a) Derivation of the energy of a straight dislocation line within a layer parallel to the growth face. (b) Illustration of the force d*F* exerted by the crystal surface upon a line segment d*l* of a straight dislocation line emerging at the surface (theorem of Lothe [51]). *With permission from Springer Science + Business Media [45].*

zero for the dislocation line segments at any depth below the surface *r*. It is plausible that a dislocation emerging at the growth face follows this direction of zero force. Using the formula

$$\mathrm{d}F = -\frac{1}{r}\left(\frac{\partial E}{\partial \alpha} + E \tan \alpha\right)\mathrm{d}l, \tag{27.9}$$

(theorem of Lothe), it can be shown that both approaches lead to the same preferred directions.

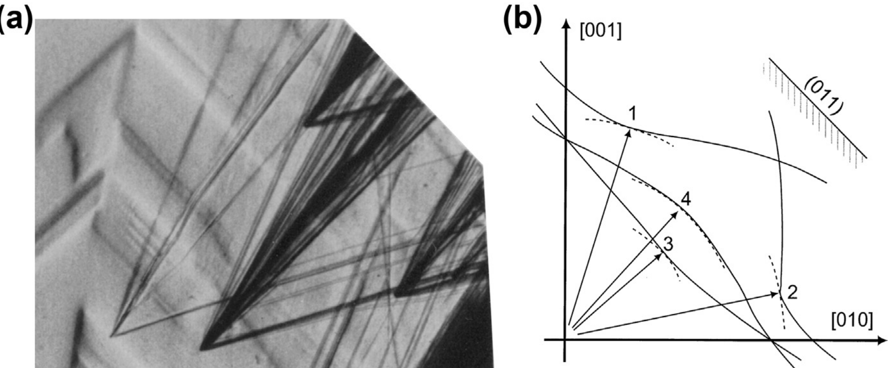

FIGURE 27.9 (a) This section (≈8.5 × 14 mm^2) of an X-ray topograph (reflection 200, Ag-Kα radiation) of a potassium dihydrogen phosphate (KDP) (100) plate (thickness ≅ 1.5 mm) shows bundles of dislocations with non-crystallographic preferred directions emanating from small liquid inclusions. The Burgers vectors of these dislocations can be recognized from their preferred directions. In addition, growth bands and features due to vicinal effects are visible. (b) Plots of calculated energies *E*/cos α (arbitrary units) of dislocations with Burgers vectors **b** = [001] (1), **b** = [100] (2), **b** = [011] (3), and **b** = [011] (4) in growth sector (011) of KDP (polar coordinates). The preferred directions of minimum *E*/cos α are represented by arrows. The dashed lines are circles with radii equal to the minimum values of *E*/cos α.

27.3.3.2 Verification of the Minimum Energy Approach and Examples

The minimum-energy directions of growth dislocations have been calculated for several Burgers vectors and growth sectors in various crystals grown from solution and supercooled melt [52–54] using the theory of dislocations in elastically anisotropic crystals developed by Eshelby et al. [55]. Although the calculations are only approximate by regarding the crystal as an elastic continuum and neglecting the dislocation core energy, the agreement between observed and calculated directions is satisfactory. Figure 27.9 shows the comparison of observed and calculated preferred directions of dislocations with four different Burgers vectors in the (011) growth sector of potassium dihydrogen phosphate (KDP) [56]. The agreement is excellent with deviations of 3–6°, except for dislocation 4, the observed directions of which scatter by $\pm 5^\circ$ around a direction deviating by about 20° from the calculated one. This may be due to the very flat minimum of K, which makes the minimum energy directions more subject to other influences, such as surface features and core-energy variations. Similar comparisons have been carried out for various crystals grown on planar faces from solutions and supercooled melts [53,54,57,58]. In general, the agreement of observed and calculated directions is satisfactory and confirms the validity of the above theorems.

On account of the factor $1/\cos\alpha$ in the energy term above, the preferred directions of growth dislocations are mostly normal or nearly normal to the (local) growth face. In some cases of planar interfaces, however, deviations from the growth normal of up to 30° have been observed in agreement with the calculations.

For interfaces with convex curvature, such as in Czochralski growth of oxides, the dislocation lines diverge and grow out of the crystal boule through its side faces, whereas for concave interfaces the dislocation lines are focused into the center of the crystal boule. Trajectories of growth dislocations in Czochralski gadolinium gallium garnet (GGG) have been calculated and compared with observed trajectories by Schmidt and Weiss [59]. The rounding of the interface has been taken into account by performing the calculations stepwise in small increments. Again, the agreement is satisfactory. Moreover, this allowed the assignment of Burgers vectors to the different dislocation trajectories, which were observed optically in polarized light. Preferred dislocation directions and their bending when penetrating a growth sector boundary have been observed by transmission electron microscopy in GaN grown by metal-organic vapor phase epitaxy (MOVPE) using the epitaxial lateral overgrowth (ELO) technique [60,61]. An example is shown in Figure 27.7(b).

Although the agreement of observed and calculated directions of growth dislocations is in general satisfactory, frequently discrepancies are found. The reasons for this may be due to the insufficient approximation by the model on which the calculations are based, the influence of other defects, or particular surface relief. The above calculations are based on linear anisotropic elasticity of the continuum and do not account for the discrete structure of the crystals, the dislocation core energy, or, in piezoelectric crystals, electric energy contributions.

The following four causes have been found to affect preferred directions:

1. Discrete lattice structure of the crystals and the neglect of the core energy
2. Long-range stress
3. Surface relief of the growth face (e.g., growth hillocks, macrosteps)
4. Dislocation movement and reactions after growth

Detailed discussions of these influences are given in Refs [44,45,50,52].

27.3.4 Postgrowth Dislocations

Dislocations formed in the interior of the already-grown crystal without connection to the growth front or other surfaces must be closed loops. It is practically impossible to generate closed loops in a perfect crystal by stress because the stress required for such processes would be extremely high. Inclusions, however, usually represent stress centers and form internal surfaces of the crystal. The stress in the crystal around the inclusions is relieved by the emission of concentric dislocations loops or—more frequently—of dislocation half-loops (see Section 27.5.4, equation 27.17). The half-loops are, strictly speaking, also closed loops (with a virtual closing line element inside the inclusion). Half-loops can also generate growth dislocations: if stress is built up around an inclusion just incorporated and still close to the growth front, half-loops emitted from the inclusion may "break through" to the growth interface, whereby each half-loop forms two separated dislocation lines with opposite Burgers vectors propagating with the growth front. Dislocation half-loops emitted from bubble inclusions in benzil grown from supercooled melt [58] are shown in Figure 27.10. Examples of half-loops in solution-grown crystals, revealed by X-ray topography, are given in Ref. [62] for sodium chlorate and in Ref. [63] for tetraoxane. The latter study shows the successive emission of half-loops from inclusions and their splitting into two separate dislocations when reaching the crystal surface. A very peculiar kind of dislocation loop is observed in octadecanol crystals grown from xylene solution: columns of prismatic loops are punched out from inclusions [64].

More detailed discussions are given in Refs [45,50,54,65].

27.3.5 Dislocation Dynamics (Patterning, Cell Structures, Clustering)

Dislocation dynamics describe the dynamic organization of dislocations into spatially heterogeneous substructures [66]. Bulk crystals are grown in heat fields with temperature differences (gradients) being not of ideally linear but, typically, nonlinear character. As a consequence, thermomechanical stresses are present in the growing crystal ingot [67]. Under such conditions, even at high temperatures, the existing dislocations exhibit both (1) *glide*, with a velocity proportional to the power of acting stress; and (2) *climb* motion, with a rate that is a function of applied stress, temperature, and, especially, density and diffusivity of available point defects. Dislocation motions result from both

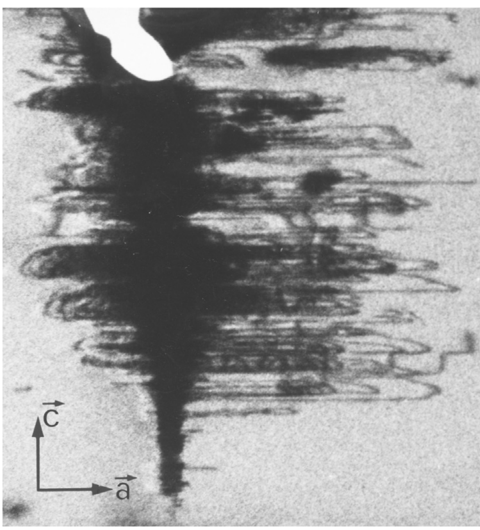

FIGURE 27.10 Postgrowth dislocation half loops in benzil (grown from supercooled melt) emitted from a trail of bubbles. Section 4.5 × 5 mm of a (0110) plate. The dislocations belong to the ⟨100⟩(0110) glide system and are purely screw in their horizontal segments [58]. *With permission from Springer Science + Business Media [45].*

long-range force fields, such as overall thermomechanical stress, and short-range reactions between individual dislocations.

When the generated thermomechanical stress within a growing crystal is of the order of the critical resolved shear stress (CRSS), the stored dislocations are shifted with a *glide velocity* of

$$v_g = v_0 \left(\tau_{eff}\right)^m \exp\left(\frac{-E_a}{kT}\right) \tag{27.10}$$

where v_0 is the empiric material constant (shear wave velocity), τ_{eff} is the effective shear stress on dislocation $= \tau - A\sqrt{\rho_0}$, A is the strain hardening factor, ρ_0 is the mobile dislocation density, m is the stress experimentally obtained from deformation experiments, E_a is the activation energy (Peierls potential), k is the Boltzmann factor, and T is the absolute temperature. Note that no obstacles, such as sessile dislocations, foreign phase inclusions, or grain boundaries, are considered in Eqn (27.10).

In addition, dislocation climb (jog dragging) is thermally activated but depends additionally on the diffusive properties of the material, particularly the diffusion of native point defects (vacancies, interstitials), being more mobile than glide, known as *climb velocity*:

$$v_c = v_{0cl} \left(\tau_{eff}\right)^{N_c} \exp\left(\frac{-E_{SD}}{kT}\right) \tag{27.11}$$

Here, $v_{0cl} \sim n_j \ D_i/\lambda$ is the characteristic climb velocity depending on point defect diffusivity, in which D_i is the distance between equilibrium point defect concentration

and dislocation line λ. The concentration of jogs per unit length of dislocation $n_j = n_0 \exp(-E_j/kT)$, where n_0 is the thermodynamic equilibrium number of atom sites per unit length of dislocation and E_j is the characteristic jog energy (n_j/n_0 is of the order of 10^{-3} at $T = 1000$ K [68]). N_c is the climb exponent and E_{SD} is the activation energy for self-diffusion.

Generally, in the course of enthalpy minimization, the long-range character of dislocation interaction produces agglomerates and patterns by mutual attraction, ensuring a *screening effect*. At the same time, a dislocation density thinning via annihilation takes place when the Burgers vectors are of opposite signs. Therefore, the total *interaction energy* between dislocations within a cylindrical crystal with radius R and mean distance between homogeneously distributed starting dislocations $\rho_0^{-1/2}$ consists of the following [69]:

$$E_i = -\int_{\rho_0^{-1/2}}^{R} 2\pi r f_a(r,\rho)\left(Gb^2/2\pi\right)\ln(r/r_0)dr \tag{27.12}$$

where $f_a(r,\rho)$ is the distribution function considering dislocation annihilation, whereupon $2\pi r f_a(r,\rho)dr$ is the difference between the number of dislocations with Burgers vector of opposite sign to that of similar sign between distances r and $r + dr$. G is the shear modulus, $\mathbf{b}$ is the Burgers vector, r is the radial position, and r_0 ($\approx 2 - 4b$), which is the dislocation core within which the linear-elastic theory breaks down.

As it was found experimentally, there are also nonlinear interactions between dislocations, which are phenomenologically described as rate processes rather than force-displacement relationships. Some of these reactions are immobilization, annihilation, dipole formation, junction formation, and dislocation multiplication. For instance, if the stress on a mobile dislocation falls below the friction stress or the dislocation is pinned at a mesoscopic obstacle (impurity conglomerate, second-phase inclusion, grain boundary), it becomes immobile. In particular, barriers caused by point defect agglomerations and grain boundaries produce often *dislocation clusters* of quite increased energy content, which produces prismatic dislocation loops or even microcracks.

Annihilation is the cancellation of two dislocations of opposite Burgers vectors, which approach each other along a given crystallographic plane within a certain critical distance. For two screw dislocations, this distance is $y_s^* \approx \mu b/2\pi\tau$, with μ being the shear modulus and τ being the shear stress required for dislocation glide. In comparison, two edge dislocations annihilate at much smaller critical distances on the order of 1–2 nm. However, they can achieve a stable configuration at a distance greater than the critical distance for annihilation. Such configuration is known as a *dipole*, being stable when the stress on a dislocation is less than the passing shear stress for a dipole $\tau_{dp} \approx \mu b/8\pi\ (1-\mu)y$, with y being the slip plane spacing.

Another important dynamic event is the energetically favorable junction formation. When many mobile dislocations are approaching each other, they can form jog intersections leading in ensemble to well-patterned dislocation networks. In particular, the energetic interplay between edge dislocations of opposite Burgers vector evoke their gathering in dislocation walls. As a result the energy of each individual dislocation within the wall reduces by a factor of three or four compared to its energy within a statistical initial arrangement. Finally, besides the cross-glide of screw dislocations, multiplication occurs by pinning of the dislocation, bowing out, and wrapping around the pinning points, known as the *Frank-Read mechanism*.

When glide and climb motions are competitive, dislocation cell structures form. This process of self-organization minimizes the internal enthalpy of the growing crystal in the course of plastic relaxation. In addition, the continuously acting flows of heat and stress put the crystal in a state somewhat outside the thermodynamic equilibrium accompanied by dissipative structuring via steady entropy production. Thus, the presence of heterogeneous dislocation substructures in as-grown crystals is not an abnormality but rather a common fact.

Cell patterning is studied best in metals under external load but also in postdeformed elemental semiconductor single crystals, such as silicon, and semiconductor compounds, such as III-BVs and II-VIs [70]. They are observed in melt-grown Czochralski [71], horizontal [72], and vertical Bridgman crystals [73], as well as in samples grown from solution [74] and vapor [75] (see Figure 27.11). However, the growth-related process of dynamical structuring, even in semiconductor compounds, has not yet been studied with such profundity as in postdeformed specimens. Of course, this is mainly due to the current impossibility of in situ stress measurements. Thus, the best possible global modeling of the present acting thermomechanical stress field in each given growth situation is increasingly coming to the fore [76].

There is a growing need for clarification of such features in semiconductors and dielectric crystals because they markedly influence the device quality. For instance, in as-grown semi-insulating GaAs, which is important for the production of low-noise high-frequency devices, a mesoscopic resistivity variation occurs due to the accumulation of As_{Ga} antisite defects (EL2) along the low-angle grain walls, which requires a sophisticated after-annealing step. Further, the wide application of $Cd_{1-x}Zn_xTe$ crystals as the most promising candidates for radiation-detection systems is still hindered by the charge-transport nonuniformities along such cellular substructures [77]. In multicrystalline silicon (mc-Si) for PV, an enhanced recombination occurs due to metal decoration in combination with oxygen at the subgrain boundaries, leading to degradation of the carrier lifetime and, thus, solar cell efficiency. Finally, as it is well known in crystals for optical applications, such as CaF_2 for ultraviolet photolithography, subgrain networks impair the transparency and resolution quality.

In general, dislocation cell structures consist of walls with high dislocation density separated by interiors of markedly dislocation-reduced or even dislocation-free material. The detailed analysis by X-ray synchrotron topography of dislocation cells in as-grown 6″

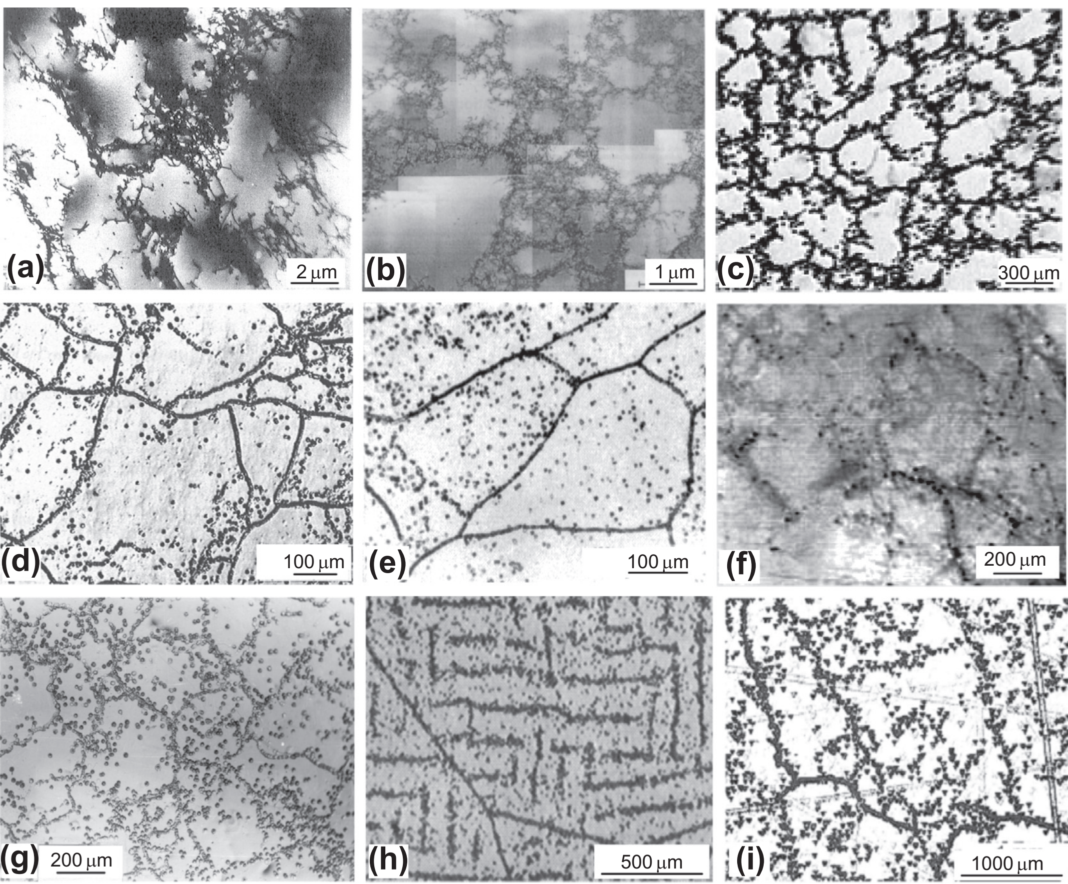

FIGURE 27.11 Dislocation patterns formed in various crystals under differing stress conditions. (a) Mo 12% deformed at 493 K; (b) Cu–Mn crystal deformed at 68.2 MPa; (c) GaAs crystal grown by VCz; (d) CdTe crystal grown by VB; (e) mc-Si crystallized bei VGF; (f) SiC crystal grown by sublimation; (g) $Cd_{0.96}Zn_{0.04}Te$ crystal grown by VB; (h) NaCl crystal with labyrinth structure deformed by 150 MPa at $T/T_m = 0.75$; (i) CaF_2 crystal grown by VB. *Adapted from Ref. [70].*

vapor-pressure-controlled GaAs crystal showed that the dislocations are accumulated in fuzzy walls [78]. Typically, numerous junctions and pins form a sessile dislocation jungle, which is rather stable against postgrowth annealing [79]. Only very small mean tilt angles around 10 arcsec exist between the cells. In comparison, in CdTe, PbTe, mc-Si, and CaF_2, the matrix contains numerous isolated dislocations and the cell walls are much sharper, consisting of only one row of dislocation pits that can be ascertained by transmission electron microscopy [75]. Such behavior is well known from the standard type of polygonized low-angle grain boundaries (primary subgrain formation), containing only the excess dislocations of similar Burgers vector after the annihilation is completed. Tilt angles of 60–120 arcsec were reported for such crystals [34]. Obviously,

compared with GaAs in these materials, the substructure reacts much more sensitively to variations of the stress field acting during crystal growth. Additionally, in II–VI and IV–VI substances, the dislocation mobility is markedly enhanced compared with III–Vs due to the much higher bond ionicity.

By ascertaining the mean cell diameter using the rules of correspondence, which are valid for most materials [80], we are able to estimate the value of once-acting thermomechanical stress. At first, after Holt's relation [69], the cell diameter is approximately given by $d \approx K\rho^{-1/2}$ (K-similitude coefficient); there is a correlation between cell size and dislocation content. Next, according to the rule of Kuhlmann-Wilsdorf [81], $d = K\,G\,\mathbf{b}\,\tau^{-1}$, the cell diameter also correlates with the acting shear stress. For instance, a mean cell diameter of 100 μm in an as-grown crystal correlates with a former τ of about 3–5 MPa. Finally, Taylor's rule [82], $\tau = K\,G\,\mathbf{b}\,\rho^{1/2}$, shows the relationship between stress and expected dislocation density (Figure 27.12). Of course, from these relationships follows that substructures should be damped by adherence of the lowest possible thermomechanical stress during growth—that is, assurance either of even or, as it was postulated by Indenbom [67], polynomial-shaped isotherms.

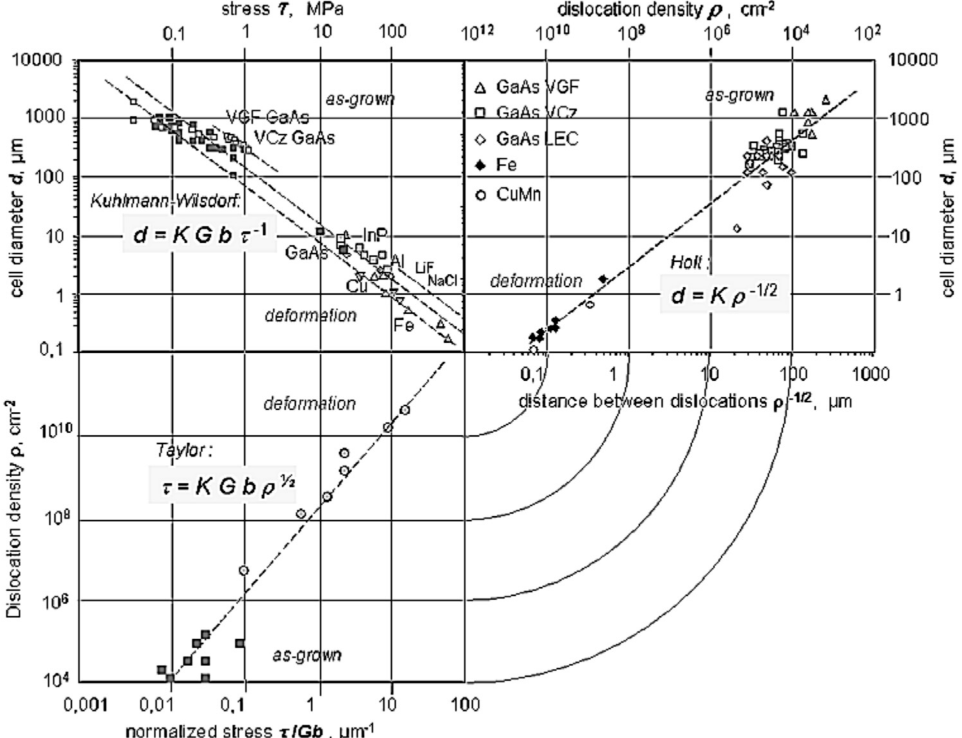

FIGURE 27.12 Kuhlmann-Wilsdorf's $d(\tau)$, Holt's $d(\rho)$, and Taylor's $\rho(\tau)$ dependencies of similarities with inserted experimental points from deformation tests and crystal growth (d-cell diameter, G-shear modulus, $\mathbf{b}$-Burgers vector, τ-shear stress, ρ-dislocation density, K-similitude constant ≈ 7.5) [83].

Dislocation clustering (bunching) is a well-known harmful defect mode in as-grown and loaded crystals that has been a long-term subject of investigation. This phenomenon is not only typical in dislocation containing semiconductor crystals, such as mc-Si or III–Vs, but also in metals, alloys, and dielectrics. They are most intensively studied on metals under load with high dislocation densities. Usually, they are related to acting mechanical and thermomechanical stresses. However, they also correlate with polycrystallinity, such as in the presence of large-angle grain boundaries. Further, dislocation clustering can appear even in crystals with low defect density, especially when foreign-phase inclusions are presented (Figure 27.13). Dislocation bundles are also formed during crystallization if concave–convex and morphologically unstable melt-solid interfaces are obtained. Even in the concave part, the minimum energy theorem, shown in Section 27.3.3.1, is responsible for dislocation bundling. In sum, their appearance and origins are versatile and often of stochastic character.

For instance, in mc-silicon ingots for PV crystallized by directional solidification, dislocation clustering is a hotly debated object due to its continuous presence and harmfulness. About 10% of the surface area of commercially available mc-wafers is covered with such clusters of diameters between 0.1 and 1.0 mm containing dislocation densities of 10^6–10^8 cm^2 [84]. They degrade the minority carrier life and, hence, the solar cell efficiency by more than 3–4 percentage points [85]. Once they are formed, they mostly follow the propagating solidification interface through the whole crystal, remembering veins. Due to their ability as getters for highly diffusive metallic impurities, the shorting of p-n junctions is most likely. Therefore, their avoidance in solar cells is of highest priority. It has been demonstrated that in multicrystalline (mc) Si ingots consisting of multigrains of uniform small size, dislocation clusters can be localized in intragrains and often disappear when those grains are overgrown by others. Accordingly, the defect multiplication is easily terminated. Such so-called high-performance mc-Si has high industrial applicability for photovoltaics, mainly because the solar cell efficiency is 17.8%, which is comparable with more defect-inherent large-grain-size material [86].

Dislocation clusters are formed around presented second-phase particles (inclusions, precipitates; see Section 27.5.3). Mostly during the solidification of nonstoichiometric

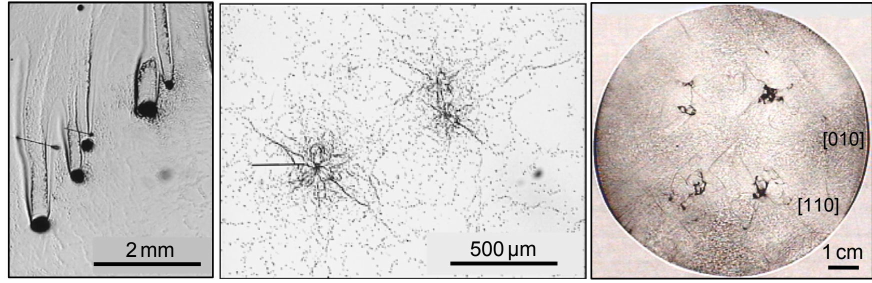

FIGURE 27.13 Dislocation clustering around Ga inclusions in GaAs (left), in directionally solidified mc-Si (middle), and at concave interface regions in an LEC GaAs crystal (right). *Images by U. Juda from IKZ Berlin.*

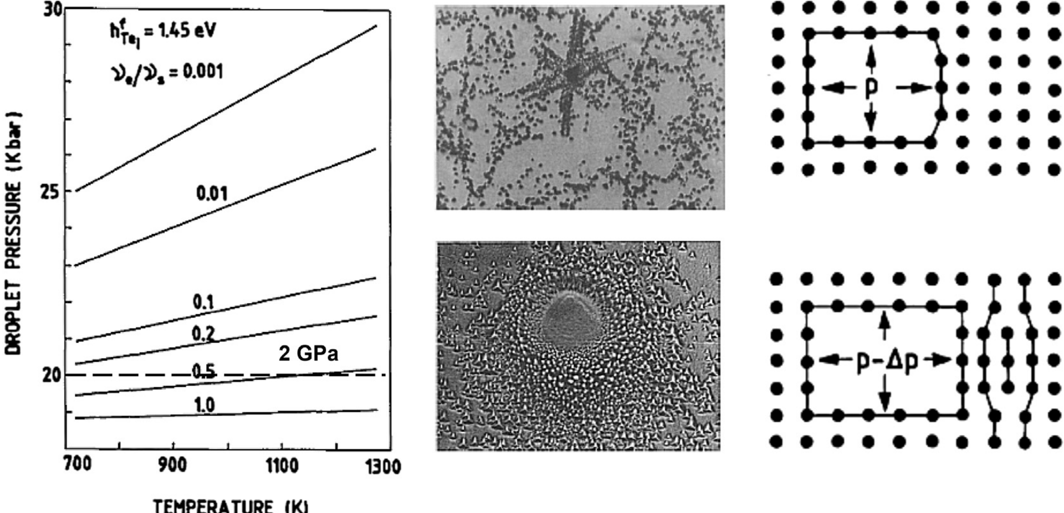

FIGURE 27.14 *Left*: Te droplet pressure p versus T curves in CdTe (h^f_{Te}-Te interstitial formation energy; ν_l/ν_s-liquid to solid vibrational frequency). *Middle*: dislocation bundling around Te precipitates with nearly spherical morphology (below) and with crystallographically regular (triangular) cross-section (above). *Right*: schematic illustration of Greenwood–Foreman–Rimmer mechanism of interstitial dislocation loop punching (above) before and (below) after a loop is punched. *Adapted with permission from Ref. [89].*

compounds, the excess component is incorporated as small liquid inclusions, crystallizing at a much lower temperature than the matrix (Figure 27.14). Different thermal expansion coefficients, volume expansion, and lattice misfits before and after the inclusion are solidified, causing marked stress that generates dislocations at the boundary to the matrix (see e.g., Refs [87,88]), which can be explained by the Greenwood–Foreman–Rimmer mechanism [89] (see Section 27.5.4).

An inhomogeneous dislocation redistribution takes place when unfavorable convex–concave (W-shaped) interfaces are present, mostly in cylindrical crystals growing from the melt. The lowest dislocation density is found at the inflection point with a concave minimum of $d\tau/dx = 0$ [90]. There, a characteristic clustering appears, with assembly symmetry according the Schmid factor. After Shibata et al. [91], effective depression of such dislocation bunching is successful when the ratio between the crystal diameter D and the radius of interface curvature r is >0.5.

Another important clustering effect, observed even in polycrystals with large-angle grain boundaries, is the dislocation pile-up. In fact, the predominant portion of dislocation bunching in mc-Si samples is observed at such boundaries [84]. If a series of dislocations with the same Burgers vector all lying in the same slip plane meet a hard obstacle, such as large-angle grain boundary, the dislocations mostly pile up behind the leading dislocation. Large long-range stress is produced at the head of the pile-up, increasing with the involved dislocation number. It can cause dislocation multiplication by cross-slip of screw dislocations held up at obstacles such as precipitates, thus

forming a dislocation gnarl. For comparison, a near screw aggregation was ascertained at the grain boundary in mechanically loaded titanium [92]. In particular, the pile-up of dislocations at grain boundaries generates a back stress; this tends to suppress further activation of the dislocation source and a stress intensification ahead of the pile-up, thus promoting grain boundary fracture, slip transfer, or twin nucleation into the neighboring grain.

As we can see, the dislocation dynamics within a growing crystal are quite manifold and complex. It is worth noting that the above-mentioned particular events must not be taken out of context. There exists a strong correlation between the dislocation dynamics and other defect types of lower and higher orders.

What about the state-of-the-art of dislocation dynamics and its modeling? Good progress has been made in the field of metal physics, especially metallurgy and cold forming of alloys, as summarized in the book by Kubin [83]. In comparison, the full ascertainment of dislocation dynamics in growing crystals is still uncertain. Consider the explanation of the dynamic processes evoking characteristic dislocation rearrangements in all stressed materials, such as the ones found in as-grown crystals. According to Kubin [83], in either case, the plastic flow is not uniform at a fine scale, such as along a pile-up band as discussed above. The inhomogeneous release of elastic energy gives rise to the emission of acoustic waves (avalanches) interplaying with stored sessile dislocations and micro-obstacles (precipitates, vacancy condensations). In the course of cooling down, sporadic clouded dislocation patterns are frozen up (Figure 27.15), recalling the well-known cluster structures in mc-silicon, for example (Figure 27.11). Thus, it will be hard for the crystal grower to maintain perfect homogeneously distributed stored dislocations.

27.3.6 Dislocation Engineering

Dislocation engineering deals with practical measures of control of dislocation density and patterns or even their in situ prevention during the crystal growth process.

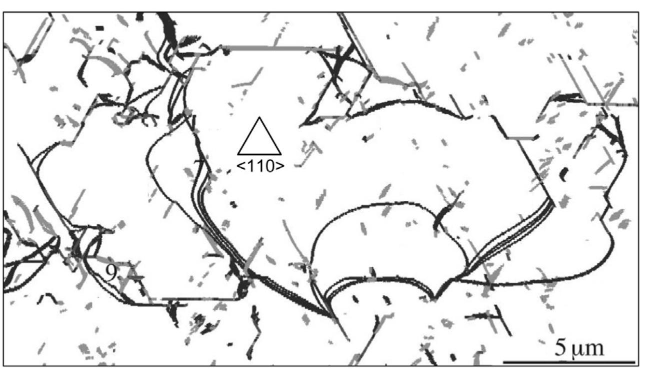

FIGURE 27.15 Modeled avalanches on the [011](111) slip system of a stressed [001] thin copper layer, sporadically pinned at obstacles. The contour of the expanding avalanche is shown in black. The light gray lines are forest dislocations and junctions formed between primary and forest dislocations. *From Devincre et al. [162].*

Generally, for dislocation-reduced growth of compound and mixed crystals with large diameters, the proper combination of the following conditions are required [19]:

1. Use of a *dislocation-free seed* crystal, preventing a thermal shock when it contacts the melt in order to avoid grown-in dislocations, which are the most serious sources for dislocation multiplication
2. Achievement of a strongly *uniaxial heat flow* with very small temperature gradients—that is, nearly flat isotherms at all stages of the growth process
3. If possible, *omission of fluid encapsulants* (boric oxide), the presence of which introduces markedly thermomechanical stresses at the crystal periphery and, possibly, its replacement by a detached growth mode [93],
4. In situ *stoichiometry control* by partial vapor pressure regulation over the melt in order to reduce the intrinsic point defect content, which promotes high-temperature dislocation multiplication by climb and also cell structure formation
5. Prevention of *constitutional supercooling* at the interface by proper selection of a noncritical G_T/v ratio
6. Minimization of atmospheric *pressure fluctuations* around the growing crystal to minimize heterogeneous dislocation rearrangements

The highest temperature nonlinearities and, hence, related thermal stress values (which increase very sensitively with diameter) appear in liquid-encapsulated Czochralski (LEC) crystals [47]. The situation can be improved by using the VCz method, which has been successfully tested not only for growth of semiconductor compounds [40] but also oxide materials [42].

However, the lowest dislocation density in compound materials is obtained by VGF, which has been investigated on industrial scales since the mid-1990s as the most promising growth variant for important semiconductors (InP, GaAs, CdTe), fluorides (CaF_2), and oxides (sapphire, BGO, PMNT, PZNT), as well as quasi-mono PV silicon (see Volume IIA, Chapters 9 and 10). The decisive technological measure is the maintenance of uniaxial heat flow through the growing crystal during the whole growth run by proper control of the cooling rate between a top and bottom heater flanked by a booster heater to avoid radial heat outflow [94]. Using solution hardening by doping, even the lowest dislocation densities (<10 cm^{-2}) can be achieved [95].

Another phenomenon to be controlled in situ is dislocation cell patterning. Independently of the materials used, the cell formation can be reduced very effectively by doping. No cell structuring was observed in GaAs crystals doped with In or Si at concentrations greater than 10^{18} cm^{-3} [19]. Such an effect is due to the impurity gettering at the dislocation core. In consequence, the yield stress is enhanced by dislocation locking. No low-angle grain structure was found in CdTe and PbTe crystals when solution hardening by mixing components Se ($x > 0.4$) and Sn ($x > 0.15$) was provided, respectively. However, there is the drawback of segregation when dopants are added to the melt and the danger of morphological interface instability by constitutional supercooling. Obviously, the best way to exclude dislocation patterning is the reduction of the

dislocation density by minimization of the thermomechanical stress. In undoped VGF GaAs at ρ values $<5 \times 10^3/\mathrm{cm}^2$, the cell structure began to disappear [41]. Also, the minimization of the native point defect content by in situ control of stoichiometry during growth can depress the dislocation cell patterning. The stoichiometry can be regulated by the partial pressure of the volatile component over the melt, applying an extra heat source within the growth chamber [40], which has been tested by HB growth [96], the hot-wall Czochralski method [97], and VCz [40]. Using a VCz arrangement without a boric oxide encapsulant, the cellular structure could be suppressed in undoped GaAs crystals when the stoichiometry is controlled by growth from a Ga-rich melt composition [14,41]. This result was confirmed by numeric simulations of the cell-structuring phenomenon in face-centered cubic (fcc) metals [98].

The pile-off and dissolute cell structures after annealing is a complicated tool. As was demonstrated by high-temperature real-time X-ray tomography, annealing in a homogeneous temperature field only 100 K below the melting point of GaAs crystals [79] did not change or rearrange the cell pattern. Only heat treatments combined with temperature differences and/or mechanical bending can be used, as described elsewhere (e.g., Ref. [99]).

27.4 Grain Boundaries

A grain boundary is the interface between two near-perfectly-built structural regions in solid materials. Their presence can influence the material properties markedly. Grain boundaries correlate with other defect types, such as dislocations and point defects, collecting them at the boundaries and therefore evoking the unfavorable qualities of inhomogeneities. It is convenient to separate grain boundaries by the misorientation angle between the two grains. *Low-angle grain boundaries* are those with a misorientation that is less than approximately 11° [99]. Generally speaking, they are composed of an array of dislocations, and their properties and structure are functions of the misorientation. In particular, the grain boundary energy γ_{GB} depends on the tilt angle between grains θ_{GB}-that is, $\mathrm{d}\gamma_{\mathrm{GB}}/\mathrm{d}\theta_{\mathrm{GB}} > 0$. In contrast, the properties of *large-angle grain boundaries*, whose misorientation is larger than approximately 11° (depending on the material, this angular limit varies from 10° to 15° [99]), are normally found to be independent of the misorientation; mathematically expressed, $\mathrm{d}\gamma_{\mathrm{GB}}/\mathrm{d}\theta_{\mathrm{GB}}$ becomes 0. From these observations, material scientists willingly differentiate between monocrystallinity ($\theta_{\mathrm{GB}} < 10°$) and polycrystallinity ($\theta_{\mathrm{GB}} > 10°$).

27.4.1 Dynamic Polygonization-Low-Angle Grain Boundaries

Low-angle grain boundaries are formed during cooling down of as-grown crystals in course of plastic relaxation tightly coupled with the previously discussed dislocation dynamics. With this in mind, the dislocation cellular structuring proves to be a process of structural matching to the thermal field situation. The larger the thermal inhomogeneities—that is, the thermoelastic stress—the greater is the driving force of

fragmentation of the bended crystal lattice into subregions (cells, domains), with ideal structures differing in orientation from each other by the tilt angle θ_{GB} in the region of some arcsec to arcmin. On the whole, the fragment sizes decrease and their misorientations increase with increasing plastic deformation.

The geometrically necessary dislocations (GNDs) [100] involved in the accommodation are usually concentrated at the boundaries of the crystal fragments. Higher-density GNDs of one sign at the boundaries lead to higher crystallographic misorientation of the corresponding crystal fragments. During crystal bending by thermomechanical stress in the initial stage of plastic relaxation, the mechanism of dynamic polygonization (DP) begins, correlating with dislocation slip mode only (easy-glide stage). During DP, vertical walls of dislocations perpendicular to the dislocation slip plane are formed. Unlike static polygonization (SP), which is the point-defect-assisted formation of misoriented block dislocation structures at elevated temperatures, the DP is observed down to relatively moderate temperatures. Therefore, the DP is also called *slip polygonization* because the formation of walls consisting of dislocations does not involve diffusive dislocation climb, in contrast to the case of SP [101]. As a result, by DP, a dynamic polygon structure arises in the form of a periodic system of tilt walls of dislocations (Figure 27.16). Of course, the dislocation distribution in the form of walls corresponds to a minimum energy of the dislocation array. This can be proven by comparing the dislocation self-energy E_s for initial random distributions, which is equal to the sum of the self-energies of the dislocations and their interaction energy and the total energy of GNDs, E_n, forming a system of $n = L/\lambda_w$ vertical walls (where L is the crystal width and λ_w is the average spacing between walls) [101]:

$$E_s = \frac{Gb^2}{2\pi(1-\mu)}\rho \ln\frac{1}{r_0\rho^{1/2}} \leftrightarrow E_n = \frac{Gb^2}{2\pi(1-\mu)}\rho \ln\frac{h_n}{r_0} \tag{27.13}$$

Using the relationship $\rho = (h_n\lambda_w)^{-1}$, the difference in energy (gain) between single dislocations and GNDs within the wall becomes

$$E_s - E_n = \frac{1}{4}\frac{Gb^2}{\pi(1-\mu)}\rho \ln\frac{\lambda_w}{h_n} > 0 \tag{27.14}$$

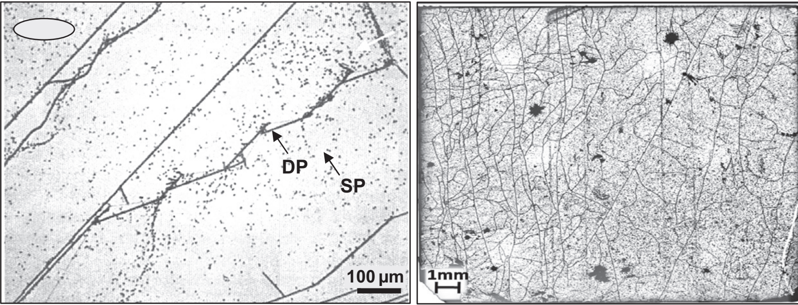

FIGURE 27.16 Dynamically polygonized dislocation walls together with statically polygonized dislocation cells in mc-Si and THM CdTe. *From Refs [163,164], respectively.*

where G is the shear modulus, b is the Burgers vector, μ is the Poisson ratio, ρ is the dislocation density, $\rho^{-1/2}$ is the mean spacing between dislocations of the random distributed configuration, r_0 is the dislocation core radius, and h_n is the distance between dislocation in walls. This result is due to the fact that the dislocation interaction energy decreases with decreasing spacing between dislocations when $\rho^{-1/2} > h_n$. The misorientations of the corresponding crystal fragments increase for the reverse relationship as $\theta_s < \theta_n$, where $\theta_s = b\rho^{1/2}$ and $\theta_n = b/h_n$.

Figure 27.16 shows both typical dislocation walls obtained by DP and dislocation cells formed at a higher T in the course of SP.

In numerous melt-grown compound crystals, such as in as-grown CdTe, PbTe, and CaF_2, for example, the cell arrangement resembles the classic low-angle grain boundary structure, with relatively high tilt angles on the order of arcmin, obviously originated by DP. The grain matrix usually contains some residual dislocations but the walls are formed very abruptly, consisting of only one dislocation row of identical Burgers vector [102]. On the other hand, there are materials with fuzzy cell walls of some thickness consisting of many tangled dislocations, such as Cu and GaAs [78], indicating SP assistance by high point defect diffusivity. They show relatively low tilt angles, around 10–20 arcsec. Additionally, there are crystals consisting of both somewhat elongated one-row dislocation walls and cellular substructures (Figure 27.16).

Finally, low-angle grain boundaries need a certain ripening time, which is not only influenced by the acting stress and cooling rate but also by the material properties, such as dislocation mobility and given content of point defects.

Note that there is also a totally different origin of formation of low-angle grain boundaries, which are not so easy to differentiate from DP in as-grown crystals. In case of morphological instabilities of the propagating melt-solid crystallization fronts caused by constitutional supercooling [103], characteristic cellular-shaped interfaces appear. They produce columnar grain boundary patterns similar to polygonized cell structuring, because the growing-in dislocations are assembled by their line bending toward the concave cusps (i.e., along the column boundaries). This has been very clearly observed by real-time synchrotron X-ray topography on Al-0.73 wt% Cu alloy [104].

27.4.2 Large-Angle Grain Boundaries-Polycrystallinity

As mentioned, large-angle grain boundaries are a characteristic feature of polycrystallinity, with tilt angles between the grains of more than 11°. A markedly disoriented grain ensemble appears when no monocrystalline seed is used to initiate a directional solidification. For instance, in metallurgical casting processes, multicrystalline ingots are intentionally produced by spontaneous nucleation of the solid phase within the melt in order to obtain enhanced mechanical strengths and macroscopic parameter homogeneity. In the field of monocrystal growth, however, it is the cardinal aim to prevent large-angle grain structures that impair the favorable anisotropic, electronic, and optical

qualities. The pioneering works aimed insert a seed into the solution tanks, dip a seed into the melt crucibles, or ensure grain selection by container necking. Many experiments have focused on grain coarsening based on the Gibbs–Thomson effect, whereupon grains of small dimension disappear due to their heightened chemical potential compared to the larger ones. To enhance the coarsening effect, an alternative remelting of the growing interface has been achieved (e.g., Refs [105,106]). In some materials, such as Te or Bi_2Te_3, the grain selection is even intrinsically supported due to the high anisotropy of thermal conductivity, favoring the overgrowth of the grains of highest conductivity along the growth direction. However, there are also materials where the artificial seeding fails. For example, CdTe and ZnSe have stable melt structuring due to their high bond ionicity, which prefers self-orientation around ⟨110⟩⟨111⟩, even when a spontaneously nucleated first-to-freeze region is present [34].

With the increasing importance of directional solidification of the cheapest mc-Si ingots for PV, the control of large-angle grain growth comes to the fore. Grains formed by spontaneous nucleation at the container bottom (Figure 27.17(a)) may markedly degrade solar cell efficiency, especially when a high density of dislocations and impurities are captured. Such structures can be avoided by grain selection via initiating the crystallization in a bottom nozzle [107] or at the bottom corner of the crucible [108], by supporting grain coarsening via interface oscillation [106], as well as by

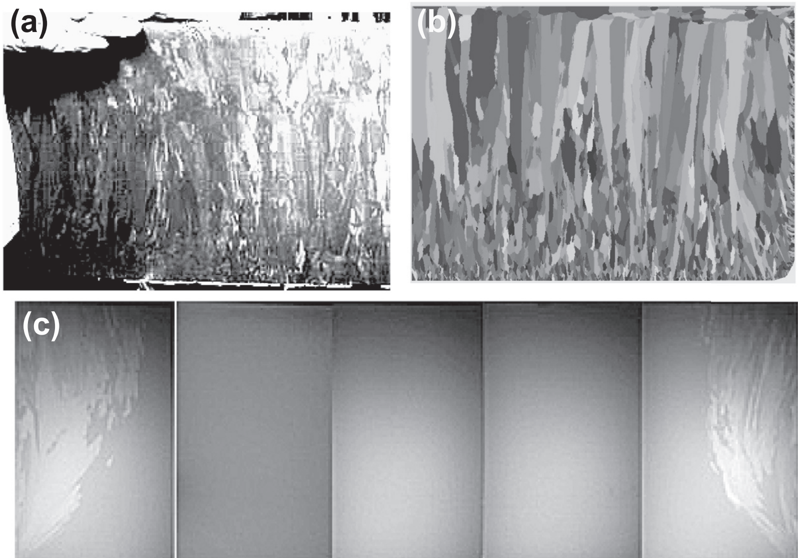

FIGURE 27.17 (a) Characteristic large-angle grain structure in a mc-Si ingot obtained by spontaneous nucleation at the container bottom; (b) simulated grain structure of case *a*; (c) cross-sectional photo from a G5 quasi-mono Si ingot directionally solidified from parquet-arranged dislocation-free Czochralski seed plates on the container bottom. As can be seen from *c*, in the course of solidification from bottom to top the polycrystalline growth is still induced at the container walls and spreading toward the volume. *Figures (a) and (b) are taken from Ref. [165] with permission; (c) is taken from Ref. [144] with Elsevier's permission.*

quasi-monocrystalline growth beginning on inserted seed plates [109]. In a study of the growth conditions for predominant grain orientations, Fujiwara [110] found that ⟨111⟩-oriented grains prevail for low-interface undercooling (low growth rate), whereas ⟨100⟩- and ⟨110⟩-oriented grains dominate at high undercooling (high growth rate).

Large-angle grain boundaries can also appear when the heat balance between melt and solid phases is disturbed, such as when the mechanically or electronically enforced moving rate of the isotherm exceeds the maximum thermal equilibrated growth velocity [111]. Also, prenucleations within the constitutionally supercooled diffusion boundary layer along the propagating interface may be responsible for disoriented growth. To avoid this, the criterion of Tiller [103] has to be obeyed.

27.5 Foreign Phase Particles

The presence of microparticles of foreign phase (second phase) or microvoids (bubbles) within the matrix of single crystals has been the object of research due to its harmful character. Such features are observed in nearly all crystalline materials. Microparticles affect the optical transmission, electrical carrier life, and structural perfection. They are sites of misfit stress and therefore of dislocation bunching; they are also sources of out-diffusing of embedded impurities. Characteristic microvoids in silicon crystals appearing at economically favorable high growth rates affect the wafer quality for epitaxial processes onto them.

There are two main origins of microparticle/microvoid generation:

1. Native *point defect condensation,* which during cooling leads to the nucleation of precipitates and microvoids via interstitial and vacancy agglomeration, respectively
2. *Incorporation* in favorable sites along the propagating crystallization front

Usually, both kinds of foreign phases differ in size. Whereas precipitates show characteristic dimensions in the range of 10–1000 nm, inclusions are typically of diameters >1 μm [34]. This classification, however, is only approximate and cannot serve as an exact criterion of distinction. The size of both kinds of microparticles or voids depends on various parameters, such as the concentration ratio of the components, degree of supersaturation, interface instabilities, and growth and cooling rates, which markedly influence the ripening time and extent. Nevertheless, the two features are treated separately in the following sections because of their usually differing backgrounds.

27.5.1 Precipitates (Retrograde Solidus, Defect Decoration)

One of the most serious consequences of compound crystal growth under conditions of native point defect formation is their condensation in precipitates and microvoids. This phenomenon is due to the retrograde behavior of the boundary of the compound

existence region (solidus) and therefore is related to nonstoichiometry. As the as-grown crystal is cooling down, the solidus is crossed and nucleation of the second phase takes place. Favored sites of precipitate ripening are dislocations, as has been concluded from infrared laser scattering tomography in GaAs crystals grown under As-rich conditions (e.g., Ref. [112]). Average tellurium precipitate densities of about 10^{8} cm^{-3} and up to 10^{12} cm^{-3} have been found in CdTe [34]. Typical sizes between 10 and 100 nm have been determined for As precipitates in GaAs [113] and Te precipitates in CdTe [114]. Half-empty precipitates have been found by transmission electron microscopy in GaAs [115] and CdTe [116], probably caused by vacancy condensation in one of the sublattice components accompanied by conglomeration of excess atoms of the opposite sublattice.

Precipitates of both components are observed in most compound crystals, such as Te and Cd in CdTe and (Cd,Zn)Te (e.g., Ref. [117]), depending on the composition of the melt from which the crystal was grown (Te- or Cd-rich, respectively); in melt-grown GaAs crystals, only As precipitates were observed [112]. This is due to the different widths and positions of the compound homogeneity region against the stoichiometry. In CdTe, like in most compounds, they extend to both sides of stoichiometry [118]. On the contrary, in GaAs the phase extent region is completely located on the As-rich side [13], being comparable with the phase diagram of SnTe [12]. Thus, in order to reduce the precipitate content and size, the stoichiometry control during growth is of cardinal importance [34,35].

Many authors propose postgrowth wafer annealing as the most effective controlling step for producing stoichiometric and, hence, precipitate-free materials (e.g., Ref. [38]). Today, it is the industrial standard of GaAs crystal production to anneal the whole as-grown boule a few degrees below the melting point to obtain the dissolution of precipitates and their rediffusion from dislocation cell walls into the interiors during this first step. Then, a second step of a cooling shock of approximately 100 K downstops their ripening and back diffusion toward dislocations, thus keeping their size at an electronically compatible dimension of $<$100 nm [119].

27.5.2 Solvent Inclusions

Solvent inclusions are very common in crystals grown by all variants of solution growth (aqueous and organic solvents, flux). Two main origins are distinguished: faceting ("capping") of rounded surfaces and fluctuation of growth conditions (growth accidents).

27.5.2.1 Faceting ("Capping") of Rounded Surfaces

In general crystals grow from solutions with planar faces (habit faces), whereby faces with low surface energies grow slowly and determine the final morphology of the crystal (Wulff's theorem [120]). If surfaces are rounded (e.g., of the seed crystal or after redissolution), during first growth facets of habit faces and (between them) terraces of these faces are formed. The facets become larger and the terraced regions grow out until

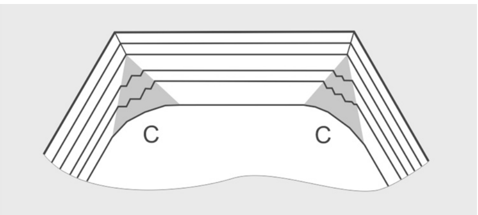

FIGURE 27.18 Faceting and "capping" on rounded crystal surfaces. The shaded regions C of terraced growth favor the entrapment of liquid inclusions. They grow out and finally form the growth-sector boundary between the main habit faces. *With permission from Springer Science + Business Media [45].*

a single edge between the two habit faces engaged is formed (see also "growth on spheres" [121], p. 130), as is shown in Figure 27.18. The "healed-out" regions often have the shape of caps (capping region). The growth on terraced surfaces favors the entrapment of solvent inclusions, which may lead in extreme cases to a spongy structure of the capping region. This usually happens during first growth on seed crystals, which are usually rounded due to final etching (which is necessary in order to remove surface impurities and defects) before seeding-in. Therefore, the zone of first growth around seed crystals is usually more or less disturbed by liquid inclusions. These inclusions, however, can be largely avoided by a very slow (and thus time-consuming) growth under low supersaturation during the seed-faceting period.

A conspicuous example of capping is provided by KDP grown in aqueous solution on (001) seed plates (Figure 27.19). KDP develops habit faces {100} (tetragonal prism) and {101} (tetragonal dipyramid), but {001} is not a habit face. Thus, in the first stage of growth on (001) seed plates, a spongy capping zone in the form of a tetragonal pyramid {101} over the (001) seed plate as basis is formed, followed by clear further growth on {101} pyramid faces (Figure 27.19). Detailed descriptions of this (001) capping process in

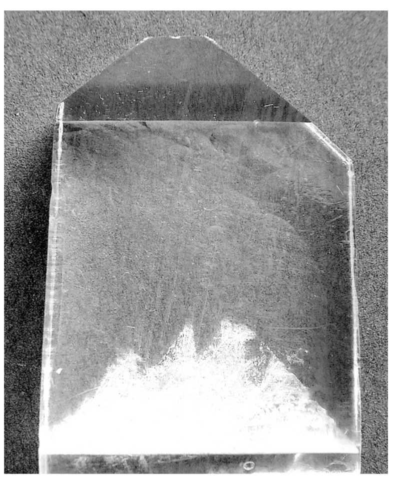

FIGURE 27.19 A potassium dihydrogen phosphate crystal (length 45 mm) with {011} capping pyramid on a (001) seed plate. *With permission from Springer Science + Business Media [45].*

KDP and ammonium dihydrogen phosphate crystal growth are presented by Zerfoss and Slawson [122] and Janssen-Van Rosmalen et al. [123].

27.5.2.2 Fluctuation of Growth Conditions (Growth Accidents)

A sufficiently strong change of growth conditions (e.g., of supersaturation, stirring rate, stirring direction) may introduce—due to local variations of supersaturation—a (temporary) instability of growth faces. Regions of retarded and promoted growth occur, leading to elevations and depressions on the growth face. Finally, overhanging layers spread over the depressions and close them, thus trapping nutrient solution. Usually, a group of inclusions arranged in a plane parallel to the growth face is formed ("zonal inclusions", Figure 27.4). If all growth faces of the crystal are affected by the same growth disturbance, inclusions are formed on all faces. After stabilization of growth conditions and further clear growth, the inclusions are visible by scattered light (if the crystal is transparent) and reveal the shape of the crystal in the instant of the disturbance ("phantom crystal" in mineralogy).

The tendency to form solvent inclusions may strongly depend on the type of growth face {hkl}. In general, the formation of solvent inclusions is favored on faces with high surface (attachment) energy and therefore high growth rate. An instructive example is provided by potassium alum growing from aqueous solution: fluctuations of growth conditions pronouncedly lead to liquid-inclusion entrapment on the smaller and fast-growing cube faces {100}, whereas the slow and morphologically dominant octahedron faces {111} resist the formation of inclusions, even for strong changes of growth parameters. The reason for the preferred inclusion trapping of certain growth faces is their specific surface structure, which favors the incorporation of solvent (and other) molecules. This phenomenon corresponds to the so-called hourglass inclusions, which have been studied in detail for potassium sulfate (e.g., Ref. [121], p. 415–420; Vetter et al. [124]; and Kahr et al. [125,126]).

The hydrodynamics of the solution flow around the growing crystal may also play a significant role in the formation of liquid inclusions (e.g., Chernov et al. [127]). A particularly interesting example of this influence in the growth of KDP crystals was reported by Janssen-Van Rosmalen and Bennema [128], Janssen-Van Rosmalen et al. [123], and van Enckevort et al. [129]. In their experiments, the growing KDP crystals (shape: tetragonal prism {100} terminated on both side by dipyramid {011}) were rotated on a lever in the solution in such a way that the solution flow was toward one (front) pyramid and off the other (rear) pyramid. On the pyramid faces of the rear side, solvent inclusions are often formed in a quasi-periodic sequence (Figure 27.5), whereas at the front side inclusions do not appear. This phenomenon is explained by the hydrodynamic situation at the rear-side pyramid face: in the wake "behind" the crystal, a swirling region with no or strongly reduced liquid exchange with the bulk mother solution is formed. Thus, the saturation locally decreases and growth is retarded compared to neighboring regions, leading to a depression in the growth face. After some amount of further growth, the flow situation changes and supersaturation is restored. This causes an overgrowth of the cavity, forming

a solvent inclusion. As is shown in Figure 27.5, this process is repeated several times in a quasi-periodic manner. A detailed study of this effect, including flow simulation experiments in a model system, was presented by Janssen-Van Rosmalen et al. [128] and van Enckevort et al. [129], who also reported that the formation of these inclusions is avoided by stronger stirring. In any case, strong stirring smoothes out supersaturation differences on the growth face and thus may largely avoid interface instabilities.

27.5.3 Melt Growth Inclusions

Second-phase inclusions may appear when a segregation-driven diffusion boundary layer is formed in front of the growing interface. If the enriched impurity concentration exceeds the solubility limit, microparticles are nucleated and very likely incorporated. Chernov [18] estimated undercritical growth rates at which such particles and gas bubbles should be rejected by the propagating solid front. However, he assumed an ideal flat interface. In reality, when both the diffusion boundary layer and low-temperature gradient are simultaneously present, the front region is constitutionally undercooled and the interface shape becomes morphologically instable. As a result, microgrooves are formed, transforming into cellular or facetted structures with favorable sites of particle capturing [19]. Note that trapping interfacial nooks can also form by coinciding grain boundaries, typically for mc-Si growth [130,131]. Hence, during silicon crystallization, SiC and Si_3N_4 precipitates are nucleated when the solubility limit of carbon (5×10^{18} cm^{-3}) and nitrogen ($\sim 1 \times 10^{19}$ cm^{-3}) is exceeded. It is always preferable to counteract against the diffusion boundary layer by complete melt mixing, such as by using a nonsteady magnetic field, inert gas sparkling, or mechanical vibration [132].

27.5.4 Structural Consequences of Second-Phase Particles

During the cooling-down process, both precipitates and inclusions induce mechanical stress due to their differing crystallographic structure and thermal expansion compared to the matrix configuration. Moreover, the particle components can exhibit a lower melt temperature than the matrix and remain in the molten (or vapor) state down to the eutectic point. In case of volume increase during their solidification, additional stress is generated. These effects were treated in various publications. A representative example is reported in the theoretical paper by Yadava et al. [89], which deals with Te precipitation in CdTe crystals.

Consider the temperature region where the incorporated second-phase particle is still a droplet. The net pressure at the interface with the solid matrix is

$$p' = p - \frac{2\gamma_{IF}}{r_d} \tag{27.15}$$

where p is the internal droplet pressure, γ_{IF} is the surface tension of the liquid Te–solid CdTe interface, and r_d is the droplet radius. In general, $p' \neq 0$; therefore, the interface will be mechanically unstable. To attain mechanical equilibrium, the isotropic droplet

volume will decrease by the amount of $\Delta V_{\mathrm{rel}} = 3/4\, p'(V/G)$, where V is the unstressed droplet volume and G is the shear modulus. This process will generate strain in the surrounding matrix and in the interface.

Using a thermodynamic approach, the included droplet pressure is given by [89]

$$p = kT\rho_l x + 2Z\varepsilon\rho_l\left[\left(1 - \frac{kT}{2Z\varepsilon}\right)x^5 - x^3\right] \tag{27.16}$$

where k is the Boltzmann constant, ρ_l is the liquid density of Te at given T (temperature), $x = \rho/\rho_l$ is the liquid density normalized with respect to the density at 1 atm (for droplets to be in compression, $x > 1$), Z is the average coordination number in liquid Te ≈ 3.1, ε is the pair association energy (≈ 1.2 eV), and k is the Boltzmann constant. The calculated dependence of the Te droplet pressure on the temperature for various interstitial concentrations is shown in Figure 27.14. Taking the precipitated Te interstitial number per droplet as a quantity of size, it follows from the figure that the pressure increases with particle volume.

The Greenwood–Foreman–Rimmer mechanism of interstitial dislocation loop punching is one of the possible processes that can effectively reduce the overall free energy. The mechanism is schematically illustrated in Figure 27.14 (right). The excess internal pressure p' (Eqn (27.16)), acting outwardly on the droplet/matrix interface, produces shear strain in the neighboring solid region; above a threshold level, this punches a part of an atomic layer and places it as a platelet of the interstitials sandwiched between two adjacent regular atomic planes. Of course, the punching occurs on the energetically-most-favorable atomic planes. In the process, the droplet volume increases and, thus, the pressure decreases. Theoretically, it is shown that the loop punching will occur if [89]

$$p' = p - \frac{2\gamma_{IF}}{r_d} \geq \frac{G_m b}{2\pi r_d}\ln\left(\frac{r_d}{b}\right) \tag{27.17}$$

where b is the Burgers vector of the dislocation loop and G_m is the shear modulus of the matrix. All another parameters are specified in Eqns (27.15) and (27.16).

27.6 Faceting and Twinning

27.6.1 Faceting during Growth

In general, crystals grow from solutions, supercooled melts, and vapor phases with planar faces (habit faces), whereby faces with low surface energies grow slowly and determine the final morphology of the crystal (Wulff theorem [120]). A crystal that has fully grown on the habit faces consists of growth sectors—that is, regions grown on different habit faces and separated by growth-sector boundaries (Figure 27.20). These boundaries are formed by the path of the edges between neighboring habit faces during growth. Due to their different growth directions and often also different crystallographic (i.e., symmetrically nonequivalent) nature, growth sectors usually exhibit slightly different, growth-induced

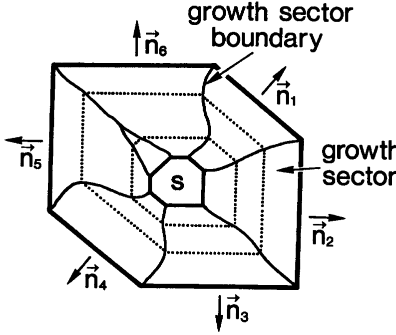

FIGURE 27.20 Fully faceted crystal, divided into growth sectors (i.e., regions grown on different habit faces). They are separated by growth-sector boundaries, which are internal surfaces generated by the movement of the edges joining neighbored faces during growth. The vectors $\mathbf{n}_i$ indicate the growth directions. Dashed lines: contours of the crystal at different stages of growth. One of the growth sectors has "grown-out." *With permission from Springer Science + Business Media [45].*

physical properties, such as different optical birefringence ("optical anomaly" [133]). Due to this phenomenon, growth sectors are sometimes misinterpreted as twins.

Similar features can be observed at crystal growth from melts, especially in materials with atomically smooth (i.e., singular) planes. Most dielectrics show such planes parallel to lattice planes of small Miller's indices. The common semiconductor materials, with their covalent bonding, tend also to form facets during melt growth, although only on their most closely packed (i.e., {111}) planes [1].

27.6.2 Growth Twins and Postgrowth Twins

A twin is a frequently occurring aggregate or intergrowth of two or more crystals of the same species (same chemical composition and crystal structure) with a defined crystallographic orientation relationship (determining the orientation states of the twin components), which in mineralogy is called the "twin law". Besides the twin law, the boundary between twin domains (the contact relation) plays a decisive role: twins occur in those crystals in which boundaries of low energy can be formed. This has quantitatively been proven by Gottschalk et al. [134], who showed that the ease and frequency of the formation of (111) spinel twins (Figure 27.24) in the zinc blende structure of III–V semiconductor compounds is correlated to the (111) stacking fault (twin-boundary) energy: the lower the stacking fault energy, the more frequent the twinning. There is, however, also a theory stating that the boundary energy is of minor importance and that kinetic influences play a decisive role in the formation of twins [135]. This approach, however, has been critically discussed [136,137].

Twins are mainly classified by morphological features (dove-tail, contact, penetration, sector, polysynthetic twins, etc.), their genetic origin (growth, transformation, mechanical or deformation twins), and their lattice coincidence features, such as

merohedral twins (full or partial three-dimensional lattice coincidence, also called CSL lattice in the treatment of grain boundaries). Reviews on twinning are presented in many textbooks of mineralogy and crystallography (e.g., Refs [138,139]). A comprehensive treatment has been provided by Hahn and Klapper [140] (see here especially for growth twinning, p. 412–14). A survey of X-ray topographic characterization of twinned crystals was given by Klapper [141].

In the growth of technologically significant crystals, the spinel twins of cubic crystals with twin law "reflection plane" (111) or "twofold axis" [111] require particular attention. They occur as growth twins in crystals with diamond structures (Si, Ge), zinc blende structures (e.g., ZnS, GaAs, InP, CdTe [134,142]), and sodium chloride structures (photographic materials AgCl and AgBr [143]). They are characterized by a partial lattice coincidence of one-third of the lattice points (so-called Σ3 twins), which form a hexagonal sublattice, with its principal axis along the threefold axis [111] common to both twin components. Preferred twin boundaries are planes {111} and {112}. The typical shapes of spinel twins grown from solutions are shown in Figure 27.21. For semiconductor crystals grown from melts, see, for example, Refs [1,145,146].

In many cases, twins are formed during the first stage of spontaneous nucleation, possibly before the subcritical nucleus reaches the critical size necessary for stable growth. This formation is strongly evidenced for penetration and sector twins, where all domains are of similar size and originate from one common, well-defined point in the center of the twinned crystal, which marks the location of the spontaneous nucleus

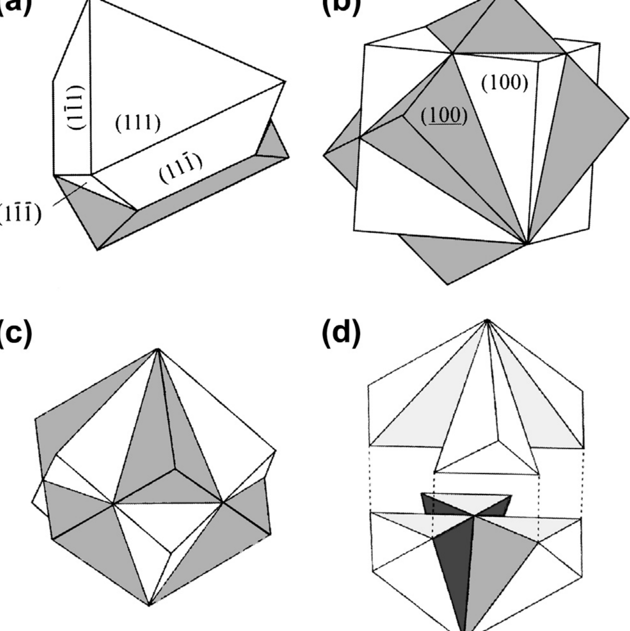

FIGURE 27.21 Spinel twins of cubic crystals with twin reflection plane (111) or twofold twin axis [111] (or alternatively ±60° rotation around [111]). The domains of the two orientation states are white and shaded. (a) Contact twin with (111) contact plane (two twin components). (b, c) Penetration twin (idealized) with one [111] and three $\{11\bar{2}\}$ contact planes (12 twin components, six of each orientation state) in two different views: (b) with one [001] axis vertical, (c) with the axis [111] common to both domains (twin axis) vertical. (d) Skeleton of the six components (exploded along [111]) of the shaded orientation state of (c). *With permission from Springer Science + Business Media [45].*

(Figure 27.22). Other prominent examples are the penetration twins in rhombohedral crystals such as corundum (aluminum oxide, Al_2O_3 [147]) or iron borate ($FeBO_3$, calcite structure [141]), and sector twins of pseudo-hexagonal crystals such as ammonium lithium sulfate (Figure 27.22), potassium sulfate [140], and aragonite $CaCO_3$, which form twins with three orientation states. The origin of twinning by nucleation must also be assumed for contact twins (Figure 27.21(a)) if both partners of the final twin have roughly the same size, or if all spontaneously nucleated crystals in one batch are twinned. For example, all crystals of monoclinic lithium hydrogen succinate precipitated from aqueous solution are without exception dove-tail contact twins.

An approach to the twin formation during crystal nucleation has been advanced by Senechal [148], who proposed that the crystal nucleus first formed has a symmetry that is not compatible with the lattice of the (macroscopic) crystal. This symmetry may even be noncrystallographic. It is assumed that, after the nucleus has reached a critical size beyond which the translation symmetry becomes decisive, the nucleus collapses into a twinned crystal with domains of lower symmetry and continues to grow as a twin. This idea of twin formation from noncrystallographic nuclei has been experimentally substantiated by high-resolution transmission electron microscopy investigations of nanocrystalline diamond-type and fcc cubic crystals, such as Ge, Ag, and Ni [149].

According to Hurle [145], also in zincblende crystals, the twinning starts at two-dimensional nucleation on the {111} facets during CZ and VGF growth when such

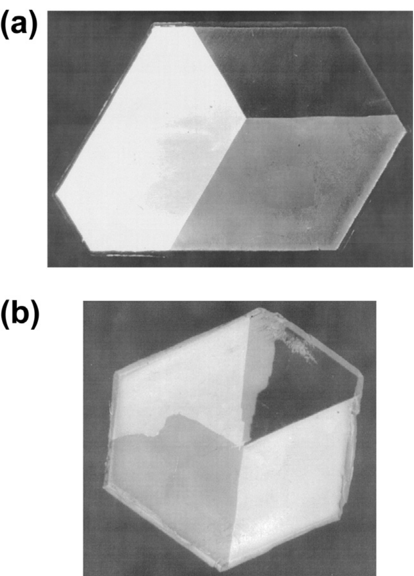

FIGURE 27.22 Photographs of (001) plates (approximately 20-mm diameter, 1-mm thick) of orthorhombic pseudo-hexagonal NH_4LiSO_4 between crossed polarizers, showing sector growth twins. (a) Nearly regular threefold sector growth twin (three orientation states, three twin components). (b) Irregular sector twin (three orientation states, but five twin components). *With permission from the internat. Union of Crystallography (IUCr) [140, p. 413].*

planes are adjacent to the three-phase boundary of melt, crystal, and ambient. This model demonstrates that, because of the orientation dependence of interfacial energies in the presence of facets, there is a configuration of the three-phase boundary for which, for sufficiently large supercooling, the free energy of formation of a critical nucleus is actually lowered by forming that nucleus at the three-phase boundary in twinned orientation (i.e., specified by a rotation of the lattice by 60° about a $\langle 111 \rangle$ axis). Such a twinned nucleus is thermodynamically favored if the supercooling exceeds a critical value. Rudolph [34] postulated that even a residual melt association in the form of tetrahedra can promote a false stacked nucleation. This fluid configuration appears demonstrably, especially in melts of high ionicity such as II–VIs (CdTe, ZnSe) [150,151] but also in InP, which shows the highest ionicity (>40%) and lowest stacking fault energy of III–Vs.

As for dislocations (see Section 27.3.2), inclusions are also frequently sources of twins. It is assumed that a nucleus in twinned orientation forms at the inclusion and proceeds in this orientation during further growth. An instructive experimental key study of this process was presented by Sunagawa et al. [152] for Dauphiné and Brazil twins in synthetic quartz. Amethyst quartz contains much more Dauphiné and Brazil twins than normal (colorless) quartz. The higher frequency of twin formation is doubtlessly due to its relatively high content of iron [153]. Sunagawa et al. [152], and references therein, grew amethyst quartz hydrothermally in various solutions containing ferric iron on amethyst seed plates of various orientations. They studied the twinning generated on as-grown faces, on etched growth faces, and on cut surfaces by light-microscopic methods. In all cases, the Dauphiné and Brazil twins originated from solid inclusions containing iron (probably as Goethite, FeOOH). In some cases, the Brazil twins are associated with dislocations originating from the same inclusion.

There are two causes for the formation of postgrown twins during cooling to room temperature after growth: *phase transitions* and ferroelastic switching [154].

Crystals often can only be grown at elevated temperatures where they crystallize in another (high-temperature) phase, of usually higher symmetry than what they adopt at room temperature. On cooling below the transition temperature, the twin domains are formed, whereby the lost symmetry elements of the mother phase act as twin elements (twin laws) relating the twin domains. For instance, lithium niobate $LiNbO_3$ is grown from the melt at $T_m = 1275\,°C$ and undergoes a paraelectric–ferroelectric transition at $T_c \approx 1140\,°C$, whereby ferroelectric domains are formed. The high-temperature superconductor $YBa_2Cu_3O_{7-\delta}$, usually grown from flux, is subject to a transition at approximately 750 °C from the tetragonal parent phase into an orthorhombic modification, whereby it develops two nearly orthogonal systems of twin lamellae parallel to the two $\{110\}$ mirror planes of the tetragonal mother phase, lost in the transition [155]. These lamellae are ferroelastic and can be changed or even removed (detwinned) by mechanical stress. A similar case was reported by Rudolph et al. [156]: ZnSe crystals underwent a phase transition from wurtzite to zinc blende structure at $\sim$100 K below the melting point $T_m = 1520\,°C$. Thus, during the cooling down of melt-grown crystals,

numerous twin lamellae were formed. An example related to mineralogy is provided by quartz, which is stable in its trigonal phase below 575 °C (α-quartz, point group 32) and hexagonal (β-quartz, point group 622) above this temperature. The transition from the hexagonal to the trigonal modification invariably leads to the formation of Dauphiné twinning (loss of the twofold axis in the sixfold axis). The shape and arrangement of twin domains generated by crystal growth or by phase transformation (e.g., for Dauphiné twins) is quite different. In mineralogy, these different features of twin textures are very helpful for the determination of the conditions of mineral formation. Brazil twins of quartz and his homeotypes (e.g., gallium phosphate $GaPO_4$) cannot be generated by the phase transition; they are always growth twins.

The twin domains of ferroelastic crystals switch by mechanical stress from one orientation state into the other. This occurs quite easily at elevated temperatures where the coercive stress is strongly reduced. Thus, in a ferroelastic crystal grown without twinning, twin domains may be introduced by stress developed during cooling to room temperature. Here again, inclusions forming stress centers are the main reason. The ferroelastic twin pattern is often correlated to the growth defects of the crystal, such as with growth striations ([157], Figure 100; [141], p. 379). Postgrowth formation of twins by *ferroelastic switching* has been observed, for example, in ammonium sulfate $(NH_4)_2SO_4$ [158] and Rochelle salt ([157], p.184), which are both grown from aqueous solution.

27.6.4 Measures to Avoid Twinning

In most cases, twinning of technologically important crystals seriously impairs their usability for technical devices. This is largely avoided by optimizing the growth conditions. For solution growth, the most important measure is to use twin-free seed crystals and avoid inclusions.

A more serious and recurrent problem is given by facet-induced twins of melt-grown crystals. Many LEC and Bridgman experiments have demonstrated that the twin probability is reduced markedly if the temperature oscillations of the growth system, and therefore undercoolings with related excursions of the angle of the contacting meniscus, are minimized. This is due to the reduced probability of encountering the critical angle when the meniscus angle fluctuations are reduced [1,145]. In fact, Hosokawa et al. [159] succeeded in twin-free InP crystal growth with diameters up to 100 mm by careful maintenance of thermal stability during growth assisted by convection damping of the magnetic field around the melt.

Neubert et al. [146] accentuated the importance of growth rate stability during LEC and VGF. They proposed highly sophisticated and robust model-based feedback control to avoid crystallization velocity fluctuations and, thus, reduce twin frequency in compound semiconductor growth [160]. Rudolph et al. [156,161] obtained a minimized twin density in CdTe and ZnSe melt-grown Bridgman crystals when the fluid phase was markedly overheated before the crystallization started. They attributed this effect to the reduced

degree of melt association, preventing the probability of false stacking sequences when associated species, such as tetrahedra are still present and being incorporated.

27.7 Concluding Remarks

The most important defect types and possible origins during crystal growth from melt and solution have been discussed in this chapter. Today, most of the defect-forming mechanisms are well understood. However, some important questions remain to be solved. For instance, the influence of the melt configuration on the growth kinetics, which probably plays an essential role in II–VI systems, it is not yet fully understood. Furthermore, the dislocation patterning and bunching mechanisms related to the growth conditions have not yet been decoded completely. Also, the main twinning origin has not yet been revealed.

Eminent success has been achieved in technological developments. Computer-controlled VGF has become the leading industrial production method for semiconductor compound crystals. However, that is not to say that all defects can be avoided. For example, the relatively poor thermal conductivity and low yield stress of III–V and II–VI compounds as compared with Ge and Si mean that it is not possible to reduce thermal stress to a sufficiently low level to avoid dislocations.

Scaling up to achieve cost reduction is an ever-present pressure. Increasing crystal diameter also increases the thermal stresses experienced during cooling. Avoiding increased dislocation density requires ever-increasing refinement of furnace design; here, computer modeling plays a key role.

An additional problem posed by scaling-up is the increased turbulence that occurs in the melt. The use of magnetic fields or another external force is being exploited to achieve damping of this turbulence [132]. In many chapters of this book, the correlation between growth parameters and all previously discussed defect types, as well as measures of prevention, are discussed.

References

[1] Hurle DTJ, Rudolph P. J Cryst Growth 2003;264:550.

[2] van Bueren HG. Imperfections in crystals. Amsterdam: North-Holland Publ.; 1960.

[3] Pick H. Naturwissenschaft 1954;41:346. in German.

[4] Kröger FA. The chemistry of imperfect crystals. Amsterdam: North-Holland Publ.; 1964 and 1973.

[5] Mattsson AE, Wixom RR, Armiento R. Phys Rev B 2008;77:155211.

[6] Voronkov VV. J Cryst Growth 2008;310:1307.

[7] von Ammon W. In: Müller G, Metois JJ, Rudolph P, editors. Crystal growth – from fundamentals to technology. Amsterdam: Elsevier; 2004. p. 239.

[8] Itsumi M. J Cryst Growth 2002;237–239:1773.

[9] Hurle DTJ. In: Müller G, Metois JJ, Rudolph P, editors. Crystal growth – from fundamentals to technology. Amsterdam: Elsevier; 2004. p. 323.

[10] Rudolph P. Cryst Res Technol 2003;38:542.

[11] Erdei S, Ainger FW. J Cryst Growth 1997;174:293.

[12] Rogacheva EI. Inorg Mater 1991;27:194.

[13] Dreyer W, Duderstadt F. On the modelling of semi-insulating GaAs including surface tension and bulk stresses, Treatise No. 995. Berlin: Weierstraß-Institut; 2004.

[14] Rudolph P, Kiessling F-M. J Cryst Growth 2006;292:532.

[15] Rosenberger F. Fundamentals of crystal growth I. Berlin: Springer; 1979.

[16] Berding MA. Phys Rev 1999;60:8943.

[17] Jackson KA. Kinetic processes. Weinheim: Wiley-VCH; 2004.

[18] Chernov AA. Modern crystallography III. Berlin: Springer; 1984.

[19] Rudolph P. In: Dhanaraj G, Byrappa K, Prasad V, Dudley M, editors. Handbook of crystal growth. Berlin-Heidelberg: Springer; 2010. p. 153.

[20] Motooka T, Nishihira K, Oshima R, Nishizawa H, Hori F. Phys Rev B 2002;65:813041.

[21] Rudolph P. In: Fornari R, Paorici C, editors. Theoretical and technological aspects of crystal growth. Switzerland: Trans Tech Publications; 1998. p. 1.

[22] Burton JA, Prim RC, Slichter WP. J Chem Phys 1987;21:1991.

[23] Müller G, Ostrogorsky A. Convection in melt growth. In: Hurle DTJ, editor. Bulk crystal growth – growth mechanisms and dynamics, vol. 2b. Amsterdam: Elsevier; 1994. p. 709.

[24] Dornberger E. [thesis]. Universite Catholique de Louvain; 1997.

[25] Hurle DTJ. J Appl Phys 1999;85:6957.

[26] Rudolph P, Rinas U, Jacobs K. J Cryst Growth 1994;138:249.

[27] Northrup E, Zhang SB. Phys Rev B 1993;47:6791.

[28] Neugebauer J, Van de Walle CG. Phys Rev B 1994;50:8067.

[29] Boguslawski P, Briggs EL, Bernholc J. Phys Rev B 1995;51:17255.

[30] Luken KM, Morrow RA. Semicond Sci Technol 1996;11:11556.

[31] Dornberger E, Virbulis J, Hanna B, Hoelzl R, Daub E, von Ammon W. J Cryst Growth 2001;229:11.

[32] Rudolph P, Kiessling FM. Cryst Res Technol 1988;23:1207.

[33] Monberg E. In: Hurle DTJ, editor. Handbook of crystal growth, vol. 2a. Amsterdam: Elsevier; 1994. p. 51.

[34] Rudolph P. Prog Cryst Growth Charact Mater 1995;29:275.

[35] Kiessling F. In: Capper P, Rudolph P, editors. Crystal growth technology. Weinheim: Wiley-VCH; 2010. p. 75.

[36] Rudolph P, Kawasaki S, Yamashita S, Yamamoto S, Usuki Y, Konagaya Y, et al. J Cryst Growth 1996; 161:28.

[37] Biswas K, Du M-H. New J Phys 2012;14:063020.

[38] Franc J, Sedivy L, Belas E, Bugar M, Zazvorka J, Pekarek J, et al. Cryst Res Technol 2013;48:214.

[39] Oda S, Yamamoto M, Seiwa M, Kano G, Inoue T, Mori M, et al. Semicond Sci Technol 1992;7:215.

[40] Neubert M, Rudolph P. Prog Cryst Growth Charact Mater 2001;43:119.

[41] Kiessling F-M, Rudolph P, Neubert M, Juda U, Naumann M, Ulrici W. J Cryst Growth 2004;269:218.

[42] Borovlev UA, Ivannikova NV, Shlegel VN, Vasiliev YaV, Gusev VA. J Cryst Growth 2001;229:305.

[43] Pfeiffer E, Rudolph P. Patent DD 290 226; 1989.

[44] Klapper H. Mater Chem Phys 2000;66:101.

[45] Klapper H. In: Dhanaraj G, Byrappa K, Prasad V, Dudley M, editors. Springer handbook of crystal growth. Berlin-Heidelberg: Springer; 2010. p. 93.

[46] Völkl J. In: Hurle DTJ, editor. Handbook of crystal growth, vol. 2b. Amsterdam: Elsevier; 1994. p. 821.

[47] Prasad V, Pendurti S. In: Dhanaraj G, Byrappa K, Prasad V, Dudley M, editors. Springer handbook of crystal growth. Berlin-Heidelberg: Springer; 2010. p. 1335.

[48] Neuroth G. [Ph.D. thesis]. University of Bonn; 1996.

[49] Forty AJ. Adv Phys 1954;3:1.

[50] Klapper H. In: Tanner BK, Bowen DK, editors. Characterization of crystal growth defects by X-ray methods. New York: Plenum Press; 1980. p. 133.

[51] Lothe J. Phys Nor 1967;2:154.

[52] Klapper H, Küppers H. Acta Crystallogr 1973;A29:495 (correction: read K/cos α instead of K cos α).

[53] Klapper H. Phys Status Solidi A 1972;14:99.

[54] Klapper H. Phys Status Solidi A 1972;14:443.

[55] Eshelby JB, Read WT, Shockley W. Acta Metall 1953;1:251.

[56] Klapper H, Fishman Yu M, Lutsau VG. Phys Status Solidi A 1974;21:115.

[57] Klapper H. In: Karl N, editor. Crystals: growth, properties and characterization, vol. 13. Berlin-Heidelberg: Springer; 1991. p. 109.

[58] Scheffen-Lauenroth T, Klapper H, Becker RA. J Cryst Growth 1981;55:557.

[59] Schmidt W, Weiss R. J Cryst Growth 1978;43:515.

[60] Venégues P, Beaumont B, Bousquet V, Vaille M, Gibart R. J Appl Phys 2000;87:4174.

[61] Gradezcak S, Stadelmann P, Wagner V, Ilegems M. Appl Phys Lett 2004;85:4648.

[62] Klapper H. In: Authier A, Logomarsino S, Tanner BK, editors. X-ray and neutron dynamical diffraction: theory and applications. Proc. NATO ASI, Erice 1996, NATO science series B, vol. 357. Plenum Publ. Corp.; 1997. p. 167.

[63] Watanabe T, Izumi K. J Cryst Growth 1979;46:747.

[64] Izumi K. Jpn J Appl Phys 1977;16:2103.

[65] Klapper H. Mater Sci Forum 1998;276–277:291.

[66] Amoedo RJ, Ghoniem NM. Dislocation dynamics I and II. Phys Rev 1990;41:6958–68.

[67] Indenbom VL. Krist Tech 1979;14:493 [in German].

[68] Hull D, Bacon DJ. Introduction to dislocations. 5th ed. Amsterdam: Elsevier; 2011.

[69] Holt DL. J Appl Phys 1970;41:3197.

[70] Rudolph P. Cryst Res Technol 2005;40:7.

[71] Mullin JB. J Cryst Growth 2004;264:578.

[72] Shimizu A, Nishizawa J, Oyama Y, Suto K. J Cryst Growth 2001;229:119.

[73] Bünger Th, Behr D, Eichler St, Flade T, Fliegel W, Jurisch M, et al. Mater Sci Eng B 2001;80:5.

[74] Genzel C, Gille P, Hähnert I, Kießling FM, Rudolph P. J Cryst Growth 1990;101:232.

[75] Durose K, Russel GJ. J Cryst Growth 1988;86:471.

[76] Frank-Rotsch Ch, Juda U, Kiessling F-M, Rudolph P. Mater Sci Technol 2005;21:1450.

[77] Bolotnikov AE, Camarda GS, Cui Y, Yang G, Hossain A, Kim K, et al. J Cryst Growth 2013;379:46.

[78] Tuomi T, Knuuttila L, Riikonen J, McNally PJ, Chen W-M, Kanatharana J, et al. J Cryst Growth 2002;237:350.

[79] Gröschel A, Will J, Bergmann Ch, Grillenberger H, Eichler St, Scheffer Czygan M, et al. Solid State Phenom 2011;178–179:360.

[80] Zaiser M. In: Müller G, Metois J, Rudolph P, editors. Crystal growth – from theory to technology. Amsterdam: Elsevier; 2004. p. 215.

[81] Kuhlmann-Wilsdorf D. Metall Trans A 1985;16A:2091.

[82] Taylor GI. J Inst Met 1938;62:307.

[83] Kubin LP. Dislocations, mesoscale simulations and plastic flow. Oxford: Oxford University Press; 2013.

[84] Ryningen B, Stokkan G, Kivambe M, Ervik T, Lohne O. Acta Mater 2011;59:7703.

[85] Sopori B, Li C, Narayanan S, Carlson D. Mater Res Soc Symp Proc 2005;864:233.

[86] Yang YM, Yu A, Hsu B, Hsu WC, Yang A, Lan CW. Prog Photovolt Res Appl 2013. http://dx.doi.org/10.1002/pip.2437.

[87] Rudolph P, Engel A, Schentke I, Grochocki A. J Cryst Growth 1995;147:297.

[88] Yang G, Bolotnikov AE, Fochuk PM, Kopach O, Franc J, Belas E, et al. J Cryst Growth 2013;379:16.

[89] Yadava RDS, Badai RK, Borle WN. J Electron Mater 1992;21:1001.

[90] Rudolph P, Frank-Rotsch Ch, Juda U, Eichler St, Scheffer-Czygan M. Phys Status Solidi C 2007;4:2934.

[91] Shibata M, Suzuki T, Kuma S, Inada T. J Cryst Growth 128(193):439.

[92] Benjamin Britton T, Wilkinson AJ. Acta Mater 2012;60:5773.

[93] Duffar T, Dusserre P, Picca F, Lacroix S, Giacometti N. J Cryst Growth 2000;211:434.

[94] Althaus M, Sonnenberg K, Küssel E, Naeven R. J Cryst Growth 1996;166:566.

[95] Müller G, Birkmann B. J Cryst Growth 2002;237–239:1745.

[96] Parsey JM, Thiel FA. J Cryst Growth 1985;73:211.

[97] Tomizawa K, Sassa K, Shimanuki Y, Nishizawa J. J Electrochem Soc Solid State Technol 1984;131:2394.

[98] Bako B, Groma I, Györgyi G, Zimanyi G. Comp Mater Sci 2006;38:22.

[99] Gottstein G. Physikalische Grundlagen der Materialkunde, 3. Auflage. Berlin: Springer; 2007.

[100] Ashby MF. Philos Mag 1970;21:399.

[101] Malygin GA. Phys Solid State 2002;44:1305. Translated from Fiz Tverd Tela 2002;44:1249.

[102] Sabinina IV, Gutakovski AK, Milenov TI, Lykakh NN, Sidorov YG, Gospodinov MM. Cryst Res Technol 1991;26:967.

[103] Tiller WA, Jackson KA, Rutter JW, Chalmers B. Acta Metall 1953;1:428.

[104] Grange G, Billia B. J Phys Fr 1994;4:293.

[105] Scholz H. Solid State Commun 1976;19:429.

[106] Koji Arafune, Eichiro Ohishi, Hitoshi Sai, Yoshio Oshita, Masafumi Yamaguchi. J Cryst Growth 2007;308:5.

[107] Li TF, Yeh KM, Hsu WC, Lan CW. J Cryst Growth 2011;318:219.

[108] Kiessling F-M, Frank-Rotsch Ch, Dropka N, Rudolph P. Patent DE 10 2011 076 860 (2011).

[109] Takahashi I, Usami N, Kutsukake K, Stokkan G, Morishita K, Nakajima K. J Cryst Growth 2010;312:697.

[110] Fujiwara K, Obinata Y, Ujihara T, Usami N, Sazaki G, Nakajima K. J Cryst Growth 2004;266:467.

[111] Rudolph P. In: Wang M, Tsukamoto K, Wu D, editors. Selected topics on crystal growth – the 14th International Summer School on crystal growth in Dalian, China. Melville (New York): AIP Conf. Proc. No. 1270; 2010. p. 107.

[112] Steinegger T, Naumann M, Jurisch M, Donecker J. Precipitate engineering in GaAs studied by laser scattering tomography. Mater Sci Eng B 2001;80:215.

[113] Fornari R, Frigeri C, Gleichmann R. J Electron Mater 1989;18:185.

[114] Rai RS, Mahajan S, Mc Devitt S, Johnson DJ. J Vac Sci Technol B 1991;9:1892.

[115] Sonnenberg K. IFF Bull Forschungszent 1997;51:14.

[116] Shen J, Aidun DK, Regel L, Wilcox WR. J Cryst Growth 1993;132:250.

[117] Brion HG, Mewes C, Hahn I, Schäufele U. J Cryst Growth 1993;134:281.

[118] Greenberg J. Thermodynamic basis of crystal growth. Berlin: Springer; 2002.

[119] Jurisch M, Flade T, Hoffmann B, Köhler A, Korb J, Kretzer U, et al. Mater Sci Eng B 1997;44:198.

[120] Wulff G. Z Krist 1901;34:449–512.

[121] Buckley HE. Crystal growth. London, New York: Wiley; 1961.

[122] Zerfoss S, Slawson SI. Am Mineral 1956;41:598.

[123] Janssen-Van Rosmalen R, van der Linden WH, Dobinga E, Visser D. Krist Tech 1978;13:17–28.

[124] Vetter WM, Totsuka H, Dudley M, Kahr B. J Cryst Growth 2002;241:498.

[125] Kahr B, Guerney RW. Chem Rev 2001;101:893.

[126] Kahr B, Vasquez L. Cryst Eng Commun 2002;4:514.

[127] Chernov AA, Kuznetsov Yu G, Smolskii IL, Rozhanski VN. Sov Phys Crystallogr 1986;31:705.

[128] Janssen-Van Rosmalen R, Bennema P. J Cryst Growth 1977;42:224.

[129] van Enckevort WJP, Janssen-Van Rosmalen R, Klapper H, van der Linden WH. J Cryst Growth 1982;60:67.

[130] Fujiwara K. Int J Photoenergy 2012;2012:1.

[131] Nadri A, Duterrail-Couvat Y, Duffar T. J Cryst Growth 2013. http://dx.doi.org/10.1016/j.jcrysgro.2013.04.013.

[132] Rudolph P, Kakimoto K. MRS Bull 2009;34:251.

[133] Kahr B, McBride JM. Optically anomalous crystals. Angew Chem Intern Ed 1992;31:1.

[134] Gottschalk H, Patzer G, Alexander H. Phys Status Solidi A 1978;45:207.

[135] Donnelly TW. Am Mineral 1967;52:1.

[136] Carstens H. Am Mineral 1968;53:342.

[137] Donnelly TW. Am Mineral 1968;53:344.

[138] Bloss FD. Crystallography and crystal chemistry. New York: Rinehart & Winston; 1971. p. 324.

[139] Giacovazzo C. Fundamentals of crystallography. Oxford: University Press; 1992. p. 80 and 133.

[140] Hahn Th, Klapper, H. International Tables for Crystallography, vol. D. 1. Edition: Dordrecht, Kluver Academic Publishers, 2003. pp. 393–448. 2. Edition: John Wiley & Sons, Inc., 2014, pp. 413–483.

[141] Klapper H. In: Krishna P, editor. Progress in crystal growth and characterization, vol. 14. Oxford: Pergamon; 1987. p. 367.

[142] Faust JW, John HF. J Phys Chem Soc 1964;24:1407.

[143] Bögels G, Meekes H, Bennema P, Bollen D. J Cryst Growth 1998;191:446.

[144] Gu X, Yu X, Guo K, Chen L, Wang D, Yang D. Sol Energy Mater Sol Cells 2012;101:95.

[145] Hurle DTJ. J Cryst Growth 1995;147:239.

[146] Neubert M, Kwasniewski A, Fornari R. J Cryst Growth 2008;310:5270.

[147] Wallace CA, White EAD. In: Peiser HS, editor. Crystal growth. Oxford: Pergamon Press; 1967. p. 431.

[148] Senechal M. Sov Phys Crystallogr 1980;25:520.

[149] Hofmeister H. Cryst Res Technol 1998;33:3 [especially sect. 4].

[150] Prigent G, Bellissent R, Ceolin R, Fischer HE, Gaspard JP. J Non Cryst Solids 1999;250–252:297.

[151] Godlevsky VV, Jain M, Derby JJ, Chelikowsky JR. Phys Rev B 1999;60:8640.

[152] Sunagawa I, Taijing L, Balitsky VS. Phys Chem Miner 1990;17:320.

[153] MacLaren AC, Pitkethly DR. Phys Chem Miner 1982;8:128.

[154] Janovec V, Přívratská J. In: Authier A, editor. International tables for crystallography, vol. D. Dordrecht: Kluwer; 2003. p. 449.

[155] Roth G, Ewert D, Heger G, Hervieu M, Michel C, Raveau B, et al. Z Phys B 1987;69:21.

[156] Rudolph P, Schäfer N, Fukuda T. Mater Sci Eng 1995;R15:85.

[157] Zheludev IS. Physics of crystalline dielectrics. Vol. 1: Crystallography and spontaneous polarisation. New York: Plenum Press; 1971.

[158] Docherty R, El-Korashi A, Jennissen H-D, Klapper H, Roberts KJ, Scheffen-Lauenroth T. J Appl Crystallogr 1988;21:406.

[159] Hosokawa Y, Yabuhara Y, Nakai R, Fujita K. In: Indium Phosphide and related materials, 1998, IPRM IEEE international conference on 11–15 May 1998. Tsukuba (Japan), p. 34.

[160] Winkler J, Neubert M, Rudolph J. J Cryst Growth 2010;312:1019.

[161] Rudolph P, Koh HJ, Schäfer N, Fukuda T. J Cryst Growth 1996;166:578.

[162] Devincre B, Hoc T, Kubin L. Science 2008;320:1745.

[163] Ervik T, Kivambe M, Stokkan G, Ryningen B, Lohme O. Acta Mater 2012;60:6762.

[164] Buis C, Cros d'aillon E, Marrakchi G, Lafford TA, Brambilla A, Verger L. IEEE Trans Nucl Sci 2013;60(Part 2):199.

[165] Wu B, Scott S, Stoddard N, Clark R, Sholapurwalla A. Miner Met Mater Soc.

28

Automation of Crystal Growth from Melt

Jan Winkler[1], Michael Neubert[2]

[1]INSTITUT FÜR REGELUNGS- UND STEUERUNGSTHEORIE, TECHNISCHE UNIVERSITÄT DRESDEN, DRESDEN, GERMANY; [2]LEIBNIZ INSTITUTE FOR CRYSTAL GROWTH (IKZ), BERLIN, GERMANY

CHAPTER OUTLINE

28.1 Introduction **1144**
28.2 Basics about Control Systems **1145**
28.2.1 Modeling in Crystal Growth Analysis and Control 1146
28.2.2 Reference Trajectory Generator 1147
28.2.3 State Estimator 1147
28.2.4 Feed-Forward Controller 1149
28.2.5 Feedback Controller 1150
28.2.5.1 Proportional-Integral-Derivative Controller 1150
28.2.5.2 Model-Based Control 1151
28.2.5.3 Model Predictive Control 1152
28.3 Cz Process **1153**
28.3.1 Process Characteristics and Control Objectives 1153
28.3.1.1 Importance of the Meniscus Region 1154
28.3.1.2 Lumped Parameter Modeling 1155
28.3.1.3 Stability 1156
28.3.2 State Estimation 1156
28.3.2.1 Weighing Technique 1157
28.3.2.2 Detection of the Bright Meniscus Ring 1159
28.3.3 Feed-Forward Control 1160
28.3.4 Conventional PID-Based Control 1161
28.3.4.1 PID-Based Control Using Optical Diameter Estimation 1161
28.3.4.2 PID-Based Control Using Weight Measurement 1161
28.3.4.3 Improvements and Optimizations 1162
28.3.5 Model-Based Control 1163
28.3.5.1 Lumped Parameter Model-Based Control 1163

Handbook of Crystal Growth. http://dx.doi.org/10.1016/B978-0-444-63303-3.00028-6
Copyright © 2015 Elsevier B.V. All rights reserved.

28.3.5.2 Distributed Parameter Model-Based Control 1164
28.3.5.3 Model Predictive Control 1165
28.4 Vertical Bridgman and Vertical Gradient Freeze Process **1165**
28.4.1 Process Characteristics and Control Objectives 1166
28.4.2 Conventional Control 1167
28.4.3 Model-Based Control 1167
28.4.3.1 Temperature Control and Interface Shape Detection 1168
28.4.3.2 Flow Speed Control 1169
28.5 Detached Bridgman Process **1169**
28.5.1 Process Characteristics and Control Objectives 1170
28.5.1.1 Choice of the Manipulated Variable 1171
28.5.1.2 Lumped Parameter Model 1171
28.5.1.3 Stability and Operational Limits 1171
28.5.2 PI-Based Control 1172
28.5.3 Model-Based Control 1173
28.6 Floating Zone Process **1174**
28.6.1 Process Characteristics and Control Objectives 1174
28.6.2 Measurement Techniques 1174
28.6.3 Reference Trajectory Planning and Conventional Control 1175
28.6.4 Model-Based Control 1176
28.7 Kyropoulos Process **1176**
28.7.1 Process Characteristics and Control Objectives 1176
28.7.2 Control Approaches 1177
28.8 Conclusions **1178**
References **1178**

28.1 Introduction

The demand for crystals of well-defined structural, chemical, optical, and electrical properties produced with a maximum level of yield and reproducibility is the motivation to develop highly sophisticated automatic control systems. For example, the better a crystal meets its desired diameter and the better the diameter constancy in the cylindrical part of the crystal, the less material has to be cut off after growth. On the other hand, strong diameter changes influence the structural properties of the crystal [1–4]. Hence, ensuring the desired diameter is a main purpose of control systems in processes in which no shaping devices or forming containers are available. Not only the diameter but also other quantities like the crystal growth rate are of special importance. For example, the growth rate directly influences the properties of the growing crystal. It correlates with the amount of imperfections, like the amount of native point defects,

residual impurities and that of intentionally introduced dopants or higher dimensional defects like dislocations, twins, precipitates, or inclusions. Consequently, for process technology there is also a huge interest in growth rate control. A typical example can be found in Czochralski (Cz) silicon crystal growth where the relation between growth rate and thermal gradients at the interface is of great importance in order to ensure an extremely low content of native point defects [5–9]. More recently, the focus of control design has been extended to maintain additional degrees of freedom that affect crystal quality as well as crystal shape, for example, in Cz growth also during the neck, shoulder, and tail sections in addition to the main body [10–16].

When designing a control system the first task is to characterize the dynamic relations between the inputs and the outputs of the process to be controlled, usually by means of a mathematical model. Secondly, the control objectives have to be defined, which are mainly determined by the desired material requirements. They are specified as the particular process phenomena that have to be controlled [17]. Based on these results a control structure is chosen. Here, different levels of mathematical complexity, questions about linear or nonlinear control design, robustness, and real time capability come into play. In any case and no matter which control strategy is chosen to address these issues, crystal growth processes are usually an extremely challenging control object.

This chapter will give a broad overview of the approaches found for different bulk crystal growth processes from melt with respect to topics like model-based analysis, process characteristics, open- and closed-loop control, reference trajectory design, and state estimation. Of course, it is impossible to cover all crystal growth processes from melt in this chapter. As examples, the Cz , the Floating Zone, the Bridgman, the Detached Bridgman, and the Kyropoulos methods are treated. Of all of these, the Cz system is by far the most thoroughly investigated one in the literature. Please note that additionally a state-of-the-art control system approach for the Floating Zone technique is discussed in detail in Vol. IIA, Chapter 7 of this handbook.

28.2 Basics about Control Systems

The purpose of a control system is to keep a set of process quantities, in the following referred to as the *controlled variables*, on a certain set point or to track them along a given *reference trajectory*. This is done by appropriately manipulating the inputs of the process, in the following referred to as the *manipulated variables*. It can be achieved by predetermined knowledge of the process (*open-loop control*) and/or by feedback of certain measured process information (*closed-loop control*). The intention of this section is to introduce some of the basic concepts used in control technology as far as they are required for an understanding of the numerous strategies for control of the discussed crystal growth processes. For this purpose, the essential components of a control system are briefly summarized according to [14,18,19]. A broader introduction can be found in [20,21], and a graphical overview showing all essential components of a control system is given in Figure 28.1. Since modeling and computer simulation play an important role in

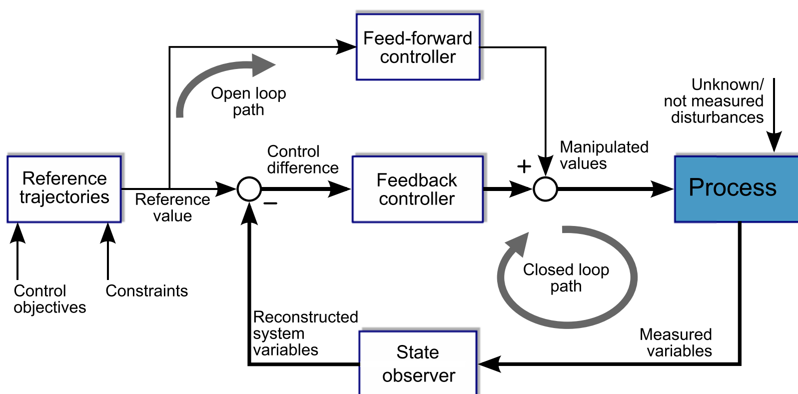

FIGURE 28.1 Sketch of a modern feedback control loop.

crystal growth process design as well as in control applications, a short comparison of how models are used in automatic control in contrast to numerical approaches in crystal process design will be given first. The approaches and requirements differ quite a lot [19] between both fields.

28.2.1 Modeling in Crystal Growth Analysis and Control

A mathematical model that takes the spatial distribution as well as the time dependency of material parameters into account leads to a system of coupled *partial* differential equations with the corresponding initial, boundary, and compatibility conditions. They belong to the so-called *infinite dimensional* or *distributed parameter* systems. Such systems are usually solved numerically using finite element methods (FEMs). Using this approach one can obtain results reflecting the reality rather accurately. FEM is an absolutely essential resource in solving problems in plant design, thermal and stress analysis, etc. However, computational effort increases dramatically depending on the accuracy required, especially for solving *time-dependent* problems.

The approach used in control technology, especially in model-based control (cf. Section 28.2.5), is to keep the models as simple as possible. This is achieved by partitioning the system under consideration into domains that may reasonably well be considered as homogeneous, i.e., the material parameters of which are assumed to be constant. Heat and mass transfer between these domains is calculated from appropriate mass and energy balance equations. Since any spatial dependence of the parameters is neglected, one ends up with a set of *ordinary* differential equations. Such approaches are called *finite dimensional* or *lumped parameter* models. They can be used to calculate the basic system behavior leading to a qualitatively and quantitatively sufficient insight into the process. Powerful methods for controller and observer design (cf. Section 28.2.3), trajectory planning, and dynamic analysis exist for this class of models. The lack of accuracy can be admitted by the introduction of feedback. Another advantage of these

models is the fact that one is able to run them on the limited computer hardware usually available at the growth furnaces.

The big challenge in applying model-based control strategies to problems in crystal growth technology is that the dynamics of these processes are mainly driven by complex nonlinear radiative, conductive, and convective heat transport phenomena. They cannot be fully captured by either a linear or a nonlinear lumped parameter model. Above all, melt growth processes are systems with free boundaries (at least the solid–liquid interface, in case of processes where the crystal grows freely from the melt, e.g., in Cz growth, also the crystal shape) making it even more complicated to solve the underlying dynamic equations. Many unknown physical parameters and the complex structure of the inner assemblies worsen the situation. Here, from a control technological point of view, one has to find a balance between accuracy and real time capability of the models [10,14,22].

28.2.2 Reference Trajectory Generator

The *reference trajectory generator*, cf. Figure 28.1, calculates reference values for the main variables to be controlled, e.g., crystal diameter, crystallization rate, or other useful quantities. Usually the independent parameter of this calculation is the growth time or the crystal length. These reference values are used in the feed-forward and the feedback controllers of the control system. Planning of trajectories has to consider the physical properties of the system in order to avoid not realizable or not favorable values for the manipulated variables. Furthermore, one cannot request physically impossible behavior from the system, such as steps in any of the system quantities or their derivatives. For example, in Floating Zone crystal growth it is reasonable to keep the crystal diameter and the zone length in a certain range in order to maintain a stable melt zone. Also, the crystal growth rate in Bridgman growth must be kept below a critical value to ensure perfect growth of the crystal.

Such constraints must be carefully considered during reference trajectory planning. It may be useful to reschedule the reference trajectories during growth to guarantee smooth behavior of the controller.

28.2.3 State Estimator

It is not always possible to measure the controlled variable directly using a sensor. As will be shown in the next sections, this is the case in a lot of crystal growth processes. For example, in Cz growth usually the force measured by a load cell or the diameter of a bright ring on the meniscus is the only measured quantity available while one is interested in the control of crystal diameter and growth rate. In Bridgman process nothing can be measured directly describing the state of the growing crystal. In such cases one might reconstruct the required variables from measured variables by means of a state estimator, often called an *observer*. This is possible if a suitable model of the system is available and the system is observable (a certain system property, cf. [23,24]).

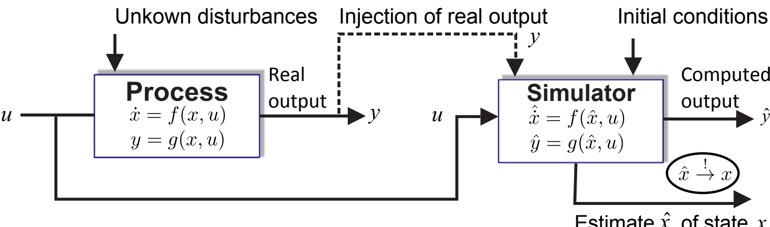

FIGURE 28.2 Working principle of a state estimator.

An observer is based on the following idea, cf. Figure 28.2, also. Assume a lumped parameter mathematical model

$$\dot{x}(t) = f_1(x(t), u(t)), \quad y(t) = f_2(x(t), u(t)), \quad x(0) = x_0$$

of a process with $(x(t), u(t)) \in \mathbb{R}^n \times \mathbb{R}^r$ and $y(t) \in \mathbb{R}^m$. If some components of x are not directly measured, one might implement a "copy"

$$\dot{\hat{x}}(t) = f_1\left(\hat{x}(t),\ u(t)\right), \quad \hat{y}(t) = f_2\left(\hat{x}(t),\ u(t)\right), \quad \hat{x}(0) = \hat{x}_0$$

of the system model with the estimated state $\hat{x}$ in a computer program. The trajectories of the manipulated variables u acting on the real system are fed into this computer program, too. Then one has access to all components of $\hat{x}$. However, since the initial values of $\hat{x}$ are not known, i.e., $\hat{x}_0 \neq x_0$, and because of model inaccuracies as well as disturbances acting on the system, generally the values calculated for $\hat{x}(t)$ will not be equal to the real values $x(t)$. However, under certain circumstances it is possible to inject the error $\hat{y} - y$ between the estimated value $\hat{y}$ and the measured value y in such a way that the difference between the estimated value $\hat{x}$ and the real value x will converge to zero as time advances [23]. In this case the system

$$\dot{\hat{x}}(t) = h\left(\hat{x}(t), u(t), \hat{y}(t) - y(t)\right), \quad \hat{x}(0) = \hat{x}_0$$

$$\hat{y}(t) = f_2\left(\hat{x}(t), u(t)\right)$$

is called an *observer*.

Design and dimensioning of the injection of the error related to the measured variable is the key task when developing an observer. However, it is important to know if it is possible to reconstruct a quantity from the measured variable at all. This property is commonly referred to as "observability." If the stochastic properties of the process are incorporated into the design of such an observer, it is usually called Kalman filter or extended Kalman filter [25]. An introduction to practical observer design is given in Ref. [26]. Especially for Cz growth, many approaches deal with this topic (cf. Section 28.3.2 for more details).

28.2.4 Feed-Forward Controller

The *feed-forward controller* calculates the manipulated values (like heater powers or crystal/crucible/feed rod translation rates) from the reference values of the controlled variables (e.g., crystal diameter) generated by the reference trajectory generator. This can be done empirically or by means of a mathematical model describing the system behavior. In crystal growth, a common method in practice is to determine the feed-forward control by careful analysis of repeated growth runs, resulting in a trajectory for the manipulated variables that can then be used as part of the process recipe in the following runs.

While this method is widely accepted, it suffers from the fact that it is extremely time consuming and, thus, expensive. It functions only if the same conditions are repeatedly met and there are no significant variations from run to run. However, any change in plant setup or change in reference values for the controlled variables means repeating this procedure. Finally, not all details of the system dynamics can be determined by this empirical approach.

If a sufficiently exact model of the process is available, this model can be used as a basis for determining proper feed-forward control trajectories that then can be fine-tuned in an empirical manner afterward. A short example is given as follows illustrating this strategy [19]. One may have a system with the manipulated variable $u \in \mathbb{R}$ (for example, a heater power), the output variable $y \in \mathbb{R}$ (which has to be controlled, e.g., a bright meniscus ring diameter in Cz growth), and two internal states $x_1, x_2 \in \mathbb{R}$ (e.g., the crystal diameter and a value describing the cone angle). Its dynamics may be captured by the following very simple, fictive lumped parameter model of order 2:

$$\dot{x}_1 = x_2 \tag{28.1a}$$

$$\dot{x}_2 = x_1^2 + (x_2 + 2)u \tag{28.1b}$$

$$y = x_1. \tag{28.1c}$$

From this model, a model-based feed-forward control can be easily calculated. Solving Eqn (28.1b) for the heater power u one obtains:

$$u = \frac{\dot{x}_2 - x_1^2}{x_2 + 2}. \tag{28.2}$$

Now, one would like to steer the system, namely the diameter y, along a reference trajectory $t \mapsto y_{\mathrm{ref}}(t)$. This reference trajectory is assumed to be two times continuously differentiable, i.e., $\dot{y}_{\mathrm{ref}}(t)$, $\ddot{y}_{\mathrm{ref}}(t)$ exist. Since according to system (28.1) one has $x_1 = y$, $x_2 = \dot{x}_1 = \dot{y}$, and $\dot{x}_2 = \ddot{y}$ the resulting reference trajectory for the manipulated variable u reads (cf. Eqn (28.2)):

$$u_{\mathrm{ref}} = \frac{\ddot{y}_{\mathrm{ref}} - y_{\mathrm{ref}}^2}{\dot{y}_{\mathrm{ref}} + 2}. \tag{28.3}$$

Using the calculated feed-forward control, one might be able to *steer* the system along its reference trajectory if the system is stable, only small perturbations are acting on the system, and the model is accurate enough.

The example given above demonstrates the general design procedure of a lumped parameter model-based feed-forward control. However, the dynamics of crystal growth process will certainly never be captured sufficiently by such simple models. Hence, this example also reveals one of the main problems in control system design for crystal growth—finding the appropriate balance between simple models suitable for control system design and accuracy of the models describing the system dynamics. The sections dealing with the control of the particular growth processes will focus especially on this topic.

28.2.5 Feedback Controller

Obviously, the main component of the control system is the *feedback controller*. Its purpose is to compensate for disturbances acting on the process and to correct inaccuracies in trajectory tracking resulting from imprecise feed-forward control. This is achieved by feedback of the measured variable (or its estimate, cf. Section 28.2.3) and a correction of the manipulated variable.

28.2.5.1 Proportional-Integral-Derivative Controller

It is common practice to realize feedback control by means of a proportional-integral-derivative (PID) controller. The PID controller processes a deviation $e(t)$ between the reference and the real value of the controlled variable in order to calculate a change $\Delta u(t)$ of the manipulated variable:

$$\Delta u(t) = K_\mathrm{P} e(t) + K_\mathrm{I} \int_{t_0}^{t} e(\tau)\mathrm{d}\tau + K_\mathrm{D} \frac{\mathrm{d}e}{\mathrm{d}t}(t). \tag{28.4}$$

The dynamic behavior of the PID controller is determined using the three real-valued constants K_P, K_I, and K_D. It is an implementation of the following natural assumptions: (1) The larger the control deviation, the more one has to counter steer, an implication that is covered by the proportional part $K_\mathrm{P} e(t)$. (2) The longer the control deviation is pending, the more the manipulated variable has to be changed in order to reduce it. This behavior is realized by the integral part parameterized using the factor K_I, the second term in Eqn (28.4). (3) The faster the control deviation changes, the stronger one has to counteract—this is covered by the third term in Eqn (28.4)—the differential part with parameter K_D. To avoid the influence of measurement noise, usually this differentiation is combined with a first-order low-pass filter. A detailed introduction and discussion of the application of PID controllers under industrial conditions can be found in [27–29].

The PID controller is suitable for a wide range of technological systems found in practice and has some advantages: its operating principle is simple and it can be easily implemented. If certain conditions hold, it can be adjusted using some simple rules [30,31]. Typical examples for its application are all kinds of temperature control, flow rate control, or position tracking in which only small perturbations occur. However, there are some drawbacks: Its parameterization is adjusted for a certain operating point of the process. If

one does not have a steady state operating point, parameters have to be continuously changed. This is usually the case in crystal growth processes. Furthermore, the performance of PID controllers is limited if the system shows nonlinear behavior. The reason for this is the fact that a change of the manipulated variable results in an "unexpected" nonlinear response of the system. The situation worsens if the system contains time delays (dead times). Then, a reaction y of the system to a change of the manipulated variable u appears delayed by the delay time $\tau > 0$, for example, $y(t) = u(t - \tau)$. Dead times must not be mixed up with a time constant T of a dynamic system, e.g., in a first-order low-pass filter: $T\dot{y}(t) = -y(t) + u(t)$. Time delays may result in an undamped increasing integral of the PID algorithm (cf. Eqn (28.4)). For example, in Cz crystal growth, the liquid-encapsulated Czochralski (LEC) process with its boron–oxide layer covering the melt belongs to the class of delay systems, cf. Section 28.3.1.1.

28.2.5.2 Model-Based Control

Fortunately, theory and application of control systems have been developed very rapidly in the last decades. Increasing capacity of microcontrollers and programmable logic controllers (PLC) combined with powerful mathematical control design methods prepared the ground for the use of sophisticated model-based controllers in practice. A model-based controller uses a mathematical model of the system, i.e., its structure and parameters fit to the system. This means that the controller can be used in a wide range of operating points and reflects the nonlinear system characteristics as well as time delays. In addition, parameterization effort is dramatically reduced. Refer to Ref. [32] for a broad overview of nonlinear model-based strategies. Such controllers show good performance only if the underlying model matches the structure and the parameters of the system appropriately. This is the crucial point when trying to enhance the capability of conventional control systems.

In order to make the strategy of model-based control more clear, the design of a simple nonlinear feedback controller based on the lumped parameter model (28.1) from Section 28.2.4 is sketched. Exactly how this type of model-based controller design is successfully applied, for example, is shown in the Cz method (Section 28.3.5.1) and in the Detached Bridgman method (Section 28.5.3). If one wants to make the output y (e.g., a diameter) follow a reference trajectory $y_{\mathrm{ref}}(t)$, the controller is designed in such a way that the tracking error $y - y_{\mathrm{ref}}$ satisfies the linear second-order differential equation

$$\left(\ddot{y} - \ddot{y}_{\mathrm{ref}}\right) + k_1\left(\dot{y} - \dot{y}_{\mathrm{ref}}\right) + k_0\left(y - y_{\mathrm{ref}}\right) = 0 \qquad (28.5)$$

with $k_0,\ k_1 > 0$.

The values of $y_{\mathrm{ref}},\ \dot{y}_{\mathrm{ref}}$, and $\ddot{y}_{\mathrm{ref}}$ are defined by the reference trajectory. If one desires the dynamics of the tracking error to satisfy Eqn (28.5), the second time derivative of the output y must behave as

$$\ddot{y} = \ddot{y}_{\mathrm{ref}} - k_1\left(\dot{y} - \dot{y}_{\mathrm{ref}}\right) - k_0\left(y - y_{\mathrm{ref}}\right). \qquad (28.6)$$

This can be achieved by a proper choice of the input u because by inserting the right-hand side of Eqn (28.6) in the equation used for calculation of u (cf. Eqn (28.2)) one obtains

$$\begin{aligned} u &= \frac{\dot{x}_2 - x_1^2}{x_2 + 2} = \frac{\ddot{y} - y^2}{\dot{y} + 2} \\ &= \frac{\ddot{y}_{\text{ref}} - k_1\left(\dot{y} - \dot{y}_{\text{ref}}\right) - k_0\left(y - y_{\text{ref}}\right) - y^2}{\dot{y} + 2}. \end{aligned} \tag{28.7}$$

This equation determines the manipulated variable u (e.g., the heater power) in such a way that the tracking error satisfies the given error dynamics Eqn (28.5). The coefficients k_0, k_1 in Eqn (28.5) are the controller parameters defining the dynamical behavior of the tracking error, i.e., the way the error converges to zero (e.g., fast with an overshooting or slowly creeping). The real value inputs are $y, \dot{y},$, and the desired value inputs are $y_{\text{ref}}, \dot{y}_{\text{ref}}, \ddot{y}_{\text{ref}}$.

28.2.5.3 Model Predictive Control

The model-based strategy presented so far relies on an *analytical* expression of the control law, cf. Eqn (28.7) as a possible example. A special model-based approach currently becoming more and more important is the so-called *model predictive control* strategy that is often used in process technology. Roughly speaking, in this approach no analytical control law is derived. Instead, the way of calculating values for the manipulated variable is based on optimization methods, cf. Figure 28.3. For this purpose, in each time step the set of control activities recorded so far is evaluated (i.e., the manipulated variables and the resulting controlled or measured variables) in order to

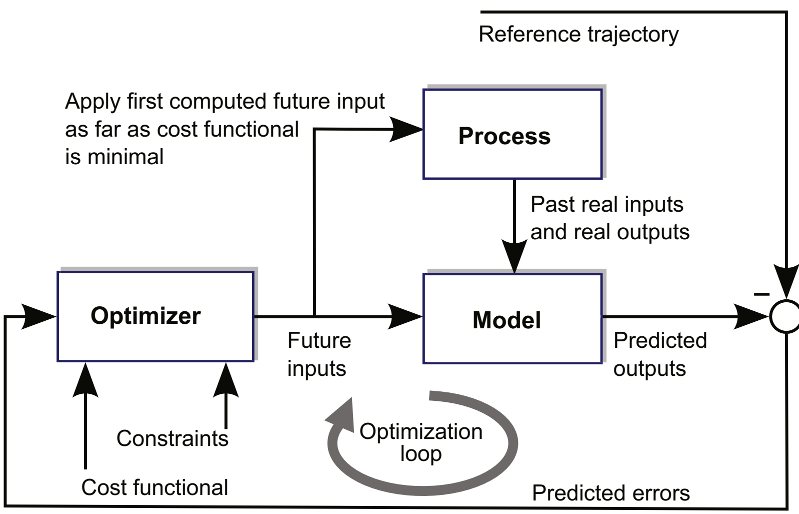

FIGURE 28.3 Model predictive control.

predict the values of the manipulated variable over a finite prediction horizon by means of a dynamic mathematical model of the process. Now, the basic idea is to repeat this calculation until an optimization criterion is minimized. Then, the first predicted manipulated value is applied to the process. In the next time step, this procedure is repeated. The optimization criteria, in some sense the "parameters" of a model predictive controller, reflect, for example, the dynamics of the deviation between desired and real values and the control effort. The solution of such optimization problems is well known and widely used in mathematics.

The advantage compared to the analytical model-based approaches presented above is that the underlying models can be arbitrarily complex as long as they can be *repeatedly numerically solved* in each time step over a finite time horizon. This is, of course, the limiting factor—one has to keep in mind that for computing a new set point value of the manipulated variables, several time-dependent solutions of the model are required. Another advantage of this method is that it is easy to account for constraints on the system states or the manipulated variables. A disadvantage is that it is more difficult to prove the stability of the closed-loop system because of the "trial and error" character of the method. A detailed introduction into this method can be found in Refs [33,34]. Application examples of this control method can be found for Cz growth in Section 28.3.5.3 and for Floating Zone growth in Section 28.6.

28.3 Cz Process

The Cz process is one of the most important crystal growth technologies used in the industrial mass production of single crystals, cf. Vol IIA, Chapters 2–4 of this handbook. Accordingly, a large amount of literature exists that deals with modeling, analysis, and control of this process.

28.3.1 Process Characteristics and Control Objectives

In Cz, as it is mostly practiced nowadays, the crystals are grown freely from the melt, i.e., there are no shaping devices ensuring a constant or well-defined diameter, which is mainly important in matters of technological requirements.[1] Next to the diameter, the crystal growth rate is also an important quantity that should be controlled, cf. Section 28.1. As manipulated variables, the power of one or several heaters and the vertical translation rates of the pulling rod as well as of the crucible are available. The rotation rates of the crucible and the crystal can be used to affect the growth, too. However, these

[1]In the past, especially in III–V semiconductor growth, a so-called coracle—a ceramic silicon nitride ring floating on the melt—was applied. Besides a thermal stabilization of the meniscus region, a self-stabilization effect due to the conical shape of the coracle and nonwetting conditions between melt and coracle was utilized, see e.g., Refs [35–38]. However, this was only an episode because of upcoming automatic diameter control.

are barely used in automatic control systems but under certain circumstances might be helpful for skilled operators to quickly influence the process.

28.3.1.1 Importance of the Meniscus Region

The key task when automating this process is an exact control of the meniscus region, the interconnection between melt and crystal, cf. Figure 28.4. The meniscus and its shape result from gravitational forces and surface tension. Its shape can be determined by numerically solving the Laplace–Young equation [39,40] or by suitable analytical approximations, e.g., by Hurle [41], Boucher and Jones [42,43], or Landau [44]. Furthermore there exist widely used analytical approximations for the meniscus height h_i itself derived by Tsivinskii [45], Boucher and Jones [42,43], or Johansen [46]. At the meniscus upper end, the so-called phase boundary, or interface, is located where crystallization takes place. Thereby the latent heat is released. Because the crystal is pulled upward into colder regions of the furnace, a temperature gradient is established, leading to a heat flow by conduction from the hot interface into the colder crystal [47]. By this mechanism, crystallization is maintained throughout the growth process. The amount of heat transported into the crystal consists of the amount of heat transported from the meniscus region into the interface and the amount of heat released by crystallization. In general, the following relation holds for the vector $\vec{v}_g$ of the growth rate along the phase boundary described by $z = \mathsf{Z}(r), r \in [0, r_i]$ (keep in mind that the vector v_g is directed in negative z-direction):

$$\vec{v}_g(r, \mathsf{Z}(r)) = \frac{1}{\rho_s \Delta H_f}(\lambda_m \nabla T_m(r, \mathsf{Z}(r)) - \lambda_s \nabla T_s(r, \mathsf{Z}(r))), \quad r \in [0, r_i]. \tag{28.8}$$

In this equation one has the heat of fusion ΔH_f, the density ρ_s of the solid at melting point temperature, and the crystal radius r_i at the interface. The heat conductivities of the solid and the melt are denoted by λ_s and λ_m, respectively, and $T_s(r, z)$ and $T_m(r, z)$ represent the temperatures of the solid and the melt. A necessary condition for growth is that the heat flux is directed from the melt into the crystal.

Changes in the temperature gradients on the melt or solid side of the phase boundary lead to an immediate change of the growth rate, as can be easily seen from Eqn (28.8).

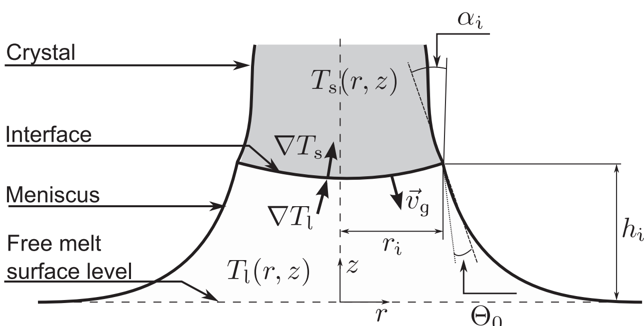

FIGURE 28.4 Sketch of the interface region with important physical quantities.

On the one hand, a local change of the growth rate results in a deformation of the phase boundary and in a change of the crystal diameter if this deformation is located at the rim of the interface. On the other hand, a change in interface geometry again initiates a change in heat transport. Furthermore, the shape of the meniscus depends nonlinearly on the radius r_i of the crystal at the interface as well as on the growth angle $\alpha = \Theta_0 + \alpha_i$ with the equilibrium growth angle Θ_0 and the crystal slope angle α_i [39,42,48], cf. Figure 28.4. Consequently, the demand of growing crystals of well-defined shape requires exact control of the thermal conditions in the interface region. Without any precise measurements characterizing the state of this region, this is an overwhelming task. An approach trying to realize such a direct control by blowing inert gas around this region is presented by Brice et al. [49]. However, usually any measurements available at the process are more or less distant to this region, complicating the control of the process.

A big challenge in achieving a proper control of the thermal situation in the meniscus region arises from the so-called "batch character" of the Cz process. This means that it does not have a steady state operating point, mainly resulting from the fact that the whole system configuration changes during the growth—while one has a crucible filled with melt in the beginning, it is nearly empty at the end of the process and the melt mass is transferred into the crystal. The falling melt level leads to a continuously changing heat entry form the heaters into the system. Thus, the process dynamics changes heavily throughout the process. Understanding the influence of these variations on the process dynamics provides a foundation for developing a robust process control system. Detailed discussions on these subjects can be found in Refs [17,22,50,51].

Besides that, variants of the process are even more difficult to control. In the LEC method [52], the liquid boron–oxide layer upon the melt introduces time delays (cf. end of Section 28.2.5.1) into the process [53–56]. In the so-called vapor pressure–controlled Czochralski (VCz) method [57] with intentionally reduced axial and radial temperature gradients, diameter control is even more difficult [4].

28.3.1.2 Lumped Parameter Modeling

First analyses of the principal system behavior of the Cz process were published by Bardsley, Hurle et al. in the 1970s [58–62] in order to improve diameter feedback control. A *global* lumped parameter model of the overall Cz crystal growth system was first presented by Steel et al. [63]. In order to simplify and improve parameterization of PID controllers, they analyzed a linearized model in terms of a transfer function in several growth stages. The central idea of their approach consists in partitioning the Cz system into the four areas: melt—meniscus—crystal—ambient. This is still the basis of all lumped parameter models of the Cz process used to date. In Ref. [64] Hurle presents a method for experimentally determining a lumped parameter model (in the form of a transfer function) of the Cz process. Other models suitable for system analysis and control system design on a lumped parameter basis have been presented by Hurle

[22,36,65], Satunkin [66,67], Looze [53], Gevelber [10], and Sveshtarov [68–70]. A more in-depth analysis using FEM methods has been presented by Derby, Brown, et al. [47,71–74].

28.3.1.3 Stability

An important matter in control theory is the question whether the system under consideration is stable or not, since unstable systems have a limitation to achievable control performance. When discussing this subject it is very important which type of model is used for stability analysis and which physical effects are included in the model. Surek's initial stability analysis was only of the capillary problem, i.e., for the meniscus region [75]. He came to the conclusion that the capillary system is unstable. However, if the heat fluxes are taken into account, one comes to a different conclusion, depending on the assumptions made during modeling. Tatarchenko [76–78], Surek [48], Hurle [65], as well as Derby [73] show stable behavior of the growth system under certain operating conditions. Nevertheless, Crowley [79] and Johansen [80] show that the system is unstable for the cases they evaluated, even if the thermal effects are included in the analysis. A more recent in-depth analysis and summary of this problem is provided by Tatarchenko in Ref. [81].

28.3.2 State Estimation

The quantities that one would like to control are mainly the crystal diameter and the crystal growth rate. Unfortunately, they cannot be directly measured. However, three different approaches exist to acquire indirect information about at least the crystal diameter:

1. Evaluation of the force acting on a load cell mounted at the top of the pulling rod, originally presented by Levinson and Rummel [82,83], discussed in detail by Bardsley et al. [58,60–62]. Alternatively, weighing of the crucible is possible [84,85].
2. Capturing of the meniscus shape, typically by detecting and evaluating the bright meniscus ring resulting from reflections of the hot glowing heaters [86–90].
3. Image processing of the whole crystal [91–93].

The third method has no technological relevance because on the one hand it is very complicated to be realized and on the other hand because changes in the growth are detected not until they have already influenced the crystal [94]. (This is actually not the case when using the first and second technique where changes in the meniscus precede a change in the crystal diameter).

Consequently, the first two approaches are widely used in industry. Which one is chosen depends on the constraints given by the process and plant setup; since silicon has a large Laplace constant (i.e., high surface tension and low density resulting in large meniscus heights) and because of its metallic reflectivity, this material is an obvious candidate for the second technique. In the LEC process the boron–oxide layer covering

the melt prevents optical detection of the meniscus. Hence, in this process the weighing method is used. The same holds for the growth of oxides with their high melting points. There the inner assemblies required for a good insulation prevent a sufficient view on the meniscus from the top of the growth furnace. Additionally, more light is emitted from the crucible, making it difficult to detect the bright ring on the meniscus. A combination of both approaches is proposed by Bruni in Ref. [95].

28.3.2.1 Weighing Technique

The idea behind the weighing technique is that, at a first glance, the rate of change of the force acting on the load cell—the so-called differential weight gain signal—might be proportional to the crystal cross-section area at the growing interface. This can be evaluated by a controller. The gravitational force F_c of a rotationally symmetric crystal of length l and density ρ_s can be calculated by

$$F_c = \pi g \rho_s \int_0^l r_i^2(\lambda) d\lambda \tag{28.9}$$

with crystal radius r_i and gravitational acceleration g. However, the force measured by the load cell is not equal to F_c of the crystal in Eqn (28.9) and, hence, the differential weight signal is not equal to the time derivative of Eqn (28.9). In fact, it is also influenced by forces resulting from the surface tension of the meniscus, the hydrostatic pressure of the melt raised over the melt level [58], and in case of LEC by the buoyancy forces resulting from the liquid boron oxide [54]. For this reason, things become considerably more complicated as it might seem from a first glance at Eqn (28.9).

A major problem when using this method occurs if the density of the solid is smaller than the density of the liquid. Then, a well-known anomaly comes into play, which consists of the fact that, e.g., an increase of the crystal diameter is not necessarily accompanied by an increase in the differential weight gain signal. The reason for this effect is that an increasing crystal diameter first results in a decrease of the meniscus height and of its volume (cf., Figure 28.5, middle). Hence, since the density of the melt is larger than the density of the solid, a decreasing meniscus volume makes the differential weight gain signal decrease at first although the crystal diameter is increasing (cf., Figure 28.5, bottom). For materials that do not completely wet their solids, i.e., $\Theta_0 \neq 0$, a similar effect can be observed since an increase in crystal diameter ($\alpha_i > 0$) leads to a reduction of the vertical component of the surface tension acting on the crystal (it is proportional to $\cos(\Theta_0 + \alpha_i)$) [60]. Unfortunately, all commonly grown semiconducting materials show this effect. A detailed discussion on this topic can be found in Ref. [60,96,97] for the standard Cz process and in Ref. [55,56] for the LEC process.

The anomaly also leads to crucial problems during the transfer from the shoulder into cylindrical growth, cf., Figure 28.6 (top)—a sudden increase of the derivative of the force acting on the load cell with respect to time is observed just before the crystal diameter reaches the cylinder. This behavior can be explained by the fact that the height (and

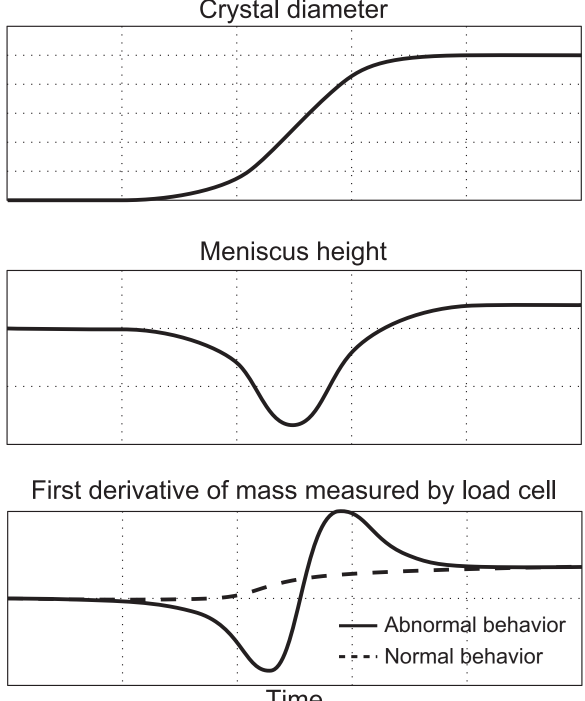

FIGURE 28.5 A slight change of the crystal diameter (top) results in a temporary break of the differential weight gain signal (bottom). The reason for that is the reduction of the meniscus height during the diameter transfer (middle).

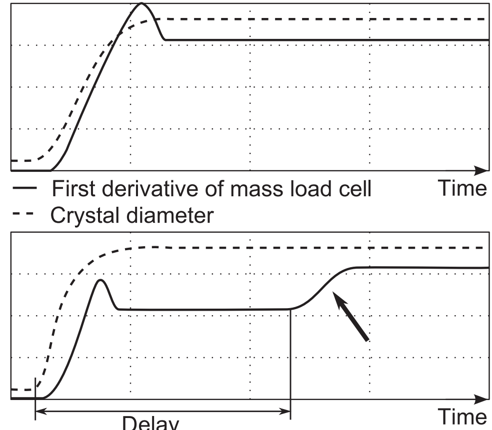

FIGURE 28.6 Top: Increase of the derivative of the differential weight gain signal before the crystal reaches the phase of cylindrical growth. Bottom: The impact of the time delay (or "dead time", cf. Section 28.2.5.2) is illustrated in the case of the LEC process: An "aftershock" occurs in the differential weight gain signal when the crystals emerge from the boron oxide layer. The dashed curves represent the corresponding diameter trends.

thus, volume) of the meniscus changes significantly at this phase of the process. More detailed discussion with respect to this subject can be found in Refs [11,66,97]. The strength of the effect depends on several factors discussed in detail in Ref. [61]. Especially the growth rate is of great importance. Roughly speaking, the lower the pulling speed, the stronger the effect.

In case of LEC growth, additionally the influence of the boron–oxide layer comes into play. One has to take into account the buoyancy as well as the time delay introduced by the emerging crystal, resulting in additional dynamical effects. For example, Figure 28.6 (bottom) shows an "aftershock" occurring in the differential weight gain signal when the crystal begins to emerge from the boron–oxide layer. These effects are discussed in Refs [54–56] and must be carefully considered during control system design.

Yet another factor limiting the weighing technique is the diameter of the crystal body. The larger it is the larger the measured force at the load cell. However, the larger the nominal load cell capacity, the worse the absolute resolution for small loads. This is problematic especially during the initial phase of the process. A discussion of the load cell dynamics and its consideration in the control system can be found in Ref. [66].

The reconstruction of the crystal diameter and other quantities by means of an observer (cf. Section 28.2.3) from the weighing signal is the subject of several publications. Satunkin and Leonov discuss the question of observability in case of Cz and LEC growth in Ref. [66]. A Kalman filter approach can be found in [98]. In both cases, the discussion is based on a linearized model of the overall process, which is bound to the knowledge of some thermodynamic parameters. An elegant approach is presented in Refs [99,100] where, roughly speaking, an iterating algorithm is used that fits the theoretically calculated mass of the load cell to its real value by heuristically changing the crystal diameter in every step. However, this algorithm contains a parameter that must be empirically determined to guarantee convergence. A reduced order nonlinear tracking observer for the Cz and the LEC system including full meniscus dynamics is presented in Ref. [15]. As far as the system is tracked along its reference trajectory, this approach produces very accurate results.

If the influence of the changing meniscus can be more or less neglected, a simple approach is presented in Refs [101,102]. Here the basic idea is to exclude the meniscus dynamics from the model, making it easy to solve the remaining equations for the radius. This method is useful for reconstruction of the radius during cylindrical growth and for crystals with slowly increasing diameter in the cone. If one is obliged to grow crystals with large slope angles in the shoulder, this method fails, especially when fading into the cylinder. Another approach modulates the crystal pulling velocity with a small sinusoidal signal with a period much shorter than the dominant time constant of the process. In such a setup it is possible to reconstruct the diameter by a versatile algorithm [103,104].

28.3.2.2 Detection of the Bright Meniscus Ring

The idea behind this measuring technique is based on the fact that light emitted by the red-hot heaters is reflected in an upward direction from the meniscus surface. These

reflections can be seen and detected by an optical camera as a so-called “bright ring.” Then, image processing software is able to determine the diameter of the ring in real time [105,106]. This can be achieved in a similar way by measuring the radiation intensity using a pyrometer [87,90,107]. The determined diameter of the bright ring, scaled by an empirically determined factor accounting for the difference between measured bright ring radius and expected crystal radius, is used as the measured variable in the control system. Hence, although the crystal radius itself is not measured, this technique is widely and successfully used especially in silicon Cz growth. However, one has to take into account that the measure is the diameter of the meniscus at a certain height, not the crystal diameter at the three-phase boundary. This means that the anomaly discussed above comes into play again—if the crystal radius begins to decrease, first the meniscus height will increase. This means that the diameter of the bright meniscus ring will increase, which might result in incorrect reactions of the controller if it is not adapted to this behavior [17]. A detailed discussion on how to obtain an estimate of the real crystal diameter from the camera system under these constraints is given in Refs [108,109].

28.3.3 Feed-Forward Control

Model-based lumped parameter approaches are presented in Ref. [50] (4″ silicon), Ref. [102] (InP), and Ref. [110]. Since the underlying models neglect the spatial distribution of system properties (cf. Section 28.2.1), most often some empirical corrections (e.g., in Ref. [102]) are introduced to fit the result to reality. An approach trying to circumvent this problem is proposed in Ref. [111], based on a mathematical description regarding the most important qualitative dependencies between the relative changes of manipulated and controlled variables during growth. For a certain thermal setup this approach allows easy calculation of reference trajectories for different crystal shapes, growth, and crucible translation rates.

In order to overcome such limitations one may describe the system behavior without neglecting the spatial dependence of some of the system properties. Then one is confronted with the problem of numerically solving a set of time-dependent 2D/3D partial differential equations with free boundary conditions. Even though powerful FEMs for solving such problems exist, and computational performance has dramatically increased in the last several years, this still is one of the most challenging tasks [112,113]. The situation gets even worse if feed-forward trajectories need to be rescheduled in real time during growth, for instance, in order to react to some perturbations. Extensive studies on this task can be found in Refs [114–117], presented for the examples of growth of large diameter silicon and germanium crystals. To reduce the computational effort, one might restrict the problem to the quasi-stationary case. The feed-forward trajectory is then generated piecewise. This very powerful strategy has been presented in detail by Derby and Brown in Refs [47,72]. An approach using a simplified 2D model especially designed for control purposes can be found in Ref. [118].

A proper reference trajectory planning for the controlled variables is essential to obtain suitable feed-forward control trajectories. A good introduction into this subject w.r.t. Cz growth is given by Satunkin in Ref. [119].

28.3.4 Conventional PID-Based Control

28.3.4.1 PID-Based Control Using Optical Diameter Estimation

When designing a control system that tracks crystal diameter and growth rate, one has to reflect the different time constants that the manipulated variables have on the system: (1) Changes in pulling speed are affecting the system quite quickly; (2) Changes in heater power need some time depending on the thermal conditions occurring in the system [11,17]. Therefore, most often a cascaded control structure is chosen assuming that pulling speed v_p is more or less equal to the growth rate (cf. Figure 28.7) [120]. Deviations Δr_i from the reference value $r_{i,ref}$ of the crystal radius r_i are fed into a PID controller manipulating the reference value $v_{p,ref}$ of the pulling speed by an amount of Δv_p. This value, indicating a deviation of the real pulling speed trajectory from its precalculated reference value, is fed into a second PID controller manipulating the reference value P_{ref} of the heater power by an amount ΔP. By this strategy it is ensured that the system is able to react quite quickly on perturbations occurring in crystal diameter. Accumulated deviations in the pulling speed trajectory lead to a change of the heater power trajectory ensuring that the system is kept in its reference state in a long-term manner. Especially the pulling speed is brought back to its reference. This control approach requires very careful planning of the feed-forward trajectories, especially for the pulling speed needed to obtain a certain growth rate trajectory.

28.3.4.2 PID-Based Control Using Weight Measurement

If one does not have the possibility to capture the diameter of the bright meniscus ring, the usual control strategy is to use the crystal or the crucible "weight" as measured variable. When growing crystals from volatile melts, crystal weighing is preferred

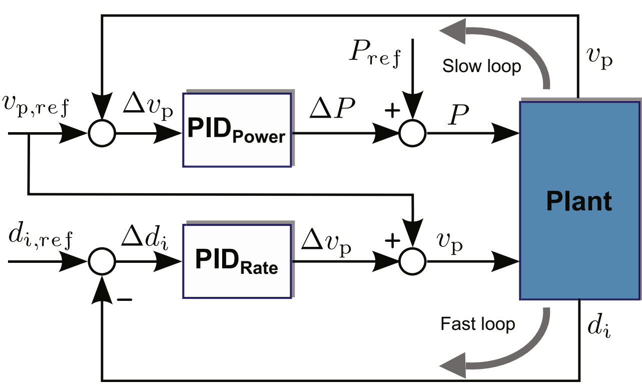

FIGURE 28.7 Cascaded PID-based control scheme utilizing pulling speed $v_{p,ref}$ and heater power (P) for diameter (d_i) control. Reference values are denoted by the subscript ref.

compared to crucible weighing because melt evaporation falsifies the signal in the latter one. The same holds when using rf-heaters where additional vertical forces induced in the crucible susceptor come into play [36]. One has to distinguish between two modes of operation [36,58]:

Weight mode: The weight measured by the load cell is compared to the reference value and the difference is used as an error signal for the PID controller. Hence, in this mode the controller tries to keep the weight on its reference value, meaning that a previous error in crystal radius later results in an error of opposite sign. This, on the one hand, is usually not preferable when trying to grow a crystal of well-defined shape. On the other hand, this mode circumvents noise generation by numerical differentiation of the force raw signal as required in differentiated weight mode.

Differentiated weight mode: The force raw signal is differentiated with respect to time and then compared to the reference value resulting from the predefined shape of the crystal. If one neglects the dynamics of the meniscus, this signal is proportional to the crystal radius, i.e., this mode tries to keep the radius on its reference value without being influenced from the past. The differentiation of the raw signal leads to a phase advance in the control system, which tends to make the system “more stable”. On the other hand, sophisticated signal processing and filtering methods as well as high resolution load cells are required.

The most crucial part in this technique is the *anomalous* behavior of the signal, cf. Section 28.3.2. The consequence of this anomaly is that the performance of the control system is fundamentally limited [10]. The controller “is only allowed to respond carefully” to any sort of perturbation since they could be of opposite direction, not indicating what really goes on at the interface.

28.3.4.3 Improvements and Optimizations

In this section some approaches trying to compensate for the problems mentioned above are sketched.

In Refs [61,62] Bardsley, Hurle, et al. present a sophisticated control algorithm containing a method to overcome the problems resulting from the anomalous behavior. They try to estimate the anomalous components in the measured weight gain signal and subtract them from the signal. The estimation is done using a linear model calculating the radius change δr_i induced by changes in heater power. This value can be used for calculating an estimate of the anomalous component of the signal. Experimental results demonstrate the performance of this approach. However, it is restricted to the knowledge of a sufficiently precise model of the process, especially of the thermal conditions in the furnace.

A challenging task in this control approach is the choice of the parameters of the PID controller. Most often this is done by trial and error. However, there are some interesting approaches trying to determine optimal parameters of the PID controller on the basis of the model knowledge available. Satunkin et al. [66,121] propose an approach based on a cost functional for adjusting parameters in a single, as well as, multiloop control system utilizing heater power and pulling speed as manipulated variables. The same authors

present a modeling approach focusing on inaccuracies of the weight sensor and the consideration of these in the control system [66].

As already mentioned, the dynamic characteristic of the process changes during crystal growth. As a consequence, parameters of the PID controller determined for one set point may not produce acceptable results as the process proceeds. The strategy to overcome this problem is to change the parameters on relevant intervals. This strategy is commonly known as *parameter* or *gain scheduling* in the field of adaptive control [122,123]. An approach for Cz growth can be found in Ref. [16].

28.3.5 Model-Based Control

28.3.5.1 Lumped Parameter Model-Based Control

In Refs [10–13] Gevelber et al. propose a model-based multiloop control system. The first two publications of this series are based on a seventh-order model of the process, while the latter ones make use of a more refined model of order 34. In these publications, a multiloop control system is proposed not only to ensure a correct diameter during the process but also to compensate identifiable disturbances before they affect the growth dynamics. Two main disturbances are identified, both related to the melt drop: the thermal state of the melt, which changes the heat flux entering the interface; and the thermal environment that the crystal is exposed to, affecting the heat flux from the interface and thus the growth dynamics. By adding a closed loop around the melt temperature, the impact of this disturbance is significantly reduced, enabling tighter control of diameter and thus minimizing growth rate variations in a robust manner. Additionally, this work analyzes the importance of controlling the interface shape in addition to the crystal diameter. This requires the use of additional actuators, and an important part of the design task is to select an actuator set that can control both degrees of freedom relatively independently. To further obtain design insight, Gevelber et al. derive a model that especially reflects the influence of radiation heat transfer within the furnace as exactly as possible within a lumped parameter model.

Further model-based approaches have been presented by Satunkin [98] (using a linear state space controller), Sabanskis [118] (using a 2D approximation), and Riedling [124] (combining heuristic and deterministic techniques in the 4″ growth of GaAs crystals using the LEC method).

The bottleneck of the lumped parameter model-based approaches is the appropriate modeling of the thermal effects. An elegant solution to circumvent this is the following approach [14]: for the Cz process, a relatively simple second-order lumped parameter model of the meniscus dynamics only can be derived if rotational symmetry and a planar solid–liquid interface is assumed [14]. It reads:

$$\dot{r}_i = v_g \tan(\alpha_i) \tag{28.10a}$$

$$\dot{\alpha}_i = \frac{v_p - v_c - c_{\alpha z}(r_i, \alpha_i) v_g}{c_{\alpha n}(r_i, \alpha_i)}. \tag{28.10b}$$

In these equations, r_i denotes the crystal diameter at the solid–liquid interface, α_i the cone angle (cf. Figure 28.4), v_p the crystal pulling rate, v_c the crucible translation rate,

and v_g the crystal growth rate. Furthermore, $c_{\alpha z}$ and c_{an} are some nonlinear functions that can be found in Ref. [14]. The growth rate results from the thermal situation in the furnace, cf. Eqn (28.8), but is considered as unknown in this approach.

Although this capillary model does not cover the complete process dynamics, it can be utilized to derive a partial model-based control system [14,15]. Considering the relation $\dot{x}/v_g = (dx/dt)/(dl/dt) = (dx/dl) = x'$ in which l is the crystal length and x an arbitrary quantity, one can divide the differential equations of the model (10) by the growth rate $v_g = dl/dt$. As a result, one obtains a model that is parameterized in crystal length instead of time:

$$r_i' = \tan(\alpha_i) \tag{28.11a}$$

$$\alpha_i' = \frac{v_z - c_{\alpha z}(r_i, \alpha_i)}{c_{\alpha n}(r_i, \alpha_i)} \quad \text{with} \quad v_z := \frac{v_p - v_c}{v_g}. \tag{28.11b}$$

The dimensionless quantity v_z is denoted as the *lift ratio*. Now, a model-based control law can be derived according to the procedure described in Section 28.2.5, Eqns (28.5)–(28.7) with $y = r_i$ and $\dot{y} = r_i' = \arctan(\alpha_i)$. One obtains:

$$\begin{aligned} v_{z,\text{ref}} &= \nu \frac{c_{\alpha n}(r_i, \alpha_i)}{1 + (r_i')^2} + c_{\alpha z}(r_i, \alpha_i) \quad \text{with} \\ \nu &= r''_{i,\text{ref}} - k_1\left(r_i' - r'_{i,\text{ref}}\right) - k_0\left(r_i - r_{i,\text{ref}}\right). \end{aligned} \tag{28.12}$$

This model-based controller calculates desired values $v_{z,ref}$ for the intermediate quantity v_z. Since one lacks a model of the thermal behavior, PID controllers are placed around this model-based controller, transforming this intermediate value into the real inputs pulling speed v_p and heater power P available at the process. This approach is sketched in Figure 28.8. A nonlinear state estimator provides values for r_i, α_i [15]. Parameter scheduling for the PID parameters and the proper assignment of the manipulated variables to the controlled variables are discussed in Ref. [16]. By this strategy, a large amount of lumped parameter model knowledge is introduced into the control system. A similar procedure can be found in model-based control of the Detached Bridgman process, cf. Section 28.5.3.

In all cases discussed in this section, the overall closed-loop performance is considerably enhanced, however, because of the lumped parameter character, some more or less strict constraints exist with respect to process setup, model validation, or trajectory planning.

28.3.5.2 Distributed Parameter Model-Based Control

Some publications try to overcome the limitations resulting from the lumped parameter approach by directly working on the partial differential equations of the distributed parameter models. Such approaches, for example presented by James Ng et al. in Refs [125–127] and Wang in [128], are fundamentally important for understanding the dynamics of the process, especially when focusing on the effects related to heat transport phenomena or variable phase boundary problems. However, for an implementation

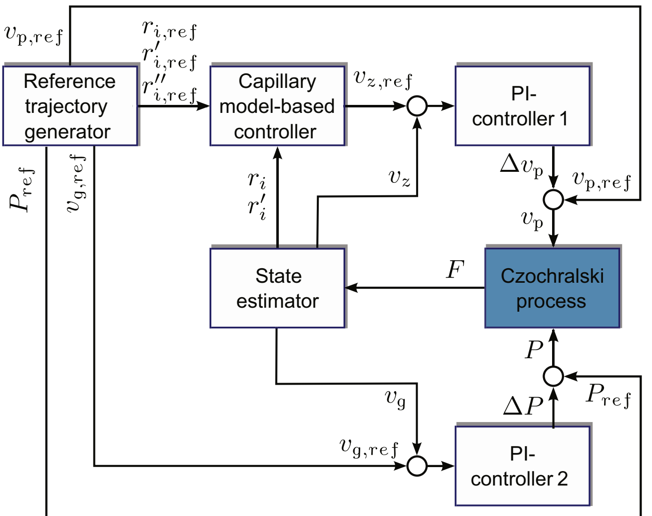

FIGURE 28.8 Combination of model-based and PID control. *Adapted from Refs [14,15].*

under real world conditions and controller parameterization they are not suitable. The reason for this is that in these models the manipulated variables are also spatially distributed, e.g., a temperature distribution on the heater surface. But, what the controller actually manipulates is the current entering the heater, which is a lumped quantity being connected to the temperature distribution on the heater surface in an unknown way.

28.3.5.3 Model Predictive Control

An interesting approach based on this strategy can be found in Refs [129,130]. The model used in this approach is of lumped parameter type. It includes melt convection, which requires very strict assumptions to be fulfilled in order to make the model applicable. Another approach to establish such a model-based control on the basis of a lumped parameter model has been published by Voronkov et al. [9,120]. It is closely related to the v_{g}/G theory [5,7], which requires very precise tracking of the growth rate v_{g}.

28.4 Vertical Bridgman and Vertical Gradient Freeze Process

From a control technological point of view, the Vertical Bridgman (VB) and the Vertical Gradient Freeze (VGF) crystal growth processes (cf. Vol. IIA, Chapter 9) are outstanding challenging tasks. On the one hand, one has—compared to other processes—a relatively large number of strongly coupled manipulated variables, and on the other hand, one has exactly zero measurement information about the most important process quantities.

28.4.1 Process Characteristics and Control Objectives

Common to both processes is the continuous movement of a (more or less) fixed temperature gradient in vertical direction of an ampule or crucible containing the molten material. This movement is done in such a way that crystallization inside the ampule takes place in a well-defined manner from the bottom toward the top. In the VB process this is realized by the relative mechanical movement between ampule and the axially arranged heaters, independently, which of both is really moved. In contrast, in the VGF process the movement of the temperature gradient is solely realized by an appropriate tracking of the heater powers.

The key problem when trying to establish a feedback control for the Bridgman process is the fact that no measurement information about the variables that should primarily be controlled is available. The most prominent candidate for the controlled variable would be the growth rate (the crystal shape is already fixed by the ampule). Assuming a flat interface shape, it could be treated in a lumped parameter sense as done in the Cz process above. However, in real systems the interface represents the melting point isotherm inside of the furnace and is never completely flat. The deflection of the interface, its convex or concave shape, directly influences the crystal quality. Usually a slightly convex interface shape is preferred in order to avoid a concentration of grown-in defects (cf. Vol. IIA, Chapter 9). To achieve this goal, the interface shape has to be detected in situ and feedback controlled. However, besides manually detecting the position of the interface [131] (which may lead to contamination issues and mechanical generation of structural defects at the interface) or using a transparent ampule [132] (which is limited to few materials) up to now no feasible method for an in situ measurement under industrial conditions of this process quantity is known. The most promising technique for this task seems to be the application of ultrasound. Here the basic work was done by Parker and Manning [133] followed by Carter et al. [134] (Germanium) and Schmachtl [135] (metal alloys) first presented acceptable resolutions. A modern approach is presented, e.g., by Azizi et al. [136] for multicrystalline PV silicon normal freezing and for FZ in Dold et al. [137]. Achieved growth rate resolutions were roughly in the range of $\pm$ (1…2) mm/h. This is acceptable to have approximate information about the position of the phase boundary. However, for Bridgman growth with its low growth rates just in that range of several mm/h, the resolution has to be better by a factor of 5–10 for using it in a robust feedback control system.

In both processes, the heater powers are important manipulated variables. The correct adjustment of the heater powers in order to maintain the required temperature field is a challenging task. In the VB process, the heaters have to be controlled in such a way that despite the moving ampule and the phase transformation in it, the temperature field remains constant. In the VGF process, the temperatures of the heaters have to be continuously changed in a predefined manner in order to establish the movement of the temperature gradient. In both cases, only very small tolerances are acceptable. The main problem here is that one has a system of several heaters that are responsible for the

temperature and its dynamics at several points of the furnace. However, each heater does influence the *whole* temperature field. Hence, when designing a temperature control system, one deals with a typical multi-input-multi-output (MIMO) system with a strong cross-coupling. Because of this, controller design is much more complicated compared to single-input-single-output (SISO) systems. An additional control task in VB growth is the proper tracking of the relative motion between ampule and heaters.

28.4.2 Conventional Control

As stated above, in the majority of applications the primary system quantities, especially the interface shape, cannot be directly measured. However, because a certain interface shape and interface position is directly connected to a certain temperature field within the ampule [138], which itself is characterized by a certain temperature distribution on the ampule's boundary, it makes sense to content oneself with a proper feedback control of the heater temperatures [139] and/or the movement of the ampule. Such an "indirect" control system uses the temperatures of thermocouples installed on the surface of the ampule as the controlled variables and the heater powers as the manipulated variables. For its function, one has to calculate the required boundary temperature distribution using a suitable model of the process. Because of the complexity of the models and possible ambiguities of the solutions, this calculation has to be done a priori. The result is used as a reference for conventional real time MIMO PID feedback control. Control design for such coupled systems using PID controllers is a well-matured task in control technology. A general introduction of the control of such systems is given, for example, in Refs [140–142] and especially for multizone heating systems in Refs [143,144].

The key problem of this indirect control strategy is the correct and unambiguous calculation of the reference temperature profile and/or translation rate of the ampule. This requires not only appropriate model knowledge, usually by means of high order FEM models, but also time-consuming experimental effort to match the models to the relevant plant setup. Furthermore, under industrial conditions, *all* plants have to be kept in exactly the state that has been used for this matching ("copy exactly", cf [145]). A wide range of modeling approaches for this purpose exists in literature; Kuppurao, Derby, et al. [146,147] may be used as a starting point.

28.4.3 Model-Based Control

Only a few publications exist for the model-based control of the VB/VGF process. Apart from the measurement issues, this is due to the fact that models of the system appropriate for *control purposes* are of distributed parameter type, cf. Section 28.2.1. For example, the controlled variable "interface shape" cannot be described by a single variable but by a functional relation. The same holds for the temperature distribution at the ampule boundary. Only the heater powers are of lumped type. The feedback control of such distributed parameter systems with lumped inputs is currently a highly dynamic

subject of investigation in control theory [148,149]. An approach for a very simple model of the VGF process detailing this strategy can be found in Refs [150,151].

Apart from that, model-based approaches exist focusing on subordinate problems and trying to reduce the problem to the control of some lumped parameter quantities. They are detailed in the next two sections.

28.4.3.1 Temperature Control and Interface Shape Detection

The model-based temperature control of the Bridgman processes has been the subject of several publications by Batur et al. In Refs [132,152] a method for the identification of a linear lumped parameter MIMO model of the heating zone system is proposed. The model is used for the design of a self-tuning linear state space controller for tracking of the zone temperatures. Experimental results from an eight-zone VB system with three thermocouples in each zone are provided showing the importance of the consideration of the cross-coupling between the heaters in the controller design. In the investigated setup, a transparent ampule for the growth of lead bromide has been used. This makes it possible to directly detect the interface shape and to close the feedback path. An appropriate algorithm for the detection of the interface from the camera pictures is provided in the mentioned publications as well as in Ref. [153]. Of course such an approach is not possible when growing crystals of nontransparent materials in nontransparent ampules, which is the case in the majority of VGF-grown elemental and compound semiconductors. The controllers used in this approach are of quite complex structure due to the MIMO character of the system and the strong cross-coupling between the zones. Therefore, in Ref. [154] the same authors present reduced-order controllers based on so-called projective control strategies [155].

A much more refined approach is presented by Batur et al. in Ref. [139] on simulation studies, cf. Figure 28.9. Again it is assumed that a certain desired interface shape requires

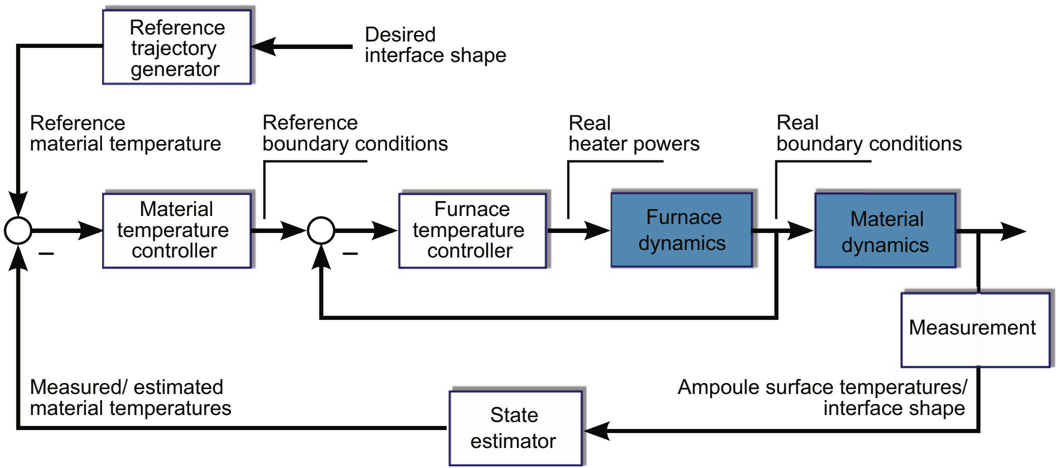

FIGURE 28.9 Bridgman crystal growth control system. *Adapted from Ref. [139].*

a corresponding temperature distribution inside the material. The task of the interface shape control loop is to establish this temperature distribution and can be accomplished by manipulating the boundary conditions around the material. These boundary conditions are established by the furnace temperature controller. If the interface shape or the inside material temperatures can be measured, it is compared with the desired interface shape or the reference material temperatures, and the resulting error signal is sent to the material temperature controller. The required boundary conditions, or equivalently the furnace (or heater) temperatures, are determined by the material temperature controller. The boundary conditions are used as the reference temperatures for the furnace temperature controller. The actual boundary conditions established by the furnace temperature controller determine the temperatures inside the material through the dynamics of the crystal growth mechanism. The approach provides the possibility to estimate the shape of the interface if it cannot be measured directly (cf [156]).

28.4.3.2 Flow Speed Control

In Refs [157,158] Sonda, Yeckel, and Derby present a model-based approach for controlling the melt flow. In their system, the meridional melt speed S is used as the controlled variable. This is the spatial root-mean-square average of the velocity magnitude, defined as

$$S = \sqrt{\frac{1}{V}\int_{(V)} \left(v_r^2 + v_z^2\right) \mathrm{d}V}$$

where v_r and v_z denote the magnitude of the velocities in the radial and axial directions, respectively and V is the total melt volume. The crucible rotation speed is used as the manipulated variable. By this choice, a SISO-controller design procedure is possible. A nonlinear input–output feed-forward controller combined with a state feedback controller [159] is chosen by the authors to address the problem. The model-based controller approach is tested by simulation on models provided by Kim et al. [160,161], Müller et al. [162], and Derby et al. [163,164] assuming two configurations: melt at the top of the ampule (“stable configuration”) and melt at the bottom of the ampule (“unstable configuration”). The results are further compared to simple linear P- and PI-controllers. It has been shown that flow oscillations in the melt could be attenuated by a significant amount. Due to the lack of any measurements, especially of S, the approach is of theoretical interest only. However, by such studies one gains deep insight into the process dynamics and the correlation between different process phenomena.

28.5 Detached Bridgman Process

The Detached Bridgman crystal growth process is a promising candidate for the production of bulk, single-crystal semiconductors of extraordinarily quality because it provides zero container contact of the crystal (as in Cz growth) and low thermal stress (as in Bridgman growth) (see Chapter 19 of Volume IIB). Thorough investigations of this

process especially with respect to process control have been provided by Yeckel and Derby [165–167], on which this section is mainly based.

28.5.1 Process Characteristics and Control Objectives

Detached growth occurs when the crystal solidifies into the melt without contacting the ampule wall, cf. Figure 28.10. Hence, a narrow gap that is usually filled with inert gas between the crystal and the ampule remains. In stable detached growth, the melt is in contact with the ampule above the crystal. The gap between the ampule wall and the triple-phase line is bridged by a small liquid meniscus. The primary control task is to achieve a stable growth regime with constant crystal diameter under terrestrial conditions, i.e., the crystal neither contacts the ampule wall nor grows away from it during growth. Compared to zero-gravity conditions, this is more complicated because of the continuously decreasing static weight of the melt on top of the growing crystal. Hence, this effect must be robustly compensated [165]. Another control task would be the regulation of the crystal growth rate or the interface shape as in conventional Bridgman growth. Here, for growth rate control the same issues and limitations exist, cf. Section 28.4, and up to now no publications are available dealing with the feedback control of this important process quantity. Anyway, a proper control of the crystal diameter or equivalently of the gap width is of superior priority since it enables one to maintain the detached state over the full process duration. It has to be noticed that no method for the in situ detection of the gap width has been developed so far. Against this background

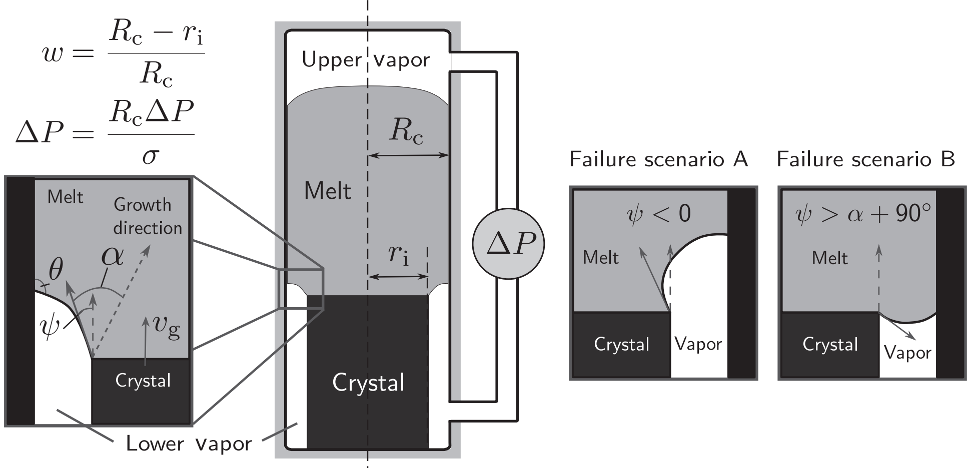

FIGURE 28.10 Sketch of a detached Bridgman growth furnace. One has the growth angle α, the wetting angle Θ, the gap width w, the crystal radius r_i, the inner ampule radius R_c, the melt surface tension σ, and the pressure difference ΔP between the upper and the lower vapor space. The angle between the vertical and the meniscus at the three-phase-line (TPL) is denoted by ψ. The two figures to the right show situations in which stable growth tends to fail because of inadequate values of the manipulated variable ΔP: (a) $\Delta P \ll 0$ (too much suction); (b) $\Delta P \gg 0$ (too much pressure downward). *Adapted from Refs [166,168].*

the following explanations are of more theoretical value, however, they may be helpful in understanding the process and its dynamics in more detail.

28.5.1.1 Choice of the Manipulated Variable

In order to control the crystal diameter and to stabilize the system, an appropriate manipulated variable must be available. Several methods have been developed for this purpose. Duffar et al. [168,169] propose a system in which a second vapor space above the melt is introduced. Then, gas is injected into the upper and lower vapor space in such a way that a stable growth regime is achieved. This configuration is depicted in Figure 28.10. In this case the manipulated variable is the pressure difference ΔP between the two vapor spaces. A similar method is proposed by Palosz [170]. Pätzold [171] alternatively manipulated the pressure on the meniscus by controlling the temperature of the vapor space in the bottom of the ampule.

28.5.1.2 Lumped Parameter Model

Fortunately, it is possible to derive a simple first-order lumped parameter model of the capillary part of the system as appropriate for control purposes if one uses the pressure ΔP as the manipulated variable. It is very similar to that employed in Cz growth. With the denotations from Figure 28.10 one has:

$$\dot{w} = v_g \tan(\alpha - \psi) \quad (28.13a)$$

$$\psi = \arccos\left[\left(\frac{\Delta P}{2} - \cos\Theta\right)(1 - w) - \frac{\Delta P}{2(1 - w)}\right]. \quad (28.13b)$$

The growth rate v_g depends on the thermal situation at the interface (cf. Eqn (28.8)) and has to be calculated from a model of the thermal system.

28.5.1.3 Stability and Operational Limits

When designing the control system the most important question to be answered is under which conditions stable growth occurs. As in Cz growth, the answer depends on the effects included in the model on which the stability analysis is performed, cf. Section 28.3.1.3. First studies on this topic neglecting any thermal effects and the shape of the crystal–melt interface can be found in Ref. [168] under zero gravity and under terrestrial conditions in Refs [169,171,172]. The influence of the gap width on the interface shape is studied in [173,174]. A linear stability analysis of Epure [175] shows that gravity may have a stabilizing effect on the process, while in Ref. [176] it is shown that mechanical perturbations to the meniscus may lead to dewetting. The most rigorous analysis under zero gravity based on a full thermocapillary model has been provided by Yeckel et al. in Ref. [165]. Their approach interestingly confirmed the basic stability criterion $\Theta + \alpha > \pi$ derived originally by Duffar without regarding thermal effects (refer to Figure 28.10 for an explanation of the symbols). From this stability criterion, it follows that when growing typical semiconductors with growth angles α in the range of $10°...30°$ a strongly non-wetting ampule material with $\Theta > 150°...170°$ is required. Apart from that, this stability criterion combined with the capillary model (13) provides further insight into the system

characteristics important for controller design as carried out in Ref. [166]: Stationary growth with respect to the gap width (i.e., $\dot{w}=0$) occurs if $\alpha=\psi$. The corresponding pressure difference ΔP_e depending on the gap width w follows from Eqn (28.13b):

$$\Delta P_e = -\frac{2(1-w)}{w(2-w)}(\cos(\alpha)+(1-w)\cos(\Theta)). \tag{28.14}$$

The pressure difference ΔP^* below which no equilibrium exists is characterized by the condition $\psi=0$. From Eqn (28.13b) it follows:

$$\Delta P^* = -\frac{2(1-w)}{w(2-w)}(1+(1-w)\cos(\Theta)). \tag{28.15}$$

The difference $\Delta P^* - \Delta P_e$ defines the largest possible perturbation of the manipulated variable and forms a strong restriction on the controller performance. On the other hand, the gap width w_e for stationary growth reads

$$w_e = 1 - \frac{\cos(\alpha) \pm \sqrt{\cos^2(\alpha)+\Delta P(\Delta P - 2\cos(\Theta))}}{\Delta P - 2\cos(\Theta)} \tag{28.16}$$

with shape stable solutions for the positive sign and shape unstable solutions $(\alpha+\Theta<\pi)$ for the negative sign. Here, two cases of instability must be distinguished—perturbing the gap width to a smaller value may cause reattachment of the crystal to the ampule; perturbing it to larger values may lead to necking of the crystal.

The gap with w^* at which the dewetting failure occurs is obtained by setting $\psi=0$ in Eqn (28.13b):

$$w^* = 1 - \frac{1 \pm \sqrt{1+\Delta P(\Delta P - 2\cos(\Theta))}}{\Delta P - 2\cos(\Theta)} \tag{28.17}$$

with the positive sign for $\Delta P > \cos(\Theta)$ and the negative sign for $\Delta P < \cos(\Theta)$. By a similar procedure, the maximum allowed interval for the wetting angle of the ampule wall can be determined. If the wetting angle increases due to a chemical or physical heterogeneous ampule wall, the meniscus will deform in an upward direction to maintain the pressure balance. This might violate the ΔP^* border. This critical angle Θ^* results from Eqn (28.13b) with $\psi=0$ and using Eqn (28.14) to eliminate ΔP. Hence, the maximum allowed perturbation $\delta\Theta$ of the wetting angle reads

$$\delta\,\Theta = \arccos\left(\frac{\cos(\alpha)+(1-w)\cos(\Theta)-1}{1-w}\right) - \Theta. \tag{28.18}$$

Equations (28.15), (28.17), and (28.18) form the basis to determine the operational limits $\Delta P > \Delta P^*$, $0 < w < w^*$, $\delta\Theta$ of a control system.

28.5.2 PI-Based Control

In a first step, it is natural to address the gap width control by means of a P- or PI-controller (cf. Section 28.2.5) with the gap width as the controlled variable and the pressure difference as the manipulated variable. A comprehensive discussion on this

strategy is presented in Ref. [166]. It turns out that due to the strong nonlinearity of the process and the restricted operational limits (cf. previous section) a robust control of this system based on such linear controllers is not favorable. For example, in closed-loop mode a certain *minimum* gap width occurs, making diameter control more complicated. Furthermore, solution multiplicities are introduced. Hence, the applicable controller gain K_P (cf. Eqn (28.4)) is limited. The key problem here is the fact that the P- or PI-controller naturally does not have any model knowledge, which enables it to account for the very restricted limitations of the system. Thus, the possibility is relatively large that the controller drives the system into a state in which immediate detaching failure occurs. This issue can only be addressed by tuning the controller very weakly or by introducing hard limits on its output. This, on the other hand, results in slow actuator performance and, hence, in poor disturbance rejection.

28.5.3 Model-Based Control

The very simple capillary lumped parameter model (13) of the system enables one to derive a nonlinear model-based controller for the system. The procedure in doing so is exactly the same as in the introductory example in Section 28.2.5 and in Cz growth (Section 28.3.5.1). Since the restrictions derived in Section 28.5.1 result from this model, such a controller will account for them. This approach has been published by Yeckel et al. [167] for the case of microgravity and will be sketched in the following:

In order to derive the controller, the control error in the gap width is introduced as $z = (w - w_{\text{Ref}})/w_{\text{Ref}}$ with the reference gap width w_{Ref}. One wants the tracking error to fulfill a stable first-order dynamics, which is defined as

$$k_0\dot{z}(t) + z(t) = 0 \quad \Leftrightarrow \quad z(t) = z(0)\mathrm{e}^{-\frac{t}{k_0}} \tag{28.19}$$

with the characteristic time $k_0 > 0$, the controller parameter determining how quickly the control error converges to zero (cf. Eqn (28.5) also). Substituting Eqn (28.13a) into Eqn (28.19) and using Eqn (28.13b), one obtains the control law

$$\begin{aligned} \Delta p &= -\frac{2(1-w)}{w(2-w)}(\cos(\alpha-\beta) + (1-w)\cos(\Theta)) \quad \text{with} \\ \beta &= \arctan\left(\frac{w_{\text{Ref}} - w}{k_0}\right) \end{aligned} \tag{28.20}$$

which provides the pressure difference required for the correction of disturbances in the gap width. Note that ΔP will always exhibit or equal the pressure limit given in Eqn (28.15). Furthermore, this control law naturally reduces to the relation of the equilibrium pressure (Eqn (28.14)) if $w = w_{\text{Ref}}$. A method on how to increase robustness with respect to bias errors by introducing an additional integral part and an in-depth discussion of the proper choice of the parameter k_0 as well as of controller performance can also be found in Ref. [167]. Additionally, it is shown that errors resulting from the static weight of the melt in case of terrestrial growth are accounted for by the controller, too.

28.6 Floating Zone Process

The Floating Zone (FZ) technique is favored if high material purity is required that cannot be ensured by, for example, the Cz method, because of melt contamination by the crucible material. The method itself is explained in detail in Vol. IIA, Chapter 7 of this handbook where a modern model predictive control system is also presented. The next chapter gives a more general overview of FZ control issues.

28.6.1 Process Characteristics and Control Objectives

The primary task of an FZ control system is to ensure a stable molten zone between the feed rod and the growing crystal. Among other parameters it is defined by the diameters of the feed rod and the crystal, respectively, and its height, the so-called zone length. The crystal diameter and the zone length are the controlled variables. A proper control of these quantities is a key issue because inappropriate values may lead at least to a reduced crystal quality and in the worst case to leakage of the melt zone or melt-inductor contact. As manipulated variables, the vertical translation rates of the feed rod (responsible for the melt flux into the molten zone) as well as the heat induced in the molten zone are available. The latter one is usually provided by single coil electromagnetic heaters, i.e., the current entering the inductor is the third manipulated variable. The translation rate of the crystal is usually kept constant in order to support a constant growth rate. This system is of strongly coupled nature—on the one hand, an increase of the heater power will increase the zone height because the amount of melt that is molten is increased. As a result of this, one will observe a temporary diameter deflection until a new steady state is reached. On the other hand, an increase of the feed rod translation rate in the downward direction will decrease the zone height, which results in an increase of the material molten from the feed rod per time unit. Hence, since the volume of the molten zone cannot increase beyond certain limits, the crystal diameter will increase to a new steady state value. These interrelationships are extremely sensitive with respect to the corresponding manipulated variables and require highly skilled operators for manual control or carefully adjusted control systems.

As in Cz growth, a first stability analysis of the Fz process has been provided by Surek in Ref. [75] focusing only on the capillary problem. From this point of view, the system is always inherently stable. A more in-depth analysis has been given by Tatarchenko in Ref. [78] (also briefly summarized in Ref. [81]), including also dynamic effects and the influence of the heat flows in the system. Especially, it has been shown that from a system theoretical stability point of view pulling downward should be preferred compared to pulling upward (pedestal growth). Further investigations on this topic can be also found in Ref. [98].

28.6.2 Measurement Techniques

A big advantage in Fz growth is the fact that the parts of the melt zone that are not hidden by the inductor coil can properly be monitored through a camera system.

The determination of the crystal diameter and the zone length as well as of the phase interfaces from such an imaging system are described in a Siemens patent from 1963 [177]. Additional information can be gathered if one tries to determine the tangent to the melt surface at certain points of the melt zone. This is described in Ref. [178]. Capturing of the *whole* visible molten zone shape enables one to reconstruct information about the state of the process, which is far beyond that gathered from the diameter and zone height, for example, the crystal cone angle or the melt angle. These quantities can be useful in a model-based control system. With respect to this, Lie et al. [179] and Wünscher [180] provided a set of methods for the calculation of the surface shape of the molten zone, including the electromagnetic pressure. One may also consult the contributions of Shyy and Rao [181] and the Kalman-based method by Werner (cf. [182] and Vol. IIA, Chapter 7).

28.6.3 Reference Trajectory Planning and Conventional Control

In the Fz process the planning of the reference trajectories is of special importance. For example, the diameter of the inductor hole limits the size of the melt neck to an upper value since one has to avoid short circuits due to contact of the melt with the heater. On the other hand, the melt neck must not be too thin since this may (in the worst case) result in detaching of the melt from the feed rod [182]. These constraints have to be considered during planning of the reference trajectories for the crystal diameter and the zone length. The size of the latter is also limited to ensure a stable melt zone. This topic is discussed by Heywang [183].

Keeping these constraints in mind, it is possible to implement a control system using standard PI or PID controllers (cf. Section 28.2.5.1). A first control approach was proposed by Rowton in 1965 [184] for a silicon refinement process. There, a relation between the diameter deviation of the feed rod and the inductor frequency is derived. Then, the measured inductor frequency is used as controlled variable. A cascaded control regime ensures proper diameter tracking, in some sense similar to that usually used nowadays in Cz growth (cf. Section 28.3.4). A deviation in the frequency drives a PID controller manipulating the heater power, and the deviation of the heater power is used for a correction of the translation rates in order to keep the disturbances of the ingot diameter away from the refined rod. Such an indirect control regime is also proposed by Otani et al. [185] for the growth of refractory metals. Today, crystal diameter and zone height are directly measured. Hence, a two-loop control system can be established; in this, a first PID controller is responsible for keeping the diameter on its reference value using the heater power as manipulated variable, and a second PID controller uses the feed rod translation rate for keeping the zone length on its reference value. Such an approach is discussed in detail, for example, by Chan et al. [186] for the growth of TiC, and is also claimed by the Shin-Etsu patents [187–189].

28.6.4 Model-Based Control

As in Cz growth, the performance of PID-based control regimes is fundamentally limited due to the nonlinearity and the batch character of the process. Hence, a variety of model-based strategies is proposed in the literature. A model predictive control approach (cf. Section 28.2.5.3) has been presented in a patent by Wacker [190]. There, a reduced order model derived from a high order one is used to perform the required real time optimization calculations. The patent illustrates the basic idea of such an approach rather than providing a realizable model. A linear fourth-order lumped parameter model suitable for controller design (in a certain set point) is derived by Satunkin in Ref. [98]. Werner proposes an eleventh-order nonlinear model in Ref. [182]. Based on this model, a sophisticated nonlinear model predictive control strategy is established, which is also sketched in Vol. IIA, Chapter 7 of this handbook.

28.7 Kyropoulos Process

The Kyropoulos growth method was intentionally designed to grow crystals under extremely low thermal stress. It has tended to be sidelined for decades, but nowadays it is experiencing a kind of renaissance, e.g., for sapphire growth [95,191]. Similarly, new applications occur for the growth of multicrystalline silicon for PV applications [192]. Hence, the demand for a proper control of this process is increasing. Unfortunately, only very few publications exist dealing with this topic. Thus, the following compilation may be useful as a starting point for further research.

28.7.1 Process Characteristics and Control Objectives

The setup of the Kyropoulos technique is sketched in Figure 28.11. In the initial stage of the process, after seeding, the crystal grows into the melt with a sharply convex interface shape, driven by the cooling of the seed crystal. Later, as the diameter increases and the release of latent heat reaches a significant amount, the temperature field inside of the growing crystal and the melt is manipulated by the heater power in such a way that crystallization is maintained. During growth, the crystal is nearly not, only slightly, or moderately pulled in an upward direction [194,195]. The exact translation rate is a question of technological requirements like internal transport of heat, shape control, etc. In modern approaches for sapphire growth – for example – the trend is toward extremely slow movement of the pulling rod [195,196] or to no translation/rotation at all [197]. At least in cases where the crystal is additionally rotated [194], the remaining difference to Cz is that the crystal grows far below the melt surface, i.e., no melt meniscus is present. The submerged growth of the crystal provides very low axial and radial thermal gradients. The finished crystal is irregularly shaped and occupies almost the entire crucible. Usually the crucible is touched by the crystal at the bottom region only. Critical stages of the process are the seeding and initial expanding phase of the shoulder and the end of the process when the crystal reaches the crucible bottom [197]. A process control system

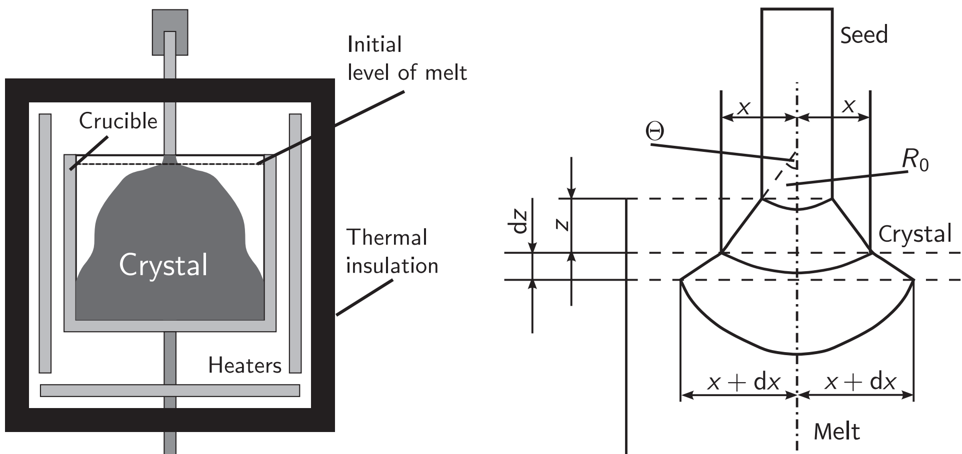

FIGURE 28.11 Sketch of a Kyropoulos plant (left) and geometrical abstraction of the process (right). *Adapted from Ref. [193].*

has to ensure that the crystal diameter does not increase too fast during the initial phase and is kept on a more or less constant value for the rest of the process. Furthermore, a sudden freezing of the melt has to be avoided. Because of the very low thermal gradients in the furnace, this is a challenging task.

28.7.2 Control Approaches

The manipulated variables are the power of one or several heaters, and the preferred controlled variable would be the crystal diameter. Instead, usually the force acting on a load cell connected to the seeding rod is used as the controlled variable [191,198]. For a proper design of the control system using a lumped parameter model, one has to derive a relation between the force acting on the load cell and the evolution of the crystal diameter. Because of the strongly convex interface shape and the irregular growth of the crystal preventing any symmetry assumptions and other simplifications in the models, this is a much more complicated task than in Cz growth where usually a planar interface and rotational symmetry can be assumed for such calculations. The situation still worsens because strong buoyancy effects of the (partially) submerged crystal have to be considered.

First investigations on calculating the crystal shape in Kyropoulos growth were published by Singh [193] using also results from Schönherr [199]. Their technique is based on a pure mass transfer approach assuming that the crystal interface shape can be described as spherical or as an ellipsoid of rotation. Although the influence of the heat transfer and melt convection is not considered in their approach, the results have been verified with acceptable limits of error by numerous experiments. Furthermore, for materials not showing a density anomaly, it is shown that the crystal radius reaches a limit value $r_{\max} = R_c\sqrt{\rho_m/\rho_s}$ with the crucible radius R_c and the densities ρ_m, ρ_s of the

melt and the crystal, respectively. A more refined (also purely geometrical) approach is given by Zhang et al. [196,200].

A common approach for controlling the Kyropoulos process is to numerically calculate the evolution of the temperature field in the furnace, which represents the desired growth of the crystal. The time evolution of the temperature field can be represented by trajectories of the heater powers. Hence, one can apply a feed-forward control regime using these heater power trajectories. A discussion related to this topic can be found, for example, in Refs [201,202]. This approach is similar to that in Bridgman growth, cf. Section 28.4.2. However, because the force on the load cell is available as measurement information about the process state, one is able to add a feedback control loop to the system compensating for the inaccuracies of the feed-forward control. Such an approach is presented by Kokh et al. in Ref. [198].

28.8 Conclusions

In this chapter, different approaches for the control of selected crystal growth processes from melt have been discussed. It has been shown that a deep understanding of the process dynamics makes controller design considerably easier. Here, model-based strategies are a key tool since they reveal the most critical characteristics of the process that have to be considered in the determination of the reference trajectories as well as for open- and closed-loop control design. On the other hand, it has also become apparent that the lumped parameter strategies usually used in control theory hit their limits in these processes. This is mainly because of the complex nonlinear thermal and convective phenomena in these systems that cannot be captured sufficiently by low order lumped parameter models. While they provide insight into subordinate problems, e.g., when dealing with the capillary phenomena, cf. Section 28.3.5.1 (partially model-based control of the Cz process) or Section 28.5.1.3 (operational limits of the Detached Bridgman process), the approach fails where a global treatment of the system quantities is inevitable, for example, in the case of Bridgman growth (cf. Section 28.4.3). With respect to this, the authors are of the opinion that model predictive control strategies (cf. Section 28.2.5.3) are the key for further development of control systems in crystal growth since they are able to rely on more accurate (but much more complex) models of the process. A necessary condition for this is that computational power increases insofar as to solve the underlying full transient high-order models in real time. Model reduction strategies keeping the principal system dynamics are an important discipline that should be involved for this purpose, too. The scientific community is encouraged to follow the path in this sense.

References

[1] Jordan, Caruso R, von Neida A, Nielsen J. J Appl Phys 1981;52:3331.

[2] Jordan, von Neida A, Caruso R. J Cryst Growth 1984;70:555.

[3] Motakef S, Kelly K, Koai K. J Cryst Growth 1991;113:279.

[4] Neubert M, Rudolph P. Prog Cryst Growth Charact Mat 2001;43:119.

[5] Voronkov V.V. J Cryst Growth 1982;59:625.

[6] Hurle D. In: Chambers R, Enderby J, Keller A, Lang A, Steeds J, editors. Sir Charles Frank, OBE, FRS: an 80th birthday tribute. Bristol: Adam Hilger; 1991.

[7] Falster R, Voronkov V. Mater Res Soc Bull 2000;73:28.

[8] Gevelber M, Wilson D, Duanmu N. J Cryst Growth 2001;230:217.

[9] Voronkov V, Mutti P. US Patent Nos US 2002043206 and US 6726764; 2004.

[10] Gevelber M, Stephanopoulos G. J Cryst Growth 1987;84:647.

[11] Gevelber M, Stephanopoulos G, Wargo M. J Cryst Growth 1988;91:199.

[12] Gevelber M. J Cryst Growth 1994;139:271.

[13] Gevelber M. J Cryst Growth 1994;139:286.

[14] Winkler J, Neubert M, Rudolph J. J Cryst Growth 2010;312:1005.

[15] Winkler J, Neubert M, Rudolph J. J Cryst Growth 2010;312:1019.

[16] Neubert M, Winkler J. J Cryst Growth 2012;360:3.

[17] Gevelber M, Wargo M, Stephanopoulos G. J Cryst Growth 1987;85:256.

[18] Winkler J, Neubert M, Rudolph J, Duanmu N, Gevelber M. In: Crystal growth processes based on capillarity. John Wiley & Sons; 2010.

[19] Winkler J, Neubert M, Rudolph J. Acta Phys Pol A 2013;124(2):181.

[20] Marlin T. Process control. McGraw-Hill; 2000.

[21] Kumar AA. Control systems. Prentice-Hall; 2007.

[22] Hurle D, Joyce G, Ghassempoory M, Crowley A, Stern E. J Cryst Growth 1990;100:11.

[23] Luenberger DG. IEEE Trans Mil Electron 1964;8(2):74.

[24] Luenberger D. IEEE Trans Autom Control 1971;16(6):596.

[25] Grewal MS, Andrews AP. Kalman filtering – theory and practice using MATLAB. 3rd ed. Wiley; 2008.

[26] Ellis G, Ellis CD. Observers in control systems: a practical guide. Academic Press; 2002.

[27] Visioli A. Practical PID control, advances in industrial control. London: Springer; 2010.

[28] Astrom KJ, Hagglund T. Advanced PID control. ISA – The Instrumentation, Systems, and Automation Society; 2005.

[29] Johnson MJ, Moradi MB, editors. PID control: new identification and design methods. London: Springer; 2010.

[30] O'Dwyer A. Handbook of PI and PID controller tuning rules. London: Imperial College Press; 2003.

[31] Graf J. PID control: Ziegler–Niccols tuning. CreateSpace Independent Publishing Platform; 2013.

[32] Khalil HK. Nonlinear systems. 3rd ed. Prentice-Hall; 2001.

[33] Allgower F, Zheng A, editors. Nonlinear model predictive control, progress in systems and control theory. Birkhauser Verlag; 2007.

[34] Camacho E, Bordons C. Model predictive control, advanced textbooks in control and signal processing. Springer; 2004.

[35] Kokubun Y, Washizuka S, Ushizawa J, Watanabe M, Fukuda T. Appl Phys Lett 1982;41(9):841.

[36] Hurle D. J Cryst Growth 1977;42:473.

[37] Cole M, Ware R, Whitaker M. In: The 5th international conference on crystal growth, Boston; 1977.

[38] Hadamovsky HF, editor. Werkstoffe der Halbleitertechnik. VEB Deutscher Verlag für Grundstoffindustrie; 1990.

[39] Mika K, Uelhoff W. J Cryst Growth 1975;30(1):9.

[40] Braescu L, Epure S, Duffar T. In: Duffar T, editor. Crystal growth processes based on capillary. Wiley; 2010.

[41] Hurle D. J Cryst Growth 1983;63:13.

[42] Boucher E, Jones T. J Chem Soc Faraday Trans 1 1980;76:1419.

[43] Boucher E, Jones T. Rep Prog Phys 1980;43:497.

[44] Landau LD, Lifschitz EM. Hydrodynamik, Lehrbuch der theoretischen Physik, vol. 6. Berlin: Akademie Verlag; 1991.

[45] Tsivinskii S. Inzheherno Fiz. Zh. Akad. Nauk. Bellorussk SSR 1962;5(9):59. in Russian language.

[46] Johansen T. J Cryst Growth 1994;141:484.

[47] Derby J, Brown R. J Cryst Growth 1986;74(3):605.

[48] Surek T, Coriell S, Chalmers B. J Cryst Growth 1980;50(1):21.

[49] Brice J. J Cryst Growth 1968;2:393.

[50] Kim K, Kran A, Smetana P, Schwuttke G. J Electrochem Soc 1983;130(5):1156.

[51] Duanmu N. [Ph.D. thesis]. College of Engineering, Boston University; 2006.

[52] Mullin J, Straughan B, Brickell W. J Phys Chem Solids 1965;26(4):782.

[53] Looze D, Farzin A, Bernstein B. J Cryst Growth 1995;148(1–2):79.

[54] Jordan A, Caruso R, von Neida A. Bell Syst Tech J 1983;62:477.

[55] Johansen T. J Cryst Growth 1987;84(2):609.

[56] Johansen T. J Cryst Growth 1992;123(1–2):188.

[57] Azuma K. Jap. Patent No. 60-11299; 1983.

[58] Bardsley W, Green G, Holliday C, Hurle D. J Cryst Growth 1972;16:277.

[59] Bardsley W, Frank F, Green G, Hurle D. J Cryst Growth 1974;23:341.

[60] Bardsley W, Cockayne B, Green G, Hurle D, Joyce G, Roslington J, et al. J Cryst Growth 1974;24/25: 369.

[61] Bardsley W, Hurle D, Joyce G. J Cryst Growth 1977;40:13.

[62] Bardsley W, Hurle D, Joyce G, Wilson G. J Cryst Growth 1977;40:21.

[63] Steel G, Hill M. J Cryst Growth 1975;30(1):45.

[64] Hurle D, Joyce G, Wilson G, Ghassempoory M, Morgan C. J Cryst Growth 1986;74:480.

[65] Hurle D. J Cryst Growth 1993;128(1–4):15.

[66] Satunkin G, Leonov A. J Cryst Growth 1990;102(3):592.

[67] Satunkin G. J Cryst Growth 1995;154(1–2):172.

[68] Sveshtarov P, Gospodinov M. Cryst Res Technol 1995;30(1):27.

[69] Sveshtarov P, Gospodinov M. Cryst Res Technol 1995;30(2):243.

[70] Sveshtarov P, Gospodinov M. Cryst Res Technol 1995;30(3):405.

[71] Derby J, Brown R. J Electrochem Soc 1985;132(2):470.

[72] Derby J, Brown R. J Cryst Growth 1986;75(2):227.

[73] Derby J, Brown R. J Cryst Growth 1987;83:137.

[74] Thomas P, Derby J, Atherton L, Brown R. J Cryst Growth 1989;96:135.

[75] Surek T. J Appl Phys 1976;47:4384.

[76] Tatarchenko V, Brener E. J Cryst Growth 1980;50:33.

[77] Babkin G, Brener E, Tatarchenko V. J Cryst Growth 1980;50(1):45.

[78] Tatarchenko YA. Shaped crystal growth, fluid mechanics and its applications, vol. 20. Dordrecht, Boston, London: Kluwer Academic Publishers; 1993.

[79] Crowley A. IMA J Appl Math 1983;30(2):173.

[80] Johansen T. J Cryst Growth 1991;114(1–2):27.

[81] Tatarchenko VA. In: Duffar T, editor. Crystal growth processes based on capillary. Wiley; 2010.

[82] Levinson J. US Patent No. 2,908,004; 1959.

[83] Rummel T. US Patent No. 3,259,467; July 5, 1966.

[84] Zinnes A, Nevis B. J Cryst Growth 1973;19:187.

[85] Valentino, Brandle C. J Cryst Growth 1974;26:1.

[86] Digges T, Hopkins R, Seidensticker R. J Cryst Growth 1975;29:326.

[87] Patzner E, Dessauer R, Poponiak M. Solid State Technol 1967;10:25.

[88] Gross U, Kersten R. J Cryst Growth 1972;15:85.

[89] Lorenzini R, Nuff F, Blair D. Solid State Technol 1974;2:33.

[90] Turovskii, Shenderovich I, Shubskii G. Inorg Mater 1977;13:948.

[91] van Dijk H, Jochem C, Scholl G, vander Werf P. J Cryst Growth 1974;21:310.

[92] van Dijk H, Goorissen J, Gross U, Kersten R. Acta Electron 1974;17:45.

[93] Bachmann K, Kirsch H, Vetter K. J Cryst Growth 1970;7:290.

[94] Joyce G, Hurle D, Vaughan Q. J Cryst Growth 1993;132:1.

[95] Bruni FJ. In: Scheel HJ, Capper P, editors. Crystal growth technology. Weinheim: Wiley-VCH; 2008.

[96] Johansen T. J Cryst Growth 1987;80(2):343.

[97] Johansen T. J Cryst Growth 1992;118(3–4):353.

[98] Satunkin G. Prog Cryst Growth Charact Mater 2010;56:1.

[99] Rossolenko S, Pet'kov I, Kurlov V, Red'kin B. J Cryst Growth 1992;116:185.

[100] Abrosimov N, Kurlov V, Rossolenko S. Prog Cryst Growth Charact Mat 2003;46(1–2):1.

[101] Kubota E. Cryst Res Technol 1999;34(4):539.

[102] Masi M, Carra S, Polli M, Ratti M, Guadalupi G. Mater Chem Phys 2000;66:236.

[103] Eidelman L, Goriletsky V, Protsenko V, Radkevich A, Trofimenko V. J Cryst Growth 1993;128(1–4): 1059.

[104] Kasimkin P, Moskovskih V, Vasiliev Y, Shlegel V, Yuferev V, Vasiliev M, et al. J Cryst Growth 2014; 390:67.

[105] Aufreiter J, Briiss D, Altekrueger B. US Patent 5853479 A; 1998.

[106] Aufreiter J, Brass D, Altekrueger B, Kalkowski K. US Patent 6341173 B2; 1998.

[107] Domey K. Solid State Technol 1971;10:41.

[108] Kimbel S. [Ph.D. thesis]. Washington University; 2000.

[109] Kimbel S, O'Sullivan J. Process imaging for automatic control. Proc SPIE – Int Soc Opt Eng 2001; 4188. pp. 45.

[110] Nalbandyan H. J Cryst Growth 1984;67:115.

[111] Neubert M, Winkler J. J Cryst Growth 2014;404:210.

[112] Brown G, Kinney T, Sackinger P, Bornside D. J Cryst Growth 1989;97:99.

[113] Voigt A, Hoffmann KH. Optimal control of complex structures, vol. 139. ISNM International Series of Numerical Mathematics; 2002. 259.

[114] Dornberger E, von Ammon W, van den Bogaert N, Dupret F. J Cryst Growth 1996;166:452.

[115] van den Bogaert N, Dupret F. J Cryst Growth 1997;171:65.

[116] van den Bogaert N, Dupret F. J Cryst Growth 1997;171:77.

[117] Olivari E, Jacmin P, van den Bogaert N, Wertz V, Dupret F. J Cryst Growth 1997;180:627.

[118] Sabanskis A, Bergfelds K, Muiznieks A, Schröck T, Krauze A. J Cryst Growth 2013;337:9.

[119] Satunkin G, Rossolenko S, Kurlov V, Reg'kin B, Tatarchenko V, Avrutik A. Cryst Res Technol 1986;21(10):1257.

[120] Voronkov V, Mutti P. U.S. Patent No. US 2002/0043208 A1; 2002.

[121] Satunkin G, Rossolenko S. Cryst. Res Technol 1986;21(9):1125.

[122] Åström KJ, Wittenmark B. In: Adaptive control. Prentice Hall; 1994.

[123] Warwick K, Rees D, editors. Industrial digital control systems. IEEE control Engineering solutions, vol. 37. Peter Peregrinus Ltd; 1988.

[124] Riedling K. J Cryst Growth 1988;89(4):435.

[125] Ng J, Dubljevic S. J Process Control 2011;21(10):1361.

[126] Ng J, Dubljevic S. Chem Eng Sci 2012;67(1):111.

[127] Ng J, Aksikas I, Dubljevic S. Int J Control 2013;86(9):1467–78.

[128] Wang P. Optim Control Appl Methods 1995;16:305.

[129] Irizarry-Rivera R, Seider WD. J Cryst Growth 1997;178(4):593.

[130] Irizarry-Rivera R, Seider WD. J Cryst Growth 1997;178(4):612.

[131] Buzniak J, Prunier V. Apparatus and method for monitoring and controlling crystal growth, Tech. Rep., U.S. Patent US 7 959 732 B1; 2011.

[132] Batur, Sharpless RB, Duval WMB, Rosenthal BN. In: Proceedings of the 1991 American Control Conference, Boston, USA; 1991. p. 1722.

[133] Parker R, Manning J. J Cryst Growth 1986;79:341.

[134] Carter JN, Lam A, Schleich DM. Rev Sci Instrum 1992;63:3472.

[135] Schmachtl M, Schievenbusch A, Zimmermann G, Grill W. Ultrasonics 1998;36:291.

[136] Azizi M, Meissner E, Friedrich J. In: Proceedings of the 5th world conference on photovoltaic energy conversion, Valencia, Spain; September 2010. p. 1520.

[137] Dold P, Heidler M, Drevermann A, Zimmermann G. J Cryst Growth 2001;256:352.

[138] Lan W, Ting CC. Chem Eng Comm 1996;145:131.

[139] Batur, Srinivasan A, Duvalt WMB, Singh NB. Prog Cryst Growth Charact 1995;30:217.

[140] Wang QG, Cai EJ, Ye Z, Hang CC. PID control for multivariable processes, lecture notes in control and information sciences. Springer; 2009.

[141] Albertos P, Sala A. Multivariable control systems – an engineering approach, advanced textbooks in control and signal processing. Springer; 2004.

[142] Skogestad S, Postlethwaite I. Multivariable feedback control. 2nd ed. Wiley; 2005.

[143] Abraham R, Lunze J. J Robust Nonlinear Control 1992;2(2):107.

[144] Klein J, Curreri V, DuBois J, Larson D. Advanced thermal control system for a programmable multizone crystal growth furnace. Tech. rep., SAE technical paper 911557; 1991.

[145] Jurisch M, Börner F, Bünger T, Eichler S, Flade T, Kretzer U, et al. J Cryst Growth 2005;275:283.

[146] Kuppurao S, Brandon S, Derby JJ. J Cryst Growth 1995;155:93.

[147] Kuppurao S, Brandon S, Derby JJ. J Cryst Growth 1995;155:103.

[148] Rudolph J. Flatness based control of distributed parameter systems. Aachen: Shaker Verlag; 2003.

[149] Benoussan A, Prato GD, Delfour MC, Mitter SK. Representation and control of infinite dimensional systems, systems and control: foundations & applications. Birkhäuser; 2007.

[150] Rudolph J, Winkler J, Woittennek F. Flatness based control of distributed parameter systems: examples and computer exercises from various technological domains. Berichte aus der Steuerungs- und Regelungstechnik. Aachen: Shaker Verlag; 2003.

[151] Rudolph J, Winkler J, Woittennek F. In: Meurer T, Graichen K, Gilles E, editors. Control and observer design for nonlinear finite and infinite dimensional systems. Lecture notes in control and information sciences, vol. 322. Springer-Verlag; 2005.

[152] Batur R, Sharpless W, Duval B, Rosenthal, Singh N. J Cryst Growth 1992;119:371.

[153] Kasparian V, Batur C, Duval WM, Rosenthal BN, N.S. J Cryst Growth 1994;141(3–4):455.

[154] Batur, Duval MB, Bennett RJ. In: Proceedings of the 1999 American control conference, San Diego, California, USA; 1999. p. 4101.

[155] Medanic J, Uskokovic Z. Int J Control 1983;37:809.

[156] Seidensticker R, Rosch W, Mazelsky R, Hopkins R, Singh N, Coriell S, et al. J Cryst Growth 1999; 198–199(2):988.

[157] Sonda P, Yeckel A, Daoutidis P, Derby J. J Cryst Growth 2004;266(1–3):182.

[158] Sonda P, Yeckel A, Derby J, Daoutidis P. Comput Chem Eng 2005;29(4):887.

[159] Daoutidis P, Kravaris C. AIChE J 1999;35:1602.

[160] Kim K, Witt A, Gatos H. J Electrochem Soc 1972;119(9):1218.

[161] Kim K, Witt A, Lichtensteiger M, Gatos H. J Electrochem Soc 1975;125(3):475.

[162] Müller G, Neumann G, Weber W. J Cryst Growth 1984;70:78.

[163] Sonda P, Yeckel A, Daoutidis P, Derby JJ. Chem Eng Sci 2005;60(5):1323.

[164] Sonda P, Yeckel A, Daoutidis P, Derby JJ. J Cryst Growth 2004;260:263.

[165] Yeckel A, Derby J. J Cryst Growth 2012;314(1):310.

[166] Yeckel, Daoutidis P, Derby J. J Cryst Growth 2012;356:33.

[167] Yeckel, Daoutidis P, Derby J. J Cryst Growth 2012;361:16.

[168] Duffar T, Dusserre P, Picca F, Lacroix S, Giacometti N. J Cryst Growth 2000;211:434.

[169] Duffar T, Dusserre P, Giacometti N. J Cryst Growth 2001;223:69.

[170] Palosz W, Volz M, Cobb S, Motakef S, Szofran F. J Cryst Growth 2005;277:124.

[171] Patzold O, Jenkner K, Scholz S, Croll A. J Cryst Growth 2005;277:37.

[172] Braescu L. J Colloid Interf Sci 2008;319:309.

[173] Sylla L, Duffar T. J Cryst Growth 2007;303:187.

[174] Epure S, Duffar T, Braescu L. J Cryst Growth 2008;310:1559.

[175] Epure S, Duffar T, Braescu L. J Cryst Growth 2010;312(8):1416.

[176] Braescu L. J Cryst Growth 2010;312(8):1421.

[177] Stut H. US Patent 3243509 A (Siemens AG); 1963.

[178] Stut H. US Patent 3757071 A (Siemens AG).

[179] Lie K, Walker J, Riahi D. J Cryst Growth 1990;100(3):450.

[180] Wünscher M, Lüdge A, Riemann H. J Cryst Growth 2011;314:43.

[181] Shyy W, Rao MM. Int J Heat Mass Transf 1995;38(12):2281.

[182] Werner N. [Ph.D. thesis]. Berlin: Technische Universität; 2014.

[183] Heywang W. Z Naturforscher 1956;11a:238.

[184] Rowton E. IEEE Trans Ind Electron Control Instrum 1965;IECI-13(1):66.

[185] Otani S, Tanaka T, Ishizawa Y. J Cryst Growth 1990;106(4):498.

[186] Chan Y, Mailloux PA. Rev Sci Instrum 1993;64(9):2643.

[187] Ikeda Y, Ohara N, Suzuki K, Watanabe M. US Patent 4866230 A (Shin Etsu Ltd); 1987.

[188] Watanabe M, Ohhara N, Taguchi K. US Patent 4876438 A (Shin Etsu Ltd); 1988.

[189] Taguchi K, Watanabe M. US Patent 4931945 A (Shin Etsu Ltd); 1988.

[190] Dornberger, von Ammon W, Ölkrug H, Wasmeier F. US Patent 5868831 (Wacker AG); 1997.

[191] Bliss F. In: Feigelsen RS, editor. 50 years progress in crystal growth. Elsevier; 2004.

[192] Nakajima K, Murai R, Morishita K, Kutsukake K, Usami K. J Cryst Growth 2012;344:6.

[193] Singh, Ghosh B, Deshpande R. Cryst Res Technol 1981;16(11):1239.

[194] Perner, Kvapil J, Stransky V, Kvapil J. Cryst Res Technol 1979;14(6):661.

[195] Xu M, Zhang S, Meng J, Han G, Wang, Zuo H. Cryst Res Technol 2007;42(8):751.

[196] Zhang L, Zuo H, Sun J, Wang X, Han J, Xing D, et al. Cryst Res Technol 2012;47(2):175.

[197] Akselrod MS, Bruni FJ. J Cryst Growth 2012;360:134.

[198] Kokh AE, Vlezko VA, Kokh KA. Instrum Exp Tech 2009;52(5):747.

[199] Schönherr. J Cryst Growth 1968;3–4:265.

[200] Zhang L, Zuo H, Sun J, Wang X, Han J, Xing D. Cryst Res Technol 2011;46(10):1019.

[201] Demina S, Bystrova E, Lukanina M, Mamedov V, Yuferev V, Eskov E, et al. Opt Mater 2007;30:62.

[202] Demina S, Bystrova E, Postolov V, Eskov E, Nikolenko M, Marshanin D, et al. J Cryst Growth 2008; 310:1443.

29

Fundamentals of Crystal Growth from Solutions

Igor Pritula[1], Keshra Sangwal[2]

[1]INSTITUTE OF SINGLE CRYSTALS, NATIONAL ACADEMY OF SCIENCES OF UKRAINE, KHARKOV, UKRAINE; [2]DEPARTMENT OF APPLIED PHYSICS, LUBLIN UNIVERSITY OF TECHNOLOGY, LUBLIN, POLAND

CHAPTER OUTLINE

29.1 Introduction **1186**
29.2 Low-Temperature Solution Growth **1187**
29.2.1 Basic Concepts of Low-Temperature Crystallization 1187
29.2.1.1 Driving Force for Crystallization 1187
29.2.1.2 Metastable Zone Width 1189
29.2.1.3 Temperature Dependence of Solubility 1191
29.2.2 Selection of Solvents 1192
29.2.3 Crystal Growth Techniques 1193
29.2.3.1 Temperature-Changing Technique 1194
29.2.3.2 Solvent Evaporation Technique 1194
29.2.3.3 Temperature Gradient Techniques 1195
29.2.3.4 Growth from Boiling Solutions 1196
29.2.4 Different Factors Affecting Crystal Growth 1196
29.2.5 Crystal Growth Rates and Dead Supersaturation Zone 1199
29.2.5.1 Basic Concepts of Impurity Effects 1199
29.2.5.2 Effect of Organic Additives on Crystal Growth 1204
29.2.6 Effect of Mechanical Impurities on Crystal Growth 1206
29.2.6.1 Growth of Water-Soluble Crystals with Embedded Organic Molecules 1206
29.2.6.2 Growth of Water-Soluble Crystals with Embedded Nanoparticles 1208
29.3 High-Temperature Solution Growth **1210**
29.3.1 Principle of the Method 1211
29.3.2 Composition of Fluxes and Their Selection 1211
29.3.3 Some Properties of High-Temperature Solvents 1215
29.3.4 Crystal Growth Techniques 1219

Handbook of Crystal Growth. http://dx.doi.org/10.1016/B978-0-444-63303-3.00029-8
Copyright © 2015 Elsevier B.V. All rights reserved.

29.3.4.1 Slow-Cooling Method 1219
29.3.4.2 Solvent Evaporation Method 1220
29.3.4.3 Temperature Gradient Methods 1221
29.3.4.4 Other Methods 1222
29.3.5 Growth Instability and Facet Formation 1223
29.4 Summary and Outlook 1223
Acknowledgment 1224
References 1224

29.1 Introduction

Crystallization of substances from supersaturated solutions at normal pressure conditions in suitable nonreactive solvents in which they are fairly soluble is usually referred to as *crystal growth from solutions*. The solvents used for the crystallization of different substances are usually water, various organic liquids and their mixtures, and melts of some chemical compounds and/or their mixtures. Water and organic liquids and their mixtures are in the liquid state under the usual laboratory pressure and temperature conditions, whereas chemical compounds and/or their mixtures are in the liquid state at elevated temperatures. From a consideration of the growth temperature when the solvent used is in the liquid state, one differentiates between crystal growth from low- and high-temperature solutions. In growth from low-temperature solutions, the crystallization temperatures generally do not exceed 70–80 °C; in growth from high-temperature solutions, the crystallization temperatures rarely exceed 1200–1300 °C. In both low- and high-temperature growths, the highest possible growth temperature is the boiling point of the solvent used.

Crystallization from supersaturated solutions devoid of foreign particles with deliberately introduced seeds always occurs in two stages: formation of three-dimensional (3D) microscopic nuclei and development of these 3D nuclei into large entities visible to the naked eye. These two stages are called homogeneous 3D nucleation and crystal growth, respectively. Foreign particles (usually called impurities) in solutions facilitate the formation of 3D nuclei (heterogeneous nucleation) and can change their subsequent growth, whereas seeds introduced in solutions eliminate the nucleation stage and enable crystals to grow without 3D nucleation. Crystallization is usually understood as the nucleation and development of crystalline product, but the term *growth* is used for large-sized crystals with or without the nucleation stage. A necessary condition for the crystallization of a solid mass dissolved in a pure or mixed solvent is the creation of supersaturation in the solution.

In this chapter, the principles and experimental techniques for the growth of crystals from low- and high-temperature solutions are described. The contents of this chapter are an extended and revised version based on a review published previously [1].

29.2 Low-Temperature Solution Growth

Crystal growth from low-temperature solutions is well suited for materials that decompose in the melt or in the solid at high temperatures and that undergo structural transformations while cooling from the melting point. It also allows crystals of the same substance to grow in a variety of morphologies and polymorphic forms by variations of growth conditions or of the solvent. Consequently, materials ranging from micrometer-sized crystalline organic pharmaceutical chemicals to large-sized inorganic nonlinear optical crystals are grown from low-temperature solutions. The method is widely used because: (1) the growth apparatus is relatively simple and cheap; (2) in contrast to other methods involving melts, low growth temperature introduces small thermal stresses (and hence a low concentration of equilibrium defects and dislocations) in the crystals; and (3) the crystals obtained usually have well-developed faces (growth habit) that make it possible to investigate crystal growth processes, including in situ observations of the surfaces and capture of impurities.

Crystal growth from low-temperature solutions has been reviewed in several monographs and reviews [1–9]. The list of compounds grown from low-temperature solutions can be found in the monographs [3,6,7].

29.2.1 Basic Concepts of Low-Temperature Crystallization

29.2.1.1 Driving Force for Crystallization

Crystallization of a compound always occurs from its supersaturated solutions in the metastable zone. The metastable zone is the region between curves representing solubility (solid curve) and supersolubility (dashed curve), shown schematically in Figure 29.1. The supersolubility curve indicates the limiting value of solute concentration when instantaneous 3D nucleation (i.e. precipitation) occurs in the solution.

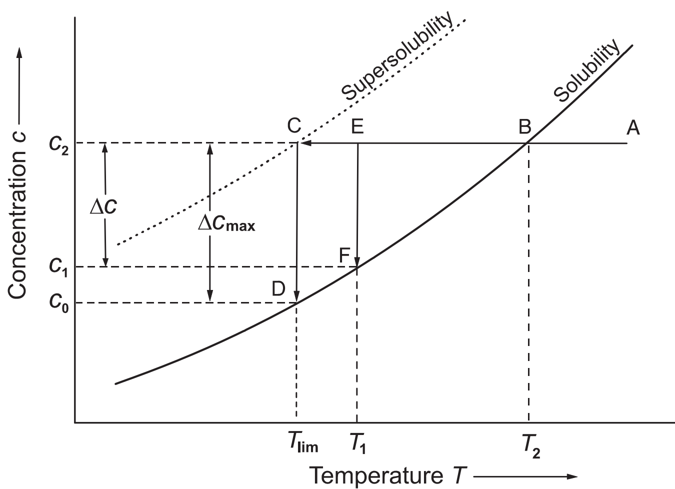

FIGURE 29.1 Schematic illustration of the dependence of solute concentration in a solute–solvent system on solution temperature. Solid and dashed curves represent solubility and supersolubility curves, respectively. See text for details. *Adapted from Ref. [12].*

From Figure 29.1, three areas can be distinguished: (1) stable undersaturated zone, (2) metastable zone, and (3) unstable supersaturated area. In area (1), which lies below the solubility curve, the actual concentration c of a solute in the solution at a given temperature, say T_{lim}, is lower than the corresponding equilibrium concentration c_0 represented by the solubility for the solute–solvent system. In an undersaturated solution, more solute will dissolve. In areas (2) and (3) lying above the solubility curve, the actual solute concentration c at the temperature T_{lim} is higher than its solubility c_0. In these areas, the solution is supersaturated. However, the processes of 3D spontaneous nucleation and crystal growth occur in the region lying between the solubility and supersolubility curves—that is, in the metastable zone. Obviously, the supersolubility curve represents the concentration when 3D spontaneous nucleation ceases to occur.

Deviation in the concentration of a dissolved salt from its equilibrium value at a given temperature or deviation in the temperature of the solute–solvent system of a given equilibrium concentration from a saturation temperature is a measure of the driving force for crystallization. In Figure 29.1, it is the concentration difference $\Delta c = c_2 - c_1$ corresponding to the saturation concentration c_1 at temperature T_1 or the temperature difference $\Delta T = T_2 - T_1$ corresponding to the saturation concentration c_2 at temperature T_2. In terms of solute concentrations in the solution, the driving force for crystallization is the dimensionless supersaturation ratio $S = c_2/c_1$, and the degree of supersaturation or simply supersaturation $\sigma = \ln S \approx \Delta c/c_1$. Obviously, $S < 1$, $S > 1$, and $S = 1$ for undersaturated, supersaturated, and saturated solutions, respectively. In terms of the solubility of a solute, when 3D nucleation of the new phase occurs instantaneously, as shown schematically by the dashed curve in Figure 29.1, the driving force for crystallization is the limiting value of metastable zone.

The metastable zone width can be described by a polythermal or isothermal method. In the polythermal (also called non-isothermal) method, the metastable zone width is measured as the maximum supercooling $\Delta T_{max} = (T_2 - T_{lim})$, with reference to a constant concentration c_0 corresponding to the saturation temperature T_{lim} (Point D), by cooling the solution at a constant cooling rate R from a temperature somewhat above T_2 (Point A in Figure 29.1) to a temperature T_{lim} at which first crystals are detected in the solution (Point D). With reference to the temperature T_{lim} corresponding to the maximum solute concentration c_2, this metastable zone width is the maximum concentration difference $\Delta c_{max} = (c_2 – c_0)$. The isothermal method, on the other hand, consists of attaining solution supersaturation as fast as possible, followed by the measurement of time period for the appearance of first detectable nuclei in the solution. When the appearance of detectable nuclei occurs immediately after attaining the predefined supersaturation corresponding to the limiting temperature T_{lim}, one defines the maximum supersaturation ratio $S_{max} = (c_2/c_0)$ and the maximum supersaturation $\ln S_{max} = \ln(c_2/c_0)$ as the width of the metastable zone width with reference to T_{lim}.

When c_{max} is the solute concentration corresponding to the saturation temperature T in Figure 29.1, one obtains the traditional relations for maximum supersaturation ratio $S_{max} = c_{max}/c_0$ and maximum supersaturation $\sigma_{max} = (c_{max} - c_0)/c_0$. Then, with reference

to the saturation temperature T in Figure 29.1, the temperature difference $\Delta T_{max} = (T - T_{lim})$ is the maximum undercooling. Alternatively, with reference to the limiting temperature T_{lim}, $\Delta T_{max} = (T - T_{lim})$ is the maximum supercooling and defines the metastable zone width.

29.2.1.2 Metastable Zone Width

The polythermal technique is the most widely used method for determining the metastable zone width. In fact, investigation of solubility and metastable zone width of various solute–solvent systems has been a field of intensive research activity for over four decades [10]. However, since 2008 several papers have been devoted to the understanding of the effect of various experimental factors on the metastable zone width. The developments in the understanding of metastable zone width of solute–solvent systems have recently been reviewed [11].

According to the self-consistent Nývlt-like approach [12], the relationship between the maximum supercooling ratio $\Delta T_{max}/T$ and cooling rate R may be given by

$$\ln(\Delta T_{max}/T) = \Phi + \beta \ln R, \tag{29.1}$$

where Φ is the extrapolated value of $\ln(\Delta T_{max}/T)$ when $\ln R \to 0$, and $\beta = 1/m$ (m is the nucleation order). However, according to the approach based on the three-dimensional nucleation theory [13], the relationship between $\Delta T_{max}/T$ and R is of the form

$$\left(\frac{T}{\Delta T_{max}}\right)^2 = F(1 - Z \ln R), \tag{29.2}$$

where F is the extrapolated value of $(T/\Delta T_{max})^2$ when $\ln R \to 0$, and the constant Z is characteristic for a solute–solvent system. Both Eqns (29.1) and (29.2) predict that, at a given saturation temperature T, the quantities $\ln(\Delta T_{max}/T)$ and $(\Delta T_{max}/T)^{-2}$ decrease linearly with an increase in $\ln R$.

The parameters Φ and $\ln(F^{1/2})$ as a function of saturation temperature T may be described by an Arrhenius-type relation, written in the following form [12,13]:

$$\ln y = \ln y_0 - E_{sat}/R_G T, \tag{29.3}$$

where $\ln y$ denotes $-\Phi$ and $\ln(F^{1/2})$; the factor $\ln y_0$, associated with the pre-exponential factor y_0 of the Arrhenius-type relation, denotes the extrapolated values of $-\Phi$ and $[\ln(F^{1/2})]$ when $1/T \to 0$, R_G is the gas constant; and E_{sat} is the activation energy associated with the diffusion of solute molecules in the solution.

Irrespective of the cooling rate R, with an increase in saturation temperature T, the value of maximum supercooling $\Delta T_{max} = T - T_{lim}$ decreases for some solute–solvent systems, it remains practically constant for some others, and it increases for the remaining solute–solvent systems. Typical examples showing such trends are shown in Figure 29.2. This means that the supercooling ratio $\Delta T_{max}/T$ decreases, increases, or remains constant with increasing saturation temperature T. Analysis of the experimental data revealed [11,14,15] that the nature of solute–solvent system is related to the activation energy E_{sat} for diffusion of nucleating species in the solution. When the value of

E_{sat} is comparable with the value of activation energy E_D for diffusion of ideal species, the supersolubility curves are roughly parallel to the solubility curves (i.e., $\Delta T_{max}/T$ is independent of T). When $E_{sat} > E_D$, $\Delta T_{max}/T$ decreases with an increase in T_0. However, when $E_{sat} < E_D$, $\Delta T_{max}/T$ increases with an increase in T.

In the polythermal method, the rate of creation of supersaturation in a solute–solvent system and its metastable zone width are determined by controlling the rate of cooling of the solution at a constant rate. However, this method can be used only for substances whose solubility increases with temperature (i.e., for substances that have a positive temperature coefficient of solubility). Irrespective of the temperature coefficient of solubility, supersaturation in the saturated solution of a solute in a solvent can also be generated by mixing another miscible solvent, usually called antisolvent or nonsolvent, in which the solute is insoluble or poorly soluble. This is associated with the fact that, at a given temperature, the solubility of a solute in different solvents is different. The rate of creation of supersaturation in the solution and its metastable zone width are associated here with the rate of addition of miscible antisolvent. In recent years, there has been a steady interest in understanding the metastable zone width in antisolvent crystallization [16].

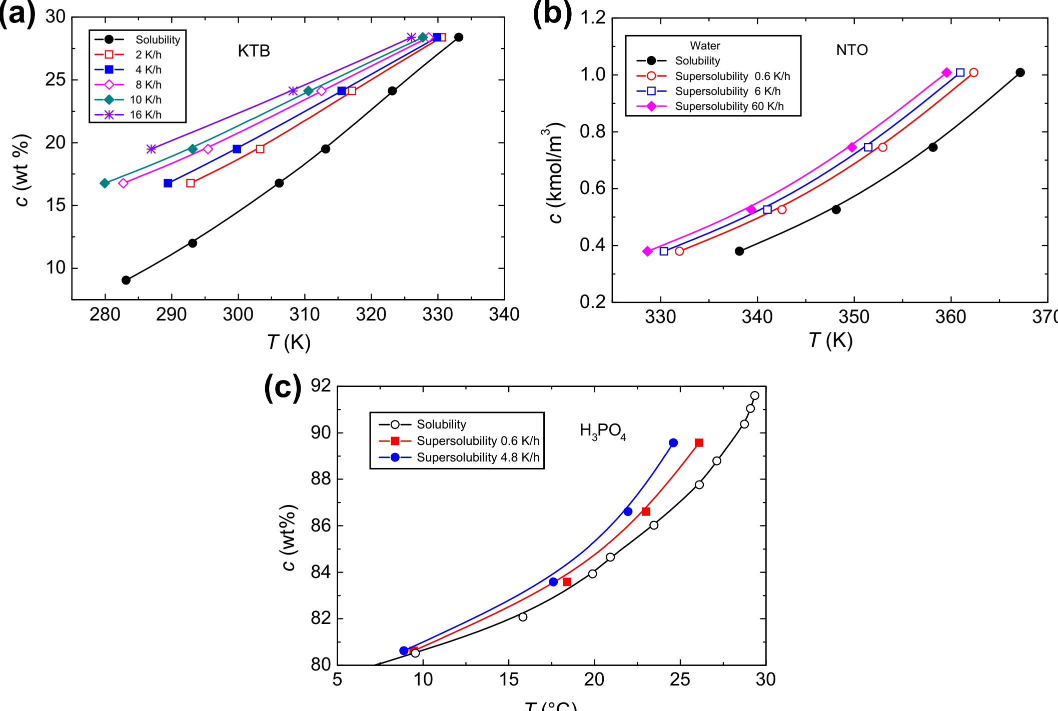

FIGURE 29.2 Typical examples of solubility and supersolubility curves for different systems: (a) KTB (potassium tetraborate tetrahydrate)–water [11], (b) NTO (3-nitro- 1,2,4-triazol-5-one)–water [11], (c) H_3PO_4–water. Supersolubility curves are for various cooling rates [15]. *Reproduced with permission of (a) Royal Chemical Society and (b) Elsevier.*

29.2.1.3 Temperature Dependence of Solubility

The experimental data of the solubility c of a compound in a solvent as a function of temperature T is described satisfactorily according to the empirical relation [16,17]

$$c = C_0 + C_1 T + C_2 T^2, \tag{29.4}$$

where the solubility c is expressed as mass of solute per given mass of solvent or solution; the temperature T is expressed in °C or K; and C_0, C_1, and C_2 are empirical fitting parameters. The data of the temperature dependence of solubility, such as those shown in Figure 29.2, can be represented by Eqn (29.4) in the entire investigated range of temperature. Another relation, based on the theory of regular solutions, that can equally be used to describe the above data is of the form [16,17]

$$\ln c = A - \frac{\Delta H_s}{R_G T}, \tag{29.5}$$

where solubility c is expressed in mole fraction, A is a constant, R_G is the gas constant, and ΔH_s is the enthalpy of dissolution of the solute in the solvent. For ideal solutions, the constant $A = \Delta H_m / R_G T_m$, where T_m is the melting point of the solute and the enthalpy of melting $\Delta H_m = \Delta H_s$. However, for regular solutions, $A \neq \Delta H_m / R_G T_m$ and $\Delta H_m \neq \Delta H_s$.

Although Eqns (29.4) and (29.5) are commonly used to describe the temperature dependence of solubility, they are not satisfied in the entire range of the investigated temperature. Figure 29.3 illustrates typical examples of the temperature dependence of solubility c for some common inorganic compounds in water in the temperature interval 0–100 °C. As seen from the figure, in certain temperature intervals the solubility of different compounds either increases or decreases with an increase in temperature.

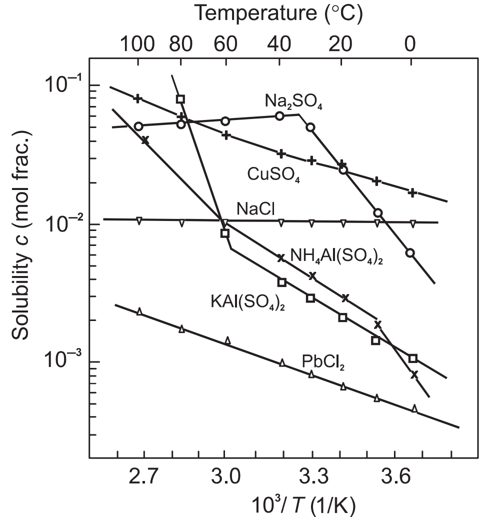

FIGURE 29.3 Examples of the temperature dependence of solubility c for some common inorganic compounds in water. *Adapted from Ref. [9].*

The increasing or decreasing trends of the dependence of solubility c on temperature T are usually discussed in terms of positive or negative temperature coefficient of solubility (i.e., $\partial c/\partial T$) in a particular temperature range. Depending on the nature of solute–solvent system, the solubility coefficient can be high or low and can vary in different temperature intervals.

29.2.2 Selection of Solvents

The first step for crystallization is the choice of solvent. Solution is a homogeneous mixture of a solute in a solvent. Solute is a component that is usually present in a smaller quantity than the solvent in the solution. For a given solution, there may be different solvents. At the growth temperature, an ideal solvent should ensure a sufficient solubility and a good temperature gradient of solubility in it; have low vapor pressure, low toxicity, low flammability, and low viscosity; not corrode the growth apparatus; and be inexpensive.

The most commonly solvent used in low-temperature growth is water because at least 90% of the crystals produced by low-temperature solution methods are soluble in water. It is not toxic and is less volatile than organic solvents, which are generally toxic, volatile, and flammable. Moreover, in comparison with most organic solvents, it is easily available in the pure state and is inexpensive. Because its boiling point is higher than that of most of the organic solvents commonly used for the growth, it provides a reasonably wide range for the selection of the growth temperature. However, water is not a reversible solvent for some materials. It hydrolyzes some materials and introduces water of crystallization to other compounds, which may be desired in the anhydrous form or in the hydrated form of particular composition.

A simple rule of thumb for the proper selection of a solvent is chemical similarity between the solvent and the compound to be grown. For example, crystals of nonpolar organic compounds can be grown easily from nonpolar organic solvents. Chemical similarity also defines solute solubility in the solvent.

The solvent from which a material is crystallized influences the crystal morphology and growth rate. These effects of the solvent on the morphology and growth rates of crystals from solutions are related to the solubility of the crystallizing compound in the solvent and to the nature of crystal–solution interface. High solubility of the solute leads to high viscosity of the solution, which hinders mass transfer at the crystal–solution interface. The crystal–solution interface for a solute–solvent system can be rough at a given temperature as a result of high solubility of the solute in the solvent (thermodynamic roughening) and high supersaturation of the solution (kinetic roughening). Both of these yield high growth rates of crystals and high density of defects. Therefore, to ensure good crystal growth of a substance, it is necessary to use (1) a solvent in which the substance is moderately soluble, (2) medium solution supersaturation, and (3) nonturbulent stirring conditions.

Most crystallized inorganic materials are ionic. This means that dissociation reactions, ionic interactions, and solution acidity (pH) determine the solubility of

inorganic compounds in aqueous solutions. In the case of organic compounds and inorganic compounds in nonaqueous solvents, a wide variety of solvents and solvent mixtures are usually employed. The differences in the solubility of different compounds in various solvents are associated with solute–solvent interactions, which are determined by solute concentration in the solution, solution temperature, composition of the solvent, and impurities present in the solution.

Experiments suggest that a solvent in which the compound has a solubility between 10% and 60% at a given temperature is economically suitable for crystal growth. These growth rates from solutions fall in the range of 0.1–1 mm/day. Very low and very high solute solubilities provide low growth rates due to low solute concentration and increased viscosity, respectively. Therefore, in both cases, it is desirable to use additives to change the solute solubility in a solvent or solution viscosity. Additives not only change the properties of solutions but also lead to changes in crystal growth habits.

29.2.3 Crystal Growth Techniques

Crystal growth methods differ in the way the supersaturation is generated and maintained constant during a growth run, and 3D nucleation is initiated. In general, the selection of a method for the growth of a compound can be made from a consideration of temperature coefficient of its solubility (see Figure 29.3). If a compound has a reasonable temperature coefficient of solubility in a certain temperature interval and does not undergo phase changes, it can be grown by changing the temperature, with simultaneously maintaining the required supersaturation for growth (temperature changing method). In principle, substances with both positive as well as negative temperature coefficients of solubility can be grown by this technique (by decreasing and increasing temperature, respectively), but usually substances having positive temperature coefficients of solubility are grown by it. These substances can also be grown by maintaining a temperature gradient between zones of crystal growth and solute supply (temperature gradient methods). If a compound undergoes phase transition at a particular temperature, the above methods cannot be used. Instead, one can use a method in which both temperature and supersaturation are maintained constant (constant temperature and supersaturation method). However, when the solubility remains practically constant with a change in temperature, the supersaturation can be created by evaporating the solvent (solvent evaporation method).

The importance of selecting an appropriate method lies in the fact that the same crystallization performed under different conditions can yield crystals of different properties (size, morphology, chemical purity, polymorphic form, etc.). However, the design of a cost-effective crystallization process requires many types of data, including mass transfer and equilibrium solubility as a function of the solvent, temperature, and pH. Surface and bulk supersaturation should be made as close as possible to the kinetic regime by suitably stirring solutions so that diffusion processes of supply of solute to the growing crystal do not limit the growth rate (see Section 29.2.4).

29.2.3.1 Temperature-Changing Technique

In this method, the value of supersaturation necessary for the growth of crystals is achieved due to slow temperature reduction, which, as a rule, is controlled by a special program. The mass of the substance Δm depositing during the reduction of temperature by ΔT may be calculated from the relationship

$$\Delta m = \frac{\mathrm{d}c}{\mathrm{d}T} V_0 \Delta T, \tag{29.6}$$

where c is the concentration of the substance in the solution, $\mathrm{d}c/\mathrm{d}T$ is the solubility coefficient, and V_0 is the solution volume. This relationship follows from Eqn (29.4) and holds in a small temperature interval.

Typical vessels for crystal growth by the temperature changing method involve large glass containers with several seeds suspended in the supersaturated solution. For growth, a solution saturated at a temperature T is poured into the crystallizer and heated a few degrees above the saturation temperature to avoid spurious nucleation due to the cooling of its walls during its transfer to the outer water bath. When the solution temperature is slightly above the saturation temperature, the seeds are suspended in the solution and the crystallizer is hermetically sealed. Then, the temperature is lowered to the growth temperature in the metastable zone and solution cooling is commenced at a preassigned rate such that the growing crystals remain the supersaturated solution. After the completion of growth with the temperature steadily decreasing to a terminal temperature, 10–15 °C above the room temperature, the crystals are gently taken out of the crystallizer, wiped, and stored.

The temperature-decreasing method is widely used for commercial crystal growth [3,18]. However, its inherent drawback is variation in the temperature during a growth run, which results in considerable changes in growth rate, adsorption of the impurity on the faces, and capture of the impurities by the growing crystal.

The possibility of obtaining large high-quality single crystals by the temperature reduction method using “point seeds” has been reported [19–21]. In this case, the final size of the crystal does not depend on the size of the seed.

29.2.3.2 Solvent Evaporation Technique

In this technique, the supersaturation required for the growth is produced by evaporating the solvent at a constant temperature [3]. Therefore, the growth rate is regulated by controlling the evaporation rate. Excess mass of the substance for crystallization is created from a consideration of the solubility of the compound in the solvent and the evaporation rate of the solvent. In most cases, the pressure of the solvent vapor over the solutions is higher than that of the solute. This enables one to evaporate solvent vapor into the atmosphere or withdraw it as condensate using water-cooled coils. Therefore, the supersaturation necessary for crystal growth can be maintained by controlled evaporation of the solvent. For nontoxic solvents such as water, solvent evaporation into the atmosphere is permissible; for toxic and flammable

solvents, precautions are taken to avoid the leakage of solvent vapor into the atmosphere.

The mass of the deposited substance Δm is proportional to the volume ΔV of the solvent removed from the solution and to the concentration c of the substance in the solution. Therefore, crystal growth rate is controlled by changing the rate of evaporation of the solvent. During growth by this method, the solution always contains a reserve of the crystallized substance. However, as the amount of the solvent diminishes and the crystal grows, concentration of impurities increases in the solution. Consequently, as growth proceeds, impurity concentration also increases in the crystal. To reduce such an effect, it is necessary to use large volumes of the solvents. However, in this method, it is difficult to maintain constant supersaturation during a long growth run. As the solution volume decreases, the value of supersaturation available in the solution increases when the evaporation is maintained constant. High evaporation rates lead to spurious nucleation followed by mass crystallization in the solution. Spurious nucleation usually occurs on the solution meniscus, where regions of high supersaturation may be formed locally by evaporation of the solvent.

29.2.3.3 Temperature Gradient Techniques

Temperature gradient techniques are based on the creation of two zones of different temperatures. In one of these zones, at a lower temperature T_2 the crystal is grown onto an introduced seed; in the other zone, at higher temperature T_1 the solute is dissolved to obtain saturated solution. The solution supersaturation can be controlled by changing the temperature difference $\Delta T = T_1 - T_2$. Material transport may be ensured by natural, thermal, or forced convection. In growth involving natural convection, the saturation region of temperature T_1 is at the top whereas the growth region at temperature T_2 is at the bottom of the growth setup such as a cylindrical crystallizer. When the growth zone at T_2 is at the top and the nutrient zone of T_1 is at the bottom, material transport occurs by thermal convection. In two-tank crystallizers based on forced convection, solution is pumped between separate tanks for solutions kept at different temperatures. The solution is forced to circulate from one tank to the other through connecting pipes.

The common difficulty with two-tank crystallizers is the occurrence of parasitic nucleation in the connecting pipes; this may result in the cessation of solution circulation. This necessitates running the tubes and pumps at relatively high temperatures. This difficulty is overcome by inserting an additional tank at a temperature $T_3 > T_1$ between the nutrient tank at temperature T_1 and the growth tank at temperature T_2. The additional tank serves as a reservoir of a subsaturated solution, which is pumped to the growth tank and again back to the nutrient tank to be reheated and resaturated. The first well-known three-tank system for crystal growth is due to Walker and Kohman [2]. Nowadays, three-tank crystallizers are widely used for crystal growth from low-temperature solutions [19].

The main advantages of the above method involve economy of solvent and growth of crystals of good quality. However, because the growth rate depends on the temperature

difference between the nutrient and the crystal growth zones, temperature changes have to be kept to a minimum. Moreover, the entire solute in the nutrient tank is not grown as crystals. A method has been introduced [22] to achieve a 100% solute–crystal conversion efficiency. The experimental setup for crystal growth by this method consists of a growth ampoule made of glass with seed mounting pad at its base and a ring heater located at the top of the growth ampoule facilitates solvent evaporation. The main advantages of this method are: (1) the experimental setup is simple, (2) crystal growth occurs essentially at room temperature, (3) it enables the growth of bulk single crystals along specific orientations, and (4) it prevents microbial growth. Because the temperatures in the top and bottom zones essentially remain stable during a growth run and the crystal grows at room temperature, growth occurs at controlled supersaturation and there are minimum thermal stresses in the crystals, resulting in their good quality.

29.2.3.4 Growth from Boiling Solutions

To grow a substance in a given phase and/or composition and at a reasonable rate, the choice of an optimum temperature interval is an important factor in low-temperature solution growth. As in other processes, the growth at elevated temperatures takes place faster. However, at elevated temperatures, smooth growth necessitates better temperature control, while increased vapor pressure creates problems connected with the control of supersaturation and spurious nucleation. These difficulties may be overcome during crystal growth from boiling solutions.

Crystal growth from boiling solutions has features of temperature-changing, evaporation, and temperature gradient methods. Constant supersaturation is developed by withdrawing a known amount of the solvent evaporated from the solution saturated at the boiling point that is constant during growth. Stirring is ensured by bubbles generated in the volume of the solution.

The greatest advantages of the method are constant temperature of boiling and stirring provided by bubbles nucleating at the walls of a reactor without an additional mechanical device. Moreover, the crystals grown from boiling solutions are less defective than those grown at low temperatures. The main drawback of the method stems from the relatively high temperature, which gives rise to problems of leakage of solvent vapor at the joints of the growth assembly. Another difficulty is nonuniform temperature in the growth vessel owing to uncontrolled sources of bubbling, because each bubble origin gives a temperature gradient along the direction of its movement. The principle of the technique, experimental apparatus for growth, and applicability of the method are described in a review [8].

29.2.4 Different Factors Affecting Crystal Growth

Among the important parameters affecting the growth rate and quality of crystals are pH, temperature, and supersaturation of the solution. Change in the composition and, consequently, in the solution pH is one of the parameters that enables control of the

process of crystal growth. In particular, by choosing the acidity of a saturated solution, one can control the growth rate either of one of the crystal faces or of the whole crystal, thereby changing the external shape (also called habit or morphology), and can regulate the incorporation of impurities in the crystal.

There are several explanations of the effect of pH on crystallization. For example, it has been suggested that the presence of free acids or bases modifies the nature and concentration of ions in the solution [2]. The effect of pH on the growth of potassium chloride crystals has been explained in terms of the structure of aqueous solutions involving hydration of ions [23].

Growth rates of different morphologically important faces at temperature T_g usually increase with increasing supersaturation σ at a given pH of the solution of saturation temperature T or supercooling defined in terms of temperature difference $\Delta T = T - T_g$. For instance, it has been observed [24] that the growth rates R of both prismatic and pyramidal faces of potassium dihydrogen phosphate (KDP) crystals increase with increasing supercooling ΔT at different pH of solutions, but for different values of supercooling the highest growth rates for these faces occur at pH of 4.2. The results also indicate that the growth of prismatic faces always occurs above a minimum supercooling for all values of pH, and the lowest value of this critical supercooling for growth for the solution is pH of approximately 4. However, the growth of pyramidal faces occurs practically without the appearance of this minimum supercooling. The region of supersaturation or supercooling where no growth occurs is usually called the dead supersaturation zone; the threshold supersaturation and threshold supercooling are denoted by σ_d and ΔT_d, respectively. The higher value of supersaturation or supercooling for the growth of prismatic face of KDP crystals is associated with the fact that this face is very sensitive to the adsorption of the growth sites by impurities.

Investigation of the effect of temperature on the growth of crystals from solutions has always been of interest. It is well known that the growth temperature has pronounced effects on the quality and morphology of crystals even in the same solvent. In fact, it is a general observation that the crystals grown at relatively high temperatures usually have a better quality than those grown at a low temperature. The effect of temperature is associated with the process of integration of growth species into the surface of a growing crystal. This process becomes favorable at increased temperature.

Crystallization can be regarded as a two-stage process: (1) supply of solute from solution to the crystal surface through a diffusion boundary layer of thickness δ between the growing crystal and the solution by molecular and convective diffusion, and (2) integration of solute ions/molecules into the crystal. The former is rate-limiting if the supersaturation at the crystallization surface is lower compared with the bulk supersaturation. In this case, the growth is said to proceed in the diffusion regime. The second stage is rate-limiting if the bulk supersaturation and crystal surface supersaturation are similar. In this case, the growth regime is said to be kinetic. Crystals are generally considered to grow in a mixed diffusion–kinetic regime. Following Chernov [5], the basic ideas of kinetic and diffusion regimes are given below.

Assuming that a spherical crystal of radius r_x grows in an isotropic environment such that its growth is determined by kinetic coefficient β and the solute concentration in the bulk solution phase and at the crystal surface, separated by distance x, is c and c_0, respectively, the relationship between the resultant growth rate R of the crystal, the concentration difference $(c-c_0)$ across the diffusion layer, and the effective kinetic coefficient β_{eff} for the growth of crystal surface and the rate D/r_x of solution diffusion is given by [5]

$$R = \beta_{\text{eff}}\Omega(c - c_0), \tag{29.7}$$

where the effective kinetic coefficient β_{eff} of growth of crystal surface is defined in terms of the sum of resistances due to the two contributions β and D/r as

$$\frac{1}{\beta_{\text{eff}}} = \frac{1}{\beta} + \frac{r_x}{D} = \frac{1}{\beta}\left(1 + \frac{\beta r_x}{D}\right), \tag{29.8}$$

where D is the solute diffusion coefficient in the solution and Ω is the solute molecular volume ($\Omega = 1/\rho$; ρ is the solute density).

Crystal and environment interact through the medium of the boundary layer, the thickness of which may vary from the minimum (e.g., in stirred solutions) virtually to infinity in unstirred solutions under certain conditions. From Eqn (29.8) the following two extreme cases may be distinguished.

1. *Kinetic regime*. When $\beta r_x/D \ll 1$, the contribution due to diffusion can be neglected. In this case, the rate $R = \Omega\beta(c-c_0)$ does not depend on crystal size, which increases as $r_x = \Omega\beta(c-c_0)t$. Since the kinetic coefficient β depends on supersaturation, it reflects the reaction of the growing surface to the deviations from equilibrium. The specific response, in turn, depends primarily on the interface roughness and defect structure of the surface, which define its growth mechanism: layer (by screw dislocations or two-dimensional nucleation) or continuous (normal).
2. *Diffusion mode*. When $\beta r_x/D \gg 1$, the rate-limiting step is solute diffusion transfer across the boundary layer $\delta \approx r_x$. In this case, the crystal size increases as $r_x = [2\Omega(c-c_0)D]^{1/2}t^{1/2}$ and the rate decelerates as $R = \Omega(c-c_0)D/r_x$. Steady state is never reached in this regime. The main feature here is that, after exceeding a certain critical size that decreases with increasing supersaturation, the crystal loses morphological stability and the starving surface disintegrates into separate sinks for the insufficient nutrient. Morphologically, the event is marked by the onset of hopper and dendritic growth.

In recent years, numerous investigations of surface morphological evolution have been carried out on crystals grown from solutions [25–27]. The results of these studies have been analyzed within the formalism of BCF theory [28] and its subsequent modifications [29], and have led to a broad understanding of the mechanics of dislocation-controlled crystal growth. For example, the growth rate of KDP crystals depends on many parameters, such as growth temperature, supersaturation of growth solution, and impurities. Typically, these KDP crystals grow on vicinal hillocks formed by dislocations.

The normal growth rate R of a crystal face growing by the screw dislocation mechanism is given by the geometrical relation

$$R = pv \tag{29.9}$$

where p is the slope of dislocation hillock and v is the tangential velocity of the elementary steps. According to Eqn (29.9), there are two ways to increase the growth rate: either increase the step velocity v or the slope p of the dislocation hillock.

We consider a composite hillock composed of m equally-spaced dislocations of Burgers vector h, arranged along a line of length L. The slope p of the hillock in this case is given by the relation [28,29]:

$$p = \frac{mh}{y + 2L}, \tag{29.10}$$

where the interstep distance $y = 19r^*_{2\mathrm{D}}$, with the radius of the critically-sized two-dimensional given by

$$r^*_{2D} = \frac{\gamma\Omega}{k_B T\sigma} \tag{29.11}$$

where γ is the solute–solvent interfacial energy, which is related to the linear edge free energy γ_l by the relationship $\gamma_l = \gamma a^2$ (the growth unit dimension $a \approx \Omega^{1/3}$); σ is the supersaturation.

As seen from Eqn (29.10), the hillock slope p (and hence R) can be increased by increasing either σ or T or by changing the number m of dislocations in the growth source. In the kinetic regime, the step velocity v is given by the following [27,29]:

$$v = b\beta\sigma \tag{29.12}$$

with the constant b related to the solubility c_0 and the kinetic coefficient

$$\beta = \beta_0 \exp(-E_A/k_B T), \tag{29.13}$$

where β_0 is a constant, E_A is the activation barrier of the slowest stage of growth, and T is the temperature. Thus, the step velocity (and hence R) can equally be increased either by increasing T or σ.

It should be mentioned that direct control of the growth rate by changing the dislocation structure is difficult because of the complicated relationship between the structure of a dislocation source σ and T. However, as was shown by De Yoreo et al. [30], in contradiction to the predictions of simple BCF models, for $\sigma > 5\%$ the activity of a growth hillock is dominated by the presence of strain-induced dislocation cores and is nearly independent of σ.

29.2.5 Crystal Growth Rates and Dead Supersaturation Zone

29.2.5.1 Basic Concepts of Impurity Effects

Growth of crystals occurs by the attachment and detachment of adatoms at kinks in the steps (ledges) present on their flat faces (F faces). Under ideal conditions, growth on a vicinal F face proceeds by step flow, with steady motion of a uniform train of steps.

However, the addition of small concentrations of impurities can greatly change the properties, morphology, and kinetics of the growing crystal, with important consequences in materials applications. Consequently, the effects of impurities on the growth kinetics of crystals have been studied intensively, both theoretically and experimentally. Here, the kinetic effects of impurities are briefly described. For more details, the reader is referred to Ref. [31].

Impurities are usually more effective at low supersaturations due to the favorable competition of impurity species with low concentration of solute particles for the adsorption and occupation of same growth sites available on the growing face. This results in a threshold supersaturation σ_d, below which no growth takes place; this is usually revealed in the dependence of the displacement rate v of steps on the F faces and face growth rate R of crystals growing from solutions containing a certain amount of impurity on supersaturation σ. The value of the threshold supersaturation σ_d increases with increasing impurity concentration c_i in the solution. The occurrence of a dead supersaturation zone induced by impurities has been reported for many crystals growing from solutions. Typical examples are KH_2PO_4, paraffin, $K_2Cr_2O_7$, ammonium oxalate monohydrate [$(NH_4)_2C_2O_4 \cdot H_2O$; AO], and KCl.

Bredikhin et al. [32] reported extensive data on the existence of dead zone in the case of the supersaturation dependence of the linear growth rate R of the (100) face of KDP crystals grown from aqueous solutions containing different concentrations of Al^{3+} and Fe^{3+} ions under the conditions of free convection. These authors observed two different supersaturation barriers σ_d and σ^* for these impurities, such that for $\sigma < \sigma_d$, there is no growth; for $\sigma_d < \sigma < \sigma^*$, the growth rate slowly increases following the classical Burton–Cabrera–Frank (BCF) parabolic law: $R = b(\sigma - \sigma_d)^n$, where b is an empirical constant and the exponent $n = 1$ or 2; while for $\sigma > \sigma^*$, the growth rate rapidly increases following an $R[(\sigma - \sigma^*)^{5/4}]$ dependence.

Rashkovich and Kronsky [33] studied the effect of trivalent cations on the supersaturation dependence of displacement velocity v of steps on the (100) and (101) faces of KDP crystals and made observations similar to those described above. These authors found three regions of $v(\sigma)$ dependence: (1) there is no growth for $\sigma < \sigma_d$; (2) the velocity v increases slowly with σ for $\sigma_d < \sigma < \sigma^*$; and (3) for $\sigma^* < \sigma < \sigma^{**}$, v steeply increases with σ above σ^*. In the region $\sigma > \sigma^{**}$, the $v(\sigma)$ curve becomes a straight line passing through the origin, as expected from the theoretical linear dependence, and the step velocity v in the presence of attains a value equal to the velocity v_0 for the system without impurities occurs at a threshold supersaturation σ^{**}. These authors attributed the behavior of the $v(\sigma)$ curves to the effect of impurities at low values of σ. The appearance of these different threshold supersaturations is illustrated schematically in Figure 29.4.

The origin of the appearance of the above threshold supersaturations σ_d, σ and σ^* may be explained in terms of adsorption of impurity particles at kinks in step ledges (Kubota–Mullin model) and on the surface terrace between successive ledges (Cabrera–Vermilyea model). These two models differ in the way impurity particles arriving from the bulk medium at the terraces between the ledges on an F face are

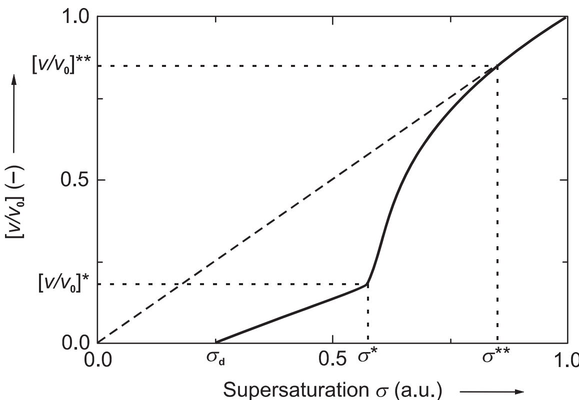

FIGURE 29.4 Schematic presentation of the above $v(\sigma)$ data illustrating the appearance of different threshold supersaturations at a hypothetical concentration c_i of an impurity. *Adapted from Ref. [15].*

adsorbed. Once they are adsorbed, they physically block the motion of advancing step ledges (pinning mechanism), as illustrated in Figure 29.5. This figure shows two steps from an array of steps, moving from left to the right, with an average distance y_0 and an average distance x_0 between the kinks in a step.

There are two extreme cases for the impurity particles to block the motion of steps. When the adsorbed impurities are sufficiently mobile on the surface, they can reach some of the kinks in the step ledges instantaneously (mobile impurities). These adsorbed impurity particles not only block the integration of solute molecules in the advancing step ledges but also physically block their movement by the pinning mechanism. However, the impurity particles can also be firmly adsorbed onto the surface terrace as soon as they reach there (immobile impurities). When the advancing step contacts an impurity particle, it tends to curl around it. The step will stop when the average distance between the adsorbed particles $L < 2r^*_{2D}$, while it will squeeze between a pair of neighboring particles when $L > 2r^*$. The critically sized two-dimensional nucleus radius r^*_{2D} on the surface is given by expression (29.11). The configuration of the advancing steps is thus changed by the adsorbed impurity particles and their average velocity v in the presence of the impurity become smaller than the velocity v_0 in the absence of the impurity. The mechanism of blocking of the movement of a step ledge by two firmly adsorbed particles is shown in Figure 29.5.

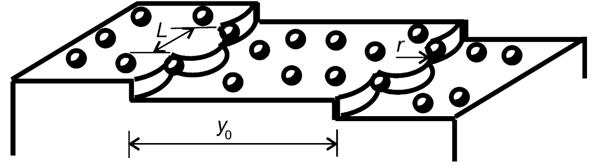

FIGURE 29.5 Illustration of blocking of movement of step ledge by two firmly attached impurity particles. *Adapted from Ref. [31].*

Using the relationship between the advancement velocity v_r of a curved step and the radius r of the curvature of the step, given by [34]

$$v_r/v_0 = 1 - r_{2D}^*/r, \tag{29.14}$$

one obtains the minimum velocity $v_{\min}$ corresponding to the curvature $r = L/2$ in the form

$$v_{\min}/v_0 = 1 - 2r_{2D}^*/L. \tag{29.15}$$

In the absence of impurity when $L \to \propto$, $v_{\max} = v_0$. In Eqn (29.15) when v is taken as the arithmetic mean velocity $v = (v_{\min} + v_0)/2$ and the geometric mean velocity $v = (v_{\min}v_0)^{1/2}$, one obtains [28,31,35]

$$v/v_0 = 1 - r_{2D}^*/L = 1 - \sigma_{\mathrm{dl}}/\sigma, \quad \text{Kubota – Mullin model;} \tag{29.16}$$

$$v/v_0 = \left(1 - r_{2D}^*/L\right)^{1/2} = (1 - 2\sigma_{\mathrm{ds}}/\sigma)^{1/2}, \quad \text{Cabrera – Vermilyea model.} \tag{29.17}$$

In Eqns (29.16) and (29.17), σ_{dl} and σ_{ds} are the threshold supersaturation barriers by Kubota–Mullin and Cabrera–Vermilyea models, respectively, given by

$$\sigma_{\mathrm{dl}} = \frac{\gamma_l a}{k_B T L} = \left(\frac{\gamma_l a}{k_B T x_0}\right)\theta_l, \tag{29.18}$$

$$\sigma_{\mathrm{ds}} = \frac{\gamma_l a}{k_B T L} = \left(\frac{\gamma_l a}{k_B T \lambda}\right)\theta_s^{1/2}, \tag{29.19}$$

where x_0 is the average distance between kinks in a step; λ is average distance between possible adsorption sites on the surface terrace, the fractional linear coverage $\theta_l = x_0/L$, and fractional surface coverage $\theta_s = (\lambda/L)^2$; and the terms given in the brackets are measures of impurity effectiveness. Because x_0 is much larger than $\lambda \approx a$, for a solute–impurity system the impurity effectiveness and the threshold supersaturation σ_{dl} according to the Kubota–Mullin mechanism is always much lower than σ_{ds} predicted by the Cabrera–Vermilyea mechanism.

According to the above concept, growth proceeds according to the usual growth mechanism after the occurrence of the threshold supersaturation barrier σ_{d}, up to a particular value of supersaturation σ^* when impurity adsorption on the growing surface becomes time dependent. However, in the case of time-dependent impurity adsorption at kinks, there is a time constant τ characterizing the upper limit when impurity adsorption ceases to be time-dependent [28,35–37]. This upper limit corresponds to a third threshold supersaturation σ^{**} when the step velocity v approaches the value v_0.

The theoretical interpretation of effect of impurities and threshold supersaturations σ_{d} and σ^* relates step velocity v with supersaturation σ for crystal growth, but no theoretical relationship between face growth R and supersaturation σ has been reported. However, in comparison with the $v(\sigma)$ data, there is a large amount of published data on face growth R as a function of supersaturation σ, where threshold supersaturations have been observed.

The $\sigma_d(c_i)$, $\sigma^*(c_i)$, and $\sigma^{**}(c_i)$ data for different impurities used during the growth of crystals may be described by the following dependences [28,31,37]:

$$\frac{1}{\sigma_c^{1/\rho}} = Q^{1/\rho}\left(1 + \frac{1}{K_L c_i}\right), \tag{29.20}$$

$$\sigma_c^{1/\rho} = B_0 + B_1 c_i, \tag{29.21}$$

which are derived by using Langmuir and Freundlich adsorption isotherms, respectively. In these equations, K_L is the Langmuir constant, the constants B_0 and B_1 are related to the parameters of Freundlich isotherm, the exponent $1/\rho = 1$ or 2, and Q is a parameter related to the value of step velocity v corresponding to the type of threshold supersaturation. Figure 29.6 presents the plots of σ_d, σ^* and σ^{**} for the (100) face of KDP crystals against the concentration c_i of different trivalent impurities, according to Eqn (29.21).

Analysis of the data according to Eq. (29.21) revealed [36] that the average interkink distance x_0 corresponding to the three threshold supersaturations σ_d, σ^* and σ^{**} follows the trend: $x_0(\sigma_d) > x_0(\sigma^*) > x_0(\sigma^{**})$. These distances correspond to three different values of supersaturation representing three average distances $y_0 = 19r^*_{2D}$ between successive steps (cf. Eqn (29.11)): (1) when the steps are completely stopped, $y_0 \geq l_d$; (2) when the steps squeeze out through the fence of adsorbed impurity particles as a result of decreasing r^*_{2D} until $y_0 = l^*$; and (3) when the steps essentially become straight and impurity adsorption no longer takes place on the steps. Steady-state (or instantaneous) and unsteady-state (or time-dependent) impurity adsorption occur in the supersaturation regions $\sigma < \sigma^*$ and $\sigma > \sigma^*$, respectively. Finally, impurity adsorption becomes time independent at $\sigma > \sigma^{**}$.

The above conclusion of three distances corresponding to the three threshold supersaturations is consistent with the concept advanced by Rashkovich and Kronsky [33]. According to these authors, the barrier σ_d occurs at $2r^*_{2D} = l_d$ when the steps are

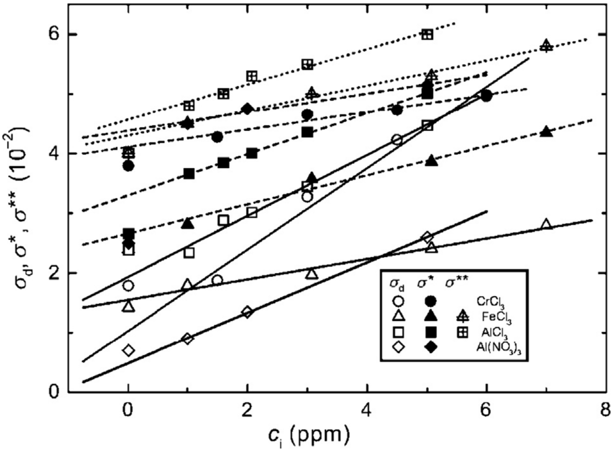

FIGURE 29.6 Example of the plots of σ_d, σ^* and σ^{**} for the (100) face of KDP crystals against the concentration c_i of different trivalent impurities, according to Eqn (21). *From Ref. [37], reproduced with permission of Wiley-VCH.*

completely blocked, while the origin of σ^* is associated with the burial of adsorbed impurity particles as a result of curling of advancing steps around them when the depth of the bent steps reaches a depth δ. The burial of impurity particles occurs when the critical nucleus diameter $2r^*_{2D} \propto \sigma^{-1}$ (see Eqn (29.11)) becomes equal to l^* between the adsorbed impurity particles. The threshold supersaturation σ^{**} corresponds to l^{**}, when the burial of impurity particles is complete and the successive steps are parallel to each other.

In the late 1950s, Frank [38] and Cabrera and Vermilyea [39] used the concept of time-dependent impurity adsorption to explain the origin of kinematic waves and step bunching in terms of relationships between flux of steps passing across a point and the density of steps on the surface. According to this concept, at given concentration of an impurity its adsorption is time-dependent at low density of steps but the impurity adsorption becomes time independent at high density of steps (i.e., low interstep distance y_0). Later, van der Putte et al. [40] suggested that adsorption of an impurity remains time independent at high concentrations of the impurity.

In a study of the effect of Fe(III), Cr(III), and Al(III) ions on the growth of KDP, Land et al. [41] proposed that recovery of crystal growth beyond the dead supersaturation zone in KDP is accompanied with the propagation of macrosteps (bunches of monolayer steps) in contrast to the growth of elementary steps considered in the Cabrera–Vermilyea model. Weaver et al. [42] suggested an improved model for describing impurity effects on crystal growth by synergizing the Langmuir model of adsorption dynamics along with the Cabrera–Vermilyea model.

Extensive studies on the growth kinetics of AO crystals from pure aqueous solutions and from aqueous solutions containing various impurities revealed that the appearance of different threshold supersaturations is associated with the nature of solute–additive–solvent system [36,43–47]. It was found that, for a given impurity concentrations, the face growth rate R approaches a value corresponding to pure solutions for supersaturation $\sigma > \sigma^{**}$, a behavior similar to that for KDP crystals [33]. Analysis of the experimental data on the kinetics of growth of different faces of the crystals in solutions containing Cr(III) impurity suggested that the appearance of threshold supersaturations at $\sigma > \sigma_d$ occurs when there is a transition in the mechanism of adsorption of an impurity from Cabrera–Vermilyea to Kubota–Mullin mechanism.

29.2.5.2 Effect of Organic Additives on Crystal Growth

Foreign substances inherently present in a growth medium or deliberately added to it affect growth rates in different ways. They can change the properties of the growth medium, whereby the equilibrium saturation concentration (i.e., solubility) of the solute and, hence, the supersaturation available for the formation of 3D nuclei and their subsequent growth in the medium, are altered. The affect of foreign substances on the growth of crystals is associated with kinetic and thermodynamic terms involved in the growth models. The kinetic parameters involved in the growth models are connected with the density of kinks and obstructions provided by impurity particles in the

movement of step ledges on the surface, whereas the thermodynamic parameter in these models is the crystal–medium interfacial energy γ. The kinetic effects of impurities were discussed in the preceding section, where no attention was paid to the thermodynamic parameters on growth kinetics. In fact, the above treatment holds when the interfacial energy γ remains unchanged during growth.

It is well known that the solubility c_0 of various substances in aqueous solutions is related to their interfacial energy γ [10]. The higher the solubility c of a substance in a solvent, the lower is its interfacial energy γ, and, consequently, the higher is the step velocity v and the face growth rate R of its crystals. Following this line of argument, it can be concluded that the usual retardation of step velocity v or face growth rate R by an impurity leads to an increase in the solute–solvent interfacial energy γ. However, consideration of the adsorption process in terms of adsorption isotherms and reversible adsorption equilibrium shows that adsorption of foreign substances decreases the value of γ [48,49]. This decrease in γ will, consequently, lead to an increase in v and R. Impurity particles firmly adsorbed at step ledge and onto the surface terrace can also serve as sources of additional kinks for the integration of solute molecules, thereby leading to an increase in v and R [31].

The above considerations show that, at relatively low concentrations of an impurity, one expects opposite effects of kinetic and thermodynamic parameters on growth kinetics. The kinetic parameter tends to decrease v and R, whereas the thermodynamic parameter tends to increase them. Thus, at low supersaturations that ensure a low density of kinks in the step ledges, the rates increase for small impurity concentrations and decrease as the impurity concentration is increased. However, at relatively high supersaturations when a high density of kinks is available in the step ledges, impurity adsorption always decreases v and R for all values of impurity concentrations c_i. With an increase in impurity concentration c_i, an initial increase and then a decrease in R passing through a maximum at a particular impurity concentration c_i were first observed by Bliznakov and Kirkova [50] for the growth rates of the (100) and (111) faces of $Pb(NO_3)_2$ crystals grown from aqueous solutions in the presence of methyl blue.

For many crystals, the ionic surface structure of different faces is fundamentally different. Therefore, organic additives interact differently with different crystal faces [51]. For example, in the case of KDP crystals, the {101} faces are terminated by a layer of K^+ ions whereas the {100} faces by a layer of both K^+ ions and $H_2PO_4^-$ groups. Consequently, because alcohols contain hydroxyl groups, adsorption of alcohols onto the {100} faces through the formation of H-bonds between the alcohols and $H_2PO_4^-$ groups is more favorable than that onto the {101} faces. Similarly, the effect of urea is less pronounced on the growth rate than that of alcohol. Enqvist et al. [52] showed that the negative charge on O atoms of alcohols containing the hydroxyl group is about 1.6 times higher than that of urea containing the carbonyl group. Therefore, the adsorption of alcohols on the {101} faces is more favorable than that of urea. Consequently, alcohols inhibit the growth of the {101} faces more than that of urea.

Small amounts of organic impurities can also cause a growth promoting effect. The positive effects of organic additives on crystal growth and quality have been reported by several authors [53–56]. For example, during ADP and KDP crystal growth, the addition of ethylene glycol, glycerol, and ethylenediamine tetra-acetic acid (EDTA) significantly increases the width of the metastable zone and the crystal growth rate in comparison with those from pure solutions [55,56]. These observations are usually explained by the ability of formation of complexes of additive molecules with multivalent ions inherently present in growth solutions.

29.2.6 Effect of Mechanical Impurities on Crystal Growth

Nonlinear optical (NLO) materials capable of second harmonic generation (SHG) have received a great deal of attention due to their commercial importance in optical communication, signal processing, sensing, and instrumentation. Systematic investigations of NLO materials are devoted to inorganic and semiorganic crystals such as KDP, K_2SO_4, KAP, and LAP with embedded organic molecules and inorganic nanoparticles. These impurities offer mechanical obstruction during growth. The studies were aimed at correlating structural properties to the nonlinear responses with the ultimate goal being the possibility of "tuning" the structure to enhance the nonlinear properties. Therefore, crystallization of some inorganic and semiorganic salts in the presence of organic molecules and inorganic nanoparticles is an important process still under careful examination by several research groups.

29.2.6.1 Growth of Water-Soluble Crystals with Embedded Organic Molecules

Gliko et al. [57] studied the morphology and growth kinetics of the pyramidal face of KDP crystals in the presence of the dye Chicago Sky Blue. The crystals were grown in crystallizers of about 10 L volume at the initial temperature of about 60 °C and impurity concentration $c_i = 1.4$ ppm ($1.4 \cdot 10^{-6}$ mol/mol KDP). It was found that staining of the crystal begins only at temperatures below 35 °C when the crystal already reaches a sufficiently large size. This observation is a consequence of a sharp increase in dye adsorption with decreasing temperature.

Figure 29.7 shows the dependence of normal growth rate R of dislocation hillocks on supersaturation σ of aqueous solutions containing different dye concentration c_i. It may be seen from the figure that the measured values of normal growth rate R in the pure solution and in the presence of the dye are close. The minor difference between them can be attributed to the difference in the activity of dislocation sources and influence of temperature. The experimentally derived dependence of velocity v of movement of steps on supersaturation σ, shown in Figure 29.8, has a character that is unusual for pyramidal faces. The $v(\sigma)$ dependence is sublinear for the shallow sector below $\sigma \approx 0.035$ (top curve), whereas v is nearly proportional to σ for steep sectors in the whole region of supersaturation (bottom curves). From the figure, it may also be seen that the dye concentration does not noticeably affect the velocity of the growth layer's movement.

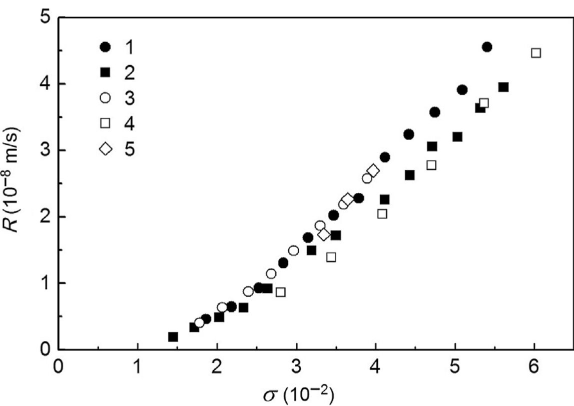

FIGURE 29.7 Dependence of normal growth rate R of dislocation hillocks on supersaturation σ of aqueous solutions containing different dye concentration c_i: (1,2) no additive, (3) 1 ppm, (4) 1.5 ppm, and (5) 2 ppm. Saturation temperature: (1,3) ca. 33 °C, and (2,4,5) ca. 37.5 °C. *Adapted from Ref. [57], with permission of the Materials Research Society.*

The fact that the capturing of a dye starts only at a sufficiently high velocity of the step in the case of the shallow sector composed of array of parallel steps with large interstep distance y_0, but it is not captured by the steepest vicinal sectors comprised of arrays of parallel steps with small y_0, is evidence of a short lifetime of dye molecules on the surface. Another observation in support of this argument is the occurrence of capturing impurity particles only at sufficiently high concentration in the solution. Gliko et al. [57] explained the observation of the capture of dye particles in the framework of a model [58], describing the movement of a step and its morphological stability in the presence of mobile impurity stoppers.

In an *in situ* atomic force microscopy (AFM) study of potassium sulfate (K_2SO_4) crystal growth in the presence of acid fuchsin and pyranine, Moret [59] found that these polysulfonated dyes adsorb onto the {110} and {010} faces, producing strong habit

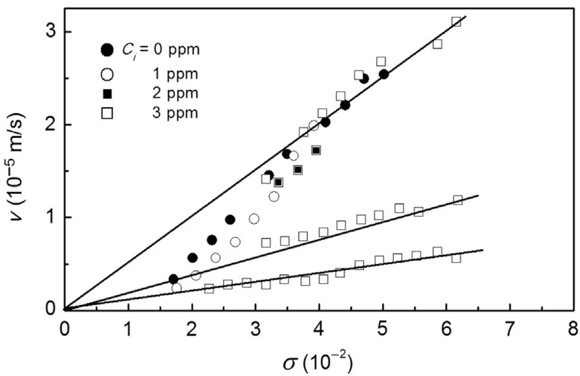

FIGURE 29.8 Dependence of velocity v of moving growth layers in three vicinal sectors on supersaturation σ. Saturation temperature about 37.5 °C. *Adapted from Ref. [57], with permission of the Materials Research Society.*

modification and changes in the surface micromorphology of the crystals. The main observations of this study were the following:

1. The presence of dye molecules at concentrations as low as about $2 \cdot 10^{-6}$ and $4 \cdot 10^{-4}$ M for pyranine and acid fuchsin, respectively, produces significant changes in the step morphology and growth rates.
2. Bunching of steps occurs as a result of absorption of impurities binding to the crystal surface.
3. Additive molecules attach to the terraces pinning the growing front and lead to the roughening of edges of the growing steps.
4. At a given supersaturation, there exists a critical value of dye concentration above which crystal growth is stopped along particular crystallographic directions (i.e., dead supersaturation zone).
5. At low supersaturations, layers grow by step flow at preexisting steps by the addition of growth units at the step edges.

The first four observations may be explained by the Caberera–Vermilyea mechanism, whereas the last observation suggests that growth is controlled by volume diffusion.

The validity of Cabrera–Vermilyea mechanism in the above study is associated with the adsorption behavior of acid fuchsin and sulfonated pyrene molecules on the two faces of K_2SO_4 crystals. Acid fuchsin and sulfonated pyrene are strong polyelectrolytes that can adsorb on terraces because of the high number of simultaneous attaching points on a molecule (three/four sulfonated groups) strongly interacting with the surface via long distance electrostatic forces. This class of molecules should remain practically immobile once adsorbed onto the surface due to the strong interactions with the host surface, provided that sulfonate–sulfonate distances reasonably match the distance between the sulfate ions on the surface host lattice and with sulfonate groups substituting for surface anions. This should particularly hold for pyranine due to its conformational rigidity, and its effects on K_2SO_4 are indeed significantly stronger than those produced by acid fuchsin.

A major goal in crystal growth studies is to ascertain whether the additives adsorb onto the surface terraces between steps or at kink sites on the steps. For example, correlation of distribution of foreign molecules inside the host crystal with surface microtopography can shed light on the relationships between surface structure, growth mechanism, and additive incorporation. For layer growth, specific affinity for dye incorporation into a growing surface is associated with its detailed structural features (i.e., density of kinks and ledges). Because nonequivalent crystallographic directions have different structural properties, they differ in their affinities toward the capture of an additive.

29.2.6.2 Growth of Water-Soluble Crystals with Embedded Nanoparticles

The methods of growth of single crystals with inclusions of the second fine-crystalline phase (of nanometric dimensions) are of great interest for designing new composite

crystalline materials with new valuable properties. Examples of such materials are the so-called combined nonlinear–optical media based on inorganic matrix (single crystal) with incorporated nanoparticles [60,61,62]. In the case of KDP crystals, SiO_2 and CdTe nanoparticles of size up to 250 nm were found to be captured [60,63].

Rudneva et al. [60] carried out an interesting study devoted to the nature of interaction of nanocrystals and crystalline SiO_2 particles with the growing face and the mechanism of their incorporation into KDP crystal. This study showed that in unstirred solutions the capture of nanocrystals and crystalline SiO_2 particles by a growing crystal face takes place at a growth rate exceeding a certain critical value which depends on particle size. The smaller the particles, the higher is the growth rate. Crystal growth from stirred solutions in the presence of solid particles showed that capture of particles by a growing crystal is also possible. As in the case of growth from unstirred solutions, the probability of capture of particles depends mainly on particle size and decreases with decreasing particle size. The specific feature of the experiments on crystal growth under the conditions of solution stirring was the formation of long channels during the capturing of particles. Such channels are not observed from unstirred solutions. It was found that at the growth rates exceeding the critical values the influence of supersaturation and growth rate of a crystal on the probability of the particle capture is insignificant.

Pritula et al. [61] carried out a similar study on the growth of KDP crystals from aqueous solution in the presence of TiO_2 nanoparticles by the temperature reduction method onto a point seed. The authors found that, under the conditions of intense stirring, TiO_2 nanoparticles are captured predominantly by the pyramidal growth sector and, to a considerably lesser extent, by the prismatic sector. Difference in the nature of interaction of the nanoparticles with the {100} and {101} growth faces is obviously caused by differences in the structure of the two faces and the nature of adsorption of impurity particles onto them. These differences are responsible for the threshold value of supersaturation necessary for the growth of the faces.

Capture of mechanical impurities in crystal growth from solutions may be explained from a consideration of two forces [5]: (1) force pressing impurity (e.g. SiO_2 particles) at the crystallization front against the crystal surface, and (2) repulsive force of disjoining pressure arising in a thin (10^{-5}–10^{-7} cm) solution layer between a particle and a crystal. The pressing force, in addition to the hydrodynamic component, also has a component related to the effect of the particle entrainment by a diffusion flow. The disjoining pressure arises mainly because of the molecular (van der Waals) and electrostatic (Debye) forces and the structural component of the disjoining pressure due to partial ordering of the liquid in the vicinity of solid surfaces. According to this concept [5], if the distance between a particle of radius r and a crystal surface becomes less than a certain critical distance ca. $0.1r$, the particle screens the surface of a growing face from the diffusion flow. This decreases solution supersaturation under the particle, which, in turn, leads to the formation of a V-like depressions on the growing face. At certain critical growth rate, the conditions for capture of a foreign particle by the crystal are created and a channel filled with mother solution is formed.

Pritula et al. [62] showed the possibility of creating a composite material on the basis of KDP crystal with incorporated $Al_2O_3 \cdot nH_2O$ (NAO) nanoparticles. These authors investigated the effect of NAO nanoparticles on the growth kinetics of KDP crystal faces and showed predominant interaction of the nanoparticles with the {100} crystal faces. KDP:NAO crystals were grown from aqueous solutions containing 1–100 ppm NAO impurity (with respect to KH_2PO_4) by the temperature reduction method. It was found that the nature of the $R(\sigma, \Delta T)$ curves for the {101} and {100} faces of KDP in the presence of NAO nanoparticles and their incorporation in different sectors is similar to that observed in the case of TiO_2 nanoparticles discussed above and trivalent cationic impurities [32,33].

29.3 High-Temperature Solution Growth

Complex multicomponent compounds usually have high melting points, high vapor pressure, or decompose incongruently before melting. It is difficult to grow such substances from conventional methods such as growth from their melts. Crystallization of these compounds is carried out from high-temperature solution where temperature for their growth is much lower than their melting points.

High-temperature solution growth has features similar to those of growth of substances from low-temperature solutions. The compound to be crystallized, or components reacting to form it, is first dissolved in a solvent at high temperature. Then, a supersaturation in the solution is attained by slow cooling of the solution or evaporation of the solvent such that crystals nucleate and grow in the supersaturated solution. Supersaturation can also be attained by creating a temperature difference between the locations of growing crystal and nutrient. Growth is carried out either in the air or in any other suitable atmosphere. The growth temperature is usually between 300 and 1800 °C, and the concentration of the solute in the high-temperature solution is between 1 and 30 wt%.

The main advantage of the method is that practically any material can be grown in some solvent whose composition may be found from a knowledge of the composition of solvents used for the crystallization of chemically similar compounds. Because the growth temperature in this method is lower than that in melt growth, technically the control of growth temperature is easier and the quality of the crystals is better in terms of dislocation densities and point defects. The main disadvantage of the method is that the solvent provides a variety of impurities, which can be incorporated into the grown crystals either substitutionally as solvent ions or as solvent inclusions.

Crystallization from high-temperature solutions has been described before in excellent books [3,64,65] and reviews [66–69]. The reader is referred to these literature sources for more information on experimental procedures for growth, characterization methods, and the materials crystallized before 1998.

29.3.1 Principle of the Method

High-temperature solution growth method employs the fact that complex compounds with high melting points have high solubilities in appropriate molten salts and oxides used as solvents. Once appropriate solvents are found for substances to be grown, crystal growth is carried out on seeds spontaneously nucleated in the bulk molten solution or on seeds introduced into the solution, using some procedures to achieve supersaturation.

The range of substances grown as single crystals from high-temperature solutions extends from elements, such as diamond and metals; semiconducting compounds, such as GaP, GaN, and AlGaAs; borates; and various oxides. Table 29.1 lists some examples of substances grown from high-temperature solutions. This table contains examples of fluxes published in the literature in recent years.

A usual growth experiment consists of weighing and mixing of required constituent materials, loading them into a crucible, tightly closing the crucible to avoid solvent losses by evaporation, placing the crucible in a furnace initially heated to the maximum temperature, holding the crucible for several hours of soaking time to dissolve and homogenize the solution, slow cooling of the furnace to the desired temperature to create supersaturation for nucleation and growth of crystals, fast cooling down of the furnace to room temperature, and finally leaching out the crystals. The crystals obtained after growth can also be separated from the solution by decanting it. The typical procedure used for crystal growth from high-temperature solutions is summarized in Figure 29.9.

29.3.2 Composition of Fluxes and Their Selection

The selection of a suitable solvent for the material to be grown from high-temperature solutions is also a critical step in this method. In the selection of a solvent, both its physical and chemical properties are important. At the growth temperature, a solvent should ensure a sufficient solubility of the compound and its components, and the solubility should show sufficient change with temperature. The compound to be crystallized should also be stable in the solvent. The solvent should have low melting point, low vapor pressure (low volatility), low viscosity, and low toxicity. It should also not corrode the growth apparatus (crucible and furnace) and should be cheaply available in the pure state.

There is no universal high-temperature solvent that satisfies all of the conditions mentioned above. Most of the solvents used for crystal growth are various individual chemical compounds or their mixtures, and up to about 1990 they were selected by a trial-and-error method. However, in later years the composition of solvents for the growth of different materials have been established from knowledge of solvents proposed before for the crystal growth of similar compounds.

For the growth of oxides from high-temperature solutions, the following fluxes are commonly used: (1) compounds containing lead and bismuth; (2) borates; (3) vanadates,

Table 29.1 Some Examples of Single Crystals Grown by Different High-Temperature Methods[a]

Crystal	Solvent/Solution	Method	Ref.
KTP	$K_8P_6O_{19}$–BaF_2	Top-seeded solution growth; Pt crucible, homogenization at 1100 °C, cooled at 40 °C/h to about 900 °C, seed introduced at about 10 °C above saturation temperature, temperature decreased at 0.2–1 °C/day until end of growth; rotation rate 60–120 rpm with rotation direction reversed every 120 s with interval pause of 5 s; after growth crystal, withdrawn from solution and furnace cooled to room temperature at 20 °C	[70]
KTP:Zr	K_2O–P_2O_5–TiO_2–ZrF_4	Slow cooling method; Pt crucibles, homogenization at 1100 °C for 10 h, cooled to 750 °C at 3 K/h	[71]
NdP_5O_{14}	$H_2P_4O_7$	Slow solvent evaporation; platinum crucible, growth temperature 500 °C	[72]
$KNbO_3$	K_2CO_3–NbO_5	Micropulling down; Pt crucible, cooling rate 30 °C/min, pulling rate 0.5 mm/min	[73]
$LaMn_{1-x}Co_xO_3$	Cs_2MoO_4–MoO_3	Electrochemical growth; Pt crucible, anode current density 5–10 mA/cm^2, 80–100 h	[74]
$LiNbO_3$	$(Li_2O:Nb_2O_5)-K_2O$	Czochralski method; pulling rate 2 mm/h, rotation rate 20 rpm	[75]
β-$FeSi_2$	Sn	Temperature gradient solution growth; quartz ampoule, $T_G = 880$ °C, $T_S = 920$–960 °C, temperature gradient 40 K/cm	[76]
PZN–PT (6–10 mol% PT)	1.7–3.0 mol% TiO_2 +($ZnO:Nb_2O_5:PbO =$ 19:11:68)	Temperature gradient method; Pt crucible, homogenization at 1160 °C for 8 h, self-nucleation, cooling at 0.5–0.75 °C/h to 890 °C, crucible cooling in 70 h	[77]
3C-SiC	Si	Top-seeded dipping method (LPE); graphite crucible, growth on dipping 6H-SiC(0001) seed mounted at the end of graphite rod at 1300 °C for 50 h	[78]
$BaAlBO_3F_2$	$LiF:B_2O_3:NaF = 5:2:0.6$	Middle-seeded solution growth; Pt crucible, homogenization at 950 °C for 24 h, slowly cooled to, temperature 10 K above melting, insertion of seed, mounted on Pt rod, temperature decrease at 0.6–2.6 K/day, rotation rate 20–40 rpm with inversion; grown crystal withdrawn from solution surface by 10 mm, cooled down to RT at 10 K/h	[79]
$KBi(WO_4)_2$	80% $K_2W_2O_7$	Top-seeded solution growth; Pt crucible, homogenization at about 800 °C for 24 h; b-oriented seed, crucible rotated slow cooling at 10 rpm; after 10 days of growth at 730 to, 720 °C, crystal cooled to room temperature at rate 10 K/h	[80]
$Y_{1-x}Ca_xBa_2Cu_3O_{7-\delta}$	Y:Ba:Cu	Top-seeded solution growth; mixtures of Y_2O_3, $BaCO_3$, $CaCO_3$ and CuO homogenized in air in alumina crucible at 880 °C for 2 days; growth in ZrO_2 crucible on MgO seed, temperature gradient 15 K/cm above melt in air or oxygen; soaking temperature ca. 1050 °C; seed and crucible rotated at 40 rpm in opposite directions	[81]

Table 29.1 Some Examples of Single Crystals Grown by Different High-Temperature Methods[a]—cont'd

Crystal	Solvent/Solution	Method	Ref.
$La_2CaB_{10}O_{19}$(LCB)	LCB:CaO:Li_2O:B_2O_3	Top-seeded solution growth; solution homogenization at 1000 °C for 48 h, seed introduced into solution 10 °C above T_S, after initiation of growth temperature decreased between 0.24 and 0.5 °C/day, crystal rotation rate 15–45 rpm	[82]
NBT–KBT (5% KBT)	Na_2CO_3–K_2CO_3–Bi_2O_3 (20% excess flux)	Top-seeded solution growth; Pt crucible, homogenization at 1360 °C, growth on seed mounted on a rod, pulling rate 1.0–1.5 mm/day, rotation rate 5–10 rpm, crystal withdrawn, from melt, furnace cooled down to room temperature at 30–50 °C	[83]
$CsLiB_6O_{10}$	Cs_2CO_3:Li_2CO_3:H_3BO_3: NaF (1:1:12:0.5)	Top-seeded solution growth; Pt crucible, homogenization at 850 °C for 24 h, z-oriented seed introduced in melt, for growth cooling rate 0.1–0.6 °C/h, rotation rate 20–40 rpm, crystal withdrawn from melt, furnace cooled to room temperature at 10–15 °C/h	[84]

[a]Abbreviation: T_S, saturation temperature.

molybdates, and tungstates; and (4) various chlorides and fluorides. Fluxes from the first group are very effective for growth. They are volatile, toxic, and relatively active with platinum crucibles. They dissolve in hot aqueous HNO_3 solutions. Fluxes from the group of borates have relatively low melting points but they are very viscous (see Figure 29.10) and have a strong tendency to creep out of the crucible. They also dissolve in hot diluted HNO_3, whereas some of them also dissolve in water. Vanadium, molybdenum, and tungsten oxides are good solvents but they are very volatile at high temperatures. Consequently, their salts (i.e., vanadates, molybdates, and tungstates) are usually used.

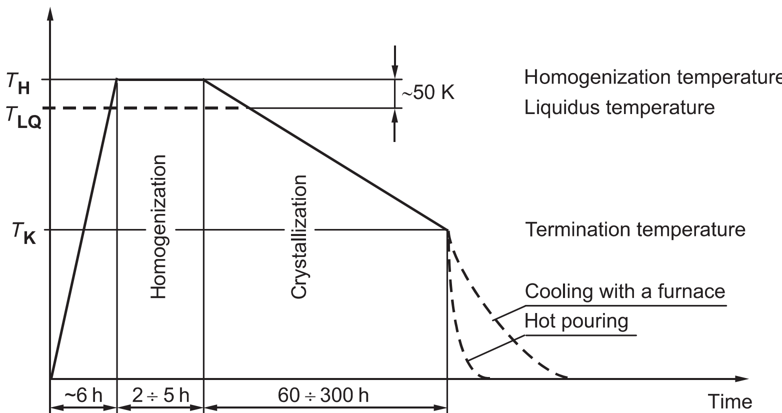

FIGURE 29.9 Typical procedure for crystal growth from high-temperature solutions. *Adapted from Ref. [68].*

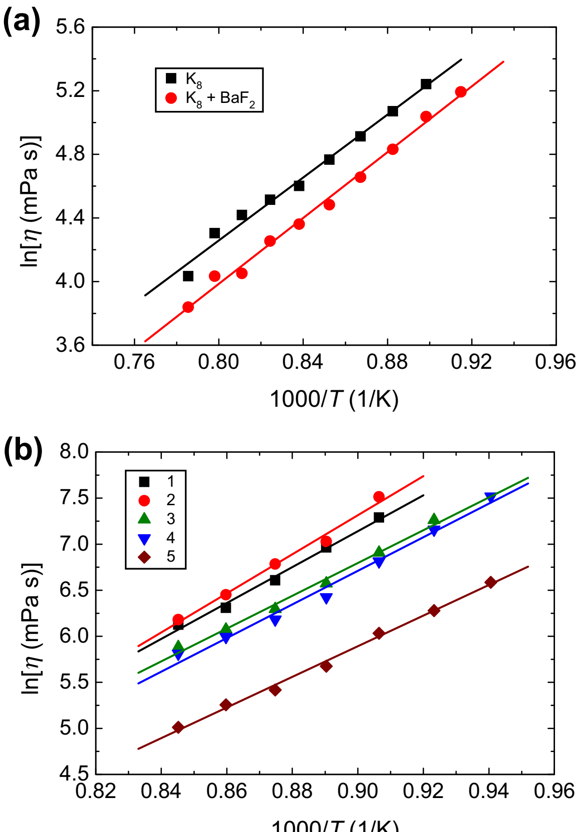

FIGURE 29.10 Plots of ln η on 1/T according to Eqn (29.16) for the data of viscosity η of two different solutions of (a) KTP in K_8 and K_8–BaF_2 solvents and (b) $CsLiB_6O_{11}$ (CLBO): (1) Cs_2CO_3:Li_2CO_3:H_3BO_3 = 1:1:12, (2) Cs_2CO_3:Li_2CO_3:H_3BO_3 = 1:1:11, (3) Cs_2CO_3:Li_2CO_3:H_3BO_3:NaF = 1:1:12:0.5, (4) Cs_2CO_3:Li_2CO_3:H_3BO_3:NaF = 1:1:12:0.667, and (5) Cs_2CO_3:Li_2CO_3:H_3BO_3:NaF = 1:1:12:2. *Original data from: (a) Ref. [70] and (b) Ref. [88].*

They all dissolve in aqueous solutions of acids and alkalis. Chlorides and fluorides are good solvents with low viscosity but they are volatile (see Figure 29.11). Fluorides dissolve in acids, whereas chlorides in hot water.

Oxide superconductors usually have complex composition and have two or more oxide components. As the complexity of composition of oxide superconductors increases, they become increasingly less stable. It is known that practically all high-temperature T_c oxide superconductors decompose before melting. Consequently, these materials are usually grown from high-temperature solutions. Three types of fluxes are used for their growth [69]: (1) self-fluxes, (2) partial self-fluxes, and (3) other fluxes. When components of the composition of an oxide superconductor serve as a solvent for growth, they are said to be the self-fluxes. When one of the components of the oxide superconductor is a part of its chemical structure while the other is partially

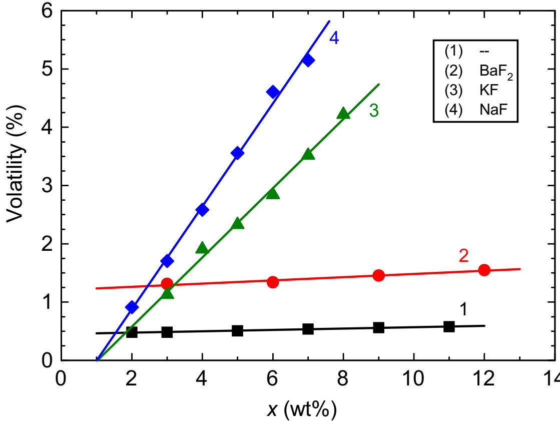

FIGURE 29.11 Volatility of KTP in four fluxes as a function of additive content *x*: (1) K_8 ($K_8P_6O_{19}$), (2) K_8–BaF_2, (3) K_8–KF, and (4) K_8–NaF. Additives to the pure solvent K_8 are given in the inset. *Adapted from Ref. [70].*

or entirely related to its structure, one talks of partial self-flux. However, when the solvent is completely unrelated to the chemical composition of the superconductor, it is categorized as other flux. For the growth of $YBa_2Cu_3O_{7-\delta}$ (YBCO), for example, CuO, CuO–BaO, and In_2O_3 are self-flux, partial self-flux, and other flux, respectively.

For the growth of crystals of complex phosphates, such as potassium titanyl phosphate ($KTiOPO_4$; KTP), potassium polyphosphates ($K_6P_4O_{13}$ and $K_8P_6O_{19}$, popularly abbreviated as K_6 and K_8 solvents, respectively) are known as good fluxes. A common problem with these fluxes is that they have high viscosity (Figure 29.10). Introduction of additives such as alkali and alkaline-earth fluorides are well known to reduce solution viscosity and increase solute solubility. However, these additives lead to an increase of their volatility, which strongly increases with the additive content in the solvent (see Figure 29.11). The increase in the flux volatility is enormously high in the fluorides of alkali metals.

29.3.3 Some Properties of High-Temperature Solvents

The solubility of a substance in a given flux and the width of the metastable zone width are associated with the formation of ions and complexes [67,85,86]. Consequently, composition of the components of the original flux and addition of impurities, usually known as additives, determine the solubility curve and metastable zone width in it for a given compound.

Garnets ($A_3B_5O_{12}$), spinels (AB_2O_4), and perovskites (ABO_3) are usually grown at high temperatures from solvents composed of oxides and fluorides (see Table 29.1). These solvents are characterized by the dissociation of oxide supplying O^{2-} ions to the solution (basic behavior) and association of O^{2-} ions to the second component (acidic behavior) [87]. Successful growth of the compounds takes place in a wide range of composition of the solvents and the ratio of the garnet-forming oxides, and there is a correlation

between oxygen ion concentration (OIC) and the range of crystallization of primary phases of a garnet, spinel, or perovskite.

Volatility of a flux used for growth of a compound has an adverse effect on the quality of crystals grown from solutions and causes problems associated with spurious nucleation on the solution meniscus, decomposition of seed crystals, and unstable growth. Therefore, while selecting the composition of a flux suitable for the growth of a compound, knowledge of the volatility of the flux is very important.

Volatilization of the solution may be determined from the weight loss of the charged crucible during each crystal growth experiment [70]. Figure 29.11 shows an example of the volatility of four fluxes used for the growth of KTP ($KTiOPO_4$) crystals as a function of the content x of K_8 ($K_8P_6O_{19}$), and three fluoride additives (BaF_2, NaF and KF) in the starting high-temperature solution for volatility experiments. The parameter x defines the weight fraction of K_8 (curve 1) or fluoride additive (curves 2–4) in the K_8–KNT–additive solution. As seen from this figure, the volatility of different solutions increases practically linearly with increasing x of K_8 as well as of all fluoride additives. As indicated by the slope of the plots of the volatility of different substances against their initial content x, above approximately 3 wt%, the volatility of NaF and KF additives increases very rapidly with an increase in their content, and the volatility of NaF is much higher than that of KF. However, as in the case of K_8 solvent, the volatility of BaF_2 increases poorly with its content in the solution.

In the above study, the authors [70] used working seeds mounted on a platinum seed-rod for crystal growth. They observed deposition of volatilized mass on seed-rod in the case of NaF and KF additives, but no such deposition was found on the seed-rod in BaF_2 additive. These results suggest that pure K_8 solvent and BaF_2 additive contained in K_8 are favorable for the growth of KTP crystals.

As in the case of different low-temperature solutions and solvents, the viscosity of high-temperature solutions decreases with an increase in temperature. The viscosity of high-temperature solution strongly depends on solution composition. For example, the viscosity of halide-free solutions used for the growth of KTP and CLBO crystals differs by a factor of about 5, and solutions of the CLBO system are more viscous than those of the KTP system. Moreover, fluoride additives, as a rule, decrease the viscosity of different systems and the relative decrease in the viscosity of the solution usually increases with increasing concentration of the fluoride additive.

The viscosity of different liquids usually follows the Arrhenius relationship:

$$\eta = \eta_0 \exp(E_a/R_G T), \tag{29.22}$$

where η_0 is a constant and E_a is the activation energy for viscous flow. Figure 29.10(a) and (b) show the viscosity of solutions of solute KTP in solvent K_8 or K_8–BaF_2 in the weight ratios between 0.4 and 0.5 and of flux composition used for the growth of $CsLiB_6O_{11}$ (CLBO) crystals, respectively, in the form of plots of $\ln \eta$ against $1/T$ according to Eqn (29.22). The calculated values of the pre-exponential factor η_0 and the activation energy for E_a viscous flow are given in Table 29.2. Obviously, the activation energy for

Table 29.2 Calculated Values of Parameters *A* and E_a for Growth Solutions for KTP and CLBO

Crystal	Solution	ln η_0	η_0 (mPa s)	E_a (kJ/mol)
KTP	K_8	-3.65 ± 0.35	$2.6 \cdot 10^{-2}$	82.2 ± 3.5
	$K_8 + BaF_2$	-4.28 ± 0.25	$1.4 \cdot 10^{-2}$	86.0 ± 2.5
CLBO	Cs_2CO_3:Li_2CO_3:H_3BO_3 (1:1:11)	-11.77 ± 1.11	$7.7 \cdot 10^{-6}$	176.3 ± 10.5
	Cs_2CO_3:Li_2CO_3:H_3BO_3 (1:1:12)	-10.40 ± 0.90	$3.0 \cdot 10^{-5}$	162.0 ± 8.5
	Cs_2CO_3:Li_2CO_3:H_3BO_3:NaF (1:1:12:0.5)	-9.22 ± 0.73	$9.9 \cdot 10^{-5}$	147.9 ± 6.9
	Cs_2CO_3:Li_2CO_3:H_3BO_3:NaF (1:1:12:0.67)	-9.69 ± 0.84	$6.2 \cdot 10^{-5}$	151.5 ± 7.9
	Cs_2CO_3:Li_2CO_3:H_3BO_3:NaF (1:1:12:2)	-9.07 ± 0.47	$1.2 \cdot 10^{-4}$	138.3 ± 4.4
$KLu(WO_4)_2$	$KLu(WO_4)_2$:$K_2W_2O_7$ (12:88)	0.68 ± 0.38	1.96	28.0 ± 4.0

viscous flow for solvents of different composition varies in a wide range. The highest activation energy is encountered for multicomponent solvents and its value is decreased by the alkali fluoride additives and their concentration.

Figure 29.12 shows the dependence of solubility *c* of KTP in KTP–$K_8P_6O_{19}$ and KTP–$K_8P_6O_{19}$–BaF_2 solutions on temperature. In the study, the solubility of the solute KTP was determined from its known weights dissolved in the solution at different temperatures by using the traditional method of introducing trial seeds and changing the solution temperature. The saturation temperature of the solution was identified when the seed size remained unchanged. In the figure, open and filled squares represent solubility data from two different studies and are somewhat different from each other. They are represented by a single curve drawn for the data shown by open squares. The other two curves are for KTP solubility in solutions prepared from solid-reacted and solution-reacted materials. Solid-reacted solutions were prepared by homogenizing KTP solute with K_8 or K_8–BaF_2 solvents in weight ratio between 0.27 and 0.42 (filled squares

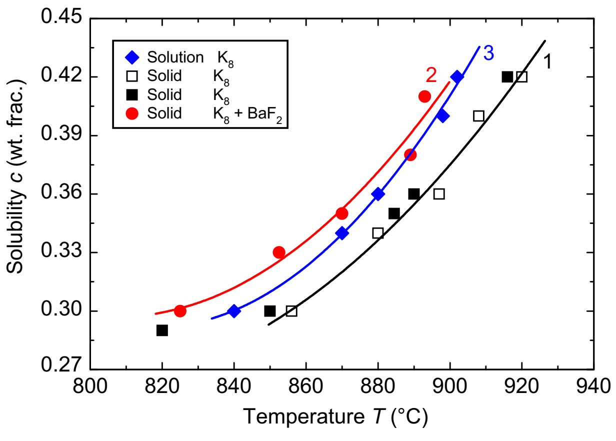

FIGURE 29.12 Temperature dependence of solubility *c* of KTP in (1,3) KTP–$K_8P_6O_{19}$, and (2) KTP–$K_8P_6O_{19}$–BaF_2 solutions. Curves (1, 2) and (3) are for KTP solubility in solutions prepared from solid-reacted and solution-reacted materials, respectively. *Data represented by filled squares and circles are from Ref. [70], whereas those shown by filled diamonds and open squares are from Ref. [88].*

and circles) and between 0.30 and 0.42 (open squares) at a temperature of about 50 °C above the saturation temperature for 24 h [70,88]. However, solution-reacted materials were prepared by reacting a solution of tetrabutyl titanate dissolved in ethanol with appropriate amounts of KH_2PO_4 and K_2CO_3 dissolved in water, which gave a white precipitate [88]. The excess amount of water was evaporated by heating the precipitate; finally, the material was dried at 50 °C for 24 h and grinded into powder in an agate mortar (filled diamonds).

From Figure 29.12, one notes differences in the solubility c of KTP obtained not only from solid- and solution-reacted materials (compare data of filled diamonds with those of open and filled squares) but also from two different solid-reacted solutions (compare open and filled squares). Moreover, the solubility of KTP is increased by BaF_2 additive (compare data of filled and open squares with those of filled circles). It may be seen that the solubility of KTP in solution-reacted materials is higher than that in the solid-reacted materials, whereas it is somewhat different in the two different solid-reacted materials. The former observation is due to small amounts of TiO_2 insoluble in high-temperature solutions [88], whereas the latter observation is associated with the difference in the initial composition of the solutions. BaF_2 additive increases the solubility of KTP at all temperatures. Using relation (29.5), these solubility differences can be analyzed from the plots of ln c against $1/T$, as shown in Figure 29.13. The values of the pre-exponential factor A and the enthalpy of dissolution ΔH_s obtained from the plots are given in Table 29.3. Obviously, the differences in the solubility for the three systems are reflected by the values of A and ΔH_s. Because for ideal solutions $A = \Delta H_s / R_G T_m$, from the values of A and ΔH_s listed in Table 29.3, one finds $T_m \approx 700$ K. This temperature is much lower than the saturation temperature T_s for the above systems, so one may conclude that high-temperature solutions are regular.

Dependence of the solubility of a solute on the composition of flux is intimately connected with the complexing properties of solute and solvent molecules/atoms. In the

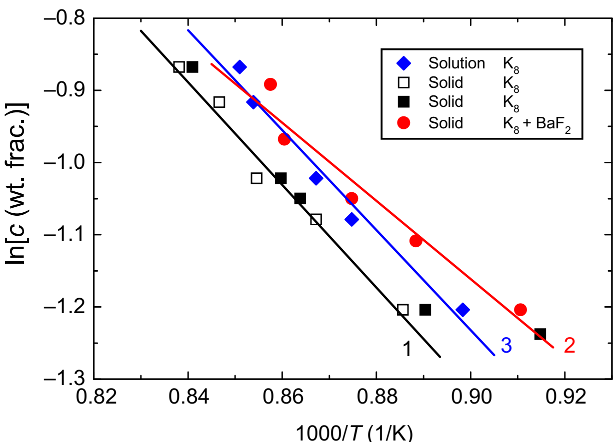

FIGURE 29.13 Plots of ln c against $1/T$ for KTP in different solvents according to Eqn (29.5). *Data from Figure 29.12.*

Table 29.3 Parameters A and ΔH_s for Solubility of KTP Prepared from Solution and Solid in K_8 and $K_8 + BaF_2$ Solvents

Solute Origin	Solvent	A	ΔH_s (kJ/mol)	T_m (K)
Solution	K_8	5.0 ± 0.54	57.6 ± 5.1	722 ± 78
Solid	K_8	5.09 ± 0.49	59.1 ± 4.8	715 ± 68
	$K_8 + BaF_2$	3.71 ± 0.63	45.0 ± 5.9	685 ± 116

case of temperature dependence of solubility of a solute in different solvents, the solubility difference is reflected by the enthalpy of dissolution ΔH_S. For example, the increase in the solubility of KTP due to the addition of BaF_2 to K_8 solvent leads to a decrease in ΔH_S. The relationship between ΔH_S and solvent composition is associated with solute–solvent interactions. The increase in the solubility of a solute with an increase in one of the components of high-temperature solvents is also associated with these solute–solvent interactions.

29.3.4 Crystal Growth Techniques

Depending on the method of achieving supersaturation in the solution, the techniques of growing crystals from high-temperature solutions may be grouped into three types. These are temperature reduction (i.e., slow cooling of the solution), solvent evaporation, and temperature gradient methods. In these methods, the driving force (i.e., supersaturation) for growth is ensured by the values of the cooling rate of the solvent, the solvent evaporation rate, and the temperature difference between saturated and growth zones, respectively. In the slow-cooling method, the cooling rate is typically around 1 K/h.

Crystal growth in high-temperature solutions may be carried out on spontaneously nucleated seeds as well as on seeds grown and prepared independently. Growth involving spontaneously nucleated seeds is usually carried out in slow cooling and solvent evaporation methods, but the crystals obtained by these methods are relatively small. These small crystals developed on self-nucleated seeds are subsequently used as seeds to grow large samples by temperature gradient methods.

29.3.4.1 Slow-Cooling Method

Crystal growth by slow cooling is commonly used for producing small specimens. The method has the advantage that the apparatus is simple (a furnace, a crucible, and a temperature programmer) and a growth run requires poor attention after the beginning of the growth process. Conventional horizontal muffle furnaces and small crucibles are usually sufficient for crystal growth by this method.

The main difficulties of growth by slow cooling are that the flux introduces strain in the crystals due to its different thermal expansion coefficient than that of the crystal, and the high nucleation density results in small size of crystals. The former difficulty is overcome by draining away the flux before starting fast cooling. The latter difficulty may

be solved by using small temperature oscillations at the nucleation stage or by initiating nucleation in a small region by localized cooling by blowing a stream of cold air (cold finger technique).

A silicon carbide heating element furnace, with a recrystallized alumina tube lining, in a vertical configuration ensures the growth of large single crystals of high melting-point materials [89]. The main components of this growth arrangement are silicon carbide heating element, crucible support, and double crucible system. For the growth of crystals of relatively low melting-point materials, a kanthal-wire bound furnace operating up to about 1200 °C can be used instead of a silicon carbide heating element.

The furnace arrangement enables one to grow crystals of different materials and composition by changing the muffle and crucible support. The double crucible system involves an inner, smaller crucible containing a crystal growing mixture and a bigger crucible placed inverted over the smaller one. After the completion of growth when this system is inverted, the solution left over in the inner crucible is drained out into the outer bigger crucible and the cooling program is commenced to cool the crucible to room temperature. This procedure enables one to obtain big crystals free of flux adhering to them.

It should be mentioned that horizontal muffle furnaces have traditionally been used for the growth of different materials by the slow-cooling method. After the completion of a growth run, the grown crystals are extracted from the unused flux by dissolving in water or in some acid or alkali.

29.3.4.2 Solvent Evaporation Method

The solvent evaporation method is usually used to grow single crystals of substances that are stable over a narrow temperature range. A simple horizontal muffle furnace to maintain a constant temperature and a crucible containing the chemicals are sufficient for crystal growth experiments. Unlike in the case of slow-cooling method, even a temperature programmer is not required. Because growth occurs at a constant temperature, the concentration of equilibrium defects and the incorporation of solvent ions as impurities remains constant in a growing crystal. The main problem is of control of the rate of evaporation of the solvent (and hence the growth rate), and the poisonous and/or corrosive nature of the solvent vapor released when an open growth system without provision of collection of solvent vapor is used.

The above problem is overcome in closed systems (Figure 29.14) in which the evaporation rate is controlled by varying the temperature T_2 at which solvent condensation takes place. In these closed systems, a crystal is made to grow in the lower part of the crucible where the temperature $T_1 < T_2$. Consequently, mass transport to the growing crucible is possible mainly by solutal convection. Therefore, growth is solutal diffusion controlled unless stirring is applied. For closed systems, this can be achieved by the accelerated crucible rotation technique (ACRT). In this arrangement, the evaporation rate is determined by the dimensions r_1 and r_2 and by the temperatures T_1 and T_2.

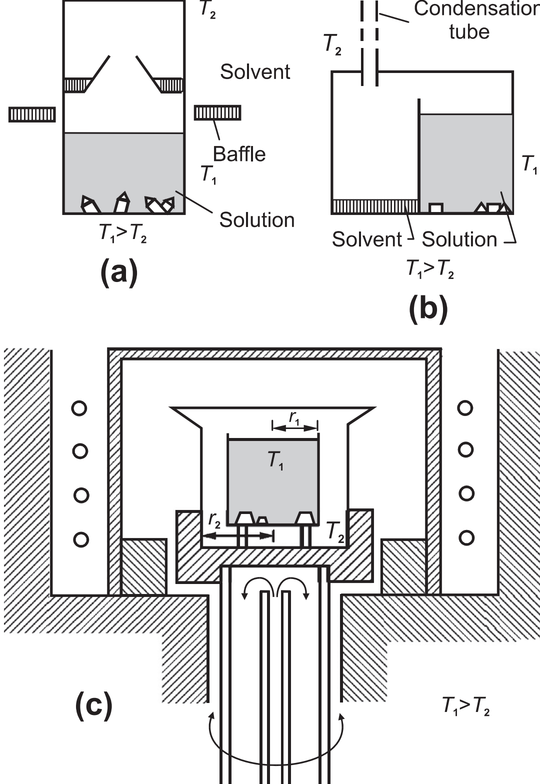

FIGURE 29.14 Arrangement for growth by flux evaporation: (a) system with collection of condensed solvent, (b) condensation of solvent in a tube, and (c) flux evaporation–condensation system with ACRT stirring. *From Ref. [64], with permission of Elsevier.*

29.3.4.3 Temperature Gradient Methods

In the temperature gradient methods, nutrient (solute) is held at a temperature T_1, whereas a growing crystal is held at a temperature T_2 such that $T_1 > T_2$. Due to the temperature difference, the solution is supersaturated and growth takes place on self-nucleated seeds or on an appropriately mounted seed surface in the supersaturated solution. Solute transport to the seed is ensured by natural or forced convection. Depending on the direction of the temperature gradient, crystal growth may be carried out either at the bottom of the crucible/ampoule or in the top part of the solution.

In the temperature gradient methods, introduction of the seed in the top part of the solution is popular. This method is known as the top-seeded solution growth (TSSG) method. An example of the apparatus used for such a growth is presented schematically in Figure 29.15 [90]. It consists of a vertical muffle furnace heated by a resistance heater, a platinum crucible, and a seed rotating system. The platinum crucible is placed on an alumina support and the furnace top is covered by an alumina lid with observation

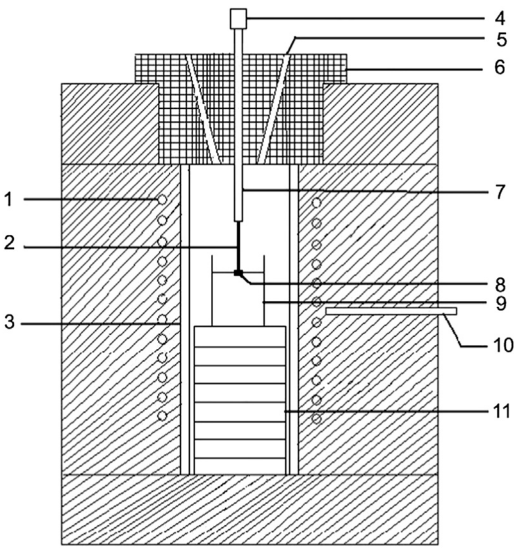

FIGURE 29.15 Schematic diagram of apparatus used for top-seeded solution growth: (1) resistance heater, (2) platinum rod, (3) alumina tube, (4) seed rotator, (5) observation hole, (6) alumina lid, (7) seed holding rod, (8) mounted seed, (9) platinum crucible, and (10) alumina support. *From Ref. [90], with permission of Elsevier.*

holes. Instead of large alumina support (10), crucible support bases on a long rods passing through the furnace bottom have also been proposed [79,84].

In some cases, the mounted seed has also be allowed to grow in the interior of the solution instead of keeping it in the top layer. This type of growth technique has been called the dipping solution technique [91]. The high growth yield in this arrangement of the seed in the solution is due to the high-temperature gradient in the lower part of the solution.

29.3.4.4 Other Methods

Among the other methods of crystal growth from high-temperature solutions are electrocrystallization and micropulling-down method. The principle of electrolytic crystallization from high-temperature solutions is essentially the same as used in conventional electrocrystallization from low-temperature solutions. The most difficult step is the selection of a solvent for growth. However, once a solution composition is known, crystallization can be carried out at constant current, constant potential difference between cathode and anode, or at a constant overpotential. Materials as diverse as bronzes, elemental and compound semiconductors, high T_c oxide superconductors, borides, CeS, ThS, MoS_2, Mo_2C, and lanthanum manganates have been grown by this method. However, the method has been poorly explored. For further details, the reader is referred to the literature [69,92–98].

A micropulling-down method from molten solutions has been proposed for the growth of high-quality fiber crystals [73,99]. The principle of the method is similar to

crystal pulling. Crystalline fiber of the desired material nucleated at the tip of a platinum pipe is pulled down from the central part of the bottom of a crucible containing molten solution of appropriate composition. Growth of $KNbO_3$ fiber crystals has been reported by this method.

29.3.5 Growth Instability and Facet Formation

It is usually observed that crystals grown by top-seeded solution growth show a tendency to develop faceting at the crystal–liquid interface. The faceting planes are usually the slowest growing, low-index planes. Faceting leads to deterioration of the quality of the growing crystal as a result of trapping of inclusions of solution and bubbles and release of internal stresses related to facet formation. Therefore, knowledge of optimum experimental parameters ensuring facet-free growth from high-temperature solution is useful.

An interesting study devoted to origin of facet formation was carried out by Szaller et al. [100], who grew stoichiometric lithium niobate (sLN) along the z-direction from 12.3 mol% K_2O and $Li_2O/Nb_2O_5 = 1$ in the starting liquid. Growth was carried out with a pulling rate of 0.2 mm/h and constant rotation rate in the range of 8–28 rpm, as well as a gradually decreasing rotation rate starting from $30-45$ rpm at the shoulder down to 26 rpm at the end. In the experiments, a cone angle of 120 and 75° maintained the crystal-to-crucible diameter ratio at approximately 1:2 at the cylindrical part, whereas height-to-diameter of the crucible was 40/50 mm. Evolution of crystal quality was studied on the (0001) slices cut perpendicular to the growth direction.

This study showed that the degree of structural perfection in the crystals is strongly affected by the necking process and that growth ridges on the shoulder surface and facets on the growth front are the main sources of crystal defects. After the introduction of seed, crystal grows with conically increasing diameter on a strongly convex growth front until the desired diameter is attained. Increases in the crystal diameter and ridge formation depend on the cone angle, whereas stresses associated with large ridges favor both cracking and mechanical twinning of the as-grown crystal during its final cooling down.

It was found [100] that growth of high-quality, facet-free stoichiometric lithium niobate crystals was possible by applying gradually variable rotation rate. Optimal conditions for the growth of good-quality crystals was achieved for $Gr/Re^2 > 1$, where the dimensionless Grashof number $Gr = g\beta\Delta TR^3/v^2$ is characteristic for buoyancy and the Reynolds number $Re = \omega r^2/v$ is characteristic for forced convection. In these relationships, R is the crucible radius, r is the crystal radius, β is the volume expansion coefficient of the crystal, g is the acceleration due to gravity, ΔT is the radial temperature difference at the melt surface, v is the kinematic viscosity of the melt, and ω is the crystal rotation speed.

29.4 Summary and Outlook

Crystallization in a laboratory, in an industrial plant, or in nature always occurs in a fluid medium of known or unknown composition in which a solid crystalline phase is

produced. In all these cases, an understanding of the processes involved in the formation of the solid crystalline phase is important. Intensive studies devoted to the understanding of crystallization processes started in the 1960s, with simultaneous rapid development in the techniques of growing single crystals due the increasing demand of materials for technological applications. These studies resulted not only in improvement in our general understanding of crystallization processes but also provided insight into the processes responsible for the nucleation and growth of crystals and the dependence of nucleation and growth rates on various external and internal factors. However, despite a long history and broad application of solution growth, a complete understanding of the detailed mechanisms that determine how crystal surfaces grow from a surrounding solution still remains elusive.

A strong influence of growth of single crystals from solutions in the present-day technology is evident from recent advances in the fields of the production of materials ranging from micrometer-sized, crystalline organic pharmaceutical chemicals to mass-scale, large inorganic nonlinear optical crystals. The growth of large single crystals from aqueous solutions is of interest for essentially two reasons. First, these large crystals find applications in the area of high-power laser technology. Second, research into this area of crystal growth and the corresponding in-depth examination of several key systems provides fundamental case studies generating theory and technology applicable to all of solution crystal growth, including new aqueous growth systems and high-temperature solution growth. Moreover, rapid-growth techniques developed during recent years have stimulated studies on the processes of single-crystal growth from solution at high supersaturations and have revealed new phenomena that were difficult to see before in crystals growing slowly at low supersaturations.

Acknowledgment

The authors express their gratitude to Dr K. Wójcik for preparing several figures presented in this chapter.

References

[1] Sangwal K. In: Encyclopedia of materials science: science and technology. Amsterdam: Elsevier; 2001. p. 3670.

[2] Buckley HE. Crystal growth. New York: Wiley; 1951.

[3] Brice JC. The crystal growth from liquids. Amsterdam: North-Holland; 1973.

[4] Petrov TG, Treivus EB, Punin Yu O, Kasatkin AP. Vyrashchivanie Kristallov iz Rastvorov [Crystal growth from solutions]. Leningrad (Russia): Nedra; 1983.

[5] Chernov AA. Modem crystallography III, crystal growth. Berlin: Springer-Verlag; 1984.

[6] Wilke K-Th, Bohm J. Kristallzüchtung. Berlin: VEB Deutscher Verlag der Wissenschaften; 1988.

[7] Henisch HK. Crystals in gels and Liesegang rings. Cambridge: Cambridge University Press; 1988.

[8] Rodriguez-Clemente R, Veintemillas-Verdaguer S, Rull-Perez F, Sangwal K. Prog Cryst Growth Charact 1988;17:1–40.

[9] Sangwal K, Sokołowski T, Wiktorowska B. In: Sangwal K, editor. Elementary crystal growth. Lublin: Saan Publishers; 1994. p. 255 [chapter 8].

[10] Nývlt J, Söhnel O, Matuchova M, Broul M. The kinetics of industrial crystallization. Prague: Academia; 1985.

[11] Sangwal K. CrystEngComm 2011;13:489.

[12] Sangwal K. Cryst Res Technol 2009;44:231.

[13] Sangwal K. Cryst Growth Des 2009;9:942.

[14] Sangwal K. J Cryst Growth 2011;318:103.

[15] Sangwal K. J Cryst Growth 2010;312:3316.

[16] Sangwal K, Mielniczek-Brzóska E, Barylska S. Chem Eng Res Des 2014;92:491.

[17] Mullin JW. Crystallization. 4th ed. Oxford: Butterworth-Heinemann; 2001 [chapter 5], p. 181–215.

[18] Yokotani A, Koide H, Yomanuro K, Sasaki T, Yamanaka T, Yamanaka C. Rev Laser Eng 1983; 11:162.

[19] Sasaki T, Yokotani A. J Cryst Growth 1990;99:820.

[20] Zaitseva NP, Rashkovich LN, Bogatyreva SV. J Cryst Growth 1995;148:276.

[21] Zaitseva NP, DeYoreo JJ, Dehaven MR, Vital RL, Montgomery KE, Richardson M, et al. J Cryst Growth 1997;180:255.

[22] Sankaranarayanan K, Ramasamy P. J Cryst Growth 2005;280:467.

[23] Mohameed HA, Ulrich J. Cryst Res Technol 1996;31:27.

[24] Sharma SK, Verma S, Shrivastava BB, Wadhawan VK. J Cryst Growth 2002;244:342.

[25] Rashkovich LN, Mkrtchyan AA, Chernov AA. Sov Phys Crystallogr 1985;30:219.

[26] Maiwa K, Tsukamoto K, Sunagawa I. J Cryst Growth 1990;102:43.

[27] Vekilov PG, Kuznetsov Yu G, Chernov AA. J Cryst Growth 1992;121:643.

[28] Burton WK, Cabrera N, Frank FC. Philos Trans R Soc Lond A 1951;243:299.

[29] Chernov AA. Sov Phys Uspekhi 1961;4:116.

[30] De Yoreo JJ, Land TA, Rashkovich LN, Onischenko TA, Lee JD, Monovskii OV, Zaitseva P. J Cryst Growth 1997;182:442.

[31] Sangwal K. Additives and crystallization processes: from fundamentals to applications. Chichester: Wiley; 2007.

[32] Bredikhin VI, Ershov VI, Korolikhin VV, Lizyakina VN, Potapenko SYu, Khlyunev NV. J Cryst Growth 1987;84:509.

[33] Rashkovich LN, Kronsky NV. J Cryst Growth 1997;182:434.

[34] Sangwal K. J Cryst Growth 2002;242:215.

[35] Kubota N, Yokota M, Mullin JW. J Cryst Growth 2000;212:480.

[36] Sangwal K, Mielniczek-Brzóska E. J Cryst Growth 2002;242:421.

[37] Sangwal K. Cryst Res Technol 2005;40:635.

[38] Frank FC. In: Doremus RH, Roberts BW, Turnbull D, editors. Growth and perfection of crystals. New York: Wiley; 1958. p. 411.

[39] Cabrera N, Vermilyea DA. In: Doremus RH, Roberts BW, Turnbull D, editors. Growth and perfection of crystals. New York: Wiley; 1958. p. 393.

[40] van der Putte P, van Enckevort WJP, Giling LJ, Bloem J. J Cryst Growth 1978;43:659.
[41] Land TA, Martin TL, Potapenko S, Palmore GT, DeYoreo JJ. Nature 1999;399:442.
[42] Weaver ML, Qiu SR, Hoyer JR, Casey WH, Nancollas GH, DeYoreo JJ. Chem Phys Chem 2006;7:2081.
[43] Mielniczek-Brzóska E, Giełzak-Koćwin K, Sangwal K. J Cryst Growth 2000;212:532.
[44] Sangwal K, Mielniczek-Brzóska E. Cryst Res Technol 2001;36:837.
[45] Sangwal K, Mielniczek-Brzóska E. J Cryst Growth 2001;233:43.
[46] Sangwal K, Mielniczek-Brzóska E, Borc J. Cryst Res Technol 2003;38:103.
[47] Mielniczek-Brzóska E, Sangwal K. Cryst Res Technol 2004;11:993.
[48] Kern R. In: Sheftal NN, editor. Rost Kristallov (Growth of crystals), vol. 8. Moscow: Nauka; 1967. p. 5.
[49] Davey RJ. In: de Jong EJ, Jancic SJ, editors. Industrial crystallization. New York: North-Holland; 1979.
[50] Bliznakov GM, Kirkova EK. Z Phys Chem 1957;206:271.
[51] De Vries SA, Goedtkindt P, Bennett SL, Huisman WJ, Zwanenburg MJ, Smilgies D-M, et al. Phys Rev Lett 1998;80:2229.
[52] Enqvist Y, Partanen J, Louhi-Kultanen M, Kallas J. Trans IChemE 2003;81:1354.
[53] Kern R, Dassonville R. J Cryst Growth 1992;116:191.
[54] Kim WJ, Kim SD, Jung HS, Hayhurst DT. Micropor Mesopor Mater 2002;56:89.
[55] Kuznetsov V, Okhrimenko T, Rak M. J Cryst Growth 1998;193:164.
[56] Srinivasan K, Meera K, Ramasamy P. J Cryst Growth 1999;205:457.
[57] Gliko O, Zaitseva N, Rashkovich LN. Res Soc Symp Proc 2001;620. M9.9.1.
[58] Voronkov VV, Rashkovich LN. J Cryst Growth 1994;144:107.
[59] Moret M. Mater Chem Phys 2000;66:177.
[60] Rudneva EB, Manomenova VL, Voloshin AÉ, Kaminskiĭ AA, Vasil'ev AB, Mchedlishvili BV. Crystallogr Rep 2006;51:142.
[61] Pritula I, Gayvoronsky V, Kolybaeva M, Puzikov V, Brodyn M, Tkachenko V, et al. Opt Mater 2011; 33:623.
[62] Pritula IM, Kosinova AV, Vorontsov DA, Kolybaeva MI, Bezkrovnaya ON, Tkachenko VF, et al. J Cryst Growth 2012;355:26.
[63] Bensouici A, Plaza JL, Halimi O, Boudine B, Sebais M, Dieguez E. J Optoelectron Adv Mater 2008; 10:3051.
[64] Elwell D, Scheel HJ. Crystal growth from high-temperature solutions. London: Academic Press; 1975.
[65] Timofeeva VA. Rost Kristallov iz Raztvorov-Razplavov (Crystal growth from the flux). Moscow: Nauka; 1978.
[66] Wanklyn BM. In: Pamplin BR, editor. Crystal growth. Oxford: Pergamon; 1975. p. 217.
[67] Görnert P, Voigt F. In: Kaldis E, editor. Current topics in materials science, vol. 11. Amsterdam: North-Holland; 1984. p. 1.
[68] Dąbkowska HA. In: Sangwal K, editor. Elementary crystal growth. Lublin, Poland: Saan; 1994. p. 303 [chapter 9].
[69] Chen C-K. Prog Cryst Growth Charact Mater 1998;36:1.
[70] Hu J, Hu Z-G. J Cryst Growth 2009;311:4235.

[71] Ivanenko VI, Zatovsky IV, Slobodyanik NS, Nadgornyi PG, Baumer NV. Cryst Res Technol 2008;43:355.

[72] Watanabe K. Cryst Res Technol 1999;34:47.

[73] Chani VI, Shimamura K, Fukuda T. Cryst Res Technol 1999;34:519.

[74] Khalyavin DD, Shiryaev SV, Bychkov GL, Barilo SN, Istinovich SN, Szymczak H, et al. Cryst Res Technol 2003;38:748.

[75] Sun DL, Hang Y, Zhang LH, Luo GZ, Zhu SN, Lim PK, et al. Cryst Res Technol 2004;39:511.

[76] Udono H, Matsumura K, Osugi IJ, Kikuma I. J Cryst Growth 2005;275:e1967.

[77] Dąbkowski A, Dąbkowska HA, Greedan JE, Ren W, Mukherjee BK. J Cryst Growth 2004;265:2004.

[78] Ujihara T, Seki K, Tanaka R, Kozawa S, Alexander, Morimoto K, et al. J Cryst Growth 2011;318:389.

[79] Yue T, Hu Z, Chen C. J Cryst Growth 2008;310:1264.

[80] Xie HD, Shen DZ, Xie CZ, Wang XQ, Shen GQ. Cryst Res Technol 2006;41:961.

[81] Lin CT, Liang B, Chen HC. J Cryst Growth 2002;237:778.

[82] Jing F, Wu Y, Fu P. J Cryst Growth 2006;292:454.

[83] Sun R, Li X, Zhang Q, Fang B, Zhang H, Lin D, et al. J Cryst Growth 2012;341:34.

[84] Yu X, Hu Z-G. J Cryst Growth 2010;312:2415.

[85] Wanklyn B. J Cryst Growth 1983;65:533.

[86] Görnert P, Sinn E. In: Kaldis E, editor. Crystal growth of electronic materials. Amsterdam: Elsevier; 1985. p. 23.

[87] Sinn E, Linzen D, Fischer K. Cryst Res Technol 1985;20:965.

[88] Lu Y, Jie W, Wang T, Zheng X, Xu Y, Luan L. J Cryst Growth 2012;355:33.

[89] Rao SM, Wu MK, Srivastava JK, Monk BH, Yen NY, Lin HY, et al. Cryst Res Technol 2006;41:859.

[90] Yu X, Yue Y, Yao J, Hu Z-G. J Cryst Growth 2010;312:3029.

[91] Ujihara T, Maekawa R, Tanaka R, Sasaki K, Kuroda K, Taeda Y. J Cryst Growth 2008;310:1438.

[92] Elwell D. In: Kaldis E, Scheel HJ, editors. Current topics in materials science, vol. 2. Amsterdam: Elsevier; 1977. p. 605.

[93] Elwell D. J Cryst Growth 1981;52:741.

[94] Feigelson RS. Adv Chem 1980;186:243.

[95] Elwell D, Feigelson RS. Sol Ener Mater 1982;6:123.

[96] Elwell D, Rao GM. J Appl Electrochem 1988;18:15.

[97] McCarroll WH, Ramanujachary KV, Greenblatt M, Cosandey F. J Solid State Chem 1998;136:322.

[98] McCarroll WH, Fewcett ID, Greenblatt M, Ramanujachary KV. J Solid State Chem 1999;146:88.

[99] Yoon DH, Yonenaga I, Fukuda T, Ohnishi N. J Cryst Growth 1994;142:339.

[100] Szaller Zs, Peter A, Polgar K, Szabo Gy. J Cryst Growth 2012;360:181.

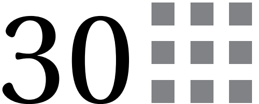

Crystallization Mechanisms of High Critical Temperature Superconductors

Yuh Shiohara, Teruo Izumi

SUPERCONDUCTIVITY RESEARCH LABORATORY, INTERNATIONAL SUPERCONDUCTIVITY TECHNOLOGY CENTER, KAWASAKI, KANAGAWA, JAPAN

CHAPTER OUTLINE

30.1 Introduction **1230**
30.2 High T_c Oxide Superconductors **1231**
30.2.1 Variety of HTSC Materials 1231
30.2.2 Crystal Structure and Characteristic Properties of YBCO System 1232
30.3 Requirement for Applications of HTSC Materials; Key Factors for Higher J_c **1233**
30.4 Phase Diagram of HTSC Material **1233**
30.4.1 Phase Diagrams of Y-Ba-Cu-O and RE-Ba-Cu-O Systems 1234
30.4.2 Quasi-ternary Phase Diagram 1235
30.4.3 Standard Gibbs Free Energy Change for Formation 1236
30.5 Bulk Crystal Growth Methods from the Melt **1239**
30.5.1 Melt Texture Growth 1239
30.5.2 Quench and Melt Growth and Melt Powder Melt Growth 1240
30.5.3 Seeding Method 1240
30.5.4 Directional Solidification Method 1242
30.6 Single Crystal Growth Methods from the Solution **1243**
30.6.1 Flux Method 1243
30.6.2 Traveling Solvent Floating Zone Method 1244
30.6.3 Top-seeded Solution Growth Method (Solute-rich Liquid Crystal-Pulling Method) 1244
30.6.3.1 SRL-CP Method 1244
30.6.3.2 Enlargement of Single Crystal Size in SRL-CP Method 1246
30.6.3.3 Other RE-123 Single Crystal Growth 1248

Handbook of Crystal Growth. http://dx.doi.org/10.1016/B978-0-444-63303-3.00030-4
Copyright © 2015 Elsevier B.V. All rights reserved.

30.7 Controlling Factors of Crystal Growth from the Melt and Solution 1248
30.7.1 Supersaturation as a Driving Force for Crystal Growth 1248
30.7.2 Faceted Growth 1249
30.7.3 Experimental Measurements of Anisotropic Growth Rate 1249
30.7.4 Trapping Phenomena of High-temperature Stable Phase (Y-211) Particles into Y-123 Crystal 1250
30.8 Crystal Growth Mechanism 1251
30.8.1 Rate-Limiting for Crystal Growth 1251
30.8.2 Solute Diffusion Model for Unidirectional Solidification 1252
30.8.2.1 Basic Growth Mechanism 1252
30.8.2.2 Driving Force of Solute Diffusion 1253
30.8.2.3 Flux Provided by Dissolution of Y-211 Particle 1255
30.8.2.4 Flux Required for Y-123 Growth 1255
30.8.2.5 Steady State Growth Rate 1256
30.8.2.6 Macrosegregation Mechanism of Pushing/Trapping Model 1256
30.8.3 Crystal Growth Mechanism of SRL-CP Method 1257
30.8.3.1 Basic Growth Mechanism of Solute Diffusion Model with Interfacial Kinetics 1257
30.8.3.2 Interface Kinetics Estimated from Spiral Growth 1259
30.8.4 Crystal Growth Mechanism Using Ternary Phase Diagram 1261
30.9 Tetragonal to Orthorhombic Phase Transition (Twin Formation) 1263
30.9.1 Experimental Measurements of Oxygen Diffusion Coefficient in $REBa_2Cu_3O_{7-\delta}$ (RE: Y & Nd) Crystal 1264
30.9.2 Diffusion Mechanism 1265
30.9.3 Twins and Tweed Pattern Due to Strains in Orthorhombic Phase 1268
30.9.4 Detwinning and Twin-free Crystal by Mechanical Stress 1269
30.10 Conclusion 1270
Acknowledgments 1271
References 1271

30.1 Introduction

The discovery of high critical temperature (T_c) superconducting (HTSC) materials with superconductivity characteristics above 30 K in the La-Ba-Cu-O system by Bednorz and Müller [1] in 1986 initiated great excitement in the field of superconductivity research and spurred an unprecedented effort by many research groups to discover and/or explore materials with a higher T_c. Some exhibit superconductivity above the boiling point of liquid nitrogen, which is much less expensive, easier to handle, and has a higher heat capacity than liquid helium, and can be used as a coolant.

The disappointing low critical current density (J_c) for HTSC systems worried many scientists about future potential for application. In particular, the critical current (I_c) and T_c characteristics were regarded as important benchmarking characteristics for HTSC applications, and these initial findings temporarily quelled the superconductor fever. Together with the opinions held by renowned physicists from around the world, *Science*, a world-class science magazine, published a shocking abstract entitled, "Superconductivity: is the party over?" [2]. Since J_c and I_c are strongly microstructure dependent rather than the intrinsic property of T_c, the control of the microstructure is very important. In principle, high J_c applications require a structurally perfect matrix of bulk superconductors. Consequently, understanding and R&D of crystal growth are indispensable especially in the field of HTSC.

Of the many HTSC materials discovered so far, $YBa_2Cu_3O_{7-\delta}$ (Y-123) [3] or RE $Ba_2Cu_3O_{7-\delta}$ (RE-123), in which RE represents a rare earth element, is the most widely studied. In this chapter, we review the progress in HTSC crystal growth research concerning the solidification process, and crystal growth mechanisms of Y-123 and other RE-123 superconducting oxides. Some of the problems related to crystal growth and epitaxy of HTSC compounds were reviewed by H. J. Scheel. [4]

30.2 High T_c Oxide Superconductors

30.2.1 Variety of HTSC Materials

Since Bednorz and Müller discovered high T_c oxide superconductors (La-Ba-Cu-O system) [1], a variety of attempts have been made to find new high T_c superconducting materials. This has led to the rapid discovery of superconducting materials above the boiling point of liquid nitrogen (77 K), first in the Y-Ba-Cu-O (YBCO) system ($T_c \sim 90$ K) [3], later in the Bi-Sr-Ca-Cu-O (BSCCO) ($T_c \sim 110$ K) [5], Tl-Sr-Ca-Cu-O (TSCCO) ($T_c \sim 120$ K) [6], and Hg-Ba-Ca-Cu-O (HBCCO) ($T_c \sim 130$ K) [7] systems. These compounds possess perovskite or oxygen-deficient perovskite structures. Furthermore, numerous new superconductors have been discovered including MgB_2 ($T_c \sim 39$ K) [8] and $LaFeAs(O_{1-x}F_x)$ ($T_c \sim 26$ K) [9] systems, although their T_c values are below 77 K.

The following specific characteristics are common in high T_c superconductors, at least in oxide superconductors:

1. the compounds consist of a number of elements including copper and have layered CuO_2 structures;
2. the two-dimensionality (anisotropy) in characteristics is large;
3. the coherence length (ξ), which is the characteristic length determining the superconducting property, is extremely short (less than 20 Å).

These three factors must be considered to fabricate the superconducting crystalline materials [10].

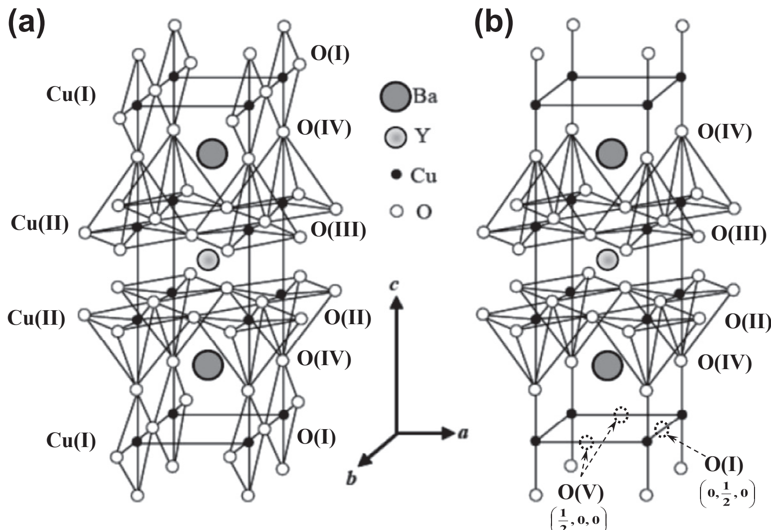

FIGURE 30.1 Crystal structure of $YBa_2Cu_3O_{7-\delta}$: (a) orthorhombic phase ($\delta < 0.5$); (b) tetragonal phase ($0.5 < \delta < 1.0$).

30.2.2 Crystal Structure and Characteristic Properties of YBCO System

YBCO materials have a distorted oxygen-deficient perovskite structure of $YBa_2Cu_3O_{7-\delta}$ (Y-123), where $\delta = 0 \sim 1$. $YBa_2Cu_3O_{7-\delta}$ is orthorhombic (Figure 30.1(a)) when the δ value is smaller than approximately 0.6, but when δ increases more than about 0.6, a transition occurs to form a tetragonal structure (Figure 30.1(b)) [10,11]. The tetragonal phase is not superconducting and shows a temperature dependence of resistivity similar to that of semiconductors and/or insulators; the orthorhombic phase is a superconductor below T_c and exhibits a metallic resistivity trend above T_c, as shown in Figure 30.2. T_c value strongly

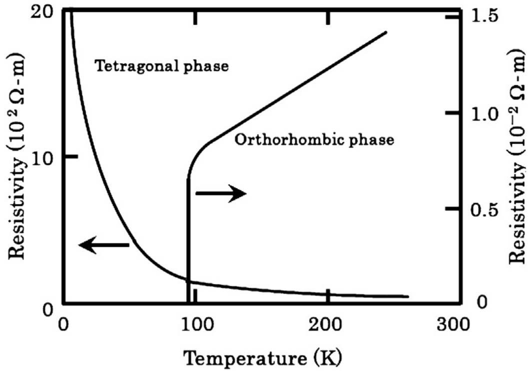

FIGURE 30.2 Temperature dependence of the resistivity for orthorhombic and tetragonal phases in Y-123 [12]. *© 1987. The Japan Society of Applied Physics.*

depends on oxygen concentration of 7-δ in the orthorhombic Y-123 [13,14]. The phase transition from tetragonal to orthorhombic depends on oxygen partial pressure in the atmosphere (P_{O_2}) and temperature (T) [15,16]. At higher T and/or low P_{O_2}, the tetragonal phase is stable. The Y-123 materials fabricated by high temperature processes, including sintering, melt growth, and vapor deposition with high substrate temperatures, have a tetragonal phase. Accordingly, the materials should be slowly cooled or post-annealed in an oxygen atmosphere for oxygenation to obtain an orthorhombic phase with high T_c, as was mentioned by H. J. Scheel [17].

Most rare earth (RE) elements can be substituted for yttrium (Y) without any destructive effects on the superconducting characteristics of Y-123 crystal. For example, the T_c value of Nd-123 reached about 96 K, which is several degrees higher than that of Y-123. In general, T_c and peritectic temperature (T_p) increase with increasing ionic radius [10]. This is because RE^{3+} ions easily substitute into the Ba^{2+} site [18–20].

30.3 Requirement for Applications of HTSC Materials; Key Factors for Higher J_c

Even in the best prepared high density bulk sintered samples, the J_c values remain very low (of the order of 10^3 A/cm^2 at 77 K) in zero applied magnetic field and decrease drastically when a magnetic field is applied, even though the T_c values are the same [10]. This can be considered to be mainly due to the random orientation of grains, i.e., the existence of high angle grain boundaries. This is supported by the fact that single crystals exhibit one or two orders of magnitude larger J_c values than polycrystalline samples [21]. We call the grain boundaries "weak links," which decrease J_c. Dimos et al. [22] have shown that J_c decreases with increasing misorientation angle between the neighbored grains, and such behavior is independent of the preparation method. This result suggests that a high angle grain boundary is intrinsically weak links, which is due to an extremely short coherence length (ξ) in oxide superconductors.

The following are dominant factors required for fabrication of high J_c materials [10]:

1. fewer weak links (no secondary inclusion at the grain boundary);
2. highly oriented texture (grain alignment);
3. presence of effective magnetic flux pinning;
4. highly and appropriately doped oxygen content (higher T_c).

30.4 Phase Diagram of HTSC Material

Equilibrium phase diagram is a useful tool to optimize a parameter used in the fabrication processes of materials and to understand crystal growth mechanisms. The following difficulties in determination of reliable phase relations were pointed out [23]: (1) the complexity of the ternary or multicomponent systems, (2) the valency change of Cu^{2+} and Cu^{+} and the very slow oxygenation of the investigated sample to the

saturated amount for the equilibrium state even with a high external oxygen partial pressure, (3) the sluggish reactions typical for peritectic systems and for large melting point differences of constituent oxides, and (4) corrosion of all candidates of commercial crucibles [24].

In the field of HTSC materials, much effort has been made to determine the thermodynamically stable and metastable phases as a function of temperature and oxygen partial pressure [25–30]. Most these investigations were concentrated for the solid state. However, for better understanding of crystal growth from the liquid (melt), the detailed information about a higher temperature phase diagram, including liquid phase, is extremely important.

30.4.1 Phase Diagrams of Y-Ba-Cu-O and RE-Ba-Cu-O Systems

The calculated isothermal sections of the Y_2O_3-BaO-CuO ternary system are reported by B. J. Lee and D. N. Lee [31,32] on the basis of the results obtained by Lay and Renlund [29] and Lindemer et al. [16]. The two-phase equilibrium composition region of liquid and $YBa_2Cu_3O_{7-\delta}$ is reduced rapidly by increasing temperature because of evolution of Y_2BaCuO_5. To show this more effectively, a vertical section containing Y_2BaCuO_5 (Y-211), $YBa_2Cu_3O_{7-\delta}$ (Y-123), and a mixture of $3BaCuO_2$ and 2CuO is shown in Figure 30.3. This figure shows that the liquidus line of liquid/Y-123 is very steep over the temperature range from 1237 to 1275 K. Krauns et al. [33] have experimentally measured the liquidus compositions of yttrium in the $Ba_3Cu_5O_8$ solvent (melt), which are superimposed in Figure 30.3 [10].

As for most rare earth elements (RE≡Y, Yb, Dy, Gd, Sm, Nd, etc.), yttrium can be substituted with the 123 structure. Although the RE-123 phase is formed by similar peritectic reactions to the Y-Ba-Cu-O system, the high temperature stable phase in the

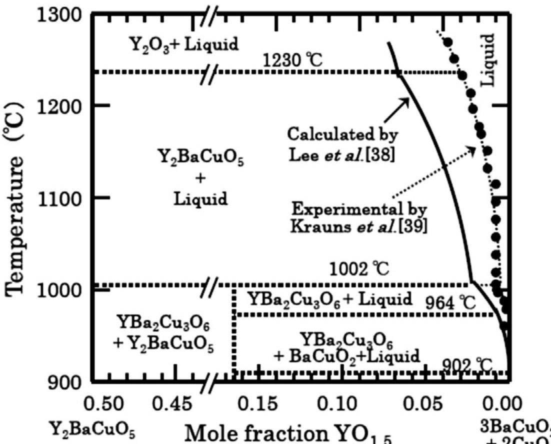

FIGURE 30.3 Calculated vertical section of the Y_2O_3-BaO-CuO_X system at 0.21 atm oxygen pressure and experimental results of liquidus line [10,33].

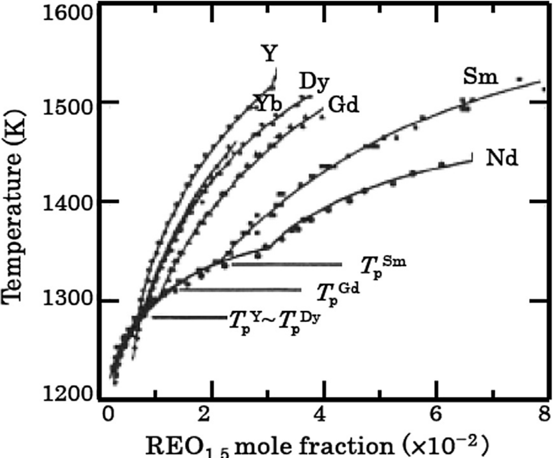

FIGURE 30.4 Liquidus lines (solubility) of RE elements in the $Ba_3Cu_5O_8$ melt under an air atmosphere. RE≡Y, Yb, Dy, Gd, Sm and Nd [10,33–35].

Nd-Ba-Cu-O system is not the same stoichiometric composition ratio as that of Y-211 but $Nd_4Ba_2Cu_2O_{10}$(Nd-422). Figure 30.4 shows the liquidus lines of the rare earth elements in the $Ba_3Cu_5O_8$ solvent (melt) in the air atmosphere [33–35]. The peritectic temperature (T_p) increases with the atomic number of the RE element (i.e., ionic radius). Near the T_p temperatures, the slopes of the liquidus decrease and the RE solubility increases with the atomic number of RE elements.

The effects of oxygen partial pressures on the liquidus lines were also reported [36]. The results indicate that decreasing the oxygen pressure decreases the T_p and increases the steepness of the slope of the liquidus lines near the T_p, which means a similar tendency could be observed when increasing oxygen partial pressure and/or when increasing the atomic number of RE elements.

30.4.2 Quasi-ternary Phase Diagram

The phase relations in the neodymium (Nd) system have been intensively investigated [30,37–40]. For the purpose of fabricating a crystal of Nd-123 crystals through melt processing, quasi-ternary phase diagrams of the $NdO_{1.5}$-BaO-CuO_x system at the temperatures near the T_p of the Nd-123 phase were reported [41,42].

Figure 30.5(A) and (B) show the quasi-ternary phase diagrams of the $NdO_{1.5}$-BaO-CuO_x system near the CuO_x corner near the T_p temperatures (1073 °C and 1030 °C) in the air atmosphere [41]. As the temperature decreases, the two-phase field of the "Nd-123 + liquid" becomes large. The substitution content, i.e., Nd^{3+} ions substitute Ba^{2+} ions, in the Nd-123 crystals decrease as the BaO/CuO ratios of the liquid composition increase, and this tendency is emphasized at lower temperatures. This fact indicates that $Nd_{1+x}Ba_{2-x}Cu_3O_{6+\delta}$ (Nd-123) crystal with x ≈ 0 could be fabricated in the air atmosphere by using the higher BaO/CuO composition ratios of the liquid.

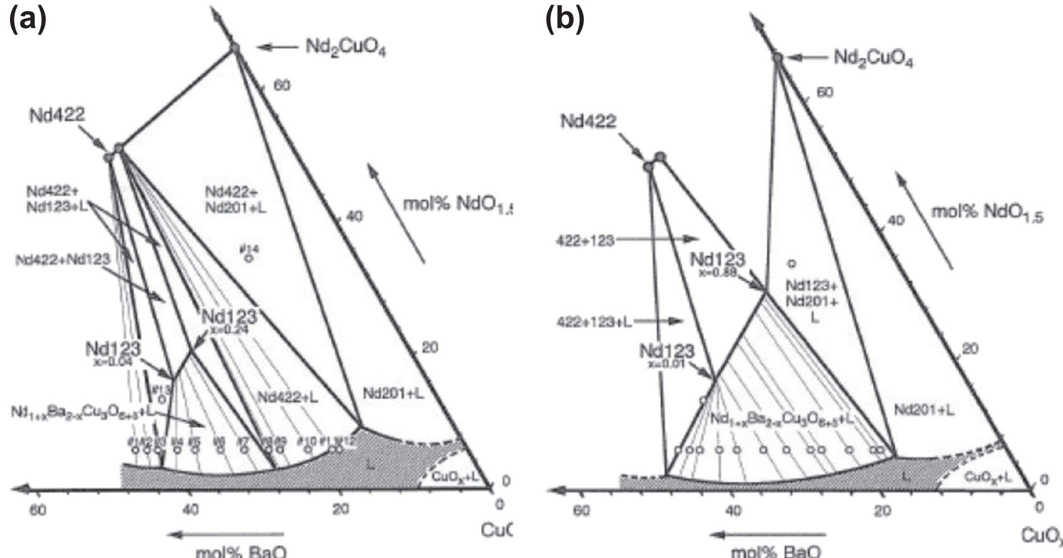

FIGURE 30.5 Quasi-ternary phase diagrams of the $NdO_{1.5}$-BaO-CuOx system near the CuOx corner at/around the peritectic temperatures. (a) 1073 °C, and (b) 1030 °C in air of the $Nd_{1+x}Ba_{2-x}Cu_3O_{6+\delta}$ (Nd-123) solid solution phase [41]. © *1998 Wiley-Blackwell.*

Another significant feature in the RE-Ba-Cu-O systems is the existence of a solid solution in the RE-123 phase of $RE_{1+x}Ba_{2-x}Cu_3O_{6+\delta}$, for light RE elements such as RE ≡ La, Nd, Sm, Eu, Gd, while Y-123 is a stoichiometric compound for cations [18,37,38]. This is considered to be due to the relatively large radii of the RE ions. It was reported that the solid solutions of $Nd_{1+x}Ba_{2-x}Cu_3O_{6+\delta}$ and $Nd_{4+y}Ba_{2-y}Cu_2O_{10+z}$ and that the solubility limits were $x < 0.6$ and $y < 0.2$, respectively, and oxygen contents of $6 + \delta$ and $10 + z$ change accordingly [37].

Effects of the oxygen partial pressure in the atmosphere on the temperature range of the solid solution of the Nd-123 phase are shown in Figure 30.6 [42]. The solubility range of Nd-123 under 0.01 atm of P_{O_2} is quite narrow. On the contrary, in the 1.00 atm of P_{O_2}, the range is wider than that in air.

30.4.3 Standard Gibbs Free Energy Change for Formation

Standard Gibbs free energy changes ($\Delta G°$) for syntheses of $YBa_2Cu_3O_{6.5+x}$, Y_2BaCuO_5, and $Y_2Cu_2O_5$ were reported with experimental results by using chemical thermodynamic methods [43]. For the reaction where $YBa_2Cu_3O_{6.5+x}$ was synthesized by the $Y_2Cu_2O_5$-$BaCO_3$-CuO mixture with the discharge of the CO_2, the equilibrium temperature and the relations of the partial pressure of CO_2 were examined by thermal gravimetric analysis. The equilibrium temperature (1080–1190 K) was determined by observing the change of sample weight at a given temperature in a stream of a CO_2-O_2-N_2 gas mixture. A similar experiment was carried out for the synthesis of Y_2BaCuO_5 from a $Y_2Cu_2O_5$-Y_2O_3-$BaCO_3$

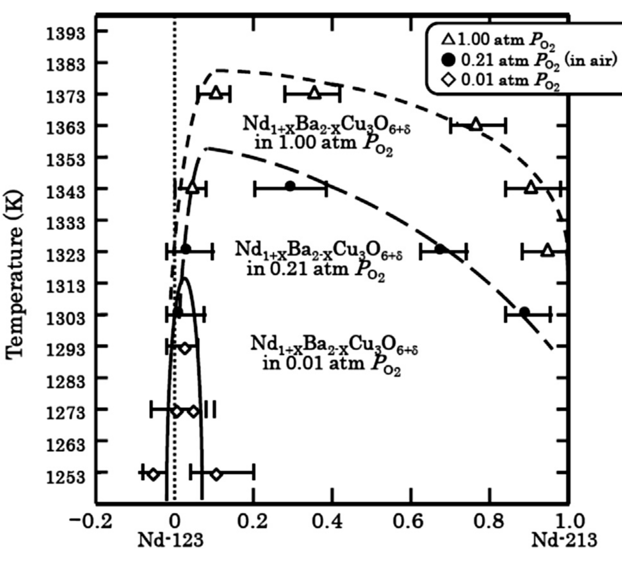

FIGURE 30.6 Solubility limit of the $Nd_{1+x}Ba_{2-x}Cu_3O_{6+\delta}$ in the temperature-composition section for different partial oxygen pressure atmospheres. ($P_{O_2} = 0.01$, 0.21, 1.00 atm) [42].

mixture. Measurements of electromotive force of the galvanic cell with a zirconia solid electrolyte were conducted for the synthesis of Y_2BaCuO_5 from Y_2O_3 and CuO. The standard Gibbs free energy change for formation of Y_2BaCuO_5 was derived from the partial pressure of O_2 in the equilibrium among Y_2BaCuO_5, Y_2O_3, and Cu_2O. By combining these results, the standard Gibbs free energy changes for formation of $YBa_2Cu_3O_{6.5+x}$ and Y_2BaCuO_5 from Y_2O_3, $BaCO_3$, and CuO were obtained.

$YBa_2Cu_3O_{6.5+x}$ decomposes to liquid and Y_2BaCuO_5 at about 1280 K in the air atmosphere. Effects of the oxygen partial pressure (P_{O_2}) on the decomposition were also examined by means of powder X-ray diffraction analysis, thermal gravimetric analysis, and differential thermal analysis [44]. The relation between $YBa_2Cu_3O_{6.5+x}$ and temperature when the decomposition occurred was expressed as:

1.

$$x = 0.00353T - 5.08 \quad (1218 - 1313\ \mathrm{K}) \tag{30.1}$$

Several reactions and standard Gibbs free energy changes related to the formation of $YBa_2Cu_3O_{6.5+x}$ are summarized as follows [43–45]:

2.

$$\frac{1}{2}Y_2Cu_2O_5 + 2BaCO_3 + 2CuO + \frac{x}{2}O_2 = YBa_2Cu_3O_{6.5+x} + 2CO_2 \tag{30.2-a}$$

$$\Delta G_1^\circ = -2RT\ln\frac{P_{CO_2}}{P^\circ} + \frac{x}{2}RT\ln 0.21 = 480000 - 341T \pm 6000\ (\mathrm{J/mole}) \quad (1080 - 11190\ \mathrm{K}) \tag{30.2-b}$$

3.

$$\frac{1}{2}Y_2Cu_2O_5 + \frac{1}{2}Y_2O_3 + BaCO_3 = Y_2BaCuO_5 + CO_2 \tag{30.3-a}$$

$$\Delta G_2^\circ = 273000 - 205T \pm 4000\ (\text{J/mole}) \quad (1090 - 1210\ \text{K}) \tag{30.3-b}$$

4.

$$\frac{1}{2}Y_2BaCuO_5 + \frac{3}{2}BaCO_3 + \frac{5}{2}CuO = YBa_2Cu_3O_{6.5} + \frac{3}{2}CO_2 \tag{30.4-a}$$

$$\Delta G_3^\circ = 34600 - 241T \pm 7000\ (\text{J/mole}) \quad (1090 - 1210\ \text{K}) \tag{30.4-b}$$

5.

$$Y_2O_3 + 2CuO = Y_2Cu_2O_5 \tag{30.5-a}$$

$$\Delta G_4^\circ = 9100 - 14T \pm 1000\ (\text{J/mole}) \quad (1025 - 1220\ \text{K}) \tag{30.5-b}$$

6.

$$\frac{1}{2}Y_2O_3 + 2BaCO_3 + 3CuO = YBa_2Cu_3O_{6.5} + 2CO_2 \tag{30.6-a}$$

$$\Delta G_5^\circ = 482000 - 344T \pm 6500\ (\text{J/mole}) \quad (1080 - 1190\ \text{K}) \tag{30.6-b}$$

7.

$$Y_2O_3 + BaCO_3 + CuO = Y_2BaCuO_5 + CO_2 \tag{30.7-a}$$

$$\Delta G_6^\circ = 278000 - 212T \pm 4500\ (\text{J/mole}) \quad (1090 - 1210\ \text{K}) \tag{30.7-b}$$

8.

$$\frac{1}{2}Y_2O_3 + 2BaCO_3 + 3CuO + \frac{x}{2}O_2 = YBa_2Cu_3O_{6.5+x} + 2CO_2 \tag{30.8-a}$$

$$\Delta G_7^\circ = 485000 - 348T \pm 6500\ (\text{J/mole}) \quad (1080 - 1190\ \text{K}) \tag{30.8-b}$$

9.

$$\begin{aligned} &YBa_2Cu_3O_{6.5} = Y_2BaCuO_5 + \text{Liquid} + O_2 \\ &\text{Liquid}: YO_{1.5}(2.0\ \text{mol\%}), BaO(37.0\ \text{mol\%}), CuO + CuO_{0.5}(61.0\%) \end{aligned} \tag{30.9-a}$$

$$\begin{aligned} \Delta G_8^\circ = -RT\ln\left(P_{O_2}/P^\circ\right) = 965000 - 736T\ (\text{J/O}_2\text{mole}) \quad (1080 - 1190\ \text{K}) \\ P^\circ = 1.013 \times 10^5\ \text{Pa(1atm)} \end{aligned} \tag{30.9-b}$$

10.

$$\frac{1}{2}Y_2BaCuO_5 + \frac{3}{2}BaCuO_2 + CuO = YBa_2Cu_3O_{6.5} \tag{30.10-a}$$

$$\Delta G_9^\circ = -3500 + 6.65T\ (\text{J/(123)mole}) \tag{30.10-b}$$

11.

$$2CuO = Cu_2O + \frac{1}{2}O_2 \tag{30.11-a}$$

$$\Delta G^\circ_{10} = 146300 + 25.5T \log T - 185T \text{ (J/mole)} \tag{30.11-b}$$

12.

$$Nd_4Ba_2Cu_2O_{10} + \text{Liquid} + O_2 = NdBa_2Cu_3O_{7-\delta} \tag{30.12-a}$$

$$\Delta G^\circ_{11} = 779T - 1077000 \text{ (J/(O}_2\text{)mole)} \tag{30.12-b}$$

30.5 Bulk Crystal Growth Methods from the Melt

Although sintering was very common and showed a lot of advantages in ceramics processing, it was not able to produce oxide superconductors with the high values of critical current densities (J_c) primarily due to the existence of weak links at the grain boundaries as mentioned before. It was pointed out that a high angle grain boundary was intrinsically the weak link due to a combination of a small coherence length and large anisotropy. The melt solidification process has overcome this weak link problem by grain alignment leading to high J_c superconductors. Solidification methods for synthesis of bulk HTSC crystals could be classified into two groups [10]:

1. solidification from semisolids (i.e., liquid + Y-211 phase) provides high J_c Y-123 bulk crystals;
2. solidification from solution (i.e., liquid) provides high crystallinity bulk single crystals.

We must make the various phenomena, which are caused with the phases (liquid, liquid + solid, solid), clear to control the microstructures of HTSC materials, which have an influence on crystallinity as well. Microscopically, the similar phase transitions take place in nondirectional solidification processing, including melt-texture-growth (MTG) [46], quenched-melt-growth (QMG) [47], and melt-powder-melt-growth (MPMG) [48] methods and the solute rich liquid crystal pulling (SRL-CP) method [49,50]. The SRL-CP method was developed for pulling a Y-123 single crystal, which is in fact a modified top-seeded solution growth (TSSG) technique.

30.5.1 Melt Texture Growth

Melt processing of Y-123 was initiated by Jin et al. [46], and it was named the MTG process. As shown in Figure 30.3, there are two peritectic reactions in the Y-Ba-Cu-O system. At high temperatures above 1200 °C, the Y_2O_3 solid phase and Y-deficient Ba-Cu-O liquid phase are stable. On cooling, these two phases transform peritectically to produce Y_2BaCuO_5 (Y-211). At around 1000 °C, Y-211 reacts with liquid to produce $YBa_2Cu_3O_{7-\delta}$ (Y-123).

In the case of the MTG process, precursor samples with a stoichiometric formula of $YBa_2Cu_3O_{7-\delta}$ are slowly cooled through either of these two peritectic reactions, or at least the latter reaction in the presence of the temperature gradient of 20–50 °C/cm in an oxygen atmosphere. The MTG sample so produced exhibits a dense structure consisting of locally aligned, long, needle-shaped grains and higher transport J_c (above 10^4 A/cm^2) at 77 K in a zero applied magnetic field than that (several hundreds A/cm^2) of typical sintered (bulk) materials [46].

30.5.2 Quench and Melt Growth and Melt Powder Melt Growth

The QMG and MPMG methods were developed to control the size of the dispersed Y-211 particles as effective magnetic flux pinning centers in order to increase J_c in magnetic fields [47,48]. First, the sintered sample is heated to the Y_2O_3 + liquid region and splat quenched using cold copper blocks. The quenched sample consists of Y_2O_3 particles and the solidified liquid phases (a mixture of $BaCu_2O_2$, CuO, and amorphous phases). The quenched plates are then reheated to the Y-211 + L region, where the Y-211 phase is formed by a peritectic reaction between Y_2O_3 and the liquid. Then, the sample is cooled to form a crystal of the Y-123 phase. By the QMG method, Y_2O_3 particles tend to segregate due to sedimentation, which causes nonuniform distribution of the Y-211 phase particles. By the MPMG method, melt quenched plates are crushed into fine powders and mixed well in order to refine the Y_2O_3 particles with uniform distribution. The pellets are then rapidly heated to the Y-211 + L region. After an appropriate holding time, the sample is rapidly cooled to the temperature just above T_p and then slowly cooled. It is remarkable that the size of the Y-211 phase crystals is much finer and their distribution is much more uniform than those in the MTG and QMG sample, resulting in high J_c-B characteristics, i.e. high critical current density in magnetics fields of B.

30.5.3 Seeding Method

The nucleation of the crystal is affected by the frequency of occurrence of nucleation events for the Y-123 phase. Accordingly, multiple nucleation takes place, resulting in the existence of several grains within a small pellet. The control of crystal orientation and number of grains is also required, since HTSC materials are highly anisotropic and possess weak links due to high angle grain boundaries, which reduce the J_c values.

It was shown that certain materials, such as Y_2O_3 powder, Sm_2O_3 powder, Nd_2O_3 powder, ZrO_2 powder, MgO single crystal, and various oxide thin films could be employed as heterogeneous nucleation reagent seeds for Y-123 [51]. However, the single domain of RE-123 can rarely be obtained. Morita et al. [52] and Sawano et al. [53] demonstrated that single crystals or quasi-single crystals of other RE-123 systems, such as Sm-123 and Nd-123, which have higher peritectic temperatures than Y-123, could act as seeds for crystal growth because the seed remains in a solid form when Y-123 is

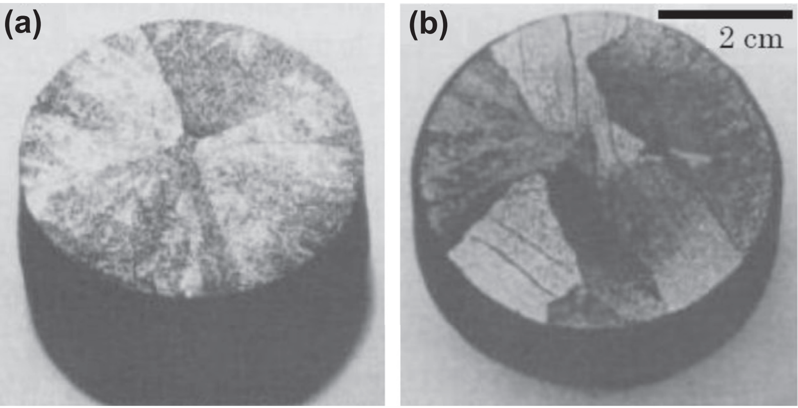

FIGURE 30.7 Appearance of (a) single-grained and (b) poly-grain melt grown bulk crystals. Note that in the single-grained crystal, the growth started at the center of the sample where a seed crystal was placed [53]. © *1991 The Japan Society of Applied Physics.*

heated above T_p. On subsequent cooling, a Y-123 crystal grows epitaxially from the seed. The entire pellet with a seed is composed of only one grain due to the elimination of the multiple nucleations as shown in Figure 30.7. The seeding method has been widely used to produce melt-textured YBCO and NdBCO samples [54–56].

Researchers all over the world have investigated several oxide seed materials that are suitable for Y-123 epitaxial growth. The fundamental criterion for the epitaxial growth is defined by the crystal lattice mismatch, ϕ, which can be given by:

$$\phi = (\lambda_c - \lambda_s)/\lambda_s \tag{30.13}$$

where, λ_c and λ_s are the crystal lattice parameters of the crystal and the substrate (seed), respectively.

For the case of $SrTiO_3$ seed crystal ($\lambda_a = 3.905$ Å), as an example, for the c-axis epitaxial growth, the lattice mismatch with the lattice parameter of the Y-123 crystal (3.8578 Å) is calculated as in the following Eqn (30.14), which is explained before in Eqn (30.13):

$$\frac{3.8578\ \text{Å} - 3.905\ \text{Å}}{3.905\ \text{Å}} \times 100\% \approx -1.21\% \tag{30.14}$$

Consequently, it is possible to select a seed material with less lattice mismatch to the Y-123 crystal lattice. Pseudocubic lattice parameters in Table 30.1 were defined as the following Eqn (30.15):

$$\lambda_{a_{cubic}} = \lambda_{b_{cubic}} = \frac{\sqrt{\left(\frac{\lambda_{a_{cubic}}}{2}\right)^2 + \left(\frac{\lambda_{b_{cubic}}}{2}\right)^2}}{2} = \lambda_{110} \quad or \quad \frac{\lambda_{a_{cubic}}}{n \times \sqrt{2}} \tag{30.15}$$

where n is integer. Pythagoras' theorem from the actual cubic lattice parameters could provide the pseudocubic lattice parameters. For the case of Y_2O_3 seed crystal

Table 30.1 Structure, Lattice Mismatch Data for *c*-axis Epitaxial Growth of YBCO for Various Seed Crystals

	Structure Type		% Lattice Mismatch
Buffers Layer Material	Cubic Lattice Parameter Å	Pseudocubic Å	vs YBCO
$BaCeO_3$	4.377		−11.86
MgO	4.203		−8.21
$BaZrO_3$	4.193		−7.99
La_3TaO_7	11.054	3.908	−1.30
$SrTiO_3$	3.905		−1.28
$YBa_2Cu_3O_{7-\delta}$	3.8578		0
Eu_2O_3	10.868	3.842	0.41
$NdGaO_3$	5.431	3.840	0.46
CeO_2	5.411	3.826	0.83
Gd_2O_3	10.813	3.823	0.91
$La_2Zr_2O_7$	10.786	3.813	1.17
$LaAlO_3$	5.364	3.793	1.71
Ga_3NbO_7	10.659	3.769	2.36
Y_2O_3	10.604	3.749	2.90
$Gd_2Zr_2O_7$	5.264	3.722	3.65
Y_3NbO_7	5.250	3.712	3.93
Yb_2O_3	10.436	3.690	4.55
YSZ($Y_2O_3$13%–$ZrO_2$87%)	5.125	3.624	6.45

($\lambda_a = 10.604$ Å), as an example, the pseudocubic lattice parameter is calculated as in the Eqn (30.16),

$$\frac{10.868\ \text{Å}}{2 \times \sqrt{2}} = 3.749\ \text{Å} \tag{30.16}$$

and the lattice mismatch with the lattice of the c-axis epitaxially grown Y-123 crystal is calculated as in the following equation:

$$\frac{3.8578\ \text{Å} - 3.749\ \text{Å}}{3.749\ \text{Å}} \times 100\% \approx 2.90\% \tag{30.17}$$

30.5.4 Directional Solidification Method

Meng et al. [57] fabricated a bar of the Y-123 compound with grain alignment by moving a sintered sample in a horizontal tube furnace with a temperature distribution almost equivalent to the temperature history at the time of crysta1 growth in the QMG/MPMG process. McGinn et al. [58–60] produced textured polycrystals in extruded Y-123 wires by zone melting in a vertical tube furnace. Izumi and Shiohara [61] applied a horizontal Bridgman method and a floating zone melting method to the YBCO system and obtained $J_c = 2 \times 10^4$ A/cm^2 at 77 K and 1 T of the applied magnetic field. Figuredo et al. [62] used

a laser-heated floating zone technique, which can provide higher temperature gradient (G) above 1000 °C/mm compared with a resistance heater, and J_c values larger than 10^5 A/cm^2 at 77 K and self field were achieved.

The temperature gradient (G) and the growth rate (R) are important process parameters to control microstructures in directional solidification. In general, G/R and $G \times R$ affect the crystal grain alignment and the grain size. In the Y-Ba-Cu-O system, the effect of the G/R ratio on the changes in the morphology of the growth interface was examined by Izumi et al. [63]. Although no nucleation ahead of the interface was recognized in the samples grown at high growth rates, the Y-123 phase crystal grains were discontinuous and possessed equiaxed-like and blocky structures. In contrast, the samples grown at slow rates with higher G (i.e., high G/R) showed continuous growth and a cellular structure composed of very well-aligned grains. Faceted interfaces were recognized in the samples, and the cell spacing increased with decreasing growth rate R. The morphological change from the equiaxed-like to the planar with increase of the G/R ratio accords with the theory of constitutional supercooling [64], at least its tendency. As a result, the increase in the J_c values of zone-melted samples with increasing G/R could be recognized even at the same cooling rates ($G \times R$) [63,65].

30.6 Single Crystal Growth Methods from the Solution

High quality single crystals have been fabricated by the flux method, but their size is limited due to uncontrollable nucleation events, the very low solubility of yttrium in the BaO-CuO flux melt, and the steep slope of the liquidus line in the equilibrium phase diagram for the primary phase crystallization temperature range. Therefore, continuous growth processes, i.e., TSFZ and TSSG methods, have been applied widely to the Y-Ba-Cu-O system, enabling fabrication of large-sized Y-123 crystals.

30.6.1 Flux Method

The flux method is one of the most commonly used processes to produce bulk single crystals in the case of incongruent melting systems such as Y-123 phase crystals [66–73]. The commonly used solvent is composed of CuO and BaO, which is called the "self-flux method." Schneemeyer et al. and others [73–76] grew single crystals. The crystals form with a layer-type morphology, similar to mica, but generally with square corners. Wolf et al. [73] optimized the melt composition and the cooling rate to obtain thick crystals, using a melt composition of Y:Ba:Cu = 1:7.5:16.5 and the cooling rate below 0.5 °C/h.

Other solvents have been tried, e.g., In_2O_3 [77], B_2O_3 [78], and KCl-NaCl [69]. The crystals grown using a KCl-NaCl f1ux were found to be relatively large in size, although they seemed to have poor crystallinity with a large number of defects [69].

In addition to the restriction in selection of suitable solvents, the progress in the growth process has also been hampered by the pronounced reactivity of the melt with

most crucible materials, which tends to contaminate the growing Y-123 crystals. Many kinds of crucible material have been used for the f1ux method, such as platinum, gold, $A1_2O_3$, ThO_2, ZrO_2, MgO, etc. Liang et al. and others [79–81] have systematically investigated the crucible materials. It was concluded that yttria-stabilized zirconia (YSZ) and yttria (Y_2O_3) crucibles are good choices for Y-123 crystal growth, preventing contamination from the crucible materials during growth.

30.6.2 Traveling Solvent Floating Zone Method

The traveling solvent floating zone (TSFZ) method is a valuable growth technique for the fabrication of high quality, large single crystals that melt incongruently. Several kinds of RE-123 crystals have been fabricated using the TSFZ method by Oka and Ito [82]. In the TSFZ method, the RE solute in the solvent required for growth of the RE-123 crystal is steadily supplied into the solvent by dissolving the RE-123 feed rod.

One of the main advantages of the TSFZ method involves containerless crystal growth, which can prevent contamination from the crucible material. At the same time, however, problems of keeping the molten zone stable during the crystal growth of RE-123 arise. Since the viscosity of the solvent composed of BaO-CuO is low, the solvent easily falls onto and penetrates deeply into the feed rod, and the solvent composition varies with time. Oka and Ito [82] have overcome this problem using high density crystallized feed rods prescanned at a high pulling rate of 2–15 mm/h.

30.6.3 Top-seeded Solution Growth Method (Solute-rich Liquid Crystal-Pulling Method)

Crystal pulling has a significant advantage in growing large single crystals. The top-seeded solution growth (TSSG) method, which is one of the crystal-pulling methods for incongruent melting materials, had not been applied to RE-123 compounds, because the promising solvent BaO-CuO flux melt is very reactive with crucible materials and cannot be maintained for a long time. Yamada and Shiohara [49] succeeded in growing Y-123 single crystals by a pulling method using a BaO-CuO solution with Y-211 solid, placed at the bottom of the yttria crucible, which supplies Y solute steadily into the solvent. This modified TSSG method has been named the solute-rich liquid crystal-pulling (SRL-CP) method, since the solute content in the solution is steadily enriched from the Y-211 solid.

30.6.3.1 SRL-CP Method

Figure 30.8 shows a schematic drawing of the configuration of the SRL-CP method. Y-211 powder was placed at the bottom of the crucible and BaO-CuO composite (Ba to Cu cationic ratio is 3:5) was placed on the layer of Y-211 powders. A temperature gradient was provided in the melt to satisfy the conditions that the temperature at the melt surface (about 1000 °C) is lower than the peritectic

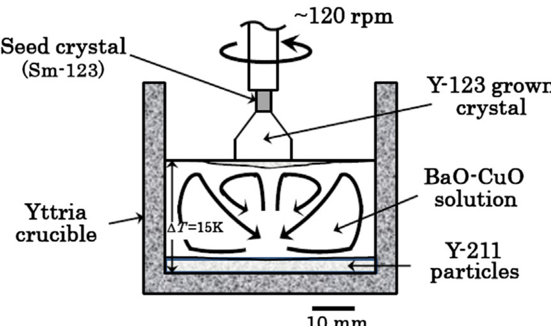

FIGURE 30.8 Configuration in the crucible during Y-123 single crystal growth using the SRL-CP method [49]. © *1993 Elsevier Science B.V.*

temperature ($T_p = 1010\,^\circ C$) of Y-123 and the temperature at the bottom of the melt (about 1015 °C) is higher than T_p. Accordingly, Y-211 solid can exist at the bottom of the crucible as a source of the solute. The surface of the melt was supersaturated by yttrium. In this method, the transport of the solute from the bottom of the crucible to the growing crystal is a key factor in obtaining higher crystal growth rates than those in flux methods. The solute was mainly transported by convection in the melt. In terms of the mass balance, the solute supplied from the Y-211 solid and the solvent $Ba_3Cu_5O_8$ react and form only the Y-123 phase crystal without the generation of any other by-products.

$$Y_2BaCuO_5 + Ba_3Cu_5O_8 \rightarrow 2YBa_2Cu_3O_{7-\delta} \tag{30.18}$$

A Y-123 single crystal or thin film prepared separately was used as a seed crystal. The Y-123 crystal was grown at a rotation rate of about 120 rev/min (rpm). This is relatively fast, enhancing forced convection in the melt. Since the high speed rotation makes the surface fluid flow away from the center and toward the crucible wall, it prevents the floating crystals from attaching to the growing crystal.

By optimizing the various growth conditions of the SRL-CP method, large-sized, high quality bulk single crystals of Y-123 were reproducibly fabricated. The shape of the grown Y-123 single crystal pulled along the *c*-axis in the air atmosphere is shown in Figure 30.9(A). The grown crystal is bulky and the typical size is about $14.5 \times 14.5 \times 13$ mm [83]. The square shape observed from the bottom reflects the symmetry of the *c*-axis, showing a strongly faceted nature of the crystal habit. The bottom surface is a (001) plane and the Y-l23 crystals grow epitaxially from the seed crystal. The as-grown surface was examined by atomic force microscopy (AFM), which revealed continuous beautiful spiral growth patterns as shown in Figure 30.9(B). The step height of about a few nanometers is equivalent to one or two unit cell lengths (lattice parameter) of the Y-123 crystal structure along the *c*-axis. Similar macroscopic growth spirals were observed in the films fabricated by liquid phase epitaxy (LPE) [84].

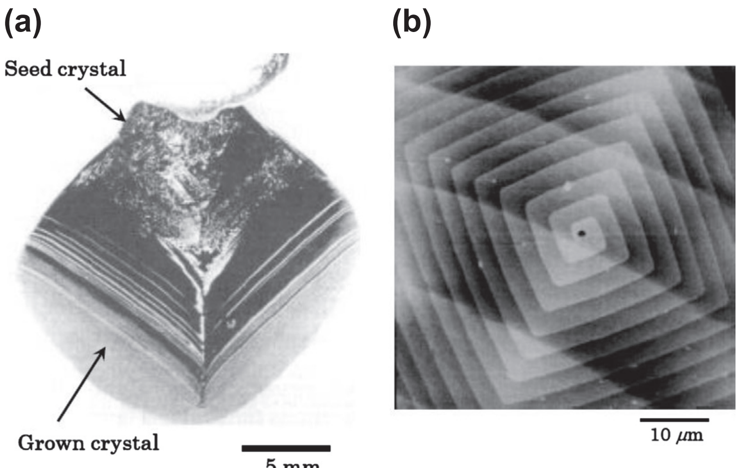

FIGURE 30.9 (a) Photo of grown Y-123 single crystal pulled along the *c*-axis from the Sm-123 seed crystal and (b) AFM image of the surface (growth interface) of the as-grown single crystal showing typical spiral growth [10,83].
© *Springer-Verlag Tokyo 1995.*

30.6.3.2 Enlargement of Single Crystal Size in SRL-CP Method

1. Increase of growth time

In the SRL-CP method, the probability of the nucleation events at the crucible wall can be hardly neg1ected. Floating particles generated on the melt surface may cause po1ycrystalline growth and the surface is finally covered with floating particles, and further growth may become impossible. However, the high speed rotation prevents the floating crystals/particles from attaching to the growing crystal as it makes the surface fluid flow away from the center to the crucible wall.

Similar to other oxide melts, the BaO-CuO flux has high viscosity, a high Schmidt number (Sc), and a high Prandtl number (Pr). Therefore, the Y solute is transferred from Y-211 placed at the bottom of the crucible to the growing Y-123 crystal mainly by melt convection, which may be affected by many factors, such as the crystal rotation rate, size of the grown crystal, temperature gradient, and crucible size.

Figure 30.10 shows the results of numerical simulations using a finite difference method for a two-dimensional axis-symmetric viscous fluid system [85]. The left part and right part of each figure show the streamlines of the melt and isotherms, respectively, within the right halves of the vertical section of the crucible. Forced convection exists below the growing crystal, which is induced by the crystal rotation and natural convection near the crucible wall. As the crystal rotation rate and/or crystal diameter increases, the forced convection becomes stronger and the meeting point of the forced and natural convection near the melt surface moves from the growing crystal to the crucible wall. The isotherms couple strongly to the

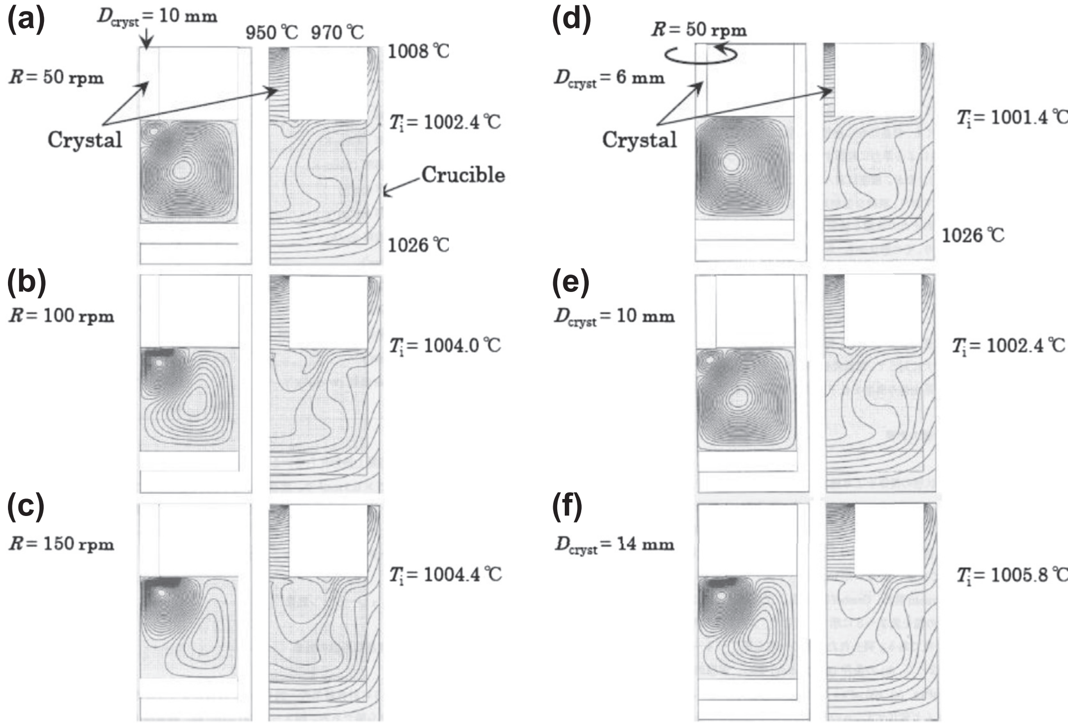

FIGURE 30.10 Numerical calculation results for 10 mm (a–c) and 6, 10, and 14 mm (d–f) diameter crystals; (a), (b), (c) show the results with crystal rotation rates of 50, 100, 150 rev/min and (d), (e), and (f) show 50 rev/min, respectively. The left part of each figure shows the stream-lines of melt convection, and right side shows the isotherms within the right halves of the vertical section of the crucible [85]. © *1996 Materials Research Society.*

convection, and the temperature at the crystal growth interface increases with increasing forced convection, i.e., crystal rotation rate, as well as with increasing the size of the crystal.

During Y-123 crystal growth, the diameter of the crystal increases with increasing the growth time, which causes a change in the crystal growth conditions. In order to maintain constant crystal growth conditions, control of the crystal rotation rate with increasing the crystal diameter is effective. Another way to circumvent this problem is to use a large crucible to make the system insensitive to the change in the crystal diameter.

2. Enhancement of growth rate
Larger single crystals can be obtained within a shorter time if the growth rate is enhanced significantly. To achieve this, supersaturation, which is the driving force for crystal growth, should be increased, e.g., simply by decreasing the surface temperature of the growing Y-123 crystal. In this case, however, the problem of floating particles comes into the picture, resulting in polycrystalline growth. Yao et al. [86]

have grown a large Y-123 crystal of 19.8 × 19.5 × 16.5 mm in size and 20 g in weight by the SRL-CP method under the high oxygen pressure atmosphere ($P_{O_2} = 1$ atm). The growth rate for $P_{O_2} = 1.0$ atm is about twice that for an air atmosphere. This was explained by the fact that, in $P_{O_2} = 1.0$ atm, the solubility of yttrium in the solvent is higher, the slope of the liquidus is lower (see Section 30.4.1), and the crystallization temperature is higher than those at $P_{O_2} = 0.21$ atm.

30.6.3.3 Other RE-123 Single Crystal Growth

The SRL-CP method has also been applied to other $RE_1Ba_2Cu_3O_{7-\delta}$ materials (RE, rare earth ≡ Sm, Nd). It has been found that bulk single crystals of several cubic millimeters in size could be repeatedly produced by the SRL-CP method after optimizing the growth conditions, such as the growth temperature, composition of the solution (melt), crucible materials, etc. [87,88].

In the case of Sm-123, the growth rate is about a factor of five faster than that of Y-123, which could be explained by the fact that the solubility of Sm in the solvent is higher, the slope of the liquidus is lower, and the crystallization temperature is higher than those for Y-123, as shown in Figure 30.4, resulting in higher mass and heat transfer for growth and easy achievement of higher supersaturation for interfacial kinetics.

Contrary to the Sm-123 crystal pulling, Nd-123 single crystals have been fabricated by the ordinary TSSG method. In this case, the high temperature stable phase (Nd-422 phase for NdBCO system) was not placed at the bottom of the crucible, and the Nd solute required for Nd-123 crystal growth was supplied only from the Nd_2O_3 crucible due to the high solubility of Nd in the Ba-Cu-O liquid phase [88].

Solid solutions are known to exist in these systems, which are described as $RE_{1+x}Ba_{2-x}Cu_3O_y$, whereas the Y-123 phase is a stoichiometric compound. In fact, the compositions of these grown crystals were measured by ICP-AES to be $Nd_{1+x}Ba_{2-x}Cu_3O_y$ ($0.01 < x < 0.1$) in which the substitution value (x) depends on the atmosphere during the growth. A low oxygen partial pressure atmosphere during crystal growth was found to be effective for minimizing the substitution of Nd^{3+} into the Ba^{2+} sites as can be seen in Figure 30.6 [88].

30.7 Controlling Factors of Crystal Growth from the Melt and Solution

30.7.1 Supersaturation as a Driving Force for Crystal Growth

In the Y-Ba-Cu-O system, a Y-123 crystal grows from the melt. The crystal melts incongruently and the solubility of yttrium in Ba-Cu-O (solvent) is very small. In the case of crystal growth from dilute solution, the driving force for crystallization is represented by supersaturation (σ) defined as:

$$\sigma = (C - C_e)/C_e \tag{30.19}$$

where C and C_e are the practical and the equilibrium concentrations of the solute in the solution, respectively.

30.7.2 Faceted Growth

The Y-123 phase crystals grown by solidification processing show clearly faceted crystal habits. According to the Jackson model [89], the faceted or nonfaceted habits of the growth interface could be roughly estimated by α (Jackson parameter):

$$\alpha = \zeta(L/k_B T) \tag{30.20}$$

where ζ is a factor (less than unity) depending on the crystallographic anisotropy, L is the latent heat of melting or dissociation, k_B is Boltzmann's constant, and T is the absolute temperature. The values of α with less than two can be taken to imply a tendency to nonfaceted crystal growth, while higher α values imply that faceted growth forms will be produced. The value of α for Y-123 crystals has been estimated to be about 20 [90]. Consequently, the growth interface of the Y-123 and/or RE-123 crystals is considered to be flat in an atomic scale.

30.7.3 Experimental Measurements of Anisotropic Growth Rate

Nakamura et al. [91], Muller and Freyhardt [92], and Imagawa and Shiohara [93] have investigated the anisotropic growth rate of Y-123 crystal, the R_a/R_c ratio, in which R_a and R_c are the growth rates of the {100} faces and the {001} faces, respectively.

In order to obtain the knowledge about the interfacial kinetics of Y-123 crystal growth, Endo et al. [94] used a seeding method using a seed of an Sm-123 crystal, combined with a constant undercooling solidification method, which has the advantages of proper control over the crystal orientation and appropriate estimation of the interfacial temperature. The Y-123 crystals were grown at several different undercoolings (ΔT). Here, ΔT is defined as the temperature difference between the T_p of the Y-123 phase ($T_p = 1010\ ^\circ C$) and the growth temperature (T_g). The dependence of ΔT on R_a is different from that on R_c, as shown in Figure 30.11. The relations between the growth rates and undercooling are described in the following power law equations:

$$R_a = 4.5 \times 10^{-7} \Delta T^{1.9} (\text{mm/s}) \tag{30.21a}$$

$$R_c = 2.8 \times 10^{-6} \Delta T^{1.3} (\text{mm/s}) \tag{30.21b}$$

The growth rate perpendicular to the *ab* plane (R_c) has been reported to be faster than that perpendicular to the *ac* plane (R_a) for Y-123 crystals grown by unidirectional solidification and the interface undercooling at a growth rate of about 1 mm/h was 30–40 K [90]. Equations (30.21a) and (30.21b) indicate that, with undercooling higher than 27 K, R_a becomes larger than R_c. Therefore, the results of the constant undercooling method are not in conflict with those of unidirectional solidification by considering the difference in undercoolings.

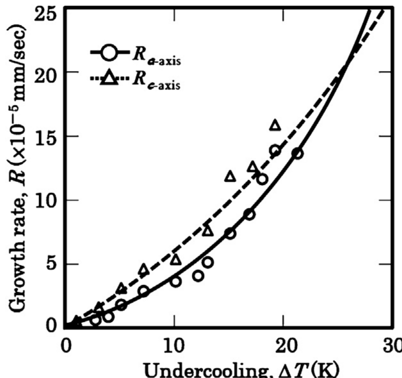

FIGURE 30.11 Relationships between the growth rate and undercooling for the growth direction of *a*-axis and *c*-axis [94]. © *Springer-Verlag Tokyo 1995.*

30.7.4 Trapping Phenomena of High-temperature Stable Phase (Y-211) Particles into Y-123 Crystal

Y_2BaCuO_5, (Y-211) inclusions are considered to act as strong magnetic flux pinning centers. In order to retain the Y-211 phase particles (inclusions) in the crystallized Y-123 grains, an overall composition shifted toward the Y-211 phase from the stoichiometric composition of Y-123 (i.e., Y-123 + x Y-211, $x > 0$) has been used. It has been assumed that the amount of excess Y-211 is completely trapped during the peritectic reaction. Macrosegregation of Y-211 particles in Y-123 crystals, observed by several groups, has stimulated interest in the investigation of the trapping phenomena of Y-211 particles [95–100].

Varanasi et al. [96,99] have observed the inhomogeneous distribution of Y-211 particles, delineating distinguishable patterns in textured Y-123 crystals with platinum additions. Kim et al. [98] also reported that fine particles were pushed out of the advancing Y-123/liquid interface toward the liquid phase in the Y-Ba-Cu-O system with metal oxide (CeO_2, SnO_2, and ZrO_2) addition. In both cases, the observed patterns of Y-211 segregation seem to exist along the boundaries between different growth directions. Investigations on the segregation of Y-211 particles have been systematically carried out by Endo et al. [97,100], which showed that the macrosegregation was dependent on the growth rate (R) as a function of the undercooling (ΔT) as well as on the growth direction.

The effect of R on the macrosegregation of Y-211 partic1es was reported using the results of two different kinds of heat treatment: constant undercooling and continual cooling by Sm-123 top-seeding melt texture method [94]. As shown in Figure 30.12, the amount of trapped Y-211 with high undercooling (e.g., $\Delta T = 30$ K; i.e., large R) is larger than that with low undercooling (e.g., $\Delta T = 10$ K; i.e., small R), especially in the c-direction [97]. The macrosegregation of Y-211 partic1es and their size in Y-123 crystals depends on the growth rate of the Y-123 crystals and their growth direction. The continual cooling method, such as QMG and MPMG [47,48], is commonly used for melt

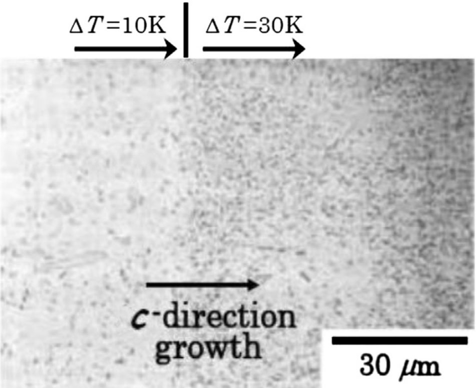

FIGURE 30.12 Cross-sectional microstructures of the grown crystal in the quenched sample. Undercooling of the sample was changed from 10 K to 30 K during the two-step undercooling method, showing drastic change in the amount of trapped Y-211 particles (dark particles in the photograph) from the 10 K undercooled region to the 30 K undercooled region [97]. © *1996 Materials Research Society.*

texture growth in the YBCO system. The distribution of Y-211 particles in the Y-123 bulk samples fabricated by this method might be inhomogeneous.

30.8 Crystal Growth Mechanism

The melt-textured Y-123 materials show a highly aligned structure, which is formed by a peritectic reaction between solid Y-211 phase particles and the liquid phase. Therefore, many studies have been performed to clarify the peritectic solidification mechanism of Y-123 crystals [63,101,102]. The solidification model is generally limited by interfacial kinetics and/or mass transport.

30.8.1 Rate-Limiting for Crystal Growth

Once a nucleus is formed, it will continue to grow. Such growth may be limited by the kinetics of atom attachment to the growth interface including its surface migration, diffusion of the solute from the environmental phase, and diffusion of latent heat for crystallization. Figure 30.13 illustrates the spatial distribution of the concentration of the solute near the growth interface during crystal growth. Initially, the solution has a uniform concentration C_0, then, as a result of cooling, a corresponding change in the equilibrium concentration C_e takes place. If the liquid concentration at the crystal growth interface, C_i, equals to C_0, the growth rate is controlled by an interface reaction process (interface control) as shown in (a) in Figure 30.13. In another extreme case, which is the case, C_i equals to C_e, the growth rate is fully controlled by diffusion in the solution (diffusion control) as shown in (C) in Figure 30.13. When the rate of incorporation of growth units to the crystal is balanced by their diffusion in the solution, C_i is not equal to either C_e or C_0 as shown in (B) in Figure 30.13 [10,103].

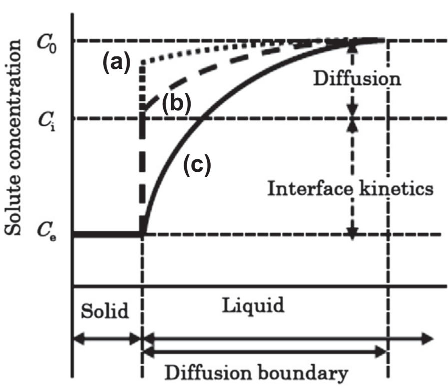

FIGURE 30.13 Solute concentration profile in the liquid in front of the growing crystals, showing the driving forces of diffusion and interfacial kinetics [10]: (a) interfacial control; (b) mixed control; (c) diffusion control.

Although the heat transfer during the crystallization is also an important factor, it could be simplified since the growth rate is sufficiently small compared with the thermal conduction in the case of Y-123 growth, suggesting that heat dissipation is relatively rapid and the assumption of an isothermal or a steady state constant temperature gradient is reasonably acceptable.

30.8.2 Solute Diffusion Model for Unidirectional Solidification

30.8.2.1 Basic Growth Mechanism

At almost the same time, three different groups proposed similar crystal growth models to explain the growth of Y-123 crystals in the directional solidification process controlled by solute diffusion [63,101,102].

Generally, in metallic alloy systems, the required solute from the high temperature stable phase solid for peritectic reaction is transferred through the solid by diffusion as shown in Figure 30.14(A). In some special cases of metallic alloys, such as Al-Mn and Cu-Sn peritectic systems, it was proposed that a part of the solute is diffused through the liquid [104,105]. A sharp faceted growth interface and a drastic change in the Y-211 volume from the semisolid region to the Y-123 crystals are observed in the sample quenched during unidirectional solidification, as shown in Figure 30.15 [63]. This observation supports the fact that the required solute for the peritectic reaction is provided by the liquid diffusion for the crystallization of the Y-123 phase. Assuming the liquid diffusion for Y-123 peritectic crystal growth as shown in Figure 30.14(B), the diffusion zone may exist in front of the planar (faceted) Y-123 interface. The liquid-diffusion-rate-limiting model for the Y-123 peritectic solidification was developed by Izumi, Nakamura, and Shiohara [63]. This so-called INS model is based on the following assumptions:

1. the rate-limiting stage for the growth of the Y-123 crystal is yttrium diffusion in the liquid since the yttrium solubility in the liquid is extremely low;

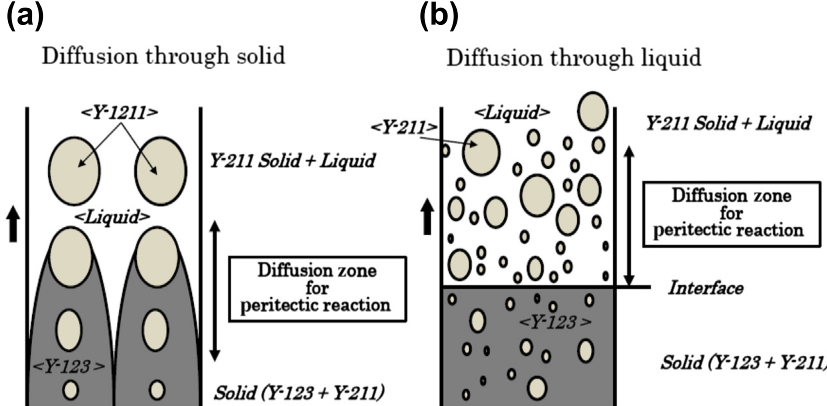

FIGURE 30.14 The expected structure around the interface in two different systems of peritectic reactions [10,61]: (a) required solutes for Y-123 growth are transported through the solid; (b) required solutes for Y-123 growth are provided through the liquid. © *1992 Materials Research Society.*

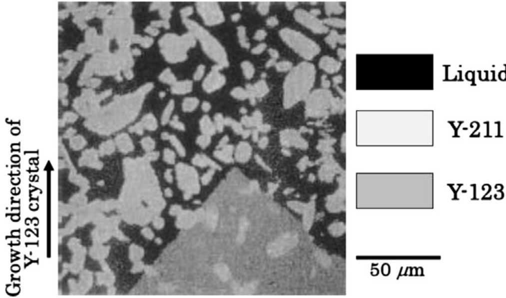

FIGURE 30.15 Y composition mapping image around the Y-123 growth interface of a sample grown at 1 mm/h. The white particles are the Y-211 phase, the gray region is the growing Y-123 phase crystal, and the black matrix is the liquid phase before quenching [63]. © *1993 Elsevier Science Publishers B.V.*

2. the interface of the growing Y-123 crystal is planar, and Y-211 particles are spherical;
3. peritectic reaction takes place isothermally;
4. thermophysical properties are constant;
5. no interaction exists between the Y-211 particles (even among particles of different sizes, e.g., Ostwald ripening).

30.8.2.2 Driving Force of Solute Diffusion

Figure 30.16 shows the principle of the liquid-diffusion-rate-limiting model. The yttrium diffusion flux for Y-123 phase crystal growth from Y-211 particles dispersed in the liquid ahead of the growth interface of the Y-123 crystal was estimated. This diffusion flux was derived from the composition difference in the liquid at the two different interfaces: liquid/Y-211 and liquid/Y-123. This composition difference consists of three origins in

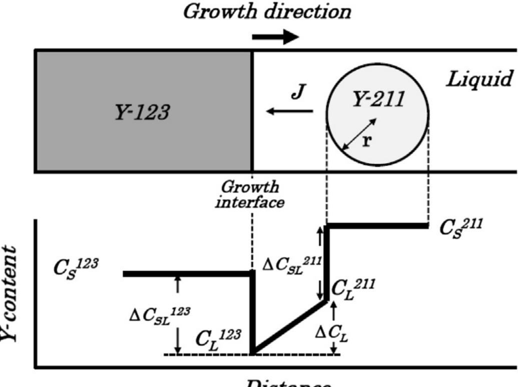

FIGURE 30.16 Sketch of the principle of the INS peritectic solidification model. The composition difference, as a driving force providing the required solute for Y-123 growth, is indicated in the composition profile [63]. *© 1993 Elsevier Science Publishers B.V.*

the case of directional solidification: the curvature effect of the dispersed Y-211 particles in the liquid, ΔC_1; undercooling, ΔC_2 [101]; and the temperature gradient, ΔC_3. When the Y-211 particles approach the interface very c1osely, the temperature gradient term, ΔC_3, becomes negligibly small. Accordingly, the total composition difference, ΔC, is the sum of $\Delta C_1 + \Delta C_2$. The concept of these three origins is shown schematically in the phase diagram (Figure 30.17). ΔC can be derived from the following equation:

$$\Delta C = \frac{1}{m_L^{211}}\left(\frac{2\Gamma^{211}}{r} + G_z\right) + \left(\frac{1}{m_L^{123}} - \frac{1}{m_L^{211}}\right)\Delta T \tag{30.22}$$

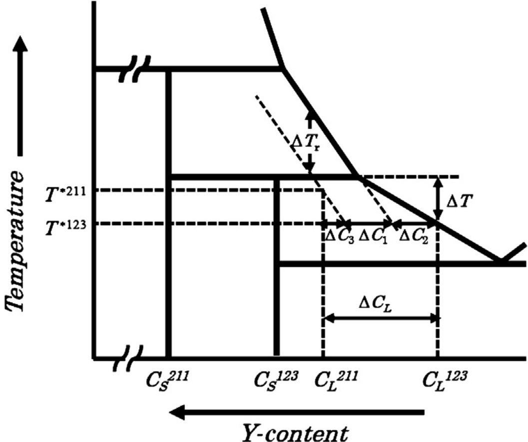

FIGURE 30.17 Origin of the composition difference used in the INS model. In this figure, T*211 and T*123 are the temperatures at the Y-211 interface and the Y-123 interface, and ΔC_1 is the supersaturation (undercooling) due to the change in chemical potential caused by the curvature of the Y-211 particle (Gibbs–Thomson effect) [63].

where m_L^{211} and m_L^{123} are the slopes of liquidus lines of the Y-211 and Y-123 phases, respectively, Γ^{211} is the Gibbs–Thomson coefficient ($\sigma_{211}/\Delta S_f$), σ_{211} is the Y-211/liquid interfacial energy, ΔS_f is the volumetric entropy of fusion, r is the radius of the Y-211 particle, G_z is the temperature gradient at the distance, z, from the Y-123 interface, and ΔT is the undercooling at the Y-123 growth interface.

30.8.2.3 Flux Provided by Dissolution of Y-211 Particle

The diffusion flux, $J_{r,z}$, from one Y-211 particle with a radius of r at a certain distance, z, from the Y-123 interface was calculated using Fick's first law:

$$J_{r,z} = D_L \frac{\Delta C}{z} = \left(D_L \frac{\Delta C}{\delta_c} \right) \tag{30.23}$$

where D_L is the diffusivity. Here the diffusion zone for peritectic reaction was assumed to be within the region between the maximum effective length δ_c and the Y-123 growth interface. The δ_c could be estimated as the characteristic diffusion length for planar steady state growth, D_L/R.

When the diffusion flux reaches the maximum flux (J_{max}), which is limited by the rate of decomposition of the Y-211 partic1es, the distance is defined as the critical length δ_c. A constant J_{max} as $4\pi r^2 k_{max}$ was assumed within δ_c using the maximum decomposition rate of the Y-211 partic1es (k_{max}). If the size distribution of the Y-211 partic1es in the region, which is out of the diffusion zone, is given initially, the total yttrium diffusion flux (J_{211}) from the Y-211 particles can be estimated by integrating the flux from the individual Y-211 particles (J or J_{max}) with respect to z and r within the diffusion zone:

$$\begin{aligned} J_{211} &= N \int_0^{\infty} \int_0^{\delta_c} J_{r,z} \Psi(r_0(r,z)) dz dr \\ &= N \int_0^{\infty} \pi r^2 \left[4k_{max}^{211} \int_0^{\delta *} \Psi(r_0(r,z)) dz + D_L \int_{\delta *}^{\delta_c} \frac{\Psi(r_0(r,z))}{z} \Delta C_L dz \right] dr \end{aligned} \tag{30.24}$$

N is the number of Y-211 particles per unit volume described as follows:

$$N = \frac{3V_f^{211}}{4 \int_0^{\infty} \pi r_0^3 \Psi(r_0) dr_0} \tag{30.25}$$

where V_f^{211} is the volume fraction of the Y-211 phase out of the diffusion zone, which can be calculated from the initial composition using the equilibrium lever rule, $\Psi(r_0(r,z))$ is the size distribution function of the Y-211 particles in the diffusion zone.

30.8.2.4 Flux Required for Y-123 Growth

According to Figure 30.13, the composition difference ΔC_{SL}^{123} at the growth interface of the Y-123 crystal can be calculated from the yttrium concentration of the Y-123 solid (C_S^{123}) and that of the liquid at the liquid/Y-123 interface (C_L^{123}), and described as follows:

$$\Delta C_{SL}^{123} = C_S^{123} - C_L^{123} = C_S^{123} - C_L^e + \frac{\Delta T}{m_L^{123}} \tag{30.26}$$

where C_L^e is the yttrium concentration of the liquid at the T_p. Then, the diffusion flux per unit area J_{123} required for Y-123 crystal growth is calculated as:

$$J_{123} = (C_S^{123} - C_i)R = \left(C_S^{123} - C_L^e + \frac{\Delta T}{m_L^{123}}\right)R \tag{30.27}$$

where R is the growth rate of the Y-123 crystal.

30.8.2.5 Steady State Growth Rate

In the steady state growth of the Y-123 crystal, the total flux from the Y-211 particles described in Eqn (30.24) should be equated with the flux indicated in Eqn (30.27). Then, the steady state growth rate, R, is given by:

$$R = \frac{3V_f^{211}\int_0^{\infty} r^2\left[4k_{\max}^{211}\int_0^{\delta^*}\Psi(r_0(r,z))dz + D_L\int_{\delta^*}^{\delta_C}\frac{\Psi(r_0(r,z))}{z}\Delta C_L dz\right]dr}{4\left(C_S^{123} - C_L^e + \frac{\Delta T}{m_L^{123}}\right)\int_0^{\infty} r_0^3\Psi(r_0)dr_0} \tag{30.28}$$

The order of magnitude of the calculated growth rates is several millimeters per hour, which is in good agreement with the experimentally confirmed growth rate for continuous growth. This model can also be used to estimate the change in size distribution of the Y-211 partic1es from the liquid to Y-123 crystals [63].

30.8.2.6 Macrosegregation Mechanism of Pushing/Trapping Model

The macrosegregation phenomenon of Y-211 particles in Y-123 crystals is similar to the pushing/trapping behavior of foreign particles at an advancing solid–liquid interface during solidification, which has been observed in various materials by many investigators [106–116]. Several theories on pushing/trapping phenomena have been proposed by considering the interaction between an inactive particle and an advancing solid–liquid interface.

Figure 30.18 is schematic drawings showing a particle in front of the solid–liquid interface and the forces acting on the particle. There are two dominant forces: the drag

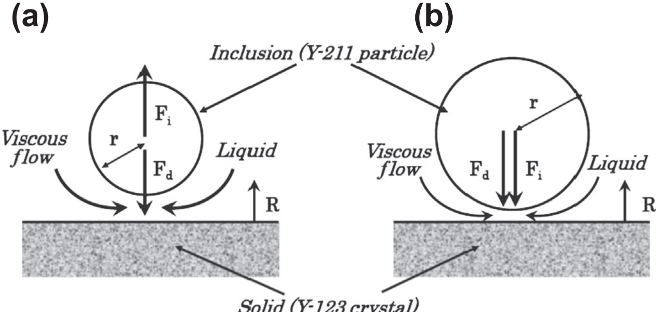

FIGURE 30.18 Schematic drawings showing a particle in front of the solid–liquid interface and the necessary condition of particle pushing [10]. (a) For $\Delta\sigma_0 > 0$. The force (F_i) due to the interfacial energy ($\Delta\sigma_0$) is conductive to pushing. (b) For $\Delta\sigma_0 < 0$. F_i is conductive to trapping. The drag force (F_d) is always conductive to trapping. *© 1997 Elsevier Science S.A.*

force (F_d) due to viscous flow around the particle, which moves together with the interface at the growth rate, R, and the force (F_i) due to the interfacial energy ($\Delta\sigma_0$).

The condition for particle pushing can be described as shown in Eqn (30.29) [106]:

$$\Delta\sigma_0 = \sigma_{SP} - \sigma_{LP} - \sigma_{SL} > 0 \tag{30.29}$$

where σ_{SP}, σ_{LP}, and σ_{SL} are the solid–particle, liquid–particle, and solid–liquid interfacial energies, respectively. F_i is conducive to pushing if $\Delta\sigma_0 > 0$, while F_d is always conducive to trapping as shown in Figure 30.18. Since the results of microstructural observations in melt growth processes indicate that Y-123 heterogeneous nucleation rarely takes place on the surface of Y-211 in the supersaturated liquid [117], it is suggested the relation of $\Delta\sigma_0 > 0$ in the Y-123/Y-211 system.

According to the pushing/trapping theory, the critical size (r^*) of a particle, larger than that trapped by the growing solid crystal, is roughly determined by the critical growth rate (R^*) and interfacial energy ($\Delta\sigma_0$):

$$R* \propto \frac{\Delta\sigma_0}{\eta r*} \tag{30.30}$$

where η is the melt viscosity. The relationship between the growth rate and the radius of the inclusion is derived to be $R^* \times r^* = \text{constant}$ using Eqn (30.30).

One should be careful when applying the pushing/trapping theory to the Y-123/Y-211 system, because this theory was proposed to explain the phenomena between inclusions, which are inert for both liquid and solid, and nonfaceted material. Actually, Y-211 partic1es are reactive inclusions as they supp1y Y solute to Y-123 by decomposition for faceted growth of Y-123 materials via peritectic transformation.

30.8.3 Crystal Growth Mechanism of SRL-CP Method

The growth mechanism of the SRL-CP method proposed by Yamada et al. [118] is basically the same as the melt texture process described in Section 30.8.2.1–30.8.2.5. Major differences between these processes include the distance between the Y-211 phase and the growth interface of the Y-123 phase crystal and the solute-transport mechanism.

30.8.3.1 Basic Growth Mechanism of Solute Diffusion Model with Interfacial Kinetics

Figure 30.19 shows the quasi-binary phase diagram illustrating the solute transport path in the melt for the SRL-CP method [119]. T_b and T_i indicate the temperatures at the bottom of the crucible and at the Y-123 growth interface, respectively. The equilibrium compositions are C_L^{123} and C_L^{211}. It was assumed that the Y concentration is uniform in the bulk liquid maintained by the natural and forced convections, except in the diffusion boundary layer near the growth interface of Y-123 phase crystal. The thickness, δ_c, of the solute diffusion boundary layer could be estimated, which is different from the above mentioned D_L/R (see Section 30.8.2.3.). Under the Cochran flow assumption [120], which

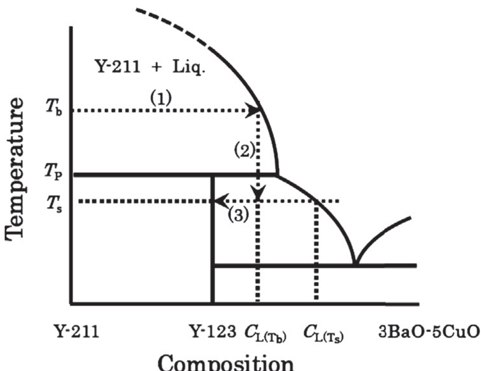

FIGURE 30.19 Phase stability and solute transportation processes shown on a schematic quasi-binary phase diagram [119]. © *1996 Elsevier Science B.V.*

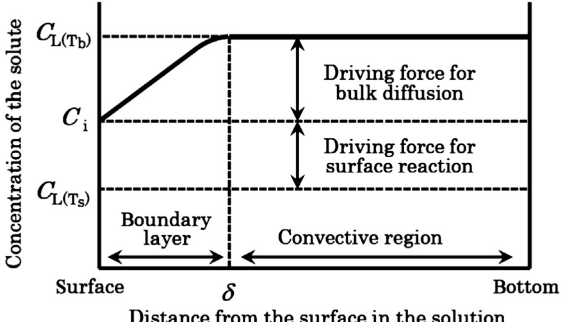

FIGURE 30.20 Schematic illustration of the solute concentration profile in front of the growing interface [118]. © *1995 Materials Research Society.*

is the fluid flow near a rotating disk, Burton et al. [121] introduced the solute boundary layer thickness as:

$$\delta_c = 1.6 D_L^{1/3} \nu^{1/6} \omega^{-1/2} \tag{30.31}$$

where D_L, ν, and ω are the diffusion coefficient of the solute, the kinematic viscosity, and the angular velocity of the rotating crystal, respectively. The Y concentration profile in the solution is schematically shown in Figure 30.20 [118].

The steady state growth rate in the SRL-CP method could be estimated similarly from the mass balance, as described before in Section 30.8.2.1–30.8.2.5. The solute flux from the solution through the boundary layer, δ_c, can be described as the same equation of Eqn (30.23) and the required flux for the Y-123 phase crystal growth is also

the same as Eqn (30.27). The steady state growth rate, R, can be given by equating both diffusion fluxes:

$$R = \frac{D_L}{\delta_c}\frac{\left(C_L^{211} - C_i\right)}{\left(C_s^{123} - C_i\right)} \tag{30.32}$$

Assuming that C_i is equal to C_L^{123}, which means that the effect of the interfacial kinetics for crystal growth are negligibly small, the growth rate reaches the maximum; the value, R_{max}, is estimated to be 5×10^{-4} mm/s by substituting the physical constants/parameters of the typical values of molten oxide and experimental conditions. The value of the R_{max} is larger than the experimental growth rate ($R = 2.8 \times 10^{-4}$ mm/s). If the composition at the interface, C_i, corresponding to supersaturation for interfacial kinetics is estimated using the experimentally measured growth rate, C_i is about 0.64 at%. By converting this value of C_i to the kinetic undercooling (ΔT_k) using the liquidus slope of the Y-123 phase, $\Delta T_k \approx 7$ K. This indicates that Y-123 single crystal growth might be controlled both by the interfacial kinetics and solute diffusion [10,118].

30.8.3.2 Interface Kinetics Estimated from Spiral Growth

1. Growth by screw dislocation (spiral growth)
   According to Cabrera and Levine [122] following the BCF theory [123], a better approximation of the step width, λ, of the spiral dislocation is given by:

$$\lambda = 19\rho_c = 19\frac{\gamma a}{k_B T \sigma} \tag{30.33}$$

   where ρ_c is the critical radius of the two-dimensional nucleus, γ is the step energy per unit length, and a is the distance between growth units.

   The relations between the growth rate and supersaturation can be written as:

$$R \propto \sigma^2, \quad \sigma < \sigma_1 \tag{30.34a}$$

$$R \propto \sigma, \quad \sigma > \sigma_1 \tag{30.34b}$$

   where the relation between σ and σ_1 is given by:

$$\frac{\sigma}{\sigma_1} = \frac{2x_s}{\lambda} = \frac{x_s}{9.5\rho_c} = \frac{\sigma}{(9.5\gamma a)/(x_s k_B T)} \tag{30.35}$$

   where x_s is a mean diffusive distance of the adsorbed atom.
   It should be noted that the equations described in this section are evaluated only for simple growth from vapor. When we discuss the interfacial kinetics of Y-123(RE-123) crystal growth from solution (liquid) precisely, it is necessary to consider complicated structures and multicomponent systems as well as the effect of desolvation on surface diffusion, which has been proposed by Bennema [124,125].
2. Growth by screw dislocation in SRL-CP method
   As shown previously, the single crystals grown by the SRL-CP method grow by a spiral growth (Figure 30.9). Kanamori and Shiohara [126] investigated the relation between the composition at the interface and the growth rate, R, from the observed

spiral patterns, including the step width, step height, and shape of Y-123 crystals grown by the SRL-CP method.

According to the approximation by Cabrera and Levine [122], the relation between the terrace width and the supersaturation, σ, is given by Eqn (30.19) and is defined as:

$$\sigma = \frac{C_i - C_L(T_i)}{C_L(T_i)} \tag{30.36}$$

C_i can be obtained from Eqn (30.13) using the experimental results R and $C_L(T_b)$. $C_L(T_i)$ is assumed to be equal to the Y concentration at the temperature, T_s, at the surface of the melt interface, since T_i could not be measured precisely. Consequently, the supersaturation, σ, can be calculated by substituting C_i and $C_L(T_i)$ into Eqn (30.36). The terrace width of spiral growth under each condition from AFM images is plotted as a function of the supersaturation in Figure 30.21 [126]. Also, by choosing the appropriate value (0.13 nm) of $\gamma a/k_BT$ so as to satisfy Eqn (30.33), it is clearly shown that the terrace widths observed on the as grown *ab* plane of the Y-123 single crystals satisfy the BCF theory [123].

In the case of sufficiently small supersaturation, the growth rate taking into account the interfacial kinetics was described in the Eqn (30.34a) and is given by:

$$R = k\sigma^2 \tag{30.37}$$

where k is the kinetic coefficient and expressed by the following equation [10]:

$$k = dfe^{-W/k_BT}\frac{1}{(19/x_s)(\gamma a/k_BT)} \tag{30.38}$$

where d is the lattice constant, f is the frequency of the molecule, W is the dissolution energy of the attached molecule from the surface of the crystal.

Substituting $d \approx 10^{-7}$ (cm) which is the lattice parameter of the c-axis of the Y-123 sing1e crystal, $W \approx 50$ (kcal/mol), which was estimated to be several times larger than

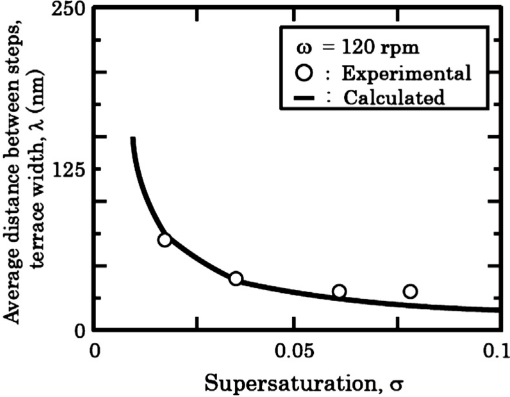

FIGURE 30.21 Supersaturation dependence of the average distance between the steps for YBCO single crystal growth [126]. © *1996 Materials Research Society.*

the value for growth from the vapor, $x_s \approx 100a \approx 4 \times 10^{-6}$ (cm) in which a is the lattice parameter of the a-axis of the Y-123 single crystal, $f \approx k_B T/3h \approx 10^{13}$ (s^{-1}) in which h is Planck's constant and the coefficient 1/3 indicates that the oscillation of the solute molecule is taken into account only in the direction perpendicular to the surface of the crystal and $\gamma a/k_B T = 0.13$ nm into Eqn (30.38), $k = 1 \times 10^{-3}$ (cm/s) was calculated as the interfacial kinetic coefficient. The relation between the growth rate and the supersaturation for the experimental and calculated results is in good agreement with each other [10,126]. Consequently, it is clear that the crystal growth of Y-123 single crystals pulled along the c-axis by the SRL-CP method can be explained by the bulk diffusion model combined with interface kinetics for surface diffusion (BCF theory).

30.8.4 Crystal Growth Mechanism Using Ternary Phase Diagram

In the previous section, the growth mechanism of Y-123 crystals prepared by the SRL-CP method was discussed on the basis of the pseudobinary phase diagram. In the case of the Y-123 system without substitution, this is sufficient because the compositions of the solid and the coexisting liquid are uniquely determined at a certain temperature by assuming that the interfacial kinetics are negligibly small (so-called monovariant system). However, in the case of solid solution systems, a ternary phase diagram should be used due to the increase in freedom (so-called divariant system). A model for the determination of the composition of the solid solution in the SRL-CP method was proposed for the Nd-Ba-Cu-O system as an example, which is modified from the model for the case of the Pr-Ba-Cu-O system [10,127].

The compositions of the solid solution and the coexisting liquid are determined by the tie-line, which links the same chemical potential for the respective solid solution and liquid solution, on the isothermal section of the Nd_2O_3-BaO-CuO ternary phase diagram at the growth temperature such as shown in Figure 30.5. The temperature dependence of the tie-line should be taken into account in the SRL-CP process. Figure 30.22 shows the condition in the crucible and the corresponding ternary phase diagram when the temperature at the bottom of the crucible is higher than the peritectic temperature. T_b, T_p, and T_s are the temperature at the bottom of the crucible, the peritectic temperature of NdBCO, and the temperature at the surface of the liquid, respectively. C_i^0, C_i^{422}, C_i^{ss}, $C_i^L(T_b)$, and $C_i^L(T_s)$ ($i \equiv$ Nd, Ba, and Cu) are the mole fractions of each cation in the initial starting composition, in the Nd-422 phase, in the NdBCO solid solution, in the liquid at T_b, and in the liquid at T_s, respectively. At first, it is considered that the liquid composition in the crucible, except in the solute boundary layer thickness, $\delta_{c,i}$, is uniform due to natural and forced convections. Then, C_i^0 is located on the tie-line connected with C_i^{422} and $C_i^L(T_b)$. The liquid of $C_i^L(T_b)$ is transferred to the solute boundary layer by natural and forced convections. Accordingly, the liquid near the solute boundary layer is supersaturated for NdBCO crystal growth because the temperature around the growing crystal is lower than the peritectic temperature T_p. This supersaturation is the driving

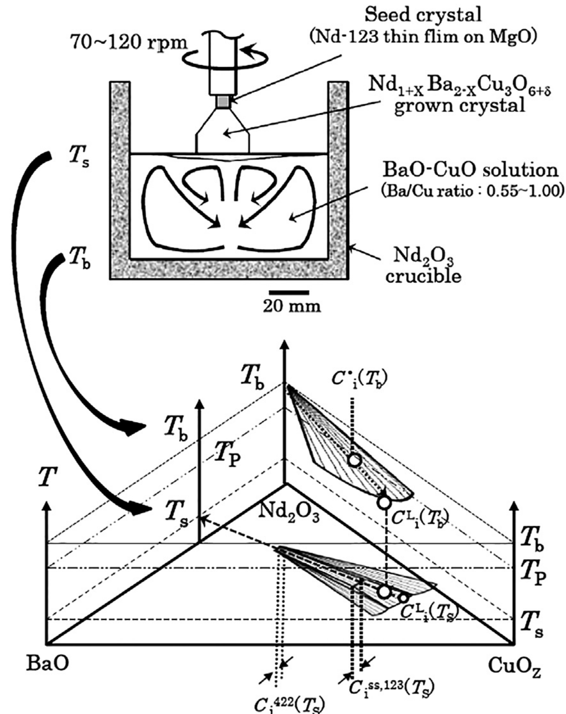

FIGURE 30.22 Condition in the solution (in the crucible) during crystal growth and the corresponding Nd_2O_3-BaO-CuO_Z ternary phase diagram.

force for NdBCO crystal growth. However, it is still uncertain which tie-line on the ternary phase diagram is selected at the growth interface in this system. Then the flux balance for each element is considered to determine the tie-line.

The following assumptions are made to simplify this problem:

1. local equilibrium is assumed at the interface between the crystal and the liquid, i.e., diffusion-controlled growth;
2. steady state solidification occurs only at the surface of the grown single crystal, and no nucleation or growth occurs at other sites (e.g., crucible walls or in the bulk liquid);
3. dilute solution approximation is permitted for the diffusion of Nd;
4. activities of Ba and Cu in the liquid follow Raoult's law;
5. difference between the unit volume of the crystal and that of the Ba-Cu-O solvent is negligibly small, the supersaturation estimated for the mole fraction causes crystallization of the same volume fraction, and the crystal growth rate can be calculated from the supersaturation in the solution given by the mole fraction;
6. crystal growth front is planar;
7. thermophysical properties are constant.

On the basis of these assumptions, the following flux balance equations for each element are derived:

$$R\{C_{Nd}^{SS} - C_{Nd}^{L}(T_S)\} = D_{Nd}\frac{\{C_{Nd}^{L}(T_b) - C_{Nd}^{L}(T_S)\}}{\delta_c} \quad (30.39)$$

$$R\{C_{Ba}^{SS} - C_{Ba}^{L}(T_S)\} = \tilde{D}\frac{\{C_{Ba}^{L}(T_b) - C_{Ba}^{L}(T_S)\}}{\delta_c} + \frac{C_{Ba}^{L}(T_S)}{1 - C_{Nd}^{L}(T_S)}(D_{Nd} - \tilde{D})\frac{\{C_{Nd}^{L}(T_b) - C_{Nd}^{L}(T_S)\}}{\delta_c} \quad (30.40)$$

$$R\{C_{Cu}^{SS} - C_{Cu}^{L}(T_S)\} = \tilde{D}\frac{\{C_{Ba}^{L}(T_b) - C_{Ba}^{L}(T_S)\}}{\delta_c} + \frac{C_{Cu}^{L}(T_S)}{1 - C_{Nd}^{L}(T_S)}(D_{Nd} - \tilde{D})\frac{\{C_{Nd}^{L}(T_b) - C_{Nd}^{L}(T_S)\}}{\delta_c} \quad (30.41)$$

where R is the growth rate, D_{Nd} is the diffusion coefficient of Nd in the liquid, and $\tilde{D}$ is the interdiffusion coefficient between barium and copper in the liquid. C_i^{SS} and $C_i^L(T_s)$ satisfying Eqns (30.39)–(30.41) simultaneously and uniquely give us a tie-line at the growing interface.

According to these equations, the selected tie-line is dependent on $\tilde{D}$ and D_{Nd}. In the case of $D_{\mathrm{Nd}} = \tilde{D}$, $C_i^L(T_b)$ is located on the tie-line (from C_i^{422} to $C_i^L(T_s)$), whereas in the case of $D_{\mathrm{Nd}} \neq \tilde{D}$, the tie-line is shifted by the relationship between D_{Nd} and $\tilde{D}$. Assuming that D_{Nd} is $\tilde{D}$, although these diffusion coefficients are uncertain at present, the composition of the grown single crystal of the NdBCO solid solution can be estimated. The estimated values using this model are in good agreement with the experimental results for various starting compositions. As in the Y-Ba-Cu-O system, the growth model should take into account the interfacial kinetics. Using the SRL-CP method, NdBCO single crystals were grown in the air atmosphere by controlling the liquid composition of the cationic ratio of Ba and Cu (Ba/Cu) to be approximately 0.80. The size of grown NdBCO single crystal was 24×24 mm as shown in Figure 30.23. The crystal exhibits high T_c value of about 95 K with a sharp transition width ΔT of less than 0.5 K [128]. This result indicates that the high Ba/Cu ratio in the liquid leads to the low amount of substitution of Nd^{3+} for Ba^{2+}, and consequently results in high superconducting properties.

30.9 Tetragonal to Orthorhombic Phase Transition (Twin Formation)

Y-123 materials have a distorted oxygen-deficient perovskite structure of $YBa_2Cu_3O_{7-\delta}$, as mentioned in Section 30.2.2. The Y-123 crystals grown by high temperature processes have a tetragonal phase, which behaves semiconductive. To attain superconductive characteristics for the crystals, an appropriate heat treatment is required at around 500 °C in an oxygen atmosphere. In this annealing process, the tetragonal-orthorhombic structural phase transition occurs and the obtained crystal composed of the twin structure. In this case, *a*-axes of the tetragonal phase separated into the *a*-axis and the *b*-axis of the orthorhombic phase, and this separation occurs randomly, resulting in formation of a twin structure.

FIGURE 30.23 As grown 1-inch-class size NdBCO single crystal produced by continuous pulling for 67 h from $Ba_3Cu_5O_8$ solvent melt in the Nd_2O_3 crucible in the air atmosphere. Its size is 24×24 mm^2 in the *ab*-plane and 21 mm in the *c*-axis direction [128]. © *1997 The Japan Society of Applied Physics.*

30.9.1 Experimental Measurements of Oxygen Diffusion Coefficient in $REBa_2Cu_3O_{7-\delta}$ (RE: Y & Nd) Crystal

For understanding of the twin formation process, knowledge of kinetics of the oxygen diffusion in both the tetragonal phase and the orthorhombic phase during annealing is important for optimizing superconductive characteristics. A considerable number of studies have been done on the oxygen diffusions in $YBa_2Cu_3O_{7-\delta}$ (Y-123) crystals [129–135] and Nd-123 crystals [136,137], in which diffusion coefficients were estimated by means of the O^{18} isotope tracer and SIMS measurements [129,130,136], the internal friction measurements [126,132], the dynamic and isothermal thermogravimetry [133], the in situ electrical resistivity measurements [134], and in situ observations of twin propagation front [135]. Application of these different evaluation techniques explains the discrepancy of numerical values in literature, which is shown in Figure 30.24.

Diffusion of oxygen in $REBa_2Cu_3O_{7-\delta}$ is anisotropic due to crystallographic anisotropy of their orthorhombic unit cells. Therefore, diffusion in such crystals should be described by (at least) three independent diffusion coefficients along the principal crystallographic directions [129]. The anisotropy is expected to be rather large since the oxygen ion vacancies are concentrated exclusively in CuO basal planes (*ab*-plane), i.e., diffusion in the perpendicular direction (*c*-axis) could be much slower than that in the *ab*-plane. The diffusion is affected by many factors, including $P_{O_2} - T - \delta$ phase-diagram considerations (Rudnyi et al. [138], chemical substitutions in $REBa_2Cu_3O_{7-\delta}$ (RE-ion effect, etc.), grain size, surface quality (Kemnitz et al. [139], Claus et al. [140], Tretyakov and Goodilin [141]), internal stress, availability of oxygen vacancies for diffusion jumps in the almost oxygenated state ($\delta_{\lim} \approx 0.003$–$0.08$ according to data of

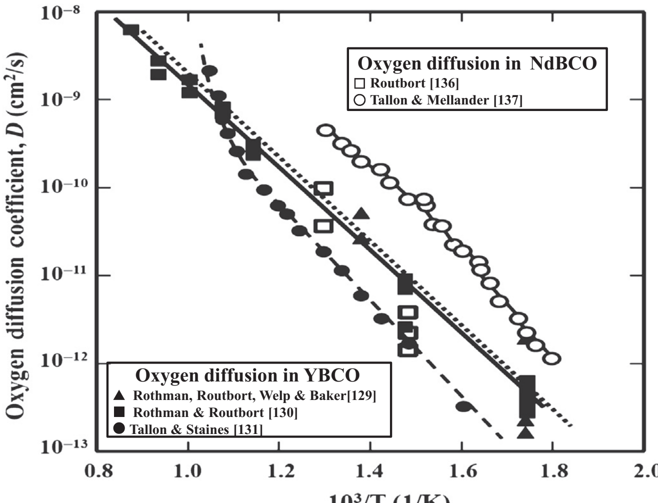

FIGURE 30.24 Summarized Arrhenius plots of the reported oxygen diffusion coefficient in the solid Y-123 and Nd-123 crystals [129–131,136,137].

different authors, Rothman et al. [129], Kruger et al. [142]), etc. Therefore, the overall mechanism of diffusion and, consequently, fitting parameters (pre-exponential factor D_o, activation energy ΔE etc., $D = D_o\ exp(-\Delta E/(kT))$ are usually different depending on experimental conditions (Bokshtein et al. [143]). However, from a practical point of view it is important to note that the chemical (D_{chem}) and self-diffusion (D_{self}) coefficients may differ by several orders of magnitude, $D_{chem} = D_{self}\ \Phi$, where Φ is a thermodynamic factor, which is nearly constant between $1 \leq \delta \leq 0.8$ (Erb et al. [144]). Usually the observable rate of in-diffusion is faster than the rate of out-diffusion because a surface-controlled process of some kind may take place especially for polycrystalline samples (Tu et al. [134], Erb et al. [144]). The intrinsic mechanism of oxygen diffusion was studied, for example, by Xie et al. [145], Rothman et al. [129], and Bredikhin et al. [146].

Reported self-diffusion coefficients and chemical diffusion coefficients of oxygen in solid RE-123 crystals are summarized in Tables 30.2 and 30.3.

30.9.2 Diffusion Mechanism

The diffusion mechanism in the Y-123 crystal should be consistent with the following experimental facts:

1. Arrhenius plot is straight;
2. diffusion coefficient is independent of P_{O_2}
3. $D_b >> D_a$, D_c at least at 300 °C; and
4. defect configuration involved in diffusion is of a type that would also give rise to an internal friction peak [129].

Table 30.2 List of Reported Self Diffusion Coefficients of Oxygen in Solid RE-123 Crystals

Diffusivity	Self Diffusion Coefficient (cm^2/s)	Method and Temperature	References
D_{self} (in *ab* plane)	$\approx 10^{-9} \sim 10^{-13}$, $D_{self} = 1.4 \times 10^{-4}$ exp (0.97 eV/kT)	Ortho- & tetra-Y-123 O^{18} tracer, 350 ~ 850 °C	Rothman et al. [129]
	1.7×10^{-13}, 6.7×10^{-13}, 2.9×10^{-12}, 1.3×10^{-11}, 5.3×10^{-11}, 1.7×10^{-10}	Internal friction 400 °C, 450 °C, 500 °C, 550 °C, 600 °C, 650 °C	Xie et al. [145]
	$\approx 3 \times 10^{-12}$, $3.8 \sim 10 \times 10^{-11}$	NdBCO, O^{18} tracer, 400 °C, 500 °C	Routbort [136]
	$8 \times 10^{-13} \sim 10^{-9}$	Y-123, 350 ~ 645 °C	Tallon & Mellander [137]
	$2 \times 10^{-11} \sim 2 \times 10^{-9}$	Gd-123, 350 ~ 610 °C	
	$3 \times 10^{-11} \sim 2 \times 10^{-9}$	Nd-123, 350 ~ 564 °C	
D_{self}	$\approx 10^{-16} \sim 10^{-17}$ (in *c*-direction)	Single crystal, 400 °C	Claus et al. [140]
	$\approx 2 \times 10^{-12}$ (in *b*-direction)	Untwinned, 300 °C	LaGraff & Payne [147]
	$\approx 5 \times 10^{-14} \sim 5 \times 10^{-15}$ (in *a*-direction)	300 °C	Rothman et al. [129]
	$D_{ab} \approx (10^4 \sim 10^6)\ D_c$, $D_b \approx 100\ D_a$, $D_{ab} \approx D_{poly}$, $D_b \approx 10\ D_{ab}$		Shiohara & Goodlin [148]
D_{self} (estimated)	$D_{ab} \approx 10^{-10}$, $D_c \approx 2 \times 10^{-16}$, $D_{ab} \approx 7 \times 10^{-10}$, $D_c \approx 2 \times 10^{-15}$	450 °C, 530 °C	Tsukui et al. [149]
	$D_{ab} \approx 3 \times 10^{-12}$, $D_c \approx 4 \times 10^{-17}$ $D_{ab} \approx 7.8 \times 10^{-9}$, $D_c \approx 6.2 \times 10^{-11}$	400 °C, 800 °C	Bredikhin et al. [146]

The first of these criteria suggests that diffusions in both the orthorhombic and tetragonal phases take place by the same type of oxygen atom jump. The second suggests that the diffusion coefficient is independent of the concentrations of oxygen ion vacancies and interstitials. The third of these criteria is related to the structure in the *ab*-plane. The combination of a straight Arrhenius line over the entire temperature range and the finding that $D_b >> D_a$ at 300 °C suggests that $D_b >> D_a$, should hold over the entire temperature range.

The theories of Bakker et al. [153,154] assume that the vacancies on O(I) and the oxygen ions on O(V) occur randomly. Diffusion via randomly arranged single vacancies at high δ values would lead to strong correlation effects and a curved Arrhenius plot. Accordingly, it was believed that diffusion via isolated vacancies is not the mechanism for the diffusion of oxygen in $YBa_2Cu_30_{7-\delta}$. The Monte Carlo calculations of Salomons and deFontaine [155] are based on the ordering of oxygen ions at $\delta < 1$, but still yield a strong P_{O_2} dependence of D.

The strong anisotropy of diffusion in the *ab*-plane was suggested by Ronay and Nordlander [156]. The diffusion coefficient may show only a weak dependence on P_{O_2} for the following reason [157]. If only the oxygen ions at the ends of the chains are mobile,

Table 30.3 List of Reported Chemical Diffusion Coefficients of Oxygen in Solid RE-123 Crystals

Diffusivity	Chemical Diffusion Coefficient (cm^2/s)	Method and Temperature	References
$D_{chem,\ poly}$ (in *ab* plane)	$\approx 10^{-10}$	TGA, 500 °C	Tang & Lo [132]
	$10^{-11} \sim 10^{-9}$	In-diffusion, 400 ~ 600 °C	Tu et al. [134]
	5×10^{-8}	94% dense Y-123 solid-state electrochemical cell, 500 °C	O'Sullivan & Chang [150]
	$5 \times 10^{-8} \sim 5 \times 10^{-7}$	Out-diffusion, 350 ~ 600 °C	LaGraff & Payne [147]
	$\approx 5 \times 10^{-5}$	450 ~ 600 °C	Elschner [151]
	7.5×10^{-7}, 1.9×10^{-6}, 3.4×10^{-6}, 6.2×10^{-6}, 1.3×10^{-5}, 1.8×10^{-5}, 2.8×10^{-5}	In- & out-diffusion in air 300 °C, 400 °C, 500 °C, 600 °C, 700 °C, 800 °C, 900 °C	Shi et al. [152]
$D_{chem,\ single\ X'tal}$ (in *ab* plane)	$\approx 10^{-7}$	Twin propagation front	Yamada & Shiohara [49]
	$\approx 10^{-5}$	In-diffusion, 725 °C	LaGraff & Payne [147]
	$\approx 10^{-6}$	Out-diffusion, 725 °C	
	$Gd_{0.8}Y_{0.2}Ba_2Cu_3O_z$ 4.94×10^{-5} exp ($0.52eV/kT$)	In-situ resistivity measurement	Erb et al. [144]
	$\approx 3 \times 10^{-8}$	550 °C,	
	$\approx 8 \times 10^{-9}$	420 °C	
	4.5×10^{-8}, 5×10^{-7}, 7×10^{-7}, 10^{-6}, 3×10^{-8}, 2×10^{-7}, 4×10^{-7}, 4.5×10^{-7}	(Nd-123) 300, 400, 500, 600 °C (Y-123) 300, 400, 500, 600 °C	Oka & Shiohara [135]

and the number of chains stays constant with stoichiometry, the number of mobile atoms will be independent of P_{O_2}. In this model, the length of the chains changes with stoichiometry, and the oxygen atom jump distance will also change. The mechanism suggested is that an oxygen ion at the end of a row of O(I) sites jumps into an O(V) site, moves along O(V) sites until it comes to another row end, and attaches itself there. It could be concluded on the basis of the experimental data that diffusion in $YBa_2Cu_3O_{7-\delta}$ probably does not take place by the random movement of vacancies in the CuO plane but rather by the movement of oxygen ion over O(V) sites between the rows of oxygen ions.

From the viewpoints of atomic mechanisms of chemical oxygen diffusion, the diffusion coefficient, D_{chem}, is given by [130]

$$D_{chem} = \frac{1}{2} d^2 \omega f \left(1 + \frac{\partial \ln \gamma}{\partial \ln c}\right) \tag{30.42}$$

where d is the jumping distance of oxygen atoms, ω is the exchange frequency between oxygen atoms and the neighboring vacancies, f is a correlation factor, γ is the oxygen activity coefficient, and c is the oxygen concentration. Assuming the independent chemical oxygen diffusion coefficient with oxygen concentration, D_{chem} is represented

by the first term on the right side of Eqn (30.42). Comparing the factors in Eqn (30.42) for the Nd-123 with those for the Y-123, the jumping distance of oxygen atoms, d, for the Nd-123 single crystals is only about 2% larger than that for the Y-123 single crystals, which was predicted from the lattice parameters of the Nd-123 and Y-123 crystals [148]. The exchange frequency between oxygen atoms and the neighboring vacancies, ω, for the Nd-123 single crystal is about 50 times larger than that for the Y-123 single crystals, which was predicted from the internal friction measurements [137]. Therefore, further assuming that the correlation factor, f, is equal to unity for both the Nd-123 and Y-123 single crystals, the chemical diffusion coefficient, D_{chem}, of the Nd-123 single crystals should also about be 50 times larger than that of the Y-123 single crystals. However, some of the coefficients obtained experimentally are different from that predicted from Eqn (30.42) as described before.

For the reason why the experimental and predicted values of the chemical oxygen diffusion coefficients were different, it should be noted that the Nd-123 crystals are easy to form a nonstoichiometric composition by substitution of a portion of the Nd^{3+} ions for Ba^{2+} ion sites during the fabrication process because of similar radii of Nd^{3+} ion and Ba^{2+} ion to each other as described before in Section 30.4.2 [18,37,88]. It should be noted that this substitution causes different oxygen activities due to different valencies. This nonstoichiometric composition in the Nd-123 crystals should affect the oxygen diffusion during annealing.

30.9.3 Twins and Tweed Pattern Due to Strains in Orthorhombic Phase

The transition of the tetragonal to the orthorhombic RE-123 phase due to oxygen in-diffusion on cooling is normally accompanied by the spontaneous formation of twin domains because the internal strains are relieved [158]. It has been suggested [159] that the spacing of the twins, $\Delta\lambda$, varies as the square root of the size G of the transforming region:

$$\Delta\lambda = \sqrt{\frac{128\pi\gamma G}{ES^2}} \tag{30.43}$$

where γ is the twin boundary energy per unit area, S is the orthorhombicity ratio, and E is the elastic modulus of the material. It is obvious that the twins can be negligibly small and undetectable in tiny particles, however, in large single crystals these twin domains are visible and give contrasted images in polarized optical microscopy.

Lin and coworkers [160] suggested that annealing the orthorhombic phase above the transition temperature at high oxygen partial pressure for a short period of time followed by quenching could result in a tetragonal oxygen-rich phase. Since the oxygen-rich tetragonal phase is a nonequilibrium state, the intrinsic strains can manifest themselves as orthogonally modulated structure distortions with a length of several tens to hundreds of angstroms (tweed structure). They demonstrated the existence of the tweed tetragonal phase in oxygen-rich pure $YBa_2Cu_30_{7-\delta}$ ($\delta < 0.6$) prepared by a similar method. The samples were superconducting with a sharp transition.

Two types of twin structures were observed in the whole range of the $Nd_{1+x}Ba_{2-x}Cu_3O_z$ solid solution: due to the tetragonal-to-orthorhombic phase transition in the region $x < 0.3$, and due to peculiarities of the crystal growth mechanism at $x > 0.6$. Additionally, the tweed structure can be observed near $x = 0.3$ and $x = 0.6$. A strong confirmation of the as-grown nature of the twins in $Nd_{1.85}Ba_{1.15}Cu_3O_z$ can be found by high temperature (hot-stage) in situ optical microscopy [135]. This is a powerful method for visualizing the twin behavior and for a kinetic study of processes in any desired environment and conditions (at certain T, P_{O_2} and applied uniaxial compression). They demonstrated the stability of the twin structure in $Nd_{185}Ba_{1.15}Cu_3O_z$ crystals even at 900 °C in low- P_{O_2} atmosphere. The twins do not disappear after this high-temperature-low-P_{O_2} anneal, contrary to the usual behavior of twins in the $x = 0$ case. To eliminate the twin structure in $Nd_{185}Ba_{1.15}Cu_3O_z$, it is necessary to destroy the crystals or to obtain them without twins under some other growth conditions. At the same time, detwinning in the $x = 0$ single crystals occurs for several minutes depending on the temperature and P_{O_2}.

30.9.4 Detwinning and Twin-free Crystal by Mechanical Stress

In the annealing process, to attain superconductivity, the *a*-axes of a tetragonal phase separate into the *a*- and *b*-axis of the orthorhombic phase, and this separation occurs randomly, leading to the twin structure. Small crystals ($\sim$1 mm^2) can be obtained in a twin-free form [161], while larger crystals demand a special detwinning procedure. Since tile stiffness of the materials becomes minimal in the middle of the structural transformation, this phenomenon allows one to obtain a twin-free orthorhombic phase starting with the tetragonal one. This process originates from the idea of ferroelasticity [162] and has been widely investigated [163–168]. Only a few practical examples will be given here. In thin (about 100 μm) flux-grown crystals, the twin structure changes under uniaxial compression of a few MPa, starting from a temperature 200–300 °C. The single-domain crystals obtained in this way show a “memory effect” [164,167], i.e., they retain internal stresses and become retwinned under subsequent annealing without uniaxial compression. The configuration of the twin-domain walls returns to its initial state as predetermined by microstructural defects. Thick crystals (e.g., produced by the SRL-CP method; see in Section 6.3.) cannot be detwinned at such low temperatures. In contrast, when raising the temperature to 500–700 °C, complete detwinning occurs without returning to the initial twin structure. The Ar preheating favors “memory cleaning” because it anneals the defects and cures microcracks of the as-grown crystals as well as homogenizes the oxygen contents and removes it from rare twins if present. Therefore a typical procedure of detwinning is as follows [166,167]. A rectangular piece is cut off from a large single crystal. Uniaxial compressive stress of about 6 MPa is applied. Then, the sample is heated under this uniaxial compression in an argon gas flow up to 600 °C. Then, the gas is changed to oxygen and the sample is cooled at a rate of about 6 °C/h. The resulting microstructure according to polarized optical microscopy observation consists of about 99.9% surface fraction of the twin-free orthorhombic $YBa_2Cu_30_7$ phase [167].

Kutami et al. [166] pressed a single crystal ($1 \times 1 \times 0.3\ mm^3$) with a tetragonal structure at 1000 kgf/cm^2 for 120 h in an oxygen atmosphere. As a result, the crystal annealed with the uniaxial compression was an orthorhombic phase without twins as confirmed by Laue X-ray backscattering, TEM observation, and T_c measurements. Onset of $T_{c,0}$ of the twin-free crystal was about 92 K and the J_c value at 1 T was one-fifth that of the twinned crystal, which indicates a high crystallinity.

30.10 Conclusion

We have reviewed the development of bulk crystal growth of high T_c superconducting (HTSC) oxides especially focusing on $YBa_2Cu_3O_{7-\delta}$ (Y-123) and $REBa_2Cu_3O_{7-\delta}$ (RE-123), the most widely studied HTSC material. By first considering the basic and fundamental solidification processes of the HTSC oxides, we have established physical models of the state of our understandings of the growth process. The Y-123 oxide solidifies (crystallizes) via peritectic reactions from its melt, i.e., incongruent melting. Although some progress has been made in the understanding of peritectic growth, much of the work is rather qualitative, and the rate-limiting stage is considered to be solid diffusion at least in most metallic alloy systems. A unique idea of its reaction with the rate-limiting stages of liquid diffusion as well as interface kinetics was reviewed. Based on a series of experimental results, the model for the peritectic reaction with the particle pushing/trapping mechanism for controlling the microstructures and understanding of the behavior of the high temperature stable solid phase was also reviewed.

With these ideas, we have then reviewed the effects of various process parameters on the bulk oxide crystal growth process, including oxygen partial pressure, growth temperature, liquid compositions, crucible materials, and crystal rotation/pulling rates for controlling the fluid flow, i.e., convections in the liquid solution. Furthermore, a unique crystal pulling process reported for fabrication of the single crystals, and a developed crystal growth model for the ternary component system to control the crystal composition in the solid solution by means of mass and flux balance equations with a local equilibrium assumptions using ternary equilibrium phase diagram together with tie-lines, were reviewed. Although modeling has been successful at least in treating the compositional partitioning of cationic elements at the interface between the solid solution and the liquid solution for the ternary systems, there is no complete theory for quaternary and high-order systems including anionic oxygen. Since oxygenation of grown crystals is necessary to enhance superconductivity, and this is a very delicate procedure in the case of single crystals, oxygen diffusion and twin formation are also reviewed. Obviously, further work is necessary for better understanding of the basic crystal growth processes to achieve a much better control of the fabrication of the superconducting oxides.

Acknowledgments

The authors wish to express their sincere gratitude to all scientists of SRL-ISTEC, and to many collaborative research scientists in the universities, industries, and research institutions all over the world. Parts of the original research reported in this chapter were supported by the New Energy and Industrial Technology Development Organization (NEDO) in Japan.

References

[1] Bednorz JG, Müller KA. Z Phys B Condensed Matter 1986;64:189–93.

[2] Pool R. Science May 26, 1989;244:914–6.

[3] Wu MK, Ashburn JR, Torng CJ, Hor PH, Meng RL, Gao L, et al. Phys Rev Lett 1987;58:908–10.

[4] Elwell D, Scheel HJ. Crystal growth from high-temperature solutions. Chapter 11. London, New York, San Fransisco: Academic Press; 2011. 635.

[5] Maeda H, Tanaka Y, Fukutomi M, Asano T. Jpn J Appl Phys 1988;27:L209–10.

[6] Sheng ZZ, Hermann AM. Nature 1988;332:138–9.

[7] Schilling A, Cantoni M, Guo JD, Ott HR. Nature 1993;363:56–8.

[8] Nagamatsu J, Nakagawa N, Muranaka T, Zenitani Y, Akimitsu J. Nature 2001;410:63–4.

[9] Kamihara Y, Watanabe T, Hirano M, Hosono H. J Am Chem Soc 2008;130:3296–7.

[10] Shiohara Y, Endo A. Mater Sci Eng 1997;R19:1–86.

[11] Izumi F, Asano H, Ishigaki T, Ono A, Okamura FP. Jpn J Appl Phys 1987;26:L611–2.

[12] Hatano T, Matsushita A, Nakamura K, Sakka Y, Matsumoto T, Ogawa K. Jpn J Appl Phys 1987;26: L721–3.

[13] Ito T, Takenaka K, Uchida S. Phys Rev Lett 1993;70:3995–8.

[14] Ando Y, Segawa K, Lavrov AN, Komiya S. J Low Temp Phys 2003;131:793–801.

[15] Cava RJ, Batlogg B, Chen CH, Rietman EA, Zahurak SM, Werder D. Nature 1987;329:423–5.

[16] Lindemer TB, Hunley JF, Gates Jr JE, Sutton AL, Brynestad J, Hubbard CR, et al. J Am Ceram Soc 1989;72:1775–88.

[17] Scheel HJ. MRS Bull September 1994:26.

[18] Wada T, Suzuki N, Maeda T, Maeda A, Uchida S, Uchinokura K, et al. Appl Phys Lett 1988;52: 1989–91.

[19] Yoo SI, Sakai N, Takaichi H, Higuchi T, Murakami M. Appl Phys Lett 1994;65:633–5.

[20] Murakami M, Yoo SI, Higuchi T, Sakai N, Weltz J, Koshizuka N, et al. Jpn J Appl Phys 1994;33: L715–7.

[21] Worthington TK, Gallagher WJ, Kaiser DL, Holtzberg FH, Dinger TR. Phys C 1988;153–155:32–7.

[22] Dimos D, Chaudhari P, Mannhardt J. Phys Rev B 1990;41:4038–49.

[23] Scheel HJ, Licci F. Thermochim Acta 1991;174:115.

[24] Scheel HJ, Sadowski W, Schellenberg L. Supercond Sci Technol 1989;2:17.

[25] Aselage T, Keefer K. J Mater Res 1988;3:1279–91.

[26] Oka K, Nakane K, Ito M, Saito M, Unoki H. Jpn Appl Phys 1988;27:L1065–7.

[27] Erb A, Biernath T, Müller-Vogt G. J Cryst Growth 1993;132:389–95.

[28] Ahn B, Lee VY, Beyers R. Phys C 1990;167:529–37.

[29] Lay KW, Relund GM. J Am Ceram Soc 1990;73:1208–13.

[30] Ng WW, Cook LP, Paretzkin B, Hill MD, Stalik JK. J Am Ceram Soc 1994;77:2354–62.

[31] Lee BJ, Lee DN. J Am Ceram Soc 1989;72:314–9.

[32] Lee BJ, Lee DN. J Am Ceram Soc 1991;74:78–84.

[33] Krauns Ch, Sumida M, Tagami M, Yamada Y, Shiohara Y. Z Phys B 1994;96:207–12.

[34] Kambara M, Nakamura M, Shiohara Y, Umeda T. Phys C 1997;275:127–34.

[35] Yao X, Shiohara Y. Supercond Sci Technol 1997;10:249–58.

[36] Nakamura M, Krauns Ch, Yamada Y, Shiohara Y. J Mater Res 1996;11:1076–81.

[37] Yoo SI, McCallum RW. Phys C 1993;210:147–56.

[38] Daeumling M, Seuntjens JM, Larbalestier DC. Nature 1990;346:332–5.

[39] Osamura K, Zhang W. Z Metallkd 1993;84:522–8.

[40] Oka K, Unoki H. J Cryst Growth 1990;99:922–4.

[41] Kambara M, Yao X, Tagami M, Goodlin EA, Shiohara Y, Umeda T. J Am Ceram Soc 1998;81(8):2116–24.

[42] Yoshizumi M, Kambara M, Shiohara Y, Umeda T. Phys C 2000;334:77–86.

[43] Shimpo R, Nakamura Y. J Jpn Inst Met (in Japanese) 1990;54:549–55.

[44] Kimura S, Shimpo R, Nakamura Y. J Jpn Inst Met (in Japanese) 1992;56:1145–51.

[45] JANAF Thermochemical Table. 3rd ed. J Phys Chem Ref Data 1985;14.

[46] Jin S, Tiefel TH, Sherwood RC, van Dover RB, Davis ME, Kammlott GW, et al. Phys Rev B 1988;37:7850–3.

[47] Murakami M, Morita M, Doi K, Miyamoto K. Jpn J Appl Phys 1989;28:1189–94.

[48] Fujimoto H, Murakami M, Gotoh S, Shiohara Y, Koshizuka N, Tanaka S. Proc 2nd ISS ’89 Adv Supercond 1989;1:285–8.

[49] Yamada Y, Shiohara Y. Phys C 1993;217:182–8.

[50] Nakamura M, Yamada Y, Shiohara Y. J Mater Res 1994;9(8):1946–51.

[51] Kondoh A, Kagiya S, Takaichi H, Sakai N, Murakami M, Fujimoto H, et al. Proc. Int. workshop on superconductivity, ISTEC-MRS, Honolulu, Hawaii; 1992. p. 272.

[52] Morita M, Takebayashi S, Tanaka M, Kimura K. Proc 3rd ISS ’90 Adv Supercond 1991;3:733–6.

[53] Sawano K, Morita M, Tanaka M, Sasaki T, Kimura K, Takebayashi S, et al. Jpn J Appl Phys 1991;30:L1157–9.

[54] Gao L, Xue YY, Ramirez D, Huang ZL, Meng RL, Chu CW. Appl Phys Lett 1993;63:260.

[55] Blohowiak KY, Garrigus DF, Luhman TS, McCray KE, Strasik M, Akway IA, et al. IEEE Trans Appl Supercond 1993;3:1049–52.

[56] Lo W, Cardwell DA, Dung SL, Bater RG. J Mater Sci 1995;30:3995–4002.

[57] Meng RL, Kinalidis C, Sun YY, Gao L, Tao YK, Hor PH, et al. Nature 1990;345:326–8.

[58] McGinn PJ, Chen W, Zhu N, Balachandran U, Lanagan MT. Phys C 1990;165:480–4.

[59] McGinn P, Zhu N, Chen W, Sengupta S, Li T. Phys C 1991;176:203–8.

[60] McGinn P, Chen W, Zhu N, Varanasi C, Tan L, Balkin D. Phys C 1991;183:51–6.

[61] Izumi T, Shiohara Y. J Mater Res 1992;7:16–23.

[62] Figueredo AM, Cima MJ, Flemings MC, Haggerty JS, Hara T, Ishii H, et al. Phys C 1995;241:92–102.

[63] Izumi T, Nakamura Y, Shiohara Y. J Cryst Growth 1993;128:757–61.

[64] Rutter JW, Chalmers B. Can J Phys 1953;31:15–39.

[65] Flemings MC. Solidification processing. New York: McGraw-Hill; 1974. p. 290.

[66] Sun BN, Schmid H. J Cryst Growth 1990;100:297–302.

[67] Drake A, Abell JS, Sutton SD. J Less-Common Met 1990;164-165:187–92.

[68] Katsui A, Hidaka Y, Ohtsuka H. Jpn J Appl Phys 1987;26:L1521–3.

[69] Gencer F, Abell JS. J Cryst Growth 1991;112:337–42.

[70] Wang Y, Bennema P, van der Linden P. J Cryst Growth 1990;106:483–6.

[71] Watanabe K. J Cryst Growth 1990;100:293–6.

[72] Watanabe K. J Cryst Growth 1991;114:269–78.

[73] Wolf Th, Goldacker W, Obst B. J Cryst Growth 1989;96:1010–8.

[74] Schneemeyer LF, Waszczak JV, Siegrist T, van Dover RB, Rupp LW, Batlogg B, et al. Nature 1987;328:601–3.

[75] Asaoka H, Takei H, Iye Y, Tamura M, Kinoshita M, Takeya H. Jpn J Appl Phys 1993;32:L1091–6.

[76] Takei H, Asaoka H, Iye Y, Takeya H. Jpn J Appl Phys 1991;30:L1102–5.

[77] Ono A, Nozoki H, Ishizawa Y. Jpn J Appl Phys 1988;27:L340–3.

[78] Wanklyn BM, Chen C, Watts BE, Haycock P, Platt F, de Goot PAJ, et al. Solid State Commun 1988;66:441–3.

[79] Liang R, Dosanjh P, Bonn DA, Baar DJ, Carolan JF, Hardy WN. Phys C 1992;195:51–8.

[80] Holtzberg F, Field C. J Cryst Growth 1990;99:915–21.

[81] Dembinski D, Gervais M, Odier P, Coutures JP. J Less-Common Met 1990;164-165:177–86.

[82] Oka K, Ito T. Phys C 1994;227:77–84.

[83] Namikawa Y, Egami M, Shiohara Y. Proc 7th ISS ’94 Adv Supercond 1995;7:595–600.

[84] Klemenz C, Scheel HJ. J Cryst Growth 1993;129:421.

[85] Namikawa Y, Egami M, Shiohara Y. J Mater Res 1996;11:288–95.

[86] Yao X, Mizukoshi T, Egami M, Zama H, Nakamura M, Shiohara Y. Jpn J Appl Phys 1996;35:2126–32.

[87] Nakamura M, Krauns Ch, Yamada Y, Shiohara Y. J Cryst Growth 1996;166:859–62.

[88] Nakamura M, Kutami H, Shiohara Y. Phys C 1996;260:297–304.

[89] Jackson KA. Liquid metals and solidification. Cleveland: American Society for Metals; 1958. p. 174.

[90] Nakamura M, Krauns Ch, Shiohara Y. J Mater Res 1996;11:1076–81.

[91] Nakamura Y, Furuya K, Izumi T, Shiohara Y. J Mater Res 1994;9:1350–6.

[92] Muller D, Freyhardt HC. Phys C 1995;242:283–90.

[93] Imagawa Y, Shiohara Y. Phys C 1996;262:243–8.

[94] Endo A, Chauhan HS, Nakamura Y, Furuya K, Shiohara Y. Proc 7th ISS ’94 Adv Supercond 1995;7:689–92.

[95] Kim CJ, Kim KB, Won DY, Moon HC, Suhr DS, Lai SH, et al. J Mater Res 1994;9:1952–60.

[96] Varanasi C, McGinn PJ. Phys C 1993;207:79–84.

[97] Endo A, Chauhan HS, Egi T, Shiohara Y. J Mater Res 1996;11(4):795–802.

[98] Kim CJ, Kim K-B, Hong G-W. J Mater Res 1995;10:1605–10.

[99] Varanasi C, Black MA, McGinn PJ. J Mater Res 1996;11:565–71.

[100] Endo A, Chauhan HS, Egi T, Shiohara Y. J Mater Res 1996;11:795–803.

[101] Cima MJ, Flemings MC, Figueredo AM, Nakade M, Ishii H, Brody HD, et al. J Appl Phys 1992;72:179–90.

[102] Mori N, Hata H, Ogi K. J Jpn Inst Met 1992;6:648–55.

[103] Pamplin B. In: Pamplin B, editor. Crystal growth, science of the solid state. Oxford: Pergamon; 1980. p. 16.

[104] Kerr HW, Cissé J, Bolling GF. Acta Metall 1974;22:677–86.

[105] Fredriksson H, Nylen T. Met Sci 1982;16:283–94.

[106] Uhlmann DR, Chalmers B, Jackson KA. J Appl Phys 1964;35:2986–92.

[107] Bolling GF, Cissé J. J Cryst Growth 1971;10:56–66.

[108] Cissé J, Bolling GF. J Cryst Growth 1971;10:67–76.

[109] Cissé J, Bolling GF. J Cryst Growth 1971;11:25–8.

[110] Chernov AA, Temkin DE. Capture of inclusions in crystal growth. In: Kaldis E, editor. Current topics in material science, vol. 2. Amsterdam: North-Holland; 1977. pp. 3–77.

[111] Chernov AA, Temkin DE, Mel'nikova AM. Sov Phys Crystallogr 1976;21:369–73.

[112] Chernov AA, Temkin DE, Mel'nikova AM. Sov Phys Crystallogr 1977;22:656–8.

[113] Shangguan D, Ahuja S, Stefanescu DM. Metall Trans A 1992;23:669–80.

[114] Grigoryan SG, Oganesyan AS, Sarkisyan AG. Kristallografiya 1983;28:782–5.

[115] ötoschke JP, Rogge V. J Cryst Growth 1989;94:726–38.

[116] Fedorov OP. Interaction of crystals growing in the melt with inclusions and concentration inhomogeneities. In: Growth of crystals. New York: Consultant Bureau; 1992. p. 169.

[117] Rodriguez MA, Chen B-J, Snyder RL. Phys C 1992;195:185–94.

[118] Yamada Y, Krauns Ch, Nakamura M, Tagami M, Shiohara Y. J Mater Res 1995;10:1601–4.

[119] Kanamori Y, Shiohara Y. Phys C 1996;264:305–10.

[120] Cochran WG. Math Proc Cambridge Philos Soc 1934;30:365–75.

[121] Burton JA, Prim RC, Slichter WP. J Chem Phys 1953;21:1987–91.

[122] Cabrera N, Levine MM. Philos Mag 1956;1:450–8.

[123] Burton WK, Cabarera N, Frank FC. Philos Trans R Soc A 1951;243:299–358.

[124] Bennema P. J Cryst Growth 1968;3-4:331–4.

[125] Bennema P. J Cryst Growth 1969;5:29–43.

[126] Kanamori Y, Shiohara Y. J Mater Res 1996;11:2693–7.

[127] Tagami, Shiohara Y. J Cryst Growth 1997;171:409–14.

[128] Yao X, Kambara M, Umeda T, Shiohara Y. Jpn J Appl Phys 1997;36:L400–2.

[129] Rothman SJ, Routbort JL, Welp U, Baker JE. Phys Rev B 1991;44:2326.

[130] Rothman SJ, Routbort JL, Baker JE. Phys Rev B 1989;40:8852.

[131] Tallon JL, Staines MP. J Appl Phys 1990;68:3998.

[132] Tang TB, Lo W. Phys C 1991;174:463.

[133] Shi LT, Tu KN. Appl Phys Lett 1989;55:1351.

[134] Tu KN, Tsuei CC, Park SI, Levi A. Phys Rev B 1988;38:772.

[135] Oka A, Koyama S, Shiohara Y. Phys C 1998;305:213.

[136] Routbort IL. Phys C 1993;214:408.

[137] Tallon JL, Mellander B-E. Science 1992;258:781.

[138] Rudnyi EB, Kuzmenko VV, Voronin GE. J Phys Chem 1998:855.

[139] Kerrmitz E, Galkin AA, Olesch T, Scheurell S. J Therm Anal 1997;48:997.

[140] Claus J, Borchardt G, Weber S, Scherrer S. Phys Chem 1998;206:49.

[141] Tretyakov YD, Goodilin EA. Russ Chem Rev 2000;69:3.

[142] Kruger Ch, Conder K, Schwer H, Kaldis E. J Solid State Chem 1997;134:356.

[143] Bokshtein BS, Bokshtein SZ, Zhukhovitskii AA. Thermodynamics and kinetics of diffusion in solids. Moscow: Metallurgiya Publishers; 1973. translated from Russian, Amerind Publishing (1985) 310.

[144] Erb A, Greb B, Muller-Vogt G. Phys C 1996;259:83.

[145] Xie XM, Chen TG, Wu ZL. Phys Rev B 1989;40:4549.

[146] Bredikhin SI, Emelchenko GA, Shechtman VSh, Zhokhlov AA. Phys C 1991;179:286.

[147] LaGraff JR, Payne DA. Phys C 1993;212:470.

[148] Goodilin EA, Oleynikov NN, Antipov EV, Shpanchenko RV, Popov GY, Balakirev VG, et al. Phys C 1996;272:65.

[149] Tsukui S, Yamamoto T, Adachi M, Shono Y, Kawabata K. Phys C 1991;185:929.

[150] O'Sullivan EJM, Chang BR. Appl Phys Lett 1988;52:1441.

[151] Elschner S, Becket W, Bestgen H, Brand M. Phys C 1992;202:401.

[152] Shi D, Krucpzak J, Tang M, Chen N, Bhadra R. J Appl Phys 1989;66:4325.

[153] Bakker H, Westerveld JPA, Lo Cascio DMR, Welch DO. Phys C 1989;157:25.

[154] Bakker H, Westerveld JPA, Welch DO. Phys C 1988;153:848.

[155] Salomons E, de Fontaine D. Phys Rev B 1990;41(11):159.

[156] Ronay M, Nordlander P. Phys C 1988;153-155:834.

[157] Hong DJL, Mehta A, Peng P, Smyth DM. Ceram Trans 1990;13:129.

[158] Shiohara Y, Goodilin EA. In: Gschneidner Jr KA, Eyring L, Maple MB, editors. Handbook on the physics and chemistry of rare earth, vol. 30. Elsevier; 2000. p. 67 [Chapter 189].

[159] Shaw TM, Shinde SL, Dimos D. J Mater Res 1989;4:248.

[160] Lin CT, Chrosch J, Yan Y, Liang WY, Salje EKH. Phys C 1995;242:105.

[161] Rice JE, Ginsberg DM. J Cryst Growth 1991;109:432.

[162] Aizu K. Phys Rev B 1970;2:754.

[163] Schmid H, Burkhardt E, Sun BN, Rivera JE. Phys C 1989;157:555.

[164] Voronkova VI, Wolf T h. Phys C 1993;218:175.

[165] Asaoka H, Kazumata Y, Takei H, Noda K. Phys C 1996;268:14.

[166] Kutami H, Yamada Y, Koyama S, Nakagawa Z, Shiohara Y. Proc. ISS'96, Sapporo, Japan. In: Nakajima S, Murakami M, editors. Advances in superconductivity, vol. IX. Tokyo: Springer; 1997. p. 689.

[167] Rykov A, Jang A,WJ, Unoki H, Tajima S. Proc. ISS'96, Sapporo, Japan. In: Nakajima S, Murakami M, editors. Advances in superconductivity, vol. IX. Tokyo: Springer; 1997. p. 341.

[168] Oka A, Koyama S, Izumi T, Shiohara Y. Phys C 1999;314:269.

31 Crystallization in Gels

Abel Moreno[1], Ma Eugenia Mendoza[2]

[1]INSTITUTO DE QUÍMICA, UNIVERSIDAD NACIONAL AUTÓNOMA DE MÉXICO, MEXICO; [2]INSTITUTO DE FÍSICA, BENEMÉRITA UNIVERSIDAD AUTÓNOMA DE PUEBLA, PUEBLA, MEXICO

CHAPTER OUTLINE

31.1 Introduction **1277**
31.1.1 Gel Growth History 1280
31.1.2 Gel Properties and Characterization 1282
31.1.3 Diffusion versus Convective Transport 1285
31.1.3.1 Diffusion Coefficient and Size of the Clusters 1288
31.1.3.2 Experimental Methods to Evaluate the Diffusion Coefficient and the Gel–Matrix Interaction 1289
31.1.4 Gel Growth Applications 1294
31.2 Hydrogels, Organic Gels, and Aerogels **1295**
31.2.1 Synthesis and Characterization of Hydrogels and Organic Gels 1295
31.2.2 Synthesis and Characterization of Xerogels and Aerogels 1299
31.3 Crystal Growth in Gels of Small Molecules, Minerals, and Biological Macromolecules in Gels **1302**
31.4 General Remarks and Future of Crystal Growth in Gels **1302**
References **1307**

31.1 Introduction

The crystallization of biomacromolecular crystals is of increasing interest in different applications. To date, the growth investigations have been focused mostly on proteins due to their importance for medicine, biochemistry, biology, and biotechnology. However, applications in industrial or technological processes are also possible, such as an alternative to zeolites and in the development of molecular devices, such as solar cells (photovoltaics), using proteins [1]. Many works also have been devoted to the development of new nanodevices using of protein nanocrystals. At present, crystallized protein molecules are mainly investigated for the determination of their atomic structure by X-ray analysis. For that, additional efforts are focused on the further development of X-ray procedures to optimize data collection by using a variety of cryoprotectors. In

Handbook of Crystal Growth. http://dx.doi.org/10.1016/B978-0-444-63303-3.00031-6
Copyright © 2015 Elsevier B.V. All rights reserved.

addition to such improvements in the understanding of the crystallographic three-dimensional (3D) structure, there are certain works focused on increasing the understanding of the crystallization process. Even with precise X-ray diffraction (XRD) analysis, single crystals of high quality are required. Systematic studies on the interaction between chemical or physical growth variables and their influence on the yield of size and high structural quality are still rare. A review was published by Otalora and Garcia-Ruiz [2]; there is also a book chapter about crystal growth and the analysis of this crystal perfection using XRD [3].

High-quality single crystals of a size large enough for X-ray analysis are still difficult to achieve in 3D structure determination. However, novel methods have been recently developed to obtain crystals in small droplets, in a shorter time, using robotic drop-dispenser machines. There is also an additional effort focused on developing procedures to optimize the process of X-ray data using personal computers. Nevertheless, few works are focused on understanding the crystallization process and the kinetics of protein crystallization, or even the physical and chemical parameters that affect protein crystallization behavior. Only a few systematic studies are available to understand how these chemical and physical variables influence the outcome in terms of a crystal's size and high structural quality. It is well known that by reducing the convective transport, high-quality single crystals can be obtained. To achieve this objective, there are currently three main possibilities: (1) to grow crystals in microgravity conditions, (2) to grow crystals in thin capillary tubes, and (3) to grow crystals in gels.

A beneficial influence on the growth properties was expected from the fact that gels reduce convection in the growth medium, prevent sedimentation, suppress foreign nucleation, and reduce twinning [4]. Indeed, the number of nuclei and also the defects of the crystals were reduced. Most growth experiments in gels demonstrated structural and physical crystal qualities comparable with those of samples grown under microgravity conditions. Not yet clarified in detail is the nucleation step. Furthermore, theoretical treatments still have to incorporate the growth-specific gel properties.

Currently, there are two basic methods (at the atomic level) for determining the 3D structure of small molecules, including biological macromolecules: nuclear magnetic resonance (NMR) and XRD/neutron diffraction (ND). For the first method, the experiment needs to be performed in solution or solid state (amorphous powder); for the second method, millimeter-sized single crystals are needed (single crystals) or crystalline powder for proper biocrystallographic work. However, for a protein crystallographic project via single-crystal XRD, from nanometer-sized [1] up to millimeter-sized (for ND) crystals are necessary to know the 3D structure [5,6]. X-ray powder diffraction for proteins is not well-developed yet, although there have been some recent advances [7]. For biological macromolecules (proteins, nucleic acids, and polysaccharides), the larger the size, the higher the amount of mass that is required to obtain a proper crystal for X-ray crystallography.

Recombinant technologies based on gene expression using molecular biology techniques have allowed researchers to obtain recombinant proteins for this type of research,

as mass availability is no longer a limiting step within the crystallographic project [8,9]. Additionally, the use of synchrotron radiation facilities [10,11] has improved not only the time for data collection (exposing the crystals to less radiation damage), but has also reduced the crystal size (in the scale of microns) needed to obtain X-ray data for structural purposes.

In any of these cases, there is still a remaining issue, which is the bottleneck in protein crystallography: obtaining high-quality single crystals with near-to-perfect habits made of molecular arrangements with minimum defects that can produce well-resolved and intense diffraction patterns. There are three basic methods to grow crystals with these near-to-perfect characteristics; in all of them, the basic idea to obtain proper crystals for XRD is to minimize (or to eliminate) solutal convection. The first method is to grow crystals in microgravity conditions, although currently this requires very expensive equipment for the experiment and is a time-consuming procedure [12,13]. It has been demonstrated that crystals grown in gel and under microgravity conditions show higher crystal quality than earth-grown crystals [14]. The second possibility is to grow crystals in thin capillary tubes, with diameters less than 0.3 mm. This capillary method has been demonstrated to yield high-quality single crystals of a variety of biological systems, using either of two basic experimental setups: the gel acupuncture method [15,16] or the counterdiffusion method [17,18]. The third method is to grow crystals in gels. This method is the most practical and effective way to obtain high-quality crystals for X-ray crystallography, with a considerable improvement in the internal order of atoms and molecules that constitute the 3D crystal network. A gel is a semi-solid material rich in liquid, which contains a 3D structure full of pores where atoms or molecules can diffuse and work as multiple crystal growth cells. In gels, the transport control is driven by diffusion processes, as has been demonstrated in a variety of publications [4,19–23].

The improvement in crystal quality is thus independent from the M_r particle. These improvements in the crystal quality are attributed to the gel-growth method for the following reasons: (1) within the hydrogel, mass transport is essentially controlled by diffusion; and (2) the protein concentration gradient (depletion zone) generated by each crystal during its growth is not destroyed by density-driven convective flow or by sedimentation [24–26]. Whereas a very low concentration of agarose (0.04% m/v) in solution is sufficient to overcome buoyancy and crystal sedimentation, a slightly higher one (0.12% m/v) is required to obtain a viscoelastic gel and to avoid mass and heat convective transport [27]. In 0.15–0.5% (w/v) gels prepared at low ionic strength, the pore diameter ranging from 300 to 900 nm [28] is compatible with the diffusion of the greatest known icosahedral viruses. Pore size distribution is broader at lower concentration or at higher ionic strength [29,30]. The randomly distributed polysaccharide fibers revealed by scanning electron microscopy (SEM) might explain why they do not appreciably affect the diffraction quality of crystals [31]. In a gel, the pore network is confined by polymer chains that change their conformation as a function of temperature, solvent, concentration, pH, etc. Therefore, for a specific type of gel, the diffusion of the substance to be

grown and the growth process will depend on these physical and chemical variables. It is possible that anomalous diffusion can be observed when large particles become entrapped in the pores network [27].

31.1.1 Gel Growth History

The usefulness of gels for the crystallization of small inorganic compound crystals is well known. However, the crystal size and quality of many materials could be improved markedly. The first applications of gels to the growth of protein crystals were reported by Robert and Lefaucheux [22], Provost and Robert [32] and Miller et al. [33] in the late 1980s and early 1990s. The crystallization of inorganic molecules in gels dates back to the end of the 19th century, when inorganic compounds were crystallized in either gelatin or gels made of siloxane [4,21,22,34,35]. The pioneering experiment related to crystal growth in gels started in 1896 by Liesegang, who obtained for the first time a group of periodic rings of inorganic compounds grown in gelatin [36]. This early description of repetitive pattern formation by Liesegang focused on the chemical reaction occurring in gels between counterdiffusing electrolytes. Liesegang noticed that stratification of parallel precipitation bands originates from anions (outer electrolyte) diffusing in a capillary containing a gel impregnated with cations (inner electrolyte). The formation of bands resulting from the precipitation of the weakly soluble salt occurs rhythmically and is separated by clear gel instead of forming a continuous precipitation zone, as one would have expected. Wilhelm Ostwald was the first to propose an explanation for the phenomenon observed by Liesegang [37,38]. His hypothesis was based on the propagation of a supersaturation wave; it belonged to the prenucleation theories, in contrast to more recent postnucleation theories [39], in which repetitive patterns are produced in essentially homogeneous and continuous colloids. Both theories use equations derived from Fick's law of diffusion [39,40].

Liesegang patterns obtained in gels are routinely described by four laws: the spacing law [41], the time law [42], the width law, and the Matalon–Packter law [43]. An experimental setup similar to Liesegang's experiments in gel has been used for several decades for protein crystallization by the method of counterdiffusion in capillaries [16,18,44]. Crystals of biological receptors (Toll) as well as Liesegang-like patterns with rings formed of protein crystals using agarose gels have been reported [45]. However, for applications in the crystal growth of proteins, the gel-method started to be used conventionally to grow a variety of single crystals after it was proven to be useful to obtain high-quality crystals for X-ray investigations. The first report on the crystal growth of proteins (albumin) in gelatin was published in the mid-1950s [20]; it took a long time before hydrogels, inorganic-gels (mostly hydrogels), and organic gels (organogels) were reintroduced for protein crystallization [22,46,47]. At that time, the gel method led a nonconventional way to grow crystals, with fewer defects and higher crystal quality. Indeed, protein and virus crystals grown in such gels have enhanced diffraction properties, including sharper Bragg reflections, higher diffraction intensities with regard to

the background noise, and a higher diffraction limit with regard to that of crystals that are grown in solution [14,30,48]. Despite the discovery and plenty of publications related to the gel method and its benefits, protein crystal growers and protein crystallographers poorly exploit the gels [30,49].

Figure 31.1 shows the four basic techniques to grow crystals using the gel-growth method (as described in [4]). The first technique uses a U-tube; on it, two solutions containing two soluble salts A and B diffuse along both sides of the tube. Nearly in the central part, an insoluble salt C is crystallized. The second technique consists of having compound A inside the gel, and a solution of salt B is poured onto the top of the gel. When the diffusion of B throughout the gel is happening, the crystallization process of compound C takes place inside the gel network; this C compound is not soluble in water if the gel is a hydrogel. The third technique is a kind of chemical complexation or chemical decomplexation reaction. At the beginning, a soluble complex AB diffuses throughout the gel network; then molecule B is complexed with molecule D, forming a new compound. The final technique is basically a counterdiffusion process; both substances are included in the gel network, then both counterdiffuse. The place where the synthesis of the new compound will take place will be the area of the compound with the smaller diffusion coefficient.

Another powerful procedure to grow crystals of high quality is the application of magnetic fields to the crystal growth process, which has attracted increasing attention. Metals and semiconductors with relatively high electrical conductivity are subject to a Lorentz force when melt movements takes place. Natural convections and flow oscillations can be damped effectively, leading to structural and chemical homogeneity improvements of the growing crystals [50]. In the case of organic fluids (e.g., proteins)

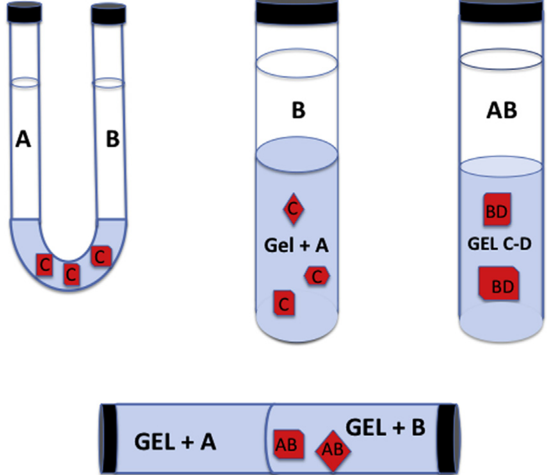

FIGURE 31.1 The four basic procedures to grow crystals in gels. The "U" tube was one of the first devices designed to grow insoluble salts. The other three techniques are use mostly to synthesize new compounds.

with much lower electrical conductivities, the question of the impact efficiency of a magnetic field arises. The existence of anisotropy of the diamagnetic susceptibility has been properly investigated in biological macromolecules, specifically protein molecules; from these, the anisotropy of diamagnetic susceptibility is high due to the existence of alpha-helices and peptide bonds. Here, the orientation/alignment effect comes to be very remarkable in terms of orientation and enhancement of crystal quality. Obviously, the positive effect is due to the alignment of the crystallization units within the magnetic field and the homogeneous transport mode in gel being an exclusively diffusion-controlled process. However, there are also some contradictory reports showing no influence at all, generally when the experiments are performed in solution and using a low-magnetic field. This fact requires further investigation of the decisive effecting parameters.

Pioneering works of the influence of strong stationary magnetic fields on protein crystallization were done by Sazaki et al. [51] and Ataka et al. [52]. A correlation to the crystal alignment within the field was found. Alternating magnetic fields have been also used [53]. An enhancement of the enzymatic reactions was also observed [54]. The first coupling of growth in gels with magnetic fields was carried out by Kinoshita et al. [55], aimed at the improvement of quality and harvest period of protein crystals for structure-based drug design. Using XRD, Lübbert and coworkers [56] analyzed rocking-curve measurements for the differences in mosaicity between lysozyme crystals grown with and without a homogeneous magnetic field of 2.4 T, as well as with and without agarose gel.

31.1.2 Gel Properties and Characterization

In general, a gel is defined as a semi-solid rich in liquid, with a pore-size distribution and structure that depends on the method of its preparation and chemical precursors [4]. Most gels display thixotropy, which is a property that turns them into fluid when agitated but causes them to resolidify when resting. Another property is syneresis, which is a chemical process related to the contraction of a gel accompanied by expulsion of liquid (in small amounts). Hence, the expelled water or organic liquid is called the water/solvent of syneresis. Most of the crystals grown in gels show higher crystal quality than those crystals grown in solution. For many years, direct observation of the gel structure in terms of the pore-size distribution was a difficult task for many researchers. One of the first images of these large pores was obtained at the end of the 1990s by Moreno et al. [26], by means of using SEM (see Figure 31.2).

It is well known that the pore size depends on the preparation conditions of the gels. For example, sodium silicate (SS) prepared by the neutralization method and tetramethyl orthosilicate (TMOS) or tetraethyl orthosilicate (TEOS) gels prepared by hydrolysis showed pores with sizes ranging from 50 to 150 nm for SS gels [26], and from 150 to 250 nm for TEOS gels [57]. The fact that bigger crystals are usually obtained in gels is explained in terms of the size of the pores. Different sizes of crystals are obtained in different types of

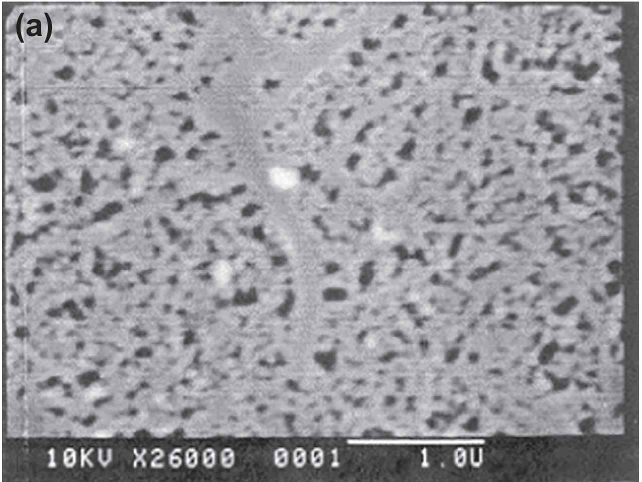

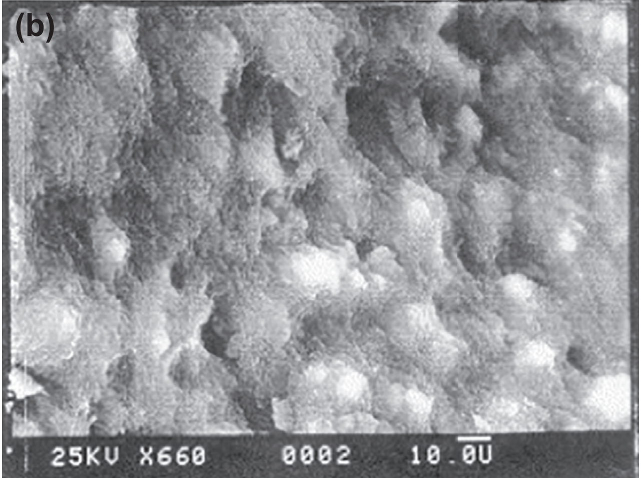

FIGURE 31.2 SEM micrographs of gels from sodium metasilicate solutions. They correspond to silica gel: (a) pH 6.0 and (b) pH 10. *Reprinted from J Cryst Growth 1999;205:375–81, with permission from Elsevier.*

gels, which is explained in terms of the relationship between gel preparation, transport processes, and pore size distribution. This has been demonstrated in previous publications focused on transport processes and protein nucleation control by varying agarose concentration [27]. The control of pore size distribution (randomly or homogeneous pore size distribution) was applied to control the number of protein crystals in the gel acupuncture setup [26]. This control, combining microgravity and gel growth, was also used to obtain large (1 mm from apex-to-apex) and high-quality single crystals of thaumatin grown in agarose gels [14]. These pores, which contain nuclei inside, work as large crystal growth cells. The mechanism of gel structure formation is different in SS or TMOS/TEOS gels. The TEOS gels, for instance, have a conglomerate of multifractal-like structure beads [57], whereas SS gels usually show a lumpy structure [26] (Figure 31.2).

Particularly, gels obtained from TMOS or TEOS hydrolysis are not easily characterized. Their characterization depends on expertise and on the technique used for this purpose. Figure 31.3 shows the peculiar shape of the pores (granular shaped) observed by coupling small angle X-ray scattering (SAXS), atomic force microscopy, and SEM techniques. These polysiloxane gels (TMOS or TEOS) are inert in most inorganics and organics, but sparingly inert for proteins usually prepared in pH buffer solutions. Besides this lack of inertness for biological macromolecules in water, smart mixing strategies allowed their successful use for proteins [21]; more recently, new synthetic strategies, using these TMOS gels compatible with a variety of buffer solutions (usually for proteins), have been published [58].

The first high-resolution micrograph of the structure of agarose gel via SEM of a red algal galactan of different sulfation levels was published in 2008 [59]. The most important characteristic of red algal galactans is their gel-forming ability—that is, the ability to form well-ordered spatial structures during cooling of their hot polymeric solution. The

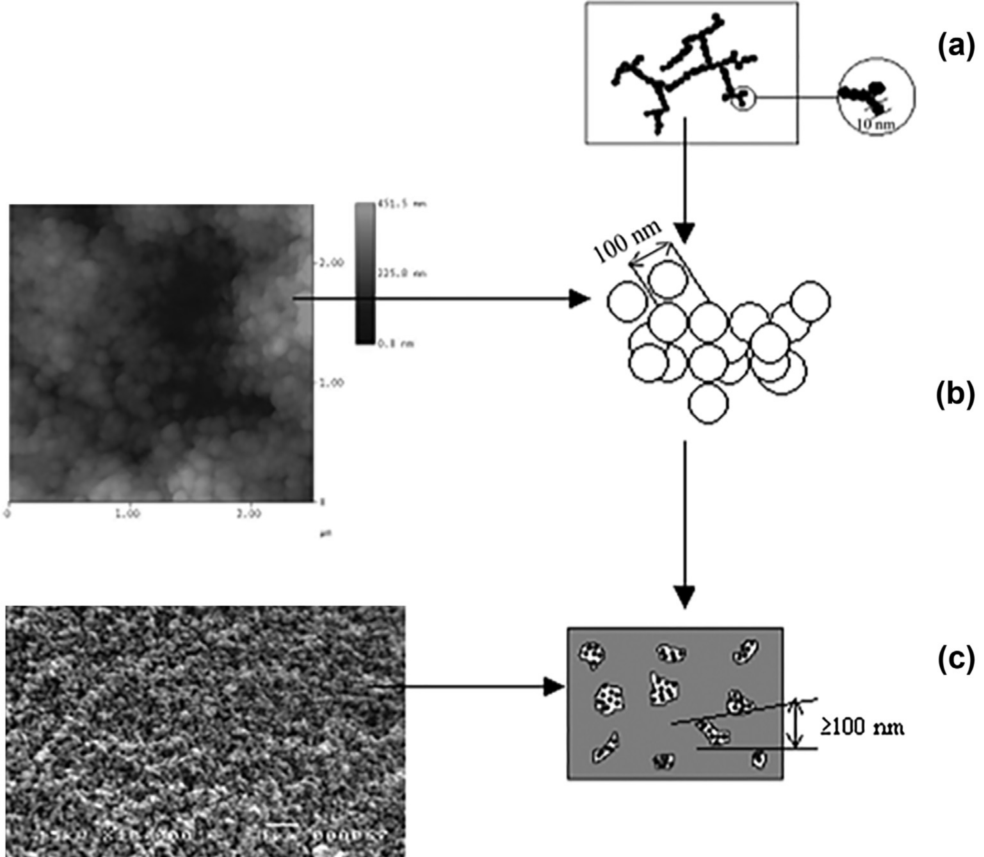

FIGURE 31.3 Multifractal investigation of TEOS silica hydrogels and aerogels. (a) First-generation clusters, as evidenced by SAXS measurements. (b) Second-generation aggregates from atomic force microscopy imaging. (c) Third-generation by SEM observation. *Reprinted from Silicon Chem 2003;2:247–54, with permission from Springer.*

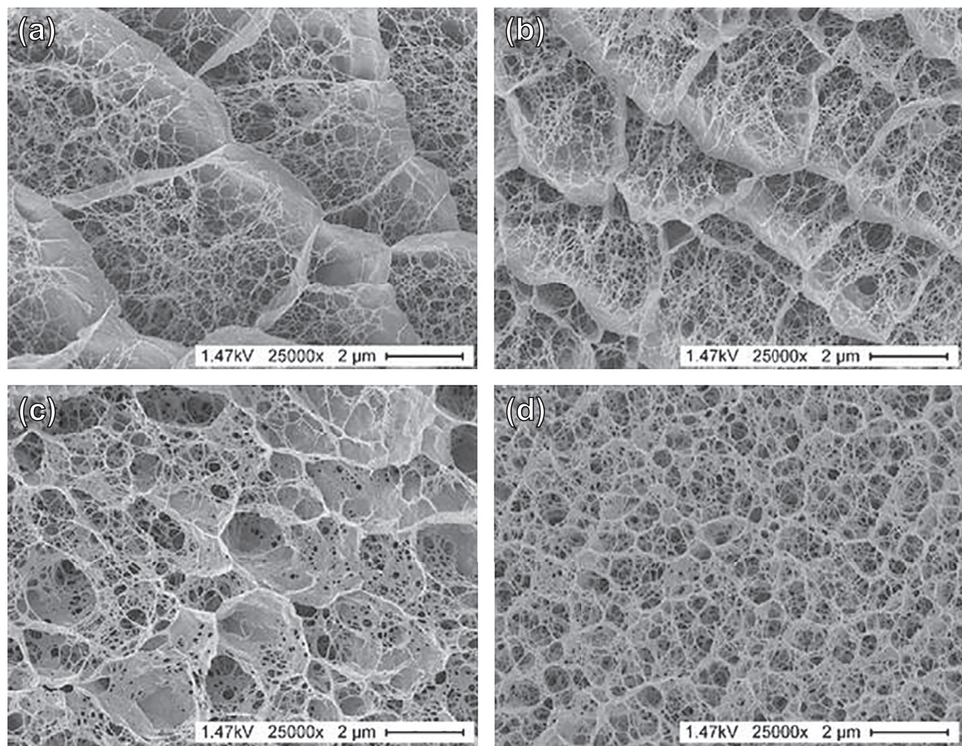

FIGURE 31.4 SEM images of 2% agarose gel network structures at (a) 70 °C, (b) 40 °C, (c) 30 °C, and (d) 20 °C. *Reprinted from J Appl Phycol 2008;20:527–35, with permission from Springer.*

pore-size distribution is in agreement with the models of gel formation described by Anderson et al. [60] for all types of agarose gels obtained from different algae. Figure 31.4 shows these images of low-melting-point agarose at 2% (w/v) concentration, and four different temperatures for gel preparation. It is important to remark that the agar is a mixture of two polysaccharides (agaropectin) and agarose, whereas agarose is a highly pure polysaccharide for hydrogel preparation (see Figure 31.4(d)).

Gels made from purified agarose have a relatively large and homogeneous pore-size distribution, making them useful for size separation of large molecules, such as proteins or protein complexes >200 kDa or DNA fragments >100 base pairs. These hydrogels are suitable for growing protein crystals and also to enhance the crystal quality for X-ray crystallographic research.

31.1.3 Diffusion versus Convective Transport

For growth to occur, the solute species must move from the bulk solution to the crystal surface, be adsorbed on the crystal surface, move to a step, and finally move to a kink on the step. If ionic species are involved, then dehydration and chemical reaction may also be required. The latent heat of crystallization must also move back into the solution because, in solution growth, the crystal is generally surrounded by the solution and there

is no sink within the crystal. The net effect is that the surface of the crystal must be at slightly different temperature from the bulk of the solution. The movement of solute from the bulk solution to the crystal surface by a combination of molecular diffusion and convection (solution movement) occurs under the general title of mass transfer. The processes that occur on the surface may be lumped together under the general title of surface integration [61].

When a crystal is grown in solution, it takes the solute from the solution, thus reducing the concentration of the solution around it. To allow the crystal to keep growing, fresh solute concentrations must be withdrawn from the bulk of the solution, and lead molecules have to move toward the crystal surface of the growing crystal. This motion of the solute is usually referred to as the mass transfer process. In the absence of convection in the bulk of the solution for a gelled system, these molecular motion processes cause mass transference in a controlled manner. These processes are very slow in solids and in gels and sparingly slow in liquids, so any small amount of convection is more than enough to increase the velocity of mass transfer. When the system is in thermodynamic equilibrium, the velocity of mass transfer toward the crystal surface should be exactly like the incorporation of the solute molecules inside the crystal. This velocity is governed by surface processes, the kinetics of mass transport, or both. If the convective transport increases, there is a reduction of the mass transport resistance; then, the influence of the surface kinetics on the crystal growth increases [62].

The crystal growth process depends on transport phenomena such as fluid motion (convection), heat, and mass transfer. All these processes have a strong influence on the crystal growth velocity, crystal morphology, and defect formation, even in gel growth [26,63,64]. Mass transfer, for instance, comes from the concentration gradients, but it can be also caused by thermal gradients (called the Soret effect), electric or magnetic fields, gravity forces, or gravity acceleration. In general, mass transfer in solutions increases due to convective transport; the motion of the solution itself carries out material from the solution. Several driving forces can cause convective transport, such as pressure gradients, mechanical forces, levitation, and electric fields, even by the crystal growth process per se. Convective transport deals with the transport in three directions of any physical property due to fluxes in different directions; we can say then that there is a convective flux [17,21]. On the other hand, the flux growth is the name given to crystal growth from high-temperature solutions, where the flux is typically a molten salt or oxide used as solvent; this method is used to grow single crystals of incongruently melting compounds [65]. The principle of flux growth does not differ significantly from that of growth in solution: temperature is higher and related to the melting temperature of the flux (solvent).

Crystal morphology depends on the kinetics of different faces of a crystal. Surface kinetics and resistance to mass transference are different for each face of the crystal. The crystal habit depends on mass transport and can depend on the amount or on any direction of convective transport inside the solution. The crystal quality will depend also on these transport processes. To increase this crystal quality, from the beginning, the crystal growth process should proceed through diffusion control. Adolf Fick empirically

obtained the basic equations for diffusion transport in 1855; these equations are equivalent to the thermal conductivity proposed by Fourier in 1822, which states that the time rate of heat transfer through a material is proportional to the negative gradient in the temperature and to the area, at right angles to that gradient, through which the heat is traveling [66].

The diffusion of macromolecules through a porous medium is important in many fields of the biological sciences. The phenomenon is relevant to biotechnological separation methods, such as electrophoresis and size exclusion chromatography. Moreover, it has important implications for understanding how macromolecular drugs and naturally occurring macromolecules are transported in living tissue. Diffusive transport is the process by which the matter is transported from one part of the solution to another via random motion at the atomic or molecular scale. In this process, atoms or molecules travel in one direction, eliminating concentration differences and making the concentration homogeneous around crystal growth. These atoms or molecules can be set in motion by applying voltages or external forces to the system [39,40,67].

Table 31.1 shows a comparison of diffusion coefficients in water and in gels for some ions, low-molecular-weight organic compounds, and high-molecular-weight organic compounds such as proteins, ribosomes, and virus particles. In some cases, the diffusion

Table 31.1 Comparison between Diffusion Coefficients of Some Molecules in Water and in Gels

Substance or Biomolecule	M_r (g/mol)	Diffusion Coefficient (cm^2/s) in H_2O	Diffusion Coefficient (cm^2/s) in Gel	References
Cl^-	35.45	2.03×10^{-5}	7.22×10^{-6}	[4]
K^+	39.10	1.98×10^{-5}	2.64×10^{-6}	[4]
KCl	74.50	1.92×10^{-5}	0.493×10^{-5}	[4,68]
Glycerol	92.00	1.3×10^{-5}	2.37×10^{-6}	[69]
Glucose	180.16	7.00×10^{-6}	1.55×10^{-6}	[70]
Sucrose	342.30	5.23×10^{-6}	1.04×10^{-6}	[70]
Ribonuclease	12,640	1.31×10^{-6}	1.20×10^{-6}	[68,71,72]
Lactalbumin	14,178	1.14×10^{-6}	2.37×10^{-7}	[72–74]
Lysozyme	14,500	1.18×10^{-6}	1.04×10^{-6}	[72,75,76]
Thaumatin	22,000	9.40×10^{-7}	N.A.	[72]
Ovalbumin	45,000	4.20×10^{-7}	1.60×10^{-7}	[72–74]
Bovine serum albumin (pH 6.78)	67,000	6.40×10^{-7}	2.45×10^{-7}	[68,72–76]
γ-Globulin	170,000	4.60×10^{-7}	4.4×10^{-7}	[72,77]
Apoferritin	440,000	3.20×10^{-7}	2.50×10^{-7}	[72,78,79]
Ribosome 70S *Escherichia coli*	3,000,000	1.83×10^{-7}	N.A.	[72,80,81]
DNA	6,000,000	1.30×10^{-8}	1.0×10^{-8}	[72]
Satellite tobacco mosaic virus	50,000,000	1.07×10^{-8}	6.00×10^{-10}	[72,82]

N.A. = Not available.

coefficient varies by even one or two orders of magnitude. It is clear that in the particular case of diffusion in gels, the transport and pore size distribution of molecules along the gel network depends on the concentration or method of synthesis of the gel.

31.1.3.1 Diffusion Coefficient and Size of the Clusters

Diffusion of particles in gels is one of the most important issues in transport processes. The molecules are in constant motion; their trajectory from the center of the mass is described in terms of a vector, R(t). If the origin of the coordinates is selected as the location of the particle at $t = 0$, the square displacement is given by $R \times R$. If the trajectory is followed many times for some elapsed time τ, the mean-square displacement is found to be proportional to the elapsed time. The Brownian diffusion law is

$$<R^2> = 6D_s\tau \tag{31.1}$$

where D_s is the self-diffusion coefficient. If the particle is a sphere of radius R_h, the self-diffusion coefficient is inversely proportional to R_h and directly proportional to the temperature of the solution. The explicit formula for the self-diffusion coefficient can be calculated by the method of Brownian dynamics [83].

The solvent is treated as a viscous continuum of dynamic viscosity η and absolute temperature T. A particle in such a solution is subjected to three types of forces: (1) viscous force; (2) external forces, such as gravity, electrical fields, or magnetic fields; and (3) a random movement of ions, atoms, or molecules. On the other hand, the mean-squared displacement of a particle in a solution subjected to no external forces can be expressed as

$$<R_h^2> = 6\left[(k_bT)/\varsigma\right]\tau \tag{31.2}$$

where k_b is the Boltzmann constant and ς is the friction coefficient for a spherical particle given by

$$\varsigma = 6\pi\eta R_h, \tag{31.3}$$

hence, it is a consequence within the limit of the length of elapsed time. This means that the self-diffusion coefficient of a particle in solution is

$$D_s = k_bT/\varsigma \tag{31.4}$$

This last equation is well known as the Stokes–Einstein equation. However, for a particle of arbitrary shape, it is customary to define the hydrodynamic radius in terms of the measured friction coefficient, as follows:

$$\varsigma = 6\pi\eta R_H \tag{31.5}$$

So, finally, the Stokes–Einstein equation becomes in its conventional form:

$$D_s = k_bT/6\pi\eta R_H \tag{31.6}$$

This equation is very useful for investigations related to dynamic or static light scattering methods [84]. By measuring the diffusion coefficient in protein solutions, we could derive the hydrodynamic radius and, as a consequence, the growth of the embryo can be experimentally detected. However, by means of Fick's laws, the diffusivity or diffusion

coefficient can be estimated. Then, Kratochvil's equation [85] can be used to measure the molecular weight of any biological macromolecule, the protein–protein interactions (based on the second virial coefficient) and the radius of the cluster can be investigated [84], all based in the Brownian motion of macromolecules.

In that sense, the determination of the diffusion coefficient of small and large biomolecules by means of different modern techniques is crucial to investigate, not only for transport phenomena research in biological systems, but also to measure useful and important parameters in protein crystal growth research.

31.1.3.2 Experimental Methods to Evaluate the Diffusion Coefficient and the Gel–Matrix Interaction

The purpose in this section is to review some of the experimental methods used in recent years to evaluate the diffusion coefficient and the molecule–gel matrix interactions, as well as the theoretical and the numerical models used to explain these experimental results.

31.1.3.2.1 EXPERIMENTAL METHODS

The experimental methods are generally based on the utilization of at least one appropriate chemical probe. This chemical probe is introduced into the gel to measure one physical property that is related, either directly or indirectly, to the diffusion of the probe. These experimental methods can explore the gel matrix–molecules or the ions, as well as their interactions at a microscopic level. They can therefore show us different parameters in real materials, such as the heterogeneity of porosity and the chemical composition, etc.

I. Single molecule spectroscopy, also called single molecule tracking methods, includes several methods such as beam- and sample-scanning confocal microscopy and wide-field imaging. The molecule probe is usually a dye. The detection of isolated molecules is achieved by using nanomolar (nM) concentrations ranging from approximately 0.01 to 1 nM of the dye probe, and an ultrasmall detection volume of approximately 1 fL. In sample-scanning experiments, the emission features, either time- or spectrally resolved, are registered for each spot. On the other hand, in wide-field imaging experiments, the motion of individual molecules in space and time are registered, taking several images of the same area [86,87]. The effect of confinement in the orientational motion of probe molecules in nanosized pores is performed by single-molecule emission and transmission dichroism. The experiments must be performed simultaneously in two orthogonal polarizations [88] (Figure 31.5).

These techniques have helped researchers to determine that the main interactions between gel matrix components are ionic, hydrogen bonding, and have hydrophobic and steric effects. In silica gels, the ion interaction happens between the deprotonated silanol sites on silica surface and the cationic part of the probe molecules. Data analysis of single molecule trajectory and orientation is performed by orthogonal regression methods [87–89].

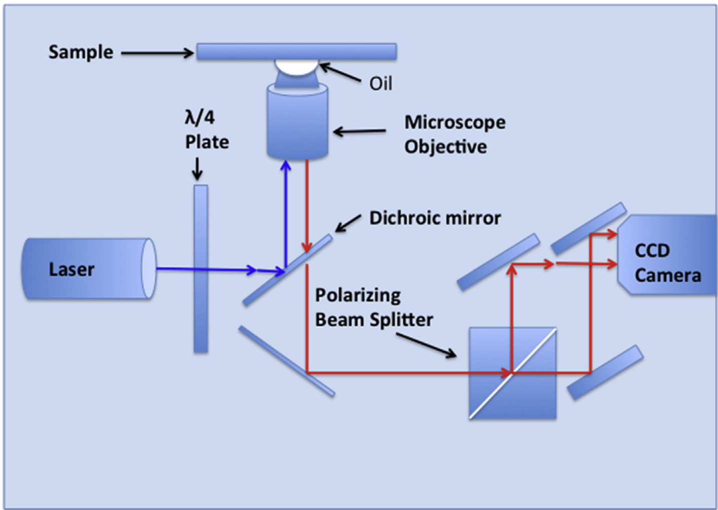

FIGURE 31.5 Schematic setup for the single molecule tracking method. *Reprinted (adapted) with permission from Rajib Pramanik, Takashi Ito and Daniel A. Higgins. J. Phys. Chem C 2013,117, 3668-3673. Copyright 2014, American Chemical Society.*

II. Electron spin resonance (ESR) and electron paramagnetic resonance (EPR): ESR or EPR methods are based on the strong environmental dependency of the electronic properties [89–91]. This makes it suitable for the study of confined species in porous media. In this method, the sample is exposed to a variable magnetic field in order to split the spin states of unpaired electrons. The separation between the lower and the higher energy states is given by $\Delta E = g_e \mu_B B_0$, where g_e is the g-factor = 2.0023 for the free electron, μ_B is the Bohr magneton, and B_0 is the strength of magnetic field. By either absorbing or emitting a photon of energy $h\nu$, an unpaired electron can move between the two energy states, obeying the resonance condition $\Delta E = h\nu = g_e \mu_B B_0$. The frequency (9–10 GHz), and the magnetic field (0.35 T) are usually employed in EPR or ESR experiments (Figure 31.6).

One important drawback of this method is the need of at least one unpaired electron in the sample paramagnetic species that is called a *spin probe*. The use of either ESR or EPR to investigate surface interactions in mesoporous materials, employing functionalized spin probes such as molecular nitroxides or 3-carboxy-proxyl, has enabled researchers to estimate the surface interaction enthalpies, the rotation correlation times, the rotation activation, and the position within the pore. These methods are sensitive to changes in polarity and in microviscosity around the paramagnetic group, and have also been used in the study of organogels. Only the amino-TEMPO spin probe was sensitive to the diffusion process in the organogel 12-hydroxystearic acid (12-HSA). However, EPR or ESR spectra were independent of the 12 Human Serum Albumin (12-HSA) concentrations [92].

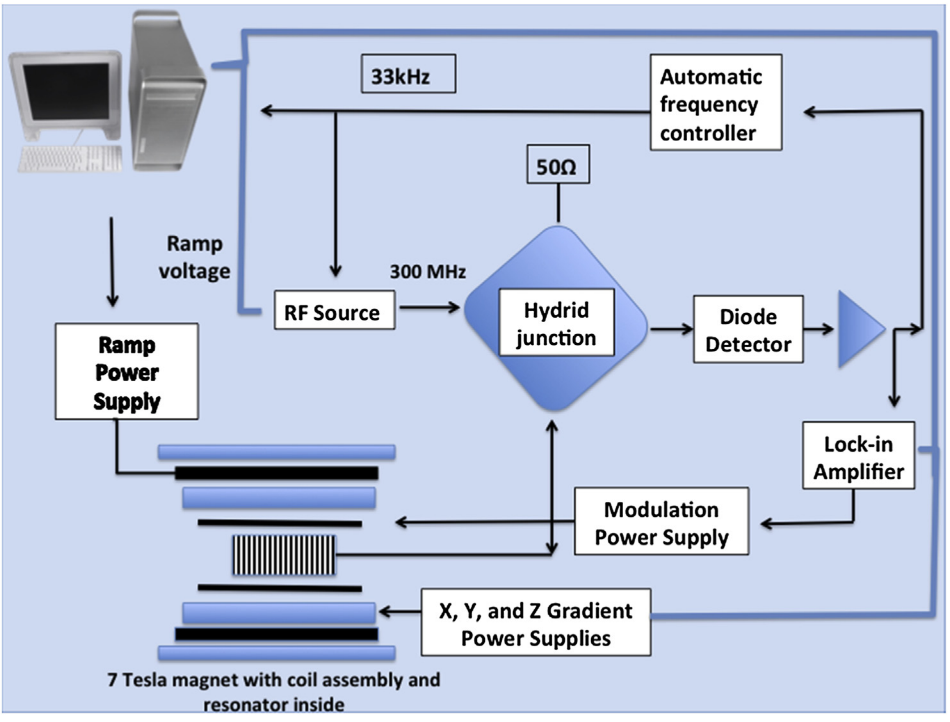

FIGURE 31.6 General setup for Electron Spin Resonance (ESR). *Reprinted (Adapted) with permission from reference A J Fagan, D J Lurie Annual Reports on NMR Spectroscopy 56 (2005) 97-140.*

III. Electron spin resonance imaging (ESRI), a method associated with ESR, has been used to study the distribution of paramagnetic molecules in the sample along the direction of the magnetic field gradient, additionally to the external magnetic field generated in the spectrometer. The spectrum measured under these conditions is a superposition of the spectra of all individual paramagnetic molecules in various positions inside the sample. ESRI allows the study of the diffusion process of a paramagnetic probe from the surface of the sample, by applying the magnetic field gradient in the direction of diffusion. Some of the spin probes used were low-molecular-weight nitroxide and spin-labeled poly(ethylene) oxide (PEO) oligomers, in 2-hydroxyethyl methacrylate (HEMA) hydrogels. It has also been found that the diffusion coefficients depend on the molecular weight of the spin probe, where the systems studied were three different probes in three hydrogels, prepared with different ratios of HEMA and 2-(2-hydroxyethoxy)ethyl methacrylate monomers. Other experiments were performed to determine the diffusion coefficients of low-molecular-weight probes in polystyrene gels cross-linked to various degrees and swollen with the same solvents. Here, the most important result was the dependence of the diffusion coefficients on the degree of crosslinking of polystyrene [93].

IV. Pulsed magnetic gradient spin echo is a method that allows measurement of the displacement of the observed spins by means of the attenuation of the echo signal that arises from the echo pulse sequence containing a magnetic field gradient pulse in each period [67]. Self-diffusion and mutual diffusion coefficients of small analytes in hydrogels have been measured by ^{13}P-NMR. It was found that the coefficients were also reduced by 30%, similarly to those measured in solutions. This could be due to the interaction at the molecular level. Another result shows that, at the mesoscopic level, the open structure of the gel has little influence [94]. The study of rotational and translational motion of the cationic-end of the ionic liquid 1-buthyl-3-methylimidazolyum-bistrifluoromethylsulfonimide, in bulk and confined in mesoporous silica, has recently been reported by pulsed field gradient NMR experiments. These experiments show that the rotational and translational motions of the ionic liquid are reduced at the silica surface, thus allowing the estimation of the mole fractions of fast (bulk) and of the slow populations of the ionic liquid in the partially filled pores of silica [95].

V. NMR imaging is a method in which the spatial resolution is obtained by a magnetic field gradient. A magnetic field gradient G is superimposed to a static field B_0. The frequency ω is shifted, whereas the spatial coordinate corresponds to the resonance frequency of the signal, such that $\omega = \gamma(B_0 + G)$, where γ is the gyromagnetic ratio. Therefore, for ω for a given spin, there is a function of the identity of the spin and of the local field. In NMR-I experiments, the frequency axis is considered as space axis by applying the gradient field in the direction of the desired profile. In the case of a 3D image, however, this has to be done in the *x*, *y*, and *z* directions. The spatial resolution depends on the power of the gradient field and on the width of the resonance line. The magnitude of both parameters in polymer gels is 500 mT/m and $\Delta\omega$ between 0.1 and 2 kHz, given a spatial resolution in gels on the order of 50 μm [96] (Figure 31.7).

31.1.3.2.2 THEORETICAL AND NUMERICAL SIMULATIONS

Hydrodynamic convection is eliminated in gel systems. Several physical obstacles as well as several chemical species can be immobilized in a gel matrix. Charged gels can interact electrostatically with ions prodding changes on their diffusion coefficients [97]. Dynamic surface tension analysis (in agarose gels) showed that the gel network inhibits the nucleation of lysozyme. This was observed by the enhancement of the repulsion and the interfacial structure mismatched between foreign bodies and lysozyme crystals. This produces a reduction of the diffusion process of the protein molecules that cluster towards the crystal–fluid interface, where their rearrangement is inhibited [98]. On this contribution, a detailed study of the kinetics of surface assembly in agarose based on a two-dimensional self-assembly mechanism has been performed.

Another method that we have reviewed is the lattice Boltzmann method (LBM), which is a numerical method used in computational fluid dynamics. Kang et al. extended the LBM method to pore-scale system, including advection, diffusion, homogeneous, and

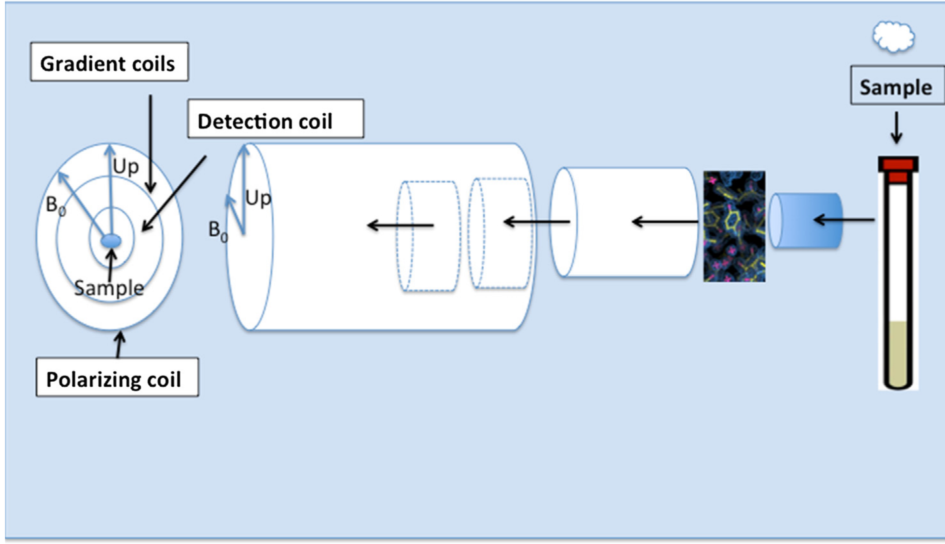

FIGURE 31.7 Schematic arrangement for nuclear magnetic resonance (NMR) imaging. *Reprinted (adapted) with permission from A Mohoric, G Planinsic, M Kos, A Duh, and J Stepisnik Instr. Sci. Technol. 32 (2004) 655.*

heterogeneous reactions, resulting in geometrical changes in pore space (cited in [98,99]). The porous structure of the gel matrix provides the nucleation sites for the heterogeneous nucleation of C, an intermediate colloidal phase. A lower gel concentration (or larger porosity) means fewer nucleation sites [98].

Numerical simulations techniques are very useful tools to support experimental data, even in complex systems such as gels. It is possible to classify them into two groups: those concerning the calculation of atomic-scale interactions that underlie the formation of the gel network and others that are focused on mass transport in the system. In the first group of methods, the gels are considered as a low-density disordered fractal network of interactive molecules with slow relaxation dynamics at low temperatures.

Molecular dynamics (MD) simulations have been used to simulate polymerized silica aerogels with a reactive charge transfer of three-body interaction potential. The calculated fractal dimension depends on the process by which the network is generated [100]. Another example of MD is the study of equilibrium and nonequilibrium routes to gel formation in a wide region of volume fractions of the dispersed phase. This was considered as the anisotropy of interactions, showing that the Arrhenius-type decay for the diffusivity was due to the bonding between colloidal particles [101]. The out-of-equilibrium gels have been explored by MD, constructing a fractal initial configuration by means of a purely kinetic particle diffusion algorithm, considering later an interaction potential between the particles and allowing the relaxation of the initial structure, which is finally followed by the dynamic of the system by means of constant-temperature MD [102]. An alternative approach to equilibrium dynamics was performed by modifying the three-body interactions of the Stillinger–Weber potential for

silicon; the aforementioned interactions can be expressed in terms of angles formed by triplets of particles, which stabilize open network structures in which the particles have very small connectivity [103].

Monte Carlo (MC) simulations of diffusion of nanoparticles in agarose gels have been reported to evaluate the fractal exponent of diffusion, its variation with the reduced hydrodynamic radius R_A/R_C. A systematic offset of the experimental fractal exponent of diffusion as compared to MC simulations could be related to nonspecific van der Walls interactions between diffusing particles and the polymer network [104,105].

Brownian simulation of solute diffusion in a 3D polymer hydrogel structure was reported by using an adaptive time stepping algorithm. The obstruction effect from the gel strands of water and diffusion of dendrimers of different sizes were determined by simulations. The interactions between dendrimers and the gel matrix were done by means of a sticky boundary condition [106].

Mass transport. One interesting contribution to the problem of simulation of mass transport in gels has been published by Zhang et al. [107]. Considering that mass transport is possible due to the elastic properties of the 3D network that enable the gel to retain its shape after deformation, and to the fact that the solvent molecules interact between themselves and with the gel network by physical bonds, a finite method element approach was finally developed. The authors combine some aspects, such as the kinematics of the network, the conservation of the solvent, the conditions of local equilibrium, and the kinetics of migration. The method is implemented in ABACUS/ standard finite element program.

pH-Redox-Equilibrium (PHREEQC) is a program used to simulate mass transport in complex multicomponent systems. The numerical simulation is performed as a function of time-dependent ion concentration gradients and saturation indices. This depends on the initial location of the calcium carbonate precipitate in the additive-free experiment, as well as on the study of the crystallization parameters of calcium carbonate in an agarose viscous sol by using counterdiffusion experiments [108].

31.1.4 Gel Growth Applications

Inorganic gels are widely studied for applications in daily lives [109], catalysis [110], electronics [111–113], thermal insulation [114], sensors [115], ceramics [116], protective and optical films [117], molecular separation [118], and pharmaceuticals [119,120]. Tetra-alkoxysilanes particularly have been used as starting materials for preparing glasses and glass ceramics by the sol–gel process and advanced silica-based materials [121,122].

Hydrogels and organic gels that limit the diffusion of solutes and of proteins have numerous applications in different areas, not only for protein X-ray crystallography but also for biotechnological fields ranging from cell encapsulation, through chromatographic separation, to controlled drug delivery in pharmaceuticals. In all of these applications, the hydrogel acts as a means of retarding the diffusion of the molecule

[123]. Other types of gel applications are, for instance, polyacrylamide gels used as dialysis membranes [124–126]. In biochemistry, agarose gels and polyacrylamide gels have been used for direct protein crystallization in the gel electrophoresis setup [26,46]. Agarose gels have been used to control the transport processes in microgravity experiments for protein crystallization [14] and for the orientation of crystals in the presence of strong magnetic fields [50,127], as well as to grow membrane proteins [128,129] to crystallize biomacromolecular complexes, such as the Toll receptor of *Drosophila melanogaster* to obtain Liesegang-like patterns [45]. One application of the gel method has been the reinforcement of protein crystals, incorporating silica fibers (TMOS gel) inside the crystal network, which can be very useful in nanobiotechnological applications and to protect crystals against radiation damage [130].

Novel and practical strategies have been published to apply classic gels to small organic molecules [131], and even to biological macromolecules, using TMOS/TEOS hydrogels [58]. Agarose gels have been used to promote nucleation at different concentrations, ranging from 0.4% to 0.8% (w/v) for protein crystallization [132]. The first suggestion about the use of agarose gels for protein crystallization dates back to the end of the 1990s [47]. The use of agarose gel with different types of additives, compatible with a variety of biological macromolecules for crystallization, was published afterwards [133]. One interesting application for protein crystallization was to screen directly in a gel electrophoresis set up using acrylamide gels [26]. Particularly, for the crystallization of proteins, nucleic acids, and viruses, a full review with plenty of recipes for gel preparation has been published [30]. Novel organic gels based on polyvinyl alcohol (PVA) and PEO have been suggested for the crystallization of soluble proteins and membrane proteins [129]. Organic gels, such as PEO, have been synthetically optimized. The PEO gel was has been suggested for crystal growth in gelled organic solvents of small molecules, either for organic or inorganic compound crystallization [131].

31.2 Hydrogels, Organic Gels, and Aerogels

31.2.1 Synthesis and Characterization of Hydrogels and Organic Gels

Gels are classified as physical or chemical gels when the temperature is the main parameter to be considered for the gelling process or a chemical reaction is carried out for the gelling process, respectively. The synthetic pathways to obtain hydrogels from the neutralization of SS solution are as follows:

$$\mathrm{Na_2SiO_3 + 3H_2O = H_4SiO_4 + 2NaOH} \tag{31.7}$$

$$\mathrm{2H_4SiO_4 \rightarrow (HO)_3{-}Si{-}O{-}Si(OH)_3 + nH_2O} \tag{31.8}$$

$$\mathrm{\rightarrow\rightarrow\rightarrow ((HO{-}Si{-}O)_n{-}Si)){-}(O{-}Si{-}OH)_n + nH_2O} \tag{31.9}$$

or by hydrolysis of TMOS or TEOS (Moreno et al., 1999):

$$Si(–O–CH_2–CH_3)_4 + H_2O \rightarrow H_4SiO_4 + nH_2O + EtOH \quad (31.10)$$

Then;

$$2H_4SiO_4 \rightarrow (HO)_3–Si–O–Si–(OH)_3 + nH_2O \quad (31.11)$$

and finally

$$\rightarrow\rightarrow (HO–Si–O)_n–Si–(O–Si–OH)_n + nH_2O \quad (31.12)$$

This reaction is the same for:

$$Si(–O–CH_3)_4 + H_2O \rightarrow H_4SiO_4 + nH_2O + MeOH \quad (31.13)$$

In both cases (reactions (31.10 and 31.13), the polymerization reaction is a two-step process: hydrolysis (rapid, stirring needed) and polycondensation (slow, solidifies when resting).

Physical gels: Algal polysaccharide agarose forms a thermo-reversible gel; its chains melt above a critical temperature (T_m) and gellation occurs below a characteristic temperature (T_{gel}, gelling point) [134]. Miller et al. [30] used agarose to grow crystals of horse serum albumin in the laboratory, which were of large size and excellent crystallographic quality and almost as good as crystals grown in solution under microgravity, where the driving gradient is limited by the concentration of the solute rather than by the heat gradient (called solutal convection) [30]. Afterwards, crystals of small model proteins grown in agarose gel have been reported to be frequently bigger and always better than reference crystals grown in solution. The former are well-facetted and develop in three dimensions because they are trapped in the network and cannot sediment, have excellent optical properties and have less defects in their lattices, as indicated by their smaller mosaicity, or are not twinned at all [135–139].

The limits for minimization of the impurity effects on the agarose network [140,141], through the formation of a stable impurity depleted zone surrounding the growing crystal [64,142], have been investigated. To characterize the threshold of impurity that can be segregated in a 0.2% m/v gel, an isoform present in trace amounts in thaumatin batches served as a marker. Mass spectrometry analyses have been performed to verify the ratio of two isoforms present in a single batch of thaumatin [143]. In other words, the impurity filtering effect operates only if structural dissimilarities are strong enough. This was the case of hen and turkey lysozymes that have a close M_r (14,313 vs 14,209) but differ by seven amino acids by a net charge of 1, and consequently in solubility [140]. Another example where the effect is amplified is that of ironless apoferritin contaminated by dimers of holoferritin, where each particle contains about 4500 iron atoms [142]. Whether agarose was working as an impurity or an impurity filter was clarified by using laser confocal microscopy combined with differential interference contrast microscopy [144].

Chemical gels: Polysiloxane hydrogels have been used for many years as a crystal growth medium [4] because their porous network permits diffusion of ions and large polymers, such as polyethylene glycols. They have been applied less frequently than

agarose because a chemical reaction is needed. Several macromolecules, including proteins, a virus, and an RNA transfer, have been crystallized in such gels [145,146]. Extensive studies on the model protein, hen lysozymes, have shown that crystal growth in polysiloxane hydrogels minimizes the effects of impurities [140]. Small-angle neutron and quasi-planar X-ray topography investigations have indicated that the gel inhibits nucleation partially [47] and decreases mosaicity [147]. In counterdiffusion or batch conditions, incorporation of the polymer into the crystal lattice at high gel concentrations (2–22%) reinforces the crystals [148]. Furthermore, polysiloxane hydrogel appears to be more effective than agarose [146]. In the peculiar case of hen lysozyme, crystals grown in the former have a lower mosaicity than those grown in agarose [147].

Moreno et al. [26] determined the pore size distribution of the flexible polymer network obtained by neutralization of sodium metasilicate using SEM (Figure 31.2). They found that pore diameter ranges from 50 to 150 nm. Hydrogels formed at pH 10 have a more homogeneous pore-size distribution than those formed at pH 6. The pore in TMOS hydrogels at 10% and 20% v/v measure 150–250 nm and 50–100 nm, respectively [26]. In the gel acupuncture method, this property of the gel matrix has been exploited to control the diffusion of the precipitant and, consequently, the nucleation rate of thaumatin crystals in solution within cylindrical capillaries [26]. SAXS analyses on TEOS hydrogels have shown that their pore-size distribution is random; their polymerization occurs via the interaction of particles whose size and fractal dimension depend on the synthesis pathway and on the final location of the latter between the surface and the heart of the gel [57,149].

A typical classification of gels in general can be summarized as follows:

GELS
- **Physical Gels** (Like agarose, PVA, gelatin, Gel Gro®)
- **Chemical Gels** (Like SS, TMOS/TEOS, acrylamide, etc)

The second classification is related to the nature of the chemical structure (i.e., atoms or molecules chemically bound to form an inorganic or an organic gel network). This depends on the chemical structure of the chain of the polymer.

GELS
- **Inorganic** (SS, TMOS/TEOS, etc)
- **Organic** (Agarose, acrylamide, carboxymethylcellulose, etc).

Novel organic hydrogels: Novel gels (other than agarose and polysiloxanes), such as PVA and PEO, have been suggested for the crystallization of a variety of compounds (including proteins), which can be dispensed into the medium prior to crystallization and easily removed from crystals [129,131]. For each of these gels, the solubility, the concentration required, the corresponding pH, and the effect of pH neutralization

should be determined. Particularly, for applications in the crystallization of biological macromolecules, compatibility with the growth medium is a highly complicated task. Investigations have concentrated on the synthesis and compatibility of PEO gels for the crystallization of small organic molecules [131]. The synthesis pathway to obtain PEO gels, which are promising gels for the crystallization of complex organic or organometallic compounds, follows.

HO–(CH2CH2–O–CH2CH2)n–OH → 1) 1,2-dichloroethane 2) Mix with any organic solvent → **PEO GEL** (ORGANOGEL)

(Poly (Ethylene) Oxide

However, in the particular case of proteins, after establishing the proper mixing conditions for any gel precursor, it is mandatory to determine how to remove this gel-cover from the crystals. The gel should allow the cryoprotectant to get into the crystalline structure for high-resolution X-ray crystallography and avoid radiation damage.

A cubic phase (usually called cubic lipid phase) of monoolein [150–152] has been the key to the successful preparation of membrane proteins [153–160]. The peculiar organization of lipids in cubic phases does not restrict their use for solubilization and crystallization of hydrophobic macromolecules. Polar proteins crystallize very well in such media [161,162]. So far, this convectionless crystallization method has not been applied outside the membrane protein crystal grower community [163].

Crystals grown in gels usually demonstrate benefits, such as occurring in fewer numbers or larger sizes. For instance, in 1995, Patel et al. suggested a kind of universal gel based on chromatography theory. They explored the possibility to crystallize various proteins, nucleic acids, and viruses in the presence of soluble polymers, such as carboxymethylcellulose [164]. Currently, there is no universal gel synthesized for the crystallization of all types of biological macromolecules (proteins, nucleic acids, and polysaccharides). In macromolecular crystallization, this universal gel (polymer or high-viscosity fluid) should not interfere with the crystal quality [26].

Several publications demonstrated that crystallization of a biological macromolecule in a hydrogel [6,139] might have at least some advantage over crystallization in pure solution for either proteins (Figures 31.8 and 31.9) or low-molecular-weight compounds [131]. Altogether, the results from the literature and the new ones here presented indicate that crystals grown in gel can be less mosaic and yield more intense diffraction patterns than those prepared in solution. Despite these benefits, a limited number of protein structures at high or atomic resolution have been obtained with crystals grown in agarose gel by vapor diffusion [14,165–167].

Crystallization in gels through the control of mass transport by diffusion mimics in part the microgravity environment and allows one to obtain fewer crystals and larger sizes in some cases. This has been demonstrated for agarose gels, where the critical

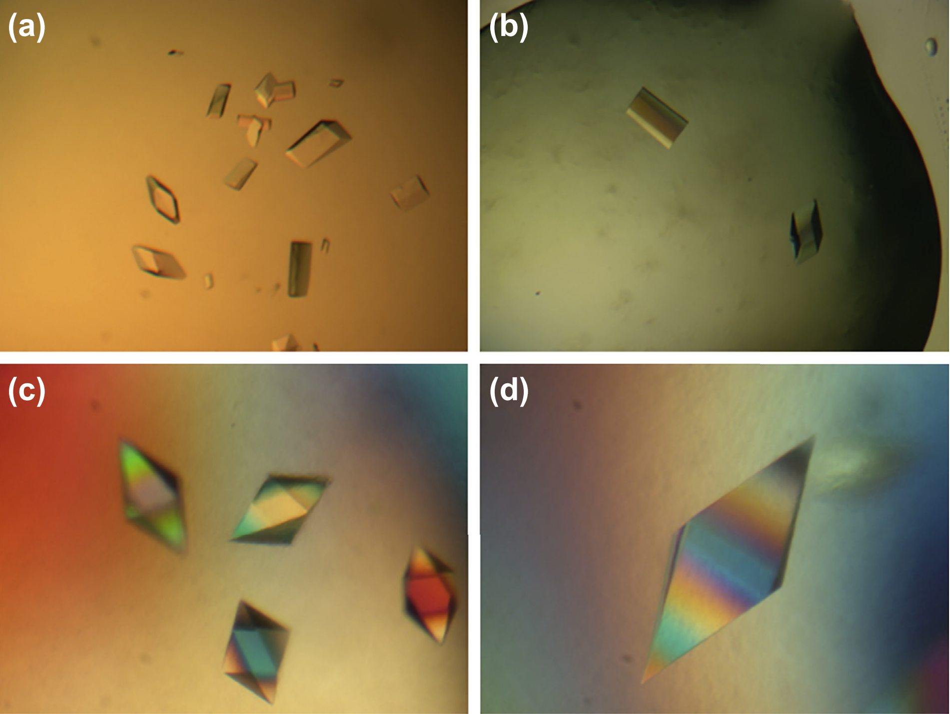

FIGURE 31.8 Pictures of aspartyl-t-RNA synthetase from *Thermus thermophilus*. (a) solution-grown, (b) gel-grown, (c) plant thaumatin crystals grown at 20 °C in solution, and (d) gel-grown single crystal. The size of the largest crystal is 500 μm and is the reference in scale for the other crystals.

concentrations were determined for the crystallization of proteins [132]. Other chemicals that form gels in aqueous solution are being synthesized every day; some of them, such as viscous polymers [164], oriented macroporous polyacrylamide gels [168], hydrogels for tissue engineering [169], supramolecular neutral hydrogels [170], and water gellators [171], may be useful for the crystallization of biological macromolecules. An alternative is the combination of gels and oils [172]. Finally, diffusion-controlled macromolecular interactions are as crucial for optimal crystal growth in gels as for biological reactions occurring in the living cells [173].

31.2.2 Synthesis and Characterization of Xerogels and Aerogels

Depending on the type of solvent (or gas/air) included inside the gel network, gels are classified as organogels (organic solvent, mineral oil, or vegetable oil inside), hydrogels (if water is inside), xerogels (which are dried gels), and aerogels containing different gas or air inside the 3D structure [174]. This third classification includes four main types of gels, which are summarized as follows.

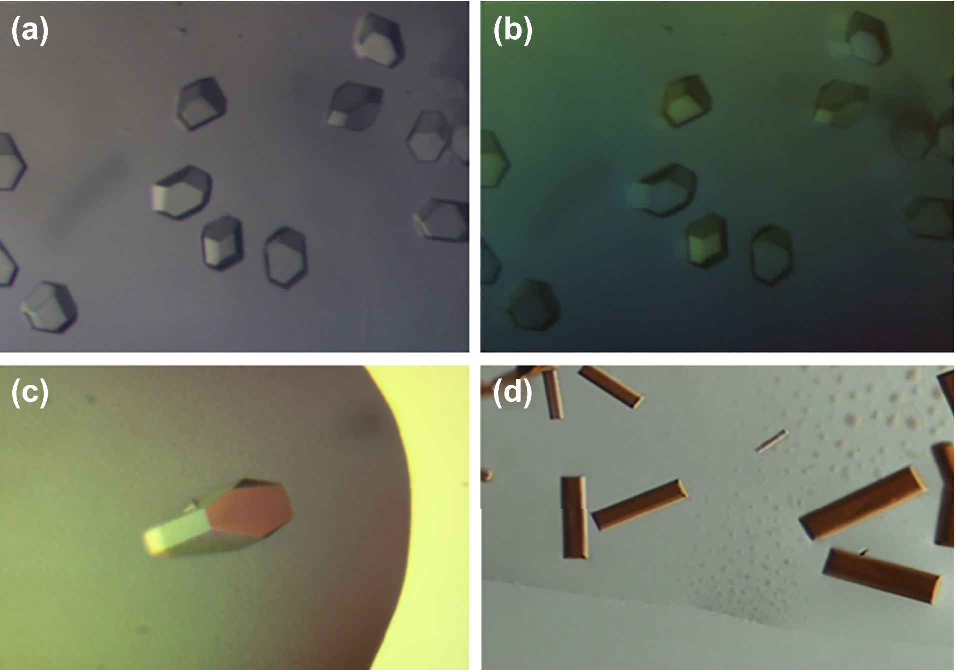

FIGURE 31.9 Pictures of different protein crystals. (a) glucose isomerase, (b) glucose isomerase in polarized light, (c) orthorhombic aspartyl-t-RNA synthetase from *Thermus thermophilus*, and (d) cytochrome C from bovine heart. The size of the largest crystal is 400 μm and is the reference in scale for the other crystals.

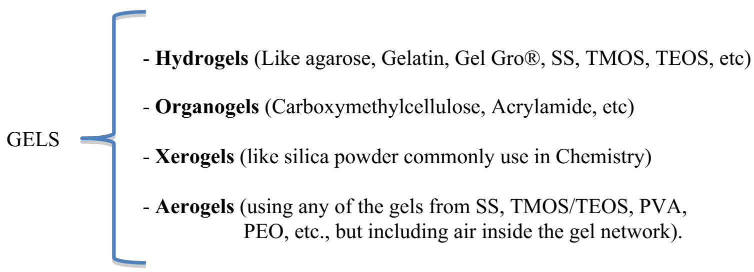

A xerogel is a solid formed from a gel by drying with unhindered shrinkage; these gels usually retain high porosity and an enormous surface area, along with very small pore-size distribution [175]. An aerogel is formed when solvent (organic or water) removal occurs under supercritical conditions; the structure does not shrink, is highly porous, and is made of low-density material [57]. During drying of xerogels, the collapse of smaller pores may occur due to the higher capillary tension developed in

the evaporation process. This phenomenon results in a contraction of the solid network, making it denser than that of aerogels. In supercritical fluids, during the drying process, the solvent is removed as a supercritical fluid; this avoids the formation of a meniscus and decreases the effect of surface tension, allowing for the preservation of the porous network [149]. Xerogels have important applications as pharmaceutical drug carriers [176].

The synthesis based on the polymerization of alkoxysilanes, such as TMOS or TEOS, allow one to obtain hydrogels. The process occurs in two steps, hydrolysis and condensation, as shown previously. Therefore, controlling these processes is an important aspect in the development of advanced materials, such as aerogels, with important biotechnological applications using the hydrophilic (for the removal of organic solvents) or hydrophobic properties for the removal of poorly water-soluble pollutants [177]. Because the properties of silicon-containing materials are very dependent on structure, it is of crucial importance to investigate hydrogel, organogel, and aerogel organization and morphology, as shown in Section 31.1.2. This fact allows one to control the pore-size distribution and sol–gel processes for applications to advanced silica-based materials [122].

During the last few years, the bulk structure of silica aerogels has been extensively studied, mainly by scattering techniques (neutrons, X-rays, light). It has been shown that porous silica aerogel has a fractal backbone structure [178]. Its spatial extension and fractal dimension are strongly dependent on the chemical (polymerization) and physical (colloid aggregation) growth process [179]. The typical length of these fractal structures ranges from 1 to 10 nm, and in some cases goes up to 100 nm [180].

The most relevant properties of silica aerogels are the high porosity (75–99.9%), resulting in a low density (3–500 kg/m^3), high specific surface area (800–1000 m^2/g), and pore size in the range of 1–100 nm [181]. The combination of their high porosity with the very small size of their pores leads to unique properties, such as low thermal conductivity (0.01–0.02 W/(m K)) and great accessibility to the internal surface through the porous network [182,183]. In some chemical systems, the porosity of xerogels can reach values close to those of aerogels, as occurs in cases where the liquid inside the pores does not exhibit appreciable interaction with the solid structure of the material. This effect is seen when the synthesized gels, before undergoing drying, have a highly hydrophobic solid network [175]. Additionally, the low density and thermal conductivity values make aerogels attractive for building insulation and for spacecraft components, whereas their very high and controlled porous structure make aerogels excellent candidates for catalysts, sensors, and filters for gaseous pollutants [114,184]. Other aerogel applications include impact absorption, cosmic particles trap, dielectrics, and spacers for vacuum electrodes [185,186]. Recently, carbon aerogels have attracted much attention because of their extraordinary properties and potential uses in a wide variety of technological applications [187].

31.3 Crystal Growth in Gels of Small Molecules, Minerals, and Biological Macromolecules in Gels

Basic research on anisotropic physical properties requires crystalline samples of high quality. Crystal growth in gels is an ideal method to provide this kind of specimen, mostly when the salts to be grown are sparingly soluble in water. The nucleation kinetics and the crystal growth itself depends on gel characteristics such as density, pH, aging time, and salt concentrations. It is important to note that SS is one of the most popular gels used to grow crystals of inorganics (low-molecular-weight compounds). In general, the gel from SS shows some general features: pH ranging from 3 to 5 and density between 1.03 and 1.06 g/cm^3.

Table 31.2 provides a list of inorganic compounds and minerals grown in gels for a variety of applications, which have ferroelectric, ferroelastic, piezoelectric, or nonlinear optical properties, such as second harmonic generation. Table 31.3 shows a few examples as well as the use of other types of gels used to grow these compounds.

Four basic crystallization methods are presently at the disposal of crystal growers to grow such crystals and introduce gel as a growth medium. Crystallization assays can be set up either (1) in batches, (2) by diffusion of vapor between hanging (or sitting) droplets and a reservoir of precipitant, (3) by dialysis across a semipermeable membrane, or (4) with free interface diffusion at the interface of two liquids [242–246]. The most popular gel incorporated into all of these crystallization methods for the crystallization of biomolecules has been agarose (see Table 3 in Ref. [30]). Gels prepared by means of polysiloxanes (alkoxysilanes), such as TMOS or TEOS, have also been suggested since their introduction in the field of protein crystal growth [239]. However, a few biomacromolecular crystals have been crystallized either using these alkoxysilanes [58] or gels prepared from the neutralization of solutions from sodium metasilicate.

Table 31.4 summarizes the protein and biomacromolecular complexes crystals directly grown in these types of gels. Figures 31.9 and 31.10 show the beauty of these protein crystals. Some of them were grown in different types of gels than those mentioned in this chapter.

31.4 General Remarks and Future of Crystal Growth in Gels

The gel method—a practical method to grow large and high-quality protein single crystals—has been poorly explored for many years, despite the large efforts from many groups to prove its effectiveness in obtaining high-quality crystals. Excellent reviews covering the crystallization of small and large molecules in gels have been published by Robert and Lefacheux [22], Garcia-Ruiz [21], Sauter et al. [14], Biertümpel et al. [23], and Lorber et al. [30]. Publications are available on combining gels and capillary tubes in counterdiffusion methods [18], protein crystallization in hydrogel

Table 31.2 Physical Properties of Crystals

Crystal	Dielectric	Optical	Ferroelastic	Piezoelectric	Ferroelectric	Magnetic Behavior	References
Sr-oxalate					X		[187,188]
Cd-oxalate					X	Diamagnetic	[189–191]
$CdMgHPO_4$					X		[192]
Nd-hepthamolybdate					X		[193]
La-hepthamolybdate	X				X		[194]
Cu-succinate	X						[195]
Cu-tartrate						Diamagnetic	[195]
Cu-(IDA)-(bypy)·$6H_2O$							[131]
$[Co(Him)_6]\ Cl_2$							[131]
Ba-oxalate					X		[196]
Sr-tartrate•$5H_2O$					X		[197]
Ba + Sr-tartrate					X		[198]
$Ba_xCa_{(1-x)}(IO_3)_4$				X			[199]
Ca-tartrate					X		[200]
Gd-Ba molybdate					X		[201]
Mn + Ba tartrate					X		[202]
KDP					X		[203]
KDP					X		[204]
Gd-Nd oxalate			X		X		[205]
Sm-tartrate					X		[206]
Y-tartrate					X		[206]
Zn phospate[a]							[207]
Cd malonate							[208,209]
Fe tartrate						Diamagnetic	[210,211]
Cu,Fe tartrate						Paramagnetic	[210,211].
KNO_3					X		[212]
(La,Nd,Pr,Sm) heptamolybdate			X	X	X		[213,214]
Pr molybdate			X	X	X		[213,214]
Ce-tartrate	X			X	X		[215]
Nd-tartrate	X			X	X		[216]
Ca-tartrate					X		[217]
K tartrate; Li-doped K tartrate		SHG		X	X		[218]
Ba oxalate							[190]
Ba tartrate	X	SHG		X	X		[219,220]
Ca + Cd tartrate					X		[219,220]
Ca + Sr tartrate					X		[221]
Sr + Ca tartrate		SHG		X	X		[222]

(Continued)

Table 31.2 Physical Properties of Crystals—cont'd

Crystal	Dielectric	Optical	Ferroelastic	Piezoelectric	Ferroelectric	Magnetic Behavior	References
Ba-tartrate					X		[223]
Metal phosphonate							[224]
Ca tartrate doped with Ba, Sr, Co, Ni, Mn, Zn, Cd					X		[225]
Gd tartrate$\cdot 3H_2O$		SHG		X	X		[226,227]
Yb tartrate$\cdot H_2O$		SHG		X	X		[226,227]
Ho tartrate		SHG		X	X		[227]
PbI_2							[228]
K, Mg phosphate							[229]
CuI							[230]
Fe, Mg, Co tartrate					X		[202]
Zn, Cd thiocyanate		SHG					[206]
Cd, Hg thiocyanate		SHG					[231]
$PbCl_2$		AcO					[206]
Ca tartrate					X		[232]
$CaHPO_4 \cdot 2H_2O$							[233]
$Ca_{10}(PO_4)_6(OH)_2$							[234]
$(Ba, Pb)SO_4$							[235]
Na, K bitartrate				X	X		[210,211]
Cu, Fe tartrate							[210,211]
$PbCO_3$							[221]
$Ba,MgHPO_4$							[236]
La,Nd oxalate							[237]
Bi_2IO_3		SHG					[238]

SHG = second harmonic generation, AcO = acousto-optical.
[a]anticorrosive.

Table 31.3 Gels Used to Grow Different Materials (Inorganic and Small Molecules)

Composition	Crystals	References
Sodium metasilicate	Oxalates, tartrates, phosphates, etc.	Listed in Table 31.1
Agar	Yb tartrate	[226]
Poly(ethylene)oxide	Cu-(IDA)-(bypy)$\cdot 6H_2O$	[131]
Polyacrylamide	$Ca_{10}(PO_4)(OH)_2$	[234]
Alginate	Metal-phosphonate	[224]

Table 31.4 Proteins or Macromolecular Complexes Directly Grown in Silica Gel or Alkoxysilanes-Made (TMOS or TEOS) Hydrogels

Protein or Macromolecular Complex	Precipitating agent	Type of gel (sodium metasilicate or TMOS/TEOS)	Resolution (Å)	References
HEW lysozyme	NaCl	Sodium metasilicate gel	ND	[239]
HEW lysozyme	NaCl	TMOS	ND	[240]
Thaumatin (*Thaumatococcus daniellii*)	NaK tartrate (pH 6.5)	Sodium metasilicate gel	ND	[146]
HEW lysozyme	NaCl	Sodium metasilicate gel	1.5 Å	[148]
HEW lysozyme, turkey lysozyme,Thaumatin	NaCl (pH 4.5), Na Tartrate (pH 6.5)	Sodium metasilicate gel as growth media and working as a filter for impurities separation	2.1 Å (lysozyme), 2.2 Å turkey lysozyme) and 3.0 Å (thaumatin)	[141]
Thaumatin (*Thaumatococcus daniellii*)	NaK tartrate	TMOS (5%)	ND	[172]
Heme proteins	Potassium Phosphate (pH 6.0–7.0) and PEG-8000	TEOS	ND	[241]
HEW lysozyme Thaumatin (*Thaumatococcus daniellii*) Ferritin	NaCl (pH 4.5) NaK tartrate (pH 6.5) $CdSO_4$ (pH 5.6)	Silica sols (2–22%) TMOS (8–18%)	1.2 Å–1.5 Å (low gel concentrations) Up to 2.6 Å (higher concentrations of silica gel and TMOS)	[130]

ND, Not determined; TMOS, tetramethyl orthosilicate; TEOS, tetraethyl orthosilicate; HEW, hen egg-white.

beads [247], the use of femtosecond laser-induced nucleation in protein crystals grown in agarose gels [248,138], combining electric fields and gels [249], and electric and magnetic fields using the gel-growth technique [127,250]. The use of smart hydrogels either for protein crystallization or for crystal gardens has been suggested [251]. Hydrogels have been used to prevent osmotic shock in protein crystals in drug design technology [252].

The use of agarose for protein crystallization has made this method more popular among the protein crystallography community for the last few years due to the convincing results not only in the crystallization and crystal quality enhancement of large biomolecules or biomacromolecular complexes [132,139,248,253,254], but also due to the easy preparation of these hydrogels and the existence of new types of low-melting-point agarose. There is still a lack in the availability of organic gels for organic molecules where strong organic solvents are used. Additionally, the gel method has been scarcely

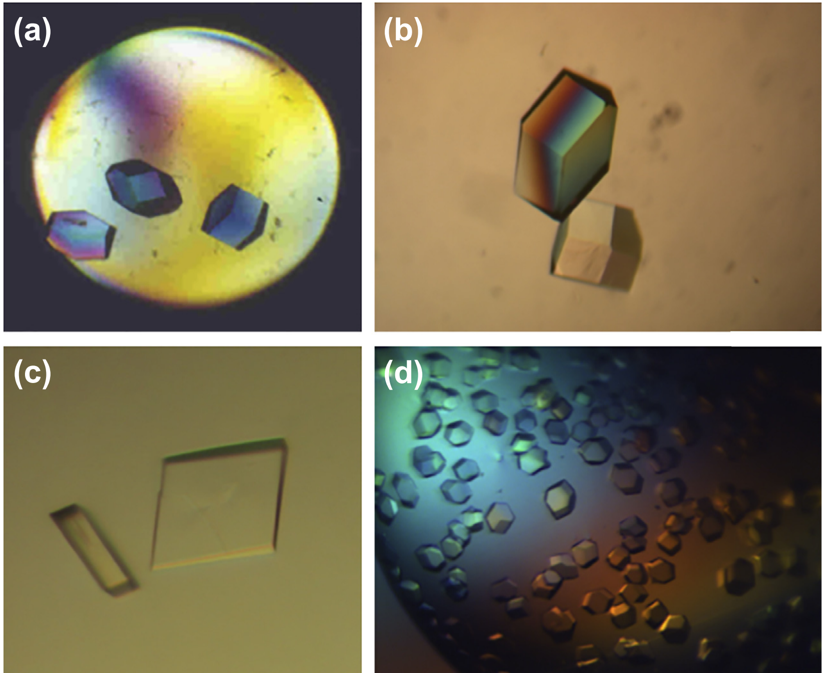

FIGURE 31.10 Pictures of different protein crystals. (a) lysozyme grown in batch method, (b) lysozyme grown in gel, (c) Monoclinic aspartyl-tRNA synthetase from *Thermus thermophilus* and (d) glucose isomerase grown at 4 °C. The size of the largest crystal is 200 μm and is the reference in scale for the other crystals.

used for membrane protein crystallization. There are not many choices for the polymer chemistry; however, the joint effort between crystal growers and synthesis scientists is the next and promising step of crystal growth in gels.

Scientists should understand the great advantages of using the gel method to grow crystals; there is a lot of chemistry and physics, as well as materials science, behind the knowledge of gels (synthesis and structure). The theory, protocols, recipes, and strategies to incorporate gels into the growth solution, where the solute (biological macromolecules) will crystallize, are now available in excellent chapters and published books, which are now classic contributions for crystal growth in gels; for example, see Chapter 6 in Refs [4,243], Chapter 10 in Ref. [244], and p. 226 in Ref. [242]. Chapter 4 in *Crystal Growth: From Fundamentals to Technology* [3] includes a section on macromolecular crystals grown by counterdiffusion (comparing solution and gel growth) and their characterization. A book published by Chayen et al. [246] reviews the different methods of macromolecular crystallization (including the gel method; see Part I, Section 8), and it also provides the theoretical basis and experimental tools to analyze the quality of biomacromolecular crystals for X-ray crystallography. In the previous edition of this handbook, Chapter 46, written by Narayana and Natarajan [255],

discusses crystallization from gels, mostly applied for biomineralization processes and human diseases.

The aim of this short chapter was to update the reader on new discoveries and approaches in the gel method. Nature has taken a long time to grow beautiful gems such as sapphires, rubies, and diamonds, but the gel-growth method allows us to play a game that has been coined as “instantaneous mineralogy” [4]. This gel method has even demonstrated the growth of large crystals of very interesting biological macromolecules that have not been easily crystallized by any other methods.

We hope that this chapter will inspire young scientists to explore gel methodology and obtain large and beautiful single crystals. It is also our goal to reach the chemical synthesis community, who usually deal with difficulties in the structure of complicated molecules (organic or inorganic), to adopt the method—or even join us in the synthesis of new gels. Many laboratories around the world are looking for new and original strategies to crystallize difficult compounds, nonintrinsically ordered proteins, and even large macromolecular complexes of biomolecules, such as ribosomes.

Today, there are still a lot of challenges to obtaining crystals of many membrane proteins, large DNA-protein, or RNA-protein complexes by the gel method, or to obtain crystals for X-ray crystallographic research. The idea of synthesizing a universal gel is still a difficult dream to come true, but there will be wonderful surprises in the coming years. This gel method is one of the areas that inspired our life as scientists, particularly for one of the authors of this chapter, for whom the gel method has been a strong tool to grow high-quality protein crystals—although they were sometimes difficult to achieve in his life as a protein crystal grower and protein crystallographer.

References

[1] Emma P, Akre R, Arthur J, Bionta R, Bostedt C, Bozek J, et al. Nat Photonics 2010;4:641.

[2] Otalora F, Garcia-Ruiz JM. Chem Soc Rev 2014;43:2013.

[3] García-Ruiz JM, Otalora F. Macromolecular crystals-growth and, characterization. In: Müller G, Métois J-J, Rudolph P, editors. Crystal growth from fundamentals to technology. Elsevier; 2004.

[4] Henisch HK. Crystals in gels and Liesegang rings. Cambridge: Cambridge University Press; 1988.

[5] Tomanicek SJ, Standaert RF, Wiess KL, Ostermann A, Schrader TE, Ng JD, et al. J Biol Chem 2013;288:4715.

[6] Matsumura H, Sugiyama S, Hirose M, Kakinouchi K, Maruyama M, Murai R, et al. J Synchrotron Rad 2011;18:16.

[7] Margiolaki I, Wright JP. Acta Crystallogr 2008;A64:169.

[8] García-Caballero A, Gavira J, Pineda-Molina E, Chayen N, Govada L, Khurdish S, et al. Cryst Growth Des 2011;11:2112.

[9] Ruggiero A, Smaldone G, Squeglia F, Berisio R. Proteins Pept Lett 2012;19:732.

[10] Maginn S. Analyst 1998;123:19R.

[11] Stojanoff V, Northrup P, Pietri R, Zhong Z. Protein Pept Lett 2012;19:761.
[12] Bosch R, Lautenschlager P, Potthast L, Stapelmann J. J Cryst Growth 1999;122:310–6.
[13] Lorber B, Ng JD, Lautenschlager O, Giege R. J Cryst Growth 2000;208:665.
[14] Sauter C, Lorber B, Giegé R. Proteins: Struct Funct Genet 2002;48:146.
[15] García-Ruiz JM, Moreno A, Viedma C, Coll M. Mat Res Bull 1993;28:541.
[16] García-Ruiz JM, Moreno A. Acta Crystallogr 1994;D50:484.
[17] García-Ruiz JM. Methods Enzymol 2003;368:130.
[18] Otalora F, Gavira JA, Ng JD, Garcia-Ruiz JM. Prog Biophys Mol Biol 2009;101:26.
[19] Bradford SC. Biochem J 1923;17:230.
[20] Low BW, Richards FM. J Am Chem Soc 1954;76:2511.
[21] Garcia-Ruiz JM. Key Eng Mater 1991;58:87.
[22] Robert M-C, Lefaucheux F. J Cryst Growth 1988;90:358.
[23] Biertümpel C, Basquin J, Suck D, Sauter C. Acta Crystallogr 2002;D58:1657.
[24] Otalora F, Novella ML, Rondon D, Garcia-Ruiz JM. J Cryst Growth 1999;196:649.
[25] Otalora F, Garcia-Ruiz JM, Carotenuto L, Castagnolo D, Novella ML, Chernov AA. Acta Crystallogr 2002;D58:1681.
[26] Moreno A, Juárez-Martínez G, Hernández-Pérez T, Batina N, Mundo M, McPherson A. J Cryst Growth 1999;205:375.
[27] García-Ruiz JM, Novella ML, Moreno R, Gavira JA. J Cryst Growth 2001;232:165.
[28] Pernodet N, Maaloum M, Tinland B. Electrophoresis 1997;18:55.
[29] Maaloum M, Pernodet N, Tinland B. Electrophoresis 1998;19:1606.
[30] Lorber B, Sauter C, Théobald-Dietrich A, Moreno A, Schellenberger P, Robert M-C, et al. Prog Biophys Mol Biol 2009;101:13.
[31] Gavira JA, Garcia-Ruiz JM. Acta Crystallogr 2002;D58:1653.
[32] Provost K, Robert M-C. J Cryst Growth 1991;110:258.
[33] Miller TY, He XM, Carter DC. J Cryst Growth 1992;122:306.
[34] Halberstadt ES, Henisch HK. J Cryst Growth 1968;3–4:363.
[35] Wilke K-Th. Kristallzüchtung. Frankfurt/Main: Verlag Harri Deutsch; 1988. p. 938.
[36] Liesegang RE. Naturwiss Wochenschr 1896;11:353.
[37] Oswald W. Z Phys Chem 1897;22:289.
[38] Oswald W. Kolloid-Z 1925;36:380.
[39] Colfen H. Nat Mater 2010;9:960–1.
[40] Henisch KH, García-Ruiz JM. J Cryst Growth 1986;75:203.
[41] Morse HW, Pierce GW. Phys Rev 1903;17:129.
[42] Jablczinsky K. Bull Soc Chim Fr 1923;4:592.
[43] Matalon R, Packter A. J Colloid Sci 1955;10:46.
[44] Ng JD, Gavira JA, Garcia-Ruiz JM. J Struct Biol 2003;142:218.
[45] Gangloff M, Moreno A, Gay NJ. J Appl Crystallogr 2013;46:337.
[46] Dondi PG. Biochem J 1975;149:475.
[47] Vidal O, Robert M-C, Boué F. J Cryst Growth 1998;192:271.

[48] Maes D, Gonzalez-Ramirez LA, Lopez-Jaramillo J, Yu B, De Bondt H, Zegers I, et al. Acta Crystallogr 2004;D60:463.

[49] Yunzhu G, Huiling C, Jin H, Chao C, Ziging W, Dachuan Y. Cailiao Daobao 2013;27:85.

[50] Moreno A, Quiroz-García B, Yokaichiya F, Stojanoff V, Rudolph P. Cryst Res Technol 2007;42:231.

[51] Sazaki G, Yoshida E, Komatsu H, Nakada T, Miyashita S, Watanabe K. J Cryst Growth 1997;173:231.

[52] Ataka M, Katoh E, Wakayama NI. J Cryst Growth 1997;173:592.

[53] Koizumi H, Fujiwara K, Uda S. Cryst Growth Des 2009;9:2420.

[54] Sakai Y, Oishi A, Takahashi F. Biotechnol Bioeng 1999;62:363.

[55] Kinoshita T, Ataka M, Warizaya M, Neya M, Fujii T. Acta Cryst 2003;D 59:1333.

[56] Lübbert D, Meents A, Weckert E. Acta Cryst 2004;D60:987.

[57] Vinograda EV, Moreno A, Lara VH, Bosch P. Silicon Chem 2003;2:247.

[58] Gonzalez-Ramirez LA, Caballero AG, Garcia-Ruiz JM. Cryst Growth Des 2008;8:4291.

[59] Tuvikene R, Truus K, Kollist A, Volubujeva O, Mellikov E, Pehk T. J Appl Phycol 2008;20:527.

[60] Anderson NS, Campbell JW, Harding MM, Rees DA, Samuel JWB. J Mol Biol 1969;45:85.

[61] Wilcox W. Fundamentals of crystal growth. In: Arend H, Hulliger J, editors. Crystal growth in science and technology; 1987. p. 119. NATO series.

[62] Prieto M, Viedma C, López-Acevedo V, Martín-Vivaldi JL, López-Andrés S. J Cryst Growth 1998; 92:61.

[63] Garcia-Ruiz JM, Novella ML, Otalora F. J Cryst Growth 1999;196:703.

[64] Otalora F, Novella ML, Gavira JA, Thomas BR, García-Ruiz JM. Acta Crystallogr 2001;D57:412.

[65] Elwell D. Fundamentals of flux growth. In: Arend H, Hulliger J, editors. Crystal growth in science and technology; 1987. p. 133. NATO series.

[66] Cheng KC, Fujii T. Heat Transf Eng 2007;19:9.

[67] Price WS. Diffusion Fundamentals 2005;2:112.1.

[68] Kapur V, Charkoudian J, Anderson JL. J Membr Sci 1997;131:143.

[69] D'Errico G, Ortona O, Capuano F, Vitagliano V. J Chem Eng Data 2004;49:1665.

[70] Venancio A, Teixeira JA. Biotechnol Tech 1997;11:183.

[71] McGuinness ET. J Chem Edu 1973;50:826.

[72] Tyn M, Gusek TW. Biotechnol Eng 1990;35:327.

[73] Pluen A, Netti PA, Rakesh KJ, Berk DA. Biophys J 1999;77:542.

[74] Tao L, Nicholson C. Neuroscience 1996;75:839.

[75] Kempe H, Persson P, Axelsson A, Nilsson B, Zachi G. Interscience. Wiley; 2005. http://dx.doi.org/10.1002/bit.20738.

[76] Gutenwik J, Nilsson B, Axelsson A. Biochem Eng J 2004;19:1.

[77] Bosna JC, Wesselingh JA. J Chromatogr B 2000;243:169.

[78] Stefanini S, Chiancone E, Arosio P, Finazzi-Agro A, Antonini E. Biochemistry 1982;21:2293.

[79] Andrews P. Biochem. J 1965;96:595.

[80] Gabler R, Wethead EW, Ford NC. Biophys J 1974;14:528.

[81] Stellwagen N, Gelfi C, Righetti PG. Electrophoresis 2002;23:167.

[82] Lai BE, Geonnotti AR, DeSoto MG, Montefiori DC, Katz DF. Antiviral Res 2010;88:143.

[83] Patterson G. Physical chemistry of macromolecules. CRC Press. Taylor, and Francis Group; 2007. p. 57–59.

[84] Asherie N. Proteins Pept Lett 2012;19:708.

[85] Procházka O, Kratochvíl P. J Polym Sci Polym Phys 1980;18:2369.

[86] Ye F, Collinson MM, Higgins DA. Phys Chem Chem Phys 2009;11:66–82.

[87] Higgins DA, Tran-Ba KH, Ito T. J Phys Chem Lett 2013;4:3095.

[88] Pramanik S, Ito T, Higgings GA. J Phys Chem 2013;C117:3668.

[89] Maeda K, Mizubayashi H. In: Czichos H, Saito T, Smith L, editors. Handbook of metrology and testing. Berlin (Heilderberg): Springer; 2011.

[90] Chiesa M, Giamello E, Che M. Chem Rev 2010;110:1320.

[91] Wessig M, Drescher M, Polarz S. J Phys Chem 2013;C117:2805.

[92] Rogozea A, Savonea F, Ionita G. Rev Roum Chim 2012;57:693.

[93] Pilar J. Dynamic processes in polymer systems studied by electron spin, resonance spin label technique [Ph.D. thesis]. Praha: Akademie ved Ceske Republiky; 2004.

[94] Gagnon MA, Lafleur M. J Phys Chem 2009;B113:9084.

[95] Han KS, Wang X, Dai S, Hagaman EW. J Phys Chem 2013;C117:15754.

[96] Arndt KF, Krahl F, Richter S, Steiner G. In: Gerlach G, Arndt KF, editors. Hydrogel sensors and actuators. Springer series on chemical sensors and biosensors, vol. 6. Berlin (Heidelberg): Springer Verlag; 2009.

[97] Yamaguchi T, Kuhnert L, Nagy-Ungvarai Z, Muller SC, Hess B. J Phys Chem 1991;95:5831.

[98] Chen L, Kang Q, He Y-L, Tao W-Q. Langmuir 2012;28:11745.

[99] Chen L, Kan Q, Robinson BA, He Y-L, Tao W-Q. Phys Rev 2013;E87:043306.

[100] Bhattacharya S, Kiefer J. J Chem Phys 2005;122:094715.

[101] Tartaglia P. In: AIP conference proceedings, 982; 2008. p. 295.

[102] Suarez MA, Kern M, Pitard E, Kob W. J Chem Phys 2009;130:194904.

[103] Saw S, Ellegaard NL, Kob W, Sastry S. J Chem Phys 2011;134:164506.

[104] Fatin-Rouge N, Starchev K, Buffle J. Biophys J 2004;86:2710.

[105] Kang Q, Moran W, Mukherjee PP, Lichtner PC. Adv Mech Eng 2010. http://dx.doi.org/10.1155/2010/142879.

[106] Kvarnstrom M, Vestergard A, Lorén N, Nydén M. Phys Rev 2009;E79:016102.

[107] Zhang J, Zhao X, Suo Z, Jiang H. J Appl Phys 2009;105:093522.

[108] Sancho-Tomás M, Fermani S, Durán-Olivencia MA, Otálora F, Gómez-Morales J, Falini G, et al. Cryst Growth Des 2013;13:3884.

[109] Kajiwara K, Osada Y. Gels handbook. London: Academic Press; 2001.

[110] Schneider M, Baiker A. Catal Rev Sci Eng 1995;37:515.

[111] Baskaran S, Liu J, Domansky K, Kohler N, Li X, Coyle C, et al. Adv Mater 2000;12:291.

[112] Hikmet RAM, Michels I. Adv Mater 2001;13:338.

[113] Hikmet RAM. Gels of liquid crystals and ion-Conducting fluids. In: Weiss RG, Terech P, editors. Molecular gels with self-assembled fibrillar networks. Springer; 2006. p. 773–92.

[114] Yoldas BE, Annen MJ, Bostaph J. Chem Mater 2000;12:2475–84.

[115] [a] Simonian AL, Grimsley JK, Flounders AW, Schoeniger JS, Cheng T-C, DeFrank JJ, et al. Anal Chim Acta 2001;442:15;
[b] Thiessen KJ. Acta Crystallogr 1994;D50:491.

[116] Mackenzie JD. J Non-Cryst Solids 1981;48:1.

[117] Klein LC. Sol–gel technology for thin films, fibers, preforms, electronics, & speciality shapes. Park Ridge (NJ): Noyes; 1998.

[118] Lenza RFS, Vasconcelos WL. J Non-Cryst Solids 2000;273:164–9.

[119] Anand B, Pisal SS, Paradkar AR, Mahadik KR. J Sci Industrial Res 2001;60:311.

[120] Escobar-Chavez JJ, Lopez-Cervantes M, Naik A, Kalia YN, Quintanar-Guerrero D, Ganem-Quintanar A. J Pharm Pharm Sci 2006;9:339.

[121] Brinker CJ, Scherer GW. Sol–gel science: the physics and chemistry of, sol–gel processing. San Diego: Academic Press; 1990.

[122] Ciriminna R, Fidalgo A, Pandarus V, Béland F, Ilharco L, Pagliaro M. Chem Rev 2013;113:6592.

[123] Amsden B. Polym Gels Networks 1998;6:13.

[124] Littke W, John C. Science 1984;225:203.

[125] Zeelen JPh, Wierenga RK. J Cryst Growth 1992;122:194.

[126] Yuefang L, Guo D, Zheng B. RSC Adv 2012;2:4857.

[127] Surade S, Ochi T, Nietlispach D, Chirgadze D, Moreno A. Cryst Growth Des 2010;10:691.

[128] Prudnikova T, Gavira JA, Rezacova P, Pineda-Molina E, Hunalova I, Sviridova E, et al. Cryst Growth Des 2010;10:3391.

[129] Pietras Z, Lin H-T, Surade S, Luisi B, Slattery O, Pos KM, et al. J Appl Cryst 2010;43:58.

[130] Gavira JA, Van Driessche AES, García-Ruiz JM. Cryst Growth Des 2013;13:2522.

[131] Choquesillo-Lazarte D, Garcia-Ruiz JM. J Appl Crystallogr 2011;44:172.

[132] Tanabe K, Hirose M, Murai R, Sugiyama S, Shimizu N, Maruyama M, Takahashi Y, et al. Appl Phys Express 2009;2:125501.

[133] Sauter C, Ng JD, Lorber B, Keith G, Brion P, Hosseini MW, et al. J Cryst Growth 1999;196:365.

[134] Guenet JM. Thermoreversible gelation of polymers and biopolymers. London: Academic Press; 1992.

[135] Sica F, Demasi D, Mazzarella L, Zagari A, Capasso S, Pearl LH, et al. Acta Crystallogr 1994; D50:508.

[136] Lorber B, Sauter C, Ng JD, Zhu DW, Giegé R, Vidal O, et al. J Cryst Growth 1999;204:357.

[137] Lorber B, Sauter C, Robert M-C, Capelle B, Giegé R. Acta Crystallogr 1999;D55:1491.

[138] Murai R, Yoshikawa H, Takahashi Y, Maruyama M, Sugiyama Sh, Sazaki G, et al. Appl Phys Lett 2010;96. 043702/1.

[139] Matsumura H, Sugiyama S, Hiroaki A, Kazufumi T, Satoshi M, Inohue T, et al. Bio Ind 2011;28:30.

[140] Provost K, Robert M-C. J Cryst Growth 1995;156:112.

[141] Robert M-C, Vidal O, Garcia-Ruiz J-M, Otalora F. In: Ducruix A, Giegé R, editors. Crystallization of nucleic acids and proteins: a practical approach. 2nd ed. Oxford, U.K: IRL Press; 1999. p. 149.

[142] Robert M-C, Capelle B, Lorber B, Giege R. J Cryst Growth 2001;232:489.

[143] Lorber B, Giegé R. J Cryst Growth 2001;231:252.

[144] Van Driessche AES, Otalora F, Gavira JA, Sazaki G. Cryst Growth, Des 2008;8:3623.

[145] Robert M-C, Provost K, Lefaucheux F. In: Ducruix A, Giegé R, editors. Crystallization of nucleic, acids and proteins, A practical approach. 1st ed. Oxford: IRL Press; 1992. p. 127–43.

[146] Cudney R, Patel S, McPherson A. Acta Crystallogr 1994;D50:479.

[147] Vidal O, Robert MC, Arnoux B, Capelle B. J Cryst Growth 1999;196:559.

[148] Garcia-Ruiz JM, Gavira JA, Otalora F, Guasch A, Coll M. Mat Res Bull 1998;33:1593.

[149] Vinogradova E, Estrada M, Moreno A. J Colloid Interface Sci 2006;298:209.

[150] Darmanin C, Conn Ch, Newman J, Mulet X, Seabrook Sh, Liang Y-L, et al. ACS Comb Sci 2012;14:247.

[151] Zabara A, Mezzenga R. Soft Matter 2012;8(2012):6535.

[152] Wallace E, Dranow D, Laible PD, Christiansen J, Nollert P. PLoS One 2011;6:e24488/1.

[153] Rummel G, Hardmeyer A, Widmer C, Chiu ML, Nolert P, Locher GP, Pedruzzi I, Landau EM, Rosenbusch JP. J Struct Biol 1998;121:82.

[154] Luecke H. In: Grisshammer R, Buchanan SK, editors. Structural biology membranes; 2006. p. 173–91.

[155] Johansson LC, Woehri AB, Katona G, Engstroem S, Neutze R. Curr Opin Struct Biol 2009;19:372.

[156] Liu W, Hanson MA, Stevens R, Cherezov V. Biophys J 2010;98:1539.

[157] Joseph J, Liu W, Kunken J, Weiss TM, Tsuruta H, Cherezov V. Methods 2011;55:342.

[158] Caffrey M. Biochem Soc Trans 2011;39:725–32.

[159] Cherezov V. Curr Opin Struct Biol 2011;21:559.

[160] Li D, Boland C, Walsh K, Caffrey M. J Vis Exp 2012;66:e4000.

[161] Landau EM, Rummel G, Cowas-Jacob SW, Rosenbusch JP. J Phys Chem 1997;B101:1935.

[162] Laczko-Dobos H, Szalontai B. Biochemistry 2009;48:10120.

[163] Topiol S. Expert Opin Drug Discov 2013;8:607.

[164] Patel S, Cudney R, McPherson A. Biochem Biophys Res Comm 1995;205:819.

[165] Gaboriaud C, Juanhuix J, Gruez A, Lacroix M, Darnault C, Pignol D, Verger D, Fontecilla-Camps JC, Arlaud GJ. J Biol Chem 2003;278:46974.

[166] Sauter C, Lorber B, Théobald-Dietrich A, Giegé R. J Cryst Growth 2001;232:399.

[167] Sauter C, Otalora F, Gavira JA, Vidal O, Giegé R, Garcia-Ruiz JM. Acta Crystallogr 2001;D57:1119.

[168] Charlionet R, Machour-Merlet N, Leclerc S, Malandain J-J. Electrophoresis 1997;18:1133.

[169] Lee KY, Mooney DJ. Chem Rev 2001;101:1869.

[170] Percec V, Bera TK, Butera RJ. Biomacromolecules 2002;3:272.

[171] Estroff LA, Hamilton AD. Chem Rev 2003;104:1201.

[172] Moreno A, Saridakis E, Chayen NE. J Appl Cryst 2002;35:140–2.

[173] Berg OG, von Hipple PH. Ann Rev Biophys Biophys Chem 1985;14:131.

[174] Morosanova EI. Talanta 2012;102:114–22.

[175] Durães L, Ochoa M, Rocha N, Patrício R, Duarte N, Redondo V, et al. J Nanosci Nanotechnol 2012;12:6828.

[176] Alcala-Alcala S, Urban-Morlan Z, Aguilar-Rosas I, Quintanar-Guerrero D. Int J Nanomedicine 2013;8:2141.

[177] Liu H, Sha W, Cooper AT, Fan M. Colloids Surf A 2009;347:38.

[178] Shaefer DW, Keefer KD. Phys Rev Lett 1986;56:2199.

[179] Knoblich B, Th Gerber. J Non-Cryst Solids 2001;296:181.
[180] Marlière C, Despetis FP, Etienne P, Woignier T, Dieudonne P, Phalippou J. J Non-Cryst Solids 2001; 285:148.
[181] Kroschwitz JI, Hawe-Gant M, editors. Kirk-othmer encyclopedia of, chemical technology. 4th ed. New York: John Wiley & Sons; 1998. p. 1.
[182] Štandeker S, Novak Z, Knez Ž. J Hazard Mater 2009;165:1114.
[183] Štandeker S, Veronovski A, Novak Z, Knez Ž. Desalination 2011;269:223.
[184] Yan Zh. Appl Mech Mater 2013;253–255:564.
[185] Gurav JL, Rao AV, Nadargi DY, Park HH. J Mater Sci 2010;45:503.
[186] Biener J, Stadermann M, Suss M, Worsley MA, Biener MM, Rose KA, et al. Energy Environ Sci 2011;4:656.
[187] Shen J, Guan D-Y. In: Aegerter MA, editor. Aerogels handbook, advances in sol–gel, derived materials and technologies. Springer, Science Business; 2011 [Chapter 36].
[188] Dalal PV, Saraf KB. Bull Mater Sci 2011;34:377.
[189] Arora SK, Kothari AJ, Patel RG, Chauhan KM, Chudasama BN. J Phys Conf Ser 2006;28:48.
[190] Raj AME, Jayanthi DD, Jothy VB, Jayachandran M, Sanjeeviraja C. Cryst Res Technol 2008;43:1307.
[191] Chauhan KM, Arora SK. Cryst Res Technol 2009;44:189.
[192] Bamzai KK, Gupta R, Suri S, Singh V. Adv Mater Lett 2014;5:89.
[193] Bhat S, Khosa SK, Kotru PN, Tandon RP. Cryst Res Technol 2006;30:267–73.
[194] Bhat S, Khosa SK, Kotru PN, Tandon RP. Mat Sci Eng 1995;B30:7.
[195] Binitha MP, Pradyumnan PP. Phys Scr 2013;87:065603.
[196] Dalal PV, Saraf KB, Shah S. Cryst Res Technol 2009;44:36.
[197] Firdous A, Quasim I, Ahmad MM, Kotru PN. Cryst Res Technol 2008;43:1015.
[198] Freeda MM, Delphine SM, Priya RK, Freeda TH, Almusallam AW. Rec Res Sci Technol 2010;2:9.
[199] Garud SL, Mahajan NK, Saraf KB. Bull Mater Sci 2009;32:187.
[200] Gon HB. J Cryst Growth 1990;102:501.
[201] Hangloo V, Tickoo R, Bamzai KK, Kotru PN. Mat Chem Phys 2003;81:152.
[202] Joshi SJ, Tank KP, Parekh BB, Joshi MJ. Cryst Res Technol 2010;45:303.
[203] Joshi MS, Antony AV. J Mat Sci 1978;13:939.
[204] Moreno-Cárcamo A, Mendoza-Alvarez ME, Silva-González R, Tabares C. Rev Mex Fís 1992;39:443.
[205] Korah I, Joseph C, Ittyachen MA. J Min Mat Char Eng 2010;9:1081.
[206] [a] Kumari PNS, Kalainathan S, Bhagavannarayana G. Cryst Res Technol 2008;43:276–81; [b] Kumari PNS, Kalainathan S. Cryst Res Technol 2008;43:413–6.
[207] Mangalam G, Das SJ. Arch Phys Res 2010;1:54.
[208] Joseph J, Mathew V, Abraham KE. Optoel Adv Mat 2008;2:707.
[209] Mathew V, Joseph J, Jacob S, Varughese PA, Abraham KE. Ind J Pure Appl Phys 2009;47:691.
[210] Mathivanan V, Haris M. Spectrochim Acta 2013;A102:341.
[211] Mathivanan V, Haris M. Pramana 2013;81:177.
[212] Mukund MR. Int J Adv Sci Res Tech 2012;2:500.
[213] Pandita S, Tickoo R, Bamzai KK, Kotru PN. Mat Sci Eng 2001;B87:122.

[214] Pandita S, Hangloo V, Bamzai KK, Kotru PN, Sahni N. Int J Inorg Mat 2001;3:675.

[215] Patil HM, Sawant DK, Bhavsar DS, Patil JH, Girase KD. Arch Phys Res 2011;2:239–45.

[216] Patil HM, Sawant DK, Bhavsar DS, Patil JH, Girase KD. J Therm Anal Calorim 2012;107:1031.

[217] Prananto YP, Khunur MM, Tjahjanto RT, Sakdi I, Basori MC. J Trp Life Sci 2011;2:1.

[218] Quasim I, Firdous A, Sahni N, Khosa SK, Kotru PN. Phys Stat Solidi 2009;A206:2791.

[219] Sawant DK, Bhavsar DS. Arch Phys Res 2012;3:8.

[220] Sawant DK, Patil HM, Bhavsar DS, Patil JH, Girase KD. J Therm Anal Calorim 2012;107:1047.

[221] Sawant DK. Chim Sin 2013;4:1.

[222] Selvapandiyan M, Sundaramoorthi P. Bulg J Phys 2013;40:78.

[223] Shah A, Patel IB. AIP Conf Proc 2010;1249:192.

[224] Stavgianoudaki N, Papathanasiou KE, Colodrero RMP, Choquesillo-Lazarte D, García-Ruiz JM, Cabeza A, et al. Cryst Eng Commun 2012;14:5385.

[225] Torres ME, López T, Stockel J, Solans X, García-Vallés M, Rodrígez-Castellón E, et al. J Solid State Chem 2002;163:491.

[226] [a] Want B, Ahmad F, Kotru PN. Mat Sci Eng 2006;A431:237;
[b] Want B, Ahmad F, Kotru PN. Cryst Res Technol 2006;41:1167.

[227] Want B, Ahmad F, Kotru PN. Cryst Res Technol 2007;42:822.

[228] Bhavsar DS, Saraf KB, Seth T. Cryst Res Technol 2002;37:225.

[229] Chauhan CK, Vyas PM, Joshi MJ. Cryst Res Technol 2011;46:187.

[230] Gao P, Gu M, Lin-Liu X. Cryst Res Technol 2008;43:496.

[231] Kumari PNS, Margaret MB, Kalainathan S. Cryst Res Technol 2009;44:177.

[232] Parekh BB, Joshi VS, Pawar V, Thaker VS, Joshi MJ. Cryst Res Technol 2009;44:31.

[233] Rajendran K, Keefe CD. Cryst Res Technol 2010;45:939.

[234] Ahymah-Joshy MI, Elayaraja K, Suganthi RV, Narayana KS. Cryst Res Technol 2010;45:551.

[235] Fernandez-González A, Pedreira VB, Prieto M. J Cryst Growth 2008;310:4616.

[236] Sundaramoorthy P, Kanchana G, Kalainathan S. Spectrochim Acta 2008;69:1154.

[237] Want B. J Cryst Growth 2011;335:90.

[238] Patil TK. Int J Sci Res Manag 2013;1:24.

[239] Lefaucheux F, Robert M-C, Bernard Y, Gits S. Cryst Res Technol 1984;19:1541.

[240] Robert M-C, Berthau J. Comptes Rendus de l'Academie des Sciences, Serie II: Mecanique, Physique, Chimie, Sciences de la Terre et de l'Univers 1987;305:847.

[241] Ronda L, Bruno S, Faggiano S, Bettati S, Mozzarelli A. Methods Enzymol 2008;437:311–28.

[242] Bergfors TM. Protein crystallization. Biotechnology series. La Jolla (USA): Int. Univ., Line; 1999.

[243] Ducruix A, Giegé R. Crystallization of nucleic acids and proteins: a, practical approach. 2nd ed. Oxford: IRL Press; 1999.

[244] McPherson A. Crystallization of biological macromolecules. 1st ed. New York: Cold, Spring Harbor Laboratory Press; 1999.

[245] Giegé R, McPherson A. In: Rossmann MG, Arnold E, editors. International table for crystallography, vol. F. Int. Union of Crystallography, KluwerAcad. Pub; 2001. p. 81.

[246] Chayen N, Helliwell JR, Snell EH. Macromolecular crystallization, and crystal perfection. IUCr-Oxford Science Publications, Oxford University, Press; 2010.

[247] Willaert R, Zegers I, Wyns L, Sleutel M. Acta Crystallogr 2005;D61:1280–8.
[248] Sugiyama Sh, Tanabe K, Hirose M, Kitatani T, Hasenaka H, Takahashi Y, et al. J Appl Phys 2009;48:075502/1.
[249] Sazaki G, Moreno A, Nakajima K. J Cryst Growth 2004;262:499.
[250] Moreno A, Sazaki G. J Cryst Growth 2004;264:438.
[251] Whitcombe MJ. Nat Chem 2011;3(211):657–8.
[252] Sugiyama Sh, Maruyama M, Sazaki G, Hirose M, Adachi H, Takano K, et al. J Am Chem Soc 2012;134:5786.
[253] Lei W, Liu X-Y. Biophys J 2008;95:5931.
[254] Ochi T, Bolanos-Garcia VM, Stojanoff V, Moreno A. Prog Biophys Mol Biol 2009;101:56–63.
[255] Narayana K, Natarajan S. Crystallization from gels. In: Springer handbook of crystal growth; 2010. p. 1607.

32 Fundamentals of Industrial Crystallization

Joop H. ter Horst[1,3], Christiane Schmidt[2], Joachim Ulrich[2]

[1]INTENSIFIED REACTION & SEPARATION SYSTEMS, PROCESS & ENERGY DEPARTMENT, DELFT UNIVERSITY OF TECHNOLOGY, DELFT, THE NETHERLANDS; [2]MARTIN-LUTHER-UNIVERSITÄT HALLE-WITTENBERG, ZENTRUM FÜR INGENIEURWISSENSCHAFTEN, HALLE, GERMANY; [3]EPSRC CENTRE FOR INNOVATIVE MANUFACTURING IN CONTINUOUS MANUFACTURING AND CRYSTALLISATION, STRATHCLYDE INSTITUTE OF PHARMACY AND BIOMEDICAL SCIENCES, UNIVERSITY OF STRATHCLYDE, GLASGOW, U.K.

CHAPTER OUTLINE

32.1 Introduction **1317**
32.2 Product Quality **1319**
32.3 Crystallization **1322**
32.3.1 Solubility and Supersaturation 1322
32.3.2 Crystallization Techniques 1324
32.4 Crystal Nucleation **1325**
32.4.1 Primary Nucleation 1327
32.4.2 Secondary Nucleation 1332
32.5 Crystal Growth **1333**
32.6 Crystallization Process Configuration **1337**
32.6.1 Continuous Crystallization 1339
32.6.2 Batch Crystallization 1341
32.7 Ensuring Product Quality in the Future **1343**
References **1346**

32.1 Introduction

Thinking of an industrial crystallization process, the instant association is a large-scale production facility for a particulate product such as table salt (Figure 32.1). Another prominent example for industrial crystallization can be found in the sugar industry, which had an annual production rate in 2011 of 168 million tons of the solid particulate sugar. Also in the pharmaceutical industry, many drug production lines incorporate at least one but usually several crystallization processes.

Handbook of Crystal Growth. http://dx.doi.org/10.1016/B978-0-444-63303-3.00032-8
Copyright © 2015 Elsevier B.V. All rights reserved.

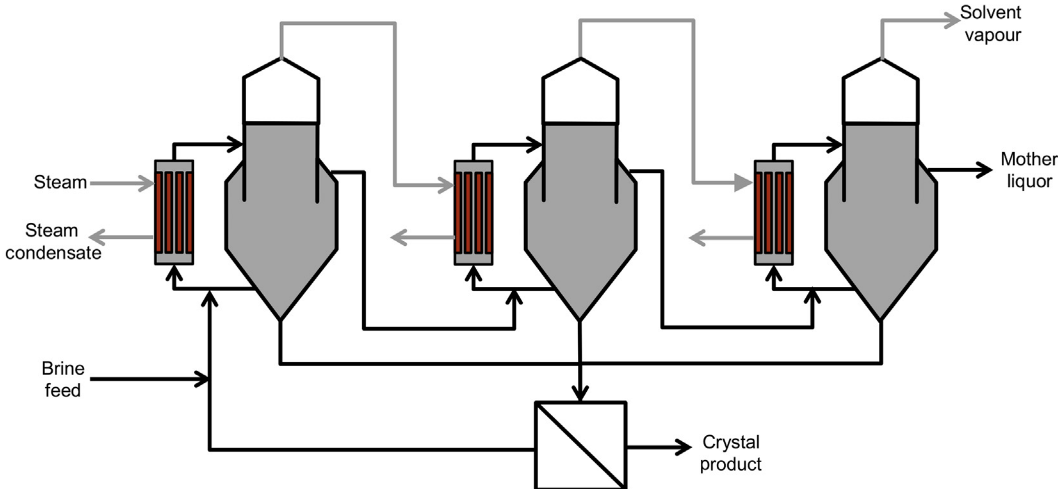

FIGURE 32.1 A cascade of three forced-circulation crystallizers in sequence, each with an external heat exchanger and a circulation pump. A brine is separated into table salt (NaCl-crystal product), water vapor, and a remaining mother liquor. Heat integration is used for the reduction of energy demands: the hot vapor leaving the crystallizer is used for heating in the next crystallizer. In a filtration system, the suspension is separated into a wet crystalline product to be dried and the remaining liquid to be recycled back into the process.

Industrial crystallization is a separation technology that exploits the first-order phase transition between liquid and solid [1,2]. By pushing the system away from equilibrium in a multicomponent liquid, a driving force for crystallization of a specific solid can be created. During crystallization, a suspension of crystals in the solution is formed which after filtration and drying leads to the desired particulate product. The resulting particulate product is usually seen as an advantage. Another advantage that lets crystallization stand out compared to other separation techniques is that the obtained product usually is close to 100% pure, even in a single process step. To achieve high purities in distillation processes, many equilibrium steps are usually needed. Further, auxiliary phases such as the solvent in extraction are often not needed in crystallization processes.

Even on industrial scales with large production rates, crystallization generally remains a molecular-level process [3]. During the growth of each crystal in the supersaturated suspension, molecules or ions incorporate at kinks of steps on the crystal surfaces (see the simplified version in Figure 32.2). These molecular level processes challenge the control over the particulate product from industrial crystallization processes.

Each crystalline product nowadays has to fulfill specific sets of demands of costumers as well as of manufacturers. The demands are not only concerned with the production rate and yield; they further may include specifications on product dissolution behavior, product stability during storage under humid conditions, particulate flow properties, color, and many others while they vary from product to product. The last 25 years showed a focus change in industrial crystallization research from bulk chemicals to fine and pharmaceutical products, showing the increasingly important molecular-level processes even on industrial scales. It is nowadays crucial to control the industrial

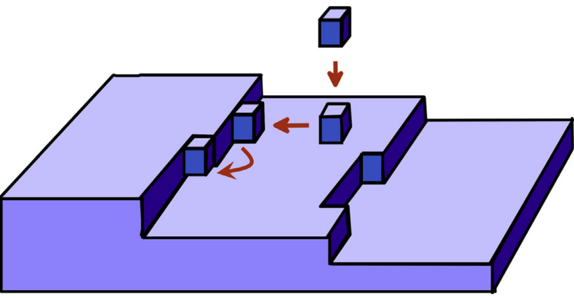

FIGURE 32.2 A simplified schematic of the molecular level process of crystallization. During crystal growth, solute molecules or ions incorporate at kinks of steps on the crystal surface. In solution crystallization next to the solute and solvent, many components can be present. Even though ideally only the solutes are incorporated, also all other components present might have a substantial effect on the crystallization behavior through disruption of the molecular level process.

crystallization process to robustly and reproducibly obtain the crystalline product in a sustainable way. In this chapter, the fundamental basis for industrial crystallization is given, highlighting product quality and the determining crystallization subprocesses. In our view, important achievements in the field of industrial crystallization in the past 20 years or so will be highlighted.

32.2 Product Quality

Figure 32.3 shows *ortho*-amino benzoic acid crystals obtained from a cooling crystallization. These crystals have a specific form, size, shape, and purity. Customer and manufacturer demands for a crystalline product can usually be traced back to these four product quality aspects.

The crystal *form* that is produced is related to the molecular or ionic arrangement in the crystals (crystal structure) and impacts on properties such as solubility, shelf life, drug

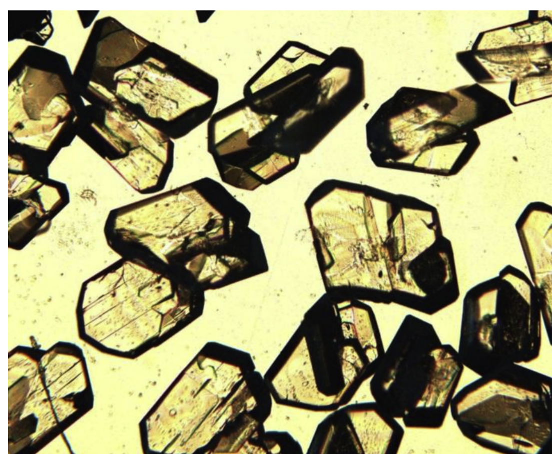

FIGURE 32.3 A crystal product from a small-scale cooling crystallization of ortho-amino benzoic acid.

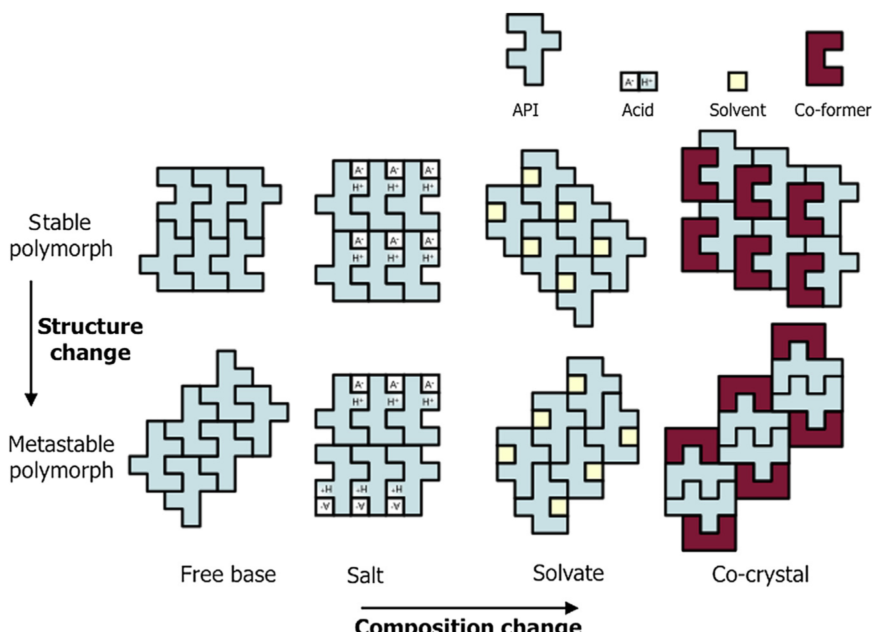

FIGURE 32.4 A chemical compound such as an active pharmaceutical ingredient could form different crystal structures either on its own (polymorphism) or together with other compounds (salt, co-crystal, solvate) which in turn also could form polymorphs or related but stoichiometrically different compounds.

stability, bioavailability, and color. Figure 32.4 shows crystal structures of different forms of a model active pharmaceutical compound. A chemical compound that is able to crystallize in different molecular or ionic arrangements in the crystal structures is named a polymorph [4]. The inability to control polymorphism in industrial crystallization processes and in the crystalline product can cause challenging problems in the pharmaceutical industry [5]. If a solvent molecule is additionally present in the crystal structure, one speaks of solvates. In the case of included water, this is termed a hydrate. Often solvates and hydrates are unwanted due to their instability. In recent years, co-crystals attained substantial attention as a route toward adjustable and improved solid-state properties of pharmaceutical compounds [6]. Co-crystals are multicomponent crystals of components that are, in their pure form, crystalline at room temperature. If the organic components of multicomponent crystals exchange charge or hydrogen, they are characterized as organic salts. These definitions of different forms might overlap: a multicomponent crystal containing a pharmaceutical compound, a singly dissociated dicarboxylic acid and a solvent would be characterized as a co–crystal salt solvate [7].

The crystal *shape* can be vital for the flow and storage properties of a product. Filtration of a suspension after crystallization containing needle-like crystals, furthermore, might become a time consuming step when the needles plug the filter and form an impassable barrier for the liquid. The terms crystal habit and crystal morphology are evident for the description of the crystal shape (Figure 32.5). The crystal habit is linked to

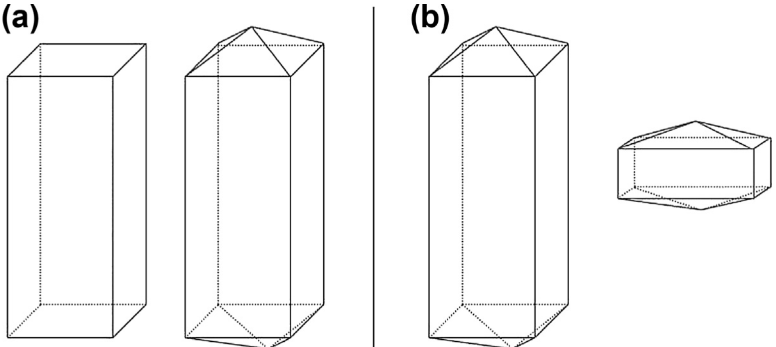

FIGURE 32.5 (a) Two crystals having the same habit but a different morphology; (b) Two crystals having a different habit, but the same morphology. *Adapted from Ref. [8].*

the outer geometrical appearance of a crystal, regardless of the crystal structure. Terms as cubic, acicular, plate-like or tabular are commonly used for the description of the crystal habit. In contrast, the term crystal morphology corresponds to a description related to the crystal structure [8]. The morphology refers to groups of crystal faces having the same relation to the elements of symmetry and can be described in terms of Miller indices. Further details on the relation between morphology and crystal structure is described elsewhere [9,10].

A crystal size distribution (CSD) gives information on the collection of crystal sizes in the product [11,12]. A CSD can be measured with the aid of a number of techniques all capturing a different characteristic length scale of the crystalline product [13]. For the same crystalline product, drastically different CSDs are obtained when using techniques that, for instance, capture a number-based or a volume-based CSD (Figure 32.6). It is, therefore, important to report what kind of CSD is measured or what technique is used to measure the CSD.

Costly downstream processing such as sieving or grinding could be avoided if an optimal CSD is obtained directly from the crystallization process. Often a narrow size

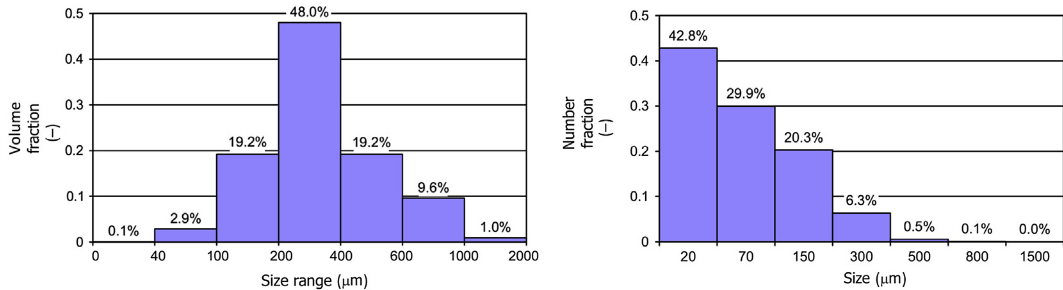

FIGURE 32.6 Volume-based and number-based crystal size distribution of the same crystal product. The majority of the crystals are small and, therefore, are prominently present in the number based CSD (right). The volume of the small crystals, however, is hardly contributing to the total volume and therefore they do not impact the volume-based distribution (left).

distribution has such optimal behavior. The CSD of the product crystals can be responsible for a specific dissolution and flow behavior of the solid crystals. During storage, a classification of the different size fractions may occur where the larger particles will be found towards the bottom and the smaller ones towards the top of the container.

The presence of a very fine, powder-like fraction may lead to caking, due to electrostatic interactions of the particles or humid conditions. During caking, the crystals grow together and form a thick lump of crystals. During caking, impurities and mother liquor are trapped within the caked crystals.

Predominantly in the food, pharmaceutical and fine chemical industries high levels of *purity* are desired. For instance, impurities from side reactions during the synthesis of an active pharmaceutical ingredient could lead to unwanted additional biological activity of the administered drug if they end up in the final product. Impurities can be located on several positions in the final product. First, they could be located on lattice positions. That could occur if the impurity molecule strongly resembles the product molecule. Second, they could be present in small pockets (inclusions) of mother liquor within the interior of the crystals. Third, an agglomerated collection of crystals is often relatively impure since impurities collect within the intergrown regions of the particles. Finally, the impurities can be located on the surface of the crystals if the washing step is not optimal.

32.3 Crystallization

32.3.1 Solubility and Supersaturation

The solubility of a crystalline compound forms the basis for crystallization process design. It describes at which temperature a specific solution composition is in equilibrium with a specific crystalline phase. Now that commercial equipment from several companies is readily available solubility data for a variety of multicomponent systems becomes accessible [14,15]. The solubility is a function of the solvent composition and the temperature, while also other compounds present in significant amounts may affect solubility. For bulk chemicals and proteins, the solvent usually is water; pharmaceutical compounds often are crystallized using organic solvents and solvent mixtures.

The solubility curve of a number of crystalline compounds in water [1] is shown in Figure 32.7. The different compounds show a wide variety of solubilities. While the NaCl solubility is close to constant as a function of temperature, that of KNO_3 shows a strong dependence on temperature. Most organic compounds such as active pharmaceutical ingredients show an increasing solubility with temperature in organic solvents. This solubility often can be described sufficiently accurate using the van't Hoff equation.

$$\ln x = -\frac{\Delta H}{R}\left(\frac{1}{T} - \frac{1}{T_m}\right) \tag{32.1}$$

The van't Hoff equation describes ideal solubility behavior through the heat of fusion ΔH and the melting temperature T_m [16]. Within a sufficiently small temperature region,

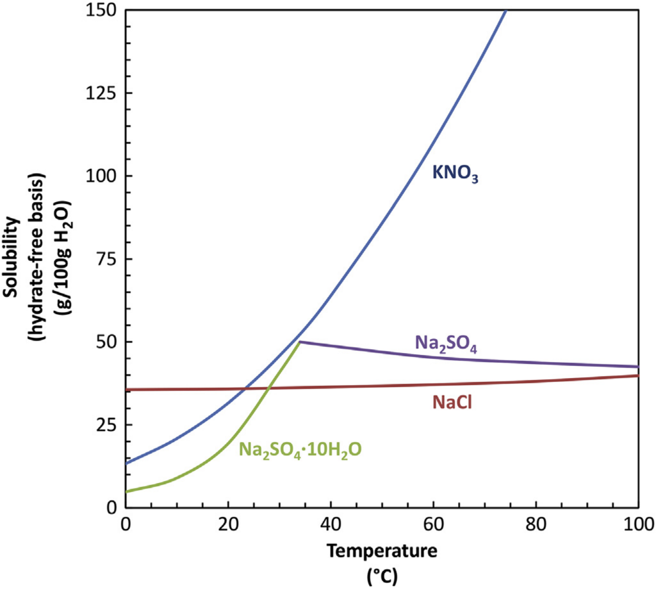

FIGURE 32.7 Solubility as a function of temperature for a number of crystalline compounds in water. While the NaCl solubility is close to constant as a function of temperature, that of KNO_3 shows a strong dependence on temperature. At low temperatures, the hydrated form of Na_2SO_4 has a lower solubility and thus is more stable than the anhydrate. At higher temperatures, this is reversed. *Constructed from data in Ref. [1]*

these could be used as fitting parameters. The nonideality of the system causes the fitted values to deviate from the actual heat of fusion and melting temperature and poor fits in too wide temperature regions.

The driving force for crystallization can be represented by the chemical potential difference between the prevailing out-of-equilibrium state of the system and the corresponding equilibrium state [11,17]. This chemical potential difference thus is a function of both concentration c and solubility c^* at a specific temperature and pressure. Therefore, the driving force for crystallization is usually represented by the supersaturation ratio S:

$$S = \frac{c}{c^*} \tag{32.2}$$

The supersaturation can be increased by, for instance, a concentration increase through solvent evaporation or a solubility decrease by decreasing the temperature. Crystal growth would reduce the solution concentration and thus the supersaturation.

The most stable polymorph has the lowest solubility $c_{\mathrm{I}}^* < c_{\mathrm{II}}^*$. If this is so in the entire temperature region from 0 K to melting temperature one speaks of a monotropic system. In an enantiotropic system, there exists a transition temperature below which one form is stable and above which the other is stable temperature. This means that in an equilibrated suspension of metastable polymorph II $(S_{\mathrm{II}} = 1)$ a supersaturation $S_{\mathrm{I}} = c/c_{\mathrm{I}}^* > 1$ exists towards the stable form I. In time, such a system would transform to

a suspension of form I crystals in equilibrium with a solution at concentration c_I^* through nucleation and growth of form I and dissolution of metastable form II. However, this could take a considerable amount of time if nucleation and growth are sufficiently small. A pharmaceutical product consisting of a metastable polymorph then could be stable enough to market as a drug. However, usually the most stable form is preferred as the product.

32.3.2 Crystallization Techniques

Industrial crystallization techniques [11,17,18] are defined by the way supersaturation is created. In case of *evaporative crystallization*, solvent is removed by evaporation from a boiling solution. Upon evaporation of the solvent, the solute concentration increases, which increases the supersaturation. The supersaturation, in turn, is consumed by the growing crystals. Evaporative crystallization thus is operated close to a three-phase equilibrium point where vapor, solution and solid phase are in equilibrium. The solution volume is reduced by transferring solvent to the vapor phase and solute to the solid phase. The operating temperature can be substantially adjusted through changing the pressure-dependent boiling temperature.

Evaporative crystallization can be applied on a large scale in continuous bulk chemical production for products such as table salt [19] and sugar [20]. Evaporative crystallization is chosen if the solubility does not show a strong positive dependence on temperature, for instance in the case of table salt (Figure 32.7). Often the choice for evaporative crystallization is made if the temperature dependence of the solubility is less than 0.005 g/g °C [21]. A recycle stream in a continuous evaporative crystallizer is used to remove crystal product from the remaining solution. A cascade of evaporative continuous crystallizers (Figure 32.1) is used to increase yield while reducing energy consumption: the vapor from a crystallizer is used to evaporate the solvent in a subsequent one.

Cooling crystallization can be chosen if the solubility shows a strong positive dependence on the temperature, larger than 0.005 g/g °C, and if the solubility at the lowest possible temperature is sufficiently low [21]. Upon decreasing the temperature of an equilibrated suspension, the solubility is decreased, and supersaturation is created which is reduced again by the growing crystals in the suspension. Usually cooling crystallization is applied in batch mode. Scaling on cooling surfaces may be an issue in continuous cooling crystallization due to the large temperature differences needed for a substantial production rate.

Another way to create supersaturation is to add an antisolvent. Although an antisolvent dilutes the mixture and reduces the concentration, it also strongly reduces the solubility in the mixture. If the solubility reduction exceeds that of the concentration then a supersaturation can be created which induces crystallization. Precipitation is sometimes named reactive crystallization. Upon mixing two streams, a reaction occurs which results in a sparingly soluble solute. If sufficiently high concentrations are used, the concentration is much higher than the solubility and supersaturation is created.

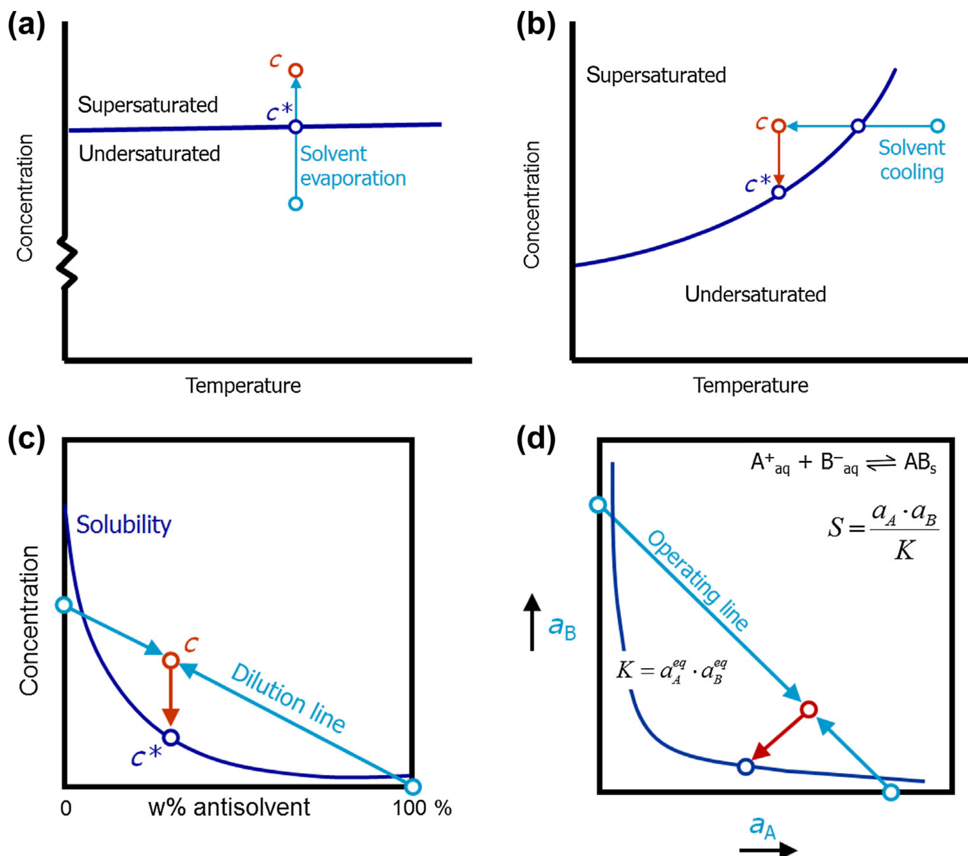

FIGURE 32.8 The phase diagrams, solubility lines, and operating points for the different crystallization techniques: (a) evaporative crystallization; (b) cooling crystallization; (c) antisolvent crystallization; (d) precipitation.

Both antisolvent crystallization and precipitation involve mixing of process streams. This mixing usually coincides with large, local supersaturations close to the inlet points. Therefore, usually locally at the flow inlets nucleation occurs after which the crystals grow out upon suspension in the bulk solution. Due to these mixing effects and local variations in process variables, it is difficult to control such processes.

Figure 32.8 shows the phase diagrams from the different crystallization techniques. It also shows how supersaturation is created and the relation between concentration, solubility and supersaturation ratio $S = c/c^*$.

32.4 Crystal Nucleation

Crystal nucleation is the start of a phase transition towards the crystalline solid phase [22]. It is thus the subprocess of crystallization with which crystals come to existence, and it takes place in a supersaturated mother phase (solution, melt, and vapor, solid).

Since this subprocess determines the number of crystals between which the crystalline material is divided during the crystallization, it plays a key role in determining the CSD: for the same mass crystallized, a higher number of crystals formed during the nucleation stage results in a smaller average product size. It is also thought that crystal nucleation is responsible for the kind of crystalline material formed: if the nucleation rate of a metastable phase is larger than the stable phase the metastable polymorph would dominantly form if the growth rate is not substantially smaller.

Within an industrial crystallization process, crystals can be formed from an initially clear solution (primary nucleation) or due to the presence of parent crystals (secondary nucleation). In turn, primary nucleation generally is divided into homogeneous and heterogeneous nucleation. During heterogeneous primary nucleation, the crystals form at surfaces such as dust particles, crystallizer wall, air-solution interface or deliberately added template particles. Homogeneous primary nucleation takes place in the absence of heterogeneous particles in a clear solution. It is important to note that in the laboratory and more so in large-scale processes on an industrial scale, the presence of many different heterogeneous particles or surfaces is impossible to avoid. Despite their importance, usually no information is available on the amount and kind of heterogeneous particles that are finally responsible for the occurrence of heterogeneous nucleation.

Thus, while an unseeded batch cooling crystallization process usually relies on primary nucleation to provide the crystals, during a continuous crystallization process the omnipresent crystals continuously generate more crystals through secondary nucleation. Only in extreme cases are there indications that homogeneous nucleation is the dominant nucleation mechanism. This is summarized in Figure 32.9. Since primary and secondary nucleation are strikingly different processes, controlling and predicting crystal size from these processes thus need completely different approaches.

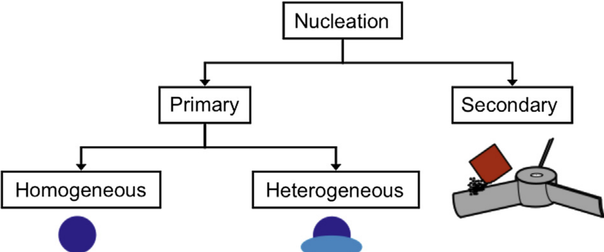

FIGURE 32.9 Crystal nucleation is divided into primary and secondary nucleation. Primary nucleation occurs in a clear liquid either in the absence (homogeneous primary nucleation, HON) or in the presence (heterogeneous primary nucleation, HEN) of heterogeneous particles. Secondary nucleation occurs in the presence of crystals. New crystals can be, for instance, created due to collisions of parent crystals with the stirrer (attrition), but other secondary nucleation mechanisms are also possible.

32.4.1 Primary Nucleation

When cooling down a solution to below its saturation temperature it becomes supersaturated and growth can commence if crystals are present. However, crystals are only detected when already a substantial supersaturation is generated (Figure 32.10). Since this cannot be only attributed to the delayed detection of macroscopically large crystals due to the detectable crystalline amount and the growth rate, it shows that a substantial free energy is needed for nucleation to occur. Thus, there is an energy barrier for nucleation, which is named nucleation work.

Starting with the work of Gibbs, classical nucleation theory (CNT) has served already for almost 150 years to describe the nucleation work and the resulting kinetics of the barrier crossing. This shows CNT is a powerful theory that needs strong, convincing evidence to be put aside. There are, however, some serious issues with the theory, an important one inevitably being the inability to accurately predict crystal nucleation rates [23]. Primary nucleation, its issues and recent advances, will be discussed in the current section from the viewpoint of industrial crystallization.

Although heterogeneous nucleation (Figure 32.9) is the dominant mechanism in industrial crystallization, the nucleation rate equation following from CNT can be best explained through homogeneous nucleation. This equation then can also be used to describe the mechanism that is assumed to be dominant: heterogeneous nucleation. Homogeneous nucleation is a balance between a free energy gain and loss. The gained results from the thermodynamics that drive the system towards the more stable crystalline state through the supersaturation, determined by the chemical potential difference between the two bulk states (bulk solution and bulk crystalline solid) and the

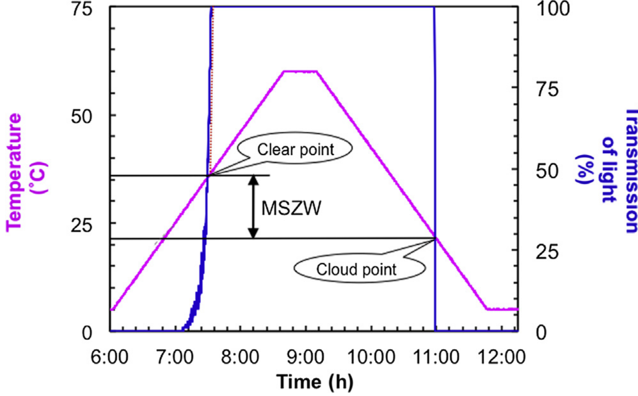

FIGURE 32.10 A measurement of the metastable zone width (MSZW). A sample is heated and cooled with a specific rate while the transmission of light through the sample is recorded. If the transmission is smaller than 100%, crystals are present; if it is 100%, a clear solution is present. The clear point is the temperature at which a suspension turns into a clear solution upon increasing the temperature. For this sample, the clear point is measured to be around 36 °C. The cloud point is the temperature at which a clear solution turns into a suspension upon decreasing the temperature. For this sample, the cloud point is measured to be around 22 °C. The difference between clear and cloud point is the metastable zone width (MSZW).

cluster volume. The loss is due to the surface that has to be created between the formed crystal and the supersaturated solution, and this loss is thus related to the interfacial energy of the solid–solution interface and the interfacial area.

At small cluster sizes, a substantial fraction of the molecules in the cluster are positioned at the surface, and the interfacial term is dominant over the volume term: there is a free energy loss upon creating the cluster. At large cluster sizes, there are many molecules within the bulk of the cluster and the volume term dominates: there is a free energy gain upon creating the cluster. Thus, there is an intermediate cluster size at which the free energy loss is maximum, and this is the nucleus size (sometimes named the critical nucleus size). This is shown in Figure 32.11.

Equations for the nucleus size n^* and nucleation work W^* can be derived from the expressions for the interfacial and volume terms [22]:

$$n^* = \frac{32\pi v^2 \gamma^3}{3k^3 T^3 \ln^3 S}; \quad W^* = \frac{16\pi v^2 \gamma^3}{3k^3 T^3 \ln^3 S} \tag{32.3}$$

With the interfacial energy γ between crystal and solution, the shape factor c relating surface area and volume, molecular volume v of the solid, and supersaturation ratio S. At increased supersaturations and decreased interfacial energies the nucleation work W^* is lower: it becomes energetically easier to nucleate. It should be noted that here the crystal is considered isotropic: the interfacial energy is constant in all directions. As is known for macroscopic crystals this usually is not the case, especially for crystalline material with a high melting temperature and low or moderate solubility: interfacial energies are

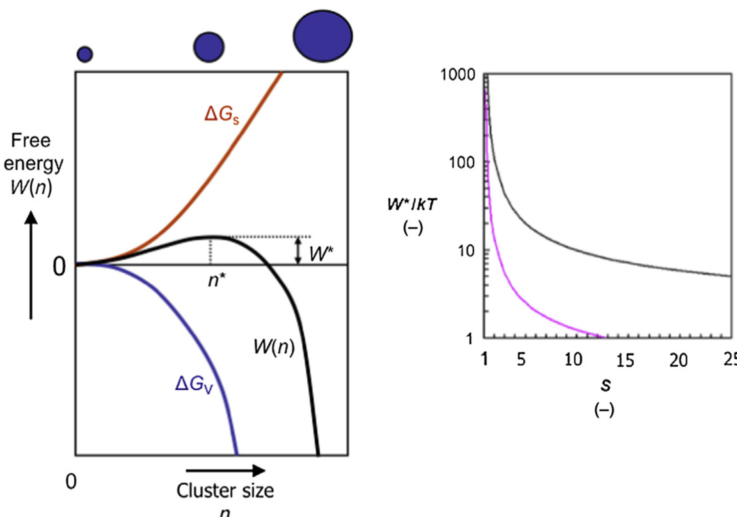

FIGURE 32.11 Left: The free energy associated with the formation of a cluster as a function of the cluster size n at a constant supersaturation S. At the nucleus size n^* the free energy of formation is maximum, which is the nucleation work W^*. Right: The decrease of the nucleation work W^*/kT as a function of the supersaturation ratio S for both HON (upper solid line) and HEN (lower solid line) for typical nucleation parameters.

relatively low for specific crystal surfaces due to the lower number and size of broken bonds at these crystal surfaces. These low interfacial energy surfaces will be dominantly present in the crystal morphology, striving to a low overall interfacial energy.

Thus, crystal nucleation is an activated process with the nucleation work W^* as the free energy barrier. The nucleation rate J, defined as the number of crystals generated per unit of time and volume, then can be described with an Arrhenius-type of equation [22]:

$$J = A\exp\left(-W^*/kT\right) = A\exp\left(-B/\ln^2 S\right) \tag{32.4}$$

While the exponential term describes the thermodynamics of the activated process of nucleation, the pre-exponential term deals with the kinetics of the barrier crossing. In order to describe the pre-exponential factor A, the model behind it has to be physically understood. A supersaturated solution consists of building units that can associate into larger clusters through a stochastic process involving a large amount of random single building unit attachments and detachments. The nucleus is a cluster consisting of n^* building units for which the attachment frequency is equal to the detachment frequency of building units. Clusters smaller than the nucleus size tend to dissolve while clusters larger than the nucleus size tend to grow to become macroscopically large crystals. The nucleus, thus in metastable equilibrium with the supersaturated solution, has about 50% chance to grow out rather than to decay.

The stationary nucleation rate then can be defined as the flux of particles through the nucleus size n^* towards larger size. This flux is defined by the concentration of nuclei $X^*(n^*)$, the attachment frequency f^* of building units to the nucleus making clusters of a size $(n^* + 1)$ and the probability $p(n^* + 1)$ that a cluster of size $(n^* + 1)$ grows out rather than dissolves.

$$J = p(n^* + 1) \cdot f^* \cdot X^*(n^*) \tag{32.5}$$

The *attachment frequency* f^* of building units to nucleus is reported to be an important factor in controlling nucleation and also growth. Molecules can self-associate and form different types of building blocks for different types of crystal structures (polymorphs), as can be seen in Figure 32.12. Several techniques are available to

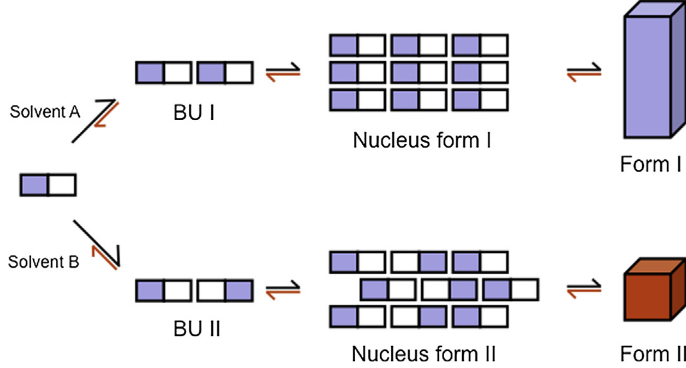

FIGURE 32.12 Effect of self-association on crystal nucleation processes.

determine the kind of association that occurs in solutions [23]. More and more literature reports show that solvents determine the association process and cause solutes to be dominantly present in specific associates that lead to the crystallization of specific polymorphic compounds [24,25].

Unfortunately, the concentration of nuclei $X^*(n^*)$ in a supersaturated solution is not known. Since in case of equilibrium the flux of particles through the nucleus size would be zero, the concentration $C^*(n^*)$ of nuclei is known that develops if equilibrium would be achieved between the supersaturated solution and the nucleus size. This is just a function of the nucleation work and the concentration C_0 of nucleation sites in the system.

$$C^*(n^*) = C_0 \exp(-W^*/kT) \tag{32.6}$$

A relation between the actual concentration $X^*(n^*)$ and the hypothetical equilibrium concentration $C^*(n^*)$ of nuclei can also be derived and the nucleation rate can be written as:

$$J = z \cdot f^* \cdot \; C_0 \exp(-W^*/kT) \tag{32.7}$$

The Zeldovich factor z accounts for the fraction of clusters of size $(n^* + 1)$ that dissolve rather than grow out as well as for the difference between $X^*(n^*)$ and $C^*(n^*)$. The *Zeldovich factor* z can be expressed as a function of the supersaturation ratio and the exponential term B:

$$z = \frac{\ln^2 S}{\sqrt{12\pi kTB}} \tag{32.8}$$

For a value of $z = 1$, an attachment of a building unit to the nucleus would reduce the possibility to zero for the cluster to dissolve. Furthermore, the concentration $X^*(n^*) = C^*(n^*)$. This would only occur at very high supersaturation ratios for which it is unlikely that nucleation occurs but rather spinodal decomposition. Therefore, reported values for z should lie below one and are usually in the range of 0.001–1.

Equation (32.7) is valid for homogeneous stationary nucleation where nuclei form in a clear solution in the absence of heterogeneous particles. However, in industrial settings such heterogeneous particles cannot be avoided, and it is usually assumed that heterogeneous nucleation (HEN) occurs under these conditions due to the much lower nucleation work $W^*_{\mathrm{HEN}} << W^*$ associated with heterogeneous nucleation, although the concentration $C_a << C_0$ of nucleation sites in heterogeneous nucleation is lower as well.

$$J_{\mathrm{HEN}} = zf^* \, C_a \exp(-W^*_{\mathrm{HEN}}/kT) \tag{32.9}$$

Since in case of heterogeneous nucleation, the nucleus forms on a heterogeneous particle there are now three interfacial energies involved: next to the interfacial energy between crystal and solution the interfacial energy between heterogeneous particle and crystal and between the particle and the solution have to be considered. Usually not much is known about these interfacial energies due to the ill-defined character of the

heterogeneous particles, and the interfacial effects are captured in an activity factor $0 < \xi < 1$.

$$\gamma_{HEN} = \xi \gamma \tag{32.10}$$

The activity factor reflects the apparent reduction of the interfacial energy between solution and crystal due to the formation of the crystal on the heterogeneous particle.

The *concentration C_0 of nucleation sites* is another variable determined by the heterogeneous particles present. Since the nucleus cannot form everywhere in the solution but only on the heterogeneous particles the concentration of nucleation sites decreases for heterogeneous nucleation $C_a << C_0$ to a value related to the concentration of heterogeneous particles present:

$$C_a = C_{HEN} a_{HEN} \tag{32.11}$$

where C_{HEN} is the concentration of heterogeneous particles and a_{HEN} is the number of nucleation sites per heterogeneous particles.

For the heterogeneous nucleation rate J_{HEN} following the CNT, it follows that [22]:

$$J_{HEN} = zf^* C_a \exp\left(-\frac{16\pi v^2 \xi^3 \gamma^3}{3k^2 T^2 \ln^2 S}\right) = A_{HEN} \exp\left(-\frac{B_{HEN}}{\ln^2 S}\right) \tag{32.12}$$

This then can be used to put next to experimental data on crystal nucleation rates from solution. Recently, a number of different crystal nucleation rate measurement methods were developed based on the double pulse method [26] and microfluidic devices [27] usually in unstirred solutions and turbidity measurements [28,29] in stirred solutions. Once nucleation rates are obtained as a function of supersaturation, they can be analyzed using the nucleation rate equation from Eqn (32.12) giving values for the pre-exponential factor A_{HEN} and the exponential factor B through a fitting procedure. While the low values reported for B_{HEN} indicate heterogeneous nucleation, the low values for A_{HEN} show that either the attachment frequency f^* of building units or the concentration C_a of heterogeneous particles is lower than expected [30,31].

Unfortunately, since usually nothing is known about the kind of heterogeneous particles the obtained values for A_{HEN} and B_{HEN} cannot be analyzed further to obtain molecular information on the crystal nucleation process which then would lead to fundamental understanding of crystal nucleation processes and better nucleation theories and nucleation rate predictions. Currently, more and more research becomes available studying the effect of well-defined heterogeneous particles on nucleation rates under well-defined conditions, which would enable a molecular interpretation. Also, simulation processes of nucleation of larger and more realistic systems become possible.

Next to association processes and heterogeneous particles, a third possibility is to use external energy sources for influencing and possibly controlling nucleation processes. For instance, lasers were used to align molecules in solutions to facilitate the nucleation of specific polymorphs [32]. Lasers were also used to induce cavitation that enabled crystal nucleation [33]. Other external energy sources include electric [34] and magnetic fields [35] and ultrasound [36,37].

There are many discrepancies between classical nucleation theory and observations from experiment and simulations. One of the main assumptions in CNT is that clusters have the same crystal structure and interfacial energy as the macroscopically large crystal. Only the reports of nucleus sizes between one and 1000 molecules already indicate that this may deviate considerably from that of a macroscopically large crystal. In fact, losing the assumption of structured nuclei is the main driver of recently introduced nonclassical nucleation mechanisms such as the two-step nucleation mechanism [38,39].

Molecular simulations [40] gave a first indication that on the transition from solution to crystalline phase it is energetically more favorable to form a liquid-like cluster in which only at larger sizes a structure is introduced. Protein nucleation experiments lead to the observation of a two-step nucleation mechanism where liquid-like clusters with a high protein density form followed by the formation of crystalline nuclei in these liquid-like clusters [38]. This would be a two-step mechanism because a barrier for nucleation exists for both the liquid-like and crystalline phase. Especially for inorganic compounds, it is argued based upon experimental evidence that larger crystalline metastable clusters form that then coagulate to form larger crystals [41,42].

Recent advances in analytical tools, molecular simulations, and measuring techniques continue to boost nucleation research. In the coming years, it is, therefore, expected to see a substantial increase in crystal nucleation knowledge. This will positively influence the industrial crystallization process control and the control over product quality from these processes.

32.4.2 Secondary Nucleation

In stirred solutions in small volumes of around 1 mL, it appeared that often only a single nucleus formed which grows out before other crystals form [43]. When the single crystal is large enough, it initiates secondary nucleation where new crystals originate from this parent crystal. This single crystal was visually observed [44] but earlier also was reported to cause chiral symmetry breaking during the crystallization of sodium chlorate, an achiral compound that crystallizes in a chiral space group [45,46]. This single nucleus mechanism indicates that possibly secondary nucleation mechanisms play an important role in determining the crystal size distribution and polymorphic form, not only in continuous crystallization processes, but even in unseeded batch cooling crystallization processes.

Secondary nucleation, exemplified by attrition in Figure 32.9, takes place in the presence of larger crystals in the suspension. Next to attrition, which seems to be the dominant secondary nucleation mechanism in industrial crystallizers [18], several other mechanisms for secondary nucleation have been identified: initial breeding, needle breeding, fracture, fluid shear, and contact [47].

Attrition causes secondary nucleation fragments due to collisions of the parent crystals with each other, the walls, and the stirrer. The stirrer tip is playing a dominant

role in this process because of its high velocity in respect to the suspension, leading to high-energy collisions of the parent crystals with the stirrer tip. A high tip speed of the stirrer thus is associated with a high attrition rate due to the large parent crystal collision frequency. However, high tip speeds are needed in order to have the crystals suspend through the solution sufficiently well. The balance between the attrition rate and suspension is a major challenge in crystallization scale-up while keeping control over the crystal size distribution.

Another way to influence parent crystal collision frequency is through the crystal mass fraction in the suspension. A higher fraction is often related to a higher number of crystals in the suspension, which in turn then would be related to a higher collision frequency.

Also, the parent crystal size is of influence: above a certain size the large parent crystals do not follow the fluid streamlines such as smaller crystals would do, and the stirrer collision probability increases. Sometimes the attrition size can be estimated from microscopic pictures of the interior of the attritted parent crystals submerged in a liquid with the same refractive index such that the crystal surface does not cloud the view on the crystal interior [48]. This attrition size may be influenced by the density difference between crystalline phase and solution.

The collisions cause fragments that may be strained and stressed and thus contain an increased chemical potential compared to an unaffected crystal. This indicates that some fragments after formation may experience an undersaturation, even though the solution is supersaturated towards the crystalline compound. This means that the supersaturation ratio is another factor influencing secondary nucleation rate: a higher supersaturation increases the probability that attrition fragments survive [49].

Next to the crystallization process conditions, many other parameters may be of influence on the secondary nucleation rate due to attrition of parent crystals with the stirrer. The material properties of crystals such as hardness and Young's modulus may play a role in the attrition propensity in a crystallizing system [50,51]. The geometry of the crystallizer and the type of stirrer, as well as the draft tube and baffle position in relation to the stirrer, can be important factors in determining the attrition rate [52]. Depending on the material, process conditions and process equipment, attrition seems to generate fragments in the range of 1–10 μm [48,53–56].

32.5 Crystal Growth

Crystal growth rates are of key importance to the engineer since they determine the crystal residence time in the crystallizer to achieve a specific crystal size and, therefore, the size of the crystallizer and the investment costs.

The linear growth rate of a specific hkl face is often denoted as R_{hkl}. For faceted crystals, the linear growth rate between hkl faces can be drastically different. The growth rate is different between faces because the surface construction differs from face to face and thus also the integration process into the kink sites is different. The growth rates of

the top faces of a needle-like crystal are usually much larger than the side faces. There is thus a relation between the crystal shape and the linear growth rate: the slowest growing hkl faces determine the shape. Linear growth rates in solution crystallization are in the order of 10^{-7} to 10^{-9} m/s. For melt layer growth, the processes can feature growth rates in the range of 10^{-5} to 10^{-7} m/s while in precipitation processes even smaller growth rates than 10^{-9} m/s could prevail.

Different definitions of growth rates are in use. In case a CSD is recorded during a crystallization process, the increase per unit of time of the characteristic crystal size L is often referred to as an overall growth rate G_L. Growth rates are sometimes also measured in terms of mass increase per surface area per unit of time resulting in a deposition rate G_m. These growth rates can be interconverted provided the crystal shape remains constant during crystal growth (Figure 32.13).

Figure 32.2 shows the route a solute molecule travels from the bulk solution to the integrated state in a kink site of a step on the crystal surface. This involves several steps. Usually the growth process is controlled by either volume diffusion or solute integration. Then the growth process is referred to as respectively volume diffusion controlled growth and integration-controlled growth. In both cases, the crystal growth rate is greater the higher the supersaturation. Only in the case of volume diffusion, the growth rate would be influenced by fluid dynamics since the volume diffusion boundary layer between crystal and bulk solution becomes thinner at higher fluid dynamics.

During growth and also nucleation, the release of the heat of crystallization causes an increased temperature at the surface [57,58]. Usually in solution crystallization this heat can be dissociated quite rapidly from the surface due to the large amount of solvent present that can act as a heat sink. In melt crystallization, this heat can be considerable and strongly affect growth rates [59,60]. Other steps that may play a decisive role in growth rate are the solvent shell removal around the solute and the volume diffusion of solvent and impurities away from the growing surface.

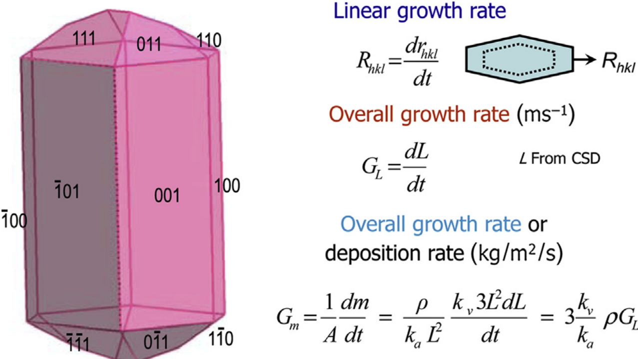

FIGURE 32.13 The relation between the linear growth rate R_{hkl} of a specific hkl face, the overall growth rate G_L, and the deposition rate G_m for a faceted crystal.

Growth rates thus depend not only on the prevailing supersaturation in the solution but may also be a function of temperature, pressure, and composition of the mother liquor, but also of fluid flow conditions, crystal growth history, and the presence of additives or impurities.

Steps and kinks (Figure 32.2) on crystal surfaces are energetically favorable sites to adsorb molecules. One way to introduce a step on a flat surface is to create a two-dimensional nucleus on the flat surface. At the periphery of the nucleus then molecules can be incorporated. This combination of two-dimensional nucleation and lateral growth of the two-dimensional islands on the surface is termed the birth and spread mechanism [61]. Since nucleation is involved, the birth and spread mechanism is a strong nonlinear function of supersaturation. For this mechanism, this leads to zero growth rates at low supersaturations and an exponential rise in the growth rate above that.

At small supersaturation, no growth would occur via the birth and spread mechanism because the energy barrier for two-dimensional nucleation is too large. Experimentally it is, however, observed that crystals grow at small supersaturations. This is explained by the spiral growth mechanism [62]. The presence of lattice imperfections such as screw dislocations in the crystal cause steps on the surface. These steps provide energetically favorable access points for incorporating molecules. Since the step originates from a fixed position of the dislocation at the surface, the incorporating molecules make the step spiral around this dislocation.

For the birth and spread mechanism at higher supersaturations the energy barrier for nucleation decreases. At some upper limit of the supersaturation, the energy barrier for nucleation becomes so low that the thermal energy within the system can overcome the barrier and molecules can freely, without energy penalty, incorporate at any position at the surface without the need of two-dimensional nucleation. The face then becomes rough, and the crystal growth mechanism is referred to as rough growth. The transition from birth and spread to a rough growth mechanism due to supersaturation is termed kinetic roughening. Its counterpart is thermal roughening where the crystal face in equilibrium shows a transition from flat to rough when increasing only temperature. More fundamental details on growth kinetics are given in Volume I of this Handbook.

A simple empirical relation for the linear growth rate R_{hkl} can be given as:

$$R_{hkl} = K(S-1)^n \tag{32.13}$$

where K is an empirical kinetic constant and the power n is the growth order. In case of surface integration-controlled growth, the value of K and n depend on the growth mechanism that occurs. Complex expressions derived from more accurate descriptions exist for the three growth mechanisms, but they all can be simplified to Eqn (32.13) by lumping the complexity in both K or n. The spiral growth, birth and spread, and linear growth mechanism have growth orders n of respectively two, larger than two and one.

In case of volume diffusion controlled growth, often it is more convenient to use the deposition rate G_M in an expression equivalent to Eqn (32.13). The kinetic constant then

is determined by the diffusion coefficient, the boundary layer thickness and the solubility, which makes it a function of for instance temperature and fluid dynamics. Usually a growth order $n = 1$ is taken for volume diffusion controlled growth.

If surface integration and volume diffusion result in competitive rates, neither can be neglected and an appropriate expression accounting for both should be used.

Since the construction of the crystal surface plays an important role in the growth rate the crystal growth history of the crystals is an important factor. The perfection or lack thereof of the surface can influence the growth rate, either accelerating or suppressing crystal growth. Often the growth history of crystals in a suspension is not equal leading to equally sized crystals having a different growth rate. These individual rates fluctuate around an average growth rate but could even lead to dissolution of specific crystals under supersaturated conditions. When crystals display individual growth rates despite identical supersaturation conditions is termed growth rate dispersion (GRD) [63]. Sometimes this is modelled using Size Dependent Growth where the growth rate varies as a function of size.

Foreign compounds such as solvents, impurities, and additives can have a drastic effect on the growth rate [64]. Figure 32.14 shows the effect of an impurity on the growth and dissolution rate of a crystalline compound [65]. Both the dissolution and the growth rate are reduced by the presence of an impurity. The more of the impurity is present, the more the growth rate is reduced. Interestingly, in this case the effect on dissolution and growth rate of the impurity is the same. There are reports that additives lead to increased growth rates [66].

The crystal shape is determined by the faces with the smallest growth rates (Figure 32.15). Growth rates are a function of the supersaturation and, therefore, an

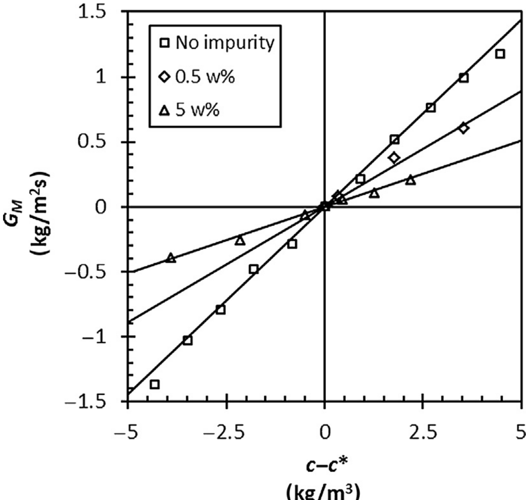

FIGURE 32.14 Growth and dissolution rates of $MgSO_4 \cdot 7H_2O$ in the absence and presence of the impurity borax. Lines are drawn as a guide to the eye. *Figure adapted from Ref. [65].*

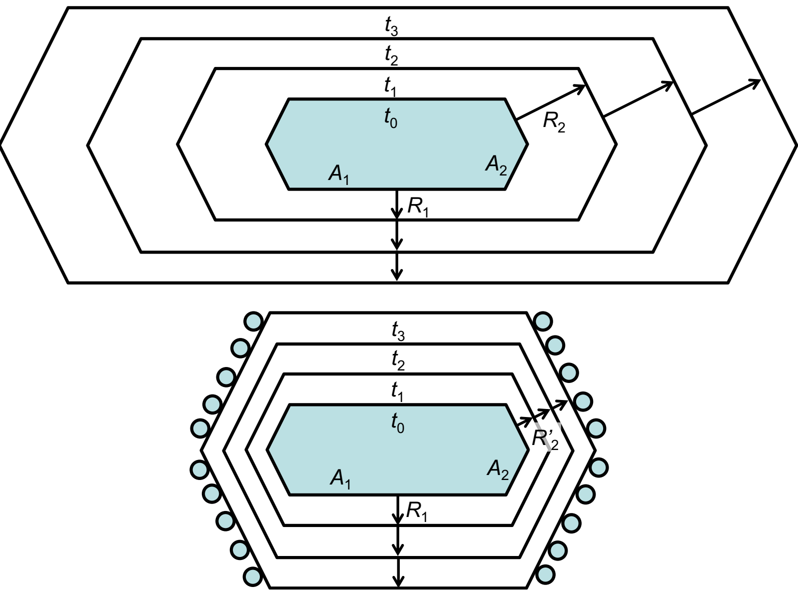

FIGURE 32.15 Impurity induced habit changes due to inhibited growth. Top: In the absence of the impurity the crystal shape does not change and the linear growth rate $R_2 > R_1$. Bottom: In the presence of the impurity on surface two from time t_0 the growth rate of face two is reduced ($R_2' < R_2$) while that of face one remains unchanged resulting in a shape change. *Adapted from Ref. [67].*

effect of the supersaturation on the shape can be anticipated. Usually, more needle-like shapes are obtained at higher supersaturations.

Since growth rates are also influenced by foreign compounds such as solvents [64], impurities, and additives, the crystal shape is also influenced by their presence. Specific crystal faces may experience growth inhibition and as a consequence, the crystal shape changes (Figure 32.15). Tailor-made additives then can be used to induce a preferred crystal shape [67]. Top faces of a needle-like crystal could specifically be inhibited with such an additive in order to considerably reduce the needle aspect ratio and in such a way prevent filtration issues or other problems.

32.6 Crystallization Process Configuration

More than 90% of active pharmaceutical ingredients (API) are crystals of small organic molecules [68]. Industrial suspension crystallization is intended to result in the preferred product quality having a good operational efficiency [69]. This means that from a product point of view (1) a sufficiently pure product should be produced of (2) the specified crystal form, having (3) the right particle size distribution and particle shape. Operational efficiency nowadays demands that the process results in (4) a high yield at (5) a high volume productivity using (6) reasonable cycle times.

Conventionally this is achieved by optimizing a limited number of different commercially available crystallizers. There are some excellent books dealing with conventional industrial crystallizer types, choice, and optimization [11,17] and, therefore, this chapter will not deal with that topic. Choosing an existing piece of equipment for a new crystallization process (usually some type of stirred vessel) would mean that the range of product quality and operational efficiency is limited and only incremental changes can be achieved through optimization once the type of equipment is chosen. This is mainly due to the many tasks that have to be performed within the stirred vessel during crystallization. Important tasks are supersaturation generation, crystal nucleation, crystal growth, secondary nucleation, and classification, all subprocesses that are optimally executed in a specific conditional and compositional operating window. These operational windows often do not overlap for optimal operational efficiency and product quality resulting in an optimized industrial crystallizer but not in an optimized crystallization process.

Therefore, nowadays one approach within industrial crystallizer design research is based on the optimization of the different subprocesses (task-based design [70]). The optimization research of the different tasks will in future lead to a toolbox of functional process building blocks for a specific crystallization task. Furthermore, these functional building blocks for different crystallization tasks can be designed into a single crystallization process or even an innovative crystallizer design especially optimized for a specific compound.

Using this task based design approach, it is investigated how to come to large crystal sizes from a crystallization process. A solution lies in having dedicated a growth compartment in the crystallizer of the future in which crystal primary and secondary nucleation are prevented. A promising candidate for a growth compartment is an airlift crystallizer [71], which uses air bubbles rather than a stirrer to cause fluid dynamics. The mild fluid dynamics cause secondary nucleation to be almost absent in the dedicated growth compartment, even for large crystal sizes.

The task supersaturation generation can, for instance, be isolated by using a membrane unit to remove solvent in a recycle loop [72]. In a state of the art evaporative crystallizer, the surface area available for evaporation is limited which also limits the rate of supersaturation generation. Evaporative crystallization processes consume a lot of energy since the heat of evaporation should be provided. To prevent scaling through crystallization, the solvent removal can take place at a higher temperature at which the solubility exceeds the concentration and thus the solution is undersaturated. Cooling down the concentrated solution creates supersaturation with which the crystal growth task can be performed.

Crystal nucleation is possibly the key process to control for good control of industrial crystallization processes. Over the years, many investigators studied possibilities to control crystal nucleation among others by providing structure (solvent [24,25], template surfaces [73]) and energy (laser light [74,75], electric fields [34], ultrasound [37]). Often, a good optimization starts with having a sound and rigorous fundamental understanding of the subprocess investigated.

Another approach to come to well-controlled product quality is by using continuous rather than batch crystallization. Continuous industrial crystallization processes (Figure 32.1) for bulk chemicals such as salt and sugar have already existed for a long time [11,17,76]. Currently, batch crystallization processes are still the preferred process configuration in the pharmaceutical industry. Batch crystallization processes are easily implemented and maintained while they produce relatively large crystals if performed well. Although batch crystallization processes seem simple, the underlying process control is highly complex. This can lead to inconsistent product specifications and batch-to-batch variations [77] as well as to problems in downstream processing and formulation. Milling of a crystalline product is, therefore, a common unit operation in the pharmaceutical industry.

Continuous crystallization would lead to improved manufacture in the chemical and pharmaceutical industry through more efficient use of reagents, solvents, energy, and space while minimizing waste production and crystallizer downtime and maximizing yield. Other advantages mentioned for continuous processes are shorter downtimes, fewer scale-up issues, better control potential for optimal process conditions, improved process safety, and economy, good reproducibility of results and smaller equipment size, which reduce capital and operating costs [78,79]. Severe scale-up problems may be prevented since pharmaceutical quantities can be achieved on benchtop scale. However, sometimes encrustation, slow achievement of steady state, and operational instability are issues to be solved for continuous crystallization processes.

32.6.1 Continuous Crystallization

Current continuous crystallization research focuses on three different process configurations. Historically, the mixed suspension mixed product removal (MSMPR) crystallizer [47] already is well known, especially for precipitation and antisolvent crystallization processes. In an MSMPR crystallizer, a feed stream is continuously fed to the crystallizer vessel and mixed with the already present suspension. An action is required to generate supersaturation, which can be done by solvent evaporation, solution cooling, antisolvent addition or by the addition of reagents that result in a low soluble reaction product. The generated supersaturation causes crystal nucleation, growth, and other subprocesses to occur in the suspension. Also, continuously a suspension stream is leaving the MSMPR crystallizer in which a variety of crystal sizes will be present if no action is taken to selectively remove crystals with the suspension stream. After a start-up period (usually taken as a substantial number of residence times), the suspension composition reaches the stationary state and, in principle, the obtained product quality should be stable.

Even slow growing crystals that need long residence times in the crystallizer to achieve the preferred size can be produced in such MSMPR crystallizers using a single process step. It appears to be relatively easy to switch from batch to continuous operation by applying MSMPR crystallizers.

A way to increase yield is to introduce a recycle stream. After filtering the suspension stream one is left with a solution, which still contains a substantial amount of the

dissolved product if the solubility of the product is relatively high. This solution can be combined with the feed stream in order to remove the remaining product. When using antisolvent crystallization or cooling crystallization, however, an action is required to respectively remove the antisolvent or concentrate the solution so that still a supersaturation can be achieved upon feeding the combined feed and recycle to the MSMPR crystallizer.

Another way to boost yield while increasing the product size is to connect several MSMPR crystallizers in a cascade [80]. In the subsequent crystallizers, the product then is grown to larger sizes. As an example, Figure 32.16 show a cascade of three continuous MSMPR cooling crystallizers with a recycle. Apart from cooling crystallization, also evaporative crystallization, antisolvent crystallization, and precipitation can be performed using MSMPR cascades.

Connecting a large number of continuously operating MSMPR crystallizers approaches a plug flow to some extent [77]. In principle, a plug flow (PF) crystallizer is a long tube to grow out the crystals that nucleate inside the tube. In a PF crystallizer, narrow residence time distributions and narrow crystal size distributions can be achieved if it is operated in true plug flow. For true plug flow conditions, turbulence is required, and that can only be achieved at high flow rates. This means that in order to achieve long residence times for large crystals, long plug flow tubes are needed. Therefore, a PF crystallizer is less suited for slow-growing crystals. Also due to the large amount of crystallizer surface present in the small diameter tube, scaling and clogging of the tube can be a severe issue [78].

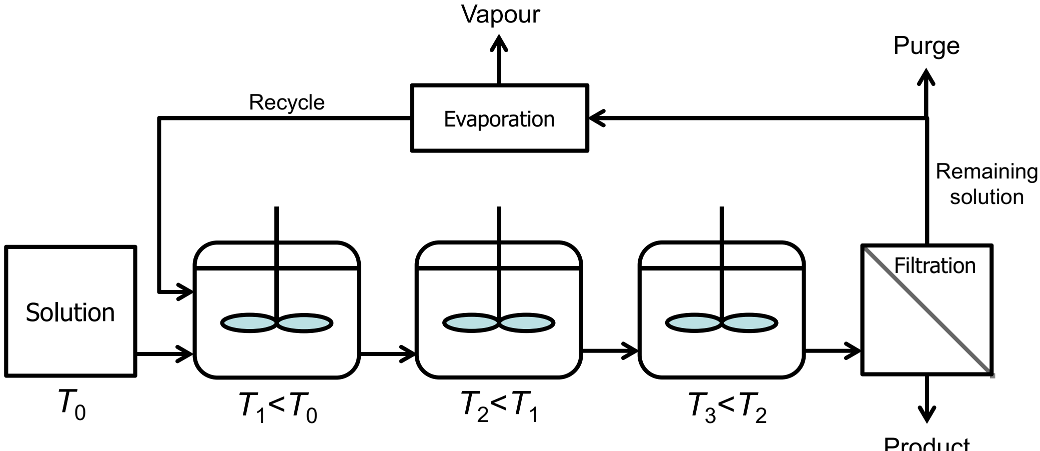

FIGURE 32.16 A cascade of three continuous MSMPR cooling crystallizers in series. Each subsequent crystallizer operates at a lower temperature to enforce a driving force for crystallization in order to increase the suspension density through nucleation and growth. The filtration step continuously separates the crystal product from the remaining solution. To increase the yield, the remaining solution is recycled back into the process after a concentration step through evaporation. A purge stream enables impurities to leave the system. *Adapted from Ref. [80].*

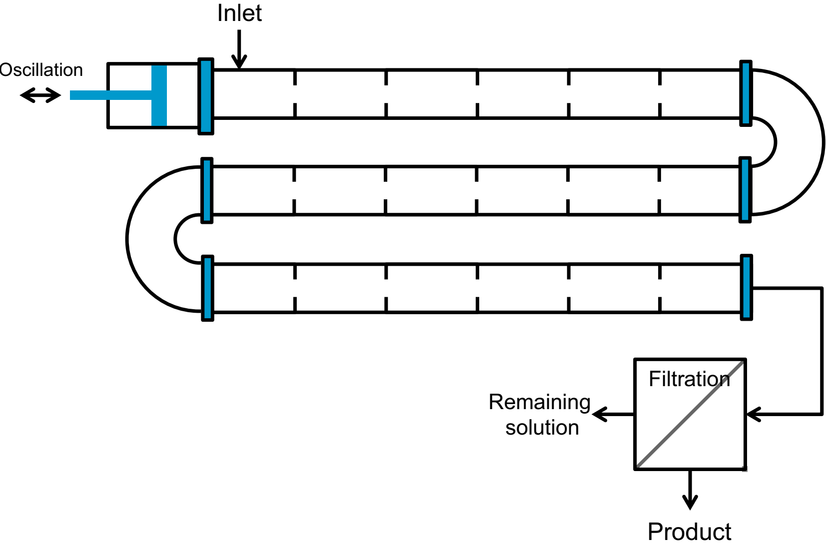

FIGURE 32.17 An oscillatory baffled crystallizer is a tubular crystallizer with periodically spaced orifice baffles. An oscillation is superimposed on the net flow for improved mixing and mass transfer. A driving force for crystallization can be imposed by, for instance, a temperature profile along the length of the tube. The filtration step continuously separates the crystal product from the remaining solution. The remaining solution can be recycled back into the process. *Adapted from Ref. [77].*

In an oscillatory baffled (OB) crystallizer [77], a tubular crystallizer is equipped with periodically spaced orifice baffles (Figure 32.17). An oscillatory flow motion is superimposed on the net flow through the tube. This gives improved mixing and mass transfer compared to the PF crystallizer at lower flow rates. In both a PF and OB crystallizer, the driving force can be controlled through the cooling profile imposed along the length of the tube. Also, solvent or other components can be added at inlets along the length of the tube in order to create the driving force.

32.6.2 Batch Crystallization

During a batch crystallization process, the process conditions change so that the supersaturation needed to grow the crystals is maintained. For instance, during a batch cooling crystallization process the temperature is decreased gradually in order to constantly increase the supersaturation which in turn is constantly reduced by crystal growth. Also, the other crystallization techniques can be performed batch-wise.

Seeding is a way to prevent primary nucleation at the start of a batch crystallization process. In a slightly supersaturated solution within the metastable zone where no nucleation occurs, seeds are added in order to grow them out. The generated supersaturation during the batch is only used for growth and because of the known amount and size of the seeds, the final product size can be controlled if agglomeration and secondary nucleation of the growing seed crystals can be prevented. The crystal size

distribution of the final product depends on the nature of the seeds introduced into the process [11,81–83].

If it is assumed that nucleation and agglomeration do not occur after seeding, the number of crystals remains constant during the batch crystallization. Then it is possible, through the number of crystals, to relate the seed mass M_s to the mass M_p produced during the batch crystallization [11]:

$$M_s = M_p \frac{L_s^3}{L_p^3 - L_s^3} \tag{32.14}$$

where L_s and L_p are seed and product size, respectively. This then can be used to determine the seed mass M_s needed to obtain a certain product size L_p during seeded batch crystallization. Due to the power of three in Eqn (32.14) the seed mass can be very small while still a substantial product size L_s can be achieved. If the seed size $L_s = 10$ μm and the required product size is $L_p = 100$ μm, the seed mass to be used is around 0.1% of the produced mass.

The seed quality depends to some extent on the origin of the seed crystals and how the seeds are added. Fines in the seeds and seed surface irregularities and imperfections can be removed by suspending the seeds in a slightly undersaturated solution and adding them as a suspension rather than a dry powder. This increases the control over the final product quality.

If the metastable zone width is small in batch cooling crystallization, primary nucleation already occurs only a few degrees below the saturation temperature. The temperature region for seeding is relatively small, and seeds could be added too early causing dissolution of the seeds or too late, after primary nucleation already occurred. In both cases, control over product quality is lost. Usually seeding is done at moderate supersaturation entering not more than 30–40% into the metastable zone.

The crystal growth rate determines the batch time since the seeds have to grow out from the seed size L_s to the product size L_p. For instance with a growth rate $R_{hkl} = 10^{-8}$ m/s, the time to grow the seeds from $L_s = 10$ to $L_p = 300$ μm is then estimated to be 4 h. Of course, the supersaturation available for growth can be adjusted through the cooling rate in order to speed up the process.

Three types of temperature profiles for cooling are commonly used in seeded batch cooling crystallization: natural cooling, linear cooling, and parabolic cooling [84–90]. The type of temperature profile has a significant impact upon the resulting crystal quality. During the batch, the crystal size increases and more crystal surface becomes available to consume the supersaturation. Therefore, the crystallizing system can handle larger cooling rates toward the end of the batch. As the crystal surface area is quadratically related to the crystal size, the temperature should, ideally, follow a parabolic function using a slow cooling rate at the start and higher cooling rates toward the end of the batch [11]. When properly controlled, a parabolic temperature profile results in a constant supersaturation and a constant crystal growth rate throughout the duration of the batch process (Figure 32.18), which usually is related to a good crystal quality.

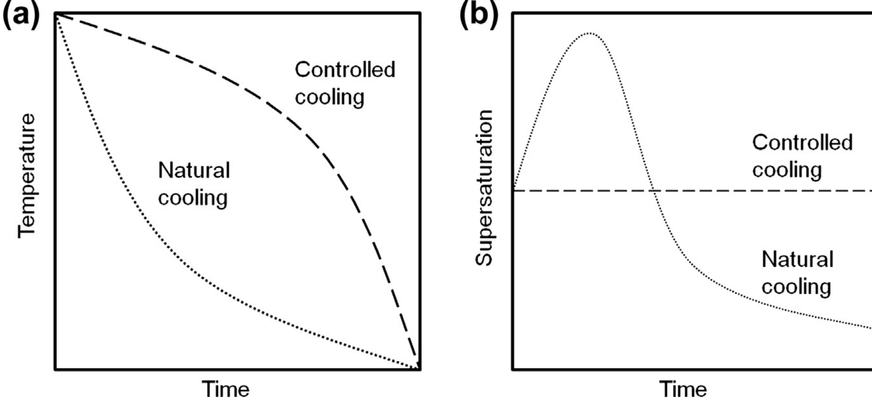

FIGURE 32.18 Temperature profiles (a) and resulting supersaturation profiles (b) for natural and controlled cooling in batch crystallization. *Adapted from Ref. [92].*

The linear and natural cooling profile both have a relatively fast cooling rate in the initial stages of the batch crystallization process. When the cooling rate is too fast during the initial stages of a seeded batch cooling crystallization, the seed crystals cannot consume the generated supersaturation sufficiently fast. Consequently, the supersaturation builds up to a point indicated in Figure 32.18 that extensive secondary nucleation can proceed. At that point, control is lost over the number of crystals and thus over the resulting product quality. If the attrition propensity of a compound is high then secondary nucleation might occur already at relatively low cooling rates, especially if the growth rate is relatively slow [91].

Agglomeration is the aggregation and intergrowth of crystals during crystallization. When agglomeration occurs during the batch, the number of particles in the suspension will decrease. The agglomeration rate depends on the number of crystal–crystal collisions, the growth rate and the agglomeration tendency. If the agglomeration tendency of a compound is high gently mixing and low supersaturations during crystallization might prevent severe agglomeration.

32.7 Ensuring Product Quality in the Future

Industrial crystallization (Figure 32.19) is a subset of processes of primary nucleation, crystal growth, secondary nucleation, and agglomeration. These processes are steered by the solution properties, fluid dynamics, and the prevailing supersaturation. The interplay between the different subprocesses and the process conditions determines the product quality defined from the kind of material produced (form), crystal size distribution, crystal shape, and purity.

Nowadays there are a number of inline process analytical tools [13] available to monitor crystallization characteristics. Raman spectroscopy [93] is a tool that can make a distinction between different forms in the suspension. Sometimes, in parallel the

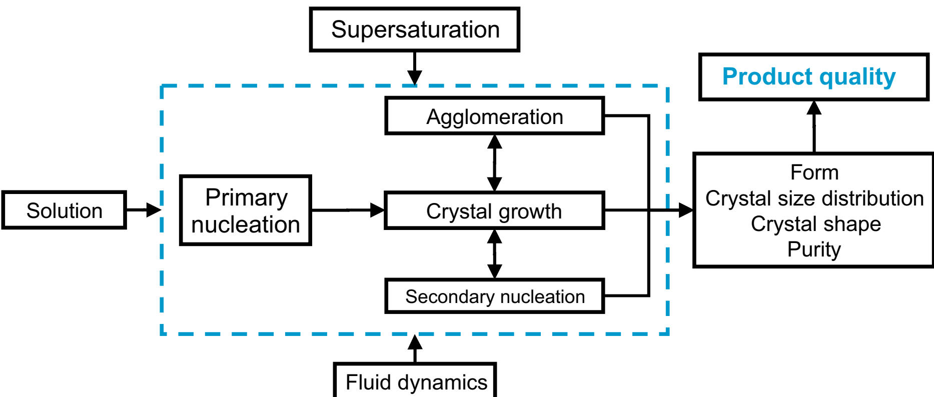

FIGURE 32.19 The crystal product quality is determined by the form, CSD, shape, and purity of the crystalline phase. This in turn is determined by the subprocesses of crystallization: primary nucleation, crystal growth, agglomeration, and secondary nucleation. The subprocesses in turn are determined by the solution, prevailing supersaturation, and fluid dynamic conditions.

solution concentration can be determined as well [94]. Other tools are infrared spectroscopy, particles size, and cord length measurement techniques, conductivity, sound velocity turbidity, and online particle tracking by laser light [13].

These process analytical tools enable process control [95]. For instance, dynamic control over the CSD in batch cooling crystallization processes can be obtained by using an in situ cord length measurement technique [96]. Unintended secondary nucleation outbursts can be detected and with controlled heating combined with an accurate process model these secondary nuclei can be dissolved again. In order to come to true process control, the signal of the process analytical tools should be translated into a process action that has a very specific effect. This means that fundamental understanding of the subprocesses is needed to feed into rigorous process models that enable the accurate prediction of how the system responds to process actions such as temperature profiles.

New active pharmaceutical ingredients show an increasingly larger molecular weight indicating that product molecules become larger while containing more functional groups. This trend toward more complex molecules, but also to more complex and multicomponent product materials, will surely proceed into the future.

A crystalline product has to fulfil certain specifications (e.g., color, stability) that are related to the product quality aspects defined in this chapter: form, size, shape, and purity. Relations between product quality aspects, process conditions, and the molecular components in the product continue to be discovered and understood. However, the resulting product quality is still difficult if not impossible to predict a priori.

One important reason for this is that the relation between the crystallizing molecules and the crystal structure is still not well understood. It is, therefore, still not possible to

reliably know whether specific stable and metastable multicomponent crystal exists. Pushed by demands from the pharmaceutical industry and the world of crystal engineering, crystal structure prediction methods did make a giant leap forward in the last few years [97,98]. At the same time, preparation methods and thermodynamic insight in multicomponent crystals lifted off by discoveries in, for instance, the co–crystal research field [15]. However, an accurate prediction of phase diagrams including multicomponent effects is still not possible. In coming years, the current knowledge should be enlarged and combined into an on-demand joint simulation and experimental approach for the discovery and use of such kind of multicomponent crystals.

Another reason is the inability to predict size, shape, and purity of a crystalline product from an industrial crystallization without experimental information. This predictability is, for instance, limited by the level of understanding of the key process of industrial crystallization, and crystal nucleation [23]. Predictions of nucleation rates with current theories are still orders of magnitude off from those measured in experiments. However, several new measurement methods became available the last few years. Also, newly developed analytical tools can be used to capture the initial stages of crystal nucleation. Molecular simulations, furthermore, become more and more powerful and can handle realistic nucleating systems. This means that the coming years interesting developments in this field can be expected.

Design, operation, and control of large industrial crystallization processes are extremely complex and challenging due to the determining molecular processes that make that all crystalline compounds show different crystallization behavior. The increasing complexity and size of the product components in the future implies that the complexity of the underlying processes will increase as well. At the same time, process technology nowadays strives to sustainable processing which puts limits to waste production, energy, and raw materials. All this brings new separation and particulate challenges also for industrial crystallization processes. The design challenges will be tackled in the future, for instance, by the task-based design approaches mentioned in the section on crystallization process configurations. Another way to overcome many of the problems is to develop continuous crystallization processes.

Increased complexity can also lead to opportunities. For instance, the combination of a racemization reaction and grinding of a conglomerate system in Viedma ripening leads to an enantiopure crystalline product [99]. In other instances, co-crystallization was proposed as a separation technology, for instance, to remove a small concentration of the product from a complex fermentation broth [100]. The use of co-crystals rather than pure component crystals enabled the in situ product removal at much lower concentrations.

The authors hope this chapter is convincing in showing that the solution to future challenges has to be found in a fundamental understanding of the crystallization subprocesses such as crystal nucleation and growth. This fundamental understanding in turn results in the identification of innovative, integrated, and intensified crystallization processes and equipment.

References

[1] Henley EJ, Seader JD, Roper DK. Separation process principles, international student version. 3rd ed. New Jersey: John Wiley; 2011.

[2] de Haan A, Bosch H. Industrial separation processes: Fundamentals. Berlin: De Gruyter; 2013.

[3] Davey RJ, Garside J. From molecules to crystallizers. New York (USA): Oxford University Press Inc.; 2000.

[4] Bernstein J. Polymorphism in molecular crystals, IUCr monographs on crystallography, 14. Oxford (GB): Oxford Science Publishers; 2002.

[5] Lee AY, Erdemir D, Myerson AS. Annu Rev Chem Biomol Eng 2011;2:259.

[6] Fleischman SG, Kuduva SS, McMahon JA, Moulton B, Bailey Walsh RD, Rodrıguez-Hornedo N, et al. Cryst Growth Des 2003;3:909.

[7] Aitipamula S, Banerjee R, Bansal AK, Biradha K, Cheney ML, Choudhury AR, et al. Cryst Growth Des 2012;12:2147.

[8] Hartman P. In: Hartman P, editor. Crystal growth – an introduction. Amsterdam: North-Holland Publ.; 1973. p. 367.

[9] Bennema P. Growth and morphology of crystals: integration of theories of roughening and Hartman-Perdok theory. In: Hurle DTJ, editor. Handbook of crystal growth, 1a. Amsterdam: Elsevier; 1993 [chapter 7].

[10] Sunagawa I. Crystals — growth, morphology and perfection. Cambridge (UK): Cambridge University Press; 2005.

[11] Mullin JW. Crystallization. 4th ed. Oxford (UK): Butterworth-Heinemann; 2001.

[12] Rhodes M. Introduction to particle technology. 2nd ed. UK: Wiley; 2008.

[13] Chianese A, Kramer HJM. Industrial crystallization process monitoring and control. Weinheim: Wiley-VCH Verlag GmbH & Co. KGaA; 2012.

[14] Alsenz J, Kansy M. Adv Drug Delivery Rev 2007;59:546.

[15] ter Horst JH, Deij MA, Cains PW. Cryst Growth Des 2009;9(3):1531.

[16] Nordström FL, Rasmuson ÅC. Eur J Pharm Sci 2009;36:330.

[17] Myerson AS. Handbook of industrial crystallization. Oxford (UK): Butterworth-Heinemann; 2002.

[18] Mersmann S. Crystallization technology handbook. New York (USA): Marcel Dekker, Inc.; 2001.

[19] Westphal G, Kristen G, Wegener W, Ambatiello P, Geyer H, Epron B, et al. Sodium chloride, Ulmann's encyclopedia of industrial chemistry, vol. 33. Weinheim: Wiley-VCH Verlag GmbH; 2012. 319–365.

[20] Schiweck H, Clarke M, Pollach G. Sugar, Ulmann's encyclopedia of industrial chemistry, vol. 34. Weinheim: Wiley-VCH Verlag GmbH; 2012. 557–628.

[21] Kramer HJM, Bermingham SK, van Rosmalen GM. J Cryst Growth 1999;198:729.

[22] Kashchiev D. Nucleation: basic theory with applications. Oxford: Butterworth-Heinemann; 2000.

[23] Davey RJ, Schroeder SLM, ter Horst JH. Angew Chem 2013;52:2166.

[24] Davey RJ, Allen K, Blagden N, Cross WI, Lieberman HF, Quayle MJ, et al. CrystEngComm 2002; 4:257.

[25] Kulkarni SA, McGarrity ES, Meekes H, ter Horst JH. ChemCommun 2012;48:4983.

[26] Galkin O, Vekilov PG. J Phys Chem B 1999;103:10965.

[27] Ildefonso M, Candoni N, Veesler S. Cryst Growth Des 2011;11:1527.

[28] Jiang S, ter Horst JH. Cryst Growth Des 2011;11:256.

[29] Nordström FL, Svärd M, Rasmuson ÅC. CrystEngComm 2013;15:7285.

[30] Kashchiev D, van Rosmalen GM. Cryst Res Technol 2003;38:555.

[31] Kulkarni SA, Kadam SS, Meekes H, Stankiewicz AI, ter Horst JH. Cryst Growth Des 2013;13(6):2435.

[32] Zaccaro J, Matic J, Myerson AS, Garetz BA. Cryst Growth Des 2001;1(1):5.

[33] Soare A, Dijkink R, Rodriguez Pascual M, Sun C, Cains PW, Lohse D, et al. Cryst Growth Des 2011; 11(6):2311.

[34] Hammadi Z, Astier JP, Morin R, Veesler S. Cryst Growth Des 2009;9(8):3346.

[35] Sazaki G, Yoshida E, Komatsu H, Nakada T, Miyashita S, Watanabe K. J Cryst Growth 1997; 173(1–2):231.

[36] Kallies B, Ulrich J, König A. Chem Eng Res Des 1997;75(2):142.

[37] Virone C, Kramer HJM, van Rosmalen GM, Stoop AH, Bakker TW. J Cryst Growth 2006;294(1):9.

[38] Vekilov PG. Cryst Growth Des 2004;4(4):671.

[39] Erdemir D, Lee AY, Myerson AS. Acc Chem Res 2009;42(5):621.

[40] ten Wolde PR, Frenkel D. Science 1997;277:1975.

[41] Gebauer D, Coelfen H. Nano Today 2011;6:564.

[42] Baumgartner J, Dey A, Bomans PHH, Le Coadou C, Fratzl P, Sommerdijk NAJM, et al. Nat Mater 2013;12(4):310.

[43] Kadam SS, Kulkarni SA, Coloma Ribera R, Stankiewicz AI, ter Horst JH, Kramer HJM. Chem Eng Sci 2012;72:10.

[44] Kadam SS, Kramer HJM, ter Horst JH. Cryst Growth Des 2011;11:1271.

[45] Kondepudi DK, Kaufman RJ, Singh N. Science 1990;250:975.

[46] McBride JM, Carter RL. Angew Chem Int Ed Engl 1991;30:293.

[47] Randolph AD, Larson MA. Theory of particulate processes. New York: Academic Press; 1971.

[48] O'Meadhra R, Kramer HJM, Van Rosmalen GM. AIChE J 1996;42:973.

[49] Virone C, ter Horst JH, Kramer HJM, Jansens PJ. J Cryst Growth 2005;275:1–2. e1397.

[50] Gahn C, Mersmann A. Chem Eng Sci 1999;54(9):1273.

[51] Gahn C, Mersmann A. Chem Eng Sci 1999;54(9):1283.

[52] Mueansichai T, Flood AE, Stelzer T, Ulrich J. Cryst Res Technol 2013;48:38.

[53] van der Heijden AEDM, van der Eerden JP, van Rosmalen GM. Chem Eng Sci 1994;49(18):3103.

[54] Nienow AW, Conti R. Chem Eng Sci 1978;33:1077.

[55] Youngquist GR, Randolph AD. AIChE J 1972;18(2):421.

[56] Garside J, Rusli IT, Larson MA. AIChE J 1979;25(1):57.

[57] Matsuoka M, Garside J. Chem Eng Sci 1991;46(1):183–92.

[58] ter Horst JH, Bedeaux D, Kjelstrup S. J Chem Phys 2011;134:054703.

[59] Arkenbout GF. Melt crystallization technology. Western Hemisphere: Technomic Publishing Company; 1995.

[60] Ulrich J, Glade H. Melt crystallization: fundamentals, equipment and applications. Aachen: Shaker Verlag, GmbH; 2003.

[61] Söhnel O, Garside J. Precipitation: basic principles and industrial applications. Oxford: Butterworth-Heinemann Ltd.; 1992.

[62] Burton WK, Cabrera N, Frank FC. Philos Trans R Soc Lond 1951;A243:299.

[63] Ulrich J. Cryst Res Technol 1989;24:249.

[64] ter Horst JH, van Rosmalen GM, Geertman RM. Additives: molecular design. In: Encyclopedia of separation science. Academic Press; 2000. p. 931.

[65] Al Jibbouri S, Ulrich J. Cryst Res Technol 2004;39:540.

[66] Dowling R, Davey RJ, Curtis RA, Han G, Poornachary SK, Shan Chow P, et al. Chem Commun 2010;46:5924.

[67] Addadi L, Berkovitch-Yellin Z, Domb N, Gati E, Lahav M, Leiserowitz L. Nature 1982;296:21.

[68] Alvarez AJ, Myerson AS. Cryst Growth Des 2010;5:2219.

[69] Variankaval N, Cote AS, Doherty MF. AIChE J 2008;54(7):1683.

[70] Menon AR, Pande AA, Kramer HJM, Jansens PJ, Grievink J. Ind Eng Chem Res 2007;46(12):3979.

[71] Soare A, Lakerveld R, van Royen J, Zocchi G, Stankiewicz AI, Kramer HJM. Ind Eng Chem Res 2012;51(33):10895.

[72] Kuhn J, Lakerveld R, Kramer HJM, Grievink J, Jansens PJ. Ind Eng Chem Res 2009;48(11):5360.

[73] Aizenberg J, Black AJ, Garetz BA, Whitesides GM. Nature 1999;398(6727):495.

[74] Matic J, Sun X, Garetz BA, Myerson AS. Cryst Growth Des 2005;5(4):1565.

[75] Okutsu T, Furuta K, Terao M, Hiratsuka H, Yamano A, Ferté N, et al. Cryst Growth Des 2005;5(4):1393.

[76] Hofmann G, Melches C. Continuous crystallization [chapter 11]. In: Beckmann W, editor. Crystallization: basic concepts and industrial applications. Weinheim: Wiley-VCH Verlag GmbH & Co. KGaA; 2013.

[77] Lawton S, Steele G, Shering P, Zhao L, Laird I, Ni Xiong-Wei. Org Proc Res Dev 2009;13(6):1357.

[78] Eder RJP, Schmitt EK, Grill J, Radl S, Gruber-Woelfler H, Khinast JG. Cryst Res Technol 2011;46:227.

[79] Chen J, Sarma B, Evans JMB, Myerson AS. Cryst Growth Des 2011;11(4):887.

[80] Alvarez Alejandro J, Singh Aniruddh, Myerson Allan S. Cryst Growth Des 2011;11(10):4392.

[81] Kubota N. Powder Technol 2001;121(1):31.

[82] Kubota N, Doki N, Ito M, Sasaki S, Yokota M. J Chem Eng Jpn 2002;35(11):1078.

[83] Zhang GGZ, Grant DJW. Cryst Growth Des 2005;5(1):319.

[84] Hu Q, Rohani S, Wang DX, Jutan A. Powder Technol 2005;156(2–3):170.

[85] Costa CBB, Maciel Filho R. Chem Eng Process 2005;44:727.

[86] Mohamed HA, Abu-Jdayil B, Al Khateeb M. Chem Eng Process 2002;41:297.

[87] Miller SM, Rawlings JB. AIChE J 1994;40(8):1312.

[88] Nyvlt J. Chem Eng Process 1988;24:217.

[89] Mullin JW, Nyvlt J. Chem Eng Sci 1971;26:369.

[90] Jones AG. Chem Eng Sci 1974;29:1075.

[91] Ulrich J, Jones MJ. Seeding technique in batch crystallization. In: Chianese A, Kramer HJM, editors. Industrial crystallization process monitoring and control. Weinheim: Wiley-VCH Verlag & Co. KGaA; 2012. p. 127.

[92] Omar W, Zur Bestimmung von kristallisationskinetiken auch unter der einwirkung von additiven mittels Ultraschallmeßtechnik, Dissertation, Universität Bremen, 1999.

[93] Ono T, ter Horst JH, Jansens PJ. Cryst Growth Des 2004;4(3):465.

[94] Cornel J, Lindenberg C, Mazzotti M. Ind Eng Chem Res 2008;47(14):4870.

[95] Barrett P, Smith B, Worlitschek J, Bracken V, O'Sullivan B, O'Grady D. Org Proc Res Dev 2005;9(3):348.

[96] Nagy ZK, Aamir E, Rielly CD. Cryst Growth Des 2011;11(6):2205.

[97] Day GM, Cooper TG, Cruz-Cabeza AJ, Hejczyk KE, Ammon HL, Boerrigter SXM, et al. Acta Crystallogr B 2009;65:107.

[98] Bardwell DA, Adjiman CS, Arnautova YA, Bartashevich E, Boerrigter SXM, Braun DE, et al. Acta Crystallogr B 2011;67:535.

[99] Noorduin WL, van der Asdonk P, Bode AAC, Meekes H, van Enckevort WJP, Vlieg E, et al. Org Proc Res Dev 2010;14:508.

[100] Urbanus J, Roelands CPM, Mazurek J, Verdoes D, ter Horst JH. CrystEngComm 2011;13:2817.

Index

Note: Page numbers followed by "b", "f" and "t" indicate boxes, figures and tables respectively

A

A-center, 83
A-form nitrogen, 679
A-swirl defect, 88
A+ wafers, 398–399
A++ wafers, 398–399
A3+ wafers, 399–400
A4+ wafers, 399–400
Accelerated crucible rotation technique (ACRT), 188, 344–345, 469, 497–498, 821, 952–953, 955, 1011, 1028, 1220
  on acceleration/deceleration, 955–956
  Bridgman/ACRT growth, 961f
  in CdTe/$Cd_{1-x}Zn_xTe$ growth, 964–967
  CMT growth, 959–960
  in group-IV growth, 967–968
  high-x CMT material, 960–964
  in material system, 968
  parameters, 959t
  rotation sequence, 957f
Acidic mineralizers, 595–596
ACRT. *See* Accelerated crucible rotation technique
Active pharmaceutical ingredients (API), 1337
Additives, 1215
Advanced Photon Source (APS), 702
Advection, 803
AE model. *See* Atomic emission model
Aerogels, 1296–1301
AFM. *See* Atomic force microscopy
Agarose gels, 1295
Agglomeration, 1343
AHP method. *See* Axial heat processing method
Alcothermal process, 536–537
AlN. *See* Aluminum nitride
$3Al_2O_3$ $2SiO_2$. *See* Mullite
Alternating magnetic field (AMF), 68, 389, 928, 932–934
Aluminosilicates, 427–428
Aluminum berlinites, 556–558
Aluminum nitride (AlN), 595, 622–623. *See also* Crystal growth
  bulk crystal, 623
    growth setups, 624f
    single crystals, 635f
  growth on SiC seeds, 634–635
  powder, 624–625
  spiral growth, 631
  structural defects, 638–640
AMF. *See* Alternating magnetic field; Automatic mirror furnace
Ammonium chloride (NH_4Cl), 648
Ammono-acidic mineralizer. *See* Acidic mineralizers
Ammono-basic mineralizer. *See* Basic mineralizer
Ammonothermal
  process, 536–537
  solution chemistry, 602–604
Ammonothermal growth techniques. *See also* High nitrogen pressure solution growth method (HNPS method)
  historical development, 595–600
  method, 600–602
  properties, 610–612
  prospects and future developments, 613
  solubility in, 604–607
Angular vibration technique (AVT), 344–345
Anisotropic growth rate, 1249
Annealing process, 1269
Annihilation, 1113
Antimonides, 121, 347
API. *See* Active pharmaceutical ingredients

APS. *See* Advanced Photon Source
Aquamarine, 562–563
Arcing, 252–253
Arrhenius-type relation, 1189
Arsenides, 119
Artificially grown crystals, 716
Astrocrystallization, 37
Atomic emission model (AE model), 185–187
Atomic force microscopy (AFM), 1207–1208, 1245
ATR. *See* Attenuated total reflection
Attenuated total reflection (ATR), 703
Autoclaves, 549t
Automatic mirror furnace (AMF), 493
AVC. *See* Axial vibrational control
AVC-assisted
  floating zone method, 979
  zone melting method, 979–980
AVC-assisted Bridgman technique (AVC-Br technique), 973, 977–978, 978f
AVC-assisted Czochralski technique (AVC-Cz technique), 973
  Cz-I method, 974, 976f
  Cz-II method, 977
Avogadro constant, 259–260
Avogadro crystal, 259–260
Avrami formulation, 17
AVT. *See* Angular vibration technique
Axial heat processing method (AHP method), 343
Axial magnetic fields, 68, 914–919
Axial vibrational control (AVC), 344–345, 952–953, 968–969
  on crystal growth, 971–980
  crystal materials, 980
  physical nature, 969–971
Axisymmetric formulations, 769–770

B
Ba-Cu-O system, 1234–1235
$Ba_2Cu_3\ O_{7-\delta}$ material (RE-123 material), 1231
Band approximation, 814
Barium metaborate (BBO), 188–192
Baroclinic instability, 862
BARS equipment, 677, 677f
Basic mineralizer, 595–596
Batch crystallization process, 1339, 1341–1343
Batch reactors, 539, 551
Bayer’s process, 538–539
BBO. *See* Barium metaborate
BC. *See* Boundary condition
Bell-curve furnace profile, 829–832
Belt-type apparatus, 675, 676f. *See also* Multi-anvil apparatus; Toroid-type apparatus
BEM. *See* Boundary element method
BEN. *See* Bias-enhanced nucleation
Bénard cells, 119–120
β angle, 445
β-BaB_2O_4. *See* Barium metaborate (BBO)
β-Ga_2O_3, 212–218
BGO. *See* Bismuth germinate
Bi-Sr-Ca-Cu-O system (BSCCO system), 1231
$Bi_4Ge_3O_{12}$. *See* Bismuth germinate (BGO)
Bias-enhanced nucleation (BEN), 694
BiB_3O_6. *See* Bismuth triborate (BiBO)
BiBO. *See* Bismuth triborate
Binder, 429
Biologically induced crystallization, 11
Biomineralization, 11
Biominerals, 11
Bismuth germinate (BGO), 152, 154–157
Bismuth triborate (BiBO), 201–202
Boiling solutions, 1196
Boron, 70, 684
  Boron-doped type IIb diamond, 684–685
  influence of boron impurities, 685
  oxide, 347
Boule growth approach, 654
Boundary condition (BC), 264, 803–805
Boundary element method (BEM), 263
Boundary layer, 864–865
BPS theory. *See* Burton–Prime–Slichter theory
BR method. *See* Bridgman method
Bridgman method (BR method), 416–417, 796, 1050, 1074, 1147–1148
Bridgman-Stockbarger methods (BS methods), 137–138
Bright meniscus ring detection, 1159–1160
“Bright ring”, 1159–1160

Brownian simulation, 1294
BS methods. *See* Bridgman-Stockbarger methods
BSCCO system. *See* Bi-Sr-Ca-Cu-O system
Bubbles. *See* Microvoids
Bulk borate NLO crystal growth
  BiBO, 201–202
  KBBF, 199–201
  LiB_3O_5 family of crystals, 192
  low-temperature phase of barium metaborate, 188–192
Bulk growth, 654
  activities, 952
  crystal growth methods, 1239–1243
  crystalline material, 794
Bulk single crystals, 1050
  dislocations in, 1074–1088
  growth process, 1079–1081
  thermal stress in, 1050
    calculating methodology, 1051–1060
    cracking by, 1069–1073
    thermal stress analysis examples, 1060–1069
Bulk spiral formation mechanism, 180–187
Bunching. *See* Dislocation clustering
Buoyancy convection, 62, 119, 881–882
Burgers vector analysis, 358
Burton–Prime–Slichter theory (BPS theory), 916, 997, 1012–1014

C

Cabrera–Vermilyea model, 1200–1201, 1208
Cadmium mercury telluride (CMT), 955, 959–960
  high-x CMT material, 960–964
Cadmium telluride (CdTe), 820
Cadmium tungstate (CWO), 152, 157–158
Cadmium zinc telluride (CZT), 820
  bell-curve furnace profile, 829–832
  Bridgman growth, 820
  crystals, 964–967
  experimental validation, 828–829
  heat transfer analysis, 822–828
  motivation, 820–822
CaF_2 crystal. *See* Calcium fluoride crystal
CAFÉ numerical method. *See* Cellular automaton finite element numerical method
Calcite, 560–561
Calcium carbonate ($CaCO_3$), 139–140
Calcium fluoride crystal (CaF_2 crystal), 137–138. *See also* Large fluoride crystals
  annealing process, 146
  double-crucible system, 142–146
  growth
    apparatus, 140
    technique, 138–139
  starting materials, 139–140
  technical challenges, 140–142
Caloric fluid, 799
Capillarity for crystal grower
  catching and horizontal conditions, 768
  growth angle, 764–766
  Marangoni convection, 762–764
  surface and cohesion energies, 761–762
  wetting angle, 766–767
  Young–Laplace equation, 764
Capillarity-driven processes, 760–761
Capillary convection, 63
Carbon, 81, 866–867
  conversion methods, 673–674
  doping mechanism, 515–519
  P-T phase diagram, 673f
  particles, 640
  precipitates, 381–382
Carbon-bonded carbon fiber (CBCF), 633
Carbonate rocks, 11
Carbonate-silicate systems, 688–689
Carbonothermal process, 536–537
Carousel magnetic fields (CMF), 389
Catching conditions, 768
Cathodoluminescence (CL), 651
CBCF. *See* Carbon-bonded carbon fiber
CBO. *See* Cesium triborate
CC model. *See* Combined convection model
CCD. *See* Charge-coupled devices
CCz technique. *See* Continuous Czochralski technique
$Cd_{1-x}Zn_xTe$. *See* Cadmium zinc telluride (CZT)
CdTe. *See* Cadmium telluride

$CdWO_4$. *See* Cadmium tungstate (CWO)
Ce^{3+}-doped fluorides, 150–152
Cell patterning, 1114
Cellular automaton finite element numerical method (CAFÉ numerical method), 452–453
Centrifugal effects, 852–854
Centrifuge, 496
Ceramic rod preparation, 290–291
CERN. *See* European Organization for Nuclear Research
Cesium lithium borate (CLBO), 197–199, 1216–1217
Cesium triborate (CBO), 195–197
Charge-coupled devices (CCD), 857
Chechevitsa (lentil), 676
Chemical complexation reaction, 1281
Chemical decomplexation reaction, 1281
Chemical gels, 1297–1298
Chemical vapor deposition (CVD), 348, 673
  DC Arc-Jet, 695–696
  DC Plasma, 695
  diamond CVD process, 692f
  diamond specialties, 703–704
  hot filament, 695
  MPCVD, 696–698
  principles, 692–694
Chemical vapor transport (CVT), 213
Chemomechanical polishing process (CMP process), 749
Chirped-pulse amplification, 152
Chondrules, 37–38
CHPA. *See* Cubic high pressure apparatus
Chuck-less process, 748
CL. *See* Cathodoluminescence
Classical nucleation theory (CNT), 1327
CLBO. *See* Cesium lithium borate
Closed-loop control, 1145–1146
Clusters, 383–385
CMF. *See* Carousel magnetic fields; Cusp-shaped magnetic field
CMP process. *See* Chemomechanical polishing process
CMT. *See* Cadmium mercury telluride
CNT. *See* Classical nucleation theory
Co-crystals, 1319–1320
Coalescence growth technique, 527–531
Cochran–Levich solution, 997
C–O–H system, 690
Cohesion energies, 761–762
Coincidence site lattice (CSL), 379–380
Cold finger, 822–825
Cold pressing, 290–291
Cold traveling heater method (CTHM), 473–474
Colloidal silica, 429
Colored quartz crystals, 555–556
Columnar defective region, 651
Columnar grains, 419–420
Combined convection model (CC model), 998, 1016
Combined mass transfer coefficient, 1016–1018
Complex coordinated crystals, 565–566
Composition
  diagrams, 543–544
  zonation, 9–10
  zoning, 25–28
Conduction, 801
Conductive HNPS-MFS-GaN crystals, 589–593
Conical growth channel, 636
Constitutional supercooling, 300–301
Continuous crystallization, 1339–1341
Continuous Czochralski technique (CCz technique), 62–63, 73–74
Continuous-wave (cw), 703–704
Control system, 1145–1146
  control loop, 1146f
  crystal growth analysis and control, 1146–1147
  feed-forward controller, 1149–1150
  feedback controller, 1150–1153
  model-based control, 1163–1165
  reference trajectory generator, 1147
  state estimator, 1147–1148, 1148f
Controlled variables, 1145–1146
Convection, 388–389, 803, 1040–1042
  convection–diffusion equation, 1001
  convective flow, 58–69
  mass flux, 1006–1009

Convective heat and mass transfer, 1005
correlations for Nusselt numbers, 1009–1010
flow patterns in crystal growth, 1005–1006
melt convection classification, 1010–1012
phenomenological approach, 1009–1010
Convective transport
convective–diffusive transport, 854–855
diffusion transport *vs.*, 1285–1295
Conventional control, 1167, 1175
Cooling crystallization, 1324
Cooling-down process, 1129
COP. *See* Crystal originated particles
Corundum (Al_2O_3), 428–429, 561–563
Counting method, 436–437
Coupled vibrational stirring (CVS), 344–345, 982–983
Crack-free thick HVPE-GaN layers, 652–653
Cracks, 302, 1069–1073
Critical Marangoni number, 882–884
Critical resolved shear stress (CRSS), 109–111
Critical Reynolds number (Re_c), 958t
Critical temperature (*Tc*), 1230
CRSS. *See* Critical resolved shear stress
Crucible(s), 348–349
configuration, 825–828
crystal growth drawbacks, 758–760
rotation, 64
rate, 64–65
Crucibleless techniques, 760–761
Crystal
anisotropy, 1050–1051, 1060–1062
defects, 356–365
enlargement, 634–636
morphology, 12, 1286–1287
nucleation, 1325–1326, 1326f, 1338
primary nucleation, 1327–1332
secondary nucleation, 1332–1333
self-association on, 1329f
perfection determination, 444–447
product quality, 1343–1345, 1344f
pulling, 1244
rotation, 64
shape, 1320–1321, 1336–1337
shoulder, 55–56
Crystal growth, 1333–1337. *See also* Aluminum nitride (AlN); Czochralski growth (Cz growth); Defect generation during crystal growth; Diamond crystal growth; Silicon carbide (SiC)
analysis and control, 1146–1147
case of giant crystals, 21–24
controlling factors, 1248–1251
deciphering geological information, 12–16
decoding
disequilibrium mineral patterns, 24–32
polycrystalline textures, 16–21
from deep earth to outer space, 36–39
early earth mineral growth, 32–35
flow patterns in, 1005–1006
geological scenarios for, 4–11
growth rate and surface growth mechanism, 13f
by high temperature dissociative sublimation
anisotropic growth, 630–631
considerations from growth theory, 627–628
crystal habit, 630–631
dissociative sublimation, 628–630
growth conditions, 625–627
rate-limiting species, 628–630
high temperature sublimation growth technology
crystal enlargement, 634–636
doping, 636–638
growth setup and process, 631–633
hot-zone materials, 633–634
seeded growth, 633–634
high-temperature solution growth, 1219–1223
low-temperature solution growth
mechanical impurities effect, 1206–1210
rates, 1199–1206
techniques, 1193–1196
Marangoni convection in, 886–904
mechanism, 1251–1263
origin of life, 32–35
primitive life detection, 32–35
process, 1145, 1286

Crystal growth (*Continued*)
control system, 1145–1153
Cz process, 1153–1165
detached Bridgman process, 1169–1173
FZ technique, 1174–1176
Kyropoulos process, 1176–1178, 1177f
VB process, 1165–1169
VGF process, 1165–1169
from solutions, 1186
high-temperature solution growth, 1210–1223
low-temperature solution growth, 1187–1210
Crystal originated particles (COP), 89
Crystal size distribution (CSD), 1321
Crystalline solid, 795
Crystallization, 24, 1186, 1197
building blocks, 846
Crystallographic orientation, 444–447
CSB_3O_5. *See* Cesium triborate (CBO)
CSD. *See* Crystal size distribution
CSL. *See* Coincidence site lattice
$CSLIB_6O_{10}$. *See* Cesium lithium borate (CLBO)
CTHM. *See* Cold traveling heater method
Cubic high pressure apparatus (CHPA), 678, 678f
Cubic single crystal
elastic constant matrix, 1052–1053, 1052f
thermal strain vector, 1058
Curie's symmetry principle, 954
Cusp-shaped magnetic field (CMF), 914, 923–927
CVD. *See* Chemical vapor deposition
CVS. *See* Coupled vibrational stirring
CVT. *See* Chemical vapor transport
cw. *See* Continuous-wave
CWO. *See* Cadmium tungstate
Cylindrical growth channel, 636
Czochralski growth (Cz growth), 46, 215–216, 849–850, 872–873, 910, 972–973, 998, 1029, 1050, 1074, 1144–1145, 1153
axial magnetic field, 914–917
CMF, 924–927
control objectives, 1153–1156
convective flow in Si melt, 61–66
conventional PID-based control, 1161–1163
crystal growth system, 886–892
economic aspects, 94–95
impact cycle time and costs, 96–97
special issues, 97–98
yield of dislocation-free Cz-grown crystals, 95–96
feed-forward control, 1160–1161
growth kinetics and interface shape, 59
heat and species transfer modeling, 66
heat transfer and growth rate, 59–60
industrial-like silicon Czochralski puller, 47f
intrinsic point defects and aggregates
calculation, 92–93
importance, 88–90
impact of impurities, 93–94
incorporation, 90–91
influence of crystal growth parameters, 91–92
magnetic fields, 67–69
with mixed convection, 1031–1034
principle, 47–48
procedure, 51–58
process characteristics, 1153–1156
RMF in, 929–930
segregation under steady forced convection, 1029–1030
of silicon crystals, 46
silicon Czochralski pulling apparatus setup, 48–51
state estimation, 1156–1160
TMF in, 936–937
transport and incorporation
considerations, 69
constitutional supercooling, 75–76
segregation coefficient, 69–72
species distribution in crystal, 72–75
striations, 76–77
unintentional impurity incorporation, 79–81
transverse magnetic field, 920–922
Czochralski method (CZ method). *See* Czochralski growth (Cz growth)
CZT. *See* Cadmium zinc telluride

D

DAC devices. *See* Diamond anvil cell devices
Dai-ichi Kiden Corporation (KDN), 396–397
DAP. *See* Donor acceptor pair
DC Arc-Jet CVD, 695–696
DC Plasma CVD, 695
DDG. *See* Double-disk grinding
Dead supersaturation zone, 1199–1206
Decoding disequilibrium mineral patterns, 24–32
Decoding polycrystalline textures, 16–21
Decoration precipitates (DP), 363
Deep ultraviolet (DUV), 209–210
Defect generation during crystal growth, 1094
  defect-forming mechanism, 1094
  dislocations, 1105–1121
  faceting, 1130–1136
  foreign phase particles, 1125–1130
  grain boundaries, 1121–1125
  point defects, 1096–1104
  twinning, 1130–1136
Defect selective etching method (DSE method), 585
Defect-free silicon, 46–47, 67
DEG. *See* Diethylenglycole
Dendritic casting method, 392–397
"Denuded zone" technique, 82
Detached Bridgman process, 1169–1170, 1170f. *See also* Vertical Bridgman growth (VB growth)
  control objectives, 1170–1172
  model-based control, 1173
  PI-based control, 1172–1173
  process characteristics, 1170–1172
Detwinning, 1269–1270
DFT. *See* Direct film transfer
Diamond, 672. *See also* High pressure high temperature (HPHT)
  boron-doped type IIb, 684–685
  classification, 678–679
  nitrogen-containing type I, 679–682
  nitrogen-free type IIa, 683–684, 683f
Diamond anvil cell devices (DAC devices), 702
Diamond crystal growth. *See also* High pressure high temperature (HPHT)
  conversion methods, 673–674
  high pressure diamond synthesis and growth methods
    synthesis with metallic catalysts, 674
    TGG method, 675
  high pressure equipment, 675
    belt-type apparatus, 675, 676f
    high pressure cell, 678, 679f
    multi-anvil apparatus, 676–678
    toroid-type apparatus, 676, 677f
  high pressure growth
    boron-doped type IIb diamond, 684–685
    diamond classification, 678–679
    nitrogen-containing type I diamond, 679–682
    nitrogen-free type IIa diamond, 683–684, 683f
Diamond growth from gas phase, 691–692
  CVD principles, 692–694
  epitaxial growth and treatment
    doping, 701
    high speed growth, 698–699
    lift-off process, 699
    mosaic structures, 700
    postgrowth treatment, 700–701
  gas activation methods, 694–698
Dichroism, 234–235
Diethylenglycole (DEG), 719–720
Differential thermal analysis (DTA), 284
Differentiated weightmode, 1162
Diffusion, 846–848
  layer, 300–301
  mechanism, 1265–1268
  mode, 1198
  transport, 1285–1295
Diffusion-limited aggregation (DLA), 30
Dipole, 1113
Dipropylenglycole (DPG), 719–720
Direct film transfer (DFT), 745–746
Direct numerical simulation (DNS), 886–888
Directional crystallization, 585
Directional heat dissipation, 421
Directional solidification method (DS method), 374, 938–941, 998, 1242–1243

Directionally solidified castings (DS castings), 414. *See also* Single crystal castings (SC castings)
ceramic shell molds for, 425–429, 431–434
elements and wax model assemblies, 430–431
investigation methods
crystal perfection determination, 444–447
crystallographic orientation, 444–447
macro and microstructure, 436–442
mechanical properties testing, 435–436
porosity investigation, 442–444
manufacturing methods, 415–418
numerical modeling, 447
analytical thermal analysis, 448–451
nucleation and grain growth, 452–454
temperature field, 451–452
parameters for, 421–423
Disk-driven forced convection, 1018–1021
Dislocation(s), 173, 356–359, 383–385, 686–687, 1105
annihilation, 1084–1085
in bulk single crystals, 1074–1088
clustering, 1117
density, 357
qualitative estimation, 1074–1075
quantitative estimation, 1075–1082
dynamics, 1111–1119
engineering, 1119–1121
free, 53–55
growth dislocations, 1105–1111
multiplication, 109–111
postgrowth dislocations, 1111
reduction process, 522–523
Dissociative sublimation, 628–630
Distributed parameter
model-based control, 1164–1165
system, 1146
Divariant system, 1261
DLA. *See* Diffusion-limited aggregation
DNS. *See* Direct numerical simulation
Donor acceptor pair (DAP), 610
Dopants, 302
distribution, 916, 920–922, 926
Doping, 352–356, 636–638, 657–659, 701
elements, 70
striations, 1045
Double donors, 84
Double-crucible system, 142–146
Double-disk grinding (DDG), 748
DP. *See* Decoration precipitates; Dynamic polygonization
DPG. *See* Dipropylenglycole
Droplet oscillation method, 876
DS castings. *See* Directionally solidified castings
DS method. *See* Directional solidification method
DSE method. *See* Defect selective etching method
DTA. *See* Differential thermal analysis
DUV. *See* Deep ultraviolet
Dynamic Bond number, 881–882
Dynamic magnetic fields, 858
Dynamic polygonization (DP), 358–359, 1095, 1121–1123, 1122f
Dynamic stability, 782–785

E

EBSD. *See* Electron back-scatter diffraction
EDAX. *See* Energy dispersive X-ray analysis
EDG. *See* Electrodynamic gradient freeze
Edge-defined film-fed growth (EFG), 760–761, 872–873, 897
crystal growth system, 902–904
technique, 745
EDTA. *See* Ethylenediamine tetra-acetic acid
EEM method. *See* Elastic emission machining method
Effective segregation coefficient, 379–380, 1000–1001, 1018
in zone purification, 1038
EFG. *See* Edge-defined film-fed growth
Ekman flow, 956
Elastic constant matrix, 1051–1057
Elastic emission machining method (EEM method), 750
Electrical power, 631–632
Electrical resistance heating, 462–463
Electro-magnetic-field-Czochralski method (EMCZ), 68, 858–859

Electrodynamic gradient freeze (EDG), 798–799, 821
Electrolytic crystallization, 1222
Electromagnetic CZ method-transverse magnetic fields (EMCZ-TMF), 858–859
Electromagnetic field (EM field), 263–264, 268, 858–859
Electron back-scatter diffraction (EBSD), 324
Electron paramagnetic resonance (EPR), 681–682, 1290
Electron probe microanalysis (EPMA), 305
Electron spin resonance (ESR), 1290, 1291f
Electron spin resonance imaging (ESRI), 1290–1291
Electronic-grade polysilicon, 69
Elliptical mirror furnaces, 466
ELOG. *See* Epitaxial lateral overgrowth
EM field. *See* Electromagnetic field
EMCZ. *See* Electro-magnetic-field-Czochralski method
EMCZ-TMF. *See* Electromagnetic CZ method-transverse magnetic fields
Emerald, 561–563
Enclosure analysis, 808–810
Energy dispersive X-ray analysis (EDAX), 305
Energy equation, 800–803
EPD. *See* Etch pits density
Epitaxial lateral overgrowth (ELOG), 520, 652–653, 659, 1110
EPMA. *See* Electron probe microanalysis
EPR. *See* Electron paramagnetic resonance
Equilibrium phase diagram, 1233–1234
  Ba-Cu-O system, 1234–1235
  of HTSC materials, 1234
  quasi-ternary phase diagram, 1235–1236
  RE-Ba-Cu-O system, 1234–1235
  standard gibbs free energy change, 1236–1239
Equilibrium temperature, 1236–1237
ESR. *See* Electron spin resonance
ESRF. *See* European Synchrotron Radiation Facility
ESRI. *See* Electron spin resonance imaging
Etch pits density (EPD), 215, 383–384
Ethyl silicate, 429
Ethylenediamine tetra-acetic acid (EDTA), 1206
ETP. *See* Exterior triple point
EURECA-1 mission, 493
European Organization for Nuclear Research (CERN), 158–159
European Synchrotron Radiation Facility (ESRF), 702
Eutectic solidification, 303
Evaporative crystallization, 1324
Existence region, 1098
Experimental methods, 1289–1292
Experimental validation, 828–829
Exterior triple point (ETP), 260
External fields
  dynamic magnetic fields, 858
  electromagnetic fields, 858–859
  static magnetic fields, 855–858
  vibrational effects, 859–860
Extrinsic point defect incorporation, 1100–1101

F

Face-centered cubic metals (fcc metals), 1120–1121
Faceted dendrites, 392–393
Faceted growth, 1249
Faceting, 1130–1136
Facets, 58, 121–124, 349–352
  formation, 1223
FB. *See* Flat belt
fcc metals. *See* Face-centered cubic metals
FE. *See* Free exciton
Fe-Ni-C system, 675
Feed rod, 251–252
Feed-forward controller, 1149–1150
Feedback controller, 1150–1153
FEM. *See* Finite element method
Fermi-level effect, 356, 1102
FET. *See* Field-effect transistor
FG. *See* Film growth
FIB technique. *See* Focused ion beam technique
Fick’s law, 628, 1007
Fickian diffusion, 90

Field-effect transistor (FET), 703
Film growth (FG), 674
Film thickness formulation, 1008–1009
Finite dimensional model, 1146–1147
Finite element formulation, 1059–1060
Finite element method (FEM), 264, 452–453, 1146
First law of thermodynamics, 799
Fixed abrasive sawing, 721–722, 728–729, 735–737. *See also* Slurry-based sawing
Flame fusion method. *See* Verneuil method
Flat belt (FB), 675
Floating zone silicon crystal growth (FZ silicon crystal growth), 243, 246–249. *See also* Multicrystalline silicon (mc-Si)
  crucial FZ details
    feed rod, 251–252
    induction coil and arcing, 252–253
    molten zone and growth angle stability, 251
    origin and analysis of failures, 249
    rotation and pull rates, 250
  crystal morphology, 253
  development, 254–255
  doping techniques, 253–254
  exemplary results, 267–276
  floating zone process automation, 255–260
  historical overview, 262–263
  impurity distribution, 253–254
  mathematical models, 263–267
  numerical simulation, 260
  setup, 245–246
  zone melting purification, 243–245
Floating zone technique (FZ technique), 82, 914, 967–968, 1016, 1050, 1074, 1174
  application, 773
  automation
    Avogadro crystal, 259–260
    choice of reference and manipulated variables, 258–259
    measurement system description, 256–257
    modeling, 257–258
    motivation, 255–256
  axial magnetic field, 918–919
  CMF, 927
  control objectives, 1174
  conventional control, 1175
  measurement techniques, 1174–1175
  model-based control, 1176
  process characteristics, 1174
  reference trajectory planning, 1175
  RMF in, 931–932
  transverse magnetic field, 923
Floating-zone growth (FZ growth), 872–873
  crystal growth system, 892–897
  single crystal growth of intermetallic compounds, 313
    manganese silicides, 321–323
    RuAl, 318–319
    TiAl, 319–320
    TiNb, 323–326
    two-phase inductor and characteristics, 315–316
Flow control
  electromagnetic fields, 341–343
  vibrations, 344–345
Flow instability
  Baroclinic instability, 862
  Rayleigh–Bénard instability, 860–862
  turbulence, 862–863
Flow speed control, 1169
Fluid dynamics
  diffusion, 846–848
  external fields, 855–860
  flow instability, 860–863
  impurity transfer, 864–868
  natural and forced convections, 848–855
Fluid motion, 979
Fluids, 8
Fluorination process, 146–147
Flux. *See* Solvent
Flux growth, 1286
Flux method, 213, 224, 1243–1244
Flux tubes, 301
Focused ion beam technique (FIB technique), 321, 520–521
Forced convection, 61, 64, 496–498, 848–855, 1011
  correlations for disk-driven, 1018–1021
  Cz growth segregation under steady, 1029–1030

disk-driven, 1018–1021
empirical correlations for natural convection, 1021–1023
regimes, 496–498
segregation without, 1023–1028
Foreign phase particles, 1125
melt growth inclusions, 1129
precipitates, 1125–1126
second-phase particles, 1129–1130
solvent inclusions, 1126–1129
Fourier number, 999
Fourier transformed infrared spectroscopy (FTIR spectroscopy), 381, 610
Fourier's first law, 801
Fractal dendrites, 30–32
Frank-Read mechanism, 1114
Frank–van der Merwe growth, 405–406
Freckles formation, 441
Free exciton (FE), 610
FTIR spectroscopy. *See* Fourier transformed infrared spectroscopy
Full width at half maximum (FWHM), 176, 214, 524, 585
Furnace heat transfer, 814–816
FZ growth. *See* Floating-zone growth
FZ silicon crystal growth. *See* Floating zone silicon crystal growth
FZ technique. *See* Floating zone technique

G

Gadolinium gallium garnet (GGG), 812
Gadolinium orthosilicate. *See* Gadolinium silicate (GSO)
Gadolinium silicate (GSO), 152, 160–163, 1055, 1069
Gain scheduling, 1163
Gallium arsenide, 730
Gallium berlinites, 556–558
Gallium nitride (GaN), 133–134, 578, 622
ammonothermal growth techniques
historical development, 595–600
method, 600–602
properties, 610–612
prospects and future developments, 613
solubility in, 604–607
ammonothermal solution chemistry, 602–604
crystal growth, 506–507
condition, 507–509
Na effects, 509–513
doping under ammonothermal conditions, 608–610
growth rates and morphology, 607–608
LPE growth
characterization, 524–525
dislocation behavior, 520–523
GaN. *See* Gallium nitride
$[Ga(NH_3)_5Cl]Cl_2$. *See* Pentaaminechlorogallium (III) dichloride
Garnets ($A_3B_5O_{12}$), 1215–1216
Gas activation methods, 694
DC Arc-Jet CVD, 695–696
DC Plasma CVD, 695
hot filament CVD, 695
MPCVD, 696–698
Gas bubbles, 303
Gas cooling casting (GCC), 415, 418
Gas porosity, 442
Gas-to-solid condensation, 38–39
Gaseous species, 644
GCC. *See* Gas cooling casting
Gd_2SiO_5. *See* Gadolinium silicate (GSO)
Gebhart's analysis, 811–812
Gel, 1279
Gel–matrix interaction, 1289
Gels, crystallization in
aerogels, 1296–1301
biological macromolecules in, 1301–1304, 1305t
crystal
growth, 1301–1307
physical properties, 1302t–1303t
quality, 1279–1280
diffusion *vs*. convective transport, 1285–1295
gel growth
applications, 1295–1296
history, 1280–1282
properties, 1278
gel properties and characterization, 1282–1285

Gels, crystallization in (*Continued*)
  hydrogels, 1296–1301
  organic gels, 1296–1301
  recombinant technologies, 1278–1279
Geometric model materials, 452
Geometrically necessary dislocation (GND), 1122
Geomicrobiology, 563–564
Germanium, 78
gFZ method. *See* granulate FZ method
GGG. *See* Gadolinium gallium garnet
Giant crystals, 21–24
Gibbs–Thomson effect, 58
Global heat transfer, 58–69
Glycothermal process, 536–537
GND. *See* Geometrically necessary dislocation
Golden beryl, 562–563
Grain boundaries, 1121
  large-angle, 1123–1125
  low-angle, 1121–1123
Grain control, 391–406
Grains selector, 418–420
Granoblastic rocks, 8–9
granulate FZ method (gFZ method), 254–255
Grashof number, 62, 142
Gravitational effects, 850–852
Greenwood–Foreman–Rimmer mechanism, 1130
Grey-Loc sealing, 540
Grid system, 848
Grinding, 748–750
Grown crystal, 1245
Growth
  condition fluctuation, 1128–1129
  dislocations, 1105
    propagation of, 1106–1111
    sources of, 1105–1106
  kinetics, 645–647
  parameters, 654–655
  region, 512
  speed, 291–292
  twins, 1131–1135
Growth accidents. *See* Growth conditions fluctuation
Growth angle, 764–766
  stability, 251
GSO. *See* Gadolinium silicate
GT Advanced Technologies (GTAT), 374
Gulliver–Scheil equation, 1002

H
4H-SiC growth, 626–627, 639–640
6H-SiC boules, 626–627
HAADF-STEM. *See* High angle annular dark field–scanning transmission electron microscopy
HAB. *See* High angle boundaries
HAS model. *See* Hassen–Alexander–Sumino model
Hassen–Alexander–Sumino model (HAS model), 388, 1075–1076
  modified, 1083–1088
  for multiaxial stress state, 1077–1079
  for uniaxial stress state, 1076–1077
Hastelloy, 549
HB method. *See* Horizontal Bridgman method
HBCCO system. *See* Hg-Ba-Ca-Cu-O system
Heat exchanger method (HEM), 338
Heat field rotation method (HFRM), 188
Heat transfer, 954
  modeling, 66
Heat transfer analysis, 822–828
  boundary conditions, 803–805
  energy equation, 800–803
  experimental practice, 796–799
  fundamentals, 799
  in melt crystal growth, 805–816
  research vignette, 820–833
  theoretical developments, 817–820
Heat transport, 846
Heat treatment process, 423–425
Heater powers, 1166–1167
Heater-magnet module (HMM), 389
HEM. *See* Heat exchanger method
2-HEMA. *See* 2-hydroxyethyl methacrylate
HEMT. *See* High electron mobility transistor
HEN. *See* Heterogeneous nucleation
HEpiGANS. *See* Hydride Epitaxial GaN Simulator

Hertz–Knudsen equation, 627–628
Heterogeneous nucleation (HEN), 1330
Heterogeneous nucleation, 1327–1328
Heterosolvents, 470
HF. *See* Hydrogen fluoride
HFRM. *See* Heat field rotation method
Hg-Ba-Ca-Cu-O system (HBCCO system), 1231
High angle annular dark field–scanning transmission electron microscopy (HAADF-STEM), 304
High angle boundaries (HAB), 441
High critical temperature superconductors (HTSC), 1230
  applications of, 1233
  bulk crystal growth methods, 1239–1243
  crystal growth
    controlling factors, 1248–1251
    mechanism, 1251–1263
  high *Tc* oxide superconductors, 1231–1233
  phase diagram, 1233–1239
  single crystal growth methods, 1243–1248
  twin formation, 1263–1270
High electron mobility transistor (HEMT), 578
High energy physics, 164–165
High frequency heater, 135–136
High nitrogen pressure solution growth method (HNPS method), 579
  method and experimental setup, 579–581
  perspective for, 594–595
  seeded growth, 585–594
  spontaneous crystallization, 584–585
  thermodynamic and kinetic aspects, 581–583
High pressure cell, 678, 679f
High pressure high temperature (HPHT), 673
  diamond crystallization in non-metallic systems, 688
    carbonate-silicate systems, 688–689
    C–O–H system, 690
    diamond formation through redox reactions, 690–691
    phosphorus-carbon system, 691
    sulfide-carbon system, 689–690
    sulfur-carbon system, 689–690
  diamond crystals
    extended defects, 686–688
    morphology, 685–686
  diamond CVD process, 692f
  diamond specialties, 701–703
  NPD rods, 693f
  ultra-high pressure synthesis of bulk diamond, 691
High pressure solution growth method (HPSG method), 506, 509
High rate solidification method (HRS method), 414
High speed growth, 698–699
High *Tc* oxide superconductors
  HTSC materials, 1231
  YBCO system, 1232–1233
High-performance mc-Si, 397–403
High-pressure method, 347
High-temperature recovery mechanism, 1083
High-temperature region, 646
High-temperature solution growth, 1210. *See also* Low-temperature solution growth
  crystal growth techniques, 1219–1223
  facet formation, 1223
  fluxes composition and selection, 1211–1215
  growth instability, 1223
  high-temperature solvents properties, 1215–1219
  principle of, 1211
  single crystals, 1212t–1213t
HMF. *See* Horizontal magnetic field
HMM. *See* Heater-magnet module
HNPS method. *See* High nitrogen pressure solution growth method
Homoepitaxial seeded growth (HPSG), 654–656
Homogeneity region, 1098
Homosolvents, 470
Horizontal Bridgman method (HB method), 335, 872–873, 898–899, 914, 1006, 1103–1104
  crystal growth system, 898–902, 900f
Horizontal conditions, 768
Horizontal disks, 1022–1023
Horizontal magnetic field (HMF), 914

Hot filament CVD, 695
Hot zone, 50–51, 337, 632–633
  design, 385
    control of growth front, 386–387
    control of impurities, 389–391
    convection, 388–389
    growth rate, 387–388
    segregation, 388–389
    thermal stress, 388
  materials, 633–634
Hot-wall chemical vapor deposition (HT-CVD), 623
HPHT. *See* High pressure high temperature
HPSG. *See* Homoepitaxial seeded growth
HPSG method. *See* High pressure solution growth method
HRS method. *See* High rate solidification method
12-HSA. *See* 12 human serum albumin; 12-hydroxystearic acid
HT-CVD. *See* Hot-wall chemical vapor deposition
HTSC. *See* High critical temperature superconductors
HTW. *See* Hydrothermal wave
12 human serum albumin (12-HSA), 1290
Hurle's model, 362
HVPE. *See* Hydride vapor phase epitaxy
HVPE-GaN seeds, 588–589
HVPE-grown bulk GaN technique doping, 659
HVPE-grown nitrides, 656–657
Hydride Epitaxial GaN Simulator (HEpiGANS), 649
Hydride vapor phase epitaxy (HVPE), 578, 622. *See also* Aluminum nitride (AlN); Silicon carbide (SiC)
  growth kinetics, 645–647
  growth on foreign substrates
    bulk growth, 654
    characteristics, 649t
    HPSG, 654–656
    quasi-bulk single-wafer growth, 651–653
    substrates and buffers, 649–650
    template growth, 650–651
  growth related properties
    doping, 657–659
    native defects, 656–657
    residual impurities, 656–657
    structural defects, 659–661
  growth thermodynamic analysis, 641–644
  laboratory and industrial setups, 647–649
  nitride semiconductors, 641
  ternary nitride growth, 641–644
Hydrogels, 1295–1301
Hydrogen, 78
Hydrogen fluoride (HF), 139–140
Hydrothermal environments, 9–10
Hydrothermal growth process, 536–537
  advantages, 537–538
  apparatus, 548
    general purpose autoclaves, 551–553
    Morey autoclave, 549–551
    Tuttle–Roy cold-cone seal autoclaves, 551
  crystals, 553–566
  current trends in hydrothermal research, 538–541
  experimental investigations, 544–547
  fine to nanocrystals, 566–571
  history, 538–541
  intelligent engineering, 542
    phase formation principles, 543–544
    physicochemical and hydrodynamic principles, 542–543
    thermodynamic calculations, 547
  kinetics of crystallization, 544–547
  solubility, 544–547
  solution, 544–547
Hydrothermal method, 220–221
Hydrothermal wave (HTW), 884–886
2-hydroxyethyl methacrylate (2-HEMA), 1290–1291
12-hydroxystearic acid (12-HSA), 1290

I

Iceland spar, 560
ICP. *See* Inductively coupled plasma
ID. *See* Inner diameter
IDP. *See* Interplanetary dust particle
IGT. *See* Industrial gas turbines
III-nitride HVPE growth, 648

IISB. *See* Institute of Integrated Systems and Device Technology
Image furnace, 283
Immersion-seeded solution growth (ISSG), 188
Impurities, 302, 1101–1102
  distribution, 265–266, 270–271
  effects, 1199–1204
    mechanical impurities, 1206–1210
  transfer
    boundary layer, 864–865
    gas and melt mass transfer, 866–868
    mass transfer in gases, 865–866
IMS. *See* Institute for Molecular Science
In_2O_3. *See* Indium oxide
Inclusions, 362–365, 482–485
  melt growth, 1129
  solvent, 1126–1129
Indium oxide (In_2O_3), 223–227
Induction coil, 252–253
Inductively coupled plasma (ICP), 162–163
Industrial crystallization, 1317
  crystal growth, 1333–1337
  crystal nucleation, 1325–1333
  crystalline product, 1318–1319
  crystallization techniques, 1324–1325
  ensuring product quality, 1343–1345, 1344f
  molecular level process, 1319f
  process configuration, 1337–1343
  product quality, 1319–1322
  separation technology, 1318
  solubility, 1322–1324
  supersaturation, 1322–1324
  three forced-circulation crystallizers, 1318f
Industrial gas turbines (IGT), 414
Infinite dimensional system, 1146
Infrared (IR), 955
Infrared transmission (IRT), 961–962
Ingot annealing process, 1081–1082
Ingot growth methods
  casting and directional solidification, 374–377
  crucible and coating, 377–379
  impurities and defects, 379–385
Injection method, 347
InN formation, 643–644
Inner diameter (ID), 716, 899–900
Inner liner. *See* Protective inner layer
Inoculation, 796
Inorganic gels, 1295
Institute for Molecular Science (IMS), 148–150
Institute of Integrated Systems and Device Technology (IISB), 825
Integration-controlled growth, 1334
Intentional doping. *See also* Czochralski growth (Cz growth); Unintentional impurity incorporation
  co-doping of solar-grade Si, 78–79
  donors and acceptors, 77–78
  elements, 78
Interface
  effect, 818
  flipping, 807–808
  roughening, 806–807
  shape, 266, 272–274
    detection, 1168–1169
Interfacial kinetics
  solute diffusion model, 1257–1259
  from spiral growth, 1259–1261
Intermediate phase, 608
Intermetallics, 313–314
Internal radiation, 808–809, 812–814
Internal triple point (ITP), 260
International Hydrothermal Symposium, 540–541
International Space Station (ISS), 1004
International standard crystal lattice defects, 1094
Interplanetary dust particle (IDP), 38–39
Interstitials, 88
Intrasectorial zoning, 25
Investment casting process, 430
Ion implantation technologies, 745–746
IR. *See* Infrared
Iron borate ($FeBO_3$), 1132–1133
IRT. *See* Infrared transmission
Isolated substitutional nitrogen (C-centers), 679

Isothermal method, 1188
Isotherms, 487, 801
condition, 807
Isotropic analysis, 1061
ISS. *See* International Space Station
ISSG. *See* Immersion-seeded solution growth
Itinerant antiferromagnet compound, 321
ITP. *See* Internal triple point

J

Jackson factor, 349–350, 350t
Jackson parameter, 1249
Johnson-Mehl-Avrami-Kolmogorov model, 16
Joulean heat sources, 265

K

Kanthal heater, 339
KBBF. *See* Potassium beryllium borate fluoride
$KBe_2BO_3F_2$. *See* Potassium beryllium borate fluoride (KBBF)
KDN. *See* Dai-ichi Kiden Corporation
KDP. *See* Potassium dihydrogen phosphate
Kerfless technologies, 745
KGT model. *See* Kurz–Giovanola–Trivedi model
Kinetic Monte Carlo simulation, 693–694
Kinetic regimen, 1198
Kinetic roughening, 807
Kratochvil equation, 1288–1289
KTA. *See* Potassium titanyl arsenate
$KTiOPO_4$. *See* Potassium titanyl phosphate (KTP)
KTP. *See* Potassium titanyl phosphate
Kubota–Mullin model, 1200–1202
Kurz–Giovanola–Trivedi model (KGT model), 453–454
Kyropoulos process, 1176–1178, 1177f

L

L-pit defect. *See* A-swirl defect
La-Ba-Cu-O system, 1231
LAB. *See* Low angle boundaries
LAGBs. *See* Low-angle grain boundaries
Lang topogram, 350, 350f
Lapping, 748–750
Large fluoride crystals, 146–147. *See also* Scintillator crystals
As-grown crystals, 148
chirped-pulse amplification, 152
growth technique, 147–148
solid-state lasers, 150–152
transmission properties, 148–150
Large Hadron Collider (LHC), 158–159
Large-angle grain boundaries, 1095, 1123–1125
Large-eddy simulation (LES), 886–888
Laser chemical processing, 747–748
Laser crystals, 170
Tm-and Ho-Doped GGG, 171
crystal growth, 171–174
laser properties selection, 176–178
vanadate crystals, 178
bulk spiral formation mechanism, 180–187
crystal growth and quality, 179–180
properties, 187
Laser-induced damage threshold (LIDT), 199
LASSCGM. *See* Levitation-assisted self-seeding crystal growth method
Latent heat, 808
Lateral convection, 1006
Lateral photovoltage scanning method (LPS method), 249
Lateral segregation, 1039
convection, 1040–1042
curved solid–liquid interface, 1039–1040
local Nusselt numbers, 1044
nonequilibrium segregation, 1043–1044
Lattice Boltzmann method (LBM), 1293
Laue diffraction indexing, 445
Laue method, 304, 444–445
Layer transfer process from porous silicon, 746–747
LBM. *See* Lattice Boltzmann method
LBO. *See* Lithium triborate
Leach bauxite, 538–539
Lead fluoride (PbF_2), 138, 144–146
Lead magnesium niobate–lead titanate (PMNT), 983
Lead molybdate (PMO), 1056
thermal stress analysis, 1065–1069

Lead tungstate (PWO), 152, 158–160
LEC technique. *See* Liquid-encapsulated Czochralski technique
LED. *See* Light-emitting diodes
LES. *See* Large-eddy simulation
LEVB method. *See* Liquid encapsulation vertical Bridgman method
LEVGF method. *See* Liquid encapsulation vertical gradient freezing method
Levitation-assisted self-seeding crystal growth method (LASSCGM), 225
LHC. *See* Large Hadron Collider
LiB_3O_5. *See* Lithium triborate (LBO)
LID. *See* Light-induced degradation
LIDT. *See* Laser-induced damage threshold
Liesegang structures, 28–29
Lift-off process, 699
Light scattering tomography (LST), 89
Light-emitting diodes (LED), 133–134, 505–506, 578, 624
Light-induced degradation (LID), 381
Limit theories, 1001–1005
$LiNbO_3$. *See* Lithium niobate (LN)
Liquid Al. *See* Aluminum nitride (AlN)—powder
Liquid encapsulation, 347–348
Liquid encapsulation vertical Bridgman method (LEVB method), 338
Liquid encapsulation vertical gradient freezing method (LEVGF method), 338
Liquid metal cooling method (LMC method), 414, 418
Liquid phase epitaxy (LPE), 962, 1245
  growth
    multifeed seed configuration, 587–594
    single seed configuration, 585–587
Liquid-encapsulated Czochralski technique (LEC technique), 106, 1120, 1150–1151, 1155
  CdTe, ZnTe, and ZnSe, 118
  GaAs, 113–114
  GaP, 114–118
  growth constraints to crystal quality
    B_2O_3 role, 126–127
    evaporative group V loss, 119–120
    facets, 121–124
    nonstoichiometric and alloy melts growth, 124–126
    point defects, 120–121
    twinning, 121–124
  historical background, 106–107
  InAs, 113–114
  InP, 114–118
  semiconductor properties, 107–108
$LiTaO_3$. *See* Lithium tantalate (LT)
Lithium niobate (LN), 1054
  thermal stress analysis, 1063–1065
Lithium tantalate (LT), 1054
  thermal stress analysis, 1063–1065
Lithium triborate (LBO), 192–195
LMC method. *See* Liquid metal cooling method
LN. *See* Lithium niobate
Local equilibrium, 998–999
Local interface shape, 349–352
Local Nusselt numbers, 1044
Local vibration modes (LVM), 83
Longitudinal concentration profiles, 72–73
Loose abrasive sawing technique, 718, 733–735
Low angle boundaries (LAB), 441
Low pressure/high temperature annealing (LPHT annealing), 700–701
Low-angle grain boundaries (LAGBs), 636, 1095, 1121–1123
Low-temperature
  crystallization, 1187–1192
  region, 645–646
Low-temperature solution growth, 1187. *See also* High-temperature solution growth
  crystal growth
    mechanical impurities effect, 1206–1210
    rates, 1199–1206
    techniques, 1193–1196
  dead supersaturation zone, 1199–1206
  factors affecting crystal growth, 1196–1199
  solvents selection, 1192–1193
Low-thermal-gradient CZ technique (LTG CZ technique), 156–157
LPE. *See* Liquid phase epitaxy

LPHT annealing. *See* Low pressure/high temperature annealing
LPS method. *See* Lateral photovoltage scanning method
LST. *See* Light scattering tomography
LT. *See* Lithium tantalate
LTG CZ technique. *See* Low-thermal-gradient CZ technique
Lumped parameter model, 1146–1147, 1155–1156, 1171
  model-based control, 1163–1164
Lutetium, 163
LVM. *See* Local vibration modes
Lyapunov method, 782
Lyothermal process, 536–537

M
Macrosegregation mechanism, 1256–1257
Magmatic environments, 5–8
Magnetic fields (MF), 67–69, 910, 1028
  in crystal growth process, 944t
  electric currents *vs*., 941–943
  magnetohydrodynamics, 911–913
  nonsteady magnetic fields, 928–941
  steady magnetic fields, 914–927
Magnetic liquid–encapsulated Kyropoulos (MLEK), 119
Magnetic resonance imaging (MRI), 164
Magnetohydrodynamics, 911–913
Manganese silicides, 321–323
Manipulated variables, 1145–1146
Marangoni convection, 762–764, 873, 884, 1012
  in crystal growth
    Bridgman method, 897–904
    CZ crystal growth system, 886–892
    EFG crystal growth system, 902–904
    FZ crystal growth system, 892–897
  HTW, 884–886
  Marangoni–Benard instability, 882–883, 882f
  thermo-solutocapillary convection, 878–882
Marangoni effect, 63, 872, 872f
Marangoni flow. *See* Thermocapillary convection
Marangoni number, 764
Marangoni–Benard instability, 882–883, 882f
Mass transfer, 954
  convection coefficient, 1009
  gas and melt, 866–868
  in gases, 865–866
  process, 1286
Mass transport, 846, 1294–1295
Material transport coefficient, 485
Mathematical model, 1146
Matrix precipitates (MP), 363
MBE. *See* Molecular beam epitaxy
mc. *See* Multicrystalline
MC simulations. *See* Monte Carlo simulations
mc-Si. *See* Multicrystalline silicon
MD. *See* Molecular dynamics
Mechanical
  ball milling, 290–291
  machining, 748–749
  stirring, 954
MEG. *See* Monoethylenglycole
Melt
  convection, 388–389, 910
    classification, 1010–1012
    lateral melt convection model, 1015–1016
  equilibrium, 999–1000
  flow, 265, 270–271, 997
  growth inclusions, 1129
  melt-grown compound crystals, 1123
  melt-textured Y-123 materials, 1251
  melting rate, 257
  mixing, 910
Melt crystal growth, heat transfer in, 805–816
Melt-powder-melt-growth (MPMG), 1239–1240
Melt-texture-growth (MTG), 1239–1240
Meniscus region, 1154–1155
Mercury cadmium telluride (HgCdTe), 825
MESFET. *See* Metal-semiconductor field-effect transistor
Metal organic chemical vapor deposition method (MOCVD method), 515, 612
  growth, 652–653
Metal-organic vapor phase epitaxy (MOVPE), 1110

Metal-semiconductor field-effect transistor (MESFET), 703
Metallic alloy system, 1252–1253
Metamorphic
  environments, 8–9
  grade, 8–9
  rocks, 8–9
Metastable phase. *See* Intermediate phase
Metastable zone width (MSZW), 1188–1190, 1327f
MF. *See* Magnetic fields
MFS. *See* Multifeed seed
Micro-pulling-down method (μ-PD method), 773–776, 1222–1223
Microgravity
  environment, 873, 877
  growth, 493
Microparticle generation, 1125
Micropipes, 639
Microsegregation, 1044–1045. *See also* Lateral segregation
Microvoids, 1125
  generation, 1125
Microwave plasma chemical vapor deposition (MPCVD), 696–698
Milne–Eddington approximation, 814
MIMO. *See* Multi-input-multi-output
Mineral morphology, 12
Mineral pattern formation, 24–25
Minimum-energy theorem, 1108, 1110–1111
Mixed convection, 1012, 1017
  CZ process with, 1031–1034
  segregation model with, 1016–1018
Mixed suspension mixed product removal crystallizer (MSMPR crystallizer), 1339, 1340f
MLEK. *See* Magnetic liquid–encapsulated Kyropoulos
Mobile dislocation immobilization, 1083, 1086–1088
MOCVD method. *See* Metal organic chemical vapor deposition method
Model predictive control, 1152–1153, 1152f, 1165
Model-based control, 1151–1152
  control system, 1163–1165
  detached Bridgman process, 1173
  FZ technique, 1176
  lumped parameter approach, 1160
Molding system, 431
Molecular beam epitaxy (MBE), 612
Molecular dynamics (MD), 1293–1294
Molten
  material surface tension, 873–878
  oxide surface tension, 878
  salt electrolysis, 225
  semiconductor surface tension, 877–878
  silicon surface tension, 873–877, 876f
  zone stability, 251
Molybdenum (Mo), 133
Mono-ellipsoid furnaces, 466
Mono-like casting, 403–406
Monoclinic single crystal
  elastic constant matrix, 1055, 1055f
  thermal strain vector, 1059
Monoethylenglycole (MEG), 719–720
Monovariant system, 1261
Monte Carlo simulations (MC simulations), 1294
Morey autoclave, 549–551
Morganite, 562–563
Morphology, 1320–1321
Mosaic structures, 700
MOVPE. *See* Metal-organic vapor phase epitaxy
MP. *See* Matrix precipitates
MPCVD. *See* Microwave plasma chemical vapor deposition
MPMG. *See* Melt-powder-melt-growth
MPS-GaN sub. *See* Multipoint-seed-GaN substrate
MRI. *See* Magnetic resonance imaging
MS focus. *See* Multistable focus
MSMPR crystallizer. *See* Mixed suspension mixed product removal crystallizer
MSZW. *See* Metastable zone width
MTG. *See* Melt-texture-growth
MTHM. *See* Multipass traveling heater method
Mullite, 427–428

Multi-anvil apparatus, 676–678. *See also* Belt-type apparatus; Toroid-type apparatus
Multi-input-multi-output (MIMO), 1166–1167
Multi-wire sawing process, 717
  mono-and multicrystalline silicon process investigations, 722–723
    fixed abrasive sawing, 728–729
    slurry-based sawing, 723–728
  technologies, 718–722
    crystal structures, Vickers and Mohs hardness, 719t
    fixed abrasive sawing, 721–722
    slurry-based sawing, 718–720
Multiaxial stress state, 1077–1079
Multicrystalline (mc), 1117
Multicrystalline silicon (mc-Si), 374, 866–867, 1114. *See also* Vertical Bridgman growth (VB growth)
  crystal growth, 374
  grain control, 391–406
  hot-zone design, 385–391
  ingot growth methods, 374–385
  nucleation, 391–406
  PV industry, 374
Multifeed seed (MFS), 585
Multipass traveling heater method (MTHM), 475
Multipass zone melting, 1039. *See also* Single-pass zone melting
Multipoint-seed-GaN substrate (MPS-GaN sub), 527–528
Multipulling, 48
Multistable focus (MS focus), 27

N

n-type wide band gap semiconductor, 564
Na flux method
  GaN crystal growth, 506–507
    condition, 507–509
    Na effects, 509–513
  GaN LPE growth
    characterization, 524–525
    dislocation behavior, 520–523
  nitrogen dissolution mechanism investigation, 513–515
  nucleation control, 515–519
  point seed and coalescence growth technique, 525–531
Na-flux point seed technique (SPST), 525–527
Nanomolar (nM), 1289
Nanopolycrystalline diamond rods (NPD rods), 693f
Native elements, 563–565
Native point defect thermodynamics, 1096–1098
Natural convection, 61, 628, 1011, 1015–1016, 1023
  centrifugal effects, 852–854
  computation, 848
  convective–diffusive transport, 854–855
  crucible rotations, 849–850
  crystal rotations, 849–850
  empirical correlations for, 1021–1023
  gravitational effects, 850–852
  vanishing, 1024–1028
Navier–Stokes equations (N–S equations), 265, 997, 1001, 1009
  momentum equation, 851
Nd. *See* Neodymium
ND. *See* Neutron diffraction
Near infrared (NIR), 234, 293–294
Necking, 53–55
Needle-eye FZ growth process, 262
Negative coefficient, 606
Neodymium (Nd), 1235
Neodymium-Doped Single Vanadate Crystals, 186t
Neumann principle, 187
Neutron diffraction (ND), 1278
New donors, 84
Newton’s iteration scheme, 487
Newton’s law of cooling, 804–805
Nickel-based superalloys, 423–425
NIR. *See* Near infrared
Nitrogen, 78
  dissolution mechanism, 513–515
  doping, 637
  nitrogen-containing

synthetic diamond crystals, 687–688
type I diamond, 679–682
nitrogen-free type IIa diamond, 683–684, 683f
precipitates, 381
NLO crystals. *See* Nonlinear optical crystals
nM. *See* Nanomolar
NMPC. *See* Nonlinear model predictive control
NMR imaging. *See* Nuclear magnetic resonance imaging
"No-mixing" diffusion-controlled segregation, 1003–1005
Nobel Symposium, 540–541
Non-isothermal method. *See* Polythermal method
Noncontact crucible method, 405–406
Nonequilibrium, 999
in melt, 999–1000
segregation, 1043–1044
Nonlinear model predictive control (NMPC), 256
Nonlinear optical borate crystals, 187–202. *See also* Laser crystals
Nonlinear optical crystals (NLO crystals), 187–188, 1206
Nonmetallic inclusions, 439
Nonsteady magnetic fields, 928. *See also* Steady magnetic fields
AMF, 932–934
RMF, 928–932
TMF, 934–941
Nonstoichiometric point defects, 1098
Novel organic hydrogels, 1298
NPD rods. *See* Nanopolycrystalline diamond rods
N–S equations. *See* Navier–Stokes equations
Nuclear magnetic resonance imaging (NMR imaging), 1278, 1292, 1292f
Nucleation, 391–406
Nucleation control, carbon doping for, 515–519
Nucleus, 1329
Numerical simulations, 1005, 1292–1295
Nusselt number, 1009–1010, 1018
correlations
for disk-driven forced convection, 1018–1021
for natural convection, 1021–1023
segregation model with, 1016–1018
Nutrient composition concentration diagrams (NC diagrams). *See* Composition—diagrams

O

OB crystallizer. *See* Oscillatory baffled crystallizer
Observability, 1148
Observer, 1147–1148
OD. *See* Outer diameter
OFZ technique. *See* Optical floating zone technique
Ohm's law, 912
OIC. *See* Oxygen ion concentration
One-dimensional defects, 1094–1095
One-dimensional perpendicular convection, 1005
Open-loop control, 1145–1146
Optical diameter estimation, 1161
Optical floating zone technique (OFZ technique), 213, 283, 285t–288t
advantages and disadvantages, 284
ceramic rod preparation, 290–291
congruently and incongruently melting oxides, 298–299
constitutional supercooling, 300–301
crystal
characterization, 301–305
growth termination and cooling, 298
crystallization, 300–301
experimental setup, 288–290
growth
atmosphere, 296–298
conditions, 291–292
overpressure, 296–298
rotation, 294–295
temperature distribution, 292–294
Optical heating, 465–466
Organic additives, 1204–1206
Organic gels, 1295–1301
Orowan's law, 1084

Orthorhombic phase transition, 1263–1270
Orthorhombic single crystal
  elastic constant matrix, 1057
  thermal strain vector, 1059
Oscillatory baffled crystallizer (OB crystallizer), 1341
Oscillatory techniques, 953
  ACRT, 955–968
  AVC, 968–980
  constant-speed rotation in melts, 953–954
  CVS, 982–983
  USV, 981–982
Oscillatory zoning, 25–26
OSF. *See* Oxidation-induced stacking fault
Out-of-specification losses, 96
Outer diameter (OD), 899–900
Oxidation-induced stacking fault (OSF), 76, 86–88
Oxide crystal growth, 888–892
Oxide superconductors, 1214–1215
Oxygen
  diffusion coefficient, 1264–1265
  precipitates, 381
    density, 85–86
    formation, 84–85
  in silicon, 79–88
    atomistic configurations, 82–83
    diffusivity, 83–84
    formation, 84
    OSF, 86–88
    reaction and aggregation, 84–86
    solubility, 83
    technical relevance of oxygen effects, 82
  source, 916–917
Oxygen ion concentration (OIC), 1215–1216

P
P-T conditions. *See* Pressure-temperature conditions
Pacific Northwest National Laboratory (PNNL), 825–826
Parameter scheduling, 1163
Parasitic nucleation, 578
Passivated emitter and rear cell (PERC), 399–400
PB. *See* Pressure balancing
$PbMoO_4$. *See* Lead molybdate (PMO)
PBN. *See* Pyrolytic boron nitride
$PbWO_4$. *See* Lead tungstate (PWO)
PCVM. *See* Plasma chemical vaporization machining
PDAS. *See* Primary dendrite arm spacing
PDG method. *See* Pendant drop growth method
Péclet number, 802–803, 1011–1012
PEG. *See* Polyethylenglycol
Pegmatites, 7–8
Pendant drop growth method (PDG method), 774
Pentaaminechlorogallium (III) dichloride, 603–604
PEO. *See* Poly(ethylene) oxide
PERC. *See* Passivated emitter and rear cell
“Perfect mixing” diffusion-controlled segregation, 1001–1003
Perfect silicon. *See* Defect-free silicon
Peritectic solidification, 1251
Perovskites (ABO_3), 1215–1216
Perpendicular convection, 1006
PET. *See* Positron emission tomography
PF crystallizer. *See* Plug flow crystallizer
Pfann’s segregation function, 479
pH-Redox-Equilibrium (PHREEQC), 1295
Phase, 543
  formation principles, 543–544
  phase-change interface, 805–808
Phenomenological approach, 1009–1010
Phosphides, 119
Phosphorus-carbon system, 691
Photomultiplier tube (PMT), 153
Photovoltaic industry (PV industry), 374
PHREEQC. *See* pH-Redox-Equilibrium
Physical gels, 1296–1298
Physical vapor transport (PVT), 218, 623, 625–631, 865–866
PID controller. *See* Proportional-integral-derivative controller
“Pint-point” inclusions, 687
Plasma chemical vaporization machining (PCVM), 749–750

PLC. *See* Programmable logic controllers
Plug flow crystallizer (PF crystallizer), 1340
PMNT. *See* Lead magnesium niobate–lead titanate
PMO. *See* Lead molybdate
PMT. *See* Photomultiplier tube
PNNL. *See* Pacific Northwest National Laboratory
Point defects, 120–121, 356
complex formation, 1101–1103
dynamics, 1098–1100
engineering, 1103–1104
extrinsic point defect incorporation, 1100–1101
native point defect thermodynamics, 1096–1098
Polarity, 603
Polishing, 748–750
Poly(ethylene) oxide (PEO), 1290–1291
Polyacrylamide gels, 1295
Polycrystallinity, 1123–1125
Polyethylenglycol (PEG), 719–720
Polyscale crystal form, 536–537
Polythermal method, 1188–1190
Polyvinyl alcohol (PVA), 1295–1296
Poor man's gemstones. *See* Colored quartz crystals
Population density, 17–19
Porosity investigation, 442–444
Positron emission tomography (PET), 152, 164
Postgrowth
dislocations, 1111
processes, 484
treatment, 700–701
twins, 1131–1135
Potassium beryllium borate fluoride (KBBF), 199–201
Potassium dihydrogen phosphate (KDP), 1110
Potassium sulfate (K_2SO_4), 1207–1208
Potassium titanyl arsenate (KTA), 559–560
Potassium titanyl phosphate (KTP), 558–560
Power down method, 415–416
Power law equation, 1249
Prandtl number (Pr), 802–803, 971, 1246–1247
Precipitates, 362–365, 482–485, 1125–1126
Preferred direction theory, 1106–1109
Pressure balancing (PB), 106
Czochralski growth, 108
LEC technique, 113–118
MLEK, 119
VCz techniques, 109–111
Pressure-temperature conditions (P-T conditions), 673–674
Pressurized cold crucible method, 221
Preston equation, 723
Primary dendrite arm spacing (PDAS), 423
Primary nucleation, 480. *See also* Secondary nucleation
Process control, 267
Process' Theory, 479
Programmable logic controllers (PLC), 1151
Proportional-integral-derivative controller (PID controller), 1150–1151
conventional PID-based control, 1161–1163
Protective inner layer, 602
Protein crystallization, 1305, 1306f–1307f
Pseudocubic lattice parameters, 1241–1242
Pull rates, 96, 250
Pulling systems, 466–467
Pulsed magnetic gradient spin echo, 1291–1292
Purification, 480–482
Pushing/trapping model, 1256–1257
PV industry. *See* Photovoltaic industry
PVA. *See* Polyvinyl alcohol
PVT. *See* Physical vapor transport
PWO. *See* Lead tungstate
Pyrolusite dendrites, 30
Pyrolytic boron nitride (PBN), 338, 348, 822, 825–826
Pythagoras' theorem, 1241–1242

Q

Quartz, 553–556
sand, 48
Quasi-bulk single-wafer growth, 651–653
Quasi-mono casting. *See* Mono-like casting
Quasi-ternary phase diagram, 1235–1236
Quenched-melt-growth (QMG), 1239–1240

R

Radiation heat transfer, 808–814
Radio frequency (RF), 221, 294
  heating, 463–465
Rafting, 438
Rapid prototyping methods, 430–431
Rapid tooling method (RT method), 430–431
Rare earth (RE), 1233
  ions, 609
  vanadates, 563
Raw powder materials, 139–140
Rayleigh convection. *See* Buoyancy convection
Rayleigh–Bénard
  convection, 1023
  instability, 860–862
RE. *See* Rare earth
RE-123 single crystal growth, 1248
RE-Ba-Cu-O system, 1234–1235
Ready-to-use crucibles, 378–379
Recombinant technologies, 1278–1279
Reconstitution technique, 675
Red sapphire, 132, 561–563
Red zone, 377
Reference trajectory
  generator, 1147
  planning, 1175
Refined approach, 1168–1169
Relative supersaturation, 627
Repetition effect, 482
Resistance heating (RH), 136, 463
Retarded doping, 353
Retrograde solubility. *See* Negative coefficient
Reynolds number, 802–803
RF. *See* Radio frequency
RGS method. *See* Ribbon growth on substrate method
RH. *See* Resistance heating
Ribbon growth on substrate method (RGS method), 745
Ridges, 57–58
RMF. *See* Rotating magnetic field
Rock-forming minerals, 1–2
Rossby number, 862
Rotating magnetic field (RMF), 68, 342, 389, 494–496, 856–857, 928–932
Rotation rates, 250
Rough growth, 1335
Rough interface, 59
Rounded crystal surfaces
  capping, 1126–1128
  faceting, 1126–1128
RT method. *See* Rapid tooling method
Ruby. *See* Red sapphire
Runge-Kutta algorithm, 772–773
Ruthenium aluminides (RuAl), 318–319

S

S-C system. *See* Sulfur-carbon system
S-L. *See* Solid–liquid
Sagging of crucible wall, 49
Sapphire single crystals, 132
  growth
    apparatus, 134–135
    technique, 135–136
  properties, 133t
SAW. *See* Surface acoustic wave
Sawing mechanisms, 738. *See also* Wafer processing
  slurry-based sawing, 738–745
    elastohydrodynamic behavior of slurry and wire, 742–744
    material removal rate, 740–742
    roughness and subsurface damage, 744–745
SAXS. *See* Small angle X-ray scattering
SC. *See* Scattering center
SC castings. *See* Single crystal castings
Scalable compact rapid ammonothermal technique (SCoRA technique), 596–600, 602
Scanning electron microscopy (SEM), 173, 520–521, 1279–1280
Scattering center (SC), 142
SCF technology. *See* Supercritical fluid technology
Scheil's equation, 72–73, 355
Schmidt number (Sc), 1246–1247
Scintillator crystals, 152
  applications, 163–165
  BGO, 154–157

CWO, 152, 157–158
GSO, 152, 160–163
lutetium and silicates, 163
PWO, 152, 158–160
SCoRA technique. *See* Scalable compact rapid ammonothermal technique
Screening effect, 1113
Second harmonic generation (SHG), 558–559, 1206
Second phase particles. *See* Foreign phase particles
Second-phase particles, 1129–1130
Secondary ion mass spectrometry (SIMS), 320
Secondary nucleation, 1332–1333
Sectorial structure, 12
Sectorial zonation, 25
Sedimentary environments, 10–11
Seed
fixation, 635
orientation, 189–190
Seeded growth, 634–636, 654
Seeding, 492–493, 1240–1242, 1341–1342
Segregation, 352–356, 388–389, 475–479, 997. *See also* Lateral segregation; Microsegregation
coefficients, 69–72, 997–1001
convective heat and mass transfer, 1005–1012
CZ process, 1029–1034
without forced convection, 1023–1028
limit theories, 1001–1005
model with mixed convection, 1016–1018
Nusselt number
correlations for, 1018–1023
model with, 1016–1018
theories on solute layer thickness, 1012–1016
ZM, 1034–1039
Selenides, 347
Self-flux approach, 299, 1243
SEM. *See* Scanning electron microscopy
Semi-insulating GaN bulk substrates, 659
Semi-insulating HNPS-MFS-GaN crystals, 593–594
Semiconductor materials, 622
Semitransparent media, 812
Sessile drop method, 766
Seya-Namioka monochromator, 148–150
SF. *See* Stable focus
Shape stability analysis, 776
capillary stability and applications to dewetting, 779–782, 785–788
dynamic stability, 782–785
heat transfer and growth rate importance, 777–779
practical stability, 785–788
static stability, 776–777
Shaping processes, 773–774
Sherwood number (Sh), 1010
SHG. *See* Second harmonic generation
Shrinkage porosity, 442–443
SiC. *See* Silicon carbide
Siemens process, 251–252
Σ3 twins, 1132
Silicon, 716–717
crystal growth, 886–888
Silicon carbide (SiC), 622, 719–720, 865–867. *See also* Crystal growth
bulk crystal, 623
for blue LED production, 624
cross-section drawings of hot zone setups, 623f
industrial synthesis, 623–624
bulk single crystals, 635f
chemical attachment, 636
precipitates, 381–382
spiral growth, 631
structural defects, 638–640, 639f
Silicon on sapphire (SOS), 133
Simple oxides, 563–565
SIMS. *See* Secondary ion mass spectrometry
Simulation tool for atom technology (STATE), 513, 518
Single crystal castings (SC castings), 414. *See also* Directionally solidified castings (DS castings)
grains selector, 418–420
solidification from seed, 420–421
Single crystal growth methods, 1243–1248. *See also* Bulk crystal growth methods
Single indentation tests
fixed abrasive sawing, 735–737

Single indentation tests (*Continued*)
loose abrasive sawing, 733–735
Single molecule spectroscopy, 1289
Single molecule tracking method. *See* Single molecule spectroscopy
Single scratch tests, 735f, 736
Single-component material, 794
Single-crystal dendrites, 30
Single-input-single-output (SISO), 1166–1167
Single-pass zone melting
"partial" mixing, 1038
"perfect" mixing, 1037–1038
Single-phase inductor, 313–314, 314f
SISO. *See* Single-input-single-output
Slicing technologies, 745. *See also* Wafer processing
ion implantation technologies, 745–746
wafering technologies
laser chemical processing, 747–748
layer transfer process from porous silicon, 746–747
Slip polygonization. *See* Dynamic polygonization (DP)
Slivers, 441–442
sLN. *See* Stoichiometric lithium niobate
Slow-cooling method, 1219–1220
Slurry-based sawing, 718–720, 738–745. *See also* Fixed abrasive sawing
dependence on slurry properties, 724–726
elastohydrodynamic behavior of slurry and wire, 742–744
force in ingot feed direction, 723
friction forces, 723–724
material removal rate, 740–742
roughness and subsurface damage, 744–745
saw marks, 727–728
wafer thickness, wire diameter, and particle size distribution, 727
wire tension, 726
Small angle X-ray scattering (SAXS), 1284
SnO_2. *See* Stannic oxide
Sodium flux method, 579
Sodium silicate (SS), 1282–1283
Solar system formation, 37
Solar-grade polysilicon (SoG polysilicon), 375
Solid state recrystallization (SSR), 475, 498
Solid-state lasers, 150–152
Solidification kinetics, 794–795
Solidification path, 5–6
Solid–liquid (S-L), 911
interface, 1039–1040
Solubility, 1322–1324
temperature dependency, 1191–1192
Solute, 1192
Solute diffusion model, 1252–1257
with interfacial kinetics, 1257–1259
Solute layer thickness, segregation theories on, 1012
BPS theory, 1012–1014
lateral melt convection model, 1015–1016
natural convection model, 1015–1016
Wilson–Garandet's model, 1014–1015
Solute-rich liquid crystal-pulling (SRL-CP), 1239, 1244
crystal growth mechanism, 1257–1261
enlargement of single crystal size, 1246–1248
method, 1244–1245
RE-123 single crystal growth, 1248
Solution crystallization, 1333–1334
Solution growth, 794
Solution-stirring technique (SS technique), 199
Solutioned castings, 423
Solutocapillary
convection, 880
flow, 873, 901–902
Solvent, 299
inclusions, 1126–1129
selection, 1192–1193
Solvent evaporation technique, 1194–1195, 1220
Solvothermal process, 536–537
Soret effect, 1286
SOS. *See* Silicon on sapphire
SP. *See* Static polygonization
Sparry calcite, 11
Species distribution, 72
CCz technique, 73–74
lateral nonuniformity, 74–75
longitudinal concentration profiles, 72–73

species transfer modeling, 66
species transport, 69
numerical modeling, 72
Spin probe, 1290
Spinels (AB_2O_4), 1215–1216
Spiral grain selectors, 420
Spiral growth, 631, 631f, 1259–1261
Spiral shearing flow, 956
Spontaneous crystallization, 584–585
Spontaneous nucleation, 491–492
Spontaneously nucleated single crystals, 630f
SPST. *See* Na-flux point seed technique
SRL-CP. *See* Solute-rich liquid crystal-pulling
SS. *See* Sodium silicate
SS technique. *See* Solution-stirring technique
SSR. *See* Solid state recrystallization
Stability, 1156
phase diagram, 27f
Stable focus (SF), 27
Standard gibbs free energy change, 1236–1239
Stannic oxide (SnO_2), 228–230
STATE. *See* Simulation tool for atom technology
State estimation, 1156–1160
State estimator, 1147–1148, 1148f
Static
magnetic fields, 493–494, 855–858
stability, 776–777
Static polygonization (SP), 1122
Steady magnetic fields, 67, 914
axial magnetic field, 914–919
CMF, 923–927
transverse magnetic field, 919–923
Steady state
growth rate, 1256
segregation, 1004
STHM. *See* Sublimation traveling heater method
Stirring effect, 344
Stoichiometric lithium niobate (sLN), 1223
Stokes–Einstein equation, 1288
Strain grains, 441
Stress, 274–275
Striations, 76–77, 303
"String ribbon" method, 745
"Stucco" method, 431–433
Sublimation traveling heater method (STHM), 470
Submerged heater, 343–344
Sulfide-carbon system, 689–690
Sulfides, 563–565
Sulfur-carbon system (S-C system), 689–690
Supercritical ammonia, 595
Supercritical fluid technology (SCF technology), 552
Supersaturation, 1247–1249, 1322–1324, 1339
Surface, 871
energies, 761–762
energy, 761
radiation, 809–812
reaction control, 511
tension, 871–872
of molten materials, 873–878
Surface acoustic wave (SAW), 1063
Surface-active impurities, 685–686
effect, 685–686
Syneresis, 1282
Synthetic diamonds, 677–679
mixed type Ib þ IaA, 682
morphology, 685
nickel and cobalt impurities, 682
sources of nitrogen, 679–680

T

Tammann-Ströber method. *See* Vertical gradient freezing (VGF)
Tantalum carbide (TaC), 633
Taylor number, 862
TC diagrams. *See* Temperature *vs.* concentration diagrams
TCO. *See* Transparent conducting oxide
TCP phases. *See* Topologically close-packed phases
TEDDI. *See* Tomographic energy dispersive diffraction imaging
Tellurides, 347
TEM. *See* Transmission electron microscopy
Temperature
control, 1168–1169
field, 264–265, 269

Temperature (*Continued*)
fluctuations, 96
gradients, 190
techniques, 1195–1196, 1221–1222
Temperature gradient growth method (TGG method), 675
Temperature gradient zone melting (TGZM), 460–462
Temperature *vs*. concentration diagrams (TC diagrams), 543–544
Temperature-changing technique, 1194
Template growth, 650–651
Ternary phase diagram, 1261–1263
Tetraethyl orthosilicate (TEOS), 1282–1284
Tetragonal single crystal
elastic constant matrix, 1056
thermal strain vector, 1059
Tetramethyl orthosilicate (TMOS), 1282–1284
Texture of rock, 16
TGG method. *See* Temperature gradient growth method
TGZM. *See* Temperature gradient zone melting
Theoretical simulation, 1292–1295
Thermal
budget, 96–97
donors, 84
field rotation, 954
strain vector, 1058–1059
stress analysis in bulk single crystals, 1050–1073
Thermo-solutocapillary convection, 878–882
Thermocapillary convection. *See* Marangoni convection
Thermocapillary flow, 63
Thermocapillary Reynolds number, 880–881
Thermodynamic approach, 1130
Thermomechanical stress, 266–267
Thermovibrational convection. *See* Fluid motion
Thin-film technologies, 210
Thixotropy, 1282
THM. *See* Traveling heater method
Three-dimensional defects, 1095
Three-dimensional flow patterns, 1006
Three-phase boundary (TPB), 359–360
Three-phase junction line (TPL), 349
Three-point bending tests, 1070–1071
THZR. *See* Traveling heater zone refining
Time of flight (TOF), 163
Time-dependent
creep deformation, 1076–1077
magnetic fields, 68
Titanium Aluminides (TiAl), 319–320
Titanium Niobium (TiNb), 323–326
Tl-Sr-Ca-Cu-O system (TSCCO system), 1231
TMAl. *See* Trimethylaluminum
TMF. *See* Traveling magnetic field
TMOS. *See* Tetramethyl orthosilicate
TOF. *See* Time of flight
Tomographic energy dispersive diffraction imaging (TEDDI), 545–546
Top-seeded solution growth (TSSG), 188, 1244–1248. *See also* Solute-rich liquid crystal-pulling (SRL-CP)
Topologically close-packed phases (TCP phases), 437
Toroid-type apparatus, 676, 677f. *See also* Belt-type apparatus; Multi-anvil apparatus
Total thickness variation (TTV), 731–733, 744
TPB. *See* Three-phase boundary
TPL. *See* Three-phase junction line
Transient Couette flow, 955–956
Transient modeling, 267, 275–276
Transition metals, 382–383
Transmission edge, 148–150
Transmission electron microscopy (TEM), 89, 218, 520–521
Transparent conducting oxide (TCO), 209–210
Transparent semiconducting oxide (TSO), 209–210
basics, 210–212
electrical and optical properties, 230–235, 232t–233t
growth techniques, 212–230
Transverse magnetic field, 914, 919–923
Trapping phenomena, 1250–1251
Traveling heater method (THM), 931–932, 964, 460
advantages and issues, 461–462

inclusions, 482–485
mass and heat transport, 485–491
materials, 478
precipitates, 482–485
principle, 460–461
purification, 480–482
segregation, 475–479
single crystal growth, 491
forced convection regimes, 496–498
under magnetic fields, 493–496
microgravity growth, 493
seeding, 492–493
SSR, 498
technology, 462
feed material, 468
pulling systems, 466–467
zone heating mode, 462–466
versatile, 468–475
Traveling heater zone refining (THZR), 480
Traveling magnetic field (TMF), 68, 342, 389, 913, 928, 934–941, 934f
Traveling solvent floating zone technique (TSFZ technique), 284, 299, 1244
Traveling solvent method (TSM), 460
Trigonal single crystal
elastic constant matrix, 1054, 1054f
thermal strain vector, 1058
Trimethylaluminum (TMAl), 637–638
TSCCO system. *See* Tl-Sr-Ca-Cu-O system
TSFZ technique. *See* Traveling solvent floating zone technique
TSM. *See* Traveling solvent method
TSO. *See* Transparent semiconducting oxide
TSSG. *See* Top-seeded solution growth
TTV. *See* Total thickness variation
Tungsten (W), 133, 634
Turbulence, 862–863
Turbulent flows, 1020–1021
Tuttle–Roy cold-cone seal autoclaves, 551
Tweed pattern, 1268–1269
Twin formation, 1263–1270
"Twin law", 1131
Twin-free Crystal, 1269–1270
Twinning, 121–124, 1130–1136
Twins, 359–362, 1131–1132, 1132f
Two-dimensional defects, 1095
Two-dimensional flow patterns, 1006
Two-dimensional formulations, 769–770
Two-phase inductor, 315–316
Two-step epitaxial lateral overgrowth (2S-ELOG), 652–653

U

Ultra-high pressure synthesis of bulk diamond, 691
Ultrasonic sound velocity measurement technique, 324
Ultrasonic vibration (USV), 981–982
Ultraviolet light sources (UV light sources), 146–147
Ultraviolet Synchrotron Orbital Radiation (UVSOR), 148–150
Uniaxial stress state, 1076–1077. *See also* Multiaxial stress state
Unidirectional solidification method, 866–867, 1252–1257
Uniform suction flow, 1003–1004
Unintentional impurity incorporation, 79
carbon, 81
oxygen, 79–81
Unstable focus (UF), 27
Upgraded metallurgical silicon (UMG), 381

V

Vacancies, 302
Vacuum ultraviolet applications (VUV applications), 139–140
van't Hoff equation, 1322–1323
Vapor phase reaction, 223–224
Vapor pressure–controlled Czochralski techniques (VCz techniques), 106, 109–111, 1104, 1155
Vapor transport growth, 622
VB growth. *See* Vertical Bridgman growth
VCz techniques. *See* Vapor pressure–controlled Czochralski techniques
Velocity magnitude, 1169
Verneuil method, 213, 783

Vertical Bridgman growth (VB growth), 335, 902, 914, 917–918, 1006, 1103–1104
  axial magnetic field, 917–918
  binary compound semiconductors
    crucibles, 348–349
    crystal defects, 356–365
    doping, 352–356
    facets and local interface shape, 349–352
    inorganic compound semiconductors, 332, 333t
    liquid encapsulation, 347–348
    segregation, 352–356
    synthesis, 346–347
  bottom-seeded, 1028
  equipment
    basics, 336–338
    specifics, 338–345
  hardware of, 336
  III-V and II-VI compounds, 335
  optimization and control, 345–346
  optoelectronic devices, 332–334
  problem in, 335
  process, 1165, 1168f
    characteristics, 1166–1167
    control objectives, 1166–1167
    conventional control, 1167
    model-based control, 1167–1169
  RMF in, 930–931
  TMF in, 937–938
  transverse magnetic field, 922–923
Vertical Gradient Freeze process (VGF process), 137–138, 336–337, 914, 1016, 1103–1104, 1165
  axial magnetic field, 917–918
  control objectives, 1166–1167
  conventional control, 1167
  model-based control, 1167–1169
  process characteristics, 1166–1167
  RMF in, 930–931
  TMF in, 937–938
  transverse magnetic field, 922–923
Vertical magnetic field (VMF), 914
Vertical walls, 1021–1022
Very hard materials, 730
VGF process. *See* Vertical Gradient Freeze process
Vibrational effects, 859–860
Viscous fingering, 31–32
VMF. *See* Vertical magnetic field
Void defect, 89
Volume diffusion
  control, 511
  controlled growth, 1334
von Mises stress, 267
Vorobyevite. *See* Morganite
VUV applications. *See* Vacuum ultraviolet applications

W

Wafer processing, 716
  compound and dielectric materials, 729–730
  economic issues and future development, 717
  electronic grade silicon, 729
  grinding, lapping, and polishing, 748
    EEM method, 750
    mechanical machining, 748–749
    PCVM, 749–750
  multi-wire sawing process, 717–730
  wafer properties, 730
    fracture behavior, 737–738
    single indentation tests, 733–737
    surface properties, 731–738
Washington State University (WSU), 825–826
Water-soluble crystals growth
  with embedded nanoparticles, 1208–1210
  with embedded organic molecules, 1206–1208
Water/solvent of syneresis, 1282
Wax model assemblies, 430–431
Weakest link, 737
Weighing technique, 1157–1159
Weight measurement, 1161–1162
Weight mode, 1162
Wetting angle, 766–767
White sapphire, 132
Wide bandgap materials, 622
  high temperature sublimation growth
    bulk SiC and AlN growth, 623–625
    crystal growth, 625–631

high temperature sublimation growth technology, 631–638
structural defects in PVT-grown SiC and AlN bulk crystals, 638–640
Wilson–Garandet's model, 1014–1015
Wire breakage, 728
Wrinkles, 442
WSU. *See* Washington State University

X

X-ray analysis, 1278
X-ray computed tomography (X-ray CT), 152, 163–164
X-ray diffraction (XRD), 585, 1277–1278
X-ray free-electron laser oscillator (XFELO), 702
X-ray rocking curve (XRC), 585
Xerogels, 1300–1301

Y

Y-123 phase crystals growth, 1249–1251
flux requirement, 1255–1256
steady state growth rate, 1256
Y-211 phase crystals growth, 1250–1251
dissolution of, 1255
Y-Ba-Cu-O system (YBCO system), 1214–1215, 1231–1233, 1248–1249
YAG. *See* Yttrium aluminumgarnet
$YBa_2Cu_3O_{7-\delta}$ material (Y-123 material), 1231
YBCO system. *See* Y-Ba-Cu-O system
Young's moduli, 324
Young–Laplace equation, 764
approximations, 770–772
axisymmetric formulations, 769–770
floating zone process application, 773
meniscus shape in Czochralski configuration, 770–772
micro-pulling-down methods, 773–776
nonlinearity, 769
ribbon thickness in pendant drop growth, 773–776
Runge-Kutta algorithm, 772–773
two-dimensional formulations, 769–770
Yttria-stabilized zirconia (YSZ), 1243–1244
Yttrium (Y), 1233
Yttrium aluminumgarnet (YAG), 812

Z

Zebra grains, 442
Zero-dimensional defects, 1094
Zero-force theorem, 1108–1109
Zinc fluoride (ZnF_2), 144–146
Zinc oxide (ZnO), 218–223
Zirconium dioxide, 429
Zirconium silicate ($ZrSiO_4$), 425–426
Zonal structure, 12
Zone melting (ZM), 243, 998, 1034–1039
mode, 462–466
Zone purification, 1038